Wolfgang Becker

The bh TCSPC Handbook

11th Edition

Time-Correlated Single Photon Counting Modules

SPC-130EMN, SPC-130EMNX
SPC-130IN, SPC-130INX
SPC-150N, SPC-150NX, SPC-150NXX
SPC-160
SPC-160PCIE
SPC-180N, SPC-180NX, SPC-180NXX
SPC-QC104, SPC-QC106, SPC-QC008

Detectors, Lasers and Peripheral Devices

Simple-Tau Systems

Technical Principles

TCSPC Applications

FLIM Systems

Applications in Life Sciences

Clinical FLIM Applications

SPCM Software

SPCImage NG Data Analysis Software



Dr. Wolfgang Becker
Tel. +49 / 30 / 212 800 2 - 0
FAX +49 / 30 / 212 800 2 -13
http://www.becker-hickl.com
email: becker@becker-hickl.com

Becker & Hickl GmbH
Nunsdorfer Ring 7-9
12277 Berlin
Germany
Tel. +49 / 30 / 212 800 2 - 0
FAX +49 / 30 / 212 800 2 -13
http://www.becker-hickl.com
email: info@becker-hickl.com

11th Edition, January 2026

This handbook is subject to copyright. However, reproduction of small portions of the material in scientific papers or other non-commercial publications is considered fair use under the copyright law. It is requested that a complete citation be included in the publication. If you require confirmation please feel free to contact Becker & Hickl GmbH.

Preface

Time-correlated single photon counting (TCSPC) is an amazingly sensitive technique for recording low-level light signals with picosecond resolution and extremely high precision. TCSPC originates from the measurement of excited nuclear states and has been used since the late 60s [847, 1367]. For many years TCSPC was used primarily to record fluorescence decay curves of organic dyes in solution. Due to the low intensity and low repetition rate of the light sources and the limited speed of the electronics of the 70s and 80s the acquisition times were extremely long. More important, classic TCSPC was intrinsically one-dimensional, i.e. limited to the recording of the waveform of a periodic light signal.

Light sources ceased to be a limitation when the first mode-locked Argon lasers and synchronously pumped dye lasers were introduced. For the recording electronics, the situation changed with the introduction of the SPC-300 modules of Becker & Hickl in 1993. Due to a new analog-to-digital conversion principle these modules could be used at photon count rates almost 100 times higher than the classic TCSPC devices. Moreover, the modules were able to record the photons of a large number of detectors simultaneously. They were thus able to record a photon distribution not only versus the time in a fluorescence decay but also versus a spatial coordinate or the wavelength of the photons. Multi-dimensional TCSPC was born.

Within a few years, more dimensions were added to multidimensional TCSPC. Fast sequential recording was introduced with the SPC-430 in 1995, fast scanning with the SPC-535 in 1997. Time-tag recording was introduced with the SPC-431 in 1996; multi-module TCSPC systems followed in 1999. Since then, the Becker & Hickl TCSPC systems became bigger, faster and more flexible. Recent TCSPC modules, like the SPC-150NX or the SPC-180, can be configured for sequential recording, imaging, or time-tag recording by a simple software command. Multi-module systems, like the SPC-134EM and SPC-154, can be used for scanning at unprecedented count rates and acquisition speeds.

Nevertheless, TCSPC still has the reputation to be an extremely sluggish technique unable to record any fast changes in the fluorescence or scattering behaviour of a sample. The multi-dimensional features of modern TCSPC are not commonly understood. Thus, many users do not make efficient use of their SPC modules. However, if appropriately used, multi-dimensional TCSPC techniques not only deliver superior results but also solve highly sophisticated measurement problems.

This handbook is an attempt to help existing and potential users understand and make use of the advanced features of modern TCSPC.

After an introduction into the bh TCSPC devices and associated detector, laser, and experiment control modules the principles of advanced TCSPC techniques are described. These include multidetector TCSPC, multiplexed TCSPC, sequential recording techniques, scanning techniques, parameter-tag recording, and multi-module TCSPC techniques. The next chapter describes the architecture of the bh SPC modules. A chapter about detectors gives a review of detector principles and of the parameters used to characterise detectors. It describes a number of detectors commonly used for TCSPC and gives advice about obtaining best performance from them.

The implementation of bh SPC devices is described in the next part of the handbook. It includes principles and wiring diagrams for typical experiments, guidelines for first system setup, and advice for system optimisation. It describes dead-time, counting loss, and pile-up effects, detector effects, and effects related to the optical system.

The next chapter of the handbook is dedicated to TCSPC applications. The first part of this chapter describes the measurement of fluorescence and anisotropy decay curves, multi-spectral lifetime experiments, recording of transient fluorescence lifetime phenomena, and

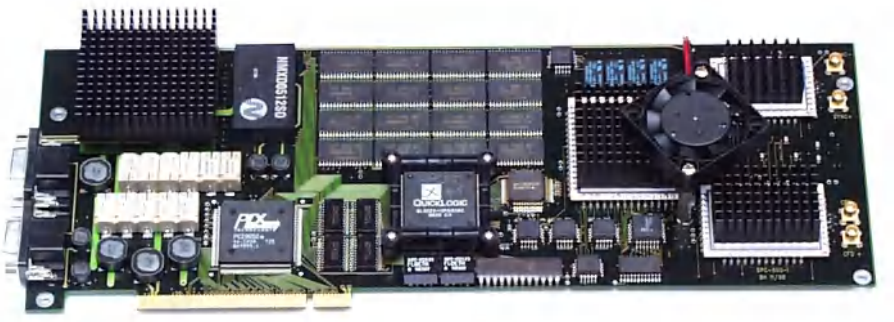
measurements of phosphorescence decay curves. The second part of the chapter is dedicated to time-resolved laser scanning microscopy. It contains sections on a wide variety of fluorescence-lifetime imaging (FLIM) experiments and procedures, such as FLIM with various excitation principles, excitation sources, and detection principles, high-speed and time-series FLIM, Z-stack FLIM, simultaneous fluorescence and phosphorescence lifetime imaging (FLIM/PLIM), fluorescence lifetime-transient scanning (FLITS), and FLIM with special microscope configurations. A third part contains FLIM background knowledge: Signal-to-noise ratio, acquisition time, the effect of counting loss and pile-up, photobleaching, and fluorescence depolarisation on the recorded data.

The book contains a large chapter on TCSPC applications, most of them in Biology. It contains sections on FLIM of molecular environment parameters in tissue, FLIM-based FRET measurements in cells, autofluorescence FLIM of biological tissue, plant physiology, and clinical FLIM applications. A section about diffuse optical tomography (DOT) by NIRS techniques includes breast imaging, static and functional brain imaging, perfusion measurement in the human brain, diffuse tissue spectroscopy, and small-animal imaging. Picosecond photon correlation, fluorescence correlation spectroscopy, burst-integrated fluorescence lifetime techniques, and photon counting histogram techniques are reviewed in the next sections. The last part of the application chapter gives an review of non-biological TCSPC applications like positron lifetime measurement, measurement of barrier discharges, remote sensing, metrological applications, and characterisation of detectors. The application chapter also includes practical hints about optical systems, detectors, and other technical aspects of the applications described.

Another large chapter describes the SPCM operating software of the bh SPC modules. It describes the various user interface configurations, operation modes, the system and control parameters, the handling and display of the multidimensional data recorded by the modules, and the associated data file structure.

The TCSPC Handbook also contains a chapter on the SPCImage NG fluorescence decay and FLIM data analysis software. It describes the general principles of fluorescence decay analysis, the calculation of fluorescence decay parameters and lifetime images by various decay models, pseudo-global and global analysis, multi-wavelength FLIM analysis, batch-processing of FLIM series, and analysis of PLIM data.

The handbook ends with a list of more than 1200 references related to TCSPC, most of them being applications of the bh SPC devices.



The legendary SPC-830 TCSPC / FLIM module. Introduced in 2001, it was the first TCSPC device capable of single-curve recording, time-tag recording, FCS, single-molecule detection, and FLIM

Contents

Overview on bh TCSPC Instrumentation 1
General Features of the bh TCSPC Devices 1
TCSPC Modules 7
Simple-Tau TCSPC Systems 15
MaxTau 12-Channel TCSPC System 15
Power-Tau TCSPC Systems 16
Other Time-Resolved Photon Counting Devices 17
Measurement Modes of the bh TCSPC Modules 18
bh DCS-120 Confocal and Multiphoton FLIM Systems 32
FLIM Systems for Zeiss LSM 710, 780, 880, 980 Family Microscopes 50
FLIM Systems for Leica SP2, SP5, and SP8 MP Laser Scanning Microscopes 68
FLIM Systems for Olympus FV 300 and FV 1000 68
FLIM Systems for Nikon C1 and A1 Microscopes 70
FLIM Systems for Sutter MOM Microscopes 71
FLIM Systems for Abberior STED System 71
PZ-FLIM-110 Piezo-Scanning FLIM System 72
FASTAC Fast-Acquisition FLIM System 73
Picosecond Diode Lasers 75
Laser Optics 80
Laser Control Electronics 80
Detectors 81
Detector Electronics 88
Experiment Control 91
Connecting Electronics 92
SPCM 64-bit Instrument Software 94
SPCImage NG FLIM Data Analysis 95
Express-FLIM Software 98
SPCDynamics 98
Burst Analyzer Single-Molecule Data Analysis 99
Classic Time-Correlated Single Photon Counting 101
Single-Photon Detection 101
Principle of Time-Correlated Single Photon Counting 102
The Classic TCSPC Architecture 106
Reversed Start-Stop 107
Modern Implementations of Classic TCSPC 108
TAC / ADC versus TDC Principle 109
Direct Start-Stop Operation 109
Buildup of the Photon Distribution in the Computer 109
Applications of the Classic TCSPC Principle 110
Multi-Dimensional TCSPC 112
Principle of Data Acquisition 112
Architecture of Multi-Dimensional TCSPC 113
Multi-Dimensional TCSPC Implementations 116
Multi-Detector and Multi-Wavelength TCSPC 116
Multiplexed TCSPC 119
Sequential Recording 121
Fluorescence Lifetime Imaging (FLIM) 124
Multi-wavelength FLIM 125
TCSPC FLIM with Excitation Wavelength Multiplexing 126
Mosaic FLIM 127
FLITS 129
Dual Time-Base Recording 130
Recording Parameter-Tagged Photon Data 132
Fluorescence Correlation Spectroscopy (FCS) 133
Calculation of FCS from Parameter-Tag data 133
Using the Micro-Time of TCSPC in FCS 135
Single-Molecule Burst Analysis 136
Multi-Module TCSPC Systems 137
Architecture of the bh TCSPC Modules 139

General Principle 139
CFD circuits 139
TAC and ADC 140
TDC 141
'Channel' Register 142
Sequencer 142
Memory Control 142
Detailed Description of Building Blocks 147
Constant-Fraction Discriminators 147
Time-to-Amplitude Converter 149
Analog-to-Digital Conversion 151
ADC Error Correction 151
Variable ADC Resolution 152
ADC Zoom 153
Detectors for TCSPC 154
Detector Principles 154
Conventional PMTs 154
Channel and Microchannel PMTs 155
Hybrid PMTs 155
Single-Photon Avalanche Photodiodes 157
Silicon Photomultipliers (SIPMs) 159
Superconducting Single-Photon Detectors 159
Detector Parameters 160
Gain 160
Single-Electron Response 160
Pulse Height Distribution 161
Signal Transit Time 163
Transit Time Spread and Timing Jitter 163
Cathode Efficiency 164
Dark Count Rate 166
Afterpulsing 167
Prepulses 168
Description of Selected Detectors 169
R3809U MCP PMTs 169
Hamamatsu R5600 and R7400 Miniature PMTs 171
Hamamatsu H5783 and H5773 Photosensor Modules 172
H11900 / H11901 and H10720 / H10721 Photosensor Modules 173
PMH-100, PMC-100, PMZ-100 174
PMC-150 PMT Modules 175
PMCS-150 PMT Modules 175
Hamamatsu H7422 and H10770A 176
Hamamatsu H7421 177
Hamamatsu H15620-45 NIR PMT 177
Hamamatsu R10467 Hybrid PMT 178
HPM-100 Hybrid Detector Modules 178
Conventional PMTs 185
Detection Efficiency Comparison 186
Influence of Magnetic Fields 187
PML-16-C and PML-16-C GaAsP Multichannel Detector Heads 189
Single-Photon Avalanche Photodiodes 193
SPAD-8 Eight-Channel SPAD Module 197
Gated SPADs 198
Id 220 InGaAs SPAD 199
id-230 InGaAs SPAD 201
NbN Superconducting Single-Photon Detectors (SSPDs) 204
Preamplifiers and Detector Control 211
Preamplifiers 211
The DCC-100 Detector Controller 212
DCU-400 and DCU-800 Detector Controllers 213
Block Diagram of the DCC-100 and DCU-400/800 devices 213
Safety Recommendations for Detectors 215

Implementation of the bh TCSPC Technique 217
The Classic TCSPC Implementation 217
Reference Signal 217
Detector Signal 219
Delayed-Stop Operation 220
Synchronisation to Random Signals 221
Multi-Detector Operation 222
Multi-Wavelength TCSPC 223
System Connection 223
Single-Detector Systems 223
Multi-Detector Systems 227
Multi-Wavelength Systems 228
Multi-Module Systems 229
Phosphorescence Systems 229
Using the Experiment Trigger 230
Resolving Cable Conflicts 232
FLIM Systems 234
Cable Diagrams of FLIM Systems 237
Piezo-Stage Systems 240
DCS-120 Confocal and Multiphoton FLIM System 242
System Architecture 242
DCS-120 System Connections 244
System Setup 249
Setup and Training Service 249
Single-Detector Systems 249
Routing Systems 254
Multi-Wavelength Systems 255
Multi-Wavelength Systems - F(xyt) Mode 256
Scanning Systems 258
Multi-Wavelength FLIM Systems 263
Multi-Wavelength FLIM by Mosaic FLIM Function 265
Setup Procedure for Other TCSPC Applications 267
System Optimisation 269
Detector Operating Conditions 269
CFD and SYNC Inputs 269
DCC Gain and CFD Threshold 271
Dependence of the Time Resolution on the Detector Gain 273
Maximum Count Rate of the Detector 274
CFD Zero Cross Level 274
Counting Background 275
Detector Operation at High CFD Threshold 277
SYNC Parameters 279
SYNC and CFD Signal Path Length for SPC Modules 279
TAC Parameters 282
SYNC and CFD Signal Path Length for SPC-QC Modules 283
TDC Offset and TDC Range Parameters 284
Excitation Source 285
Electromagnetic Shielding 285
Differential Nonlinearity 288
Dead Time 290
Counting Loss 292
Dead-Time Compensation 293
Pile-Up 294
Classic Pile-Up 294
Inter-Pulse Pile-Up 295
Avoiding Pile-Up Errors 297
Multiplexing of Lasers 298
Optimising a Photomultiplier 300
Voltage Divider 300
Illuminated Area 300
Dark Count Rate 301

Checking the SER of PMTs....301
Quick Test of a PMT....302
Optical System....303
Lenses....303
Absorptive Colour Filters....303
Interference Filters....303
Monochromators and Polychromators....304
Optical Fibres....305
Baffles and Aperture Stops....306
Avoiding Optical Reflections....306
Fluorescence Depolarisation....307
Re-Absorption and Re-Emission....309
Non-Scanning TCSPC Applications....311
Measurement of Luminescence Decay Curves....311
Excitation Sources....311
Filter-Based Systems....312
Recording Fluorescence Decay Curves with a FLIM System....317
Monochromator-Based Systems....319
Time-Resolved Spectra....320
Multi-Spectral Lifetime Experiments....322
Multi-Wavelength Tissue Lifetime Spectrometers....324
Fibre-Based TCSPC Systems....325
Micro-Spectrometers....326
Multi-Wavelength Micro Spectrometers....327
Measurement of Time-Resolved Fluorescence Anisotropy....328
Lock-in TCSPC....331
Transient Fluorescence Phenomena....333
Chlorophyll Transients....333
Stopped Flow Techniques....337
Continuous Flow Mixing Techniques....338
Simultaneous Measurement of Fluorescence and Phosphorescence Decay....340
Time-Resolved Laser Scanning Microscopy....343
Introduction....343
The Advantage of Scanning....344
The Laser Scanning Microscope....345
One-Photon Excitation....345
Two-Photon Excitation....346
Excitation Lasers....348
Detectors....350
Confocal FLIM with Diode-Laser Excitation....352
Confocal FLIM with Tuneable-Excitation....353
Multiphoton NDD FLIM....357
Live Cell and Tissue Imaging....359
Ultra-High Resolution FLIM Systems....362
High Resolution FLIM for Zeiss NLO Systems....362
High Resolution FLIM for DCS-120 MP Systems....362
NADH FLIM with Ultra-Fast Detectors....365
Multispectral FLIM....366
Confocal Multispectral FLIM....366
Multiphoton Multispectral NDD FLIM....367
Multi-Spectral FLIM with GaAsP Detectors....369
Applications of Multi-Spectral FLIM....370
Excitation-Wavelength Multiplexing....371
Metabolic Imaging by Simultaneous FLIM of NADH and FAD....375
Metabolic FLIM with One-Photon Excitation....375
Metabolic FLIM with Two-Photon Excitation....378
Tryptophan FLIM....381
Near-Infrared FLIM....384
Confocal NIR FLIM....384
NIR Multiphoton NDD FLIM with OPO Excitation....389
Infrared FLIM....392

Lifetime Imaging of Singlet-Oxygen Phosphorescence 394
High-Speed Parallel-Channel FLIM 395
Time-Series FLIM 398
Mosaic FLIM 400
Lateral Mosaic FLIM 400
Z Stack Mosaic Imaging 401
Multi-Wavelength Mosaic 401
Temporal Mosaic FLIM 402
Moving Objects 403
Z Stack FLIM by Record-and-Save Procedure 406
Recording with Z-Plane Trigger 406
Z Stack FLIM by Integrated Microscope Control 408
Fast FLIM Techniques 409
Triggered Temporal Mosaic FLIM 409
Calcium Transients 409
FLITS: Fluorescence Lifetime-Transient Scanning 410
Principle 410
Chlorophyll Transients 412
Calcium Transients 415
Fast Online FLIM with Standard bh TCSPC Systems 415
Fast FLIM Recording by the bh FASTAC System 420
Express FLIM 424
Fast FLIM by Time-Tag Recording and Off-Line Image Buildup 427
Lifetime-Intensity FLIM 428
DIC FLIM 430
Bi-Directional Scanning 432
Simultaneous FLIM/PLIM 434
Principle 434
Examples 436
FLIM with Special Scanning Techniques 439
FLIM of Macroscopic Objects 439
Imaging in the Primary Image Plane of a Scanner 439
Scanning through Endoscopes 443
Combination of Beam Scanning with a Motorised Sample Stage 446
Scanning of Well Plates 446
FLIM of a Rotating Object 447
Polygon Scanners 449
Multi-Beam Scanning Techniques 451
Scanning Systems with Piezo Stages 451
Stimulated Emission Depletion Microscopy (STED) 454
Time-Resolved Optical Near-Field Microscopy (NSOM) 458
Wide-Field FLIM 460
FLIM Background Knowledge 467
What is Important to FLIM of Biological Objects? 467
Signal-to-Noise Ratio of FLIM 470
Why Does FLIM Need More Photons than ‘Normal’ Imaging? 471
Photobleaching and Photodamage 472
Acquisition Time of TCSPC FLIM 474
Counting Loss and Pile-Up Effects 477
Spatial Binning of Decay Data 479
Image Area 480
IRF Recording 481
Effect of Fluorescence Depolarisation on Measured Decay Curves 485
Scan Rate 488
Biological FLIM Applications 491
Why Use the Fluorescence Lifetime? 491
Molecular Parameters Accessible by FLIM 493
Measurement of Local Environment Parameters 498
pH Imaging 498
Calcium Imaging 499
Chloride Imaging 500

Local Viscosity 501
Membrane Potential 502
Oxygen Concentration Measurement by FLIM 504
Other Environment Parameters 504
Förster Resonance Energy Transfer (FRET) 507
Intensity-Based FRET 507
Lifetime-Based FRET 508
Double-Exponential FLIM FRET Analysis 510
FRET Parameters from Double-Exponential Decay Analysis 511
Using Information from the Acceptor Decay Function 514
Multi-Spectral FLIM FRET Approaches 516
Dark Acceptors 516
FRET Between Endogenous Fluorophores 517
Homo FRET 518
Ultra-Fast Energy Transfer 518
Practical Hints for FRET Measurements 518
FRET Literature 522
Label-Free FLIM of Cells and Tissues 527
Metabolic Imaging 527
Basics of Metabolic FLIM 527
Indicators Characterising the Cell Metabolism 531
Metabolic Imaging with the bh FLIM Systems 535
Principle 535
Metabolic Imaging of Excised Human Bladder Tissue 537
Using the FAD FLIM Data for Clinical Diagnosis 540
Metabolic Imaging by Macro FLIM 542
Metabolic Imaging Combined with pH Imaging 543
Complex Decay Behaviour of NADH and FAD 545
NADH: Additional Decay Components 545
FAD: The FMN Problem 547
Unmixing NAD(P)H / FAD Fluorescence Components 549
Review of NAD(P)H / FAD FLIM Literature 550
Two-Photon FLIM of Mammalian Skin 556
FLIM of Other Endogenous Fluorophores 559
Drug Delivery and Diffusion of Nanoparticles in Skin 559
Autofluorescence of the Ocular Fundus 560
Ultra-Fast Fluorescence Decay in Biological Material 561
Mushroom Spores 561
Pollen Grains 562
Carotenoids 563
Human Hair 565
Malignant Melanoma 566
Fossil Micro-Organisms in Flint Stone 569
Decay Analysis by SPCImage NG 570
Image Segmentation by Phasor Plot 570
Oxygen Sensing by Phosphorescence Lifetime Measurement 572
Phosphorescence 572
Oxygen Sensing by PLIM 573
Simultaneous Recording of Oxygen and NAD(P)H Images 573
Delayed Fluorescence of PpIX 574
Applications 576
Plant Physiology 577
Other Biological FLIM Applications 583
Clinical Applications of FLIM 587
Multiphoton Tomography of Human Skin 587
Dermainspect Instrument 587
MPT FLEX 589
Ophthalmic FLIM (FLIO) 590
Biomedical Background 590
System Architecture 591
Heidelberg Engineering FLIO System 593

Results and Applications 594
Data Analysis 596
FLIO Analysis by SPCImage NG 598
Analysis FLIO Data of a Cataract Patient 600
Analysis of FLIO Data of a Normal Patient 602
Other Attempts to Suppress the Lens Fluorescence 603
Phasor Plot 604
FLIO with Two-Photon Excitation 604
Diffuse Optical Tomography: DOT, NIRS and fNIRS 605
General Principle 605
Scanning Mammography 608
Static Brain Imaging 611
Functional Brain Imaging 613
Perfusion Measurements by ICG Boli 615
Perfusion Measurement by Diffuse Optical Correlation (DCS) 619
DOT Experiments at Small Source-Detector Distance 620
Fibre-Based DOT Endoscopes 620
Tissue Spectrometers 621
Fibre-Based System for Brain Activation Measurement in Mice 622
Tissue Scanning System with Laser Wavelength Multiplexing 623
Muscle and Bone Studies 626
Fluorescence Lifetime Detection in DOT 626
Small-Animal Imaging 627
Technical Issues of DOT 629
Picosecond Photon Correlation 635
Antibunching 636
Technical Aspects 637
Fluorescence Correlation Spectroscopy (FCS) 639
Principle 639
Calculation of FCS curves from the TCSPC data 640
Using Micro-Time Information in Combination with FCS 643
FCS System Parameter Setup 645
Gated FCS 650
FCS with Laser Scanning Microscopes 651
FCS with the LSM 510 651
Zeiss LSM 710/780/880/980 651
Zeiss LSM 880 655
FCS with the DCS-120 confocal FLIM System 656
FCS in Live Cells 658
Practical Tips 659
Time-Resolved Single-Molecule Spectroscopy 665
Burst-Integrated Fluorescence Lifetime (BIFL) Techniques 665
Multi-Parameter Single-Molecule Burst Analysis 667
Single-Molecule FRET Experiments 672
Identification of Single Molecules 674
Correlation of Lifetime Fluctuations 674
Photon Counting Histograms 675
Other TCSPC and FLIM Applications 679
FLIM of Semiconductors 679
Barrier Discharges 681
Principle 681
Scanning with Galvanometer Mirror 682
Two-Photon Excitation by Picosecond Diode Lasers 685
Measuring the Laser-Pulse Duration in Two-Photon Microscopes 686
Positron Lifetime Measurements 687
LIDAR Systems 689
Basic Principle 689
Early Implementations 689
Modern Implementation of a TCSPC-LIDAR System 691
Characterisation of Detectors 694

Measurement of the IRF of a Detector 694
Spatially Resolved Characterisation of SPADs 695
Light Emission from SPADs 697
Measurement of Absolute Detector Quantum Efficiency 698
Photon-Number Sensitive TCSPC 699
Optical Oscilloscope 701
SPCM Software 703
Overview 703
SPCM Main Panel 704
'Dark' and 'Light' Versions 705
Changing Between Different Instrument Configurations 706
Measurement Functions 707
Display of TCSPC Data 708
Display, Trace Parameters and Window Parameters 709
Cursors in the Display Windows of the Main Panel 710
Trace Statistics 711
System Parameters 712
System Parameter Settings from the Main Panel 712
Module Select (Multi-SPC Systems) 712
Status Information 713
Application Options 714
Software Start 716
Main 718
Load Panel 718
Save Panel 720
Predefined Setups 723
Multi-File View 724
Data Export and Import: Convert Functions 724
Link to SPCImage Data Analysis 728
Print 728
Sleep policy 728
System Parameters - SPC Series 731
System Parameters - SPC QC Series 731
Operation Modes 732
‘Single’ Mode 733
Oscilloscope Mode 734
f(txy) Mode 735
f(t,T) Mode 737
f(t,EXT) Mode 739
fi(T) Mode 742
fi(EXT) Mode 744
Continuous Flow Mode 747
Scan Sync Out Mode 750
Sequential Recording in the Scan Sync Out mode 752
Scan Sync In Mode 753
Scan XY Out Mode (SPC-700/730 only) 760
FIFO Imaging Mode 762
Delay Correction for 16-Channel Detectors 768
FIFO Mode 770
Wide-Field FLIM 777
Control Parameters (Photon Distribution Modes) 779
Stop Condition and Overflow Handling 779
Steps 780
Cycles and Autosave 780
Accumulate 780
Repeat 780
Trigger 780
Display After Each Step and Each Cycle 781
Add/Sub Signal 781
Measurement Timing Control Parameters 781
Collection Time 781

Repeat Time 782
Display Time 782
Dead Time Compensation 783
CFD Parameters 783
SYNC Parameters 784
TAC Parameters for SPC Modules 784
TDC Parameters for SPC-QC Modules 786
Data Format 787
Page Control 790
'More' Parameters 792
Adjust Parameters 793
Parameter Management for Multi-Module SPC Systems 795
Module Selection 795
Trigger Master and Clock Master Function 795
Display Functions 797
Display of 2D Data 798
Display of 3D Data 803
Display of FLIM Data 806
Definition of the Display Windows 806
Intensity Images from FLIM Data 809
Time-Gated Intensity Images 814
Colour-Coded Lifetime Images 815
Images from Lifetime-Intensity Mode 819
Simultaneous FLIM/PLIM Images 819
Display of Decay Data in Point or Region of Interest 821
Resizing and Positioning the Display Windows 822
Display Parameters 825
General Display Parameters 825
2D Display Parameters 826
3D Display Parameters 826
Displaying Subsets of Multidimensional Data 828
Display Parameters for Different Display Windows 829
2D Trace Parameters 831
Trace Parameters for 2D Curve Mode 831
Trace Parameters for 2D Block Mode 833
Block Info 834
Export of Trace Data 834
3D Trace Parameters 836
Window Intervals 839
Time Windows 839
Routing X and Y Windows 841
Scan X and Y Windows 844
Auto Set Functions 845
Starting and Stopping a Measurement 847
Exit 848
Operation of Experiment Control Devices from the SPCM Software 849
Scanner Control via the GVD-120 Card 849
DCC-100 Detector Controller Card 854
Control of the Zeiss Axio Observer Z1 856
DB-32 SYNC Delay Box 856
DDG-210 Pulse Generator Card 857
Ti:Sa Laser and AOM Control 858
Motor Stage 859
SPCImage NG Data Analysis Software 861
Overview 861
Main Panel 861
Images of Decay Parameters 863
Phasor Plot 865
Maximum-Likelihood Algorithm 865
Modelling of the Instrument-Response Function 866
Decay Models 866

GPU Processing ... 866
Parameter Histograms ... 867
2-D Histograms ... 868
ROIs ... 868
Image Segmentation ... 869
Analysing FLIM Data with SPCImage ... 871
Loading the FLIM Data into SPCImage NG ... 871
Calculating the Lifetime Image ... 875
Model Functions ... 877
IRF Options ... 881
Fit Algorithm ... 883
Fit Control Parameters ... 884
Fit Quality Indicators ... 886
Display of Decay Data ... 889
Display of Colour-Coded Images ... 891
General Configuration ... 891
Intensity Parameters ... 892
Colour Parameters ... 893
Parameter Histogram ... 896
Intensity Histogram ... 897
ROI Definition ... 899
Rectangular ROI ... 899
Polygonal ROI ... 899
Lines of Interest ... 900
ROIs from 2D Histograms and Phasor Plots ... 900
Pixel Masks ... 901
Decay-Parameter Histograms in ROIs and Masks ... 902
2D Histograms ... 904
Phasor Plot ... 906
Model Parameters ... 909
Preferences ... 912
Configurations ... 913
Analysis of Special Data Types ... 915
Single-Curve Data ... 915
Pseudo-Global Analysis ... 917
Global Analysis ... 918
Multi-Wavelength Lifetime Images ... 919
Spatial and Temporal Mosaic FLIM Data ... 921
INT FLIM Data ... 921
Phosphorescence Lifetime Images ... 923
Batch Processing ... 927
Saving SPCImage Data ... 928
Export of Data ... 928
Special Commands ... 929
Supporting Information ... 930
Spatial Binning ... 930
Temporal Binning ... 931
The Convolution Integral ... 932
Decay Models ... 933
Fit Procedures ... 936
How Many Exponential Components Are Needed? ... 938
Over-Determined Models ... 939
Instrument Response Function ... 942
Parameters of the Decay Functions and their Use in SPCImage ... 949
Phasor Plot ... 955
Assistance through bh ... 959
External Control Signals ... 961
SPC-600/630 ... 961
SPC-700/730 and SPC-830 ... 962
SPC-130, SPC-134 ... 966
SPC-130EM, SPC-130EMN, SPC-150, SPC-150N, SPC-160 ... 967

SPC-180N, SPC-180NX, SPC-180NXX, SPC-130IN, SPC-130INX 970
SPC-QC-104 and SPC-QC-106 modules 970
GVD-120 Scan Controller 971
DCC-100 Detector Controller 972
Specifications 973
Absolute Maximum Ratings (for all SPC modules) 973
Acknowledgements 973
References 975
Index 1034

Overview on bh TCSPC Instrumentation

Over the past three decades, bh have developed a large number of TCSPC devices and measurement systems based on them. This chapter gives an overview on the bh TCSPC and TCSPC/FLIM devices and related components, such as detectors, lasers, optical components, and experiment control devices. It describes essential features of the bh TCSPC modules, operation modes, associated data acquisition and data analysis software, and typical applications. It also gives a summary on the bh DCS-120 confocal and multiphoton laser scanning systems, the bh FASTAC system, and on the combination of the bh devices with laser scanning microscopes of other manufacturers.

General Features of the bh TCSPC Devices

Ultra-High Resolution Photon Timing

The bh SPC series TCSPC/FLIM devices use an ultra-high resolution TAC/ADC principle. The bh TCSPC modules deliver a far better time resolution for fast detectors than any other TCSPC product. The internal timing jitter is on the order of 2.7 ps (rms, root mean square) for the standard modules SPC-150N and SPC-180N modules, 1.6 ps for the SPC-150NX and SPC-180NX modules, and about 1.1 ps for the corresponding -NXX modules. The internal IRF widths are 6.6 ps, 3.5 ps, and 2.8 ps (fwhm, full-width at half maximum, see Fig. 1). The minimum time channel width is 810 fs for the standard boards, 405 fs for the -NX boards, and 202 fs for the -NXX boards.

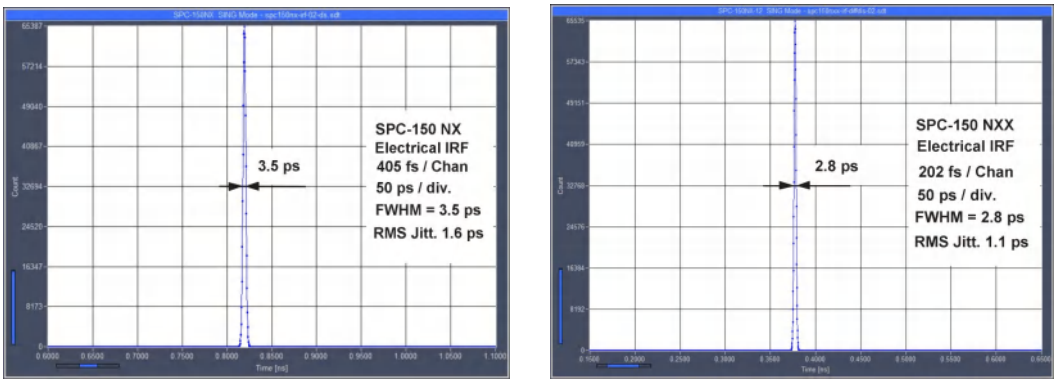


Fig. 1: Electrical time resolution of SPC-150NX (left) and SPC-150NXX (right)

The full-width-half-maximum instrument response of the entire TCSPC system with fast hybrid detectors or MCP PMTs is in the sub-20 ps range. This includes the transit-time spread of the detector, the internal jitter of the TCSPC module, and possible synchronisation jitter. With superconducting NbN detectors 17.8 ps fwhm has been achieved, with a single-nanowire detector even 4.4 ps fwhm. A few examples are shown in Fig. 2.

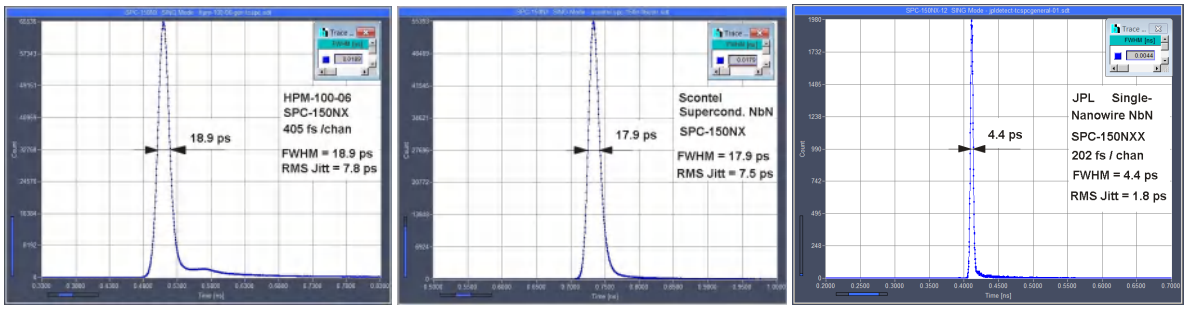


Fig. 2: System-IRFs for a fast HPM-100-06 hybrid detector, a superconducting NbN detector, and a superconducting single-nanowire NbN detector.

Parallel Recording Channels

The SPC-QC devices are designed for recording in parallel TCSPC channels. This required minimisation of board space and power consumption. The SPC-QC boards therefore use a fast TDC (Time-to-digital) conversion principle. The boards do not reach the time resolution as the SPC boards but, with electrical IRF widths of 30 to 40 ps, they are still fast for common standards. Moreover, the SPC-QC boards are able to record at photon rates exceeding 100 MHz per channel. The SPC-QC boards are therefore used in many applications that require high throughput but not necessarily ultimate time resolution. The electric IRF of an SPC-QC-104 module and system IRFs of an SPC-QC-104 with an HPM-100-40 and an HPM-100-06 hybrid detector are shown in Fig. 3.

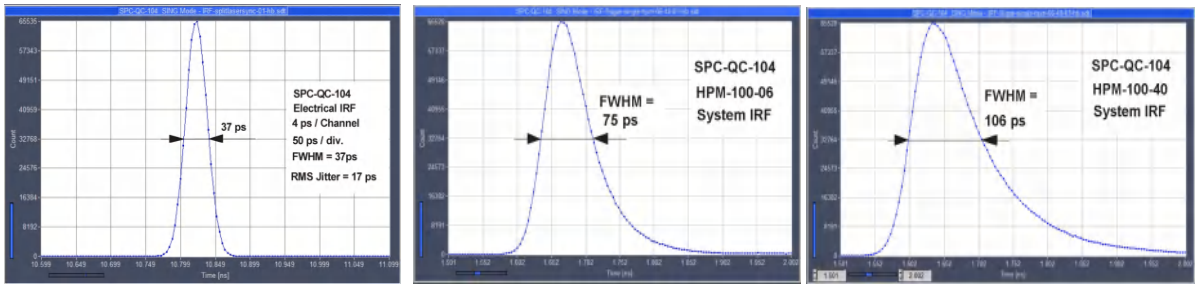


Fig. 3: Left: Electrical IRF of an SPC-QC-104. Right: System IRF with an HPM-100-40 hybrid detector. Time scale 50 ps / div, same as in Fig. 2.

Unprecedented Timing Stability

The bh TCSPC devices are virtually free of IRF drift or low-frequency timing wobble. IRF drift, if perceptible at all, remains below the electrical IRF width over minutes or even hours. That indirectly means that the IRF neither broadens in an experiment of long acquisition time nor shifts over a longer series of recordings. Fig. 4, left and right, shows a series of 100 IRF recordings over 100 seconds. The horizontal axis is the TCSPC time axis, the vertical axis is the time into the series. The variance in the time of the IRF centroid is less than 0.4 ps. Overall timing drift of a real measurement system is shown in Fig. 5. It shows two IRFs of an SPC-150NX system with a superconducting NbN detector, recorded 5 minutes apart. The timing drift is less than the time-channel width (405 fs).

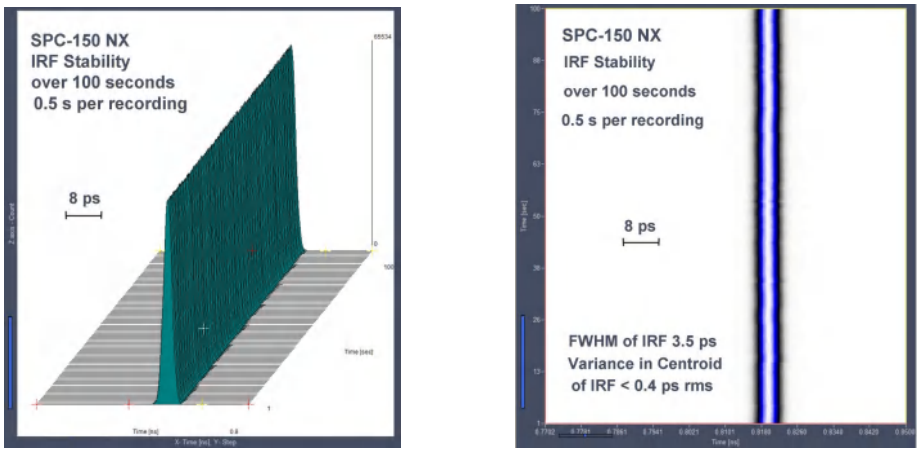


Fig. 4: Series of 100 (electrical) IRF recordings for an SPC150NX over 100 seconds. Left: Result displayed as series of curves. Right: Colour-Intensity display. The horizontal axis is the TCSPC time axis (bar indicates 8 ps), the vertical axis is the time into the recording sequence. The variance in the centroid of the IRF is less than 0.4 ps rms.

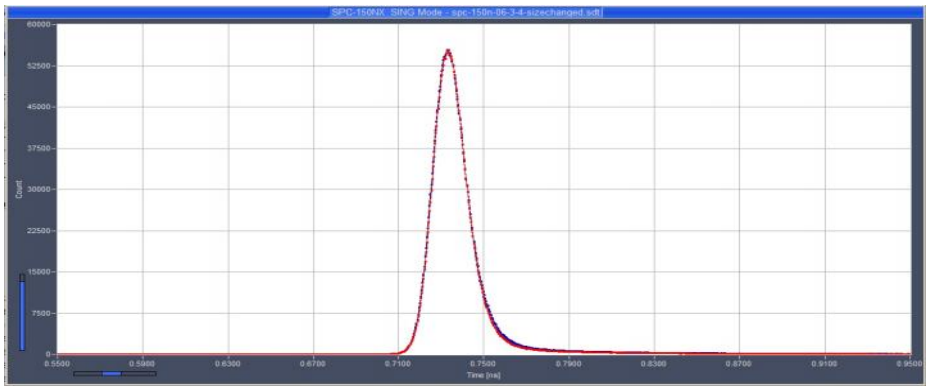


Fig. 5: Two IRFs of an SPC-150NX TCSPC system with a superconducting NbN detector, recorded 5 minutes apart (black and red dots). The drift is less than one time-channel (405 fs).

The timing stability for an SPC-QC-104 is shown in Fig. 6. The timing drift is less than 5 ps over 640 seconds.

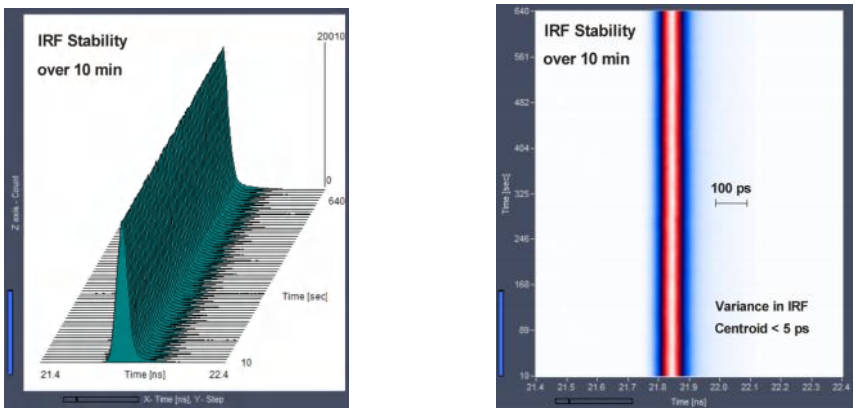


Fig. 6: Series of 64 (electrical) IRF recordings for an SPC-QC-104 over 640 seconds. Left: Result displayed as series of curves. Right: Colour-Intensity display. The horizontal axis is the TCSPC time axis (bar indicates 100 ps), the vertical axis is the time into the recording sequence. The variance in the centroid of the IRF is less than 5 ps rms.

Multi-Dimensional TCSPC

The bh TCSPC modules are using a multi-dimensional TCSPC process. Unlike classic TCSPC devices, they record photon distributions not only over the time in the excitation pulse period, but also over additional parameters that can be associated to the individual photons. This can be the wavelength of the photons, the spatial location where they come from, the time from the start of an experiment, the time within the period of a stimulation of the sample, the time within the period of a modulation of the excitation laser, or any other parameters that are determined during the recording process. As a result, the bh SPC modules can be used for the classic fluorescence decay applications as well as for fluorescence lifetime imaging (FLIM), multi-wavelength fluorescence decay measurement, multi-wavelength FLIM, simultaneous fluorescence and phosphorescence decay measurement, simultaneous FLIM and PLIM, fast time-series fluorescence decay recording, fast time-series FLIM, fluorescence correlation spectroscopy (FCS), single-molecules experiments, anti-bunching experiments, and many other multi-dimensional photon recording tasks.

FLIM at Unprecedented Image Size

FLIM images can be recorded at a maximum data size of 4096 x 4095 pixels x 64 time channels, 2048 x2048 pixels x 256 time channels, or 1024 x 1024 pixels x 1024 time channels. Several such images can be recorded in parallel. An example is shown in Fig. 7.

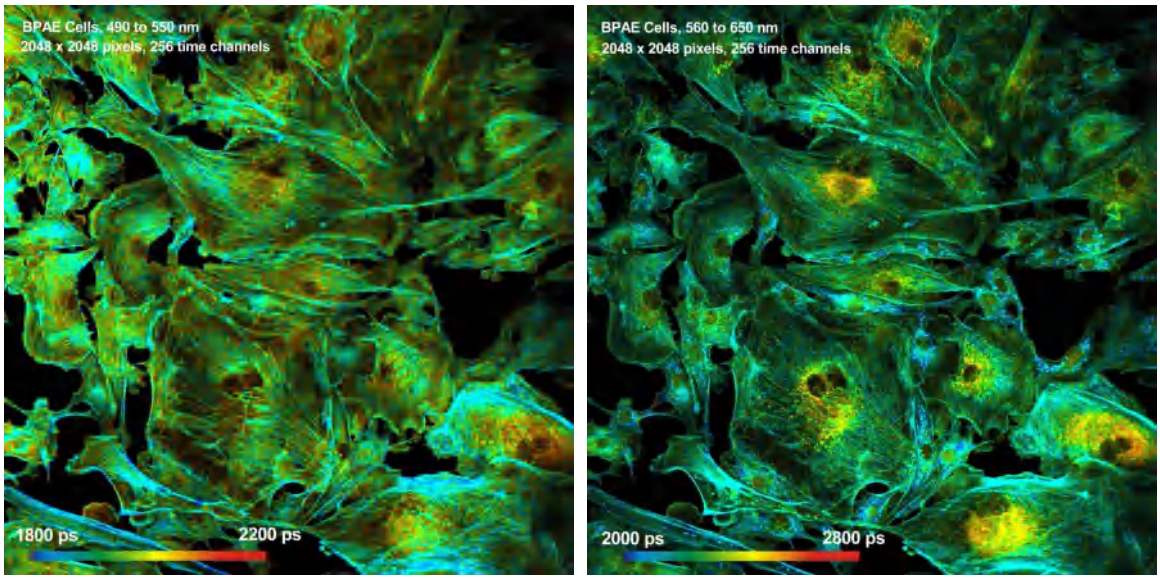


Fig. 7: FLIM images with 2048 x 2048 pixels and 256 time channels per pixel, recorded by a dual-channel SPC-160 pcie system.

All Electronics on Board

The bh SPC modules contain complete electronics for recording fast light signals by multi-dimensional TCSPC on single PC boards. All the building blocks, such as constant-fraction discriminators, time-to-amplitude converter, analog-digital converter, TDC, data processing logics, data memory and data buffer, and the associated control circuitry are integrated.



Fig. 8: SPC-180NX TCSPC/FLIM module. The complete electronics for recording multi-dimensional TCSPC data is integrated on a single circuit board.

Parallel Operation of Modules

Up to four bh TCSPC modules of similar type can be operated in parallel and controlled by the device software. Up to 12 modules can be operated in an extension box connected to one computer.

Online Data Display

Decay curves, multi-wavelength decay data, FCS curves, photon counting histograms, intensity images, and FLIM and PLIM images are displayed online. Intermediate results are displayed in programmable time intervals. For multi-dimensional data two-dimensional sub-sets can be defined and displayed during the measurement.

High Throughput Rates

The boards have saturated count rates on the order of 10 to 12.5 MHz, and can be used at count rates in excess of $5 \cdot 10^6$ photons/s. Thus, fluorescence decay curves or other optical waveforms can be recorded at acquisition times in the ms range. The speed can further be increased by operating several TCSPC modules in parallel. This way, saturated count rates of 40 MHz can be reached; experiments can be run at count rates of 20 MHz.

Hardware and Software Accumulation Modes

The boards can be operated both in a hardware accumulation mode, in a software accumulation mode, or in a single-photon parameter-tag mode. In the hardware-accumulation mode, the boards build up photon distributions directly in the device memory. These can be single fluorescence decay curves or other optical waveforms, anti-bunching curves, multi-wavelength decay data, time-series of decay curves, or FLIM data. Since the data acquisition occurs in the hardware of the TCSPC module the recording process does not require any computer interaction during the measurement. Photons can thus be recorded up to a sustained count rate of up to 10 MHz per SPC module, independently of the speed of the system computer.

In the software accumulation mode, the photon data are transferred into the system computer photon by photon, and the photon distributions are built up by software. Due to the large memory space available, large photon distributions can be built up, such as FLIM images with 2048 x 2048 pixels and 256 time channels per pixel. The large memory space is also an advantage when complex photon distributions are built up, for example for spatial or temporal mosaic FLIM, fast FLIM time series, or multi-wavelength FLIM. The software accumulation mode is also used to record FCS, combined FLIM / PLIM, or photon counting histograms. Please see section 'Multi-Dimensional TCSPC' for an overview.

Parameter-Tag Recording

In the software accumulation modes, parameter-tagged single-photon data can be stored instead or in parallel with the build-up of photon distributions. Such data are used especially for single-molecule spectroscopy. The transit of single molecules through a laser focus can be identified in the data, spectroscopic information be derived from the photon data of the individual molecules, and the properties of the molecules be statistically analysed.

Complex Systems for a Wide Range of Applications

bh TCSPC systems have a high degree of modularity. By combining TCSPC modules, experiment control modules, detectors, bh picosecond and CW diode lasers, titanium-sapphire lasers, super-continuum lasers, motorised sample stages, optical scanners, microscopes, and other optical components time-resolved optical recording systems for a wide range of experiment tasks are feasible. bh deliver complete one-photon and multiphoton FLIM laser scanning microscopes, FLIM systems for laser scanning microscopes of a wide variety of manufacturers, scanning systems for macroscopic FLIM systems, fibre-based systems for metabolic

measurements in animals, and sub-systems for diffuse near-infrared imaging (NIRS and fNIRS).

64-Bit Instrument Software

All functions of the SPC modules and of peripheral devices are controlled by 64-bit SPCM 'Multi SPC Software'. The software provides functions such as measurement control, online calculation and display of data, set-up of measurement parameters, 2-dimensional and 3-dimensional display of measurement results, mathematical operations, selection of subsets from multi-dimensional data sets, loading and saving of results and system parameters, and control of the measurement in the selected operation mode. The SPCM software includes also the control of the bh DCS-120 confocal scanning FLIM system, resulting in a seamless interaction of TCSPC operation and scanning. The 64-bit SPCM Software runs under Windows 10 and Windows 11, 64 bit.

Fluorescence Decay and FLIM / PLIM Data Analysis Software

The SPCM software has a direct link to the SPCImage NG fluorescence-decay and FLIM data analysis. SPCImage calculates fluorescence decay parameters and lifetime images by various decay models. It runs analysis of single fluorescence decay curves, analysis of single- and multi-wavelength FLIM data, batch-processing of FLIM time series an FLIM Z stacks, and analysis of PLIM data.

Wide Range of Application

Due to their superior time resolution all bh TCSPC devices are an excellent choice for the traditional fluorescence lifetime experiments. However, their true strength are advanced applications, such as multi-spectral fluorescence lifetime spectroscopy, single- and multi-wavelength FLIM, simultaneous FLIM and PLIM of cell metabolism and oxygen partial pressure, fast sequential recording of time-of-flight distributions in diffuse optical tomography, measurement of transient fluorescence lifetime effects in biological systems, combined fluorescence correlation (FCS) and lifetime spectroscopy, and spectroscopy of single molecules, quantum dots and semiconductor nano-structures by FCS, FIDA, MFD, and BIFL techniques.

TCSPC Modules

SPC-180N Series Modules

The SPC-180N series has ultra-fast timing electronics and GHz-bandwidth constant-fraction discriminators to achieve maximum time resolution for a given single-photon detector. The SPC-180N series modules have a high-speed PCI-Express (pcie) interface. The new interface achieves extremely high data transfer rates. With the SPC-180N, bus saturation and FIFO overflow in fast FLIM applications are unlikely to occur. To facilitate fast FLIM, the modules of the SPC-180N series have a fast counter in parallel to the TCSPC timing electronics. This allows the data acquisition software to build up FLIM images the intensity of which remains linear up to the highest count rates. Please see page 428.

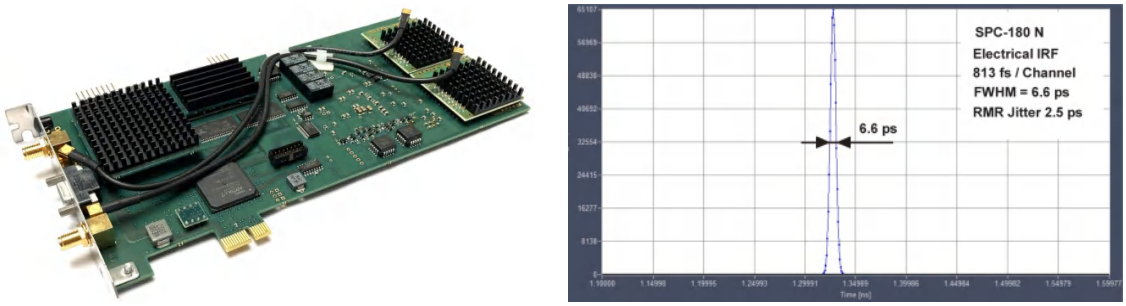


Fig. 9: SPC-180NXX Module. Right: Electrical IRF

SPC-180 NX Modules

The SPC-180 NX is a resolution-enhanced version of the SPC-180N. The minimum time-channel width is 405 fs in comparison to 810 fs for the SPC-180N. The electrical IRF width is 3.5 ps FWHM, the rms timing jitter 1.6 ps RMS. The SPC-180NX is recommended especially for applications with high-resolution detectors, such as superconducting single photon (SSPD) detectors, MCP PMTs, and fast hybrid detectors [115, 117, 122]. The SPC-180NX achieves sub-20 ps (full-width-half maximum) IRF width with these detectors.

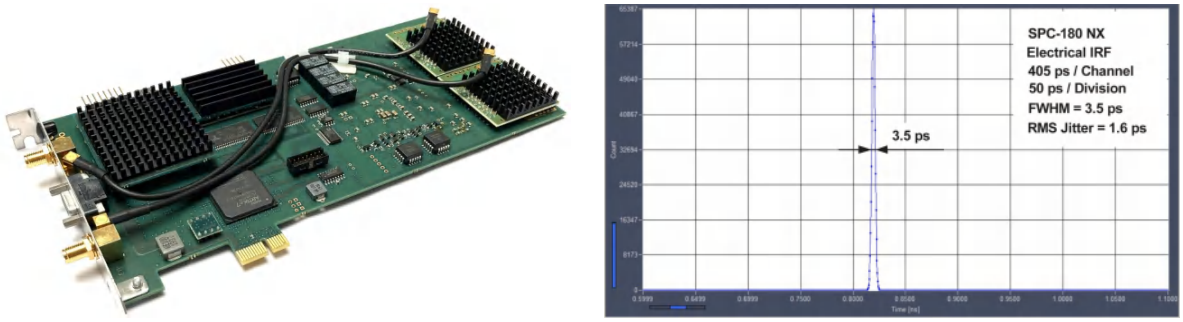


Fig. 10: SPC-180NX Module. Right: Electrical IRF

SPC-180 NXX Modules

The SPC-150NXX is a version of the SPC-150NX with ultimate time resolution. The minimum time-channel width is 202 fs. The electrical IRF width is typically 2.8 ps, full width at half maximum, the rms timing jitter 1.1 ps. The SPC-180NXX is recommended especially for applications that require ultimate time resolution from superconducting single-photon (SSPD)

detectors. With an SPC-150NXX and a single-superconducting nanowire detector a system IRF of 4.4ps fwhm has been reached [117], see page 204.

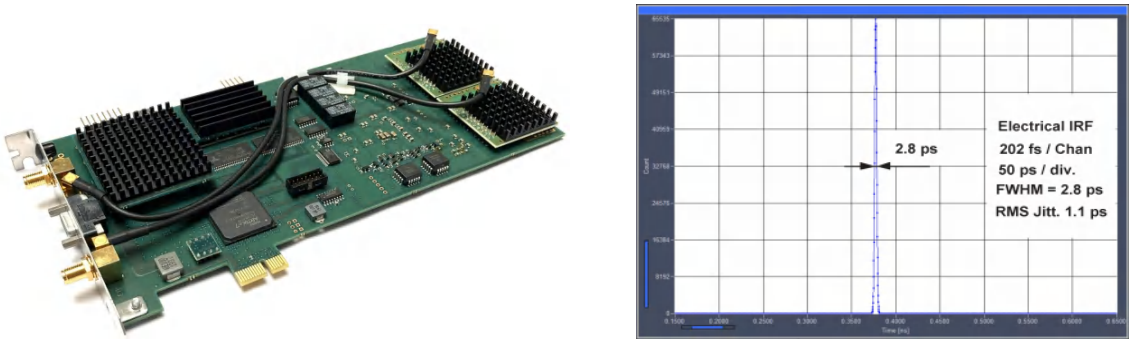


Fig. 11: SPC-180NXX Module. Right: Electrical IRF

SPC-130 IN, INX, INXX

The SPC-130 IN, INX, and INXX are TCSPC modules for non-imaging applications. The SPC-130 IN, INX, and INXX modules use SPC-180N technology. The modules have the same fast pcie interface, and the same time resolution as the SPC-180N, NX, and NXX modules.

SPC-QC-104

The SPC-QC-104 TCSPC / FLIM module has four absolute time-tagging channels or three parallel TCSPC / FLIM channels on a single PCI-express board. A reduced function-set module without FLIM, the SPC-QC-004, is available as well. The SPC-QC-104 uses the fast constant fraction discriminators of the SPC-180N series but a different time-measurement technique. Instead of the TAC-ADC principle of the SPC-180 series, the SPC-QC modules use a direct Time-to-Digital Conversion (TDC) process to determine photon times. The TDC process does not reach the same time resolution as the TAC/ADC process used in the SPC modules. Nevertheless, the SPC-QC modules feature high temporal and extraordinarily high timing stability. The electrical IRF width is 37 ps FWHM; the timing jitter is about 17 ps RMS. The timing stability over 10 minutes is better than 5 ps RMS, including a bh BDS-SM ps diode laser and a bh HPM-100-06 detector. An advantage of the SPC-QC series is that it has extremely short dead time and, therefore, can reach peak count rates on the order of 100 MHz. In addition to the usual single-curve, oscilloscope, time-tagging, and FLIM modes the SPC-QC has a coincidence mode for recording coincidence curves for photons detected in different pairs of its four detection channels. Details of the SPC-QC-104 are described in a separate handbook [75].

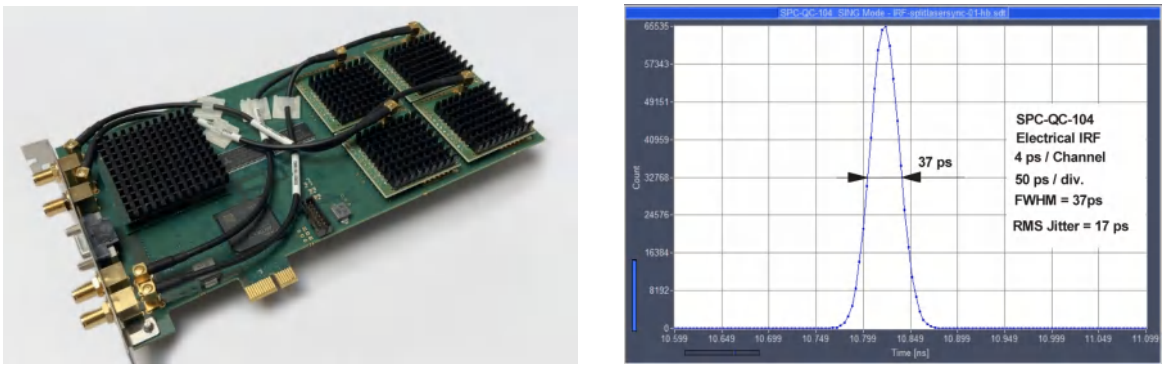


Fig. 12: SPC-QC-104 module. Right: Electrical IRF

SPC-QC-106

The SPC-QC-106 is similar to the SPC-QC-104 but has 6 absolute time-tagging channels or 5 parallel TCSPC / FLIM channels on a single PCI-express board. Applications are quantum-correlation experiments and high-throughput FLIM with four or five parallel detector channels.

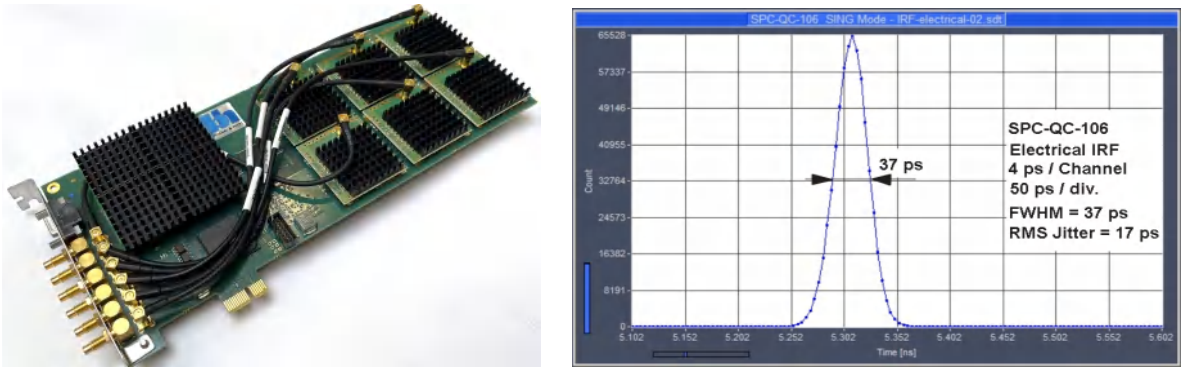


Fig. 13: SPC-QC-104 module. Right: Electrical IRF

SPC-QC-008

The SPC-QC-008 has 8 timing channels on a single PCI-express board. It is used for quantum-correlation experiments and parallel-channel TCSPC experiments. For absolute time-tagging experiments all 8 channels can be used. For TCSPC one channel is used as a reference channel, the other seven are photon channels. Due to restrictions in space and power consumption the SPC-QC-008 has leading edge discriminators instead of the constant-fraction discriminators of the SPC-180 series and the SPC-QC-104 and -106. This is not a problem for SPAD detectors and hybrid detectors. The discriminators have GHz bandwidth and do not have an influence of the time resolution of these detectors. However, for conventional PMTs and other detectors with large pulse-amplitude fluctuations the time resolution can be slightly lower than for the modules with CFDs. The SPC-QC-008 is decribed in a separate handbook [59].

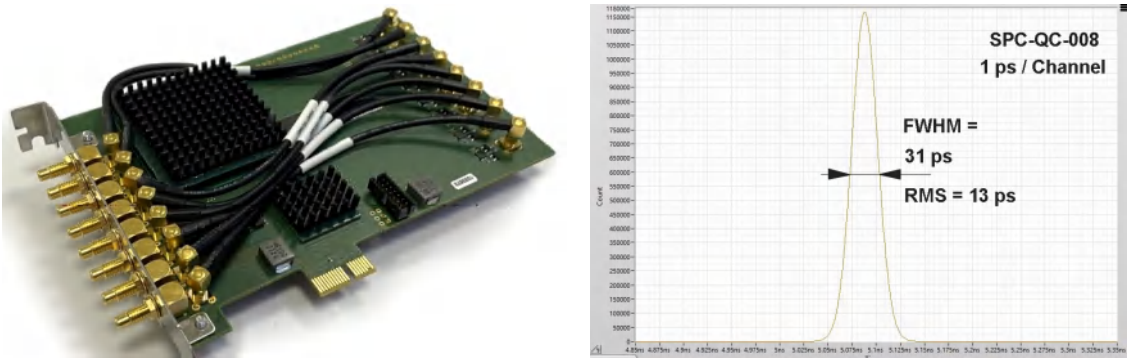


Fig. 14: SPC-QC-008 module. Right: Electrical IRF

Multi-Module TCSPC Packages

All SPC modules are available as two-channel, three-channel, and four-channel packages. The devices are used in applications where several optical signals have to be recorded simultaneously, and maximum throughput is required. Typical examples are bh FLIM systems, which normally have two parallel SPC channels. Three- and four-channel systems are commonly

used in near-infrared diffuse optical imaging applications. A package of four SPC-QC-008 modules in one computer is shown in Fig. 15.

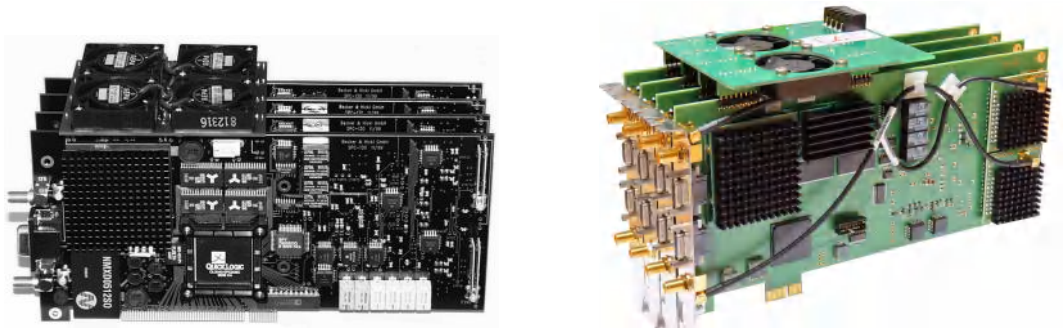


Fig. 15: SPC-134 (left) and SPC-184NX (right) four-channel TCSPC packages



Fig. 16: Parallel operation of four SPC-QC-008 modules in one computer, view on the input connectors. The system provides 32 parallel timing channels.

Older TCSPC Modules

There is a number of SPC modules that are still in use in large quantities but which are no longer recommended for new systems.

SPC-150N Series Modules

The SPC-150N is an all-purpose TCSPC and FLIM module with PCI bus interface. The SPC-150N differs from the older SPC-150 in that it has ultra-fast discriminators in the detector- and synchronisation inputs. This allows the module to obtain superior time resolution with detectors that both have low transit time spread and an extremely fast single-photon response. They are recommended especially for superconducting detectors, MCP PMTs, and ultra-fast hybrid detectors. The SPC-150N equals or surpasses the older SPC-150 in all parameters. In 2020, the SPC-150N and its faster siblings (see below) have replaced the SPC-150.



Fig. 17: SPC-150N board. Right: Electrical IRF

SPC-150NX Module

The SPC-150NX is a resolution-enhanced version of the SPC-150N. The minimum time-channel width is 405 fs in comparison to 810 fs for the SPC-150 and SPC-150N. The SPC-150NX is recommended especially for applications that require ultimate time resolution from superconducting detectors, MCP PMTs, and fast hybrid detectors. The SPC-150NX achieves sub-20 ps (full-width-half maximum) IRF width with these detectors.



Fig. 18: SPC-150NX board. Electrical IRF shown on the right.

SPC-150NXX Module

The SPC-150NXX is a version of the SPC-150NX with further resolution enhancement. The minimum time-channel width is 202 fs. The SPC-150NXX is recommended especially for applications that require ultimate time resolution from superconducting detectors, MCP PMTs, and fast hybrid detectors. The electrical IRF width is typically 2.8 ps, full width at half maximum. With an SPC-150NXX and a single-superconducting nanowire detector a system IRF of 4.4ps fwhm has been reached [117].



Fig. 19: SPC-150NXX board. Right: Electrical IRF

SPC-130EMN, EMNX, EMNXX

The SPC-130EMN is a TCSPC module with PCI interface for non-imaging applications. It uses SPC-150N technology. The electrical time resolution for the EMN version is 6.6 ps, The electrical time resolution is 6.6 ps FWHM for the EMN version and 3.5 ps FWHM for the EMNX version.

SPC-160 Modules

The SPC-160 modules have a large internal memory and a fast bus interface, combined with the largest set of functions and operating modes of all bh TCSPC modules. The SPC-160 modules have the fast discriminators of the SPC-150N. Moreover, they have an additional parallel photon counting channel in the FIFO Imaging (FLIM) mode. The SPC-160 modules are thus able to record intensity images up to a detector peak count rate of about 10 MHz. Intensity information from the parallel counter channel and lifetime information from the TCSPC imaging channel are combined to obtain FLIM images that have a linear intensity scale up to extremely high count rates.



Fig. 20: SPC-160 board

As the SPC-150 and SPC-150N, the SPC-160 modules can be used for traditional fluorescence lifetime experiments, diffuse optical tomography, stopped flow experiments, single molecule spectroscopy, FCS and FCCS recording, FLIM, multi-wavelength FLIM, Mosaic FLIM, and simultaneous FLIM / PLIM.

SPC-160pcie Modules

The SPC-160pcie is a PCI-Express-bus version of the SPC-160. The range of functions and operation modes is the same as for the SPC-160.



Fig. 21: SPC-160pcie

SPC-130 Modules

The SPC-130 modules were optimised for small size and low price. They were the first boards which could reasonably be operated in packages of four modules. The SPC-130 boards have all standard photon distribution modes, the continuous-flow mode, and the FIFO (time-tag) mode implemented. However, the boards have no imaging modes. The SPC-130 board can thus be used for traditional fluorescence lifetime experiments, diffuse optical tomography, stopped flow experiments, single molecule detection and combined FCS/lifetime experiments. The disadvantage of the SPC-130 is that it has a relatively slow bus interface and limited routing capabilities. It has therefore been replaced with the more advanced SPC-130EM and SPC-130EMN modules.

SPC-130EM Modules

The SPC-130EM module is an improved version of the former SPC-130. It has all standard photon distribution modes, the continuous-flow mode, and the FIFO (time-tag) mode, but no imaging modes. However, it got the faster bus interface, the large memory, and the full routing capability of the SPC-150. The SPC-130EM board can be used for traditional fluorescence lifetime experiments, diffuse optical tomography, stopped flow experiments, single molecule detection and combined FCS/lifetime experiments. Since 2020, the SPC-130EM has been replaced with the more advanced SPC-130EMN series modules. These modules have ultra-fast discriminators and thus offer improved time resolution for ultra-fast detectors.



Fig. 22: SPC-130EM board

SPC-150 Modules

The SPC-150 modules have a large internal memory and a fast bus interface, combined with a large set of functions and operating modes. The difference to the new SPC-150N series modules is that the SPC-150 has discriminators with 'only' 1 GHz bandwidth. That means the time resolution with fast detectors is lower.



Fig. 23: SPC-150 board

The SPC-150 board can be used for traditional fluorescence lifetime experiments, diffuse optical tomography, stopped flow experiments, single molecule spectroscopy, FCS and FCCS recording, FLIM, Mosaic FLIM, FLITS, and combined FLIM / PLIM. One or more SPC-150 modules are used the bh DCS-120 confocal FLIM system. For many years, SPC-150 modules have also been the basis of the FLIM systems for the Zeiss LSM 880, 780, 710 and 510 microscopes and various other confocal and multiphoton laser scanning microscopes. Since 2020, the SPC-150 has been replaced with the more advanced SPC-150N series modules. These modules have ultra-fast discriminators and thus offer improves time resolution for ultra-fast detectors.

SPC-830

The SPC-830 combines the functions of the older SPC-630 and the SPC-730 modules. It has a memory four times as large as the SPC-730 and an fast bus interface. The SPC-830 was the first module covering the complete range of applications from the traditional fluorescence lifetime and anisotropy decay experiments, photon correlation experiments, confocal and two-

photon fluorescence lifetime microscopy, single molecule lifetime, anisotropy and fluorescence correlation, cross-correlation, and burst-integrated lifetime experiments.

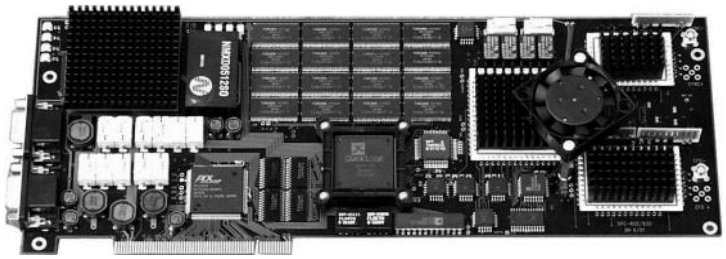


Fig. 24: SPC-830 module

SPC-600/630

The SPC-600/630 modules were the first TCSPC devices that had both the photon distribution modes and the single-photon parameter-tag mode implemented.

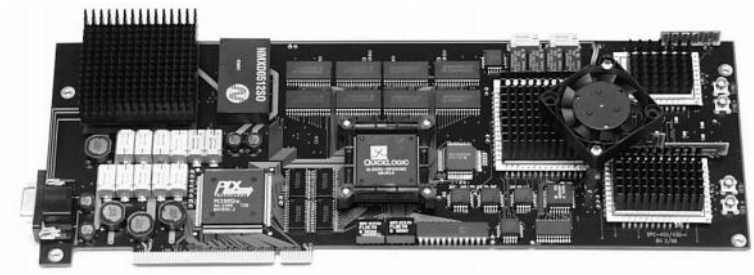


Fig. 25: SPC-630 module

Thus, the modules can be used for the complete range of applications from the traditional fluorescence lifetime and anisotropy decay experiments, photon correlation experiments, and single-molecule spectroscopy by FCS, FIDA and BIFL techniques. The SPC-600/630 modules have a dual memory structure for simultaneous measurement and data readout. A 'Continuous Flow' mode is available to record extremely fast and virtually infinite sequences of waveforms. Thus, the SPC-600/630 modules can be used to record transient phenomena in the absorption, scattering and fluorescence parameters of a sample.

SPC-700/730

The SPC-700/730 modules were the first devices designed for TCSPC imaging with laser scanning microscopes. They combine the features of the earlier SPC-500/530, SPC-505/535 and the SPC-506/536 modules.

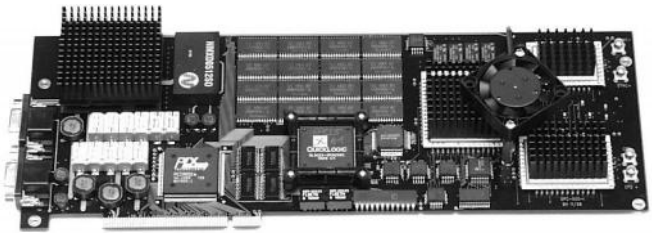


Fig. 26: SPC-730 module

The disadvantage is the (for modern standards) small device memory and the lack of a FIFO imaging mode. Images recorded with the SPC-730 therefore do not reach pixel numbers higher than 256 x 256. The manufacturing of the SPC-730 boards has been discontinued. Nevertheless, the boards are still supported by bh SPCM device software, and the data can be processed by SPCImage data analysis software.

Simple-Tau TCSPC Systems

The Simple-Tau systems are compact table-top systems based on a lap-top computer and a bus-extension box. The box contains the TCSPC and experiment control electronics.

There is a wide variety of Simple-Tau systems with different TCSPC boards, different numbers of TCSPC boards, and different experiment control modules. The ‘small’ Simple Tau systems (see Fig. 27) have space for four PCI modules. Most of the systems contain two SPC-150 TCSPC FLIM modules and one DCC-100 detector controller. Systems for FLIM can also contain a GVD-120. They are used for DCS-120 confocal or multiphoton scanning systems. However, also systems with SPC-130 modules are in use. Older SPC-130 or SPC-150 Simple-Tau systems can be upgraded with SPC-150N, SPC-150NX, SPC-130EMN or SPC-130EMNX cards.

For applications requiring more than four PCI modules a ‘big’ Simple-Tau version is available, see Fig. 27, right. The electronics boxes of these systems provide space for 8 cards.

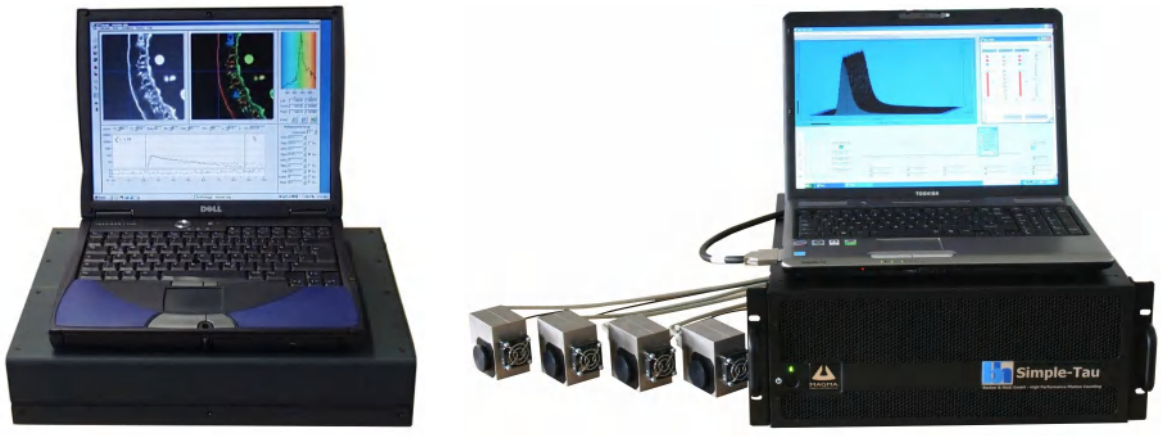


Fig. 27: Simple-Tau systems. Left: Standard version. Right: Simple-Tau BIG version with space for 8 cards.

MaxTau 12-Channel TCSPC System

The bh MaxTau system contains 12 parallel SPC-150N or SPC-150NX channels in a single 19” case. The entire system is connected to a standard PC or a laptop computer via a bus extension cable. Two extension boxes can be connected to one computer, resulting an a system with up to 24 parallel TCSPC / FLIM channels.

The system offers extremely high throughput rate without any crosstalk between the channels. Time resolution, IRF stability, and time channel width are the same as for the SPC-150N or SPC-150NX. A typical application of the system is diffuse optical tomography by near-infrared spectroscopy (NIRS). The system and a 12-channel fluorescence decay result are shown in Fig. 28 and Fig. 29.



Fig. 28: MaxTau 12-channel TCSPC system

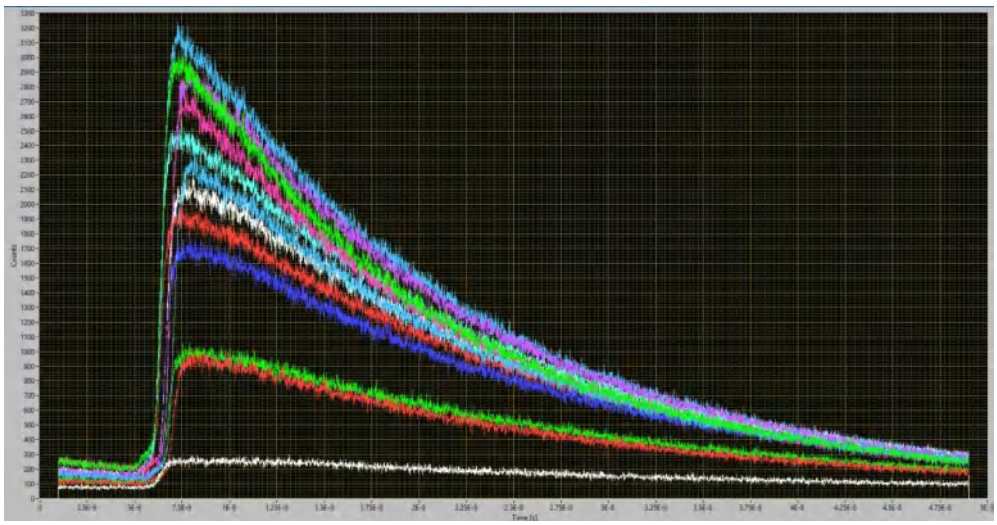


Fig. 29: 12 signals recorded in parallel by the bh MaxTau system

Power-Tau TCSPC Systems

The Power-Tau TCSPC systems are used in applications where maximum computation power, maximum memory space, and maximum data throughput rate are required. Up to six TCSPC or measurement control cards are operated in a high-performance PC. The cards communicate with the CPU directly via the computer bus, thus avoiding any bottleneck in the data transfer by interface or data transmission lines. The Power-Tau systems are especially used for multi-module systems, such as the SPC-154, SPC-154N, or SPC-164. Typical applications are high-throughput FLIM, clinical FLIM, and diffuse optical imaging.



Fig. 30: Power-Tau system, shown with optical scanner, ps diode laser, and several detectors

Other Time-Resolved Photon Counting Devices

DPC-230 16-Channel Photon Correlator

The DPC-230 [80] targets at a new type of fluorescence correlation spectroscopy that records correlation over a time range of 10 orders of magnitude [442]. Thus, singlet decay rates, rotational relaxation rates, rate constants of conformational changes, triplet transition and decay rates, and diffusion times of free fluorophores and fluorophores bound to proteins, lipids or nanoparticles can be obtained within a single measurement. Another application may be diffuse optical correlation experiments which require autocorrelation in a large number of detection channels.

The DPC-230 photon correlator card (Fig. 31) records absolute photon times in up to 16 parallel detection channels. The time resolution of the recording is 165 ps per time channel. Depending on how the photons are correlated, fluorescence correlation (FCS), fluorescence cross correlation (FCCS), or photon counting histograms are obtained. A fluorescence correlation curve from 160 ps to 1 ms is shown in Fig. 31, right.

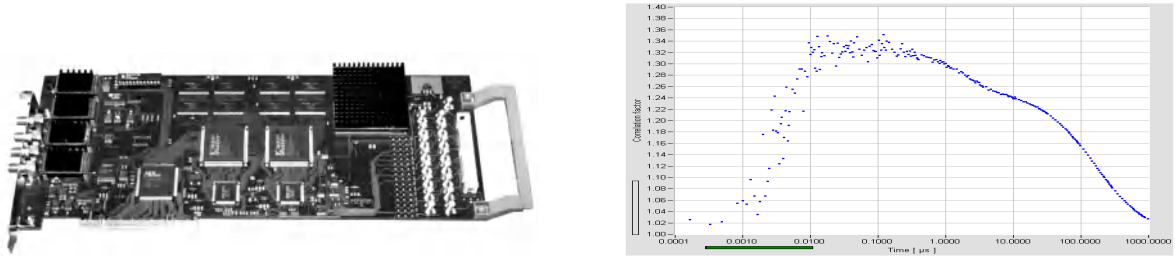


Fig. 31: DPC-230 16 channel correlator (left) and fluorescence cross-correlation function of two detector channels recorded at ps resolution (right)

Moreover, the DPC-230 can be used for recording luminescence decay curves and fluorescence lifetime images from the sub-nanosecond to the millisecond range, for LIDAR experiments, time-of flight mass spectroscopy, or any other experiments based on acquiring the temporal distribution of detection events in a large number of detector channels. Details of the DPC-230 are described in a separate handbook [80]. The DCS-230 has been discontinued in 2023. Please use the SPC-QC-008 or the SPC-QC-106 instead.

PMS-800

The PMS-800 is a 4-channel gated photon counter / multiscaler with a time-channel resolution of 4 ns. It replaces the older PMS-400 2-channel device. Compared to the PMS-400 the PMS-800 has 2 more parallel channels, higher time resolution, and higher throughput rate. The PMS-800 uses SPC-QC-008 hardware with modified on-board signal processing logics. The PMS-800 is described in a separate handbook [60]. A photo is shown in Fig. 32.



Fig. 32: PMS-800 board. The PMS-800 uses SPC-QC-008 hardware with modified on-board signal processing logics

Measurement Modes of the bh TCSPC Modules

'Single' Mode

The 'Single' mode records the waveform of an optical signal in the ps or ns range (usually a fluorescence decay curve), see Fig. 33, left. The 'Single' mode is equivalent to the traditional TCSPC procedure used in classic TCSPC devices. However, the bh modules are able to record at much higher pulse repetition rates and count rates. Thus, results can be obtained within acquisition time intervals far less than one second. More importantly, the bh TCSPC modules can record the signals of several detectors or detector channels simultaneously. With the bh PML-Spec and MW-FLIM detectors a signal is recorded in 16 wavelength intervals, see Fig. 33, middle and right. The same principle can be used to record signals excited by several multiplexed lasers.

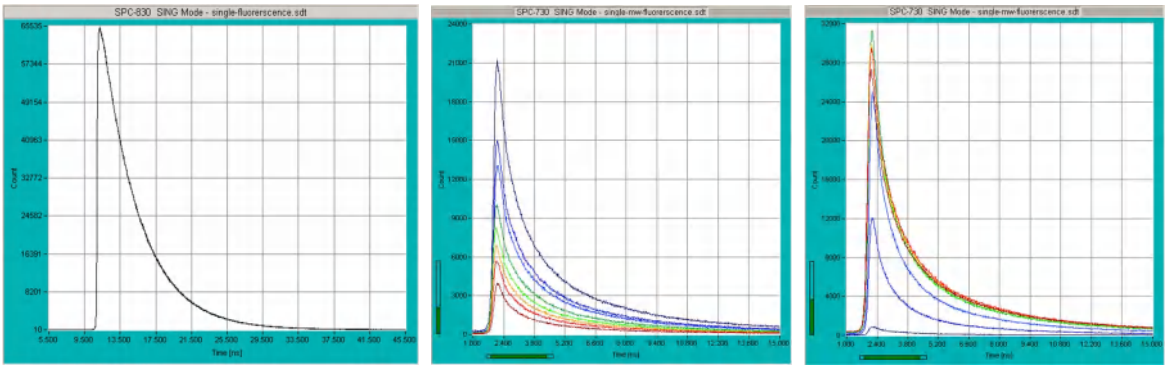


Fig. 33: 'Single' mode. Left: Fluorescence decay curve detected by one detector. Middle and Right: 16 fluorescence decay curves detected simultaneously at different wavelength (Curves 1 - 8 and 9 -16, PML-SPEC detector)

The memory of the TCSPC modules can be divided into several 'measurement pages'. The pages hold data of different measurements with the same system parameters. That means, several measurements can be performed one after another, the data be recorded into different pages, and stored together in a single data file. The 'Single' mode has a 'page stepping', a 'cycle' and an 'autosave' function. Using the page stepping function, several measurements can be performed automatically and the data be stored into subsequent pages. The recorded data set can be saved into a single file at the end of the procedure. The entire procedure can be repeated by the cycle function and subsequent data sets be saved in subsequent data files.

Oscilloscope Mode

The 'Oscilloscope' mode performs a fast repetitive measurement and displays the results in short intervals. The measurement and display update rate can be on the order of 50 measurements per second and faster. Thus, the TCSPC device works like an oscilloscope. However, compared with a measurement with fast photodiode and an oscilloscope the sensitivity and the time resolution are orders of magnitude higher. As described for the 'Single' mode, the signals of several detectors or several multiplexed lasers can be measured and displayed simultaneously. Fig. 34 gives an impression of the performance of the bh SPC modules in the oscilloscope mode.

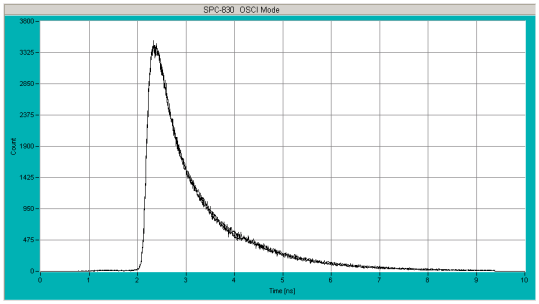


Fig. 34: Oscilloscope mode. Measurement and display update rate 0.1 s. Three subsequent curves were overlaid to reproduce the visual appearance.

f(t,x,y) Multidimensional TCSPC Mode

The 'f(t,x,y)' mode is used for measurements with one-dimensional or two-dimensional detector arrays or for other multi-dimensional recording tasks. The principle of data recording is the same as in the 'Single' mode. However, the results are interpreted as a multi-dimensional photon distribution over the time in the excitation pulse sequence, the coordinates of the elements of a detector array, or one or two other variables encoded in the digital 'routing' input signals of the SPC module. A number of different display modes is available to display these multi-dimensional results. Two examples are shown in Fig. 35.

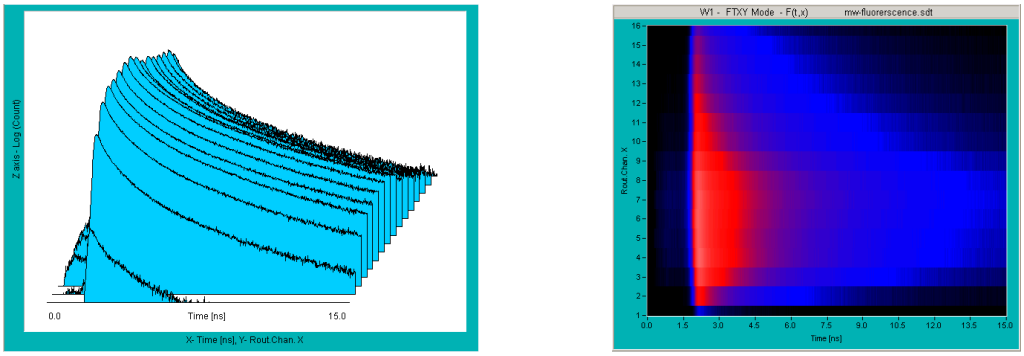


Fig. 35: f(t,x,y) mode: Decay curves recorded for 16 wavelengths simultaneously

f(t,T) Time-Series Mode

In the 'f(t,T)' mode the measurement is repeated in specified time intervals, and the results are written into subsequent memory pages of the SPC module. The result is a sequence of waveforms (usually fluorescence decay curves). With several detectors or a PML-SPEC multi-wavelength detector every step of the time-series delivers decay curves in several wavelength intervals. An example is shown in Fig. 36.

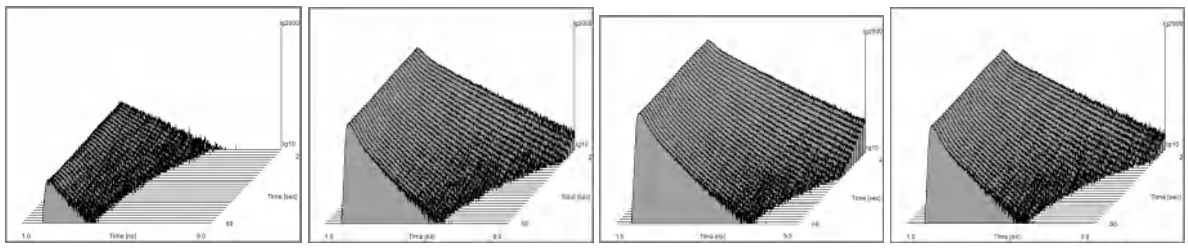


Fig. 36: Time-series of decay curves recorded in the f(t,T) mode. Fluorescence of live plant after start of exposure, time series starts from the back. Simultaneous recording in four wavelength intervals.

f(t,ext) Mode

In the 'f(t,EXT)' mode an external parameter is assigned to the steps of the series. The parameter may be the wavelength selected by a monochromator, the sample temperature varied

via an external controller, a voltage or electrical field strength, or any other parameter. The results represent the change of the waveform as a function of the external parameter.

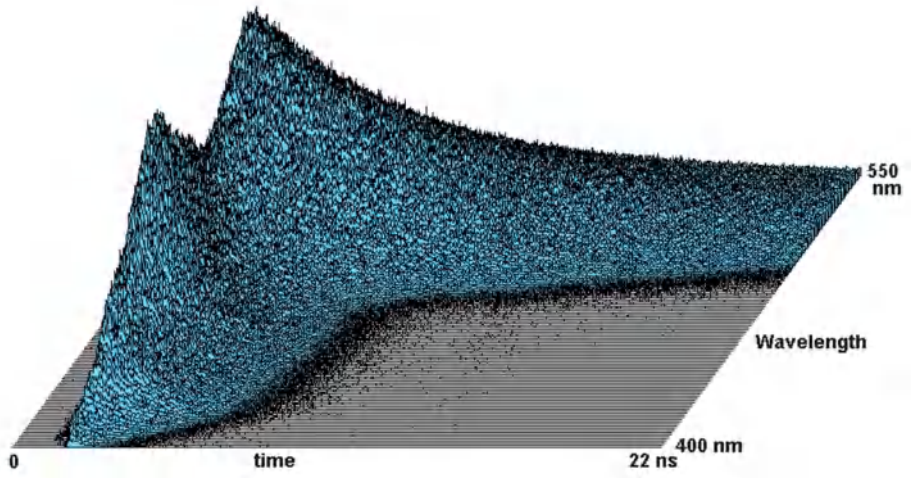


Fig. 37: Series of decay curves recorded during a wavelength scan of a monochromator

fi(T) and fi(ext): Spectrum Scan Modes

The 'fi(ext)' and 'fi(T)' modes record a time-controlled sequence of decay curves. However, instead of storing the complete decay curves, gated intensities in selectable time windows are stored. Up to eight independent time windows can be defined on the measured waveforms. The intensities within these windows are displayed as functions of time or of an externally variable parameter. The mode is also called spectrum scan mode because it was originally introduced to record time-resolved spectra.

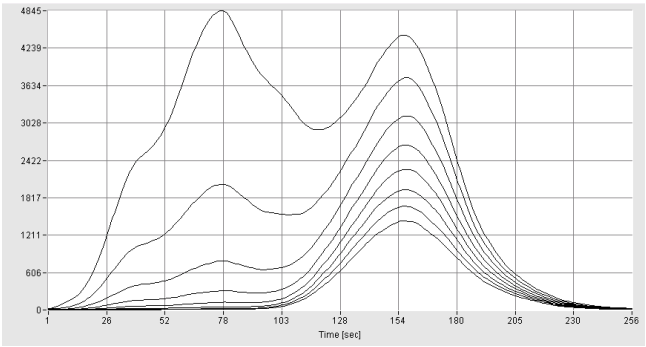


Fig. 38: fi(t,T) mode: Time resolved spectra in 8 time-windows, recorded during a wavelength scan of a monochromator

Continuous Flow Mode: Unlimited Time-Series Recording

The 'Continuous Flow' mode records an unlimited sequence of decay curves or other optical waveforms. The memory of the SPC module is split into two banks. Each bank provides space for a large number of recordings. The continuous flow modes writes the waveforms (either from a single detector or from an array of detectors) in subsequent memory blocks of the current memory bank. When one bank is full the banks are swapped, and the recording is continued in the other bank. In the meantime the results from the first bank are read and written to the hard disc of the computer. Thus, a virtually infinite sequence of waveforms can be measured. Unlike f(t,T), the Continuous Flow mode is strictly hardware controlled and thus provides an extremely fast and accurate recording sequence. The Continuous Flow mode was originally developed for single molecule detection or DNA analysis in a gel electrophoresis setup. Now the mode is mainly used for functional brain imaging by optical tomography techniques, for stopped-flow measurements, measurements of the Kautski effect in living plants, and other applications which require a large number of decay curves to be recorded in short

and exactly defined time intervals without time gaps between subsequent recordings. An example is shown in Fig. 39.

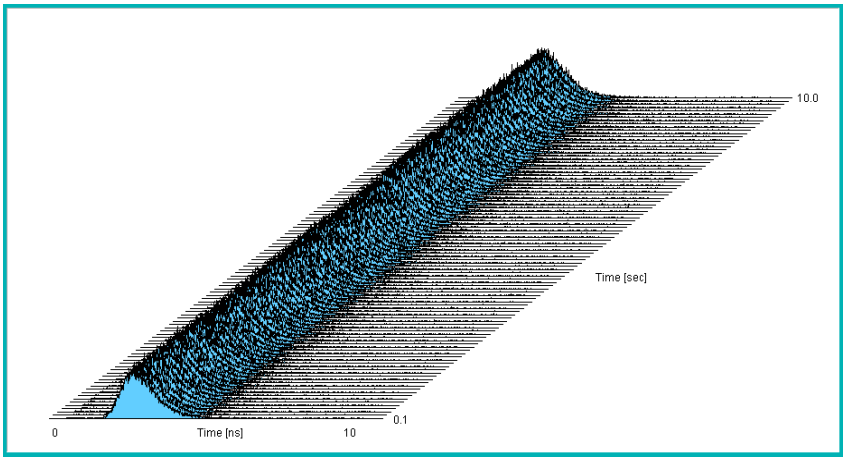


Fig. 39: Part of a Continuous-Flow sequence

Scan Sync Out Mode: Ultra-Fast Triggered Time Series

The Scan Sync Out mode was originally designed to record images with piezo scan stages. The SPC module controls the scan by sending synchronisation pulses to the scan controller and, pixel by pixel, builds up a photon distribution over the coordinates of the scan, the times of the photons in the laser pulse sequence, and a detector number or the wavelength of the photons. Since piezo scanner have widely been replaced with galvanometer scanners the Scan Sync Out mode has come out of use for imaging applications. It is now mainly used to accumulate ultra-fast triggered time series. An example is shown in Fig. 40.

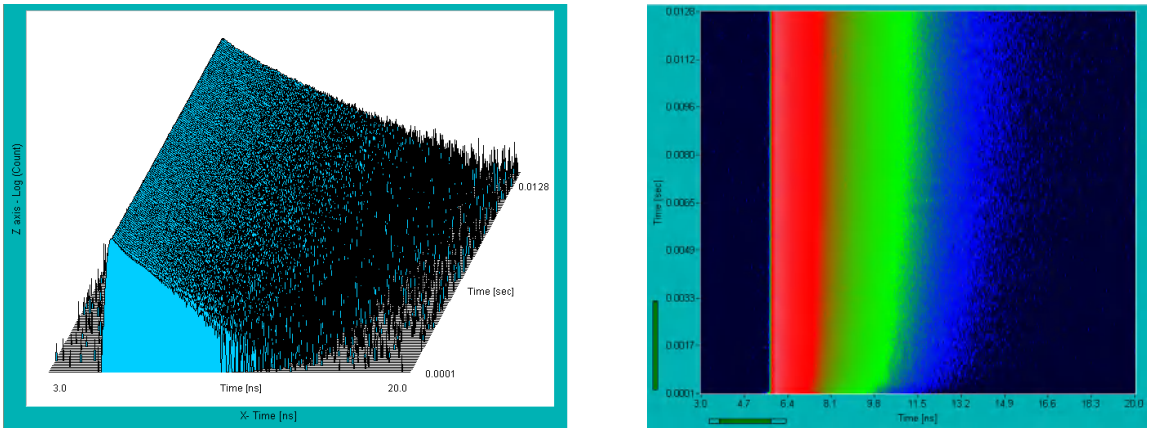


Fig. 40: Photochemical quenching transient of chlorophyll in living plant. Scan Sync Out mode, accumulated triggered time series, 100µs per curve.

Parameter-Tag Recording: The 'FIFO' Mode

In the parameter-tag (or 'FIFO') mode the hardware of the SPC module does not build up photon distributions but records the full information about each individual photon. Each photon delivers three pieces of information: the time in the signal period, or 'micro time', the number of the detector channel where the photon was detected, and the time from the start of the experiment, or 'macro time'. Additional information can be fed in via additional 'routing bits' and by encoding external events into four 'marker' bits. These data are put into in a first-

in-first-out (FIFO) buffer. During the measurement the FIFO is continuously read. The photon data are processed online or stored in the computer memory or on the hard disc.

The FIFO mode is mainly used for single molecule experiments. The results are used to calculate fluorescence correlation (FCS) curves, fluorescence decay curves, and photon counting histograms (PCH), and intensity (MCS) traces over specified time intervals within the measurement interval or as a function of time. These data can be calculated both off-line or online in the incoming data stream, see Fig. 41.

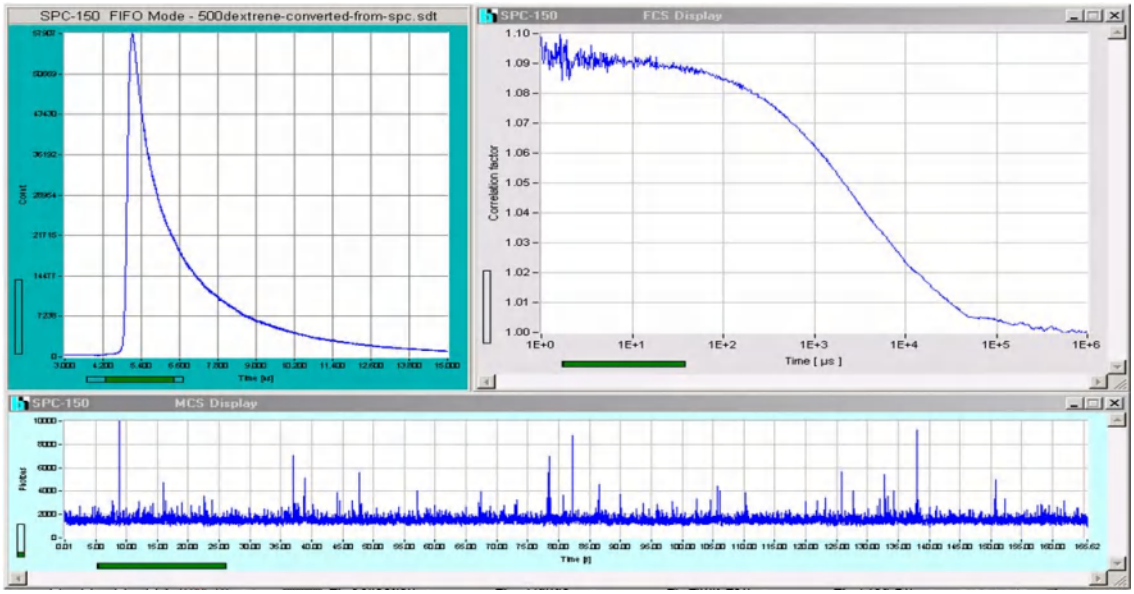


Fig. 41: Decay function, FCS curve, and MCS trace recorded and displayed online in the FIFO mode.

Moreover, FIFO data are used to obtain Burst Integrated Fluorescence Lifetime (BIFL) and Multiparameter Fluorescence Detection (MFD) data. The data delivered are compatible with the MFD analysis software of the University Düsseldorf [443].

The FIFO mode is also the basis of FLIM recording with large pixel numbers, for recording optical waveforms on the microsecond and millisecond time scale, and for simultaneous FLIM / PLIM.

The FIFO mode is available for all active bh SPC modules. It is also available in the SPC-830, with the restriction that the ‘marker’ inputs are available only in modules manufactured later than May 2007.

Coincidence Measurements

The Coincidence (Absolute Timing) Mode of the SPC-QC module records coincidences between photons arriving in different detection channels. Photon times in one channel are determined with reference to photon times in another channel, not with reference to laser pulses. Each photon is characterised by its time from the start of the experiment, and, if necessary, by a number of other parameters which are encoded in the routing information of the photon. The SPC-QC creates a data stream of time- and parameter-tagged single photon data and sends them to SPCM. SPCM stores these data for further analysis, and/or builds up coincidence curves, auto- and cross-correlation curves, or time traces (or Multichannel Scaler, MCS curves) from them. An example is shown in Fig. 42.

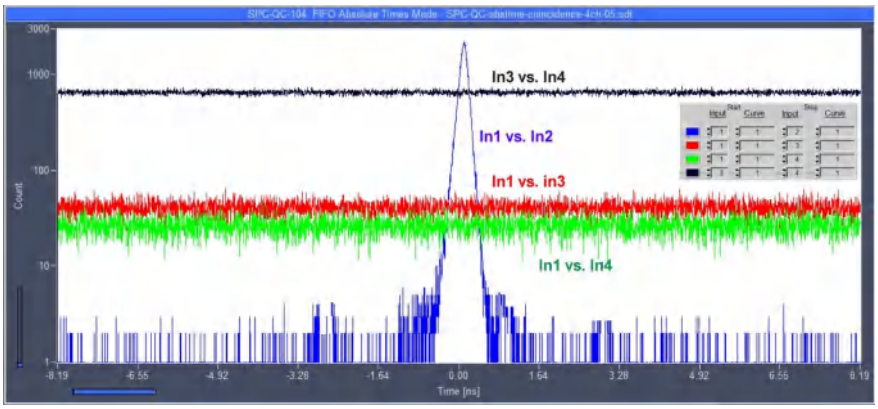


Fig. 42: Coincidence curves recorded with the SPC-QC-104. Blue input 1 versus input 2, red input 1 versus input 3, green input 1 versus input 4, black input 3 versus input 4. There is temporal coincidence of the events at input 1 versus input 2. There are no coincidences in channel 1 versus the other channels, and no coincidences at inputs 2, 3, and 4 against each other.

Microsecond and Millisecond Luminescence Decay

Already with the SPCM software version 9.0 of April 2010 'Triggered Accumulation MCS' acquisition has been added to the FIFO mode. The mode builds up the distribution of the photons versus their macro times after an excitation pulse. The time of the excitation pulse is inserted in the photon data stream via one of the 'marker' inputs of the SPC-150 or SPC-830 modules. The Triggered Accumulation MCS mode is used to record luminescence decay curves in the microsecond or millisecond range. The mode can be combined with fluorescence decay recording and with scanning, see Fig. 57.

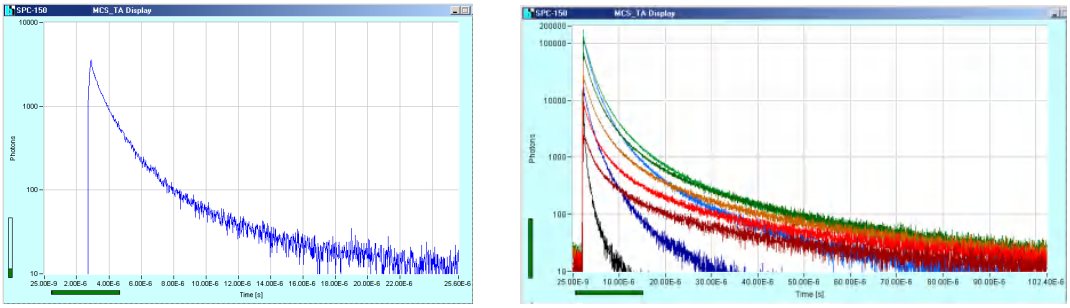


Fig. 43: Microsecond luminescence decay curves recorded in the Triggered Accumulation MCS mode. Left: Single PMC-100 detector. Right: PML-SPEC multi-wavelength detector, 8 of 16 channels displayed

FLIM: Scan Sync In Mode

The 'Scan Sync In' mode was implemented for recording fluorescence lifetime images in conjunction with fast scanning devices. The mode not only works with piezo scan stages but also with fast galvanometer or even fast polygon and resonance scanners. In the 'Scan Sync In' mode the data acquisition is controlled by receiving synchronisation pulses from a free-running scanner. The SPC module builds up a photon distribution over the coordinates of the scan, the times of the photons in the laser pulse period, and a detector number or the wavelength of the photons. The recording process works at any combination of photon rate and scan rate. In particular, it is *not* required that a sufficient number of photons is recorded within the dwell time of the scanner in a single pixel. For fast scanning, the data are accumulated over a large number of frames, therefore the number of photons depends on the total acquisition time, not on the pixel dwell time.

The problem of the Scan Sync In mode is that the image size - both in the number of pixels and the number of time channels - is limited by the memory capacity of the TCSPC module. Therefore, the Scan Sync In mode has more and more replaced by FIFO imaging. Nevertheless, it is still used to acquire images with pixel dwell times down to 100 ns, and to obtain preview images at high count rate. Different than in the FIFO Imaging mode, high count rates do not saturate the data transfer from the TCSPC module into the computer. An example of an image recorded in the Scan Sync In mode is shown in Fig. 44.

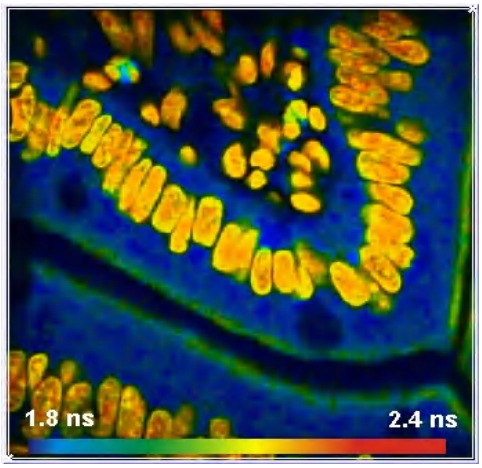


Fig. 44: Fluorescence lifetime image recorded in the Scan Sync In mode

Multi-Wavelength FLIM by Scan Sync In

Both the Scan Sync In and the Scan Sync Out can be used in combination with multi-wavelength detection. An example is shown in Fig. 45. Please note that the recording process does not use any time gating or wavelength scanning. Thus, multi-wavelength lifetime images are obtained with near-ideal efficiency and minimum sample exposure.

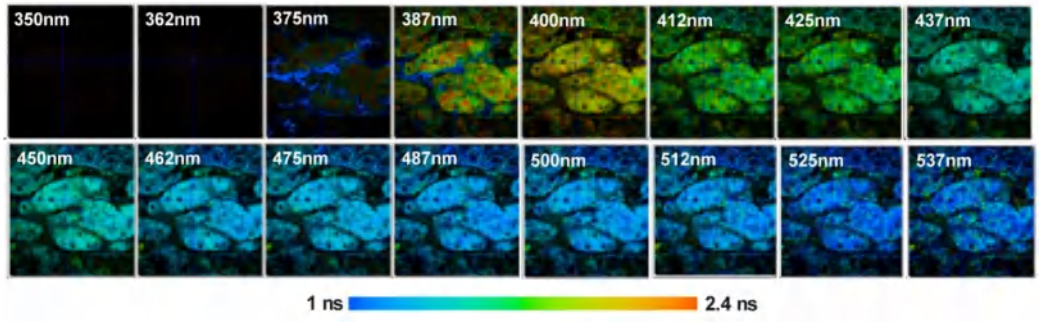


Fig. 45: Multi-wavelength fluorescence lifetime image recorded in the Scan Sync In mode

Continuous Flow Imaging: Fast FLIM Time Series

The SPC-150, SPC-150N, SPC-160, SPC-160pcie, SPC-180N modules and the corresponding multi-module packages are able to combine Scan Sync In imaging with the Continuous Flow (memory swapping) technique. The memory is split in two banks. The banks are swapped periodically, and during the image acquisition in one bank the data from the other bank are read and written on the hard disc. Because the data readout and the data acquisition are performed in different memories photons can be recorded at a sustained rate up to the saturated count rate of the SPC module. Fig. 46 shows a time series of images recorded at a rate of 2 frames per second.

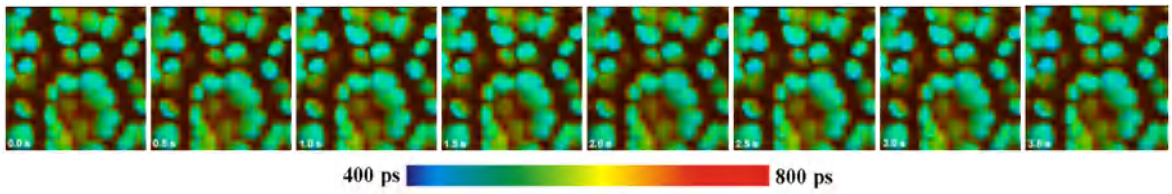


Fig. 46: Continuous flow imaging sequence, recorded at rate of 2 imager per second. Lifetime images of chloroplasts in a leaf.

FIFO Imaging Mode

The FIFO Imaging mode combines parameter-tag recording with fast scanning and imaging. From 2007 on, it is implemented in all bh TCSPC modules and in the corresponding multi-module packages. An example of a FIFO-mode image is shown in Fig. 47.

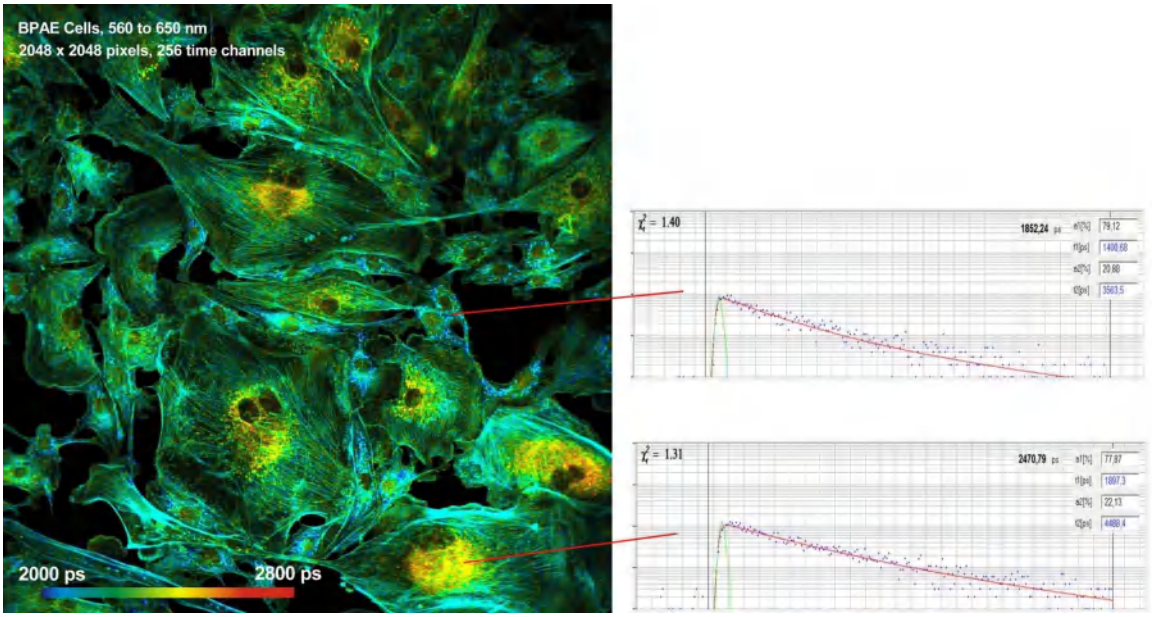


Fig. 47: Image recorded in the FIFO imaging mode. BPAE cells, 2048 x 2048 pixels, 256 time channels. Decay data in selected spots of the images are shown on the right.

In contrast to the Scan Sync In mode, the FIFO Imaging mode does not build up a photon distribution in the memory in the SPC module. Instead, it transfers parameter-tag data of the individual photons and of the scan clock pulses into the computer. The lifetime images are built up from these data in the memory of the computer. Thus, the size of the images, i.e. the number of pixels and time channels, is not limited by the size of the on-board memory of the TCSPC module. FIFO imaging can therefore record images with enormous pixel numbers. The image shown in Fig. 47 has 2048 x 2048 pixels and 256 time channels per pixel. The instrument software can be adapted to a wide variety of scan procedures and scan clock definitions, including bi-directional scanning. Several such images can be recorded simultaneously by a parallel-channel FLIM system.
In addition to online calculation of intensity images and lifetime images, the time-tag data themselves can be stored for off-line analysis, e.g. to obtain correlation data or sequences of images in individual frames of the scan.

Multi-wavelength FLIM

The FIFO imaging mode can be used in combination with multi-wavelength detection. As for the Scan Sync In mode, the data in all wavelength intervals are recorded simultaneously, i.e. without any wavelength scanning or time gating. An example is shown in Fig. 48.

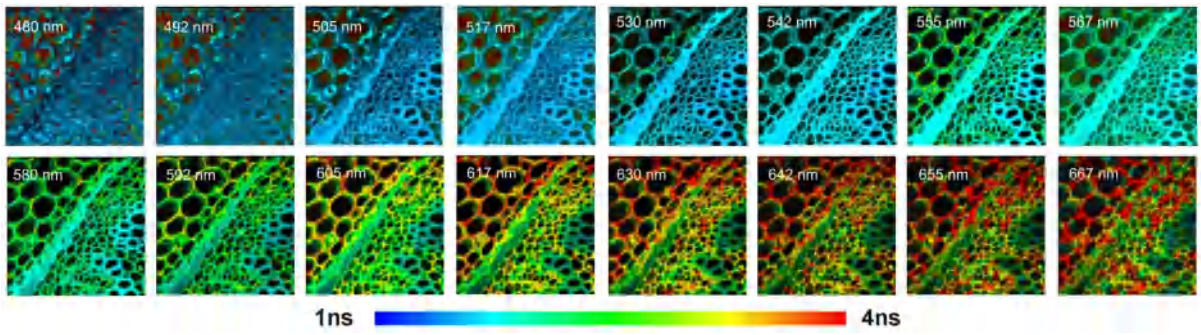


Fig. 48: Multi-wavelength FLIM of a *convallaria* sample.

Excitation-wavelength multiplexing FLIM

Several lasers or laser wavelengths can be multiplexed on a pixel-by-pixel, line-by-line, or frame-by-frame basis, and separate images be recorded within the same scan. The high multiplexing rate avoids artefacts by photobleaching or dynamic effects in the sample. In the bh DCS-120 scanning system excitation wavelength multiplexing is integrated in the scanner control [68]. An example of a wavelength-multiplexed recording is shown in Fig. 49. Please see also page 371 of this handbook.

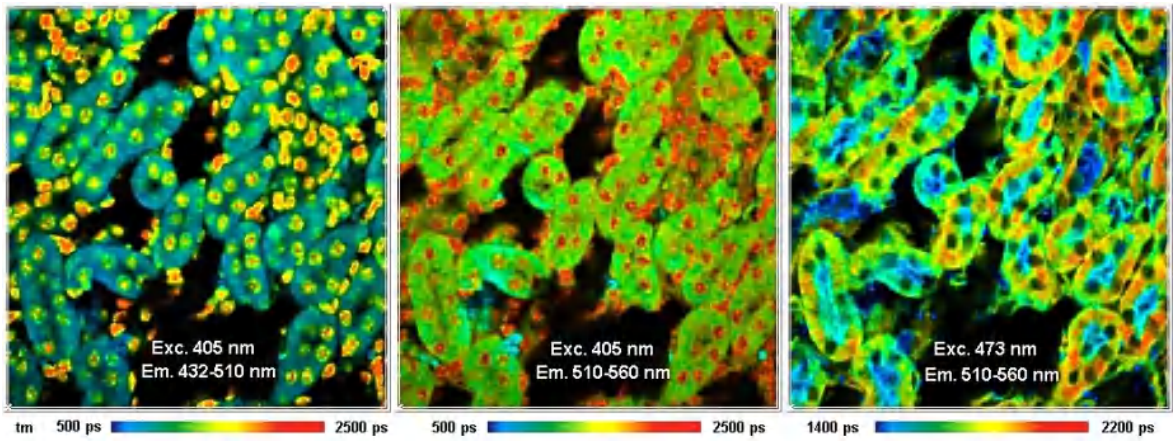


Fig. 49: Excitation wavelength multiplexing, 405 nm and 473 nm. Detection wavelength 432 nm to 510 nm and 510 nm to 550 nm. Mouse kidney section, stained with Alexa 488 WGA, Alexa 568 phalloidin, and DAPI.

Z Stack FLIM

Z stack FLIM acquires FLIM images in a large number of subsequent focal planes of a confocal or multiphoton laser scanning microscope. FLIM Z stacks can be obtained by controlling the microscope from the SPCM software [68], or by running a Z sequence in the microscope and running a triggered series of FLIM acquisitions in the TCSPC system [69, 96]. Plane by plane of the sample is scanned for a selected acquisition time, FLIM data are built up for the subsequent planes, and saved into consecutive data files. Please see page 406 of this handbook. An example is shown in Fig. 50.

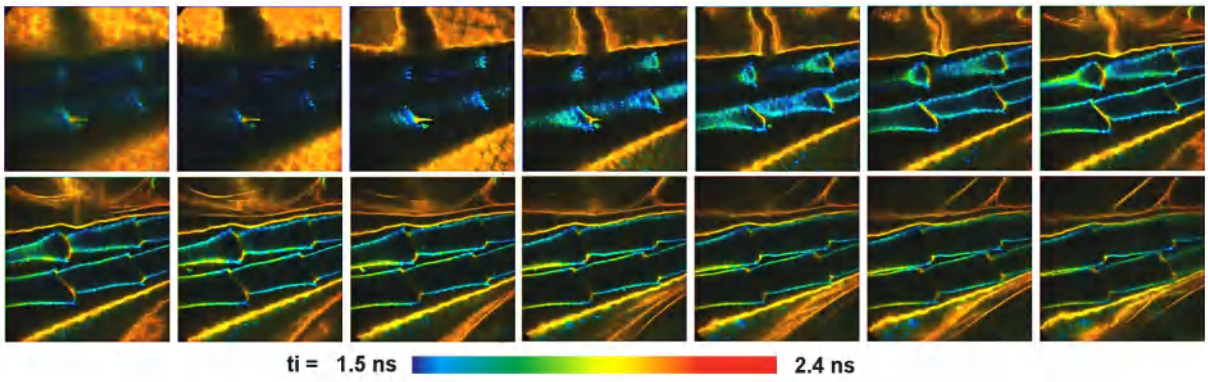


Fig. 50: Z stack recording, part of a water flee, autofluorescence. Images 256x256 pixels, 256 time channels.15 steps in Z, step width 4 µm. bh DCS-120 confocal scanning FLIM system with HPM-100-40 hybrid detector.

In most instances, FLIM Z stacks are recorded only for a moderate number of planes. However, technically a Z stack is not limited in the number of Z planes. An example is shown in Fig. 51. A drosophila fly was scanned by a bh DSC-120 MP system, and images in 128 subsequent planes were acquired and saved into subsequent files. The data in the files were analysed by SPCImage's Batch Processing function, and the results were assembled into a 3-D animation by Image J software.

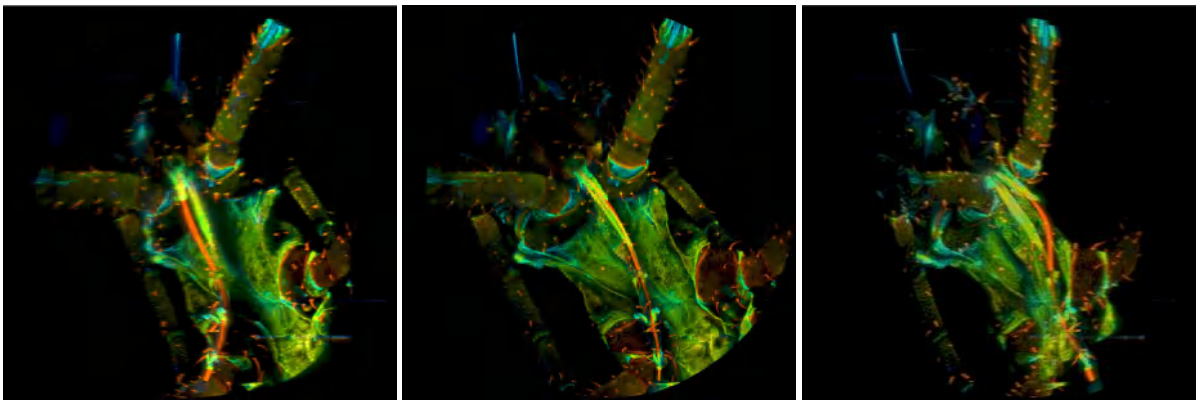


Fig. 51: FLIM Z stack with 128 planes, bh DCS-120 system. Drosophila fly, autofluorescence, different aspect angles of the same data.

Mosaic FLIM

Mosaic FLIM records an array of FLIM images. The individual elements of the array can represent a spatial array of images obtained by a sample-stepping device, images in different wavelength channels of a multi-wavelength detector, images in different depth of a sample, or images at different times after a stimulation of a sample. The entire mosaic is recorded into one single, large photon distribution. The advantage of Mosaic FLIM is that there are no readout times between the recordings of the mosaic elements, and that the entire data set can be analysed in a single data analysis run. This makes it possible to perform a fit with global parameters, please see data analysis chapter of this book. A lateral mosaic is shown in Fig. 52 left, a Z stack recorded by mosaic FLIM in Fig. 52, right.

Because there is no readout time between the recording of the individual mosaic elements the procedure can be used to record fast time series. An example of ‘Temporal Mosaic FLIM’ is shown in Fig. 53. The figure shows the change of the fluorescence lifetime of the chloroplasts in a moss leaf for different time after the start of illumination.

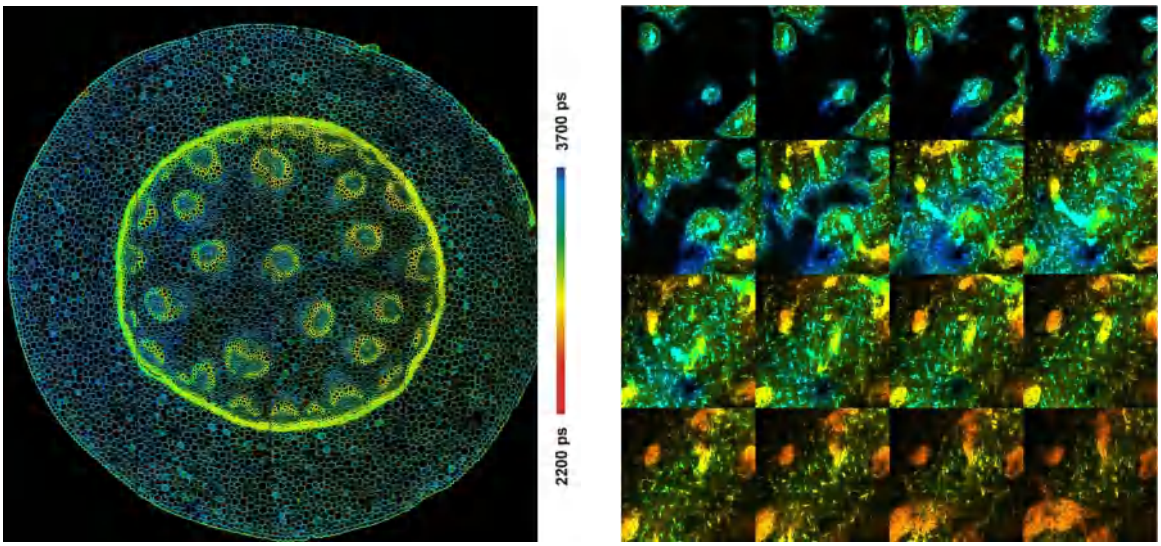


Fig. 52: Examples of Mosaic FLIM. Left: Spatial mosaic, *convallaria* sample, 16 elements of 512 x 512 pixels each, 256 time channels, entire mosaic is 2048 x 2048 pixels x 256 time channels. Right: Z Stack recorded by Mosaic FLIM. Pig skin, stained with cyanine dye, each element 512 x 512 pixels x 256 time channels

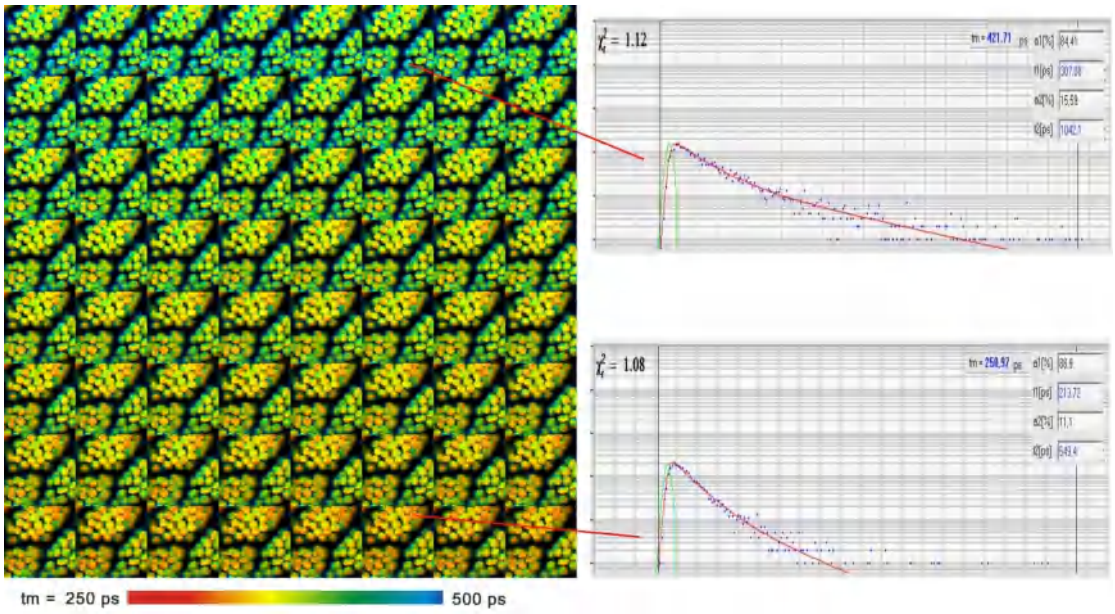


Fig. 53: Temporal mosaic, lifetime change of chlorophyll in a leaf, 64 elements of 128 x 128 pixels, time per element 1 second. Time is running upper left to lower right. Decay curves for two identical spots at different time after the start of the illumination are shown right.

Mosaic FLIM with Triggered Accumulation

An important feature of temporal mosaic FLIM is that the sample can be stimulated periodically and the data be accumulated. This allows extremely fast image sequences to be recorded without the need of trading lifetime accuracy against the speed of the sequence. An example is shown in Fig. 54. The figure shows the change in the calcium concentration in a culture of live neurons after stimulation with an electrical pulse. Please see 128 and page 402 for details.

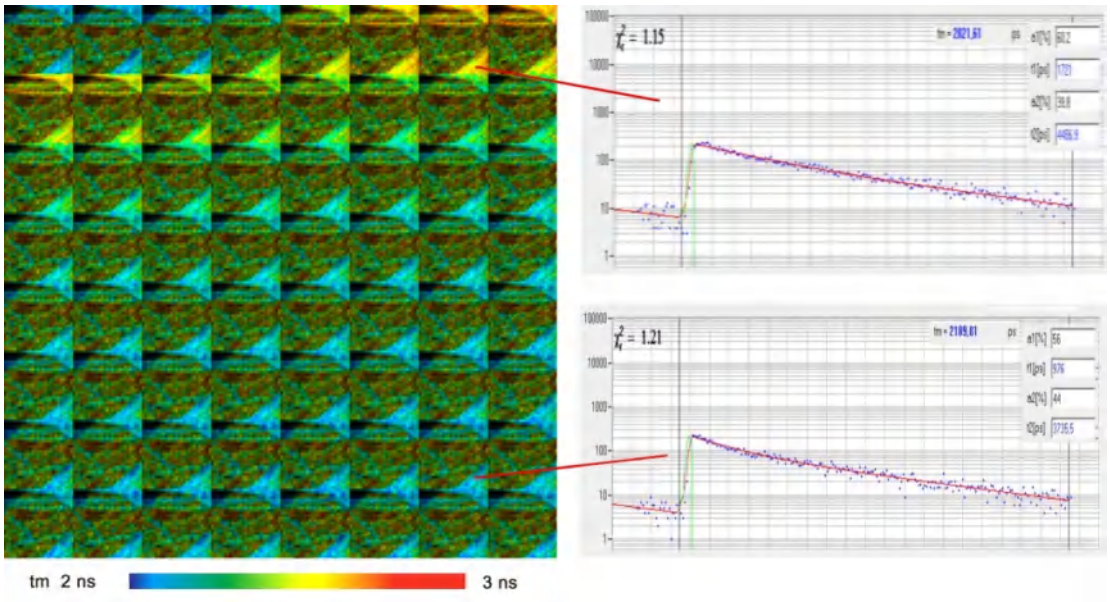


Fig. 54: Ca^{2+} transient in cultured neurons, incubated with Oregon Green. Electrical stimulation, stimulation period 3 s, data accumulated over 100 stimulation periods. Scan time per mosaic element 38 ms.

FLITS: Fluorescence Lifetime-Transient Scanning

FLITS records transient effects in the fluorescence lifetime of a sample along a one-dimensional scan. The maximum resolution at which lifetime changes can be recorded is given by the line scan time. With periodic stimulation and triggered accumulation transient lifetime effects can be resolved at a resolution of about one millisecond [113, 162].

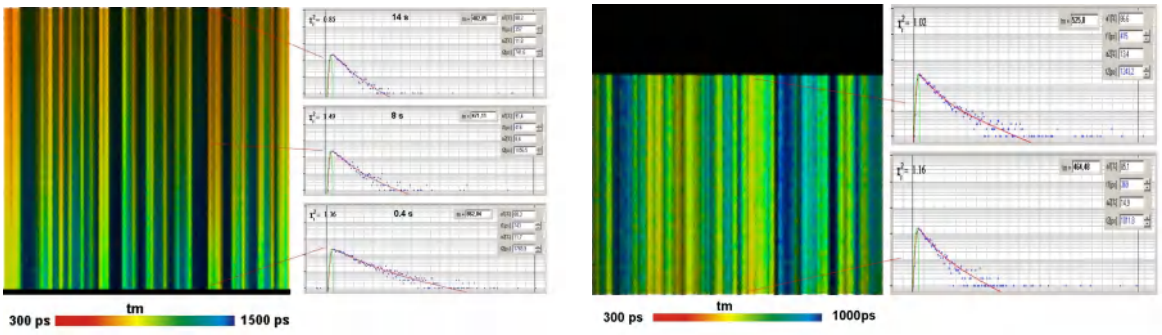


Fig. 55: FLITS of chloroplasts in a grass blade, change of fluorescence lifetime after start of illumination. Experiment time runs bottom up. Left: Non-photochemical transient, transient resolution 60 ms. Right: Photochemical transient. Triggered accumulation, transient resolution 1 ms.

Express FLIM

The bh Express-FLIM technique is based on fast confocal or multiphoton scanning, single-photon detection and timing, and calculation of fluorescence decay times in the TCSPC hardware. At the end of every pixel, the TCSPC hardware determines a (single-exponential) fluorescence-decay time and the number of photons within the pixel time. Only these two values are transferred to the computer. Compared to the normal FIFO-imaging procedure, the amount of data that has to be transferred is much smaller. Moreover, the amount of data does not depend on the count rate. The count rate is therefore not limited by the data transfer rate from the TCSPC module into the computer, and extremely fast image sequences can be recorded. Subsequent images from a Express-FLIM sequence are shown in Fig. 56.

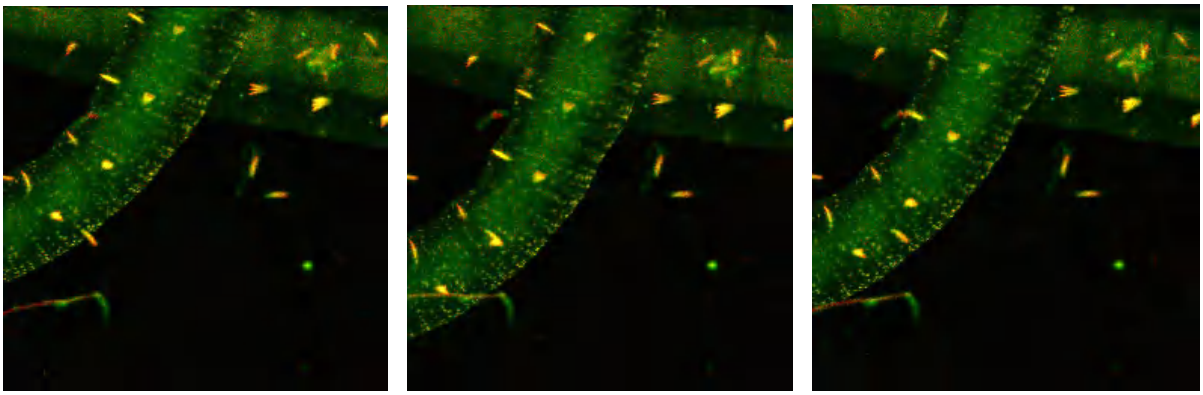


Fig. 56: Three subsequent FLIM images from an Express-FLIM sequence. Enchytraeus albidus, autofluorescence. Image rate 5 frames / second.

Microsecond and Millisecond FIFO Imaging (PLIM)

With the SPCM software version 9.0 of April 2010 phosphorescence lifetime imaging (PLIM) in the microsecond and millisecond range has been introduced [104, 161]. PLIM is performed in the FIFO Imaging mode. However, instead of the micro time of the photons it uses the macro time to build up the photon distribution. Minimum time-channel width is 25 ns. An example is shown in Fig. 57.

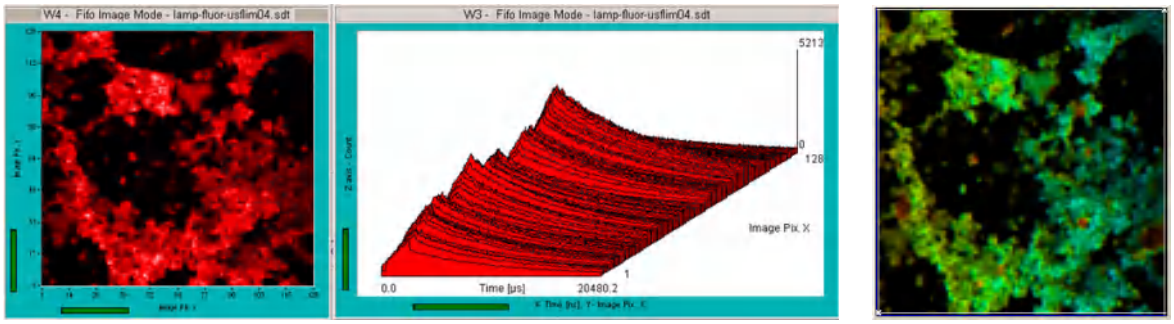


Fig. 57: Luminescence lifetime image of an inorganic fluorophore. Left to right: Intensity image, phosphorescence decay functions of pixels along a horizontal stripe of the image, lifetime image, red to blue corresponds to a range of 10 to 15 ms.

Simultaneous FLIM / PLIM

Phosphorescence lifetime imaging can be run simultaneously with FLIM. The technique is based on on/off modulation of a high-frequency pulsed laser. It is performed in the FIFO Imaging mode. For each photon both the time in the laser pulse period and the time in the modulation period are determined. PLIM is obtained from the times of the photons in the modulation period, FLIM from the times of the photons in the laser pulse period. To avoid aliasing of the laser modulation with the pixel frequency the modulation period is synchronised with the pixels of the scan. An example is shown in Fig. 58. Please see page 130 or page 434 for details.

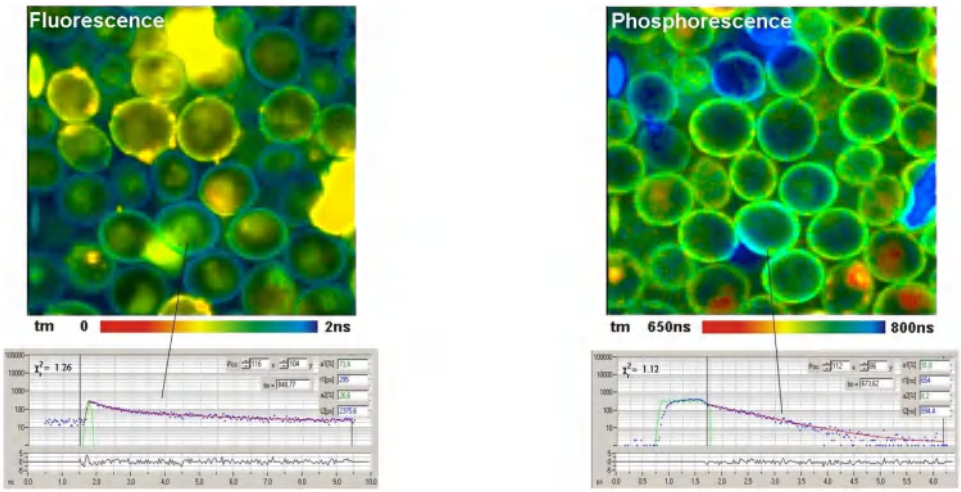


Fig. 58: Simultaneous FLIM and PLIM of yeast cells. Autofluorescence of the cells (left) and phosphorescence of a ruthenium compound (right)

Wide-Field FLIM

The Wide-Field FLIM mode requires three SPC-150N, SPC-160 or SPC-160pcie modules with special discriminators and a position-sensitive detector with delay-line anode [121, 172]. The first module measures the times of the photons in the laser pulse period. The second and third module measure the time differences of the pulses at the outputs of the X and the Y delay lines of the detector. The detection events, i.e. the times, t, and the time differences, t_x and t_y, are transferred into the computer photon by photon. From these data the software builds up a photon distribution over the coordinates x, y, and the times, t. This is the usual photon distribution of FLIM: It is an array of pixels, each of which contains a fluorescence decay curve consisting of photon numbers in consecutive time channels. The data can thus be analysed by SPCImage FLIM data analysis software. For parameter setup and other technical details please see page 460 and page 777 of this book.

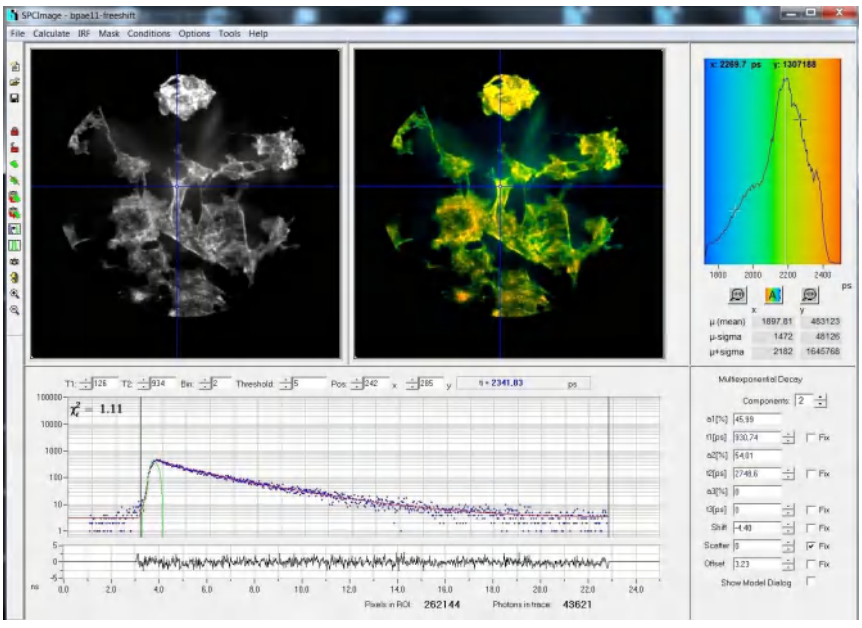


Fig. 59: Wide-Field FLIM, data analysis by SPCImage. Invitrogen BPAE cells, 512 x 512 pixels, 1024 time channels per pixel.

bh DCS-120 Confocal and Multiphoton FLIM Systems

The DCS-120 [65, 68] is a family of complete confocal or multiphoton laser scanning microscope system for fluorescence lifetime imaging. The basic system uses picosecond diode laser excitation, scanning by fast galvanometer mirrors, confocal detection, bh's multi-dimensional TCSPC technique, and 64-bit SPCM data acquisition software. The multiphoton systems use a Ti:Sa laser or one or two femtosecond fibre lasers for excitation. Instead of a confocal beam path the multiphoton versions use a non-descanned beam path. Data analysis is performed by bh's legendary SPCImage NG software [68, 69, 78].

The DCS-120 system has been introduced in 2007. Since then, it has been upgraded constantly with new detectors, new lasers, new TCSPC / FLIM modules, and new scanner optics.

Two of the early DCS-120 confocal versions are shown in Fig. 60. A DCS-120 system with an inverted microscope is shown on the left, a system with an upright microscope on the right.

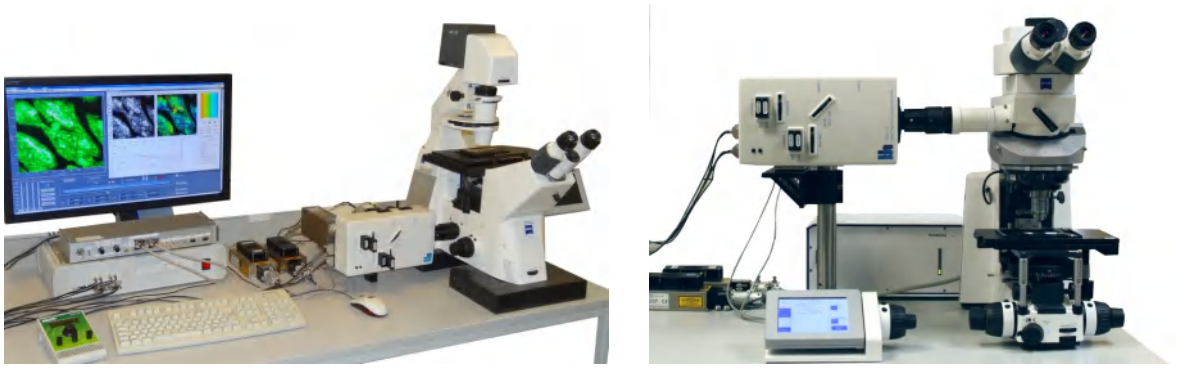


Fig. 60: DCS-120 Confocal Scanning FLIM system. Left: Inverted version with Zeiss Axio Observer. Right: Upright version with Zeiss Axio Examiner

The detection system of the DCS-120 uses two HPM-100-40 or -06 hybrid detectors, and two fully parallel TCSPC FLIM channels. Early systems used two SPC-150 modules, later systems two SPC-150NX modules. Recent DCS-120 systems use two SPC-180NX modules or one SPC-QC-104 module. For all versions multi-wavelength FLIM with one or two PML-16 GaAsP detectors is available.

The scanner and the lasers are controlled by a GVD-120 or GVD-140 scan controller card. The user interface for scanner and laser control is integrated in the SPCM software of the bh TCSPC systems. For more technical details please see DCS-120 handbook [68], DCS-120 Overview Brochure [65], and chapter 'DCS-120 Confocal and Multiphoton FLIM System', page 242 of this handbook.

Confocal Systems

Recent DCS-120 versions are shown in Fig. 61 through Fig. 64. Fig. 61, left, shows the basic confocal DCS-120 system. It has two BDS-SM ps diode lasers, two detection channels with HPM-100-40 or HPM-100-06 hybrid detectors, two SPC-180NX or one SPC-QC-104 TCSPC/FLIM module, and an upgraded optical scanner module. The new scanner has improved optical and mechanical stability, improved transmission, a super-stable main dichroic beamsplitter which can be replaced by the user, and electronic pinhole alignment. An upscaled version of the basic DCS-120 system is the DCS-120 CMI Molecular Imaging System. It has four lasers of different wavelength, and is able to multiplex them for simultaneous FLIM of fluorophores of different excitation spectra. The DCS-120 CMI is shown in Fig. 61, right.

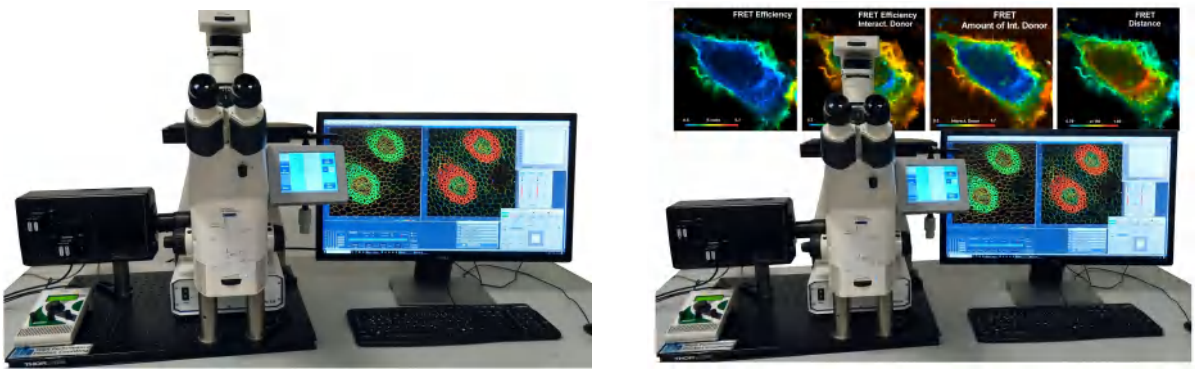


Fig. 61: DCS-120 Confocal Scanning FLIM systems. Left: Basic version with two lasers and two detection channels. Right: DCS-120 CMI Molecular Imaging Confocal FLIM System. Four lasers and up to four parallel detection channels

Multiphoton Versions

Multiphoton versions of the DCS-120 are shown in Fig. 62. On the left, the figure shows the basic DCS-120 MP multiphoton system. It uses a 785 nm Toptica femtosecond fibre laser (either a Femto Fibre Pro or a Femto Fibre Smart) for excitation. With these fibre lasers the system is not only the least expensive multiphoton FLIM microscope in the world, it is also the one easiest to use. The system is ready for use immediately after turn-on, the sample is positioned visually through the eyepieces, and fine focusing is done in the Preview Mode of the SPCM software. The excitation wavelength is not only ideal for label-free imaging with NAD(P)H, FAD, carotenoids and melanin, it also works for metabolic FLIM and molecular imaging FLIM with most of the commonly used exogenous fluorescence probes. Another outstanding feature is time resolution. Because the laser pulse is much shorter than the detector response, the system reaches less than 20 ps fwhm IRF width with the fast HPM-100-06 hybrid detectors.

Fig. 62, right, shows the DCS-120 DMP Dual Multiphoton Excitation system. The DCS-120 DMP uses two Toptica femtosecond fibre lasers of 785 nm and 880 nm. The lasers can be multiplexed for simultaneous FLIM of NAD(P)H and FAD. With this capability, the DCS-120 DMP is the ideal multiphoton metabolic FLIM system. It can also be used for NAD(P)H or FAD metabolic FLIM in combination with exogenous fluorescence probes or oxygen measurement by PLIM. Also here, the time resolution with the ultra-fast HPM-100 detectors is better than 20 ps fwhm.

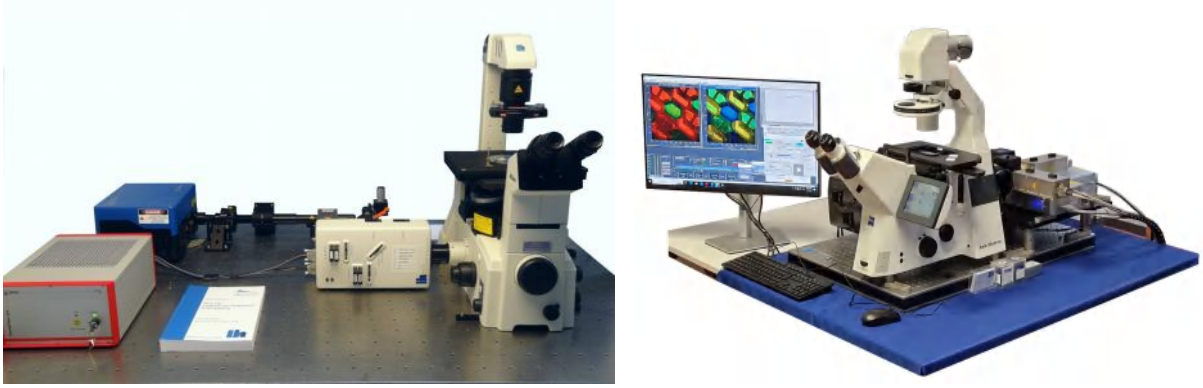


Fig. 62: Left: DCS-120 MP system. Excitation by femtosecond fibre laser of 785 nm. Right: DCS-120 DMP system. Excitation by two multiplexed femtosecond fibre lasers of 785 and 880 nm.

Fig. 63 shows another unique FLIM system of the DCS family, the DCS-120 Super MPC. The system uses a Ti:Sa laser for tuneable multiphoton excitation or the SHG of the Ti:Sa

laser for visible tuneable excitation. Multiphoton FLIM is performed via a non-descanned beam path, one-photon excitation via a confocal beam path. The DCS-120 Super MPC can be used for deep-tissue FLIM and single-cell imaging as well. The time resolution with HPM-100-06 detectors is better than 20 ps fwhm not only for multiphoton NDD but also for confocal FLIM with visible excitation.

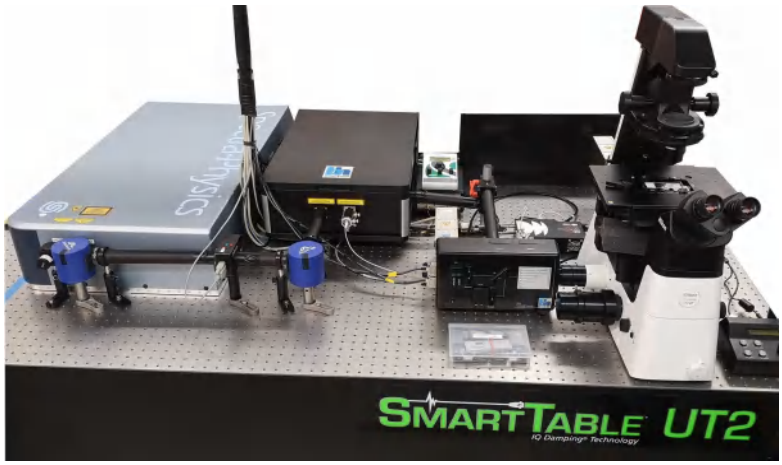


Fig. 63: DCS-120 Super MPC system. Multiphoton FLIM by Ti:Sa laser combined with tuneable confocal FLIM via SHG of Ti:Sa laser

DCS-120 MACRO System

The DCS-120 MACRO system records images of macroscopic objects directly in the image plane of the scanner. FLIM images of objects as large as 15 mm can be scanned directly, larger images by mosaic FLIM in combination with a motorised sample stage. Like the basic DCS system, the DCS-120 MACRO uses two ps diode lasers for excitation and two HPM-100 hybrid detectors for detection. With lasers of 375 nm and 445 nm, the system is perfectly suited for metabolic imaging with laser multiplexing. Main application is inspection of excised tissue during tumor surgery.

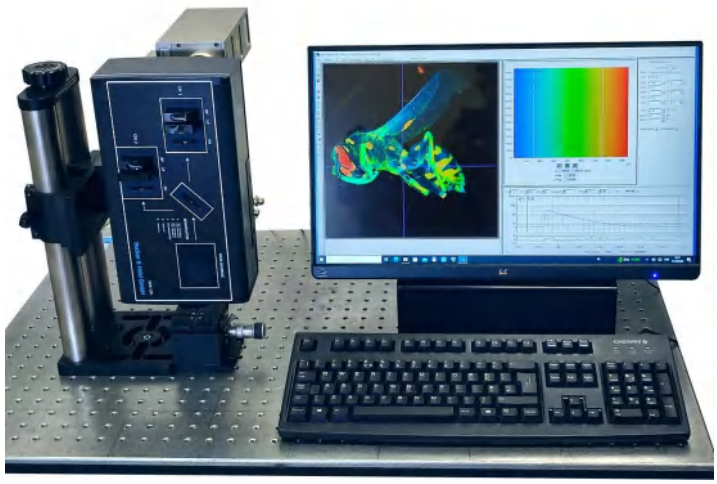


Fig. 64

Essential Features of the DCS-120 family FLIM systems

Confocal Detection Suppresses Out-of-Focus Light

The DCS-120 scan head contains the complete beam deflection and confocal detection optics. The principle is shown in Fig. 65. The laser beams are deflected by fast-moving galvanometer

mirrors, and sent down the microscope beam path. The axis of the galvanometer mirrors is projected into the plane of the microscope lens. With the motion of the galvanometer mirrors the laser focus thus scans over the focal plane in the sample. The emission light is collected back through the microscope lens. The emission beam is descanned by the galvanometer mirrors, separated from the excitation beam, split into two channels of different wavelength or different polarisation and focused into pinholes in a plane conjugate with the focal plane in the sample. Out-of-focus light is not focused into the pinholes and thus suppressed. Please see page 242 of this handbook or [68] for details of the optical system. The confocal detection principle efficiently suppresses out-of-focus light and laterally scattered light. It thus avoids contamination of the recorded decay functions in the individual pixels by decay components from other sample planes or other pixels.

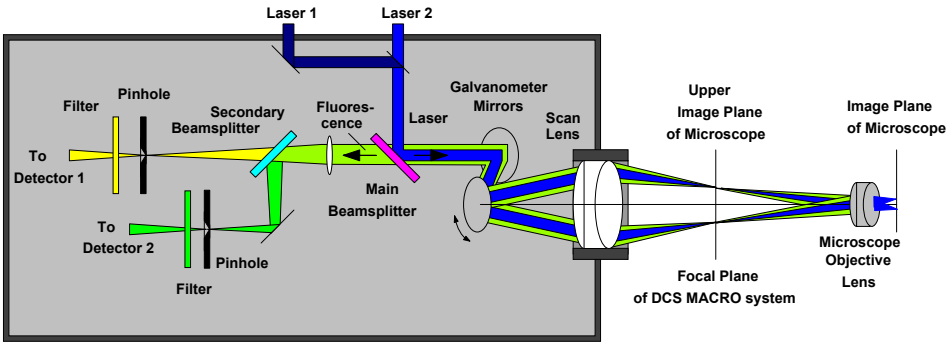


Fig. 65: Optical diagram of the DCS-120 scan head. Simplified, please see page 242 for details

Multiphoton Excitation Delivers Clean Images of Deep Sample Layers

Different than confocal imaging, which avoids out-of-focus detection, multiphoton imaging avoids out-of-focus excitation. Near-infrared excitation penetrates much deeper into biological objects than UV or visible excitation. Moreover, because no pinhole is needed to suppress out-of focus fluorescence, light diffusely scattered on the way out of the sample can be detected by 'Non-Descanned Detection'. Multiphoton excitation is therefore the key to deep-tissue FLIM. The principle is shown in Fig. 66.

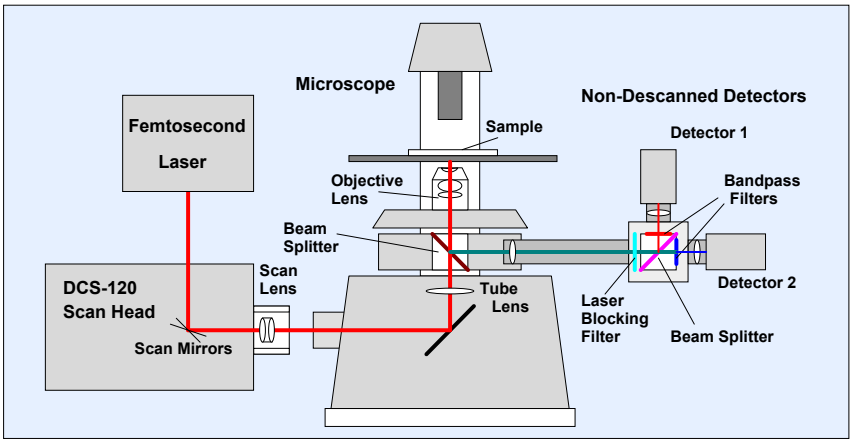


Fig. 66: DCS-120 MP Multiphoton System, optical principle

Fast Beam Scanning - Fast Acquisition

The DCS-120 uses fast beam scanning by galvanometer mirrors. A complete frame is scanned within a time from 100 ms to a few seconds, with pixel dwell times down to one microsecond. Compared with sample scanning by a piezo stage, beam scanning is not only much faster, it avoids also induction of cell motion by exerting dynamic forces on the sample. Moreover, live cell imaging requires a fast preview function for fluorescence images for sample positioning

and focusing. This can only be provided if the beam is scanned at a high frame rate. With its fast scanner and its multi-dimensional TCSPC process the DCS system achieves surprisingly short acquisition times, an example is shown in Fig. 67. In most cases the acquisition speed is not limited by the recording process but by the photostability of the sample. For large scan areas with low-magnification objective lenses the laser power is distributed over a large area, and excellent FLIM images can be obtained within a second or less. Please see Fig. 68.

Please see also 'Fast Online FLIM with Standard bh TCSPC Systems', page 415, and 'Time-Series FLIM', page 398.

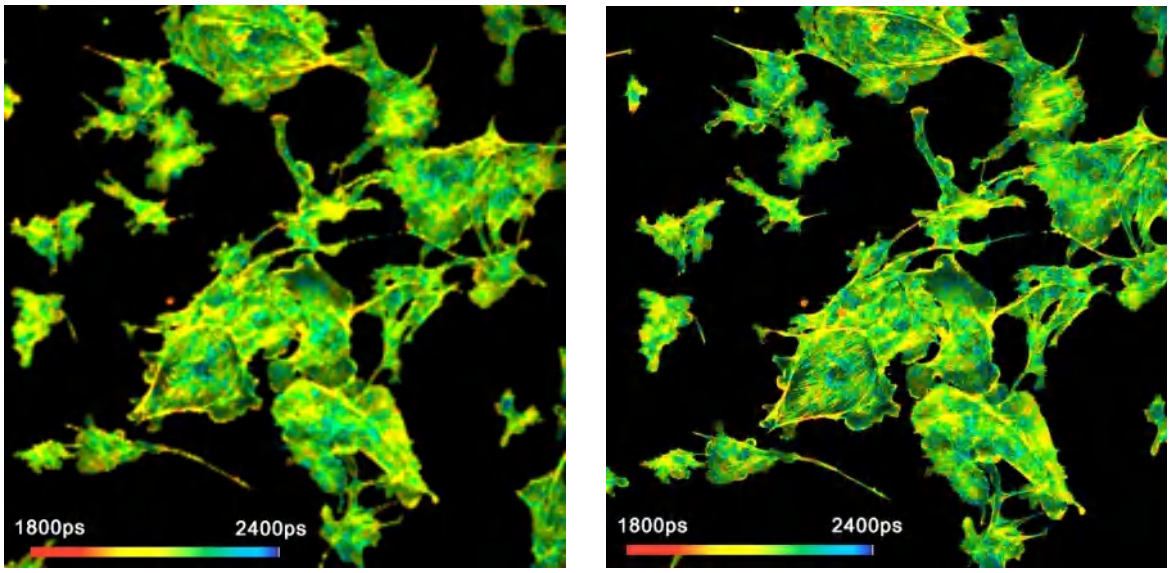


Fig. 67: FLIM images recorded within 5 seconds acquisition time. 256 x 256 pixels (left) and 512 x 512 pixels (right), both with 256 time channels.

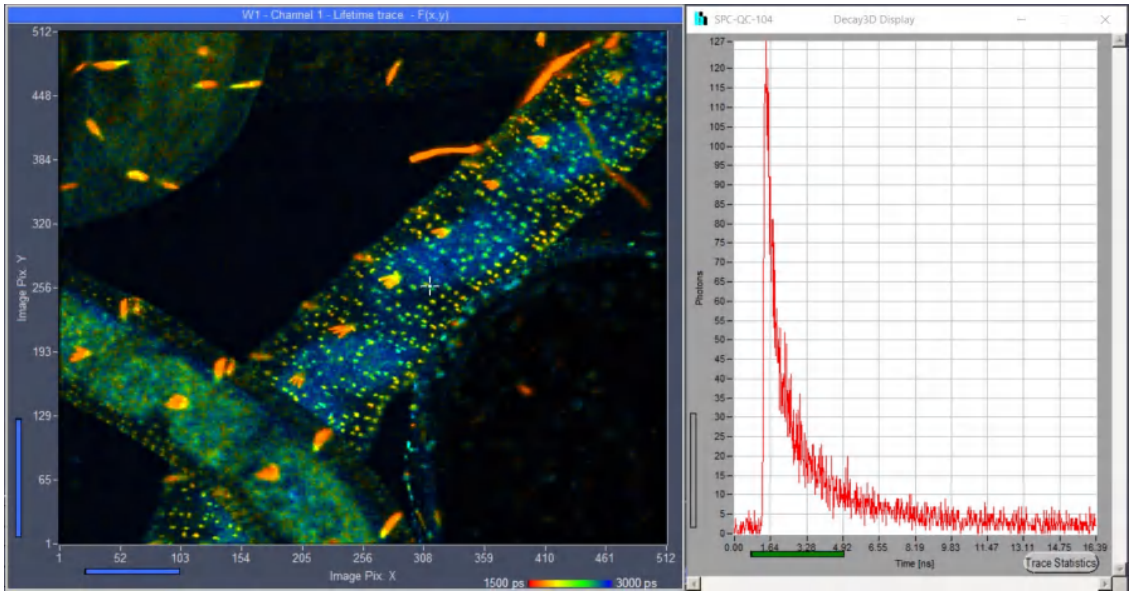


Fig. 68: Enchytraeus Albidus, Autofluorescence, Acquisition Time 1 second, Image Area 1mm x 1mm. Online-lifetime display of SPCM software. Right: decay curve in selected spot of the image.

Data Acquisition Software

The DCS-120 series FLIM systems use bh's SPCM data acquisition software. SPCM includes the management of the measurement and measurement control parameters, user-interface configuration parameters, and parameters for online data visualisation. Load and save functions are provided to handle measurement and setup data. A large part of SPCM provides display functions for multi-dimensional data. There are display functions for decay curves, series and

arrays of decay curves, images, and arrays of images. Display functions also contain online calculation and display of pseudo-colour fluorescence-lifetime images and display of decay curves from ROIs within lifetime images. SPCM also controls external devices such as the scanner of the DCS-120 system, motor stages, microscopes, and the detectors of the DCS-system. A direct link is provided for communication with SPCImage NG FLIM analysis software. An example of the SPCM software panel is shown in Fig. 69. For details please see chapter SPCM Software, page 703.

Fully Integrated Scanner Control

The control of the DCS-120 scanner is fully integrated in the SPCM data acquisition software, see Fig. 69. The scanner control panel allows the user to select the image format, scan rate, and scan area, and to control the lasers. Changes in the scan parameters can be made at any time, even without stopping the scan. The DCS-120 has automatic scan speed control. It automatically selects the fastest possible scan rate available for the scan parameters used.

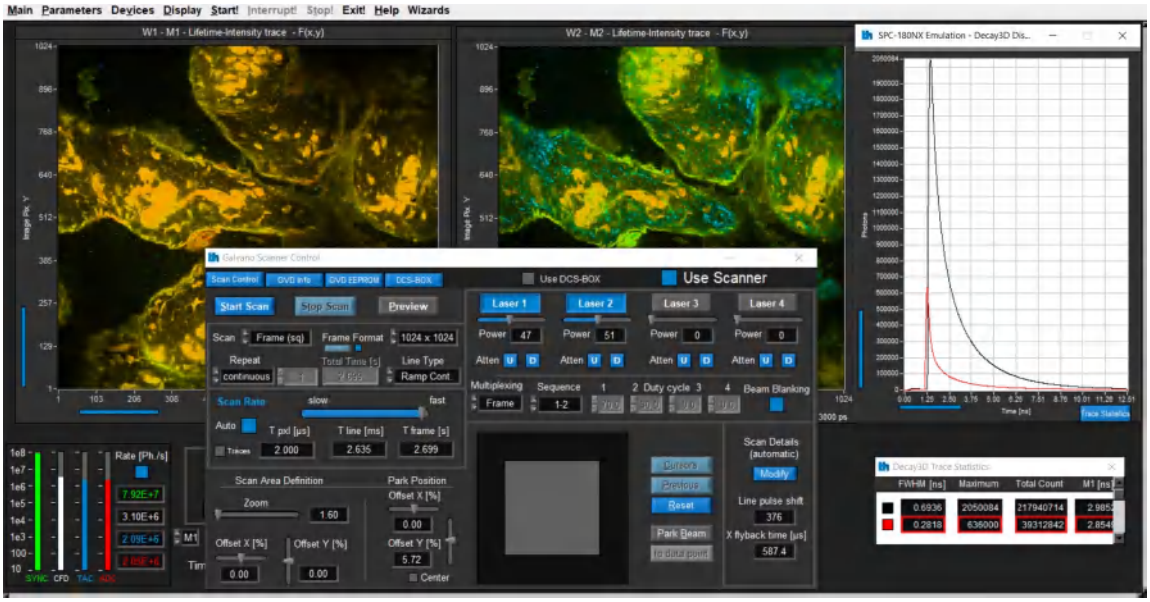


Fig. 69: SPCM Version 9.92 data acquisition software with integrated scanner control

Fast Preview Function and Interactive Scanner Control

The DCS-120 has a fast preview function that scans the sample at high speed, and displays fluorescence images in intervals of one second or less. With the preview function it is easy to bring the sample into focus, shift it in the desired position, and select the region to be scanned. Scanner control is fully integrated in the SPCM data acquisition software. The zoom factor and the position of the scan area can be adjusted via the scanner control panel or via the cursors of the display window. The scanner can be operated in the raster-scan mode, in the line mode, or in the single-point excitation mode. Changes in the scan parameters are executed online, without stopping the scan.

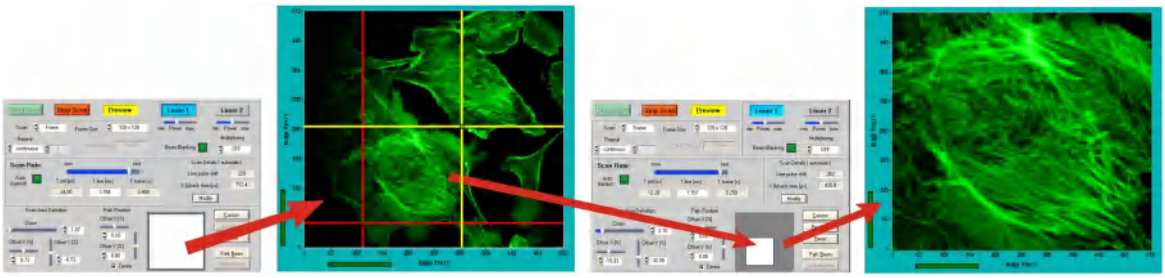


Fig. 70: Preview function with interactive scanner control

Easy Change Between Instrument Configurations

Frequently used instrument configurations are stored in a ‘Predefined Setup’ panel. Changing between the different configurations and user interfaces is just a matter of a single mouse click, see Fig. 71.

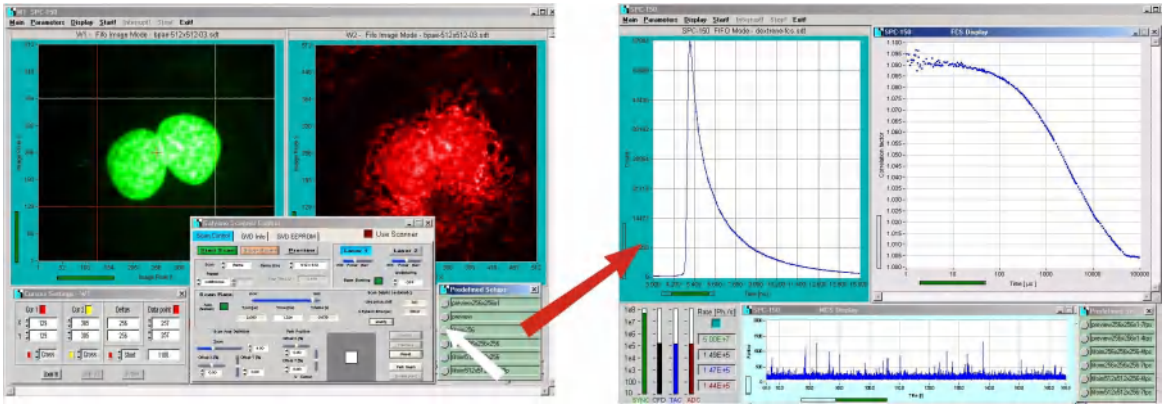


Fig. 71: Changing between different instrument configurations: The DCS-120 system switches from a FLIM configuration into an FCS configuration by a simple mouse click

Online-Lifetime Display

The DCS-120 system displays lifetime images online, both during the accumulation of FLIM data and for the individual steps of a fast image sequence, please see 'Fast Online FLIM', page 415. The calculation of the lifetime images is based on the first moment of the decay data in the pixels of the images. The first-moment technique combines short calculation times with near-ideal photon efficiency. Importantly, it does not require to reduce the time resolution (time channels per pixel) to obtain high image rates. Even if the fast online lifetime function is used during the FLIM acquisition the data can later be processed by precision SPCImage multi-exponential data analysis.

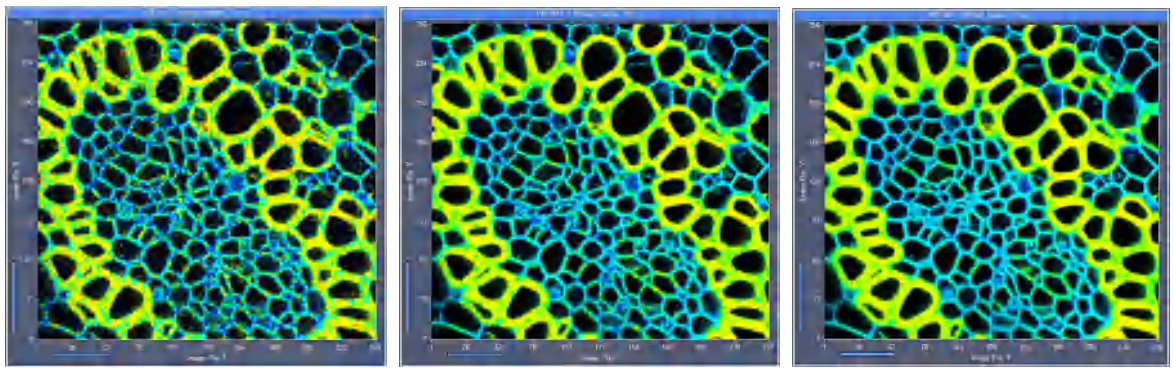


Fig. 72: 256x256-pixel images obtained by SPCM online FLLIM function. Acquisition time 0.2s, 0.5s, and 2s.

Express-FLIM Function

The DCS-120 system is able to run bh's Express FLIM procedure. Express FLIM requires nothing than loading a special software. With this software, the DCS-120 system is able to record FLIM sequences as fast as 5 images per second. The results are saved into a sequence of PNG files, please see Fig. 73. Importantly, adding Express FLIM to a DCS system does not require replacing any part of the hardware. That means a DCS-120 system with Express FLIM option is still able to run 'normal' high-resolution FLIM.

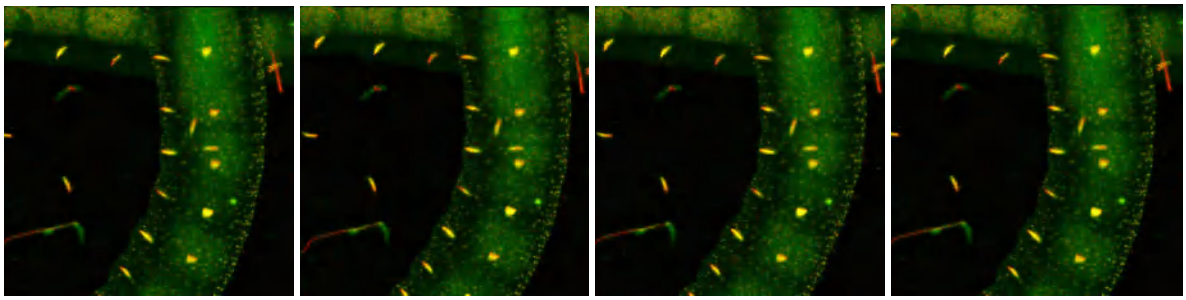


Fig. 73: Express-FLIM of a live Enchytraeus albidus. Autofluorescence, four subsequent images from a 5-frames/second sequence. DCS-120 system with SPC-QC-104. Photon Rate about $10 \cdot 10^6$ s^{-1}.

Simultaneous FLIM / PLIM: Fluorescence / Phosphorescence Lifetime Imaging

The DCS-120 is able to simultaneously record fluorescence and phosphorescence lifetime images. The technique is based on modulating the ps diode laser synchronously with the pixel clock of the scanner. Fluorescence is recorded during the on time, phosphorescence during the off time of the laser. Please see [104, 161] and page 434 of this handbook.

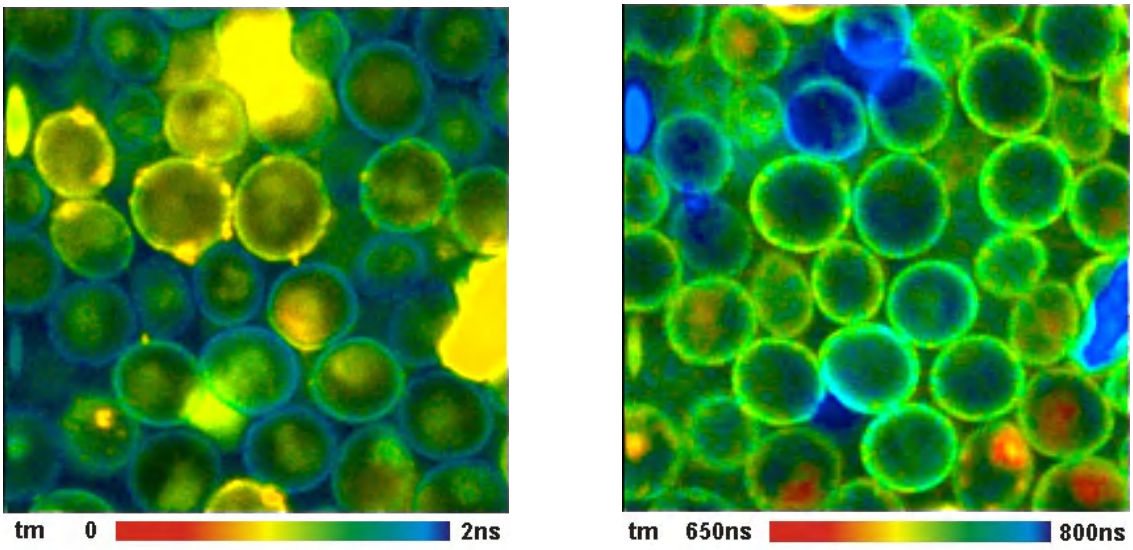


Fig. 74: FLIM (autofluorescence, left) and PLIM (2,2'-bipyridyl) dichlororuthenium (II) hexahydrate, right) yeast cells. Excitation 473 nm, 256x256 pixels.

Megapixel FLIM Images

With 64-bit SPCM software, pixel numbers can be increased to 2048 x 2048 pixels, with a temporal resolution of 256 time channels. Two such images are recorded simultaneously in different wavelength channels. Fig. 75 and Fig. 76 show an example.

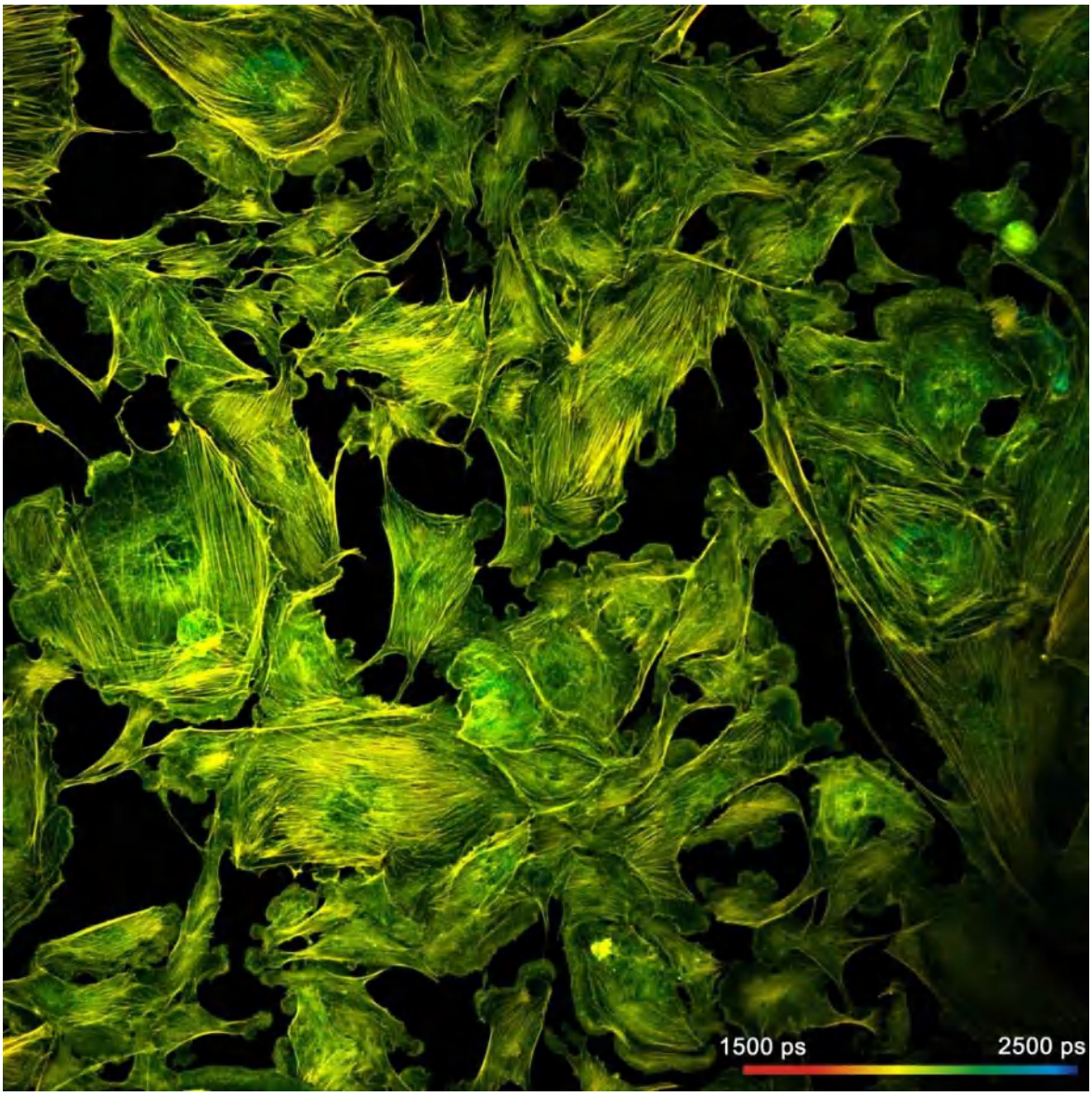


Fig. 75: BPAE sample (Invitrogen) scanned with 2048 x 2048 pixels. Green channel, 485 to 560 nm

The large pixel numbers available in SPCM 64 bit allow the full field of view of even the best microscope lenses to be scanned with an oversampling factor of two or more. In other words, extremely large image areas can be scanned without compromising spatial resolution.

Large pixel numbers are especially important for tissue imaging. They are also useful in cases when a large number of cells have to be investigated and the FLIM results to be compared. Megapixel FLIM records images of many cells simultaneously, and under identical environment conditions. Moreover, the data are analysed in a single analysis run, with identical IRFs and fit parameters. The results are therefore exactly comparable for all cells in the image area.

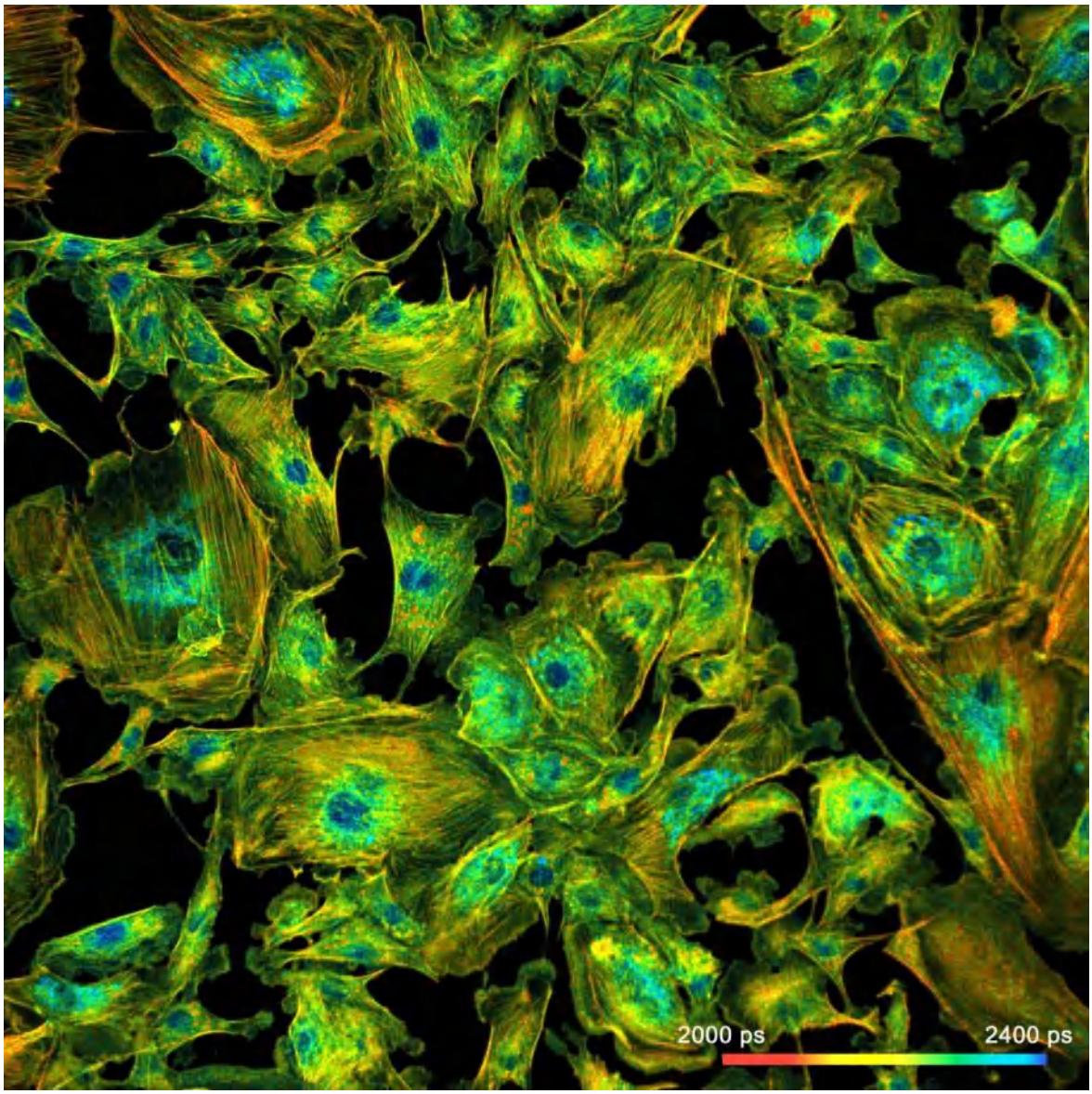


Fig. 76: BPAE sample (Invitrogen), scanned with 2048 x 2048 pixels. Red channel, 560 to 650 nm

Mosaic FLIM

The DCS-120 system is able to record spatial mosaics of FLIM images. These can be lateral mosaics to increase the image area beyond the field of view of the microscope lens, multi-wavelength images, or Z stacks of images. The control functions for the sample stage and the Z drive of the microscope are fully integrated in the software of the DCS system. Examples are shown in Fig. 51 and Fig. 52, page 27. Another application of Mosaic FLIM is the recording of very fast time series of FLIM images. An example for temporal mosaic FLIM is shown in Fig. 594, page 402.

Multi-Wavelength FLIM

With the bh multispectral FLIM detectors the DCS-120 records FLIM simultaneously in 16 wavelength channels [145, 156]. The images are recorded by a multi-dimensional TCSPC process which uses the wavelength of the photons as an additional coordinate of the photon distribution. There is no time gating, no wavelength scanning and, consequently, no loss of

photons in this process. The system thus reaches near-ideal recording efficiency. Moreover, dynamic effects in the sample or photobleaching do not cause distortions in the spectra or decay functions. Multi-wavelength FLIM got an additional push from the new 64-bit SPCM software, and from the introduction of a highly efficient GaAsP multi-wavelength detector. 64-bit software works with enormously large photon distributions, and the GaAsP detector delivers the efficiency to fill them with photons. As a result, images in 16 wavelength channels can be recorded at a resolution of 512 x 512 pixels and 256 time channels. An example is shown in Fig. 546.

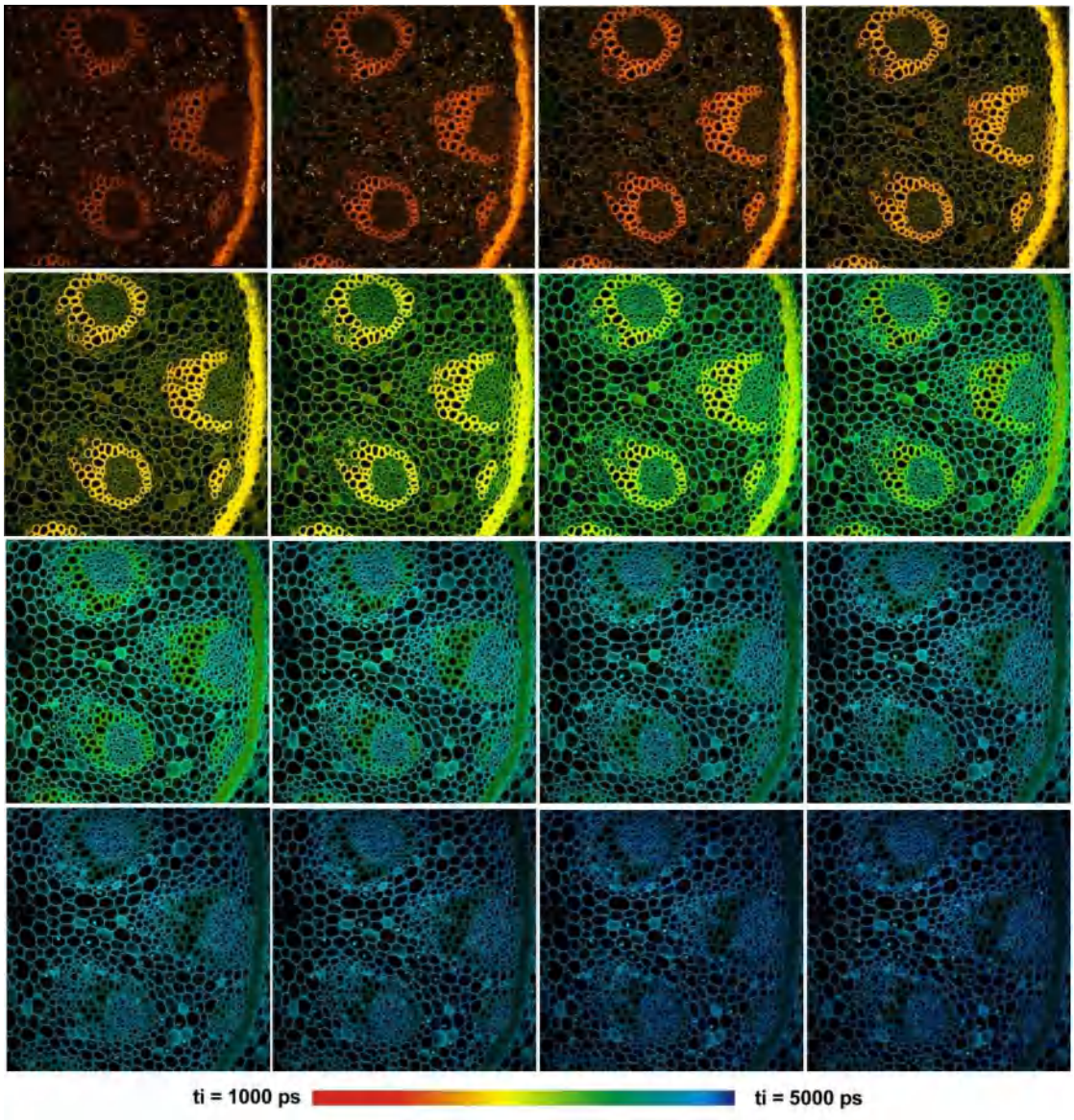


Fig. 77: Multi-wavelength FLIM with the bh MW-FLIM GaAsP 16-channel detector. 16 images with 512 x 512 pixels and 256 time channels were recorded simultaneously. Wavelength from upper left to lower right, 490 nm to 690 nm, 12.5 nm per image. DCS-120 confocal scanner, Zeiss Axio Observer microscope, x20 NA=0.5 air lens.

Fig. 547 demonstrates the true spatial resolution of the data. Images from two wavelength channels, 502 nm and 565 nm, were selected form the data shown Fig. 546, and displayed at larger scale and with individually adjusted lifetime ranges. With 512 x 512 pixels and 256 time channels, the spatial and temporal resolution of the individual images is comparable with what previously could be reached for FLIM at a single wavelength. Decay curves for selected pixels of the images are shown in Fig. 548.

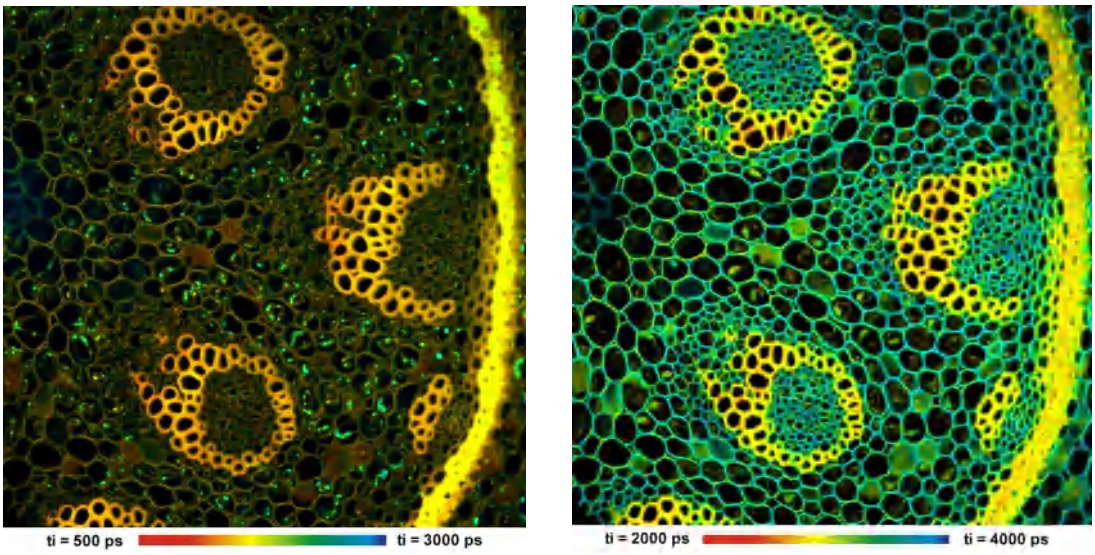


Fig. 78: Two images from the array shown in Fig. 546, displayed at larger scale and with individually adjusted lifetime range. Wavelength channels 502 nm (left) and 565 nm (right). The images have 512 x 512 pixels and 256 time channels.

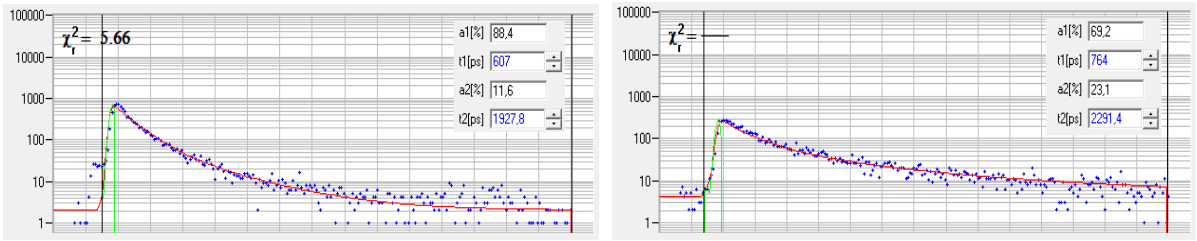


Fig. 79: Decay curves at selected pixel position in the images shown above. Blue dots: Photon numbers in the time channels. Red curve: Fit with a double-exponential model.

Laser Wavelength Multiplexing

The two ps-diode lasers of the basic DCS-120 system or the four lasers of the DCS-120 CMI system can be multiplexed on a pixel-by-pixel, line-by-line, or frame-by-frame basis. Laser multiplexing helps discriminate the signals of several fluorophores, or excite several fluorophores quasi-simultaneously while recording the signals in separate images. An example is shown in Fig. 80.

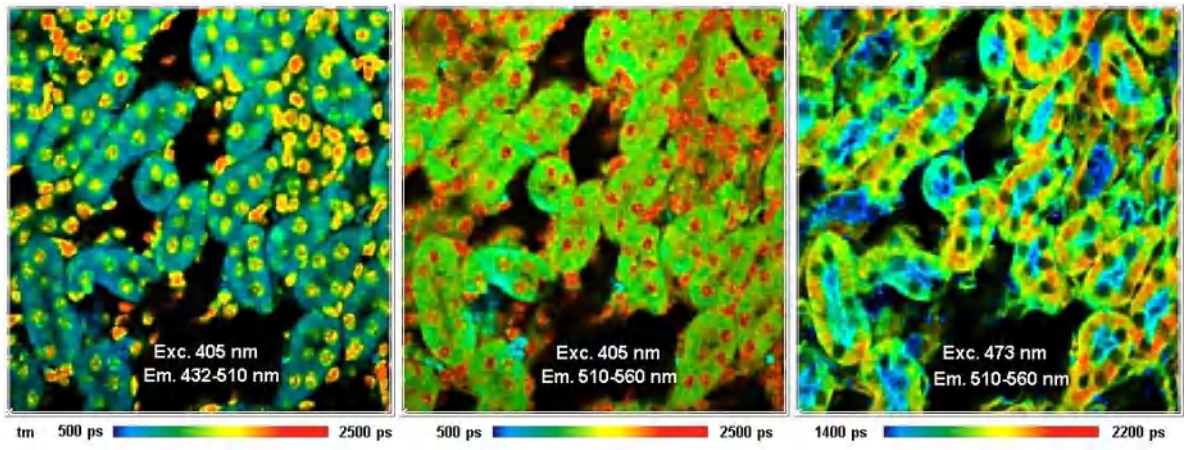


Fig. 80: Excitation wavelength multiplexing, 405 nm and 473 nm.

Metabolic FLIM

Metabolic FLIM is based on recording fluorescence-decay parameters of NADH and FAD, see 'Metabolic Imaging ', page 535. In the DCS-120, NADH and FAD images are acquired quasi simultaneously by laser-wavelength multiplexing and dual-channel detection. Images recorded with the DCS-120 are shown in Fig. 81.

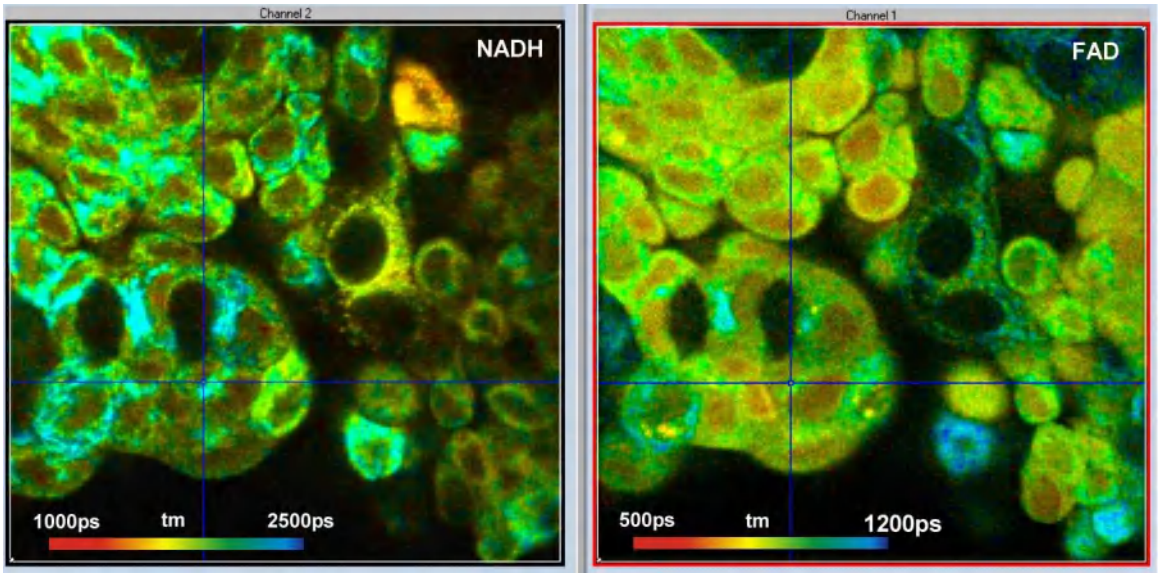


Fig. 81: Metabolic Imaging. Laser-multiplexed FLIM of NADH and FAD.

Time-Series FLIM

Traditional time-series FLIM is available for all system versions, and all detectors. Time series as fast as 2 images per second can be obtained [652]. A time series taken at a moss leaf is shown in Fig. 82.

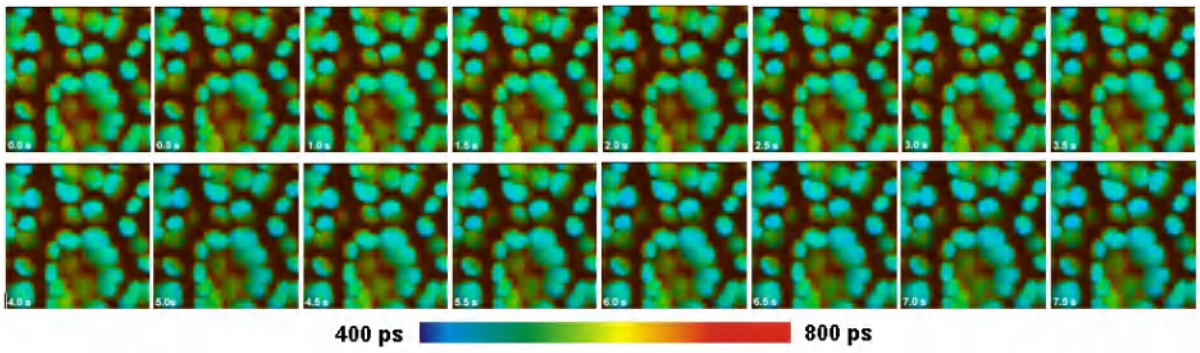


Fig. 82: Time-series FLIM, 2 images per second. Chloroplasts in a leaf, the fluorescence lifetime of the chlorophyll decreases with the time of exposure.

Time-Series Recording by Temporal Mosaic FLIM

Exceptionally fast time series of FLIM images can be recorded by the Mosaic FLIM function of the SPCM software. Temporal Mosaic FLIM records a large number of subsequent FLIM images into a single data array. The advantage of Mosaic FLIM over a traditional record-and-save procedure is that there are no readout times between the recordings of the mosaic elements, and that the data can be accumulated. This allows extremely fast image sequences to be recorded without the need of trading lifetime accuracy against the speed of the sequence. With the DCS-120 scanner and temporal mosaic FLIM, time series at a speed of 100 ms per image can be recorded. An example is shown in Fig. 594, page 402.

Z Stack Recording

In combination with the Zeiss Axio Observer Z1 microscope the DCS-120 system records Z-stacks of FLIM images. The sample is continuously scanned. For each plane, a FLIM image is acquired for a specified 'collection time'. Then the data are saved in a file, the microscope is commanded to step to the next plane, and the next image is acquired. The procedure continues for a specified number of Z planes. A Z stack of autofluorescence images taken at a water flee is shown in Fig. 83.

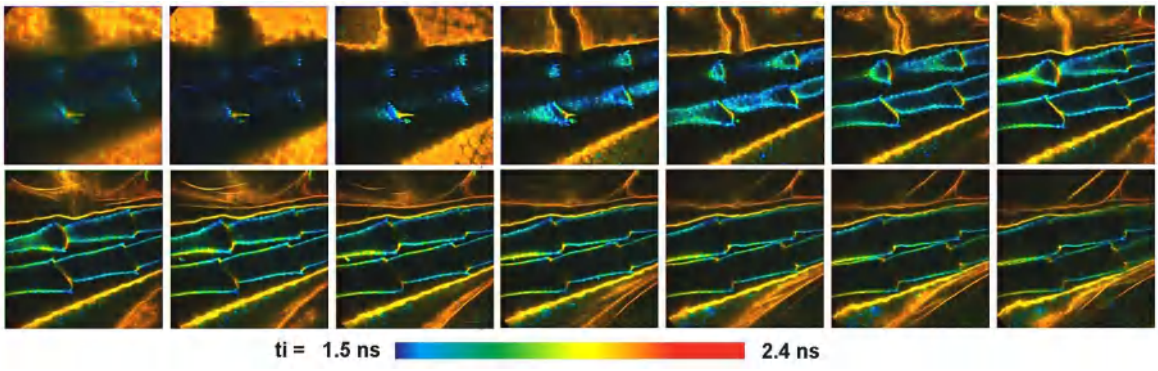


Fig. 83: Z stack recording, part of a water flee, autofluorescence. 15 steps in Z, step width 4 um.

Tuneable Excitation

The basic DCS-120 version can be used with tuneable excitation. Images obtained with a Toptica Ichrome laser [998] are shown in Fig. 84. Another option is the DCS-120 Super MPC system, where wideband visible excitation is obtained by frequency-doubling the output of a Ti:Sa laser. Please see Fig. 63, page 134.

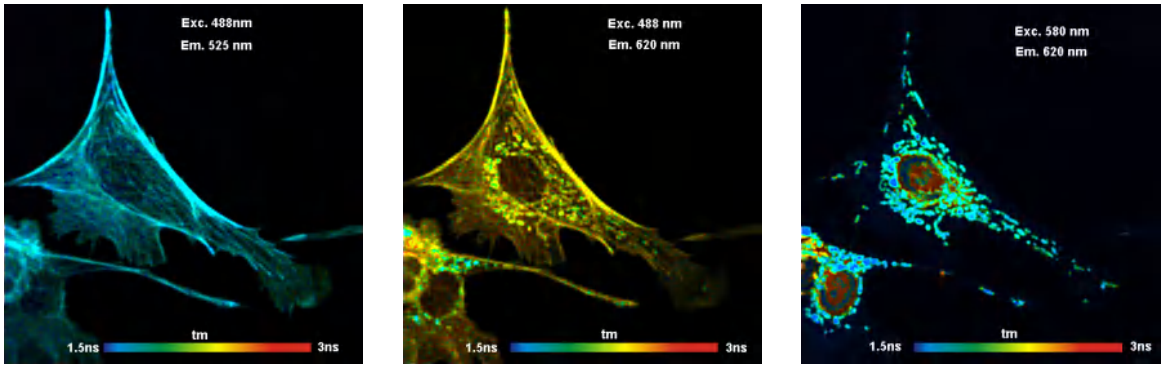


Fig. 84: Tuneable excitation with DCS-120 WB and Toptica Ichrome laser. Left to right: Excitation 488 nm emission 525±15 nm, excitation 488 nm emission 620±30 nm, and excitation 580 nm emission 620±30 nm.

DCS-120 MP: Multiphoton FLIM with Ti:Sa or Femtosecond Fibre Laser

Multiphoton FLIM is used when images from deep layers of biological tissue have to be imaged. A two-photon FLIM image of *Artemia salinas* (a small shrimp) recorded by the DCS-120 MP system is shown in Fig. 85. The image was recorded with the Femto-Fibre-Pro (fibre-laser version) of the DCS-120 MP [128].

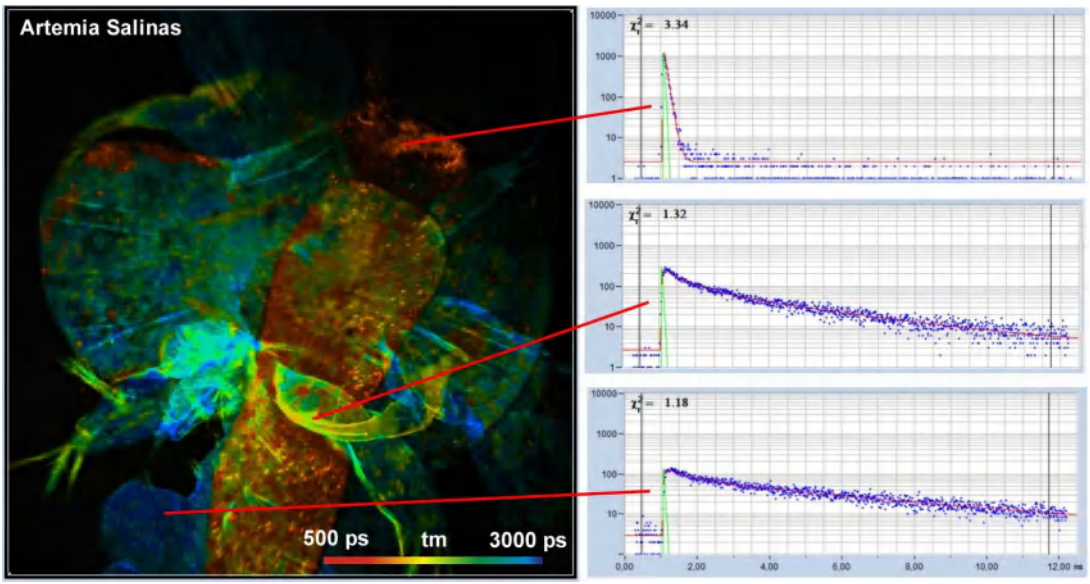


Fig. 85: Autofluorescence FLIM image of a brine shrimp, *artemia salinas*. Mean (amplitude-weighted) lifetime of double-exponential decay. Decay functions of selected areas shown on the right.

FLIM images of pig skin in different depth of the tissue are shown in Fig. 86. The images were recorded by a DCS-120 MP with a Ti:Sa-Laser.

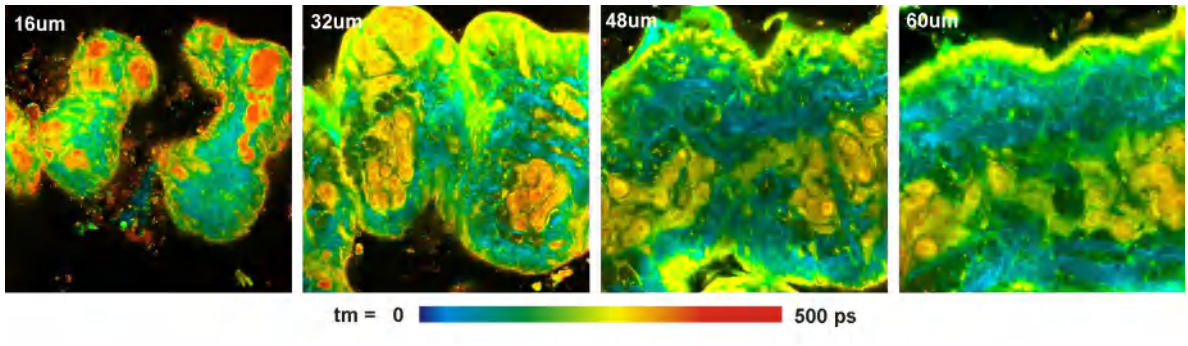


Fig. 86: Pig skin, autofluorescence, image in different depth in the sample. Amplitude-weighted lifetime of triple-exponential decay model

Recording of Ultra-Fast Fluorescence Decay

When used with the HPM-100-06 and -07 hybrid detectors the DCS-120 MP systems deliver extremely high temporal resolution. An example is shown in Fig. 87. The image shows mushroom spores of *Boletus edulis* [177]. The image was recorded by a DCS-120 MP with a Femto-Fibre-Pro laser (Toptica), ultra-fast HPM-100-06 detectors, and SPC-150NX TCSPC modules. The data show clearly a decay component of 20 ps lifetime.

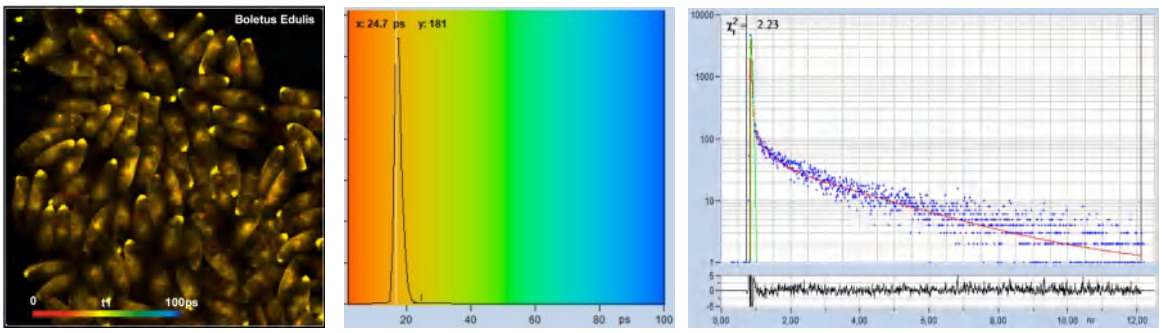


Fig. 87: Spores of *Boletus edulis*. Left to right: Image of fast decay component, t_1, of triple-exponential decay model, histogram of t_1, and decay curve in selected spot. Data from [177].

Near-Infrared FLIM

The DCS-120 is able to record lifetime images with near-infrared (NIR) fluorophores, see page 384 of this book. NIR fluorophores often display large variations of their fluorescence lifetimes depending on the binding target. Moreover, because both the excitation and the emission wavelengths are in the near infrared a high penetration depth is obtained. NIR FLIM is therefore another promising technique to obtain molecular information from deep layers of biological tissue. An image of a pig skin sample incubated with 3,3'-diethylthiatricarbocyanine is shown in Fig. 88.

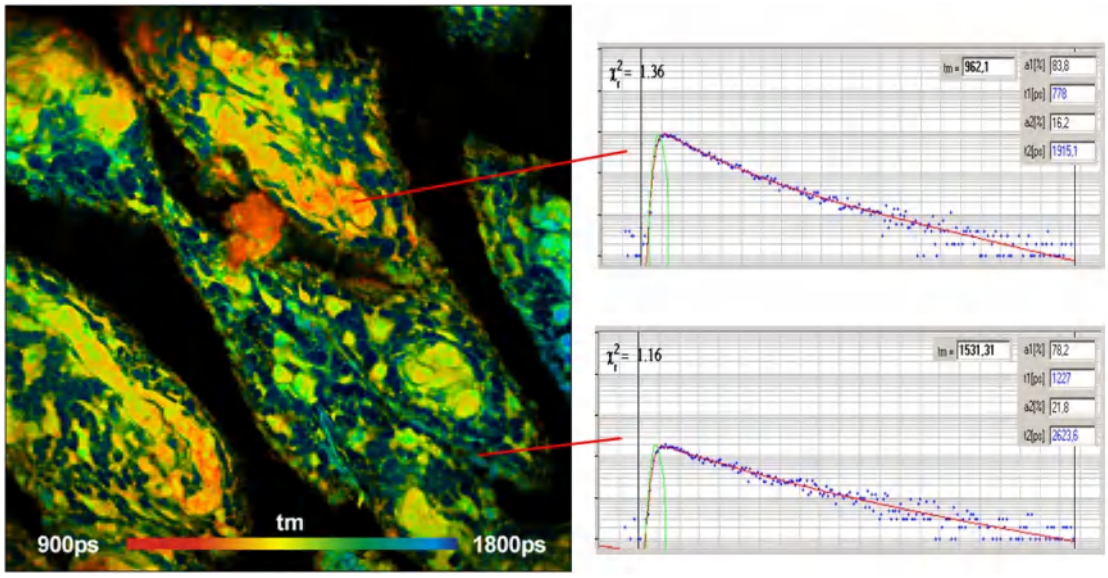


Fig. 88: Near-Infrared FLIM. Pig skin sample stained with 3,3'-diethylthiatricarbocyanine, detection wavelength from 780 nm to 900 nm.

DCS-120 MACRO: Scanning Macroscopic Objects

The DCS MACRO version of the DCS system scans objects directly in the focal plane of the scanner. Objects up to a size of 15 mm can be imaged at high resolution. Fig. 89 shows a leaf with a fungus infection.

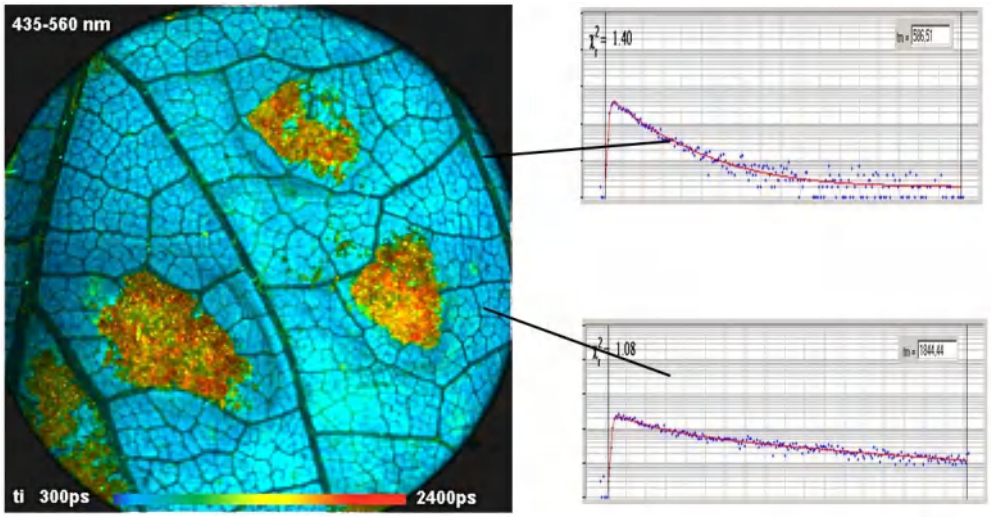


Fig. 89: Leaf with a fungus infection. ps diode laser excitation, 405 nm, scan format 512 x 512 pixels. Right: Decay functions of healthy and infected areas.

DCS MACRO with Motor Stage

The image area of the DCS MACRO can be extended by a motorised sample stage. With the motor stage, images of objects as large as 10 cm can be recorded by spatial mosaic FLIM. An example is shown in Fig. 90.



Fig. 90: Mosaic FLIM image of a $20 bill

FLITS: Fluorescence Lifetime-Transient Scanning

FLITS records transient effects in the fluorescence lifetime of a sample along a one-dimensional scan. The maximum resolution at which lifetime changes can be recorded is given by the line scan time. With repetitive stimulation and triggered accumulation transient lifetime effects can be resolved at a resolution of about one millisecond [113, 162, 68]. Please see also page 410 of this handbook.

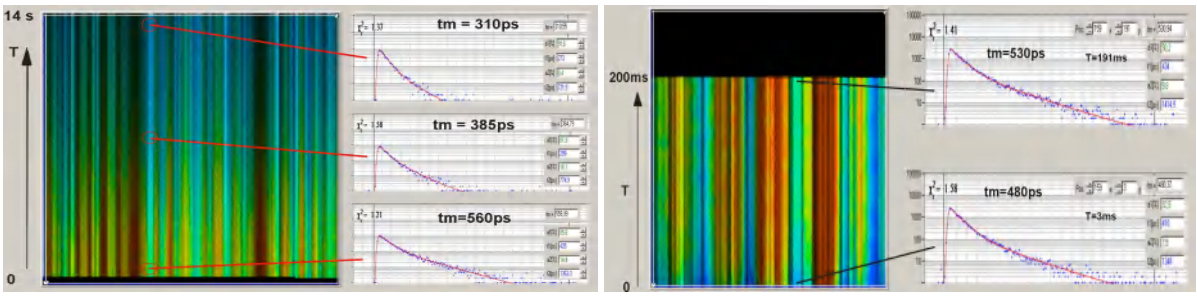


Fig. 91: FLITS of chloroplasts in a grass blade, change of fluorescence lifetime after start of illumination. Left: Non-photochemical transient, transient resolution 60 ms. Right: Photochemical transient. Triggered accumulation, transient resolution 1 ms.

FCS

Due to the superior performance of the HPM-100-40 hybrid detectors the DCS-120 system delivers highly efficient FCS. There is no afterpulsing peak in autocorrelation data [159]. Thus, accurate diffusion times and molecular-brightness parameters are obtained from a single detector. Compared to cross-correlation of split signals, correlation of single-detector signals yields a four-fold increase in correlation efficiency. The result is a substantial improvement in the signal-to-noise ratio of FCS recordings. Gated FCS is possible by hardware gating

via the TAC limits of the TCSPC modules, FCCS by cross-correlating the signals of the two DCS channels.

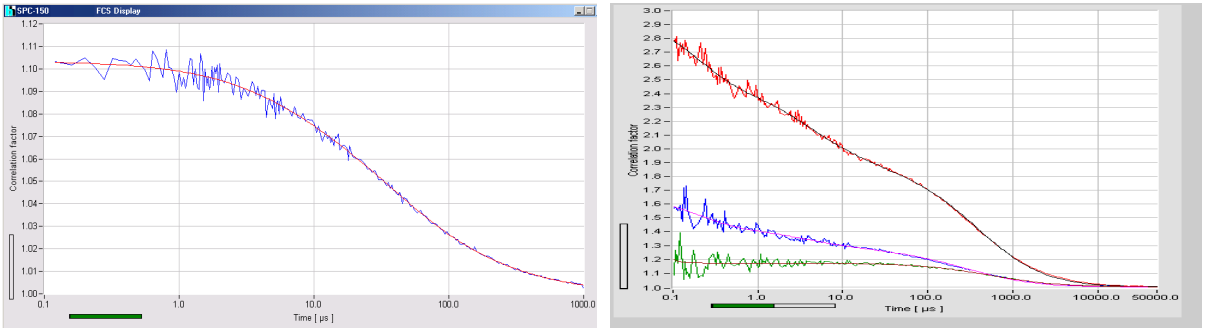


Fig. 92: Left: FCS curve recorded by a single HPM-100 detector. The data are free of an afterpulsing peak. Right: Dual-colour FCS, autocorrelation blue and red, cross-correlation green. Online fit with SPCM software.

FLIM Systems for Zeiss LSM 710, 780, 880, 980 Family Microscopes

bh deliver FLIM systems for the Zeiss LSM laser scanning microscopes since 2000 [142, 143, 146]. Since then, several generations of LSM family laser scanning microscopes, and several generations of bh FLIM modules have been introduced. As a result, a wide variety of bh FLIM systems and of FLIM system configurations is in use. The excitation light source can be the Ti:Sapphire laser of a multiphoton microscope, a picosecond diode laser attached to or integrated in the microscope, or a visible-range tuneable solid state laser. The fluorescence light may be detected via a confocal port of the scan head or via a non-descanned port of a multiphoton microscope. Signals may be detected by one detector, simultaneously by two, three, or four detectors, or by the 16 channels of a bh multi-wavelength detector. Since 2008, bh FLIM systems are using highly efficient GaAsP hybrid detectors. By combining extremely high efficiency with large active area, high counting speed, high time-resolution, and low background, these detectors have triggered a breakthrough in FLIM recording. Another step was made by the introduction of 64-bit data acquisition software [103]. Recent bh FLIM systems for Zeiss LSMs are recording data at unprecedented pixel numbers, high dynamic range, short acquisition time, minimum exposure of the sample, and unprecedented time resolution. New hardware and software functions have resulted in advanced FLIM functions, like time-series FLIM, Z stack FLIM, spatial and temporal Mosaic FLIM, combined fluorescence and phosphorescence lifetime imaging (FLIM / PLIM), and fluorescence lifetime-transient scanning (FLITS). New bh / Zeiss FLIM systems are available with bh's new integrated SPCConnect software. It combines bh SPCM software and Zeiss ZEN software by TCP (Transmission Control Protocol). SPCM is then running in the framework of ZEN, with both components freely exchanging commands, system parameters, and data. Please see www.becker-hickl.com.

Optical Configuration

Typical FLIM configurations for the LSM 710/780/880/980 family microscopes are shown in Fig. 93 through Fig. 95. Fig. 93 shows FLIM configurations for inverted microscopes. The configuration on the left uses multiphoton excitation by a femtosecond titanium-sapphire laser. The fluorescence light is detected via a non-descanned detection (NDD) beam path. Typically, the light is split in two spectral components by a Zeiss 'T Adapter', and detected by two parallel detectors and TCSPC channels. The configuration shown on the right uses picosecond diode lasers. The sample is excited by one-photon excitation. The fluorescence light is detected back through the confocal beam path of the scanner and sent out of the scan head via an optical port. It is split into two spectral channels by a bh beamsplitter module and fed into two FLIM detectors. The single-photon pulses from the detectors are recorded by two separate TCSPC channels of the FLIM system.

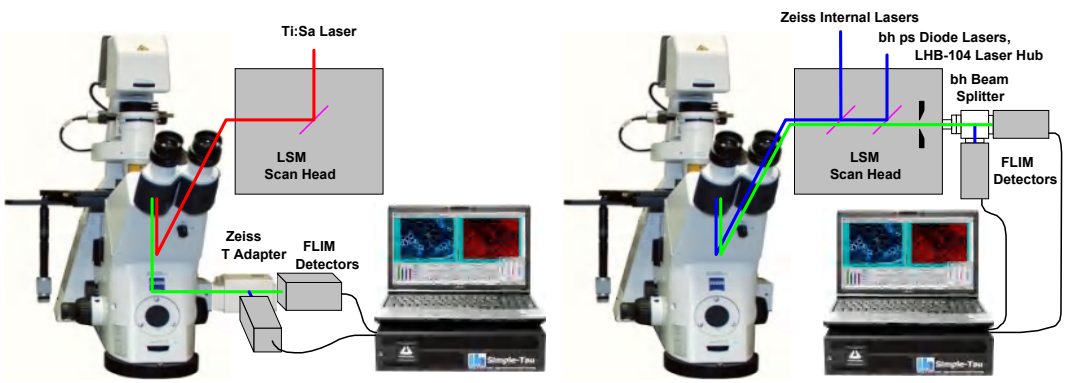


Fig. 93: LSM 710 to 980 family FLIM systems, inverted microscopes. Left: Multiphoton-excitation FLIM with non-descanned detection. Right: One-photon FLIM with confocal detection.

The detectors and detector assemblies for the confocal port are compatible with those for the NDD port. That means the detectors can be moved between the two ports. It is also possible to attach detectors to both ports permanently. The desired pair of detectors can then be selected from the SPCM data acquisition software.

Fig. 97 shows FLIM at an LSM 710/780/880/980 in the upright version. The configuration on the left uses multiphoton excitation and non-descanned detection, the configuration on the right uses one-photon excitation and confocal detection.

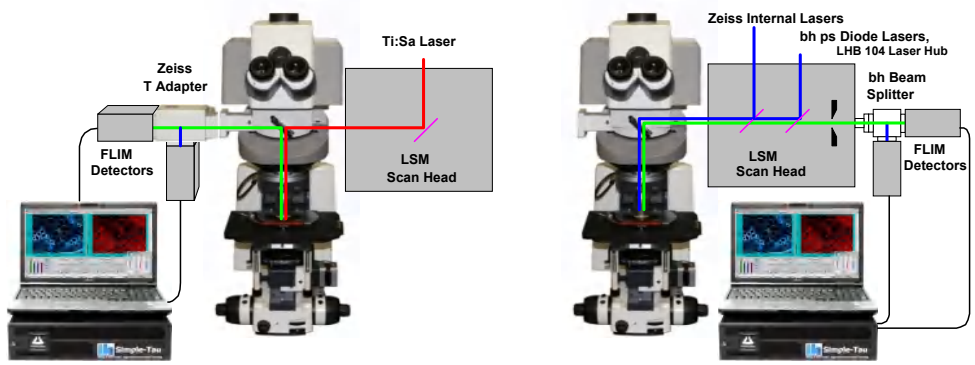


Fig. 94: Zeiss LSM 710/780/880/980 family FLIM systems, upright microscopes. Left: Multiphoton-excitation FLIM with non-descanned detection. Right: One-photon excitation FLIM with confocal detection.

Multiphoton and one-photon FLIM configurations for the LSM 880 and LSM 980 with Airy-Scan detectors are shown in Fig. 95, left and right. For the multiphoton system there is no difference to the standard system. The Airy-Scan detector rests at the confocal port and does not interfere with the FLIM detectors at the NDD port. For the one-photon FLIM system the FLIM detectors are connected to a beam switch between the scan head and the Zeiss Airy-Scan detector, see Fig. 95, right.

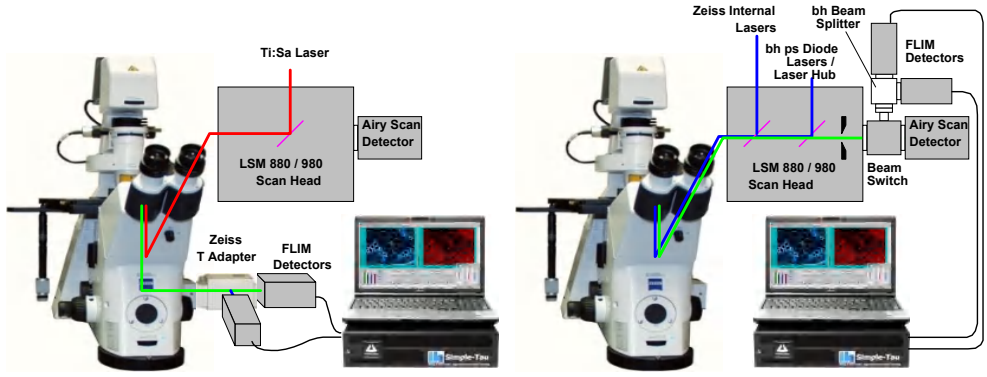


Fig. 95: Zeiss LSM family FLIM systems, inverted microscopes. Left: Multiphoton-excitation FLIM with non-descanned detection. Right: One-photon excitation FLIM with confocal detection.

Standard bh FLIM systems for the LSM 710, 780, 880, and 980 use the bh HPM-100-40 or -06 hybrid detectors [160], see section 'HPM-100 Hybrid Detector Modules', page 178. However, the bh systems work also with the Zeiss BIG 2 detector [102], with the NIR versions and the ultra-fast versions of the HPM-100 detectors [100, 169], and with the bh MW-FLIM GaAsP multi-spectral FLIM detectors (see 'PML-16-C and PML-16-C GaAsP Multichannel Detector Heads', page 189). The optical configuration for multiphoton multi-wavelength FLIM is shown in Fig. 96. The light is collected from an NDD port by a fibre bundle. The light is dispersed spectrally, and detected by a bh PML-16 GaAsP (16-channel) PMT module. Similarly, the multi-wavelength FLIM detector assembly can be attached to the confocal port of the scan head.

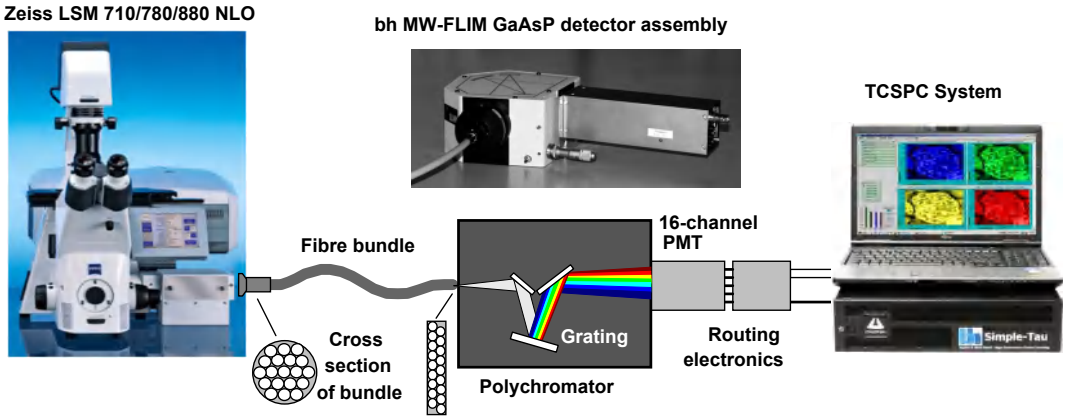


Fig. 96: Multi-wavelength FLIM

Fig. 97: LSM 710 family FLIM systems, upright microscopes. Left: Multiphoton-excitation FLIM with non-descanned detection. Right: One-photon excitation FLIM with confocal detection.

Detectors

The FLIM systems for the Zeiss LSMs use bh HPM-100-40 or HPM-100-06 hybrid detectors. Detectors with adapters for the NDD ports and the confocal ports of the Zeiss LSM family microscopes are shown in Fig. 98.



Fig. 98: HPM-100 hybrid detector and a dual-detector assembly with adapter to the optical ports of the Zeiss LSM systems

LSM 880 and LSM 980 confocal microscopes often have the 'Airy Scan' detector attached to the confocal port of the scan head. In these cases, the bh confocal-FLIM detectors are connected to a beam switch that is inserted between the san head and the Airy Scan detector, see Fig. 99. The beam switch is available from Zeiss.

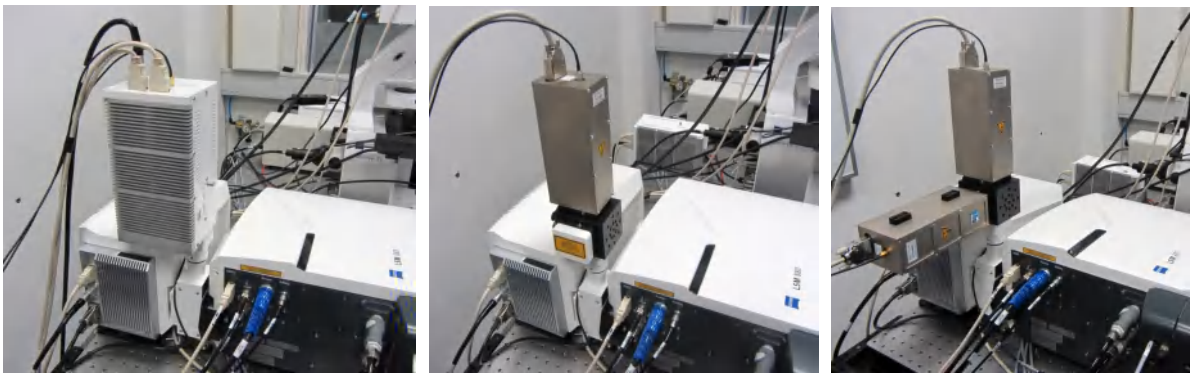


Fig. 99: LSM 880, confocal FLIM detectors. Left to right: BIG-2 detector, one HPM-100-40 hybrid detector, two HPM-100-40 detectors

More details of the FLIM systems for the Zeiss LSM 710/780/880/980 and LSM 510 families are described in a separate 240-page handbook [69], an 18-page addendum for the LSM 980 microscopes [70], and in a 68-page overview brochure [71].

Lasers for Confocal FLIM

bh FLIM systems for the Zeiss LSM 710, 780, and 880 confocal microscopes had one or two ps diode lasers. These were integrated in the hardware and software of the Zeiss LSM systems. With just two laser wavelengths and limited control over the laser function, these systems were limited both in excitation wavelength and recording functions. The LSM 980 confocal FLIM systems are coming with four ps diode lasers of different wavelength [70]. The lasers are contained in the bh LHB-104 'Laser Hub' [74], shown in Fig. 100. The lasers are coupled into the LSM 980 scan head via a single-mode fibre with a standard Zeiss / Lasos fibre coupler. The lasers can be switched on and off on demand, multiplexed in time for excitation-wavelength multiplexed FLIM, or on/off modulated for simultaneous FLIM / PLIM.



Fig. 100: LBH-104 'Laser Hub'. Output of four wavelengths via single fibre with Zeiss / Lasos coupler, demonstrated by reflection off an optical grating.

Laser for Multiphoton FLIM

The bh FLIM systems work both with the confocal versions and with the multiphoton versions of the Zeiss LSMs. The excitation source in multiphoton systems is normally a Ti:Sa laser. The FLIM systems are perfectly compatible with these lasers. In principle, they also work with femtosecond fibre lasers, should one of these be used in combination with a Zeiss LSM.

FLIM Data Acquisition

FLIM data acquisition is performed by two parallel SPC-150NX, two parallel SPC-180NX or one SPC-QC-104 TCSPC FLIM Module in combination with bh's 64-bit SPCM Software. Acquisition is based on bh's multi-dimensional TCSPC process. Based on parameter-tagged photon data and scan clock pulses delivered by the TCSPC modules, the SPCM software builds up the photon distributions for the two detection channels or, if multi-spectral FLIM is used, for the 16 spectral channels of the bh MW FLIM detector. During the FLIM acquisition intermediate results are displayed in predefined intervals, usually every few seconds. The acquisition can be stopped after a defined acquisition time, or by a user command when the desired signal-to-noise ratio has been reached.

Data Acquisition Software

The bh FLIM systems for the Zeiss LSMs use bh's SPCM data acquisition software. SPCM includes the management of the measurement and measurement control parameters, user-interface configuration parameters, and parameters for online data visualisation. Load and

save functions are provided to handle measurement and setup data. A large part of SPCM provides display functions for multi-dimensional data. There are display functions for decay curves, series and arrays of decay curves, images, and arrays of images. Display functions also contain online calculation and display of pseudo-colour fluorescence-lifetime images and display of decay curves from ROIs within lifetime images. The SPCM software is also able to record FCS and FCCS, or to deliver parameter-tagged photon data for single-molecule spectroscopy. Moreover, it records combined fluorescence/phosphorescence lifetime images (FLIM / PLIM) and Fluorescence Lifetime-Transient Scanning (FLITS) data. A direct link is provided for communication with SPCImage NG FLIM analysis software. An example of the SPCM software panel is shown in Fig. 101. For details please see chapter SPCM Software, page 703.

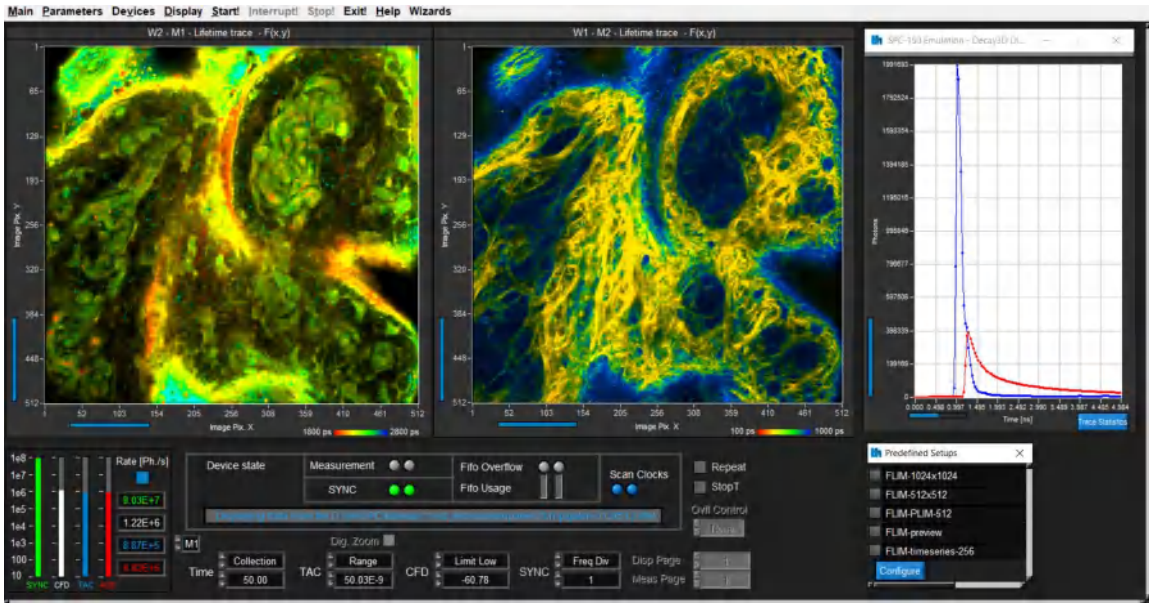


Fig. 101: SPCM software panel for Zeiss FLIM. FLIM in two detection channels. Right: Decay functions in selected areas of images

ZEN-Integrated FLIM Software

The new bh / Zeiss FLIM systems for the LSM 980 are available with bh's new integrated SPCConnect software. It connects bh SPCM software and Zeiss ZEN software by a TCP (Transmission Control Protocol). That means SPCM is running in the framework of ZEN, with both components freely exchanging commands, system parameters, and data. Compared to an integration on the DLL level TCP integration has the advantage that, in addition to basic FLIM, functions like Z-stack recording, time-series recording, fast triggered accumulation, FLITS, and simultaneous FLIM / PLIM are available. Upgrades on either side become immediately available to the user. As usual, data analysis is performed by bh's legendary SPCImage data analysis software. It performs single, double and triple decay analysis and directly delivers lifetimes, component amplitudes, and biologically relevant parameters such as metabolic ratios, FLIRR, FRET efficiencies, and FRET distances. SPCImage runs on a GPU, delivering FLIM results within seconds even for images in the megapixel range. With these features, the new bh/Zeiss FLIM systems are excellently suitable for the whole range from entry-level FLIM to high-end multidimensional molecular imaging applications. An example of the combined software panel is shown in Fig. 102.

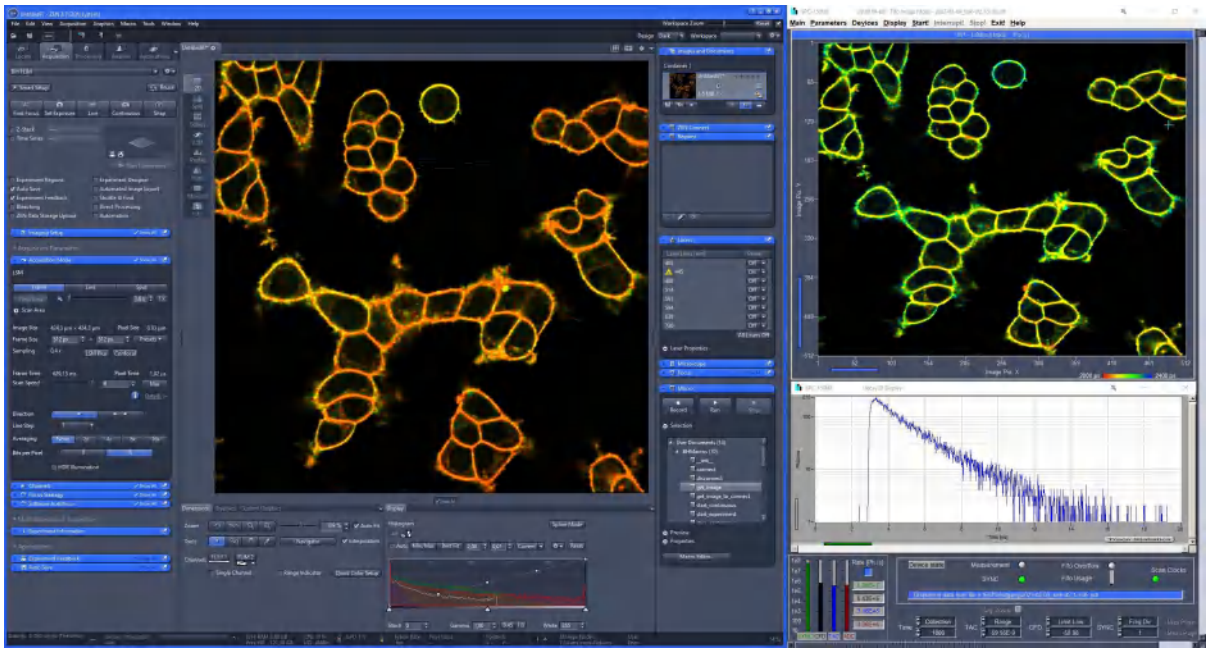


Fig. 102: ZEN / SPCM integrated FLIM software

Fast Preview Function

The FLIM systems have a fast preview functions for sample positioning, focusing, laser power adjustment, and region-of-interest selection. The preview function displays images in intervals on the order of 1 second and less, see Fig. 103.

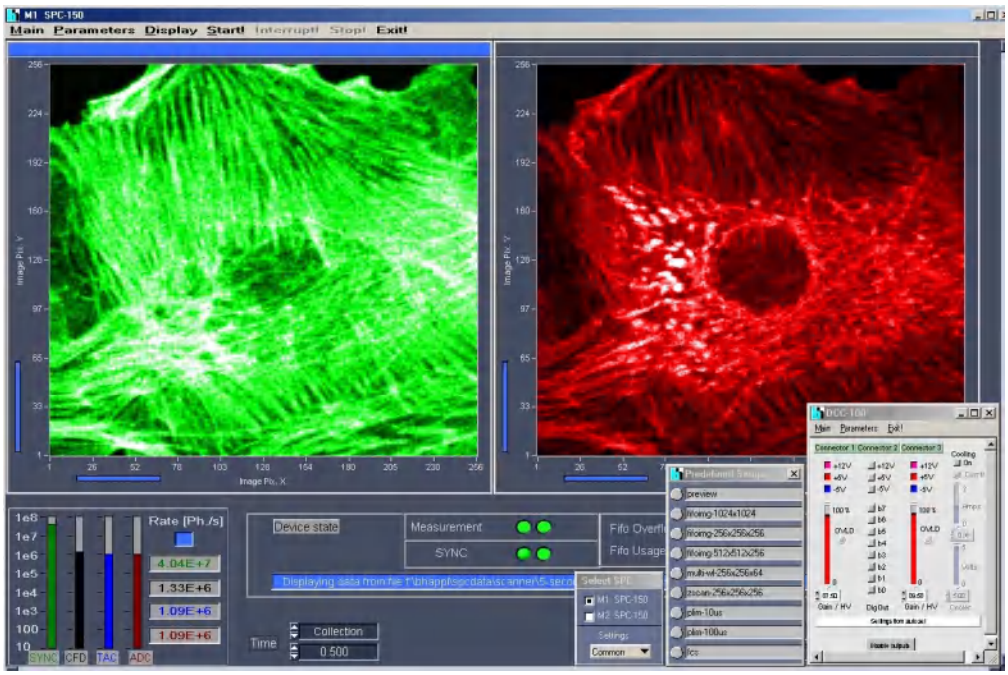


Fig. 103: SPCM software in fast preview mode. 1 second per image.

Any change in the microscope parameters, such as sample position, scan area, the zoom factor, depth of focal plane, pinhole size or laser power, becomes immediately visible in the preview images, see Fig. 104.

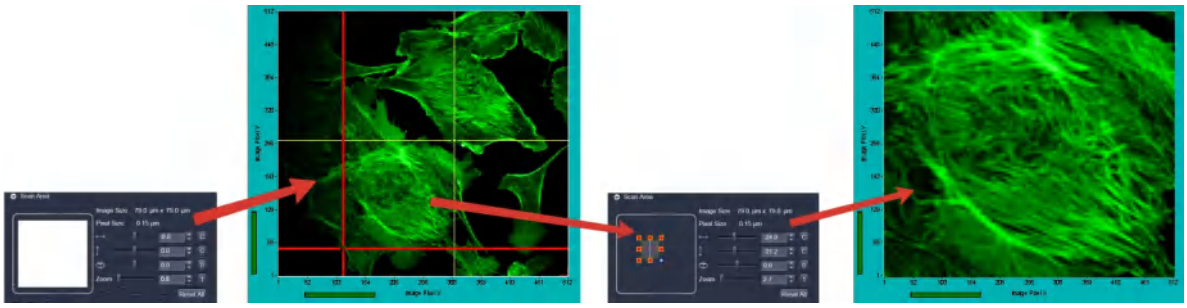


Fig. 104: When the scan area definition in the Zeiss ZEN software is changed the result becomes visible in the images immediately.

Easy Switching Between Acquisition Modes

Frequently used operation modes and user interface configuration can be selected from a panel of predefined setups. Switching between Preview modes, FLIM acquisition, different pixel and time-channel numbers, time-series recording, Z-stack recording, FCS, or any other conceivable recording procedure is a matter of a single mouse click, see Fig. 105.

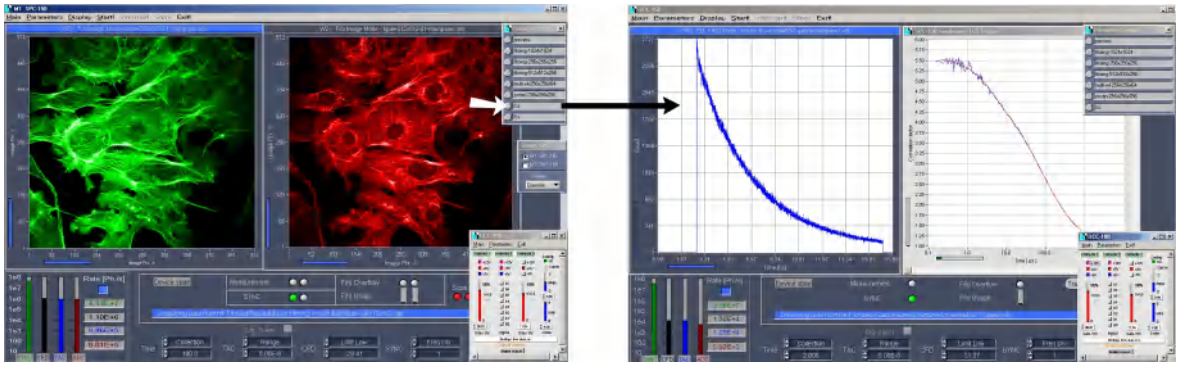


Fig. 105: Switching the instrument configuration via the 'Predefined Setup' panel

Fast Beam Scanning - Fast Acquisition

The bh FLIM systems are perfectly compatible with the fast beam scanning used in the Zeiss microscopes. Frame times can be from about 50 ms to a few seconds, with pixel dwell times down to one microsecond. The multi-dimensional TCSPC process used in the bh FLIM systems delivers identical results for different scan rates, provided the total acquisition time is the same. FLIM can be acquired at short acquisition time. Fig. 106 shows lifetime images of a BPAE cell recorded within 5 seconds acquisition time.

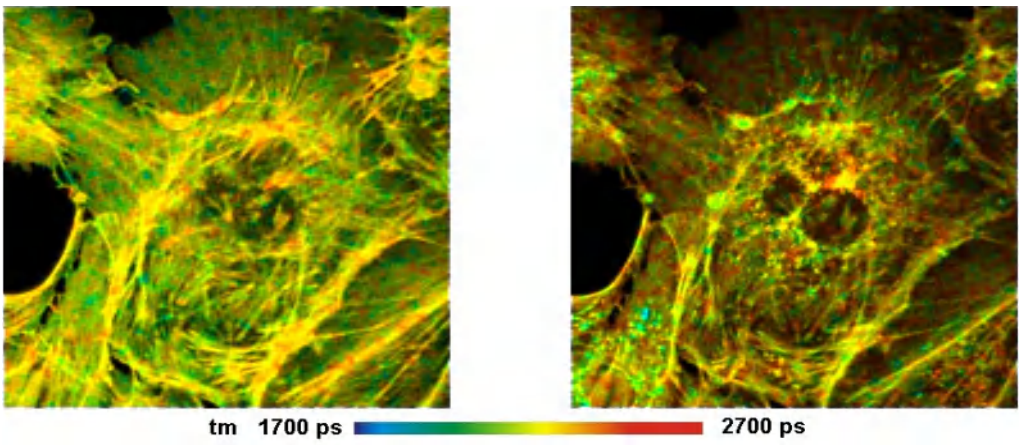


Fig. 106: FLIM acquired within 5 seconds of acquisition time. Left 485 to 560 nm, right 560 to 650 nm. BPAE cell stained with Alexa 488 and Mito Tracker Red.

Online FLIM Display

Starting from Version 9.72 SPCM software the FLIM systems for the Zeiss LSM 710 / 780 / 880 / 980 family are able to display lifetime images online, both during the accumulation of FLIM data and for the individual steps of a fast image sequence, see page 415 of this book. An example is shown in Fig. 107. The calculation of the lifetime images is based on the first moment of the decay data in the pixels of the images. The first-moment technique combines short calculation times with near-ideal photon efficiency. It does not require to reduce the time resolution (time channels per pixel) to obtain high image rates. That means the data can later be processed by precision SPCImage multi-exponential data analysis.

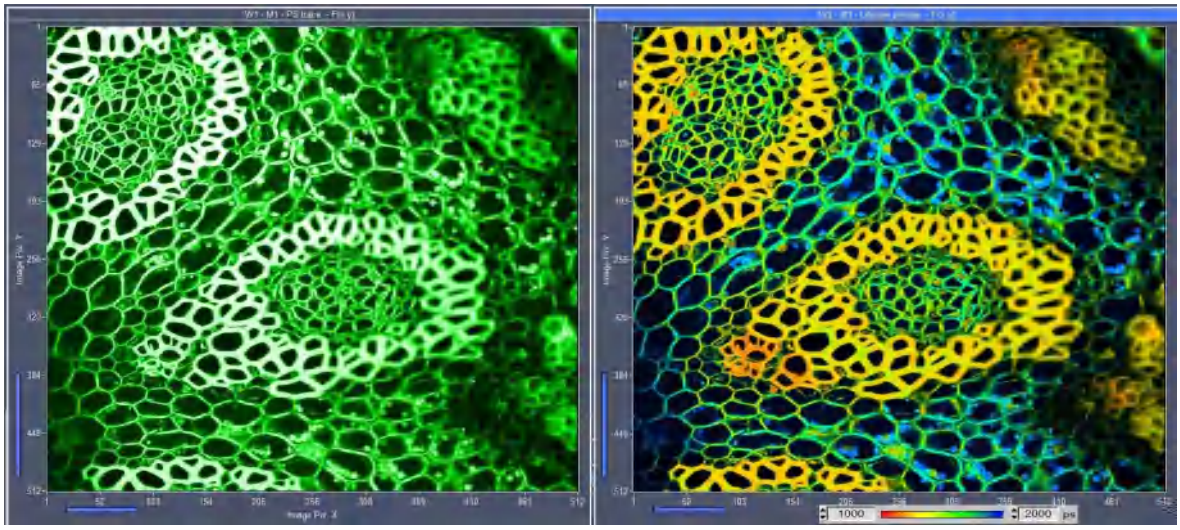


Fig. 107: Intensity image (left) and lifetime image (right) calculated online by SPCM software

Bi-Directional Scanning

With Version 9.73 SPCM Software, the bh TCSPC / FLIM systems are able to record FLIM with bidirectional scanning. As usual, data recording is synchronised with the scanning by frame clock, line clock, and pixel clock pulses from the scanner. Each first line clock pulse indicates the beginning of a forward scan, each second one the beginning of a backward scan. The recording procedure automatically reverses the data from the backward scan and compensates for the line shift caused by the dynamic behaviour of the scanner. The FLIM data structure is the same as for unidirectional scanning. Thus, standard online intensity and lifetime display functions of the SPCM software are available, and data can be analysed by SPCImage as usual.

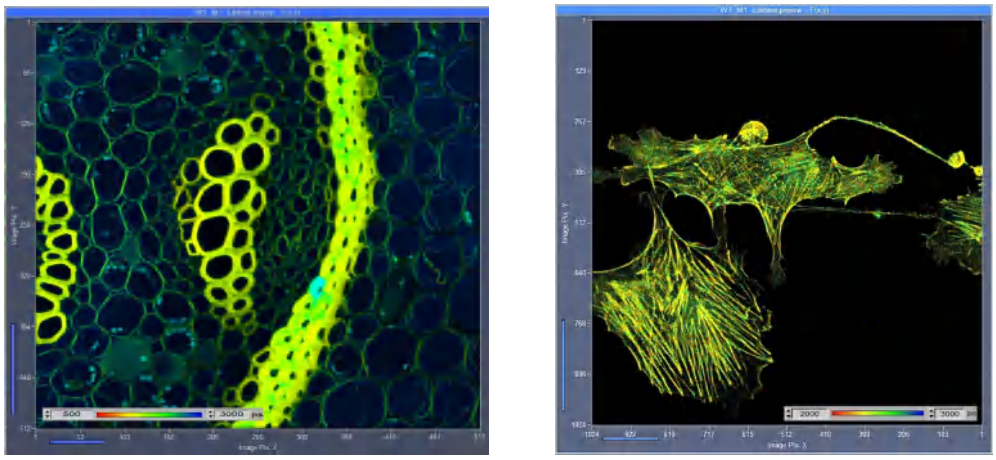


Fig. 108: FLIM of Convallaria sample (left, 512 x 512 pixels) and BPAE Cell sample (right, 1024x1024 pixels), recorded with bidirectional scanning. Images created by online-lifetime function of SPCM software.

High-Resolution Images

Pixel numbers of FLIM data can be increased up to 2048 x 2048. Fig. 109 shows a FLIM image of a BPAE sample recorded at a resolution of 1024 x 1024 pixels. The image on the left shows the entire area of the scan. The image on the right have been selected from the full-area scan by the zoom function of SPCImage data analysis software.

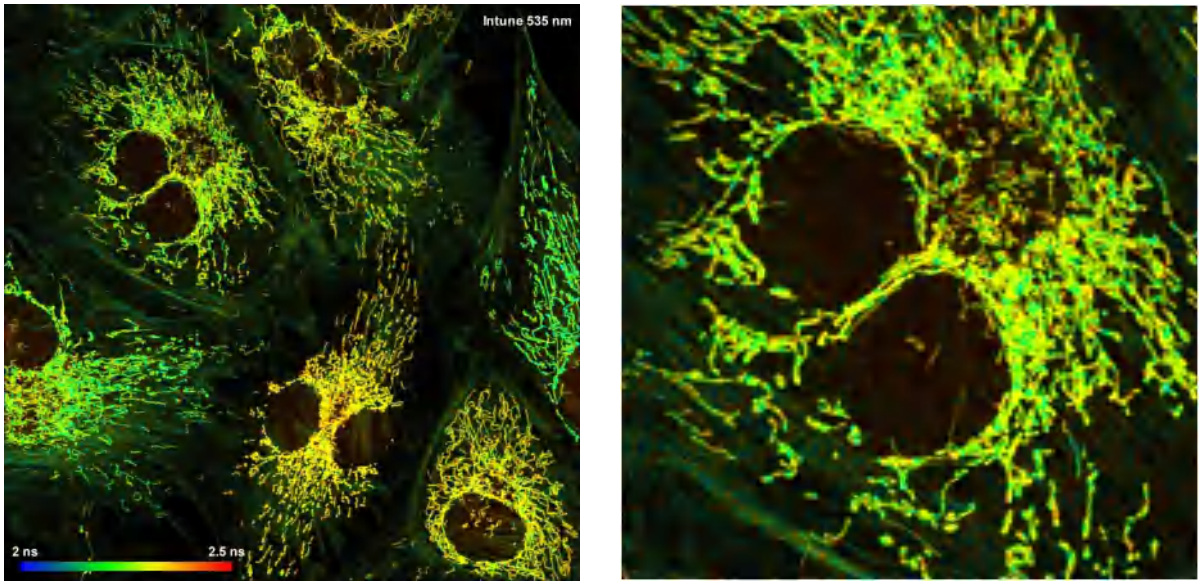


Fig. 109: Left: Image recorded with 1024 x 1024 pixels. Right: Digital zoom into the data of Fig. 109, showing the two cells on the upper left. Effective resolution 256 x 256 pixels. LSM 710 Intune system, excitation 535 nm, emission from 550 nm up. BPAE cell stained with Alexa 488 and Mito Tracker Red.

Two Fully Parallel TCSPC FLIM Channels

Standard bh FLIM systems record in two wavelength intervals simultaneously. The signals are detected by separate detectors and processed by separate TCSPC modules. There is no intensity or lifetime crosstalk. Even if one channel overloads the other channel is still able to produce correct data.

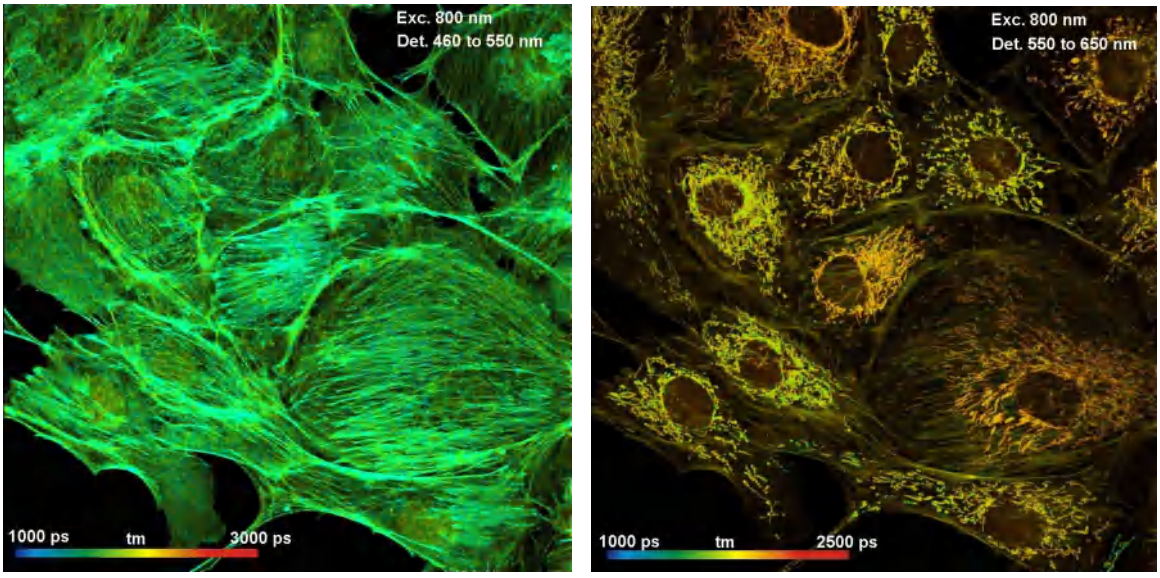


Fig. 110: Dual-channel detection. BPAE cells stained with Alexa 488 phalloidin and Mito Tracker Red. Left: 460 nm to 550 nm. Right: 550 nm to 650 nm.

Laser Wavelength Multiplexing

FLIM systems using the bh 'Laser Hub' can be operated in a fast excitation-wavelength multiplexing mode. Multiplexing can be performed frame-by frame, line by line, or even pixel by pixel. The advantage over pulse-interleaved excitation (PIE) is that there is absolutely no overlap between the multiplexing phases. Consequently, there is no intensity or lifetime crosstalk between signals excited by different wavelength. An example is shown in Fig. 550.

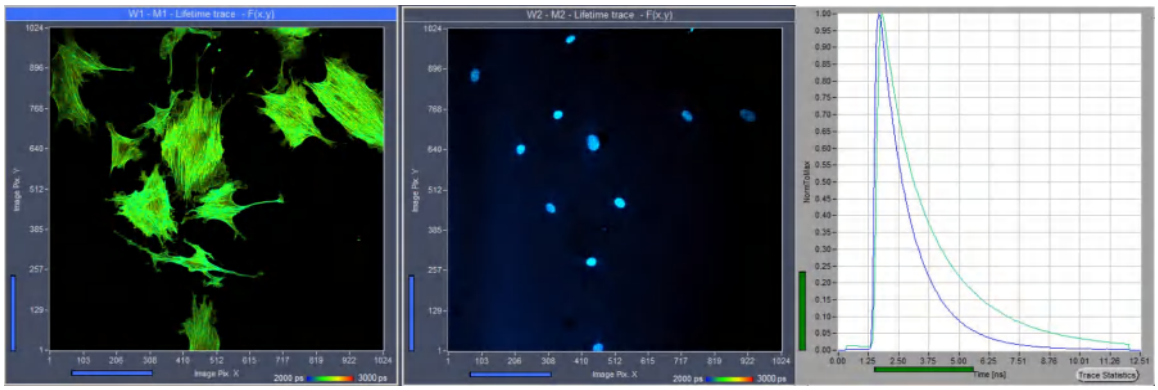


Fig. 111: FLIM with laser-wavelength multiplexing, 480 nm and 405 nm, Alexa 488 and DAPI. LSM 980 confocal system with bh LHB 104 laser hub

Multiphoton NDD FLIM: Deep Tissue Imaging

The bh Multiphoton FLIM systems use the non-descanned detection (NDD) path of the LSM 710/780/880/980 NLO or LSM 7 MP microscopes. With non-descanned detection, fluorescence photons scattered on the way out of the sample are detected far more efficiently than in a confocal system. The result is that clear images are obtained from deep tissue layers. An example is shown in Fig. 112.

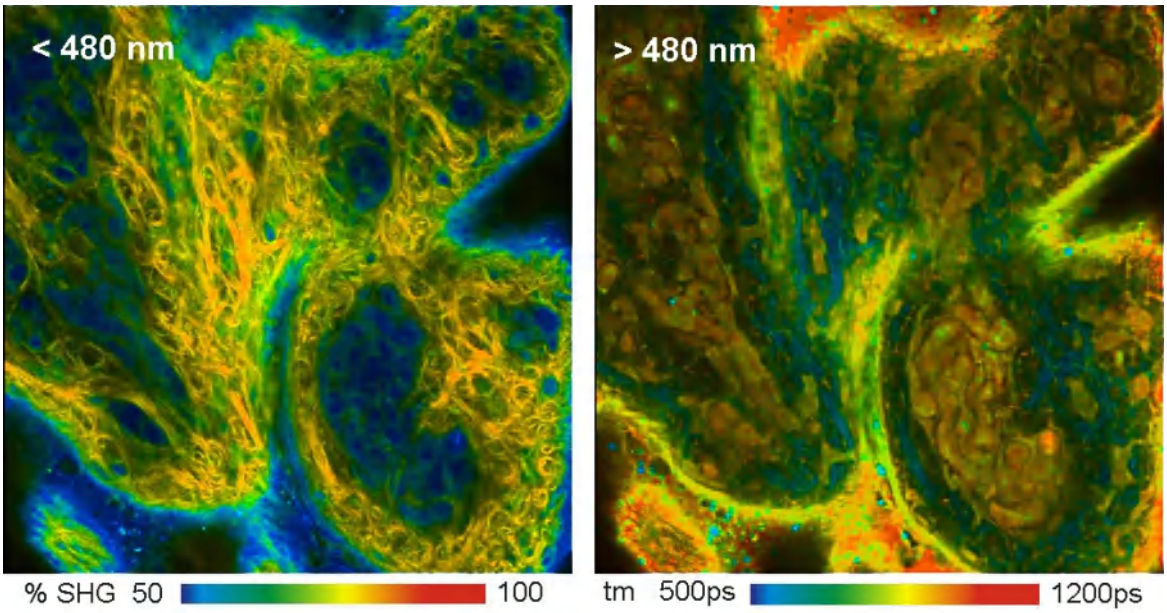


Fig. 112: Two-photon FLIM of pig skin. LSM 710 NLO, excitation 800 nm, HPM-100-40, NDD. Left: Wavelength channel <480 nm, colour shows percentage of SHG in the recorded signal. Right: Wavelength channel >480 nm, colour shows amplitude-weighted mean lifetime.

FLIM with Ultra-Fast Detectors

The instrument-response function of a multiphoton FLIM system with HPM-100-06 detectors has a full-width at half maximum (FWHM) of less than 20 ps [122]. The fast response greatly improves the accuracy at which fast decay components can be extracted from a multi-exponential decay. Applications are mainly in the field of metabolic FLIM, which requires separation of the decay components of bound and unbound NADH, and in the range of FRET, which requires the separation of interacting and non-interacting donor components. An NADH FLIM image recorded with an ultra-fast FLIM system on a Zeiss LSM 880 NLO is shown in Fig. 112. Images of the images of the amplitude ratio, a1/a2 (unbound/bound ratio), and of the fast (t_1, unbound NADH) and the slow decay component (t_2, bound NADH) are shown in Fig. 541.

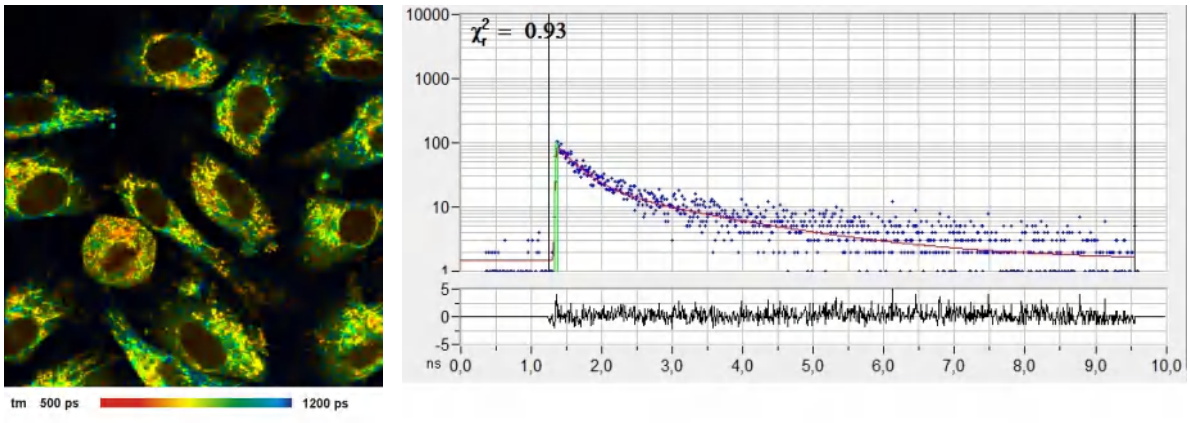


Fig. 113: Left: NADH Lifetime image, amplitude-weighted lifetime of double-exponential fit. Right: Decay curve in selected spot, 9 x 9 pixel area. FLIM data format 512 x 512 pixels, 1024 time channels. The IRF width is 19 ps, the time-channel width 10 ps.

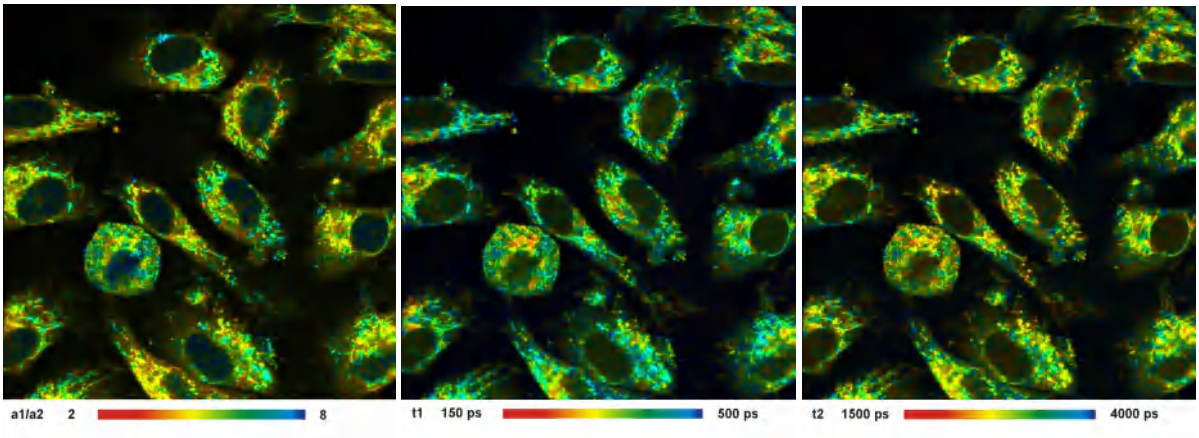


Fig. 114: Left to right: Images of the amplitude ratio, a_1/a_2 (unbound/bound ratio), and of the fast (t_1, unbound NADH) and the slow decay component (t2, bound NADH). FLIM data format 512 x 512 pixels, 1024 time channels. Time-channel width 10 ps.

With the fast detectors, the FLIM system is able to record lifetime images from fluorophores which have long be considered 'non-fluorescent'. Ultra-fast fluorescence decay in biological material is far more frequent than commonly believed. Prominent examples are carotenoids, which play a role in virtually all live organisms, and melanin, which is important to protect organisms from UV light. Please see sections 'Ultra-High Resolution FLIM Systems', page 362 and 'Ultra-Fast Fluorescence Decay in Biological Material', page 561 of this handbook.

Fig. 115 shows mushroom spores of *Cortinarius Mucosus*. An image of the amplitude-weighted lifetime, t_m, is shown on the left, a decay curve on the right. t_m is in the range from

20 to 40 ps, the lifetime of the fast component, t_1, in the range from 10 to 20 ps. No FLIM system of any other manufacturer is able to resolve such fast decay processes quantitatively.

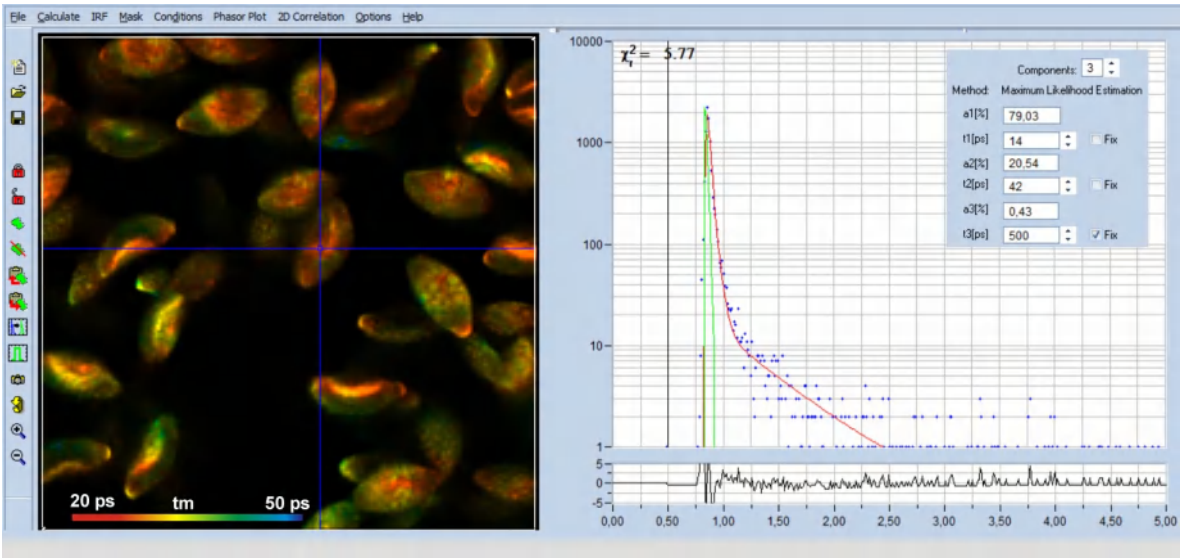


Fig. 115: Mushroom spores, *Cortinarius mucosus*, 2p excitation at 760 nm. Image of the amplitude-weighted lifetime, t_m, and decay curve at cursor position. t_m is in the range from 20 to 40 ps, t_1 is in the range from 10 to 20 ps.

Metabolic FLIM

Multiphoton Metabolic FLIM can be performed with all bh-Zeiss FLIM systems, for an NADH image please see Fig. 113 and Fig. 114. For NADH, the excitation source can be the Ti:Sa laser of an NLO system (tuned to 750 nm), or the 375-nm laser of a bh Laser Hub connected to an LSM 980 can be used. For FAD the Ti:Sa laser has to be tuned to 900 nm, or the 440 nm laser of the Laser Hub can be used. With Ti:Sa laser NADH and FAD images must be recorded sequentially, with the Laser Hub NADH and FAD recording can be multiplexed [70, 74].

Multiphoton Multispectral NDD FLIM

bh's MW FLIM is the world's first simultaneously detecting multiphoton multispectral NDD FLIM system. It uses an optical interface that connects to the NDD ports of the LSM 710/780/880/980 NLO microscopes [156]. A typical result is shown in Fig. 116.

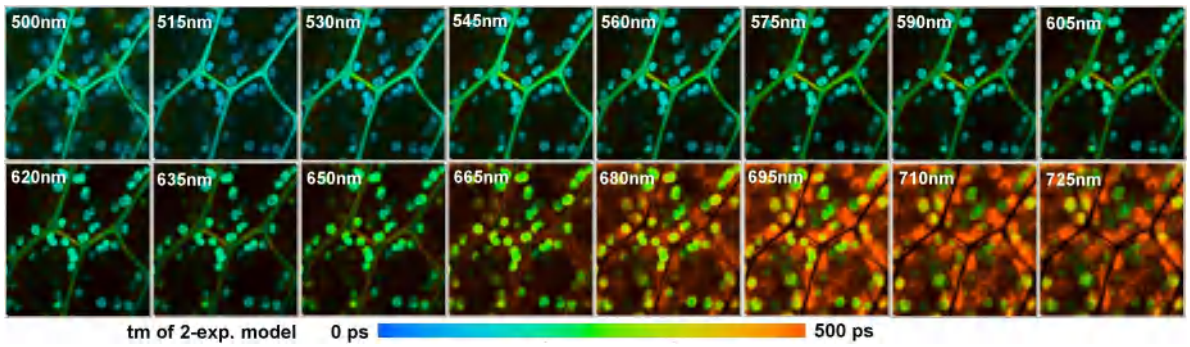


Fig. 116: Multiphoton Multispectral NDD FLIM. LSM 710 NLO, bh MW FLIM detector

Tuneable-excitation FLIM with Intune laser

Tuneable-excitation FLIM uses the 'Intune' laser of the Zeiss LSM 710/780 systems. FLIM of the same sample at different excitation wavelength can provide additional information on the composition of the fluorophores contained in it. In the past, beautiful FLIM images were obtained with the 'Intune' laser of the Zeiss LSM 710 systems. Examples are shown in Fig. 117. Regrettably, the Intune system has been discontinued by Zeiss. There is currently no system that delivers similar performance. The only system that comes close to it is the LSM 980 confocal FLIM system with the bh LHB-104 'Laser Hub', see Fig. 118.

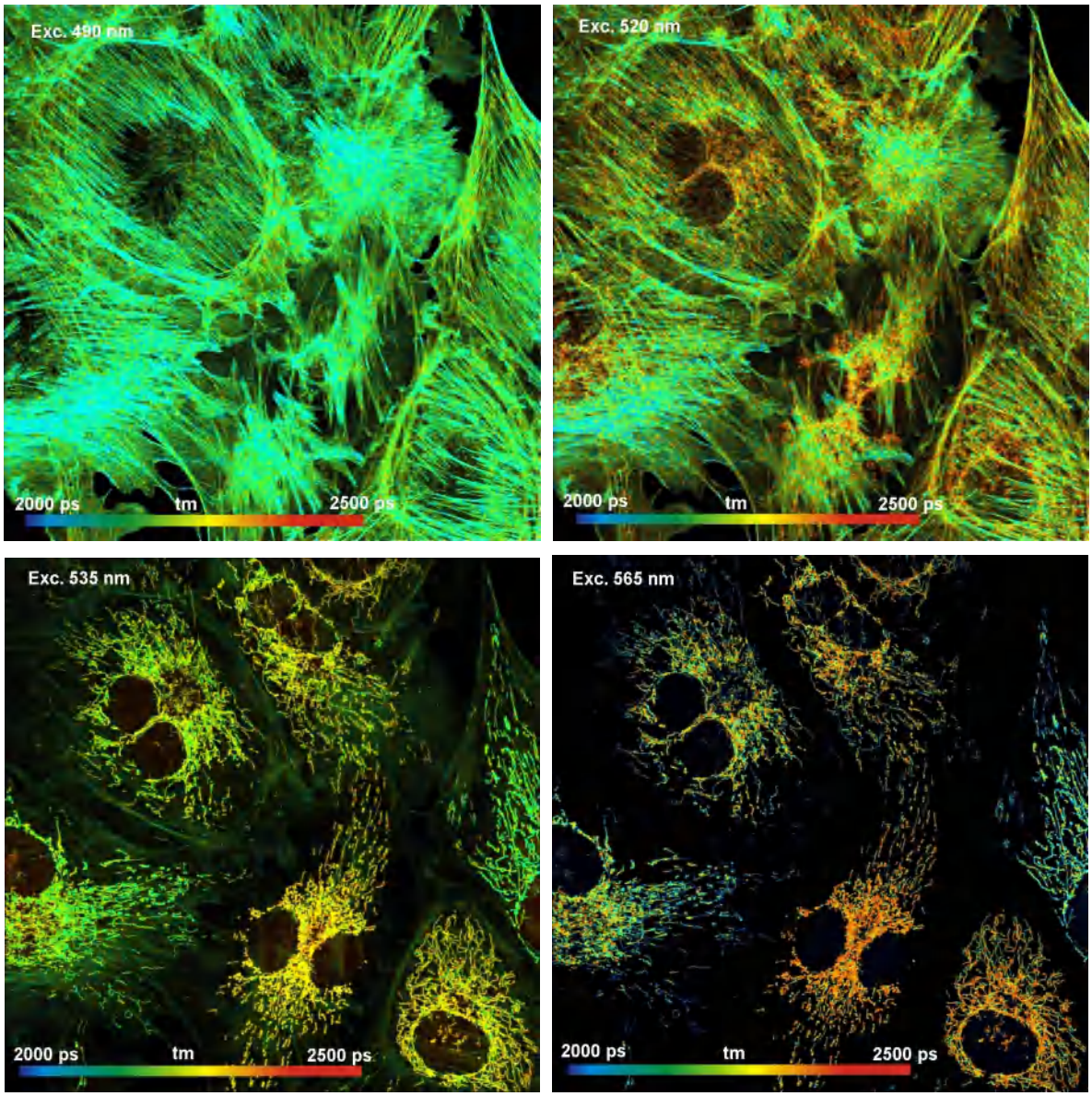


Fig. 117: Confocal FLIM with tuneable 'Intune' laser. BPAE cells stained with Alexa 488 phalloidin and Mito tracker red. Left to right: Excitation at 490 nm, 520 nm, 535 nm, and 556 nm.

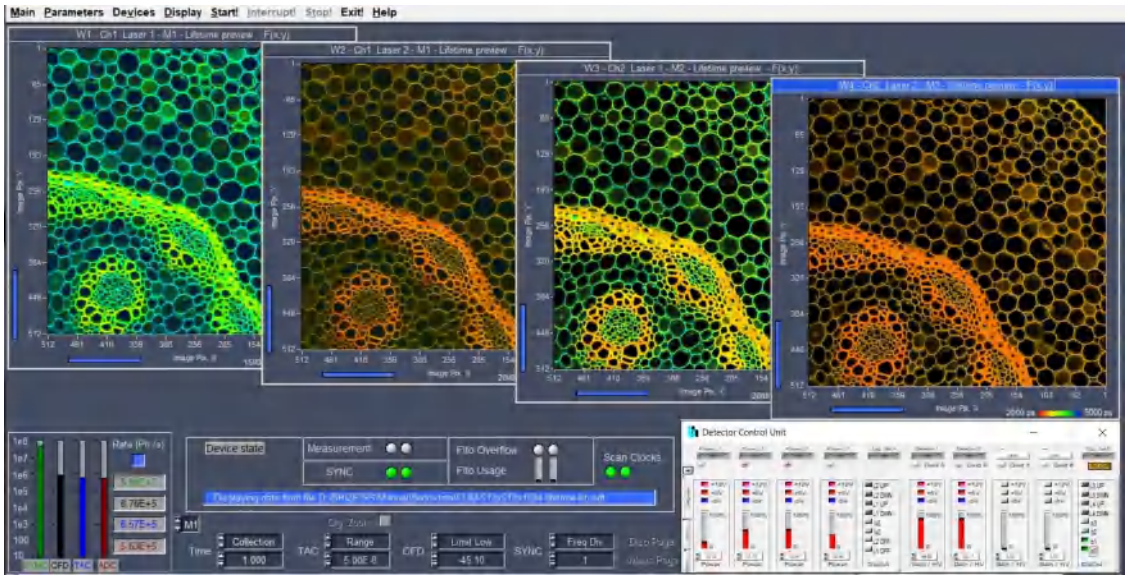


Fig. 118: FLIM at four combinations of excitation and emission wavelength. LSM 980 FLIM system with bh Laser Hub.

Z-Stack FLIM

For many years, Z-stack FLIM had been prevented by photobleaching and photodamage caused by the high excitation dose. With the LSM 710 to 980 family microscopes and the new GaAsP hybrid detectors photobleaching is no longer a problem. The FLIM system automatically acquires FLIM in consecutive Z planes and saves the data into a sequence of files. Z-stack FLIM is particularly interesting in combination with the deep-tissue imaging capability of multiphoton NDD FLIM. It can, however, be used also in combination with diode-laser FLIM and Intune FLIM. An example is shown in Fig. 119.

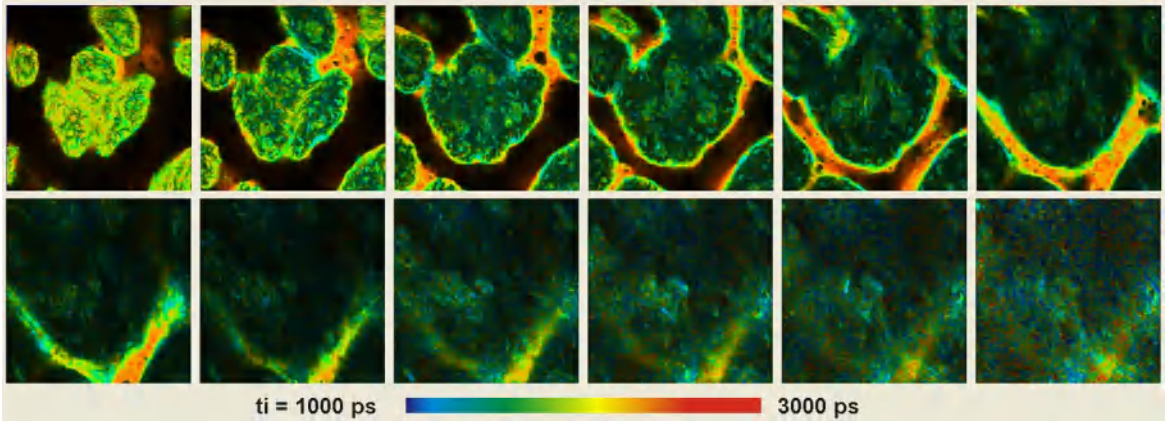


Fig. 119: Z-stack of FLIM images. Pig skin, autofluorescence, 5 µm to 60 µm below the surface. LSM 710 Multiphoton NDD FLIM, GaAsP hybrid detector

Time-Series FLIM

Time-series FLIM by the traditional record-and-save procedure is available for all system versions, and all detectors. Time-series FLIM can be recorded at a rate fast as 1 images per second, see Fig. 120.

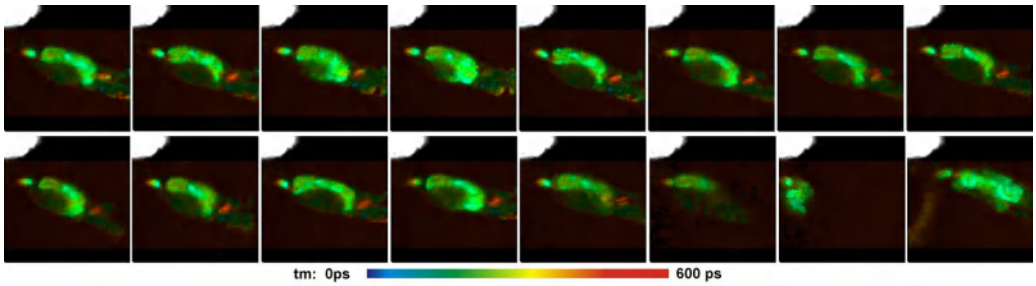


Fig. 120: Moving amoeba. Autofluorescence, acquisition time 0.5 s, image rate 1 image per second.

Mosaic FLIM

Mosaic FLIM records an array of FLIM images. The 'elements' of the mosaic may represent images for different lateral offset obtained by a sample-stepping device, images in different wavelength channels of a multi-wavelength detector, images in different depth of a sample, or images at different times after a stimulation of a sample. The entire mosaic is recorded into one single, large photon distribution. Mosaic FLIM can thus be used to increase the field of view of a high-NA microscope lens, to record multi-wavelength FLIM data, to record FLIM Z-stacks, or to record fast FLIM time series. An advantage is that no time for readout operations has to by reserved. This allows extremely fast time series to be recorded. A time series can even be accumulated, thus avoiding the need of trading lifetime accuracy against speed of the sequence. Examples of a spatial and a temporal mosaic are shown in Fig. 121. A Z stack recorded by mosaic FLIM is shown in Fig. 123.

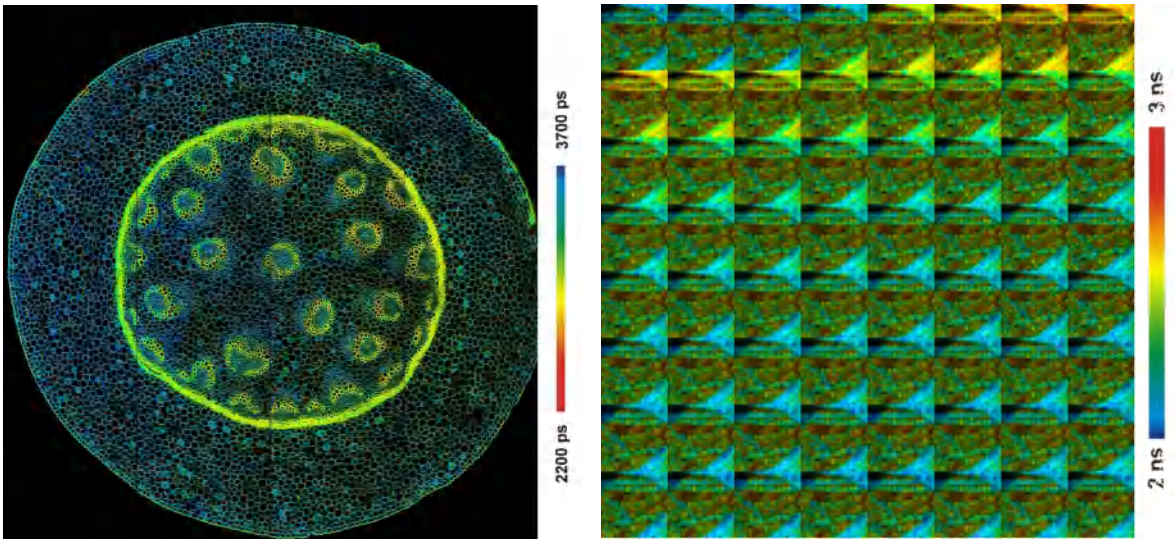


Fig. 121: Mosaic FLIM with the Zeiss LSM 710 / 780 / 880 microscopes. Left: Spatial mosaic, *convallaria* sample, 16 elements of 512 x 512 pixels, 256 time channels, entire mosaic is 2048 x 2048 x 256. Right: Temporal mosaic, Ca^{2+} transient in cultured neurons, electrical stimulation, 64 elements of 64 x 64 pixels, time per element 38 ms. 100 stimulation periods accumulated. Time runs from upper left to lower right, the stimulation was applied during the 4th element.

Near-Infrared FLIM

Near-infrared FLIM can be performed by using the Ti:Sa laser of a multiphoton (NLO) microscope as a one-photon excitation source [100, 169] or by two-photon excitation with an LSM 780 OPO system [101]. Please see page 384 for details. Images are shown in Fig. 122. Because near-infrared light penetrates thick layers of tissue images from deep sample layers

are recorded. This makes NIR FLIM especially attractive in combination with Z stack recording. An example is shown in Fig. 123.

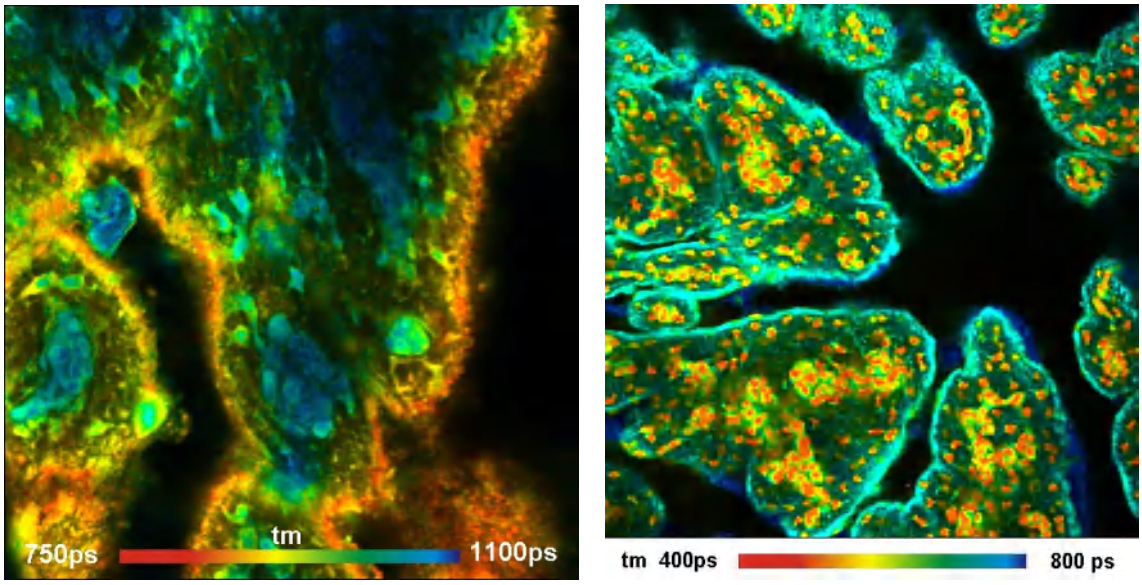


Fig. 122: Left: Pig skin sample stained with DTTCC. Zeiss LSM 710 NLO, one-photon excitation with Ti:Sa laser. Right: Pig skin stained with methylene blue. OPO system, two-photon excitation at 1200 nm

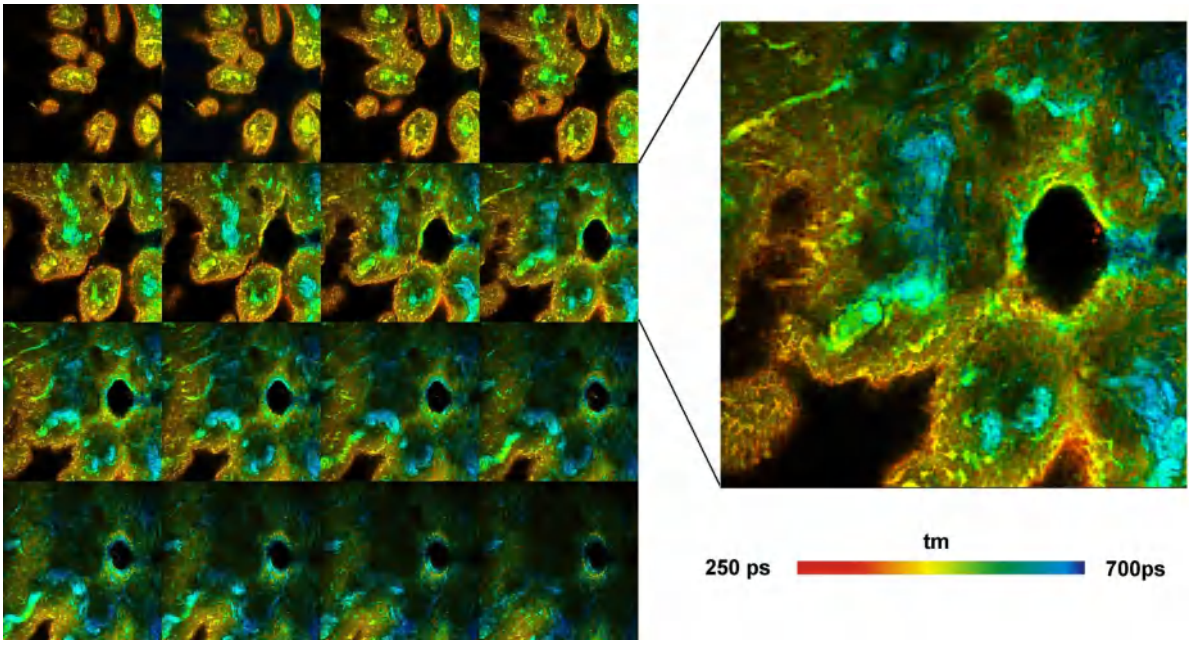


Fig. 123: Z stack recorded at a pig skin sample stained with Indocyanin Green. OPO excitation, Z-stack recorded by Mosaic FLIM, 16 planes from 0 to 60 µm from top of sample, each plane 512 x 512 pixels, 256 time channels.

Simultaneous FLIM / PLIM

In combination with the LSM 710 / 780 / 880 / 980 family multiphoton microscopes the bh FLIM systems are able to simultaneously record fluorescence and phosphorescence lifetime images. The technique is based on modulating the excitation laser synchronously with the pixel clock of the scanner. Photon times are determined both with reference to the laser pulses and the laser modulation pulse [104, 161]. Please see page 434 for details. A typical result is shown in Fig. 124.

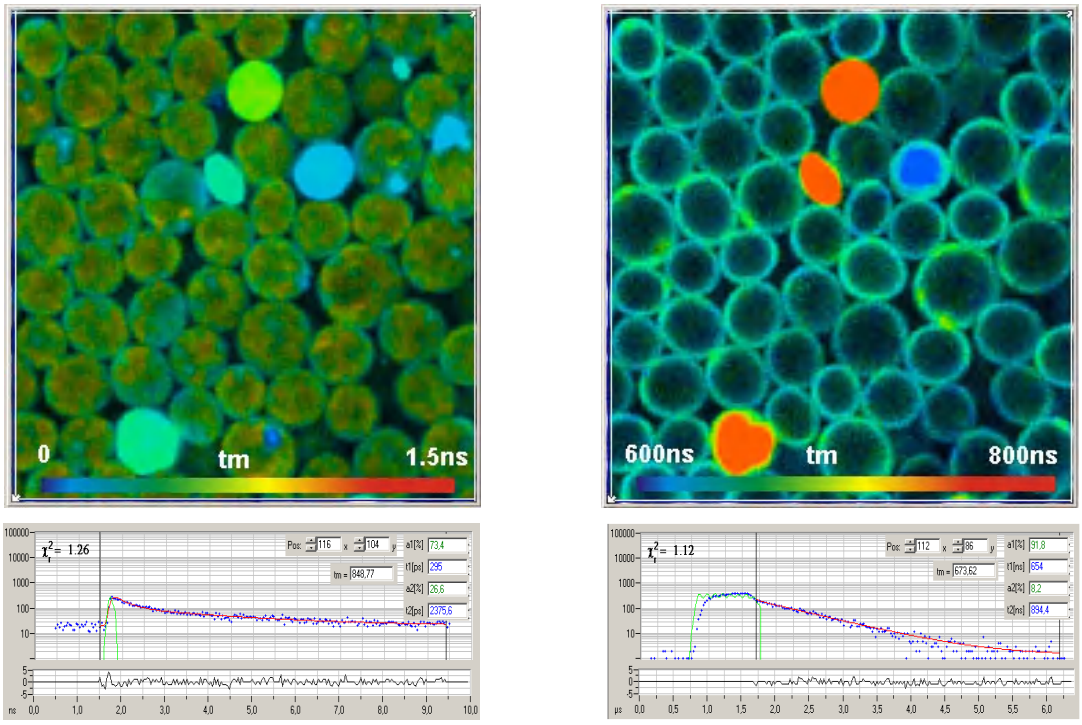


Fig. 124: Yeast cells stained with a Ruthenium dye. Left: FLIM image and fluorescence decay curve in selected spot. Right: PLIM image and phosphorescence decay curve in selected spot.

FLITS: Fluorescence Lifetime-Transient Scanning

FLITS records transient effects in the fluorescence lifetime of a sample along a one-dimensional scan. The maximum resolution at which lifetime changes can be recorded is given by the line scan time. With repetitive stimulation and triggered accumulation transient lifetime effects can be resolved at a resolution of about one millisecond [69, 113, 162]. Please see page 410. FLITS of the Ca^{2+} transients in cultured neurons on electrical stimulation is shown in Fig. 125.

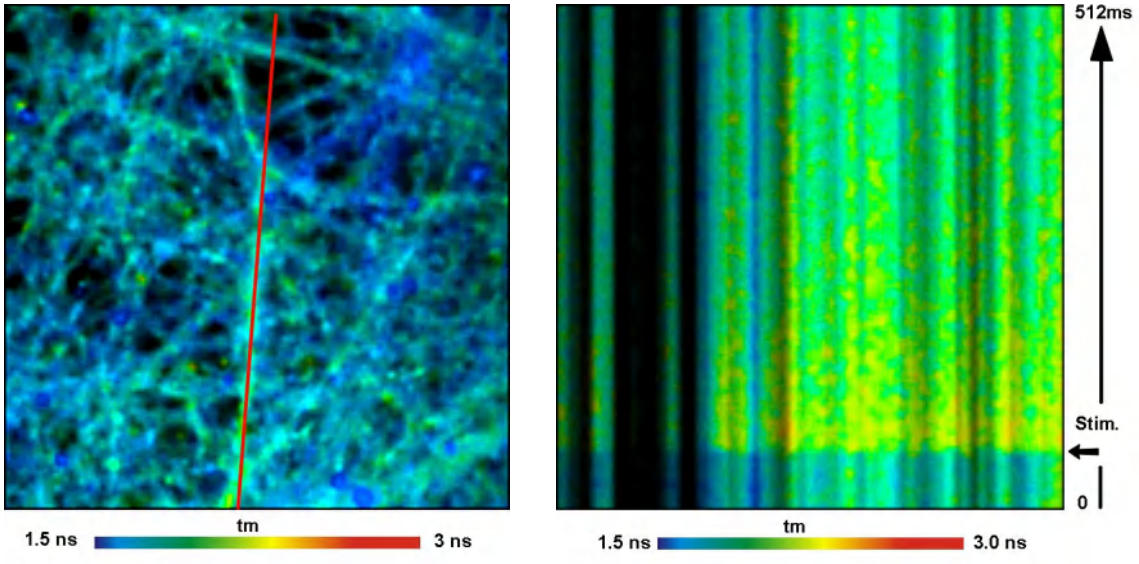


Fig. 125: FLITS of Ca^{2+} transient in cultured neurons. Left: FLIM image, location of one-dimensional FLITS scan indicated. Right: FLITS image, FLITS time scale 0 to 512 ms, resolution 2 ms, 200 stimulation periods accumulated.

FCS

The GaAsP hybrid detectors of the bh FLIM systems deliver highly efficient FCS. Because the detectors are free of afterpulsing diffusion times are obtained from a single detector, without the loss in correlation events that occurs when the signals from two detectors are cross-correlated. FCS can be obtained with the diode-laser systems, the Intune system, with the CW lasers of the LSM, and with the Ti:Sa laser of the multiphoton systems.

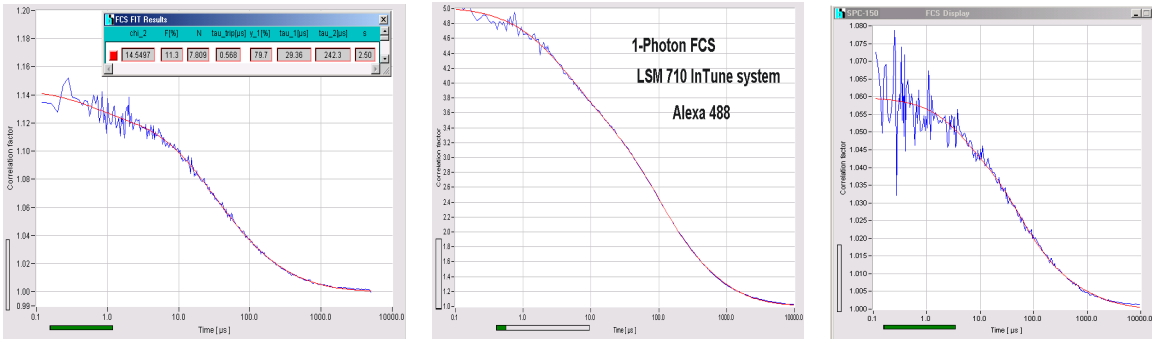


Fig. 126: FCS with GaAsP hybrid detectors. Left to right: Confocal FCS with ps diode laser, Confocal FCS with Intune laser, Two-photon NDD FCS

Data Analysis

SPCImage NG FLIM data analysis (see page 861) is integrated in the TCSPC software package delivered with the systems. For single-molecule burst-analysis bh 'Burst Analysis' software is available. Please see Fig. 179, page 95 and Fig. 187, page 99.

FLIM Systems for Leica SP2, SP5, and SP8 MP Laser Scanning Microscopes

Earlier FLIM systems for the Leica SP2, SP5 and SP8 MP [76, 87, 89] used bh HPM-100-40 hybrid detectors which were attached to the RLD port or to the X1 port of the microscopes. Recent FLIM systems use the Leica Hyd hybrid detectors. The single-photon pulses from these detectors are directly compatible with the inputs of the bh TCSPC FLIM modules. A non-descanned FLIM detector is shown in Fig. 127, left, a FLIM image recorded from a BPAE sample in Fig. 127, right.

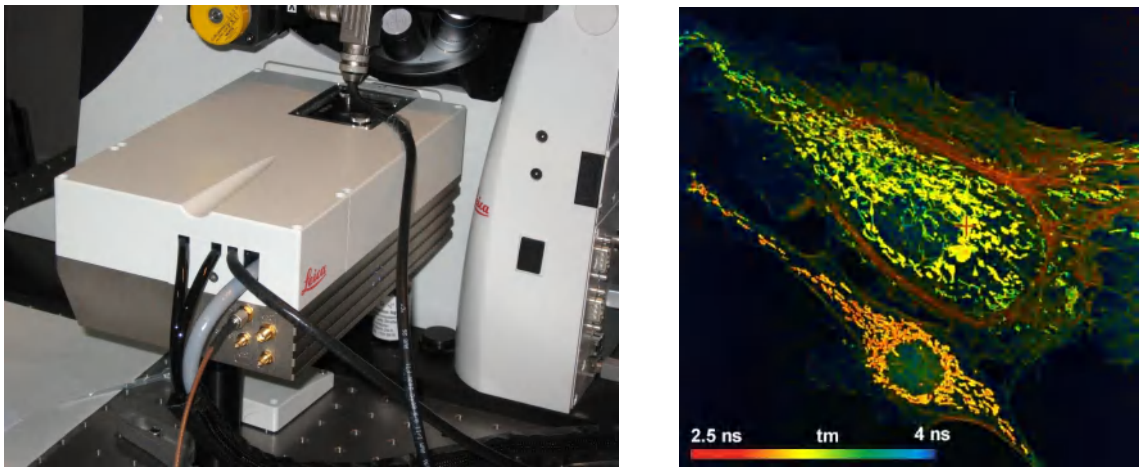


Fig. 127: Left: Leica dual-channel hybrid detector with FLIM outputs, at the non-descanned (RLD) port of an SP8 multiphoton microscope. Right: FLIM image recorded from a BPAE sample, 512 x 512 pixels, 256 time channels. bh Simple-Tau 152 TCSPC FLIM system

A frequent concern is that the sinusoidal scan used in the Leica SP5 and SP8 microscopes may cause a nonlinearity in the x coordinate of the FLIM images. This is, however not the case. The microscopes compensate for the nonlinearity of the scan by a variable pixel clock period. Since the bh FLIM systems use the pixel clock from the microscope to synchronise the acquisition with the scan the x coordinate of the image remains a linear function of the x coordinate of the sample [90, 168].

FLIM Systems for Olympus FV 300 and FV 1000

One-photon confocal FLIM systems

One-photon FLIM systems for the FV 1000 use one of the fibre inputs of the scan head to connect a bh BDL-SMC or -SMN picosecond diode laser [77, 81, 82]. The FLIM detectors are connected to a confocal output from the FV 1000 scan head. A wide variety of detectors can be used. PMTs are coupled directly, i.e. without any optical fibre, to the FV 1000. The fibre adapter is removed (or not installed altogether), and an a direct coupling optics attached instead. The FLIM beam pass contains a long-pass or bandpass filter and, in case of the R3809U detector, an electronically controlled shutter. Details are shown in Fig. 128.

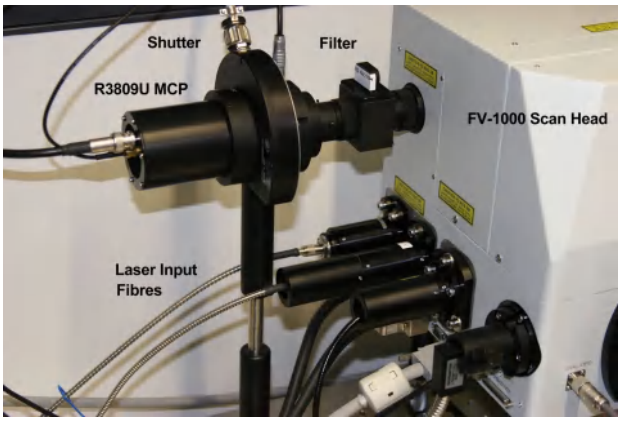


Fig. 128: Coupling an R3809U MCP PMT to the FV 1000 scan head

Multi-wavelength FLIM is possible by using the PML-SPEC spectral detection assembly [62], see page 189 and page 367 of this handbook. The PML-SPEC assembly can be connected both via the fibre output from the FV 1000 scan head or via a fibre bundle attached to the FLIM adapter for PMTs.

Multiphoton NDD FLIM Systems

Non-descanned FLIM systems are available for the inverted (IX) versions of the FV 300 and FV 1000 multiphoton microscopes. Once the Olympus NDD port is installed, the PMC-100 detector, the R3809, the HPM-100-40, or the MW FLIM detector can be used as shown in Fig. 129. A lifetime image obtained by a bh standard FLIM system attached to an FV 300 multiphoton is shown in Fig. 130. Please see [87, 91] for details.

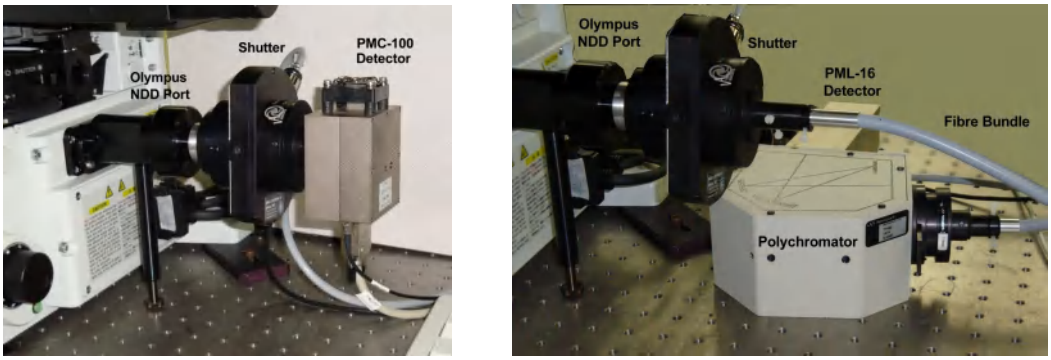


Fig. 129: FLIM detectors at the non-descanned port of an Olympus scanning microscope. Left: PMZ-100 detector. Right: Multi-wavelength FLIM detector.

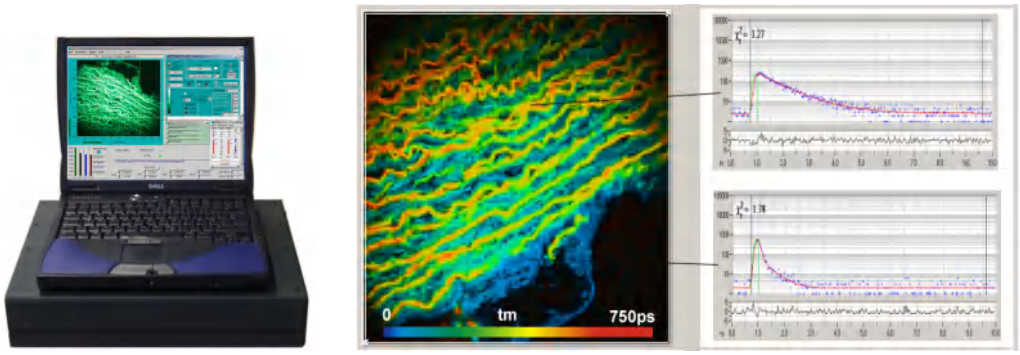


Fig. 130: Left: Simple-Tau 150 system for Olympus FV 300 or FV 1000 MP. Right: FLIM of heart tissue sample, fluorescence from endogenous fluorophores and SHG from the collagen in the tissue.

FLIM Systems for Nikon C1 and A1 Microscopes

bh FLIM systems are also available for the Nikon C1 and A1 laser scanning microscopes. One-photon FLIM systems use one or several BDL-SMN ps diode lasers for excitation. The lasers are connected to a fibre input port of the scan head. In confocal systems bh HPM-100-40 hybrid detectors are connected to the fibre output of the scanner, see Fig. 131, left. In multiphoton systems the detectors are preferably connected to an optional C-Mount NDD port at the Nikon non-descanned detector module, see Fig. 131, right. Multi-wavelength detectors are either coupled to the confocal port via a single optical fibre or to the NDD port via a fibre bundle.

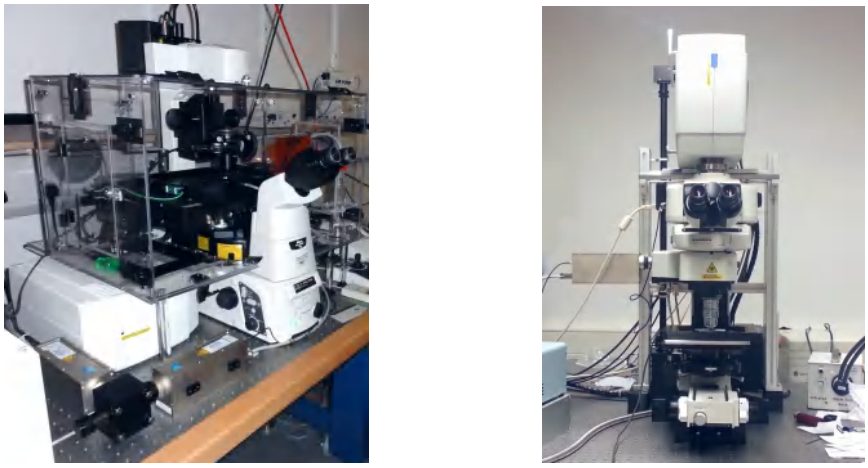


Fig. 131: Left: Confocal A1 system. Two hybrid detectors (lower left) connected to the confocal fibre port of the A2. Right: A2 multiphoton system. Hybrid detector (left) connected to the NDD detector module.

Nikon A1 Integrated FLIM Systems

FLIM operation with the bh TCSPC/FLIM modules has been implemented in the new 'NIS-Elements' software of the Nikon A1+ confocal laser scanning microscopes. The systems use one or two bh BDS-SM picosecond diode lasers, two bh HPM-100 hybrid detectors, and two fully parallel SPC-150N or NX TCSPC data recording channels. All FLIM components are controlled directly from Nikon's NIS-Elements software. Intensity images, FLIM images, and decay curves from regions of interest are displayed online. For precision multi-exponential data analysis, the system incorporates bh's SPCImage NG FLIM data analysis software. An example of the A1$^+$ instrument software panel with two FLIM channels opened is shown in Fig. 132. Details are described in [126], the application to FLIM-FRET measurements in [280].

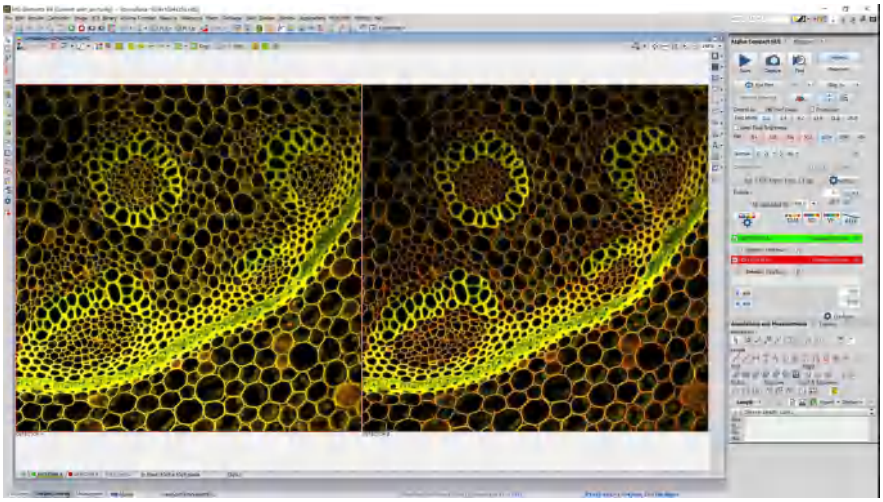


Fig. 132: Implementation of FLIM in Nikon's NIS-Elements software. Convallaria sample, scanned with 1024 x 1024 pixels, Lifetime by First-Moment analysis, images of both FLIM channels displayed.

FLIM Systems for Sutter MOM Microscopes

The Sutter Instrument MOM microscope [1213] is a modular platform for imaging deeply within live samples. It uses multi-photon excitation by a titanium-sapphire laser in combination with non-descanned detection. Due to its pulsed excitation source and its high modularity the MOM system can easily be combined with the bh TCSPC FLIM systems [106]. Up to four FLIM detectors can be attached to the system. The signals are processed in up to four entirely parallel TCSPC FLIM channels. A setup with two detectors is shown in Fig. 133. Due to the parallel system architecture, high photon count rates and short acquisition times can be achieved. FLIM data can be recorded with up to 1024 x 1024 pixels and 1024 time channels.

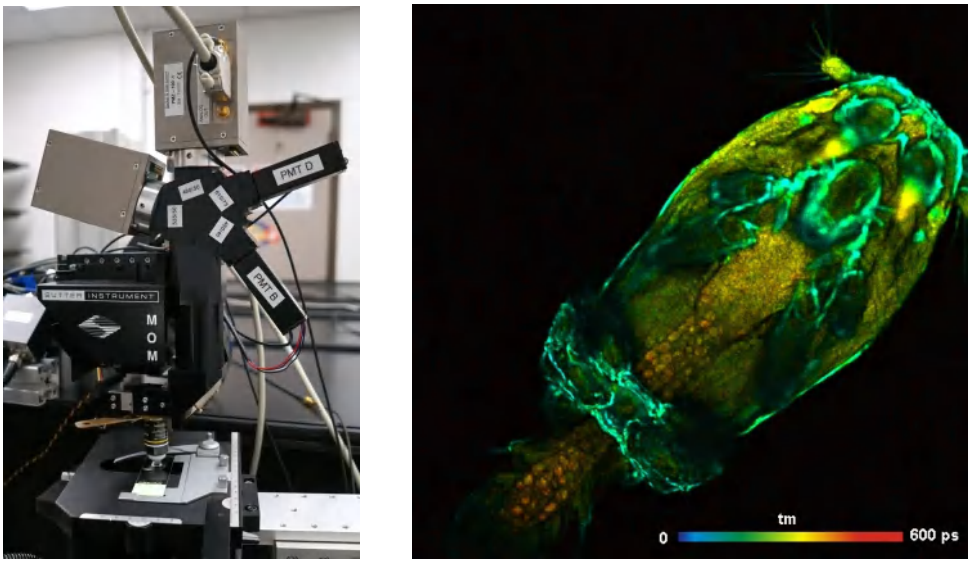


Fig. 133: Left: Two FLIM detectors attached to Sutter MOM microscope. Right: Salmon louse (*Lepeophtheirus Salmonis*), 512 x 512 pixels. Autofluorescence, excitation wavelength 750 nm, detection wavelength 440 to 480 nm. Amplitude-weighted lifetime of double-exponential decay.

The combination of the bh TCSPC-FLIM system with the Sutter MOM microscope is an efficient and flexible solution to fluorescence lifetime imaging of live cells and live tissues. The system can be used for all the typical FLIM applications, such as metabolic imaging by recording the fluorescence of NADH and FAD, protein interaction experiments by FLIM-FRET techniques, and ion concentration measurements with environment-sensitive fluorescent dyes. With an additional DDG-210 pulse generator card it can also record simultaneous FLIM / PLIM. For technical details and parameters setup please see [106].

FLIM Systems for Abberior STED System

The combination of the Abberior STED system [2] with the bh Simple-Tau TCSPC FLIM system records FLIM data at a spatial resolution of better than 40 nm [111, 112]. The FLIM system can either be integrated in the Abberior microscope software or operated independently via bh SPCM software. The image format can be as large as 2048 x 2048 pixels with 256 time channels per pixel. An image area of 40 x 40 micrometers can thus be covered with <20 nm pixel size, fully satisfying the Nyquist criterion. The system especially benefits from Windows 64-bit technology used both in the Abberior and in the bh data acquisition software, and the high data throughput of up to four parallel TCSPC FLIM channels. The system uses fast galvanometer scanning, and achieves peak count rates in excess of 5 MHz per FLIM channel, resulting in unprecedented signal-to-noise ratio and short acquisition time. The system can thus be used with the online-FLIM display function of the SPCM software. Technical

details are described in [111] and [112]. Please see also page 454 of this book. To our knowledge, the Abberior systems achieves the best spatial resolution and the best sensitivity of all STED systems currently available. This is probably a result of the dynamic wavefront correction used in the Abberior optics. A typical image is shown in Fig. 134.

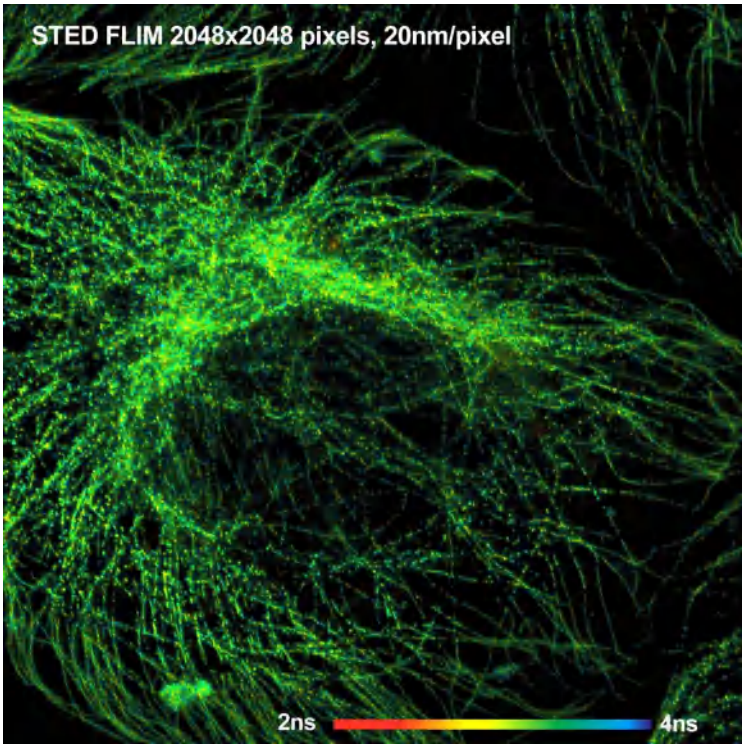


Fig. 134: FLIM image recorded with the Abberior - bh combination. Tubulin fibres in a BPAE cell, recorded with 2048 x 2048 pixels and 256 time channels per pixel.

PZ-FLIM-110 Piezo-Scanning FLIM System

The PZ-FLIM-110 Piezo Scanning FLIM system uses bh's multi-dimensional TCSPC technique in combination with a piezo scanner. The scanner is controlled via a bh GVD-120 scanner control card, the FLIM data are recorded by an SPC-150, SPC-150N, SPC-160, or SPC-180N TCSPC / FLIM module. Data acquisition is controlled by 64-bit bh SPCM TCSPC software. The system is able to run X-Y scans, X-Z (vertical) scans, and to record simultaneously FLIM and PLIM data. Maximum FLIM data formats are 512 x 512 pixels, 4096 time channels, or 2048 x 2048 pixels, 256 time channels.

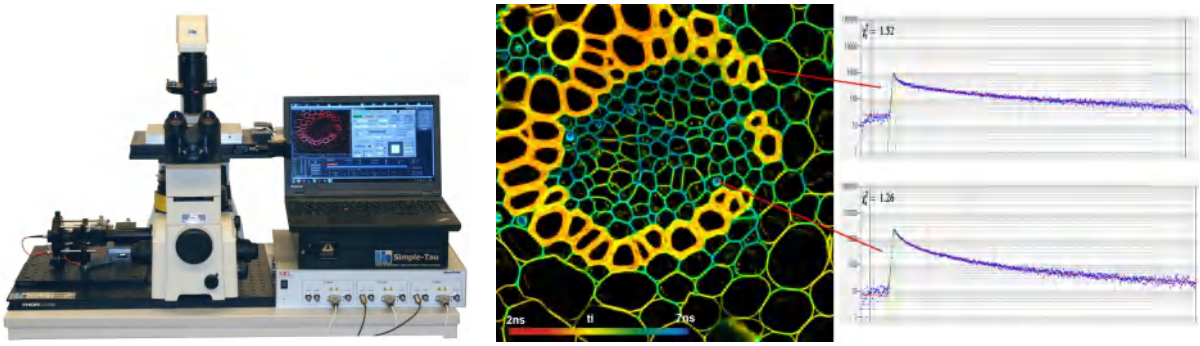


Fig. 135: Left: Photo of the bh PZ-FLIM-110 piezo scanning system. Right: Lifetime image of a convallaria sample. 512 x 512 pixels, 1024 time channels per pixel.

Sample scanning yields high efficiency and good optical resolution. Problems do, however, arise from the slow scan speed of the piezo stage. Under typical imaging conditions, the acquisition time is determined by the speed of the scanner, not by the time needed to acquire the

desired number of photons. Frame times for 512 x 512 pixel images are on the order of 100 seconds, frame times for 2048 x 2048 pixel images are at least 6 minutes. These scan times may be acceptable for high quality FLIM but not for imaging dynamic effects in a life sample. Moreover, the slow scan rate makes focusing into a defined image plane within a sample difficult. If these restrictions are taken into account the PZ-FLIM-110 is a cost-efficient alternative to a DCS-120 galvanometer scanner system. Please see [120] and page 451 of this book for technical details.

FASTAC Fast-Acquisition FLIM System

The bh Fast-Acquisition FLIM system uses four parallel TCSPC channels and a device that distributes the photon pulses of a single detector into the four recording channels. The principle is shown in Fig. 136, left. As usual, the photon pulses from the detector are passing a constant-fraction discriminator, CFD. The pulses from the CFD control a four-way switch that distributes the pulses to four TCSPC modules. Please see 'Fast FLIM Recording by the bh FASTAC System', page 420 for technical details.
The system features an electrical IRF width of less than 7 ps (FWHM), and a time channel width down to 405 fs. The optical time resolution with an HPM-100-06 or -07 hybrid detector is shorter than 25 ps (FWHM). FLIM data can be recorded at acquisition times down to the fastest frame times of the commonly used galvanometer scanners. The data are recorded with the TCSPC-typical number of time-channels of up to 4096, and with pixel numbers from 128 x 128 to 2048 x 2048 pixels. The system is therefore equally suitable for fast FLIM and precision FLIM applications [109, 110, 116].

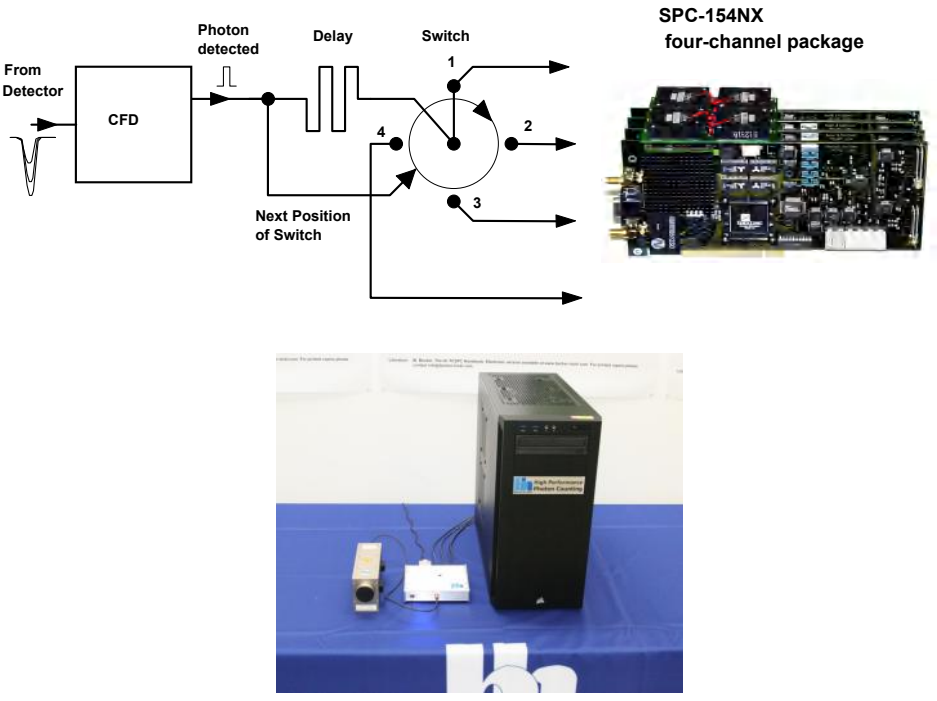


Fig. 136: FASTAC FLIM system.

The system runs in combination with any laser scanning system that uses fast beam scanning. Fig. 138, shows an images recorded in combination with a Zeiss LSM 880 NLO (1024 x 1024

pixels, 1024 time channels, Fig. 138 an image recorded with a DCS-120 MACRO system. The acquisition time was 10 seconds and 2 seconds, respectively.

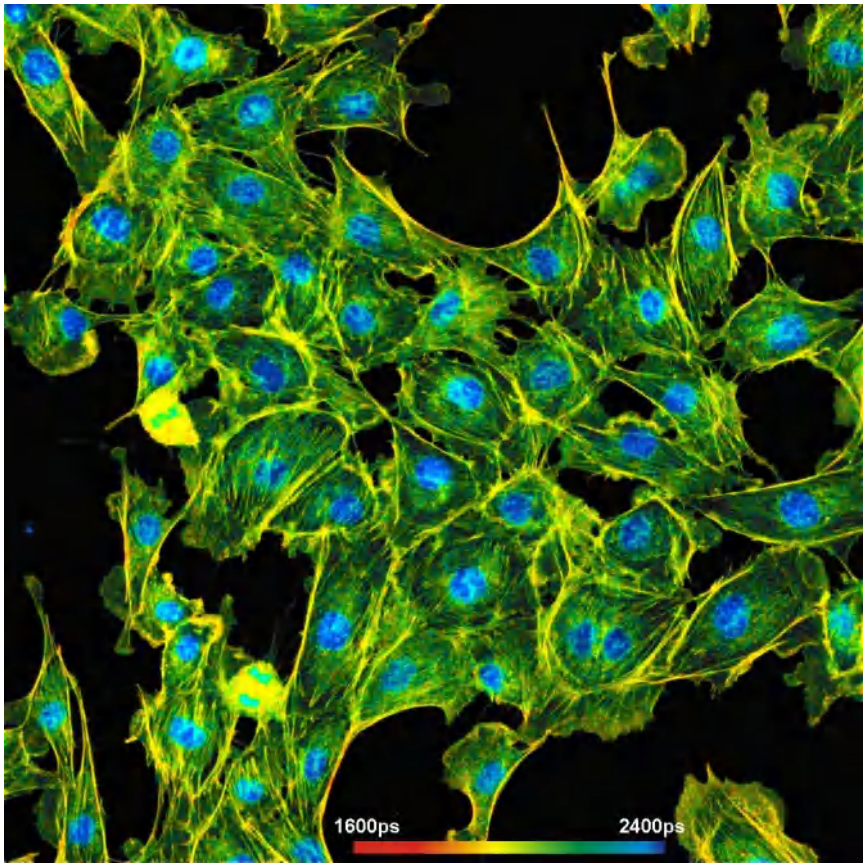


Fig. 137: FASTAC 1024x1024-pixel image recorded with a Zeiss LSM 880 NLO Acquisition time 10 seconds

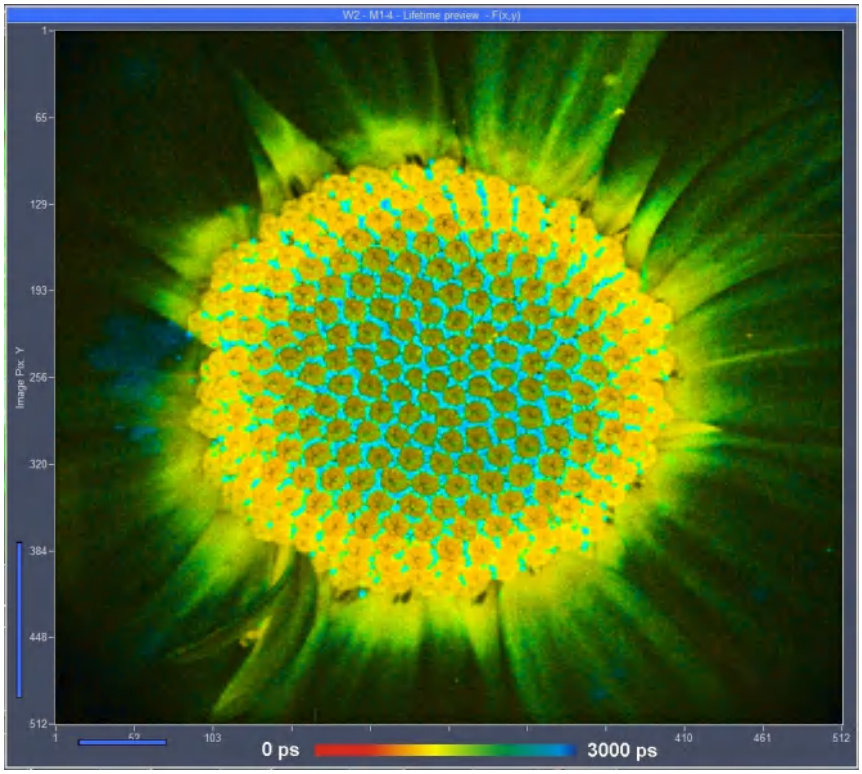


Fig. 138: 512 x 512-pixel image recorded with a DCS-120 MACRO system. Acquisition time 2 seconds.

Picosecond Diode Lasers

BH deliver a number of picosecond diode lasers with wavelengths from the NUV to the NIR [82, 81]. All lasers feature simple +12 V power supply, high repetition rate, short pulse width, and an extremely low electrical noise level. The complete driver electronics is integrated in the laser module. All bh diode laser modules are directly compatible with the bh TCSPC modules.

BDL-SMC Series Lasers

The bh BDL series lasers are manufactured in cooperation of bh and Lasos GmbH, Jena, Germany. The lasers are available for all the typical Diode laser wavelengths: 375 nm, 405 nm, 440 nm, 473 nm, 488 nm, 515 nm, 640 nm, 685 nm, and 785 nm [81]. The BDL lasers can be switched between three repetition rates and CW operation. The typical pulse width in the pulsed mode is 50 to 90 ps, see Fig. 139, right. The available power varies with the mode, the repetition rate, and the wavelength version. In the pulsed mode, the power for near-Gaussian pulse shape is in the range of 0.4 to 2 mW at 50 MHz repetition rate. The power in the CW mode is 20 to 60 mW. It is stabilised by an internal regulation loop to minimise drift and noise in the optical power. The lasers have the complete driver and control electronics integrated. They are running from a simple +12 V power supply. The bh BDL-SMC lasers are especially designed for application in laser scanning microscopy. They have a fast on/off control input to turn off the laser during the beam fly-back of the scanner, and to multiplex several laser of different wavelength. For efficient fibre coupling and for free-beam coupling into microscope systems the BDL-SMC series lasers have beam-profile and astigmatism correction, see Fig. 139. The beam is almost circular, with a diameter of 1 mm.

The corrected beams of the BDL-SMC lasers can be efficiently coupled into single-mode fibres. The coupling efficiency is 50 to 70 %. Versions with a Point-Source compatible fibre coupler [981], a Lasos coupler and with a permanently attached ('pig tail') fibre is available. A BDL-SMC laser, the beam profile, and typical pulse shapes are shown in Fig. 139. Lasers with different fibre coupling are shown in Fig. 140.

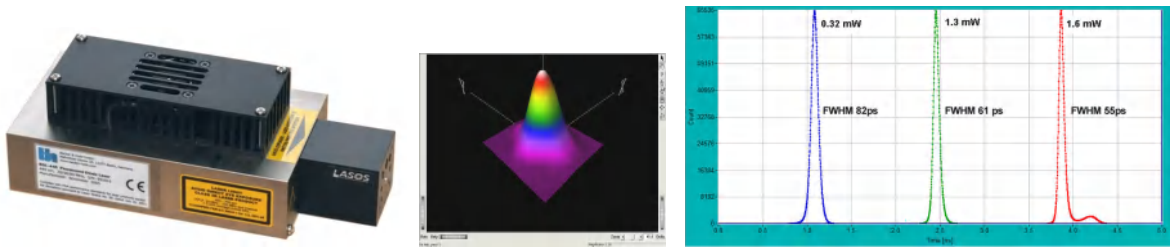


Fig. 139: BDL-SMC laser with beam-profile corrector (left), beam profile (middle) and typical pulse shapes for different average power at a repetition rate 50 MHz (right)

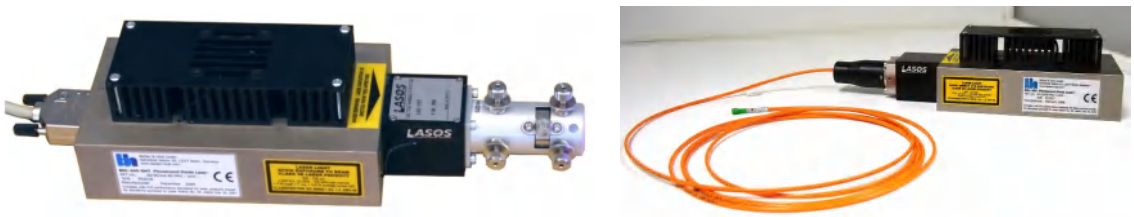


Fig. 140: BDL-SMC series laser with single-mode fibre coupler (left), and with fibre pigtail (right)

Since 2013, the BDL-SMC lasers have been more and more replaced with the more advanced BDL-SMN version. Please see section below.

BDL-SMN Series Lasers

The BDL-SMN lasers [81] are advanced successors of the BDL-SMC lasers. As the BDL-SMC lasers, they are manufactured in cooperation of bh and Lasos. The SMN lasers have the same mechanical dimensions, the same beam correction optics, and the same control features as the SMC-Lasers. However, there are several advanced features.

The optical power is stabilised by an internal regulation loop also in the pulsed mode. The result is low optical noise and excellent power stability both in the CW and in the pulsed mode, and a strictly linear power control characteristic. The SMN lasers use improved driver electronics, resulting in improved pulsed shape at high pulse power. The SMN lasers can thus be run at substantially higher power than the SMC lasers. For some laser wavelengths, an average power of 8 mW (at 80 MHz) can be reached. The pulse width at medium power is typically 50 to 80 ps. It usually stays below 200 ps up to 4 to 8 mW. Please see Fig. 142.

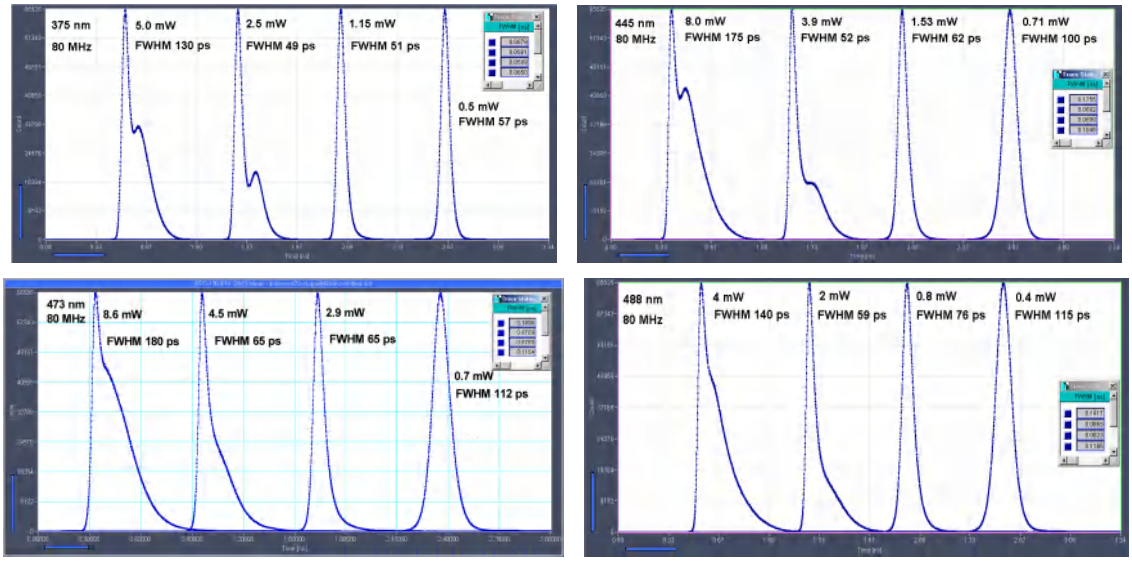


Fig. 141: BDL-SMN laser, pulse shapes for four typical laser wavelengths. 80 MHz, power measured in free beam.

The lasers have a synchronisation output to bh TCSPC modules, and a trigger input for synchronisation with other BDL-SMN lasers or other pulsed excitation sources. As the SMC lasers, the SMN version is available with a free-beam output and with various single-mode fibre couplers, see Fig. 141.



Fig. 142: BDL-SMN lasers

The BDL-Series lasers are part of the bh FLIM systems for laser scanning microscopes [69, 76, 77]. The are also used in the bh DCS-120 Confocal Scanning FLIM System [68]. There are separate manuals for the BDL-SMC and the BDL-SMN lasers, please see [81] and [82].

BDS-SM Series Lasers

The BDS-SM lasers [83] are OEM Modules with a size of only 40 mm x 40 mm x 110 mm. The lasers contain the entire driver electronics. They are operated from a simple +12 V power supply.

The BDS ps diode lasers are available both with free-beam and single-mode fibre output. The pulse width is on the order of 50 to 90 ps, the pulse repetition rate can be switched between 80 MHz, 50 MHz, 20 MHz, and CW. All the typical diode laser wavelengths from 375 nm to 785 nm are available. The BDS lasers use the same driver principle as the BDL-SMN lasers. Thus, high optical power at good pulse shape is available, see Fig. 143. The output power is stabilised by an internal regulation loop, and fast on-off switching is implemented. The lasers have a synchronisation output to the bh TCSPC modules and a trigger input for synchronisation with other pulsed lasers.

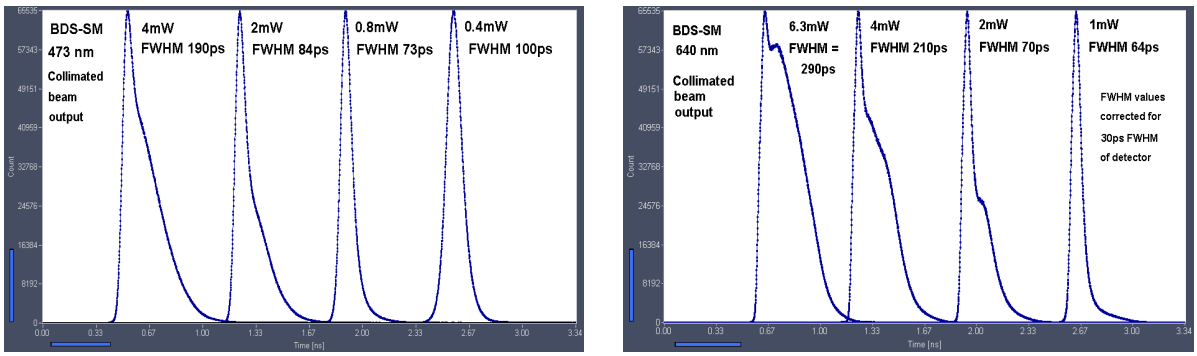


Fig. 143: BDS-SM laser, pulse shape for different output power. 473 nm and 640 nm, power measured at fibre output.



Fig. 144: BDS-SM series laser with pig-tail single-mode fibre, Qioptiq Kineflex adapter, Lasos Precision Connector, and free-beam output through C-Mount adapter

40-ps BDS-SM Versions

Over several years, improvement in laser diode performance has resulted in a constant decrease in the pulse width of the BDS-SM lasers. Currently, the 375 nm, 405 nm, and 445 nm versions achieve pulse widths of less than 40 ps. These pulse widths are achieved in an inten-

sity range where the lasers deliver clean pulse shapes, without much afterpulsing or large shoulders. Examples are shown in Fig. 145.

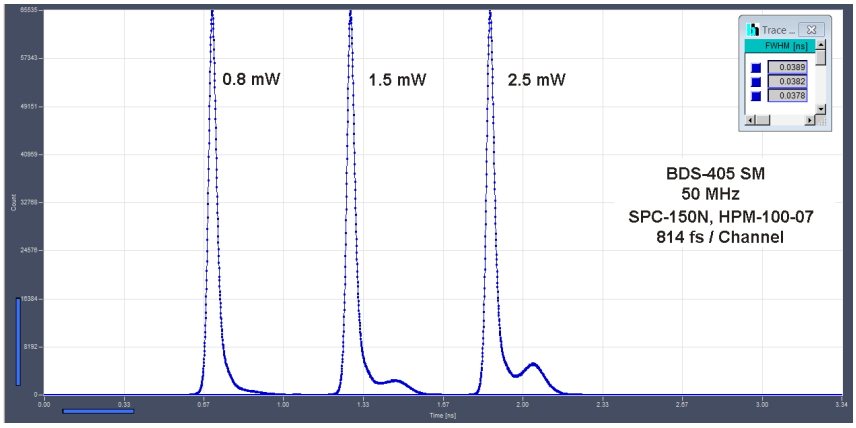


Fig. 145: Pulse shapes of a 405 nm BDS-SM laser. SPC-150N with HPM-100-07 detector. The recorded FWHMs are below 40 ps, corrected for the detector IRF of 19 ps the laser pulse width is about 35 ps.

BDU-SM Lasers

The BDU-SM family picosecond / CW diode lasers are fully controlled and powered via a USB interface. Available wavelengths range from 375 nm to 780 nm. The lasers are available with elliptical or circular free-beam output, and with single-mode fibre output. As the BDS-SM family lasers, the BDU laser feature extraordinarily high timing stability and intensity stability. Repetition rates are 20, 40, 80 MHz, or CW. Optical power at 80 MHz is typically 3 to 5 mW. Pulse width is 40 ps to 300 ps, depending on the wavelength version and selected power. A BDU-SM laser, a typical pulse shape, and the software-control panel are shown in Fig. 146.

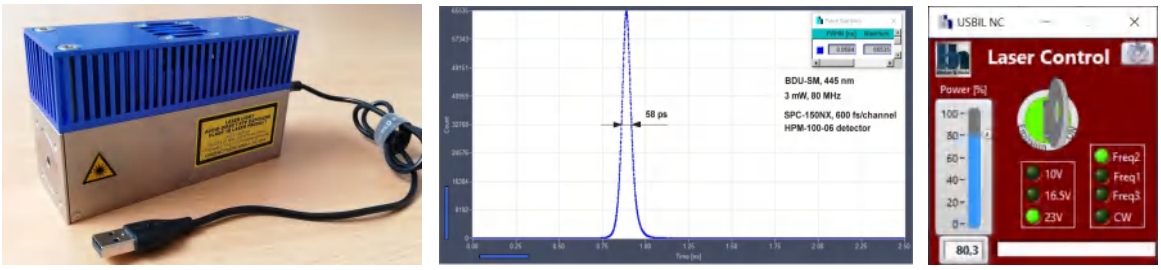


Fig. 146: BDU-SM laser, pulse shape of 445-nm laser at 80 MHZ, 3 MW, software panel

BDS-MM Series Lasers

The BDS-MM lasers [84] are multi-mode versions of the BDS-SM lasers. Depending on the wavelength version, the CW equivalent power at 50 MHz repetition rate can be as high as 20 to 50 mW. In most cases, the pulse shape remains free of tails and afterpulses up to more than 10 mW. A few compromises had to be made, however: Due to limitations in power dissipation the MM lasers have no CW mode, and no 80 MHz range. The output beam is not single-mode, and cannot be focused into a diffraction-limited spot. It is thus difficult to focus into optical fibres. Single-mode fibre coupling is not possible at all. If possible, the BDS-MM lasers should be used with free-beam optics or, if fibre coupling is unavoidable, with multi-mode fibres with core diameters of 200 µm or larger.

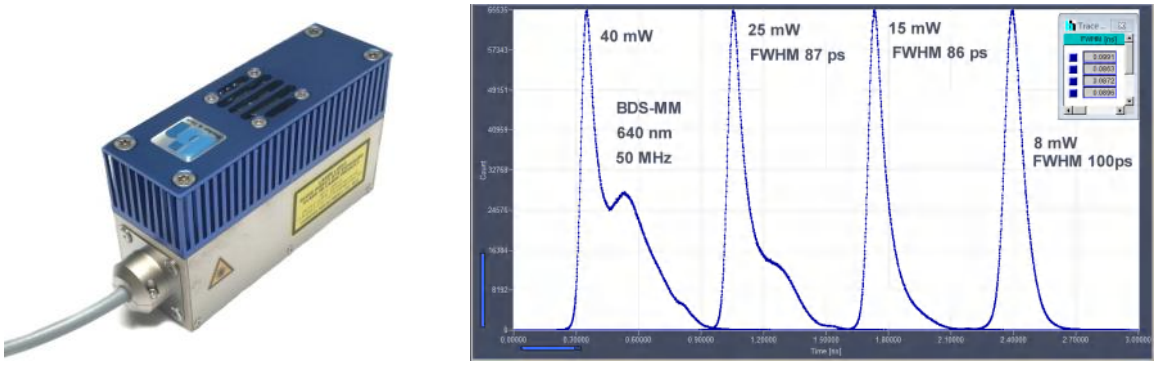


Fig. 147: Left: BDS-MM laser, with 200 µm fibre. Right: Pulse shape for a 640-nm version. Indicated power is for 50 MHz repetition rate, and measured in free beam.

LSB-C and LSB-C2 Laser Switch Boxes

LSB-C and LSB-C2 laser switch boxes provide control signals to one or two BDS or BDL lasers. The devices contain an intensity regulator, a switch to select the repetition rate, the mandatory key switch, and inputs for various external control signals. The LSB-C and LSB-C2 switch boxes are shown in Fig. 148.



Fig. 148: LSB-C and LSB-C2 laser switch boxes for one and two BDS or BDL lasers

LHB-104 'Laser Hub'

The LHB-104 ‘Laser Hub’ contains up to four BDS-SM lasers. The beams of the individual lasers are combined into a single free-beam output or into a single optical (single-mode) fibre. The box contains control electronics equivalent to the LSB-C and LSB-C2 Laser Switch boxes. In addition, it contains wavelength-multiplexing electronics, inputs for control signals, and outputs for the synchronisation and routing signals to SPC modules. The LHB-104 is part of the bh FLIM systems for the Zeiss LSM 980 microscopes [70], see page 50. The LHB-104 'Laser Hub' is shown in Fig. 149, a handbook [74] is available at www.becker-hickl.com.



Fig. 149: LHB-104 'Laser Hub'

Laser Optics

Laser Beam Combiner

A laser beam combiner is available for up to four lasers of different wavelength. The beams from four single-mode fibres are combined into a single collimated output beam or a single-mode fibre. The beam combiner is permanently aligned.

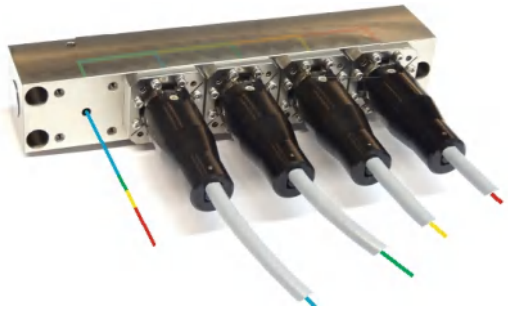


Fig. 150: Beam combiner for four lasers

Acousto-Optical Modulator for Ti:Sa Laser

An AOM (Acousto-Optical Modulator) for the Ti:Sa lasers of multiphoton laser scanning microscopes is available from bh, see Fig. 151, left. The AOM is part of the DCS-120 MP system but can also be used for other applications that require control or modulation of a femtosecond laser. The control of the Ti:Sa laser and the control of the AOM are integrated in the same SPCM software panel, see Fig. 151, right. This way, the driver frequency of the AOM is automatically adjusted to the wavelength of the laser. Please see page 858 for details.

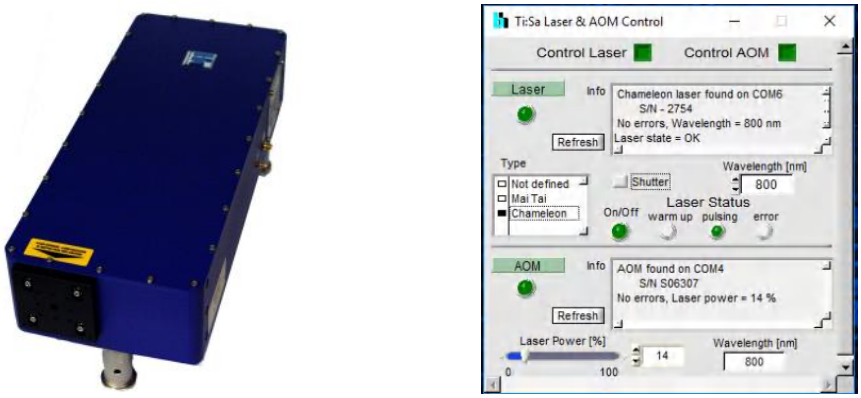


Fig. 151: Left: AOM for Ti:Sa lasers. Right: Control panel in the SPCM data acquisition software.

Laser Control Electronics

Laser Power Control via DCC-120 Module

The DCC-100 card (see Fig. 166, page 88) is able to control the output power of one or two bh ps diode lasers. For systems with one laser and one detector both can be controlled by a single DCC-100 card. For details, please see page 212 and page 854 of this handbook.

Laser Multiplexing by DDG-210 Module

For on-off modulation and multiplexing of the BDL and the BDS series lasers the DDG-210 and DDG-220 digital delay generators are available. The devices provide on/off signals for up to four lasers and the corresponding routing signals for the TCSPC module.



Fig. 152: DDG-210 and DDG-220 digital delay generators

On/off modulation is used to record fluorescence signals, time-of-flight distributions, and FLIM images for several excitation wavelengths simultaneously. It is also used for simultaneous fluorescence and phosphorescence decay detection and simultaneous FLIM / PLIM. Please see page 434 and page 857 of this handbook.

The frequency of the multiplexing sequence and the duty cycle of the individual lasers within the sequence are fully programmable. The sequence can also be triggered, such as to synchronise laser on/off operation with the pixel clock of a scanner.

Laser Control via GVD-120 Scan Controller

bh ps diode lasers can also be controlled by the GVD-120 scan controller card. The GVD-120 controls both axis of a galvanometer scanner, and two lasers. It provides for intensity control, beam blanking in the flyback phases of the scanner, laser multiplexing within one pixel, or between subsequent lines and subsequent frames. Pixel-synchronous on-off modulation for FLIM / PLIM is provided within the individual pixels. A photo of the GVD-120 is shown in Fig. 172, page 91. For a description of the GVD functions please see [68] and page 849 of this handbook.

Detectors

The bh TCSPC modules can be used with almost any photon counting detector. For reasonable operation it is only required that the detector delivers a reasonably fast and stable single-electron response. This section gives a brief description of the detectors typically used with the bh photon counters. For a detailed description and discussion of the parameters of various detectors please see section 'Detectors for TCSPC'.

PMT modules

In earlier TCSPC applications often the bh PMH-100 detector head was used, see Fig. 153, left. This device contained a fast, small PMT, the high voltage generator and a preamplifier in a 32 x 38 x 92mm housing. The PMH-100 was powered directly from an SPC module or a DCC-100 card. By now, the PMH-100 has almost entirely been replaced with more advanced detectors.

The PMC-100, shown in Fig. 153, middle, is a cooled version of the PMH-100. The PMC-100 is fully controlled via the bh DCC-100 detector controller, see Fig. 166. The DCC-100 provides for power supply, gain control, and overload shutdown. The PMC detector comes in

different cathode versions. The PMC-100-0 has a bialkali cathode with good efficiency in the wavelength range from 330 to 600 nm. The PMC-100-1 has a bialkali cathode. This cathode can be used from about 330 to 800 nm. UV-sensitive versions are available as well. The PMC-100-20 has a 'high efficiency extended-red' multialkali cathode. This cathode works up to almost 900 nm and red and near-infrared range yields a noticeably higher sensitivity than the conventional multialkali cathode.

Since 2016, there is an improved version of the PMC-100 detectors. The new PMC-150 detectors are functionally identical with the PMC-100 but contain PMTs with higher cathode efficiency and better time resolution. Please see page 175 of this book.

The PMZ-100 (Fig. 153, right) was originally designed as a FLIM detector for the NDD ports Zeiss LSM 710 NLO microscopes. It has its active area very close to the front face, and an adapter to the LSM 710 NDD ports. In the meantime, it has almost entirely been replaced with HPM-100 hybrid detectors. Currently, the PMZ-100 modules are used as FLIM detectors for the Sutter MOM microscopes where the HPM-100 detectors are to large and heavy. Also the PMZ-100 has been upgraded by new PMTs, and thus got improved sensitivity and time resolution.

The PMCS-150, shown in Fig. 154, has been designed for TCSPC systems with a large number of parallel channels. In these applications it is important that the detector is physically small and does not require external control signals. The PMCS therefore has pre-set cooling, pre-set gain and internal overload shutdown. It runs off a simple +12 V power supply. Size is 40 x 40 x 120 mm.

All these detectors have an exceptionally stable timing response function at high count rates, see [154]. Please see chapter 'Detectors for TCSPC' of this handbook.



Fig. 153: Left to right: PMH-100, PMC-150 and PMZ-100 PMT modules



Fig. 154: PMCS-150 detector.

Microchannel Plate PMTs

For several decades, fastest available single-photon detectors were MCP PMTs of the Hamamatsu R3809U family. An detector-shutter assembly with an R3809U is shown in Fig. 155. The R3809U needs a high-voltage power supply that delivers an operating voltage of -3000 V. A power supply module is available from bh, see Fig. 155, right. The module is controlled via the bh DCC-100 detector controller.



Fig. 155: R3809U MCP PMT (left) and bh HVM-100 power supply module (right)

The R3809U is commonly believed to deliver about 25 to 30 ps (FWHM) instrument response width in TCSPC applications. Recent experiments with the bh SPC-150NX modules have shown that the detectors are even faster: IRF measurements with a 100 fs fibre lasers showed than an IRF width of <20 ps can be achieved [122]. Please see page 169 of this book.

HPM-100 Hybrid Detector Modules

Hybrid detectors are currently the most promising light sensors for TCSPC. The detectors are extremely sensitive, have a clean TCSPC response function, and are free of afterpulsing background [85, 159]. Recently, it turned out that some hybrid detectors (with bi-alkali and multialkali cathodes) yield sub-20 ps FWHM instrument response width [122]. Please see section 'Description of Selected Detectors' of this handbook. Bare hybrid detector tubes are difficult to use because the output pulse amplitude is low, and a cathode voltage of -8000 V is needed. The detectors can only be reasonably used if the tube, the preamplifier, and the high voltage generators are integrated in a perfectly shielded housing. bh deliver several versions of hybrid detector modules: The HPM-100-40 with a GaAsP cathode, the HPM-100-50 with a GaAs cathode, and the HPM-100-06 and HPM-100-07 with bi-alkali and multialkali cathodes. The HPM-100 modules are available with different diameter of the active area, with C-Mount adapters, with fibre adapters, and with adapters to the Zeiss LSM 710/780/880 family laser scanning microscopes. Cooled versions are available as well, see Fig. 156. All HPM-100 detectors are controlled by the DCC-100 detector controller. Please see page 178 for details.



Fig. 156: bh HPM-100 hybrid detectors

Multi-Channel PMTs and Multi-Wavelength Detectors

For multichannel measurements, e.g. spectrally resolved lifetime measurements, the bh PML-16-C detector head is available [62]. The PML-16-C is shown in Fig. 157, left. It contains a 16-channel multi-anode PMT and the routing electronics that connects all PMT channels to a single TCSPC channel. The PML-16-C has an internal high-voltage generator, i.e. no external high-voltage power supply is required. The PML-16-C is fully controlled via the DCC-100 detector controller, which provides for power supply, gain control, and overload shutdown. The PML-16-C detector is the basis of the PML-SPEC multi-wavelength detection modules and the MW-FLIM multi-spectral FLIM detection assembly.

The PML-Spec consists of a bh PML-16-C sixteen-channel PMT module [62] and a polychromator. With a bh TCSPC module 16 wavelength channels are recorded simultaneously. Typical applications of the PML-Spec are single-point autofluorescence measurements of biological tissue and multi-spectral time-resolved laser scanning microscopy. The MW-FLIM system, shown in Fig. 157, right, is a spectral detection module optimised for direct (non-descanned) detection in multi-photon laser scanning microscopes. The multi-spectral detection modules can be used in all bh FLIM systems, including the DCS-120 confocal scanning FLIM system, and the FLIM systems for the Zeiss, Leica, Olympus and Nikon microscopes.

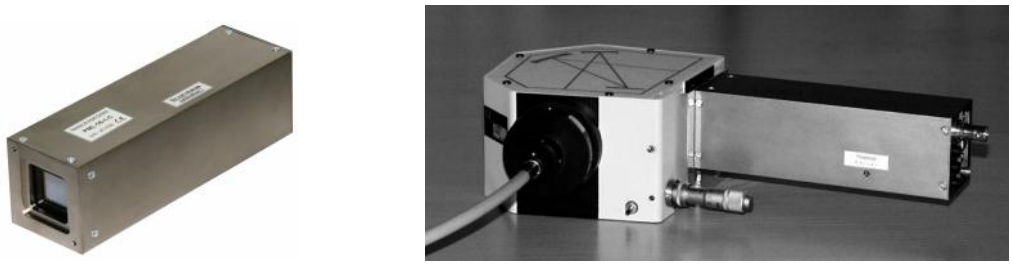


Fig. 157: Left: PML-16-C multi-channel PMT module. Right: MW-FLIM 16-channel spectral detection unit for laser scanning systems

Since 2014 a PML version with a GaAsP cathode (PML-16 GaAsP) is available. The PML-16 GaAsP and the MW-FLIM GaAsP multi-wavelength FLIM detectors based on it have about five times the efficiency of the PML and MW FLIM versions with bi-alkali and multi-alkali cathodes. The IRF width is between 200 and 250 ps. An instrument response function and a fluorescence signal recorded by the MW FLIM GaAsP are shown in Fig. 158.

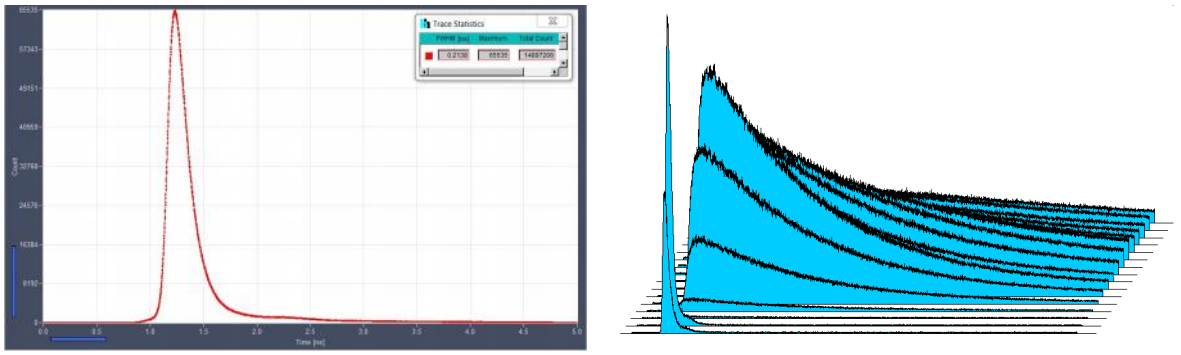


Fig. 158: Instrument response function (FWHM 212 ps, left) and fluorescence signal recorded with MW-FLIM GaAsP detector (right)

The PML-16-C, the PML-SPEC, and the MW-FLIM system are described in a separate handbook [62].

Single-Photon Avalanche Photodiodes (SPADs)

For measurements that require both high sensitivity and high time-resolution single-photon Avalanche diodes (SPADs) can be used. A SPAD from id Quantique is shown in Fig. 159, a SPAD from Micro Photon Devices in Fig. 160. The IRFs for a 20 µm version of id Quantique and for a 100 µm version of MPD are shown on the right. The id-100 is connected to the SPC module via an electrical attenuator and an A-PPI pulse inverter, see Fig. 176, the PDM-100 is coupled directly via its fast timing (Lemo connector) output.



Fig. 159: id100 SPAD. Left: C-mount adapter. Middle: Fibre-coupled version. Right: IRF measured with a 20 ps diode laser at 785 nm. Corrected for the pulse width of 20 ps, the IRF width is 40 ps, FWHM.

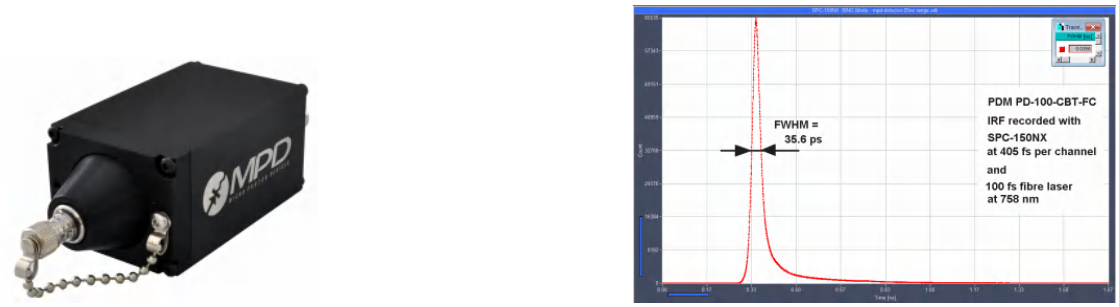


Fig. 160: Left: SPAD module from Micro Photon Devices (from www.micro-photon-devices.com). Right: Instrument response function of a PDM PD-100-CBT-FC measured with SPC-150NX TCSPC module and 100 fs fibre laser. The IRF width is 35.6 ps.

The bh SPC modules also work with other SPADs, such as the SPCM-AQR modules of Perkin Elmer / Excelitas or the COUNT modules of Laser Components. These modules have large area and high NIR sensitivity but do not reach the time resolution of the idQ or MPD modules.

Eight-Channel SPAD Module

The bh SPAD-8 module contains 8 parallel SPAD channels. It contains an id150-1x8, a generator for the SPAD operating voltage, and the routing electronics for multi-dimensional TCSPC. The device is controlled via the bh DCC-100 detector controller and connects directly to the bh SPC modules. Please see page 197 for details.

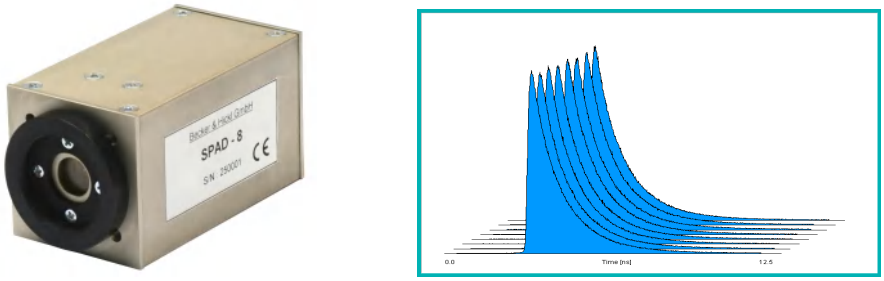


Fig. 161: Left: SPAD-8 eight-channel SPAD module. Right: Instrument response function.

InGaAs SPADs

InGaAs SPADs work in the spectral range from 900 nm to 1700 nm. For TCSPC operation, the devices must work in a continuous (none-gated) mode. This is the case for the id Quantique id 220 [98], and id 230 detectors [114]. The ID230 delivers an instrument re-

sponse width of 80 ps FWHM with the bh SPC-150 TCSPC module. So far, this is the fastest TCSPC response reported for any commercially available InGaAs SPAD. The detector we tested had less than 300 dark counts when operated with a dead time of 40 µs. Optical signals as weak as 800 photons per second count rate could be detected at high signal-to-background ratio [114]. For details please see [114] or pages 199 and 201 of this handbook.

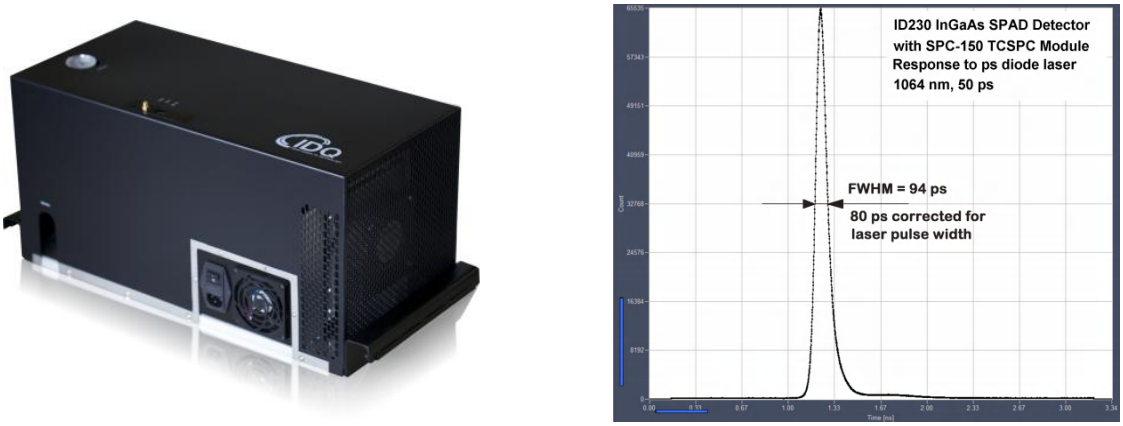


Fig. 162: Left: id 230 InGaAs SPAD detector. Right: Instrument response function with SPC-150

Superconducting NbN Detectors

Superconducting NbN single-photon detectors (SSPDs) compatible with the bh SPC modules are available from SCONTEL, Moscow. With an FWHM of 17.8 ps, the combination of an SCONTEL TCORPS-UF-10 with the SPC-150NX has delivered the fastest TCSPC response reported for any commercially available SSPD detector so far [115]. An even faster IRF has been obtained with a single-nanowire detector made by MIT in collaboration with JPL [117], please see 'TCSPC with a Single-Nanowire ', page 207.

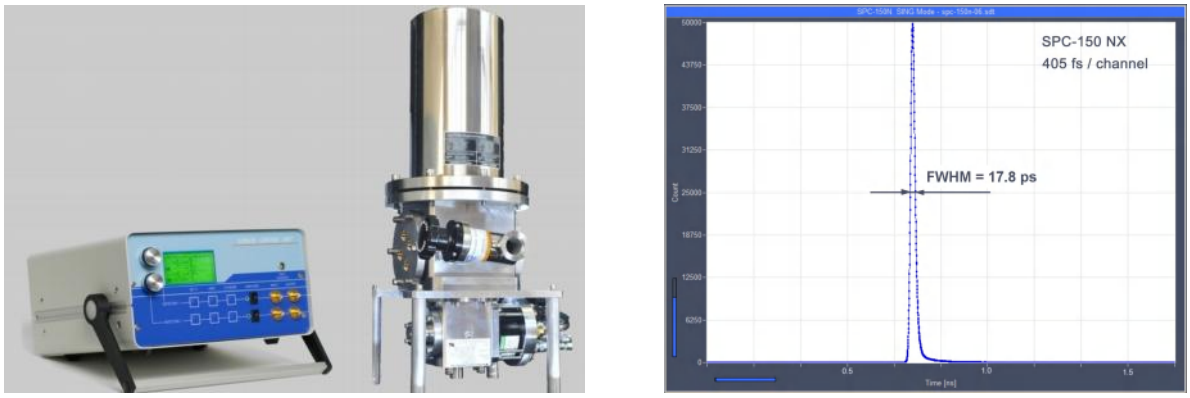


Fig. 163: Left: SCONTEL TCORPS-UF-10 detector. Right: Instrument response function with SPC-150NX

Detector, Shutter and Beam Splitter Assemblies for TCSPC Microscopy

Photon counting detectors, especially MCP-PMTs, can easily be damaged or destroyed by overload. Even when an MCP or PMT is switched off the cathode performance is impaired temporarily if the cathode is exposed to a high light intensity [723]. Especially in microscopy applications the microscope lamp - usually a mercury, xenon or halogen lamp - is a potential source of detector damage. A simple operator error can destroy one or several detectors. BH deliver detector/shutter/beamsplitter assemblies for one, two, and four detectors. The assemblies contain a field lens for efficient light transfer from the non-descanned beam path of two-

photon laser scanning microscopes. The assemblies can also be used with fibre adapters at the inputs. They can be used with a wide variety of detectors, including the R3809U, the H7422, the PMH-100, the PMC-100, and the PML-16C. Although primarily developed for laser scanning microscopes, the detector assemblies can be used for any application in which extreme detector overload cannot be reliably excluded. Please see [137].

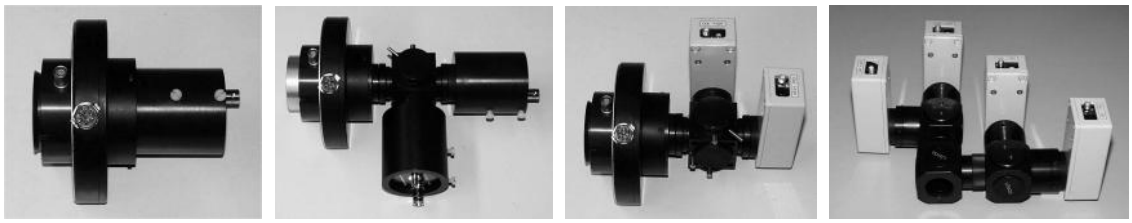


Fig. 164: Detector assemblies. Left to right: One R3809U MCP with shutter, two R3809U with shutter and beamsplitter, the PMH-100 with shutter and beamsplitter, four PMH-100 with three beamsplitters

A beamsplitter assembly for the BIG port of the Zeiss LSM 710 family microscopes is shown in Fig. 165, left. It uses standard microscopy beamsplitter cubes (Zeiss type) that can be configures with different dichroic mirrors and filters. The same assembly is available with a C-mount thread input, see Fig. 165, right.



Fig. 165: Left: Beamsplitter assembly for BIG port of Zeiss LSM 710 family microscopes. Right: Beamsplitter with C-Mount thread input. Both shown with HPM-100 hybrid detectors.

Detector Electronics

DCC-100 and DCC-100PCIE Detector/Laser Control Module

The bh DCC-100 and DCC-100 pcie modules [63] are used to control detectors and lasers in conjunction with bh photon counters. The DCC-100 provides power supply, gain control, and overload shutdown for two detectors. For cooled PMT modules the DCC also delivers the current to the thermoelectric coolers. It can be used to operate a wide variety of detectors, including the bh PMC-100 and PMC-150, the bh PMCS-150, the bh PML-16-C and PML-16 GaAsP, the Hamamatsu H7422, H5783, H6773 or the Hamamatsu R3809U. The DCC-100 and DCC-100PCIE provide also high-current digital outputs for controlling shutters or electromagnetic actuators. Due to its versatility the DCC modules are part of almost any bh TCSPC system. The DCC-100 is a PCI module, the DCC-100PCIE a PCI Express module for IBM compatible computers, see Fig. 166. The modules work under Windows 10 and Windows 11.



Fig. 166: DCC-100 and DCC-100PCIE detector controllers. The DCC modules provide power supply, cooler current, gain control, shutter control and overload shutdown for two detectors. The control panel is shown on the right.

DCU-400 Detector/Laser Controllers with USB Interface

Different than the DCC-100 modules, the DCU-400 is connected to the system computer via a USB interface. The DCU-400 controls four and detectors or lasers. The control software is integrated in bh's SPCM software. Please see Fig. 167.



Fig. 167: DCU-400 Detector/Laser Controller with USB interface. Software panel shown right.

Preamplifiers

For TCSPC experiments with some PMTs and MCP PMTs preamplifiers are required. For safe operation of MCPs and PMTs the HFAC-26 (26 dB, 1.6 GHz) and the HFAH amplifiers (26 dB, 1.6 GHz or 40 dB, 500 MHz). These amplifiers indicate overload conditions in the detector by a LED and by a TTL signal. In combination with the DCC-100 detector controller overload shutdown for the detector is provided. For multidetector measurements the HFAM-26 with eight amplifier channels is available. Other amplifiers are the ACA-2 and ACA-4 devices with gains from 10 dB to 40 dB and a bandwidth up to 2 GHz.

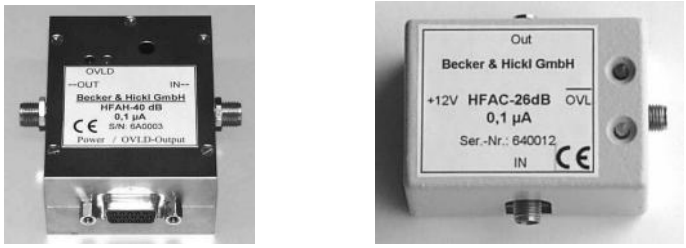


Fig. 168: HFAH series and HFAC series preamplifiers

Routing Devices for Multi-Detector Operation

The HRT-41 and HRT-81 routers are used to connect up to four (or eight) individual PMTs or MCPs to one bh SPC module. For SPAD modules with TTL and low-level TTL outputs the HRT-82 router is available. With the HRT devices, all detector channels work simultaneously and the detected photons are 'routed' into individual memory blocks. Please see individual manual [61] or data sheets. In 2013 the HRT-41 got an upgrade. The internal discriminator threshold was made adjustable to better adapt the router to detectors with different single photon response, see Fig. 169, right. Connection diagrams are given in chapter 'System Connection', page 223 and 'Cable Diagrams of FLIM Systems', page 237.



Fig. 169: HRT-81 (left) and HRT-41 (middle and right) routers. The routers connect several detectors to a single TCSPC module

Photon-Number-Sensitive Routing

Hybrid detectors, such as the bh HPM-100 modules, deliver output pulses the amplitude of which depends on the number of simultaneously detected photons. This feature can by used to identify detection events as single-, double-, or triple-photon events and route then into different memory blocks of the SPC device. The principle is described in [125]. Please see also page 699 of this handbook.

Reference Photodiodes

To generate the synchronisation signal for SPC modules from a laser pulse sequence fast photodiode modules are available. The bh PHD-400 and the bh PDM-400 use fast PIN photodiodes. The modules use single +12 V power supply which is provided by the SPC card, the DCC-100 detector controller, or by a wall-mounted AC-DC adapter.



Fig. 170: PHD-400 photodiode module

A new development became necessary for Ti:Sa lasers with wide tuning range. Over the tuning range, the output power of the laser changes by at least one order of magnitude. Simultaneously, the efficiency of the photodiode changes by almost the same ratio, i.e. the signal from a simple photodiode would change over a range of 1:100. That means the optical power needed to generate a reasonable synchronisation signal by a simple photodiode had to be adjusted depending on the wavelength. This inconveniency is avoided by the APS-100 Sync module. The APS-100 delivers an almost constant output signal over an intensity range of about 1:100. Gain regulation in the APS-100 is achieved by keeping the average photodiode current constant. That means, a constant pulse frequency in the range of 70 MHz to 90 MHz is required for the module to work properly. The APS-100 contains a beamsplitter that directs a few percent of the laser power into the photodiode, and lets the rest pass to the experiment. The device is shown in Fig. 171, left. The laser beam enters from the back and leaves the beamsplitter to the front. The output signal for an 80 MHz laser pulse sequence is shown in Fig. 171, right.

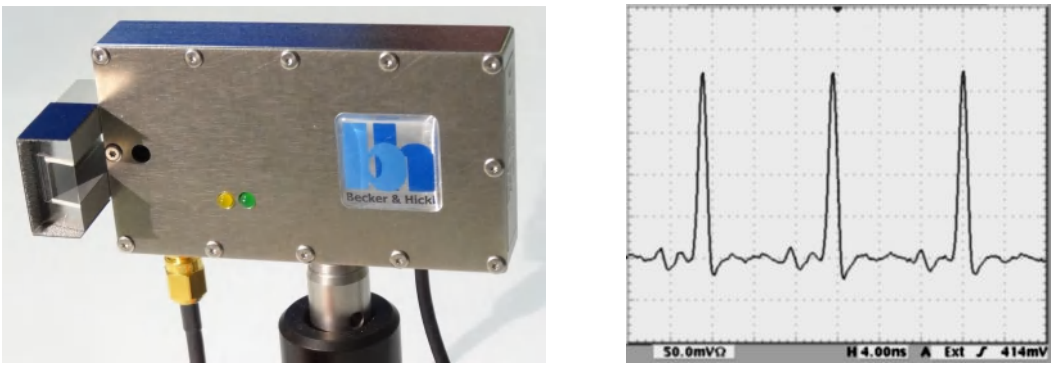


Fig. 171: APS-100 Synchronisation module. Right: Output pulses for an 80 MHz laser pulse sequence.

Experiment Control

GVD-120 Scan Controller

The GVD-120 card generates the x and y deflection signals for galvanometer scanners and piezo scan stages. The card is shown in Fig. 172. The x-y signals are generated by the hardware of the GVD module, the software is only used to load different waveforms or scan parameters in the scan controller. The waveforms are therefore independent of the computer speed and of software reaction times. The DCS-120 uses a cycloid trajectory for the fly-back of the scanner (see Fig. 172, right). This minimises mechanical resonances and thus allows the scanner to be operated at high scan rates. The GVD-120 also generates the scan synchronisation pulses for bh TCSPC modules, and the beam blanking, multiplexing, and intensity control signals for two bh BDL-SMC, BDL-SMN, or BDS-SM ps diode lasers. The control of the GVD card is fully integrated in the SPCM software of the bh TCSPC systems. The GVD-120 is available in a PCI version and in a PCI-express version.



Fig. 172: GVD-120 scan controller card (left) and scan waveforms (right)

GVD-140 Scan Controller

The GVD-140 scan controller is an extended version of the GVD-120. Different than the GVD-120 it controls up to four lasers. Any pair of the lasers can be multiplexed, and variable attenuators of the lasers can be controlled. A photo and the software-control panel are shown in Fig. 173.



Fig. 173: GVD-140 scan controller, photo and software panel

DDG-210 and DDG-220 pulse generator cards

The DDG-210 and DCC-220 pulse generator cards are used to multiplex lasers in complex TCSPC system, and to on-off modulate lasers for combined FLIM / PLIM in bh FLIM systems, see page 81. The cards can be operated via a control panel integrated in the bh SPCM software or by its own control software. In the second case, it can be used not only for laser modulation and multiplexing but also for a wide variety of other experiment control tasks.

The DDG-210 has a PCI interface, the DDG-220 a PCI-express interface. Photos of the DDG-210 card and the DDG-220 card are shown in Fig. 174.



Fig. 174: DDG-210 card (left) and DDG-220 card (right) for laser multiplexing and FLIM / PLIM laser control.

DB-32 Delay Switch Box

The DB-32 Delay Switch Box allows the user to electronically adjust the temporal relationship of the detector signals and the laser reference pulses, see page 279. 32 delay steps are available, the step width is 500 ps. The box is also able to select signals from two different sources. The advantage of using the DB-32 is that delay and the Sync source for different system configurations are kept in the setup files of the SPCM data acquisition software. Thus, the correct delay for a particular instrument configuration is set automatically when a setup is recalled from the 'Predefined Setup' panel.

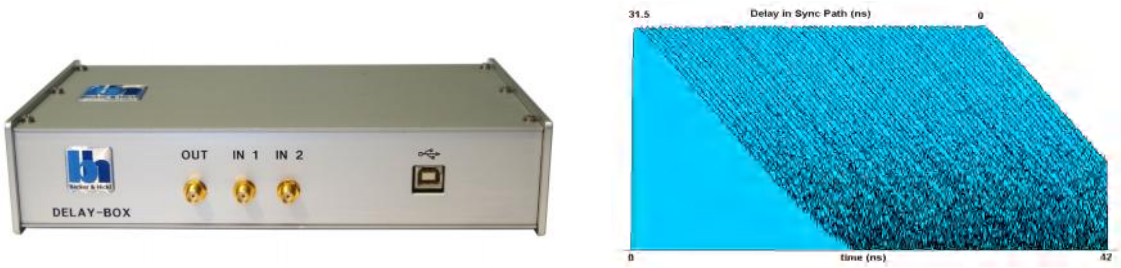


Fig. 175: USB-controlled delay switch box. Right: Fluorescence decay functions recorded with different SYNC delay.

Connecting Electronics

To connect signals from different detectors to the bh SPC modules a wide variety of cables and adapters are available. This includes attenuators and inverting transformers for TTL signals (e.g. from single-photon avalanche photodiode modules), power splitters, attenuators, cables, and various adapters, see Fig. 176. All bh SPC modules are delivered with a reasonable set of cables and adapters.



Fig. 176: Left to right: A-PPI-D pulse inverter, 1:2 and 1:4 power splitters, attenuator, cable with SMA connectors, SMA-to-SMA adapters, SMA-to-BNC adapter

To simplify the signal connections in complex TCSPC systems, such as multi-module systems, multi-detector system, or FLIM systems a number of connection boxes are available, see Fig. 177.



Fig. 177: BOB-101 and BOB-104 ‘breakout boxes’ for signal distribution in complex TCSPC systems

Connection diagrams for typical TCSPC systems are given in chapter ‘System Connection’, page 223 and ‘Cable Diagrams of FLIM Systems’, page 237.

SPCM 64-bit Instrument Software

All bh TCSPC devices use the same SPCM data acquisition software. The software operates up to four parallel SPC modules and peripheral devices such as scanners, detectors, lasers, and microscopes. Data and setup parameters can be freely exchanged between different TCSPC devices. Upgrading an experiment with a more advanced TCSPC module, or adding more TCSPC modules to the same experiment therefore does not require new instrument software or entirely different setup parameters. Moreover, the data recorded before and after upgrading an instrument remain compatible.

The user interface of the SPCM software is configurable. Thus, the software can be adapted to totally different experiments, or different operation modes within the same experiment. The user can change between different instrument configurations by a single mouse click. Examples are shown in Fig. 178.

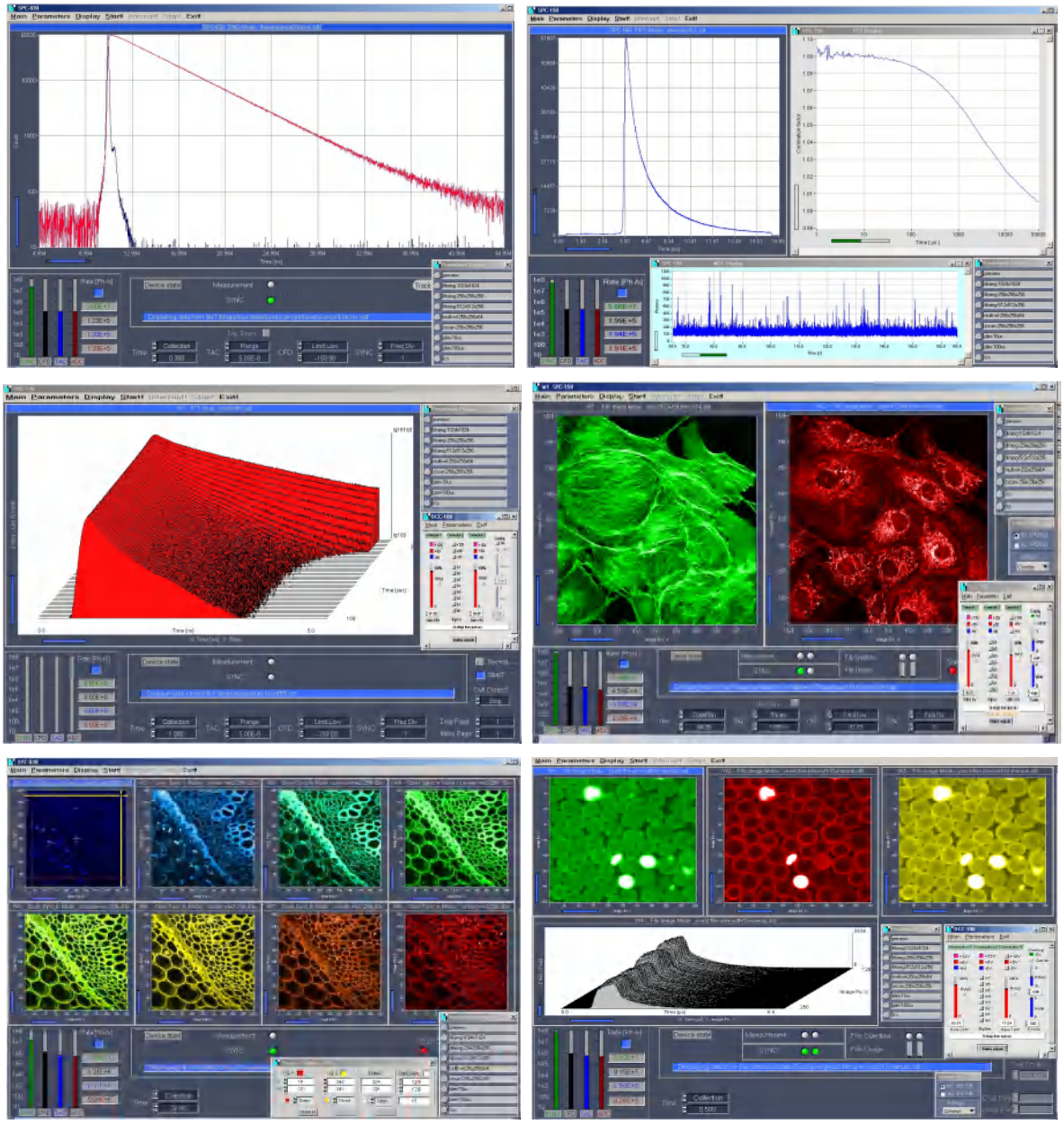


Fig. 178: Configurations of the SPCM instrument software: Fluorescence decay measurement, FCS measurement, fluorescence decay time series, dual-channel FLIM, multi-wavelength FLIM, simultaneous FLIM / PLIM.

Since 2014 the SPCM software is available in a 64-bit version. It runs under Windows 10 and Windows 11. In the 64-bit environment, a much larger amount of memory can be addressed. As a result, 'Megapixel' FLIM images can be recorded, and new functions like spatial and temporal Mosaic FLIM [103, 1198] or simultaneous FLIM / PLIM [104, 105] are available. Recent SPCM versions are also able to calculate colour-coded lifetime images online during the measurement [108], record FLIM with bi-directional scanning [107], and control external devices like motor stages, Ti:Sa lasers, and an AOM. Version 9.78 has functions to combine the channel data for the FASTAC fast-acquisition FLIM system, version 9.82 uses extended multi-threading for fast readout of data from multi-module systems. Please see Chapter 'SPCM Software', page 703 for a detailed description.

SPCImage NG FLIM Data Analysis

SPCImage NG is a new generation of bh's TCSPC-FLIM data analysis software. It combines time-domain and frequency-domain analysis, uses a maximum-likelihood (MLE) algorithm to calculate the parameters of the decay functions in the individual pixels, and accelerates the analysis procedure by GPU processing. 1D and 2D parameter histograms are available to display the distribution of the decay parameters over the pixels of the image or over selectable ROIs. Image segmentation can be performed via the phasor plot. Pixels with similar phasor signature can be combined for high-accuracy time-domain analysis. SPCImage NG provides decay models with one, two, or three exponential components, incomplete-decay models, and shifted-component models. Parameters of multi-exponential decays can be left floating, fixed to known values, or defined as global parameters. Another important feature is advanced IRF modelling, making it unnecessary to record IRFs for the individual FLIM data sets. For detailed description please see chapter 'SPCImage NG Data Analysis Software' or SPCImage NG Overview Brochure [78]. A typical main panel of SPCImage NG is shown in Fig. 179.

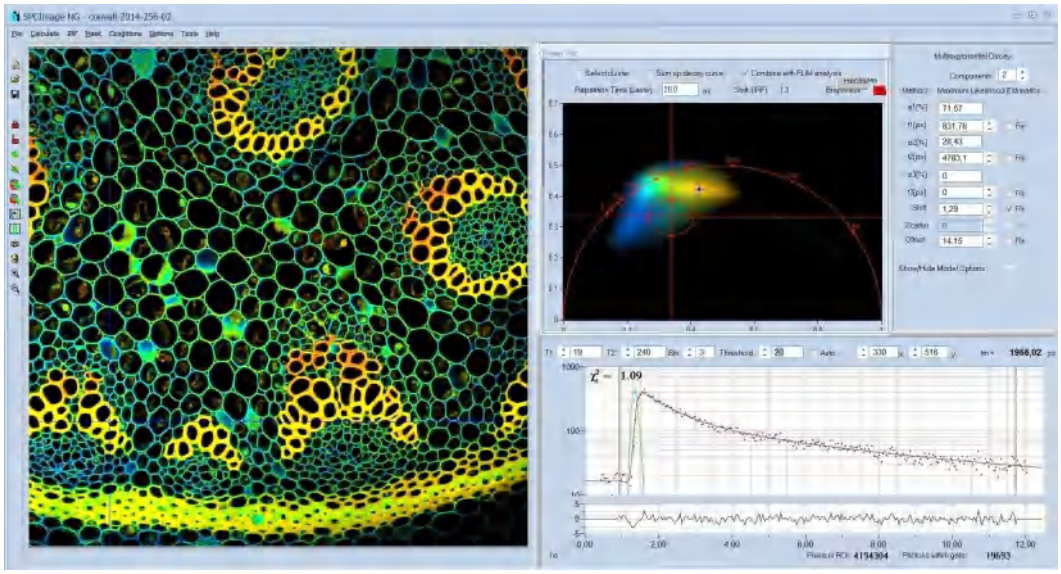


Fig. 179: Example of SPCImage NG main panel. Combination of time-domain analysis (left and lower right) and phasor plot (upper right)

Deconvolution and Fit Procedure

SPCImage NG runs an iterative fit and de-convolution procedure on the decay data of the individual pixels of the FLIM images. In the simplest case, the result is the lifetime of the decay functions in the individual pixels. For complex decay functions the fit procedure deliv-

ers the lifetimes and amplitudes of the decay components. SPCImage then creates colour-coded images of the amplitude- or intensity-weighted lifetimes in the pixels, images of the lifetimes or amplitudes of the decay components, images of lifetime or amplitude ratios, and images of other combinations of decay parameters, such as FRET intensities, FRET distances, bound-unbound ratios, or the fluorescence-lifetime redox ratio, FLIRR. A few examples are shown in Fig. 180 and Fig. 181. For details please see chapter 'SPCImage NG Data Analysis Software' of this handbook. Please see also [78, 68, 69].

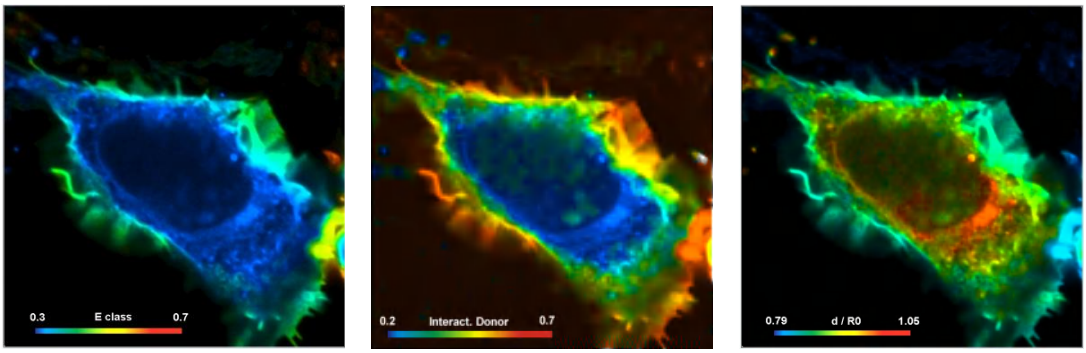


Fig. 180: Cell with interacting proteins, labelled with a FRET donor and a FRET acceptor. Left to right: Classic FRET efficiency, fraction of interacting donor, FRET distance

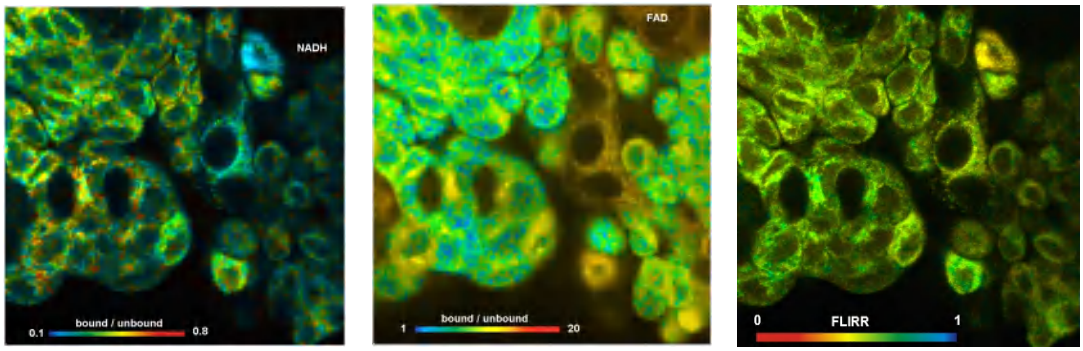


Fig. 181: Metabolic FLIM. Bound-unbound ratio of NADH, Bound/unbound ratio of FAD, Fluorescence-Lifetime Redox Ratio, FLIRR.

Maximum-Likelihood Algorithm

Unlike previous SPCImage versions, SPCImage NG uses a maximum-likelihood algorithm (or maximum-likelihood estimation, MLE) for fitting the data. In contrast to the usual least-square fit, the MLE algorithm takes into account the Poissonian distribution of the photon numbers. Compared to the least-square method, the fit accuracy is improved especially for low photon numbers, and there is no bias toward shorter lifetime as it is often observed for the least-square fit. For comparison with older data sets the weighted least-square fit and the first-moment algorithms of the previous SPCImage versions are still available in SPCImage NG.

Instrument-Response Function

SPCImage NG avoids troublesome recording of an instrument response function (IRF) for each FLIM measurement. This is achieved by modelling the IRF with a generic function. The parameters of this function are determined by fitting it to the FLIM data together with the selected decay model. The results of this procedure are so good that an accurate IRF is obtained even for decay functions containing ultra-fast components, see Fig. 182. For details please see chapter 'SPCImage NG Data Analysis Software' in this handbook.

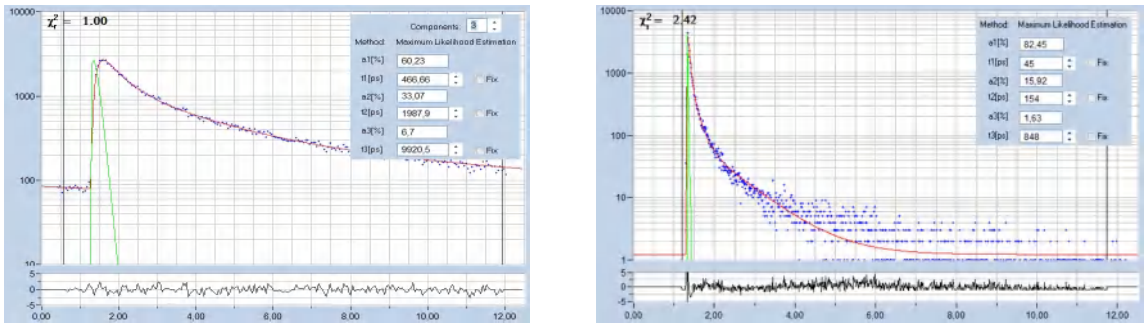


Fig. 182: Synthetic IRF. Left: Autofluorescence of cells, ps diode laser, HPM-100-40. Right: Sample with extremely fast decay component, femtosecond fibre laser, HPM-100-06

Phasor Plot

SPCImage NG combines time-domain multi-exponential decay analysis with a phasor plot. In the phasor plot, the decay data in the individual pixels are expressed as phase and amplitude values in a polar diagram [383]. Independently of their location in the image, pixels with similar decay signature form clusters in the phasor plot. Different phasor clusters can be selected, and the corresponding pixels back-annotated in the time-domain FLIM images. The decay functions of the pixels within the selected phasor range can be combined into a single decay curve of high photon number. This curve can be analysed at high accuracy, revealing decay components that are not visible by normal pixel-by pixel analysis [124]. An example is shown in Fig. 183.

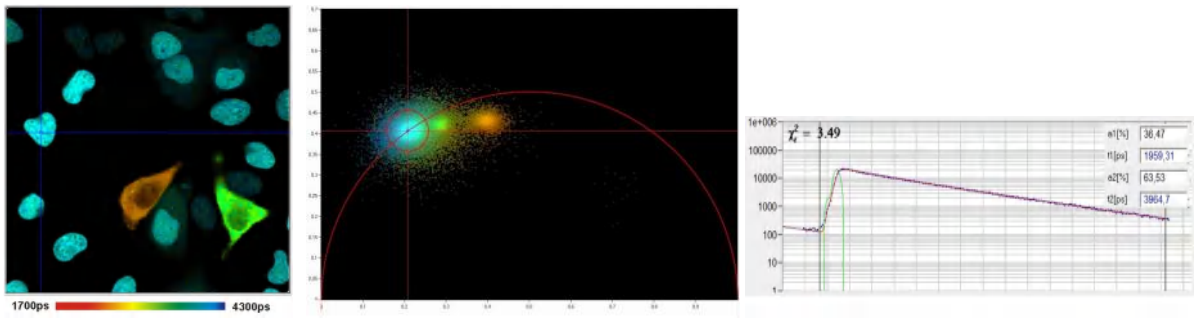


Fig. 183: Combination of time-domain analysis with phasor plot. Left to right: Lifetime image, phasor plot, decay curve of combined pixels within selected phasor range

GPU Processing

SPCImage NG uses GPU (Graphics Processor Unit) processing. GPU processing is running on NVIDIA cards and a number of other NVIDIA-compatible devices. The TCSPC data are transferred into the GPU, which then runs the de-convolution and fit procedure for a large number of pixels in parallel. This way data processing times for large images are reduced from several minutes to a few seconds.

Single-Curve Analysis

SPCImage can also be used to analyse single decay curves, The data can come from traditional cuvette experiments, or from the combined pixels of a FLIM recording. An example is shown in Fig. 184.

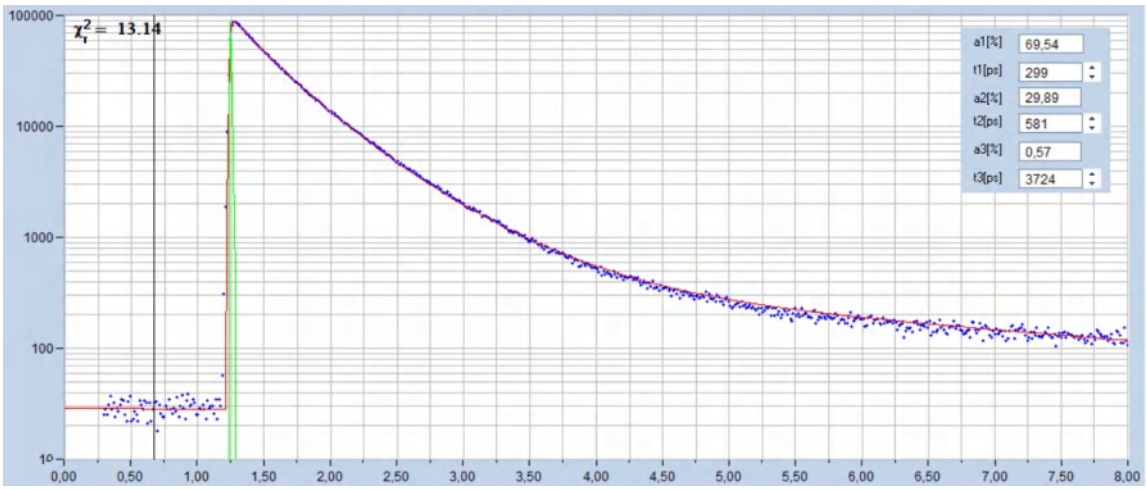


Fig. 184: SPCImage used for fluorescence decay analysis of single curves. NADH dissolved in water, recorded with bh DCS-120 MP FLIM system.

Express-FLIM Software

The bh Express-FLIM system runs on special software. The user interface is shown in Fig. 185. The Express-FLIM software provides for parameter setup, measurement control, and fast display of image sequences. It is even able to stream the image sequence in a video file. The operation of the Express FLIM system is described in a separate handbook, please see [72].

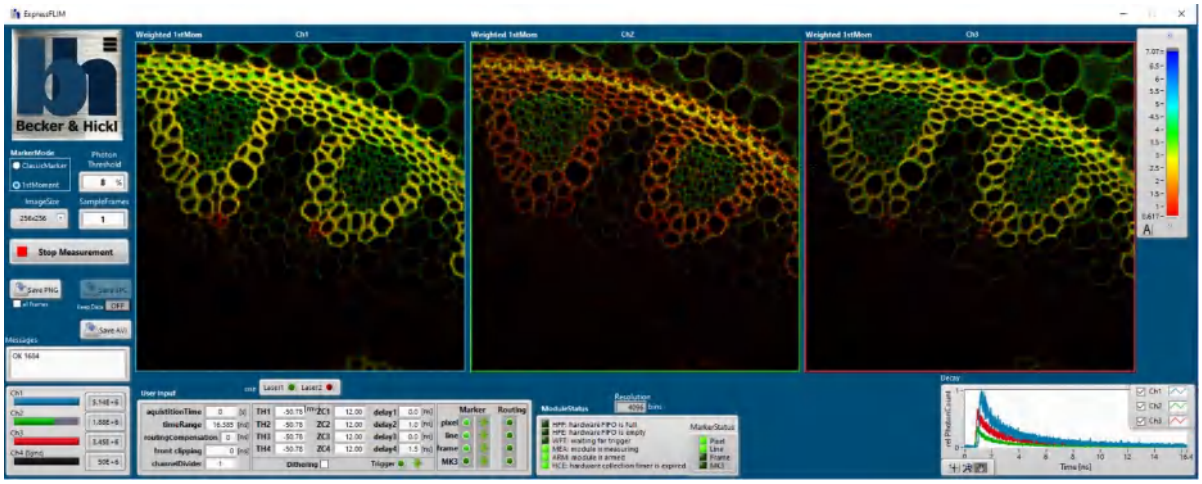


Fig. 185: Express FLIM software, main panel

SPCDynamics

SPCDynamics has been designed for analysis of .spc time-tag data created by SPCM Software. Typical applications are statistical analysis of photon-burst data, decay analysis of moving particles, single molecule spectroscopy, and analysis of dynamic effects within TCSPC FLIM recordings. The user interface of SPCDynamics is shown in Fig. 186. A handbook is available on www.becker-hickl.com [73].

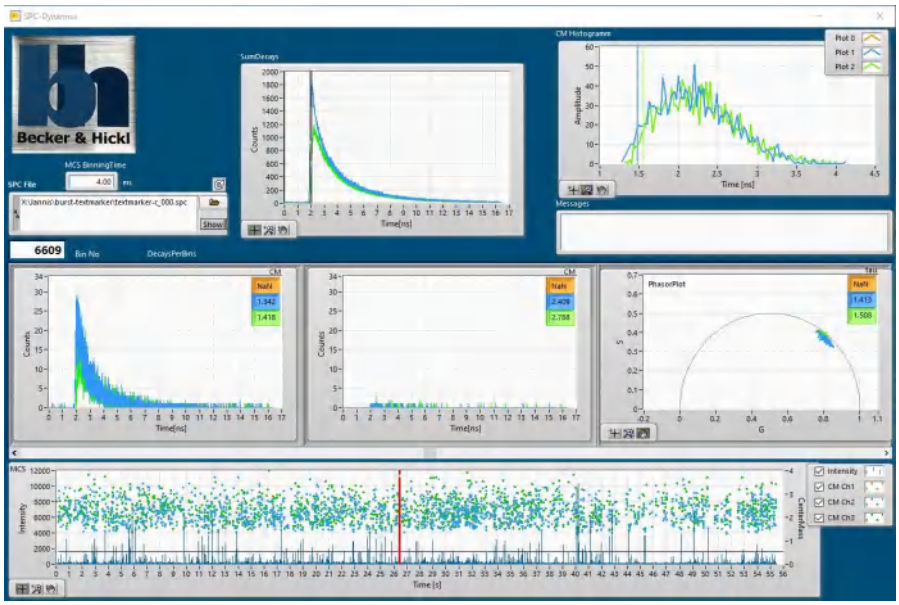


Fig. 186: User interface of SPCDynamics

Burst Analyzer Single-Molecule Data Analysis

The bh 'Burst Analyser' software is used for data analysis of single-molecule fluorescence. It uses parameter-tag data files recorded in the FIFO mode of the SPC-630, SPC-130EM, SPC-150, SPC-150N, SPC-160, or SPC-180N TCSPC modules. Photon bursts from single molecules travelling through a femtoliter detection volume are identified in the parameter-tag data. Within the bursts, intensities, intensity variations, fluorescence lifetimes, and ratios of these parameters between several detection channels of a routing system, different channels of a multi-module TCSPC system, or different time windows of a PIE recording are determined, and histograms of the parameters are calculated. The results are used to obtain histograms and time traces of FRET efficiencies, and to calculate FCS and FCCS data. The Burst Analyser is described in a separate handbook, see [79].

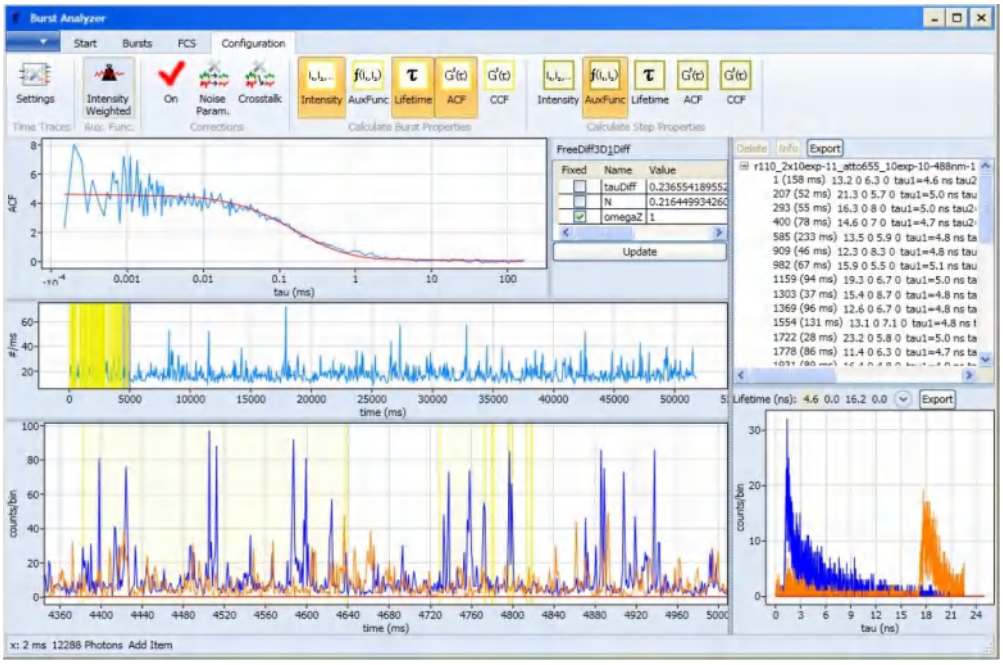


Fig. 187: bh Burst Analyzer software for single-molecule data analysis

Classic Time-Correlated Single Photon Counting

Single-Photon Detection

Photon counting techniques consider the detector signal a random sequence of pulses corresponding the detection of the individual photons. Fig. 188, left, shows the output pulses of a Hamamatsu R5900 PMT for a photon detection rate of 10^7 photons per second. The figure left shows the pulses at a time scale of 1 ns per division. The same signal of the same PMT at a time scale of 100 ns per division is shown right.

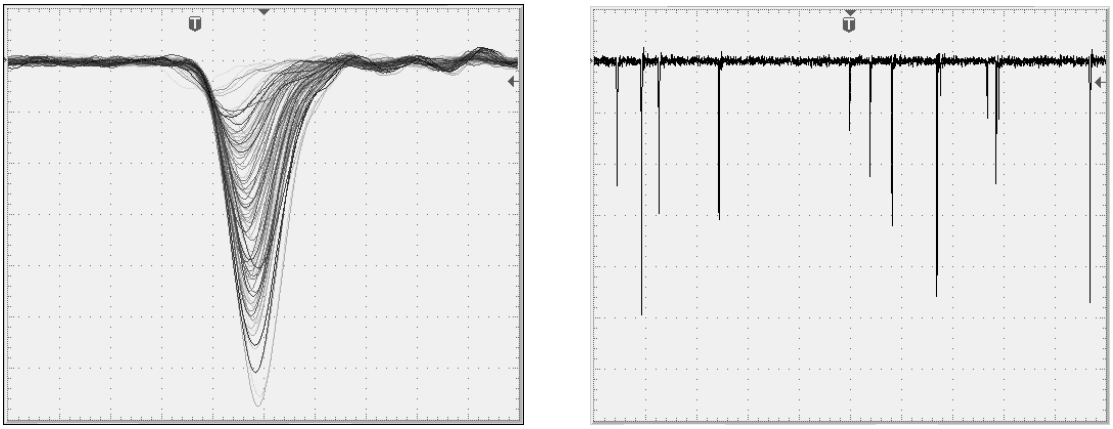


Fig. 188: Single-photon pulses delivered by a R5900 PMT (left, 1 ns / div) and output signal of the PMT at a photon detection rate of 10^7 s^{-1} (right, 100 ns / div). Operating voltage -900 V, signal line terminated with 50 Ω.

The individual single-photon pulses have a duration of less than 2 ns. Therefore, the detector signal is a random sequence of single-photon pulses rather than a continuous waveform (Fig. 188, right). The light intensity is represented by the density of the pulses, not by their amplitude. Obviously, the intensity of the light signal is obtained best by counting the pulses in subsequent time channels.

Photon counting has a number of advantages over analog recording techniques. Fig. 188, left, shows that the single photon pulses have a considerable amplitude jitter. The amplitude jitter - or 'gain noise' - is a result of the random amplification process in the PMT. It is present in all high-gain detectors. When the signal is recorded by an analog technique the gain noise contributes to the noise of the measurement. Photon counting results are free of gain noise. Also electronic noise does not contribute to the result as long as its amplitude is smaller than that of the photon pulses. Photon counting techniques therefore obtain a shot-noise-limited signal-to noise ratio down to the background count rate of the detector.

Another unique feature of photon counting results from the fact that the arrival time of a photon pulse can be determined with high precision. The bandwidth of a photon counting experiment is limited only by the transit time spread of the pulses in the detector, not by the width of the pulses. The transit-time distribution is usually an order of magnitude narrower than the width of the single-photon pulses. For the same detector, photon counting therefore obtains a significantly higher time-resolution than any analog recording technique. This feature is more or less inherent to all photon counting techniques, but is found in its extreme form in time-correlated single photon counting, or TCSPC.

Principle of Time-Correlated Single Photon Counting

Time-correlated single photon counting, or TCSPC, is based on the detection of single photons of a periodic light signal, the measurement of the detection times, and the reconstruction of the waveform from the individual time measurements [154, 924].

Technically, TCSPC was derived from the 'Delayed Coincidence' method used in nuclear physics to determine the lifetime of unstable nuclei. The earliest publication on the use of the method to detect the shape of light pulses dates back to 1961 [233], the first applications to spectroscopy of excited molecules were published in the 1970s [334, 759, 768, 1086, 1367].

TCSPC makes use of the fact that for low-level, high-repetition rate signals the light intensity is low enough that the probability to detect more than one photon in one signal period is negligible. The situation is illustrated in Fig. 189.

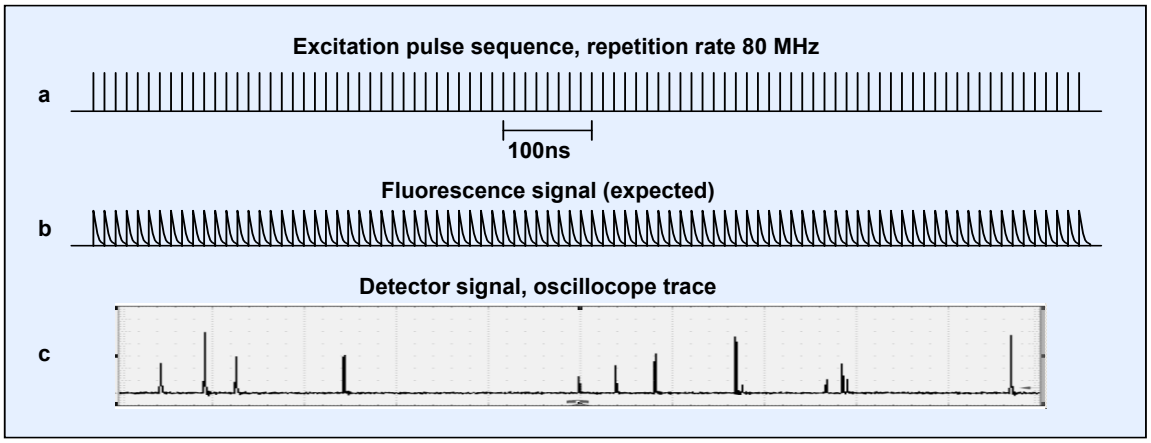


Fig. 189: Detector signal for fluorescence detection at a pulse repetition rate of 80 MHz

Fluorescence of a sample is excited by a laser of 80 MHz pulse repetition rate (a). The expected fluorescence waveform is (b). However, the detector signal, (as measured by an oscilloscope) has no similarity with the expected fluorescence waveform. Instead, it is a sequence of extremely narrow pulses randomly spread over the time axis (c). A signal like this often looks confusing to users not familiar with photon counting. However, there is a simple explanation to the odd signal shape: The pulses represent single photons of the light signal arriving at the detector. The shape of the pulses has nothing to do with the waveform of the light signal. It is the response of the detector to the detection of a single photon. Please note that the photon detection rate of (c) was about 10^7 s^{-1}. This is on the order of the maximum permissible detection rate of most photon counting detectors. Even at a detection rate this high, the detector signal is far from being a continuous waveform.

There are two conclusions from the signal shape in Fig. 189 (c). First, the waveform of the optical signal is not the detector signal. Instead, it is the distribution of the detector pulses over the time in the excitation pulse period. Second, the detection of a photon within a particular excitation pulse period is a relatively unlikely event. The detection of two or more photons is even more unlikely. Therefore, only the first photon within a particular pulse period has to be considered. The build-up of the photon distribution over the pulse period then becomes a relatively straightforward process. The principle is shown in Fig. 190.

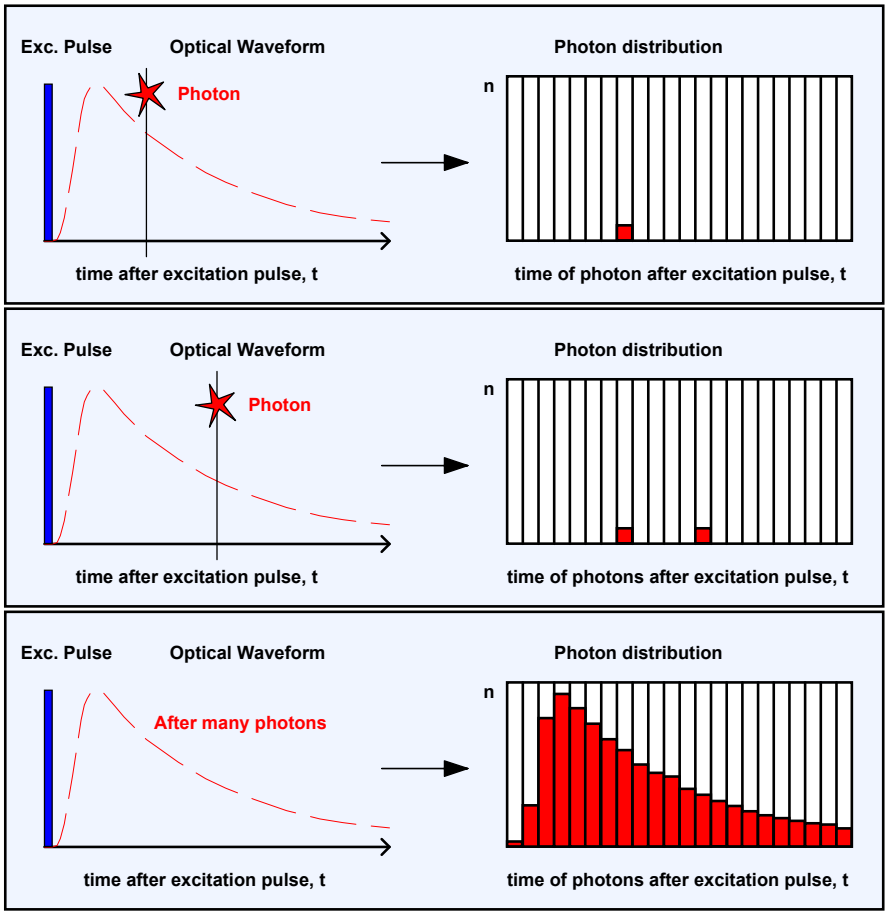


Fig. 190: Principle of TCSPC. The recording process builds up the distribution of the photons over their times after the excitation pulse

When a photon is detected, the arrival time of the corresponding detector pulse in the signal period is measured. The events are collected in a memory by adding a '1' in a memory location with an address proportional to the detection time. After many signal periods a large number of photons has been detected, and the distribution of the photons over the time in the signal period builds up. The result represents the 'waveform' of the optical pulse. (Please note that there is actually no such waveform, only a distribution of the photon probability, see Fig. 189). Although this principle looks complicated at first glance, it has a number of fascinating features.

Extremely High Time Resolution

The time resolution of an analog signal recording technique is limited by the bandwidth of the detector. The width of the instrument response function cannot be shorter than the single-photon response (see Fig. 188, left). For TCSPC the time resolution is much better. The explanation is given in Fig. 191. The times of the photons are derived from the arrival times of the detector pulses. These times can be measured at an accuracy much better than the width of the pulses. Thus, the 'instrument response function', or IRF, of a TCSPC system is essentially given by the transit time dispersion (or transit time spread, TTS) of the photon pulses in the detector. The TTS can be more than 10 times narrower than the single-photon response of the detector. The IRF is therefore much narrower than the single-photon response, see Fig. 191, right.

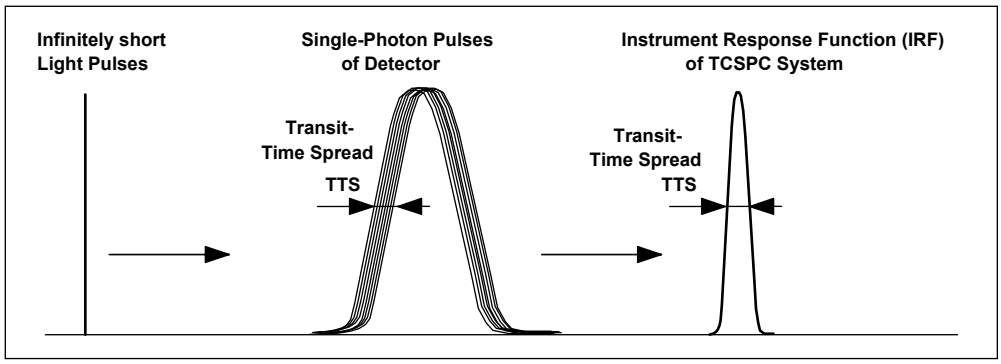


Fig. 191: Response of detector to infinitely short light pulses and instrument response of TCSPC system.

A practical example is shown in Fig. 192. The single-photon response of an HPM-100-06 hybrid detector is shown left. It has a width of about 1 ns. The TCSPC IRF is shown right. The width is 18.9 ps, i.e. more than 50 times shorter than the SER!

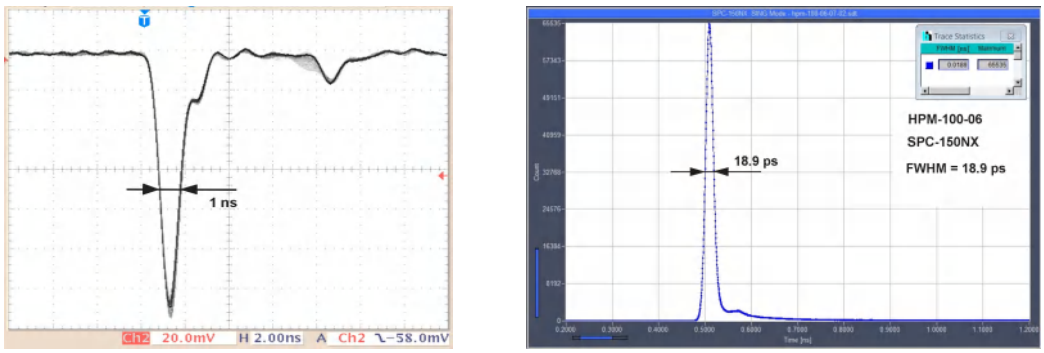


Fig. 192: Single electron response (SER, left) and TCSPC Instrument response function (IRF, right) for a bh HPM-100-06 hybrid detector. The TCSPC IRF is more than 50 times faster than the SER. Note the different time scale.

The TCSPC instrument response function (IRF) for a number of typical detectors is given in chapter 'Detectors for TCSPC'. All are substantially shorter than the single-photon pulses of the detectors.

Timing Stability

A carefully designed TCSPC device can achieve a timing stability in the sub-ps range. This can be extremely important in distance-measurement and diffuse-optical imaging applications, where changes in the mean time-of-flight of the photons on the order of a few ps are recorded over tens of minutes. The bh TCSPC devices address the needs of these applications by an extraordinarily low timing drift and timing wobble. Examples are given in Fig. 4, and Fig. 5, page 2.

High Photon Efficiency - High Lifetime Accuracy

An important feature of TCSPC is that there is no loss of photons in the recording process. Provided the timing electronics is fast enough, every photon seen by the detector arrives in the photon distribution. TCSPC therefore reaches a near-ideal photon efficiency [680].

The high photon efficiency of TCSPC translates directly into accuracy for fluorescence lifetime recording. Under ideal conditions a single-exponential fluorescence lifetime can be determined with a signal-to-noise ratio, SNR, of

$$SNR = \sqrt{N}$$

from a number, N, of detected photons. This is the same SNR as it is obtained for an intensity measurement based on the same number of photons [497, 680]. In a TCSPC device operated at reasonable count rate all detected photons contribute to the result. There is no counting loss

due to 'gating' as in 'Boxcar' devices or gated image intensified CCDs, and no variable weight as in sine-wave modulation techniques [154, 278, 968]. In combination with the fact that TCSPC delivers the shortest possible IRF for a given detector it yields the best lifetime accuracy (or 'Photon Efficiency') for a given number of detected photons [46, 680].

Recording of Complex Decay Profiles

TCSPC records the entire waveform of an optical signal into a large number of time channels. This is important especially in bio-medical applications. Fluorescence decay profiles in these applications are usually complex. The information is not simply in an average 'fluorescence lifetime' but in the parameters of the multi-exponential decay function, i.e. amplitudes and decay times of the decay components. TCSPC data are able to deliver these parameters, and the high time resolution and the high photon efficiency make it possible to determine them from a limited number of photons available from a sample.

No waveform distortion by dynamic changes in the optical signal

There is also a third advantage that has been noticed only recently. If there is variation in the optical signal waveform over the time the data are acquired TCSPC records an *average waveform*. This can be important in biomedical applications where the optical waveforms may vary due to metabolic processes. A technique based on temporal scanning, i.e. by shifting a time-gate over the signal, would record a distorted waveform in these cases.

The 'Pile-Up' Effect'

As a serious drawback of TCSPC it is often stated that the technique can record only one photon per signal period. If the light intensity is high a possible second or third photon in the same excitation pulse period with the first one is lost. The result is a distortion of the recorded signal waveform. It is often stated that, to avoid pile-up distortion, the photon detection rate must be no higher than 0.1% of the excitation pulse rate. *This is wrong.* The limit of 0.1% probably originated from a typo in the early TCSPC literature.

A derivation of the systematic error in the detected fluorescence lifetime has been given in [154]. The lifetime error induced by pile-up is surprisingly small: Even for an average detection rate of 20% of the excitation rate the lifetime error is no larger than 5%. (Please see 'Pile-Up', page 294) For excitation with a Ti:Sa laser (80 MHz) it would correspond to a detection rate of 16 MHz. This is much more than the detection rates in typical TCSPC experiments. With state-of-the-art laser sources and TCSPC electronics the count rate - and thus the available acquisition speed - is rather limited by the photostability of the samples. This is especially the case in fluorescence lifetime microscopy where the fluorescence comes from a pico- or femtoliter sample volume.

Count Rate and Acquisition Time

The TCSPC technique is often believed to suffer from slow count rate, slow recording speed and long acquisition times. This reputation comes from early fluorescence lifetime spectrometers which indeed needed acquisition times of several minutes or even hours to record a single fluorescence decay curve. The reason was the low repetition rate of the light sources used and the long 'dead time' of the electronics of the 1980s. At a repetition rate of a few 10 kHz (typical of the nanosecond flash lamps used) pile-up indeed limited the count rates to no more than

1000 photons per second. The acquisition times were correspondingly long. Another limitation was the slow signal processing speed of the electronics. The 'dead time' after the detection of a photon was on the order of 20 µs, which precluded the recording of more than a few 10^4 photons per second.

These limitations do not longer exist in modern TCSPC setups. Modern light sources can be operated at repetition rates of 50 to 80 MHz. Moreover, the bh TCSPC devices employ a new AD conversion principle that results in processing times about 100 times shorter than in the traditional TCSPC setups (see 'Analog-to-Digital Conversion', page 151). TCSPC devices from Becker & Hickl have dead times of 80 to 125 ns and are able to record photons at a rate of about $5 \cdot 10^6$ photons per seconds. Fig. 193 shows a fluorescence decay curve of plant tissue recorded within an acquisition time of 100 ms. About 400.000 photons were recorded within this time. Reasonable fluorescence lifetimes can be derived from 1000 photons, which can be obtained within less than 1 ms. Advanced TCSPC devices can therefore be used for high speed applications such recording of chlorophyll transients, dynamic brain imaging by diffuse optical tomography, spectroscopy of single molecules, or fluorescence lifetime imaging by fast scanning techniques.

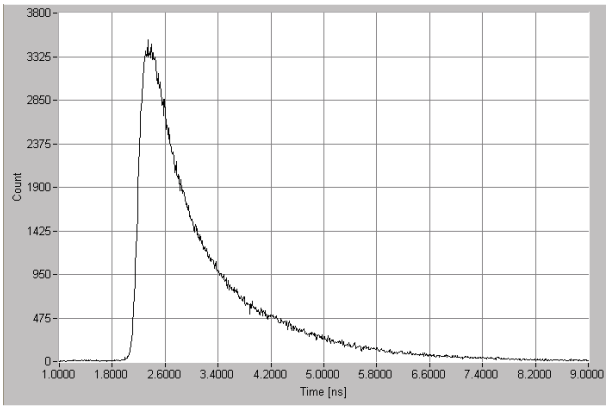


Fig. 193: Fluorescence decay curve of plant tissue, count rate $4 \cdot 10^6$ s-1, acquisition time 100 ms. SPC-140 TCSPC module.

The Classic TCSPC Architecture

The architecture of a classic TCSPC device [334, 924, 1367] is shown in Fig. 194.

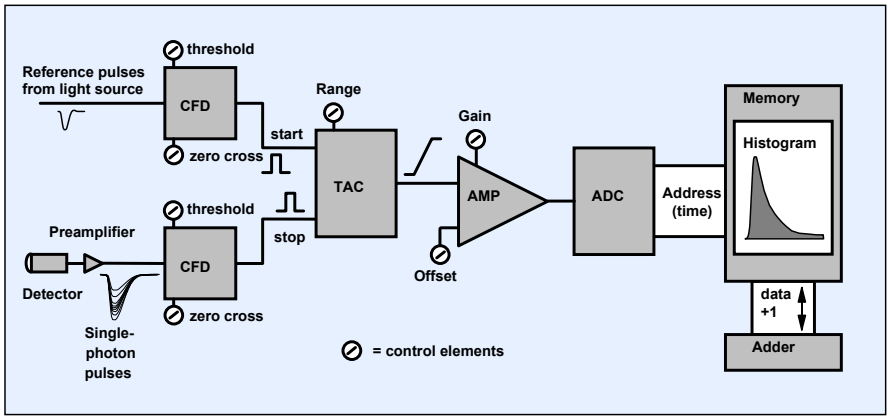


Fig. 194: Architecture of a classic TCSPC device

The detector delivers pulses for the individual photons of the repetitive light signal. The pulses are detected by a fast discriminator. Due to the random amplification mechanism in the detector, the single-photon pulses can have a considerable amplitude jitter. If a simple lead-

ing-edge discriminator was used, it would trigger when the leading edge of the input pulse reached a defined threshold. Even if the discriminator were infinitely fast, the amplitude jitter would induce a timing jitter on the order of the pulse rise time. Therefore a 'Constant Fraction Discriminator', CFD, is used to trigger on the PMT pulses. The CFD triggers at a constant fraction of the pulse amplitude, thus avoiding pulse-height induced timing jitter. Practical implementations of CFDs trigger at the baseline transition of a re-shaped pulse, which is equivalent to constant fraction triggering. The details of constant-fraction triggering are described in chapter 'Detailed Description of Building Blocks' page 147.

A second CFD is used to obtain a timing reference pulse from the light source. The reference signal is usually generated by a photodiode or by a PMT operated at medium gain. Thus also the reference pulses may have some amplitude fluctuation or amplitude drift. The use of a CFD in the reference channel prevents these fluctuations from causing timing jitter or timing drift.

The output pulses of the CFDs are used as start and stop pulses of a time-to-amplitude converter, TAC. The TAC generates an output signal proportional to the time between the start and the stop pulse. Conventional TACs use a switched current source charging a capacitor. The start pulse switches the current on, the stop pulse off. If the current in the start-stop interval is constant, the final voltage at the capacitor represents the time between start and stop. This principle works with remarkable accuracy, and time differences of a few ps can be clearly resolved.

The TAC output voltage is sent through a 'Biased Amplifier', AMP. The amplifier has a variable gain and a variable offset. It is used to select a smaller time window within the full-scale conversion range of the TAC.

The amplified TAC signal is fed to the Analog-to Digital Converter, ADC. The output of the ADC is the digital equivalent of the photon detection time. The ADC must work with an extremely high precision. Not only must it resolve the amplified TAC signal into thousands of time channels, but the time channels must also have the same width. Any non-uniformity of the channel width results in a systematic variation of the numbers of photons in the channels, creating noise or curve distortion.

The ADC output is used as an address word for the measurement data memory. When a photon is detected, the ADC output word addresses a memory location corresponding to the time of the photon. By incrementing the data contents of the addressed location the photon distribution over time is built up.

Reversed Start-Stop

The principle described above measures the time from the reference pulse, which is usually a pulse from an excitation light source, to the detection of a photon. Of course, there are many pulse periods in which no photons are detected. In these periods the TAC is started but not stopped. Consequently, there must be a circuit in the TAC that detects the out-of-range condition, and resets the TAC for the next signal period. The frequent start-only events and subsequent resets are no problem at low pulse repetition rates.

However, for light sources of 50 to 100 MHz repetition rate, like titanium-sapphire lasers or pulsed diode lasers, the principle described above is not applicable. The TAC must be reset each 10 or 20 ns, while measuring some rare detection events between the reset pulses. Therefore, high-repetition rate systems work in the 'reversed start-stop' configuration [665, 1338], see Fig. 195.

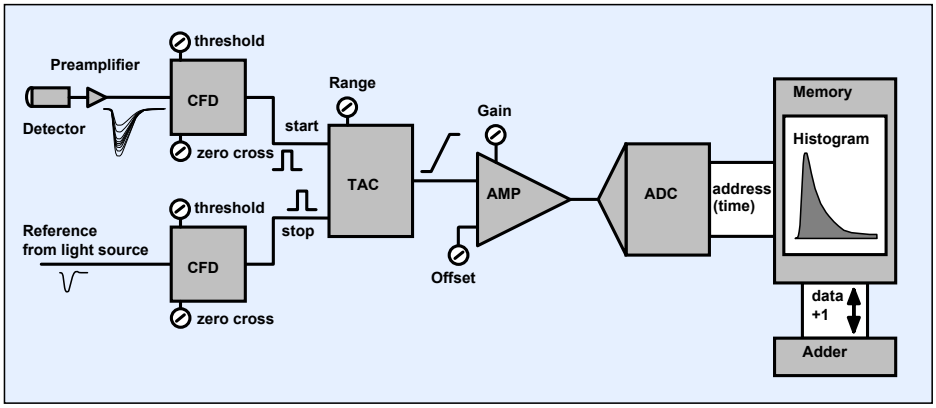


Fig. 195: Reversed start-stop configuration of TCSPC

In the reversed start-stop configuration, the TAC is started when a photon is detected and stopped with the next reference pulse from the light source. Consequently, the TAC has to work only at the rate of the photon detection events, not at the much higher rate of the excitation pulses. In the reversed start-stop mode the TAC output voltage decreases for increasing arrival times of the photons. The reversal of the time axis can be compensated by inverting the signal in the biased amplifier, by inverting the ADC bits, or simply by reversed readout of the data memory.

The setup shown in Fig. 195 is based on the presumption that the period of the excitation pulses is constant and free of jitter down to the order of 1 ps. If there is a pulse period jitter it adds to the transit time spread of the detector. The reversed start-stop configuration can easily be made insensitive to pulse period jitter by introducing a passive delay line in the reference channel. With an appropriate delay in the reference channel the time of the photon is measured against the laser pulse from which the detected photon originated. This removes the effect of any pulse period change on the timing (see ‘Delayed-Stop Operation’ page 220).

The setup shown in Fig. 194 and Fig. 195 is often complemented by passive delay lines in the detector and reference channels, by rate meters that display the start and stop rates, and by a suitable computer interface for data readout [924]. Classic TCSPC setups were usually built from nuclear instrumentation (NIM) modules. The CFDs, the TAC, the biased amplifier, the ADC, and accessories like rate meters or delay lines were individual plug-in modules. The large size of these modules and the large number of cable connections made the devices relatively bulky. The system parameters had to be set by manual controls. The long dead times of the TAC and ADC limited the available count rates. However, the most severe limitation of classic TCSPC was that it was intrinsically one-dimensional, i.e. restricted to the recording of the waveform of the light signal. The solution to that problem is ‘Multi-Dimensional TCSPC’, described in the next chapter.

Modern Implementations of Classic TCSPC

In applications where only a single optical waveform has to be recorded, or the experiment allows a series of waveforms to be recorded sequentially the classic principle is still used to a large extend. Of course, this does not mean that electronics from the last century has to be used. All bh TCSPC devices can be well used in the classic modes, taking advantage of the high time resolution and high count rates. Beyond that, there may be other differences to the classic TCSPC instruments: The time conversion can be performed also by direct time-to-digital (TDC) conversion, the time measurement can be performed in the direct start-stop mode, and the photon distribution can be built up in the memory of a computer.

TAC / ADC versus TDC Principle

In the modern implementation, the time measurement for the individual photons is not always performed by the classic TAD / ADC principle. Also a Time-to-Digital Converter, or TDC can be used.

The two principles are illustrated in Fig. 196. The TAC / ADC principle is shown left. It uses a linear voltage ramp between a start pulse (usually the photon) and a stop pulse (usually a reference from the laser). The voltage is converted in a digital data word which expresses the time of the photon in the laser pulse sequence. The advantage of the TAC / ADC principle is the extremely high time resolution. The IRF width of the SPC-150 NXX and -180 NXX modules is 2.8 ps fwhm (full width at half maximum), the effective timing jitter is about 1.5 ps (rms). The time-channel width can be as small as 200 femtoseconds. A resolution on this level is not reached by any other TCSPC device. It is more than 13 times higher than for the TDC principle.

The TDC principle is shown on the right. The photon pulses from the detector and the reference pulses from the laser are sent through chains of digital delay elements. The timing logics looks at the data in the delay chains, identifies start-stop pairs of photons and laser pulses, and this way determines the temporal positions of the photons in the laser pulse sequence. The time resolution of the TDC principle is significantly lower than that of the TAC/ADC principle. The advantage of the TDC principle is that it works up to extremely high photon rates, and that the electronics is less power consuming. Several timing channels can therefore be implemented on a single PC board.

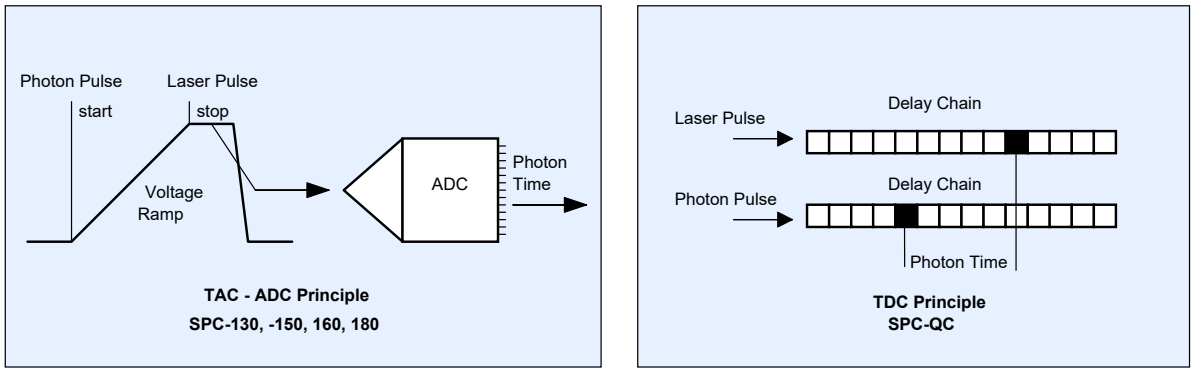


Fig. 196: Principles of time measurement. Left: TAC/ADC principle. Right: TDC principle

Direct Start-Stop Operation

For the TDC it is not required that the photon pulse comes before the reference pulse from the light source. A TDC-based TCSPC module can therefore be used in the direct start-stop configuration. This makes the module easier to use, especially when the time range of the measurement is very long.

Buildup of the Photon Distribution in the Computer

The classic TCSPC implementation builds up the photon distribution in a memory in the TCSPC device, see Fig. 194. The memory is read at the end of the measurement. Modern TCSPC devices, both with TAC/ADC and TDC time measurement, can also transfer the data photon by photon, and build up the photon distribution in the memory of the computer. This 'FIFO' operation had become possible by a dramatic increase in data transfer rate and computer speed.

Applications of the Classic TCSPC Principle

In applications were only a single optical waveform has to be recorded, or the experiment allows a series of waveforms to be recorded sequentially the classic principle is still used to a large extend. Of course, this does not mean that electronics from the last century has to be used. The bh TCSPC devices can be well used in the classic modes, taking advantage of the high time resolution and high count rates.

The typical classic application is the recording of fluorescence decay curves. Examples are shown in Fig. 197. Fig. 197, left, shows fluorescence decay curves of quinine sulphate quenched by Cl^- ions. The fluorescence lifetime changes with the quencher concentration [742]. Fig. 197, right shows decay curves of DODCI (3,3'diethyloxadicarbocyanine iodide) for different wavelength. The data were obtained by scanning the detection wavelength by a monochromator and recording the decay curves sequentially.

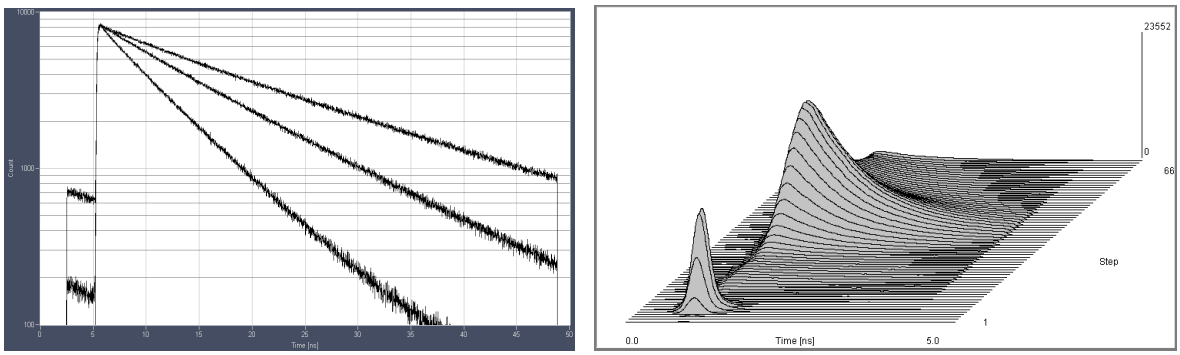


Fig. 197: Fluorescence decay measurement by TCSPC. Left: Fluorescence decay curves of quinine sulphate for different quencher concentration. Right: Fluorescence decay curves of DODCI recorded for different wavelengths

The classic TCSPC principle is often used to record fluorescence anisotropy decay times. For details please see chapter 'Measurement of Time-Resolved Fluorescence Anisotropy', page 328. An example is shown in Fig. 198. Fluorescein in a water-glycerol solution was excited at 474 nm. The blue curve shows the fluorescence decay measured at a polarisation parallel, $I_{par}(t)$, the red curve the fluorescence decay at a polarisation perpendicular to the excitation, $I_{perp}(t)$. The black curve shows the anisotropy, $R(t)$, (arbitrary units) calculated by

$$R(t) = I_{par}(t) - I_{perp}(t) / I_{tot}(t)$$

$I_{tot}(t)$ is the total intensity. For measurement in a 90-degree parallel-beam configuration it is $I_{tot}(t) = I_{par}(t) + 2\, I_{perp}(t)$ [742, 1292, 1293]. Please see section Fluorescence Depolarisation, page 307.

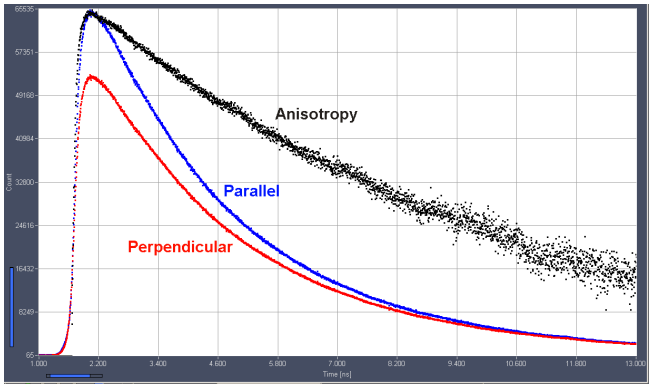


Fig. 198: Fluorescence anisotropy measurement. The fluorescence of a sample was measured parallel and perpendicular to the excitation; the anisotropy was calculated by $R(t) = I_{par}(t) - I_{perp}(t) / I_{tot}(t)$.

Another application of the classic principle is recording of anti-bunching effects. A single optical emitter, such as a single molecule or a quantum dot, can only emit a single photon within its fluorescence decay time. The experiment is run in the classic 'Hanbury-Brown-Twiss' setup [552]: The light is split in two detection channels, and the detection events in one detector are used as a start, the ones in the other as a stop signal for TCSPC. The resulting curve has a dip at the time at which the events coincide. An example is shown in Fig. 199.

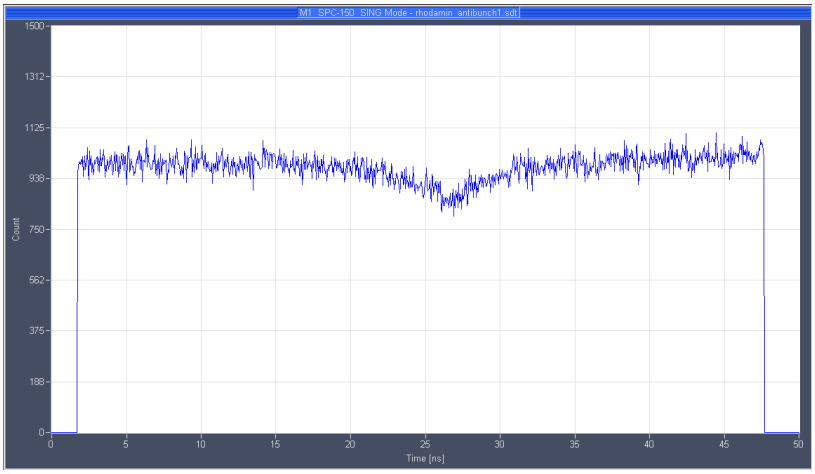


Fig. 199: Anti-bunching curve recorded at a diluted solution of fluorescein in a confocal microscope. On average, about 7 molecules are in the focus at a time.

Until today, some of these basic applications are performed by TCSPC setups based on the classic NIM (Nuclear Instrumentation Module) architecture [924]. Of course, the bh SPC devices can be well used in these traditional applications. Even in simple applications as the ones shown above the modern devices have advantages over NIM-based instruments: They have higher time resolution, work at higher pulse repetition rates and higher count rates, achieve shorter acquisition times, and are fully computer controlled. The real advantage of the modern implementation is, however, that the recording process is multi-dimensional. As a result, experiments can be performed which are entirely out of the reach of the classic design. Please see next chapter.

Multi-Dimensional TCSPC

In 1993 bh introduced a new generation of TCSPC devices. It abandoned the NIM technique entirely and integrated all building blocks on a single printed circuit board (PCB). The enormous size reduction became possible by surface mount PCB technology, hybrid circuits, and field programmable gate arrays (FPGAs). The single-board design relaxed the interconnection problems between the individual building blocks so that the speed of new analog and logic ICs could be fully exploited. The electronic system was optimised as a whole, resulting in time-shared operation of TAC, ADC and memory access. Together with new time-to-digital conversion principles the count rate of TCSPC was increased by two orders of magnitude.

Compared with the very limited capacity of the more or less discrete control electronics of classic TCSPC systems, the use of FPGAs also led to a breakthrough in functionality. Advanced TCSPC devices use a multi-dimensional recording process [154, 167]. The idea behind multi-dimensional TCSPC is illustrated in Fig. 200.

Principle of Data Acquisition

The classic TCSPC principle, shown Fig. 200, left records a photon distribution over the time in the signal period. The result is one-dimensional, i.e. a curve that represents the waveform of the optical signal. If the shape of the curve is to be observed in dependence of a additional parameter the experiment has to be repeated for different values of that parameter. This is time-consuming, and, if the parameter cannot be actively controlled, inefficient.

Multi-dimensional TCSPC is shown right. It records the photon density not only as a function of the time in the signal period, but also of one or more additional parameters, P. These can be the wavelength, spatial coordinates, location within a scanning area, the time from the start of the experiment, or any other parameter that describes the individual photons, or the state of the system investigated.

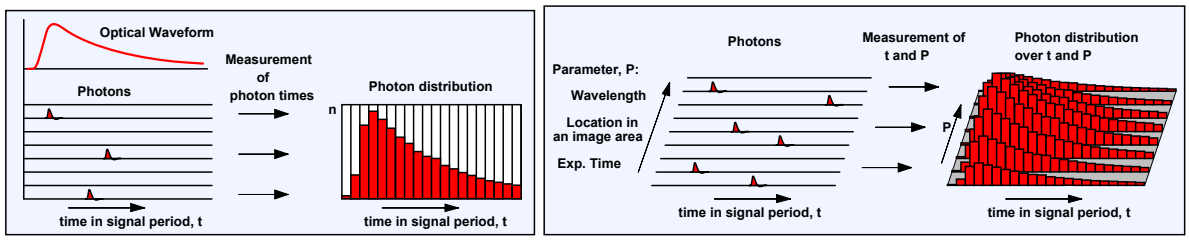


Fig. 200: Left: Principle of classic TCSPC. The result is a one-dimensional photon distribution over the time in the signal period. Right: Multi-dimensional TCSPC. The result is a multi-dimensional distribution over the time in the signal period and one or several additional parameters determined for the individual photons.

Depending on which and how many additional parameters are used, different photon distributions are obtained. Three possibilities are shown in Fig. 201. Wavelength-resolved fluorescence decay data (shown left) are obtained by using the wavelength as additional recording parameter. Dynamic fluorescence decay data (middle) are obtained by using the time from a stimulation event. Fluorescence lifetime imaging uses the location of the excitation beam, x,y, in a scan area as additional parameters.

Please note that there is no need to control the additional parameters actively, or change them at a given rate. It is only needed that the values of the parameters can be determined in the moment of the photon detection. The recording process then puts the photon into a memory location depending on the time in the signal period, and the values of the parameters. Thus, the process works for any rate of parameter variation, and even for parameters varying randomly.

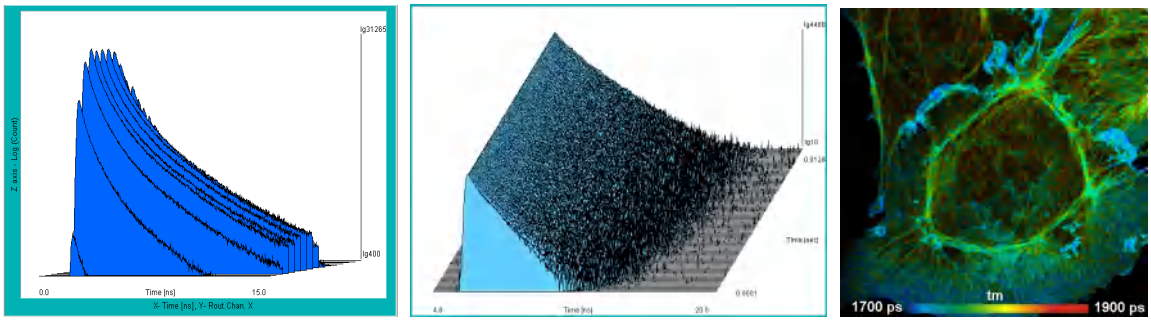


Fig. 201, left to right: Wavelength resolved fluorescence decay, dynamic change of fluorescence decay with time of exposure in the µs range, fluorescence lifetime image.

It is sometimes believed that the same results can also be obtained by classic TCSPC. The parameter of interest would be varied and a sequence of waveforms be recorded. This is correct, but there is an important difference. The classic procedure would have to acquire a full waveform until the value of the parameter is changed, and then start a new recording. That means, any change in any of the additional photon parameters had to be slow, and predictable.

Multi-dimensional TCSPC is free of this limitation. Any parameter of the photon distribution can vary at any speed. It can even vary randomly. Every photon is just put into its place in the photon distribution according to its time after the excitation pulse and the values of the additional parameters in the moment of the photon detection. As the parameters keep varying, the photon distribution is just accumulated until enough photons have been collected for any particular combination of parameters. In other words, the rate at which the parameters are varying is decoupled from the rate at which the photons are recorded.

Typical examples are the results shown in Fig. 201. The wavelength of the photons in Fig. 201, left, was determined by a multi-wavelength detector. It varies randomly, and is different for every photon. The variation in the fluorescence decay functions in Fig. 201, middle, is induced by a stimulation of the sample. The recording procedure runs through the 128 curves of the photon distribution at a rate of 100 µs per curve. This is not enough to record a reasonable amount of photon per curve. However, the two-dimensional recording process accumulated the photons over a large number of stimulation periods. Thus, a high signal-to noise ratio was obtained despite of the microsecond stepping time. The lifetime image on the right was recorded by scanning the sample with a pixel dwell time of one microsecond. At an average photon rate on the order of 10^6 s^{-1} one would expect that the result would contain no more than a few photons per pixel. Fluorescence decay data acquired this way would be useless. However, because the photons were accumulated over a large number of frames of the scan, and an excellent accuracy of the decay time is obtained.

Architecture of Multi-Dimensional TCSPC

The general architecture of a TCSPC device with multi-dimensional data acquisition is shown in Fig. 202. The core of the TCSPC device is the time measurement block. This block receives the single-photon pulses from a detector, and the timing reference pulses from a pulsed light source. The time is measured from a start pulse to a stop pulse. With the time-conversion principle used in the bh TCSPC modules the time between start and stop can be measured at an accuracy down less than 3 ps (rms).

The time measurement block delivers the photon time, t, relative to the stop pulse as a digital data word. The data word addresses the time-channel in a selected waveform data block in the memory. The photon is added in the addressed memory location. As more and more photons are detected the waveform of the optical signal builds up.

Up to this point the function of the TCSPC device is identical with classic TCSPC. The difference is that the memory of a multi-dimensional TCSPC device has space for a large number of waveform data blocks, and that these blocks can be addressed via additional building blocks of the TCSPC device. The address part delivered by these blocks carries additional information related to the individual photons. Photon parameters available directly as digital data words are fed into the TCSPC device via the 'Channel' register. Examples are the wavelength channel in which a photon has been detected by a multi-wavelength detector (see Fig. 207 and Fig. 208), or the number of one of several multiplexed lasers that was active when the photon was detected (see Fig. 209 and Fig. 210).

Additional parts of the address can be generated by a 'Sequencer' block. The sequencer generates an address word either by counting synchronisation pulses from an external experiment control device (e.g. an optical scanner), or by counting pulses from an internal clock.

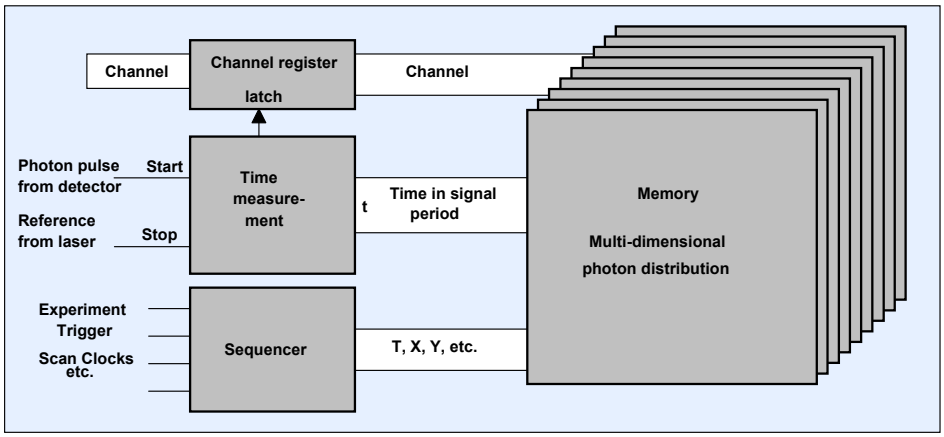


Fig. 202: Multi-dimensional TCSPC architecture, photon distribution built up in the internal memory of the TCSPC device

In the architecture shown in Fig. 202 the photon distribution is built up by on-board logics in the memory of the TCSPC device. The advantage of this principle is that the acquisition runs virtually without interaction by the measurement control software.

A second architecture is shown in Fig. 203. Here, the parameters of the individual photons are directly transferred into the system computer. To buffer the information for periods when the computer is not able to read the data a FIFO (first-in-first-out) buffer is inserted in the data path. The computer builds up the photon distribution by software or directly stores the data of the individual photons for further processing.

When data of individual photons are generated there is no need to use a sequencer to direct photons into different waveform data blocks of the memory. The function of the sequencer is therefore performed by 'Event Identification' logics. This block adds an absolute time (from the start of the recording) to the data words of the individual photons. Moreover, it puts external events, such as trigger pulses from an experiment or synchronisation pulses from a scanner, into the data stream and marks them with an absolute time and an identifier.

The advantage of this architecture is that more memory size is available to build up the photon distributions, and that more complex data operations can be performed. Because the principle in Fig. 203 uses a stream of data for photons marked with detection times and other parameter it is also called 'time tag' or 'parameter-tag' mode.

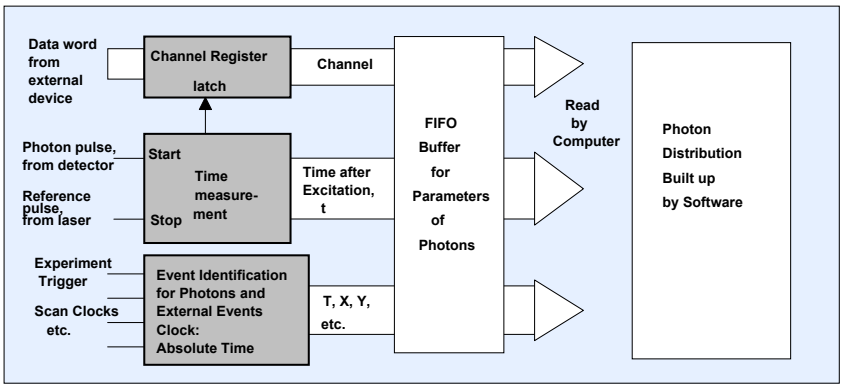


Fig. 203: Multi-dimensional TCSPC architecture, photon distribution built up in computer

Depending on the information fed into the 'channel' input and the information generated in the sequencer or event identification block, a number of advanced signal acquisition principles is available:

- Classic TCSPC: If the channel register and the sequencer are not used the device works as a classic TCSPC device. Compared with the early TCSPC systems based on NIM electronics the recordable count rates are considerably higher.
- Multi-detector operation: Several individual detectors or several channels of a multi-anode PMT are used. A 'router' generates a 'channel' information that indicates which of several detectors detected the current photon. Depending on the optical system, spectral resolution, spatial resolution, or separation of photons of different polarisation can be obtained.
- Multiplexed detection: Several lasers of different wavelength, different excitation positions, different samples or different sample positions are multiplexed. The 'channel' signal indicates the number of the particular laser, the sample, or the position in the sample in the moment when the photon was detected.
- Multi-parameter detection: The 'channel' information comes from one or several external ADCs. The ADCs deliver data words for externally measured sample parameters, such as temperature, pressure, or electrical or magnetic field strength.
- Sequential recording: Controlled by an internal clock oscillator, the sequencer counts through a range of subsequent address words. The result is a sequence of waveform measurements. The individual measurements can be multi-dimensional themselves, due to the capabilities of the 'channel' control. The sequence can be recorded at almost any rate. It can be triggered by an 'experiment trigger', and a specified number of triggered sequences can be accumulated.
- TCSPC imaging with a scanning device: The sequencer synchronises the recording with the action of an external scanner. The sequencer delivers two additional dimensions, X and Y. Synchronisation with the scanner is obtained either by sending to or receiving clock pulses from the scanner. The result is a spatial array of data blocks, each of which can be multi-dimensional itself, due to the capabilities of the 'channel' control. TCSPC scanning is able to work at extremely high scan rates, even at pixel rates much higher than the count rate.
- Dual-time-base recording: The TCSPC process can be configured to record two waveforms or two images containing data at different time scales. One of them uses the photon times after the excitation pulses (determined by the time-measurement block), the other the times from the event identification block.
- The photon density of a single detector signal or of several detector signals can be correlated on a time scale determined by the event identification block.

Multi-Dimensional TCSPC Implementations

Multi-Detector and Multi-Wavelength TCSPC

Multi-detector and multi-wavelength TCSPC use the number of an individual detector within a linear array of detectors as an additional dimension of the photon distribution. When the optical signal is split spectrally, and the spectrum is projected on the detector array, the detector number represents the wavelength of the photons. The result is a photon distribution over time and wavelength, see Fig. 204.

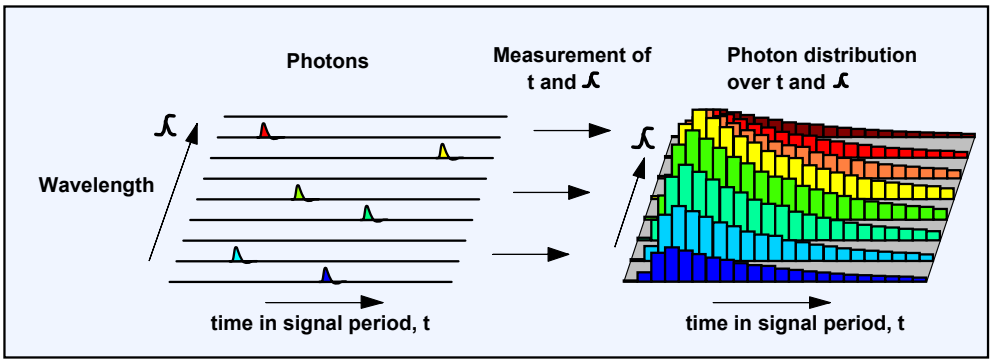


Fig. 204: Multi-wavelength TCSPC determines the wavelengths of the individual photons and builds up a distribution over the arrival time in the signal period and the wavelength.

To understand how multi-detector or multi-wavelength detection works, please remind that the average number of photons detected per signal period is less than one, see 'Principle of Time-Correlated Single Photon Counting', page 102. How much less than one it has to be is subject of discussion. Many sources (incorrectly) state a limit of 0.001 photons per signal period. However, a detection rate up to 0.1 or even 0.2 per signal period can normally be tolerated [154, 167], see Fig. 453, page 295. In any case, the detection of several photons per period remains an unlikely event.

Now consider an array of detectors over which the same photon flux is spread. Because it is unlikely that the complete array detects several photons per period it is also unlikely that several detectors of the array will detect a photon in the same signal period. This is the basic idea behind multi-detector TCSPC. Although several detectors are *active simultaneously they are unlikely to deliver a photon pulse in the same signal period*. The times of the photons detected in all detectors can therefore be measured in a single TAC [140, 144, 154, 167]. The technical principle is illustrated in Fig. 205.

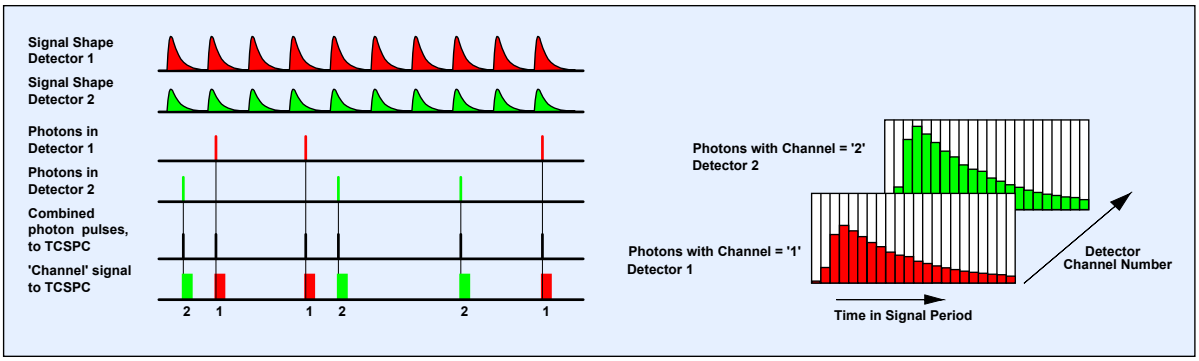


Fig. 205: Principle of TCSPC multi-detector operation. The photon pulses from both detectors are combined, and the times of the pulses are measured in a single TAC. A ‘Channel’ signal indicates which of the detectors detected the current photon.

The photons of all detectors are combined into a common timing pulse line. Simultaneously, a detector number signal is generated that indicates in which of the detectors a particular photon was detected. The combined photon pulses are sent through the normal time measurement procedure of the TCSPC device. The detector numbers are used as a ‘channel’ (or ‘routing’) signal for multi-dimensional TCSPC. The TCSPC device uses this signal to route the photons from the individual detectors into different waveform-memory sections. In other words, the detector-channel number is used as a second dimension of the photon distribution recorded.

Routing was already used in classic NIM-based TCSPC setups [210, 211, 1202]. Each of the detectors had its own CFD. The CFD output pulses were combined into one common TAC stop signal, and simultaneously used to control the destination memory block in the MCA. Because separate CFDs were used for the detectors, the number of detector channels was limited.

The modern implementation uses a single CFD for all detector channels. A ‘router’ combines the single-photon pulses into one common timing pulse line, and generates a 'channel' signal that indicates at which of the detectors the current photon arrived [140, 144, 154].

A block diagram of the router is shown in Fig. 206. The routing module consists of a number of amplifiers, A_1 through A_n, connected to discriminators, D_1 through D_n, a digital encoder circuit, and a summing amplifier, A_s. The amplifiers, A_1 through A_n, amplify the single-photon pulses of the detectors, typically to several hundred mV. When a detector detects a photon, the corresponding discriminator responds and the subsequent encoder generates the 'channel' byte that indicates which detector detected the photon. Simultaneously, the photon pulse propagates through the summing amplifier, A_s, and appears at the photon pulse output of the routing module.

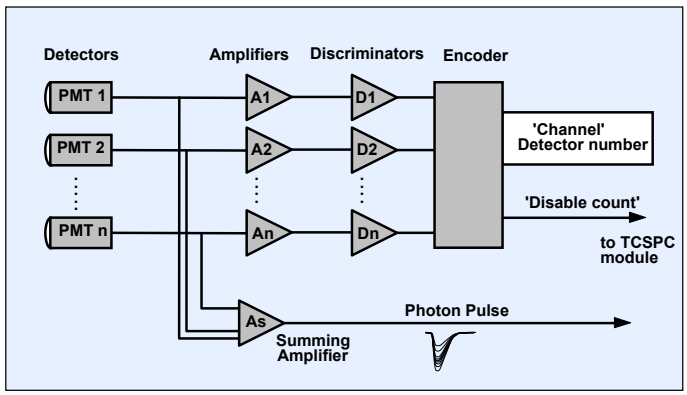


Fig. 206: Routing module for multi-detector TCSPC. For each photon, the routing module delivers the photon pulse and a ‘channel’ signal that indicates in which detector the photon was detected.

The function of the router is based on the assumption that the detection of several photons in *different* detectors within the response time of the amplifiers and discriminators is unlikely. The detection of several photons is, however, not impossible. The encoder is unable to deliver a valid routing information for such events. It does, however, easily detect them. It then delivers a ‘disable count’ signal, which suppresses the recording of the double event in the TCSPC module. Because simultaneous recording of several photons is more likely to happen in different detectors than in one a routing setup reduces pile-up effects (see section ‘Pile-Up Effects’, page 294).

Fig. 207 shows how the router works in combination with the TCSPC module. The CFD of the TCSPC module receives the single-photon pulse from the router, i.e. the amplified pulse of the detector that detected the photon. When the CFD detects this pulse, it starts a normal time measurement sequence for the detected photon. Furthermore, the output pulse of the CFD loads the ‘channel’ information from the router into the channel register. The informa-

tion loaded into the channel register controls the memory block in which the photon is stored. In other words, it is used as an additional dimension in the recording process. Thus, in the TCSPC memory separate photon distributions for the individual detectors build up.

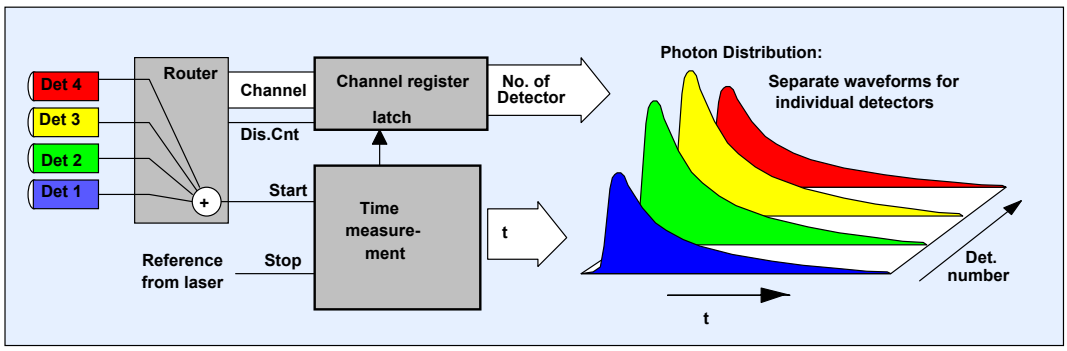


Fig. 207: TCSPC multidetector operation, several individual detectors. By the 'channel signal' from the router, the photons of the individual detectors are routed into separate memory blocks.

In the simplest case, these photon distributions are single waveforms. However, if the sequencer is used, the photon distributions of the individual detectors can be multidimensional themselves, see Fig. 214 or Fig. 218.

In practice, noise sets a limit to the number of individual PMTs that can be connected to a router. The cables connecting the PMTs to the router must be matched with 50 Ohm resistors. Even with a near-perfect summing amplifier, the noise from the matching resistors would be added to the output signal. Even worse is noise from the environment picked up by the detectors. While resistor noise adds by a square-root law, noise from the environment is more or less in phase for all detectors and therefore adds linearly. In practice, no more than eight individual PMTs are connected to one routing device.

A higher number of channels can be obtained if a multi-anode PMT is used. The system architecture is shown in Fig. 208.

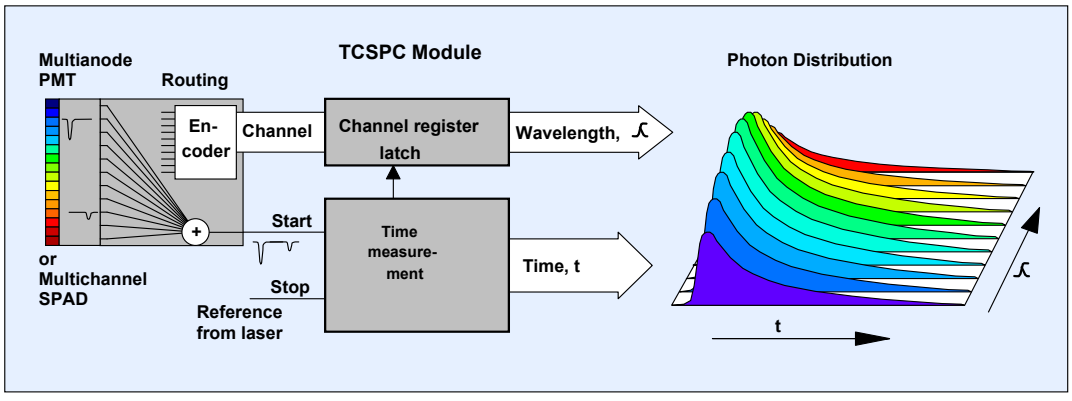


Fig. 208: TCSPC multidetector operation, multi-anode PMT

In a multi-anode PMT the photon pulses of all channels can be derived from the last dynode. The combination of the pulses works therefore without introducing noise. Using this method, devices with 32 channels and even 64 channels appear feasible. In practice the number of channels is limited mainly by the power dissipation of the routing electronics. Routers for multi-anode PMTs are combined with the PMT tube into a common detector housing. Heat from the electronics increases the temperature of the PMT and thus the background count rate. TCSPC multichannel detector heads are currently available for 16 channels [62].

Please note that the multidetector technique does not use any detector switching or multiplexing. Thus the multi-detector technique can considerably improve the counting efficiency of a TCSPC system. This is especially the case if a fluorescence signal has to be recorded with

spectral resolution. With a single detector several measurements have to be performed one after another, usually by scanning the spectrum by a monochromator. Most of the photons emitted by the sample are then lost. In a multidetector TCSPC system the signals of all wavelength intervals are detected simultaneously and loss of photons is avoided. Multi-detector TCSPC, especially multi-wavelength detection, has therefore become a commonly used technique of fluorescence lifetime imaging of biological samples and a standard technique of single-molecule spectroscopy.

Of course, the multidetector technique does not increase the maximum count rate (or the throughput rate) of a TCSPC system. In any TCSPC device there is a small but noticeable loss of photons due to the 'dead time' of the processing electronics. The dead time of the bh TCSPC devices is of the order of 100 ns, and for count rates above 1 MHz the counting loss becomes noticeable (see 'Counting Loss', page 292). The counting loss for a multi-detector TCSPC system is the same as for a single detector system operated at the total count rate of the detectors of a multi-detector system.

The multi-detector technique was first implemented in 1993 in the SPC-300 module of Becker & Hickl [140]. Although an amazingly efficient and versatile technique, it was first used widely only when diffuse optical tomography (DOT) began to require a large number of time-resolved detection channels [919, 920]. Other applications of the multidetector technique are time-resolved laser scanning microscopy, fluorescence correlation spectroscopy, single molecule spectroscopy, and multi-spectral measurement of transient fluorescence lifetime effects.

An alternative to the multi-detector technique is parallel operation of several independent TCSPC channels, which increases the total counting capability at the expense of higher system cost. Please see 'Multi-Module TCSPC Systems', page 137.

Multiplexed TCSPC

The routing capability of TCSPC can be used to multiplex several light signals and record them quasi-simultaneously. Multiplexing can be achieved on the excitation or on the detection side. Multiplexed excitation can be obtained by on-off modulating several ps diode lasers or changing the wavelength of the AOTF of a super-continuum laser. Multiplexing in the detector path is possible by rotating elements in the beam path [138], see Fig. 495, page 330 or by fibre switches, see 'Functional Brain Imaging', page 613.

Excitation Wavelength Multiplexing

The most common application of multiplexed TCSPC is quasi-simultaneous recording of signals excited by several multiplexed lasers. Diode lasers can be switched electronically via their 'laser on' inputs [81, 83, 84]. Other lasers may be multiplexed by acousto-optical modulators or by fibre switches. Multiplexing requires that a digital signal is available to indicate which laser is active. This signal is connected to the 'channel' signal input of the TCSPC module. Consequently, the photons of the different signals are routed into separate photon distributions. The principle for four multiplexed signals (or lasers) is shown in Fig. 209.

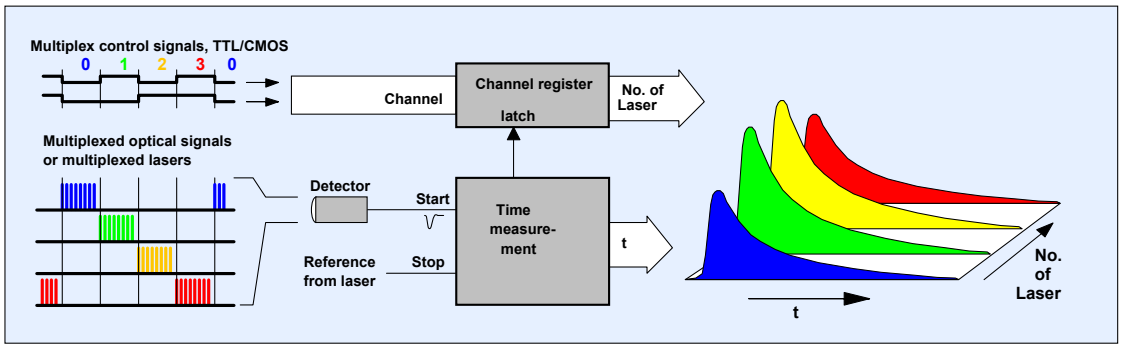


Fig. 209: Multiplexed TCSPC operation. Several signals, usually excited by several lasers, are actively multiplexed into the detector. The destination in the TCSPC memory is controlled by a multiplexing signal at the 'channel' input.

Multiplexing is similar to multi-detector operation (compare Fig. 207 and Fig. 209) in that it uses the routing capability of the SPC modules to send photons into different memory blocks. There is, however, a basic difference: Multiplexed recording actively switches between different signals, and controls the destination of the photons by a determinate signal from some kind of experimental control device. Multi-detector operation is random. The destination of a photon in the memory is controlled by a property of the photon itself, such as wavelength, polarisation, or position or direction in space.

Fast multiplexing has a number of advantages over consecutive recording of the same signals. The most obvious one is that slow changes in the sample do not cause direct artefacts in the results. Any change in the sample acts the same way on the signals for all multiplexing channels. Even if there is a change during the collection time the results remain comparable.

Moreover, there is practically no limitation of the multiplexing rate on the TCSPC side. If multiplexing in the experiment can be made fast, and a correct multiplexing status signal is provided, multiplexing periods in the ms and µs range can be used.

Multiplexed recording can be used in combination with multi-detector operation, sequential recording, or scanning (see sections below). In these cases, the memory blocks into which the multiplexing signal routes the photons are multi-dimensional photon distribution themselves. Each memory block represents a number of fluorescence decay curves (or other signal waveforms) for different detection wavelength, consecutive times after a stimulation event, or for different location in a scanning area. Multiplexed TCSPC for multi-dimensional data is shown in Fig. 210.

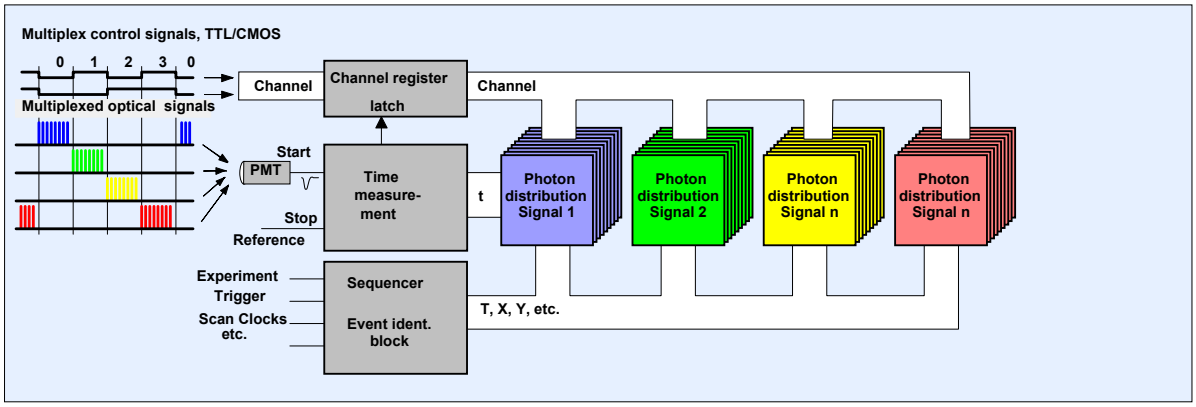


Fig. 210: Multiplexed TCSPC operation for multi-dimensional data. Several signals are actively multiplexed into the detector. The destination in the TCSPC memory is controlled by a multiplexing signal at the 'channel' input, and by additional information from the sequencer or event identification block.

Spatial Multiplexing

A combination of wavelength multiplexing and spatial multiplexing is used in diffuse optical tomography (DOT). The principle is shown in Fig. 211. Several picosecond diode laser beams are combined into a single optical fibre and multiplexed. The fibre with the combined lasers is connected to the input of a fibre switch, or split into several parts which are connected to several fibre switches. The fibre switch multiplexes the laser light (which by itself consists of several multiplexed laser wavelengths) consecutively into a large number of optical fibres which deliver the light to different sample positions. The diffusely transmitted light is recorded by a large number of detectors at other locations at the sample [633]. The detector signals are recorded by parallel TCSPC modules the 'Channel' inputs of which are used to record the signals of different source positions and laser wavelengths into different waveform memory blocks. To increase the number of detector positions the setup can be extended by routers. Please see 'Diffuse Optical Tomography', page 605.

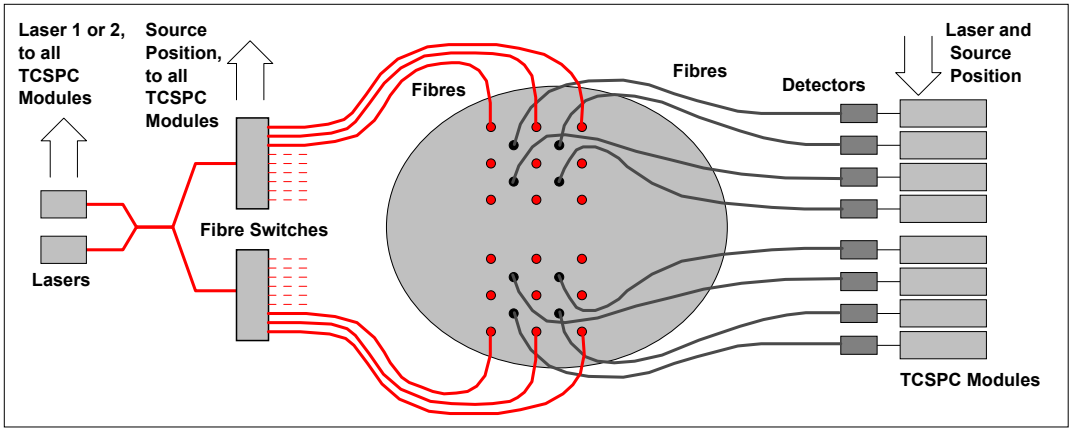


Fig. 211: Laser wavelength multiplexing and spatial multiplexing in time-resolved systems for diffuse optical tomography

Sequential Recording

Single Sequence

Sequential recording, also known as 'double kinetic mode' [190] or 'time-lapse recording', adds a second temporal dimensions to the photon distributions recorded by a single-detector, multi-detector, or multiplexed TCSPC system, see Fig. 212.

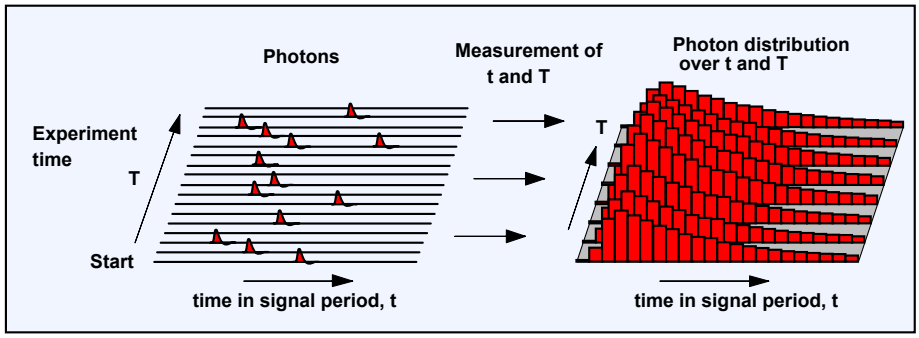


Fig. 212: Sequential recording: The TCSPC device builds up a distribution over the time in the signal period and the experiment time.

The technical principle for a single-detector system is shown in Fig. 213. Controlled by its internal clock oscillator, the sequencer switches through a specified number of waveform memory blocks.

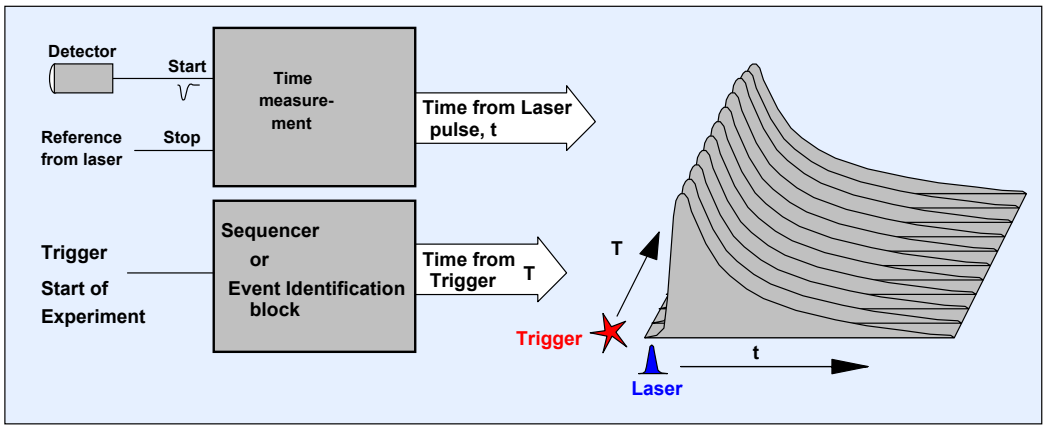


Fig. 213: Time-series recording with a single detector

The sequence can simply be started by an operator command. However, in practice the response of the measurement object to a stimulation event is investigated. The stimulation can be a strong laser pulse, a temperature jump, a change in an electric field applied across the sample, or the switch-on of the excitation source. The recording is then started by a trigger pulse that coincides with the stimulation. After being started, the sequencer steps through a defined (usually large) number of waveform memory blocks.

Instead of single waveforms (as shown in Fig. 213) the memory blocks may contain data that are complex photon distributions themselves. Sequential recording is possible for multi-wavelength data recorded by several detectors, data obtained by laser-wavelength multiplexing, time-resolved images, and even time-resolved multi-wavelength images. An example of a multi-detector setup is shown in Fig. 214.

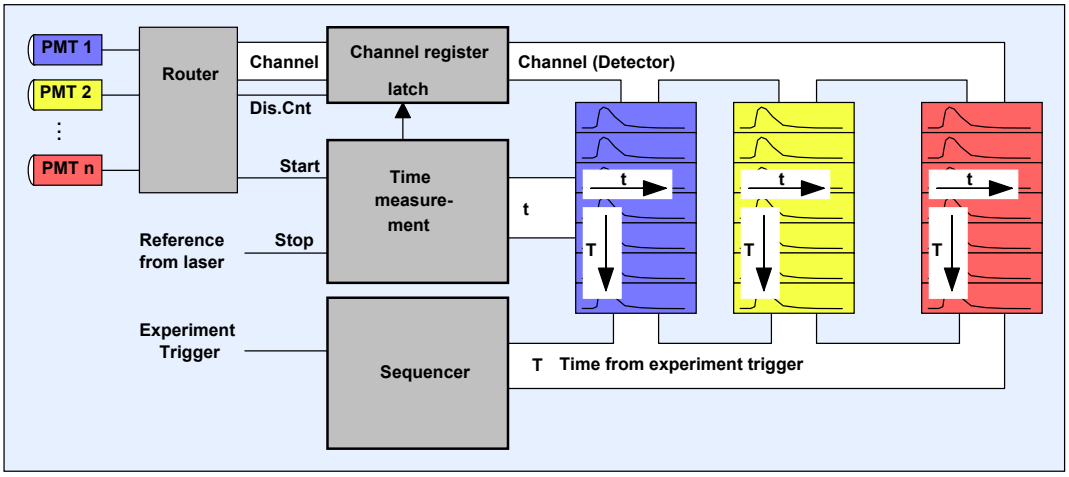


Fig. 214: Sequential recording. Triggered by the experiment trigger, the sequencer switches through a large number of memory blocks. Each block contains the photon distribution over the time in the signal period, t, and over the detector channels.

Triggered Accumulation of a Sequence

An obvious limitation of the procedure shown above is that the time increment of the experiment time, T, must be long enough to record a reasonable number of photons within this time. The problem can be avoided by ‘triggered accumulation’. Triggered accumulation requires that the stimulation of the measurement object is repeatable. The measurement object is then stimulated repeatedly, and each stimulation starts a sequence of recordings along the experiment-time (T) axis. After a large number of accumulations a photon distribution over t and T builds up, see Fig. 215.

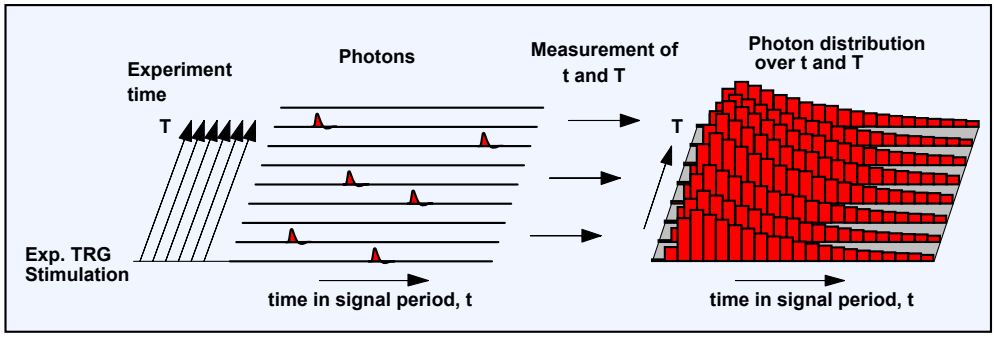


Fig. 215: Triggered accumulation of a sequence

With triggered accumulation, there is no longer a connection between the T increment and the signal-to-noise ratio. A photon distribution of the desired signal-to-noise ration will be obtained at any count rate and T increment, if only the number of accumulations (the total acquisition time) is made large enough.

High resolution in T does, of course, require full hardware control of the recording procedure. Depending on the SPC module type either the 'Scan Sync Out' or the 'Continuous Flow' mode can be used. Both modes achieve a T resolution of less than one microsecond. Please see page 747 and page 750 for system parameter setup.

Please note that the bh SPC devices also have an 'F(t,T)' mode for software-controlled sequencing. This mode should not be used for triggered accumulation of fast sequences. Stepping faster than 100 ms per step by software control becomes inaccurate, which makes an accumulation of sequences impossible.

'Continuous Flow' Recording

In the SPC-130, 150, and 160 devices a 'Continuous Flow' mode is implemented to record a virtually unlimited number of waveforms. The sequencer of the continuous-flow mode uses two independent data memory banks; see Fig. 216.

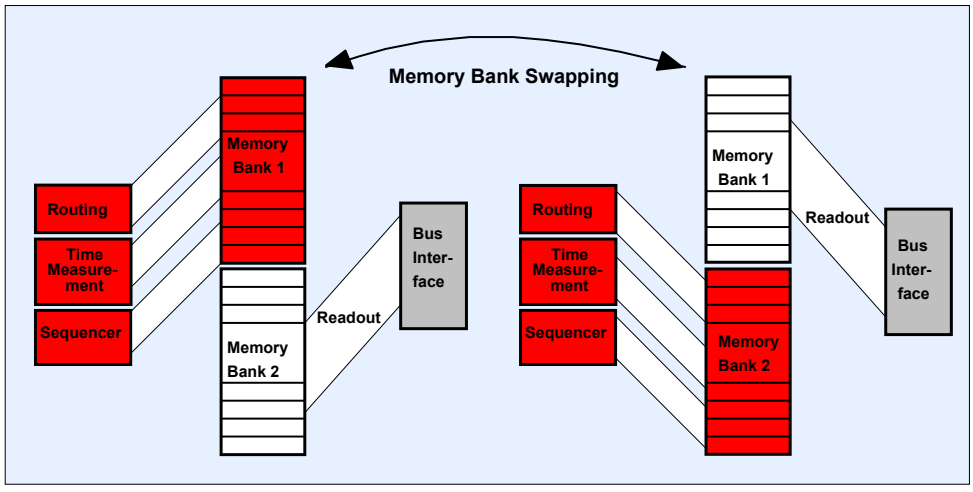


Fig. 216: Unlimited sequential recording by memory bank swapping. When one memory bank is full, the sequencer swaps the banks. While the sequencer writes into one bank, the other bank is read by the computer

After a trigger pulse or a start command by the operator, the sequence starts in the first memory bank. The sequencer switches through the memory blocks of the current bank. Again, each memory block provides space for a full photon distribution versus the time in the signal period, and the detector and multiplexing channel numbers. When the current memory bank is full, the sequencer swaps the memory banks and continues recording. While the measurement is running in one memory bank, the results of the other bank are read and stored to the hard

disk. Thus, a virtually unlimited number of decay curves can be recorded without any time gaps between the subsequent steps of the sequence [141].

The 'Continuous Flow' mode was introduced 1996 with the SPC-430 modules of bh. It was originally developed for DNA analysis and single-molecule detection in a capillary gel electrophoresis setup [141]. Now it is routinely used for dynamic brain imaging by diffuse optical tomography (DOT) techniques [784, 785, 786], see 'Diffuse Optical Tomography', page 605. The continuous flow mode can be used with a trigger signal that starts either the recording of each bank or the recording of each data block within the current bank. It is also possible to run triggered accumulation within one memory bank, and, after a defined number of accumulations pass to the next bank. With these options, the Continuous Flow mode provides fast and efficient recording procedures for a wide range of complex experiments.

In the SPC-150 modules Continuous Flow recording is even available in combination with imaging. Continuous Flow imaging delivers extremely fast time-series of fluorescence lifetime images [652], please see 'Time-Series FLIM', page 398.

Fluorescence Lifetime Imaging (FLIM)

The principle of a TCSPC FLIM system [143, 148, 154, 165, 167, 410] is shown in Fig. 217. A laser scanning microscope (or another scanning device) scans the sample with a focused beam of a high-repetition-rate pulsed laser. Depending on the laser used, the fluorescence in the sample can either be excited by one-photon or by multiphoton excitation. The TCSPC detector is attached either to a confocal or non-descanned port of the scanning microscope. For every detected photon the detector sends an electrical pulse into the TCSPC module. From this pulse, the TCSPC module determines the time, t, of the photon within the laser pulse sequence (i.e. in the fluorescence decay). Moreover, the TCSPC module receives scan clock signals (pixel, line, and frame clock) from the scan controller of the microscope. The sequencer of the TCSPC module is configured as a scanning interface. It contains two counters, X,Y, for the x and y location in the scanning area. Synchronously with the scanning action, the sequencer counts through x and y.

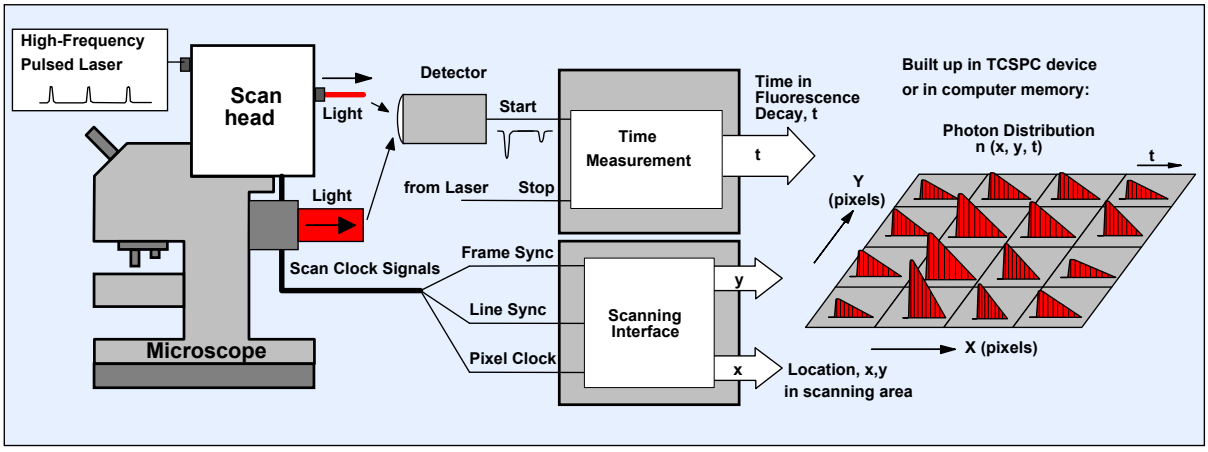


Fig. 217: Multidimensional TCSPC architecture for FLIM

For each photon pulse from the detector, the TCSPC module determines the time within the laser pulse period (i.e. in the fluorescence decay) and the location within the scanning area, x and y. The photon times, t, and the spatial coordinates, x and y, are used to address a memory in which the detection events are accumulated. Thus, in the memory the distribution of the photon density over x, y, and t builds up. The result is a data array representing the pixel array of the scan, with every pixel containing a large number of time channels with photon numbers for consecutive times after the excitation pulse. In other words, the result is an image that contains a fluorescence decay curve in each pixel [148, 154, 167].

In contrast to conventional slow-scan techniques, multi-dimensional TCSPC does not require that the scanner stays in one pixel until enough photons for a full fluorescence decay curve have been acquired. It is only necessary that the *total pixel acquisition time*, over a large number of frames, is large enough to record a reasonable number of photons per pixel. Thus, TCSPC FLIM works even at the highest scan rates available in laser scanning microscopes (see 'Polygon Scanners', page 449). At the pixel rates used in practice, the recording process is more or less random: A photon is just stored in a memory location according to its time in the fluorescence decay, its detector channel number, and the location of the laser spot in the sample in the moment of detection.

In early TCSPC FLIM systems the photon distribution was built up directly in the hardware of the TCSPC module (Fig. 202, page 114). The advantage of hardware accumulation is that the acquisition works independently of the computer. It can therefore be run at extremely high photon rates and scan speeds. The disadvantage is that the available memory space is limited. A typical application of hardware-accumulation is the 'Preview' mode of FLIM systems where images must be recordable up to almost any count rate and displayed at high image rate, but with a relatively moderate number of pixels and time channels.

The way to obtaining larger images is to use software accumulation, i.e. the configuration shown in Fig. 203, page 115. The TCSPC device transfers the data of the individual photons and the clock pulses to the computer, and the photon distribution is built up by software. The required hardware architecture and suitable acquisition modes were available even in early TCSPC modules, for instance the SPC-435 and the SPC-630. However, the bus transfer speed and the processing capabilities of the PCs of the 1990s was insufficient for this kind of operation. At count rates above 100 kHz and pixel rates on the order of 1 MHz, as they are routinely used in FLIM, the computer was not able to read the data from the SPC module and simultaneously process them to build up a photon distribution.

The situation changed with the introduction of fast multi-core PCs. The tasks of data transfer and data processing could now be shared between the CPU cores. Count rate in the parameter-tag mode was no longer a problem. Modern TCSPC FLIM system therefore use almost exclusively software accumulation. Typical images sizes with 32-bit operating systems were 512 x 512 pixels, with 256 time channels per pixel, see Fig. 47, page 25. With the introduction of 64-bit operation systems and corresponding 64-bit data acquisition software, the maximum image size for the bh FLIM modules increased to 2048 x 2048 pixels x 256 time channels and more [103, 1198]. Pixel numbers this large are enough to record images of the maximum field of view even of the best microscope lenses. FLIM applications running on 64-bit SPCM software are therefore rarely limited by memory size.

Multi-wavelength FLIM

Multi-wavelength FLIM uses a combination of the FLIM architecture shown in Fig. 217 with the multi-wavelength detection principle described in Fig. 208, page 118. A spectrum of the fluorescence light is spread over an array of detector channels. In addition to the times of the photons and the positions, x, and y, of the scanner, the TCSPC module determines the detector channel that detected the photon. These pieces of information are used to build up a photon distribution over the time of the photons in the fluorescence decay, the wavelength, and the coordinates of the image [154, 156, 165, 167]. The result is an image that contains several decay curves for different wavelength in each pixel, see Fig. 218, right.

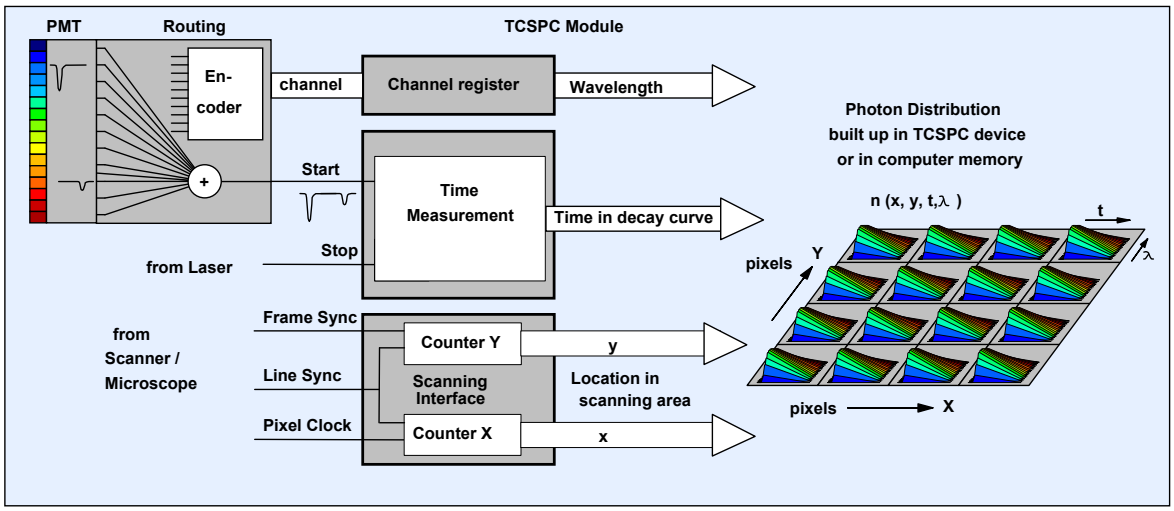


Fig. 218: Multi-wavelength FLIM. The recording process builds up a photon distribution over x,y,t, and λ in the device memory. The result is an array of pixels, each containing a number of fluorescence decay curves for different wavelength.

Multi-wavelength FLIM requires a large amount of memory. Already for images of 128 x 128 pixels, 256 time channels, and 16 wavelength channels 134 MB of memory space are required. Multi-wavelength FLIM can therefore performed at reasonable pixel numbers only by building up the photon distribution in the computer memory. Significant progress has been made with the introduction of 64-bit data acquisition software. In the 64-bit environment, data with 16 wavelength channels can be resolved into images of 512 x 512 pixels, and 256 time channels [103, 1198]. Please see Multispectral FLIM, page 366.

TCSPC FLIM with Excitation Wavelength Multiplexing

FLIM can be combined with excitation wavelength multiplexing. The extension of the principle of TCSPC FLIM to excitation-multiplexed FLIM is shown in Fig. 219. Excitation at different wavelength is achieved by multiplexing (on/off switching) of several lasers, or by switching the wavelength of the acousto-optical filter (AOTF) of a super-continuum laser. A multiplexing signal that indicates which laser (or laser wavelength) is active is fed into the routing input of the TCSPC module. The signal represents the excitation wavelength. The TCSPC module is running the normal FLIM acquisition process: It builds up a photon distribution over the coordinates of the scan area, the photon times, and the excitation wavelength. The result is a data set that contains images for the individual excitation wavelengths. It can also be interpreted as a single image that has several decay curves for different excitation wavelengths in its pixels.

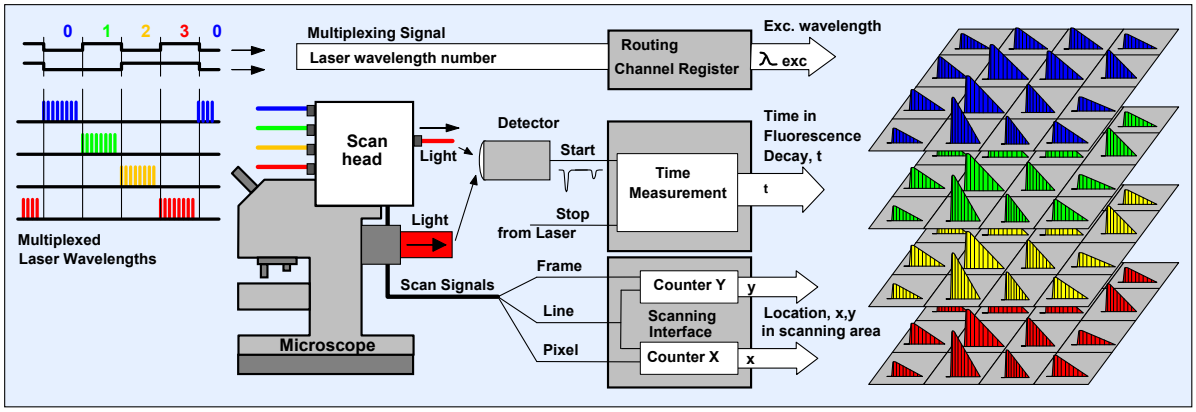


Fig. 219: FLIM with laser wavelength multiplexing

To avoid interference of the multiplexing frequency with the pixel, line, or frame frequency of the scanner, multiplexing is normally synchronised with the pixels, the lines, or the frames of the scan. Images for different combinations of excitation and emission wavelengths can be obtained by using several detectors and a router. Modern implementations normally use several parallel TCSPC modules, running on the same multiplexing signal. Examples are shown in Section 'Excitation-Wavelength Multiplexing' page 371.

Excitation wavelength multiplexing can also be performed by 'Pulse-Interleaved Excitation', or 'PIE'. PIE does not use the laser wavelength as a dimension of the photon distribution. Instead, the pulse trains of several (usually two) lasers are interleaved pulse by pulse, and the fluorescence decay functions excited by both lasers are recorded into a single waveform. The recorded waveform contains the fluorescence decay excited by one laser followed by the decay excited by the other. The data of the two excitation channels are selected by time-gating in the data analysis. Data for different combinations of excitation and emission wavelengths are recorded by using several parallel TCSPC channels or a single TCSPC channel with a router.

The advantage of PIE in FLIM applications is that it is also applicable to lasers that cannot be on-off modulated at high speed. The disadvantage is that PIE is not entirely free of crosstalk. The tails of the fluorescence decay excited by one laser may extend into the decay excited by the other. Moreover, there is intensity crosstalk due to counting loss, and mutual influence by detector afterpulsing. For a comparison of PIE and laser multiplexing please see 'Multiplexing of Lasers', page 298.

Mosaic FLIM

Spatial Mosaic FLIM

The Mosaic FLIM function was introduced in 2014 in conjunction with the new SPM 64-bit data acquisition software. Originally, Mosaic FLIM was designed to operate with the 'Tile Imaging' function of laser scanning microscopes. The microscope scans an image at one position of the sample, then offsets the sample by the size of the scan area, and scans a new image. The process is repeated, and the images of the individual frames are stitched together. This way, a sample area larger than the field of view of the microscope lens can be imaged. The TCSPC FLIM process of Mosaic FLIM is illustrated in Fig. 220.

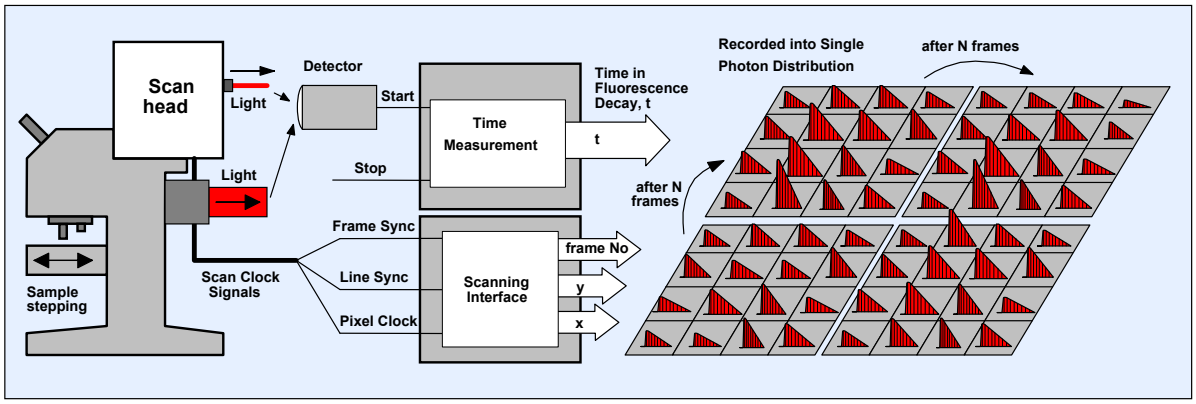


Fig. 220: Mosaic FLIM, recording of a X-Y mosaic

The microscope scans the sample, and performs a raster stepping ('Tile stepping') of the sample. For every step the sample is scanned for a defined number of frames. The TCSPC device records the data by its normal FLIM procedure. However, the memory is configured to pro-

vide space not only for a single image of the defined frame format but for the entire mosaic of images of the tile stepping. The TCSPC FLIM process starts in the first mosaic element. After a defined number of frames the recording passes to the next mosaic element. Provided the number of frames per tile of the microscope stepping and the number of frames per mosaic elements are the same the TCSPC module records the complete tile array into a single photon distribution. The recorded photon distribution represents a FLIM image of the entire array. An example is shown in Fig. 591, page 400.

Of course, Mosaic FLIM requires an extraordinarily large amount of memory. Therefore, it can be performed only with software accumulation and with 64-bit software [103, 1198].

Z Stack Recording

The idea that Mosaic FLIM records several images into a single photon distribution leads to a more general concept of Mosaic FLIM: The transition from one mosaic element in the FLIM data to the next can be associated not only to tile stepping but also to other parameters of the experiment. An obvious application is Z-stack FLIM. In that case, the microscope performs steps in Z (the depth in the sample), and the mosaic elements represent images in different depth of the sample. The procedure is the same as for Tile Imaging, except for the fact that the meaning of the data is different. For results please see Fig. 576 to Fig. 578, page 391.

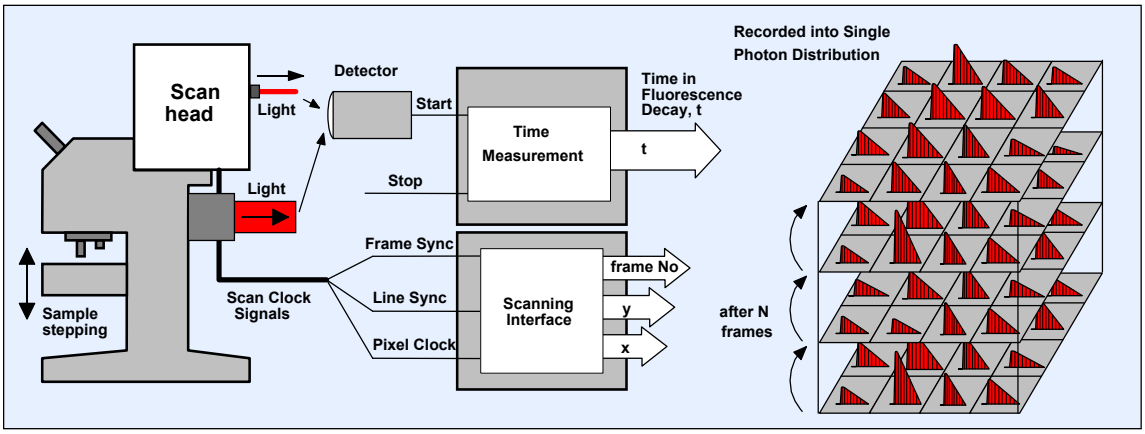


Fig. 221: Z Stack recording by the Mosaic FLIM

It should be noted that Z stack recording can also be performed by a conventional record-and-save procedure, see Fig. 602, page 407. In that case, consecutive recordings are performed for different depth in the sample, and the results are saved in separate files. The advantage of Mosaic-based recording is that no time (and no frame of the scan) is lost during the save operations, and that the entire Z stack can be analysed in a single computation run. This makes it easier to analyse the data with global parameters (see ‘Analysing FLIM Data with SPCImage’, page 871).

Temporal Mosaic FLIM

Mosaic FLIM also provides an excellent way to record fast FLIM time series. The sample is scanned in the same spatial position, but subsequent images are recorded in consecutive elements of the FLIM mosaic. The result is a time series, the time step of which is a multiple of the frame time. The principle is shown in Fig. 222.

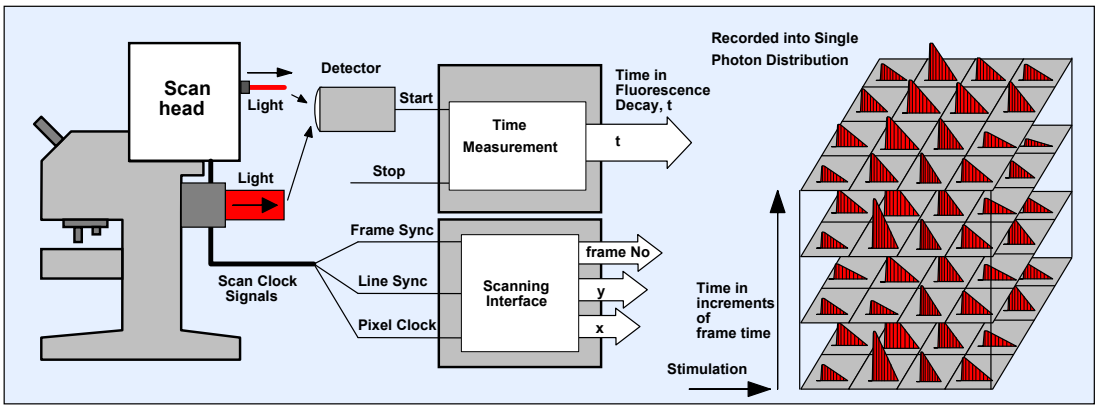


Fig. 222: Temporal Mosaic FLIM

Compared to the conventional record-and-save procedure the Mosaic procedure has several advantages: No time has to be reserved for the save operations, and the data can be better analysed with global-parameter fitting. The biggest advantage is, however, that mosaic time series data can be accumulated: A sample would be repeatedly stimulated by an external event, and the start of the mosaic recording be triggered by the stimulation. With every new stimulation the recording procedure starts a run through all elements of the mosaic, and accumulates the photons. Accumulation allows data to be recorded without the need of trading photon number and lifetime accuracy against the speed of the time series. Consequently, the time per step (or per mosaic element) is only limited by the minimum frame time of the scanner. For pixel numbers on the order of 128 x 128 pixels and small scan areas galvanometer scanners reach frame times on the order of 50 milliseconds. Resonance scanner are even faster. This brings the time-series resolution into the range where even lifetime changes by Ca^{2+} transients in neurons can be recorded, see ‘Temporal Mosaic FLIM’, page 402. Previously, this was only possible by FLITS, i.e. recording the decay functions within the pixels of a line scan [164, 463], see below.

FLITS

Temporal Mosaic FLIM is able to record a FLIM time series at a time per image down to the frame time of the optical scanner. Faster effects can be resolved by a combination of TCSPC and line scanning. The technique has been named ‘FLITS’, fluorescence *lifetime-transient* scanning [162, 164, 463]. FLITS is based on building up a photon distribution over the distance along the line of the scan, the experiment time after a stimulation of the sample, and the arrival times of the photons after the excitation pulses. The principle is shown in Fig. 608.

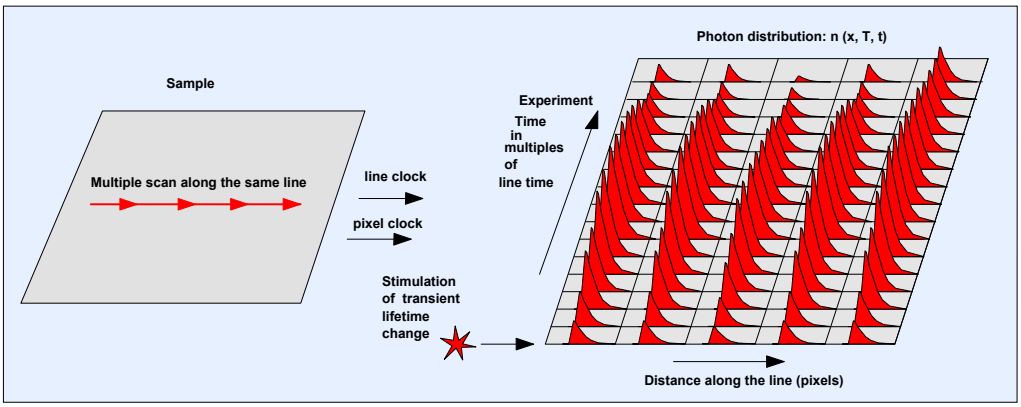


Fig. 223: Principle of FLITS. A sample is scanned along a line, the TCSPC system builds up a photon distribution over the distance along the line, the time after a stimulation of the sample, and the times of the photons after the excitation pulses.

FLITS uses the same recording procedure as FLIM. Similar as for FLIM, the result is an array of pixels, each of which contains a fluorescence decay curve in the form of photon numbers in subsequent time channels. The recording is synchronised with the scan by pixel clock pulses (which indicate the transition to the next pixel of the line) and line clock pulses, which indicate the transition from the end of the line back to the start. The procedure differs from FLIM in that the frame clock pulses do not come from the scanner but from an external event that stimulates a fluorescence-lifetime change in the sample. The TCSPC module thus records a photon distribution which has the Y coordinate of FLIM replaced with a coordinate that represents how often the scanner scanned along the line since the stimulation. In other words, the Y coordinate is the time after the stimulation, given in multiples of the line time.

As long as the stimulation occurs only once the recording process is simple: The sequencer of the TCSPC module starts to run with the stimulation, and puts the photons from the subsequent line scans in consecutive lines along the T axis. The result is identical with a time-series of line scans.

However, there is an important difference: The data are still in the memory (either in the onboard memory of the TCSPC module or in the computer) when the sequence is completed. Thus, the recording process can be made repetitive: The sample would be stimulated periodically, and the start of T triggered by the stimulation. The recording then runs along the T axis periodically, and the photons are accumulated into one and the same photon distribution.

With repetitive stimulation of the sample, it is no longer necessary that each T step acquires enough photons to obtain a complete decay curve in each pixel and T channel. No matter when and from where a photon arrives, it is assigned to the right location in x, the right experiment time, T, and to the right arrival time, t, after the laser pulse. As in the case of FLIM, a desired signal-to-noise-ratio is obtained by simply running the recording process for a sufficiently long acquisition time. Obviously, the resolution in T is limited by the period of the line scan only, which is about 1 ms for the commonly used galvanometer scanners. For resonance scanners and fast polygon scanners the line time can be made even shorter.

FLITS is therefore an elegant way to record fast changes in the fluorescence lifetime of a sample with - though only one-dimensional - spatial resolution. FLITS can be performed in the normal FLIM modes of a TCSPC module. It does neither require an extraordinarily large amount of memory nor extremely high computation power. The data can be analysed by normal FLIM data analysis software. The application to Ca^{2+} transients in live neurons has been published in [164, 463], details are described in Section ‘FLITS: Fluorescence Lifetime-Transient Scanning’, page 410.

Dual Time-Base Recording

A bh TCSPC module can, in principle, record an optical waveform simultaneously on two different time scales. One time scale comes from the TAC, the other from the sequencer. By timing the photons both by the TAC times and the sequencer times, simultaneously photon distributions on the picosecond and on the microsecond time scale can be build up.

The technique is used to record fluorescence and phosphorescence decay data simultaneously. The principle is shown in Fig. 224. A high-frequency pulsed laser is on-off modulated with a period in the microsecond or millisecond range. The TCSPC module determines photon times, t, within the laser pulse period, and photon times, T, within the laser modulation period. Fluorescence decay curves are obtained by building up a photon distribution over t, phosphorescence decay curves by building up a the photon distribution over T. The technique solves a number of problems of phosphorescence decay measurement. The most significant one is that for phosphorescence decay measurement the duration and the period of the excitation must be long. This conflicts with the capabilities of the available lasers, and with the re-

quirement that for fluorescence decay measurement the pulses and the pulse period must be short. With the principle shown in Fig. 224, the effective excitation pulse for the phosphorescence measurement is the laser-on period, but for fluorescence it is the single laser pulse. Examples of simultaneous fluorescence and phosphorescence decay recording are shown in Section 'Simultaneous Measurement of Fluorescence and Phosphorescence Decay', page 340.

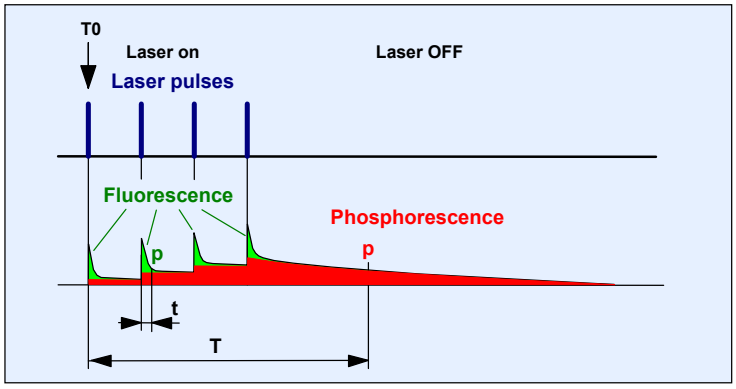


Fig. 224: Build-up of phosphorescence within a burst of laser pulses

To combine the technique shown in Fig. 224 with imaging the scan coordinates must be included in the parameters of the photon distributions. A phosphorescence lifetime image (PLIM) is obtained by recording the photons versus the times, T, in the laser on-off period and the scan coordinates, a fluorescence lifetime image (FLIM) by recording the photons versus the TAC times, t, and the scan coordinates. Both processes can be run simultaneously. The TCSPC system architecture for simultaneous FLIM / PLIM is shown in Fig. 225.

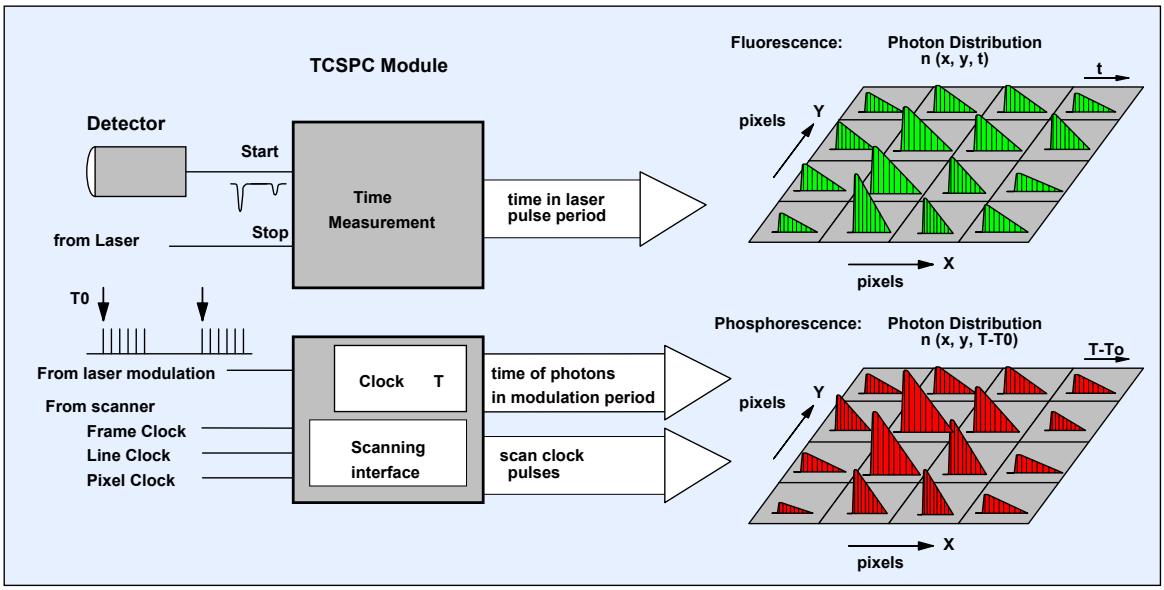


Fig. 225: Simultaneous fluorescence and phosphorescence lifetime imaging in the parameter-tag mode

The procedure can be refined by using the laser on/off information as a routing signal to better separate the fluorescence in laser-on phases from the phosphorescence in the laser-off phases. Please see page 434 in the application part of this handbook. For parameter setup see 'Microsecond Lifetime Imaging: MCS FLIM', page 767.

Recording Parameter-Tagged Photon Data

Many of the TCSPC configurations described above transfer parameter-tagged single-photon data into the system computer which immediately processes the data to builds up photon distributions. Once a photon has been put into the photon distribution the information associated to it is no longer needed and, normally, discarded.

Parameter-tagged photon data may, however, be used to build up other results than multi-dimensional photon distributions. At the time of the experiment it may even not be clear how exactly the photon data are to be processed. User-interaction during the data processing may be required, or the processing may require so much computation power that it cannot be performed online. In these cases the single-photon data can be saved for later off-line processing. The bh TCSPC modules can save parameter-tagged data in the FIFO mode and in the FIFO Imaging mode. The general structure of parameter-tagged single-photon data and the use of such data in a few typical applications will be described below.

SPC Module Architecture

The architecture of a TCSPC device in the Parameter Tag mode is shown in Fig. 226, the structure of the parameter-tagged data in Fig. 227. The TCSPC configuration is identical with the configuration shown in Fig. 203, page 115. Each photon is tagged with its time after the excitation pulse (the 'micro time'), the time from the start of the recording (the 'macro time'), and the data word from the 'channel' register of the TCSPC device. External events, such as transitions of scan clock signals, are also put in the stream. Several identifier bits mark a particular entry either as a photon or as an external event. Of course, the entries of external events do not contain valid micro time information. The micro time bits of external events may therefore be used to transfer other information.

The macro-time clock has normally a resolution of 25 or 50 ns. However, an experiment can be run over a time of seconds, minutes, or even hours. Because the number of macro time bits in the photon data word is limited the macro time will overflow in regular intervals during the recording. To allow the data processing software to account for the overflows these are marked in the data. Macro time overflow marks can either be attached to the photon data words or be put in the data stream the same way as external events.

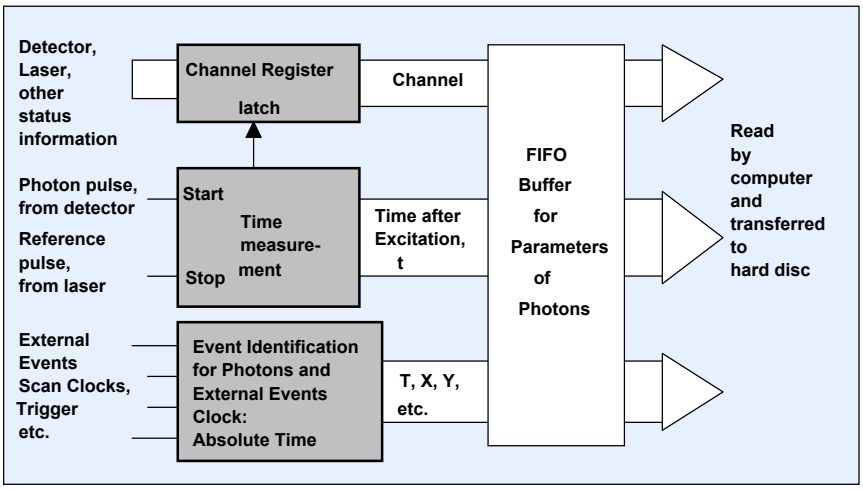


Fig. 226: TCSPC configuration in the Parameter-Tag mode

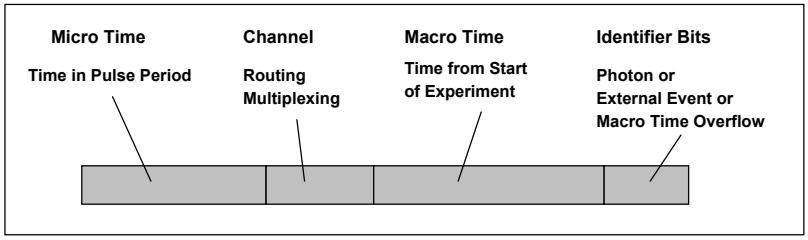


Fig. 227: Structure of parameter-tagged photon data

The source of the macro time clock can be an internal quartz oscillator of the module, the macro time clock from another TCSPC module, or the reference (SYNC) signal from the laser. Thus, fully synchronous macro-time clocks in several TCSPC modules can be obtained. This allows the photon times of several TCSPC modules to be cross-correlated, see chapter 'Fluorescence Correlation Spectroscopy' page 639. Photon data can even be cross-correlated down to the ps time scale [442] see 'FCS Down to the Picosecond Time Scale', page 644.

It is, of course, imperative that the computer reads the photon and marker data at a rate higher than the average photon count and event rate. The requirements to the readout rate are relaxed by the large size of the FIFO buffer. Both the detection rate and the readout rate are not constant. In many applications the count rates vary over time, or bursts of photons may appear on a background of low count rate. The FIFO buffers temporarily high photon rates, and buffers the data during periods when the computer does not read data. With a sufficiently large FIFO the computer has to read the data only at an *average readout rate* equal to the *average photon rate*. In the bh SPC modules FIFO sizes of 128,000 to 8 million photons are used. Average readout rates are on the order of several million photons or events per second. Readout rate was a limitation in the 1990s but has ceased to be a problem since fast multi-core PCs an multi-thread processing were introduced.

A remark should be made here about attempts to use the parameter-tag, FIFO, or time-tag mode in *any* application. It is correct that the result of any multi-dimensional TCSPC measurement can, in principle, be extracted from parameter-tagged data. Parameter-tagged single-photon data would just be recorded, and then analysed to squeeze out as much as possible information. However, this does not mean that such procedure is efficient or even feasible. There is an increasing number of biomedical TCSPC applications which record at high count rate, and in a large number of parallel TCSPC channels. Dynamic effects in the recorded optical signals (if there are any) are on the time scale from 100 ms to tens of seconds. Recording such dynamics with 25 to 50 ns resolution of the FIFO mode would result in extreme requirements to the computing power and unacceptably large data files.

Applications that require recording of parameter-tag data are mainly in single-molecule spectroscopy. Common applications are briefly described below. For details please see application chapters of this book.

Fluorescence Correlation Spectroscopy (FCS)

Calculation of FCS from Parameter-Tag data

Fluorescence Correlation Spectroscopy (FCS) is based on the recording of fluorescence from a limited number of fluorescing molecules in a small sample volume, and correlating intensity fluctuations caused by the motion of the molecules [151, 153, 1011]. The data processing procedure for FCS is usually described by the correlation functions

$$G(\tau) = \lim_{T\to\infty} \frac{1}{2T} \int_{-T}^{+T} I(t)\, I(t+\tau)\, dt \qquad G_{12}(\tau) = \lim_{T\to\infty} \frac{1}{2T} \int_{-T}^{+T} I_1(t)\, I_2(t+\tau)\, dt$$

where $G(\tau)$ is the autocorrelation function of a single signal, $I(t)$, and $G_{12}(\tau)$ the cross-correlation function of two signals, $I_1(t)$ and $I_2(t)$.

For TCSPC parameter-tag data the definition above is not very useful. TCSPC data are not analog waveforms but photon counts, N, in consecutive, discrete time channels. In that case $G(\tau)$ and $G_{12}(\tau)$ can be obtained by calculating

$$G(\tau) = \sum N(t) \cdot N(t+\tau) \quad \text{and} \quad G_{12}(\tau) = \sum N_1(t) \cdot N_2(t+\tau)$$

The procedures for FCS calculation from TCSPC parameter tag data are described in detail in Chapter 'Fluorescence Correlation Spectroscopy', page 639.

An example of FCS calculated from parameter-tagged data is shown in Fig. 228. The data were recorded by a bh DCS-120 confocal FLIM system [68]. On average, about 0.4 molecules were in the detection volume at a time. The average count rate was about 5000 photons per second.

Fig. 228, top, shows an intensity trace of the recorded signal. The time bin width is 10 µs, the time over shown part of the trace is 10 ms. At a count rate of 5000 s^{-1} there are about 50 photons over a period of time of 10 ms. Consequently, the trace consists of random single-photon detection events. Most of the time bins are empty, and there are no time bins with more than a single photon.

The autocorrelation function is shown at the bottom of Fig. 228. Note that the τ scale of the FCS curve was selected similar to the time scale of the intensity trace. However, the FCS curve was calculated over the complete acquisition time of the measurement, in this case 120 seconds. It shows a clear correlation of the intensity fluctuations caused by diffusion of the molecules.

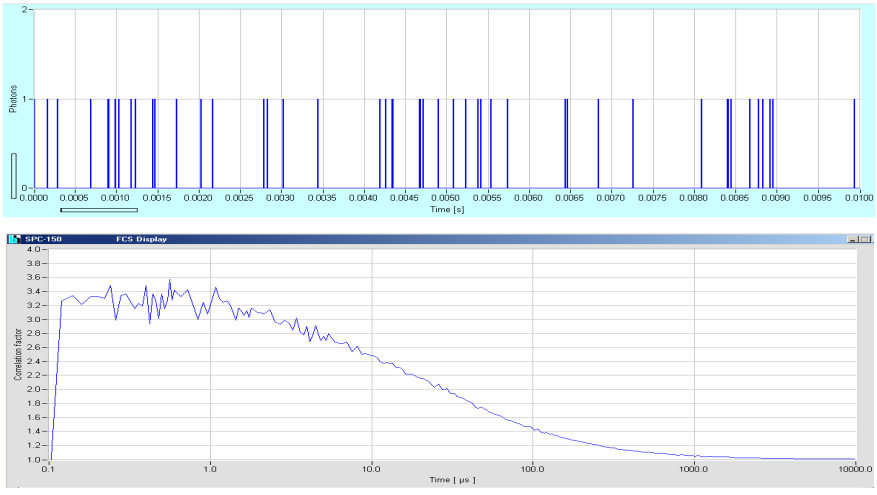


Fig. 228: Top: Intensity trace, time bin width 10 µs, displayed time interval 10 ms. Bottom: Autocorrelation curve from the same signal, correlation time from 100 ns to 10 ms. Calculated over acquisition time of 120 seconds.

That a correlation curve is obtained from the data shown in Fig. 228, top, may surprise at first glance. It is a result of the fact that the data have been correlated over a period of 120 seconds, not only over the time interval shown in the intensity trace in Fig. 228, top. This is another example that the signal-to-noise ratio in single-photon counting experiments depends on

the total acquisition time, not on the number of photons within the time channels of the raw data.

Most FCS applications aim at the estimation of the size of labelled biomolecules, on the detection of interaction between biomolecules, and on determination of the number of fluorescent molecules attached to a special biomolecule. The size of the molecules can be derived from the diffusion time, i.e. the point of the autocorrelation function at it which drops to 50 % of its maximum. More accurately, the diffusion time is obtained by fitting the autocorrelation function with an appropriate model. Interaction of molecules is derived from the cross-correlation functions. Different biomolecules are labelled with fluorophores of different absorption and emission spectra. The cross-correlation (FCCS) function of the two signals indicates whether the constructs diffuse together or independently. Please see Chapter 'Fluorescence Correlation Spectroscopy', page 639. The number of fluorescent molecules linked to a biomolecule is derived from the 'molecular brightness' which is the average number of photons detected for a single labelled biomolecule.

The correlation function is also used for perfusion measurements in diffuse optical imaging. The technique is based on correlating intensity fluctuations of photons scattered in the blood flowing in the tissue [298]. The technique is described in Chapter 'Diffuse Optical Tomography: DOT, NIRS and fNIRS'.

In terms of TCSPC data acquisition FCS and FCCS are very simple applications. They even do not need the micro-times of the photons, and do not need a pulsed excitation source. FCS and FCCS are, however, anything but simple in respect to the optical system and the detectors: Excellent optical efficiency, low chromatic and spherical aberration, excellent alignment of the confocal optics, and excellent detection efficiency are necessary to obtain good FCS results. Please see Chapter 'Fluorescence Correlation Spectroscopy' for technical details.

Using the Micro-Time of TCSPC in FCS

The calculation of FCS by the algorithms shown above are based exclusively on the macro times of the photons. FCS and Cross-FCS can therefore also be obtained by excitation with CW lasers. If the fluorescence is excited by pulsed lasers the micro time of the photons can be used in several ways.

Simultaneous Recording of FCS and Fluorescence Decay Functions

Obviously, fluorescence decay curves can be obtained in parallel with the FCS measurement. All that is necessary is to build up a photon distribution over the micro times of the photons. From the combined data, information on the size of a biomolecule, on its structure, on its interaction with the molecular environment, on possible protein aggregation, and on the number fluorophore molecules linked to it can be derived. Please see 'Simultaneous Recording of FCS and Fluorescence Decay Functions', page 643.

Time Gating

FCS signals are sometimes contaminated by Raman scattering. Raman light shows up as a sharp peak at the beginning of the fluorescence decay. The peak can be gated off, either by setting a time gate in the TCSPC hardware, or by excluding photons with macro times outside a selectable time window. Time gating can also be necessary when FCS is recorded with pulse-interleaved excitation (PIE). Please see 'Time Gating of FCS', page 644.

Filtered FCS

Micro times can be used to separate FCS signals of fluorophores of different fluorescence decay times. In that case, the photons are weighted with a coefficient derived from the micro time via a filter function [231, 444].

Global Fit of FCS and Decay Data

Another way to improve the separation of diffusion components of different species in FCS analysis has been developed by Anthony and Berland [23, 24]. The idea is to fit all parameters, i.e. the fluorescence lifetimes, the component amplitudes, and the diffusion times of the FCS components by single, global fit routine. This greatly improves the separation of the diffusion components of different fluorescing species.

FCS down to the Picosecond Time Scale

By including the micro times, photons can be correlated down to the picosecond time scale. The principles has been introduced by Felekyan et. al. in 2005 [442]. It uses two synchronised TCSPC modules. The internal macro time clock is synchronised to the signal at the stop inputs of the TCSPC modules [154]. Please see 'FCS Down to the Picosecond Time Scale', page 644.

Single-Molecule Burst Analysis

Consider a solution of fluorescent molecules, excited by a focused laser beam through a microscope lens, with the emitted photons being detected through a confocal pinhole that transmits light only from a volume of diffraction limited size. When the concentration of fluorescent molecules is low enough only one molecule will be in the detection volume at a time. As the molecule diffuses through the excitation/detection volume it emits photons. Thus, the detection signal consist of bursts of photons caused by individual molecules, see Fig. 229.

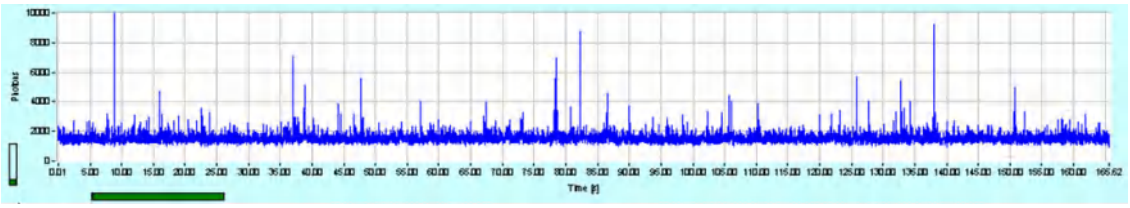


Fig. 229: Photon bursts from single molecules travelling through a femtoliter-size detection volume

The idea behind single-molecule burst analysis is to identify the bursts in the intensity traces, determine as many as possible fluorescence parameters for the individual bursts, and build up multi-dimensional histograms of the frequency of the bursts versus the parameter values. It is even possible or record changes of fluorescence parameter within the individual bursts [378, 426, 986, 378, 936, 991, 991, 1336]. Please see 'Multi-Parameter Single-Molecule Burst Analysis', page 667.

Multi-Module TCSPC Systems

The maximum count rate of a single TCSPC channel is limited by the counting loss due to the 'dead time' of the TCSPC channel, by pile-up effects, and by the counting capability of the detector.

Compared with classic systems, the dead time of advanced TCSPC systems has been considerably reduced. It is however, still on the order of 80 to 150 ns. Further reduction of the dead time is technically difficult. It is even not desirable in some instances because it leads to an increase in the afterpulsing background, see 'Counting Background', page 275. The fraction of photons lost in the dead time - the 'counting loss' - becomes noticeable at detector count rates higher than 10% of the reciprocal dead time (see 'Counting Loss', page 292).

Pile-up is caused by the detection (and loss) of a second photon within the same signal period with a previous one. Because a second photon is more likely to be detected in the later part of a signal period, pile-up causes a distortion of the signal shape (see 'Pile-Up', page 294). The pile-up distortion is smaller than commonly believed (see Fig. 453, page 295). Reasonable results can be obtained up to a detector count rate of 10 to 20% of the signal repetition rate. Nevertheless, pile-up sets a limit to the applicable count rate.

The third limitation, the counting capability of the detector, depends on the detector type used, the voltage divider design of a PMT, and on the requirements to the IRF stability, the long-term gain stability, and the detector lifetime. For conventional PMTs the practical limit for TCSPC is of the order of 5 to 10 MHz. For MCP-PMTs the maximum count rate is 200 kHz to 2 MHz, depending on the MCP gain used. SPADs (single-photon avalanche photodiodes) can be used up to a count rate of a few MHz.

Because of pile-up, and detector effects, a breakthrough in the counting capability of TCSPC cannot be achieved by simply making the signal processing electronics of the TCSPC device faster.

The solution to the count-rate problem is multi-module operation. Splitting the light into several detectors connected to independent TCSPC modules proportionally increases the counting capability. Of course, multi-module operation also increases the system cost and can cause space and power supply problems in the host computer. These problems have at least partially been solved with the SPC-134, SPC-154N and SPC-164 four-channel packages of bh. The SPC-134 and SPC-154NX packages are shown in Fig. 230.

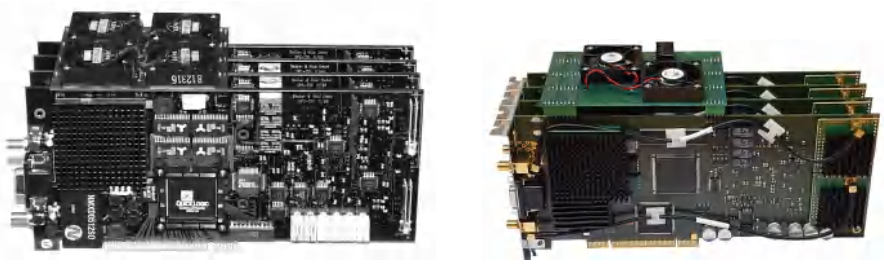


Fig. 230: Packages of four fully parallel TCSPC channels. SPC-134 (left) and SPC-154NX (right)

Two-channel and four-channel systems are available in an small-size extension box to a laptop computer, see Fig. 231, left. Systems with up to 12 channels require a larger extension box, please see Fig. 231, middle and right.

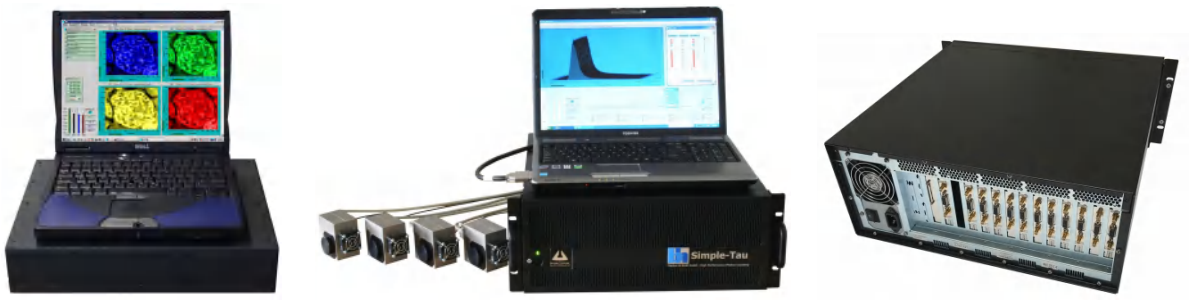


Fig. 231: ‘Simple-Tau’ multi-TCSPC systems based on bus extension boxes

With a dead time of 100 ns per TCSPC channel, the total saturated count rate of a four-channel system is 40 MHz. Useful count rates on the order of 20 MHz can be achieved. The high count rate and the high number of channels make multi-module TCSPC systems exceptionally useful for diffuse optical tomography [144, 633, 784, 785] and high count rate applications in laser scanning microscopy [68, 69, 149, 158, 652]. Details are described under ‘Diffuse Optical Tomography’ and ‘Time-Resolved Laser Scanning Microscopy’.

Another application of multi-module systems is in correlation spectroscopy of single molecules. If the photons detected in different detectors are recorded in different modules, the minimum correlation time is no longer limited by the dead time. By synchronising the macro-time clocks of the modules, a correlation down to the macro time clock period is possible. By including the TAC time (micro-time) in the correlation continuous correlation functions from the picosecond to the millisecond scale can be achieved [442], see ‘FCS Down to the Picosecond Time Scale’, page 644.

Architecture of the bh TCSPC Modules

General Principle

The bh SPC modules contain all the building blocks of TCSPC on a single PCI or PCI-express-compatible PC board. The general principle of the modules is shown in Fig. 232 and Fig. 233. Module with TAC-ADC principle is shown on the left, modules with TDC principle on the right. The modules can be operated in two different modes. In the photon distribution modes (Fig. 232) the modules build up photon distributions in their internal memories. In the Time / Parameter Tagging modes the data of the individual photons are buffered in a FIFO (first-in-first out) memory. From there they are transferred to the computer for further processing.

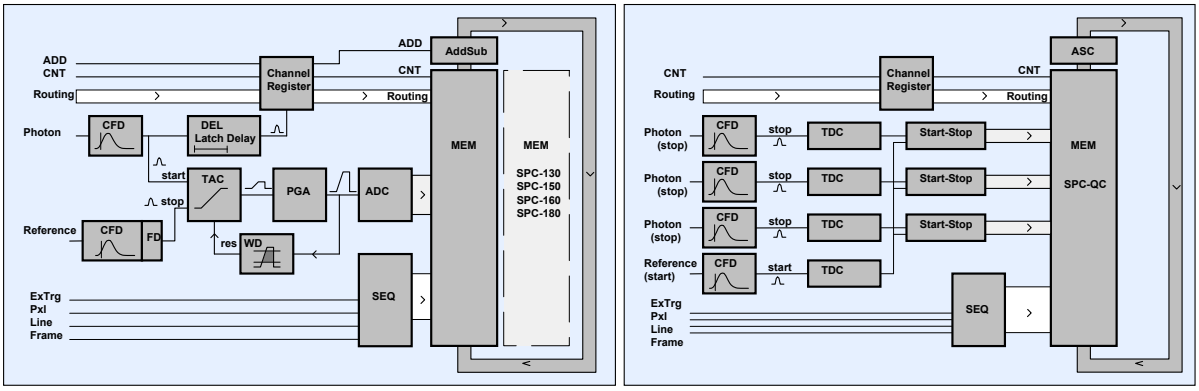


Fig. 232: Electronic building blocks of the bh TCSPC modules. Photon-Distribution Modes. Left: Module with TAC-ADC principle. Right: Module with TDC principle, three relative timing channels.

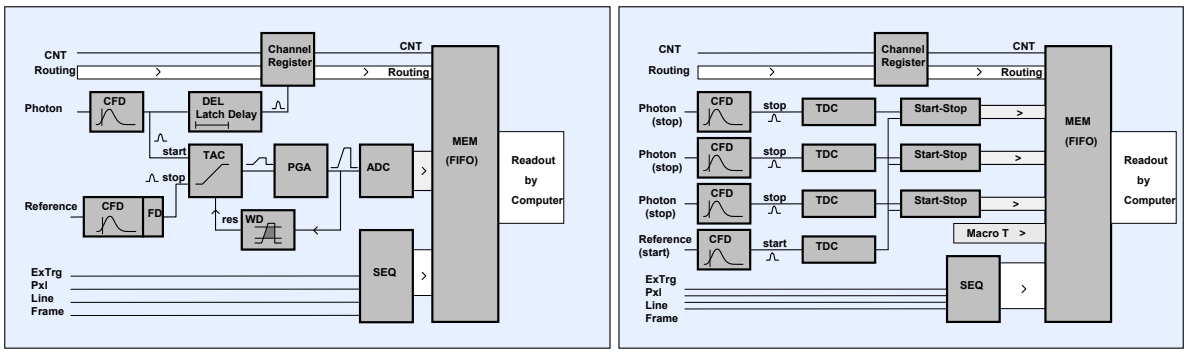


Fig. 233 Electronic building blocks of the bh TCSPC modules. Time/Parameter Tagging Modes. Left: Module with TAC-ADC principle. Right: Module with TDC principle, three absolute timing channels.

CFD circuits

TCSPC is based on the measurement of the time differences between the single-photon pulses from a detector (or from a number of detectors) and reference pulses. For fluorescence decay measurements the reference pulses are derived from the excitation pulse sequence; in photon correlation experiments the reference pulses are single-photon pulses from an additional detector. Accurate time measurement means accurate triggering on the single-photon pulses of the detectors and the reference pulses from the light source. Unfortunately, these pulses are far from being stable. The single-photon pulses have a considerable amplitude jitter due to the random amplification mechanism in the detectors (see Fig. 188, page 101), and the pulse amplitude of the light source may change due to intensity fluctuations. A simple leading-edge discriminator cannot be used to trigger on such pulses. The amplitude jitter would introduce a timing jitter on the order of the pulse rise time (Fig. 234, left).

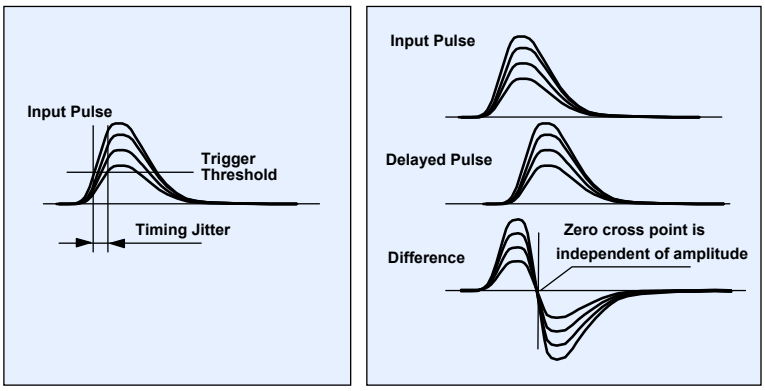


Fig. 234: Leading-edge triggering (left) and constant-fraction triggering (right)

Therefore constant-fraction discriminators (CFDs) are used both at the detector and at the reference input. A CFD triggers at a constant fraction of the pulse amplitude, thus avoiding pulse-height-induced timing jitter. Technically, constant-fraction triggering is achieved by triggering on the zero cross point of the sum of the input pulse and the delayed and inverted input pulse, see Fig. 234, right. Since the temporal position of the crossover point is independent of the pulse amplitude, this timing method minimises the time jitter caused by the amplitude jitter of the detector pulses. Furthermore, the CFD contains a discriminator that rejects input pulses smaller than a selectable discriminator threshold. The threshold is adjusted to reject noise from the environment, noise from preamplifiers or small background pulses from the detector.

The general architecture of the CFDs in the detector channel and the Sync channel is the same. However, the SYNC CFD of the SPC boards has a selectable frequency divider behind its CFD. In the SPC-QC the frequency divider is in the TDC. Controlled by the software, the internal SYNC frequency can be reduced by a factor of 1...16, see SYNC Parameters, page 784. With the divider set to ratios greater than one several periods of the light signal are recorded. Recording several periods is used to record signals of high repetition rates and to check the time-calibration of a TCSPC module.

TAC and ADC

The time-to-amplitude converter, TAC, measures the time of a detected photon from the pulse at the detector input to the next pulse at the reference input. This 'reversed start-stop' method is the key to process high photon count rates at high pulse repetition rates. It reduces the speed requirements to the TAC because its working cycle (start-stop-reset) has to be performed only at the photon detection rate instead of the considerably higher laser pulse repetition rate, see Fig. 195, page 108.

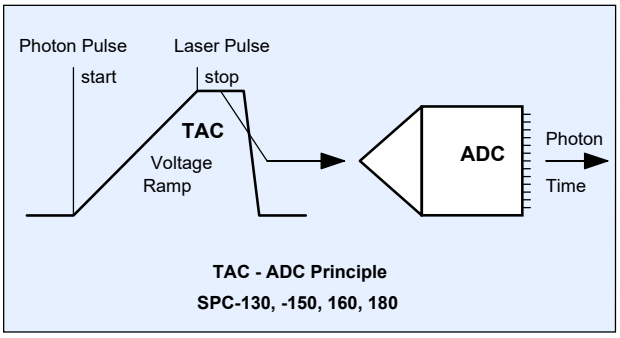


Fig. 235: Time conversion by TAC/ADC principle. The TAC generates a linear-ramp voltage between a start and a stop pulse. This voltage is converted into a digital number by an ADC.

When the TAC is started by a pulse at the start input, it generates a linear ramp voltage until a stop pulse appears at the stop input. Thus the TAC generates an output voltage depending linearly on the temporal position of the photon. The TAC output voltage is fed to a programmable gain amplifier, PGA. The PGA is used to stretch a selectable part of the TAC characteristic over the complete measurement time window. To increase the effective count rate at high PGA gains, the output voltage of the PGA is checked by the window discriminator WD which rejects the processing of events outside the time window of interest. For details of the TACs of the bh SPC modules, see 'Detailed Description of Building Blocks', page 147.

The analog-digital converter, ADC, converts the amplified TAC signal into the address at which the corresponding photon is stored in the memory, MEM. The challenge of the analog-to-digital conversion is that it has to work with an extremely high accuracy. The ADC has to resolve the TAC signal into 4096 time channels, and the width of the particular channels must be equal within 1% or better. ADC chips are usually specified by a 'non-missing code accuracy' which defines the number of bits for which the ADC characteristic is still monotonous. 12-bit conversion with a channel uniformity of 1% requires a non-missing code accuracy of 19 bits. Although ADCs with such a high accuracy exist, they are far too slow for TCSPC applications. Therefore, in the early TCSPC systems, the ADC was the bottleneck both in terms of speed and channel uniformity.

The breakthrough was achieved by an error correction technique introduced by bh in 1993. The technique is based on a modified 'dithering' process [139, 141, 144]. By adding an auxiliary signal to the ADC input and subtracting the digital equivalent of it from the ADC output the non-uniformity of the ADC channels is averaged out. Thus, an ADC with 12 bit non-missing code accuracy is sufficient to convert the TAC signal. 12-bit ADCs are available with high speed so that the ADC does not longer limit the available count rate of the TCSPC module. The error correction is described under 'Analog-to-Digital Conversion', page 151.

TDC

Different than the SPC series modules the SPC-QC modules use time-to-digital converters for time measurement. The principle of the TDCs is shown Fig. 236. The photon pulses from the detector and the reference pulses from the laser are sent through chains of digital delay elements. The timing logics looks at the data in the delay chains, identifies start-stop pairs of photons and laser pulses, and this way determines the temporal positions of the photons in the laser pulse sequence. The time resolution of the TDC principle is lower than that of the TAC/ADC principle. The advantage of the TDC principle is that it works up to extremely high photon rates, and that the electronics is less power consuming. Several timing channels can therefore be implemented on a single PC board.

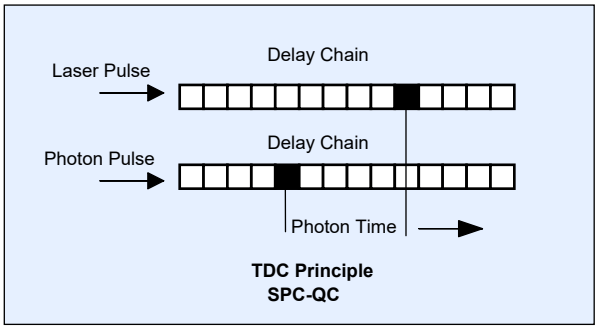


Fig. 236: Start and stop pulses are sent through chains of delay elements, the start-stop time is the difference of the position of the pulses in the chains

'Channel' Register

The channel register receives the ‘channel’ data used for multi-detector operation and multiplexing (see also Fig. 205 and Fig. 206). Except for the SPC-130 and SPC-134, the channel data are loaded into the channel register with an adjustable delay. The delay is used for multi-detector operation with an external router. It takes the router a few 10 ns to encode the channel data word. Thus, the channel signal arrives at the TCSPC module after the single-photon pulse. The ‘latch delay’ compensates for the delay in the router and loads the channel data within the time interval when the router delivers a valid channel data word.

Sequencer

The sequencer generates address bits for one or two additional dimensions of the recording process. The sequencer is a block of counters which are driven either by an internal clock signal, by a signal derived from the synchronisation signal of the TCSPC module, or by a number of clock or trigger signals from the external experiment setup. Depending on the clock signals used and on the number and configurations of the counters the sequencer can generate different information:

In the sequential recording modes the sequencer data word is the time from the start of the experiment or the number of experiment trigger pulses received at the ‘experiment trigger’ input. In the scan modes, the sequencer delivers the X and Y coordinates for the currently detected photon. In the FIFO mode the sequencer is used as a ‘Macro Time Clock’. It delivers the Macro Time, i.e. the time from the start of the experiment for the time tagging of the individual photons. Details of the sequencer function are described below under ‘Memory Control’.

Memory Control

In the photon distribution modes the memory of the TCSPC module is used to add the individual photons in a memory location according to the time in the signal period, the detector channel number, the time from the start of the experiment, or other coordinates delivered be the sequencer. In the time-tag (or FIFO) modes the memory buffers the corresponding data for the individual photons. The structure of the memory and the way it is controlled is thus different for different operation modes of the TCSPC module.

Different modules differ considerably in memory size. Moreover, the available range of the ADC resolution, i.e. number of time channels per waveform block, is different. Some values for the number of available waveform blocks are given in the table below.

ADC resolution, channels	Number of waveform blocks (curves) in the device memory				
	SPC-130	**SPC-130EM**	**SPC-150, -150N**	**SPC-QC-104**	**SPC-QC-106**
4096	32	1024	1024	256	128
256	512	16384	16384	4096	2048
16	--	262,144	262,144	65,536	32,768
1	--	4,194,304	4,194,304	65,536	65,535

To get an overview about the number of available waveform channels, detector channels, multiplexing channels, or pixels of a scan we recommend to load the SPCM operating software (available from www.becker-hickl.com) and check the available combinations.

Recording of single curves

In the simplest case the SPC module is used as a conventional one-dimensional TCSPC device. The 'channel' data word is ignored, and the sequencer delivers a constant address offset from the beginning of the memory. When a photon is detected the ADC delivers an address proportional to the time of the photon in the signal period. The addressed memory location is

read, the data word is incremented in the addition/subtraction circuit, ASC, and the result is written back into the same memory location. After the detection of many photons the waveform of the light signal, e.g. a fluorescence decay curve, is built up.

The adder/subtractor delivers an overflow signal when the memory contents of the addressed memory location has reached a maximum of 65535 counts. In this moment the measurement can be stopped automatically (‘stop on overflow’ function).

The incremetation of the memory contents can be done by any number from 1 to 255. Of course, count increments greater than one do not improve the sensitivity of a measurement. Values >1 are, however, useful to vary the number of photons for which a ‘stop on overflow’ is obtained. Different recordings can thus be normalised to their maxima.

By changing the address offset from the sequencer by software, a number of ‘pages’ in the memory are available. Consequently, several signals can be recorded one after another and the results be held in different pages of the memory.

Multi-Detector Operation

The addressing of the memory for multi-detector operation is shown in Fig. 237. The router delivers a 'channel' signal that indicates which of the detectors detected the current photon. The detector channel number is loaded into the channel register of the TCSPC device. When a photon is added into the memory the bits of the channel data word are used as higher address bits of the memory address. Thus the memory provides space for as many waveforms as there are detectors. The memory location within one waveform block is determined by the ADC data word, i.e. by the time of the photon in the signal period. The waveform block is determined by the bits in the channel register, i.e. by the number of the detector that detected this photon.

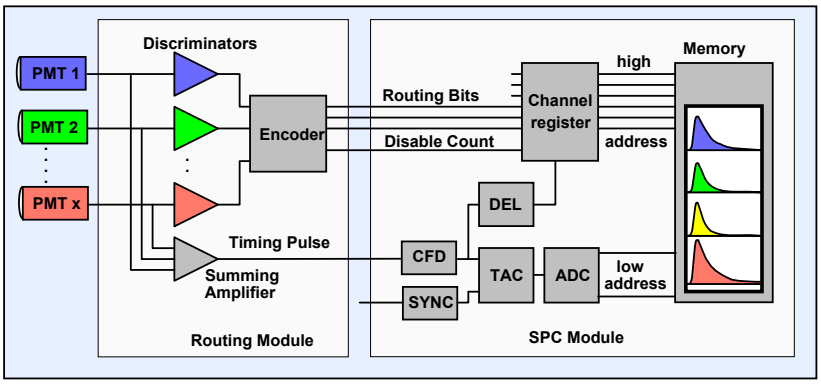


Fig. 237: Memory addressing for multidetector operation

The number of channel bits that are loaded into the channel register can be defined by the parameters ‘routing channels x’ and ‘routing channels y’. Together with the parameter ‘ADC resolution’ these parameters are used to automatically configure the memory into the right number of waveform blocks and time channels.

The discriminators and the encoder of the router need 10 to 20 ns to deliver a valid detector channel number. Therefore, the loading of the data into the channel register must be delayed. The delay is adjustable by the parameter ‘Delay’, see 'System Parameters', ‘Page Control’, page 790. The delay of the higher address bits does not conflict with the memory access as long as the delay is shorter than the conversion time in the TAC and the ADC. Only for latch delays greater than 100 ns the memory access is delayed. Because this reduces the maximum count rate unnecessarily large latch delays should be avoided.

At high count rates the probability of detecting several photons in different detector channels within the response time of the router cannot be neglected. Of course, the router is unable to deliver a valid channel data word in this case. It does, however, detect such multi-photon events and activates the 'disable count' signal. The 'disable count' bit is loaded together with the channel data word. When 'disable count' is active the storing of the corresponding photon in the memory is suppressed.

Multiplexed TCSPC

Multiplexing works in the same way as routing. However, the channel bits come from external experiment control electronics. The most frequent application is multiplexing of several diode lasers see 'Chlorophyll Transients', page 333, and 'Diffuse Optical Tomography', page 605. The channel bits then indicate which of the lasers is active. Multiplexing can, however, also be used for multiplexing several detection light paths (see Fig. 495) or to record photons into a large number of waveform blocks depending on the state of an externally measured signal (see 'Barrier Discharges', page 681).

Multiplexing can be used in combination with multi-detector operation. Normally the lower channel bits are used for the detector number from the router, the higher bits for the multiplexing signal.

Sequential Recording

As routing and multiplexing, sequential recording uses higher address bits of the memory. However, for sequential recording these bits are generated by an internal logic block, the sequencer. The number of bits (or accessible memory blocks) is not limited by the number of externally available routing bit lines. The only limitation is the number of address bits of the memory, i.e. the memory size. Within reasonable limits, sequential recording can therefore be combined with multi-detector operation and multiplexing. For sequential recording the sequencer switches through a defined number of subsequent data blocks of the memory. One data block can be a single waveform, a number of waveforms for different detectors, or a number of waveform blocks for multiplexed signals.

Because the switching though the memory blocks is strictly hardware-controlled an extremely accurate sequence is obtained. The start of the sequence can be triggered by an external 'experiment trigger'. The trigger is normally used to synchronise the start of the sequence with a stimulation event. Triggered sequential recording can be combined with accumulation, i.e. a large number of sequential recording cycles is performed and the data of the individual waveform, routing, or multiplexing data blocks are accumulated. Triggered accumulation does not require a large number of photons to be recorded within a single step of a sequence. It works even at count rates lower than the step rate of the sequence. The recording then becomes a random process, i.e. a detected photon is stored in a memory location according to its time in the signal period, its detector channel, and the current state of the data word delivered by the sequencer. The recording is continued until the desired number of photons per time channel of the waveform has been accumulated. Consequently, triggered sequences can be recorded with times down to about one microsecond per step (see 'Transient Fluorescence Phenomena', page 333).

Sequential recording can also be obtained by triggering the individual steps of the sequence. Step triggering is used to synchronise the recording with an experiment control device, i.e. a scan stage or a monochromator drive.

A number of different sequential modes are available in the bh TCSPC modules. The SPC-630, SPC-130, SPC-150 and SPC-160 have the 'Continuous Flow' mode implemented which can be used to record virtually unlimited sequences (see paragraph below).

Special cases of sequential recording are the ‘Scan Sync In’ and ‘Scan Sync Out’ modes of the SPC-730, -830, SPC-150, and SPC-160 modules. These modes are actually designed to scan images with fast optical scanners. They can, however, also be used for sequential recording (see ‘Sequential Recording in the Scan Sync Out mode’, page 752).

Continuous Flow Mode

In the SPC-630, SPC-130, SPC-150, SPC160, and SPC-180 modules a ‘Continuous Flow’ mode is implemented. The mode is designed for sequential recording of a virtually unlimited number of waveforms, or routing/multiplexing blocks. The Continuous Flow mode makes use of the two independent memory banks which are implemented in the modules.

Subsequent waveforms or waveform blocks are measured in intervals of ‘Collection Time’. The measurement is repeated while the sequencer switches through all memory blocks of one memory bank. When one bank is full the sequencer swaps the memory banks. While the measurement is running in one memory bank, the results of the other bank are read and stored to the hard disk. Thus, a virtually unlimited number of decay curves can be recorded without any time gaps between subsequent curves. The principle is illustrated in Fig. 216, page 123.

The continuous flow mode can also be used with a limited number of sequencer steps. If the number of steps is smaller than the number of waveform blocks of one memory bank the mode can be used for triggered accumulation of a fast sequence.

Scan Modes

In the Scan modes the TCSPC module records the photons into a large two-dimensional array of waveform blocks. A waveform block may contain a single waveform, or a number of waveforms for different detector or multiplexing channels. Each waveform block represents a pixel of the image. The sequencer controls the higher address bits of the memory and thus addresses the individual pixels of the image. Moreover, the sequencer synchronises the recording with the action of an external scanner. The sequencer can be used to control the scanner actively (‘Scan Sync Out’ or ‘Scan XY Out’ modes), or the scanner can be used to control the sequencer (‘Scan Sync In’ mode). Fig. 238 shows how the sequencer switches through the pixels of the image.

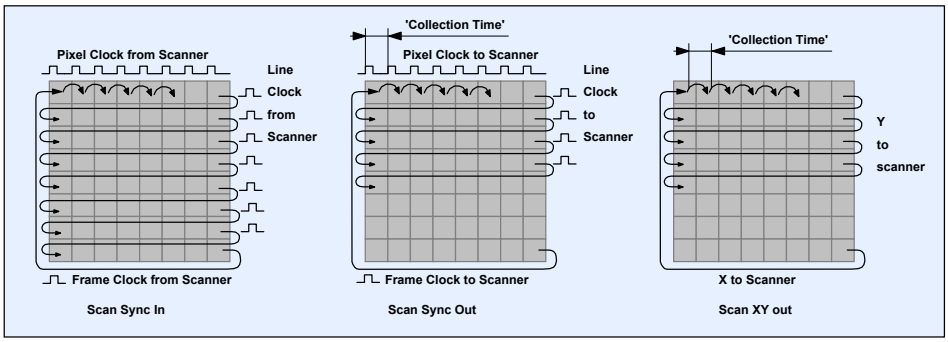


Fig. 238: Sequencer operation in the scan modes. Left: Scan Sync In, Middle: Scan Sync Out, Right: Scan XY Out

In the Scan Sync In mode the sequencer receives scan clock pulses from a scanner. A ‘pixel clock’ sets the waveform block address to the next pixel, a ‘line clock’ pulse to the beginning of the next line, and a ‘frame clock’ pulse back to the first pixel of the frame. The pixel dwell time is determined by the scanner. The measurement is started by an operator command or by an experiment trigger pulse. The measurement is stopped after the specified ‘collection time’ has been reached or the measurement is stopped by the operator. Thus, any number of frames of a repetitive scan can be accumulated.

Dynamic effects in galvanometer mirrors often preclude reasonable recording in the first pixels after a frame or a line fly-back. These pixels can therefore be excluded from being recorded by two additional counters. The excluded pixels are defined by the system parameters ‘upper boarder’ and ‘left boarder’, see 'System Parameters'.

In the Scan Sync Out mode the sequencer controls the scanner. The pixel dwell time is specified by the parameter ‘collection time’. After each collection time interval the sequencer proceeds to the next waveform block address and sends a pixel clock pulse to the scanner. When the scanner receives this pulse it proceeds to the next pixel. At the end of a line the sequencer sends a line clock pulse which causes the scanner to return to the beginning of the next line. When a frame is completed the sequencer sends a frame clock, which resets the scanner to the first pixel of the image. The number of pixels per line and the number of lines per frame is defined by the system parameters ‘Scan pixels X’ and ‘Scan Pixels Y’. Dynamic effects in the scanner can be reduced by defining a ‘flyback x’ and a ‘flyback y’ time.

The Scan XY Out mode is available only in the SPC-700/730. It is similar to the Scan Sync Out mode except for the scanner control. Instead of sending clock pulses to the scanner the sequencer sends complete data words of the X and Y position. The Scan XY out mode is an easy way to control a scanner. However, the number of pixels is limited by the number of available output lines for the X and Y bits. The largest image is therefore 128 by 128 pixels.

CNT and ADD Control

Additional control over the measurement process is possible by the signals CNT and ADD. CNT is a ‘Count Enable’ signal, i.e. a photon is stored only if CNT is ‘1’ in the moment of its detection. The CNT signal is used to suppress photons for which no valid routing information is provided or to confine the recording to externally controlled time intervals.

The ADD signal controls whether a photon is added or subtracted. This allows the user to combine the TCSPC recording with a digital lock-in technique. By using an optical system with light choppers or rotating sector mirrors background or scattering signals can be suppressed [138] (see also ‘Lock-in TCSPC’, page 331).

All external control signals are read via the ‘Channel’ register. The signals are latched at an adjustable delay time after the start pulse. By adjusting this delay it can be assured that every photon be processed with the correct state of the control signals.

Time / Parameter Tagging (FIFO) Mode

The Time-Tagging, or FIFO Mode, is used to record information about each individual photon. The mode is available in all SPC modules starting from the SPC-830 and in the SPC-QC modules. The principle is shown in section ‘Recording Parameter-Tagged Photon Data’, page 132. The sequencer delivers the time from the start of the recording, and the memory is configured as a FIFO (first-in-first-out) buffer. For each photon the time in the pulse period (measured by the TAC and the ADC), the time from the start of the recording (delivered by the sequencer), and the channel data word (delivered by a router or a laser multiplexing device) are stored into the FIFO.

At the output, the FIFO memory is continuously read by the software. The data are written into a buffer in the main memory of the computer and from there on the hard disc. Due to the buffering in the FIFO of the SPC module it is not required that the computer reads the data continuously. Even strong bursts of photons can be detected with the maximum count rate of the SPC module as long as the number of photons in the burst does not exceed the size of the FIFO.

For photon numbers larger than the FIFO size the maximum average count rate is determined by the rate at which the computer is able to read the FIFO. If the computer does not read the data faster than they are recorded FIFO overflow can occur. FIFO overflow causes loss of photons and other information written into the FIFO by the measurement procedure. Data loss by FIFO overflow has become rare since faster computers are available. It is almost entirely avoided by the extended multithreading functions used in version 9.82 SPCM software and later.

Detailed Description of Building Blocks

Constant-Fraction Discriminators

Principle

The single-photon pulses of most photon-counting detectors have a substantial amplitude jitter. The amplitude jitter (or amplitude 'noise') is not caused by any noisy element, it is a result of the electron multiplication process in the detector. In a PMT the source of amplitude jitter is obvious: The photoelectron is accelerated towards the first dynode, where it releases several (typically 4 to 10) secondary electrons. As everything in the quantum world, secondary-electron emission is a random process. The number of secondary electrons therefore varies for the individual photoelectrons, and so does the amplitude of the photon pulses. The amplitude noise is lower in hybrid detectors because the photoelectrons are accelerated to an energy of 7000 to 8000 eV before they reach the avalanche diode at the output of the detector, see 'Hybrid PMTs', page 155. The multiplication factor by the impact into the avalanche diode is on the order of 1000 and more. Consequently, the relative variation in the number of generated electron-hole pairs is low. It is not zero, however, probably because of locally different gain of the avalanche diode. Only single-photon avalanche diodes (SPADs) deliver output pulses which are entirely free of amplitude jitter. The reason is that SPAD modules have internal discriminators. The output pulses from the discriminator are free of amplitude jitter, even though the SPAD itself is not.

Single-photon pulses from a PMT are shown in Fig. 239, left. If the pulses would be sent through a normal discriminator the amplitude jitter would cause a timing jitter, Δt, on the order of the duration of the leading edge the photon pulses, see Fig. 239, right. For normal (high-speed) PMTs this would be about 1 ns - too much for the standards of TCSPC.

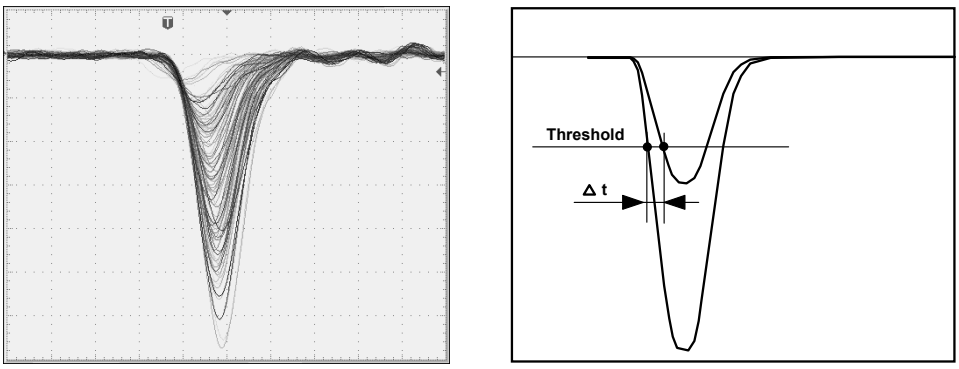


Fig. 239: Left: Single-photon pulses from a normal PMT. Right: When the pulses are received by a normal discriminator the amplitude jitter would induce a timing jitter, Δt.

Obviously, a TCSPC device needs a discriminator which triggers at a constant fraction of the pulse amplitude, see Fig. 240, left. If the discriminator threshold is varied in a way that it is a

constant fraction of the pulse amplitude the timing variation, Δt, would vanish. Fig. 240 reproduces the usual description of the CFD principle. Unfortunately, its implementation hits a problem. When the leading edge of the pulse crosses the threshold the actual threshold level is not known yet. Moreover, for very small pulses the threshold approaches zero. The discriminator would then oscillate or trigger on spurious noise. The practical implementation is therefore different, see Fig. 240, right.

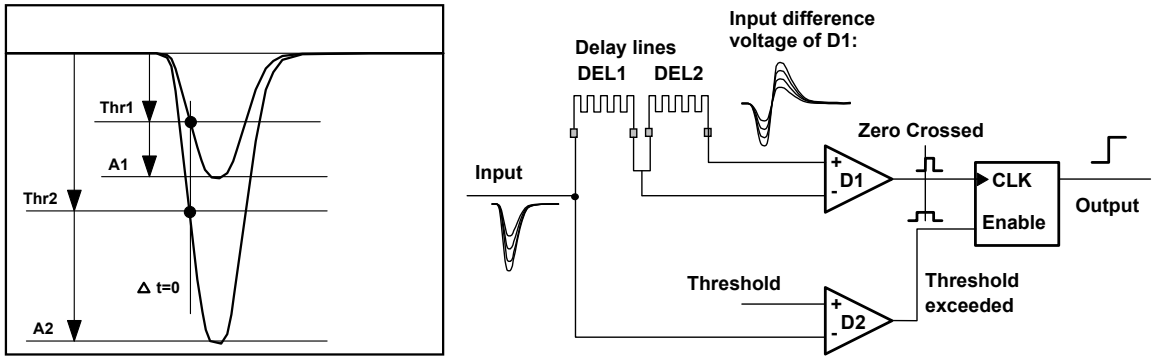


Fig. 240: Principle of a CFD (left) and practical implementation (right)

The CFD has two delay lines, DEL1 and DEL2, and two discriminators, D1 and D2. D2 receives the direct input pulse. It triggers when the input voltage exceeds an adjustable threshold. D2 is a simple leading-edge discriminator, it just detects the arrival of a pulse with an amplitude that exceeds the threshold. Simultaneously, the input pulse propagates through the delay lines, DEL1 and DEL2. It arrives at the inverting input of D1 about a nanosecond after it has reached D2. A short time later it also arrives at the non-inverting input of D1. Thus, D1 sees the difference of the input pulse and a copy of the input pulse delayed by DEL2. The resulting signal has a baseline transition whose temporal position does not depend on the pulse amplitude. D1 triggers at this transition and produces a L/H transition at its output. If the transition is within the output pulse of D2 it triggers a D flip-flop. The appearance of a L/H transition at the output of the flip-flop indicates the detection of a photon pulse with an amplitude larger than the threshold of D2. The temporal position is related to the pulse edge from D1 and therefore does not depend on the pulse amplitude. The practical implementation may look different than the principle in Fig. 240, left, but in fact it is functionally similar. The signal at the inverting input of D1 represents the amplitude-proportional threshold, and the signal at the non-inverting input of D1 the photon pulse.

Implementation in the SPC modules

The CFD implementation in the bh TCSPC modules is shown in Fig. 241. Identical CFDs are used in the detector input and the sync input. The CFDs of the older SPC modules (SPC-300 through SPC-830) follow the same general principles but are different in detail. Please see TCSPC Handbook 7th edition or earlier.

The architecture of the CFDs of the SPC-130 and SPC-150 is shown in Fig. 241, left. It essentially follows the principle shown in Fig. 240, right. The zero cross point of D1 can be adjusted by applying a differential 'Zero Cross' voltage to the discriminator inputs. The Zero Cross adjustment is used to optimise the timing performance. The SPC-130 and SPC-150 CFDs are implemented on the boards of the modules. The delay lines can be replaced to adapt the CFDs for different detectors. Please see 'System Optimisation' page 269 for details.

The CFDs of the SPC-160, SPC-150N, SPC-180N family and the SPC-QC-105 and -106 are shown in Fig. 241. The CFDs of these module use ultra-fast discriminators made in SiGe technology, and an additional flip flop, FF2. The SiGe discriminators yield improved zero-cross timing for detectors with ultra-fast single-photon pulses. A side effect of the fast discriminators is that the output of the leading edge discriminator, D2, can be so fast that it has

already switched back when the zero-cross transition from D1 arrives. The additional flip-flop, FF2, stores the 'Threshold Exceeded' signal until the zero-cross transition has arrived and triggered FF1. The SPC-160, SPC-150N, SPC-180N, and SPC-QC CFDs are separate modules which are plugged onto the SPC boards, see Fig. 241, bottom.

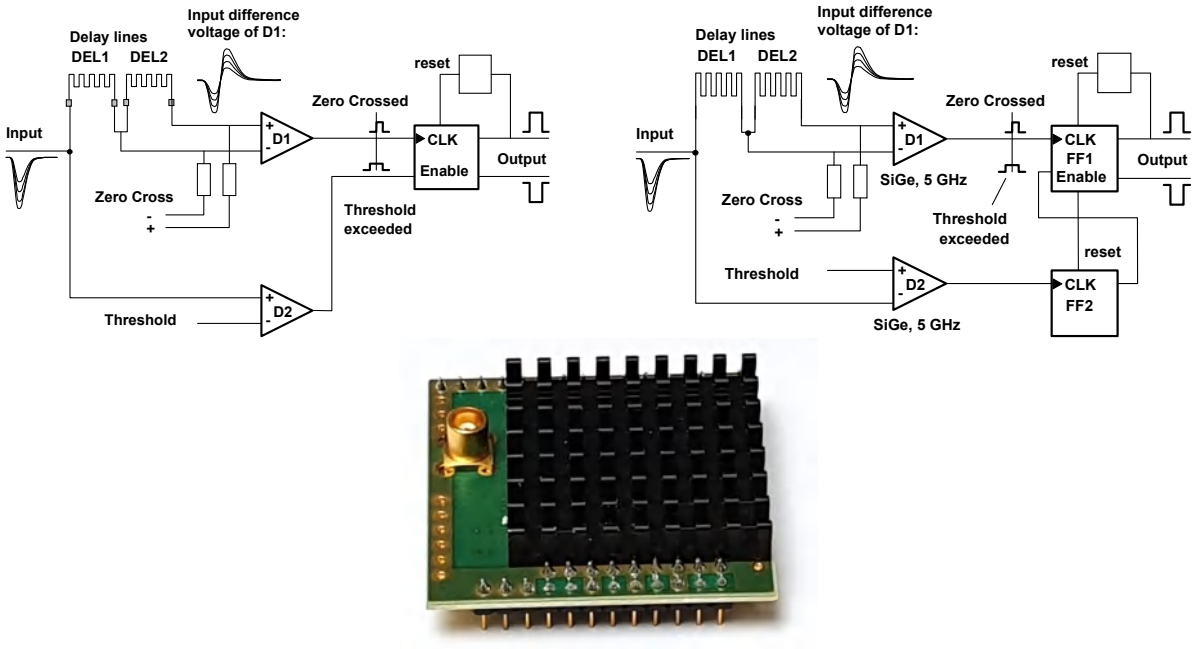


Fig. 241: Top left: Principle of the SPC-130 and SPC-150 CFDs. Top right: Principle of the SPC-150N, SPC-180N, and SPC-QC-104 and -106 CFDs. Bottom: CFD of an SPC-180N

Time-to-Amplitude Converter

The time to amplitude converter (TAC) converter the times of the photons from their detection to a reference pulse form the light source. The TAC of the bh modules has been optimised together with the subsequent ADC to obtain high count rates, low differential nonlinearity, extremely small time channel width and extremely low timing jitter.

Compared with direct time-to-digital conversion (TDC) [312, 640, 749] (and compared with the SPC-QC) the circuitry of a TAC/ADC system is relatively complicated. However, the time resolution (IRF width) of a TAC/ADC system is on the order of 3 to 6 ps, full width at half maximum, which is currently about 20 times faster than for a TDC. The principle of the TAC of the bh TCSPC modules is shown in Fig. 242.

The TAC contains a linear ramp generator, a biased amplifier with variable gain, several comparators to check the conversion result and the associated control circuitry.

The ramp generator, RPG, is started when a pulse from the CFD in the start channel arrives at the start input of the TAC. Once started, the ramp voltage increases until a stop pulse from the CFD in the stop (Sync) channel arrives at the TAC stop input. After the stop pulse the voltage remains constant until the TAC is reset. The slope of the ramp (and thus the conversion range of the TAC) is variable via the control software, see 'TAC Parameters', page 784.

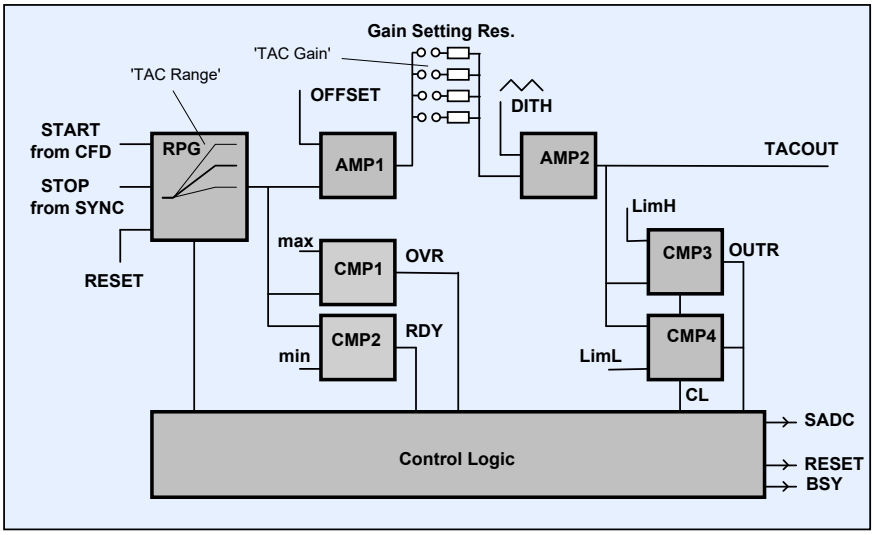


Fig. 242: Principle of the TAC

An amplifier, AMP1, adds an adjustable offset voltage to the ramp voltage. A second amplifier, AMP2, has variable gain. The offset and the gain are used to define a smaller conversion time interval within the total range of the ramp generator. Both the offset and the gain of AMP1 are set via the control software, see ‘TAC Parameters’, page 784.

The ‘Dithering’ signal, DITH, is used for the ADC error correction. It shifts the TAC output voltage periodically up and down at the ADC characteristic (see below, ‘ADC Error Correction’).

CMP3 and CMP4 are latched comparators. They check whether the ramp voltage is inside the a window selected by ‘TAC Limit L’ to ‘TAC Limit H’ (see ‘TAC Parameters’, page 784). The comparator latch pulse, cl, is generated by the TAC control logic. It is derived from the delayed stop pulse. If the ramp voltage is outside the selected window in the moment of the cl pulse an OUTR (outrange) signal is generated.

If the ramp voltage is inside the selected window (i.e. OUTR not active) the control logic generates the SADC (start ADC) pulse. This pulse starts the ADC and the signal processing in the digital part of the TCSPC module. After about 40 ns the control logic generates a reset signal for the ramp generator. The reset signal remains active until the comparator CMP2 detects the reset of the ramp voltage. The reset signal is also used to reset the CFD.

If the TACOUT amplitude is not inside the selected window the control logic does not generate a SADC pulse but immediately initiates a reset sequence. Thus, no further time is wasted for converting photons with TAC signals outside the selected TAC range.

If the stop pulse from the SYNC does not arrive within the time of the selected TAC range the comparator CMP1 detects an OVR (overrange) condition. To avoid that the TAC is blocked by missing stop pulses the OVR signal initiates a reset sequence.

The bh TCSPC modules have a ‘dead time compensation’ that can (but need not) be used to obtain an intensity-proportional counting result even at extremely high count rates when a substantial fraction of photons is lost in the dead time. The dead-time compensation extends the acquisition time (‘collection time’) by the accumulated dead time during the measurement. To determine the dead time the control logic of the TAC delivers a BSY (‘BUSY’) signal. This signal is used to stop the 'Collection Time' timer during the times the TAC is unable to convert a new photon. Thus, the effective collection time increases by the sum of the dead time over the whole measurement, resulting in a linear intensity scale up to count rates on the order of the reciprocal dead time. (See ‘Dead-Time Compensation’, page 293)

The TACs of the SPC-6, -7, and -8 modules differ slightly from the TACs used in the SPC-130, 150, and 160 modules. The visible difference is that the TAC of the SPC-6, 7 and 8 modules is a module built in hybrid technique whereas the TACs of the SPC-130, 150, and 160 modules are built in standard printed circuit board technique. Moreover, the SPC-130, 150, and 160 TACs do not contain the comparators CMP3 and CMP4. Instead, the TAC window is set by comparators in the digital signal processing circuitry of the modules.

Analog-to-Digital Conversion

ADC Error Correction

The high maximum count rate of the bh SPC modules is achieved by a fast flash ADC in conjunction with a proprietary error compensation technique [139, 144, 154]. The error compensation improves the accuracy of the ADC by several bits without any loss in speed or channel resolution. The technique is essential to the operation of the module. The following description helps to understand the principle of the technique and the side-effects associated with its application.

The error compensation in the bh modules is based on a modified ‘dithering’ process . Dithering is a technique to enhance the resolution of an ADC by accumulating a large number of samples with a digitally generated noise (the dither signal) added to the input signal. The digital equivalent of the dither signal is later subtracted from the ADC output bytes. In TCSPC the principle of dithering is reversed. The ADC input signal is random, and a determinate dither signal is used. The principle is shown in Fig. 243.

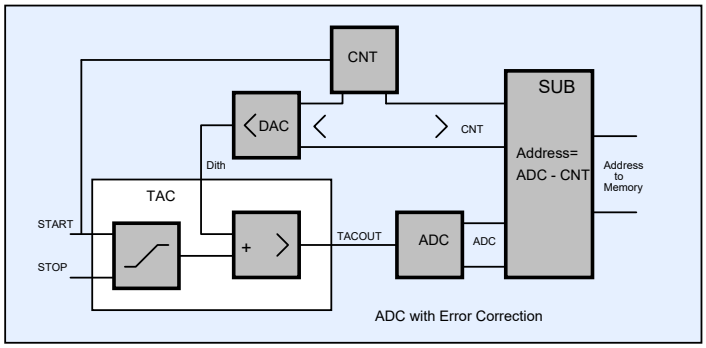


Fig. 243: TAC/ADC principle used in the bh TCSPC modules

A DA converter, DAC, is used to shift the TAC output voltage up and down on the ADC characteristic. The DAC is controlled by a counter that counts the start pulses of the TAC. Consequently the DAC generates a sawtooth voltage that increases by one DAC step at the recording of each photon. The DAC voltage is added to the TAC output voltage. The resulting signal is converted by the ADC. The ADC data word corresponds to the sum of the DAC and the TAC voltage. To restore the correct address byte for the memory the digital equivalent of the DAC voltage is subtracted from the ADC value in a digital subtraction circuit, SUB.

Of course each address byte still contains the unavoidable deviation of the particular ADC step from the correct value. But there is a significant difference to a direct ADC conversion in that the error is now different for different photons - even if these photons appeared at equal times in the signal periods and caused equal TAC voltages. For a large number of photons the non-uniformity of the ADC channels is averaged. The result is that the effective ADC characteristic is smoothed.

For an ideal DAC, the smoothing of the ADC characteristics does not cause any loss in signal detail. In practice, gain and linearity errors of the DAC cause a slight broadening of the re-

corded signal. The broadening is, however, smaller than 1 or 2 ADC steps or 0.8 to 1.6 ps in the fastest TAC Range, see Fig. 244.

The improvement in conversion accuracy depends on the number of ADC steps, $N_{dac,}$ over which the signal is shifted by the DAC voltage (see system parameter 'Dither Width') and on the distribution of the errors of the ADC characteristic. If there is no correlation between the errors of adjacent ADC step the improvement is $N_{dac}^{1/2}$. However, in practice the errors of flash ADCs are more or less periodical, i.e. near a big ADC step a smaller one occurs and vice versa. In this case the accuracy improvement is considerably larger than $N_{dac}^{1/2}$. In Fig. 244 shows that the principle yields an enormous improvement of the ADC. The differential nonlinearity of an SPC-130 TCSPC channel is shown for 'Dither Width' = 0 (original ADC characteristics), 'Dither Width' = 1/32 or 7 ADC bits and 1/8 of the conversion range or 9 ADC bits. Interestingly, it took 15 years until the principle was taken up by other designers of TCSPC electronics, see Resnati et al. [1004].

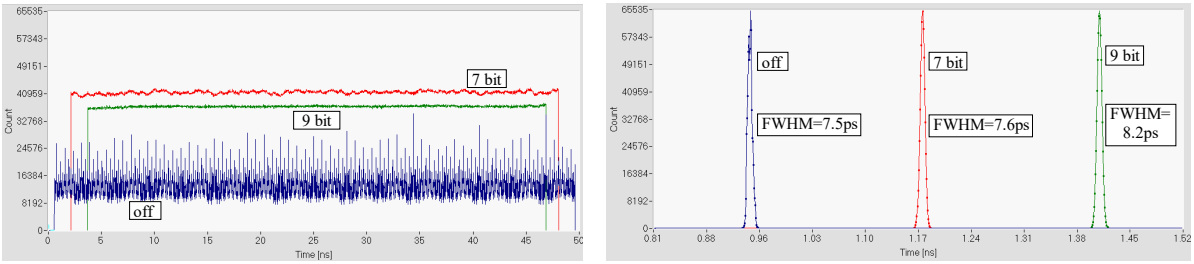


Fig. 244: Left: Unmodulated light recorded without error reduction, and with a counter data width of 7 bit and 9 bit. Right: Corresponding instrument response function of the module (electrical test signal)

The price that has to be paid for the accuracy improvement is that the outer parts of the ADC characteristic cannot be used. The sum of the TAC and the DAC signals is clipped at the ends of the ADC range. The clipped parts are visible as artefacts at both ends of the ADC range. However, except for a few very special applications the loss in conversion range is not essential. With the system parameter 'Dither Width' the shift width can be selected to make an trade-off between ADC accuracy and useful ADC range.

Variable ADC Resolution

The ADC of all bh SPC modules resolves the TAC voltage into 4096 discrete values. In the photon-distribution modes this yields 4096 time channels per curve. There are, however, applications where such a high number of time channels is not needed. In these cases it is often useful to reduce the number of time channels to decrease the required memory space, to increase the available number of curves or scan pixels in the memory, or to obtain more photons per time channel. Therefore in all bh TCSPC modules a specified number of ADC channels can be combined (binned) into one time channel, see Fig. 245.

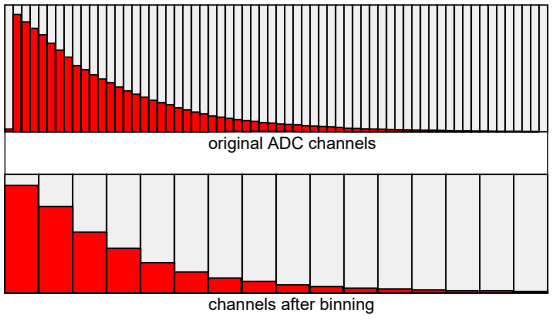


Fig. 245: Variable ADC resolution by binning several ADC channels

The bh SPC modules can be used with a resolution of 4096, 1024, 256, 64, 16, 4, and 1 time channels. Working with only one time channel, i.e. discarding the time information at all, may appear useless at first glance. The setting can, however, be used to turn a TCSPC FLIM system into an extremely sensitive steady state photon counting imager.

ADC Zoom

Another possibility to reduce the number of time channels is the 'ADC Zoom'. The ADC zoom feature is implemented in the SPC-830, SPC-130, SPC-150 and SPC-160 modules. It assigns the original ADC channels of a selectable part of the ADC characteristics to a full scale recording with a reduced number of channels. The principle is shown in Fig. 246.

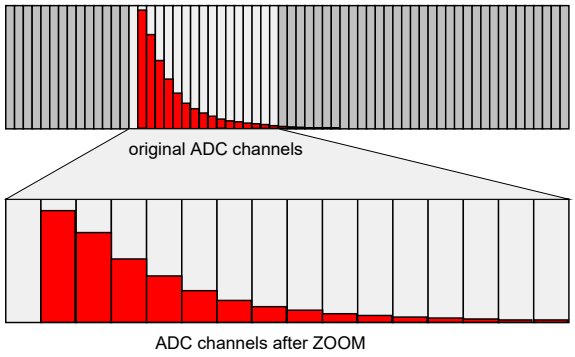


Fig. 246: ADC Zoom

The ADC Zoom feature is useful in imaging and other multi-curve applications if very fast fluorescence decays are recorded with a fast detector. The photons then fill only part of the available conversion range. Zooming this range into a full-scale time axis makes it possible to record a large number of curves (or pixels) at extremely high time resolution.

Detectors for TCSPC

Detectors for photon counting must have sufficient gain to deliver a useful output pulse for a single detected photon. The output pulse must be short enough to resolve the individual photons at high count rate, and the transit time jitter in the detector should be small to achieve a good time resolution. There is a wide variety of photomultiplier tubes (PMTs), photomultiplier modules, hybrid detectors, and single-photon avalanche photodiode (SPAD) modules that meet these general requirements [723, 1368]. However, these devices are far form being ideal single-photon detectors. Knowledge about the different principles of detectors, their typical performance, and possible side effects is therefore important to obtain best results from a TCSPC experiment. The following section gives an introduction into the general principles of detectors and the parameters which characterise them. Moreover, it describes a number of frequently used detectors and gives advice about selecting the right detector and getting best performance from it.

Detector Principles

Conventional PMTs

PMTs, or photomultiplier tubes, are around since to 40s of the last century. A photomultiplier tube (PMT) is a vacuum device which contains a photocathode, a number of dynodes (amplifying stages) and an anode which delivers the output signal [558, 723, 847]. The principle is shown in Fig. 247.

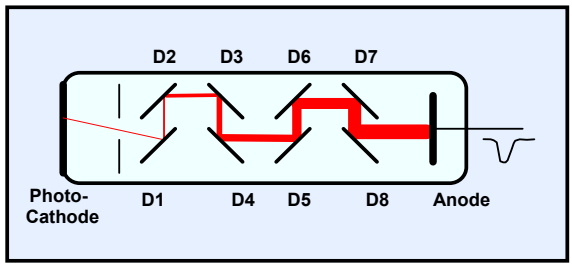


Fig. 247: Principle of a conventional PMT

The operating voltage builds up an electrical field that accelerates the electrons from the photocathode to the first dynode D1, further to the next dynodes, and from D8 to the anode. When a photoelectron hits D1 it releases several secondary electrons. The same happens for the electrons emitted by D1 when they hit D2. The overall gain reaches values of 10^6 to 10^8. The secondary emission at the dynodes is very fast, therefore the secondary electrons resulting from one photoelectron arrive at the anode within a few ns. Due to the high gain and the short response a single photoelectron yields an easily detectable current pulse at the anode.

A wide variety of dynode geometries has been developed. Some of the designs are in use for more than 50 years [558]. Of special interest for photon counting are the ‘linear focused’ type dynodes, the ‘fine mesh’ and the ‘metal channel’ types [723]. Linear-focused dynodes are designed to obtain similar transit time for different electron trajectories. Thus, linear-focused PMTs have a short transit-time spread and a fast single electron response. A fast response can also be obtained by keeping the pathways of the electrons extremely short. Because fine mesh and metal channel PMTs can be built in extremely small sizes they deliver similar or even faster response than the larger linear focused devices. Moreover, the fine mesh and metal channel design can be combined with an array of anodes to obtain spatial resolution.

Channel and Microchannel PMTs

A similar gain effect as in the conventional PMTs is achieved in the Channel PMT (Fig. 248, left) and in the Microchannel PMT (Fig. 248, right). These detectors use channels with a resistive coating. A high voltage is applied along the channels. The walls of the channels work as secondary emission targets. The principle can be used in a single macroscopic channel or a microchannel plate (MCP). A microchannel plate contains a large number of channels with a diameter of 3 to 15 µm. Two or three channel plates can be arranged in series to obtain a high gain. Due to the small distance between the photocathode and the first MCP and the small size of the channels the transit time spread of the photoelectrons can be as short as 25 ps [1, 723, 724, 1356]. Moreover, the microchannel plate technique can be used to build position-sensitive detectors and image intensifiers.

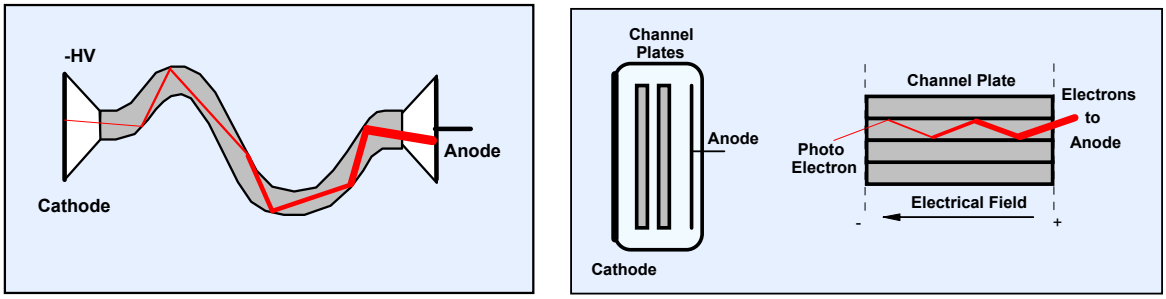


Fig. 248: Channel plate PMT (left) and microchannel PMT (right)

To obtain position sensitivity, the single anode can be replaced with an array of individual anode elements (Fig. 249). By individually detecting the pulses from the anode elements the position of the corresponding photon on the photocathode can be determined. Multi-anode PMTs are particularly interesting in conjunction with the multi-detector capability of the bh TCSPC modules.

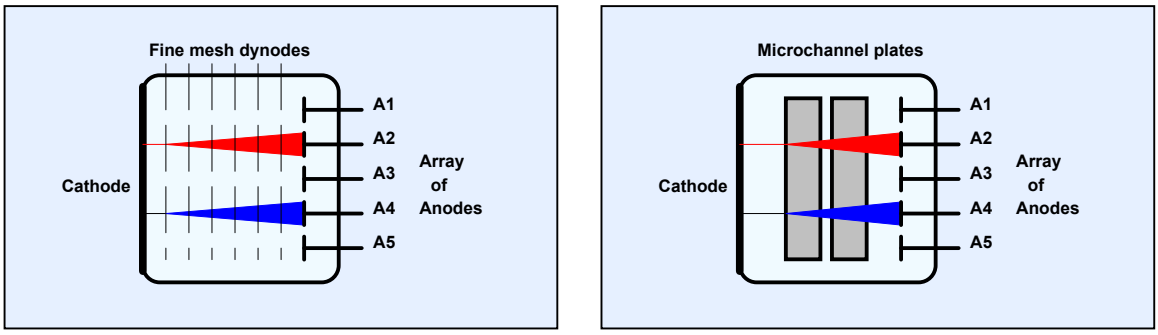


Fig. 249: Multi-anode PMTs for position-sensitive detection. Fine-mesh PMT (left) and MCP-PMT (right)

Hybrid PMTs

The basic principle of a hybrid PMT is shown in Fig. 250. The photoelectrons emitted by a photocathode are accelerated by a strong electrical field and injected directly into a silicon avalanche diode [469, 470 , 750]. When an accelerated photoelectron hits the avalanche diode it generates a large number of electron-hole pairs in the silicon. These carriers are further amplified by the linear gain of the avalanche diode.

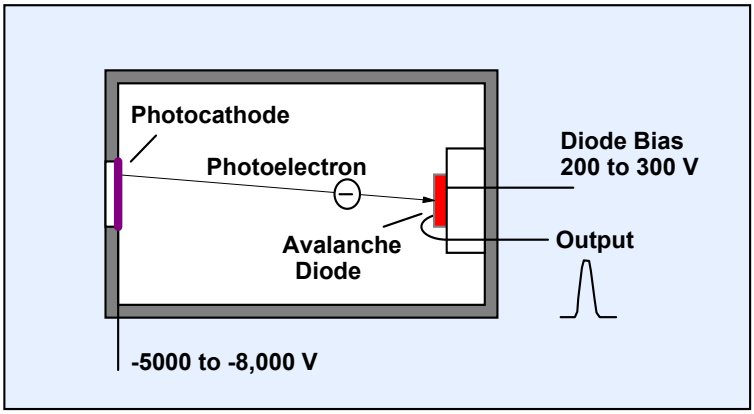


Fig. 250: Principle of a hybrid PMT

The principle of the hybrid PMT has a number of advantages over other detector principles. An obvious advantage of the hybrid PMT is that a large part of the gain is obtained in a single step. Hybrid PMTs therefore deliver single-photon pulses with a narrow amplitude distribution. The devices can thus be used to distinguish between one, two, or even more photons detected simultaneously [750], see also section 'Photon-Number Sensitive TCSPC'. In normal TCSPC applications the low amplitude fluctuation virtually eliminates the influence of the CFD circuitry on the timing jitter.

More important for TCSPC, the high acceleration voltage between the photocathode and the APD results in low transit time spread [469, 470]. With an acceleration voltage of 8 kV the transit-time spread of the electron time-of-flight is less than 50 ps [469, 470, 549]. Moreover, the TCSPC instrument response of a hybrid PMT is very clean, without significant tails, bumps, or secondary peaks.

Compared with a conventional PMT, the hybrid PMT has also an advantage in terms of counting efficiency. In a conventional PMT, a fraction of the photoelectrons is lost on the first dynode of the electron multiplication system [154]. Instead of being multiplied electrons may also get absorbed or reflected. There are no such losses in the hybrid PMT: A photoelectron accelerated to an energy of 8 keV is almost certain to generate a signal in the avalanche diode. With a high-efficiency GaAsP cathode a hybrid photomultiplier reaches the efficiency of a single-photon APD (SPAD), but with a cathode area several orders of magnitude larger.

The perhaps most significant advantage of the hybrid PMT has been recognised only recently: The hybrid PMT is virtually free of afterpulsing [85, 159]. Afterpulsing is the major source of counting background in high-repetition-rate TCSPC applications, and a known problem in fluorescence correlation measurements. Background has a detrimental effect on the accuracy of fluorescence lifetime determination [680]. Afterpulsing in FCS results in a false peak at correlation times shorter than a few µs. So far, the afterpulsing peak could only be suppressed by splitting the light and recording cross-correlation between two detectors.

The absence of afterpulsing in a hybrid PMT is inherent to its design principle. In conventional PMTs afterpulsing is caused by ionisation of residual gas molecules by the electron cloud in the dynode system. In single-photon avalanche photodiodes afterpulsing results from trapped carriers of the previous avalanche breakdown. Both effects do not exist in the hybrid PMT: Ionisation is negligible because only single electrons are travelling in the vacuum, and there is no avalanche breakdown in the avalanche diode.

On the downside, there are also a few disadvantages of the hybrid PMT. The extremely high cathode voltage is difficult to handle. The APD reverse voltage must be very stable, and be correctly adjusted. The most significant problem is the low gain of the hybrid PMTs. Earlier devices reached a gain on the order of only 10^4. At a gain this low, the single-photon pulse amplitude is in the µV range. Therefore electronic noise from the termination resistor and

from the preamplifier impaired the time resolution of single photon detection. Until recently, hybrid PMTs were therefore not routinely used for TCSPC experiments. The situation changed with the introduction of the R10467 hybrid PMTs of Hamamatsu [549]. The devices reach a total gain on the order of 10^5. The single-photon pulse amplitude is on the order of several 100 µV, the pulse width about 800 ps. A high bandwidth, low-noise preamplifier is able to amplify the pulses into an amplitude range where they are detected by the constant-fraction discriminator of a TCSPC module. Initial tests have shown the superior performance of the R10467 compared to previously existing detectors [85, 159]. However, in practice RF noise pickup from the environment, noise from the high voltage power supplies, and low-frequency currents flowing through ground loops make the bare R10467 tube difficult to use in TCSPC experiments. bh have therefore designed a compact detector module that contains the -8 kV power supply for the cathode voltage, the power supply for the AD voltage, and a low-noise preamplifier [159]. Please see ‘HPM-100 Hybrid Detector’, page, 178.

Single-Photon Avalanche Photodiodes

PMTs use the emission of photoelectrons from a photocathode, i.e. the ‘external photo effect’, as a primary step of detection. The drawback of the external photo effect is that the photoelectrons are emitted in all directions, i.e. also back into the photocathode. Therefore the quantum efficiency, i.e. the probability that a photon releases an photoelectron, is smaller than 0.5. The best cathodes reach a quantum efficiency of about 0.4 between 400 and 500 nm [548].

Semiconductor detectors use the ‘internal photo effect’. That means that the photons generate electron-hole pairs inside the semiconductor. Theoretically the internal photo effect works with a quantum efficiency of 1. In practice the quantum efficiency of a good silicon photodiode reaches 0.8 around 800 nm. In photodiodes and photo-conductors an electrical field separates the electrons and holes, so that a photocurrent flows through the device when it is illuminated. Of course, the photocurrent caused by a single electron-hole pair is far too small to be recorded directly. Single photons can therefore be detected only if the semiconductor detector has an internal gain mechanism that does not introduce any thermal noise background. A suitable gain mechanism exists in the ‘avalanche effect’. A photodiode is operated at a reverse voltage so high that the carriers moving through the semiconductor break off new electron-hole pairs from the lattice of the semiconductor material. The avalanche effect is used in standard avalanche photodiodes (APDs) and delivers a stable gain on the order of 10^2 to 10^3.

A gain of 10^3 is still too low to detect single photons with the time resolution required for TCSPC. Unfortunately, higher gain normally results in instability, i.e. the avalanche becomes self-sustaining and destroys the diode. Nevertheless, photon-induced avalanche breakdown can be used for single photon detection. The reverse voltage of the diode is set several volts above the breakdown voltage. To avoid the avalanche destroying the diode, an active or passive quenching circuit restores normal operation after each photon [335, 337, 733]. The principle is often termed ‘Geiger mode’, because of the similarity with the Geiger-Müller counter. The principle of a single-photon avalanche photodiode (SPAD) operating in the Geiger mode is shown in Fig. 251.

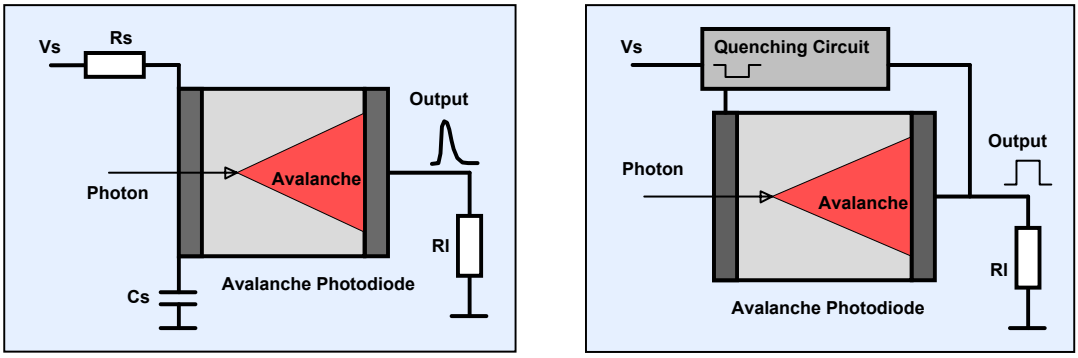


Fig. 251: Single photon avalanche photodiode (SPAD). Left Passive quenching, right active quenching

Passive quenching is obtained by operating the diode via a series resistor, R_s, which is typically a few hundred kΩ. C_s is the stray capacitance of R_s and the diode leads to ground, or an additional capacitor of a few pF. When an avalanche breakdown occurs, C_s is discharged within a time on the order of a nanosecond. The discharge current flows through the diode and the load, producing a correspondingly short output pulse. Simultaneously, the voltage across the diode drops below the breakdown voltage and the avalanche stops. The voltage across the diode then increases and eventually reaches the supply voltage. Full recovery of the reverse voltage normally takes several microseconds. Consequently, passive quenching can be used only at count rates below 1 MHz, and some count-rate dependence of the timing performance and efficiency must be expected.

Active quenching uses an electronic quenching circuit [335, 338, 431, 733]. The quenching circuit may be integrated with the SPAD on the same chip [1024]. When a breakdown occurs, the output pulse of the diode triggers the quenching circuit, which reduces the reverse voltage of the diode below the breakdown level for a time of typically 20 to 50 ns. After the quenching pulse the reverse voltage is restored within a few ns, and the diode resumes normal operation. Thus a much higher count rate can be obtained than for passive quenching. Nevertheless, also actively quenched photodiodes often show some count-rate-dependent timing shift and change in efficiency.

APDs suitable for single-photon detection must be free of premature breakdown at the edge of the junction or at local lattice defects. Therefore, the use of standard Si APDs in the breakdown mode is usually not successful. However, Si SPAD detectors with especially manufactured diodes are commercially available and increasingly used [607, 858, 967, 1115]. The active areas are small, typically 20 to 150 µm in diameter. However, the time resolution of many Si SPADs is on the order of 30 ps and less, and the efficiency in the visible range is high. For detection in the infrared region the situation is less favourable. A few TCSPC applications of liquid-nitrogen cooled Germanium APDs in the Geiger mode have been reported [927], but have not resulted in commercially manufactured detectors. The operation of InGaAs APDs in the Geiger mode has long been hampered by strong afterpulsing and high dark count rate. Therefore, the devices could only be operated in the gated mode and were not suitable for TCSPC. Now InGas SPADs for continuous operation are available. The time resolution is on the order of 90 ps, the efficiency on the order of 25%. Please see page 201.

A problem often associated with quenched breakdown operation is light emission from the diode. The effect is normally not noticeable in standard fluorescence lifetime applications. It can, however, be a problem for correlation experiments and quantum cryptography [728, 1273]. Please see page 697 of this handbook.

Silicon Photomultipliers (SIPMs)

A Silicon Photomultiplier, or SIPM, consists of an array of a large number of SPADs on a common silicon chip, see Fig. 252, right. The individual SPADs are passively quenched and the outputs connected in parallel, see Fig. 252, left. The individual diodes are biased above the breakdown voltage. If one of the SPADs receives a photon it breaks down and initiates a current pulse at the output of the SIPM. The typical pulse shape is shown in Fig. 252, middle. It consists of a fast part from the discharge of the capacity of the SPAD cathode versus Vcc, and a slow part from the recharge of the junction capacitance of the SPAD via its quenching resistor, R_Q. The fast part of the pulse can be used for single-photon timing.

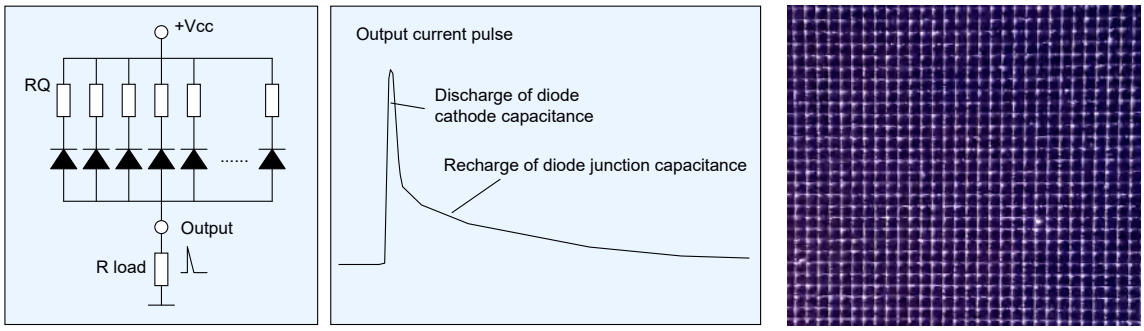


Fig. 252: Silicon Photomultiplier (SIPM). Left: Principle. Right: Micrograph of a SIPM

When many photons are reaching the SIPM within a short period of time they are unlikely to hit the same SPAD. The dead time of the individual SPADs is therefore not an issue. The output pulses initiated by the photons simply overlap, creating a signal that looks more or less like the output signal of a PMT. With tens of thousands of SPADs connected as shown in Fig. 252, right, the total active area of a SIPM can be as large as several cm^2, i.e. of the same size as the cathode of a PMT. Like a PMT, a SIPM can therefore be used for recording light that emerges from a large area.

The downside of the large active area is the large dark count rate. For a 1-cm^2 detector it is on the order of 10^7 counts per second at room temperature. This is more than the saturated count rate of most TCSPC devices, and in the pile-up range for even the highest signal repetition rates used in fluorescence decay measurements. For TCSPC application, SIPMs must therefore be cooled down to temperatures below 0° Celsius. Moreover, there is a considerable amplitude jitter of the output pulses. It is caused by the nonuniformity of the breakdown voltage of the individual diodes. To obtain reasonable time resolution the TCSPC module must therefore have a CFD in the photon input channel.

Superconducting Single-Photon Detectors

Superconducting single photon detectors (SSPDs) are made of an ultra small and ultra-thin meander or a single nanowire of niobium nitride on an isolating substrate, see Fig. 253. The device is cooled down to a temperature below 3 Kelvin so that the NbN structure becomes superconducting. A DC current of a few µA is sent through the structure. When a photon is absorbed somewhere within the meander superconductivity is temporarily lost. The voltage across the device temporarily increases, and the corresponding voltage pulse indicates the detection of a photon. The pulse amplitude into a load of 50 Ω is on the order of 0.5 to 1 mV. Therefore, a high-gain ultra-wideband amplifier is necessary to increase the amplitude to a level that triggers the CFD of a TCSPC module.

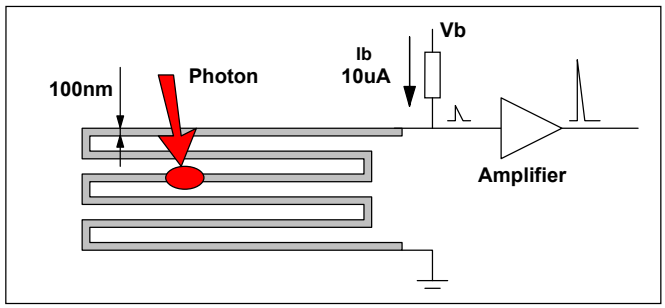


Fig. 253: Principle of a superconducting single-photon detector.

The time resolution obtained from SSPDs can be in the sub-10ps range. SSPDs are sensitive from the visible spectral range up to almost 10 µm. The dark count rate is on the order of a few pulses per second. The problem of the SSPD in spectroscopy applications is the extremely small active area. The entire active area is no larger than a few micrometers. Considering that the SSPD is located inside a cryostat, it is not easy to project the light on the detector. SSPDs are therefore normally fibre coupled. To maintain the intrinsic time resolution of the detector a single-mode fibre must be used. This solves the problem of transferring the light into the cryostat and onto the detector but simultaneously creates a problem on the fibre-input side. A single-mode fibre has a diameter of a few micrometers. Injecting light into the fibre is not an easy task. For TCSPC with SSPDs please see page 204 of this handbook.

Detector Parameters

Gain

A linear detector, such as a PMT, MCP PMT, or hybrid PMT must have sufficient gain that a single photoelectron emitted from the photocathode yields a detectable pulse at the detector output. The gain depends on the number of amplification stages and the acceleration voltage. In PMTs, the secondary emission coefficient at the dynodes depends on the material of the dynodes and the energy of the primary electron. The gain of a photomultiplier tube therefore changes strongly with the operating voltage. For typical interstage voltages on the order of 100 V the secondary emission coefficient is between 4 and 10 and changes with the 0.7th to 0.8th power of the voltage [558]. For a 10 stage PMT the total gain increases with the 7th or 8th power of the total voltage. For miniature PMTs with 6 to 7 dynodes, such as the Hamamatsu photosensor modules, the increase of the gain with the voltage is less dramatic, but still depends on the 4th power of the operating voltage. The gain of hybrid PMTs depends only moderately on the acceleration voltage, but dramatically on the APD reverse bias voltage. For gain setting of hybrid detectors please see page 273 of this handbook.

PMTs of the same type but with different cathode materials may differ considerably in gain. Highly efficient cathode materials are also good secondary-electron emitters. During the manufacturing process the cathode material spills into the dynode system, with the result that the secondary emission depends on the cathode type.

Single-Electron Response

The detector output pulse for a single photoelectron is called the ‘Single-Electron Response’ or ‘SER’. Approximate SER shapes for typical detectors are shown in Fig. 254.

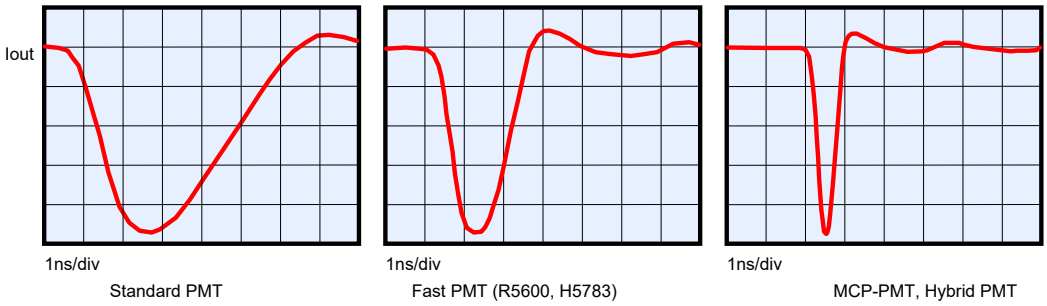


Fig. 254: Single electron response (SER) of different photomultipliers

Due to the random nature of the detector gain, the pulse amplitude varies from pulse to pulse. The pulse-height distribution can be very broad, up to 1:5 to 1:10. The average peak current of the SER is approximately

$$I_{SER} = \frac{G \cdot e}{T_{FWHM}},$$

with G = PMT Gain, e=1.6 · 10^{-19} As, T_{FWHM}= SER pulse width, full width at half maximum. The table below shows some typical values. I_{SER} is the average SER peak current and V_{SER} the average SER peak voltage when the output is terminated with 50 Ω. I_{max} is the maximum permitted continuous output current of the PMT.

PMT type	PMT Gain	FWHM	I_{SER}	V_{SER} (50 Ω)	I_{max} (cont)
Standard	10^7	5 ns	0.32 mA	16 mV	100µA
Fast PMT	10^7	1.5 ns	1 mA	50 mV	100µA
MCP PMT	10^6	0.36 ns	0.5 mA	25 mV	0.1µA
Hybrid Detector	10^5	0.8 ns	0.2 mA	10 mV	10 µA

There is one conclusion from this table: If a detector is operated near its full gain the peak current I_{SER} from a single photon is much higher than the maximum continuous output current. Consequently, for steady state operation the PMT always delivers a train of random photon pulses rather than a continuous signal (see also Fig. 188, page 101).

Pulse Height Distribution

The secondary emission coefficient at a particular dynode depends on the dynode material and energy of the primary electrons. For typical inter-dynode voltages used in PMTs, the secondary emission coefficient, n, is between 4 and 10. Because the secondary emission is a random process the number of the generated secondary electrons varies from electron to electron. The width of the distribution can be expected at least of the size of the standard deviation, $n^{1/2}$, of a Poissonian distribution of the secondary emission coefficient, n. Therefore the single-photon pulses obtained from a PMT have a considerable amplitude jitter. For TCSPC applications it is important that the pulse amplitudes of the majority of the pulses are well above the unavoidable noise background.

Because the gain of a PMT may vary over a wide range, the total width of the distribution may vary for different tubes and different supply voltages. However, despite the different materials and shapes of the dynodes in different PMTs, the general shape of the distribution is more or less similar.

A pulse amplitude distribution measured for a Hamamatsu H7422P-40 PMT module at different gain is shown in Fig. 255. There is a broad peak at high amplitudes and a secondary peak at low pulse amplitudes. The high amplitude peak contains the regular single-electron pulses.

The low-amplitude peak is at least partially related to the light. Its relative height does not appreciably depend on the count rate. It is possibly caused by photoelectrons scattered at the first dynode and reaching the second dynode without amplification. Another source of the small-amplitude peak is photoelectron emission on the first dynode. If the discriminator threshold is set low enough an extremely high peak appears at very low amplitudes. This peak does not originate in the PMT but is caused by electronic noise of the preamplifier and noise pickup from the environment. For some photomultipliers a 'peak to valley' ratio is specified, which indicates how much higher the main peak is compared to the valley between the main and the secondary peak.

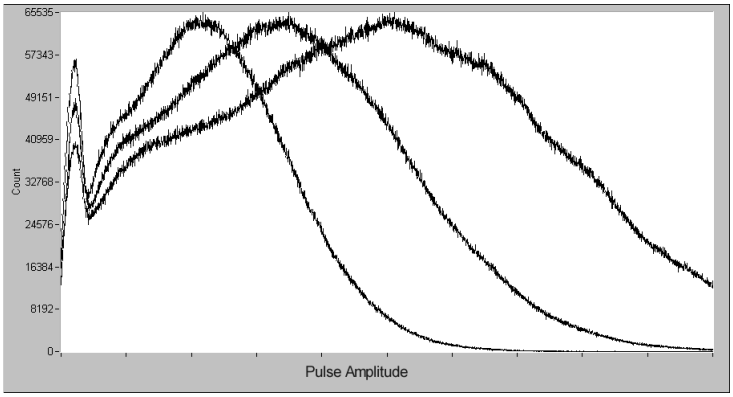


Fig. 255: Pulse amplitude distribution of a H7422P-40 for different gain.

The pulse height distribution at high detector gain often shows a sub-structure (see Fig. 255), probably due to the discrete numbers of secondary electrons emitted at the first dynode.

The shape of the main peak of the amplitude distribution is almost the same for the photon pulses and the dark pulses, see Fig. 256. This is not surprising because the secondary emission process makes no difference between electrons emitted at the cathode thermally or optically. However, the secondary peak at low amplitudes is more pronounced for the dark pulses, probably because some of the thermal electrons are emitted at the dynodes.

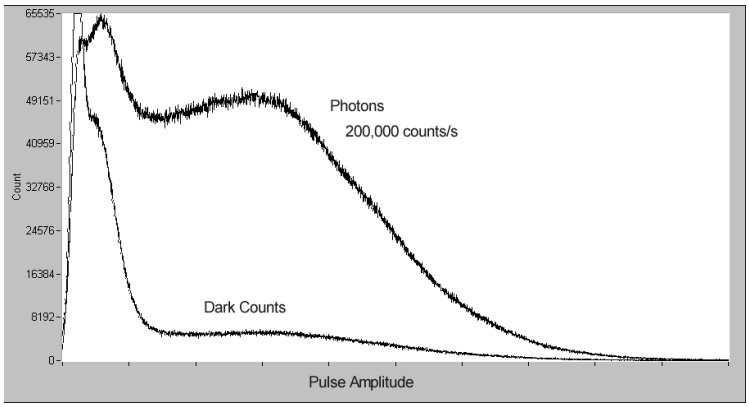


Fig. 256: Pulse amplitude distribution for dark pulses and photon pulses of an R5600P-01 PMT

For reasonable TCSPC operation, a discriminator threshold must be found that rejects the electronic noise background and the pulses in the low-amplitude peak, but counts as many of the regular photon pulses as possible. Moreover, the threshold should be considerably above the electronic noise level so that the smallest detected pulses still have a good signal-to-noise ratio. For photon counting it is therefore essential that a sufficient gain can be achieved within the permissible operating voltage of the PMT.

It is often believed that the width of the pulse amplitude distribution depends on the cathode material. Certainly there are differences in the peak ratios of the main peak and the low-amplitude peak, and in the peak-to-valley ratio. However, the differences are not very large,

and the relative width of the main peak does not vary appreciably. It seems that detectors of different cathode type differ mainly in gain, rather than in the shape of the distribution. Consequently, the problem of most PMTs of poor photon counting performance is lack of gain, especially at the first dynode, not so much an odd shape of the amplitude distribution.

Signal Transit Time

The signal transit time in a PMT is almost entirely determined by the transit time of the electrons through the PMT. It is therefore proportional to the reciprocal square root of the supply voltage. Typical transit times for a number of frequently used PMTs are shown in the table below.

Detector	Operating voltage (Gain control voltage)	Transit Time	Transit Time per % Change in operating or gain control voltage
Hybrid detector	8000V, 400V	< 1 ns	<10 ps
R3809U MCP-PMT	3000 V	< 1 ns	3 ps
R7400 and R5600 TO8 PMTs	900 V	5.4 ns	21 ps
H5773 Photosensor module	(0.9 V)[1]	5.4 ns	21 ps
H7422 PMT module	(0.9 V)[1]	6.5 ns	27 ps
R928 side window PMT	900 V	22 ns	100 ps
XP2020 44 mm linear focused PMT	2500 V	28 ns	140 ps

[1] Gain control voltage. Controls operating voltage of PMT.

The transit time has to be taken into account when choosing the cable length in the detector and reference signal path of a TCSPC system (see ‘SYNC and CFD Signal Path Length, page 279). More important than the transit time itself is the variation of the transit time with the detector supply voltage. To keep the average transit time of a conventional PMT stable within 1 ps a stability of the operating voltage on the order of 0.05% to 0.01% is required.

Transit Time Spread and Timing Jitter

The delay between the absorption of a photon at the photocathode and the output pulse at the anode of a PMT varies from photon to photon. The effect is called ‘transit time spread’, or TTS. There are tree major TTS components in conventional PMTs and MCP PMTs - the emission at the photocathode, the variation in the electron transit times, and the timing jitter of the subsequent electronics.

The time constant of the photoelectron emission at a traditional photocathode is small compared to the other TTS components and usually does not noticeably contribute to the transit time spread. However, high efficiency semiconductor-type photocathodes (GaAs, GaAsP, InGaAs) are much slower and can introduce a transit time spread on the order of 100 to 150 ps.

The photoelectrons are emitted at the photocathode of a photomultiplier at random locations, with random velocities and in random directions. Therefore, the time they need to reach the first dynode or the channel plate is slightly different for each photoelectron (Fig. 257, left). Since the average initial velocity of a photoelectron increases with decreasing wavelength of the absorbed photon the transit-time spread is wavelength-dependent.

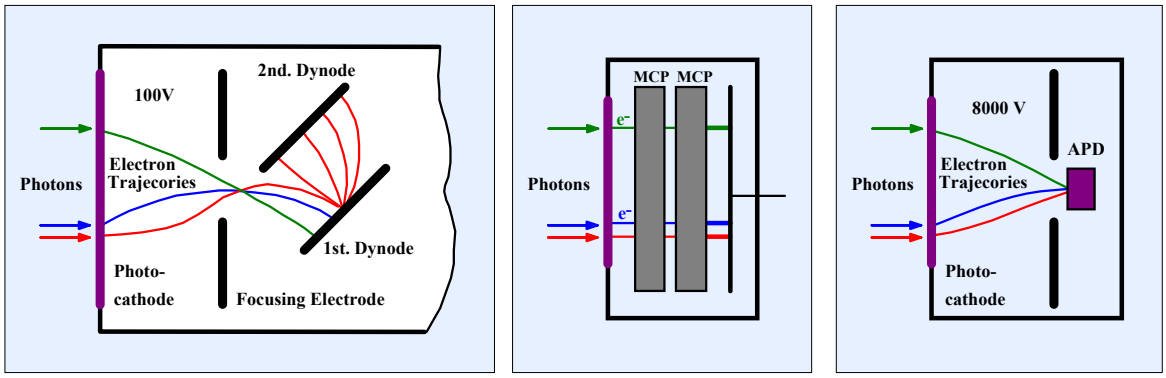


Fig. 257: Electron trajectories in a PMT(left), an MCP-PMT, and a hybrid detector (right)

Also the secondary electrons emitted at the first dynodes of a PMT or in the channel plate of and MCP PMT have a wide range of start velocities and start directions. The variation in the time they need to reach the next dynode adds to the transit time spread in the cathode space.

In an MCP PMT (Fig. 257, middle) the electron trajectories are short, straight, and differences in the direction of the photon emission have little effect on the transit time. MCP PMTs therefore have very low transit time spread.

In a hybrid detector (Fig. 257, right) the same basic effects are at work, but the acceleration voltage is 8000 V. The electron trajectories are therefore much straighter, and the transit times shorter. Correspondingly smaller is the transit-time variation for different start velocity of the photoelectrons. The transit-time spread in hybrid detectors is therefore very small.

TTS does exist also in single-photon avalanche photodiodes. The main reason of TTS in SPADs is the different depth in which the photons are absorbed. This results in different conditions for the build-up of the carrier avalanche and in different avalanche buildup times. Because the average depth where the photons are absorbed depends on the wavelength also the TTS depends on the wavelength. Moreover, if high count rates are used, the reverse voltage may not have completely recovered from the breakdown caused by the previous photon. The result is a shift in the TTS with the count rate.

Cathode Efficiency

Several different definitions are used to specify the efficiency of a PMT cathode. Often the sensitivity of a PMT is specified in units of ‘cathode luminous sensitivity’. This is the cathode current per lumen incident light from a tungsten lamp operated at a temperature of 2856 K. Because the intensity maximum of the lamp is at about 1000 nm, the luminous sensitivity may not represent the efficiency at a given wavelength. Photocathodes of different spectral sensitivity are therefore not directly comparable. Moreover, the cathode luminous sensitivity does not include the efficiency of the electron transfer from the cathode into the dynode system and the possible loss of photon pulses due to incomplete resolution of the pulse height distribution.

In the test sheets of PMTs, the manufacturers occasionally specify the measured ‘anode luminous sensitivity’ instead of the cathode sensitivity. The anode sensitivity is the cathode sensitivity (including the electron transfer efficiency) multiplied by the gain of the tube. Because almost any gain can be obtained by increasing the supply voltage, the anode luminous sensitivity cannot be used to compare the photon-counting performance of PMTs.

The ‘cathode radiant sensitivity’ is the cathode current per watt of incident power at a given wavelength. It is usually given as a plot versus the wavelength. The cathode radiant sensitivity does not include the efficiency of the electron transfer from the cathode into the dynode system or the possible loss of photon pulses due to poor resolution of the pulse height distri-

bution. Nevertheless, the cathode radiant sensitivity is useful for comparing different detectors and different cathode versions.

The most useful parameter for characterising the efficiency of a photon-counting detector is the quantum efficiency. The quantum efficiency, *QE*, of a photocathode is the probability of the emission of a photoelectron per incident photon. It is directly related to the radiant sensitivity, *S* :

$$QE = S\,\frac{hc}{e\lambda} = \frac{S}{\lambda}\cdot 1.24\cdot 10^{-6}\,\frac{\mathrm{Wm}}{\mathrm{A}}$$

with h = Planck constant, e = elementary charge, λ = wavelength, c = velocity of light.

Usually quantum efficiencies given for detectors refer to the emission of a photoelectron or, in avalanche photodiodes, the generation of an electron-hole pair. The 'detection efficiency' in PMTs or SPADs is smaller for the reasons mentioned above: Not all photoelectrons cause a detectable anode current pulse in a PMT, and not all electron-hole pairs trigger an avalanche in a SPAD. An exception is the hybrid PMT: A photon emitted at the cathode is accelerated to such a high energy that it almost certainly generates an output pulse in the avalanche diode.

The efficiency of the commonly used photocathodes is shown in Fig. 258. The QE of the conventional bialkali and multialkali cathodes reaches 20 to 25% between 400 and 500 nm. GaAsP cathodes reach 45 to 50% and work up to 700 nm. The GaAs cathode works up to 900 nm. Tt significantly surpasses conventional cathodes in sensitivity above 700 nm.

Generally, there is no significant difference between the efficiency of similar photocathodes in different PMTs and from different manufacturers. The differences are of the same size as the variation between different tube of the same type. Reflection type cathodes are a bit more efficient than transmission type photocathodes. However, reflection type photocathodes have non-uniform photoelectron transit times to the dynode system and therefore cannot be used in ultra-fast PMTs. An overview about the spectral characteristics of PMT cathodes is given in [723].

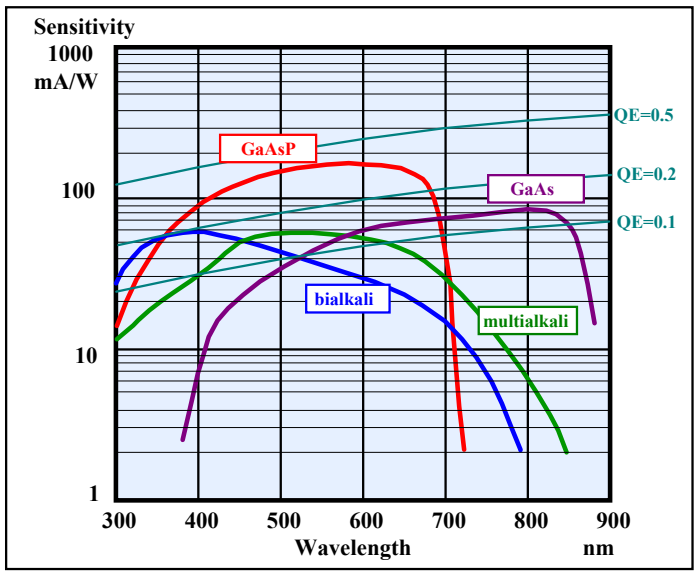


Fig. 258: Sensitivity of different photocathodes, after [723]

The typical efficiency of the Perkin Elmer SPCM-AQR single photon avalanche photodiode module (now from Excelitas) is shown in Fig. 259 (after [967]). The wavelength dependence follows the typical curve of a silicon photodiode and reaches more than 70% at 700 nm. However, the active area of the SPCM-AQR is only 0.18 mm wide, and the diameters of other

SPADs are as small as 20 µm. Therefore the high efficiency of a SPAD can only be exploited if the light can be focused into such a small area.

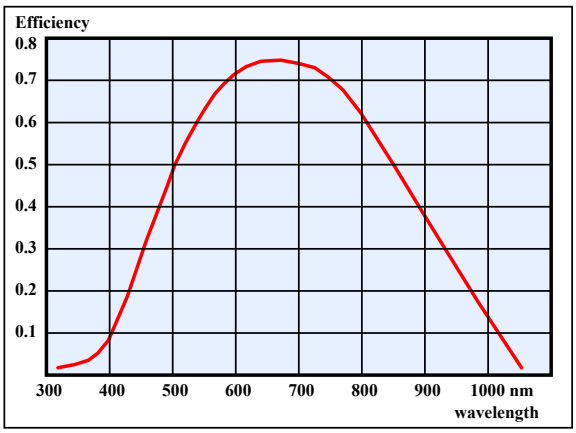


Fig. 259: Quantum efficiency vs. wavelength for a Perkin-Elmer SPCM-AQR SPAD module [967]

Dark Count Rate

The dark count rate of a PMT depends on the cathode type, the cathode area, and the temperature. The dark count rate is highest for cathodes with high sensitivity at long wavelengths. Depending on the cathode type, the dark count rate decreases by factor of 3 to 10 for a 10 °C decrease in temperature. The most efficient way to keep the dark count rate low is thermoelectric cooling. Reducing the temperature by 5 or 10 °C is often sufficient to obtain a substantial decrease in dark count rate. Of course, any heat sources, such as the voltage divider resistors, amplifiers connected to the output, or electrically driven shutters should be thermally decoupled from the tube.

Exposing the cathode of a switched-off PMT to daylight increases the dark count rate for a longer period of time. For the traditional cathodes the effect is reversible, but full recovery can take several hours, see Fig. 260. Semiconductor cathodes should not be exposed to full daylight at all.

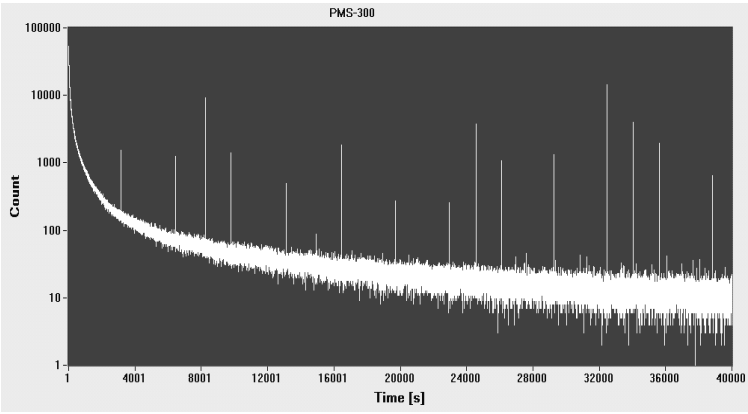


Fig. 260: Decrease of dark count rate (counts per second) of a H5773P-01 photosensor module after the cathode had been exposed to daylight. The device was operated at an ambient temperature of 5°C.

After extreme overload, e.g. daylight on the cathode of an *active* PMT, the dark count rate can be permanently increased by several orders of magnitude. The tube is then damaged and does not recover.

Many PMTs produce random single pulses of extremely high amplitude or bursts of pulses with extremely high count rate. Such bursts are responsible for the peaks in Fig. 260. The peaks may indicate beginning instability in the tube and disappear if the gain is slightly re-

duced. However, irregular bursts can also originate from dust on the cathode window, scintillation effects by radioactive decay in the vicinity of the tube, in the tube structure itself, by cosmic ray particles or from tiny electrical discharges in the cathode region. Therefore not only the tube, but also the materials in the cathode region must be suspected to be the source of the effect. Generally, there should be some mm clearance around the cathode region of the tube.

Afterpulsing

Photon-counting detectors have an increased probability of producing background pulses within a few microseconds following the detection of a photon. These afterpulses are detectable in almost any conventional PMT. It is believed that they are caused by ion feedback [319], or, by a smaller amount, by luminescence of the dynode material and the glass of the tube. Afterpulsing exists also in SPADs. Afterpulsing of SPADs is caused by electrons and holes from a previous avalanche. The carriers are trapped in lattice imperfections; the duration of afterpulsing in SPADs therefore depends on the temperature. The only detectors that are free of afterpulsing are hybrid detectors [159], see 'HPM-100 Hybrid Detector', and 'NbN Superconducting Single-Photon Detectors' [867, 1189, 1190].

Afterpulses are difficult to identify in a standard TCSPC fluorescence lifetime setup. The afterpulses appear within a few microseconds after the detection of a photon. However, TCSPC records only one detector pulse per signal period. An afterpulse is recorded only if it appears in a new signal period and after the dead time caused by the previously detected photon.

The afterpulsing probability versus the time after a regular single-photon pulse can be measured by illuminating the detector by a source of continuous classic light, such as an incandescent lamp or an LED, and recording the detector pulses in the FIFO (time-tag) mode of a TCSPC module. Afterpulsing reveals itself in the autocorrelation function of the photon density over time. For continuous classic light, the autocorrelation function is a horizontal line. Afterpulsing shows up as a peak at times shorter than a few microseconds. An example is shown in Fig. 261.

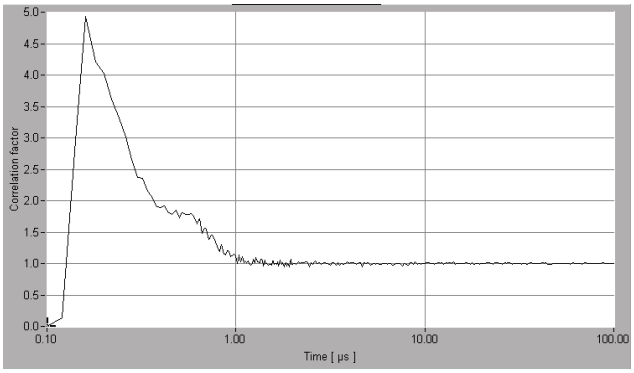


Fig. 261: Afterpulsing of an R5600P-1 PMT. Autocorrelation of the photon density recorded for a continuous light, count rate 10.000 /s.

The height of the afterpulsing peak depends on the count rate. The reason is that the probability of detecting the afterpulse of a previously detected photon is constant, whereas the probability of detecting another photon increases with the count rate. To make the results directly comparable different detectors must be tested at the same count rate.

The density of the afterpulses, as a function of time after a light pulse, can be recorded directly with a multichannel scaler. The PMT is illuminated with light pulses at a pulse period

in the µs range, and the PMT pulses are recorded over a time interval of a few microseconds. An example is given in [154].

Afterpulsing can be a problem in high-repetition rate TCSPC applications, especially with Ti:Sapphire lasers or diode lasers. At high repetition rate, the afterpulses from many signal periods pile up and cause a considerable signal-dependent background. The total afterpulsing rate can easily exceed the dark count rate of the detector by an order of magnitude (see 'Fig. 425', page 276). In fluorescence correlation spectra, afterpulsing results in a typical 'afterpulsing peak' at times shorter than a few µs (see Fig. 906, page 660). The amount of afterpulsing depends on the PMT gain. It can be reduced, yet not entirely removed, by decreasing the operating voltage of the PMT and using a preamplifier of a correspondingly higher gain.

The average amplitude of the afterpulses is higher than of the regular single-photon pulses. The higher amplitude can result in a number of confusing effects. One of them is that the apparent background of a detector may increase with increasing discriminator threshold. The reason is, of course, not a real increase of the background count rate. Instead, the afterpulsing background remains almost constant while the signal count rate decreases. In extreme cases almost all photon pulses are suppressed, and only afterpulses are recorded, see Fig. 427, page 278.

A remark appears indicated about the bumps that are commonly found in the TCSPC IRF of photomultipliers. These bumps (see, for example Fig. 264 or Fig. 267) are sometimes called 'afterpulsing' or 'afterpulses'. They have, however, nothing to do with the effect described here: The bumps are caused by regular photoelectrons that are scattered at the first dynode of a PMT or at the front face of the channel plate of an MCP PMT, and re-enter the amplification system with a delay of few 100 ps or a few ns. The difference compared to true afterpulses is that such scattered photoelectrons are *not related to a previously detected photon*. They are thus recorded, and, because they are delayed, cause said bumps in the IRF. True afterpulses occur after the detection of a regular photon. Afterpulses occurring closer than about 100 ns after a photon a are not detected because they fall into the dead time of the photon. They do thus not cause a bump in the IRF.

Prepulses

In some detectors a bump in the TCSPC instrument response function (IRF) appears a few ns before the main peak. The size of the bump depends on the discriminator threshold. Normally the bump can be suppressed or reduced in size by increasing the discriminator threshold. The effect is probably caused by photoelectron emission from the first dynode. The corresponding pulses reach the anode prior to the photons from the cathode, and have a lower amplitude. An example is shown in Fig. 262. Similar effects can arise from an inappropriate zero cross level in a CFD. If the zero cross level is too close to the signal baseline, the zero cross comparator may oscillate and produce a double structure in the IRF. Therefore the CFD parameters should be checked before a PMT is suspected of producing pre-pulses.

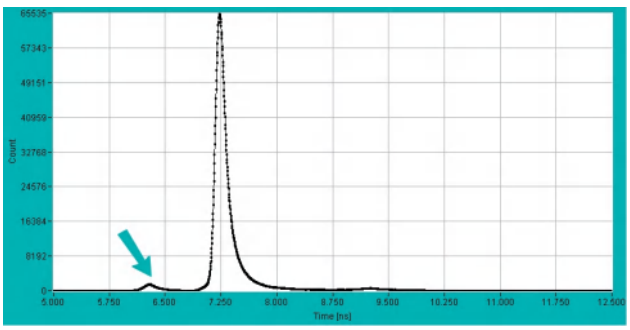


Fig. 262: Prepulses in IRF of a PMT

Description of Selected Detectors

R3809U MCP PMTs

For many years, the Hamamatsu R3809U (Fig. 263) was the fastest detector in terms of TCSPC time resolution. TCSPC devices with the R3809U routinely achieve an IRF width below 30 ps [544]. The R3809U is available with conventional bialkali, multialkali, and extended-red multialkali cathodes. Recently, R3809 versions with high efficiency GaAs and GaAsP cathodes and versions for the spectral range above 1000 nm have become available.

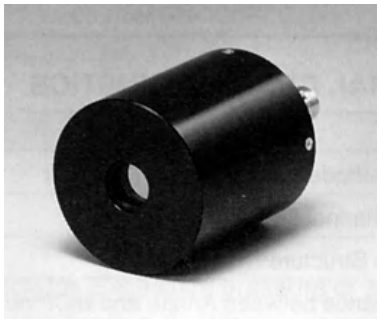


Fig. 263: Hamamatsu R3809U MCP

An instrument response function of an R3809U measured with a bh SPC-630 TCSPC module is shown in Fig. 264. At an operating voltage of -3 kV an IRF width of 28 to 30 ps (FWHM) is obtained. The detector was operated with a 1.8 GHz preamplifier of 26dB gain. The CFD threshold was adjusted to a level that did not suppress more than 20% of the pulses. The IRF width decreases to about 25 ps if the operating voltage is increased to the maximum permitted value of -3.4 kV. The IRF has a shoulder of about 0.5 ns duration and 1 to 2% of the peak amplitude, see Fig. 264, right.

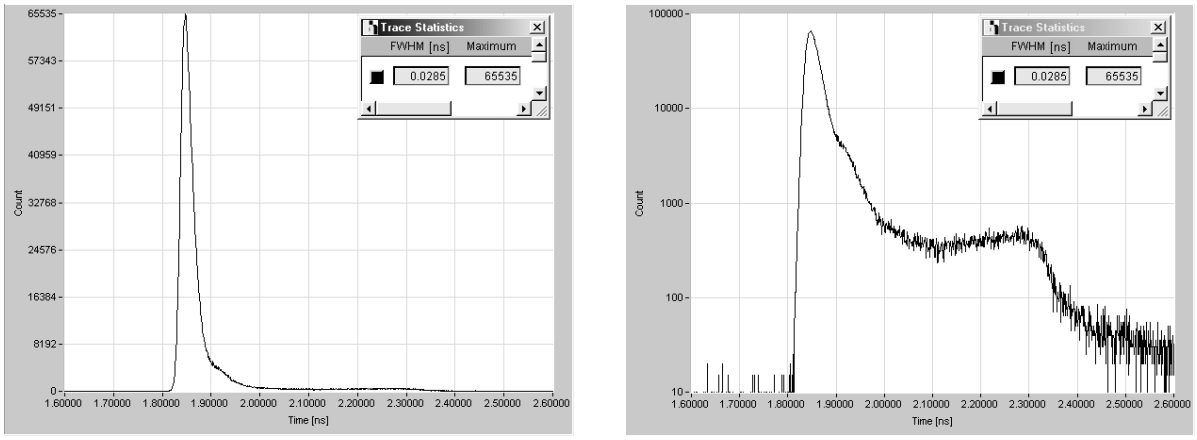


Fig. 264: IRF of an R3809U at -3 kV operating voltage. Linear scale (left) and logarithmic scale (right). Measured with Ti:Sapphire laser and SPC-630 TCSPC module. Time channel width 820 fs, time per division 100 ps.

For a long time, an IRF width of 25 to 30 ps FWHM was considered the best that could be reached at a reasonable CFD threshold, without suppressing more than 50% of the photon pulses. Occasional reports about shorter IRF width were (probably correctly) attributed to the use of exceedingly high CFD thresholds. Operation in this regime results in low detection efficiency, and bears the risk of multiphoton detection and count-rate dependent IRF by saturation of the microchannels.

The situation changed with the introduction of the bh SPC-150N and, in particular, SPC-150NX modules. These modules have CFDs with an input bandwidth of 5 GHz, compared to about 1 GHz of the SPC-630, 830, 130, and 150 modules. The new discriminators therefore 'see' the leading edge of the single-photon pulses with a faster rise time than the old ones. Consequently, amplitude fluctuations and amplifier noise have less influence on the time resolution. We tested an R3809U-50 / SPC-10NX combination with a Toptica FemtoFerb (100 fs) fibre laser. Details of the test setup are described in [122]. With the SPC-150NX the R3809U-50 delivers an IRF width around 20 ps and below. The IRF shape for two different CFD thresholds is shown in Fig. 265. left, the dependence of the IRF width and the efficiency on the CFD threshold in Fig. 265, right.

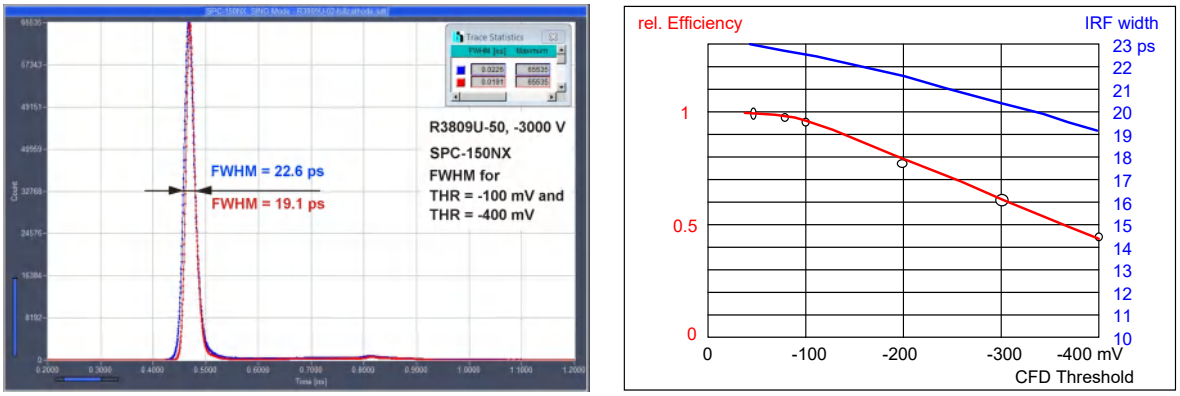


Fig. 265: IRF of R3809U-50 with SPC-150NX. Left: IRF shape for CFD threshold of -100 mV (blue) and -400 mV (red). Right: IRF width and efficiency as a function of CFD threshold. The operating voltage of the R3809U was -3000 V

It should be noted that the IRFs shown in Fig. 265 were recorded at a detector operating voltage of only -3000 V, and with the entire photocathode illuminated. Under these conditions, a count rate of several MHz can be achieved. An even shorter IRF width may be possible at the maximum operating voltage of -3400 V, and with a smaller illuminated area. The count rate is then limited by saturation of the microchannels and by the maximum permitted output current of the detector (see below). Nevertheless, operation in this range may be a solution to low-count-rate applications.

MCP PMTs are commonly believed to be unable to work at count rates higher than a few 10^4 photons per second. This is not correct if the detector is operated correctly [155]. IRF curves for a Hamamatsu R3809U at different count rate with illumination of the full cathode and -3 kV operating voltage are shown in Fig. 266, left. Up to a count rate of 3.3 MHz there is neither a change in IRF position nor in IRF shape. The first moment of the IRF does not change by more than 3 ps.

Fig. 266, right, shows the IRF of a Hamamatsu R3809U MCP for an illuminated area of about 1/10 of the cathode area. The count rates were 100 kHz, 1.4 MHz, and 3.3 MHz. There is indeed a noticeable change in the IRF, with a shift in the first moment of almost 20 ps. The IRF shift is most likely an effect of the saturation of the microchannels. The output of a single microchannel saturates when a single photon enters the input [723]. The recovery time of the channel is in the microsecond range. If a large number of photoelectrons is concentrated on a limited number of microchannels these do not fully recover, and the IRF changes. A simple extrapolation from the spot area of 10 mm^2 in Fig. 266, left, to smaller areas shows that the useful count rate can indeed drop to the 10-kHz range.

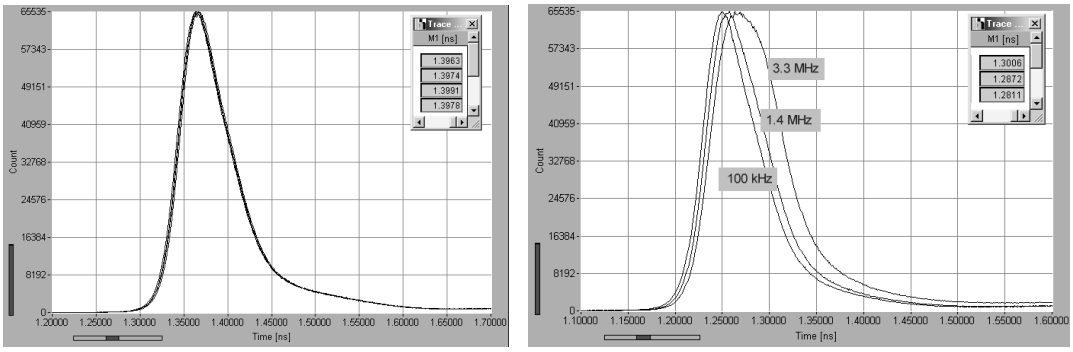


Fig. 266: IRF of an R3809U MCP-PMT for different count rates. Illumination by diode laser, pulse width 50 ps. Operating voltage -3 kV, 20 dB preamplifier gain, CFD threshold -80 mV. Left: Full cathode area illuminated, count rates 3.3 MHz, 1.8 MHz, 480 kHz, and 25 kHz. Right: Illuminated area 2 x 5 mm, count rates 3.3 MHz, 1.4 MHz, 100 kHz.

These results show that MCP PMTs can be used for count rates close to the maximum useful count rate of currently available TCSPC systems. It should be noted, however, that the output current at a count rate of 3.3 MHz and an operating voltage of 3 kV is a few time higher than the maximum rating of 100 nA. This is certainly not a problem in applications where high count rates appear only temporarily, as in laser scanning microscopy. The lifetime of an MCP PMT at a continuous count rate of more than 3 MHz is not known.

MCP PMTs are expensive and can be damaged by overload. It is also believed that the conductive counting of the microchannels gradually degrades by sputtering under the impact of the electrons. This is no problem when the detector is operated within the limits given by Hamamatsu. However, unnecessarily high count rates over longer periods of time should be avoided. To provide maximum safety for the detector we recommend to use the bh HFAC-26-01 or HFAH-26-01 preamplifiers (see ‘Preamplifiers’, page 211), the bh DCC-100 detector controller card (see ‘The DCC-100 Detector Controller’, page 212), and a high-voltage power supply that is controlled by the DCC-100. A high-voltage power supply module for the R3809U is available from bh, see Fig. 155, page 83. In situations where severe overload can occur the R3809U can be protected by a shutter, see Fig. 164, page 87 and Fig. 370, page 237.

The R3809U-50 and -52 have been found almost free of afterpulsing [136, 154]. This makes the detector well suitable for fluorescence decay measurements over a wide dynamic range. In this respect, the performance is only surpassed by hybrid detectors and superconducting single-photon detectors (SSPDs).

Hamamatsu R5600 and R7400 Miniature PMTs

The Hamamatsu R7400 and the older R5600 are miniature PMTs in a TO-8 size housing. The R7400 PMTs are the basis of the H5773 and H5783 photosensor modules, see paragraph below. Due to their small size, the tubes yield a fast TCSPC instrument response. The typical IRF width for multialkali and bialkali tubes is between 150 and 180 ps fwhm. Increasing the voltage between the cathode and the first dynode makes the response even faster. It is unknown how far the voltage can be increased without the tube breaking down. A test tube worked stable at 1 kV overall voltage with a cathode-to-dynode voltage 3 times as high as the dynode-to-dynode voltage. The decrease of the response width is shown in Fig. 267.

The metal-channel design of the R5600 and R7400 results in slight periodical variations of the efficiency and the IRF over the active area, see Fig. 268, right. Consequently, either the entire active area should be illuminated or the position of the illuminated spot should be kept stable.

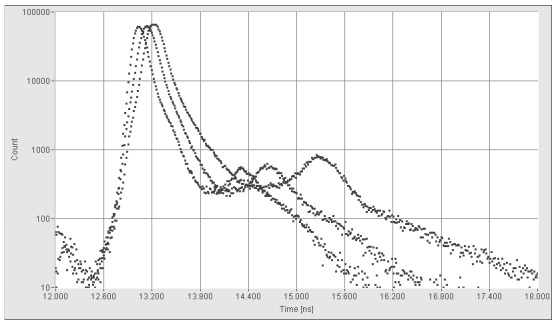


Fig. 267: R5600P-1, -1kV supply voltage: TCSPC response for different voltage between cathode and first dynode. Left to right: 3, 2 and 1 times nominal voltage. Entire cathode area illuminated, time scale 600 ps/div.

The afterpulsing probability of the miniature PMTs is relatively high, especially for the NIR-sensitive versions. However, the afterpulsing ceases after one microsecond and can, as usual, be reduced by operating the tube at reduced gain.

The performance of the R7400 and R5600 tubes with the standard voltage divider is the same as for the Hamamatsu H5773 and H5782 photosensor modules (see below). It is questionable whether the slightly lower price compensates for the inconvenience of building a voltage divider and using a high voltage power supply. Moreover, a R5600 or R7400 with a standard voltage divider does not yield the same high timing stability as the photosensor modules.

Hamamatsu H5783 and H5773 Photosensor Modules

H5783 and H5773 are miniature optical sensors containing a TO-8-size PMT together with a high-voltage power supply. The modules are operated from a simple +12 V to + 15 V power supply. The operating voltage of the PMT is controlled by a 0 to +0.9 V gain control signal. The modules are available in different cathode and window versions. A 'P' version selected for high gain and good pulse height distribution is available for the bialkali and multialkali tubes.

The typical IRF of an H5773P-0 is shown in Fig. 268. The output pulses were amplified by a HFAC-26-10 preamplifier, and the response to 50 ps pulses from a 650 nm diode laser was recorded by an SPC-730 TCSPC module.

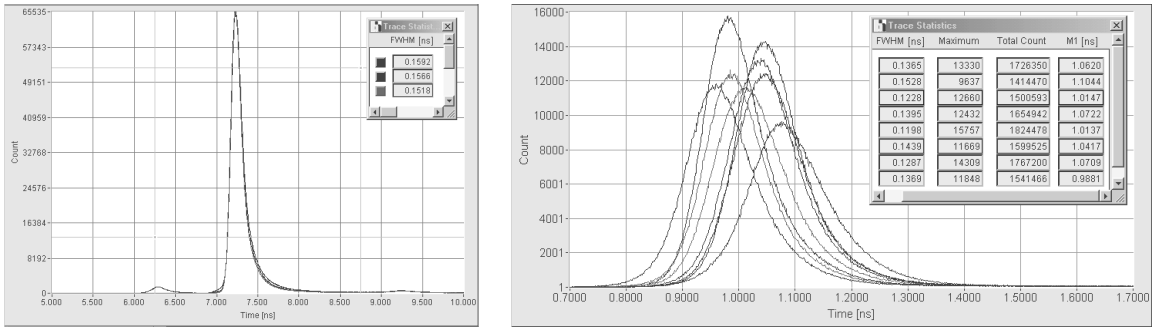


Fig. 268: H5773P-0. Left: TCSPC IRF, time scale 500 ps/div. Gain control voltage 0.9 V, preamplifier gain 20dB, discriminator threshold -100 mV, -300 mV and -500 mV. Right: Variation of the IRF and the efficiency over the cathode area.

The response function has a pre-peak about 1 ns before and a secondary peak 2 ns after the main peak. The pre-peak is caused by low amplitude pulses, probably by photoemission at the first dynode. It can be suppressed by properly adjusting the discriminator threshold. The secondary peak is independent of the discriminator threshold.

The variation of the IRF for an H5773-20 over the active area is shown in Fig. 268, right. The FWHM of the IRF varies from about 120 ps to about 140 ps, and the first moment shifts over 90 ps (see insert). This means that the IRF width for small spots can be substantially shorter

than for the full active area. However, the improved resolution can only be exploited if the location of the illuminated spot is kept stable within less than 0.1 mm. If timing stability is important it is probably better to spread the light over the full cathode area. There is also some variation in the efficiency, see total count numbers in the insert of Fig. 268, right.

The H5783 and H5773 photosensor modules have an exceptionally good timing stability at high count rates [155]. A test result for a Hamamatsu H5773P-20 photosensor module is shown in Fig. 269.

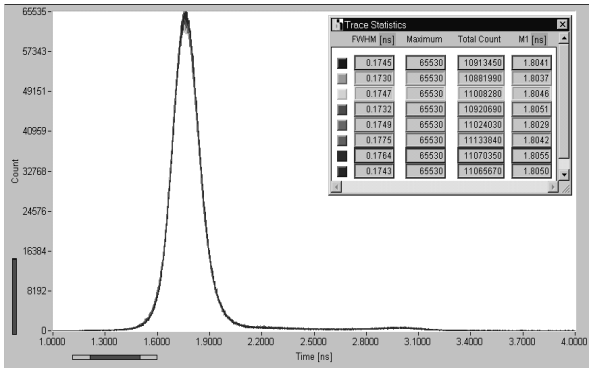


Fig. 269: IRF of an H5773-20 photosensor module for recorded count rates of 30 kHz, 300 kHz, and 4 MHz. The shift between 30 kHz and 4 MHz is <2 ps and not discernible in the IRF curves. Insert: First moments of the curves.

For (recorded!) count rates varying from 30 kHz to 4 MHz the shift in the first moment of the IRF is <2 ps and not discernible in the IRF curves. The surprisingly high timing stability may in part be a result of the Cockroft-Walton voltage-divider design of the H5773 and H5783 modules [547].

Surprisingly, the internal high voltage generator of the H5783 and H5773 does not induce much noise at the output of the modules. Some ripple is detectable, especially at a load impedance of 1 MΩ, but the amplitude is much smaller than the amplitude of the single-photon pulses.

Unfortunately the housings of the H5783 and H5773 modules do not provide good RF shielding. Apparently there is no low-impedance connection between the internal signal ground and the housing. To obtain reasonable photon counting operation, the modules must be operated in an additional shielding box.

To improve the noise immunity and to provide safety against damage by overload the photosensor modules should be used with an HFAC-26-10 preamplifier. The +12 V supply voltage can be taken from the sub-D connector of the SPC module. The gain control voltage can be obtained from a simple voltage divider. A more comfortable solution is the DCC-100 detector controller of bh [63] (see ‘The DCC-100 Detector Controller’, page 212). The DCC-100 provides software-controlled gain setting, detector on/off switching and overload shutdown in conjunction with a bh HFAC-26 preamplifier.

H11900 / H11901 and H10720 / H10721 Photosensor Modules

Recently, Hamamatsu have introduced new photosensor modules. The H11900 / H11901 and H10720 / H10721 modules are functionally compatible with the H5783 and H5773 but have higher cathode efficiency and shorter transit-time spread. The H1190 and H10720 have pin connections, the H1190 and H10720 have cables, see Fig. 270.

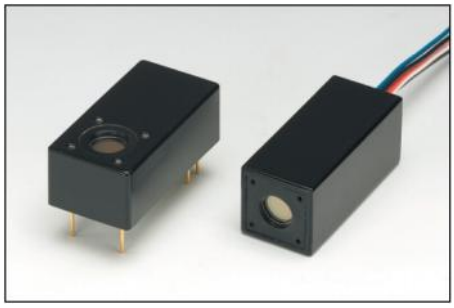


Fig. 270: Hamamatsu H11900 (left) and H11901 (right) photosensor modules

The modules can be used in combination with the bh TCSPC modules. To avoid detector or discriminator damage by overload or high pulse current we recommend to use the detectors with an HFAC-26-10 preamplifier and to control them from a DCC-100 detector controller. The H11900 modules are used in the new PMC-150 PMT modules of bh. Please see 'PMC-150' for a characterization.

PMH-100, PMC-100, PMZ-100

The PMH-100, PMC-100, and PMZ-100 detector modules of bh contain a Hamamatsu H5773 photosensor module together with a preamplifier. The PMC-100 also contains a thermoelectric cooler. The detectors are shown in Fig. 271.



Fig. 271: PMH-100 (left), PMC-100 (middle) and PMZ-100 detector modules

The PMH module (shown left) was the standard detector for the early SPC-300, SPC-400, and SPC-500 modules. The PMH was operated from the +12 V output at the sub-D connector of the SPC module or from a wall-mounted AC/DC adapter. The disadvantage of the PMH-100 was that it had no overload shutdown. In the years after 2000, the PMH-100 modules have been almost entirely replaced by PMC-100 detectors.

The PMC-100 is an improved version of the PMH-100. It has a thermoelectric cooler and internal overload detection. The PMC-100 requires the DCC-100 detector controller for proper operation. The DCC-100 delivers the current for the Peltier cooler and provides overload shutdown of the detector. Due to the cooling, even the NIR-sensitive versions of the PMC-100 deliver low dark count rates.

The PMZ-100 has been designed for the non-descanned output ports of the Zeiss LSM 710 NLO multiphoton laser scanning microscopes. The beam path of these microscopes requires the PMT cathode to be extremely close to the optical adapter. Also the PMZ-100 is operated via the DCC-100. It has overload shutdown but no thermoelectric cooler.

The IRF of the PMH, PMC and PMZ modules is identical with the IRF shown for the H5773 in Fig. 268. Moreover, the detectors feature the same exceptionally IRF stability at high count rates, see Fig. 268. Due to the high IRF stability and the high NIR sensitivity the PMC-100-20

is currently the best detector for DOT applications. For microscopy applications, the PMC-100 is available with a non-descanned port adapter and electro-mechanical shutter.

PMC-150 PMT Modules

The PMC-150 PMT modules are functionally identical with the PMC-100 but contain new Hamamatsu The H11900 photosensor modules with a higher cathode efficiency, shorter transit-time spread, and less IRF variation over the cathode area. Two IRFs recorded for a PMC-150-110 are shown in Fig. 272. The IRF width is 118 ps for an illuminated spot of 1 mm diameter, and 128 ps for illumination of the entire photocathode.

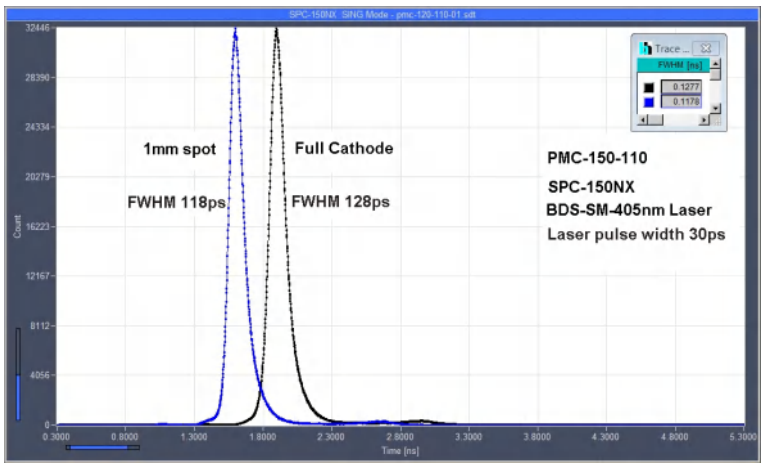


Fig. 272: IRF for a PMC-150-110 (bi-alkali cathode). 1 mm spot and full photocathode illuminated. Time scale 500 ps per division. Curves shifted to make them better distinguishable.

IRFs for different location on the photocathode are shown in Fig. 273. The left figure shows the IRF as a function of the shift in x direction, or perpendicular to the venetian-blind elements. The right figure shows the IRF as a function of y, parallel to the elements. The largest shift occurs in x and is about 40 ps over the entire diameter of the cathode. The shift in y is about 18 ps.

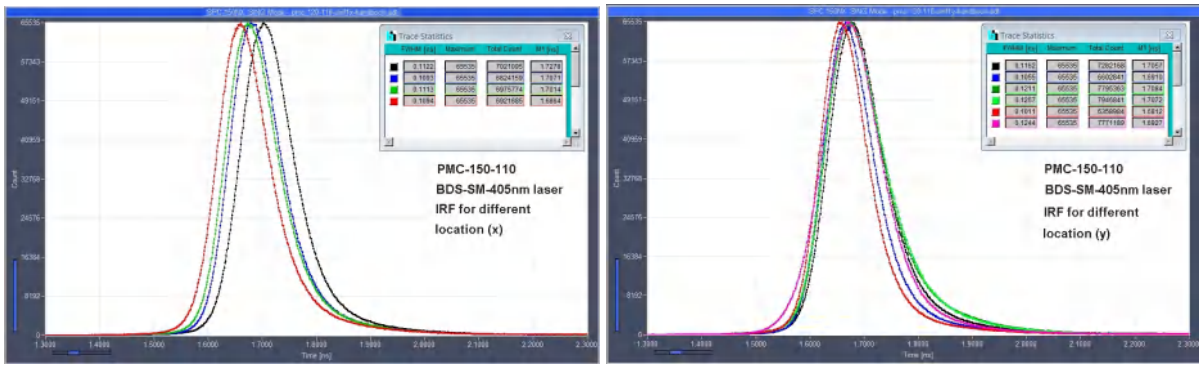


Fig. 273: Left: IRF as a function of location, x, on the photocathode. Right: IRF as a function of location, y, on the photocathode. Time scale 100 ps per division.

PMCS-150 PMT Modules

The PMCS-150 is a small-size (40 x 40 x 120 mm) version of the PMC-150. It was designed with special regard to the bh 12-channel MaxTau system. The PMCS-150 has active cooling, internal high-voltage generation, and an internal preamplifier. A difference is that the PMCS-150 can be operated without being controlled from a DCC-100 detector controller. To run independently of a DCC card, the PMCS has pre-set gain and internal overload-shutdown

circuitry. When overload occurs the detector regulates down its gain until the output current is within the safe range. When the overload is removed the gain regulates up to the pre-set value, and the detector resumes normal operation. The PMCS-150 module is shown in Fig. 274, left, the IRFs for illumination of a 1-mm spot and for illumination of the entire cathode are shown in Fig. 274, right. The IRF widths are 120 ps and 130 ps, respectively.

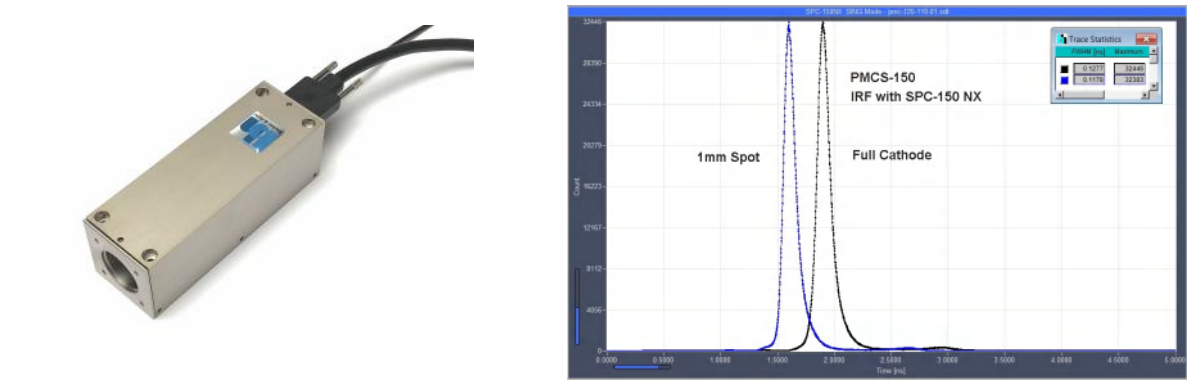


Fig. 274: PMCS-150 detector (shown left) and IRF with SPC-150NX (shown right)

Hamamatsu H7422 and H10770A

The H7422-40, the H7422-50 and the H8632 are high-speed, high-sensitivity cooled PMT modules [548]. The modules feature excellent sensitivity in the red and near-infrared region. They contain an GaAsP or GaAs photomultiplier along with a thermoelectric cooler and a high voltage generator. The resolution in the TCSPC mode is typically 200 to 350 ps [136, 154]. The H7422 comes in different cathode versions for the wavelength range up to 900 nm.

The H7422-40 has a GaAsP cathode and can be used from about 300 nm to 700 nm. The cathode quantum efficiency reaches 40% in the visible range of the spectrum. The IRF measured for three different specimens of the H7422-40 is shown in Fig. 275. The width varies from about 200 ps to 350 ps. An uncooled version, the H10770A-40 is smaller in size. It has the same IRF but higher dark count rate.

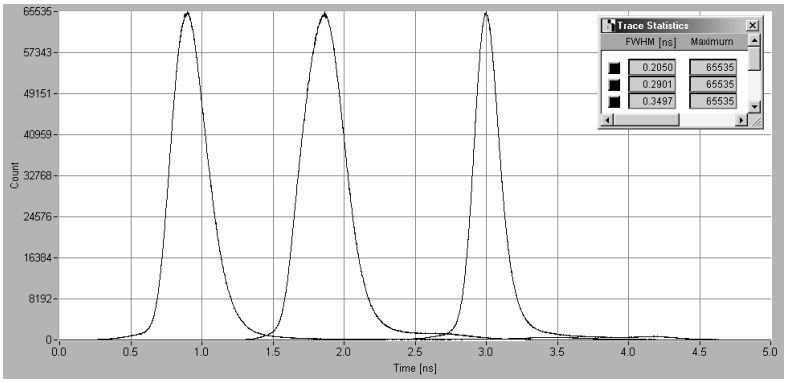


Fig. 275: IRF for three different specimens of the H7422-40. Gain control voltage 0.81 V, preamplifier HFAC-26-1 (20 dB), CFD threshold -150 mV, 650 nm diode laser of 45 ps pulse width, SPC-630 TCSPC module, Time scale 500 ps/division

For the wavelength range up to 900 nm the H7422-50 can be used. The timing behaviour is about the same as for the H7422-40. Due to its high NIR sensitivity the H7422-50 is frequently used for diffuse optical tomography. There are also special versions of the H7422 with cathodes for wavelengths up to 1100nm. Please contact Hamamatsu for details.

The modules must be handled with care because the cathodes can easily be damaged by overload. Exposure to bright daylight is not allowed even when the devices are switched off. The maximum output current is 2 µA. Therefore the H7422 and H107701 detectors should be used with an HFAC-26-1 or -2 preamplifier. Power supply, gain control, overload shutdown and cooling current for H2422 modules is provided by the bh DCC-100 detector controller [63].

Before the introduction of hybrid detectors the H7422s and H10770s were widely used in FLIM, FCS, and single-molecule spectroscopy applications. Now they have been almost entirely replaced by HPM-100 hybrid detectors.. If you are using a FLIM system that uses an H7422 or H10770 please check whether you can replace it with an HPM-100. What you gain is a three-times shorter IRF and complete absence of afterpulsing.

Hamamatsu H7421

The H7421 is a TTL output version of the H7422. As the H7422, the modules feature excellent sensitivity in the red and near-infrared region and come in different cathode versions for the wavelength range up to 900 nm. The H7421 can be connected to the SPC boards via an A-PPI pulse inverter and a 20 dB attenuator. The internal discriminator of the H7421 has a fixed threshold. Moreover, the discriminator is not of the constant fraction type. That means that the H7421 has poor time resolution when used in TCSPC applications. The typical IRF width is 600 to 700 ps, and a noticeable dependence of the IRF on the count rate was found [136, 154].

Hamamatsu H15620-45 NIR PMT

The Hamamatsu H15620-45 detector contains a small PMT together with a high-voltage generator, a thermoelectric cooler, a heat sink, and a cooling fan. The active area is 2 mm^2, the detection wavelength range is from 950 to 1400 nm. The detector needs a +5 V power supply, a 0...+0.9 V gain control voltage, and a 1...4 A current source for the thermoelectric cooler. These voltages and the thermoelectric-cooler current are supplied by a bh DCC-100 detector controller module. The only voltage which is not available from the DCC is the supply voltage for the cooling fan. Together with a bh HFAC-26-1 26-dB preamplifier the DCC-100 also provides for overload shutdown. The single-photon pulses from the preamplifier have an amplitude of -100 to -400 mV. This is compatible with the CFD input of the bh SPC series TCSPC / FLIM modules. The IRF of the detector and an IR scan of the palm of a human hand are shown in Fig. 276. With a cooler current of 2 A the dark count rate of our test device was about 4000 counts per second. Details are described in [185].

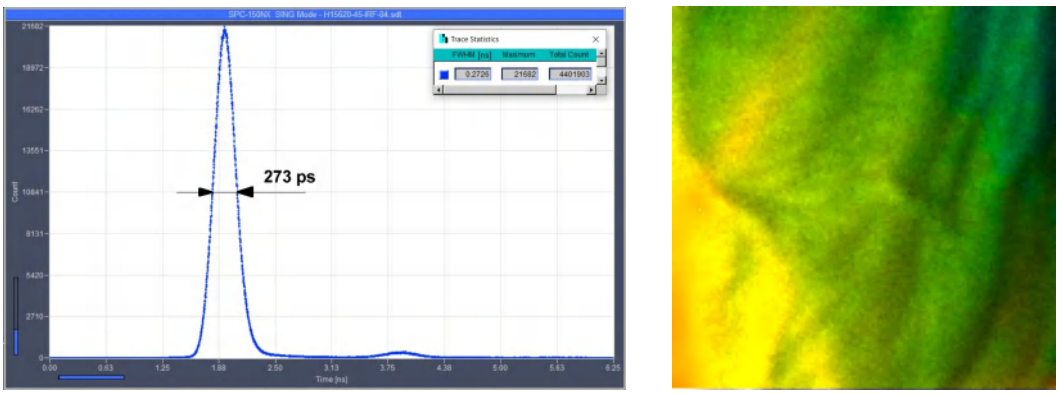


Fig. 276: Left: IRF of the H15620-45 detector, recorded with SPC-150NX TCSPC module and BHL-150, 1300 nm picosecond diode laser. Right: IR transmission scan of the palm of a human hand. Combined intensity / propagation-time image. Colour shows the average propagation time, yellow to green refers to 900 to 1100 ps.

Hamamatsu R10467 Hybrid PMT

The Hamamatsu R10467 [549] is the first hybrid PMT suitable for TCSPC operation. In a hybrid PMT, the photons are detected by a photocathode, the photoelectrons are accelerated by a voltage of 8000 V, and directly injected into an avalanche diode, see Fig. 250, page 156. The R10467 has a gain on the order of 10^5, and a single-electron (SER) amplitude on the order of a few 100 µV. With a preamplifier of 40 dB gain the amplitude is sufficient for TCSPC operation. The active area of the cathode is 3 mm, a version with 5 mm diameter is available since 2014. The R10467 comes in different cathode versions. The -40 version (GaAsP cathode) works from 300 to 720 nm, the -50 version (GaAs cathode) from 400 to 900 nm, and the -06 version (bi-alkali cathode) from 300 to 600 nm. Recently, a -7 version (multialkali cathode, 250 to 800 nm) and a -41 version (extended GaAsP, 300 to 800 nm) have been added. A photo of the R10467 is shown in Fig. 277.

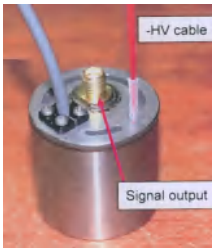


Fig. 277: Hamamatsu R10467 hybrid PMT tube

The detectors are small cylinders of about 30 mm diameter. They have an SMA connector at the back, and wires for the supply voltages for the cathode (7 to 8 kV) and the avalanche diode (about 400 V).

The detectors feature excellent sensitivity and short TCSPC IRF width. Remarkably, the detectors are free of afterpulsing. However, the low output amplitude, the high cathode voltage, and the requirement of perfect shielding make it difficult to use the bare R10467 in an open laboratory environment. bh therefore integrated the R10467 tube together with the high-voltage power supply, the avalanche-diode power supply, and the preamplifier in a compact housing. The result was the HPM-100 detector module described in the section below.

HPM-100 Hybrid Detector Modules

When Hamamatsu released their H10467-40 hybrid PMT in 2009 bh were the first to notice that the detector was likely to open a new era of TCSPC operation [85, 86, 159, 160]. Detection efficiency of almost 50%, large active area, fast and stable IRF without bumps and tails, absence of afterpulsing and, consequently, large dynamic range of fluorescence decay recording, made it almost ideal for fluorescence lifetime, fluorescence lifetime imaging, FCS, and single-molecule experiments. To make the R10467 practically useful for TCSPC applications the R10467 tube, the -8000 V power supply for the cathode voltage, the power supply for the AD voltage, and the preamplifier were integrated in a compact, carefully shielded housing. The entire device is controlled by the bh DCC-100 detector controller. The DCC-100 provides for power supply, overload shutdown, and, in the cooled versions, for operation of a thermo-electric cooler. The bh HPM-100 module pulled off an unprecedented success story. It replaced almost all the PMT and MCP PMT detectors in the high-end TCSPC applications. More than 800 pieces were manufactured since 2009. With the introduction of GaAs cathode versions the application was extended into NIRS spectroscopy [86]. Finally, with the ultrafast bialkali and multialkali versions, the HPM-100 modules joined the exclusive club of sub-20-ps detectors, which previously was entirely governed by SSPDs [122].

Photos of the HPM-detector are shown in Fig. 278. It comes with a C-Mount adapter, an adapter to the BIG and NDD ports of the Zeiss LSM 710/780/880 family laser scanning microscopes, and with fibre adapters. A cooled version is available as well.



Fig. 278: Left: bh HPM-100 hybrid PMT module. Left to right: Versions with C-Mount adapter, version with Zeiss BIG adapter, fibre-version, version with thermoelectric cooler

As the R10467, the HPM-100 modules come in different cathode versions. These are listed in the table below.

	Cathode Type	Wavelength Range, nm	IRF Width, ps
HPM-100-06	Bialkali	300 - 600	< 20
HPM-100-07	Multialkali	250 - 800	< 20
HPM-100-40	GaAsP	300 - 720	100 - 130
HPM-100-41	GaAsP	300 - 800	100 - 130
HPM-100-50	GaAs	400 - 900	130 - 190

A characterisation of the HPM-100 modules is given in the paragraphs below. Please see also [85, 86, 159, 160].

Instrument-Response Function

HPM-100-40

The instrument response function of an HPM-100-40 module (R10467-40 tube, GaAsP cathode) is shown in Fig. 279. The recorded IRF width is 130 ps. Corrected for the laser pulse width of 60 ps, the true IRF width is about 120 ps. The response function is remarkably clean, as can be seen in the logarithmic plot on the right.

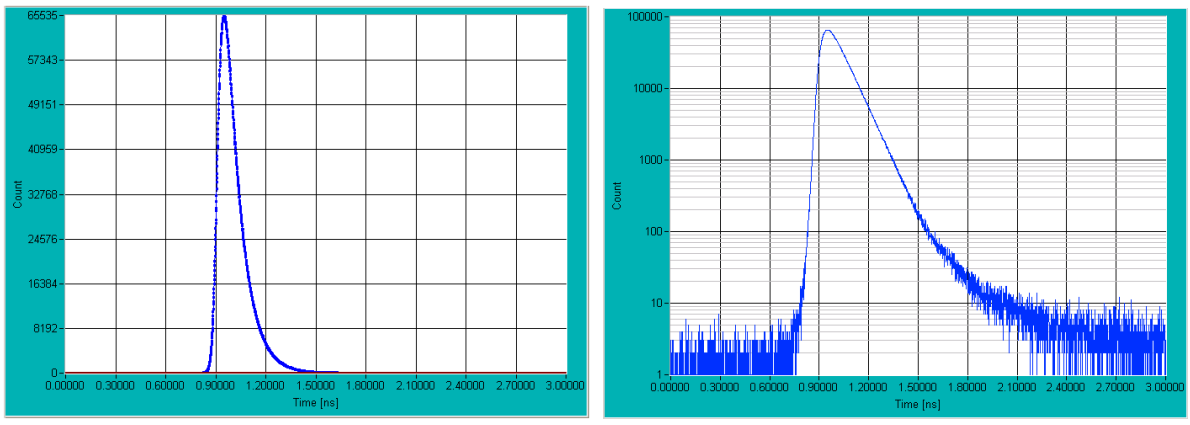


Fig. 279: Instrument response function of the HPM-100-40, time scale 300 ps/div. Left: linear scale. Right: Logarithmic scale. bh BDL-445 SMC picosecond diode laser, bh SPC-830 TCSPC module.

With about 120 ps FWHM, the IRF of the HPM-100-40 is not super-fast. However, the relatively large FWHM is partly compensated by the fact that it has no bumps and tails. A comparison of the IRF of an HPM-100-40 with an R3809U MCP PMT is shown in Fig. 280. Although the IRF of the HPM has a larger FWHM (full-width at half-maximum) it does not

have any bumps or tails, and the width at the 1% level is smaller. Late photons in the recorded waveform of a light signal are therefore recorded at the same or even at better accuracy. A fluorescence decay containing a weak slow component may therefore by determined at a better accuracy than with the faster detector.

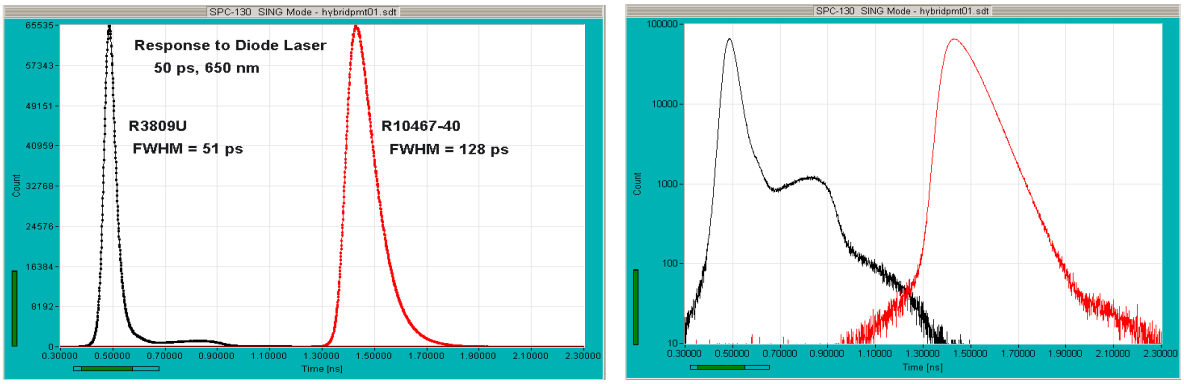


Fig. 280: Comparison of HPM-100-40 with R3809U. Left: linear scale. Right: Logarithmic scale. Red curve: R10467-40. Black curve: R3809U MCP PMT. bh SPC-130 TCSPC module, time-channel width 820 fs, time scale 200 ps/div.

HPM-100-50

The IRF of an HPM-100-50 (GaAs cathode) is shown in Fig. 281. The FWHM of the device tested was 130 ps. Over 4 orders of magnitude, the falling edge of the IRF is almost single exponential, and without bumps or tails.

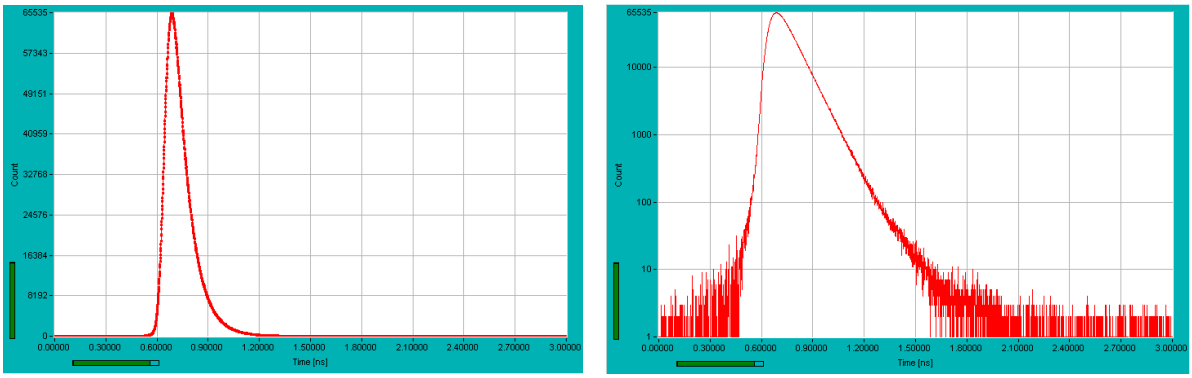


Fig. 281: IRF of an HPM-100-50. FWHM is 130 ps

The HPM-100-50 detector is an excellent solution to time-resolved NIRS spectroscopy. In these applications, light travels diffusely through thick layers of biological tissue. The pulse shape (or the 'distribution of times of flight', DTOF) of the detected signal contains information on the tissue properties, see chapter 'Diffuse Optical Tomography: DOT, NIRS and fNIRS' of this book. Most information is in the late photons, which have travelled the longest way through the tissue. To separate these photon form early ones a clean IRF is essential.

Different than the HPM-100-40, the -50 (GaAs) versions show a relatively large variation in IRF width. We can only speculate about the reasons. It is probably a result of the cathode-formation process. Attempts to increase the cathode quantum efficiency lead to a thicker layer of the cathode material, and a longer electron lifetime in the GaAs. This leads to longer electron diffusion times in the cathode, and thus to a longer IRF. An IRF for a 'slow' -50 detector is shown in Fig. 282. The IRF width is 190 ps, but the trailing edge is still single exponential over 3 orders of magnitude.

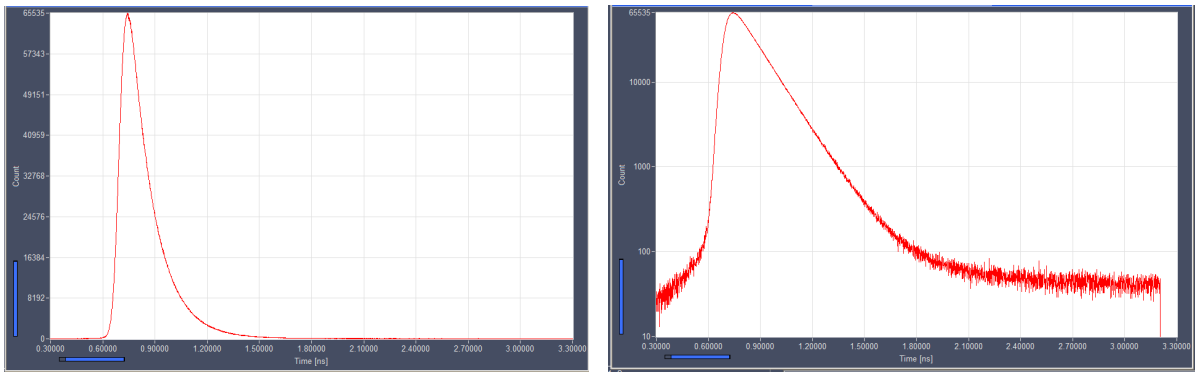


Fig. 282: The -50 versions show noticeable variation in IRF width. The IRF width of this device is 173 ps, but the trailing edge is still single-exponential over three orders of magnitude.

HPM-100-06 and -07 Versions

GaAsP and GaAs cathodes have an intrinsic time constant caused by the diffusion of the photoelectrons in the cathode. The IRF of the -40 and -50 hybrid detectors thus contains a component due to this effect. The fact that the falling edge of the IRF is almost single exponential (see Fig. 279, right) indicates that diffusion in the cathode is the dominating component of the IRF.

It can be expected that the IRF of the -06 and -07 versions (with bialkali and multialkali cathodes) does not contain this component, and that the detectors are faster. This is indeed the case. Already diode-laser based measurements had shown that the IRF of the HPM-100-06 is faster than 40 ps. To find out how fast the detectors really are we recorded IRFs with a Toptica FemtoErb Laser (pulse width 100 fs) and an SPC-150NX module [122]. The result is shown in Fig. 283.



Fig. 283: Left: IRF of HPM-100-06 (bi-alkali cathode). Right: IRF of HPM-100-07 (multi-alkali cathode). The full with at half maximum is 18.9 ps and 19.4 ps, respectively. Toptica FemtoErb laser, 785 nm, 100 fs pulse width, and SPC-150NX, 100 ps/div, 405 fs/channel

For both detectors the IRF width is faster than 20 ps. We suspected that the extremely short IRF may be a result of the long detection wavelength. Therefore we repeated the measurements at the second harmonics of the laser wavelength, i.e. 392 nm. The result was essentially the same, see Fig. 284.

There are small differences in the shape and the FWHM but these mainly depend on the illumination geometry. In all cases, the IRF width remains shorter than 20 ps. That means the -06 and -07 HPMs are the second-fastest detectors next to superconducting single-photon detectors!



Fig. 284: IRF of HPM-100-06 (left) and HPM-100-07 measured at 392 nm

Afterpulsing

The afterpulsing probability can be characterised by the autocorrelation function of the photons of a continuous light signal detected at a known count rate [154]. Fig. 285 compares the autocorrelation function of an HPM-100-40 at 10 kHz count rate with that obtained from a Hamamatsu H5773-1 PMT module.

While the H5773-1 shows the typical afterpulsing peak, the autocorrelation for the HPM is flat down to the dead time of the SPC-830 TCSPC module. Comparable performance has been achieved so far only for NbN superconducting single-photon detectors. However, these detectors have active areas with µm extensions and need to be operated in a liquid-He cryostat [867, 1189, 1190].

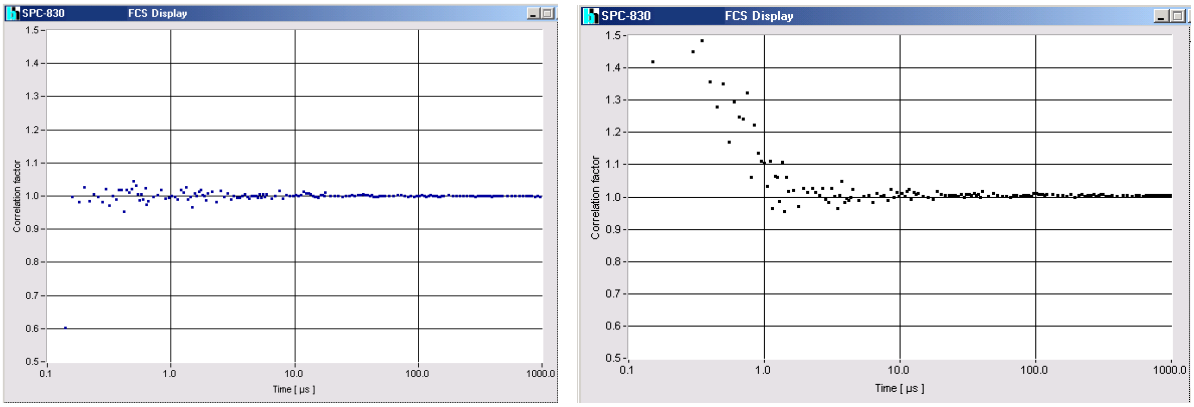


Fig. 285: Autocorrelation function of a continuous light signal of 10 kHz count rate. Left: HPM-100-40. Right: H5773-1. The autocorrelation function measured with the HPM is flat down to 125 ns, indicating that no afterpulses are detected.

Fig. 286 shows an FCS curve measured at a solution of fluorescein in water. The data were recorded by an HPM-100-40 connected to one of the confocal channels of the bh DCS-120 confocal scanning FLIM system. Because there is no afterpulsing peak, diffusion and triplet times are obtained merely by autocorrelation of the photons detected in a single detector.

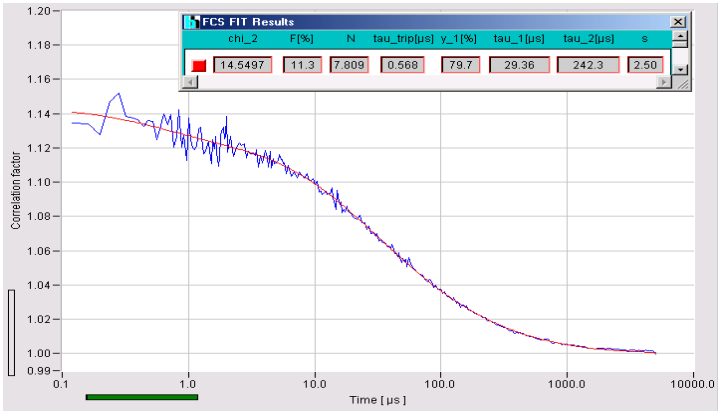


Fig. 286: Fluorescence correlation function of fluorescein molecules in water. Recorded with HPM-100-40, connected to bh DCS-120 confocal scanning FLIM system

The absence of afterpulsing results in a significantly improved dynamic range of fluorescence decay measurements. An example is shown in Fig. 287. It shows the fluorescence decay of fluorescein recorded at a laser pulse repetition rate of 20 MHz. The signal was detected by a HPM-100-40 (left) and a H5773-1 PMT module (right). Both detectors have approximately the same dark count rates. For the HPM-100, the dark count rate is the only source of background. Because the dark count rate is only a few 100 counts per second an extraordinarily high dynamic range is obtained. For the H5773-1 the background is dominated by afterpulsing. The background is thus substantially higher, and the dynamic range of the decay curve is far smaller than for the HPM-100-40.

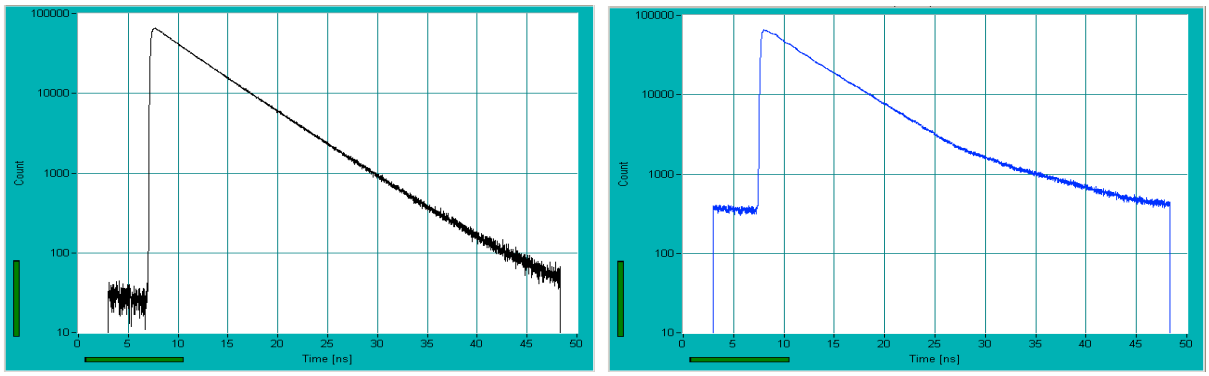


Fig. 287: Fluorescence decay curves for fluorescein recorded at a laser repetition rate of 20 MHz. Left: HPM-100-40. Right: H5773-01

Sensitivity

Quantum efficiency curves given for the R10467-40, -50, -06 and -07 by Hamamatsu are copied in Fig. 288. We had no possibility to verify these data quantitatively. What we could verify, however, is that the detection efficiency of the HPM-100-40 is slightly higher than for the Hamamatsu H7422P-40. The H7422P-40 (see page 176) has the same GaAsP cathode as the R10467-40 but uses a conventional PMT design. Before the hybrid detectors were introduced the H7422P-40 was the ultimate in sensitivity for large-area detectors. The HPM-100-40 reaches at least the same efficiency at a far better time resolution, with a clean IRF, and without afterpulsing.

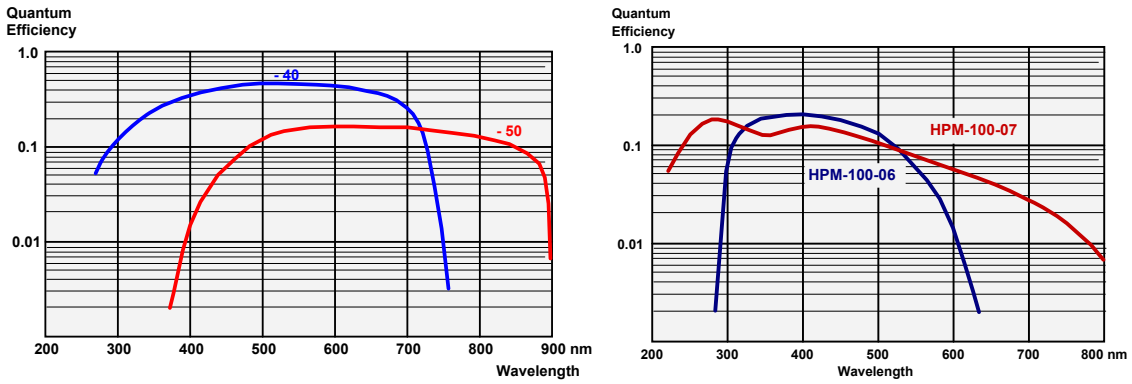


Fig. 288: Left: Detection quantum efficiency for HPM-100-40 and -50. Right: Detection quantum efficiency for HPM-100-06 and -07. After Hamamatsu R10467 data sheets [549].

Dark Count Rate

For low-level light detection the limiting parameter is often not only the efficiency but also the dark count rate. Typical curves of the dark count rate versus temperature are shown in Fig. 289.

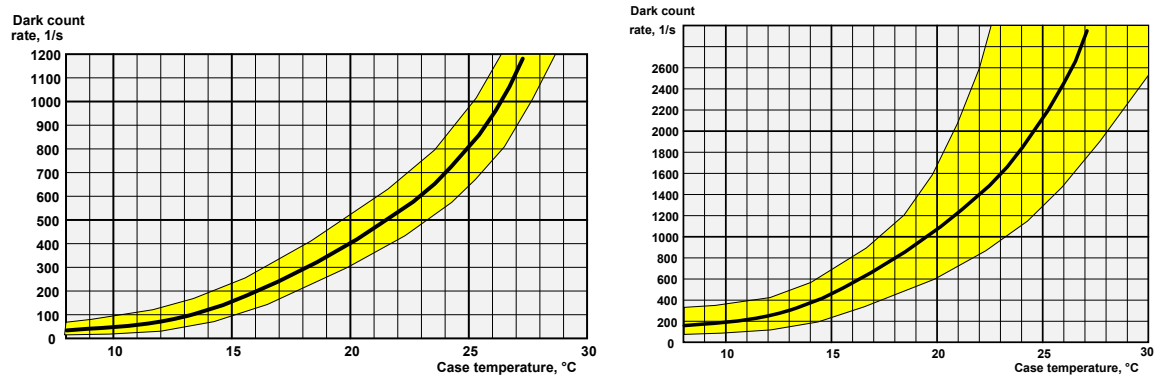


Fig. 289: Dark count rate versus case temperature. Left HPM-100-40, right HPM-100-50. Black curve: Average of 8 detectors. Yellow area: Range of variation.

On average, the values we found are a bit lower than the numbers in the Hamamatsu test sheets of the R10467 tubes, and significantly lower that the values reported in [855]. The reasons are not clear. It should be noted that low dark count rates are only obtained if (a) the reverse voltage of the avalanche diode is selected below the breakdown level and (b) the tube has been kept in the dark for several hours after exposure to daylight.

Important: The dark count rate can be reduced by selecting an especially good detector or by cooling. However, the significance of the dark count rate is often over-estimated. In most of the TCSPC experiments the counting background is dominated by afterpulsing of conventional PMTs or by leakage of environment light into the experiment setup. In the first case the use of an HPM solves the problem automatically. In the second case the leakage must be found and removed. Only when these sources have been reliably excluded the use of a selected or cooled detector should be considered.

Active Area

In most TCSPC applications it is difficult or even impossible to concentrate the light to be on an extremely small detector area. A typical case is multiphoton microscopy. Multiphoton microscopy is used to obtain images from image planes deep in a sample. The fluorescence photons from these layers are scattered on the way out of the sample and emerge from a large area of the sample surface. Although these photons can be transferred to a detector by ‘non-

descanned detection' they cannot be concentrated on an area smaller than a few mm in diameter [87]. The diameter of the active area of the HPM-100 hybrid detector is 3 mm, and thus compatible with NDD detection in multiphoton microscopes. A version with a larger cathode diameter (5 mm) is available since 2012. The IRF width was found to be 150 ps as compared to 128 ps for the 3 mm version.

A detector-area problem can even exist in a confocal microscope. Confocal detection uses a pinhole in a plane conjugate with the image plane in the sample. One might presume that the light from the pinhole is easy to focus an a small detector, such as a single-photon avalanche diode (SPAD). Unfortunately, in practice this is often not the case. Normally scan heads of laser scanning microscopes have additional magnification built in so that the physical pinhole size is on the order of millimeters. De-magnifying the pinhole to the size of a SPAD by a single lens can be impossible. This is especially the case when larger pinholes, on the order of tens of Airy Units, are used. There is no such problem for the hybrid detector: The light can easily be concentrated on the 3 mm cathode area.

An example is shown in Fig. 290. Both lifetime images were recorded at a pinhole size of 3 Airy Units. Data recorded with the HPM-100 are shown left, data recorded with an id-100-50 SPAD right. Despite the fact that the quantum efficiencies of the detectors do not differ substantially the image recorded with the HPM contains about twice the number of photons as the image recorded with the SPAD.

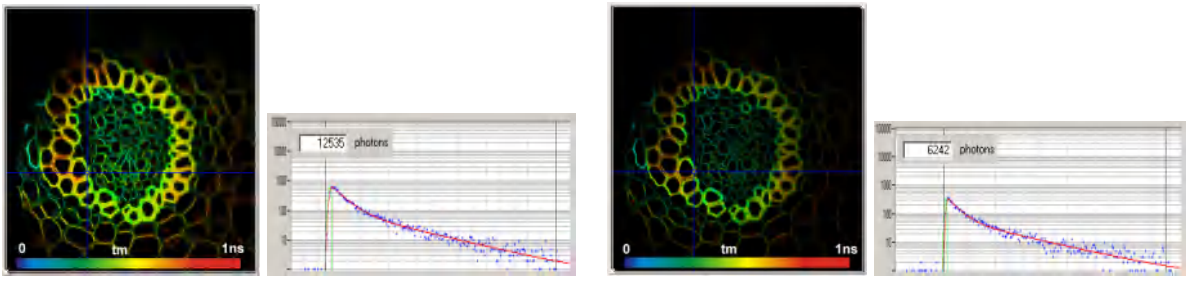


Fig. 290: Fluorescence lifetime images recorded with an HPM-100-40 hybrid detector (left) and with an id-100-50 SPAD (right). Images and decay functions at selected cursor position.

Conventional PMTs

Compared to the H5783 and the PMH-100, conventional PMT tubes have poor timing performance and are therefore not recommended for the SPC modules. The least objectionable are short-time PMTs, such as the XP2020, with high gain and single-photon specification. Due to the high gain and output current, these tubes work well without preamplifiers. Nevertheless, preamplifiers should be used to protect the CFD inputs of the SPC module against damage by high-amplitude pulses. The IRF width is about 200 to 350 ps (FWHM), but depends strongly on the wavelength and the illuminated area of the photocathode [154].

Sometimes older PMTs (such as the 56 UVP) were built up with voltage dividers with an extremely high cross current (10 mA and more). We strongly discourage to use such devices. They require high-power HV supplies which are extremely dangerous. Furthermore, the detector current can become very high and the PMT be easily damaged at higher light levels. For most TCSPC applications a voltage divider current of a few 100 µA is sufficient.

Simple side-window PMTs (R928, R931 etc.) were reported to yield a time resolution below 300 ps FWHM in the TCSPC mode [273, 666, 848]. This is correct - with some serious re-

strictions. A short response is obtained only if the light is focused into a spot of less than 1 mm on the PMT cathode and the best location on the cathode is selected (see Fig. 291).

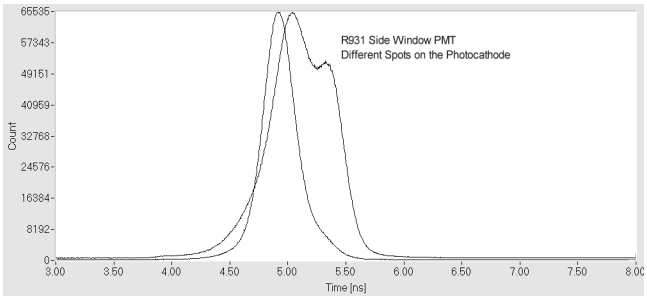


Fig. 291: IRF of an R931 side-window PMT

There is a considerable 'Colour Delay', i.e. a change of the delay and the shape of the response as a function of the wavelength. Furthermore, there is usually a long tail in the response with an ugly bump some ns after the main peak. Therefore, we do not recommend to use such tubes for TCSPC. The exception are cases when a complex instrument with side-window PMTs, such as a laser scanning head, has to be upgraded with TCSPC.

Detection Efficiency Comparison

A comparison of the detection efficiency of different detectors is shown in Fig. 292. The detectors were tested with the collimated beam of a BDL-SMN 480 nm laser. A wavelength of 480 nm was used because it is close to the emission wavelength of important fluorophores, such as NADH, Cerulean, and GFP. The beam diameter was 1 mm. The laser beam was pointed on the photocathode through a package of neutral-density filters, see Fig. 292, left. The signals were recorded with an SPC-150N TCSPC module. A CFD threshold of -63 mV was used for all detectors. The detector gain was adjusted individually so that the count rates were in the plateau of the cont-rate-gain function. A collection time of 5 seconds was used for all measurements. A comparison of the recorded photon numbers is shown in Fig. 292, right. The photon numbers were normalised to the photon number obtained with the HPM-100-40.

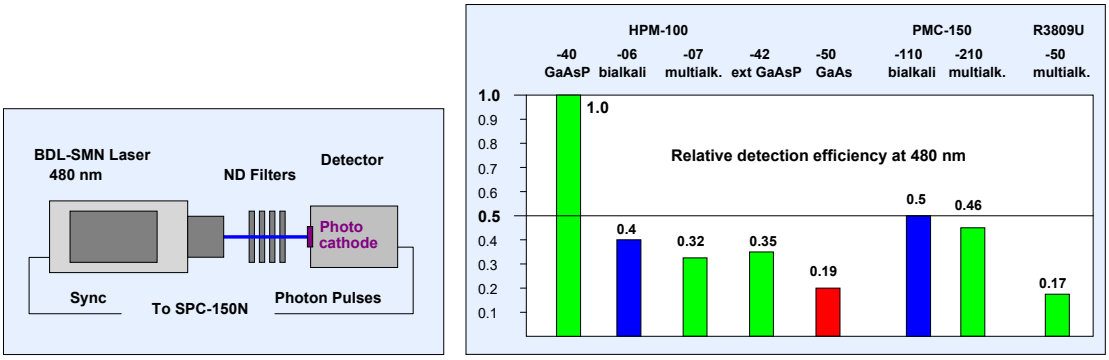


Fig. 292: Efficiency comparison of detectors. Left: Test setup. Right: Relative detection efficiency at 480 nm, normalised to efficiency of HPM-100-40.

As expected, the HPM-100-40 (GaAsP) has the highest detection efficiency at the test wavelength. The -06 and -07 versions (bialkali and multialkali) have 2.5 to 3 times lower efficiency. This is expected because the tubes have conventional photocathodes. The -50 (GaAs) version has about 19% of the detection efficiency of the -40 version. The -50 is optimised for NIR detection, and has its efficiency maximum at longer wavelength. The values measured are in agreement with the spectral sensitivity data given by Hamamatsu (see Fig. 258, page 165).

Surprisingly, the PMC-150 detectors have a slightly higher detection efficiency than the HPM-100-06 and -07 versions. We do not have an explanation for that. In fact, the HPMs should have a higher electron transfer efficiency from the photocathode into the multiplication system, and thus a higher detection efficiency. The reason may be in the cathodes themselves. The cathode formation process has a large effect on the cathode sensitivity, and it is different for different detectors.

The relatively low detection efficiency of the R3809U MCP PMT was expected. In an MCP PMT, not all photoelectron enter the microchannels of the michrochannel plate. This results in a sub-ideal electron-transfer efficiency, and, consequently, lower detection efficiency.

Please note that the tests were performed at a wavelength of 480 nm. This wavelength is clearly in favour of the HPM-100-40 detectors. To estimate the efficiency ratios at other wavelength, please refer to the spectral quantum efficiency curves for the individual cathode types, please see Fig. 258, page 165.

Influence of Magnetic Fields

It is commonly known that magnetic fields influence the detection efficiency and the temporal response of PMTs. For conventional PMTs the effects are so large that careful magnetic shielding is recommended. Understandably, users of TCSPC systems with PMTs or other vacuum-tube detectors are concerned that the temporal instrument-response function (IRF) of their system may change in the presence of magnetic fields. We therefore tested the bh HPM hybrid detector modules and the bh PMCS PMT detector modules for possible IRF changes by externally applied magnetic fields.

The IRFs were recorded with a bh SPC-150NX TCSPC module, with an electrical IRF of about 3.5 ps FWHM. As a test light source we used a FemtoFibre pro femtosecond-fibre laser from Toptica. The wavelength was 780 nm, the beam diameter 1.5 mm. The laser beam was attenuated by a package of ND filters and, without other optical elements, projected to the photocathode of the detector. Details are described in [127].

As a source of the magnetic field we used DD2 type disc magnets from K&J Magnetics, Inc., see Fig. 293, left. The magnet has a field perpendicular to the plane of the disc, with a surface strength of 1940 Gauss. For the tests we placed the magnet close to the detector under test. The field strength at difference distance from the magnet was calculated by the ‘K&J Magnetic Field Calculator’, available on www.kjmagnetics.com\fieldcalculator.asp. The field configuration is shown in Fig. 293, right.



Fig. 293: Left: Magnet used for the test. Right: Field configuration and field strength at the magnetic axis 25 mm from the magnet . Both figures from www.kjmagnetics.com

For testing the HPM-100-07, the magnets were applied with their magnetic axis perpendicular to the detector axis and under 45 degrees to it. The test geometries are shown in Fig. 294.



Fig. 294: Magnetic-field geometries tested. Field direction from detector axis: Left (a) 90 deg horizontal, middle (b) +45 degree vertical, right (c) -45 degree vertical

Results are shown in Fig. 295. The black curves are reference curves recorded without the magnetic field. One curve was recorded at the beginning, the other at the end of the experiments. The FWHM is 16.3 ps and 16.5 ps, an the difference in the first moment is 0.5 ps. This is within the natural low-frequency timing wobble of the laser sync output and the photon timing in the SPC module. The blue curve shows the IRF for field configuration a, i.e. with the field axis horizontally and perpendicular to the axis of the detector. The shift in the first moment versus the averaged reference curves is 1.75 ps, the FWHM is 16.5 ps. The green and the red curves show the IRF for the +45-degree and -45-degree configurations. The shifts are 9.45 ps and 14.4 ps. The FWHMs increased slightly to 18.4 ps and 17.7 ps, respectively.

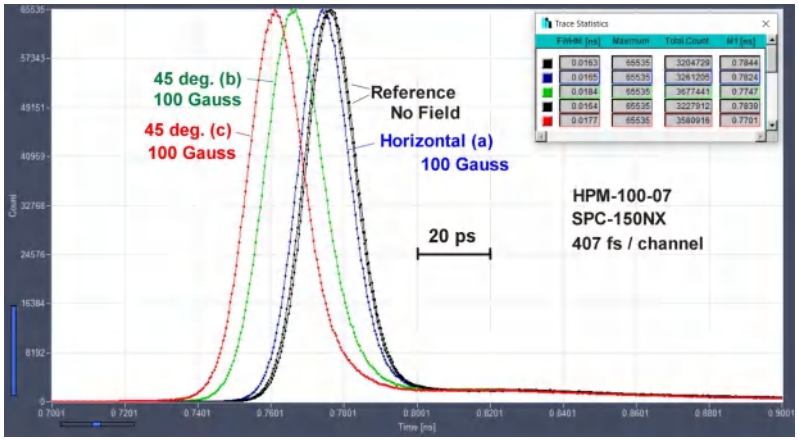


Fig. 295: IRFs recorded for the field-free case and for configurations a , b, and c. Time scale 20 ps / division.

Similar measurements were performed on a bh PMCS-150 detector. The field configurations were 90 degree horizontal, 90 degree vertical, and +45 degrees, see Fig. 296. Due to the smaller size of the PMCS module, the magnet comes closer to the detector. The field strength in the axis of the detector was therefore 150 Gauss, i.e. slightly higher than for the HPM module. The results are shown in Fig. 297. The ‘no field’ IRF and the two 90-degree IRFs are indistinguishable. The IRF widths are about 97 ps FWHM. The 45-degree IRF is shifted by 9.7 ps toward later times, and the FWHM is increased to 109 ps.

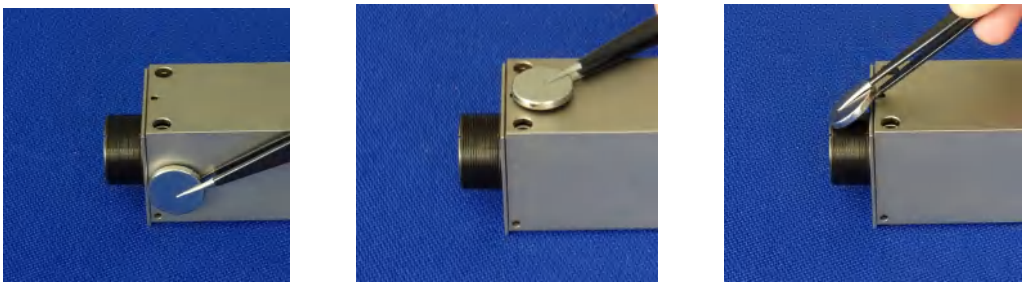


Fig. 296: Magnetic-field test configurations for the PMC-150 detector. Field direction from detector axis: Left (a) 90 deg horizontal, middle (b) 90 degree vertical, right (c) +45 degree vertical

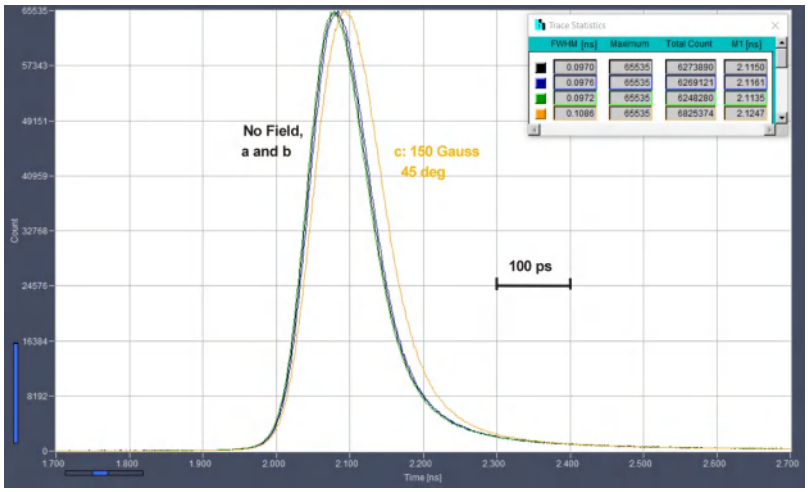


Fig. 297: Magnetic-field dependence of IRF of PMCS-150 detector. Time scale 100 ps / div. Note different time scale than in Fig. 295

As can be seen from Fig. 295 and Fig. 296, the IRF shifts induced by the magnetic field are surprisingly small. Considering the fact that the field strength used in the tests was much higher than normally encountered in a typical operation environment, it can be concluded that magnetic fields are unlikely to impair normal fluorescence decay or FLIM measurements with these detectors.

PML-16-C and PML-16-C GaAsP Multichannel Detector Heads

The bh PML-16C and PML-16 GaAsP detectors provide 16 simultaneously recording detection channels for TCSPC. The detectors are shown in Fig. 298, left and second left. Multi-wavelength detection assemblies with the PML-16 detectors are shown in Fig. 298, second right and right.

The PML-16 detectors contain a Hamamatsu R5900-L16 [545] or R12309U-40 [546] multi-anode PMT together with 16-channel routing electronics (see Fig. 208, page 118), a preamplifier, and the high-voltage power supply for the PMT. The detectors are controlled by a bh DCC-100 card, which provides for power supply, gain control, and overload shutdown.

The channel arrangement of the PML-16-C and the PML-16 GaAsP is 1-by-16, the IRF width 150 to 250 ps FWHM [62, 136]. The PML-16-C comes in a bi-alkali (-0) and a multi-alkali (-1) version, the PML-16 GaAsP has a GaAsP cathode.

The PML detectors can be connected directly to the SPC-6, -7, -8 -140, -130EM, -150 , 150N, -150NX, and the SPC-160 modules. The photons from the individual detector channels are routed into different blocks of the SPC memory, see Fig. 208, page 118. The measurement yields a separate decay function for each PMT channel. The advantage of the PML detectors compared to single-detector wavelength-scanning solutions is the dramatically increased detection efficiency. Typical applications are optical tomography, multi-wavelength FLIM microscopy, stopped flow experiments, and classic multi-wavelength fluorescence lifetime experiments. Details of the detectors and their application are described in a separate handbook [62].



Fig. 298: Left to right: PML-16C, PML-16 GaAsP, PML-SPEC assembly, MW-FLIM assembly

Instrument-response Function

IRFs for the PML-16-C and the PML-16 GaAsP are shown in Fig. 299. The IRF width is 150 ps FWHM for the PML-16-C, and 203 ps for the PML-16 GaAsP. The slightly broader IRF of the PML-16 GaAsP results from the non-zero diffusion time of the photoelectrons in the cathode material. Both IRFs have a secondary peak about 1 ns after the main peak. Such peaks are common in conventional PMTs. They probably result from photoelectrons that are reflected at the first dynode and then forced back to the dynode by the electric field. The amplitude of the secondary peak is about 1% of the main peak and thus does not pose a problem to fluorescence lifetime measurements.

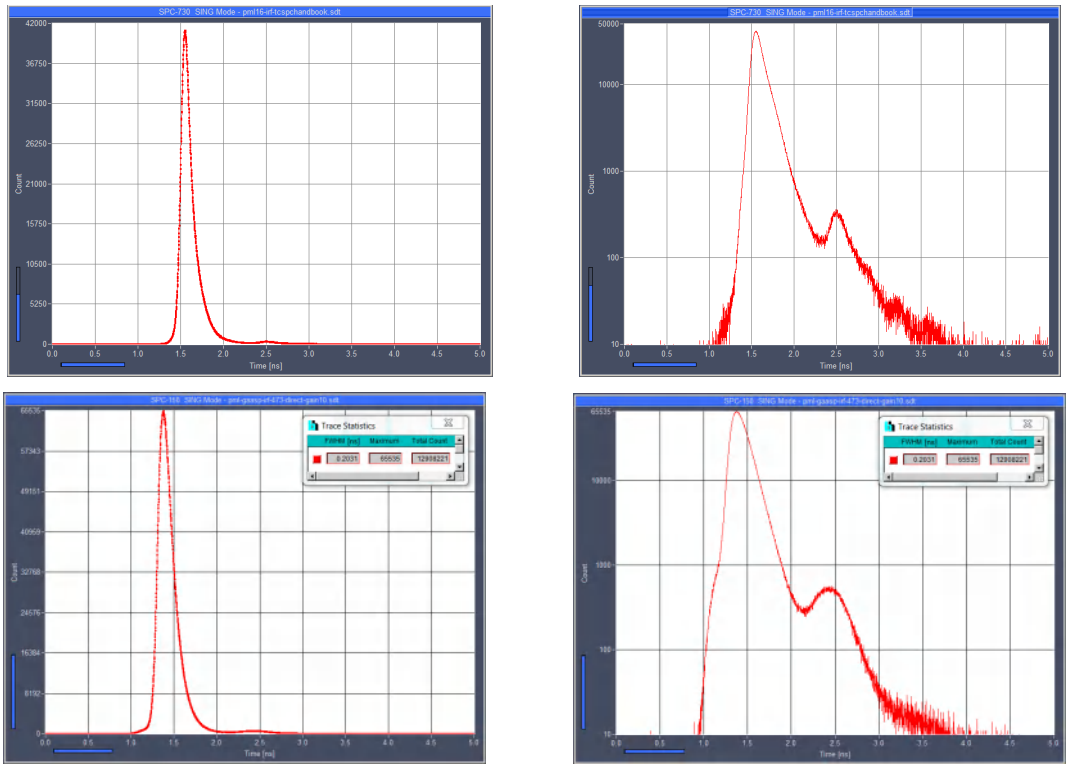


Fig. 299: IRF of PML detectors, single channel. Top: PML-16C, linear and logarithmic scale. FWHM is 150 ps. Bottom: PML-16 GaAsP, linear and logarithmic scale. FWHM is 203 ps.

Transit-Time Variation

Photomultipliers of the metal-channel type commonly have some variation of the transit time with the location on the photocathode, see Fig. 268, right. The R5900 tube and the R12309U-40 tubes used in the PML-16 detectors are no exception. Fig. 300 shows that there is a systematic wobble in the transit time of the channels. In the FIFO mode and the FIFO Imaging mode the shift of the transit times can be corrected during recording, see 'Delay Correction for 16-Channel Detectors', page 768. Alternatively, the effect can be taken into account in the data analysis, either by determining individual IRFs for the channels or by including a shift

parameter in the fit procedure. Please see chapter 'SPCImage NG Data Analysis Software', page 861.

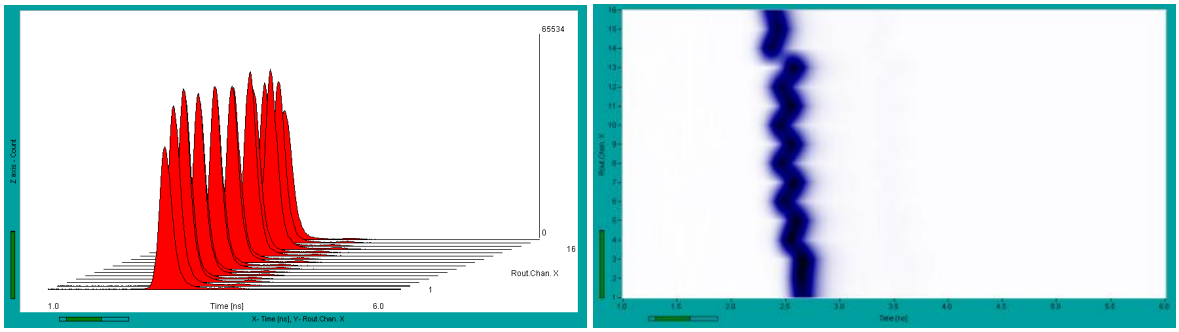


Fig. 300: Instrument response functions of the PML-16 C channels. Response to 50 ps diode laser pulses at 650 nm. Left: curve plot. Right colour-intensity plot, vertical axis is the channel number.

Sensitivity

A comparison of the sensitivity of the PML-16C-01 and the PML-16 GaAsP is given in Fig. 301 and Fig. 302. Between 500 and 700 nm, the sensitivity of the PML-16 GaAsP is about 6 time higher. FLIM images recorded with the PML-16 GaAsP are correspondingly brighter.

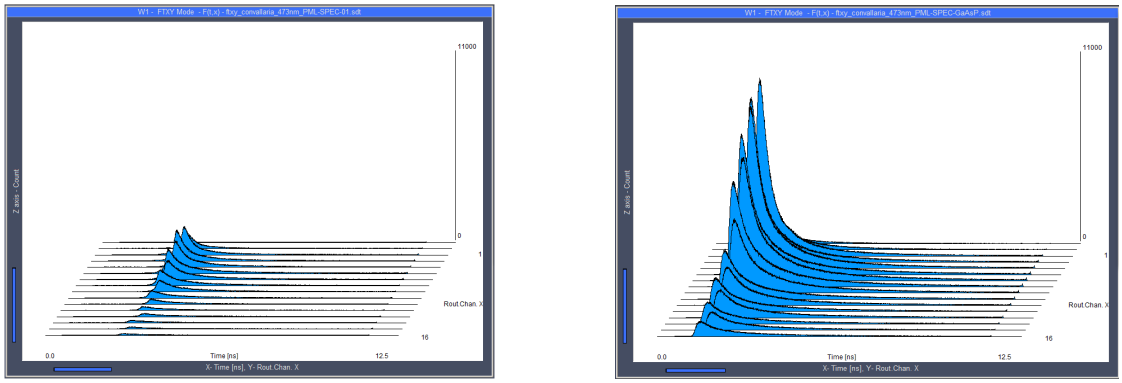


Fig. 301: Multi-wavelength fluorescence decay measurement with PML-16-1 (multi-alkali, left) and PML-16 GaAsP (right). Same acquisition time, same intensity scale, 500 to 700 nm, long wavelength is at the front.

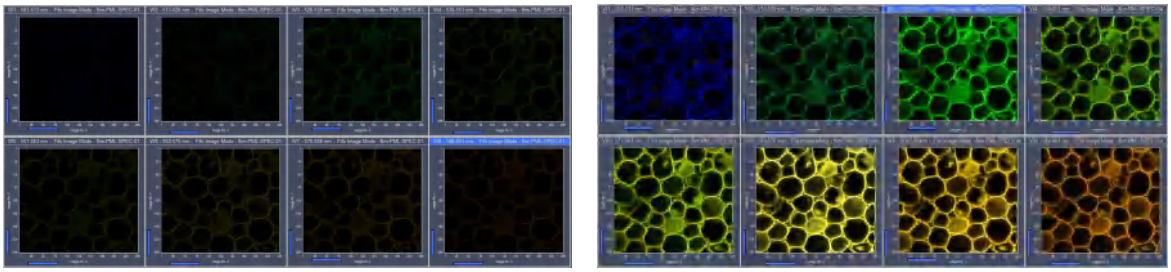


Fig. 302: Multi-wavelength FLIM, 8 of 16 channels shown. Left: PML-16-C-01. Right: PML-16 GaAsP. Same acquisition time, same intensity scale.

PML-SPEC and MW-FLIM Systems

The PML-16C and the PML-16 GaAsP are part of the bh PML-SPEC spectral detection systems and the bh multi-wavelength MW-FLIM systems. These systems include the detector, a grating polychromator (spectrograph) for spectral dispersion, and an optical fibre or fibre bundle to transfer the light into the input plane of the polychromator. The PML-SPEC is shown in

Fig. 303, the MW FLIM in Fig. 304. For details, please see handbook of the PML-16C [62] or handbooks of the bh FLIM systems [68, 69, 76, 77].

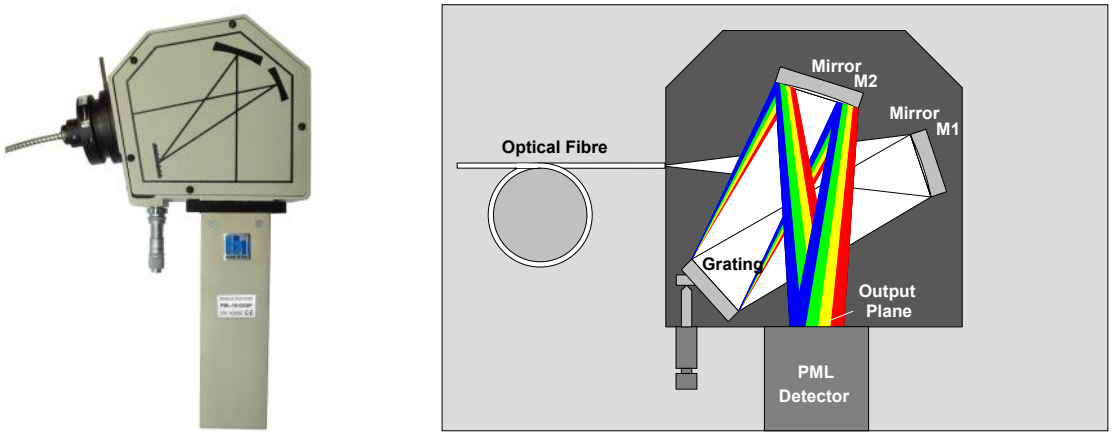


Fig. 303: PML-SPEC detector. The light is coupled into the polychromator input by an optical fibre.

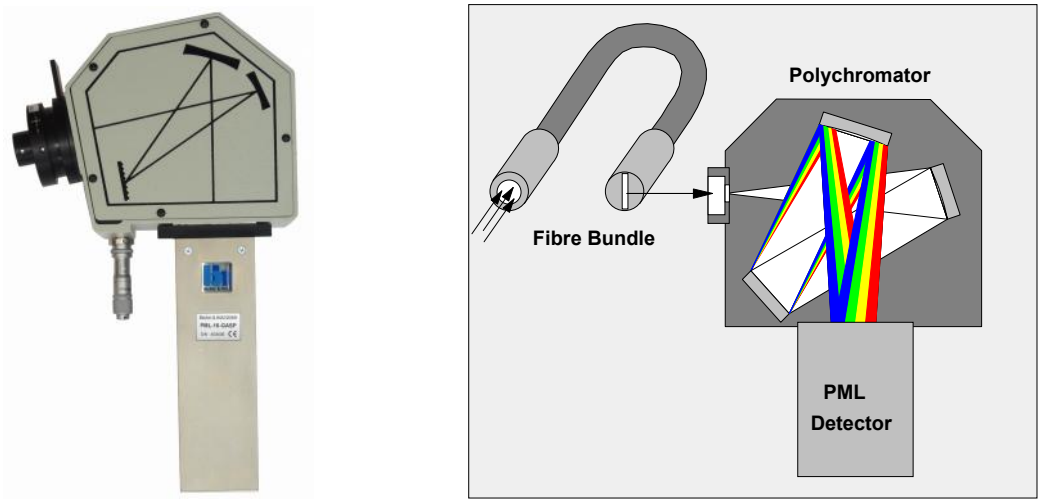


Fig. 304: MW FLIM detector. The light is transferred into the polychromator by a fibre bundle.

Single-Photon Avalanche Photodiodes

Single-Photon Operation of Standard APDs

There is a large number of inexpensive avalanche photodiodes (APDs) for use as high-sensitivity linear light detectors. The diodes are operated below the breakdown voltage, and the internal gain is on the order of a few 100. Single-photon detection cannot be obtained this way. It would require operation in the 'breakdown mode', i.e. at a reverse voltage above the breakdown voltage. A singe photon absorbed in the depletion layer of the diode would the causes an avalanche breakdown, and an easily detectable output pulse, see Fig. 251, page 158. Single-photon operation of standard silicon APDs in simple passive and active quenching circuits has been reported since 1981 [335, 431, 733]. However, there is no off-the-shelf APD for which single-photon operation is guaranteed. Standard APDs should therefore not be confused with Single-Photon Avalanche Photodiodes, or SPADs. Only these are designed to work reliably above the breakdown voltage.

Deep-Junction SPADs

For a long time the only commercially available single photon avalanche photodiodes (SPADs) were the SPCM-AQR modules from Perkin Elmer (now Ecxelitas) [967]. The SPCM-AQR modules have a high efficiency in the near infrared. They are available in different dark count classes down to 25 counts per second. The output pulses are positive, with TTL/CMOS levels and a pulse width of several 10 ns. The pulses can be coupled into CFD inputs of the bh TCSPC devices via an A-PPI inverting transformer (see Fig. 176) or via a HRT-82 router. Due to their high efficiency and low afterpulsing probability, the SPCM-AQR modules are preferentially used in FCS and single-molecule experiments.

Unfortunately, the timing performance of the SPCM-AQR varies over a relatively wide range. The IRF of an unselected SPCM-AQR is shown in Fig. 305, left. The pulse width of the laser was about 50 ps, i.e. much shorter than the detector response. The measurements show that not only was the TTS of the tested detector relatively wide, but also there was a considerable change with the count rate. Fig. 305, right shows the IRF of an SPCM-AQR selected for low timing jitter. The IRF of this module was shorter than 300 ps, and the dependence of the IRF on the count rate was reduced.

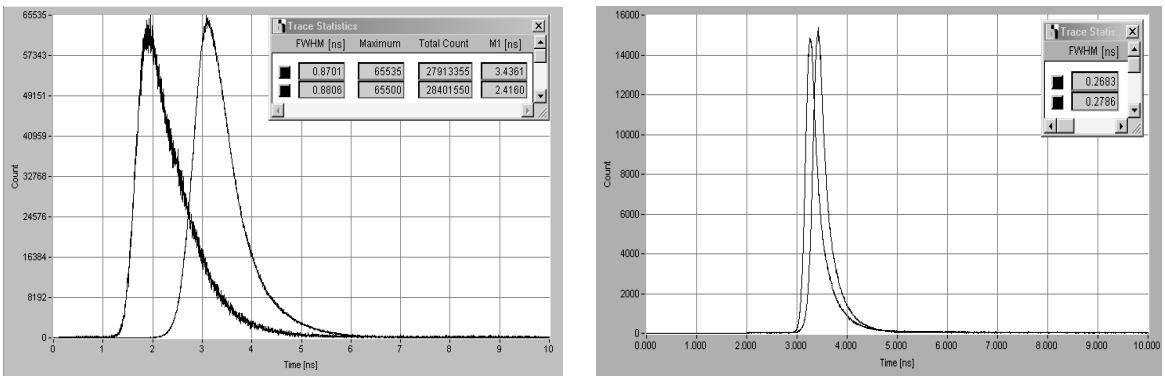


Fig. 305: TCSPC IRF of two SPCM-AQR modules, 1 ns/div. Left: Unselected modules, measured at 650 nm, 50 kHz, and 500 kHz count rate. Right: Module selected for low timing jitter, measured at 496 nm, 50 kHz and 500 kHz count rate.

Shallow Junction Epitaxial SPADs

In the last years it became possible to manufacture silicon SPADs by standard epitaxial processes as they are used for high-speed CMOS devices. The diodes are characterised by a small thickness of the depletion region. The thin depletion region results in a relatively low breakdown voltage, high time resolution, and low dark count rate. The drawback of the thin depletion region is a reduced quantum efficiency in the near infrared.

Fig. 306 shows IRF recordings for an id 100-20 detector of id Quantique [607, 1024] (left) and for a PDM 50 CBT detector of Micro Photon Devices [858] (right). The test light source was a bh BHL-600 785 nm diode laser of 24 ps pulse width; the signals were recorded by bh SPC-140 TCSPC module. For both detectors the detector count rate was varied from a few 10 kHz up to several MHz.

The three curves for the id 100 (Fig. 306, left) were recorded at detector count rates of 61 kHz, 2.7 MHz, and 8.1 MHz. The recorded pulse width (FWHM) is 49 ps, 48 ps and 45 ps, respectively. Corrected for the laser pulse width, the detector IRF width is 43 ps, 42 ps, and 38 ps. The shape of the IRF is remarkably clean, without any secondary peaks. Compared to a count rate of 61 kHz, the IRF shifts by 13 ps and 27 ps for 2.7 MHz and 8.1 MHz, respectively.

The curves for the PDM 50 CBT were recorded at a detector count rate of 750 kHz, 1.7 MHz, 3.2 MHz, and 4.1 MHz. Surprisingly, the detector tested had a dead time longer than the dead time of the SPC-140 (100 ns). A detector dead time longer than the TCSPC dead time can cause tails and secondary peaks in the recorded response, especially if the end of the dead time interval coincides with a laser pulse. The IRFs of the PDM 50 CBT were therefore recorded by an SPC-150 with the module dead-time adjusted to about 140 ps. The detector then showed a clean response with extraordinary low shift in the first moment. The shift in the first moment is 1.1 ps for 1.7 MHz, 6.5 ps for 3.2 MHz, and 8.8 ps for 4.1 MHz. For count rates of 750 kHz, 1.7 MHz, 3.2 MHz, and 4.1 MHz the recorded pulse width was 43 ps, 47 ps, 64 ps, and 67 ps, respectively.

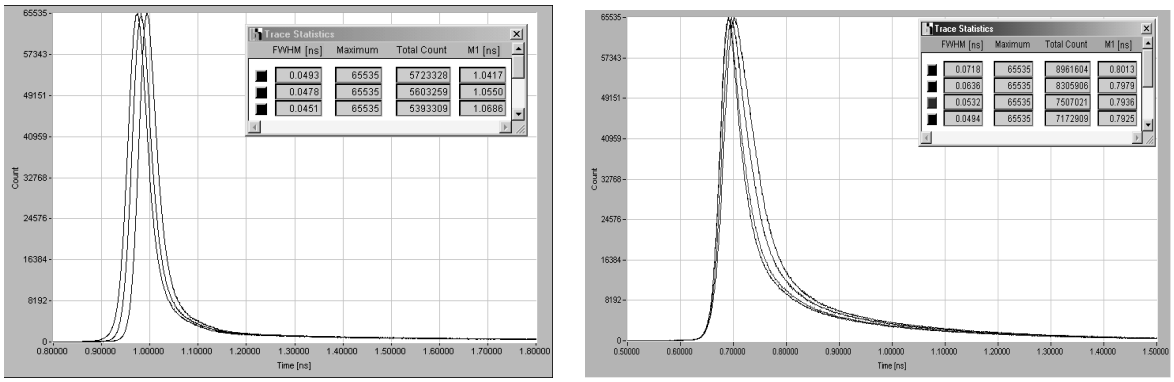


Fig. 306: IRF shapes of epitaxial SPADs. Response to diode laser pulses, wavelength 785 nm, pulse width 24 ps. Time channel width 814 fs, 100 ps / division. Left: id 100-20 at detector count rates of 61 kHz, 2.7 MHz, and 8.1 MHz. Right: PDM 50 CBT at detector count rates of 750 kHz, 1.7 MHz, 3.2 MHz, and 4.1 MHz.

Fig. 307 compares the response of two epitaxial SPADs (id 100-20 of id Quantique [607] and PDM 50 CT of Micro Photon Devices [858]) with the response of an R3809U-50 MCP PMT for a detection wavelength of 785 nm. There is a slow tail in the response measured at 785 nm. This ‘diffusion tail’ is typical of APDs operated at long wavelengths. It is caused by photons which penetrate the depletion layer and generate photons in the neutral regions nearby.

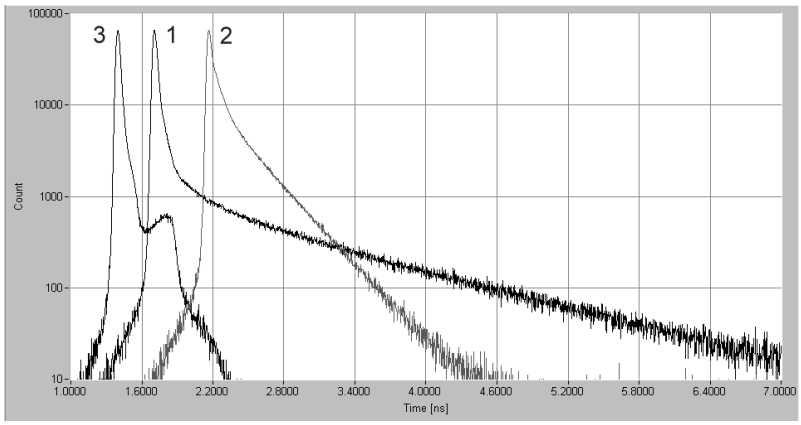


Fig. 307: Response of an id 100-20 SPAD (1), an PDM 50CT SPAD (2), and an R3809U MCP PMT (3). Wavelength 785 nm, optical pulse width 24 ps, time scale 600 ps/div.

The diffusion tails in the SPAD responses are almost single-exponential. The single-exponential profile and the fact that the tail is not present at short wavelength can be a pitfall in fluorescence decay measurements, where the diffusion tail is sometimes mistaken for a fluorescence component.

The dependence of the IRF on the wavelength is shown in detail in Fig. 308. Not only is there a considerable change in the amplitude of the diffusion tail but also a change in the width on the main peak and consequently in the FWHM, see especially Fig. 308, right. Caution is therefore indicated if SPADs are used at variable wavelength.

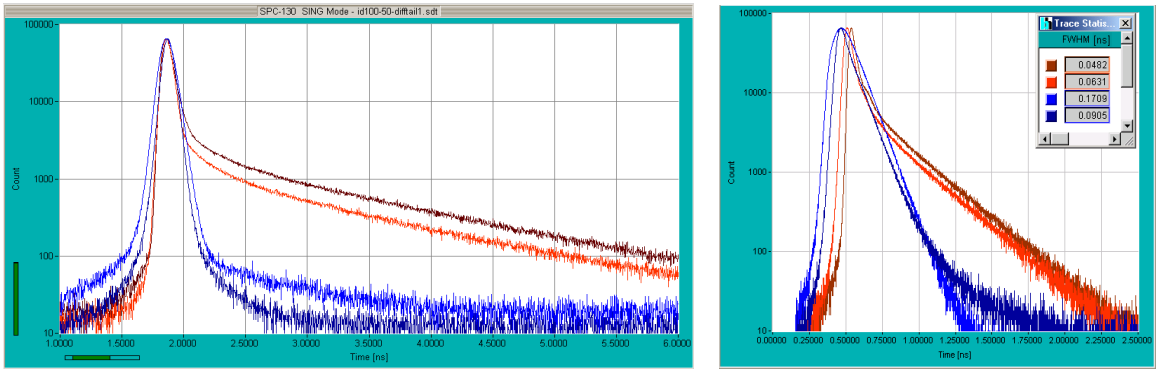


Fig. 308: Wavelength dependence of the IRF of an id 100-50 (left, 500 pd/div) and a PDM 50 CBT SPAD (right, 250 ps/div). 785nm (dark red), 650 nm (red), 446 nm (blue), 405 nm (dark blue)

Shallow Junction SPADs with Larger Area

Fast SPADs with active areas larger than 50 µm in diameter are manufactured by Micro Photon Devices (MPD). We tested a PDM PD-100-CBT-FC (diameter 100 µm) with an SPC-150NX TCSPC module and a 100 fs FemtoErb fibre laser from Toptica. The attenuated laser pulses were injected directly, without a fibre, into the FC fibre coupler of the detector. The result is shown in Fig. 309. The IRF has an FWHM of 35.6 ps. This is surprisingly fast for a 100-µm SPAD. The logarithmic display (Fig. 309, right) shows the typical diffusion tail. However, the tail decays entirely within about 1.5 ns. The dynamic range from the top of the IRF to the background level is about 4 orders of magnitude. This indicates that the PD-100-CBT-FC also had low afterpulsing.

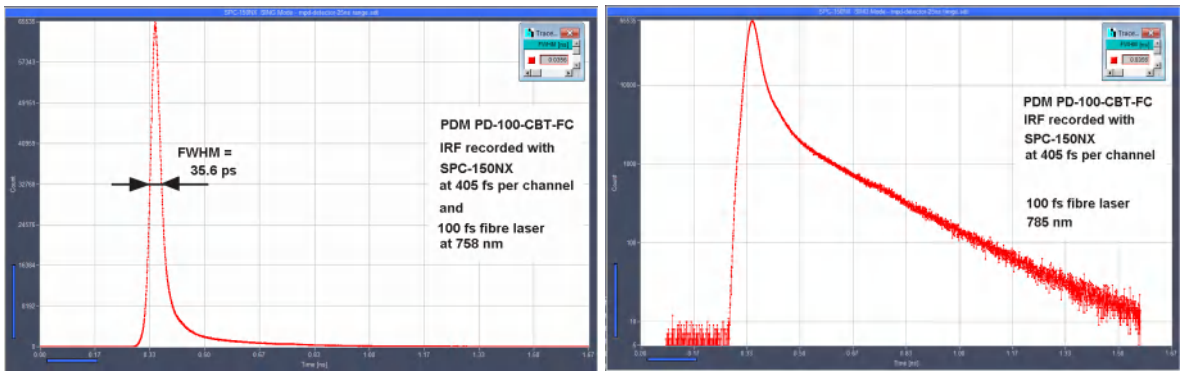


Fig. 309: IRF of a PDM PD-100-CBT-FC of MPD, recorded with SPC-150NX and Toptica Femto-Erb fibre laser. Total time range of recording 1.67 ns, TCSPC time channel width 405 fs.

Ultra-Fast SPADs

We tested an ultra-fast four-element low-jitter Si single-photon avalanche diode (SPAD) of EPFL, Neuchâtel, for TCSPC time resolution and timing jitter. The test setup followed the usual design principle. As a test light source we used a Toptica Femto Fibre Pro femtosecond fibre laser with a wavelength of 780 nm and a repetition rate of 40 MHz. The beam was widened to about 3 mm diameter and attenuated by absorptive ND filters. Optical elements which could introduce temporal pulse dispersion were strictly avoided. The attenuated beam was fed directly to the SPADs. The associated detector electronics delivers photon pulses of about ±200 mV at four separate differential outputs [521]. The photon-pulse signals of the diode under test were connected to the inputs of a bh SCP-150 NXX TCSPC module. To exploit the differential-output capability of the SPAD we used a differential discriminator in the TCSPC module [131]. Results are shown in Fig. 310.

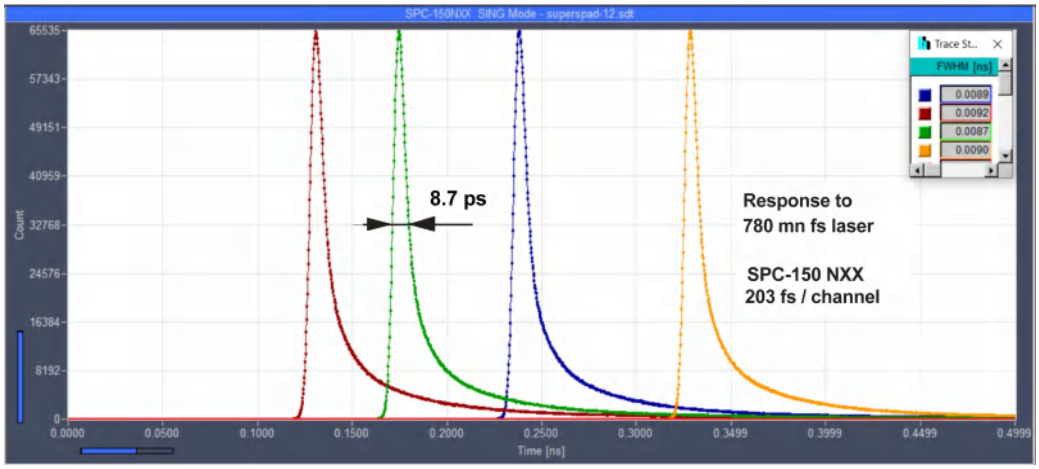


Fig. 310: Response of SPADs to 780-nm femtosecond laser. SPC-150 NXX TCSPC Module with 203 femtoseconds per channel, display scale 50 ps per division. FWHM of fastest SPAD is 8.7 ps.

We obtained IRF (instrument-response function) widths of 8.7 ps to 9.2 ps FWHM for the individual detector elements. These values correspond to a single-photon timing jitter of about 5.2 ps RMS. With these values, the detector is the fastest high-performance SPAD currently known, surpassed only by superconducting single-photon detectors (SSPDs). Details are described in [132].

Silicon Photomultipliers (SIPMs)

SIPMs are arrays of thousands on SPADs integrated on a single silicon chip. The SPADs passively quenched by individual series resistors, and their outputs connected into a single signal output, see Fig. 252, page 159. Since recently, SIPM chips are available directly from a semi-

conductor manufacturer [255]. Active areas range from 1 mm^2 to more than 4 cm^2. A test result for a SIPM of 0.5 cm^2 is shown in Fig. 311.

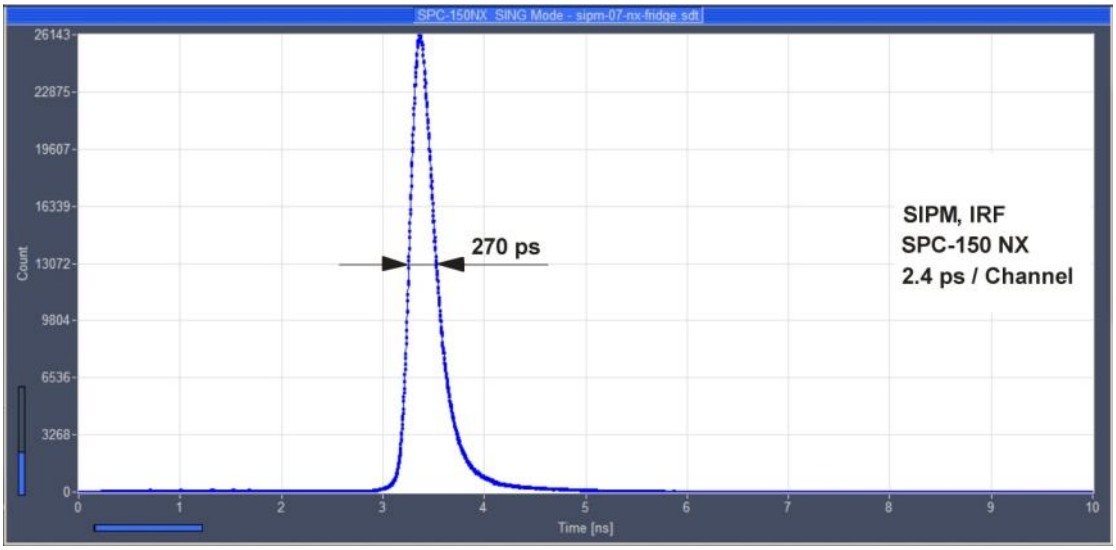


Fig. 311: IRF of a SIPM, active area 0.5 cm^2. FWHM is 270 ps.

The FWHM of the detector tested was 270 ps. This is not extremely fast but well within the range where applications appear possible. Due to their large areas SIPMs have extremely large dark count rates. At room temperature, the detector tested had a dark count rate of several 10^6 counts per second. The test measurements were performed at 14° C. The dark count rate at this temperature was 85,000 counts per second. It can certainly be reduced to TCSPC-typical values by cooling to about 0° C.

Spatial Variation of IRF

IRF measurements on SPADs often deliver contradictory results. The reason is not only a possible wavelength dependence of the IRF but also spatial variation over the active area. The shape and the width of the IRF then depends on where and how tightly the light is focused on the detector. A way to measure such variations is shown in the applications chapter of this book, see page 695.

Light Emission from SPADs

The avalanche breakdown in a SPAD generates light. This ‘breakdown flash’ can cause trouble in correlation experiments and in quantum cryptography setups [728, 1273]. Please see page 697 for measurements of the effect.

SPAD-8 Eight-Channel SPAD Module

The bh SPAD-8 module is based on an id150-1x8 multichannel SPAD of id Quantique [608]. The id150-1x8 contains eight actively quenched SPAD pixels on a single silicon chip. The bh SPAD-8 module contains an id150-1x8, the generator for the SPAD operating voltage, and the routing electronics for multi-dimensional TCSPC. For each photon, the SPAD-8 module delivers a timing pulse and the number of the SPAD pixel that has detected the photon. The SPC module builds up a photon distribution versus the time and the pixel number, or stores the individual photons as time-tag data, see Fig. 208, page 118 or Fig. 227, page 133. Power supply, SPAD excess-voltage control, and current for the TE cooler are provided by a bh

DCC-100 detector controller card. The detector and the pixel arrangement are shown in Fig. 312. The IRF with a BDL-SMC 405 nm laser and a BHL-600 650 nm laser are shown in Fig. 313. The DCC control panel is shown on the right.

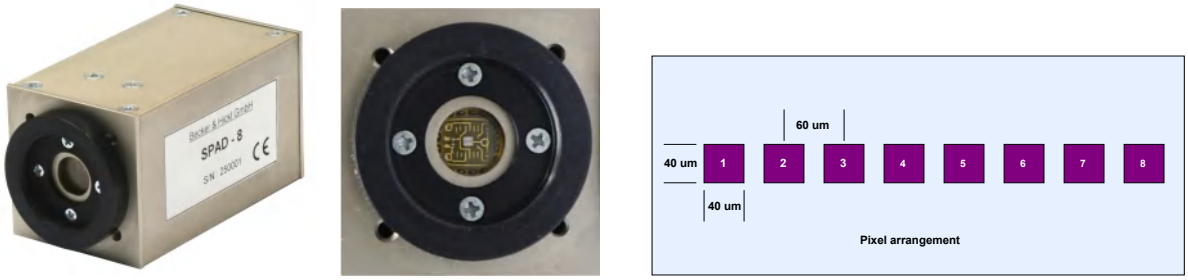


Fig. 312: SPAD-8 Eight-channel SPAD detector. Left to right: Side view, front view, and arrangement of pixels on detector chip

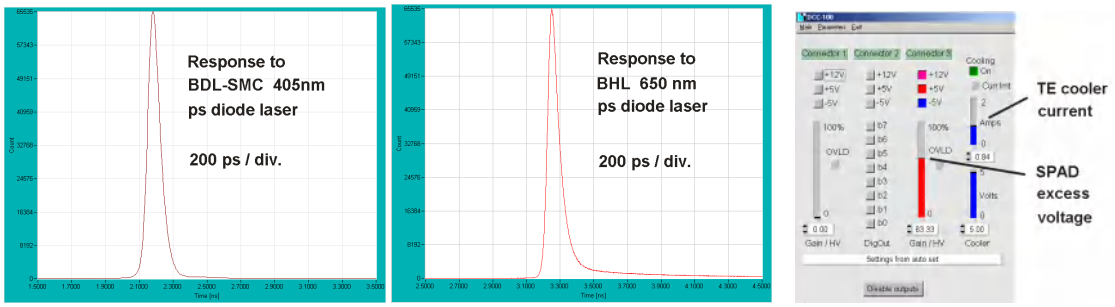


Fig. 313: IRF at 405 nm (left), and 650 nm (middle). The DCC panel for detector control is shown on the right.

Fig. 314 shows a test of the device with a fluorescence signal. The light was distributed evenly over the SPAD pixels. As can be seen from Fig. 314 the sensitivity of the channels is surprisingly uniform, with no more than 5% difference for the individual channels.

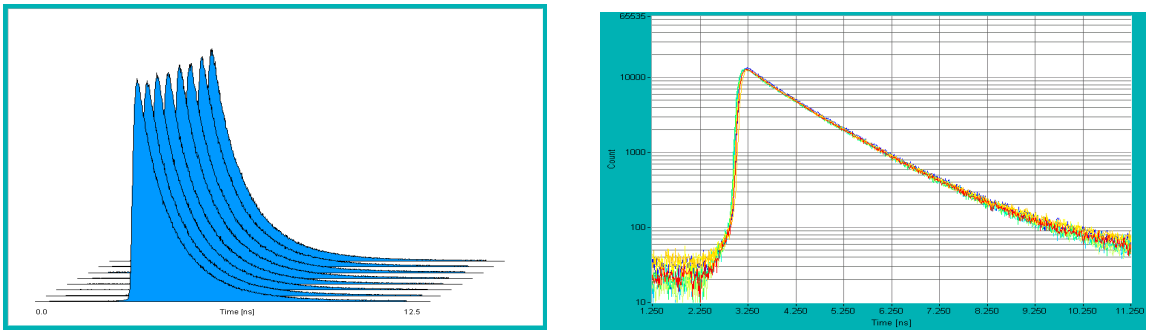


Fig. 314: Recording of a fluorescence signal. The sensitivity of the channels does not vary by more than 5%.

Gated SPADs

SPADs can be gated by switching the reverse voltage between a level above (‘on’ state) and below the breakdown voltage (‘off’ state). Although the principle is straightforward the electronic implementation is not. The breakdown voltage at the high end of the diode is between about 25 V for shallow junction SPADs and 300 V for deep-junction SPADs. It is not easy to overlay a clean modulation pulse to this voltage without causing spurious signals on the signal on the low-voltage end of the diode. Moreover, the voltage during the ON phase must be absolutely free of ringing to avoid modulation of the detection efficiency. Therefore most SPADs - if gateable at all - can be gated only with on-off times on the order of 50 ns and longer. Nevertheless, Tosi, Boso and Zappa have managed to build a SPAD that can be gated with on-off times in the sub-ns range [240, 1260].

The applicability of the device to diffuse optical reflectance measurement has been demonstrated by Dalla Mora et al. and Pifferi et al. [351, 975]. Several TCSPC recordings of a diffusely reflected signal from a scattering medium are shown in Fig. 315. The grey curve is a recording of the un-gated signal. The red, green, blue, cyan, brown, and magenta curves are gated recordings with different gate-on delay. As can be seen from the recordings, most of photons before the gate-on transition are indeed suppressed. The suppression is not perfect, however. There is a 'memory effect' due to carriers generated in the substrate by early photons. These diffuse into the active layer after the gate-on and cause the overshoot seen in the gated curves. There is also a change of the background due to signal-dependent amount of afterpulses [352]. Considering the fact that the intensity in the gate-off period was orders of magnitudes higher than in the gate-on phases these effects are very small, see the scale at the left of Fig. 315. The detector therefore provides an excellent solution to the dynamic-range problem in diffuse optical imaging experiments with zero source-detector distance [835].

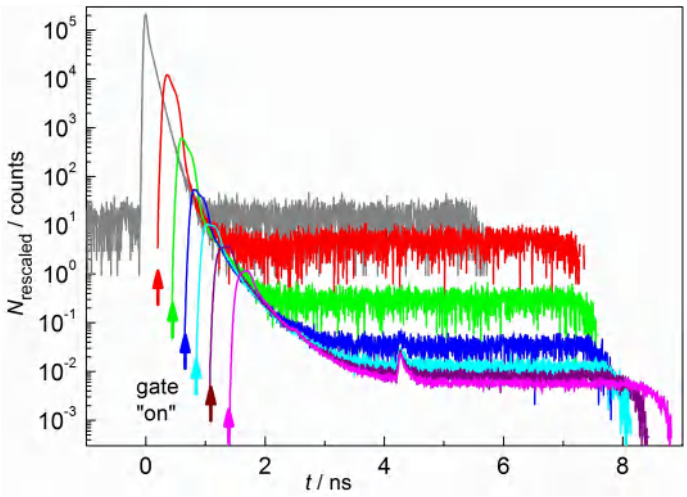


Fig. 315: Gated SPAD, detecting the light pulse returned from a scattering medium. Grey curve: Un-gated recording. Red, green, blue, cyan, brown, magenta: Waveforms recorded with gating, different 'gate on' times. Recorded with SPC-150, same data as in [1307].

Id 220 InGaAs SPAD

For many years, a problem of TCSPC was the lack of suitable single-photon detectors for the infrared region. The situation improved with the availability of single-photon avalanche diodes (SPADs) based on InGaAs material. These detectors achieve a quantum efficiency of about 20% at a wavelength 1300 nm. The sensitivity range goes from 900 nm to about 1700 nm. The problem of early InGaAs SPADs was the high dark count rate, and the strong afterpulsing. To avoid instability, the devices could only be operated in a gated mode: The reverse voltage was increased above the breakdown level for a period of 10 to a few 100 ns, and then decreased below the critical level for several microseconds. This kind of operation is not compatible with most TCSPC applications.

Standard TCSPC detection in the IR became possible with the introduction of the Id Quantique id220 detector [609]. The id220 was the first InGaAs SPAD that could be operated in a continuous mode. It thus could be used for TCSPC without any restrictions. The detector is shown in Fig. 316.



Fig. 316: Id 220 InGaAs SPAD detector

For a test of the id220 in combination with the bh TCSPC modules we used the setup shown in Fig. 317. A bh BDS-SM picosecond diode laser generates a 50 MHz train of picosecond light pulses at a wavelength of 1064 nm. The optical output from the laser is via a single-mode fibre. The end of the fibre was brought in contact with a cuvette containing a dye solution or a scattering medium. The light from the sample was collected by a multi-mode fibre and transferred to the detector. The TCSPC system was a bh Simple-Tau 150, containing an SPC-150 TCSPC module. The detector output pulses were adapted to the input voltage range of the SPC module by an attenuator and an A-PPI-D pulse inverter. The synchronisation of the TCSPC module comes directly from the laser.

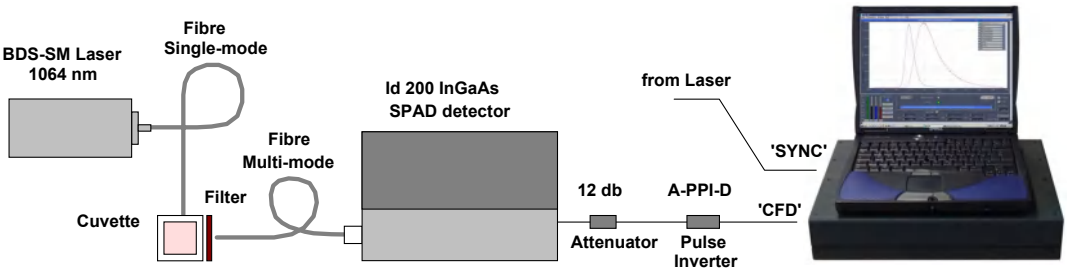


Fig. 317: Test setup for id-220 InGaAs SPAD

Typical waveforms recorded with the system are shown in Fig. 318. The curves show signals obtained from diluted milk (black curve), IR1061 (Aldrich, brown curve), and undiluted milk (red curve). The curve from the diluted milk (black curve) can be expected to reproduce the temporal IRF. It is surprisingly fast: The full width at half maximum (FWHM) is 230 ps. This includes the laser pulse width, the transit time differences in the 1 cm cuvette, and the transit time spread in the detector fibre. A deconvolution of the decay recorded for the IR1061 fluorophore from this IRF delivers about 50 ps. This is in agreement with the fluorescence decay time measured with an ultra-fast NbN SSPD detector, see Fig. 328, page 208.

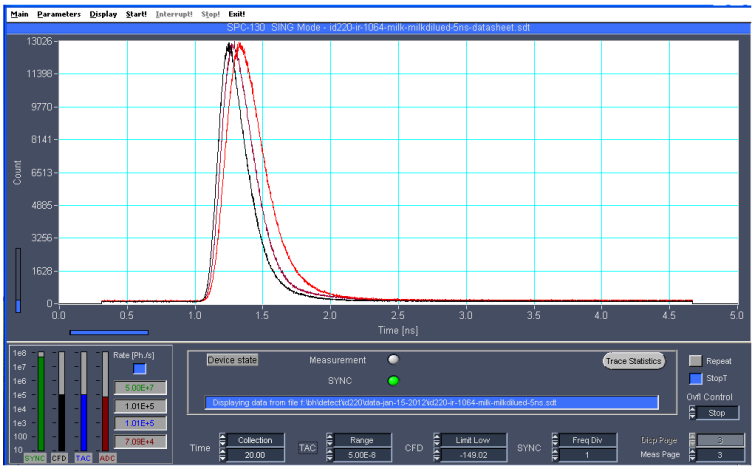


Fig. 318: Waveforms recorded with the setup shown in Fig. 317. Black curve : Diluted Milk. The curve can be expected to reproduce the temporal IRF. Brown curve: Fluorescence decay of IR1061. Red curve: Photon migration in milk, undiluted. Time axis 0 to 5 ns, 500 ps per division, 1.22 ps per data point.

In the meantime, the id-220 detector has been replaced with an improved version, the id-221. It yields a slightly higher time resolution and lower dark count rate.

The id-221 detectors come with software which allows the user to optimise the detector parameters for the intended experiment. Both the detection efficiency and the dead time (quenching time after detecting a photon) can be modified. We made test measurements with various parameter combinations. The best TCSPC results were obtained with the detection efficiency set to the maximum of 20%, and a dead time of 5 µs. Reducing the detection efficiency results in lower dark count rate. However, the efficiency drops by the same ratio as the dark count rate. Moreover, lower detection efficiency results in a broader IRF. Reducing the detection efficiency is therefore not recommended. The dead time of 5 µs was found to be a compromise between counting speed and afterpulsing background. Dead time settings larger than 5 µs unnecessarily reduce the saturated count rate, dead times shorter than 5 µs result in a noticeable increase of the signal-dependent counting background. Please note that a dead time of 5 µs is much longer than the dead time of the bh TCSPC modules, and much longer than the dead time of visible-range detectors. For 5 µs dead time, the saturated count rate is 200 kHz. The recording rate should therefore be kept below 100 kHz.

id-230 InGaAs SPAD

The new ID Quantique id-230 InGaAs SPAD delivers an instrument response width of 80 ps FWHM with the bh SPC-150 TCSPC module. Compared to its predecessor, the id-220, the id-230 also has a much lower dark count rate. The id 230 is shown in Fig. 319.



Fig. 319: id 230 InGaAs SPAD detector of id Quantique

We have tested the id-230 with a bh BDS-SM-1064 nm picosecond diode laser of 50 MHz repetition rate and about 60 ps pulse width [114]. The TCSPC system was a standard bh Simple-Tau 150, containing an SPC-150 TCSPC module. The detector output pulses were adapted to the input voltage range of the SPC module by an attenuator and an A-PPI-D pulse inverter. The synchronisation signal for the TCSPC module was obtained directly from the Sync output of the BDS-SM laser. An IRF recorded with this setup is shown in Fig. 320.

The width of the recorded photon distribution is 94 ps. These 94 ps contain a contribution from the laser pulses. The width of laser pulses is not exactly known since we had no fast reference detector for a wavelength of 1064 nm. However, BDS-SM lasers of sub-1000 nm wavelength have pulse widths in the range of 50 to 60 ps. Assuming the same width for the pulses at 1064 nm the real IRF width of the detector-TCSPC combination can be expected in

the range of 72 ps to 80 ps. To our knowledge, this is the fastest TCSPC response reported for any commercially available InGaAs SPAD yet.

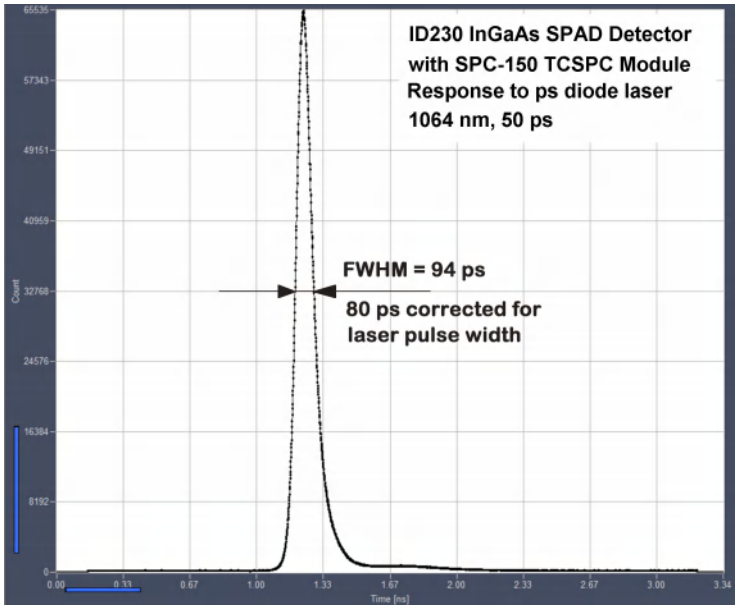


Fig. 320: Laser pulse recorded with the id-230 SPAD. BDS-SM-1064nm ps diode laser, SPC-150 TCSPC module. Detection efficiency 25%, dead time 5 µs. Laser pulse width is 50 ps to 60 ps.

The ID230 detector comes with software that allows the user to adapt the detector parameters to the conditions of the experiment. Both the detection efficiency and the dead time (quenching time after detecting a photon) can be modified. As for the id-220, the best TCSPC results were obtained with the detection efficiency set to the maximum of 25%. Reducing the detection efficiency results in a broader IRF and is therefore not recommended.

Unlike the detection efficiency parameter, the dead time selection in the id-230 software is important to optimise the TCSPC performance for different experiments. Shorter dead time results in higher saturated count rate and less counting loss but also in higher background and stronger afterpulsing. For typical applications with count rates in the 10 kHz to 100 kHz range a dead time of 5 µs was found to be the best compromise. For low-count-rate applications longer dead times can be used. At count rates in the range of a few kHz or below an increase in dead time does not cause noticeable loss of photons. It does, however, result in a dramatic decrease of the counting background. An increased dead time thus increases the dynamic range of the recording.

An example is shown in Fig. 321. The laser was attenuated until a count rate of only 800 counts per second was obtained. This signal was recorded with a detector dead time of 40 µs. At 800 counts per second, the loss of photons in the 40 µs following a previously recorded photon is negligible. However, the increased dead time reduces the dark count rate from several 1000 down to less than 300 counts per second. The dynamic range therefore increases, and the signal is recorded at high signal-to-background ratio. The result shows that the ID230 can indeed be used down to extremely low light intensities.

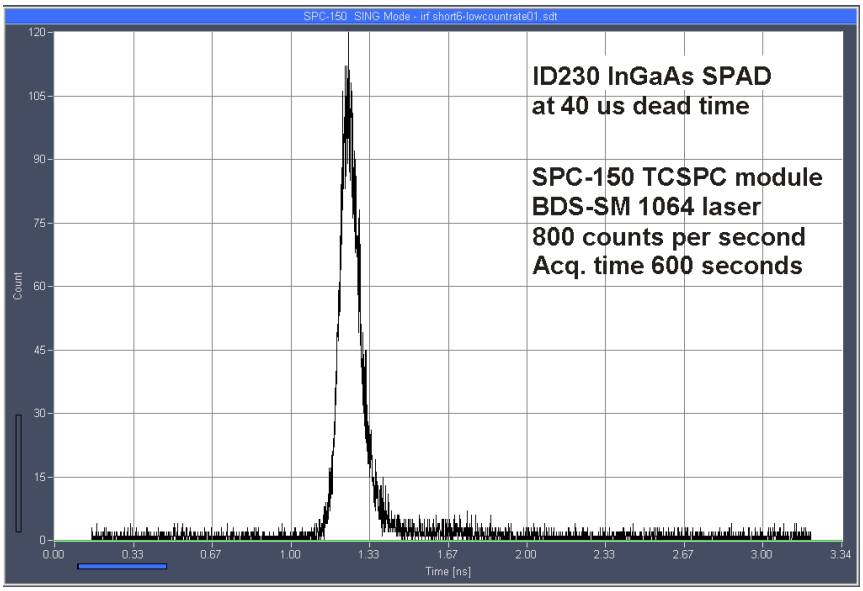


Fig. 321: Laser pulse recorded at a count rate of 800 photons per second. id-230 dead time 40 µs, acquisition time 600 seconds. The long dead time decreases the counting background and thus results in a high signal-to-background ratio.

NbN Superconducting Single-Photon Detectors (SSPDs)

Superconducting single-photon detectors (SSPDs) detectors offer sensitivity up to micrometer wavelengths and time resolution in the sub-20 picosecond range. The detectors are based on a nano-structured ultra-thin layer (‘nanowire’) of niobium nitride, see Fig. 253, page 160. The structure is cooled down to a temperature of a few Kelvin so that the NbN film is superconducting. A DC current is sent through the device. When the NbN structure absorbs a photon superconduction is temporarily lost. Te corresponding decrease of the current causes a voltage pulse across the load resistor. The amplified voltage pulse is the single photon pulse of the detector.

Test results obtained with a time-resolved detection system composed of a superconducting detector made by Karlsruhe Institute of Technology [590], Germany, and a Simple-Tau 130 EM TCSPC system have been published by Tousaint et al. [1261, 1262]. The basic setup of the system is shown in Fig. 322.

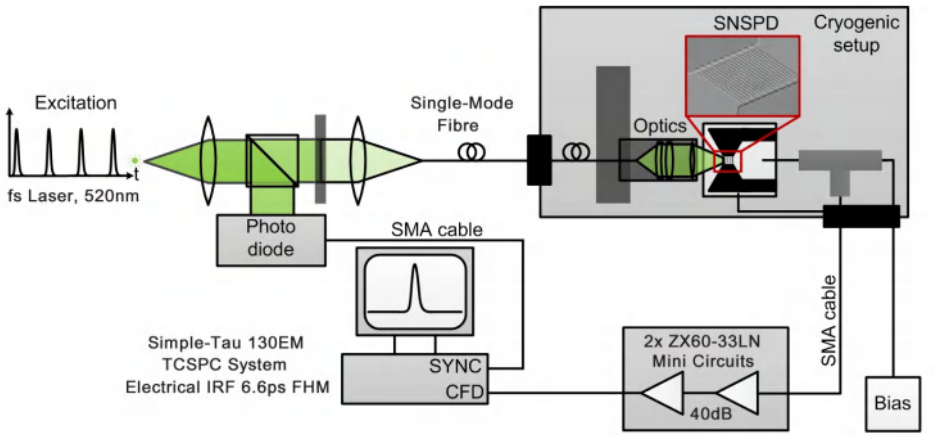


Fig. 322: Setup of detection system with superconducting detector, Courtesy of Julia Toussaint, IPHT Jena, Germany

Light from a femtosecond laser (pulse width 150 fs, repetition rate 75 MHz, wavelength 520 nm) was coupled into the detector via a single-mode fibre. The output pulses from the detector were amplified by two Mini Circuits ZX60-33LN amplifiers. The total gain was about 40 dB, the bandwidth about 1 GHz. The reference signal for the SPC-130EM module was generated by a photodiode. The TCSPC instrument response function (IRF) obtained with this setup is shown in Fig. 323.



Fig. 323: IRF of Simple-Tau 130 EM TCSPC system with superconducting detector. Optical wavelength 520 nm. Time channel width 813 fs, the recorded FWHM is 22.2 ps. Linear scale (left) and logarithmic scale (right). Data courtesy of Julia Toussaint, IPHT Jena, Germany

The IRF width is 22.2 ps (FWHM). The IRF contains the laser pulse width (150 fs, negligible), possible broadening in the optics (not known), the electrical IRF width of the SPC module (6.8 ps), the real IRF of the detector, and a contribution from the noise of the amplifiers. The contribution of the amplifier noise can be estimated from the electrical response of the amplifier-SPC combination (10.6 ps). It is about 8 ps. Thus, the timing noise induced by the amplifier noise forms a noticeable contribution of the IRF width. A reduction of this term is difficult. The amplifiers used in the setup have a noise figure of typically 1.1 dB. That means the noise is not significantly larger than the unavoidable noise of the internal matching resistor (50 Ω). A reduction is only possible by cooling the amplifiers down to extremely low temperature.

To test the detector for afterpulsing an autocorrelation (FCS) curve of the photon density was recorded simultaneously with the IRF data, see Fig. 324. The count rate was 100 kHz. As expected, no afterpulsing peak is visible in the data.

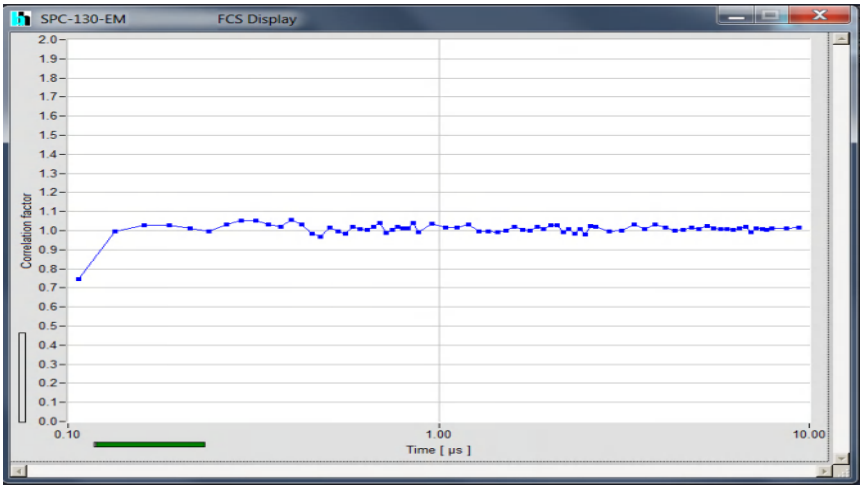


Fig. 324: Autocorrelation of the detection rate over an acquisition time of 10 seconds. Count rate 100 kHz. No afterpulsing peak is visible in the data.

A detector consisting of a linear array of NbN nanowire structures connected in series via delay lines was described in [588]. The detector can be used for position-sensitive detection of photons, provided the arrival times of the photons are known.

Single Quantum Eos X10 CS

Another test was performed with an Eos X10 CS superconducting detector of Single Quantum, Delft, the Netherlands. The general principle of the test setup was similar to the one shown in Fig. 322, except that a Fianium supercontinuum laser was used as a light source. A wavelength of 1300 nm was selected by a filter and injected into the input fibre to the detector. The pulse shape recorded with an SPC-150N module is shown in Fig. 325. left.

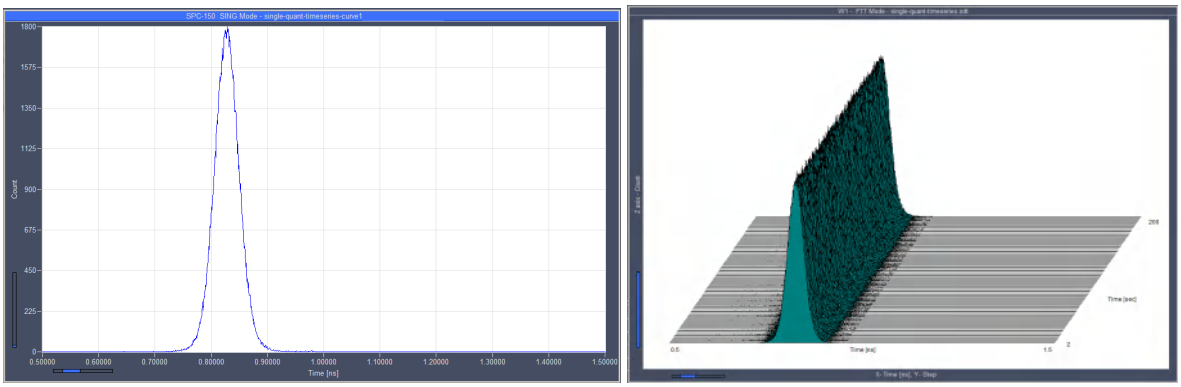
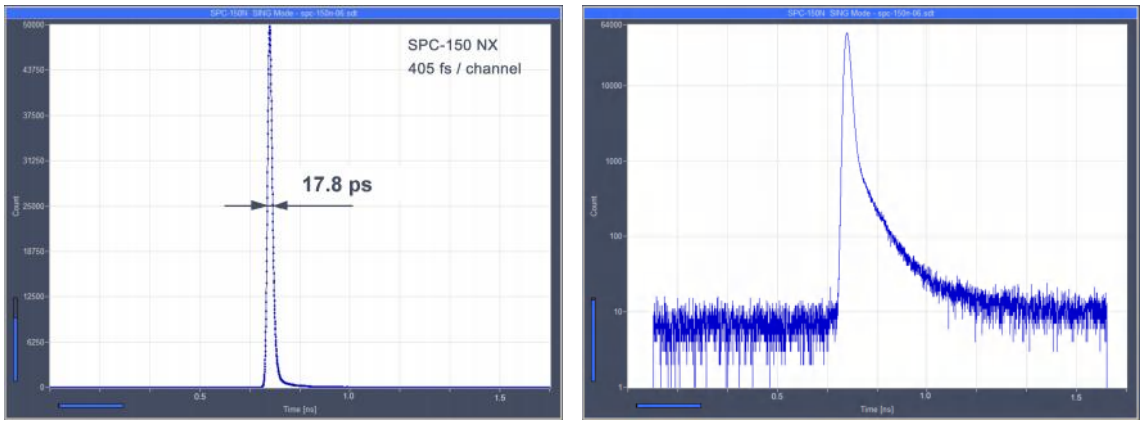


Fig. 325: Pulses of a Fianium supercontinuum laser recorded with a Eos X10 CS detector. Wavelength 1300 nm, time channel width of TCSPC module 813 fs. Left: Single pulse. Right: Time-series recorded in 2-second intervals over 200 seconds. We thank Gabriele Bulgarini and Sander Dorenbos of Single Quantum, Delft, for their cooperation.

Different than in the measurements performed with the fs laser at University of Jena, the pulse width of the supercontinuum laser is not negligible. Thus, the recorded pulse width is longer than with the fs laser. The recorded width is 48 ps. This is consistent with the assumption that the laser pulse and the detector IRF have an FWHM of 40 ps and 25 ps, respectively. However, this is mere speculation because the exact pulse width of the laser at 1300 nm is not known. A time-series recording of the pulses is shown in Fig. 325, right. The timing stability is excellent: The centroid (first moment) is stable within less than a picosecond.

SCONTEL TCORPS-UF-10 Detector

The fastest IRF we have obtained so far from a *commercially available* SSPD is from the NbN detector of SCONTEL, Moscow [1109]. Details are described in [115] and [1129]. The test light source was an AVESTA Project EFO-80 laser with a wavelength of 1550 nm and a pulse width of 300 fs. The TCSPC module was an SPC-150NX module, with high bandwidth discriminators, an electrical IRF of 3.8 ps FWHM, and a time-channel width of 405 fs. The result is shown in the figure below. The IRF of the detector-TCSPC combination has an FWHM of 17.8 ps.



IRF of the NbN detector of SCONTEL, Moscow, Russia, recorded with an SPC-150NX TCSPC module. Left: Linear Scale. Right: Logarithmic scale. The IRF of the detector-TCSPC combination has an FWHM of 17.8 ps. This is world record in TCSPC time resolution!

We believe that the 17.8 ps FWHM we obtained with the SCONTEL detector can be further reduced. Theoretical considerations show that the timing jitter in the buildup of the quasiparticle avalanche may be well below 10 ps FWHM. The electrical response of the SPC-150NX module (for noise-free input pulses) is less than 4 ps FWHM. We therefore believe that the largest part of the timing uncertainty is induced by electronic noise. Using pre-

amplifiers with lower noise figure does not significantly improve the situation. Good amplifiers have a noise figure of less than 2 dB. That means the input-referred noise is only 25% higher than the thermal noise of the 50-Ohm input matching resistor. In other words, most of the noise comes from this resistor. The only way to reduce it is cooling. Resistor noise scales with the square root of the temperature. The most rigorous way to reduce the noise would be to integrate the amplifier in the cryostat of the detector. Already moderate cooling with liquid nitrogen (70 K) reduces the noise by a factor of two. Normally the entire amplifier has to be cooled because the matching network is part of the amplifier chip. This leads to another complication: Only FET-based amplifiers or amplifiers in SiGe technology can be used, Si bipolar transistors do not work well at low temperature.

Another way to improve the resolution would be to increase the amplitude of the single photon pulse of the detector itself. However, simply increasing the detector bias current does not help. Above a certain level, the dark count rate increases steeply [1109, 1285], and at higher current superconductivity is lost altogether. It is possible that the amplitude can be increased by deeper cooling or modified detector design but this has not been practically proved yet.

TCSPC with a Single-Nanowire SSPD

An NbN superconducting nanowire single photon detector (SNSPD) has been used to perform time-correlated single photon counting (TCSPC) with an instrument response function (IRF) width of 4.4 ps, full width at half maximum (FWHM). The detector was developed collaboratively by Massachusetts Institute of Technology (MIT) and the Jet Propulsion Laboratory (JPL) [695]. The TCSPC module was a bh SPC-150NXX device. Details of the test setup are described in [117]. By carefully eliminating all sources of temporal pulse dispersion, we obtained an IRF width of 4.4 ps FWHM, see Fig. 326.

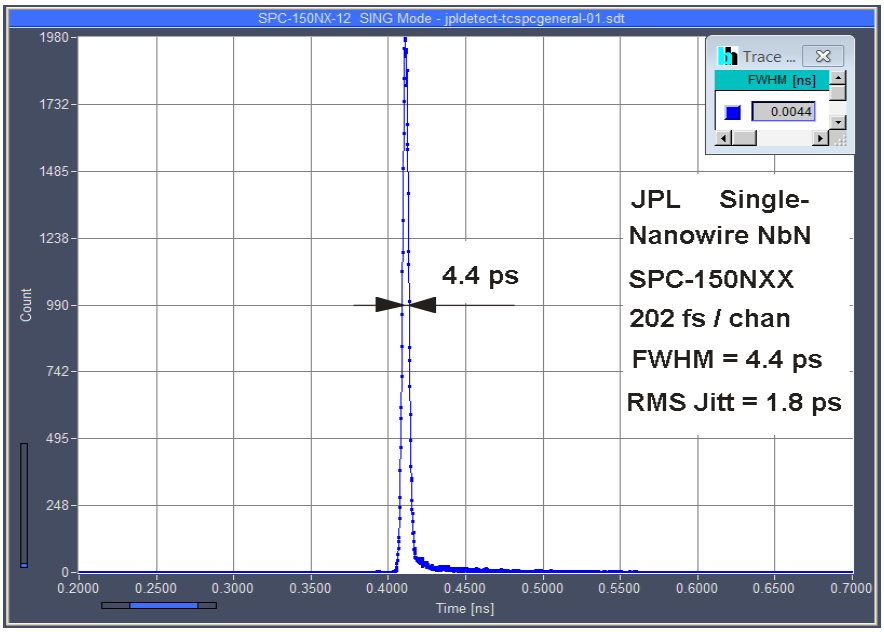


Fig. 326: IRF of the single-nanowire detector with an SPC-150NXX TCSPC module

It is sometimes believed that a single-nanowire detector is of no practical use because it is impossible to focus a reasonable amount of light on it. Fig. 328, shows that this is not necessarily correct. Using the optical setup shown in Fig. 327, we recorded the fluorescence decay of IR 1061 (an IR dye from Signal Aldrich). We used a 10-mm glass cuvette which had walls

of 4 mm thickness on two opposite sites. The horizontal cross section of the liquid volume is thus 2 mm by 8 mm. The laser beam was focused into the cuvette by an IR apochromate, L1. Fluorescence emitted by the dye solution is collected by another apochromate, L2. The beam is collimated by L2, and focused on the detector by an achromatic lens, L3. Two mirrors, M1 an M2, are used for alignment. To avoid pulse broadening by transit time effects it is important that the laser beam is focused correctly into the centre of the cuvette and that the fluorescence from exactly the focal volume is projected onto the detector. The detector then forms a confocal system with the excited spot. The fluorescence decay curve of IR 1061 recorded with the setup is shown in Fig. 328.

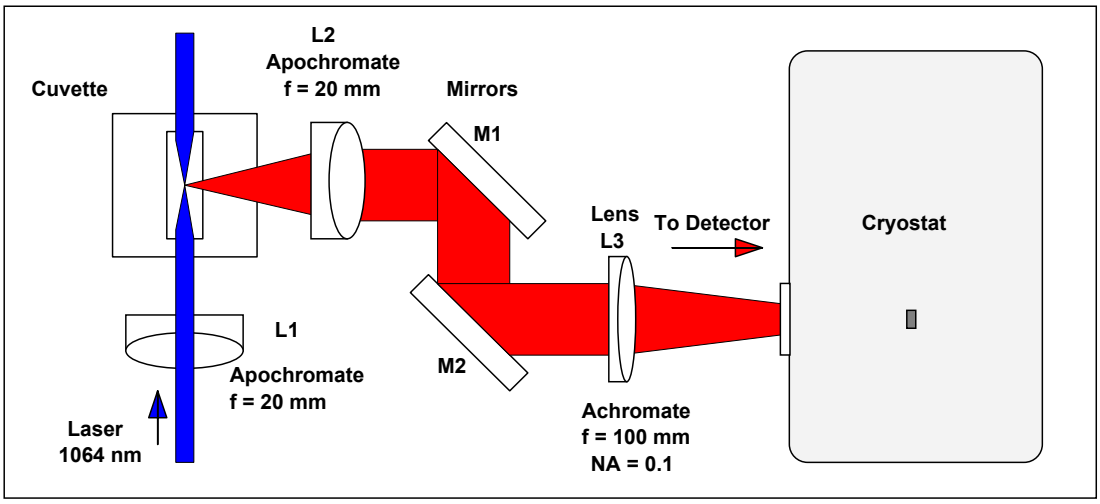


Fig. 327: Optical setup for fluorescence decay measurement with the NbN detector

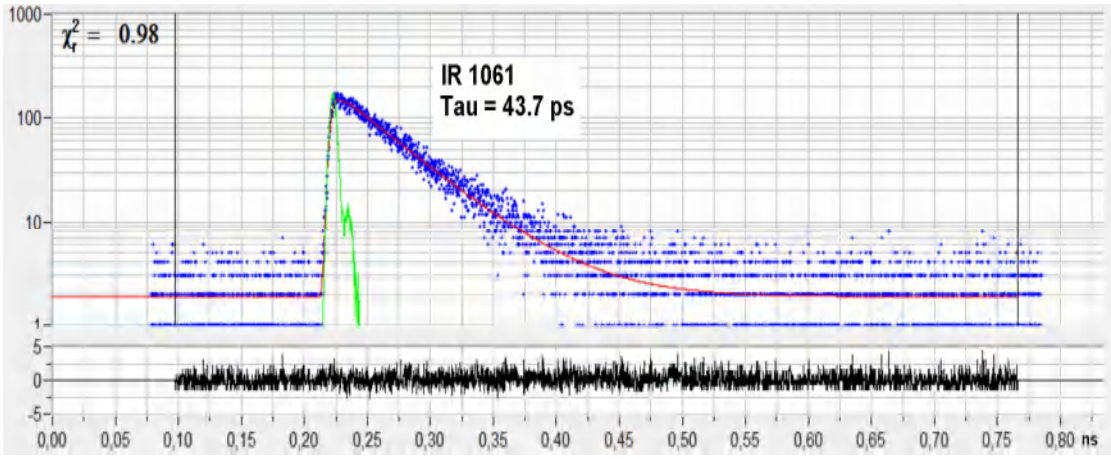


Fig. 328: Fluorescence decay curve of IR 1061, dissolved in dichloromethane. SPCImage determined a fluorescence lifetime of 43.7 ps.

At the high time resolution of the SNSPD, the decay function of IR1061 looks almost like that of a 'normal' fluorescent dye, such as fluorescein, recorded by a standard lifetime spectrometer. However, the fluorescence lifetime is 43.7 ps (determined by SPCImage), i.e. about 100 times shorter than that of fluorescein.

The detector - TCSPC combination described above has been used for scanning three-dimensional objects. Time-resolved imaging is performed in the FIFO Imaging mode of the SPC-150NXX. Resolution in x and y is obtained from the scan, resolution in z from the transit time of the photons. Due to the short IRF, only a few photons per pixel are needed to obtain sub-millimeter depth resolution [696].

Reduction of Geometric Jitter

In SSPDs with sizes on the order of 20 x 20 µm the geometric jitter limits the time resolution to typically 40 ps, FWHM. The geometric jitter can be cancelled by deriving output pulses from both ends of the meander and using the difference voltage for timing. A setup like this has been tested in combination with the SPC-150NXX. Differential readout was obtained both by a differential discriminator and by a balun (a small HF transformer) in front of the normal CFD input. The setup delivered an FWHM of 13.1 ps with the differential discriminator and 9.7 ps with the balun [321].

Preamplifiers and Detector Control

Preamplifiers

Most MCPs and PMTs deliver pulses of 20 to 50 mV into a load of 50 Ω when operated at maximum gain. Although these pulses can easily be detected by the input discriminators of the bh SPC modules a preamplifier can improve the time resolution, the noise immunity, the threshold accuracy and, importantly, the safety against damaging the SPC input. Furthermore, it can extend the lifetime of an MCP PMT because the detector can be operated at a lower average output current. The strongest argument is, however, that a properly designed preamplifier can protect the detector against overload. The principle is shown in Fig. 329.

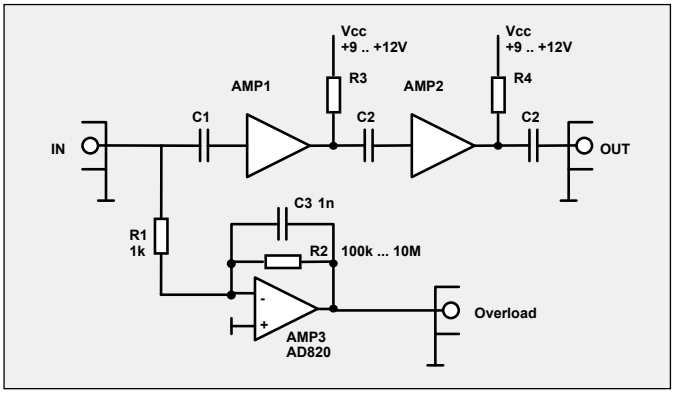


Fig. 329: Preamplifier with overload signal output

AMP1 and AMP2 are AC coupled high-frequency amplifiers as they are used in communication devices. To avoid signal inversion, either two inverting amplifiers are used in series or one non-inverting amplifier is used. Many types of amplifier chips are available, with similar designs but different gains and bandwidths. Depending on the amplifier chips used, AMP1 and AMP2 deliver a total gain between 12 dB and 40 dB, at a bandwidth between 500 MHz and several GHz. The DC component of the detector current is fed into AMP3. AMP3 is an operational amplifier with FET input. It converts the input current into a voltage with a transimpedance determined by R2. The output voltage of AMP 3 is proportional to the detector current. If it becomes too high it activates an overload warning, e.g. turns on a LED or an acoustic signal, and activates an overload signal that commands the detector controller to shut down the detector. The amplifiers are shown in Fig. 330.



Fig. 330: HFAC-26 (left) and HFAH-26 preamplifiers (right)

It should be noted that a preamplifier using the principle shown Fig. 329 is a much better overload indicator than a rate meter that monitors the detector count rate. Monitoring the count rate is not safe because the discriminator threshold can be wrong, or the detector gain may be set too low for the CFD of the SPC module to see individual photons. Moreover, the counting may break down at extreme overload. An inexperienced user may then increase the

light intensity even more. Overload detection via the detector current responds properly in all these situations.

Please note that the amplifiers come with different overload thresholds. The recommended overload thresholds for different detectors are:

R3809U MCP PMT	0.1 µA
R5600 and R7400 Miniature PMTs	10 µA
H5773 and H5783 Photosensor Modules	10 µA
H7422-40 and -50 Modules	2 µA
R928, R931, etc. Side Window PMTs	10 µA
XP2020 Linear focused PMTs	100 µA

In applications where high count rates occur only temporarily the overload thresholds can be increased by a factor of 3. The recommended amplifier Gain is 20 to 26 dB, i.e. 10 to 20. Higher gain is rarely needed for PMTs and MCP PMTs. It could even cause problems with the noise of the internal high voltage generator of photosensor modules. A gain higher than 20 should therefor4e not be used for the H5773, H5783, and H7422 photosensor modules.

Please note that preamplifiers are not needed for the bh *detector modules*, such as the PMH, PMC, PMZ, HPM, or PML detectors. These modules have internal preamplifiers that use the principle shown in Fig. 329. An additional external preamplifier would result in an exceedingly high amplifier gain, with the result that noise from the internal amplifier or from the power supply would trigger the CFD.

The DCC-100 Detector Controller

The DCC-100 module is used to control detectors in conjunction with the bh photon counters [63]. The DCC-100 provides power supply to two detectors and controls their gain via the PMT operating voltages. In conjunction with bh detectors or bh preamplifiers, it provides overload shutdown of the detectors. Furthermore, the DCC-100 delivers the current for thermoelectric coolers, e.g. for the Hamamatsu H7422, the bh PMC-100, and cooled HPM-100 modules. Moreover, the DCC-100 has high-current digital outputs for controlling shutters or actuators. In addition to controlling detectors, the DCC-100 can also be used to control the output power of bh BDL-SMC picosecond diode lasers. The operation of the DCC-100 is integrated in the SPCM data acquisition and system control software.

The DCC-100 is available as a PCI module and as a PCI-express module for IBM compatible computers, see Fig. 166, page 88. The software of the DCC-100 is included in the TCSPC installation package (please see ‘Software Installation’). The DCC-100 control panel is shown in Fig. 331, right. The use of the DCC-100 for a number of frequently used detectors and detector configurations is described under ‘System Connection’ and ‘FLIM Systems’.



Fig. 331: DCC-100 detector controller, software panel for detector control. Left: Normal operation, both detectors enabled. Right: Overload in one detector, detector shut down.

DCU-400 and DCU-800 Detector Controllers

For TCSPC systems which have more than two detectors or BDL or BDS series diode lasers the DCU-400 and DCU-800 controllers are available. The devices are separate boxes which are connected to the TCSPC system computer via USB, see Fig. 167, page 88. The DCU-400 has four outputs to detectors or lasers, the DCU-800 has eight. The software control panel for a DC-800 is shown in Fig. 332. It is shown in the configuration for the Zeiss LSM 980 confocal FLIM system [70]. It controls the four lasers of a LHB laser hub and two confocal detectors.

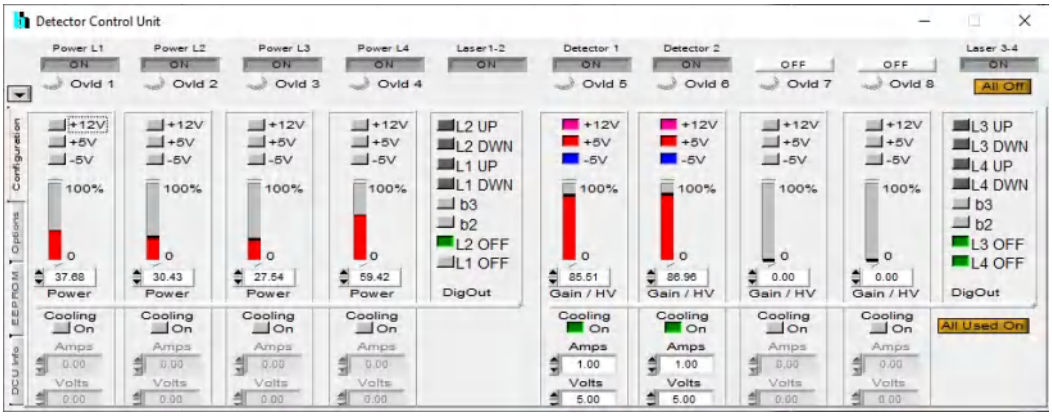


Fig. 332: DCU 800 software panel. In the configuration shown it controls four lasers and two detectors of the bh FLIM system for the Zeiss LSM 980.

Block Diagram of the DCC-100 and DCU-400/800 devices

The block diagram of the DCC-100 is shown in Fig. 333. The DCC-100 contains two detector control blocks and one general purpose power switch block.

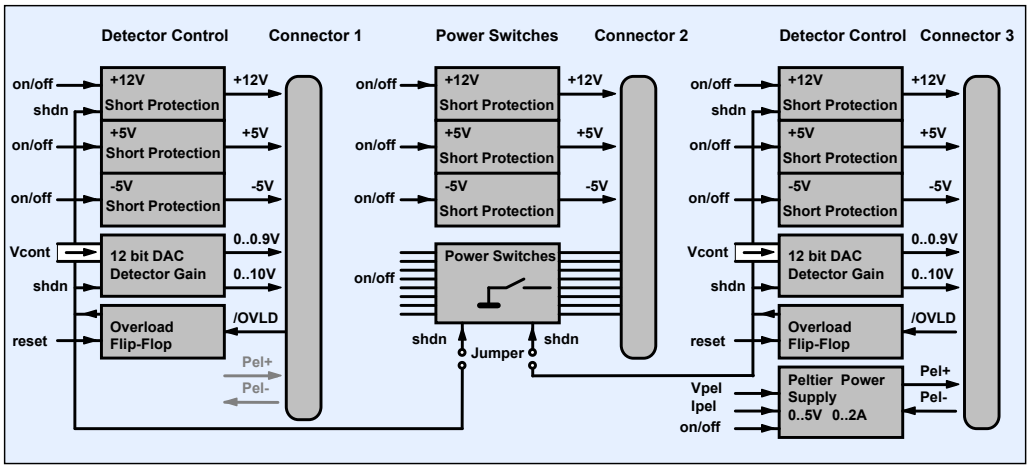


Fig. 333: Block diagram of the DCC-100 detector controller

Detector Control Blocks

The detector control blocks contain power supply outputs for detectors, a digital-to-analog converter (DAC) for detector gain control, and an overload shutdown circuit. The power supply outputs are short-circuit-protected and deliver +12 V, +5 V and -5 V. The outputs can be switched on and off by software. A 12 bit DAC is used to control the gain of the detector. It delivers the 0 to +0.9 V control voltage required for Hamamatsu photosensor modules (H7422, H5783, H5773 etc.) and the bh PMC-100 detector. A 0 to +10 V control voltage is available for FuG high voltage power supplies.

Both detector control blocks have a detector overload shutdown function. The shutdown function works in conjunction with bh HFAC-26 and HFAH-26 preamplifiers, and with the PMC-100 detector module. If the preamplifier or the detector module detects an overload condition it sends an active low overload signal (/ovld) to the DCC-100. This signal sets the overload flip-flop which shuts down the detector control voltage and the +12 V detector power supply. Furthermore, it can be used to deactivate the switches in the power switch block (see below).

High-Current Switch Block

The high-current switch block contains power supply outputs for detectors and preamplifiers and eight high-current MOSFET switches to operate shutters, motors or magnetic actuators.

The power supply outputs are short-circuit-protected and deliver +12 V, +5 V and -5 V. The outputs can be switched on and off by software. The MOSFET switches are able to switch currents up to 2 A and voltages up to 20 V. One side of each switch is connected to ground, the other side is available at the output connector. The switches are **not** short circuit protected.

The high-current switches can be shut down (i.e. set into the non-conducting state) by one or both overload signals from the detector control blocks. The configuration is set by jumpers on the DCC-100 board, see DCC-100 manual [63].

Power supply for thermoelectric cooler

Current supply for thermoelectric coolers is provided at connector 3 or at connector 1 and 3. The configuration differs for DCCs manufactured before and after June 2014. In earlier DCCs coolers supplied from connector 1 and 3 the are connected on series. The configuration is set by jumpers on the DCC board. In the new versions coolers connected to connector 1 and 3 are driven by independent power supply circuits.

The cooler drivers deliver up to 5 V and 2 A. Both voltage and current can be selected by software. The device automatically controls either the output voltage or the output current. Voltage control is active as long as the current through the load is smaller than the current limit set by the software. When the current through the load reaches the current limit the device automatically switches to current control. A block diagram is shown in Fig. 334.

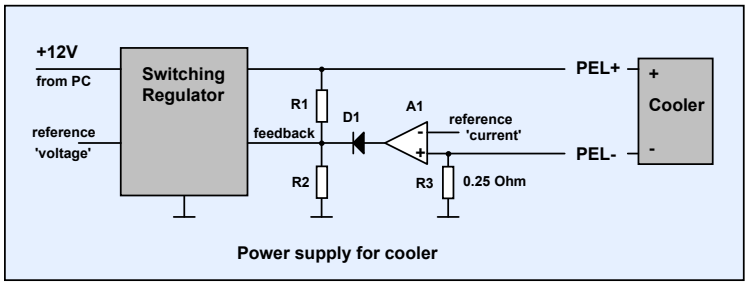


Fig. 334: DCC-100, control of the cooling current

A switching regulator is used to generate the supply current for the cooler. The cooling current flows through the sensing resistor R3. As long as the voltage at R3 is smaller than the reference voltage at A1 (‘current’ reference) A1 is inactive and the switching regulator works as a normal voltage stabiliser. If the voltage at R3 exceeds the reference voltage at A1, the amplifier becomes active, and, via D1, overwrites the feedback voltage of the switching regulator. This causes the regulator to reduce the output voltage until the voltage at R3 equals the reference of A1.

For more information, please see DCC-100 data sheet and DCC-100 manual, available on www.becker-hickl.com.

Safety Recommendations for Detectors

PMTs are operated at a voltage in the range of 800 to 3500 V, and the operating voltage of avalanche photodiodes can be as high as 300 V. Therefore it is necessary to obey to the usual safety rules for handling high voltage. An extremely important but often neglected issue is the ground return path to the power supply. A typical situation is illustrated in Fig. 335.

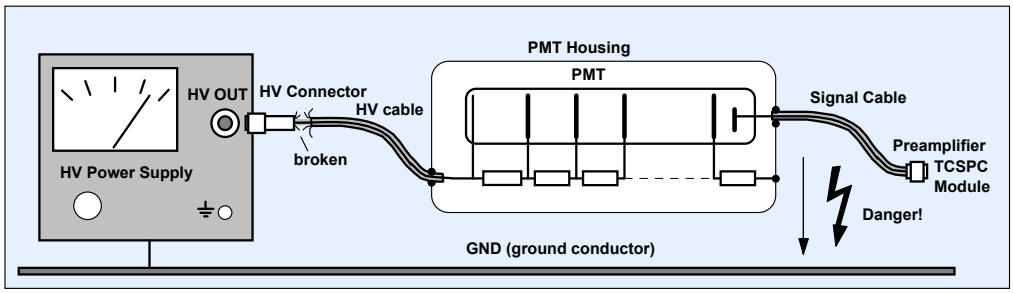


Fig. 335: Effect of a broken ground return path to the high voltage power supply

The cable that connects the voltage divider of the PMT to the high voltage power supply has a broken outer conductor. The inner conductor still connects the 'hot' side of the voltage divider to the high voltage. However, because the outer connector is broken, the current through the voltage divider resistors cannot flow back to the power supply. Therefore the current flows through the preamplifier, the TCSPC module, the computer, and the ground conductor of the power socket back to the power supply. Nothing happens, but the setup is not safe: When the signal cable is disconnected from the SPC input, there is a high voltage between the signal cable and the TCSPC module. Fortunately the resistors in the PMT voltage divider limit the current so that a broken HV cable will probably not deliver a fatal shock; but nevertheless the effect can be surprising.

The setup can easily be made safe by providing an auxiliary ground return path from the PMT housing to the high voltage power supply. Unfortunately, most PMT housings and many power supplies do not provide any connectors for an additional ground connection. Therefore: Do not disconnect the PMT signal cable from the SPC module when the high voltage is switched on, and do not use any cables with broken or unreliable screen or ground connectors.

High voltage safety is not the only reason why a PMT cable should not be connected or disconnected when the high voltage is on. The situation is illustrated in Fig. 336.

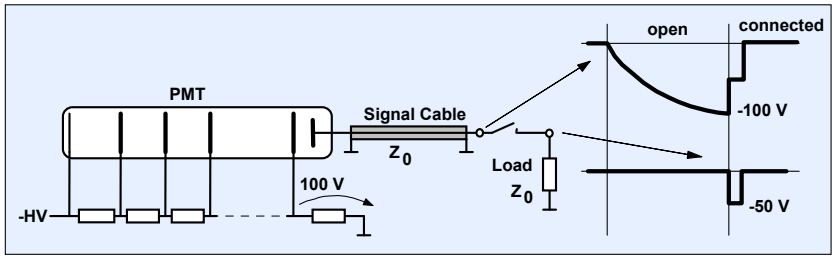


Fig. 336: Discharging a charged PMT signal cable into a resistive load

If the load is unconnected, the output current of the PMT charges the signal cable until the voltage reaches approximately the voltage at the last dynode. This voltage can be as high as several hundred Volts. When the load is connected, the cable discharges into the load. For a load impedance equal to the characteristic impedance of the cable, the amplitude of the resulting pulse is half the voltage to which the cable was charged. The pulse duration is twice the cable transit time. The pulse can be enough to destroy an amplifier or a CFD. Normally the limiter diodes at the input of the amplifier or CFD will prevent a destruction. However, a ca-

ble discharge will stress the diodes enormously so that absolute safety is not given. Therefore, be careful and don't tempt fate.

If possible, you can connect a resistor of about 100 kΩ from the PMT anode to ground inside the PMT case. This will prevent the cable from being charged and thus provide protection against preamplifier or CFD damage.

Summary: Do not connect or disconnect a photomultiplier to or from the SPC module or a preamplifier when the high voltage is switched on! Never connect a photomultiplier to the SPC module or a preamplifier if the high voltage was switched on before with the PMT output left open! Never use switchable attenuators between the PMT and the SPC! Never use cables and connectors with bad contacts! The same rules should be applied to photodiodes which are operated at internal reverse voltages above 20 V.

Implementation of the bh TCSPC Technique

The Classic TCSPC Implementation

The classic TCSPC setup consists of a light source that excites a sample, a detector that detects single photons of the light emitted by the sample, and a TCSPC module that measures the times of the photons in the laser pulse period and builds up the photon distribution over the time in the signal period. bh systems normally also contain a detector controller that provides for reproducible detector operating conditions and detector shutdown in case of overload. A system like this is shown symbolically in Fig. 337.

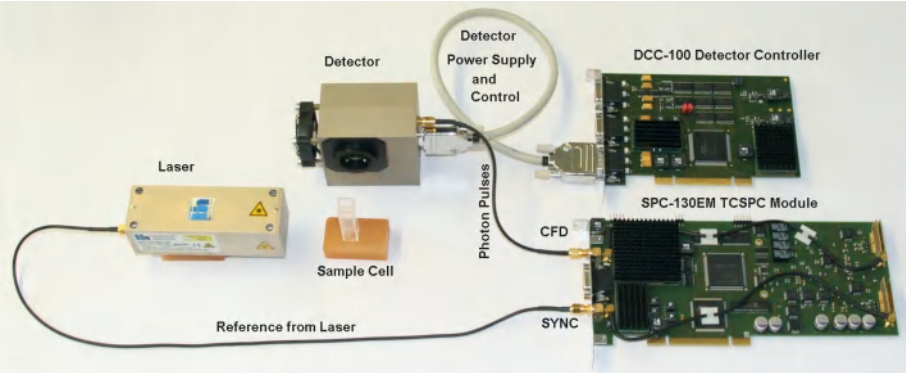


Fig. 337: Classic TCSPC system for fluorescence decay measurement

The setup shown above uses a BDS-SM picosecond diode laser, a PMC-100 or -150 detector, and an SPC-130EM TCSPC module. This does not mean, however, that exactly these components have to be used. Other light sources, such as the BDL-SMN or BDL-SMC lasers, supercontinuum lasers, fibre lasers, or Ti:Sa lasers can be used as well. Instead of the PMC detector an HPM-100 hybrid detector or an MCP PMT can be used. Other SPC modules can be used as well - even older modules such as the SPC-630 and SPC-730 can be operated in the classic TCSPC configuration.

Reference Signal

Reference from the Laser

The TCSPC module needs a timing-reference signal that is synchronous with the pulses of the excitation light source. The signal is connected to the 'SYNC' input of the TCSPC module. In many cases a suitable signal is available directly from the laser. All bh picosecond diode lasers deliver a SYNC signal for the SPC modules. An example is shown in Fig. 338.



Fig. 338: Timing reference signal from bh BDS-SM ps diode laser

Timing-reference (Sync) pulses are also available from most Ti:Sa lasers, from super-continuum lasers, and from many fibre lasers. For direct connection into the Sync input of the SPC module the polarity must be negative, and the amplitude in the range from -50 mV to -500 mV. Positive pulses must be inverted with an A-PPI-D pulse inverter (see Fig. 176. page 92). Pulse amplitudes larger than -500 mV are not immediately dangerous as long as they remain below about -2 V. The inputs of all bh SPC modules are overvoltage-protected by diodes that limit the input amplitude to about 1.5 V. The diodes withstand pulse input currents up to 2 A (100 V from a 50-Ohm source) for times < 1 µs. DC input currents must not exceed 100mA (5 V from a 50-Ohm source). Nevertheless, exceedingly large amplitudes should be avoided because they can cause crosstalk into the detector signal. We therefore recommend to keep the amplitude in the correct range by an electrical attenuator.

Reference from Photodiode modules

If the excitation source does not deliver a suitable Sync signal it must be generated by a fast photodiode. Complete photodiode modules are available from Becker & Hickl. These modules get their +12 V supply voltage from the SPC module or the DCC module so that no special power supply is required. The most frequently used one is the PHD-400, see Fig. 339, left. It incorporates an indicator of the average photodiode current for convenient optical alignment. The indicator current range is adapted to the average signal current typically flowing at pulse repetition rates from 40 to 100 MHz.



Fig. 339: Photodiode modules for Sync signal generation. Left: PHD-400. Right: APS-100

A Sync problem can occur for Ti:Sa laser with wide tuning range. Over the tuning range, the laser power can change over a factor of 10 or more. Simultaneously, the sensitivity of the photodiode changes - unfortunately in the same direction as the laser power. With a simple photodiode module, such as the PHD-400, the optical power at the photodiode needs to be adjusted depending on the laser wavelength. We therefore designed a photodiode module with internal amplitude regulation Fig. 339, right. The APS-100 delivers a constant output amplitude over an intensity range of about 1:100. Electrical output signals of the PHD-400 and the APS-100 are shown in Fig. 340. Please note that the output signal lines of the photodiodes must be matched with 50 Ω. This is the case when the modules are connected to the Sync input of an SPC module but not necessarily when they are connected to an oscilloscope.

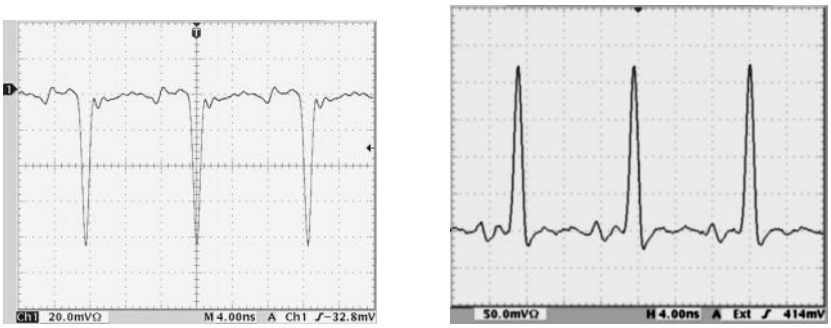


Fig. 340: Output signals from a PHD-400 (left) and an APS-100 (right). 80 MHz repetition rate, time scale 4 ns / division

There are a few cases where a photodiode is not sensitive enough to generate reference pulses of sufficient amplitude. Typical cases are luminescence decay measurement by ns flashlamps [1367], positron lifetime experiments [709], experiments of sono-luminescence [47, 376, 511], the measurement of the decay time of scintillators by particles from radioactive decay [233], or the measurement of electrical barrier discharges [1309, 1310] (see 'Barrier Discharges', page 681). In these cases it may be required to use a PMT to generate the reference signal. A good choice for reference generation are the Hamamatsu H5773 and H5783 photosensor modules, or PMC-100 or -150 PMT modules operated a low gain.

PMTs or SPADs at the reference (stop) input are also used as stop detectors for photon correlation experiments, see 'Picosecond Photon Correlation', page 635. The situation differs from the cases described above in that the PMT or SPAD is used as a single-photon detector. The requirements to the single-photon pulses and the way the detector are connected are the same as described for the detectors at the CFD (start) input.

In multi-module systems it may be required to distribute a reference signal to several TCSPC modules. For this purpose, reflection-free power splitters should be used. Suitable splitters for 1:2 and 1:4 signal distribution are available from bh, see Fig. 176, page 92. It should, however, be taken into regard that the signal amplitude for 1:2 and 1:4 distribution drops by a factor of 2 and 4, respectively.

Detector Signal

The SPC modules accept input pulses from a wide range of detectors. Of course, the detector must have single-photon sensitivity, and detector pulses must represent the detection of single photons of the light signal to be measured. The single-photon pulses from the detector are connected to the 'CFD' input of the SPC module (see Fig. 337).

The single-photon pulses of most detectors have a considerable amplitude jitter. In a normal discriminator the amplitude jitter would induce a temporal jitter in the discriminator output pulses. To avoid the influence of the amplitude jitter the SPC modules have constant-fraction discriminators (CFDs) which trigger independently of the input pulse amplitude (see Fig. 417, page 269).

For correct CFD function, the detector pulses must be negative, with an amplitude of -50 to -500 mV. For best time resolution, the leading edge of the pulses should be steeper than 1 ns. If possible, single-photon pulses from PMTs should be no longer than about 2 ns. Photon pulses from SPADs can be several 10 ns long. Such pulses have no amplitude jitter so that perfect constant-fraction triggering is not required. The leading edge should be steeper than 1 ns. If a SPAD delivers positive pulses the polarity must be reversed by an A-PPI-D pulse inverter. Single-photon pulses for a few frequently used detectors are shown in Fig. 341.

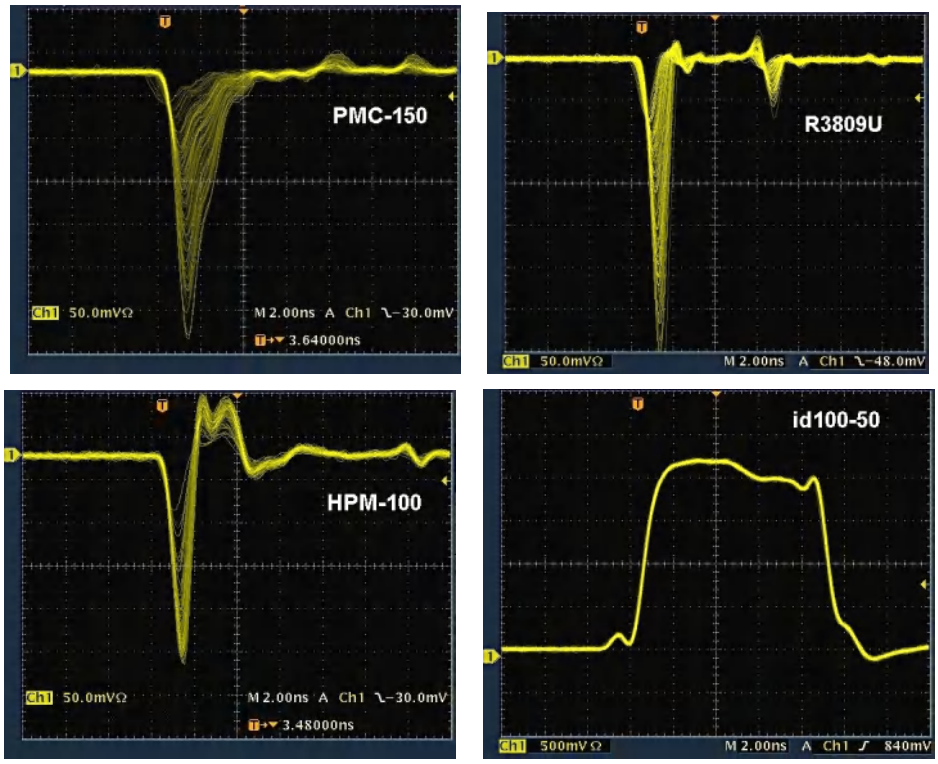


Fig. 341: Single-photon pulses of typical TCSPC detectors. Upper row: PMC-150 PMT module, R3809U MCP PMT (with HFAC-26 preamplifier). Lower row: HPM-100 hybrid detector, id-100-50 (different vertical scale)

Delayed-Stop Operation

The typical TCSPC setup measures the times of the individual photons of an optical signal exited by some kind of pulsed light source. The photon times are measured relative to synchronisation pulses derived from the light source. The bh SPC devices are normally working in the 'reversed start-stop' mode, see Fig. 195, page 108. The pulse period of the light source is considered to be constant, and the time measurement is performed from the photon to the next laser pulse. For a laser with a constant pulse period on the order of 10 to 50 ns this mode of TCSPC operation is easy to implement and delivers perfect results.

However, not all lasers can be expected to have negligible pulse-period jitter. If the photon times are measured from the photon to the next laser pulse the pulse period this jitter adds to the transit-time jitter of the detector, and the time resolution of the measurement decreases. The period of the excitation pulses may also be variable, as it is the case for ps diode lasers or Ti:Sa lasers with pulse pickers. The result of a change in the laser pulse period is a shift of the recorded photon times with the repetition rate, which is at least inconvenient. Moreover, the pulse period may simply be too long to measure reasonable photon times by stopping with the next pulse.

The problem can easily be avoided by delayed-stop operation of the TCSPC module. A delay line is inserted in the SYNC path of the SPC module. This places the SYNC pulse behind the pulse of a photon that originated from the corresponding laser pulse. The principle is shown in Fig. 342.

The upper part of the figure shows stopping with the next laser pulse. The laser pulse that generated the detected photon is marked black. If the pulse period changes (upper part, left and right) the measured photon time changes correspondingly.

With an appropriate delay in the reference channel the time of the photon is measured against the laser pulse that initiated the detected photon. The measured photon time does then not

depend on the pulse period, see lower part of Fig. 342. TCSPC with delayed stop operation can even be used to record the shape of entirely random light pulses, see paragraph below.

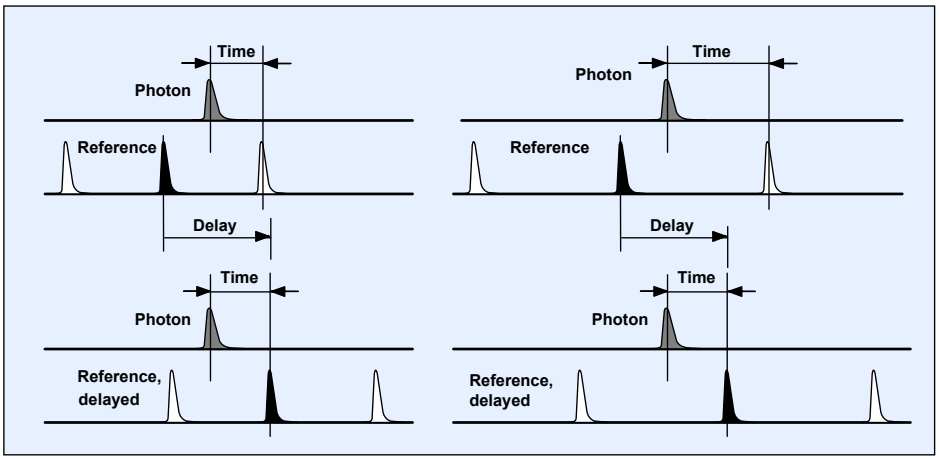


Fig. 342: Upper part: Stop with the undelayed laser pulse, different period of laser pulses. The laser pulse which released the photon is marked black; the measured photon time depends on the laser period. Lower part: Stop with the delayed laser pulse. With an appropriate delay in the reference channel the time of the photon is measured against the laser pulse that generated the photon. The measured photon time does not depend on the signal period.

The required delay in the reference channel can easily be provided by a cable in the reference (SYNC) path, see Fig. 343. The delay should be approximately the desired measurement time interval, plus the difference in the transit times of the detector and photodiode path. A good reference delay to start with is 10 ns or 2 m cable for an MCP PMT or hybrid detector, and 20 ns or 4 m cable for TO-8 PMTs, photosensor modules, or the bh PMC-100 and PMC-150 detectors. Adjusting the delay cable length is described at page 279. Please note also that bh deliver a USB-controlled 'Delay Switch Box' to provide an adjustable Sync Delay from 0 to 32 ns, please see Fig. 175, page 92.

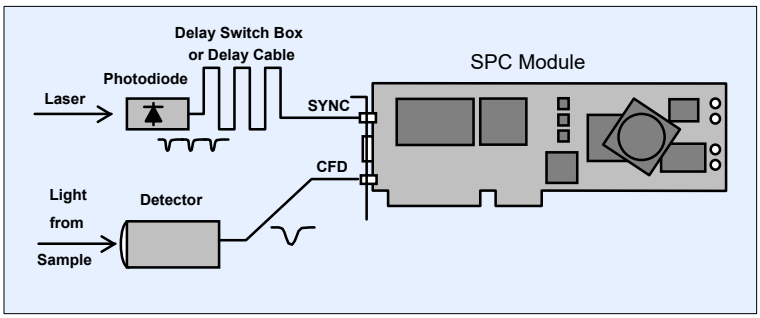


Fig. 343: Delayed stop operation

Synchronisation to Random Signals

There are a few TCSPC applications where the light pulses appear at entirely random times. Typical examples are experiments on electrical barrier discharges, positron lifetime experiment, and sono-luminescence. Because the light pulses are not generated by an external event, such as a laser pulse, an independent timing reference signal does not exist. Nevertheless, TCSPC can be used to record the shape of such signals. The principle is shown in Fig. 344.

PMT 1 is the reference PMT. It is operated at a relatively low gain and receives a strong signal from the sample. Consequently, it delivers a signal roughly corresponding to the true shape of the optical pulse. These reference pulses are delayed and fed into the SYNC input of the TCSPC module. Even if the pulses vary in amplitude, the constant fraction discriminator

of the SYNC channel produces a timing signal that is reasonably correlated with the centroid of the light pulses.

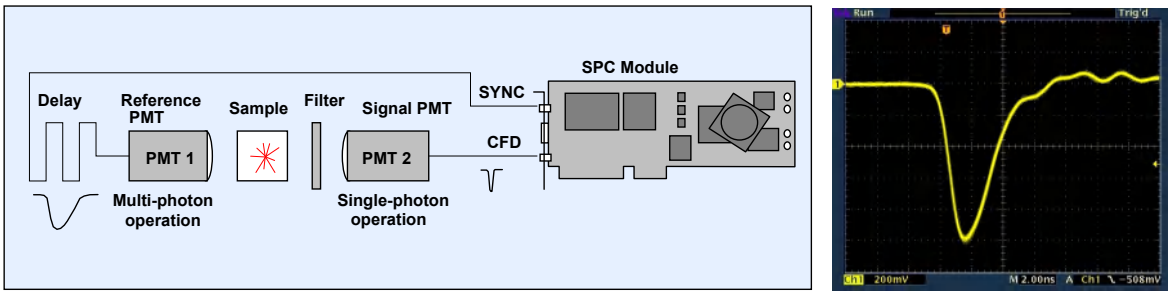


Fig. 344: Recording random light pulses by a TCSPC module. Right: Sync signal from PMC-100 detector operated at low gain.

PMT 2 receives the light through a set of filters, a monochromator, or another optical element that transmits only a small fraction of the photons. The gain of PMT 2 is high. Therefore it delivers single-photon pulses. If the intensity at PMT 2 is low enough correct single-photon operation is achieved, and the TCSPC module records the shape of the light pulses emitted by the sample.

Multi-Detector Operation

The classic setup shown in Fig. 337, page 217 can be extended for simultaneous operation of several detectors. The system components are shown in Fig. 345.

The principle is called ‘routing’, see 'Multi-Detector and Multi-Wavelength TCSPC', page 116. An external device - the router - receives the single-photon signals of several detectors. It combines the single-photon pulses of all detectors in a common timing pulse line. The combined signal is fed into the CFD input of the SPC module. Simultaneously, the router determines which detector has delivered the corresponding photon pulse. The number of the detector is sent into the ‘routing’ input of the SPC module. In the recording process, the SPC module sends the photons from the individual detectors into separate memory data blocks. The TCSPC process thus delivers separate curves for the signals detected by the individual detectors. An implementation for two PMC-100 or PMC-150 detectors and an SPC-130EM module is shown in Fig. 345.

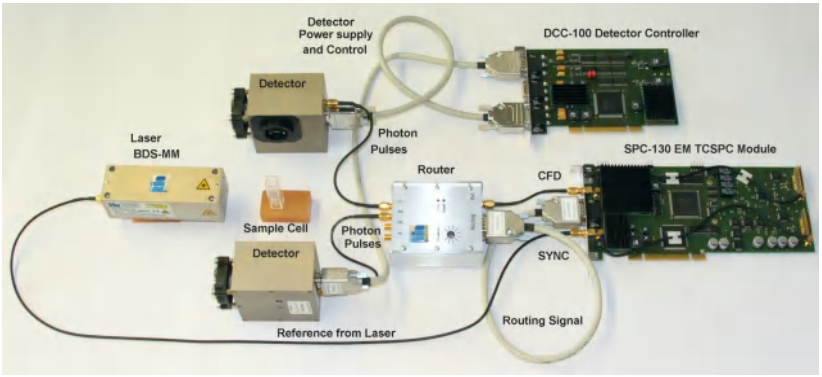


Fig. 345: Components of a routing system with two detectors

The requirements for the detector and synchronisation signals are the same as for the classic single-detector setup. System parameter setup for routing systems is described at page 254. Important is that the number of routing channels is correctly defined and the ‘Latch delay’ (the time after the detection of a detector pulse at the CFD when the routing signal is read) is appropriately set. For cable diagrams for routing systems please see page 227.

Multi-Wavelength TCSPC

A symbolic setup of a multi-wavelength TCSPC system is shown in Fig. 346. The principle is described in section ‘Multi-Detector and Multi-Wavelength TCSPC’, page 116. The light from the sample is detected by a PML-SPEC or MW FLIM multi-spectral detection assembly. The polychromator of the detection assembly projects a spectrum of the light signal on the cathode of a PML-16-C or PML-16 GaAsP 16-channel detector. The routing electronics of the PML generates a photon-pulse signal and a routing signal. The photon pulses are fed into the CFD input of the SPC module, the routing signal into the routing input. The SPC module then records 16 separate waveforms for the individual anode elements of the PML-16. Since these are related to the spectrum of the light the recording delivers separate optical waveforms for different spectral intervals. Software-parameter setup is described at page 255.

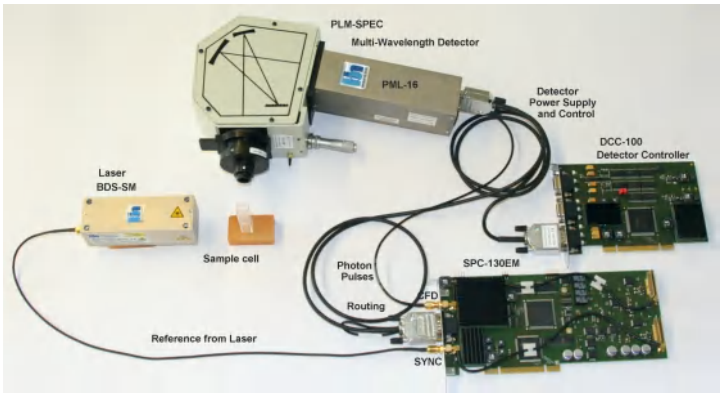


Fig. 346: Multi-wavelength TCSPC system

System Connection

bh TCSPC systems are highly modular. Based on the general system configurations shown above a large number of TCSPC systems with different lasers, different detectors, different number of detectors, different SPC modules, and different numbers of SPC modules are possible. Cable diagrams for a few frequently used TCSPC configurations are described in the following sections.

Single-Detector Systems

Extremely simple systems can be built with the PMC-100 or PMC-150 detectors and a bh picosecond diode laser, see, for example Fig. 337, page 217. A cable diagram for TCSPC system with a PMC-100 or PMC-150 detector is shown in Fig. 347.

The detector is controlled via a DCC-100 detector controller. The detector is connected to the DCC-100 via its standard power supply cable. The cable connects the +12 V power supply and the gain control signal from the DCC-100 to the detector, and the overload signal from the detector to the DCC-100. The DCC-100 delivers also the power supply for the Peltier cooler of the PMC-100 or PMC-150. The photon-pulse output of the PMC-100 or PMC-150 is connected directly - without an additional amplifier - to the ‘CFD’ input of the TCSPC module. The reference signal comes directly from the laser. Any of the bh BDS-SM, BDS-MM, or BDL-SMN lasers can be used. The BDL-SMC lasers deliver positive pulses and require the A-PPI or A-PPI-D pulse inverter (see Fig. 176). All cables and the A-PPI-D inverter are included in the standard cable set delivered with the SPC module and the PMC-100 or PMC-150.

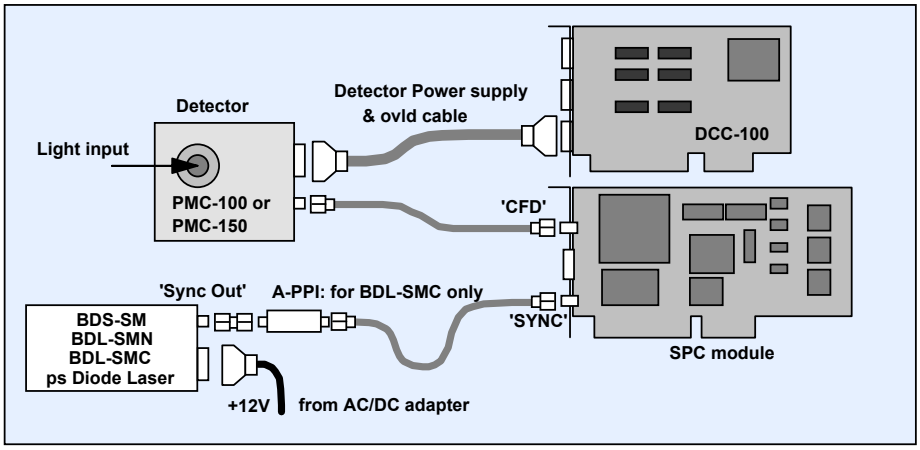


Fig. 347: Classic TCSPC system with a PMC-100 or PMC-150 detector

Similar systems can be set up with the HPM-100 hybrid detectors. The system architecture is exactly the same, see Fig. 348. The only difference is the detector, and, possibly, a slightly longer detector or shorter Sync cable to compensate for the shorter signal transit time in the HPM-100. A TCSPC setup can thus be upgraded with a new detector without replacing the entire TCSPC system.

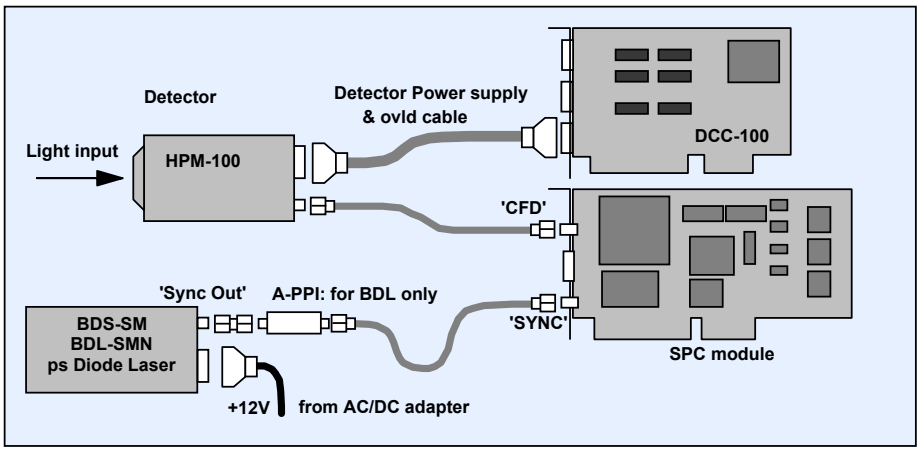


Fig. 348: Classic TCSPC system with a HPMH-100 hybrid detector

Important: Monitor cables for PCs have the same connectors as the power supply cables of the PMC-100. However, some of these cables have not all lines connected, or even have some pins connected in parallel. This can cause malfunction of the detectors or even damage the DCC-100 module. Therefore, please use only the detector cables delivered with the bh SPC or detector modules.

Fig. 349 shows how a Hamamatsu H7422 module [548] is connected to a bh TCSPC system. The +12 V power supply, the gain control signal, and the Peltier cooler current are delivered by the DCC-100 via the H7422-DCC power supply cable. Because the H7422 does not contain a preamplifier a HFAC-26-2 amplifier is used in the photon pulse path. The overload signal from the HFAC-26 is connected to the DCC-100; the power supply for HFAC-26 comes from the routing connector of the SPC module.

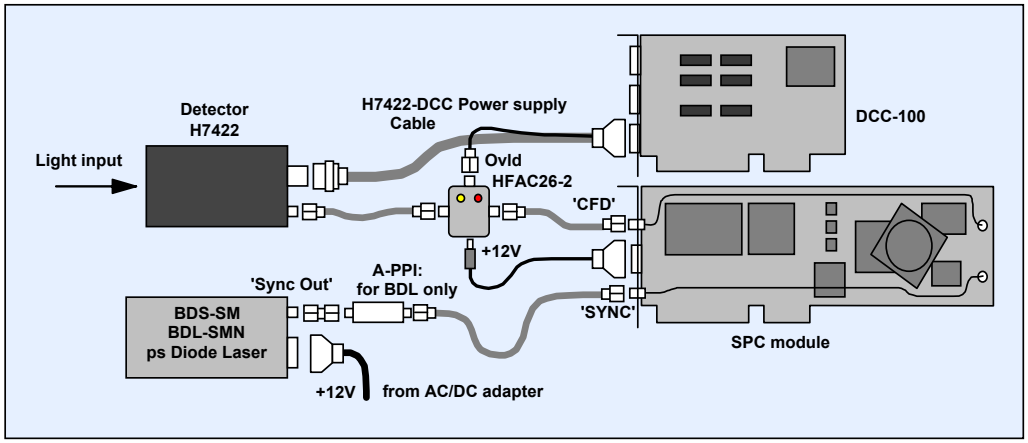


Fig. 349: Connecting an H7422 PMT module to a bh TCSPC system.

A TCSPC system with an R3809U MCP PMT [544] is shown in Fig. 350. The high voltage for the R3809U is delivered by an FuG HCN14-3500 power supply. The HCN14-3500 is controlled by a signal delivered by the DCC-100. The single photon pulses of the MCP PMT are amplified by a HFAC-26-01 preamplifier. The overload signal of the HFAC-26 is connected to the DCC-100. If the overload signal becomes active the DCC shuts down the operating voltage of the R3809U.

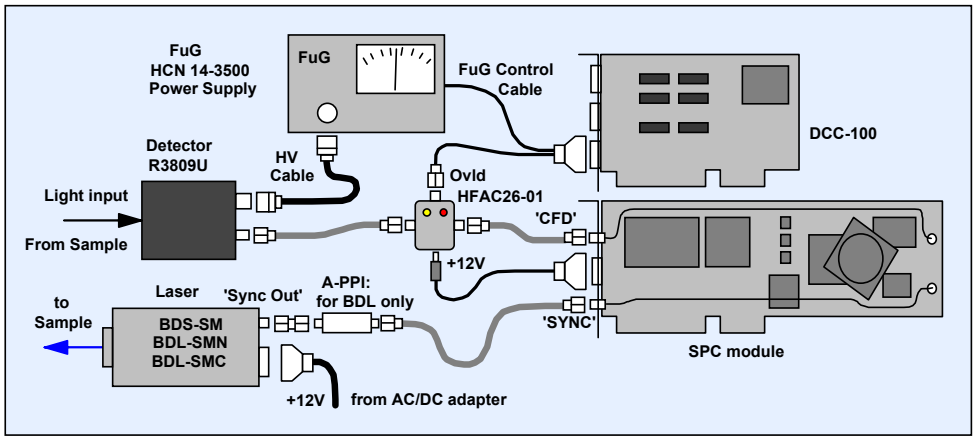


Fig. 350: Operation of an R3809U MCP PMT in a bh TCSPC system. Voltage for R3809 from FuG HCN 14-3500 power supply.

Alternatively, the high voltage of the R3809U can be generated by a bh HVM-3000 high-voltage module. The connection diagram is shown in Fig. 351.

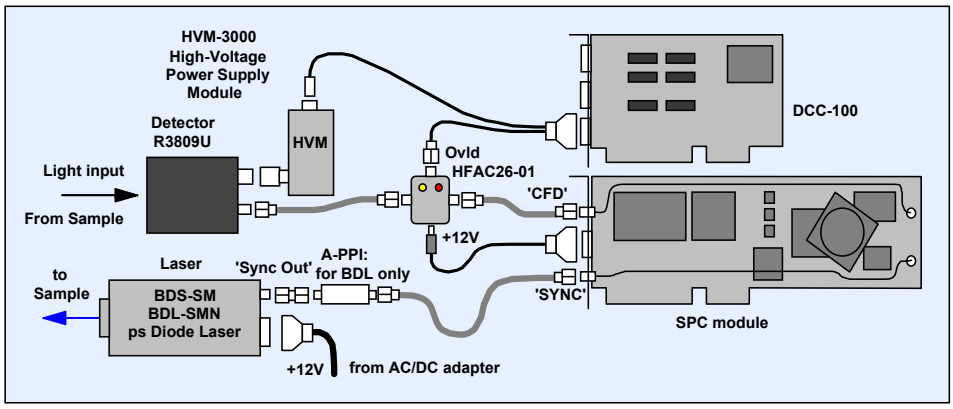


Fig. 351: Operation of an R3809U MCP PMT in a bh TCSPC system. Voltage for R3809 from HVM-3000 module.

A TCSPC system with an id Quantique id-100 SPAD module [607] is shown in Fig. 352. The id-100 modules deliver low-voltage TTL (LVTTL) pulses into a load of 50 Ω. The pulse duration is about 20 ns, the amplitude about 2 V. To connect the positive pulses to the input of the SPC module the polarity must be reversed by an A-PPI-D pulse inverter. The pulse amplitude is reduced by an attenuator of 10 to 20 dB. The appropriate CFD settings are CFD limit Low = -100 to -200 mV and CFD Zero Cross = -30 mV. The id-100 SPAD module is overload-proof. A DCC-100 module is therefore not needed.

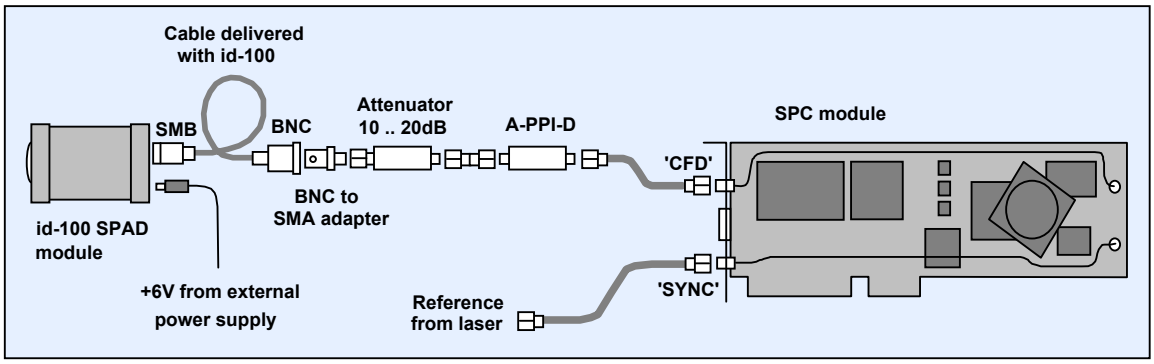


Fig. 352: Connecting an id Quantique id-100 SPAD module

The PDM-50 SPADs of MPD [858] can be connected directly to a bh SPC module. Use the 'Timing' output of the PDM module, and connect it as shown in Fig. 353. The pulse amplitude is about -500 mV. An attenuator in the signal line can be helpful to avoid reflections but is not absolutely required. As the id-100 of id Quantique, the PDM modules of MPD are overload-proof. The module can therefore left turned on all the time the TCSPC system is used.

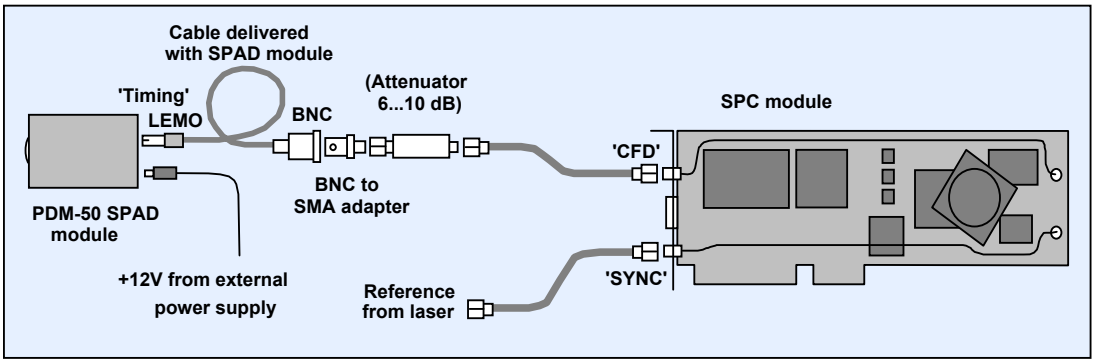


Fig. 353: Connecting an MPD PDM module

The connection of a single SPCM-AQR (SPAD) module to a bh SPC module is shown in Fig. 354. The SPCM delivers positive output pulses of about 4 V peak amplitude. Therefore, a 20-dB attenuator and an A-PPI-D pulse inverter are inserted in the detector signal line. Please note that the SPCM-AQR is *not* overload-proof.

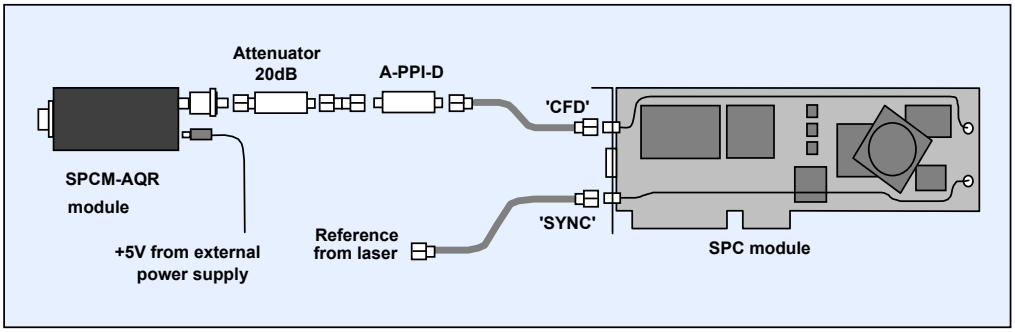


Fig. 354: Connecting an SPCM-AQR detector to an SPC module

Multi-Detector Systems

A TCSPC system with two PMC-100 or -150 detectors is shown in Fig. 355. Both detectors are controlled by a single DCC-100 card. DCC-100 modules manufactured before 2015 must be configured to connect the coolers of both PMCs in series (see DCC-100 manual). The photon pulses of the PMCs are connected to two inputs of an HRT-41 router. The combined photon pulses of the detectors are available at the timing output of the router and are connected into the 'CFD' input of the TCSPC module. The routing signal delivered by the router is connected to the 'Routing' input of the SPC module. Both the PMC-100 and the HRT41 router have internal amplifiers. The total gain of the PMC-HRT combination is about 100. A gain this high can cause problems with the noise of the high-voltage generator of the photosensor modules in the PMCs. Therefore two 12-dB attenuators are inserted in the photon pulse lines.

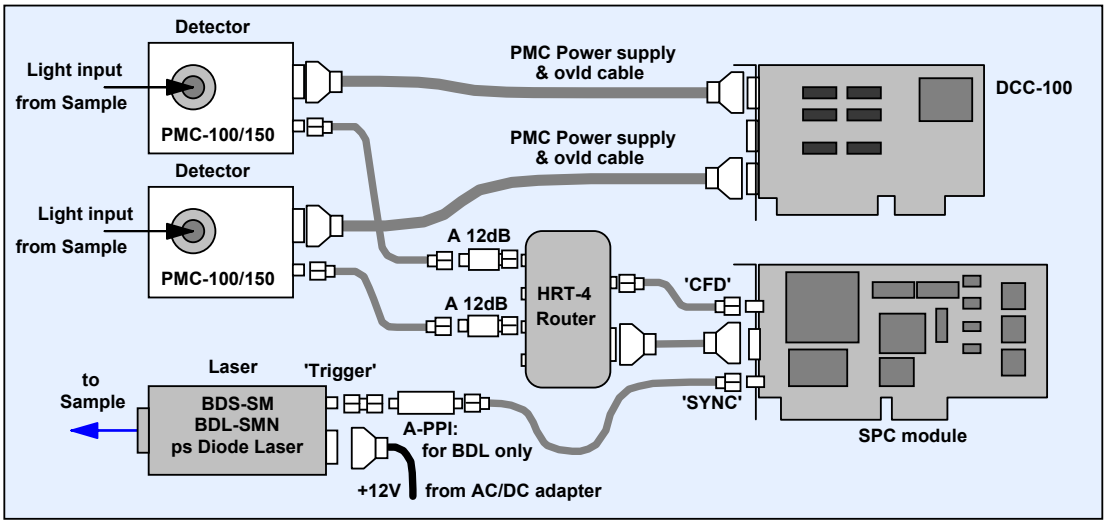


Fig. 355: Dual detector system with two PMC-100 and a HRT-4 router

The setup shown in Fig. 355 can be used with more than two detectors. With a HRT41 router up to four detectors can be connected to one SPC module. Additional PMCs can be controlled by additional DCC cards or by a DCU-104 USB detector controller.

Multidetector systems with routers have the disadvantage that they have limited throughput. They are therefore more and more replaced with multi-module systems and with the new SPC-QC-104 and -106 multi-channel TCSPC boards [75]. A setup with two parallel HPM-100 detectors is shown in Fig. 356.

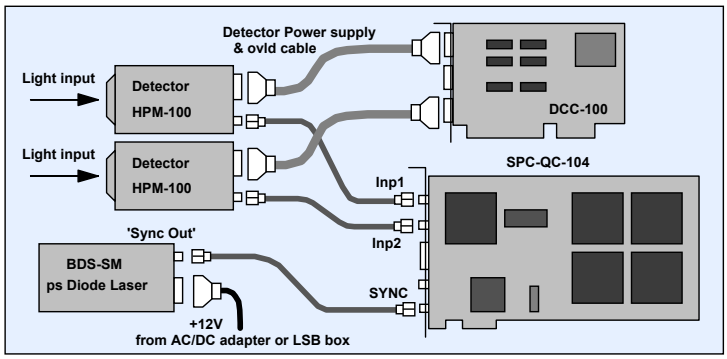


Fig. 356: Parallel dual-detector system with two HPM-100 hybrid detectors, SPC-QC-104

A three-channel SPAD system with an SPC-QC-104 [75] is shown in Fig. 357. The SPADs are simply connected to the three CFD channels of the SPC-QC. The configuration shown is for SPAD modules that deliver negative pulses. For SPAD modules with positive (TTL) out-

put A-PPI pulse inverters and attenuators have to be inserted in the signal lines, see Fig. 358. For pure correlation or coincidence measurements, a fourth detector can be connected instead of the Sync signal. With fast detectors, photons can be correlated at a resolution down to about 40 ps [75].

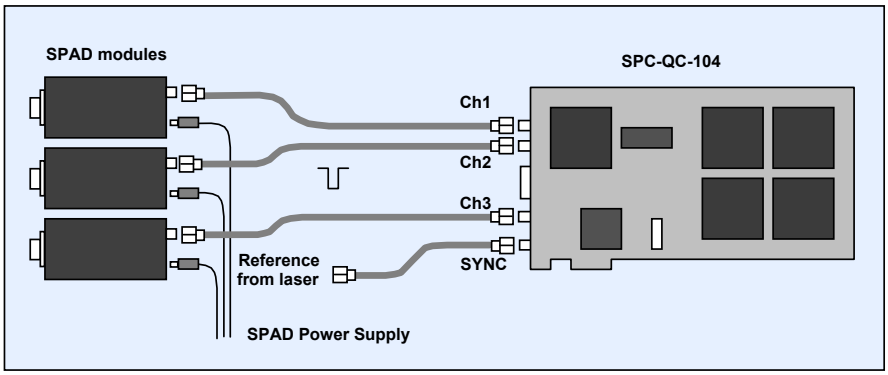


Fig. 357: Three-channel parallel detection system with three SPADs and an SPC-QC-104. Negative pulses.

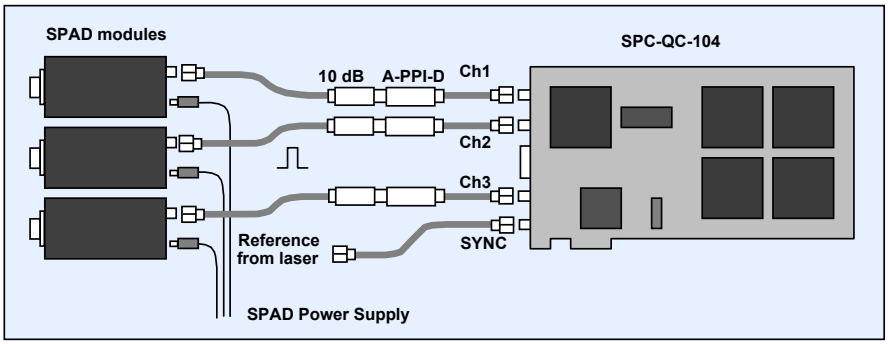


Fig. 358: Three-channel parallel detection system with three SPADs and an SPC-QC-104. Positive pulses.

Multi-Wavelength Systems

Fig. 359 shows how the bh PML-16-C and PML-16 GaAsP 16-channel detectors or the corresponding multi-wavelength detector assemblies are connected to a TCSPC system. The detector power supply comes from a DCC-100 detector controller which also provides for shutdown in case of PMT overload. The photon pulses of the detector are fed into the CFD input of the SPC module, the routing signals into the routing input.

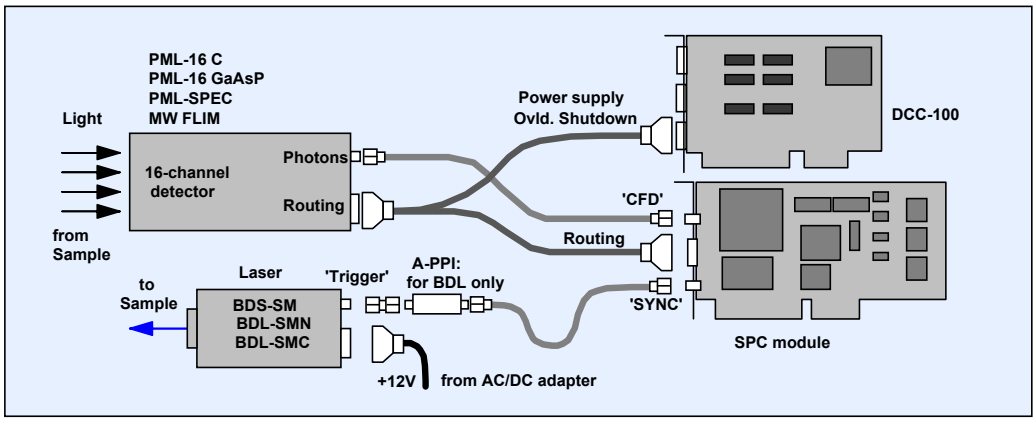


Fig. 359: 16-channel parallel detection system with the PML-16-C. The PML-16-C detector has an internal high-voltage generator and is fully controlled from the DCC-100 card.

Important: Monitor cables for PCs have the same connectors and generally the same connection scheme as the router and the power supply cables of the HRT, PMC and PML modules. However, some monitor cable have not all lines connected, or even have some pins connected in parallel. This can cause malfunction of the routers and detectors or even damage the SPC or DCC modules. Therefore, please use only the router and detector cables delivered with the SPC modules or routers.

Multi-Module Systems

A cable diagram for a system with two SPC modules is shown in Fig. 360. Two detectors are used, and each detector is connected to a separate SPC module. The detectors are controlled from the two outputs of a DCC-100 detector controller card. The SYNC signal is split into the two SPC modules by a 1:2 power splitter.

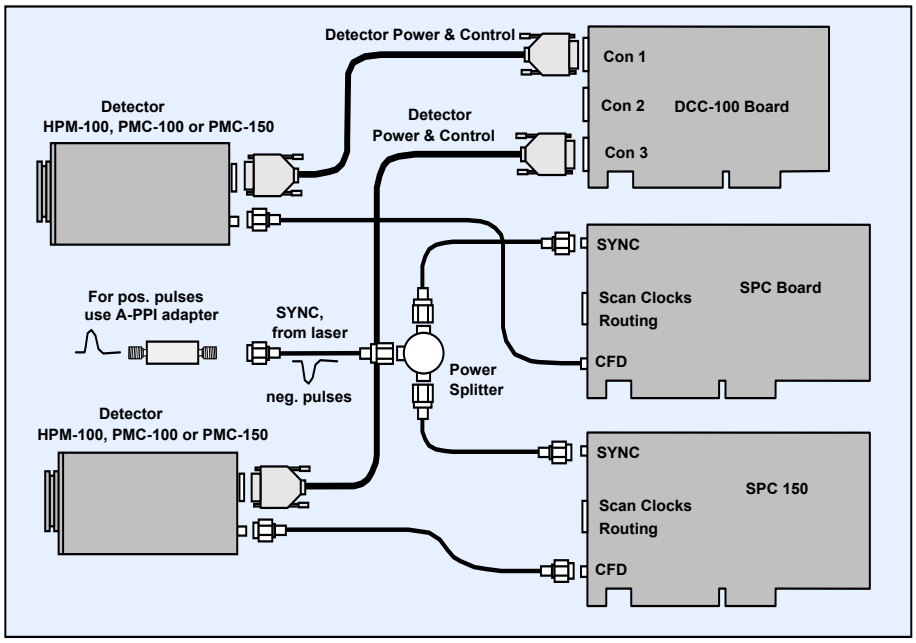


Fig. 360: Dual-module TCSPC system

Systems with up to four TCSPC channels can be built by the same principle. To operate the four detectors a second DCC-120 card must be used; the SYNC signal must be distributed by a 1:4 power splitter.

Phosphorescence Systems

The system connections for a single-detector (non-scanning) fluorescence / phosphorescence system are shown in Fig. 361. The system uses the principle described in Fig. 510, page 341. A ps diode laser is on-off modulated at the microsecond time scale, and photon times are determined both within the laser pulse period and the modulation period. Fluorescence decay curves are built up from the times in the laser pulse period, phosphorescence decay curve from the times in the modulation period.

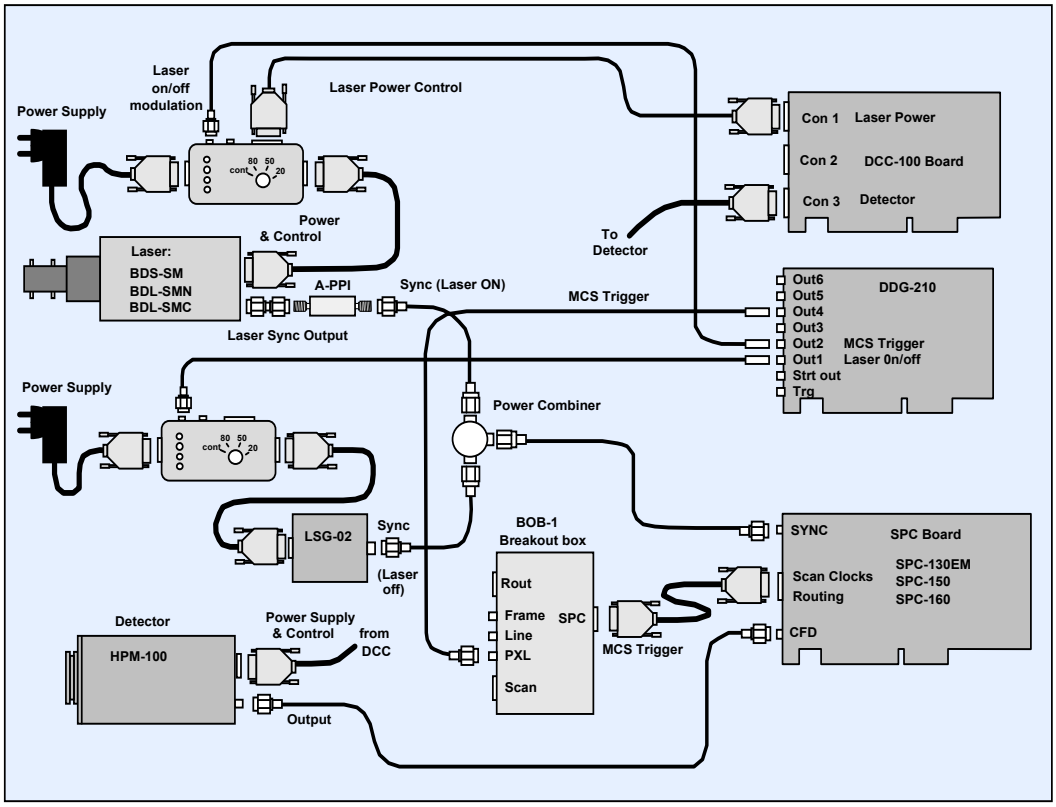


Fig. 361: Combined fluorescence / phosphorescence decay system

A BDS-SM, BDL-SMN, or BDL-SMC laser is used for excitation. The laser is on/off modulated by a signal from the DDG-210 pulse generator card. (The control of the card is integrated in the SPCM software, see 857) The power for the laser comes from a wall-mounted +12 V power supply, the intensity is controlled from a DCC-100 card. The power, the modulation signal, and the power control signal are connected to the laser through a small 'laser switch box' that comes with the laser.

During the 'laser-off' periods the laser does not deliver a SYNC signal. This signal is, however, needed for the TCSPC module to complete the recording cycle of each individual photon. An auxiliary SYNC signal is therefore generated by a LSG-02 SYNC generator module. Electronically, this module behaves like a BDL-SMC laser: It delivers pulses at a frequency controlled by a laser switch box, and can be on/off modulated by a TTL signal. The LSG-02 generator receives a control signal from the DDG-210 card that is inversed compared to that for the laser. Thus, the LSG-02 module delivers SYNC pulses when the laser does not, and vice versa.

The SYNC pulses from the laser and the LSG-02 module are combined and fed into the SYNC input of an SPC board. Any of the SPC-130EM, SPC-150, SPC-150N, and SPC-160 modules can be used. The SPC-830 can be used if it was manufactured later than May 2007 (serial number 3D0178). The timing reference ('MCS Trigger') for the times in the modulation period comes from the laser on-off modulation. It is fed into the SPC module via a BOB-1 box (see Fig. 364, page 233). The CFD pulses come from the detector. The detector should preferably be an HPM-100 hybrid detector. Conventional PMTs generate afterpulses which make it difficult to detect clean phosphorescence decay functions at times smaller than a few microseconds.

Using the Experiment Trigger

The SPC-6, -7, -8 and the SPC-130, -130EM, -150, -150N, and -160 modules have an 'Experiment Trigger' to start a measurement by an externally applied TTL/CMOS trigger signal.

The experiment trigger is a simple, but extremely powerful experiment control feature of the bh SPC modules. By using the experiment trigger complex experiment procedures can often be performed in the SPCM standard software, i.e. without the need of special DLL or LabView programming. Moreover, because the experiment trigger is a hardware function the response of the SPC modules to a trigger event is virtually immediate. The trigger can therefore be used for a number of real-time applications that are entirely beyond the capabilities of software control. A few typical applications are:

- Slow Scan applications. A sample is scanned by a step motor assembly or a piezo scan stage, or a spectrum is scanned by a step-motor-driven monochromator. After each step of the scan, the scan controller sends a trigger pulse to the SPC module. Each trigger initiates an individual measurement in the SPC module. The results can be saved in individual files, or written into a number of subsequent 'pages' of the memory. Page stepping can either be accomplished by using the page stepping function of the 'Single' of f(txy) mode, or the 'Continuous Flow' mode. Moreover, the fi(t) or fi(ext) spectrum scan modes can be used to convert the sequence of decay curves directly into time-resolved spectra.
- Measurement of signals that are present only during brief periods of time. A measurement is performed in the Oscilloscope, Single, or f(txy) mode. The measurement is started when the signal is present and continued for a 'collection time' corresponding to the typical dwell time of the signal. The results can either be accumulated, stored into subsequent memory blocks, or saved into individual files.
- Sequential recording ('double-kinetic mode'). Started by the experiment trigger, the SPC module records a hardware-controlled sequence of decay curves. In the 'continuous flow mode' or in the 'Scan Sync Out' mode the sequence can be as fast as a few µs per curve. To obtain a reasonable number of photons within a collection time this short a large number of triggers sequences can be accumulated (see 'Chlorophyll Transients', page 333).
- Starting the measurement synchronously in a multi-module system.

The electrical configuration of the experiment trigger input is shown in Fig. 362. The 51 Ω or 100 Ω series resistor and the diodes are built in for overvoltage protection. The 10 kΩ resistors provide a defined 'high' level when the input is open. Thus, the experiment trigger can either be driven from a standard TTL or CMOS gate or by a switch that connects the experiment trigger input to ground. Connecting the input to ground generates a falling, disconnecting it a rising trigger signal edge. To trigger a measurement by an optical pulse a phototransistor or photodiode can be connected from pin 13 to ground.

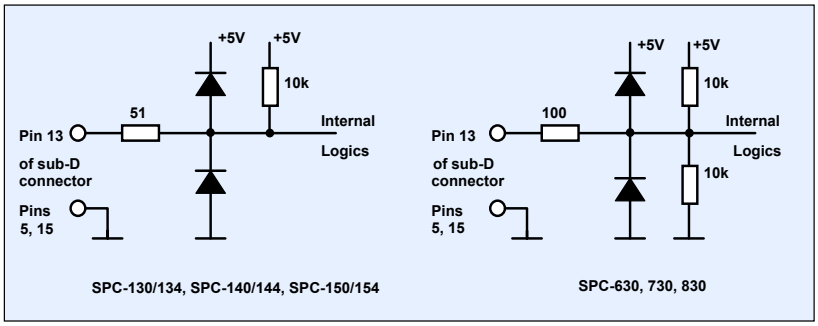


Fig. 362: Experiment trigger input

The experiment trigger input is connected to pin 13 of the 15 pin sub-D connector. For modules with two sub-D connectors, such as the SPC-830, the experiment trigger has to be connected to the *upper* sub-D connector. In some SPC modules the experiment trigger shares one pin with the 'Add/Sub' signal, see 'External Control Signals', page 961. The experiment trigger function is then only available if the system parameter 'Add/Sub Signal' is set to 'add only'. For details please see 'External Control Signals', page 961.

In SPC modules that have only one sub-D connector the experiment trigger and the routing signals have to be connected to the same sub-D connector. This can cause a cable conflict if a standard router cable is used. The conflict can be resolved by using the BOB-101 breakout box (see Fig. 364) or by a router cable with a trigger split-off. Suitable cables are available from bh, see Fig. 363.

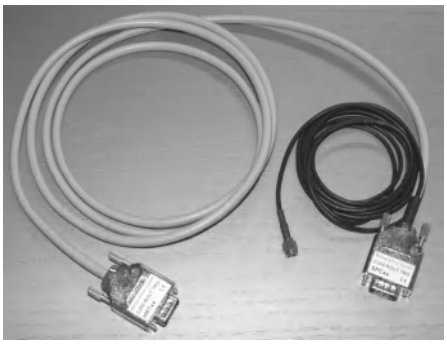


Fig. 363: Router cable with experiment-trigger split-off

To start the acquisition in a multi-module TCSPC system by an external event a trigger signal must be applied to all modules of the system. This is not only inconvenient, it is also not guaranteed that all SPC module will see the trigger pulse in exactly the same SYNC period. Therefore, the SPC-130EM, SPC-150 and SPC-160 modules have a 'Trigger Master' function. The trigger is applied to only one module (the master), but all modules are started simultaneously via an internal trigger synchronisation logics. The trigger master function is activated via the SPCM software. Important: The fan assembly for multi-module systems must be attached to the SPC modules to provide the trigger link between the modules.

Resolving Cable Conflicts

Cable conflicts may occur if signals from several sources have to be connected to one sub-D connector of an SPC module. A typical situation is when an SPC-130EM, SPC-150, SPC-150N or SPC-160 module is used in a multi-wavelength FLIM system. In this case the routing and scan clock signals have to be fed into the same sub-D connector. Problems may also occur if control signals from one source have to be distributed into several channels of a multi-module SPC system. The typical example is a multi-module FLIM system which requires the scan clocks to be connected to all SPC modules. These situations would require split cables which are difficult to build and inconvenient to handle. To allow users to build up TCSPC systems with standard cables bh deliver two 'breakout boxes'.

The BOB-101 box connects routing signals, an experiment trigger, an add/sub (or Marker 3) signal and the three scan clock signals from an optical scanner to one SPC-130EM, SPC-150, SPC-150N or SPC-160 module. The output side of the box is shown in Fig. 364, top, the input side in Fig. 364, bottom.

The BOB-104 box (Fig. 365) allows scan clock pulses and experiment trigger pulses to be distributed to four SPC modules. The output side of the box (shown in Fig. 365, top) connects to the SPC modules. An auxiliary +12 V power supply can be connected to the connector on the left. The input side of the BOB-104 box is shown in Fig. 365, bottom. From left to right, there are four connectors for routers or PML-16-C detectors, individual SMA connectors for the experiment trigger, the Add/Sub (or Marker 3) signal, and SMA connectors for the frame, line and pixel clocks from optical scanners. If the scan clocks are delivered via standard microscope scan connection cables, the can also be connected to the 15 pin 'Scan' connector. The connector on the right is a power output for the +12 V, +5 V, -5 V, and -12 V lines.



Fig. 364: BOB-101 breakout box. The box connects routing signals, an experiment trigger, an add/sub signal, and the three scan clock signals to one SPC-130EM, SPC-150, SPC-150N or SPC-160 module.

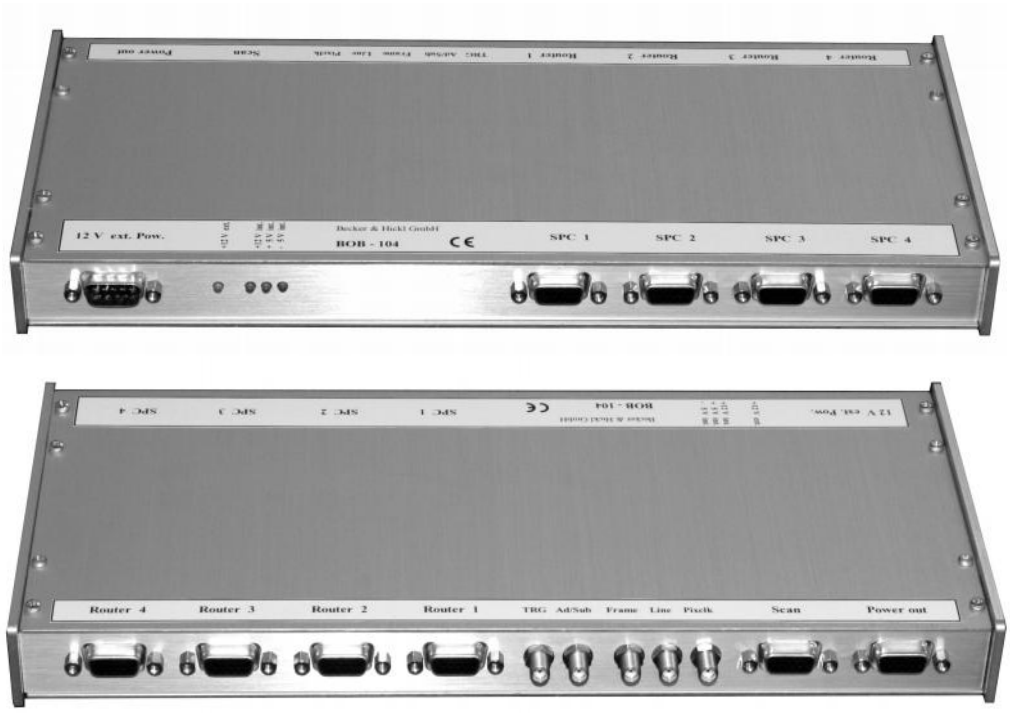


Fig. 365: BOB-104 breakout box. Top: TCSPC side. Left to right: Auxiliary +12 V input, status LEDs for power supply lines, 15 pin connectors to SPC modules. Bottom: Output side. Left to right: 15-pin connectors for routers, SMA connectors for TRG, Add/Sub or M3 and scan clock signals, 15-pin connector for scan clocks, 15 pin connector for power supply of external electronics.

FLIM Systems

TCSPC FLIM is based on scanning a sample with a focused laser beam, detecting single photons of the fluorescence light, and building up a photon distribution over the scan coordinates, and the time in the laser pulse period.

Superficially, the configuration of TCSPC FLIM systems does not differ much from the classic TCSPC implementation shown in Fig. 337. The obvious difference is that there is an additional cable connection from the optical scanner to the SPC module. The scan cable delivers pixel clock, line clock, and frame clock pulses from the scanner to the SPC card. The SPC card uses these pulses to determine the spatial location, x,y, of the laser beam in the scan area in the moment when a photon is detected. The major difference is in the optical system: The optics of a classic FLIM system records photons just records photons from a fixed spot in the sample. The optical FLIM system has to scan the sample with the beam of the excitation laser and transfer the fluorescence (or phosphorescence, see page 434) photons to the detector. The principle is shown in Fig. 366.

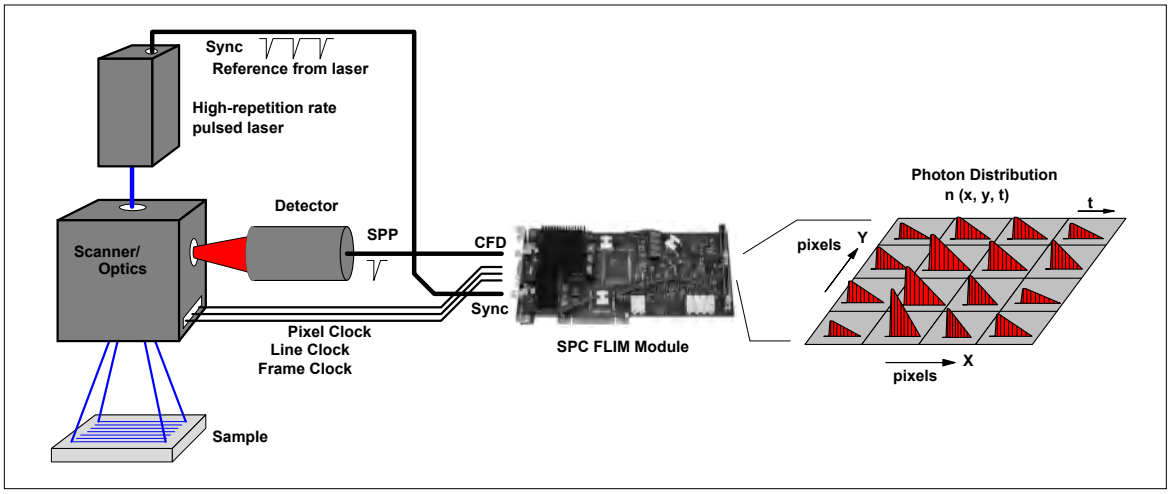


Fig. 366: Basic principle of a TCSPC FLIM system

The recording process works as described under ‘FLIM: Scan Sync In Mode’ and ‘FIFO Imaging Mode’: The scanner runs a repetitive raster scan over the sample. The SPC module tracks the scanner position by continuously counting the scan clock pulses delivered by the scanner. When the SPC module detects a photon pulse it determines the time of the photon in the laser pulse period. By doing so for a large number of photons, the SPC module builds up the distribution of the photons over the time in the laser period and the scan coordinates. The result is a data array that represents the pixels of the scan, with a large number of time channels in each pixel. The photon numbers in these time channels represent the fluorescence decay function, see Fig. 366, right.

Adding more Detector Channels: Parallel TCSPC

More detector channels can be added as shown in Fig. 367. Within the optical system, the light is split into several spectral (or polarisation) components. The components are detected by separate detectors which are connected to separate SPC modules. The advantage of using parallel TCSPC channels is that the maximum count rate of the system is multiplied by the number of modules. Moreover, there is no electrical crosstalk between the channels. Even if one TCSPC channels saturates in bright pixels, the other one still delivers correct data. Because of these advantages all bh FLIM systems with two detector channels currently use parallel TCSPC architecture [68, 69]. A system with 8 parallel channels has been described in [97] and [158].

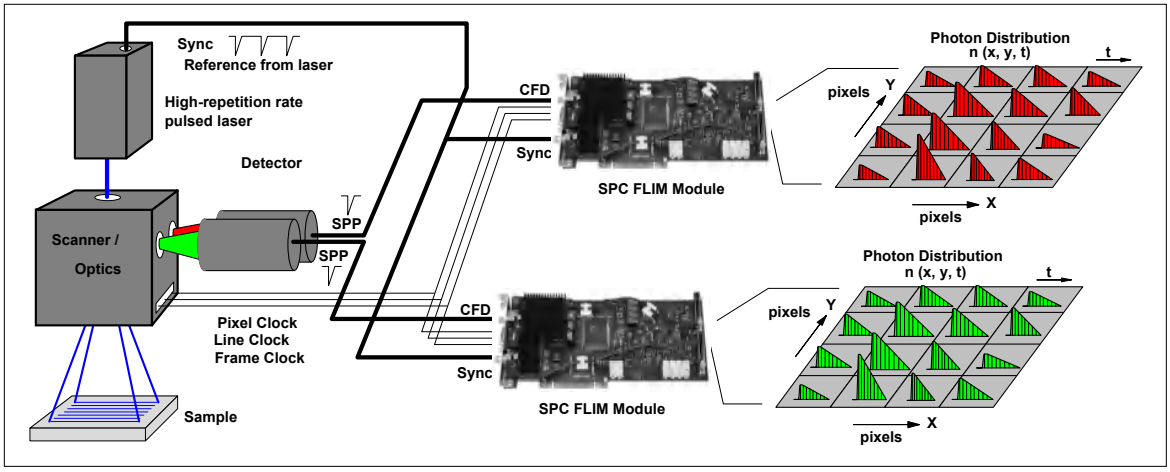


Fig. 367: Recording in two detector channels by parallel TCSPC modules

Adding More Detector Channels: Routing

A second way to simultaneously detect in several detector channels is 'Routing', see Fig. 368. A router combines the photon pulses of both detectors and marks the photons with their detector numbers. The photon are then recorded in a single TCSPC module. The TCSPC modules produces lifetime images that contain individual decay curves for each detector in their pixels. A large number of FLIM systems with routing configuration are in use. The disadvantage is that the throughput rate is that of one TCSPC modules, and that overload in a pixel of one channel can cause an artefact in other channels. Routing systems for two, three, and four detectors are therefore more and more replaced with multi-module systems. However, the advantage of the routing technique is that it makes large numbers of detector channels feasible, see below.

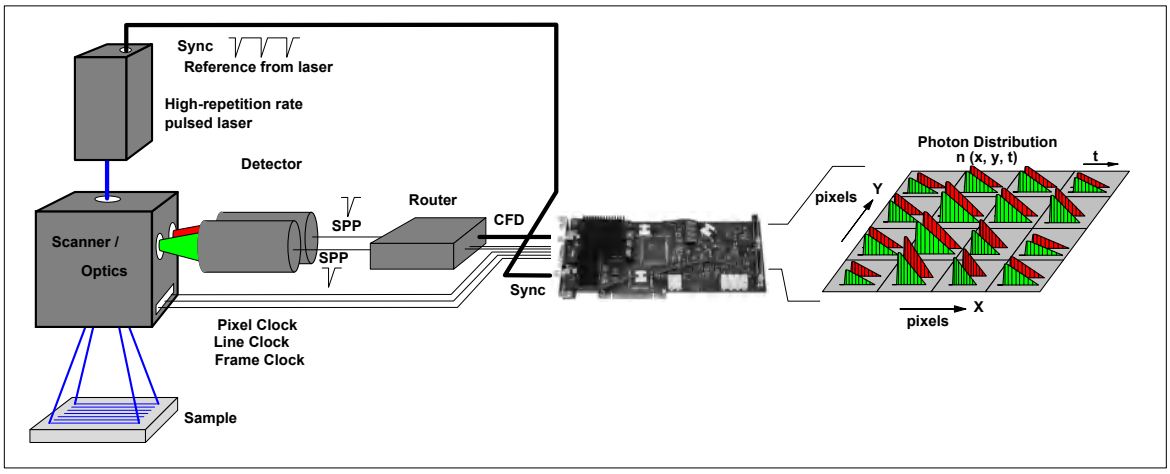


Fig. 368: Recording in two detector channels by routing

Adding More Detector Channels: Multi-Wavelength FLIM

The routing principle can be extended to multi-wavelength FLIM. The principle is shown in Fig. 369. The light from the sample is dispersed by a polychromator, and the spectrum projected on a PML-16 multi-channel PMT with routing electronics [62, 95, 156]. The SPC module builds up a photon distribution over the scan coordinates, the photon arrival time, and the wavelength of the photons. The recording principle is explained in detail in Fig. 218, page 126. Please see also 'Multispectral FLIM' and 'Multiphoton Multispectral NDD FLIM'. page 366 and 367.

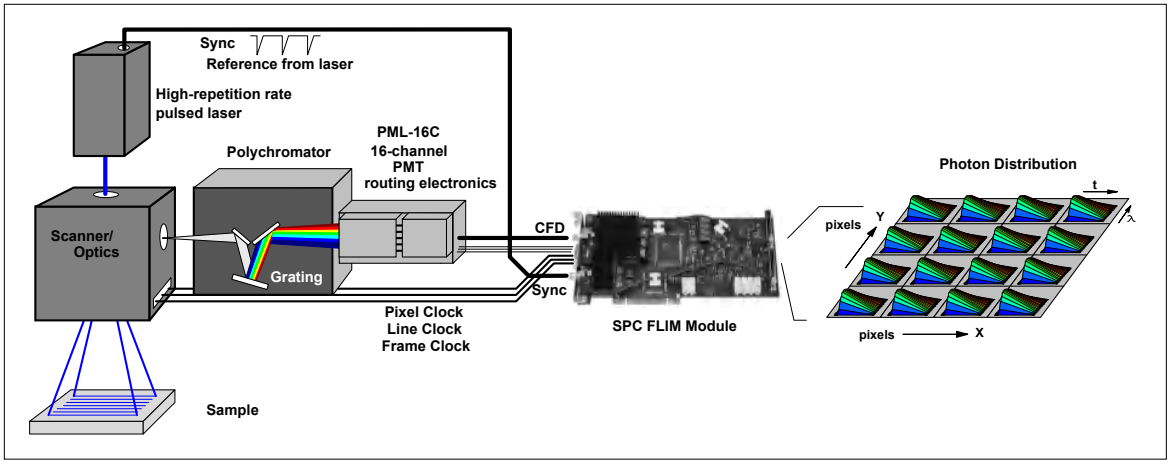


Fig. 369: Multi-wavelength recording

Beam Scanning

The preferred way of scanning is fast optical beam scanning. Normally, scanning is performed by two galvanometer mirrors. One mirror deflects the beam in x, the other in y. The motion of galvanometer mirrors can be very fast, with scan rates of about 500 lines per second. Optical scanners are relatively complex optical devices, with beam combiners for several lasers of different wavelength, a dichroic beamsplitter that separates the fluorescence signal from the excitation light, a pinhole to suppress out-of-focus light, and beamsplitters and filters for several detection beam paths. Please see 'Chapter Time-Resolved Laser Scanning Microscopy', page 343.

There are also other optical scanning principles. Resonance scanners are very similar to galvanometer scanners. The difference is that one of the mirrors - usually the on for x - is operated in a resonance mode. This way, a faster scan rate than for a galvanometer mirror can be achieved. The drawback is the scan speed cannot be changed, and that the scan trajectory is sinusoidal, not linear as in the case of the galvanometer mirror.

Polygon scanners use a fast-rotating polygon mirror for deflection in x. Polygon mirrors can be made extremely fast, with speeds of several 1000 lines per second. The disadvantage is that the scan amplitude cannot easily be changed.

For galvanometer systems, the synchronisation of the TCSPC process with the scanning is performed via pixel, line. and frame clock pulses from the scanner. Resonance scanners and polygon scanners often do not deliver a pixel clock. In these cases the bh TCSPC systems can be run at an internal pixel clock. Please see ‘Scan Sync In Mode’, page 753 and 'FIFO Imaging Mode', page 762 for system parameter setup.

Sample Scanning

Scanning can also be performed by keeping the laser beam stationary and move the sample instead. The principle is described in section 'Scanning Systems with Piezo Stages', page 451. The advantage of sample scanning (or ‘stage scanning’) is that it is optically simple. The drawback is the slow scan rate. Focusing and positioning the sample becomes a nightmare, and acquisition times are extraordinarily long. Moreover, sample scanning induces motion in the sample. It is therefore not recommended for biological applications.

Synchronisation of the SPC module with the scanner is achieved by the same scan clock pulses as for the beam scanner.

Scanner Control by GVD-120 or GV-140 Module

Scanner control is needed if a FLIM system is added to a conventional microscope. In this case, scanning is performed either by user-built scanners, or by the bh DCS-120 scanhead. To generate the scan waveforms, the pixel, line and frame clocks, and the laser on/off signals for these systems bh have developed the GVD-120 and GVD-140 scan controller cards. The cards controls both axis of a galvanometer or piezo scanner, and two ps (GVD-120) or four (GVD-140) ps diode lasers. A control panel for the GVD-120 and GVD-140 cards is integrated in the SPCM software. By using the GVD cards, that the scanner control becomes fully integrated in the data acquisition software. Please see page 849 for details.

Cable Diagrams of FLIM Systems

Cable diagrams for typical FLIM configurations are shown in the following paragraphs. Please note that bh FLIM systems are modular, and a wide variety of system configurations are possible. The diagrams in the paragraphs below provide general information but may not accurately reproduce the connections in a particular system. For wiring diagrams of standard bh FLIM systems for special microscopes please see [68, 69, 76, 77].

Single-Detector Multiphoton FLIM Systems

Fig. 370 shows two single-detector systems for a multiphoton microscope with non-descanned detection. The system shown on the left just contains a detector, a TCSPC module, and a detector controller. The detector pulses are fed into the CFD input the TCSPC module. Any FLIM-capable module can be used - the system works with the SPC-150, the SPC-150N or SPC-150NX, the SPC-160, and the SPC-180N or NX. Even older SPC-830 or SPC-730 modules work. The SYNC signal is obtained directly from the laser. In most two-photon microscopes a suitable signal is delivered by the Ti:Sapphire laser. The signal is normally positive. Therefore an A-PPI pulse inverter is inserted in the SYNC line. The scan clock signals of the microscope controller are connected to the sub-D connector of the SPC module.

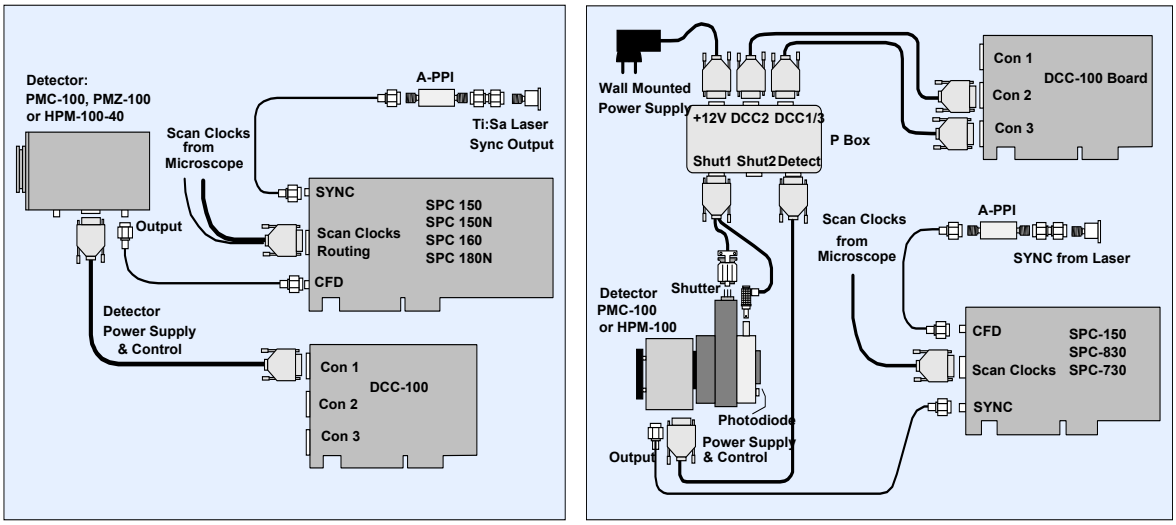


Fig. 370: Wiring Diagrams of FLIM systems for non-descanned detection. Left: Basic configuration. Detector control via DCC-100. Right: Detector protected by shutter. Detector and shutter control via DCC-100.

FLIM systems like the one shown in Fig. 370, left, have been used in large quantities for the Zeiss LSM 510 NLO multiphoton microscopes. The problem with this microscope was that, by a simple operator error, the epi-fluorescence lamp could shine directly in the detector. The systems therefore had a shutter which closed the detection beam path when the light intensity was exceedingly high. The cable diagram is shown in Fig. 370, right. Both the detector and

the shutter are controlled via the DCC-100 detector controller card. A shutter control signal is provided at connector 2 of the DCC-100. The ‘P- box’ (power saving box) reduces the current in the shutter coils when the shutter is open and thus avoids heating of the detector by the shutter. Moreover, the box combines the overload signal of the PMC-100 detector with an overload signal from a photodiode in front of the shutter. This prevents unintentional opening of the shutter when the microscope lamp is on.

Dual-Channel Multiphoton FLIM System

FLIM systems with two parallel channels are shown in Fig. 371. The system uses two detectors and two SPC-150, SPC-150N, SPC-150NX, SPC-160, or SPC-180N or NX modules. The detectors are controlled by a DCC-100 module. The SYNC signal from the laser is split by a reflection-free power splitter and fed into the SYNC inputs of the SPC modules. In Fig. 371, left, the scan clocks are connected to both SPC modules by a split cable.

The solution in Fig. 371, left, is simple and straightforward. However, there is no way to connect additional control signals to the SPC modules. This can be a problem for advanced FLIM techniques, such as Z-stack imaging, FLITS of PLIM. The system shown in Fig. 371, right, therefore connects the scan clock signals via a BOB-4 signal distribution box. If needed, the BOB-4 box combines additional control signals into the 15-line cables to the SPC modules. Moreover, the setup allows to add up to two additional detectors and SPC modules to the system.

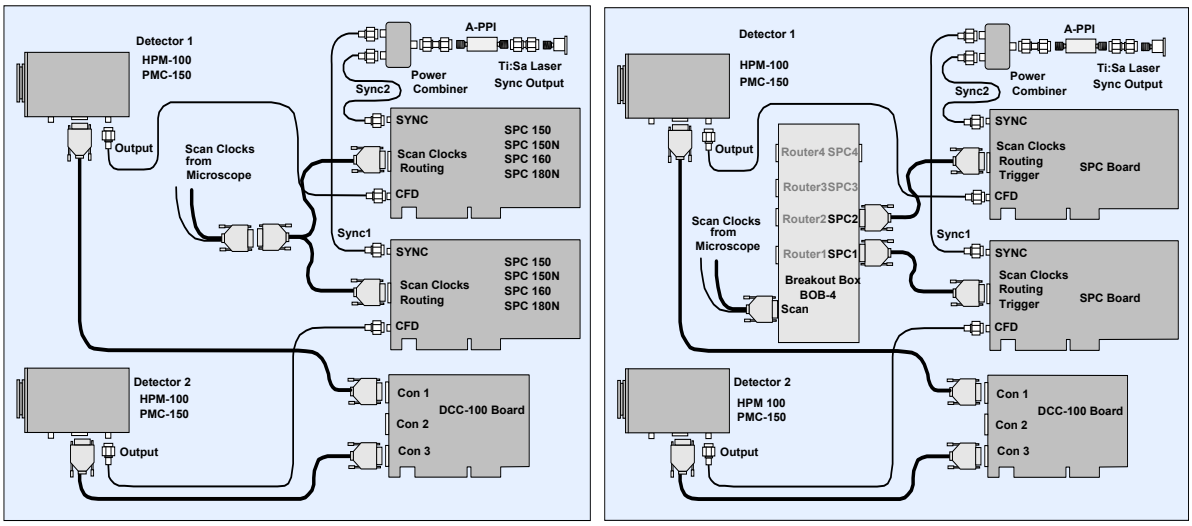


Fig. 371: Dual-Channel FLIM multiphoton FLIM systems

Confocal FLIM Systems

Two examples of confocal (one-photon) FLIM systems are shown in Fig. 372. A single-channel system is shown on the left. The basic system connections are the same as for the multiphoton system. However, a BDS-SM or BDS-SMN ps diode laser is added to the system. It is controlled from the 'Con3' and the 'Con2' ports of the DCC-100 via a LSB-C laser switch box. Con3 delivers a power control signal, Con2 an on/off signal.

Fig. 372, right, shows a one-photon system with two TCSPC channels and two lasers. Compared with the multiphoton system there are two BDS-SM or BDL-SMN lasers, and an additional DCC-100 which controls the lasers. The SYNC signals from the lasers are first combined into a single SYNC line by a power combiner, and then distributed to the SPC modules by a power splitter.

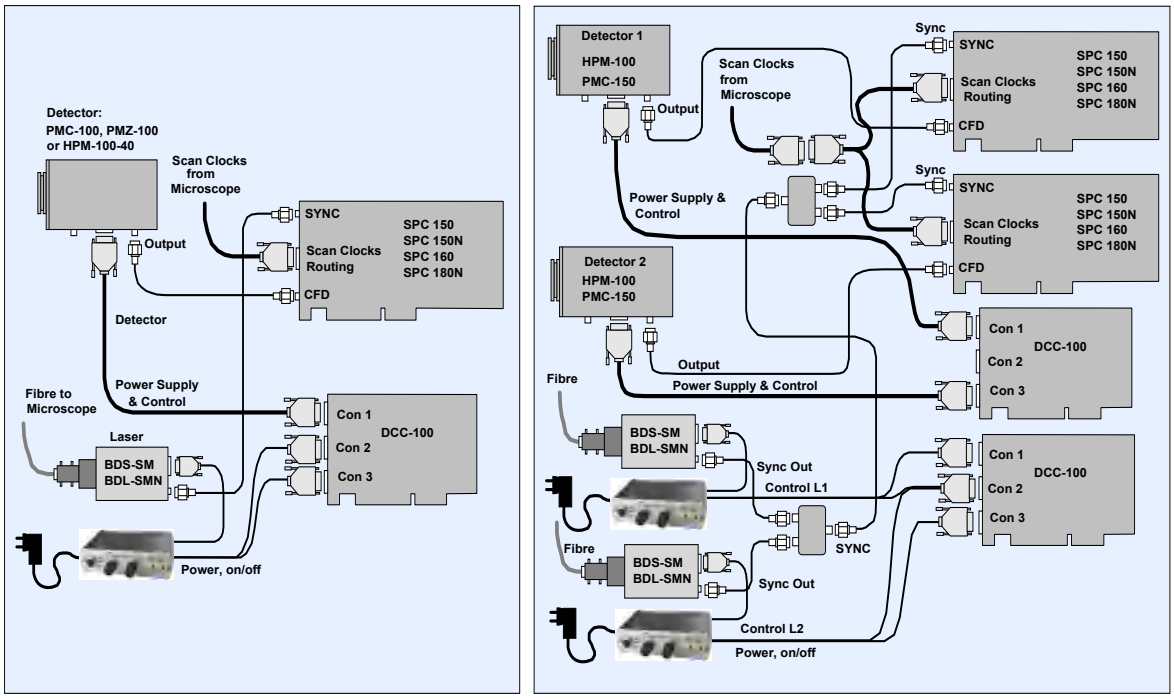


Fig. 372: Confocal FLIM systems. Left: One FLIM channel and one laser. Right: Two FLIM channels and two lasers.

Multi-Wavelength FLIM Systems

A multiphoton multi-wavelength FLIM system with an SPC-150, 150N, or 160 TCSPC module is shown in Fig. 373. The system used the PML-16-C or PML-16 GaAsP multi-wavelength detector. The photon pulse output is connected to the CFD input. The routing signals have to be fed into the 15-pin routing and control input of the SPC module. In the SPC-150 and SPC-160 the scan clocks and the routing signals share the same 15 pin sub-D connector. Therefore a BOB-1 ‘breakout box’ is used to feed both the clocks and the routing signals into this connector.

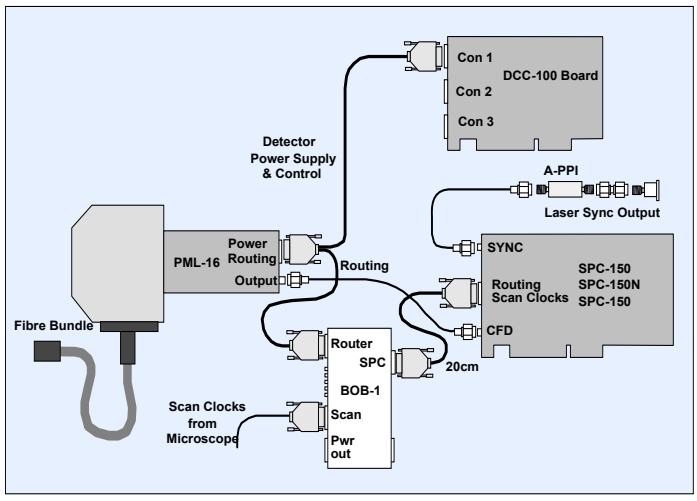


Fig. 373: Multi-wavelength NDD FLIM system with SPC-150 or SPC-160

Fig. 374 shows a multi-wavelength FLIM system with an SPC-180 module. Starting with serial number 25 SPC-180 modules have two 15-pin control connectors. Therefore a BOB-1 box is not needed. The routing signals from the detector are connected to one connector, the scan clocks to the other.

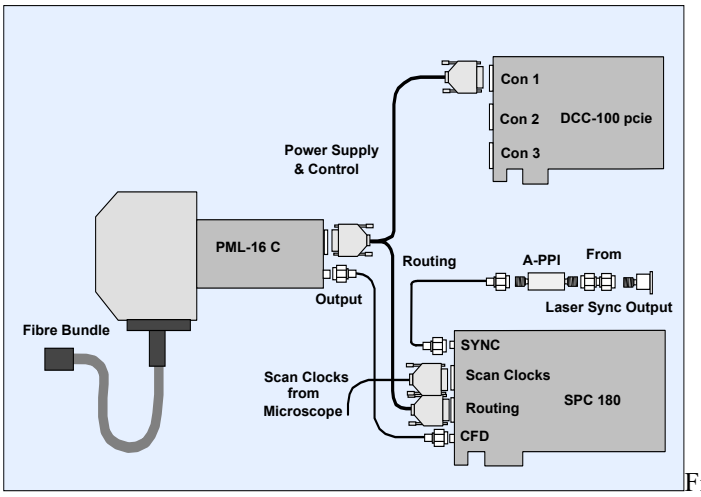


Fig. 374: Multi-wavelength NDD FLIM system with SPC-180

FLIM / PLIM System for a Two-Photon Microscope

A combined FLIM/PLIM system for a two-photon microscope is shown in Fig. 375. The modulation signal for the laser is generated by a DDG-210 card. To synchronise the laser modulation with the scanning the DDG-210 is triggered by the pixel clock of the microscope. The DDG-210 also generates a routing bit for the SPC-150 board. This bit is used to distinguish between photons in the laser-on (fluorescence) and laser-off (phosphorescence) periods [69]. A BOB-1 box is used to split off the pixel clock to the DDG card, and to combine the scan clocks from the microscope and the routing bit into the standard 15-pin cable to the SPC-150 board. The detector is an HPM-100 hybrid detector. It is controlled the usual way by a DCC-100 detector controller. The SYNC signal comes from the Ti:Sapphire laser of the laser scanning microscope. Its polarity is reversed by an A-PPI-D pulse inverter.

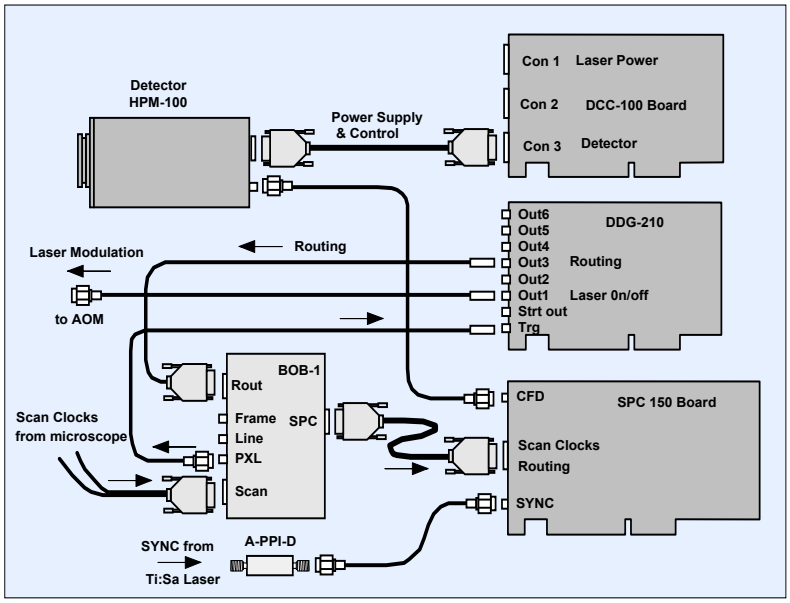


Fig. 375: FLIM/PLIM system for two-photon microscope. The AOM of the microscope is controlled from a DDG-210 pulse generator card.

Piezo-Stage Systems

A cable diagram piezo scanning system with a GVD-120 scan controller is shown in Fig. 376. The GVD-120 ramp voltages generated by the GVD-120 scan controller are connected to the driver amplifier of the piezo stage. If the driver amplifier allows for it is recommended to use

both differential signals +X, -X and +Y, -Y, for both coordinates. This suppresses possible noise from the environment.

The signal acquisition in the TCSPC board is synchronised with the scanning via frame, line, and pixel clock pulses. These signals are connected to the 15 pin connector of the TCSPC module. The GVD-120 also controls a BDL-SMC diode laser. The laser power can be adjusted and the laser can be turned on and off by the user, and the laser is switched off during the line and frame flyback of the piezo stage. If a second laser is used this can be controlled the same way. In addition, the lasers can be multiplexed for dual-wavelength excitation.

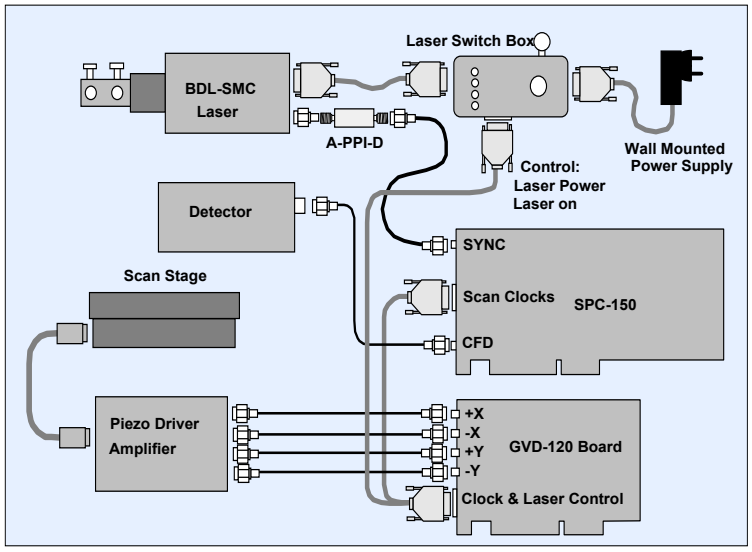


Fig. 376: Piezo stage scanning system controlled by the bh GVD-120 board.

For optical system setup please see ‘Scanning Systems with Piezo Stages’, page 451, for system parameter setup see ‘Scanner Control via the GVD-120 Card’, page 849’.

Other FLIM Systems

There are other FLIM systems, such SPC-730 or SPC-830-based systems, systems with R3809U detectors, dual-detector systems with a router, or multi-module systems with shutters. These systems are no longer manufactured. Because of space restrictions, the cable diagrams have been removed from this edition of the TCSPC handbook. If you need them, please see 8th edition.

DCS-120 Confocal and Multiphoton FLIM System

The bh DCS-120 confocal and multiphoton FLIM system [68] is a complete laser scanning FLIM microscope based on a research-grade microscope, the bh DCS-120 scan head, and bh TCSPC electronics. It uses fast scanning by galvanometer mirrors and highly sensitive and ultra-fast hybrid detectors. The one-photon versions use one or several picosecond diode lasers for excitation, the multiphoton version a Ti:Sa laser of a femtosecond fibre laser. Detectors of one-photon systems are attached to direct optical outputs of the scan head. Detectors of multiphoton systems are attached to a direct port of the microscope via non-descanned beam optics. The scanner and the lasers are controlled directly via a GVD-120 scan controller card, the detectors by a DCC-100 detector controller card. Both cards are included in the TCSPC system and controlled from bh's SPCM data acquisition software, see ‘Scanner Control’ page 849. The system can be supplemented by a software-controlled motorised sample stage for mosaic scanning and an acousto-optical beam modulator for Ti:Sa and fibre lasers, see 'Ti:Sa Laser and AOM Control', page 858.

The DCS-120 is a fully 'integrated' system, meaning that there is only one piece of operating software, and only one computer to run the system. Data analysis is performed by bh's SPCImage NG data analysis software, see chapter 'SPCImage NG Data Analysis Software'. The DCS system has a high degree of modularity. Therefore it can also be used to upgrade existing microscopes with laser scanning and FLIM, to build special scanning systems for other applications. A version of the system without a microscope is available in form of the DCS-120 MACRO system. It scans samples as large as 15 x 15 mm directly in the primary focal plane of the scan head [1131]. The following section gives an overview on the DCS-120 system, details and applications are described in a separate handbook, please see [68].

System Architecture

The optical principle of the DCS-120 scan head is shown in Fig. 377.

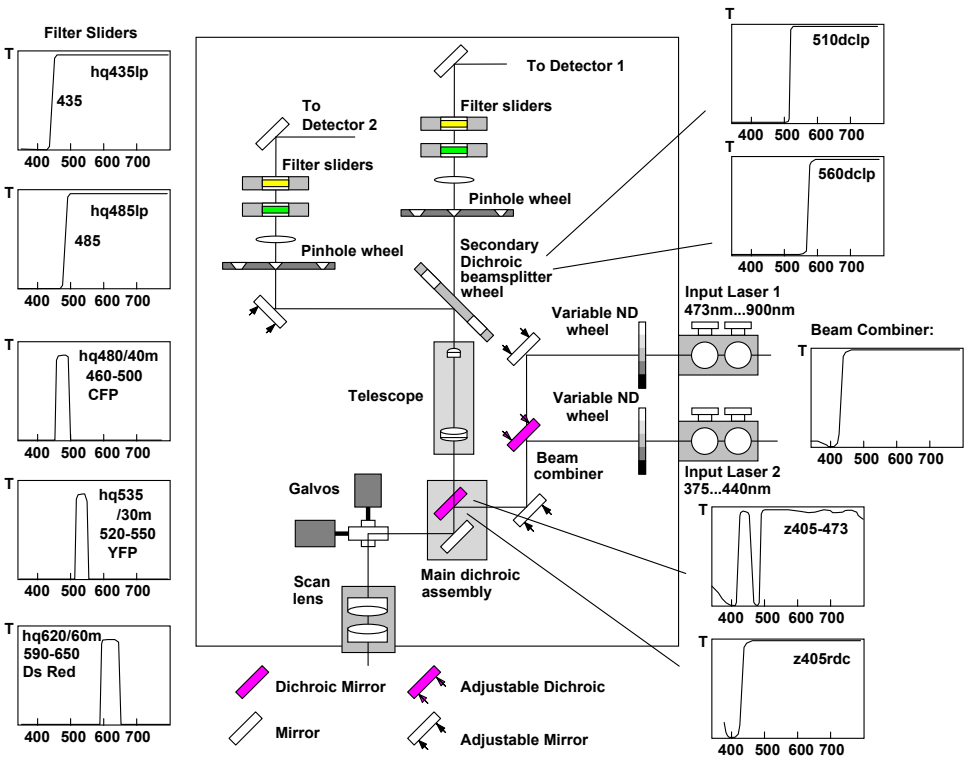


Fig. 377: Schematic diagram of the DCS-120 scan head with characteristics of standard filters and dichroics

The scan head has two input channels for bh BDL-SMC or BDS-SM lasers, two confocal detection paths, internal beamsplitters and filters, individually selectable pinholes, and two outputs for detectors. The detectors are attached to the back of the scan head. Free-beam coupling is used to minimise coupling loss and reflections. Scanning is performed by fast galvanometer mirrors. For details please see handbook of the DCS-120 system [68].

The electronic system components are shown schematically in Fig. 378. The scanner is controlled by a bh GVD-120 scan controller and a bh GDA-120 scan amplifier. The GVD-120 controls also the lasers. Laser control includes beam blanking during the flyback, laser multiplexing, on/off modulation for PLIM, and intensity regulation.

In principle, the DCS-120 system can be operated with a wide variety of detectors, e.g. the bh PMC-150, the PMCS-150, the Hamamatsu H7422-40 and R3809U, and the id-Quantique id100-50 SPADs. However, in the past 5 years, these detectors have been entirely be replaced with the bh HPM-100-40 and -06 hybrid detectors. The hybrid detectors are not only more sensitive, they also have a clean and fast IRF (19 ps for the -06 version), low dark count rate, and no background counts by afterpulsing. For systems which have both confocal and non-descanned detection a pair of HPM-100 detectors can be attached to both ports. Each pair of detectors can be activated or de-activated by software, thus achieving full software control of the system.

The only application where the HPM-100 detectors cannot be used is multi-wavelength FLIM. Multi-wavelength detection is available by using the bh MW FLIM assembly. Two MW FLIM assemblies can be coupled to the output ports of the DCS-120 scan head or to the NDD optics via the usual fibre bundle, see 'PML-SPEC and MW-FLIM Systems', see 191 [62]. The MW FLIM detectors are controlled via a DCC-100 detector controller card.

At the beginning, the TCSPC system of the DCS-120 system consisted of two parallel SPC-150 TCSPC/FLIM modules. With the introduction of new module types, the configuration changed to two SPC-150N or SPC-150NX modules, two SPC-160 modules, and, recently, to two SPC-180NX PCI-Express modules. In PCI-Express systems also the original GVD-120 and DCC-100 cards were replaced by PCI-Express versions.

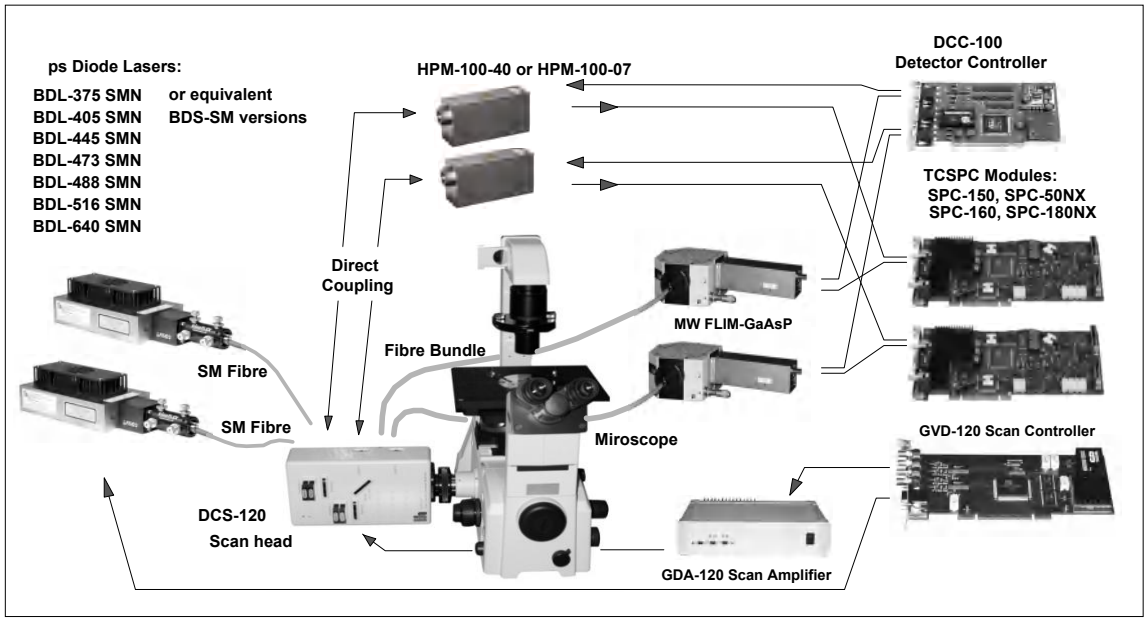


Fig. 378: DCS-120 confocal scanning FLIM system. Standard configuration with ps diode lasers and two parallel SPC-150 modules.

Since 2021 the DCS-120 confocal system can be equipped with the LHB-104 'Laser Hub'. That means, there are four laser available, two of which can be operated simultaneously and multiplexed with the pixels, lines, of frames of the scan.

An example of the main panel of a DCS-120 system is shown in Fig. 379. The system uses two SPC-180NX cards, a DCC-100PCIE detector controller, and a GVD-140PCIE scan controller. The panel is shown with online lifetime display of two images, with decay-curve display, and control of four lasers of the LHB-104 Laser Hub.

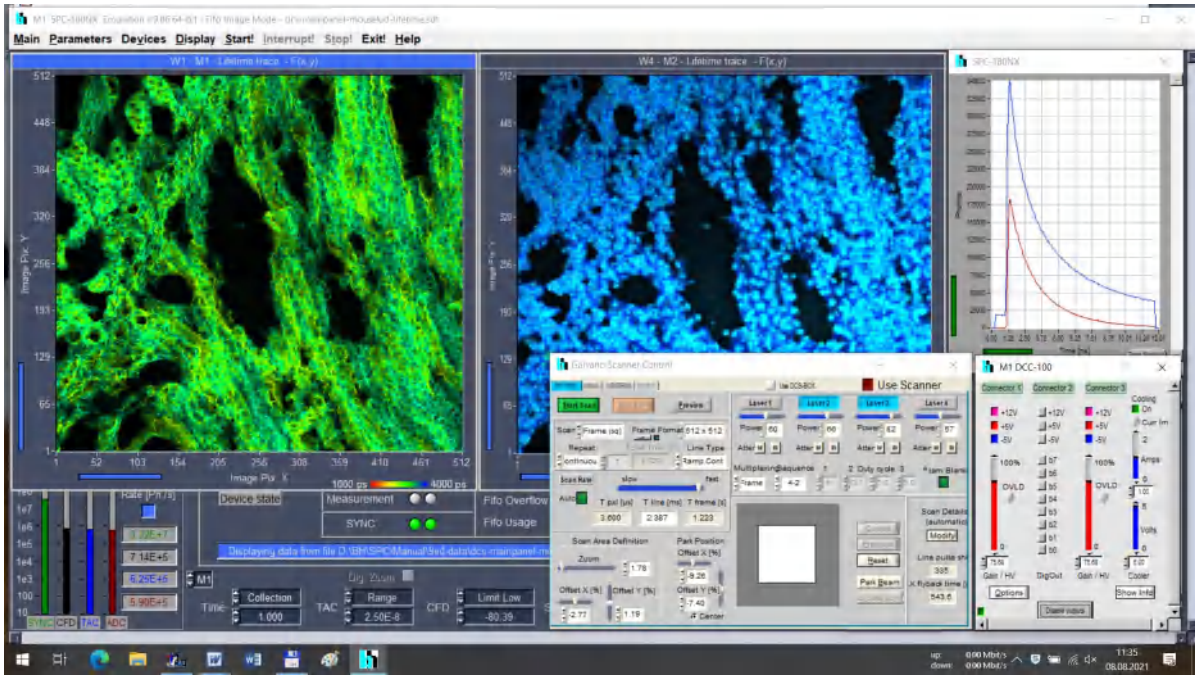


Fig. 379: SPCM main panel of a DCS-120 scanning system. Dual-SPC-180NX system with DCC-100PCIE and GVD-140PCIE. Lifetime images of both channels displayed, decay curve display, scanner control and detector control panels open

DCS-120 System Connections

As shown in Fig. 378 the DCS-120 FLIM systems contain a DCS-120 scan head, a GVD-120 scanner control card, a scan amplifier, one or two BDL-SMN diode lasers, one or two single-wavelength or multi-wavelength detectors and one or two TCSPC modules. The GVD card sends position signals to the scanner, power control and on/off signals to the lasers, and scan clocks to the TCSPC modules. There may be routing signals sent from multi-wavelength detectors to the TCSPC modules, and a laser multiplexing signal from the GVD-120. The connections are different for different system configurations, resulting in a confusing variety of different cables. The DCS-120 system therefore comes with a ‘DCS Box’ which makes the system setup straightforward and provides for some amount of system flexibility. The box is shown in Fig. 380.



Fig. 380: Connection Box of the DCS-120 system, front side (left) and rear side (right)

The DCS Box distributes the scan clock pulses of the GVD-120 scan controller to the TCSPC modules and the on/off and power control signals to the lasers. The DCS Box has also the

function of the ‘Laser Switch Box’ of the BDL-SMN or BDS-SM lasers [81] integrated. The lasers are therefore connected to the DCS Box directly, i.e. without the laser switch box.

The DCS Box also provides flexibility in combining the routing signals of PML-16 detectors or routers with a routing bit from the laser multiplexing control logics of the GVD-120. Moreover, two external experiment control bits may be added to the routing data. The way the signals are fed into the routing lines of the SPC modules is configured by a ‘Configuration’ switch at the DCS box. This switch is factory-set depending on the configuration of the FLIM system. *Please do not change the switch setting unless you have good reasons to do so*. The switch positions for different routing and multiplexing configurations are shown in Fig. 380.

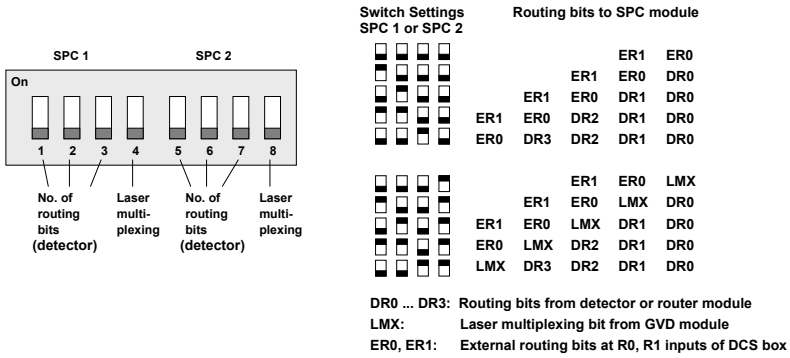


Fig. 381: Configuration switch of DCS Box

DCS boxes manufactured from October 16, 2009 or Ser. No. B30012 can be configured electronically from the scan control panel, see Fig. 382. The electronic configuration overwrites the DIP switch settings. The configuration date are stored in the .sdt and .set data and setup files. When a system configuration is loaded via the predefined setup panel, or a new setup or data file is loaded the DCS box configuration changes automatically.

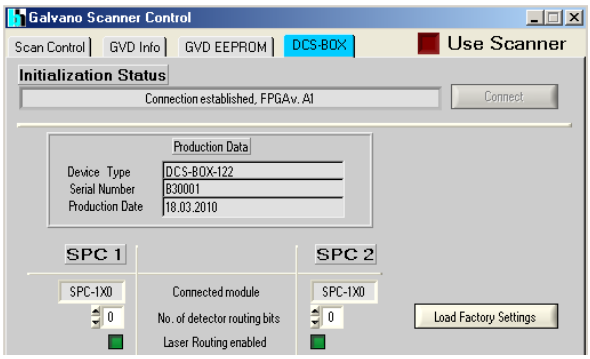


Fig. 382: Configuration panel of the DCS switch box

With the DCS Box most of the system connections are provided by standard 15-pin cables, see Fig. 383. Please use only the 15-pin cables delivered by bh. There are PC monitor cables with the same connectors. These often do not have all pins connected, or some pins may even connected in parallel. Using such cables may result in malfunction or even damage of components of the DCS system.

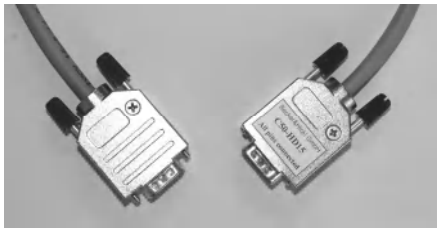


Fig. 383: Standard 15 pin cable for connecting subsystems of the DCS-120 system

A wiring diagram of a typical DCS-120 confocal scanning FLIM system is shown in Fig. 384. The system has two BDL-SMN or BDS-SM lasers and two PMC-100 detectors. The signals of the two detectors are processed in two parallel SPC-150 TCSPC modules.

Systems with one detector and one SPC-150 module are similar, except for the fact that one detector, one SPC-150 and the power splitter at the SPC end of the SYNC cable are omitted. For systems with one laser the second laser is omitted, and the SYNC cable is connected to the TRG output of the laser directly, i.e. without the power splitter.

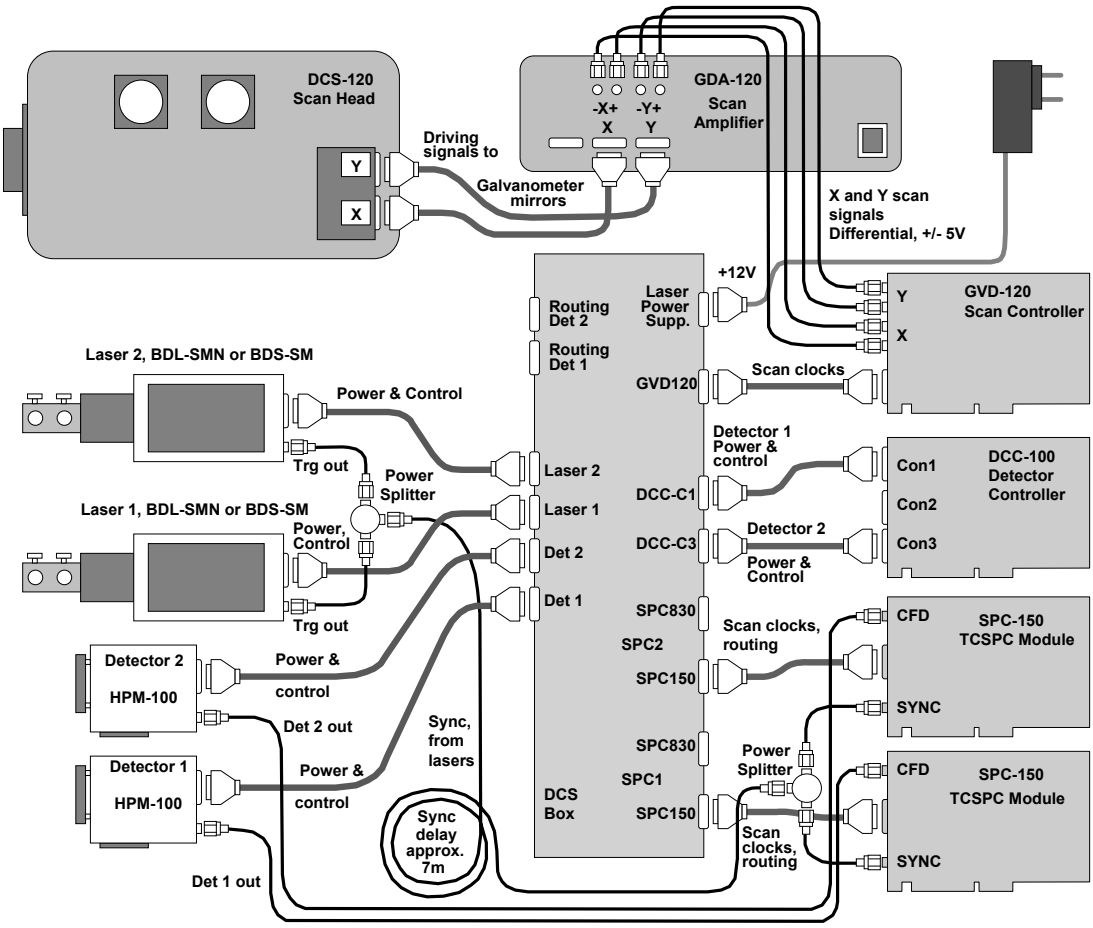


Fig. 384: DCS-120 system with two lasers, two PMC-100 detectors, and two SPC-150 TCSPC channels

The configuration switch setting of the DCS Box is shown in Fig. 385. Each SPC-150 module works with one detector, the number of detector routing bits is thus zero. The laser multiplexing bit is enabled.

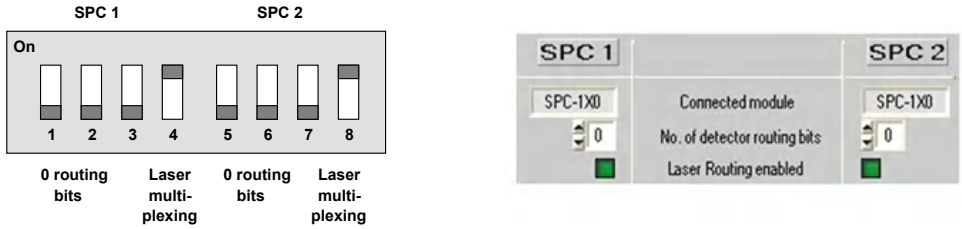


Fig. 385: Configuration switch settings of the DCS box. Left: By DIP switches. Right: By software. Dual-SPC-150 system with two single-wavelength detectors

A wiring diagram of a DCS-120 system with two MW FLIM multi-wavelength detectors is shown in Fig. 386. The MW detectors have the usual 15-pin connector for the power supply and control inputs for bh detector modules. However, they also deliver a 4-bit routing signal. This routing signal is delivered at different pins of the same 15-pin connector. The routing signal is therefore derived from the connector via a split cable. The end marked with ‘Routing

/ SPC' is connected to the routing input of the DCS box, the end marked with 'Power / DCC' is connected to the 'Detector 1' and 'Detector 2' outputs of the box. Inside the box, the routing signals are fed into the signal lines of the 15 pin (SPC-150 / lower SPC-830) connectors.

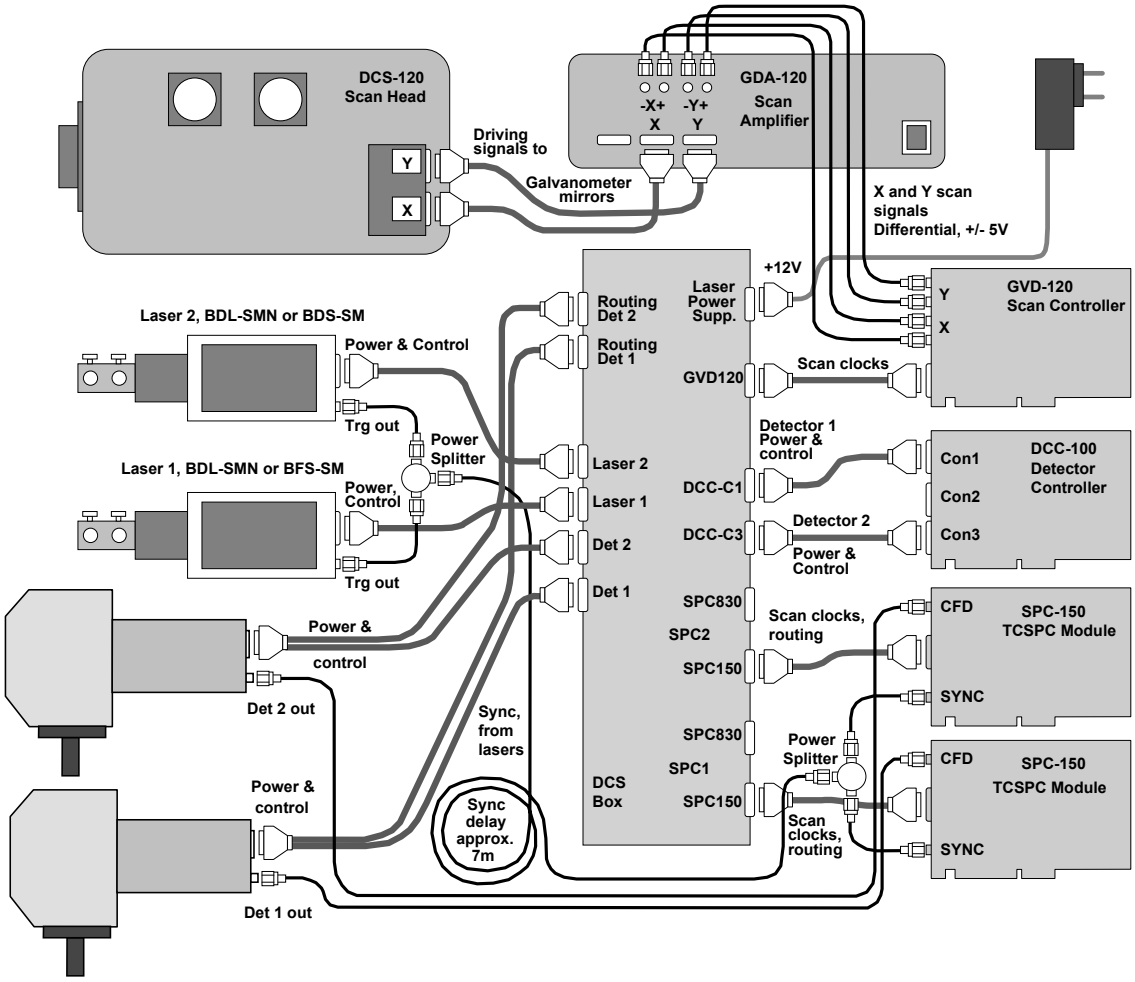


Fig. 386: DCS-120 system with two lasers, two PML-16 detectors, and two SPC-150 TCSPC channels

The corresponding configuration switch settings of the DCS box are shown in Fig. 387. Because the SPC-150 modules have only four inputs for routing bits multi-wavelength detection cannot be used in combination with laser multiplexing. (The combination would be problematic also for optical reasons.) The number of detector channels is 16; the number of detector routing bits is thus four. The laser multiplexing bit is disabled.

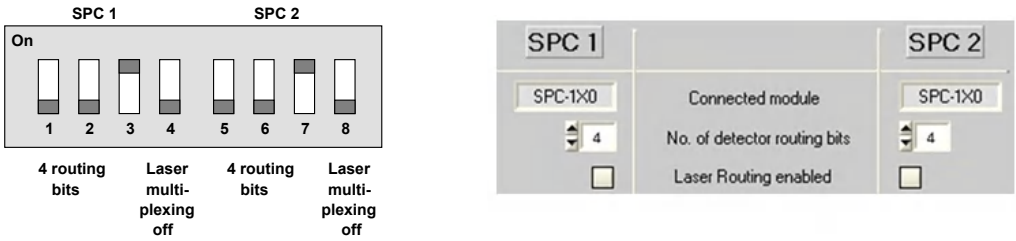


Fig. 387: Configuration switch settings of the DCS box. Left: By DIP switches. Right: By software. Dual-SPC-150 system with two multi-wavelength detectors

A cable diagram of a DCS-120 MP multiphoton system is shown in Fig. 388. The configuration switch setting is the same as shown in Fig. 385 for the dual-SPC-150 system.

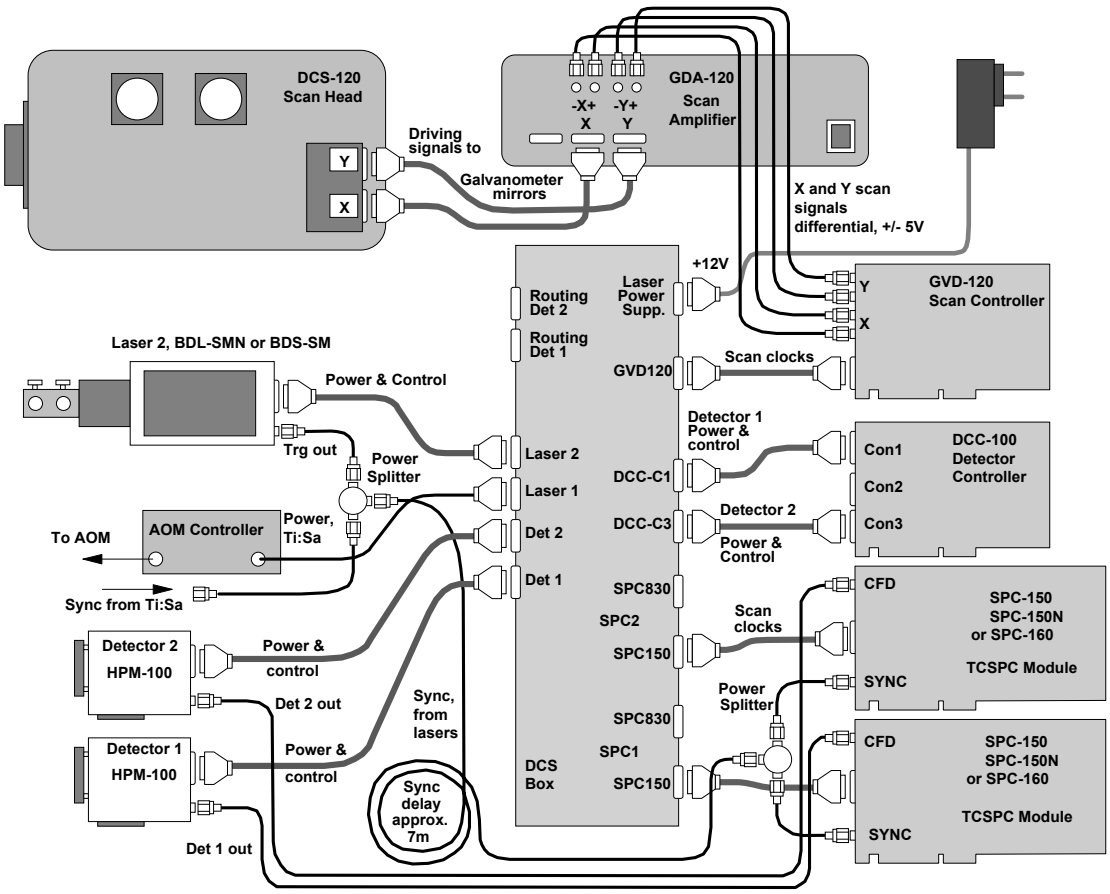


Fig. 388: DCS-120 MP system with a diode laser, a Ti:Sa laser, two HPM-100 detectors, and two SPC-150, 160, or -180 TCSPC modules

The system contains a Ti:Sa laser for multiphoton excitation and a ps diode laser for one-photon excitation. The Ti:Sa laser is controlled via the ‘Laser 1’ output of the GVD. The signal is fed through the DCS connection box, and connected to the input of the AOM controller. Laser 2 is the ps diode laser. It is connected to the ‘Laser 2’ control lines as usual. The synchronisation signal for the SPC modules comes either from the Ti:Sa laser or from the diode laser. Additional NDD detectors can be controlled by a second DCC card. The output signals of the NDD detectors are combined with those of Detector 1 and Detector 2 via power combiners. The combination of the signals is possible because the confocal detectors and the NDD detectors are not used simultaneously and only one pair of detectors is used at a time.

System Setup

Setup and Training Service

Becker & Hickl offer a setup and training service for all TCSPC and FLIM systems. It includes system setup, optimisation of the system parameters, configuration of the main panels according to the application and preferences of the user, definition of setups for special experiments planned by the users, definition of the predefined setups, etc. An important point is user training and discussion of the experiments the FLIM system is intended for. *Unless you are perfectly familiar with the TCSPC system you have ordered we strictly recommend to take advantage of the setup service.*

The following section contains supplementary information for experienced users and for setup engineers. It may also help users get the system running when a part of the system has been replaced or the system has been moved, modified or partly re-installed.

Single-Detector Systems

General System Checks

Please make sure that the software recognises the SPC modules, the DCC-100 detector controller, and other PC cards which are possibly in your system. The SPCM software must run in the 'hardware mode', see 'Software Start', page 716.

Check that the detectors are correctly connected. Most detectors have a 15-pin power supply and control cable, and a 50Ω cable for the single photon pulses. The control cable must be connected to Connector 1 (upper) or Connector 3 (lower) of the DCC card, the 50Ω cable must be connected to the 'CFD' input of the SPC module. Please see cable diagrams in the previous sections. For detector with external amplifiers, please make sure that the power supply of the amplifier is connected (it usually comes from the DCC or SPC module) and that the 'Overload' line is connected. If the connection is missing detector overload remains unnoticed, and the detector can be damaged.

System Parameters

For the first steps, we recommend to use the 'Oscilloscope Mode', with the system parameters shown in Fig. 389, left. The discriminator thresholds (see CFD and SYNC parameters) are set to values which most certainly will allow the SPC module to detect the synchronisation from the laser and the single-photon pulses from the detector. The number of data points (ADC Resolution) in the curve is 4096. Photons will by collected over a Collection Time interval of 0.5 seconds, the measurement repeated, and a new curve be displayed at the end of every collection time interval.

The trace attributes, Fig. 389, upper right, are chosen to display the results in the first eight 'Measurement Pages' no matter into which of the pages you record the data. The Display Parameters, Fig. 389, lower right, are set to display the curve in logarithmic scale. Autoscale is active to guarantee that something will be displayed, regardless of the photon rate detected by the detector.

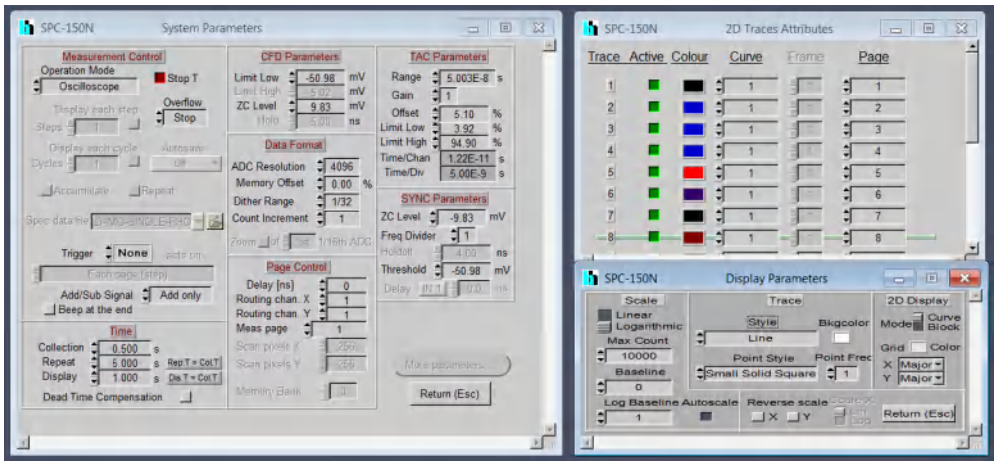


Fig. 389: Parameter settings recommended for startup: System Parameters (left), Trace Parameters (upper right), Display Parameters (lower right)

The parameters are shown for an SPC-150N module. The panels for other modules may differ slightly, but are not significantly different.

Main Panel Configuration

Configure the main panel as shown in Fig. 390. Keep the display and trace parameter panels open, and resize and place the panels as shown in Fig. 390. Make sure that the ‘Rate’ button in the main panel is switched on. ‘Measurement Page’ should be ‘1’.

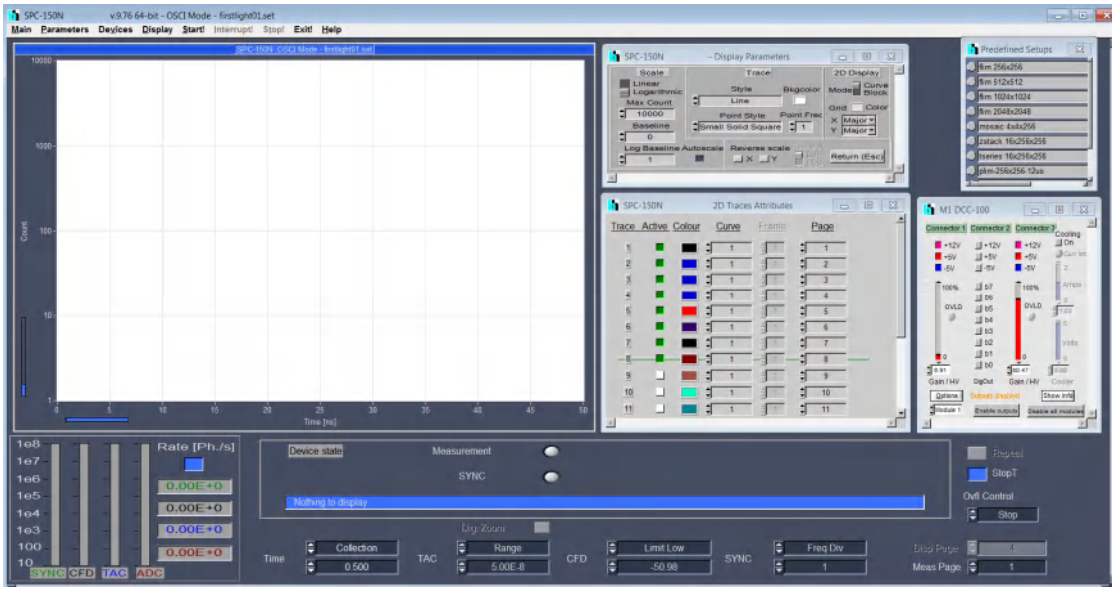


Fig. 390: Recommended configuration of the SPCM software panels for startup

Synchronisation with the Light Source

Turn on the excitation light source. Make sure that it is really pulsing: If it is a ps diode laser integrated in a FLIM just turning it on electrically may not be enough. You may also have to enable it in the scan control panel and start the scanning. Please refer to the instructions for the particular system. When the laser is running the SPCM software should display a SYNC rate, see Fig. 392, left. If it doesn’t please check that the Sync polarity is correct (insert an A-PPI if it isn’t) and that the Sync cable is connected from the correct output of the laser to the Sync input of the SPC module.

Detector Control

Most bh TCSPC or TCSPC FLIM systems contain a DCC-100 detector controller. The software panel for detector control is shown in Fig. 391, left. If the panel does not show up please open the 'Application Options', activate 'Detector Control',see Fig. 391, right.

Pull down the detector gain sliders (Gain/HV) to 10% or less, activate all operating voltage buttons (+12 V, +5 V, -5 V). If you have one detector, make sure to which output it is connected. Connector 1 is upper connector, Connector 3 is lower connector, the middle connector (Connector 2) is for controlling shutters. If you have a shutter in your system find out which of the button is used to control it (it is usually b0). If you don't know, click on 'Enable Outputs' and click on the buttons. Usually you can hear the shutter opening and closing.

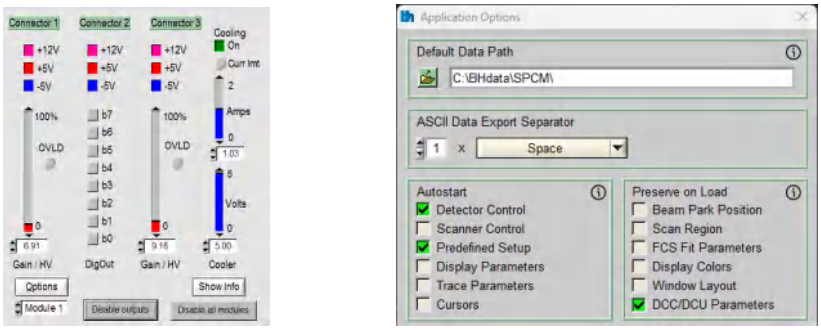


Fig. 391: DCC panel (left) and Application Options relevant for DCC (right)

Detector Gain

Start the measurement in the SPCM software. Enable the DCC outputs by clicking on the 'Enable Outputs' button. Make sure the detector operating voltages are turned on, see Fig. 392, left. Slowly pull up the Gain/HV slider for the DCC output (Connector 1 or 3) to which the detector is connected (Fig. 392, left). At a certain Gain, the SPC module should start to detect photon pulses. A CFD, TAC, and ADC rate is displayed, and counts become visible in the decay curve window, see Fig. 392. Even if there is no light on the detector some dark counts should be detected.

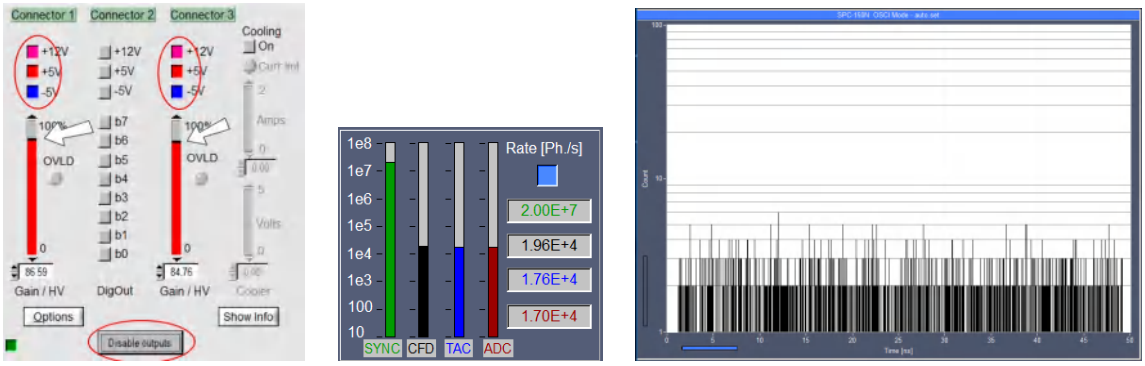


Fig. 392: Left: DCC settings. Middle: CFD, TAC, and ADC rates are displayed when photons are detected. Right: Single photons show up in the decay curve window.

If you don't see counts please check whether you pulled up the correct gain slider. The detector may not be connected to the corresponding DCC output. Or, you have two TCSPC modules with separate detectors and look at the count rate of the wrong TCSPC module. In that case, switch the count rate display to the correct modules, as shown in Fig. 395, right.

When you see counts, increase the gain of the detector. For most detectors, the count rate comes saturates at a certain detector gain. This gain region (the 'counting plateau') is the desired operating point of the detector.

Two things can happen during the gain adjust procedure. A hybrid detector may shut down without having reached a substantial count rate before, see Fig. 422, page 273. In that case, the operating voltage of the avalanche diode inside the detector has been driven into the breakdown region. Pull the gain down by a few clicks when this happens, and click on the 'Reset' button. Or, the count rate increases into the 10 MHz range, and the detector shuts down. In that case, the light intensity on the detector is too high. In most cases the high count rate is caused by daylight leakage. Find the leak and close it.

When the detector delivers reasonable counts, don't attempt fine adjustments at this stage. This can better be done later, when the entire system is working.

Sync Delay and TAC Offset

Send a real measurement signal to the detector. It can be the laser pulse itself. However, the laser wavelength may be blocked by a filter in the optical system. It may therefore be better to use a fluorescence signal. Start the measurement. If you are lucky the curve looks as shown in Fig. 393.

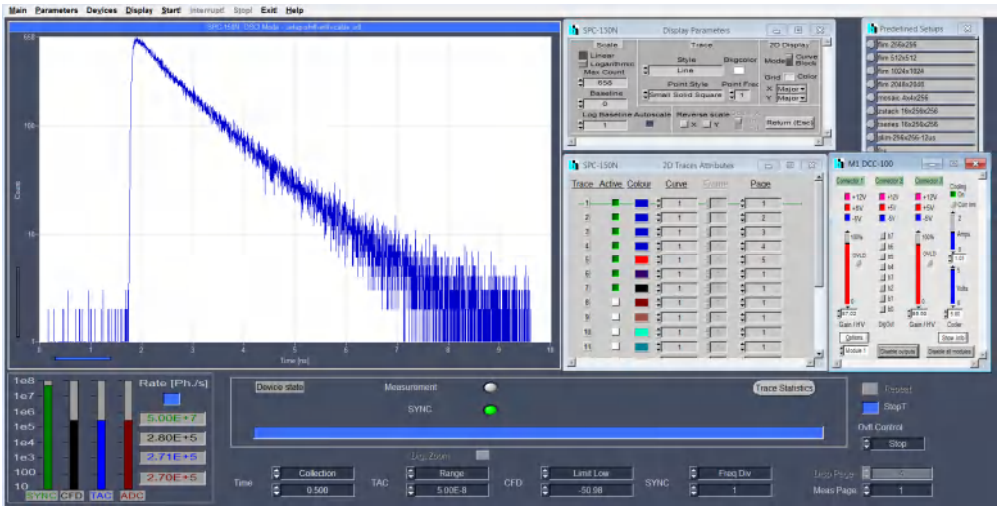


Fig. 393: Main panel in the oscilloscope mode. Detector enabled, laser pulsing, fluorescence is detected

In most cases, however, the curves will appear badly shifted, see Fig. 394, left and middle. In that case, you have to change the signal transit time in the SYNC path from the laser. If there is a SYNC Delay Box (see Fig. 175, page 92) in the system this is easy: Click into Sync, Delay, and change the delay until the curve is perfectly placed in the display window, see Fig. 394, middle.

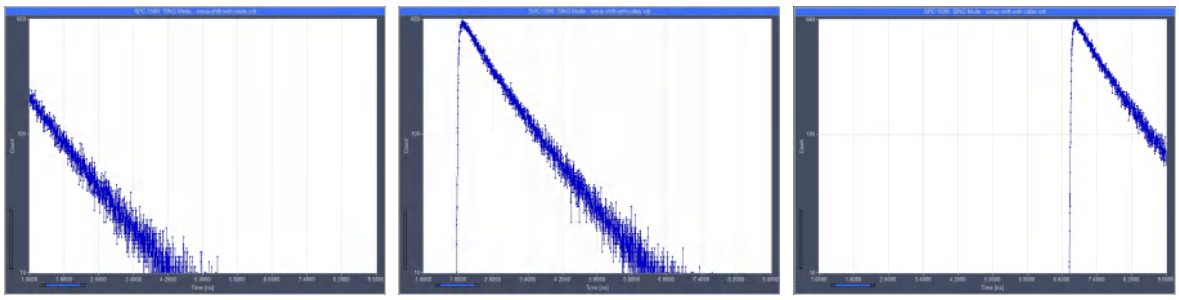


Fig. 394: Effect of the SYNC cable length. Left: Decay curve too far left. Decrease Sync cable length. Middle: Decay curve correctly placed in recorded time interval. Cable length correct. Right: Decay curve too far right. increase Sync cable length. (Decay curves displayed in logarithmic scale.)

Without the delay switch box you have to add or remove cable length in the sync line. Adding cable shifts the curve left, removing cable shifts it right. 20 cm (8 inch) of cable shifts it by one nanosecond. Please see also 'SYNC and CFD Signal Path Length', page 279. Fine alignments can be achieved by changing the TAC offset. However, the correction margin may be

limited: You can shift the curve only within the laser pulse period. For example, with the typical pulse period Ti:Sa laser, 12,5 ns, and a recording time window of 10 ns (TAC Gain = 5) there is only about 2.5 ns room for adjustment.

Time Scale of Recording

Select the desired time scale for your measurements. A typical decay curve should reasonably fill the display window. You can achieve this by changing TAC Gain and TAC Offset, see 'TAC Parameters', page 282. Save the result as an .sdt or .set file. If necessary, create several parameter setups and save them.

Multi-Module Systems

In TCSPC systems with several TCSPC modules, use a 'Trace Parameter' setup that displays curves from all modules. An example for a four-module system is shown in Fig. 395. With the parameters shown, SPCM displays two subsequent pages for each of the four TCSPC modules. To see the count rate of the module you are interested in, click in the 'Select SPC' panel, an select the corresponding SPC module. Please see Fig. 395, right.

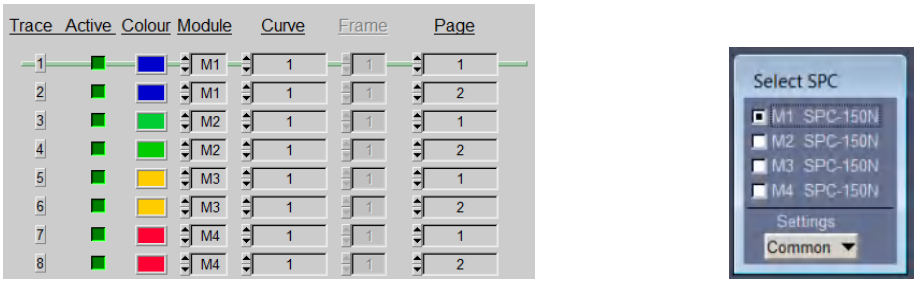


Fig. 395: Left: Trace Parameters for a four-module SPC system. Right: Select SPC Panel, to select the module for which the count rate is displayed.

CFD and Detector Gain Fine Adjustment

When the system is working you can possibly improve the time resolution and the efficiency by fine adjusting the CFD parameters and the detector gain. Please see 'Detector ', page 269.

Locking the Detector Gain

When the final detector working conditions have been established we recommend to lock the Gain in the DCC parameters. Please see Fig. 396.

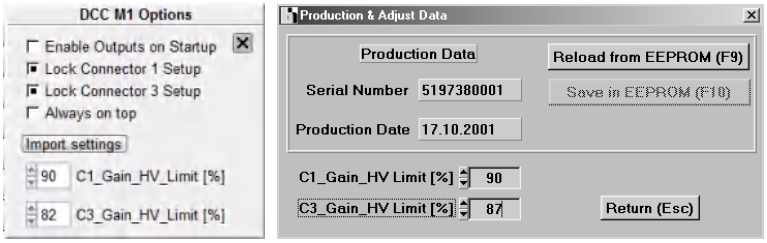


Fig. 396: Locking the detector parameters and Gain/High Voltage Limits

For systems where the detector gain is being frequently changed a maximum gain can be defined for each of the detectors. This provides safety against unintentional overvoltage, with possible detector instability and detector damage.

Saving the setup parameters

When you have found the correct parameters, save them as .sdt or .set files, see ‘Save Panel’ page 720. Create an entry for the setup in the predefined setup panel, see ‘Predefined Setups’, page 723.

Routing Systems

For routing systems with two, three, or four individual detectors (see Fig. 345, page 222) use the system parameters as shown in Fig. 389, but set ‘Routing Channels X’ to the number of connected detectors. ‘Delay’ should be 20 ns for the first tries. In the 2D trace parameters, define traces for Curve 1, Curve 2, Curve 3 or Curve 4, depending on how much detector you have. The system parameters and trace parameters for a routing system with two detectors are shown in Fig. 397. The main panel is shown in Fig. 398.

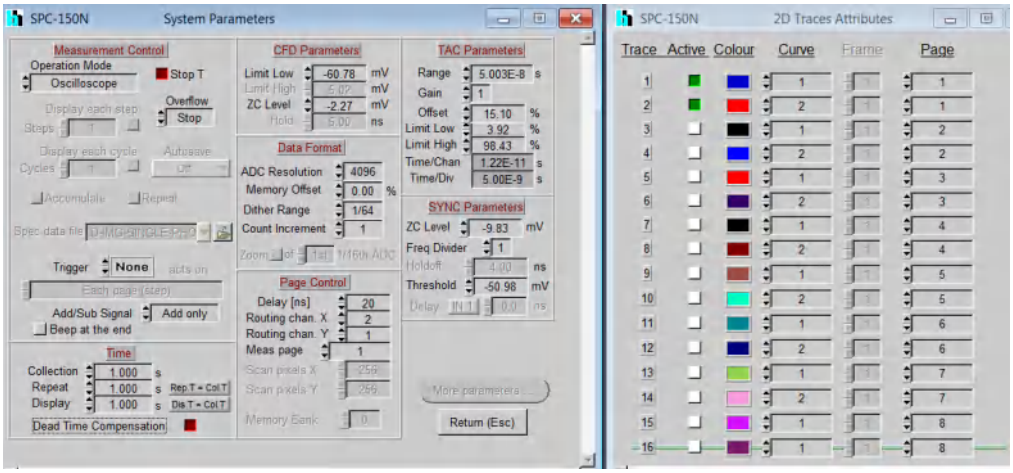


Fig. 397: System parameters and trace parameters for a routing system with two detectors.

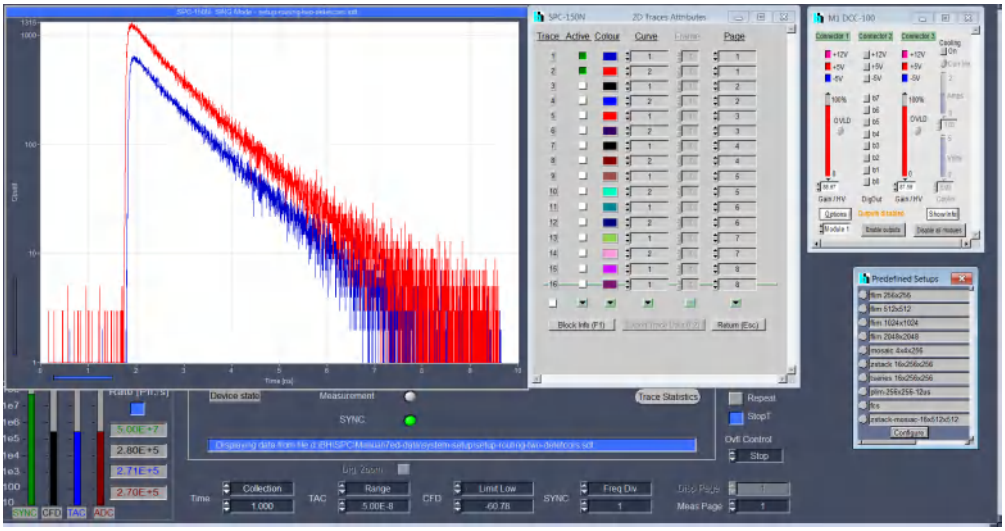


Fig. 398: Main panel for a routing system with two detectors. Shown with data of the two routing channels.

To get the photons from the two detectors correctly separated into two channels the ‘Latch Delay’ in the Page Control section of the system parameters must be correct. A value of 20 ns works with most systems, but the best value depends on the length of the routing cable and the signal cable from the router to the CFD input of the SPC module. We recommend to start with 20 ns, optimise the TAC parameters as described for single-detector systems and then vary the Latch Delay until the signals are optimally recorded.

Important: If you connect a detector directly to the CFD input (bypassing the router) the 15-pin routing cable must be disconnected from the SPC module. If the router does not see the detector signal (because the detector is not connected to it) it cannot generate a routing signal, and without a valid routing signal the SPC does not record photons.

Multi-Wavelength Systems

System Parameters

For the setup of systems with PML-16-C and PML-16 GaAsP detectors use the system parameters and the trace parameters shown in Fig. 399. Most of the parameters are the same as for a single-detector system. Operation mode is Oscilloscope, collection time 0.5 seconds, Stop T is set. The recommended CFD threshold (Limit Low) is higher than for the single-detector system to prevent detection of noise from the routing electronics. To send the photons of the individual detector channels into separate photon distributions 'Routing Chan. X' is set to 16 routing channels. The latch delay for the routing signals is 20 ns. The best value may depend on the length of the detector signal and routing cables. It can range from 10 ns to 50 ns, but 20 ns is a good value to start with. The 2D trace attributes are defined to show all curves of the 16 detector channels.

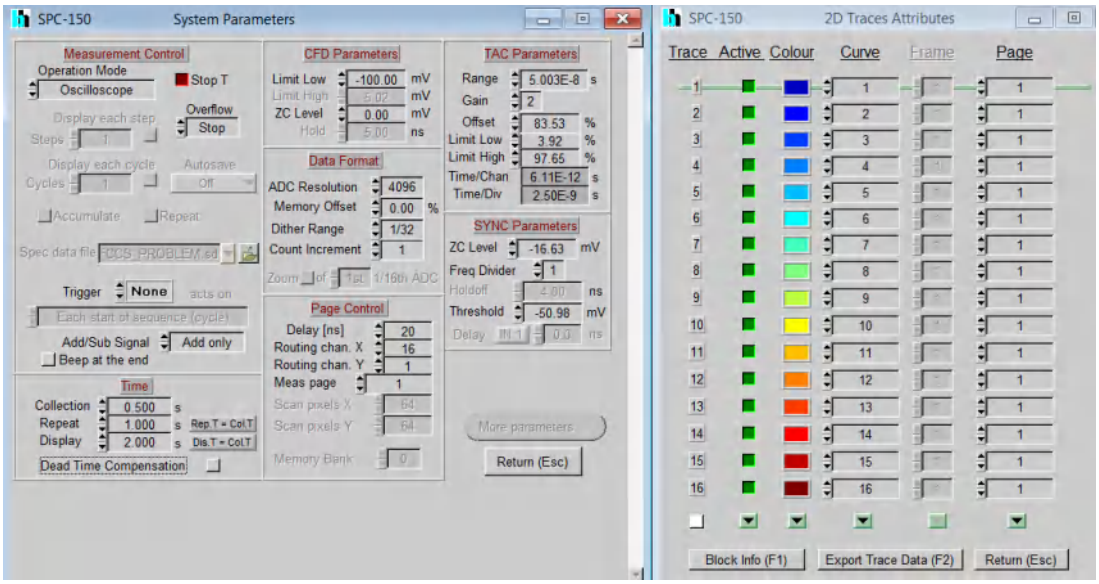


Fig. 399: System parameters and trace parameters for a multi-wavelength system with a PML-16-C or PML-16 GaAsP detector.

Main Panel Configuration

The main panel configuration is shown in Fig. 400. The decay-curve Window has been place on the left, the trace parameters and the DCC-100 panel are open on the right. Measurement page is '1'. You can use other pages, e.g. to record several sets of data and save them in one file. However, the Page in the trace parameters must be the same as in the lower right of the main panel to get the data displayed.

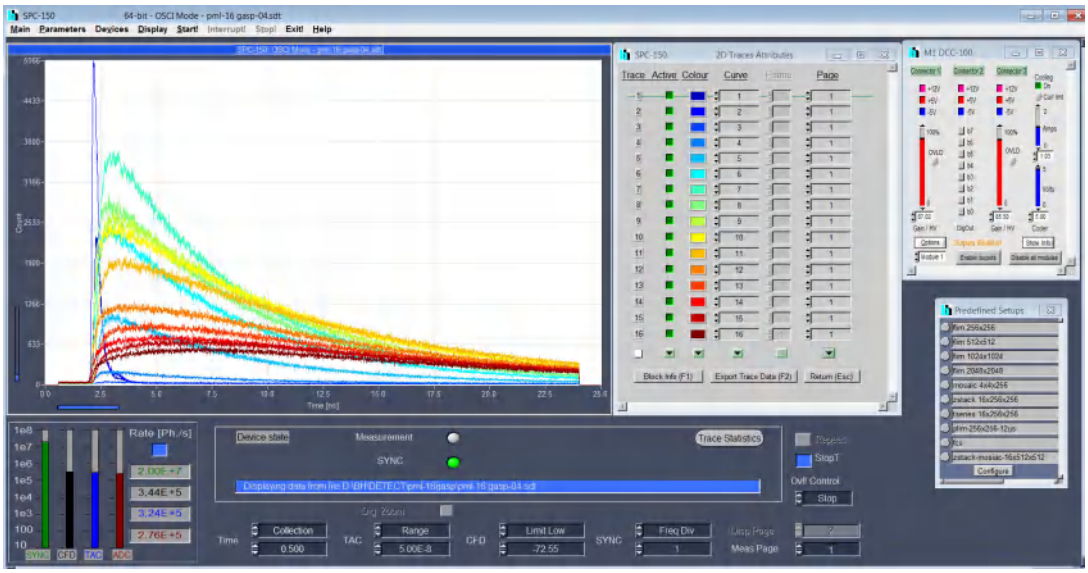


Fig. 400: Main-panel configuration for multi-wavelength detector

Detector Control

The detector control and detector gain setting is the same as for a single-channel detector, please see Fig. 391 and Fig. 392. Enable the detector and pull up the gain slider until you detect photons.

Sync Delay and TAC Offset

Please follow the instructions given for single-channel detectors, see Fig. 394.

Optimisation of Latch Delay

Latch Delay (see Fig. 399, first parameter under ‘Page Control’) determines when after the arrival of a photon pulse the routing signal from the detector is read by the SPC module. The best value can vary for different detectors, SPC modules, and connection cable length. To find the correct value, run an oscilloscope mode measurement as described above and change the Latch Delay. Find the delay range where the curves of all channels are recorded, and set a Latch Delay in the middle of that range.

Multi-Wavelength Systems - F(xyt) Mode

Multi-wavelength recording can also be performed in the F(xyt) mode. The data recorded in this mode are compatible with 16-channel data recorded in the Oscilloscope mode or in the Single mode with 16 routing channels. That means you can switch between the modes even after you have recorded the data. SPCM configuration and system parameters for the F(xyt) mode are described in the following section.

SPCM Main Panel Configuration

The f(xyt) mode displays the curves of the 16 channels of the detector in a quasi-three-dimensional graph. The recommended main panel configuration is shown in Fig. 401. The results are displayed in the upper left part of the main panel. The DCC-100 detector control panel, the display parameter panel, and the predefined setup panel are open on the right.

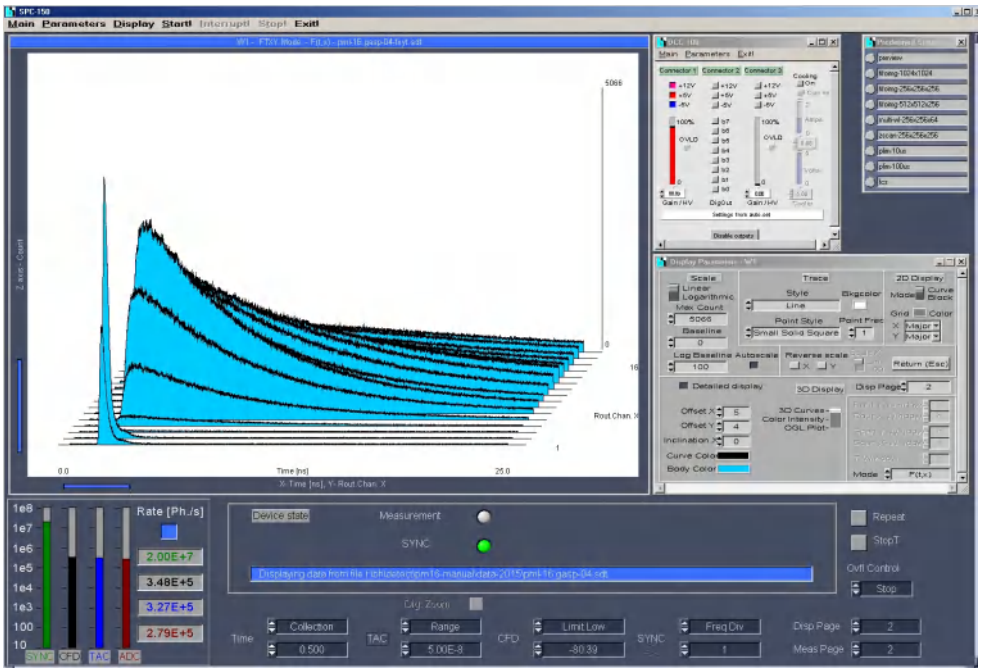


Fig. 401: SPCM Main panel for the f(xyt) mode

The style of the data display is defined by the display parameters. A linear or logarithmic scale can be used, the upper and the lower display limit are defined by Max Count, Baseline, and Log Baseline. Maxcount can be determined automatically by the Autoscale function. Offset X and Y determine the offset of the curves of the subsequent channels in the display. Please see software chapter for details.

System Parameters

The TCSPC system parameters for the f(xyt) mode are shown in Fig. 402. With the parameters shown, the SPC module performs a single measurement for the 16 channels of the PML-16-C or PML-16 GaAsP detector. Data are collected until an overflow occurs or the measurement is stopped by the operator. Intermediate data are displayed in intervals of 'Display Time'.

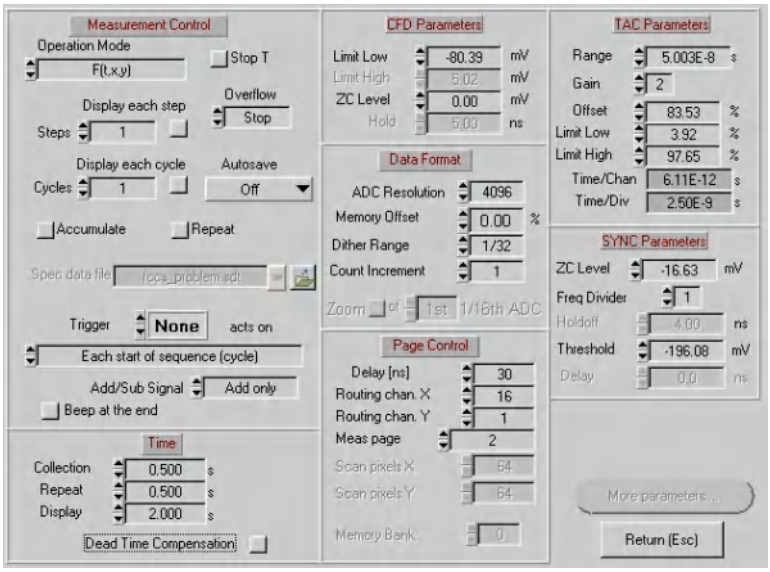


Fig. 402: system parameters for f(xyt) mode. A single measurement is performed, data are collected until an overflow occurs or the measurement is stopped by the operator. Intermediate data are displayed in intervals of 'Display Time'.

Scanning Systems

The details of the parameter setup for a scanning (FLIM) system largely depend on the particular scanner. We can therefore give only general instructions here. For details, please refer to the handbooks of the particular FLIM system. The instructions given in this section are for a dual-channel FLIM system with two SPC-150N modules. Setups for other modules types or for single-detector systems are not significantly different.

First Photons

The initial steps for the setup of scanning (FLIM) systems are as described in the previous section. Please note that it may be necessary to enable the excitation laser in the scanner software. Please see individual handbooks. In most systems the laser turns on only when the system is scanning. Also the detection beam path may be blocked until scanning is started. When you start the scanning, it can happen that you get an immediate detector shutdown. There are three possible reasons for that:

1. Too much room light gets into the detection light path. This happens especially for non-descanned detectors in multiphoton microscopes. If room light is the reason of shutdown, darken the room and cover the critical parts of the microscope with black cloth. Note that light can also shine through the sample. Cover the back of the sample with a piece of cardboard.

2. There are wrong filters in the detection beam path. The laser wavelength is not sufficiently blocked. In two-photon microscopes, a bandpass filter in the detection path is not enough. The laser must be locked by a special short-pass filter of high extinction ratio.

System Parameters for Scanning

Older FLIM systems used the ‘Scan Sync In’ mode. Recent systems almost exclusively use ‘FIFO Imaging’. The following instructions therefore refer to the FIFO Imaging mode. The general system parameters for imaging are shown in Fig. 403, left. We recommend to start from the parameters set established as described under ‘Single-Detector Systems’, page 249. For imaging, change the operation mode to FIFO Imaging, Runtime Display / Configure ‘ps FLIM’. ADC resolution 256 and Image Pixels X and Y 512 x 512 is the default resolution used in most scanning microscopes. If necessary, set the microscope image size to 512 x 512 pixels. The configuration of the scanning interface must be defined under ‘More Parameters’. The exact configuration depends on the particular scanner. For the first tries you can set the parameters as indicated. Most likely this will record *some* image. If it is not the correct one, corrections can be made later.

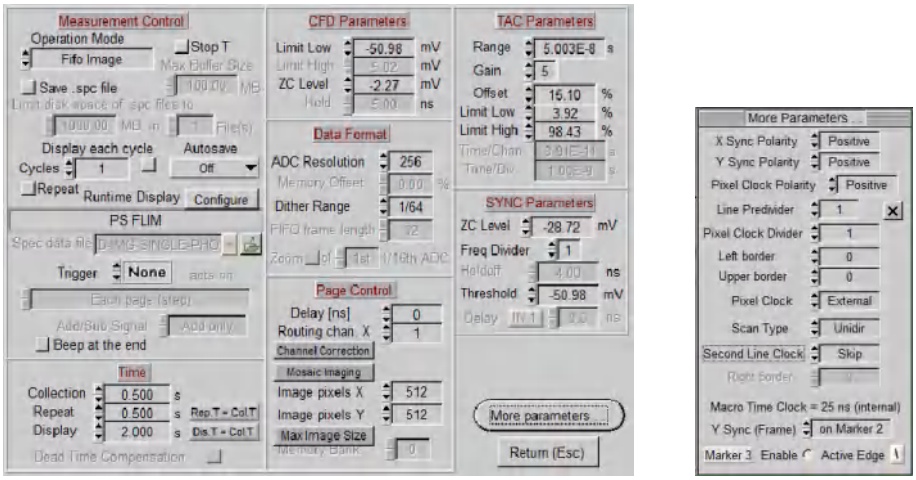


Fig. 403: System parameters for the FIFO Imaging mode. Right: Scanning interface configuration.

Window and Trace Parameters

The SPCM software is able to display several images simultaneously. The images can be from different SPC modules, different detector channels of a multi-detector or multi-modules system, or from different time windows within the time range recorded. The corresponding definitions are made by the 3D Trace parameters and the Window parameters. Please refer to the software chapter of this handbook. For the first steps please start with the parameters shown in Fig. 404.

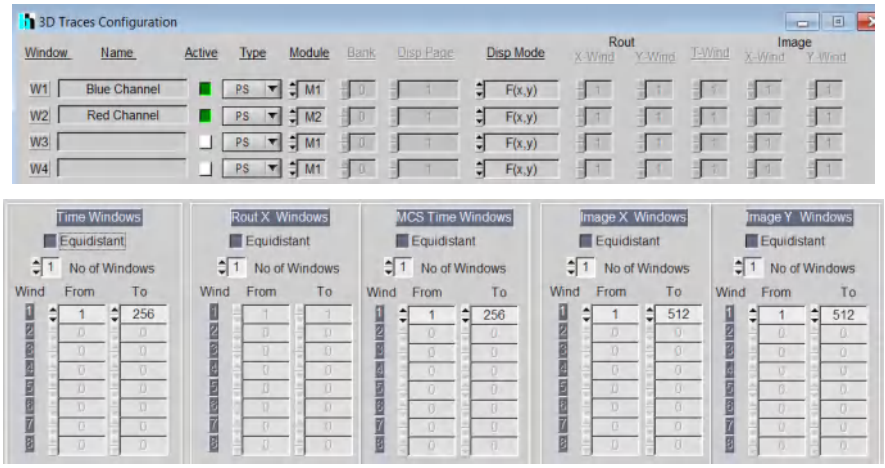


Fig. 404: 3D Trace Parameters (Top) and Window Parameters (Bottom)

Display Parameters

The display parameters define how the data of the images should be displayed. They can be displayed as images, as time-gated images, as curves of the intensity versus t, x, or y, and in different colours. Please see software chapter for details. For the first steps please use the parameters shown in Fig. 405. Note that there are two display windows defined in the 3D trace parameters. Consequently, there are also two separate display parameters sets, as shown in Fig. 405.

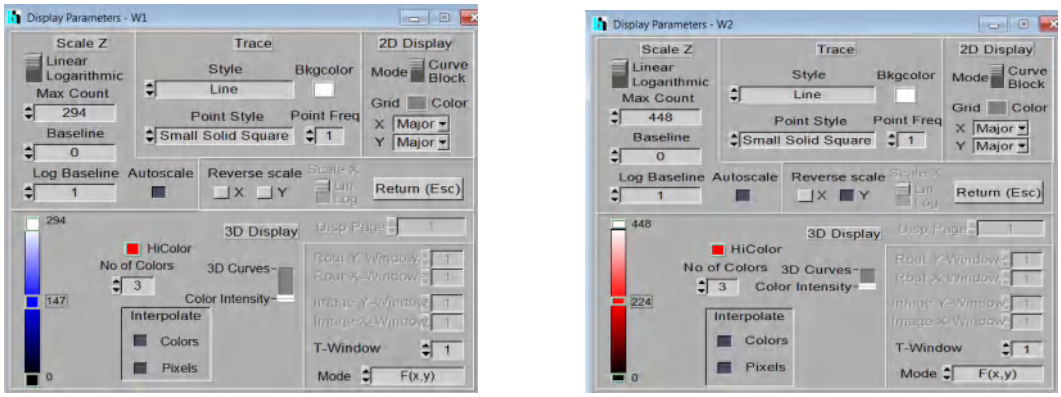


Fig. 405: Display parameters for Imaging. Note there are separate display parameters for the individual images

Main Panel Configuration

Configure the main panel as shown in Fig. 406. Images for both FLIM channels are displayed (shown with data here). The detector control panel has been placed in the lower right.

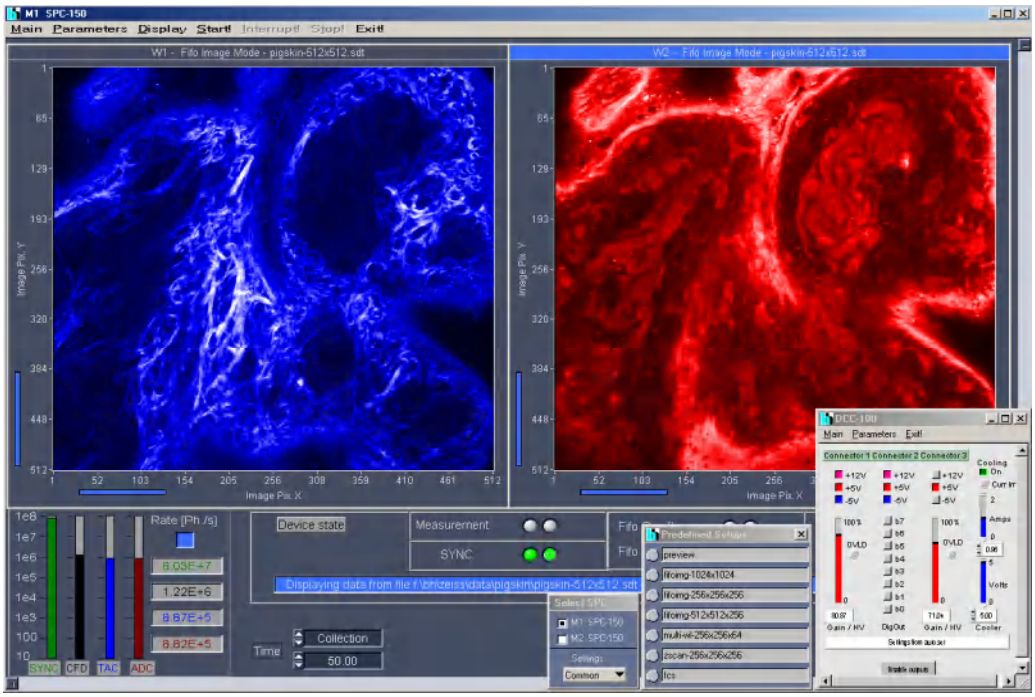


Fig. 406: Main panel configuration for two-channel FLIM

Scan Clock Pulses

To synchronise the recording with the scanner the SPC module needs the frame clock, line clock, and pixel clock pulses from the scanner. There are different cables for different laser scanning microscopes. In some systems the scan clocks are connected directly to the sub-D connector of the SPC modules, in other cases they are connected via a BOB-1, BOB-4, or DCS switch box. Please see cable diagrams under 'Cable Diagrams of FLIM Systems' and 'DCS-120 System Connections'.

To check whether the scan clocks arrive, start the scanning in the microscope (or in the DCS-120 scanner panel, if the scanner is a DCS-120). The scan clock indicators in the lower part of the main panel (they may be hidden behind another panel) should turn green, indicating that the scan clock arrive. The Frame clock indicator may cycle between green and red if the frame rate is slower than one second. If one or both indicators are permanently red one or several of the clocks are missing. To find out which ones these are, place the mouse cursor on the indicator. This displays the status of frame, line, and pixel clock.

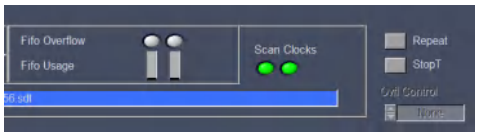


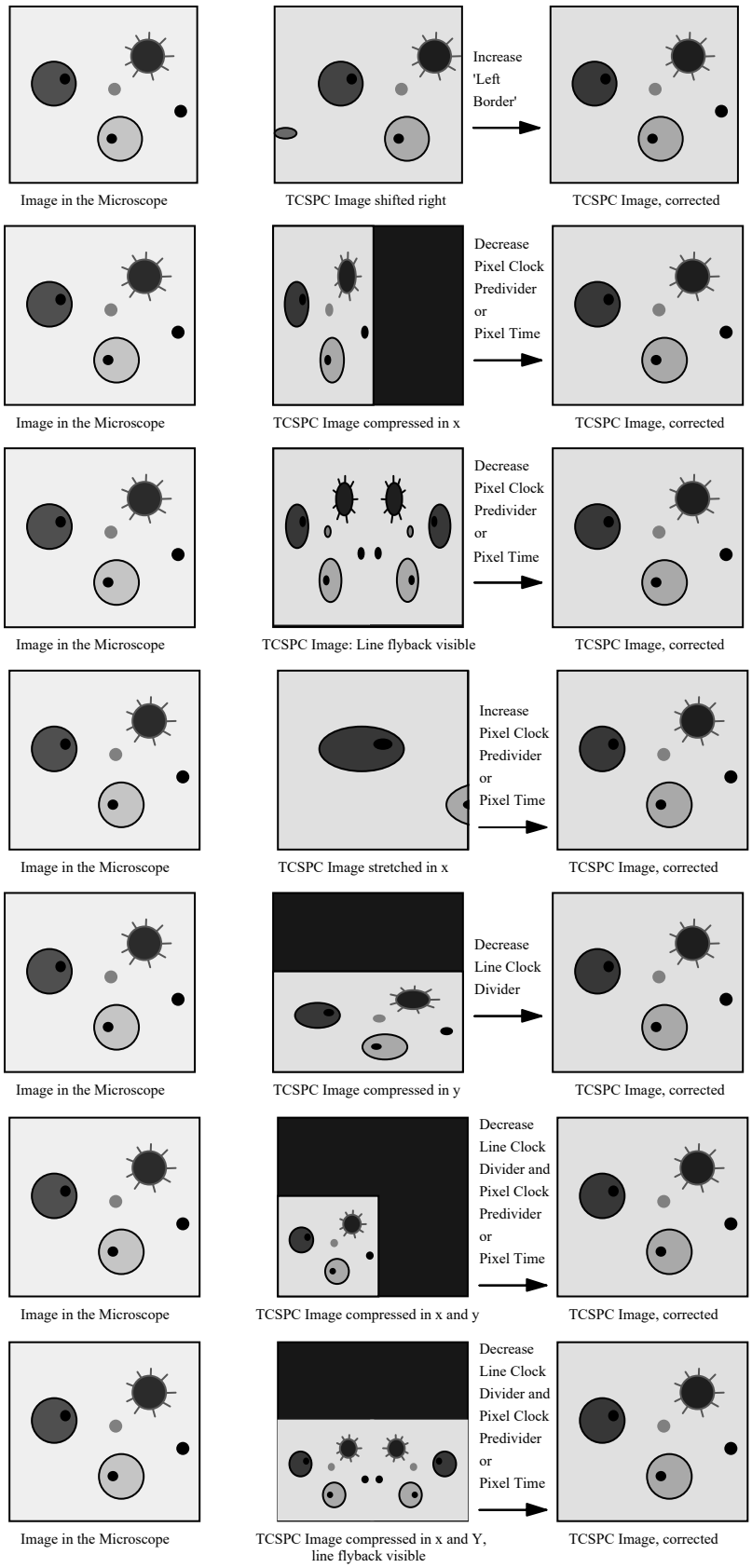
Fig. 407: Scan clock indicators

First Images

Make sure that the detectors are turned on in the DCC-100 panel. Start continuous scanning in the microscope, and start the measurement in SPCM or vice versa. The recording in the SPC modules starts with the next frame clock from the scanner. The status changes to ‘Recording’, and first images should show up after 2 seconds (the ‘display time’ in the system parameters. The photons of subsequent frames are accumulated. Because ‘Autoscale’ is active in the display parameters the image intensity will stay the same. However, as more photons are recorded, the signal-to-noise ratio of the images become higher and higher.

Correcting the Scan Interface Parameters

It can happen that the recorded images are reversed, distorted, or otherwise confused. This is a normal situation - there are as many different scan clock definitions as there are laser scanning microscopes. Some typical cases and the method of correction are shown in Fig. 408.



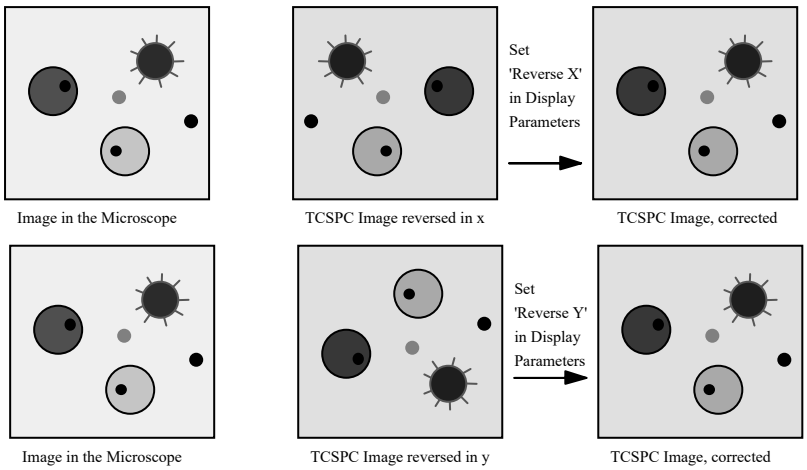


Fig. 408: Typical cases of distorted images and methods of correction

Some microscopes have an option to use a bi-directional scan. In that case, you may get an image as shown in Fig. 409, middle. Using a bidirectional scan with the bh SPC modules is, in principle, possible. If you want to work with bidirectional scanning, please set the scan parameters as described under 'FIFO Imaging Mode', 'Scan Synchronisation Parameters' page 766. However, bidirectional scanning has more disadvantages the advantages. If possible, you should better switch the microscope to unidirectional scanning.

Some microscopes deliver pixel clock pulses both at the start and at the end of each line also for unidirectional scanning. The result is the same. You get a mirrored image from the beam flyback, which is superimposed on the image of the forward scan. You can correct for the effects by selecting 'Skip second Line clock' in the scan parameters.

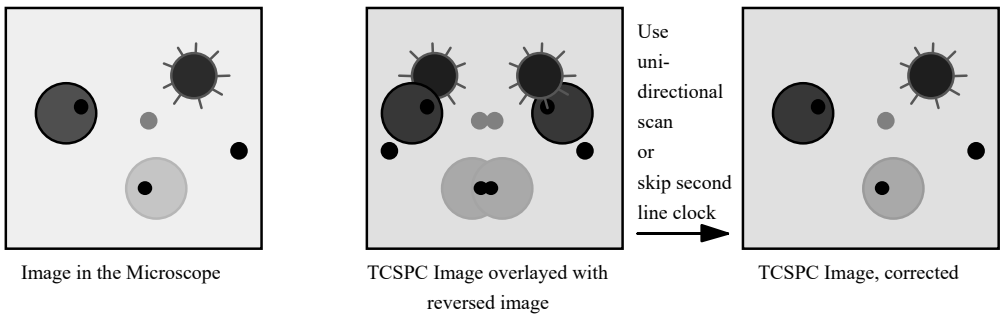


Fig. 409: Images obtained with pixel clocks at both ends of the line, or with bi-directional scan

When you have obtained the correct images, save the setups and load them into the predefined setup panel, see ‘Predefined Setups’ page 723.

Final Refinements

Record an image and send the data to SPCImage. Check whether the decay curves are located correctly in the decay window. The temporal system parameters have been set on an early stage of the setup and may have been changed unintentionally.

Make a number of setups for different pixel numbers. 512 x 512 pixels with 256 time channels is the most frequently used one. However, you may also need 1024 x 1024 or even 2048 x 2048 pixels for high-resolution images. When acquisition time is an issue 256 x 256 pixels may be an option. Moreover, for NAD(P)H FLIM with ultra-fast detectors you may want a setup with 512 x 512 pixels and 1024 time channels, see 'NADH FLIM with Ultra-Fast Detectors', page 365.

We recommend to create a setup also for a ‘fast preview’ mode. The usual setup for fast preview is 256 x 256 pixels, 1 time channel, a collection time of 0.5 seconds, and the ‘repeat’ function turned on. The FLIM system then displays a fast sequence of images.

With the setup parameters suggested in this section SPCM displays intensity images of the FLIM data. You can also display lifetime images instead. Please see section 'Display of FLIM Data', 'Colour-Coded Lifetime Images', page 815.

Multi-Wavelength FLIM Systems

For multi-wavelength FLIM system please follow the general instructions for single-detector TCSPC systems (page 249) and single-detector FLIM systems (page 258). To display the images in different wavelength intervals use the SPCM configuration and the setup parameters described in the following sections.

SPCM Main Panel Configuration

The SPCM main panel recommended for multi-wavelength FLIM is shown in Fig. 410. Eight images are displayed, each for two subsequent channels of the MW-FLIM detector. The data shown in Fig. 410 were recorded by a bh DCS-120 confocal scanning system. Therefore, the DCS-120 scanner control panel is open on the lower right. The predefined-setup panel and the detector control panel are open on the upper and middle right.

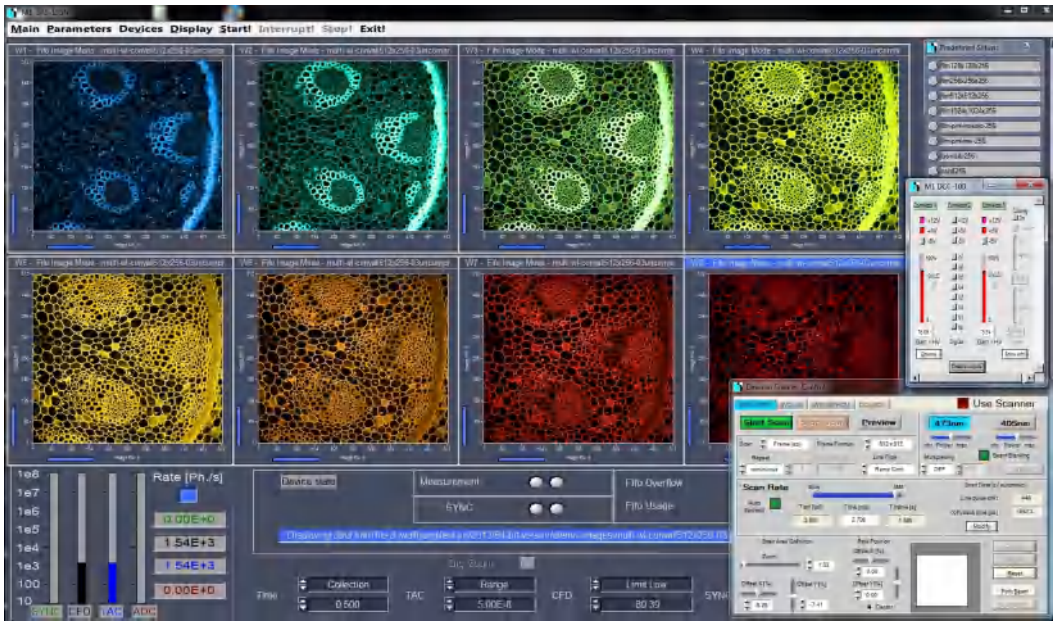


Fig. 410: SPCM main panel for multi-wavelength FLIM. Eight images are displayed, each containing the combined data of two wavelength channels

System Parameters

The TCSPC system parameters of a FLIM measurement with the MW-FLIM detectors are shown in Fig. 411. The measurement mode is FIFO Imaging. The measurement runs until it is stopped by the operator. Intermediate results are displayed every 4 seconds.

The image size and the number of wavelength channels are specified under ‘Page Control‘. At the times of 32-bit Windows, the image format was limited by the amount of memory provided Windows. Typical data formats were 256 x 256 pixels and 64 time channels, or 128 x 128 pixels and 256 time channels. With the introduction of Windows 64 bit and SPCM 64 bit the memory limitation does no longer exist [1198]. With the system parameters shown

in Fig. 411 the DCS-120 system delivers images of 512 x 512 pixels and 256 time channels for all 16 wavelength channels.

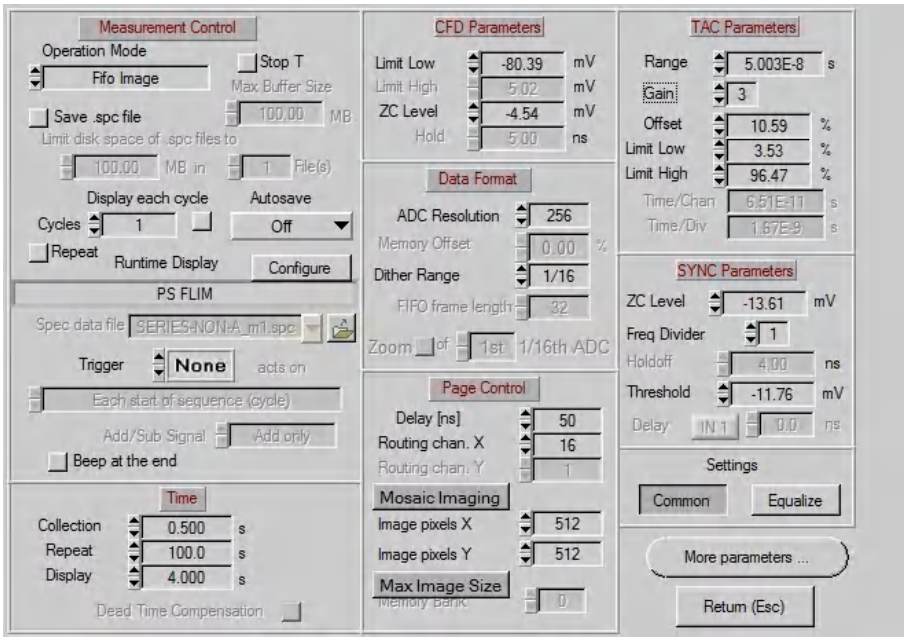


Fig. 411: System parameters for a multi-wavelength FLIM measurement, FFO Imaging Mode, 16 detector channels, 512 x 512 pixels, 256 time channels

Window Parameters and 3D Trace Parameters

The Window Parameters and 3D Trace Parameters define how many images are displayed in the SPCM main panel, and which data they contain. The Window Parameters for multi-wavelength FLIM differ from those for single-detector FIFO imaging in that several routing windows are defined. The routing windows define wavelength intervals in which images are to be displayed. The window parameters shown in Fig. 412 define eight routing windows, each containing two subsequent wavelength channels.

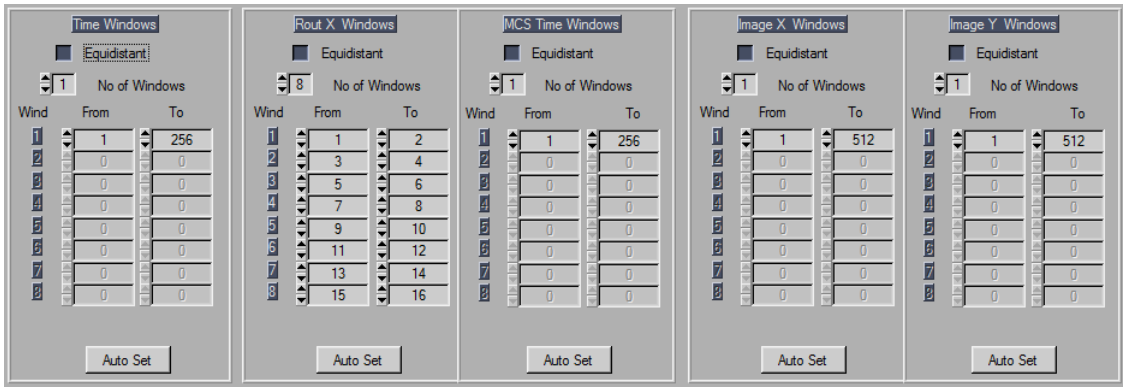


Fig. 412: Window parameters for multi-wavelength FLIM

The 3D Trace parameters shown in Fig. 413 define independent display windows for the eight routing windows. With the settings shown eight images for subsequent wavelength intervals are displayed. Each image contains the data of two wavelength channels.

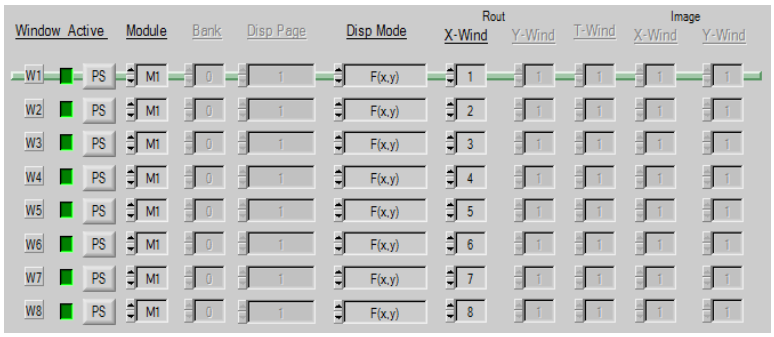


Fig. 413: 3D Trace parameters for multi-wavelength FLIM

The setups shown in Fig. 412 and Fig. 413 assume that there is only one MW detector, and that it is connected to SPC module M1. In principle, it is possible to use a second MW detector and connect it to a second SPC module (Module M2). The number of routing windows then should be reduced to four, and four images be defined for each detector.

Please note that the combination of the detector channels by the window intervals act *only on the way the data are displayed*. The .sdt files produced by the SPCM software contain the data of all individual wavelength channels, for all detectors, and for all SPC modules used.

Display Parameters

The display parameters define the intensity scale and the colour of the images. Display mode is 'Colour-Intensity', and F(x,y). Every window defined in the 3D trace parameters has its own set of display parameters. The display parameter panel is shown in Fig. 414.

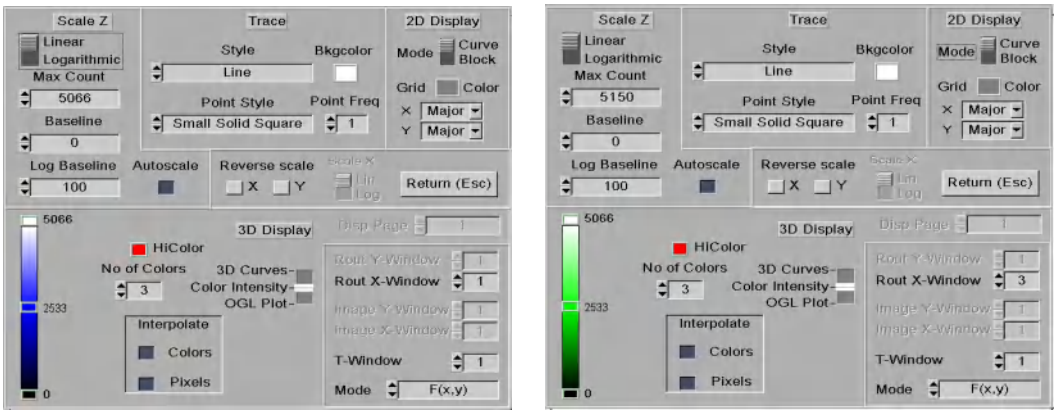


Fig. 414: Display parameters for FIFO Imaging mode. Every display window defined in the 3D parameters has independent display parameters. The figure shows the parameters for Window 1 and Window 2.

Multi-Wavelength FLIM by Mosaic FLIM Function

SPCM Main Panel

The FIFO Imaging with the parameters shown above records multi-wavelength FLIM data that are structured as a set of 16 individual images for different wavelength. With the Mosaic FLIM function multi-wavelength data can be recorded into a single image that is considered a mosaic of the images of the individual wavelength channels. The SPCM main panel configuration is shown in Fig. 415. The image on the left is a mosaic of the images recorded in the 16 wavelength channels of the PML-16 detector. 512 x 512 pixels and 256 time channels are

recorded for each of the 16 detector channels. The entire mosaic therefore has 2048 x 2048 pixels, each with 256 time channels.

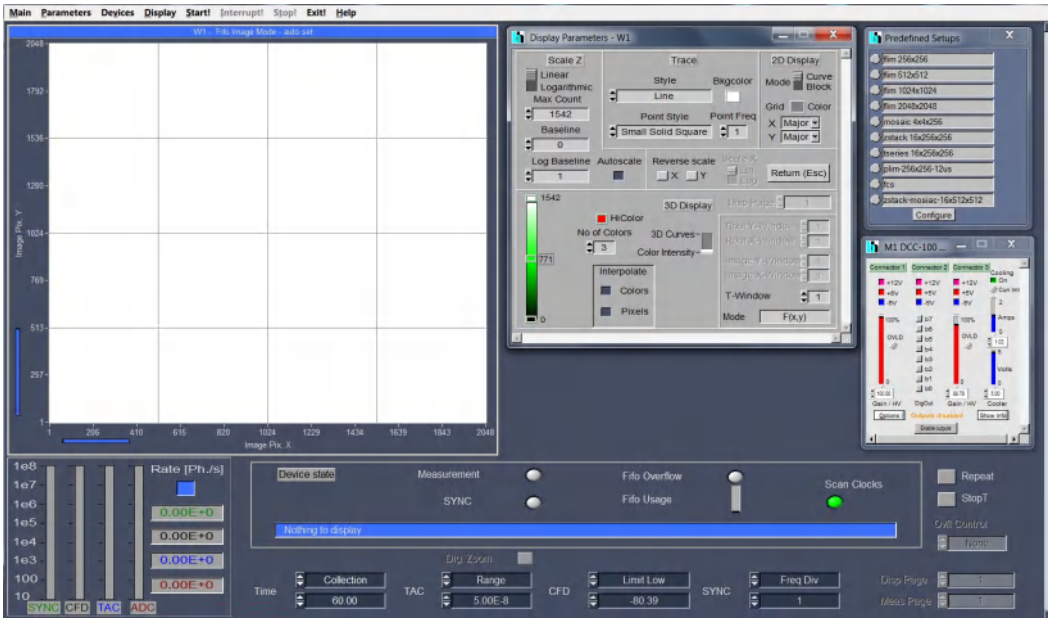


Fig. 415: Main panel for multi-wavelength FLIM by the mosaic function

System Parameters

The system parameters for multi-wavelength mosaic FLIM are essentially the same as for normal multi-wavelength FIFO imaging, see Fig. 416, left. With the parameters shown data with 512 x 512 pixels and 256 time channels are recorded for each of the 16 detector channels.

A click on the ‘Mosaic Imaging’ button opens the mosaic imaging configuration panel shown on the right. The mosaic type is ‘Routing Channels’, the layout of the mosaic is 4x4. This yields a mosaic of 16 elements, each containing a 512 x 512 pixel image for one detector channel.

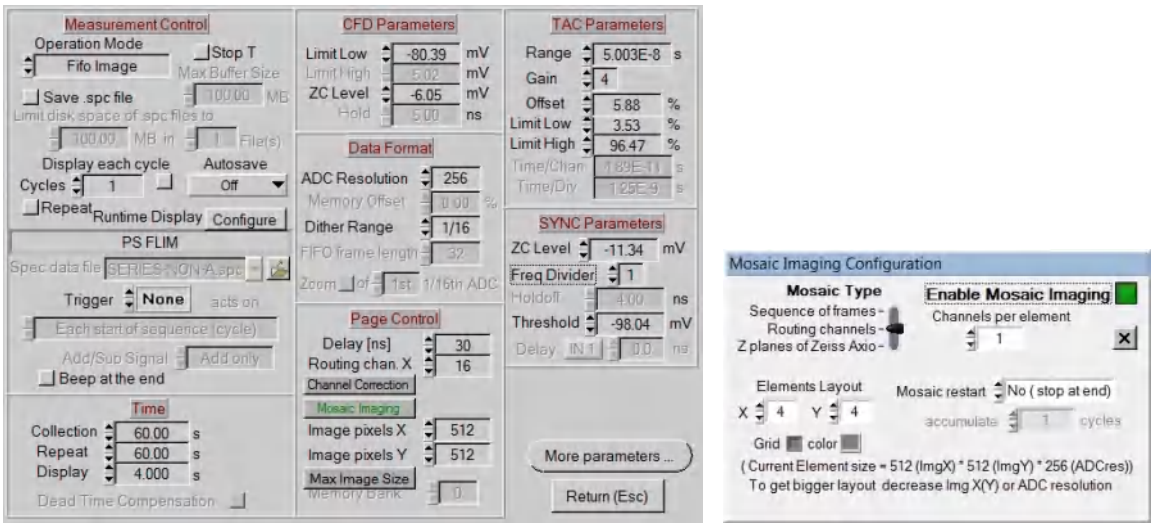


Fig. 416: System parameters for FIFO imaging with the mosaic function. Mosaic configuration panel shown on the right.

Channel Delay Correction

Mosaic data are analysed as a single, large image. Consequently, the data analysis uses the same instrument response function for the analysis of all wavelength channels. Systematic

variation of the channel delay in the detector (see Fig. 300, page 191) then induces a systematic variation in the fluorescence decay times calculated for individual wavelength channels. The variation in the decay time is the same as the delay variation, which is on the order of 100 to 200 ps. Mosaic multi-wavelength FLIM should therefore be used with channel delay correction. For parameter setup please see 'Delay Correction for 16-Channel Detectors', page 768 in the software chapter.

Setup Procedure for Other TCSPC Applications

There are other TCSPC applications such as simultaneous FLIM/PLIM, FLITS, FCS, and Picosecond Photon Correlation. Special parameter setup for these experiments is described in the corresponding application sections. For general TCSPC setup please proceed as described under ‘Single-Detector Systems’, page 249.

System Optimisation

Optimisation of a TCSPC system is sometimes considered a complicated process, exposing the user to numerous mysteries and pitfalls. This may have been true for classic TCSPC systems built from NIM modules. For a bh SPC system the only optimisation steps that are really important are to set the correct operating conditions of the detector and the correct signal transit time in the synchronisation and detection path.

However, there are a few more things which influence the performance of a TCSPC system. An excitation laser of appropriate pulse repetition rate should be used, and deliver pulses with stable pulse shape and peak power. The optical system must be properly designed, without reflections or temporal dispersion in the excitation and detection beam path. The pickup of electronic noise from the environment and electrical crosstalk between the laser and the detectors should be minimised.

The optimisation of a bh TCSPC system can be done efficiently in the 'Oscilloscope Mode'. In the Oscilloscope Mode the measurement is repeated automatically at the maximum available speed. The result is displayed at the end of each measurement cycle. Furthermore, by switching on the ‘Trace Statistics’ button the total number of counts and the half-width of the measured signal can be displayed. To obtain a fast response to the adjustments you are doing we recommend a ‘Collection Time’ of 0.1 s to 0.5 s. Please see setup parameters given under ‘System Setup', Single-Detector Systems.

Detector Operating Conditions

CFD and SYNC Inputs

The function of the constant fraction discriminators in the detector and reference channel of the SPC modules is described under ‘Detailed Description of Building Blocks’, page 147. The input discriminators contain a pulse shaping network that converts the unipolar detector pulse into a bipolar pulse. The discriminator triggers on zero-transition of the shaped pulse. The principle is shown in Fig. 417.

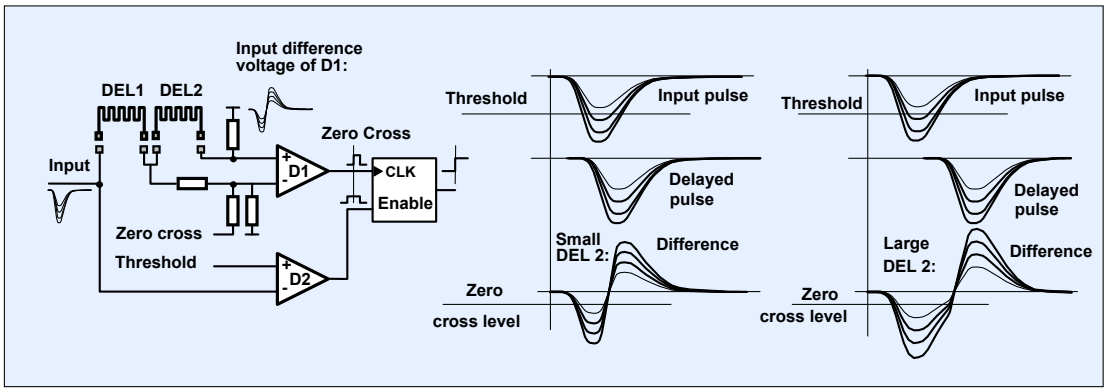


Fig. 417: Principle of constant fraction triggering

The CFD has two discriminators, D1 and D2. D1 triggers on the zero-transition of the voltage difference at the input and the output of a delay line, DEL2. D2 triggers on the input pulse itself. It triggers only when the input voltage exceeds an adjustable ‘Threshold’ voltage. When D1 has triggered, the zero-transition pulse edge of D2 triggers a D-flip-flop. The D flip flop thus delivers a pulse edge at its output when D1 has detected a sufficient input pulse am-

plitude and D2 has detected a zero transition of the shaped signal. The leading edge of the output pulse from the D flip-flop is thus related to the time of the zero transition at the input of D2. Since the temporal position of the zero transition does not depend on the input amplitude the trigger delay does not depend on the amplitude of the input pulses.

The CFD and SYNC inputs can be configured for different detector rise times by replacing the delay lines, DEL1 and DEL2, in the zero cross shaping network. In contrast to TCSPC systems of the 1980s, for the bh TCSPC modules changes in the pulse shaping network are rarely needed. The reason is probably that the discriminators of the SPC CFDs are faster and detectors of faster single-electron response are used. *For all the currently used single-photon detectors the default delay lines of the SPC modules deliver reasonably good, if not best results.*

Possible exceptions are detectors with very slow single-electron response, with pulse rise times of 5 ns or slower. If such detectors have to be used for whatever reasons changes of the delay lines can only be done by try and error. As a rule of thumb, 'Delay 2' should be approximately the same as the rise time of the SER of the detector. However, the influence of the delay lines on the shape of the zero transition is not entirely predictable, and the bandwidth of the discriminators is not exactly known. It is therefore not entirely predictable how the discriminator actually 'sees' the zero transition. A longer DEL2 may result in an unfavourable shape of the zero transition but in a higher signal amplitude. On the other hand, a short DEL2 may yield a steeper zero transition but may not improve the timing because it reduces the amplitude of the shaped signal. Therefore, the importance of correct pulse shaping should not be overestimated.

The delay lines for the CFD and SYNC inputs for SPC-630, 730, and 830 modules are shown in Fig. 418, left, the delay lines for SPC-130, 130EM, and 150 modules in Fig. 418, middle.

The SPC-150N, SPC-150N, SPC-160, and SPC-QC-104 modules have encapsulated CFD and SYNC discriminators with internal delay lines, see Fig. 418, right. For most detectors these CFDs can be used as they are. An exceptions are the multi-wavelength detectors. The single-photon pulses of these detectors have relatively slow leading edges. Moreover, there is some photon-synchronous noise from the routing electronics. The multi-wavelength detectors, both the PML and PML-GaAsP versions, therefore work better with special CFD with longer delay lines. A CFD module for the multi-wavelength detectors and other slow detectors is available from bh.

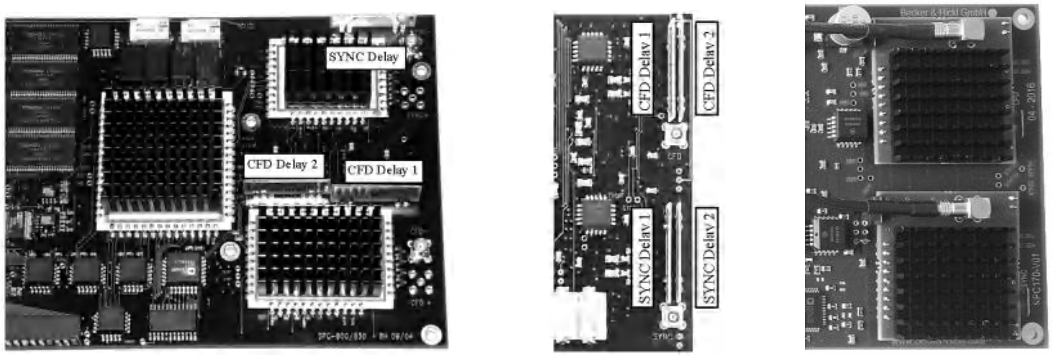


Fig. 418: Delay lines in the CFDs of the SPC modules. Left: SPC-630, 730, 830 modules. Middle: SPC-130, 130EM, 150 modules. Right: SPC-150N, SPC-160. In these modules the entire CFD can be replaced.

For the SYNC channel, the pulse shaping network has less influence on the timing stability than for the CFD (detector) channel. The Sync signal normally has negligible amplitude jitter so that amplitude-induced timing jitter is not an issue. An exception can be correlation experiments or experiments with random light pulses. However, also in these cases the default delay lines usually work well.

DCC Gain and CFD Threshold

To obtain a good counting efficiency from a given detector the CFD threshold must be correctly adjusted. Correct threshold adjustment is especially important for PMTs. On the one hand, background noise and small pulses from the dynodes of a PMT should be suppressed, on the other hand, as many as possible of the 'good' photon pulses should be detected. As shown in Fig. 188, page 101, the single-photon pulses of PMTs have a considerable amplitude jitter. The general shape of the pulse amplitude distribution is shown in Fig. 419, left (see also Fig. 255, page 162).

The pulse amplitude distribution consists of three major components. The regular single-photon pulses, i.e. the pulses originating from electron emission at the photocathode, form a wide peak at relatively high amplitudes. Thermal emission, photoelectron emission, and reflection of primary electrons at the dynodes forms a secondary peak at lower amplitudes. At very low amplitudes electronic noise, either from the preamplifier or from the environment, causes a third peak of extremely high count rate. A TCSPC system should record the regular photon pulses, but not the dynode pulses and the electronic noise background. Therefore, the optimum CFD threshold is in the valley between the regular photon pulse distribution and the peak caused by dynode emission.

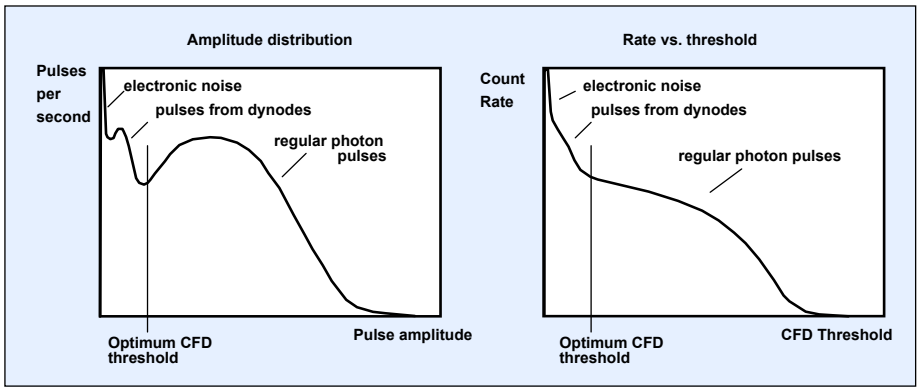


Fig. 419: Amplitude distribution of the single-photon pulses of a PMT (left) and dependence of the count rate on the discriminator threshold (right)

The corresponding dependence of the count rate on the discriminator threshold is shown in Fig. 419, right. When the PMT is illuminated with light of low intensity and the discriminator threshold ('CFD limit Low') is decreased the count rate increases. At a sufficiently low threshold the increase of the count rate flattens, and in the ideal case forms a plateau. At very low threshold the count rate increases again because the dynode pulses or electronic noise are detected. In practice the dynode peak may be not very prominent or even be hidden in the electronic noise. Also the shape of the plateau may vary for different detectors. The plateau can be almost flat and extremely wide. In other cases it may not be very pronounced. However, at least a flattening of the count rate increase should be found. The optimum CFD threshold is between the amplitude distribution of the regular pulses and the dynode pulses.

The pulse-amplitude distribution of the PMT does, of course depend on its gain. Thus, the CFD threshold is different for different detector gain: Higher detector gain requires higher CFD threshold, and vice versa. The general dependence is shown in Fig. 420.

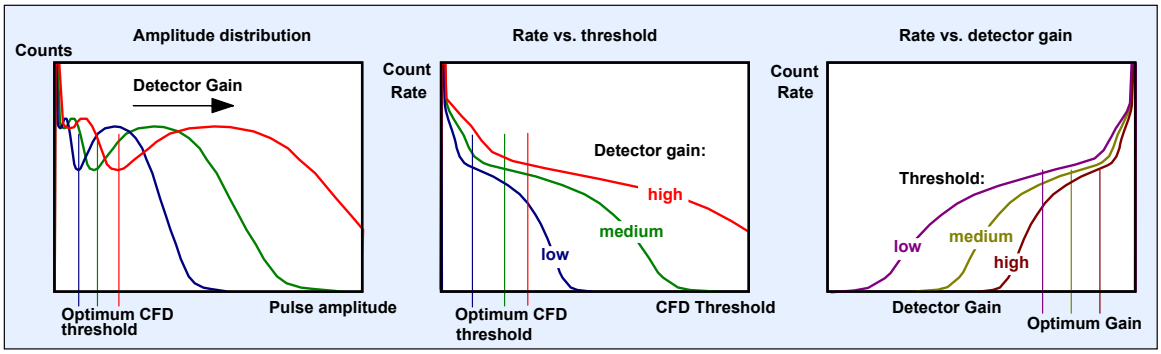


Fig. 420: Amplitude distribution of the single-photon pulses of a PMT (left) and dependence of the count rate on the discriminator threshold (right)

As can be seen from Fig. 420, middle and right, there are two strategies to optimise the operating point of the TCSPC system: You can select a reasonable detector gain and optimise the CFD threshold, or select a reasonable CFD threshold and optimise the detector gain.

We recommend to follow the second strategy. The reason is that the gain of a PMT changes steeply with the operating voltage (or the 'gain' selected in the DCC panel), and that the effective gain for different PMTs may vary considerably. To find a reasonable combination of threshold and gain we recommend to start with the CFD thresholds given in the table below.

Detector	**CFD Threshold**	**DCC Gain (Voltage)**
R3809U with FuG-HCN	-80 mV	80 to 86% (-2.9 to -3.0 kV)
R3809U with HVM-100	-80 mV	90 to 100%
PMC-100	-100 mV	80 to 90%
PMZ-100	-100 mV	80 to 90%
PMC-150	-100 mV	80 to 100%
H7422P-40	-100 mV	70 to 85%
PML-16C	-100 mV	85 to 100%
PML-16 GaAsP	-100 mV	85 to 100%
HPM-100, all versions	-50 mV	70 to 90%, see below

Send a small amount of light to the detector. It can be laser light, fluorescence from a sample, or daylight leaking into the detector light path. The count rate should be no more than 10^4 to 10^5 photons per second. Turn on the detectors in the DCC panel, as shown in Fig. 421, left. If you have two detectors, fully pull down the gain slider of the other detector. (This avoids confusing the detectors!) If you have a dual-channel system, use the 'Select SPC' panel to display the count rate of the detector to be optimised. The count rate should behave as shown in Fig. 421, middle. The optimum gain range is marked with green ellipses. It may happen that the detector switches off by overload. The reason may be that the light intensity is too high, or that the gain is so high that the PMT develops instability. In that case, reduce the light intensity or the gain, and re-activate the detector as shown in Fig. 421, right.

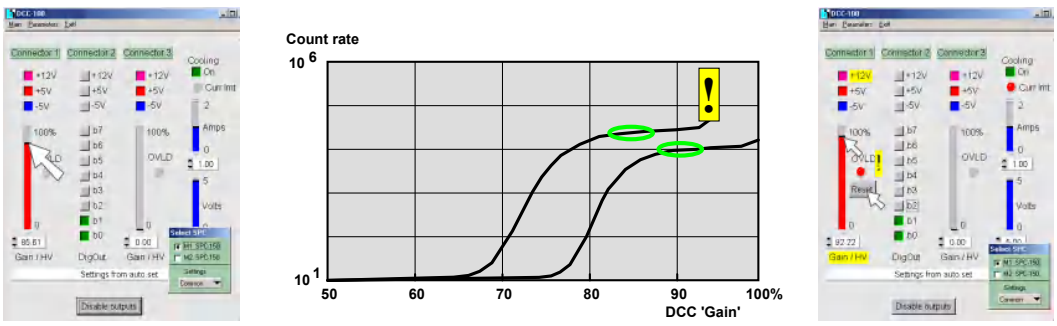


Fig. 421: Adjusting the detector gain for PMT modules. Left: DCC panel with detectors enabled. Middle: General dependence of count rate on gain. The optimum gain region is marked. Right: DCC panel after detector overload.

The procedure for the HPM-100 hybrid detectors is similar. However, the gain characteristic of a hybrid detector is extremely nonlinear. The function of the count rate versus DCC 'gain' is therefore very steep, see Fig. 422. The plateau is short but very flat. It is usually sufficient to find the point where the detector switches off by overload and then take the DCC gain back by a few percent.

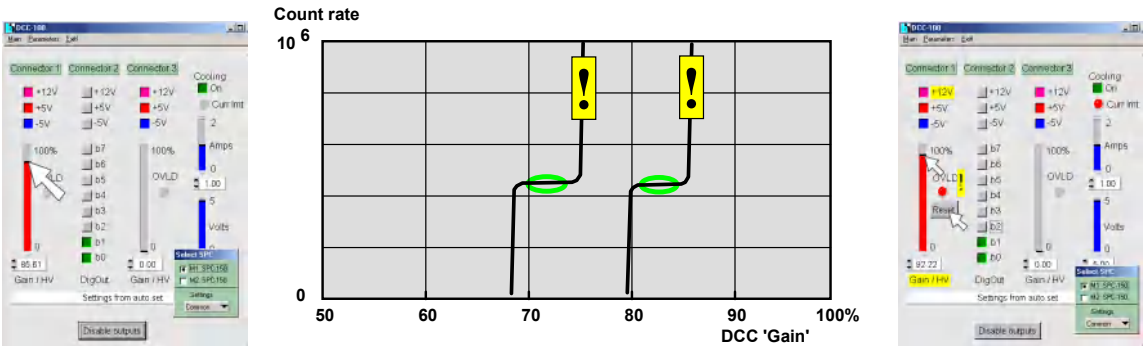


Fig. 422: Adjusting the detector gain for HPM-100 hybrid detector modules. The operating point can be found by determining the gain when the detector shuts down by overload and taking back the gain by a few per cent.

When you have found a reasonable set of CFD and DCC parameters, do not forget to save the setup parameters. Please note that recent versions of the DCC software have a 'Lock Setup' option, see Fig. 423. When 'Lock Setup' is set the detector parameters cannot be changed by the operator. We recommend use this option for systems that are used permanently with the same detectors.

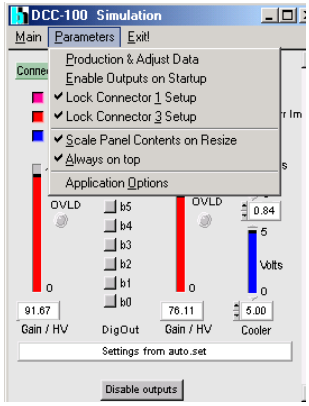


Fig. 423: 'Lock Setup' option of DCC-100 software

Single-Photon Avalanche Diodes (SPADs)

No CFD adjustments are necessary for single-photon avalanche photodiode (SPAD) detectors. These detectors have their own internal discriminators and deliver a pulse of defined amplitude and duration for each photon. Once these pulses are detected by the CFD of the SPC module further adjustment has negligible influence on the efficiency and the IRF shape.

Dependence of the Time Resolution on the Detector Gain

The timing jitter and the influence of electronic background noise is smaller for higher pulse amplitudes. Therefore higher PMT gain and higher threshold settings in general yield shorter IRF widths. The threshold is therefore often increased above the value that yields best efficiency. This is not objectionable as long as no more than 90% of the pulses are rejected and the corresponding loss in counting efficiency is taken into account. However, it should be noted that the efficiency and the IRF is less stable than in the counting plateau.

Moreover, every detector has a maximum save output current. With a high threshold, a large fraction of the detector output current is wasted for the rejected photons. The maximum safe count rate, especially for MCP PMTs, is therefore reduced.

Older SPC-300 and SPC-400 modules had an additional 'Limit High' threshold to reject pulses of high amplitude. It could help suppress afterpulses, see 'Counting Background', page 275. Also, a narrower amplitude window in principle decreases the influence of the amplitude jitter on the timing. However, the pulse amplitude distribution drops steeply at high amplitude so that the effect of the higher threshold on the time resolution is not very pronounced. If too many pulses are rejected by the higher threshold it may happen that reflections of these pulses on the signal cables trigger the CFD. The result is a second IRF peak after twice the cable transit time.

Maximum Count Rate of the Detector

The maximum output current of a photon counting detector sets a limit to the detectable count rate. For example, the maximum permissible average output current for the R3809U MCP PMTs is 100 nA. The H7422 detectors have maximum output current of a few µA. The maximum count rates are on the order of 1 MHz and 2 MHz, respectively. For a given count rate, the output current increases with the detector gain. It may therefore be appropriate to operate the detector at a gain lower than the specified maximum. This is especially the case for the MCP PMTs and for the H7422 modules.

CFD Zero Cross Level

The CFD zero cross level has an influence on the timing jitter that is induced by the amplitude jitter of the detector pulses (see Fig. 417). In early TCSPC systems the zero cross level was called 'walk adjust'. Because both the detectors and the discriminators were slow the walk adjust had an enormous influence on the shape of the instrument response function (IRF). In modern systems the influence is much smaller, sometimes even not noticeable. The reason is that detectors with faster single-electron response are used and the discriminators are faster. Therefore, the effective slope of the zero cross transition is steeper, with a correspondingly smaller influence on the zero cross level.

Theoretically the best IRF should be expected at a zero-cross level of exactly zero (see Fig. 417). However, in practice the zero-cross discriminator has an offset voltage of a few mV. Moreover, the intrinsic delay of the zero-cross discriminator depends on the speed of the zero transition. The corresponding contribution of the discriminator to the timing jitter can be compensated for by slightly offsetting the zero-cross level from the signal baseline. Therefore the best zero cross value can be some tens of mV above or below zero. A zero-cross level extremely close to the signal baseline can even cause problems. In that case, the zero-cross discriminator may trigger on to spurious signals from the synchronisation channel or may even oscillate. Of course, spurious triggering and oscillation stop when an input pulse arrives, but some after-ringing may still be present and modulate the trigger delay. The result is poor differential nonlinearity or a double-structure in the IRF.

The dependence of the IRF on the CFD zero-cross level for a PMC-150-110 detector is shown in Fig. 424. The best IRF is obtained at +25 mV, the FWHM is 116.7 ps.

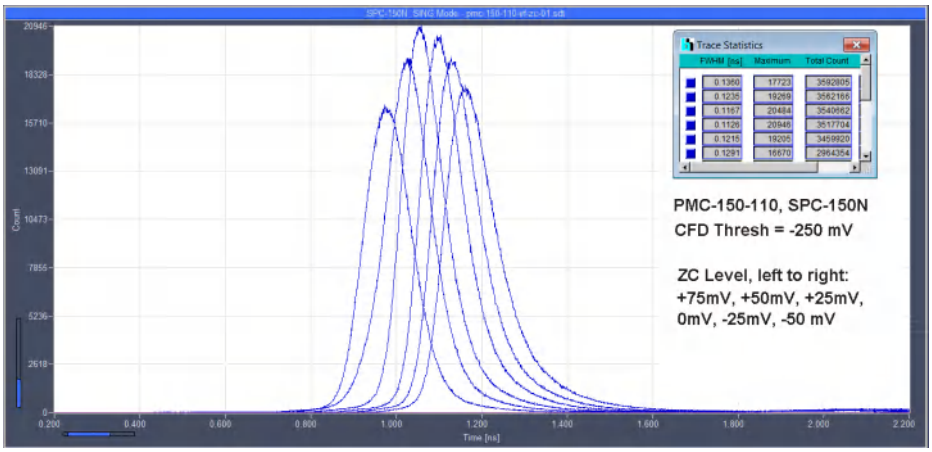


Fig. 424: IRF shape for a PMC-150-110 detector. CFD Threshold -250 mV, ZC level from +75 mV (left) to -50 mV (right). Best IRF is obtained at +25 mV, FWHM = 116.7 ps.

The Zero-Cross adjustment can be done conveniently in the 'Oscilloscope Mode'. Any change in the IRF shape becomes immediately visible. For fine tuning, turn on ‘Trace Statistics’. This opens a window which shows the FWHM, the count number in the maximum, and the total number of counts in the signal recorded. If several measurement pages are active the corresponding values for all pages are displayed. This way, FWHMs for different CFD settings, different detector gain or even for different detectors can be conveniently compared.

Counting Background

Counting background is usually attributed to thermal emission of photoelectrons in the detector. The first idea is then to use a cooled detector. However, there are at least three more sources of background in TCSPC experiments. The most trivial (but also most frequent) one is leakage of daylight into the detection light path. Another (and often the dominating) one is afterpulsing. Afterpulsing is present in all PMTs, MCP PMTs and SPADs. It forms a signal-dependent background under the recorded signal. Other possible sources of background is luminescence of lenses and filters, and spectral background of excitation lasers. The effect on the recorded signals is similar to the one caused by afterpulsing.

Thermal Background

Thermal background changes dramatically with the temperature. As a rule of thumb, the thermal dark count rate decreases by a factor of 5 for a 10 K decrease in temperature. This provides an easy way to find out whether thermal background is a problem: Run a normal measurement with an ice bag on the detector and check whether the background in the recorded signal decreases.

Afterpulsing Background

Almost all photon counting detectors have an increased probability to deliver background pulses within the first few 100 ns after the detection of a photon, see page 167. The source of afterpulsing in PMTs is ion feedback, i.e. ionisation of rest gas molecules by the electrons [319]. In SPADs afterpulses are caused by trapped carriers of the previous avalanche breakdown. MCP PMTs, especially the R3809U of Hamamatsu, have low afterpulsing rates, but only hybrid detectors and super-conducting NbN detectors are virtually free of it. In high-repetition rate experiments the afterpulses accumulate over many excitation periods and cause a count-rate dependent background.

Afterpulsing background can easily be identified. Record the normal signal, e.g. a fluorescence decay curve for a given collection time. Then block the excitation beam path and record again with the same collection time. If the background is higher in the first recording the reason is most likely afterpulsing.

An example of afterpulsing background in two different detectors is shown in Fig. 425. The figure shows recordings of a fluorescence signal (top) and of the dark counts (bottom) for a cooled H5773-20 photosensor module (left) and an R3809U-50 MCP-PMT (right). The pulse repetition rate was 50 MHz, the count rate approximately 400 kHz, the acquisition time 40 seconds.

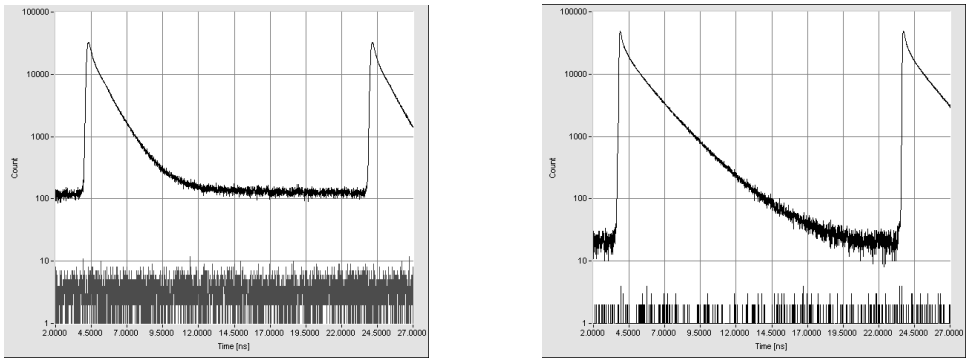


Fig. 425: Afterpulsing background. Fluorescence signals and dark counts recorded by a cooled H5773-20 PMT module (left) and a R3809U-50 MCP-PMT.

For both detectors, the background in the decay recording is more than an order of magnitude higher than the thermal background. A similar comparison for a HPM-100-40 hybrid detector and a H5773-01 PMT is shown in Fig. 287, page 183.

The afterpulsing probability in a PMT and thus the afterpulsing background can be reduced by reducing the detector gain. The reduced detector gain must be compensated for by a higher preamplifier gain or a reduced discriminator threshold. The afterpulsing probability decreases approximately with the square root of the gain. However, if the afterpulsing background is in the range of some % of the system response, no adjustment will remove the problem entirely. Such PMTs have either poor vacuum or have been stressed by overload. For tubes severely plagued by afterpulsing or even instability we recommend the same treatment which Russell W. Porter (the father of amateur telescope making) suggested for warped telescope mirrors: *'Seek out a good hard, solid hydrant. Hurl the mirror (the photomultiplier) as fiercely as possible at said hydrant. Walk home.*

Luminescence of Filters and Lenses

Long-lifetime luminescence of absorptive filters, lenses, optical fibres, and other optical elements can cause a signal-dependent background that is almost indistinguishable from afterpulsing. Therefore, if background is a problem, the optical system should also be checked. Luminescence can often be identified by recording a signal without a sample, or with a dummy sample that has normal scattering behaviour but no fluorescence. Nevertheless, finding and removing the source of the problem is not always easy. Optical elements to be suspected are especially those which are both in the excitation and in the detection beam path.

Wideband Background from Lasers

Persistent background can also come from wideband emission of lasers. For example, ps diode lasers emit slow fluorescence over a range of 50 to 100 nm on the long-wavelength side of the laser line [67]. Two examples are shown in Fig. 426.

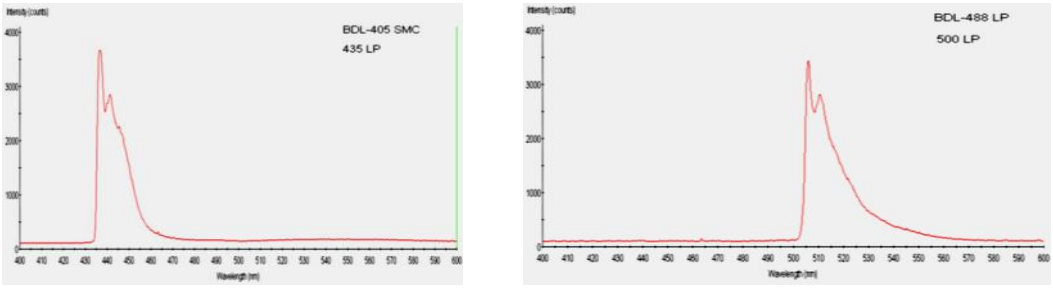


Fig. 426: Wideband emission from ps laser diodes. Laser line suppressed by long-pass filter.

The intensity of the background is much lower than that of the laser line. It becomes detectable only when the laser line is suppressed by a long-pass filter. In fluorescence applications the background can be in the spectral range where fluorescence is detected. It then passes the fluorescence filter and contaminates the detected signal. The relative amount of background in the detected signal depends on the concentration of the fluorophore and on the scattering behaviour of the sample. The effect on the recorded decay curve is therefore hard to predict. Since 2012 the bh BDL lasers have a short pass filter in the output. The filter suppresses the largest part of the background.

Wideband background must also be expected from supercontinuum lasers with acousto-optical filters. Even Ti:Sa lasers are not free of wideband background. The background often shows up in two-photon images recorded in laser scanning microscopes. It is most pronounced in systems that have no AOM for laser intensity regulation. In systems with AOM a large part of the background is suppressed by the spectral selectivity of the beam deflection in the AOM.

Problems with laser background can usually be identified and solved by inserting a cleaning filter in the laser beam path.

Detector Operation at High CFD Threshold

It is sometimes attempted to reduce the dark count rate of a detector by decreasing the gain or increasing the CFD threshold. Except for background caused by electronic noise these attempts are not promising. The amplitude distribution is the same for the photon pulses and the dark pulses, and the CFD threshold suppresses both likewise.

High CFD Threshold is also used to obtain a narrower IRF from a given detector. This works up to some point because only the fraction of photon pulses with the largest amplitudes are detected. This effectively narrows the amplitude spectrum of the recorded photon pulses and reduces the amplitude-induced timing jitter in the CFD. However, the improvement comes at a price. Since only a fraction of the pulses is used for the TCSPC recording the efficiency of the recording drops dramatically.

High CFD threshold and low detector gain may also result in other detrimental effects. One of them is an increase in afterpulsing background. A large fraction of the afterpulses have larger amplitudes than the photon pulses. That means high threshold suppresses photons more than afterpulses.

Moreover, most of the afterpulses appear within 100 ns after a photon was detected. With a CFD threshold correctly adjusted these afterpulses are suppressed by the dead time caused by the previously detected photon. However, if the CFD threshold is increased (or the detector gain decreased) too far the photon is suppressed, and the afterpulse is detected instead.

The result of exceedingly high threshold is not only a dramatic increase of the relative afterpulsing background but also a distortion of the detected signal shape by the afterpulses. An example is shown in Fig. 427. At -100 mV the PMT still performs normal, see Fig. 427, left. However, if the CFD threshold is increased to -300 mV (Fig. 427, right) the signal / background ratio becomes totally unacceptable. Moreover, the afterpulses cause an additional bump 8 ns after the main peak.

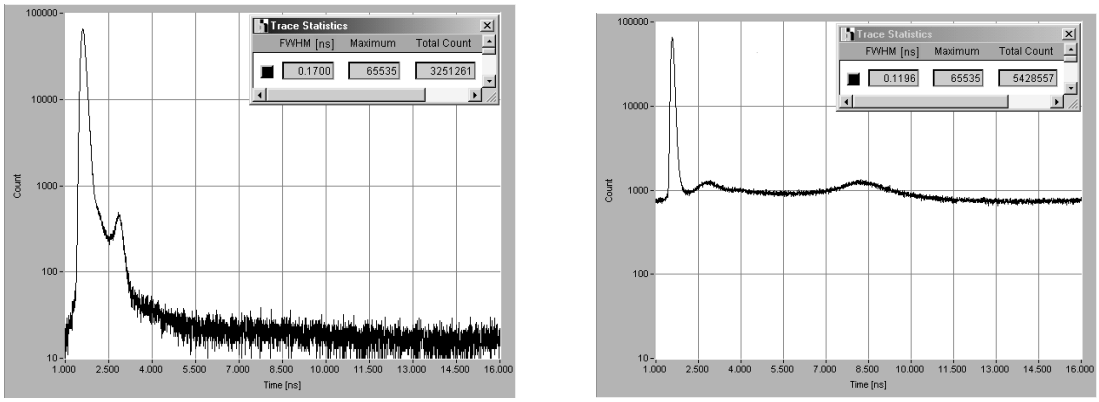


Fig. 427: Increase of afterpulsing background by setting the CFD threshold too high. Left: The PMT performs normally at a threshold of -100 mV. Right: At -300 mV mainly afterpulses are recorded.

Multi-Photon Detection

Excessively high CFD thresholds in combination with low detector gain can entirely suppress the detection of single-photon pulses. If the light intensity is increased, eventually multi-photon events are detected. Especially at low pulse repetition rates this may remain unnoticed because high peak intensities can be reached without obtaining an exceedingly high average detector current. A typical example of multi-photon detection is shown in Fig. 428.

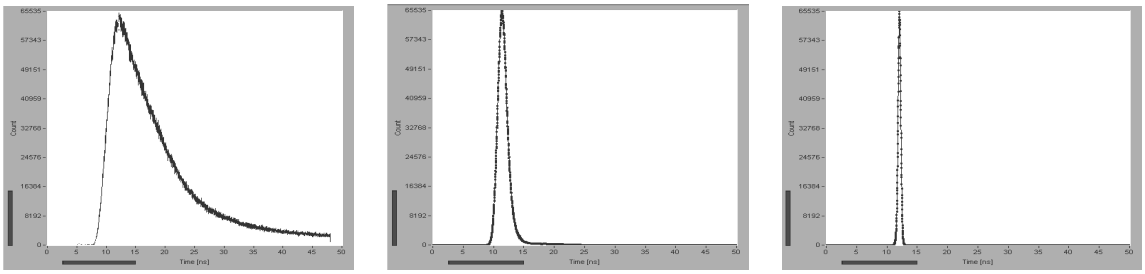


Fig. 428: Detection of multi-photon events at low detector gain. Left: Correctly recorded signal, recorded at a detector gain of 10^6 and a count rate of $3{\cdot}7{\cdot}10^4$ s^{-1}. Centre and right: The same signal recorded at a detector gain of 10^5 and 10^4. The light intensity was increased until the PMT signal triggered the CFD.

The left curve was recorded at a detector gain of 10^6 and shows the true shape of the light pulse. The curves in the middle and right were recorded at a detector gain of 10^5 and 10^4, respectively, and at high light intensity. At a gain this low a single photon does not trigger the CFD. However, if the light intensity is increased, the PMT signal eventually turns into a continuous signal representing the shape of the light pulse. If the amplitude of the signal reaches the CFD threshold, the CFD triggers. The count rate steeply increases from zero to the signal repetition rate, and extremely narrow pulse shapes are recorded. Operating the PMT in this multi-photon mode results in an extreme distortion of the recorded signal waveform. An extremely short 'IRF' of less than 20 ps duration can be obtained. This IRF is, of course, entirely useless for any waveform recording. It can, however, be used in distance-measurement and time-of-flight applications when only the distribution of the arrival times of the pulses is wanted, not the temporal shape of the pulses.

SYNC Parameters

In most cases the constant fraction discriminator of the Sync input is triggered by a reference signal from the light source. The SYNC parameters have little influence on the time resolution as long as the amplitude of the reference signal is stable. If the reference signal has amplitude fluctuations, or if the SPC modules is used for start-stop experiments with a second detector the parameters of the SYNC channel are optimised as described for the detector channel.

If the synchronisation signal has reflections, ringing, or afterpulses multiple triggering can occur. The effect on the recorded signal is shown in Fig. 429. If you see effects like these, increase the 'Sync Threshold' or 'Sync Holdoff.

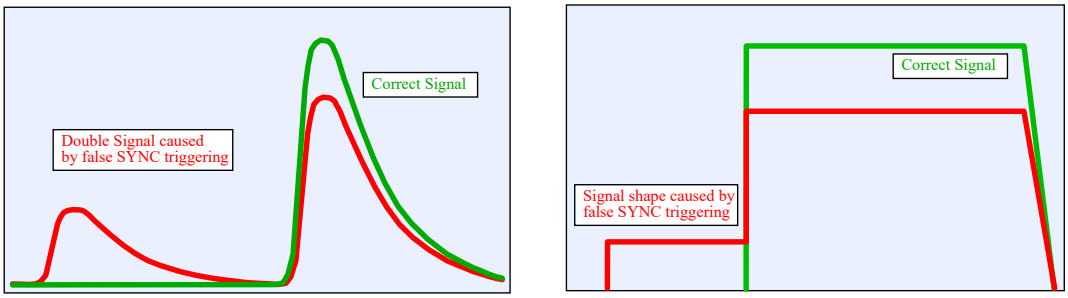


Fig. 429: Effect of false SYNC triggering on recorded signal shape. Left pulsed signal, right continuous light

The 'Sync Frequency Divider' setting determines the number of signal periods that are recorded, see Fig. 430. Values greater than one are convenient to find the signal in high repetition rate applications. Furthermore, they can be used to check or calibrate the time scale by comparing the displayed pulse distance with the known pulse repetition rate.

However, fluorescence data analysis programs usually expect data for only one signal period. Spreading the recorded photons over several periods and analysing only one means wasting at least 50% of the photons. Furthermore, recording several periods in multidimensional measurements may waste memory space. Moreover, the time from the photon detection to the next stop pulse adds to the effective dead time. Recording several signal periods thus increases the average dead time and the corresponding counting loss. Therefore, if counting efficiency or memory space are an issue, the 'Sync Frequency Divider' should be set to 'one'.

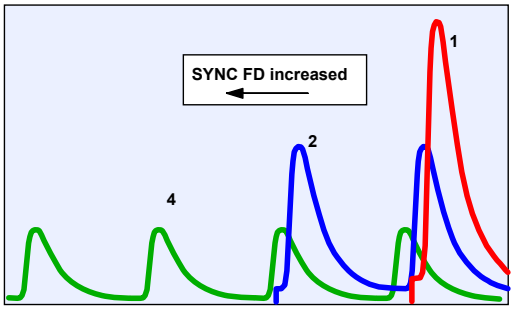


Fig. 430: High repetition rate signal recorded with different Sync Frequency Divider settings

SYNC and CFD Signal Path Length for SPC Modules

SPC-Series modules measure photon times from the photon to the next Sync pulse. When working with 'Sync Frequency Divider' = 1 and a sufficiently long TAC Range the SPC module records over an observation-time interval of one signal period minus a few ns required to start and stop the TAC. The location of the recording interval within the signal period de-

pends on the optical path lengths, the cable lengths in the CFD and SYNC channels and on the delays in the PMT and SYNC detectors. Therefore, it usually happens that the SPC does not records the desired time interval of the signal. Because of the reversed start-stop operation the effects are often confusing to TCSPC users. Some typical cases and the method of correction are shown below.

The effect of the CFD and SYNC cable length is shown in Fig. 431. The original curve is (1). A longer SYNC cable or a longer SYNC light path shifts the curve left (2), a longer CFD cable or a longer detection light path shifts the curve right (3). 1 ns corresponds to 30 cm light path or 20 cm cable length. Please note that it is not necessarily required to change cables to obtain the correct signal transit times. The same effect can be obtained by using the DB-32 USB-controlled delay switch box shown in Fig. 431, right.

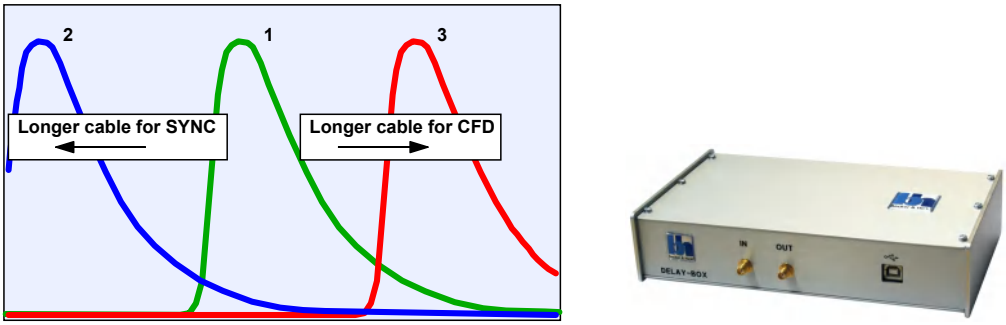


Fig. 431: Effect of the CFD and SYNC cable length. Right: Delay switch box for adjusting signal transit time.

As long as the recorded time interval is shorter than the full signal period the curve can also be shifted by changing ‘TAC Offset’, see ‘Optimising the TAC Parameters’. However, if ‘TAC Offset’ is too small the beginning of the TAC characteristic comes into view (Fig. 432, left). In the first nanosecond the TAC characteristic is nonlinear. The corresponding signal interval displays as a short peak with no photons right of it, see Fig. 432, left. If the signal photons arrive too late they are recorded in the next signal period. The corresponding part of the signal either wraps around the signal period and appears on the left or is outside the conversion range and is not recorded. The method of correction is to use a shorter CFD cable or a longer SYNC cable. The peak at the start of the TAC characteristic can be shifted out of the recorded range by increasing the TAC offset.

The opposite effects happens if a part of the signal photons arrive too early. Due to the reversed start-stop, early photons cause large TAC times. Of course, with FD = 1 TAC times larger than one signal period do not exist. The recorded waveform then drops abruptly to zero left of a TAC time corresponding to one signal period. The part of the signal left of this point is either lost or wraps around the signal period and appears at the right side of the recorded range. The method of correction is to increase the CFD cable length or decreasing the SYNC cable length.

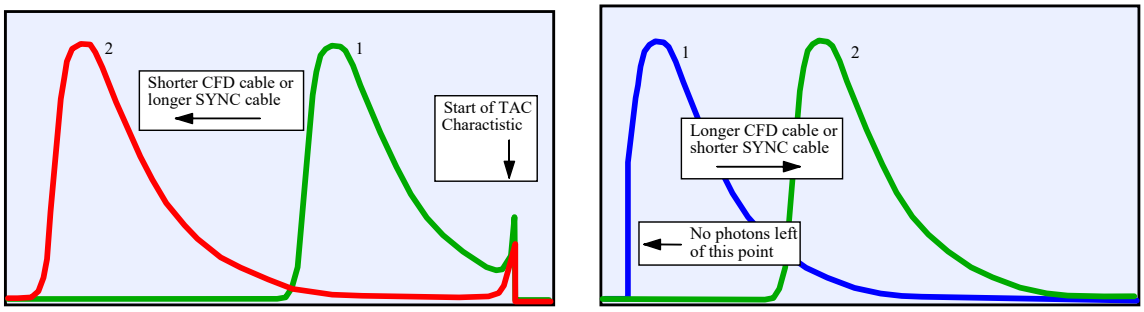


Fig. 432: Left: Photons too late and TAC offset too small, end of TAC characteristic comes into view. Right: Photons too early, no photon with TAC time larger than one signal period recorded

Reversed start-stop operation of TCSPC requires a reference pulse at the end of the signal period or at the end of the recorded time interval. If a high-repetition rate laser is used for excitation this is normally not a problem. However, it is not always clear which laser pulse actually stops the time measurement. It can happen that the stop pulse is not the same laser pulse that excited the detected photon but a pulse from a period before or after. Stopping with a pulse from a different period is no problem if the laser pulses have a constant period and no pulse-to-pulse jitter. This is certainly the case for a Ti:Sapphire laser. Diode lasers, however, may have selectable pulse periods. Moreover, the clock oscillator of a diode laser may have a pulse-to-pulse jitter of some 10 ps. If the reference pulses come from the wrong signal period the position of the recorded signal in the TAC range changes when the laser period is changed. Moreover the pulse-to pulse jitter adds to the transit time spread of the TCSPC system.

To stop the TAC with the correct laser pulse, the reference signal must be delayed so that the reference pulse arrives after a photon pulse from the same period. The correct delay in the reference channel is the detector transit time, plus the width of the recorded time interval, plus a few ns for the TAC start delay. The relation of the detector and reference delay is shown in Fig. 433.

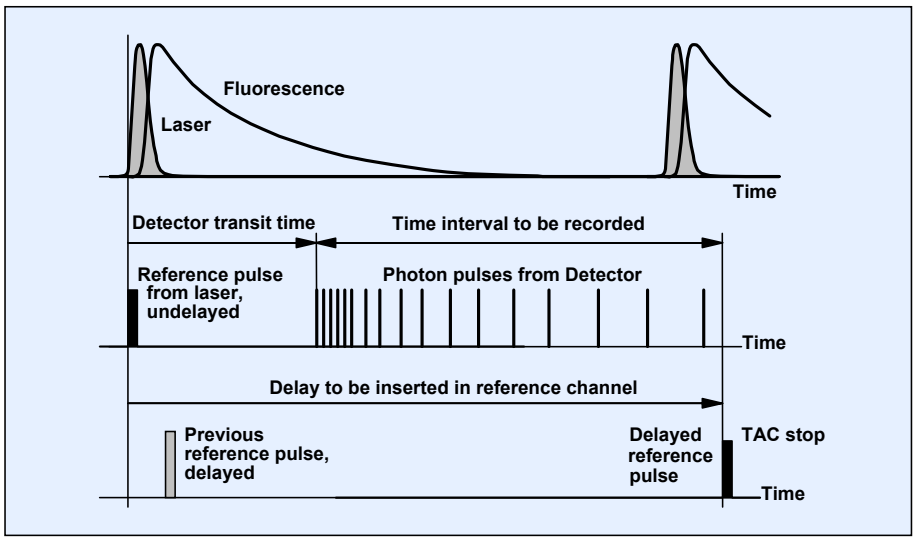


Fig. 433: Reversed start-stop should be used with a delay in the reference channel to stop the TAC with the correct laser pulse

The detector transit time is about 1 ns for an MCP, 5 to 6 ns for a TO-8 PMT or a photosensor module, and 20 to 30 ns for side-window and linear-focused PMTs (see ‘Signal Transit Time’, page 163). A good reference delay to start with is 15 ns or 3 m cable for an MCP PMT and 25 ns or 5 m cable for TO-8 PMTs.

An appropriate delay in the reference path is particularly important in experiments with pulse pickers or kHz lasers. With insufficient delay in the reference path it can happen that a time interval completely outside the signal is recorded. In other cases extremely unfavourable TAC settings are used. The signal period is a few 100 ns, and the signal photons appear in the first part of the signal period. Without a delay in the Sync channel the times of the photons are measured to the next laser pulse. This results in extremely long TAC times that vary only within a small interval. This small time interval is then magnified by an extremely large TAC Gain. The situation is illustrated in Fig. 434, left.

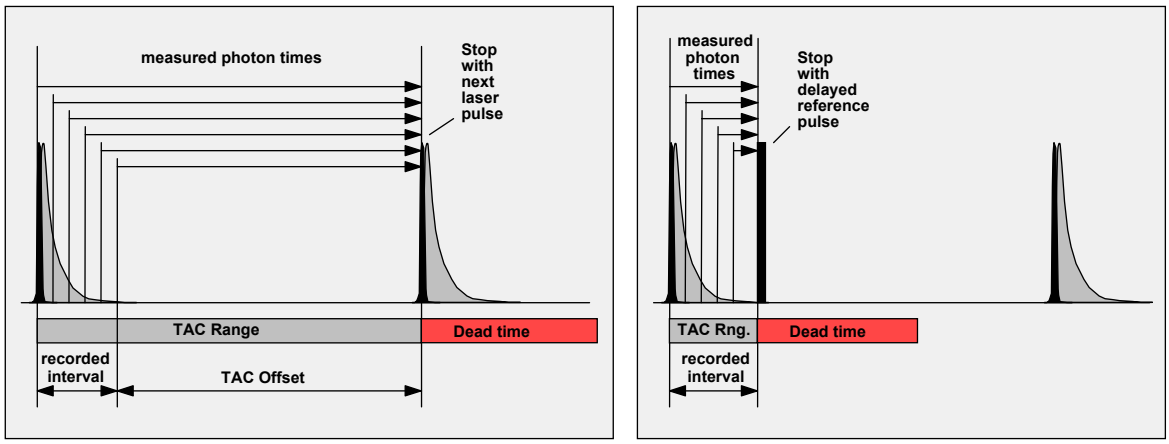


Fig. 434: Recording a short signal within a long laser pulse period. Left: Stop with the undelayed laser pulses; the TAC is stopped by the next laser pulse. Right: Stop with the delayed laser pulses.

There are several serious disadvantages of this way to operate the TAC: The electronic noise from the TAC core is unnecessarily amplified, a possible pulse-to-pulse jitter of the laser appears in the photon times, and the dead time is unnecessarily long. Moreover, the dead time extends into the next signal period. Because the photons appear only in the first part of the period the system is unable to record a photon in the next laser period. Thus, the system has an effective dead time of a full signal period.

A far better solution is to use a delay cable in the reference channel. The delay shifts the stop pulse to a time after the photons to be recorded. The photon times are shifted to smaller TAC times (Fig. 434, right). Consequently, a shorter TAC range and a smaller TAC gain can be used. The result is lower noise in the TAC signal and a correspondingly better time resolution. Because a shorter TAC range is used also the dead time is shorter (see 'Dead Time'). For long signal periods the dead time may even be entirely hidden in the last part of the signal period where no photons are recorded (Fig. 434, right). The influence of different TAC operation on the effective dead time is discussed in [154].

TAC Parameters

The TAC parameters determine the time scale and the part of the signal that is recorded. The bh SPC modules work in the 'reversed start-stop' configuration, i.e. a photon pulse from the detector starts the TAC and the next pulse from the SYNC - or the SYNC frequency divider - stops it. The direction of the time axis is corrected by reversed readout of the photon distributions. As a result, 'time zero' of the TAC is right, and shifting the TAC signal down by increasing the 'TAC Offset' shifts the curve right, see Fig. 435.

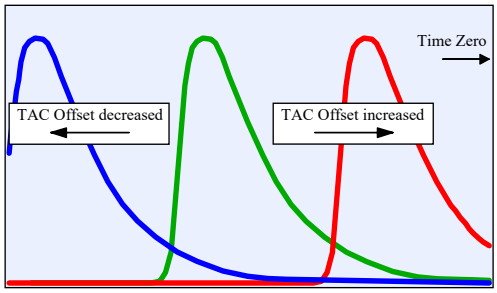


Fig. 435: Effect of TAC Offset

However, if 'TAC Offset' is too small the beginning of the TAC characteristic comes into view. Since the very first part of the TAC characteristic is nonlinear it displays as a short peak with no photons right of it (Fig. 436, left). TAC Offset should be high enough - usually a few % - to shift the beginning of the TAC characteristic out of the recorded time interval. If

the signal is too far right so that it interferes with the beginning of the TAC characteristic, change the CFD or SYNC cable length as described above under ‘SYNC and CFD Signal Path Length’.

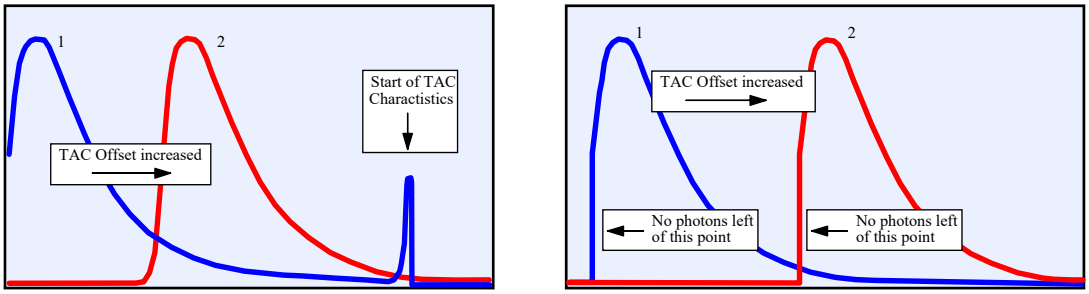


Fig. 436: Left: Increasing the TAC Offset shifts the recorded curve right, and shifts the beginning of the TAC characteristic out the recorded range. Right: No photons with times larger than the stop period are recorded.

The opposite effects happens if some of the photons arrive prior to the previous SYNC pulse. Then the recorded photon distribution drops to zero left of the time where the SYNC pulse is detected (Fig. 436, right). Although the curve can be shifted right by increasing TAC Offset, the part of the signal before the SYNC pulse cannot be detected. The method of correction is increasing the CFD cable length or decreasing the SYNC cable length while decreasing ‘TAC Offset’. (see ‘SYNC and CFD Signal Path Length’).

The parameter ‘TAC Range’ determines the time scale of the recording. The parameter works in conjunction with ‘TAC Gain’ (Fig. 437). ‘TAC Range’ sets the slope gradient of the TAC ramp, ‘TAC Gain’ the gain of the TAC output amplifier. Therefore, TAC Range determines the maximum recording interval, and ‘TAC Gain’ works as a magnifier for a part of this interval, see Fig. 437.

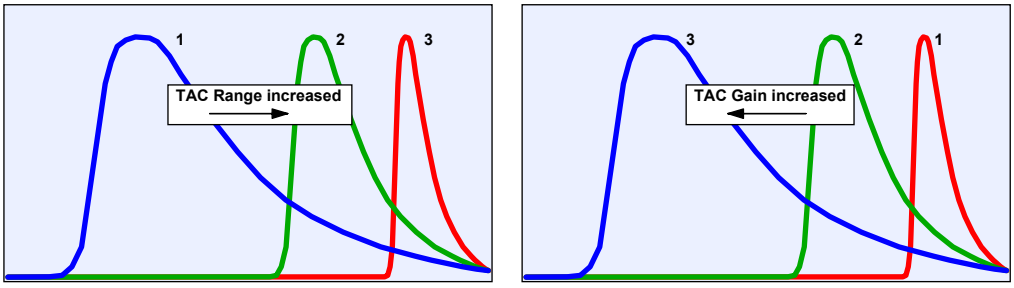


Fig. 437: Effect of TAC Range (left) and effect of TAC Gain (right)

As long as a smaller ‘TAC Range’ is available there is normally no need to use a ‘TAC Gain’ > 1 (see also ‘Dead Time’). However, to obtain maximum resolution within the minimum ‘TAC Range’ of 50 ns ‘TAC Gain’ can be increased to values up to 15.

SYNC and CFD Signal Path Length for SPC-QC Modules

The SPC-QC modules measure the photon times from the Sync pulse to the photons. The effect of signal path lengths and timing parameters is therefore different than for the SPC-series modules. Fig. 438 shows how the recorded curves shift with a change in the signal-transit time in the photon path (top) and in the Sync path (bottom).

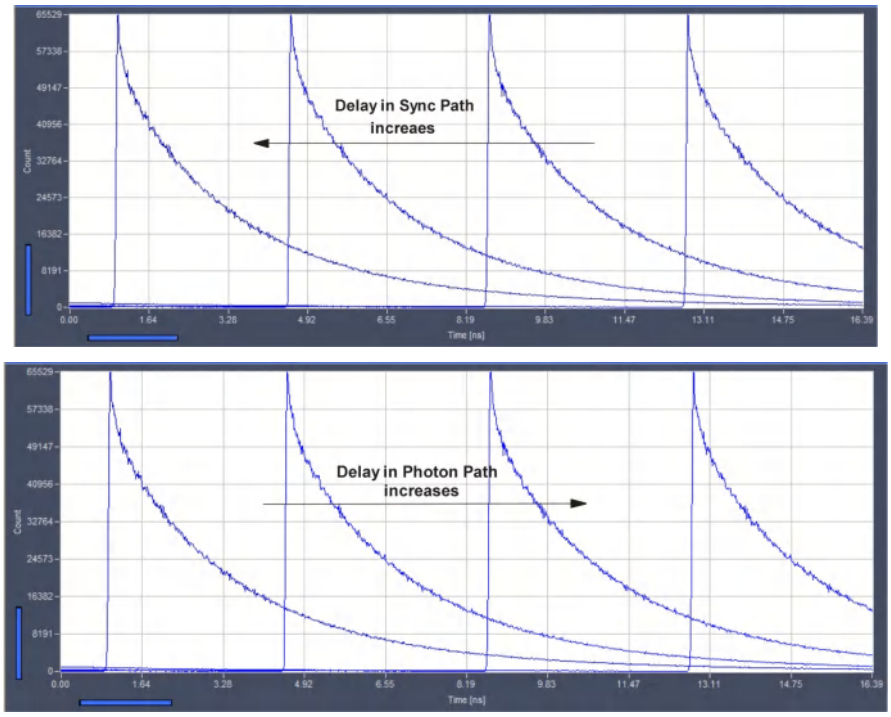


Fig. 438: Shift in the recorded curves with the delay in the photon path (top) and the Sync Path (bottom)

TDC Offset and TDC Range Parameters

A similar shift is obtained by changing the 'TDC OFFset' parameter in the system parameters, see Fig. 439. The effect of different 'TDC Range' on the curves is shown in Fig. 440. For more details, please see handbook of the bh SPC-QC modules [75].

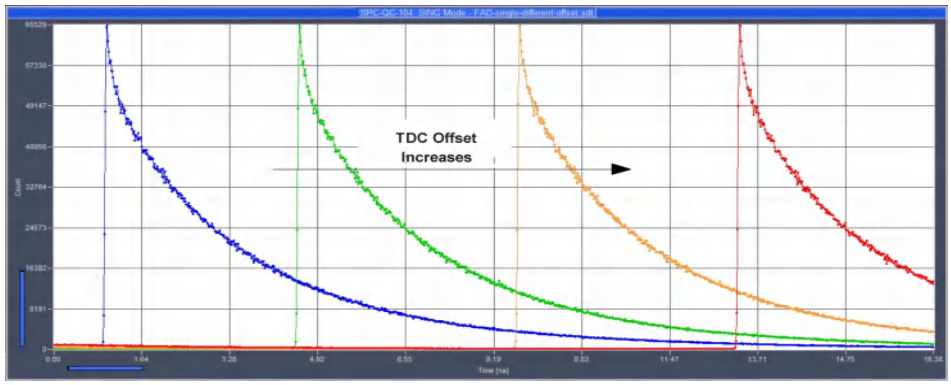


Fig. 439: Shifting the curve by the TDC Offset parameter. From left to right, the curves were recorded with increasing TDC Offset.

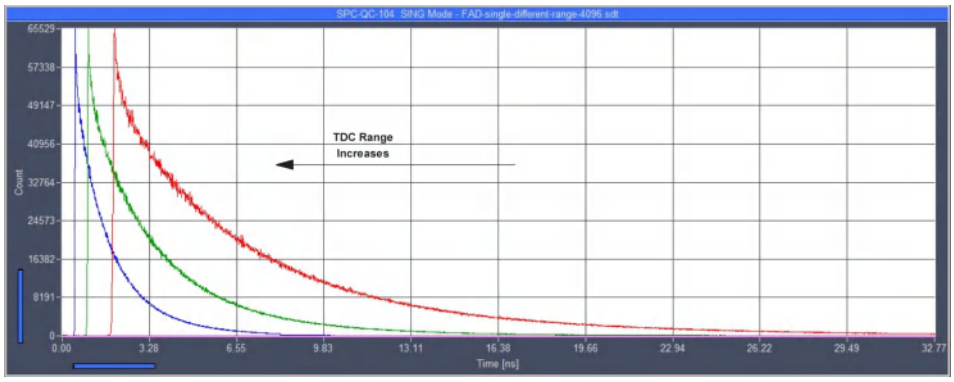


Fig. 440: Effect of different TDC Range on the recorded curves

Excitation Source

Before spending much time to optimise the instrument response function you should check the laser for pulse stability. This may be done by inspecting the pulses from the SYNC photodiode with an oscilloscope. Amplitude modulation, drift or jitter should be as small as possible. The influence of these effects on the timing will be small due to the constant fraction characteristic of the SYNC channel, but it cannot be absolutely avoided. Especially synchronously pumped dye lasers and mode locked argon lasers are prone to instability. Also poorly aligned Ti:Sapphire lasers can develop pulse amplitude jitter and amplitude drift. For such lasers we suggest to monitor the laser action by a fast oscilloscope connected to the SYNC diode or a second photodiode. It is also recommended to switch on the count rate displays in the SPC main panel and check the sync frequency. This is recommended especially if the laser system tends to produce prepulses or afterpulses. If you use active mode locking in your laser, make sure that the mode locking frequency does not interfere with the SYNC signal. This frequency is one half the repetition rate and can seriously affect the synchronisation.

If possible do not use pulse pickers or cavity dumpers. It is not only that these devices produce very unpleasant electrical noise, they also transmit satellite pulses of considerable amplitude. This can make the synchronisation difficult. If you must work with a pulse picker for whatever reason, adjust the SYNC threshold that satellite pulse do not trigger the SNC channel.

IRF Stability

A common source of IRF instability are scattering solutions or cuvettes of large diameter. If the scattering coefficient is too high pulse broadening by some 100 ps can result. Moreover, the transit time in a fully illuminated 1 cm cuvette adds almost 100 ps to the IRF with. For optimising the time resolution of a detector we recommend not to use a scattering target. It is better to put a package of absorptive ND filters in front of the PMT and to illuminate it directly by the laser.

Electromagnetic Shielding

Noise on the start and stop inputs can noticeably degrade the time resolution, counting efficiency and the differential linearity of a TCSPC system.

Noise may have different effects on the recorded signals. Asynchronous RF noise, e.g. noise from radio and television transmitters reduces the signal-to-noise ratio of the start and stop pulses. The result is poor timing accuracy, i.e. broadening of the IRF of the TCSPC system. Moreover, noise can make it impossible to use a sufficiently low CFD threshold to record all single-photon pulses within the pulse distribution of the detector. The result is a loss in counting efficiency.

RF pickup from the excitation source or crosstalk between the detector and the reference lines causes systematic timing errors. The result is a modulation of the effective CFD threshold and the effective CFD zero cross point. Modulation of the threshold modulates the detection efficiency; modulation of the zero cross point warps the time axis. In either case the result is a ripple in the recorded curves, see Fig. 447, page 289.

Improper shielding or grounding can even transform the line frequency into the input signals. Because the line frequency is usually not synchronous with the signal repetition rate, the apparent effect for long acquisition times is the same as for RF pickup. The difference shows up

if sequences of curves faster than the line frequency are recorded. The size and the temporal position of the curves are then modulated with the line frequency.

The rejection of noise is most critical for PMT signals. It is not only that the single-photon pulses of a PMT can have small amplitudes in general, there is also a wide spectrum of pulse amplitudes. Even if the average amplitude is on the order of 100 mV, there is a large amount of pulses of much smaller amplitude. These are, of course, most likely to be influenced by external noise.

Unfortunately, proper shielding of TCSPC system components is not straightforward. Like all high-speed electronics, TCSPC uses impedance-matched cables for the signal connections. These connections are relatively immune to capacitive noise pickup. Therefore, building a simple metal box around the detector or even the whole TCSPC system often does not solve the problem.

The problem in TCSPC systems usually is inductive noise coupling. RF radiation from external noise sources penetrates the setup and induces noise currents in the ground lines between different system components. Also power supply currents with RF noise components can flow in the ground system. The currents flow partially through the outer conductors of the coaxial lines connecting different system components. A part of the RF noise is transformed into the inner conductors, and thus introduced into the signal lines. If ground loops are the cause of noise pickup, simple screening of the system has little effect; the ground loops must be found and disrupted, or the noise currents must be diverted.

Fig. 441, left shows what can happen if different system components are connected to different power sockets. The power supply system in a large building forms a huge antenna. In addition, switching transients from power supplies inject large RF currents into the power lines and the ground connectors. If the sockets of the system components are connected to different power circuits of the building, huge compensation currents can flow through the ground conductors and, consequently, through the signal cables that connect the components. Of course, most of the current flows through the outer shield of the cables. However, the impedance of the shield is not zero, and some of the current flows through the signal line and the 50 Ω matching resistors as well. A simple solution is to supply all system components from only one power socket, as shown in Fig. 441, right.

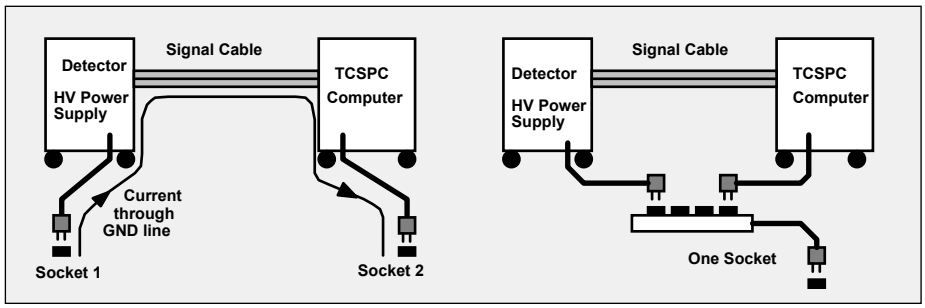


Fig. 441: Ground loop formed by connecting system components to different power sockets

A similar situation can result when a network cable is connected to the computer of the TCSPC system. Network cables often go through a large part of a building and form a huge ground loop. Although the cable has no DC connection into the computers, there is enough capacitive coupling to allow RF currents to flow. A network cable can therefore inject considerable noise currents into a TCSPC system.

RF currents can also be induced in ground systems by an RF field that penetrates the area between the ground plane and the signal cable, see Fig. 442, left. The RF field induces a current flowing through the shield of the signal cables. A part of this current may be introduced

into the detector signal. One remedy is to disrupt the ground loop by isolating the detector (Fig. 442, right).

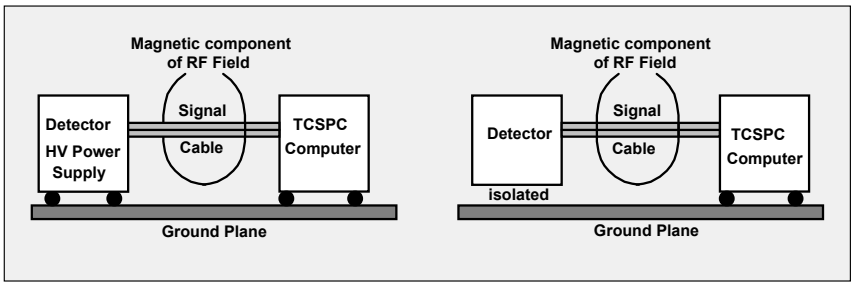


Fig. 442: Ground loop, left; avoiding it by isolating one system component from the ground, right.

If there is no closed loop there is also less RF current flowing through the cable and less noise pickup. However, the detector housing may still be enough of an antenna to send some RF current through the signal cable. Isolating it from the ground may then make the noise pickup even worse. In other cases it may not be possible to isolate the detector from the system ground because there is an additional connection to the detector power supply.

It is therefore impossible to disrupt all ground loops. Some improvement may possibly be achieved by putting ferrite ring cores on the cables. The ferrite core increases the inductance of the ground loop and thus reduces the RF current flowing through it. Ferrite cores that can be snapped on the cables are available for this purpose. However, the effect of such measures is usually small.

Therefore, the best viable strategy is to prevent RF noise from being introduced into the detector signals. This can be achieved by properly shielding the detectors. Unfortunately, shielding is anything but simple, and a large number of inefficient solutions can be found. Two wrong design principles are shown in Fig. 443.

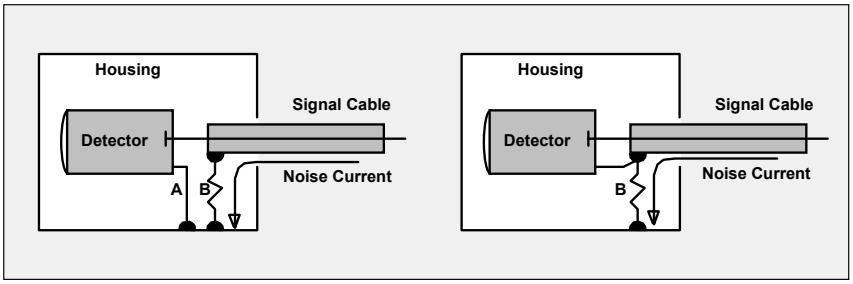


Fig. 443: Two examples of improper shielding: The noise voltage induced across the inductance of the ground connection B appears directly in the signal (left) or between the housing and the signal line (right).

In Fig. 443, left, the noise current flowing through the cable shield into the detector housing shares the ground line, B, with the signal current. The noise current generates a noise voltage across the inductance of the connection B, and this voltage appears in the signal. The same happens with any noise current injected into the detector housing. Therefore the housing has a poor screening effect. In Fig. 443, right, the noise current and the signal do not share the line B, but there is still an RF voltage across the inductance of the line B. Consequently, the housing is not shielding the detector adequately.

The correct design is shown in Fig. 444. The cable shield is connected to the housing *directly* at the point where it is fed through. The noise current is diverted directly into the housing. There is neither a noise current in a signal ground line nor any noise-induced voltage inside the housing. The best way to connect the cable shield is to build an appropriate coaxial connector into the housing.

Often additional control or power supply lines have to be fed into the housing. The best way to avoid noise injection via these lines is with a feed-through capacitor or a feed-through filter, see Fig. 444, right. If a feed-through capacitor cannot be used, i.e. for the high voltage of a PMT, a coaxial cable should be used and connected as described for the signal cable.

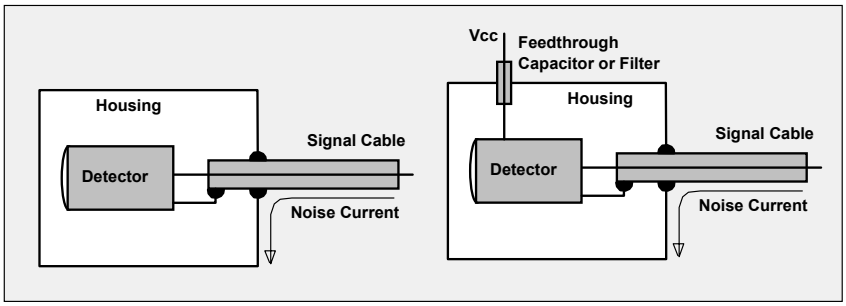


Fig. 444: Correctly designed RF shielding. The noise current flowing through the cable shield is diverted outside the housing

It is often hard to believe that there is an appreciable difference between the designs shown in Fig. 443 and Fig. 444, especially if the length of connection B is 'only a few centimetres'. However, it is precisely the wire B that makes the difference between an ineffective shielding and an effective one, even if the length is only one or two centimetres. The wrong design shown in Fig. 443 can be found in many variations, including designs with an inductor in the place of the wire B or housings with no connection to the signal ground at all. All these designs have in common that the cable shield is not connected to the housing at the point where the cable is fed through. In practice it can be difficult to correct such designs. For a signal cable, one possible solution is to scratch the outer insulation open and solder the cable shield to the housing. For a high-voltage cable such treatment cannot be seriously considered. An emergency repair that yields at least some improvement is to wrap a copper foil around the last 10 to 20 cm of the cable and solder this foil to the housing, see Fig. 445. The copper foil forms a capacitor with the outer connector of the cable, which diverts a large part of the RF noise current.

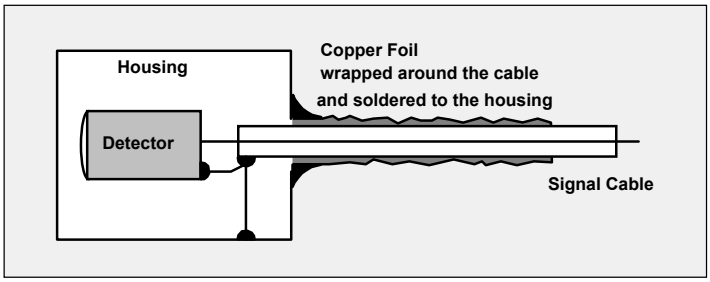


Fig. 445: 'Emergency repair' of a poorly designed RF shield. A copper foil wrapped around the cable forms a capacitor with the cable shield and diverts a part of the noise current

Differential Nonlinearity

The differential nonlinearity (DNL) of the time measurement is a common problem of TCSPC measurements.

Normally imperfect TAC and ADC performance is considered the source of differential nonlinearity. However, normally the source of the problem in not in the TAC or in the ADC. Fig. 446 shows a DNL recording of the SCP-150 ADC-TAC circuitry. Two signals from independent sources were connected directly to the start and the stop input of the TAC. As can be seen from the figure the curve is almost ideally flat.

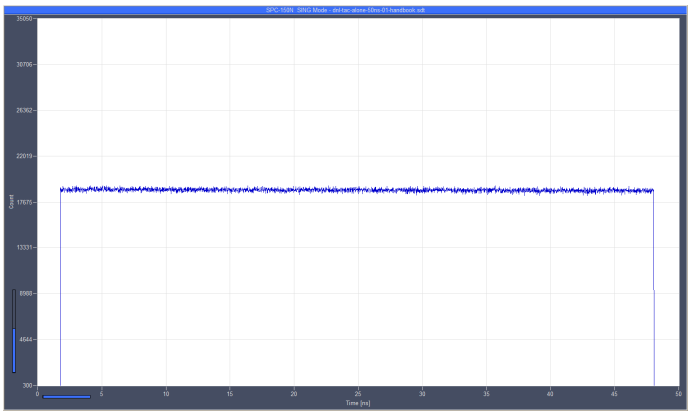


Fig. 446: DNL curve of an SPC-150, start and stop pulses from two pulse generators, directly connected to the TAC

That means deviations from the ideal time-conversion characteristic must occur before the TAC - in the CFDs or outside the TCSPC module. It turns out that the reason of sub-ideal DNL is spurious coupling of start- and stop-related signals - laser-synchronous noise pickup of the detector, coupling between the detector and synchronisation cables, coupling between the CFD and the SYNC circuits, or noise pickup of the CFD for the detector signal from stop-related signals on the SPC board. The result of such interaction is nonuniformity of the channel width and, consequently, a nonuniform count result in the particular channels. Laser-synchronous noise pickup may also modulate the effective CFD threshold, with the result that more or less photon pulses are detected at different times in the laser pulse period. The mechanism is illustrated in Fig. 447. If synchronous noise is present, the complete pulse height spectrum (shown grey in Fig. 447) is shifted up and down with the warped pulse baseline. Consequently, the probability of the photon pulses to exceed the threshold changes with the time in the signal period. The result is a modulation of the measured waveform by the spurious signal. If the detector has a narrow pulse height distribution and the threshold is adjusted correctly, the effect on the detection probability is small (Fig. 447, left). However, if the pulse height spectrum is broad or the detector is not operated in the counting plateau even a small ripple on the baseline causes serious distortions of the measured waveform (Fig. 447, right).

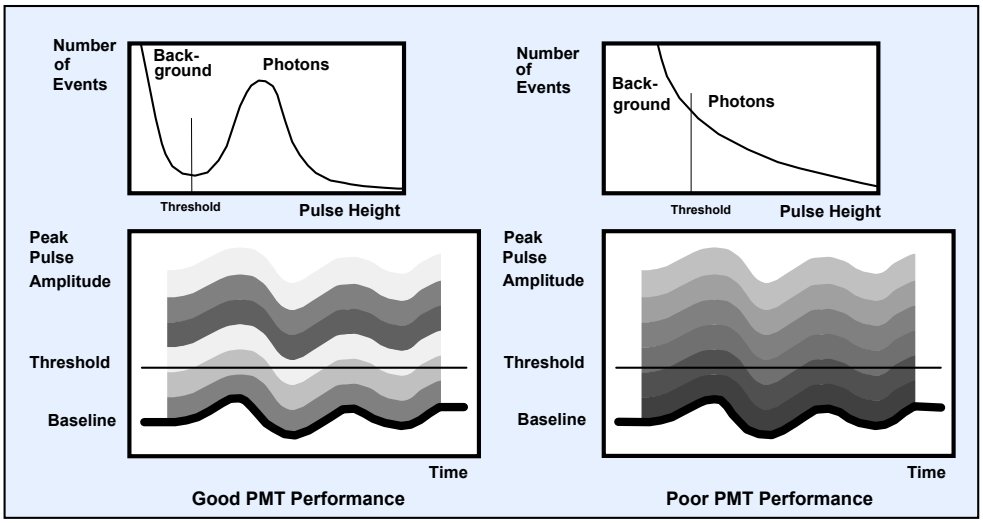


Fig. 447: Interaction of spurious signals with the PMT pulse height spectrum

Good electrical shielding of the detector is therefore extremely important. Any coupling of the SYNC signal or other excitation-related signals into the detector signal must be strictly avoided. Detector and synchronisation cables should be separated spatially. Equally important

is that noise radiation from the excitation source is avoided. Noise radiation is a problem especially for pulse pickers, cavity dumpers, and active mode-lockers. Notorious noise transmitters are poorly shielded picosecond diode lasers, and even Ti:Sa lasers may not be free of noise radiation.

When noise from the excitation source cannot be entirely avoided the detector should be operated at a gain as high as possible. If possible, a detector with a narrow pulse height distribution should be used. Such detectors are less impaired by noise because there are less pulses of small amplitude (which are more influenced by the noise from the laser) and the effect of threshold modulation (Fig. 447) is smaller. This is probably the reason that TCSPC systems with the bh HPM-100 hybrid detectors usually deliver a better DNL than systems with ordinary PMTs.

For measurements that require maximum accuracy a reference curve with a continuous light source can be recorded. The measurement results is then divided by this curve. The operation can be performed by SPCM software, see ‘2D Data Processing’, page 801. Because the reference curve has the same linearity errors as the measurement results, the division removed the DNL errors. Introducing noise of the reference measurement into the quotient can be largely avoided by smoothing the reference curve before it is used [154].

Dead Time

The ‘dead time’ is the time the system is ‘blind’ after the detection of a photon. On the one hand, the dead time of a TCSPC device has a positive in that it helps suppress afterpulses of the detector. On the other hand, the dead time sets a limit to the count rate that can be used when an optical signal is recorded. Moreover, it can introduce distortions of the signal waveform and errors in the measured intensities. The sources of the dead time, its influence of the measured photon numbers and on the recorded waveforms is discussed in the following paragraphs.

Fig. 448 shows the timing diagram of the TAC/ADC combination for a single detected photon.

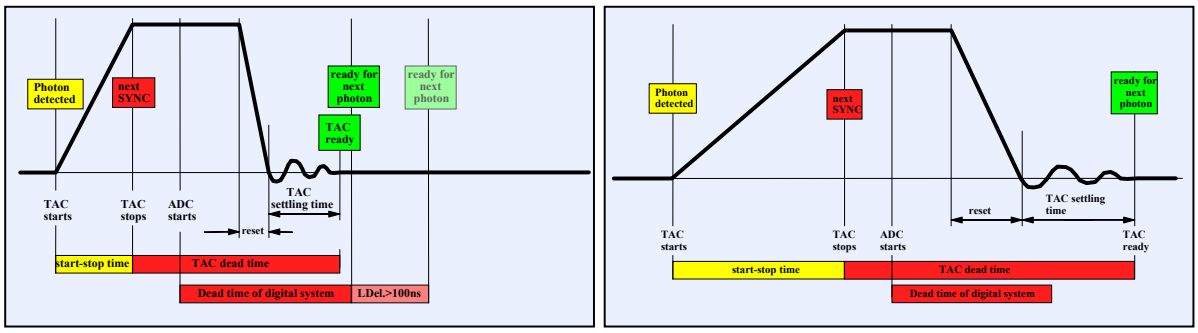


Fig. 448: Timing diagram for TAC Range < 100 ns (left) and TAC Range >100 ns (right)

When the photon is detected the TAC ramp starts until the next STOP pulse arrives at the TAC. Depending on the ‘SYNC Frequency Divider’ setting this can be the next synchronisation pulse from the light source or one of the next 2, 4, 8 or 16 pulses. Some 10 ns after the TAC has stopped the ADC is started. When the ADC is ready the TAC is reset, i.e. the TAC capacitor is discharged. After some additional recovery time needed for the TAC output amplifiers to settle the TAC is ready to convert the next photon.

With the start of the ADC, i.e. in parallel with the TAC reset the digital signal processing sequence for the current photon is initiated. The digital system sends a ‘not ready’ signal to the TAC which holds the TAC in the reset state until the next photon can be accepted.

For TAC ranges smaller than 100 ns and for a ‘Latch Delay’ smaller than 100 ns the end of the of the TAC dead time and the end of the digital signal processing are almost coincident. For ‘Latch Delay’ > 100 ns the digital dead time increases because the digital signal processing machine has to wait until the routing signal has been latched.

For longer TAC ranges the TAC reset and recovery time can be significantly longer because the TAC capacitor is larger. Approximate TAC dead times are given in the table below:

TAC Range	TAC Dead Time: SPC-6, -8	SPC-130, -150	SPC-160, -180
50 ns to 99 ns	125 ns	100 ns	80 ns
100 ns to 199 ns	150 ns	140 ns	120 ns
200 ns to 499 ns	180 ns	180 ns	160 ns
500 ns to 999 ns	260 ns	260 ns	240 ns
1 µs to 2 µs	550 ns	550 ns	530 ns

The times depend on the time difference between start and stop, because the TAC reset time increases with the TAC output voltage. The values in the table are for 50% TAC output voltage. The ‘Dead Time’ given in data sheets is normally the time from the stop pulse to the moment when the system is ready for the next photon. The effective dead time for a particular photon is this ‘Dead Time’ plus the start-stop time. The start-stop time depends on the operating conditions, particularly on the signal duration and the time from the signal to the next sync pulse. For a typical Ti:Sa laser experiment with 12 ns pulse spacing the average start-stop time is on the order of 6 ns so that the dead time is not significantly increased. However, for fluorescence decay measurements in the 100 ns range there can be a noticeable contribution of the start-stop time. Fig. 449 shows how the overall dead time depends on the start-stop time.

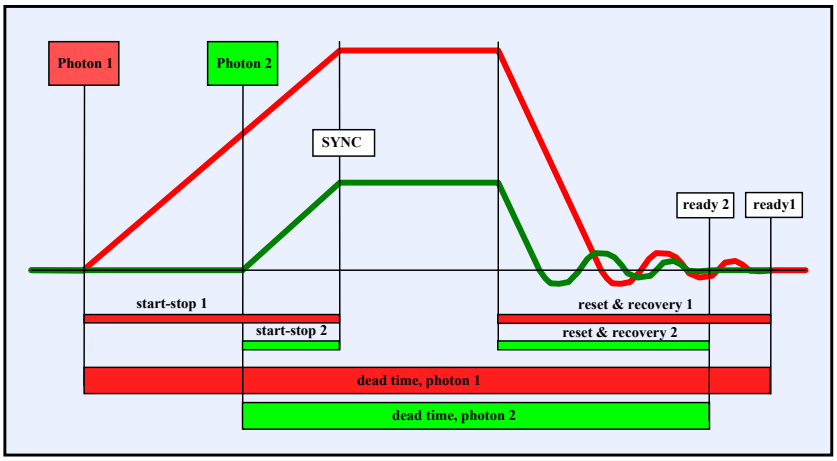


Fig. 449: Influence of the start-stop time on the overall dead time

Please note that the start-stop time not only contributes to the overall dead time, also the TAC reset time increases proportionally. To hold the effective dead time as short as possible we recommend:

- Use the smallest possible TAC range. This holds the TAC reset and recovery time short.
- Avoid unnecessarily long start-stop times. Use ‘Sync Frequency Divider’ = 1 and a ‘TAC Offset’ as small as possible. Adjust the SYNC and CFD cables to shift the signal as far as possible right.
- For measurements at low repetition rate, use a delay cable in the SYNC path. Delayed stop operation can eliminate the effect of dead time entirely, see Fig. 434.

Counting Loss

When recording a light signal the single photon pulses from the detector occur at random times. Therefore, even if the average time interval between the pulses is much longer than the dead time of the counting system, a fraction of the pulses is lost. For the calculation of the counting loss is important whether a photon lost in the dead time causes new dead time or not. In TCSPC a lost photon clearly does not cause any noticeable dead time. Under this condition the recorded rate, r, for a input pulse rate, r_0, is

$$r = \frac{r_0}{1 + r_0 t_d}, \text{ with } t_d = \text{dead time}$$

The counting efficiency, E, is

$$E = \frac{r}{r_0} = \frac{1}{1 + r_0 t_d}$$

Effect on TCSPC Results

The relation between detector count rate and recorded count rate is shown graphically in Fig. 450. The curve becomes visibly nonlinear above a detector count rate of 10% of the reciprocal dead time.

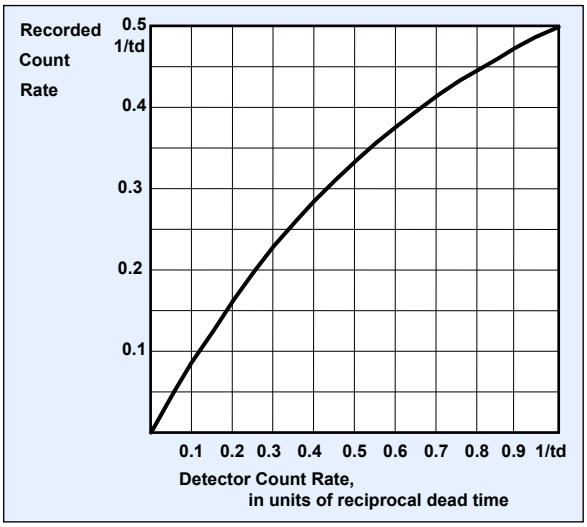


Fig. 450: Recorded count rate vs. input count rate for a counter with the dead time t_d

The nonlinear intensity scale shows up especially in FLIM images recorded at high count rates: The images look increasingly 'flat' when the count rate comes close to the reciprocal dead time. An example is shown in Fig. 698, page 478.

Fortunately, most TCSPC applications focus on recording temporal parameters, such as a fluorescence lifetime. These parameters are independent of a number of unknowns, such as concentration of fluorophores or absorbers in the sample, unstable laser power, or unstable optics. A nonlinearity of the intensity scale is therefore not normally a problem.

Maximum Count Rate

For an input count rate of the reciprocal dead time, $1/t_d$, the recorded count rate is 50% of the input count rate. bh defines the recorded count rate for 50% loss as the 'maximum useful count rate':

$$r_{mu} = 0.5 / t_d$$

The input (or detector) count rate, r_0, at the maximum useful count rate, r_{mu} is the reciprocal dead time, *1/td*.

Often data sheets of photon counters specify a ‘maximum count rate’ which is simply the reciprocal dead time. Of course this count rate can be reached only for infinite input count rate. Better the term ‘saturated count rate’ should be used, see ‘Specification’, page 973.

The consideration above assumes that the detected light signal is continuous. However, signals measured by TCSPC are usually pulsed. Moreover, the photon detection and consequently the dead time is synchronised with the signal period. The equation given above applies with satisfactory accuracy to reversed start-stop measurements at high pulse repetition rate. In other cases the counting loss depends on the operating conditions. Depending on the system configuration, there may be no dead-time related counting loss at all, or the effective dead time can be a full signal period (see Fig. 434). A detailed discussion is given in [154].

Dead-Time Compensation

The bh TCSPC modules provide an optional ‘dead-time compensation’ in the device hardware. The idea behind the dead-time compensation is to increase the collection time by the sum of all dead time intervals that occurred during the measurement. The principle is shown in Fig. 451.

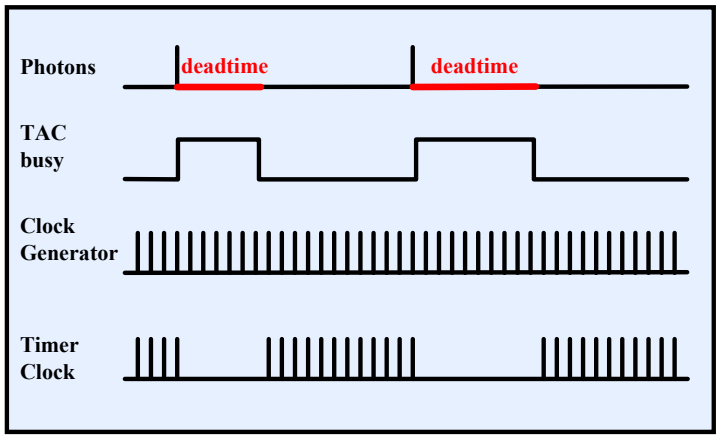


Fig. 451: Dead time compensation by gating the timer clock

The TAC delivers a ‘busy’ signal as long as it is unable to accept a new photon. A high frequency clock is gated with the ‘busy’ signal, and the gated clock is used to drive the collection timer. Thus, the collection timer is stopped in the dead-time intervals.

We recommend to use dead-time compensation for measurements that require an accurate intensity scale. However, please take into regard that the compensated collection time changes with the count rate and can be noticeably longer than the selected collection time.

The dead time compensation works with satisfactory accuracy if the photons can be considered to appear in random intervals, and in a virtually continuous stream. This is the case for reversed-start-stop measurements at high repetition rate, when the signal period is several times shorter than the dead time. The dead time compensation is not necessarily correct for measurements at low repetition rate, see Fig. 434, right. The compensation also does not work for simulated detector pulses delivered by a pulse generator at a fixed frequency.

Pile-Up

Classic Pile-Up

'Pile-Up' is the possible detection - and loss - of a second photon in the same excitation pulse period with a previous one. As a consequence, an optical waveform recorded by TCSPC gets distorted when the count rate becomes too high. The pile-up effect is often used as an argument against TCSPC and, especially TCSPC FLIM. *Please don't get confused by such statements. They are wrong.*

It is commonly believed and written over and over again that the count rate of TCSPC and TCSPC FLIM must not exceed 0.1% of the excitation rate. The limit of 0.1% stems from a typo in the TCSPC literature of the late 1970s. Since the 1980s the wrong size of the pile-up has been duly copied without ever being challenged, and been taken as a basis of technical discussion and technical development.

The correct size of the pile-up error has been calculated in [154]. It turns out that it is 100 times smaller than believed. The count rate limit dictated by pile-up is 0.1 x (or 10% of) the excitation pulse rate. With the correct value of the pile-up limit, the maximum count rate for 80 MHz repetition rate is 8 MHz (8×10^6 photons per second). This is 100 times more than commonly believed and 10 times more than typical FLIM samples can deliver without photo-induced changes in their molecular structure. It is probably a singular case in technical history that a typo has impeded the application of a technique over half a century.

How deeply the misconception of pile-up is fixed in the minds of TCSPC users becomes evident from the fact that [154] is constantly cited as a proof of the allegedly devastating effect of pile-up on TCSPC FLIM. In fact, [154] proofs the opposite. Therefore, make sure that you cite [154] in the *correct context*. If you carelessly copy the mistake you show that you either have stolen the reference from another paper, or that you were unable to grasp the point of [154] – which even sub-average intelligence should have been able to.

The pile-up effect is shown schematically in Fig. 452. Pile-up becomes noticeable when the count rate exceeds a few percent of the pulse repetition rate. Detection and loss of a second photon is more likely to occur in the later part of the signal, therefore the recorded waveform is distorted.

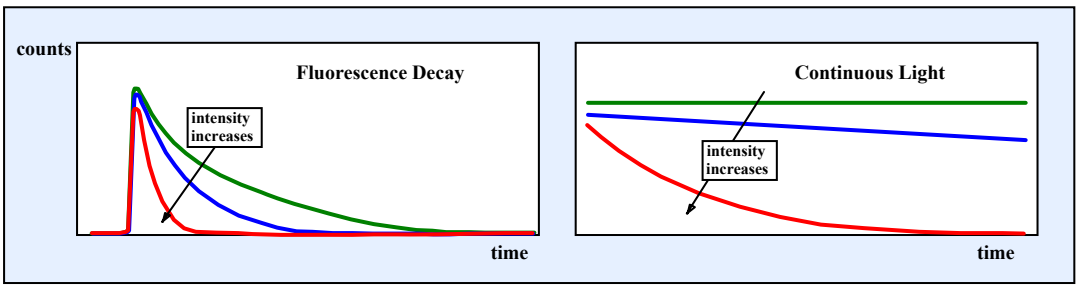


Fig. 452: Effect of classic pile-up on the waveform

Pile-up was indeed an inherent source of signal distortion in experiments with lasers or flashlamps working at a repetition rate in the kHz range [768, 759, 760, 1086, 1367]. The distortion of the signal shape by pile-up is predictable and - within reasonable limits - correctable if the detector count rate and the signal repetition rate are known [316, 317, 318, 924, 1367]. However if a flashlamp-based experiment was run at too high a count rate, extreme pile-up effects could impair the results so severely that any attempt at correction was useless. If the detector actually sees hundreds or thousands of photons per laser pulse, pile-up can even mimic signals shorter than the detector transit time spread (see 'Multi-Photon Detection', page 278).

The actual size of the pile-up effect has been calculated in [154]. Pile-up adds virtual lifetime components of $\tau/2$, $\tau/3$ ... τ/n, to the recorded waveform. A mean lifetime, τ_{meani}, of the recorded curve can be defined as an average of the lifetimes, τ_i weighted by their integral intensities, [742]:

$$\tau_{meani} = \frac{\sum a_i \tau_i^2}{a_i \tau_i}$$

with a_i = intensity coefficients of the lifetime components, τ_i .

The pile-up distorted τ_{meani} is

$$\tau_{meani} = \tau \frac{1 + \frac{1}{2}\frac{1}{2!}P + \frac{1}{3}\frac{1}{3!}P^2 + \frac{1}{4}\frac{1}{4!}P^3 + ...}{1 + \frac{1}{2!}P + \frac{1}{3!}P^2 + \frac{1}{4!}P^3 + ...}$$

with P = average number of photons per laser period [154]. For small values of P the mean lifetime is

$$\tau_{meani} \approx \tau \left(1 - P/4\right) \quad \text{or} \quad \tau_{meani} \approx \tau \left(1 - r_{phot}/4r_{laser}\right)$$

with P = average number of photons per laser period, r_{phot} = photon rate, r_{laser} = laser pulse rate.

Fig. 453 shows the recorded intensity-weighted mean lifetime as a function of the number of photons per laser period, P, relative to the correct lifetime, τ .

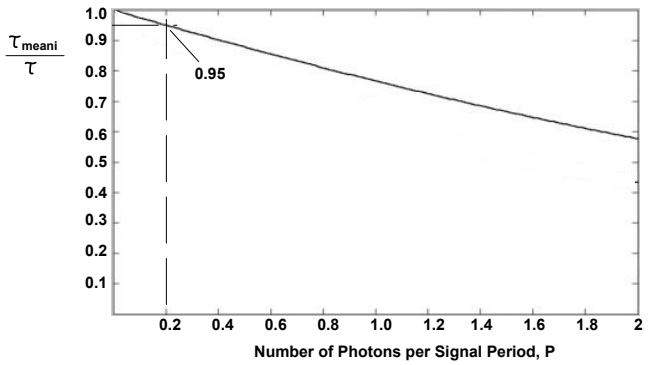


Fig. 453: Intensity-weighted lifetime as a function of the number of photons detected per signal period, P

As can be seen from Fig. 453 the influence of pile-up on the obtained lifetimes is surprisingly small. A count rate of 10% of the laser repetition rate cause lifetime change of no more than 2.5%. In many cases a 5% change in the intensity-weighted mean lifetime is tolerable. The corresponding P is then about 0.2, i.e. the detector count rate can be 20% of the pulse repetition rate. Classic pile-up is therefore not a real problem at pulse repetition rates between 50 and 100 MHz, as they are typical for titanium-sapphire lasers, fibre lasers, and picosecond diode lasers.

Inter-Pulse Pile-Up

Inter-pulse pile-up is a problem of high-repetition rate experiments. It is actually a counting-loss effect, but it causes signal distortions as the classic pile-up does. The effect is illustrated in Fig. 454. After a photon was detected the system is blind for the start-stop time and the TAC/ADC dead time. The TAC/ADC dead time starts with the next SYNC pulse and ends

somewhere in one of the next SYNC periods. Consequently, no photon can be detected in the first part of this period.

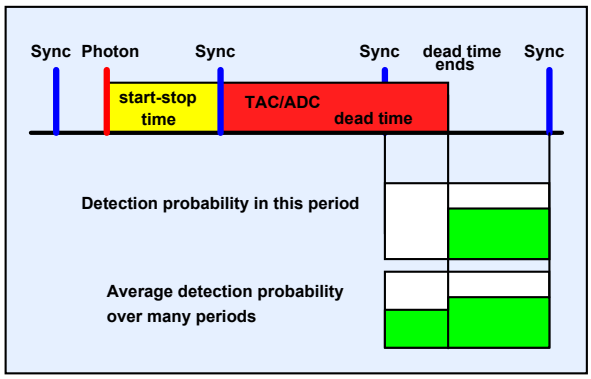


Fig. 454: Mechanism of inter-pulse pile-up

Averaged over a large number of periods, the result is a step in the recording probability. The recorded waveforms are thus distorted. The size of the distortion depends on the ratio of the count rate to the signal repetition rate and can be estimated as follows:

The probability, P, to detect a photon in a particular laser period is

$$P = r_{det} / f_{rep}$$

with r_{det} = detector count rate at the CFD input, f_{rep} = signal repetition rate. However, a photon in the early part of the period can be recorded only if no photon was detected in the signal period a dead-time interval before. The probability, p_{early}, of detecting a photon in the early part of the period is therefore

$$p_{early} = \frac{r_{\mathrm{det}}}{f_{rep}} \left(1 - \frac{r_{\mathrm{det}}}{f_{\,rep}} \right)$$

The relative size of the distortion is

$$(p_{late} - p_{early}) / p_{late} = r_{det} / f_{rep}$$

Interestingly, the size of the dead-time-related distortion does not depend on the dead time. The absolute size of the distortion is of the same order as the distortion by classic pile-up. It even counteracts the classic pile-up because it happens in the early part of the signal period. Although the size of the distortion is predictable, the actual shape of the distortion is not. If the recorded time interval is shorter than one signal period the distortion may be outside the recorded interval. It may differ from a clean step because the dead time may vary due the TAC voltage of the detected photon, and the transition from the blind into the active state may cause some ripple in the TAC characteristic for a few ns. Moreover, in practice the dead time is determined by CMOS logic circuits and active delay lines in the control circuitry of the TCSPC module. The dead time can therefore be expected to be stable within a few ns at best. The temporal position of a possible distortion is therefore not absolutely stable. Thus, it is difficult to correct for dead-time-related distortion.

In practice the distortion can be minimised in the same way as classic pile-up, i.e. by maximising the signal repetition rate, or, more precisely, maximising the TAC stop rate. The signal repetition rate should be as high as possible, and the setup should avoid frequency division in the reference channel and pulse-by-pulse multiplexing with a common stop pulse (see Fig. 456, page 299).

It should be noted here that distortions by inter-pulse pile-up have exactly the same appearance as distortions by optical reflections (see Fig. 463, page 306). In fact, the vast majority of step-like distortions is caused by optical reflections, not by inter-pulse pile-up. Therefore the optical system should be checked before a TCSPC module is suspected to produce distortions by inter-pulse pile-up.

Avoiding Pile-Up Errors

As shown in the two paragraphs above, pile-up is rarely a problem in standard fluorescence-decay and FLIM applications. For the commonly used excitation sources the excitation-pulse repetition rate is 50 to 80 MHz. With these excitation sources a TCSPC device can be operated up to a photon count rate of 5 to 8 MHz without introducing noticeable pile-up errors. Such count rates are hard to obtain in normal TCSPC and FLIM experiments. This is especially the case when biological samples are investigated.

Nevertheless, a few simple mistakes should be avoided:

- Most pile-up problems originate from the use of lasers with low repetition rate, especially lasers with pulse pickers and amplifiers. Such lasers are often selected because of their high peak power. The repetition rate of these lasers is in the 100-KHz range. Of couse, the low repetition rate causes problems with pile-up. Moreover, such laser systems are exceedingly expensive. For TCSPC they are entirely unnecessary - the pulse power from a normal fs Ti:Sa laser, a fs fibre laser, or a ps diode laser is more than enough for FLIM and classic fluorescence-decay measurements.
- Keep the laser pulse rate as high as possible. It is often feared that the excitation pulse period is too short for the fluorescence to decay completely within one pulse period of the laser. Such concerns are unnecessary. SPCImage NG data analysis can deal with such cases unless the lifetime is longer than the laser period.
- Avoid pulse-interleaved excitation. It reduces the effective excitation pulse rate for each of the signals to be recorded.
- Do not use 'Frequency Divider' settings larger than one for fluorescence-decay measurement. This reduces the effective stop rate of the TCSPC module and is thus equivalent to lower laser pulse rate.
- Do not attempt to record phosphorescence decay functions with single low-repetition rate pulses in the normal TCSPC or TCSPC / FLIM modes. Not only would a single femtosecond or picosecond pulse excite much phosphorescence, the pile-up would be extreme. Instead, use combined FLIM / PLIM with multi-pulse excitation, as described in chapter 'Simultaneous FLIM/PLIM', page 434.

Nevertheless, there remain a few TCSPC applications where the excitation pulse rate cannot be easily increased. One example are measurements of barrier discharges or positron lifetime experiments, see page 681 and page 687 of this book and LIDAR, see page 689. There may also be experiments in plasma physics which require extremely high pulse power and thus preclude the use of high repetition rate. In principle, such experiments could benefit from the pile-up rejection circuits developed in early times of TCSPC [1086, 1339]. The circuits detected a possible second photon in one signal period, and, when a second photon was detected, suppressed the storing of both photons in the memory. Consequently, only photons from signal periods with one photon were used. In practice this approach has a significant flaw. Typical fluorescence lifetimes are on the order of a few ns, i.e. in the same range as the width of the detector pulses. It is then not possible to distinguish between one or two photons within the detector pulse width.

It has been attempted to record several photons per signal period, i.e. by fast multichannel-scaler principles or by time-to-digital conversion (TDC) circuits. These solutions face the same problems as pile-up correction. Two photons detected within a fluorescence decay time of a few ns cannot be distinguished in the detector signal, and multiple triggering by ringing and reflections causes distortions in the recorded curves.

Nevertheless, there is a way to reduce the classic pile-up. If the light is spread over several detectors multi-photon events in one detector become less likely. Instead, simultaneous detection will occur in different detectors so that it can be recognised, see Fig. 455.

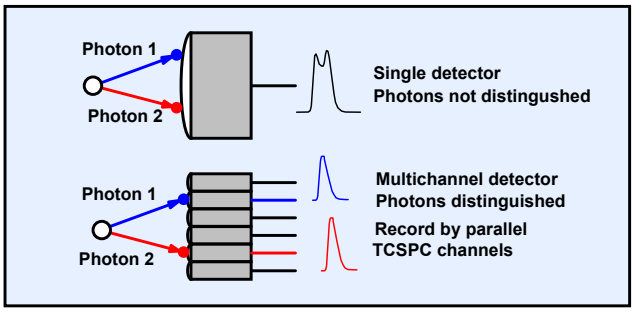


Fig. 455: Separation of photons by multi-detector setup

The light signal is spread over several detector channels. These may be individual detectors or the channels of a multi-anode PMT. If several photons appear in the same signal period they are more likely to hit different detectors channels than the same one. Photons detected at the same time in different detectors can, however, easily be separated.

The straightforward solution is to record the photons from the detector channels in several parallel TCSPC channels. This can be done by SPC-134 or SPC-154 multi-channel packages, or by an SPC-QC-104 module. Please see page 395 and page 689.

Pile-up-rejection is, however, also possible by using a single TCSPC channel with a router [1202]. The router monitors the output signal of all detector channels by fast discriminators. When a detector delivers a photon pulse the corresponding discriminator triggers and an encoder generates a digital ‘detector channel’ number (see Fig. 206, page 117). If several detectors deliver pulses within the response time of the discriminator/encoder circuitry, the encoder delivers a ‘Disable Count’ signal. This signal suppresses the storing of the complete detection event, i.e. of both photons, in the memory of the TCSPC module. Thus, waveform distortion by classic pile-up is reduced. The time interval in which several photons are recognised as a multi-photon event is usually on the order of several tens of ns.

All these approaches a able to reduce pile-up errors. However, the better solution is to plan an experiment in a way that the effective laser repetition rate is kept on a level high enough to avoid pile-up altogether.

Multiplexing of Lasers

Pulse-by-pulse multiplexing of lasers was introduced by Wijnaendts van Resandt et. al. in 1982 to simultaneously record two signals in a classic TCSPC setup [1338]. The technique has been re-invented later and called ‘pulse-interleaved excitation’, or PIE. Two ore more optical signals are given different optical delays. They are then detected through the same detection path and recorded in the same TAC range. Pulse-by pulse multiplexing can also be achieved by interlacing the pulses of several synchronised lasers. The reference signal is derived from only one of the lasers. Although pulse-by-pulse multiplexing looks elegant at first glance it has severe drawbacks when applied to signals of at high count rate and high repetition rate.

The situation is illustrated in Fig. 456, left. Compared with the detection of a single signal the effective stop rate is divided by the number of multiplexed signals. The required TAC range is multiplied by the number of signals. In practice it must even be longer because enough time between the signals must be provided to avoid overlapping of the tail of one signal into the rising part of the next. The result is increased pile-up, increased inter-pulse pile-up, and, especially, increased counting loss.

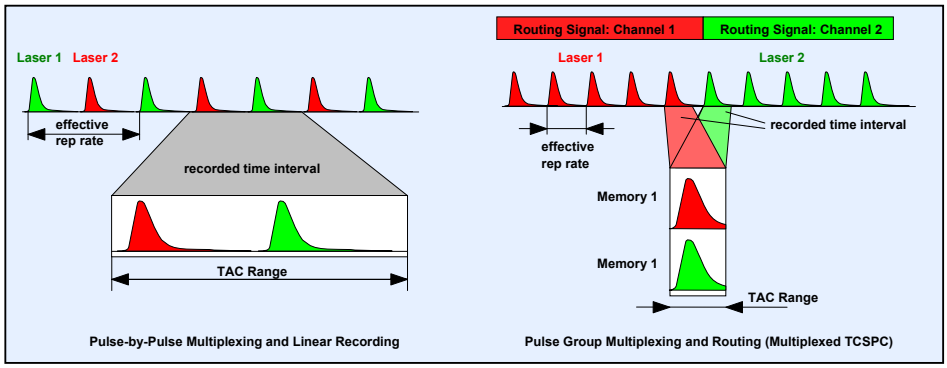


Fig. 456: Pulse group multiplexing and routing is more efficient than pulse-by pulse multiplexing and linear recording

A better way to record several signals is to use the multiplexing capability of multi-dimensional TCSPC, see Fig. 456, right. The lasers are multiplexed at microsecond rate, and the routing signals are used to send the photons into separate memory blocks (see Multiplexed TCSPC, page 119). The stop rate is the full laser repetition rate, and the TAC range does not have to be the duration of a single signal.

A practical comparison of the two multiplexing techniques is given in Fig. 457. It shows the effect of pile-up and counting loss (upper row), of optical reflections (middle row) and of detector afterpulsing (bottom row) on the recorded signals.

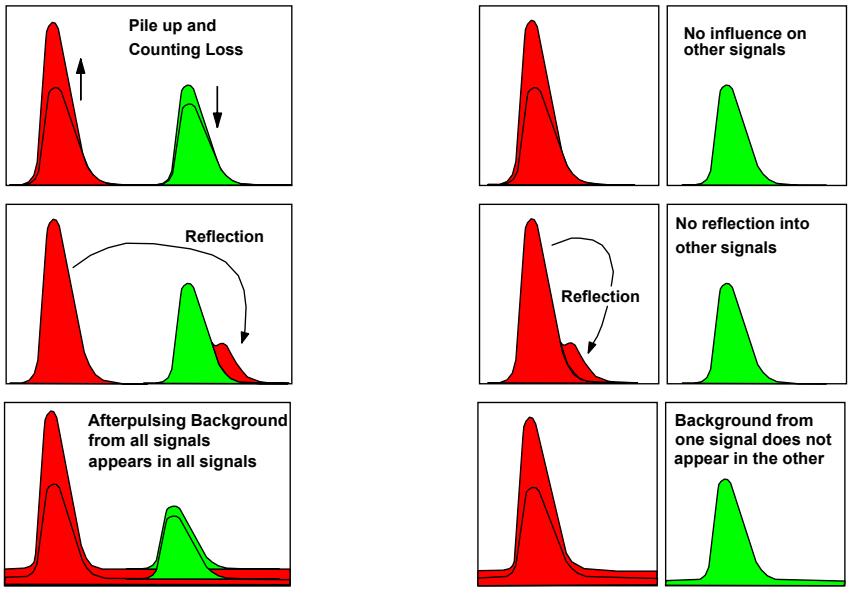


Fig. 457: Comparison of pulse-by-pulse multiplexing (left) and pulse-group multiplexing (right). Upper row: Influence of pile-up and counting loss. Middle row: influence of optical reflections. Bottom row: influence of afterpulsing.

Optimising a Photomultiplier

In older books and papers about TCSPC a numerous hints were given of how to improve the time resolution of a photomultiplier [273, 666]. Optimised voltage divider chains, changed voltages at the focusing electrodes, operation at a reduced number of dynodes, or even magnetic fields in the photocathode region were reported to improve the resolution by nearly one order of magnitude. This may be true for the PMTs of that time, especially if the optimisation started with a poorly designed voltage divider.

Now, the fastest detectors are the Hamamatsu R3809U MCPs and hybrid detectors. There is nothing you could adjust at these detectors. Another fast detector, the Hamamatsu H5783 module with its 150 ps FWHM is completely sealed. Thus, there is little you can do to improve the response of these detectors. However, sometimes PMTs of conventional design must be used because of the spectral range, the dark count rate or price constraints. For such applications some hints are given below.

Voltage Divider

Conventional fast photomultipliers often have one or more focusing electrodes between the cathode and the first dynode. The voltage at these electrodes influences the transit time spread, the 'colour shift' (dependence of the IRF on the wavelength) and the dark count rate. The adjustment can be difficult because the trim pots are at high voltage potentials. Therefore, the photomultiplier housing should contain a light protection between the voltage divider and the tube. The adjustment then need not be done in the dark and is less dangerous.

For almost all photomultipliers the time resolution improves with increasing the voltage between the photocathode and the first dynode. Increasing this voltage also reduces the 'colour shift', i.e. the dependence of the system response on the wavelength. It may also be useful to increase the voltage between the first two dynodes.

The FWHM decreases reciprocally with the square root of the voltage. The effect of the voltage between the cathode and the first dynode for an R5600 PMT is shown in Fig. 458.

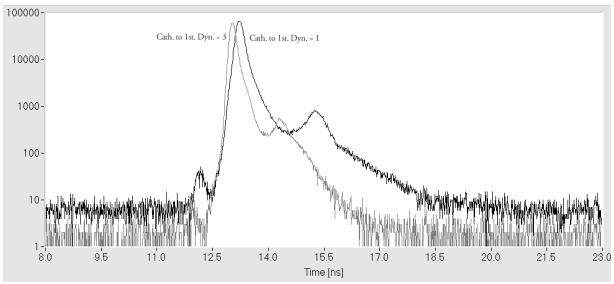


Fig. 458: Effect of the voltage between the cathode and the first dynode of an R5600 PMT

The response functions were measured with the nominal voltage divider and with a circuit applying a 3-fold increased voltage between the cathode and the first dynode. Unfortunately for most PMTs no maximum values for this voltage are given. Consequently there is some risk to damage the photomultiplier if the voltage is increased too much.

Illuminated Area

To achieve a good time resolution with a conventional photomultiplier the light has to be focused onto a small area of the photocathode. Even for a focus diameter below 1mm an effect can be detectable. Therefore, means to adjust the optical focus should be provided. Also the position of the light spot on the photocathode has an influence on the time resolution, see Fig. 268, page 172.

However, under no circumstances the light should be focused on the cathode of an MCP PMT. The lifetime of an MCP PMT is limited by degradation of the coating of the micro-channels. This degradation is caused by sputtering under the influence of the secondary electrons. In first approximation, the degradation of a channel is proportional to the overall charge it has delivered. Spreading the light over the full cathode area extends the lifetime of the MCP by reducing the load at the individual channels. Moreover, the IRF stability at high count rate improves dramatically for larger illuminates area (see Fig. 266, page 171). Therefore MCP PMTs should always be operated with the full cathode area being illuminated.

Dark Count Rate

For high-sensitivity applications a low dark count rate of the PMT is important. Attempts to decrease the dark count rate by increasing the CFD threshold are not very promising. Except for very small pulses caused by thermal emission or electron scattering at the first dynodes, the pulse height distribution is the same for dark pulses and photon pulses (see Fig. 256, page 162). Thus, with increasing threshold the photon count rate decreases by almost the same ratio as the dark count rate. To achieve a low dark count rate, the following recommendations can be given:

- The most efficient way to reduce the dark count rate is to cool the detector. For PMT cathodes which are sensitive in the infrared region (Ag-O-Cs, InGaAs) cooling is absolutely required. Unfortunately most coolers for PMTs are bulky and expensive. In many cases there is a simple and inexpensive solution to the cooling problem: Put the PMT in a fridge. This is no problem if the light is coupled through an optical fibre, or if the complete experiment can be put into the fridge. A decrease in temperature of 10 degrees Celsius typically reduces the dark count rate by a factor of five to eight. (To get paid for the fridge it may be better say it is for food supply than for spectroscopy!)
- Avoid heating the detector by the voltage divider or by step motors, shutters, preamplifiers, etc. Already a few degrees increase of temperature can double the dark count rate.
- Use a PMT with the smallest possible cathode area and with a cathode type not more red sensitive than required for your application.
- Keep the PMT in the dark even if the operating voltage is switched off. After exposing the PMT to daylight the dark count rate is dramatically increased. It can take several hours or even days until the PMT reaches the original dark count rate. An example for an H5773P-01 is shown in Fig. 260, page 166.
- Do not overload the PMT. This can increase the dark count rate permanently. Extreme overload conditions are sometimes not noticed, because the count rate saturates or even decreases at high light levels.
- Keep the cathode area clear from lenses, windows and housing parts. The cathode area is at high voltage. Contact with grounded parts can cause tiny discharges or scintillation in the glass of the PMT.
- Keep the cathode area absolutely clean.
- Avoid the contact of the PMT with helium. Helium permeates through the glass and impairs the vacuum in the tube.

Checking the SER of PMTs

If you do not know the amplitude or shape of the Single Electron Response of your PMT you can measure it with a fast oscilloscope. The oscilloscope must have sufficient bandwidth to show the correct amplitude and width of the pulses. For conventional PMTs the bandwidth must be at least 400 MHz, for MCP PMTs several GHz. Connect the PMT output to the oscilloscope. Do not forget to switch the oscilloscope input to 50 Ω. Set the trigger to ‘internal’,

'normal', 'falling edge'. Start with no light at the PMT. Switch on the high voltage and change the trigger level of the oscilloscope until it is triggered by the dark pulses. This should happen at a trigger level of -5 mV to -50 mV. When the oscilloscope triggers, give some light to the PMT until you get enough pulses to see a clear trace.

Please obey the usual safety rules for operating a PMT. In particular, do not connect or disconnect the signal cable when the high voltage is switched on. This may damage the input circuitry of the oscilloscope (see 'Safety Recommendations for Detectors', page 215).

The single photon pulses have an amplitude jitter of 1:5 or more. The amplitude jitter causes a very noisy curve at the oscilloscope display. Nevertheless, the pulse shape can be roughly estimated from the displayed curves. A typical result is shown in Fig. 459.

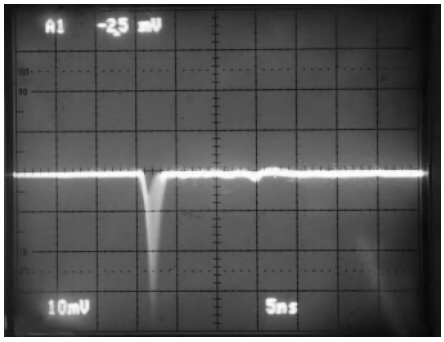


Fig. 459: SER of an R5600 PMT displayed by a 400 MHz oscilloscope

For checking the SER of an MCP PMT we recommend to use a HFAC-26-01 or HFAH-26-01 preamplifier. The preamplifier gives a warning if the maximum output current of the MCP PMT is exceeded. Moreover, the amplified signal has sufficient amplitude to be displayed by the oscilloscope.

Quick Test of a PMT

In a TCSPC system it may be necessary to test whether or not a PMT is working. A simple test can be made by a general-purpose oscilloscope. To withstand a possible accident like a discharge in a damaged tube or voltage divider, the oscilloscope should have a maximum input voltage of several hundred Volts. Nevertheless, before you apply a high voltage to the PMT, you should make sure that the cable connections are not damaged and that there is a reliable ground return path. Do not connect to or disconnect the PMT cable from the oscilloscope when the high voltage is on, see 'Safety Recommendations for Detectors', page 215.

To run the test, switch the oscilloscope input to 1 MΩ, DC, and select an input voltage range of 10 mV per division or less and a time base of 10 µs per division. Connect the PMT - without a preamplifier - to the oscilloscope input. Activate the trigger for the oscilloscope channel being used and select the 'norm' trigger mode and a trigger level of -5 to -10 mV. Make sure that there is *no* light on the PMT. Then start to increase the operating voltage of the PMT. For PMT modules with internal high-voltage generator, switch on the power supply and increase the gain control voltage. When the PMT operating voltage approaches 80% of the permitted maximum you should see the first dark pulses of the PMT. The pulses are negative and have a sawtooth shape, with a steep leading edge and an slow exponential trailing slope, see Fig. 460. Of course, this pulse shape is not the true shape of the single-photon pulse delivered by the PMT. It is simply the result of the RC time-constant formed by the sum of the PMT anode capacitance, the cable capacitance, and the oscilloscope input capacitance in conjunction with the total load resistance (1 MΩ parallel with a resistor possibly connected to ground inside the PMT housing).

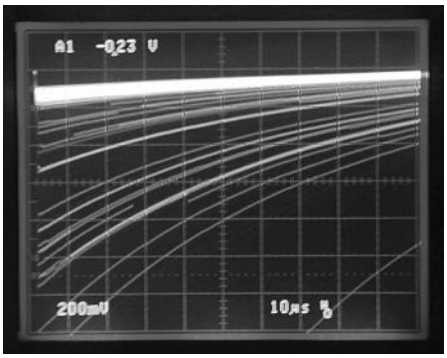


Fig. 460: Test of the general function a PMT with an oscilloscope. XP2020RU PMT, R_{load} = 500 kΩ, V = -2.9 kV, 200 mV/div

Optical System

Optical systems used for TCSPC usually collect less than 10% of the photons emitted by the sample. Consequently, if the detection efficiency is to be increased, the largest potential is in the optical system, not in the detector or in the TCSPC module. Nevertheless, TCSPC users are often more willing to spend 10,000 dollars for a detector of a slightly higher quantum efficiency or 100,000 dollars for a stronger laser than a few hundred dollars for some good lenses and other high-quality optical components. However, a good optical system often not only improves the detection efficiency dramatically, but also reduces typical error sources, such as signal distortion by reflections, pulse dispersion, instability or wavelength-dependence of the IRF, and leakage of excitation light or daylight. A description of the most frequently used optical elements and their use in optical systems for TCSPC is given in [154].

Lenses

The most frequently used optical elements are lenses. A simple spherical lens suffers from spherical and chromatical aberration. Both aberrations increase steeply with the numerical aperture or the f-number of a lens. Aberrations are considerably reduced in achromatic doublets or triplets. However, achromatic lenses contain a flint glass element and therefore turn intransparent at wavelengths below 360 nm. Therefore TCSPC optics often used single element lenses made of BK7 glass or even fused silica. The unavoidable aberrations can be minimised by using lenses of the right shape, and by inserting them into the beam path with the right orientation [154].

Absorptive Colour Filters

There are a large number of long-pass colour filters with transition wavelengths from 300 to 800 nm. Because colour filters absorb the light in the stop band they do not cause noticeable reflections. However, colour filters often show fluorescence. They should therefore be inserted in a plane of the beam path that is not conjugate with the detector plane. The fluorescence lifetimes of filters can be anywhere from a few ns to several µs [154]. Therefore, if a TCSPC system suffers from unexplained background signals, it should be checked for possible filter fluorescence.

Interference Filters

Interference filters are made by depositing a number of dielectric and metallic layers on a glass substrate. Short pass, long pass, bandpass, and notch filters are available. The transition

from the stop band into the passband can be extremely steep. Good interference filters do not show any noticeable fluorescence.

Interference filters work with their specified performance only if placed in a parallel beam of light. For oblique rays the transition wavelengths shifts to shorter values. The filters should therefore be used in a collimated beam. Baffles should be provided to prevent scattered excitation light from entering the filter at oblique angles.

Light that is not transmitted by the filter is reflected back into the beam path. Because the filter is placed in a collimated beam reflected excitation light is often perfectly focused back into the sample. This can cause noticeable afterpulses in the IRF. The size of the afterpulse may depend on the scattering coefficient of the sample and therefore be different for the IRF measurement and the measurement of the sample. To avoid multiple reflections interference filters should not be stacked.

A typical case of filter reflection is shown in Fig. 461. In the attempt to improve suppression of undesired wavelengths, two interference filters of the same wavelength were placed in the detection beam path in front of an R3809U MCP PMT. The beam was perfectly collimated and the filters inserted under exactly 90°. Both filters reflected about 20% of the light. The result is shown in Fig. 461, left. Removing the first filter and tilting the second one by 5° removed the reflections, and restored the correct IRF of the R3809U, see Fig. 461, right.

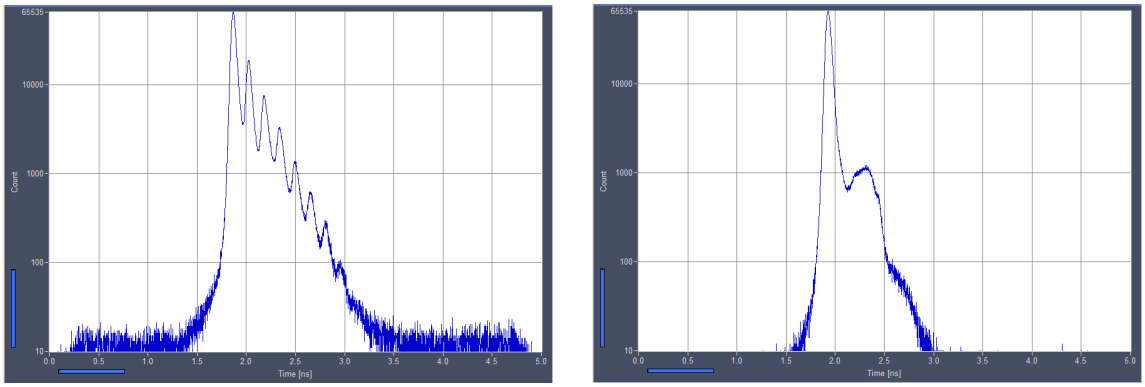


Fig. 461: Left: Two interference filters in the beam path in front of an R3809U detector. Right: First filter removed, second filter tilted by 5°.

Monochromators and Polychromators

A problem of monochromators in picosecond-spectroscopy applications is colour shift and pulse dispersion. The path length from the entrance slit to the grating and from the grating to the exit slit is different for both sides of the grating. The path length difference depends on the angle of the grating. Therefore a pulse travelling through the monochromator broadens, and the amount of broadening depends on the selected wavelength. The path length difference can be in the range of several millimeters. This may not sound much, but a 5 mm path length difference results in a pulse broadening by 50 ps. This is a lot compared to the <20 ps IRF width of an SPC-150NX system with an ultra-fast detector. The IRF change can be even more annoying if the grating is not symmetrically illuminated. This can happen in an imperfectly aligned optical system. Then the IRF shifts with the selected wavelength. A shift in the IRF translates linearly in a shift in a detected fluorescence lifetime. A shift in lifetime by 50 ps (for 5 mm path length change) with the wavelength can seriously affect the performance of a lifetime spectrometer.

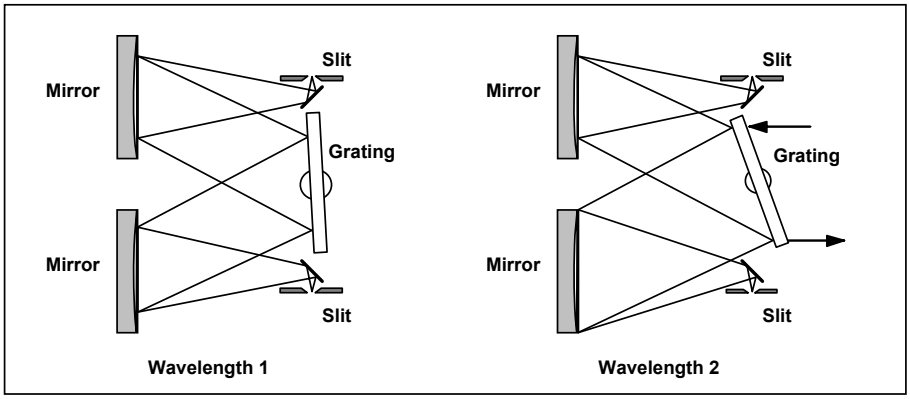


Fig. 462: Path length differences in a monochromator. There is a path-length difference between both side of the grating. The difference changes with the selected wavelength.

Pulse broadening and pulse shift can be avoided by using a double monochromator of the 'subtractive dispersion' type. In this design the second monochromator is rotated by 180 °, and the gratings are moving in opposite directions. Thus the path length differences for both sides of the gratings and for different wavelength cancel.

Similar effects are present in polychromators. A polychromator has no exit slit. It just projects the spectrum of the input light into the plane where the monochromator has the exit slit. There it is detected by a multichannel detector. Please see 'Multi-Spectral Lifetime Experiments', page 322. Because the multichannel TCSPC detectors do not have ultra-fast IRFs the transit-time effects in the polychromator are usually not visible.

The grating of the monochromator disperses the light into several diffraction orders. The light of the unused orders can cause substantial stray light and reflection problems. A monochromator should therefore always be used with an additional filter which blocks the excitation wavelength. In a polychromator light reflected form the detector photocathode can be reflected back to the detector by the zero order of the grating. In the PML-16 detectors the PMT is therefore slightly tilted so that the reflection is directed out of the beam path.

Optical Fibres

Optical fibres are increasingly used because they are convenient to send light from one place to another. Optical fibres come in different versions.

Multi-mode fibres consist of a core with a high refractive index covered by a cladding with a lower refractive index. The light stays inside the fibre core by total internal reflection. The fibres come in diameters up to several millimeters. To further increase the cross section a large number of fibres can be combined in a fibre bundle. Multi-mode fibres accept light inside a numerical aperture as large as 0.35. However, rays entering the fibre under different angles have different path lengths and, consequently, different transit times. The pulse dispersion depends on the numerical aperture (NA) of the light cone at the input of the fibre, but not on the diameter of the fibre [783]. If the full NA of a fibre is used the pulse dispersion can easily be 100 ps per meter. By changing the focal length of the lens in front of a fibre, NA can be traded against diameter. Consequently, using a fibre of large diameter at a low NA reduces the pulse dispersion.

Light leaving a multi-mode fibre is emitted from the entire core cross section, and into a cone of large NA. It is therefore not possible to focus light from a multi-mode fibre into a diffraction limited spot.

Single-mode fibres have a core diameter of only a few µm. Only a single wave-mode can propagate through the fibre. The output of a single-mode fibre can therefore be focused into a diffraction limited spot. The problem is, however, that only light of high beam quality can be efficiently coupled into a single-mode fibre. Coupling light from laser diodes requires appropriate beam shaping. Coupling fluorescence light from a cuvette or another macroscopic sample into a single-mode fibre is a hopeless enterprise.

Baffles and Aperture Stops

A good optical system has a number of circular stops and baffles to prevent scattered light from propagating through the system. As a rule of thumb, no parts of the housing, lens holders, or the insides of optical tubes should be visible from the detector. This can be achieved by circular stops that restrict either the field of view of the detector (field stops) or the effective aperture of a beam (aperture stops). The term ‘baffle’ is often used; baffles are cylindrical or conical tubes or circular stops that keep off unwanted light from the detector [250].

Avoiding Optical Reflections

Reflections in optical systems can change the shape of the TCSPC IRF noticeably. Even worse, the distortions depend on the absorption and scattering properties of the sample, on the transmission wavelength of filters and monochromators, and on neutral density filters possibly used to control the intensity. The measured IRF is therefore not necessarily the effective IRF. A deconvolution of the measurement data from the measured IRF may deliver a poor fit or plainly wrong results.

Reflections show up as secondary peaks in the IRF and, consequently, as single or multiple steps in recorded fluorescence decay curves. The typical appearance of a single reflection in a fluorescence decay curve is shown in Fig. 463. The amplitude of the reflected pulse is about 6%, the delay about 0.5 ns.

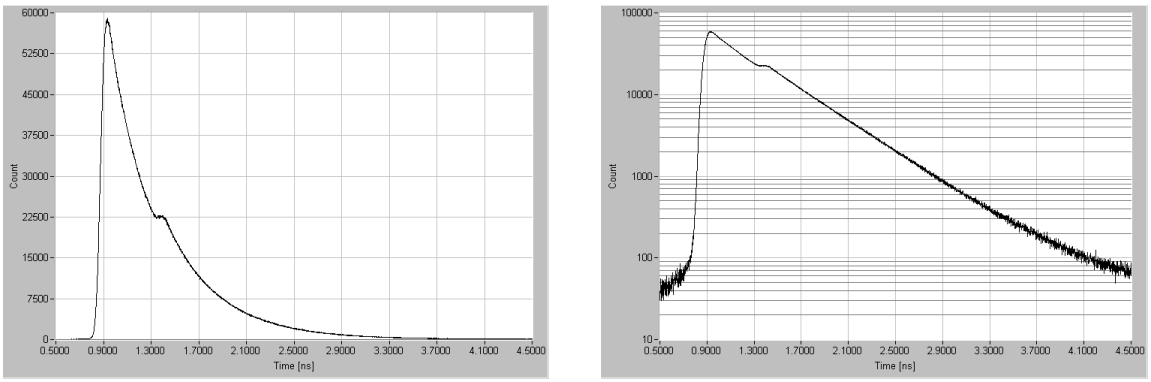


Fig. 463: Reflection in a recorded fluorescence decay curve. Time scale 400 ps per division.

Reflections are especially troublesome between two highly reflective surfaces, and between a highly reflective surface and a glass surface. Highly reflective surfaces are interference filters, reflective neutral density filters, and the cathodes of PMTs. Also the brackets of monochromator slits can reflect a large amount of light. A number of typical cases of reflections and their effect on the IRF of a TCSPC system are shown in [154]. A reflection between the

photocathode of an R3809U MCP PMT and a filter is shown in Fig. 464, left. Tilting the filter by 5° removes the reflection and restores the normal IRF of the R3809U, see Fig. 464, right.

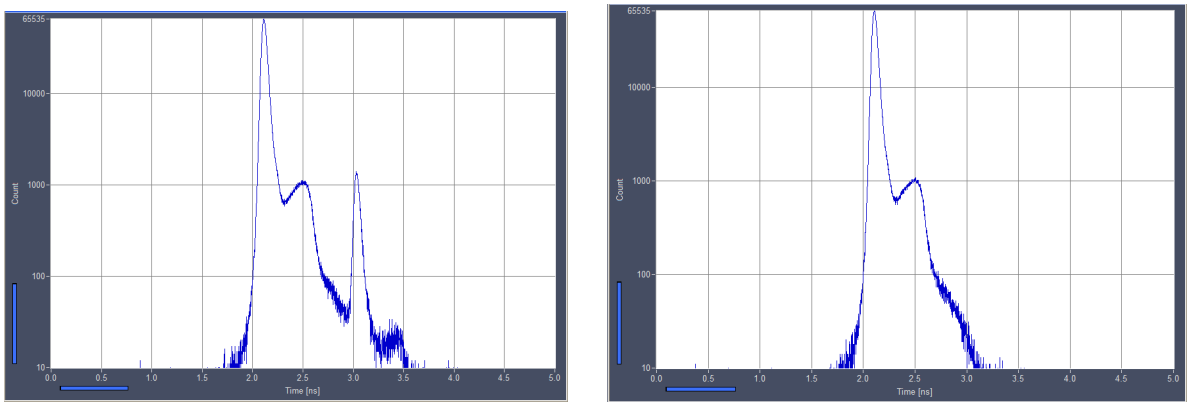


Fig. 464: Left: Reflection between a filter an the photocathode of an R3809U MCP PMT. Right: Filter tilted by 5°, the reflection is directed out of the beam path.

In practice any design is a compromise between reflections, efficiency, filter performance, and filter fluorescence. Reflections can be directed out of the detection path by tilting the critical part, or by placing it in a non-parallel part of the beam. It must be decided whether the resulting change in the characteristics of a filter can be tolerated or not. Often slight changes in the beam geometry have a large effect, especially if aperture and field stops are used in the right places.

Fluorescence Depolarisation

A general problem of fluorescence lifetime measurements arises from fluorescence depolarisation [742, 1292, 1367]. Consider a cuvette that is excited by a vertically polarised laser beam under an angle of 90° from the optical axis of detection. The laser preferentially excites molecules which have their dipoles oriented parallel with the polarisation of the laser. In the first moment after an excitation pulse the fluorescence is therefore partially polarised. Due to the random rotation of the molecules the anisotropy of the fluorescence decreases with a typical time constant in the 100 ps range. One might presume that the anisotropy decay has no effect on the fluorescence decay curve measured with a detector that does not prefer a special direction of polarisation. This is, however, not the case. The situation is illustrated in Fig. 465.

The fluorescence is excited by a beam along the Z axis and a polarisation parallel to the Y axis. I_P and I_S are the intensities of the projections of the electrical field vectors parallel and perpendicular to the excitation, in the corresponding directions of detection. Detection in X direction delivers I_{PX} and I_{SX}, detection in Z direction delivers I_{PZ} and I_{SZ}, and detection in Y direction delivers two I_{SY} components. Obviously, the rotational relaxation cancels if all these components are detected with the same efficiency. Because the angular distribution of the molecules is symmetrical around the Y axis, the intensity is the same for all I_p components and for all I_S components:

$$I_{PX} = I_{PZ} \qquad I_{SX} = I_{SY} = I_{SZ}$$

The sum of all intensity components is therefore

$$I_{SUM} = 2I_P + 4I_S$$

Consequently, a signal proportional to $I = I_P + 2I_S$ must be recorded to reject the rotational relaxation from a lifetime measurement. However, for detection along X, Z or any other direction in the X-Z plane $I_P + I_S$ is detected.

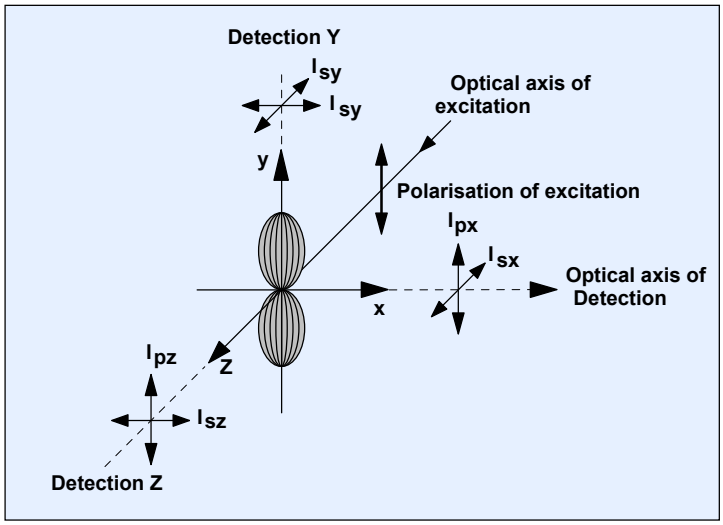


Fig. 465: Polarisation components of the signals detected along the X, Y, and Z axis

Except for a few special cases, there are similar polarisation effects for other angles between the optical axis of the excitation and the X-Z plane, different polarisation of the excitation, and even for unpolarised excitation. Methods to reject depolarisation effects from the measured decay curves in different geometric configurations are discussed in detail in [859, 924, 1171]. The commonly used solution is to place a polariser in the detection path. The polariser is rotated by 54.7° from the polarisation of the excitation, see Fig. 466. The principle is often called 'Magic Angle' detection. The detection efficiency of I_S is then twice the efficiency of I_P, resulting in the detection of a signal proportional to $I = I_P + 2I_S$.

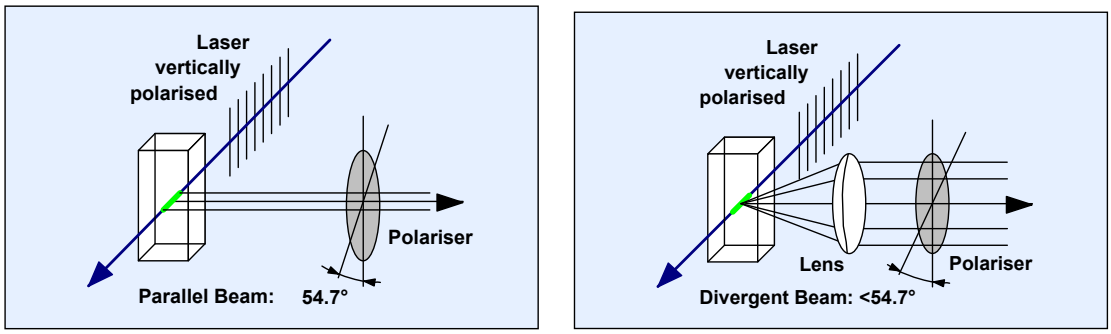


Fig. 466: 'Magic Angle' detection. Left: Excitation and detection in parallel beams. The magic angle is 54.7°. Right: Detection in a diverging beam. The magic angle is <54.7°.

It should be noted that the considerations above apply strictly only to excitation and detection by parallel beams of light. The situation is different for excitation and detection through lenses of large numerical aperture, see 'Effect of Fluorescence Depolarisation on Measured Decay Curves', page 485 in the microscopy section. For an optical axis along the Z axis high-NA focusing leads to field vectors in x and z direction [38, 45, 1005, 1152, 1153, 1370]. Detection though a high-NA lens detects also components in z direction. In other words, a high NA lens acts as an integrating sphere that more or less detects all spatial polarisation components [450, 451, 699]. The 'magic angle is then smaller than 54.7°. It reaches 45° for a lens with an NA of 1. That means, no polariser is needed in this case.

It is often presumed that excitation and/or detection with high NA just results in a drop in the measured anisotropy. This is, however, not correct. The anisotropy, *r(t)*, is

$$r(t) = \frac{I_p(t) - I_s(t)}{I(t)}$$

with *I(t)* = total fluorescence over all spatial directions

Obviously, the waveform of the anisotropy decay function is obtained correctly only if the waveform of the total intensity, *I(t)*, is correct. A simple test can be based on the fact that *I(t)* for a homogeneous solution of similar molecules should be single-exponential, i.e. free of the anisotropy decay. It has been shown experimentally that for excitation and detection through an NA=1.4 oil-immersion microscope lens the sum $I(t) = I_P(t) + 1.0\ I_S(t)$ (not the traditionally used term $I(t) = I_P(t) + 2I_S(t)$) was found free of the anisotropy decay [154].

Re-Absorption and Re-Emission

If the absorption and fluorescence spectra of the sample overlap an appreciable part of the molecules can be excited by absorbing fluorescence photons from other molecules. The result is a change in the apparent fluorescence lifetime and in the decay profile. The effect on the measured decay curve is illustrated in Fig. 467. The laser, a, excites fluorescence, b. The fluorescence, b, excites other molecules, c. The waveform, c, is the convolution of the true decay curve, b, with itself. The measured fluorescence decay, d, is the sum of b and c. The measured waveform has longer lifetime than the original fluorescence, and is no longer single exponential.

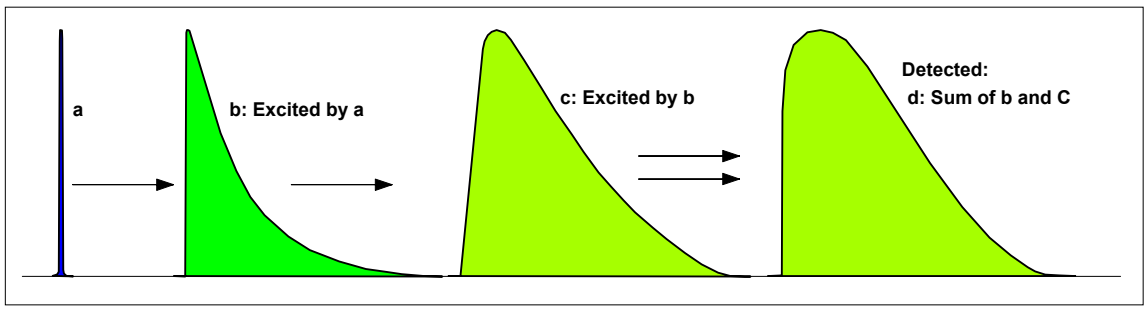


Fig. 467: Effect of re-absorption / re-emission on the detected fluorescence decay

Re-absorption is noticeable especially in highly concentrated samples and samples of large optical thickness. Moreover, if the optical system is not well aligned or plagued by serious aberrations, it can happen that the detector mainly sees light from molecules which are excited by re-absorption. Due to the high sensitivity of the TCSPC method such situations are sometimes not noticed. Therefore, check for possible re-absorption effects if you record suspiciously long fluorescence lifetimes and unexpected multi-exponential decay profiles.

Non-Scanning TCSPC Applications

Measurement of Luminescence Decay Curves

Excitation Sources

Early TCSPC fluorescence lifetime spectrometers used nanosecond flashlamps for excitation [557, 1367]. The duration of the excitation pulses was on the order of one nanosecond. Lifetimes shorter than 100 ps were therefore difficult to measure, especially if the decay functions were multi-exponential. The most severe drawback of a flashlamp is the low repetition rate and the low excitation power, both of which resulted in extremely long acquisition times. Flashlamps had, however, the benefit that almost any excitation wavelength could be selected by a monochromator in the excitation path. Flashlamp-based systems were therefore manufactured even after suitable lasers became available, and a few may even be in use today.

Modern instruments for fluorescence-decay measurement use pulsed lasers for excitation. The first ones which became available were mode-locked argon and frequency-multiplied Nd:YAG lasers. The disadvantage of the fixed wavelength was partly overcome by synchronously pumped jet-stream dye lasers. These systems delivered pulses of <100 ps duration and 80 to 120 MHz pulse repetition rate. For the first time, the temporal resolution of TCSPC could be fully exploited, and the much-feared pile-up effect was no longer a problem (see 'Pile-Up', page 294). However, the laser systems were expensive, complicated, and needed constant maintenance. A fluorescence decay curve measured in 1993 with a mode-locked Ar^+ laser and a bh SPC-300 TCSPC module and an 18 ELU FS photomultiplier is shown in Fig. 468. The IRF width of this system was about 180 ps.

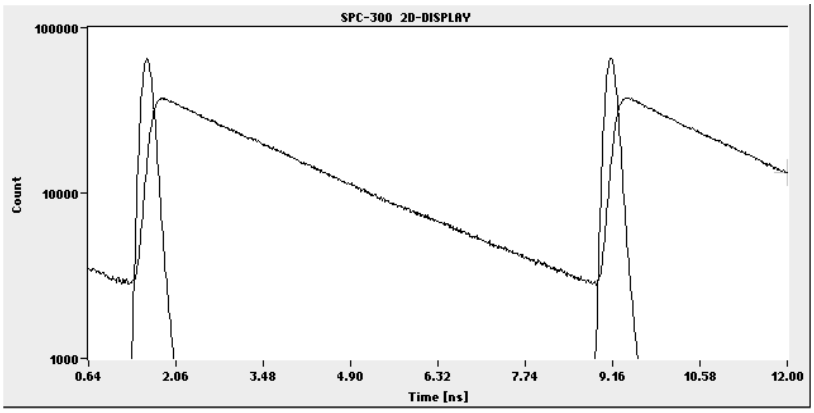


Fig. 468: Fluorescence decay recorded with a mode-locked Ar^+ laser and a bh SPC-300 module

The next improvement came with the Ti:Sa lasers. Tuneability, high repetition rate, picosecond and femtosecond pulse width, (for fluorescence measurements) virtually unlimited power and easy generation of UV wavelengths by frequency doubling and tripling made the Ti:Sa laser an almost ideal excitation source for fluorescence excitation. Only the high price of the laser was (and still is) a problem.

Recent fluorescence lifetime systems therefore mostly use picosecond diode lasers. The diode lasers are available for a wide range of wavelength. The lack of tuneability is compensated by swapping lasers of different wavelength, or by combining the beams of several lasers optically and selecting the desired laser electronically. The fact that only discrete wavelengths are available is not a severe problem. The absorption bands of most fluorophores are wide enough that a reasonable excitation wavelength can be found.

If the application demands for full tuneability (e.g. for recording of excitation spectra) supercontinuum laser are used. The desired wavelength is selected from the supercontinuum by an acousto-optical filter, by a monochromator, or by a set of excitation filters of different wavelength.

Filter-Based Systems

The wavelength at which a fluorescence-decay measurement system detects can be selected by filters or by a monochromator. In the past 10 years filter-based systems have become more and more popular because they are optically simple, inexpensive, and extremely sensitive. A simple system of this type is shown in Fig. 469. The principle of the system is shown in Fig. 470.

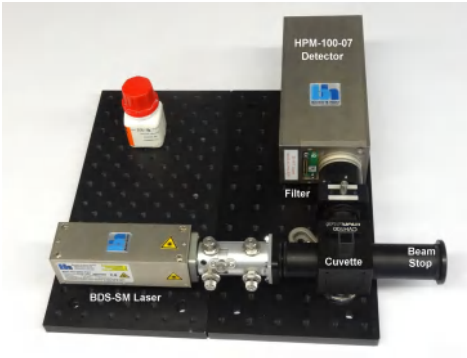


Fig. 469: Filter-based fluorescence lifetime system

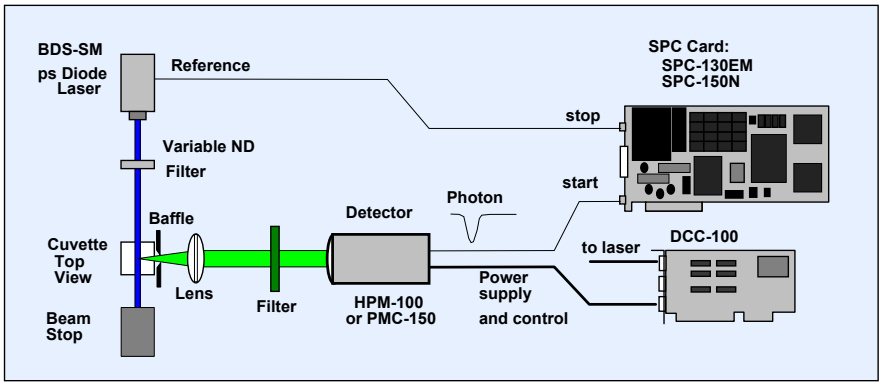


Fig. 470: Filter-based fluorescence lifetime system, principle

The system shown in Fig. 469 consists of a bh BDS-SM ps diode laser, a sample cell, a filter slider, a HPM-100-07 detector, an SPC-130EM or SPC-150N TCSPC module, and a DCC-100 detector controller.

The beam of the BDS-SM laser excites the sample. The fluorescence light from the sample is collimated by a lens. A baffle in the detection beam path restricts the detection area to a small part of the excited volume in the cuvette. This is necessary to avoid broadening of the IRF by the transit time of the laser pulses through the cuvette. An interference filter selects the desired detection wavelength interval. The setup has no magic-angle filter in the detection beam path. Instead, the polarisation of the laser is tilted from the vertical plane as shown in the photo (Fig. 469). A critical part of the system is the beam stop. It has to avoid that the laser beam is reflected or scattered back into the system and enters the sample cell a second time. Light passing the filter is detected by an HPM-100-06 or -07 hybrid detector. The detector is controlled by a DCC-100 detector controller which provides for power supply, gain control and overload shutdown.

An typical result is shown in Fig. 471. It shows a 5.5 ns fluorescence decay of a rhodamine dye. A BDS-SM 405 nm laser was used for excitation, the detector was an HPM-100-06. Due to the absence of afterpulsing in the HPM detector the decay function is cleanly recorded over a dynamic range of three orders of magnitude. The IRF is so short that it is barely visible in Fig. 471 (black curve). With the BDS-SM 405 nm laser and the HPM100-06 detector the IRF width of the entire system is about 50 ps.

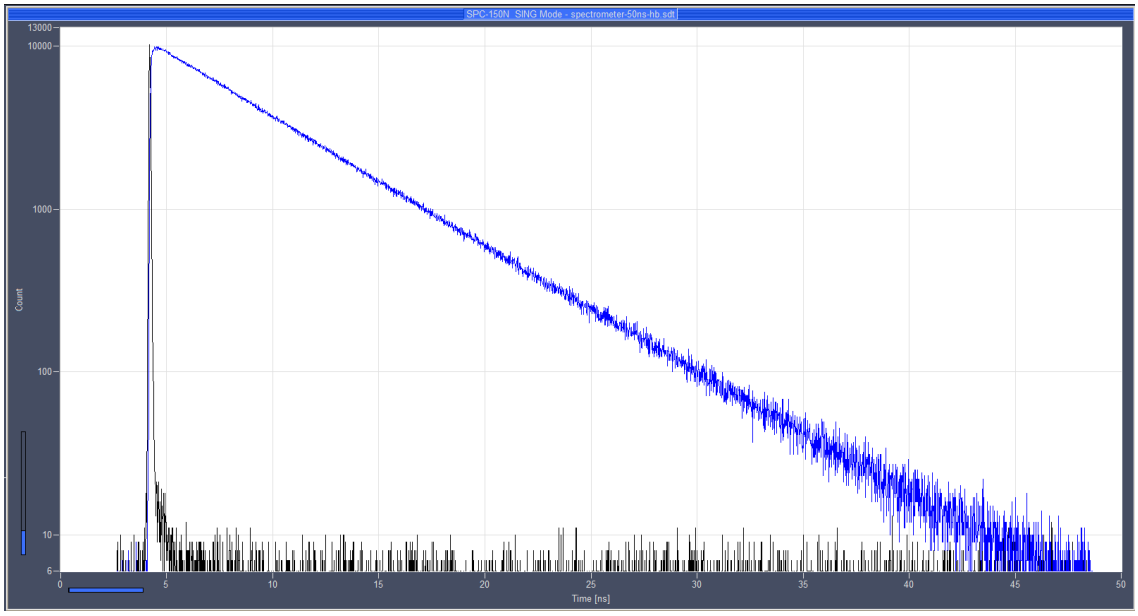


Fig. 471: Fluorescence decay of a rhodamine dye, decay time 5.5 ns. Excitation at 405 nm, HPM-100-06 detector, SPC-150N TCSPC module. Time range 50 ns, time per channel 12 ps.

Time Resolution

The true time resolution of the system is demonstrated in Fig. 472. It shows the same 5.5 ns decay recorded over a time interval of 5 ns. The system is so fast that the fluorescence decay function of the rhodamine almost looks like a phosphorescence decay.

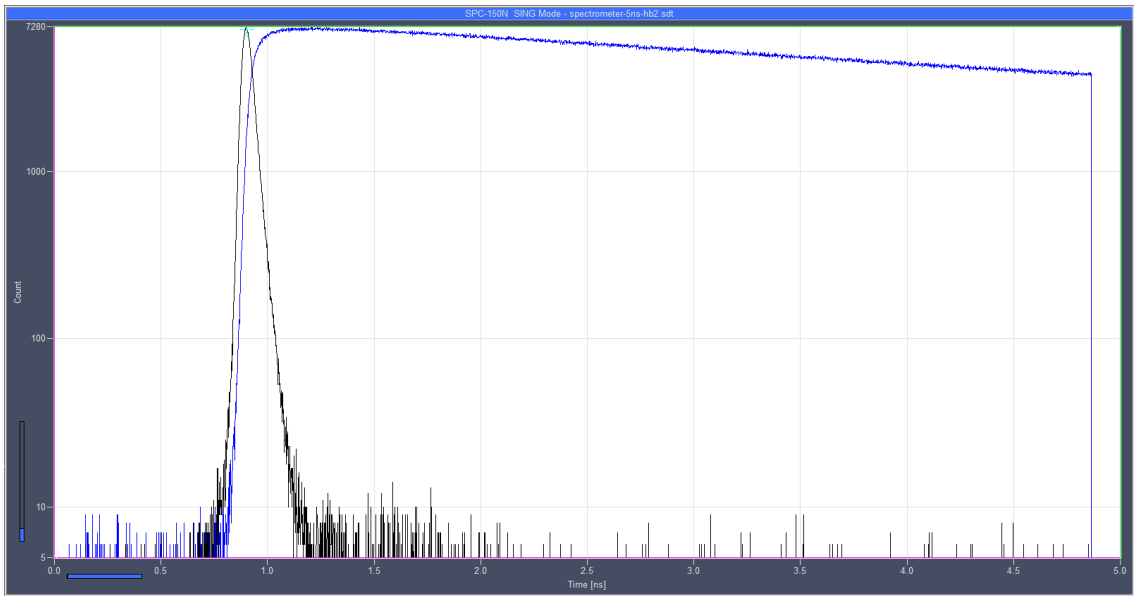


Fig. 472: Same fluorescence signal as in Fig. 471, but recorded over a time interval of 5 ns. Time per channel 1.2 ps. The FWHM of the IRF is less than 50 ps.

The IRF width of the system shown in Fig. 470 is dominated by the pulse width of the ps diode laser. With femtosecond lasers an IRF width of less than 20 ps can be achieved. An example for a Toptica FemtoErb (100 fs) laser is shown in Fig. 473. It shows a fluorescence decay function of Indocyanine Green (ICG) in water. The IRF width is 19 ps, the fluorescence decay time 170 ps.

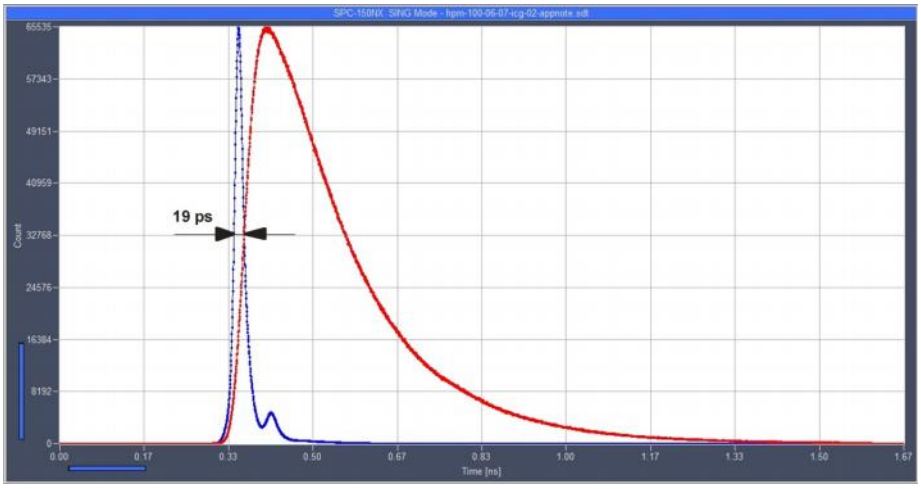


Fig. 473: Fluorescence decay of ICG, excited by Toptica FemtoErb fibre laser. The IRF width is 19 ps FWHM, the fluorescence decay time 170 ps. SPC-150NX, time scale 1.67 ns, time channel width 405 fs.

Other Detectors

Other detectors can be used instead of the HPM-100-06. If sensitivity is an issue (this is unlikely in filter-based systems) an HPM-100-40 can be used. If low cost is more important than short IRF a PMC-150-110 or -210 is a good solution. The IRF width with these detectors is about 120 ps.

In principle, also single-photon avalanche photodiodes, such as the PDM modules of MPD [858] or the id-100 of id Quantique [607] can be used. However, the active area of these detectors is tiny compared to that of the HPM or PMC. Even if the light is concentrated on the active area by an additional lens in front of the detector the sensitivity is lower than for the HPM-100 detector. Other problems can arise from the diffusion tail in the SPAD response, or from count-rate dependent IRF shift, see Fig. 308, page 195.

Polarisation

To obtain correct results of fluorescence lifetime measurements it is important to avoid that the rotational depolarisation in the solvent distorts the fluorescence decay curve, see Fig. 465, page 308. The common way of recording fluorescence decay curves is to use vertically polarised excitation and a polariser in the detection path. The polariser is rotated by 54.7° from the polarisation of excitation. However, the angle differs from the theoretical value if the fluorescence is collected by a lens, as it is the case in a fluorescence-lifetime spectrometer. The correct angle is not accurately predictable. It depends on the numerical aperture of the detection light bundle in the vicinity of the excited sample volume. It thus depends on the effective NA of the lens and on the refractive index of the solvent.

In a setup like the one described above it is often easier to cancel the depolarisation effect by tilting the polarisation plane of the laser, see Fig. 469. Also in this approach, the exact tilt angle depends on the refractive index of the solvent. It is, however, not very critical. The angle can be determined experimentally by recording a decay curve of a sample with a single-exponential decay function. The laser is rotated until the recorded curve is single-exponential. Curves for different polarisation angles of the laser are shown in Fig. 474.

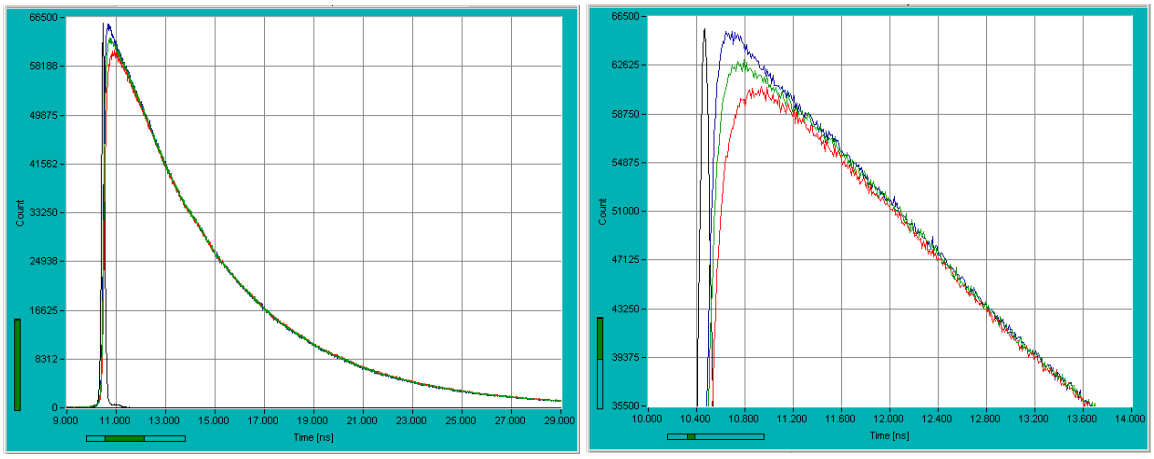


Fig. 474: Effect of the rotational depolarisation on the measured decay curve. Rhodamine 110 in water, excitation at 405 nm, polarisation of laser vertical (upper decay curve, blue), 45° (green curve, middle), and horizontal (lower curve, red). Left: full decay curve. Right: Zoom into the peak of the fluorescence decay.

The depolarisation time of small organic molecules in water is on the order of 100 to 200 ps. In Fig. 474 it is about 100 ps. With the laser polarised vertically, too much of the Ip (parallel) components is detected (see also Fig. 465). Consequently, the intensity is measured too high within the first 100 ps. With the laser polarised horizontally, almost exclusively Is recorded. The intensity in the first few 100 ps is therefore measured too low. With the laser at 45° the detection efficiency of I_s and I_p is almost balanced, and the measured decay function comes close to the correct one.

Detection at Several Emission Wavelengths

Simultaneous detection at several wavelengths can be achieved by using a system of dichroic mirrors in the detection beam path and a corresponding number of detectors. The optical setup is shown in Fig. 475. The fluorescence light is collected and collimated by lens 1. A filter blocks scattered excitation light. The fluorescence light is split spectrally by several dichroic mirrors and focused onto several detectors via lens 2 through lens 4. The numerical aperture of lens 1 can be made relatively large so that a high collection efficiency is achieved. Suitable beamsplitter / detector assemblies are available from bh, please see ‘Detector, Shutter and Beam Splitter Assemblies for TCSPC Microscopy’, page 86. In Fig. 475, the photons of all wavelength channels are detected by one TCSPC module via a router. A more advanced solution is to use parallel TCSPC modules. Parallel TCSPC is more expensive but has the advantage of higher total count rate, shorter acquisition time, and absence of any electrical crosstalk between the detection channels.

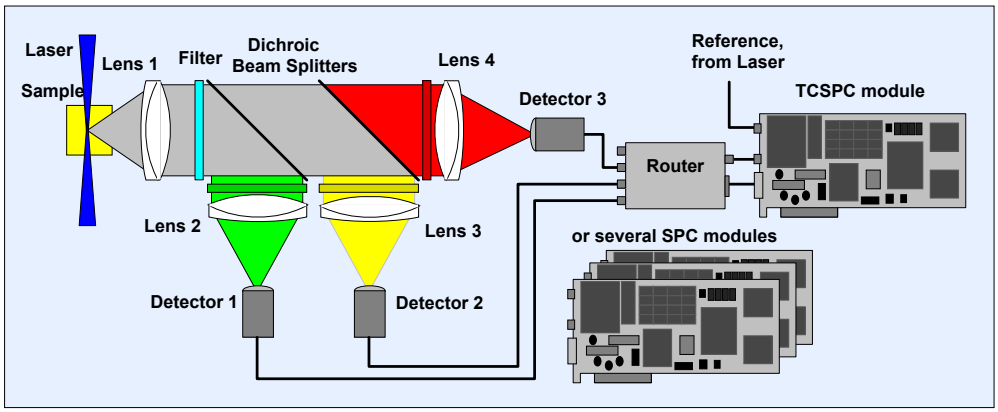


Fig. 475: Multi-wavelength detection system with dichroic beamsplitters

Time-Series Recording

The application range of a filter-based fluorescence measurement can easily extended by time-series recording. The TCSPC system is switched in the f(t,T) mode, and series of measurement steps with appropriate collection time is defined. The recording can be started manually or electronically by a trigger pulse.

An example is shown in Fig. 476. A solution of Rhodamine B in water was heated from 25°C to 80°C over a time interval of 80 seconds. The fluorescence decay time of RhB is known to change with temperature [852]. To demonstrate this, a time series over the time of the temperature ramp was recorded with 40 steps of 2 seconds acquisition time each. It can clearly be seen how the fluorescence decay time decreases with time.

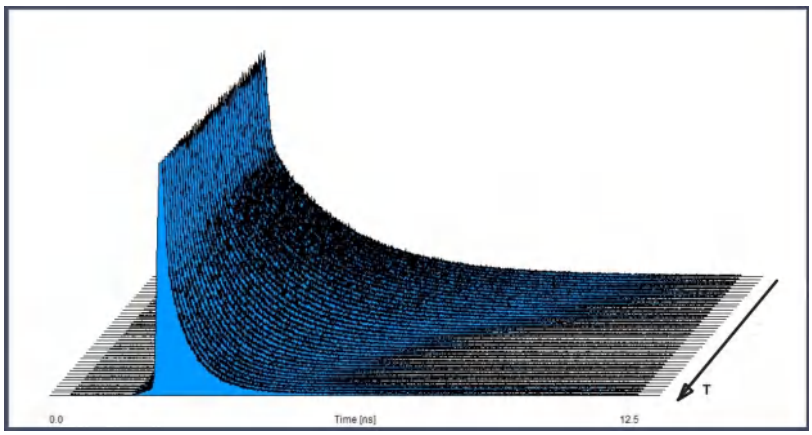


Fig. 476: Fluorescence decay of Rhodamine B, time series recorded over a temperature ramp from 25°C to 80°C.

It is often possible to stimulate a dynamic effect in a sample periodically. By triggering the start of the time series with the stimulation, the time series can be accumulated. The signal-to-noise ratio of such a recording depends on the total acquisition time, not on the time per step of the individual sequence. By accumulating many stimulation periods, fast time series can thus be recorded with high signal-to-noise ratio. Fig. 477 shows the photochemical chlorophyll transient in a live plant. It was induced by periodically turning on and off the excitation light. The recording in the SPC module was triggered synchronously with the on/off period. The time series consists of 50 steps with 50 µs collection time. 20.000 on/off periods were accumulated, resulting in an effective collection time of 20.000 x 50 µs = 1 s per step in the accumulated result. The transient effect is therefore reproduced with an excellent signal-to-noise ratio.

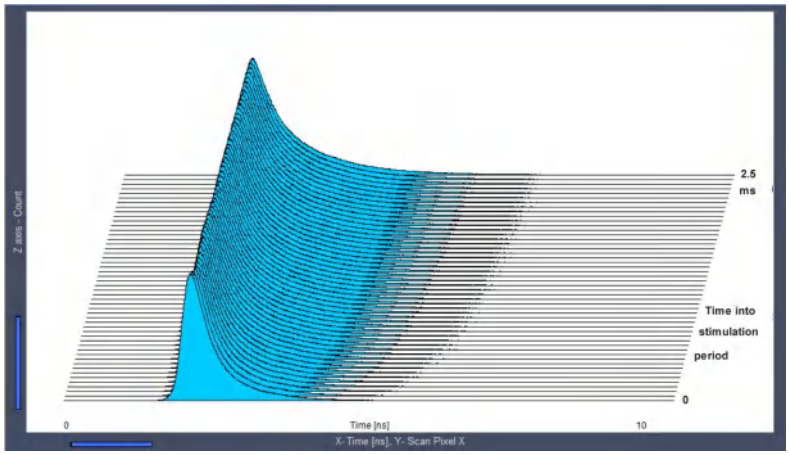


Fig. 477: Time series with triggered accumulation. Photochemical chlorophyll transient in a leaf, time per step of the sequence 50 µs, length of sequence 2.5 ms, 20.000 on-off periods accumulated.

The principle of accumulation of time series is also used in combination with scanning, see FLITS and Temporal Mosaic FLIM. An application to carotenoid-tryptophan hydrogen bonding dynamics is described in [833].

Recording Fluorescence Decay Curves with a FLIM System

FLIM experiments often have to be supported by precision measurements of the decay functions of special fluorophores. FLIM users then often resort to an additional fluorescence lifetime spectrometer for cuvette-based measurements of decay functions. In most cases, however, such fluorescence decay data can better be recorded with the FLIM system.

There are two ways to record decay curves with a FLIM system. You can use the 'Single' mode and collect the data directly in a singe curve, or you can use the 'FIFO Imaging' mode, record an image, and later combine the data of all pixel in a single decay curve.

For collecting the data into a single curve, switch the SPCM software to the ‘Single’ mode, and increase the ‘ADC resolution’ to the number of time channels you need. Leave the other system parameters as in the FLIM (FIFO Imaging) mode. Put the dye solution to be investigated in a cell dish, place it under the microscope and scan it with the laser of the desired wavelength. This is easy in an inverted microscope. In an upright microscope you can scan the dish from above through the plastic cover. The poor optical quality of the cover does not matter - you want only a decay curve, no high-resolution images. Start a scan, record the curve for a specified collection time, or use ‘Stop Overflow’ to normalise all recorded curves to the same maximum. You can record several curves into subsequent ‘Memory Pages’, as described under ‘2D Trace Parameters’, page 831. Send the curve of interest to SPCImage and analyse it with an appropriate model. A decay curve recorded this way is shown in Fig. 478 and Fig. 479.

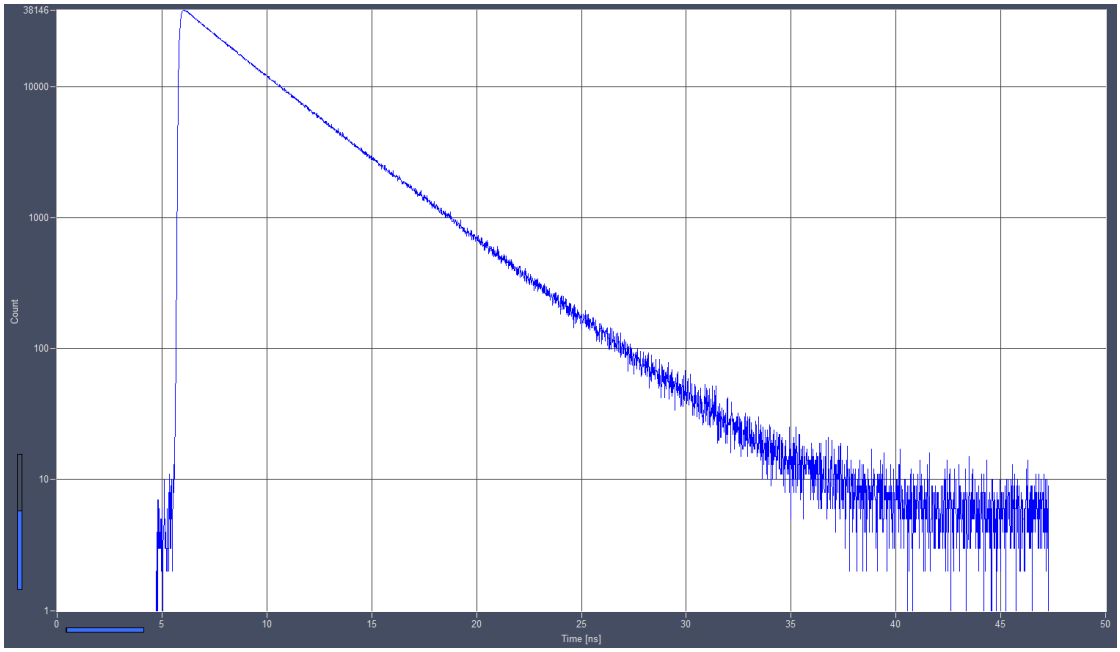


Fig. 478: Decay curve of Atto 425 recorded with DCS-120 confocal scanning FLIM system

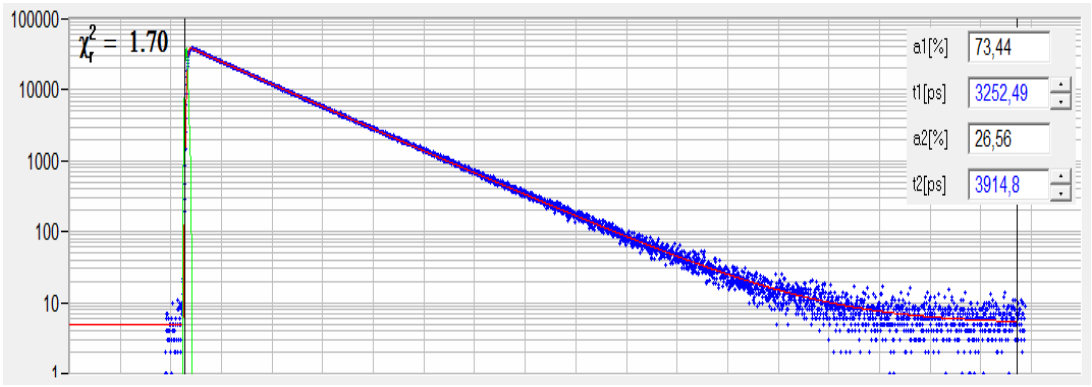


Fig. 479: Fluorescence decay curve, analysed by SPCImage

For collecting the decay data into an image, scan the dye solution with the laser of the desired wavelength and record a FLIM image. Use a FLIM data format with a large number of time channels (4096 or 1024) but a low number of pixels (128 x128). Load the data into SPCImage as described in Chapter 'SPCImage NG Data Analysis Software'. Select the entire image by the two image cursors, and click on the (Lock) button. The result is a decay curve containing the data from all pixels. Deconvolution and fitting of the combined data is performed the same way as for single pixels of a FLIM image.

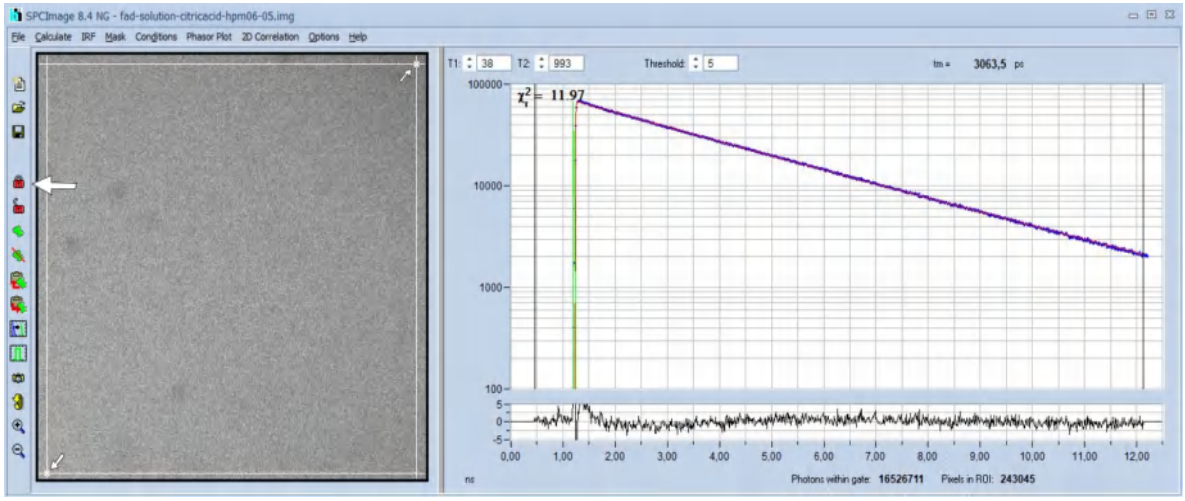


Fig. 480: Combining pixel data into a single decay curve in SPCImage NG

The procedures outlined above have the advantage that the decay curves are recorded under exactly identical conditions as in the FLIM measurement. Possible anisotropy-decay effects are cancelled by the high NA of the microscope lens, and there is virtually no re-absorption. Another advantage is the extremely high time resolution. Two-photon systems with HPM-100-06 or -07 detectors reach an IRF width of <20 ps FWHM. Compared with a standard fluorescence-lifetime spectrometer this can make the difference between accurately detecting a fast decay component or missing it. An example for an FAD solution is shown in Fig. 481. FAD has long been suspected to have a fast decay component with a lifetime around 60 ps [1280], but the component has never been detected directly. The bh DCS-120 MP system with a HPM-100-06 detector shows it without problems, see the peak at the maximum of the decay curve.

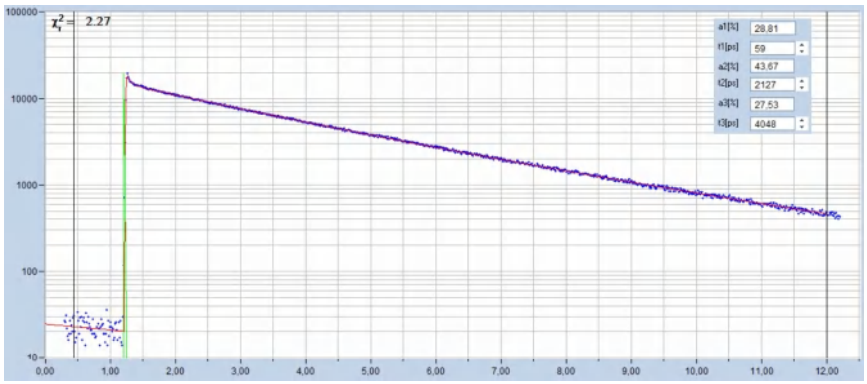


Fig. 481: Fluorescence decay curve of FAD in water, detected with bh DCS-120 MP FLIM system. The system shows that there is a 59-ps decay component with an amplitude of 29%.

Moreover, in the case of the DCS-120 system or other systems with PLIM function, phosphorescence and delayed-fluorescence decay curves can be recorded. An example for single-curve recording of the delayed fluorescence of PpIX is shown in Fig. 795, page 575.

Monochromator-Based Systems

The typical setup of a fluorescence lifetime spectrometer with a monochromator is shown in Fig. 482. The laser is vertically polarised and enters the cuvette under an angle of 90° from the optical axis of the detection system. Front-side illumination can be used for samples of high absorption or scattering. However, 90° illumination is usually preferred because fluorescence depolarisation effects (see ‘Fluorescence Depolarisation’, page 307) are easier to handle and possible fluorescence of the cuvette walls is not detected.

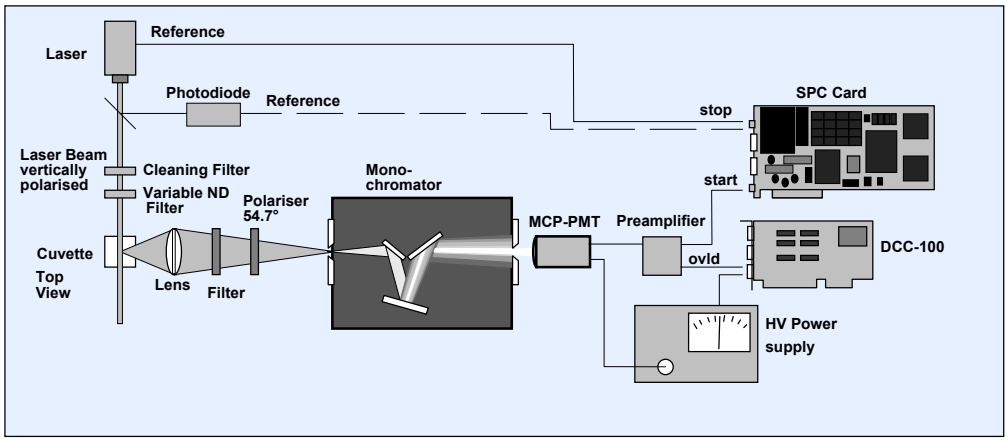


Fig. 482: Typical setup of a fluorescence lifetime spectrometer

The fluorescence light from the sample is collected by a lens and projected on the entrance slit of a monochromator. The effect of rotational depolarisation on the decay curves is removed by a polariser under the ‘magic angle’ of 54.7 degrees (see ‘Fluorescence Depolarisation’, page 307). An additional long-pass filter is recommended to block scattered excitation light.

The monochromator selects the wavelength to be detected. In many laser-based lifetime spectrometers an R3809U MCP PMT is used for detection. Its short transit-time-spread, clean IRF function, and low afterpulsing probability makes the R3809U superior to conventional PMTs. An even better time resolution can be achieved with HPM-100-06 and -07 hybrid detector modules. However, no applications of these detectors in lifetime spectrometers have been reported until now.

The single-photon pulses of the MCP PMT are amplified and fed into the start input of the TCSPC module. The stop pulses come either from a reference output of the laser or are generated by a photodiode module (see Fig. 339, page 218). Any of the bh SPC modules can be used for classic fluorescence decay measurements.

A lifetime spectrometer should include precautions against detector damage by overload. For MCP PMTs it is therefore recommended to use one of the HFAC or HFAH series preamplifiers and to control the high voltage of the detector by a DCC-100 detector controller. If overload occurs the preamplifier delivers an overload signal which causes the DCC-100 to shut down the high voltage of the PMT. A detailed connection scheme is shown in Fig. 350, page 225. PMC-100 and HPM-100 detectors have internal preamplifiers and deliver an overload signal to the DCC-100 via their standard power supply and control cables.

Applications

Classic fluorescence lifetime instruments - both filter based and monochromator based - are used for an extremely wide range of applications. The publications do not always make clear which instruments were used. The selection given below is therefore somewhat arbitrary:

Lifetime changes induced by solvent interaction, pH, conformational changes and different binding state to proteins, peptides or lipids are described in [272, 369, 669, 677, 814, 905, 945, 961]. The dependence of the lifetime on the refractive index of the environment was investigated in [402, 966, 1203, 1204].

Pressure effects on the lifetime are shown in [1233, 1234]. Electron and proton transfer are subject of [1140, 1141, 1221, 1279]. Lifetime spectroscopy on constructs relevant for photodynamic therapy is described in [539, 697, 851, 1348]. Lifetimes of fluorescent proteins were measured in [328, 333, 570, 571, 579, 1295]. Time-resolved FRET measurements and their application to protein folding are described in [283, 471, 538, 746, 1061, 1062, 1178]. Energy and charge transfer from quantum dots into organic dyes was described in [15]. Upconverting nanoparticles were studied in [551].

Enhanced radiative decay rates and enhanced photostability of dyes conjugated to metallic nanoparticles are reported in [488, 489, 814]. For indiocyanine green attached to silver colloid particles the fluorescence could be increased by a factor of 30 while the average (amplitude-weighted) lifetime decreased from 548 ps to 68 ps. Extremely short components of multi-exponential decay functions down to less than 10 ps were measured in [880, 1369]. Fluorescence decay measurements at semiconductors in the microsecond range are described in [484, 485, 486]. The influence of molecular vibrations and higher triplet levels on the intersystem crossing or metal-free organic emitters was investigated in [602].

Time-Resolved Spectra

The setup shown in Fig. 482 can be upgraded with a step motor that drives the monochromator, or a monochromator with an internal step motor drive can be used. The system can then be used to record time-resolved fluorescence spectra or complete wavelength-resolved decay profiles. The recording in the SPC module can be synchronised with the wavelength scan by running a time-controlled recording sequence in one of the sequential modes of the SPC module, or by using the repeat function of the SPC module in conjunction with an experiment trigger from the monochromator drive.

The principle of recording time-resolved spectra is shown in Fig. 483. The wavelength is scanned, and for each wavelength a fluorescence decay curve is recorded. The counts in the

time channels of the decay curve are averaged within selectable time intervals. The averaged counts are stored as functions of the wavelength. Several independent time windows can be used simultaneously; therefore several spectra in different time windows are obtained simultaneously. A suitable operation mode is implemented in all bh SPC modules, see ‘fi(EXT) Mode’, page 744.

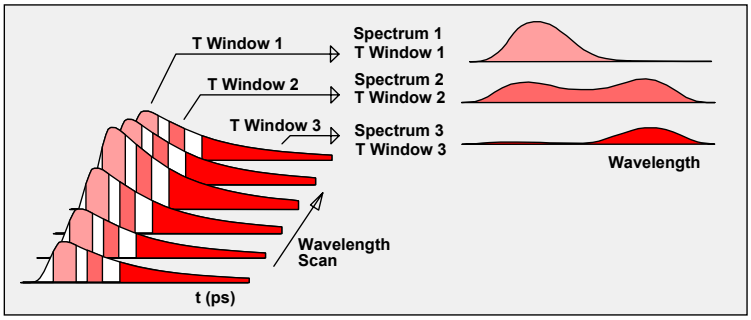


Fig. 483: Recording time-resolved spectra

Unfortunately, there are a few general objections against the gated spectrum recording technique. The problems have already been stated in [924] and result from the obvious fact that the data are not de-convoluted from the instrument-response function. The effective time window in which a spectrum is obtained is a convolution of the selected time window with the IRF. No matter how short a time interval is selected, the effective time interval cannot be shorter than the IRF.

The second objection concerns gated detection in general. Gated spectrum recording is normally used to separate the fluorescence spectra of different kinds of molecules by their fluorescence lifetimes. However, whatever gate interval is used, the integral over any time interval of the decay function contains contributions of *all* decay components present in the curve. Unless the fluorescence lifetimes are *very* different, gated detection is a poor technique to separate the fluorescence signals of different species. Theoretically the separation efficiency can be improved by using several time gates, but the choice of gate intervals is limited because they are smeared by the instrument response function.

A far better way to obtain time- and wavelength-resolved fluorescence data is to record a series of fluorescence decay curves during the wavelength scan [138, 924, 928]. All bh TCSPC devices have sequential recording modes or ‘page stepping’ implemented so that there is actually no argument for using gated spectral recording. The recording sequence in the TCSPC device can be controlled the same way as for gated detection, i.e. either by software or by a hardware sequencer and a trigger pulse from the monochromator drive. An example of a wavelength-resolved sequence is shown in Fig. 484.

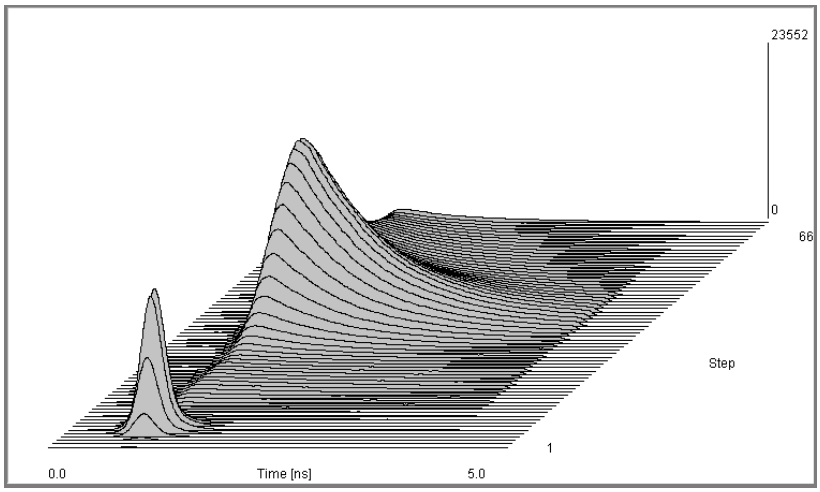


Fig. 484: Sequence of decay curves versus emission wavelength. DODCI, excited by AR^+ laser at 514 nm

Multi-Spectral Lifetime Experiments

A more detailed fluorescence spectrum is obtained by using a polychromator (or spectrograph) and recording the spectrum with a multi-anode PMT. bh delivers a complete multi-spectral detection system based on the PML-16-C and PML-16-GaAsP 16-channel detector heads and a MS 125-8M polychromator (LOT) [62]. The optical principle of multi-spectral fluorescence-decay detection is shown in Fig. 485.

The sample is excited the usual way by a high-repetition rate pulsed laser. The fluorescence light from the sample is transferred by a lens to the input slit of the polychromator. The polychromator splits the light spectrally and projects a fluorescence spectrum on the cathode of a PML-16 multichannel detector. For each photon, the routing electronics generate a timing pulse and a digital data word that indicates in which channel the photon was detected. These signals are used in the TCSPC module to build up the photon distribution over the time in the fluorescence decay and the wavelength (see also Multi-Detector and Multi-Wavelength TCSPC, page 116). Consequently, all photons detected by the PMT are used to build up the result, and the maximum possible signal-to-noise ratio is obtained for a given number of photons emitted by the sample.

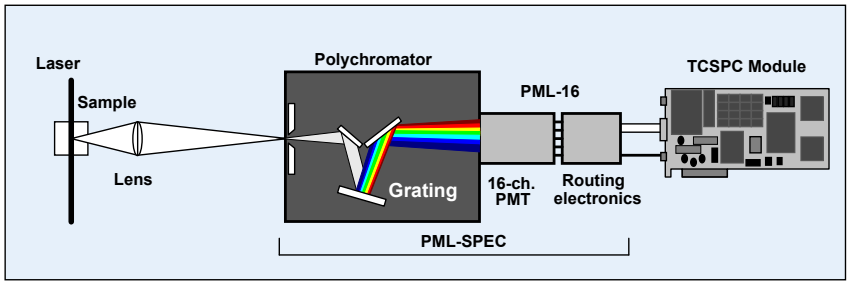


Fig. 485: Multi-wavelength fluorescence experiment

Fig. 486 shows decay curves of a mixture of Rhodamine 6G and fluorescein, both at a concentration of $5 \cdot 10^{-4}$ mol/l, recorded by a bh PML-Spec system. High concentration caused some re-absorption of the Rhodamine 6G fluorescence, resulting in a clearly visible change in the shape of the decay curves and an increased lifetime.

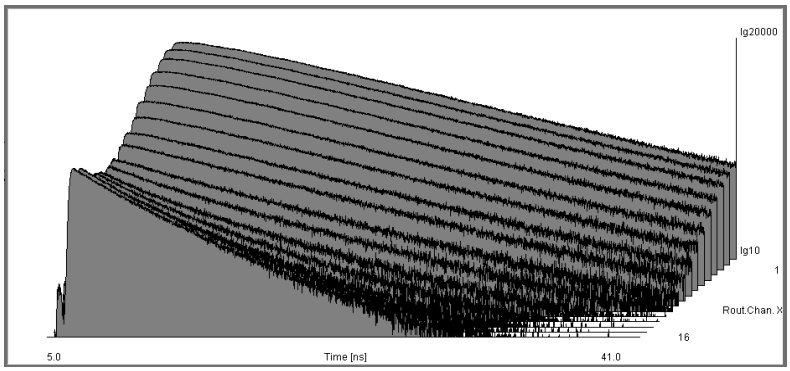


Fig. 486: Fluorescence of a mixture of Rhodamine 6G and fluorescein, simultaneously recorded over time and wavelength

A multi-wavelength system based on a polychromator is by far more efficient than a system that scans the spectrum by a monochromator. Another advantage of multi-wavelength TCSPC is that transient changes in the fluorescence lifetime or other signal parameters within the acquisition time do not induce artefacts in the fluorescence decay curves or spectra detected.

Due to its high efficiency, the principle is often used in a micro-spectrometric system to obtain multi-wavelength fluorescence decay data from single cells [293, 300, 301, 303, 304, 305]. Multi-spectral measurement of low-intensity fluorescence induced by ion beams has been described in [664]. Multi-wavelength detection in diffuse optical tomography with white-light illumination was demonstrated in [1174], multi-spectral lifetime probes and their application to tissue fluorescence in [150, 154, 363,]. Please see section below.

Multi-wavelength detection can be combined with time-series recording of transient fluorescence-lifetime effects. The recording of the time series can be made very fast if 'triggered accumulation' is used. For triggered accumulation, a transient effect in a sample is stimulated periodically, the start of the time-series triggered synchronously with the stimulation, and the data for subsequent stimulation periods are accumulated. The number of photons in the individual decay curves then no longer depends of the speed of the time series. It only depends on the total acquisition time. As a result, extremely fast time series can be recorded if only a large number of stimulation periods are accumulated. An example is shown in Fig. 487. It shows the photochemical chlorophyll transient in a live plant. The excitation light was periodically turned on and off, and the time series triggered with the off/on transition. Each off-on transition initiates a changes in the fluorescence lifetime of chlorophyll. The time per step of the time series in 50 µs, the length of the series 50 curves. 20.000 off/on periods were accumulated. Due to the accumulation the effective acquisition time per step of the series is 1 second, resulting in a high signal-to-noise ratio of the recorded series.

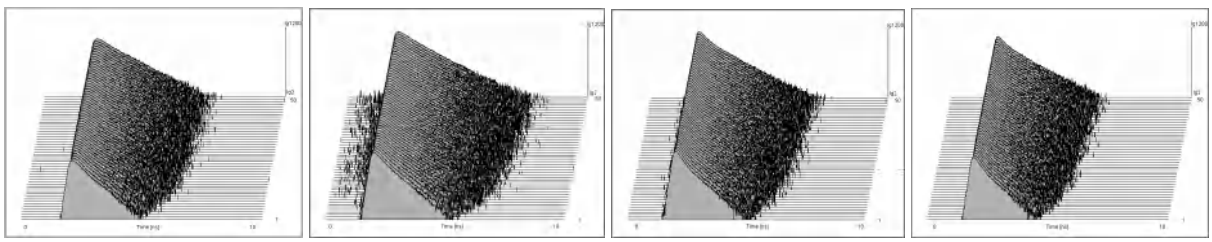


Fig. 487: Multi-wavelength recording of the photochemical transient of chlorophyll in a leaf. Triggered accumulation of time series, 50 curves, 50 µs per curve, 20,000 on/off cycles accumulated. Four selected wavelength channels from a 16-channel recording.

In principle, the result of a multi-wavelength time series is a photon distribution over the times of the photons in the laser period, the wavelength, and the photon times after the stimulation of the sample. Of course, a multi-wavelength photon distribution can also be recorded

over other parameters than the time in a stimulation period, such as the two-dimensional distance from the origin of a fast spatial scan. The principle can therefore be used for multispectral FLIM microscopy [68, 69, 76, 77, 145, 154, 156, 212]. Please see page 366 and page 367 of this handbook.

Multi-Wavelength Tissue Lifetime Spectrometers

An optical setup for multi-wavelength single-point measurements of tissue autofluorescence is shown in Fig. 488, left. The setup is based on the bh 'PML-Spec' multi-wavelength detection system [62]. It consists of a 375 nm, 405 nm, or 473 nm BDL or BDS picosecond diode laser, a fibre probe, a polychromator, a 16-anode PMT with routing electronics, and a TCSPC module [150, 154]. Multi-spectral fluorescence decay data of human skin obtained this way are shown right. The count rate was about $2 \cdot 10^6$ s^{-1}, at an excitation power of about 60 µW.

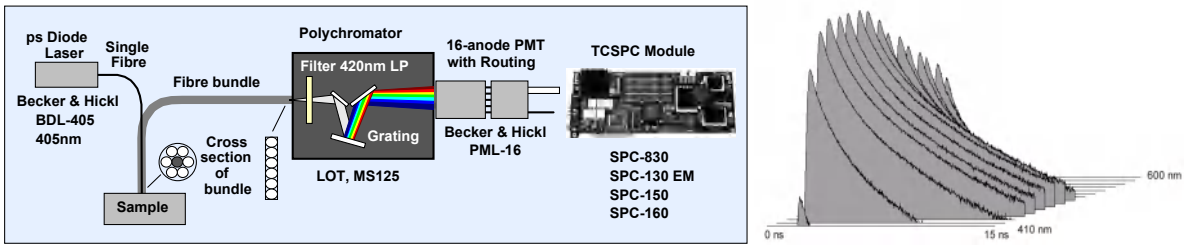


Fig. 488: Left: Optical setup for single-point autofluorescence measurement. Right: Multi-spectral fluorescence decay data of human skin.

The sensitivity of the instrument is very good. It not only records the photons in all spectral channels simultaneously it also collects the photons efficiently from the tissue: The effective numerical aperture of the detection fibres in on the order of 0.3. This is considerably more than in a cuvette spectrometer with a monochromator.

A problem of the optical design shown in Fig. 488 can by fluorescence from the polymer in the fibre bundle. The problem can be hard to identify. As long as the probe is not in contact with the sample the polymer is not exposed to excitation light, and light emitted in the polymer is not transferred into the detection fibres. This is different when the probe is in contact with a sample that scatters light: Excitation light is scattered into the polymer, and polymer fluorescence is scattered back into the detection fibres. To make things entirely confusing, the fluorescence decay functions from the polymers are usually multi-exponential with lifetime components from 0.5 to about 5 ns. The decay functions can be virtually undistinguishable from those of biological tissue. Tests with non-fluorescent scattering targets are therefore recommended.

A portable instrument of the principle shown in Fig. 488 has been described by De Beule et al. [363]. It uses two multiplexed ps lasers of 355 nm and 440 nm wavelength. The laser-multiplexing signal was connected to routing bit R4 of the SPC module. Thus, the detector routes photons of different detection wavelength into 16 separate channels, which, in turn, are routed into separate data blocks by the laser multiplexing. The result is 32 channels with different combination of excitation and detection wavelength. The instrument has later been extended by a supercontinuum laser and a prism on a translation stage for wavelength selection [412].

The spectrometer was used as a lifetime-probe for skin cancer diagnosis [363, 412]. The authors found a decreased average lifetime both for basal cell carcinoma (BCC) and squamous cell carcinoma (SCC). BCC and SCC could be discriminated by their fluorescence spectra. Melanoma could be separated from naevi by a decrease in the lifetime, and a red-shift in the spectrum. The application to excised colon samples was described by Coda et al. [320]. They

obtained statistically significant changes in the mean fluorescence lifetimes between normal and neoplastic tissue. The instrument was also used by Thompson et al. [1243] who compared tumor discrimination by multispectral fluorescence lifetime and by CW fluorescence and diffuse reflection measurement.

A similar instrument based on excitation by a supercontinuum laser was described in [820]. The instrument can be used both for measurements of cell suspensions in cuvettes and of tissue samples. The cuvette is placed directly in the beam path, for tissue measurements a fibre probe is used. Time-resolved emission spectra are obtained via the PML-SPEC multi-wavelength detector assembly, excitation spectra by scanning a slit over the spectrum of the supercontinuum radiation. Fluorescence anisotropy data from cuvettes are obtained by rotating a polarizer in the detection beam path.

Fibre-Based TCSPC Systems

A fibre-based TCSPC system with implantable tips for small-animal experiments is available from bh. The system is shown in Fig. 489, left. A BDL-SMN ps diode laser is used as an excitation source. The excitation light is delivered into an implantable fibre tip via a single-mode fibre, see Fig. 489, right. Fluorescence light from the measurement object is split off directly behind the tip, and transferred to an HPM-100-40 hybrid detector. The fluorescence decay functions are detected by an SPC-150 module in a bh Simple-Tau system. The Simple-Tau also contains a DCC-100 which controls the detector and the laser.

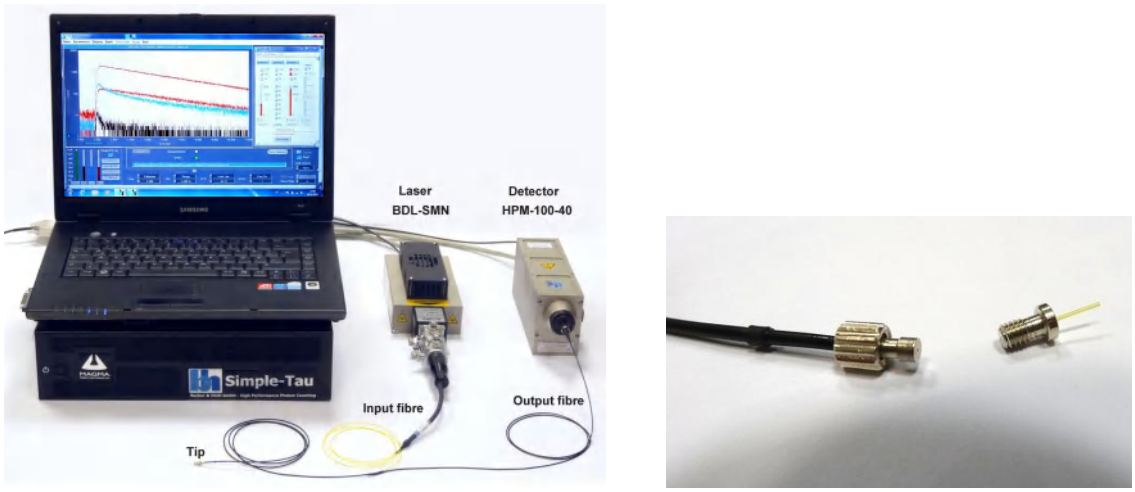


Fig. 489: Fibre based TCSPC system with implantable fibre-tip

Efficient light collection via the multi-mode fibre in combination with the high detection efficiency of the HPM-100 makes the system extremely sensitive. Decay curves measured in a 10^{-6} and 10^{-7} mol/l fluorescein solution and a decay curve measured in mammalian skin compared with the background signal of the probe itself are shown in Fig. 490. Please note that the data were recorded with only 20 µW laser power at the probe output, and within a collection time of only 0.5 seconds.

A system similar to the one shown above has been used Cui et al. [348, 349] to monitor and correlate activation of strial direct and indirect pathways during action initiation.

Other applications of fibre-based systems refer to the measurement of metabolic parameters via the fluorescence decay parameters of NADH and FAD. A system with the fibre tip formed as a biopsy needle was used by Potapova et al [982].

like this, with a BDL-SMN 375 nm laser and a phosphorescence-decay extension (see 'Simultaneous Measurement of Fluorescence and Phosphorescence Decay', page 340) was used by Lukina et al. [801] to record NAD(P)H decay curves simultaneously with phosphorescence decay curves in mouse tumors.

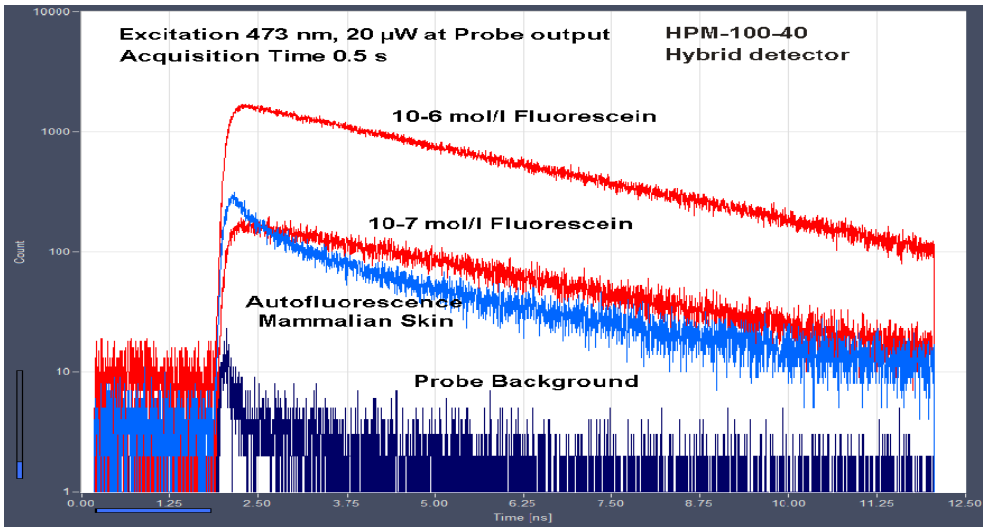


Fig. 490: Decay curves of fluorescein solution, 10^{-6} and 10^{-7} mol/l and decay curve of mammalian skin compared to background signal of the fibre probe itself. Collection time 0.5 seconds, laser power at probe output 20 µW.

Fibre-based TCSPC systems can be combined with image recording by a camera. Guided by the camera image, the fibre is moved over the sample manually, and the TCSPC data are assigned to the corresponding pixels in the camera image. To obtain a bright camera image the sample is illuminated by an LED which is multiplexed in time with the TCSPC recording. Systems of this design are described in [457, 577, 735, 736, 832, 1212, 1401].

Micro-Spectrometers

Fluorescence decay measurement is often combined with detection from a micro volume in a microscope. The optical principle is shown in Fig. 491. A laser (ps diode laser, supercontinuum laser, Ti:Sa laser) is focused into the upper image plane of the microscope lens. The laser light is projected down the microscope beam path by a dichroic mirror and focused into the sample by the microscope lens. The fluorescence from the sample is collected back through the microscope lens and focused into a pinhole in the upper image plane of the microscope. Light from outside the focal plane of the microscope lens is not focused into the pinhole. The detector thus receives only light from the focal plane. With a high-NA microscope lens a femtoliter detection volume can be achieved. Therefore, the setup shown in Fig. 491 is not only used for fluorescence lifetime measurement in micro volumes [601] but also for FCS experiments, combined FCS and fluorescence decay experiments, and single-molecule FRET experiments by burst analysis techniques [232, 407, 408, 436, 720, 897, 898,933, 1113, 1114, 1333, 1333, 1335, 1336].

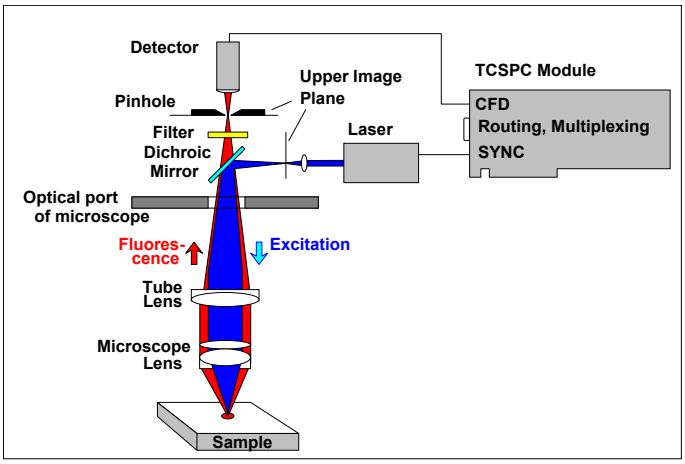


Fig. 491: Optical setup for fluorescence-lifetime microspectrometry, shown for one laser and one detector.

The lifetime micro spectrometer can be used with a piezo scan stage and a bh GVD-120 scan controller to obtain a simple FLIM system, see Fig. 670, page 452. It can also be extended with several detectors and a router or several TCSPC modules [719]. Several lasers can be multiplexed at a frequency in the 100 kHz range and the signals be recorded by multiplexed TCSPC. Lasers that cannot be on-off modulated for multiplexing can be synchronised, delayed with respect to each other, and the pulse trains be interleaved. Please see section 'Excitation-Wavelength Multiplexing', page 371.

A micro-spectrometer with pulse-interleaved excitation (PIE) and three detectors was described in [933]. A supercontinuum laser delivered the excitation light. Two beams of different wavelengths were formed via a beamsplitter and filters. One of the beams was delayed by half the laser pulse period, and then combined with the other. The combined beams (with interleaved pulses of different colour) were sent into the microscope. Three detectors were used via dichroic or polarising beamsplitters as shown in Fig. 475. The detectors were connected to an SPC-150 TCSPC module via a router. The TCSPC module thus records three waveforms, each of which is composed of a decay curve for the first laser wavelength followed by the decay curve for the second laser wavelength.

Because the instrument detects from a femtoliter sample volume it is able to deliver also fluorescence correlation (FCS) curves simultaneously with the decay data. Autocorrelation is obtained by correlating the photons of the individual channels with themselves, cross correlation by correlating photons of different channels. Please see Chapter 'Fluorescence Correlation Spectroscopy', page 639. Another application is single-molecule spectroscopy by burst analysis techniques, see Time-Resolved Single-Molecule Spectroscopy, page 665.

Multi-Wavelength Micro Spectrometers

A micro spectrometer can by combined with multi-wavelength TCSPC. The detector in the setup shown Fig. 491 would just be replaced with a PML-SPEC multi-wavelength detector assembly. Chorvat & Chorvatova used a PML-16-based micro-spectrometer to record time- and wavelength resolved fluorescence from NAD(P)H in live cardio-myocytes. The optical and electrical setup is shown in Fig. 492, details are described in [300] and [822].

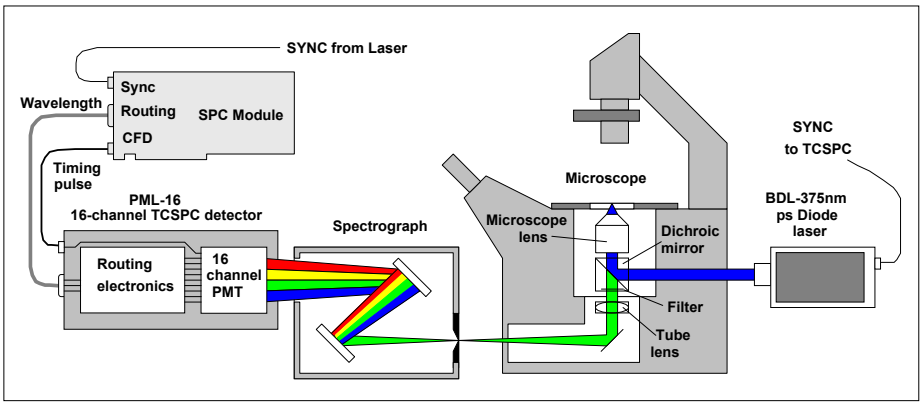


Fig. 492: Micro-spectrometry setup for time- and wavelength resolved fluorescence spectroscopy of cardiomyocytes

The authors were able to record changes in the metabolic oxidative state of the cells via analysis of the fluorescence decay components of bound and unbound NAD(P)H. They were able to detect changes induced by metabolic modulation, by the application of drugs, by various pathological and non-pathological processes, and changes during the rejection of transplanted hearts [302, 304, 305, 306, 307]. Please see [308, 822] for an overview.

Measurement of Time-Resolved Fluorescence Anisotropy

If the fluorescence of a sample is excited by linearly polarised light the fluorescence is partially polarised, see ‘Fluorescence Depolarisation’, page 307. The fluorescence anisotropy, *r*, is defined as

$$r(t) = \frac{I_p(t) - I_s(t)}{I(t)}$$

with I_p = fluorescence intensity parallel to excitation, I_s = fluorescence intensity perpendicular to excitation, I = total intensity.

The fluorescence anisotropy decays with the rotational relaxation time, τ_{rot}. Typical rotational relaxation times of free fluorophores in water are in the range from 50 to a few 100 ps. The relaxation time is an indicator of the size of the dissolved molecules, dye-solvent interactions, aggregation states, the binding state to proteins, and nanoscale diffusion constant [315, 742, 766, 909, 1239, 1292, 1367, 1395]. The anisotropy decay time is also an indicator of the flexibility of protein chains, and DNA strands and bases [745, 899, 996, 1062]. Anisotropy decay measurements are therefore often combined with protein folding experiments and sequential recording [899]. The anisotropy and the anisotropy decay is also changed by FRET. Homo FRET, i.e. FRET between similar molecules can be measured only via the anisotropy [909, 1239, 1292].

Time-resolved measurements of the anisotropy are difficult because $I_p(t)$ - $I_s(t)$ is small compared to the fluorescence components $I_p(t)$ and $I_s(t)$ themselves. Moreover, $I_p(t)$ and $I_s(t)$ are detected with different efficiency, especially if a monochromator is used. The effect depends on the angle of the grating, i.e. on the wavelength, and on the slit width and the beam geometry. If a monochromator is not really required a filter-based setup is often a better solution. Nevertheless, anisotropy measurements require calibration of the efficiency of the $I_p(t)$ and $I_s(t)$ detection channels. The relative efficiency, E_p/E_s, of the I_p and I_s detection channels is the ‘G factor’:

$$G = \frac{E_p}{E_s}$$

There are two ways to determine the G factor [742, 924]. The first way is to run a measurement with horizontal polarisation of the excitation beam. For an angle of 90° between the optical axis of excitation and emission, the excited-state distribution is oriented towards the axis of observation, see Fig. 465, page 308. Consequently equal perpendicular polarisation components are emitted into both measurement channels. The ratio of the measured intensities represents the G factor.

The second way to obtain G is 'tail matching'. A sample with a depolarisation time substantially shorter than the fluorescence lifetime is measured. The G factor is obtained from the intensities in the later parts of the decay curves. The advantage of tail matching is that it can be used also for optical systems with excitation and detection along the same optical axis.

To separate the rotational relaxation from the fluorescence decay it is essential that the correct total intensity, *I(t)* be taken for the denominator of *r(t)*. It is normally assumed that both the excitation and emission light cones have negligible numerical aperture, and that the excitation is polarised perpendicularly to the plane defined by both optical axes. The total intensity is then $I(t) = I_P(t) + 2\ I_S(t)$. The factor of 2 results from the geometrical fact that light polarised longitudinally to the optical axis of observation is not detected [742, 1367], see Fig. 465, page 308. The factor is smaller than 2 for excitation and detection through an optical system of high-NA, e.g. a microscope lens [38, 154, 450], see 'Fluorescence Depolarisation', page 307.

A wide variety of anisotropy measurement setups is used. The simplest possibility is to use a standard fluorescence setup with a polariser in the detection path, see Fig. 493. The components $I_P(t)$ and $I_S(t)$ are measured one after another with the polariser in 0° and 90° orientation. The advantage of this setup is that the instrument response function is the same for both measurements. The drawback is that two measurements are required, and drifts in the detector efficiency, photobleaching or temperature changes in the sample can impair the results. Moreover, about 50% of the photons remain unused. This can be a drawback if the photostability of the sample is an issue. Moreover, the fact that $I_P(t)$ and $I_S(t)$ are measured consecutively makes it impossible to record dynamic affects in the anisotropy and fluorescence decay times.

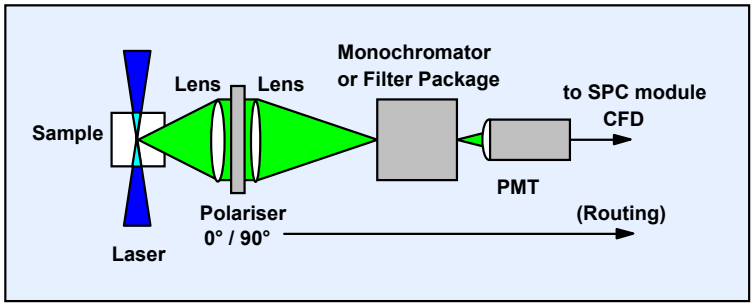


Fig. 493: Single-detector anisotropy setup

The flipping of the polariser between 0° and 90° can be combined with controlling the destination of the photons in the SPC memory via one of the routing bits. The fluorescence decay curves for I_P and I_S are then automatically stored in separate memory blocks. An instrument with periodical switching was used in [368] and [369].

Another commonly used setup for anisotropy measurements is the 'T geometry', see Fig. 494. The sample (usually a cuvette) is measured from both sides, under 0° and 90° polarisation angle. Two detectors and a router are used to detect I_P and I_S simultaneously. The T geometry has the advantage of increased efficiency. However, the instrument response functions (IRFs) of the two detectors can be different, which makes the data analysis more difficult than for the single detector setup. The IRF problem gets relaxed if extremely fast detectors, e.g.

HPM-100-06 hybrid detectors or R3809U MCPs, are used and the optical and electrical path length of both channels are carefully balanced.

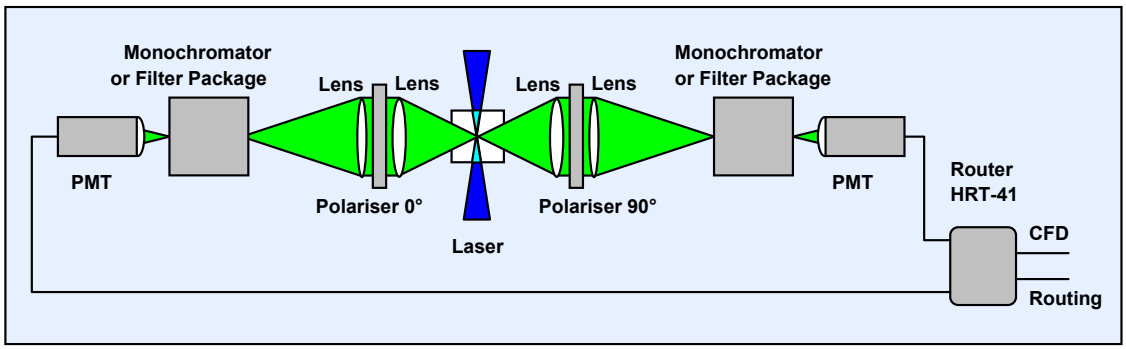


Fig. 494: 'T geometry' anisotropy setup

In cases where the light cannot be collected from both sides of the sample, i.e. in a confocal microscope setup, a 1:1 beamsplitter and two polarisers or a polarising beamsplitter can be used to separate I_P and I_S.

Multiplexed TCSPC can be used to measure I_p and I_S quasi-simultaneously. The components are separated by a beamsplitter and two polarisers (or a polarising beamsplitter) and optically multiplexed into one detector, see Fig. 495. The photons for I_P and I_S are routed into different memory blocks.

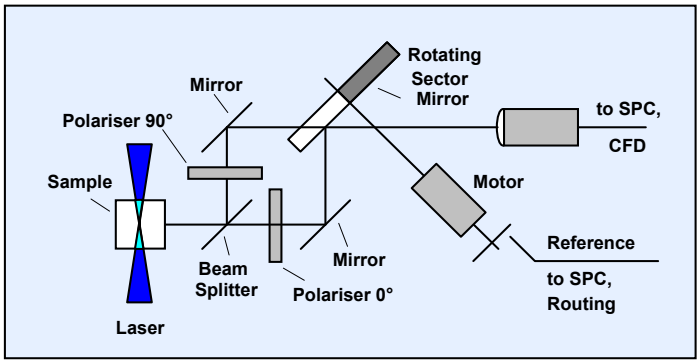


Fig. 495: Alternating measurement of I_P and I_S. Lenses and filters not shown

The advantage of the setup is that changes in the sample and changes of the detector efficiency influence I_P and I_S likewise. The drawback is that the optical system is complicated. A sector mirror is not commonly available, and it must be well aligned on the rotation axis to avoid that the reflected beam tumbles. Although the same detector is used for both light paths it is not simple to obtain exactly the same IRF in both channels. An optical system of the design shown above is described in [138].

In principle, a fluorescence anisotropy system can be built with a rotating polariser. A possible setup is shown in Fig. 496.

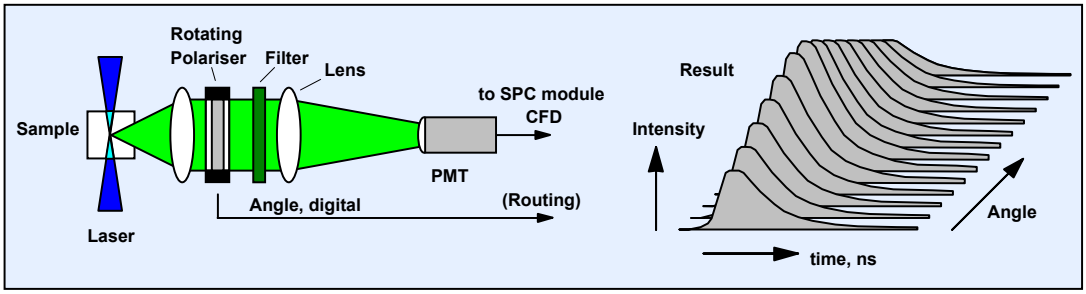


Fig. 496: Anisotropy measurement by a rotating polariser

The polariser is rotated during the measurement. The photons are recorded into a large number of curves in the SPC memory. The recording is synchronised with the rotation, so that the recorded decay curves correspond to different rotation angles. Synchronisation can be achieved by using a digital angle signal from the rotator as a routing signal or by using pulses from the rotator as synchronisation for the 'Scan Sync In' mode of an SPC-730 or -830 module. The setup shown above can be used for samples that have an intrinsic optical activity. Although a system with a rotating polariser is relatively simple no such instrument has yet been described.

Anisotropy decay measurements are not only used for macroscopic samples, such as solutions in cuvettes [745, 746, 996, 899, 1062], but also for micro-spectrometry of cells [358, 1290] and polymer films [26], in conjunction with flow experiments [207], lifetime imaging in cells [28, 323, 358] and for single molecule spectroscopy [720, 986, 1068].

A fluorometer for anisotropy measurements by two-photon excitation is described in [1294]. The quadratic characteristic of two-photon excitation results in a higher initial anisotropy than for one-photon excitation.

Lock-in TCSPC

Every detector generates a background signal which is caused by thermal emission of electrons. This background signal limits the sensitivity and degrades the accuracy of the numerical data analysis. It is possible to reduce the background by cooling, but this often causes unpleasant problems like frost on optical windows or water in the PMT voltage divider chain.

The SPC modules provide a digital lock-in technique that eliminates the background from the results. The principle is shown in Fig. 497.

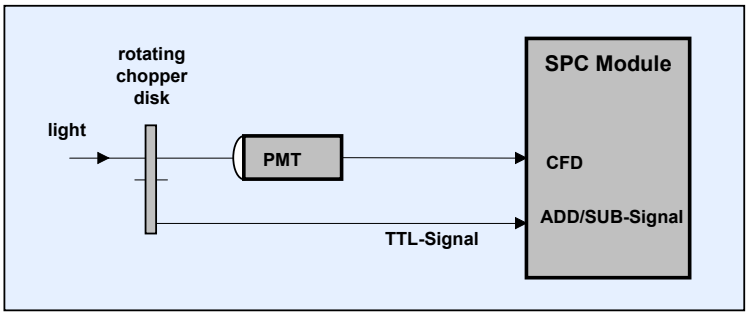


Fig. 497: Multiplexed TCSPC

The light chopper interrupts the light with an on/off ratio of 1:1. At the same time the chopper disk controls the /SUB signal which is connected to the /SUB input of the SPC module. This signal acts in a way that the photons in the bright phase are added and in the dark phase are subtracted in the memory. Because both phases have the same duration the background (but not the background noise) is eliminated from the result.

For luminescence measurements the chopper disk may be conveniently placed in the excitation light path in front of the sample cell. Similar arrangements are possible to measure two different objects (for instance the sample cell and a reference cell with the solvent) quasi-simultaneously. The excitation and luminescence light beams are handled by rotating sector mirrors or by light choppers and 50% mirrors. For early TCSPC devices Lock-in TCSPC was en elegant way to increase the sensitivity of a lifetime measurement beyond the limit set be Raman scattering or solvent fluorescence [138]. With advanced TCSPC modules lock-in TCSPC is not often used. These modules have enough on-board memory to use multiplexed detection. The fluorescence and the background are then recorded into different memory

blocks. The background is eliminated by subtracting the background measurement from the fluorescence measurement. The advantage of multiplexed measurement is that possible differences in the sensitivity or in the duration of the two multiplexing intervals can be compensated for.

Transient Fluorescence Phenomena

Many biological systems show dynamic changes in their fluorescence, absorption, and scattering behaviour. The fluorescence transients in living plants are caused by light-induced changes in the efficiency of the photosynthesis. In experiments of diffuse optical tomography (DOT, see Diffuse Optical Tomography, page 605) changes are driven by the heart beat and by the hemodynamic response to brain stimulation [785]. The associated changes in the diffusely transmitted or reflected light are usually recorded by time-series recording in the 'Continuous Flow' mode of the SPC-130 or SPC-150 modules. Protein folding and other biochemical reactions can be traced by recording time-series of fluorescence decay or anisotropy decay curves [899, 1178]. Depending on the speed of the reaction the recording may be started after adding a reagent, or be synchronised with temperature-jump, continuous flow mixing, or stopped flow mixing techniques. Other examples are electro-physiological stimulation of cells and experiments of photodynamic therapy. Some typical applications of TCSPC to transient phenomena are described in the paragraphs below.

Chlorophyll Transients

A typical example of dynamic fluorescence lifetime changes are the chlorophyll transients found 1931 by Kautsky and Hirsch [649]. The effects have been termed fluorescence induction, fluorescence transients, or Kautsky effect [516, 517, 834]. When a dark-adapted leaf is exposed to light the intensity of the chlorophyll fluorescence starts to increase. After a steep rise the intensity falls again and finally reaches a steady-state level. The rise time is of the order of a few milliseconds to a second, the fall time can be from several seconds to minutes.

The initial rise of the fluorescence intensity is attributed to the progressive closing of reaction centres in the photosynthesis pathway. Therefore the quenching of the fluorescence by the photosynthesis decreases with the time of illumination, with a corresponding increase of the fluorescence intensity. The fluorescence quenching by the photosynthesis pathway is termed 'photochemical quenching'. The slow decrease of the fluorescence intensity at later times is termed 'non-photochemical quenching'. It is believed that it is a mechanism the plant uses to protect itself from photodamage.

Non-Photochemical Transient

Measurements of the non-photochemical quenching transient by TCSPC is very simple. In most cases it is sufficient to record a sequence of fluorescence decay curves at a rate of about one curve per second. Sequences this slow can be obtained by software-controlled sequencing, i.e. in the f(t,T) mode or simply by activating the 'page stepping' function of a bh SPC module. The principle of the experiment is shown in Fig. 498.

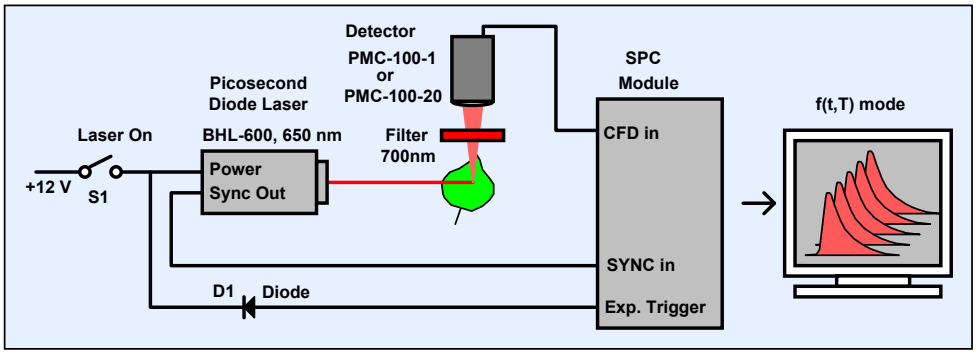


Fig. 498: Recording non-photochemical fluorescence quenching in a living plant

The fluorescence of chlorophyll in a leaf is excited by a picosecond diode laser. The fluorescence is separated from the scattered excitation light by a bandpass filter that transmits a wavelength range around 700 nm. The fluorescence light is detected by a PMC-100-1 or a PMC-100-20 detector. The single-photon pulses are connected into the 'CFD' input of the SPC module; the reference pulses come from the laser.

After the leaf has been kept a few minutes in the dark, the laser is switched on by closing the switch, S1. The operating voltage of the laser is connected to the 'experiment trigger' input of the SPC module via a small-signal diode, D1. In conjunction with the pull-up resistor of the experiment trigger input this generates a positive trigger edge. This edge triggers the start of a sequence of measurements in the SPC module.

Typical results are shown in Fig. 499. A bh BHL-600 laser module was used, with a wavelength of 650 nm, 80 ps pulse duration, and 50 MHz repetition rate. The incident power density at the surface of the leaf was approximately 1 mW/mm^2. The detection wavelength was selected by a 700 ± 15 nm bandpass filter. A sequence of fluorescence decay curves was recorded at a rate of one curve in 2 seconds. The count rate was approximately $2 \cdot 10^6$ s^{-1}. Dead time compensation was used to avoid the influence of counting loss on the recorded intensity.

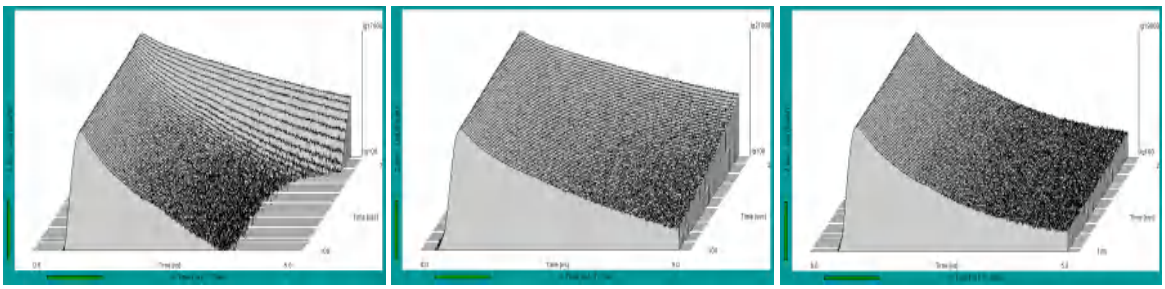


Fig. 499: Sequences of fluorescence decay curves measured at a leaf after start of illumination. Left to right: Fresh leaf, faded leaf, dried leaf. Time per curve 2 seconds, logarithmic intensity scale. The sequence starts from the back.

A result obtained from a fresh dandelion leaf is shown left. The fluorescence lifetime decreases considerably within the first 10 seconds of illumination. The peak intensity remains almost constant. This shows that the change in the fluorescence behaviour is mainly a change in the fluorescence quenching rate, not a change in the number of fluorescing molecules. In a faded leaf the lifetime change is slower and less pronounced. A dry leaf does not show any measurable lifetime change.

Photochemical Transient

Sequential recording of photochemical quenching transients requires a time resolution of better than 1 ms per step. A sequence this fast cannot be recorded by software-controlled sequencing. Moreover, it is impossible to obtain enough photons in a single-shot experiment. Therefore a hardware-controlled sequencing mode, e.g. the Continuous Flow mode or the Scan Sync Out mode, must be used. The recording of the sequence is repeated and the counts accumulated until enough photons have been collected. A suitable experiment setup is shown in Fig. 500.

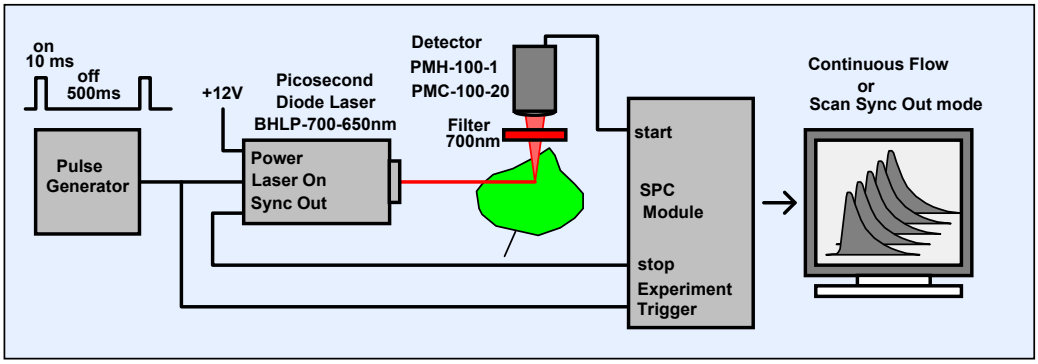


Fig. 500: Measurement of photochemical quenching transients

The setup uses a picosecond diode laser with fast on/off capability. For the results shown below a bh BHLP-700 laser with a wavelength of 650 nm was used. The laser is controlled by a pulse generator that turns the light periodically on and off. The 'on' duration is 12.8 ms, the 'off' duration 500 ms. Within the 'on' phases, the laser delivers picosecond pulses at a pulse period of 20 ns. The leaf is excited by this pulse sequence. The fluorescence photons are detected by a PMC-100-20 PMT module and recorded by an SPC-630, SPC-130 or SPC-150 TCSPC module. The SPC module is operated in the continuous flow mode. It runs a hardware-controlled sequence of recordings, with a time per curve of 100 µs and an overall number of 128 curves. The start of the sequence is triggered by the rising edge of the 'laser on' signal, and a large number of such cycles is accumulated.

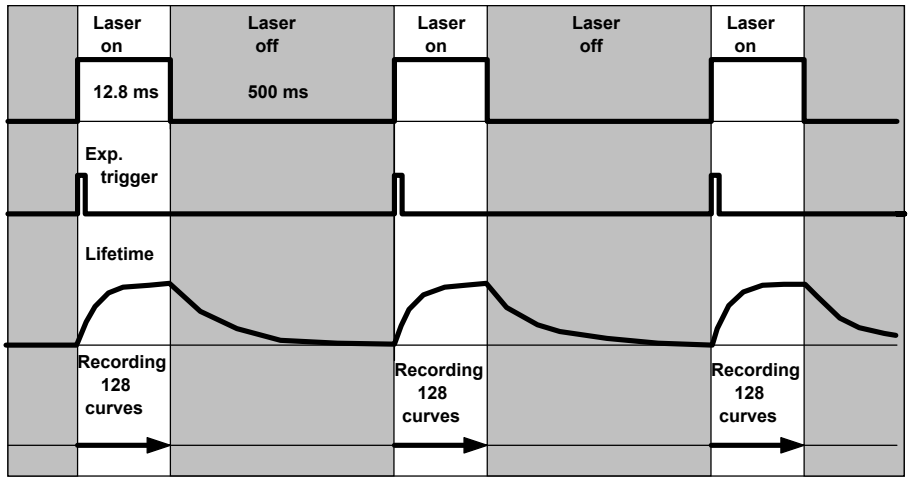


Fig. 501: Excitation sequence for recording photochemical chlorophyll transients

Each 'laser on' period initiates a normal transient of the chlorophyll fluorescence. Photochemical quenching decreases within the 10 ms 'laser on' period with a typical time constant of about a millisecond. In the subsequent 'off' period, photochemical quenching recovers to its initial state. Due to the low duty cycle of the 'laser on' signal, the average excitation intensity is low and does not cause much non-photochemical quenching. Therefore, the change of photochemical quenching can be recorded independently, if only the duty cycle of the laser on/off control signal is kept low enough. A result is shown in Fig. 502. 10,000 on/off cycles were accumulated. For system parameter setup please see 'Sequential Recording in the Scan Sync Out mode', page 752.

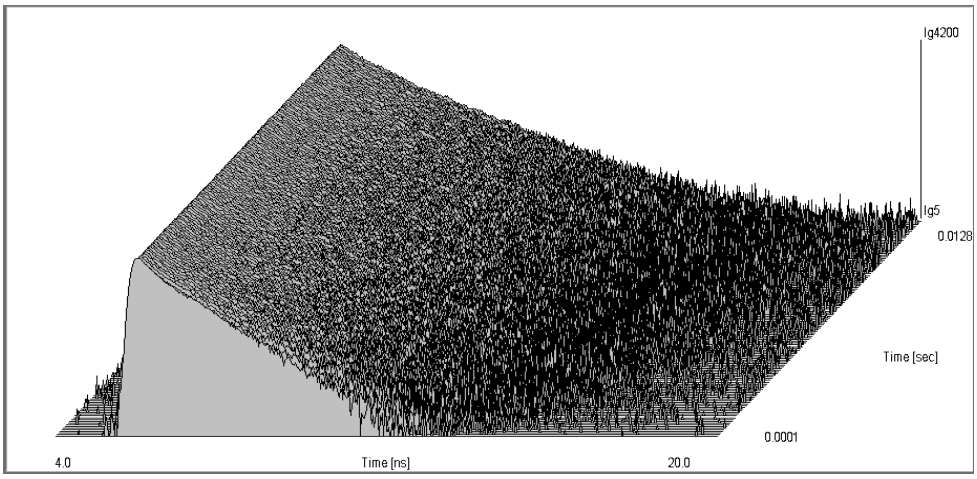


Fig. 502: Photochemical quenching transient measured in a dandelion leaf. The sequence starts at the front. Time per curve 100 µs, 10,000 on/off cycles were accumulated.

Excitation Wavelength Multiplexing

Green leaves show the typical chlorophyll fluorescence around 700 nm, and a blue-green fluorescence which originates from flavinoids. The investigate possible interactions of these signals it may be necessary to record fluorescence decay curves at different excitation and detection wavelengths. If the measurements are performed consecutively the Kautsky effect induces different lifetime changes in both measurements. It would therefore be difficult to obtain comparable lifetimes. The problem can be solved by multiplexed TCSPC. An suitable setup is shown in Fig. 503.

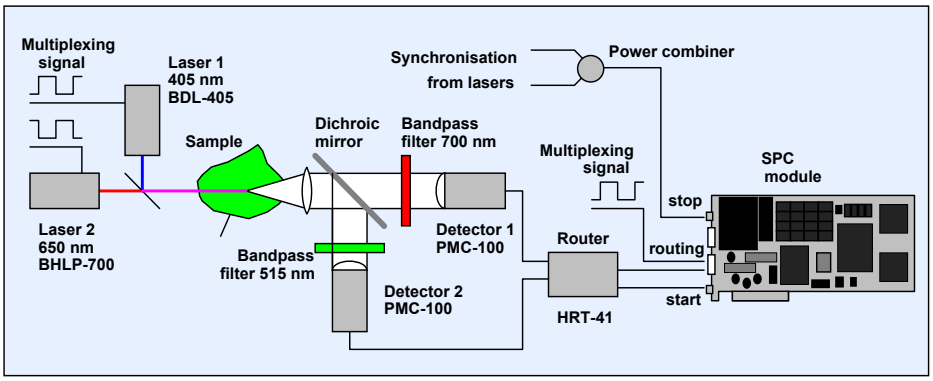


Fig. 503: Simultaneous measurement at two excitation and two emission wavelengths

The sample is excited by two lasers at 405 nm and at 650 nm. The lasers are multiplexed by a TTL signal from a pulse generator or a bh DDG-210 module. The light from the sample is split into a 515-nm and a 700-nm component by a dichroic mirror and two bandpass filters. The fluorescence components are detected by two PMT modules. The PMTs are connected to the TCSPC module via a HRT-41 router. Thus, both fluorescence components are recorded simultaneously. One routing bit is required to separate the photons of both detectors. A second routing bit is used to separate the photons excited by the two lasers. The stop signal for the TCSPC module comes from the synchronisation outputs of the lasers. Because only one laser is active at a time, the pulses can be combined by a simple power combiner.

If the multiplexing is fast there is no time for the chlorophyll lifetime to change for the different excitation efficiency at the two different excitation wavelengths. Complete suppression is obtained for multiplexing rates faster than 20 kHz. Multiplexing rates on the order of 10 to 100 Hz suppress only the non-photochemical transients. An example is shown in Fig. 504. The multiplexing period was 50 ms.

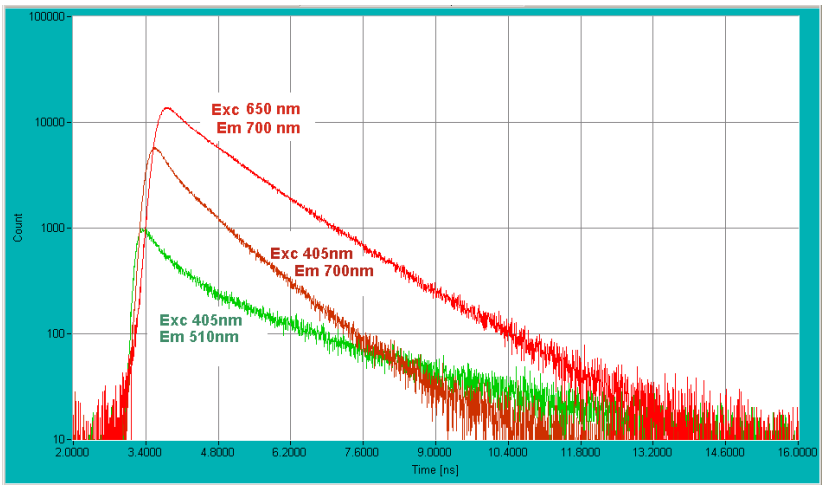


Fig. 504: Multiplexed measurement of the fluorescence of a leaf. Multiplexed excitation at 405 nm and 650 nm, simultaneous detection at 510 nm and 700 nm. Multiplexing rate 20 Hz.

Stopped Flow Techniques

Stopped flow techniques are based on the mixing of two reagents in a flow cell. The flow of the reagents is periodically stopped, and the reaction is observed by recording the transient changes in absorption, fluorescence intensity, or fluorescence lifetime. An overview about the technique is given in [1063]. The principle of a TCSPC-based detection system for stopped flow is shown in Fig. 505.

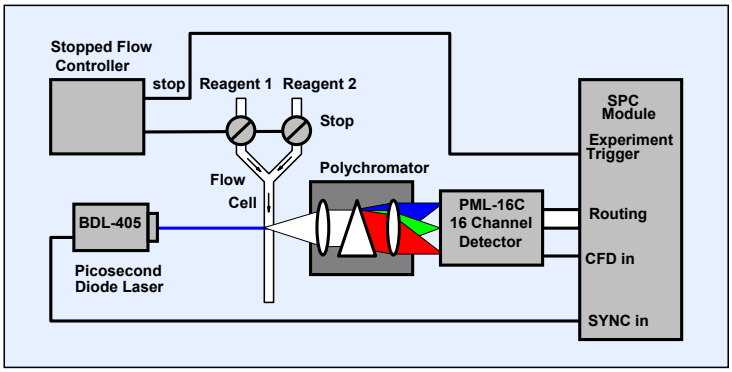


Fig. 505: Stopped Flow Experiment with TCSPC and multi-spectral detection

A laser is focused at the flow channel of the mixing cell shortly behind the mixing region, and the fluorescence from this spot is detected. The flow of the reagents through the cell is periodically stopped by two valves. Commercial instruments stop the flow within approximately one millisecond. For each stop of the flow, the TCSPC device records a sequence of fluorescence decay curves. Because the number of 'stop' events is limited by the amount of reagents available good exploitation of the fluorescence photons is important. It is therefore advisable to combine stopped flow experiments with multi-detector operation. Several PMTs can be used to detect under 0° and 90° of polarisation, or to detect in different wavelength intervals. Another possibility is multi-spectral detection, e.g. with the bh PML-16 C detector or the bh PML-Spec system, as shown in Fig. 505.

Results obtained in an SPC-630 based single-detector system have been presented in [154]. An instrument with two detectors, a router and a bh SPC-630 modules has been described in [1063]. Both instruments used sequential recording in the continuous flow mode.

Continuous Flow Mixing Techniques

The time-resolution of stopped-flow mixing techniques is limited by the speed of the valves which stop the flow. The resolution is about 1 ms. Higher resolution is obtained by continuous flow mixing techniques. Two reagents are fed into separate inputs of a flow cell under high pressure. They are combined in a mixing region and then flow through the observation channel. The observation channel is illuminated by a laser, and the absorption or the fluorescence along the channel is recorded. Because the velocity in the observation channel is known, the distance along the channel represents the time scale of the reaction. With micromachined channels, a resolution down to a 25 µs is achieved [208].

Continuous flow mixing can be combined with TCSPC by scanning the position along the flow channel and recording a fluorescence decay curve for each position, see Fig. 506. An SPC-630 based instrument and its use for investigating protein-folding reactions has been described in [208]. The basic setup is shown in Fig. 506, top. A similar instruments with two detectors and a dual-module TCSPC system was used to observe protein folding via FRET and fluorescence anisotropy [207, 650, 651, 1351], see Fig. 506, bottom.

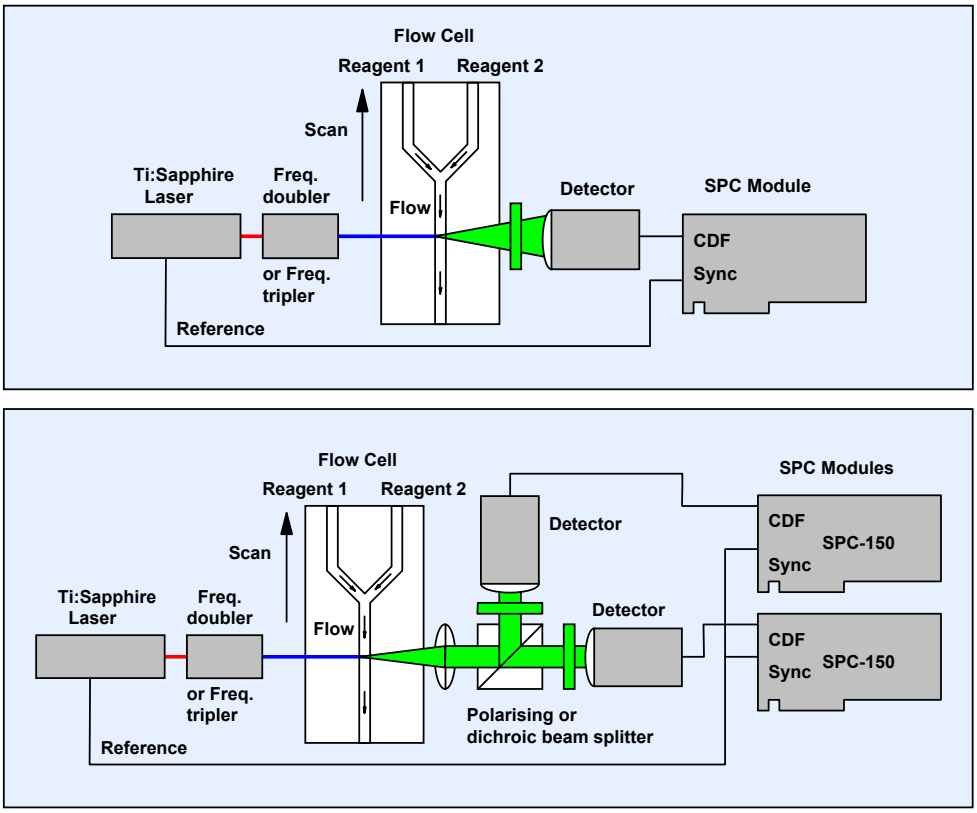


Fig. 506: Continuous flow mixing with fluorescence lifetime detection. Single-detector (top) and dual-detector setup (bottom)

The advantage of scanning the position along the flow channel is that the instrument can easily be combined with several detectors, e.g. for fluorescence anisotropy decay measurement or detection in several spectral intervals. By using the bh PML-Spec system multi-spectral detection can be achieved. A typical result is shown in Fig. 507.

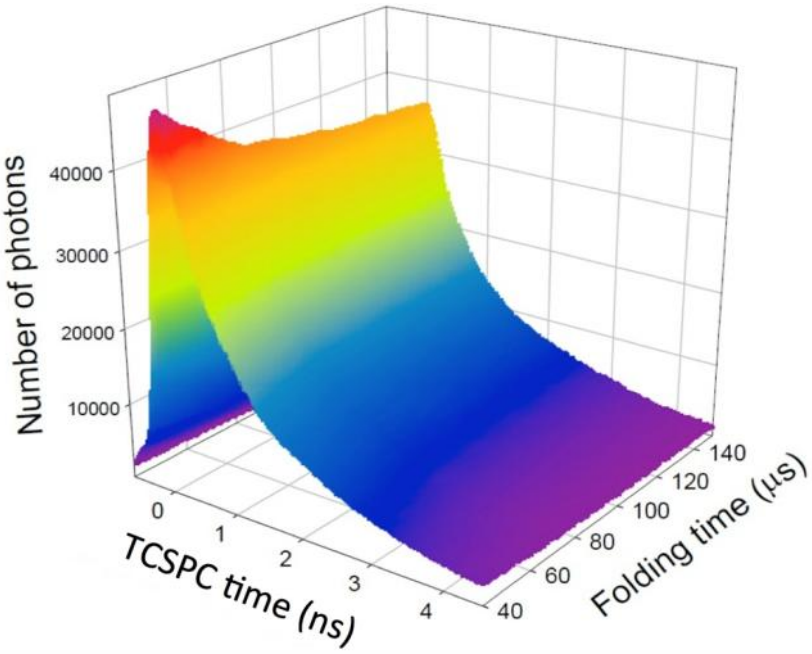


Fig. 507: Continuous-flow mixing data of the refolding of horse heart cytochrome. The 'folding time' is the distance along the flow channel divided by the flow speed. With permission from Kathuria et al. [650].

The drawback of the scanning principle is that the instrument consumes large amounts of reagents. Reagent economy can be largely improved by using multichannel detection along the flow channel. The flow channel is illuminated along its full length, and the fluorescence decay curves along the channel are detected simultaneously by a PML-16 multi-anode detector head. However, it is difficult to obtain constant excitation intensity and sensitivity along the channel. Illumination by a laser tends to produce speckles, and the sensitivity of the PML-16 channels is not uniform. Both effects are not necessarily stable over longer periods of time, so that the calibration can be difficult.

Simultaneous Measurement of Fluorescence and Phosphorescence Decay

Simultaneous measurement of fluorescence and phosphorescence decay functions is difficult because the time scales and the intensities differ by three, often six orders of magnitude. If the excitation pulses are made short enough to measure the fluorescence decay either the fluorescence in the first few ns saturates the detector or the phosphorescence is so weak that it is lost in the detector background. Reasonable phosphorescence decay functions can only be obtained with excitation pulses of long duration, which, however, make the detection of the fluorescence decay impossible.

Triggered Sequential Recording

The problem can be solved by using the triggered sequential recording capability of multi-dimensional TCSPC in combination with a picosecond diode laser with fast on/off capability. The excitation of fluorescence and phosphorescence is illustrated in Fig. 508.

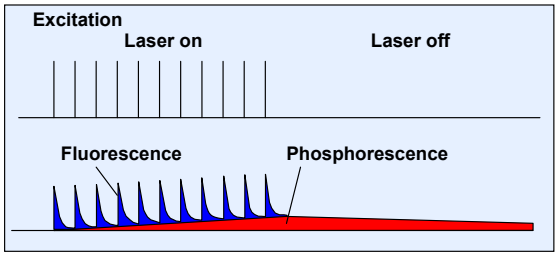


Fig. 508: Excitation of fluorescence and phosphorescence by laser on/off switching

The diode laser delivers excitation pulses at a repetition rate of 40 to 80 MHz. The laser is switched on and off at a period in the microsecond or millisecond range. In the ‘laser on’ phases normal fluorescence decay is observed. A single excitation pulse does not cause any detectable triplet population and thus no detectable phosphorescence. However, during the complete ‘laser on’ phase a noticeable triplet population is accumulated. The phosphorescence is then observed in the ‘laser off’ period.

To record the signals a TCSPC device is operated in a triggered sequential mode. Both the ‘Scan Sync Out’ and the ‘Continuous Flow’ mode can be used. The start of the sequence is triggered with the ‘laser on’ signal. The length of the sequence is slightly shorter than the complete on-off period of the laser. A large number of on/off periods are accumulated. A result is shown in Fig. 509.

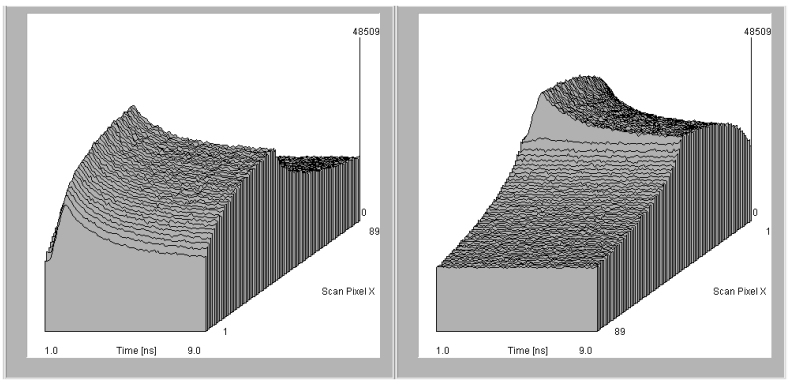


Fig. 509: Detection of fluorescence and phosphorescence by laser on/off switching and triggered sequential recording. The sequence begins with the start of the ‘laser on’ period. Left: Sequence shown from the beginning, ‘laser on’ period at the front. Right: Sequence shown from the end, ‘laser on’ period at the back

The laser on/off period was 90 ms, the duty cycle 50%. The laser repetition rate was 50 MHz. Thus, $2.25 \cdot 10^6$ laser pulses were sent into the sample during the 45 ms of the 'laser on' period. These pulses build up a substantial amount of phosphorescence. The build-up of the phosphorescence can be seen at the bottom of the sequence of fluorescence decay functions (Fig. 509, left). During the 'laser off' phases no fluorescence is excited, and the pure phosphorescence is detected (Fig. 509, right).

Fig. 509 gives an impressive demonstration of the double-kinetic recording capability of multi-dimensional TCSPC. It should be noted that the phosphorescence of the sample used for Fig. 509 was extremely strong. The sample was used to demonstrate both the build-up and the decay of the phosphorescence. In practice the 'laser on' period is often entirely dominated by the fluorescence, and the phosphorescence is lost in the afterpulsing background of the fluorescence signal. However, the decay of the phosphorescence in the 'laser off' period is not disturbed by fluorescence and observable even if the phosphorescence is weak.

Triggered-Accumulation MCS Mode

A second way of phosphorescence decay recording has been added to the SPCM software with version 9.0 of April 2010. For the FIFO mode of the SPC-150 and SPC-830 modules a 'Triggered Accumulation MCS' option is available. It builds up the distribution of the photons versus their macro times after an excitation pulse, or a burst of excitation pulses. The time of the excitation pulse is inserted in the photon data stream via one of the 'marker' inputs of the SPC-150 or SPC-830 modules. Triggered Accumulation MCS can be used to record luminescence decay curves in the microsecond or millisecond range simultaneously with fluorescence decay functions in the ps or ns range.

The general setup is shown in Fig. 510. The sample is excited by a BDL-SMC, BDL-SMN, or BDS-SM laser. The laser is periodically turned on and off by a DDG-210 pulse generator card. The result is the excitation scheme shown above in Fig. 508: During the laser-on time fluorescence is excited, and phosphorescence builds up. During the laser-off time the phosphorescence decays. The photons are recorded by an SPC-150 or SPC-830 TCSPC module. As usual, the start pulses come from the detector, the stop pulses from the laser. Because the laser does not deliver SYNC pulses in the laser-off periods an auxiliary SYNC signal is generated by a LSG-02 sync generator module. The on/off signal for the LSG-02 is reversed with respect to that of the laser. An 'MCS Trigger' is sent into the SPC module as a timing reference to the laser on/off modulation. The SPC module is operated in the FIFO mode. It builds up a photon distribution over the start-stop times (this is the fluorescence decay) and a photon distribution over the times in the laser modulation period (this is the phosphorescence decay).

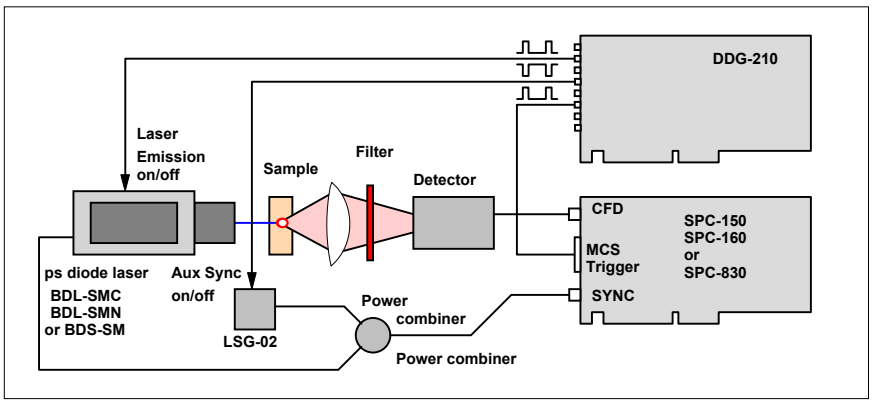


Fig. 510: Principle of simultaneous fluorescence and phosphorescence decay measurement by triggered accumulation MCS recording in the FIFO mode

A typical result is shown in 342. The sample was a solution of Fluorescein and a Ruthenium dye. The display window in the left shows the fluorescence of the Fluorescein. The window on the right shows the phosphorescence of the ruthenium dye. The time range was selected to show the full laser on/off period. The left part of the curve is the laser-on period. The signal within this time is fluorescence, and phosphorescence in the process of building up. The right part of the curve is the laser-off period. It shows the phosphorescence decay.

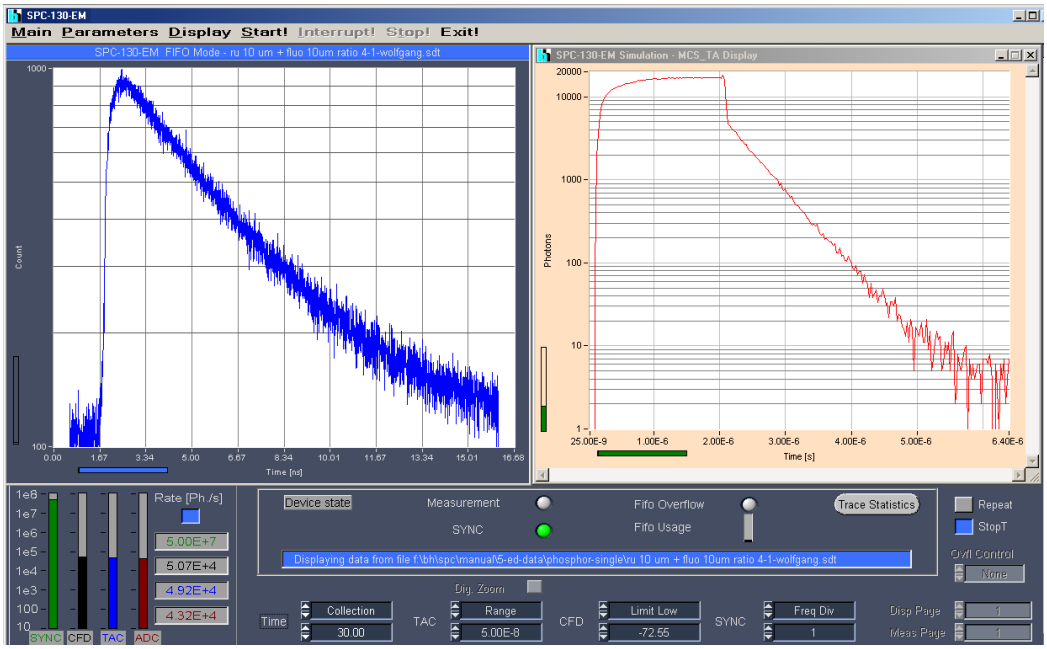


Fig. 511: Simultaneous measurement of fluorescence and phosphorescence decay

The setup can be modified for recording only phosphorescence, or for multi-wavelength detection by a PML-16 detector. Examples are shown in Fig. 512, left and right.

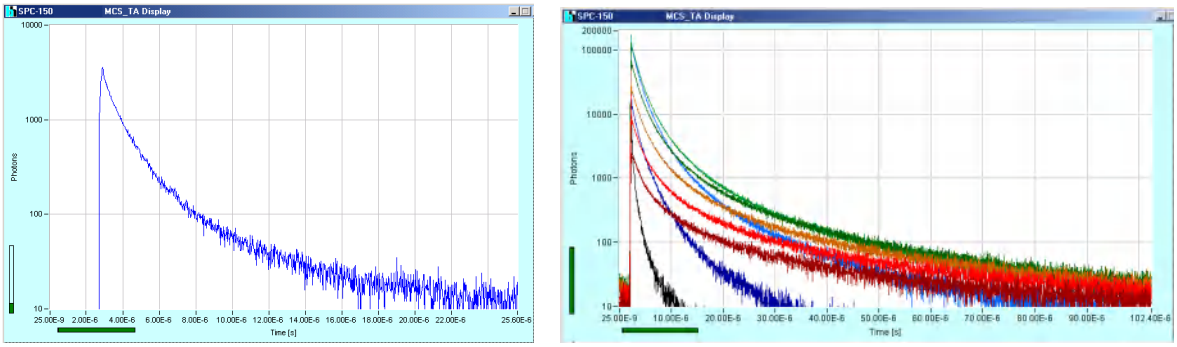


Fig. 512: Microsecond luminescence decay curves recorded in the Triggered Accumulation MCS mode. Left: Single PMC-100 detector. Right: PML-SPEC multi-wavelength detector, 8 of 16 channels displayed

A complete cable diagram for a fluorescence/phosphorescence decay system is shown in Fig. 361, page 230. For system parameter setup please see ‘Microsecond Lifetime Imaging: MCS FLIM’, page 767.

Please note that triggered accumulation MCS can be combined with scanning. For technical principle please see ‘Dual Time-Base Recording’, page 130, for application see chapter ‘Simultaneous FLIM/PLIM’, page 434 of this handbook.

Time-Resolved Laser Scanning Microscopy

Introduction

Fluorescence techniques have found broad application in live sciences because they are non-invasive, non-destructive, extremely sensitive, and deliver information about biochemical processes on the molecular scale. The development of fluorescence techniques has especially benefited from the introduction of confocal [830, 875, 1342] and multiphoton [366] laser scanning microscopes. By suppression of out-of-focus light and lateral scattering, these instruments deliver fluorescence images of unprecedented contrast. Moreover, laser scanning microscopes have made microscopy multi-dimensional: Data are obtained over three spatial dimensions [373, 952], over the wavelength [375], the experiment time, and the polarisation of the light [1292].

The combination of laser scanning with fluorescence and phosphorescence decay recording adds additional dimensions to the recording process. Unlike the fluorescence intensity, the fluorescence lifetime does not depend on the concentration of the fluorophore. In the simplest case, the fluorescence decay function, or the fluorescence lifetime, can be thus be used as an additional parameter to separate or identify the emission of different fluorophores [686, 738, 1249].

More importantly, the parameters of fluorescence decay function are direct indicators of the molecular processes in biological systems. TCSPC FLIM data thus contain a lot more information than steady-state intensity images, spectral images, or time-lapse recordings. Another outstanding feature of TCSPC FLIM is that it records several pieces of complex information simultaneously: Intensities, fluorescence spectra, fluorescence lifetimes, fluorescence lifetimes of different fluorophore fractions, relative concentrations of fluorophore fractions, and phosphorescence lifetimes can be obtained simultaneously in the same imaging process. The parameters can therefore be directly related to each other and to possible changes in the metabolism of the cells.

First bh FLIM applications date back to 1996 when bh introduced the SPC-535 modules and used them for FLIM with ophthalmic scanners [1087]. These were the worlds first combination of multi-dimensional TCSPC with fast optical scanners.

Implementation of FLIM in laser scanning microscopes started in 1998 with the introduction of the SPC-730 module. Within a short time, bh FLIM systems for the Zeiss LSM 410 and LSM 510, the Leica SP2, the Biorad MRC-600, MRC-1024, and the Olympus FV 300 were released. The FLIM systems were continuously upgraded with more powerful TCSPC modules, new detectors, and with optical and electrical interfaces for new microscope types [69, 71, 91, 92, 95, 96, 100, 101, 102, 76, 89, 90, 106, 111, 112, 123, 161, 168]. In 2007 bh introduced the DCS-120 system - the first complete confocal laser-scanning FLIM microscope with fast beam scanning, dual-channel parallel detection, diode-laser or multiphoton excitation, and simultaneous-FLIM/PLIM capability [66, 65, 68].

bh FLIM systems were constantly improved by adding new features and functions. bh were first to introduce multi-spectral FLIM [95, 145, 156]. FLIM with hybrid detectors was introduced in 2010 [159, 160], and the wavelength range was extended into the near-infrared region [100, 101, 169]. In 2013 the bh systems made the step into the 64-bit world of Windows. As a result, images with megapixel resolution were obtained [103, 111, 1198] and multidimensional data of unprecedented complexity could be recorded [101, 168]. Mosaic FLIM was introduced to record high-resolution data from large image areas and simplify Z-stack FLIM [99, 168]. Fast physiological changes in a sample could be recorded by temporal mosaic FLIM and FLITS [162, 164, 168, 463]. The metabolic state of cells and tissue could be related

to the oxygen concentration by simultaneous FLIM and PLIM [161, 637, 943, 1130]. Ultra-fast hybrid detectors were introduced in 2017. The detectors substantially improved metabolic imaging by NADH FLIM [122]. They also revealed ultra-fast decay components which had never been detected before. These and other multi-dimensional TCSPC FLIM techniques will be described in the following sections of this chapter. For overview literature on FLIM by multi-dimensional TCSPC please see [163, 165, 166, 167, 168, 171].

The Advantage of Scanning

It is commonly accepted that confocal and multiphoton laser scanning deliver images from a defined focal plane in the sample. Light from other planes is suppressed by the pinhole or, in the case of multiphoton imaging, not excited at all. This 'optical sectioning' capability is extraordinarily important in FLIM applications: The fluorescence decay functions recorded from biological objects are usually multi-exponential. The decay components have to be separated to obtain quantitative FRET results, distinguish different proteins, different metabolic states, or to derive biochemical information from autofluorescence. Separating several decay components is generally difficult and requires a large number of photons in the pixels of the image [680]. The situation becomes virtually hopeless if the pixels contain not only fluorescence of several fluorophore populations but also fluorescence from different sample layers. Suppression of out-of-focus signals is therefore a precondition for obtaining meaningful lifetime images.

However, optical sectioning capability is not the only advantage of scanning. Scanning also avoids crosstalk between the pixels by scattering. Scattering is not important for imaging of thin and transparent samples, as they are usually considered in conventional microscopy. It is, however, the dominating process of image deterioration in thick samples, such as mammalian skin, bone, or other tissues. An example is shown in Fig. 513. The left image shows a conventional image of pig skin taken through a microscope. The image shows some surface details of the sample but the internal structure is entirely hidden. The same sample imaged by scanning yields the image in Fig. 513, middle. It clearly shows the internal tissue structure. Please note that the image was not taken through a confocal pinhole, only by scanning with a focused laser beam and detecting the photons coming back through the scanner beam path. However, the contrast is still impaired by out-of-focus haze, which clearly can be seen in the image. The image in Fig. 513, right, was taken through a confocal pinhole. The pinhole also removes the out-of-focus light, which results in a clean image of the scanned sample plane.

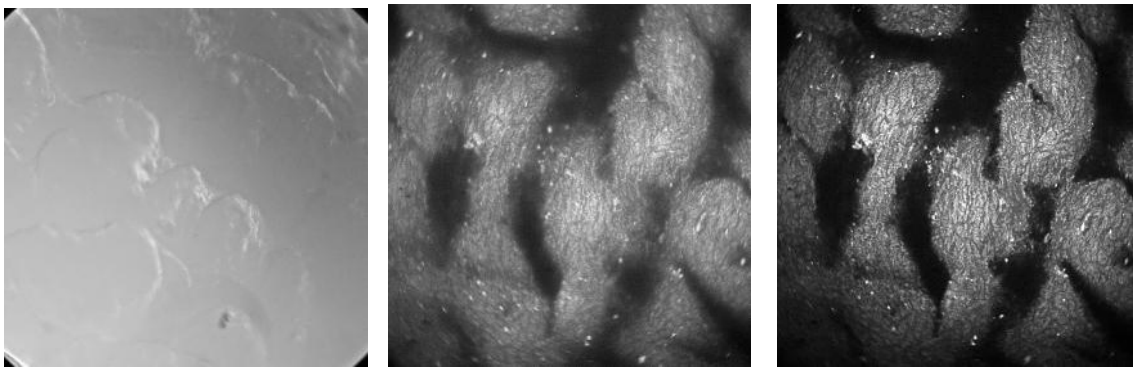


Fig. 513: Left to right: Wide-field image, non-confocal scan image, confocal image

Why is the image quality so much better for scanning? The reason is scattering. A scanning device excites only one pixel at a time. Consequently, it records scattered light *only from the scanned pixel* but not from the other pixels of the image. A wide-field imaging system excites all pixels simultaneously. In every pixel, it detects scattered light not only from *this* pixel, but also from *all other pixels* of the illuminated area. Considering the fact that a good microscopy

image has at least 500 x 500 = 250.000 pixels it becomes clear why the wide field technique is unable to image sample layers inside the tissue.

It is a lucky coincidence, or perhaps a result of the intuition of the designers, that the most accurate and sensitive technique of fluorescence decay measurement, multi-dimensional time-correlated single photon counting, is almost ideally compatible with laser scanning techniques. Multi-dimensional TCSPC is able to record images with a fully resolved decay curve in each pixel of an image. The results are independent of the scan rate of the scanning system: The signal-to-noise ratio depends only on the total acquisition time, not on the scan rate. TCSPC delivers an excellent time resolution: The IRF - the temporal point-spread function - is short and clean, and virtually free of background. Thus, the combination of laser scanning techniques and multi-dimensional TCSPC combines near-ideal resolution in space with near-ideal resolution in time.

The Laser Scanning Microscope

The general optical principle of a laser scanning microscope [373, 875, 952] is shown in Fig. 514. One-photon excitation is shown left, two-photon excitation right. Both approaches have in common that the laser beam is deflected by fast-moving galvanometer mirrors. The mirrors change the direction of the beam. The scan lens projects the axis of the galvanometer mirrors into the principal plane of the microscope lens. Thus, the direction of the laser beam in the principal plane of the microscope lens changes, and the laser spot in the focus of the microscope lens moves over the sample. The fluorescence light is collected back through the microscope lens.

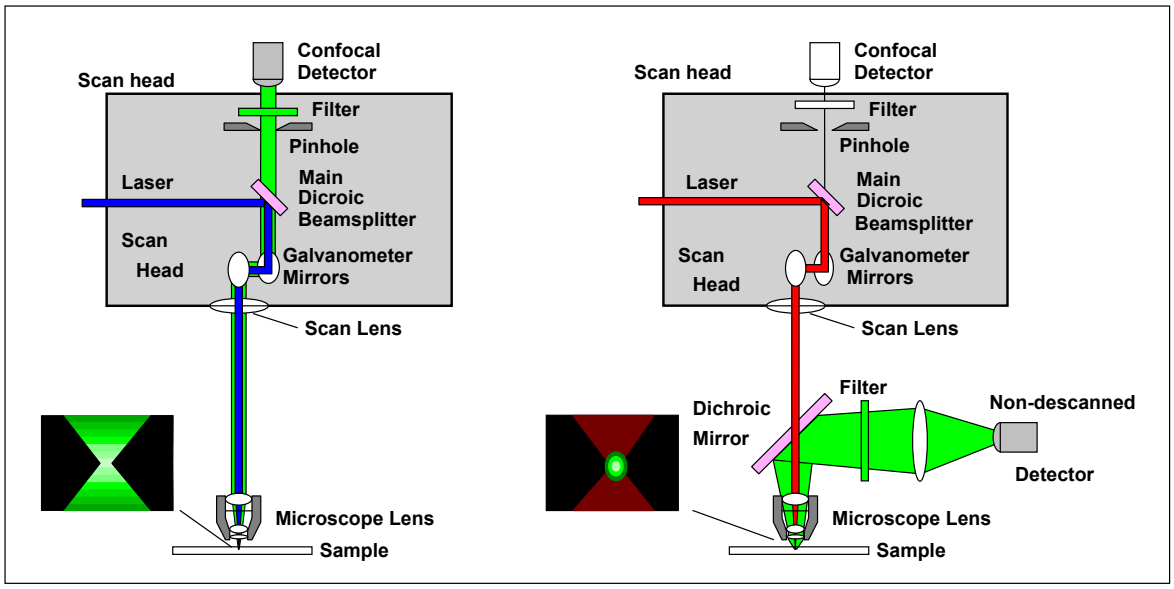


Fig. 514: One-photon FLIM (left) and multi-photon FLIM (right), light path simplified

The way the fluorescence light is transferred to the detectors is different for one-photon excitation and two-photon excitation systems.

One-Photon Excitation

One-photon excitation uses an ultraviolet or visible light laser for excitation. Fluorescence is excited via the conventional S0-S1 absorption process, i.e. the fluorescence appears at the long-wavelength side of the excitation line. Typical excitation power for biological samples is on the order of a few 10 µW in the sample plane. The laser beam excites fluorescence within a double cone throughout the whole depth of the sample, see Fig. 514, left. Detecting all the

fluorescence returned from the sample would result in a conventional microscope image, i.e. the image of the focal plane would be overlaid by blurry images of sample layers above and below the focal plane.

Confocal Detection

To confine the detection of fluorescence to the focal plane the light is focused into a confocal pinhole in the upper focal plane of the microscope. Only light from the focal plane is focused into the pinhole and thus able to pass it. Light from outside the focal plane is substantially suppressed [373, 875, 952]. To send the moving fluorescence beam into a stationary pinhole the beam must be 'descanned'. This is achieved by feeding it back through the galvanometer mirrors, see Fig. 514, left. The stationary beam of fluorescence light is separated from the excitation light by the 'main dichroic beamsplitter'.

The optical design of a confocal scanner is anything but trivial. Ideally, the pinhole has a diameter on the order of the diameter of the Airy disc in the upper focal plane. Keeping the system aligned for different scan angles, scan amplitudes, microscope lenses, wavelengths, and main dichroic beamsplitters requires extraordinary mechanical reproducibility and optical perfection. Details can be found in [68] and [1187].

To attach a confocal FLIM detector to an existing laser scanning microscope the scan head must have a suitable output port. Some scan heads have fibre ports which can be used to direct the light to external detectors. Fibre coupling of the detectors is convenient but has a few disadvantages when used for FLIM: There is some intensity loss in the fibre coupler, there is temporal pulse dispersion in the fibre, and there are reflections at the fibre faces which can distort the recorded decay curves. These problems are avoided by direct coupling of the detectors. Direct ports exist or are available for the Zeiss LSM 710/780/880/980 microscopes, the bh DCS-120 system, and for the Leica SP5 and SP8 microscopes.

Two-Photon Excitation

Two-photon microscopes use a picosecond [542] or femtosecond [367] Ti:Sa laser to excite the sample by two-photon absorption, see Fig. 514, right. Simultaneous absorption of two (or more) photons has been theoretically predicted by Maria Göppert-Mayer [509]. It has been suggested for laser scanning microscopy by Wilson and Sheppard in 1984 [1345] and practically introduced by W. Denk and J.H. Strickler [366, 367] in 1990. The efficiency of two-photon excitation increases with the square of the excitation power density. With a femtosecond Titanium-Sapphire laser the excitation process becomes so efficient that no more than a few milliwatt of laser power are required to obtain clear fluorescence images with endogenous [373, 681, 682, 683] and exogenous fluorophores [204, 1352]. 'A few milliwatt' may sound a lot of power compared to the µW power levels used for one-photon excitation. It should, however, be noted that only the absorbed power is important for possible damage effects, not the incident power. The power absorbed by the fluorophores is, however, no higher than for one-photon excitation. For sample layers outside the focal plane it is even lower.

Two photon excitation has a number of advantages over one-photon excitation. First, the absorption - both one-photon and two-photon - of the sample at the NIR wavelength of the Ti:Sa laser is very low. Also the scattering coefficient is lower than at visible or ultraviolet wavelengths. Two-photon excitation therefore goes deeper into tissue than one-photon excitation, see Fig. 515, left and middle. Two-photon excitation can be used to excite fluorescence in tissue layers as deep as 100 µm, in some cases even 1 mm [366, 373, 682, 683, 952, 958, 1161, 1240].

Second, absorption and possible sample damage occurs only within a thin plane around the focal plane of the microscope. Two-photon excitation is safe to live cells and tissues [448, 681, 682, 683, 684]. It can even be used in clinical applications [690, 692].

Third, noticeable two-photon excitation is obtained only in the focus (Fig. 515, middle). Thus, two-photon excitation is a second way to obtain depth resolution and suppression of out-of-focus fluorescence. Different from one-photon excitation with confocal detection, which avoids out-of focus *detection*, two-photon excitation avoids out-of-focus *excitation*.

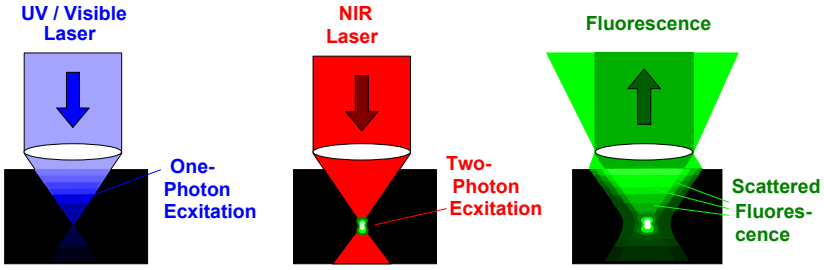


Fig. 515: Left: One-photon excitation. The effective excitation power decreases rapidly with increasing depth. Middle: Two-photon excitation. The NIR laser penetrates deeply into the sample. Right: The fluorescence from a deep focus is scattered on the way out of the sample. It leaves the back aperture of the microscope lens in a wide cone.

Non-Descanned Detection

The fact that the fluorescence signal comes only from the focus leads to a another advantage of two-photon excitation: A two-photon microscope is able to detect photons which are scattered on the way out of the sample. Scattered photons leave the back aperture of the microscope lens in a wide cone of light (Fig. 515, right). In a one-photon system with a descanned confocal beam path these photons would be lost. They can neither be fed through the narrow beam path of the scanner, nor can they be focused into a pinhole. In a two-photon microscope, however, there is no out-of focus excitation and, consequently, no need to use a pinhole. Two-photon microscopes therefore divert the fluorescence from the excitation beam directly behind the microscope lens and project it on a large-area detector, see Fig. 514, right. The principle is called non-descanned (or 'direct') detection. A two-photon microscope with non-descanned detection not only excites fluorescence in deep sample layers, it also detects these photons efficiently [57, 58, 926]. Please see Fig. 527, page 358 for optical details of the NDD beam path.

Non-descanned output ports for external detectors exist or are available for a number of two-photon microscopes, such as the Zeiss LSM 510, the Zeiss LSM 710/780/880/980, the Olympus FV1000 (inverted version) and the two-photon version of the bh DCS-120 system [91, 69, 68]. The Zeiss LSM 780/880/980 NLO and the Leica SP5/SP8 have FLIM-compatible NDD detector modules, please see [102] and [90].

A practical advantage of NDD in combination with multiphoton excitation is that the scanner is far less complicated than for confocal detection. There is no requirement to exactly cancel the beam motion for different wavelengths, scan fields, or objective lenses. It is also not necessary to focus the fluorescence in a diffraction-limited pinhole, and keep the alignment stable when filters or dichroics are replaced. All that is required for multiphoton NDD is that a laser beam of the correct diameter is cleanly transferred into the back aperture of the microscope lens and correctly scanned. The simplifications in the scanner optics at least partially compensate for the high price of a femtosecond laser. Two-photon microscopes can therefore be built by attaching the laser and an optical scanner to a conventional microscope [371] or by upgrading a one-photon system with a Ti:Sapphire laser [372, 819].

Two-Photon Excitation With Descanned Detection

For sake of completeness, it should be mentioned that two-photon excitation is also being used with descanned detection. The advantage over non-descanned detection is that the pinhole (even if opened wide) rejects daylight and optical reflections. Confocal detection may also help suppress spurious fluorescence light if there is a highly fluorescence layer close to the image plane. The disadvantage is that fluorescence photons scattered on the way out of the sample are not detected. Descanned detection therefore does not exploit the deep-tissue imaging capability of multiphoton excitation.

Excitation Lasers

TCSPC FLIM requires a pulsed excitation source which delivers picosecond or femtosecond pulses at a repetition rate in the 40 to 100 MHz range. The wavelength should be compatible with the fluorophores used in the particular FLIM application. This usually implies that several pulsed lasers must be present or that a tuneable excitation source must be used.

Picosecond Diode Lasers

Picosecond diode lasers are available for the required pulse repetition rates, an for a wide range of wavelengths. Laser scanning microscopes normally have fibre ports for the excitation lasers. Only light from single-mode fibres can be focused in a diffraction-limited spot. Therefore it is important, that the lasers have single-mode fibre outputs or that their output beams can be coupled into single-mode fibres. The bh BDL-SMC, BDL-SMN and BDS-SM lasers are available with the Qioptiq (formerly Point Source) fibre coupling system and with permanently attached single-mode fibres. They are thus fully compatible with laser scanning microscopes. Examples are shown in Fig. 516.



Fig. 516: BDL-SMC laser and BDS-SM lasers with single-mode fibre coupling

An advantage of ps diode laser is that the pulse repetition rate can be changed and that they can be on/off modulated electronically. The can therefore be directly - without an additional optical modulator - be used for combined FLIM/PLIM and for wavelength-multiplexed FLIM.

The pulse shape of a ps diode laser changes with on the electrical driving power. Within one series of experiments, the electronic power control should therefore not be used to change the excitation power at the sample. Also, a ps diode laser should not be operated at excessively high power. The pulses then develop tails or afterpulses. These pulse substructures decrease the efficiency of lifetime calculation. The effect is similar as for detector background [680]. Although operation at high power may increases the count rate nothing is gained in terms of lifetime accuracy.

A frequent concern is that the output power of the diode laser may be insufficient for FLIM. This concern is unfounded, at least for lasers with state-of-the-art fibre coupling. It rather happens that the power is too high. The laser or the scanner should therefore by equipped with some kind of variable optical attenuator.

Another concern against ps diode lasers is the limited availability of wavelengths. Fig. 517, left, compares approximate excitation spectra for a number of commonly used fluorescent

proteins with the available laser wavelengths. The curves were taken from [340] and [360]. Already with two laser wavelengths, 405 nm and 445 nm, a large number of fluorescent proteins can be excited. The most important ones are ECFP (Cerulean is almost similar), mTFP, and EGFP, because these are good FRET donors. As can be seen from Fig. 517 the 445 nm laser excites ECFP and the new mTFP [360] near their excitation maxima. It also excites EGFP at reasonable efficiency. The 405 nm laser yields good efficiency for EBFP and ECFP, and even excites the EGFP at about 20% of its maximum efficiency. The EYFP and the DsRed are normally used as FRET acceptors, and excitation is rather to be avoided then be achieved.

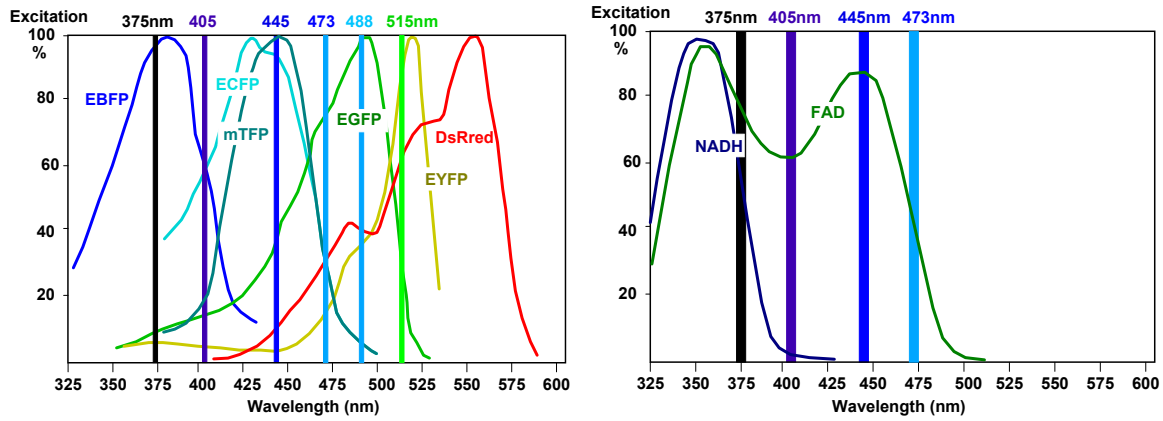


Fig. 517: Left: One-photon excitation spectra of commonly used fluorescent proteins, after [340] and [360]. Right: Excitation spectra of NADH and FAD, after [1094].

Fig. 517, right, shows excitation spectra of NADH and FAD. FAD is excited by all blue laser diodes. NADH is excited well by the 375 nm laser. The problem is not the availability of a suitable laser wavelength but the low penetration depth at this wavelength. One-photon excitation is therefore restricted to single cells. NADH FLIM of tissue is better performed by two-photon excitation.

Super-Continuum Lasers

Super-Continuum lasers with acousto-optical filters can be tuned over the entire range from 420 nm to 800 nm. For FLIM/PLIM the lasers can be on/off modulated via the filter. We have tested different devices in combination with the DCS-120 scan head and generally obtained good results [93, 94], see page 353 in this chapter. However, there can be some pitfalls. The pulses are not always as short as expected, especially at shorter wavelength. We have found pulse widths of up to 300 ps in the range below 480 nm. This is too broad to determine accurate lifetimes for fast effects, such as the bound component of FAD, or the interacting donor component in FRET experiments. Also, we occasionally encountered broadband leakage of the acousto-optical filter. This is not a problem in scanners with a single-wavelength dichroic beamsplitter. But in systems with wideband beamsplitters (which are most desirable for a tuneable excitation source) the leakage can make FLIM impossible. The only solution is then to put a cleaning filter in the excitation beam path. This has to be replaced when a different wavelength is used which is, at least, inconvenient in a tuneable-excitation system.

Titanium-Sapphire Lasers

Titanium-Sapphire lasers are the near-ideal excitation source for multiphoton excitation. They are tuneable, the short pulse width yields high efficiency of two-photon excitation. Short pulses also yield good FLIM time resolution. With the ultra-fast HPM-100-06 and -07 detectors a TCSPC instrument-response function of less than 20 ps FWHM is obtained. The combination of these features is the reason that more than 50% of the bh FLIM systems are two-

photon systems. Ti:Sa lasers cannot be modulated or power-controlled electronically. Therefore an AOM (acousto-optical modulator, see 'Ti:Sa Laser and AOM Control', page 858) must be used to control the intensity, and to modulate the laser for FLIM/PLIM. Some multiphoton systems use EOMs (Electro-Optical Modulators) to control the laser power. Our experience is that EOMs have problems at high attenuation factors (low laser power). The laser is not turned cleanly off, and there is a iris effect that reduces the beam diameter at high extinction. In the low-intensity range, where FLIM usually works, the microscope lens is no longer fully illuminated, and the microscope loses resolution.

Femtosecond Fibre Lasers

In multiphoton microscope systems, femtosecond fibre lasers have become a real alternative to the Ti:Sa lasers. The main advantage of the fibre lasers is that they are virtually maintenance-free, compact in size, and do not need warm-up time. The lasers deliver pulses of 100 to 150 fs pulse width, typically at a wavelength of 780 nm. Wavelengths of 880 nm and 920 nm are possible as well. The repetition rate is in the range of 40 to 50 MHz. This is another advantage over the Ti:Sa laser: The ratio of peak power to average power is higher, and the fluorescence has more time to decay in the excitation pulse period.

For many years the output power of fibre lasers was a limitation. Tests with a 50 mW fibre laser delivered two-photon images of the bright demonstration samples but the power was not always sufficient to excite typical FLIM samples. The reason is probably not the laser power itself but the fact that only a fraction of the laser power arrives in the focal plane of the scanning system. Currently available lasers deliver 200 mW, which is more than sufficient for two-photon excitation.

A disadvantage is that fibre lasers are not tuneable. The lack of tuneability is less a problem than commonly believed. A wavelength of 780 nm not only excites NADH efficiently but also a large number of other fluorophores. Two-photon absorption spectra are broad, and excitation is obtained also if the laser wavelength does not match the absorption maximum exactly. Especially, on the short-wavelength side there is usually enough absorption to obtain reasonable excitation efficiency. The performance of a FLIM system with a 780-nm Toptica Femto Fibre Pro laser has been demonstrated successfully, please see [128, 177, 178] and section 'Ultra-High Resolution FLIM Systems', page 362.

Toptica have recently introduced a dual-wavelength fibre laser, the Femto Fibre Dual. This laser delivers wavelengths of 780 nm and 920 nm in a single output beam. The laser contains internal AOMs to control the output power of the two wavelengths individually and to multiplex them for wavelength-multiplexed FLIM, please see section 'Metabolic FLIM with Two-Photon Excitation', page 378.

Detectors

The detectors have a large influence on the performance of a FLIM system. Of course, a good detector should have a high detection quantum efficiency (QE). However, to exploit a high detector QE in terms of lifetime accuracy the detector must also deliver low background counts, and a clean and sufficiently fast temporal ‘instrument response function’ (IRF). The IRF should also be stable, i.e. independent of the count rate and the wavelength. Moreover, a high QE is of little use if the active area is too small for the light to be concentrated on it. A brief description of the detectors typically used in FLIM is given below. For a detailed discussion of detectors and their operation in FLIM systems please see chapter ‘Detectors’.

Conventional Photomultipliers

Most conventional Photomultipliers (PMTs) are too slow for reasonable FLIM operation. Therefore, the PMTs typically integrated in laser scanning microscopes cannot be used as

FLIM detectors. Nevertheless, there is a number of PMTs that yield good FLIM results: These are miniature-size PMTs that achieve low transit time spread due to the short trajectories of the electrons through the multiplication system. PMTs of this type are used in the bh PMC-100, PMC-150 and PMZ-100 detector modules. The IRF width is on the order of 100 to 150 ps (fwhm). The diameter of the active area is 8 to 10 mm, enough for non-descanned detection in multiphoton microscopes.

Multichannel (MCP) PMTs

Multichannel (MCP) PMTs are among the fastest detectors currently available. The instrument response functions is 30 ps (fwhm) or shorter, the active area is sufficient for NDD FLIM in multiphoton microscopes. MCP PMTs are therefore frequently used for FLIM [69, 148, 154, 220, 410, 1094]. However, speed comes at a price: With about $15,000 per detector MCP PMTs are not a low-budget solution.

Single-Photon Avalanche Photodiodes

Single-Photon Avalanche Photodiodes (SPADs) are often praised as the ideal detectors. Fast SPADs reach QEs around 50%, and IRF widths down to 40 ps. However, there are a few serious drawbacks. First, the IRF shape depends on the wavelength. At wavelengths longer than 500 nm a 'diffusion tail' develops, see Fig. 308, page 195. The amplitude of the tail depends on the wavelength so that it is hard to calibrate. Even if the tail is correctly accounted for in the data analysis it reduces the accuracy at which the fluorescence lifetime is obtained. Another obstacle is the small active area, with a diameter of 50 to 100 µm: It impossible to use a SPAD as an NDD detector in a multiphoton microscope.

Hybrid Detectors

bh were the first to introduce hybrid detectors for FLIM. With a GaAsP cathode the detectors reach a quantum efficiency of almost 50%. The IRF width is on the order of 120 ps (fwhm) for GaAsP versions and <20 ps (fwhm) for versions with conventional cathodes. The IRF is extremely clean, without bumps or tails. With an active area of typically 3 mm diameter the detectors can well be used in the NDD detection path of multiphoton microscopes. The biggest advantage of the hybrid detectors over the other detectors has been discovered only recently: The hybrid PMT is free of afterpulsing. Afterpulsing is the major source of counting background in high-repetition-rate TCSPC applications. The absence of any afterpulsing background results in a considerably increased lifetime accuracy for a given number of detected photons. The hybrid detector is the best and the fastest FLIM detector currently available [159, 160, 177, 178], please see section 'Ultra-High Resolution FLIM Systems', page 362. Please see also page 178 and FLIM examples in the application part of this chapter.

Multi-Anode PMTs

Multi-anode PMTs have a segmented anode. They are thus able to detect several optical signals simultaneously. The most frequent application in FLIM is multi-wavelength detection: The light is split spectrally, the spectrum is projected at the cathode of the PMT, and the photon pulses of the anodes are recorded into separate FLIM data sets. This is usually achieved by routing the photon pulses from the individual anodes into separate photon distributions [145, 156], see page 116 and page 125. This principle is used in the bh MW-FLIM multi-wavelength FLIM detector. The efficiency of the bh multi-wavelength detectors has been dramatically increased with the introduction of the MW-FLIM GaAsP detectors. For examples please see page 366. The pulses from several anodes or anode groups can also be recorded in a parallel-channel TCSPC system. This has been demonstrated for 8 channels [158], see page 397.

Confocal FLIM with Diode-Laser Excitation

FLIM results obtained with diode-laser excitation are shown in the figures below. Fig. 518 shows a BPAE cell stained with Alexa 488 phalloidin and Mito Tracker Red. The sample was scanned by a DCS-120 FLIM system. The excitation wavelength was 473 nm, the fluorescence was detected simultaneously in two wavelength channels, from 484 nm to 560 nm (left) and 590 nm to 650 nm, right.

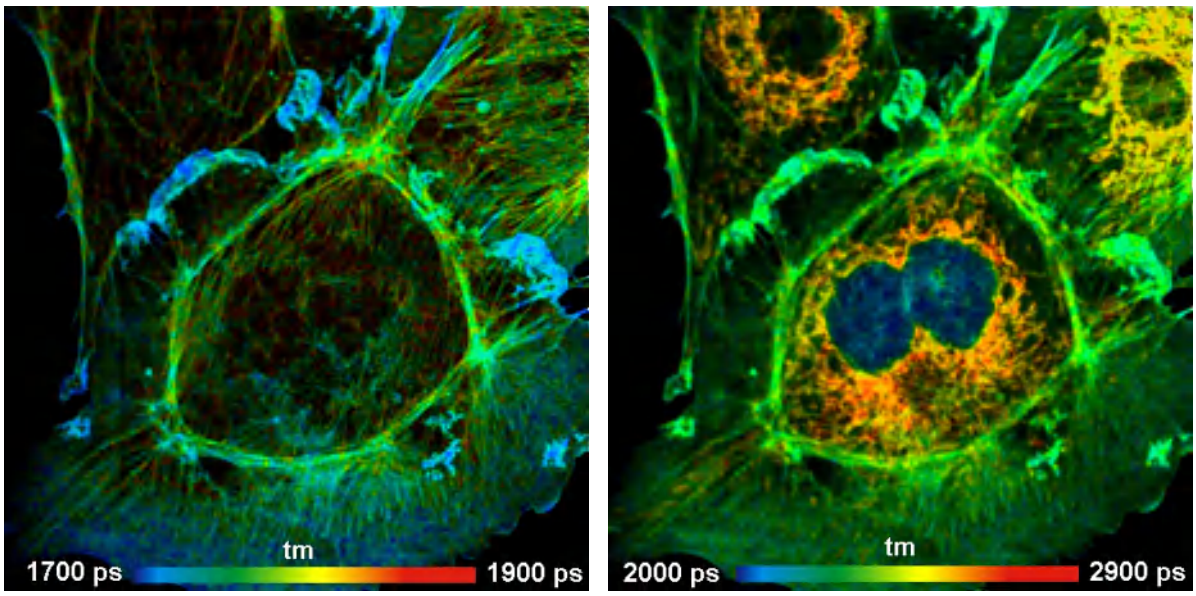


Fig. 518: Dual-wavelength detection. BPAE cells stained with Alexa 488 phalloidin and Mito Tracker Red. Left: 484 nm to 560 nm. Right: 590 nm to 650 nm. 512 x 512 pixels, mean lifetime of double-exponential decay. DCS-120 system with HPM-100-40 hybrid detector

Fig. 519 shows the result of a FRET measurement on a live cell. The donor was CFP, the acceptor YFP. The sample was excited at 405 nm. It should be noted that this is not the optimum excitation wavelength for CFP. Nevertheless, the quality was good enough to run double-exponential FRET analysis on the data. The left image shows the ratio of the lifetimes of the non-interacting and interacting donor fractions, τ_0/τ_{fret}. The distribution of τ_0/τ_{fret} over the pixels is shown on the left. An image of a/b and the distribution of N_{fret}/N_0 over the pixels are shown is Fig. 519, right. The t_1/t_2 image represents the variation in the distance , the a_1/a_2 image the relative amounts of interacting and non-interacting donor. Please see [68] and section 'Förster Resonance Energy Transfer (FRET)' of this handbook for details.

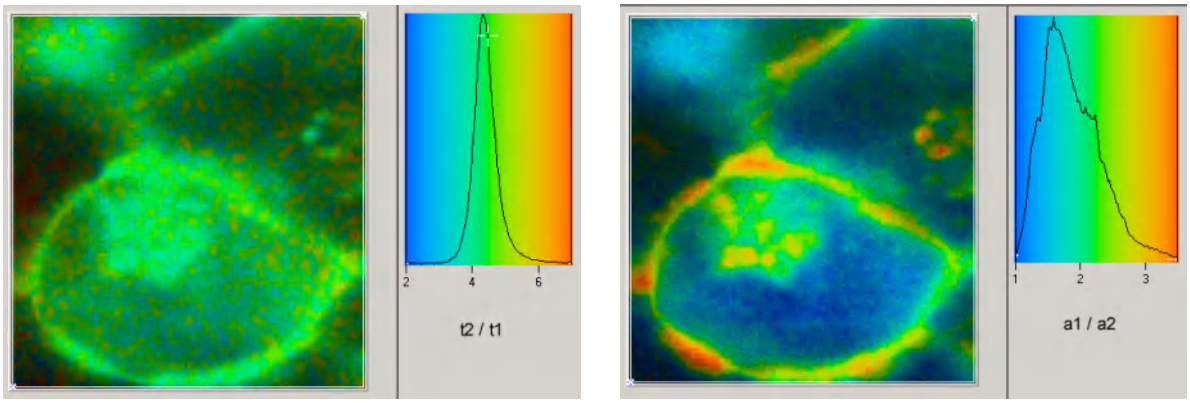


Fig. 519: FRET results obtained by double-exponential lifetime analysis. Left: Ratio of the component lifetimes, $t_2/t_1 = \tau_0/\tau_{fret}$, Right: Ratio of the interacting and non-interacting donor fractions, $a_1/a_2 = N_{fret}/N_0$. Cells courtesy of Burkhard Wiesner, Leibniz Institute of Molecular Pharmacology (FMP), Berlin, Germany

Confocal FLIM with Tuneable-Excitation

Scanning microscopy with tuneable excitation has a long history. The first confocal scanning microscope developed by Marvin Minsky [874, 875] in 1957 used wideband illumination by a conventional lamp and a 50% wideband beamsplitter, see Fig. 520. Scanning was obtained by moving the sample by an electrically driven resonance system. Minsky's microscope was, in principle, a tuneable system: By inserting different filters, the microscope could be used at any desired wavelength. Unfortunately, Minsky did not use fluorescence for image formation. The reason was certainly not the detector - photomultipliers for low-intensity detection were routinely used at this time. Presumably, the benefits of using fluorescence had just not been discovered yet.

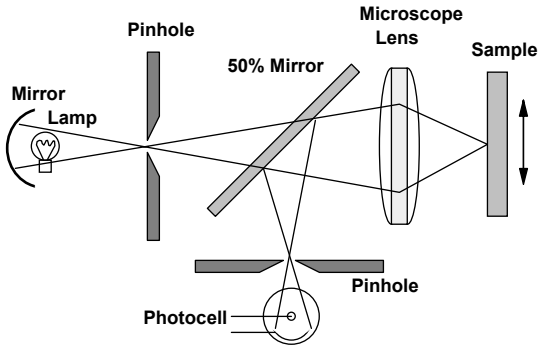


Fig. 520: Minsky's design of the first confocal laser scanning microscope

In 1962, Freed and Engle [462] described a scanning microscope that used an arc lamp as a light source. The wavelength of the illumination light was selected from the lamp spectrum by a monochromator. Also this system was described for reflected light only. Fluorescence was not mentioned although the instrument must have been able to record fluorescence images by simply inserting the right filter in the detection path.

The first tuneable excitation laser scanning fluorescence microscope was described by Van der Oord et al. They used synchrotron radiation for excitation [1281]. The excitation wavelength was selected from the wideband continuum by a filter in front of the input of the laser scanning microscope. Similar instruments were described in [900], and [327]. The latter one was even used with FLIM by parallel-gated photon counting [265].

With the introduction of light sources based on super-continuum generation in photonic crystal fibres [14, 409] a bright tuneable light source became available for laser scanning microscopy [838]. By an acousto-optical tuneable filter (AOTF) any wavelength from less than 400 nm to more than 1000 nm can be selected from the super-continuum. Supercontinuum sources with AOTFs are available from FIANIUM and NKT.

With these light sources, tuneable excitation in a laser scanning microscope may appear easy. Unfortunately it is not. The reason is shown in Fig. 521, left. The laser scanning microscope uses a dichroic beamsplitter to reflect the excitation light down to the microscope lens, and transmit the emission light to the detectors. This beamsplitter can only be made for a single, or a limited number of excitation wavelengths. If the microscope has to be used for a wide range of excitation wavelengths the beamsplitter must be replaced for every wavelength. It is possible to use several dichroic mirrors on a wheel, but this has other disadvantages: To maintain confocal alignment for different beamsplitters the mechanical reproducibility has to be excellent. This is not easy to obtain. Moreover, switching dichroics by rotating a wheel takes time. This makes fast wavelength multiplexing impossible.

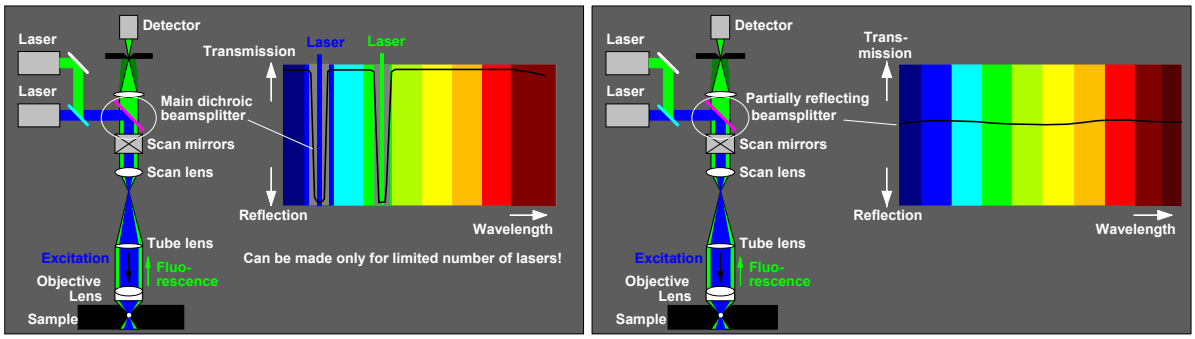


Fig. 521: Confocal scanner with dichroic beamsplitter (left) and wideband beamsplitter (right)

The easiest way to avoid these problems is to go back to Minsky's original design and use a partially reflective mirror, see Fig. 521, right. At first glance, a wideband beamsplitter may appear a very poor design: A considerable part of the emission and the excitation light would be lost. A somewhat closer look, however, shows that Minsky's approach is not so poor after all: The vast majority of TCSPC FLIM experiments (probably also of other LSM applications) is performed at less than 10% of the available laser power. Under these conditions, a loss in excitation power at the beamsplitter can easily be compensated by increasing the laser power at the input of the scanner.

The loss in detection efficiency may appear more serious: Any loss in detection efficiency either results in an increase in photobleaching, or in a decrease in fluorescence lifetime accuracy. However, also here a closer look shows that the loss can be tolerated:

Consider an 80/20 beamsplitter, with 80% transmission for the fluorescence and 20% reflection for the laser. Losing 20% of the fluorescence photons results only in a 10% decrease in lifetime accuracy. Moreover, the loss is less than the difference in collection efficiency of a microscope lens with NA = 1.0 compared to one with NA = 1.15. No one ever considers the differences in collection efficiency of lenses of slightly different NA.

bh have therefore designed a wideband ('WB') version of their confocal FLIM scanner [68]. The design was originally made for swapping diode lasers of different wavelengths [67]. It can, however, be used with any light source that has a Point-Source (now Qioptiq) compatible fibre coupler. Test results are shown in Fig. 522 and Fig. 523.

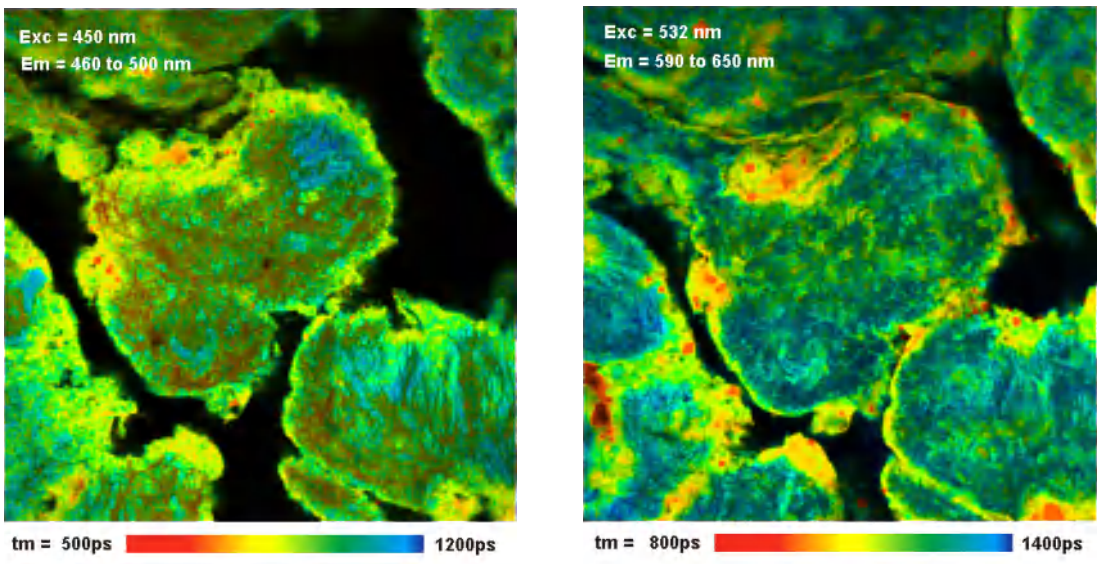


Fig. 522: Pig skin sample, autofluorescence. Left: Excitation 450 nm, detection 460 to 500 nm. Right: Excitation 532 nm, detection 590 to 650 nm. 512 x 512 pixels, 256 time channels. Amplitude-weighted lifetime of triple-exponential fit. Excitation wavelengths multiplexed via the AOTF, DCS-120 WB scanner with Fianium SC400 laser

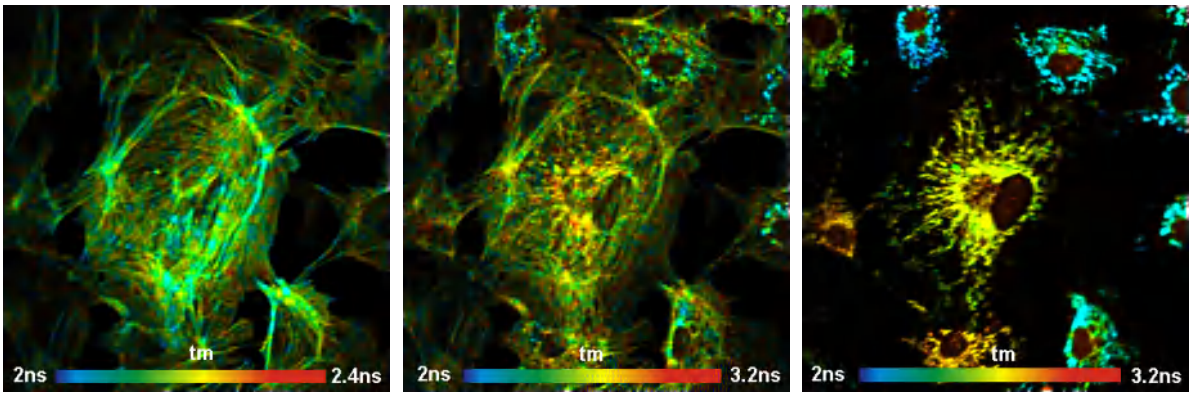


Fig. 523: BPAE Cell labelled with Alexa 488 phalloidin and Mito Tracker red. Measured by laser wavelength multiplexing via the AOTF. Left to right: Excitation 500nm emission 525±50 nm, excitation 500 nm emission 620±30 nm, excitation 580 nm emission 620±30 nm, frame-by-frame multiplexing. DCS-120 WB scanner with NKT SuperK EXTREME laser.

Despite previously published work the patent situation in the field of supercontinuum-laser scanning microscopy is controversial. Becker & Hickl do therefore not sell FLIM system with supercontinuum lasers. Publications based on TCSPC FLIM with supercontinuum laser excitation and confocal scanners can be found in [824, 839, 1207, 1266]. Supercontinuum STED-FLIM applications are described in [35, 258, 761].

A slightly different design of a tuneable laser uses wavelength conversion in a nonlinear fibre but tunes the conversion to generate only a single wavelength. The wavelength is in the NIR; visible-range emission is obtained by frequency doubling. The principle has been developed by TOPTICA and is described in [574]. Images obtained by connecting the TOPTICA IChrome laser to the DCS-120 WB system are presented in [68]. The disadvantage of the TOPTICA laser is that the wavelength is tuned mechanically so that fast wavelength multiplexing is not possible.

The Zeiss LSM 710/780 laser scanning microscopes were available with a tuneable ‘In Tune’ laser. The tuning range is 488 to 640 nm. Thus, the system can be perfectly matched to the excitation spectra of most the fluorophores used in FLIM [69]. The laser delivers pulses with a duration of a few picoseconds at a repetition rate of 40 MHz. These features make the In-Tune system a perfect match to the bh TCSPC FLIM systems. The Zeiss In Tune system comes with a scan head configuration that offers a wide range of main dichroic beamsplitters. These beamsplitters have extremely sharp transitions, and extremely low leakage. Contamination of the fluorescence signals by scattered laser light is almost entirely avoided, even if the system is operated without additional fluorescence filters.

An example of a FLIM recording with the Intune system is shown in Fig. 524. The images show BPAE cells (Molecular Probes sample) stained with Alexa 488 and Mito Tracker red. The FLIM data were recorded by a Zeiss LSM 710 with a bh Simple-Tau 150 FLIM system and a bh HPM-100-40 GaAsP hybrid detector. An image format of 1024 x 1024 pixels and 256 time channels was used. The optical parameters were: 63x NA=1.4 oil immersion lens, pinhole 1 AU, laser power 1%, detection wavelength starting from 10 nm above the excitation wavelength. The lifetime displayed is the amplitude-weighted average of a double-exponential fit to the data.

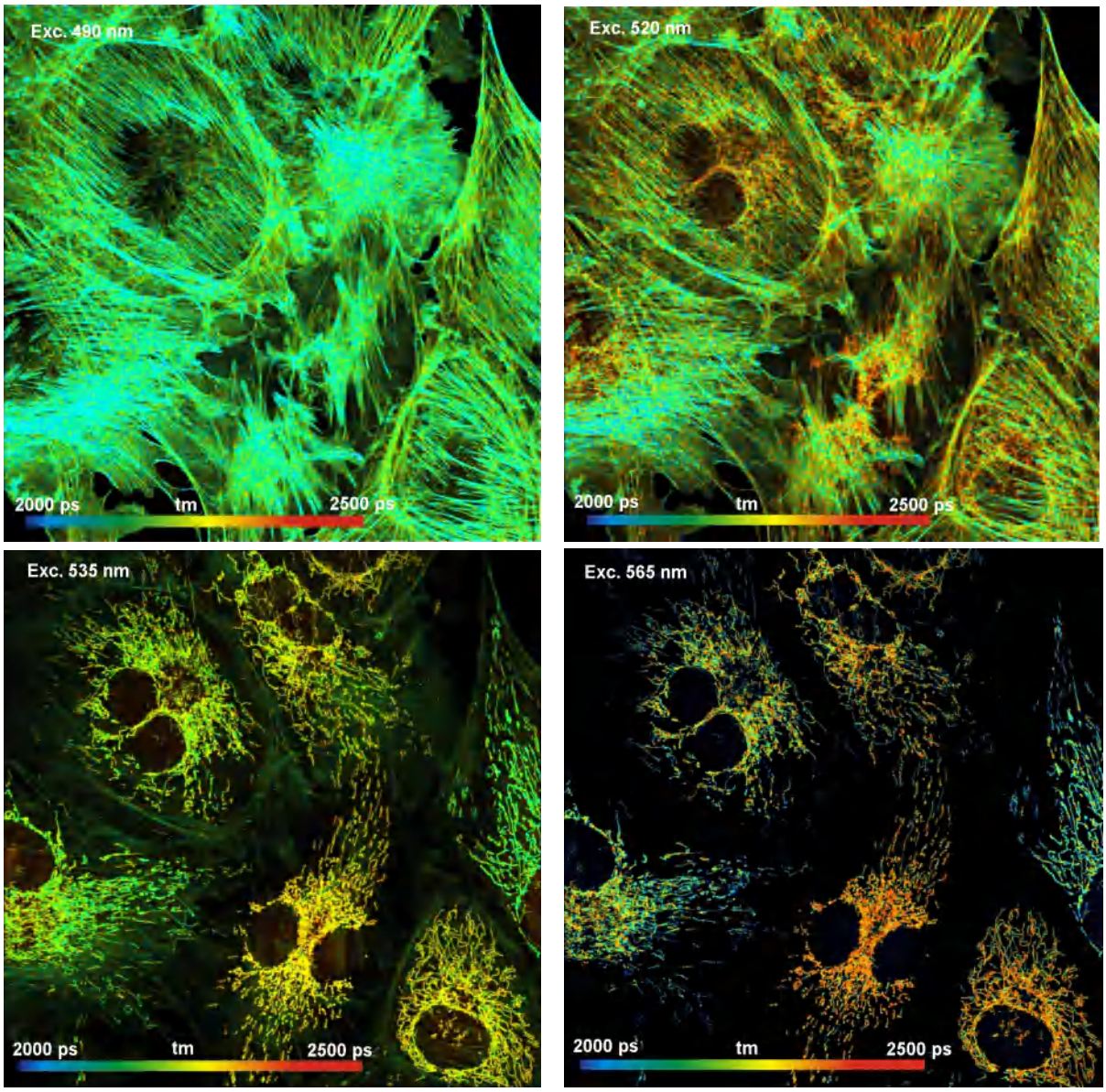


Fig. 524:Confocal FLIM with LSM 710 and tuneable 'Intune' laser. BPAE cells stained with Alexa 488 phalloidin and Mito tracker red. Excitation at 490 nm, 520 nm, 535 nm, and 556 nm as indicated in the images.

The high efficiency of the optics together with the high efficiency of the bh GaAsP hybrid detector, the tuneability, and plenty of laser power available allows one to use the system with diffraction-limited pinhole sizes. It is thus easy to obtain diffraction-limited image quality and near-ideal axial resolution.

Due to the high optical quality and the absence of background signals the In Tune system performs surprisingly well even for thick samples. Fig. 525 shows autofluorescence FLIM images of a pig skin sample. The left image is 10 µm, the right image 40 µm from the top of the sample. Both images show the amplitude-weighted lifetime, t_m, and the ratio of the amplitudes, a_1/a_2, of the lifetime components of a double exponential decay model.

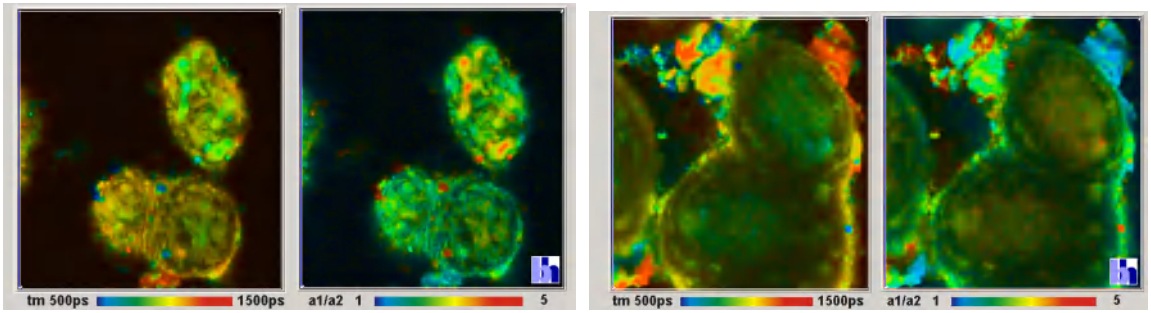


Fig. 525: Pig skin sample, autofluorescence. Double-exponential fit, amplitude-weighted mean lifetime and amplitude ratio. 10 µm (left) and 40 µm (right) from the surface of the skin. HPM-100-40 hybrid detector, SPC-150 FLIM module.

The fluorescence decay in a selected pixel of Fig. 525, left, is shown in Fig. 526. The data quality is so good that even triple-exponential analysis is feasible.

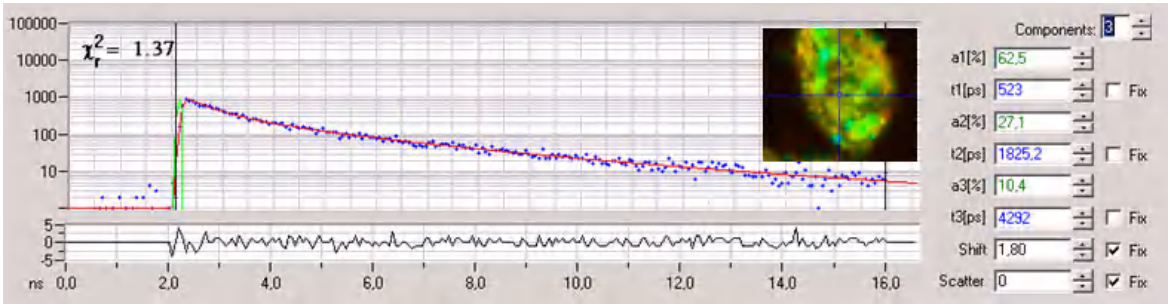


Fig. 526: Fluorescence decay in selected spot of Fig. 525. Triple-exponential analysis.

Multiphoton NDD FLIM

Multi-photon excitation with non-descanned detection (NDD) is the method of choice for FLIM of deep tissue layers. The differences to one-photon excitation are shown in Fig. 515, page 347. The laser wavelength is in the NIR, and fluorescence is excited via multi-photon (usually two-photon) process. Direct absorption at the NIR wavelength is low, therefore the excitation light reaches deep tissue layers. Different than one-photon excitation with confocal detection which *detects* only photons from the focal plane, multi-photo-excitation *excites* only in the focal plane. The fluorescence light can therefore be fed directly to a detector, without the need of a pinhole and without a long and narrow beam path through the scanner. Thus, even photons scattered on the way out of the sample are detected and assigned to the correct pixel of the image.

The optical principal of an NDD beam path is shown in Fig. 527. The fluorescence light is split off by a dichroic mirror directly behind the microscope lens. A transfer lens (or an equivalent lens system) projects an image of the back aperture of the microscope lens on a large-area detector. With a reasonably large transfer lens and a reasonably large detector area, the scattered photons arrive at the detector. Please note that detecting scattered photons does not cause any blurring because all the photons originate from the focus of the laser beam.

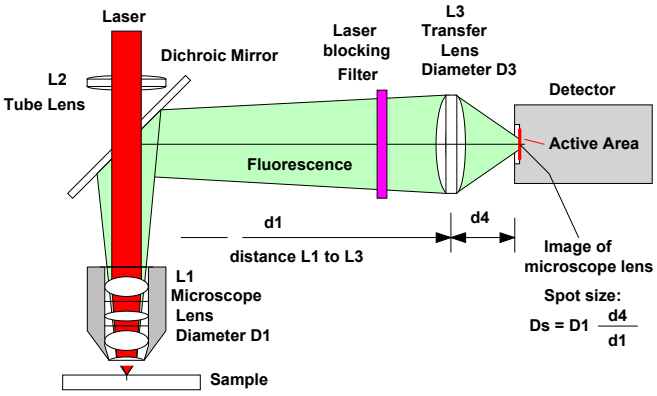


Fig. 527: Principle of an NDD beam path

A frequent mistake found in a many home-built systems is that the transfer lens projects an image of the *sample* (instead of the microscope lens) on the detector. The consequence is that the spot of fluorescence light moves over the detector surface when the sample is scanned. Inhomogeneities in the detector efficiency or dust on the detector then overlay with the image. For the same reasons, filters, lenses, or any other optical surfaces should not be placed in a plane conjugate with the sample.

Fig. 527 shows that reasonable NDD operation sets a lower limit to the active area of the detector: The diameter of the microscope lens is in the range of 5 to 10 mm. The focal length of the transfer lens, L3, cannot be made infinitely short - practically no shorter than its diameter. This leads to a minimum spot size of a few millimeters. The required active area is achieved by most conventional photomultipliers and by the HPM-100 hybrid detectors. It is not achieved by SPADs (single-photon avalanche diodes, not to be confused with linear APDs). SPADs have active areas of 50 to 200 µm diameter and are thus unable to collect the light from an NDD beam path.

Simultaneous detection in several wavelength intervals can be obtained by placing a dichroic beamsplitter in the beam path. The best place for the beamsplitter is between the laser blocking filter and the transfer lens. The beamsplitter is then placed in a near-parallel beam of light, and transfer lenses of short focal length can be placed close to the detectors. The Zeiss LSM 710/780/880/980 family microscopes use the principle shown in Fig. 528. A transfer lens inside the microscope projects the plane of the microscope lens into a plane closely in front of the beamsplitter module. Inside the module, the beam is collimated by Lens 1, split into spectral components by a normal microscope beamsplitter cube, and projected on the detectors by Lens 2 and Lens 3. The advantage of this design is that several beamsplitters can be cascaded. For application to FLIM please see handbook for the LSM 510 and 710 Family FLIM systems [69].

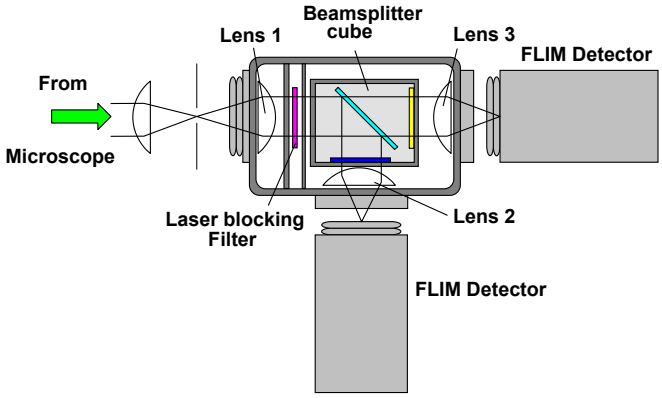


Fig. 528: Principle of NDD beamsplitter module of Zeiss LSM 710 family

Multiphoton NDD imaging has an impact on the selection of the microscope lens. To obtain a sharp laser focus the lens must be corrected for NIR wavelengths. Correction in the visible range is less important: The lens does not need to produce a sharp image of the sample at the fluorescence wavelength. The spatial resolution is determined by the NA (numerical aperture of the lens). The numerical aperture also determines the light collection efficiency. However, different than for confocal imaging also the magnification matters: High magnification (short focal length) results in a wider cone of scattered photons coming from a given volume in the sample. That means, best results are obtained with high-NA lenses of medium and low magnification [57, 58, 926].

Unfortunately, the high efficiency of detecting scattered photons has also a downside: It increases the detection efficiency photons of background light similarly. Any NDD system with TCSPC has therefore to be operated in *absolute* darkness. That means the microscope, and, especially, the sample stage must be covered by black cloth or another light-protective cover.

Problems can also arise from photons reflected at the condensor lens or in the (transmission) lamp path of the microscope. In a confocal system these photons are unlikely to pass the pinhole. In an NDD system, however, they are transferred to the detector. This is no problem for steady-state imaging because they are assigned to the correct spatial position in the sample. However, reflected photons arrive with a delay of a few nanoseconds and thus cause steps and bumps in the FLIM decay functions. The problem can be avoided by blocking the condensor light path at the back of the sample.

An example of a two-photon excited lifetime dual-channel lifetime image is shown in Fig. 529. It shows a BPAE (bovine pulmonary artery) sample. The sample was excited at 800 nm, the images were detected in two parallel TCSPC channels at 460 to 550 nm and 550 to 650 nm. The image format is 1024 x 1024 pixels, 256 time channels.

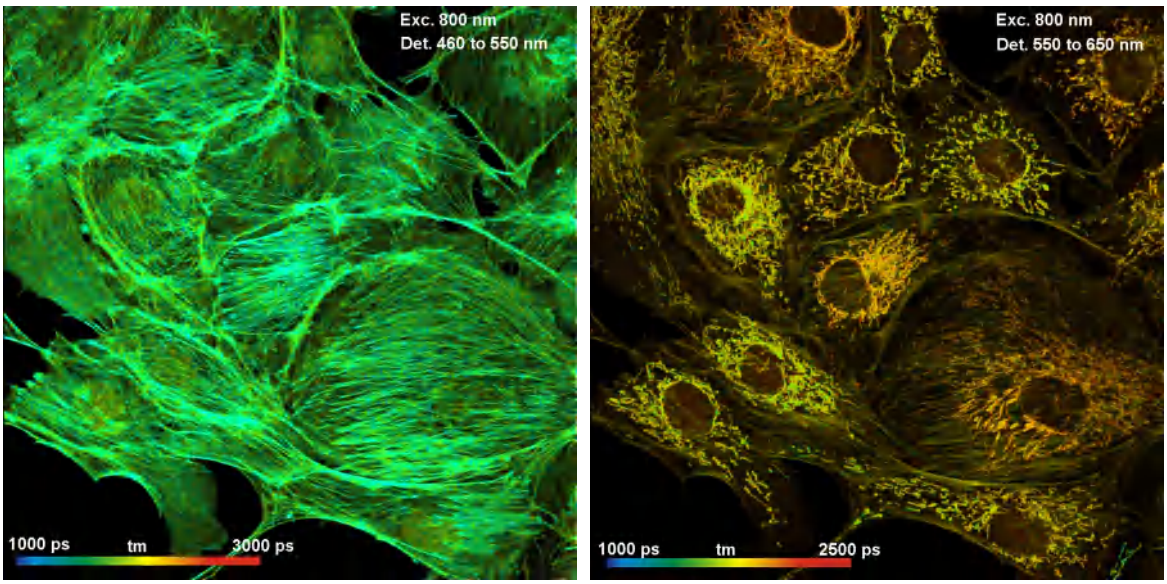


Fig. 529: Two-photon dual-channel NDD FLIM. BPAE cells stained with Alexa 488 phalloidin and Mito Tracker Red. Left: 460 nm to 550 nm. Right: 550 nm to 650 nm. Image format 1024 x 1024 pixels, 256 time channels. Zeiss LSM 710 NLO microscope, HPM-100-40 hybrid detectors, Simple-Tau 152 FLIM system

Live Cell and Tissue Imaging

Applications of multiphoton FLIM are mostly in the field of live cell and tissue imaging. It is widely accepted that 2-photon excitation is safe to live systems [448, 449, 681, 682, 684, 689, 1267]. Although there is probably more photobleaching than for one-photon excitation [391,

948] possible damage occurs only in the focal plane, not in the entire volume of the excitation-beam cone as in the case of one-photon excitation.

Another advantage is that fluorophores with excitation spectra in the UV can be reached by NIR wavelengths. This avoids the need of UV optics and avoids direct damage of proteins and DNA. It also circumvents the need of UV-compatible optics in the microscope and in the scanner. For instance, tryptophane can be reached by three-photon excitation [10, 632, 960], NADH, FAD, Melanin and a variety of other endogenous fluorophores by two-photon excitation [252].

A frequent application of two-photon FLIM is NADH imaging. One-photon excitation of NADH would require a wavelength around 370 nm which is inconvenient to use in a microscope. With two-photon excitation, NADH and other endogenous fluorophores can easily be reached at wavelengths from 750 to 850 nm [252]. NADH is especially important because its fluorescence signature bears information on the metabolic state of the cells. Consequently, there is a large number of publications in this field. Examples are the separation of the signals of bound and unbound NADH by their lifetimes and the relation of the bound/unbound ratio to metabolism [225, 501, 502, 643, 758, 1039, 1155, 1156, 1157, 1315, 1321]. The technique has been extended to monitoring the maturation of stem cells [1267], monitoring the effect of anti-cancer drugs [1316, 1317, 1318] and photodynamic therapy [1037, 1038].

The fact that 2-photon excitation and non-descanned detection systems reach into deep sample layers has resulted in a large number of tissue FLIM applications. Most of these target on tumour identification in human skin and are closely related to clinical applications [385, 386 690, 692, 947, 1022, 1047, 1049]. How rich in detail NDD FLIM images can be is shown in Fig. 530. The figure shows a pig skin sample excited by two-photon excitation at 800 nm. Two images were recorded simultaneously in two wavelength channels. The FLIM system was a Simple-Tau 152 with two HPM-100-40 hybrid detectors. The system was connected to a Zeiss LSM 710 NLO multiphoton microscope.

Fig. 530, left image shows the wavelength channel below 480 nm. This channel contains both fluorescence and SHG signals. The SHG fraction of the signal has been extracted from the FLIM data. The colour indicates the percentage of SHG in the detected signal. Fig. 530, right image shows the wavelength channel above 480 nm. It contains only fluorescence. The colour corresponds to the amplitude-weighted mean lifetime.

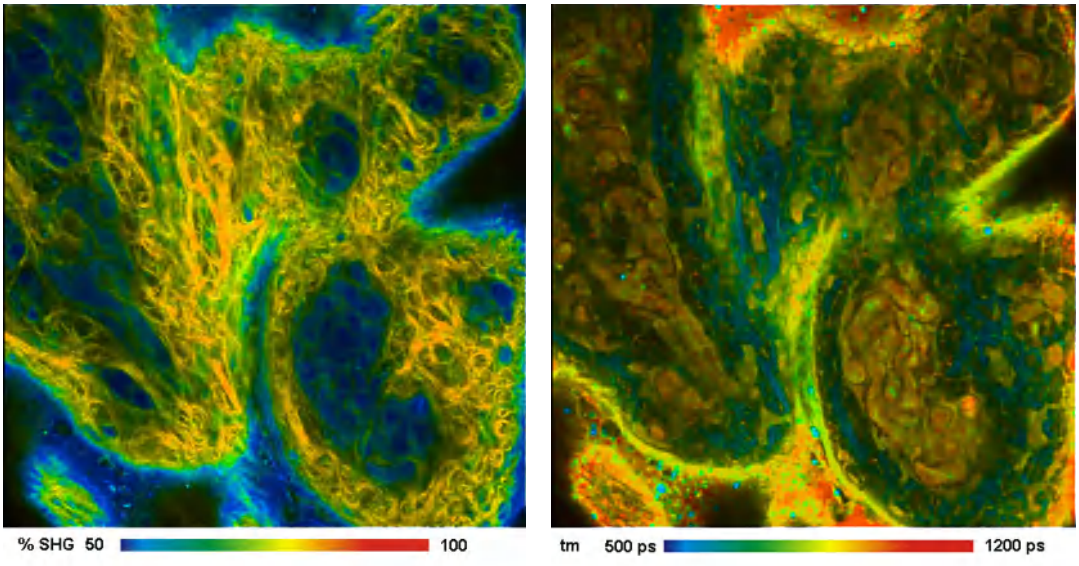


Fig. 530: Two-photon NDD FLIM of pig skin. Left: Wavelength channel <480 nm, colour shows percentage of SHG. Right: Wavelength channel >480 nm, colour shows amplitude-weighted mean lifetime.

The fluorescence image can be further analysed. Fig. 531, left to right, shows images of the lifetime of the fast decay component, t_1, of the relative amplitude of the fast component, a_1, and of the lifetime of the slow decay component, t_2.

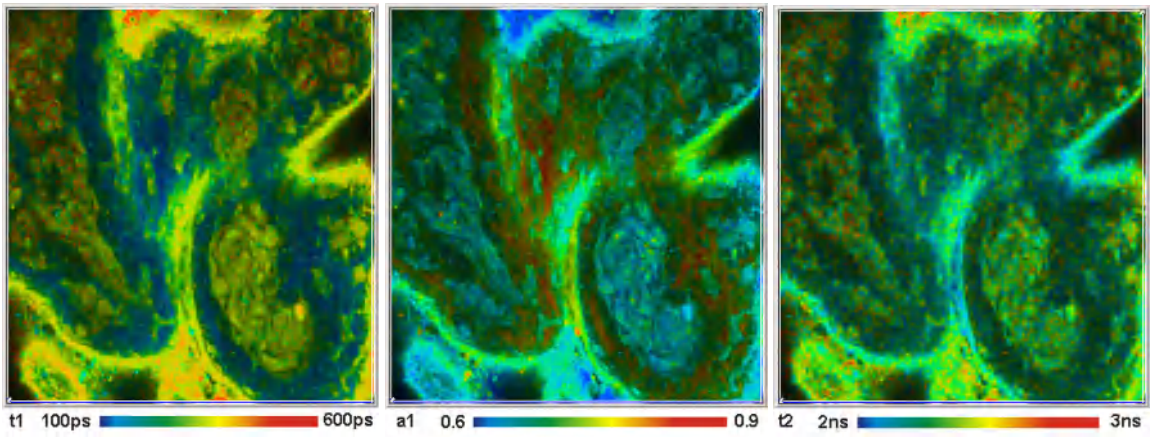


Fig. 531: Wavelength channel >480 nm, images of the lifetime of the fast decay component, t_1, the amplitude of the fast decay component, a_1, and the lifetime of the slow decay component, t_2

Two-photon NDD FLIM can also be useful to obtain clear FLIM images of plant tissue [56, 205, 237, 242, 1134]. Plant tissue is highly scattering, and has strong absorption in the visible range. The contrast and the penetration depth of confocal imaging is therefore often unsatisfactory. Two-photon lifetime images of a plant leaf are shown in Fig. 532. The wavelength channel from 450 to 550 nm shows the fluorescence of flavines in the cell membranes. The channel from 550 to 700 nm shows the chloroplasts.

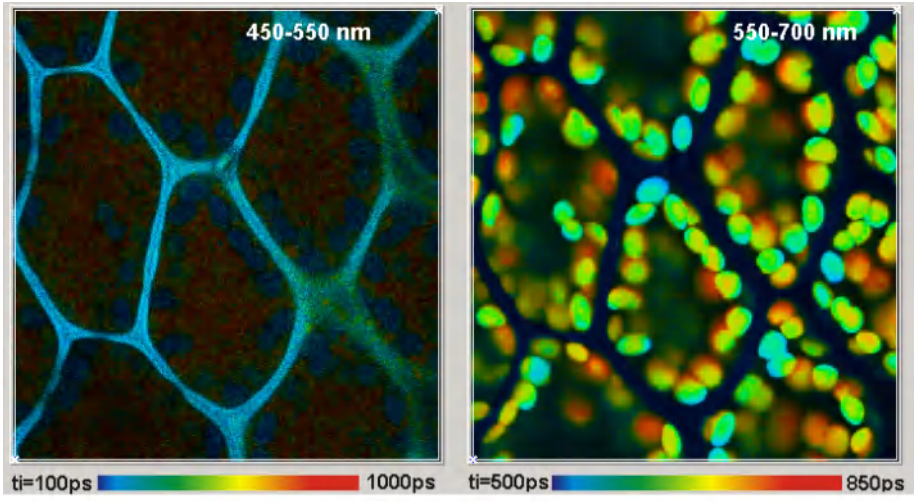


Fig. 532: Two-photon NDD FLIM of plant tissue. Left: 450 to 550 nm channel. Right: 550 to 700 nm channel. Zeiss LSM 710 NLO with Simple-Tau 152 FLIM system.

A frequent application of two-photon FLIM is the measurement of protein interaction in cells by FRET techniques. In these applications it is important that the protein structure is not changed before or during the imaging. FRET experiments are therefore preferably performed in live cells. An example is shown in Fig. 533. It shows a HEK (human embryonic kidney) cell expressing two interacting proteins labelled with CFP (donor) and YFP (acceptor). FRET occurs in the places where the proteins interact. The images are from the donor channel. The t_m image is equivalent to an image of the classic FRET efficiency. t_1/t_2 represents the distance, a_1/a_2 the fraction of interacting proteins. As usual, there is very little change in the distance. (Please remember that t_1/t_2 is proportional to d^6 !). Most of the variation in the classic FRET

efficiency is due to the variation in the fraction of interacting proteins. Please see also Fig. 732, page 511.

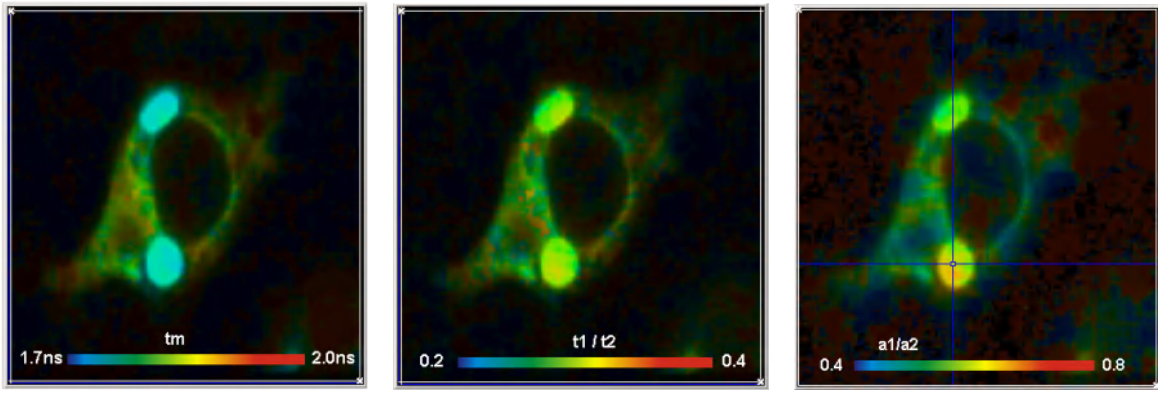


Fig. 533: Multiphoton FRET measurement, HEK cell expressing interacting proteins labelled with CFP and YFP. Images recorded in CFP channel. Left to right: Mean (amplitude weighted) lifetime, ratio of quenched and unquenched CFP lifetimes, amplitude ratio. LSM 510 NLO, SPC-830 TCSPC module.

There are hundreds of FLIM FRET papers, most of them having been performed by 2-photon FLIM. Please see chapter 'Förster Resonance Energy Transfer (FRET)' in the application part of this book.

Another application where 2-photon excitation is often useful is ion concentration measurement in cells and tissue. Some of the ion sensor dyes [491, 742, 876, 1218, 1340, 1341] (e.g. MQAE and Calcium Green) require short excitation wavelengths which can be hard to reach in normal scanning microscopes. Moreover, excitation may by required over relatively long periods of time, especially when Z stacks of tissue are taken [472, 505, 642] or electrophysiology experiments are performed [164, 463], see also Fig. 121 and Fig. 125 in this book.

Ultra-High Resolution FLIM Systems

High Resolution FLIM for Zeiss NLO Systems

With the HPM-100-06 and -07 hybrid detectors bh SPC-150NX and NXX modules and the corresponding SPC-180NX and NXX TCSPC/FLIM modules reach a time resolution of about 18 ps, FWHM. The rms timing jitter of these systems is about 8 ps. Thant means FLIM systems with these components can resolve fluorescence decay time of less than 10 ps. Of course, the resolution can be exploited only if similarly short laser pulses are used for excitation. That means that ultra-fast FLIM is done best with femtosecond lasers and multiphoton excitation. The high price of the excitation source is not a problem for FLIM systems which are attached to an existing multiphoton laser scanning microscope, such as the Zeiss LSM 780/880/980 NLO systems [70, 71]. If the FLIM system is already there the only change to obtain ultra-fast FLIM is to replace one or two detectors, please see section below.

High Resolution FLIM for DCS-120 MP Systems

Another option for high resolution FLIM is the DCS-120 MP system with a femtosecond fibre laser, such as the DCS-120 MP. The system uses a Totica Femto Fibre Pro or Femto Fibre Smart laser [128, 129]. The complete FLIM system is not significantly more expensive than a confocal DCS system with diode lasers. The DCS-MP Fibre system is probably the simplest multiphoton FLIM system in the world. The principle is shown in Fig. 534. A photo is shown in Fig. 535. An IRF of the system is shown in Fig. 536.

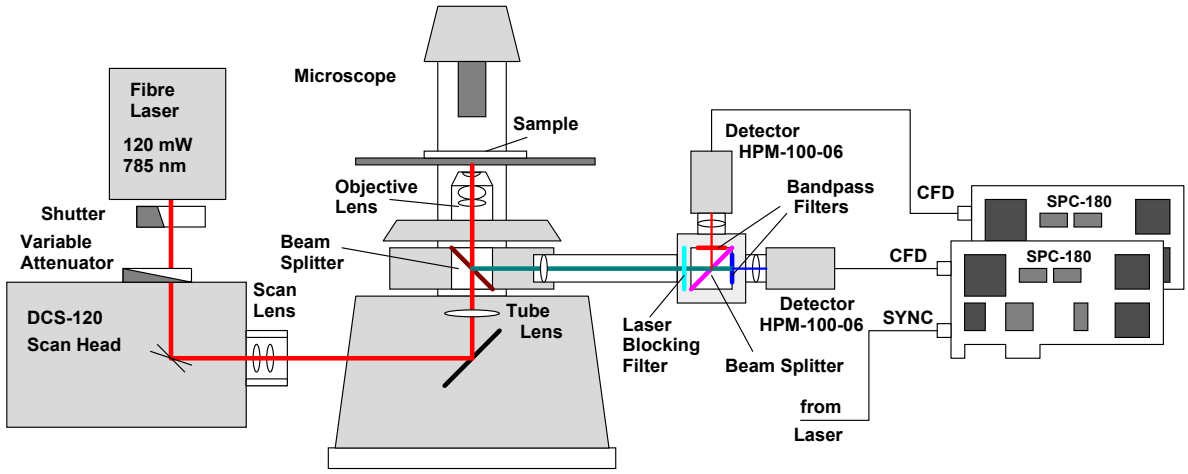


Fig. 534: Principle of the DCS-MP Fibre-Laser system

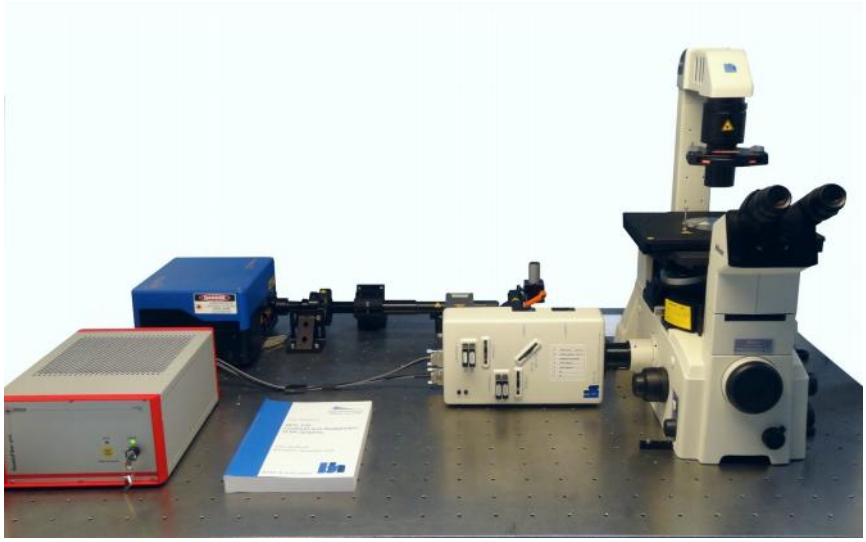


Fig. 535: DCS-120 MP multiphoton FLIM system with femtosecond fibre laser



Fig. 536: IRF of the femtosecond fibre-laser FLIM system with HPM-100-06 and -07 detectors and SPC-150NX or SPC-180NX TCSPC FLIM modules

The high time resolution of the bh multiphoton FLIM systems with these detectors makes fluorescence-decay components visible which have never been detected before. Fig. 537 shows FLIM data of mushroom spores. From left to right, images of the fast decay component, t_1, of the mean lifetime, t_m, and of the amplitude of the fast component, a_1, are shown. A decay curve at the cursor position is shown on the right. t_1 at the cursor position is 11 ps, and a1 is in the range from 98 to 100%. Please see [177] for more data.

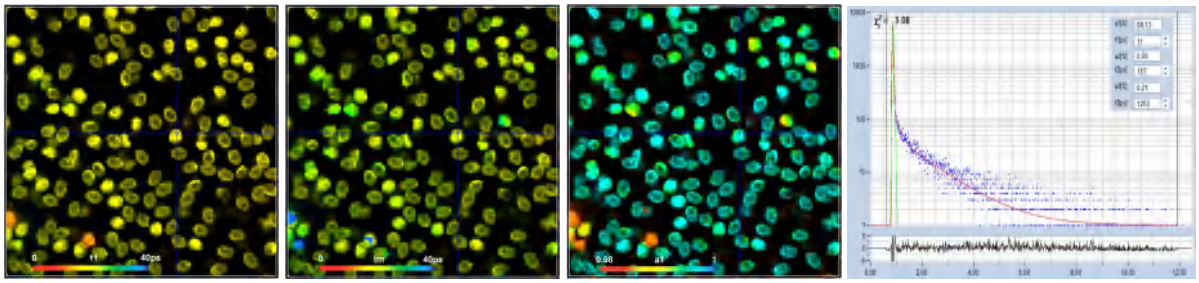


Fig. 537: 2p FLIM of Mushroom Spores of *Agaricus campestris*. The fast component has a lifetime of t_1 = 11 ps

With the SPC-150NXX or the SPC-180NXX modules, the time resolution can be driven to the extreme. Fig. 538 shows data recorded with a time-channel width of 300 femtoseconds, i.e. on a time scale 10 times faster than in Fig. 537. The number of time channels is 4096, the total observation-time interval 1,25 ns. Please see [176] for further details.

The decay data in a selected spot of the image are shown in the middle. The green curve is the IRF, the blue dots are the photon numbers in the time channels. The IRF is a real one, recorded from SHG of powdered sugar. At the time scale used, the fwhm of the IRF extends over 70 data points. The figure looks like a decay / IRF plot from a conventional lifetime spectrometer, with the difference that the time scale is 20 times faster. With the data resolved into a number of data points this high, the deconvolution routine is able to determine lifetime components considerably shorter than the IRF width. In the data shown in Fig. 538 the 11-ps component, t1, of Fig. 537 is split into two, with a t1 = 7.6 ps and t2 = 66 ps. The distribution of t1 is shown in the histogram on the right of Fig. 538.

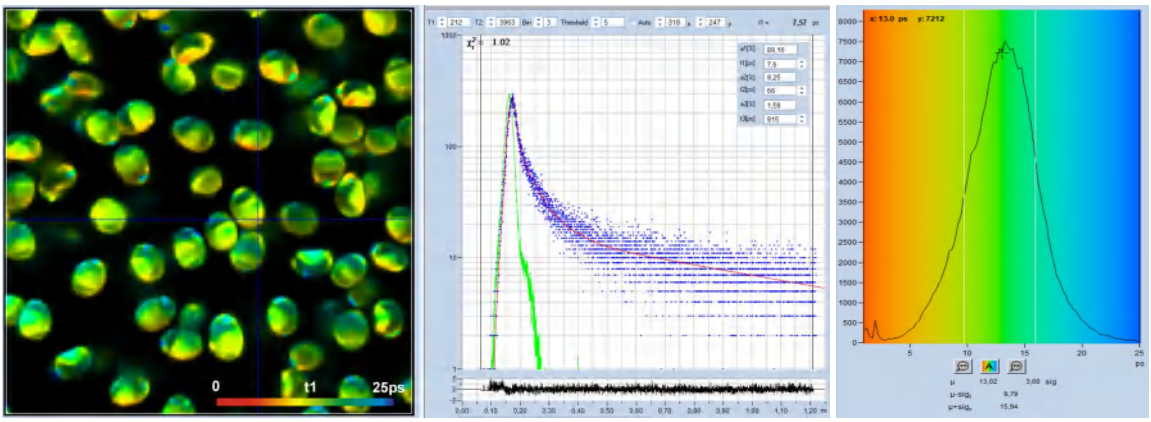


Fig. 538: Spores of *Paxillus involutus*, time-channel width 300 fs, 4096 time channels, observation-time interval 1.25 ns. Left: Image of the fast decay component, t1, colour scale 0 to 25 ps. Middle: Decay curve (blue), IRF (green), and decay parameters at the cursor position. Right: Histogram of the t1 values over the pixels of the image.

Fig. 539. shows FLIM of Pollen grains. The FLIM system detects a component with 10 ps lifetime [178], see Fig. 539. The data shown here were detected with a DCS-120 MP system using a Femto Fibre Pro Toptica femtosecond fibre laser, an HPM-100-06 detector and SPC-150NX TCSPC modules. Please see [128] for details. In principle, ultra-fast decay components are detectable also with bh FLIM systems on other multiphoton microscopes, provided the bh SPC-150NX or SPC-180NX TCSPC modules and HPM-100-06 detectors are used.

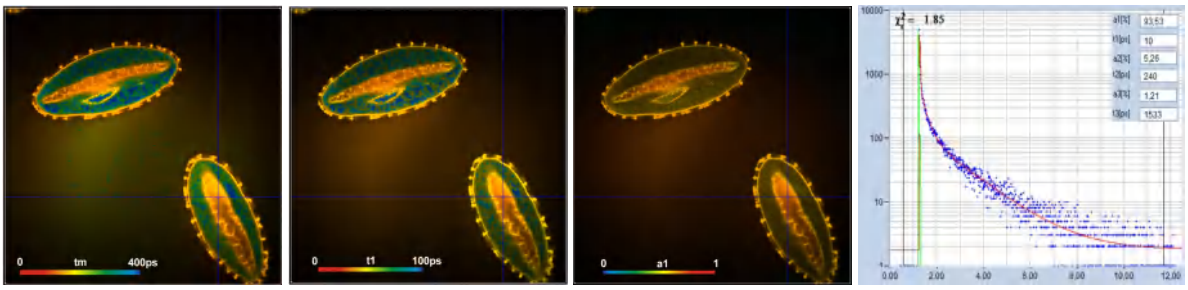


Fig. 539: 2p FLIM of Pollen Grains. The fast component has a lifetime of t_1 = 10 ps

More results, including FLIM images from malignant melanoma, are shown in section 'Ultra-Fast Fluorescence Decay in Biological Material', page 561. Please also see [177, 178, 179 180 181 [182]] for experimental procedures and more FLIM images.

NADH FLIM with Ultra-Fast Detectors

The typical IRF for the GaAsP hybrid detectors in standard FLIM systems is about 90 to 120 ps, FWHM [159, 160]. This is not much faster than the dominating decay time of the unbound NADH, which is about 300 to 500 ps [225]. It can therefore be expected that a FLIM-system with a faster IRF improves the accuracy of the fluorescence-decay analysis of NADH FLIM. This is indeed the case.

It is shown above that with femtosecond excitation the HPM-100-06 and -07 detectors deliver an IRF width of less than 20 ps with and SPC-150NX and SPC-180NX TCSPC modules. We therefore recorded NADH images with a bh FLIM system at a Zeiss LSM 880 NLO multiphoton microscope. The HPM-100-40 detectors were replaced with HPM-100-06 and an HPM-100-07 detectors. The FLIM system itself was left in the standard multiphoton configuration, with the detectors attached to the NDD output of the microscope via the usual Zeiss NDD T adapter. The signals were recorded by two SPC-150NX TCSPC modules. The system is able to record in two wavelength channels in parallel, the images shown below are from a wavelength channel from 440 nm to 480 nm. The excitation wavelength was 740 nm. The data were recorded with 512 x 512 pixels and 1024 time channels per pixel. The time channel width was 10 ps.

A lifetime image of the amplitude-weighted lifetime of a double-exponential fit is shown in Fig. 540, left. Decay data in a selected spot of 9 x 9 pixels on the right. As expected, the time resolution of the detection system is excellent. The rise of the fluorescence occurs over less than two time channels, indicating that the IRF is indeed shorter than 20 ps.

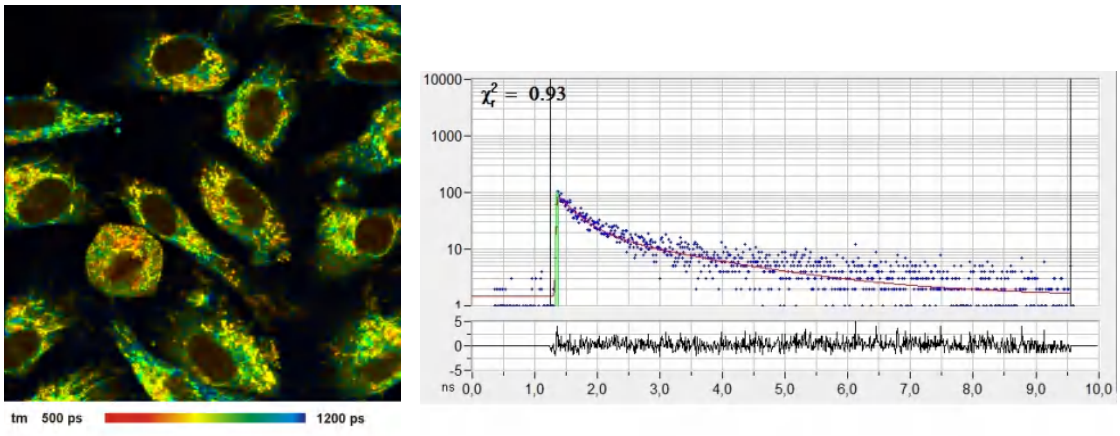


Fig. 540: Left: NADH Lifetime image, amplitude-weighted lifetime of double-exponential fit. Right: Decay curve in selected spot, 9 x 9 pixel area. FLIM data format 512 x 512 pixels, 1024 time channels.

Images of the amplitude ratio, a_1/a_2 (unbound/bound ratio), and of the fast (t_1, unbound NADH) and the slow decay component (t_2, bound NADH) are shown in Fig. 541. Such images are normally noisy, and visibly contain fitting artefacts. Not so in the data recorded with the fast detectors and SPC modules. Due to the near-ideal temporal resolution the FLIM data analysis delivers the decay components at extremely high precision, and the images are free of fitting noise and fitting artefacts.

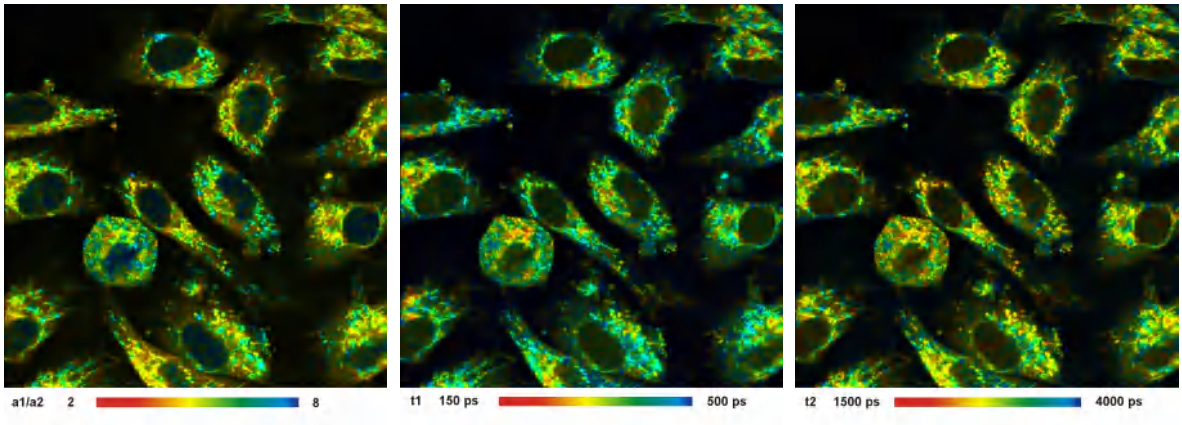


Fig. 541: Left to right: Images of the amplitude ratio, a_1/a_2 (unbound/bound ratio), and of the fast (t1, unbound NADH) and the slow decay component (t_2, bound NADH). FLIM data format 512 x 512 pixels, 1024 time channels. Time-channel width 10 ps.

The results show that the ultra-fast HPM-100-06 and HPM-100-07 hybrid detectors in combination with the SPC-150N TCSPC modules improve the accuracy of NAD(P)H FLIM dramatically. The IRF is so fast that it does no longer interfere with the decay times of the fast fluorescence components. The deconvolution process in the data analysis therefore virtually becomes a simple curve fitting, and the decay parameters are obtained at unprecedented accuracy. Even the a_1/a_2 images and the t_1 and t_2 images are virtually free of noise or fitting artefacts.

Multispectral FLIM

Confocal Multispectral FLIM

Multispectral FLIM is based on the bh PML-SPEC or MW-FLIM multi-wavelength detection assemblies, see page 189. The assemblies contain a polychromator and a bh PML-16-C multi-anode PMT module [62]. For each photon, the PML-16C delivers a single-photon pulse and a routing signal that indicates which of the channels has detected the photon. These signals are processed by multi-dimensional TCSPC, see Fig. 218, page 126.

The input of the polychromator is a slit of about 1 mm width. The fluorescence light from the optical output of the microscope must be projected into this slit. For a confocal output this is relatively easy: The fluorescence light is either transferred into the polychromator input by an optical fibre or projected into the slit plane by a lens.

Multi-wavelength TCSPC-FLIM with fibre coupling has first been demonstrated in [145]. The system described used the fibre output from an LSM 510 NLO microscope, a bh PML-SPEC assembly and an SPC-730 module. The application of the system to FRET measurements was demonstrated in [221]. Rück et. al. used a similar system attached to a Zeiss LSM 410 microscope for tracking the metabolites of 5-ALA (5-aminolevulinic acid, an approved sensitizer for photodynamic therapy) in living cells [1036, 1037] and FRET experiments [1038]. Kundu et al. used a confocal DCS-120 FLIM system with a PML multi-wavelength detector to study the dynamics of the transformation of oleate micelles into oleic

acid/oleate vesicles by a pH-sensitive fluorophore. Multi-wavelength FLIM can be combined with MACRO FLIM as has been demonstrated by Shcheslavskiy et al. and Yakimov et al. [1132, 1355].

Fibre coupling often causes optical reflections on the fibre. Also some coupling loss is inevitable. Loss and reflections can be avoided by projecting the light from a direct confocal output of the scan head directly into the input slit plane of the polychromator. The basic principle is as shown in Fig. 586, middle. Spriet and Waharte used a direct-coupled spectrograph with a PML-16 detector and an SPC-710 at the X1 confocal port of a Leica SP2 multiphoton microscope [1176, 1177, 1311].

Direct coupling to a free beam confocal port can be impossible due to spatial restrictions. The multi-wavelength assembly can then be coupled to the port by a fibre bundle, as it is used for multiphoton NDD detection, see Fig. 543. Of course, this does not entirely avoid coupling loss and reflections but at least works without additional optics and alignment. Fig. 542 shows a multi-spectral lifetime image of a stained wood sample recorded this way by the bh DCS-120 system [66, 156]. The sample delivered a count rate of several MHz without noticeable photobleaching. The image shown was therefore obtained within an acquisition time of only 20 seconds.

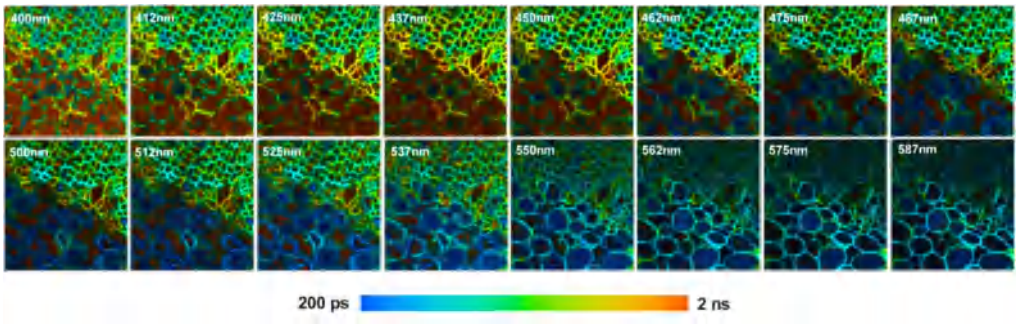


Fig. 542: Multi-wavelength lifetime image of a stained wood sample. DCS-120 confocal FLIM system, wavelength channels from 400 nm to 587 nm.

Multiphoton Multispectral NDD FLIM

A multi-spectral FLIM system for two-photon microscopes with non-descanned detection was first described in [212]. A de-magnified image of the aperture of the microscope objective lens was projected on the input of a 1-mm multi-mode fibre. The fibre delivered the fluorescence light to the polychromator of a PML-SPEC assembly. The spectrum was recorded by a bh PML-16 detector, and the 16 wavelength channels were recorded simultaneously by a bh SPC-830 module. The problem of this approach is that a lens of short focal length is required for projection into the fibre. The diameter of the lens is thus limited (a microscope lens was used in [212]), resulting in sub-optimal light collection efficiency for deep-tissue imaging. Moreover, the light is focused into the fibre at high numerical aperture. The high NA results in noticeable (and possibly alignment-dependent) pulse dispersion in the multimode fibre [783]. The pulse dispersion has been reduced by using a photonic crystal fibre to transfer the light into the polychromator [214]. However, the diameter of the fibre is too small to collect scattered photons efficiently.

The bh MW-FLIM multiphoton multi-spectral NDD FLIM systems therefore use a fibre bundle to transfer the light into the slit plane of the polychromator [62, 156]. The principle is shown in Fig. 543.

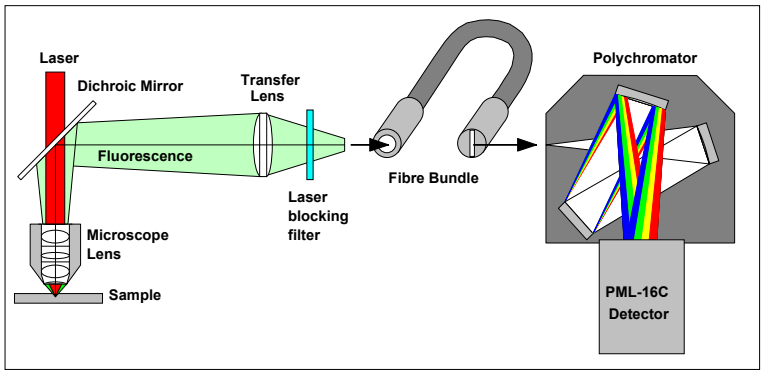


Fig. 543: Multi-spectral two-photon FLIM system with non-descanned detection

A lens projects an image of the back aperture of the microscope lens on the input of a fibre bundle. The fibre bundle has a circular cross section at the input, and a rectangular cross section at the output. The input has an area large enough to cover the whole area of the image of the microscope-lens aperture. The output of the fibre bundle is used as an input slit of the polychromator. More optical details are described in [95].

Due to the relatively large area of the fibre bundle input a field lens of large diameter can be used. The system thus yields high efficiency even for deep sample layers and highly scattering samples. Compared to the single-fibre system described in [212] the fibre bundle is used at a relatively moderate numerical aperture so that pulse dispersion is kept at a noticeably lower level.

An example of a multiphoton NDD FLIM measurement is shown in Fig. 544. The figure shows an autofluorescence image of mouse kidney tissue. The data were recorded by a bh SPC-830 with a MW-FLIM assembly attached to the NDD switch box of a Zeiss LMM 510 NLO [69]. Two-photon excitation at 750 nm was used. The acquisition time was 100 seconds. The signal-to-noise ratio of the data obtained in this time is sufficient to analyse the decay functions by double-exponential analysis, see Fig. 768, page 550.

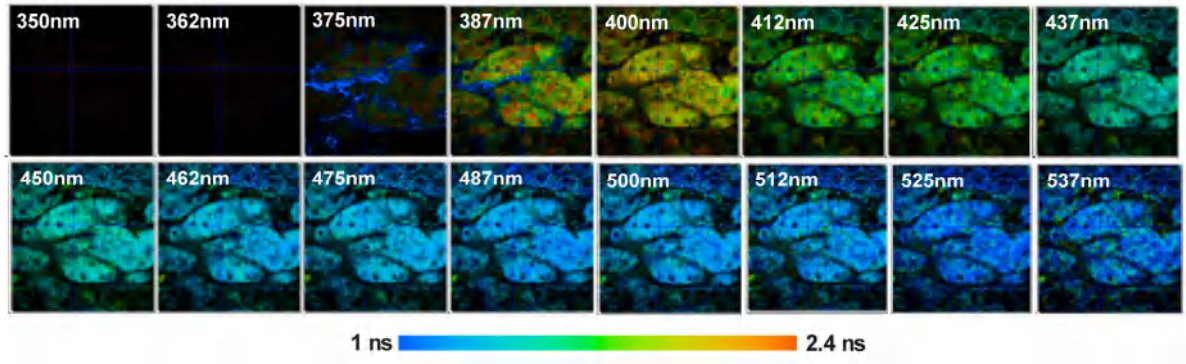


Fig. 544: Multi-spectral NDD FLIM of unstained mouse kidney tissue. Zeiss LSM 510 NLO, bh MW FLIM assembly, bh SPC 830. Two-photon excitation at 750 nm.

Fig. 545 shows multi-spectral FLIM data of a plant sample. The data were recorded by a bh Simple-Tau 510 with bh multi-wavelength FLIM assembly connected to the non-descanned output of a Zeiss LSM 710 NLO [69, 95].

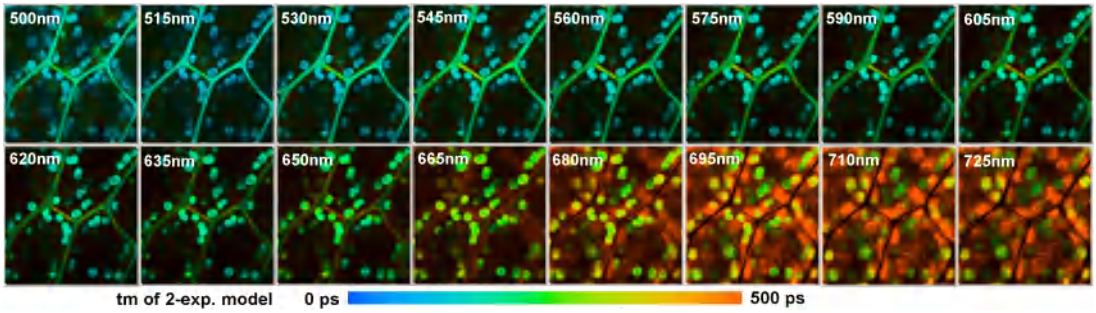


Fig. 545: Multiphoton Multispectral NDD FLIM. LSM 710 NLO, bh MW FLIM detector. FLIM images for wavelength channels from 500 nm to 725 nm. Intensities normalised to the brightest pixels in the individual wavelength intervals.

Multi-Spectral FLIM with GaAsP Detectors

The performance of multi-wavelength FLIM has dramatically improved by GaAsP detectors and 64-bit software. A example of a multi-spectral FLIM result obtained with the new PML-16 GaAsP detectors (see page 189) is shown in Fig. 546. The data were recorded in 16 wavelength channels at a resolution of 512 x 512 pixels and 256 time channels per pixel. The wavelength channel width was 12.5 nm, the centre wavelengths of the channels range from 490 nm to 690 nm. The file size of the entire multi-wavelength data is 2 GB.

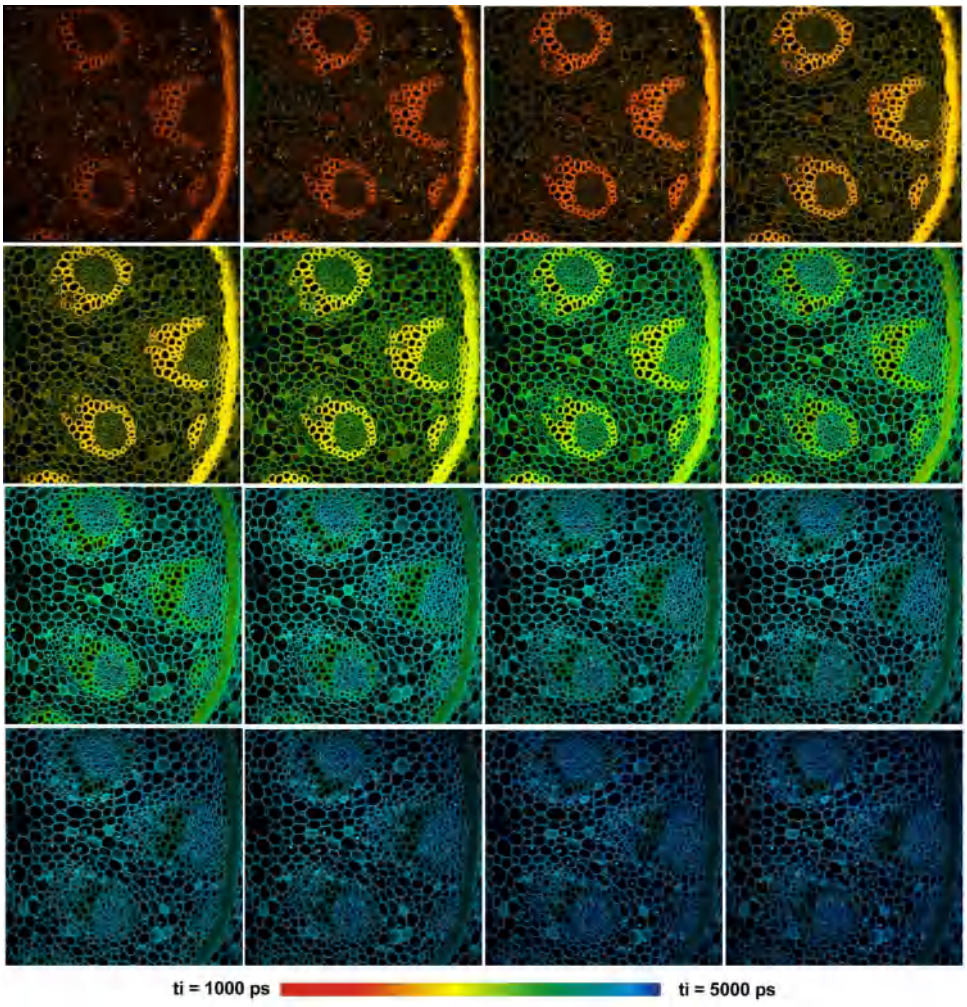


Fig. 546: Multi-wavelength FLIM with a bh MW-FLIM GaAsP 16-channel detector, DCS-120 system. 16 images with 512 x 512 pixels and 256 time channels were recorded simultaneously. Wavelength from upper left to lower right, 490 nm to 690 nm, 12.5 nm per image.

Fig. 547 demonstrates the true spatial resolution of the data. Images from two wavelength channels, 502 nm and 565 nm, of the data shown Fig. 546 are displayed at larger scale and with individually adjusted lifetime ranges. The spatial resolution is comparable with what previously could be reached for FLIM at a single wavelength. Nevertheless, the decay data are recorded at a temporal resolution of 256 time channels. Decay curves for an arbitrary selected pixel of the images are shown in Fig. 548.

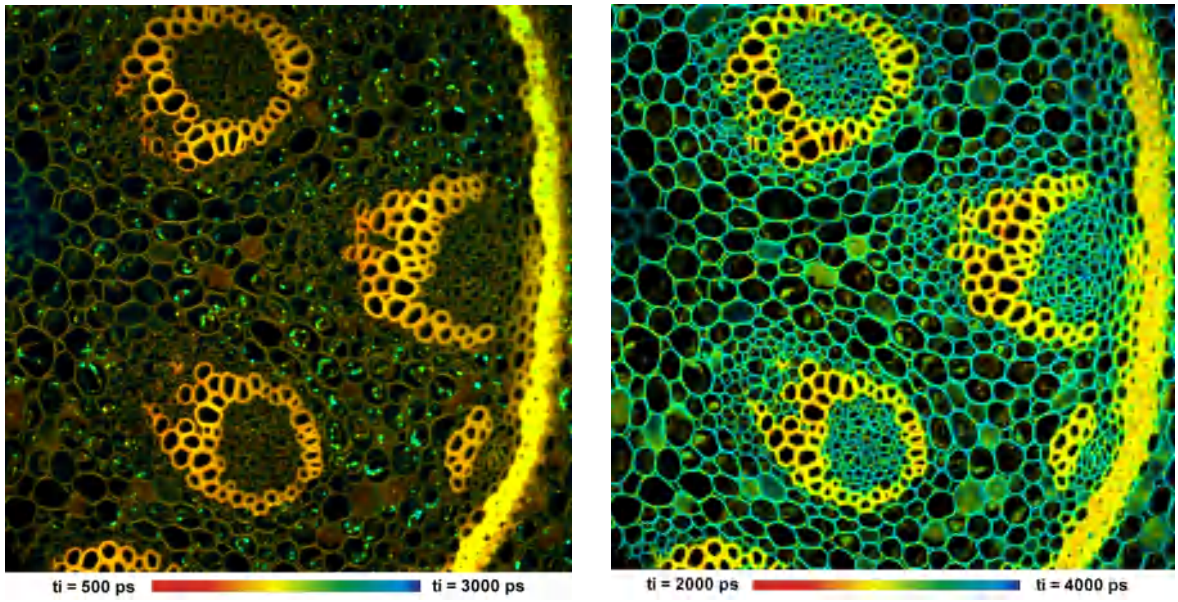


Fig. 547: Two images from the array shown in Fig. 546, displayed in larger scale and with individually adjusted lifetime range. Wavelength channels 502 nm (left) and 565 nm (right). The images have 512 x 512 pixels and 256 time channels.

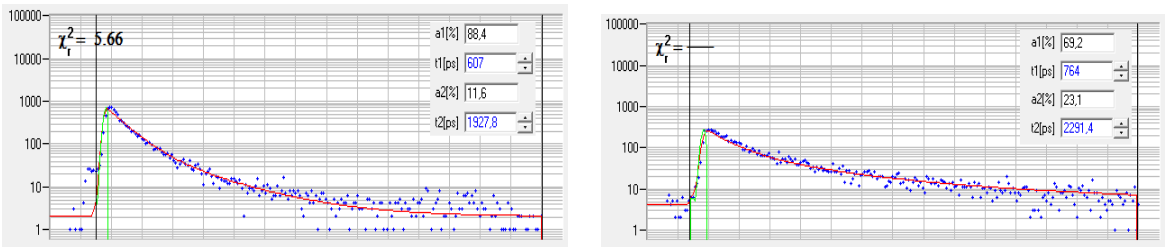


Fig. 548: Decay curves at selected pixel position in the images shown above. Blue dots: Photon numbers in the time channels. Red curve: Fit with a double-exponential model.

Applications of Multi-Spectral FLIM

Multi-wavelength FLIM was first demonstrated in 2002 by Becker et al. for recording decay data in the complete donor-acceptor wavelength range of a FRET experiment [145]. Bird et al. demonstrated the technique for lifetime imaging of stained kidney tissue samples [212]. Rück et al. used multi-wavelength FLIM for monitoring the conversion of photosensitizers for PDT and the generation of photoproducts [1037, 1038]. FRET measurements by multi-wavelength FLIM were described in [222], and [223].

The majority of multi-wavelength FLIM applications are in autofluorescence imaging, especially imaging of the coenzymes NADH and FAD [303, 771, 1039, 1359]. Chorvatova and Chorvat worked out spectral unmixing techniques based on multi-wavelength FLIM data and used them determine metabolic parameters in cardio-myocytes [300, 301, 303 304, 305, 306, 307] and investigate their response to drugs and stress conditions.

Li et al. used multi-wavelength FLIM for NADH imaging. They found different bound/unbound ratios (represented by the a_1/a_2 ratio of the amplitudes of the lifetime components) in the cytosol and in the mitochondria, and changes induced by variable concentration of deoxyglucose [771]. They also found changes in the bound/unbound ratio when cells were exposed to sub-lethal concentrations of cadmium [772, 1359].

Using two-photon excitation and multi-wavelength FLIM Li et al. were able to detect and characterise two-photon excited fluorescence from haemoglobin [1394]. Multi-wavelength FLIM was used to discriminate the haemoglobin fluorescence from fluorescence of other endogenous fluorophores. This way, haemoglobin fluorescence was used for label-free imaging of microvasculature in live tissue [776, 777].

A multiphoton multi-colour excitation system with a Titanium Sapphire laser, supercontinuum-generation in a photonic crystal fibre and a Becker & Hickl PML-16 / SPC-150 multi-wavelength FLIM system has been developed by Li et al. [773]. The system excites tryptophan and NADH simultaneously and separates the fluorescence of both compounds spectrally. The authors found that the ratio of NADH and tryptophan fluorescence is a sensitive indicator of cell metabolism. The same instrument was used to record tryptophan and NADH lifetime images in combination with SHG images in different depth of epithelial tissue [774]. The principle was also used for investigation of squamous intraepithelial neoplasia [660]. Simultaneous recording of tryptophan, SHG, NADH intensity images by the system has been described in [1209]. Other applications are autofluorescence lifetime imaging of leukocytes [1384], multi-modal label-free imaging of zebra fish [775], and skeletal muscle tissue [1209].

Multi-wavelength FLIM in combination with multiphoton tomography of human skin [690, 692, 1022] was used by Dimitrow et al. [385]. The authors found changes in the fluorescence spectra and shorter fluorescence lifetime in malignant melanoma compared to normal skin.

Excitation-Wavelength Multiplexing

Excitation wavelength multiplexing is used when the signals from two or more fluorophores are to be recorded, and these cannot be efficiently excited at only one excitation wavelength. It can also happen that the fluorophores can be excited at a single wavelength but the signals cannot be spectrally separated on the detection side. A possible solution is to run several measurements one after another with different lasers or with the laser tuned to different wavelengths. However, laser-induced changes in the sample or physiological effects can make the results difficult to compare. It is therefore desirable to multiplex the laser wavelengths, i.e. quickly switch back and forth between the laser wavelengths and record the signals quasi simultaneously. There are two ways to perform this kind of measurement: The lasers can be multiplexed (or interleaved) pulse by pulse or they can be multiplexed within a period longer than the pulse period.

Multiplexing by Pulse-Interleaved Excitation, PIE

Excitation wavelength multiplexing can be obtained by 'Pulse-Interleaved Excitation', or 'PIE'. The pulse trains of several (usually than two) lasers are interleaved pulse by pulse, and the fluorescence decay functions excited by both lasers are recorded into a single waveform, see Fig. 549. The recorded waveform contains the fluorescence decay excited by one laser followed by the decay excited by the other. The images from the two excitation channels are selected by time-gating in the SPCM display function or by time-gating in the data analysis.

Data for different combinations of excitation and emission wavelengths are recorded by using several parallel TCSPC channels or a single TCSPC channel with a router. A typical result is shown in Fig. 550.

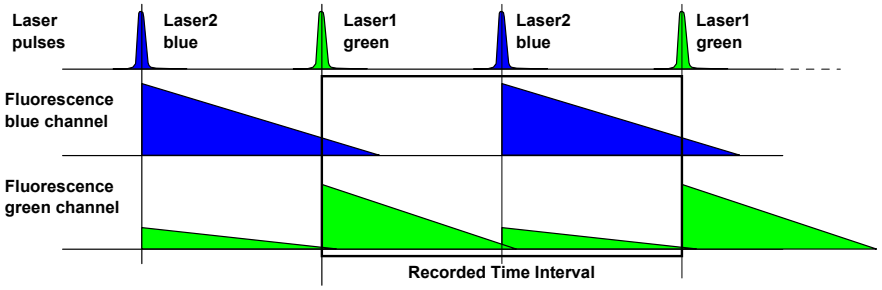


Fig. 549: Principle of laser wavelength multiplexing by pulse-interleaved excitation

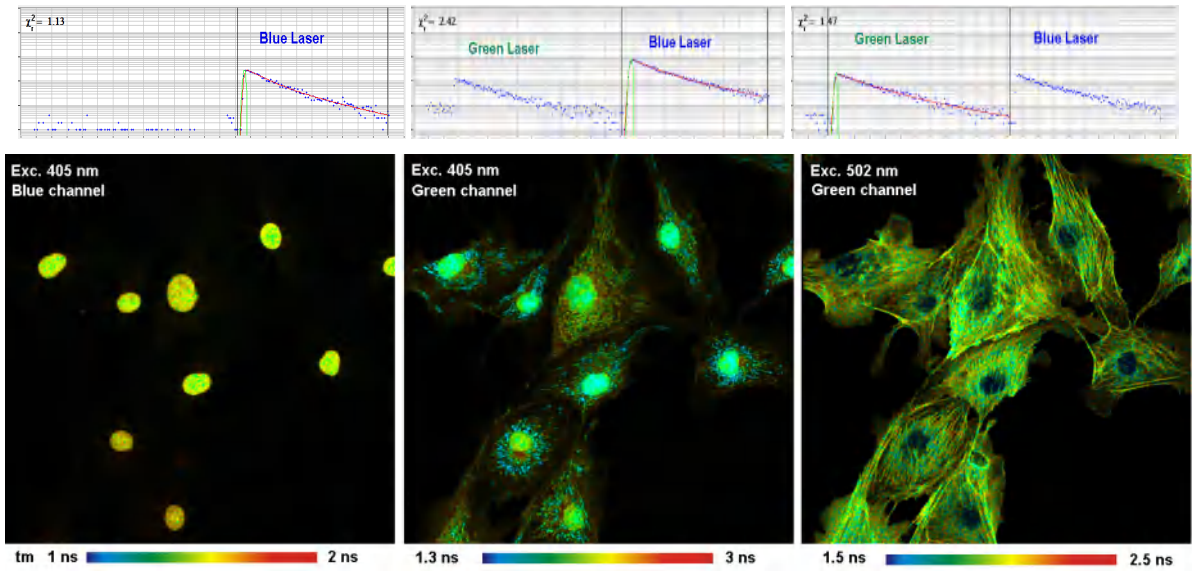


Fig. 550: FLIM by PIE. Zeiss LSM 710 Intune laser ('green laser') and 405 nm ps diode laser ('blue laser'). Images recorded by two parallel SPC-150 TCSPC modules. Left: Blue laser, blue detection channel. Middle: Blue laser, green detection channel. Right: Green laser, green detection channel. Top: Decay curves in selected pixels. Bottom: FLIM images, analysed by SPCImage, time-gated intensity.

PIE is the oldest technique of laser multiplexing, probably because it can easily be performed with classic TCSPC devices. An advantage of PIE is that it is applicable to lasers that cannot be on-off modulated at high speed. However, PIE has significant disadvantages. One of them is that PIE is not free of crosstalk. The tails of the fluorescence decay excited by one laser may extend into the decay excited by the other. Moreover, the effective Sync rate of the TCSPC device is reduced in proportion to the number of lasers. This brings the technique closer to the range where pile-up becomes noticeable. Moreover, there is intensity crosstalk due to counting loss, and mutual influence by detector afterpulsing. For a comparison of PIE and laser multiplexing please see 'Multiplexing of Lasers', page 298 .

Multiplexing by On-Off Modulation of Lasers

Multiplexing with on-off modulation of the lasers uses the multiplexing capability of multi-dimensional TCSPC. The technical principle of multiplexed TCSPC FLIM is described in section 'TCSPC FLIM with Excitation Wavelength Multiplexing', page 126. Several lasers or laser wavelengths are multiplexed synchronously with the pixels, lines, or frames of the scan. A routing signal is sent into the TCSPC module to indicate which laser or laser wavelength

was active in the moment when a photon was detected. The TCSPC module uses this information to direct the photons into different photon distributions. Multiplexing of two bh BDL-SMC, BDL-SMN, or BDS-SM ps diode lasers is integrated in the GVD-120 scan controller and the corresponding software panel. It is a standard function of the bh DCS-120 confocal and multiphoton scanning system [68]. The technical principle is illustrated in Fig. 555, page 376.

An example of wavelength-multiplexed FLIM is shown in Fig. 551. Two ps diode lasers, with wavelengths of 405 nm and 473 nm, were multiplexed synchronously with the frames of the scan. The two TCSPC channels of the DCS system recorded the images in two wavelength channels, 435 nm to 510 nm, and 510 nm to 550 nm. The sample was a mouse kidney section, stained with DAPI, Alexa 488 WGA, and Alexa 568 phalloidin. The combination of 405 nm excitation with detection at 435 nm to 510 nm shows the DAPI and the Alexa 488. Excitation at 405 nm and detection 510 nm to 550 nm shows a strong signals from the Alexa 488 and a weaker signal of the DAPI. Excitation at 473 nm and detection at 510 nm to 550 nm shows the Alexa 488 and the Alexa 568 but no trace of the DAPI.

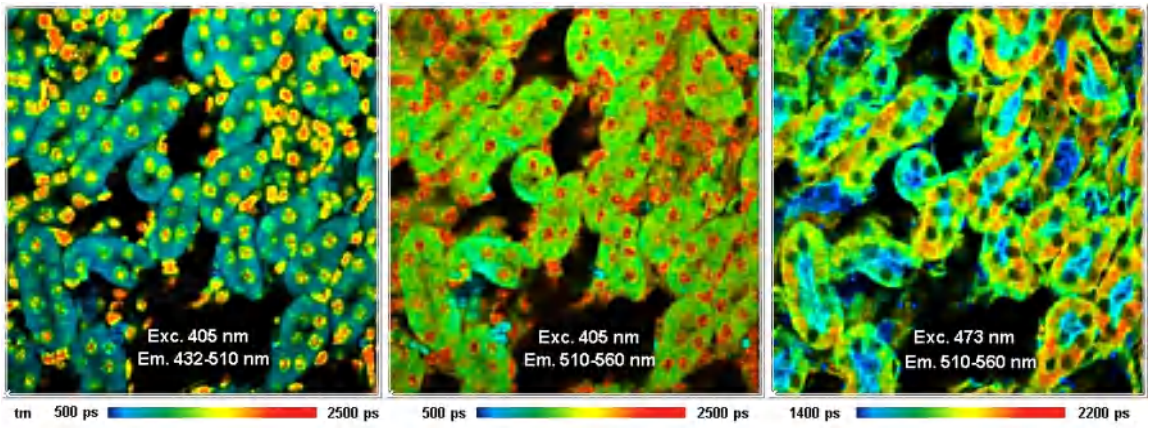


Fig. 551: Excitation wavelength multiplexing, 405 nm and 473 nm. Detection wavelength 435 nm to 510 nm and 510 nm to 550 nm. Mouse kidney section, stained with Alexa 488 WGA, Alexa 568 phalloidin, and DAPI.

Similar results can be obtained by multiplexing wavelengths selected from the emission of a super-continuum laser selected by an acousto-optical filter (AOTF). The AOTF wavelength can be controlled from the 'Laser On' outputs of the GVD scan controller. The AOTF responds within a time of a few microseconds. This is fast enough to run multiplexing on a line-by-line or frame-by-frame basis. FLIM images of a BPAE cell stained with Alexa 488, Alexa 568, and Mito Tracker red is shown in Fig. 552.

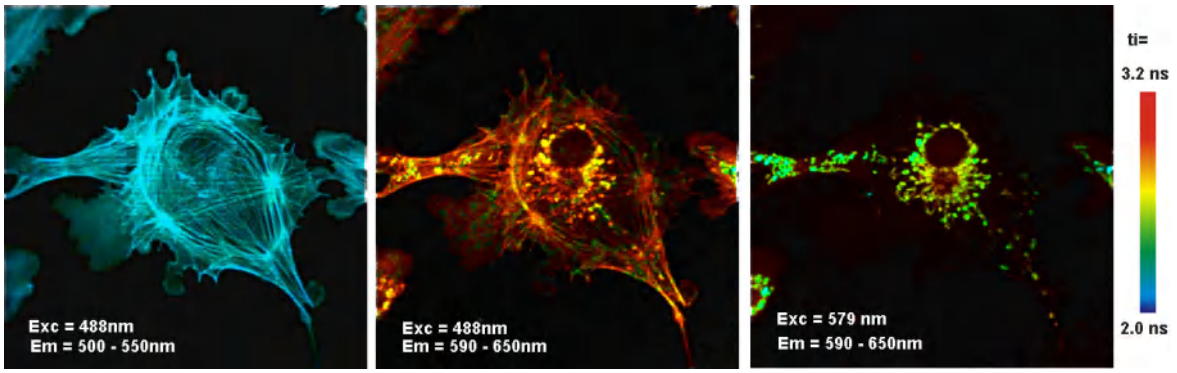


Fig. 552: BPAE sample, image recorded by wavelength multiplexing. Fianium SC400 laser with AOTF.

Another example is shown in Fig. 523, page 355. Multiplexing of 8 wavelengths in diffuse optical imaging is described in Chapter 'Diffuse Optical Tomography: DOT, NIRS and fNIRS'.

Compared with PIE, multiplexing by on/off modulation of the lasers has several advantages. There is no overlap of the tails of the decay functions from the different excitation lasers. There is no decrease in the effective sync rate with the number of laser channels and, consequently, no increase in pile-up. The principle therefore works up to the maximum count rate of the TCSPC module(s). Counting loss affects only the channel in which it occurs. It has no effect on the other laser channel(s). Two applications are described in the sections below.

Metabolic Imaging by Simultaneous FLIM of NADH and FAD

Metabolic FLIM with One-Photon Excitation

Fluorescence Decay Behaviour of NADH and FAD

Metabolic FLIM is based on the recording of lifetime images of NAD(P)H (nicotinamide adenine (pyridine) dinucleotide) and FAD (flavin adenine dinucleotide), see chapter 'Label-Free FLIM of Cells and Tissue'. NAD(P)H and FAD have to be excited at different wavelengths. Considering its relevance for cancer research and cancer diagnosis metabolic FLIM is probably the most important application of excitation wavelength multiplexing.

In biological systems both NADH and FAD exist in a protein-bound and in a free form. Bound and free forms have different decay times. For NAD(P)H the lifetime is long (a few ns) when it is bound and short (a few 100 ps) when it is free. For FAD the bound component has a short lifetime and the free component a long one. The fluorescence behaviour of NADH and FAD is illustrated in Fig. 553.

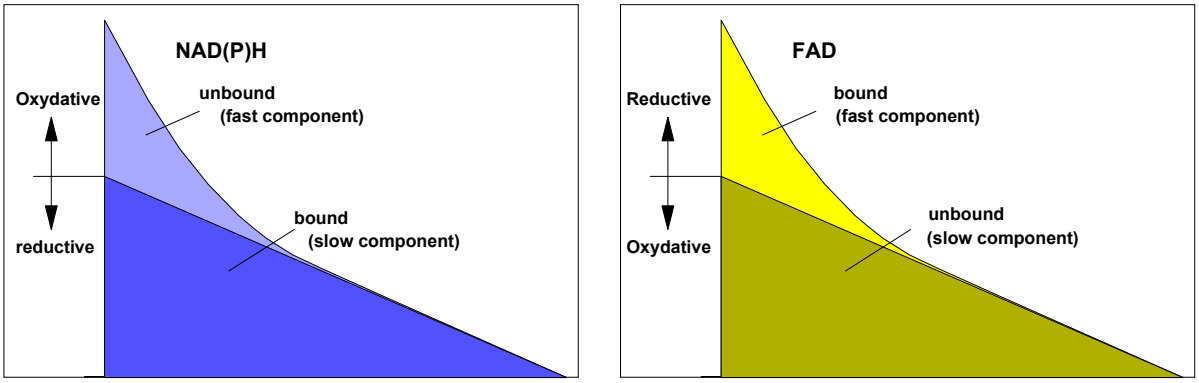


Fig. 553: Fluorescence decay behaviour of NAD(P)H and FAD

The resulting decay functions are double exponential, with the fast components originating from unbound NADH and from bound FAD. When the metabolism becomes more oxidative the amounts of bound NADH and of bound FAD increase, resulting in an increase in the amplitude of the slow decay component of NADH and of the fast decay component of FAD. When the metabolism becomes reductive the fast component of NADH and the slow component of FAD increase.

Excitation and Emission Spectra

To record lifetime images of NAD(P)H and FAD the signals from both compounds have to be separated. Approximate excitation and emission spectra of NAD(P)H and FAD are shown in Fig. 554. The spectra were taken from [742] and [1094]. The figure shows that NAD(P)H needs an excitation wavelength shorter than 380 nm. FAD can be excited all the way up from 350 nm to about 475 nm. That means, in principle, that NAD(P)H and FAD could be excited at the same wavelength, in the range from 350 to 380 nm. However, a look at the emission spectra shows that the emission signals cannot be separated in this case.

Fig. 554 shows that a clean NAD(P)H signal can be detected from about 425 to 475 nm. Above 475 nm the NAD(P)H signal is overlaid by emission from FAD. FAD emission occurs from about 480 nm to more than 600 nm. However, there is a strong overlap from the NAD(P)H emission. A clean FAD signal can therefore only be detected if an excitation wavelength above 400 nm is used, where the excitation of NAD(P)H is weak. In other words, the

signals from NAD(P)H and FAD can only be separated if different excitation wavelengths *and* different detection wavelengths are used.

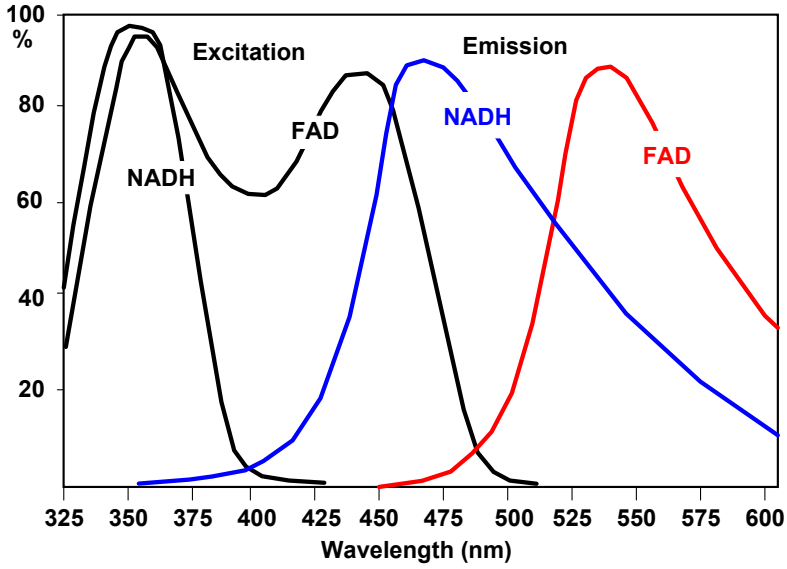


Fig. 554: Excitation and emission spectra of NADH and FAD

TCSPC FLIM Process with Laser Multiplexing

It is desirable that the data for NAD(P)H and FAD be recorded quasi-simultaneously. This way, possible focus drift, image shift, and, importantly, changes in the metabolic state of the cells induced by the imaging process itself have the same influence on both recordings. Quasi-simultaneous measurement at two excitation wavelengths is achieved by dual-channel FLIM in combination with laser multiplexing. The system architecture is shown in Fig. 555.

The FLIM system has two parallel TCSPC channels. One channel detects in the spectral range of NADH, the other in the range of FAD. Two ps diode lasers are multiplexed. The first one has a wavelength of 370 nm and excites NADH and (unavoidably) FAD. The second laser has a wavelengths of 410 nm and excites preferentially FAD. The excitation wavelengths were selected according to the available laser-diode wavelengths, and to the condition that the excitation wavelength for FAD should not be within the detection interval for NADH.

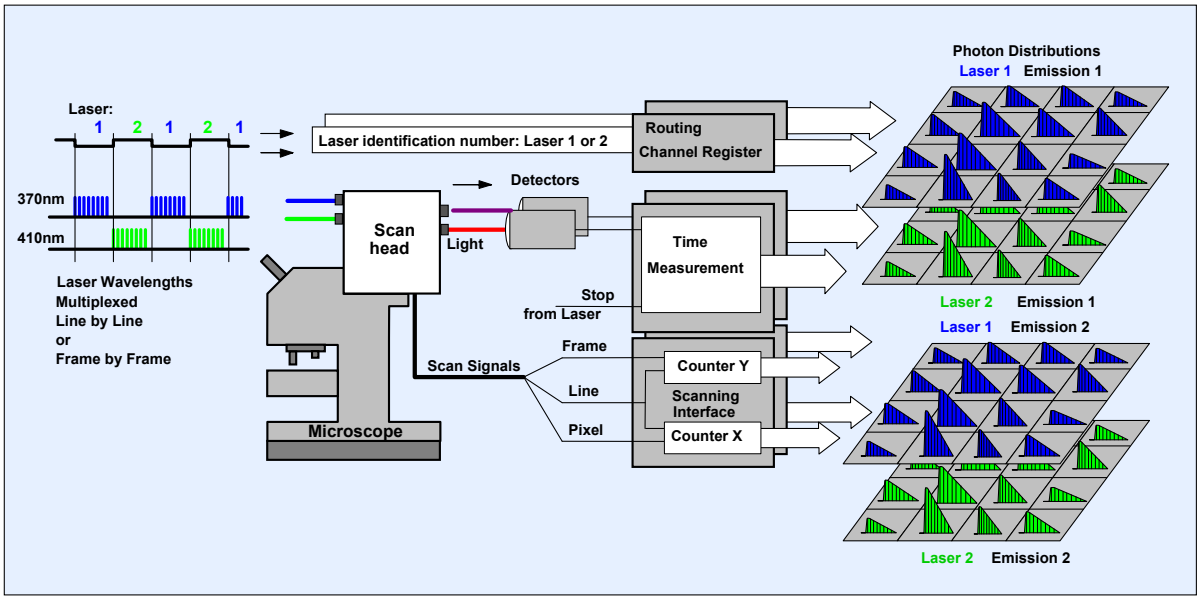


Fig. 555: Principle of simultaneous NADH / FAD FLIM

The recording process generates lifetime images for four combinations of excitation and detection wavelengths:

	Excitation	Emission	Signal detected
Image 1	375 nm	420 to 470 nm	NAD(P)H
Image 2	375 nm	490 to 600 nm	FAD + NAD(P)H, not used
Image 3	410 nm	420 to 470 nm	not used
Image 4	410 nm	490 to 600 nm	FAD

The data of interest are the ones in Image 1 (NAD(P)H) and in Image 4 (FAD). Please see [130] for more technical details.

Results

Metabolic-FLIM data were recorded with a DCS-120 confocal FLIM system in a 'Metabolic FLIM' configuration. Compared to the DCS-120 standard configuration the only difference is in the laser wavelengths: BDL-SMN lasers of 370 nm and 410 nm wavelength are used. Multiplexing of the lasers is controlled by the multiplexing functions of the GVD-120 scan controller of the DCS-120 system. For user interface, parameter setup, and other technical details please see Handbook of the DCS-120 system [68]. Images for NADH and FAD are shown in Fig. 556, left and right. The decay curves show the expected shape. The FAD displays a shorter average lifetime, τ_m, than the NADH, and has a shorter and more pronounced fast decay component. Detailed results are described in [130, 173, 1211] and in chapter 'Label-Free FLIM of Cells and Tissue'.

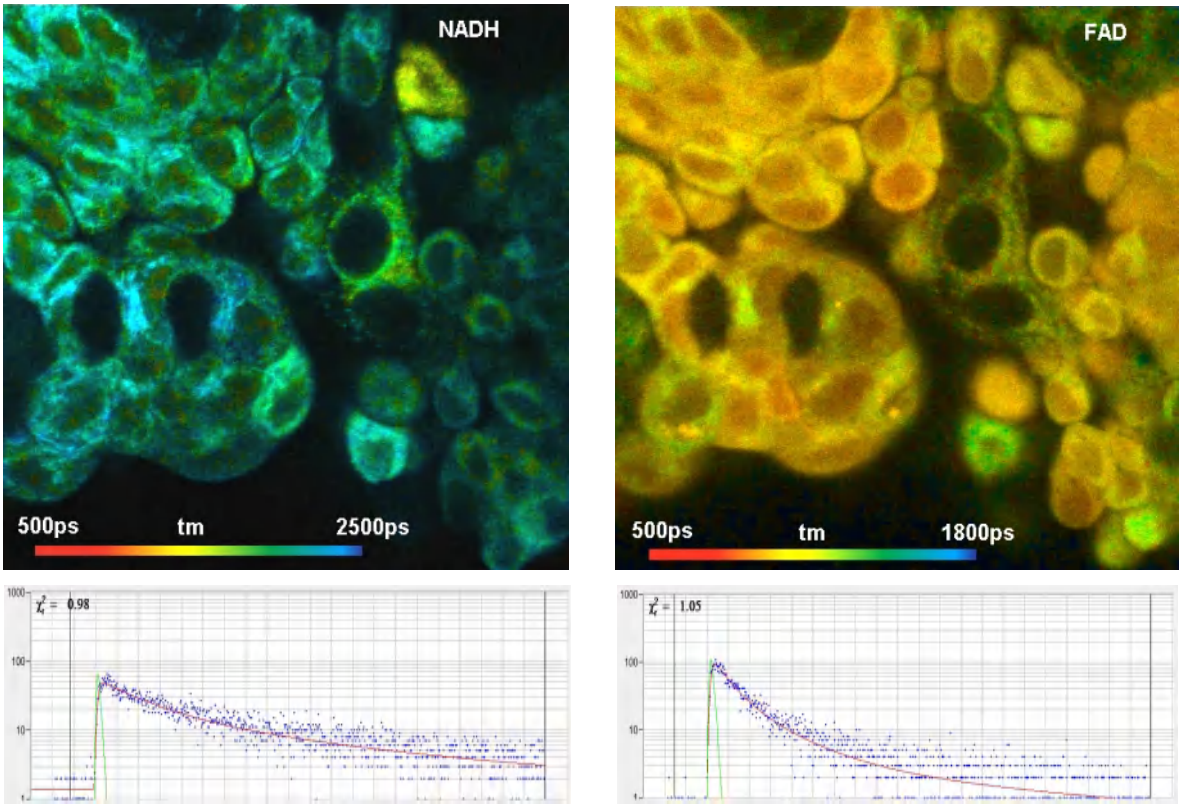


Fig. 556: NADH FLIM image (left) and FAD FLIM image recorded simultaneously by excitation wavelength multiplexing and dual-channel recording. Bottom: Decay curves in arbitrary selected spot. Data analysis by SPCImage NG.

Metabolic FLIM with Two-Photon Excitation

For metabolic imaging in deep tissue it is desirable to excite NADH and FAD by two-photon excitation. Two-photon excitation penetrates deep into tissue, and simultaneously avoids the complication of one-photon FLIM that the best FAD excitation wavelength is within the detection wavelength interval of NADH. However, there is a problem when wavelength multiplexing is to be used. A system with two femtosecond lasers would be too expensive, and tuning a femtosecond laser periodically between NADH and FAD excitation is not fast enough.

It has been attempted to solve the problem by dual-wavelength tuneable lasers, such as the Insight DS of Spectra Physics. The laser emits both at a fixed wavelength of 1041 nm and at a tuneable wavelength in the range from 680 nm to 1300 nm. NADH is excited normally at λ_1=760 nm. FAD is excited by injecting both λ_1=760 nm and λ_2=1041 nm into the sample. The combined energy of the 760-nm and the 1041-nm photons is equivalent to two-photon excitation at a single wavelength of λ_v=878 nm [1195]. 878 nm is an efficient wavelength for FAD excitation. Multiplexing can be performed by periodically turning off and on the 1041-nm beam via an AOM or EOM.

Unfortunately, the principle has a flaw. When FAD is excited by the 'virtual' wavelength of λ_v=878 nm also the NADH excitation wavelength, λ_1=760 nm, is active. That means also NADH is excited. The essential problem of FAD imaging (the overlap of the tail of the NADH emission band into the FAD band , see Fig. 554) is thus not solved, and a clean FAD signal is not obtained.

Recently, Toptica GmbH (Munich, Germany) have developed the 'FemtoFibre Dichro', a prototype of a dual-wavelength femtosecond fibre laser. The laser emits at 780 nm and at 880 nm. It contains individual AOMs for the two wavelengths. The AOMs are controlled by digital on/off (beam blanking) signals and by analog intensity signals. The laser can be directly controlled by the outputs of the bh GVD-120 scan controller. It is thus a perfect match to the bh DCS-120 MP multiphoton FLIM system [68]. The combination of both makes an almost ideal two-photon metabolic FLIM system. A photo of the system is shown in Fig. 557, left. The control of the laser is fully integrated in the SPCM FLIM data acquisition software via the scan control panel, see Fig. 557, left. The two laser wavelengths, 780 nm and 880 nm, can be turned on or off independently by the blue buttons in the upper right of the panel. The intensities are controlled via the Power sliders. The wavelengths are multiplexed by the multiplexing function of the GVD-120 scan controller. In the panel shown in Fig. 557 both wavelengths are active, and multiplexed frame by frame.

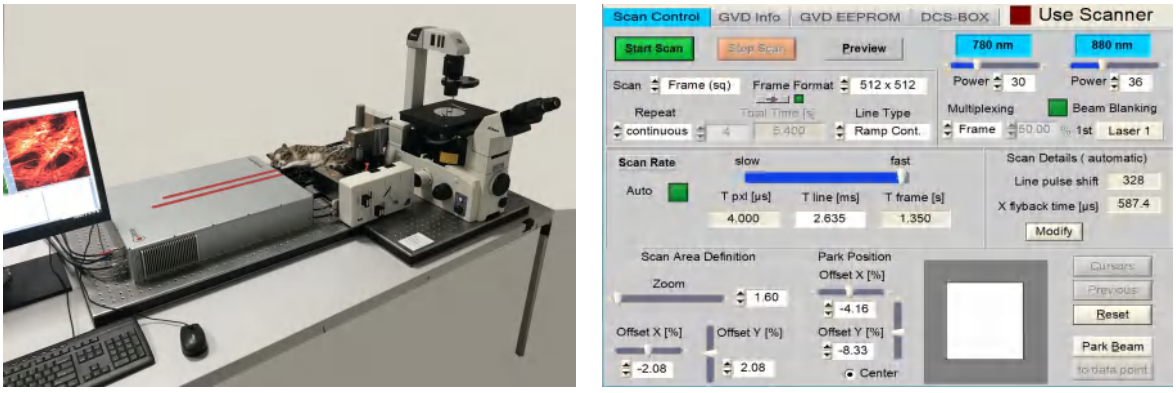


Fig. 557: DCS-120MP Metabolic FLIM System with Toptica FemtoFibre Dichro. Cover of beam path removed.

The images generated by the setup are:

	Excitation	Detection	Signal detected
Image 1	780 nm	420 to 470 nm	NAD(P)H
Image 2	780 nm	490 to 600 nm	NAD(P)H + FAD, not used
Image 3	880 nm	420 to 470 nm	Collagen, SHG of 880 nm laser
Image 4	880 nm	490 to 600 nm	FAD

Image 1 and image 4 are the desired NADH and FAD images. Image 3 contains the SHG signal from collagen, excited by 880 nm. The image provides supplementary information about connective-tissue structure, vascularisation, or skin ageing.

Typical Results

Typical results are shown in Fig. 558 through Fig. 561. Fig. 558 shows NADH and the FAD images of yeast cells recorded by the 2p metabolic FLIM system.

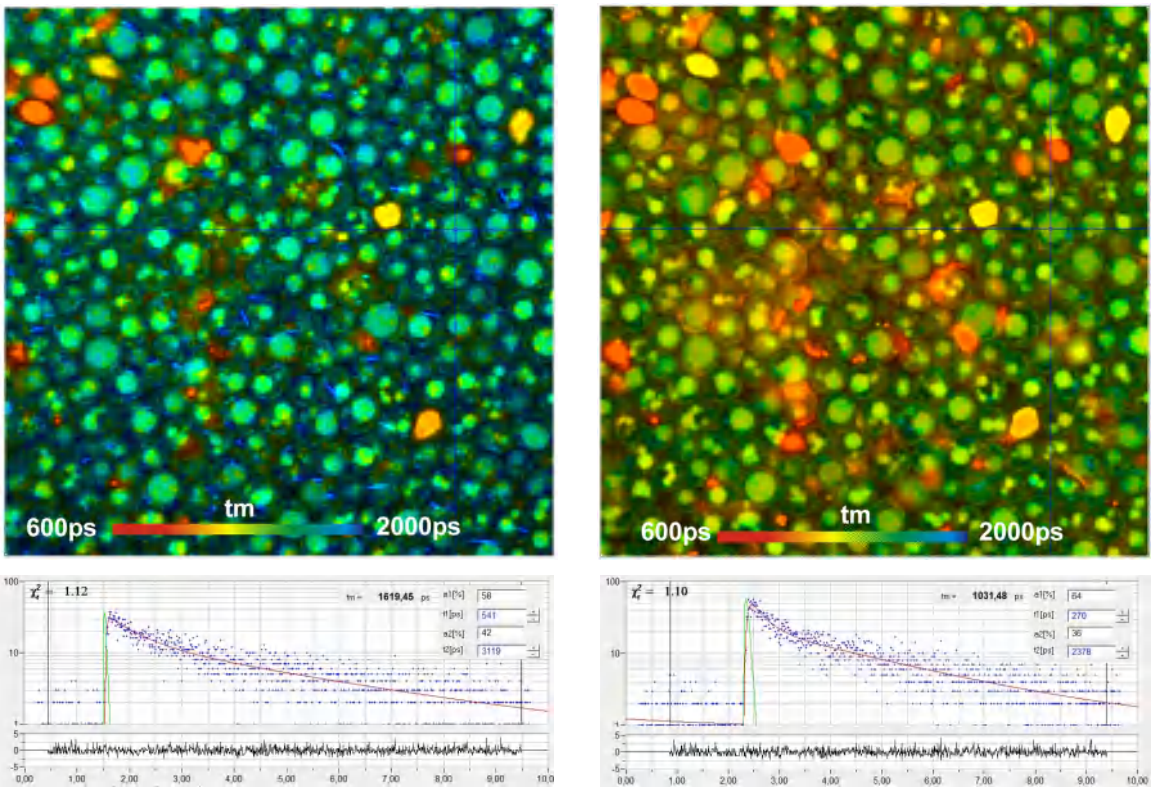


Fig. 558: 2-Photon metabolic FLIM of yeast cells, Images and decay curves at cursor position. Left: NADH. Right: FAD. Data analysis by SPCImage NG.

Fluorescence decay curves in a selected spot of 5 x 5 pixels are shown below the images. The amplitude-weighted lifetimes, t_m, for the NAD(P)H and the FAD are 1619 ps and 1031 ps, respectively. As expected, the decay components for NAD(P)H have lifetimes of 512 ps and 3119 ps. With 58%, the amplitude of the fast component is in the normal range (the cells were imaged under atmospheric pO_2). The components for FAD are 270 ps and 2378 ps, with amplitudes of 64% and 36 %, respectively.

Fig. 559 to Fig. 561 show 2-photon metabolic-FLIM images obtained from pig skin. Fig. 561 is the image from the NADH channel. The decay curve shown lower right is from a 5 x 5 pixel area around the cursor position. The decay function contains 67% of 432 ps and 33% of 2820 ps, compatible with the known lifetimes of unbound and bound fractions of NADH. Fig. 560 shows the image in the FAD channel. The decay components at the cursor position are 62% of 431 ps and 38% of 2490 ps. These values are generally compatible with FAD. It should, however, be noted that other fluorophores, such as FMN (flavin mononucleotide),

melanin, or porhyrines may contribute to the decay function. Fig. 561 is the image in the SHG channel. The signal mainly comes from collagen, and thus marks the connective-tissue structures. SHG is an ultra-fast process, therefore the 'lifetime' of the SHG signal should be zero. However, a small contribution from fluorescence is present, visible as a low-amplitude tail in the decay curve. The effective t_m averaged over the image is therefore not exactly zero, see lifetime histogram in the upper right.

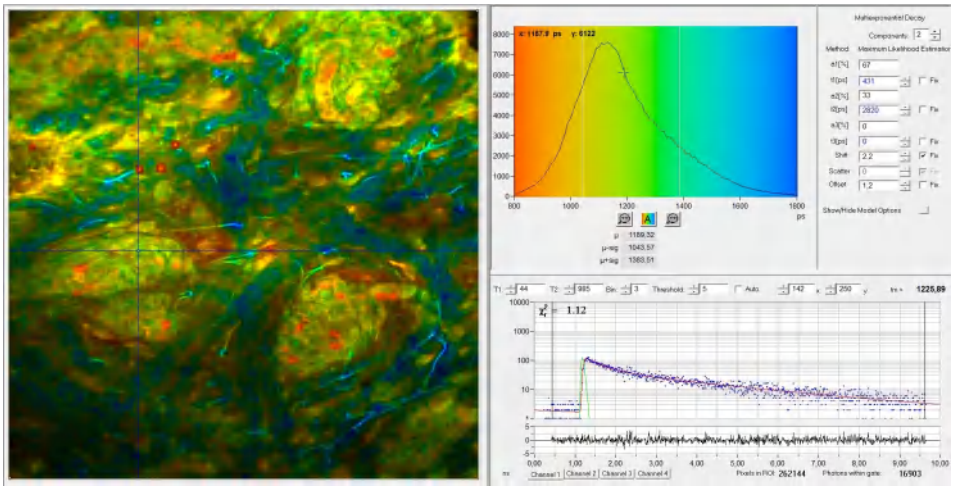


Fig. 559: 2p metabolic FLIM of Pig skin, t_m image in the NADH channel

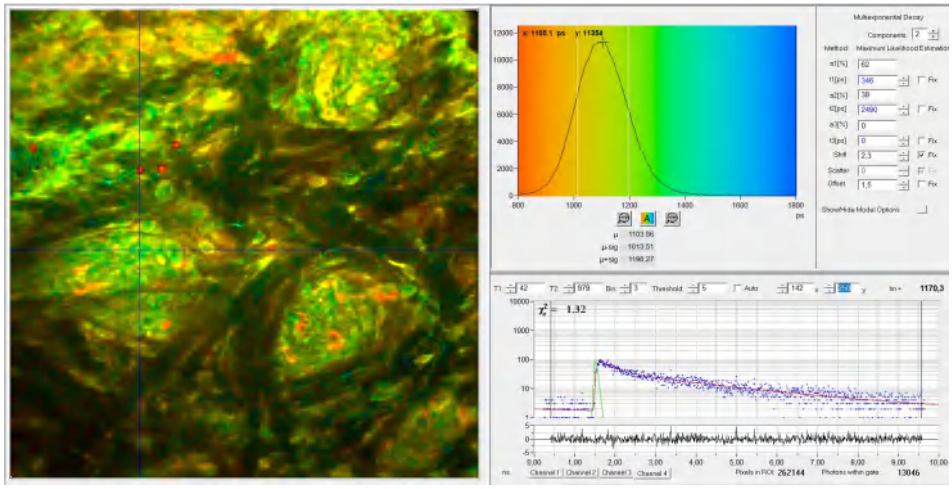


Fig. 560: 2p metabolic FLIM of Pig skin, t_m image in the FAD channel

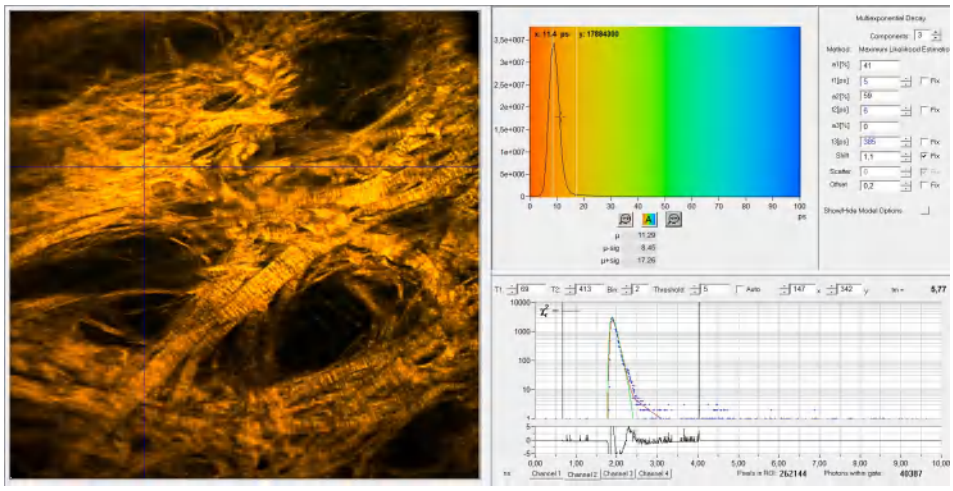


Fig. 561: 2p metabolic FLIM of Pig skin, image in the SHG channel

Tryptophan FLIM

Tryptophan is an essential amino acid. It is, together with other amino acids, a constituent of most proteins. Tryptophan is fluorescent, and its fluorescence is the dominating part of protein fluorescence. Tryptophane fluorescence is dependent on biological parameters, such as protein constitution, protein folding, and presence of other amino acids in the closer molecular environment. This dependence makes tryptophan a potential fluorescence marker for molecular parameters in biological systems.

The problem of tryptophane (TRP) fluorescence imaging is that the excitation and emission wavelengths are in the UV. The excitation maximum is around 280 nm, the emission band extends from about 300 nm up to 400 nm [742]. Tryptophan absorption and emission spectra are shown in Fig. 562.

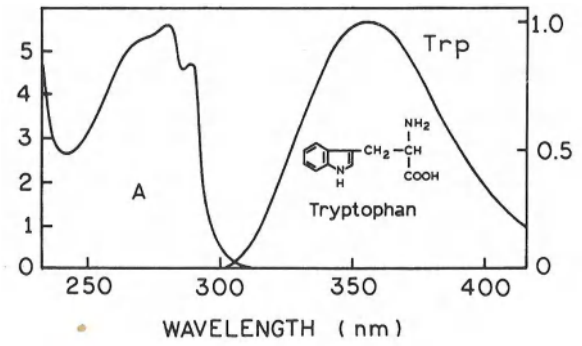


Fig. 562: Absorption (left) and emission spectra (right) of tryptophan (from [742])

Decay Curves of tryptophan fluorescence can be recorded in a conventional fluorescence spectrometer with UV-transparent optics or in a microscope with wide-field illumination by a UV-LED via a separate excitation beam path [279]. Although microscopes with a special UV objective lens have been used [770]. In a normal microscope direct excitation of tryptophan is not possible because the required excitation wavelength does not pass the objective lens and the tube lens. In a laser scanning microscope the problem is even greater because the excitation has to pass also the scanner optics.

The usual way around the UV problem is to use multiphoton excitation. It has been shown that useful results can be obtained with three-photon (3-p) excitation [10, 632]. For 3-p excitation a wavelength in the range from 750 nm to 840 nm is used. Appropriate wavelengths can easily obtained from a Ti:Sa laser.

Unfortunately, 3p excitation of tryptophane has a potential problem. 3p excitation needs high laser power, usually more than 10 mW in the focal plane. This is no problem for a tryptophane solution, but it is a problem for cells. Cells contain NADH and FAD. At 740 nm to 840 nm, the laser hits the absorption band of these co-enzymes with the full power of two-photon excitation, see Fig. 563. Published results [10, 632] were obtained with 7 mW to 8 mW at 740 nm. This is significantly more than normally used for NADH and FAD imaging, and almost certainly causes damage to the cells. Nevertheless, the count rates obtained from the cells in the TRP emission band were only 10,000 counts per second.

Another possibility is to excite tryptophan by two-photon (2p) excitation. The optimum excitation wavelength for tryptophan would then be in the range from 530 to 560 nm. There is no significant absorption of NADH or FAD at this wavelength, see Fig. 563. It can therefore be expected that photodamage will remain at an acceptable level. Suitable excitation wavelengths can be obtained from an OPO, but the price of an OPO system is high. However, a

femtosecond fibre laser with 540 nm wavelength has recently become available [1278]. With this laser, tryptophan FLIM becomes possible with a DCS-120 MP system [133].

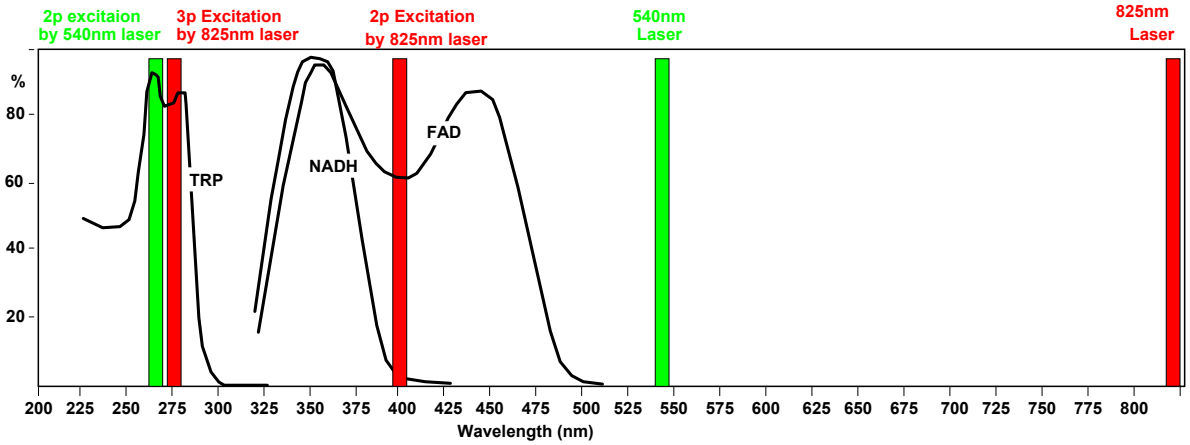


Fig. 563: Excitation of TRP by multiphoton excitation. Red: 825 nm laser. Green: 540 nm laser. It can be seen that 3p excitation at 825 nm excites also FAD. Two-photon excitation at 540 nm does not have this problem.

The optical system consists of the DCS-120 scan head, a Nikon Ti 2E microscope, a 560 nm VALO Aalto laser with SHG option [1278], and two HPM-100 hybrid detectors. The principle is shown in Fig. 564. The laser delivers 50 mW of optical power at a wavelength of 540 nm. To obtain high efficiency both for excitation and detection we used an x40 NA=1.3 oil immersion lens. The fluorescence light is collected back through the microscope lens, separated from the excitation light by a 520 nm dichroic beamsplitter in the filter carousel of the microscope, and sent out through the back port of the microscope. The light is transferred to the detectors via a normal NDD (non-descanned detection) beam path. Scattered laser light is removed by a 500 nm short pass filter. The signal is further cleaned by a 360/40 band pass filter. The signal is detected by one of the two NDD detectors of the DCS-120 MP and recorded by the usual multi-dimensional TCSPC FLIM process.

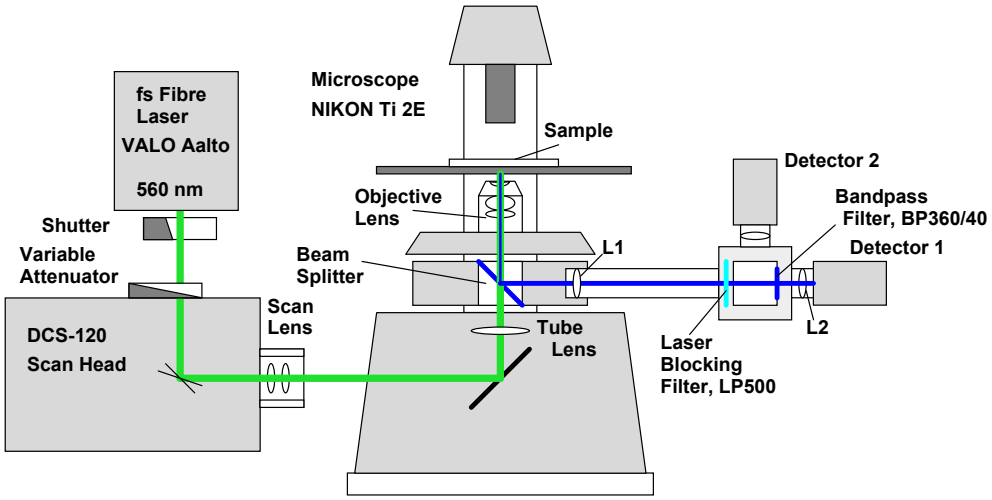


Fig. 564: Optical principle of the 2-photon tryptophan FLIM system

Fig. 565 shows a tryptophan lifetime image of live yeast cells. The excitation power was 2 mW in the plane of the sample, the acquisition time 60 seconds. With a count rate of $90 \cdot 10^3$ photons per second, 5.5 million photons were acquired within this time. The number of photons is sufficient for double-exponential decay analysis. The decay components at the cursor position are 49 % of 632 ps and 51% of 3525 ps. The amplitude-weighted lifetime is 2108 ps. These values are close to the lifetimes reported in the literature and to the lifetimes we recorded in a TRP solution [133].

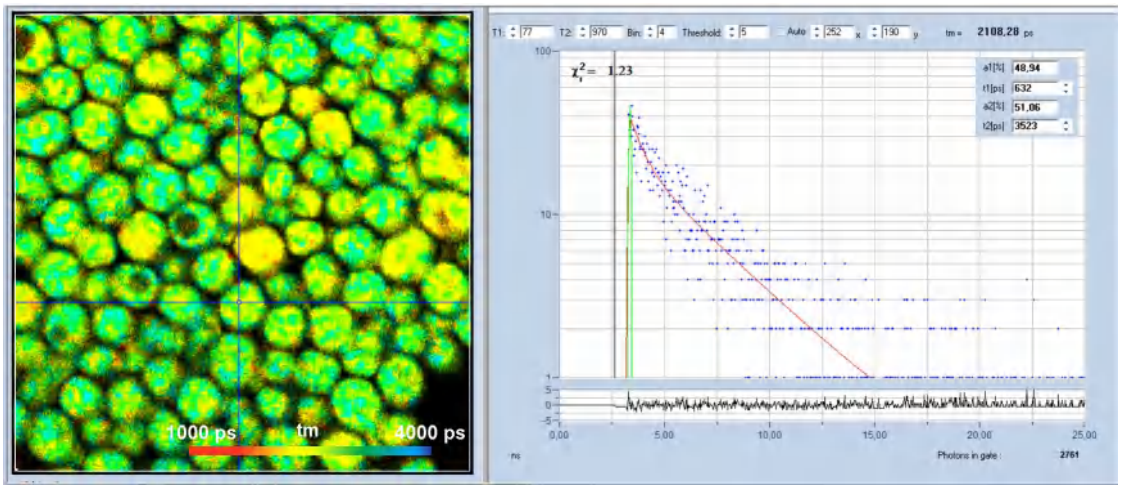


Fig. 565: Tryptophan FLIM of Yeast cells. Left: Lifetime image. Amplitude-weighted lifetime of double-exponential decay. Right: Decay function at cursor position. Image format 512 x 512 pixels, 1024 time channels, two-photon excitation at 540 nm, lifetime range from 1000 ps to 4000 ps. Analysis by bh SPCImage NG 9.0.

Fig. 566 shows a tryptophan lifetime image of live Escherichia coli (E. coli) bacteria. E. coli bacteria are not an easy target. They are small and move quickly. The image shown was recorded with an acquisition time of 90 seconds. The entire image contains about 10 million photons. The image was analysed with a double-exponential decay model. The decay components at the cursor positions are 62.7 % of 1573 ps and 37.3 % of 4740 ps. The amplitude-weighted lifetime is 2762 ps.

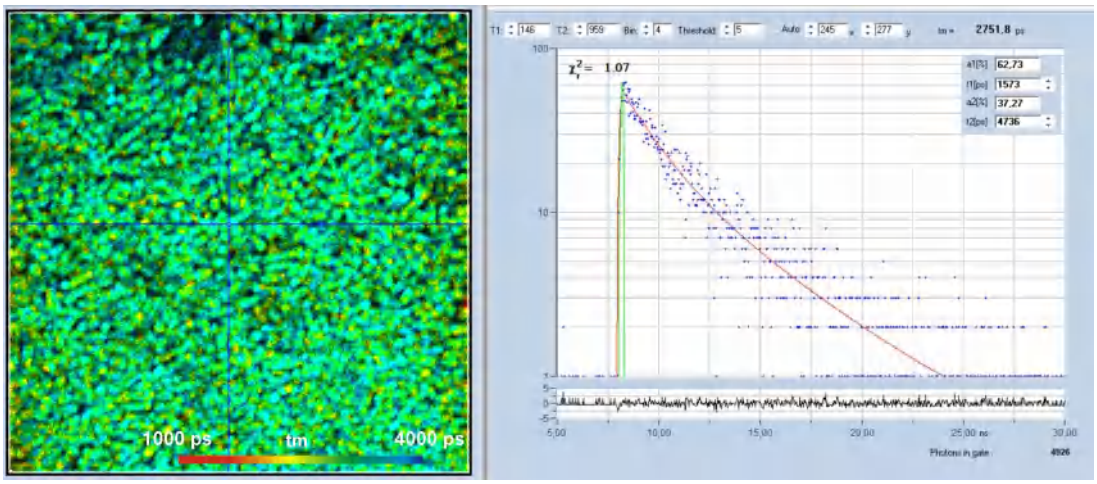


Fig. 566: Tryptophan FLIM of E. coli bacteria. Left: Lifetime image. Amplitude-weighted lifetime of double-exponential decay. Right: Decay function at cursor position. 512 x 512 pixels, 1024 time channels, two-photon excitation at 540 nm, lifetime range from 1000 ps to 4000 ps. Analysis by bh SPCImage NG 9.0.

The results show that tryptophan FLIM with two-photon excitation is possible. Still, the count rates are relatively low which may, in part, be a result of poor UV transmission of the microscope lens. Lenses with higher UV transmission may be available. But such lenses have lower NA than visible-range lenses. The collection efficiency is thus lower, and the overall result may be not better than with a high-NA visible-range lens.

Near-Infrared FLIM

Near-infrared dyes are used as contrast agents and as fluorophores in diffuse optical imaging applications [243, 657, 743, 786]. Diffuse optical imaging (or diffuse optical tomography, DOT) reconstructs internal structures and scattering and absorption parameters of tissue from diffusely transmitted photons. DOT uses the fact that the scattering and absorption coefficients decrease with increasing wavelength. By using wavelengths between 650 and 900 nm information about the tissue condition can therefore be obtained up to a depths of about 5 cm. For these applications it is important to have information about binding of the dyes to proteins, DNA, collagen, and other cell constituents available. It is also important to know whether the dyes change their fluorescence lifetimes on binding, and whether these lifetime changes depend on the binding targets [194]. Possible lifetime changes may interfere with the reconstruction of the tissue structure and tissue parameters from time-resolved data, but may also be exploitable to gain additional biological information [29, 477]. Moreover, the penetration depth in the NIR - even for a confocal system - can be expected to be noticeably higher than for visible excitation and detection.

Confocal NIR FLIM

At first glance, FLIM at NIR wavelengths should neither be a problem on the detection nor on the excitation side: FLIM detection in the 700 to 900 nm range can be achieved by bh HPM-100-50 hybrid detectors or by PMC-100-20 PMT modules. Picosecond diode lasers for the red and near-infrared range are available with 640 nm, 685 nm, and 785 nm, the Intune of the Zeiss LSM 710 can be tuned up to 645 nm, and super-continuum lasers with acousto-optical filters deliver any wavelength from the visible range to more than 1000 nm. Multiphoton microscopes have a Ti:Sapphire laser that works from about 700 nm to 1000 nm. The wavelengths available from these light sources are compatible with the (one-photon) excitation spectra of a variety of NIR dyes.

Unfortunately, there are a few pitfalls in the microscope optics: The internal beamsplitter of the scan head must reflect the excitation light towards the microscope lens, and transmit the fluorescence back from the lens to the detectors (Fig. 567, second right). Neither a normal confocal nor a multiphoton microscope has the right dichroic beamsplitter: The transition wavelengths of the beamsplitters of the confocals are too short (Fig. 567, left), and the transmission range of the multiphoton beamsplitter is at the wrong side of the excitation wavelength (Fig. 567, second left).

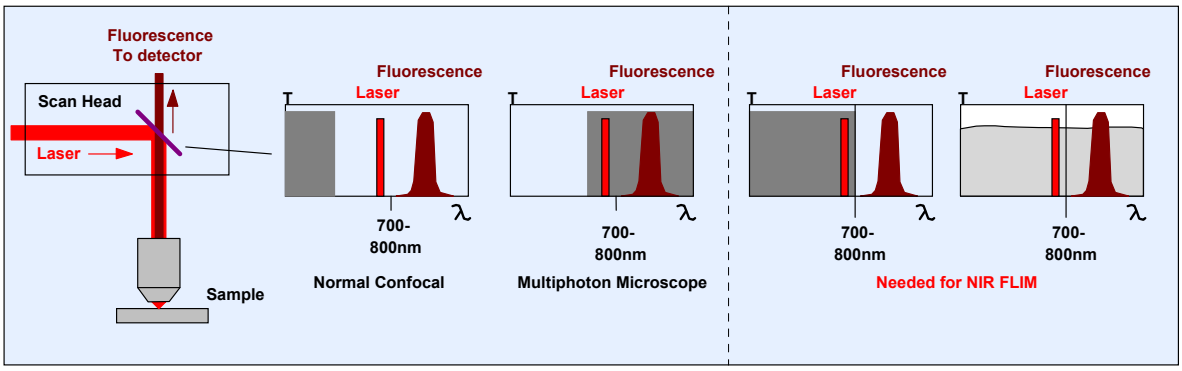


Fig. 567: Main dichroic beamsplitter of normal confocal, of a multiphoton microscope, and dichroic beamsplitter required for NIR FLIM

The problem of the internal beamsplitter is avoided by using two-photon excitation and non-descanned detection. In that case, the fluorescence is split off by a beamsplitter cube in the filter carousel directly behind the microscope lens. The cube in this place can easily be replaced and configured for the desired transition wavelength. Two-photon excitation of NIR dyes and FLIM detection by an SPC-730 FLIM module and a PMC-100-20 NIR detector has indeed been demonstrated [1371]. It requires, however, a laser or an OPO hat delivers wavelengths between 1000 and 1600 nm, see 'NIR Multiphoton NDD FLIM with OPO Excitation', page 389.

The problems can easily be solved in confocal systems that have a wideband beamsplitter available, see Fig. 567, right. A wideband beamsplitter loses some light but works at any combination of laser and fluorescence wavelength, see also 'Confocal FLIM with Tuneable-Excitation', page 353. Wideband beamsplitters are available in the bh DCS-120 system and in the Zeiss LSM 710 family microscopes.

In the DCS-120 WB system NIR excitation is obtained by connecting a BDL or BDS series ps diode laser with 640 nm, 685 nm, or 785 nm to the scanner. Any other laser of suitable wavelength and with Point-Source compatible fibre output a can be used as well [67, 68]. A system with an Olympus FV1000, a bh BDL-SMC 785 nm laser, a bh PMC-100-20 detector and a bh SPC-730 TCSPC FLIM module has been described in [916].

The Zeiss LSM 710 family microscopes have an 80/20 beam splitter in their main beam splitter wheel. There is also a near perfect solution to the excitation source: The LSM 710/780 NLO multiphoton microscopes have a Ti:Sapphire laser that delivers tuneable pulsed excitation in the NIR. The laser is used as a one-photon excitation source. The microscope must have a confocal output from the scan head to which an HPM-100-50 detector is attached [69].

Indocyanine Green (ICG)

Indocyanine Green (ICG) has an absorption maximum around 780 nm. At concentrations higher than about 50 µm/l aggregates form which have an absorption maximum at 690 nm. The fluorescence is emitted around 820 nm [370].

Fig. 568 shows images of pig skin stained with ICG. The data were recorded by a DCS-120 WB system with a wideband beamsplitter. The small stokes shift between the absorption of the monomers and the emission makes it difficult to suppress scattered laser light and wideband spectral background of the laser. Fortunately, ICG has sufficient absorption down to 630 nm. We therefore used a 640 nm BDL-SMC ps diode laser for the experiments. This provides convenient spacing between the excitation and emission wavelengths, and avoids any filter leakage problems.

The image shown in Fig. 568, left is from a focal plane about 20 µm below the top of the skin. The image on the right was taken from the back of the skin sample. Both images show the intensity-weighted lifetime of a double-exponential fit (t_i in SPCImage, see page 949 of this handbook).

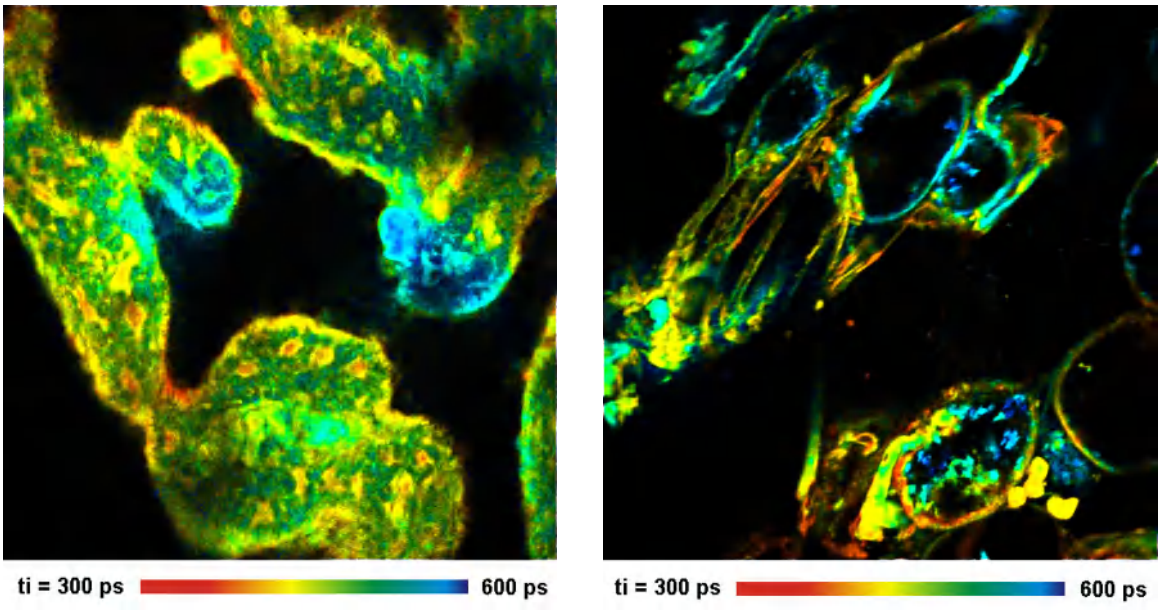


Fig. 568: Pig skin sample stained with ICG. Left: Image from the top of the skin, about 20 µm from the highest structures. Right: Image taken from the back of the skin sample. Fit with double-exponential model, intensity-weighted lifetime. DCS-120 WB system, HPM-100-50 detector.

There are surprisingly large changes in the fluorescence lifetime throughout the sample. It is known that ICG has a lifetime of about 200 ps in water, and about 600 ps when bound to serum albumin. Typical fluorescence decay functions and the corresponding decay parameters are shown in Fig. 569.

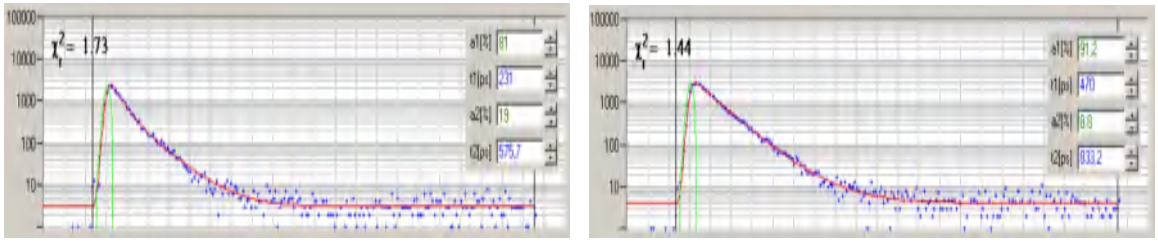


Fig. 569: Decay functions from selected 15 x 15 pixel areas of Fig. 568. Left: Short-lifetime areas (yellow-orange). Right: Long-lifetime areas (green)

In the short-lifetime areas (yellow-orange in the images) the lifetimes of the decay components are 231 ps and 576 ps. This is marginally compatible with a mixture of bound and unbound ICG. In the long-lifetime areas (green in the images) the fit delivers two decay components, with lifetimes of 470 ps and 833 ps. This is clearly incompatible with a simple mixture of bound and unbound ICG.

The results show that the assumption of an essentially invariable fluorescence lifetime (and thus quantum efficiency) of ICG in biological systems is not correct. The variability may have an impact on the reconstruction of tissue parameters in diffuse optical imaging experiments.

Diethylthiatricarbocyanine (DTTCC)

A pig skin sample stained with DTTCC (3,3'-diethylthiatricarbocyanine) is shown in Fig. 570. The image was recorded by a Zeiss LSM 710 NLO system. The Ti:sapphire laser was used as a one-photon excitation source. The laser wavelength was 780 nm. The 80/20 beamsplitter of the LSM 710 scan head was used, and the fluorescence selected by a 800 nm longpass filter in front of the HPM-100-50 detector. The general behaviour of the DTTCC is similar to that of ICG: The lifetime is short where the tissue was exposed to high dye concentration, and longer inside the tissue. This may be due to aggregation of the dye. Even though the lifetime may not reflect any biologically relevant parameters the long excitation and detection

wavelength results in high contrast images as they are not normally obtained by confocal detection in thick tissue.

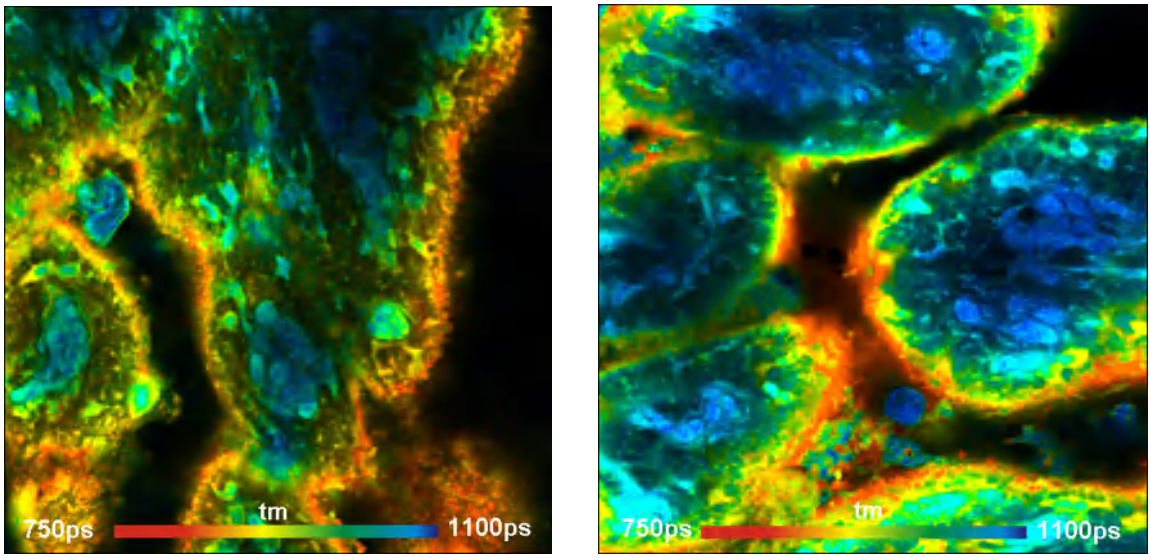


Fig. 570: Pig skin samples stained with DTTCC. Zeiss LSM 710 NLO, Ti:Sa laser used for one-photon excitation. Excitation wavelength 780 nm, detection wavelength 800 nm to 900 nm. HPM-100-50 hybrid detector, Simple-Tau 152 FLIM system. Lateral size of the images 212 x 212 µm, depth about 30 µm from surface. Note the high contrast of the images.

Methylene Blue

Methylene Blue has an absorption band from 550 to 690 nm, with a maximum at 660 nm. Fluorescence is emitted from 650 nm to 750 nm, with a maximum at 680 nm. Methylene Blue is a biomedically interesting compound. It has anti-viral and anti-bacterial effects, and it has been used as a drug against malaria [1070]. It has been used to induce apoptosis in cancer cells [1346], and to treat psoriatic skin lesions by photodynamic therapy [1044]. The use to treat Alzheimer disease is under clinical trial [843]. Fig. 571, left, shows a pig skin sample stained with Methylene Blue. As can be seen from the lifetime image and from the decay curves (Fig. 571, right) Methylene blue delivers distinctly different decay times depending on the tissue structures it binds to. Both the lifetimes of the decay components and the amplitudes change. The exact mechanism of the lifetime changes is not known. Methylene blue shows changes in its absorption spectrum on pH variation. It can be expected that these are accompanied by lifetime changes. More important, it is known that Methylene Blue is a redox indicator. It is thus possible that the changes originate from variation in the redox potential of the proteins. If this speculation is correct Methylene Blue could be a highly potent marker for the tissue state.

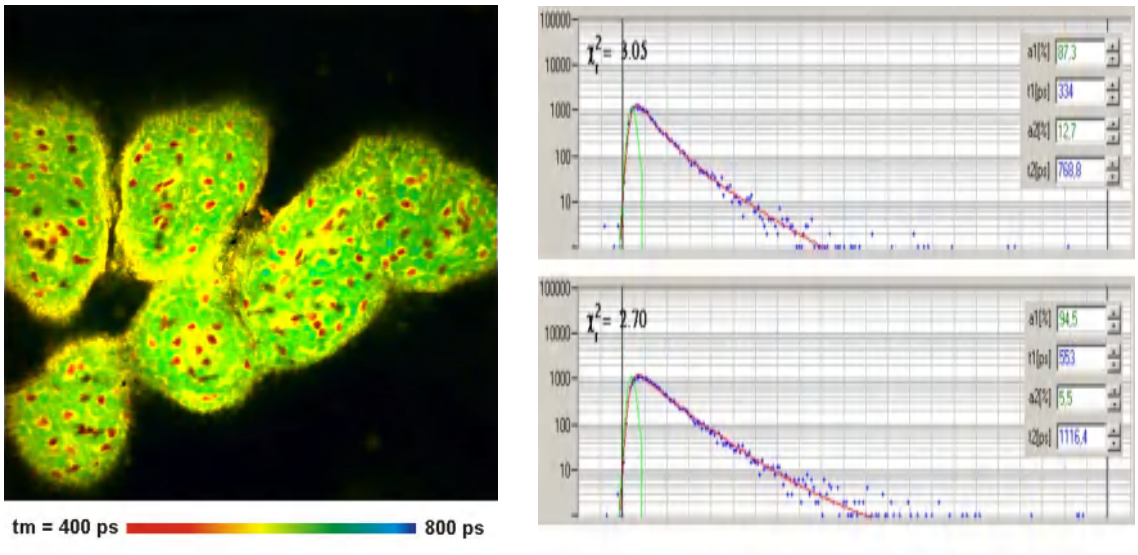


Fig. 571: Pig skin stained with Methylene Blue. Left: Lifetime image, double-exponential model, amplitude-weighted lifetime. Right: Decay curves in 3 x 3 pixel areas. Top: From red spots (fast decay). Bottom: From green areas (slow decay). DCS-120 WB system, 640 nm ps diode laser.

The absorption wavelength of Methylene Blue can be reached by the Zeiss LSM 710 Intune (tuneable excitation) system. Results obtained by this system are shown in Fig. 572. The Methylene blue was excited at 645 nm, the fluorescence was detected from 660 to about 750 nm. The results confirm the lifetime variations seen in the DCS-120 images.

The results show that even dyes known for decades may hold surprises when used for fluorescence lifetime imaging. New NIR fluorophores are constantly under development [194, 195, 515]. These should be tested for environment-dependent lifetime changes and for use as possible probes for molecular environment parameters.

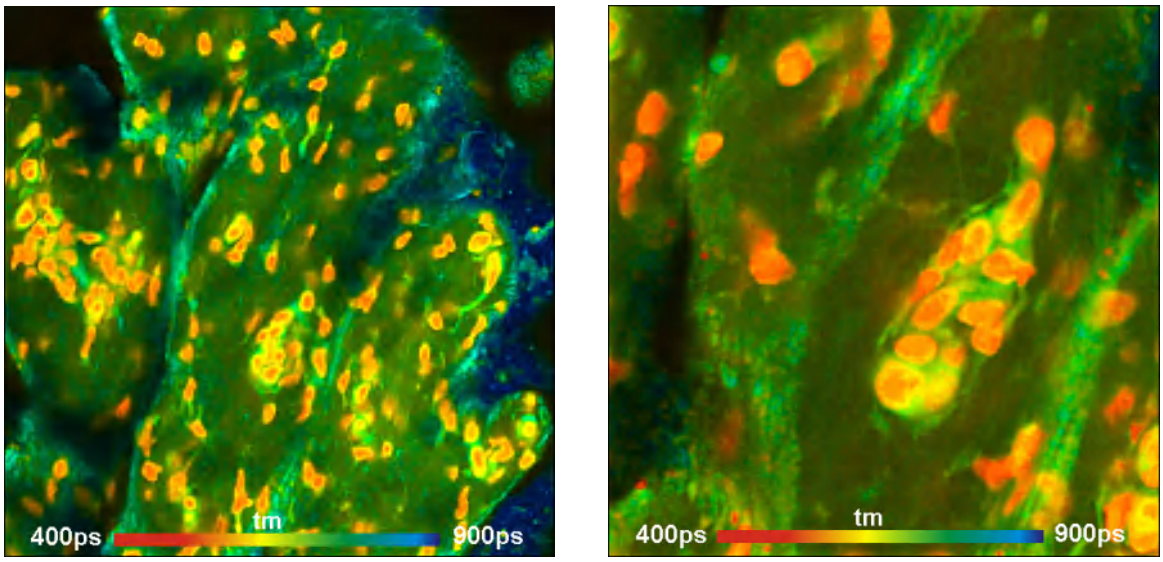


Fig. 572: Pig skin stained with Methylene Blue. LSM 710 Intune system, excitation 645 nm, detection from 660 nm up. Simple-Tau 152 FLIM system, HPM-100-50 hybrid detector. Image sizes 212 x 212µm (left) and 90 x 90µm (right)

NIR Multiphoton NDD FLIM with OPO Excitation

The excitation wavelength range of multiphoton FLIM can be extended to wavelength longer than 1000 nm by using an optical parametric oscillator (OPO) as an excitation source. A suitable system based on the LSM 710/780/880 NLO microscope family is available from Zeiss [276].

To explore the options of OPO FLIM we used this system in combination with the bh SimpleTau 150 TCSPC FLIM system. To obtain sensitivity in a wavelength range up to 900 nm the HPM-100-40 GaAsP hybrid detector of the FLIM system was replaced with an HPM-100-50 GaAs hybrid detector. The detector was attached to the NDD port of the microscope via a Zeiss T adapter [69]. To be able to detect fluorescence up to 900 nm we replaced the standard two-photon beamsplitter in the beam path at the back of the objective lens with a 980 nm dichroic mirror. The beamsplitter is not critical, an 80/20 wideband beamsplitter can be used as well. The standard 700 nm short pass (laser blocking) filter in the T adapter was replaced with a 980 nm short pass filter. The microscope objective lens was an x20/1.0 DIC VIS-IR Plan-Apochromate for water immersion.

FLIM Images with Methylen Blue

Methylene Blue has an absorption band from 550 to 690 nm, with a maximum at 660 nm. Fluorescence is emitted from 650 nm to 750 nm, with a maximum at 680 nm. It can thus be expected that two-photon excitation works well in the range from 1000 nm to 1200 nm.

A FLIM image obtained from a pig skin sample stained with Methylene Blue is shown in Fig. 573, left. The sample was excited at 1200 nm, the fluorescence was detected from 680 nm to 780 nm. Excitation was surprisingly efficient. No more than 4 percent of the available OPO power were needed to obtain a count rate on the order of 1 MHz. Decay curves from characteristic spots are shown in Fig. 573, right. The data obtained with 2-photon excitation are similar as the one-photon data shown above in Fig. 571. The decay profiles are multiexponential but can be reasonably fitted by a double-exponential decay model. The amplitude-weighted lifetime in different parts of the tissue varies by almost a factor of two.

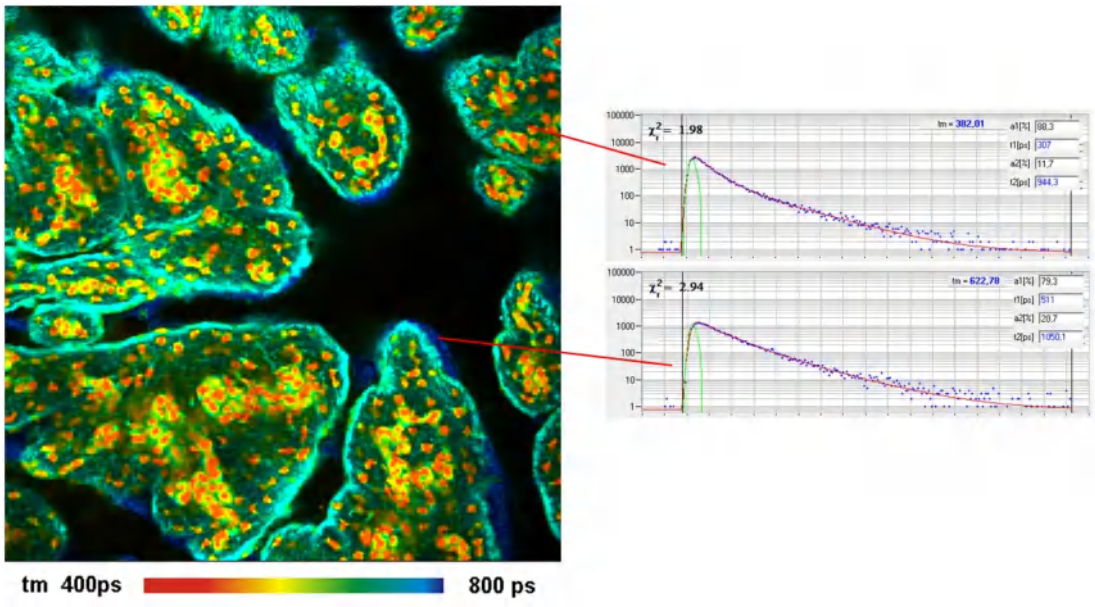


Fig. 573: Pig skin stained with Methylene Blue. Lifetime image, double-exponential decay model, amplitude-weighted lifetime, Decay curves. Two-photon excitation at 1200 nm, 512 x 512 pixels, 256 time channels.

Indocyanine Green (ICG)

FLIM Images of a similar sample stained with ICG are shown in Fig. 574. The data were analysed with a double-exponential decay model. The lifetime shown is the amplitude-weighted average of the decay components. The fluorescence was excited at 1200 nm, fluorescence was detected from 780 nm to 850 nm. As for the Methylene Blue, about 3% of the available excitation power was sufficient to obtain a count rate on the order of 1 MHz.

The range of the lifetime and its variability is in agreement with FLIM data obtained by one-photon excitation. Again, the results show that the common assumption of an essentially invariable fluorescence lifetime (and thus quantum efficiency) of ICG in biological systems is not correct.

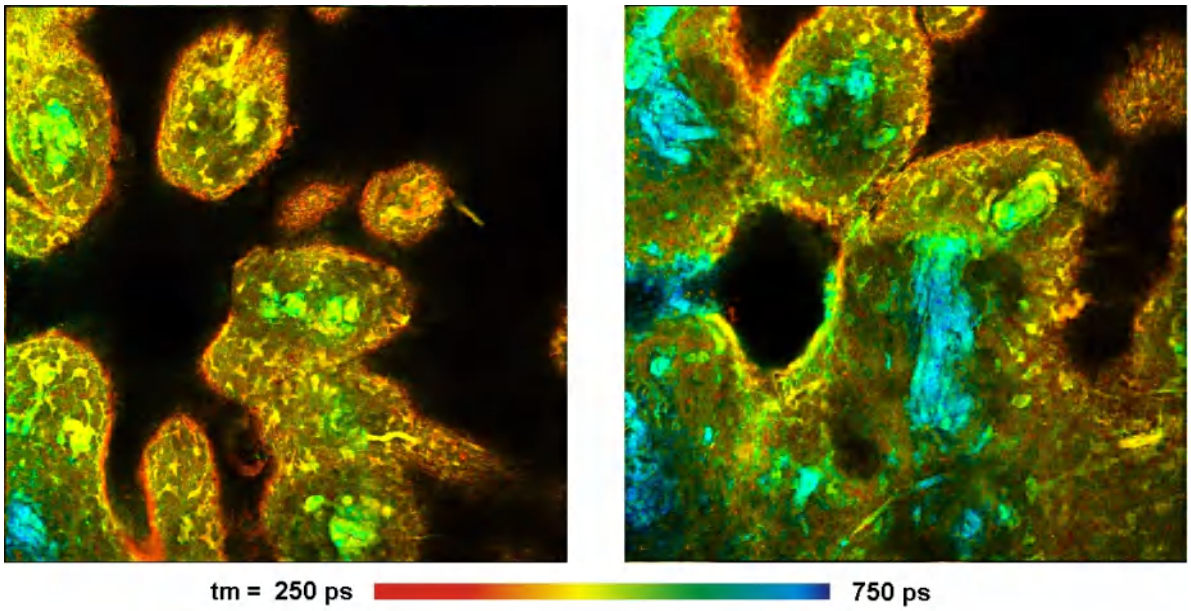


Fig. 574: Pig skin stained with Indocyanin Green. Two-photon excitation at 1200 nm, detection from 780 to 850 nm. Amplitude-weighted lifetime of double-exponential decay. Depth from top of tissue 10 µm (left) and 40 µm (right). 512 x 512 pixels, 256 time channels.

3,3'-Diethylthiatricarbocyanine (DTTCC)

A FLIM image of a pig skin sample stained with DTTCC is shown in Fig. 575. The excitation wavelength was 1200 nm, the fluorescence was detected from 780 nm to 850 nm. The excitation power was 2% of the available OPO power. The fluorescence lifetime is generally longer than for ICG. The general lifetime behaviour is the same as found for one-photon excitation. The lifetime is short where the tissue was exposed to high dye concentration. However, there is also variability inside the tissue.

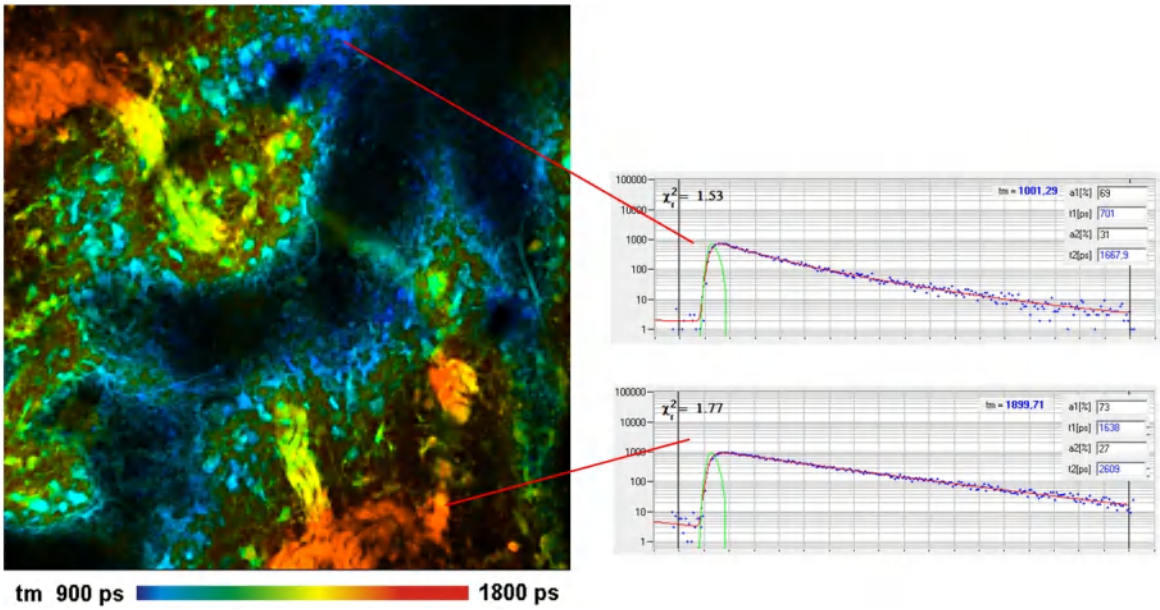


Fig. 575: Pig skin stained with DTTCC. Left: Lifetime image, amplitude-weighted lifetime of double-exponential decay model, 512 x 512 pixels, 256 time channels. Right: Decay curves in selected spots.

FLIM Z Stacks

To explore the dependence of the fluorescence decay parameters on the staining conditions we recorded FLIM Z stacks for the samples shown above. The Z stacks were recorded by the Mosaic Imaging function of the SPCM 64-bit software. Each Z stack contains 16 images from the surface of the tissue down to about 60 µm. The FLIM format for each individual Z plane is 152 x 512 pixels with 256 time channel per pixel. The results are shown in Fig. 576 through Fig. 578.

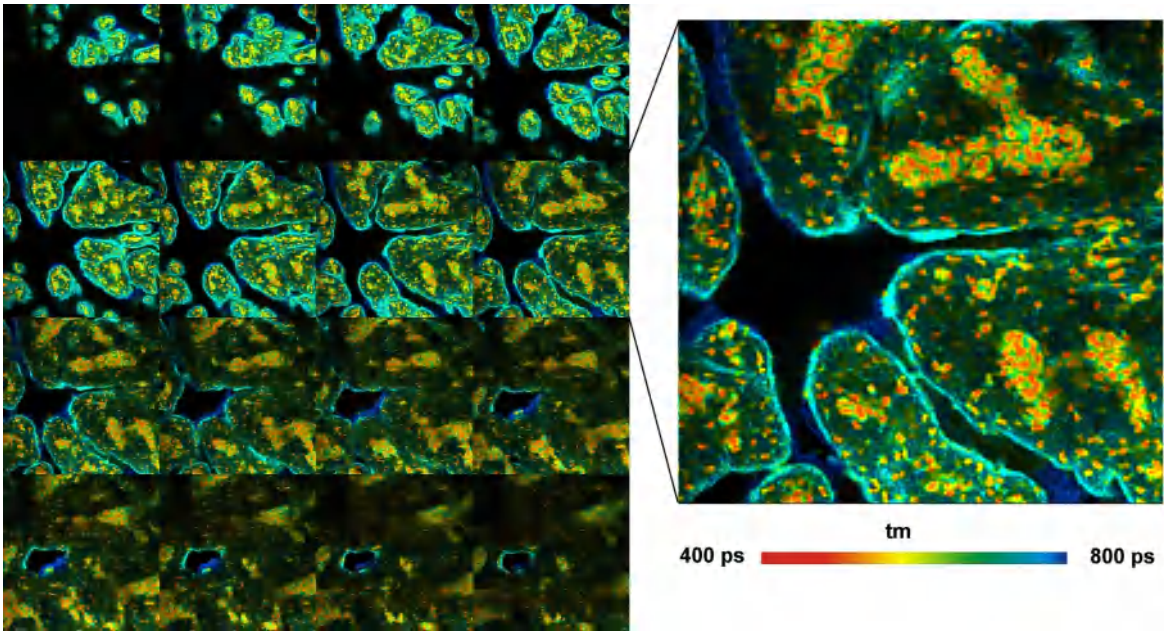


Fig. 576: Pig skin stained with Methylene Blue. Z-stack recorded by Mosaic FLIM, 16 planes from 0 to 60 µm from top of sample, each plane 512 x 512 pixels, 256 time channels. Amplitude-weighted lifetime of double-exponential decay. Plane 8 shown magnified on the right.

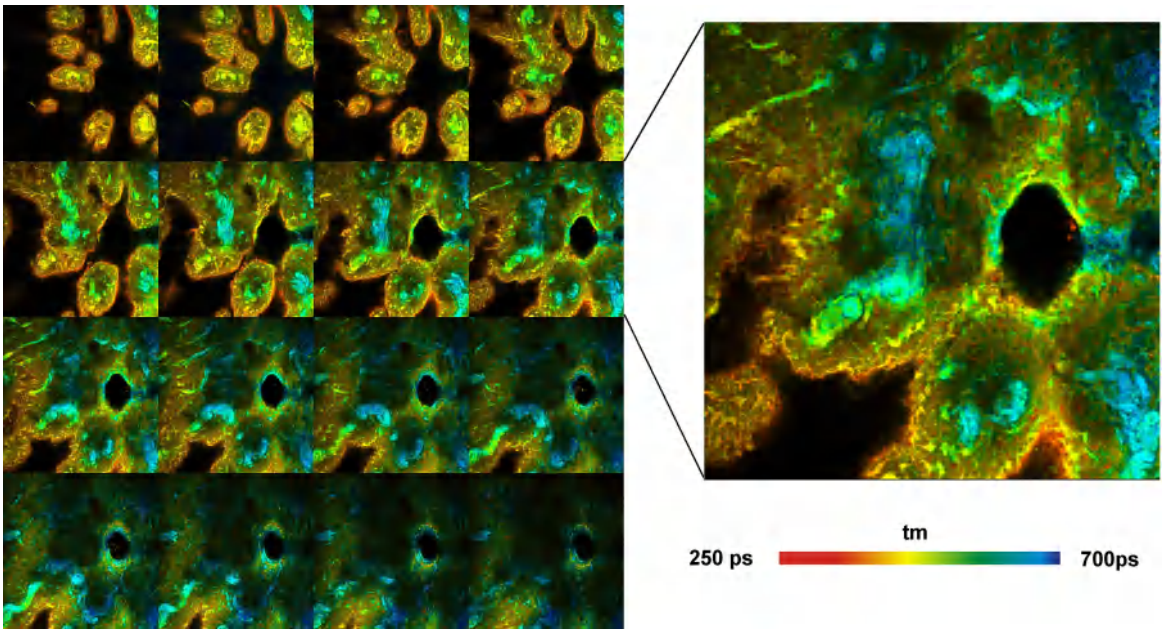


Fig. 577: Pig skin stained with Indocyanin Green. Z-stack recorded by Mosaic FLIM, 16 planes from 0 to 60 µm from top of sample, each plane 512 x 512 pixels, 256 time channels. Amplitude-weighted lifetime of double-exponential decay. Plane 8 shown magnified on the right.

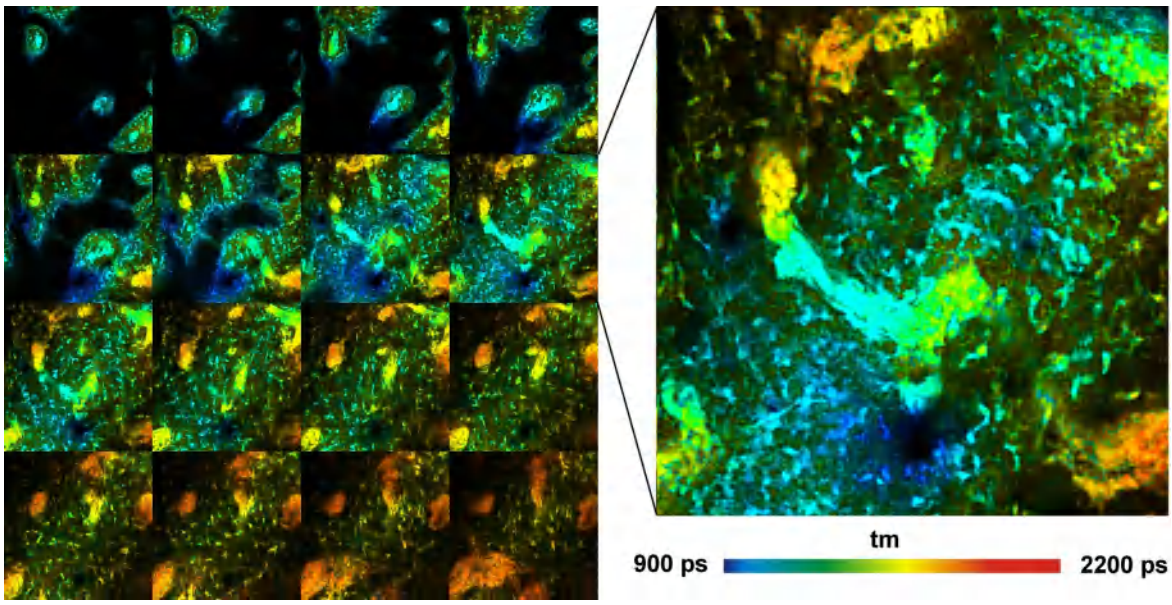


Fig. 578: Pig skin stained with DTTCC. FLIM Z stack, recorded by Mosaic FLIM, 16 planes, 0 to 60 um from top of tissue. Each element has 512 x 512 pixels and 256 time channels per pixel. Amplitude-weighted lifetime of double-exponential decay. Plane 8 shown magnified on the right.

The Z stacks show that, in the samples investigated, the lifetime changes with the depth in the tissue. We used an incubation time of only 15 minutes. It is therefore likely that the change in with the depth in the sample is caused by concentration changes or different binding efficiency due to incomplete incubation.

Infrared FLIM

Near-infrared FLIM by the optical principles described above can, in principle, be extended into the wavelength range beyond 1000 nm. Ti:Sa lasers work up to about 1000 nm, OPOs work at much longer wavelengths, and laser diodes exist for various wavelengths up to 1550 nm. To test whether fluorescence lifetime imaging at excitation and emission wavelengths above 1000 nm is possible we used the setup is shown in Fig. 579. It consists of a

Simple-Tau TCSPC system, a BDS-SM 1064 nm picosecond diode laser, a bh DCS-120 confocal scan head [68] attached to a Nikon TE 2000 microscope, and an id-220 InGaAs SPAD detector, see page 199 in the detector chapter of this book. The input face of an optical fibre (25 µm diameter) was placed in the focal plane of the first lens of the internal telescope of the DCS-120 scan head.

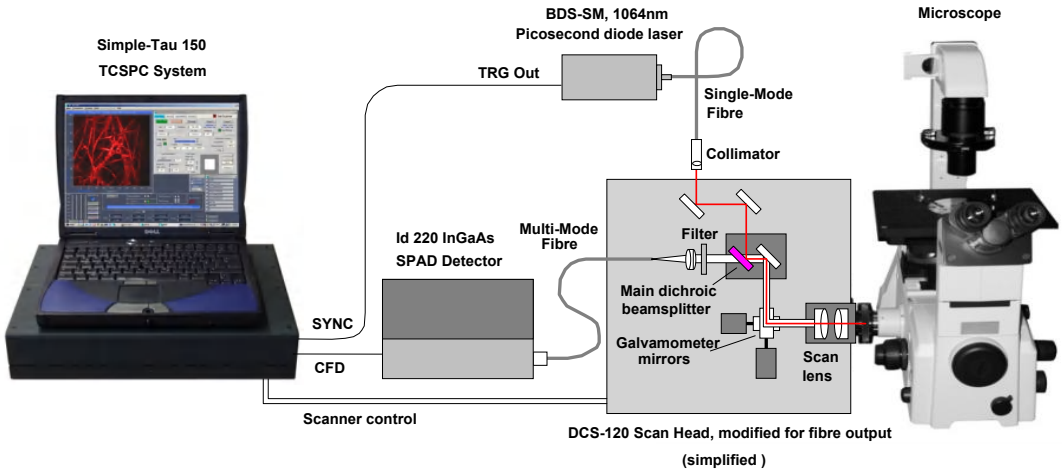


Fig. 579: Principle of FLIM setup

Technically, there was no problem to obtain a FLIM image at a detection wavelength of about 1200 nm. A result is shown in Fig. 580. The image shows cellulose fibres stained with IR 1061 from Sigma Aldrich. The image format is 512 x 512 pixels, 256 time channels per pixel. An x20, NA=0.6 microscope lens was used. The detector count rate was kept below 50 KHz to avoid saturation of the detector. The excitation power for this count rate was about 30 µW in the sample plane.

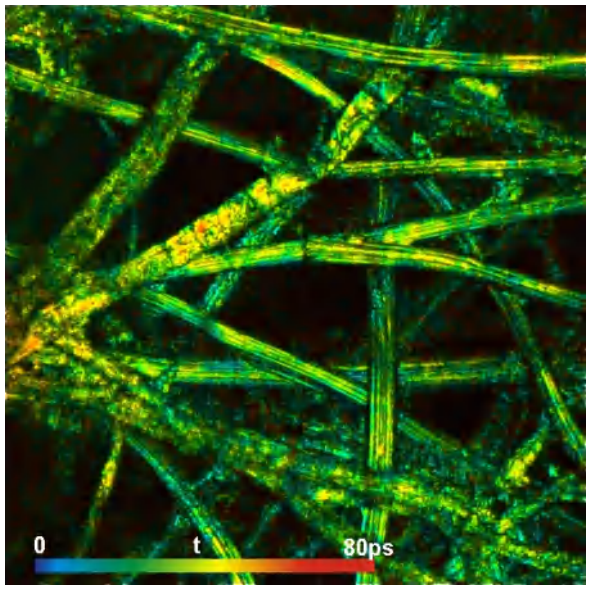


Fig. 580: Cellulose fibres, stained with IR1061 (Aldrich). Excitation 1064 nm, detection 1100 nm to 1400 nm. 512 x 512 pixels, 256 time channels per pixel. Colour represents fluorescence lifetime, lifetime range from 0 to 80 ps.

A typical decay curve from a selected pixel together with the IRF (obtained from a reflection at the cover slip) are shown in Fig. 581. The fluorescence lifetimes are extremely short. The distribution of the amplitude-weighted lifetime over the pixels peaks at about 50 ps. Nevertheless, clear lifetime differences were resolved throughout the image. This shows that both the existing optical systems and the id 220 detector are applicable to IR FLIM.

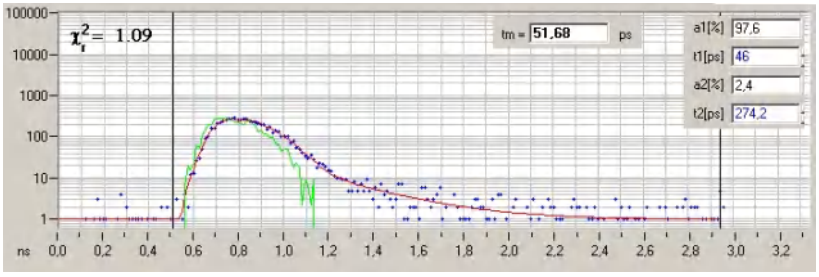


Fig. 581: Decay data (blue spots) and IRF (green) in a selected pixel

The problem of infrared FLIM are the fluorophores. There are only a few organic compounds that are known to absorb and fluoresce above 1000 nm. The fluorescence lifetimes are very short, and the fluorescence quantum efficiencies are low. Moreover, most of the dyes are not soluble in water. This makes them difficult to use in the typical FLIM applications.

Lifetime Imaging of Singlet-Oxygen Phosphorescence

Imaging of singlet-oxygen phosphorescence is a hot topic in photodynamic therapy. In principle, the intensity and the decay time of the signal show how much singlet oxygen is generated and how much it interacts with the molecular environment. In other words, singlet oxygen phosphorescence is an indicator of the efficiency of the primary step of photodynamic therapy. The problems of singlet-oxygen detection are that the intensity is very low and that the emission occurs around 1300 nm. Good detectors for this wavelength are rare. IR PMTs with suitable cathodes have low efficiency and high dark count rate. InGaAs SPADs have higher efficiency but the dark count rates are high, and afterpulsing interferes with the phosphorescence decay. Better performance can be expected from superconducting single (SSPD) NbN detectors. These detectors have high efficiency in the IR, extremely low dark count rate, and virtually no afterpulsing. The problem is the small size of the detectors, which makes it difficult to project the light on the active area. The situation is further complicated by the fact that the detector has to work at liquid-helium temperature. The only practicable solution is to couple the light into the detector by a single-mode optical fibre. This poses the problem of how to project the light from the excited spot within the sample into this fibre.

Our solution is shown in Fig. 582. The basis of the system is a modified DCS-120 scan head. In normal operation, the scan head has two laser input ports with adjustable single-mode fibre manipulators. One of these ports is used to inject the excitation laser. The laser beam is fed through the usual dichroic beam splitter, deflected by two galvanometer mirrors, and projected down the beam path of a microscope via the scan lens. The light from the sample travels back through the same beam path. Normally, it is separated from the excitation beam by the main dichroic beamsplitter and projected into the normal FLIM detectors. For singlet-oxygen detection we replaced the main beamsplitter with a mirror. The light from the sample thus travels back toward the laser ports. The beam combiner, BC, is modified to let radiation above 1000 nm pass to the second laser port. An additional filter, F, blocks residual excitation light. Light emitted by singlet oxygen in the sample arrives at the laser port. It is coupled into a single mode fibre via a normal Qioptics single mode fibre coupler. Via this fibre, it is fed into a SCONTEL SSPD detector [115, 1129]. The setup thus works as a confocal system, with the detection fibre acting as a confocal pinhole.

The recording principle is the same as described in section 'Simultaneous '. The excitation laser was on-off modulated synchronously with the pixel dwell times, and the distribution of the photons over the pixel position and the arrival time within the modulation period was built up.

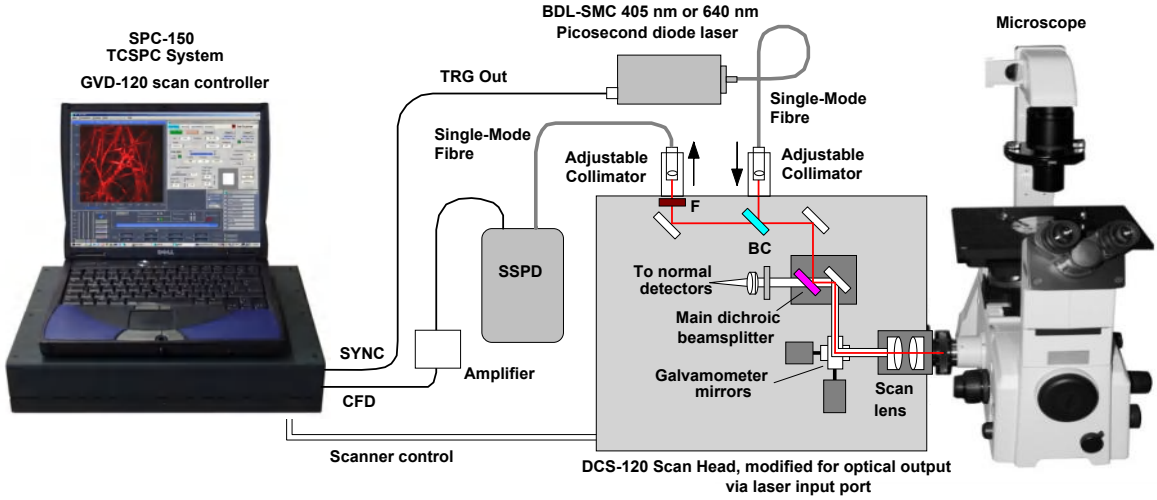


Fig. 582: Experiment setup for singlet-oxygen lifetime imaging

The system was tested with solutions of Ce6 and methylene blue, and with Ce6 in Hela cells [890]. In all cases, a weak signal of about 100 photon per second at 1300 nm was detected. The low intensity was not a problem, however, because the SSPD detector has a dark count rate of only a few counts per second. The acquisition time therefore could easily be extended to 10 minutes and more to collect enough photons. A result for a solution of methylene-blue is shown in Fig. 583. For a detailed discussion of the results please see [890].

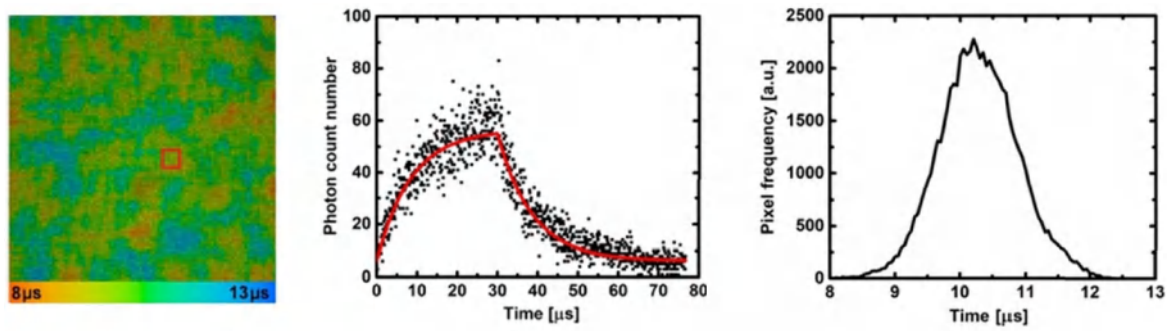


Fig. 583: Phosphorescence lifetime image of a methylene-blue solution. Colour coded image (left), waveform of the detected signal (middle) and distribution of the lifetime over the pixels of the image.

High-Speed Parallel-Channel FLIM

Most of the FLIM applications, such as FRET measurements [220], investigation of membrane proteins [358], or autofluorescence imaging [690, 1155] have in common that the fluorophore concentration is low. Moreover, the excitation power has to be kept low to avoid lifetime changes by photobleaching [589]. The count rates available from the samples are therefore on the order of 10^4 s^{-1} to 10^5 s^{-1} only. This is one to two orders of magnitude lower than the counting capability of a single TCSPC FLIM device. Consequently, the acquisition time required to achieve a given lifetime accuracy is exclusively determined by the count rate obtained from the sample, not by the counting capability of the TCSPC module. Technical efforts to increase the counting capability of the TCSPC FLIM electronics do not result in shorter acquisition times in these applications.

Count rates higher than the maximum count rate of a single TCSPC module can be obtained from demonstration samples commonly used by microscope manufacturers to demonstrate their microscopes. Although these samples produce beautiful FLIM images the results are not

very meaningful. The high dye concentration normally leads to aggregation of the dyes, and the fixing procedures change the molecular environment of the fluorophores. Both effects change the lifetimes unpredictably. The results therefore do not tell much about molecular interactions between different fluorophores or a fluorophore and its environment. At best, the results reveal the distribution of the different fluorophores in the sample.

There are, however, a few classes of FLIM experiments that can deliver high count rates. One of these is imaging of chlorophyll in plant tissue. Chlorophyll is highly photostable and emits strong fluorescence around 700 nm. The fluorescence lifetime of chlorophyll in live plants changes with the time of exposure [516]. Recording these changes requires fast FLIM [652]. Another potential application is, surprisingly, autofluorescence. Autofluorescence signals are usually weak, but exceptions do exist. Fig. 584 shows autofluorescence FLIM images of live yeast cells. The bright cells (probably apoptotic ones) are about 50 times brighter than the dim ones (visible in Fig. 584, right). Recording lifetimes for both types of cells in the same image requires the count rate of the bright cells to be kept below about 4 MHz. The count rate in the dim cells is then less than 100 kHz, resulting in long acquisition time.

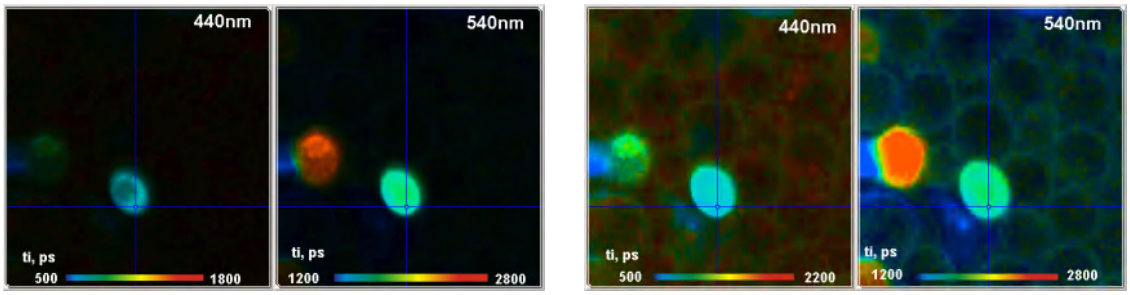


Fig. 584: FLIM images of yeast cells. Left: Intensity scale 0 to 3000 counts per pixel. Right: Intensity scale 0 to 300 counts per pixel. The bright cells are about 50 times brighter than the dim ones. Becker & Hickl DCS-120 confocal scanning FLIM system, excitation at 407 nm.

The count rate of TCSPC FLIM is limited by counting loss due to the dead time of the TCSPC electronics and the detector, and by pile-up effects, see ‘Pile-Up’, page 294. Counting loss could, in principle, be reduced by decreasing the dead time of the electronics. Pile-up-effects could be reduced by recording more than one photon per signal period. Unfortunately, both approaches have detrimental effects on the recorded decay data. Reducing the dead time increases the background caused by the afterpulsing of the detector. Recording several photons per laser period leads to an overlap of subsequent single-photon pulses and thus causes count-rate-dependent distortions of the decay curves.

A better way to increase the counting capability of TCSPC FLIM is therefore to use several parallel TCSPC channels. Currently used bh FLIM systems for the DCS-120 confocal system [68] or the Zeiss LSM 710 NLO [69] system have two parallel TCSPC channels. Both systems can reasonably be used up to a total (detected) count rate of about $10 \cdot 10^6$ s^{-1}, or a total detector count rates of $10 \cdot 10^6$ s^{-1}.Under these conditions FLIM images can be obtained in less than one second, see ‘Time-Series FLIM’, page 398.

A recorded count rates of $20 \cdot 10^6$ s^{-1}, or a detector count rate of $40 \cdot 10^6$ s^{-1}, can be reached with four-channel TCSPC systems [149]. FLIM data recorded with an SPC-144 are shown in Fig. 585. The sample was a mouse-kidney section (Molecular Probes, F-24630) stained with Alexa Fluor 488 WGA, Alexa Fluor 568 phalloidin, and DAPI. Two photon excitation at 860 nm was used. The count rate was $14 \cdot 10^6$ s^{-1}, the acquisition time 10 s. A double-exponential fit was used to analyse the data. Fig. 585 shows the mean (amplitude-weighted) lifetime and the intensity coefficient for the fast component.

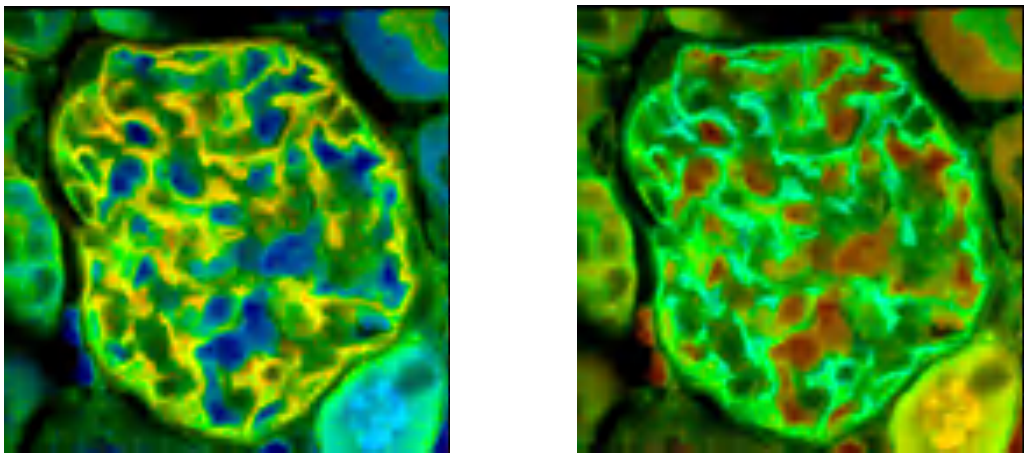


Fig. 585: FLIM recorded by a four-channel TCSPC system. Left: Colour represents the amplitude-weighted mean lifetime, blue to red = 0.7 to 1.7 ns. Right: Fraction of the fast lifetime component of double-exponential decay. The colour represents the amplitude of the fast lifetime component, blue to red = 0.1 to 0.9. bh SPC-144 with four PMH-100 detectors, Zeiss LSM 510 NLO, NA of objective lens 1.3. From [149]

It should be mentioned that the count rate of $14 \cdot 10^6$ s^{-1} was the maximum that could be obtained from the sample. The high excitation power required to reach this count rate already caused noticeable photobleaching and, consequently, changes in the observed lifetimes. Details are described in [149, 154].

The basic system components of an 8-channel parallel FLIM system [158] are shown in Fig. 586. A bh DCS-120 confocal scanner with a Nikon TE 2000 microscope was used. An LOT MS 125 polychromator was attached to one confocal output of the DCS-120 scanner. The input slit of the polychromator was removed, and the light focused into the slit plane by a lens, see Fig. 586, middle.

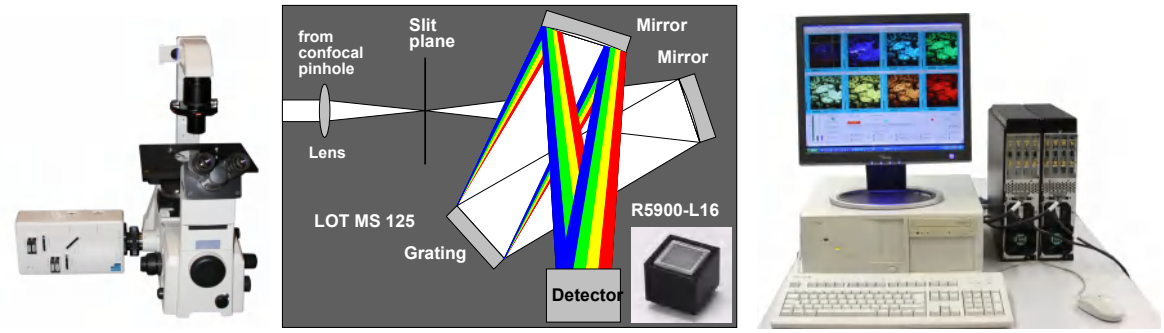


Fig. 586: Eight-channel parallel FLIM system. Left: DCS-120 scanner. Middle: Principle of spectral dispersion. Right: 8-TCSPC electronics.

The spectrum at the polychromator output was detected by a Hamamatsu R5900-L16-01 multichannel PMT. Only eight of the 16 channels of the R5900 were used; the remaining ones were terminated via 50 Ω into ground. The electronics of the 8-channel FLIM system is shown in Fig. 586, right. The system uses eight SPC-150 TCSPC modules. The modules were inserted in two bus extension boxes holding four SPC-150 modules each, see Fig. 586, right.

Fig. 587 shows wavelength-resolved autofluorescence lifetime images of a part of a drosophila eye, recorded in the setup shown above. The excitation wavelength was 407 nm, the detection wavelength was from 480 nm to 620 nm. The images show the mean lifetime (left) and the relative amplitude of the fast component of the double-exponential decay. The resolution of the FLIM data is 256 x 256 pixels x 256 time channels.

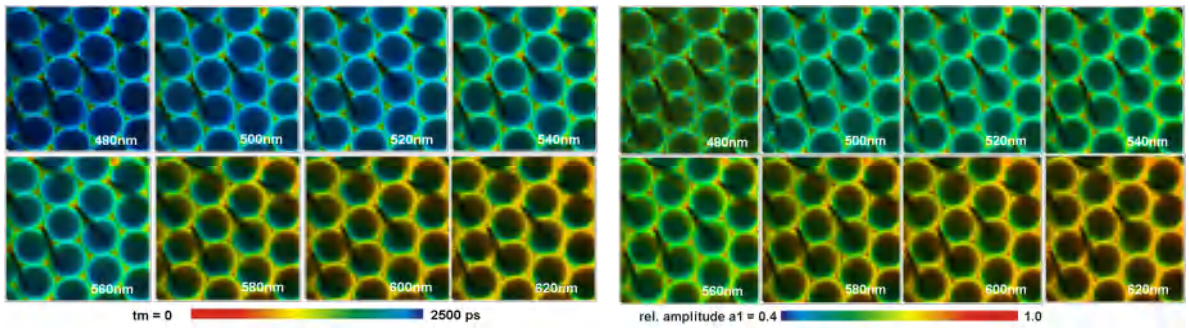


Fig. 587: Eight-channel parallel FLIM of a drosophila eye. Autofluorescence. Excitation at 407 nm, detection wavelength from 480 nm to 620 nm. Left: Mean Lifetime of double-exponential decay. Right: Relative amplitude of fast decay component. bh DCS-120 confocal scanning system.

Fig. 588 shows a time-series of wavelength-resolved FLIM data recorded at a moss leaf. The excitation wavelength was 407 nm. The images were scanned and recorded at a resolution of 256 x 256 pixels x 256 time channels. The scan rate was 4 frames per second. The detection wavelength range was from 580 nm to 720 nm. A time-series of FLIM data sets was recorded at an acquisition time of 5 seconds per step. The data were recorded in the 'FIFO imaging' mode of the SPC-150 modules. Data analysis was performed by SPCImage, see page 861. A double-exponential model was used, the lifetime was colour-coded from 200 ps (blue) to 600 ps (red). The lifetime shown is an amplitude-weighted average of the two lifetime components of the double-exponential fit. The intensity scale of all images was normalised to the intensity of the brightest pixel.

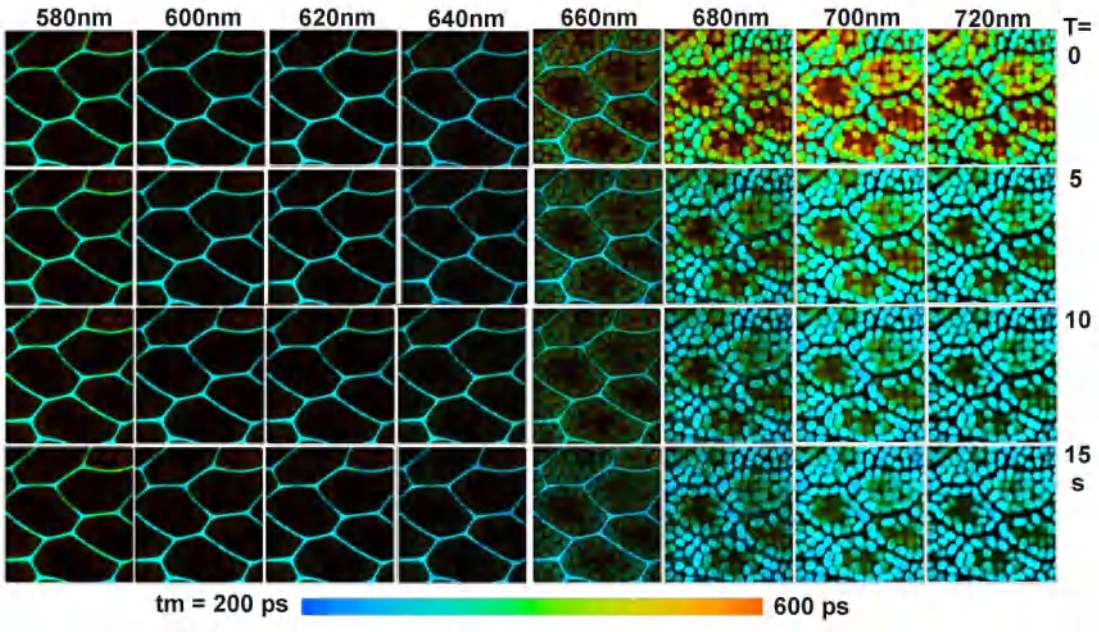


Fig. 588: FLIM images obtained from a moss leaf. Each image is 256 x 256 pixels, 256 time channels. Left to right: Wavelength, from 580 nm to 720 nm. Top to bottom: First four steps of a time series, acquisition time 5 seconds per step. Mean (amplitude weighted) lifetime of double-exponential decay.

Time-Series FLIM

Time-series FLIM is used to study the response of cells or organisms to irradiation, to a change in the chemical environment, to a temperature change, or to an electrical signal applied to it. An important application is observation of changes in the cell metabolism after induction of apoptosis or necrosis. In plant physiology chlorophyll transients can be observed and used as an indicator of the plant metabolism.

With the bh FLIM systems time-series can be recorded by using the 'Cycle' and 'Autosave' functions of the SPCM software. Provided scanning is sufficiently fast time series down to 1 or 2 seconds per image can be obtained this way. The individual steps of the measurement sequence can be triggered to obtain a 'microscope controlled time series' as described in [69].

Fig. 589 shows a time series of autofluorescence lifetime images of an amoeba. A DCS-120 system was used to acquire the data, the scan format was 128 x 128 pixels at a frame rate of 4 frames per second. The FLIM acquisition time was 0.5 second per image, i.e. two frames were accumulated into one FLIM data set. The FLIM image rate was 1 image per second, the FLIM data format 128 x 128 pixels x 64 time channels.

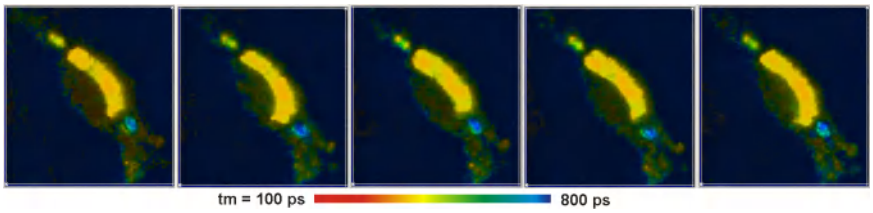


Fig. 589: Lifetime images of an amoeba, recorded at a rate of 1 image per second. Excitation 405 nm, autofluorescence. DCS-120 confocal scanning FLIM system.

Fig. 590 shows chloroplasts in moss leaf. A time series was started with the start of the illumination, and recorded at a speed of one image every two seconds. Due to the Kautsky effect [516, 517, 649, 834] the fluorescence lifetime of the chloroplasts decreases with the time of exposure. The decrease of the fluorescence lifetime can easily be seen in Fig. 590.

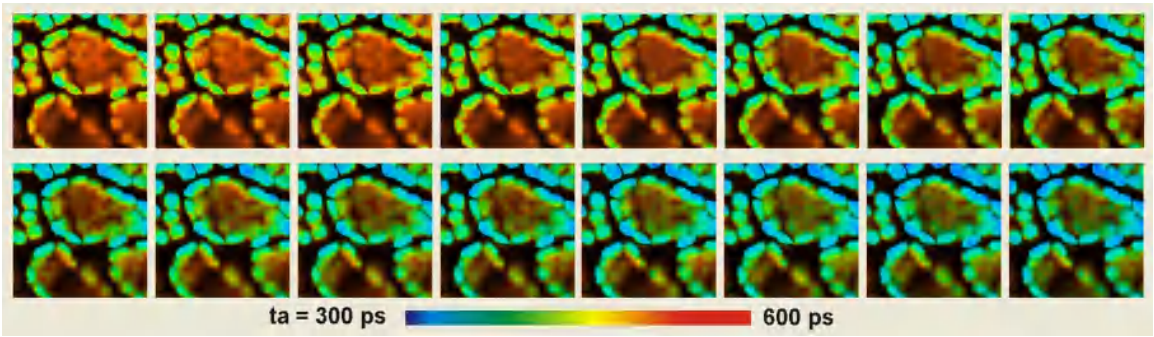


Fig. 590: Time series of the non-photochemical chlorophyll transient in the chloroplasts of a moss leaf. Recorded by a DCS-120 system, 2 seconds per image.

Relatively little has been published about applications of time-series FLIM, possibly because the possibility of obtaining fast image sequences is not commonly known. However, procedures like the ones above have been used by Bosch et al. [239] to record a sequence of FRET images during re-organisation of postsynaptic substructures in neurons, and by Iwai et. al. 612 during state transitions in the photosystem II in plant cells.

Faster sequences than with the procedure shown above can be obtained by using the 'Continuous Flow' imaging capability of the SPC-150 modules. In the Continuous Flow Imaging mode the memory of the SPC-150 is split into two halves or 'banks'. While the recording runs in one bank of the memory the data of the other bank are read. After each cycle the memory banks are swapped and the process continues. Thus, images are obtained without any time gaps caused by the save operations between the recordings [652]. The disadvantage is that the image size is restricted to pixel number of less than 128 x 128.

Another way to obtain fast time series is to use Temporal Mosaic FLIM. With triggered temporal mosaic FLIM dynamic lifetime effects can be recorded at speed that is only limited by the speed of the scanner. Please see 'Triggered Temporal Mosaic FLIM' page 409.

Mosaic FLIM

Mosaic FLIM was introduced with the transition from 32-bit to 64-bit software in 2014. Originally, it was intended only to record images larger than the maximum field diameter of the microscope lens laser scanning microscopes. However, it turned out soon that Mosaic FLIM can do much more than that: It is a way to record images from the same sample for different x-y positions, different z positions, different wavelengths, or different times in a series of recordings. By triggering a series of recordings in combination with repetitive stimulation of the sample it is even able to record time series at a speed in the millisecond range without the need of excessively high photon rate. All these techniques have in common that a large number of FLIM images with different values of an independent parameter are recorded into a single photon distribution. In other words, Mosaic FLIM is a way of recording multi-dimensional FLIM data.

Lateral Mosaic FLIM

The microscope scans an image at one position of the sample, then offsets the sample by the size of the scan area, and scans a new image. The process is repeated, and the images of the individual frames are stitched together. This way, a sample area larger than the field of view of the microscope lens is imaged. The general procedure is known from standard microscopy as ‘tile imaging’. An example of Mosaic FLIM with a Zeiss LSM 710 is shown in Fig. 591.

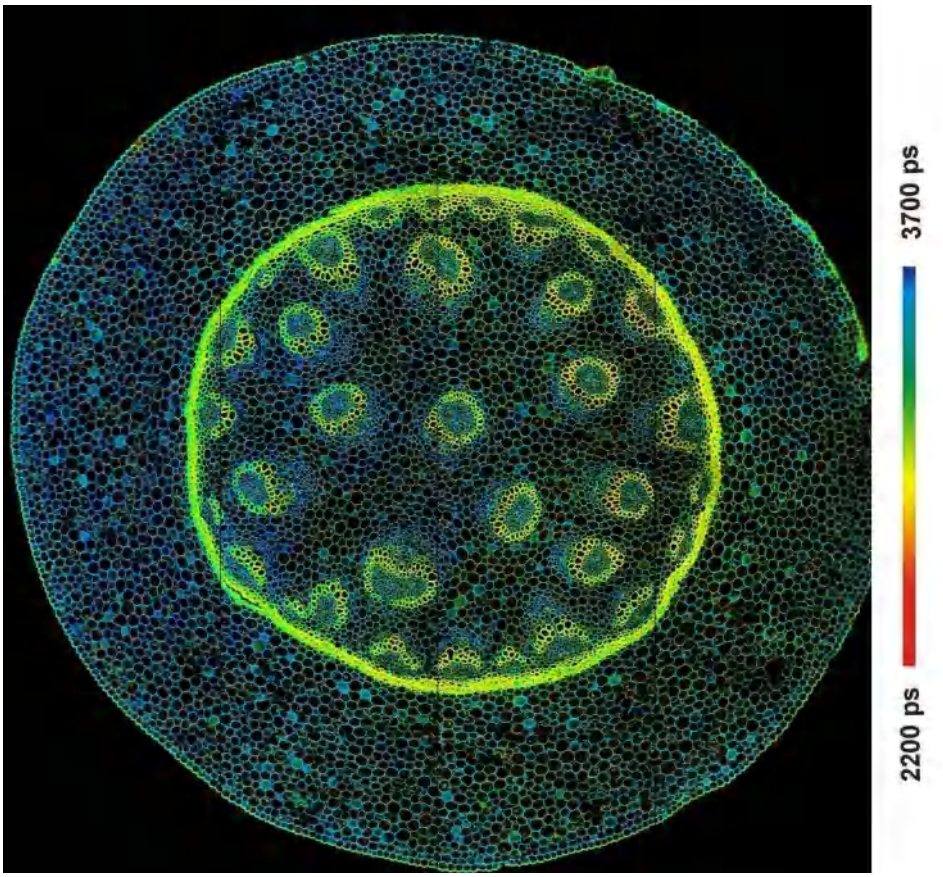


Fig. 591: Mosaic FLIM of a Convallaria sample. The mosaic has 4x4 elements, each element has 512 x 512 pixels, each pixel has 256 time channels. Zeiss LSM 710 Intune system with bh Simple-Tau 150 FLIM system.

The mosaic has 4 x 4 elements, each element has 512 x 512 pixels with 256 time channels. The complete mosaic has thus 2048 x 2048 pixels, each pixel holding 256 time channels. The sample area covered by the mosaic is 2.5 mm x 2.5 mm.

Z Stack Mosaic Imaging

A FLIM Mosaic can be recorded at the same lateral (x-y) position but for different Z positions. The data then represent a FLIM Z stack. The data set can be considered a photon distribution over x, y, z, and the times of the photons, t, after the excitation pulses. A Z stack recorded by Mosaic Imaging is shown in Fig. 592. The individual mosaic elements represent FLIM images in subsequent layers of the sample. The image on the right shows an image of one of the planes at larger scale. Another example is shown in Fig. 576, page 391.

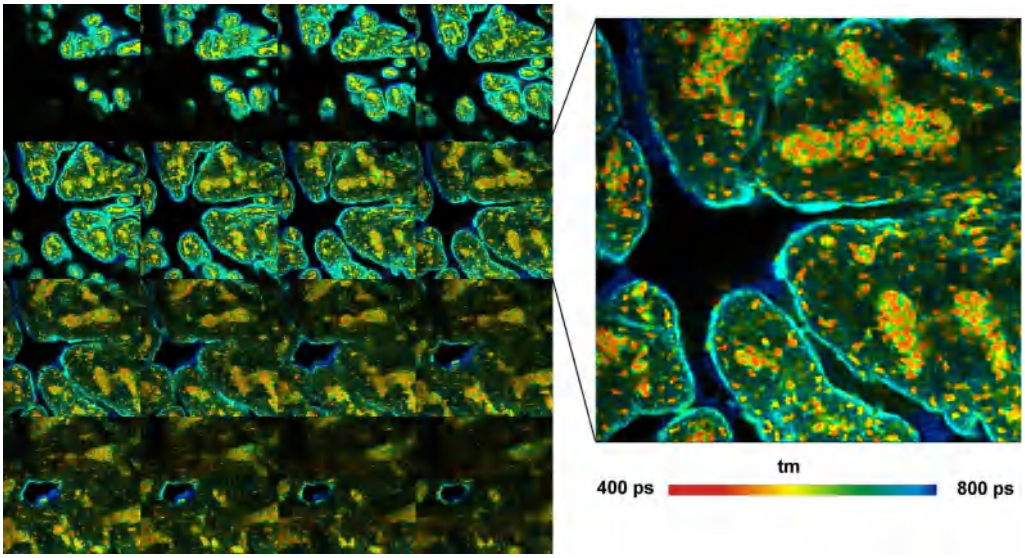


Fig. 592: Z stack of a pig skin sample stained with methylen blue

The advantage is that the entire Z stack can be analysed like a single FLIM image. This makes it easier to maintain identical fit conditions over all planes of the stack. It is also possible to run phasor analysis over the entire stack to find structures of similar decay signature and extract them for further analysis.

Multi-Wavelength Mosaic

Multi-wavelength FLIM data can be recorded in the format of a FLIM Mosaic. An example is shown in Fig. 593.

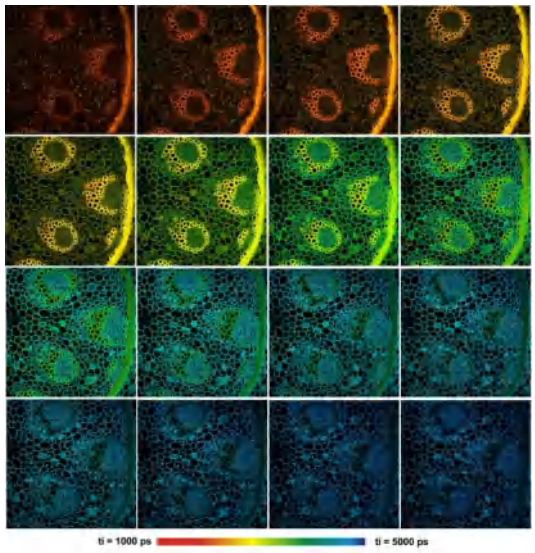


Fig. 593: Multi-wavelength FLIM recorded as Mosaic FLIM data

As for a FLIM Z stack, the entire data set can be analysed in one analysis run with identical fit parameters, and further scrutinised by the phasor plot.

Temporal Mosaic FLIM

Fast Time Series of FLIM Images

Mosaic FLIM also provides a new, extremely efficient way to record fast FLIM time series. The principle of Mosaic FLIM is described in Section Mosaic FLIM, page 127. The photons of subsequent frames (or several frames averaged) are recorded in consecutive elements of the FLIM mosaic. The result is a time series, the time step of which is the frame time or a multiple of it.

An example is shown in Fig. 594. The sample was a fresh moss leaf, the microscope a bh DCS-120 confocal FLIM system. The time runs from lower left to upper right. The excitation light causes a non-photochemical transient in the chlorophyll fluorescence [516, 517, 649], resulting in a decrease in the fluorescence lifetime with the time of exposure.

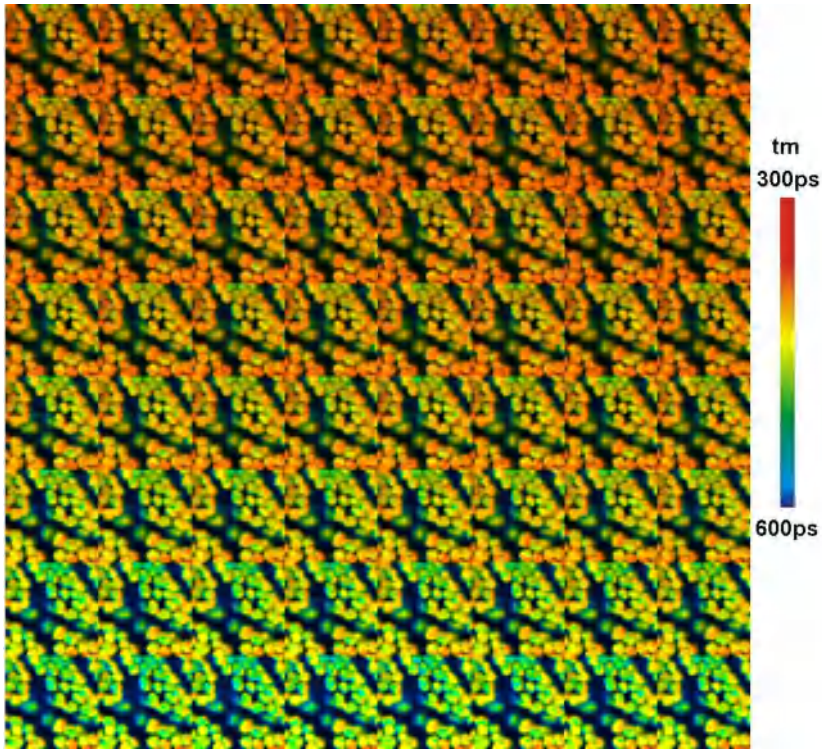


Fig. 594: Time series recorded by mosaic imaging. Non-photochemical transients in chloroplasts of a moss leaf. 64 mosaic elements for consecutive times after turn-on of excitation light. Acquisition time per element 1 second, total time of sequence 64 seconds, image size of each element 128 x 128 pixels, 256 time channels. Time runs from lower left to upper right. bh DCS-120 confocal FLIM system with SPC-150 TCSPC modules, SPCImage data analysis software.

Mosaic time-series recording has several advantages over the conventional record-and-save procedure. First, the transition from one mosaic element to the next occurs instantaneously. No time has to be reserved for saving the data of the individual steps of the series. Moreover, the result is not a sequence of files but single, large photon distribution. Standard functions of SPCImage NG (see SPCImage NG Data Analysis Software, page 861), such as analysis with fixed component lifetimes, global parameters, or analysis by the phasor plot can therefore applied to the data. Fig. 595 shows a phasor plot of the mosaic shown in the figure above. It shows the trajectory the system is taking in the phasor space. Interestingly, the trajectory remains close to the semicircle of the phasor plot, which means the fluorescence decay remains close to single exponential over the entire chlorophyll transient.

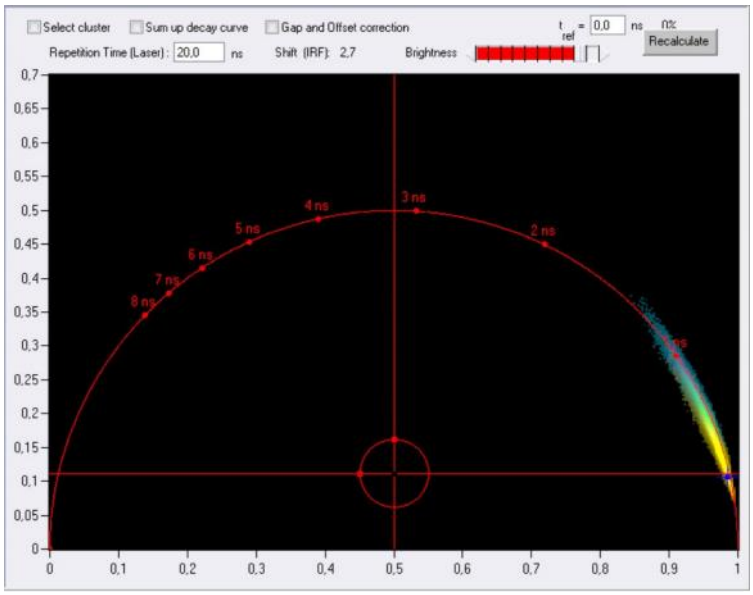


Fig. 595: Phasor plot of the mosaic time series in Fig. 594. The fluorescence decay remains close to single exponential over the entire chlorophyll transient.

Accumulation of Temporal FLIM Data

The most important advantage of temporal mosaic FLIM is that the data can be accumulated: A sample would be repeatedly stimulated by an external event, and the start of the mosaic recording be triggered by the stimulation. With every new stimulation the recording procedure runs through all elements of the mosaic, and accumulates the photons. Accumulation allows data to be recorded without the need of trading photon number and lifetime accuracy against the speed of the time series. Consequently, the time per step (or mosaic element) is only limited by the minimum frame time of the scanner. Please see 'Fast FLIM Techniques', page 409.

Moving Objects

Motion in live samples is the nightmare of any FLIM user. To acquire enough photons for precision decay analysis a large number of frames have to be accumulated. This is no problem as long as the objects in the sample stay in place for the entire acquisition time. However, if the objects under investigation are moving, as many bacteria do, the image is smeared out, and the decay data of the bacteria are mixed with signals from the substrate.

An example is shown in Fig. 596. The images show live *Escherichia coli* bacteria on the substrate they were cultured on. The data were recorded with a bh DCS-120 MP Fibre-Laser multiphoton FLIM system at 785 nm excitation wavelength. The bacteria are extremely mobile. Recorded at an acquisition time of 1.5 seconds, live bacteria are marginally visible as green-yellow spots, but there are not enough photons for reasonable lifetime analysis. Another problem that shows up in Fig. 596 is background fluorescence from the substrate. For immobile objects it is suppressed by the depth resolution of the two-photon excitation process. For objects that move during the acquisition, however, fluorescence of the background is mixed into the fluorescence of the objects. Therefore immobile (dead) bacteria stand out as blue spots in the image while the live bacteria are visible only with difficulty.

With the acquisition time increased to 24 seconds (Fig. 596, right) the motion has totally smeared out all image detail. Only dead bacteria are still visible as blue spots.

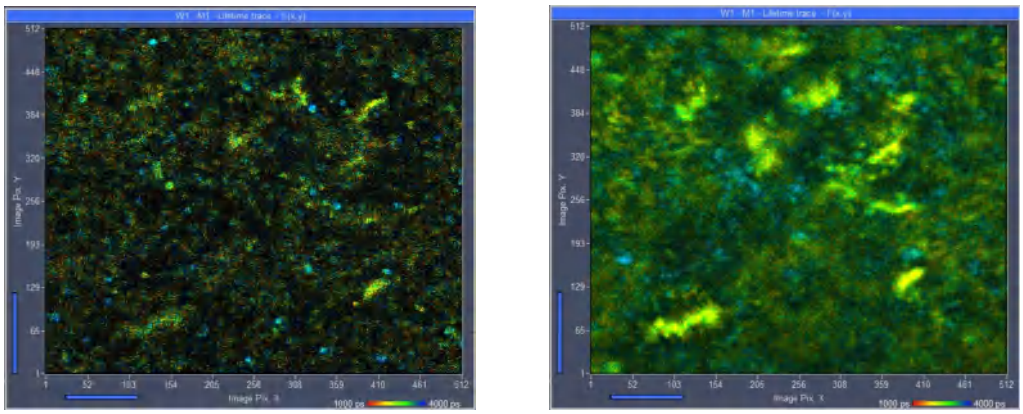


Fig. 596: Left: *Escherichia coli* bacteria culture, single scan of 1.5 second duration. Live bacteria are marginally visible as green-yellow spots, but there are not enough photons for accurate decay analysis. Right: Same sample, acquisition time 24 s. There are enough photons per pixel but motion has rendered the bacteria invisible.

It is usually attempted to solve the problem by increasing the excitation power. Higher excitation power yields, of course, a higher rate of fluorescence photons and thus a better image in a limited period of time. But this comes at a price. Fig. 597 shows a recording with 2.5 times increased excitation power. This leads to a 6.52 fold increase in photon rate. No doubt bacteria are better visible than in Fig. 596, but a large number of spots with extremely short lifetimes (red in the image) have appeared. These are burn marks which indicate that severe photodamage has occurred. Of course, there are still bacteria which appear to be intact. However, with severe photodamage present nearby, the decay data and, especially, the metabolic information derived from them cannot be trusted.

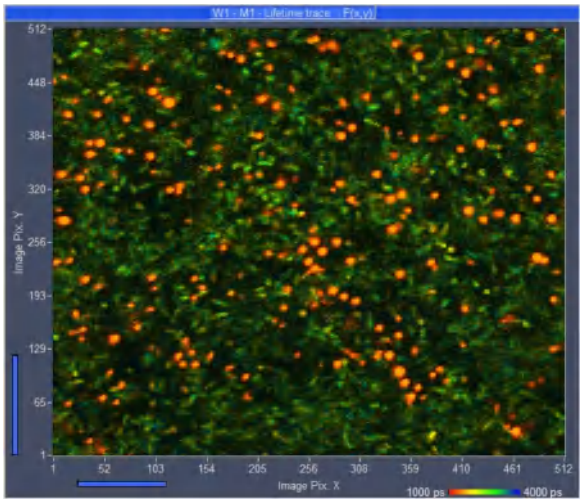


Fig. 597: FLIM recording at 2.5 x increased laser power. The red spots of ultra-short lifetime indicate sample damage. Online-lifetime display of SPCM, red to blue = 1 ns to 4 ns.

A solution to the problem is Mosaic FLIM. A mosaic of FLIM images is recorded at moderate excitation power and with an acquisition time of about 0.5 second per mosaic element. The result is shown in Fig. 598.

The entire mosaic is then loaded into SPCImage NG, a preliminary FLIM analysis is performed, and the phasor plot is opened, see Fig. 599. The phasor range occupied by the bacteria is selected and the photons of the corresponding pixels are summed up, see Fig. 599. The result is a decay curve of excellent accuracy. A fit with a triple-exponential model delivers the decay parameters of the bacteria, see Fig. 600, upper right. The fit even splits the slow fluorescence into two decay components, known to come from bound NADH and bound NADPH [225].

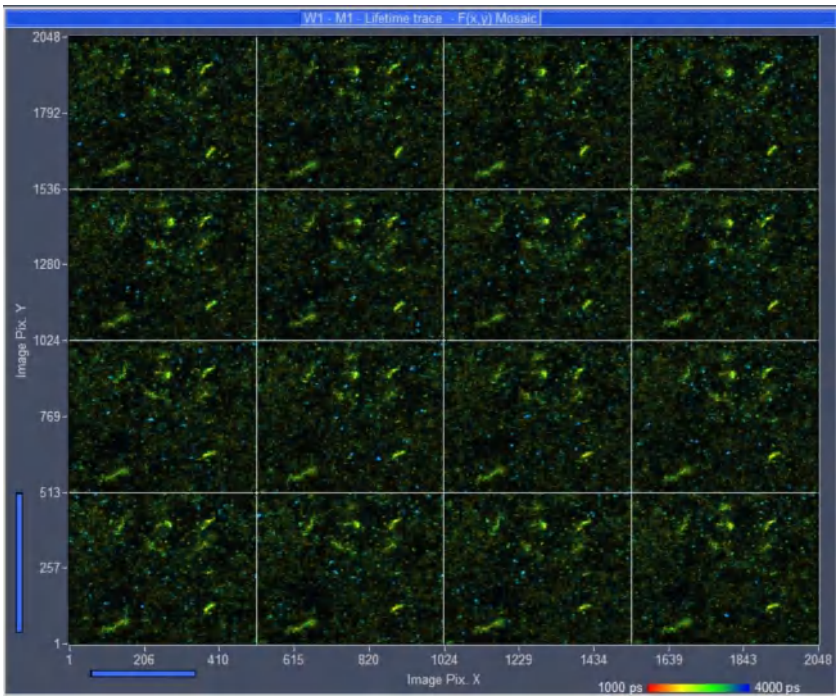


Fig. 598: 4x4 Mosaic of single scans, recorded by Mosaic Imaging function of SPCM data acquisition software. Displayed by online-lifetime function of SPCM.

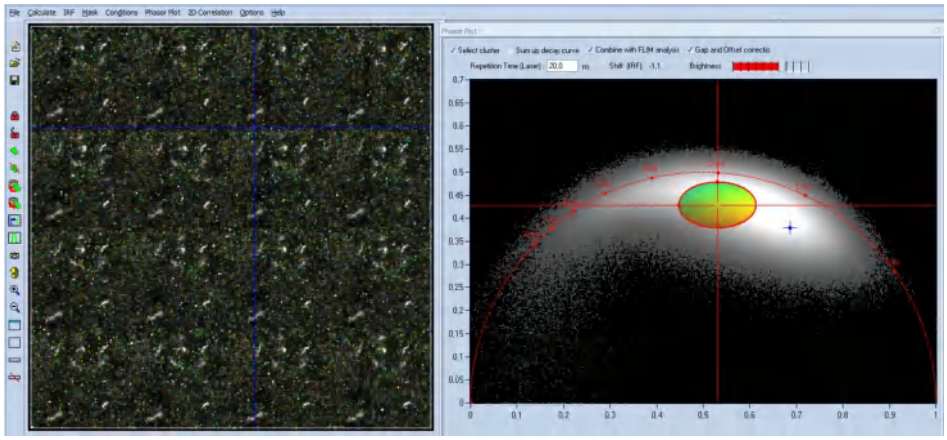


Fig. 599: 4x4 mosaic, loaded into SPCImage NG. Phasor plot enabled, phasor range of bacteria selected, selected pixels back-annotated in the FLIM image.

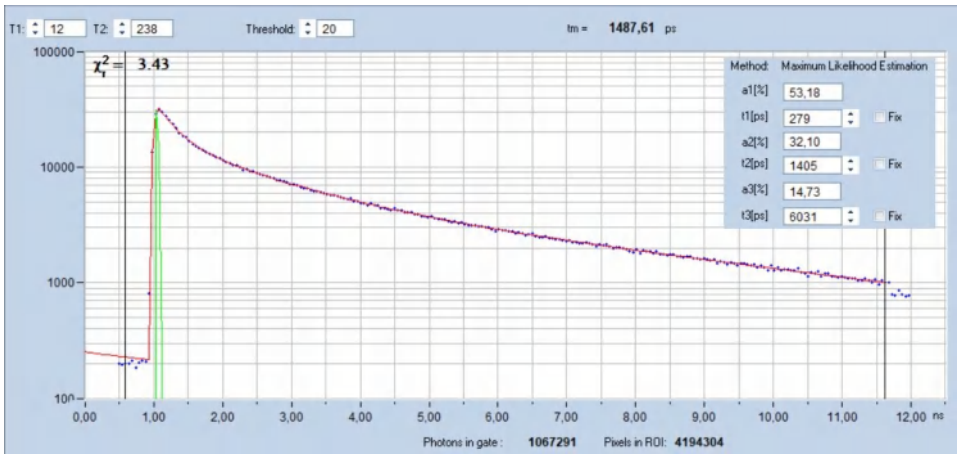


Fig. 600: Decay curve obtained by summing up decay data of pixels selected by phasor plot. Fit with SPCImage NG, triple-exponential 'incomplete-decay' model. Total number of photons 1,067,291, Decay parameters shown upper right.

Z Stack FLIM by Record-and-Save Procedure

The recording of Z stacks of images, or 'Z scanning' has been early introduced into confocal and multiphoton laser scanning microscopes [952]. The microscope scans one image plane, saves the image data, changes the depth of the focus, and scans another plane. The process is continued until the desired number of planes have been scanned, see Fig. 601. Ideally, a sufficiently large number of closely spaced z planes would be scanned to allow the three-dimensional structure of the sample to be reconstructed.

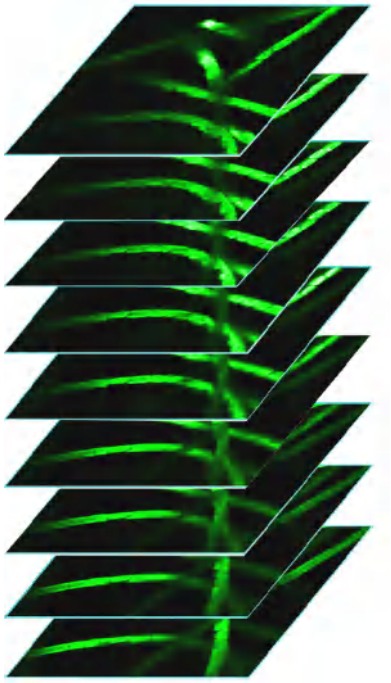


Fig. 601: Z stack of algae, recorded by bh FLIM system, intensity im-

Z stack recording faces two major problems. First, the maximum depth in the sample from which a reasonable image can be obtained is limited by absorption, scattering, refractive-index mismatch and refractive index inhomogeneity. Second, scanning a large number of planes exposes the sample to a high excitation dose. Photobleaching is therefore a severe limitation. Both problems are mitigated by using two-photon excitation. Absorption at NIR wavelengths is usually low, and scattered excitation light can be collected by non-descanned detection. Different than for one-photon excitation, photobleaching is restricted to the focal plane. Although two-photon excitation causes increased photobleaching in the focal plane [391] the total amount of bleaching for a large number of Z planes is usually lower than for one-photon excitation [405].

Despite these improvements, photobleaching has been a severe obstacle to the introduction of Z stack recording in early FLIM systems. Although FLIM data are obtained from a given number of photons at the same accuracy as intensity data FLIM usually requires a larger number of photons per pixel [154]. Moreover, a moderate amount of photobleaching can usually be tolerated for the reconstruction of spatial structures. In FLIM, however, photobleaching can cause unpredictable lifetime changes, see Fig. 693, page 473. A breakthrough came with the HPM-100-40 hybrid detectors by bh in 2009. With this detector, FLIM data are obtained at a 10 times lower sample emission rate than for the PMTs used before. Photobleaching is therefore no longer a severe problem.

Recording with Z-Plane Trigger

For recording Z stacks the recording of subsequent FLIM images has to be synchronised with the Z stepping in the microscope. For the Zeiss LSM 710 to 980 family microscopes the synchronisation problem has been solved by delivering a Z-plane trigger output to the FLIM system. The principle of the synchronisation is shown in Fig. 602.

Z stack acquisition is achieved by using the experiment trigger and autosave functions of the bh FLIM system in combination with the Z stepping and frame accumulation function of the Zeiss LSM 710. The LSM 710 real-time computer sends a plane trigger to the bh SPC-150 modules when it starts to scan a plane. Each plane is scanned repetitively, typically 4 to 16 times. The number of frames per plane, the frame time, the z step width, and the number of Z planes to be scanned is defined in the ZEN software of the LSM 710. For each plane, the FLIM system acquires FLIM data for a defined 'collection time'. The FLIM acquisition for the individual planes is synchronised the usual way via the frame clock, line clock, and pixel

clock pulses. When the collection time is over the FLIM system stops the acquisition, saves the data into a file, and waits for the next plane trigger. The acquisition continues for a number of Z planes defined by the 'cycles' parameter in the SPCM software of the FLIM system. For details of system parameter setup please see [69].

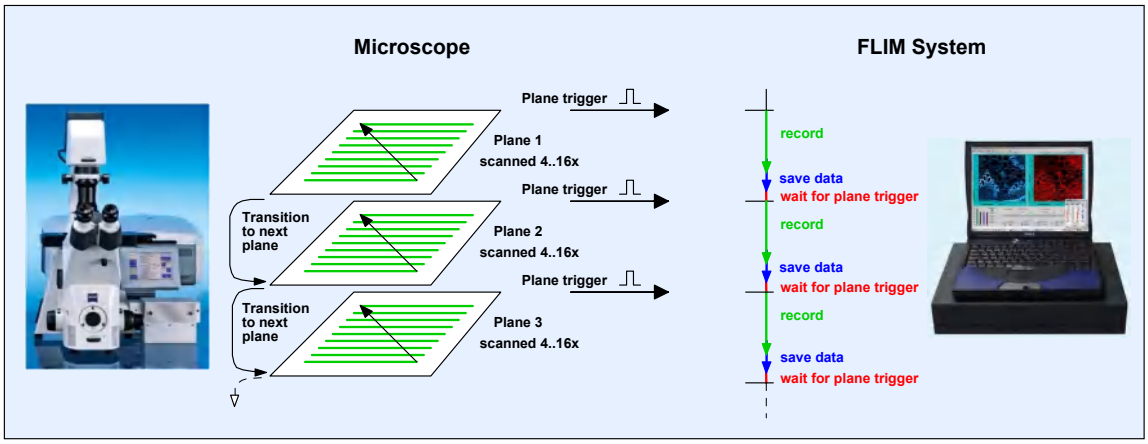


Fig. 602: Synchronisation of the FLIM system with the Z stepping

Typical results are shown in Fig. 603 and Fig. 604. Images of an (unstained) pig skin sample were recorded by a dual-channel FLIM system in an LSM 710 NLO multiphoton microscope. HPM-100-40 hybrid detectors were used at the 0° and the 90° output of the NDD T-Adapter of the LSM 710. A beamsplitter was used to simultaneously record images below and above 480 nm. The excitation wavelength was 800 nm, the laser power 2.4 %. A water apochromate 40 x, NA=1.1 was used; the scan area was 212 x 212 µm. The FLIM images of each plane were acquired at a resolution of 256 x 256 pixels and 256 time channels. The Z step interval chosen in the ZEN software was 5.09 µm. The total scan time per plane was 25 seconds. The collection time of the FLIM system was 20 seconds, i.e. 5 seconds were spared for saving the data and waiting for the next plane trigger. Fig. 603 shows the FLIM images in the wavelength interval from 480 nm to 600 nm. The intensity of the images was normalised to the intensity of the brightest pixel.

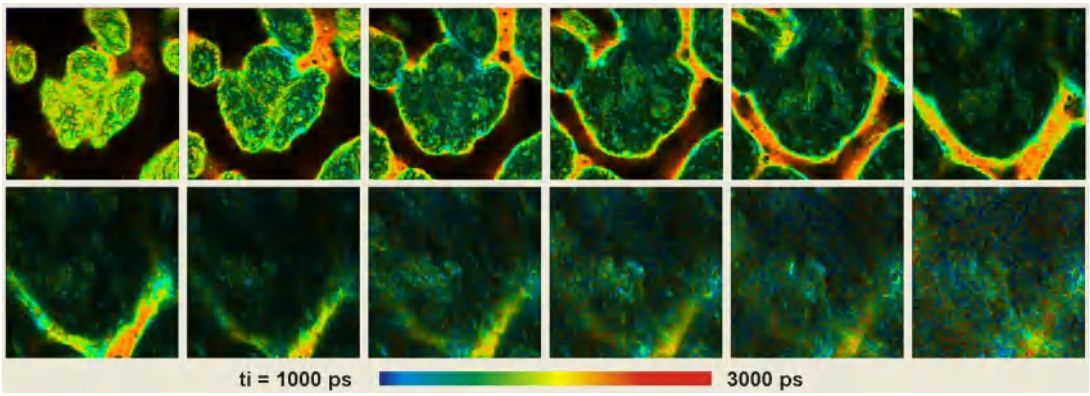


Fig. 603: FLIM Z stack recorded at a pig skin sample, Images from 5 µm to about 60µm below the surface. Intensity-weighted lifetime of a double-exponential fit. FLIM data format 256 x256 pixels, 256 time channels.

Fig. 604 shows data recorded in the wavelength interval below 480 nm. The data recorded in this interval contain both fluorescence and SHG. The SHG signal can be extracted from these data by selecting the signal component of infinitely short lifetime. Fig. 604 shows SHG images extracted from the FLIM data this way. The intensities were normalised to the intensity in the brightest pixel.

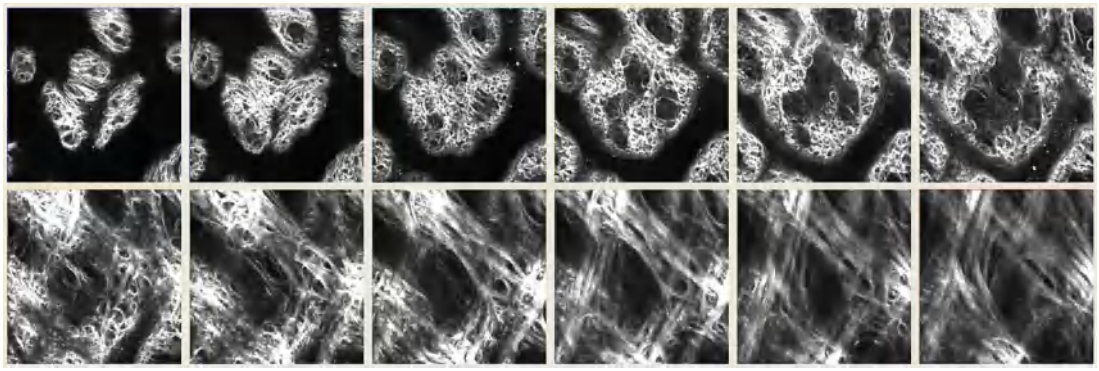


Fig. 604: Z stack recorded at a pig skin sample, excitation at 800 nm, emission below 480 nm, SHG signal, extracted by selecting photons in an early time window. Z step width is 5.09 µm, scan area 212 x 212 µm. Images from 5 µm to 60 µm depth.

Z Stack FLIM by Integrated Microscope Control

The procedure described above requires that each plane is scanned repetitively for a defined number of frames, and that the collection time of the FLIM system is made a bit shorter than the total scan time to reserve time for saving the data. Because the microscope and the FLIM systems have separate software it can be difficult to set the correct parameters. Another disadvantage is that at least one frame per plane remains unused during the time when the data are saved. A better solution is therefore to integrate the scanner and microscope control together with the FLIM data acquisition in one piece of software. Exactly this solution is implemented in the bh DCS-120 system, see Fig. 605. With the parameter shown, the system records 100 Z planes with a step width of 1 µm. The collection time is 10 seconds per plane.

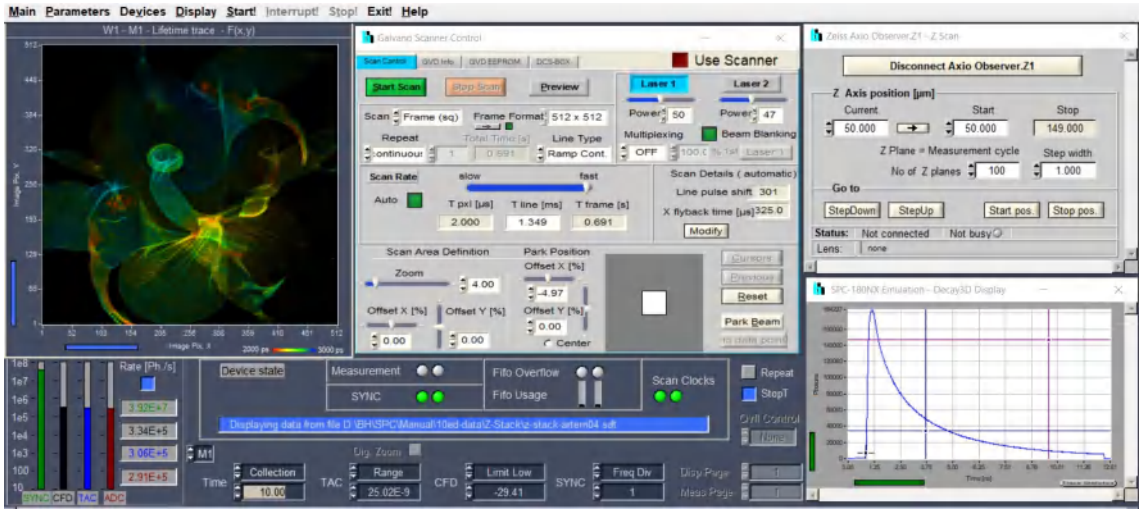


Fig. 605: S-Stack recording with the DCS-120, Axio-Observer version. 100 Z planes, 1µm per plane.

A typical result is shown in Fig. 606. A Drosophila fly was scanned with 100 planes of 512 x 512 pixels each. The files of the subsequent frames were loaded in SPCImage NG, processed by the Batch-Processing function, and exported into 100 tif files. These were loaded into Image J software and converted into the three-dimensional animation shown in Fig. 606.

Another integrated Z Stack procedure is available in the bh / Zeiss Zeiss FLIM systems. These systems are available with bh's new integrated SPCConnect software. SPCConnect combines bh SPCM software and Zeiss ZEN software by a TCP (Transmission Control Protocol). That means SPCM is running in the frame of ZEN, with both components freely ex-

changing commands, system parameters, and data. In this version, FLIM Z stacks can be recorded directly from ZEN. Please see www.becker-hickl.com.

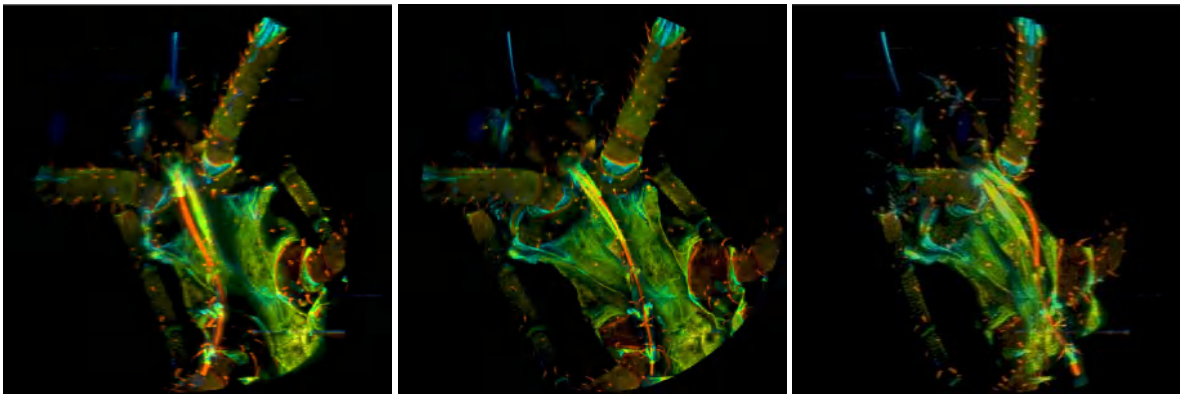


Fig. 606: FLIM Z stack of a Drosophila fly. DCS-120 MP, 100 planes, processed by SPCImage and combined into a 3D animation by Image J software. Three images from different view angles.

Fast FLIM Techniques

Triggered Temporal Mosaic FLIM

Triggered temporal mosaic FLIM is based on triggering a dynamic effect in the sample, starting a mosaic-recording cycle with the trigger, and accumulating the data of many recording cycles. Accumulation allows FLIM data to be recorded without the need of trading photon number and lifetime accuracy against the speed of the time series. Consequently, the time per step (or mosaic element) is only limited by the minimum frame time of the scanner.

For pixel numbers on the order of 128x128 pixels and small scan areas galvanometer scanners reach frame times on the order of 50 milliseconds. Resonance scanner are even faster. This brings the time-series resolution into the range where even lifetime changes induced by Ca^{2+} transients in neurons can be recorded. With that speed temporal mosaic FLIM is faster than most of the 'Fast FLIM' techniques currently flooding the market [794]. More than that, it achieves that speed without the need of excessively high photon rate or excitation power [170].

Calcium Transients

Fig. 607 shows a mosaic FLIM recording of the Ca^{2+} transient in cultured neurons after stimulation by an electrical signal. Oregon Green was used as a Calcium sensor. A Zeiss LSM 7 MP multiphoton microscope was used to scan the sample. The scan format was 64 x 64 pixels. With 64 x 64 pixels and a zoom factor of 5, the LSM 7 MP reaches a frame time of 38 ms. The FLIM data were recorded by a bh SPC-150 module. A FLIM mosaic size of 8 x 8 elements was used. The stimulation period was 3 seconds. 150 milliseconds before every stimulation a recording through the entire 64-element mosaic was started. With the frame time of 38 ms, the acquisition thus runs through the entire mosaic in 2.43 seconds. 100 such acquisition runs were accumulated. The result shows clearly the increase of the fluorescence lifetime of the Ca^{2+} sensor in the mosaic elements 4 to 6, and a return to the resting state over the next 10 to 15 mosaic elements (380 to 570 ms).

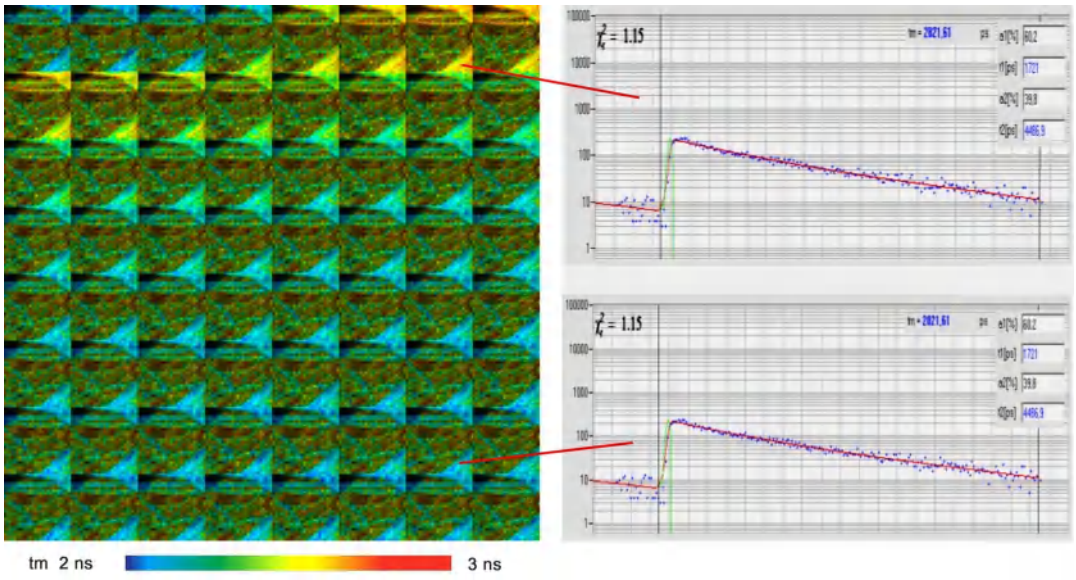


Fig. 607: Temporal mosaic FLIM of the Ca^{2+} transient in cultured neurons after stimulation with an electrical signal. The time per mosaic element is 38 milliseconds, the entire mosaic covers 2.43 seconds. Experiment time runs from upper left to lower right. Photons were accumulated over 100 stimulation periods. Recorded by Zeiss LSM 7 MP and bh SPC-150 TCSPC module. Data courtesy of Inna Slutsky and Samuel Frere, Tel Aviv University, Sackler Faculty of Medicine.

FLITS: Fluorescence Lifetime-Transient Scanning

Principle

FLITS (Fluorescence Lifetime-Transient Scanning) records transient effects in the fluorescence lifetime of a sample with spatial resolution along a one-dimensional scan. The technique is based on building up a photon distribution over the distance along the scan, the experiment time after a stimulation of the sample, and the arrival times of the photons after the excitation pulses. The maximum resolution at which lifetime changes can be recorded is given by the line scan time. With repetitive stimulation and triggered accumulation transient lifetime effects can be resolved at a resolution of about one millisecond.

Fig. 608, left, shows the photon distribution built up by normal TCSPC FLIM. It is a distribution of photon numbers over x, y, and t. In Fig. 608, right, one spatial coordinate (y) has been replaced with an 'experiment time', T. Technically, this is achieved by constantly running the scanner along the same line, and recording the photon distribution over the position in the line and the number of the individual line scan period. The experiment time, T, is thus the time after a stimulation of the sample, expressed in units of the line scan time. X is the distance along a spatially one-dimensional scan.

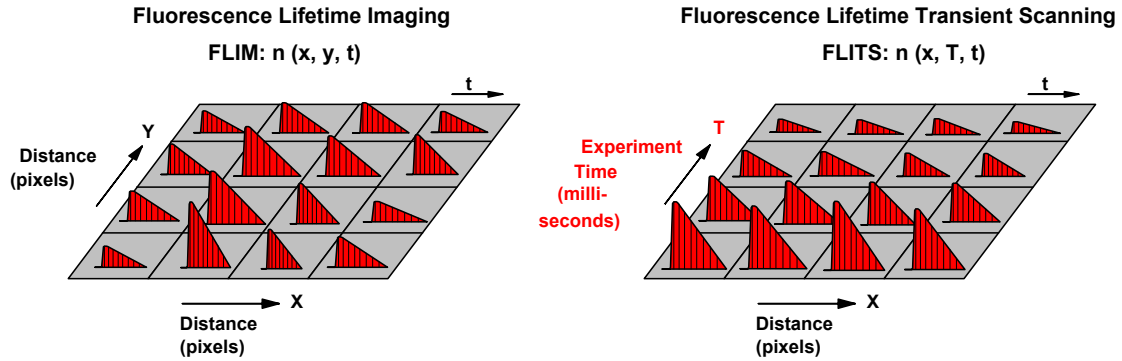


Fig. 608: Left: Photon distribution built up by standard FLIM. Right: Photon distribution built up by fluorescence lifetime-transient scanning.

As long as the stimulation occurs only once the recording process of FLITS is simple: The FLIM state machine of the TCSPC module starts to run with the stimulation, and puts the photons in consecutive time channels along the T axis. The result is equivalent to a time-series of line scans.

However, there is an important difference to a simple time series: The data of all lines are stored in a single data array. The data are still in the memory (either in the on-board memory of the TCSPC module or in the computer) when the sequence is completed. Thus, the recording process can be made repetitive: The sample would be stimulated periodically, and the start of T triggered by the stimulation. The recording then runs along the T axis periodically, and the photons are accumulated into one and the same photon distribution.

With this 'triggered accumulation' process, it is no longer necessary that each T step acquires enough photons to obtain a complete decay curve in each pixel and T channel. No matter when and from where a photon arrives, it is assigned to the right location in x, the right time T, and to the right arrival time, t, after the laser pulse. The signal-to noise ratio depends only on the total acquisition time, not on the line time. This behaviour is an equivalent of the capability of FLIM to deliver a signal-to-noise ratio independent of the pixel time if only the total acquisition time remains the same. Thus, the resolution at which FLITS resolves lifetime changes is limited only by the period of the line scan. This is about one millisecond for the galvanometer mirrors used in the DCS-120 scanner.

Technical Solution

Fluorescence lifetime-transient scanning (FLITS) can be performed in the commonly used FLIM modes of the bh TCSPC modules. That means, the SPC module records the fluorescence photons in the Scan Sync In or in the FIFO Imaging mode. The synchronisation with the scan is accomplished the usual way, via the pixel clock, line clock, and frame clock pulses. However, different than for x-y-t imaging, the frame clock for FLITS does not come from the scanner but from the stimulation of the sample. All that is needed to perform FLITS is a line scan, and a way to switch the frame clock source between the frame clock from scan controller and a trigger pulse from the source of stimulation. In the simplest case, this can be done by swapping the cable connector between the two sources. (A suitable cable is available from bh)

FLITS procedure

Before the FLITS recording is started it is recommended to run a normal FLIM acquisition to obtain an image of the sample. It is recommended to run the FLIM acquisition with the same line time that will be used for the subsequent FLITS recording. The result of the FLIM measurement is an image as shown in Fig. 609, left. Then the scanner is switched into the line mode and the location of the line scan is selected within the image recorded before. The source of the frame clock is switched to the stimulation.

Then the FLITS recording is started, and the stimulation is started. The SPC module now records a photon distribution n (x, T, t) the coordinates of which are the distance, x, along the scanned line, the transient time, T, after the event that stimulates the sample, and the time, t, of the photon after the laser pulses. The principle is illustrated in Fig. 609, right. The transient-time, T, is given in multiples of the line time.

There is no need to synchronise the start of the recording with the start of the stimulation sequence: The recording in the TCSPC modules does not start until the first frame clock arrives. It is only required that the stimulation sequence be started *after* the start of the FLITS recording.

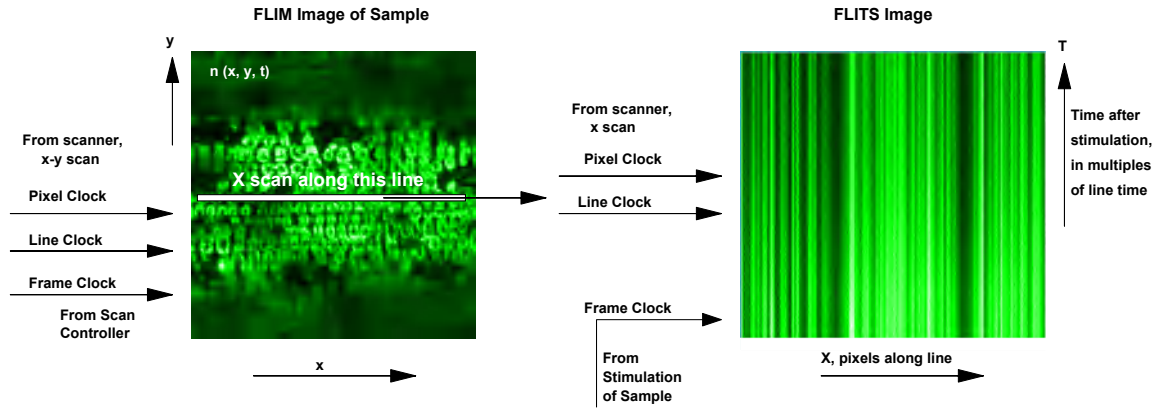


Fig. 609: Principle of recording transient lifetime effects by line scanning

The time scale of T can be varied either by varying the scan rate, or by defining 'line clock divider' values larger than one in the scan parameter section of the TCSPC system parameters, see page 754 and page 766. When FLITS data have been recorded they can be analysed by standard SPCImage FLIM analysis procedures, see page 861 of this handbook.

Chlorophyll Transients

FLITS can be demonstrated most easily by recording the 'chlorophyll transients' that occur when a live plant is exposed to light [516, 517, 834]. Upon illumination, the fluorescence lifetime (and intensity) first increases. The increase happens within a few milliseconds or tens of milliseconds. It is attributed to the progressive saturation of photosynthesis channels, and a corresponding decrease in fluorescence quenching. The increase in the fluorescence quantum efficiency is therefore called 'photochemical transient'. After a few seconds of exposure, the fluorescence lifetime starts to decrease again. At intensities comparable to sunlight, it reaches a steady-state level after a few tens of seconds. It is assumed that the decrease of the lifetime is a protection mechanism of the plant. The slow decrease is called 'non-photochemical transient'.

Non-Photochemical Transient

Recording the non-photochemical transient is relatively easy: The transient is slow and can even be recorded by time-series FLIM, see page 398. Stimulation is obtained by turning on the excitation laser.

An example of a FLITs recording is shown in Fig. 610. The sample was a fresh grass blade. The excitation intensity during the initial FLIM recording was kept low so that no noticeable lifetime change was induced. The FLITS recording was started by manually generating a single frame clock pulse. The excitation laser was switched on 180 ms later. The result is shown in Fig. 610. The horizontal coordinate is the distance along the scanned line, the vertical coordinate is the time, T, after the frame clock. The line time was 60 ms, the number of lines along the T axis is 256. Thus, the total time along the vertical axis is 15.4 seconds. It can clearly be seen that both the fluorescence intensity and the fluorescence lifetime decrease with the time of illumination.

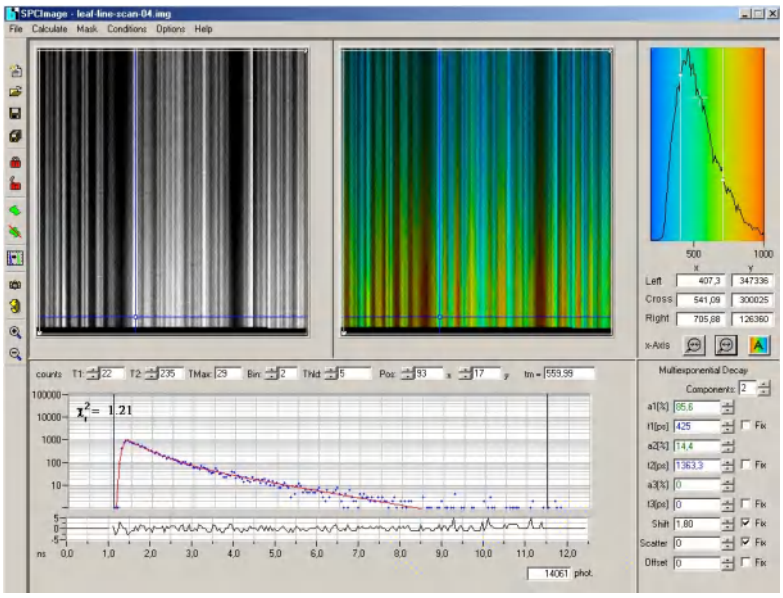


Fig. 610: FLITS image of non-photochemical chlorophyll transient. Horizontal: Distance along the line scanned. Vertical, bottom to top: Time, T, after the start of illumination. 256 pixels along the line, line time 60 ms, 256 lines, total time interval recorded 15.36 seconds. Left: Intensity image. Right Lifetime image. Colour represents lifetime, blue to red corresponds to 200 ps to 1 ns. Amplitude-weighted lifetime of double-exponential decay. Bottom: Decay curve at cursor position.

Photochemical Transient

Recording the photochemical transient requires periodical stimulation and acquisition of the data over a longer period of time. Both the laser on-off signal [81] and the FLITS frame clock were therefore generated by a bh DDG-210 pulse generator card. (Any standard pulse generator works as well.) The on-off period was 1 second, the 'on' time within the period was 200 ms. Each turn-on of the laser initiates a photochemical transient, i.e. a temporary increase in the fluorescence lifetime. In the laser-off period the leaf partially recovers, so that the next laser-on initiates a new transient. The total acquisition time was 40 seconds, i.e. 40 on-off periods were accumulated.

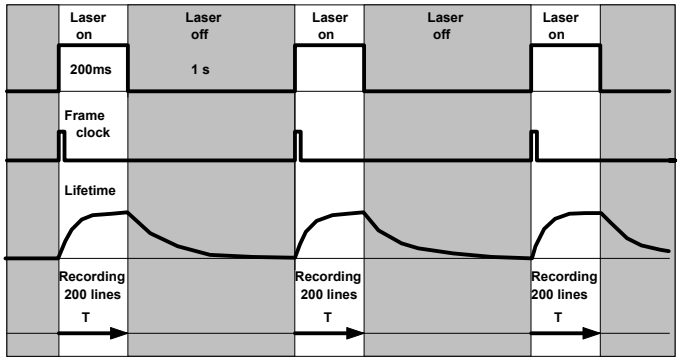


Fig. 611: Excitation sequence for recording the photochemical transient

The result is shown in Fig. 612. The intensity image is shown on the left, the lifetime image on the right, and a decay curve at the cursor position at the bottom. The horizontal axis of the images is the distance along the line scanned. The vertical axis (bottom to top) is the time after the start of illumination. The line time was 1 ms, 256 lines, i.e. 256 ms in total, were recorded in T direction. The Laser was turned on at T = 0, and turned off at T = 200 ms. The lifetime image shows the amplitude-weighted lifetime obtained from a double-exponential fit. The lifetime range is from 450 ps (blue) to 650 ps (red).

Although the lifetime change is less pronounced than for the non-photochemical transient an increase can clearly be seen. Changes occur especially in the first 10 to 20 ms after the turn-on of the laser, see bottom of the lifetime image.

Despite the small duty cycle of the laser the illumination unavoidably also causes a non-photochemical transient. When the photochemical transient is complete, activity essentially shuts down, and no non-photochemical transient is observed any more. Perfect recording of the non-photochemical transient therefore requires optimisation of the laser intensity, the laser duty cycle, and the total accumulation time.

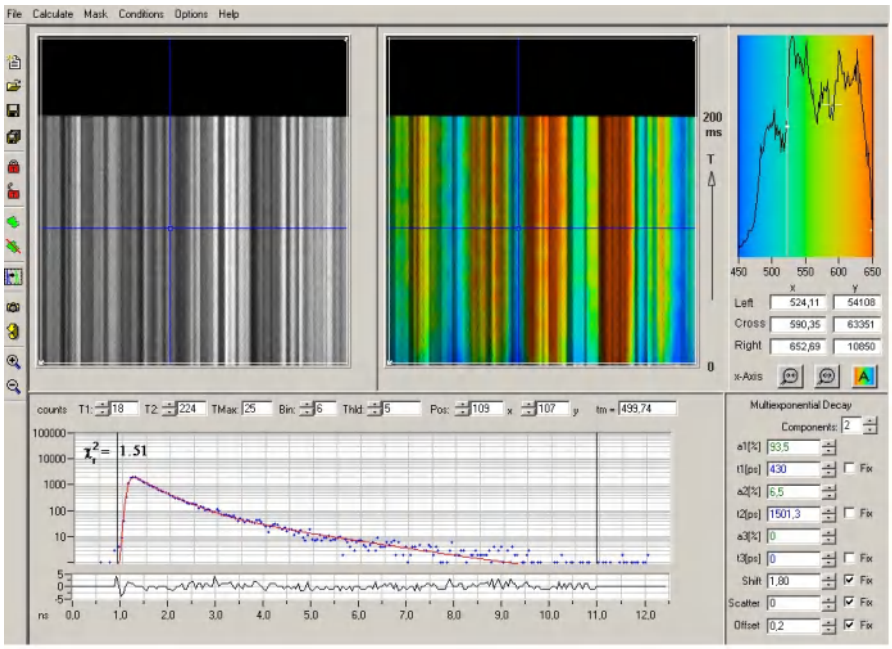


Fig. 612: FLITS image of photochemical chlorophyll transient. Horizontal: Distance along the line scanned. Vertical, bottom to top: Time, T, after the start of illumination. Line time 1 ms, 256 lines, total time interval recorded 256 ms. Laser turned on at T=0, laser-on time 200 ms. Left: Intensity image. Right Lifetime image. Colour represents lifetime, blue to red corresponds to 450 ps to 650 ps. Amplitude-weighted lifetime of double-exponential fit. Bottom: Decay curve at cursor position.

Decay curves and lifetimes for a selected pixel in the scan and for two points on the T axis are shown in Fig. 613. From T = 3 ms to T = 191 ms the amplitude-weighted lifetime of the double-exponential fit increases from 480 ps to 530 ps.

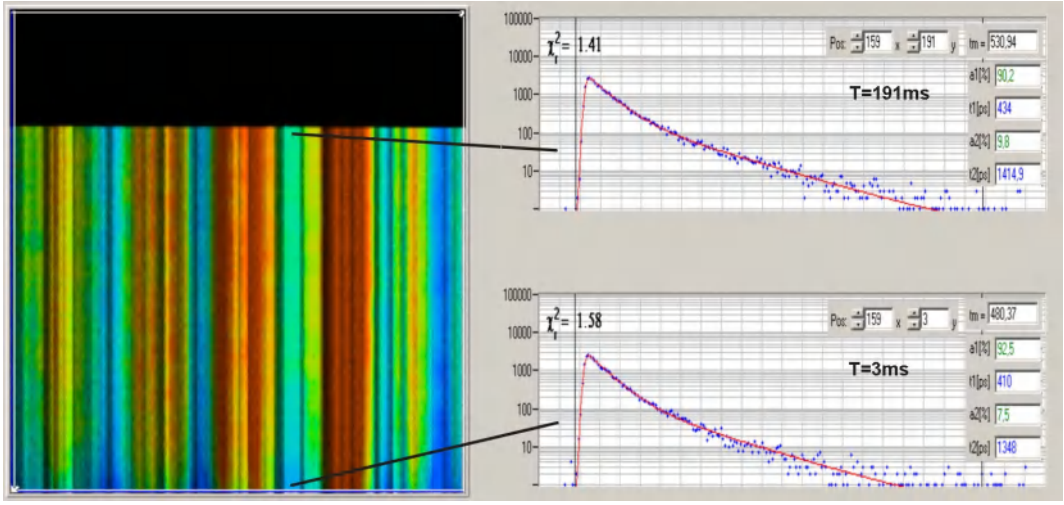


Fig. 613: Decay curves for a selected pixel (x=159) within the line for T = 3 ms and T = 191ms into the laser-on phases. Double-exponential fit. The amplitude-weighted lifetime increases from 480 ps to 530 ps

Calcium Transients

The application of FLITS to the recording of Ca^{2+} transients (changes in the concentration of free Ca^{2+}) in live neurons on electrical stimulation has been described in [164, 171] and [463]. A typical result is shown in Fig. 614. Hippocamal cultures were prepared from newborn rats and kept under physiological conditions for 12 to 18 days. The cultures were then loaded with OGB-1 AM, see [463] for details. A Zeiss LSM 7 MP multiphoton microscope with a normal Simple-Tau 150 FLIM system was used to run the FLITS experiments. The cells were stimulated synchronously with the line clock of the LSM 7 MP. To run the experiments, an intensity image was taken by the LSM 7 MP, and an appropriate location for the line scan selected. Then the LSM 7 MP was switched into the line scanning mode. The data acquisition in the FLIM system, the scanning in the LSM 7 MP, and the stimulation were started. The stimulation pulses of 1 ms duration were applied to the cell culture in intervals of 3 seconds [463]. Data acquisition was continued over about 300 seconds, i.e. photons from about 100 stimulation periods were accumulated. The result is shown in Fig. 614, left.

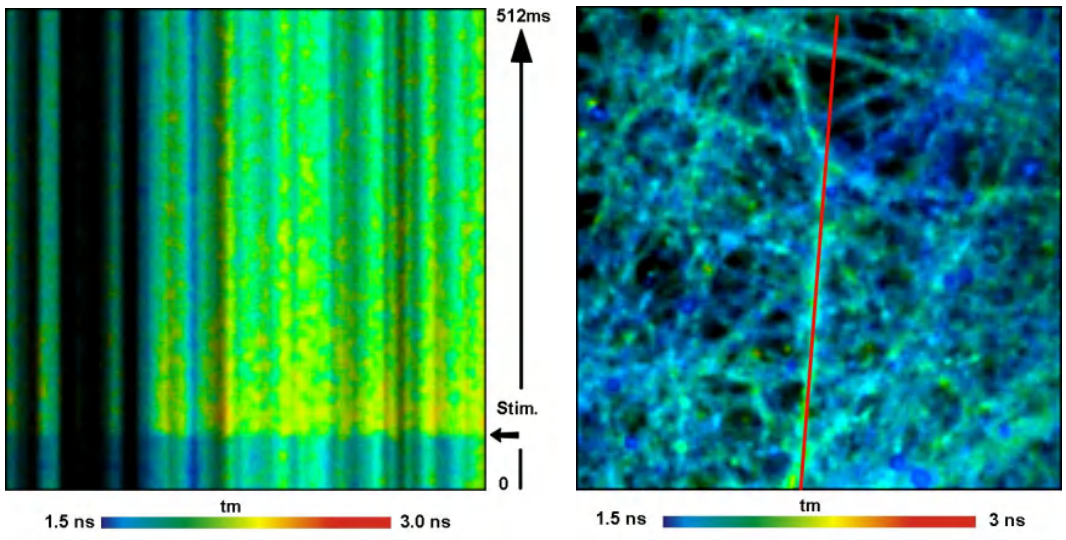


Fig. 614: FLITS of Ca^{2+} transients in live neurons. Left: FLITS image. Right: FLIM image taken after the FLITS recording. Red line indicates position of FLITS scan.

To verify that the FLITS experiment did not cause cell damage or photobleaching a FLIM image was recorded after the FLITS experiment. It is shown in Fig. 614, right. It does not show any cell damage or photobleaching effects along the scanned line. It also shows that the Ca^{2+} concentration returned to the resting level, compare bottom of FLITS image on the left.

Fast Online FLIM with Standard bh TCSPC Systems

The techniques described above are aiming at the *recording* of fast dynamic effects in the fluorescence decay parameters, not at a fast sequential *online display* of lifetime images. Online display not only requires that the FLIM data are recorded within a short acquisition time but also that the fluorescence lifetime is calculated from the decay data in a similarly short period of time. The task is complicated by the fact that the signal-to-noise ratio of a FLIM recording cannot be higher than

$$SNR_\tau = \sqrt{N} \qquad (1)$$

where N is the number of photons in the pixels. The number of photons available within a given period of time (the photon count rate) is limited by the sample itself: Excitation power

or fluorophore concentration above a certain level cause invasive effects to the sample. Count rates obtained in FLIM experiments are thus rarely higher than a few MHz. The speed of online-FLIM is therefore limited by the decrease of the signal-to-noise ratio with increasing image rate. The requirements for fast online FLIM are therefore:

- The recording technique must record the photons in a way that the SNR comes close to the ideal value. That means the decay curve must be recorded in a sufficiently large number of time channels, with a negligible IRF width, and with negligible background from detector dark counts, detector afterpulsing, or daylight pickup [680]. TCSPC comes very close to the ideal conditions, and achieves a signal-to-noise ratio very close to the ideal value.
- the calculation algorithm for the lifetime must not only be fast enough to analyse the images within a time shorter than the image period but also extract the lifetime from the recorded data at the ideal signal-to-noise ratio inherent to the TCSPC data.

First-Moment Algorithm

An almost ideal SNR from TCSPC data is obtained by calculating the lifetime via the first moment of the decay data [55]. The method has been suggested first by Z. Bay in 1950 for the determination of excited nuclear state lifetimes in coincidence experiments [55]. The first moment of a photon distribution is

$$M1 = \frac{1}{N}\sum tn(t) \qquad (2)$$

with N = total number of photons, t = time of individual time channels, $n(t)$ = photon number in individual time channels

The first moment can also be considered the average arrival time of all photons in the decay curve. For a single-exponential decay, it can easily be shown that the first moment delivers an ideal SNR: The standard deviation of the photon arrival time is τ, and the standard deviation of the average arrival time of a large number of photons is $\tau/\sqrt{N}$. The relative standard deviation, or the SNR, is thus $1/\sqrt{N}$, and the signal-to-noise ratio is $\sqrt{N}$.

The fluorescence lifetime (of a single-exponential decay approximation) is the difference of the first moment of the fluorescence and the first moment of the IRF:

$$\tau = M1_{\,fluorescence} - M1_{IRF} \qquad (3)$$

The relations are illustrated graphically in Fig. 615. The blue dots are the photon numbers in the time channels of the pixel, the green curve is the IRF. 'M1 of Fluorescence' is the first moment calculated according to (2), 'M1 of IRF' is the M1 of the IRF calculated by the same formula. 'Tau' is the fluorescence lifetime calculated according to (3). The red curve is the convolution of a single-exponential function, $f(t) = e^{-t/\tau}$, with the IRF.

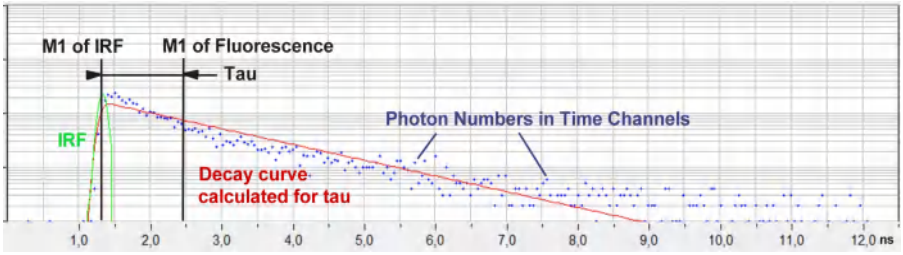


Fig. 615: First-moment calculation of fluorescence lifetime. The lifetime is the difference of the first moment of the fluorescence and the first moment of the IRF.

For a double-exponential decay, it can be shown that (3) delivers the intensity-weighted average of the lifetimes of the two components. The signal-to-noise ratio remains very close to $\sqrt{N}$ for a wide range of lifetime and intensity ratios of the components.

To obtain correct lifetimes the first moment of the IRF has to be known. This is no problem for TCSPC FLIM. $M1_{IRF}$ can be obtained either by analysing a FLIM data file with SPCImage or from decay data of a fluorophore with known lifetime. In any case, the IRF can be recorded with a high N, its uncertainty therefore does not significantly contribute to the uncertainty of τ.

Other requirements for the M1 calculation of lifetimes are that the background of the decay signal is negligible, and that the entire decay curve is recorded up to a time channel beyond which no more photons are recorded. Also this is no problem for fast online display. Due to the short acquisition time, background is low or even not detectable, and the decay function drops quickly to the point where later photons are unlikely to be detected. Examples can be seen in Fig. 616 and Fig. 617, middle.

Binning of Decay Data

Online FLIM at image rates faster than one image per second delivers very low photon numbers in the pixels. An example is shown in Fig. 616. The decay curve (shown left) is from a single pixel of a FLIM recording of 256x256 pixels, recorded at an acquisition time of 0.2 seconds (5 frames per second). The entire curve contains about 45 photons. The corresponding FLIM image is shown in Fig. 616, right. According to (1) the SNR of the fluorescence lifetime in the bright pixels of the image is about 7. The noise in the lifetime can easily be seen in Fig. 616.

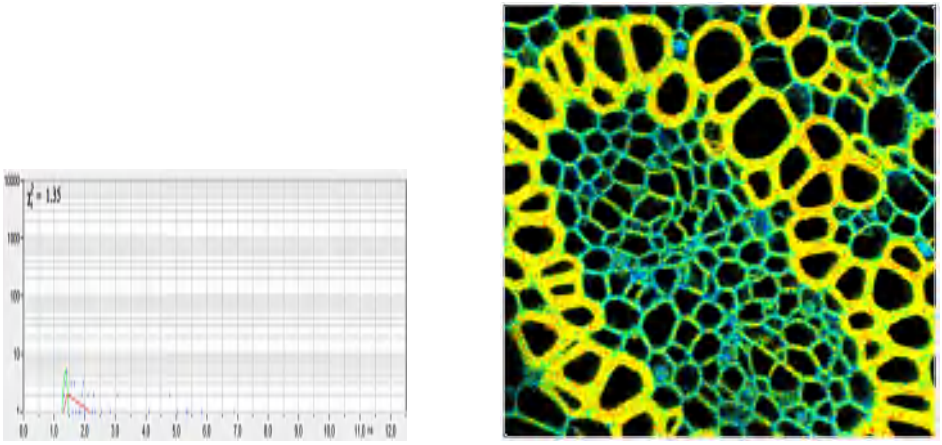


Fig. 616: Online FLIM with acquisition time 0.2 seconds (5 frames/second). 256x256 pixels, no binning. Left: Decay curve in brightest pixel, the photons are barely visible between t = 1ns ... 2ns. Right: Lifetime image calculated by M1 algorithm, red to blue = 1000 to 3000 ps.

A substantial improvement is obtained by binning the decay data for the lifetime analysis. The binning algorithm used in SPCM is the same as in SPCImage. For every pixel of the image, it uses not only the photons in this pixel but also the photons in the pixels around, see Fig. 617, left. On average, this yields a photon number 9 times larger than without binning (Fig. 617, middle), and a 3 times better SNR of the lifetime. The lifetime image is built up from the intensity data of the unbinned pixels and the lifetime data from the binned pixels. The image calculated this way is shown in Fig. 617, right.

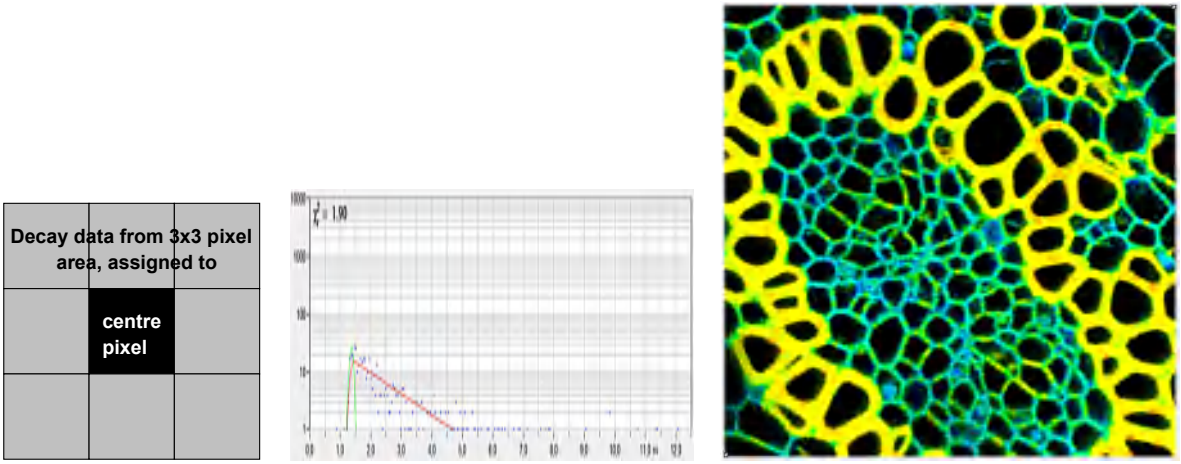


Fig. 617: Online FLIM, parameters same as Fig. 616, but with binning of lifetime data, 3 x 3 pixels. Left: Decay curve in brightest pixel. Right: Lifetime image calculated by M1 algorithm, red to blue = 1000 to 3000 ps.

The improvement in image quality is striking: The noise in the lifetime is much lower, but, surprisingly, there is no apparent reduction in image definition. This has two reasons. The first one is the way the human eye-brain combination processes images. Perception of image definition comes exclusively from the intensity, the colour is just an overlay on the intensity image. Since the intensity data have not been binned the apparent definition is not impaired by binning. The second one is the way images are recorded in microscopy. Usually, the images are oversampled, i.e. the Airy disc (or point-spread function) is imaged on an area of several pixels. Binning has, of course, little effect on data which are already smoothed by spatial convolution with the Airy disc.

Implementation in SPCM

The Online-Lifetime display function is implemented in the SPCM software, version 9.72 or later. The function is activated in the 3D Trace parameter panel, see Fig. 618, left. The parameters of the calculation procedure are defined in the Display Parameters, see Fig. 618, right. For details please see page 815 in the software chapter of this handbook.

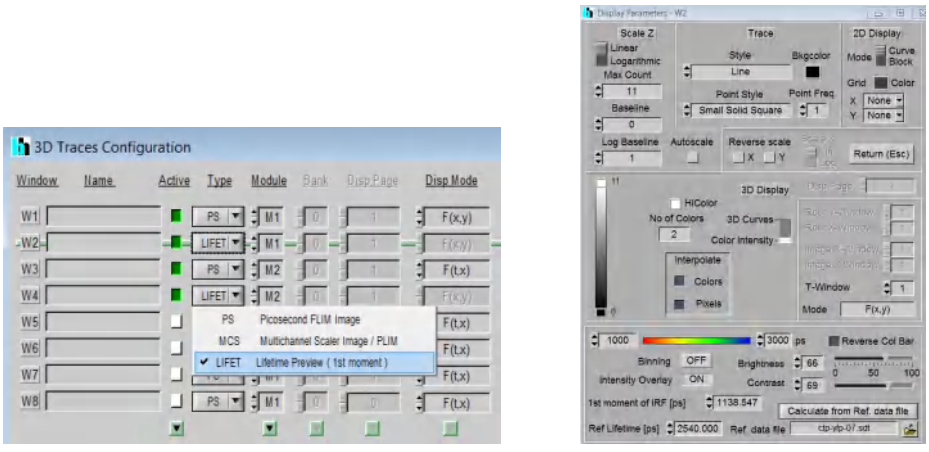


Fig. 618: SPCM Definitions for online lifetime display

Results

Fig. 619 shows 128x128-pixel images recorded with acquisition times of 0.1 s, 0.5 s, and 2 s. The upper row shows images without binning, the lower row images with 3 x 3 pixel binning of the decay data. The images show that lifetime images of reasonable quality are obtained even at an acquisition time of 100 ms, or an image rate of 10 per second.

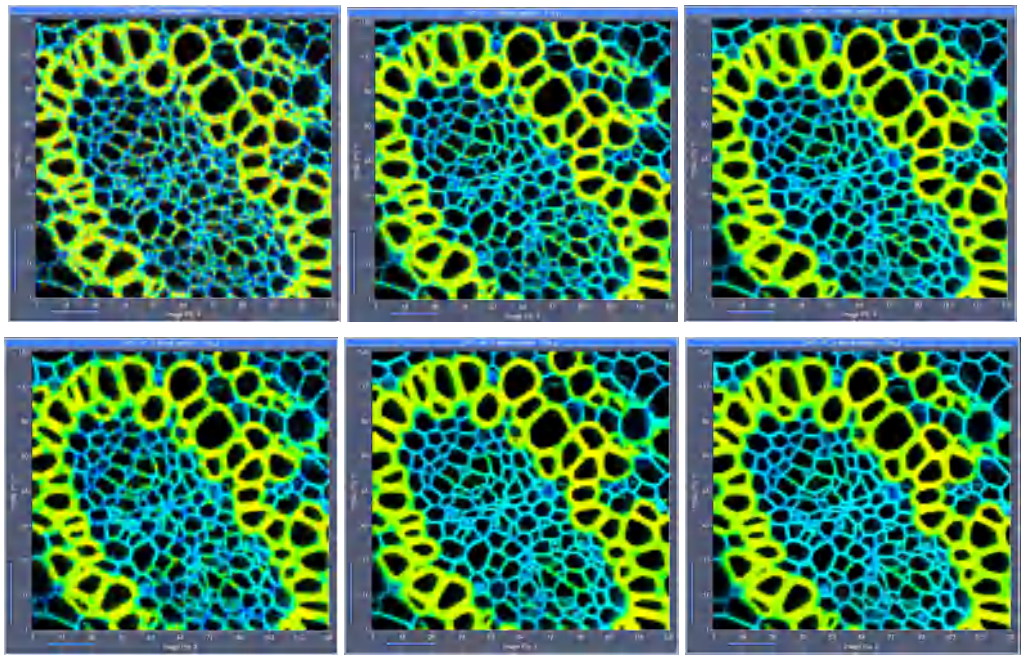


Fig. 619: 128x128-pixel images. Acquisition time 0.1s, 0.5s, 2s. Upper row: No binning. Lower row: Binning 3 x 3 pixels

Images recorded with 256 x 256 pixels are shown in Fig. 620. The acquisition time was 0.2 s, 0.5 s, and 2 s. Also here, binning reduces the lifetime noise substantially but does not cause noticeable blurring of the images.

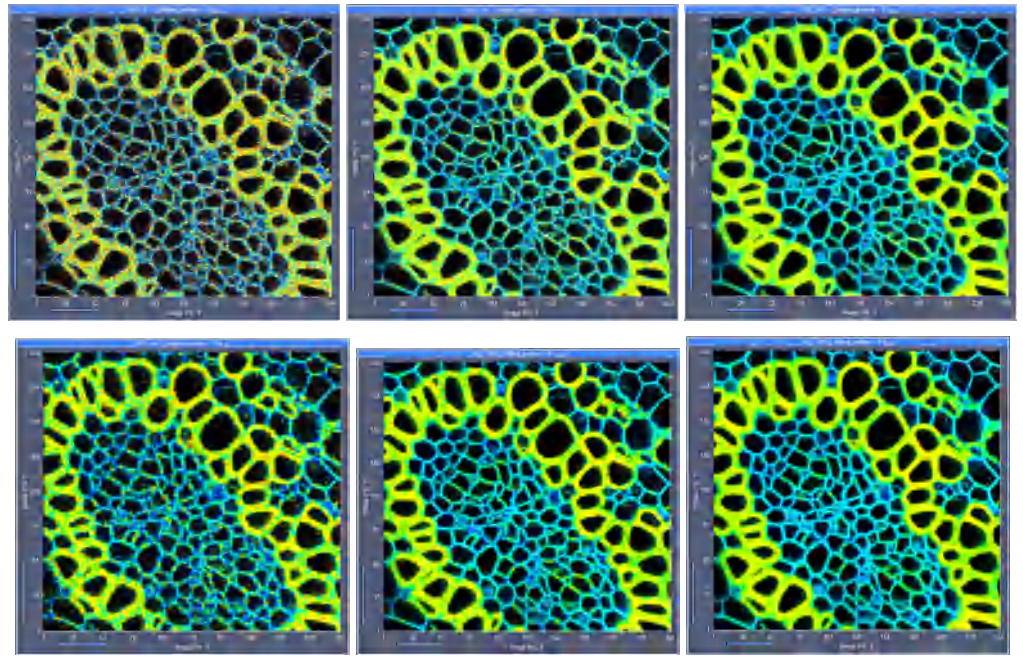


Fig. 620: 256 x 256-pixel images. Acquisition time 0.2 s, 0.5 s, 2 s. Upper row: No binning. Lower row: Binning 3 x 3 pixels

Summary

The results shown above demonstrate that fast online FLIM is feasible almost up to the maximum frame rate of the commonly used galvanometer scanners. Importantly, fast online FLIM does not require a decrease in the number of time channels per pixel. The function can thus be used during FLIM acquisition, without compromising later high-accuracy multi-exponential decay analysis. It should be noted, however, that the examples shown here were recorded with

a convallaria sample. In this sample, the lifetime varies over a range of about 1:2.5. In real-world FLIM samples the lifetime variation is often smaller. Selecting FRET-positive cells in a culture of donor-and-acceptor expressing cells requires a lifetime resolution of about 1:1.25. Obtaining images of similar quality as for the convallaria would require four times the photon number, and thus four times the acquisition time, see equation (1). This would be about 0.4 seconds for a 128 x 128 pixel image with binning. This is still an acceptable image rate. Even in clinical FLIM applications, with metabolism-induced lifetime changes on the order of 1:1.1 [637, 1049] images can probably be displayed at rates faster than one image per second.

Fast FLIM Recording by the bh FASTAC System

Motivation

There is currently a run towards faster and faster acquisition in fluorescence lifetime imaging [794]. Unfortunately, these developments usually ignore the fact that, in most instances, the limitations are in the sample rather than in the recording electronics. The fastest recording system cannot record fast if the sample is not able to deliver the photons needed to acquire the data at this speed [116]. Moreover, recording speed is usually obtained at the expense of time resolution or data complexity, such as the capability to record a fully resolved fluorescence decay function in each pixel. These are exactly the features needed in biological FLIM applications, such as metabolic imaging, protein interaction experiments, and other molecular imaging applications. Ignoring these needs by just recording a 'lifetime' in the pixels of the image means reducing the fluorescence decay function to a simple contrast parameter. In other words, the commonly used 'Fast FLIM' techniques sacrifice the most important features of FLIM for a single parameter (recording speed) which, ironically, cannot be exploited in the typical applications. This section shows a way to record FLIM at short acquisition time without compromises in time resolution or data complexity.

Principle

The bh FASTAC FLIM system uses one detector and four TCSPC modules. The photon pulses from the detector are distributed into the TCSPC modules by a module called 'Photon Spinner' [109, 110, 116]. The principle is shown in Fig. 621. As usual, the photon pulses from the detector are passing a constant-fraction discriminator, CFD. The output pulses of the CFD have a constant width and a time independent of the pulse amplitude of the detector pulses. The pulses from the CFD control a four-way switch that distributes the pulses to four TCSPC modules. Every photon pulse from the CFD rotates the switch by one position. The trick of the solution is that every photon sets the switch not for the next photon, but for itself. To do so, the photon pulses pass a delay line. Every photon arrives at the switch a short time after the switching action has been completed. This way, the 'Photon Spinner' avoids the influence of possible switching transients on the timing: Because every photon pulse arrives at the switch at a fixed time after the switching action the sum of the photon pulse and the switching transient is the same for all photons. It is also independent of the time of the photon in the laser pulse period. Therefore, the time resolution (IRF width) of the system and the differential nonlinearity of a bh FASTAC system is nearly the same as for a single-module system.

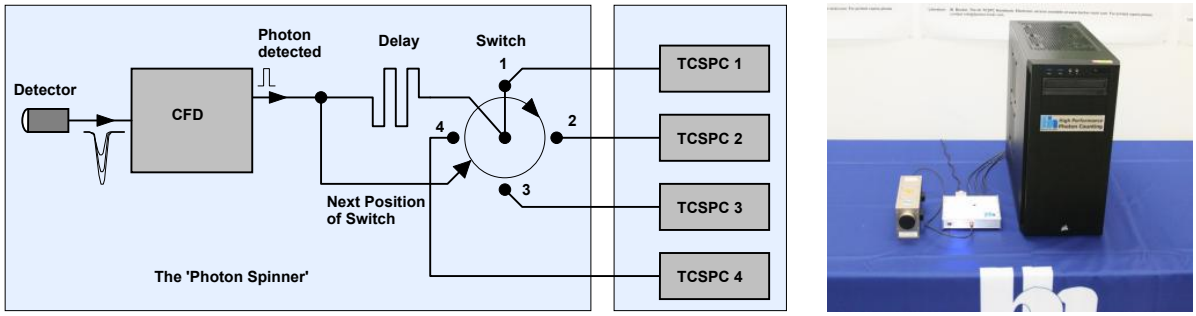


Fig. 621: Left: Principle of the bh FASTAC FLIM system. Right: Photo showing detector, photon spinner module, and PC with the four TCSPC modules.

The system features substantially smaller pile-up and counting loss than a single-channel system. As the switch spins around with the photons arriving, each of the TCSPC modules records 1/4 of the photons. Counting loss (by detecting a photon in the dead time of a previous one) is thus substantially reduced. The improvement is larger than for a system with four separate detectors because the distribution device (the 'Photon Spinner') regularises the photon arrival times. Short time intervals between the photons therefore become less likely.

The second effect of the 'Photon Spinner' is a reduction of possible pile-up errors. The pile-up reduction is larger than for a system with four detectors. If a new photon is detected in the same laser pulse period with a previous one it goes to the next TCSPC module. It thus does not cause any pile-up distortion. Only if more than *four* photons were detected within one and the same laser pulse period a pile-up error would occur. For the commonly used pulse repetition rates of 50 to 80 MHz the detection of more than four photons in the same signal period is extremely unlikely.

Another advantage of the Photon Spinner is that it works independently of the TCSPC modules. No feedback or 'ready' signal from the TCSPC modules is necessary. The device can therefore be built as a simple extension box to a TCSPC four-module package.

Time resolution

Fig. 622, left, shows the electrical instrument response functions of four SPC 150N modules with the PHDIS-04 Photon Spinner. The IRF width of the individual modules is 6.7 to 6.9 ps, i.e. only insignificantly longer than the IRF of the modules themselves (typically 6.6 ps).

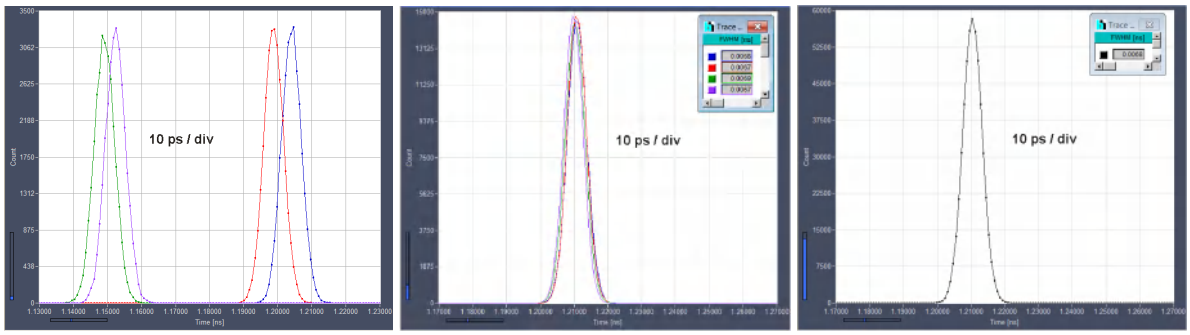


Fig. 622: Electrical IRFs of the four SPC-150N modules. Before (left) and after delay alignment (middle). The combined IRF of the four SPC-150N is shown on the right. The FWHM of the combined IRF is 6.8 ps.

Due to transit time differences in the Photon Spinner and in the connecting cables the IRFs of the four TCSPC channels appear slightly shifted, see Fig. 622, left. The shift can be corrected by using separate TAC offsets for the individual TCSPC modules. Fine alignment is achieved by tweaking the 'Zero Cross' levels of the CFDs of the modules. Different Zero Cross shifts the trigger point up and down the leading edge of the spinner output pulses, and thus acts as a delay fine adjustment. The variation in the Zero Cross has no influence on the IRF width be-

cause the output pulses of the Photon Spinner have no amplitude jitter. The IRFs of the SPC-150N modules after delay alignment are shown in Fig. 622, middle, the combined IRF of the four modules is shown in Fig. 622, right. The combined IRF still has 6.8 ps FWHM, much faster than the transit time spread of any commonly available photon detector.

The optical IRF of the entire system with an HPM-100-06 detector is shown in Fig. 623. It was recorded with a Toptica Femto Erb femtosecond fibre laser in the test setup described in [122].

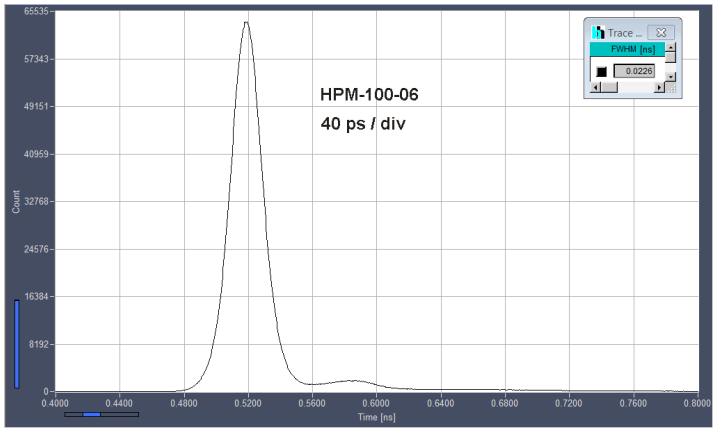


Fig. 623: Instrument response function of an SPC-154N four-module package with the Photon Spinner and an HPM-100-06 hybrid detector. FWHM is 22.6 ps.

Results

Fig. 638 shows FASTAC FLIM of a Convallaria sample. The data were recorded in combination with a bh DCS-120 confocal FLIM system, one-photon excitation by a ps diode laser was used. The acquisition time was 0.5 seconds, lifetime calculation and display of the image and the decay curve were performed by the online-display functions of SPCM.

Fig. 639 shows 2-photon images recorded in combination with a Zeiss LSM 880 NLO, see [110] for details. The left image was recorded with an acquisition time of 0.6 seconds, the right image with an acquisition time of 4 seconds. Except for different signal-to-noise ratio, the lifetimes derived from the data are the same.

Fig. 626 shows a_1/a_2 (amplitude ratio) images calculated from the same data by double-exponential decay analysis. As can be seen from the images, reasonable a_1/a_2 data are even obtained from the data acquired within 0.6 seconds.

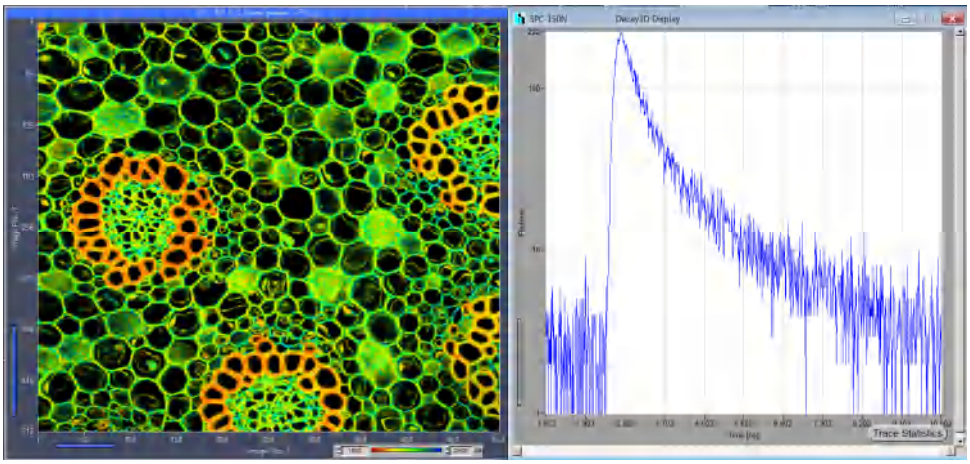


Fig. 624: 1p FLIM recorded bh FASTAC system. Left: 512 x 512 pixel image, recorded within 0.5 seconds. Right: Decay function from a 10 x 10 pixel area in the centre of the image. DCS-120 confocal FLIM system. Image and decay curve displayed by online FLIM functions of SPCM.

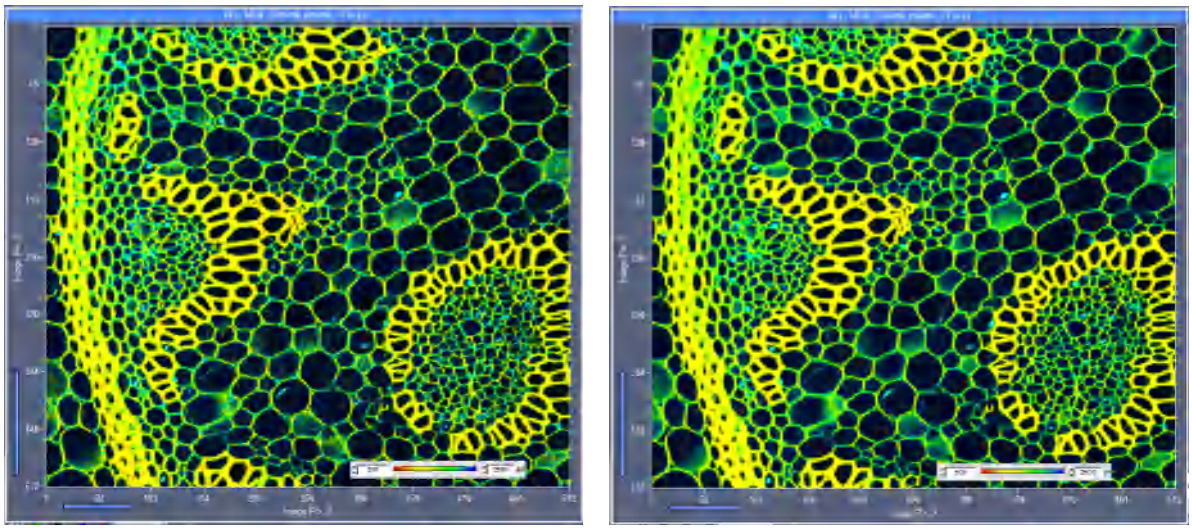


Fig. 625: 2p FASTAC FLIM of a Convallaria sample, 512 x 512 pixels, 1024 time channels. Left: Acquisition time 0.6 seconds. Right: Acquisition time 4 seconds. Images calculated and displayed by online-FLIM algorithm of SPCM.

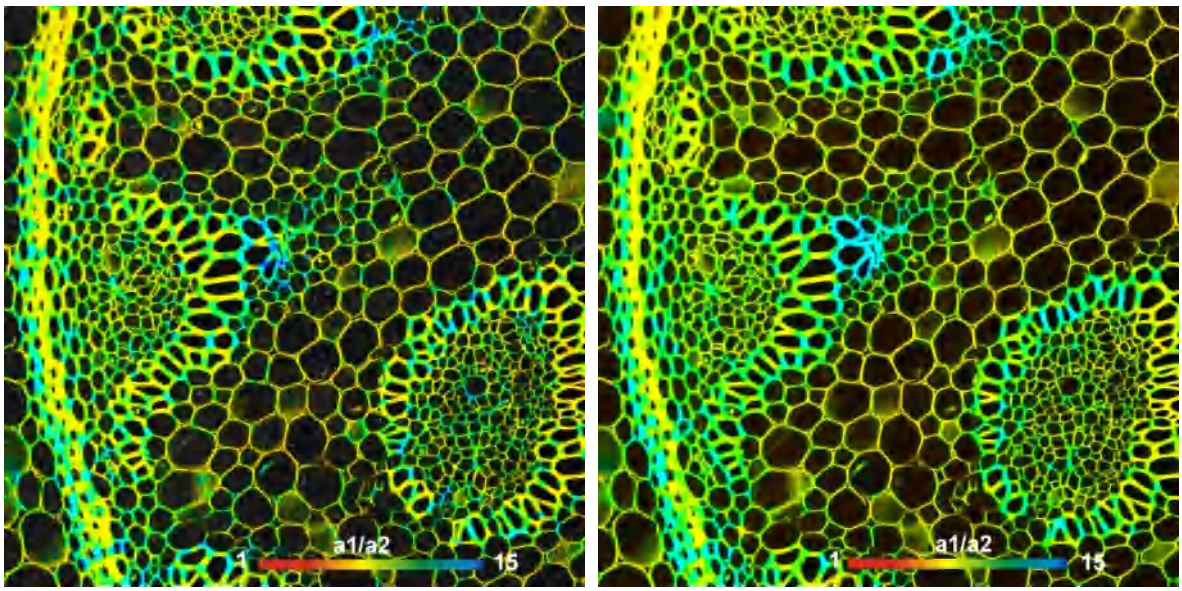


Fig. 626: a_1/a_2 (amplitude ratio) images of the data shown above. Double-exponential decay analysis by SPCImage NG, MLE algorithm, binning 4.

In 2014 bh introduced 'Megapixel FLIM' with pixel formats of 1024 x 1024 and more, without compromising the temporal resolution. Fig. 627 shows that Megapixel FLIM is also feasible with the FASTAC FLIM system. The figure shows a 1024 x 1024 pixel, 1024 time-channel image of a BPAE (bovine pulmonary artery) cell sample (stained with DAPI, Alexa 488 and Mito Tracker Red). Two-photon excitation at 800 nm was used, the image was recorded in 10 seconds.

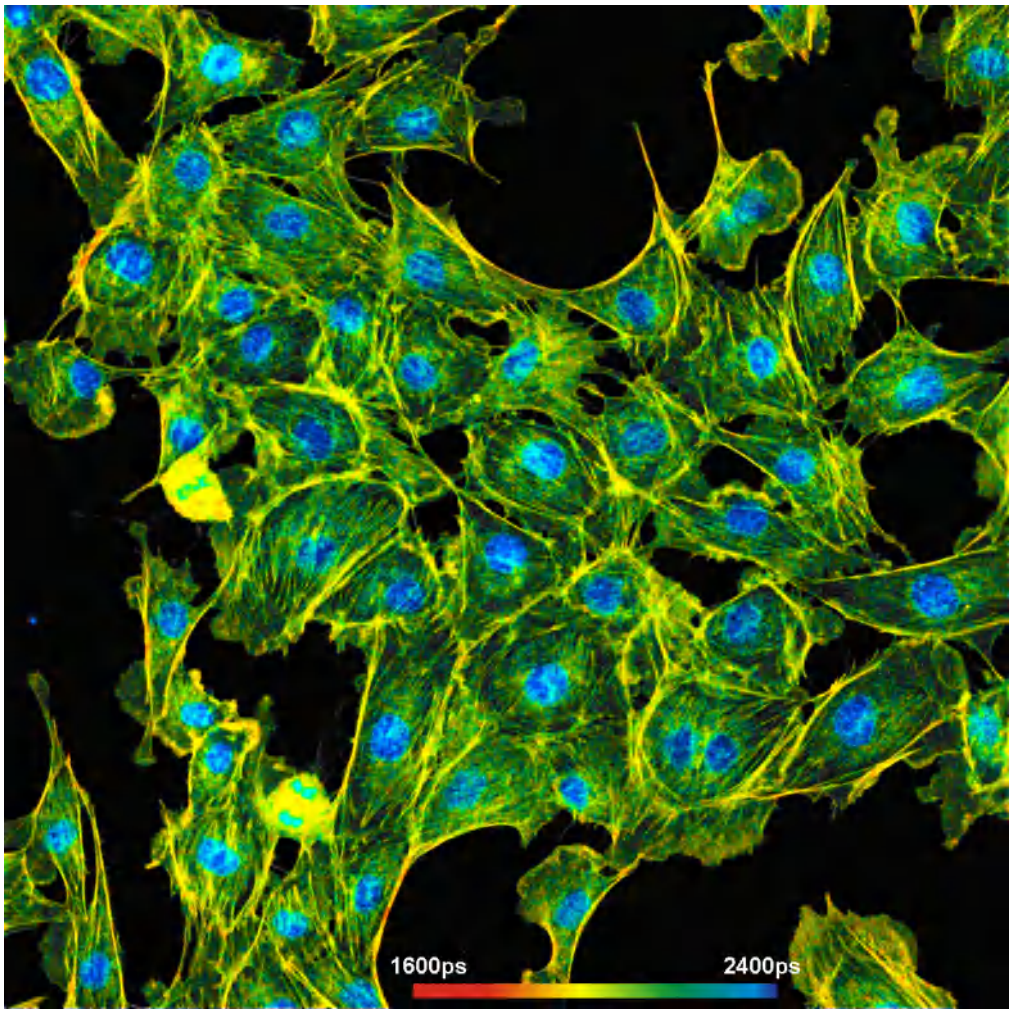


Fig. 627: FASTAC FLIM of a BPAE sample, recorded in 10 seconds. 1024 x 1024 pixels, 1024 time channels per pixel. 2p excitation at 800 nm, acquisition time 10 seconds, Zeiss LSM 880 NLO.

Summary

The bh FASTAC system is able to record FLIM at high count rates and short acquisition times. Importantly, the system reaches high count rate and short acquisition time without any reduction in time resolution. FLIM data can still be recorded at sub-ps time channel width, and sub-25 ps IRF width, thus fully exploiting the time resolution of the bh TCSPC FLIM modules and ultra-fast hybrid detectors. The system is therefore equally suitable for fast FLIM and precision FLIM applications. It can be used in combination with the bh DCS-120 confocal and multiphoton scanning systems [68], but also with laser scanning microscopes of other manufacturers [110].

Express FLIM

Limitations to the Imaging Speed of FLIM

FLIM with short acquisition time requires high photon rate. Only if the photon rate is high enough to fill the pixels with a reasonably high number of photons a reasonably high accuracy of the lifetime can be achieved. It is commonly believed that the limitation of TCSPC FLIM in terms of photon rate is the pile-up effect. This is, however, not correct. The pile-up error remains below 5% up to a count rate of 20% of the excitation rate, see 'Pile-Up', page 294. For 80 MHz excitation rate this would be 16 million photons per second - a count rate that is hard to achieve for live samples. More visible than pile up is counting loss in dead time of the TCSPC module. With increasing count rate, an increasing fraction of the photons is lost in the

dead time. As a result, the intensity scale becomes nonlinear, and the images are losing contrast. The effect is clearly visible in high-count-rate FLIM results, see 'Counting Loss and Pile-Up Effects', page 477. It has probably contributed to the myth that pile-up is a severe problem for TCSPC FLIM. In fact, it is the counting loss that causes the nonlinearity, not pile-up. In other words, the images can be taken at count rates higher than commonly believed. (Whether this is non-invasive to the sample is a different question.)

Solution

One way to avoid the intensity nonlinearity is to use Lifetime-Intensity FLIM, as described at page 428. The other way is to use an SPC-QC-104 or SPC-QC-106 module. Due to its TDC principle, the SPC-QC modules have a much shorter dead time than the SPC series modules. Therefore, nonlinearity of the intensity is virtually not visible. As an example, Fig. 628 shows a FLIM result taken at an average count rate of about 8 MHz.

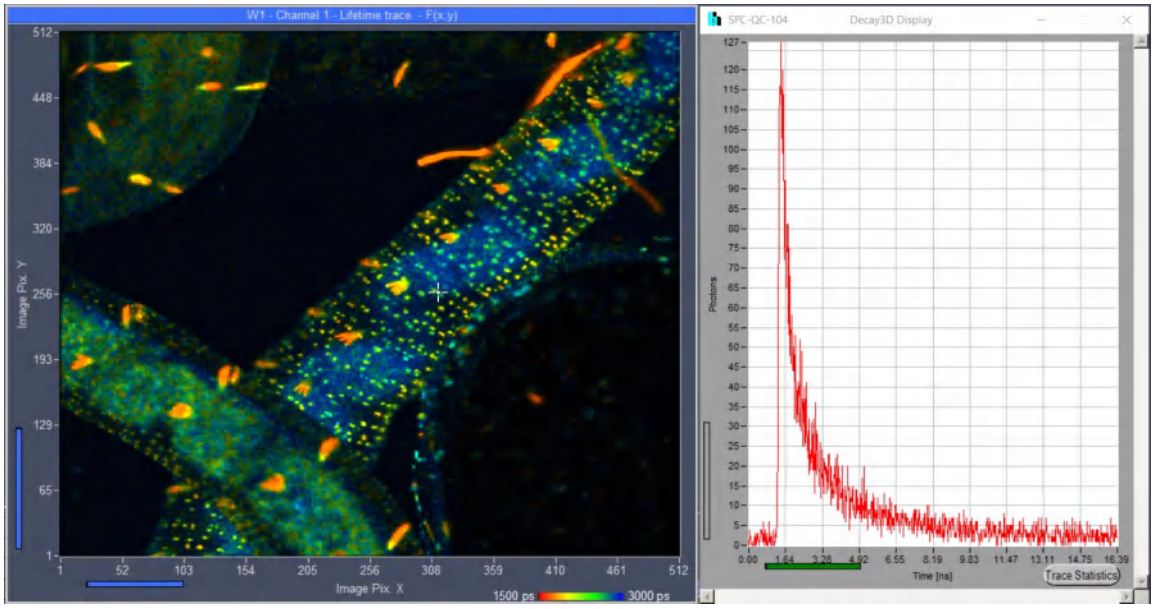


Fig. 628: Lifetime image taken from a live Enchytraeus albidus. Autofluorescence, 1 second acquisition time at 8 MHz average count rate, DCS-120 system with SPC-QC-104. Online FLIM with SPCM software.

Principle of Express FLIM

Recording an image like the one shown above requires an enormous data transfer rate from the TCSPC module to the computer. The data transfer problem increases if not only one channel but all three channels of the SPC-QC are operated at high count rate. Possible bus saturation then sets a limit to the recordable photon rate.

A solution to the data transfer problem is the bh Express FLIM technique. Express FLIM does not transfer data into the computer photon by photon. Instead, the hardware of the SPC-QC module combines the information of all photons within a given pixel into a just two numbers. One is the first moment of the decay curve, the other the number of photons within the pixel. Both numbers are transferred to the computer at the end of each pixel. Even for fast scanning, the required data transfer rate can easily be achieved. The result is a lifetime image that contains first-moment values in the individual pixels. Four subsequent images from a sequence of 200-ms recordings (5 frames per second) are shown in Fig. 629. A video of the sequence is available under https://www.becker-hickl.com/products/express-flim/.

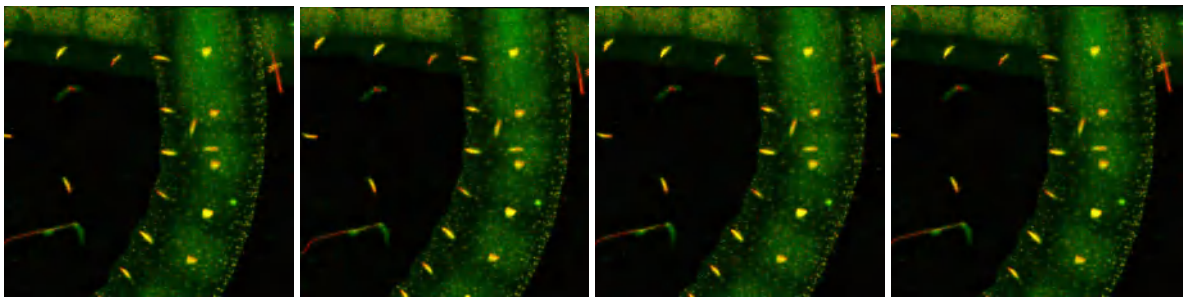


Fig. 629: Express-FLIM of a live Enchytraeus albidus. Autofluorescence, four subsequent images from a 5-frames/second sequence. DCS-120 system with SPC-QC-104. Photon Rate about $10 \cdot 10^6$ s^{-1}.

The technique delivers near-ideal photon efficiency - the standard deviation of the first moment is the square root of the photon number, $N^{1/2}$. The disadvantage is that only the 'Lifetime' of the decay data in the pixels is available. For fast imaging this is tolerable - the photon numbers in the pixels do not allow the data to be analysed with more sophisticated models, anyway.

Express FLIM uses special software, please see [72]. When you start the SPC-QC with the Express FLIM software it runs in the Express-FLIM mode. When you start it with SPCM it runs in the normal high-resolution FLIM mode. So another charm of Express FLIM is that *you are not forced to use it*. If you want precision FLIM, just start SPCM and the SPC-QC will perform like a 'normal' FLIM module, with full fluorescence decay data in the individual pixels, see Fig. 628.

The data shown in Fig. 629 were recorded with a single detector in a single channel of the SPC-QC module. It is easily possible to record data with three detectors in all three channels of the module. The data can be combined in a single FLIM image (or a single sequence of FLIM images) to reduce possible pile-up. However, at a count rate $10 \cdot 10^6$ s^{-1} as it was obtained from the Enchytraeus the pile up is negligible. Attempts to increase the count rate above $10 \cdot 10^6$ s^{-1} led into the usual problem: The worms died within a few seconds of illumination with the required laser power.

Photostability of the sample

A remark about sample photostability appears indicated here. In [116) it has been shown that count rates above about 1 MHz cause photobleaching and photodamage in the samples. Please see also Fig. 693 in this handbook. Yet the worms in the experiments shown above were imaged at count rates close to 10 MHz. What is the reason that this worked? The explanation is simple. For the standards of microscopy an Enchytraeus albidus is a huge object. The worms were imaged with an x10 lens, providing an image area of about 2 x 2 mm. The excitation power density is then much lower than for a typical image area of 50 x 50 µm, as it is used in cell imaging, and so is the damage effect on the object.

Express FLIM with the DCS-120 MACRO

If the scan area has a significant effect on the sample stability Express FLIM with the DCS-120 MACRO system should be even less invasive than microscopy at low magnification. Express FLIM experiments with the MACRO system confirmed this. Live *Hermetia illucens* larvae were imaged within a scan area of 10 x 10 mm, and with the full power of a BDS-SM 405-nm laser. The power at the input of the scanner was about 3 mW, the power in the sample plane about 0.6 mW. No detrimental effects on the worms were noticed within several minutes of scanning. Images are shown in Fig. 630.

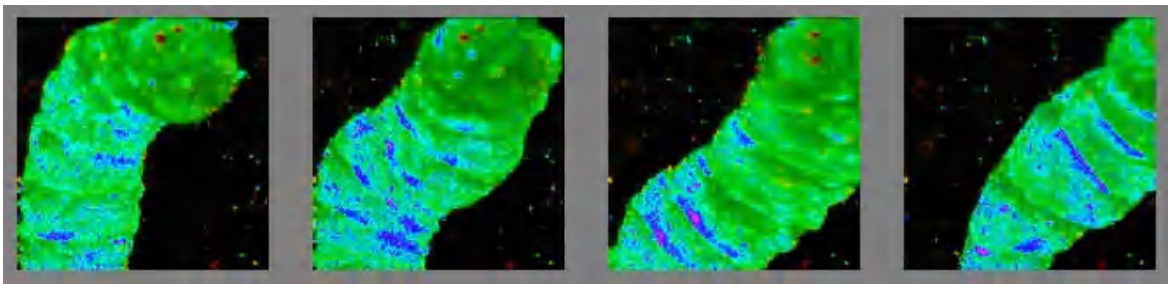


Fig. 630: Images of a *Hermetia illucens* larva, recorded at an image rate of 5 frames per second. Autofluorescence, Image area 10 x 10 mm

Fast FLIM by Time-Tag Recording and Off-Line Image Buildup

A third way of recording fast dynamic lifetime effects is to do away with building up images online and record a continuous data stream of single photons and scan clock pulses instead. The data are then processed off-line to generate a sequence of images. The procedure is similar to Fast Online FLIM (page 415) except for the fact that no time and computation power is spent on building up and displaying images. The technique is efficient especially for recording at moderate count rates when the count rate is on the order of the pixel rate. Of course, it cannot be expected that a high signal-to noise ratio is achieved under these conditions. However, it is an advantage that the speed and signal-to-noise ratio can be traded against each other just by changing the binning of subsequent frames during off-line processing. An example is shown in Fig. 631. The figure shows three subsequent FLIM images from a beating mouse heart organoid, labelled with Fluo4-AM. The frame rate of the recording was 5 frames per second. The intensity trace on the upper right shows the individual beats over a time of about 30 seconds. Cursors in the trace can be used to select individual frames or a sequence of interest from the data stream. A video of the selected part of the sequence is available on https://www.becker-hickl.com/see-the-heart-of-your-mouse-beating/.

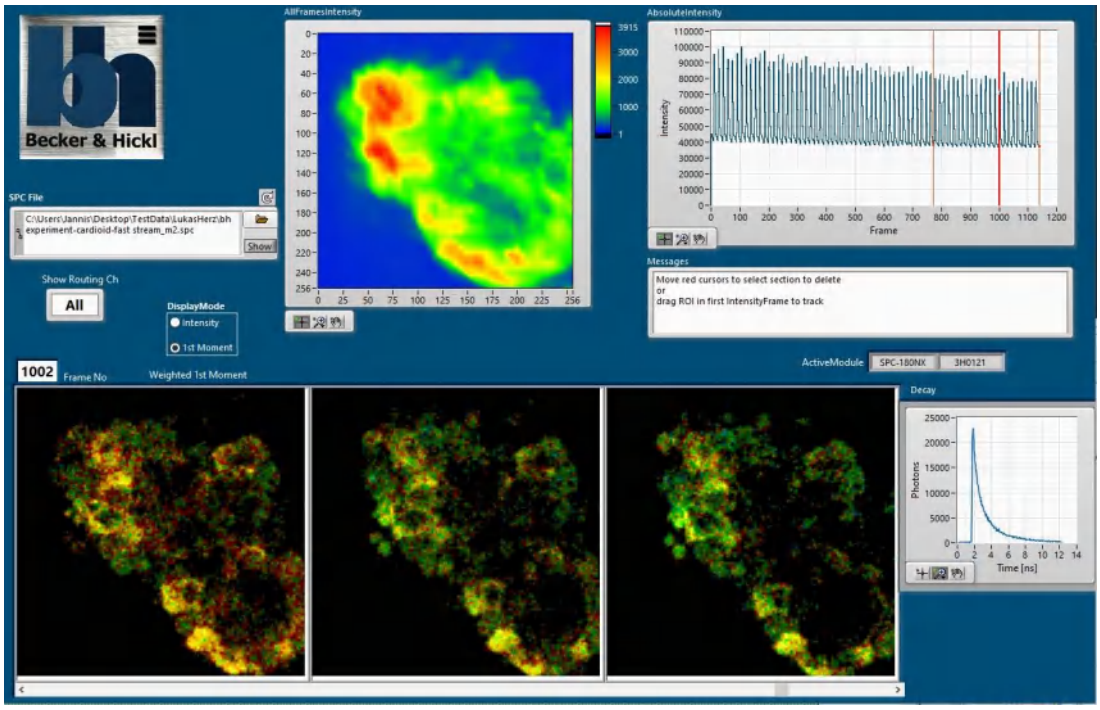


Fig. 631: Mouse heart organoid, 5 frames per second, time-tag data processed by bh SPCDynamics.

Lifetime-Intensity FLIM

TCSPC FLIM at High Count Rate

TCSPC FLIM images taken at high count rates often look unsightly, with less than ideal contrast and apparent loss in highlight detail. The source of the effect is not the 'pile-up' effect, as commonly believed. Pile-up would change the recorded lifetimes to lower values. However, a decrease of the recorded lifetime is not found in the data. This is understandable: The error in the recorded lifetime remains less than 5% up to a count rate of 20% of the excitation pulse frequency [154], see section Pile-Up, page 294. That means, for 80 MHz laser repetition rate count rates of more than 10 MHz can be used. Count rates that high are rarely encountered in FLIM measurements.

It turns out that the reason of poor contrast at high count rate is counting loss by the dead time of the TCSPC process. Counting loss causes a nonlinearity in the intensity scale [154], see 'Counting Loss', page 292. The function of the count number over intensity flattens out at high intensities, and eventually saturates. The effect is a loss in contrast in the bright parts of the image. This is exactly what is observed.

For most FLIM applications the nonlinearity of the intensity scale is a purely aesthetic problem: Information is derived from the shape of the decay curves, not from the intensities in the pixels. Instrumental solutions which sacrifice time resolution or photon efficiency for low dead time are therefore not appropriate [794]. A possible way to obtain short dead time without sacrificing temporal resolution is the bh FASTAC FLIM system [109]. However, the technical effort is high, and not normally justified to solve a purely aesthetic problem.

Technical Solution

A simple solution to the intensity-nonlinearity problem has been implemented in the bh SPC-160 and, recently, in the SPC-180 TCSPC modules. These modules have got a parallel counter that bypasses the TCSPC timing electronics. It counts the pulses directly at the output of the detector CFD, and puts the counter result for every pixel in the pixel clock entry in the parameter-tag data. The dead time of this counter is negligible - it is mainly determined by the detector and CFD dead time. This is about 5 ns. The FLIM images are built up by using the counter results as pixel intensities, and the data from the TCSPC timing electronics as pixel decay curves. The new 'Lifetime/Intensity' mode is available for the SPC-160 and the new SPC-180 family TCSPC modules.

Example

An example of the image improvement is shown in Fig. 632. The images were recorded with a DCS-120 Confocal FLIM system using SPC-180NX TCSPC modules. The sample was a stained mouse kidney section (Invitrogen F24630). The excitation wavelength was 480 nm, the detection wavelength interval 500 to 680 nm. The images were recorded with 512 x 512 pixels, and 1024 time channels per pixel. The recorded count rate averaged over the image was 5.6 MHz. The image on the left was created by the new Lifetime/Intensity mode, the image on the right by the traditional FLIM mode.

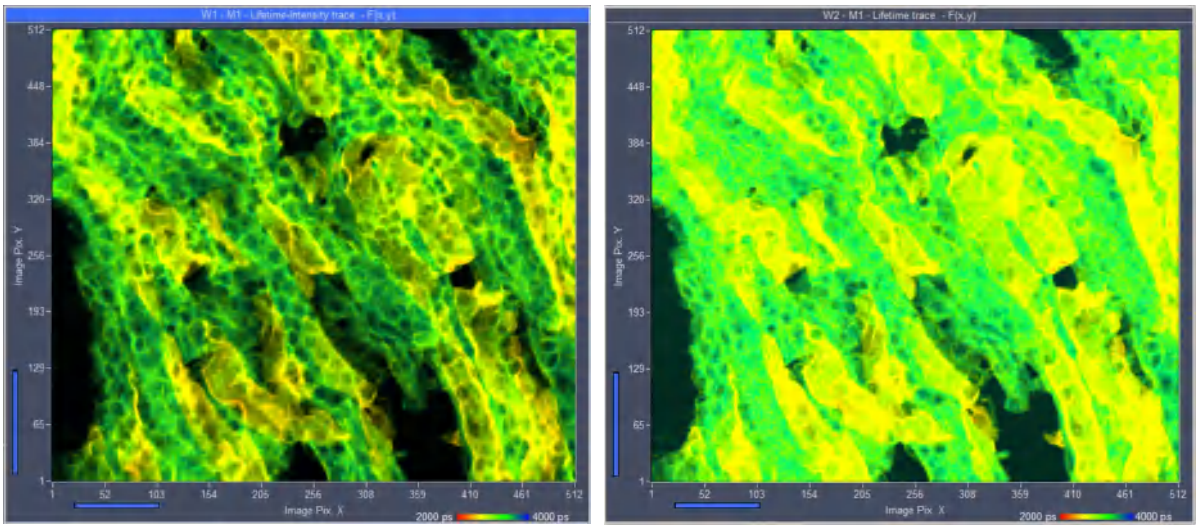


Fig. 632: FLIM images recorded from an Invitrogen F24630 Mouse kidney section. Left: New Lifetime/Intensity mode. Right: Traditional FLIM mode. 512 x 512 pixels, 1024 time channels, online-lifetime display function of SPCM software. Lifetime scale 2000 ps to 4000 ps. Average (recorded) count rate 5.5 MHz.

Parameter Setup for Lifetime-Intensity FLIM

The Lifetime/Intensity mode is available in the SPCM data acquisition software, Version 9.86 of June 8, 2021 or later. The implementation in the user interface and the parameter setup are shown in Fig. 633 and Fig. 634. In the 'System Parameters', click on 'Configure' and enable 'Intensity Image / Build Image'. This enables the parallel counter, puts the pixel intensities in the photon data stream, and instructs the software to build up an array of pixel intensities.

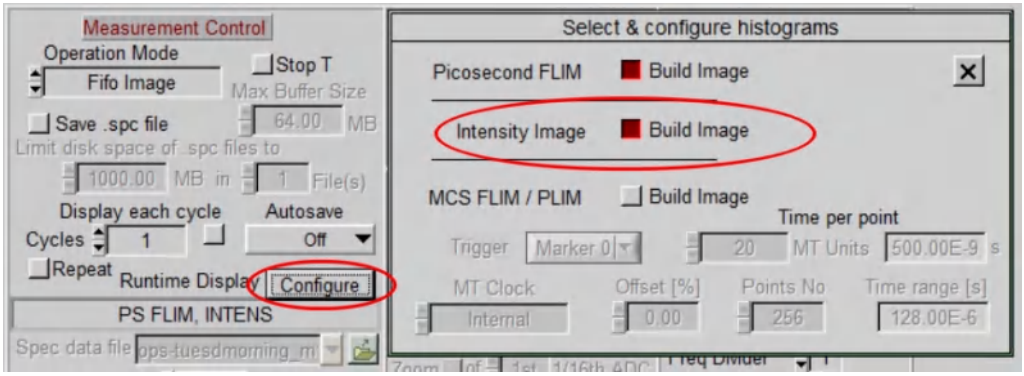


Fig. 633: System parameters for intensity imaging via the parallel counter channel. SPCM builds up an array of the pixel intensities recorded by the parallel counter.

In the 3D Trace parameters (accessible via 'Parameters' or right mouse click in an image window), select 'Lifet+I' (Lifetime + Intensity) as a data type, see Fig. 634. You can select 'Lifet+I' for one channel or for several channels simultaneously. In Fig. 634 it has been set for Display Window 1, Display Window 2 shows a 'normal' lifetime image created by the online-lifetime function of SPCM [108], see 'Fast Online FLIM with Standard bh TCSPC Systems', page 415. The images for a second TCSPC module, M2, have been turned off. With the settings shown, SPCM displays the two images shown in Fig. 632.

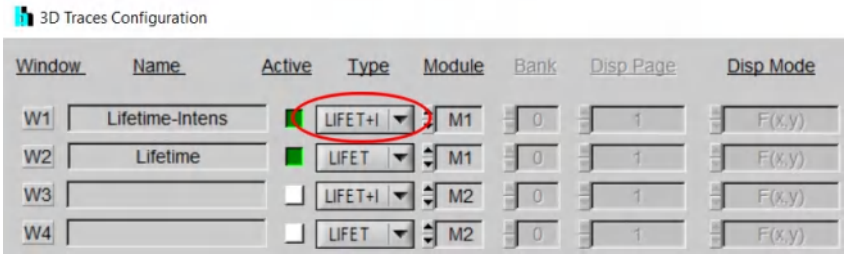


Fig. 634: Enabling the buildup of a Lifetime/Intensity image using the intensity values from the parallel counter

Analysis with SPCImage NG

Analysis of Lifetime/Intensity data is implemented in SPCImage NG, Version 8.4 or later. Data analysis is performed the usual way, see chapter 'SPCImage NG Data Analysis Software'. Right-click into the SPCM display window of interest, and select 'Send Data to SPCImage', or click into 'Main' and 'Send Data to SPCImage'. SPCImage recognises that the data are Lifetime/Intensity data, and handles them accordingly. That means, the decay curves are taken from the normal FLIM data array, but the intensities come from the array of pixel photon numbers created by the parallel counter channel. To start the data analysis, select an appropriate decay model, and start the procedure via 'Calculate', 'Decay Matrix'. The result for the data of Fig. 632, left, is shown in Fig. 635.

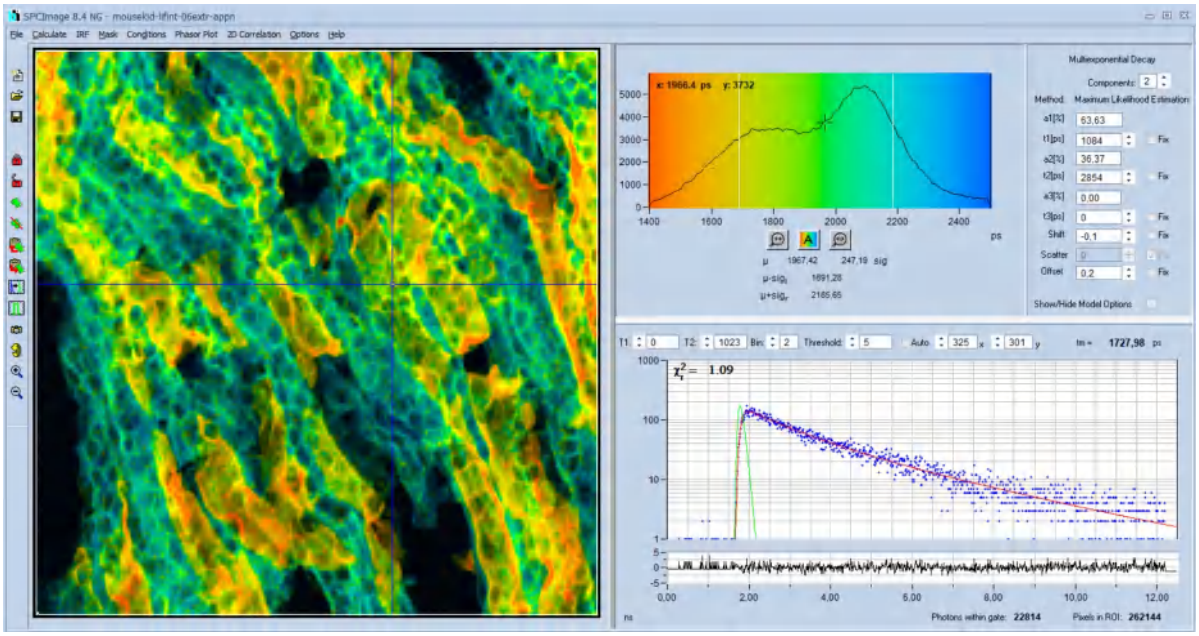


Fig. 635: Analysis of Lifetime / Intensity data by SPCImage NG. Mean lifetime of double-exponential decay, t_m, lifetime range from 1400 ps to 2500 ps.

DIC FLIM

FLIM images are usually built up by using the number of photons per pixel as brightness, and the lifetimes or other parameters of the decay functions as colour. This is not necessarily the best way to present the data. FLIM applications usually exploit the fact that the lifetime information is inherently ‘ratiometric’, i.e. independent of the concentration of the dye. The brightness information, which depends on the concentration, is either discarded altogether, or only used to help display the spatial structure of the sample. It may therefore be reasonable to replace the brightness with an another optical parameter. An extremely useful parameter has been found refractive index variation. Refractive index variation can be recorded by differen-

tial interference contrast (DIC) imaging. For optical principle please see [952]. The procedure of recording a DIC-FLIM image is as follows: In the first step a normal FLIM recording is performed by confocal scanning. Then the DIC assembly is switched into the beam path, and a lamp in the transmission path is turned on. A DIC image of the sample is scanned by the FLIM system with scan parameters identical to those of the previous FLIM recording. Thus, FLIM and DIC images are obtained at exactly the same image size, aspect ratio, and identical image distortion. The FLIM analysis software then overlays the DIC image with a colour related to the desired decay parameter of the FLIM data.

An example is shown in Fig. 636. It shows a mouse kidney sample, Invitrogen / Molecular Probes F24630, stained with Alexa 488 WGA and Alexa 468 phalloidin. The images were recorded by a Becker & Hickl DCS-120 confocal scanning FLIM system attached to a Zeiss Axio Observer. The fluorescence intensity image extracted from the FLIM data is shown left. A normal FLIM image is shown second left. It is a combination of the intensity data with the fluorescence lifetime. The DIC image is shown second right. The combination of the DIC data with the lifetime data is shown on the right.

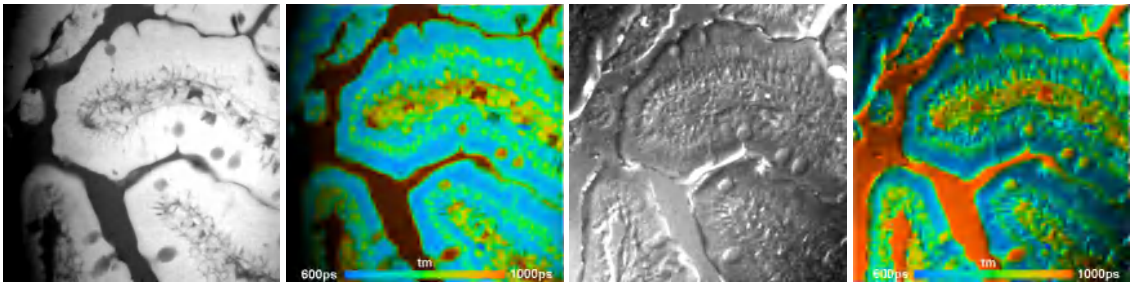


Fig. 636: Left to right: Fluorescence intensity image, FLIM image, DIC image, and combination of DIC image with lifetime data. bh DCS-120 confocal scanning FLIM system.

Bi-Directional Scanning

There are two different ways to raster-scan a sample in a laser scanning microscope. Unidirectional scanning uses a linear forwards scan and a fast 'flyback'. Data are recorded only during the forward scan. Bidirectional scanning uses a linear scan in both directions, and records data both during the forward and the backward scan. The differences are shown in Fig. 637.

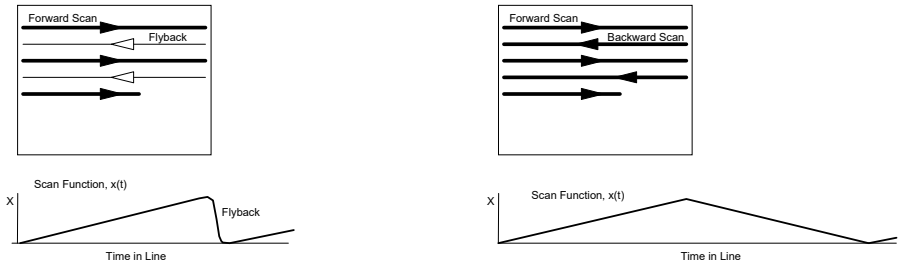


Fig. 637: Unidirectional scan (left) and bidirectional scan (right)

At first glance, a bidirectional scanning appears far more efficient than a unidirectional one. No time has to be wasted for the flyback, the acceleration forces acting on the scan mirrors are lower, and there is no need to turn off the excitation laser during the beam flyback. However, these advantages come at a price. Due to dynamic effects, there is a lag (or phase shift) of the scanner position behind the scanner control voltage. The result is a horizontal shift of the image data between the forward scan and the backward scan. The size of the shift depends on the scan speed and is thus not easy to correct. Moreover, the horizontal scan must be linear (or at least symmetrical) within 0.1% of the image size to avoid a mismatch of the forward and backward scan data. This is not easy to achieve, especially if high scan rates are desired. A unidirectional scan does not have these problems. The scanner lag does not matter and a much larger nonlinearity can be tolerated. The beam flyback can be made much faster than the forward scan. Even for the fastest scan rates, it normally requires no more than 10% to 20% of the line time. The speed advantage of a bidirectional scan is therefore smaller than commonly believed. Nevertheless, almost all laser scanning microscopes and a number of clinical scanning systems have a bidirectional scan implemented, or offer it at least as an option. A FLIM system attached to these systems should therefore be able to record data with a bidirectional scan.

FLIM data recording in combination with bidirectional scanning has been implemented with Version 9.73 of the bh SPCM software. The data are recorded in the FIFO imaging mode, the synchronisation of the recording with the scanning is defined in the 'More Parameters' panel of the FIFO Imaging mode, see page 766.

Bidirectional recording works for all bh TCSPC modules which have the FIFO Imaging (software accumulation) mode implemented. That means the function is available for all SPC-150, SPC-150N, SPC-150NX, SPC-160, and SPC-180 modules. It works also for SPC-830 modules manufactured later than May 2007 [64]. The structure of the recorded data is the same as for unidirectional scanning, and the same pixel numbers and time channel numbers can be achieved. The online intensity and lifetime image display functions of the SPCM software are available, and the recorded data can be analysed by bh SPCImage FLIM data analysis software as usual.

FLIM data recorded by bidirectional scanning are shown in Fig. 638, left and right. The data were recorded by a bh Simple-Tau 152 FLIM system, with two SPC-150 TCSPC FLIM modules, in combination with a Zeiss LSM 880 [69]. The sample was excited by the 445 nm ps diode laser of the LSM 880, the fluorescence was recorded via the confocal port of the scan

head. The image on the left shows a convallaria sample scanned with 512 x 512 pixels, the image on the right a BPAE cell sample scanned with 1024 x1024 pixels. Both were calculated by the online-lifetime function of the SPCM software [108], see 'Fast Online FLIM', page 415. No double structure or blurring of details is visible, showing that the data from the forward scan perfectly match those from the backward scan.

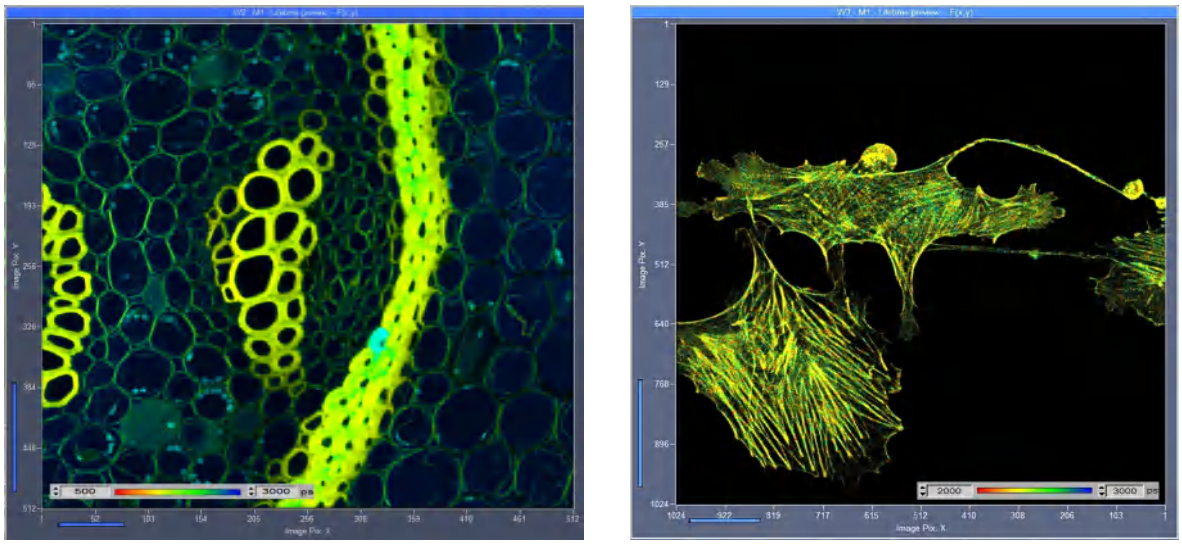


Fig. 638: Convallaria sample (left, 512 x 512 pixels) and BPAE Cell sample (right, 1024 x 1024 pixels), recorded with bidirectional scanning. SPC-150 TCSPC module, Zeiss LSM 880 in bidirectional scan mode. One-photon excitation at 445 nm. Images by online-lifetime function of SPCM software.

Fig. 639 shows the Convallaria data of Fig. 638, left, analysed by bh SPCImage FLIM data analysis software. No special adjustments were made, the data were analysed as described in Chapter 'SPCImage NG Data Analysis Software', page 861.

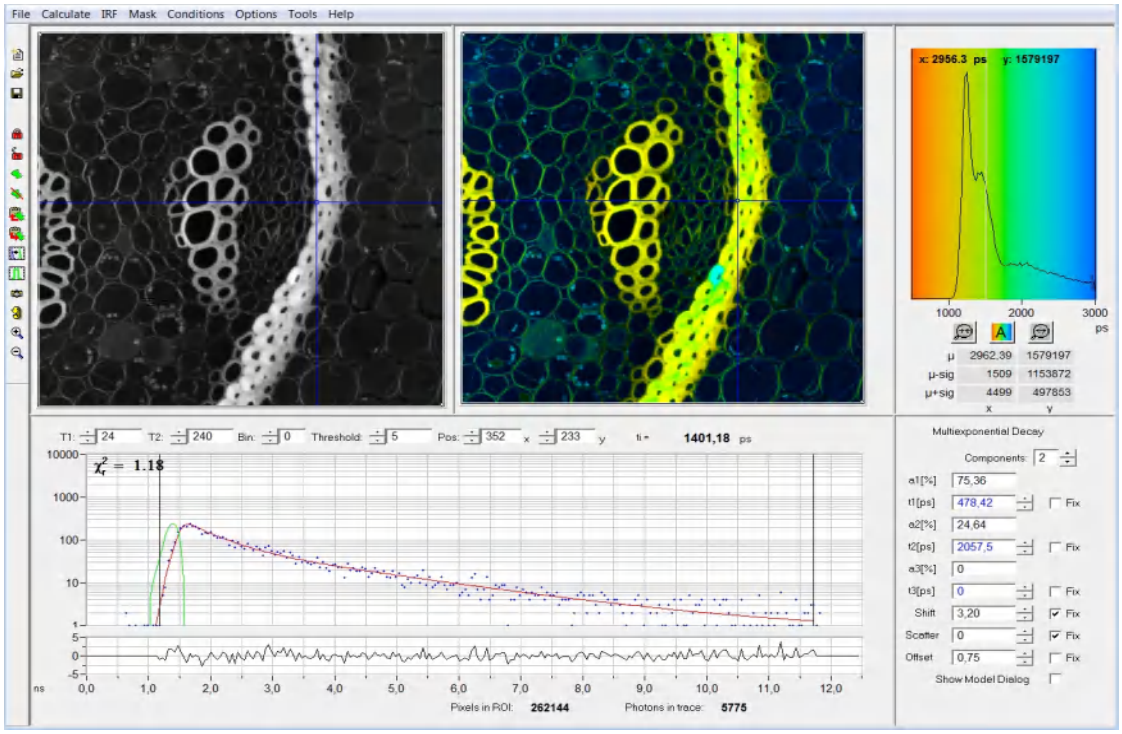


Fig. 639: Convallaria sample data as in Fig. 108, left, analysed with SPCImage. Double-exponential decay model, intensity-weighted lifetime of decay components.

Simultaneous FLIM/PLIM

There is a number of radiative relaxation mechanisms which occur on a much longer time scale than fluorescence. The commonly known one is phosphorescence, i.e. emission from the triplet state of organic dyes. Phosphorescence of organic dyes is usually weak at room temperature but can be strong at low temperatures, or if the dyes are embedded in a solid matrix. Strong emission in the microsecond and millisecond range is obtained also for lanthanide complexes [288] and organic complexes of ruthenium [597, 742], platinum [446, 742, 753, 1043, 1165, 1166], terbium, and palladium [753] and iridium [943]. Of special interest for live-cell imaging is that the luminescence of these complexes is strongly quenched by oxygen. The dyes are therefore used as oxygen sensors [496, 742, 753, 940, 941, 943, 1043, 1137]. Slow emission is also obtained from a large number of inorganic compounds, quantum dots, nanoparticles, and semiconductors. There are possible applications of these substances as sensors for local molecular environment parameters and as FRET donors [288]. Dos Santos et al. found purely organic compounds with oxygen-dependent lifetimes in the 100-ns range [1054]. Although it is not clear whether the emission comes from the singlet or from the triplet state also these compounds are potential oxygen sensors.

Principle

The measurement of long-lifetime luminescence in laser scanning FLIM faces a number of problems. The first problem is related to the excitation of the luminophore. Obviously, the laser pulse period must be longer than the luminescence lifetime. For ruthenium dyes with phosphorescence lifetimes below 1 us the reduction in laser repetition rate is still feasible, and lifetime images can be recorded in the normal FLIM acquisition modes of the bh TCSPC FLIM modules, see Hosny et al. [597]. However, the lifetimes for Platinum and Palladium-based dyes are on the order of 50 µs, and the lifetimes of Europium and Terbium dyes can be in the millisecond range. FLIM with these dyes requires a laser repetition rate no faster than 10 kHz, or a few 100 Hz, respectively. Generating such low repetition rates with pulsed lasers of a laser scanning microscopes is a problem. More important, reduction in repetition rate, for a given peak power, leads also to a reduction in average excitation power. Attempts to compensate for the drop in average power by higher peak power are limited by the capabilities of the laser, and by nonlinear effects or even ionisation in the sample. Moreover, any sample that emits phosphorescence necessarily also emits fluorescence. Because fluorescence is fast the peak power of fluorescence becomes very high. This causes transient overload effects in the detectors preventing the detection of phosphorescence in the first microseconds after the laser pulse. A better way to obtain higher average power is therefore to use longer laser pulse width. However, this is not easily possible for most of the lasers. Moreover, long laser pulse width is incompatible with multiphoton excitation.

Another problem is related to scanning. The time the scanner stays within the excited sample volume must be longer than the luminescence lifetime. If the scanner runs off the excited volume within the luminescence decay time photons in the tail of the decay function would be lost, and the recorded decay profile be distorted. Reasonable recording, even of pure intensity images, can thus only be obtained by very slow scanning. However, if both the pixel time and the pulse repetition period are long there are only a few excitation pulses within the pixel time. The number of excitation pulses in the pixels varies systematically. This induces Moiré effects in the images. The problem can be solved by synchronising the laser pulses and the pixel frequency, but there is usually no provision for this in a normal laser scanning microscope. Without synchronisation, the pixel time had to be at least 100 times longer than the laser period. This leads to unacceptably long frame times.

Excitation Sequence

The problems described above are avoided by the excitation principle shown in Fig. 640. A high-frequency pulsed laser is used. However, the laser does not run continuously. Instead, it is turned on only for a short period of time, t_{on}, at the beginning of each pixel [104, 105, 161, 1043]. For the rest of the pixel time the laser is turned off. Within the on-time, t_{on}, the laser excites fluorescence, and builds up phosphorescence. Within the rest of the pixel dwell time, t_{off}, pure phosphorescence is obtained.

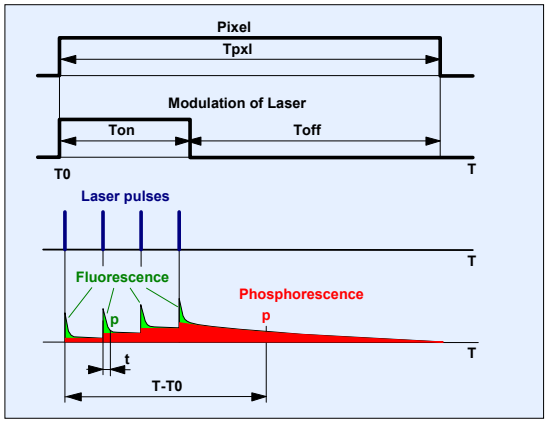


Fig. 640: Principle of Microsecond FLIM

TCSPC Recording

Lifetime images are built up by the process described in section 'Dual Time-Base Recording', page130. For each photon, the SPC module determines the time, t, within the laser pulse period, and the time, $T\text{-}T_0$, after the start of the modulation pulse. A fluorescence lifetime image is obtained by building up a photon distribution over the 'micro times', t, of the photons, and the scanner position, x,y, during the T_{on} periods. The phosphorescence lifetime image is obtained by building up a distribution over the macro-time differences, $T\text{-}T_0$, between the photon times, T, and the 'laser on' pulse edges, T_0. The spatial coordinates come from the scanner position in the moment of the photon detection. Thus, fluorescence and phosphorescence lifetime images are obtained simultaneously, in the same scan, and from photons excited by the same laser pulses. Please see Fig. 225, page 131 for further technical details. For parameter setup please see 'Microsecond Lifetime Imaging: MCS FLIM', page 767.

Laser On/Off control

Laser on-off control for the bh DCS-120 confocal FLIM system is integrated in the GVD-120 scan control card. Scan format and scan area definitions in the scanner control panel are the same as for standard FLIM. The differences are marked in Fig. 641. Both lasers are turned on. The second laser is disabled optically by turning the laser attenuator wheel at the scanner fully down. Laser multiplexing is set to 'Pixel'. The fraction of the pixel time in which 'Laser 1' is on is defined in the field left of '% for 1st laser'. This is the time when the laser is running, and fluorescence is measured. For the rest of the pixel time the laser is off, and phosphorescence is measured. 'Line Type' is set to 'Steps'. This prevents the scanner from running off the excited spot within the phosphorescence decay time. The 'Auto' button for the scan rate is disabled. The pixel time, T_{pxl}, must be few times longer than the expected phosphorescence decay time. For efficient recording, T_{pxl} should be a about the same as the 'Time Range' selected in the Configure panel, see Fig. 641, right. Please see [68] for further details.

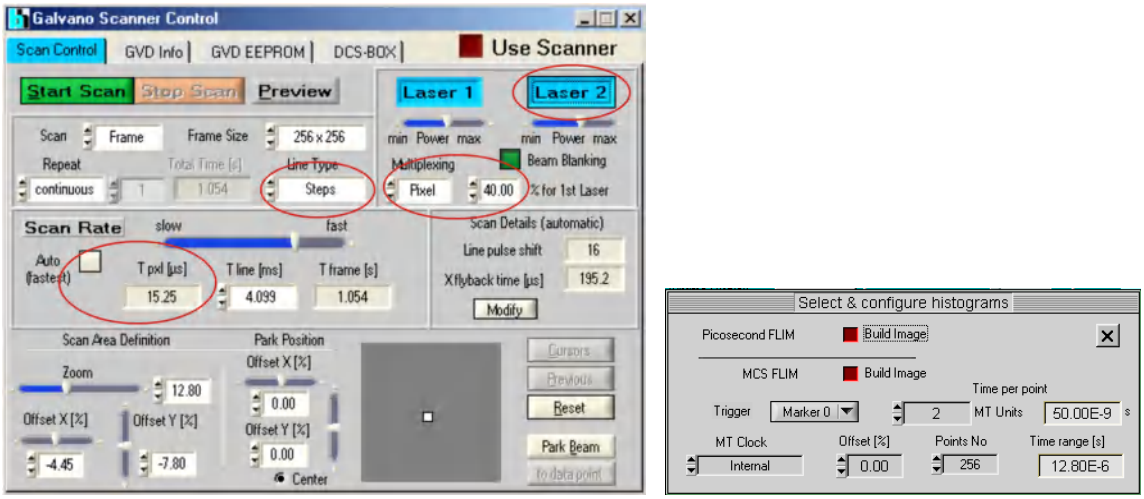


Fig. 641: DCS-120 PLIM. Left: Scan and laser control parameters. Right: PLIM timing parameters

For other microscopes, such as the Zeiss LSM 710/780/880/980 family, a bh DDG-210 card is added to the FLIM system. The card triggers on the pixel clock of the LSM, and sends a 'Laser On' signal to the laser controller of the microscope. The principle is shown in Fig. 642. The pixel clock is split off from the scan synchronisation cable and connected into the trigger input of the DDG card. The 'Laser On' signal is connected into the Laser control module of the Zeiss LSM via a 'PLIM' input. Please note that this input is optional; it has to be ordered via an 'INDIMO' (individual modification) request. A PLIM macro has to be installed to activate and de-activate the PLIM input. PLIM Laser control via the DDG-210 card has been integrated in the SPCM software, see Fig. 642, right. The laser-on time is defined on the left. The times on the right define a routing signal that is used to separate the photon from the laser-on and the laser-off times in the SPC module. The routing signal can be delayed with respect to the laser-modulation pulse to compensate for the delay in the AOM of the microscope. Please see [69] for further details.

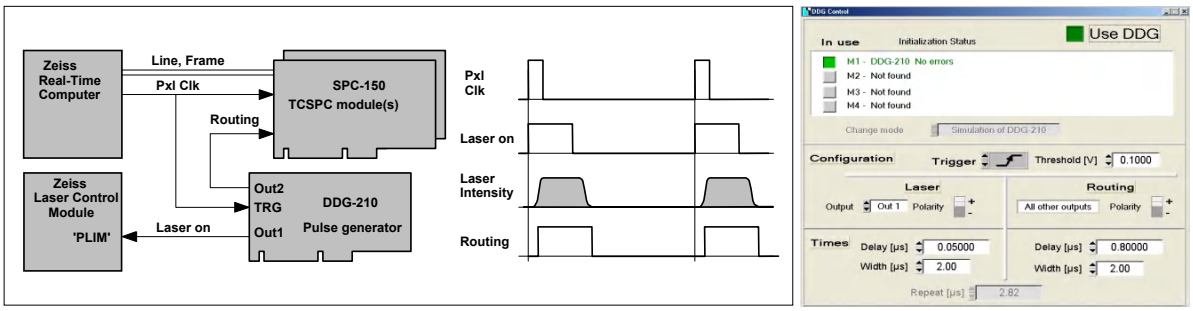


Fig. 642: Left: Principle of laser on/off control for the Zeiss LSMs. Right: Laser control panel.

Examples

Fluorescence and phosphorescence lifetime images of yeast cells stained with tris (2,2'-bipyridyl) dichlororuthenium (II) hexahydrate are shown in Fig. 74, left and right. The data were acquired by a DCS-120 system with the parameters shown in Fig. 641. The excitation wavelength was 473 nm.

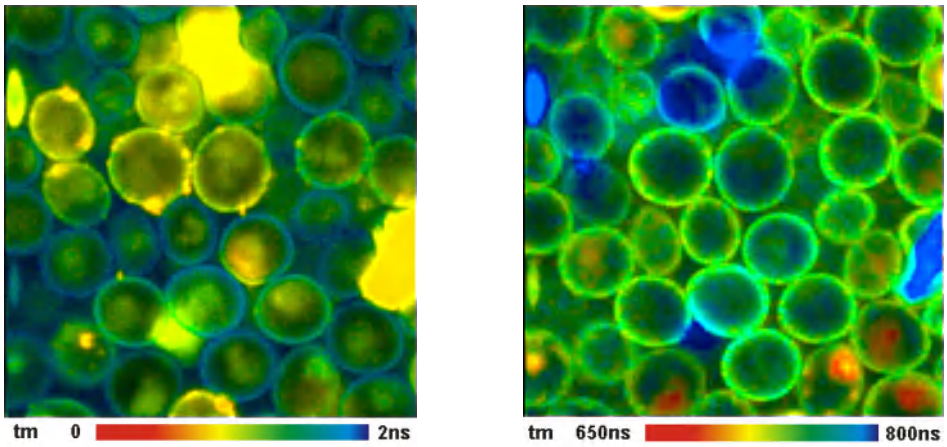


Fig. 643: FLIM and PLIM images of yeast cells stained with (2,2'-bipyridyl) dichlororuthenium (II) hexahydrate. Excitation 473 nm, 256x256 pixels. DCS-120 confocal FLIM system.

Fig. 644 shows FLIM and PLIM images of a pig skin sample stained with the same ruthenium dye as the yeast cells. The FLIM image (Fig. 644, left) shows the autofluorescence of the skin. The PLIM image (Fig. 644, right) shows the phosphorescence of the ruthenium dye. There is a clear variation in the phosphorescence lifetime, most likely caused by variation in the oxygen concentration.

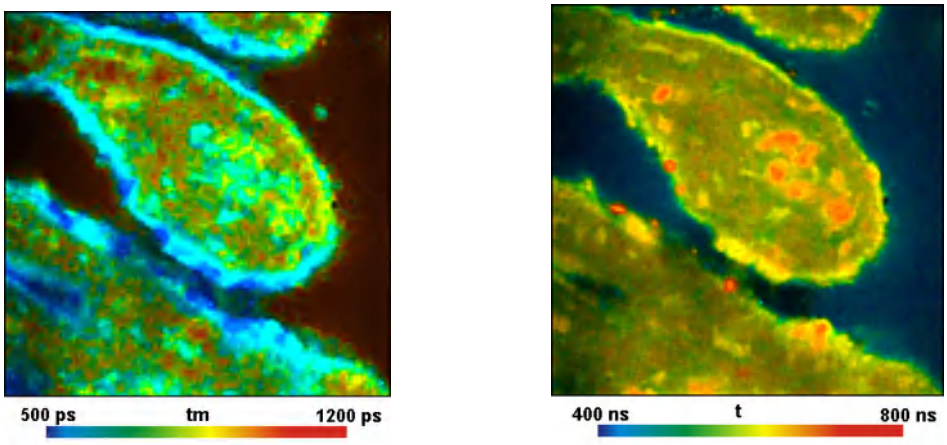


Fig. 644: Pig skin sample stained with ruthenium dye. Left: FLIM, autofluorescence. Right: PLIM

Phosphorescence is also obtained from various inorganic materials. Fig. 645 shows PLIM data of zinc oxide nanoparticles. The decay function is multi-exponential, with average (intensity-weighted) lifetimes up to 20 µs. The long lifetime can thus be used to track ZnO nanoparticles from sunscreens or cosmetic products in human skin [1049].

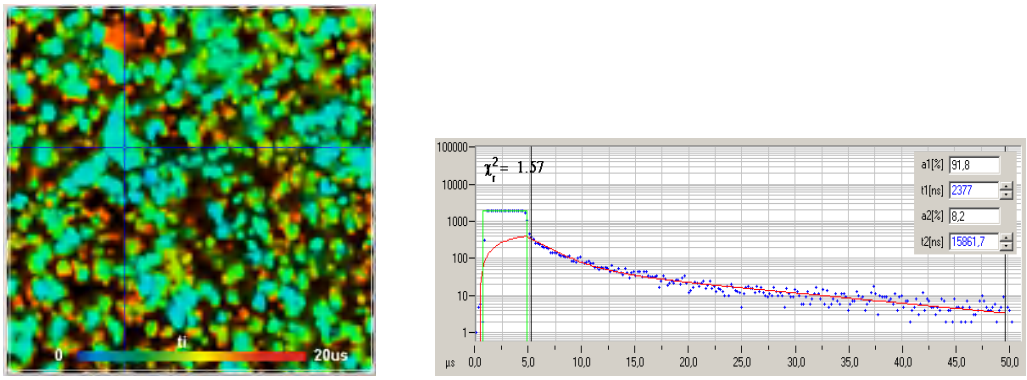


Fig. 645: PLIM of zinc oxide nanoparticles. Left: Lifetime image, intensity weighted lifetime of double-exponential fit. Right: Decay curve at cursor position. Zeiss LSM 710, two-photon excitation at 750 nm

Fig. 646 was obtained from an Autumit crystal (a uranium mineral). The phosphorescence lifetimes vary from about 100 us to 400 us. The lifetime image is shown on the left, decay curves of two selected spots on the right. The pixel time was 3.6 ms, the laser-on time 200 µs. The excitation wavelength was 405 nm, a 435 nm long-pass filter was used in the emission path. The Autumit phosphorescence was so strong that the laser power had to be reduced to the absolute minimum.

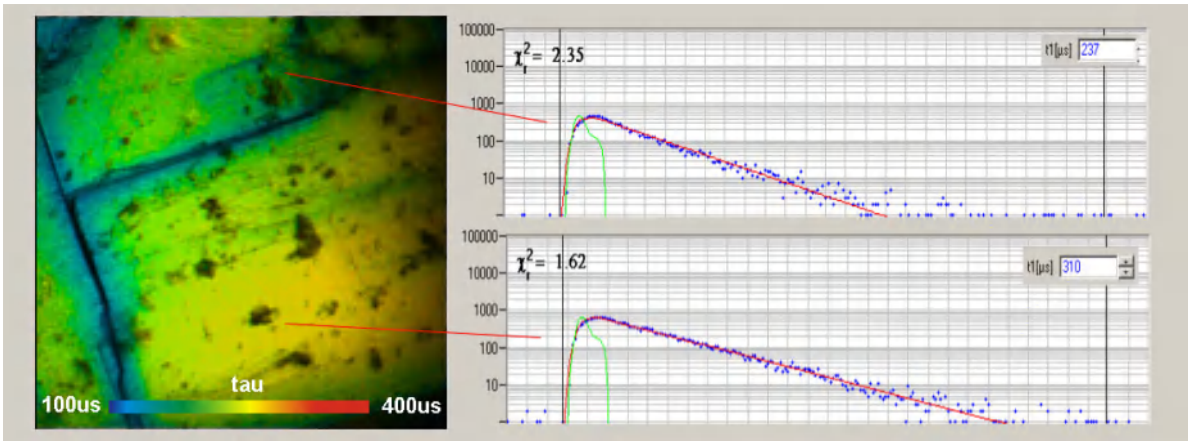


Fig. 646: PLIM image of a uranium mineral. Decay curves if two arbitrary selected spots are shown on the right. 256x256 pixels, 256 time channels, pixel time 3.6 ms, excitation 405 nm, emission filter long pass 435 nm.

Applications to oxygen measurement in live systems are described under 'Oxygen Sensing by Phosphorescence Lifetime Measurement, page 572, singlet-oxygen lifetime measurements in section 'Lifetime Imaging of Singlet-Oxygen Phosphorescence', page 394.

FLIM with Special Scanning Techniques

FLIM of Macroscopic Objects

Imaging in the Primary Image Plane of a Scanner

Macroscopic samples can be scanned in the primary image plane of a confocal scan head. The optical principle of the bh DCS-120 scan head is shown in Fig. 647, left, the complete instrument in Fig. 647, right.

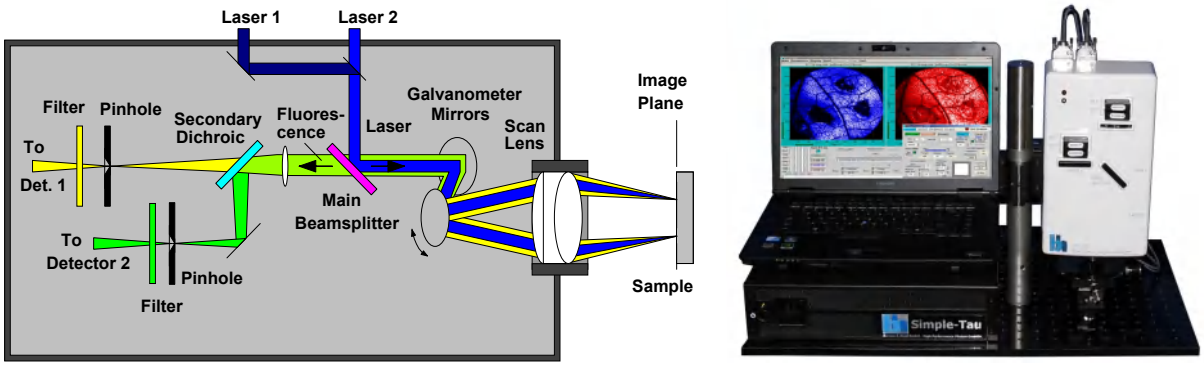


Fig. 647: Scanning of a macroscopic sample in the primary image plane of the DCS-120 scanner

The laser beam is scanned by two fast-moving galvanometer mirrors. The scan lens focuses the laser beam into an image plane shortly in front of the scanner. When the scanner is used with a microscope, the image plane of the scan lens coincides with the upper image plane of the microscope. For scanning large samples, the image plane of the scan lens is brought in coincidence with the sample surface. As the galvanometer mirrors change the beam angle the laser focus scans across the sample. Fluorescence light excited in the sample is collimated by the scan lens, de-scanned by the galvanometer mirrors, and separated from the excitation light by the main dichroic beamsplitter. The fluorescence beam is further split into two spectral or polarisation components, and focused into pinholes. Light passing the pinholes is sent to the detectors. The systems scans an image area of approximately 15 x15 mm. For imaging of objects larger than the scan area the system can be extended with a motorised sample stage. Please see [68] for further details. Applications to tumor detection in live mice are described in [1131].

Combination with Multi-Wavelength Detection

Macro FLIM can be combined with multi-wavelength detection. The principle is the same as for standard confocal FLIM through a microscope. The fluorescence is split into 16 spectral channels. These signals are detected by a PML-16 or PML-16 GASP 16-channel detector. For every photon, the detector delivers a timing pulse and a detector-channel number. Together with the scanner position in the moment of the detection the TCSPC process builds up a photon distribution over the image coordinates, the arrival time of the photon in the laser pulse period, and the wavelength of the photon. Please see 41Multi-Wavelength FLIM. Applications are described in [1355]. The selectivity of multi-wavelength FLIM can further be increased by excitation-wavelength multiplexing [1132]. Please see page 371 for details.

Examples

Fig. 648, Fig. 649 and Fig. 650 show a few examples. The samples were placed directly in the image plane in front of the scan lens of a bh DCS-120 scanner. Fig. 648 shows a leaf with a fungus infection. The fluorescence lifetimes in the infected areas is considerably longer than in the non-infected ones, see decay curves on the right.

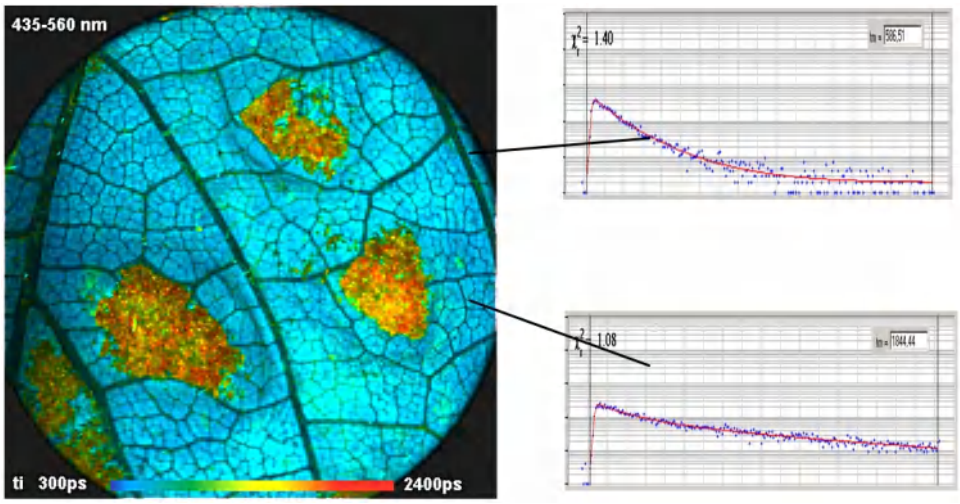


Fig. 648: FLIM in the image plane of the of a DCS-120 MACRO scanner. Leaf with a fungus infection. DCS-120 MACRO system, excitation with 405 nm ps diode laser. Image 512 x 512 pixels, 256 time channels.

Fig. 649 shows that good images can even be obtained from weakly fluorescent samples. The left image was recorded from a feather of a songbird, the image on the right from human skin. Both samples delivered about 100,000 counts per seconds when excited with the 405 nm laser.

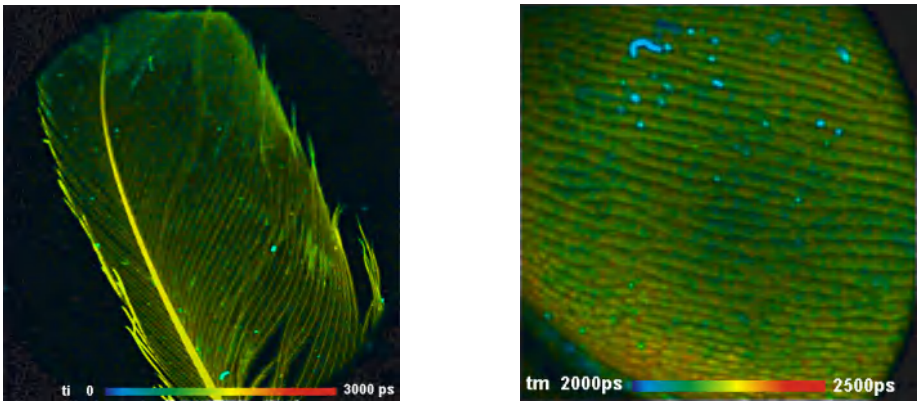


Fig. 649: Left: A feather of a songbird. Right: Lifetime image of the author's fingertip. The smudges of short lifetime are paper particles.

The DCS-120 MACRO scanner can be equipped with a wideband beamsplitter and a supercontinuum laser with a tuneable acousto-optical filter. Example images are shown in Fig. 650.

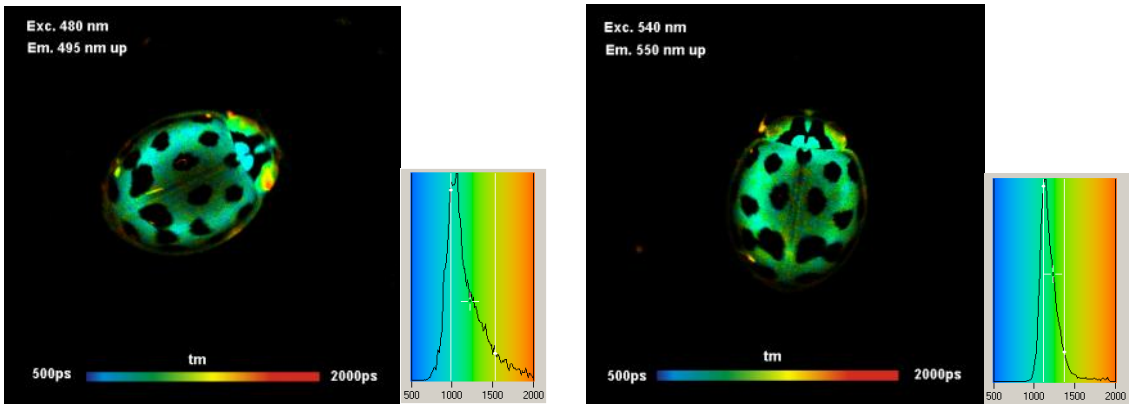


Fig. 650: *Coccinella* beetle, excited by supercontinuum laser with AOTF. Lifetime images and lifetime distributions over pixels. Excitation 480 nm (left) and 540 nm (right). 512 x 512 pixels, 256 time channels. Amplitude-weighted lifetime of double-exponential decay model.

Image Area and Spatial Resolution

The maximum diameter of the image area in the primary image plane of the scanner is about 15 mm. Smaller areas can be scanned by using the 'Zoom' function of the scanner, see [68]. The size of the laser spot in the image plane is about 15 µm. The resolution in the detection path is even higher because the numerical aperture in the focus of the scan lens is larger than for the laser beam. That means, full-size images could, in principle, be reasonably scanned with at least 1024 x 1024 pixels, for moderate oversampling even with 2048 x 2048 pixels. A high-resolution image with 2048 x 2048 pixels is shown in Fig. 651.

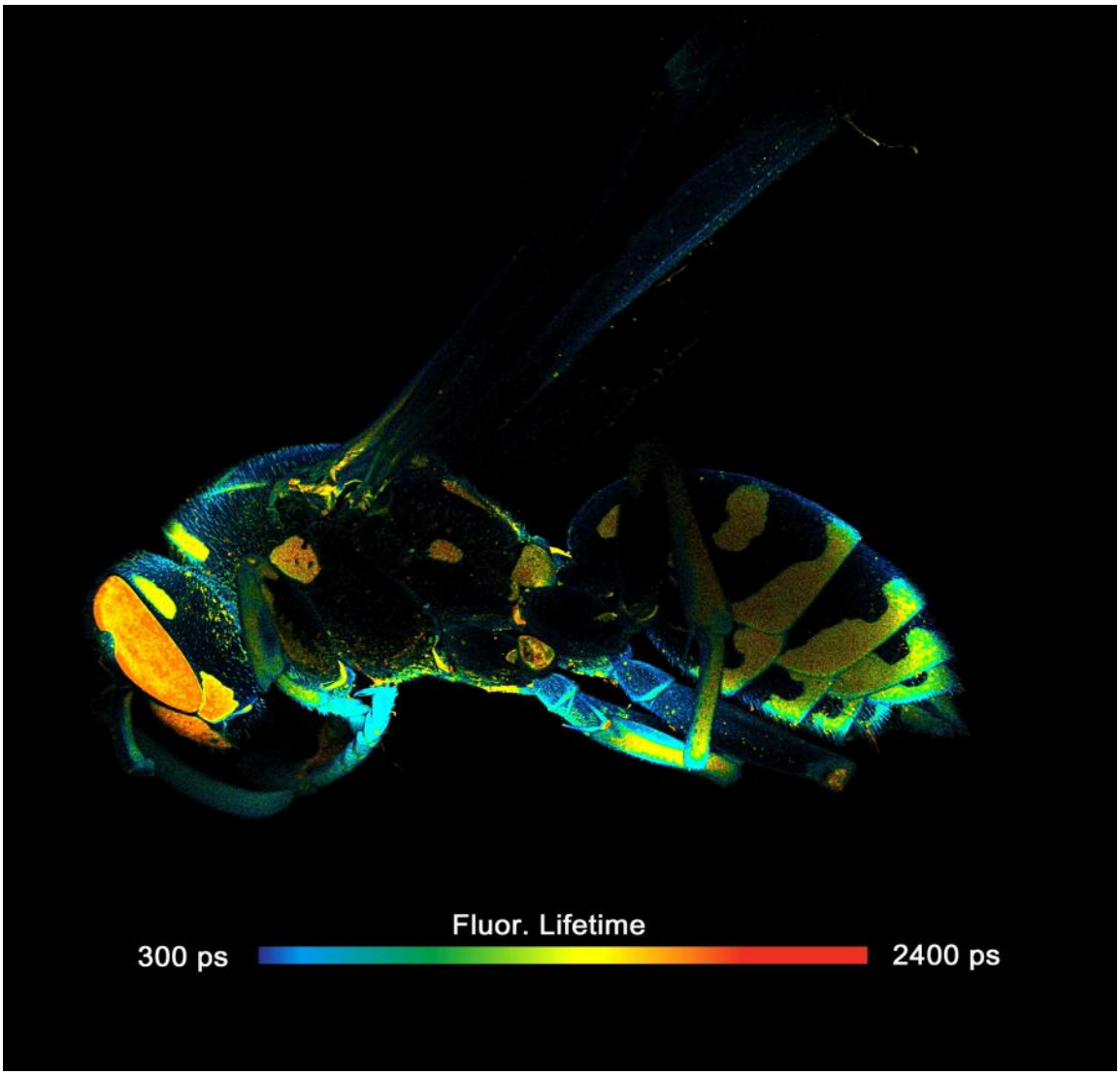


Fig. 651: High-resolution MACRO FLIM image with 2048 x 2048 pixels

Collection efficiency

The numerical aperture of the detection beam path is given by the beam path diameter (about 3 mm) and the focal length of the scan lens (40 mm). The collection efficiency is thus considerably lower than in combination with a microscope. However, macroscopic imaging can use much higher laser power, which partially compensates for low collection efficiency. Even weakly fluorescent samples, such as human skin or the feather shown in Fig. 649, deliver count rates on the order of 100,000 counts per second.

Acquisition Times

Under these conditions, a 512 x 512 pixel image of 5% lifetime accuracy is recorded within an acquisition time of about 1 minute, provided the default binning parameter of 1 (3 by s pixels) is used in SPCImage [174]. Much shorter acquisition times can be reached if the count rate is higher or the pixel number is lower. It is then even possible to run the DCS MACRO in the Express FLIM mode, please see 'Express FLIM', page 424.

Application to Metabolic Imaging

With a 375-nm BDL-SM or BDS-SM laser signals from NADH can be recorded. To determine the metabolic state double-exponential decay analysis is necessary, which requires to record about 1000 photons within the binning area in SPCImage [174]. It has been shown that this is well within the reach of the DCS MACRO system [184, 802, 803, 804, 1131, 1143, 1145, 1376]. Two examples are shown in Fig. 652, details are described in section 'Metabolic Imaging by Macro FLIM', page 542.

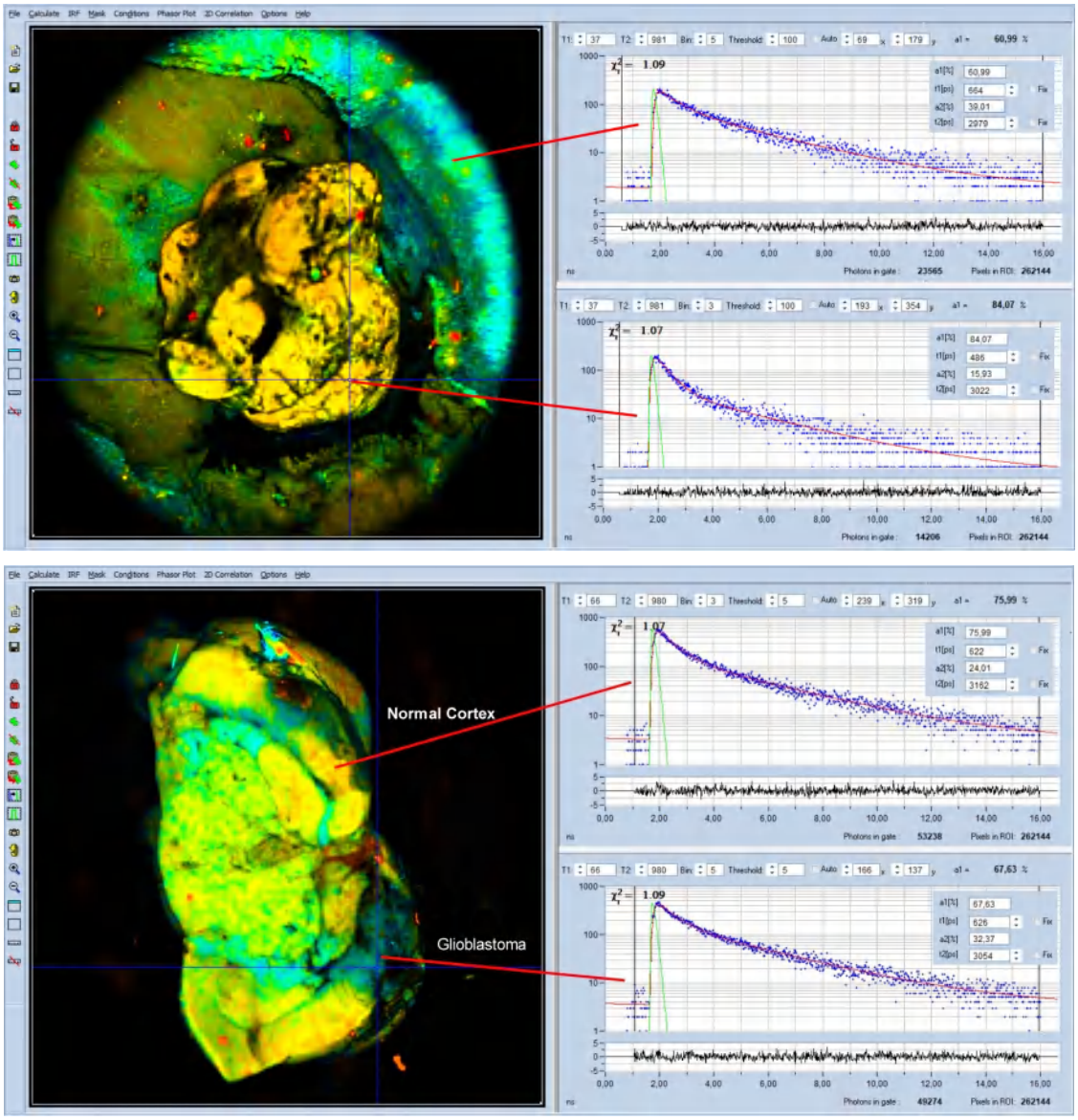


Fig. 652: Open tumor in a mouse (top) and rat brain with glioblastoma (bottom). Autofluorescence, excitation 375 nm, detection 430 to 475 nm

Scanning through Endoscopes

Scanning Through a Fibre Bundle

The principle used in the DCS MACRO system can extended to endoscopy. The laser beam is scanned over the input face of a fibre bundle endoscope, see Fig. 653. The excitation spot at the input face of the bundle is transferred to the distal bundle face. The distal face is either brought in direct contact with the sample, or imaged into deeper sample layers by a transfer lens. The fluorescence excited in the sample is transferred back to the input face, and back through the confocal scanner to the detectors. The setup has optical sectioning capability: Light from a point not in contact with the distal bundle face (or, if a transfer lens is used, not conjugate with it) does not form a sharp spot on the fibre bundle face. It is thus not focused into the pinholes.

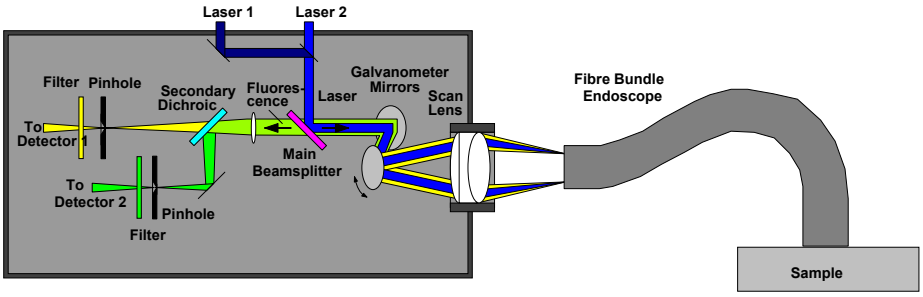


Fig. 653: Combination of a confocal scanner with a fibre bundle endoscope

An instrument of this type has been described by Kennedy et al. [656]. Excitation pulses of 488 nm wavelength were generated by frequency-doubled Ti:Sapphire laser. The excitation beam was scanned over the input face of a fibre bundle consisting of 30,000 single-mode fibres. The FLIM data were recorded by a PMH-100-1 detector and an SPC-830 TCSPC FLIM module. By terminating the distal fibre end with a miniature objective lens images at a resolution of 1.4 µm were obtained.

It should not be concealed, however, that the setup has also a few disadvantages: The effective numerical aperture of the detection channel is low, and the images get rastered by the fibre bundle structure. A significant problem is fluorescence from the fibre bundle itself, as our own experiments have painfully shown. With the commonly used image fibre bundles it is virtually impossible to record FLIM at excitation wavelengths shorter than 450 nm. The most important endogenous fluorophore, NADH, excites at wavelengths around 370 nm and is thus not accessible.

Scanning Through a Rigid Endoscope

Good results were obtained by combining the DSC scan head with a rigid periscope. The principle is shown in Fig. 654. L2 transfers the image plane scan lens into the plane of L3, L4 transfers the image in the plane of L3 into the plane of the object. L1 and L3 are field lenses: L1 forms an image of the scan lens on L3, L3 forms an image of L2 on L4. The lenses thus avoid that the field of view is obstructed by the transfer lenses, L2 and L4. The periscope is sealed with a glass plane at the distal end. The lenses in the periscope were achromatic doublets of 45 mm focal length and 8 mm diameter. The entire endoscope had a length of 38 cm and an outer diameter of 9 mm. The field of view has a maximum diameter of 6 mm.

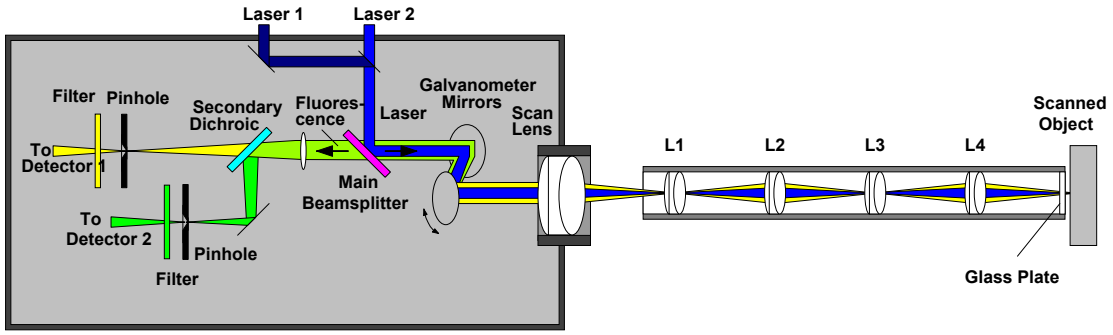


Fig. 654: Scanning through a rigid endoscope (not to scale). L2 and L4 are transfer lenses, L1 and L3 are field lenses.

Fig. 655 shows a lifetime image taken from a plant leaf. The scanned area is 5 x 5 mm, the image format is 512 x 512 pixels, 256 time channels per pixel. The excitation wavelength was 473 nm, the detection wavelength from 560 nm to 690 nm. Fig. 655 shows that the optical resolution is not impaired by the endoscope optics.

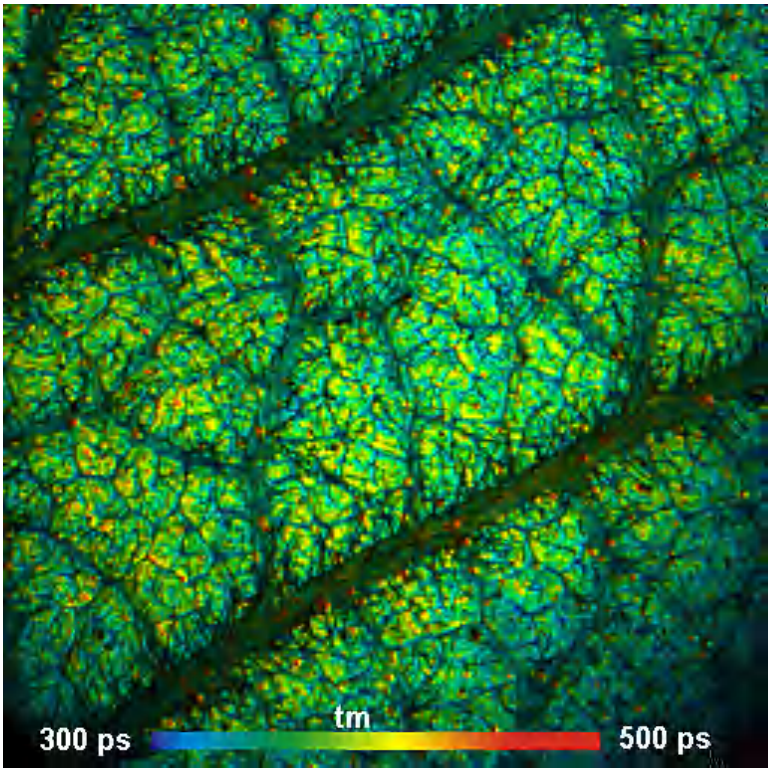


Fig. 655: Lifetime image of a leaf scanned through the endoscope. 512 x 512 pixels, 256 time channels. Amplitude-weighted lifetime of double-exponential decay. Excitation 473 nm, detection 560 to 690 nm.

Fig. 656 shows autofluorescence lifetime images of two lesions on human skin. The excitation wavelength was 405 nm. An area of 5 x 5 mm was scanned, the image format was 512 x 512 pixel, 256 time channels. The total acquisition time was 10 seconds. 10 frames were accumulated within this time. Although some blurring is caused by motion during the acquisition time the anatomical structure is still reasonably resolved. The images were recorded at an excitation power of 50 µW, measured in the sample plane. Note that this power was distributed over an area of 25 mm^2, corresponding to an excitation power of 2 µW per square millimeter. This is far below the permissible exposure for human tissue.

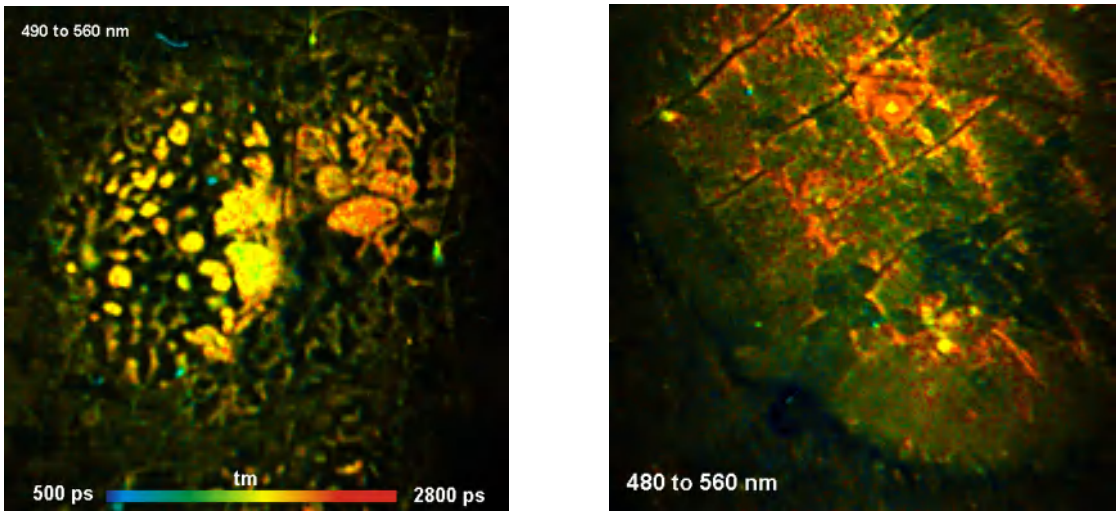


Fig. 656: Basal cell papilloma (left) and a keratomic lesion (right), scanned in vivo through the endoscope. Image size 5 x 5 mm, scanned with 512 x 512 pixels. Becker & Hickl DCS-120 confocal scanner and Simple-Tau 152 TCSPC FLIM system. Amplitude-weighted lifetime of double-exponential decay, lifetime range 500 to 2800 ps. Excitation wavelength 405 nm, detection wavelength 480 to 560 nm. Excitation power 50 µW, acquisition time 10 seconds.

2-Photon FLIM Through an Endoscope

It has been attempted to record 2-photon FLIM through an endoscope. The problem of endoscopic 2p FLIM is that reasonable excitation efficiency can only be obtained a high numerical aperture at the distal end of the endoscope. That means that either a large diameter of the entire endoscope or a short focal length at the distal end is needed. However, a short focal length means high magnification and, consequently, small field of view. Nevertheless, we have shown that 2p FLIM through an endoscope is possible, see Fig. 657 and Fig. 658. The endoscope had a numerical aperture of 0.5 at the distal end, a diameter of 10 mm and a length of 300 mm. The image shown was recorded with a DCS-120 MP system using bh SPC-150NX TCSPC/FLIM modules and HPM-100-40 hybrid detectors. The excitation wavelength was 785 nm, the detection wavelength interval 420 nm to 470 nm. The laser power at the distal end was about 5 mW.

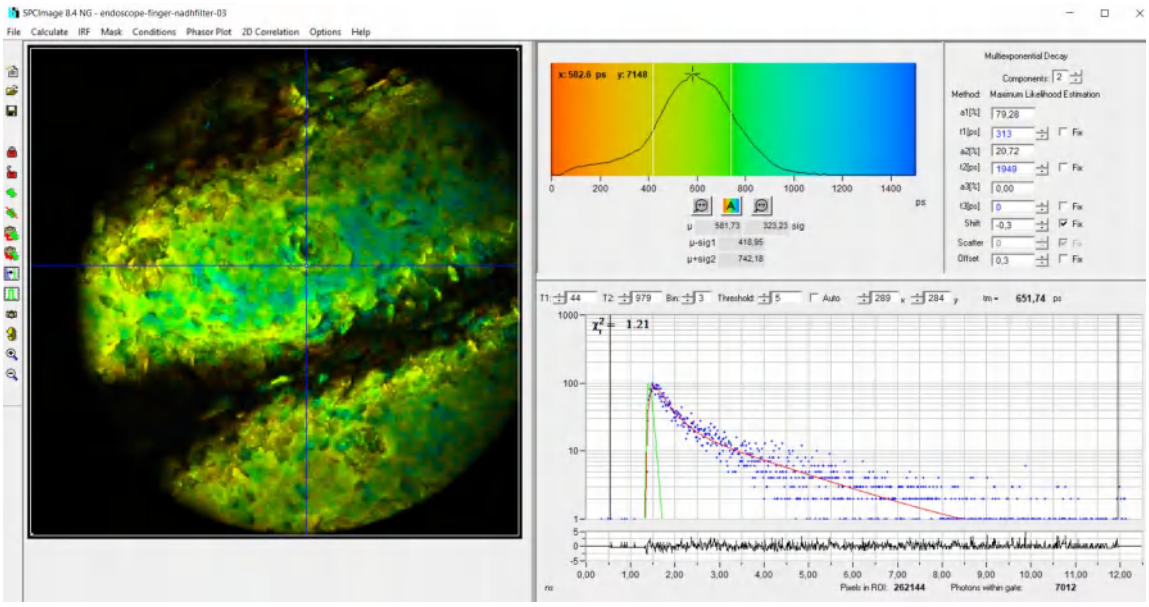


Fig. 657: 2p FLIM through an endoscope. Stratum corneum of human skin, analysis with SPCImage NG

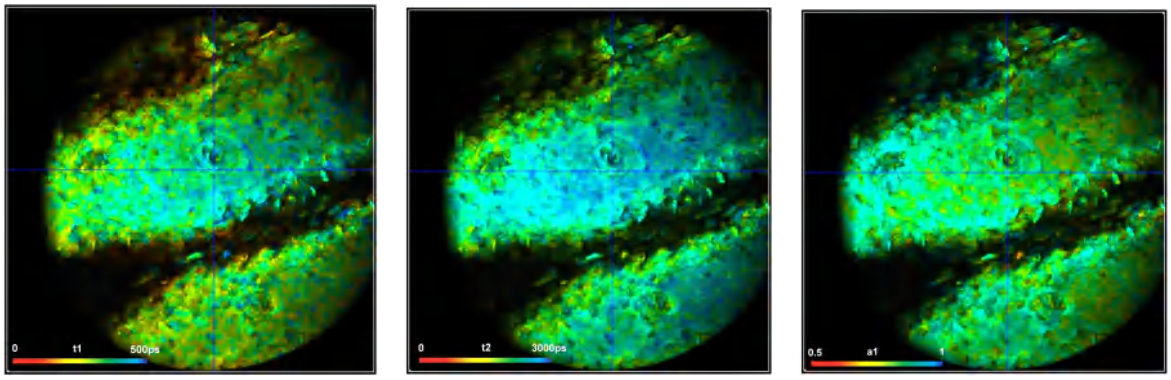


Fig. 658: 2p FLIM through an endoscope. Stratum corneum of human skin, images of decay components

Combination of Beam Scanning with a Motorised Sample Stage

Scanning in the primary image plane of a confocal scanner covers a sample area of about 15 mm diameter. In principle, a larger scan area can be obtained by inserting a lens system (a reversed telescope) between the scanner and the sample. However, the numerical aperture in the plane of the sample would decrease with increasing de-magnification factor. This is no problem for the excitation beam path. In the detection beam path, however, the amount of collected light and thus the sensitivity would decrease in proportion with the reverse scan area diameter. In principle, the NA problem can be solved by galvanometer mirrors of larger size. However larger mirrors are not only slower, they would also require an entirely new scanner design.

The problem can be solved by placing the sample on a motor stage, and run a Mosaic FLIM recording over a larger sample area. The combination of the DCS-120 MACRO system with a motor stage is shown in Fig. 659, left. The operation of the motor stage has been implemented in the SPCM software, version 9.76 of July 2017. Please see software chapter, ‘Motor Stage’, page 859 for details. An example of a large-area mosaic scan is shown in Fig. 659, right.



Fig. 659: Left: DCS-MACRO system with motor stage. Right: Large-area mosaic scan.

Scanning of Well Plates

In 2017 the bh DCS-120 confocal FLIM system has been upgraded by a software-controlled motor stage, see page 859. In this configuration, the system is able to scan well plates. The well plate is placed on the motor stage. A defined area within the first well is scanned by the optical scanner of the DCS system, then the operating software shifts the plate by the distance between the wells, and scans the next well. The advantage of confocal scanning is that data are obtained from a thin focal plane inside the wells. Therefore, the decay curves are not impaired by re-absorption and re-emission. Moreover, possible effects of rotational depolarisation are cancelled by the high NA of the microscope lens. The data are saved as a normal Mosaic-FLIM file of the SPCM operating software. A preliminary lifetime image can be dis-

played during the acquisition by the fast online-display functions of the SPCM software. Precision multi-exponential lifetime analysis is performed by bh SPCImage data analysis software.

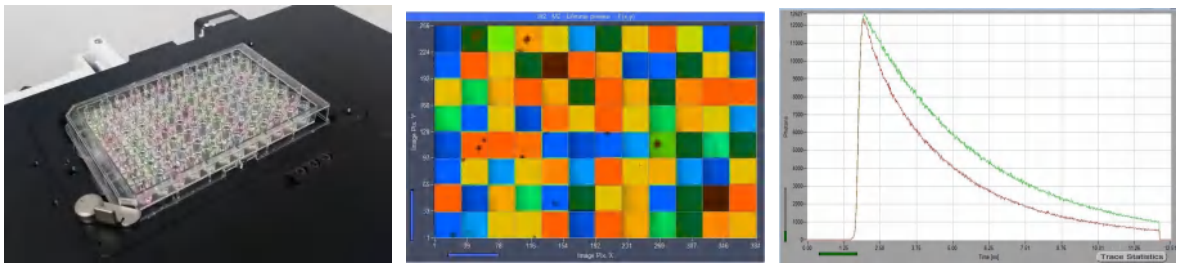


Fig. 660, left to right: Well plate on microscope stage, fluorescence-lifetime image, decay functions in wells 4 and 5, lower row.

FLIM of a Rotating Object

Small-animal tomography techniques - no matter whether optical or non-optical - often use rotation of the measurement object to obtain data for different projection angles. Although such techniques are not normally focusing on fluorescence lifetime detection they can be favourably supplemented by recording time-resolved data, especially fluorescence lifetime images or time-resolved diffuse reflection images. The fluorescence lifetime delivers direct information on molecular parameters, and time-resolved diffuse reflection data deliver scattering and absorption parameters from different tissue layers. In this section we show how fluorescence lifetime images of the entire circumferential surface of a rotating object can be obtained.

The optical principle is shown in Fig. 661. The object is placed on a table which rotates it around its vertical axis. Simultaneously, the object is scanned vertically by a fast galvanometer mirror. A bh BDS-SM picosecond diode laser is used for exciting fluorescence in the object. A lens, L1, focuses the laser beam into an intermediate image plane. A projection lens system, L2 and L3, projects this plane on the surface of the object. As the galvanometer mirror is moving, the laser spot moves up and down the surface of the object. With the rotation of the table, the entire surface of the object is scanned by the laser spot. Fluorescence emitted at the object is projected back into the intermediate image plane and collimated by L1. It is separated from the excitation light by a dichroic mirror. It then passes a long-pass or bandpass filter and is detected by a PMC-150 or HPM-100 detector. The imaging setup is shown in Fig. 662.

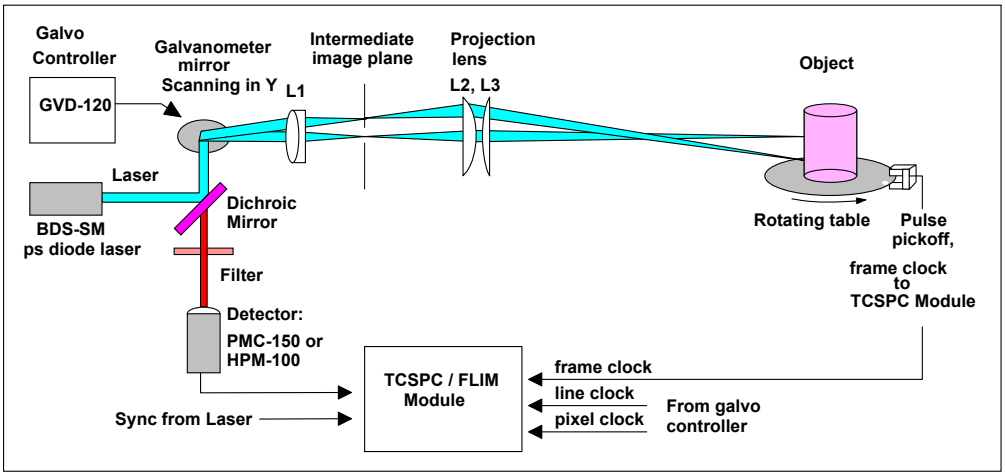


Fig. 661: Principle of the optical system

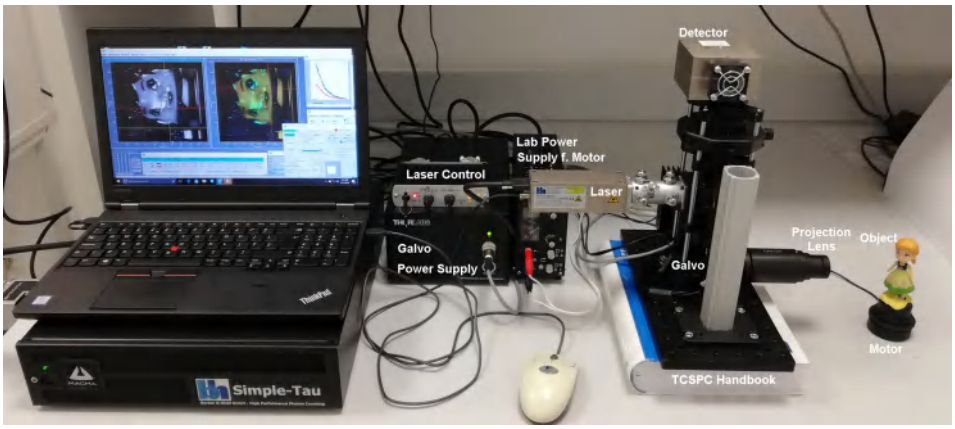


Fig. 662: Imaging setup, with laser, TCSPC system, and optical system

We tested the setup with the test object shown in Fig. 663, left. A lifetime image provided online by SPCM software is shown in Fig. 663, middle. The lifetime range is from 1000 ps (blue) to 3000 ps (red). A decay curve in a selected spot of the image is shown in Fig. 663, right.

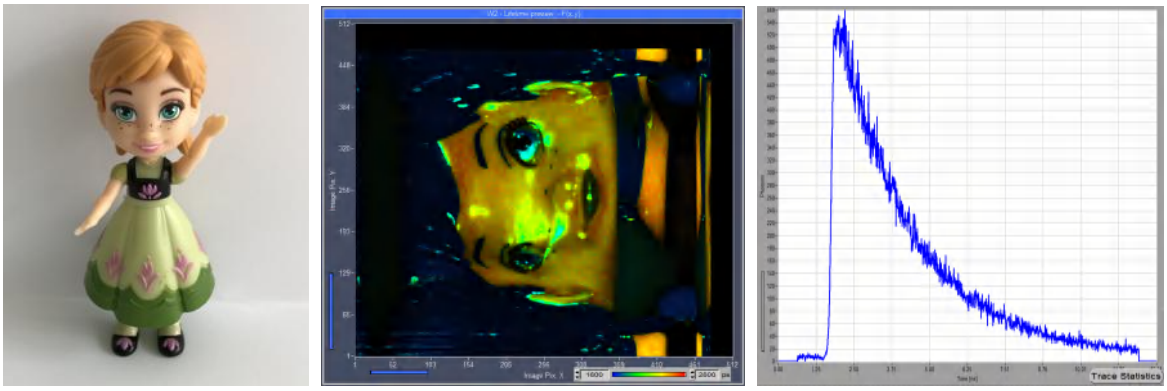


Fig. 663, left to right: Test object, lifetime image, decay curve in selected spot. 512 x 512 pixels, 1024 time channels per pixel. Image and decay curve created by online display functions of SPCM data acquisition software.

The data shown in Fig. 663 were recorded with a laser power of about 100 µW. The average count rate at this laser power was about 400,000 s^{-1} on average, and about 900,000 s^{-1} in the bright areas. The acquisition time was about one minute, i.e. photons from 12 rotations of the object were accumulated.

The setup described above provides a relatively simple and inexpensive way to record lifetime images of the entire circumferential surface of a three-dimensional object. A few non-ideal features should, however, be taken into regard.

The first one is that the path length to the surface of the object and back varies with the surface topography. One millimeter variation in surface topography causes 2 mm path length difference, and thus a difference of 6.6 ps in transit time. The transit time difference transfers directly into a shift in the measured fluorescence lifetime. The problem can, in principle, be solved by using a floating IRF in SPCImage. However, a floating IRF increases the noise in the calculated lifetime, especially for fast decay components in the range of the IRF width.

Another feature is the low collection efficiency of the optics. For a given diameter of the galvanometer mirror, there is a reciprocal relationship between the maximum diameter of the scan area and the numerical aperture of the light collection. The light collection efficiency is therefore lower than in a scanning system with a microscope. However, different than in microscopy, the excitation light is distributed over a large scan area. The excitation dose per area unit is therefore much lower. Consequently, photobleaching and photodamage are far less a

problem. The low collection efficiency can therefore partially be compensated by using higher excitation power.

Polygon Scanners

In-vivo imaging systems often use fast-rotating polygon scanners to obtain imaging at near video rate. If such systems have or can provide an input for a BDL or BDS series laser and an output to a FLIM detector they can easily be combined with bh FLIM systems, see also 'Ophthalmic FLIM', page 590. The principle of a polygon scanner and its connection to a bh FLIM system are shown in Fig. 664.

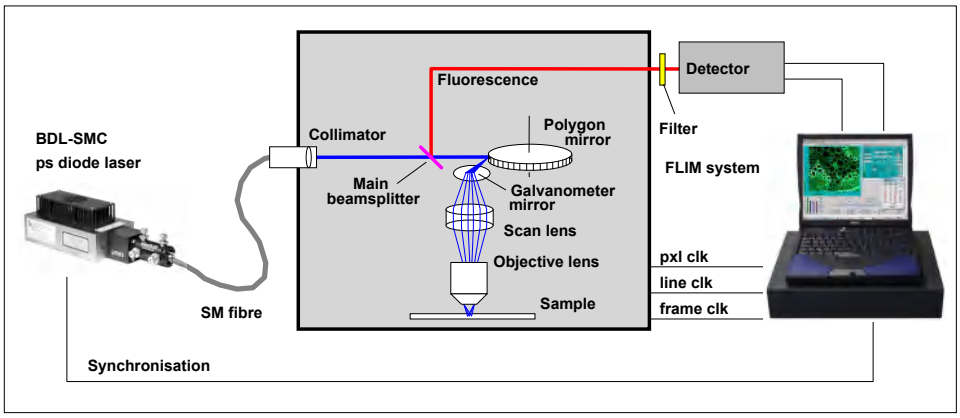


Fig. 664: FLIM with a polygon scanner

Polygon scanners achieve pixel rates on the order of 10 MHz. As long as the scanner provides correct scan clock pulses such pixel rates are no basic problem for multi-dimensional TCSPC. A problem can occur in the FIFO imaging mode with external pixel clock: The pixel clock rate can be so high that the transfer of pixel clocks alone saturates the computer bus. The problem can be solved by recording with internal pixel clock. Internal pixel clock does not cause the same inconveniencies as for galvanometer scanners because the polygon scanner runs at constant speed. A pixel clock is therefore not needed, and, in most instances, even not provided by the scanner. Fig. 665 and Fig. 666 show FLIM data obtained with a bh Simple-Tau 150 and a 'Vivascope' system of Lucid, Rochester.

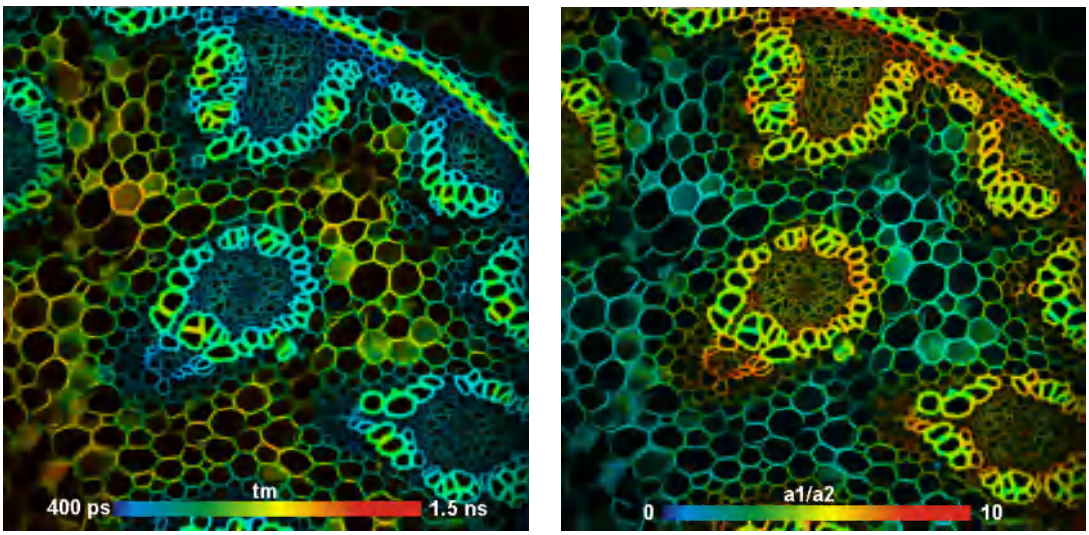


Fig. 665: Convallaria sample, 512 x512 pixels, 256 time channels. Double-exponential analysis. bh BDL-473-SMC laser and Simple-Tau 150 with Lucid Vivascope.

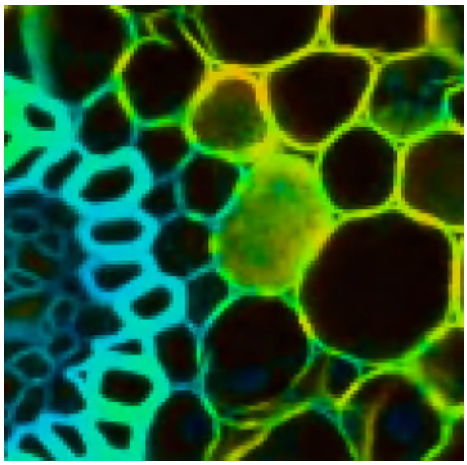


Fig. 666: Magnified detail of the image shown in Fig. 665, left. No synchronisation problems were found.

An important requirement to an optical system for time-resolved detection is that the beam path is free of optical reflections. Reflections show up as bumps in the recorded fluorescence decay profiles. No such artefacts have been found in the Vivascope, see Fig. 667.

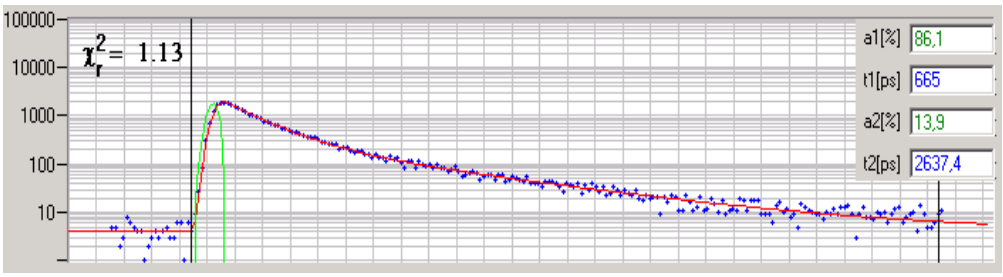


Fig. 667: Fluorescence decay in a selected spot of Fig. 665. No optical reflections are visible.

Fig. 668 shows an autofluorescence FLIM image of pig skin. A BDL-SMC-488 nm picosecond diode laser was used for excitation, FLIM was recorded by a bh Simple-Tau 150 system.

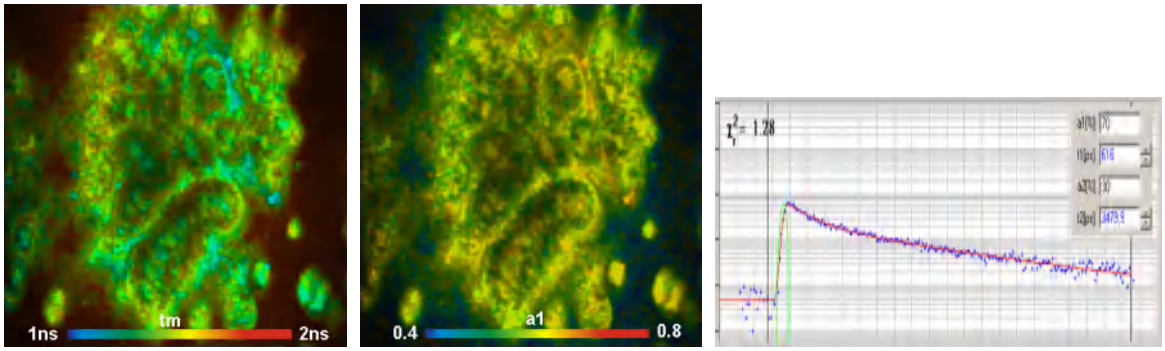


Fig. 668: Autofluorescence of Pig skin. Excitation BDL-SMC picosecond diode laser, 488 nm. Recorded by Simple-Tau 150 system with HPM-100-40 hybrid detector. Analysis by SPCImage, double-exponential decay model. Left: Amplitude-weighted lifetime, t_m. Middle: Amplitude of fast decay component. Right fluorescence decay in a 5 x 5 pixel area in the centre of the image. Data courtesy of Michael Roberts, University Adelaide.

Resolution and contrast at 488 nm excitation wavelength are excellent, and the decay data are clean, see Fig. 668, right. Sanchez et al. have therefore used a Vivascope with a bh BDL-SMC 488nm laser and a Simple-Tau 150 FLIM systems for in vivo FLIM of human skin [1049].

A problem of the Vivascope optics is loss in efficiency and resolution at excitation wavelength shorter than 450 nm: The objective lenses of the Vivascope are corrected for reflection imaging in the NIR. They cannot be expected to be free of aberrations at ultraviolet wavelengths. In principle, it should be possible to replace the objective lens with one that is cor-

rected for the blue spectral range, and thus make the instrument better suitable for excitation at 405 nm or shorter.

Multi-Beam Scanning Techniques

Multi-beam scanning was developed to obtain multiphoton images at short acquisition times. Scanning with several beams not only reduces the time required to scan one frame but also reduces photobleaching. The reduction in photobleaching rate is due to the nonlinear dependence of the photobleaching rate on the emission rate [391, 595, 948].

Typical multi-beam scanning microscopes split the excitation beam into an array of several beams, scan the sample simultaneously with this beam array, and record the image by a CCD camera. Lifetime imaging in combination with multi-beam and a gated image intensifier camera has been demonstrated by Straub et al. [1192]. However, scanning a time gate over the fluorescence decay results in poor recording efficiency. The advantage of low photobleaching is thus lost.

Kumar et al. therefore used multichannel TCSPC with a bh PML-16 detector connected to an SPC-830 TCSPC module [722]. 16 excitation beams were used, and the luminescent spots were projected on the 16 input stripes of the R5900-L16 tube of the PML-16. The data recorded require correction for the inhomogeneity in the sensitivity and the delay of the PMT channels. A result is shown in Fig. 669.

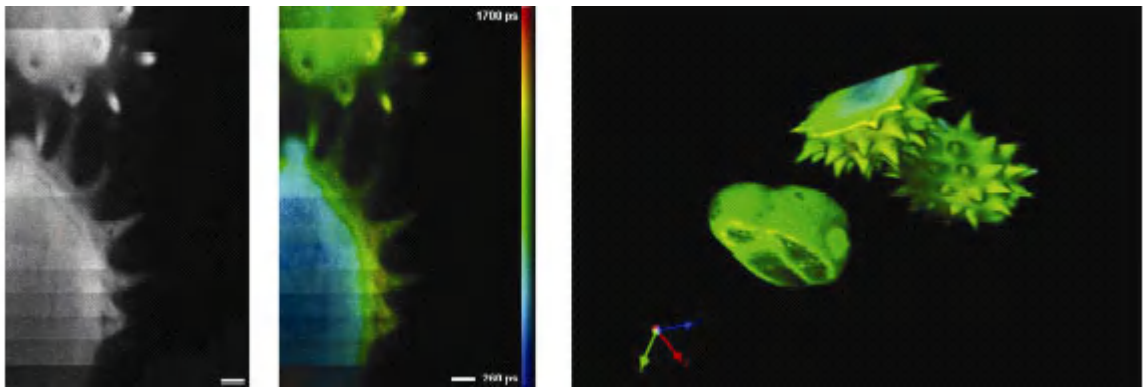


Fig. 669: TCSPC FLIM images obtained by multi-beam scanning. Left: Intensity image. Middle: Lifetime image, blue to red corresponds to 260 to 1700 ps. Right: 3-D FLIM rendering of a z stack of 250 scans in different depth of the sample. Colour scale from 260 to 1700 ps. With permission, from [722]

Scanning Systems with Piezo Stages

Optical System

The scanning systems described above use beam scanning to move the laser spot over the sample. However, scanning can also be performed by moving the sample. The optical principle of a confocal system with sample scanning is shown in Fig. 670.

The system shown on the left injects the laser beam into the microscope via the lamp port of the microscope. The beamsplitter and the emission filter are inserted in one of the standard microscope filter cubes in the filter carousel of the microscope. The detector is attached to a side port of the microscope. A pinhole in the upper image plane of the microscope suppresses out-of-focus light. The setup is easy to implement but has a few disadvantages: The lamp port cannot be used for a fluorescence lamp, and the laser beam diameter must be increased to match the size of the back aperture of the microscope lens. The most significant problem is

alignment. The laser must be focus in the sample must conjugate exactly with the pinhole. The angle of the dichroic mirror in the filter cube is therefore critical. Microscopy filter cubes are not designed for this level of precision. The setup is therefore not recommended for high-resolution imaging.

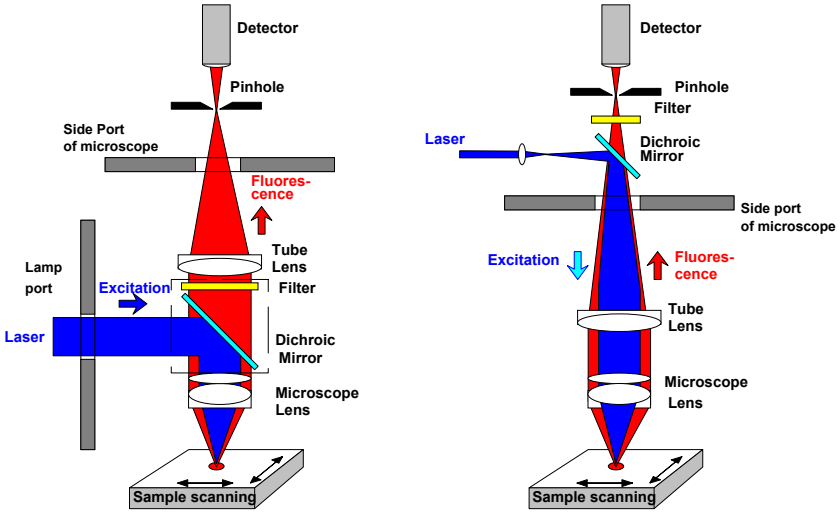


Fig. 670: Optical principle of a sample scanning system with confocal detection. Left: Beamsplitter and emission filter in microscope beamsplitter cube, pinhole and detector attached to the side port of the microscope. Right: Beamsplitter filter, pinhole and detector in compact optical assembly attached to a side port of the microscope.

The system on the right has the laser input, the dichroic, beamsplitter, the emission filter, the pinhole, and the detector integrated in a compact optical assembly. The entire assembly is attached to an optical port of the microscope. The setup makes it easier to maintain exact alignment of the laser and the pinhole.

Synchronisation of the Scanner with the TCSPC Module

Piezo scanning can be combined with multi-dimensional TCSPC the same way as beam scanning: The recording is synchronised with the scanning by pixel clock, line clock, and frame clock pulses, see section ‘Fluorescence Lifetime Imaging (FLIM)’, page 124. The only difference is in the scan rate. Stage scanning is typically 100 times slower than beam scanning. As a consequence, piezo scan data are often acquired in a single frame whereas beam-scanning data are normally accumulated over many frames. In any case, the recording process is fully integrated in the hardware and software of state-of-the art TCSPC devices and does not require any user-specific software.

One way to combine a piezo scanning with TCSPC FLIM is to run the piezo controller software in parallel with the TCSPC FLIM software. The piezo controllers can usually be programmed to generate the clock synchronisation pulses required for TCSPC.

A more elegant way of integrating a scan stage in a TCSPC system is via a bh GVD-120 scan controller card, see Fig. 376, page 241 for a cable diagram. The GVD-120 card is part of the bh DCS-120 confocal scanning system. It has analog outputs which are normally used to drive galvanometer scanners. The card can, however, be configured to run the slow scan ramps required for piezo stages. The control of the card is fully integrated in the bh SPCM data acquisition software. This way, the piezo stage gets fully integrated into the SPCM instrument software, see ‘Operation of Experiment Control Devices from the SPCM Software’, page 849. Different pixel numbers, scan formats, and scan speeds can be selected via the SPCM software. The scanner can be parked in a selected spot for FCS recording or single-molecule spectroscopy. The scan controller also controls two ps diode lasers. The lasers can

be multiplexed synchronously with the pixels, lines, or frames of the scan, or be modulated for simultaneous FLIM/PLIM operation, see page 371 and page 434.

Fig. 671 shows a typical lifetime image recorded in the setup of Fig. 670, right. A Nikon TE 2000 microscope with an 63x, NA = 1.3 oil immersion lens was used. A PI P733.3DD piezo stage with analog inputs was driven by a bh GVD-120 scan controller card. A bh BDL-488 SMN (488 nm) laser was used for excitation. The fluorescence was detected by a bh HPM-100-40 GaAsP hybrid detector, and recorded by a bh SPC-150 TCSPC FLIM module. The scanning and the recording was controlled by standard bh SPCM software. The data FLIM data were analysed by bh SPCImage software.

The sample was a convallaria preparation as it is commonly used in microscope demonstrations. The scanner was run at a line time of 3.33 seconds (including line flyback). The scan format was 512 x 512 pixels, resulting in a scan time of 1700 seconds for the entire image.

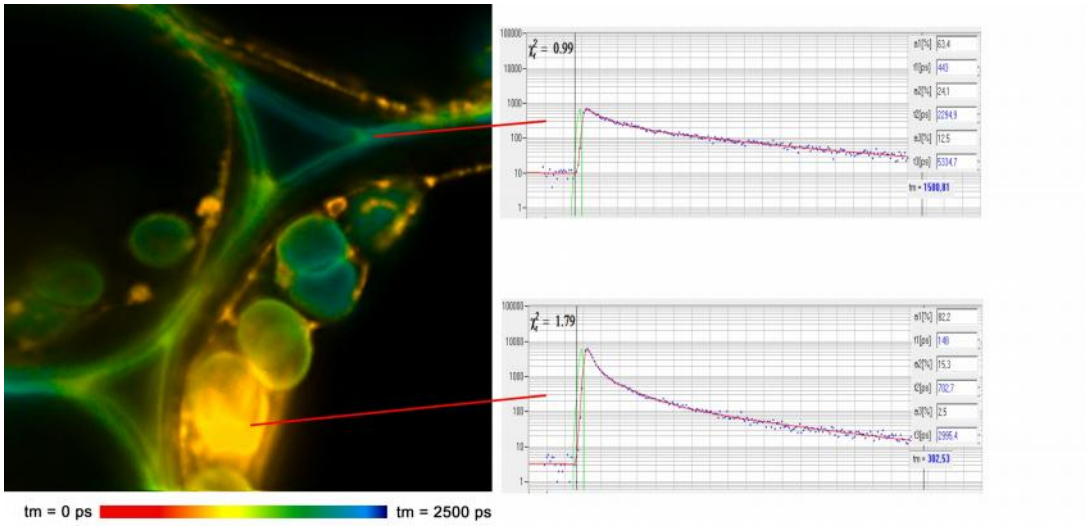


Fig. 671: FLIM image obtained piezo-stage scanning. PI P733.3DD piezo stage controlled by bh GVD-120 scan controller. Recording by bh SPC-150 TCSPC FLIM module. Image size 30 µm x 30 µm, data format 512 x 512 pixels, 256 time channels. Single scan, scan speed 5 lines per second.

The advantage of stage scanning is that there are only a few optical elements in the beam path, and there are no moving elements. The excitation and detection beams remain on the optical axis for all locations in the image. This way, aberrations and transmission losses are kept at a minimum. However, these advantages come at a price: The scanning is painfully slow, acquisition speed is limited by the scanner, a fast preview function is not available, focusing into the desired image plane is a nightmare, and deliberately selecting an image area of interest is difficult. Moreover, the scanning exerts insertion forces to the sample. Imaging of live cells in a cell culture can be a problem because the cells are shaken around by the scanning action.

Stage scanning is traditionally used in NSOM microscopy, see page 458 and in STED microscopy (see page 454). In NSOM there is indeed no way around the piezo stage: The required resolution is on the order of a nanometer, and the sample has to be moved with respect to the tip. However, no technical reason to use scan stages for STED. A galvanometer scanner easily achieves the required accuracy and allows for much faster recording. Commercial STED implementations have therefore dome away with the piezo stages and use galvanometer scanners. Please see section below.

Stimulated Emission Depletion Microscopy (STED)

Stimulated Emission Depletion (STED) microscopy exploits the nonlinearity of stimulated emission to obtain optical super-resolution [573, 671]. The fluorescence excited by the excitation beam in a scanning microscope is depleted by stimulated emission induced by a second (STED) laser beam. The wavefront of the STED beam is manipulated to obtain a diffraction pattern that either has doughnut shape laying in the x-y plane or a dumbbell shape oriented along the z axis. Fluorescence remains un-depleted in the centre part of the doughnut or the dumbbell. Because stimulated emission is highly nonlinear the un-depleted volume can be made considerably smaller than the point-spread function of the excitation beam. By scanning both beams together images with optical super-resolution are obtained.

STED FLIM Implementations

At first glance, it may appear impossible to combine STED with fluorescence lifetime imaging, because the decay curves are distorted by stimulated emission. Nevertheless, Auxorius et al. have shown that FLIM in combination with STED is possible [35]. The authors used a femtosecond Ti:sapphire laser to generate the excitation beam and the STED beam. The excitation beam was obtained by sending a part of the Ti:Sapphire laser emission through a microstructured optical fibre. The fibre generated a super-continuum from which the excitation wavelength was selected by a filter. For the STED the Ti:Sapphire pulses were broadened to 300 ps by 100 m of single-mode fibre. The broad pulses prevent re-excitation and multiphoton excitation by the STED beam. FLIM was performed the usual way by recording the photons in the Scan Sync In mode of an SPC-730 TCSPC module. A typical result is shown in Fig. 672.

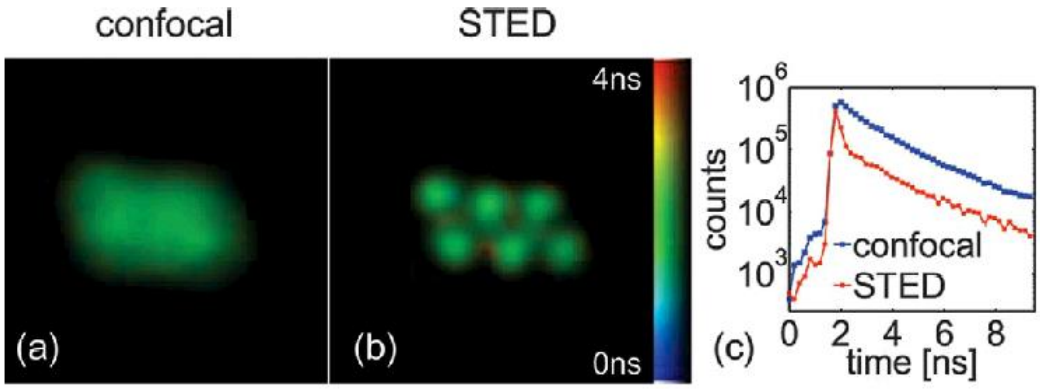


Fig. 672: Confocal (a), STED lifetime images (b), and confocal and STED decay curves (c). From [35].

The decay curves (Fig. 672, right) have a sharp peak around the time of the excitation maximum. It comes from the entire Airy disk of the excitation beam, before the outer parts are depleted by the STED beam. The decay after the STED peak has the correct decay profile as to be expected for the fluorophore used. The result shows that FLIM in combination with STED is possible.

Bückers et al. used a super-continuum laser to generate two pairs of excitation and STED beams [258]. The optical principle is shown in Fig. 673, left.

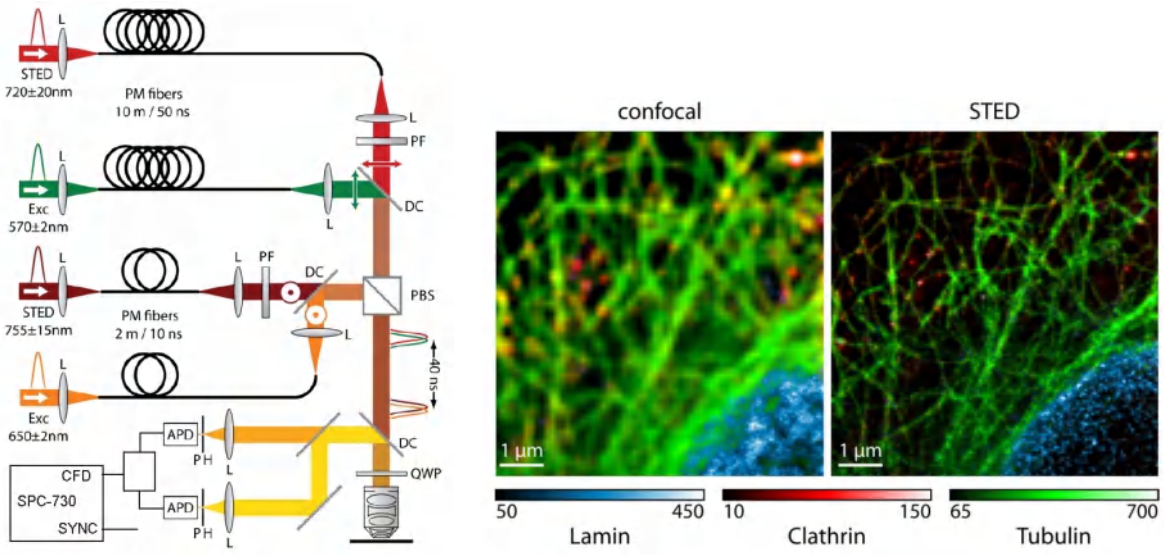


Fig. 673: Dual wavelength STED with super-continuum laser. Left: Optical principle. Right: Confocal image and STED image, combined spectral and lifetime separation. Lamin and tubulin were stained with KK 114 and ATTO 647N, respectively, which were segregated by lifetime analysis. The clathrin was stained with ATTO 590.The fluorescence of it was separated spectrally from those of the other dyes. From [258].

The pulses of the both beam pairs were offset in time by 40 ns. Both excitation / STED beams are used simultaneously to excite and deplete different fluorophores. The fluorescence signals were separated from the excitation and STED beams by a dichroic beam splitter, DC, split spectrally by a second dichroic beam splitter, and projected into confocal pinholes, PH. Light passing the pinholes was detected by Perkin Elmer SPC-AQR detectors. Scanning was performed by moving the sample by a piezo scan stage. The photon pulses from the detectors were processed by a bh SPC-730 TCSPC FLIM module via a router. The TCSPC module records separate lifetime images for the two detection wavelengths. Each pixel of each lifetime image contains two subsequent decay curves for the two excitation pulse trains. From the recorded data, images for fluorophores of different lifetimes and excitation / emission wavelengths were extracted.

Lesoine et al. [761] used the same basic optical setup. The photons were detected by an HPM-100-40 hybrid detector and the image recorded by an SPC-830 FLIM module. The authors detected lifetime changes of Alexa Flour 594 phalloidin. They attributed these changes to electron transfer between the Alexa dye as an electron acceptor and tryptophane as an electron donor.

Abberior STED System

A commercially available STED FLIM system with FLIM function is available from Abberior Systems, Göttingen, Germany. The system uses an SPC-150 module for FLIM recording. In single images the fluorescence intensity and lifetime are mapped at a lateral resolution of <30 nm. 3D FLIM stacks are recorded at a longitudinal and lateral resolution of <70 nm. Three-channel STED FLIM measurements are performed with a single depletion laser. An example of a STED FLIM image recorded by this system is shown in Fig. 674.

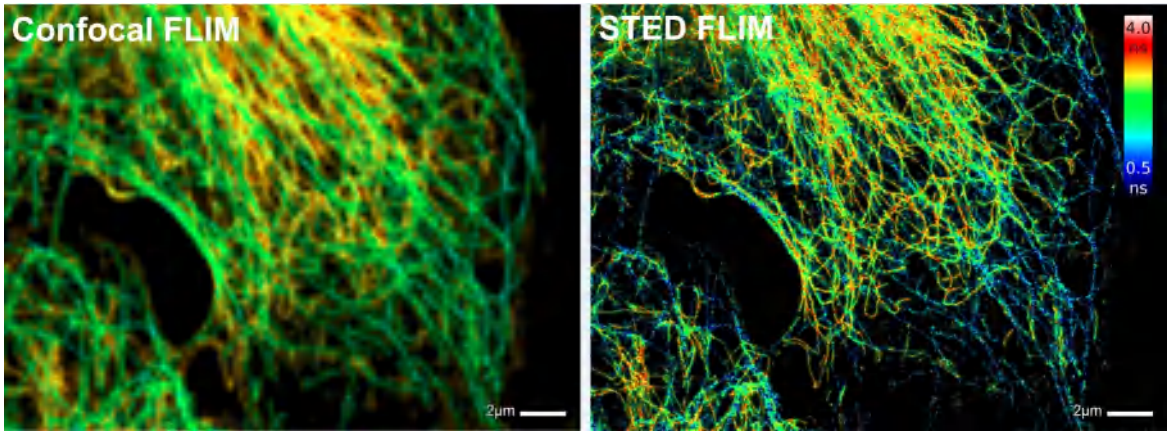


Fig. 674: Confocal (left) and STED FLIM image (right) recorded with Abberior Instruments STED FLIM system and SPC-150. Mammalian cells labelled with tubulin/ Atto647N and vimentin/ Abberior STAR 635P.

The Abberior system can be run with fully integrated FLIM or with an external bh FLIM system. An image recorded with an external SPC-150 FLIM system is shown in Fig. 675. The image was generated by the online-lifetime function of the SPCM software. An application to human neurotensin receptors in live cells has been published by Spantzel et. al. [1170].

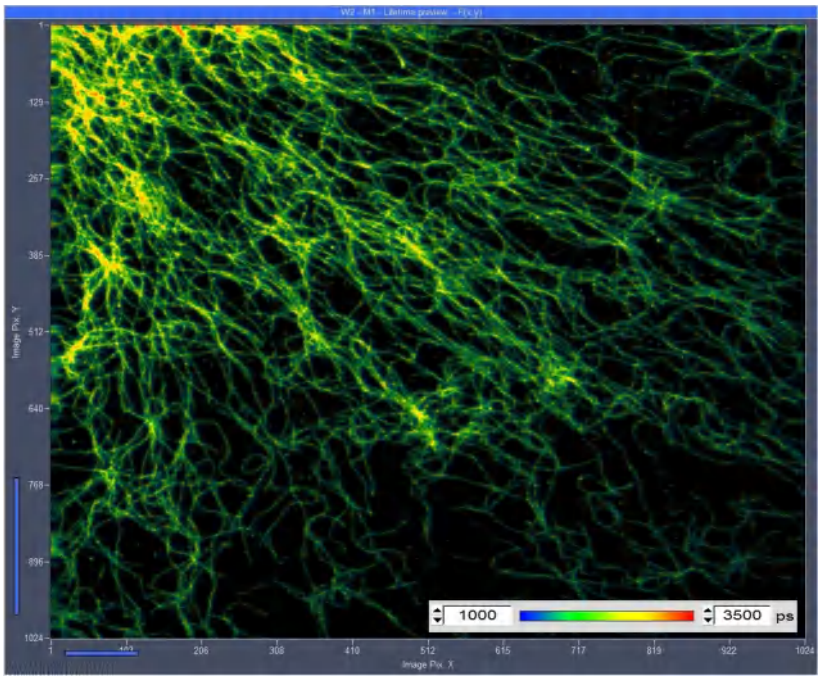


Fig. 675: STED FLIM image recorded with an Abberior STED microscope and an external SPC-150 FLIM system. Image created by the online-lifetime function of SPCM. 1024 x 1024 pixels, 256 time channels. Image recorded at 2nd Workshop on Advanced Time-Resolved Imaging Techniques at BioCev, Vestec near Prague , May 16-17, 2017. We thank Maria Olisova of BioCev for recording data of extraordinary quality.

Time-Gated STED Images

A fluorescence decay extracted from an Abberior / bh STED image is shown in Fig. 676. The shape of the decay is typical for STED. There is the initial peak of un-depleted fluorescence from the entire airy disc of the excitation laser, followed by the fluorescence decay function from the molecules in the 'hole' of the depletion disc. (A similar peak can be seen in Fig. 672, right) The contrast and resolution can therefore be improved if the fluorescence from the un-deleted part of the decay function is suppressed by time-gating.

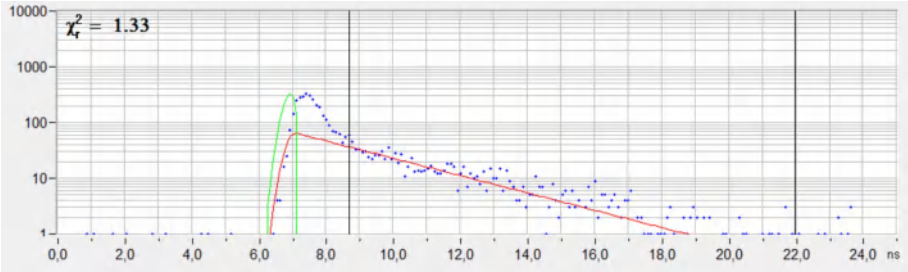


Fig. 676: Decay curve in selected spot of the STED FLIM image. The fluorescence intensity and the fluorescence decay time was derived from the time interval after the peak of the un-depleted fluorescence.

Time-gating can be achieved by defining appropriate 'Window Intervals' in the SPCM software and displaying images in the defined time windows. Time-gating acts both on online-intensity images and online-lifetime images. Since the by FLIM system records a full set of FLIM data the gate position can even be adjusted after the acquisition. A comparison between a ungated image an a gated image is shown in Fig. 677.

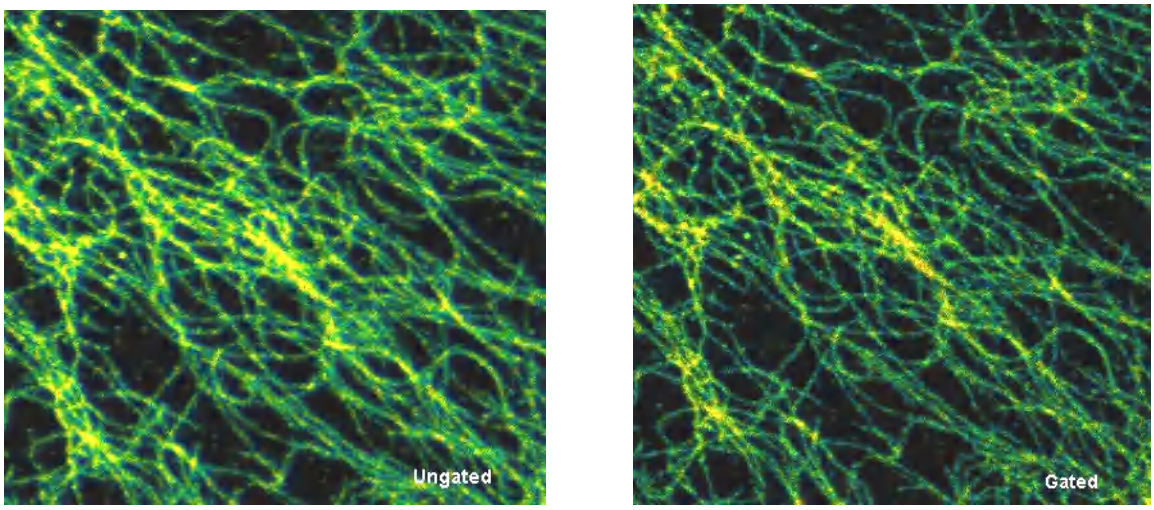


Fig. 677: Ungated (left) and gated online-FLIM image (right). Detail from the image in Fig. 675.

Other Super-Resolution Techniques

It should be mentioned here that optical super-resolution can also be obtained by techniques like PALM or STORM. These techniques are based on switchable fluorophores. The fluorophores are optically controlled so that only a small fraction of molecules is fluorescing at a time. These molecules are localised at a precision higher than the optical resolution, and the image reconstructed from the positions of the individual molecules. Super-resolution FLIM by switchable fluorophores would require a wide-field FLIM technique. Such a technique does, in principle exists, see page 460 of this handbook. A bigger problem are the switchable fluorophores. Whether the lifetimes of these fluorophores react to the molecular environment, and whether possible changes report biologically interesting parameters is not known. STED FLIM is less restricted in the choice of the fluorophores. It is currently the best technique to combine optical super-resolution with molecular imaging by FLIM.

Time-Resolved Optical Near-Field Microscopy (NSOM)

The scanning near-field optical microscope (SNOM or NSOM) combines the principles of the atomic force microscope and the laser scanning microscope [411]. A sharp tip is scanned over the sample and kept in a distance comparable to the diameter of a single molecule. The tip can be the end of a tapered fibre through which the laser is fed to the sample, see Fig. 678, left. Or, a metallic tip is illuminated by focusing the laser through the microscope objective on it. The evanescent field at the tip is used to probe the sample structure (Fig. 678, right). In both cases the fluorescence photons are collected through the microscope objective lens. Scanning is performed by a piezo-driven scan stage.

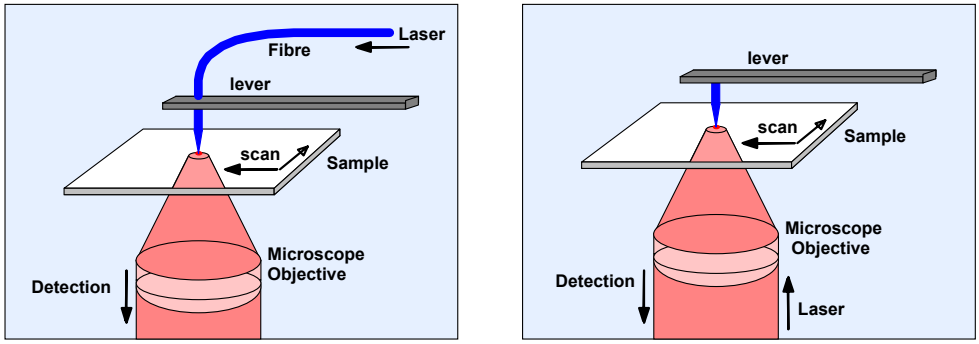


Fig. 678: Optical near-field microscope

Because NSOM uses scanning it can easily be combined with TCSPC FLIM. Because the image is obtained in a single slow scan the fluorescence decay curves are often recorded and read out on a pixel-by-pixel basis. However, a better way to record NSOM FLIM is by the usual imaging procedure of multi-dimensional TCSPC. The advantage of using multidimensional TCSPC is that no user-specific programming is necessary, that readout times during the acquisition are avoided, and that the data can be processed by standard TCSPC-FLIM analysis software. Examples of NSOM FLIM are shown in Fig. 679 and Fig. 680.

Fig. 679 shows nano islands of fluorescing material on a semiconductor surface. The AFM image is shown left, the FLIM image in the middle. The right image is a combination of the AFM data with the fluorescence lifetime data. The image was scanned with an AFM/NSOM system of Nanonics, Jerusalem. Optical excitation was performed by a bh BDL-SMN 480 nm ps diode laser, the photons were detected by an HPM-100-40 hybrid detector and recorded by an SPC-150 TCSPC FLIM mode in the FIFO imaging mode. Synchronisation with the scanning was achieved by frame, line, and pixel clock pulses delivered by the Nanonics piezo stage controller.

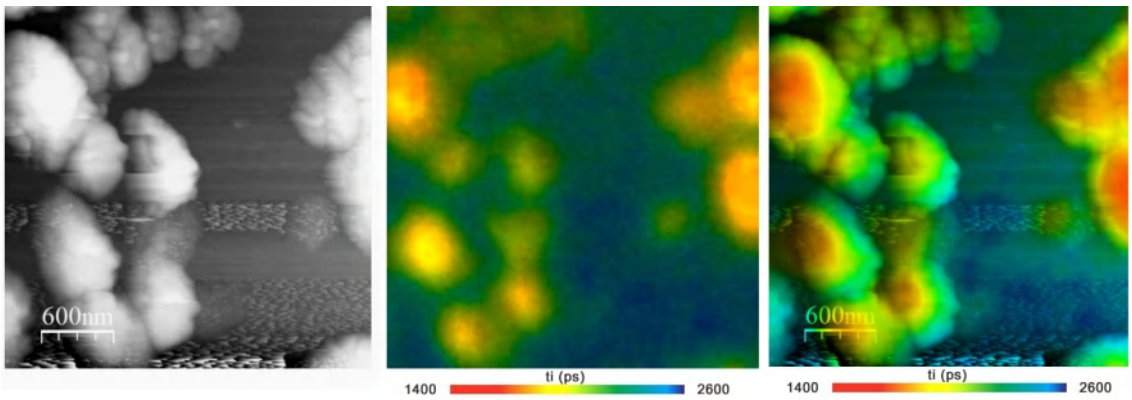


Fig. 679: NSOM FLIM of nano-islands on a semiconductor surface. Left: Topography from AFM system. Middle: FLIM. Right: Overlay of AFM topography image with lifetime from FLIM. Amplitude-weighted lifetime of double-exponential decay.

The images shown in Fig. 680 were recorded by a combination of a NTEGRA SPECTRA AFM/NSOM system of NT MDT, Moscow, and an SPC-150 TCSPC modules with a BDL-SMN 488nm ps diode laser and a HPM-100-40 detector. The FIFO imaging mode was used, with frame, line, and pixel clocks from the NTEGRA system.

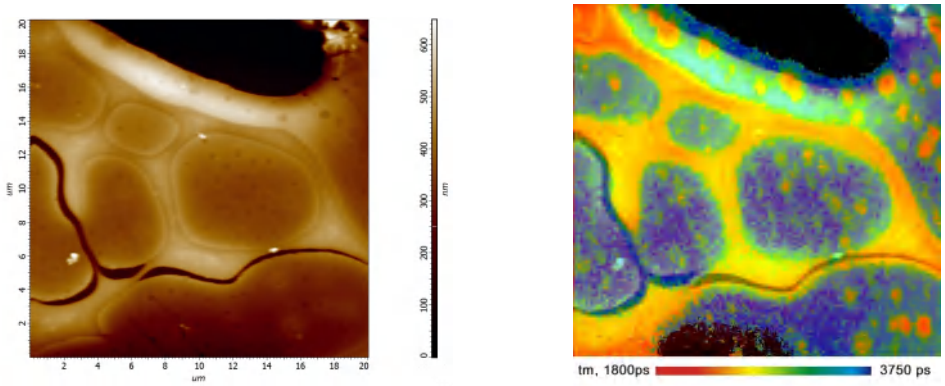


Fig. 680: NSOM FLIM of a polymer. Recorded with NTEGRA SPECTRA of NT MDT, Moscow and bh SPC-150 TCSPC FLIM module. Left: AFM topography image, lateral size 20 x 20 µm, vertical scale shown on the right. Right: Overlay of FLIM data with AFM data. Amplitude-weighted lifetime of double-exponential decay.

Although the combination of TCSPC FLIM with NSOM does not pose any substantial problems not many NSOM FLIM applications have been published yet. In [600, 857] an SPC-730 module was used; [730] used a classic TCSPC setup based on NIM modules. SNOM lifetime images presented in early publications were not very impressive. It is not clear whether the reason was lack of photons, too much detector background, inefficient data analysis and image-reconstruction software, or simply poor reproduction.

Near-field FLIM Images of good quality were presented by Cadby et al. [266]. The authors used a Veeco Aurora SNOM system upgraded with an R3809U MCP PMT and an SPC-830 TCSPC module. The system was used to investigate the nano-structure of blends of fluorescent and non-fluorescent polymers [266, 267] and to microcapillary cavities containing a fluorescent dye [4].

Gokus et al. used tip-enhanced near-field excitation to identify single carbon nanotubes and measure their fluorescence lifetime. A titanium-sapphire laser was used to excite the sample at 760 nm. The fluorescence was detected by an MPD PDM 50 SPAD, and the decay curves were recorded by a bh SPC-140 TCSPC module. The instrument response width was 27 ps (!), so that fluorescence lifetimes of 4 to 36 ps could reliably be recorded [510].

Gaiduk et al. used the SNOM principle for combined optical and force spectroscopy of single labelled DNA molecules [479, 480]. When a DNA molecule is captured between the tip and the surface simultaneous force and fluorescence data are acquired. As the tip is moved up and down complete distance cycles are recorded. The force data are added as an additional dimension in MFD (multi-parameter fluorescence detection) analysis (see Multi-Parameter Single-Molecule Burst Analysis, page 667).

In all TCSPC NSOM applications it must be expected that he proximity of the tip changes the radiative and non-radiative decay rates of the fluorophores. Therefore the obtained lifetimes do not necessarily represent the lifetimes of the undisturbed sample. Nevertheless, recording the fluorescence lifetime may help separate the change of the fluorescence intensity by the evanescent field at the tip and the change of the fluorescence intensity by variations in the decay rates.

The change of the lifetime of an emitter depending on its photonic environment has been exploited by Frimmer et al [464]. They used a spontaneous emitter attached to a scanning probe and recorded the lifetime changes by a DPC-230 card. They applied the technique to record enhancement of optical states around metal nanowires.

Wide-Field FLIM

bh deliver a wide-field TCSPC FLIM system consisting of a position-sensitive MCP PMT of the delay-line type, three SPC-150N TCSPC modules, a bh BDS-SM picosecond diode laser, an inverted microscope, and optics that projects a fluorescence image on the active area of the detector. The operation of the system is fully integrated in the bh SPCM TCSPC software, data analysis is performed by bh SPCImage. The system is described in the following section, additional details are described in [121] and [172].

Detector

The system uses Photek FGN 392-1000 Detector. The FGN 392-1000 is an MCP PMT with a position-sensitive readout structure at the anode, see Fig. 681.

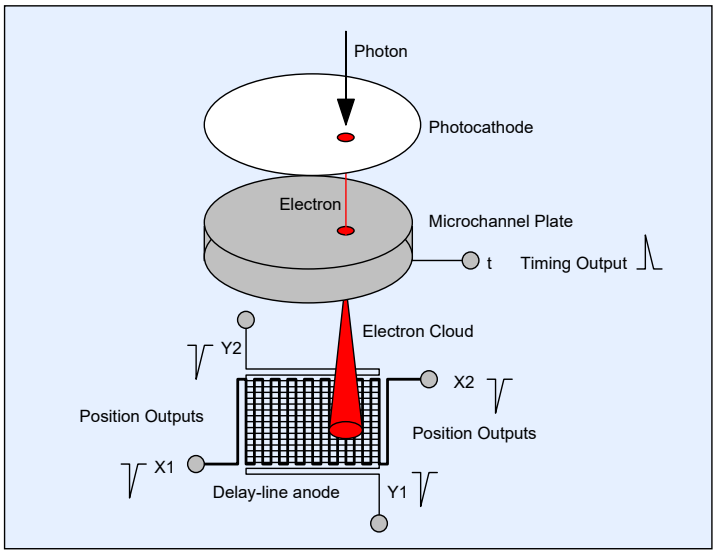


Fig. 681: Principle of position-sensitive detector: The detector has a delay-line structure as an anode. The X position of a photon is proportional to the delay between X1 and X2. The Y position of a photon is proportional to the delay between Y1 and Y2. The time of the photon is derived from a signal from the low-side of the channel plate, t.

The readout structure consists of two crossed delay lines. The x position of a photon is derived from the time difference between the outputs of the x delay line, the y position from the time difference at the outputs of the y delay line. Timing information for the individual photons is derived from a pulse from the low-side of the microchannel plate.

TCSPC System

The TCSPC system consists of three parallel SPC-150N modules, see Fig. 682. The first module measures the times of the photons in the laser pulse period. The second and third module measure the times of the pulses at the outputs of the X and the Y delay lines. Delay cables in the stop lines guarantee that the start-stop times remain positive for all X and Y positions. The SPC modules are working in the FIFO (Parameter-TAG) mode. That means the detection events, i.e. the times, t, and the positions, x and y, are transferred into the computer photon by photon together with a ‘macro time’. The macro time is an absolute time from the start of the acquisition. It is used by the software to assign the t, x, and y data delivered by different modules to a particular photon. From these data the software builds up a photon distribution over the coordinates x, y, and the times, t. This is the usual photon distribution of FLIM: It is an

array of pixels, each of which contains a fluorescence decay curve consisting of photon numbers in consecutive time channels. To make this process possible the measurement in all three modules must be started at exactly the same moment, and the macro-time clocks in the modules must be synchronised. This is achieved by the 'Trigger Master' and 'Clock Master' functions of the SPC-150N modules (see page 795 of this handbook).

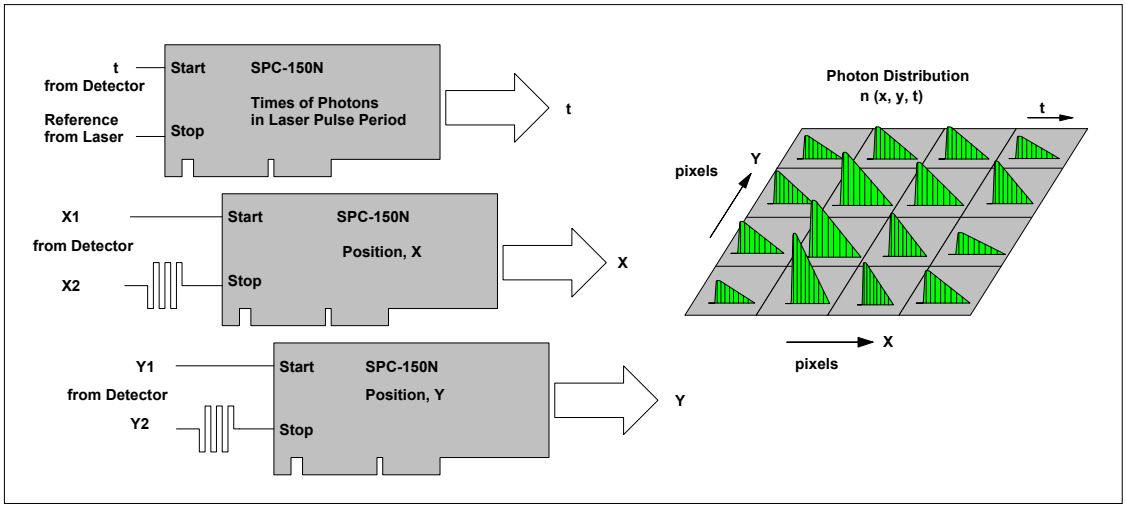


Fig. 682: TCSPC System

Constant-Fraction Discriminators

All bh SPC modules have constant fraction discriminators (CFDs) at their start and stop inputs. The CFDs not only reject noise and low-amplitude pulses but also prevent the amplitude jitter of the detector pulses from inducing timing jitter. For this purpose, the CFD circuitry shapes the detector pulses into a bipolar waveform. The zero-cross point of this pulse does not shift with the amplitude. A fast discriminator triggers on the zero-cross point and thus delivers the temporal position of the photon is independently of the pulse amplitude (see page 269 of this handbook). If the pulse shaping network is adapted to the rise and fall time of the detector pulses this principle works well for all commonly used detectors. It also works for the single photon pulses at the timing output of the Photek FGN 392-1000 detector, see Fig. 683, left. A normal CFD does not work, however, for the signals delivered by the position outputs of a delay-line detector. The signals at these outputs have nothing in common with normal single-photon pulses, see Fig. 683, middle. They resemble of a burst of pulses rather than a single photon pulse. Trying to process a signal like this by a normal CFD is hopeless.

The reason of the unusual signal shape is that the electron cloud of a single photoelectron simultaneously hits several parts of the delay line structure, see Fig. 681. Moreover, the subsequent steps of the delay line are electrically not perfectly de-coupled. The only way to obtain timing from the position outputs is to determine the centroid of the entire burst. This can be achieved by sending the signal through a low-pass filter (pulse shape shown in Fig. 683, right).

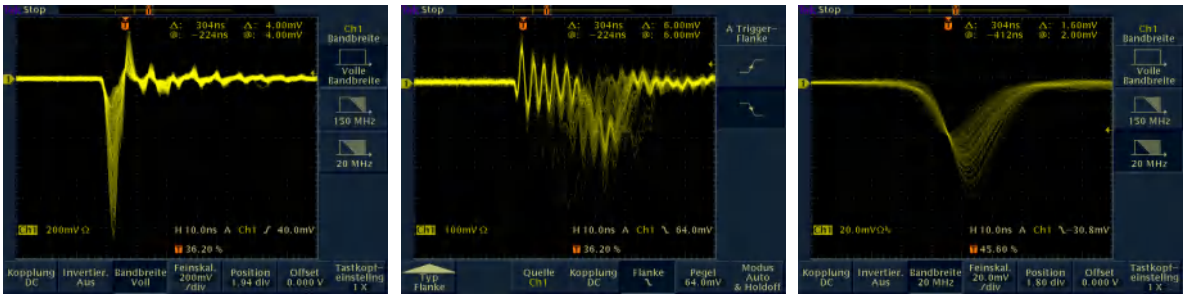


Fig. 683: Single photon pulses delivered by the Photek detector. Left: Timing output. Middle: Position output X1. Right: Signal of position output X1 after passing through a 20 MHz low-pass filter.

The required transformation of the pulse shape is performed in special CFD in the SPC-150N cards of the position channels. The CFDs have the filter function integrated in a way that the filter simultaneously works as a pulse shaping network of the zero-cross discriminator. The principle is described in [172].

Optical System

The optical part of the wide-field FLIM system is shown in Fig. 684. It consists of an inverted microscope, a BDS-SM 488nm picosecond diode laser, and a Photek FGN 392-1000 detector. The BDS-SM laser is used for excitation. A cleaning filter removes long-wavelength broad-band emission from the laser beam. The light passing the filter is delivered into the microscope by a single-mode fibre. A standard microscope beam-splitter cube reflects the laser towards the microscope lens. The fibre output delivers a diverging beam of light into the back aperture of the microscope lens. The light is thus not focused into the sample, it illuminates the entire field of view. Due to the clean beam profile at the end of the single-mode fibre the illumination is homogeneous over the entire image area.

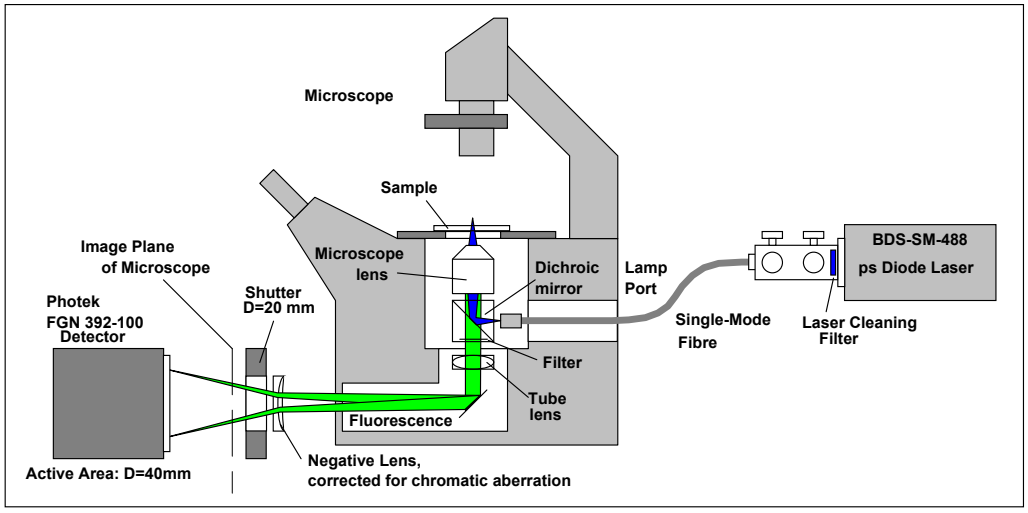


Fig. 684: Optical System

Fluorescence excited in the sample passes the dichroic mirror of the beamsplitter cube and an emission filter. It is directed out of the microscope via one of the side ports. An achromatic negative lens a few cm in front of the image plane magnifies the image to match the active area of the detector. A shutter is placed behind the lens to protect the detector and conveniently block the light path when the microscope lamp is used.

SPCM Software

Data acquisition is performed by bh SPCM software. Fig. 685 shows the main panel for wide-field FLIM. The image is shown on the left. The display parameter panel, the predefined setup panel, and the DCC-100 (detector, shutter, laser control) panel are open on the right. The display parameters define the colour, the intensity scale and the mode of the data that are dis-

played. Data can be displayed as intensity images, intensity images in several time gates, or as decay curves over selected areas of the image. For routine use we recommend the settings shown in Fig. 685. Please see SPCM software description in this handbook.

The DCC-100 panel controls the intensity of the laser, operates the shutter and controls the operating voltage of the detector.

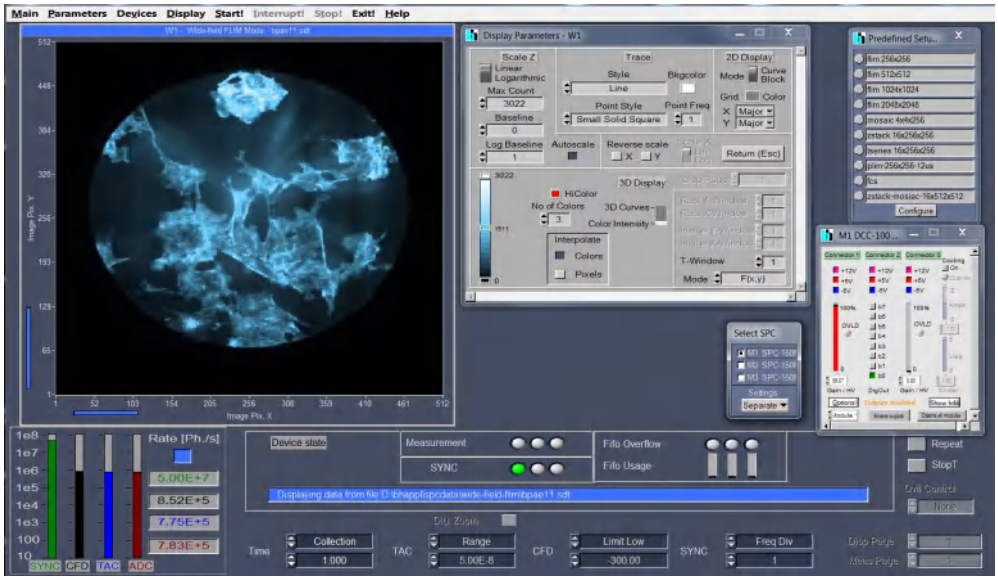


Fig. 685: Main panel of SPCM software, recommended configuration for wide-field FLIM. Image Invitrogen BPAE sample, acquisition time 1 minute.

The count rates are displayed on the lower left. The count rates have different meaning depending on which SPC module is selected in the ‘Select SPC’ panel. If module 1 is selected the Sync rate is the reference pulse frequency from the laser. The other bars are the photon rates in the at the CFD input, in the TAC, and in the ADC of the time-measurement module. For wide-field FLIM, we recommend not to exceed a photon rate of 1 MHz. This can cause detector saturation in bright parts of the image, or result in a large fraction of ‘unmatched events’ (unmatched time and position information) and, consequently, loss of photons. If M2 or M3 are selected the Sync and CFD rates show the event rates in the X1 / X2 and Y1 / Y2 position channels. All rates should be approximately the same as the CFD rate in M1.

The SPCM system parameter panel with the recommended settings is shown in Fig. 686, left. Operation mode is ‘Wide-Field FLIM’. Stop T is not set - the measurement is started and stopped by the operator. ADC resolution is 1024. That means, decay curves of 1024 time channels are recorded in the pixels. 'Image pixels Y' and 'Image Pixels Y' is 512, corresponding to an image of 512 x 512 pixels. The pixel number can be increased to 1024 x 1024 to obtain larger over-sampling factors as they are commonly used in microscopy.

To associate the events recorded in the three SPC-150N modules to the correct photons the modules must be started synchronously, and be operated from the same master clock. The definitions are shown in Fig. 686, right.

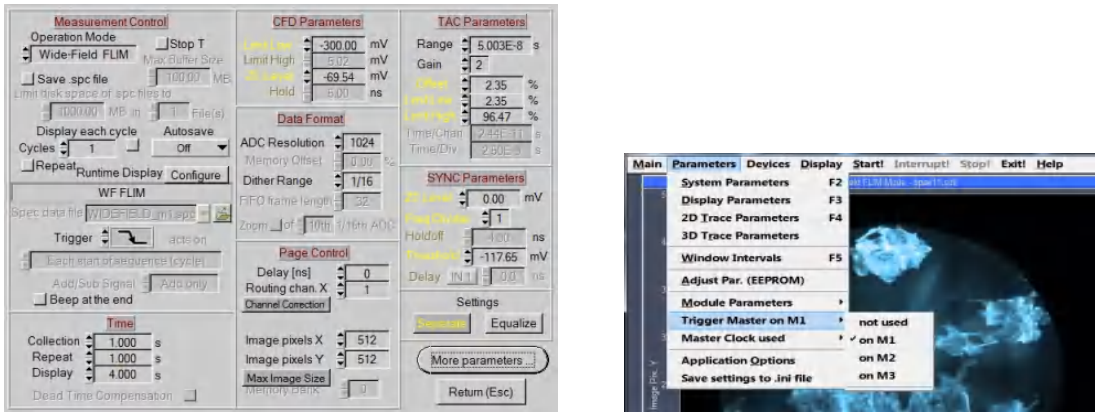


Fig. 686: System Parameters (left) and definition of Trigger Master and Master Clock function (right)

System-specific parameters are defined under ‘More Parameters’, see button in the system parameter panel, lower right. These parameters control the conversion of the times measured between the X1 and X2, and the Y1 and Y2 signals into spatial information. We recommend not to change these settings.

Data Analysis

Although the recording process of wide-field FLIM is different from scanning FLIM the recorded photon distribution is similar. It is an array of pixels, each containing a fluorescence decay function in a large number of consecutive time channels.

Data Analysis can therefore be performed by SPCImage in the usual way, see Fig. 687. An intensity image build up from the TCSPC data is shown left, a lifetime image is shown right. A decay curve for the pixel at the cursor position is shown at the bottom. The decay curve is clean, without optical or electrical reflections. The residuals (shown below the decay curve) confirm the good quality of the temporal data.

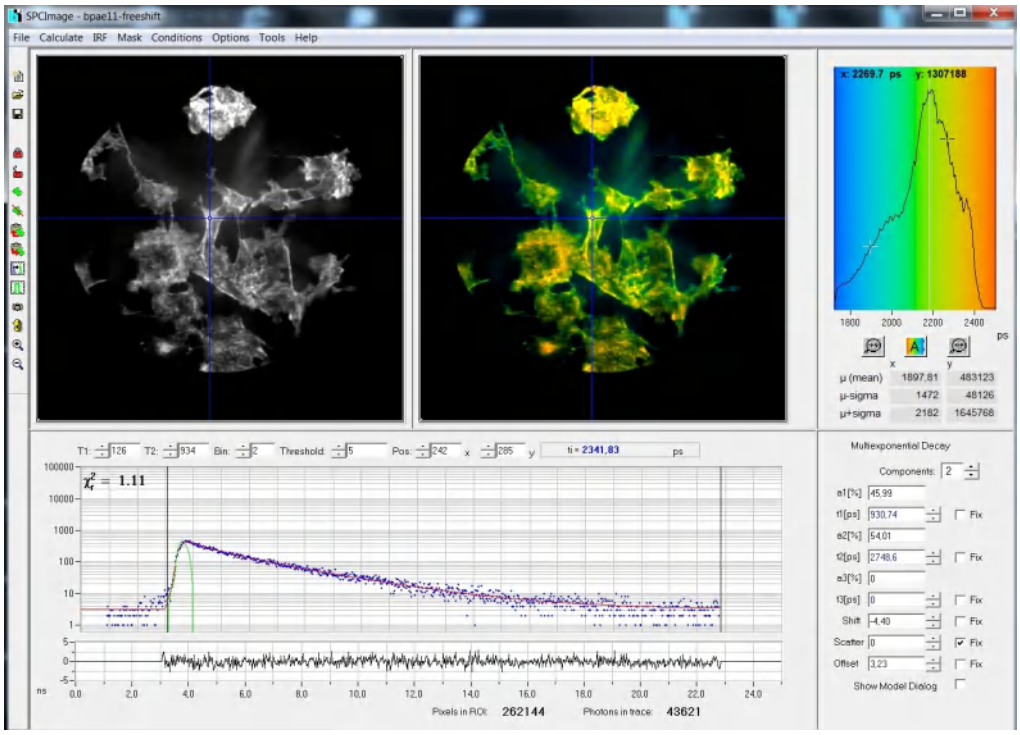


Fig. 687: Data analysis by SPCImage. Same data as shown in Fig. 685, 512 x 512 pixels, 1024 time channels per pixel. Sample Invitrogen BPAE cells.

Spatial and Temporal Resolution

A lifetime image at larger scale is shown in Fig. 688, left. The image was recorded with 512 x 512 pixels. This is more than the detector / TCSPC combination resolves. Fig. 688, right, shows a zoom into an area near the centre of the image. It can be estimated that the effective spatial resolution of the detector-TCSPC combination is about 250 x 250 pixels. The entire cathode of the detector has a diameter of 40 mm, one pixel thus corresponds to about 160 µm on the cathode.

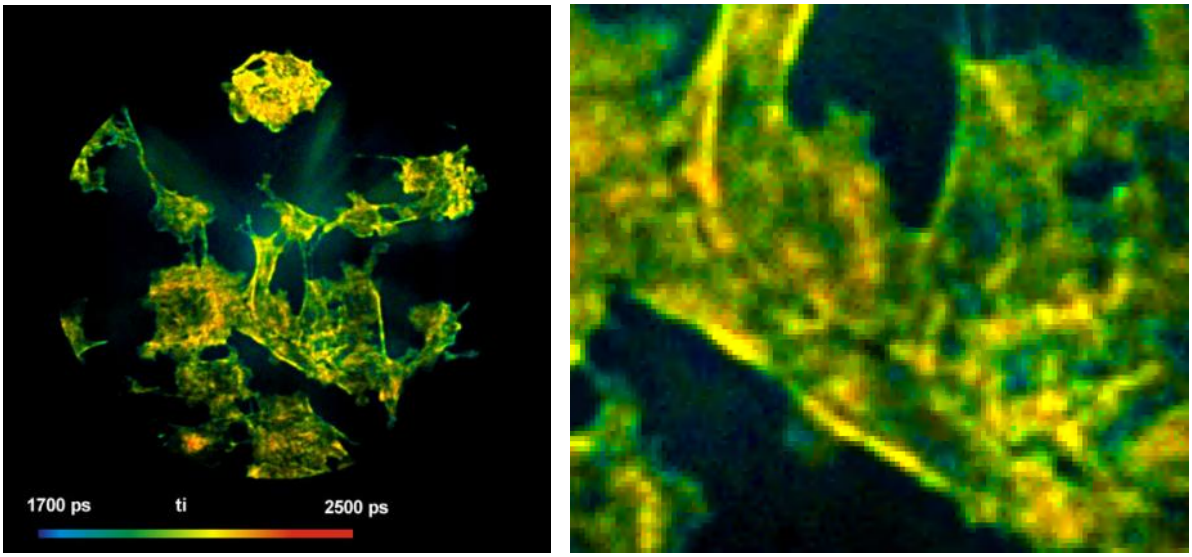


Fig. 688: Left: Wide-field FLIM image analysed with the parameters shown in Fig. 687. Right: Digital zoom into an area near the centre of the image.

The temporal instrument response function (IRF) of the detection system for different spots at the photocathode is shown in Fig. 689. To avoid saturation of the channel plates by high local intensity the IRF measurement was performed at a count rate of no more than 70 kHz.

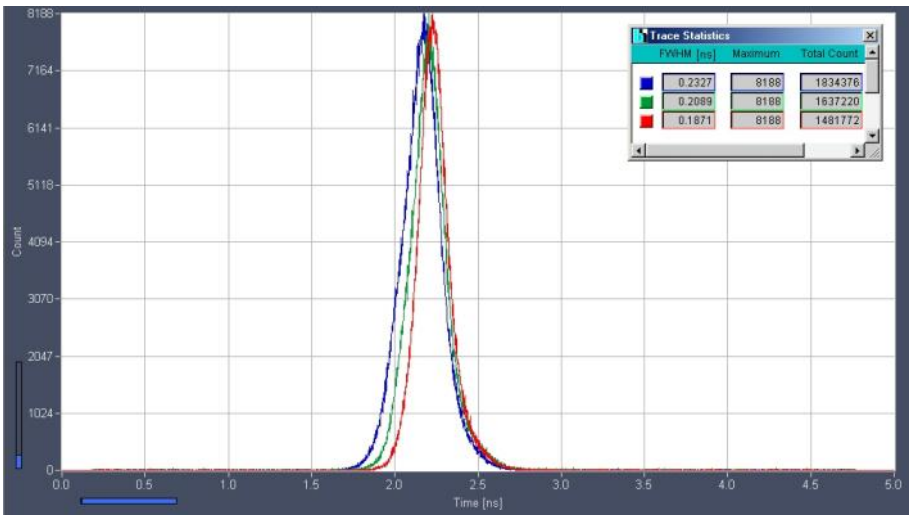


Fig. 689: Temporal instrument response function (IRF) for different x positions on the photocathode

The full-width at half-maximum (FWHM) is 187 to 233 ps. There is a slight change in the IRF shape and position with the position on the photocathode. The shift in the first moment of the IRF is about 75 ps. There are two reasons for this shift. The first one is that the timing signal is derived from only one point at the periphery of the microchannel plate. Therefore there is a non-zero propagation delay from the detection position to the output signal line. The second one is that there is a systematic variation in the shape of the electrical single-photon

pulse with the detection position. The shape variation causes a shift of the zero-cross point in the CFD. Both effects result in a dependency of the IRF on the spatial position at which the photons are detected. A shift in the first moment of the IRF induces a shift of approximately the same size in the calculated fluorescence lifetimes. For the analysis of wide-field FLIM data we therefore use a floating IRF (see SPCImage chapter).

FLIM Background Knowledge

What is Important to FLIM of Biological Objects?

FLIM technique

There is a wide variety of different FLIM techniques based on different data recording principles [148, 157, 163, 165, 166, 171, 959, 1133, 1205]. The techniques differ considerably in essential parameters, such as photon efficiency, i.e. in the number of photons required to achieve a given lifetime accuracy, time resolution, ability to resolve multi-exponential decay functions, multi-wavelength capability, acquisition time needed to reach a given lifetime accuracy, photon rate they are able to process, compatibility with laser scanning, optical sectioning capability, or compatibility with single-molecule techniques. Especially, there is currently a run on techniques which are able to achieve short acquisition times [794] for samples which deliver extraordinarily high fluorescence intensities. Often the development is purely technological: Techniques are concentrating on just one parameter of the recording process, while neglecting another. Therefore not all techniques are equally suitable for FLIM of biological objects. An attempt to compare different techniques has been made in [157] and [163]. The following paragraphs give a summary of the features that are important for FLIM of biological samples.

Time Resolution

It is sometimes believed that FLIM in cells or tissues does not require a particularly high time resolution. The argument is that the fluorescence lifetime of fluorescent dyes used in microscopy is normally on the order of a few nanoseconds. This is certainly correct. However, the recording of images of conventionally stained samples is not the main application of FLIM. Modern FLIM is a molecular imaging technique. That means it focuses on recording lifetime variations caused by different molecular environment of the fluorophores. Fluorescent probes for these applications do not always have long lifetimes. Moreover, the information is not in the average fluorescence lifetime of the probe but in the lifetimes and amplitudes of decay components. Examples are FRET experiments, where the interacting donor lifetime can be as short as 200 ps, and metabolic imaging experiments based on the fluorescence of NADH and FAD, where the lifetimes of the fast components are on the same order. Lifetimes of dye aggregates in cells have been found as short as 50 ps [652], the lifetime of fluorophores bound to metallic nano-particles [488, 814] can be 100 ps and shorter, and SHG components are infinitely fast. Recently, high-resolution TCSPC FLIM has shown that ultra-fast decay component with lifetimes in the 20-ps range are far more frequent than commonly believed [177, 178]. A good FLIM technique should therefore by able to record lifetimes down to 100 ps and below without noticeable decrease in accuracy. Moreover, it should be able to resolve the components of complex decay profiles, see below.

Fluorescence Decay Profiles of Biological Samples

The fluorophore populations in biological specimens are usually not homogeneous. Several fluorophores may be present in the same pixel, or one fluorophore may exist in different binding states or different molecular environment. The fluorescence decay functions are therefore usually multi-exponential. A few typical decay profiles are shown in Fig. 690. Even without data analysis, it is clearly visible that the decay profiles are not single exponentials.

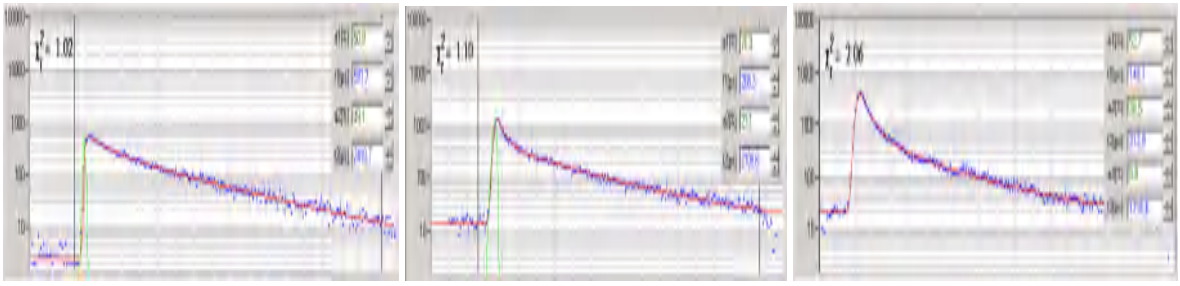


Fig. 690: Decay profiles of biological samples, total length of time axis 10 ns, logarithmic intensity scale. Left to right: CFP-YFP FRET in HEK cell at emission wavelength of CFP, autofluorescence of the stratum corneum of human skin, plant tissue sample

There are certainly cases when fitting multi-exponential decay profiles by a single-exponential decay is feasible. These may be pH imaging, oxygen quenching experiments, or ion concentration measurements. In most cases, however, describing the fluorescence of the sample by a single 'Fluorescence Lifetime' means discarding useful information or even leads to wrong results. The FLIM technique should therefore record a full fluorescence decay function in each pixel, not only a single 'lifetime' value. This is no problem for TCSPC FLIM - it records well-resolved decay profiles in the individual pixels.

Multi-Parameter Recording

Biological systems are multi-parameter systems. Moreover, the systems are dynamic. A FLIM technique for biological applications should be able to determine several parameters of a biological system simultaneously, and in their mutual dependence. This requires features like multi-exponential decay analysis, fast accumulation of time series, excitation-wavelength multiplexing, simultaneous recording in several emission wavelength intervals, or simultaneous FLIM/PLIM. In fact, only multi-dimensional TCSPC is able to meet these requirements.

Photon Efficiency

The accuracy of fluorescence lifetime detection is inevitably connected to the number of photons recorded. Under ideal conditions, the lifetime of a single-exponential decay can be obtained from the recorded data with the same accuracy as the intensity [46, 497, 680]. In both cases the signal-to-noise ration, or reciprocal relative standard deviation is $\sqrt{N}$, with N being the number of photons in the pixel considered. However, there is a significant difference: Conventional fluorescence imaging is aiming at resolving the spatial structure of a sample. This is easily possible on images of low signal-to-noise ratio: An intensity image with a standard deviation of 10%, or 100 photons per pixel, resolves the spatial structure of a sample very well. FLIM, however, is aiming at resolving molecular interactions. The lifetime changes induced by these effects are in the 10% range or below. Thus, a much lower standard deviation, or higher signal-to noise ratio, is required for the lifetime in FLIM than for the intensity in spatial imaging. Consequently, more photons are needed. These are difficult to obtain from biological samples. Therefore, photon efficiency, becomes an extremely important parameter of FLIM. The FLIM technique should not only detect the photons as efficiently possible, it should also derive a maximum of information from them. This is no problem for TCSPC FLIM: The lifetime accuracy obtained from TCSPC FLIM data is very close to the theoretical maximum, $\sqrt{N}$.

Low-Intensity Imaging

Recording many photons means either a high excitation intensity or a long acquisition time. Therefore photobleaching [391, 948] and photodamage [595, 681, 684] are important issues in precision FLIM experiments. Both effects are more troublesome for FLIM than for spatial imaging because they are likely to change the lifetimes [149, 589]. Photobleaching and photodamage are clearly nonlinear for two-photon excitation. A nonlinear component seems to be

present also for high intensities of one-photon excitation [203]. Thus, photobleaching can be reduced by recording at lower excitation power and correspondingly longer acquisition time. A good FLIM technique must not only make best use of the detected photons, it must also be able to work reliably at extremely low intensity. TCSPC FLIM works with single photons and thus delivers the best possible results at low intensities.

Single-Photon Detection Capability

Under conditions described above, the detector signal is a train of random pulses representing the detection of the single photons. A typical signal is shown in Fig. 691. The laser repetition rate is 80 MHz, the photon count rate is $10 \cdot 10^6$ photons per second. The FLIM technique has to reconstruct the decay functions in the pixels of the image from the single-photon pulses of the detector. The logical consequence is that a TCSPC technique should be used [154, 167].

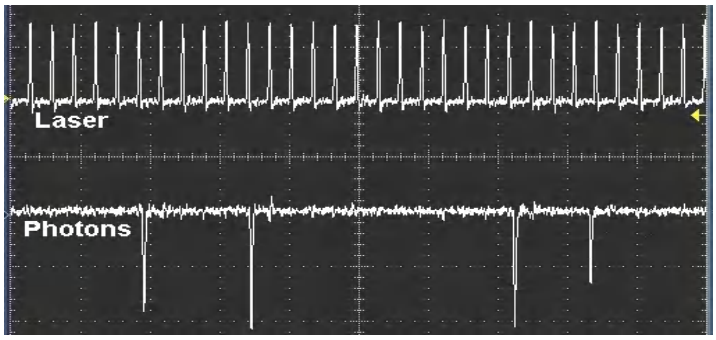


Fig. 691: Laser pulse sequence (top) and detector signal (bottom) in a typical FLIM application. Laser 80 MHz, count rate $10 \cdot 10^6$ photons per second.

Single-Molecule Detection Capabilities

The detection volume of a laser scanning microscope is on the order of femtoliters. If the fluorophore concentration is not too high the detection volume contains only a limited number of molecules. The molecules show dynamic effects, such as diffusion, rotation, conformational changes, transition between the singlet and the triplet state, and blinking. The recording technique used should not only be able to record FLIM but also be able to deliver information about single-molecule dynamics. Again, TCSPC FLIM meets these requirements.

Multi-Wavelength Detection

In many cases FLIM images are taken in several emission wavelength intervals or under different angle of polarisation. It is important that both recordings be performed simultaneously. This not only reduces the sample exposure and the associated photobleaching, it also avoids that photobleaching during the first recording changes the results of the second one. Only if both recordings are done simultaneously the results are comparable. Multi-wavelength detection is a standard feature of TCSPC FLIM and can be used with all bh FLIM systems.

Depth Resolution and Suppression of Lateral Scattering

Another important issue is longitudinal resolution. Mixing the fluorescence lifetimes of different sample planes and pixels must be strictly avoided. The only technique that delivers depth resolution and suppression of lateral scattering without loss in photon efficiency is confocal or multiphoton laser scanning. Thus, the FLIM technique must take full advantage of the capabilities of confocal and two-photon laser scanning microscopes [154, 168]. TCSPC FLIM is perfectly compatible with these instruments.

Compatibility with the Scanning Microscope

Laser scanning microscopes with standard scanners scan the sample at pixel dwell times down to about 1 µs, systems with resonance scanners even faster. Photon rates obtained from

typical samples are usually an order of magnitude smaller. It is thus impossible to obtain enough photons for lifetime analysis within the time the beam is on one pixel. Consequently, the FLIM system must be able to acquire the photons from a large number of frames scanned at a pixel rate higher than the photon detection rate. TCSPC FLIM does exactly this.

Fast Scanning

The ability to work with fast scanning is mandatory also from a practical point of view. The operator must be able to position the sample under the microscope, find the desired focal plane, adjust the scan area, the laser power, and select the right imaging parameters. For biological samples, these activities must be completed within a limited period of time and with limited exposure to the excitation light. This is only possible if the imaging system has some kind of fast preview function. A fast preview is, of course, only possible if the sample is scanned at high frame rate, and if the imaging technique is compatible with this rate. TCSPC FLIM is independent of the scan rate. The results depend only on the photon rate delivered by the sample and the total acquisition time.

Tolerance to Dynamic Effects in the Sample

Fluorescence signals from live specimens cannot be expected to remain constant over the acquisition time of the image. There may be motion in the shape of the cells, organelles may be moving, mitochondria are drifting around, or the cells may respond to variations in the oxygen or CO_2 concentration. There may even be fluctuations due to a variable number of fluorophore molecules in the laser focus. Moreover, photobleaching is often not absolutely avoidable so that the fluorescence intensity and lifetime may change slightly over the acquisition time. Such changes should not induce direct artefacts, such as distortions in the decay curves, fluorescence spectra, or images recorded. Procedures like slow scanning of time gates or wavelength scanning must therefore be avoided. TCSPC does not use any gating in time or wavelength. Instead, it builds up a photon distribution. The photon distribution always represents an average of the fluorescence decay function over the acquisition time.

Multiphoton Excitation and Non-Descanned Detection

Lifetime microscopy extends more and more into experiments using life tissue, life animals, or even into clinical applications. The only way to obtain clear images from tissue layers deeper than a few 10 µm is two-photon excitation with non-descanned detection (NDD), see page 346 of this handbook. The FLIM system must be NDD-compatible. TCSPC FLIM has no problems with two-photon excitation, and works perfectly with non-descanned detection.

Acquisition Time

Of course, a good FLIM technique should deliver a result of a given signal-to-noise ratio in an acquisition time as short as possible. Under the conditions of live cell imaging, the photon rate that can be obtained is usually limited by the photostability of the sample. Short acquisition time is therefore inevitably connected to high photon efficiency. That means, surprisingly, that TCSPC FLIM yields the shortest acquisition time under these conditions. Please see considerations below.

Signal-to-Noise Ratio of FLIM

From a single-exponential fluorescence decay recorded under ideal conditions the fluorescence lifetime can theoretically be obtained with a relative standard deviation or ‘coefficient of variation’, CV_τ, and with a signal-to noise ration, SNR, of

$$CV_\tau = \frac{\sigma_\tau}{\tau} = \frac{1}{\sqrt{N}} \qquad SNR = \sqrt{N} \qquad (1)$$

with N = number of recorded photons [46, 497, 174, 680]. In other words, the fluorescence lifetime can be obtained at the same accuracy as the intensity. Measurement under ideal condition means the decay function is recorded

- with an instrument response function that is short compared to the decay time
- into a large number of time channels
- within an observation-time interval several times longer than the decay time
- with negligible background of environment light, detector dark counts, and detector afterpulsing

Under these conditions, the equation given above can easily be verified: The average arrival time of the photons after the excitation pulse is equal to the decay time, and the variance of the arrival time of the individual photons is equal to the decay time. The variance of the average arrival time for N photons decreases with $N^{1/2}$. Consequently, the relative variance of the lifetime is $N^{-1/2}$. Correctly recorded TCSPC FLIM data come very close to the theoretical limit [68, 69, 174].

The conclusion from (1) is that the main parameter that influences the signal-to-noise ratio of the lifetimes derived from FLIM data is the photon number in the pixels, N. There are various ways to maximise N. The first idea in this direction is often to use more laser power or to increase the acquisition time. This is certainly correct, but the options are limited by the photostability of the sample. Better ways to higher N is to use detectors of high efficiency, objective lenses of high NA, perfect alignment of the optical system, exact focusing, and correct binning in the data analysis [174].

Things become complicated when the fluorescence decay is no longer recorded under ideal conditions. An investigation of the signal-to-noise ratio under non-ideal conditions has been published by Köllner & Wolfrum [680]. It turns out that the factor impairing the lifetime accuracy most dramatically is background. Also this can easily be explained: The arrival time of the background photons varies over the full recording time interval. This is usually 10 times longer than the fluorescence lifetime. That means background photons, on average, introduce 10 times more timing variation than the fluorescence photons. There are also other factors which influence the efficiency of lifetime analysis, for example length and position of the observation-time interval, laser repetition rate, number of time channels, IRF width, and amplitude and lifetime ratio of the decay components of multiexponential decay functions. For a detailed discussion and experimental demonstration of the effects please see [174].

Why Does FLIM Need More Photons than 'Normal' Imaging?

The fact that FLIM achieves the same signal-to-noise ratio as intensity imaging is in apparent contradiction with common experience: From the same sample imaged under similar excitation conditions, intensity images are obtained in a far shorter acquisition time than FLIM images. Where is the mistake?

The mistake is to implicitly assume that 'intensity imaging' (in the sense of spatial imaging) and FLIM are recording the same physical properties of the sample. This is wrong: Intensity imaging aims at resolving the spatial structure of the sample. To do so, it uses the fluorescence intensity of a fluorophore attached to the internal sample structures. In other words, intensity imaging records the spatial variation of the fluorophore concentration in the sample. Relative concentrations in stained and unstained structures of the sample can vary by 1:100 and more.

FLIM aims at resolving changes in the fluorescence lifetime, i.e. in the quantum efficiency of the fluorophore. Relative changes in these parameters are much smaller than the concentration

changes. Lifetime changes are usually in the 10% range. Consequently, a higher signal-to-noise ratio, and a higher number of photons are needed, see equation above.

The differences are illustrated in Fig. 692. The figure shows an intensity image (left) and a lifetime image (middle) derived from the same TCSPC FLIM data. The number of photons, N, in the bright pixels is about 80. The signal-to-noise ratio is about 9. However, the concentration changes are much larger than this. The spatial structure of the sample is therefore resolved very well. The signal-to-noise ratio of the lifetime in the FLIM image is on the same order as the intensity noise in the intensity image. This can be proved by the lifetime histogram on the right. (Note that the relative variance is about 1/4 of the full-width at half maximum.) However, the lifetime variation in the sample is at the limit of delectability. The reason is simply that the lifetime variation in the sample is much smaller than the concentration variation.

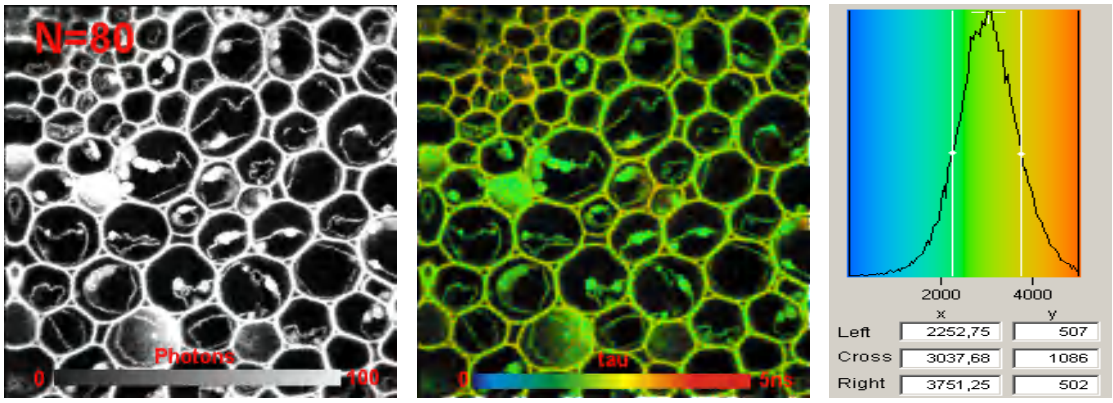


Fig. 692: Intensity and lifetime images derived from the same TCSPC data. Left: Intensity image. Middle: Lifetime image. Right: Histogram of the lifetime over the pixels of the FLIM image.

It should be noted that 'intensity imaging' may also be used to investigate molecular interactions of the fluorophores with their environment. In that case, the aim is to record variation in the fluorescence quantum efficiency of the fluorophores. The quantum efficiency and the fluorescence lifetime are directly connected. Consequently, the relative intensity changes to be recorded are the same as for the lifetime in lifetime imaging. However, the intensity also depends on the concentration. The variation in concentration must be removed from the data by reference measurements. These introduce additional noise. A practical evaluation of FLIM versus intensity measurement for FRET applications has been published by Pelet et al. [953]. The authors found that FLIM indeed delivered a better SNR than intensity-based FRET measurement.

Photobleaching and Photodamage

The problems described above are further complicated by photobleaching or even photodamage [203, 391, 595, 681, 948]. Moderate photobleaching has no effect on the spatial structure of a sample. Intensity measurements (in the sense of spatial imaging) can therefore be performed at high excitation power. It may be expected that photobleaching has no effect on FLIM as well: FLIM is independent of the fluorophore concentration. Some loss in fluorophore concentration by photobleaching therefore should not have an impact on the recorded lifetimes. Unfortunately, this is usually not the case [149, 589]. The reason is that biological samples normally contain several fluorophores, or a fluorophore in different states of interaction with the molecular environment. Different fluorophores and different fluorophore fraction bleach at different rate. Usually slow lifetime components bleach faster, the lifetime distribution changes toward shorter lifetimes, and the apparent lifetime decreases. It may also happen that photobleaching products are fluorescent themselves. In these cases the lifetime changes may become entirely unpredictable. Moreover, photobleaching generates radicals,

and these have a destructive effect on the proteins. Photobleaching may therefore not only change the fluorophores but also the molecular structure of the specimen itself. Caution is required especially in attempts to verify FLIM-FRET results by acceptor photobleaching.

An example of photobleaching is shown in Fig. 693, left and middle. A region around the centre was scanned by a 405 nm ps diode laser for 5 minutes at full power. Then a lifetime image of a larger area was recorded. The intensity image (Fig. 693, left) shows a photobleached region in the scan area of the full-power 405 nm laser. The spatial structure of the sample is still perfectly preserved. The lifetime image of the intensity-weighted lifetime, ti, is shown in the middle. It can clearly be seen that the photobleached region has a decreased lifetime.

When FLIM is performed on endogenous fluorophores the effects can be even more dramatic. Fig. 693, right, shows an NADH image of live cells. It was obtained with two-photon excitation in a Zeiss LSM-880 at 5% of the available laser power. The average count rate over the entire image was 350,000 s^{-1}. Within 20 seconds, photodamage occurred, see the bright spots of extremely short lifetime. However, even if there is no obvious photodamage the metabolic state of the cells may be changed. Alam et al. have investigated such changes and found that the metabolism had shifted towards increased OXPHOS (oxydative phosphorilation after exposure to increased laser power [11]. Interestingly, the changes were only in the a1/a2 ratio, not in the component lifetimes, τ_1 and τ_1.

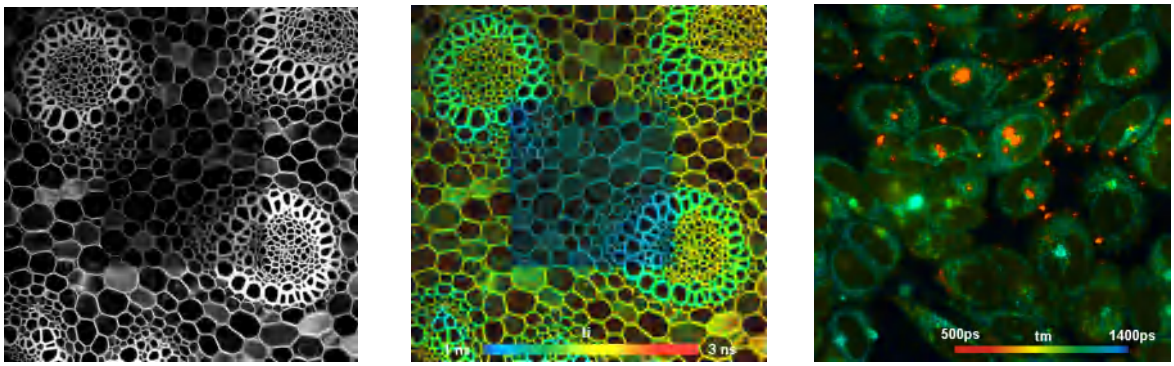


Fig. 693: Left and middle: Photobleaching in a convallaria sample. The region around the centre has been scanned with the full power of the 405 nm diode laser. The scanned region shows little change in fluorescence intensity (left), but a massive change in fluorescence lifetime (middle). Right: Two-photon NADH image of live cells. The red spots are locations of severe photodamage.

The same problem exists, of course, for intensity-based measurements of molecular parameters of the sample. The only difference to FLIM is that photobleaching and photodamage artefacts are more difficult to identify. The problem therefore often remains unnoticed.

It should be noted here that there is also another difference between FLIM and spatial imaging. Samples for spatial imaging contain high concentrations of fluorophores. Examples are samples as the one shown in Fig. 693. FLIM samples (and samples for intensity-based molecular imaging) are different. They contain no exogenous fluorophores at all or fluorophores linked to highly specific binding sites in the cells. In both cases, the fluorophore concentration is low. For a given emission rate, the molecules have to perform a higher number of absorption-emission cycles and, consequently, photobleach faster.

It is sometimes believed that two-photon excitation causes less photobleaching than one-photon excitation. This is wrong. It is certainly correct that two-photon excitation does not cause photobleaching outside the focal plane [405]. It is also correct that NIR radiation causes considerably less photodamage in live tissue than UV radiation for the same excitation power [681]. However, if the photobleaching rates within the focal plane are compared for the same

emission rate photobleaching has been found up to 20 time higher for two-photon excitation [391].

Photobleaching and photodamage are clearly nonlinear for two-photon excitation [391, 595 681, 948], and a nonlinear component probably also exists for one-photon excitation [203]. Therefore, photobleaching can usually be reduced by decreasing the excitation power and compensating for the lower count rate by an increased acquisition time.

Giving general recommendations for adjusting the count rate is difficult. On the one hand, the concentration of the fluorophore and the photostability may vary by orders of magnitude; on the other hand, the tolerance of the users to possible artefacts may differ considerably. In published FLIM results the count rates and the amount of photobleaching are rarely mentioned so that only a few examples can be given here: CFP-YFP FRET images of HEK cells presented in [148, 154] were recorded at $50 \cdot 10^3$ s^{-1}. CFP-YFP FRET in *Caenorhabditis Elegans* [253] was recorded at $< 10^5$ s^{-1}. Two-photon autofluorescence of skin delivered about $60 \cdot 10^3$ s^{-1} [685, 686, 687]. These count rates are by a factor of 40 to 100 lower than the maximum count rate of the bh TCSPC devices used. It should be expected that much higher count rates are obtained from stained tissue. Nevertheless, imaging of the pH in skin tissue by BCECF was performed at an average photon rate of only $2 \cdot 10^6$ s^{-1} [553], although the frequency-domain technique used was capable of processing much higher rates.

Acquisition Time of TCSPC FLIM

There is probably no parameter of FLIM which is discussed more controversially than the acquisition time. We have shown that the signal-to-noise ratio of TCSPC FLIM comes very close to the theoretical limit of $N^{1/2}$, [174] see also page 415 of this book. Therefore, it should be expected that TCSPC FLIM also reaches short acquisition times. Nevertheless, the technical literature is full of wrong estimations of the acquisition time needed to record a TCSPC FLIM image. The mistakes start with wrong assumptions on the size of the pile-up effect, and, consequently, the count rates that can be applied in FLIM measurements, and end with the assumption of unrealistic pixel numbers, wrong numbers of photons required per pixel, and neglecting of overlapping binning in the data analysis.

Effect of Pixel Numbers and Binning

The equation given at page 470 can be used to estimate the number of photons and the acquisition time needed to record a fluorescence lifetime image. With N being the number of photons per pixel the relative standard deviation and the signal-to-noise ration of the lifetime is

$$CV_\tau = \frac{\sigma_\tau}{\tau} = \frac{1}{\sqrt{N}} \qquad SNR = \sqrt{N}$$

With N = p T / pxl (p= photon rate, T= acquisition time, pxl=pixel number) the acquisition time is

$$T = \frac{1}{pCV_\tau^2} pxl \qquad T = \frac{SNR^2}{p} pxl$$

The acquisition time as a function of the desired standard deviation for a count rate of 10^6 s^{-1} and different pixel numbers is shown in Fig. 694, left. Even for an image of 512 x 512 pixels a relative lifetime accuracy of 0.1 (or 10%) is obtained within less than 30 seconds, for smaller pixel numbers the acquisition time is correspondingly shorter. However, an acquisition time of 2600 seconds (or 45 minutes) would be required to record lifetime image of 512 x 512 pixels with a lifetime accuracy of 1 %.

The acquisition time in the equations above and in Fig. 694, left refers to unbinned lifetime data. With binning in the lifetime analysis, and with the definition of the binning factor, *n*, used in SPCImage (see page 861 of this handbook) the effective number of pixels, pxl_{eff}, of an image with *pxl* pixels is

$$pxl_{eff} = pxl / (2n+1)^2$$

The acquisition time then becomes

$$T = \frac{1}{pCV_\tau^2} \frac{pxl}{(2n+1)^2} \qquad T = \frac{SNR^2}{p} \frac{pxl}{(2n+1)^2}$$

A diagram for 512 x 512 pixels and different binning is shown in Fig. 694. With a binning parameter of n=2 (appropriate for spatial oversampling factor 5, see 'Spatial Binning', page 930) the acquisition time for a lifetime accuracy of 1% (SNR of 100) becomes 100 seconds. For an accuracy of 10% it is only 1 second.

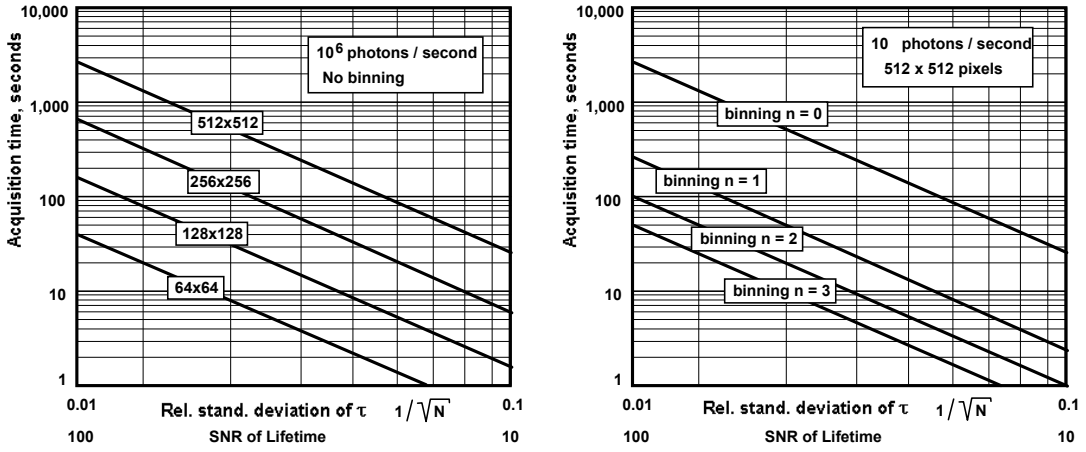


Fig. 694: Left: Acquisition time versus relative standard deviation and SNR versus pixel number for different pixel number. No binning used. Right: Acquisition time versus relative standard deviation and SNR versus pixel number for different binning in the data analysis. Count rate 10^6 s^{-1}.

The diagrams above show that FLIM with acquisition times on the order of a few seconds and below is well possible if the requirements to the lifetime accuracy are not too high. Please see [108] and 'Fast Online FLIM with Standard bh TCSPC Systems' page 415, for experimental demonstration.

This doesn't men, however, that FLIM experiments should always be performed near the minimum of the acquisition time needed to obtain a desired accuracy. The accuracy required to resolve a particular biological effect is often not known in advance, and the accuracy obtained in the lifetime analysis may be lower than $N^{1/2}$. This is especially the case when multi-exponential analysis is required, or when the data quality is impaired by non-ideal recording conditions [174].

Recording Conditions

The relation SNR = $N^{1/2}$ applies to FLIM data recorded under ideal conditions. In particular, the entire decay must be in the observation-time interval and there must be no background from environment light, detector afterpulsing, laser background or long-lifetime fluorescence. If this is not the case the required number of photons is increases, and so does the acquisition time for a given signal-to-noise ratio of the lifetime [174]. Moreover, it can happen that the optical system simply does not collect the number of photon it could. Frequently encountered mistakes are poor alignment of the optical system, inaccurate focusing, and the use of wrong microscope lenses. Examples and their influence on the lifetime accuracy are shown in [174].

Carelessness in only one of these points may not influence the results by much. However, negligence in *all* of these details can reduce the lifetime accuracy by a factor of 30, see [174]. To compensate the loss in accuracy almost 1000 times more photons from the sample would be needed. In other words, the acquisition time to obtain a given SNR becomes 1000 times longer than under optimum conditions.

Multi-Exponential Decay Functions

The required number of photons increases if double-exponential decay functions are to be resolved. However, the number of photons needed is commonly over-estimated. The misconception probably goes back to a paper of Köllner & Wolfrum [680]. They (correctly) calculated the number of photons required to resolve a double-exponential decay to be N = 400,000. The paper is therefore used as an argument that multi-exponential lifetime analysis in FLIM is impossible. However, Köllner & Wolfrum assumed a decay function with 10% of 2 ns and 90% of 4 ns. This is an extremely unfavourable situation which indeed requires an extremely high number of photons.

Fortunately, the prospects of separating two lifetime components improve dramatically with the ratio of the two lifetimes and with the amplitude of the short lifetime component. Typical FLIM applications are metabolic FLIM, with separation of the decay components of bound and unbound NADH or of bound and unbound FAD, and FRET experiments, with separation of the interacting and non-interacting donor fraction. In these cases, the component lifetimes differ by a factor of 5 to 10, and the amplitude of the fast component is 50 to 90%. Under such conditions double-exponential analysis is feasible on no more than a few 1000 photons per pixel or per binning area. An example is shown in Fig. 695 and Fig. 696.

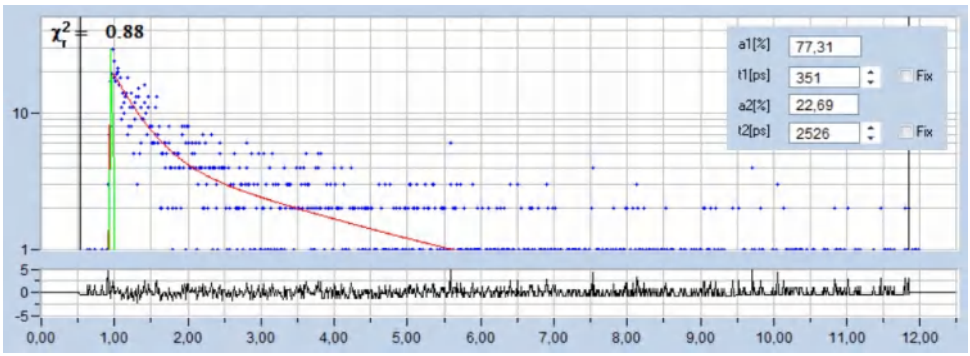


Fig. 695: Decay curve with 1700 photons, double-exponential fit. Decay curve from cursor position in Fig. 696.

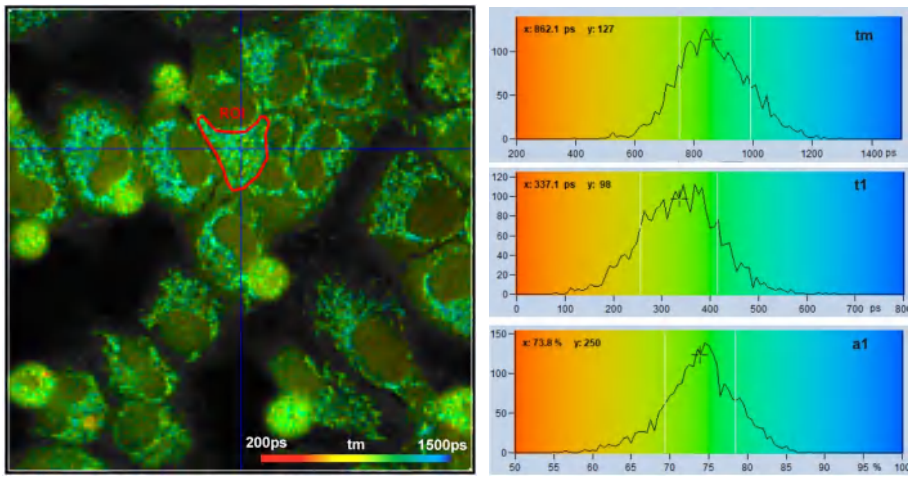


Fig. 696: Left: NADH FLIM of live cells, 512 x 512 pixels, binning = 2, about 1700 photons in binning area. Right: Distribution of decay parameters t_m, t_1, and a_1 in region of interest.

The data show autofluorescence of live tumor cells. The sample was excited by 2-photon excitation at 750 nm, the photons were detected from 440 nm to 475 nm, the acquisition time was about 40 seconds at a count rate of 500,000 photons per second. (Higher count rate caused damage to the cells) The fluorescence comes almost exclusively from NAD(P)H. Fig. 695 shows the decay curve at the cursor position of Fig. 696. The raw data contain about 70 photons per pixel. Binning = 2 was applied to the data, the curve thus contains 1700 photons. The data were fitted by a double-exponential model, see red curve. The fit results, shown in the insert, are perfectly compatible with the decay components of NAD(P)H.

Fig. 696, left, shows a lifetime image of the amplitude-weighted lifetime, t_m, of the double-exponential fit. Histograms of t_m and of the lifetime, t_1, and the amplitude, a_1, of the fast decay component are shown in Fig. 696, right. With about 1700 photons per binning area the distributions are not overwhelmingly narrow. But they are still scientifically meaningful. For example, a_1 peaks at 75%. In comparison, a normal cell has an a1 of about 65%. Clearly, the a1 histogram is compatible with a tumor cell but not with a normal cell. Thus, the data are accurate enough to distinguish between tumor cells and normal cells.

Counting Loss and Pile-Up Effects

TCSPC is based on the assumption that the light intensity at the detector is low enough so that the detection of several photons per signal period is unlikely [154, 167, 924]. If the count rate is too high ‘pile up’ occurs, and the recorded decay curves are distorted. Pile-up was indeed a problem in early TCSPC lifetime spectrometers working at pulse repetition rates in the kHz range [924]. For modern excitation sources the repetition rates are in the range of 50 to 80 MHz so that pile-up is rarely a problem [154, 167]. Please see 'Pile-Up', page 294. Nevertheless, postulated limitations of the detection rate are often used as an argument against TCSPC FLIM. Some remarks about the behaviour of TCSPC FLIM at high count rates appear therefore indicated.

For TCSPC at high signal repetition rate two instrumental effects have to be distinguished: The first one is the loss of a second photon detected *within the signal processing time* (‘dead time’) of a previous one, the second one is the loss of a second photon detected *in the same signal period* with a previous one. The first effect causes ‘Counting Loss’, i.e. a nonlinearity in the recorded intensities. The second one causes an error in the detected fluorescence lifetime. The dead time of the bh TCSPC modules are on the order of 100 ns, the signal period is on the order of 10 to 20 ns. Counting loss is therefore more likely than pile-up. (Please see page 292 and page 294 for a quantitative description of the effects.)

Counting Loss

Fig. 697, left shows oscilloscope traces of the laser pulses (80 MHz) and the single photon pulses of a PMC-100 detector (detection rate 10 MHz). As you can see, there is a non-zero probability that a photon falls into the dead time caused by a previously detected one.

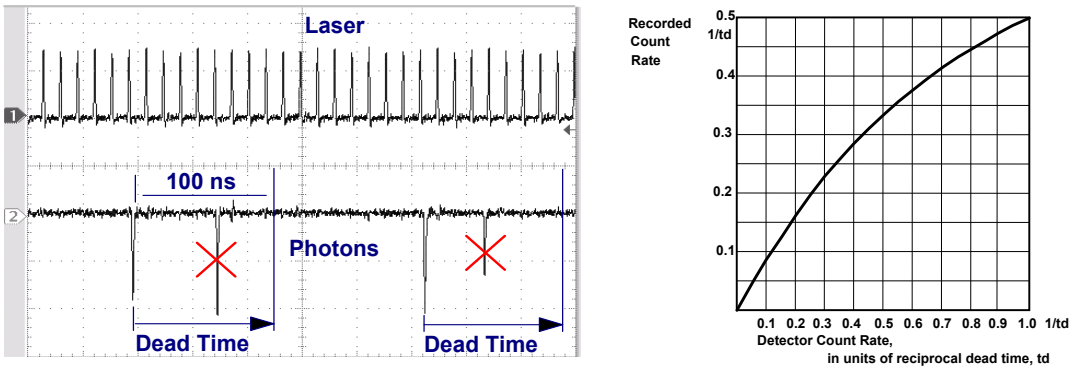


Fig. 697: Left: Detection (and loss) of a photon within the dead time caused by a previous one. Right: Nonlinearity of recorded vs. detected count rate.

Consequently, a fraction of the photons is not detected. The result is a nonlinearity in the recorded count rate versus the detector count rate, i.e. a nonlinearity in the recorded intensity, see Fig. 697, right.

For a single TCSPC module the nonlinearity becomes apparent at (average) count rates above about 1 MHz, see Fig. 698. Because the count rate in bright pixels is much higher than the average count rate these are recorded with a lower intensity than they actually have. The images start looking ‘flat’, as can be seen in Fig. 698, right.

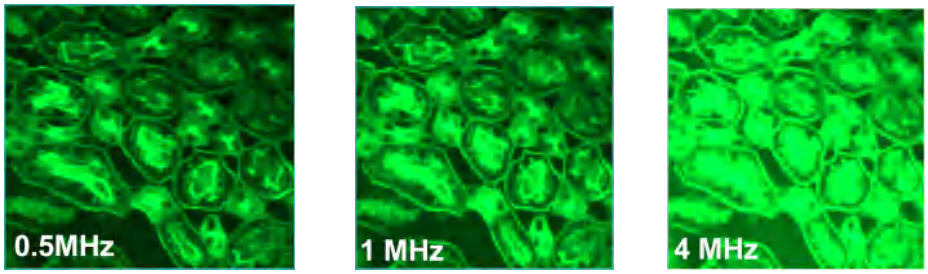


Fig. 698: Intensity images taken at average count rates of 0.5 MHz, 1 MHz, and 4 MHz. Intensity normalised on brightest pixel.

The counting loss could easily be corrected by using the curve shown in Fig. 697, right. Another way to obtain a linear intensity scale is to use intensity information from a counter that counts the detector pulses directly, without passing them through the timing electronics of the TCSPC module. The FLIM images are then constructed using pixel photon numbers from the counter and photon times from the timing electronics. The technique and the parameter setup are described in section 'Lifetime-Intensity FLIM', page 428. However, in the majority of FLIM applications the intensity is not used, and the nonlinearity of the intensity can be ignored.

Pile-Up

‘Pile-up’ means the detection (and loss) of a second photon within the same laser period of a previous one. Pile-up causes a distortion in the recorded decay profiles. As can be seen from Fig. 697 pile-up is far less likely than counting loss. Moreover, the influence on the recorded decay time is far smaller than commonly believed. The change in the lifetime of a single-exponential decay model is approximately

$$\tau_{meani} \approx \tau \left(1 - P/4\right)$$

P = average number of photons per laser period, τ = fluorescence lifetime

τ_{meani} = intensity-weighted lifetime of the measured decay profile

Thus, even with 0.2 photons per laser period the lifetime error is only 5 %, see also page 294. A detailed derivation of the pile-up distortion is given in [154]. A curve of the ratio of the

detected lifetime and true lifetime as a function of the number of photons per signal period is shown in Fig. 699.

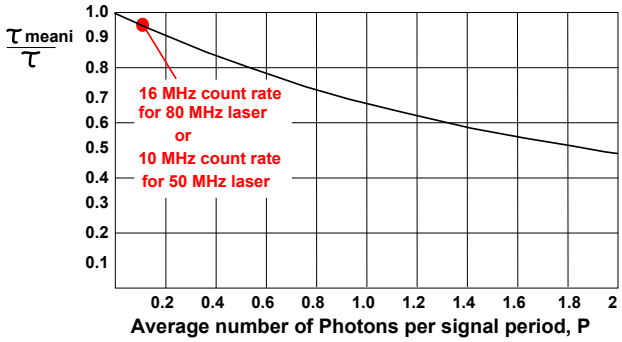


Fig. 699: Ratio of detected lifetime and true lifetime as a function of the average number of photons per laser period. The pile-up error in the lifetime at 16 MHz detection rate and 80 MHz laser repetition rate is only 5%.

Two lifetime image taken at 4 MHz and 8 MHz *average* count rate and 50 MHz laser repetition rate are shown in Fig. 700, left and right. The images show the intensity-weighted lifetime of a double-exponential decay. The 8-MHz image shows clear indications of intensity nonlinearity by counting loss. But there are no visible differences in the measured lifetime. The lifetime determined in the brightest spot is 2244 ps for the 4-MHz image versus 2207 ps for the 8-MHz image. The difference is a mere 1.7%. This shows that pile up errors are far less severe than commonly believed.

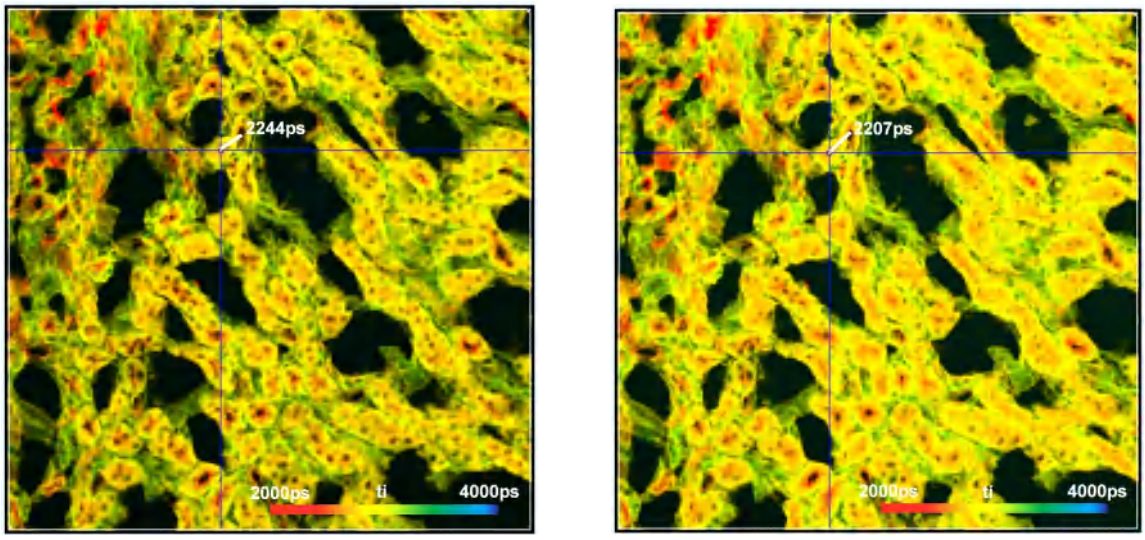


Fig. 700: Lifetime image taken at 4 MHz (left) and 8 MHz (right) average count rate. Intensity-weighted lifetime of double-exponential analysis. The lifetimes in the brightest pixel are 2244 ps versus 2207 ps, a difference of merely 1.7%. DCS-120 system with SPC-160 and HPM-100-40

Spatial Binning of Decay Data

Correct binning of the decay information during lifetime analysis is key to good lifetime images. When an image is recorded by a scanning microscope the point-spread function of the microscope lens is usually ‘oversampled’ to obtain maximum spatial resolution. As a rule of thumb, the diameter of the central part of the Airy disc should be sampled by 5 × 5 pixels, see 'Spatial Binning', page 930. In practice often higher oversampling factors are used unintentionally. The decay data in the pixels within one Airy-disc diameter are, of course, highly correlated. SPCImage data analysis [68, 69, 78] therefore uses a binning function. The lifetime images are built up from the unbinned intensity data and the binned decay data. Binning is controlled by a binning factor, n, see page 885 and page 930 in the data analysis chapter.

By using the binning function of SPCImage in the data analysis, images can (and should be) recorded with correct spatial oversampling and the loss in photon number per pixel be compensated by binning. The resulting images are much better than under-sampled images recorded with low pixel number. An example is shown in Fig. 1219, page 885. The optimum binning factor is about the radius of the point spread function, expressed in pixels. That means, for typical oversampling factors of 5 to 8 binning with n=2 or n=3 should be used. Higher binning factors are available and can be used to analyse images with low photon numbers, where a compromise between spatial resolution and lifetime accuracy must be made.

Fig. 701 shows two lifetime images obtained from 256 × 256 pixel raw data. For the left image, no binning was used (n=0), the right image was processed with binning of n=2. It can be seen that the image on the right has the same spatial resolution but a much better signal-to-noise ratio of the fluorescence lifetime.

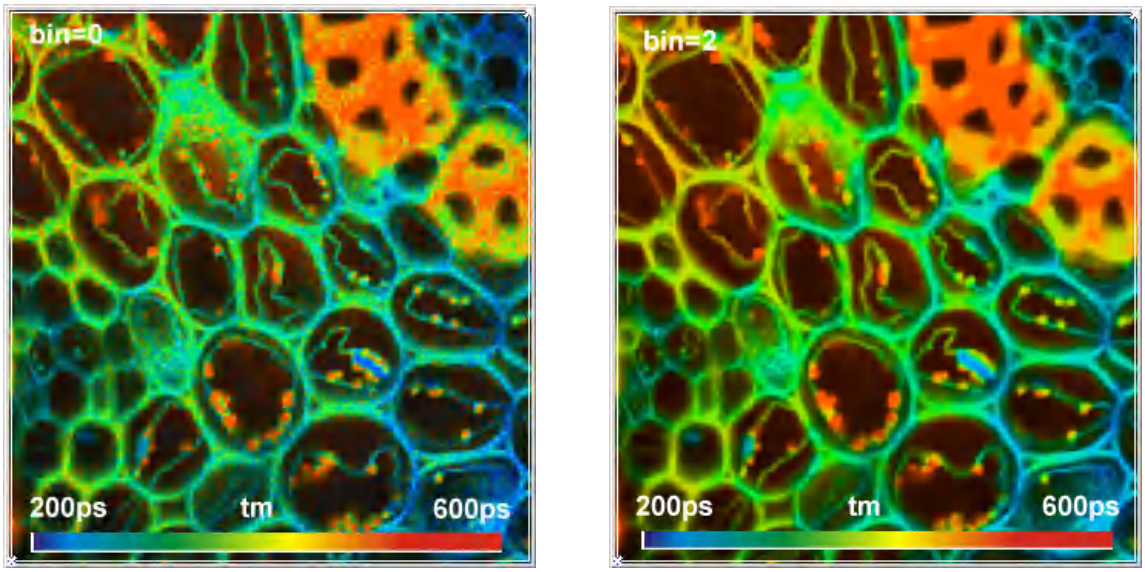


Fig. 701: Lifetime images obtained from 256 x 256 pixel data. Left Binning n=0, right Binning n=2

Image Area

The time needed to scan an image increases linearly with the number of pixels recorded. This statement may be considered trivial. Nevertheless, it is often ignored by microscope users. A laser scanning microscope scans the image area at a constant pixel dwell time, regardless whether or not the pixels contain useful information. Thus, you can decrease the acquisition time by excluding useless pixels from being recorded. The simplest way of achieving this is to zoom into the right area of the image, see Fig. 702.

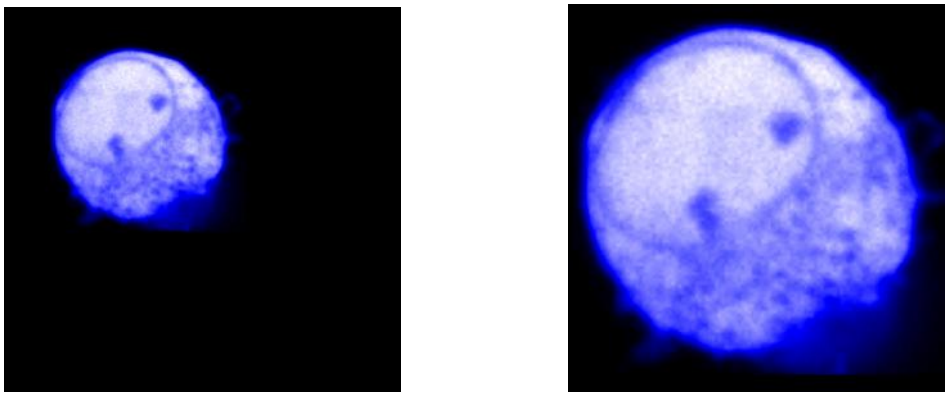


Fig. 702: Image of a single cell. Left: Without zoom; the image contains only 15% pixels with useful information. Right: After zooming into the correct region of interest 75% of the pixels are used.

The cell shown on the left fills only 15% of the total scan area. In other words, only 15% of the acquisition time are spent on recording the image of the cell. 85% of the time are spent on recording dark pixels. After zooming into the an appropriate region of interest the cell fills 75% of the scan area, and 75% of the acquisition time are used to image the cell. This is an improvement of a factor of 5 over the recording shown left. You may object that the zoomed image of the cell has also 5 times more pixels, and thus contains the same number of photons per pixel than Fig. 702, left. This is correct. However, for the image on the right you can use binning in the lifetime analysis. You then obtain an image that shows the cell with a number of pixels as Fig. 702, right, but with the same number of photon per binning area as the image in Fig. 702, left.

IRF Recording

To determine the lifetimes from TCSPC FLIM data the data analysis needs the IRF of the system. It is therefore believed (and constantly taught) that it is necessary to record the IRF of the FLIM system. However, to say it bluntly, 50% of the recorded IRF are wrong.

The following paragraphs therefore give an introduction on the role of the IRF in data analysis, its general shape in the bh FLIM systems, the problems to measure it, how to avoid errors in IRF measurement, and, if possible, how to avoid IRF measurement altogether.

What is the IRF?

The fluorescence waveform the FLIM system records is the convolution of the true fluorescence decay profile with the instrument response function, or ‘IRF’. The IRF is the function the FLIM system would record for a sample with an infinitely short fluorescence lifetime. Decay parameters are derived from the recorded waveforms by convoluting the IRF with a model function of the fluorescence decay, and fitting the result to the data, see 'The Convolution Integral', page 932. Thus, at least an approximate IRF is needed to derive fluorescence decay parameters from the detected fluorescence waveforms. Measurement and optimisation of the IRF was an important issue in early fluorescence lifetime spectrometers [924]. Therefore, users of FLIM are often concerned that inaccuracy in determining the IRF of the FLIM system might induce systematic errors in the lifetimes measured.

IRF of bh FLIM Systems

bh FLIM systems use HPM-100-06 and -40 hybrid PMTs to detect the photons. Typical IRFs for these detectors are shown in Fig. 703, left and middle. For comparison, Fig. 703, right, shows the IRF of an XP2020, which was commonly used in early lifetime spectrometers. It becomes obvious from these curves that the IRF of the hybrid detectors are much faster and cleaner than that of the XP2020. Consequently, the IRF has a far smaller influence on the analysis results than it had in the early lifetime spectrometers.

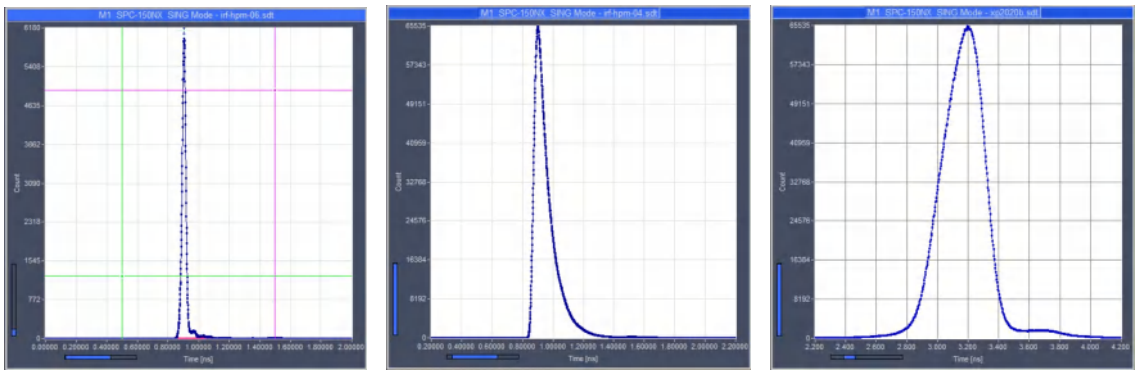


Fig. 703: IRF of the HPM-100-06 (left) and HPM-100-40 (middle) as compared to that of an XP-2020 as it was used in lifetime spectrometers 20 years ago (right). SPC-150NX TCSPC module.

Can We Measure the IRF of a FLIM System?

Recording the IRF in a (confocal) laser scanning microscope may appear simple at first glance. The sample would be replaced with a scattering medium, and a TCSPC image or a single waveform would be recorded at the wavelength of the excitation laser. Unfortunately, this procedure has a flaw. The problem is shown in Fig. 704. In a confocal microscope the light returned from the sample is separated from the laser beam by a dichroic beamsplitter. The beamsplitter is designed to reflect the laser and to transmit the fluorescence. Consequently, laser light returning from the sample is reflected toward to the laser, not toward the detector, see Fig. 704.

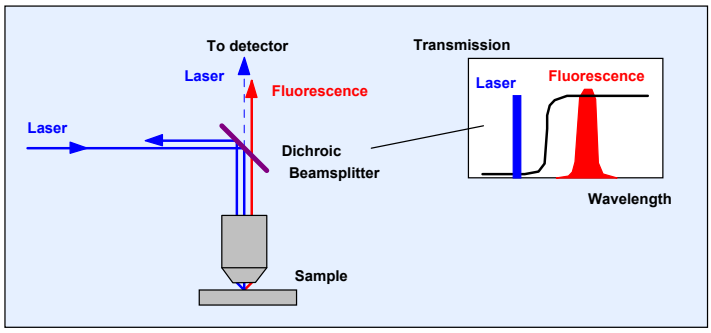


Fig. 704: Problem of recording an IRF in a confocal microscope. The laser light is reflected back to the laser, and does not reach the detector

It is often attempt to use short-lifetime fluorescence to avoid the problem. However, the lifetime had to be shorter than 10 ps. Fluorophores with decay times this short and with reasonable brightness do not exist.

Another attempt is to use the fact that a dichroic mirror has a small amount of leakage at the laser wavelength. A small amount of light scattered back from the sample can therefore be recorded. However, the efficiency is much higher at longer wavelength, and the slightest amount of fluorescence from the target makes the IRF wrong.

Microscopes that have a wideband beamsplitter do not have these problems. The DCS-120 WB version has an 40/60% beamsplitter instead of the main dichroic, and the Zeiss LSM 710/780/880/980 can switch between a dichroic an 80/20% mirror. However, also with a wide-band beamsplitter IRF recording is not free of problems. It can happen that multiple scattering in the target broadens the returned pulse shape, or that fluorescence of contaminations is recorded together with the scattered light. Therefore, use a small pinhole, and select an area for IRF definition which does not show signs of fluorescence. An IRF which was measured with the DCS-120 WB and then imported into SPCImage NG is shown in Fig. 705.

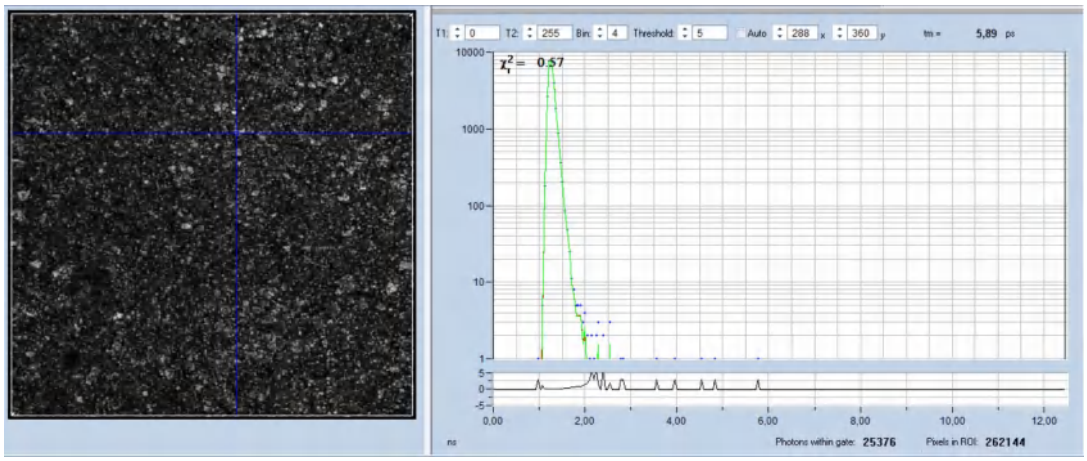


Fig. 705: IRF measured with the DCS-120 WB system. The scattering target was a ceramics plate

In a two-photon microscope the measurement of the IRF is easier. There is a number of ultrafast processes that transfer the excitation wavelength into a wavelength that passes the beamsplitters in the detection light path. The fast signal is then automatically separated from the laser light. It has been suggested to use hyper-Raman scattering from gold nanoparticles [537, 1222]. Unfortunately these are expensive and cannot be stored for longer periods of time. We recommend to use second-harmonic generation (SHG). Strong SHG signals are obtained from urea crystals and sugar crystals [88]. But also the use of SHG holds a pitfall. SHG is emitted in forward direction, not back into the microscope lens. The detected signals has been scattering in the SHG material, reflected at the microscope slide or at the cover that protects the beam path from environment light. In the sub-20 ps range, transit time differences caused by these effects have an influence on the signal shape. The detected signal may therefore not exactly represent the IRF.

Synthetic IRF

SPCImage NG avoids troublesome recording of an instrument response function (IRF) by IRF modelling. This is achieved by using a generic function which has the same general shape as the IRF of the FLIM system. The parameters of this function are determined to make it similar to the IRF. To obtain the IRF parameters, a fluorescence signal is recorded, and the convolution integral of the IRF and the model function of the fluorescence is fitted to the data. The result is a synthetic IRF, which is the best possible approximation to the IRF the fluorescence was recorded with. For details please see 'Instrument Response Function' in chapter ‘SPCImage NG Data Analysis Software’, page 942.

A comparison of FLIM analysis with a synthetic IRF and with a (correctly) measured one is given in Fig. 706. As can be seen from the figure, the results are virtually undistinguishable. The lifetime images, the lifetime distribution, and even the parameters of the two decay components are closely the same. The reason of the similarity becomes clear when the shape of the IRF (green curve in Fig. 706) is considered. Even if the IRFs are not absolutely identical, they have a width much shorter than the fluorescence lifetimes, and no low-amplitude tail. Under these conditions, the shape of the IRF has no influence on the shape of the measured decay function for times later than few 100 ps after the excitation maximum. Consequently, the lifetime analysis delivers the same results for both IRFs. *The conclusion is that the synthetic IRF should be used, and no effort be taken to use a measured IRF for standard FLIM applications.*

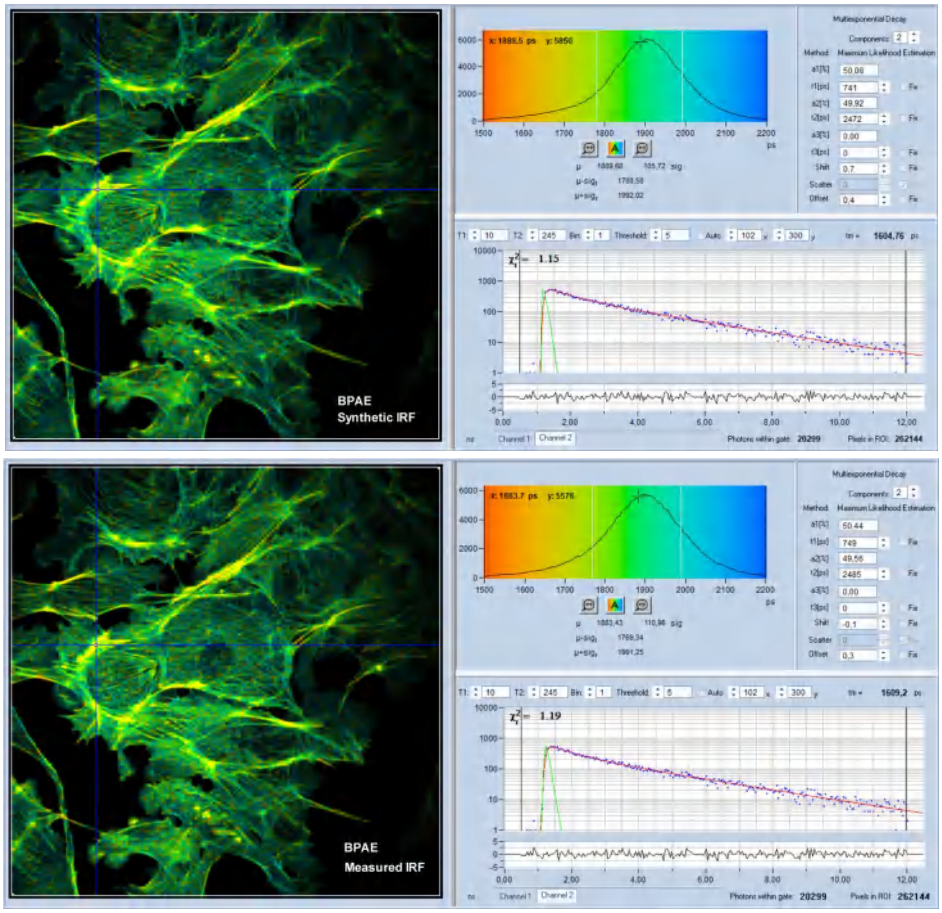


Fig. 706: Top: Analysis with synthetic IRF. Bottom: Analysis with measured IRF. The results are virtually undistinguishable. BPE cells, Alexa 488, 473 nm diode laser, 525±25 nm filter.

Measuring the IRF in a Confocal Microscope

If you have to measure the IRF for whatever reasons or if you just can't resist the temptation to do so, please follow the instructions given in the paragraphs below.

Make sure that you record the IRF under the same conditions as the FLIM data to be analysed with it. In particular, TCSPC system parameters affecting the timing and the time scale, such TAC, CFD, SYNC parameters and ADC Resolution, must be the same. Cable lengths, optical path length, delay box settings, DCC detector gain, and electrical laser power for ps diode lasers must be the same. We also recommend to use the same microscope lens because the optical path length may be slightly different for different lenses. Filters, laser attenuation, secondary beam splitters, and scan parameters can be different. They do not noticeably affect the IRF shape.

In a confocal microscope, switch to a wideband beamsplitter. Use a bandpass filter for the laser wavelength in the detection beam path. Make sure there are no other filters in the light path that block the laser wavelength. In a dual-detector setup with external beamsplitters and filter you may need to remove or replace the beamsplitter cube of the beamsplitter module.

Put a scattering target under the microscope. The target should scatter the excitation light back into the microscope beam path but should not emit noticeable fluorescence. Record am image of the scattering target. If the intensity is too high, use optical attenuation, or change the pinhole size. If this is not enough slightly defocus the sample. When the image is complete send it to SPCImage and follow the instructions given at page 944.

Measuring an IRF in a Two-Photon Microscope

Put a sample of finely ground sugar or finely ground urea under the microscope. Use emission filters which transmit the SHG wavelength (1/2 of the laser wavelength). Cover the back of the sample by black paper or black cloth. This avoids that the SHG light reaches the condensor lens and is back-reflected in the detection beam path. Run the imaging in the preview mode, focus into the right focal plane, and adjust the laser power until the count rate is in a reasonable range. Then record a FLIM image. An example is shown in Fig. 707. Send the data to SPCImage and follow the instructions under 'Measured IRF', page 944.

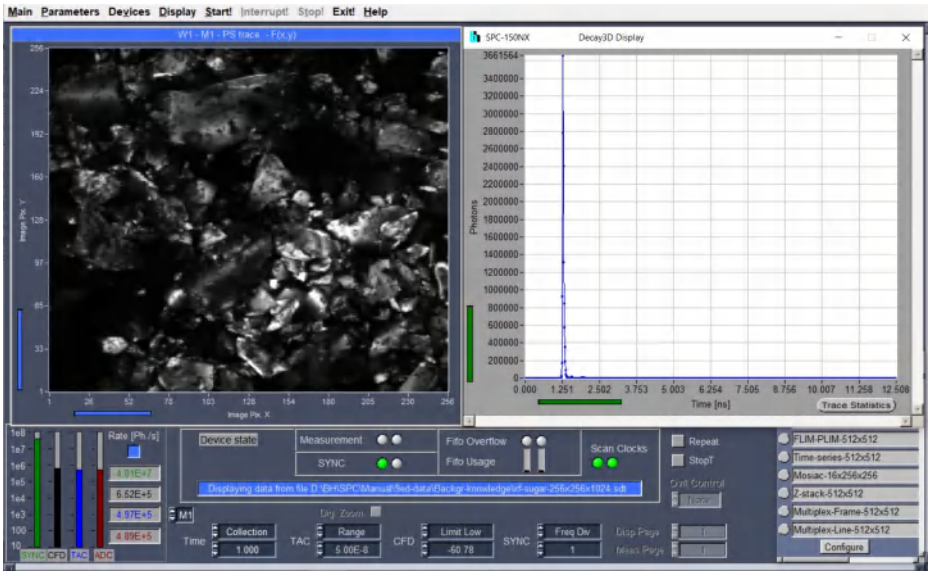


Fig. 707: IRF recorded from SHG of sugar. DCS-120 MP system with HPM-100-06 detector.

Sometimes it is possible to extract IRF data from FLIM data of the same sample of which you record the lifetime image. There is a number of SHG-active compounds in biological tissue. Often strong SHG signals from collagen or (in plant tissue) starch can be obtained by only using an emission filter which transmits the SHG wavelength and selecting an the right spot in the image. An example is shown in Fig. 1316, page 947.

Effect of Fluorescence Depolarisation on Measured Decay Curves

Fluorescence decay profiles measured without special precautions contain a contribution from the rotational depolarisation. The effect is described in section ‘Fluorescence Depolarisation’, page 307. The laser preferentially excites molecules with dipoles oriented parallel to the polarisation of the laser. Immediately after the excitation pulse the fluorescence is therefore partially polarised. Due to the random rotation of the molecules the anisotropy of the fluorescence decreases with time. For small molecules like Fluorescein or Alexa dyes dissolved in water the rotational relaxation time is on the order of a few 100 ps, for the GFPs it is several 10 ns. In conventional lifetime spectrometers the rotational depolarisation is rejected from the decay profiles by placing a polariser under the ‘magic angle’ of 54.7° in the detection light path.

It is therefore sometimes attempted to improve FLIM systems by placing a polariser under 54° from the polarisation of the laser in the detection path. Unfortunately the polariser not only blocks a large fraction of the fluorescence light, it can actually *increase* the polarisation effects. The reason is that the spatial excitation and detection conditions under a microscope lens differ from that in a lifetime spectrometer.

Fig. 708 shows the excitation (left) and the detection (right) of molecules in a parallel beam. The laser is polarised along the x axis. It excites molecules (A) oriented along the X axis, but not molecules oriented along the Y and Z axis (B and C). The fluorescence is detected from molecules oriented along X and Y (A and C) but not from molecules oriented along Z (B). Rotation of the molecules during the fluorescence lifetime leads to change in the detection efficiency and thus to a distortion of the measured fluorescence decay curve.

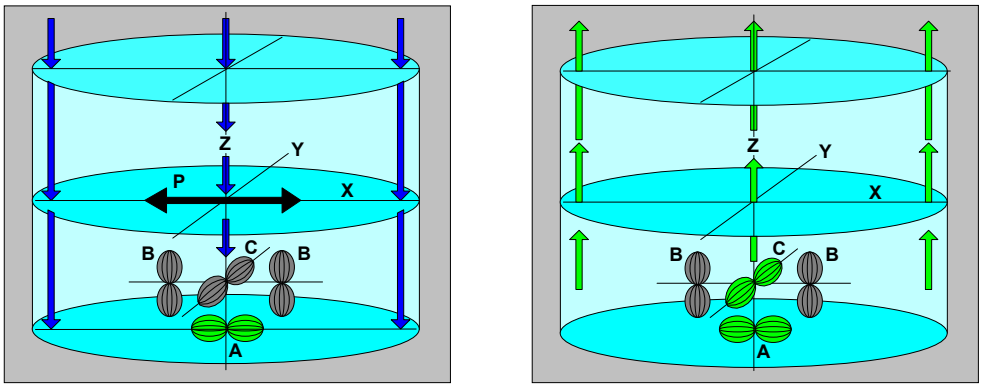


Fig. 708: Excitation (left) and detection (right) of molecules in a parallel beam of light

Excitation and detection conditions under a microscope lens of high numerical aperture are shown in Fig. 709. It is obvious that the laser in the convergent beam not only excites molecules oriented along X (A) but also molecules oriented along Z (B). Moreover, a detector looking at the sample through the microscope lens detects light from molecules of all orientations, A, B, and C. It is obvious that two spatial orientations instead of one are excited. Moreover, three orientations instead of two are detected. This reduces the polarisation effects dramatically. When the NA of the microscope lens approaches 1 light is detected from the complete half-space under the lens. Thus, molecules of all orientations are excited and detected at the same efficiency, and depolarisation effects in the decay curves disappear. Please see [450, 451, 699] for theory.

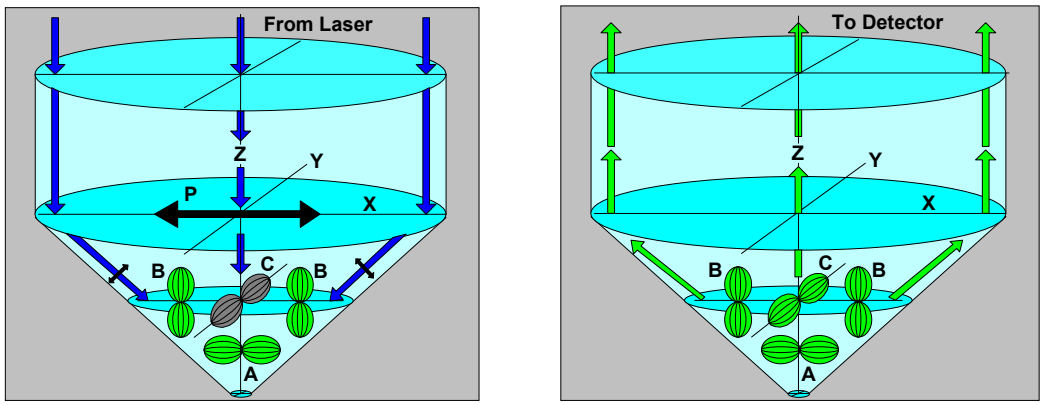


Fig. 709: Excitation (left) and detection (right) of molecules under a microscope lens

Some examples are shown in Fig. 710. Fluorescence decay curves from a solution of fluorescein in water-glycerol mixture were measured through lenses of different NA and with and without a 54.7° polariser.

The upper row show curves measured with an NA=0.3 air lens (left) and an NA= 1.3 oil immersion lens (right). It can be seen clearly that the measured decay profiles differ for detection with and without the 54.7° polariser. The difference between the curves with and without the polariser is about the same for both lenses.

The panel shown lower left compares the decay measured through the NA=0.3 lens plus polariser (red) with the decay measured through the NA=1.3 lens without polariser (blue). The curves are almost identical.

The panel shown lower right compares the fluorescence decay measured through the NA=0.3 lens and the NA=1.3 lens, both with a 54.7° polariser. It can be seen that the curve for NA=1.3 is clearly above the NA=0.13 curve, i.e. the polarisation effect is overcompensated.

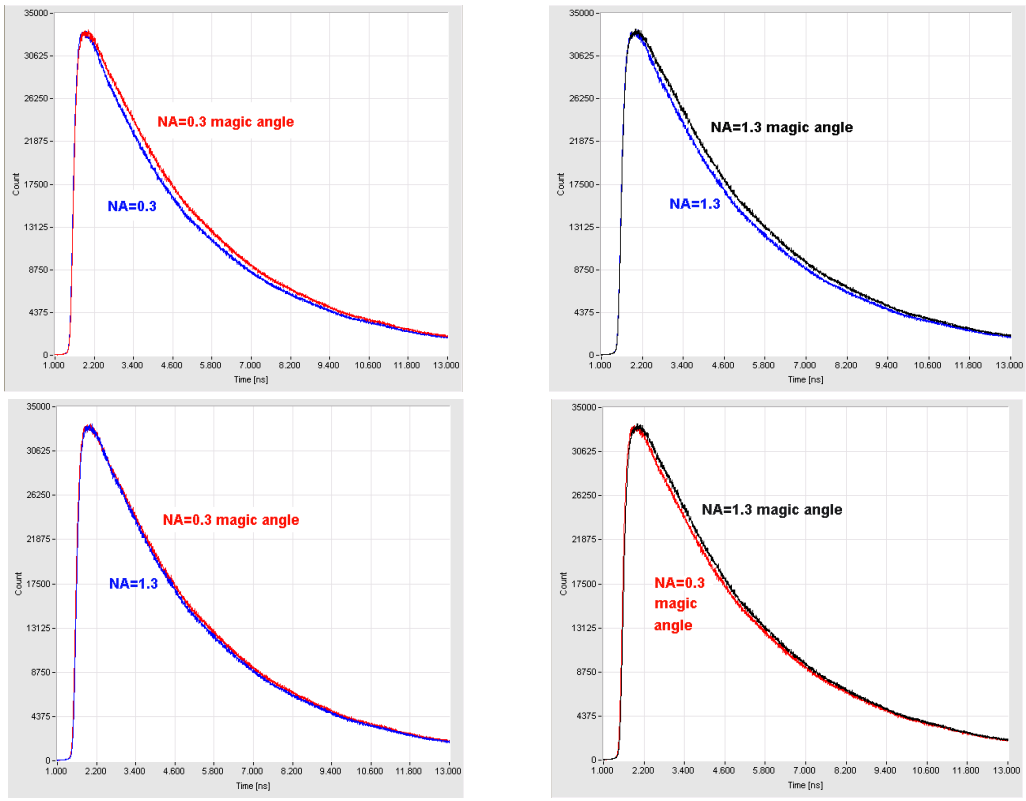


Fig. 710: Fluorescence decay of fluorescein in a water-glycerol mixture measured under different optical geometry. One-photon excitation at 473 nm.

The results presented in Fig. 710 show that the depolarisation effect on the fluorescence lifetimes can be avoided by using microscope lenses of high NA. Under no circumstances a high-NA lens should be combined with a 54.7° polariser. This would offset the lifetimes by the same amount as for an NA<<1 system without the polariser, but in reverse direction.

Please note that detection through a high-NA lens cancels the depolarisation effect only for a detection system that has the same efficiency for both directions of polarisation. For a correctly designed and correctly used FLIM detection system this is normally the case. Different efficiency for different polarisation can be introduced by a main dichroic used at the edge of the spectral transmission curve, or by a conventional (partially reflecting) main beamsplitter. Also, surface-protected aluminium mirrors used under 45° can introduce some polarisation. However, the effect becomes noticeable only if several such mirrors are in the beam path.

It should be mentioned that the influence of the depolarisation on the measured fluorescence lifetime is largest if the depolarisation time and the lifetime are of the same order of magnitude, as it was the case for the fluorescein solution used above. Green fluorescent proteins (GFPs) and their derivatives have lifetimes between 2 and 4 ns, and depolarisation times between 40 and 100 ns. The depolarisation effect on the GFP lifetime is therefore smaller than the effects shown in Fig. 710.

The fact that a high-NA objective lens detects fluorescence from molecules of any orientation has an impact on anisotropy and anisotropy decay measurements. The total intensity for high-NA detection is $I(t) = I_P(t) + I_S(t)$, not $I(t) = I_P(t) + 2I_S(t)$ as in the case of parallel-beam detection. Fig. 711 shows an example for the same fluorescein solution used for the curves shown above. The correct $I(t)$ should be free of depolarisation, i.e. show a single-exponential decay. As can be seen from Fig. 711, I_p+I_s is clearly closer to a single-exponential decay than I_p+2I_s.

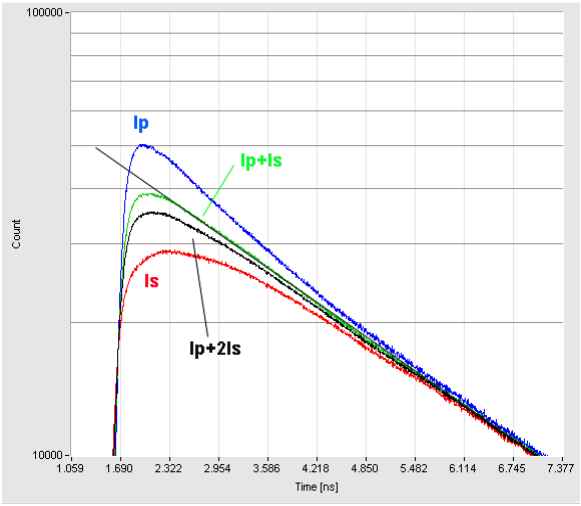


Fig. 711: Fluorescence depolarisation for a solution of fluorescein in glycerol/water. Measured curves for I_s and I_p, and curves for I_p+Is and I_p+2I_s calculated from the measured data. NA=1.3 immersion lens, one-photon excitation at 473 nm

The fluorescence anisotropy for high-NA detection is thus

$$r(t) = \frac{I_p(t) - I_s(t)}{I_p(t) + I_s(t)}, \quad \text{not} \quad r(t) = \frac{I_p(t) - I_s(t)}{I_p(t) + 2I_s(t)}$$

as in the parallel-beam case. If the wrong denominator is taken for $r(t)$ the anisotropy is normalised on a total intensity that is not free of the depolarisation effect. As a result, not only a wrong $r(0)$ is obtained but also a wrong decay profile for $r(t)$. Although $r(0)$ can be corrected by adjusting the G factor (which corrects for different sensitivity of I_s and I_p detection, see page 328), this is not the case for the shape of $r(t)$.

Scan Rate

For the bh TCSPC technique the scan rate has no direct influence on the intensity, the signal-to-noise ratio, or the time-resolution of the images. A faster scan just runs more frames within a given acquisition time. The total acquisition time per pixel remains almost the same and so does the number of recorded photons. There is just the obvious fact that you cannot obtain an image within an acquisition time shorter than the frame time. However, even if 'Collection Time' shorter than the frame time is selected, the acquisition will run until the end of the frame. Nevertheless, there are some effects of the scan rate which will be discussed below.

Triplet Accumulation

When a fluorophore molecule is excited it transits into the first excited singlet, or 'S1' state. From there it returns to the ground, or 'S0', state either by emitting a photon, by converting the energy into heat, or be transferring the energy to the molecular environment. This is the normal process of fluorescence. The molecule may, however, also cross from the S1 state into the first excited triplet, or 'T1', state. The effect is called intersystem crossing, or 'ISC'. The

transition from T1 to S0 is ‘forbidden’. Thus, the lifetime in the T1 state is very long - at room temperature usually in the microsecond range. Molecules in the T1 state do not longer cycle between the S0 and the S1 state. That means, the effective number of fluorophore molecules in the confocal volume is reduced and so is the fluorescence intensity. For high excitation power the loss can be as large as 30%.

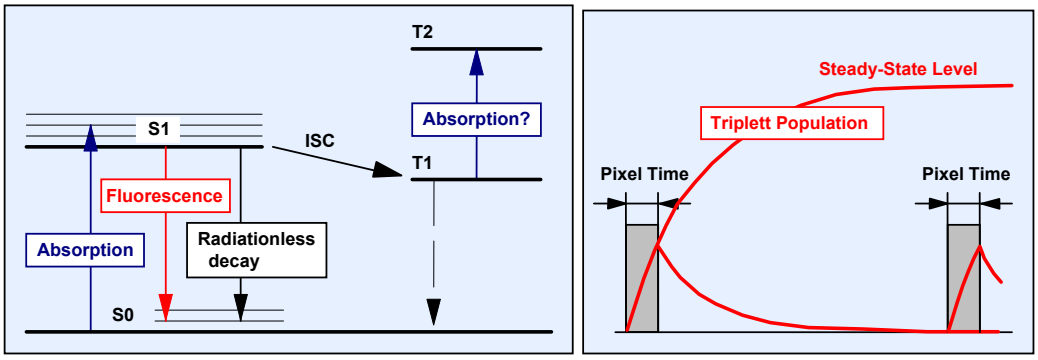


Fig. 712: Left: Intersystem crossing into the triplet state. Right: Reduction in triplet population by pixel times shorter than the triplet decay time.

The relative triplet population can be reduced by using short pixel times. If the pixel time is shorter than the T1 lifetime the T1 population does not reach the steady state level until the scanner goes to the next pixel. The molecules in T1 have then time to return to the ground state before the laser beam comes back to the same pixel for the next frame. The result is a reduction in the average triplet population during the pixel time.

Photobleaching

Avoiding large triplet population is important also for another reason. Molecules in the T1 state are chemically very reactive and therefore likely to create radicals. These, in turn, can cause photodamage and photobleaching [1169]. It may even happen that a molecule in T1 absorbs a photon of the laser wavelength and transits into a higher triplet state. It is not entirely understood what then happens, but it is likely that molecules returning from T2 trigger photochemical reactions. Fast scanning may therefore help reduce photobleaching.

Effect on Data Acquisition

There is no direct effect of the scan rate on the FLIM data acquisition. When a photon is detected the SPC module just determines its time in the fluorescence decay, its wavelength, and its XY position, and puts it into the right location of the data array recorded. That means, the recording process works at any scan rate and up to detector peak count rates of more than 10 MHz per TCSPC module.

Biological FLIM Applications

Why Use the Fluorescence Lifetime?

In microscopy everything is about 'Contrast'. Microscopists therefore constantly look for techniques that could allow them to improve the contrast in the images they are recording. Consequently, they consider the fluorescence lifetime just an additional parameter to separate the signals of different fluorophores. FLIM would then be just a contrast technique to obtain more detailed fluorescence images through a microscope. Up to some point, this seems to make sense: The fluorescence lifetime is independent of the concentration of the fluorophore, the laser power, the detector efficiency, properties of the microscope lens, and other parameters that are difficult to keep under control. However, reducing FLIM to a mere contrast technique means missing the point of FLIM. We will show soon why.

Parameters Characterising Fluorescence

Fluorescence is characterised by three main parameters, the fluorescence intensity, the fluorescence spectrum, and the fluorescence decay function, see Fig. 713. There may be a few more, such as fluorescence anisotropy or intersystem-crossing rate but we will ignore them here for sake of simplicity.

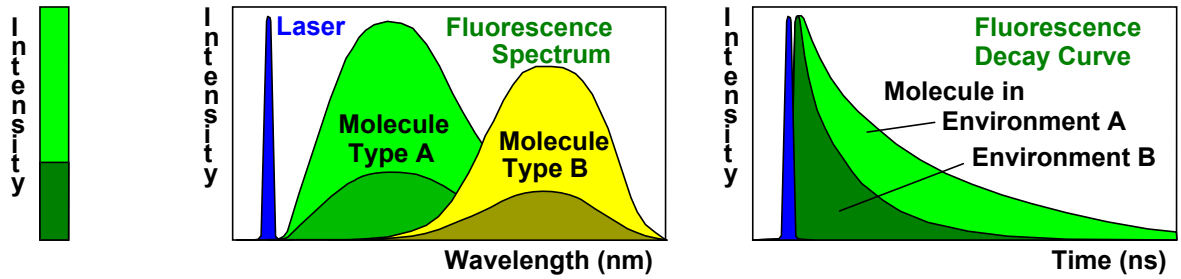


Fig. 713: Fluorescence intensity, fluorescence spectrum, and fluorescence decay curve

The *fluorescence intensity* (Fig. 713, left) gives a good impression of the spatial distribution of a fluorophore within a sample. If the fluorophore is targeted to special physiological subunits of the cell the image shows where these subunits are located. However, a pure fluorescence image does not yield reasonable information about molecular processes in the sample. The intensity just depends on too many other parameters, such a concentration, laser power, and detector gain.

The *fluorescence spectrum* (Fig. 713, middle) is much more informative. The spectrum is different for different fluorophores and thus a good parameter to distinguish different fluorophores. In many cases it is not necessary to record the complete spectrum, recording in a few different spectral channels can be enough. Spectral imaging or imaging in several spectral channels is therefore the contrast technique microscopists are looking for, and it has been successful in fluorescence microscopy for decades.

The *fluorescence lifetime*, or, better, the *fluorescence decay function* (Fig. 713, right) is different. Of course, the fluorescence lifetime is specific for a given fluorophores. However, it not only depends on the type of the fluorophores but also on the molecular environment. This makes it less suitable as a contrast parameter in microscopy. But the dependence on the molecular environment makes FLIM an excellent approach to molecular imaging. Processes on the molecular level, such as interactions of cell functions with ions, interaction with drugs,

protein interactions, or metabolic state and metabolic activity can be directly imaged by FLIM. Such effects are not directly accessible by any intensity-based imaging technique. With FLIM, they can be investigated independently of the unknown and, usually, variable fluorophore concentration [163, 196, 742, 1022].

Single-Exponential Decay Functions

In the simplest case, there is just one fluorophore which changes its fluorescence lifetime with the molecular environment. As long as the environment is homogeneous the fluorescence decay function remains single-exponential. The task is then simply to determine the lifetime and relate it to the molecular parameter in question. However, decays are strictly single-exponential only for lifetime changes caused by 'collisional' quenching [742]. In other cases the decay can become multi-exponential. In these cases it must be decided whether it is possible to work with a single-exponential approximation or better with multi-exponential decay analysis.

Multi-Exponential Decay Functions

As said above, typical FLIM applications are not primarily aiming at discriminating signals of *different* fluorophores. Instead, FLIM is used to quantify *fractions of the same fluorophore* in different states of interaction with its environment. These fractions have different fluorescence lifetimes. The resulting net decay function is multi-exponential. An example is shown in Fig. 714, left. The general composition of the decay function is illustrated in Fig. 714, right.

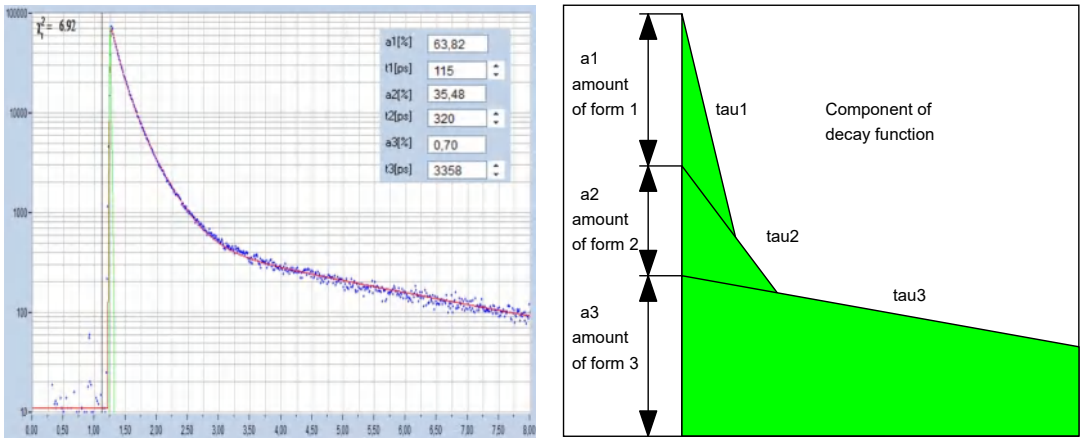


Fig. 714: Left: Real decay function recorded by a TCSPC FLIM system. The decay function is multi-exponential. Right: Exponential components of the net decay function.

The decay function is composed of several decay component (in the example three), with different amplitudes, a1, a2, a3 and different lifetimes, τ1, τ2, τ3. The amplitudes tell how much of the corresponding fluorophore fraction is there, the lifetimes tell how these fractions interact with the molecular environment. Examples are FRET measurements, where the decay components represent interacting and non-interacting donor fractions, and metabolic imaging, where the decay components represent of the bound and unbound NADH and FAD fractions.

Implications to the FLIM System

A FLIM system suitable for molecular imaging must be able to record a full fluorescence decay in each pixel of the image. Systems which record only a 'Lifetime' in the pixels are unable to deliver the right information. Moreover, the recorded data must be precise enough to run double- or triple-exponential decay analysis on them. Than means that the time resolution

(given by the IRF width) must be at least few time shorter than the lifetime of the fastest decay component. Moreover, the sensitivity (more exactly, the photon efficiency) must be high to obtain enough photons for multi-exponential decay analysis. The bh TCSPC FLIM systems match these requirements, but most of the recently introduced 'Fast FLIM' systems don't.

Molecular Parameters Accessible by FLIM

Ion Concentrations

An excited molecule can dissipate the absorbed energy by interaction with other molecules. The effect is called fluorescence quenching. The fluorescence lifetime, τ, then becomes shorter than the normally observed fluorescence lifetime, τ_0, see Fig. 715, left. One quenching mechanism is 'collisional' quenching, i.e. the collision of the excited molecule with another molecule, atom, or ion. Typical quenchers are oxygen, halogens, heavy metal ions, and a variety of organic molecules. The rate constant of fluorescence quenching depends linearly on the concentration of the quencher. The concentration of the quencher can therefore be directly derived from the decrease in the fluorescence lifetime. The classic example is quinine, the lifetime of which follows the reciprocal Cl^- concentration over two orders of magnitude. A practical example is shown in Fig. 715, right. A comprehensive overview about ion quenching can be found in [742].

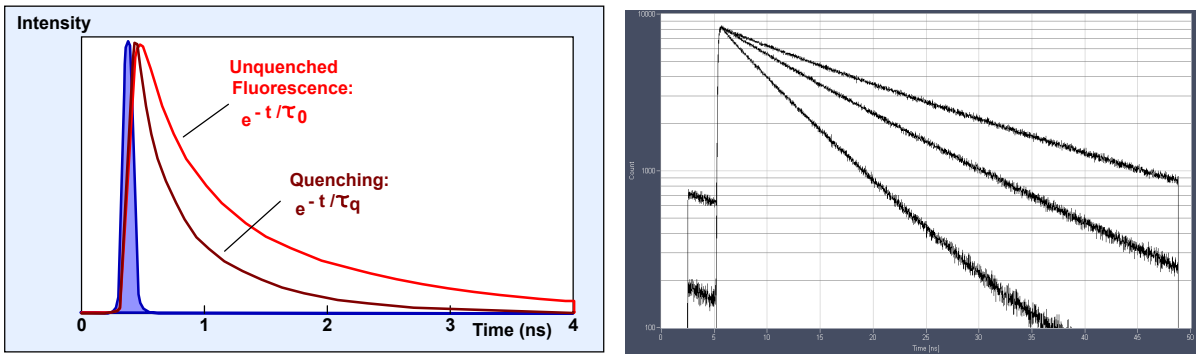


Fig. 715: Left: Fluorescence quenching. Right: Change of the fluorescence lifetime of quinine sulphate with the Cl^- concentration.

There are fluorescence sensors for a wide variety of different ions. The sensors either undergo collisional quenching by the ions, or perform conformational changes which lead to a change in the rate of radiationless decay within the molecule. Please see [224, 742, 1205] for an overview. Of particular interest to cell biology are Ca^{++} and Cl^-, both of which are important to the function of the neuronal system. The use of Ca^{2+} and Cl^- sensors is described in section 'Measurement of Local Environment Parameters', page 498. Other applications of Fluorescence-lifetime recording and FLIM to the measurement of Ca^{++} and Cl^- concentrations can be found in [164, 716, 1344] and [472, 505, 642], respectively.

pH Sensors

Many fluorescent molecules have a protonated and a deprotonated form. The equilibrium between both depends on the pH. If the protonated and deprotonated form have different lifetimes the apparent lifetime is an indicator of the pH. A typical representative of the pH-sensitive dyes is 2',7'-bis-(2-carboxyethyl)-5-(and-6)-carboxyfluorescein (BCECF) [22, 553, 560, 742, 1052]. An example is shown in the application part of this chapter. Medintz et al. presented a pH sensor based on a quantum-dot/dopamine conjugate [846]. They determined the mechanism of the lifetime change to be electron transfer within the conjugate.

Förster Resonance Energy Transfer: FRET

Förster resonance energy transfer (FRET) was first theoretically explained by Theodor Förster in 1946 [454, 455]. The effect is also called fluorescence resonance energy transfer or simply resonance energy transfer (RET). FRET is an interaction of two molecules in which the emission band of one molecule overlaps the absorption band of the other. In this case the energy from the first molecule, the donor, can transfer into the second one, the acceptor. FRET can result in an extremely efficient quenching of the donor fluorescence and, consequently, in a considerable decrease of the donor lifetime. The energy transfer rate from the donor to the acceptor decreases with the sixth power of the distance. Therefore it is noticeable only at distances shorter than 10 nm [742]. FRET is used as a tool to investigate protein-protein interaction and protein conformation. In the first case, different proteins are labelled with the donor and the acceptor, and FRET is used as an indicator of the binding between these proteins. In the second case, donor and acceptor are attached to the same protein. The intensity of FRET is then an indicator of the protein conformation. Correct FRET measurement requires double-exponential decay analysis and thus cannot be performed with FLIM systems which do not record the decay curves. Please see ‘Förster Resonance Energy Transfer (FRET)’, page 507.

Metabolic Imaging by NADH and FAD Fluorescence Dynamics

The NADH and FAD fluorescence dynamics are the basis of 'Metabolic FLIM', a technique that has emerged in the past couple of years and is rapidly expanding. Both NADH and FAD exist in a bound and an unbound form. The relative amount of bound and unbound forms varies with the type of the metabolism. With oxydative phosphorylation, the amount of the bound fractions increase, with glycolysis it decreases. The lifetime differences between the forms are substantial, and bound and unbound fractions can be easily distinguished by FLIM [741, 950]. Both the effective lifetimes of the net decay functions and the amplitudes of the decay components changes with the metabolic state [213, 301, 303, 502, 1155, 1156]. In the past it had been attempted to derive the metabolic state from the net (or apparent) decay times. This was not very successful because the component lifetimes also depend an a variety of cell parameters which are not directly related to the metabolic state. The breakthrough came with the use of double-exponential analysis and the use of the amplitudes of the decay components as an indicator of the type of the metabolism. Metabolic FLIM is described in detail in this handbook, please see chapter 'Label-Free FLIM of Cells and Tissues', page 527.

Other Endogenous Fluorophores

There are other endogenous fluorophores, such as Lipofuscin [1094, 1206], Carotenes [179], Flavines [596], Anthocyanins [287, 935], Advanced Glycation End Products (AGEs) [1094], and Melanin. Most of these fluorophores are mixtures of slightly different compounds, with almost identical spectra but different fluorescence lifetimes [1094, 1097, 1098]. The composition of the mixture may vary, and thus induce a change in amplitudes of the decay components and in the apparent lifetime. Some of the compounds, especially Carotenoids and Melanins, emit fluorescence with extremely fast decay components [179, 182], see 'Ultra-Fast Fluorescence Decay in Biological Material', page 561. The decay times are so fast that they only can be seen by TCSPC and TCSPC FLIM with ultra-fast detectors. The component lifetimes and amplitudes depend on the binding to proteins, on the oxygen concentration [1091], or other physiological parameters. FLIM of these fluorophores is the basis of ophthalmic FLIM, please see 'Chapter Ophthalmic FLIM', page 590 of this handbook. Also Melanin exists in different forms. Some of them have extremely short fluorescence lifetimes. Interestingly, an extremely fast decay component was found in malignant melanoma but not in benign pigmented skin lesions [182]. Please see 'Malignant Melanoma', page 566.

Oxygen

Oxygen is an efficient fluorescence quencher for a large number of fluorophores [742], especially those of longer fluorescence lifetime. Strong effects are observed for pyrene, anthracene, and coronene. Unfortunately these compounds absorb and emit in the UV. They are therefore of limited usefulness in microscopy. Strong oxygen quenching is also observed for the phosphorescence of organic ruthenium, europium, platinum and palladium compounds [496, 742, 753, 940, 941]. Unfortunately the phosphorescence lifetimes are so long - from hundreds of nanoseconds to many microseconds - that they are difficult to record in combination with the high laser pulse-repetition rates and fast scan rates used in modern laser scanning microscopes. bh have therefore developed a phosphorescence lifetime imaging technique based on laser modulation and dual-time-base recording [161, 1130], see Dual Time-Base Recording, page 130, and 'Simultaneous FLIM/PLIM', page 434.

Oxygen Effect on NADH and FAD Fluorescence

Oxygen has a strong effect on the fluorescence of the endogenous fluorophores NADH and FAD. Chance et al. defined a ‘redox ratio’ that is a direct indicator of the amount of oxygen used in the mitochondria of the cells [284, 285]. Indirectly, oxygen has an influence on the ratio of bound and unbound NADH [502, 300, 303]. Effects of oxygen probably exist also for other endogenous fluorophores [1091, 1094]. Oxygen-induced changes of the decay profiles of endogenous fluorophores can be expected to become important with the introduction of FLIM into clinical applications.

Binding to Proteins and other Biomolecules, Protein Configuration

Many fluorescent molecules, including endogenous fluorophores, form complexes with other molecules, in particular proteins. The fluorescence spectra of these different conformations can be virtually identical, but the fluorescence lifetimes are often different. The exact mechanism of the lifetime changes is not always clear. The most likely mechanism are fluorescence quenching, and a change in the configuration of the fluorophore which, in turn, changes the rate of internal non-radiative decay. In practice, for almost all dyes the fluorescence lifetime depends more or less on the binding to proteins, DNA or lipids [677, 742, 1035, 1282]. When a fluorophore is bound to a protein also the protein configuration may have an influence on the fluorescence lifetime [193]. Fluorescence lifetimes of flavinoids in plant cells recorded by TCSPC FLIM were found to be as short as 45 ps, probably due to extremely efficient quenching [894]. A glucose sensor based on this mechanism has been described in [1064]. An effect of target protein configuration has even been found for EGFP which had long believed to be insensitive to its environment [503]. Lifetime changes of diphenylhexatriene (DPH) depending on the cholesterol concentration were reported in [541]. Sensors based on polyethylenimine derivatives of triphenylamine and coumarin have been developed for detection of GTP and ATP Interaction [365]. Environment-dependent changes of fluorescence parameters have even been observed for quantum dots and nano-particles [277, 331, 493, 1387]. There is an enormous amount of fluorophores used in microscopy today [560, 1205], and only a few of them have been tested for target-specific lifetime changes. The most promising ones are those of medium and low quantum efficiency. These are most likely to be influenced by the local molecular environment. FLIM users are encouraged to keep eyes on lifetime changes that may be suitable as probe functions, see also page 384 of this handbook.

Local Viscosity

Local viscosity can be sensed by ‘molecular rotors’. These are fluorophores that have a high degree of internal flexibility. Rotation inside the fluorophore provides for a radiationless decay path. The non-radiative decay rate changes with the viscosity of the solvent. Viscosity measurement by FLIM with a Bodipy-based molecular rotor has been demonstrated in [721,

763, 598, 1139]. Please see page 501. In general, the fluorescence lifetime of any fluorophore of high molecular flexibility can be expected to depend on the viscosity of the environment. Lifetime variation of dialkyl-indocarbocyanines due to micro viscosity changes in cell membranes has been used in [1220].

Membrane Potential

Membrane potentials can be measured by FLIM of voltage sensitive dyes. The dyes are long chains of conjugated double bonds with an electron acceptor at one end. Within the conjugated double-bond chain the electrons can move freely. If a voltage is applied along the chain the distribution of the electron density changes and so does the fluorescence lifetime. The lifetime change over the physiological range of membrane potentials is not very large but can well be resolved by TCSPC FLIM [186, 752]. Currently, the dye with the largest relative change in lifetime is VoltageFluor VF2.1.Cl [752]. Please see section 'Membrane Potential', page 502.

Influence of Local Refractive Index

The radiative decay rate of a fluorophore depends on the local refractive index [1194]. The refractive index varies within biological cells and tissue. The lifetime changes induced by these variations can be used to gain structural information about biological specimens [1263, 1264]. Pliss et al. [977] transfected cells with GFP and used the change of the lifetime by the refractive index as an indicator of the protein condensation. By the same technique, the authors found periodic changes in the protein condensation in organelles of cell nuclei [978].

Proximity to Metal Surfaces, Binding to Nanoparticles

Extremely strong effects on the decay rates are found for dye molecules bound to metal surfaces, especially to metallic nano-particles [268, 488, 778, 814, 989, 1019]. Proximity to metal surfaces changes both the radiative and non-radiative decay rates. It can happen that the radiative rate increases dramatically. The result is a decrease in the fluorescence lifetime without a decrease (or even with an increase) in intensity, accompanied by an increase in photostability. Similarly, yet less dramatic effects have been reported also for non-metallic nanoparticles. They are interesting when such particles are used as carriers of drug delivery. TCSPC measurements on Cy3 encapsulated in calcium phosphate nanoparticles have shown reduced non-radiative and increase radiative decay rates, resulting in a 20 fold increase in brightness [888, 897]. The use of cyanine-loaded lipid nanoparticles was demonstrated in [1238], and improved fluorescence efficiency was verified by TCSPC. Changes of the fluorescence lifetime depending on the substrate a protein construct is resting on were exploited in [601].

Solvent Polarity

The molecular conformation of a fluorophore and thus its fluorescence behaviour is influenced by the solvent properties [194, 742]. In particular, the fluorescence lifetimes of many fluorophores depend more or less on the solvent polarity [562, 767]. Moreover, when a molecule enters the excited state the solvent molecules around it re-arrange. Consequently, energy is transferred to the solvent, with the result that the emission spectrum is red-shifted. Solvent (or spectral) relaxation in water happens on the time scale of a few ps. However, the relaxation times in viscous solvents and in dye-protein constructs can be of the same order as the fluorescence lifetime. The effects can be measured by TCSPC [986]; applications of spectral relaxation to cell imaging have not been reported yet.

Redox Potential

There are fluorophores that change their fluorescence behaviour depending on the redox potential of the local environment [942]. Sensors based on GFP variants are described in [554].

An improved redox sensor based on a modified GFP (roGFPiE) was developed by Avezov et al. Test results obtained in various cells by TCSPC FLIM are described in [36].

Aggregation of Fluorophores

The radiative and non-radiative decay rates depend on possible aggregation of the dye molecules. The electron systems of the individual molecules in aggregates are strongly coupled. Therefore the fluorescence behaviour of aggregates differs from that of the free molecules. Aggregation is influenced by the local environment; the associated lifetime changes can be used as a probe function. Lifetime heterogeneity due to aggregation was reported for E-Bodipy fluorophores, see [377]. Aggregation has also been used to observe the internalisation of dyes into cells [654]. Lifetime effects may also occur when dye-labelled proteins aggregate. This has been used to observe HIV-1 internalisation into cells [523], and to observe oligomerisation of labelled proteins [555]. A sensor for GTP and ATP for FLIM microscopy has been described by Delagdo-Pinar et al. [365].

Electron Transfer

At distances smaller than about 1 nm between an (electron) donor and acceptor photo-induced electron transfer can occur [459, 742]. The excited molecule can either be the electron donor or the electron acceptor. The direction of the electron transfer is determined by the oxidation potential of the donor and the reduction potential of the acceptor. Electron transfer delivers two radicals, both in the ground (S0) state. Both exited singlet states and triplet states can undergo electron transfer at high rates. In solution, the effective transfer rate is usually limited by diffusion. However, in ordered systems (e.g. complexes or adsorbates) the electron transfer rate may become extremely high. Electron transfer is a basic step in photosynthesis. It is also important to the development of organic photovoltaic devices and artificial photosynthesis systems [1164]. In biological imaging photo-induced electron transfer, and the radicals produced by it, are a source of photobleaching and photodamage. Electron transfer is a possible explanation of the fact that some fluorophores are highly photostable in solution, but rapidly photobleach when attached to proteins. It also explains why unstained cells survive high exposure to light, while the same cells stained with exogenous fluorophores do not. Although electron transfer may be the basic mechanism of a number of quenching effects it is not explicitly used as a probing function.

Second-Harmonic Generation

Second-Harmonic Generation (SHG) is an ultra-fast nonlinear process that converts two photons of the incident light into one emitted photon. The wavelength of the emitted photon is exactly one half of the wavelength of the excitation photons. Second-harmonic generation has nothing to do with fluorescence but often shows up as ultrafast component in decay curves measured in multiphoton microscopes. Second harmonic components in FLIM data give additional information about the constitution of the tissue under investigation [831]. SHG emission requires some global organisation of the molecules. In biological system it mainly comes from connective tissue, especially from collagen in animal tissue and from cellulose and starch in plant tissue. The ratio of SHG and autofluorescence intensity in mammalian skin is an indicator of skin ageing [678]. SHG may also become important to localise nanoparticles in human skin.

Measurement of Local Environment Parameters

FLIM can be used to measure local environment parameters, such as pH, oxygen concentration, concentration of physiologically important ions, binding to RNA, DNA, proteins or lipids, local viscosity, and local refractive index. There is a wide range of fluorescent probes for these parameters [224, 742, 904, 1205]. Unless the environment dependence is caused by static quenching [742] the sensors display a lifetime change with the parameter they are sensitive to. Compared with intensity-based methods fluorescence-lifetime detection has the advantage that the result gets de-coupled from the concentration of the sensor, possible absorption in the sample, intensity of the laser, focusing, detector gain and other instrumental effects.

pH Imaging

Microscopic pH imaging is achieved by staining the sample with a pH-sensitive fluorescent probe. pH probes usually have a protonated and a deprotonated form. There is an equilibrium between both forms that depends on the pH of the local environment. If both forms have different fluorescence lifetimes the average lifetime is a direct indicator of the pH [742]. A typical representative of the pH-sensitive dyes is 2',7'-bis-(2-carboxyethyl)-5-(and-6)-carboxyfluorescein (BCECF) [560]. In aqueous solution the lifetimes of the protonated form and the deprotonated form are 2.75 ns and 3.90 ns, respectively [553]. In the pH range from 4.5 to 8.5 both forms exist, and the fluorescence decay function is a mixture of both decay components. Thus, the lifetime of a single-exponential fit can be used as an indicator of the pH. An example of pH imaging of skin tissue is shown in Fig. 716. A single-exponential lifetime image is shown left, decay curves from different areas of the image are shown right. In areas of low pH fluorescence components of both protonated and deprotonated BCECF are found. The decay profile is therefore double-exponential. In areas of high pH essentially deprotonated BCECF is found, and the decay profile is single-exponential. It should be noted that the lifetimes of free BCECF differ from the lifetimes of BCECF bound in the tissue. The lifetime-pH relation must therefore be calibrated for bound BCECF.

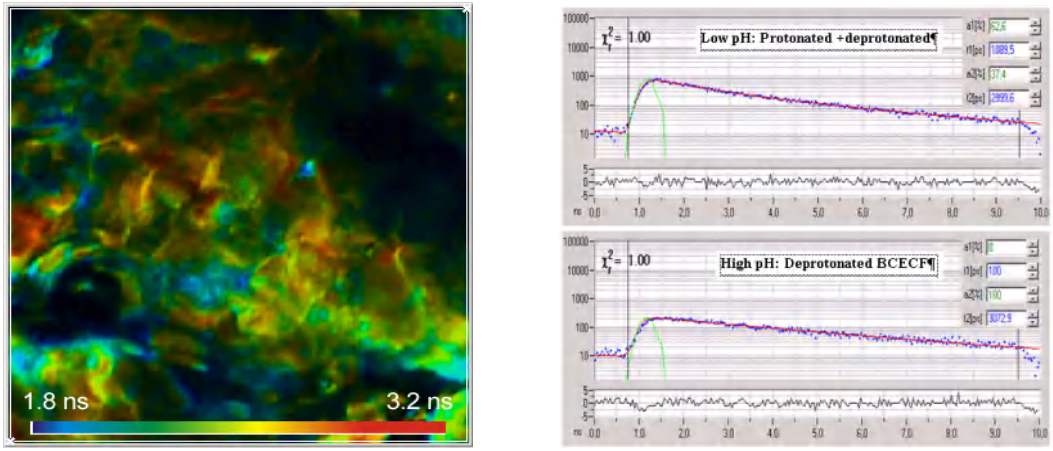


Fig. 716: Left: Lifetime image of skin tissue stained with BCECF. The lifetime is an indicator of the pH. Right: Fluorescence decay curves in an area of low pH (top) and high pH (bottom)

There are certainly more fluorophores which change their fluorescence lifetime with the pH. Aigner et. al. designed pH-sensitive perylene bismide probes which surpass BCECF in brightness and photostability, allow for efficient staining of cells, and display a large lifetime change with the change in pH [9]. A pH probe based on the phosphorescence (yes, phosphorescence!) lifetime of an Iridium(III) complex has been developed by Shakirova et al. [1123]. The authors show that the probe is applicable to the monitoring of intra- and extracellular pH.

Calcium Imaging

Ca^{2+} ions are involved in a large number of cell functions, such as intracellular transport, membrane potential, muscle contraction, gene expression, and cell differentiation. There is a wide variety of Ca^{2+} sensors [740, 742, 876]. Most likely, the mechanism of the Ca^{2+}-dependent lifetime change is that the fluorophore has a Ca-bound and an Ca-unbound form of different fluorescence quantum efficiency and thus different fluorescence lifetimes. The fluorescence lifetime of the bound form is higher than that of the unbound form. Consequently, the net fluorescence lifetime depends on the Ca^{2+} concentration. It can, however, happen that the lifetime and the quantum efficiency of the unbound form is so low that the corresponding lifetime component is no longer observed. In that case, an intensity change but no lifetime change is observed [742]. This is the case for the Fluo sensors, as has been shown for Fluo-4 [164, 463]. However, the traditional Ca^{2+} dyes, such as calcium green and Oregon green, display large lifetime changes and work beautifully for lifetime-based Ca^{2+} measurement. Examples is shown in Fig. 717 and Fig. 718.

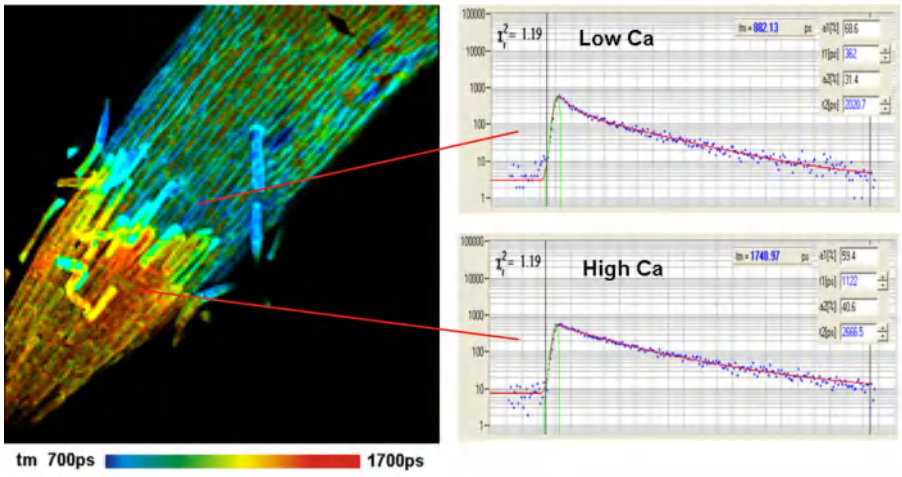


Fig. 717: Barley root tip, stained with Oregon green. Courtesy of Feifei Wang, Zhonghua Chen & Anya Salih, University of Confocal Bioimaging Facility, University of Western Sydney, Australia. Leica SP5 MP with bh SPC-150 FLIM module

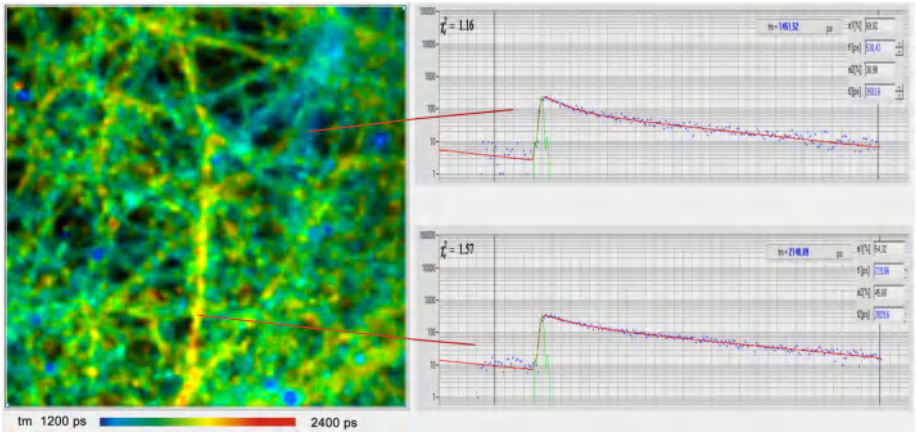


Fig. 718: FLIM image of cultured neurons stained with Oregon green OGB-1 AM. Colour range from τm = 1200 ps (blue) to 2400 ps (red). Decay curves of regions with low Ca (top) and high Ca (bottom) shown on the right. Data courtesy of Inna Slutsky and Samuel Frere, Tel Aviv University, Sackler School of Medicine.

The advantage of FLIM over intensity-based Ca^{2+} imaging is that absolute values of the Ca^{2+} concentration are obtained. This has been used to quantify calcium concentrations in astrocytes of live mice with cortical plaques by multiphoton NDD FLIM [716].

The Ca^{2+} concentration in cells can change within remarkably short periods of time. The Ca^{2+} response of live neurons to stimulation occurs within milliseconds. Nevertheless, the effects can be measured by FLITS and Temporal Mosaic FLIM [164, 463]. An example is shown in Fig. 719. Please see also Fig. 607, page 410 and Fig. 614, page 415 of this book.

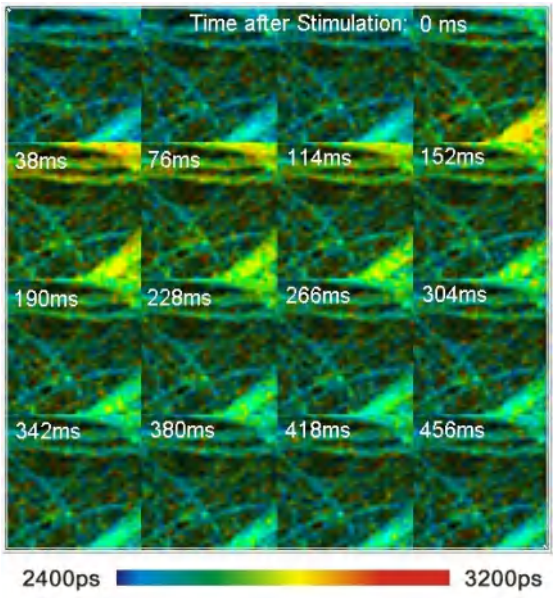


Fig. 719: Ca2+ transient in cultured neurons. Oregon Green Bapta, data recorded by temporal mosaic FLIM, 38 ms per mosaic element.

Chloride Imaging

The chloride concentration is important to the function of the neuronal system. An overview is available in [224] and [491]. Measurements of the concentration of intracellular Cl^- in olfactory sensory neurons by TCSPC FLIM were described in [642]. MQAE was used as a fluorescent probe. MQAE is quenched by Cl^- , and the concentration can be calculated from the lifetime change via the Stern-Volmer relation. A bh SPC-730 module was used in combination with two-photon laser scanning. Because 2-photon excitation does not cause photobleaching and photodamage outside the focal plane the authors were able to obtain Z stacks of the Cl^- concentration in dendrites over depth intervals up to 150 µm. Fig. 720 shows a spinal ganglion of a mouse stained with MQAE. Short lifetimes indicate high Cl^- concentration and vice versa.

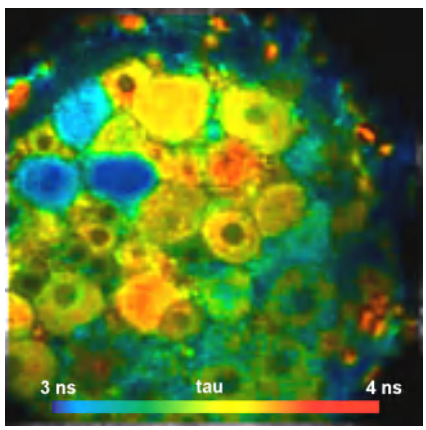


Fig. 720: Spinal ganglion of a mouse stained with MQAE. Short lifetime indicates high Cl^- concentration. Data courtesy of Thomas Gensch, Jülich Research Centre, Germany

The same technique was applied to somatosensory neurons in dorsal root ganglia of newborn mice [505]. It could be shown that the somatosensory neurons undergo a transition of Cl^- homeostasis during the first three postnatal weeks. The modulation of chloride homeostasis by inflammatory mediators was investigated in [472].

The influence of pH and Cl- concentration on the lifetime of GFP was studied in [31]. Measurements of the refractive index are described in [1203, 1204]. Although the refractive index is not directly related to biochemical parameters it can probably be used to study membrane effects, e.g. the transition of a bacterium or a virus through a cell membrane.

Local Viscosity

Local viscosity has a large influence on the rates of biochemical reactions in a cell. Changes in viscosity on the sub-cellular level have been shown to accompany a wide range of cell malfunctions. Changes in viscosity have been found for hematologic disorders, diabetes, Alzheimer disease, DNA damage, liver malfunction and cancer [311, 1138].

Viscosity on the molecular scale can be determined by 'molecular rotors'. These are fluorophores which have two more or less rigid parts connected by a single bond. The two parts can rotate one against the other. Rotation is an additional relaxation pathway which competes with radiative relaxation. Ability of internal rotation therefore shortens the fluorescence lifetime. When the rotation is hindered by high viscosity of the molecular environment this relaxation pathway becomes less efficient, and the fluorescence lifetime increases. An example of a viscosity measurement by a Bodipy-based sensor is shown in Fig. 721.

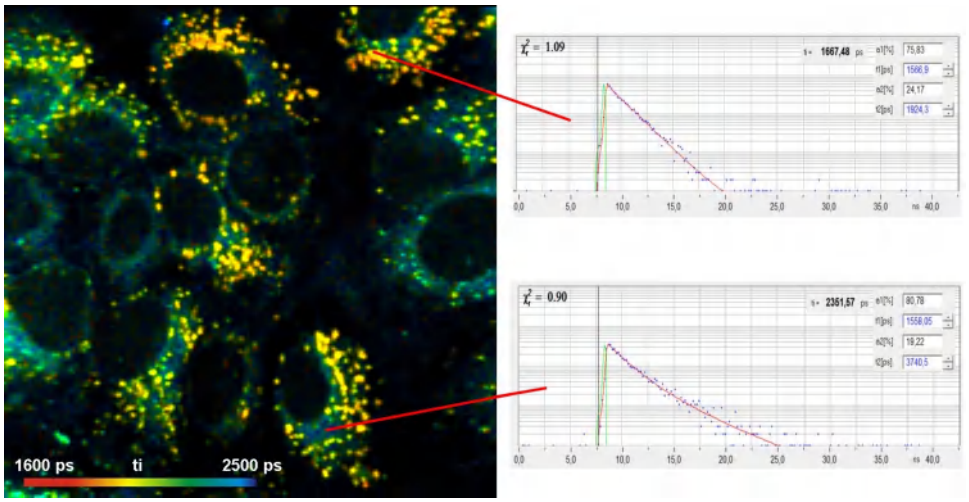


Fig. 721: Viscosity measurement by a Bodipy-based viscosity sensor. Long lifetime means high viscosity, and vice versa. Data courtesy of Marina Kuimova, Imperial College London.

There is an increasing number of publication about viscosity sensors, viscosity measurements in cells and tissues, and applications. Vysniaukas et al. used a molecular rotor to obtain spatially resolved viscosity maps of lipid photooxidation in giant unilamellar vesicles [1297]. Sherin et al. obtained microviscosity maps of the membranes of porcine eye lens cells [1136]. Mika et al. measured the viscosity of plasma membranes of Escherichia coli [866]. The results showed a high degree of lipid ordering within their liquid-phase plasma membranes. Kubánková et al. studied the assembly of proteins, including amyloid-β peptide from their monomeric forms into highly organised fibrillar states [715]. Shimolina et al. used viscosity-FLIM both on the single-cell level and in the connecting tissues of subcutaneous tumors in mice. They found viscosity imaging a potential tool of the progress of tumor treatment [1138], and give a summary of possible applications. The same authors studies changes in membrane viscosity

of cancer cells in response to treatment with Oxaliplatin [1139]. Zhou et al developed a viscosity sensor that specifically targets mitochondria [1398]. A change in mitochondrial viscosity was observed during appotosis. Clancy et al. reported on viscosity changes upon DNA damage [311].

Ponjavic et al. studied the effect of pressure on the molecular viscosity of a solvent. They took measurements of a thin liquid film between a glass substrate and a small ball pressed against it. The observed a dependence of the viscosity on the pressure and spatial heterogeneity within the fluid film [980].

The molecular rotors themselves and their reaction to viscosity, temperature, and other molecular parameters are subject of studies by A. Vyšniauskas et al. [1298, 1299]. Imaging of micro-bubbles and aerosol particles and their viscosity change upon hydration and chemical aging is described in [598, 599].

Membrane Potential

Cells have concentration gradients of ions across their membranes. These gradients produce a voltage over the membrane which is characteristic of a number of fundamental cellular processes [635]. Unfortunately, techniques for precise measurement of membrane potentials are rare. Patch-clamp techniques are highly invasive and do not deliver spatially resolved data. Optical methods based on the fluorescence intensity exist but are not quantitative. A promising solution is FLIM with a voltage-sensitive dye. Several such dyes have been developed in the past decade [868]. The dyes are long chains of conjugated double bonds with an electron acceptor at one end. Within the conjugated double-bond chain the electrons can move freely. If a voltage is applied along the chain the distribution of the electron density changes and so does the fluorescence lifetime. The lifetime change over the physiological range of membrabe potentials is not very large, however. That means high accuracy of the FLIM measurement is required. Currently, the dye with the largest relative change in lifetime is VoltageFluor VF2.1.Cl [752].

Calibration data for VF2.1.Cl are given in [752]. The sensitivity, s, is 3.5±0.08 ps/mV, and the zero-mV lifetime, τ_0, is 1.77±0.02 ns. Within the calibration range of -80 mV to +80 mV the lifetime-voltage relation is linear. A calibration curve for VF2.1.Cl is shown in Fig. 722.

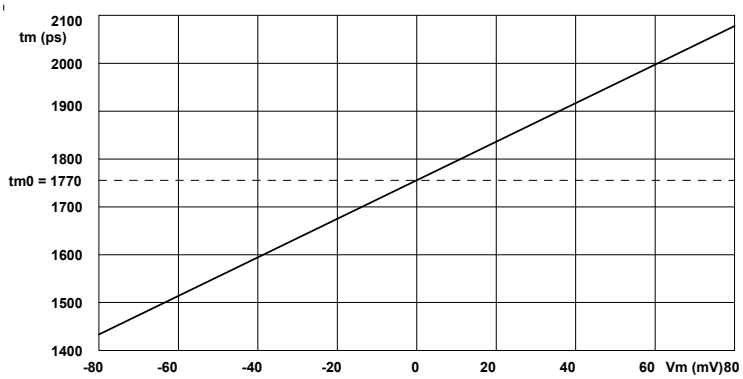


Fig. 722: Calibration curve for VF2.1.Cl, amplitude-weighted lifetime, τm, vs. membrane potential, V_m. Redrawn from [752].

The figure below shows a FLIM image of cells loaded with VoltageFluor VF2.1.Cl [752, 868]. The FLIM format is 512 x 512 pixels with 1024 time channels per pixel. The data were recorded by a standard Becker & Hickl (bh) TCSPC System on a Zeiss LSM 980 laser scanning microscope [69, 70,]. The system contains two parallel SPC-150NX TCSPC/FLIM modules with HPM-100-40 hybrid detectors. For excitation, the system contains the bh 'Laser Hub' with four ps diode lasers.

The excitation wavelength used for the measurement was 445 nm, the detection wavelength 525 nm to 550 nm. The raw data were processed by bh SPCImage NG data analysis software. Maximum-Likelihood Estimation (MLE) with a double-exponential incomplete-decay model was used to fit the decay data. The synthetic IRF of SPCImage was used for deconvolution, and a double-exponential model was used to fit the data. The image was colour-coded with the amplitude-weighted lifetime, tm. A binning radius of 6 was used to obtain a high signal-to-noise ratio of tm.

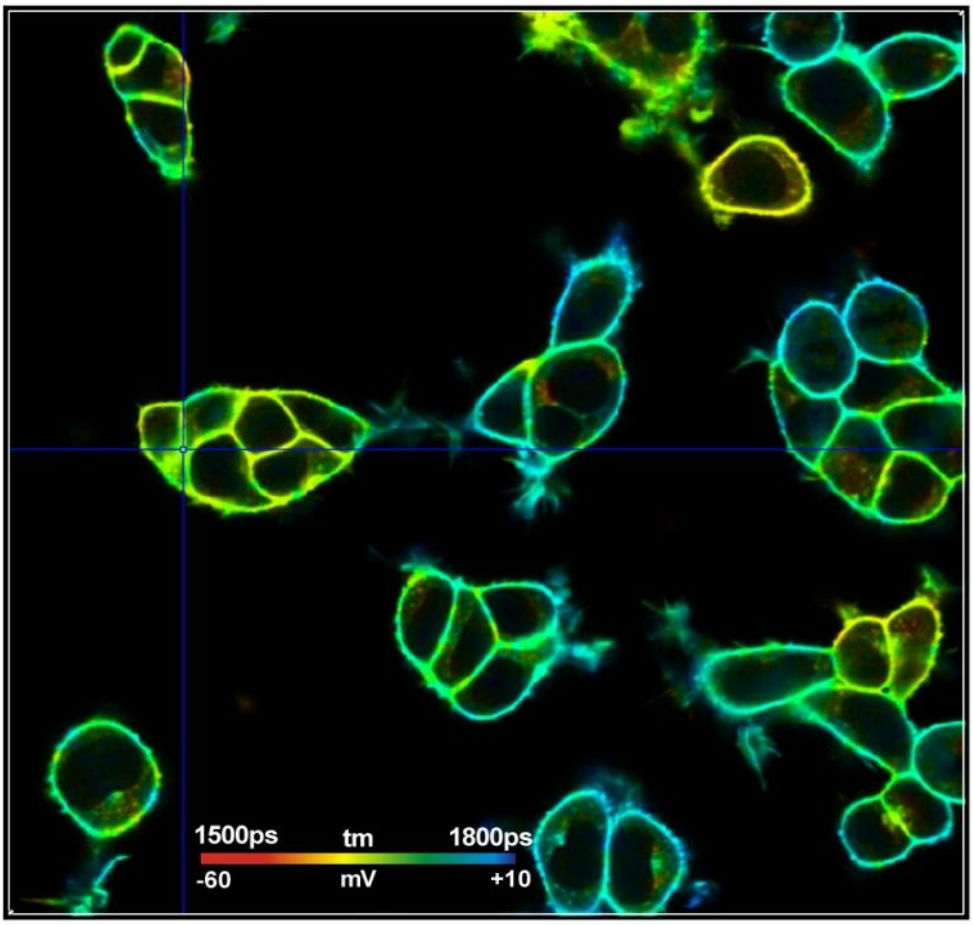


Fig. 723: FLIM image of HEK cells loaded with VoltageFluor VF2.1.Cl. Data courtesy of Susanna Yaeger-Weiss, University of Berkeley

A decay curve at the cursor position is shown in Fig. 724. The blue dots represent the photon numbers in the time channels of the decay curve, the red curve is the IRF, the red curve represents a fit with a double-exponential decay model. The decay parameters are shown upper right.

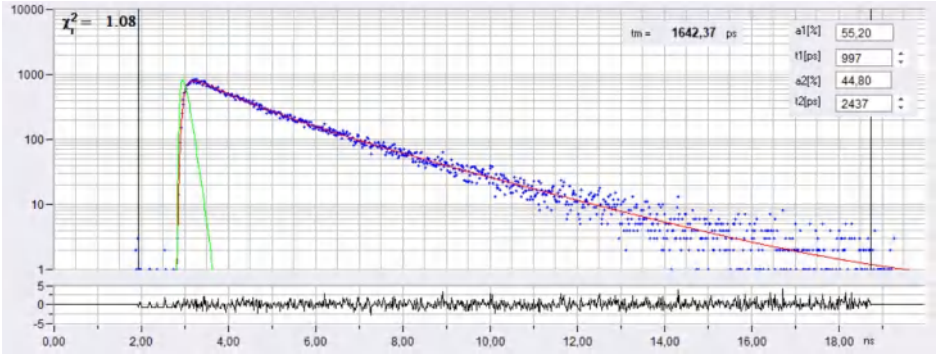


Fig. 724: Decay curve at cursor position of Fig. 723.

Both the FLIM image and the decay curve are proof of the high quality of the data. A near-perfect fit of the decay data was obtained. The tm image clearly shows heterogeneity of the lifetime, which means that different cells have different membrane potentials.

A detailed discussion of the standard deviation of the membrane potential in dependence of the number of photons per pixel and the SPCImage NG data analysis parameters can be found in [186]. Theoretical considerations and experimental data show that the membrane potential can be determined at a standard deviation of a few millivolts.

Oxygen Concentration Measurement by FLIM

The traditional way to determine the Oxygen concentration in cells and tissues is by using phosphorescence lifetimes. Phosphorescence is quenched by oxygen so that the phosphorescence lifetime changes with the oxygen partial pressure, pO_2.

Phosphorescence lifetime imaging, or PLIM, is therefore an efficient way to measure pO_2. Early implementations of PLIM had a number of problems, as stated in [955]. Most of them, such as low intensity, long acquisition time, and restriction to the measurement at only a few selected spots in a sample, have been solved by the simultaneous FLIM / PLIM technique introduce by bh [105], see chapter 'Simultaneous FLIM/PLIM', page 434. Nevertheless, a few inconveniencies remain. The necessity of staining the cells with metal-organic dyes, the inapplicability of transfection techniques to get the dye in the cells, and the production of singlet oxygen during the measurement are features not perfectly welcome to a biologist.

Penjweini et al. therefore developed an oxygen sensor that is purely based on fluorescence [955]. The sensor is a construct that has myoglobin and mCherry connected by a short linker. When the myoglobin is excited FRET from the myoglobin into mCherry occurs. Depending on the oxygen concentration more or less of the myoglobin exists in an oxydised or deoxydised state. These states have different spectra. That means the spectral overlap between the myoglobin emission spectrum and the mCherry absorption spectrum changes, and so does the Förster radius, r_0. The result is a change in the fluorescence lifetime of the myoglobin. The apparent lifetime change is from 0.9 ns to about 1.25 ns, or 30 %. Details are described in [955]. An example is shown in Fig. 725. It shows an A549 cell under different pO2 at atmospheric pressure. The lifetime distributions are shown on the right. Applications of the technique are described in [889, 956, 957, 1110].

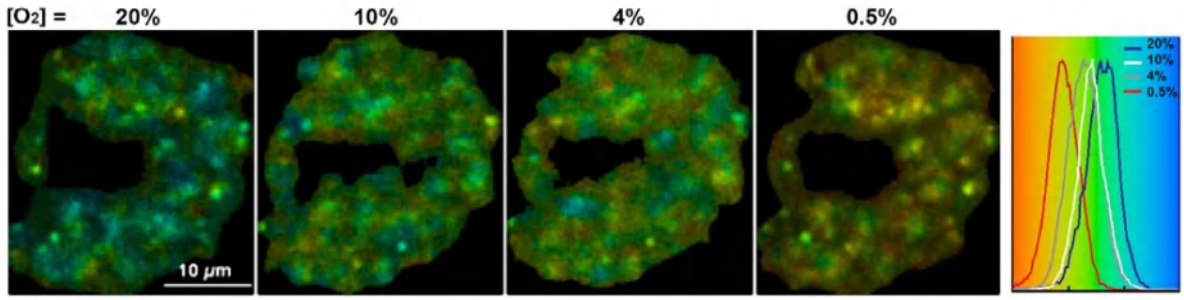


Fig. 725: Fluorescence lifetime change in an A549 cell for different pO2 at atmospheric pressure. Mean (amplitude-weighted) lifetime of double-exponential decay. Copied, with permission, from [955].

Other Environment Parameters

FLIM of cellular Na^+ with CoroNaGreen has been demonstrated by Meyer et al. [854]. The authors found differences in the Na^+ concentration in the cytosol, the nucleus, and in the peri-

nuclear region. Saxl et al. presented a glucose sensor based on Baudan bound to a glucose/galaktose-binding protein (GBP) [1064]. It was concluded that Baudan fluoresces with short lifetime for the open form of the protein and with long lifetime for the closed form of the protein. The protein configuration changes at binding to glucose, and so does the average lifetime. Kirchberger et al. [667] found changes in the decay profile of Lucifer Yellow depending on the conformation of the protein to which it was bound. Levitt et al. [767] used the fluorescence lifetime of Nile Red for measurements of the intracellular polarity.

It has been shown by van Zandvoort et al. that the fluorescence lifetime of SYTO13 is different when bound to DNA or RNA [1282]. The effect has been used to measure the RNA:DNA ratio in living bacteria cells and bacteria colonies [1312]. Douma et al. used the environment-dependent lifetime of SYTO13 and SYTO41 to differentiate between different cells and cell structures in blood vessels [403]. Davey et al. found an increase of the fluorescence lifetime of dil-C18 and Alexa-488-labelled IgE in local membrane structures [358]. Garcia et al. used a fluorescently labelled ATP analog to detect actomyosin states in muscle sarcomeres [487]. An application of environment-dependent lifetime variation to the analysis of histological samples has been described in [325] and [433].

Kuchlyan et al [718] describe an Hg^{2+} sensor based on a rhodamine-spirolactam derivate. Normally, Hg is an efficient fluorescence quencher. However, when Hg^{2+} binds to the rhodamine-based spirolactam the fluorescence intensity increases significantly, and the fluorescence lifetime increases. The authors recorded FCS and FLIM with a DCS-120 confocal scanning system to verify that the change is indeed an effect of binding to Hg^{2+}.

The exact mechanisms of the lifetime changes are not always known. The Cl^- sensitivity of MQAE is almost certainly due to classic collisional quenching, as it is known for quinine sulphate [742], see Fig. 715. In other cases the reason may be a change in the internal flexibility of the molecule, and a corresponding change in the non-radiative decay rate. This mechanism is known for ‘molecular rotors’, such as Bodipy, which respond to the viscosity of the solvent [721], see page 501. Also the polarity of the environment has an influence on the conformation of the fluorophore molecule and thus on its fluorescence lifetime [194, 196]. For dyes forming aggregates, such as ICG, the environment influences the degree of aggregation. This, in turn, changes the fluorescence lifetime. Whatever the lifetime changes are caused by, environment-dependent lifetime changes occur for a large number of fluorophores. Consequently, there is a large potential in finding lifetime-based reporters for biological environment parameters among commonly known fluorophores.

Förster Resonance Energy Transfer (FRET)

Förster resonance energy transfer (FRET) is an interaction of two fluorophore molecules (or, more exactly a fluorophore and an absorber) that are arranged in close distance to each other. If the emission band of one dye overlaps the absorption band of the other energy from the first one, the donor, can be transferred to the second one, the acceptor, Fig. 726. The energy transfer itself does not involve any light emission and absorption, it is a direct coupling of the dipoles of the two molecules. The theory of the effect was developed by Theodor Förster and published in 1948 [454, 455]. Förster resonance energy transfer (FRET), fluorescence resonance energy transfer, or resonance energy transfer (RET), are synonyms of the same effect. The term FRET is also used for experiments that are based on the FRET effect. Important is, that the FRET energy transfer rate increases with the sixth power of the inverse distance. Therefore it is noticeable only at distances shorter than 10 nm [742].

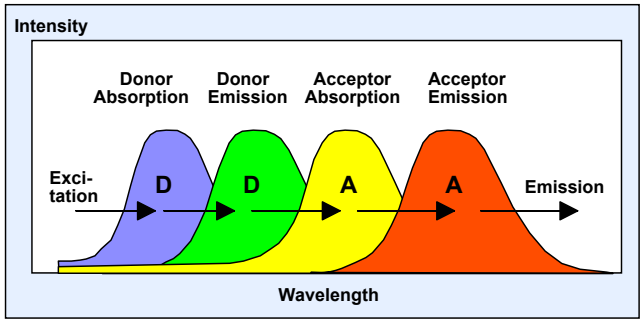


Fig. 726: Fluorescence resonance energy transfer

Because of its dependence on the distance FRET has become an important tool of cell biology [958, 959, 960, 1210]. Different proteins are labelled with a donor and an acceptor; FRET is then used to verify whether the proteins are physically linked and to determine distances on the nm scale. Donor and acceptor can also be linked to the same protein, the intensity of FRET is then an indicator of protein folding and protein conformation.

Intensity-Based FRET

In the early times of FRET experiments it was attempted to derive FRET efficiencies from the ratio of donor and acceptor intensities. However, the emission spectrum of the donor extends into the emission spectrum of the acceptor, and there is fluorescence not only from FRET-excited acceptor molecules but also from directly excited ones. These effects - the ‘donor bleedthrough’ and the ‘acceptor bleedthrough’ make it impossible to determine the net energy transfer rate (the ‘FRET Efficiency’) by a ratio measurement of the donor and acceptor intensities. Therefore, intensity-ratio FRET measurements delivered qualitative results, at best.

Nevertheless, FRET experiments can be (and in fact are) performed by pure intensity measurements. The 'FRET efficiency', is defined

$$E_{fret} = 1 - I_{DA} / I_D \qquad (1)$$

where I_{DA} is the donor intensity in presence of an acceptor and I_D the donor intensity in absence of an acceptor. By using only donor intensities, the definition avoids the problem of measuring the FRET-excited acceptor intensity. However, solving the problem of the definition does not solve the problem of the measurement. The reference intensity, I_D, cannot be obtained under identical conditions as I_{DA}. It even cannot be obtained from the same cell as I_D.

Therefore calibration measurements from different cells are required, including measurements of samples containing only the donor and only the acceptor [513, 576]. Even then, the meas-

ured intensities dependent of the laser power, the detector gain, and the focus quality. This makes the technique difficult to use and susceptible to systematic errors.

The calibration problems can partially be circumvented by the acceptor photobleaching technique. An image of the donor is taken, then the acceptor is destroyed by photobleaching, and another donor image is taken. The increase of the donor intensity is an indicator of FRET. The drawback is that this technique is invasive and destructive. Photobleaching creates radicals which can induce photochemical reactions in the sample. Moreover, once the acceptor has been bleached, the experiment cannot be repeated. The technique is also difficult to use in live cells because diffusion replenishes the photobleached acceptor. In fixed cells, however, the protein structure is changed already by the fixation so that the results are not necessarily correct. The acceptor-bleaching technique is therefore not the gold standard it is often considered.

Finally, there is a general problem of intensity-based FRET measurements. In protein-interaction experiments, there is usually a mixture of interacting and non-interacting proteins. Both the fraction of interacting proteins and the distance between the proteins influence the net FRET efficiency derived from the intensities. It therefore cannot be told whether a variation in FRET efficiency is due to a variation in the distance or a variation in the fraction of interacting proteins.

Lifetime-Based FRET

Most of the problems of intensity-FRET are avoided by lifetime-based FRET measurement [154, 148, 142]. When FRET occurs the donor is loosing part of its energy to the acceptor, with the effect that its fluorescence lifetime becomes shorter, see Fig. 727, right.

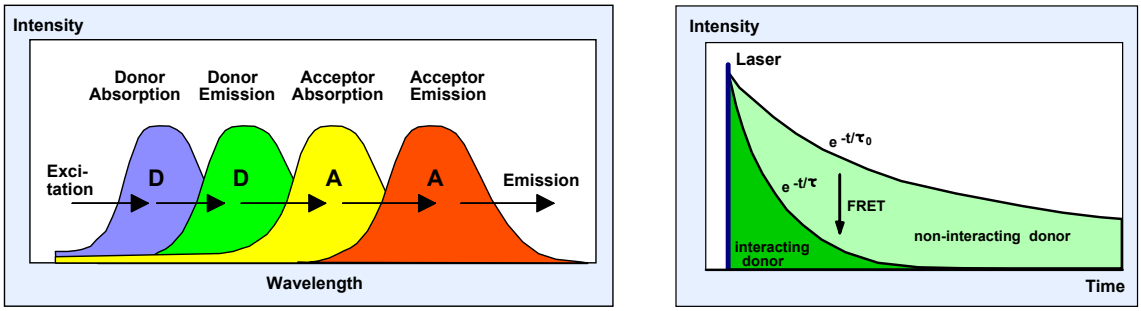


Fig. 727: Förster-resonance energy transfer. The lifetime of the donor becomes shorter when it interacts with an acceptor.

The lifetime-based FRET efficiency is:

$$E_{fret} = 1 - \tau_{DA} / \tau_D \qquad (2)$$

τ_{DA} is the donor lifetime in presence of acceptor, τ_D is the donor lifetime in absence of acceptor.

The lifetime-based FRET efficiency (2) is equivalent to the intensity-based one (1) under the presumption that the lifetimes, τ_{DA} and τ_D, are proportional to the relative intensities I_{DA} and I_D.

The use of FLIM FRET has the obvious advantage that the FRET intensity is obtained from a single lifetime image of the donor in the FRET system in combination with a reference lifetime image of the donor in absence of an acceptor. The FLIM-FRET technique outlined above is easy to use and robust. It has been used for a wide variety of protein interaction studies, see for example [40, 142, 148, 291, 410, 963, 1040]. For an overview on the FLIM FRET literature please see section 'FRET Literature', page 522.

An example is shown in Fig. 728. The cell expresses two interacting proteins, one linked to the donor, CFP, the other to the acceptor, YFP. FRET occurs in locations where the proteins interact. A lifetime image is shown on the left, an image of the FRET efficiency on the right.

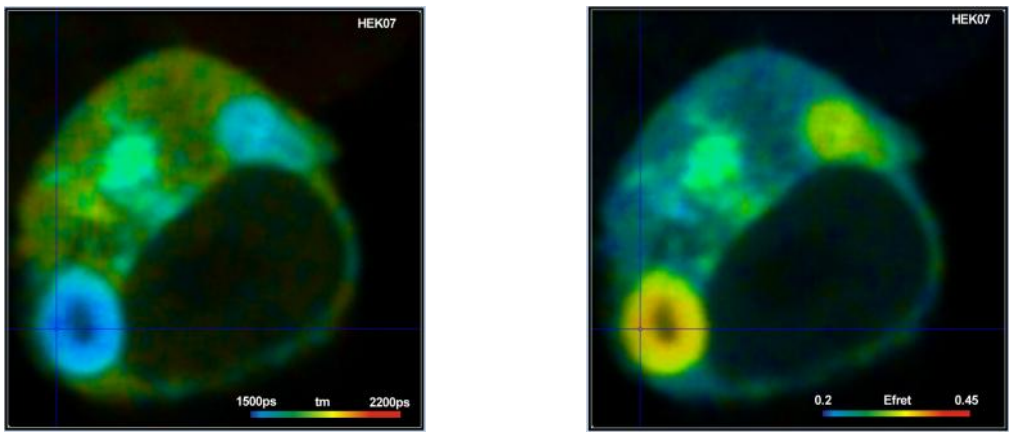


Fig. 728: HEK cell expressing two interacting proteins, one labelled with the donor, CFP, the other with the acceptor, YFP. Donor image. Left: Lifetime image. Right: Image of the FRET efficiency.

Fig. 728 shows how the FRET efficiency varies throughout the cell and, consequently, where in the cell the proteins interact. The FLIM-FRET approach is therefore commonly used for protein interaction and protein conformation experiments. However, a close inspection of the decay functions turns up a possible problem: The decay curves are not single-exponential. The deviation from single-exponential behaviour is the larger the higher the FRET efficiency is, see Fig. 729. The multiexponential behaviour therefore cannot be an intrinsic property of the donor.

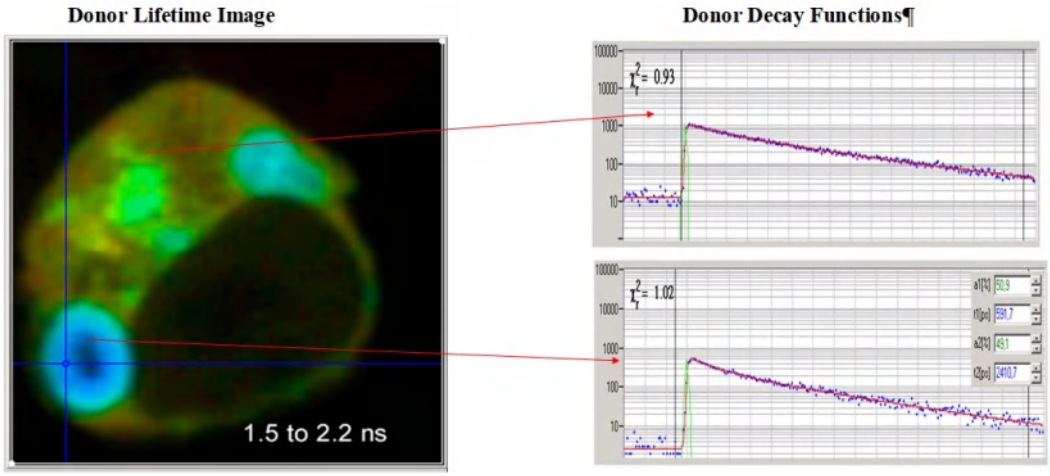


Fig. 729: HEK cell, expressing two interacting proteins, labelled with CFP (donor) and YFP (acceptor).

The multi-exponential profile of the donor decay raises questions on the interpretation of FLIM FRET data in general and on the applicability of the definition of the FRET efficiency. In particular, it requires clarification of which lifetime should be used in the definition of the lifetime-based FRET efficiency (2) [188]. There are at least two definitions of the lifetime of a double-exponential decay, the intensity-weighted lifetime, τ_i, and the amplitude-weighted lifetime, τ_m. The difference between the FRET efficiency derived from τ_i and the FRET efficiency derived from τ_m can be substantial, please see Fig. 730. The left image was calculated from τ_i, the right image from τ_m. The FRET efficiencies the at the cursor position are 0.18 and 0.39, respectively.

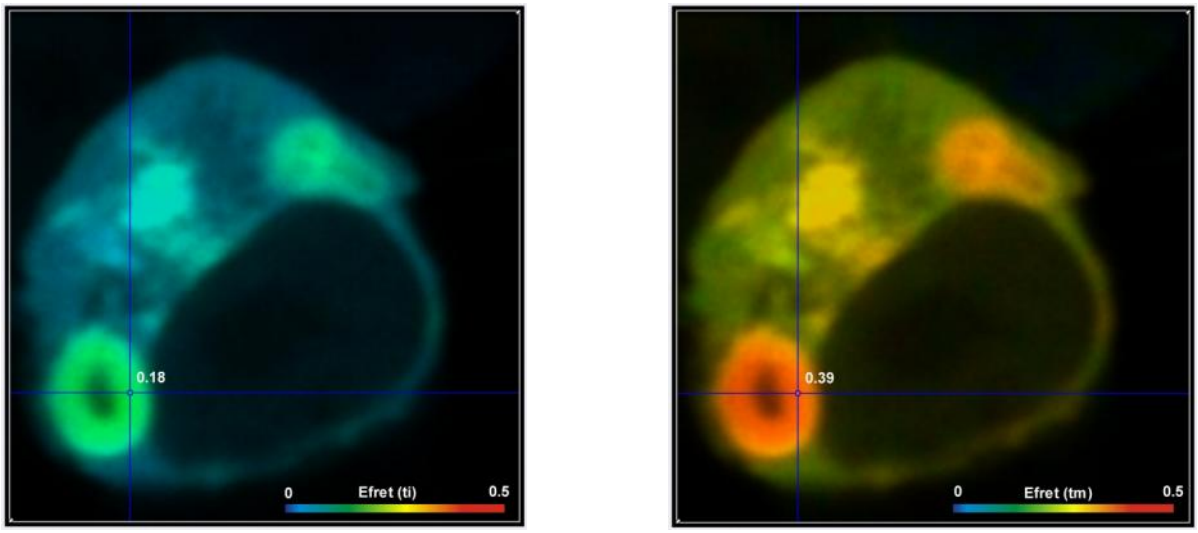


Fig. 730: FRET efficiency derived from τ_i (left) and τ_m (right)

It can be shown that the correct lifetime is τ_m, not τ_i. The reason is that the intensity scales linearly with τ_m but not with τ_i [742]. The FRET efficiency calculated from τ_m is therefore equivalent to the intensity-based FRET efficiency. The fact that τ_m has to be used has consequences: τ_m can only be obtained by double exponential analysis of the donor decay function. This, in turn, means that a FLIM system that records only lifetime values in the pixels of the image, as many 'fast' FLIM systems do, is not able to deliver correct FRET efficiencies.

Double-Exponential FLIM FRET Analysis

The double-exponential decay of the FRET donor and its implication on FRET analysis have been ignored for many years. However, double exponential decay behaviour is commonly found in FRET experiments based on multi-dimensional TCSPC [40, 142, 147, 148, 220, 269, 410, 434, 963]. Double-exponential decay profiles have also been confirmed by streak-camera measurements [218, 219].

In the past few years, the presence (but not necessarily the implications) of double-exponential donor decay has been more and more accepted. It became more and more obvious that it comes from the presence of a non-interacting and an interacting donor fraction.

The donor decay functions can thus be approximated by a double exponential model, with a fast component from the interacting donor fraction and a slow lifetime component from the non-interacting donor fraction [154, 142]. There are several reasons why a donor may not interact. Its protein may just not be linked to an acceptor protein, the acceptor protein may not be labelled with the acceptor, or the orientation between the donor and the acceptor may be wrong. Orientation is usually considered random, an taken into account by the κ^2 factor [742, 958, 959]. However, this does not solve the problem that a part of the donor is not interacting. These situations are illustrated in Fig. 731, left. Whatever the reasons of missing donor-acceptor interaction are, the result is a double-exponential decay curve, shown schematically in Fig. 731, right. The amplitudes, a and b, then represent the fractions of interacting and non-interacting donor molecules.

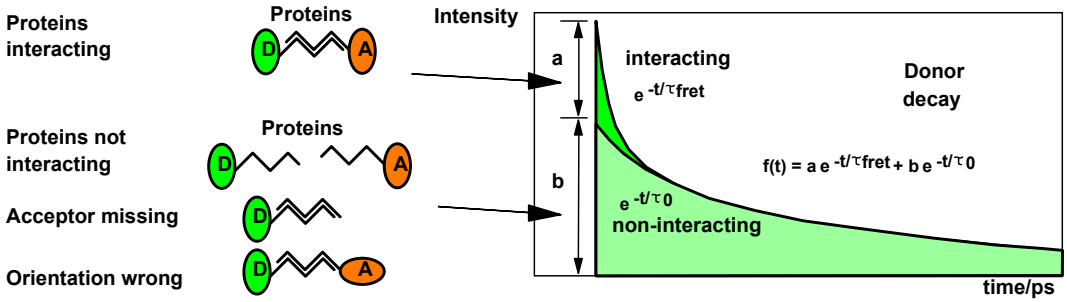


Fig. 731: Fluorescence decay components in FRET systems

Fig. 732 shows the result of a double-exponential analysis of the data of Fig. 728. The left image shows the ratio of the lifetimes of the non-interacting and interacting donor fractions, τ_0/τ_{fret}. The distribution of τ_0/τ_{fret} in different regions is shown far left. The locations of the maxima differ by only 10%, corresponding to a distance variation of about 2%. However, the variation in the intensity coefficients, a/b, is about 10:1. This shows that the variation in the single-exponential lifetime and the FRET efficiency (Fig. 728) is almost entirely caused by a variation in the fraction of interacting proteins, *not* by a change in donor-acceptor distance. In other words, interpreting variations in the single-exponential lifetime (or classic FRET efficiencies from single-exponential lifetimes) as distance variations leads to wrong results.

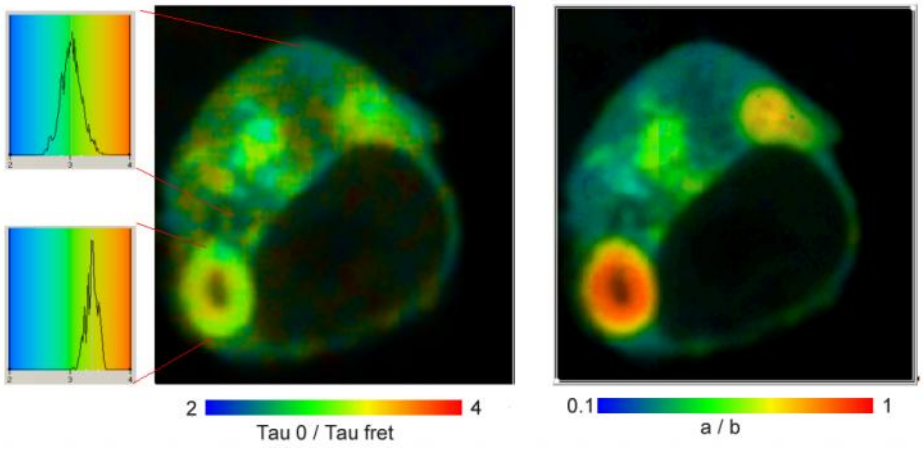


Fig. 732: FRET results obtained by double exponential lifetime analysis. Left: τ_0/τ_{fret}, Right: N_{fret}/N_0

FRET Parameters from Double-Exponential Decay Analysis

In the last decade, the capabilities of multi-exponential FLIM recording and data analysis have improved considerably. More sensitive detectors have increased the number of photons in the FLIM data [160], the time resolution of detectors and TCSPC systems has increased [122], Maximum-Likelihood Estimation (MLE) and intelligent binning have reduced the number of photons per pixel needed for double-exponential FLIM analysis [174], and GPU processing has reduced the data processing time, see chapter on SPCImage Data Analysis.

With these improvements, FLIM data analysis is able to deliver the lifetimes, τ_1 and τ_2, and the amplitudes, a_1 and a_2, of the two decay components. τ_1 is the lifetime of the interacting donor fraction, τ_2 the lifetime of the non-interacting donor fraction. The lifetime of the non-interacting donor fraction, τ_2, is identical with τ_D in the definition of the FLIM-FRET Efficiency. τ_D can therefore be replaced with τ_2. By eliminating τ_D the classic FRET efficiency E_{fret}, the true FRET efficiency of the interacting donor, $E_{interact}$ [154, 274], the ratio of the do-

nor-acceptor distance and the Förster radius, r/r_0 , and the ratio of the number of interacting and non-interacting donor molecules, N_{fret} / N_0 can be calculated exclusively from the decay parameters of the donor decay:

$E_{fret} = 1 - \tau_m / \tau_2$, with $\tau_m = a_1 \tau_1 + a_2 \tau_2$, amplitude-weighted lifetime of double-exponential decay

$E_{interact} = 1 - \tau_1 / \tau_2$

$(r / r_0) = 1 / E_{interact} - 1$ or $(r / r_0) = \tau_1 / (\tau_2 - \tau_1)$, with r_0 = Förster radius

$N_{fret} / N_0 = a_1 / a_2$

The double-exponential FRET approach has been introduced by bh already in 2004 and 2005 [154, 148] but attracted little attention. Nevertheless, it has significant advantages over the classic one.

Double-exponential FRET is free of external calibration

A significant advantage of double-exponential FRET is that it free of external calibration. It does not need external reference data from a donor-only cell. The reference lifetime is the lifetime, τ_2, of the non-interacting donor fraction. It is obtained from the same measurement, the same cell, the same pixels, and the same environmental conditions as the interacting-donor lifetime, τ_1. The double-exponential FRET approach is therefore more robust than the classic one [187]. Moreover, the double-exponential approach is much easier to use than the traditional one. Just record a FLIM data set of the sample at the donor emission wavelength, let the FLIM analysis fit the decay data and let it calculate the FRET parameters you are interested in.

Correct Classic FRET Efficiency

Another advantage is that double-exponential FRET analysis delivers correct classic FRET efficiencies. In contrast to the lifetime from a single-exponential fit, the mean lifetime, $\tau_m = a_1 \tau_1 + a_2 \tau_2$, directly follows the donor intensity so that the FLIM-FRET efficiency reproduces the intensity-FRET efficiency [188]. FRET efficiencies based on τ_m thus reproduce intensity-based FRET efficiencies.

Correct FRET Efficiency of Interacting Donor

Double-exponential analysis delivers the real FRET efficiency, $E_{interact}$, of the interacting donor. Donor-acceptor distances calculated from this efficiency are correct and independent of the ratio of the amounts on interacting and non-interacting donor. This is not the case for the classic FRET efficiency: By using an average of the donor decay components it mingles the effects of the donor-acceptor distance and the interacting / non-interacting donor ratio.

Amount of Interacting Donor

The fourth advantage is that the method delivers the relative amount of interacting donor. This is real biological information which cannot be obtained from Intensity-FRET or single-exponential FLIM FRET approaches.

Example of Double-Exponential FRET Analysis

An example of double-exponential FRET analysis is shown in Fig. 733. FLIM-FRET data were recorded by a bh SPC-150 TCSPC FLIM module with a HPM-100-40 hybrid detector on a Zeiss LSM 880. A single fluorescence-lifetime image was taken at the emission wavelength of the donor. The data were analysed by bh SPCImage NG FLIM data analysis software. The data were processed using a double-exponential incomplete-decay model and Maximum Likelihood Estimation (MLE). Colour coding of the classic FRET efficiency, E_{fret}, the FRET efficiency of the interacting donor, $E_{interact}$, the donor-acceptor distance, d/R_0, and

the relative amount of interacting donor was used to obtain images of the corresponding FRET parameters.

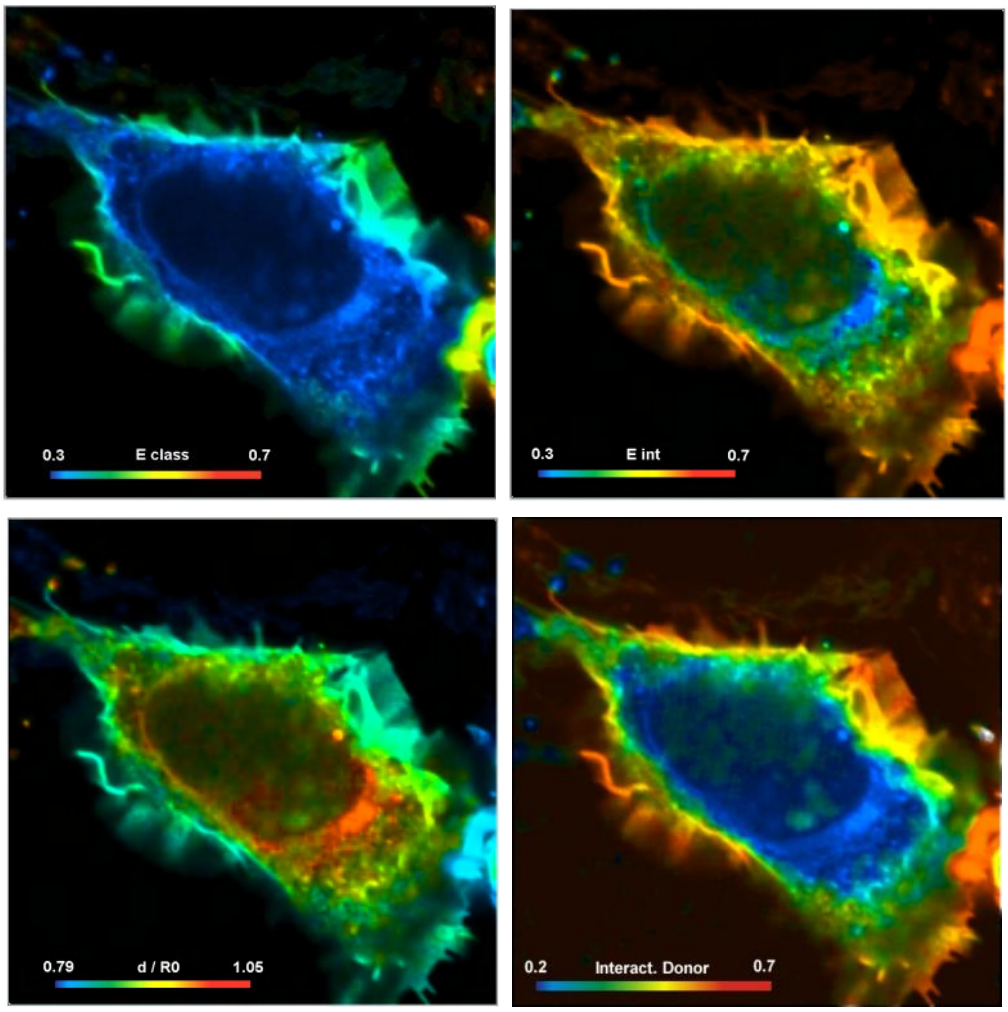


Fig. 733: HEK cell expressing two proteins labelled with Cerulean (donor) and Venus (acceptor). Interaction occurs preferentially in the cell membrane. Upper left to lower right: Classic FRET efficiency, E_{fret}, (E_{class} in SPCImage), FRET efficiency of interacting donor, $E_{interact}$, donor-acceptor distance, d/R0, relative amount of interacting donor. bh SPC-150 TCSPC FLIM module with HPM-100-40 hybrid detector, bh SPCImage NG FLIM data analysis software running on NVIDIA GPU.

Impact of Non-Ideal Effects on FRET Measurements

Although the double-exponential approach usually yields good results it should be noted that FRET experiments can be more complicated than described above. There is the problem that a protein can be expressing (or be labelled with) several donor or acceptor molecules. The effect of multi-labelling is energy migration between the donors, and an increase in the energy transfer rate due to the presence of several acceptors. For physical background and possible pitfalls please see [702, 703, 1291].

It should also be mentioned here that double-exponential FRET measurement can be faced to the problem that the fluorescence decay of the unquenched donor itself can multi-exponential. It is possible that the fluorescence decay of the donor is intrinsically multi-exponential. However the fluorescence decay of a fluorophore can only be multiexponential if it consists of molecules of inhomogeneous molecular structure. The usefulness of such donors in FRET

experiments is questionable, anyway. Other sources of multi-exponential donor decay are photoconversion by excessive excitation dose [589] or changes in the molecular structure of the sample by fixation procedures (see Fig. 740).

Even photo-induced changes in the protein conformation cannot entirely be excluded, see Fig. 742. However, over the past decades, photo-induced artefacts have been greatly reduced by better efficiency of the detectors [160], better efficiency of the microscope optics, and by new fluorescent proteins with higher photostability [360, 361]. Excitation-induced artefacts should therefore be avoidable.

The situation can be further complicated if the donor fluorescence is contaminated by autofluorescence [629]. The decay profiles of autofluorescence are multi-exponential, and can look very similar to the decay of the donor in a FRET system, see Fig. 741. Negative tests with unlabeled cells and with donor-only cells are therefore recommended.

FLIM-FRET experiments need not necessarily be performed in single cells. The same data analysis principles can, of course, be applied to fluorescence decay data obtained from protein or cell suspensions in cuvettes or micro-cuvettes [238, 471, 536, 610]. The advantage of these measurements is that photobleaching is not a problem. The disadvantage is that only average FRET parameters over the entire volume of the cells and over a large number of cells are obtained. It cannot be expected that all cells are in the same state of protein interaction, or that all cells express both the donor and the acceptor. Consequently, the result can be biased towards lower FRET efficiency, and a lower fraction of interacting proteins.

Using Information from the Acceptor Decay Function

There is constant discussion about the shape of the acceptor decay function, whether it can be used to improve the accuracy of FRET measurements, and whether FRET results can be derived form an acceptor lifetime image. Fig. 734 shows how the acceptor decay function in an ideal FRET experiment should look like. Acceptor excitation occurs via the S1 state of the interacting donor molecules. The function of the number of interacting donor molecules in the S1 state over time is represented by the fast donor fluorescence component. Consequently, this component acts as an excitation pulse to the acceptor. In other words, the observed acceptor decay function is the convolution of the fast donor decay component with the natural decay function of the acceptor. The acceptor fluorescence decay function should therefore have a slow rising edge with a time constant equal to the decay time of the interacting donor fluorescence.

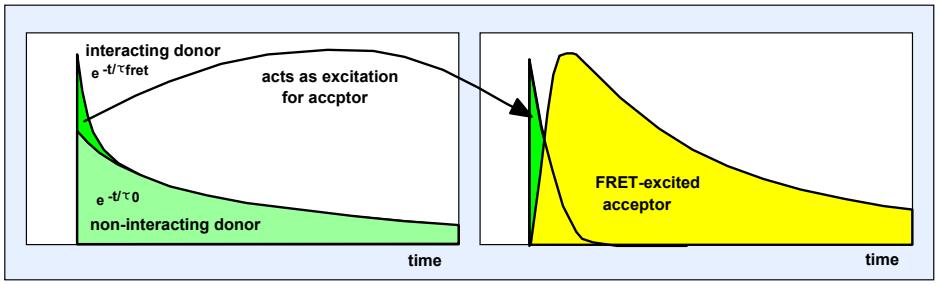


Fig. 734: Donor and acceptor decay functions expected in an ideal FRET experiment: The excitation of the acceptor comes from the interacting donor

However, nothing like this is observed in practical FLIM FRET experiments. Fig. 735 shows a lifetime image of the acceptor of the HEK cell shown in Fig. 729, page 509. The mean lifetime is between 2.3 and 2.6 ns. The fluorescence decay from the region of strong FRET has lifetime components of 2.2 ns and 3.2 ns. The shape is close to a single-exponential decay.

There is neither a trace of a slow rise, nor is there a decay component with a negative amplitude.

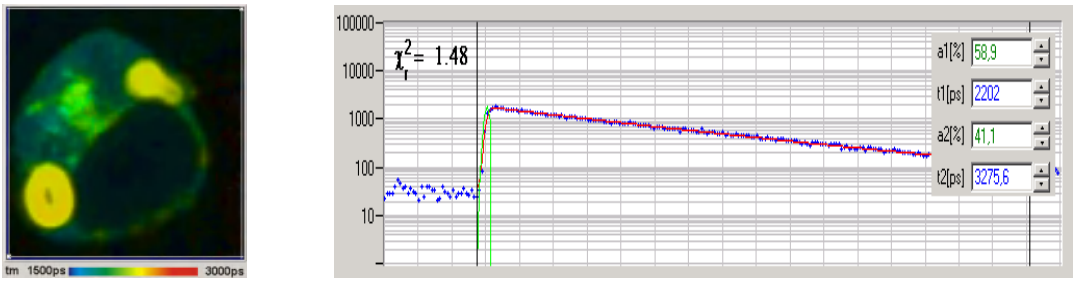


Fig. 735: Left: Acceptor lifetime image of the HEK cell shown in Fig. 729, page 509. Right: Acceptor decay function in region of strong FRET (right)

The explanation of the observed donor decay profile is in the fluorescence spectra. There is a strong overlap of the donor emission into the acceptor emission. The observed acceptor decay is therefore a sum of the decay function of the FRET-excited acceptor, the donor emission overlapping into the acceptor spectrum, and a contribution from directly excited acceptor. This is in agreement with the decay components shown in Fig. 735: The lifetimes of the decay components are close to the average lifetime of the donor, CFP, and the typical lifetime of YFP.

In CFP-YFP experiments the amount of donor fluorescence in the spectral range of the acceptor can be almost 50% of the observed acceptor fluorescence. As described above, the decay time of the fast donor component is exactly the rise time of the FRET-excited acceptor. Both effects cancel, and the result is a near-single-exponential decay function, as shown in Fig. 736.

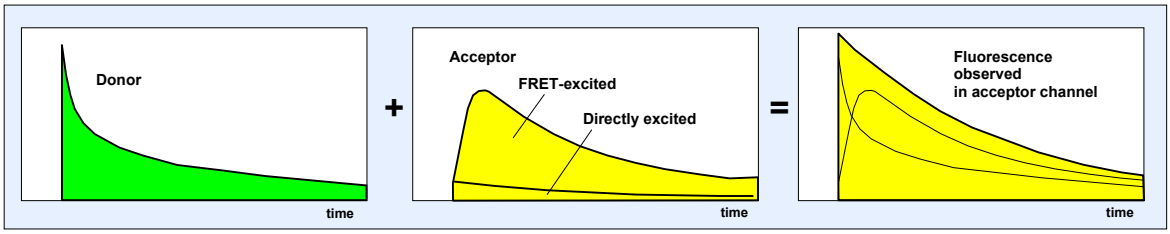


Fig. 736: The observed acceptor decay is a sum of FRET-excited acceptor fluorescence and donor fluorescence emitted in the spectral range of the acceptor.

The prospects of using the acceptor decay functions in FLIM FRET are therefore not good. It has been attempted to obtain additional FRET information from the acceptor emission measured simultaneously with the donor emission in a dual-detector TCSPC system [603]. An attempt was made in [149] to subtract the donor bleedthrough from the acceptor decay and to build up an acceptor lifetime image free of donor bleedthrough. The result showed indications of the slow-rising acceptor component but also a large amount of directly excited acceptor fluorescence. The slow rise of the acceptor fluorescence has been observed in [238] and [1196]. These measurements were performed in protein solutions in cuvettes. The reason that the slow rise of the acceptor fluorescence stands out more prominently than in the FLIM data is possibly that the cuvette experiments used more restrictive filtering: [238] detected through a 557 nm filter, [1196] in the 540 nm channel of a bh PML-16 multi-wavelength detector. Typical CFP / YFP beamsplitters used in microscopy split the signals at 510 to 520 nm and thus record more donor bleed-through.

Even if the FRET-excited component of the acceptor fluorescence is correctly extracted from the decay data as shown in [1196], all these attempts are facing the same problems as intensity FRET: It is not possible to record the FRET-excited acceptor fluorescence without accu-

rate correction of the donor bleedthrough and the contribution from directly excited acceptor fluorescence.

Multi-Spectral FLIM FRET Approaches

A more promising approach to the exploitation of the acceptor fluorescence is multi-wavelength detection [145, 156]. In the ideal case, reference spectra of the donor and the acceptor would be recorded, and the FRET fluorescence would be fitted by a model containing these spectra and the unknown intensity coefficients and lifetimes of the donor and the acceptor. However, Strat et al. demonstrated that multi-wavelength measurement and global analysis with a purely kinetic model of the donor decay, the acceptor decay and the energy transfer rate yields robust results [1193]. Thus, multi-wavelength FLIM may lead to a combination of FLIM-based and sensitised-emission FRET techniques. More multi-spectral approaches are described in [221, 222, 223, 1193, 1196].

Dark Acceptors

An exciting possibility to improve FLIM FRET results is to use a dark acceptor. The advantage of this approach is that donor-acceptor pairs with almost ideal overlap of donor emission and acceptor absorption spectra can be selected. The FRET efficiency for a given donor-acceptor distance is therefore higher than for conventional FRET pairs.

The situation for a GFP-YFP pair is shown in Fig. 737. The figure shows that the pair would be almost impossible to be used for conventional FRET: The emission of the GFP and the YFP cannot be spectrally separated, and excitation of the GFP anywhere close to its absorption maximum would also excite a large amount of YFP. However, there is an excellent overlap between the GFP emission and the YFP absorption. With a dark YFP, the GFP emission can be detected, and the FRET efficiency determined by FLIM FRET. A dark YFP mutant (called resonance energy accepting chromoprotein, REACh) has indeed been developed, and the GFP- (dark)YFP pair been used for FRET experiments [475, 476, 902, 903, 960]. FRET between mRuby2 and dark mCherry is described in [906].

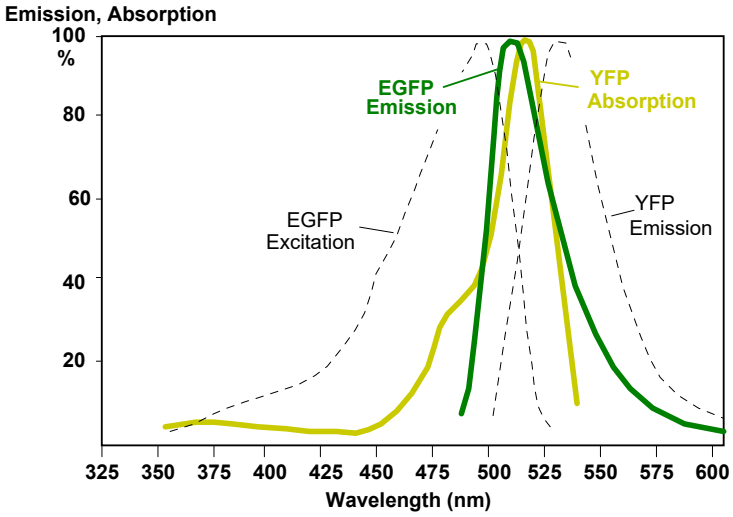


Fig. 737: Absorption and emission spectral of GFP and YFP, after [340]

An interesting approach has been used by Kuchlyan et al. [717] and Mackowski [808]. They used graphene as an acceptor. Graphene absorbs throughout the entire optical spectrum and can thus work as an acceptor for almost any fluorophore with emission in the visible spectrum.

One argument against FRET experiments with a dark acceptor is that even a 'dark' acceptor is not entirely free of fluorescence - the fluorescence is only strongly quenched. The donor emission would therefore be contaminated by an unknown amount of acceptor fluorescence. Such contamination may indeed exist. What happens in detail depends on whether the fluorescence of the acceptor is quenched dynamically or statically [742]. The effect on the measured donor decay is shown in Fig. 738, left and right. Dynamic quenching results in an extremely short fluorescence lifetime of the acceptor. The decay function of the FRET-excited acceptor is then identical with the decay component the interacting donor. Contamination would result in a slight over-estimation of the amount of interacting donor, but not in an error in the determined FRET distance. Static quenching (if incomplete) would result in a weak acceptor fluorescence with the normal lifetime. The result would be contamination by a FRET-excited or directly excited acceptor decay, and thus an over-estimation of the non-interacting donor fraction. The size of both effects can be determined by recording FLIM of acceptor-only samples.

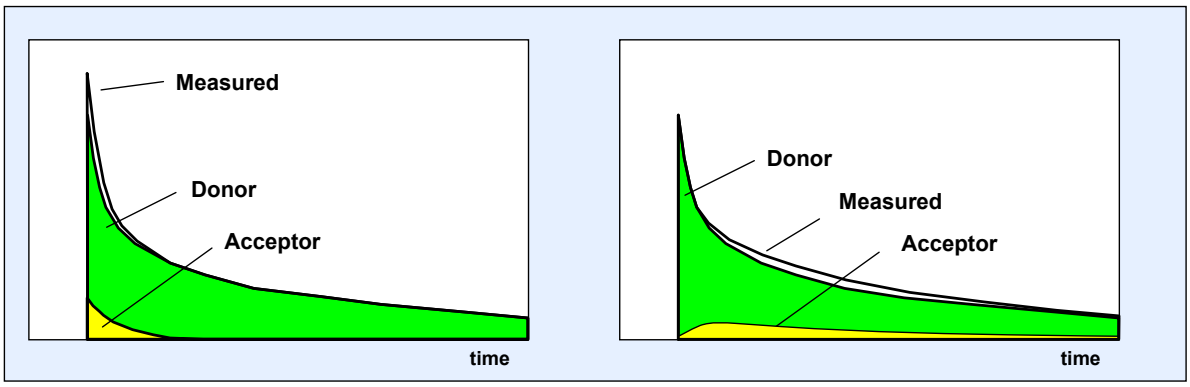


Fig. 738: Contamination by 'dark' acceptor fluorescence. Left: Acceptor quenched dynamically. Right: Acceptor quenched statically.

Another argument against dark-acceptor FRET is more serious: There is no way to prove that the cells are expressing the acceptor. If there is no acceptor a FRET signature in the donor decay will not occur, even if the donor proteins are perfectly labelled and interacting with the acceptor proteins. Consequently, the *absence* of a FRET signature in the donor decay function is no prove of the absence of protein interaction.

FRET Between Endogenous Fluorophores

There is a number of endogenous fluorophores. The emission and absorption spectra are overlapping. That means FRET may occur between the fluorophores, and make it possible to investigate interactions of the associated proteins. Serrano et al. used FRET from an amino acid (the donor) into tryptophane to detect structural heterogeneity [1117]. Tryptophane can also be used as a FRET donor. The problem of these experiments is that amino acids or tryptophan must be excited deep in the UV, around 250 nm. The optics of a normal microscope and of the scan heads of normal laser scanning microscopes is transparent only down to about 360 nm. Li and Seeger therefore built a confocal UV microscope with 266 nm excitation wavelength, a PMH-100-6 detector and an SPC-630 TCSPC module. They were able to obtain decay curves from tryptophane, and to show that the fluorescence lifetime decreases on interaction with other proteins [770]. There are currently attempts to reach tryptophane via three-photon excitation in multiphoton microscopes. The problem of this approach is that this wavelength excites NADH and FAD via two-photon excitation. At a given laser power, two-photon excitation is far more efficient than three-photon excitation. It can easily kill the cells,

as we have found in our own test experiments. Nevertheless, it has turned out that three-photon excitation of tryptophane - and the detection of its fluorescence - is possible. With UV-optimised optics in the detection beam path, hybrid detectors, and carefully adjusted laser power three-photon excited TCSPC FLIM images of tryptophane were obtained. Possible FRET would occur between the tryptophane and the bound component of the NADH. Indeed, FLIM experiments have shown a decrease in the tryptophane lifetime with the bound-unbound ratio of the NADH fluorescence [10, 274, 632, 960].

Homo FRET

The FRET technique described above is based on resonance energy transfer between *different* fluorophores. It should be mentioned, that FRET is also possible between *similar* molecules. Resonance energy transfer between similar molecules is called homo-FRET. Homo-FRET leaves the fluorescence decay profiles unchanged: The energy transferred from the first molecules to a second one is emitted by the second molecule, and the sum of the decay rates does not change. What changes, however, is the fluorescence anisotropy. Homo FRET has thus to be detected by comparing the intensities and decay profiles in two detection channels of perpendicular polarisation [909, 1292]. This is possible by using a polarising beamsplitter in the detection beam path. In most scanning microscopes these are not available as standard parts. Thaler et al. and Nguyen et al. therefore detected through the condenser beam path of an LSM 510 NLO. Their papers on structural arrangement and re-arrangement of CaMKIIα catalytic domains are based on homo FRET and can be recommended as an amazing piece of scientific detective work [1239, 909, 910].

Moreover, Nguyen et al. used a combination of Homo FRET, Hetero FRET and time-laps recording to investigate transient excited state structure associated with CaMKII-NR2B binding. They dubbed the technique 'Binary FRET' and used it to show that a transient excited-state intermediate exists where paired catalytic-domains in the holoenzyme first separate prior to subsequent NR2B association. Additionally, the holoenzyme exhibits a biochemical form of plasticity with calcium- dependent adaptation of T-site ligand binding affinity. Please see [911] for details.

Ultra-Fast Energy Transfer

It is normally believed that the energy transfer rate between fluorescent proteins is limited by the geometry of the barrel structure of the molecules. However, Kim et al. found in homo-FRET experiments that the limiting anisotropy of Venus_{a206} dimers is reproducibly lower than expected. They concluded that the dimers must behave more or less like a single emitter. They investigated the effect by spectral measurements, anisotropy-decay measurements, FSC, molecular-brightness measurements, and anti-bunching measurements. After exclusion of all other conceivable mechanisms, the results left coherent behaviour of the Venus molecules as the only possible explanation [662].

Practical Hints for FRET Measurements

FRET in Diffraction-Limited Spots

Problems may arise when FRET occurs in image details too small to be resolved by and optical microscope. To show up in the image at all, a sub-resolution structure must emit fluorescence at an intensity much higher than the environment. That means the fluorophore concen-

tration in the structure itself must be very high. High concentration bears the risk of interaction of the donor molecules with several acceptors [703]. The FRET efficiency for a given donor-acceptor distance is then higher than expected. The second problem is on the detection side. The fluorescence decay function from a sub-diffraction structure will necessarily be contaminated by fluorescence from the closer environment. If there is no FRET in the environment (which is the purpose of the experiment) the FRET efficiency and the fraction of interacting proteins may be under-estimated.

Typical cases are cell membranes or synapses between neurons. A beautiful FLIM FRET image of a live cultured neuron is shown in Fig. 739. FRET is expected to occur in synapses. As can be seen in the image on the left there are a large number of small spots with decreased lifetime. Magnified images of two typical details are displayed on the right.

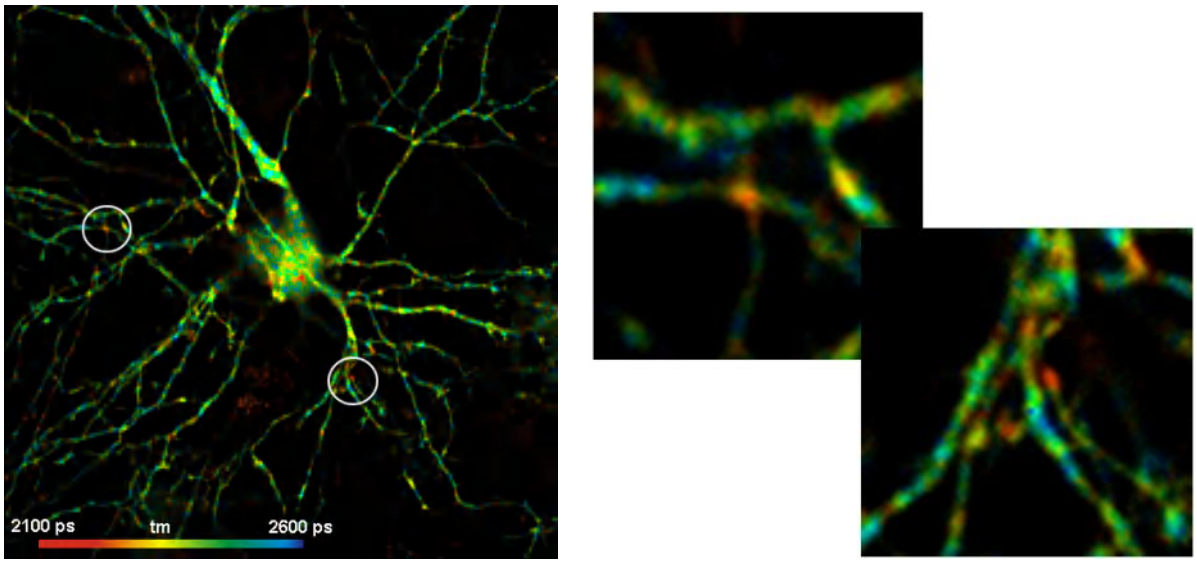


Fig. 739: Live cultured neurons. FRET expected in synapses. Left: Full image, interesting candidates marked. Right: Magnified images of details marked. Zeiss LSM 7 MP microscope with Simple-Tau 152 FLIM system and HPM-100-40 hybrid detectors. Analysis by SPCImage, incomplete decay model with two exponential components. Data courtesy of Inna Slutsky, University Tel Aviv.

The interpretation of such data is far more difficult than in a cell like the one shown in Fig. 732, page 511. The spots of decreased lifetime are hard to distinguish from photon-induced noise and from variation due to inhomogeneity of the local environment. Conclusions can only be made by correlating the spots of decreased lifetime with the morphology, by comparing a large number of measurements, and including negative tests with acceptor-free samples.

FLIM FRET in synaptic structures has been published by Bosch et al. and by Fogel et al. Bosch et al. were not only able to detect protein interaction, they could even follow the reorganisation of post-synaptic substructures during long-term potentiation by time-series FLIM [239]. Fogel et. al. [456] used a combination of intensity FRET measurement, FLIM FRET measurement, and single-molecule imaging to show that the amyloid precursor protein homodimer constitutes a resynaptic receptor that transduces a signal from amyloid-beta peptides to glutamate release. Aow et al., Dore et al. and Murokashi et al. performed FLIM-FRET experiments in single dendritic spines [27, 399, 400, 401, 902]. Zoltowska et al. used FRET to show that presenilin 1 and synaptotagmin 1 interaction modulates exocytosis and amyloid β production [1403]. Superresolution FRET imaging in dendritic spines by STED-FLIM has been described by Tardif et al. [1223]. The authors were able to discriminate different nanoclusters of synaptic proteins in different states of interaction with binding partners inside the spines.

Multi-Exponential Decay of the Free Donor

Double-exponential FRET measurements are faced with the problem that the fluorescence decay of the unquenched donor itself can be multi-exponential. This happens especially for the CFPs and, at a smaller extend, Cerulean. CFP has two lifetime component of about 1.3 ns and 2.9 ns with an amplitude of 20 to 40% and 60 to 80%, respectively [148]. Sarkar et al. [1053] found an almost similar composition (60% of 3.7 ns and 40% of 1.5 ns) for Cerulean excited at 405 nm. Interestingly, there is no trace of a second component in our own data from live cells, see Fig. 740, left. It is therefore possible that the composition of the decay depends on the molecular environment, or on the excitation wavelength.

Fortunately, in FRET experiments the fast lifetime component in the donor decay is usually in the range of 400 to 800 ps. Under these conditions a double-exponential fit routine tends to combine the 1.3 ns and the 2.9 ns component into one component of about 2.5 ns. Thus, the interacting and non-interacting donor fractions can still be distinguished.

Almost ideal single-exponential decay profiles are obtained from GFP. GFP or EGFP are therefore increasingly being used as FRET donors.

Please note that strong multi-exponential behaviour can be induced by fixation procedures. The frequent complaints about strongly multi-exponential donor decay probably result from measurements of fixed samples, see below.

Live Samples versus Fixed Samples

FRET measurements aim at measuring changes in the conformation and binding of proteins. That means, that the molecular structure of a sample must be preserved during sample preparation. In other words, FLIM measurements normally have to be performed on live cells or live tissue. Fig. 740 shows what can happen if this simple fact is ignored. Both images show cells of the same type, transfected with Cerulean only. The excitation wavelength was 445 nm, the detection wavelength 480±20 nm. The left image was obtained from a live cell, the right image from a fixed cell. Both cells were analysed by a double-exponential model.

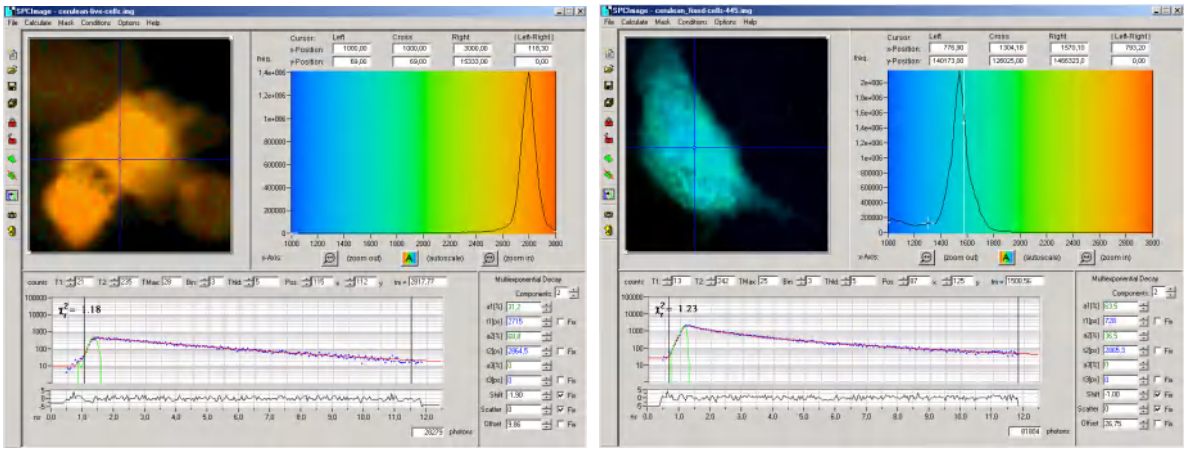


Fig. 740: Lifetime differences between a live cell (left) and a fixed cell (right). Colour-coded lifetime image, histogram of lifetimes over the pixels, decay curve in selected spot of the image, excitation 445 nm. Both cells are expressing Cerulean, without any FRET acceptor. Nevertheless, the fixed cell shows a decay profile typical for FRET.

The live cell delivers two almost identical lifetime components. This is a clear indication that the decay is almost perfectly single-exponential. The lifetime is about 2.8 ns. This is exactly what one would expect for a cell expressing Cerulean alone.

The fixed cell (Fig. 740, right) shows a strongly double-exponential decay profile, with 60% of 770 ps and 40% of 2.8 ns. The amplitude-weighted mean lifetime is around 1.56 ns. Moreover, the lifetime histogram shows a broad background of shorter lifetimes from the embedding medium. No matter what kind of experiment this result would be used for, it would lead to significantly wrong results. Consider a FRET experiment: The decay profile of the fixed Cerulean cell is similar to the decay profile of a cell showing FRET, compare Fig. 729. An inexperienced user may interpret the decay profile as 60% of interacting proteins, with a FRET efficiency of 0.725. The average FRET efficiency would be 0.44. However, the cell does not contain an acceptor, and consequently, cannot do any FRET.

Similarly wrong lifetimes and decay profiles are found also for other fluorescent proteins in fixed samples. It appears likely that the frequent complaints about strong multi-exponential decay of CFPs at large extend originate from measurements on fixed samples.

Autofluorescence

A frequent pitfall of FRET experiments is autofluorescence. If the cells are not expressing the fluorophores as expected autofluorescence dominates the FLIM signals. In the spectral range of typical FRET experiments autofluorescence mainly comes from NAD(P)H and FAD. Consequently, there is a fast and a slow decay component from the unbound and bound fraction of NADH, and from the bound and unbound fraction of FAD. The shape of autofluorescence decay functions can be very similar to those of FRET, see Fig. 741. FLIM can help to identify autofluorescence problems: If the slow decay component (circled) is not as expected for the free donor something must be wrong with the sample. However, even this is not sure. If autofluorescence wants to fool you it will, as can be seen in Fig. 741, right. Negative tests with un-transfected cells and with acceptor-free cells are therefore mandatory for proving the relevance of FRET results.

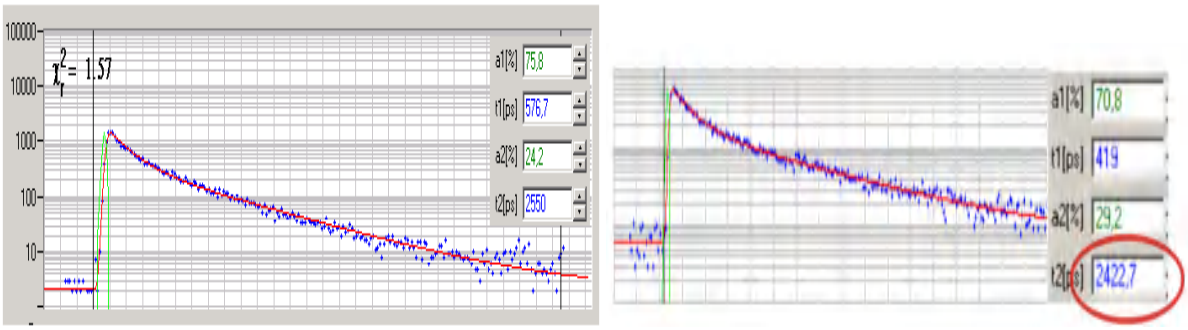


Fig. 741: Fluorescence decay from the donor of a CFP-YFP FRET system (left) and fluorescence decay of autofluorescence. The lifetime of the slow component is 2.55 ns for FRET, and 2.42 ns for autofluorescence. The difference is only 130 ps, well within the normal variation of FRET donor lifetimes.

Photobleaching

Photobleaching acts differently on the interacting and the non-interacting donor fraction. The non-interacting donor component photobleaches faster, so that the fraction of interacting donor (and thus the conventional FRET efficiency) is biased towards higher values. It is also possible that the acceptor photobleaches. In that case, photobleaching decreases the fraction of interacting donor. Moreover, photobleaching can create photoproducts that are fluorescent. Emission from these compounds can change the composition of the decay profiles unpredictably [589].

As a rule of thumb, the count rates should not decrease by more than 20% during the measurement. If it does, make sure that you have exploited all options of increasing the photon collection efficiency, please see [174] for advice. In one-photon systems, you may also try

with a larger pinhole and thus trade count rate against depth resolution. Even if you have to sacrifice a number of cells for these experiments the higher number of photons obtained at less photobleaching pays off at the end.

It should also be taken into regard that the exposure may induce real changes in the protein conformation in the cells. A possible example is shown in Fig. 742. The images shows a live-cell sample expressing interacting proteins fused with CFP and YFP.

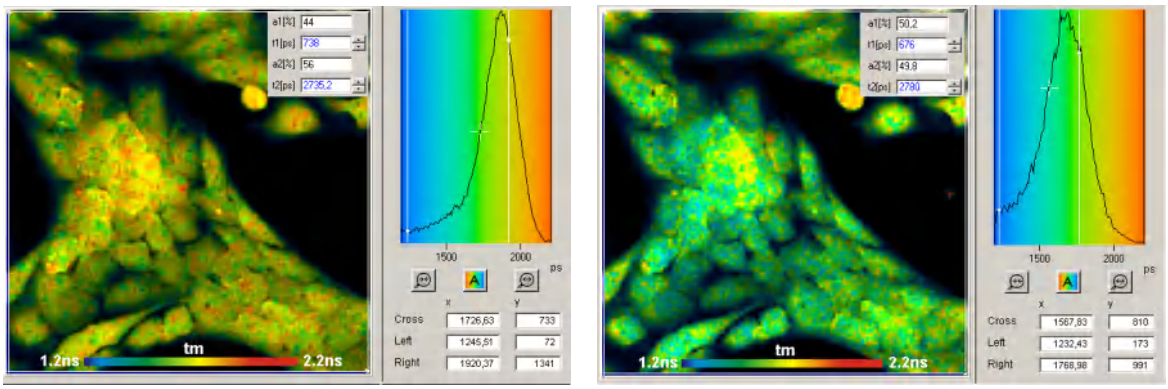


Fig. 742: Two FLIM FRET measurements of the same sample, lifetime images and lifetime histograms. Left: Initial recording, acquisition time 30 seconds. Right: Second recording, acquisition time 30 seconds, after 90 seconds of total exposure. Insert: Amplitudes and lifetimes of the decay components. Analysis by bh SPCImage, incomplete decay model with two exponential components.

Two-photon excitation at 860 nm was used, the laser power regulator of the microscope was set to 4%. This is a power commonly used in two-photon live cell imaging. Both images were recorded at the donor emission wavelength. After getting the sample into focus, a 30 seconds FLIM recording was taken. Then the scanning was continued for another 60 seconds, and another 30 second image was taken. As can be seen from the images, the lifetime (amplitude weighted lifetime, t_m) in the second recording is significantly shorter. The shorter t_m comes from a larger amplitude and a shorter lifetime of the fast decay component. The slow decay component remained virtually unchanged. This is exactly what should be expected if the protein interaction had become stronger. This interpretation may be a bit speculative, but is shows that real changes in the sample should be considered at least as a possibility.

Photobleaching, and, possibly, photo-induced changes in the samples, has been a frequent problem of FRET measurements in early FLIM systems. These systems used PMTs with conventional photocathodes and, in many cases, inefficient ports of the microscopes. In the last years the photobleaching problem has been reduced by hybrid detectors [160] and highly efficient microscope optics. There is also a continuous development of new photostable fluorescent proteins which further reduce photobleaching artefacts [360, 361].

FRET Literature

An enormous amount of FRET papers based on the bh FLIM technique has been published in the past 15 years. An overview on FRET techniques, their applications and the related pitfalls is given in [1291]. Liput et al. [765] give an overview on FLIM FRET in Neuroscience. A detailed description of a TCSPC-FLIM FRET system is given in [410]. The system was used for FRET between ECPF-EYFP and FM1-43 - FM4-64 in cultured neurones. A number of papers give a general characterisation of TCSPC-FLIM FRET for monitoring protein interactions [220, 291, 292, 963, 1160]. A combined FLIM-FRET microscope / endoscope system is described in [467]. The system simultaneously scans FLIM images through the beam path of an inverted microscope and records fluorescence from the back of the sample through a fibre

bundle. Superresolution FRET imaging by STED has been described by Tardif et al. [1223]. They were able to discriminate different nanoclusters of synaptic proteins in different states of interaction with binding partners inside dendritic spines. Elder et al. reviewed different methods of FRET signal normalization and verified them by TCSPC FLIM [432].

A comparison of the accuracy of FRET measurements by different techniques has been given by Pelet et al. [953]. The authors compared FLIM, spectral imaging, and two-channel intensity imaging with calibration of excitation and emission crosstalk. For the individual measurements they used identical optical paths, comparable data acquisition times and comparable fluorescence intensities. It turned out that the FRET results obtained from the FLIM data had a three-times smaller standard deviation than those obtained from the dual-channel and spectral measurements. Sun & Periasamy compared conventional FRET efficiencies obtained by filter-based FRET measurements with FRET efficiencies obtained by FLIM FRET [1208] and found that additional correction is needed for filter-based measurements.

The construction of FRET standards and their verification by FLIM measurement are described in [275, 1179]. Although FLIM FRET actually does not need calibration the standards are required to verify and compare the results obtained by different FRET techniques.

There is a number of FRET applications which are directly related to clinical research [844]. Because FRET yields information about protein interaction it can be used to investigate the formation - and possible dissolution - of amyloid plaques of Alzheimer's disease [40, 41, 197, 198, 199, 533, 575, 630, 792, 795, 1270]. Mechanisms of Huntington disease (a progressive neuro-degenerative disorder) were investigated in [458] and [901].

FLIM FRET in synaptic structures has been published by Bosch et al., Fogel et al. and Ueda et al. [239, 456, 1268, 1269]. These experiments are difficult because FRET occurs in subresolution volumes of the sample. The effects are therefore difficult to detect, see above, 'FRET in Diffraction-Limited Spots'. Bosch et al. were not only able to detect protein interaction, they could even observe the re-organisation of post-synaptic substructures during long-term potentiation by time-series FLIM [239]. Fogel used a combination of intensity FRET measurement, FLIM FRET measurement, and single-molecule imaging to show that the amyloid precursor protein homo-dimer constitutes a resynaptic receptor that transduces a signal from amyloid-beta peptides to glutamate release.

Wang et al. then used two-photon excited FLIM FRET to detect material transport in tunnelling nanotubes (TNTs) [1325]. The results showed that the number of TNTs have an impact on the drug treatment of cancer cells, which provided a new perspective for the involvement of TNTs in cancer treatment.

Nguyen et al. used a combination of Homo FRET, Hetero FRET and time-laps recording to investigate transient excited state structure associated with CaMKII-NR2B binding [911]. They showed that a transient excited-state intermediate exists where paired catalytic-domains in the holoenzyme first separate prior to subsequent NR2B association. Additionally, the holoenzyme exhibits a biochemical form of plasticity with calcium- dependent adaptation of T-site ligand binding affinity.

Kelleher et al. demonstrated deep tissue FLIM FRET in cancer cells and animal models. Two-photon excitation was used to obtain FRET images from layers as deep as 100 µm [655]. Kiuchi et al. [670] performed FLIM FRET between donor and acceptor labelled EGFR and ErbB4, and suggested it for clinical detection of breast cancer. Ahmed et al. studied the interaction of growth factor receptor-bound bound protein (Grb2) and Ras/mitogen-activated protein (MAP) and found a relation to normal versus oncogenic function of the cells [7].

Another potential FRET application is the investigation of infection mechanisms. The technique was demonstrated by Ghukasyan et al. for the infection of HeLa cells with enterovirus 71 [501]. Jeshtadi et al. [626], Danquah et. al. [357] and Cheung et al. [297] used FRET to investigate interaction of virus proteins with proteins of the host cell. The FRET pair was GFP-DsRed. The spreading of viruses in plant cells was studies by Amari et al. [17], fungus infection of plant cells by Shen et al. [1134].

Almost all the FLIM-FRET applications are related to interactions of various proteins or to protein organisation [5, 6, 8, 19, 218, 220, 230, 242, 239, 399, 456, 465, 466, 473, 492, 514, 617, 627, 644, 661, 676, 711, 725, 796, 797, 812, 818, 902, 923, 954, 998, 1015, 1050, 1082, 1118, 1119, 1180, 1247, 1296, 1375]. Monitoring HIV-1 protein oligomerization by FLIM FRET was described in [1006]. Protein interaction studies include detection of enzymatic activity in neuronal micro-compartments by FRET [1365], Na^+ channels [860], or intracellular transport mechanisms and membrane trafficking [359, 877, 1007]. Rochel et al. used FRET to study the role of DNA in the spatial organisation of nuclear hormone receptors (NHRs) [1025]. Interactions between the PCK and NKκB signalling pathways have been investigated in [891]. [1197] investigated the association of protein kinase C alpha (PKCα) with caveolin. FRET between GFP and RFP and FRET cascades from GFP via Cy3 into Cy5 are demonstrated in [964] and [19]. The agglutination of red blood cells by monoclonal antibodies was studied using FRET between Alexa 488 and DiI [1018]. Interaction of the neuronal PDZ protein PSD-95 with the potassium channels and SHP-1-target interaction were studied in [218, 220]. Interaction of αB-crystallin with focal adhesion kinase (FAK) was investigated in by Pereira et al. [962] and shown to confer protection to FAK against calpain mediated proteolysis in cardio-myocytes.

It has also been shown that conformational changes of proteins in cells can be monitored by FLIM FRET [269, 795]. Nanoscale Chromatin compaction was studied in [797] and [798]. Tynan et al. and Martin-Fernandez used FRET to gain insight into the structure of the human epidermal growth factor (EGFR) [824, 1266]. Mergenthaler et al. investigated the function of mitochondrial HKs in different states of metabolic deprivation during hypoxia and hypoglycemia [853]. Regulation effects during mitosis have been investigated by Hasegawa et al., Kalab et al. and Soderholm et al. [559, 636, 1162]. Kaye et al. used FLIM FRET to measure microtubule assembly [653].

A variety of papers is devoted to the conformation and interaction of SNARE proteins and mechanisms modulating their interactions [729, 844, 937, 1007, 1008, 1009, 1159, 1283]. In [1008] double-exponential FRET is used to distinguish interacting and non-interacting protein fractions. Studies of the interaction dynamics on the millisecond time scale are described in [1009].

Ariola et al. used a Bodipy-cholesterol derivate (Bdp-Chol, donor) and Dil-C12 (acceptor) to probe fluidity and lipid order in cell membranes [30]. They found a reduction in lifetime of the Bdp-Chol in ordered domain which they attributed to FRET. The results were confirmed by anisotropy decay measurement. Costa et. al. used FRET-induced and Dexter-transfer induced lifetime changes to study self-organisation of meso-substituted porhyrines in thin films [332].

The influence of shear forces on protein conformation was investigated in [271, 281, 1385]. The authors used a micro-fluidic setup to induce dynamic forces on the cells. The setup was placed under a microscope and illuminated by a frequency-doubled Titanium-Sapphire laser. The donor fluorescence was detected by a bh PML-16 multi-wavelength detector with polychromator, and recorded be an SPC-630 TCSPC module. A similar setup was used to study the influence of oxygen concentration [1383]. The Oxygen supply was turned on and off by

starting and stopping the flow in the cell. The oxygen concentration was monitored via the emission intensity of a phosphorescence probe.

FRET between ECFP and EYFP in plant cells was demonstrated in [237]. FRET measurements in plant cells can be difficult because of the strong autofluorescence of the plant tissue. The authors showed that two-photon excitation can be used to keep the autofluorescence signal at a tolerable level. The autofluorescence problem has also been solved by using the GFP mutant TSapphire and the DsRed variant mOrange as FRET donor and acceptor, respectively [56]. Protein interactions upon intrusion of fungal pathogens into plant cells were investigated in [245, 205, 1134]. Interactions between Golgi tethering factors and small GTPases was studied by Osterrieder et al. [934].

FRET is the basis of many sensors for biological parameters. The mechanism is usually that a donor and an acceptor are attached to the ends of a protein or DNA construct. The construct is able to bind to a specific target. When it binds it changes its conformation, and the FRET intensity changes. A new Ras sensor was developed and characterised by Oliveira and Yasuda [932]; Zlobovska et al. and Zherdeva et al. describe a far-red sensor for caspase-3 activity [1402, 1400]; and Strohhöfer et al. a sensor for Ca^{2+} [1196]. Burgstaller et al. presented a FRET-Based pH sensor [262], Currie et al. a sensor for crowding studies [350], and Penjweini et al. a sensor for oxygen [955]. A glucose sensor has been developed and evaluated by Diaz-Garcia et al. [374]. A review on sensors for protease activity has been given by Goryashchenko et al. [512]. Miller et al. presented a FRET sensor for ionic strength measurements [869]. It uses mCerulean3 and mCitrine. The fluorophores are linked by charged α-helices and a flexible loop. The angle between the helices changes with the ionic strength of the molecular environment, and so does the FRET efficiency. The readout is via the donor lifetime [869] or via the anisotropy of the acceptor fluorescence [28].

There is a continuing search for new FRET pairs with higher photostability, better overlap of donor emission with acceptor absorption bands, and (important for steady-state FRET techniques) less donor and acceptor bleedthrough. Please see [56, 360, 361, 1207] for new fluorescent proteins for FLIM FRET and their characterisation. An interesting approach is the use of a GFP as a donor and a dark YFP as an acceptor [475, 476].

Currently there is an increasing interest in FRET pairs with absorption and emission in the red and near-infrared region. The advantage of going to longer wavelengths is that it excites less autofluorescence and induces less direct photodamage to the systems investigated. Please see [1033] and [906].

It is also attempted to use quantum dots or combinations of quantum dots (as donors) and fluorescent proteins [845] or quantum dots and organic dyes or metal-organic complexes [15, 1191] as FRET partners. Spectroscopically, quantum dots make excellent FRET donors and acceptors. The photostability is excellent, and almost any absorption and emission wavelength can be obtained. The drawback is that quantum dots cannot be easily be linked to target proteins by transfection techniques as fluorescent proteins can.

Label-Free FLIM of Cells and Tissues

Biological tissue contains a wide variety of endogenous fluorophores [309, 504, 686, 1014, 738, 1091, 1149]. For many years, autofluorescence was just considered an unwanted background signal in the fluorescence microscopy with exogenous fluorophores. Autofluorescence (or label-free) Measurements of cells and tissues were performed - if at all - by spectrally resolved imaging techniques. A problem of purely spectrally resolved techniques is that the emission and excitation spectra of the endogenous fluorophores are broad and poorly defined. Many of the fluorophores are mixtures of closely related compounds. The shape of the spectra can therefore vary. Moreover, absorbers present in the tissue may change the apparent fluorescence spectra. It is therefore difficult to disentangle the fluorescence components by their emission spectra alone.

As in other areas of microscopy, the first use of FLIM in autofluorescence imaging was for increasing the contrast between different endogenous fluorophores. This has been demonstrated by Krasieva et al. [708] who used TCSPC FLIM and phasor plot analysis to separate the fluorescence components of different melanins, and to separate the melanin fluorescence from the NADH fluorescence. Borges da Silva who used FLIM to identify cells of bone marrow in unstained routine samples [236]. Autofluorescence imaging was also found beneficial when the reaction of tissue to optical radiation had to be investigated, such as skin ageing [1048] or photodamage and tumor induction by UV [681] and IR irradiation [689]. Such experiments forbid the use of exogenous fluorophores because energy or electron transfer between the fluorophores and the proteins can induce additional photodamage. Moreover, TCSPC FLIM has been more and more introduced into clinical applications, see chapter 'Clinical Applications of FLIM', page 587. In these applications ‘label-free’ imaging is mandatory because staining the tissue with exogenous fluorophores is either not possible or not permitted.

The real breakthrough in label-free imaging came with the use of the fluorescence lifetime as a molecular-imaging parameter. The lifetimes of many, if not all endogenous fluorophores bear information on molecular parameters, such as pH, oxygen saturation, ion concentrations, and, especially, on binding to proteins. With the use of the fluorescence lifetime to study molecular interactions, functional relationship of endogenous compounds, and their role in the metabolic processes in the cell a new era of biological research begun. The number of publications in this field increased dramatically, see, for example [213, 225, 226, 227, 272, 282, 299, 300, 323, 356, 404, 406, 556, 686, 990, 991, 690, 691, 692, 714, 1048, 1049, 1022, 1045, 793, 801, 802, 811, 878, 950, 976, 1002, 1003, 1039, 1045, 1091, 1093, 1094, 1096, 1124, 1125, 1143, 1149, 1156, 1206, 1217, 1290, 1316, 1317, 1318, 1323, 1364]. The most important applications of label-free time-resolved imaging will be described in the following sections of this chapter.

Metabolic Imaging

Basics of Metabolic FLIM

The most important argument for using lifetime imaging is that the lifetimes of many endogenous fluorophores bear information on molecular parameters, such as pH, oxygen saturation, ion concentrations, and, especially, on the binding to proteins. The most promising signals come from NAD(P)H (nicotinamide adenine (pyridine) dinucleotide) and FAD (flavin adenine dinucleotide). NAD(P)H and FAD are coenzymes involved in the cell metabolism. NAD(P)H and FAD are unique in the sense that their fluorescence intensities and fluorescence decay functions bears direct information on the metabolic state of the cells. There is an

increasing number of papers about this subject [39, 213, 225, 226, 227, 228, 270, 272, 282, 299, 300, 314, 323, 404, 406, 556, 741, 742, 793, 801, 802, 811, 878, 950, 976, 1002, 1003, 1039, 1045, 1093, 1094, 1124, 1125, 1143, 1149, 1155, 1156, 1206, 1217, 1290, 1316, 1317, 1318, 1363, 1364, 1377]. This section will give an overview on the fluorescence properties of NADH and FAD and their relationship to the metabolism of the cells.

Excitation and Emission Spectra

The signals from NAD(P)H and FAD are not easy to separate. Failure to record metabolic effects in most instances results from incorrect excitation and detection wavelengths. Also the numerous inconsistent 'tumor lifetimes' reported in the past may result in part from using wrong wavelengths.

Approximate excitation and emission spectra of NAD(P)H and FAD are shown in Fig. 743. The spectra were taken from [742] and [1094]. Both the excitation spectra and the emission spectra are overlapping. To obtain clean signals NAD(P)H must be excited in the range from 330 to 370 nm, and detected from 425nm to no more than 475 nm. FAD could, in principle be excited in the entire range from 330 to 470 nm. However, excitation below 400 nm would excite also NADH. The emission spectrum of NADH extends into that of FAD, and a clean FAD signal would not be detected. Therefore FAD should not be excited at wavelengths shorter than 400 nm. NAD(P)H excitation is then negligible, and a clean FAD signal can be obtained in the range from 500 to 600 nm. However, it is technically inconvenient to have the FAD excitation wavelength within the detection range of NAD(P)H. If the NADH and the FAD excitation are multiplexed (as in the bh metabolic FLIM systems) scattered light from the FAD excitation would shut down or damage the NADH detector. In practice this limits the FAD excitation wavelength range to the interval from 410 to 425 nm. For two-photon excitation a technical limitation for the FAD excitation does not exist. NAD(P)H can therefore be excited at 750 to 780 nm, and FAD at 860 to 900 nm.

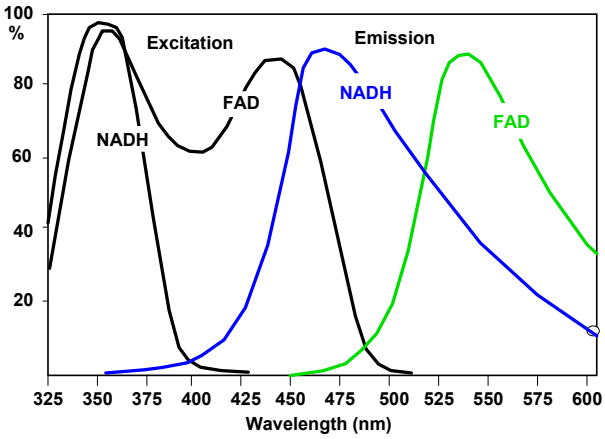


Fig. 743: Excitation and emission spectra of NADH and FAD. After [1094] and [742].

NAD(P)H and FAD Intensities

Both NAD(P)H and FAD form redox pairs. NAD(P)H is fluorescent in its reduced form but not when oxidised to NAD^+. FAD is fluorescent when oxidised to FAD^+, and loses fluorescence when reduced. The fluorescence intensity ratio of FAD and NAD(P)H therefore changes with the redox state of the tissue. The intensity ratio shows whether the metabolism in a cell is more oxidative (oxidative phosphorylation) or more reductive (glycolysis) [1158]. The redox ratio is closely related to the 'Warburg Effect': In normal cells oxidative phosphorylation dominates, in cancer cells reductive glycolysis [1326, 1327].

The influence of the redox state can be shown by recording FLIM from yeast cells. Fig. 744, left, shows yeast cells in a medium saturated with CO_2 and virtually free of oxygen. Except for a few (probably apoptotic) cells the fluorescence is extremely week. When the sample has

taken up oxygen from the air the fluorescence intensity increases, accompanied by a change in the lifetimes.

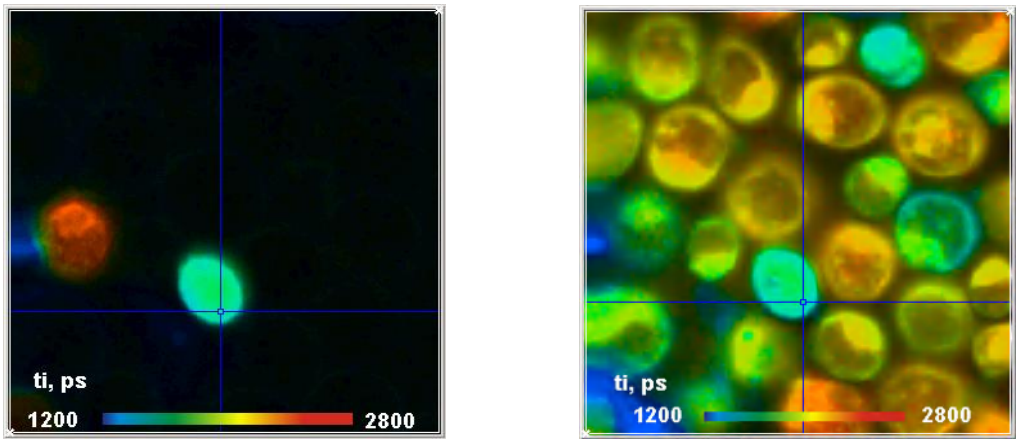


Fig. 744: FAD FLIM images of yeast cells in a cell dish saturated with CO_2 (left) and saturated with O_2 (right). Confocal FLIM, excitation 405 nm, detection by bh MW FLIM, 540 nm

Fluorescence Decay Functions

The fluorescence lifetimes of NAD(P)H and FAD depend on the binding to proteins [741, 742, 950]. Unbound NAD(P)H has a fluorescence lifetime of about 0.3 to 0.5 ns. When NAD(P)H binds to proteins the lifetime typically increases to a few ns [272, 742]. For FAD the effect of binding is opposite: Bound FAD has a lifetime of a few 100 ps, unbound FAD of a few ns. The resulting decay functions are thus (at least) double exponential. Typical decay functions of NAD(P)H and FAD in cells are shown in Fig. 745. The lifetimes and decay times of the decay components are shown in the inserts. The net lifetimes (amplitude-weighted, tm) for NADH and FAD are 1.86 ns and 0.68 ns, respectively.

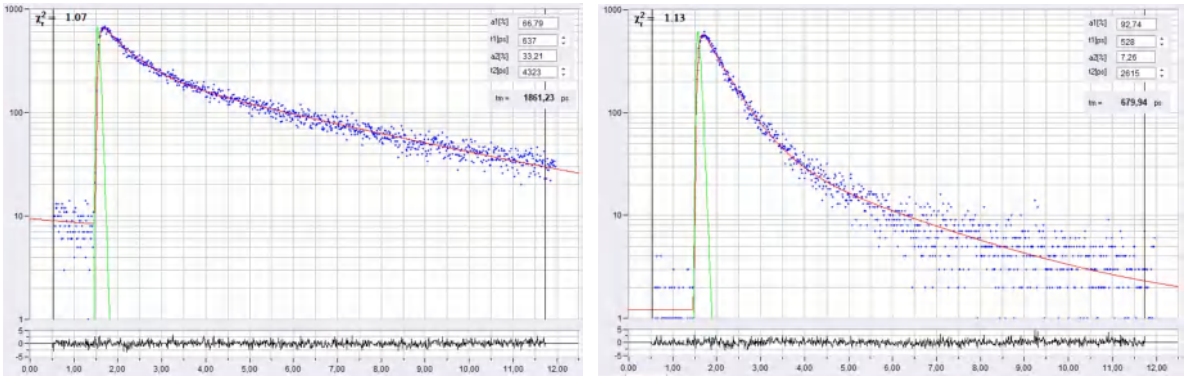


Fig. 745: Typical decay functions of NAD(P)H (left) and FAD (right). The blue dots are the data points, the red curve is a fit with a double-exponential decay model. Recorded from healthy human epithelium cells by bh metabolic FLIM system, see page 375.

Change in the Lifetimes with the Metabolic State

What happens to the decay functions when cells pass from oxydative phosphorylation to glycolysis? Pioneering work in this direction has been done by the group of Melissa Skala at Vanderbilt University (now Morgridge Institute, Madison). A result from [1156] is shown in Fig. 746. The figure shows NADH (left) and FAD (right) lifetime images for normal cells and different grades of tumors. It is clearly visible that the NADH lifetime gets shorter and the FAD lifetime longer as the tumor progresses. In other words, the lifetime changes for NADH and FAD go in opposite directions.

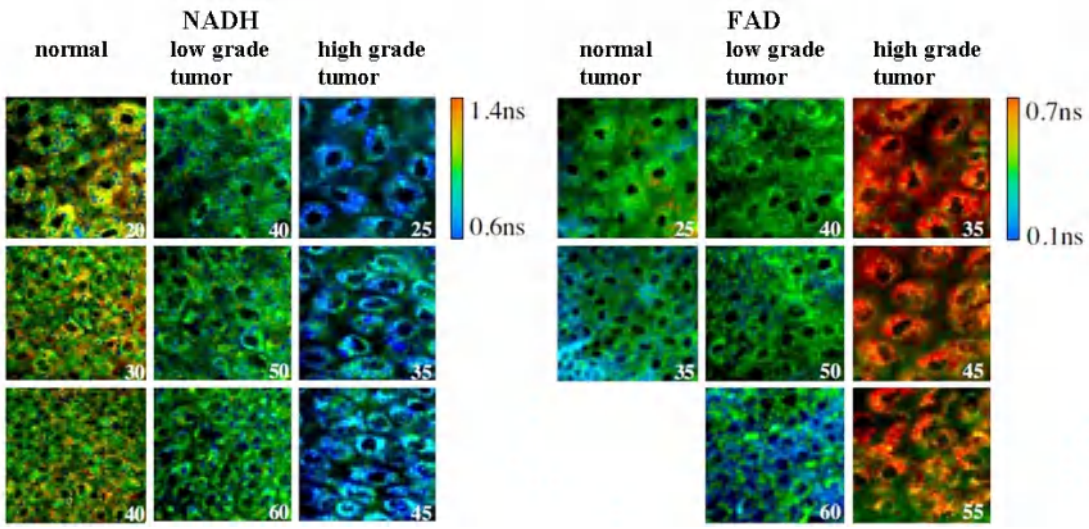


Fig. 746: Change in the mean (amplitude-weighted) lifetime of NADH and FAD with the state of the cells, from normal (oxidative phosphorylation) to high-grade tumor (glycolysis). With permission, from [1156].

Amplitudes of the Decay Components

The fluorescence lifetime does not tell whether a change in the lifetime is caused by a change in the lifetimes of the bound and/or unbound NADH and FAD or by a change in the amount of bound and unbound NADH and FAD. However, there are strong indications from biochemistry that the primary cause of the lifetime change is in the bound/unbound ratios. The bound/unbound ratio is reflected by the amplitudes, a1 and a2, of the decay components. a1 and a2 can be obtained by double-exponential decay analysis. Because the amplitudes do not depends on other cell parameters, such as mitochondrial-matrix pH [913, 1066, 1067] and extracellular pH [1073] they are better - and more quantitative - indicators of the true metabolic state than the net lifetimes.

A comparison of NADH images of the amplitude-weighted lifetime, tm and the amplitude of the fast component, a1, for different cells is shown in Fig. 747.

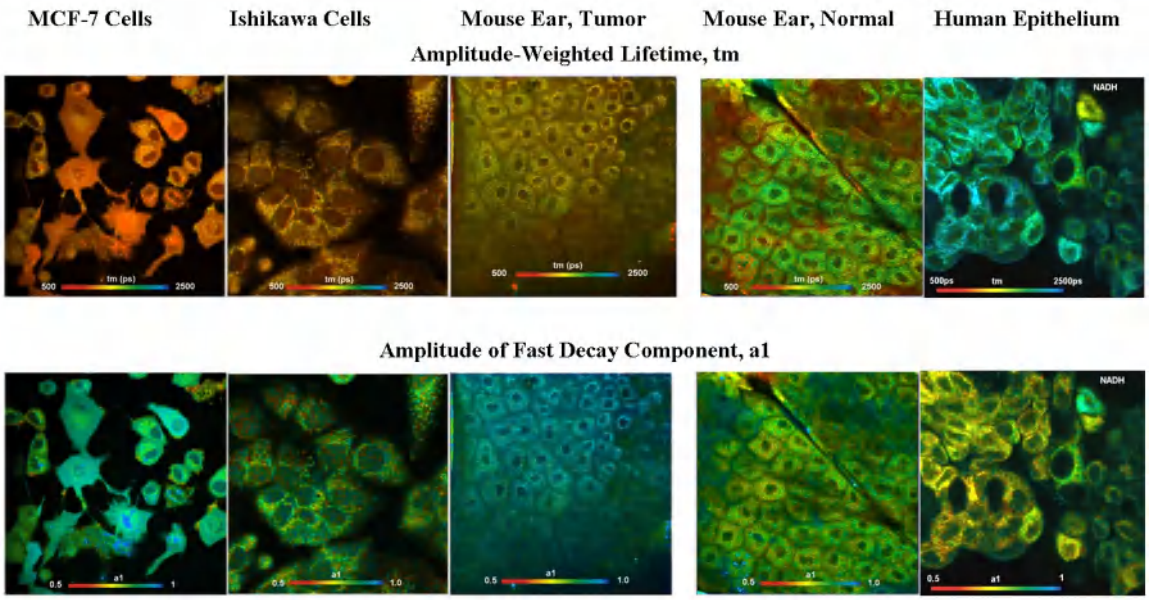


Fig. 747: Images of amplitude-weighted lifetimes, t_m, (upper row) and amplitudes, a1, of various cells. The left three cells are tumor cells, the right two are normal.

The figure shows two things: First, the change in a1 goes in step with the change in tm. Second, a1 is obtained at almost the same signal-to-noise ratio as tm. The good signal-to-noise ratio of a1 may be surprising. a1 is obtained from a double-exponential fit, which is intrinsi-

cally less stable than a single-exponential one. The explanation is in the speed of the detector. The data in Fig. 747 were recorded with fast HPM-100-40 and -06 detectors. The IRF of these detectors is several times shorter than the IRF width of the previously used H7422 detectors, and several times shorter than the lifetime of the fast decay component. The fast IRF significantly reduces the ambiguity in the fit and thus results in a high accuracy of a1.

Summary of Effects Ruling NADH and FAD Fluorescence

A summary of the mechanisms affecting the NAD(P)H and FAD fluorescence is given in Fig. 748. NAD(P)H is shown on the left, FAD on the right. Please note that the change in intensity is caused by the change in oxidised/reduced forms, not by the change in the apparent lifetime. The first effect dominates, and the intensity does not (as might be expected) change in step with the lifetime.

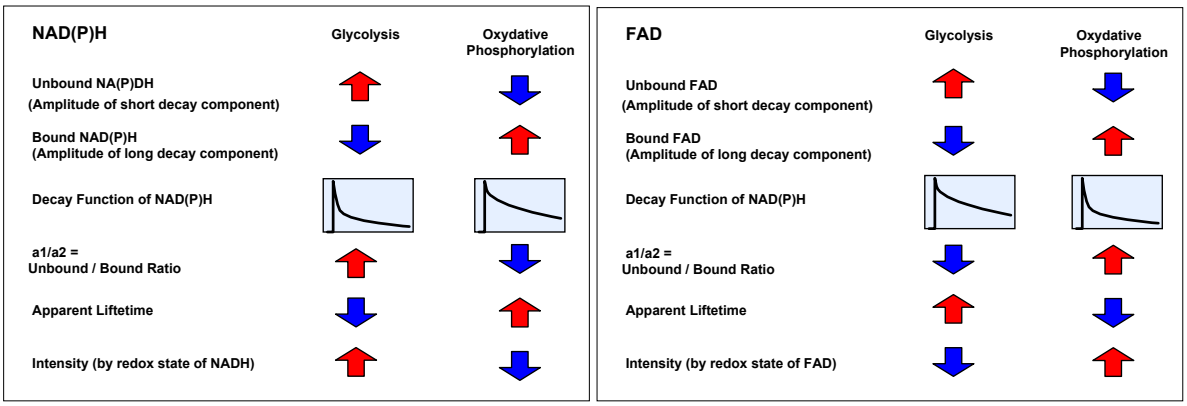


Fig. 748: Response of NAD(P)H and FAD fluorescence parameters to type of metabolism

Indicators Characterising the Cell Metabolism

As described above, there is a confusing complexity of molecular processes influencing the fluorescence of NADH and FAD. Different optical techniques have been developed that deliver insights into different aspects of the problem, but none of them is able to cover the problem in its full complexity. The technique that comes closest to the ideal is multi-dimensional TCSPC FLIM. But it is not only the technique that matters, it is also the researcher who has to understand the technical capabilities of a technique and exploit them to advantage. In this situation, it is not surprising that different approaches have been developed to quantify the metabolic state of cells. The most frequently used indicators are described below.

Redox Ratio

The Redox Ratio was introduced by Chance et al. in 1976 [284, 285]. The redox ratio is defined as

$$RR = I_{FAD} / I_{NAD(P)H} ,$$

with I_{FAD} and $I_{NAD(P)H}$ being the fluorescence intensities of FAD and NAD(P)H. There is some inconsistency in the definition of the redox ratio. Sometimes it is defined as the intensity ratio of FAD/ NADH [802], and sometimes as the intensity ratio of NADH /FAD [1158]. Sometimes also the ratio of FAD / (FAD + NADH) is used [438, 631]. Here we use the definition of Britton Chance (1979) [285], which is the intensity ratio of FAD / NADH.

The Redox Ratio makes use of the fact that both NADH and FAD exist in an oxydised and in a reduced form. NADH is fluorescent, NAD^+ is not. For FAD the effect is opposite: FAD^+ is

fluorescent, FAD is not. The fluorescence intensity ratio of FAD and NADH therefore changes with the redox state of the cell. Often, the Redox Ratio is used in combination with the fluorescence lifetime. For practical applications please see [481, 793, 801, 886, 988, 1121, 1157, 1158, 1315, 1319].

The redox ratio can, in principle, be derived from NADH / FAD FLIM data. The total number of photons in a given pixel is a measure of the intensity. Therefore the redox ratio can be determined by calculating the ratio of the photon numbers in the corresponding pixels of an FAD image and an NADH image of the same cell. This is especially attractive if NADH and FAD data are recorded simultaneously by laser-wavelength multiplexed FLIM, see 'Excitation-Wavelength Multiplexing' page 371. For calculation and display of Redox-Ratio images please see 'Classic Redox Ratio' page 952.

The problem of the redox ratio is that it depends on the ratio of the concentrations of NAD(P)H and FAD in the cells. The concentration ratio can hardly be considered to be the same for different cell types. Therefore, it is a good parameter to observe a given cell shifting its metabolism between glycolysis and oxidative phosphorylation, but it does not tell quantitatively whether a given cell is a tumor cell or a normal one.

Fluorescence Lifetimes

When the metabolism shifts from oxidative phosphorylation to glycolysis the apparent lifetime of NAD(P)H decreases, and the lifetime of FAD increases. Since the lifetimes (and the lifetime ratio of NAD(P)H and FAD) do not depend on the absolute concentrations they are more robust parameters than the redox ratio. They are therefore frequently used as indicators of the metabolic state [270, 481, 886, 990, 991, 988, 1121, 1232, 1324].

However, some pitfalls remain. The component lifetimes of NAD(P)H and FAD depend on the mitochondrial-matrix pH [913, 1066, 1067], extracellular pH [1073], temperature, and a number of other environment parameters [272, 1124]. They are clearly different in different compartments of a cell [1003, 1364], see Fig. 541, page 366.

There is increasing evidence that the primary effect of the metabolic state on the decay function is a change in the ratios of bound/unbound NADH and FAD, i.e. in the amplitudes of the decay components. However, the net lifetimes of NADH and FAD are influenced both by the amplitudes and the decay times of the components. The net lifetime is therefore not a quantitative indicator of the metabolic state.

Another source of confusion originates from the definition of the 'lifetimes'. The decay functions of NAD(P)H and FAD are double-exponential. Therefore the apparent 'lifetime' depends on the way the components are averaged. There are two definitions of this lifetime: The amplitude-weighted lifetime, t_m, and the intensity-weighted lifetime t_i. t_i and t_m are different and so are the metabolic states derived from one or the other.

Another simple mistake originates from incomplete (or missing) separation of the fluorescence signals of NADH and FAD, see Fig. 749. The many inconsistent 'tumor lifetimes' found in the literature probably originate from this mistake.

OMI Index

Skala and Walsh combined the normalised value of the redox ratio RR, the normalised amplitude-weighted fluorescence lifetime, $\tau_{m\ NADH,}$ and the normalised $\tau_{m\ FAD,}$ of NAD(P)H and FAD into a single 'Optical Molecular Imaging', or OMI index.

$OMI = RR + \tau_{m\,NADH} - \tau_{m\,FAD}$ (all parameters normalised to reference values)

The OMI index turned out to be a sensitive and robust parameter to characterise the metabolism of a cell. The authors use it successfully to check the response of human cancer cells from clinical biopsies to various anti-cancer drugs [1125, 1315, 1316, 1317, 1318, 1319].

The OMI index is, however, not free of technical problems. The problem of variable NAD(P)H and FAD concentration has already been mentioned above. OMI values are therefore difficult to compare for different cell types. Moreover, the NAD(P)H and FAD intensities have to be measured at different excitation wavelengths (see Fig. 743). That means that changes in the relative laser power, focusing errors or aberrations in the microscope lens can influence the result. That means the OMI index is a robust and sensitive metabolic indicator for a given type of cell but it is not useful to compare different types of cells.

Statistics of Cell Clusters of Different Decay Signature

Shirshin et al. used non-parametric analysis based on identification of cells in the images, and discrimination of cells of different τm, phasor values, or decay shapes [1150]. Distributions of the number of cells over the discrimination parameter were built up and used to identify different cell populations. The most successful discrimination technique was 'K-means', as it was demonstrated by simulated and measured data. Although the technique proved to be efficient in finding different cell populations it was not shown how it reacts to the pure metabolic state in presence of heterogeneity in the molecular environment, such as pH or oxygen concentration.

Mitochondrial-Cytoplasmic Ratio, MCR

Evers et el. introduced the ratio of the NAD(P)H fluorescence intensity in the mitochondria and in the cytoplasm, MCR, as an indicator of the metabolism [438]:

$$MCR = \frac{I_{NADHmitochondiral}}{I_{NADHcytoplasmic}}$$

The MCR reflects changes in the NAD(P)H concentration in the different cellular compartments.

Amplitude Ratios of NAD(P)H and FAD Decay Functions, a1/a2

After almost two decades of NADH FLIM there is more and more evidence that the primary effect of the metabolic state on the decay functions is a change in the amplitudes of the decay components. If this is correct, why not using the amplitude of the fast component or the ratio of the amplitudes as an indicator of the metabolic state? Changes in the component lifetimes, possibly induced by different molecular environment, pH, or different NADH / NAD(P)H ratio, then have no influence on the results. a1/a2 values are therefore comparable between different types of cells.

A problem of the amplitudes is that they can be difficult to extract from the decay data. Double-exponential decay analysis is required, so that the fit routine has several parameters to obtain a match of the model parameters to the data. The uncertainty in the amplitudes can therefore be higher than in a single-exponential fit of the fluorescence lifetime. This is especially the case if the IRF width is on the same order as the lifetime of the fast decay component, as it was the case for the H7422 detectors used in earlier FLIM systems. The poor signal-to-noise ratios of a_1 and a_2 obtained with these detectors have probably led to some reluctance in using the amplitudes as metabolic indicators. However, if the IRF of the FLIM system is significantly shorter than the lifetime of the fast decay component the amplitudes can be obtained with almost the same accuracy as the net lifetime of the decay. Compared with

the old H7422, the accuracy is much better for HPM-100-40 hybrid detectors, and the problem has entirely been solved with the ultra-fast HPM-100-06 (see 'NADH FLIM with Ultra-Fast Detectors', page 365) in combination with the MLE algorithm of SPCImage NG, see chapter 'SPCImage NG Data Analysis Software'.

In the past few years, the a_1/a_2 ratio (and a_1, see below) have more and more replaced the other metabolic indicators, please, see, [11, 173, 314, 404, 481, 556, 490, 613, 631, 694, 793, 802, 1045, 1046, 1122, 1143, 1145, 1211, 1287, 1362, 1376].

Amplitude of the Fast Decay Component, a_1

The a1/a2 ratio represents the unbound/bound an bound/unbound ratio of NAD(P)H or FAD. However, the a_1/a_2 ratio has a disadvantage. Because $a_1 + a_2 = 1$, the a_1/a_2 ratio can also be expressed as

$$a_1/a_2 = a_1 / (1-a_1)$$

That means, the a_1/a_2 ratio is a nonlinear function of a_1. This is no problem as long as a_1 remains in the range around 0.5 to 0.6. However, if a_1 gets higher than 0.8 (which is often the case for FAD) the function becomes highly nonlinear. The images then start to look noisy, and it is hard to evaluate the pixel histograms. These get more and more stretched toward larger a_1/a_2 values - please note that a_1/a_2 goes to infinity for a_1=1. We therefore find it more useful to base the evaluation of metabolic FLIM data on the amplitude coefficient of the fast component, a1. Of course, the amplitude of the slow component can be used as well because $a_1 + a_2 = 1$ [274, 481].

FLIRR Ratio

To navigate around the problems of the classic redox ratio Alam, Wallrabe and Periasamy defined a fluorescence-lifetime redox ratio (FLIRR) [10, 274, 1314]. It is the ratio of the fractional amplitudes of the bound decay components of NAD(P)H, $a_2/(a_1+a_2)_{NADH}$, and FAD, $a_1/(a_1+a_2)_{FAD}$.

$$\text{FLIRR} = \frac{a_2/(a_1+a_2)_{NADH}}{a_1/(a_1+a_2)_{FAD}}$$

The authors have shown that the FLIRR is a robust parameter for evaluation of the cell status. The advantage of the FLIRR is that it does not depend on the relative amounts of NAD(P)H and FAD in the cells, and not on the laser power, the focus accuracy or focus quality, or other instrument parameters. It should be noted that the FLIRR is not the same as the redox ratio. The redox ratio describes the relative amounts of oxidised and reduced NAD(P)H and FAD, the a_{1FAD} / a_{2NADH} ratio the relative amounts of bound coenzymes in the cell.

Kalinina et al. [638] have extended the definition of the FLIRR ratio. They found that the FAD decay functions often contain a noticeable contribution from FMN, see 'FAD: The FMN Problem', page 547. FMN has a fluorescence lifetime of about 4.5 ns. This is distinctly longer than the lifetime of bound FAD. The authors therefore run triple-exponential decay on the data in the FAD channel. The FMN component then constitutes the slowest component, a_3 and τ_3, and a_2 and τ_2 describe the true decay of unbound FAD. Based on the triple-exponential decay parameters in the FAD channel and using the ratios a_{2NADH}/a_{1FAD}, a_{2NADH}/a_{2FAD}, and a_{2NADH}/a_{3FAD} the authors calculate three different FLIRR ratios.

Metabolic Imaging with the bh FLIM Systems

Due to their high time resolution and clean instrument response function bh FLIM systems are excellent metabolic FLIM systems. Provided the right excitation wavelengths are available, metabolic FLIM can be performed with all bh FLIM systems that have the HPM-100 hybrid detectors. The fast and clean instrument response function in combination with the MLE fit of SPCImage data analysis software then permits efficient separation of the decay components of bound and unbound NADH and FAD - a basic requirement for metabolic FLIM. However, there is another technical feature important for metabolic FLIM with NADH and FAD. This is laser multiplexing. As shown above, NADH and FAD need different excitation wavelength to separate the signals of the fluorophores: Laser multiplexing. Laser multiplexing allows the signals of NADH and FAD to be recorded quasi-simultaneously, making the results for NADH and FAD exactly comparable. The bh DCS-120 systems therefore have a laser multiplexing function permanently integrated. bh metabolic FLIM systems are available with one-photon excitation and with two-photon excitation. One-photon systems use ps diode lasers, two photon systems use femtosecond fibre lasers. Technical descriptions of these systems are given under 'Metabolic Imaging by Simultaneous FLIM of NADH and FAD', page 375.

The sections below present typical results obtained with these systems and show details of the NADH and FAD dynamics which have not been seen by any other FLIM techniques yet.

Principle

The bh metabolic FLIM technique is based on recording the fractions bound and unbound NADH and bound and unbound FAD. FLIM data of NADH and FAD are recorded simultaneously by laser multiplexing and parallel dual-channel detection, see 'Metabolic Imaging by Simultaneous FLIM of NADH and FAD', page 375. The decay data are analysed by a double-exponential model, yielding the amplitudes, a1 and a2, and the lifetimes, t1 and t2, of the two decay components. The relationship to the metabolic state is illustrated in Fig. 749.

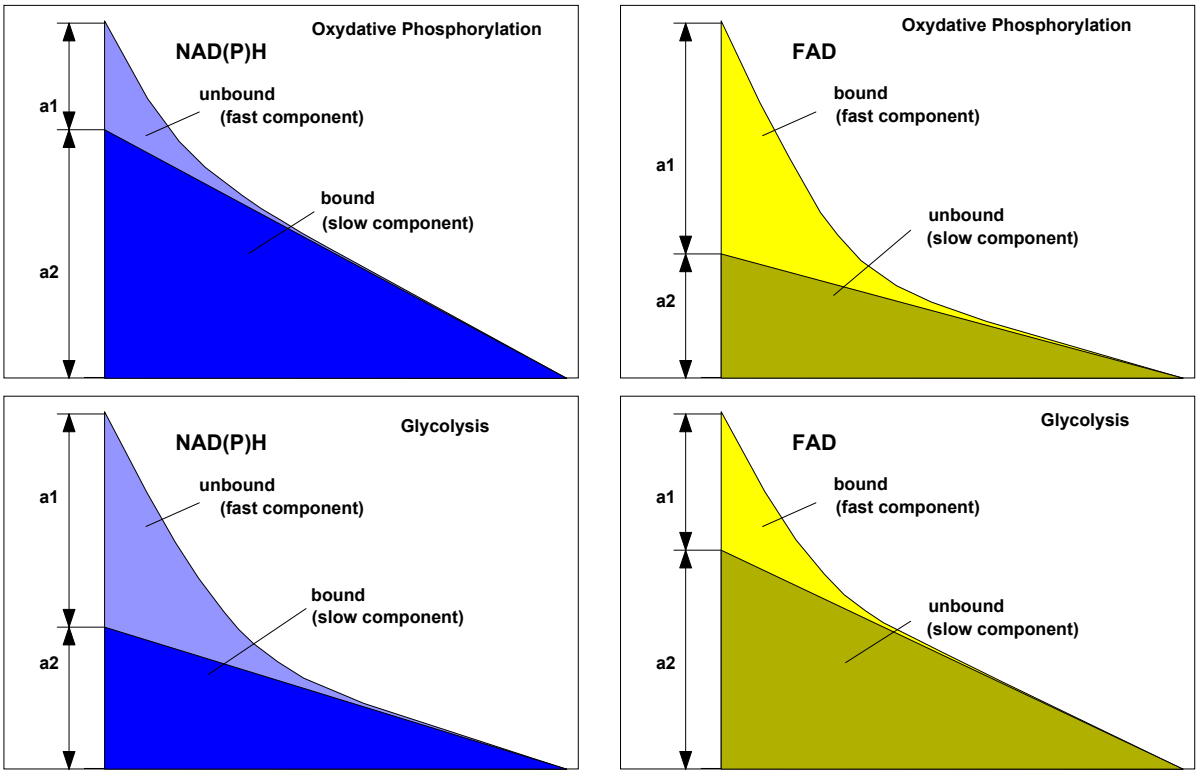


Fig. 749: The composition of the decay functions of NAD(P)H and FAD and changes with the metabolic state.

The decay components, a 1 and a2 then directly represent the fractional amount of bound and unbound NADH or FAD. The ratio of the amplitudes a_1/a_2, often called 'metabolic ratio', directly represents the concentration ratio of unbound/bound NADH or bound/unbound FAD.

The figure shows the general composition of the decay curves of NADH and FAD. In the NADH decay functions, there is a fast decay component from the unbound NADH and a slow component from the bound NADH. For the FAD it is the opposite. The fast component is from bound FAD, the slow component is from unbound FAD. The ratio of the amounts of bound and unbound NADH and FAD depends on the metabolic state. A cell can run both a oxidative metabolism (oxidative phosphorylation) and a reductive one (glycolysis). A shift from oxidative phosphorylation ('oxphos') to glycolysis is accompanied by a decrease of the bound fractions of NADH and FAD. Consequently, a shift from oxphos to glycolysis causes an increase in a1 in the NADH decay and a decrease in a1 in the FAD decay. A shift from glycolysis to oxphos results in the opposite: a1 of NADH decreases, a1 of FAD increases.

The changes in real decay data are shown in Fig. 750. The upper row shows decay functions from normal cells, NADH is shown left, FAD right. The lower row shows the corresponding decay curves for a tumor cell. The decay parameters are show in the inserts. As expected, a1 of NADH is higher in the tumor than in the normal cell. In the FAD curves, a1 is lower in the tumor than in the normal cell. This is exactly the behaviour that has to be expected for the model illustrated in Fig. 749. The differences are not very large but, nevertheless, are clearly detected by TCSPC FLIM.

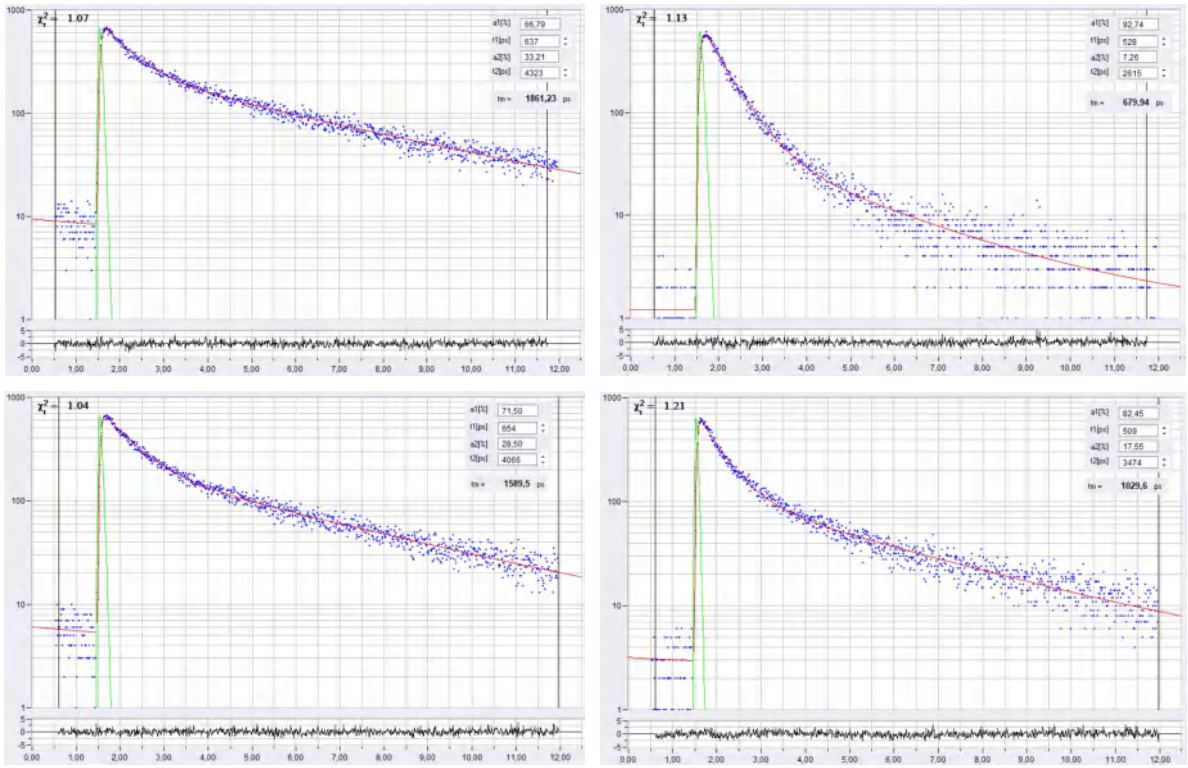


Fig. 750: Real decay data for NADH and FAD in a normal cell and in a tumor cell. Upper row: Decay curves of normal cell, NADH (left) and FAD (right). Lower row: Decay curves of tumor cell, NADH (left) and FAD (right).

The opposite changes in the decay parameters of NAD(P)H and FAD are a possible explanation of numerous discrepancies in fluorescence lifetimes measured in tumors. There have been as many reports for decreased lifetime as for increased ones. The source of the discrepancies is probably that the measurements did not cleanly separate the signals of NADH and FAD. Depending on which fluorophore dominates the net decay function the result can indeed be a

decrease or an increase of the lifetime in the tumor compared to normal tissue. Another possible pitfall is in the detection of FMN, please see 'FAD: The FMN Problem', page 547.

Metabolic Imaging of Excised Human Bladder Tissue

The principles presented above were verified using the instrument described in section 'Metabolic Imaging by Simultaneous FLIM of NADH and FAD', page 375. The instrument was placed in a hospital. FLIM data were obtained from human bladder cells excised during surgery. The patients had been diagnosed with bladder cancer or other suspicious lesions by classic endoscopy. Measurements on the excised material were performed immediately after surgery, before the material went to histology [1211]. Representative results are shown in Fig. 752 through Fig. 754.

Fig. 751 shows NAD(P)H images of the amplitude-weighted lifetime, t_m. The left image shows normal cells, the right image tumor cells. It should be noted that the image of the 'normal' cells also contains some tumor cells, and the image of the 'tumor' cells some normal cells. This is unavoidable due to the procedure by which the cells were excised. Nevertheless, the behaviour is as expected - t_m is shorter in the tumor sample.

NAD(P)H images of the amplitude, a_1, of the fast decay component are shown in Fig. 752. There is a clear difference in a1 between the normal cells and the tumor cells. The normal cells have an average a_1 of about 0.65 (or 65% of the total amplitude). The cancer cells have an a1 between 75% and 80%. We find similar values consistently in data of different cells.

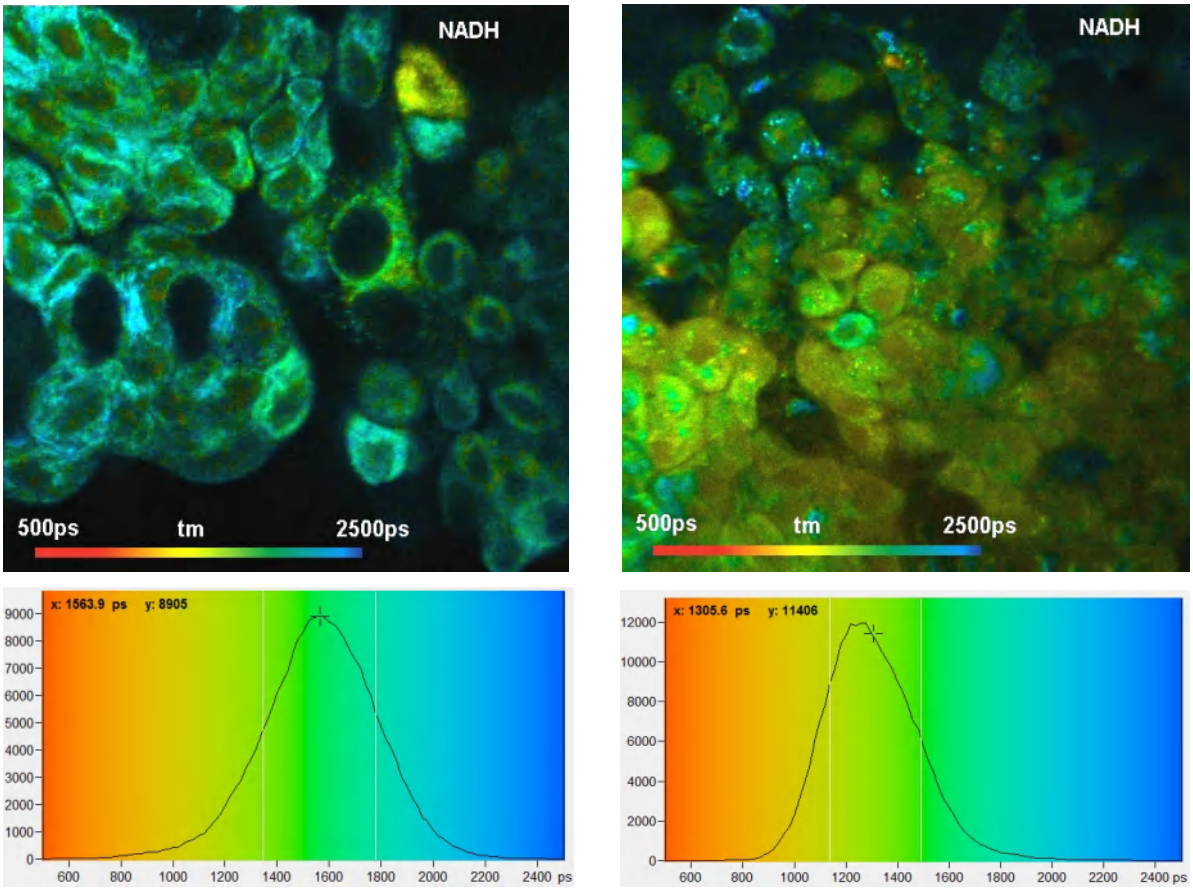


Fig. 751: NAD(P)H t_m images for normal cells (left) and tumor cells (right). Lower row: Histograms of t_m over the pixels of the images. As expected, t_m is shorter in the tumor sample.

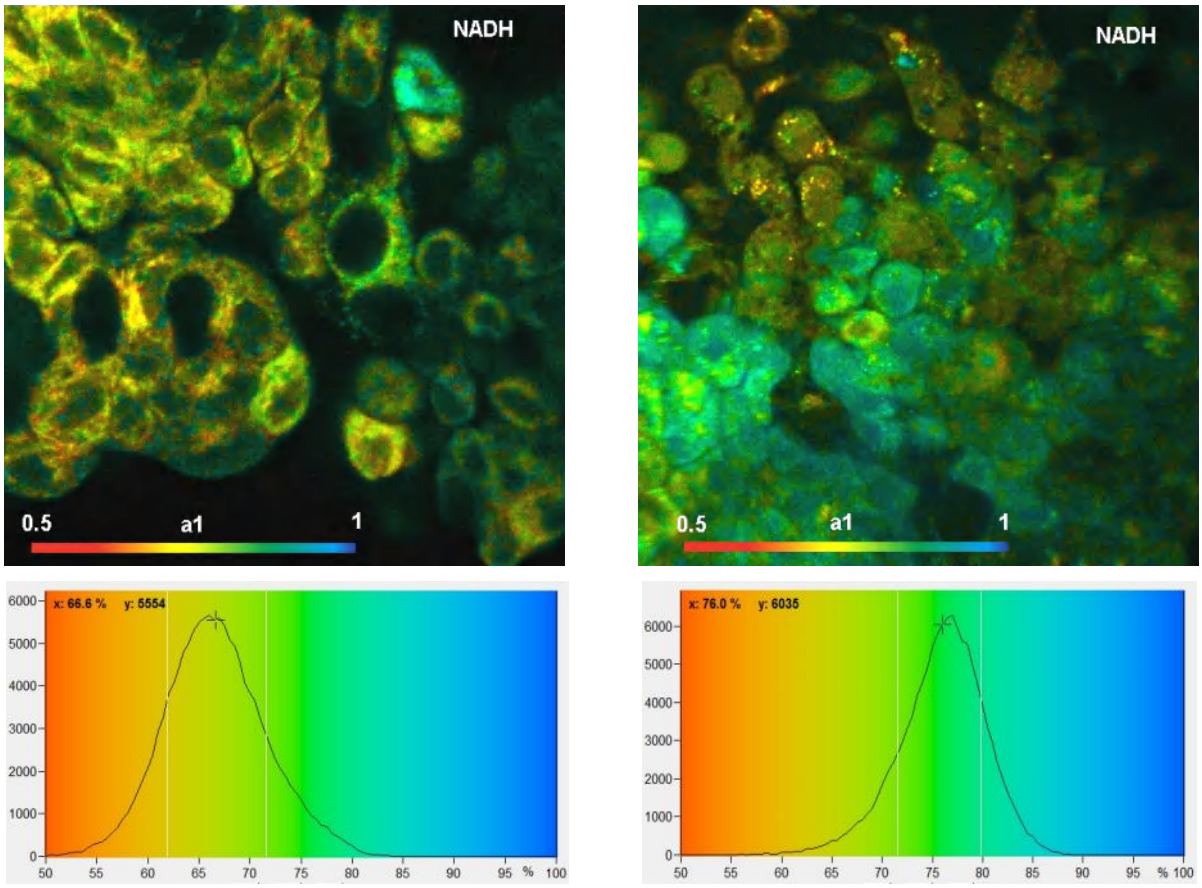


Fig. 752: NAD(P)H a_1 images for normal cells (left) and tumor cells (right). Lower row: Histograms of a1 over the pixels of the images. The histogram of the tumor sample is from lower half of the image because the upper half contains also normal cells.

FAD data are shown in Fig. 753. In general, also the FAD data show the expected trend. a_1 decreases for the cancer cells, indicating that they contain less bound FAD (note a_1 is the *bound* component of FAD). However, some details are not entirely plausible. On the one hand, cells in the upper part of Fig. 753, right, have a significantly different a_1 then the cells in the normal-cell sample (Fig. 753, left). On the other hand, in the NAD(P)H images the same cells have *the same* a_1 as the cells in the 'normal' sample (compare Fig. 752, left and right). However, there is a possible explanation. The redox ratio in the tumor sample may be so low that the FAD intensity gets extremely weak. It is then possible that residual NAD(P)H fluorescence excited by the 410-nm laser is detected in the FAD channel. The fluorescence in the yellow cells in Fig. 753 may then be from NAD(P)H, not FAD. A inspection of the decay curves in the yellow areas shows indeed that the decay functions are more compatible with NAD(P)H then with FAD. An improvement can probably be obtained by using a slightly longer excitation wavelength for FAD excitation.

Fig. 754 shows the FLIRR calculated from the same data sets. As expected, the FLIRR shifts to lower values for the cancer cells.

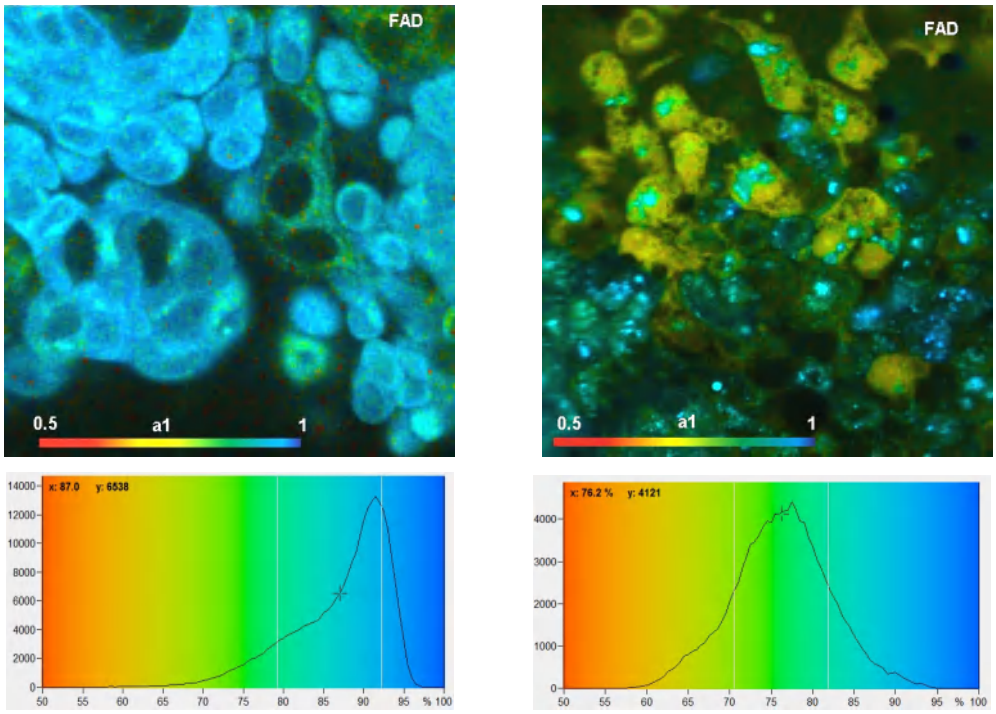


Fig. 753: FAD a1 images for normal cells (left) and tumor cells (right). Lower row: Histograms of a1 over the pixels of the images. The histogram of the tumor sample is from lower half of the image because the upper half contains also normal cells.

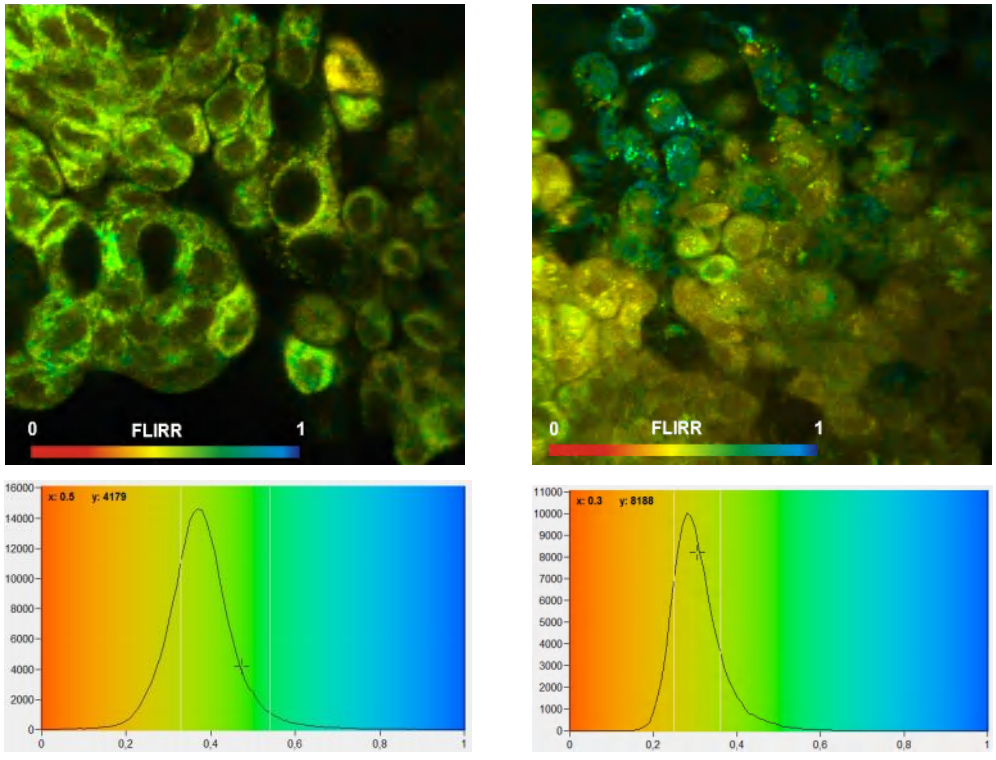


Fig. 754: FLIRR images of normal cells (left) and tumor cells (right). Lower row: Histograms of the FLIRR over the pixels of the images. The histogram of the tumor sample is from lower half of the image.

Comparison of NAD(P)H FLIM and Histology Results for Clinical Diagnosis

A comparison of the results of classic endoscopy, NAD(P)H FLIM, and histology is given in Fig. 755. FLIM data were obtained from the material from 7 patients [173, 1211]. Initial endoscopy had diagnosed two of them with non-cancer lesions, and 5 of them with cancer.

The a_1 FLIM images showed normal a1 for patients 1 and 2, a suspiciously increased a1 for patients 3, an increased a1 for some of the cells from patient 6, and a massively increased a_1 in the entire sample from patient 7. By using a selection criterion of $a_1 = 0.71$ as the tumor threshold, the FLIM-based diagnosis is as indicated in the figure. A threshold of $a1 = 0.7_1$ may appear somewhat artificial but is supported by other NAD(P)H FLIM data [406, 802, 1131].

Histology diagnosed the patients 1 and 2 as healthy, patients 2, 3, and 4 as inflammation, patient 6 as low-grade tumor, and patient 7 as high-grade tumor. The FLIM results were thus in perfect agreement with histology, and much better than the initial endoscopy results [1211]. We therefore believe that FLIM can favourably complement histology. In this respect, a substantial benefit of FLIM is that, in contrast to histology, the results are available within minutes after surgery.

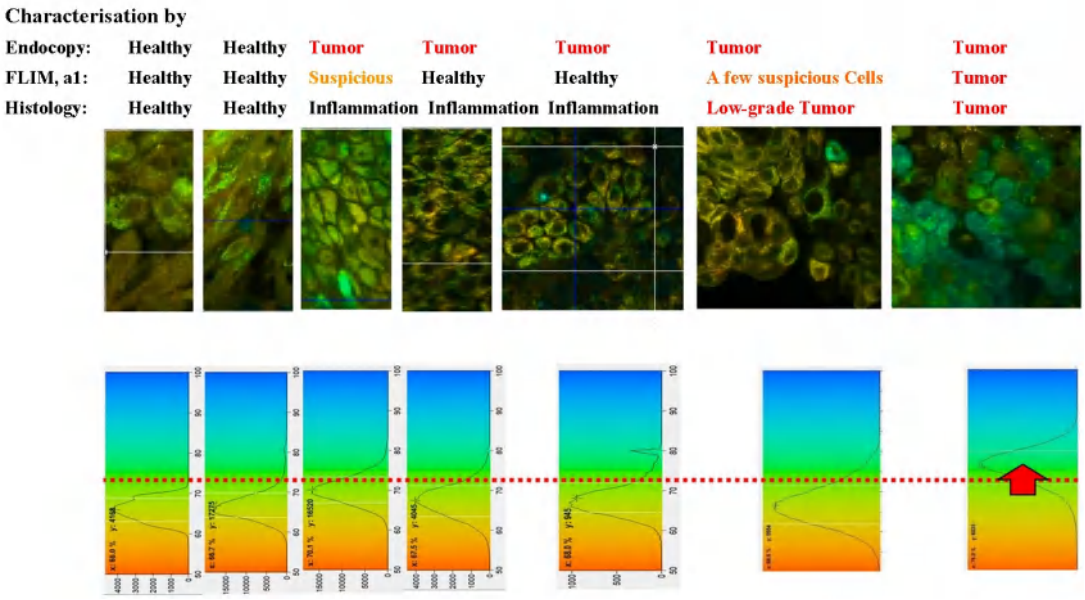


Fig. 755: Comparison of endoscopy, NAD(P)H FLIM, and histology results

Using the FAD FLIM Data for Clinical Diagnosis

Using the FAD data in combination with the NADH data turns out to be more difficult than expected. One problem is that there is a possible contribution of a decay component from of FMN, see page 547. The second problem is that the FAD signal can be extremely weak. Although the FLIM system is sensitive enough to detect images in these cases the decay data contain fluorescence of contaminations and residual fluorescence of NAD(P)H. Low FAD intensity was found especially in the data from cancer cells. Whether this is due to intrinsically low FAD concentration or extremely low redox ratio is not known. Moreover, there is still disagreement about the mechanism of the lifetime changes of FAD. Even the direction of the change with the metabolic state is discussed controversially. Be it as it may, additional research effort is required to make the FAD decay parameters a reliable indicator for clinical diagnosis.

To avoid spoiling metabolic data from NADH with possibly misinterpreted FAD data, FAD data can be used in a way that they supplement the NADH data but do not get entirely mingled with them. A possible way to do so is two-dimensional histogramming of the amplitudes. A histogram of a_1 of FAD (vertical axis) versus a_1 of NADH (horizontal axis) is calculated and displayed as shown in Fig. 756. Normal cells are characterised by low a_1 of NADH and high a_1 of FAD. They are expected to cluster in the upper left part on the histogram. Tumor cells have high a1 of NADH and low a1 of FAD. They are expected in the lower right part. If

the FAD data are of poor quality the histogram just washes out vertically, but horizontally the distribution remains conclusive.

An example of 2D histogramming is shown in Fig. 756. The data were taken from the images of the 'low-grade tumor' sample shown Fig. 755, second right. The histogram of the entire sample (Fig. 756, top) shows indeed indications of clustering.

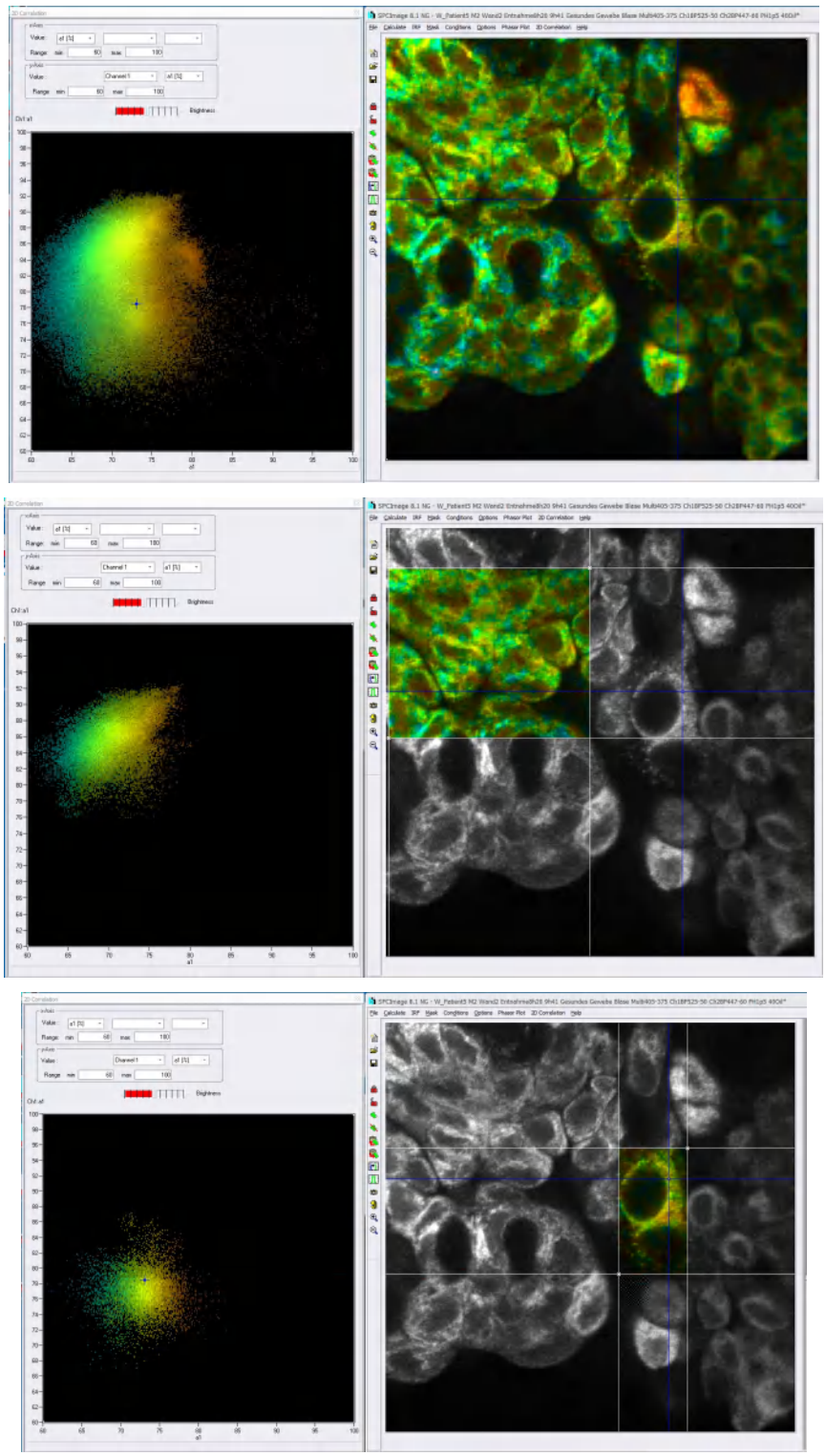


Fig. 756: Histograms of a_1 of FAD (vertical) versus a_1 of NADH (horizontal). t_m images from the NADH channel shown on the right. Top: Histogram from entire image. Middle: Histogram from mostly healthy cells. Bottom: Histogram from suspected tumor cell.

Fig. 756, middle, shows the histogram of cells in the upper left of the image. These cells are presumed normal or close to normal. Fig. 756, bottom shows the histogram from a suspected tumor cell. Interestingly, the difference in a1 of NADH (horizontal axis) between the normal cells and the tumor cells is not significant but the difference in a_1 of FAD clearly is. This shows that 2D histogramming of the two a_1 against one another is a possible way to combine the information from NADH and FAD data.

Another possibility would be to display the FAD/NAD(P)H intensity ratio on the vertical axis. If low FAD intensity, either by low concentration or low redox ratio, is a cancer indicator this would add important information to the NAD(P)H a1 data. In any case, further work appears necessary to make the FAD signal a reliable source of clinical information.

Metabolic Imaging by Macro FLIM

Metabolic FLIM can be performed with the bh DCS MACRO system, see page 439. In the simplest case, the sample is excited by a 375-nm BDS or BDL laser, and the fluorescence of NADH is detected between 440 and 470 nm. To determine the metabolic state double-exponential decay analysis is required, which requires to record about 1000 photons within the binning area in SPCImage [174]. It has been shown that this is well within the reach of the DCS MACRO system [184, 802, 803, 804, 1131, 1143, 1145, 1376]. Metabolic FLIM with the DCS-120 MACRO system is therefore a real option for the investigation of tissue samples from tumor surgery. The FLIM data would not show whether the excised tissue is cancerous or not, but also deliver valuable information on the metabolism of different tumor tissues.

Two examples are shown in Fig. 757 and Fig. 758. Fig. 757 shows an open tumor in a mouse and a freshly excised rat brain with a glioblastoma. The image is false-colour images of the amplitude of the fast (unbound) decay component, a1, of NADH. Decay curves from the tumor region and the healthy tissue are shown on the right.

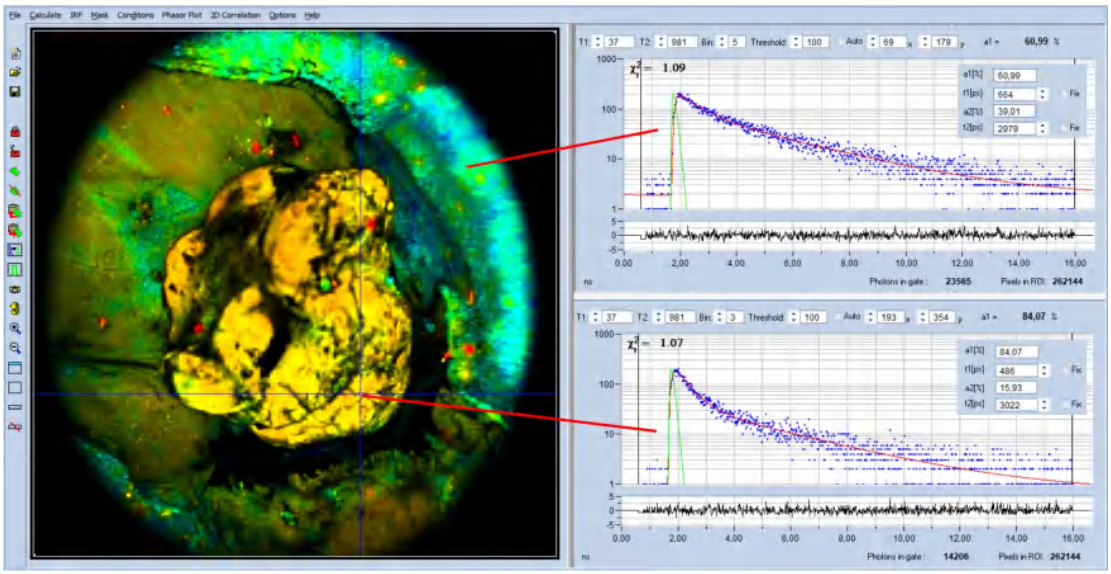


Fig. 757: Open tumor in a mouse. NADH image, excitation 375 nm, detection 430 to 475 nm. Image size 15 x 15 mm. False-colour image of the amplitude, a1, of the unbound NADH component.

Fig. 758 shows a similar image of a freshly excised rat brain with a glioblastoma. The acquisition time for both images was about 100 seconds, the data were analysed by the maximum-likelihood fit of SPCImage NG. The decay parameters of the mouse tumor are exactly as expected. The component lifetimes are the typical ones for NADH, and the amplitude, a1, is 61 % in the normal tissue and 84 % in the tumor.

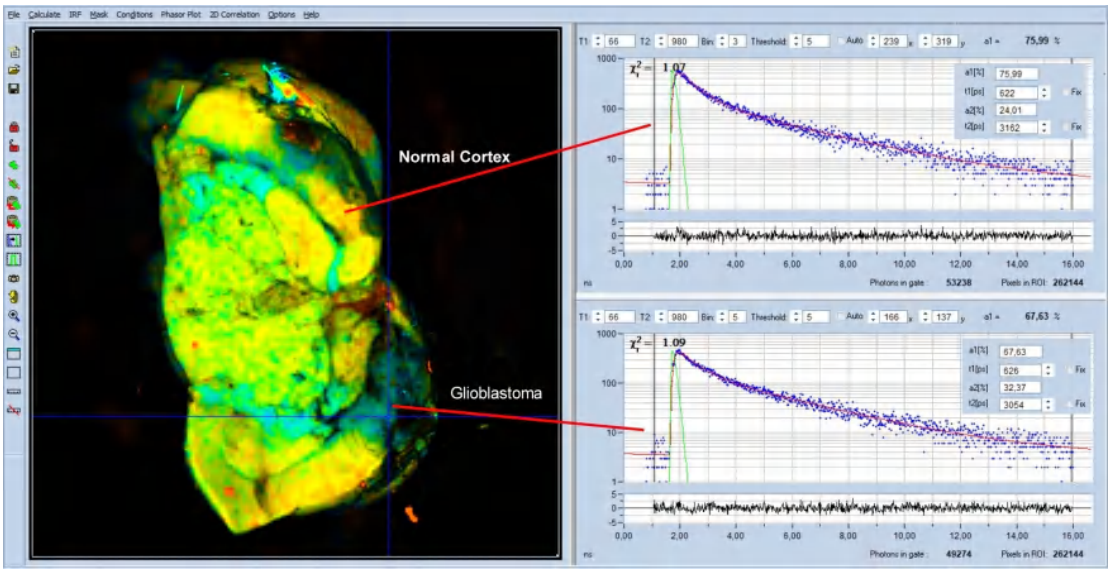


Fig. 758: Rat brain with glioblastoma (right). Autofluorescence, excitation 375 nm, detection 430 to 475 nm

The rat brain shows entirely different spectroscopic behaviour. Also here, the lifetimes are in the range expected for NADH. However, the amplitude, a1, does not follow the expected trend. It is 75% in the normal brain tissue and 67% in the tumor. This is the opposite of what has to be expected. It is not clear what causes this discrepancy. It is possible that glioblastoma just do not follow the usual trend. However, it is also possible that the unusual a_1 is a reaction of the tissues to the environment conditions. There is no perfusion, the temperature is not in the physiological range, and the partial pressure of O_2 and CO_2 is not in the correct range. Brain tissue has a high metabolic rate. From this point of view, deviations from the normal behaviour appear plausible. Especially the fact that a_1 of the normal brain tissue is in the tumor range supports the assumption that the tissue became hypoxic. The possibility of hypoxic conditions is supported also by [1376] where a_1 is in the glycolysis range (above 70%) both for the glioblastoma and the normal brain tissue. Further investigation, such as measurement of a brain by a fibre-based system, are necessary to make final conclusions. Additional information could also be derived from the recording of FAD FLIM images.

The MACRO FLIM system can be extended to simultaneous measurement of NADH and FAD. Two lasers, 375 nm and 420 nm, would be multiplexed in time, and FLIM data of the two fluorophores recorded in two spectral emission channels. Please see 'Metabolic Imaging by Simultaneous FLIM of NADH and FAD', page 375.

A inconvenience of MACRO FLIM is that the detection efficiency is lower than when the scanner is attached to a microscope. The acquisition times are therefore relatively long. The reason is the low NA of the detection light bundle in the image plane of the scanner. It could be increased by larger galvanometer mirrors in the scanner, but the options for that are limited by mechanical restrictions. The effect on the acquisition time can, however, be compensated by higher laser power. Due to the large scan are, the excitation light is distributed over a large area. An increase of the laser power by a factor of 10 or more should therefore not induce invasive effects on the sample. Suitable lasers, such as frequency-multiplied fibre lasers, OPOs or Ti:Sa Lasers are available. The only obstacle to their widespread application is the high price of these laser system.

Metabolic Imaging Combined with pH Imaging

The NAD(P)H lifetimes in the mitochondria of a cell are influenced by local pH. It has therefore been suggested to supplement metabolic FLIM measurements by pH measurement. In measurements using the fluorescence lifetime of NAD(P)H the pH can be used to correct the

results for the pH dependence, in amplitude-based measurements it delivers additional information on the status of the cell [1066]. In such experiments, it is, of course, desirable to run the pH measurement simultaneously with the measurement of the metabolic state. This requires two parallel TCSPC FLIM channels. One is used for the NAD(P)H, the other for a pH-sensitive fluorescence probe.

A good candidate for a pH probe is BCECF (2′,7′-bis-(2-carboxyethyl)-5(6) carboxyfluorescein). It has a relatively large pH dependence of its fluorescence lifetime [553], it can be excited at the same wavelength as NAD(P)H, its emission spectrum does not overlap much with the emission of NAD(P)H, and it has no toxic effects on cells and tissues.

For the experiments described here we used a DCS-120 MP two-photon FLIM system with a femtosecond fibre laser [128]. The laser has an emission wavelength of 785 nm. Two-photon excitation at this wavelength excites both the NAD(P)H and the BCECF at reasonable efficiency. The fluorescence of the two compounds was collected via a non-descanned beam path and split spectrally by a dichroic beamsplitter and filters. The signals were recorded in two parallel TCSPC FLIM channels of the DCS-120 system. With the HPM-100-40 detectors and the SPC-180NX FLIM modules used in this system the IRF width is about 85 ps, full width at half maximum.

A typical result is shown in Fig. 759. The NAD(P)H image (on the left) shows the amplitude-weighted lifetime, τ_m, as it is normally used in metabolic FLIM. For the BCECF image we used the intensity-weighted lifetime, τ_i, because it is the closest match to the phase-and-amplitude lifetime used in [553]. The τ-pH curve published in [553] therefore applies also to the BCECF lifetimes in Fig. 759, right.

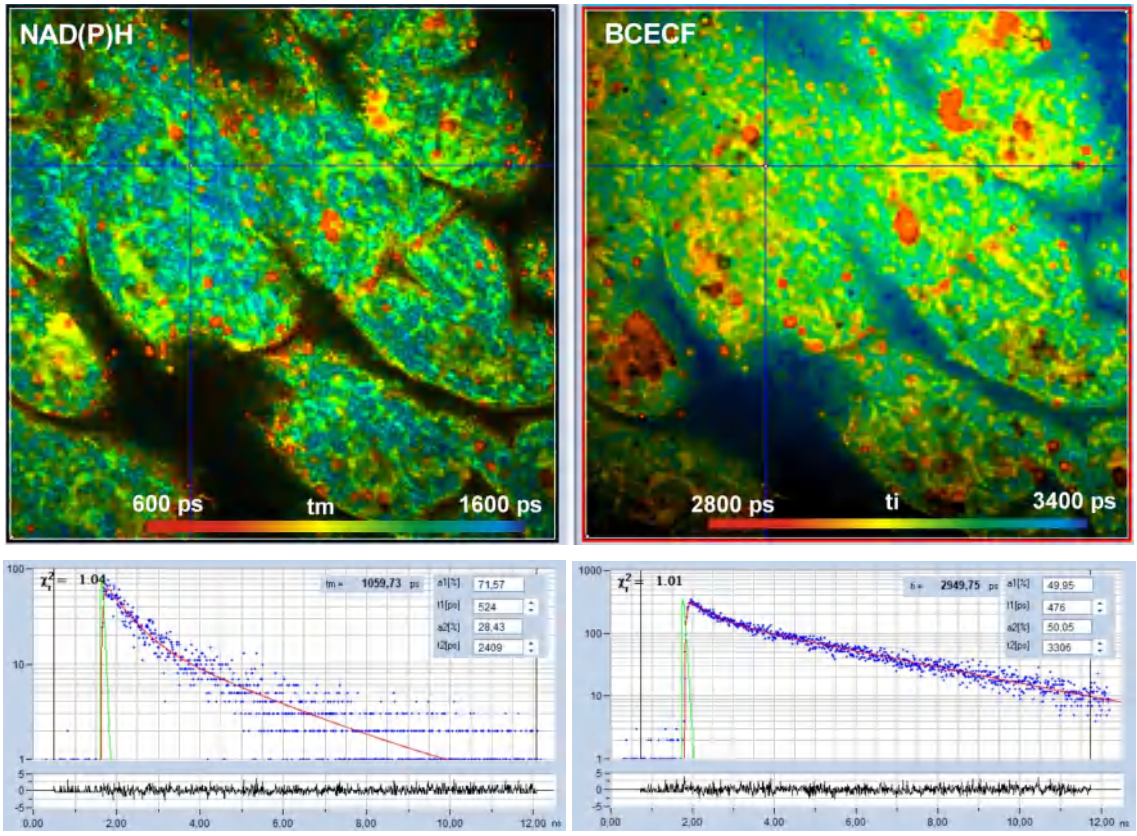


Fig. 759: Upper row: NAD(P)H image of the amplitude-weighted lifetime, t_m, and intensity-weighted lifetime image of BCECF. Lower row: Decay function of NAD(P)H and decay function of BCECF at cursor position. Both images 512 x 512 pixels, 1024 time channels. Data analysis with bh SPCImage NG, MLE fit.

Fig. 759 uses weighted averages of the component lifetimes, τ_1 and τ_2, to characterise the metabolic state and the pH of the tissue. As mentioned above, fluorescence lifetimes are not

the most reliable parameters to characterise the metabolic state. A more reliable way to characterise the metabolic state by the relative amount of free NAD(P)H, a_1, or the ratio of bound/free NAD(P)H, a_1/a_2.

A similar consideration applies also for the BCECF. Different pH induces differences in the relative amounts of protonated and de-protonated BCECF. These have different fluorescence lifetimes. As a result, a1 shows the relative amount of protonated BCECF, a1/a2 the ration of protonated and de-protonated BCECF.

Images of the amplitude, a_1, of the fast decay component for NAD(P)H and BCECF are shown in Fig. 760. For technical details and possible pitfalls please see [134].

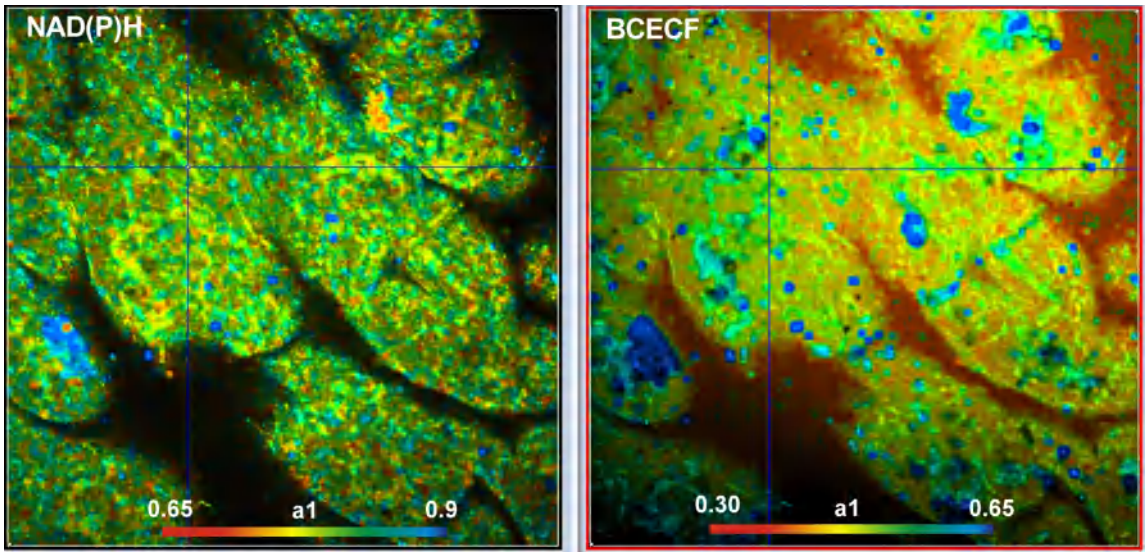


Fig. 760: NAD(P)H image (left) and BCECF image (right) of the amplitude, a_1, of the fast decay component. In the NAD(P)H image a1 represents the fraction of unbound NAD(P)H, in the BCECF image it represents the amount of protonated BCECF.

Complex Decay Behaviour of NADH and FAD

NADH: Additional Decay Components

The fact that a double-exponential model fits the decay curves of NADH well does not mean that there are only two decay components. In fact, there is direct evidence that the ‘fast’ and the ‘slow’ decay components consist of several sub-components. There are reports that the fluorescence of NAD(P)H in cells has at least three, if not four components [225, 438, 1363, 1364]. This is confirmed by data obtained with the bh ultra-fast hybrid detectors. Fig. 762 shows a 2-photon NAD(P)H image of live 'Ishakawa' cells. A double-exponential fit in an area of 5x5 pixels delivers a good fit with component lifetimes of 356 ps and 2546 ps. A triple-exponential fit splits the slow component into two, even though it does not yield a visibly better fit quality. The component lifetimes are 290 ps, 1393 ps, and 5868 ps, see Fig. 762.

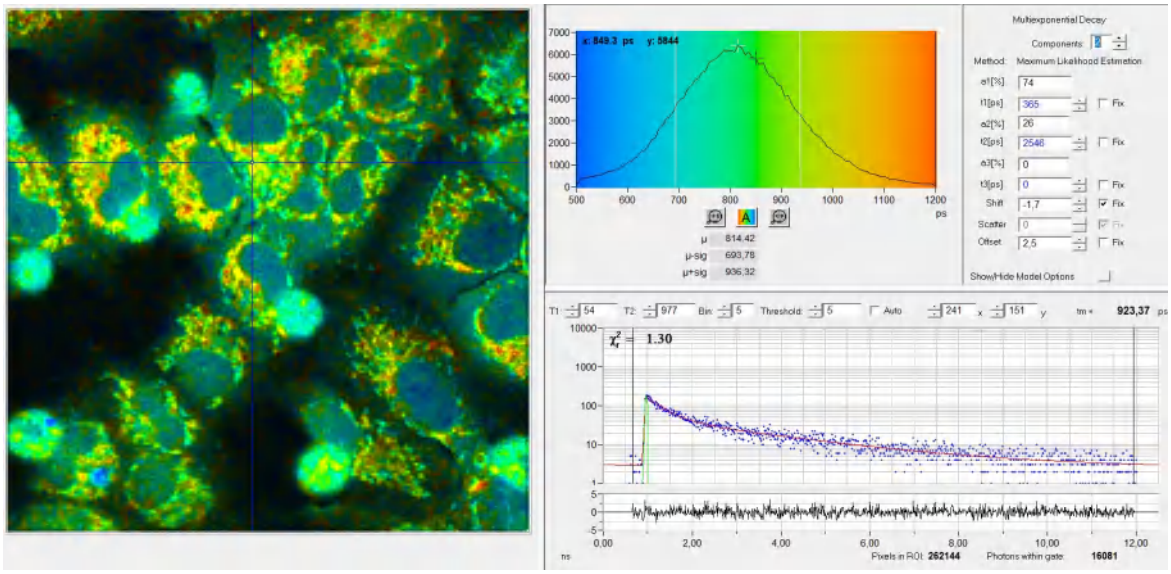


Fig. 761: NAD(P)H FLIM with ultra-fast detector, IRF width <20 ps. A fit with a double-exponential model delivers component lifetimes of 356 ps and 2546 ps.

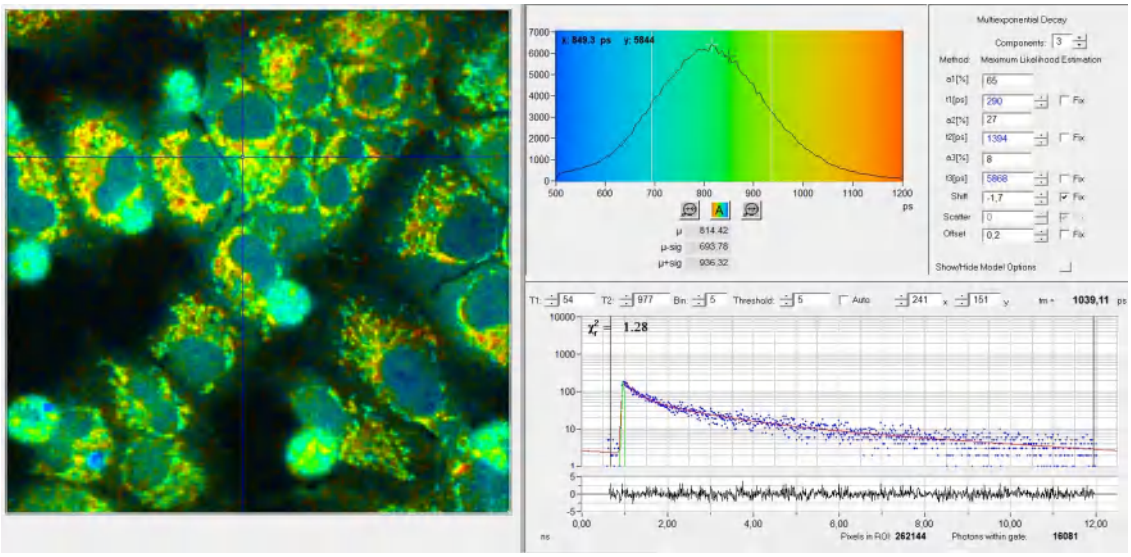


Fig. 762: NAD(P)H FLIM with ultra-fast detector, IRF width <20 ps. Triple-exponential analysis shows three decay components, with lifetimes of 290 ps, 1393 ps, and 5868 ps.

Often additional components can only be identified in data from larger areas, either by binning pixels, or by defining regions of interest and combining the decay data of the pixels. However, the component lifetimes can also be different in different compartments of the cell, and even different in different mitochondria. An example is shown in Fig. 763. It shows an image of the slow (bound) component of NAD(P)H obtained from the usual double-exponential fit. Similar differences can be found in the fast component, see 'NADH FLIM with Ultra-Fast Detectors', page 365.

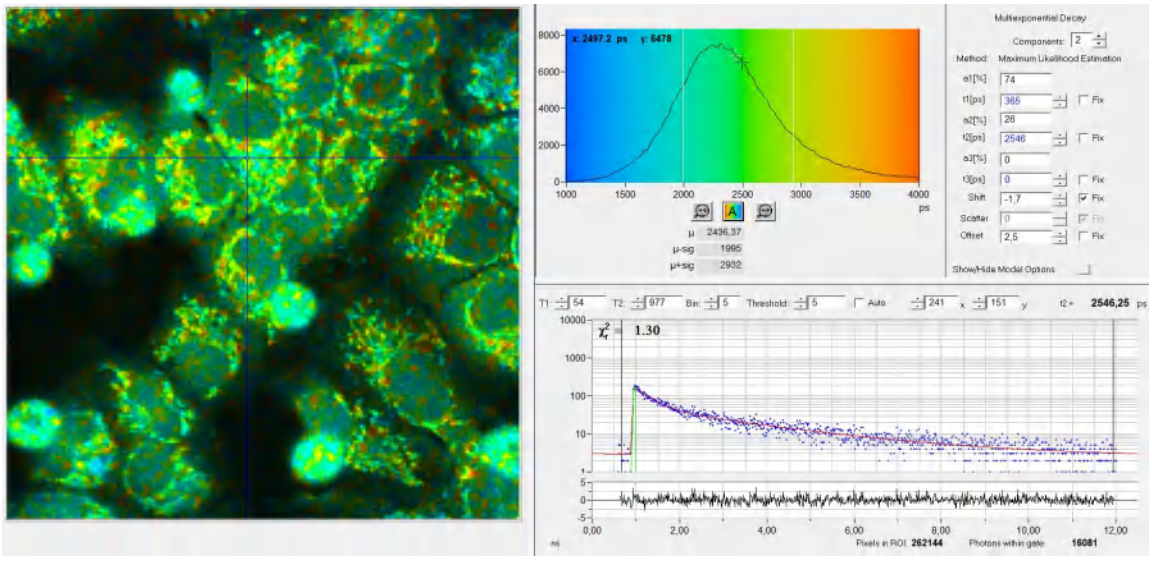


Fig. 763: Image of the lifetime of the slow component, t_2, from the double-exponential model. Different mitochondria have different t_2.

Caution is recommended when NADH FLIM is performed in tissue. Especially in skin tissue there can be other fluorophores which interfere with NADH. Especially Keratin has excitation and emission spectra which overlap those of NADH and FAD [813]. In how far contamination of the metabolic-FLIM signature can be avoided by image segmentation or by including the known lifetime of Keratin in the decay analysis as a fixed component is not know.

FAD: The FMN Problem

Also for the FAD, there are indications that the decay functions contain more than two components. More importantly, it seems that the signal recorded in the FAD channel does not always come from FAD (flavin adenine dinucleotide) alone but also from FMN (flavin mononucleotide). FMN has the same fluorescence spectrum as FAD but a longer lifetime.

Fig. 764 shows an FAD image of freshly excised human epithelial bladder cells, please see page 537 for details. The sample was imaged by laser-multiplexing and detection in an NADH channel and an FAD channel. According to the NADH images, the sample contains mostly normal cells, but also a few (possibly tumorous) cells with an enhanced fraction of free NADH. In Fig. 764, an ROI was chosen which contains only cells that qualify 'normal' in the NADH channel. The decay curve of the combined pixels within the ROI is shown on the right. Triple-exponential analysis clearly delivers a decay component of 4.8 ns, present with an amplitude of 3.9%. A lifetime of 4.8 ns cannot be attributed to FAD, but very well to FMN.

Fig. 765 shows the same data, but the ROI was set on cells which are classified as 'low grade cancer' in the NADH image. The lifetime of the third component is 3.38 ns, not much different than in Fig. 764. However, the amplitude has increased to 8.84%.

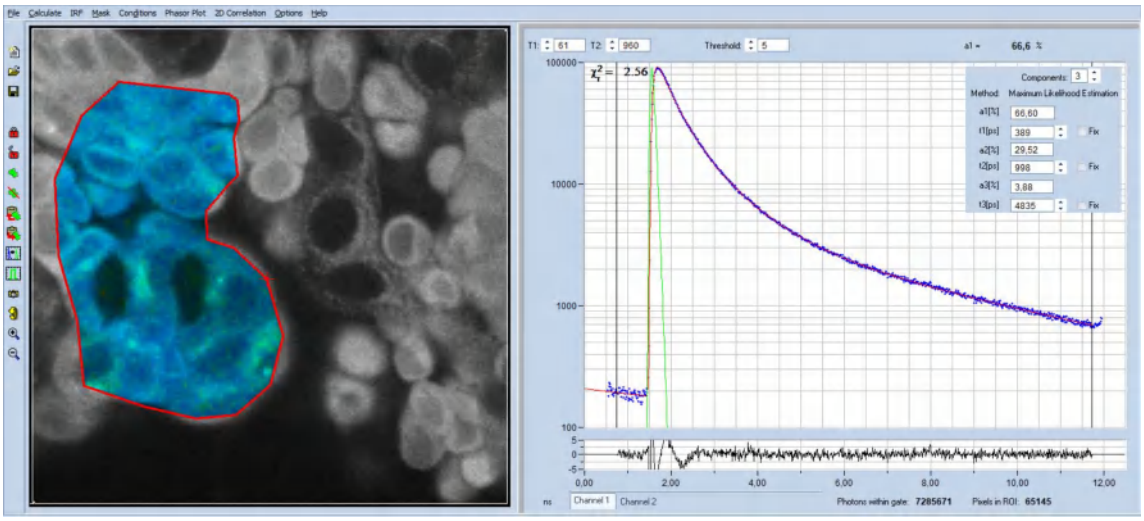


Fig. 764: Left: FAD Image of human epithelial bladder cells. The region of interest includes healthy cells only. Right: Decay curve of combined pixels in ROI, and triple-exponential fit. The third component, with t_3 = 4.83 ns and a_3 = 3.88%, is compatible with FMN.

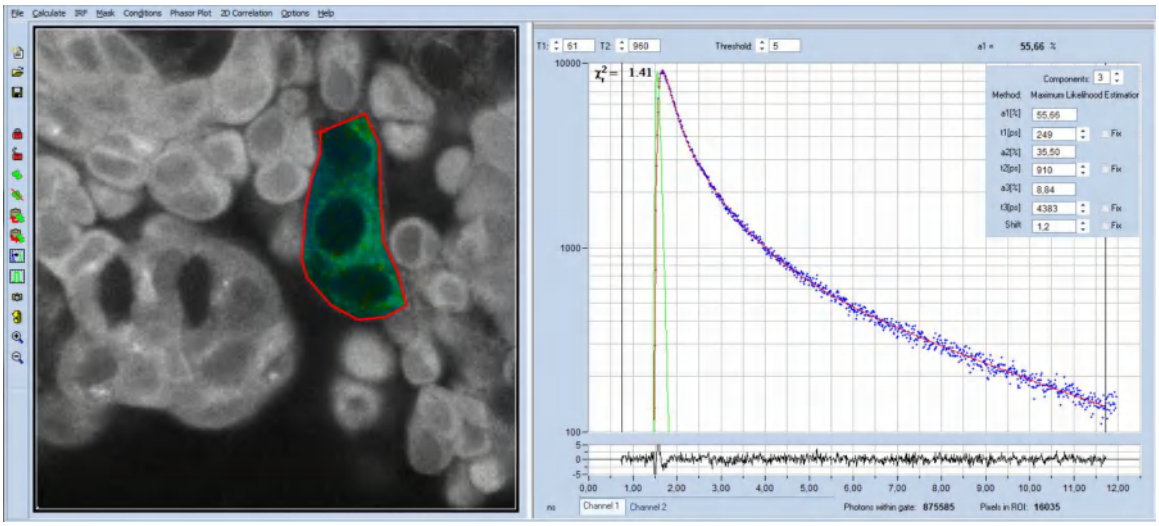


Fig. 765: Same data as in Fig. 764, but ROI on cells which are probably tumor ells. The third component is t_3 = 4.38 ns and a_3 = 8.84%.

The presence of a decay component from FMN can have implications to metabolic imaging, especially if FAD data are used for cancer diagnosis. Certainly, an amplitude contribution of 3.8% or even 8.84% from FMN does not render the FAD data useless. It can, however, introduce unpredictable shifts in the metabolic parameters. The results can then no longer be considered quantitative. The shifts have not only consequences to the amplitudes, a1 and a2 which are determined for FAD, but also on FLIRR values derived from them. Kalinina et al. therefore suggested new definitions of the FLIRR based on triple-exponential analysis of FAD [638].

In Fig. 766 an attempt was made to extract the amplitudes of bound FAD (t1), unbound FAD (t3), and FMN (t3) from FLIM data on a pixel-by pixel basis. With all three lifetimes and amplitudes freely floating the result is not satisfactory [135]. However, when the lifetimes are fixed to the most frequent values (see SPCImage, Pseudo-Global Analysis) clean images of the amplitudes are obtained.

Of course, a pseudo-global fit with fixed component lifetimes is prone to user errors. If only one component lifetime is fixed to a wrong value large errors in the other lifetimes and, even more, in the amplitudes are induced. SPCImage NG, version 9.0 therefore has a global-fit procedure implemented. The procedure fits the decay data under the assumption that the com-

ponent lifetimes are unknown, but otherwise the same in all pixels of the image. For principles and pitfalls please see [135] and section 'Global Analysis' in this book. A result is shown in Fig. 766.

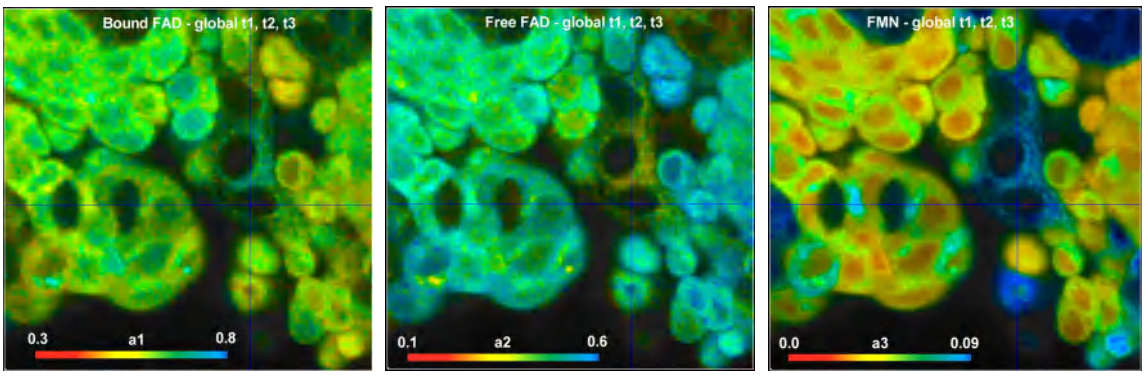


Fig. 766: Left to right: Amplitudes, a1, of bound-FAD decay component, a2, of unbound FAD component, and FMN, a3. Global Fit by SPCImage MLE.

As can be seen from Fig. 766, right, there is a large difference in the amplitude, a3, of FMN between the tumor cells and the normal cells. There may be different reasons for that. The first one is that there is simply less FAD in the tumor cells. Another plausible reason may be different redox ratio. The amount of oxydised FAD compared to reduced FAD is then lower, and so are the fractional contributions of the FAD component, a1 and a2. Since the sum of the amplitudes is $a_1 + a_2 + a_3 = 1$ the amplitude of FMN, a3, increases. A third possibility is that there is more FMN in the tumor cells. However there is no theoretical explanation for that. More research on the FAD and FMN fluorescence dynamics and its dependence on the metabolic state is required to settle these questions.

Unmixing NAD(P)H / FAD Fluorescence Components

Additional information on the NAD(P)H / FAD fluorescence can be obtained by multi-wavelength FLIM with the bh PML-16 C and PML-16 GaAsP detectors [62], see page 366. The separation of the signals from NAD(P)H and FAD can then be improved by spectral unmixing of the components, distinct spectral components within the emission spectra of NAD(P)H and FAD can be determined, and previously unknown decay components can be discovered [156, 293, 300, 301, 303 1036, 1037, 1038]. Typical multi-wavelength autofluorescence data are shown in Fig. 767. Two-photon excitation at a wavelength of 750 nm was used. This wavelength excites both NAD(P)H and FAD. Each of the images covers a wavelength range of about 12.5 nm. The colour of the images represents the lifetime obtained from a single-exponential fit.

Due to the different fluorophores present in the tissue, the lifetimes in the individual wavelength intervals are different. The third left image contains a strong SHG component. SHG reveals itself as an infinitely short lifetime component, see the blue features in the third to left image.

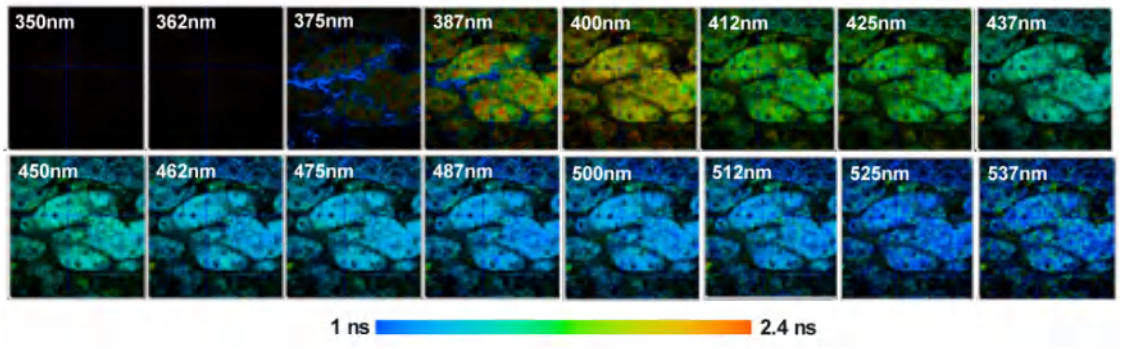


Fig. 767: Multi-wavelength fluorescence lifetime images of a mouse kidney section. Two-photon excitation at 750 nm. Images in subsequent wavelength intervals from 350 nm to 550 nm.

Fig. 768 shows the fast lifetime component, the slow lifetime component, and the amplitude ratio of both for a wavelength interval from 430 to 480 nm. The fluorescence in this interval is dominated by NADH. The lifetime of NADH is known to depend on the binding to proteins [741, 742, 950]. The images can therefore be expected to represent different binding states of NADH.

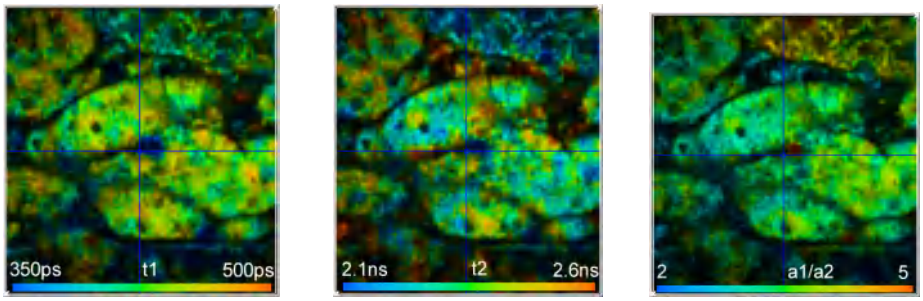


Fig. 768: Images of the lifetime components and amplitude ratio of a double exponential fit, 430 to 480 nm interval

An interesting application of multi-wavelength lifetime detection of NADH has been published by Chorvat et al. [304]: The authors used the data to detect early stages in the metabolism of isolated live cardio-myocytes in cases of rejection of transplanted hearts.

An overview about autofluorescence multi-wavelength FLIM is given in [303]. Full exploitation of multi-wavelength autofluorescence FLIM data requires a global fit with a suitable model that includes the effective spectra of the expected fluorophores. The task is extremely difficult because some of the endogenous fluorophores are in fact mixtures of slightly different compounds, with different absorption and emission spectra [1094]. Moreover, there may be absorbers of unknown absorption spectra, inhomogeneous distribution, and unknown concentration in the tissue. Nevertheless, there is currently a number of approaches that are likely to solve at least a part of the problem [300, 301, 303, 983].

Review of NAD(P)H / FAD FLIM Literature

General Evaluation of NAD(P)H Decay Parameters

An overview on NADH / FAD fluorescence dynamics has been given by Chorvat and Chorvatova [303] and by Heikal [572]. Ghukasyan and Kao [502] have shown that the NADH decay parameters, in particular amplitudes of the fast and slow lifetime components, are indicators of physiological and pathological states of the cells. Changes in the unbound-bound ratio of NADH with the shift from oxidative phosphorylation to glycolysis were confirmed by using FLIM and phasor plot analysis [744]. Differentiation between apoptosis and necrosis by the NADH lifetime components was described by Wang et al. [1321].

Early experiments of Skala et al. [1155, 1156] performed with two-photon excited autofluorescence FLIM delivered lifetime images of NADH in normal and pre-cancerous epithelia. They found a significantly decreased lifetime of the slow decay component, of the bound NADH, in precancerous tissue. A significant decrease of the lifetime of the protein-bound FAD was detected in high-grade pre-cancers [1156]. Bird et al. used a similar approach for metabolic mapping of human breast cells [213]. Yu & Heikal found statistically relevant differences in the free/bound NADH ratio in normal cells and breast cancer cells [1373]. Majumder et al. report on metabolic changes in cochlea cells upon sensorineural hearing loss [811].

Heikal et al, Vishwasrao et al, and Yu et al. showed that independent information on the unbound/bound ration of NADH can be obtained by recording fluorescence anisotropy decay data of intracellular NADH [324, 572, 1290, 1373].

Response to Laser Irradiation

Alam et al. have investigated changes in the decay parameters of NAD(P)H on exposure to the excitation laser. They found that the metabolism had shifted towards increased OXPHOS (oxydative phosphorylation) after exposure to increased laser power [11]. This is an indication that the laser power should be kept under strict control when metabolic FLIM is performed. Interestingly, the changes were only in the a1/a2 ratio, not in the component lifetimes, τ_1 and τ_1. This is another indication that the lifetimes and the amplitudes are independent parameters of the NADH fluorescence decay.

Tumor Identification, Tumor Metabolism

Metabolic imaging of melanoma progression was performed by Pastore et al. [946]. They confirm a significant increase in the unbound / bound (a1/a2) ratio of NADH with the growth of a melanoma tumor. The increase a1/a2 caused an increase in the t_m lifetime, while the lifetimes of the decay components themselves remained constant. Similar results were found in tumors of the human respirators tract [427]. Kantelhardt et al. [643] and Leppert et al. [758] recorded two-photon excited lifetime images of glioma and the surrounding brain tissue. Surprisingly, they found a significantly *increased* mean (amplitude-weighted) lifetime for the glioma cells compared to the surrounding brain cells.

Effects of a nanosecond-pulsed electric field in normal and cancer cells was investigated by Awasthi et al [37]. They found changes both in the intensity and the lifetime of NADH. The NADH FLIM signature shows that apoptosis was induced in the cancer cells. Based on these results, the authors suggest the application of pulsed electric fields for drug-free cancer therapy. An overview on exploring tumor metabolism by NADH / FAD FLIM has been given by Shirmanova et al., please see [1143]. There are many more publications on FLIM-based tumor detection, see, for example [173, 323, 324, 563, 613, 801, 803, 943, 1126, 1158, 1211].

Impact of Coenzyme Q_{10}

Wieland et al. used FLIM to study the effect of coenzyme Q_{10} on the mitochondrial metabolism [1337]. In fibroblasts of ten different donors treated with Q_{10} they found increased NADH lifetimes compared to untreated cells. This is an indication that Q_{10} caused a shift in metabolism towards oxydative phosphorylation. It is therefore possible that Q_{10} facilitates the development of good cells and impedes the development of cancer cells. This is an intriguing possibility, and it can easily be followed up by metabolic FLIM.

Response to Chemotherapy

NADH FLIM is closely related to efficiency of cancer drugs in chemotherapy. Skala and Walsh used NADH FLIM to evaluate the effect of different cancer drugs on cells from biop-

sies from patients, and to develop the best treatment strategy [506, 1126, 1315, 1316, 1317, 1318, 1319]. The cells are cultured, the cell cultures are treated with the drugs, the cells are repeatedly imaged by FLIM. The OMI index is used as an indicator of the response to the drugs [1125, 1315, 1316, 1317, 1318, 1319]. Within a few days, the most efficient drug can be determined and a treatment strategy for the patient be developed. If the technique can be transferred into clinical use it has the potential to revolutionise cancer treatment.

Shah et al. [1121] investigated heterogeneity in the response to cetuximab and cisplastin. The aim of this work was to avoid that subpopulations of cells escape the anti-cancer treatment and later cause relapse in cancer patients. Stunz et al. [1199] studied the response of cultured rat astrocytes and neurons to manganese treatment.

Shirmanova et. al. [1142] demonstrated the relationships between the intracellular pH and the metabolic state derived from NAD(P)H / FAD FLIM in response to treatment with cisplatin. They found a metabolic shift from glycolysis towards oxidative metabolism during cisplatin-induced inhibition of cancer cell growth in vitro and in vivo. Lukina et al. report on experiments with paxlitaxel [802], Yuzhakova et al. used NAD(P)H FLIM to explore the response of patient-derived glioblasoma to temozolomide (TMZ) [1377]

Using a molecular rotor, Shimolina et al. studied the change in membrane viscosity of cancer cells in response to treatment with Oxaliplatin [1139].

Sergeeva et al. [1116] performed metabolic imaging of NAD(P)H and FAD, and simultaneously used the genetically encoded pH-indicator SypHer1 and the FRET-based mKate2-DEVD-iRFP sensor for pH imaging and caspase-3 activity imaging. They found a relationship between the metabolic state derived from NAD(P)H FLIM, intracellular pH and caspase-2 activation during apoptosis. Induction of apoptosis was accompanied by a switch to oxidative phosphorylation, cytosol acidification and caspase-3 activation.

Response to Drugs

The effect of Ouabain, a pharmaceutical drug, and of 4-hydroxynonenal on live cardiomyocytes was studied by Chorvatova et al., see [305] and [306]. Alex et al. used in-vivo FLIM to study the spatial distribution and residency of a topically delivered drug in the epidermis and dermis of human patients [13]. Yuzhakova et al. used NAD(P)H FLIM to explore the response of patient-derived glioblasoma to temozolomide (TMZ) [1377]. Tasmi et al. studied metabolic changes in response to different doses of Propofol [1232].

Infection and Infection Defence Mechanisms

NADH FLIM can be used to show metabolic changes during infections. Szaszak et al. [1217] used the NADH fluorescence to track metabolic changes in the host and in the pathogen during intracellular infectious by *chlamydia trachomatis*. Buryakina et al. showed changes during infection of HeLa cells with enterohemorrhagic *Escherichia coli* [263]. Szulczewski et al. used NADH FLIM for metabolic imaging of macrophages in a tumor environment [1219], Gallego-Lopez measured metabolic changes caused by *Toxoplasma gondi* infection [481].

T Cells and Macrophages

Walsh et al. performed autofluorescence of T cells [1320]. They were able to classify the cells based on the τm of NAD(P)H, the τm of FAD, and the redox ratio. Heaster et al. [563, 564] used τm of NADH and FAD in combination with the redox ratio to assess macrophage heterogeneity on the cell level. Izosimova et al. investigated T cells in normal and tumor-bearing mice by FLIM of NADH [613]. In the tumor mice, they found an increase in a_1, i.e. an increase in free NADH. Moreover, triple-exponential analysis showed that a decay component from NADPH appeared which was not detectable in normal mice.

Wound Healing

Gehlsen et al. [490] recorded NADH lifetimes and bound/unbound NADH ratios during wound healing of corneal epithelial cells. They compared the results to lifetimes obtained at different temperature, and during suppression of mitochondrial electron transport by Rotenone. Other wound healing studies were performed by Deka et al. [364]. They showed that the 'metabolic rate' (revealed by the amplitude-weighted lifetime of NADH) increased after injury, and then gradually decreased. Simultaneously, collagen built up (revealed by SHG signal). A FLIM study on the uptake and excretion of fluorescein in hepatic reperfusion injury was presented in [1244]. Alterations in NADH FLIM data of rat aorta induced by diabetes mellitus are described by Uherek et al. [1271]. Batista et al. report on combined NADH FLIM and SHG measurements of porcine cornea [54]. Jones et al. used the redox ration and the a_1/a_2 ratio to compare wound healing diabetic and normal mice [631].

Metabolic FLIM of Oocytes

Sanchez et al. have shown that 2-photon excited FLIM of NAD(P)H and FAD can be used to differentiate normal oocytes from those with metabolic dysfunctions [1045]. The authors used the fluorescence intensities, the component lifetimes, τ_1 and τ_2, and the amplitudes of the bound component to quantify the metabolic state of mouse embryos. The authors also conducted studies of the impact of the illumination on the blastocyst development rates. They did not find a measureable differences between embryos that has been exposed to the FLIM measurement and reference embryos which had not been illuminated. More publications related to metabolic FLIM of oocytes have appeared in the following years: Metabolic FLIM combined with SHG imaging of the spindle [1046] proved useful for embryo assessment, differences in the metabolic parameters of euploid and aneuploid blastocytes [1122], variations in the metabolic parameters between different blastocytes and within the same blastocytes over time [1287], and changes with patient age and between mature and immature oocytes were found [1286]. Yang et al. developed model that relates changes in the metabolic parameters obtained by FLIM to mitochondrial metabolic pathways [1362]. A overview on non-invasive metabolic profiling of cumulus cells, oocytes, and embryos by FLIM has been given in [1288].

Liver Tissue

Thorling et al. give a review on the use of multiphoton microscopy in combination with FLIM in defining liver function [1246]. Rodimova et al. studied the metabolic state of liver tissue during the regeneration process [1030]. They found a significant increase of bound NAD(P)H during liver regeneration. This indicated a metabolic shift towards oxydative phosphorylation. In parallel, they used mass spectrometry to study the lipid and amino acid composition. During regeneration, mass spectrometry showed an increase in the triglyceride signals and cholesterol signals, and a decrease in amino acids and sphingomyelin. Another study from the same group compared double-exponential and triple-exponential analysis approaches, and evaluated the influence of contributions of FAD, collagen and elastin to the detected signals [1029]. Moreover, the authors extensively studied the influence of the preservation conditions on the FLIM results. Only with preservation of liver tissue in 10% BSA [803] and storage on ice the metabolic state remained stable within an observation time of 3 hours.

Barkanauskas et al. used nonlinear regression to estimate the lifetimes of unbound and bound forms of NAD(P)H and FAD, the amplitude ratio, a_1/a_2, and the fluorescence-lifetime redox ratio (FLIRR) [49]. They also examined the impact of image segmentation. Both the amplitude ratio and the FLIRR were found useful for discrimination of diseased liver from healthy liver. These parameters provided a far better insight into the tissue state than the global mean fluorescence lifetime, t_m.

Brain Tissue

Metabolic-FLIM for Brain tissue has produced inconsistent and often contradicting results. Kantelhardt et al. [643] and Leppert et al. [758] found a significantly increased mean (amplitude-weighted) lifetime for the glioma cells compared to the surrounding brain cells. This is in contraction to the model that tumor cells have more free NAD(P)H and, consequently, a larger amplitude, a1, of the fast lifetime component. It could be suspected that the data were biased by inappropriate storing conditions or inappropriate filtering. However, more recent results show similar inconsistencies. Lukina et al. performed FLIM measurement of macroscopic brain samples by a bh DCA-120 MACRO system [804]. The excitation wavelength was 375 nm, the detection wavelength 435 nm to 475 nm. Both samples from rat brains and from human brains were investigated. The decay data were analysed by fitting with a double-exponential model. In both cases, the lifetimes of the decay components were significantly higher than normally found for NAD(P)H in biological tissue. In the rat brains τ_1 = 0.78 to 0.94 ns and τ_2 = 3.32 to 5.03 ns was found. The values for human brain samples were τ_1 = 1.6 ns and τ_2 = 7.8 ns. These values suggest that the fluorescence does not come from NADH or NADPH alone.

In rat glioblastoma t_m in the tumor was found shorter than in the tumor-distant cortex and the tumor-distant white matter, and shorter than in the healthy brain. In glioma t_m was only insignificantly shorter than t_m in the tumor-distant cortex and the tumor-distant white matter. It was, however, substantially shorter than in the healthy brain. t_m in anaplastic astrocytoma followed the same trend. However, the a_1/a_2 ratios were inconclusive or even went in the unexpected direction, i.e. a decrease of a_1/a_2 was found in the tumor.

In human glioblastoma the t_m in the tumor, in infiltrated white matter, and in non-infiltrated white matter did not differ significantly. However, the component lifetimes in non-infiltrated white matter were shorter. The amplitude of the fast component, a1, and the amplitude ratio, a_1/a_2 were lower in the tumor, i.e. went in the expected direction. Please see [804] for details.

As can be seen from these results, the fluorescence decay behaviour of brain tumors still resists explanation. Storing conditions are unlikely a source of the problem, as was carefully checked [803] by the authors. The clue may be in the unusual lifetimes of the decay components. It appears likely that the components contain contributions from fluorophores other than NAD(P)H. The fast and slow decay component then cannot be attributed to free and bound NA(P)DH, and a_1/a_2 cannot be considered a free/bound ratio. Possible sources of additional decay components are discussed in [804]. NAD(P)H is certainly present but cannot account for the extremely long lifetimes found in the data. FMN can be excluded because it is not detected through the emission filter used. Other possible sources are collagens, myelin, cholesterol, and various phospholipids. There are several approaches to solve the problem. One of them is precision triple- and quadruple exponential decay analysis on combined pixel data. It could show whether 'normal' NAD(P)H decay functions are hidden behind the decay functions of unknown fluorophores. Also measurements at different excitation and emission wavelength with careful multiexponential decay analysis and multi-wavelength FLIM could help solve the mystery.

Neurons

Niederschweiberer et al. performed NADH FLIM measurements of neurons [913]. The authors had found earlier that the NADH decay times depend on the pH in the mitochondrial matrix [1066]. Therefore, they used two detection channels, one from 430 to 490 nm for the NADH and another for SypHer, a pH sensor. The NADH lifetimes were then corrected for the particular pH. It was found that the NADH lifetimes correlated with the overexpression strength of Alzheimer's disease-related proteins. Majumder et al. report on metabolic changes in cochlea cells upon sensorineural hearing loss [811].

Stem Cells

Gou at al. used FLIM of the decay components of NADH to distinguish human mesenchymal stem cells from differentiated progenies [535]. Uchugonowa & König applied two-photon autofluorescence lifetime imaging to human and animal stem cells [692, 693]. They found significant changes in the fluorescence lifetimes on differentiation and maturation of the cells. An example is shown in Fig. 769. The differentiated cells have smaller a_1/a_2 ratios and longer mean lifetime, t_m.

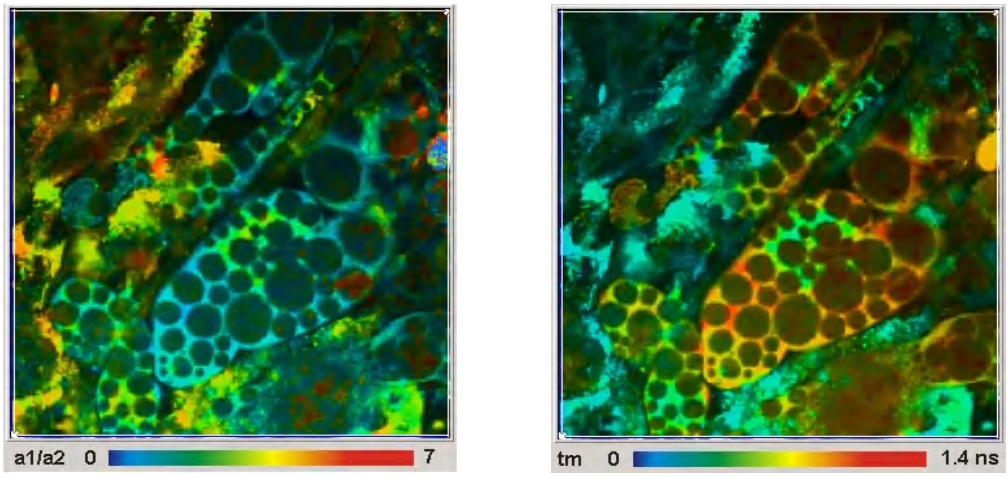


Fig. 769: FLIM of human salivary gland stem cells. Differentiated cells have significantly lower a1/a2 ratio and longer mean lifetime. Data courtesy of Aisada Uchugonova and Karsten König, Saarland University, Saarbrücken.

Meleshina et al. simultaneously tracked the redox ratio and the a_1/a_2 (unbound/bound) ratio during maturation of stem cells. For different stages of differentiation, they observed metabolic shifts both in the direction to glycolysis and to oxidative phosphorylation [849, 850]. Rodimova et al. Reported on spontaneous osteogenic differentiation on tissue-engineered constructs [1031]. Qian et al. used metabolic FLIM to track and predict the differentiation of stem cells into cardiomyocytes for regenerative medicine [988]. Molugo et al. tracked the reprogramming status of patient-derived elytroid progenitor cells to select high-quality donor-specific induced pluripotent stem cells (iPSCs) [886].

NADH / FAD FLIM with Tracking of the Cell Cycle

Shirmanova et al. developed a new variant of the cell cycle indicator FUCCI (fluorescent ubiquitination-based cell cycle indicator) [1144]. The variant, FUCCI-Red, utilises two fluorescent proteins, mCherry and mKate. Depending on the phase in the cell cycle, emission from one or the other fluorophore dominates the net fluorescence. Because the fluorescence lifetimes are different, the apparent lifetime is an indicator of the phase in the cell cycle. Different than for the original FUCCI, the fluorescence spectra of the two emission components of FUCCI-Red are closely the same. The signal can therefore be detected in a single spectral channel. Importantly, the emission is in the red region of the optical spectrum, and thus does not interfere with the emission from NADH and FAD. It is therefore possible to detect NADH FLIM, FAD FLIM, and FUCCI-Red FLIM simultaneously. As a result, the metabolic state of cells can be related to the phase in the cell cycle. The authors demonstrated the method on CT26 cancer cells.

Two-Photon FLIM of Mammalian Skin

A typical application of two-photon excited FLIM measurements of tissue autofluorescence is multiphoton optical tomography of skin [686, 1010]. The technique has been developed to the stage of clinical application [356, 690, 691, 692, 947, 1022, 1048, 1049]. Typical in-vivo images obtained at human skin are shown in Fig. 770.

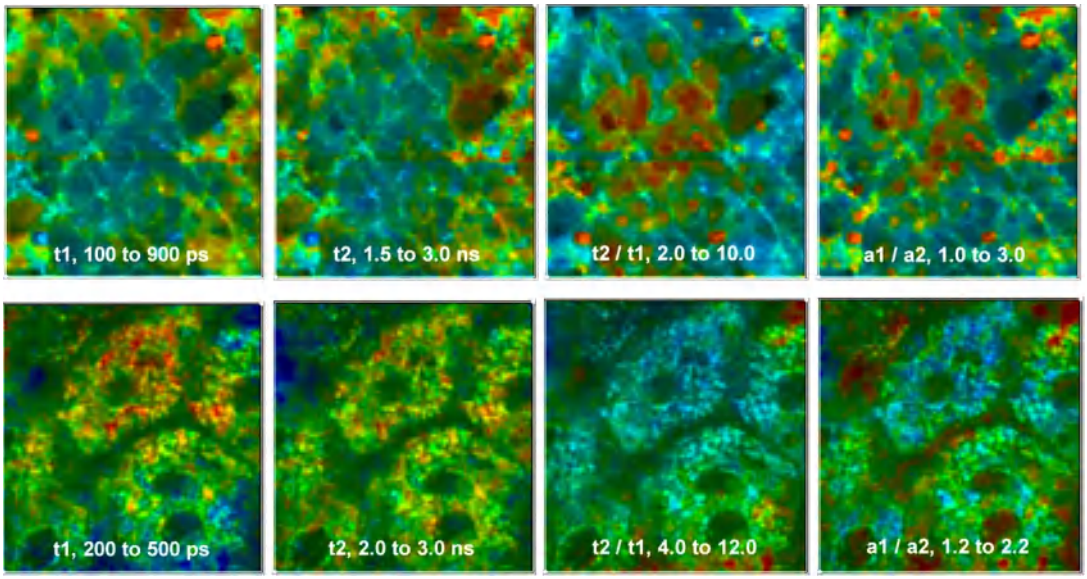


Fig. 770: Time-resolved in-vivo autofluorescence images of human stratum corneum and stratum spinosum. Left to right: Fast lifetime component, τ_1, slow lifetime component, τ_2, ratio of the lifetime components, τ_1/τ_2, and ratio of amplitudes, a_1/a_2. The indicated parameter range corresponds to a colour range from blue to red. Karsten König and Iris Riemann, Fraunhofer Institute of Biomedical Techniques, St. Ingbert, Germany.

The upper row shows the stratum corneum (upper row, 5 µm deep), the lower row the stratum spinosum (lower row, 50 µm deep). Double-exponential decay analysis was applied to the data. The colour represents the fast lifetime component, τ_1, the slow lifetime component, τ_2, the ratio of lifetime components, τ_1/τ_2, and the ratio of the amplitudes of the components, a_1/a_2.

Lifetimes, lifetime components, and intensity ratios in several spectral channels have been used by Patalay et al. to derive signatures of skin lesions [947]. They recorded skin FLIM data in a Dermainspect system with a bh SPC-830 module, see page 587. From the data of individual cells in images of several patients they built up scatter plots of component lifetimes vs. the fractional intensities of the components (note this is q_1 and q_2 in SPCImage), and of the mean (amplitude-weighted) lifetimes versus intensity ratios in different channels. They found differences in the distribution of the amplitude-weighted lifetimes for dysplastic nevi and nodular basal cell carcinoma. Differences also showed up in the scatter plots. The authors discuss whether the observed changes come from melanin or from NADH without coming to a final decision.

NAD(P)H imaging of melanoma progression was performed by Pastore et al. [946]. They confirm a significant increase in the unbound / bound (a_1/a_2) ratio of NADH with the growth of a melanoma tumor, while the lifetimes of the decay components remained constant.

FLIM measurements at human skin and the results obtained are supported by measurements with single-point tissue lifetime spectrometers [363, 1243], see page 324. An interesting result has been published by Pires et al. [976]. The authors excited human skin with two BDL-SMC ps diode lasers with wavelengths of 378 nm and 445 nm. The 378 nm predominately excites NADH, the 445 nm laser FAD. The fluorescence was detected at wavelengths of 440 nm (NADH) and 514 nm (FAD) and recorded by two SPC-150 channels. The decay curves were

analysed with a double-exponential model. This delivered the fast and slow decay times, τ_1, and τ_2, of the NADH and the FAD decay curves. With these values they plotted the frequency of the values of τ_{1FAD} versus τ_{2NADH} obtained from a large number of samples. The results delivered a clear discrimination between normal skin and melanoma, see Fig. 771.

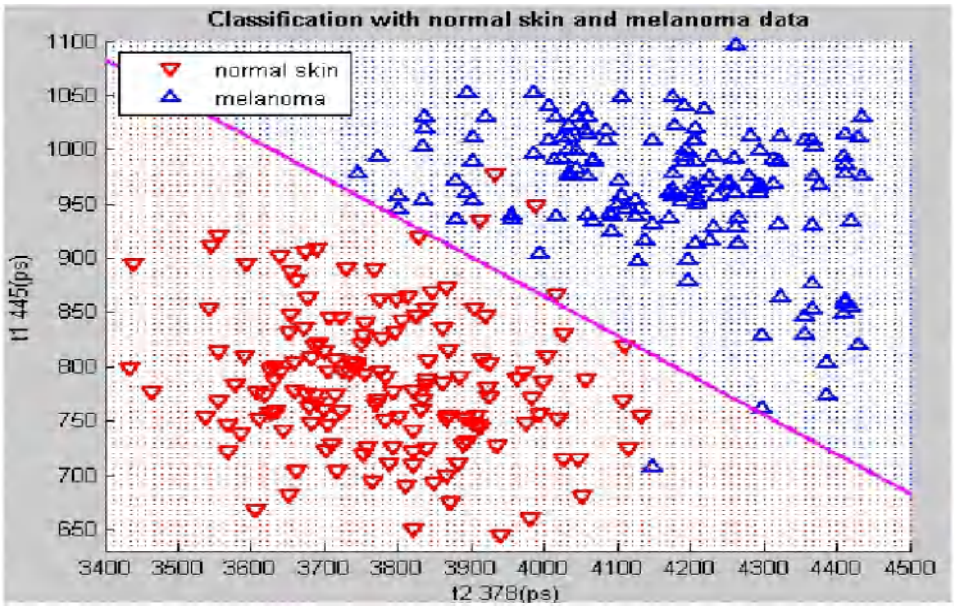


Fig. 771: Discrimination of normal skin and melanoma by a plot of τ_{1FAD} versus $\tau_{2NADH.}$ Adapted from [976]

If these results can be confirmed by FLIM experiments (they are in agreement with [10]) a similar discrimination for the individual pixels of the image, and thus of the of the tumor tissue could be achieved.

Earlier experiments of Teuchner et. al. [1237] and Eichhorn et al. [429] have shown that the fluorescence spectrum of melanin in malignant melanoma is red-shifted compared to normal skin. The result has been confirmed by Dimitrow et al. who used multiphoton multi-spectral FLIM [385]. Consequently, there is an increasing interest in lifetime imaging of melanin. FLIM of melanin fibrils by an LSM 510 with a bh Simple-Tau 150 FLIM system has been described by [842], lifetime imaging of melanin in human hair in [428]. Two-photon excitation spectra of melanin are given in [252]. For an overview please see also [690, 692].

Combination with SHG

Additional information about the constitution of tissue can be obtained from second-harmonic generation (SHG) signals. Second-Harmonic generation has nothing to do with fluorescence but often shows up as an ultrafast component in two-photon autofluorescence data. SHG emission requires some global organisation of the molecules [831]. In biological system it comes mainly from connective tissue, especially from collagen in animal tissue and from cellulose and starch in plant tissue. The ratio of SHG and autofluorescence intensity in mammalian skin is an indicator of skin ageing [678].

An example is shown in Fig. 772. The images show a pig skin sample exited by two-photon excitation at 800 nm. The left image shows the wavelength channel below 480 nm. This channel contains both fluorescence and SHG signals. The SHG fraction of the signal has been extracted from the FLIM data and displayed by colour. The right image is from the channel >480 nm. It contains only fluorescence, the colour corresponds amplitude-weighted mean lifetime.

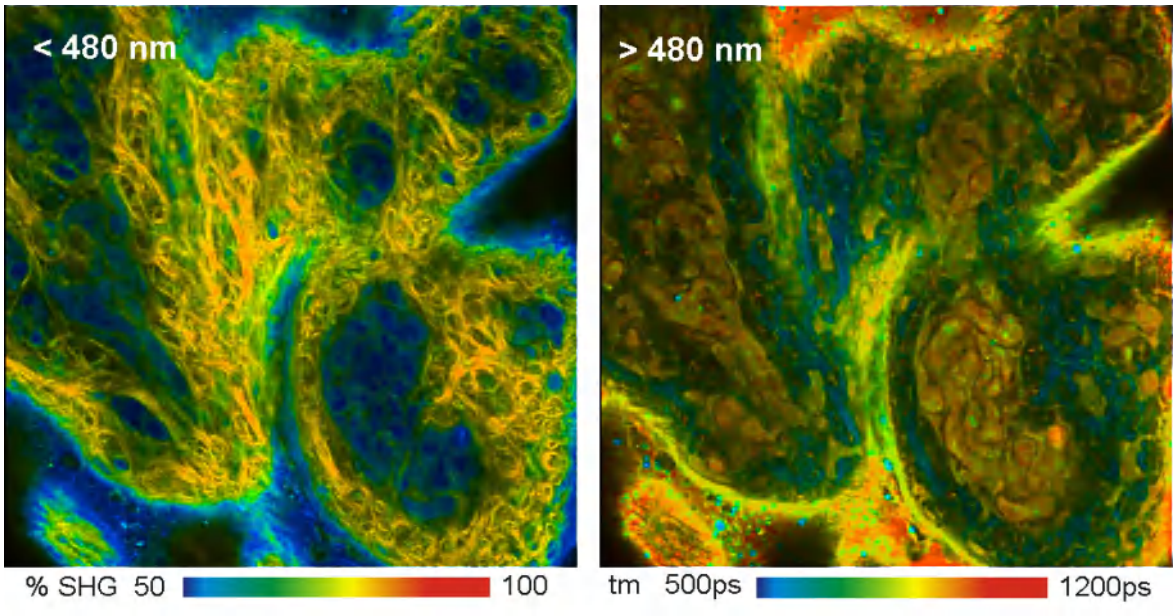


Fig. 772: Two-photon FLIM of pig skin. LSM 710 NLO, excitation 800 nm, HPM-100-40, NDD. Left: Wavelength channel <480 nm, colour shows percentage of SHG in the recorded signal. Right: Wavelength channel >480 nm, colour shows amplitude-weighted mean lifetime. Same data as in [160].

Z Stacks of Autofluorescence FLIM

Measurements as the ones described above can favourably be performed by Z stack FLIM, see page 406. Fig. 773 shows Z-stack FLIM data of a pig skin sample in the wavelength channel above 480 nm. The data were analysed by the batch-processing function of SPCImage. The colour of images shows the average (intensity-weighted) lifetime of a double-exponential fit to the decay data. The intensity of the images was normalised to the intensity of the brightest pixel.

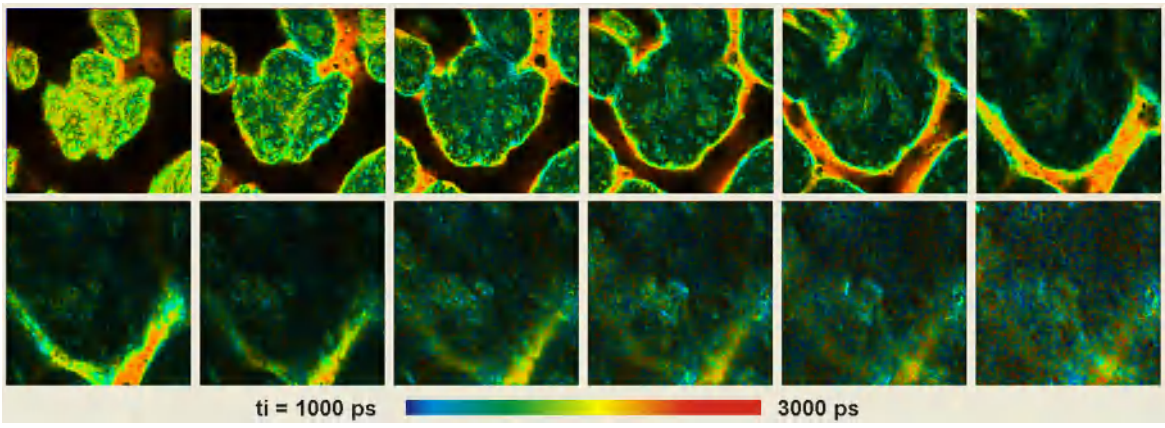


Fig. 773: FLIM Z stack recorded at a pig skin sample, excitation at 800 nm, emission above 480 nm. Z step width 5.09 µm, scan area 212 x 212 µm. Images from 5 µm to about 60 µm below the surface. Colour represents average (intensity-weighted) lifetime of a double-exponential fit. FLIM data format 256 x 256 pixels, 256 time channels. Normalised intensity.

Fig. 774 shows the SHG intensity extracted from the FLIM data in the channel below 480 nm. Also here, intensity of the images was normalised to the intensity of the brightest pixel.

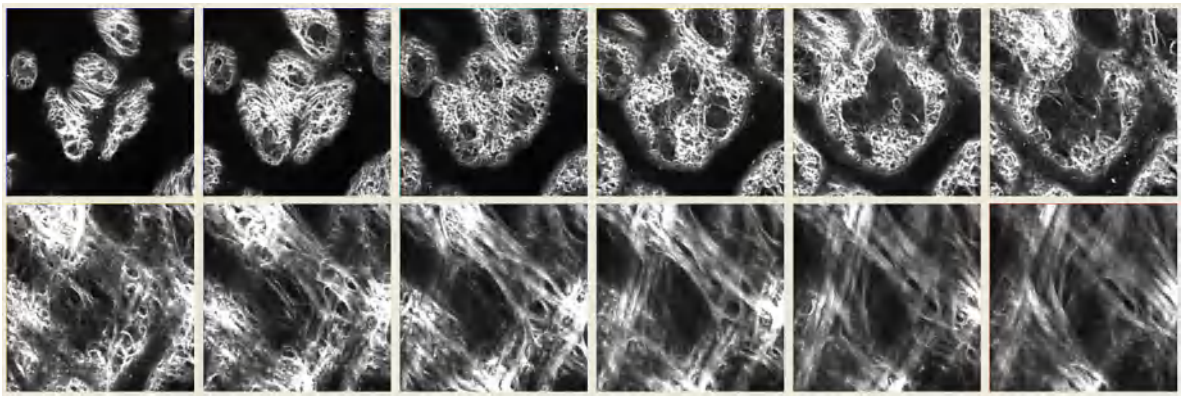


Fig. 774: Z stack recorded at a pig skin sample, excitation at 800 nm, emission below 480 nm, SHG signal, extracted by selecting photons in an early time window. Z step width is 5.09 µm, scan area 212 x 212 µm. Images from 5 µm to about 60 µm depth. Normalised intensity.

In all autofluorescence lifetime experiments it is important that the metabolism of the tissue be not changed before or during the measurement. This is critical especially for ex-vivo samples. Sanchez et al. have therefore studied the degradation of skin samples over the storage time and under different storage conditions [1047].

FLIM of Other Endogenous Fluorophores

There are other endogenous fluorophores which can possibly be used for the identification of the tissue state and of cancerous and pre-cancerous situations. Melanin at its relationship to melanoma has been described above. The use of the tryptophane fluorescence, including FRET from tryptophane into NAD(P)H has been described in [10, 632, 960]. The problem of tryptophane is that it cannot easily be excited by wavelength available in one-photon and two-photon laser microscopes. The authors therefore used three-photon excitation. FLIM with endogenous bilirubins has been described by Shen et al. [1135]. Bilirubin is present at high concentration in liver tissue. The authors excited it by two-photon excitation at 1230 nm. In differentiated hepatocellular carcinoma they found a fluorescence lifetime of 500 ps compared to 300 ps in non-tumor tissue. Endogenous fluorescence is also recorded from porhyrines. Porphyrines exhibit a strongly multi-exponential fluorescence decay which indicates that they are a mixture of slightly different compounds, different conformations, or, possibly, aggregates of different size. The composition of these mixtures may depend on the tissue state. The composition of the decay function may therefore contain biological information. Other endogenous fluorophores, such as lipofuscin or advanced glycation end products (AGEs) are important as indicators in ophthalmic FLIM, please see page 590.

Drug Delivery and Diffusion of Nanoparticles in Skin

An important issue in dermatology is diffusion of drugs and nano-particles through human skin. On the one hand, diffusion through the skin may be desirable as a pathway of drug delivery. On the other hand, nanoparticles contained in sunscreens or cosmetic products should not permeate through the stratum corneum of human skin. Moreover, it is important whether the nanoparticles cause changes in their molecular environment. The use of two-photon imaging and FLIM to study these effects has been described in [498, 592, 756, 757, 790, 817, 883, 984, 1022, 1049, 1245, 1397].

Autofluorescence of the Ocular Fundus

FLIM is being used in ophthalmic scanners, see page 590. The instruments have produced FLIM images of amazing quality. Clinical trials have show that FLIM is able to detect metabolic changes that are early indications of a number of eye diseases [414, 415, 416, 417, 1096, 1097, 1098, 1101, 1102, 1103]. The resolution of an ophthalmic scanner is limited by the low NA and the poor optical quality of the lens of the human eye. Data delivered by ophthalmic scanners have therefore to be supported by FLIM microscopy of ex-vivo samples.

Lifetime imaging of lipofuscin and melanin in retinal pigment epithelium cells has been described by Sun et al. [1206]. An autofluorescence FLIM study of retinal pigment epithelium cells under oxidative stress has been published by Miura et al. [878].

A FLIM study of extra-macular drusen has been published by Schweitzer et al. [1100]. Based on the FLIM data, the authors were able to clearly discriminate the RPE from Bruch's membrane, drusen, and choroidal connective tissue. An example of a FLIM image of the RPE with hard drusen is shown in Fig. 775. The data were acquired with the MW FLIM multi-wavelength detector. The figure shows the lifetime data in all combined wavelength channels. Triple-exponential decay analysis was used; the images show the fast decay component, the medium component, and the slow decay component. Interestingly, in the drusen and in the Bruch's membrane an extremely slow component with about 8 ns decay time occurs. The lifetimes in the RPE are much shorter.

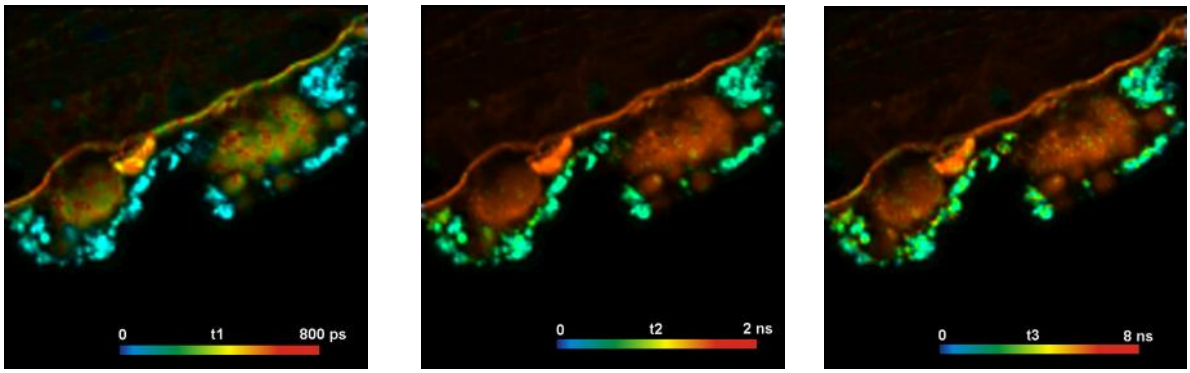


Fig. 775: Autofluorescence FLIM image of a human fundus sample. Triple-exponential analysis, left to right: Lifetimes of the fast, medium, and slow decay component. Courtesy of Dietrich Schweitzer, Martin Hammer, Sven Peters, Christoph Biskup, University Jena, Germany.

Spectrally resolved data are shown in Fig. 776. It shows single wavelength channels of the MW-FLIM detector from 450 nm to 575 nm. The lifetime shown is the amplitude weighted average of a triple-exponential decay model. The intensities were normalised to the brightest pixel.

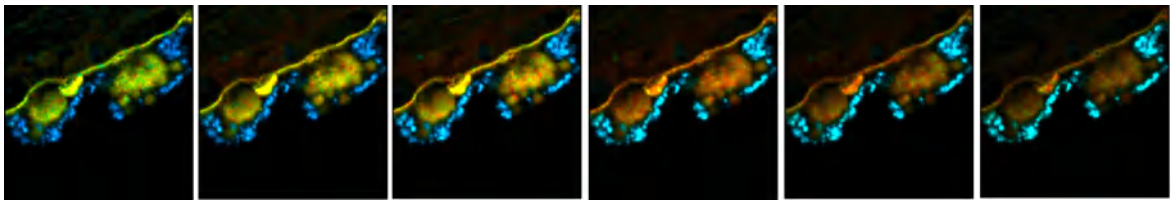


Fig. 776: Lifetime images of the amplitude-weighted lifetime, t_m, for single wavelength channels from 450 nm to 575 nm. The lifetime scale is blue to red, 0 to 2500 ps.

Ultra-Fast Fluorescence Decay in Biological Material

It is commonly believed that autofluorescence lifetimes of biological material are in the range from a few 100 ps to about 5 ns. This is supported by fluorescence-decay data of NADH, which exhibits a lifetime of about 400 ps for the free form and 3 ns for the protein-bound form, and of FAD, with about 250 ps for the bound form and 2 ns for the free form [183, 742]. Lifetimes of other endogenous fluorophores are in the same range, with fast decay components down to about 200 ps [1094]. The fact that no faster decay times are known may in part be due to the limited time resolution of the instruments. Commonly used FLIM systems have instrument response functions with a full width at half-maximum (fwhm) of about 250 ps (when using PMT detectors) and 100 ps (when using hybrid detectors with GaAsP cathodes). Faster fluorescence decay times may therefore have eluded attention, especially when they appeared as components of a multi-exponential decay.

Recently, bh have introduced ultra-fast hybrid detectors and ultra-fast TCSPC-FLIM modules to their FLIM systems [128]. In combination with femtosecond-lasers and two-photon excitation the systems deliver an IRF of <20 ps fwhm [122]. We have used the systems to look for extremely fast fluorescence decay processes in a variety of biological samples. The result was a surprise. Ultra-fast decay components were found in mushroom spores [177], pollen grains [178], in carotenoids [179], human hair [180], and even in Scottish whiskey [181]. The most interesting find was ultra-fast fluorescence decay in melanoma, which is not present in benign pigmented skin lesions [182]. Lifetimes were found as short as 10 ps, and amplitudes, a1, as large as 0.99. Ultra-fast decay times therefore should not be considered a peculiarity any more. They are a reality.

Mushroom Spores

Pieces of fresh mushroom caps were placed over 180 µm thick microscope slides to collect the spores. For FLIM measurement, the slides were placed on the sample stage of an inverted microscope. To obtain maximum resolution and photon collection efficiency we used a microscope lens with oil immersion, NA = 1.3 numerical aperture, and 40x magnification. The emitted photons were recorded via the non-descanned detection path of the DCS-120 MP system, see 'Ultra-High Resolution FLIM Systems', page 362. A Chroma SP 700 short-pass filter was used to reject scattered laser light, and a 400-nm long pass filter to suppress possible SHG light. Thus, fluorescence was detected from about 400 nm up to the upper detection limit of the detector, which is about 650 nm. A selection of typical results are shown in Fig. 777, more are available in [177]. It turns out that the lifetime, t_1, and the amplitude, a1, of the fast decay component scale strictly with the colour of the spores. The darker the spores the larger is a_1 and the shorter is t_1.

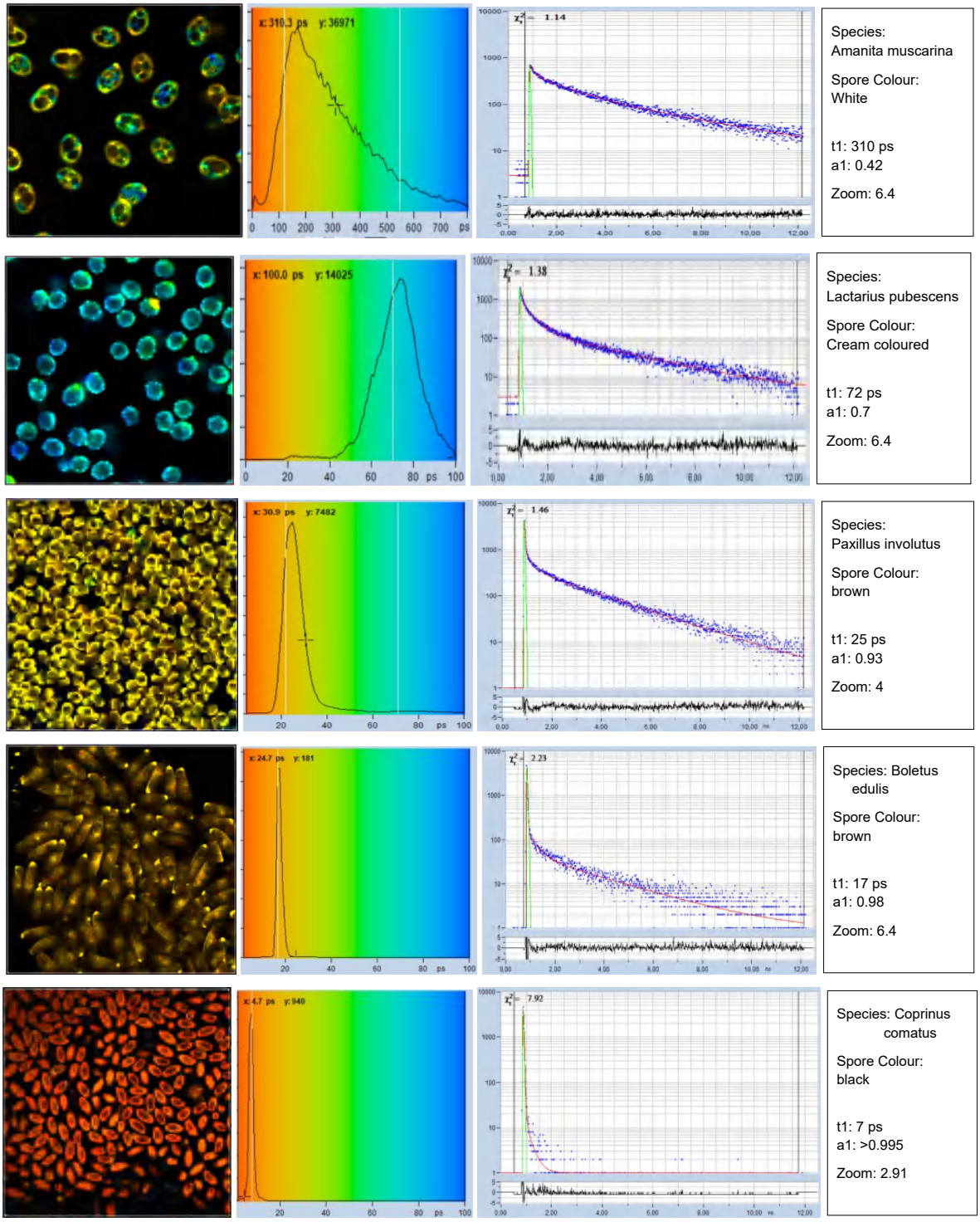


Fig. 777: Mushroom spores in order of decreasing t1. Left to right: t1 lifetime images (upper row red to blue = 0 to 800 ps, other rows 0 to 100 ps), distribution of t1 over pixels, decay curve in selected spot, and text field describing species, spore colour, t1 and a1, and zoom factor used for the recording. Field size is 500 µm / Zoom.

Pollen Grains

FLIM data of pollen grains of *Lilium orientalis* are shown in Fig. 778. Also here the general trend is that the deeper the colour the shorter the lifetime of the fast component, t1, and the larger the amplitude, a1. The shortest lifetime, 10 ps, is found in the dark-pink variant.

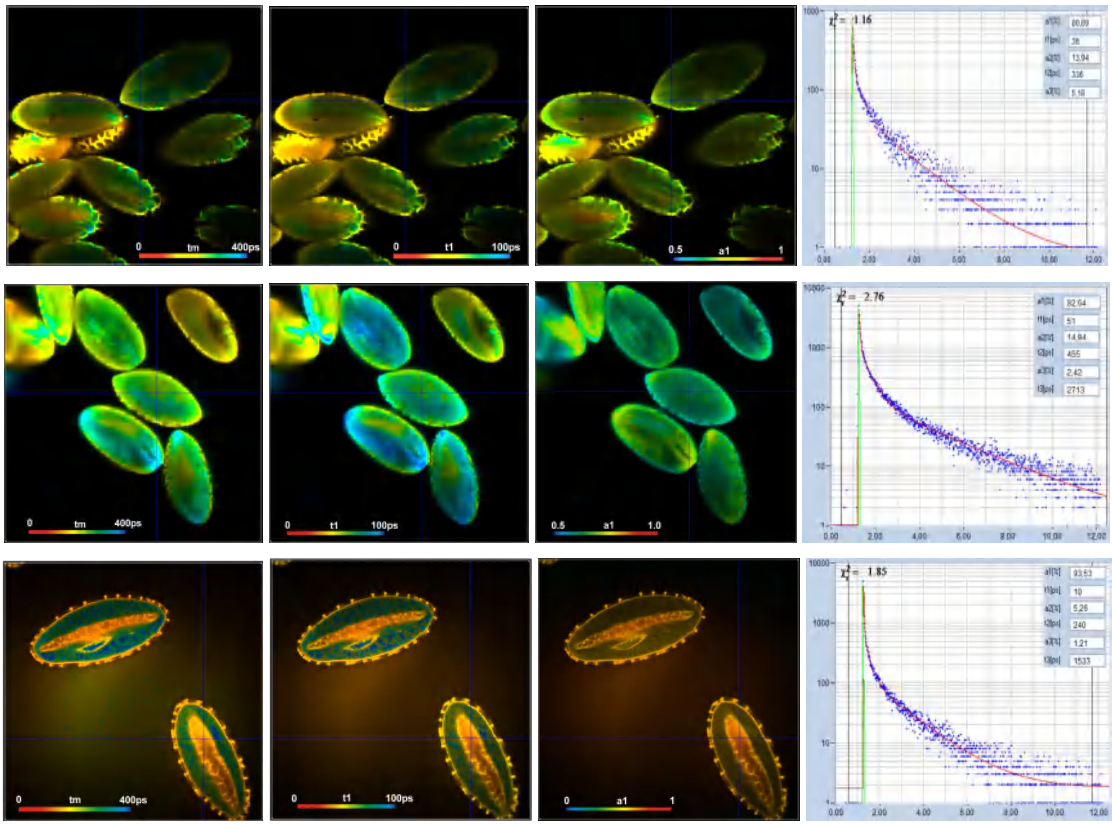


Fig. 778: Lifetime images and decay curves of pollen grains of *Lilium orientalis*. Top to bottom: White, pink, and dark pink variant. Left to right: Images of amplitude-weighted mean lifetime, tm, lifetime of the fast component, t1, amplitude of the fast component, a1, and decay curve over entire image.

Carotenoids

Carotenoids are present in almost any live species on this planet. In plants and algae, they assist photosynthesis via an additional light-harvesting complex and protect the cells against photo-oxidative stress [1069]. In animals, carotenoids and their derivatives are providing the colours of fish, reptiles, and birds. Moreover, carotenoids play a role as UV absorbers and as scavengers of reactive oxygen species. In mammals, carotenoids are present in almost all organs, such as skin, liver, brain, ovaries, prostate, and blood [445, 837, 1354]. In the eye, carotenoids present a dominating portion of the macular pigment [1094].

It is presumed - in some cases even known - that carotenoids are essential to the function of the organs. Moreover, there are indications that they act as anti-oxidative and anti-inflammatory agents, and that they have anti-bacterial, anti-viral, and even anti-cancer functions [206]. Well known is the effect of β-carotene and lutein on the macula of the human eye [206, 1094].

It would therefore be desirable to investigate these effects directly on the cell level. This can be done best by using fluorescence lifetime and fluorescence lifetime imaging (FLIM) techniques. Unfortunately, there is a problem: Carotenoids are virtually non-fluorescent. Fluorescence quantum yields are on the order of 10^{-4} to 10^{-5} [499]. The excited state (s1) lifetime of β-carotene, measured by transient absorption, has been found to be 16 ps [499]. S1 lifetimes of other carotenoids measured by the same technique were found in the range from 25 ps down to less than 2 ps [915]. That means the fluorescence lifetimes must be in the lower ps range, and can only be detected by a very fast FLIM system. With an IRF width of less than 20 ps there is a good chance that a fast bh FLIM system is able to record decay functions and

FLIM images from carotenoids and derive molecular information from these data. Fig. 780 shows that this is indeed possible.

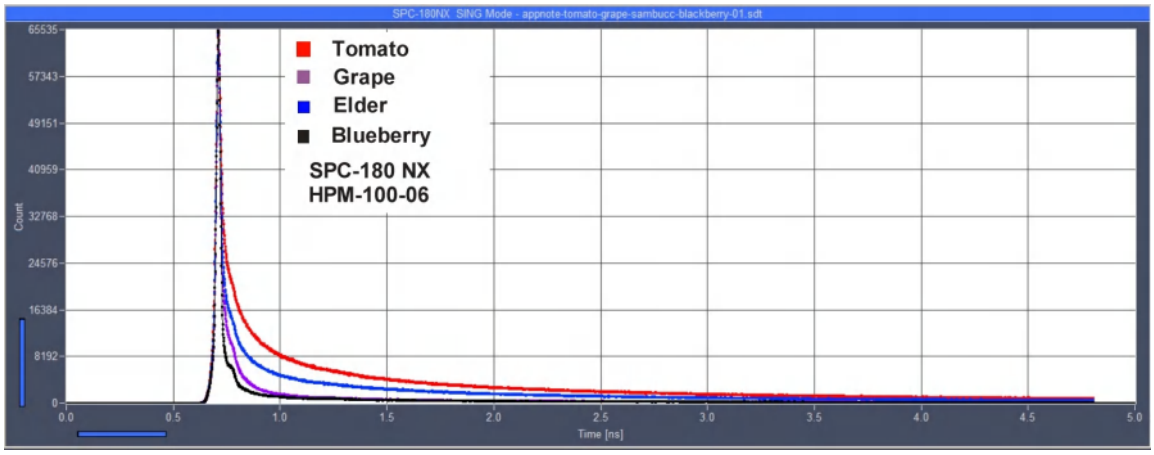


Fig. 779: Decay curves of extracts of tomato, grape, blueberry, and black elder.

The decay data of the samples investigated are summarised in Fig. 780. Based on fits of different data sets and fits with different model options we estimate that the accuracy of the fast-component lifetime, t1, is about ±2 ps, if not better.

Carrot		Tomato		Grape		Elder		Blueberry		Egg	
a1[%]	99,06	a1[%]	84,87	a1[%]	93,90	a1[%]	91,05	a1[%]	97,97	a1[%]	84,91
t1[ps]	8,6	t1[ps]	20,7	t1[ps]	14,3	t1[ps]	16,2	t1[ps]	10,5	t1[ps]	17,1
a2[%]	0,39	a2[%]	11,38	a2[%]	5,55	a2[%]	6,92	a2[%]	1,66	a2[%]	9,55
t2[ps]	296	t2[ps]	276	t2[ps]	130	t2[ps]	234	t2[ps]	180	t2[ps]	336
a3[%]	0,55	a3[%]	3,74	a3[%]	0,54	a3[%]	2,03	a3[%]	0,38	a3[%]	5,54
t3[ps]	3937	t3[ps]	2188	t3[ps]	2161	t3[ps]	2169	t3[ps]	2216	t3[ps]	2751

Fig. 780: Decay parameters of the samples investigated

For comparison, Fig. 781 shows decay curves of a number of pure carotenoids and anthocyanins. Not surprisingly, the pure substances show the same extremely fast decays as the natural samples.

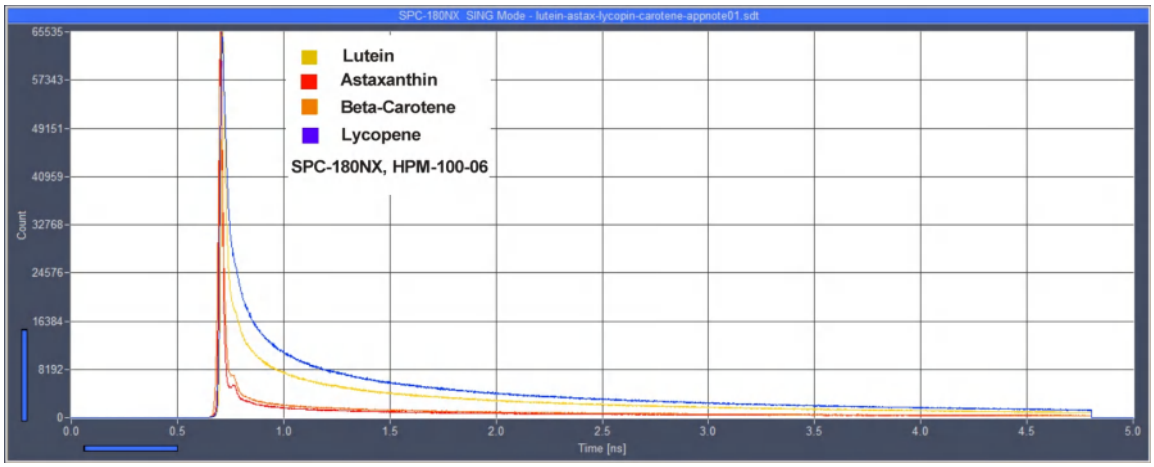


Fig. 781: Decay curves of lutein, astaxanthin, β-carotene, lypcopene

The results show that carotenoid fluorescence - and fluorescence lifetimes - can well be detected by bh fast FLIM systems. With the ability to split the decay functions into several components, the results can potentially be used to investigate molecular processes related to biological functions of carotenoids in live organisms.

Human Hair

The images shown in Fig. 782 to Fig. 784 show lifetime images of human hair. The data were recorded by the DCS-120 MP system described in section 'Ultra-High Resolution FLIM Systems', page 362. Only one channel of the system was used, with the entire light being fed to the detector in the 0° beam path. A FLIM image of black hair is shown in Fig. 782. A t_m (amplitude-weighted lifetime) image is shown on the left. The colour scale is from 20 ps (red) to 500 ps (blue). A decay curve at the cursor position is shown on the right, the insert shows the amplitudes and lifetimes of the decay components. Already at first glance, it is evident that the decay is very fast. SPCImage data analysis shows that the dominating decay component has a lifetime of 8.5 ps and an amplitude of almost 96%. The amplitude-weighted average decay time, t_m, is 19.3 ps.

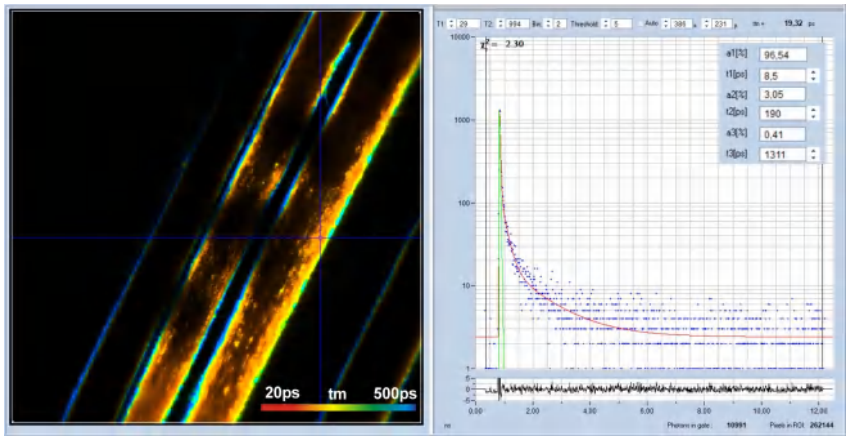


Fig. 782: Black hair, lifetime image (left) and decay function at cursor position (right). Decay components shown in the insert upper right. Triple-exponential analysis by SPCImage NG. The fastest component, t_1, has a lifetime of 8.5 ps and an amplitude of 96.5%.

Fig. 783 shows brown hair (bottom) and grey hair (top) from the same donor. Decay curves and decay components are shown upper and lower right. The brown hair has a fast decay component, t_1, of 14.2 ps lifetime and 96.5% amplitude, which is only slightly slower than for the black hair in the figure above. The fast component is not present in the grey hair, see decay curve upper right. Here, the fast component, t_1, has a lifetime of 180 ps, with an amplitude of only 45.5%. The amplitude-weighted mean lifetimes, t_m, of the brown and the black hair are 68 ps and 1300 ps, respectively.

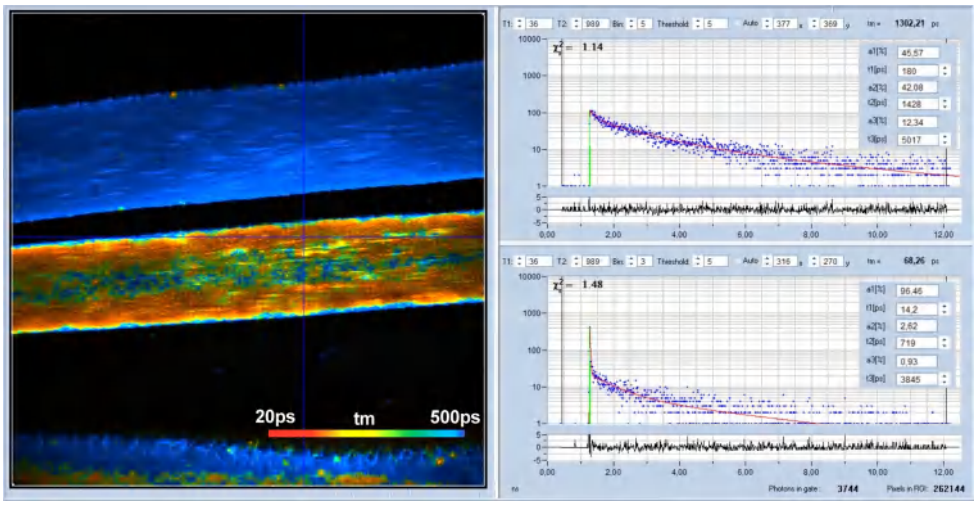


Fig. 783: Brown hair (bottom) and grey hair (top) from the same donor. Decay curves and decay components are shown upper and lower right.

Blond hair is shown in Fig. 784. The entire decay is much slower than for the black and brown hair. The lifetime of the fast component, t_1, is 54 ps, and the amplitude 58%. This is fast for average FLIM standard, but by far not as fast as for the black and brown hair. The amplitude-weighted mean lifetime, t_m, at the cursor position is 782 ps. Also this is much longer than in the figures above. Please note the different colour scale of the image.

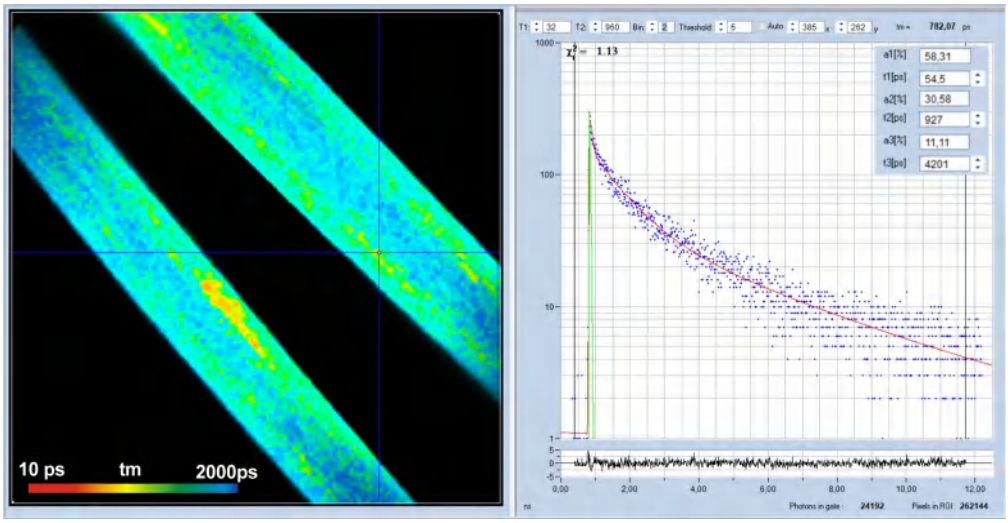


Fig. 784: Blond hair. Left: Lifetime image, tm = 10 ps to 2000 ps. Right: Decay curve at cursor position.

Malignant Melanoma

There have been earlier indications that short fluorescence lifetimes occur also in tissue of malignant melanoma. Decreased fluorescence lifetimes have been found by Dimitrow et al. [385, 386] and by Seidenari et al. [1111]. With the limited time resolution of the instruments used, it was not possible to decide whether the reported lifetimes were the true lifetime of the melanoma tissue, whether the resulting decay functions were single- or multiexponential, and which of the decay components were the source of the short apparent lifetime. Having ultrafast FLIM systems at hand, it was therefore a logical step to look for fast decay in tissue samples from malignant melanoma. Results are summarise below. Please see also [182] for further details.

For melanoma imaging we used a bh FLIM system attached to a Zeiss LSM 880 NLO multiphoton microscope in the inverted (Axio Observer) version [69]. HPM-100-06 hybrid detector modules (Becker & Hickl GmbH) were attached to the NDD port of the LSM 880 NLO via a Zeiss NDD beamsplitter module. The recording electronics consisted of two parallel SPC-150 N modules. The instrument response of the FLIM system is about 18 ps, full width at half maximum [122].

Fig. 785 shows a lifetime image of a vertical section through melanoma tissue. Superficial layers are shown on the right in the image, deeper layers on the left. Colour coding shows the lifetime of the fast decay component, t1, obtained by fitting the decay data by a triple-exponential model. Decay curves from selected spots of the image are shown on the right. The sharp peak in the decay curve from the superficial layer (bottom, right) shows visibly that there must be an extremely fast decay component. The fit delivers a lifetime, t1, of 13 ps and an amplitude, a1, of 98% for this component. The amplitude ratio, a1/(a2+a3), is about 57, which is unusually high for biological material. The peak is not present in the decay curve from deep tissue layers, see top right. The component lifetimes in these areas are in a more or less 'normal' range, and compatible with a mixture of NADH, FAD, and possibly FMN [183]. The parameters are t1 = 185 ps, a1 = 23.8%, a1/(a2+a3) = 0.31.

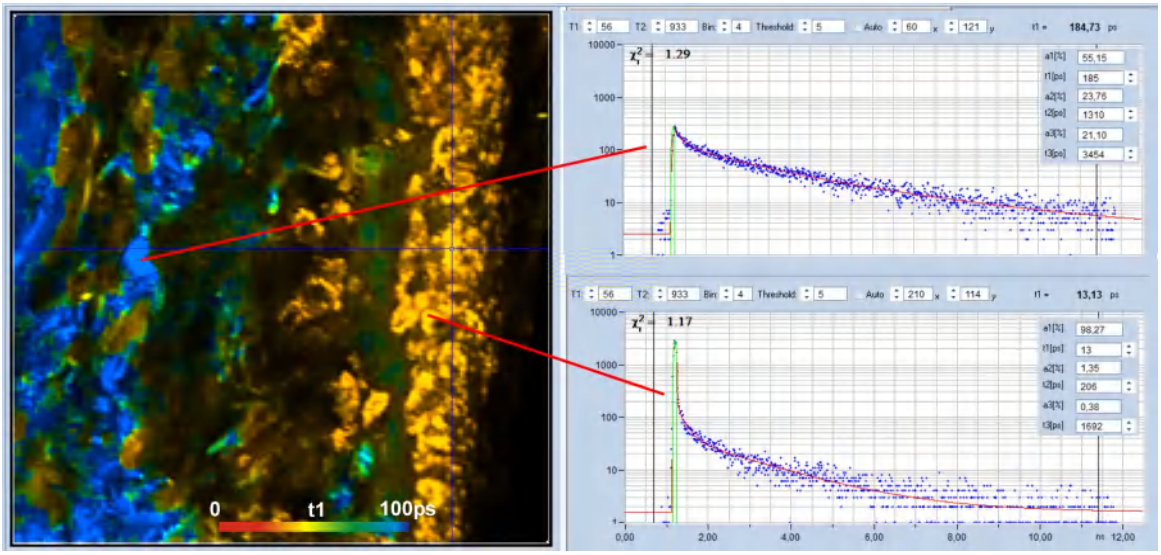


Fig. 785: Vertical section through melanoma tissue. Colour-coded image of the lifetime of the fast component, t1, of a triple-exponential fit of the data. Red to blue corresponds to 0 to 100 ps. Decay curves in characteristic spots of the image are shown on the right.

For comparison, Fig. 786 shows a FLIM image of a sample from a benign pigmented lesion recorded under similar conditions. A tm image is shown on the left, a decay curve from a selected spot on the right. As can be seen from the figure there is no ultra-fast component of high amplitude, as in the melanoma data. The fast decay component has a lifetime of 96 ps, and an amplitude of 45%. This is fast, but not as fast as in the malignant melanoma. The amplitude ratio, a1/(a2+a3), is about 0.8, i.e. 70 times smaller than for the malignant melanoma.

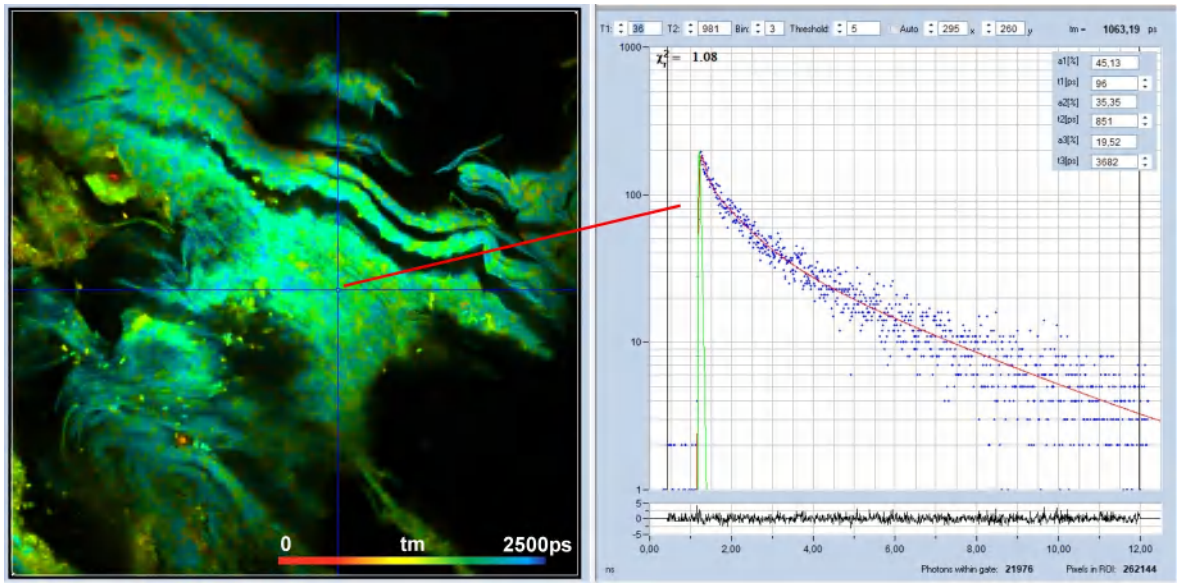


Fig. 786: Left: tm image of a sample from a benign pigments skin lesion. Red to blue corresponds to tm = 0 ps to 2500 ps. Right: decay curve in a selected spot of the image. There is no high-amplitude ultra-fast decay component.

As can be seen from the comparison of Fig. 785 and Fig. 786 there is a dramatic difference in the decay profile of the melanoma and the benign skin lesion. This fact can be used to identify malignant melanoma spectroscopically, possibly even in very early states. It may also help investigate how exactly malignant melanoma originate and grow.

As for the origin of the fast decay component in the melanoma tissue we can only speculate. It is reasonable to assume that it comes from some form of melanin. A likely source is aggre-

gates, forming by the high concentration of melanin in the melanoma. It is not unusual that aggregates exhibit extremely short fluorescence lifetimes, and it would not be surprising if the same effect occurred for melanin. However, why other material with high melanin content does not show the fast decay component remains an open question.

Fossil Micro-Organisms in Flint Stone

Laser scanning microscopy is mostly used to study biological objects. However, a laser scanning microscope can also be used to study the internal structure of minerals. On the micrometer scale, many minerals are transparent or at least translucent. A laser scanning microscope is then able to record images from defined internal layers of the material. The results show inclusions, cracks, crystal defects, trapped bacteria, or other features of interest. When combined with FLIM, the contrast to the surrounding material can be increased, and additional molecular information on the features of interest can be obtained [310]. To explore possible FLIM applications in mineralogy we used the bh DCS-120 confocal FLIM system on a number of different minerals. One of them was flint stone. Flint is partly translucent and emits surprisingly strong visible-range fluorescence with a lifetime in the lower nanosecond range. When we recorded FLIM images from flint samples we found, to our surprise, structures that, both in size and in shape, resembled single microorganisms and clusters of microorganisms [189]. Examples are shown in Fig. 787.

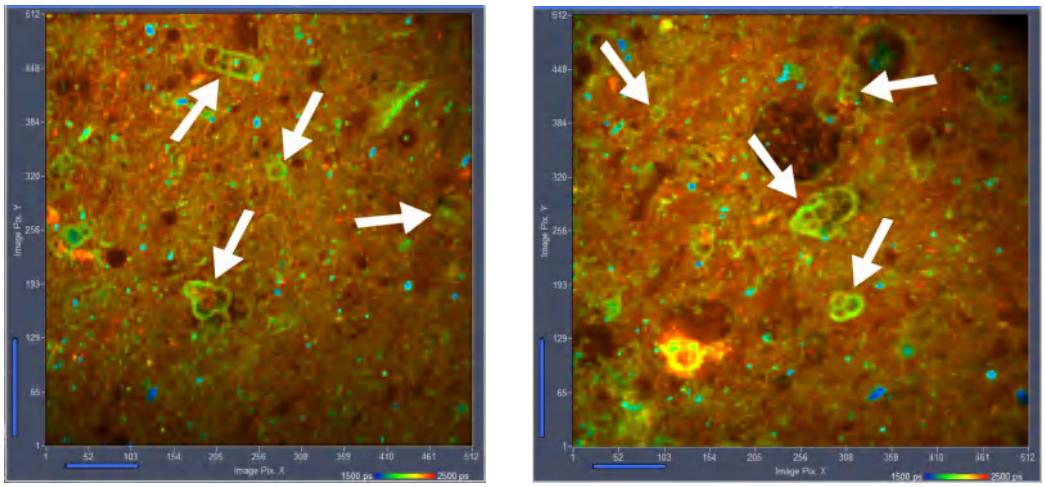


Fig. 787: Fossil micro-organisms in flint stone. bh DCS-120 Confocal Scanning FLIM system, excitation 405 nm, detection 435 nm to 650 nm. Image Size 400 x 400 µm. Objective lens 20x, NA=0.5, Pinhole size 1 AU (right). Online-display-function of SPCM data acquisition software, single-exponential approximation of decay time.

The figure shows that the bacteria-like objects have noticeably different fluorescence lifetimes and visibly different decay curves than the surrounding material. Fluorescence-decay curves of the objects and the surrounding material are shown in Fig. 788.

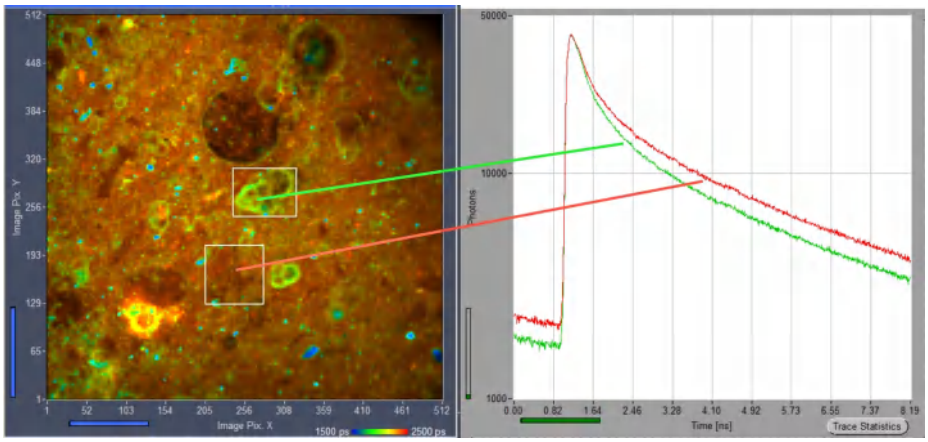


Fig. 788: Fluorescence-decay functions in regions of interest containing objects (green) and surrounding material (red)

Decay Analysis by SPCImage NG

To gain further information on the fluorescence behaviour of the enigmatic objects we applied bh SPCImage NG FLIM data analysis to our data. A lifetime image obtained this way is shown in Fig. 789. From the decay parameters and the decay curve (upper right and lower right) it can be seen that the fluorescence decay is multi-exponential. It is described well by a triple-exponential model, as can be seen from the smooth residuals below the decay curve. Please note that the lifetimes are different than in Fig. 787 and Fig. 788. SPCM uses a first-moment calculation that yields a single-exponential approximation of the lifetime, whereas SPCImage runs an MLE fit with a multi-exponential model, delivering an amplitude-weighted average of the component lifetimes. Lifetimes obtained by the two procedures are necessarily different.

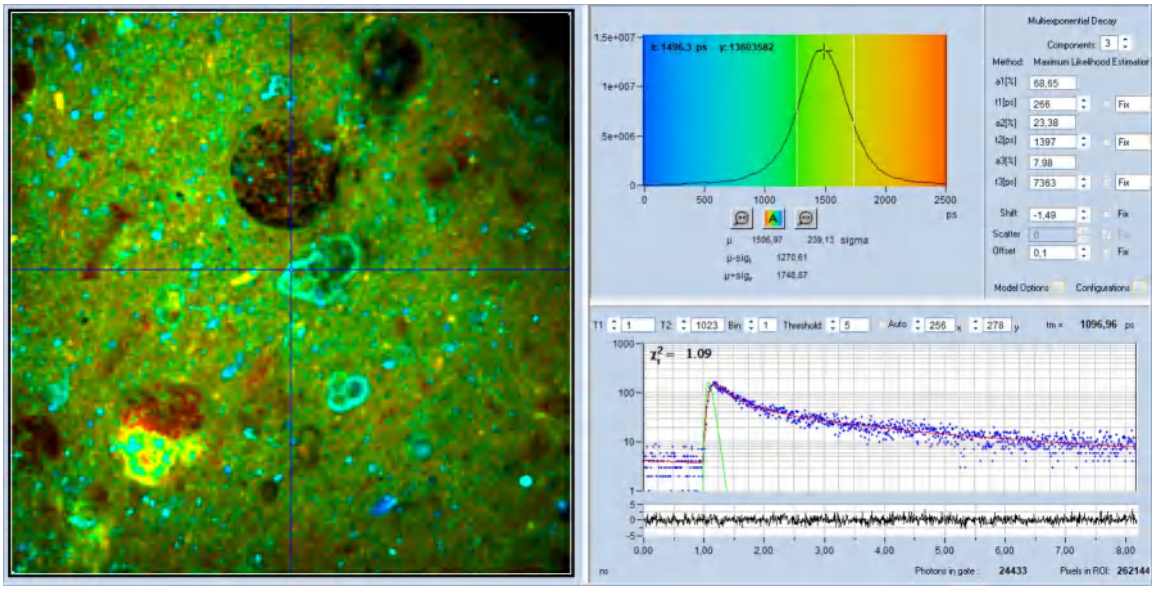


Fig. 789: Fluorescence-lifetime image created by SPCImage NG. Left: Lifetime image, showing amplitude-weighted lifetime, tm, of triple-exponential fit. MLE fit, GPU calculation. Upper right: Histogram of tm over the pixels of the image and decay parameters at cursor position. Lower right: Decay curve at cursor position. The image format is 512 x 512 pixels, with 1024 time channels per pixel.

Image Segmentation by Phasor Plot

Fig. 790 shows the use of the phasor plot of SPCIMage NG as an image segmentation tool (see Image Segmentation, page 869). In the phasor plot (upper right), a phasor range was selected which contains the phasor signature of the objects of interest. In the lifetime image (left), pixels outside the selected phasor range are displayed in grey. The 'Select Cluster' function of the phasor plot was used to combine the decay data of the selected pixels in a single decay curve. The combined decay curve is shown lower right. It contains more than 13 million photons and, therefore, can be analysed with very high precision. (Please ignore the large residuals, they are large because the number of photons is extremely high) The result shows that the decay is indeed triple-exponential, with decay components of 280 ps, 1962 ps, and 7542 ps. The amplitudes are 0.654, 0.2541, and 0.092, respectively. Interestingly, these lifetimes are compatible with the fluorescence decay of flavin adenine dinucleotide (FAD), a constituent of live cells.

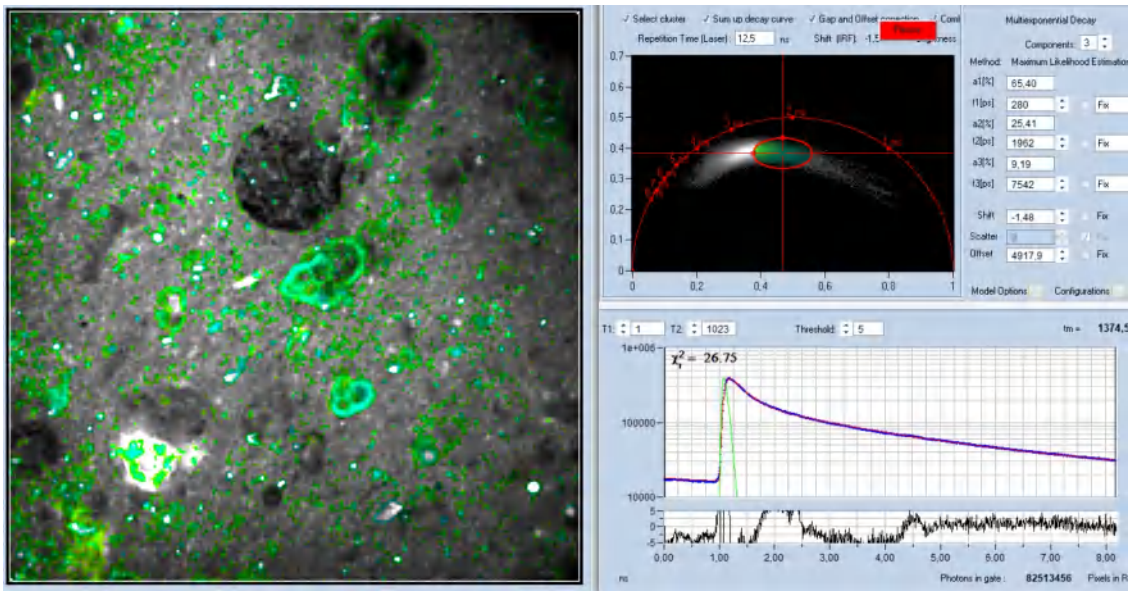


Fig. 790: Image segmentation by phasor plot, pixels with phasor signature of the cells selected. Combined decay curve for selected pixels shown lower right.

Is it possible that we indeed are seeing FAD in the flint? Flint formed in the Mesozoic, between 150 and 60 million years ago. It is thought that it formed when silicon-rich fluid filled cavities in sediment, such as holes bored by crustaceans or molluscs. With the time, the fluid became rich in silicic acid, gelled, and finally solidified to become cryptocrystalline silica [452, 453]. It is conceivable that the original fluid was inhabited by bacteria. However, silicification is a slow process. It is not clear how bacteria could stay alive or, at least, morphologically intact over such a long period of time in an increasingly hostile environment. It is even less conceivable that the FAD of the bacteria remained stable over more than 60 million years. However, if it did, the examination of flint by FLIM could be an intriguing technique to study ancient micro-organisms.

Oxygen Sensing by Phosphorescence Lifetime Measurement

Phosphorescence

Phosphorescence occurs when an excited molecule transits from the first excited singlet state, S1, into the first triplet state, T1, and returns from there to the ground state by emitting a photon [742]. Both the S1-T1 transition and the T1-S0 transition are ‘forbidden’ processes. The transition rates are therefore much smaller than for the S1-S0 transition. That means that phosphorescence is usually a weak and slow process, with low intensity and lifetimes on the order of microseconds or even milliseconds. Phosphorescence of organic dyes or endogenous fluorophores is extremely weak or even not detectable at room temperature. However, strong phosphorescence with lifetimes from the microsecond up to the millisecond range is obtained for lanthanide complexes [288] and organic complexes of ruthenium [742, 597], platinum [446, 742, 753, 1043, 1165, 1166], terbium, palladium [753], and iridium [712, 713, 881, 943 944, 1386]. Early TCSPC PLIM applications used the long lifetime of phosphorescence to suppress endogenous fluorescence of the sample [43, 44].

Of special interest for live-cell imaging is, however, that the phosphorescence of these complexes is quenched by oxygen, see Fig. 791. Phosphorescent dyes are therefore excellent oxygen sensors [496, 712, 713, 742, 753, 881, 940, 941, 943 944, 1043, 1137]. Dos Santos et al. found purely organic compounds with oxygen-dependent lifetimes in the 100-ns range [1054]. Although it is not clear whether the emission comes from the singlet or from the triplet state also these componds are potentiel oxygen sensors. Most PLIM applications are therefore aiming at the measurement of oxygen partial pressure (pO_2) in biological objects. Of special interest is the correlation of changes in the oxygen concentration with the metabolism of the cells [637, 943]. To reach this target it is necessary that PLIM and FLIM measurements are performed simultaneously [105, 161, 165, 167, 168, 943, 1130, 1054], see 'Simultaneous FLIM/PLIM', page 434. The oxygen concentration is derived from the PLIM data, the metabolic information from the FLIM data, preferably from the NAD(P)H fluorescence.

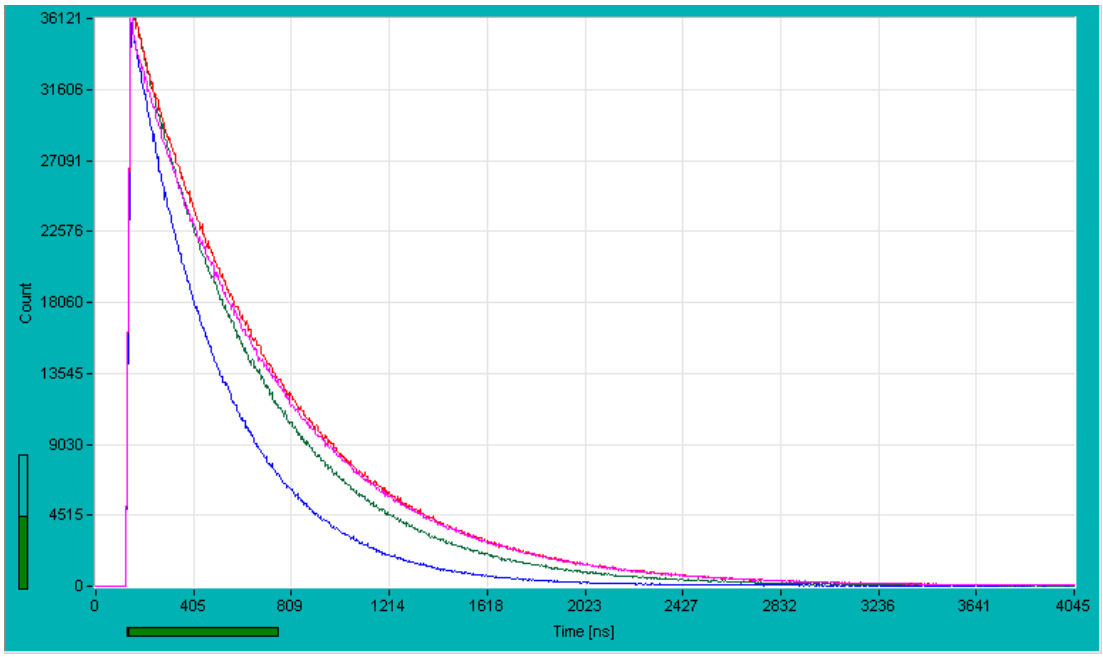


Fig. 791: Phosphorescence decay of a ruthenium dye for different oxygen concentration. Recorded with bh DPC-230

Oxygen Sensing by PLIM

Examples are shown in the figures below. Fig. 792 and Fig. 793 show cultured human embryonic kidney cells incubated with a palladium-based phosphorescence dye. Fig. 792 was recorded under atmospheric oxygen partial pressure. The maximum of the lifetime distribution over the pixels (upper right) is at 75 s. Fig. 793 was recorded under decreased oxygen partial pressure. As can be seen, the maximum of the lifetime distribution has shifted to 144 µs.

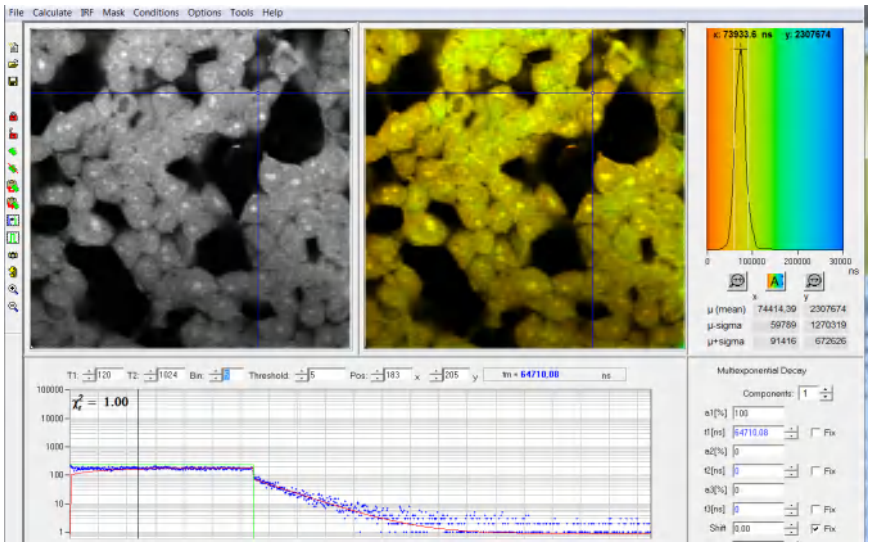


Fig. 792: HEK cells incubated with a palladium dye under atmospheric oxygen partial pressure. Recorded by bh DCS-120 confocal scanning system, data analysis by bh SPCImage. Lifetime scale 0 (red) to 300 µs (blue). Phosphorescence lifetime at the Cursor-Position 65 µs. The maximum of the lifetime distribution over the pixels is at 75 µs.

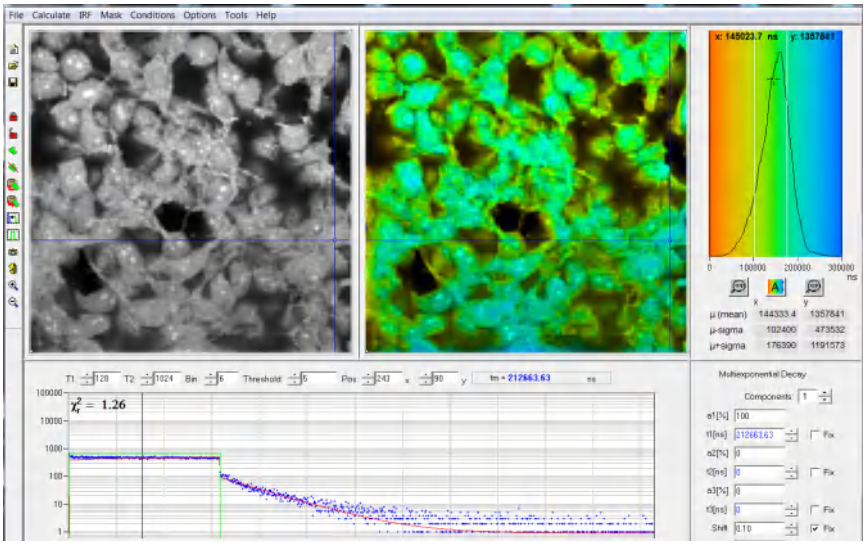


Fig. 793: HEK cells incubated with a palladium dye under reduced oxygen partial pressure. Recorded by bh DCS-120 confocal scanning system, data analysis by bh SPCImage. Lifetime scale 0 (red) to 300 µs (blue). Phosphorescence lifetime at the Cursor-Position 212 µs. The maximum of the lifetime distribution over the pixels is at 144 µs.

Simultaneous Recording of Oxygen and NAD(P)H Images

Simultaneously recorded fluorescence and phosphorescence lifetime images of live cultured human embryonic kidney cells stained with 5,10,15,20-tatrakis(4-carboxyphenyl)porphyrin-Pd(II) are shown in Fig. 794. The FLIM and PLIM images on the left were recorded under

atmospheric oxygen concentration. The images on the right were recorded after adding sodium sulphite (Na_2SO_3). Na_2SO_3 binds oxygen. The oxygen concentration in therefore low. It can clearly be seen that the phosphorescence lifetime became longer, indicating there is indeed less oxygen (please note different colour scales). In the FLIM image, it can be seen that the amplitude-weighted lifetime, τ_m, of the NADH has decreased.

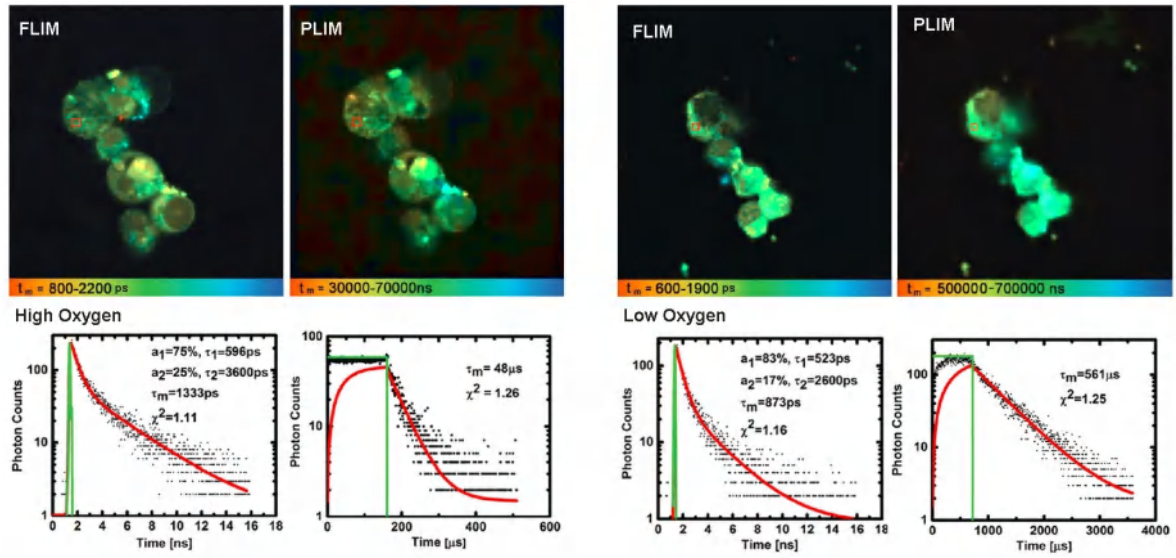


Fig. 794: Simultaneous FLIM/PLIM of human embryonic kidney cells. Left: High (atmospheric oxygen concentration). Right: Low oxygen concentration. Upper row FLIM and PLIM images, lower row decay curves in indicated position. Lifetime-colour scale given underneath the images. bh DCS-120 confocal scanning FLIM system, excitation wavelength 375 nm. Adapted from Shcheslavskiy et al. [1130].

Delayed Fluorescence of PpIX

Protoporphyrin IX (PpIX) is an endogenous porphyrin. PpIX emits delayed fluorescence in measurable amounts [864, 865]. Delayed fluorescence occurs when an excited molecule transits from the S1 state to the T1 state, and back to the S1 state. From there it emits through the normal S1-S0 relaxation process. Since the process goes through the triplet state the lifetime is long as in the case of phosphorescence. The triplet state interacts with oxygen, therefore the lifetime of delayed fluorescence has the same pO_2 dependence as phosphorescence. PpIX is there a potential (and probably the only) endogenous oxygen sensor.

Since the emission of delayed fluorescence occurs from S1 the emission spectrum is identical with that of prompt fluorescence. However, the intensity of delayed fluorescence is orders magnitude lower than that of prompt fluorescence. Delayed fluorescence is therefore difficult to record. The bh simultaneous FLIM/PLIM technique separates fluorescence and phosphorescence temporally, without the need of spectral separation. In principle, it is therefore able to record also delayed fluorescence.

To confirm the existence of delayed fluorescence a solution of PpIX was put in a cell dish and scanned with the 405 nm laser. The data were recorded by a DCS-120 system by bh's simultaneous FLIM/PLIM technique. A laser-on-off period of 412 µs was used, with a laser-on time of 95 µs. Fluorescence and phosphorescence (in this case delayed fluorescence) decay data of all pixels were combined in a singe fluorescence and delayed-fluorescence curve. The result is shown in Fig. 795. The decay function of the prompt fluorescence is shown left. The decay is strongly multi-exponential, with a mean lifetime of about 9 ns. The luminescence in the 0 to 300 µs range is shown on the right. A long-lifetime signal was indeed detected in the laser-off phases. It has a lifetime of about 25 µs, which is in agreement with [864]. The lifetime increased when we decreased the oxygen concentration by adding Na_2SO_3 to the solu-

tion. We therefore believe that the signal is indeed delayed fluorescence from PpIX. However, the signal is extremely weak - almost 3 orders of magnitude weaker that the prompt fluorescence in the laser-on phases.

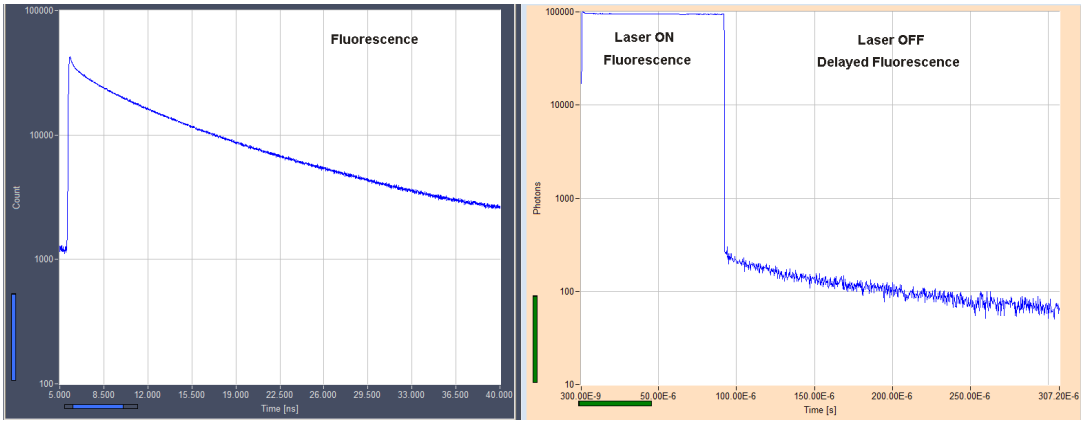


Fig. 795: Fluorescence (left) and delayed fluorescence of PpIX (right). DCS-120 system in FLIM/PLIM mode, excitation 405 nm, detection 600-700 nm.

Imaging data of the same solution are shown in Fig. 796. The figure shows the SPCImage data analysis panel, with the intensity image, the lifetime image, the decay data in a selected area of the sample, and a lifetime histogram over the pixels. Delayed fluorescence is also see in the scan data. However, the intensity is uncomfortably low. For reasonable decay analysis we had to bin the data into 20 x 20 pixel areas. Within this binning area decay data of the delayed fluorescence are obtained as shown in the figure. (The prompt fluorescence is 3 orders of magnitude stronger, and out of the scale of Fig. 796).

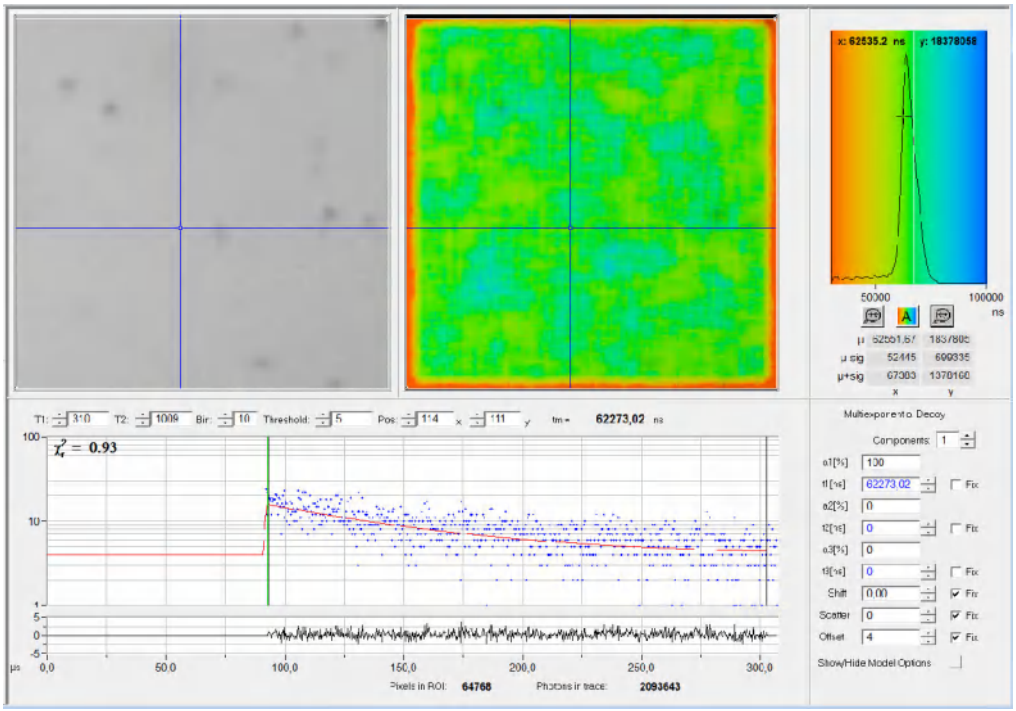


Fig. 796: Delayed fluorescence of PpIX, shown in scanning data. Total scan area 256 x 256 pixels, decay data from 20 x 20 pixel binning area. Lifetime histogram over the pixels shown upper right.

These results show that the delayed fluorescence of PpIX can be recorded. Most likely, it can be used for sensing the average pO_2 in an entire sample or in reasonably large areas of a sam-

ple. However, it is probably too weak to image pO_2 in individual compartments of a cell or in individual structures within a tissue sample.

Applications

There is an impressive amount of publications based on the bh FLIM/PLIM technique. The first publications concentrated on the characterisation of phosphorescence probes. In [395], [397] and [942] Dmitriev and Papkovski give a summary on available phosphorescent probes, their O_2 sensitivity, brightness, phosphorescence lifetimes, cell-staining capability, and toxicity.

The problem of sensitivity of phosphorescent dyes to other cell parameters, such as pH, viscosity, and oxygen diffusion time constant, is addressed by embedding the dyes in nanoparticles and nanostructured cell substrates. Phosphorescent nanoparticles, nanostructured films, scaffolds and fibres as pO_2-sensors are explored in [393, 396, 621, 622, 925, 931, 1251, 1366]. Phosphorescent gold clusters as probes for lipid droplets were described in [698].

Oxygen imaging of neurospheres is described in [392]. Applications to Giant Umbrella Cells and to healthy and inflamed colon tissue are described in [1390] and [1392]. Changes in intracellular oxygen concentration with the metabolic activity were observed by Zhdanov et al. [1391]. Jenkins et al. studied the function of SPCA ATPases in HCT116 cells. They found correlations of the expression of SPCA1 and SPCA2 with the O_2 concentration [623].

Kuroki et al. [727] provided a detailed evaluation of TCSPC PLIM with Platinum(II) 5,10,15,20-tatrakis-[4-carboxyphenyl)porphyrin. They tested the sensor with MKN45 cells, colon26 spheroids under different O_2 concentration. They were able to correlate low pO_2 regions with mitochondria, to track the change in O_2 concentration in Colon26 cells after addition of antimycin A, and to visualise the O_2 change in MIN6 cells after glucose stimulation.

Simultaneous measurements of NADH FLIM and PLIM and the correlation of metabolic parameters and O_2 concentration were published first by Kalinina et al. [637]. The authors observed changes in the NADH lifetime with the O_2 concentration and after addition of antimycin A. Changes of the NADH decay functions with the intracellular O2 concentration were also demonstrated by Shcheslavskiy et al. [1130].

Lukina et al. [801] used a fibre-based TCSPC system with implantable fibre tips (see page 325 and page 622 of this book) to record NAD(P)H decay curves simultaneously with phosphorescence decay curves of an oxygen sensor in mouse tumors. The authors found characteristic changes in the NADH decay parameters and the O_2 concentration between healthy tissue and tumor tissue.

Plant Physiology

The fluorescence of plant tissue is dominated by the emission of chlorophyll. Chlorophyll is excited at any wavelength throughout the visible spectrum. It emits strong fluorescence in the spectral range from 700 to 800 nm. The chlorophyll fluorescence is closely related to the efficiency of photosynthesis. Energy used in the photosynthesis process is not emitted as fluorescence, and energy emitted by fluorescence does not contribute to photosynthesis. The quantum efficiency of the chlorophyll fluorescence - and thus the fluorescence lifetime - is therefore an indicator of photosynthesis rate, and an indicator of plant health.

Early chlorophyll lifetime measurements have been performed by Schneckenburger et al. [1074-1080] and applied to the detection of plant diseases, especially forest decline by environment contamination.

Falkowski, Lin, and Gorbunov [439, 791] have measured the quantum yield of photochemistry and the fluorescence decay time of chlorophyll in phytoplankton. They collected 200,000 data sets at various locations in five oceans. Night time (dark-adapted) lifetimes ranged from 0.5 to 2.7 ns. From the data the authors calculated an average quantum yield of photochemistry of 0.35, and a average quantum yield of the fluorescence of 0.07. The remaining 58% of the absorbed energy is converted into heat.

Pavlinska et al. examined the responsiveness of *Dunalliela tertiolecta* algae to Cadmium, Acidification, and laser-induced photobleaching [951]. They recorded FLIM in two channels, from 500 to 550 nm, and from 650 to 710 nm. Presence of cadmium caused an increase in the intensity in the 500-550-nm channel but no change in the fluorescence lifetime. Acidification caused an increase in the intensity accompanied by an increase in lifetime. An examination of the lifetimes of *Chlorella sp.* under different acidification [823] showed a decrease in intensity and a decrease in the lifetime, τ_1, in the red channel with increasing acidity. Under severe acidification, also the lifetime, τ_2, in the green channel changed but the change went toward longer lifetime.

In addition to chlorophyll, plant tissue contains an (often unknown) number of different fluorophores, namely carotenoids and flavinoids [578, 1353, 1354]. Many of them are fluorescent but little is known about the fluorescence lifetimes and their dependence on environment conditions. FLIM measurements of plant tissue with the bh DCS-120 MP system and ultra-fast detectors have shown multi-exponential decay functions with extremely fast decay components, see Fig. 797. The fast decay component, t_1, at the cursor position has a lifetime of 33 ps, and it is present with 87% of the amplitude of the entire decay function!

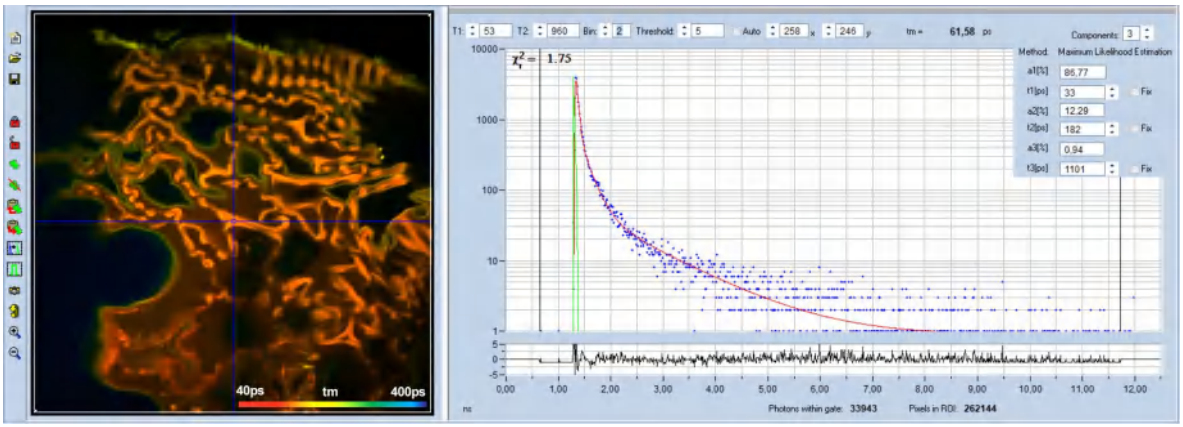


Fig. 797: Tissue in an anther of a green pine cone. Note the fast decay component, t_1, with 33 ps decay time. The component constitutes 87% of the amplitude of the entire decay.

Due to the large number of fluorophores which have to be expected it can by useful to record multi-wavelength decay or multi-wavelength FLIM data. A multi-wavelength FLIM image of plant tissue (a moss leaf) is shown in Fig. 798. The fluorescence of chlorophyll is detected above 680 nm, at the red end of the spectrum. At wavelength below 650 nm fluorescence from other compounds, presumably from flavines, is detected. The intensity of the flavin fluorescence is much lower than that of the chlorophyll fluorescence; the intensity in Fig. 798 had to be normalised to show the flavin images at all. The decay times in the flavin channels are generally short, and strongly multi-exponential.

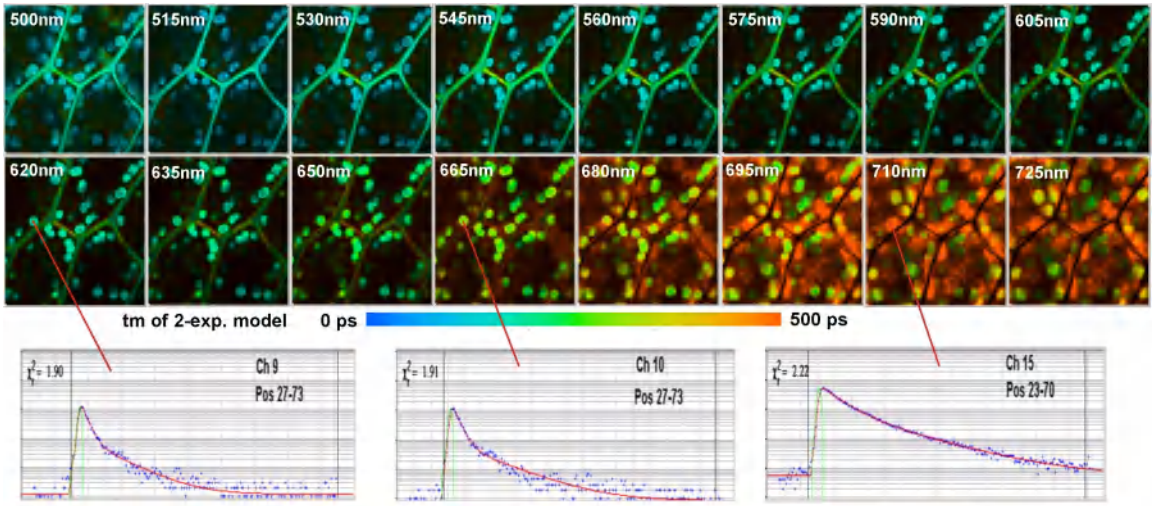


Fig. 798: Multi-spectral FLIM of plant tissue. Moss leaf, LSM 710 NLO, two-photon excitation at 850 nm. Amplitude-weighted mean lifetime of double-exponential fit. Intensity normalised to brightest pixel of each wavelength interval. Decay curves displayed for indicated spot of the 620 nm, 665 nm, and 710 nm images.

Chlorophyll Transients

The fluorescence of chlorophyll competes with the energy transfer into the photosynthesis channels. The photosynthesis rate changes with the light intensity and the time of exposure. Therefore, the fluorescence lifetime of the chlorophyll in live plant tissue not only depends on the state of the plant but also on the light intensity, and the time of exposure.

The changes in the fluorescence intensity of chlorophyll with the exposure to light have already been found 1931 by Kautsky and Hirsch [649]. The effects have been called fluorescence induction, fluorescence transients, or Kautsky effect [516, 517, 834]. When a dark-adapted leaf is exposed to light the intensity of the chlorophyll fluorescence starts to increase. After a steep rise the intensity falls again and finally reaches a steady-state level. The rise time is on the range from a few milliseconds to a second, the fall time can be from several seconds to minutes.

The initial rise of the fluorescence intensity is attributed to the progressive closing of reaction centres in the photosynthesis pathway. Therefore the quenching of the fluorescence by the photosynthesis decreases with the time of illumination, with a corresponding increase of the fluorescence intensity. The fluorescence quenching by the photosynthesis pathway is called ‘photochemical quenching’, and the associated change in the fluorescence intensity ‘photochemical transient’. The slow decrease of the fluorescence intensity at later times is termed ‘non-photochemical quenching’. Both the photochemical and the non-photochemical transient are accompanied by a corresponding change in the fluorescence lifetime [18, 500, 872].

These light-induced changes in the fluorescence lifetime in live plants are often considered an obstacle for the use of the fluorescence lifetime in chlorophyll research. The effects make it necessary that measurements are performed under exactly defined illumination, and under steady-state conditions. Researchers in the chlorophyll field therefore often consider lifetime

measurements too difficult and resort to intensity measurements. However, the chlorophyll transients can well be recorded by advanced TCSPC technique. We believe that the amplitude and the speed of the chlorophyll transients are an even better indicator of the plant state than fluorescence intensity or decay measurements under steady-state conditions.

Single-Point Measurement

Both the photochemical and the non-photochemical quenching transients can be measured by time-series TCSPC. A dark-adapted leaf is put in a standard fluorescence-decay measurement setup. The laser is switched on, and a series of decay recordings is started. A non-photochemical fluorescence transient of a leaf recorded this way is shown in Fig. 799. The time of the series runs from the back to the front. From left to right, the behaviour of a fresh leaf, a faded leaf, and a dried leaf is shown. The differences between leaves of different health state are striking. In fact, the amplitude and the speed of the non-photochemical transient are a much better indicator of the health state of the plant than the (average) lifetime itself. The figure also shows that a measurement of a single decay function of the chlorophyll fluorescence delivers unreliable results: Unless the measurement is performed under steady-state conditions, i.e. when the transient is complete, the measured decay curve would be just an average of decay profiles of an undefined time interval within the transient. Most likely, the results would depend on the acquisition time and the excitation power. More important, it would miss the most important effect, which is that the decay profile is *changing*, and that the change bears information of the health of the plant.

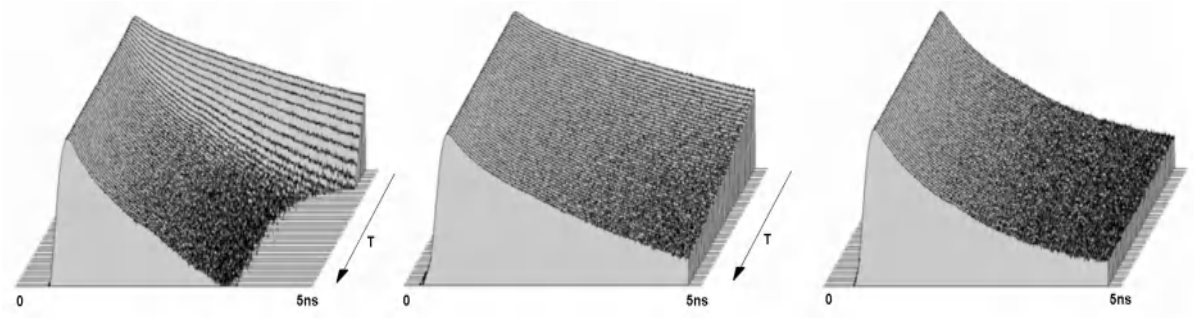


Fig. 799: Sequences of fluorescence decay curves measured at a leaf after start of illumination. Left to right: Fresh leaf, faded leaf, dried leaf. Decay time axis 0 to 5 ns, time per curve 2 seconds, logarithmic intensity scale. The sequence starts from the back.

The decay curves in Fig. 799 were recorded at speed of 2 seconds per curve. There is no problem to record enough photons for high accuracy decay analysis within this time. To record the 'photochemical transient' a much faster recoding speed has to be used. The problem is that the acquisition time per curve becomes too short to record enough photons. The solution is triggered accumulation of the sequence: The light is periodically turned on and off, a sequence of decay curve is recorded over the time of the 'ON' phases, and the photons of many on/off periods are accumulated. Technical details are described at page 333 of this handbook.

An example for the recording of a photochemical transient is shown in Fig. 800. The time per curve is 100 µs, 10,000 on/off periods were accumulated. The time of the sequence runs from the front to the back. It can clearly be seen how the fluorescence lifetime increases over the time into the laser-on period.

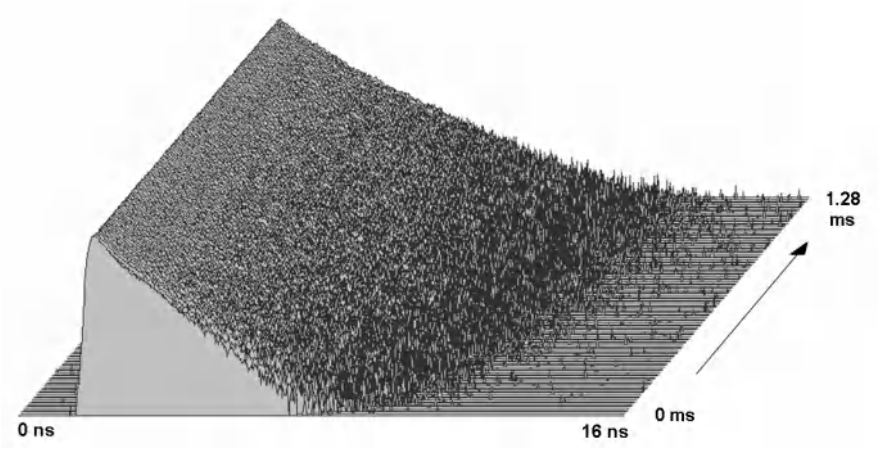


Fig. 800: Photochemical quenching transient of chlorophyll in a fresh leaf. The sequence starts at the front. Time per curve 100 us, transient-time scale 0 to 12.8 ms into laser-on periods. 10,000 on/off cycles accumulated.

FLIM of the Non-Photochemical Transient

The non-photochemical transient can be recorded by FLIM. Even with a conventional record-and-save procedure a time series can be recorded at a speed of one image per second. An example is shown in Fig. 801. The acquisition time per image was 1 second, the image size 256 x 256 pixels x 64 time channels. It can clearly be seen that the fluorescence lifetime becomes shorter over the time of exposure. Other examples have been shown in [154, 612, 652]. Holub et al. have recorded a FLIM series of the non-photochemical transient by wide-field frequency domain FLIM [593] at a rate of a few seconds per image. With a reasonably fast scanner TCSPC FLIM reaches at least the same speed, with the advantage that depth resolution is available.

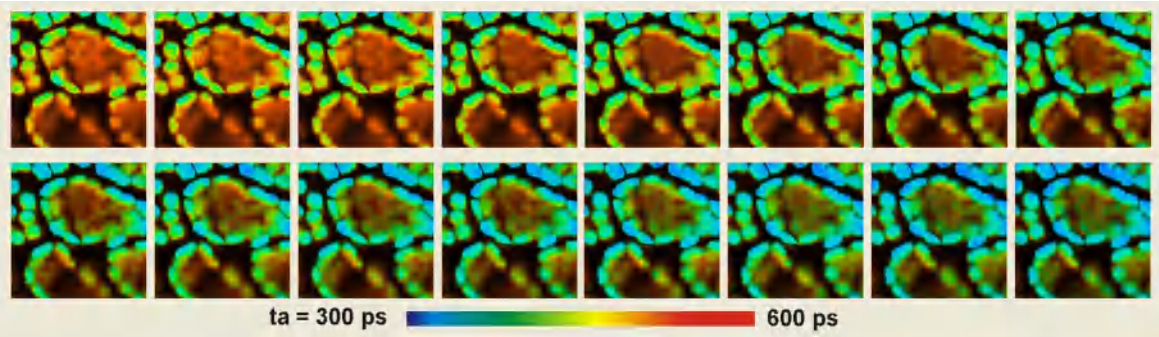


Fig. 801: Change of the fluorescence lifetime of chlorophyll with time of exposure. Moss leaf, 1-photon excitation at 445 nm, 256x256 pixels. SPC-150 autosave time-series, 1 image per second. Intensity-weighted lifetime of double-exponential fit.

Temporal Mosaic FLIM

A more advanced way of recording time-series of non-photochemical chlorophyll transients is by temporal mosaic FLIM. Time series recording is performed over the elements of a mosaic of FLIM images. Because the entire mosaic is kept in the memory the sequence is not slowed down by save operations. Please see section ‘Temporal Mosaic FLIM’, page 402. A chlorophyll series recorded by mosaic FLIM is shown in Fig. 802.

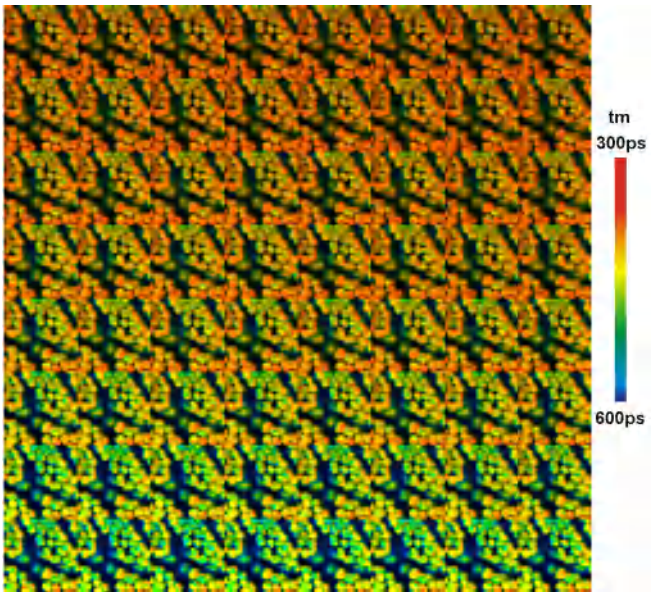


Fig. 802: Non-photochemical transients in the chloroplasts of a moss leaf, recorded by temporal mosaic FLIM. Time runs from lower left to upper right. Red means long lifetime. DCS-120 confocal scanning system.

The sequence contains 64 images (or 64 mosaic elements) for consecutive times after the turn-on of the excitation light. The acquisition time per element was 1 second, the total time of the sequence 64 seconds, the image size of each element 128 x 128 pixels, with 256 time channels per pixel.

Recording the Chlorophyll Transients by FLITS

A second way to record the chlorophyll transients with spatial resolution is by using the 'FLITS' technique [162, 164]. FLITS records the changes in the decay profile of a sample over time and along a one-dimensional scan. For technical details please see page 410 of this handbook. Procedures to record FLITS are described in [68] and [69]. An example for the non-photochemical transient is shown in Fig. 803. It shows decay curves for one selected pixel within the line scan for times of 0.5 s, 7.5 s, and 13.4 s after the turn-on of the laser. The mean lifetimes, t_m, obtained from a double-exponential fit are 560 ps, 385 ps, and 311 ps, respectively. The changes in the decay profiles are clearly visible.

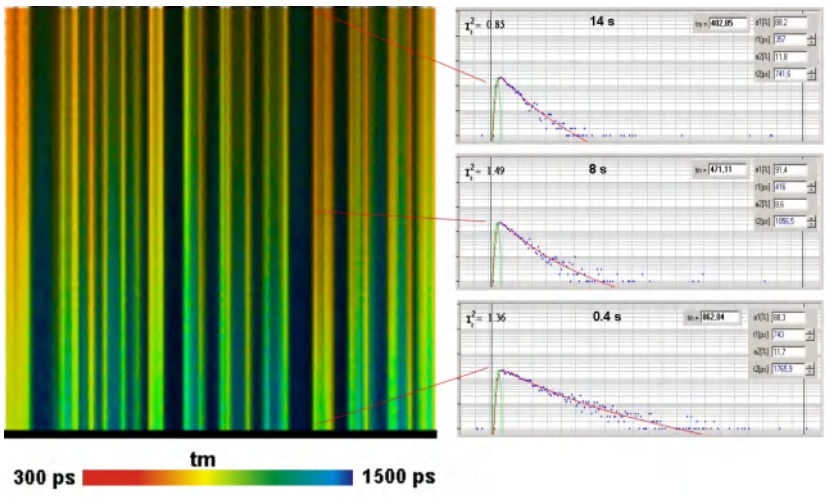


Fig. 803: FLITS of chloroplasts in a plant leaf. Non-photochemical transient, decay curves for a selected pixel within the line for times of 0.5 s, 7.5 s, and 13.4 s after the turn-on of the laser. Lifetimes are amplitude-weighted averaged of a double exponential fit to the decay data. The vertical stripes are the lifetime traces of individual chloroplasts over the transient-time.

With FLITS, a sequence fast enough for the photochemical transient can be recorded. To obtain a sufficiently high number of photons per time interval accumulation over a larger number of on/off periods must be used. An example is shown in Fig. 804.

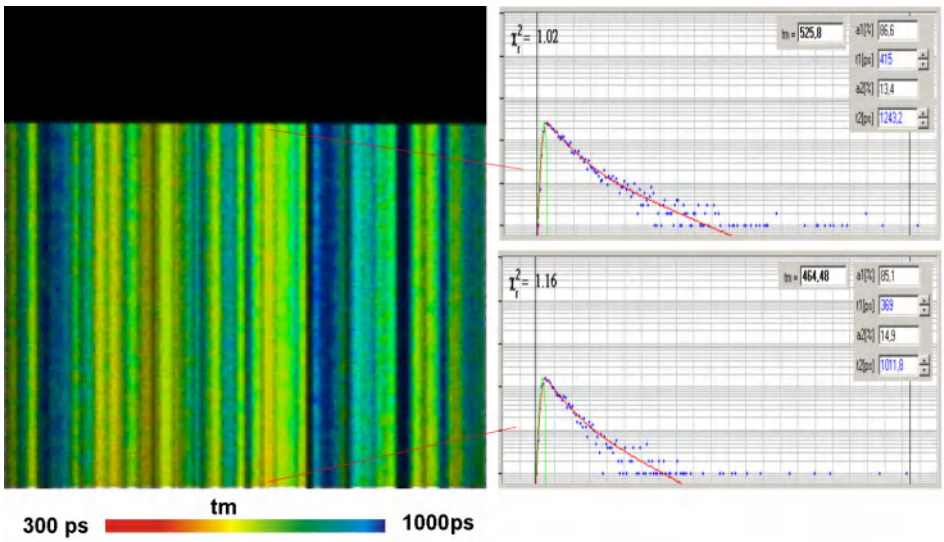


Fig. 804: FLITS of chloroplasts in a plant leaf. Photochemical transient, triggered accumulation, decay curves for a selected pixel within the line for times of 3 ms and 191 ms into the laser-on periods. Amplitude-weighted lifetime of double-exponential decay.

Other Chlorophyll-Lifetime Applications

The results presented above show that lifetime changes induced by physiological effects in plants can be recorded by various operating modes of the bh TCSPC modules. Nevertheless, very little has been published in this area. Broess recorded FLIM data of single chloroplasts [256]. Teplicky et al. [1236] recorded FLIM of Chlorella algae, aiming on a possible use of the chlorophyll lifetimes for environment monitoring. Gilmore et. al [500] showed the fluorescence lifetime changes during the non-photochemical transient, Nozue at al. [918] recorded FLIM for different laser power, and the associated changes in the chlorophyll decay parameters. Lambrev et al. [748] recorded spectrally resolved intensity changes during the transient. Miloslavina et al. [872] used TCSPC to record decay curves of dark-adapted cells, light-adapted cells, and light-adapted cells under the influence of DCMU (3-(3'4'-dichlorphenyl)-1,1-dimethylurea). Lifetime imaging of plant tissue during the non-photochemical transient was used by Holub et al. [593]. The authors used a wide-field frequency-domain technique that acquired images within 3.9-second intervals during the non-photochemical transient. Iwai et al. [612] used a bh SPC-830 TCSPC module at a Leica SP5 confocal laser scanning microscope. By using SPCImage data analysis they showed that there are distinct peaks in the lifetime distribution that change their relative amplitudes during exposure to light. Other applications aim on the construction of chlorophyll-based light harvesting complexes with of higher absorption coefficients. Grayson et al. [519] designed a YFP-enhanced reaction centre, Szalkowski et al. [1216] used chlorophyll assemblies on nanowires.

Other Biological FLIM Applications

Internalisation and Conversion of Photosensitizers for PDT

Cells incubated with photosensitizers used in photodynamic therapy (PDT) show significant changes of the fluorescence lifetime with the incubation time and the exposure time. The effects can be used to reveal the binding of the photosensitizer to different protein structures and to track the formation of photoproducts. An SPC-730 module in combination with a bh PML-SPEC system attached to a Zeiss LSM 410 microscope was used for tracking the metabolites of 5-ALA (5-aminolevulinic acid, an approved sensitizer for photodynamic therapy) or Photofrin in living cells [1036, 1037, 1038, 223]. In the cells 5-ALA converts into protoporphyrin-9, which causes clearly detectable changes in the fluorescence lifetime.

Su et al. [1200] performed PDT by 5-ALA in cells and simultaneously recorded NADH lifetime images. They found that the NADH lifetime increased when the cells died through the apoptotic pathway. By contrast, the lifetime decreased when the cells dies though necrosis.

A FLIM study of the distribution of Radachlorin in cells during PDT was performed by Belashov et al. [192]. The authors found that the fluorescence quantum yield of Radachlorin depends on the pH. Determining the distribution by pure intensity imaging can therefore lead to wrong results. They show that FLIM can be used to discriminate between areas of different pH and, in turn, correct the recorded Radachlorin distribution. Moreover, the ability of FLIM to discriminate between the fluorescence of Radachlorin and other fluorescent compounds allowed the authors to track its accumulation more accurately than by pure intensity imaging [191].

Photothermal Therapy

Rivas Aiello et al. explored the photothermal effect of HeLa cells loaded with poly(vinylpyrrolidone)-coated silver nanoplates and tracked the local temperature with Rhodamine B [1020].

Aggregation of Fluorophores, Oligomerisation

Aggregation of fluorophore molecules has an influence on the fluorescence lifetimes. Changes are observed both for aggregation of the fluorophore molecules themselves and for aggregation of the proteins they are bound to. The effect has been used to investigate the internalisation of aggregated photosensitizers by tumor cells and the monomerisation of the aggregates inside the cells [654]. Lifetime heterogeneity due to aggregation was also reported for E-Bodipy fluorophores, see [377]. Greiner et al. used the effect of oligomerisation on the fluorescence lifetime of rhodamine in rhodamine-labelled Vpr(52-96) peptides to observe HIV-1 internalisation into cells in [523]. Changes in the lifetime of Rhodamine B linked to proteins was used be Haque et al. [555] to study oligomerisation.

Blood Cells

Borges da Silva et al. used autofluorescence FLIM on red blood cells. They showed that label-free FLIM is able to intracellular polymerisation of hemoglobin in sickel cells [235].

Detection of Special Endogenous Compounds

Mueller-Harvey et al. recorded FLIM images of flavanols in plant cells [894]. Fluorescence lifetime of less than 45 ps were obtained by TCSPC FLIM with an SPC-830. Bisby et al., and Botchway et al. used a sub-picosecond laser of 630 nm to excited endogenous compound with absorption spectra in the UV. They obtained lifetime images of combretastatin [216], of propranolol [217] and of serotonin [241].

Characterisation and Use of Labels for Endogenous Compounds

Shivalingam et al. [1151] developed small-molecule based sensor for G-quadruplexes and evaluated them by fluorescence decay measurements and FLIM. Okkelman et al. [930] used lifetime changes of a common nuclear stain, Hoechst 33342, to study cell proliferation, S phase progression over several division cycles, and effects of anti-proliferative drugs. Abdollahi et al. [3] used Hoechst 34580 to visualise radiation-induced chromatin decondensation. Prions were instigated by Magnusson et al. by staining with PTAA and several structurally related oligothiophenes [810]. Kuchlyan et al. [717] and Mackowski [808] used FLIM and FCS to study graphene oxide interactions with serum albumine, with the aim to develop new biosensors. Pliss et al. [977] transfected cells with GFP and used the change of the lifetime by the refractive index of the local environment as an indicator of the local protein concentration.

Diffusion of Exogenous Compounds through Skin

There is currently an increasing amount of research related to the development of cosmetic products and sunscreens. The diffusion of anti-ageing products into the skin and the metabolic effect on the different layers of the skin must be tested. Coloration products and sunscreens must be proved to remain in the hair or in the epidermis. Because animal experiments are largely banned from these tests advanced microscopy techniques are increasingly used in the cosmetics industry. Related work on multiphoton lifetime imaging of human hair has been described in [428]. The migration of ZnO particles of sunscreens in skin has been studied in [498, 790, 984].

FRAP

FLIM has been used in combination with FRAP (fluorescence recovery after photobleaching) [604]. A region of the sample is photobleached, and then the diffusion of into that region is observed by time-series FLIM. Compared to intensity measurements FLIM has two advantages: The FLIM data help distinguish a possible bound and an unbound fluorophore fraction, and may show possible damage to the tissue via changes in the autofluorescence lifetimes.

Metabolisation of Exogenous Compounds

Changes in the fluorescence lifetimes of exogenous fluorophores can be used to track metabolic activity or transport phenomena. The transport and conversion of fluorescein in rat liver has been described in [1021].

Temperature Measurement in Cells

Okabe et al. designed a temperature probe that reports the local temperature in cell organelles via its fluorescence lifetime [929]. By using TCSPC FLIM they found temperature differences inside cells. The nucleus was, on average, warmer than the cytoplasm by 0.96 °C. They also found that the temperature difference depends on the cell cycle. The temperature was also increased in centrosomes, and in the mitochondria. The technique is especially interesting because it yields information about metabolic activity. It could complement metabolic imaging via the NADH fluorescence. Viger et al. used the temperature-dependent lifetime of fluorescein to monitor the temperature of water confined in drug-loaded nanoparticles on near-infrared-induced heating. A lifetime change of 500 ps over a temperature range from 20 to 70 Celsius was found [1289].

Hayashi et al. developed a temperature sensor based on a fluorescent polymer. The sensor yields a temperature resolution of 0.05 to 0.54 degrees, and works within a range from 28 to 38 °C. FLIM analysis in cells showed a temperature difference between the nucleus and the cytoplasm and heat production near the mitochondria [561].Protocols of using the sensor are described in [611].

Jenkins et al. [624] describe a sulforhodamine temperature sensor. The sensor is cell-permeable, localises in the cytoplasm, and has a temperature response of 0.037 ns/K. They evaluated the sensor for temperature imaging in combination with pO_2 imaging by PLIM.

Discrimination of Unwanted Fluorescence Components

In some cases, FLIM is just used to suppress unwanted fluorescence components by multi-exponential decay analysis. This has been used in experiments of protein folding, dynamic protein interactions, and binding of dyes to DNA strands, in microfluidic channels. A problem of these experiments is often that a fraction of the fluorophore binds to the channel walls. The fluorescence lifetime of the bound fluorophore molecules is different from that of the molecules in solution. FLIM is thus able to discriminate the two fractions via double-exponential decay analysis [965, 1023].

Imaging of Lignin in Wood

Lignin in wood has technical importance because it gives the wood its mechanical strength. Lignin imaging has also a relation to bio-fuel production. Donaldson and Radotic used a Leica SP5 with a bh SPC-830 FLIM module to detect difference in lignin composition [398].

FLIM of Solid-State Materials

FLIM of diamond has been described by Liaugaudas et al. [779, 780]. They used a Leica SP2 laser scanning microscope with a 467 nm ps diode laser and an SPC-830 TCSPC FLIM module. They found different lifetimes and decay profiles for different colour centres. Intensities were generally low, and FLIM required acquisition times of several ten minutes. Kalinushkin and Uvarov [639] used FLIM to map the charge-carrier lifetime in semiconductor materials.

Other applications are related to photovoltaic devices and new semiconductor materials. In particular, there is currently an increase of research on perovskite and perovskite-like materials. FLIM of Nb- and La-doped $RsTiO_3$ substrates was reported by Rodenbücher et al. [1026]. The same authors used FLIM in combination with AFM [1027] and FLIM in combination with phase contrast and fluorescence-intensity microscopy [1028] for the investigation of SrTiO3. Schultz et al. studied the influence of laser-based patterning on the carrier lifetimes in $Cu(In_x,Ga_{1-x})Se_2$ films [1083]. The optical emission from this material occurs around 1300 nm, therefore an id-200 InGaAs SPAD was used as a detector. Lifetime images were scanned with a modified DCS-120 scan head.

Brovelli et. al. [257] used FLIM to investigated energy transfer in semi-conducting polymers. McNeil et al. [841] used bulk fluorescence decay measurements to investigate charge transport in dye-sensitised nanoparticle films. Cadby et al. [266, 267] studied polymer blends by NSOM FLIM, see page 458.

Luminescence lifetimes of inorganic materials can be very long, see FLIM images of zinc oxide particles, and of Autumit, page 438. It can therefore by useful to combine FLIM with PLIM, see page 434.

FLIM with Quantum Dots

Quantum dots are increasingly used as markers and sensors in fluorescence lifetime microscopy. Carlini and Nadeau [277] report on possible use of quantum dots as sensors of the molecular environment, and on the uptake and processing in the cells. Tu et al. [1265] used antibody conjugated silicon quantum dots with long fluorescence lifetime to discriminate fluores-

cence from organic fluorophores. Zhang et al. [1389] described quantum dots with specific fluorescence lifetimes and fluorescence spectra as markers for different for cell structures.

Forensic FLIM Applications

There are also possible FLIM applications in forensic science. Microscopy techniques are commonly used in forensics and any additional contrast parameter is welcome. The application of FLIM to detection and identification of gunshot residue is described in [215]. Another application is the detection of drugs, poisons or coloration products in human hair. The substances may be enclosed in the keratin fibre structure of the hair [428] and remain there for a longer period of time, holding a record of the exposure of a person to different drugs or chemicals.

Combination with Micro MRI

Stark et al. Combined two-photon excited autofluorescence and SHG imaging and autofluorescence FLIM with MRI micro-imaging. The method was demonstrated on barley embryos [1181].

Clinical Applications of FLIM

Multiphoton Tomography of Human Skin

Multiphoton tomography of human skin exploits the fact that two-photon excitation in combination with non-descanned detection delivers optically sectioned images of tissue layers as deep as 100 µm. The three-dimensional tissue structure can be reconstructed from the data at sub-cellular resolution. The technique goes back to the work of Gratton, König, Masters, So and Tromberg who showed that in-vivo two-photon imaging of cells and, especially, human skin is possible without impairing the viability [681, 684, 827, 828]. Please see also [829] for a selection of early multiphoton imaging papers.

Dermainspect Instrument

Of course, a normal laser scanning microscope is inconvenient or even impossible to use at a human patient. A commercial instrument for clinical skin inspection has therefore been designed by Jenlab, Jena, Germany. The 'Dermainspect' is based on excitation by a Ti:Sapphire laser, a fast optical galvanometer scanner, and non-descanned detection. FLIM is integrated by a bh SPC-830 TCSPC module. FLIM is detected in three spectral channels by separate detectors, or in 16 channels by a bh MW FLIM detector. The instrument is shown in Fig. 805.



Fig. 805: 'Dermainspect' system of Jenlab GmbH, Jena, Germany. Karsten Koenig and Peter So are demonstrating the instrument.

An impressive number of papers is related to FLIM data obtained by this instrument and its successors, please see [13, 356, 385, 427, 498, 507, 592, 643, 686, 687, 688, 690, 691, 692, 714, 756, 757, 758, 790, 815, 946, 947, 984, 1010, 1021, 1022, 1047, 1048, 1049, 1148, 1149, 1146, 1244, 1245, 1397]. A summary of clinical multiphoton tomography of skin is given in [690 and 1049]. The combination with micro-endoscopes described in [691].

Earlier Dermainspects used a single SPC-830 TCSPC FLIM module with a router for three or four detector channels. To record at higher count rates (and thus achieve shorter acquisition times) the instruments can be upgraded with more recent SPC-153 (three-channel) or SPC-154 (four-channel) parallel TCSPC systems. The general principle is shown in Fig. 806. The principle is that of a multiphoton microscope with non-descanned detection, compare Fig. 514, page 345. The fluorescence light collected by the microscope lens is split off by a dichroic mirror, split into three (or four) spectral components by dichroic mirrors, and detected by three or four detectors. The detector signals are recorded by parallel TCSPC channels. The TCSPC modules work in the normal FLIM acquisition mode, see section Fluorescence Life-

time Imaging (FLIM), page 124. An image recorded by this system is shown in Fig. 807. It shows the Stratum granulosum of a human volunteer. The excitation wavelength was 750 nm.

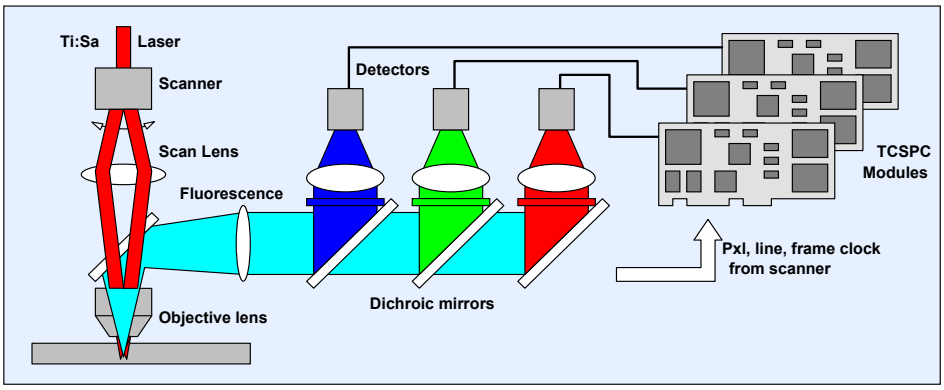


Fig. 806: Optical principle of the Dermainspect (upgraded with three parallel SPC-150 TCSPC channels)

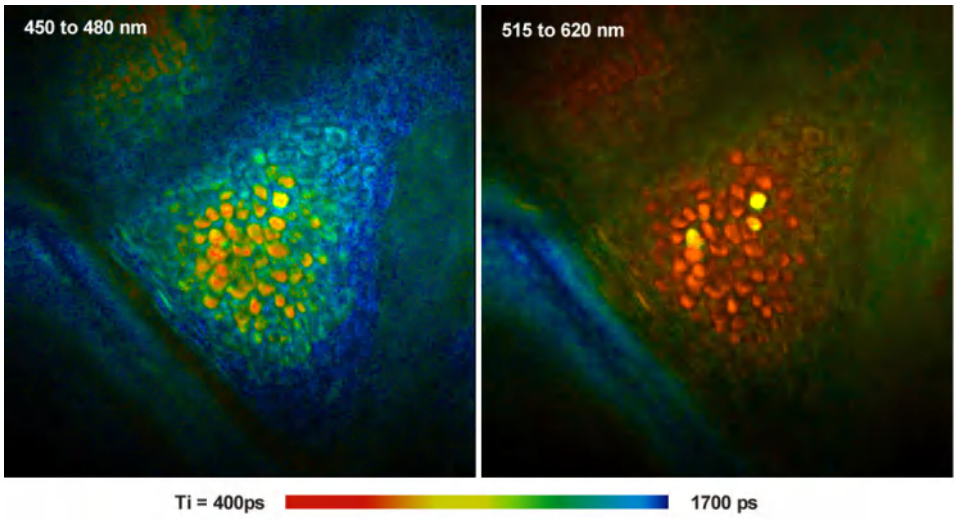


Fig. 807: FLIM of the stratum granulosum at the forearm of a human volunteer. Data courtesy of Washington Sanchez and Michael Roberts, University of Queensland, Brisbane, Australia.

The Dermainspect has been used with the MW-FLIM multi-wavelength FLIM detector based on the PML-16 16-channel detector. Fig. 808 shows a typical result. Lifetime images were recorded simultaneously in eight wavelength intervals from 400 nm to 600 nm. Images of the mean (amplitude-weighted) lifetime of a double-exponential fit are shown left, images of the amplitude ratio right. The images were still recorded with the older PML-16-1 (multi-alkali) detector and 32 bit SPCM software. With the new PML-16 GaAsP and 64-bit software the resolution can be improved to the level of Fig. 807.

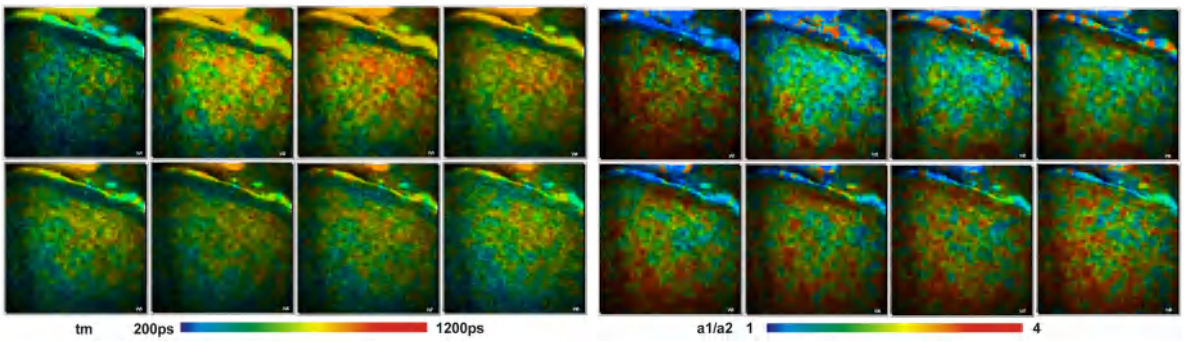


Fig. 808: Multi-wavelength multi-photon lifetime images of human skin. Wavelength from 400 to 600 nm. Left: Mean (amplitude-weighted) lifetime of double-exponential fit. Right: Ratio of the amplitudes of the decay components.

MPT FLEX

Recently, Jenlab has introduced the 'MPT FLEX' which has the scan head on a flexible arm. The instrument is show in Fig. 809, left. The MPT FLEX combines autofluorescence intensity imaging, SHG imaging, CARS, and FLIM [1331]. An intensity image and a lifetime image of human skin (both recorded by an SPC-830 module) are shown in Fig. 809, middle and right. It can clearly be seen that the FLIM image contains information not visible in the intensity image. Please see also chapter 'Label-Free FLIM of Cells and Tissue', page 527.

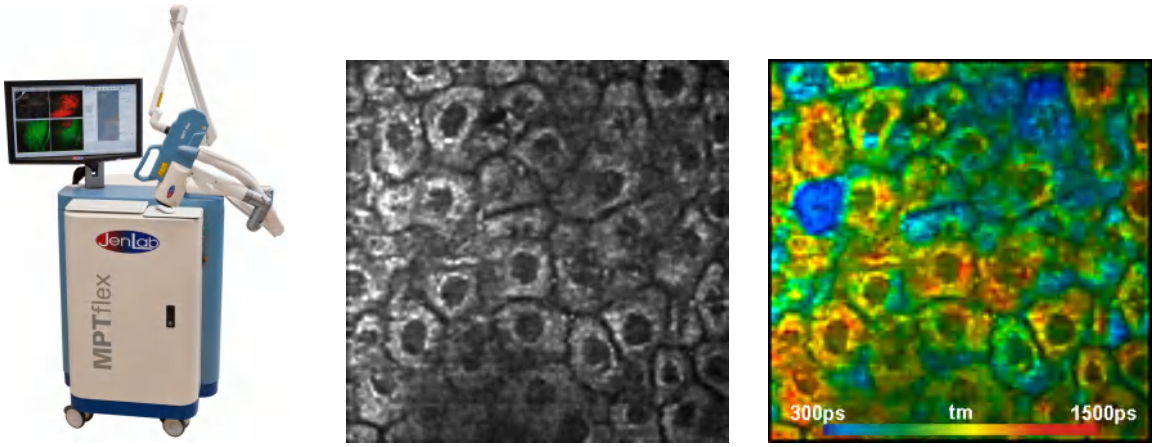


Fig. 809: MPT FLEX system. Middle and Right: Intensity image and FLIM image of human skin.

Comparison with NIR Reflection Imaging

It should be mentioned that deep images of human skin can also be obtained by NIR reflection imaging. These systems scan the sample with a focused beam of NIR light, and detect the backscattered light through a confocal pinhole.

Steven et al. compared the Dermainspect with a confocal system for reflection ophthalmic imaging [1188]. The general difference of the systems is that the Dermainspect (and the MPT FLEX) use fluorescence while the ophthalmic scanner uses reflected (or scattered) NIR light for imaging. Reflection imaging has, of course, the advantage that high-intensity signals are obtained. The acquisition times are therefore short. The authors point out correctly that multiphoton fluorescence imaging has the advantage of delivering information about metabolic processes and separating of different fluorescent species, while the reflection system only delivers morphological information.

The same differences should be noted for another reflection imaging system, the Vivascope of Lucid Inc. The Vivascope uses NIR lasers to obtain confocal reflection images of tissue in vivo [994]. The instrument delivers morphological information with excellent resolution at high image rate. However, the metabolic information contained in fluorescence or fluorescence lifetime data is not accessible.

The lack of molecular information in reflection imaging data has initiated attempts to upgrade reflection scanning systems with fluorescence and fluorescence lifetime detection. Fluorescence lifetime images recorded with the Vivascope are shown in Fig. 665, page 449.

Ophthalmic FLIM (FLIO)

Biomedical Background

Reflection and fluorescence imaging of the ocular fundus is an established tool of diagnosing eye diseases [594, 799, 1163, 1032]. Reflection imaging is performed at near-infrared wavelength where the sensitivity of the retina is low. Therefore high signal intensities and high images rates are obtained. However, reflection imaging delivers only morphological information. Autofluorescence intensity imaging yields additional information but is limited by the usual problems: The fluorescence signals contain components of several fluorophores which cannot be clearly separated in intensity images. More important, intensity variations by metabolic alterations cannot be distinguished from variations in the concentration of the fluorophores.

Fluorescence lifetime imaging improves the situation considerably: Metabolic changes or pathological alterations in the tissue constitution induce changes in the fluorescence lifetimes. These are observed independently of the variable concentration of the fluorophores and of possible absorbers. Ophthalmic FLIM is therefore a potential technique of diagnosing eye diseases. However, FLIM of the human retina faces a number of problems.

The most obvious one is that the excitation power must be very low. The maximum permitted excitation power is on the order of 100 µW. Compared to FLIM microscopy this may sound a lot. However, the numerical aperture at which the fluorescence is collected is limited by the lens of the eye and thus much smaller than in microscopy. Consequently, the collection efficiency is much lower and so is the detected fluorescence intensity.

The second problem is eye motion. It is impossible for the patient to keep the eye fixed at one point for longer than a few seconds. The imaging system must therefore track the eye motion and assign the detected photons to the right pixels.

The third problem is the transmission of the ocular media. The transmission of the eye lens drops dramatically below 450 nm and is almost zero at 400 nm [1094, 1095]. The transmission curve shifts to longer wavelength with increasing age. In practice, the ocular transmission prevents excitation of NADH in the retina of an intact eye. Although indications of weak excitation of NADH at 450 nm have been found [1099], neither the ratio of bound and unbound NADH [1155, 1156] nor the redox ratio, i.e. the intensity ratio of NADH and FAD fluorescence [284, 285], can be used as an imaging parameter.

Most of the observable fluorescence of the fundus comes from FAD and components of Lipofuscin. Lipofuscin is a mixture of 10 slightly different fluorophores. The most relevant component is A2E, a by-product of the visual cycle that accumulates in the retinal pigment epithelium. However, there is also contribution from AGE (advanced glycation end products) and from the collagen and elastin in the connective tissue [1093, 1094, 1095, 1096, 1097, 1098, 1101, 1102, 1103]. All these fluorophores exist in several configurations with different decay components. Some of these have very short lifetimes. The decay profiles are thus multiexponential. Lifetimes and amplitudes of the decay components for different fluorophores and tissue types are given in Table 1.

Substance	t_1 (ps)	a_1 (%)	t_2 (ps)	a_2 (%)
Collagen 1	670	68	4,040	32
Collagen 2	470	64	3,150	36
Collagen 3	345	69	2,800	31
Collagen 4	740	70	3,670	30
Elastin	380	72	3,590	28
A2E	170	98	1,120	2
Lipofuscin	390	48	2,240	52
Melanin	280	70	2,400	30
FAD	330	18	2,810	82
AGE	865	62	4,170	28
NADH	387	73	3,650	27
Ocular tissue				
Retina	260	90	2,790	10
RPE	210	96	1,800	4
Choroid	500	70	3,400	30
Sclera	450	65	3,110	35
Cornea	570	70	3,760	30
Lens	490	69	3,600	31

Table 1: Fluorescence lifetimes and amplitudes of decay components for endogenous fluorophores in the fundus and for various tissue types. From [1094], bi-exponential approximation of decay profiles

To resolve these lifetime components the FLIM system must have high efficiency, high time resolution, and a clean and stable IRF. Moreover, it must be able to resolve multi-exponential decay profiles. The FLIM system has to work at the high scan rates used in ophthalmic scanners. Multi-dimensional TCSPC is clearly the best FLIM technique for fluorescence lifetime imaging of the retina [1087, 1089, 1091, 1093, 1094].

System Architecture

Ophthalmic imagers normally use a scanning technique with the pupil of the eye placed in the exit pupil of the scanning system [1128]. This reduces image distortion and blurring due to the poor optical quality of the lens of the eye. Moreover, confocal detection is used to suppress reflection, scattering, and fluorescence signals from the lens of the eye. A suitable instrument has been developed by Schweitzer and Hammer [152, 1089, 1091, 1093]. The general principle of the instrument is shown in Fig. 810.

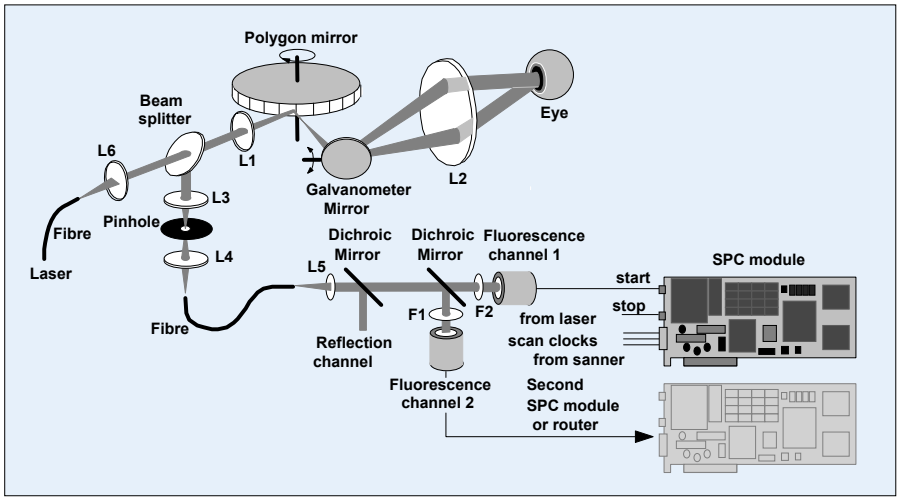


Fig. 810: Principle of an ophthalmic FLIM system [152, 1091]

The instrument uses one or two SPC-830 or SPC-150 TCSPC modules in combination with a modified scanning ophthalmoscope. The scanner has optical fibres both for the input of the excitation light and the output of the light returned from the fundus. Thus, it can relatively easily be combined with different light sources and detectors.

The optical system is based on a modified CLSo ophthalmic scanner from Zeiss, Germany. A 445 nm or a 473 nm picosecond diode laser is used for fluorescence excitation. Scanning in X is performed by a fast polygon scanner, scanning in Y deflection a galvanometer mirror.

A lens, L1, forms a focus approximately halfway between the polygon mirror and the galvanometer mirror. A second lens, L2, (the scan lens) sends a parallel beam of light into the eye. The beam wobbles with the scanning, with a virtual pivot point in the pupil of the eye. The lens of the eye focuses this beam on the retina. The light returned from the retina leaves the eye via the same beam path, travels back via the scan mirrors, and is separated from the laser light by a wideband splitter. It is focused into a pinhole by a third lens, L3, and transferred to the detectors by an optical fibre.

The returned signal is split into three components. The reflection component is used to co-record reflection images at high rate. The fluorescence component is split further into two wavelength intervals [152]. The best transition wavelength has been found around 560 nm. The short-wavelength channel then records FAD and AGE, the long wavelength channel A2E. The photons are detected by two Hamamatsu R3809U MCP PMTs. The FLIM data are by an SPC-830 module with a router.

The FLIM images are built up by a modified FIFO imaging process. The photons and the scan clock pulses are marked with their times in the fluorescence decay, the detector channel, and the time from the start of the recording. These data are transferred into the computer. The imaging procedure receives also the shift vector from the reflection channel. The lifetime images are built up over the scan coordinates corrected by the shift vector.

The typical count rates obtained by this system were on the order of 1000 to 10,000 s^{-1}. Therefore acquisition times of about 100 to 200 seconds were required to record useful data.

Results

A result obtained with the CLSo scanner is shown Fig. 811. The figure shows lifetime images of the amplitude-weighted average lifetime, τ_{av}, of the fast lifetime component, τ_1, and of the slow lifetime component, τ_2. The fluorescence decay and the result of the fit for the pixel at the cursor position are shown in the lower part of the figure.

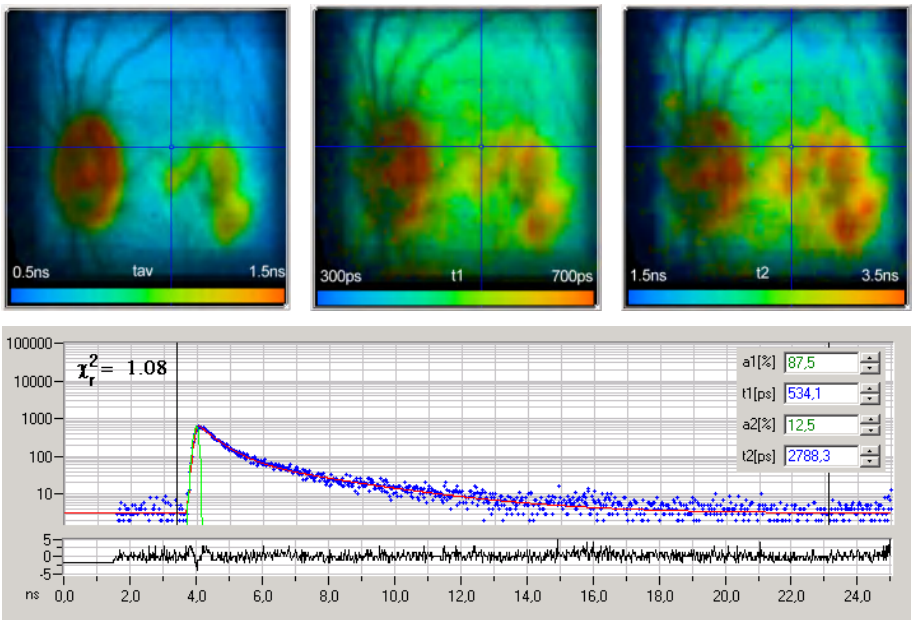


Fig. 811: TCSPC lifetime images of the human ocular fundus Upper left: Average lifetime. Upper middle: Fast lifetime component. Upper right: Slow lifetime component. Lower part: Decay curve in the selected spot and fit results. From [154] and courtesy of Dietrich Schweitzer, Friedrich Schiller University Jena, Germany

Heidelberg Engineering FLIO System

The weakness of the old Zeiss CLSo scanner optics was low optical efficiency. It resulted from the fact that it was not designed for fluorescence imaging. The system thus had considerable losses both in the excitation and in the detection light path.

An entirely new system was designed in cooperation of Heidelberg Engineering, the University of Jena, and Becker & Hickl. The instrument is based on the optics of a Heidelberg HRT III ophthalmic scanner. The scanner uses a fast resonance scanner for X, and a galvanometer mirror for Y deflection. The optical system is optimised for fluorescence detection. The main beamsplitter is a dichroic mirror, and all reflective surfaces have low-loss dielectric coatings.

The fluorescence-detection part uses bh BDL-SMC or BDL-SMN ps diode lasers for FLIM excitation, two HPM-100-40 hybrid detectors for FLIM detection, and two SPC-150 or SPC-160PCIE TCSPC FLIM modules for recording the FLIM data. With these improvements, the detected count rate increased by a factor of 50 to 100.

Another advance is the eye-motion compensation system. Infrared reflection images are recorded frame by frame and analysed by the system computer. The analysis procedure delivers a shift vector that is transferred into the image-buildup procedure of the FLIM system. The FLIM uses the shift vector to assign the photons to the correct pixels, independently of the eye motion. As a result, the FLIM system records images which are not blurred by eye motion. The optical principle is shown in Fig. 812, a prototype of the new FLIO Spectralis instrument in Fig. 813.

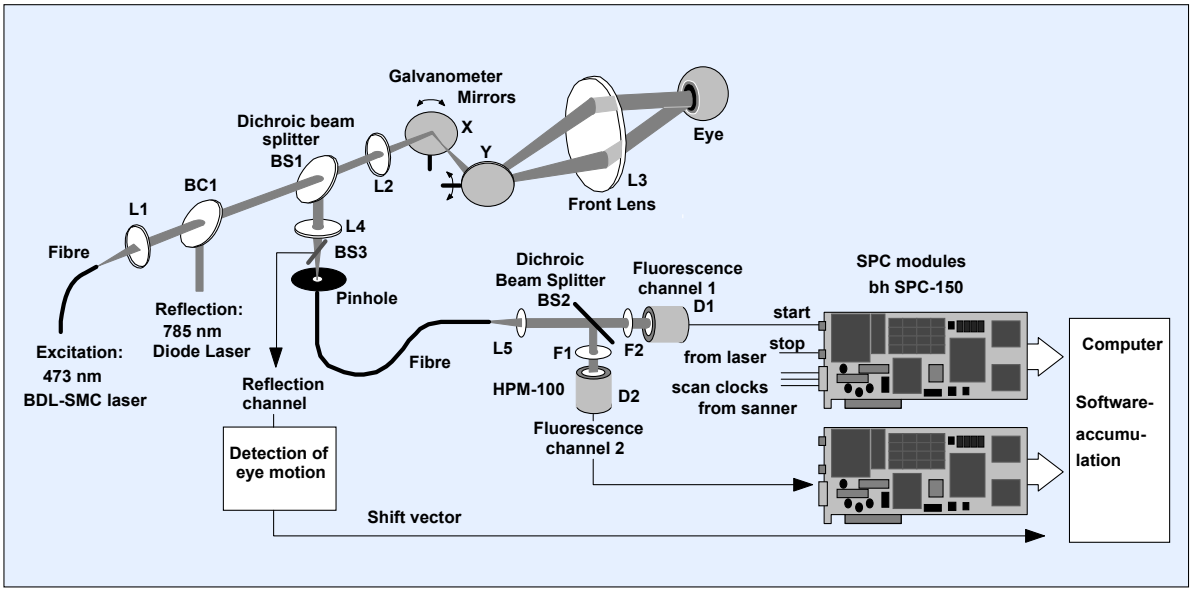


Fig. 812: Principle of the FLIO system of Heidelberg Engineering

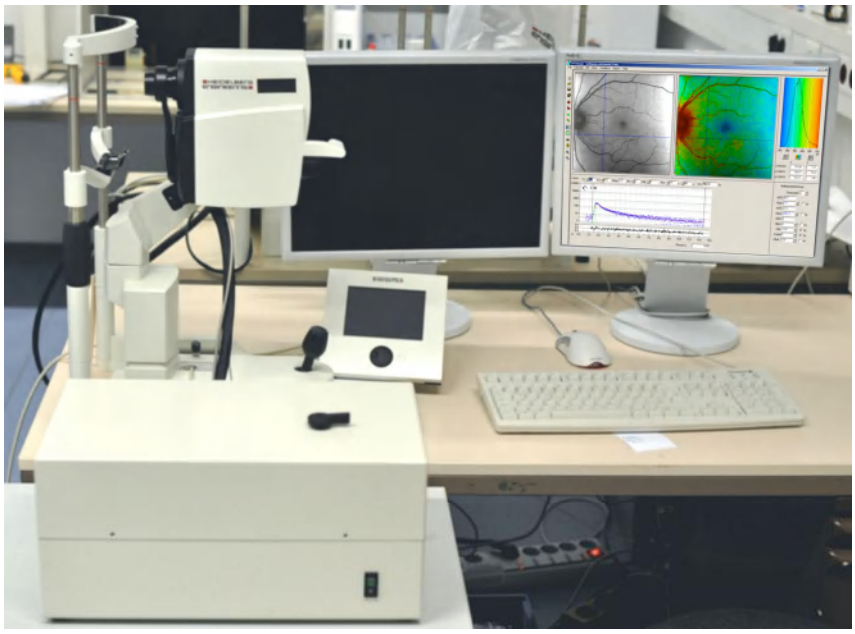


Fig. 813: FLIO-Spectralis ophthalmic FLIM system. Photo courtesy of Heidelberg Engineering.

The Heidelberg Engineering FLIO instrument delivers fundus FLIM images of amazing quality. Fig. 814 shows a FLIM images of the author's left eye. It shows more or less normal behaviour: The lifetime is long in the optic disc, short and uniform in the macula, and very short in the fovea. The FLIM image reveals some deposits along the blood vessels. These are not visible in the intensity image.

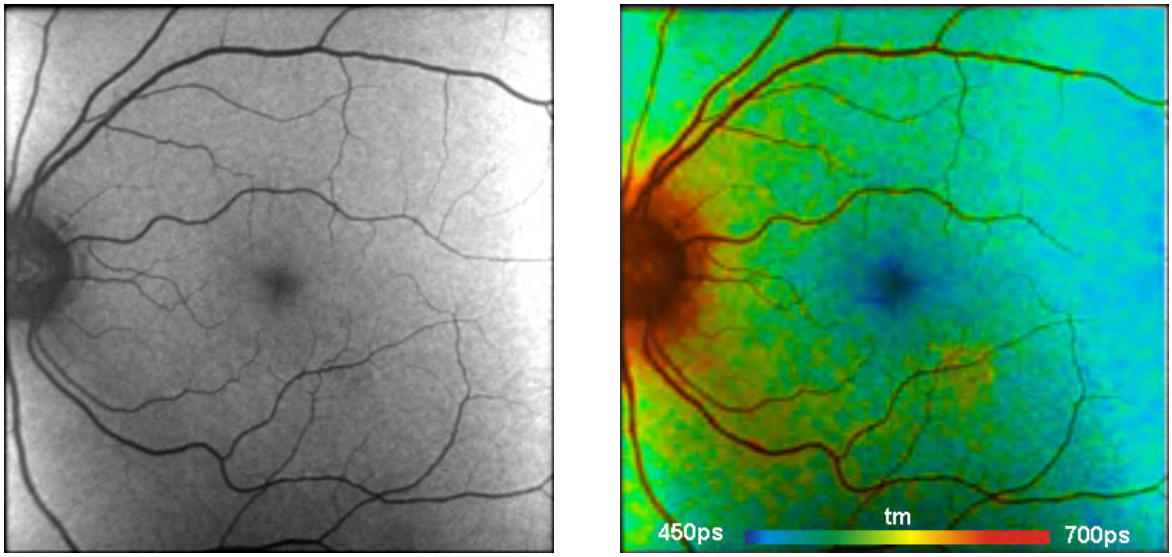


Fig. 814: The author's left eye. Left: Fluorescence intensity image. Right: FLIM image. SPCImage data analysis, amplitude-weighted lifetime, t_m.

Results and Applications

Fig. 815 show images of a patient suffering from advanced AMD (age-related macula degeneration). The macula is almost entirely destroyed, and there is long lifetime almost anywhere in the active area of the ocular fundus. Fig. 816 shows images of the relative intensity contributions, q_1, q_2, and q_3, of the fast, medium, and slow decay component.

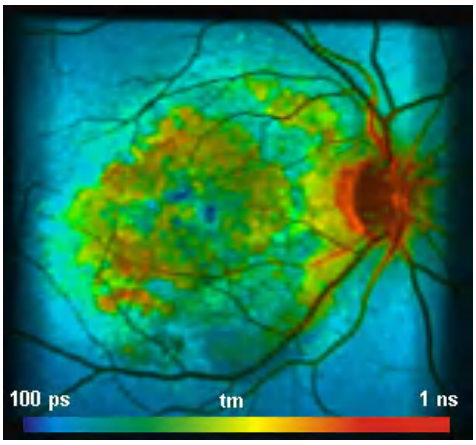


Fig. 815: Fundus FLIM image of a patient suffering from advanced AMD. SPCImage data analysis, amplitude-weighted lifetime, t_m.

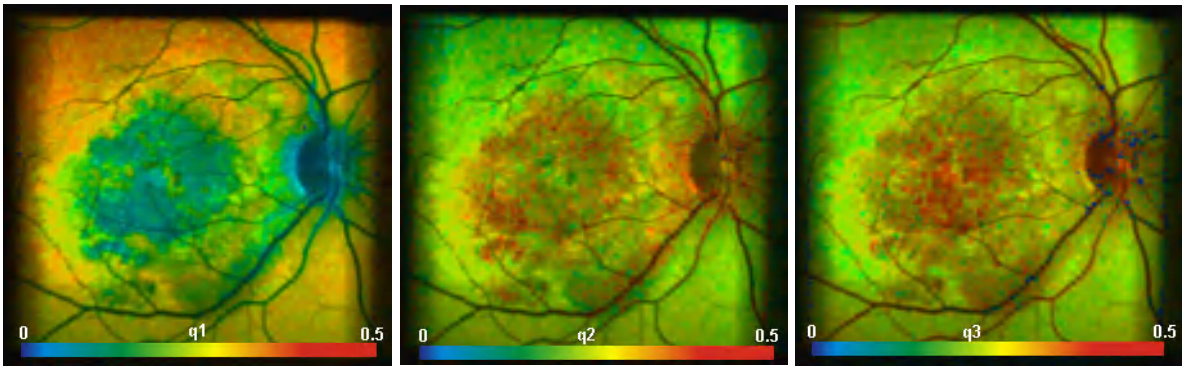


Fig. 816: Images of the intensity contributions of the fast, medium, and slow lifetime component. SPCImage data analysis, q_1, q_2, and q_3

Schweitzer et al. have shown that the decay components and intensity contributions can be associated to different fluorophores and to different tissue layers [1094, 1095]. They could also show that the lifetimes are dependent on the oxygen saturation, as has been proved by oxygen breathing experiments [1091]. Most importantly, they found significant differences in the fast and slow lifetime components of the retina fluorescence for healthy volunteers and patients with age-related macular degeneration (AMD) [1091].

A review on FLIM ophthalmoscopy can be found in [417]. General clinical studies with the FLIO instrument are described in [414, 1059, 1057], pre-clinical studies on mice in [420, 415, 1235]. Distinct signatures of the decay parameters were found for early and late AMD, for under-supplied regions after arterial branch occlusions, and for metabolic alterations due to diabetes mellitus [550, 1084, 1085, 1096, 1097, 1098, 1101, 1102, 1103, 1104]. Other publications report on FLIO of retinitis pigmentosa [21], stargard disease [416], arterial occlusion [418], retinal pigment atrophy [419], central serous chorioretinopathy [421], mydriasis [732], glaucoma [995], macular telangiectasia [1055], noneexudative AMD [1056], macular holes [1058], pigment epithelial detachments [1060] and diabetic retinopathy [1072]. Jaggi et al. showed that FLIO may serve as a prediction of the outcome in Macula-Off rhegmatogenous retinal detachment [615]. Dysli et al. report on the lifetime distribution in phakic and pseudophakic healthy eyes [422]. The influence of smoking on the fluorescence lifetime of the ocular fundus has been described by Sonntag et al. [1168]. Klemm et al. [674] investigated bleaching effect in the retina before and after irradiation with light of 3200 cd/m^2. Lifetime changes were less than 10% which is less than the changes found for pathological processes. Lifetime changes after irradiation with strong laser pulses and during subsequent wound healing were studied by Sonntag et al. and Hutfilz et al. [1167, 605].

Semenov et al. used a bh DCS-120 FLIM system to study the influence of Lipofuscin on cultured RPE cells [1112]. The found an increase of Lipofuscin lifetime after illumination with white light. The authors attribute the change to photo-induced oxydation of Lipofuscin, with possible oxidative stress to the RPE cells. Addition of Zeaxanthin suppressed the lifetime increase. They conclude that Carotenoids can shield Lipofuscin from oxydation, and thus help protect the RPE from oxydative stress.

An interesting application of ophthalmic FLIM is the possible detection of Alzheimer's disease. Alzheimer's disease is related to the expression of the phospho tau 181 protein. This protein is present in the eye and can be detected via its fluorescence. In the FLIO data it shows up as an increased intensity contribution of the medium lifetime component [625, 1102]. Sadda et al. performed a study on 28 eyes of 15 subjects 7 of which had Alzheimer's disease. They found longer τ_m in the Alzheimer group than in the control group.

Another way is to use a ligand that develops special fluorescent properties upon binding to Amyloid β. Kerbage et al. described this approach and an instrument based on it [659]. The optical system is based on a BDS-SM ps diode laser of 473 nm wavelength, a galvanometer scanner that scans the lens of the eye, a SPAD detector, and an SPC-150 TCSPC module. A sufficiently accurate decay signature is obtained within an acquisition time of one second. The results of a clinical trial have demonstrated that the system is able to discriminate between healthy volunteers and patients with Alzheimer's disease.

Data Analysis

Analysis of FLIO data is an extremely demanding task. Fundus lifetimes are on the order of a few 100 ps, with relevant decay components as short as 80 ps. Due to their extraordinary timing stability (see 'Unprecedented Timing Stability' page 2) the bh modules are well able to measure such lifetimes, and SPCImage data analysis is able to extract them from the data. However, this is only possible if the shape and, especially, the temporal position of the system IRF are known, and if the decay model is correct [119]. Both prerequisites are not given for FLIO data. The problems are illustrated in Fig. 817 and Fig. 818.

Shape of the IRF

It has been attempted to improve FLIO analysis by recording a system IRF and using it for analysis of the decay data. However, the IRF has to be measured on a scattering target. Scattering in the target tends to broaden the IRF. Moreover, the IRF has to be recorded through the optical system which is designed to block the laser wavelength. The slightest amount of fluorescence either from the target itself or from contaminations at its surface further broadens the IRF. The measured shape of the IRF is therefore rarely correct.

Variable Optical Path Length between the Scanner and the Fundus

In FLIO measurement the optical path length from the scanner to the fundus and back is not constant. It depends on the patient's head profile and on the optical length of the eye. Differences of 1 cm in the distance (or 2 cm in the path length) are not unusual. This translates in a transit-time difference of 67 ps. The uncertainty in the transit time results in an uncertainty of the same size in the recorded lifetimes. That means lifetimes on the order of 100 ps cannot be determined without shifting the IRF into the correct temporal position. The data analysis routine has to estimate the position of the IRF before it starts the fit algorithm.

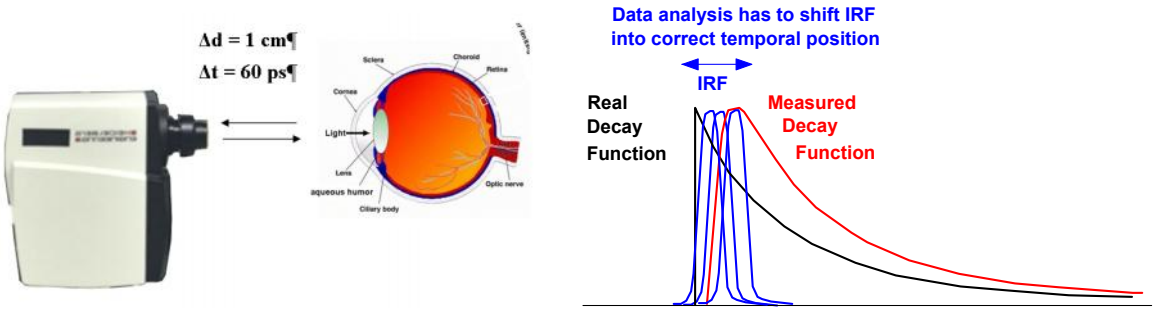


Fig. 817: The path length between the scanner and the eye varies (left). The data analysis has to correct for the associated transit time variation (right).

Model Function

For many years, FLIO analysis used the commonly known triple-exponential model function in the form of

$$f(t) = a_1 e^{-t/\tau_1} + a_2 e^{-t/\tau_2} + a_3 e^{-t/\tau_3}$$

This model ignores the fact that the fluorescence from the fundus is overlaid by fluorescence from the lens of the eye. The lens fluorescence arrives 120 to 150 ps before the fundus fluorescence. It not only adds an unwanted decay component to the net decay function in every pixel, it also causes a distortion in the rising edge of the fluorescence pulse (Fig. 818, left). The triple-exponential model is not able to describe the rising edge correctly (Fig. 818, right).

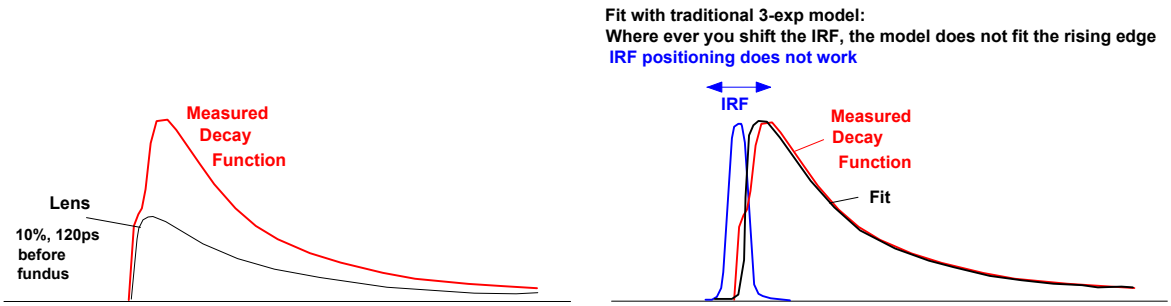


Fig. 818: Left: measured decay function in the presence of lens fluorescence. Right: The traditional model function is not able to describe the rising edge correctly.

The inadequate modelling of the decay functions in combination with the inaccurately known IRF has several consequences.

- The poor fit of the rising edge results in a broad χ^2 minimum, ambiguity of the fit, and fit instability.
- There is no clear χ^2 minimum for different IRF positions. The fit routine is thus unable to find the correct IRF position. Moreover, the optimisation procedure tries to compensate for the distortion in the rising edge by modifying the IRF position. Thus, even if an IRF position with minimum χ^2 is found it is not the correct one.
- The shape of the rising edge depends on the relative amount of lens fluorescence detected. The shape has an influence on the IRF position obtained, and thus on the lifetime determination. As a result, the fundus lifetimes obtained from the fit tend to depend on the focusing, and on the quality of the patient's eye lens, in particular on the amount of astigmatism, and, importantly, on the fluorescence properties of the lens. In particular, there is a problem for cataract patients. These have extraordinarily high lens fluorescence.

It has been attempted to solve these problems by excluding the rising edge from the fit, i.e. by fitting only the part of the decay functions after the maximum. This way, a good χ^2 is obtained for the falling part of the decay functions. However, the results depend on the selection of the fit range and still contain an uncertainty from the ambiguity of the IRF position. Moreover, fast decay components are not obtained with the best possible accuracy. Information on these components is contained mainly in the early part of the decay functions, i.e. in the part which is excluded from the fit. All these attempts to get more reliable FLIO data were therefore in vain. For a detailed analysis of the problem, please see next section.

FLIO Analysis by SPCImage NG

Synthetic IRF

FLIO analysis has to accept the fact that it is virtually impossible to measure an accurate IRF for a FLIO system. SPCImage NG therefore provides a mathematical model for the IRF. Basis of the model is a function

$$f(t) = t/t_0 \cdot e^{-t/t0}$$

A comparison of the real IRF of the IRF of a HPM-100-40 / SPC-150N combination and the function $f(t) = t/t_0 \cdot e^{-t/t0}$ is shown Fig. 819.



Fig. 819: Comparison of the IRF of the HPM-100-40 detector (left) and a function $f(t) = t/t_0 \cdot e^{-t/t0}$ (right)

The function not only models the real IRF reasonably well, it is also characterised by one single parameter, t_0. A fit procedure therefore has to determine only this one parameter.

The IRF is further refined by convoluting it with a function

$$f(t) = e^{-(t/tl)^2}$$

describing the shape of laser pulse. The width parameter, t_l, is specific for the laser. It is given by design. Therefore a fixed value is used for it.

To obtain the final IRF SPCImage NG fits the parameter t_0 together with the selected model of the fluorescence decay to the measured data. The results are so good that a measurement of the IRF is no longer necessary. In fact, the synthetic IRF usually yields a better fit of the FLIO data than a measured one. Please see [175].

Shifted-Component Model

The problems described above can only be solved by using a correct IRF *and* a correct model function [119]. SPCImage NG therefore provides a 'shifted-component' model. The traditional triple-exponential model function is extended with a parameter, t_{d3}, which describes a shift of one of the fluorescence components. The new model function is:

$$f(t) = a_1\, e^{-t/\tau 1} + a_2\, e^{-t/\tau 2} + a_3\, e^{(-t+td3)/\tau 3}$$

a_1, a_2, a_3, τ_1, τ_2, τ_3 are fit parameters. t_{d3} is the transit time from the lens of the eye to the fundus and back. A model like this has already been suggested by D. Schweitzer [1102]. Implementing the model in FLIO data analysis was not successful, however, probably because the delay was used as a fit parameter. This caused instability of the fit. SPCImage NG therefore assumes that t_{d3} is known and constant. In reality, it may vary slightly with the length of the eye. Our tests have shown, however, that the value of t_{d3} is not critical. A t_{d3} of 120 ps to 150 ps works well for all adults. The principle of data analysis with the shifted-component model is illustrated in Fig. 820.

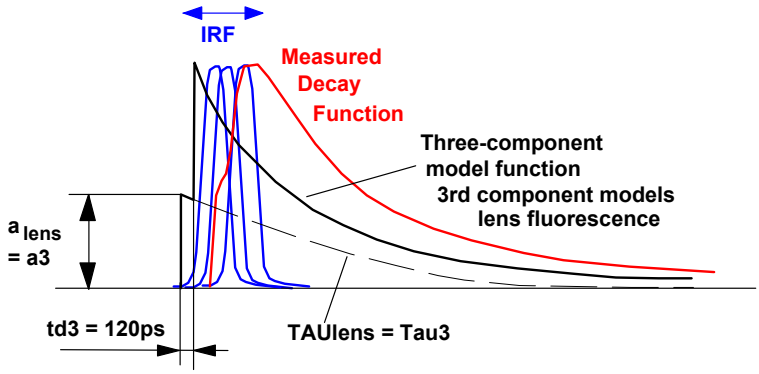


Fig. 820: Modelling the eye fluorescence with the shifted-component model.

A practical example of FLIO analysis with the shifted-component model and the synthetic IRF is shown in Fig. 821. The image was recorded with an ultra-fast HPM-100-06 detector. Due to the fast IRF the step in the rising edge of the fluorescence can clearly be seen. As also can be seen in Fig. 821, the model fits the step accurately. The χ^2 distribution (shown below the decay curve) is virtually free of bumps in the vicinity of the rising edge of the fluorescence pulse.

Importantly, fitting the data with the new model does not require any tweaking of fit conditions or fit-interval boarders. The fit interval is just set to the beginning and the end of the recorded decay data. Small changes in the cursor positions have no visible influence on the results as long as the left cursor remains left of the rising edge and the right cursor in the region where the fluorescence has decayed to reasonably low intensities.

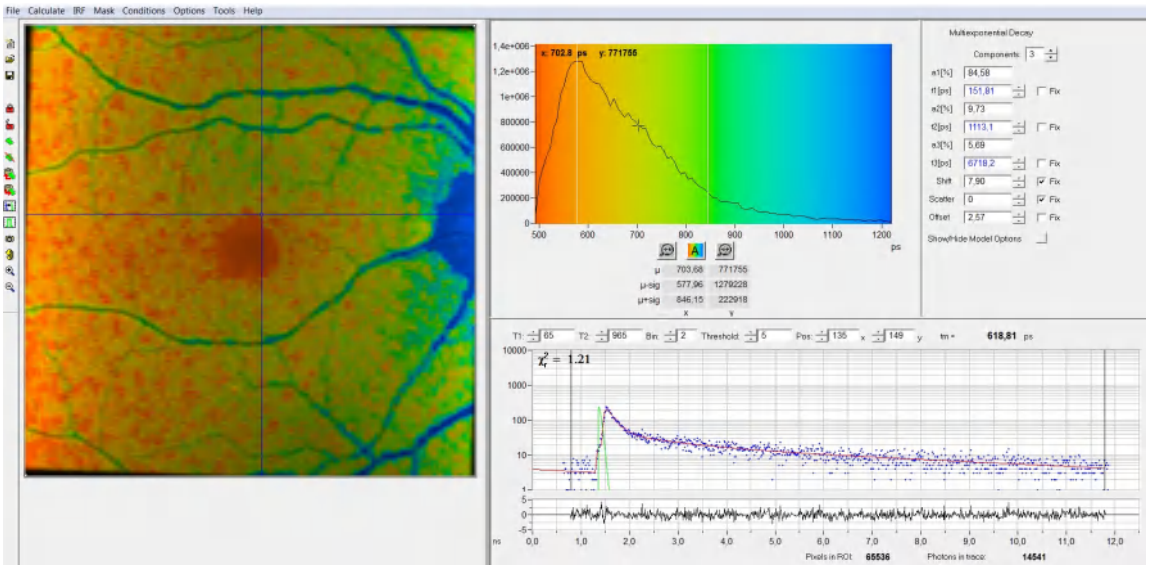


Fig. 821: Test data recorded with ultra-fast hybrid detector. Analysis with shifted component model and synthetic IRF.

Suppression of lens decay component

With the new model, the fit delivers two decay components, t_1 and t_2, from the fundus, and a third component, t_3, from the lens. Thus, the shifted component model not only delivers an accurate fit of FLIO data with a correctly positioned IRF, it also allows us to remove the contamination of the fundus data by the lens decay component. This is achieved by calculating an average (amplitude weighted) lifetime, t_{m12}, only from the first two decay components, t_1 and t_2, and their amplitude factors, a_1 and a_2:

$$t_{m12} = \frac{t_1 a_1 + t_2 a_2}{a_1 + a_2}$$

The application of t_{m12} to FLIO data with strong lens fluorescence will be demonstrated below.

Analysis FLIO Data of a Cataract Patient

We applied the new analysis approach to data from a cataract patient. The patient obtained a cataract surgery, i.e. got an artificial lens implanted. The natural lens of a cataract eye is highly fluorescent, whereas the artificial one is not. FLIO data were recorded before and after the surgery. The results are shown in Fig. 822 through Fig. 826. All data are courtesy of Lydia Sauer, University of Utah. Fig. 822 though Fig. 824 are pre-surgery, Fig. 825 and Fig. 826 are post-surgery images. The images are from the short-wavelength channel, for the long-wavelength channel please see [118]. All images are shown in normal FLIM style, i.e. with the fluorescence intensity as brightness the fluorescence lifetime as colour. Ophthalmology style is different in that only the lifetime information is shown. We used the normal FLIM style to give an impression of the contrast improvement obtained by the new model.

Fig. 822 is a pre-surgery image showing the amplitude-weighted lifetime, t_m, of the traditional triple-exponential model. As can be seen from the figure, the lifetime is entirely off range. The lifetimes are massively biased toward long times by the strong contribution from long-lifetime lens fluorescence.

Fig. 823 is a t_{m12} image from the same data set. t_{m12} contains only t_1 and t_2, i.e. decay components from the fundus. t_{m12} is in the range of normal fundus data. Moreover, t_{m12} is very close to the t_m of the post-surgery image, Fig. 825. The similarity of the lifetimes indicates that t_{m12} of the pre-surgery image is indeed associated to the fundus. Several small spots (barely visible in the t_m image), show up clearly in the t_{m12} image. The spots have increased lifetime, a possible indication of beginning Stargard disease.

Of course, the large contribution of lens fluorescence has also an effect on the pixel intensities. The lens fluorescence is spatially unspecific, and thus causes a decrease in image contrast. The contrast can be improved by using time-gated pixel intensities from the early part of the decay. This part is dominated by the fundus fluorescence and thus delivers higher contrast. The result is shown in Fig. 824.

Fig. 825 shows a post-surgery image of the normal amplitude-weighted average lifetime for all three decay components. The t_m lifetimes in the post-surgery images closely match the fundus lifetimes, t_{m12}, in the pre-surgery image. That means the assumption that t_{m12} comes from the fundus is generally correct. Fig. 825 still shows a decay component, t_3, that is associated to the front part of the eye. This is indicated by the kink in rising edge and the perfect it of it. The lifetime is 1.47 ns, compared to 3.64 ns in the pre-surgery data. The component probably comes from other anatomic structures in the front part of the eye. As shown for the lens fluorescence, the component can be rejected by using t_{m12} as imaging parameter.

The result is shown in Fig. 826. It can be assumed that Fig. 826 is virtually free of fluorescence from the front end of the eye. The lifetime histogram has a maximum at about 200 ps.

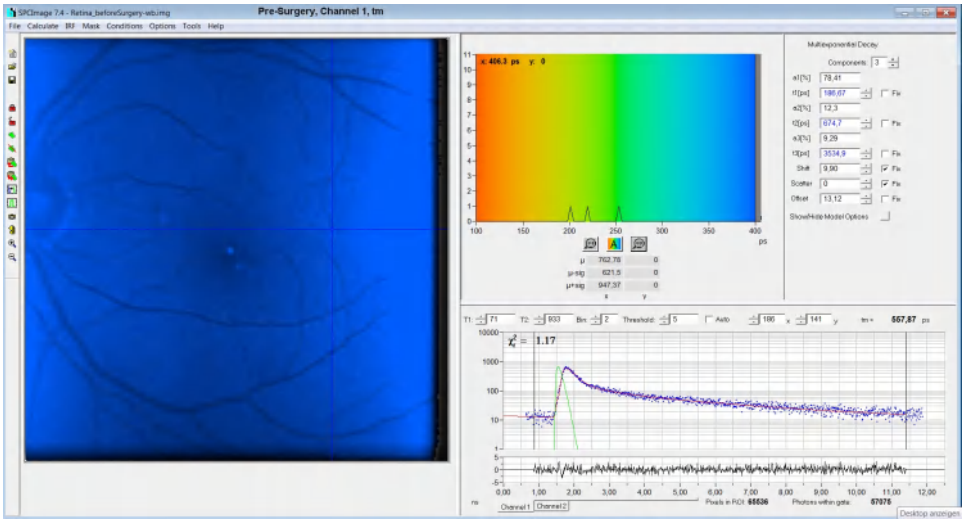


Fig. 822: Pre-surgery t_m image. The lifetime is entirely off range due to strong lens fluorescence

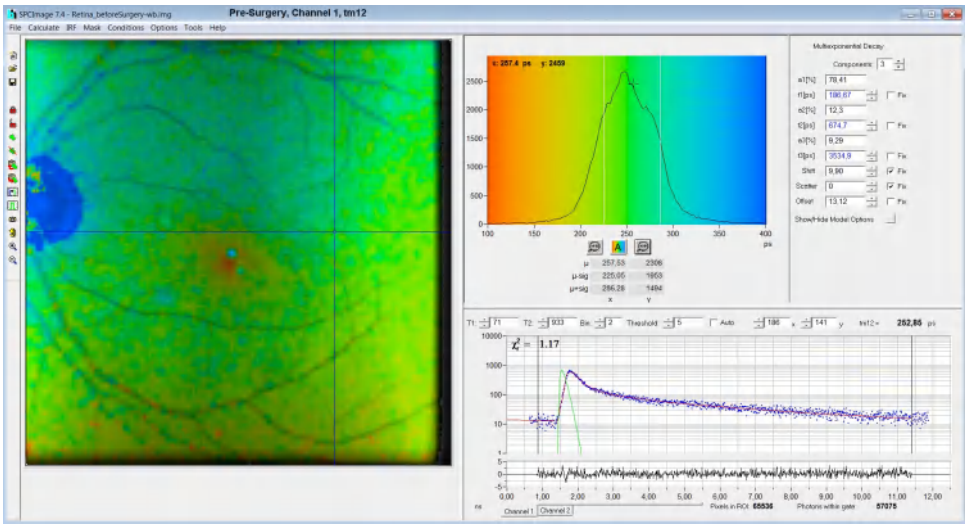


Fig. 823, pre-surgery t_{m12} image: The lifetime is in the normal range, and close to the post-surgery value.

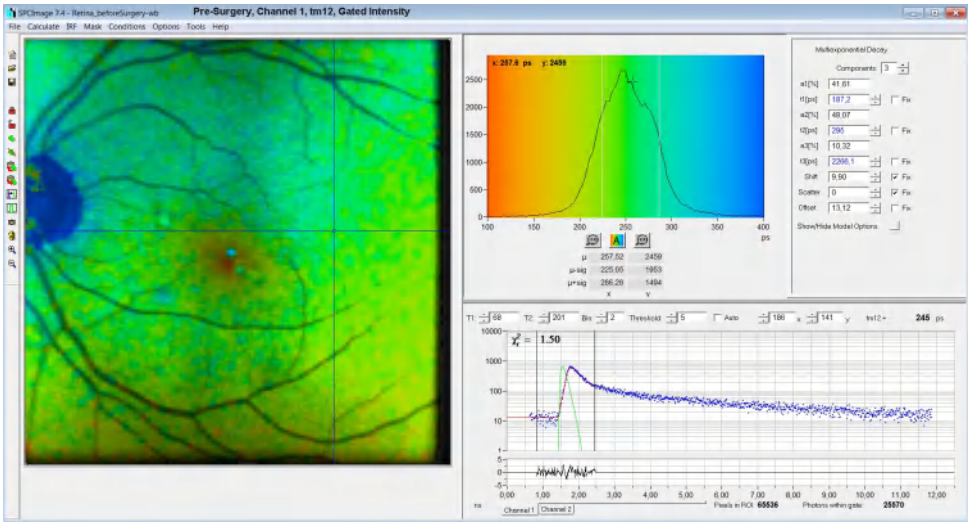


Fig. 824, pre-surgery t_{m12} image, time-gated intensity: Increased contrast by rejecting most of the lens fluorescence

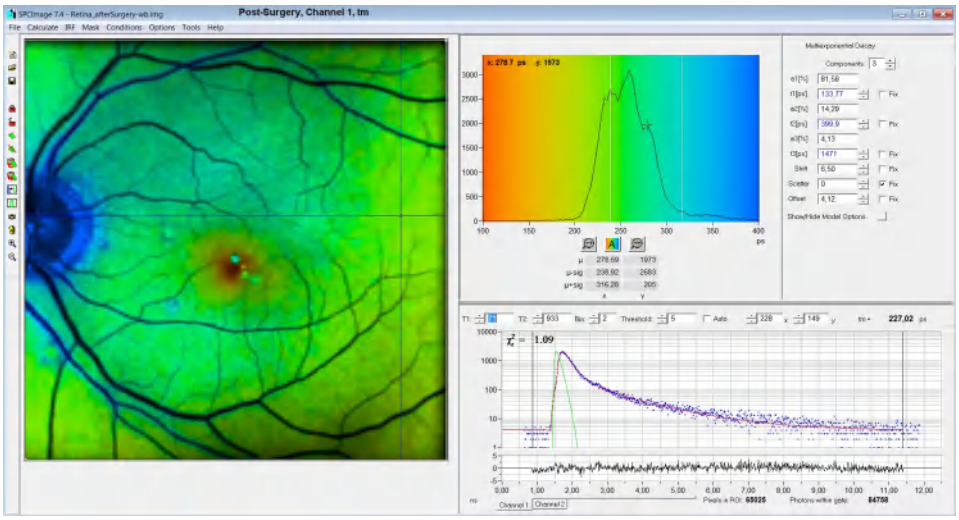


Fig. 825, post surgery t_m image. The lifetime matches the pre-surgery t_{12} image. A shifted slow component, t_3, is still detected. However, the amplitude is far smaller than in the pre-surgery image.

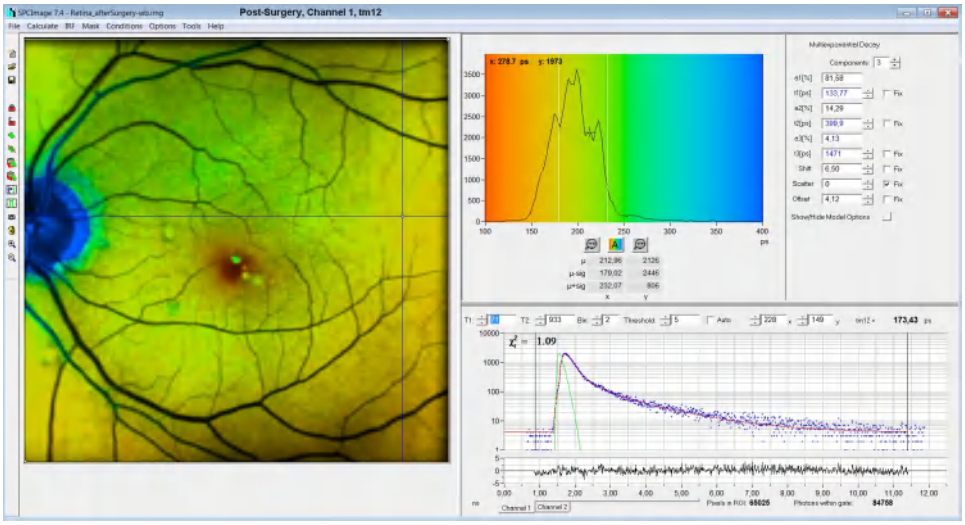


Fig. 826, post surgery t_{m12} image. In t_{m12}, the slow component, t_3, is not included. Therefore t_{m12} is shorter than t_m. It is also shorter than tm12 of the pre-surgery image. It is possible that the component is not present in the pre-surgery image, or that it is too weak to show up in the pre-surgery data.

The results show that the problem of the lens fluorescence can be solved by the shifted-component model. It should be noted however, that the technique works only if a correct IRF is used. It should therefore be used with the synthetic IRF. Convolution with a wrong IRF does not reproduce the rising edge of the fluorescence correctly, and a correct IRF position and a correct amplitude of the lens component are not obtained. This results is a wrong estimation of the fundus decay components. Please see [175] for details.

Analysis of FLIO Data of a Normal Patient

The results shown above indicate that the real fundus lifetimes may be offset by lens fluorescence also for normal eyes. This would mean that the real fundus lifetimes are shorter than previously assumed. This suspicion is indeed supported by FLIO data. Fig. 827 shows FLIO images of a 25-year old subject. At this age, the lens fluorescence is weak. Both images were analysed with the shifted-component model and a synthetic IRF. The fit is excellent, see the smooth residuals underneath the decay curve. Importantly, the rising edge of the fluorescence is fitted correctly. That means that the model fits the lens fluorescence correctly. A τ_m image is shown on the left, a τ_{m12} image on the right. The maximum of the τ_m histogram is at 250 ps, the maximum of the τ_{m12} histogram is at 180 ps. This is a difference of 28 %.

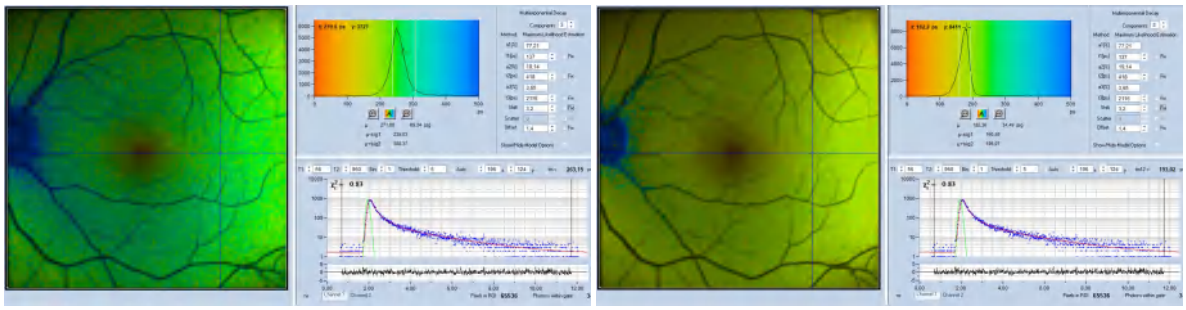


Fig. 827: FLIO images of a 25-year old subject. Analysed with shifted-component model. Left: τ_m image, including lens fluorescence. Right: τ_{m12} image, excluding lens fluorescence. The maximum of the lifetime histogram shifts from 250 ps to 180 ps.

The difference between the results should be kept in mind when FLIO images are compared. More importantly, it should be noted that the amount of lens fluorescence increases with age. There is a common believe that the fundus lifetime increases with the age of the subject. This effect may not be real after all. Instead, it may be induced by an increasing amount of lens fluorescence. Please see [175].

Other Attempts to Suppress the Lens Fluorescence

It has been suggested to measure the decay function of the crystalline lens via an independent optical channel and include the lens decay data in the data analysis of the fundus fluorescence [673, 1092]. These methods are difficult, if not impossible, to implement in existing ophthalmoscopes. Moreover, the lens-measurement channel delivers only the lifetime of the lens fluorescence, not its relative amplitude and time compared to the fundus decay components. The lens data are therefore difficult to include in the data analysis.

The problem of lens fluorescence and its impact on the measured fundus lifetimes are discussed in detail by Lincke et al. [764]. The authors found that the change in measured lifetimes scales with the degree of lens opacity. They attribute the change in the lifetimes mainly to lens opacity. This is most likely not correct and not supported by FLIO decay data. The results presented in [764] confirm, however, that the fundus lifetimes got back to the normal values after cataract surgery. The authors suggest a correction of the fundus lifetimes depending on the degree of lens opacity. The problem of such correction would be that it can be applied only to the mean lifetime, τm, and not to the lifetimes and amplitudes of the decay components.

Brauer et al. adopted the shifted component model to their FLIMX data analysis software. In addition, they implemented models with four exponential components, one of them being shifted by the transit time between lend and fundus [249]. They tested the models on the data of several patients who had obtained cataract surgeries. They found that the 3-exponential model and one of the 4-exponential models (with the shift parameter in the 4th component) worked, yet not equally well for all subjects.

We didn't encounter similar problems with SPCImage NG. One reason may be that Brauer et al. used a measured IRF. We found that most measured IRFs are too long, and the shifted-component model works perfectly only with the correct IRF. Moreover, SPCImage NG uses MLE fitting, which has different properties than the WLS fit used by Brauer et al. There may also be a problem if the slowest fundus component becomes slower than the lens fluorescence. SPCImage has a mechanism that allows the slow component of the fundus, τ_2, to become longer than the lens fluorescence, τ_3. However, we found that this only happens in the optical disc, not in the other parts of the fundus.

Phasor Plot

Another way to solve the data analysis problem of FLIO is possibly to do away with the need of absolute determination of the lifetimes. If information is derived from the relative variation of the lifetime and lifetime components over the anatomical structures of the fundus the accuracy problem would be relaxed. A possible solution is the combination of time-domain analysis with the phasor plot provided by the new SPCImage versions. With the new functions, different anatomical structures can be associated to different areas in the phasor plot. Diseases may then show up by the location of the phasors of suspicious spatial structure in the phasor plot. The requirement to obtain absolute lifetime values for decay components shorter than 100 ps may then be relaxed.

Phasor plots of a 25-year old and a 62-year old patient are shown in Fig. 828, left and right. There are clear differences in the two plots. Not only that the general lifetimes are longer for the older patient (lens fluorescence?), the phasor cluster from the fovea (marked) is also pointing in different directions.

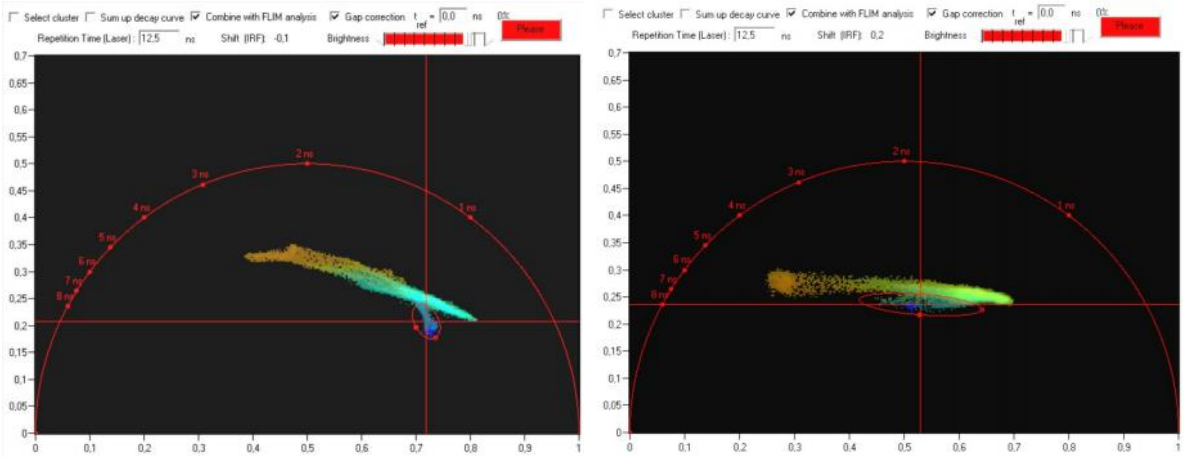


Fig. 828: FLIO phasor plots of a 25-year old (left) and of a 62-year old patient (right)

FLIO with Two-Photon Excitation

The lens of the eye is intransparent at wavelengths shorter than 400 nm. This precludes the use of the metabolically and spectroscopically most relevant fluorophore, NAD(P)H.

In principle, the problem can be solved by two-photon excitation. The excitation is than in the range of 750 to 780 nm, and easily passes the lens. However, there are a few problems. Efficient two-photon excitation requires high NA, and perfect focus quality. The NA of the lens of the eye is on the order of 0.15. This is almost by a factor of 10 lower than the NA of the microscope lenses used for two-photon microscopy. Moreover, the optical quality of the fully dilatated eye lens is extremely poor. Nevertheless, it has been shown that two-photon excitation of fluorescence in the fundus can be achieved if the aberrations of the eye are compensated by adaptive optics [1127]. The spatial resolution of the instrument is so good that individual rods and cones are clearly resolved. First FLIM results from animal experiments have been presented by Feeks et al. [441]. Huynh et al. were able to show different lifetime signature in S cones, M/L cones, and rods [606].

Diffuse Optical Tomography: DOT, NIRS and fNIRS

General Principle

Diffuse optical tomography, or DOT, aims at the resolution of the spatial distribution of optical properties in highly scattering media. Near-Infrared Spectroscopy (NIRS) is a synonym for the same technique. NIRS used for functional imaging of brain activity is usually called Functional Near-Infrared Spectroscopy, fNIRS. Biomedical applications of DOT are based on illumination of thick tissue by NIR light, detection of diffusely transmitted or reflected light, or fluorescence of endogenous or exogenous fluorophores [294, 949, 1343]. Typical applications of DOT techniques are optical mammography, brain imaging, and non-invasive investigations of drug effects in small animals.

Scattering and Absorption in Biological Tissue

Scattering in biological tissue is not isotropic. A considerably larger amount of light is scattered forward rather than in reverse [882, 1343]. For describing the penetration of light into thick tissue it is, however, sufficient to assume isotropic scattering with a reduced scattering coefficient. The reduced scattering coefficient, μ'_s, is

$$\mu'_s = \mu s\,(1 - g)$$

with g being the average cosine of the scattering angle. For biological tissue g is typically in the range from 0.7 to 0.9 [344]. Reduced scattering coefficients for various types of tissue are given in [882].

Typical values of μ'_s are around 10 cm^{-1}. Consequently, there are practically no unscattered or 'ballistic' photons for tissue thicker than 1 cm. Instead, the photons must be considered to diffuse through the tissue. Consequently, the spatial resolution of DOT images is extremely poor and cannot compete with positron emission, X ray and MRI techniques.

The NIR absorption in tissue is dominated by oxy-haemoglobin, deoxy-haemoglobin, lipids, and water [344]. There is an absorption minimum from approximately 650 to 900 nm. Therefore, NIR light can be transmitted and detected through tissue layers as thick as 10 cm. Absorption coefficients for various types of tissue are given in [882].

In spite of the poor spatial resolution, DOT in the NIR has the benefit that the measured absorption coefficients are related to the biochemical constitution of the tissue, such as haemoglobin concentration and blood oxygenation [344, 840]. If exogenous markers are used, the absorption or fluorescence delivers additional information about blood flow, blood leakage, ion concentrations, or protein binding state.

In images obtained by continuous illumination and detection it is difficult to distinguish between the effects of scattering and absorption. The situation is much better if pulsed or modulated light is used to transilluminate the tissue and the pulse shape or the amplitude and phase of the transmitted light are recorded. The general effect of variations in the scattering and absorption on the shape of the transmitted pulses is shown in Fig. 829.

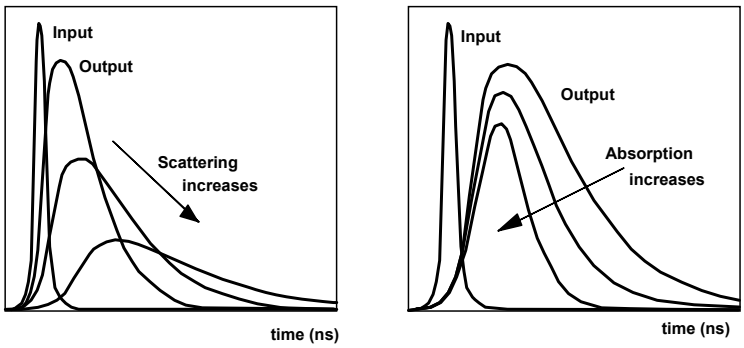


Fig. 829: Effect of scattering and absorption on the shape of a pulse transmitted through thick tissue

Both increased scattering and increased absorption decrease the integral output intensity. However, increased scattering increases the pulse width, while increased absorption decreases it. Therefore, the shape of the 'time-of-flight distribution' of the photons in combination with the intensity can be used to distinguish between changes in scattering and absorption.

Spatial Resolution

DOT is targeting not only at recording scattering and absorption coefficients but also at resolving their spatial distribution. Of course, scattering acts as a spatial low-pass filter, and quickly smoothes out details with increasing depth in the tissue. Reconstruction of the internal tissue structure is normally limited to details no smaller than the depth in which they are located.

The options of reconstructing are improved by using temporal resolution: Photons arriving at early times have travelled a shorter distance in the tissue than later photons. On average, they have taken a more direct path through the tissue. Images built up from early photons therefore yield a noticeably better spatial resolution, see [754, 914, 1276, 1300].

Moreover, in diffuse reflection experiments (i.e. with the source and the detectors at the same side of the tissue) the depth of scattering and absorption changes in the tissue can be derived from time-resolved data much better than from intensity data [565, 1183].

The computation of the spatial distribution of absorption and scattering can be considerably simplified by using the first and second moments, i.e. the mean time of flight and the variance of the time of flight [782, 785]. It has been shown that variations of the absorption and scattering coefficients calculated from the moments are obtained from considerably larger depth than such calculated from the intensity. The situation is shown qualitatively in Fig. 830.

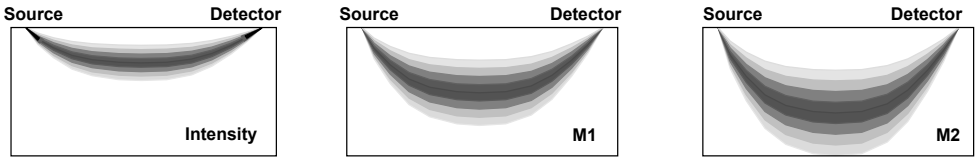


Fig. 830: Diffuse reflection experiment, depth in the tissue from which changes in the absorption and scattering coefficients are obtained. Left calculation from intensity data, middle calculation from M1 (mean time of flight), right calculation from M2 (variance of time of flight)

The banana-shaped pattern shows the depth from which absorption and scattering changes are obtained. Please note that it does *not* represent anything like the mean path of the photons. For a detailed discussion and Monte-Carlo calculations please see Wabnitz et al. [1303].

The complete reconstruction of tissue structures and optical properties from time resolved data is extremely demanding and not entirely solved yet. A number of different approaches are used to solve the 'inverse problem' of DOT [32, 33, 296, 437, 440, 478, 922, 969, 1255, 1300].

Instrumental Approaches

All approaches use a large number of time-resolved detection channels of different wavelengths, source-detector distance, or different location or transillumination angle. The time-channel width required to quantify absorption and reduced scattering coefficient is on the order of 10 ps [922]. Moreover, low-noise data are required to reconstruct the tissue properties from the relatively small intensity and pulse shape changes. This requires to record a large number of photons. Because the illumination intensity and the measurement time for in vivo measurements are limited a high detection efficiency is essential. Detection efficiency becomes even more important if fluorescence is to be detected in combination with normal DOT. Therefore the instruments normally use simultaneous detection in many time-resolved channels. Two typical setups used in DOT are shown in Fig. 831.

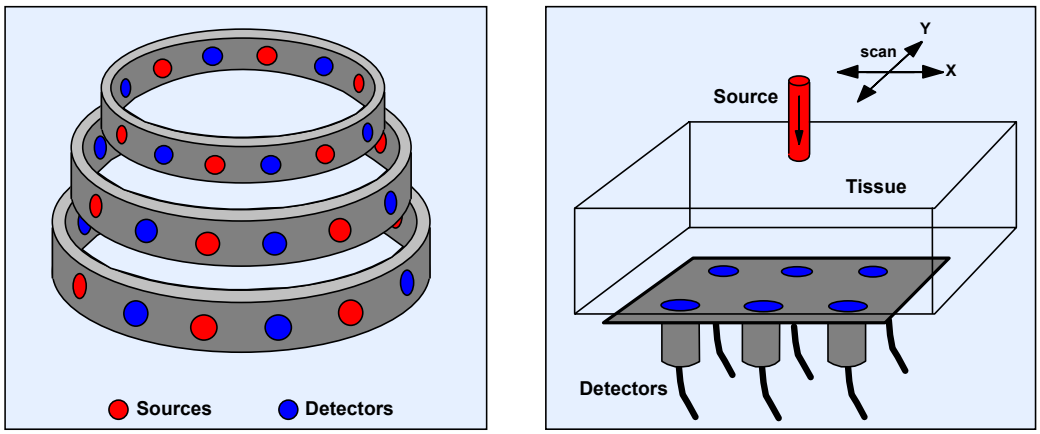


Fig. 831: Source-detector setups for optical tomography. Left: Circular arrangement of sources and detectors. Right: Scanning setup with one source and several detectors. Source and detectors are scanned simultaneously across the sample.

The traditional tomography setup is shown left. A large number of sources and detectors are arranged around the sample. The light sources are switched on one after another. For each source, time-of-flight distributions are recorded by all detectors [34, 483, 566, 920, 1071]. The setup is used for breast imaging and infant brain imaging. Because the setup is compact, mechanically simple, and can be built from purely non-metallic materials it is also used for optical tomography in conjunction with MRI imaging [919, 921]. When the setup is used for adult brain imaging, the detectors opposite to the source do not detect reasonable signals. Therefore detectors and sources are arranged at only side of the head. The configuration can be considered a sub-set of the arrangement shown in Fig. 831, left.

The right setup uses a scanning technique. Several lasers of different wavelength are multiplexed into a single optical source. The light source and the detector, or a number of detectors, are scanned simultaneously across the sample. The scanning technique is successfully used for optical mammography [347, 525, 526, 528, 970, 1017, 1224, 1225, 1254, 1255]. A scanning setup for small-animal imaging is described in [474]. The benefit of scanning is that it obtains a high spatial density of data points. Therefore the Nyquist condition is fulfilled for both spatial dimensions. However, problems can arise from edge effects. Not only can the detectors be damaged if the scan runs over the edge of the sample, but also the reconstruction of the sample properties has to cope with different photon migration near the edge. The problem can be solved by immersing the sample into a matching fluid [1301].

In both setups different wavelengths are multiplexed into the optical source channels. The wavelengths can be multiplexed on a pulse-by pulse basis and recorded in the same TAC interval or in longer intervals and recorded in different memory blocks by using the multiplexing capability of the SPC modules. The advantage of the second technique is that there is no

crosstalk between the wavelength channels and reduced signal distortion due to pile-up effects. Please see Multiplexing of Lasers, page 298.

On the detection side, frequency domain instruments using modulation techniques are competing with time-domain instruments using gated image intensifiers, and instruments based on TCSPC. An overview on TCSPC-based DOT techniques has been given in [154], an overview on frequency-domain DOT techniques can be found in [286]. It is now commonly believed that TCSPC instruments are more complex, but superior in terms of efficiency and sensitivity. The excellent results obtained with TCSPC-based instruments under clinical conditions clearly confirm the applicability of TCSPC to DOT [528, 529, 786, 1017, 993, 1224, 1225].

Many TCSPC-based DOT instruments still use single lasers or several multiplexed lasers and record in a single SPC-330 or SPC-630 channel [342, 526, 527, 528, 529, 782, 971, 1017, 1254]. Multi-detector operation of up to eight detectors connected to a single SPC-330 or SPC-630 channel was used in [343, 346, 347, 920, 921, 1256]. A system with 32 fully parallel TCSPC channels based on conventional NIM modules was described in [1071] and used for breast and brain imaging [566, 567, 569].

Recent TCSPC-based instruments use the bh SPC-134 or SPC-154 packages of four, in some cases eight parallel TCSPC devices [144, 633, 785, 786, 970, 972, 1224, 1225, 1255, 1284, 1301, 1302]. The number of detector channels is often increased by routers, see for example [326].

Optical tomography techniques for human medicine are currently at the stage of clinical tests. This causes a data compatibility problem between the different instruments. Optical mammographs and brain imagers are complex instruments with their own data acquisition and data processing software. Even if the instruments are based on time-resolved detection by TCSPC they may not use exactly the same procedures and data processing algorithms. To keep the clinical data obtained by different instruments comparable exact protocols for quality assessment have to be defined [973, 1304, 1305].

Scanning Mammography

A recent overview on Time-Resolved Optical Mammography has been given by Quarto et al. [993]. The principle of a typical TCSPC-based scanning mammograph is shown in Fig. 832.

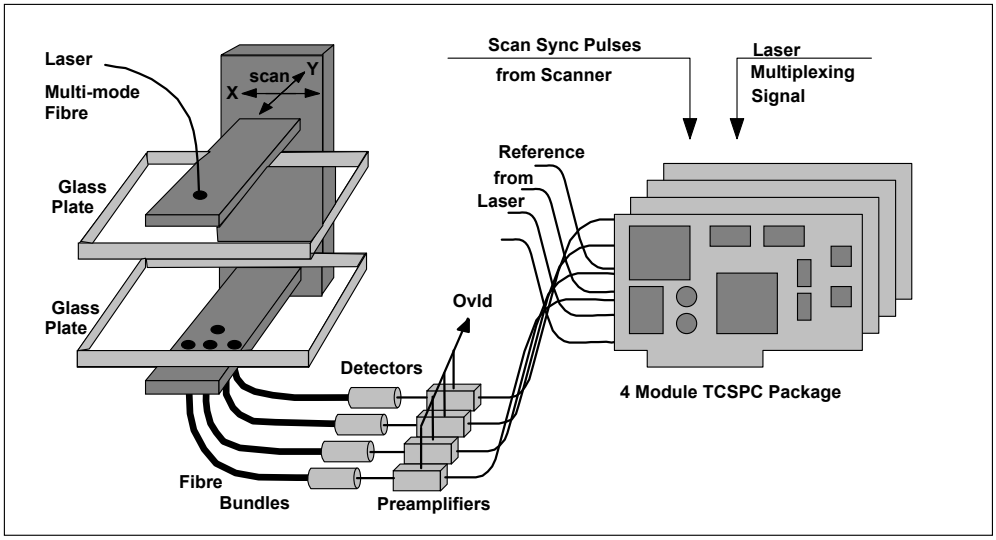


Fig. 832: General principle of a TCSPC scanning mammograph

The breast is slightly compressed between two glass plates. Due to the high sensitivity of TCSPC compression to about 6 cm is sufficient to obtain enough signal at the detectors.

The laser light is delivered via a multi-mode fibre. The transmitted light is collected by four fibre bundles and fed into four detectors. Fibres and fibre bundles are certainly not a favourable solution in terms of pulse dispersion, timing stability and detection efficiency. However, they decouple the electrical part of the system from the patient. The fibres are therefore an important part of the system to satisfy safety regulations for medical instruments.

Both the source fibre and the detection fibre bundles are assembled on a scanning stage. One scan typically contains 1000 to 5000 pixels, enough to avoid artefacts due to spatial undersampling. The scan amplitudes and the shape of the scanning area are different for different patients. To ensure that the detectors are not damaged by overload, the scanner must be prevented from running beyond the edge of the breast. This is achieved by using preamplifiers with overload detection (see 'Preamplifiers and Detector Control', page 211). When the detector currents exceed a reasonable limit the scan direction is reversed.

The four detector signals are connected into individual channels of a four-module TCSPC system. In practice, variable neutral-density filters and long-pass filters are placed in front of the detectors to compensate for different intensity at different breast thickness and to reduce the daylight sensitivity.

Usually several laser wavelengths are multiplexed into a single source fibre. Typical wavelengths used in mammography are between 685 and 785 nm. However, in the last few years more and more wavelengths have been added: 635 nm is used to obtain better general absorption contrast [1225]. Wavelengths from 905 nm to 975 nm deliver information about water and lipid contents [1224]. Recently even 1060 nm has been used to detect collagen in the breast tissue [1228, 1229]. An application to the identification of healthy subjects who are at risk to develop breast cancer was described in [1231].

The wavelengths can be multiplexed on a pulse-by pulse basis and recorded in the same TAC interval [528, 970, 1017, 1224, 1225, 1254, 1255] or in intervals of 50 to 200 µs (2500 to 10.000 pulses) and recorded in different memory blocks by using the routing capability of the SPC modules (see Fig. 456, page 299). The benefit of the second technique is that there is no crosstalk between the wavelength channels, and signal distortion due to pile-up effects is reduced.

The number of wavelength channels can be increased by generating a super-continuum in a photonic crystal fibre and TCSPC multi-wavelength detection [51, 52, 1174, 1201]. The technique delivers superior spectral data. As long as Titanium-Sapphire lasers had to be used to excite the super-continuum the technique was too expensive for routine application. Recently introduced super-continuum sources based on fibre lasers have changed the situation [1201]. These light sources can be used in not only in combination with multi-wavelength TCSPC but also with wavelength multiplexing via tuneable acousto-optical filters, see section 'Tissue Scanning System with Laser Wavelength Multiplexing' in this chapter.

The recording in the TCSPC channels can be synchronised with the scanning by software. In this case the time-of-flight distributions are read out from the TCSPC modules for each individual pixel. The bh SPC-630 and SPC-130/134 modules can avoid devoting time to readout during the scan by using sequential recording in the Continuous Flow mode (see 'Sequential Recording' page 121). Another convenient mode is hardware-controlled scanning (see 'Tissue Scanning System with Laser Wavelength Multiplexing', page 623) and synchronisation of the data acquisition via the Frame, line and pixel clock pulses. In this mode the TCSPC modules hold the time-of-flight distributions of all pixels of a scan in their memories. The data are read out when the scan is completed. It must, however, be taken into account that the length of the lines of the scan varies since the return points of the scan are controlled by the detector over-

load signals. Therefore, the scan software must store the positions of the return points and the number of pixels between. These positions are used later to adjust the lines horizontally.

In the last few years it is increasingly attempted to use fluorescence of contrast agents in addition to diffuse reflectance or transmittance. A scanning system that records images of the time-resolved fluorescence, diffuse fluorescence, diffuse transmittance, and fluorescence from both sides of an object was described in [243]. The data in the four channels were recorded by an SPC-134 TCSPC system. The instrument was demonstrated on phantoms containing a fluorescent inclusion but is, in principle, be applicable also to breast imaging.

If fluorescence is to be detected in combination with DOT, detection efficiency may become a crucial point. The detection efficiency increases with the total detection area and, therefore, with the number of detectors. It can therefore be advantageous to use more than the four detectors shown in Fig. 832. In that case, several detectors are connected to one TCSPC channels via a router.

Fig. 833, left, shows the time-of-flight distributions for four detectors detecting at different projection angles at a single pixel of a breast scan. The acquisition time was 100 ms per pixel. The source-detector geometry is shown at right. The time offsets between the curves are due to different delays in the fibre bundles, detectors, and TCSPC channels. Mammograms were calculated from the photons in the 8th of 10 equidistant time windows spread over the time-of-flight distribution. The result [144] is shown in Fig. 834.

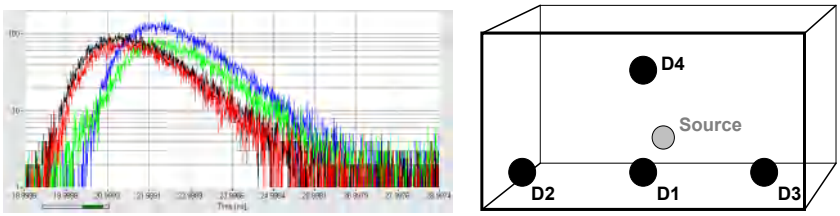


Fig. 833: Left: Time-of-flight distributions in one pixel of a breast scan. Different projection angels, acquisition time 100 ms per pixel. Right: Detector and source configuration. D1 is the direct detector, D2, D3 and D4 are offset by 2 cm.

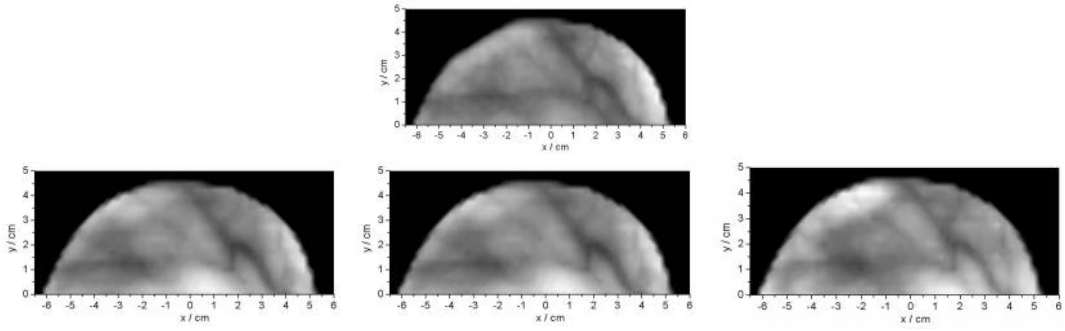


Fig. 834: Mammograms of a healthy volunteer recorded simultaneously at four projection angles. The images were generated from photon counts in a late time window. The arrangement of the mammograms corresponds to that of the detectors D1-D4 in Fig. 833. From [144]

Images in early and late time windows show qualitatively the scattering and the absorption in the tissue [341]. They can therefore be used to distinguish tumours in breast tissue. Most tumours have increased absorption due to increased haemoglobin content and blood leakage. These tumours are therefore prominent in the late time window. Cysts have decreased scattering and are visible in early time windows [1224]. An additional benefit of the late time window is that the images are almost free of edge effects [526].

Breast imaging has also been performed in a two-dimensional modification of the classic tomography setup. A technical system based on an SPC-134 and fibre switches for the source

and detector position has been described by Gao et al. [1388], reconstruction algorithms was by Yang et al. [1361], a pilot study has been presented by Zhang et al. [483].

When quantitative data of the absorption and reduced scattering coefficients are needed this requires the application of an appropriate analytical model [296, 295, 1300]. The modelled distribution is convoluted with the IRF and fitted to the measured time-of-flight distributions in the individual pixels at several wavelengths [526, 528, 1173, 1255]. A comparison of the accuracy of scattering and absorption coefficients obtained by a time-window technique and by fitting a homogeneous diffusion model to the data is given in [341]. In-vivo applications and results of clinical studies were presented in [528, 529, 530, 531, 532, 540, 979, 993, 1016, 1017, 1224, 1226, 1230, 1231].

Static Brain Imaging

Structural tomography data of the brain are acquired in the traditional tomography setup, see Fig. 831, left. For each source position time-of-flight distributions are recorded for all laser wavelengths in all detector channels. Switching between the source positions is performed by fibre switches. The time-of-flight distributions at the detector positions can be recorded sequentially by another fibre switch as described by Gao et al. and Lu et al. [483, 800]. An improved architecture that uses the four parallel TCSPC channels of an SPC-134 and multiplexes four signals into the detector of each channel by 4:1 fibre switches has been described in [482]. Both instruments have been used for phantoms but are basically capable of recording static brain images. Fibre switching is a cost-efficient way to record at many source and detector positions. However, it makes the measurement slow and inefficient in terms of photon efficiency. The measurement can be made faster and the efficiency be increased by recording the time-of-fight distributions all detector positions in parallel. For static brain imaging this is usually performed by several TCSPC modules and routers, as shown in Fig. 835.

A recent instrument of this type has been described by Cooper et al. [331]. Named ‘MONSTIR II’, the instrument has 4 SPC-150 TCSPC modules, four HRT-81 routers, and 32 detectors. 4 wavelengths of an SC450 Fianium supercontinuum laser are multiplexed via AOTFs. All in all, 128 signals for different combinations of laser wavelength and detector position are recorded for every source position.

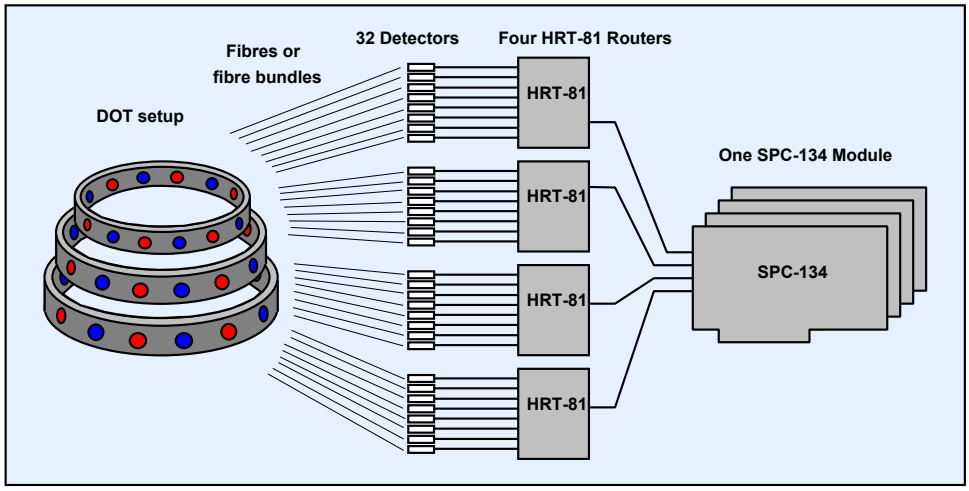


Fig. 835: Connecting a 32-channel tomography setup to an SPC-134 for-channel TCSPC package

In systems like the one shown above the count rates in the individual detector channels may differ over a wide range depending on the distance from the source. For channels directly adjacent to the current source position, the count rate can be as high as several MHz. The PMTs

can even be driven into overload. On the other hand, channels opposite to the source position may not collect any reasonable number of photons at all. In a TCSPC system with routers, the overloaded detector may block the router to which it is connected and thus prevent other signals from being recorded. Therefore, if the count rate of a detector becomes too high, either this detector must be switched off or an automatic intensity regulator of some kind must be placed in front of the detectors.

Typical time-of-flight distributions are shown in Fig. 836. The curves were recorded with a bh BHLP-700 diode laser of 2.5 mW power, 785 nm wavelength, and 50 MHz repetition rate. The detector was a bh PMC-100-20. The curves show the time-of-flight distribution for two different locations at the forehead together with the instrument response function. The source-detector distance was 6 cm. The acquisition time was 20 s, the count rates were between 800 kHz and 1 MHz.

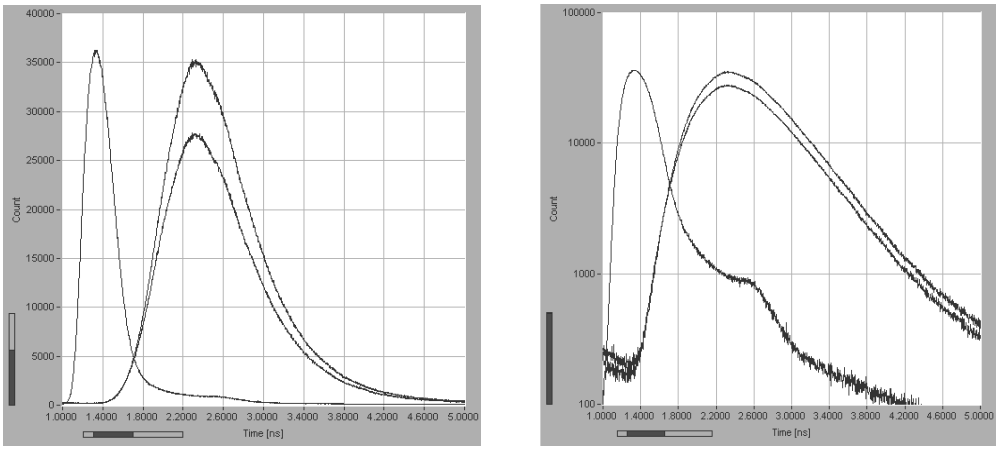


Fig. 836: Time-of-flight curves for two different source and detector positions at the forehead, and instrument response functions. Left linear scale, right logarithmic scale. Source-detector distance 6 cm, Laser 2.5 mW, 785 nm, 50 MHz. Acquisition time 20 s, ADC resolution 4096 channels.

The obtained count rates drop dramatically with increasing source-detector distance. With a laser power of a few mW, meaningful signals can be recorded diametrically through an infant head. For an adult head this is impossible. However, weak signals can be detected from temple to temple, as shown in Fig. 837. With a BHLP-700, 2.5 mW, 785 nm laser and a PMC-100-20 detector a total number of photons of 29,000 and 107,000 was acquired within an acquisition time of 60 s.

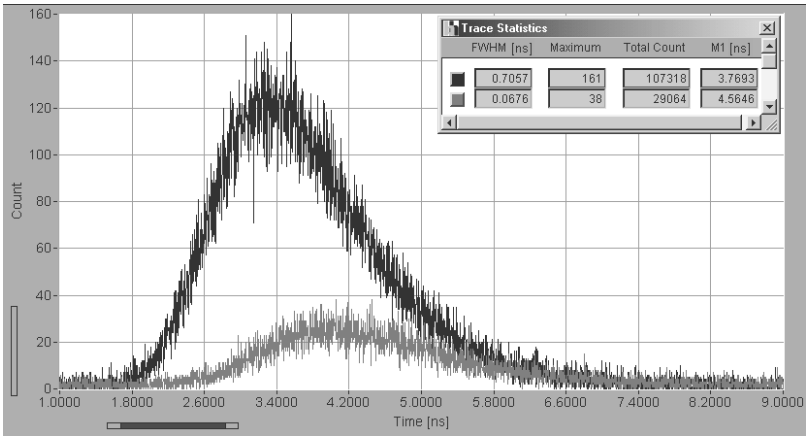


Fig. 837: Time-of flight curves detected from temple to temple through an adult head. Slightly different source and detector positions. Laser power 2.5 mW, wavelength 785 nm, PMC-100-20 detector, acquisition time 60 s, ADC resolution 4096 channels.

Functional Brain Imaging

Dynamic changes in the time-of-flight distributions are caused by the heart beat, variable oxy- and deoxyhemoglobin concentration induced by brain activity, and effects of associated physiological regulation. The haemodynamic response to brain stimulation is on the time scale of a few seconds [413, 460, 461, 1252, 1253].

Recently Liebert et al. have demonstrated that advanced TCSPC is able to record effects of brain activity with 50 ms time resolution, clear separation of scattering and absorption, and better depth resolution than CW or frequency-domain techniques. In particular, moment analysis and time-window analysis of TCSPC data provide a way to distinguish between perfusion changes in the brain and the scalp [330, 620, 781, 784, 785]. Please see [755, 786, 884, 885, 992, 1000, 1051, 1185, 1186] for technical details, applications, and clinical results. An overview has been given in [789], a comprehensive review can be found in [1259].

Time-domain functional brain imaging instruments normally use bh SPC-154 or SPC-134 four-channel TCSPC systems with four individual detectors and several multiplexed laser diode lasers. A fast sequence of time-of-flight distributions was recorded in consecutive time intervals of 50 to 100 ms. More results obtained with similar instruments are described in [807, 1184, 1304].

Quaresima et al. used a single SPC-630 channel and a multi-anode PMT to record sequences of time-of-flight curves in eight parallel channels [992]. The acquisition time per step of the sequence was 166 ms. The data of five steps were averaged. Values of μ_s' and μ_a were calculated from the averaged data by using a standard model of diffusion theory. An improved instrument of this type used an SPC-134 package with HRT-41 four-channel routers connected to each TCSPC channel [329, 330]. Thus, simultaneous detection in 16 detector channels was achieved. Two lasers were multiplexed by pulse interleaving; 16 source positions were multiplexed by fibre switches. Applications to functional brain imaging are described in [264, 884, 1258].

An instrument with 8 fully parallel TCSPC channels has been described in [633]. The setup uses two SPC-134 packages in one industrial computer. The optical architecture is shown in Fig. 838.

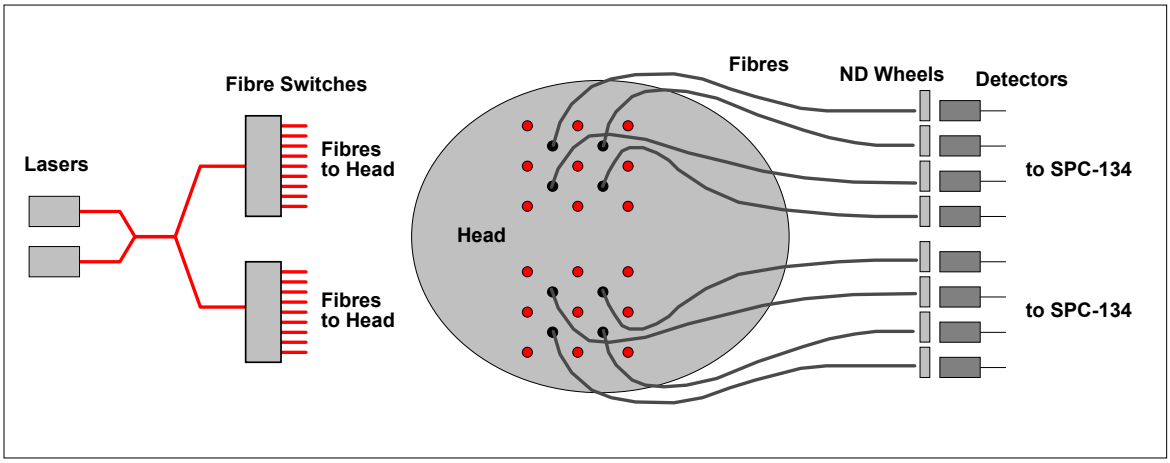


Fig. 838: Optical architecture of the 8-channel parallel DOT system described in [633]

The DTOFs at both sides of the head are recorded simultaneously. For every source position the DTOFs are acquired for 95 ms. One switching cycle through all 9 source positions is completed within 0.9 seconds. Variations of the optical properties in the brain are derived from the intensity and the first and second moments of the time-of-flight distributions [782].

An instrument that multiplexes also the lasers by fibre switches has been described by Re et al. [999]. The system avoids crosstalk of different laser wavelengths by reflections, pile-up, counting loss or detector afterpulsing, see page 298. An application to heamodynamics of the human brain is described by Aletti et al. [12]. The authors show how signal components caused by skin vasomotion and by cerebral perfusion can be separated.

Fig. 839 shows how dynamic DOT data look like. Time-of flight curves of photons transmitted through a forehead were recorded in the continuous flow mode of an SPC-134 system. 20 subsequent time-of-flight curves from the continuous-flow sequence are shown in Fig. 839. The acquisition time was 100 ms per curve, the ADC resolution 1024 channels. The left sequence was detected at a source-detector distance of 5 cm, the right sequence at a distance of 8 cm. The count rates were $1.8 \cdot 10^5$ s^{-1} and $4.5 \cdot 10^6$ s^{-1}, respectively.

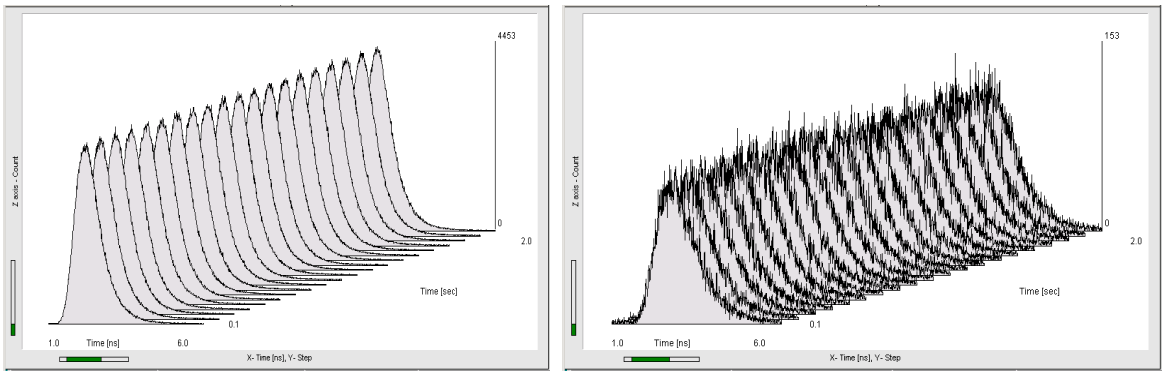


Fig. 839: 20 steps of a TOF sequence recorded in the Continuous Flow mode of an SPC-134. Acquisition time 100 ms per curve, ADC resolution 1024 channels. Left: Source-detector distance 5 cm, count rate $4.5 \cdot 10^6$ s^{-1}. Right: source-detector distance 8 cm count rate $1.8 \cdot 10^5$ s^{-1}

It should be noted that a count rate of $4.5 \cdot 10^6$ s^{-1} is at the very limit of currently available TCSPC devices. Intensity measurements at rates this high require a correction for counting loss (see 'Counting Loss', page 292). The first and second moments of the time-of-flight distributions are not noticeably influenced by counting loss. This is another benefit of the moments technique developed by Liebert et. al.

The standard deviation of the photon numbers and the first moments of the data in Fig. 839, left, is about 0.15 % and 800 fs, respectively. These values are substantially lower than the typical changes caused by the haemodynamic response. In principle, useful response curves could therefore be obtained by recording only a moderate number of stimulation events. However, in practice there is a strong variation in the data due to heart beat and respiration. The haemodynamic brain response can only be separated from these effects by recording a TOF sequence over a large number of stimulation events. Therefore, all the experiments mentioned above used the 'continuous flow' mode of the SPC-134 or SPC-630.

Typical results of haemodynamic response measurements performed by Liebert et al. [781, 785] are shown in Fig. 840. Visual stimulation was used. An annular black and white checkerboard alternating at 8Hz on a computer screen was shown to the patient. During the rest period a dark grey screen was presented while fixation was maintained. The stimulation periods lasting 30s were repeated 20 times separated by 30s of rest. Signals from 20 stimulation periods were averaged. Three multiplexed laser wavelengths were used. The photons were detected by four R7400 PMTs at different source-detector positions. The TOF curves were recorded by an SPC-134 system in the continuous-flow mode. Fig. 840, left to right, shows the intensity change, the change in the mean time of flight, and the change in the variance of the time of flight over the stimulation period. Depth-resolved intra- and extra-cerebral changes of the oxy- and deoxyhemoglobin concentrations calculated from the data of the four detectors at the three wavelengths are shown in Fig. 841.

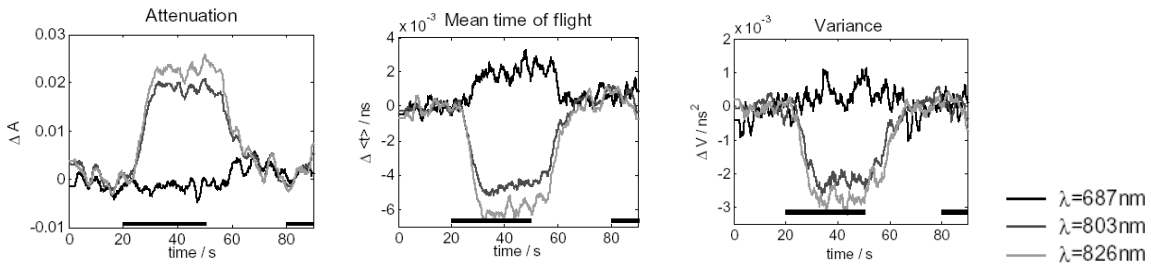


Fig. 840, Left to right: Intensity change, change in the mean time of flight, and change in the variance of the time of flight over the stimulation period. The horizontal bars indicate the periods of stimulation. From Liebert et. al., Proc. SPIE 5138. [781].

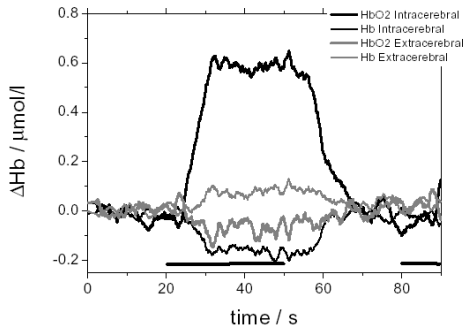


Fig. 841: Intra- and extra-cerebral changes of oxy- and deoxyhemoglobin concentrations during visual stimulation obtained from DTOFs measured at 3 wavelengths and four source-detector separations. The horizontal bars indicate the stimulation period. From [781], Liebert et. al., Proc. SPIE 5138.

Mackert et al. and Sander et al. combined time-resolved reflectance measurement with magneto-encephalography [807, 1051]. They used the setup described in [785]. This way, the vascular response could exactly be correlated with the neuronal response.

Perfusion Measurements by ICG Boli

Exogenous absorbers can be used by detecting either their absorption or their fluorescence. The only NIR dye currently approved for use at human patients is indocyanine green (ICG) [370, 887]. Absorption spectra of ICG in water are shown in Fig. 842, left.

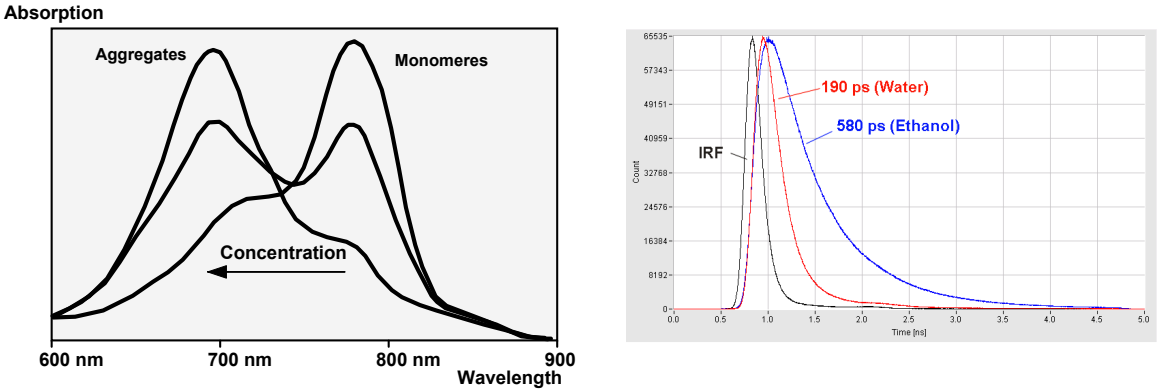


Fig. 842: Left: Absorption spectra for ICG in water, after [370]. Right: Fluorescence decay of ICG in water and ethanol, BHL-600-650 laser, PMC-100-20 detector and SPC-630 TCSPC module.

ICG absorbs strongly between 650 and 820 nm. The absorption of ICG monomers peaks at about 780 nm. In water ICG tends to form aggregates which cause a second absorption band around 700nm. In blood ICG binds to the serum albumin. Aggregation is then largely sup-

pressed, and the absorption around 780 nm dominates. Due to the binding to albumin ICG stays in the blood. It is therefore used as a contrast agent to mark blood vessels.

Fluorescence decay curves of ICG are shown in Fig. 842, right. The fluorescence lifetime in Ethanol is about 580 ps. In water the lifetime is about 190 ps. In both cases the decay functions are multi-exponential, probably due to the presence of monomeric and aggregated forms. The short lifetimes indicate that the fluorescence quantum efficiency is low. Values given in the literature are around 4% [370].

Absorption

In brain imaging ICG can be used to detect blood-flow dynamics. Liebert et al. used the technique for bed-side assessment of cerebral perfusion in stroke patients [786]. A bolus of ICG was injected and the subsequent absorption changes in the tissue monitored. The instrument was essentially the same as used for motor-stimulation experiments [781, 785] (results see Fig. 841). Two multiplexed lasers and four detectors connected to the four TCSPC channels of an SPC-134 package were used. By using the Continuous Flow Mode of the SPC-134, time-of-flight distributions were recorded at a rate of 50 ms per curve. From the time-of-flight distributions the changes in the attenuation, in the mean time of flight, and in the variance of the time of flight were calculated. Fig. 843 shows results for two healthy volunteers, subject 1 and subject 2, and two stroke patients, patient 1 and patient 2 [786]. The curves are sliding averages over 20 subsequent 50-ms recordings. The moments were scaled to a range from 0 to 1 by subtracting the minimum value and normalising the result to its maximum value.

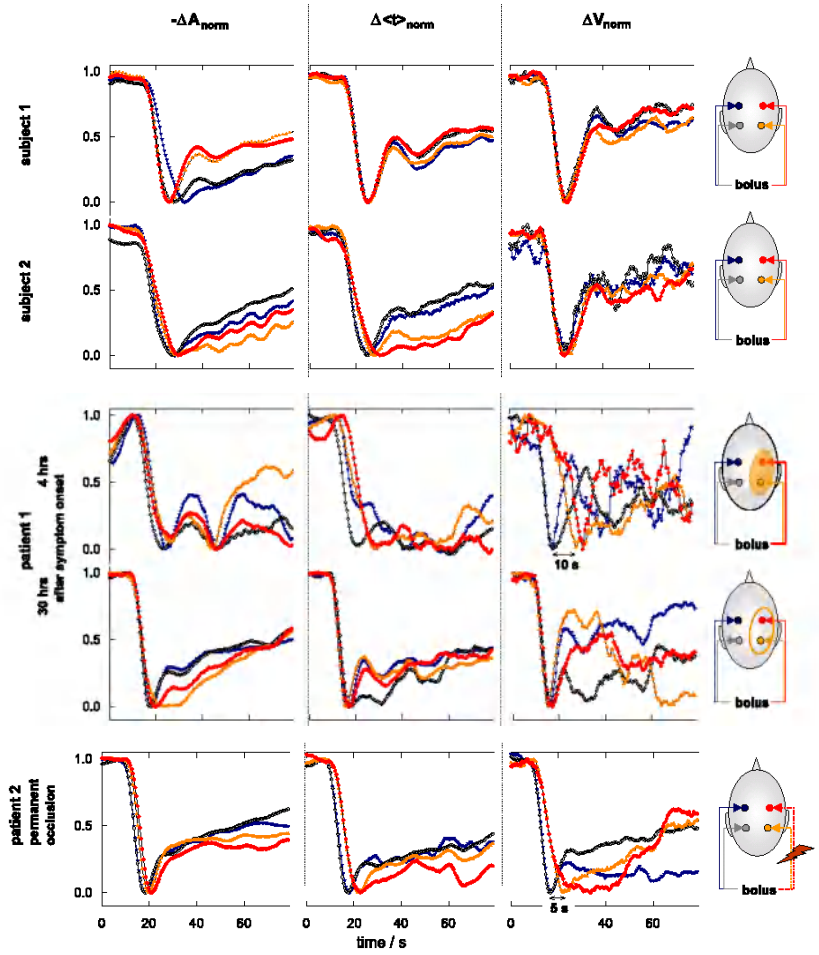


Fig. 843: Changes of the normalised attenuation, $-\Delta A_{norm}$, the mean time of flight, $\Delta\langle t\rangle_{norm}$, and the variance of the time of flight, ΔV_{norm} for two healthy subjects and two stroke patients. The curves were scaled to a range from 0 to 1 by subtracting the minimum value and normalising the result to its maximum. From [786].

For the healthy subjects the changes in the moments appear virtually simultaneously in both brain hemispheres. For the stroke patients the changes in the moments at the location of the stroke are delayed. The delay is most pronounced in the variance, ΔV_{norm}. A thrombolytic therapy of patient 1 resulted in normal perfusion after 30 hours. Patient two had a permanent occlusion.

Absorption changes are not only caused by inflow dynamics of the ICG bolus but also by physiological effects like heart beat, breathing, and blood pressure variations. These effects can be seen as quasi-periodic oscillations in Fig. 843. The mechanisms of these effects and their impact on NIR tissue spectroscopy are discussed in [668].

Diop et al. [387, 388] used the ICG bolus technique to determine cerebral blood flow in piglets under normocapnia, hypercapnia, and carotid occlusion. They compared time-resolved (TCSPC) and CW data recorded under similar conditions. Although the general correlation of the TR and CW data was good the authors also found systematic differences. After discussing possible instrumental effects the authors conclude that the techniques deliver information from different depth in the brain. This is supported by the fact that in the time-resolved data the amplitude of the attenuation change during the bolus is larger for late-arriving photons.

Recently, Liebert et al. described an instrument that records ICG concentration changes at extremely large source-detector distance [788]. By using high incident power from a Ti:Sa laser, and placing a detector directly at the surface of the tissue they were able to record at 9 cm source-detector distance. The instrument was used both on phantoms and on human volunteers. The phantom consists of a fish tank filled with a mixture of milk, water and an absorber. The tank contained a transparent flow-tube through which the same mixture was pumped. In ICG bolus was simulated by injecting ICG in the flow system. The authors showed that the ICG bolus was detectable down to a depth of 5 cm. Measurements at the human head confirmed this result in that they showed physiological effects expected in deep brain layers.

Fluorescence

For a given number of recorded photons, a fluorescence measurement in general yields a better intrinsic SNR than an absorption measurement. The reason is that the dye concentration obtained via fluorescence is directly related to the number of detected photons, whereas the concentration derived from absorption or diffuse reflection is the difference of two photon numbers. However, compared to the diffusely transmitted or reflected intensity the fluorescence intensity is much lower. The SNR actually obtained depends on the efficiency of the optics and the detection system, the tissue thickness, the fluorophore concentration and quantum yield, and the acceptable acquisition time. Milej et al. compared fluorescence and diffuse reflection measurements in phantom experiments. They used a phantom that had tubes for dynamic inflow of indocyanine green (ICG) inserted at different depths. They showed that the use of fluorescence signals delivered better sensitivity and signal-to-noise ratio compared to the use of diffuse reflectance data. A similar study for a fluorescent inclusion within non-fluorescent and weakly fluorescent phantoms came to the same result [634].

Liebert et al. and Milej et al. have shown that the fluorescence of ICG can well be detected from inside the human brain [787, 870, 871]. They used two or four channels of an SPC-134 package. One channel detected the diffusely reflected light, the other the fluorescence. Measurements were performed at a rate of 10 s^{-1}. A result is shown in Fig. 844.

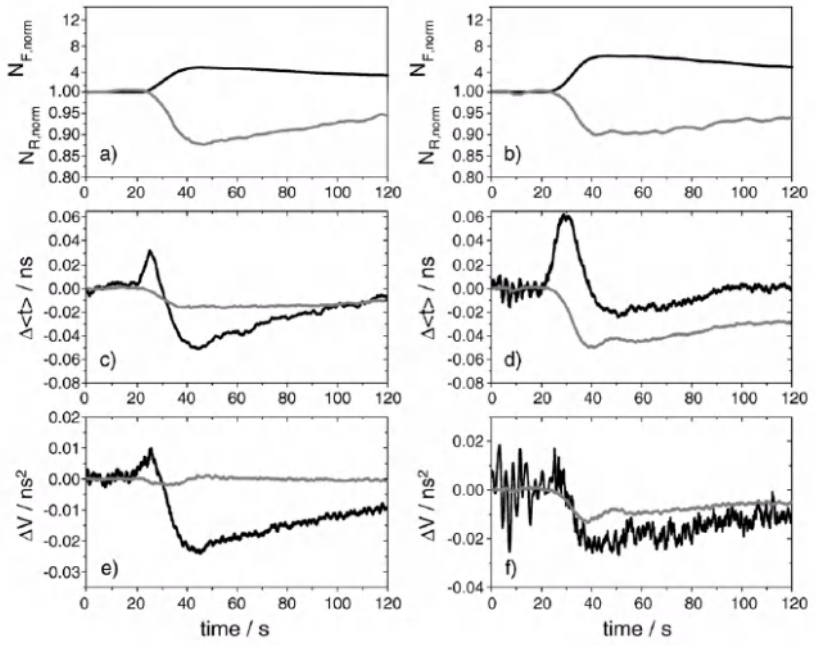


Fig. 844: Normalised number of photons, N_{Rnorm} and N_{Fnorm}, changes in mean time of flight, $\Delta\langle t\rangle$, and changes in variance of time of flight, ΔV, after injection of an ICG bolus. Both hemispheres of brain. Gray curve: Diffuse reflection. Black curve: Fluorescence. From [787], copyright Elsevier Ltd.

The shapes of the curves of the mean time of flight and the variance are significantly different for the fluorescence and the diffuse reflectance. The authors attribute these differences to the time differences of the inflow of the ICG in the intra- and extra-cerebral compartments.

Intra- and extra-cerebral fluorescence components during an ICG bolus have been investigated in detail by Jelzow et al. [619]. The authors present an algorithm to separate these components based on the bolus function and on changes in the DTOFs over the bolus time.

Gerega et al. [495] have demonstrated multi-wavelength fluorescence detection of ICG boli. The authors used a PML-SPEC (MW FLIM) 16-channel detector connected to an SPC-830 TCSPC module. The light from the tissue was collected by a fibre bundle and transferred into the input slit of the PML-SPEC polychromator, see Fig. 845, left. A time-series of multi-wavelength recordings was performed in the Scan Sync Out mode of the SPC-830 module. A result is shown in Fig. 845, right. The authors discuss the effects of absorption, re-absorption, ICG concentration, and depth in the tissue on the recorded data. Please see also a general investigation and discussion of the spectral and temporal fluorescence behaviour of ICG in simulated physiological environment by the same authors [494].

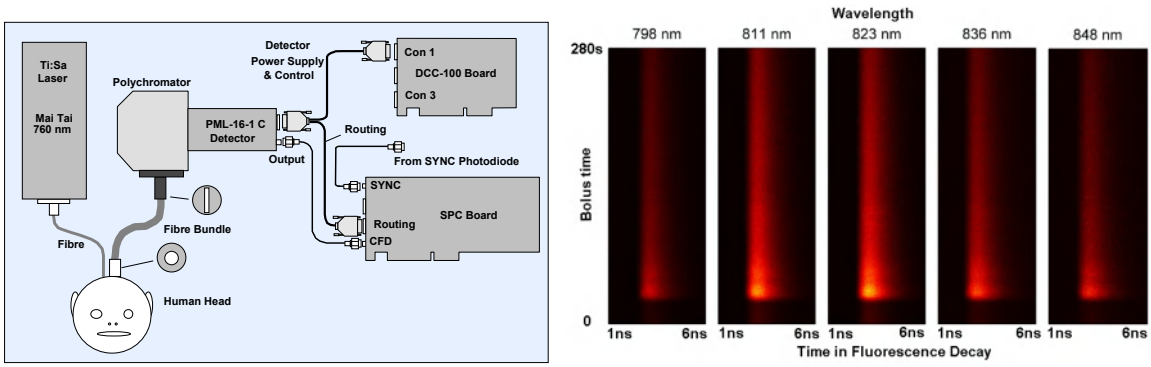


Fig. 845: Setup for time- and wavelength-resolved bolus detection used by [495]

Perfusion Measurement by Diffuse Optical Correlation (DCS)

Perfusion measurements in tissue are also possible by correlating intensity fluctuations of photons scattered in the tissue [298, 389, 1372, 1396]. A laser injects light into the tissue via a fibre. The light at a different spot is collected by another fibre and detected by a photon counting detector. An autocorrelation function of the intensity is calculated from the absolute times of the photons. To obtain a useful correlation function it is required that the laser have a coherence length longer than the average path length in the tissue, and that the fibres have diameters on the order of 20 µm or less. For a test of the principle we used the setup shown in Fig. 846.

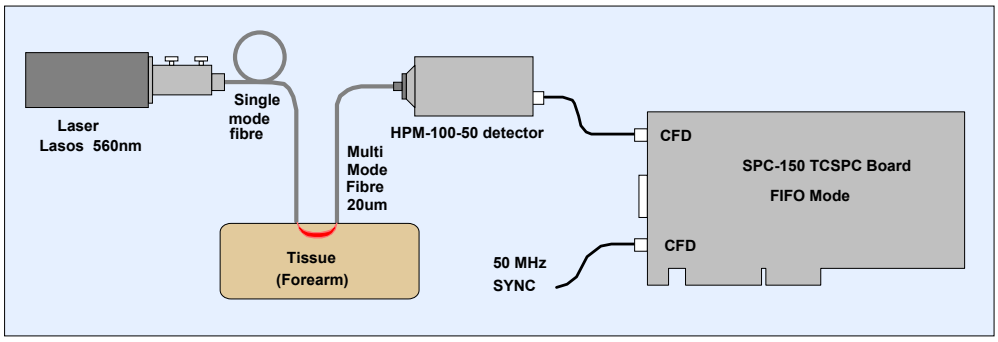


Fig. 846: Test setup for diffuse correlation

Long-coherence length light was delivered by a LASOS DPSS series 561 nm laser. It was injected into the tissue by a single-mode fibre. Diffusely scattered light was collected by a 20 µm multi-mode fibre and detected by an HPM-100-50 hybrid detector. The photons were recorded by an SPC-150 card in the FIFO mode. An autocorrelation function was calculated by the online correlation function of the SPCM software (see page 640). A result is shown in Fig. 847. Because of the unfavourable laser wavelength (we had no long-coherence length laser of longer wavelength) we obtained a count rate of only 25 kHz at a source-detector distance of 3 mm. Nevertheless, there is a clear correlation in the data. The result shows that diffuse correlation can, in principle, be recorded by equipment typically used in TCSPC time-domain DOT.

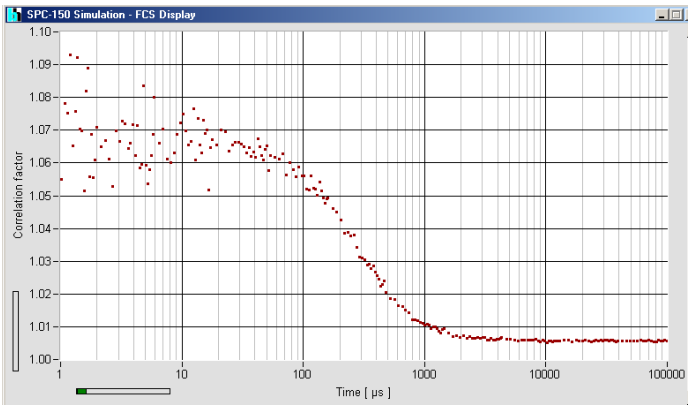


Fig. 847: Correlation curve obtained in the setup shown above. Human forearm, source-detector distance 3 mm, detected count rate 25 kHz.

The setup can easily be extended to 8 detection channels by using a router in front of the SPC-150 card. Correlation can also be obtained by a bh DPC-230 correlator card as has been shown by Diop et al. [389]. In that case, autocorrelation in up to 16 channels can be obtained. An instrument composed of an SPC-134 TCSPC system and a DPC-230 card was used to

combine time-resolved NIRS and DCS for quantification of the cerebral metabolic rate of oxygen consumption [1284].

DOT Experiments at Small Source-Detector Distance

An important parameter of a DOT system of the diffuse reflection type is the maximum depth at which tissue parameters or dynamic variations can be detected. The practical limitation is the rapidly increasing extinction of the optical signal with the path length in the tissue. Theoretically, the path length for a given depth can be reduced by reducing the source-detector distance. Unfortunately, reducing the source-detector system creates another problem: Most of the photons return to the detector after having travelled only a short way through the tissue. The signal intensity in the first few 100 ps after the laser pulse becomes extremely high. The intensity of the later part of the signal, i.e. of the part that has travelled through deep tissue layers, is many orders of magnitude lower. Detecting these photons by the normal time-resolved techniques is impossible: Even if the detector and the TCSPC system could deal with the enormous intensity ratio the photons would be lost in the tail of the IRF and in the after-pulsing of the detector.

It is therefore attempted to suppress the first part of the signal by gating the detector. Fast gating can be obtained in single-photon avalanche diodes (SPADs). However, the on-off ratio of the gating must be on the order of 10^5. Also, the detector must deliver a clean photon timing only a few 100 ps after the 'gate-on' transition. In particular, no electron-hole pairs from the 'gate-off' period must be trapped in the detector and cause avalanche breakdown in the 'gate-on' period. Unfortunately, a lot of such carriers exist in the 'diffusion tail' of a SPAD. Gated detection for zero-distance measurement therefore required substantial improvements in the SPADs and in the quenching and gating circuitry. Other problems are caused by reflections and scattering in the optical system. Also scattered and reflected photons can arrive after the gate-off period and interfere with the 'late photons' returning from deep sample layers. Improvements in SPAD design, theoretical considerations and results of zero-distance DOT can be found are described in [351, 734, 835, 975, 1172, 1175, 1257, 1260]. Please see also 'Gated SPADs, page 198'

Fibre-Based DOT Endoscopes

Laidevant et al. have designed a fibre-based tissue probe arranged around the ultrasound transducer of an endoscopic ultrasound probe [737]. The principle is shown in Fig. 848.

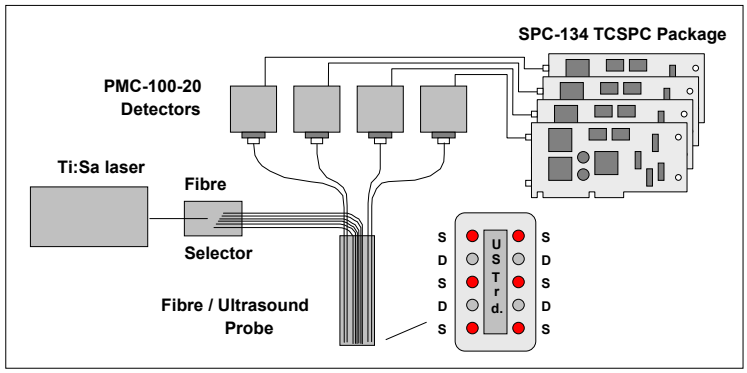


Fig. 848: Fibre based tissue probe with time-resolved detection

6 source fibres and 4 detector fibres are arranged around the ultrasound transducer of the endoscope. The laser is switched periodically through the 6 source fibres. The signals returned through the detector fibres are detected by four PMC-100-20 detectors, and recorded by the four TCSPC modules of an SPC-134 package. The system was tested for fluorescence detec-

tion. By using the temporal data of the four detection channels for the 6 laser positions spatially resolved detection a small ICG inclusion in a scattering medium could be localised at good precision. The optical information is then used to complement the information from the ultrasound transducer.

Tissue Spectrometers

Application of diffuse optical tomography to clinical problems requires that the general optical parameters of different tissue types and their dependence on the wavelength be known. These parameters are determined by recording time-of-flight curves for different source-detector distances at different wavelengths and fitting diffusion models to the results. Because there is no need to resolve fast physiological effects measurements at different source-detector distances and different wavelength are usually performed sequentially. The principle is shown in Fig. 849.

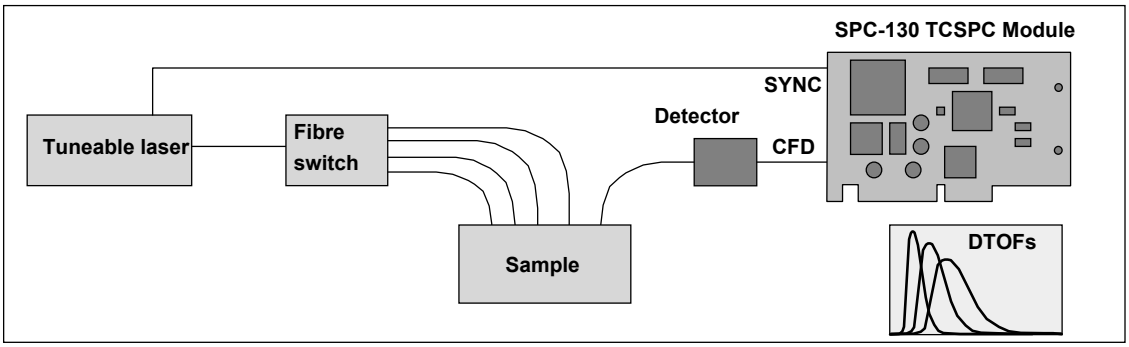


Fig. 849: Principle of a tissue spectrometer with a tuneable laser

A tuneable laser provides light of selectable wavelength. Tissue spectrometers of this type use titanium-sapphire lasers, supercontinuum radiation generated by titanium-sapphire lasers in photonic crystal fibres, supercontinuum lasers with tuneable filters, or tuneable dye lasers pumped by Nd:YLF lasers.

As second way of obtaining spectral information is to illuminate the sample with supercontinuum radiation directly and detect the DTOFs by multi-wavelength TCSPC [51, 354, 508], see Fig. 850.

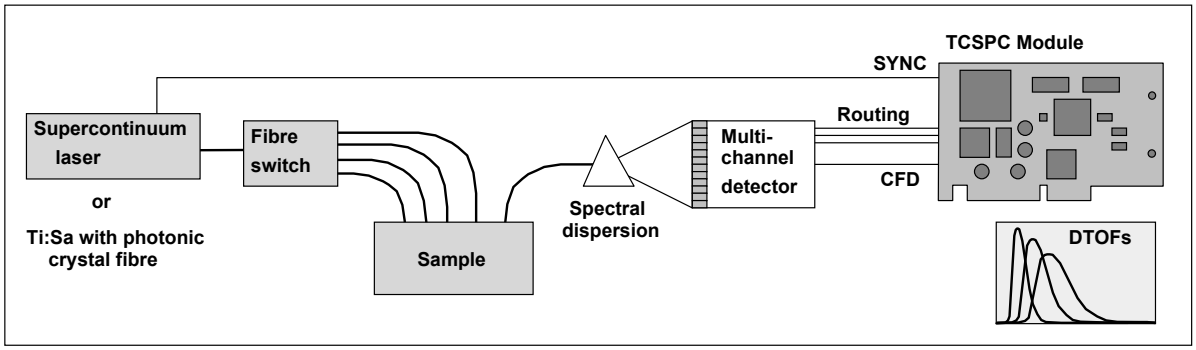


Fig. 850: Principle of a tissue spectrometer with wideband illumination and spectrally resolved detection

Instruments and applications are described in [51, 53, 322, 354, 508, 972, 974, 1227, 1228, 1229, 1214, 1215, 1229]. Gerega et al. used a multi-wavelength detection setup to determine the fluorescence dynamics of ICG in under simulated physiological conditions [492], and discuss the influence of absorption, re-absorption, scattering, and aggregation on the decay profiles at different excitation and emission wavelength. Tissue spectrometers have also been

used in non-medical applications, such as to determine the moisture content of wood, or the quality of food [353, 355, 912, 1250, 1404].

Fibre-Based System for Brain Activation Measurement in Mice

Cui et al. used a fibre-based excitation and detection system to record brain activation in mice during complex tasks [348, 349]. The mice were kept in a compartment which had a food magazine and a lever on each side of the magazine to open it. To open the magazine, the mice had to touch either the left or the right lever. The animals expressed a genetically encoded Ca^{2+} indicator in the brain. The fluorescence of the Ca^{2+} indicator was excited and detected via fibres implanted in the brain. The principle of the fibre-based excitation and detection system is shown in Fig. 851.

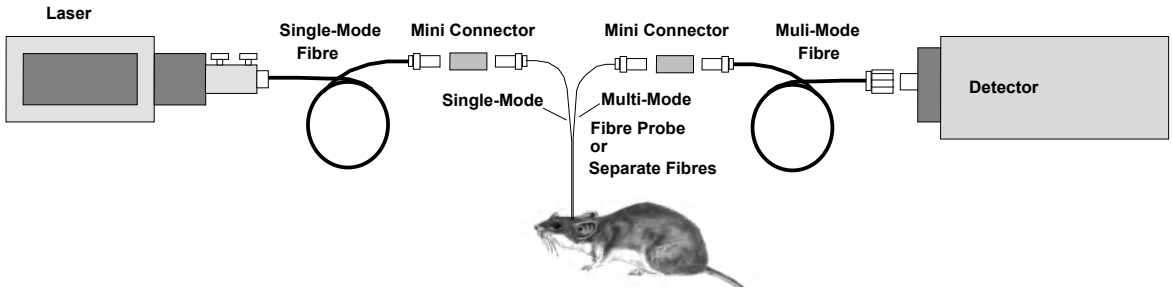


Fig. 851: Principle of fibre excitation and detection system

The excitation light must be transmitted into the brain by a single-mode fibre. A multi mode fibre would generate a speckle pattern the structure of which changes with bending of the fibres and thus induce motion artefacts. The detection fibres are multi-mode to increase the light-collection efficiency. Intensity changes by mode fluctuations do not occur on the detection side because the fluorescence signal is diffusely coupled and has a wide optical spectrum. Excitation and detection fibres (provided by bh) are shown in Fig. 852. The excitation and detection fibres are either separate (Fig. 852, left), or the fibres are mounted in a single excitation/detection probe (Fig. 852, right).

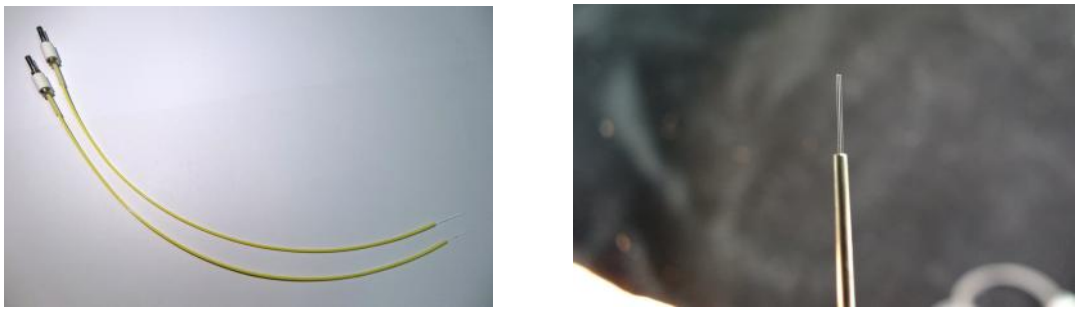


Fig. 852: Excitation and detection fibre (left), combined excitation/detection fibres (right)

For in-vivo applications it is important that the excitation and detection system can be connected and disconnected from the animal. This is achieved by small-size light-weight fibre connectors, Fig. 852, left, upper left. Details of the connectors are shown in Fig. 853. The total weight of the fibre connection is less than 2 g.

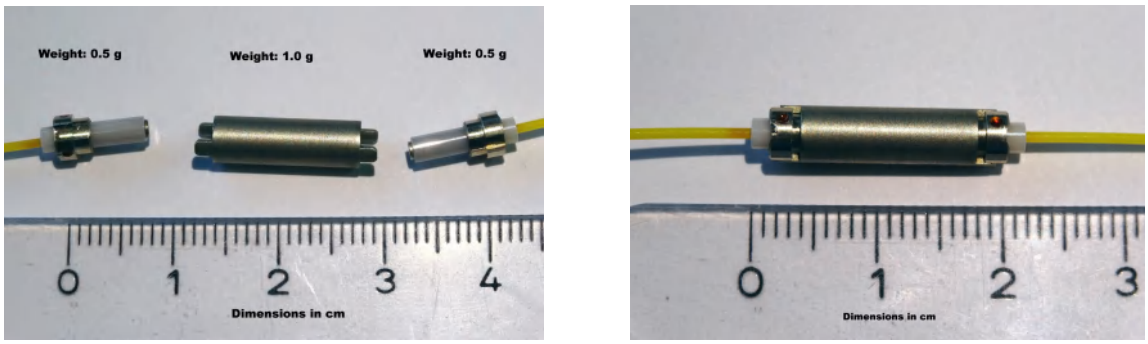


Fig. 853: Fibre mini connectors for excitation and detection fibres. Unconnected (left) and connected (right)

The system was used to detect concurrent activation of the strial direct and indirect pathway during motor activation. The authors were able to record clear differences in the Ca^{2+} signal when the mouse operated either the left or the right lever. Amazingly, the signal was observed about 100 ms before the mouse started to move. That means it was related to the decision to use one or the other lever. Details are described in [348, 349].

Recently, bh have developed a fibre probe with a removable tip, see Fig. 854. the laser is delivered via a single-mode fibre, the fluorescence is detected through a multi-mode fibre. In the tip, both are combined into a short piece of multi-mode fibre. The advantage of this design is that, when the animal is de-coupled from the experiment only the tip remains in it. The disadvantage is possible fluorescence from the tip itself, and from contamination at the interface of the fibres with the tip. Both are transilluminated by the laser, and fluorescence excited in at the interface or in the tip is transferred to the detector. This is no problem for experiment with exogenous fluorophores. For autofluorescence it is, however, critical. By using special glass for the tip, the fluorescence has been kept at a level two orders of magnitude lower than autofluorescence of mammalian tissue. The interface between the fibres and the tip has to be kept absolutely clean. A speck of dust, a single pollen grain, or a fingerprint of the surfaces can make autofluorescence detection impossible. A application has been described in [801].

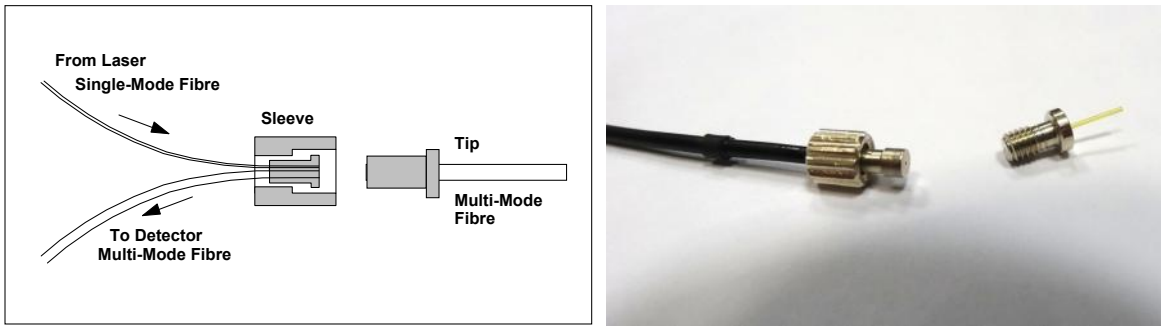


Fig. 854: Fibre probe with a removable tip

Tissue Scanning System with Laser Wavelength Multiplexing

Most TCSPC DOT data are under-sampled in space and in wavelength: The optical signals are collected by fibres or fibre bundles at a moderate number of spatial positions, and a few lasers (usually two) of different wavelength are multiplexed. Undersampling poses a significant problem to spatial reconstruction. For small-animal imaging the problem has been partially solved by moving the detector setup and the subject, see Fig. 859 and Fig. 860.

A setup for scanning stationary objects in space and wavelength has been built and tested in cooperation of bh and the Physikalische Bundesanstalt Berlin (PTB). We thank Michail Mazurenka and Heidrun Wabnitz for their cooperation. The principle is in Fig. 855.

The measurement object is scanned by a laser beam via a fast galvanometer scanner. The scanner is driven by a bh GVD-120 scan controller the same way as in the bh confocal FLIM systems [68]. The light returning from the sample (diffuse scattering or fluorescence) is separated from the excitation beam by a beam splitter. The light passes a filter and a pinhole, and is detected by an HPM-100-50 hybrid detector. The single-photon pulses from the detector are recorded by an SPC-150 TCSPC FLIM module. The pixel, line, and frame clock pulses for synchronisation with the scan are delivered by the GVD-120 scan controller.

A supercontinuum laser delivers the pulsed excitation light. We used a Fianium SC400 laser (40 MHz version) with an AOTF-V1-HP tuneable acousto-optical filter (AOTF). The AOTF is able to select between eight programmable wavelengths by signals applied to the 'MOD' inputs of the AOTF controller. These signals are provided by a counter that is driven by the frame clock pulses of the scan controller. The result is that the AOTF cycles through the 8 wavelengths for subsequent frames of the scans. Simultaneously, the routing inputs of the SPC-150 module are driven by signals from the counter outputs. Thus, the SPC module builds up separate images for the individual laser wavelengths.

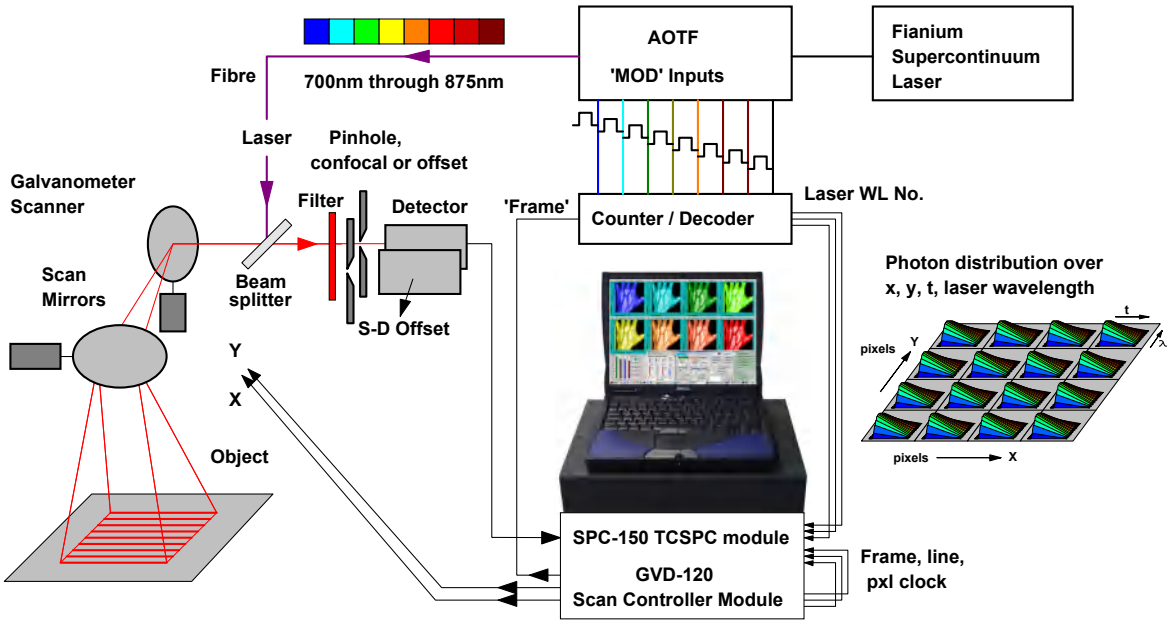


Fig. 855: Scanning system with wavelength multiplexing

The detector and the pinhole can either be made confocal with the laser spot in the sample plane, or offset by a few millimeters. A filter in front of the detector selects either diffusely scattered light or fluorescence. A typical result is shown in Fig. 856.

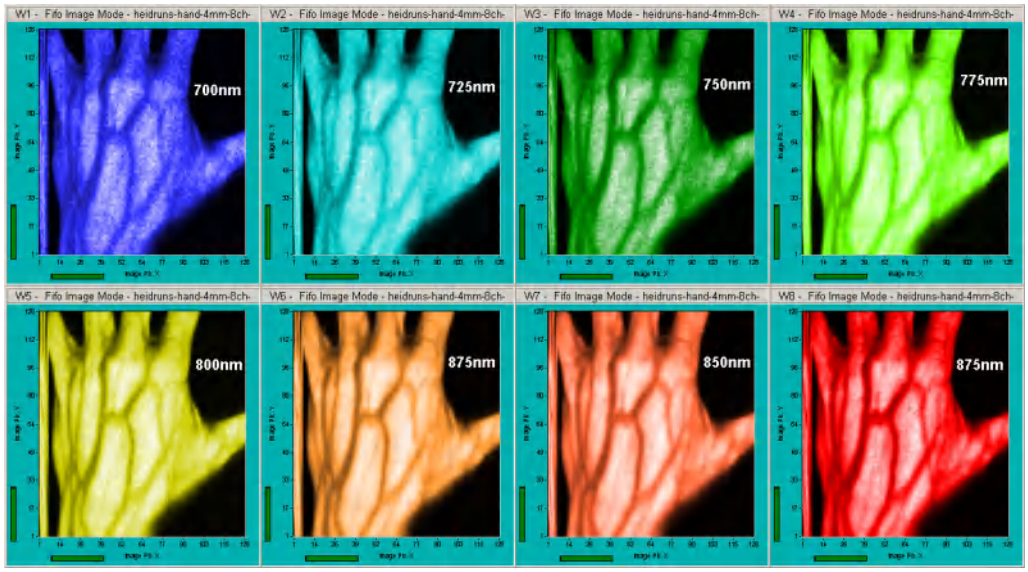


Fig. 856: Diffuse-reflection scan of a human hand. Source-detector offset 4 mm, wavelengths indicated in the images. False colour, selected to indicate the different laser wavelength.

Fig. 857 shows two images analysed by bh SPCImage FLIM analysis software. Both are from the 820-nm channel, and show the first moment, M1, coded in colour. The left image is for a source-detector distance of d = 0 mm, the right one for a distance of d = 4 mm. Both images show differences in M1 between the blood vessels and the surrounding tissue. As expected, the difference depends on the source-detector distance: For d = 0 it is only 3.5 ps, whereas it is almost 22 ps for d = 4 mm.

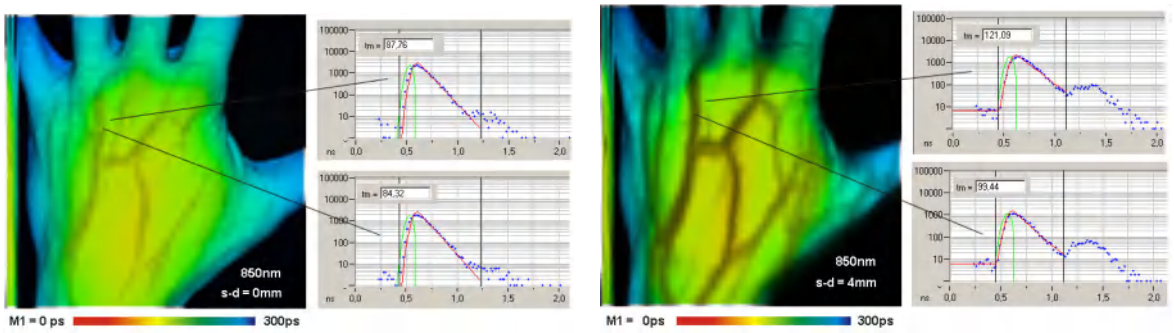


Fig. 857: M1 images of the data in the 820-nm channel. d = 0 (left) and d = 4 mm (right). Analysis by bh SPCImage FLIM analysis software.

Fig. 857 shows also two problems of the setup. The first one is that the measurement object is not flat. Consequently, there are path length differences that show up in the M1 data. This problem can be solved by taking a reference scan at d = 0 and using it as a reference for scans at larger distances. The path-length can also be eliminated by using the second moment, M2. Another problem is reflection and scattering in the optical setup. The laser is scattered and reflected at any optical surface in the beam path. Because excitation and detection use the same beam path reflections show up in the time-resolved data, see bumps at late times in the DTOFs shown in Fig. 857. The reflections can only be minimised by carefully selecting the optical components, by using anti-reflection coatings, and by avoiding optical surfaces in planes conjugate with the pinholes.

Another way to mitigate the influence of optical reflections is to use a time-gated SAPD (see Gated SPADs, page 198) as a detector. To explore the options of time-gated detection a single-point (non-scanning) setup was built up and evaluated [835]. This setup was then upgraded with scanning and multiplexing of two wavelengths [836] by the principles shown in

Fig. 855. Results were presented in [836] and [1307]. A characterisation of the system has been given in [390].

Optical reflections are not a problem when the scanner is used to detect fluorescence. They are then suppressed by the fluorescence filter. An example of fluorescence recording is shown in Fig. 858. Interestingly, the ICG lifetime is not constant, see also FLIM images in Fig. 568, page 386.

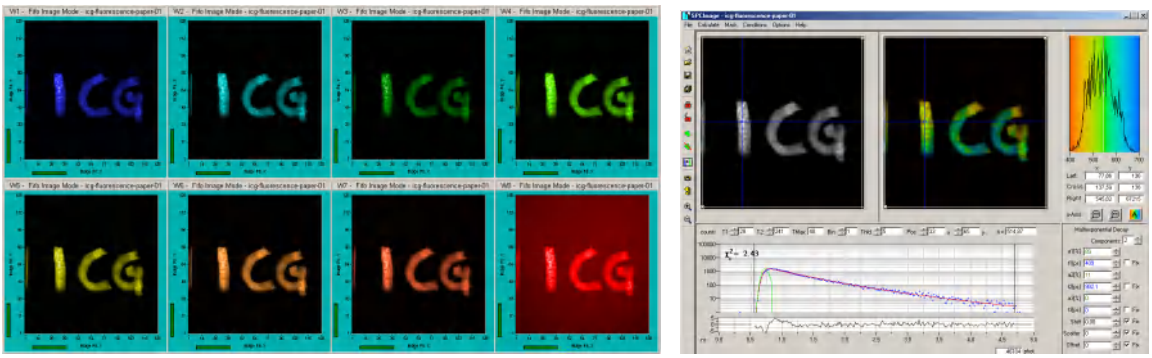


Fig. 858: Left: Fluorescence images of ICG on paper. Excitation wavelengths from 701 nm (upper left) to 780 nm (lower right). Fluorescence was detected from 800 nm to 850 nm. Right: Lifetime analysis with SPCImage, excitation channel 770 nm.

Muscle and Bone Studies

Time-resolved DOT is sometimes used for optical biopsy of bone tissue, and to track heamodynamics and oxygen kinetics in muscle tissue. Compared with instruments used for structural brain imaging the number of source and detection channels is normally considerably reduced.

Instruments described in [343, 346, 1256] used two lasers multiplexed pulse-by-pulse and eight detection channels routed into a single SPC-630 channel. An instrument described in [51] used super-continuum generation in a photonic crystal fibre and a multi-wavelength TCSPC system based on a PML-16 and an SPC-630. Absorption and scattering coefficients were obtained at 16 wavelengths simultaneously. Binzoni et al. describe an instrument based on an SPC-130, a supercontinuum laser, and wavelength multiplexing by a rotating filter wheel. The instrument was used for characterisation of bone tissue phantoms [209].

An instrument for optical biopsy of bones based on a diode laser and a single SPC-330 TCSPC channel was described in [423, 424]. Other instruments use a tuneable synchronously pumped dye laser and a Ti:Sapphire laser [971]. The lasers are switched into a single source fibre by a fibre switch. A single SPC-630 channel records the diffusely reflected light and a reference signal split off from the source fibre.

Fluorescence Lifetime Detection in DOT

The fluorescence lifetime of a fluorophore depends on its local environment. The lifetime of many fluorophores changes upon binding the protein and DNA. Extremely large changes can be obtained from FRET probes that contain a donor and an acceptor at the ends of a protein chain. The lifetime of the donor then depends on the folding of the protein chain. The folding changes upon binding to other proteins, and so does the lifetime of the donor. It is expected that such probes can be constructed to mark specific binding targets.

Fluorescence DOT as a diagnostic tool of human medicine is in an early stage, mainly because potential probes are not approved for the application to human patients. So far, only indocyanine green (ICG) can be used. ICG in water has a fluorescence quantum yield of about 4% [370]. The fluorescence lifetime of ICG bound to human serum albumin (HSA) in water was determined to be double exponential, with contributions of 84% of 615 ps and 16% of 190 ps [488, 814]. Please see also section 'Near-Infrared FLIM' page 384 in this book. The lifetime is clearly dependent on the solvent; for pure ICG in ethanol 550 to 650 ps are obtained, see Fig. 842. Lifetimes this short are difficult to separate from the time-of-flight distribution in thick, inhomogeneous tissue. It is therefore difficult to exploit possible lifetime changes of ICG for tissue characterisation.

Another problem is the extraction of fluorescence lifetimes from DOT data. The extraction of pH-induced fluorescence lifetime variations from time-of-flight curves recorded by TCSPC was studied in [477]. The fluorescence of beads stained with IRD38 (Li-Cor, Inc.) embedded in agarose phantoms was recorded by TCSPC. A femtosecond titanium-sapphire laser was used for excitation, and a H7422-50 PMT module for detection. The decay curves were recorded by an SPC-730 TCSPC module. The authors show that the fluorescence decay can be separated from the instrument response function and the time-of-flight distribution of the bulk medium.

Small-Animal Imaging

Small-animal imaging is not limited by the strict constraints placed on DOT in human patients. Thus a large number of exogenous fluorophores can be used [1120]. Moreover, the typical tissue thickness is only a few millimeters, so that the excitation wavelength is not restricted to the NIR only. Visible and UV excitation can be used to excite not only exogenous, but also a large number of endogenous fluorophores, including NADH, or GFP and its mutants in transgenic organisms. The non-invasive character of DOT allows one to track the growth of a tumor, angiogenesis, invasion and metastasis, the progress of photodynamic therapy, or the effect of drugs [345, 1120].

A complete time-resolved small-animal imager was available from ART Advanced Research Technologies Inc., Montreal, Canada. The animal (a mouse or a rat) was placed on a platform mounted on a translation stage. Scanning in the X direction was accomplished by moving the translation stage. In the Y direction the laser beam is scanned by a galvanometer mirror. The fluorescence light was collected by a lens, descanned by a second galvanometer mirror, and detected by a PMT. The signal was recorded by an SPC-130 TCSPC module. First results were presented by Gallant et al. [474]. Detection of a tumor in a mouse was demonstrated in [229]. A dye-labelled hexapeptide was used as a tumor marker. The marker accumulated in the tumor and the major excretion organs. In the tumor a fluorescence lifetime of 1.03 ns was found, compared to 800 ps in other tissue. Unfortunately, ART went out of business, and this wonderful instrument disappeared from the market.

A system that records steady-state fluorescence images and time-resolved fluorescence data in single points by an SPC-130 card was described in [1275]. The authors used the instrument to observe the effect of vascular disruption agents on tumors in mice.

A scanning system that records the images of the time-resolved fluorescence, diffuse fluorescence, diffuse transmittance, and fluorescence from both sides of a sample was described in [243]. The data in the four channels were recorded by an SPC-134 TCSPC system. The instrument was demonstrated on phantoms containing a fluorescent inclusion.

An instrument developed by Gao et al. uses the four parallel TCSPC channels of an SPC-134 and multiplexes four signals into the detector of each channel by 4:1 fibre switches [482, 805]. The laser was multiplexed into several source positions by another fibre switch. The instrument was demonstrated on small-animal-sized phantoms but was certainly capable of being used on the animals themselves. Image reconstruction procedures for the recording geometry used were described by Ma et al. [805] and Yang et al. [1361].

A small-animal system of the classic tomographic architecture has been built by Kepshire et al. [657, 658]. The principle of the system is shown in Fig. 859.

The specimen is illuminated by a single laser beam. A gantry with five collection lenses is rotated around the specimen. The collected light is projected into optical fibres which transfer the light to the detectors. The light of each channel is split into a transmission and a fluorescence component. Both components of each channel are detected by H7422P-50 PMT modules. The PMT pulses are fed into three routers and processed by three TCSPC channels of the SPC-134 package. The forth TCSPC channel records a reference pulse from the laser. The signal is used to eliminate intensity variations and temporal drift.

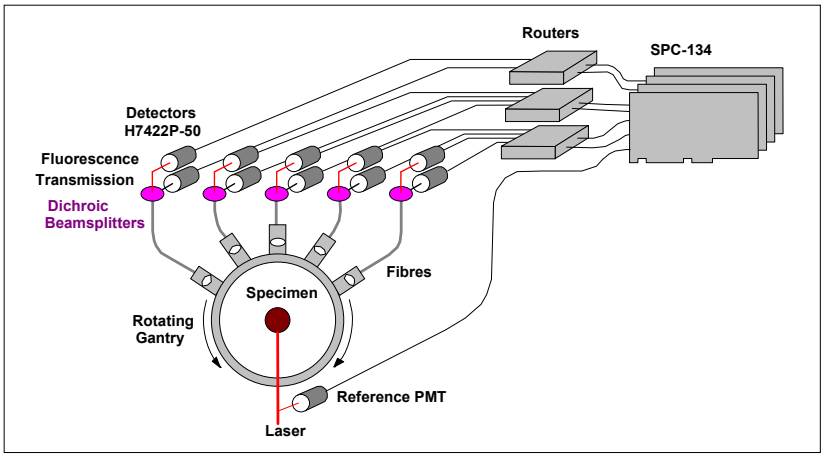


Fig. 859: Small-animal fluorescence tomography system used by Kepshire et al.

The system was used for tomographic imaging of a glioma tumor in a mouse. The authors exploited the fact that glioma tumors have increased concentration of protoporphyrin IX (PpIX). The concentration was further enhanced by administration of aminolevulinic acid (ALA). PpIX was excited at 635 nm and detected from 650 nm to 700 nm. The setup was sensitive enough to detect a clear signal form the PpIX. The tumor image was reconstructed from the ratio of the fluorescence and transmission intensities. Because fluorescence and transmission data are acquired simultaneously this ratio is resistant to most calibration errors, distance changes, and tissue inhomogeneities. The data obtained this way were combined with micro CT data obtained from the same animal. Please see [657, 658] for details.

Another non-contact tomographic system with 7 fluorescence channels and 7 reflection channels has been built by Lapointe, Pichette, and Berube-Lauziere [743]. The basic optical architecture is shown in Fig. 860, left. The subject is placed on a shaft that can be rotated and shifted vertically. Fluorescence is excited by the beam of a Ti:Sapphire laser. Each optical detection channel contains a lens system that projects a small area of the subject on two PMC-100-20 detectors. One detector is used for fluorescence, the other for reflection. A dichroic beamsplitter in the beam path splits the light into a the two channels; filters are blocking unwanted spectral signal components. Adjustable irises in front of the detectors are used for regulation of the active detection area. The photon pulses from all 14 detectors are routed into the four TCSPC channels of an SPC-134 package.

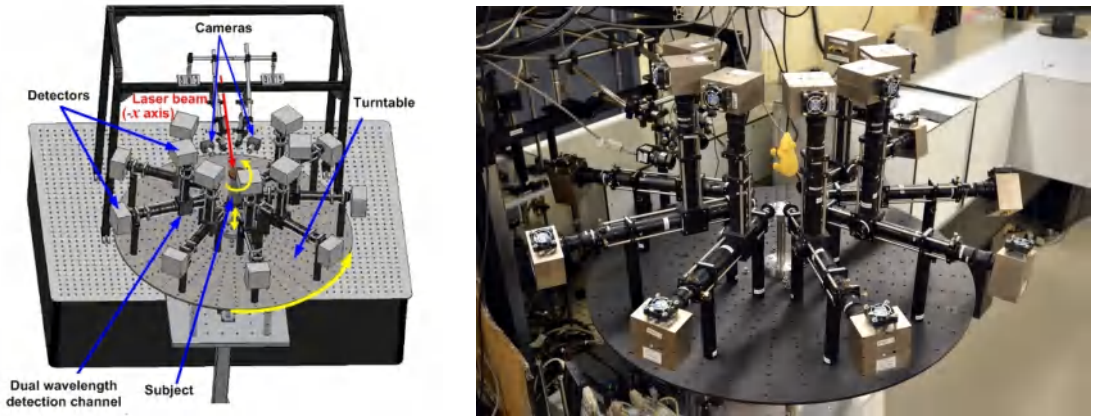


Fig. 860: Fluorescence tomography setup of Lapointe, Pichette, and Berube-Lauziere. 7 detection channels containing a fluorescence and a reflection detector each can be rotated around the sample.

Mu, Pera and Niedre built a dual-channel multi-wavelength fluorescence and diffuse reflection imaging setup [893]. It consists of a supercontinuum laser, two nested motorized rotation stages, two PML-16-C multichannel detectors, and two SPC-130 TCSPC modules. The rotation stages move both the sample and the detector positions so that tomographic imaging under different projection angles is performed. From the laser, two illumination beams are derived. The first one is used for fluorescence imaging, and has a spectrum from 630 to 680 nm. The second one is used for diffuse reflection imaging, and has a spectrum from 550 to 850 nm. The principle is shown in Fig. 861, left, a photo of the setup is shown in Fig. 861, right.

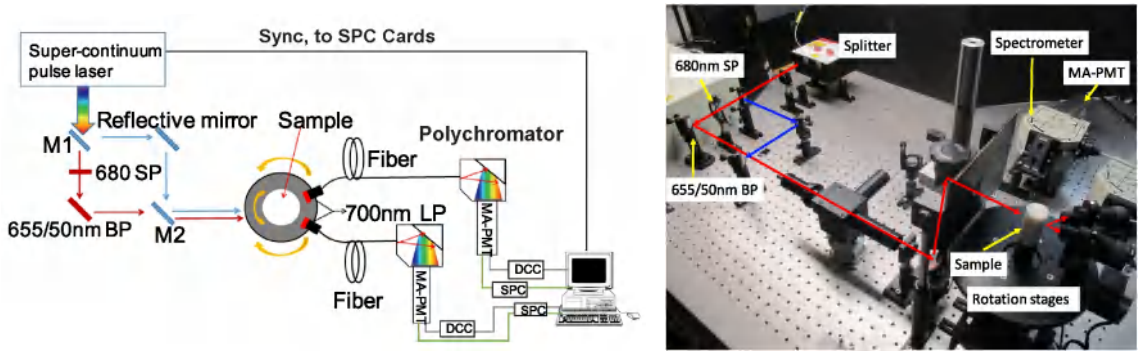


Fig. 861: Multi-wavelength fluorescence and diffuse reflection imaging setup of Mu, Pera and Niedre. Adapted from [893].

The authors verified the instrument and the data analysis algorithms with phantoms, and demonstrated that they obtain homographic images for four fluorophores with 1 mm or better spatial resolution. An similar setup with two SPAD detectors instead of the 16-channel PMTs is described in [892].

Technical Issues of DOT

Pulse Dispersion in Optical Fibres

Almost all devices for diffuse optical tomography are using fibres or fibre bundles to transmit the light from the lasers to the patient and to feed the diffusely transmitted or reflected light from the patient into the detectors. The fibres do not only simplify the optical setup but also decouple the patient electrically from the recording electronics. Unfortunately the temporal dispersion in the fibres noticeably impairs the time resolution. Moreover, the effective instru-

ment response function (IRF) depends on the numerical aperture of the light cone coupled into the fibres. The effective aperture can be different for the recording of the IRF and the time-of-flight distribution at the patient, and severe errors in the determined optical properties can result [783]. A solution to the dispersion problem is to use a thin diffuser for IRF recording. The diffuser is placed in front of the detector fibres and illuminates the fibre with the same aperture as the sample. Because a thin diffuser does not broaden the IRF noticeably the recorded IRF shape has been found very close to the correct one [783].

Any other optical elements that can change the effective numerical aperture at the entrance or exit if a fibre or fibre bundle have to be strictly avoided. Under no circumstances an iris should be used for intensity regulation. However, also absorptive and reflective neutral density filters yield different attenuation for rays of different obliquity.

Changes of the effective NA can be particularly strong if a narrow-band interference filter is placed in the light cone in front of the fibre. The transmission wavelength of an interference filter shifts to shorter wavelength for oblique rays. With a narrow-band filter in a divergent or convergent beam, the outer part of the useful NA of the fibre can be entirely blocked by the filter. The correct solution is to put the filters into a collimated part of the beam.

Collimation of the filter beam path is important also for fluorescence detection in a DOT setup. To separate the fluorescence from the much stronger excitation light, an extremely steep long-pass interference filter has to be used. If this filter is not used in a parallel beam, the filter transition broadens towards shorter wavelengths, with disastrous effect on the blocking of the excitation light.

Laser Multiplexing

Most of the currently existing DOT systems multiplex lasers pulse-by-pulse. This technique has a number of serious drawbacks: It reduces the effective stop rate of the TCSPC modules by the number of laser. This increases possible pile-up effects. Moreover, pile-up and counting loss in the signal of one laser influences all signals later in the multiplexing period. The result is intensity crosstalk between the laser channels. There is also crosstalk by optical reflections on the fibres. A reflection from one laser channel normally shows up in the time interval of another channel. The result is warp in the waveform recorded in this channel dependent on the signal size of the channel that causes the reflection. Finally, thee is also crosstalk due to detector afterpulsing. The afterpulsing background is proportional to the total signal. However, the afterpulsing background of the detector is recorded in all laser channels. Consequently, there is also a crosstalk in the background. The effects are shown graphically in section ‘Multiplexing of Lasers’, page 298.

A better way to record signals excited by several laser is to use the multiplexing capability of multi-dimensional TCSPC, see ‘Multiplexed TCSPC’, page 119 or ‘Multiplexing of Lasers’, page 298. The lasers are multiplexed in microsecond or millisecond intervals, and the routing signals are used to send the photons into separate memory blocks. The stop rate is the full laser repetition rate, and the TAC range needs not to be no longer than the signal duration. Pile-up, counting loss, reflections, and afterpulsing in one channel does not influence other channels. Another advantage is that that multiplexing on the microsecond or millisecond time scale can be used with the AOTFs of supercontinuum lasers, as shown in Fig. 855, page 624.

Detectors

Time Resolution

The typical width of the time-of-flight distributions recorded in DOT is on the order of a few ns. Therefore a detector IRF width of 150 to 300 ps is normally sufficient. Even longer detector IRFs are sometimes tolerated, especially if the pulse dispersion in long fibre bundles dominates the IRF width. It can, however, be expected that the stability of a curve fitting procedure and the standard deviation of the first and second moments of the recorded signal shape decrease dramatically when the IRF width reaches or exceeds the true width of the time-of-flight distribution.

More important than the IRF width is the IRF stability. To reveal effects of brain activity, variations corresponding to changes in the first moment (M1) of a few ps must be reliably recorded. Maintaining a timing stability of a few ps over a wide range of count rates is anything but simple. The most critical parts of the system are the PMT and its voltage divider.

Extremely good timing stability has been obtained with the H5773, H5783 photosensor modules and, consequently, with the bh PMC-100 detectors that are based on these modules (see Fig. 269, page 173). Also the H7422 modules yields good timing stability [154].

Background

Detector background has a detrimental effect on any time-resolved optical measurement. As an example, Fig. 862 shows a distribution of time-of-flight (DTOF) recorded with 1 % background. The influence of the background does not look dramatic, and one might presume that the effect can be ignored.

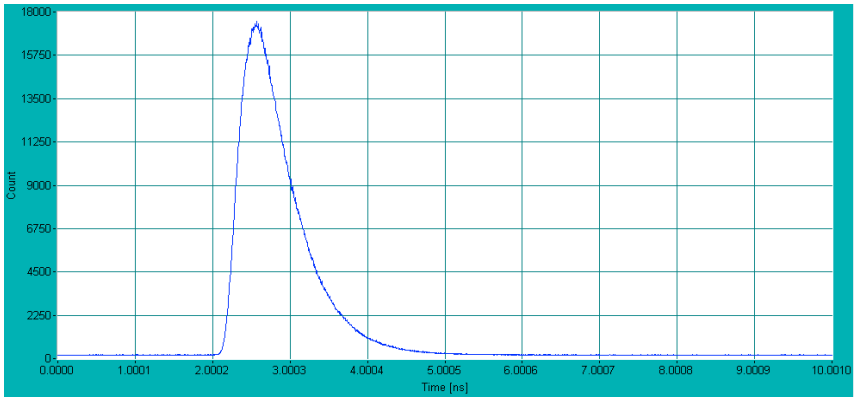


Fig. 862: DTOF recording with a background of 1% of the peak intensity

Now consider what happens when the first moment of the DTOF is calculated: The FWHM of the DTOF is 0.7 ns, and it contains approximately $3{\cdot}10^6$ photons. The FWHM of the background is 10 ns. There are approximately 425,000 photons in the background.

When the first moment is calculated the arrival times are added and divided by the number of photons. The absolute noise of the sum of the arrival times for the photons in the DTOF and in the background is about $FWHM\sqrt{N}$. One might presume that the background does not add much noise because it contains far less photons than the DTOF. However, the FWHM of the background is 10 ns, whereas the FWHM of the DTOF is only 0.7 ns. The absolute noise contributions are thus

$0.7ns\sqrt{3{\cdot}10^6} = 1212$ ns for the DTOF photons and

$10ns\sqrt{425000} = 1955$ ns for the background photons

In other words, the timing noise contribution from the background is larger than the noise induced by the statistics of the DTOF photons!

Subtraction of the background does not help because it does not reduce the contribution of the timing noise to M1. Keeping the recording (or calculation) time interval as small as possible may help a bit, but the only efficient way to obtain near-ideal signal-to-noise ratio of M1 is to reduce the frequency of background counts.

Unfortunately, attempts to reduce the background by cooling the detectors are only partially successful: Most of the background in PMTs and SPADs comes from afterpulsing. The reason of afterpulsing in PMTs is ionisation of rest gas molecules, in SPADs it is trapping and diffusion of electrons and holes of the previous avalanche breakdown. Although afterpulsing can be slightly reduced by optimising the detector operating voltages a dramatic improvement is only possibly by special detector design.

The only large-area detector free of afterpulsing background known so far is the hybrid PMT. Fig. 863 shows a DTOF recording by a HPM-100-50 hybrid detector module (left) and by a R7400 PMT (right). The better dynamic range of the HPM recording is due to the absence of afterpulsing.

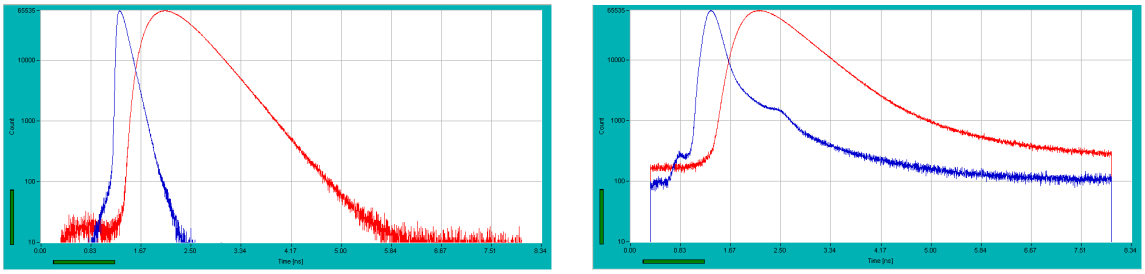


Fig. 863: DTOF recorded with a bh HPM-100-50 hybrid detector module (left) and with an R7400 PMT (right). The DTOF is shown red, the IRF blue.

Efficiency

TCSPC-based DOT requires PMTs with a high efficiency in the NIR. Although the commonly used multi-alkali cathode works up to 820 nm, the efficiency above 750 nm is not satisfactory. Reasonable sensitivity above 750 nm can be obtained from ‘extended-red’ multi-alkali cathodes. PMTs with these cathodes work up to 850 nm.

Recently, Hamamatsu has developed a ‘high efficiency extended red’ cathode, the NIR efficiency of which comes close to that of the GaAs cathode. The new cathode is available in the H5773-20 and H5783-20 photosensor modules. The high timing stability, the short IRF, and the relatively low price of these modules make them the most useful single channel DOT detectors currently available. However, reasonably low dark count rates can be obtained from these detectors only when they are cooled. Therefore, the bh PMC-100-20 detector module contains a thermoelectric cooler attached to an H5773-20 photosensor module.

The most efficient cathodes in the wavelength range of DOT are GaAs cathodes. Although the cathode efficiency of different devices may differ considerably, a factor of 10 can be gained at 800 nm compared to a conventional multi-alkali cathode. The GaAs PMT module most frequently used in DOT is the H7422-50 [548].

The best DOT detector currently available is the bh HPM-100-50 hybrid detector module. It is based on the new Hamamatsu H10467-50. The detector has a GaAs cathode. Although direct comparisons have not been made yet the efficiency of the HPM-100-50 can be expected even a bit higher than for the H7422-50. Please see ‘HPM-100 Hybrid Detector’, page 178.

Detector Area

In DOT experiments the light is diffusely emitted from a large area of the sample. Whatever optics are used, the intensity per area unit cannot be made higher than at the surface of the sample. That means good sensitivity can only be obtained with a detector of large active area. This is no problem for PMTs which have active areas of at least a few millimeters in diameter.

Active area is, however, a problem to SPADs. Fast SPADs have diameters of 50 to 100 µm [607, 858]. Compared with a PMT of 5 mm diameter the area is 2500 to 10,000 times smaller and so is the detected signal. Although SPADs have good quantum efficiencies in the NIR they cannot compete with PMTs in terms of sensitivity.

Fig. 864 shows a comparison of an MPD PDM-50 SPAD with a HPM-100-50 hybrid detector module. The SPAD has an active diameter of 50 µm, the hybrid detector of 3 mm. The quantum efficiencies are approximately the same.

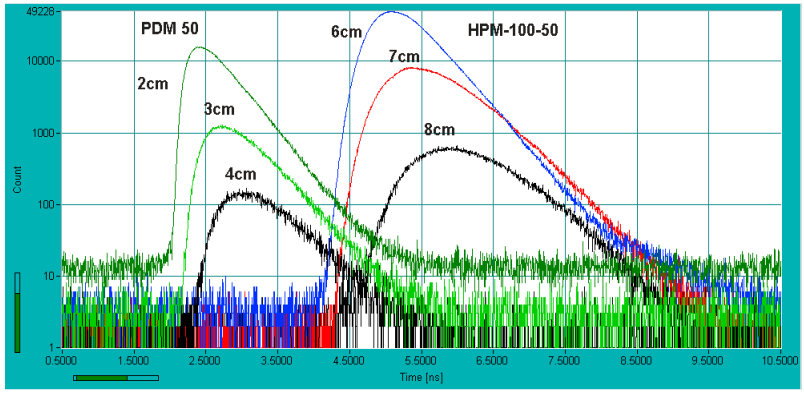


Fig. 864: Comparison of a 50µm SPAD with a hybrid PMT of 3mm active diameter. Phantom measurement, numbers indicate source-detector distance

The comparison was done at a phantom with realistic optical properties. With the SPAD, reasonable signals were obtained for source-detector distances of 2, 3 and 4 cm. With the hybrid detector good signals were obtained for 6, 7, and 8 cm. Shorter distances were not used because the signals caused overload in the detector. (Of course, signals at shorter distance can be recorded with ND filters.) The results are interesting in several respects.

First, the results confirm a general rule of thumb of optical tomography: The intensity drops by about an order of magnitude for every centimetre increase in source-detector distance.

Second, from the results it can be estimated that the HPM-100-50 detects about 10,000 times more photons than the SPAD.

Third, this huge increase in sensitivity translates into an increase of the applicable source-detector distance by a only factor of two. A factor of two may be a lot when penetration depth into tissue is considered but it is ridiculous considering a sensitivity ratio of four orders of magnitude. This should be kept in mind when different detectors are compared: Sensitivity differences have minuscule influence on the maximum source-detector distance unless they are larger than an order of magnitude. Even the SPADs with their tiny area deliver good results if the source-detector distance in no larger than 4 cm.

The dependence of the intensity on the source-detector distance should be kept in mind also when laser power is considered. Compensating for intensity drop at increased source-detector distance by increased laser power soon leads to unrealistic (and unsafe) power levels.

Picosecond Photon Correlation

Classic light sources emit photons randomly, independent of each other. Typical examples are thermal sources or fluorescence from a large number of molecules. The distribution of the time intervals between successive photons drops exponentially for increasing time intervals.

For light generated by nonlinear optical effects and fluorescence of single molecules [50], single quantum dots [856, 1242, 1374, 1405] or other semiconductor nano-structures this is not necessarily the case. A molecule cannot perform a new absorption-emission cycle before the previous one is completed. Similar effects are observed in semiconductor nanostructures. Thus the fluorescence photons are no longer independent of each other - the distribution of the photons drops at times shorter than the lifetime of the excited state. The opposite can happen by nonlinear optical effects in crystals. An example is parametric downconversion. Such effects can literally split one photon of the pump radiation into two, which are then highly correlated [861, 862, 863]. Investigation of all these effects requires the detection and correlation of photons on the ps and ns scale.

Picosecond photon correlation experiments have some similarities with fluorescence correlation spectroscopy (FCS). FCS investigates the fluctuations of the fluorescence intensity of a small number of molecules confined in a small sample volume (see ‘Fluorescence Correlation Spectroscopy’, page 639). The intensity fluctuations are correlated on a time scale from microseconds to milliseconds. Therefore, FCS differs from typical picosecond correlation experiments in the way the photons are correlated. Moreover, FCS effects are driven by diffusion, intersystem crossing, conformational changes, or other sample-internal effects, while typical picosecond correlation effects are driven by the dynamics of the photons of the excitation and emission light.

Optically driven photon correlation experiments normally require confining the detection or the excitation to a sample volume on the order of femtoliters. This is achieved either by confocal detection or two-photon excitation in a microscope. The optical principles are the same as in confocal and two-photon laser scanning microscopes, see ‘Time-Resolved Laser Scanning Microscopy’, page 343. However, most correlation experiments do not require fast scanning and can be performed in relatively simple microscopes.

The classic photon correlation experiment records a histogram of the time intervals between the photons of the investigated signal [50, 552]. Unfortunately, the detector dead time makes it impossible to detect the photons in a single detector and to measure the times between the photons on the ps time scale. Moreover, ringing in the detector, reflections in the detector signal, and afterpulsing preclude a reasonable correlation of the pulses from a single detector on a time scale below 100 ns. The problem of the detector dead time is avoided by the Hanbury-Brown-Twiss, or HBT, setup [552]. This setup is the basis of almost all TCSPC photon correlation experiments.

The principle is shown in Fig. 865. The investigated light signal is split by a 1:1 beam splitter, and the two light signals are fed into separate detectors. One detector delivers the start pulses, the other the stop pulses of a TCSPC device. The stop pulses are delayed by a few ns to place the coincidence point in the centre of the recorded time interval. The setup delivers a histogram of the time differences between the photons at both detectors. Because separate detectors are used for start and stop, there is no problem with the detector dead time. Moreover, the photons are recorded in a classic TCSPC channel. By using SPC-180NX or SPC-150NX modules with HPM-100-06 or -07 hybrid detectors HBT experiments of unprecedented time resolution are possible.

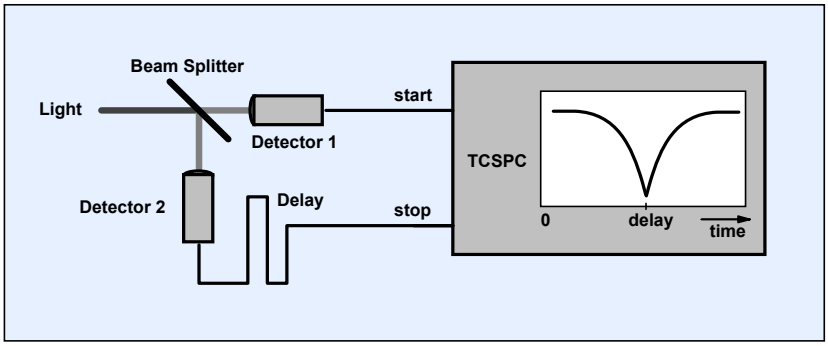


Fig. 865: Dual-detector (Hanbury-Brown Twiss) photon correlation setup

Antibunching

In fluorescence experiments the Hanbury-Brown-Twiss setup can be used with continuous excitation or with excitation by picosecond pulses. Continuous excitation of a small number of fluorescent molecules delivers the typical 'antibunching' curve [50]. An example is shown in Fig. 866. The curve was recorded with two H7422-40 PMT modules (Hamamatsu) connected to to the start and stop inputs of an SPC-130 TCSPC Module.

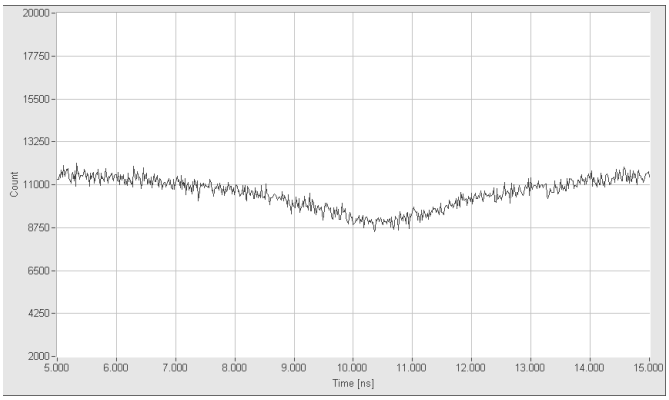


Fig. 866: Antibunching curve for Rhodamine 110, CW excitation, one SPC-134 channel, H7422-40 detectors, 1 ns/div

Similar TCSPC-based antibunching experiments have been used to investigate single photon emission from optically [1242, 1405] and electrically [468, 1374] driven quantum dots.

The setup shown in Fig. 865 is also used for experiments based on parametric downconversion. A nonlinear crystal produces photon pairs the energy of which is equal to the energy of the pump photons. The measurement then delivers a correlation peak on a baseline of randomly detected background photons. The effect can be used for tests of quantum mechanics and a number of metrological applications [248]. The measurement of absolute detector quantum efficiencies by using photon pairs generated by parametric downconversion [731, 861, 862, 863, 997, 1329] is shown in Fig. 955, page 698.

Antibunching experiments with pulsed excitation are described in [442], [662] and [1334]. The measurement delivers a number of correlation peaks spaced by the laser pulse interval. If the laser pulse width is much shorter than the fluorescence lifetime there is almost no chance that a single molecule is excited several times within one laser pulse. Consequently, the emission of two photons from a single molecule within a time shorter than the excited-state lifetime becomes extremely unlikely. The ratio of the height of the central coincidence peak to the adjacent peaks is therefore an indicator of the number of the molecules in the excited volume, see Fig. 867.

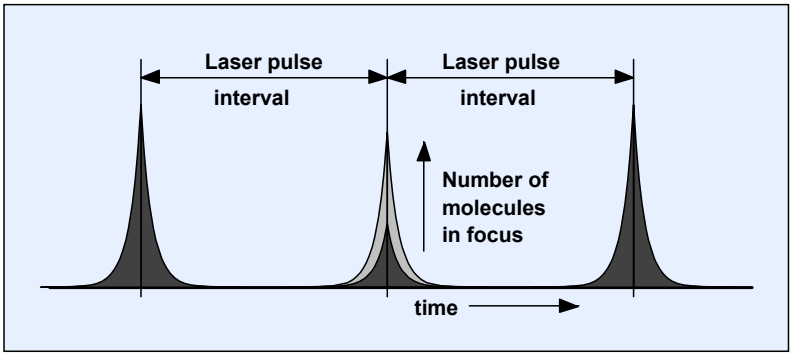


Fig. 867: Antibunching with pulsed excitation. The result is a train of correlation peaks spaced by the laser pulse period. The height of the central correlation peak depends on the number of molecules in the focus.

Technical Aspects

Because the correlation experiments described above are simple start-stop experiments they can be performed with any bh TCSPC module. For experiments with PMTs the SPC-x30 modules should be preferred because these have identical CFDs in the start and the stop channel.

The coincidence rate (the rate of complete start-stop events) of the Hanbury-Brown-Twiss experiment is normally very low. At the light intensity obtained from typical samples, it is relatively unlikely that two photons appear within a time interval of a few nanoseconds. Consequently the coincidence rate depends on the square of both efficiency of the optical system and the detector efficiency. The design of the optical system and the selection of the detectors are therefore crucial points of photon correlation experiments.

Most photon correlation experiments use single photon avalanche photodiodes (SPADs), especially the SPCM-AQR detectors of Perkin Elmer [967]. However, these detectors often experience timing shift and transit time jitter dependent on the wavelength and the count rate. Although the timing drift of both detectors of a Hanbury-Brown-Twiss experiment may partially compensate, it is difficult to obtain a time resolution better than 0.5 ns or to investigate changes in the correlation function versus intensity.

A troublesome effect of SPADs is light emission from the APD. When an avalanche is triggered in the APD, a small amount of light is emitted. The effect and its implications for photon correlation experiments and quantum key distribution are described in detail in [1273] and [728]. If the detectors are not carefully optically decoupled, false coincidence peaks appear. The effect on TCSPC correlation measurements and the way to avoid artefacts are discussed in [154].

Timing instability and optical crosstalk can be avoided by using PMTs with high-efficiency GaAsP photocathodes, such as the Hamamatsu H7422-40 module [548]. The IRF of these has a width of 200 to 350 ps. The IRF is almost independent of the wavelength and remains stable up to count rates in the MHz range. The quantum efficiency reaches 40% around 500 nm, see Fig. 258, page 165. Better time resolution is obtained with hybrid detectors, please see page 155 for principles. When used with an SPC-180NX or -NXX module the bh HPM-100-40 detector has an IRF width of about 100 ps, and a cathode efficiency of almost 50%. The HPM-100-06 reaches an IRF width of less than 20 ps at an efficieny of about 20%. Please see page 178.

Fluorescence Correlation Spectroscopy (FCS)

Principle

Fluorescence correlation spectroscopy (FCS) is based on exciting a small number of molecules in a femtoliter volume, detecting the fluorescence photons, and correlating the fluctuations of the fluorescence intensity. The fluctuations are caused by diffusion, rotation, intersystem crossing, conformational changes, or other random effects. The technique dates back to a work of Magde, Elson and Webb published in 1972 [809]. Theory and basic applications of FCS are described in [201, 1011, 1012, 1013, 1106, 1107].

The required femtoliter detection can only be achieved in the focus of a high-NA microscope lens. That means FCS measurements must be performed in a microscope or a similar optical setup. Excitation and detection from a sufficiently small volume can be achieved by confocal detection or by two-photon excitation. The principle is the same as in a laser scanning microscope, see 'Time-Resolved Laser Scanning Microscopy', page 343.

In a confocal microscope a laser beam is focused into the sample through the microscope objective lens, see Fig. 868, left. The laser excites fluorescence by the conventional one-photon absorption process. The fluorescence light from the sample is collected back through the microscope lens, separated from the laser by a dichroic mirror, and fed through a pinhole in the upper image plane of the microscope lens. Fluorescence light from above or below the focal plane is not focused into the pinhole and therefore substantially suppressed. With a high-aperture objective lens the effective sample volume is of the order of a femtoliter, with a depth of about 1 µm and a width of about 300 nm.

A similarly small sample volume can be obtained by two-photon excitation, see Fig. 868, right. A femtosecond laser is used to achieve the required power density. Different than one-photon excitation and confocal detection (which suppresses out-of focus detection) two-photon excitation avoids out-of-focus excitation. The fluorescence light therefore need not be sent through a pinhole. It can be sent directly to a detector.

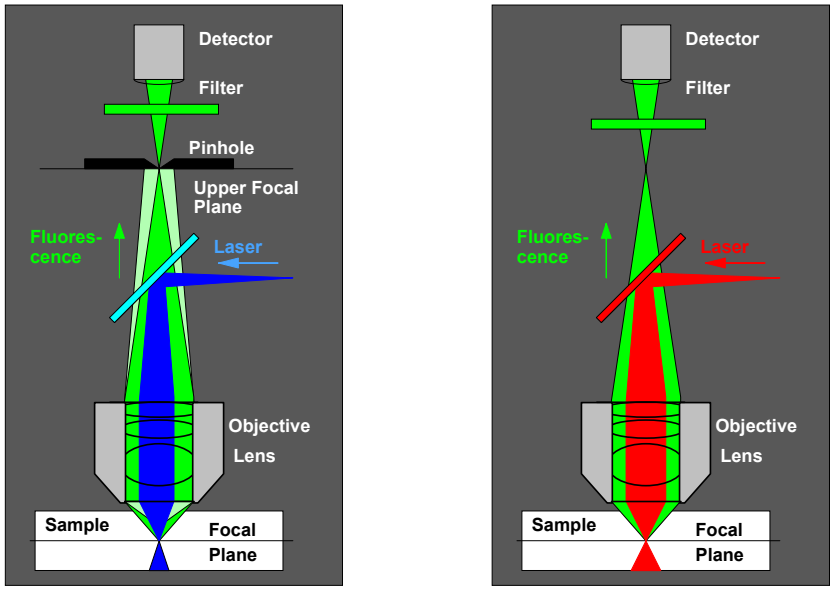


Fig. 868: Left: One-photon excitation and confocal detection. A pinhole in the upper focal plane of the microscope suppresses light from outside the focal plane in the sample. Right: Two-photon excitation. Excitation occurs only in the focus of the laser. The fluorescence light is projected directly on the detector.

Instead of a single detector several detectors detecting in different wavelength intervals or under 0° and 90° of polarisation can be used. It is also possible to use two lasers simultaneously to excite different fluorophores.

The single-photon pulses from the detector are recorded by a TCSPC Module in the parameter-tag mode, Fig. 226, page 132. In setups with several detectors the photon pulses of the detectors are either connected to a single TCSP module via a router or to separate TCSPC modules. The router setup is used for system which are primarily used for FCS. The limited count rate of a single TCSPC channel is then not a problem. Systems which are used for FLIM and FCS normally use a parallel-channel architecture. In these systems the detectors are connected to separate TCSPC modules.

Calculation of FCS curves from the TCSPC data

The (un-normalised) autocorrelation function $G(\tau)$ of an analog signal $I(t)$ and the cross-correlation function, $G_{12}(\tau)$, of two signals $I_1(t)$ and $I_2(t)$ are

$$G(\tau) = \lim_{T\to\infty} \frac{1}{2T} \int_{-T}^{+T} I(t)\, I(t+\tau)\, dt \qquad G_{12}(\tau) = \lim_{T\to\infty} \frac{1}{2T} \int_{-T}^{+T} I_1(t)\, I_2(t+\tau)\, dt$$

For photon counts, N, in consecutive, discrete time channels $G(\tau)$ and $G_{12}(\tau)$ can be obtained by calculating

$$G(\tau) = \sum N(t) \cdot N(t+\tau) \qquad G_{12}(\tau) = \sum N_1(t) \cdot N_2(t+\tau)$$

For a randomly fluctuating signal, $I(t)$, the autocorrelation function $G(\tau)$ assumes high values only if the intensity values, I, at a given time, t, and at a later time, $t+\tau$ are correlated. Uncorrelated fluctuations of I cancel over the integration time interval. Similarly, $G12(\tau)$ assumes high values if the fluctuations in both signals, $I_1(t)$ and $I_2(t+\tau)$, correlate with each other. The drop of $G(\tau)$ and $G_{12}(\tau)$ over the shift time, τ, shows how far the fluctuations are correlated in time. The general behaviour of the auto- and cross-correlation functions is illustrated in Fig. 869.

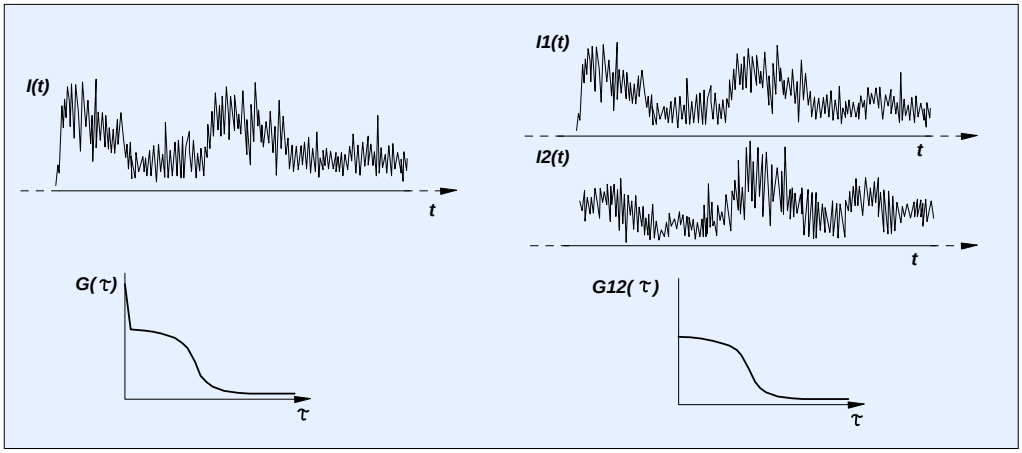


Fig. 869: General behaviour of the autocorrelation function, $G(\tau)$,of a signal I and the cross-correlation function, $G_{12}(\tau)$, of the signals I_1 and I_2

The autocorrelation (shown left) has a sharp peak at $\tau = 0$. (The function correlates perfectly with itself). The slow fluctuations in I(t) represent themselves in a high correlation at medium τ. For τ longer than the typical time of the slow fluctuations $G(\tau)$ drops to very low values.

The cross-correlation function of the two signals, I_1 and I_2, is shown right. The slow fluctuations in I_1 and I_2 have the same general appearance. However, the noise in I_1 and I_2 is different. Therefore only the fluctuations correlate and give a noticeable contribution to $G_{12}(\tau)$.

The equations shown above are appropriate to calculate correlation functions from analog signals. They do, however, not well apply to time-tagged photon counting data recorded by TCSPC. Such data do not display a continuous waveform as shown in Fig. 869 but are rather a random sequence of individual detection events.

The general correlation procedure for parameter-tagged photon data is illustrated in Fig. 870. In typical TCSPC data, the time-channel width, T, is shorter than the dead time of the detector/photon counter combination. Therefore only one photon can be recorded in a particular time channel. Consequently, $N(t)$ and $N(t + \tau)$ can only be 0 or 1. The calculation of the autocorrelation function therefore becomes a simple shift, compare, and histogramming procedure. The times of the individual photons are subsequently shifted by one time-channel interval, T, and compared with the original detection times. The coincidences found between the shifted and the unshifted data are transferred into a histogram of the number of coincidences, G, versus the shift time, τ. The obtained $G(\tau)$ is the (un-normalised) autocorrelation function.

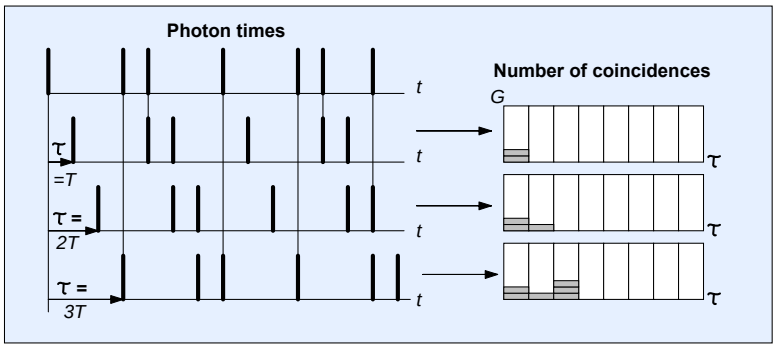


Fig. 870: Calculation of the autocorrelation function from TCSPC time-tag data

The cross-correlation function between two signals is obtained by a similar procedure. However, the photon times of one detector channel are shifted versus the photon times of another channel.

The result of the shift-and-compare procedure is not normalised. Normalisation can be interpreted as the ratio of the number of coincidences found in the recorded signal to the number of coincidences expected for an uncorrelated signal of the same count rate. The normalised autocorrelation and cross-correlation functions are

$$G_n(\tau) = G(\tau)\,\frac{n_T}{N_P^2}$$

with n_T = total number of time intervals, N_p = total number of photons, and

$$G_{12n}(\tau) = G_{12}(\tau)\,\frac{n_t}{N_{P1}N_{P2}}$$

with n_T = total number of time intervals, N_{p1} = total number of photons in signal 1, N_{p2} = total number of photons in signal 2.

The procedure illustrated in Fig. 870 yields $G(\tau)$ in equidistant τ channels. The width of the τ channels is equal to the macro time clock period of the SPC module, T. The algorithm is known as the 'Linear Tau' algorithm. The equidistant τ channels result in an easily predictable statistics. This is a benefit if a model function is to be fitted to the correlation function.

Unfortunately, for long correlation times the algorithm would result in an extremely large number of τ channels in $G(\tau)$, and in intolerably long calculation times.

The SPCM operating software of the SPC module therefore applies binning steps to the photon data during the correlation procedure. The general procedure is illustrated in Fig. 871.

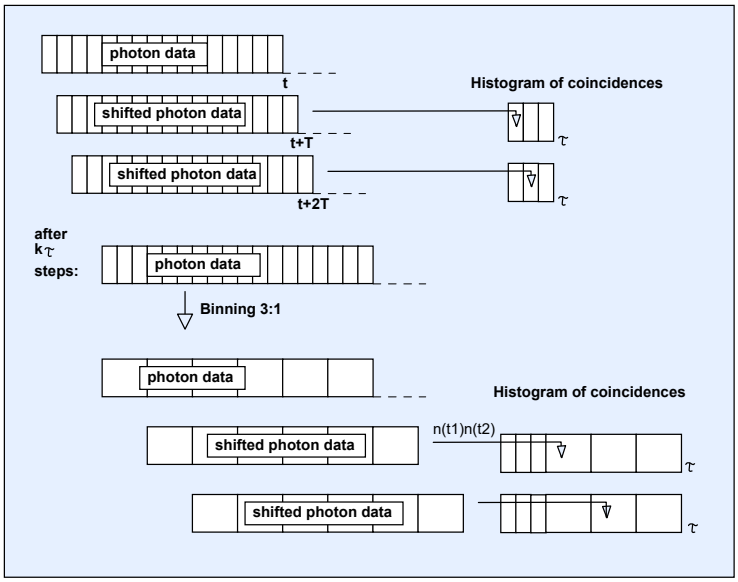


Fig. 871: Correlation procedure with progressive binning

The procedure starts with a number of shift-and-compare operations as shown in Fig. 870. However, after a number, k_τ, of shift-and-compare operations the remaining photon data are binned by a factor of three. (The factor of three is used to keep the new time intervals centred at multiples of the original time channel width, T.) Then the shift-and-compare operation is continued on the binned data. After every k_τ operations a new binning step is performed. Thus, the width of the τ channels increases progressively. The progression is the faster the smaller the progression parameter, k_τ is chosen. The procedure shown in Fig. 871 delivers similar results as the 'multi-τ algorithm' commonly used in conventional correlators [679]. The results have the typical logarithmic scale of the correlation time and the typical signal-to-noise behaviour caused by the progressive binning, see Fig. 872.

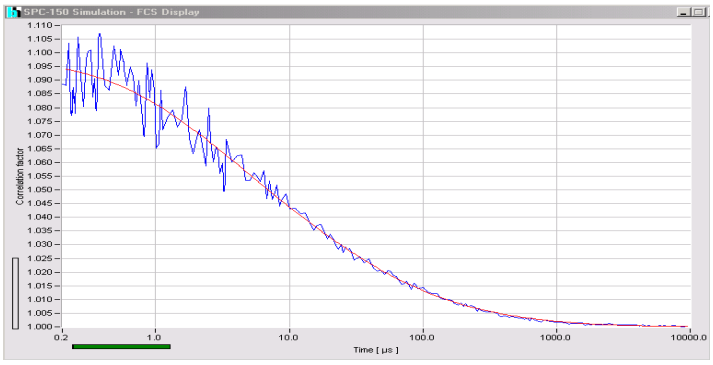


Fig. 872: FCS curve obtained by the progressive-binning algorithm. Data recorded by SPC-150 module and HPM-100-40 hybrid detector, FCS curve calculated online. The red curve is a fit with a two-component diffusion model.

The calculation of FCS by the algorithms shown above are based exclusively on the macro times of the photons. FCS and Cross-FCS can therefore also be obtained by excitation with CW lasers. There is only one technical requirement: The TCSPC module needs a pulse at its Sync input after each photon to complete the TAC-ADC time conversion cycle. The sync pulse can come from an LSG-02 auxiliary Sync generator module or from a pulsed laser of

the microscope system that is electrically active but optically turned off. Please see Fig. 905, page 659.

Applications of FCS aim at the estimation of the size of labelled biomolecules, on the detection of interaction between biomolecules, and on the determination of the number of fluorescent molecules linked to a special biomolecule. The size of the biomolecules can be derived from the diffusion time, i.e. the point of the autocorrelation function at which drops to 50 % of its maximum. More accurately, the diffusion time is obtained by fitting the autocorrelation function with an appropriate model. Interaction of molecules is derived from the cross-correlation functions. Different biomolecules are labelled with fluorophores of different absorption and emission spectra. The cross-correlation (FCCS) function of the two signals indicates whether the constructs diffuse together or independently. The number of emitters in a biomolecule is obtained via its 'molecular brightness', i.e. the photon rate divided by the number of molecules in the detection volume. Please see [436, 897, 898, 933, 1113, 1114, 1333, 1333, 1335] for applications in conjunction with TCSPC.

Using Micro-Time Information in Combination with FCS

If the fluorescence is excited by pulsed lasers the micro time of the photons can be used in several ways.

Simultaneous Recording of FCS and Fluorescence Decay Functions

Obviously, fluorescence decay curves can be obtained in parallel with the FCS or FCCS measurement. All that is necessary is to build up a photon distribution over the micro times of the photons, see Fig. 873.

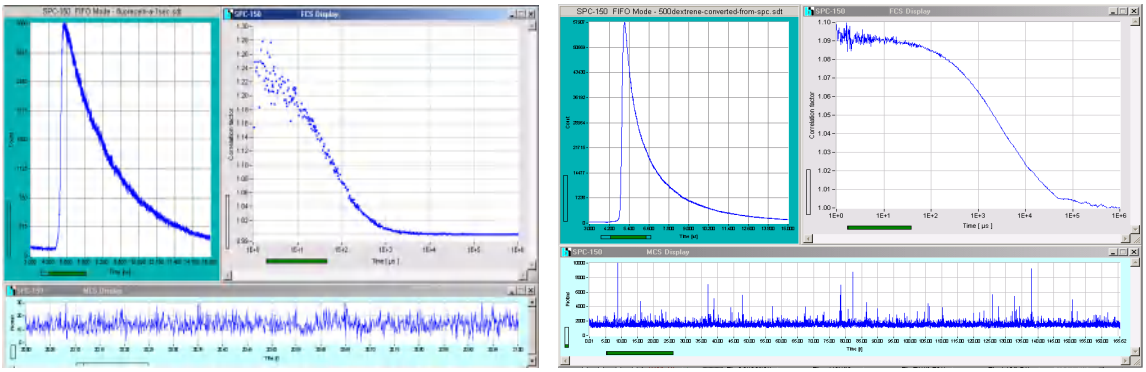


Fig. 873: Combined FCS and Fluorescence Decay recording. Left: Free Na-fluorescein in water. Right: Dextrane labelled with Alexa 488 in water. The fluorescein has a longer decay time than the Alexa but diffuses much faster than the large dextrane-alexa constructs.

A typical application is the study of protein structure, where the donor lifetime of a FRET pair attached to the protein delivers the folding state and the diffusion time the overall size of the molecule [933, 1333]. FCS in combination with decay measurement in two polarisation channels is used to combine FCS with fluorescence anisotropy and anisotropy decay measurement. FCS delivers the diffusion time and the molecular brightness. These values deliver information on the size of the molecule, on possible protein aggregation, and on the number fluorophore molecules linked to the protein. The anisotropy and the anisotropy decay show homo-FRET between the fluorophore molecules and thus deliver structural information [707, 909, 1239]. Even if the fluorescence decay functions are not used to derive information on the molecules investigated they can helpful to identify problems, such as contamination by fluorescent contamination, autofluorescence, or Raman scattering.

Time Gating of FCS

FCS signals are sometimes contaminated by Raman scattering. Raman light shows up as a sharp peak at the beginning of the fluorescence decay. The Raman light can be suppressed by time-gating. Time gating can be achieved either by setting a time gate in the TAC parameters of the TCSPC hardware, or by excluding photons with macro times outside a selectable time window in the FCS calculation. Time gating can also be necessary when FCS is recorded with pulse-interleaved excitation (PIE).

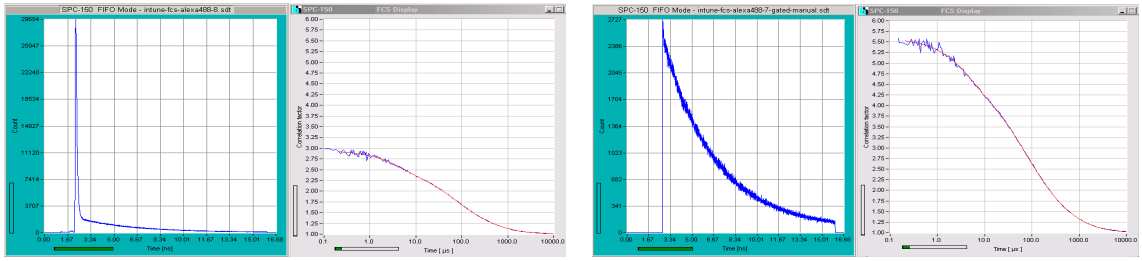


Fig. 874: Gated FCS, detected light contains Raman scattering. Left: Fluorescence decay with Raman peak, FCS curve calculated from entire signal. Right: Raman peak gated out, FCS calculated inside selected time window. Note the increased FCS amplitude. Zeiss Intune system, Becker & Hickl SPC-150 TCSPC-FLIM module with HPM-100-40 hybrid detectors.

Filtered FCS

Micro times can be used to separate FCS signals of fluorophores of different fluorescence decay times. In that case, the photons are weighted with a coefficient derived from the micro time via a filter function [231, 444]. The technique can also be used to reject detector background signals, Raman scattering, or unwanted background fluorescence.

Global Fit of FCS and Decay Data

Another way to improve the separation of several diffusion components in FCS analysis has been developed by Anthony and Berland [23, 24]. Assume there are several fluorescing species of similar or nearly similar excitation and emission spectra. These species diffuse at different speed. In principle, the two diffusion components can be separated by fitting the FCS data with a model that contains two diffusion components. The problem is that, unless the diffusion times are very different, the components can be separated only at limited accuracy. However, if the two species have different fluorescence lifetimes the relative amplitudes can be obtained via double-exponential decay analysis. The amplitudes can then be used in the FCS analysis to obtain a more reliable fit. An even more robust fit is obtained if all parameters, i.e. the fluorescence lifetimes, the component amplitudes, and the diffusion times of the components are determined by a global fit [23, 24].

FCS Down to the Picosecond Time Scale

A single TCSPC channel is able to deliver FCS data down to a correlation time of the module dead time, i.e. about 100 to 125 ns. Cross correlation is obtained down to the macro time resolution, i.e. 25 to 50 ns, depending on the SPC module type.

By including the micro times, photons can be correlated down to the picosecond time scale. The principles has been introduced by Felekyan et. al. in 2005 [442]. They used two synchronised TCSPC modules in the setup shown in Fig. 875, left. Fluorescence in the sample is excited by a CW laser in a femtoliter sample volume. The fluorescence light is split into two detectors, the signals of which are recorded by two TCSPC modules. The stop pulses for the time measurement come from an external 80 MHz clock generator. The internal macro time clock is synchronised to the signal at the stop inputs of the TCSPC modules [154]. The TCSPC modules work in the parameter-tag-mode; the single-photon data are constantly read by the system computer. By using both the micro times and the macro times FCS data were

obtained at a resolution of about 20 ps. The algorithm is described in [442], and included in a single-molecule analysis software package of the University of Düsseldorf [443].

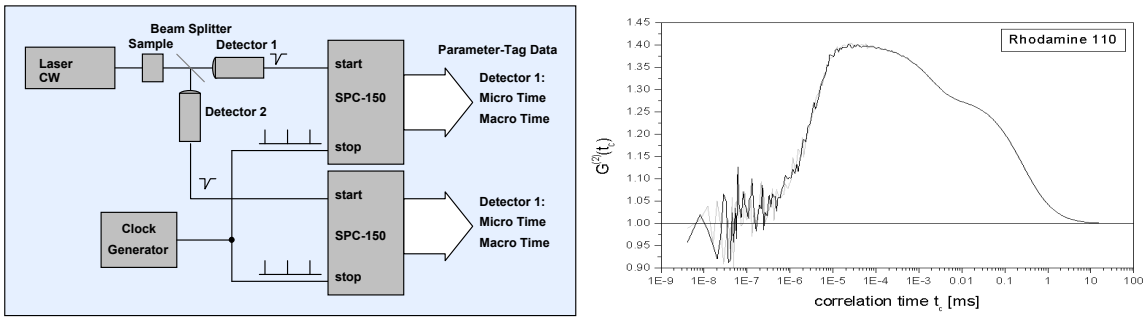


Fig. 875: Picosecond fluorescence correlation with two synchronised TCSPC modules. Courtesy of S. Felekyan, R. Kühnemuth, V. Kudryavtsev, C. Sandhagen, and C.A.M. Seidel, University Düsseldorf

At first glance, it may look surprising that this method works: The TCSPC modules used in the setup determine the micro times by an advanced TAC/ADC principle. This delivers high resolution micro times at excellent stability. However, the time scales of the micro time and the macro time are not strictly comparable, and there may be minor overlaps or gaps in the two time scales. It can also happen that photons with arrival times too close to a stop pulse are not recorded. However, all these effects are correlated with the signal from the *external clock oscillator*. They are *not* correlated with the photons. The correlation of the photon data therefore delivers correct results.

Applications of picosecond correlation to dye-exchange dynamics of R123 in micellar solutions and supra-molecular cyclodextrin-pyronin complexes are described in [917] and [16]. Combined with FRET measurement, the method has been used to study conformational changes in a yellow chameleon Ca^{+} sensor [238]. It has also been used to study complexes of adamantane and cyclodextrin [518], and micellar exchange dynamics [234].

Picosecond correlation is easy with TCSPC devices using direct time-to-digital conversion by TDC chips, especially if the chips contain several channels operated by the same internal clock. A picosecond correlation curve recorded by a Becker & Hickl DPC-230 photon correlator is shown in Fig. 876.

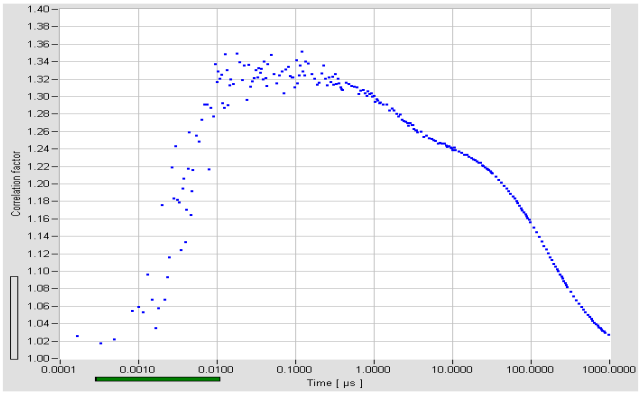


Fig. 876: Picosecond photon correlation by DPC-230 photon correlator

FCS System Parameter Setup

Typical system setup parameters for FCS measurements with the bh SPC-150 and SPC-830 modules are shown in Fig. 877 through Fig. 880. The parameters may slightly differ for different TCSPC module types, but the general features are the same.

Measurement Control Parameters

The measurement control part of the System Parameters is shown in Fig. 877. 'Operation Mode' is set to 'FIFO'. The settings shown on the left calculate and display decay curves, FCS curves, and an MCS (intensity) trace online. The time-tag data are *not* saved. The settings shown on the right calculate the curves online, but simultaneously save the time-tag data into a file 'fluorescein-a.spc'. The maximum file size is 100 MB. The measurement stops when this file size is reached. The measurement can also be stopped after a defined acquisition time. Please activate the 'Stop T' button if you want to stop after a specified time.

'Max Buffer Size' defines a buffer in the RAM of the computer. If enough RAM is available the buffer size should be as large as or larger than the specified file size. The SPCM software then stores the time-tag data into the RAM before it writes them on the hard disc. The data readout is then not slowed down by hard disc operations.

The experiment trigger is not used; the setting is 'None'. You may use the experiment trigger if you want to start the recording synchronously with an external event. Please note that you have to use the trigger if you want to cross-correlate photons recorded in different SPC-830 modules of a two-module system. For a dual-SPC-150 (SPC-152) system this is not necessary. The start of the recording in both modules is synchronised via a signal line on the fan assembly board.

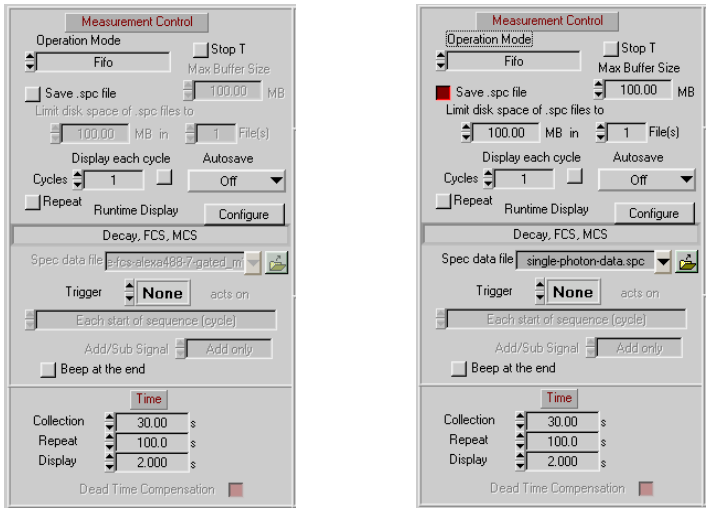


Fig. 877: FCS: Measurement control part of the 'System Parameters' panel. Left without, right with saving of the single-photon data.

'Collection Time' defines the acquisition time for the 'Stop T' option. 'Display Time' is the update interval for the online display.

The online calculation of FCS is configured via the configure panel shown in Fig. 880. With the settings shown, decay curves, FCS curves, and an MCS (intensity) trace are shown. FCS curves are calculated by a multi-tau algorithm, and within a correlation time window of 10 ms. The MCS trace is displayed at a resolution of 1 ms per point.

TCSPC System Parameters

The TCSPC parameter section of the system parameters is shown in Fig. 878. The left panel shows a setup for an SPC-150 (single-channel) or an SPC-152 (dual-channel) system. The number of routing channels is 1, because there is only one detector per module. The right panel is for an SPC-830 that has two detector connected via a router. The number of routing channels is therefore two. Please note that the FIFO mode always records with 4096 time channels. 'ADC Resolution' is therefore disabled.

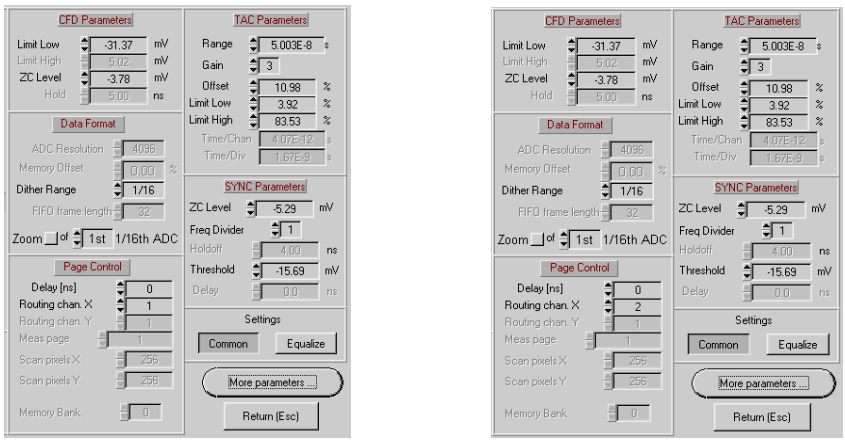


Fig. 878: TCSPC parameter section of the system parameters. Left: SPC-150 or SPC-152, one detector per SPC module. Right: SPC-830, two detectors connected

Source of Macro Time Clock

For FCS experiments with pulsed lasers it is recommended to use the SYNC frequency from the laser as a macro time clock. This avoids artefacts by aliasing of the laser repetition frequency with the internal macro time clock. The macro time source is defined under ‘More Parameters’ in the System Parameters panel.

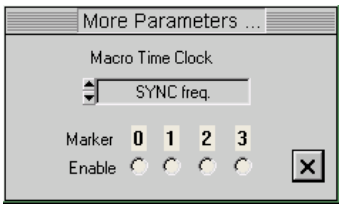


Fig. 879: Definition of the laser frequency as a macro time source

FCS FIT

SPCM is able to run a fit on the calculated FCS data. The setting shown in Fig. 880, left, are without, the settings shown right with an FCS fit. The model contains two diffusion times, tau_1 and tau_2, and a triplet time, tau trip. F is the relative triplet population, N the number of molecules in the detection volume, and Y the relative amplitude of the slow diffusion component. For the online fit we recommend to use a simple model, preferably one diffusion time and a triplet time. The start values of the fit procedure are defined on the right of the ‘Configure’ panel.

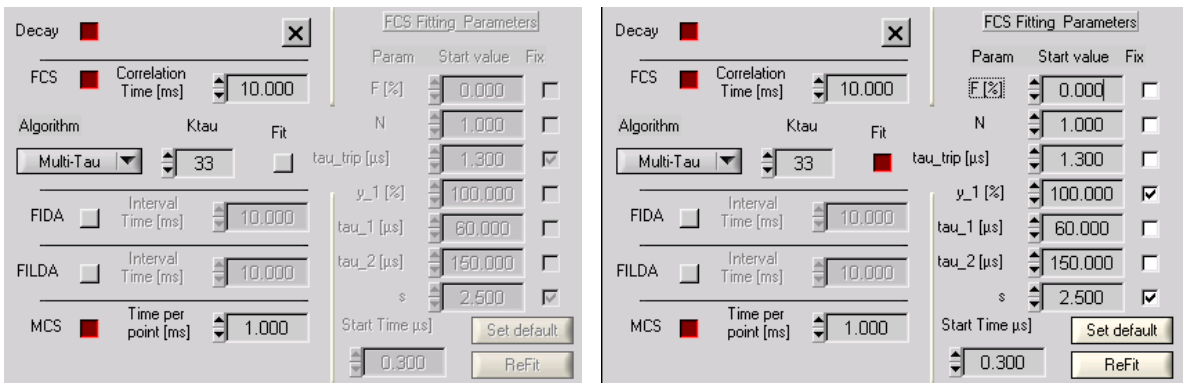


Fig. 880: Configuration of the online display. Decay curves, FCS curves, and an MCS trace are displayed. The left setup is without, the right setup with an FCS fit.

When 'FCS' is turned on a panel opens where the curves are displayed. When 'Fit' is enabled also a fit curve with the selected model parameters is displayed. Please see Fig. 883 and Fig. 884 for configuration parameters. The fit results are displayed when 'Trace Statistics' is turned on in the main panel. The FCS curve panel with an FCS curve, a fit curve and the fit results is shown in Fig. 881.

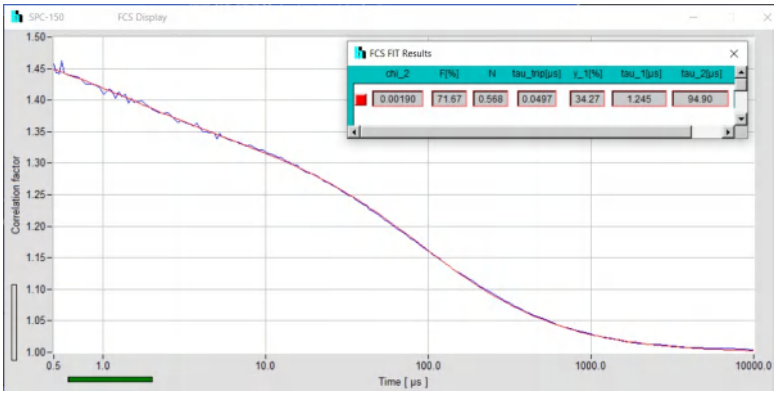


Fig. 881: FCS panel with FSC curve (blue), fit curve (red) and fit results. To see the fit results, click the 'Trace Statistics' button in the main window.

SPCM Main Panel

Panel Configuration

With the online display configured for decay, FCS, and MCS the main panel of the SPCM software assumes a configuration as shown in Fig. 882. The window sizes may be different when the panel is configured the first time, but can be resized according to the requirements of the user. We recommend to switch on ‘Scale Contents on Resize’ option under ‘Display’.

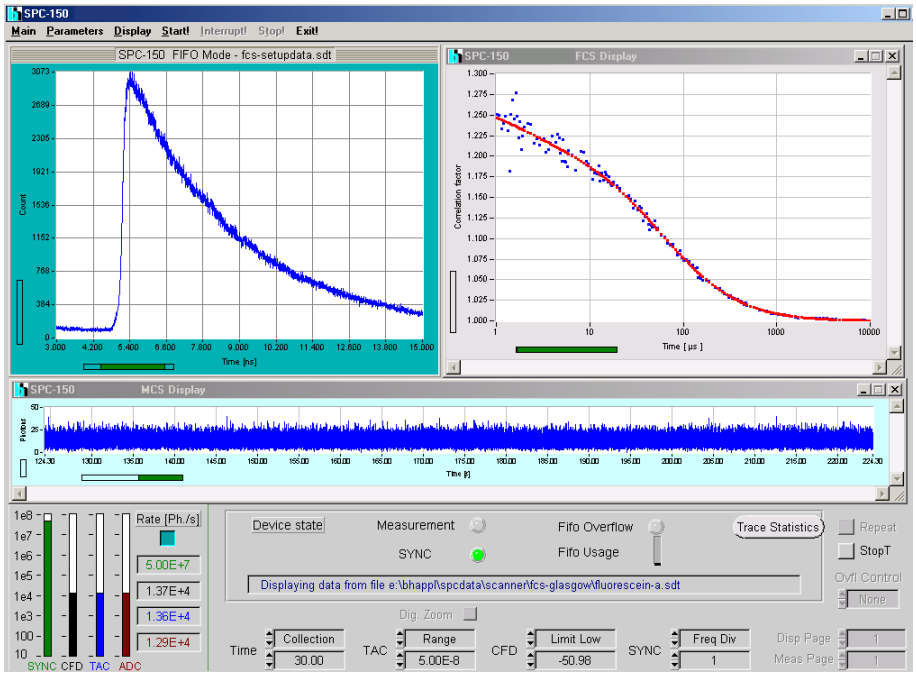


Fig. 882: Main panel with decay curve, FCS, and MCS trace windows.

Trace Parameters

The curves to be displayed in the three curve windows are defined under ‘Trace Parameters’. Each curve window has its own trace parameters. To open the trace parameters, click on ‘Display’, ‘Trace Parameters’. A click into one of the curve windows selects the correspond-

ing trace parameter set. The panels for the decay curve window and the FCS window are shown in Fig. 883, left and right. The panels show the simple case that the decay curve of one detector, and the autocorrelation and the fit for the same detector are to be displayed.

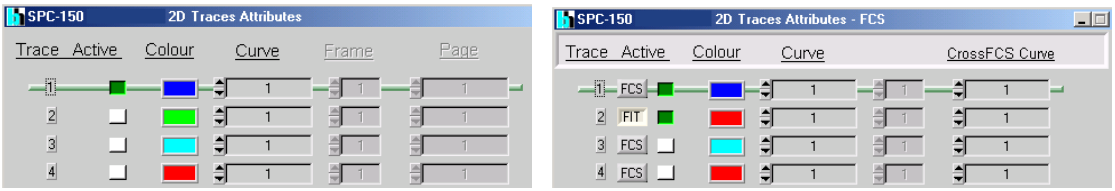


Fig. 883: Trace parameters. Left for decay window, right for FCS window. One detector channel, autocorrelation.

The FCS trace parameters for cross-correlation is shown in Fig. 884. The left setup is typical of an SPC-152 system. It has two parallel TCSPC modules. The trace parameters define correlation of the data of Module 1 with those of Module 1, and correlation of the data of Module 2 with those of Module 2. These are the autocorrelation curves. The third curve is correlation of Module 1 versus Module 2. This is the cross-correlation. The fit is run on the cross-correlation data.

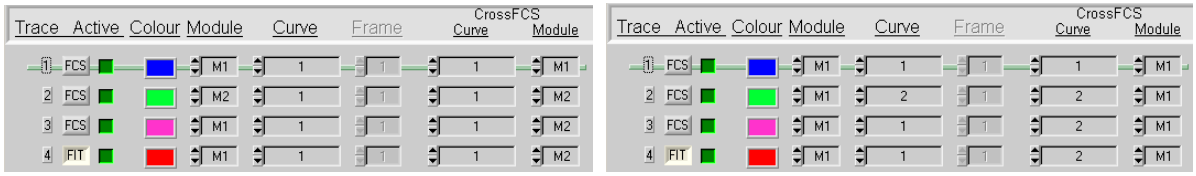


Fig. 884: Trace parameters for dual-channel system. Left: Dual-module system. Right: Single-module system with routing. Both parameters sets define autocorrelation of both channels, cross-correlation between both channels, and a fit of the cross-correlation data.

The setup shown in Fig. 884, right, is for a single-TCSPC system with routing. It calculates autocorrelation of Detector 1 (Curve 1 vs. Curve1), autocorrelation of detector 2 (Curve 2 vs. Curve 2), and cross-correlation (Curve 1 vs. Curve 2). The fit is run on the cross-correlation data.

Synchronous Start of Several TCSPC Modules

For cross-correlation of photons recorded in different TCSPC modules it is required that these not only work on the same macro-time clock period but also start their recordings synchronously. Identical macro time clock periods can be achieved by using the laser sync, see Fig. 879. Simultaneous starting of several SPC-150 modules is achieved by declaring one module as a ‘Trigger Master’, see Fig. 885, left. Cross-correlation of several SPC-830 channels requires the modules to started via the ‘Experiment Trigger’, see Fig. 885, right.

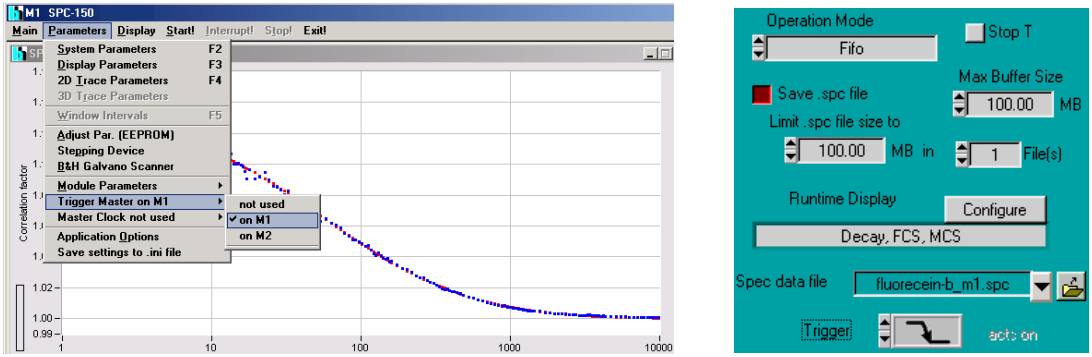


Fig. 885: Left: Synchronous start of several SPC-150 modules via the trigger master function. Right: Synchronous start of SPC-830 modules by the experiment trigger.

Display Parameters

The display scale (linear or logarithmic) and the curve style (curves, points, connected points) are defined in the 'Display Parameters'. As for the trace parameters, every display window has its own display parameters. The display parameter panels for the decay and the FCS window are shown in Fig. 886.

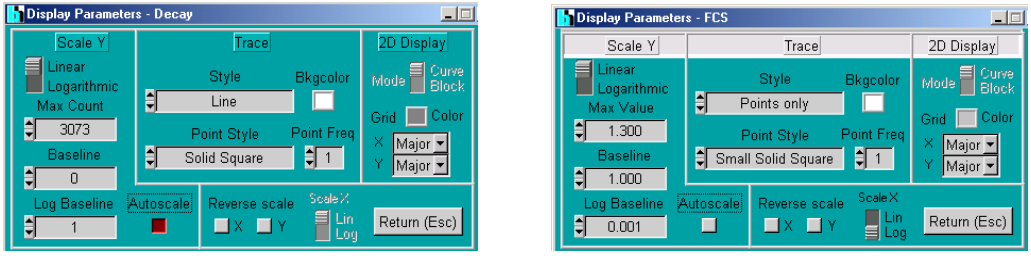


Fig. 886: Display parameters. Left for decay window, right for FCS window

Gated FCS

Time-gating of FCS can either be achieved offline by bh Burst Analyzer software or online by using the TCSPC hardware gating function. Hardware gating was achieved by defining appropriate values for 'TAC Limit Low' and 'TAC Limit High' parameters as shown in Fig. 887. By reducing 'TAC Limit High' photons within the Raman peak were excluded from being recorded, see Fig. 888, right. Similarly, 'TAC Limit Low' can be used to suppress late photons that are caused by detector background.

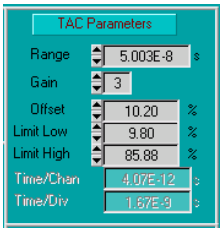


Fig. 887: Suppression of a Raman peak by the parameter 'TAC Limit High'.

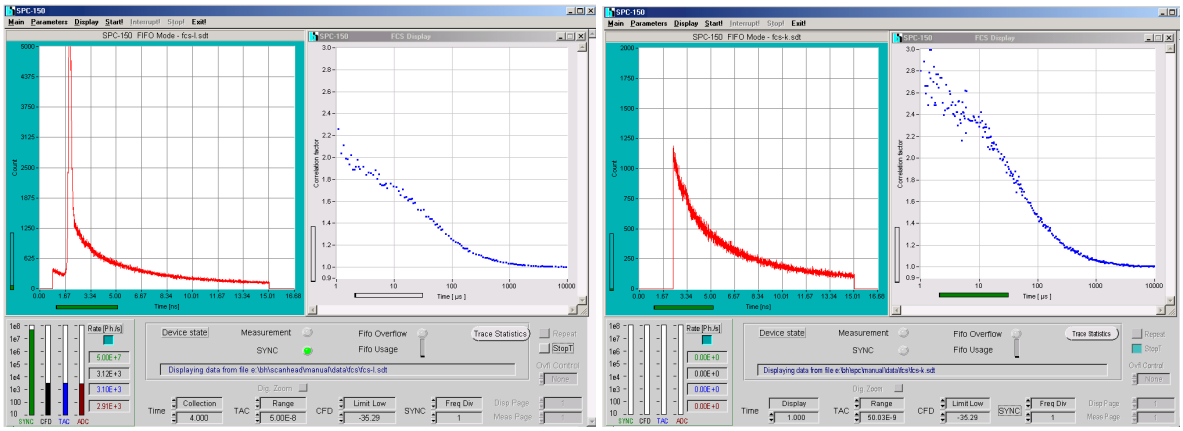


Fig. 888: Left: Un-gated FCS recording. The sharp peak in the decay curve is caused by Raman scattering. Right: Gated FCS recording. The Raman peak is suppressed, with a corresponding increase of the correlation coefficient.

Fig. 888, left, shows the un-gated signal. The Raman signal is visible as a sharp peak at the beginning of the fluorescence decay. In Fig. 888, right, the Raman peak has been gated off. The correlation amplitude is clearly higher than in the un-gated case.

FCS with Laser Scanning Microscopes

FCS can be obtained in any confocal or two-photon laser scanning microscope that has a bh FLIM system with SPC-830, SPC-150, or SPC-160 TCSPC modules. It is, however, required that the laser scanning microscope is able to stop its scan in a spot of interest and keep the beam position stable without noticeable spatial jitter. Beam jitter was the weak point of older laser scanning microscope. Some of them had a 'Spot' mode which in fact did not stop the scan but only reduced the scan area to the minimum possible value. The scan amplitude was usually larger than the Airy disc diameter of the microscope lens. The result was that decay data were recorded but no correlation showed up in the FCS data. Another reason of failure to record FCS is misalignment of the optics. If the pinhole of a confocal microscope does not correctly coincide with the focus of the laser the sensitivity goes dramatically down, the effective confocal volume increases, and the FCS signal is lost. The FCS performance of a few typical laser scanning microscopes is demonstrated below.

FCS with the LSM 510

Unfortunately neither the NDD nor the confocal detection path of the LSM 510 was perfectly suitable for FCS detection. The confocal output from earlier 510s was an optical fibre. The efficiency was low, and no signals were recorded from samples with FCS-typical concentrations. Late LSM 510s had a direct-beam output from the scan head. This output had good efficiency. However, it was difficult, if not impossible, to connect additional lasers to the LSM 510. FCS could therefore by recorded only with the internal CW lasers.

The LSM 510 multiphoton systems could be used for FCS. The fluorescence was excited by two-photon excitation and detected by H7422-P40 detectors at the two of the Zeiss NDD (non-descanned detection) module. A typical result is shown in Fig. 889.

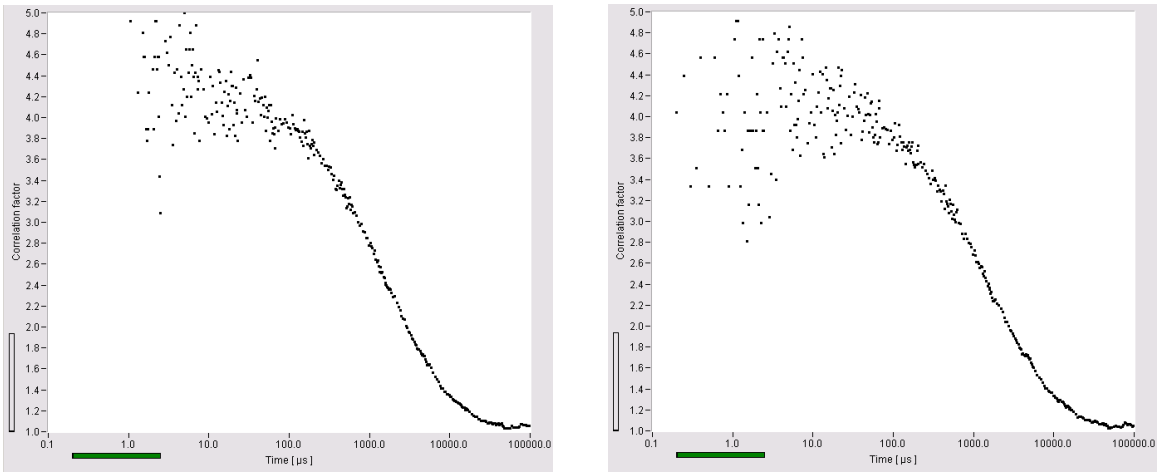


Fig. 889: FCS functions measured in an LSM 510 NLO multiphoton microscope. SPC-830 FLIM module, HRt-41 router, two H7422P-40 detectors. Two-photon excitation at 860 nm, detectors attached to the Zeiss NDD module. Left: Autocorrelation of one detector. Right: Cross-correlation between both detectors.

Zeiss LSM 710/780/880/980

The LSM 710/780/880/980 microscopes have excellent efficiency both for the confocal detection path and the NDD path. The LSM 710 can thus be used both for confocal (one-photon) FCS and for two-photon FCS. FCS applications of the LSM 710 FLIM systems especially benefit from the superior performance of the HPM-100-40 detectors [160].

ZEN Software Setup

FCS requires that the laser beam is pointed to a defined spot in the sample and kept there for the time FCS data are acquired. The laser must be turned on for the same period of time. The ZEN software has no special mode for this kind of operation. FCS recording can, however, be obtained with the setup shown in Fig. 890.

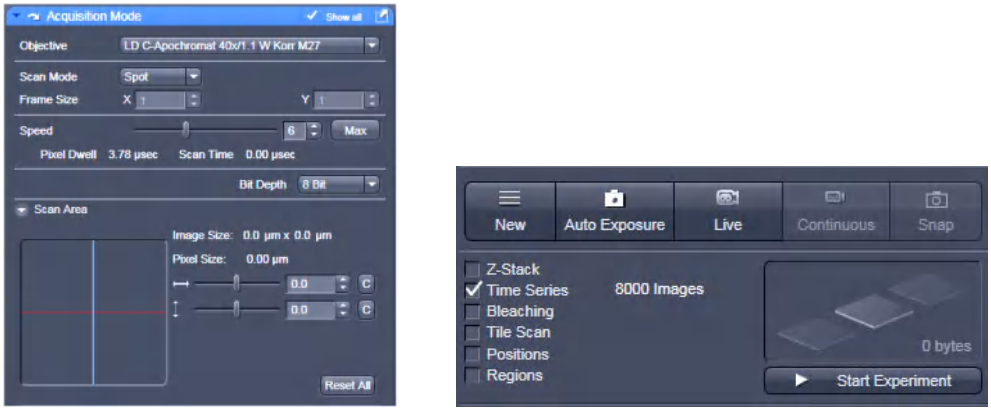


Fig. 890: General setup of the LSM 710 ZEN software for FCS recording

The Scan Mode in the Acquisition Mode Windows is set on ‘Spot’ as shown in Fig. 890, left. The ‘Scan Speed’ is reduced to values of 6 or less. It has no influence on the position of the beam, it only influences the period of time the laser remains turned on after the experiment has been started. To achieve a sufficiently long laser-on time a ‘Time Series’ with a large number of ‘Images’ is defined, see Fig. 890, right. The laser is turned on by clicking on the ‘Start Experiment’ button.

FCS with the LSM 710/780 InTune Laser

The LSM 710 Intune FLIM system is an excellent instrument for FCS measurement. Tuneability of the excitation wavelength, abundance of laser power, excellent optical efficiency, high efficiency and absence of afterpulsing for the HPM-100-40 hybrid detector result in unprecedented speed and data quality. An example is shown in Fig. 891. An Alexa 488 solution was excited at 490 nm, at a laser power of 5%. The objective lens was an x 63, NA = 1.2 water ‘C Apochromate’. No emission filter was used when the data were recorded.

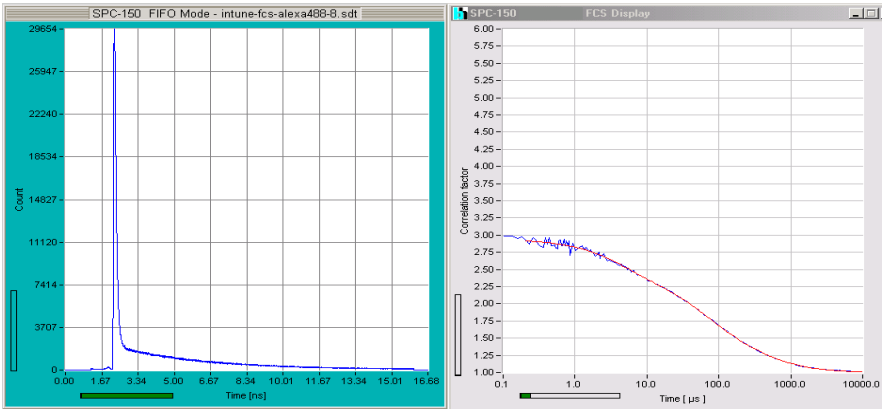


Fig. 891: FCS with the LSM 710 Intune system. Un-gated FCS, the signal contains Raman light. Alexa 488 in water, excitation 490 nm, laser power 8%, HPM-100-40 detector.

The decay function (shown left) contains a substantial amount of Raman light from the water. The Raman signal has no intensity fluctuations. The FCS function of the combined fluorescence and Raman signal shows the correct diffusion time, but a reduced correlation amplitude. In the recording shown in Fig. 892 the Raman peak was gated off by the ‘TAC Limit High’ parameter of the SPC-150 module. (Please note different intensity scale of decay win-

dow.) The gated recording contains only fluorescence photons and thus shows the correct FCS curve, with an amplitude of about 4.5 compared to 2 in the un-gated recording.

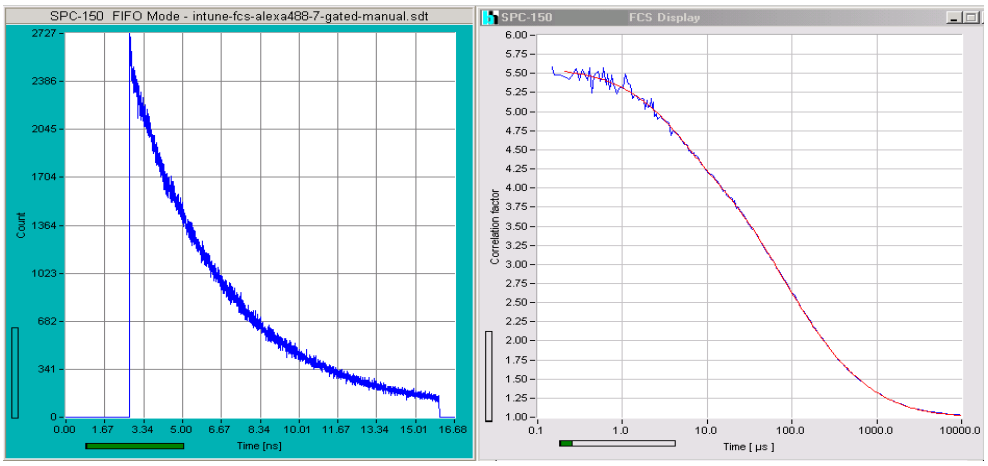


Fig. 892: Gated FCS, the Raman peak has been gated off. Same sample as in Fig. 891. Note the increase in correlation amplitude compared to the un-gated recording.

Gating is very effective with the HPM-100-40 and the Intune system: The detector response is fast, without any bumps or tails, and the laser pulse width does not broaden the system IRF. Consequently, only a negligible part of the fluorescence is lost if the Raman peak is gated off. In cases where the fluorescence overlaps with a strong Raman line gating may therefore be more efficient than spectral filtering.

The available laser power in the Intune system is so high that saturation can occur. This is shown in Fig. 893. The left recording was taken at a laser power of 8%. If the power is increased above 10% the fluorescence starts to saturate. The central part of the Airy disc gets depleted of active fluorophore: Most of the molecules are in the triplet state. The effective confocal volume gets larger, the FCS amplitude decreases, and the apparent diffusion time gets longer. These effects can clearly be seen in Fig. 893, right, taken at a laser power of 30%.

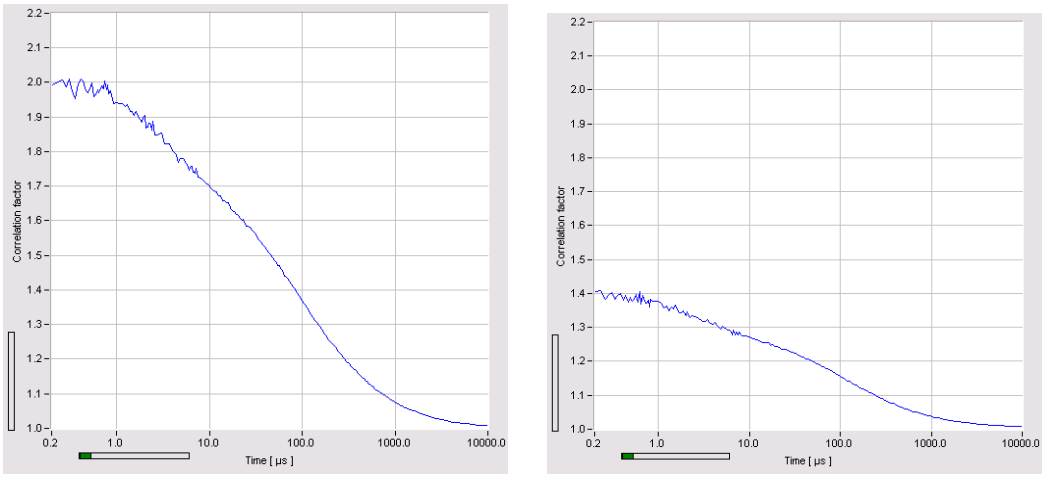


Fig. 893: FCS of an Alexa 488 solution, excitation at 490 nm. Left: Laser power 8%. Right: Laser power 30%. NA=1.2 Water C Apochromate, HPM-100-40 detector.

FCS with the ps Diode Laser

Good FCS results are obtained also with the ps diode lasers of the LSM 710/780 family. The setup parameters are identical with these used with the Intune laser. An example is shown in Fig. 894.

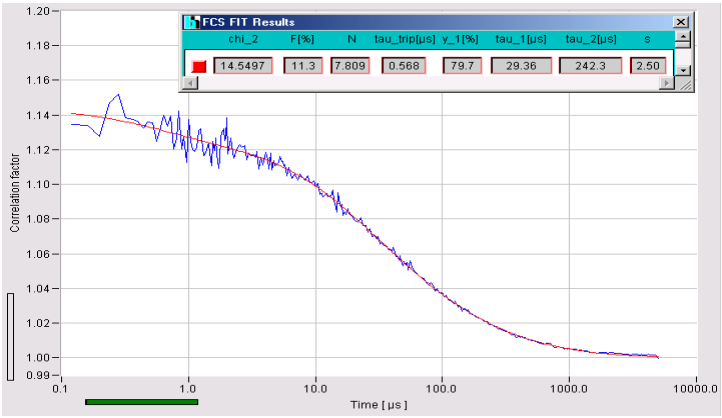


Fig. 894: FCS recorded with a ps diode laser. Fluorescein in water, HPM-100-40 detector, NA=1.2 Water C-Apochromate. FCS curve (blue) fit curve (red) and fit results.

FCS with LSM 710/780/880 CW Lasers

The available wavelengths of the picosecond diode lasers may not always match the excitation maxima of the fluorophores commonly used for FCS. In such cases a CW lasers of the LSM 710 can be used for excitation. Because the SPC module needs a sync (stop) pulse to complete its recording cycle an artificial sync signal (‘pseudo sync’ signal) is required. The pseudo sync can usually be obtained from one of the pulsed lasers. The laser is turned on electrically, but its optical output is not used.

An example is shown in Fig. 895. A Rhodamine 123 solution was excited by a CW laser at 488 nm. The laser power was 5 mW. A 40x NA=1.2 water C-Apochromate lens was used; the acquisition time was 160 seconds.

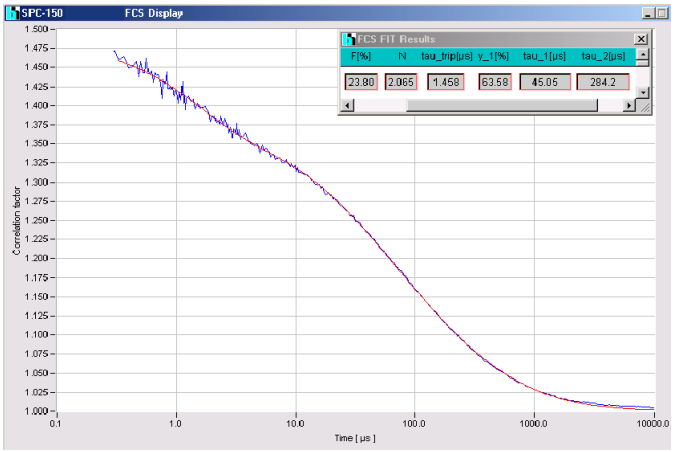


Fig. 895: FCS of Rhodamine 123. NA = 1.2 Water C Apochromate, CW excitation 488 nm 5 mW, acquisition time 150 s. The blue curve shows the FCS data, the red curve is a fit with two diffusion times and a triplet time.

Of course, FCS measurements with CW lasers do not deliver fluorescence decay data. Thus, gated FCS is not available. Possible Raman signals have to be suppresses by optical filters.

Two-Photon FCS via NDD detectors

Two-photon excited FCS via the non-descanned detection path is shown in Fig. 896. An Alexa 488 solution was excited at 900 nm, with 30% of the available laser power.

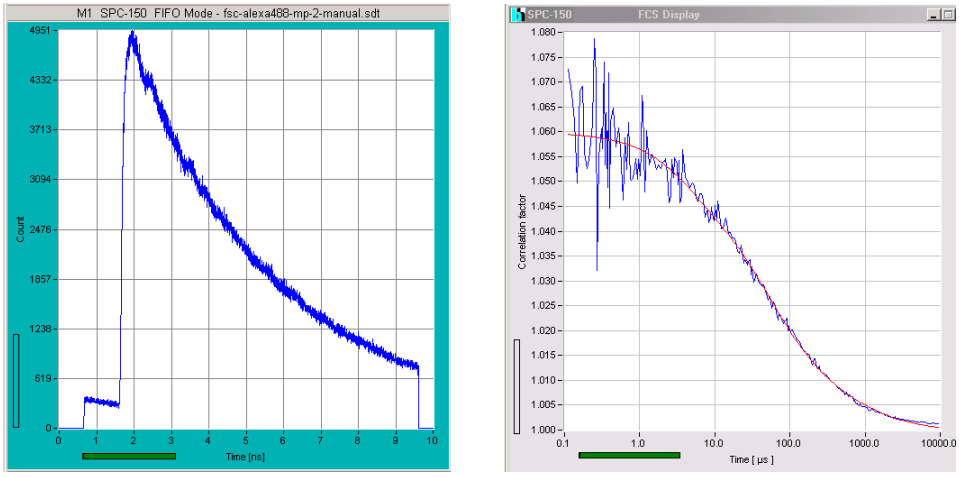


Fig. 896: Two-photon FCS of an Alexa 488 solution. Excitation at 900 nm, laser power 30%. HPM-100-40 hybrid detector, non-descanned detection, Water C-Apochromate, x 63, NA = 1.2

Two-photon excitation with some of the commonly used FCS dyes may face the problem that the excitation maximum is too far in the IR. This is even the case for Alexa 488, which has its 2p excitation maximum around 1100 nm. Nevertheless, useful excitation can often be obtained at shorter wavelengths, as the curves in Fig. 896 show. The higher laser power required at wavelengths outside the excitation maximum usually does not cause increased photobleaching or photodamage because it is not absorbed. An overview about two-photon excitation spectra is given in [204].

Zeiss LSM 880

We have tested the new Zeiss LSM 880 for FCS. The LSM 880 has the same scan head as the LSM 710/780. The difference is that most of the 880s have the Zeiss ‘Airy Scan’ detector attached to the scan head. Zeiss has a beam switch that can be inserted between the scan head and the Airy Scan detector. The beam switch diverts the output beam from the Airy Scan detector the a bh HPM-100 hybrid detector, to a dual HPM detector/beamsplitter assembly, or to a Zeiss ‘BIG-2’ detector, see Fig. 99, page 52.

FCS results recorded with the BIG-2 detector were excellent. Fig. 897 shows decay curves and FCS curves of Atto 425 excited with the 405 nm ps diode laser, Fig. 898 an FCS curve of Rhodamine 110, excited by the 488 nm CW laser.

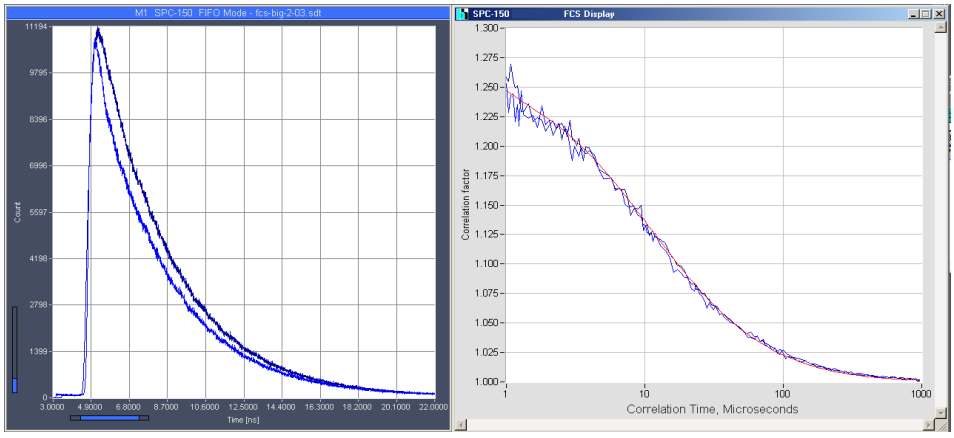


Fig. 897: Fluorescence decay functions and FCS curves detected in the two channels of the BIG-2 detector. Atto 425, excitation by 405 nm ps diode laser. Simple-Tau 152 dual-channel FLIM system. The red cure is a fit with two diffusion terms and a triplet term.

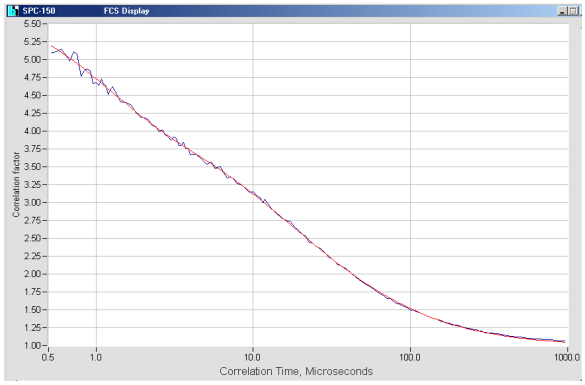


Fig. 898: FCS of Alexa 488 excited by 488 nm CW laser. Blue: FCS data. Red: Fit with two diffusion terms and a triplet term.

FCS with the DCS-120 confocal FLIM System

System Parameter Setup

FCS measurements are performed in the 'FIFO' mode of the SPC module(s) and in the 'Beam Park' mode of the DCS-120 scanner. Typical TCSPC system setup parameters are shown under 'FCS System Parameter Setup', page 645. For the scanner setup parameter parameters please see Fig. 1154, page 852. The beam-park position can also be selected in an image recorded before, see Fig. 1155, page 852.

Two examples of FCS recordings are shown in Fig. 899. FCS of fluorescein in water is shown left. For comparison, Fig. 899, right, shows an FCS recording of dextrane labelled with Alexa 488. Please note the long diffusion time of the macro-molecules compared to the small fluorescein molecules.

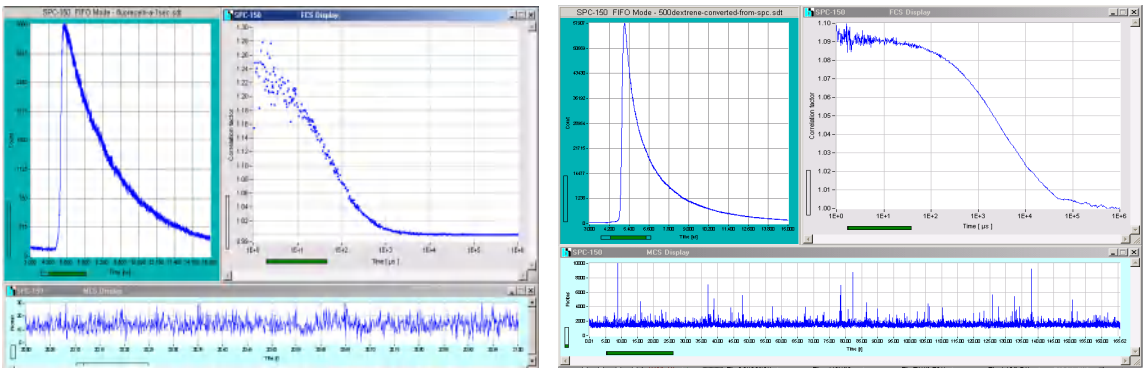


Fig. 899: DCS-120 FCS. Left: Fluorescein in water. Right: Dextrane labelled with Alexa 488 in water

Two-Colour FCS

The basic optical setup for a dual-colour FCS experiment with the DCS-120 is shown in Fig. 900. Two BDL-SMC diode lasers, 488 and 647 nm, were used to excite fluorescence in the sample. Both lasers were operated in the CW mode. The sample contained two fluorophores, Atto 488 and Atto 647N, each of them excited by one of the lasers. The scanner was put in the 'park beam' mode with the beam in the middle of the field of view. The fluorescence was detected by two HPM-100-40 detectors at the outputs of the DCS-120 scanner through different filters. The detection (macro) times of the photons were recorded by two TCSPC channels. The photons of the channels were auto-correlated and cross-correlated by the SPCM software.

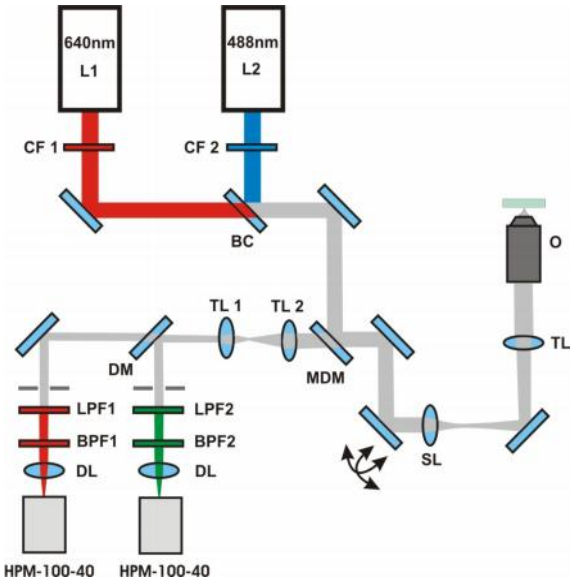


Fig. 900: Dual-colour FCCS setup based on BDL-SMN lasers and DCS-120 confocal FLIM system. L1, L2: BDL-SMN picosecond/CW diode laser, operated in CW mode. BC: beam combiner. MDM: Dual-wavelength dichroic mirror, 488/647 nm. SL: scan lens of DCS-120 scan head. TL: tube lens of microscope. O: Microscope objective lens. TL1, TL2: Lenses, forming a telscope projecting the beam into comfocal pinholes. DM: Dichroic mirror, splits the light of the two fluorophores. LPF1, LPF2: Long-pass filters. BPF1 and BPF2 band-pass filters. DL: Lens centering the light on the detectors.

Auto- and cross-correlation functions of free Atto 488 and Atto 647N fluorophores are shown in Fig. 901, left. There is autocorrelation for the signals from both fluorophores (Red and blue curves) but no cross-correlation between the signals (green). Curves for a 40-base pair double-stranded DNA labelled with Alexa 488 and Cy5 are shown in Fig. 901, right. There is a significant cross-correlation (green curve) showing that DNA strands labelled with different fluorophores are partially linked to each other.

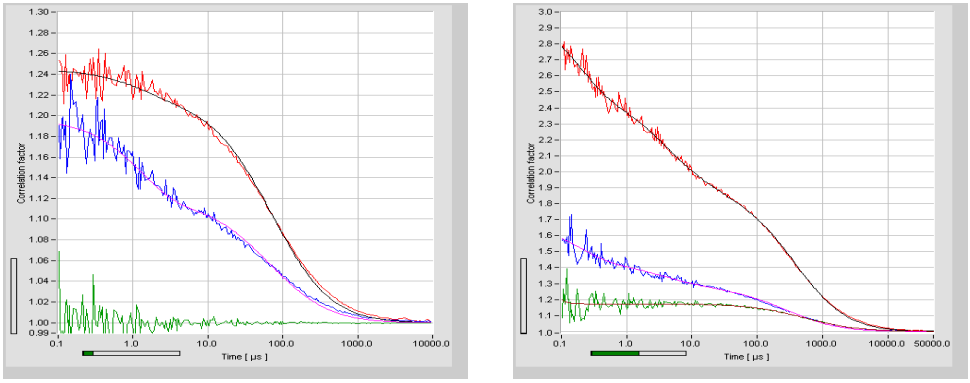


Fig. 901: Left: Atto 488 and Atto 647N, molecules not linked. Right: Alexa 488 and Cy5 partially linked by double-stranded DNA. Blue and Red: Autocorrelation. Green: Cross-correlation.

Picosecond FCS

With the highly efficient HPM-100-40 detectors the DCS-120 can be used for picosecond correlation. The laser is switched into the CW mode, and the photons in both detection channels are cross-correlated. Cross-correlation is either be calculated between the data of the two SPC-150 channels [442, 443], or a DPC-230 correlator module is connected in parallel with the SPC-150 modules [80]. Fig. 902 was recorded by a DPC-230.

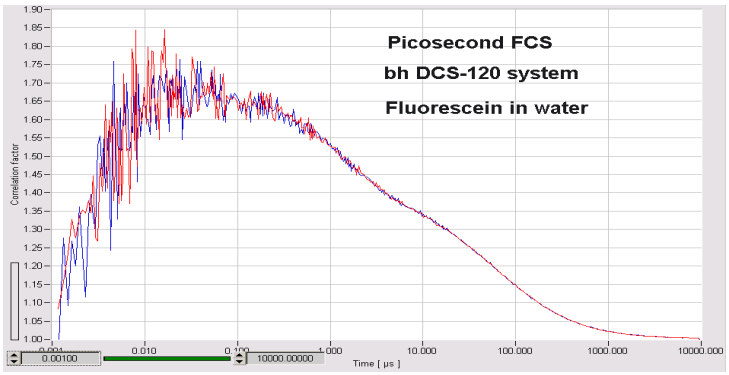


Fig. 902: Picosecond FCS with the DCS-120 system. Two HPM-100-40 detectors, DPC-230 correlator module.

FCS in Live Cells

FCS in cells is much more difficult than in solution. There is background fluorescence from endogenous fluorophores, the concentration of the fluorophore for FCS cannot be accurately controlled, and there is motion in the cell. The results therefore usually have low correlation amplitude and poor signal to noise ratio.

Fig. 903 shows FSC recorded from a cell by an SPC-830 module and a custom made two-photon laser scanning microscope [151, 153]. The detector was a Perkin Elmer SPCM-AQR. The FLIM image o the left was obtained in the Scan Sync In mode. After the FLIM recording the laser beam was pointed into the marked spot, and an FCS recording in the parameter-tag (FIFO) mode started. The acquisition time for the data shown was 130 s, the average count rate $15 \cdot 10^3$ s^{-1}. A fluorescence decay curve and an FCS curve in a selected spot are shown in the middle and at right. Please note the small amplitude of the FCS curve. The correlation amplitude is only 0.016, compared to 1.2 for a GFP solution recorded in the same setup, see Fig. 904.

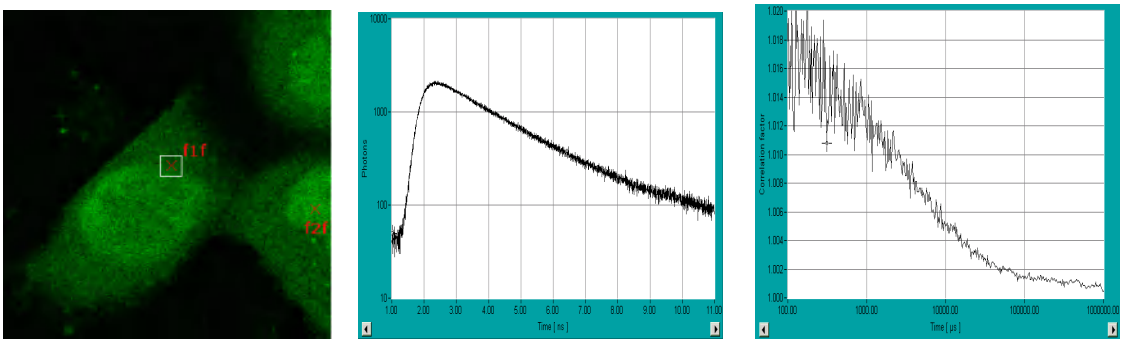


Fig. 903: FLIM image (left), decay curve (middle) and FCS curve (right) recorded in a selected spot (1). Home-made laser scanning microscope, two-photon excitation, SPCM-AQR detector, SPC-830 TCSPC module. [151] and courtesy of Zdenek Petrasek and Petra Schwille, Biotec TU Dresden.

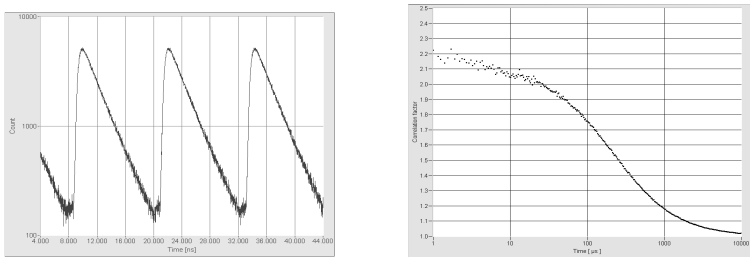


Fig. 904: Fluorescence decay curve over three laser pulse periods (left) and FCS curve (right) of a GFP solution, recorded in the same setup as Fig. 903. Count rate 5 to 7 kHz, acquisition time 980 s. From [151, 154].

Practical Tips

TCSPC-FCS with CW Excitation

When FCS is recorded with a CW laser the TCSPC module needs a synchronisation pulse at its SYNC input to finish the recording cycle for each photon. In laser scanning microscopes that have a ps diode laser or a Ti:sapphire laser this is no problem: The ps laser is used to generate the SYNC signal, while the sample is excited by one of the CW lasers of the microscope, see Fig. 905, left. If there is no pulsed laser in the system a SYNC signal can be generated by a pulse generator. e.g. a LSG-02 module. See Fig. 905, middle.

It is also possible to split the detector signal electrically and use one part for the CFD, the other for the SYNC input of the SPC module (Fig. 905, right). Note that the macro-time clock source in the TCSPC system parameters must be 'internal' in this case. If several modules are used these must be synchronised via the 'Master Clock' option in the 'Parameters' menu.

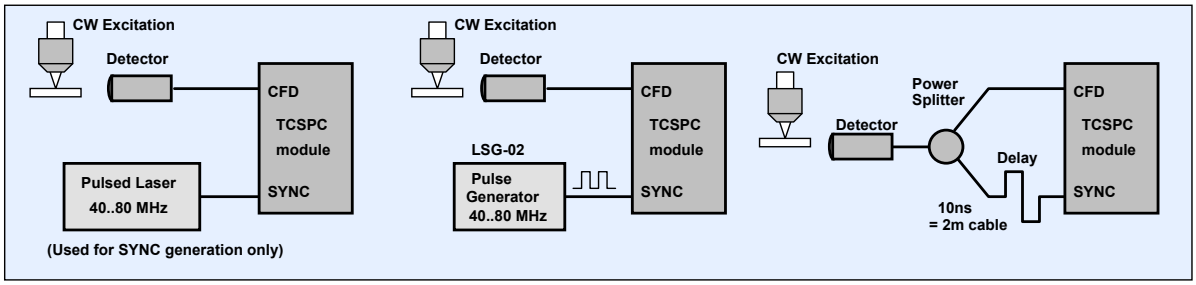


Fig. 905: Stop pulse generation for TCSPC-FCS with a continuous laser

Interference of the Laser Period with the Recording Clock

If FCS experiments are excited by a pulsed laser the laser pulse repetition frequency can interfere with the macro time clock frequency. The result is a periodical variation of the number of laser pulses per macro-time period. The same period shows up in the correlated intensity. Periodicity can appear on any time scale, depending on the difference of the laser and macro-time clock frequencies or their harmonics. The problem is most pronounced if both frequencies are almost identical. In the bh SPC-830, SPC-130/134, SPC-140/144 and SPC-150/154 modules the problem has been solved by providing an optional clock path from the timing reference (SYNC) input to the macro time clock, see 'FIFO Mode', page 770. The macro time clock can then be synchronised with the laser pulse repetition rate, which removes the problem entirely. Moreover, using the SYNC signal as a macro time clock is a simple way to synchronise several TCSPC channels of a multi-module system. Of course, using the Sync input as a clock source for FCS requires that the SYNC signal is free of glitches.

Detectors

Compared to fluorescence decay measurements, the efficiency of FCS measurements is relatively low. For a given number of photons, N, the SNR of a fluorescence decay measurement is proportional to $N^{1/2}$, whereas the SNR of FCS is proportional to N itself. This somewhat surprising behaviour results from the fact that two photons are needed to obtain one macro-time coincidence in the correlation histogram. The strong dependence of the SNR on the count rate makes detection efficiency an important issue in FCS.

Most FCS setups therefore use single photon avalanche photodiodes [769, 1001], usually SPCM-AQR detectors from Perkin Elmer [967]. The SPCM-AQRs have a quantum efficiency that reaches almost 80% at 800 nm. However, the SPCM-AQRs often have a timing delay dependent on wavelength and count rate. The changes can be of the order of 1 ns, see Fig.

305, page 193. Recording a fluorescence decay curve with a detector this unstable delivers questionable results.

Better timing stability can be achieved with SPADs manufactured in epitaxial processes, such as the id 100-20 of id Quantique [607] and the PDM 50 CT of Micro Photon Devices [858]. The quantum efficiency up to 550 nm is comparable, above 650 nm lower than for the SPCM-AQR.

Timing problems are also avoided by using PMTs with high-efficiency GaAsP photocathodes, such as the Hamamatsu H7422-40 module [548]. The modules have a stable and almost wavelength-independent transit time spread of about 300 ps duration. The quantum efficiency reaches 40% at 550 nm, see Fig. 258, page 165.

The best solution to the detector problem is the hybrid PMT. Hybrid PMTs are vacuum devices that accelerate the photoelectrons from a photocathode into an avalanche photodiode [469]. There is virtually no loss of photoelectrons in these devices. The Hamamatsu R10467-40 uses a GaAsP photocathode and thus reaches an unprecedented counting efficiency. The transit time spread is about 100 ps. Amazingly, the R10467-40 is virtually free of afterpulsing, see Fig. 908. Please see also page 178, 'HPM-100 Hybrid Detector'.

Afterpulsing of Detectors

All conventional PMTs and the commonly used SPADs show a more or less pronounced afterpulsing (see 'Afterpulsing', page 167). Afterpulsing causes a steep rise of the autocorrelation function towards short times in the range below one microsecond.

The absolute amount of afterpulsing in PMTs increases with the gain. Reducing the operating voltage of a PMT while increasing the preamplifier gain therefore helps, but does not remove the problem entirely. Moreover, the height of the afterpulsing peak in the autocorrelation function is proportional to the reciprocal count rate. The reason is that the probability of detecting an afterpulse of a previously detected photon is constant, whereas the probability of detecting another photon increases with the count rate. The effect of the count rate on the afterpulsing peak in the correlation function is shown in Fig. 906.

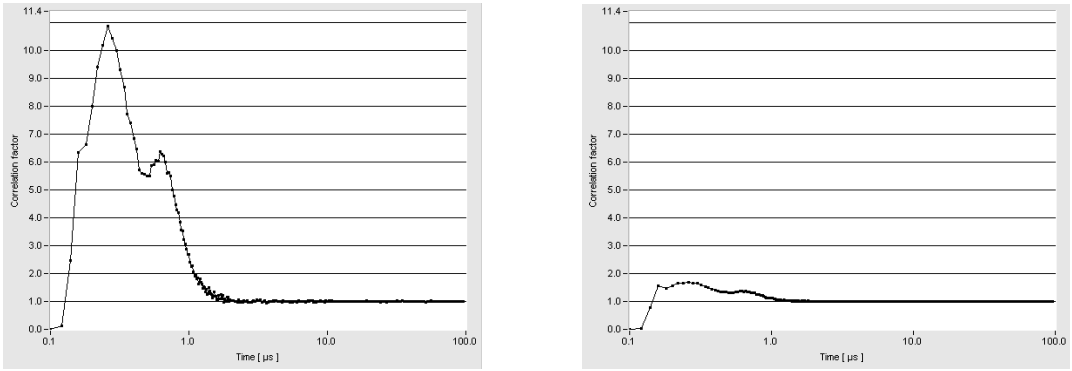


Fig. 906: Effect of the count rate on the height of the afterpulsing peak. H74222-40 detector, count rate 10 kHz (left) and 100 kHz (right)

Afterpulsing can be almost entirely rejected from FCS results by cross-correlation. The light is split into two equal beams that are detected by individual detectors. Afterpulses in one detector are not correlated with any counts in a second detector and therefore do not noticeably change the cross-correlation function. An example for two H7422-40 detectors is shown in Fig. 907. Curves a and b are the autocorrelation curves of the individual detectors. Curves c and d are cross-correlation curves of the signals of detector 1 against detector 2 and vice versa. The afterpulsing is almost entirely removed in the cross-correlation.

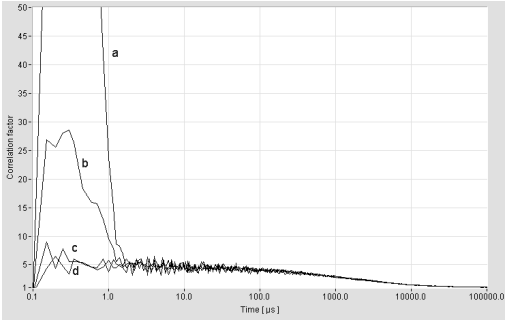


Fig. 907: Rejection of detector afterpulsing by cross correlation. GFP solution, two H7422-40 detectors, 2-photon excitation, LSM 510 NLO microscope in beam-stop mode. Curves a and b: Autocorrelation of the signals of the two detectors. Curves c and d: Cross-correlation detector 1 against detector 2 and vice versa.

Until recently, the only detectors that were free of afterpulsing have been NbN detectors based on superconduction [867, 1189, 1190]. This seems to have changed with the introduction of the Hamamatsu R10467-40 hybrid PMTs [469, 549] and the bh HPM-100-40 hybrid detector modules based on them. Our tests have shown that the detectors are virtually free of afterpulsing down to a time scale of 100 ns. The autocorrelation function for a conventional light signal at a count rate is shown in Fig. 908, left. Except for the noise, the curve is flat down to 100 ns. Fig. 908, right shows the autocorrelation function obtained from a fluorescein solution. Because there is no afterpulsing peak the data from a single detector can be used to obtain both the triplet lifetime and population, and the diffusion time.

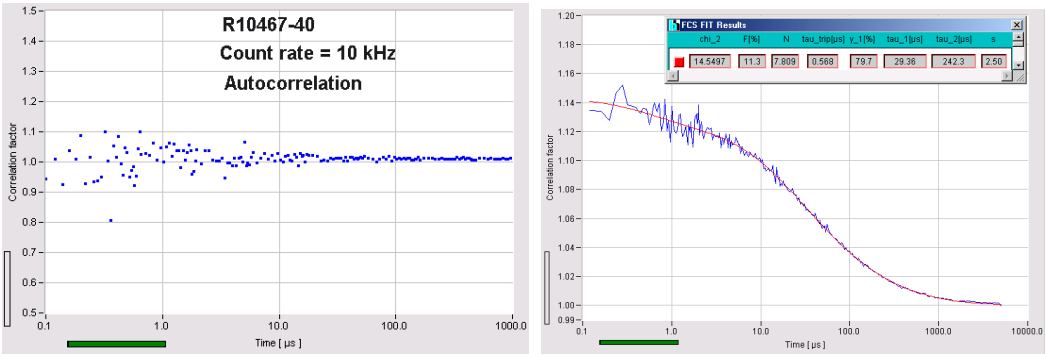


Fig. 908: R10467-40 hybrid PMT. Left: Autocorrelation function of an uncorrelated signal. Right: Autocorrelation function of fluorescein solution (blue) and fit with a model containing the triplet transition and diffusion time. Fit: bh SPCM TCSPC operating software. Optics: bh DCS-120 confocal scanning FLIM system.

Autocorrelation of photons detected in a single detector has a significant advantage: Compared with a system that splits the signal into two channels and cross-correlates the photons the number of correlations increases by a factor of four. That means, either a given signal-to noise ratio is obtained in a four-times shorter acquisition time, or the signal-to-noise ratio is two times better for a given acquisition time. Moreover, the relative number of dark counts is lower for the single-detector correlation. Thus, also the influence of the dark counts on the FCS amplitude is smaller. A comparison of autocorrelatation and cross-correlation of the same signal is shown in Fig. 909. Autocorrelation is shown left. Cross-correlation of the components of the same signal split on two detectors is shown right. The higher signal-to-noise ration and the higher amplitude of the autocorrelation is clearly visible.

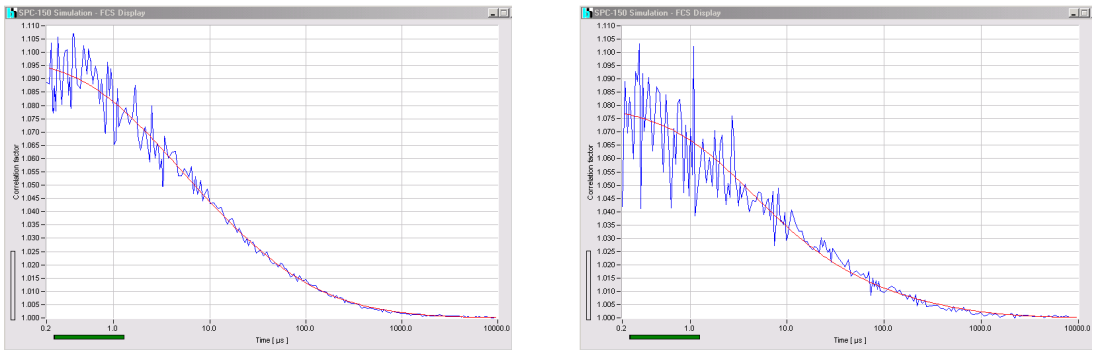


Fig. 909: FCS with the HPM-100-40. Left: Single detector, autocorrelation. Right: Light split on two HPM-100-40 detectors, cross correlation. Note the higher SNR and higher correlation amplitude for autocorrelation.

Background Signals

Background signals are a frequent source of failure in attempts to record FCS curves. Background signals may result from detector background, leakage of daylight, leakage of excitation light, emission of LEDs within the microscope, spurious laser emission at different wavelengths, or long-lifetime fluorescence of lenses or filters. The background reduces the apparent correlation coefficient or even makes the fluorescence correlation entirely undetectable.

It is often difficult to identify the sources of the background. In pulsed excitation systems, the amount of background can easily be estimated from the recorded fluorescence decay: Any intensity that remains after the fluorescence has decayed is caused by background effects. Leakage from room lights has a strong correlation at the line frequency. The light can therefore be identified by checking the autocorrelation function in the 20-ms range. Other sources of background light can often be removed by bandpass filters in the excitation and detection beam path. In two-photon systems background light can often be reduced by using a pinhole in a conjugate focal plane. Although the pinhole is not required for two-photon FCS it suppresses background signals which do not come from the excited sample volume.

Beam Jitter

Instability of the beam position results in a distortion of the FCS curves or, in most cases, in a de-correlation of the fluorescence signal. Complete de-correlation occurs if the beam jitters is larger than the airy disc diameter and faster than the average photon count rate. Subsequent photons then come from different molecules and are no longer correlated. Beam jitter was a problem in early laser scanning microscopes but has virtually been eliminated in modern scanning systems.

Sample Volume

Fluorescence correlation functions can, of course, only be obtained if the focal volume is small enough. For two-photon excitation through a good microscope lens this is achieved (almost) automatically. For one-photon excitation a pinhole must be placed in a plane conjugate with the focus in the sample. The diameter of the pinhole depends on the magnification on the way from the sample to the pinhole. High-end microscopes have objective lenses corrected for infinite conjugate ratio, i.e. the fluorescence light leaves the back aperture of the lens in a parallel beam. The light is focused into the eyepiece plane by a tube lens. A pinhole placed in this plane should have a diameter that is approximately the Airy disc diameter multiplied by the magnification power of the objective lens.

Optical Aberrations

It should be noted here that FCS recording requires a near-perfectly working optical system. FCS works only if the detection volume is reduced to less than one femtoliter. A focal volume this small is obtained only with a high NA objective lens and correct matching of the refrac-

tive indices. Because FCS is done in aqueous solutions or living cells normally a water immersion lens is required. The lens must be corrected both for the excitation and the detection wavelength. For FCS recording with the Zeiss LSM microscopes and with the DCS-120 attached to a Zeiss Axio Observer we recommend the NA=1.2 'C-Apochromate' water immersion lens.

FCS measurements in solution are sometimes attempted in the setup shown in Fig. 910, left. A cover slip is placed directly on top of the microscope lens of an inverted microscope. A droplet of a diluted dye solution is placed on the cover slip. We discourage to use this setup for several reasons. First, the dye solution can easily spoil the microscope lens. Second, the optimum resolution of the microscope lens may not be reached. The lens is corrected for a beam path that has a space (the 'working distance') between the lens and the cover slip, see Fig. 910, right. This gap is filled with the immersion fluid. In the setup of Fig. 910, left, however, the working distance is above the cover slip, i.e. in the dye solution. The dye is normally dissolved in water, or a solvent of similar index of refraction. The setup of Fig. 910, left, therefore works only for a water immersion lens. For an oil immersion lens the mismatch of the refractive index is so severe that a reasonably small focal volume is not obtained. Consequently, a TCSPC FIFO measurement shows a fluorescence decay curve, but no fluorescence correlation.

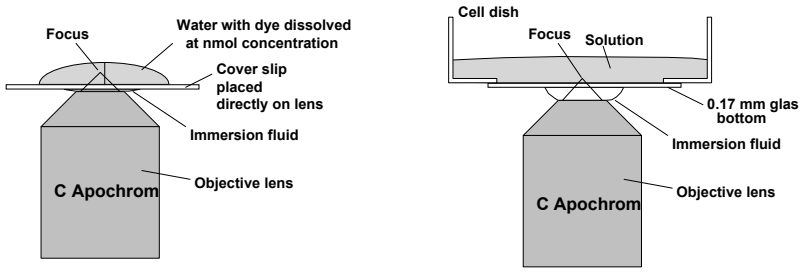


Fig. 910: FCS measurement of a dye solution. Left: Cover slip placed directly on microscope lens, sample solution placed on cover slip. A large part of the beam path is in the sample. Right: Correct optical configuration, the beam path is in the immersion fluid.

A correct setup is shown in Fig. 910, right. One of the commonly used cell dishes contains the dye solution. Use a cell dish with a glass bottom of the thickness your microscope lens is specified for. The space between the microscope lens must be filled with the immersion fluid. Unless you go deeper into the solution than a few µm the setup works reasonably well even with an oil immersion lens.

FCS measurements in solution are often attempted in well plates, as shown in Fig. 911, left. Unfortunately these plates often have poor optical quality, wrong bottom thickness, or wrong refractive index. We obtained better results in cell dishes with glass bottom, see Fig. 911, right.

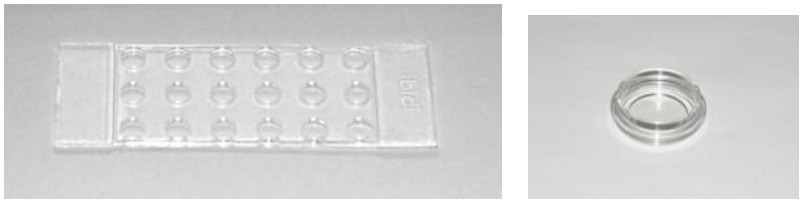


Fig. 911: Well plate (left) and cell dish (right) for fluorescence measurement in solution

Time-Resolved Single-Molecule Spectroscopy

The techniques described under ‘Picosecond Photon Correlation’ and ‘Fluorescence Correlation Spectroscopy’ exploit the correlation between the photons emitted by single molecules or by a small number of molecules. Picosecond photon correlation techniques investigate effects driven by the absorption of a single photon of the excitation light. The effects investigated by FCS are driven by Brownian motion, rotation, diffusion effects, intersystem crossing, or conformational changes. Because of these random and essentially sample-internal stimulation mechanisms, correlation techniques do not necessarily depend on a pulsed laser.

A second way to obtain information about single molecules is time-resolved spectroscopy with pulsed excitation at high repetition rate. The borderline between correlation techniques and time-resolved single-molecule spectroscopy is flowing and somewhat artificial. In general, time-resolved single-molecule spectroscopy delivers spectroscopic information about *individual* molecules by recording the fluorescence in a short period of time. Photon correlation techniques normally derive average molecular properties from the observation of *different* molecules over a longer period of time.

The optical systems used for both techniques are essentially the same. A small sample volume is obtained by confocal detection or two-photon excitation in a microscope. Several detectors are used to detect the fluorescence in different spectral ranges or under different angles of polarisation. Therefore correlation techniques can be combined with fluorescence lifetime detection, and the typical time-resolved single-molecule techniques may use correlation of the photon data. This paragraph focuses on single-molecule experiments that not only use, but are primarily based on pulsed excitation and time-resolved detection. An overview of time-resolved single-molecule spectroscopy is given in [154].

Burst-Integrated Fluorescence Lifetime (BIFL) Techniques

Molecules diffusing in a solution or travelling through a capillary are in the focus of a microscope lens for a time of a few hundred microseconds to a few milliseconds. Immobilised molecules under high excitation power cycle between the S0/S1 (singlet) states and the non-fluorescent triplet state. The fluorescence signal therefore consists of random bursts corresponding to the transit of individual molecules through the focus or to the dwell time in the singlet state. Under typical conditions, from a highly fluorescent molecule a few hundred photons are detected within a single burst. The idea behind burst-integrated fluorescence lifetime detection, or BIFL, is to identify the bursts of the molecules, obtain spectroscopic information within the bursts, and thus characterise the individual molecules.

BIFL by Sequential Recording

Lifetime detection within individual bursts was accomplished even with early PC-based TCSPC modules, such as the SPC-300 and SPC-330 [896, 1378]. Software-controlled sequencing or an external counter connected to the routing inputs was used to record a sequence of fluorescence decay curves. The time per curve was typically 10 ms, the number of curves per sequence 128. Of course, a resolution of 10 ms per curve did not yield reliable information about the burst duration and the burst size. Therefore, often intensity tracing and FCS recording were performed in parallel by a multi-channel scaler (MCS) and a correlator [1379]. The technique was applied to single-molecule identification in a capillary [1379] and to the identification of antigen molecules in human serum [1065].

Far better burst resolution was obtained by bh TCSPC modules with an internal sequencer. In particular, sequencing in combination with memory swapping (the ‘continuous flow’ mode)

was used to record a virtually infinite sequence of decay curves in time intervals of 100 µs and shorter [141, 1248]. A part of a sequence recorded this way is shown in Fig. 912.

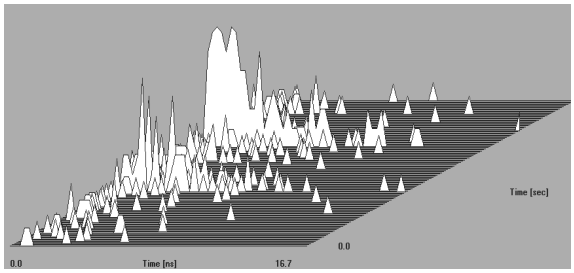


Fig. 912: Bursts of single molecules. Part of a longer sequence recorded by sequencer-controlled memory swapping. 1 ms per step of the sequence, 64 ADC channels.

A burst is identified by detecting more than a defined number of photons in several successive steps of the sequence. For fluorescence-lifetime calculation, the photon distributions of all time-steps within the burst are accumulated and the lifetime is obtained by a maximum-likelihood algorithm [328, 677, 680, 1068]. A histogram of the lifetimes obtained in a large number of bursts yields information about the homogeneity of the molecules and their local environment. Information about the quantum efficiency or 'molecular brightness' is obtained by building up a histogram of the burst size. For freely diffusing molecules the diffusion time constant can be estimated from a histogram of the burst duration. In a capillary the histogram of the burst duration is an indicator of the speed of the molecules.

Burst-recording in the continuous-flow mode can be combined with multi-detector operation. The detectors can be used to record the fluorescence in different wavelength intervals or under different angles of polarisation. This 'multi-parameter' detection technique delivers the lifetime, the angle of polarisation, the fluorescence anisotropy, and the emission wavelength within the individual bursts [1068, 1248].

For a burst resolution around 1 ms, detection by the continuous flow mode is relatively efficient in terms of data size. The drawback of the continuous-flow mode is that the burst resolution is limited by the increase of the data size and, and consequently, by the available data readout rate [154].

BIFL by Time-Tag Recording

BIFL results with a burst resolution down to the laser pulse period can be obtained by recording the photons in the 'FIFO' or 'time-tag' mode of TCSPC, see 'Recording Parameter-Tagged ', page 132. Because the full information about all photons is recorded time-tag data are extremely flexible. Conformational dynamics, rotational relaxation, and intersystem crossing can be investigated at almost any time scale [425, 426, 720, 1248].

An early impressive demonstration of the technique was given in [986]. A frequency-doubled mode-locked Nd-YAG laser delivers pulses of 532 nm wavelength, 150 fs pulse width, and 64 MHz repetition rate. The laser is coupled into the beam path of a microscope and focused into the sample. The sample is mounted on a piezo-driven sample stage. The fluorescence light from the sample is collected by the microscope lens and separated from the excitation light by a dichroic mirror and a notch filter. The light is split into its 0° and a 90° components. The 0° component is further split into a short-wavelength and a long-wavelength component. The signals are detected by SPAD modules and recorded by a single bh SPC-431 TCSPC module via a router. The TCSPC module records the photons in the FIFO mode.

The molecules to be investigated were embedded in polymethylmethacrylate (PMMA). An image of the sample was obtained by scanning and assigning the photons to the individual pixels by their macro times. Based on this image, appropriate molecules were selected for further investigation.

These molecules were then brought into the focus and time-tag data were acquired. By analysing these data a surprisingly large number of spectroscopic parameters can be determined. The intersystem crossing yield is obtained from a histogram of the number of photons in the bright periods. The histogram of the dark periods reflects the triplet decay and delivers the triplet lifetime. The fluorescence lifetime is obtained by building up the fluorescence decay functions from the micro times.

The polarisation of the fluorescence is obtained by comparing the counts in the SPAD detecting under 0° polarisation with the counts in both SPADs detecting the 90°. The anisotropy decay can be calculated from the micro times of the photons in these detector channels. The authors showed that there is some rotational relaxation, in spite of the solid matrix in which the molecules are embedded. They derived the initial and final anisotropy, the angle of the cone of wobbling, and the rotational correlation time.

The authors managed even to observe the spectral relaxation of single molecules. They placed a dichroic mirror between two SPADs, with a transition in the centre of the fluorescence band of the molecule being investigated. The spectral relaxation is obtained from the ratio of the counts of these detectors in the individual time channels. For the spectral relaxation of an Alexa 546 molecule conjugated to a single protein a spectral shift of 4 nm and a spectral relaxation time of 0.3 ns was found [986].

The same instrument was used to monitor conformational changes in the citrate carrier CitS [645]. A version of the instrument uses an annular aperture stop in the beam path of the microscope. With this stop, different Airy disks are obtained for different orientation of the dipoles of the molecules [1152, 1153]. Comparing the observed intensity patterns of the molecules with calculated diffraction patterns makes it possible to derive the 3D orientation of the molecules. In [710] the lifetime of DiI molecules in a 20 nm polymer film at a glass surface is investigated by this technique. The lifetime varied between 4.7±0.7 ns and 2.11±0.1 ns, depending on the orientation of the molecules to the surface.

Fiore et al. used four parallel channels of an SPC-134 system. Four SPCM-AQR SPADs were used to detect 0° and 90° polarisation in two wavelength channels. Single-molecule studies of freely diffusion RNA constructs are described in [447] and [583].

Multi-Parameter Single-Molecule Burst Analysis

The idea behind Multi-Parameter Fluorescence Detection, or MFD, is to simultaneously record several parameters of the fluorescence of a sample, take a large number of measurements, and build up two-dimensional or multi-dimensional histograms of the frequency of the results versus the fluorescence parameters [426, 719, 720, 1336]. The parameters used are normally intensity ratios in different spectral intervals, the fluorescence lifetime in different spectral intervals, and the fluorescence anisotropy. The technique differs from the method [986] described in the previous paragraphs in that it not only records several parameters of the fluorescence simultaneously but also analyses the fluorescence data in a multi-dimensional parameter space.

The principle is illustrated in Fig. 913. Consider a series of measurements taken from a sample. Each measurement delivers fluorescence intensities and fluorescence lifetimes at two wavelengths, λ_1 and λ_2. A TCSPC measurement like this can easily be performed by four detectors, a dichroic beamsplitter, and two polarising beamsplitters. The results from these measurements are used to build up a histogram of the intensity ratio λ_1 and λ_2 versus the lifetime at λ_1, a histograms of the intensity at λ_1 versus the intensity λ_2, and the lifetime at λ_1 versus the lifetime at λ_2. It is obvious that the histograms would represent a signature of the

fluorophore in sample. Moreover, because the measurement results are obtained by photon counting, the standard deviation of the parameters obtained is predictable. Any wider distribution found in the histograms indicates that there were fluctuations in the sample within the measurement time [25] (see also 'Photon Counting Histograms', page 675).

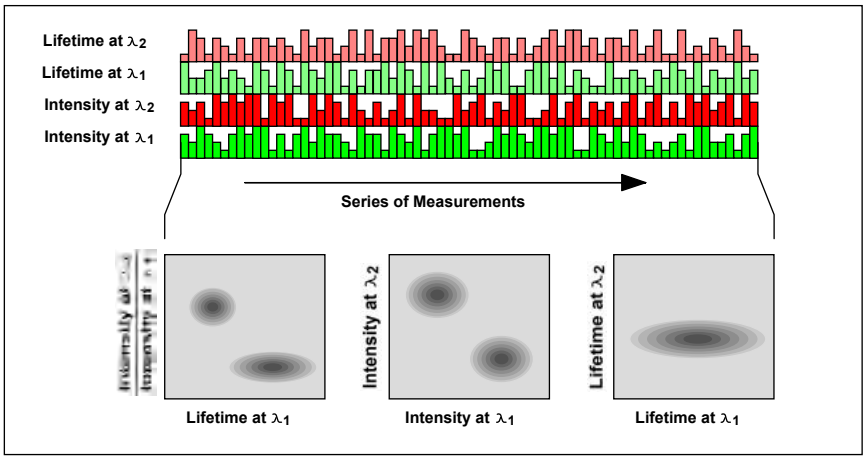


Fig. 913: Principle of multi-parameter fluorescence detection and analysis

The selectivity can be further improved by selecting measurements within a special pattern in one histogram, and using only these measurement for other histograms.

Multiparameter detection and analysis was originally developed for burst-integrated fluorescence lifetime measurement at single molecules. In that case, the fluorescence data are recorded by time-tag TCSPC, and the individual measurements shown in Fig. 913 represent the photon bursts of the individual molecules. If the fluorophore concentration is such that only a single molecule is in the detection volume at a time molecules with different fluorescence signature would produce different spots in the histograms. For instance, with the parameter used in Fig. 913 FRET effects would be likely to show up. Obviously, the interacting donor molecules would display different signatures than free donor or free acceptor molecules.

Molecules in Solution

An impressive demonstration of the capabilities of MFD for single-molecule FRET has been given by Widengren et al. [1336]. The principle of the experiment is shown in Fig. 914.

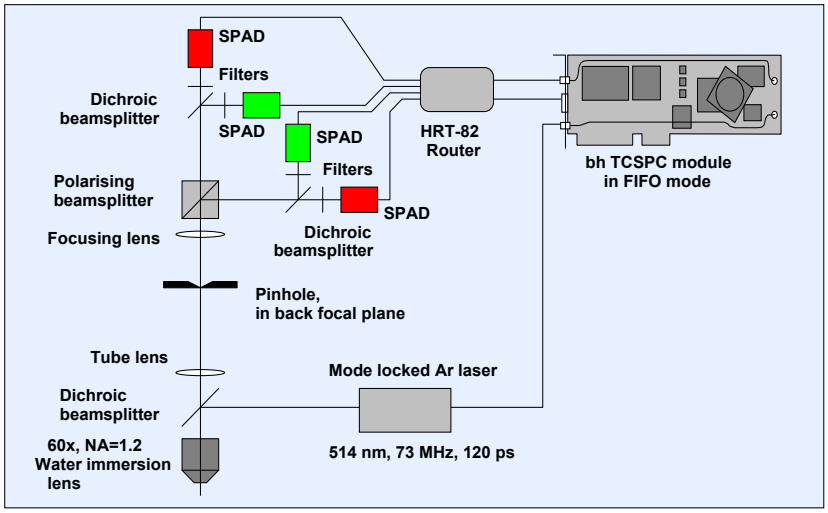


Fig. 914: Principle of MFD experiment

The typical confocal setup is used. The excitation laser is reflected down the beam path via a dichroic mirror. The confocal volume is confined by a pinhole in the upper focal plane of the microscope. The fluorescence light is split into 0° and 90° components of polarisation. Both

polarisation components are split into two wavelength intervals by dichroic mirrors and filters. The two wavelength intervals were selected to detect the donor and the acceptor of the FRET constructs to be investigated. Four detectors, in this case SPCM-AQRs, received the light signals. The output pulses of the detectors were connected to a single bh TCSPC module via an HRT-82 router. The router / TCSPC combination could, in principle, be replaced with a four-channel TCSPC package. However, the higher counting capability of the four-channel system would pay off only for burst count rates exceeding 1 MHz which are rarely obtained.

The FIFO mode (parameter-tag) data delivered by the TCSPC module are first analysed to identify the bursts of the molecules diffusing through the confocal volume. Once a burst is identified the analysis software determines

- average count rates in the donor (green) and acceptor (red) channels over the burst duration
- the anisotropies in the donor (green) and acceptor (red) channel
- the fluorescence lifetimes in the donor and acceptor channel

To demonstrate their MFD technique Widengren et al. used a deoxyoligonucleotide containing 27 nucleo bases in a random sequence [1336]. The 5'-d of the deoxyoligonucleotide was labelled via a C6 amino link with a FRET donor. Either Cy3 or Rh6G were used. The FRET acceptor was linked to a defined position on a complementary deoxyoligonucleotide. Either Cy5 or BP650/656 were used. The data analysis steps were as follows:

A histogram of the frequency of bursts versus the lifetime and the anisotropy in the donor channel was calculated, see Fig. 915. Both CY3 and Rh6G have high anisotropy when they are linked to the oligonucleotide. However, there is a number of bursts with low anisotropy. These come either from free donor molecules or from impurities. Bursts below the red line in Fig. 915 were therefore excluded from further analysis.

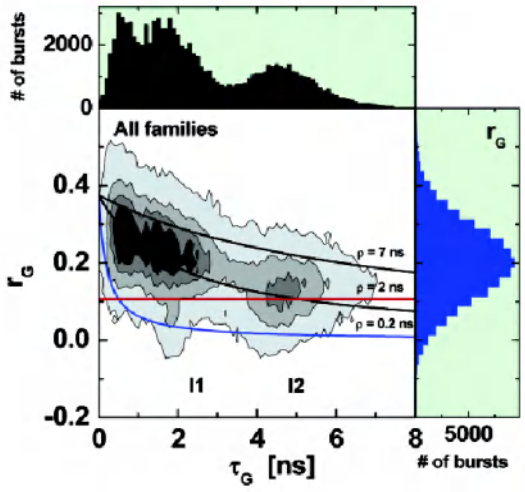


Fig. 915: Histogram of burst frequency in a histogram of donor anisotropy versus donor lifetime. With permission, from [1336]

From the remaining bursts data donor/acceptor-intensity ratio versus donor-lifetime histograms were built up, see Fig. 916. For a single FRET pair, these showed clearly the populations of donor-only constructs (black ellipses) and donor-acceptor constructs (yellow ellipses). The location of the donor-acceptor pattern varied clearly with the donor-acceptor distance, compare location of donor-acceptor events, left to right.

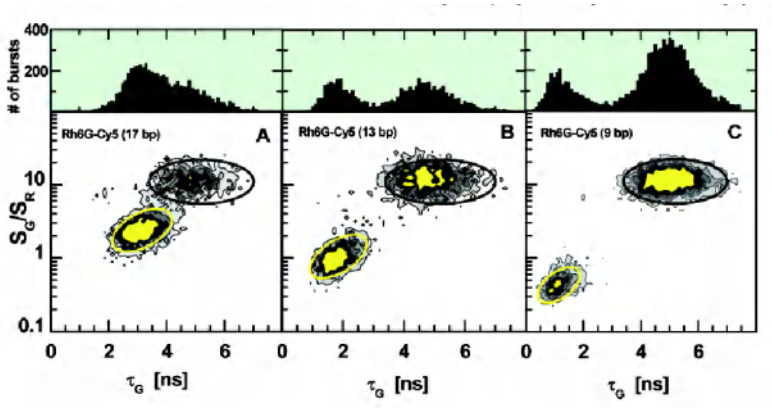


Fig. 916: Frequency of bursts in a histogram of the donor/acceptor intensity ratio versus the donor lifetime. The black ellipses mark donor-only events, the yellow ellipses donor-acceptor events. Left to right: Donor-acceptor distance 17, 13, and 9 base pairs. With permission, from [1336].

Mixtures of oligonucleotide labelled with different donors and acceptors were separated by plotting the frequency of bursts in donor/acceptor-intensity versus donor-lifetime histograms, see Fig. 917, left. Further analysis by using a donor/acceptor-intensity versus acceptor-lifetime histogram separated also constructs with different acceptors, see Fig. 917, right, A and B.

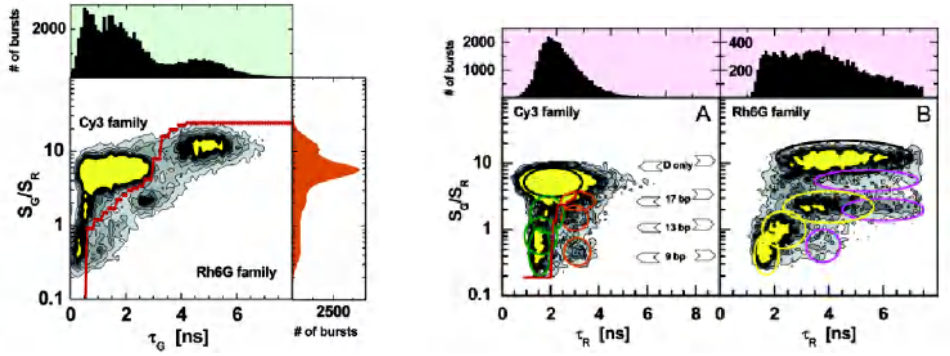


Fig. 917. Left: Frequency of bursts in a histogram of the donor/acceptor intensity ratio versus the donor lifetime. The red line shows the separation between the oligonucleotides labelled with Cy3 and Rh6G donors. Right: Frequency of bursts in a histogram of the donor/acceptor intensity ratio versus the acceptor lifetime, after separation of the different donors. A: Donor Cy3, green ellipses Cy3-Cy5, red ellipses C3-BP650/656, black Cy3 only. B: Donor Rh6G, yellow ellipses Rh6G-Cy5, pink ellipses Rh6G- BP650/656, black Rh6G only. With permission, from [1336].

Applications of the MFD technique to single-molecule FRET experiments are described in [25, 1347]. A combination of picosecond fluorescence correlation [442] and MFD was used to investigate dye-exchange dynamics in micellar solutions of Rhodamine 123 [917]. Orientational and dynamical heterogeneity of Rhodamine 6G attached to DNA was investigated in [908]. Stefani et al. used a similar histogramming technique to study changes of singlet and triplet decay rates of single molecules induced by a nearby gold film [1182].

The University of Düsseldorf provides a data analysis package for MFD analysis of bh SPC FIFO mode data. For details please see [443].

Cell Imaging

The principle of MFD analysis can, of course, be applied to any kind of multiple-measurement data. These may be single, dual- or multi-wavelength FLIM data recorded in the Scan Sync In mode, time-tag FLIM data recorded in the FIFO Imaging mode, sequential FLIM data recorded by Continuous-Flow FLIM, single-point time-tag data, or single-point Continuous-Flow data.

Kudryavtsev et al. used MFD for live cell imaging [719]. They combined the setup shown in Fig. 914 with a piezo-scan stage. The image data were acquired in a single slow scan. The spectral range detected was 510 to 556 nm for the green channel and 660 to 800 nm for the red channel. TCSPC time-tag data of the photons and the scan clocks were acquired by two bh SPC-130 modules via routers. (Please note that the SPC-130 has not been designed for FLIM. The synchronisation with the scanner is considerably easier with SPC-830, SPC-150 or SPC-160 modules!) The pixel dwell times were from 20 ms to 300 ms, large enough to obtain fluorescence anisotropy, fluorescence lifetime, and FCS amplitudes and times in the individual pixels. Fig. 918 shows *Schizosaccharomyces pombe* yeast cells expressing Mal3-pk-GFP fusion proteins. The cells were excited at 1.7 µW; The integration time per pixel was 20 ms. The images show the fluorescence intensity in the green channel, the fluorescence intensity in the red channel, and the fluorescence lifetime and fluorescence correlation amplitude in the green channel (left to right).

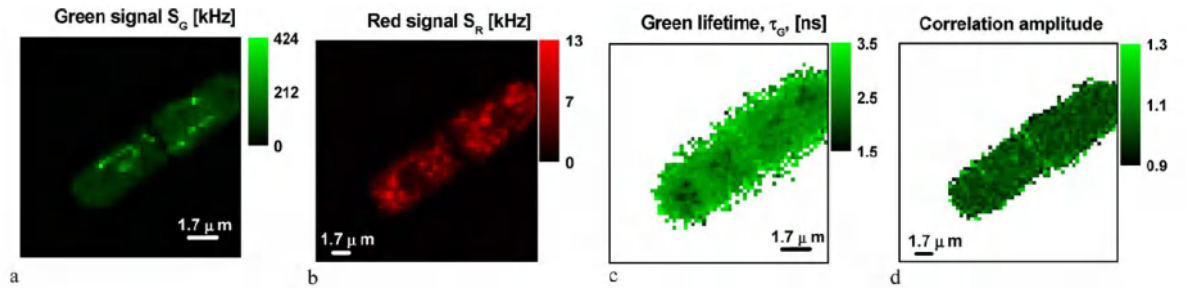


Fig. 918: MFD imaging of Mal3-pk-GFP proteins in *Schizosaccharomyces pombe* yeast cells. a) Intensity image of a the green signal, S_G. b) Intensity image of the red signal, the red signal, S_R. c) green fluorescence lifetime, τ_G. d) correlation amplitude. From [719], copyright Springer.

Multi-parameter analysis [443] of the data is shown in Fig. 919. A 2-D histogram of the pixels frequency versus the lifetime in the green channel and the green/red intensity ration is shown on the left. The red box selects pixels of short lifetime, τ_G, and low green-to-red intensity ratio, S_G/S_R. The corresponding pixels are highlighted red in the intensity image of the green channel (second left). A 2D histogram of the pixels frequency versus correlation time and amplitude is shown second left. The red box selects pixels of high correlation amplitude. An intensity image of the green channel with the corresponding pixels highlighted is shown on the right.

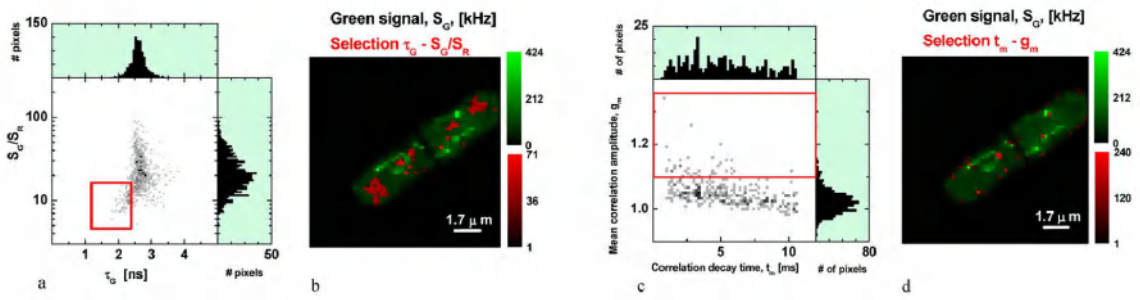


Fig. 919: MFD selection of subspecies according to their MFD parameters. a) Selection of short lifetime, τ_G, low green-to-red intensity ratio, SG/SR, in a 2-D histogram (red box). b) The corresponding pixels are highlighted red in the intensity image of the green channel. c) Selection of high correlation amplitude. d) The corresponding pixels are highlighted in the intensity image of the green channel. From [719], copyright Springer.

Applications to detecting heterogeneity of diffusion of Rhodamine 110 in sepharose beads and to protein interaction studies in HEK cells and plant cells are described in [1330]. Both stage scanning by a piezo stage and beam scanning by the bh DCS-120 system were used.

Single-Molecule FRET Experiments

An important application of burst analysis is the detection of conformational changes in biomolecules by single-molecule FRET techniques [378, 407, 408, 618, 628, 821, 936, 1380, 1381]. Two representative applications of the technique will be described below.

Pallikuth et al. [936] used the technique to detect conformational changes in the sarcoendoplasmic reticulum of calcium ATPase (SERCA). Two constructs were used. One was had Cerulean at the N-terminus and an EYFP intra-sequence tag in the nucleotide-binding domain (CY-CERCA, Fig. 920, A). The other was labelled with GFP in the N-domain and a TagRFP in the N-terminus (Fig. 920, B). The molecules were freely diffusing through the laser focus of a Leica SP5 two-photon microscope. Fluorescence was detected simultaneously in two emission wavelength intervals corresponding to the emission spectra of Cerulean and GFP. The photons were recorded by a bh SPC-830 TCSPC module via a router. Parameter-tag data were recorded and analysed as shown in Fig. 920, C to F.

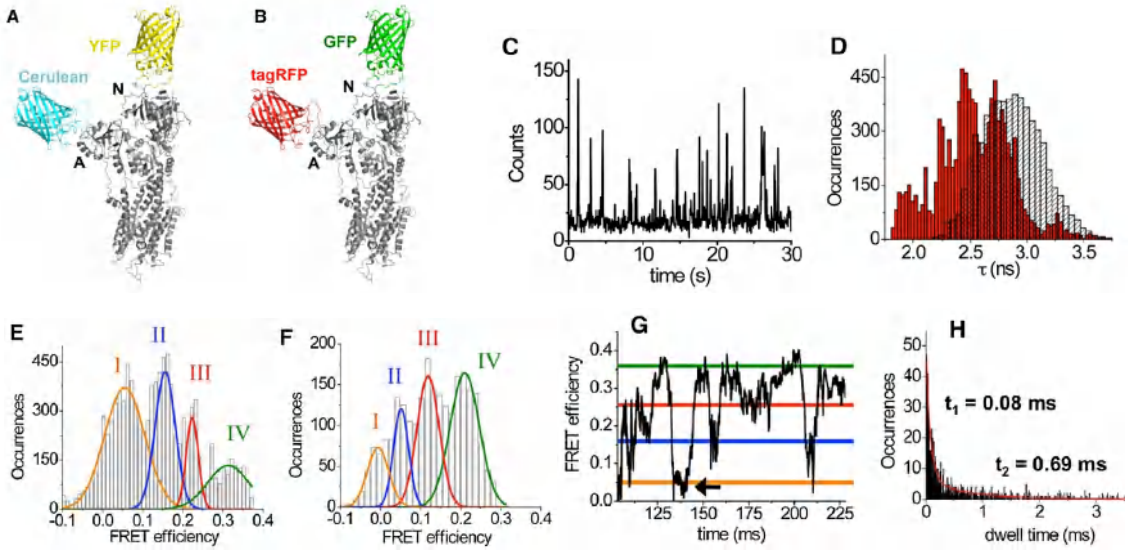


Fig. 920: Single-molecule FRET of SERCA. A: CY-SERCA comprises a Cerulean FRET donor fused to the N-terminus of SERCA (grey) in the actuator, or A-domain, and an intrasequence FP inserted in the nucleotide-binding, or N-domain. B: RG-SERCA is an analogous construct composed of a TagRFP acceptor fused to the N-terminus in the A-domain and GFP (green) donor inserted in the N-domain. C: Time-trace of fluorescence bursts from single molecules. D: Histogram of the fluorescence lifetimes obtained from RG-SERCA(red) or control GFP-SERCA (black). E: Histogram of the FRET efficiency calculated from the lifetime measurements shown in panel D. A Gaussian fit reveals subpopulations consistent with four discrete conformations of SERCA. F: CY-SERCA also exhibited four discrete RET states. The reduced FRET efficiency of these states (compared to panel E) was consistent with a larger Förster radius. G: RG-SERCA single-molecule FRET time trajectory. The horizontal lines indicate States I–IV (orange through green) identified by Gaussian analysis of the distributions of the FRET efficiency. H: Analysis of the dwell time for SERCA-sampling States I–IV revealed a biphasic distribution of dwell times characterized by fast (t_1) and slow (t_2) kinetics. With permission, from [936].

Fig. 920, C, shows the intensity bursts caused by the transition of the molecules through the laser focus. The bursts were identified in the data stream and a lifetime analysis performed in the individual bursts. A histogram of the lifetimes obtained over a large number of bursts is shown in Fig. 920, D. Changes in the conformation of the molecules results in different FRET efficiency and thus in different fluorescence lifetimes. The lifetimes were therefore translated into FRET efficiencies. Histograms of the FRET efficiencies are shown in Fig. 920, E and F. Four different FRET states are visible in the figures. The FRET efficiencies were extracted by fitting the distributions with four Gaussian distributions. Fig. 920, G shows the fluctuations of the FRET efficiency within a single burst. Also here, four different FRET efficiencies can be identified.

Fig. 920, H shows a distribution of the duration the molecules spent in each FRET state. The distribution was fitted with a bi-exponential model. This revealed two characteristic times, t_1 and t_2, the system stayed in the individual FRET states.

The experiments were extended to SERCA-expressing cultured rabbit cardio myocytes. Also here, four discrete structural states were found. The relative populations of these states oscillated with electrical pacing. Low-FRET states were most populated in the low-Ca phase (diastole), high-FRET states correlated with high Ca (systole).

Burst analysis of single-molecule FRET data has also been used for detecting conformational changes also in F_0F_1-ATP synthase. Early experiments based on a bh PMS-300 card had shown different conformations of F_0F_1-ATP synthase via variations in the FRET intensity [1399]. Later approaches used SPC-150 TCSPC modules [1380] and Hidden Markov Models to identify conformational states [1381, 1382] of the molecule. These experiments gave a detailed picture of the function of the molecular rotor of F_0F_1-ATP synthase [407, 408, 1154].

The principle of these experiments is shown in Fig. 921. EGFP was fused to the C terminus of subunit α, and Alexa 568 attached to residue E2C at one of the c subunits, see Fig. 921, left. FRET occurs between the EGFP and the Alexa 568. The entire C ring (blue) rotates against the upper part of the structure. This causes a change in the distance between the EGFP and the Alexa 568 and, consequently, a change in the FRET efficiency. The FRET efficiency was determined by recording fluorescence in a red (acceptor, Alexa) and a green (donor (EGFP) detection channel and calculating ratios of the count numbers. Bursts from constructs containing both the donor and the acceptor were selected by wavelength-multiplexed excitation and analysing the count numbers in both channels. Intensity traces and FRET distances for two selected bursts are shown in Fig. 921, right.

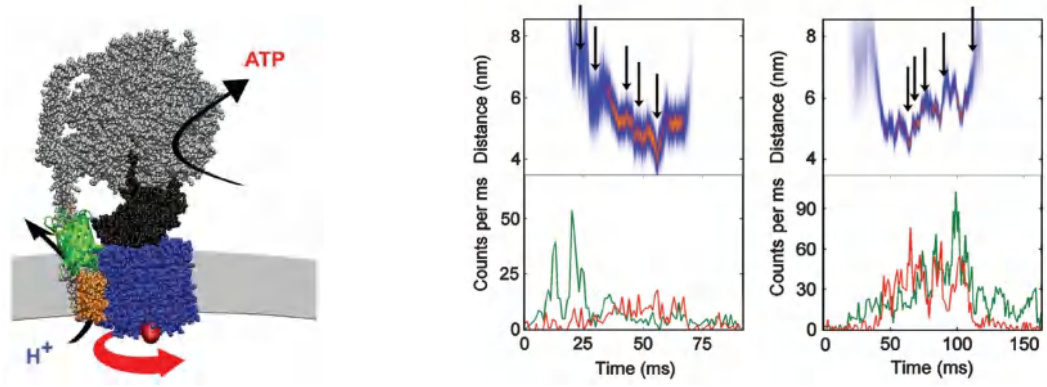


Fig. 921: Left: Model of *E. coli* F0F1-ATP synthase labelled with EGFP (donor, green, fused to the C terminus of subunit α, orange) and Alexa 568 (acceptor, red, at residue E2C at one of the c subunits (blue). Right: Counts in green (donor) and red (acceptor) detection channel (bottom) and donor-acceptor distances derived from FRET intensities for two selected photon bursts. The arrows mark steps in the FRET distance. From [408].

There are two different models of the rotation of the C ring against the upper part of the structure. One model predicts a step size of the rotation of 120°, the other a step size of 36°. To decide between the two models the distances of subsequent FRET states were identified in the data. The distances for subsequent states were determined, and the density plot of distances shown in Fig. 922 was built up. It shows the frequency of data pairs for subsequent FRET states (one distance versus the subsequent one). The results is compatible with the prediction for 36° step size (white line) but not with 120° step size (black line). Please see [232] for more details.

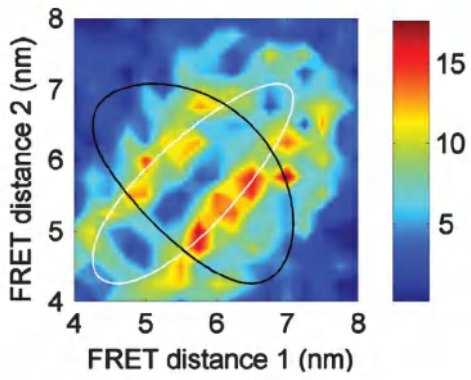


Fig. 922: FRET transition density plot. Distance pairs for subsequent FRET states, distance 1 and distance 2. The result is compatible with the prediction for 36° step size (white line) but not with 120° (black line). With permission, from [408].

Identification of Single Molecules

Identification of single molecules has relevance for spectroscopic DNA sequencing and drug screening. Molecules can be identified by using the fluorescence lifetime, the fluorescence anisotropy, the lifetime in conjunction with the emission wavelength, and the burst size and duration.

Identification purely based on the fluorescence lifetime is described in [435]. The true shape of the signal, i.e. the convolution of the IRF with the expected decay function, is pre-calculated for different molecules. The photon distributions in the individual bursts are then compared with these pre-calculated functions. The Rhodamine derivatives JF9, JA67, and JA53 were identified with an error rate between 0.1 and 0.01.

The problem of pure lifetime identification is that the lifetime differences are often relatively small. Moreover, there may be some variation in the lifetime of a single type of molecule due to different local environments. It is therefore useful to add more parameters to the identification algorithm. By using the fluorescence anisotropy, Rhodamine 133 and EYFP were identified with only 1% misclassification [1068].

Prummer et al. used the lifetime and the emission wavelength for on-line classification of molecules [985]. A dichroic mirror split the fluorescence into two wavelength intervals, which were detected by two SPAD modules (SPQ141, EG&G). The pulses of the APDs were connected into a bh SPC-402 module via an HRT-82 router. Classification was performed online in the incoming FIFO data stream. The procedure uses a lookup table that returns the probability that a photon originates from a particular type of molecule as a function of the micro time and the wavelength channel. The identification procedure starts when the time lag between 50 consecutive counts is below 2 ms. The probabilities are accumulated for successive photons until the molecule is identified or the time lag between 50 consecutive counts exceeds 2 ms. The technique was demonstrated for the dyes Rhodamine 6G (R6G), sulforhodamine B (SRB), dibenzanthranthene (DBATT), and 1,1′-dioctadecyl-3,3,3′,3′,-tetramethylindocarbocyanine perchlorate (DiI). Identification required less than 300 photons per molecule.

Correlation of Lifetime Fluctuations

Spontaneous conformational fluctuations of biomolecules are closely related to fluctuations in the enzymatic rate constant and have therefore become subject of a large number of single-molecule experiments. The fluctuations occur in a wide range of time scales from microsec-

onds to hundreds of seconds. Conformational changes can be investigated by single-molecule FRET techniques or by optically induced electron transfer between an electron donor and an electron acceptor within the same biomolecule. The corresponding changes in the fluorescence can be investigated by BIFL techniques, FCS, or by recording photon counting histograms within different sampling time intervals. Direct information about the rate of the fluctuations can be obtained by correlating fluorescence lifetimes obtained from single molecules within millisecond sampling time intervals. The technique was demonstrated by Yang et al. [1360]. The lifetime changes were attributed to electron transfer between FAD and nearby residues, such as Trp and Tyr. For every 100 photons a fluorescence lifetime was obtained by a maximum likelihood estimation. The lifetimes were converted into electron transfer rates and distances, which were correlated subsequently. A similar experiment with electron transfer in a fluorescein-tyrosine pair within a single protein complex was described in [873].

Photon Counting Histograms

The photon counting histogram (PCH) of an optical signal is obtained by recording the photons within successive sampling-time intervals and building up the distribution of the frequency of the measured counts versus the count numbers. For a light signal of constant intensity the PCH is a Poisson distribution. If the light fluctuates, e.g. by fluctuations of the number of fluorescent molecules in the focus of a laser, the PCH is broader than the Poisson distribution. A characterisation of the PHC was given in 1990 by Qian and Elson [987]. The technique is also called fluorescence intensity distribution analysis, or FIDA. The principle is explained in Fig. 923.

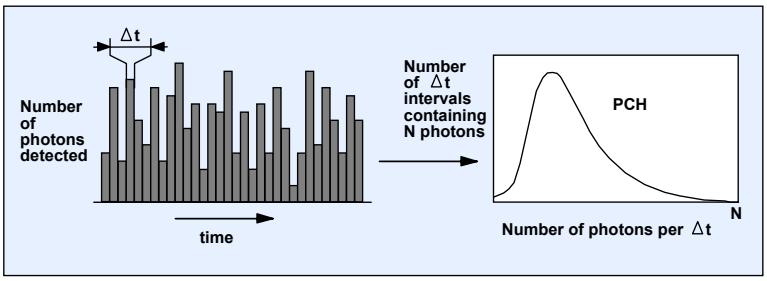


Fig. 923: Photon counting histogram. Left: Photons counted in successive sampling time intervals. Right: Histogram of the number of time intervals containing N photons

The optical setup for PCH experiments is the same as for BIFL, MFD, or one-photon or two-photon FCS. The sample is excited by a laser through a microscope objective lens. The effective sample volume is confined to a few femtoliters by two-photon excitation or by confocal detection. PCH recording requires a high-efficiency detector and a multichannel scaler that records either the photon counts in successive time bins or the time-tag data for the photons.

The optimum sampling time interval depends on the time-scale of the fluctuations and is usually in the 10 µs to 1 ms range. Recording directly into fixed time bins yields relatively compact data sets. Time-tag recording yields more flexibility and is usually preferred. Time-tag data can be used to calculate several PCHs in different sampling time intervals, and to calculate FCS curves and PCHs from the same data. A photon counting device for PCH measurement is described in [430].

The PCH delivers the average number of molecules in the focus and their molecular brightness. Several molecules of different brightness can be distinguished by fitting a model containing the relative brightness and the concentration ratio of the molecules to the measured PCH. The technique is also called ‘fluorescence intensity distribution analysis’, or FIDA. The theoretical background is described in [289, 290, 646, 648, 895, 938, 939, 987].

The PCH/FIDA technique can be extended for two-dimensional histograms of the intensity recorded by two detectors in different wavelength intervals or under different polarisation. 2D FIDA delivers a substantially improved resolution of different fluorophores [647, 648]. Further improvement is achieved by using pulsed excitation and using the fluorescence lifetime as an additional dimension of the histogram. The techniques is termed 'Fluorescence Intensity and Lifetime Distribution Analysis' or FILDA [648, 938]. Of course, accurate lifetimes cannot be obtained from the small number of photons within the individual sampling time intervals. However, useful lifetime information may be obtained from the photon arrival times in the laser period averaged over the sampling time interval. The average arrival time is directly related to the first moment of the decay function and therefore to the fluorescence lifetime.

FIDA, 2D-FIDA and FILDA do not directly deliver information about the diffusion times of the fluorescent species. Diffusion times can, however, be obtained by calculating the PCHs in different sampling time intervals and fitting the result with a model that contains both the molecular brightness and the diffusion time [648].

In principle, FIDA, 2D-FIDA, and FILDA are possible by using any bh TCSPC module that has the FIFO mode implemented. The data recorded in the FIFO mode contain the individual arrival time of each photon in the laser pulse sequence, the time from the start of the experiment, and the number of the detector that detected the photon. Thus, both decay curves, FCS curves and PCHs can be calculated from these data. The PCHs can obtained for each individual detector and for virtually any sampling-time interval. Data measured at a solution of Rhodamine 6G molecules attached to a protein are shown in Fig. 924.

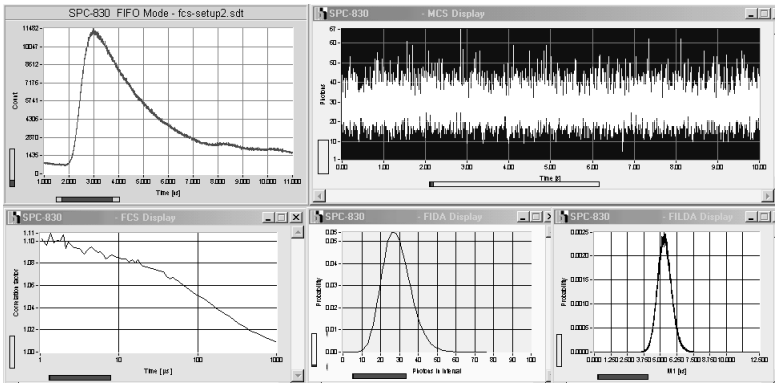


Fig. 924: Decay curve, intensity (MCS) trace, FCS curve, photon counting histogram and lifetime histogram for a Rhodamine 6G solution. Sampling times for photon counting and lifetime histograms 1 ms, time per channel of MCS trace 1 ms. Two-photon excitation, SPC-830 TCSPC module with SPCM software, acquisition time 490 s, count rate $28 \cdot 10^3$ s^{-1}.

Fig. 925 shows distributions of the average photon arrival time for different sampling time intervals. The average arrival time is identical with the first moment of the photon distribution and, except for a constant offset, represents the fluorescence decay time. The width of the distribution contains both the statistical variance of the arrival time and the real inhomogeneity of the lifetimes of the molecules. If the sampling time is reduced, the number of photons per time interval decreases, and distribution of the arrival time becomes wider. For very small sampling time intervals most of the time intervals contain either no photon or one photon. The distribution of the arrival time then converges into the fluorescence decay curve. Multi-exponential analysis of the decay curve is, in principle, a second way to reveal inhomogeneity of the lifetimes.

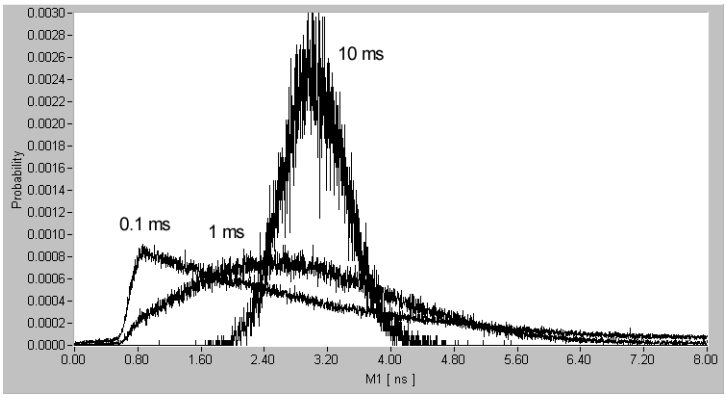


Fig. 925: Distribution of the first moment, M1, of the photon arrival times, calculated from TCSPC time-tag data. Sampling time interval 100 µs, 1 ms, and 10 ms. SPC-830 TCSPC module, count rate 3000 photons per second.

Although TCSPC is used successfully for BIFL experiments, little has been published about applications for FIDA. The reason is probably that the dead time of TCSPC is considered a drawback. However, a simple consideration shows that the detectable burst rate is not substantially reduced by the dead time of the TCSPC device. The commonly used detectors lose 50% of the photons at an input rate of about $16 \cdot 10^6$ s^{-1} [967], fast TCSPC modules (SPC-140/144) at $10 \cdot 10^6$ s^{-1}. This means the dead time of the TCSPC module is only slightly shorter than the dead time of the detector. The use of TCSPC for PCH experiments therefore does not result in a considerable increase of dead-time-related errors. Moreover, BIFL applications have shown that the burst count rates are well within the counting capability of TCSPC.

Other TCSPC and FLIM Applications

FLIM of Semiconductors

Charge-Carrier Lifetime in Semiconductors

Semiconductors with direct recombination emit luminescence when the charge carriers recombine. Laser-induced luminescence can therefore be used to map the charge-carrier lifetime in semiconductor materials. Kalinushkin and Uvarov [639] described the use of FLIM to map the charge-carrier lifetime in ZnSe and other direct-gap semiconductor materials. Brovelli et. al. [257] used FLIM to investigate energy transfer in semi-conducting polymers. McNeil et al. [841] used bulk fluorescence decay measurements to investigate charge transport in dye-sensitised nanoparticle films. Schultz et al. studied the influence of laser-based patterning on the carrier lifetimes in $Cu(In_x,Ga_{1-x})Se_2$ films [1083]. The optical emission from this material occurs around 1300 nm. For the experiments, a bh DCS-120 system with an id-200 InGaAs SPAD detector, an IR-modified DCS-120 scan head and an SPC-150N TCSPC/FLIM module was used. For excitation a bh BDS-SMC picosecond diode laser of 474 nm wavelength was used. The system was able to scan image with 512 x 512 pixels and 1024 time channels, or to record single luminescence-decay curves in selected positions of the sample.

Perovskite

Most applications of FLIM in semiconductor research are currently related to photovoltaic devices. In particular, there is currently an increase in research on perovskite and perovskite-like materials. Perovskite is a group of minerals based on TiO_3 in combination with calcium ($CaTiO_3$), Barium ($BaTiO_3$) or Strontium ($SrTiO_3$). The efficiency of the devices is, of course, directly related to the carrier lifetime. The longer light-induced carriers stay in the semiconductor the larger is the chance that they create an electrical current in an external electrical circuit. The carrier lifetime is reflected by the luminescence decay time which, therefore, is an indicator of the efficiency.

FLIM of Nb- and La-doped $SrTiO_3$ substrates was reported by Rodenbücher et al. [1026]. The same authors used FLIM in combination with AFM [1027] and FLIM in combination with phase contrast and fluorescence-intensity microscopy [1028] for the investigation of SrTiO3.

Time-resolved luminscence experiments are conducted either by recording decay curves in single points of a semiconductor sample or by FLIM through a microscope. Single-point measurements deliver accurate decay curves of selected spots, FLIM data show where possible defects are located, how large they are, and how frequently they occur.

For inspection of photovoltaic devices it is, however, desirable to record FLIM over a larger area than a microscope can cover. FLIM Images of appropriate size can be obtained with the DCS-120 MACRO system, see 'FLIM of Macroscopic Objects', page 439. For the data shown below we used a standard bh DCS-120 MACRO system with a 475-nm laser and a HPM-100-50 hybrid detector. The use of a hybrid detector is recommended to avoid afterpulsing. In the expected range of decay times up to a few 100 ns afterpulsing could otherwise offset the decay times considerably.

A FLIM image of a perovskite photoelement is shown in Fig. 926. The image shows one 5x5-mm element from an array of 6 similar elements. The element was operated with shorted terminals. The data were analysed with SPCImage NG. A triple-exponential model was used for the fit. The image shows the amplitude-weighted mean lifetime, tm. Fig. 926 shows a slight gradient over the area of the element but otherwise good homogeneity. The lifetime is

3.77 ns in the upper part of the element, and 4.6 ns in the lower part. Please note that these are not the intrinsic lifetimes of the Perovskite - the measured lifetimes are significantly shorter than the intrinsic values due to the short-circuit operation of the element.

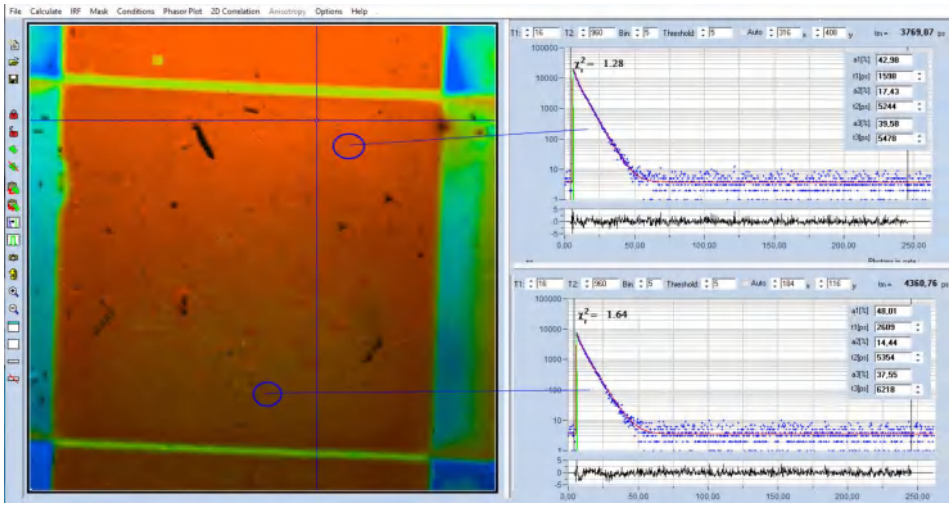


Fig. 926: FLIM image of a 5x5-mm Perovskite photoelement, short-circuit operation. Recorded by DCS-120 MACRO system, excitation 475 nm, detection from 500 nm to 900 nm. Triple-exponential decay analysis by SPCImage NG. Decay curves of two characteristic regions shown on the right. Component lifetimes and amplitudes shown as inserts in the decay curve panels.

When photoelements are used as solar cells they are neither operated short circuit nor open circuit but with a certain load across their electrical terminals. Consequently, a voltage across the terminals develops in response to the illumination. It is therefore desirable to record FLIM data as a function of voltage across the elements. Voltage-dependent FLIM can be achieved by the Mosaic Imaging function of the bh TCSPC/FLIM modules, see 'Mosaic FLIM', page 127.

The principle is illustrated in Fig. 927. The desired region of the Perovskite sample is continuously scanned by the DCS-120 system. A DDG-201 signal generator module generates a voltage for the Perovskite element. With every frame of the scan, the voltage is increased by a programmable increment. Simultaneously, the DDG-201 sends routing signals to an SPC-QC-104 TCSPC / FLIM card. These signals determine into which element of the FLIM Mosaic the photons are stored. When the last step of the voltage ramp is finished, the voltage switches back to zero, and the sequence starts from the beginning. The process is continued until a sufficient number of photons has been recorded in the FLIM Mosaic.

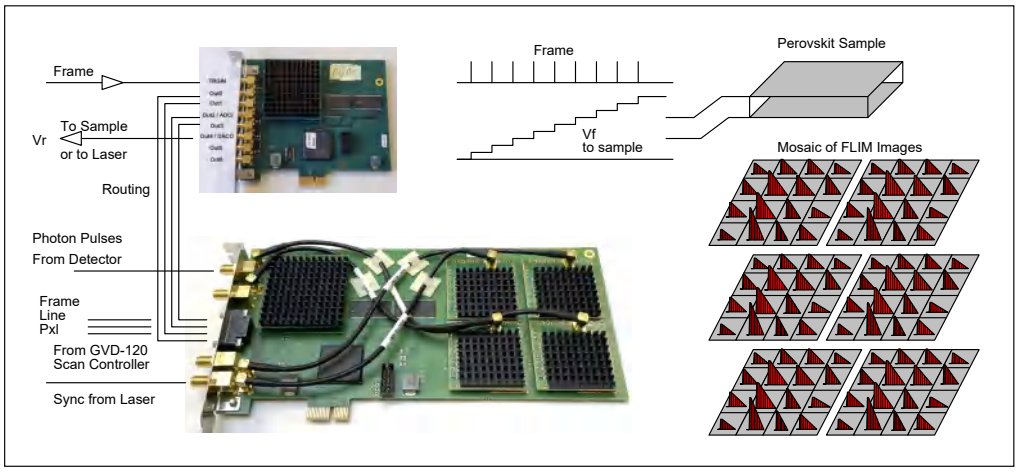


Fig. 927: Recording of voltage-dependent Perovskit-FLIM data.

A result is shown in Fig. 928. The recording starts in the lower left with DDG voltage $V_f = 0$. With every frame of the scan the recording switches to the next Mosaic element, and the voltage, V_f, increases by 60 mV. This continues until Mosaic element 16 and $V_f = 0.96$ V are reached. Then the recording switches back to $V_f = 0$ and Mosaic element 1. The process is continued until a sufficient number of photons has been recorded.

In Fig. 928 the scan range has been adjusted to scan two adjacent elements of the Perovskit sample. The left one of the two Perovskit elements gets the voltage from the DDG 201, the right element is left unconnected. This way, the change of the lifetime with the voltage can clearly be seen and compared to the open-circuit situation.

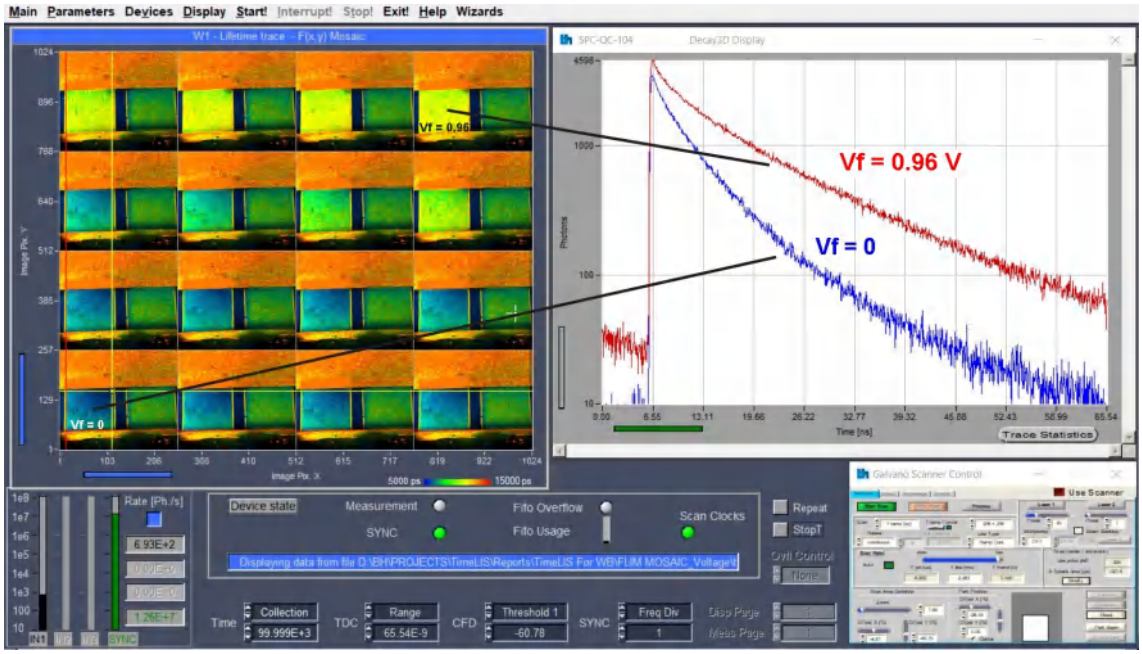


Fig. 928: Voltage-dependent Perovskite FLIM. Recording starts lower left in Mosaic element 1 with $V_f = 0$ and proceeds up to Mosaic element 16 upper right. Then it starts again in Mosaic element 1. Decay curves for Mosaic element 1 and 16 shown on the right.

Barrier Discharges

The study of barrier discharges (also referred to as dielectric barrier discharges or silent discharges) is important for understanding mechanisms of degradation and breakdown of insulators as well as the reactions in the gas of the discharge. A barrier discharge consists of a large number of micro-discharges of nanosecond duration. The investigation of the discharges is difficult: The individual discharges occur at random times, the duration of the light pulses is on the order of a few nanoseconds, and the intensity is low. Ideally, it would be desirable to record the shapes of the optical pulses as a function of the gap voltage and the distance along the gap for selectable wavelength. Exactly this task can be solved by multi-dimensional TCSPC.

Principle

The general principle of a barrier-discharge experiment [244, 584, 675, 704, 705, 706, 1308, 1309, 1310] is shown in Fig. 929. The barrier discharge occurs between two glass-coated electrodes. The electrical field between the electrodes is driven by a high-voltage transformer.

The input signal of the transformer is generated by a digital waveform generator, in this case a bh PPG-100.

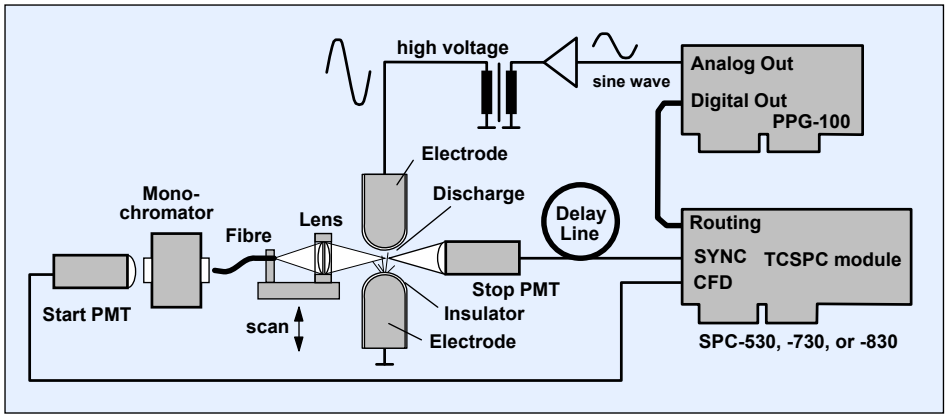


Fig. 929: Detection of barrier discharges. The pulse shape is recorded as a function of the voltage across the discharge gap, the wavelength, and the location in the discharge gap

Because the discharges occur at random times the stop signal for the TCSPC module is generated from the light pulses themselves. The stop detector is a bh PMH-100 module operated at a gain below the single-photon detection level. It delivers a timing reference signal of relatively low jitter (see 'Synchronisation to Random Signals', page 221). The pulses of the stop PMT are delayed and fed into the SYNC (stop) input of the TCSPC module.

The light from the other side of the discharge gap is focused on the input of an optical fibre and fed into a monochromator. The light of the selected wavelength is detected by the start PMT. Due to the low numerical aperture and narrow wavelength interval transmitted by the monochromator, the light intensity at the detector is much lower than at the stop detector. Therefore the start PMT detects single photons at a rate considerably lower than the average rate of the discharge pulses. The single-photon pulses are used as start pulses of the TCSPC module and processed in the ordinary way.

The waveform generator feeds a digital equivalent of the sine-wave voltage into the routing input of the TCSPC module. When a photon is detected, it is written into in a memory block corresponding to the momentary voltage and into a time channel corresponding to its time referred to the stop pulse. Therefore the TCSPC module records the photon distribution over the voltage across the discharge gap and the time within the discharge duration. A large number of such distributions are obtained sequentially by scanning the monochromator wavelength or the fibre position along the discharge gap.

An overview of typical results is given in [154]. The setup shown Fig. 929 is in use for more than 15 years, and, to our knowledge, still producing good results, please see [244, 584, 675, 704, 705, 706, 1308, 1309, 1310]. Understandably, many of the components shown in Fig. 929 have become obsolete in 15 years.

Scanning with Galvanometer Mirror

A recent implementation of the barrier discharge system is in Fig. 930. The system contains a GVD-120 scan controller card, an SPC-150, SPC-150N, or SPC-180N TCSPC FLIM module, and a DCC-100 detector controller card (not shown).

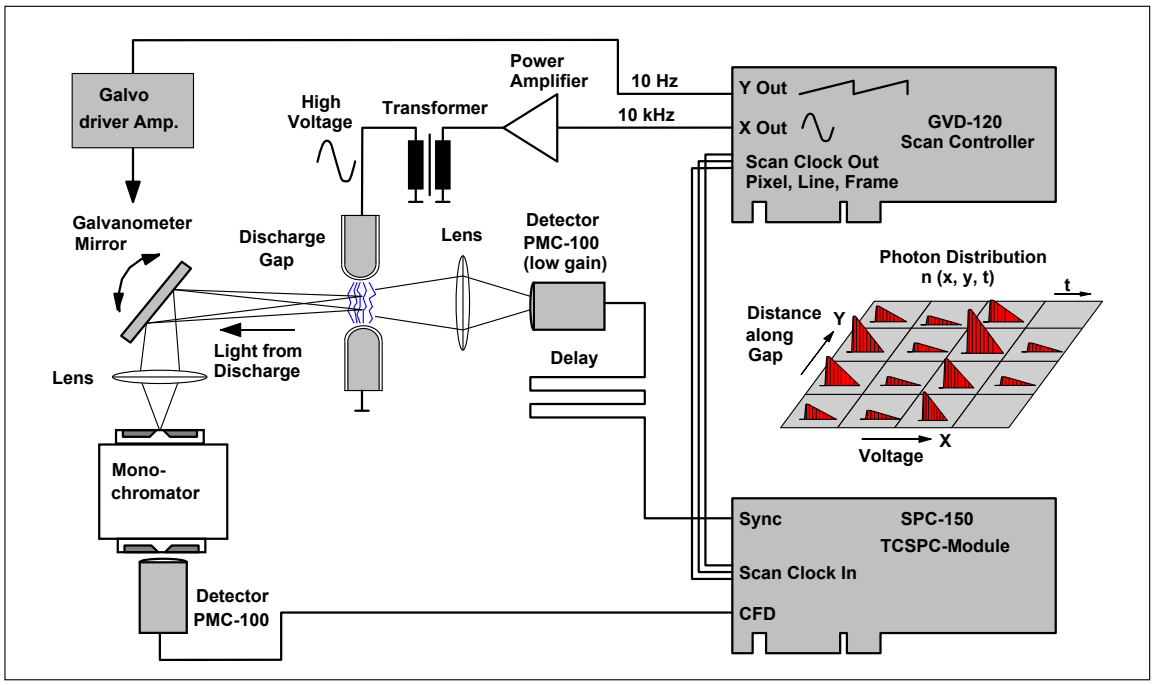


Fig. 930: Modern implementation of the barrier discharge setup. The discharge voltage is generated by a GVD-120 scan controller that also drives a galvanometer mirror. The SPC-150 FLIM module records a photon distribution over the voltage across the discharge gap, the distance along the gap, and the times of the photons within the optical pulses.

The X output of GVD-120 card delivers a sinusoidal output voltage. The voltage is amplified, transformed to a voltage in the 10 kV range, and applied across the discharge gap. The Y output of the GVD-120 drives a galvanometer mirror. The galvanometer mirror periodically scans the spot from which the light is detected along the discharge gap. A monochromator selects the desired detection wavelength. Single photons of the selected signal are detected by a PMT module. The photon pulses are connected to the start input of an SPC-150 TCSPC module.

The stop input for the TCSPC module comes from a second PMT. This PMT detects light from the entire discharge gap in a wide spectral range. For every discharge, it detects about 1000 photons. Operated at a relatively low gain, it delivers a timing reference for the TCSPC module. The recording process is synchronised with the operation of the scan controller via scan clock pulses from the scan controller. Consequently, the TCSPC module records a photon distribution over the phase of the gap voltage (X), the distance along the discharge gap (Y), and the times of the photons in the optical pulses generated by the discharges.

Fig. 931, left and right, shows the waveform of the optical pulses as a function of the distance over the gap integrated over the positive and the negative half-waves of the gap voltage. It can be seen that the optical pulse varies along the gap. It also differs between the positive and the negative half-wave of the gap voltage.

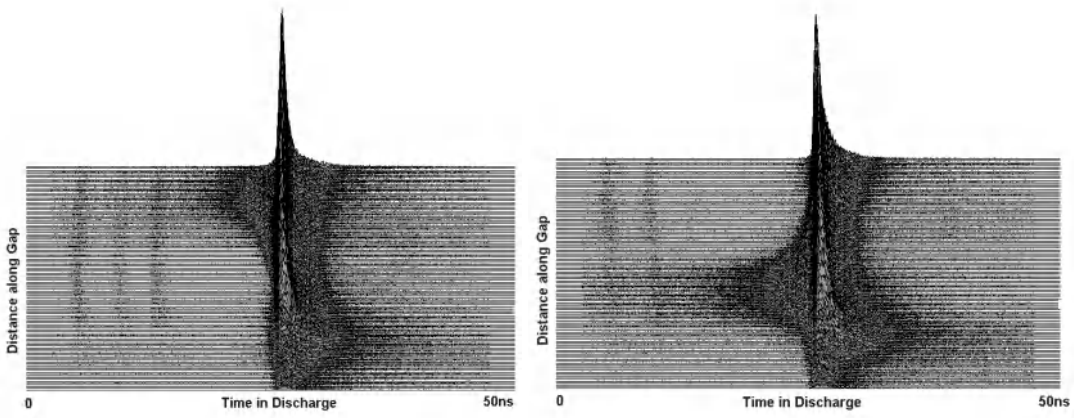


Fig. 931: Waveform of optical pulses for different distance along the gap for positive (left) and negative (right) half-wave of the gap voltage. Data courtesy of Ronny Brandenburg, INP Greifswald, Germany

Fig. 932 shows the intensity over the time in the optical pulse and the distance along the gap for four different phases in the gap voltage, Fig. 933 the intensity over the time in the pulse and the phase in the gap voltage for four subsequent distance intervals along the gap. The images reveal a complex behaviour of the light pulses. The shape varies both with the location in the gap and with the gap voltage at which the discharges occur. There are also pre-pulses that occur some 10 ns before the main pulse.

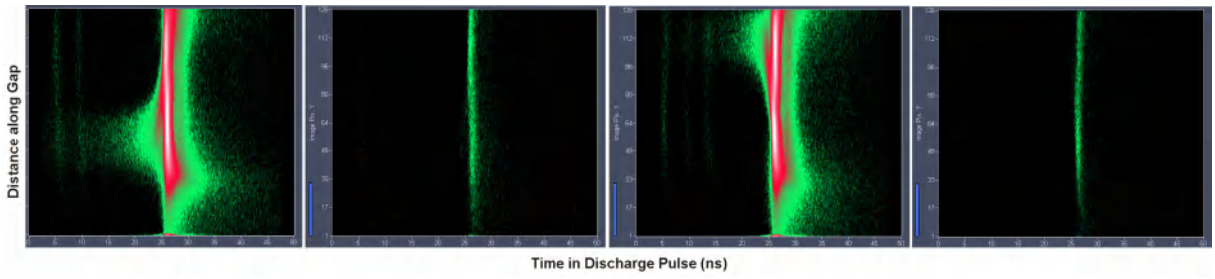


Fig. 932: Intensity over time in discharge pulse and distance along the gap for four subsequent phase intervals (quarter waves) in the gap voltage. Horizontal scale 0 to 50 ns. Data courtesy of Ronny Brandenburg, INP Greifswald, Germany

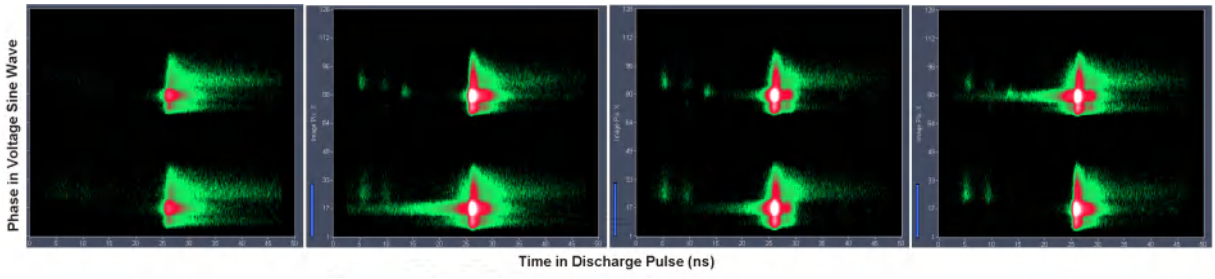


Fig. 933: Intensity over time in the discharge pulse and phase in the gap voltage for four subsequent distance intervals along the gap. Horizontal scale 0 to 50 ns. Data courtesy of Ronny Brandenburg, INP Greifswald, Germany

Similar as the other multi-dimensional TCSPC applications, the principle shown above has no inherent limitation of the rate at which an experiment parameter are modulated. This is very important for barrier-discharge measurements: The frequency of the gap voltage must be in the 10 kHz range, and matched to the resonance frequency of the transformer-gap combination. Sequential recording of the voltage-dependence - e.g. by keeping the voltage constant until enough discharges have occurred and enough photons been recorded - is therefore not an option.

Barrier-discharge systems exist in several variants. Some are using sub-sets of the principle shown above, e.g. point measurements at selected location in the gap, or slow scanning along the gap distance. Other are using two parallel TCSPC and detector channels. However, all are using the phase of the gap voltage as a parameter of a multi-dimensional TCSPC process. Please see [246, 247, 524, 585, 586, 675, 704, 705, 706, 907, 1308, 1309, 1310] for technical details and for results.

Two-Photon Excitation by Picosecond Diode Lasers

Two-photon excitation has become a standard technique in laser-scanning microscopy and fluorescence correlation spectroscopy. The excitation wavelength is twice the absorption wavelength of the molecules to be excited. Because two photons of the excitation light must be absorbed simultaneously, the excitation efficiency increases with the square of the excitation power density. The technique requires pulsed excitation with high peak power, i.e. femtosecond pulses, and focusing into a diffraction limited volume within the sample. In most cases Ti:Sapphire lasers are used for two-photon excitation [366, 1294, 1295].

Two-photon fluorescence excitation with a picosecond diode laser cannot be expected to work with the same efficiency. The average intensity is only a few mW. Moreover, the pulse duration is of the order of 100 ps, so that the peak power is many orders of magnitude lower than for a femtosecond Ti:Sapphire laser. The question whether two-photon excitation at a noticeable level can be obtained by a picosecond diode laser may therefore appear a bit academic. However, two-photon excitation by a diode laser may be reasonable, e.g. for fluorescence excitation deeply within a highly absorbent sample.

It can indeed be demonstrated that two-photon excitation by a picosecond diode laser delivers fluorescence signals that can easily be detected by TCSPC [154]. A result is shown in Fig. 934.

A bh BHLP-700 laser was used for excitation. The laser emits at a wavelength of 785 nm. The average power of the laser was adjusted to approximately 10 mW. The pulse width at this power was about 300 ps FWHM. The laser beam was focused into a 1-mm sample cuvette by a microscope objective (NA = 0.4). The relatively low NA was used to obtain a convenient working distance to the sample cuvette. The fluorescence light was detected from the back of the cuvette. 6 mm of Schott BG39 filter glass was used to block the laser light from the detector. The fluorescence light was detected by a Hamamatsu H7422P-40 photomultiplier module connected to a bh SPC-730 TCSPC module.

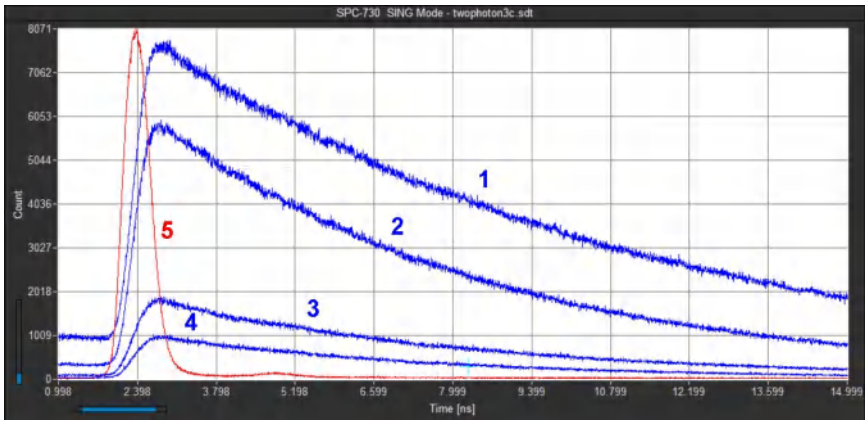


Fig. 934: Fluorescence decay curves obtained by two-photon excitation. 1) Rhodamine 6G, 10^{-3} mol/l in ethanol, 2) Rhodamine 6G 10^{-4} mol/l in ethanol, 3) Fluorescein Na 10^{-3} mol/l in pH 7.4 buffer, 4) Fluorescein Na 10^{-4} mol/l in pH 7.4 buffer, 5) Laser pulse

Curves 1, 2, 3 and 4 are the recorded decay functions of Rhodamine 6G, 10^{-3} mol/l, Rhodamine 6G 10^{-4} mol/l, Fluorescein 10^{-3} mol/l and Fluorescein 10^{-4} mol/l. Curve 5 is the laser pulse, detected through ND filters without the NIR blocking filters. The count rates were 4500 s^{-1}, 900 s^{-1}, 3000 s^{-1} and 400 s^{-1}, respectively. The overall acquisition time was 3000 s each. The fluorescence lifetimes are 5.4 ns and 7.9 ns for the 10^{-4} mol/l and 10^{-3} mol/l Rhodamine 6G solutions, and 4.7 ns and 5.6 ns for the 10^{-4} mol/l and 10^{-3} mol/l Fluorescein solutions. The increase of the lifetime with the concentration can be explained by re-absorption. Re-absorption is more critical for two-photon than for one-photon excitation, because locations much deeper in the sample can be excited.

The efficiency can certainly be improved by using a lens of higher NA, by using a low-pass filter with a steeper transition than the BG 39, and by matching of the laser wavelength and the absorption maximum of the fluorophores. All in all, an improvement in the detected count rate by a factor of 10^2 to 10^3 appears feasible. If this is correct, two-photon diode-laser-excited fluorescence can be detected from a large number of marker dyes in biologically relevant concentrations.

Measuring the Laser-Pulse Duration in Two-Photon Microscopes

For constant average power, the efficiency of two-photon excitation is proportional to the reciprocal square of laser pulse duration. The pulse duration is normally measured by a fs correlator, a device which overlays two fractions of the laser beam with variable optical decay and monitors the intensity of an SHG signal generated in a nonlinear crystal. The problem is that it is difficult, if not impossible, to pick up light from the focal plane of the microscope and feed it back into the correlator. The correlator therefore delivers the pulse width at the input of the scanner. The result does not reflect the pulse width in the sample plane. Kim & Vogel therefore developed a technique which is based on an SHG signal generated directly in the focal plane and its detection via the FLIM detectors [663]. The principle is shown schematically in Fig. 935.

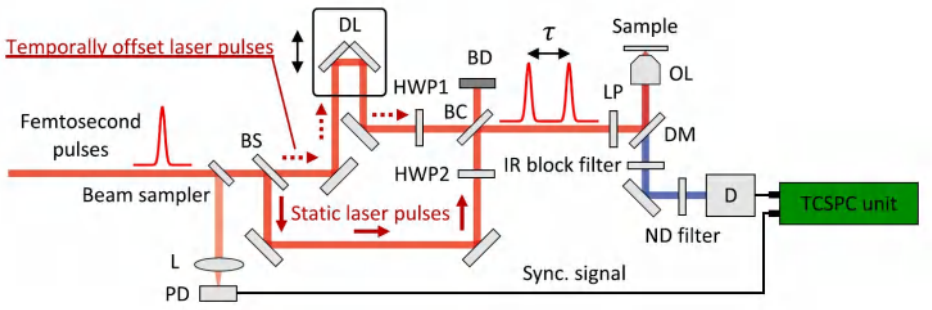


Fig. 935: Measurement of pulse duration in a two-photon microscope. BS beam splitter, HWP half-wave plate, L lens, LP linear polariser, DL delay line, D FLIM detector, PD reference photodiode, BC beam combiner, OL objective lens, DM dichroic mirror, BD beam dump. From [663].

The laser beam is split in two parts, marked 'Static laser pulses' and 'Temporally offset laser pulses'. Both are combined by a beam combiner, BC. The combined beam excites SHG in the sample. The SHG signal is detected back through the microscope objective lens, OL, and fed to the FLIM detector, D. The signal is detected by the TCSPC device. For each part of the laser beam, the waveform of the detected signal is the IRF of the detector / TCSPC combination. When the delay line, DL, is set for the two pulses to overlap the IRFs of the two channels overlap. When the delay is within the laser pulse duration, the intensity of the detected signal increases. Course adjustment (down to a 10 ps) can easily be obtained by watching the detected pulse shape. By synchronising the shift of the delay with a TCSPC recording in the

f(t,T) or f(t, ext) mode, a photon distribution over the TCSPC time and the delay time is recorded. The cross section in 'Delay' direction is the autocorrelation of the laser pulse shape, see Fig. 936. In the raw data it is overlaid by an interference pattern, which is removed by fitting the data with a Gaussian function.

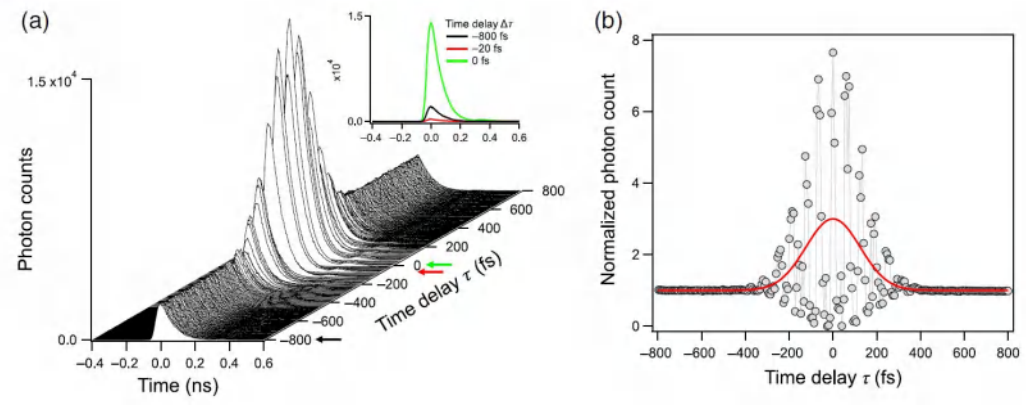


Fig. 936: (a) Time-resolved SHG curves over delay time. (b) Autocorrelation function with Gaussian fit (red curve). From [663].

Positron Lifetime Measurements

Positron lifetime measurements can be used to investigate the type and the density of lattice defects in crystals [709]. In solid materials positrons have a typical lifetime of 300 to 500 ps until they annihilate with an electron. When positrons diffuse through a crystal they may be trapped in crystal imperfections. Since the electron density in these locations is different from the density in a defect-free crystal the positron lifetime depends on the type and the density of the crystal defects.

The positrons for the lifetime measurement are conveniently obtained from the β^+ decay of ^{22}Na. In ^{22}Na a 1.27 MeV γ quantum appears simultaneously with the positrons. This 1.27 MeV quantum is used as a timing reference for the positron lifetime measurement.

When a positron annihilates with an electron two γ quanta of 511 keV are emitted. The γ quanta can easily be detected by a PMT and a scintillator. The general experimental setup is shown in Fig. 937.

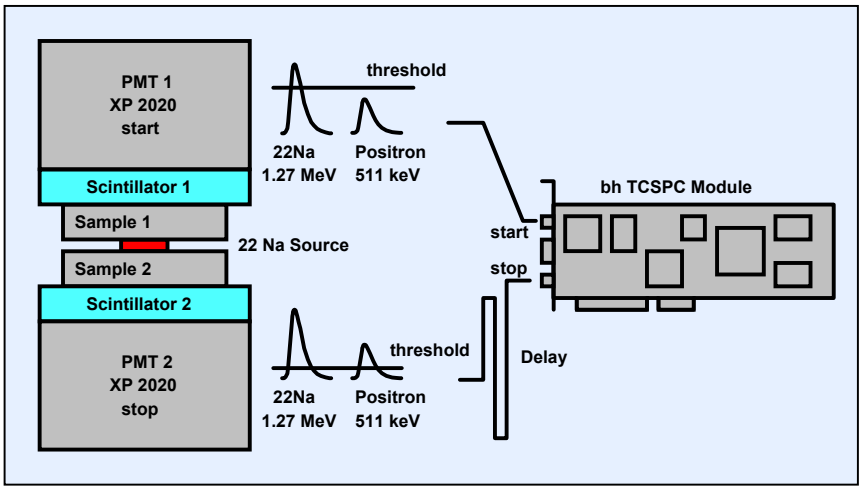


Fig. 937: Positron lifetime experiment

The ^{22}Na source is placed between two identical samples. Two XP 2020 photomultipliers equipped with scintillators are attached directly to the two samples. The pulses from the photomultipliers are used as start and stop pulses for the bh TCSPC module. The pulses from PMT 2 are delayed by a few ns so that a stop pulse arrives after the corresponding start pulse. The TCSPC module can be any SPC-x30, i.e. a module with a discriminator threshold in the SYNC channel. The amplitudes of the photomultiplier pulses are proportional to the energy of the particle that caused the scintillation. The discriminator thresholds for start and stop are adjusted in a way that the stop channel detects all, the start channel only the larger ^{22}Na pulses. The rate of the ^{22}Na events is on the order of a few kHz or below. Therefore it is unlikely that a time measurement is started and stopped by two subsequent ^{22}Na events. The by far most likely event is the detection of a ^{22}Na decay in the start PMT followed by the detection of a positron in the stop PMT. The distribution of these events gives the desired positron lifetime distribution. A typical result is shown in Fig. 938.

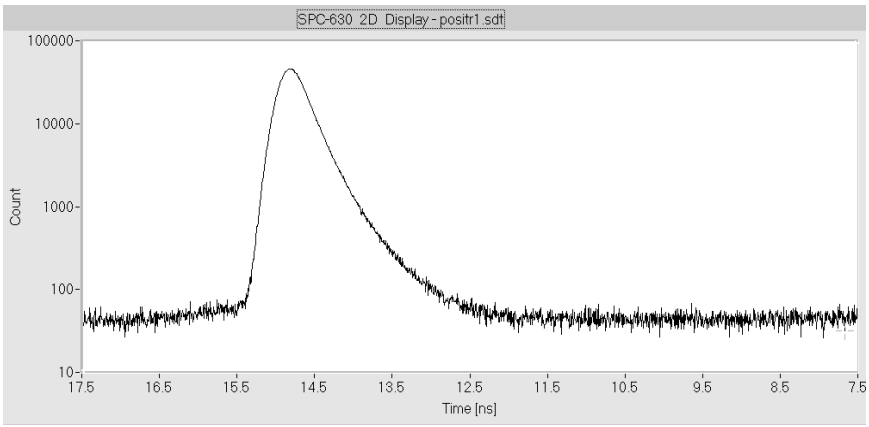


Fig. 938: Result of a positron lifetime measurement. TCSPC Module SPC-630, PMTs XP2020. Acquisition time 20 minutes

LIDAR Systems

Basic Principle

The distance to a distant objet can be measured by sending laser pulses to it, detecting light reflected or scattered at the object and determining the propagation time of the pulses to the object and back. The technique is called Light Detection and Ranging, or LIDAR. The principle is illustrated in Fig. 939.

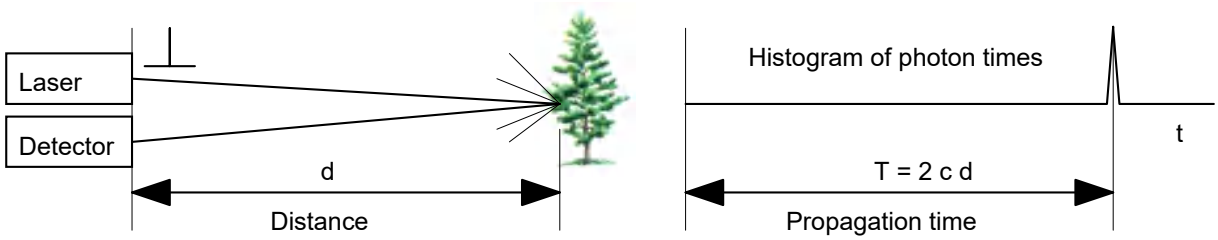


Fig. 939: Principle of LIDAR

The intensity of the light reaching the detector decreases with the distance of the object. For distances in the 100-m range and above and moderate laser power the intensity quickly drops to the single-photon level. A histogram of the photon times then shows a peak at a time $T = 2\ c\ d$ after the laser pulse, see Fig. 939, right. Time-correlated single photon counting (TCSPC) or related techniques are then the techniques of choice.

The instrument-response function (IRF) of a TCSPC-based LIDAR system is given by the convolution of the laser pulse shape, the transit-time spread function of the detector, and the electrical instrument-response function of the TCSPC device. Even with medium-speed TCSPC devices, medium-speed detectors, and picosecond diode lasers an IRF width below 100 ps (FWHM, full width at half maximum) or 40 ps (RMS, root mean square) can be reached. Ultra-fast TCSPC devices with high-speed detectors can be 5 times faster than that [122].

The actual resolution of a LIDAR experiment can be much higher. The reason is that not only one photon is used to build up the photon distribution. The standard deviation of the first moment of the propagation time distribution then decreases (and the accuracy increases) with the square root of the number of photons. For example, for a system IRF of 40 ps (RMS) and 10,000 photons the standard deviation of the transit time becomes 0.4 ps, and the standard deviation of the distance is 60 µm. With a resolution that high not only the distance can be determined very accurately, but also optical properties, such as surface texture, photon migration times within the object, or fluorescence lifetimes the can be determined.

Early Implementations

The high time resolution of the bh SPC modules in conjunction with fast detectors has been exploited to build up high-resolution ranging and three-dimensional imaging systems. A early TCSPC ranging system has been described in [261, 825, 826, 1313]. It used a 20 ps diode laser, a very fast actively quenched avalanche photodiode [338] and a bh SPC-300 TCSPC module. The photons reflected from the target and a reference pulse were recorded within the same TAC range. A slow scanning procedure was employed, i.e. the photons for one pixel of the image are collected, the time-of-flight distribution was read out from the SPC module, and then the next pixel was scanned.

The system achieved a distance repeatability of 10 µm and 30 µm for a 1 m and 25 m stand-off, respectively. The distance accuracy corresponds to a time accuracy of about 66 fs to 200 fs. The authors used a fitting algorithm [1274] which is reported to give a better timing accuracy than the usual centroid (first moment?) estimation. Although it is not clear how the statistical accuracy of the first moment can be surpassed, the high resolution is explained by the fact that the average timing jitter of a large number of detected photons decreases with the square root of the photon number. Of course, an accuracy this good can only be achieved with short laser pulses, a detector of low transit time spread, efficient cancellation of system drifts, and with a TCSPC time-channel width short enough to sample the IRF adequately.

TCSPC can also be used for ranging systems for longer distances. The application to distributed 'non-cooperative' targets are described in [260, 261, 1328]. The authors used JMCMC (Jump Markov Chain Monte Carlo) processing of the data. They were able to identify multiple targets within the instrument response function, and reflections from targets hidden below the background count level.

Another potential application of long-distance TCSPC is the measurement of target properties, such as fluorescence decay functions or photon-migration time profiles. With a suitable optical system TCSPC is able to record such signals over remarkable distances. The setup shown in Fig. 940 records the fluorescence of chlorophyll in plants over a distance of several 100 meters.

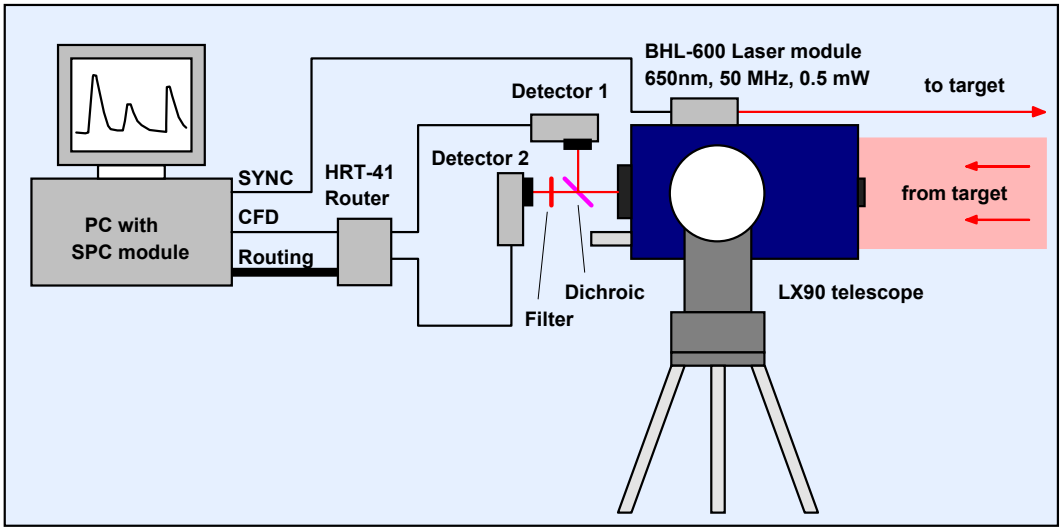


Fig. 940: Fluorescence measurement over large distance

A bh BHL-600 laser sends a beam of ps pulses to the target. The repetition rate of the laser pulses is 50 MHz, the average power 0.5 mW. An 8-inch telescope (Meade LX90 EMC) is used to collect the photons from the target. The fluorescence and the reflected light are separated by a dichroic mirror and a 700±15 nm bandpass filter and detected simultaneously by two PMH-100 detectors. Consequently, detector 1 detects the diffusely reflected laser, detector 2 the fluorescence of the leaves. Despite the low laser power chlorophyll fluorescence is detected over a distance of several 100 meters, with count rates on the order of 1000 photons per second. At a count rate this low the background signal is an important issue, which implies that reasonable results can only be obtained at night. A typical result is shown in Fig. 941.

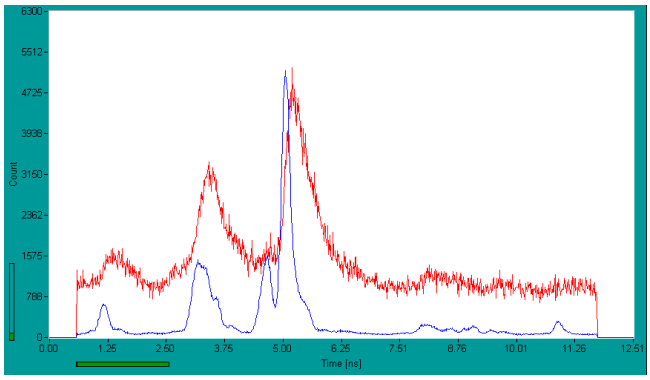


Fig. 941: Fluorescence and reflectance of leaves in a forest 300 meter away

The telescope and the laser were pointed into a forest approximately 300 m away. The red curve is the detected fluorescence, the blue curve the reflected laser. It is almost impossible to hit only one leaf over a distance this long. Therefore the signals from several leaves in different distances are detected. Moreover, the signal intensity fluctuates considerably at the scale of seconds, due to the motion of the leaves in the wind. However, because the reflectance and the fluorescence signals are detected simultaneously, the reflectance can be used as an approximation of the instrument response function to analyse the fluorescence data. This approach is not absolutely correct because the reflected photons can come from non-fluorescent target components too. It does, however, deliver fluorescence decay times of reasonable accuracy [154].

Modern Implementation of a TCSPC-LIDAR System

A modern implementation of a TCAPC LIDAR system uses the bh SPC-QC-104 module [75]. The SPC-QC-104 has an electrical IRF of 38 ps FWHM, or about 18 ps RMS. Importantly, it can record more than one photon within the start-stop time [75]. The possible detection of background photons therefore does not suppress the detection of a target photon at later times. Moreover, the time scale is locked to the frequency of an internal quartz oscillator. It thus has an absolute accuracy of a few 10 ppm. A photo of the optical setup is shown in Fig. 942.



Fig. 942: Optical setup

As a light source we used a BDS-SM 640-nm ps diode laser. The laser was pulsed externally at a repetition rate of 250 kHz. The average power at this repetition rate is less than 10 µW, the pulse energy is about 40 pJ. Photons from the target were collected by a Meade LX90 (20 cm) telescope and detected by a bh PMC-150-20 photomultiplier module attached to the eye-piece holder.

The low laser power and the low pulse energy used in our setup helps avoid laser-safety problems. However, it creates a problem with the pickup of environment light. The experiments were therefore performed at night. Even at night, light pollution turned out to be a problem. The pickup of ambient light was therefore reduced by a bandpass filter in front of the detector.

Despite the low laser power a clean signal was picked up from the target. The bump on the left is from the side-lobes of the laser beam diffusely scattered at a nearby tree, the peaks after the main peak are from trees behind the primary target.

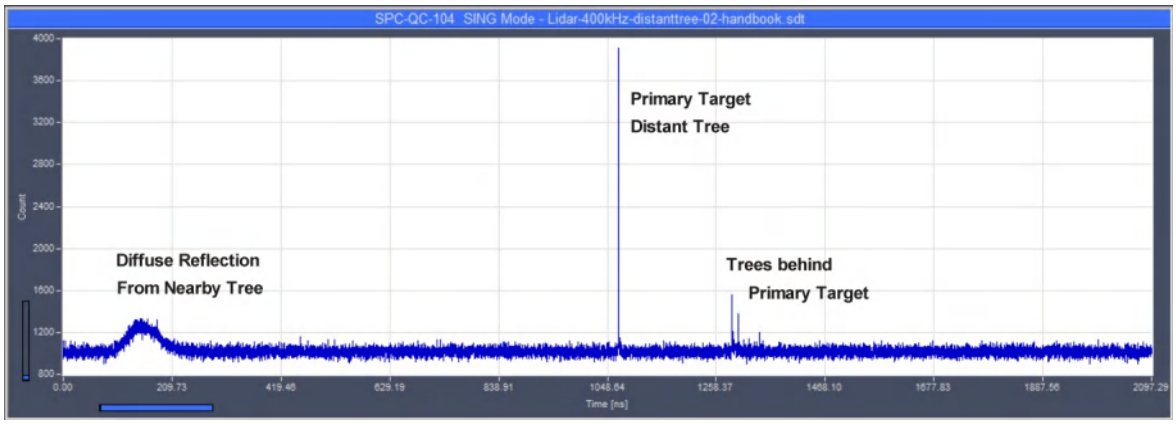


Fig. 943: LIDAR result obtained with the setup shown in Fig. 942. Laser repetition rate 250 kHz, laser pulse energy 40 pJ.

A zoom into the data around the primary-target peak is shown in Fig. 944. The time of the maximum of the peak is 1070.21 ns, corresponding to a distance of 160.53 m.

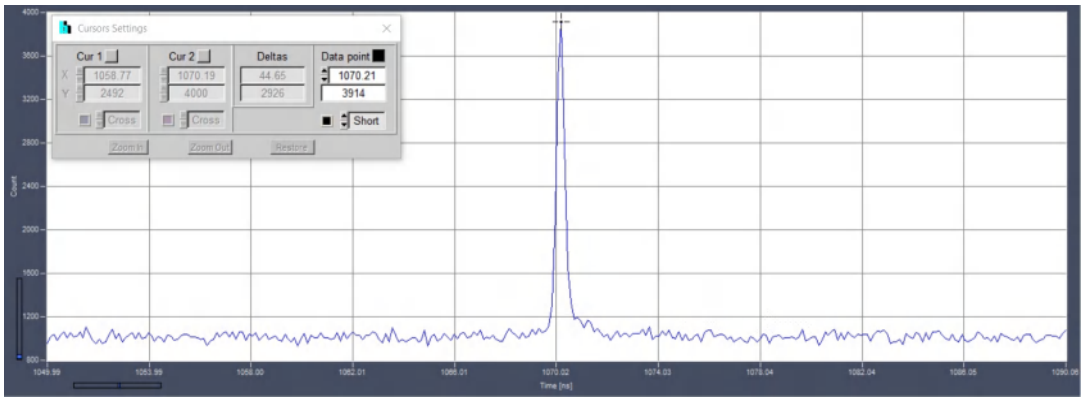


Fig. 944: Zoom into the region around the primary-target peak. The peak time is 1070.21 ns, corresponding to a target distance of 160.53 m.

The success in recording scattered light from trees over a distance of more than 160 m prompted us to try recording of fluorescence decay functions of chlorophyll over the same distance. For a given average laser power, the intensity of fluorescence is several orders of magnitude lower than that of scattered laser light. However, the loss in intensity can be compensated by increasing the laser pulse repetition rate. There is no need of low repetition rate to avoid ambiguity, as in the case of distance measurement. The laser can therefore be run at its nominal repetition rate of 50 MHz, effectively increasing the average power by a factor of

200. The bandpass filter was replaced with a 680-nm long-pass filter, and the TCSPC recording-time window decreased to 16 ns. The time-channel width was set to 4 ps, and the number of time channels to 4096. The result was striking: The count rate increased to about 300,000 photons per second, and fluorescence decay curves showed up almost instantly. An example is shown in Fig. 945.

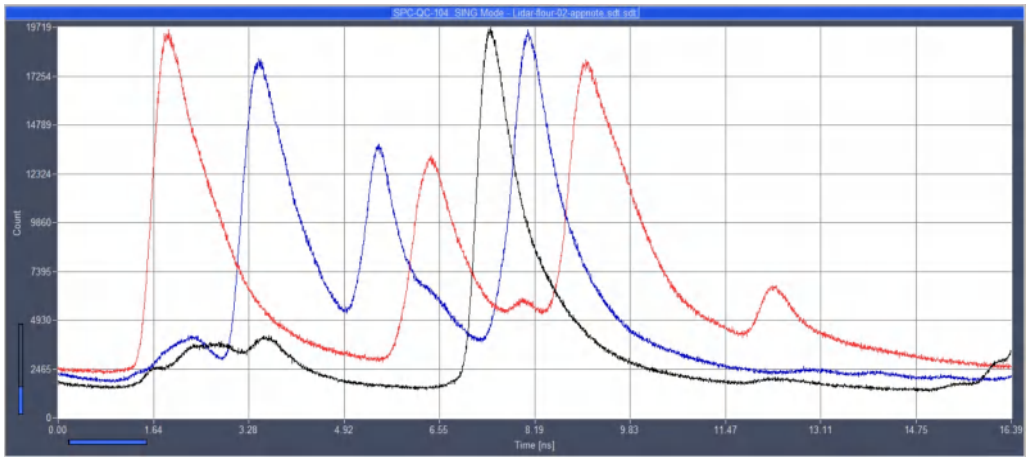


Fig. 945: Fluorescence decay curves of chlorophyll recorded from a tree 160 m away. The three curves were recorded from slightly different locations. The laser beam illuminated several leaves simultaneously, therefore several decay profiles are present in each curve.

Three curves (red, blue and black) were recorded from slightly different spatial locations. Moreover, the laser beam hit several leaves in slightly different distance. Therefore, several overlaid decay profiles are visible in each curve.

An attempt to de-convolute a decay curve with SPCImage NG is shown in Fig. 946. The black curve of Fig. 945 was sent to SPCImage NG, and the fit range restricted to the decay curve in the centre. A double-exponential model and a synthetic IRF were used for the fit. The fit of the rising edge is not perfect, probably because there are small signal contributions from leaves in different distances. Nevertheless, reasonable decay times and amplitudes are obtained. The decay components are shown in the insert in the upper right of the figure.

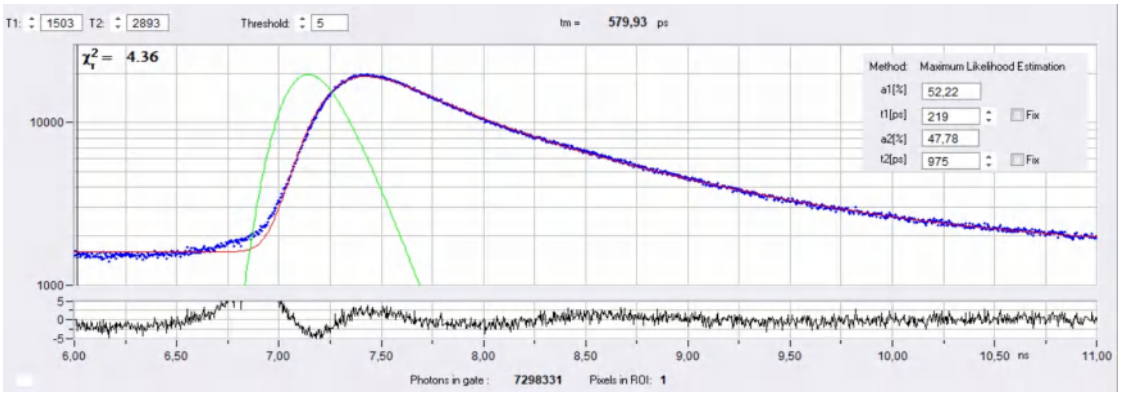


Fig. 946: De-convolution of the decay in the middle of the black curve in Fig. 945. Double-exponential model, synthetic IRF. Decay components shown in the insert upper right. The green curve is the IRF.

The decay times of the two components are $t_1 = 219$ ps and $t_2 = 975$ ps, the amplitude-weighted lifetime is tm = 580 ps. This is a short lifetime for chlorophyll. The short lifetime explains by the fact that the leaves are fully dark adapted, and the excitation power density is extremely low. Under these conditions, the photosynthesis channels are fully open, and the fluorescence is quenched by photosynthesis reactions.

Characterisation of Detectors

Measurement of the IRF of a Detector

The IRF of the detector is the limiting factor of the time resolution of a TCSPC system. How fast a TCSPC device is ever used for the experiments - the IRF of the system cannot be faster than the IRF of the detector. Detectors are usually not characterised by their IRF but by their transit-time-spread function, or TTS. Both are identical, but there are subtle differences: The TTS function is normally described by the root-mean square (rms) of the transit-time jitter, the IRF is described by its full width at half maximum (fwhm). For typical shapes of the TTS function or IRF the rms value is 2.5 to 1.7 times smaller than the fwhm value. Please keep this in mind when comparing detector (and TCSPC!) specifications. Some manufacturers use rms values for the IRF width to make their devices look better.

A typical setup for detector-IRF measurement is shown in Fig. 947. IRF measurement requires a laser with a pulse width much shorter than the TTS to be measured, and a TCSPC module with an electrical IRF much shorter than the TTS. In most instances, that means a femtosecond laser has to be used. A diode laser is not fast enough for most TCSPC detectors. The laser beam is attenuated by a package of ND filters and pointed to the active area of the detector.

On the recording side, a fast TCSPC module must be used, e.g. the SPC-150 NX or the SPC-180 NX, or the even faster SPC-150 NXX or the SPC-180 NXX. These modules have an electrical IRF width of 2.5 to 3.5 ps (fwhm), and a time channel width of 200 to 400 ps. With these parameters, the IRF of virtually all detectors is reasonably resolved.

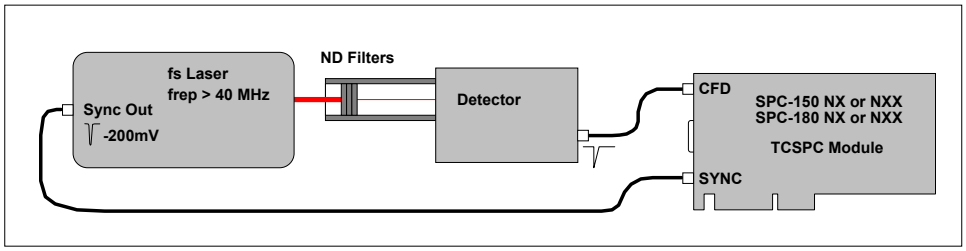


Fig. 947: Setup for IRF (TTS) measurement

IRFs for a variety of detectors measured in this setup are given in the detector chapter of this book. An IRF for a fast hybrid detector is shown in Fig. 948.

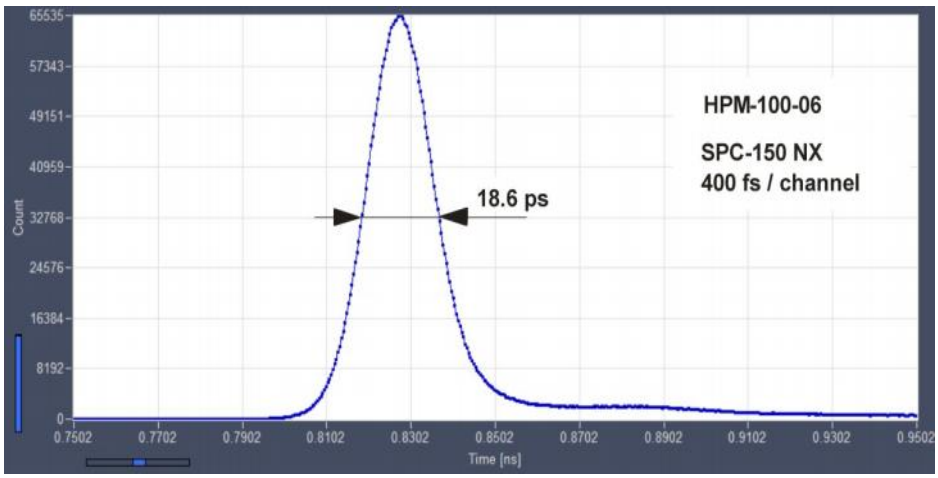


Fig. 948: IRF (TTS) of a bh HPM-100-07 hybrid detector

Although TTS measurement is more or less straightforward there is room for number of mistakes:

Don't use optical fibres in the measurement setup. Pulse dispersion in one meter of a multimode fibre can be as large as 100 ps. If you want to test detector with a fibre-connector input, inject the laser bean directly in the connector.

Make sure you illuminate the active area in the same configuration as used in the final experiment setup. The TTS depends on the illuminated area.

Use a wavelength close to the wavelength the detector will be used at in the final experiment. Don't use a wavelength outside the normal sensitivity range of the detector.

Don't use lasers with low repetition rate, or, if you have to, be extremely careful with the intensity. If the pulse intensity is too high every electrical output pulse contains a large number of photons. A TTS measured under these conditions would be entirely wrong.

Spatially Resolved Characterisation of SPADs

SPAD detectors are increasingly used in TCSPC applications because they have high detection quantum efficiency and low transit time spread. However, the typical diameter of the active are is on the order of 20 µm to 100 µm only. The full performance of a SPAD can therefore only be exploited if the light is focused on an extremely small area. In practice, the size and the location of the focused spot on the diode chip may change due to alignment errors, variation of optical properties of the sample, or pinhole size and scanner position in a confocal scanning system. It is therefore important to know by how much the sensitivity and the IRF shape of a SPAD vary across the active area.

Experiment Setup

A setup for spatially resolved characterising SPAD detectors is shown in Fig. 949. The setup uses the bh DCS-120 confocal scanning FLIM system [68], see page 32 of this handbook.

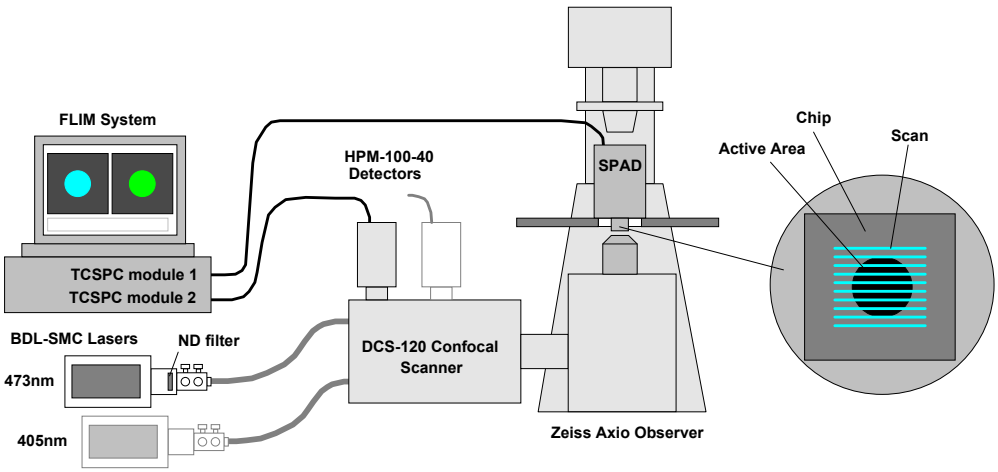


Fig. 949: Experiment setup. The SPAD is placed in the focal plane of a DCS-120 confocal scanning FLIM system. The laser beam scans the active area of the SPAD. One FLIM detector is disconnected from its TCSPC module, and the SPAD is connected instead of it. The TCSPC module thus records an image of the active area of the SPAD via the SPAD's own output. The image contains an IRF for each pixel of the image.

The SPAD chip is scanned by the focused ps diode-laser beam of the DCS-120 system. One of the two detectors of the DCS system is disconnected from its TCSPC module. Instead, the output of the SPAD is connected to this module. The corresponding FLIM channel thus re-

cords an image of the active area of the SPAD via the SPAD's own output. The images obtained this way contain the local IRF of the SPAD at the pixel position.

For the experiments described here we used the 473 nm laser of the DCS system. Of course, the intensity of the laser is far too high to be directly detected by a SPAD. An additional ND filter must therefore placed in the input collimator of the laser fibre.

Spatial Distribution of Sensitivity and IRF Shape

An image of the active area of an id-100-50 epitaxial SPAD (50-µm, id Quantique) is shown in Fig. 950. The brightness of the pixels corresponds to the number of photons detected, the colour shows the first moment of the IRF.

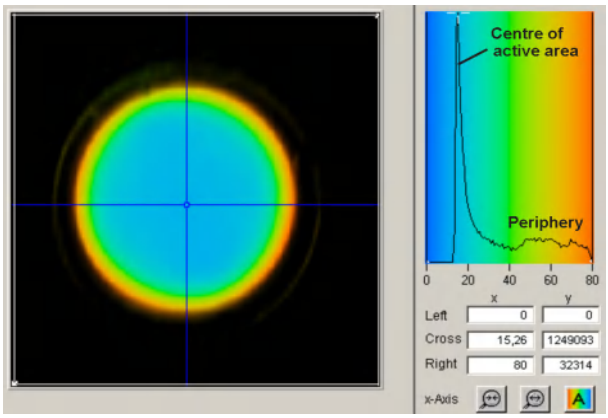


Fig. 950: Active area of a 50 µm epitaxial SPAD. The colour shows the first moment (M1) of IRF, the intensity shows the number of detected photons. The distribution on the right is the frequency of pixels of a given M1, multiplied by the corresponding photon numbers.

The sensitivity is surprisingly uniform within the entire active area. The temporal response is less stable. The first moment of the IRF is uniform up to a radius of 90% from the centre but changes by about 40 ps in the outer parts of the area.

More detailed diagrams are shown in Fig. 951. The intensity plot (shown left) confirms the uniformity of the sensitivity over the active area. The IRF plots (middle and right) show that the IRF shape is indeed stable up to the last 10% to the rim. Then it gets broader and shifts to later times. There is also some sensitivity entirely outside the active area, probably due to scattered light.

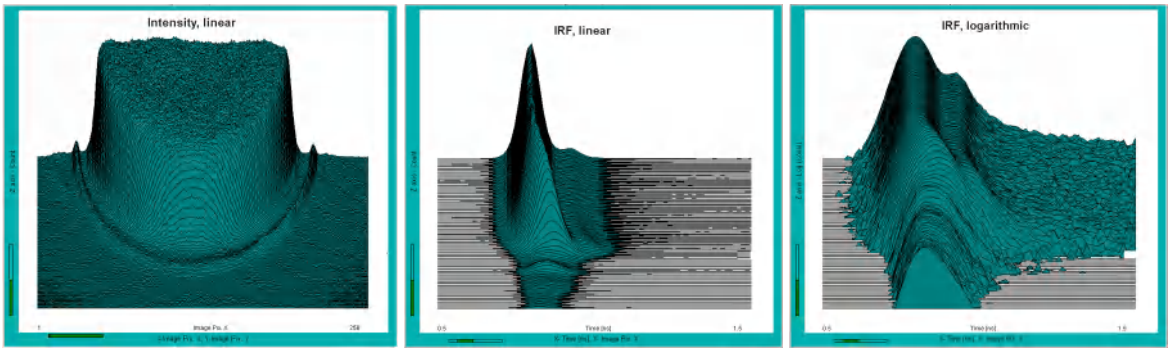


Fig. 951: Left: Sensitivity for lower half of the active area. Middle and right: IRFs over a stripe 8 pixels wide, going from the front of the scan area to the centre of active area. Displayed time interval 1 ns wide. Middle linear scale, right logarithmic scale.

Light Emission from SPADs

SPADs are known to emit light during the avalanche breakdown. This 'breakdown flash' can be a problem in correlation experiments [154], and is a potential weakness of quantum cryptography systems [728, 1273]. The intensity and duration of the light emission is therefore another parameter that should be known.

Light emission can be measured in a start-stop setup as shown in Fig. 952. The SPAD is illuminated by an attenuated laser beam. Emission from the SPAD is reflected towards a PMT module via a dichroic (or partially reflecting) beamsplitter. Scattered laser light is blocked from the PMT module by a long-pass filter. The SPAD pulses are used as stop (SYNC) pulses for the SPC module. The setup thus records the waveform of the breakdown emission of the SPAD, see Fig. 952, right.

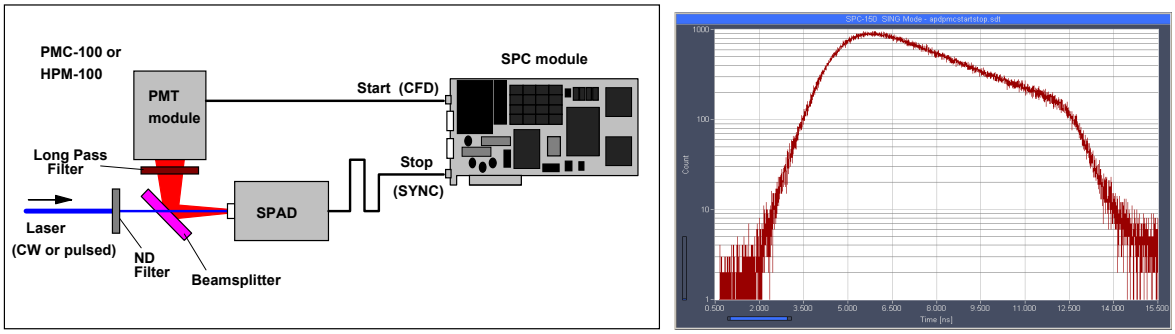


Fig. 952: Measurement of breakdown emission from a SPAD. Left: TCSPC setup. Right: Breakdown emission from an SPCM-AQR SPAD. Logarithmic intensity scale, Time scale 500 ps / div.

Light emission from a SPAD can also be measured in the scanning setup shown in the paragraph above, see Fig. 949. The active area of the SPAD is scanned by an attenuated laser beam, and an image is taken through one of the confocal detectors of the DCS-120 system. Results for an id-100-50 SPAD are shown in Fig. 953. The confocal images were taken through a 600 - 660 nm bandpass filter. The left two images were recorded with the SPAD being turned on, the two right images with the SPAD turned off.

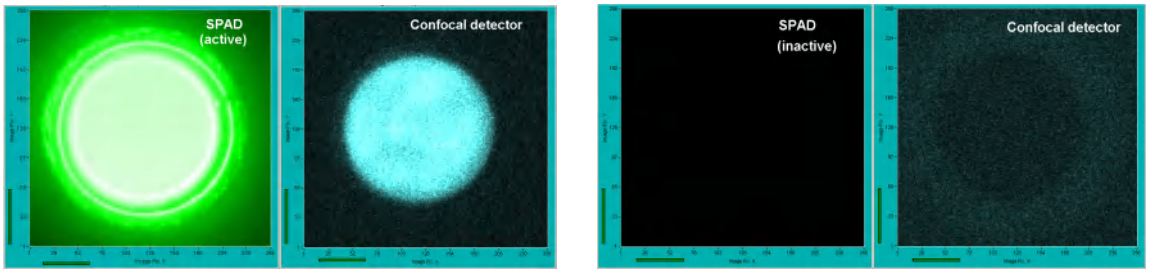


Fig. 953: Light emission from SPAD. Left two images: SPAD turned on, image delivered by SPAD, and image delivered by confocal detector. Right two images: SPAD turned off. Count rate of SPAD 4 MHz, acquisition time 180 seconds.

The fact that the confocal detector detected a signal from the active SPAD, but no signal from the inactive one indicates that there was indeed breakdown emission. However, it was surprisingly weak. Although the SPAD was operated near its maximum count rate, an average of only 40 photons per pixel was recorded within an acquisition time of 180 seconds. The emission was thus far weaker than reported for an SPCM-AQR deep-junction SPAD [728]. The reason may be the thinner depletion layer and faster quenching of the epitaxial SPAD. It should also be noted that we recorded the emission through a diffraction-limited pinhole, i.e. from the illuminated spot only. It is not known how far the breakdown avalanche spreads out

laterally. It is possible that the avalanche region is larger than the region from which the light passes the pinhole.

The temporal shape of the breakdown emission is shown in Fig. 954. The duration is much shorter than for the SPCM-AQR (less than 500 ps). The first moment, M1, of the pulse is relatively uniform over the active area.

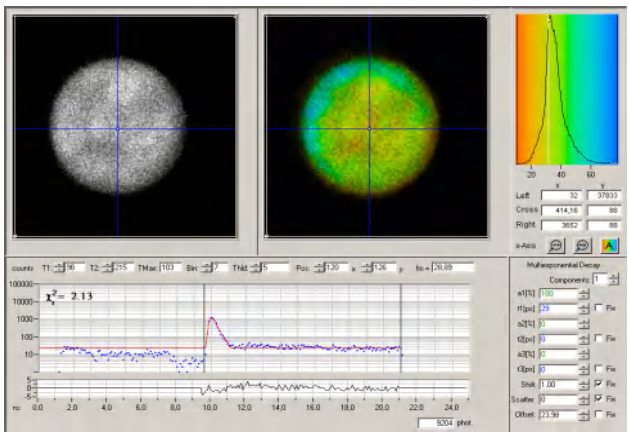


Fig. 954: Light emission from id-100-50 SPAD. Intensity image, M1 image, and waveform at the cursor position.

Measurement of Absolute Detector Quantum Efficiency

A technique for measuring the quantum efficiency of a photon counting detector without a calibrated reference detector was described in [731, 861, 862, 863, 997, 1329]. The technique is based on the generation of photon pairs by parametric downconversion. The principle is shown in Fig. 955.

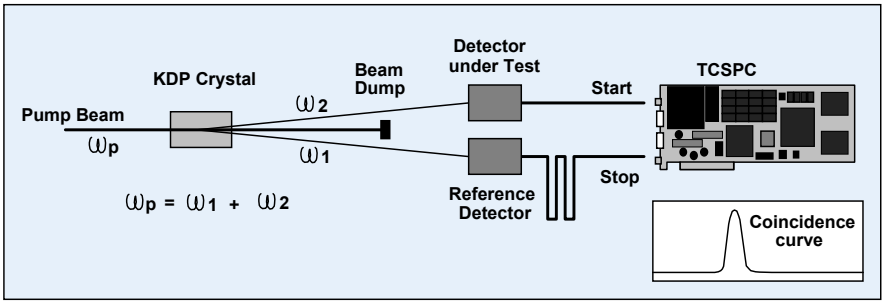


Fig. 955: Absolute measurement of the detector quantum efficiency by parametric down-conversion

A NUV laser pumps a KDP (potassium dihydrogen phosphate) crystal. Down-conversion in the crystal generates photon pairs with a total energy equal to the energy of the pump photons. The photons of a pair leave the crystal in slightly different directions and can therefore be separated spatially. One photon is sent to the detector being tested, the other photon to a timing reference detector. A photon pulse from the reference detector indicates that a photon pair has been produced. The quantum efficiency of the detector being tested is the probability that it detects the other photon of the pair. The result does not depend on the efficiency of the reference detector.

Scattered pump light is blocked by interference filters in front of the detectors. These filters are the only parts of the system that need calibration. Because the transmission is in the 10 to 90% range, a highly accurate calibration is possible. Errors due to detector background and possible filter leakage are avoided by using the pulses of the detectors as the start and stop of a TCSPC device. The result is a coincidence curve that can be clearly separated from uncorrelated background signals.

Photon-Number Sensitive TCSPC

Principle

There is a number of TCSPC applications which would benefit from the ability to determine whether a detection event has been caused by a single photon, or by two or more photons. Typical examples are basic research on entangled photons, quantum key distribution, and development of single-photon light sources. The ability to distinguish between one or several simultaneously detected photons may also help suppress background in LIDAR experiments.

In principle, the amplitude of the output pulses of a (linear) high-gain detector bears information on the number of photons that caused a particular pulse. Several photons detected at the same time generate several photoelectrons, which, in turn, cause a larger output pulse. Unfortunately, classic PMTs and MCP PMTs deliver a single-photon pulse amplitude spectrum much wider than 1:2. That means, the amplitude of a single pulse cannot be used to determine the number of photons.

The options to distinguish multiphoton detection events are much better for hybrid detectors. The pulse-amplitude spectrum of the output pulses is much narrower than for a classic PMT (see Fig. 341, page 220). Output pulses for one, two, three or even more simultaneously detected photons stand out clearly in the amplitude spectrum [751]. Hybrid detectors are therefore promising candidates as detectors for photon-number-sensitive TCSPC.

Routing by Photon Number

To obtain photon-number-sensitive TCSPC the 'Routing' technology described at page 116 of this book is used. However, the router is modified so that the destination of the photons is not determined by the source channel of the individual photon pulses but by their amplitude. The principle of a 'photon-number router' is shown in Fig. 956. The router splits off a part of the detector signal, amplifies it, and feeds it into several discriminators, D1 to D4. The discriminators are operated at different reference voltages. The voltages are adjusted in a way that D1 responds if the input amplitude corresponds to one photon, D2 if the amplitude corresponds to two photons, and so on. The discriminators are very fast (<1 ns) so that several photons detected in intervals of a few ns are not interpreted as multi-photon events. The discriminator outputs are encoded to form a routing signal that indicates how many photons a particular detection event contained.

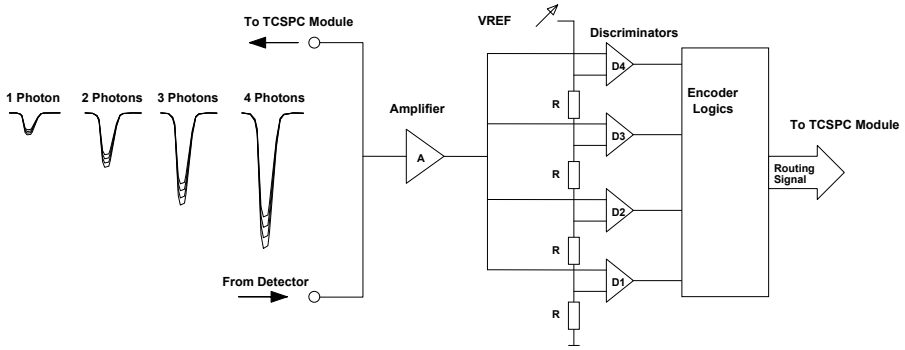


Fig. 956: Principle of Photon-number-sensitive routing

Test Result

A BDS-405 ps diode laser, an HPM-100-07 hybrid detector, a routing device of the principle shown in Fig. 956, and an SPC-150N TCSPC module were used to test the principle. The detector gain was changed to obtain different pulse amplitudes, simulating the simultaneous

detection of one, two, three, and four photons. The result is shown in Fig. 957. The detector pulse amplitude increases from top to bottom, the routing channel increases from left to right.

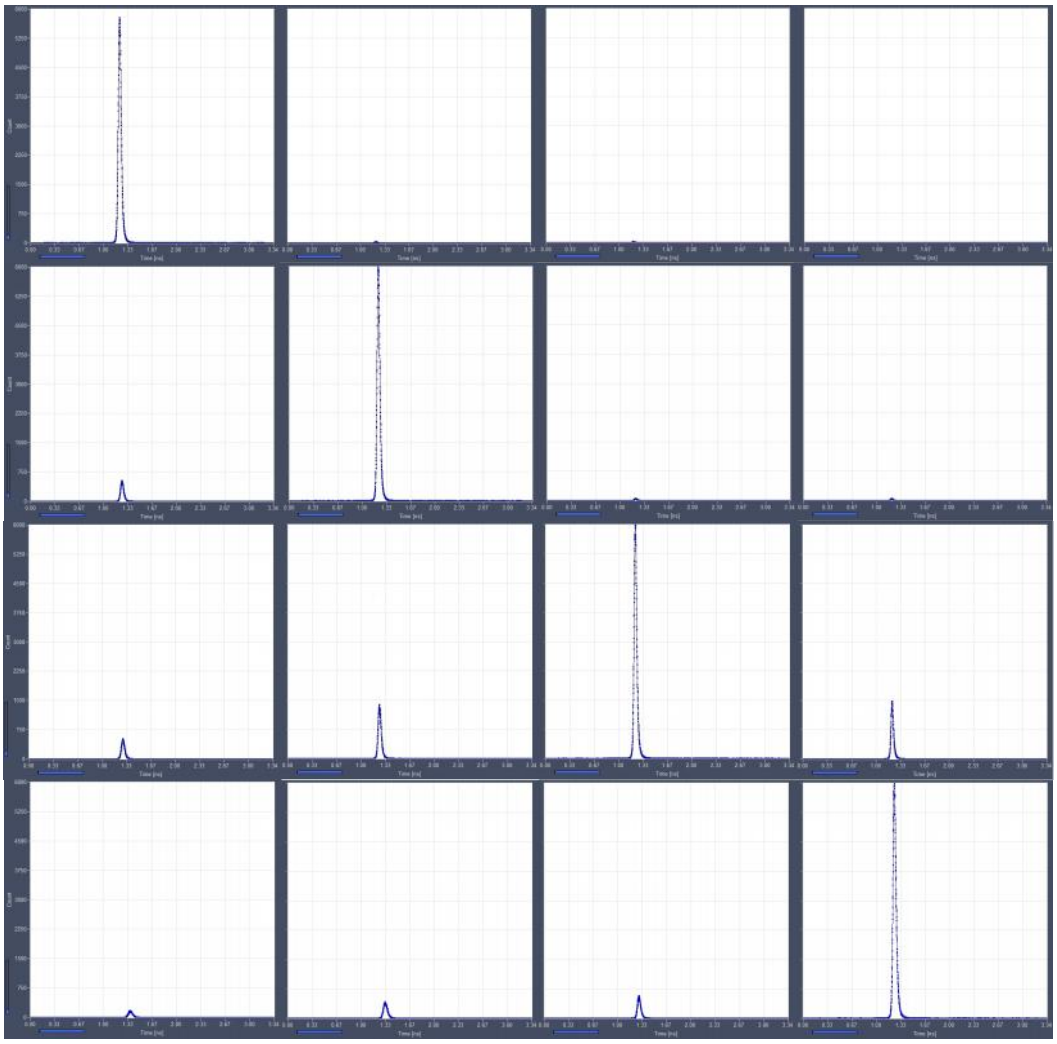


Fig. 957: Test results obtained with bh HPM-100 hybrid detector and SPC-150N TCSPC module. Detector gain changed to simulate different photon number. The detector pulse amplitude increases from top to bottom, the routing channel increases from left to right. Light pulses from BDS-405 nm picosecond diode laser.

It can be seen that the detected pulse shifts through consecutive routing channels with increasing amplitude of the photon pulses. The results show that photon-number-sensitive routing is able to distinguish between detector pulses with amplitudes corresponding to one, two, three, and four photons. So far, we had no chance to test the device with real photon pairs or other multiphoton events of known photon number. Since it is known that the hybrid detector translates photon number into pulse amplitude, there is no doubt that real multiphoton-detection events can be identified by the device. It should be noted, however, that identifying multiphoton *detection events* is not the same as identifying *photon multiples in the light signal*. The detection efficiency for every photon is less than one. Currently, it is about 50% for the best photocathodes (GaAsP). That means the probability to correctly distinguish a photon pair from a single photon in the incoming light is 50% at best. Therefore some calibration of the system may be required to quantitatively determine the true fraction of photon multiples.

Optical Oscilloscope

At a count rate of 10^5 to 10^6 photons per second a reasonably accurate waveform is recorded within less than 100 ms. All bh TCSPC modules can therefore be used as optical oscilloscopes. A repetitive measurement cycle is performed in short intervals and the recorded photon distribution versus time is displayed. Even with a low-cost PMT module, e.g. the Hamamatsu H5783, an IRF width of about 150 ps is achieved; SPADs yield an IRF width of about 40 ps. These IRF widths correspond to signal bandwidths of about 2 GHz and 9 GHz, respectively. The time channel width can be made as short as a picosecond, which results in an equivalent sample rate of 1000 GS/s.

Fig. 958 shows an example of a TCSPC oscilloscope measurement. The fluorescence of chlorophyll in a leaf was recorded at a count rate of $4{\cdot}10^6$ photons per second and an acquisition time of 100 ms. Two successive traces were overlaid to reproduce the visual impression.

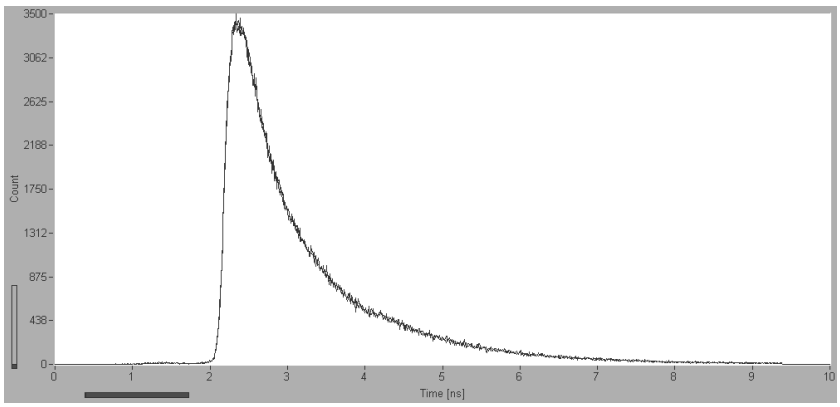


Fig. 958: Fluorescence signal recorded in the oscilloscope mode. SPC-140 module in a 'Simple-Tau' system, detector count rate 6 MHz, recorded count rate 4 MHz, 1024 time bins per curve, acquisition time and screen update rate 100 ms. To reproduce the visual impression, two successive traces were overlaid.

Convenient detectors for oscilloscope application are the Hamamatsu H5783 or H5773 modules, or the bh PMC-100 detector heads based on these modules. The modules have a built-in high-voltage generator so that any handling of high voltage is avoided. This is an important feature for practical use.

Recently fast and relatively inexpensive SPAD modules have become available, such as the id-100-20 of id Quantique [607], the PDM 50 CT of Micro Photon Devices [858]. The detectors have an active area of 20 to 100 µm diameter and are overload-proof. The IRF width is about 40 ps, resulting in an equivalent signal bandwidth of about 9 GHz. Although the small active area can cause some alignment problems, these detectors are excellently suitable for TCSPC oscilloscopes.

The oscilloscope mode has become an indispensable tool for a large number of technical jobs. Alignment and optimisation of optical systems often requires not only maximising the efficiency but also localising and removing optical reflections, leakage of excitation light, or pulse dispersion. The oscilloscope mode is also used to optimise the operation conditions of detectors and the driving conditions of picosecond diode lasers. Furthermore, the oscilloscope mode is a convenient way to optimise TCSPC system parameters, such as signal delay, CFD zero cross and threshold, and TAC parameters.

SPCM Software

Overview

SPCM runs the data acquisition in the various operation modes of the SPC modules while controlling peripheral devices, such as detectors, lasers, scanners, or motor stages. Operation modes are available for almost any conceivable TCSPC application. There are modes for fluorescence and phosphorescence decay recording, multi-wavelength decay recording, laser-wavelength multiplexing, recording of time series, FCS and photon counting histograms, and anit-bunching and photon-correlation experiments. There are operation modes for FLIM, Multi-Wavelength FLIM, Excitation-Wavelength Multiplexed FLIM, Mosaic FLIM, Time-Series FLIM, Z stack FLIM, and simultaneous FLIM/PLIM. Since July 2019 SPCM comes with extended multi-threading capabilities, greatly improving the throughput rate even in case of complex online data and display operations.

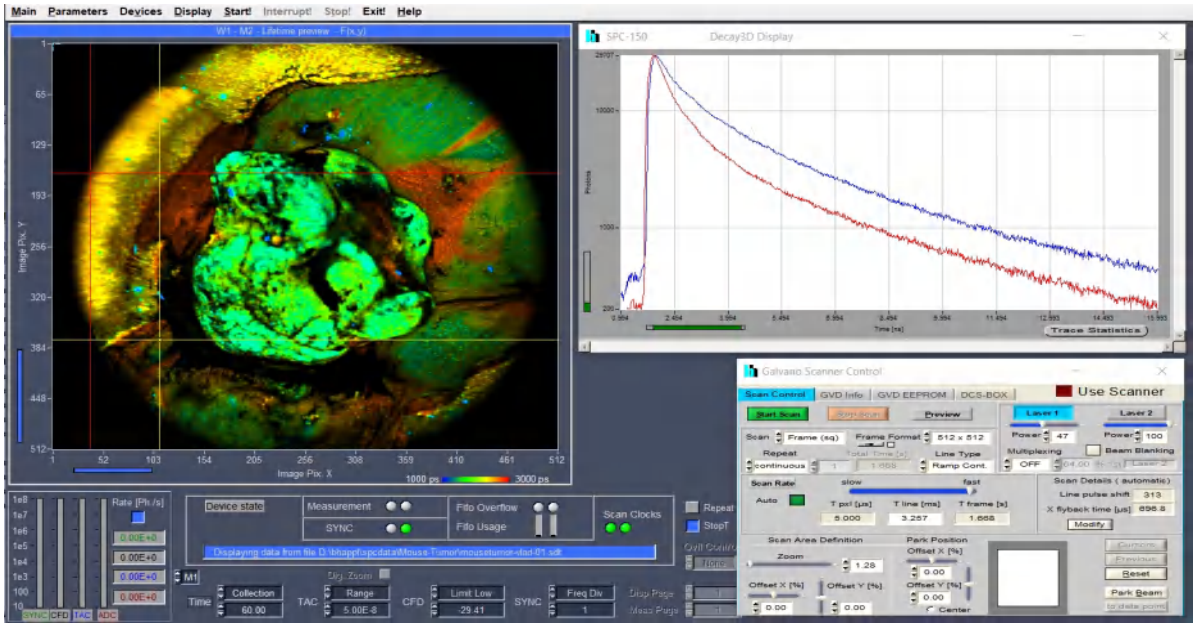


Fig. 959: Example of SPCM Main panel. Other examples see Fig. 960.

SPCM includes the management of the measurement-control parameters, user-interface configuration parameters, and parameters for online data visualisation. Load and save functions are provided to handle measurement and setup data. A large part of SPCM provides display functions for multi-dimensional data. There are display functions for decay curves, series and arrays of decay curves, images, and arrays of images. Different projections can be used to create images from selected planes within a multi-dimensional data array. Display functions also contain online calculation and display of pseudo-colour fluorescence-lifetime images and display of decay curves from ROIs within lifetime images. A direct link is provided for communication with SPCImage NG FLIM analysis software.

SPCM runs under Windows 10 and Windows 11. SPCM is a true 64-bit application. Provided the computer has enough memory there is virtually no limitation in the data size of TCSPC-FLIM results. SPCM thus records 'Megapixel' FLIM data with unprecedented pixel numbers. Moreover, the large data space available in the 64-bit environment allows SPCM to record data of high complexity, such as multi-wavelength or multi-excitation wavelength FLIM data, dynamically variable FLIM data, spatial FLIM mosaics, or data scanned with a combination of an optical scanner and a motor stage.

SPCM Main Panel

The user interface of SPCM is configurable by the user. Different configurations can thus be created for different applications and measurement tasks. Examples of typical SPCM Main Panel configurations are shown in Fig. 960.

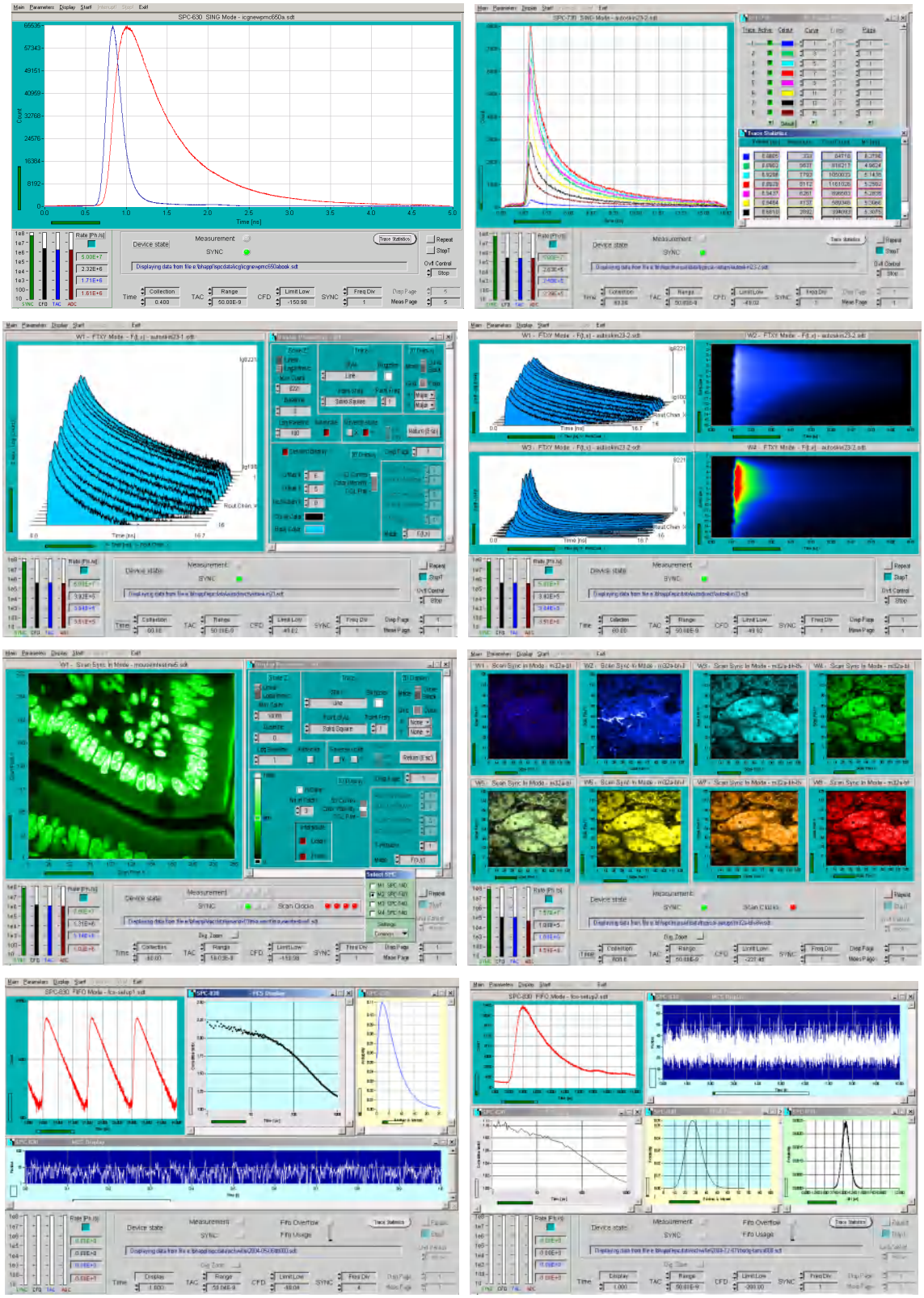


Fig. 960: Main panel of the SPCM software, examples of different configurations. Upper row measurement of single and multi-wavelength decay curves; Second row multi-detector or sequential measurements, three dimensional display, third row Fluorescence lifetime imaging, lower row single molecule spectroscopy, with decay curves, FCS curves, photon counting histograms and intensity (MCS) traces.

The upper row shows configurations typically used for traditional fluorescence decay measurements. For a single-detector setup often a display window is used that fills the upper part of the main window entirely (upper row, left). The curves displayed are the instrument response function and one or several fluorescence measurements. The displayed traces are defined in the ‘Trace Parameters’ which are accessible via the menu bar.

Often several measurements are performed one after another in subsequent memory pages, or a number of decay curves are recorded simultaneously by using the multi-detector capability of the SPC modules. It may then be convenient to have the trace definitions directly available (upper row, right). The display window has therefore been reduced in size, and the ‘Trace Parameter’ panel is kept open and placed right of the display window. The FWHM, the maximum and total counts, and the first moments of the curves are displayed by keeping the 'Trace Statistics' open.

The second row shows typical configurations for multi-wavelength measurements. The left panel shows a three-dimensional graph of the decay curves in the subsequent wavelength channels. The graph is controlled by the ‘Display Parameters’ which are kept open in the right part of the main panel. Other options are shown in the main panel configuration on the right. Four display windows are defined. The same data set is shown in linear and logarithmic scale, and as a three-dimensional curve and a colour-intensity plot. Similar panel configurations can be used for sequential measurements.

The configurations shown in the third row are typical of FLIM measurements. The configuration shown left uses one display window. To change between images in different time windows or different detector channels, the ‘Display Parameter’ panel is kept open; different TCSPC channels of a multi-module system can be selected by the ‘Select SPC’ panel. The main panel configuration shown right is used for multi-wavelength FLIM. Eight display windows are used to display images in subsequent wavelength intervals. The same configuration can be used to display subsequent images of page-stepping sequence.

The last row shows configurations for single-molecule spectroscopy. The left panel displays the decay function, the FCS curve, a photon counting histogram and a curve of the recorded intensity over a selected time interval of the measurement. Photon counting lifetime histograms can be displayed as well, see lower row right, lower right curve.

A wide variety of user interface configurations can be defined, for examples see [68, 69]. The configuration data are stored in the setup and data files of the SPCM software. Different user interface configurations can be loaded by recalling them from a list of ‘predefines setups’, or by loading setup or data files.

'Dark' and 'Light' Versions

Since version 9.92 SPCM comes in a 'dark' and a 'light' version. The configuration is selected in the 'Application Options', see page 714. Examples of the two versions are shown in Fig. 961.

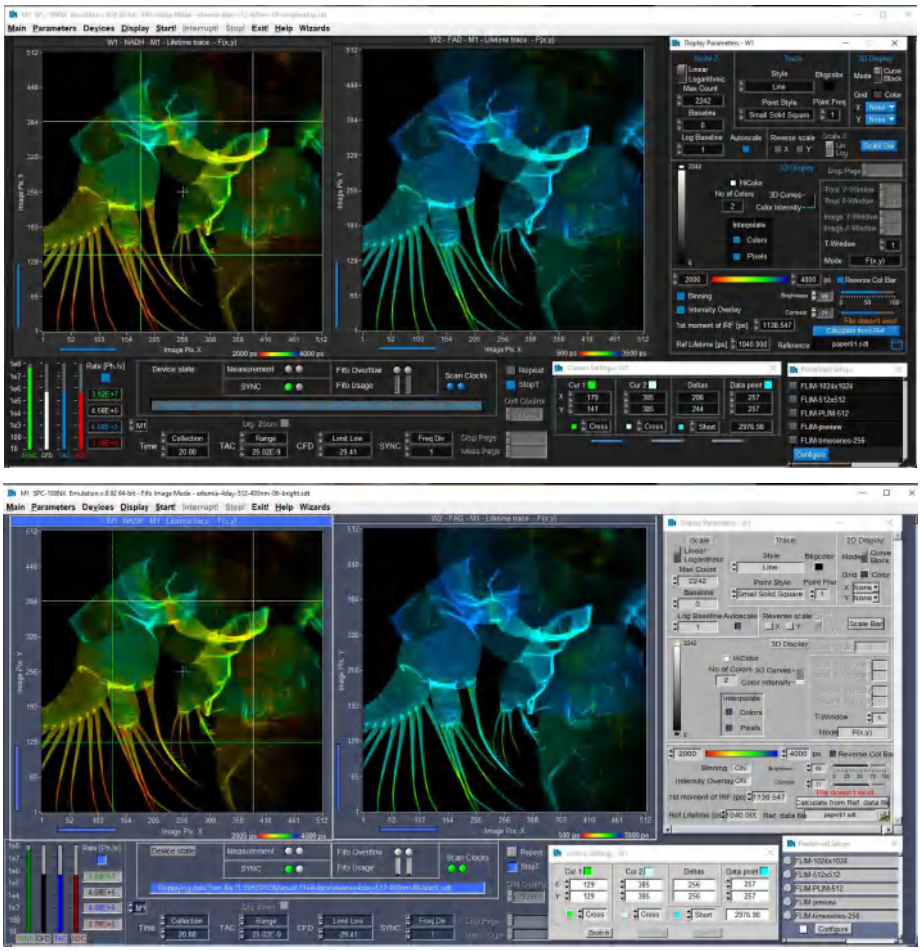


Fig. 961: 'Dark' and 'Bright' versions of the SPCM main panel

Changing Between Different Instrument Configurations

The complete instrument configuration is saved together with the data or setup files. Thus, the main panel configuration used for a particular experiment is restored when the corresponding measurement or setup data are loaded. To simplify switching between different configurations you can put the data or setup files into a list of 'Predefined Setups', see Fig. 962. To open the predefined-setup panel, click on 'Main', 'Load Predefined Setups'. For creation of the panel please see page 723.



Fig. 962: Predefined-Setup panel. You can change between different instrument configurations by a single mouse click

With the Predefined-Setup panel switching between different instrument configurations is merely a matter of a mouse click, see Fig. 963.

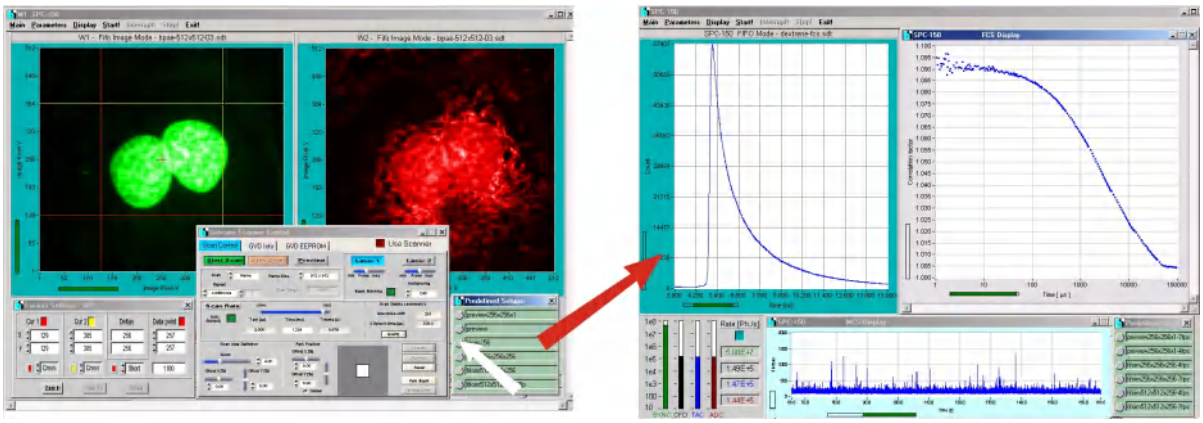


Fig. 963: Example of using the predefined setup panel: The instrument switches from a FLIM configuration into an FCS configuration by a simple mouse click

Measurement Functions

The bh SPC and SPC-QC modules provide a wide variety of measurement functions. These include the traditional recording of fluorescence decay curves or other optical waveforms, phosphorescence decay curves, FCS curves, time series or other sequences of decay curves, triggered ultra-fast time series, multi-detector data or multi-wavelength data, FLIM, multi-wavelength FLIM, time series FLIM, FLIM Z stacks, lateral FLIM mosaics, FLIM time series, fast triggered FLIM time series, PLIM, and simultaneous FLIM and PLIM, and combinations of these. Consequently, SPCM contains a large number of measurement control parameters, display parameters, online-calculation, and user-interface setup parameters. As an overview, a few of the corresponding software-configuration panels are shown in Fig. 964. For details, please see description of the individual panels.

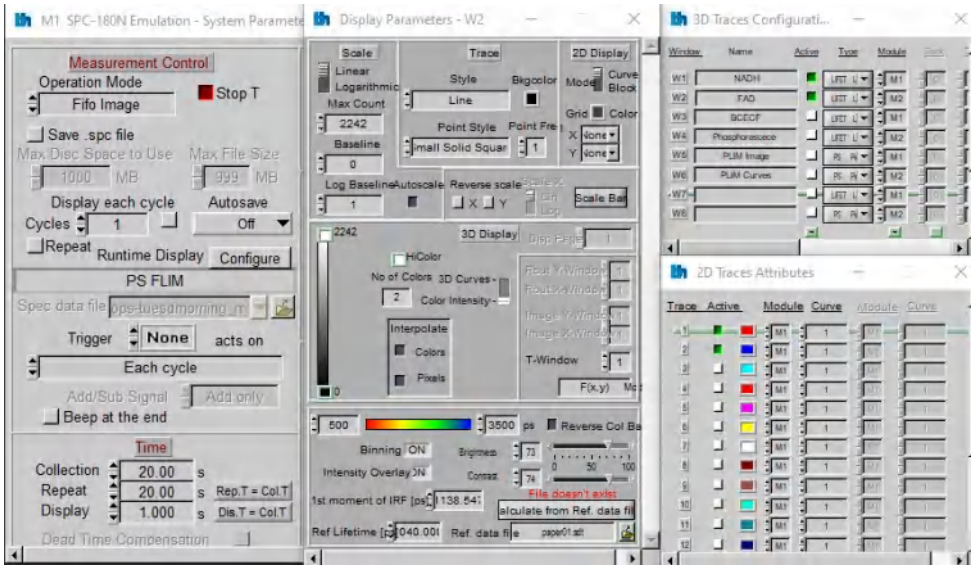


Fig. 964: Measurement control and system configuration parameters

Fig. 965 shows measurement results for a few frequently used SPCM measurement functions. The upper row shows results of fluorescence decay measurement, multi-wavelength fluorescence decay measurement, and fast accumulation of time series. The second row shows FCS, phosphorescence decay, and an intensity trace from single molecules. The third row shows

FLIM, Mosaic FLIM, and PLIM. There are many other possibilities, please see 'System Parameters' for details and system setup.

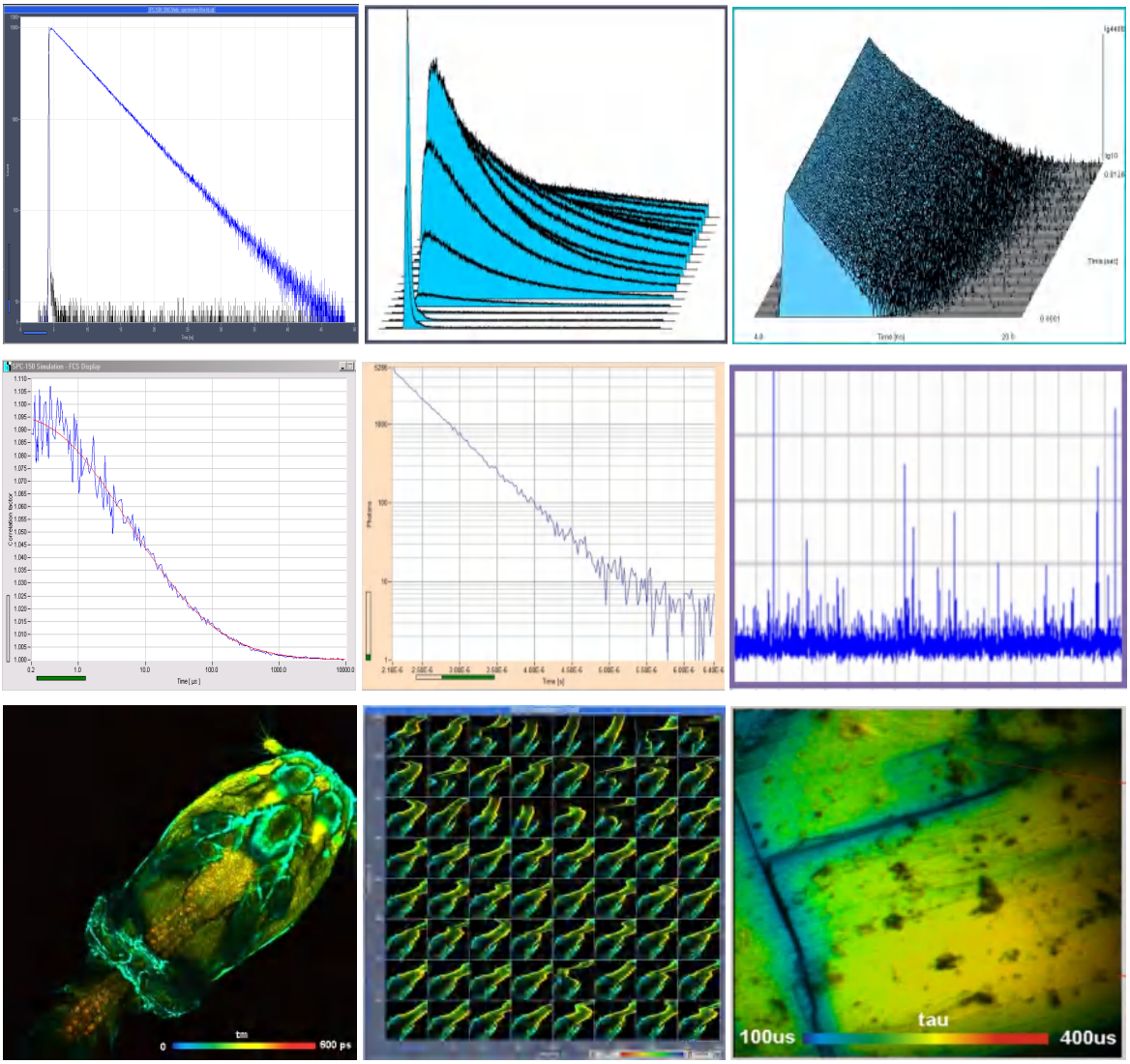


Fig. 965: Examples of frequently used measurement functions. Upper row: Fluorescence decay, Multi-wavelength fluorescence decay, fast accumulated time series. Middle row: FCS, phosphorescence decay, intensity trace (from single molecules). Lower row: FLIM, Mosaic FLIM, PLIM.

Display of TCSPC Data

SPCM has various display functions to display the results of TCSPC measurements. The three basic display modes are illustrated in Fig. 966. The 2D display function shows up to 16 decay curves (or other optical waveforms) in the same diagram. The 3D curve display function displays 3D patterns of curves, such as multi-wavelength decay data or results of sequential measurements. The 3D image display function displays intensity images of FLIM data or colour-coded lifetime images as shown in Fig. 966, right. Please see 'Display Functions', page 797.

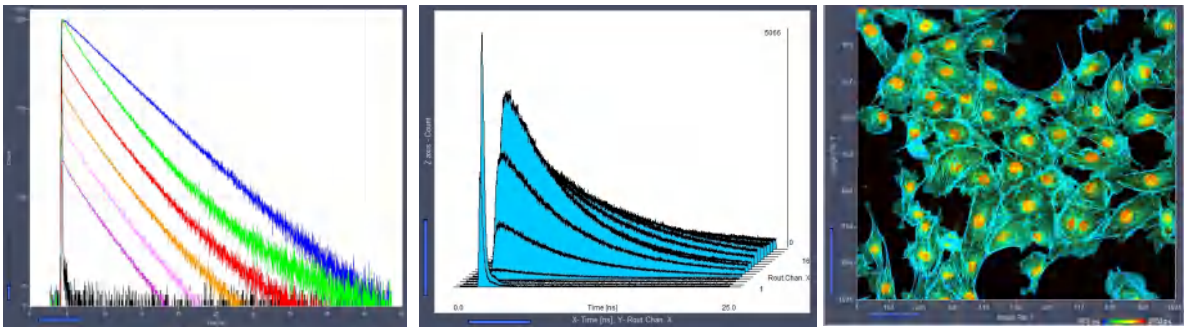


Fig. 966: Three basic display modes of SPCM: Curves in a common diagram, 3D pattern of curves, lifetime image.

Images and other multidimensional data can be displayed in different projections. These projections represent images within a selected time interval (time-gated images), decay curves along a vertical or horizontal stripe of an image, or images within a selected wavelength interval of multi-wavelength FLIM data. Data from different SPC modules, from different routing channels, or different representations of the same data can be displayed in parallel in up to eight display windows. The display functions of SPCM are controlled by the Trace Parameters, Display Parameters, and Windows parameters. An overview is given in the section below, for detailed information please see chapter 'Display Functions' page 797.

Display, Trace Parameters and Window Parameters

The display windows of the main panel are configured by the ‘Display Parameters’ the ‘2D Trace Parameters’, and the ‘3D Trace Parameters’. The corresponding panels are shown in Fig. 967.

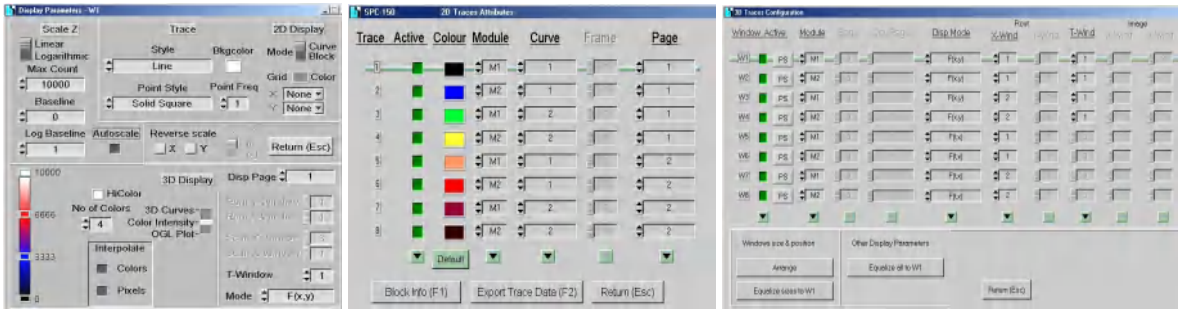


Fig. 967: Left to right: Display parameters, 2D Trace parameters, and 3D Trace Parameters

The *Display Parameters* (shown left) allow you to define how your results will be displayed. The range of the count numbers to be displayed can be defined upper left. The style of the curves displayed can be defined under ‘Trace’ and ‘2D display’. The lower part of the Display Parameters applies mainly to multi-dimensional data sets as they are obtained in the imaging and sequencing modes. A 3D curve mode and a colour-intensity mode are available. Sub-sets of multi-dimensional data sets can be selected in the lower right part of the panel. For details, please see ‘Display ’, page 797.

As shown in Fig. 960, the main panel may have several display windows open. The windows have separate Display and 2D Trace Parameters. To select the right set of display parameters, click into the top bar of the particular display window.

The *2D Trace Parameters* define the curves displayed by the 2-dimensional display modes. Curves from different modules of a multi-module TCSPC system (‘Module’), individual curves from a multi-detector measurement (‘Curve’), and from different measurements or steps of a measurement sequence (‘Frame’ or ‘Page’) can be selected. A curve may also con-

tain accumulated data of several detector channels or measurement steps. Please see ‘2D Trace Parameters’, page 831.

The *3D Display Parameters* define up to eight display windows for multi-dimensional measurements. For each window, the display mode can be defined individually. Thus, images in time windows, sequences of curves in spatial windows of an image, or in windows of the detector number can be defined. Each window has separate display parameters. Thus, windows showing results in the curve and colour intensity mode and in different display scale can be created. For details, please see ‘3D Trace Parameters’, page 836.

The *Window Parameters* are used to define and display subsets of multi-dimensional TCSPC data. Data can be displayed in selectable time windows (of the TCSPC time), routing (usually wavelength) windows, MCS time windows (time in a phosphorescence decay) and over selectable X and Y windows (stripes of an image). Please see 'Display Functions' page 797.

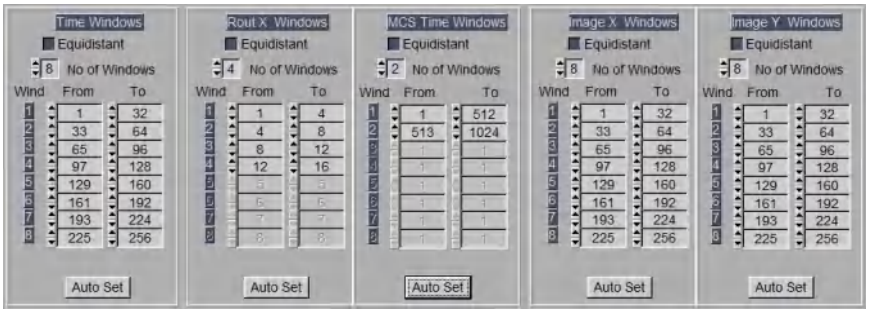


Fig. 968: Window Parameters, used for defining subsets of multidimensional data for display.

Cursors in the Display Windows of the Main Panel

Cursors in the display windows of the main panel are enabled by clicking into the window with the right mouse key. This opens a small panel in which the cursors functions can be enabled or disabled, see Fig. 969, left. A display window with cursors is shown in Fig. 969, middle. Two cursors and a ‘data point’ are available.

When the cursors are enabled a window with the cursor settings is displayed, see Fig. 969, right. The cursor settings window can be placed anywhere in the screen area. It can be closed by clicking on the ‘close’ symbol in the upper right corner, and re-opened by a right mouse click into the display window and selecting ‘Cursor Settings’.

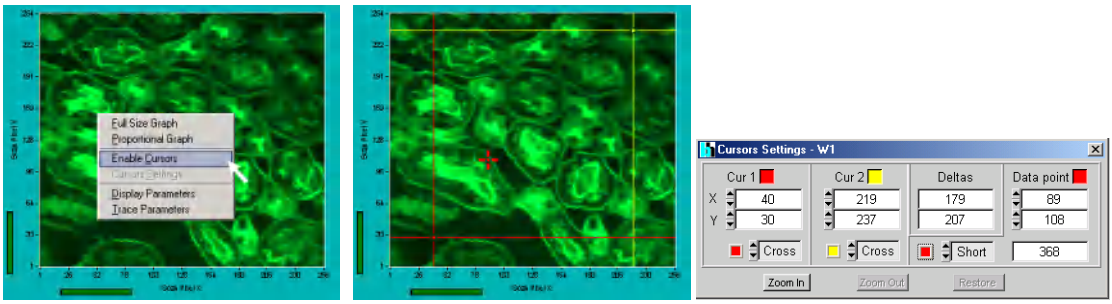


Fig. 969: Cursors in the display windows of the main panel

The cursors and the data point can be shifted by the mouse cursor, or by changing the cursor positions in the cursor settings window. Furthermore, the style and the colour of the cursors can be changed and a zoom function is available. The function is the same as for the cursors in the 2D and 3D Display, see 'Display Functions' page 797.

The cursors in the main window interact with the parameters of the DCS-120 scanner. A region in a previously recorded image is selected by the cursors, and the scan parameters are automatically adjusted to scan this area. Please see Scanner Control, page 849.

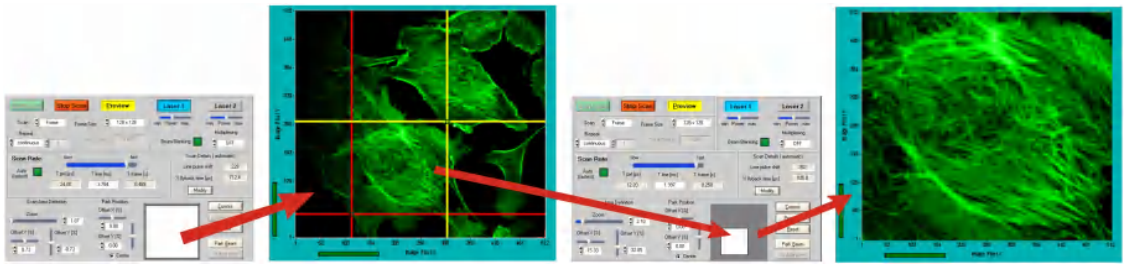


Fig. 970: Interactive scanner control

Trace Statistics

Clicking on the 'Trace Statistics' button opens a window which displays information about the data shown in the curve windows. For decay curves or other waveforms the FWHM values, the peak counts, the total counts and the first moment of the photon distribution are displayed, see Fig. 971, left. For an FCS window the trace statistics window displays the results of the fit, see Fig. 971, right.

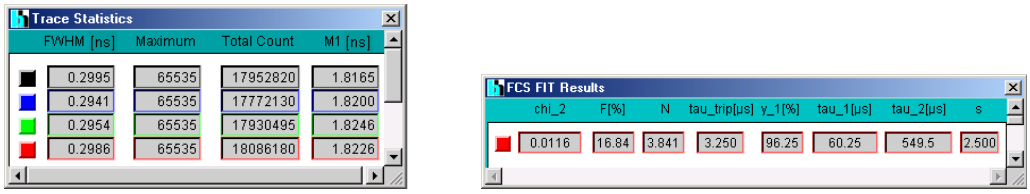


Fig. 971: Trace statistics panel. Left for a waveform window, right for an FCS window

The window can be placed anywhere in the screen area. Please note that the trace statistics window works also in the oscilloscope mode. The window is thus an efficient tool to adjust the system for best time resolution, correct signal transit time, counting efficiency, or IRF stability.

System Parameters

Parameters controlling the TCSPC hardware and the measurement procedures are accessible through the 'System Parameters' panel. To open the panel, click in into 'Parameters' of the top bar and select 'System Parameters'. The System Parameter panel is slightly different for different operation modes. Two examples are shown in Fig. 972. For details please see chapter 'System Parameters', page 731.

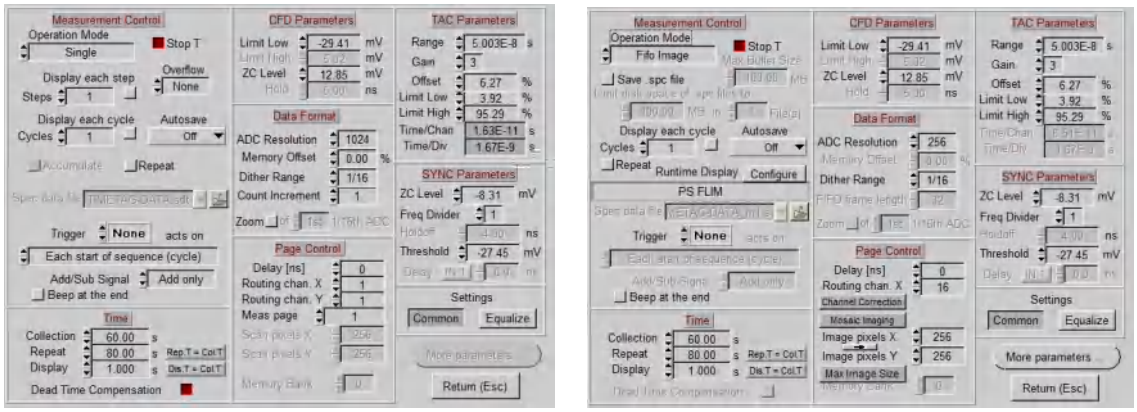


Fig. 972: System parameter panel. 'Single' mode (left) and FIFO Imaging mode (right).

System Parameter Settings from the Main Panel

To simplify on-line adjustments the essential hardware and measurement control parameters are accessible directly from the main panel, see Fig. 973. The complete system parameter set is accessible under ‘System Parameters’, see ‘System Parameters’, page 731.

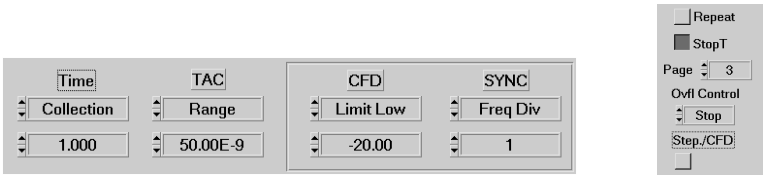


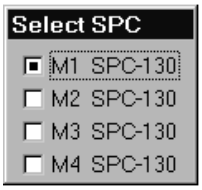
Fig. 973: Access to system and control parameters from main panel

Parameters directly accessible are:

- Time: Collection Time, Display Time, Repeat Time
- TAC: Range, Gain, Offset, Limit Low, Limit High
- CFD: ZC Level, Hold, Limit Low, Limit High (SPC-x00 only)
- SYNC: Freq Divider, ZC Level, Holdoff, Threshold (SPC-x30 only)
- Ovfl Control: None, Stop on Overflow, Correct Overflow
- Page: Memory area (destination) for measurement data
- Repeat: Repeat measurement
- Stop T: Stop after Collection Time

Module Select (Multi-SPC Systems)

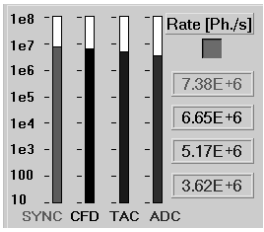
The SPCM Software is able to control up to four TCSPC modules. Many (though not all) system parameters can be set differently in the individual modules. The parameters shown in the ‘Main Panel’ and in the ‘System Parameters’ panel belong to the modules that is selected in the ‘Select SPC’ panel, see figure below. This small panel can be placed anywhere in the screen area.



Status Information

Count Rate Display

The rate display informs about the count rates the CFD, the SYNC rate, the TAC rate and the ADC rate. The CFD rate represents all pulses with an amplitude greater than 'CFD Limit Low'. The TAC rate is the working rate of the TAC. It can be slightly smaller than the CFD rate because the TAC is not started by photon pulses within the dead time of a previously detected photon. 'ADC Rate' is the conversion rate of the ADC. It represents the events inside the selected TAC window and, in case of FLIM, inside the selected scan area.



Count Rate Display

Device State

'Device state' informs about the status of the device, see Fig. 974.

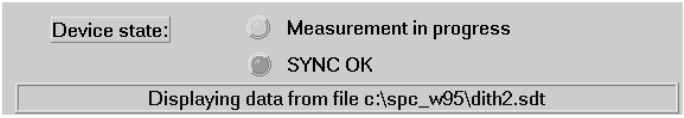


Fig. 974: Device status information

The most important status messages are

Collecting Data:	Measurement running
Displaying Data:	Measurement finished, final result is displayed
Displaying data from file:	Displaying data loaded from an SPC data file
No SYNC:	No synchronisation signal detected
SYNC OK:	Synchronisation signal present
SYNC Overload:	Synchronisation amplitude too high
FIFO Overflow:	The FIFO has run full, not all photons could be recorded
Waiting for Trigger:	Measurement started, waiting for experiment trigger
Waiting for Scan Signals:	Scan measurement started. Waiting for next frame clock to start or to stop the measurement

Status of the Scan Control Signals

When the SPC-730, SPC-830, SPC-150 and SPC-160 modules are operated in the ‘Scan Sync In’ or the 'FIFO Imaging' mode the status of the scan control signals - frame clock, line clock and pixel clock - is displayed, see Fig. 975.

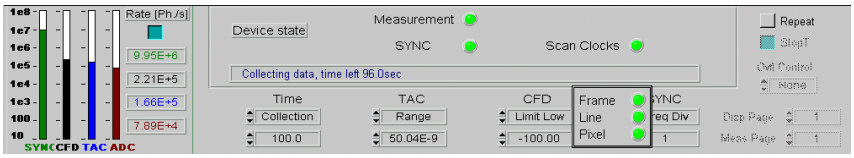


Fig. 975: Status of the scan clocks

The ‘Scan Clocks’ lamp turns on when all used scan control pulses - i.e. Frame and Line Clock for internal pixel clock and Frame, Line and Pixel Clock for external pixel clock - are present. To display the state of the individual clocks, move the mouse cursor on the ‘Scan Clocks’ lamp. This opens a window with indicators for the individual clocks.

Important: The lamps indicate only whether the signals are pulsing or not. They do not indicate that the frequency of the clocks is correct. Furthermore, the state is read once per second. Therefore the ‘Scan Clock’ and the ‘Frame’ pulse indicator may flash if the frame clock is slower than one pulse per second.

Application Options

Additional configuration data can be defined in the Application Options panel, see Fig. 976. In the left part you can define which control panels should open automatically when the SPCM application is started. Please note that there is an option to start the DCC-100 detector controller automatically. The fields for the TAC, CFD and SYNC parameters in the SPCM main panel can be enabled or disabled. The upper right part defines features of the DCS-120 scanner control: The measurement can be started and stopped with scanning, and scanning can be started and stopped with the measurement. Scanning can also be stopped if no measurement has been running for a given period of time.

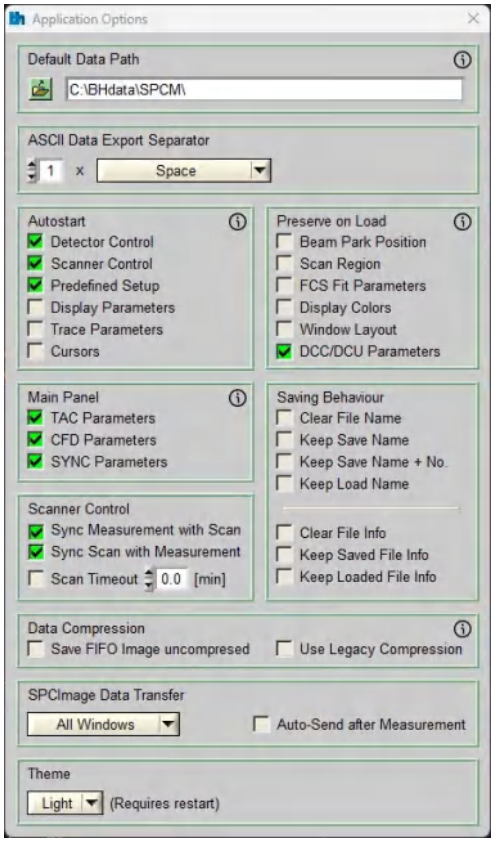


Fig. 976: Application options

Other options are for loading saving files. The load options are important especially for changing the instrument configuration: In a DCS-120 system it may be important that the scanner beam park position or the scan area be maintained when new system setup parameters are loaded. It may also be desired to maintain the display panel positions or display colours.

Since 2011 there is an option to save compressed data files in the FIFO imaging mode. Saving compressed files is the default option. You can turn it off to keep files compatible with earlier versions, or to increase the speed of the saving operation.

Different options can also be used for sending decay curves or FLIM data to SPCImage. Data can be sent automatically at the end of each measurement. and data can be sent from all display windows or only from a selected one.

Important: The application options are stored in the registry of Windows, not in the SPCM data files.

Software Start

Normal SPCM Start

When the SPCM software starts it displays the initialisation status window shown in Fig. 977. It shows the SPC modules found by SPCM and displays them with their type and serial number. Simply click 'OK' in this situation to proceed to the SPCM main panel.

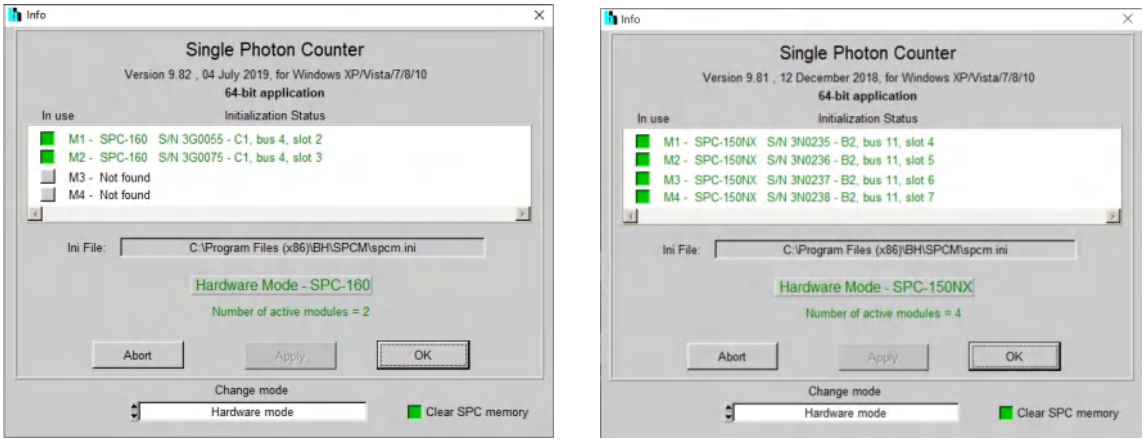


Fig. 977: Initialisation panel. Two SPC modules (left) and four SPC modules (right)

De-Selection of Modules

You can de-select modules from the panel if you do not want to use them. This can be desired if one or several modules are not connected to the Sync or Scan clock signals, or if there are modules of different types in the system. Examples are shown in Fig. 978. De-select the unused module(s) as shown and proceed with 'OK'.

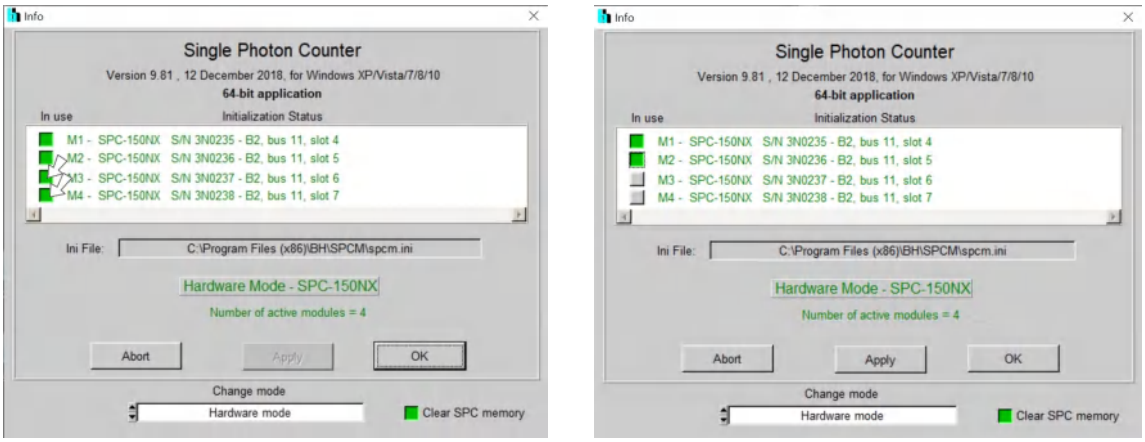


Fig. 978: De-selecting modules from the initialisation panel

Device Already in Use

In the case of a software crash or when a second SPCM application is started accidentally it can happen that SPCM finds that the SPM modules are already being used by another application. The initialisation panel then comes up as shown in Fig. 979, left. In most cases, you can continue by clicking on the 'In Use' buttons and 'OK'. The modules will then be enabled for the SPCM instance being opened and disabled for other applications or SPCM instances.

Hardware Error

SPCM runs a brief hardware test of the digital building block on start-up. In case it detects a hardware error it comes up as shown in Fig. 979, right. You can try to continue by clicking

the 'In Use' and the 'OK' button. If the error is non-fatal the software will proceed. However, please be aware of the possibility that the module will not work correctly.

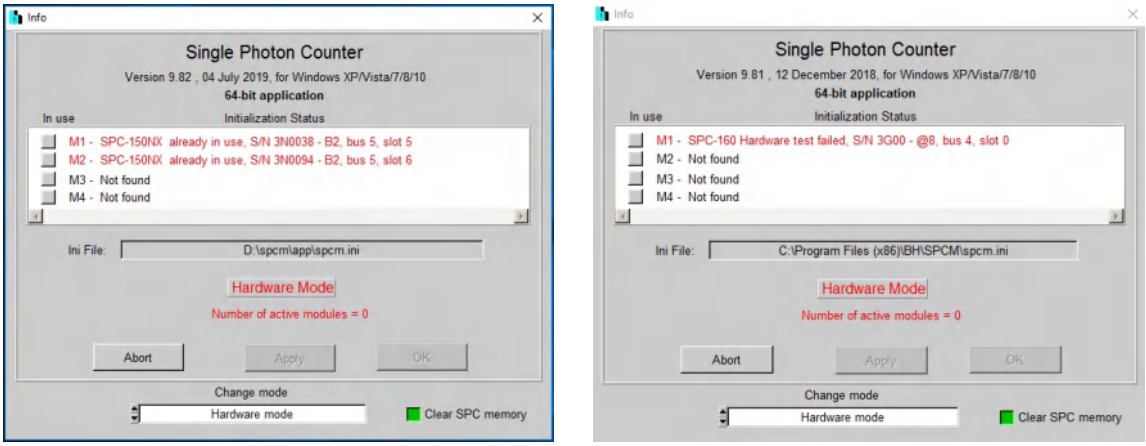


Fig. 979: Initialisation panel in case of errors. Left: Module used by other windows application. Right: Hardware error

Emulation Mode

Without an SPC module the software starts in the ‘Emulation Mode’, see Fig. 977. You can use the emulation mode to load, display, or manipulate data in a computer without SPC hardware. Select the type and the number of SPC modules you want to emulate and start with 'Apply' and 'OK'.

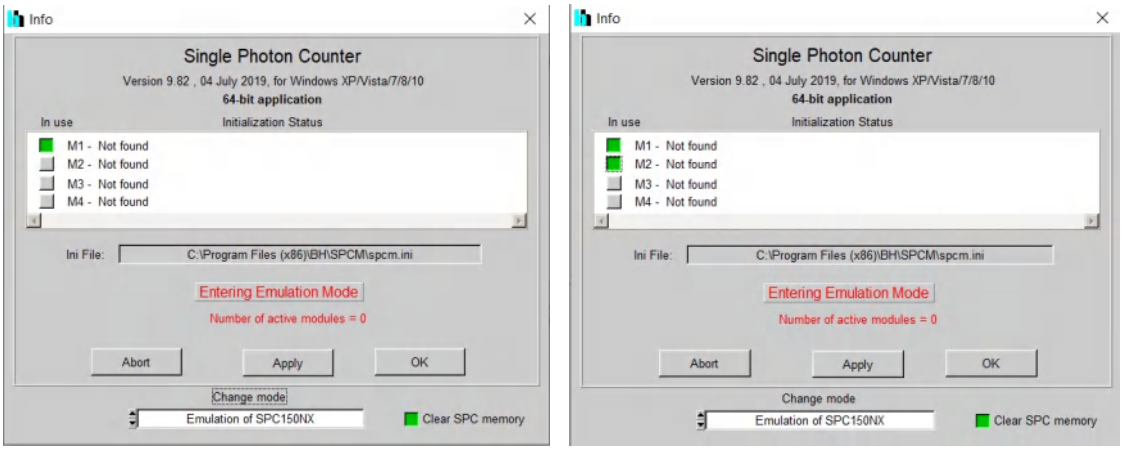


Fig. 980: Initialisation panel for emulation mode. One module (left) and two modules (right)

Main

The functions for loading, saving and converting data and the print functions are available under ‘Main’.

Load Panel

The ‘Load’ menu is shown in Fig. 981. It contains fields to select different file types, to specify a file, to display information about the file selected, and to select different load options.

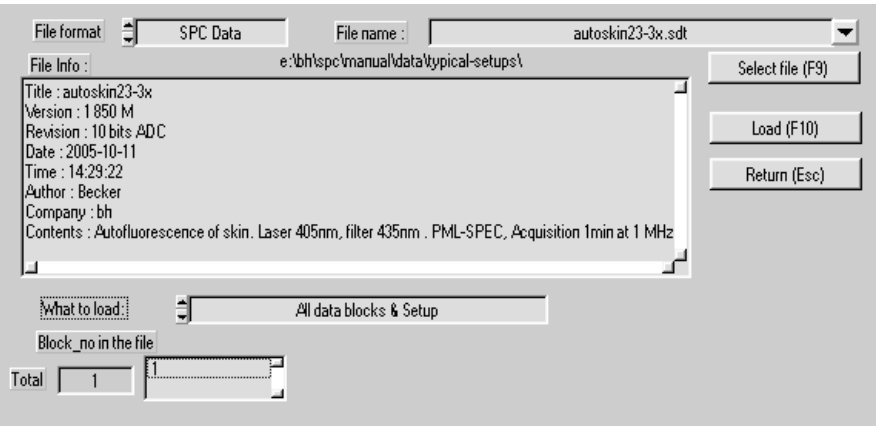


Fig. 981: Load panel

File Format

You can chose between ‘SPC Data’ and ‘SPC Setup’. The selection refers to different file types. With ‘SPC Data’, .sdt files are loaded. These files contain both measurement data and system parameters. Thus the load operation restores the complete system state as it was in the moment when the file was saved.

If you chose ‘SPC Setup’, .set files are loaded. These files contain the system parameters only. The load operation sets the system parameters, but the actual measurement data are not influenced.

Note: Measurements in the ‘FIFO’ (time tag) mode deliver an .spc file that contains the micro time, the macro time, and the detector channel for each individual photon. These files are loaded by using the ‘Convert’ routines, see ‘Converting FIFO Files’, page 725.

File Name / Select File

The file to be loaded can is selected in ‘File Name’ field. ‘Select File’ opens a dialog box that displays the available files. These are ‘.sdt’ files or ‘.set’ files depending on the selected file format. A history of previously loaded files is available by clicking on the ▼ button.

File Info

The file info window displays information about the file selected. The first three lines of the file info are inserted automatically when a file is saved. The last three items can be typed in by the operator, see ‘Save Panel’.

Block Info

Activating a data block in the ‘Block Number in File’ field enables a ‘Block Info Button’. Clicking on this button opens a list that contains the device number of the SPC modules by which the data were recorded, the time and data of the recording, and all system parameters, see Fig. 982. At the end of the block information the minimum and maximum count rates of

the corresponding measurement are shown (see Fig. 982, right). The block info often helps to recover the exact recording conditions of an older measurement.

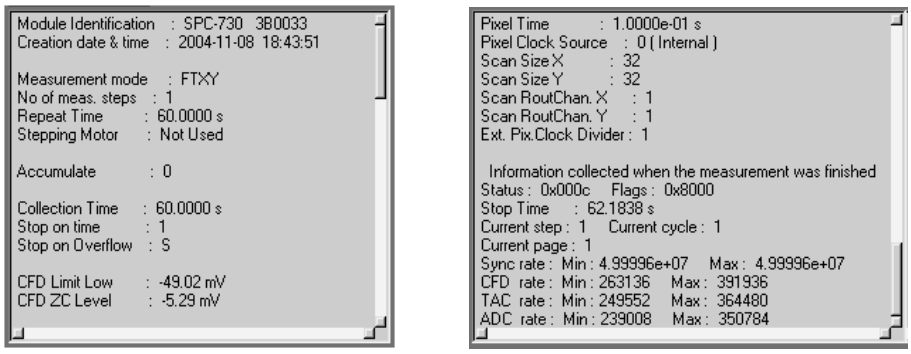


Fig. 982: Block info window of the load panel

Load Options

Under ‘What to Load’ the options ‘All data blocks & setup’, ‘Selected data blocks without setup’ or ‘Setup only’ are available. The default setting is ‘All data blocks & setup’, which loads the complete information from a previously saved data file. *Except for special cases (see below) we recommend to use the ‘All data blocks & setup’ option.*

Loading selected Parts of a Data File

‘Setup only’ loads the setup data only, the measurement data in the SPC memory remains unchanged.

With ‘Selected data blocks without setup’ a number of selected curves or data sets out of a larger .sdt file can be loaded. A data set is a number of curves measured with identical hardware parameters, e.g. a decay curve stored on one ‘page’ of a ‘Single Mode’ measurement, or the decay curves of all pixels of a ‘Scan’ mode measurement.

For ‘Selected data blocks without setup’ the lower part of the ‘Load’ menu changes as shown in Fig. 983.

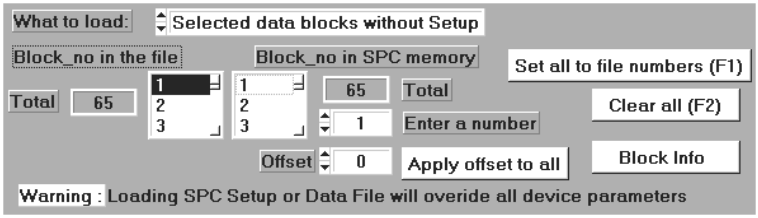


Fig. 983: Selecting data blocks to be loaded from a larger data set

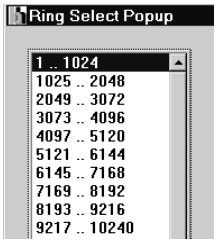
The list ‘Block no in the file’ shows the curves (or data sets) available in the file. Under ‘Block no in the memory’ the destination of the data blocks (curves or sets of curves) in the memory is shown. With ‘Set all to file numbers’ the destination in the memory can be set to the same block numbers as in the file. To set the destination of the data to locations different from the block numbers in the file, click on the a block number in the ‘Block no in the memory’ list and change the number in the ‘Enter Number’ field. ‘Clear all’ clears the ‘Block no in the memory’ list.

For the SPC-134, SPC-144, or other multi-SPC systems operated by the Multi-SPC Software, the block designator contains the module number and a curve number (module_curve).

'Apply offset to all' loads data with a constant offset referred to the file block numbers. It can be used to conveniently load large data blocks to a memory location different from the location in the file.

A sequence of blocks can be selected by pressing the 'Shift' key and clicking on the start and stop number.

Creating the 'Block No' list can take some time, especially on slow computers. Therefore, for high number of blocks the list is created on demand by clicking on the 'Detail' button. When the list is switched on, a menu can be opened from which the location in the block number list can be selected in groups of 1024 blocks.



'Block Info' opens a new window which gives information about the data in a selected data block. An example for the block information window is given in the section 'Trace Parameters'.

Loading Files from older Software Versions

Older software versions may contain less system parameters than newer ones. Therefore, loading older files into a newer software (or vice versa) can cause warnings of missing or unknown parameters. To load the file, click on the 'Continue' button until the file is loaded. Unknown parameters are ignored, and missing parameters are replaced with default values. To avoid further problems with such a file, we recommend to save it in the current software version (Use option 'All used data blocks', see 'Save Panel').

Save Panel

The 'Save' menu is shown in Fig. 984. It contains fields to select different file types, to select or specify a file, to display information about existing file, and to select between different save options.

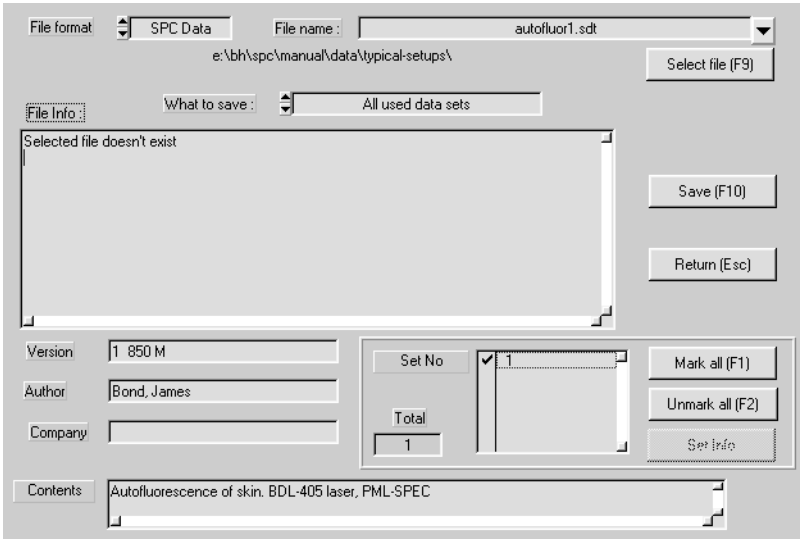


Fig. 984: Save panel

File Format

You can chose between ‘SPC Data’ and ‘SPC Setup’. The selection refers to different file types. With ‘SPC Data’ files are created which contain both measurement data and system parameters. When this file is loaded not only the measurement data are restored but also the complete system setup. With ‘SPC Setup’ files are created that contain the system parameters only. When such files are loaded the system setup is restored, but no data are loaded. Files created by ‘SPC Data’ have the extension ‘.sdt’, files created by ‘SPC Setup’ have the extension ‘.set’.

File Name / Select File

A file name can be written into the ‘File Name’ field. ‘Select File’ opens a dialog box that allows you to change or create directories. Moreover, it shows the names of existing files. These are ‘.sdt’ files or ‘.set’ files, depending on the selected file format. If you want to overwrite an existing file you can select it in the ‘File Name’ field. A history of previously saved files is available by clicking on the button.

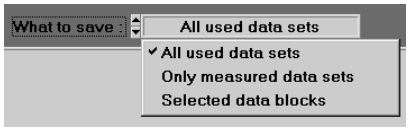
File Info

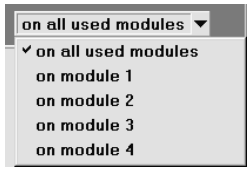
After selecting the file text can be written into the ‘Author’, ‘Company’ and ‘Contents’ fields. Both for ‘SPC data’ and ‘SPC setup’ the file information is saved in the file. The file information helps considerably to later identify a particular measurement among a large number of data files. We therefore strongly recommend to spend a few seconds on typing in a reasonable file information.

If you have selected an existing file the file information contained in it is displayed in the ‘File info window’. If you want to overwrite this file you can edit the existing file information.

Selecting the data to be saved

Under ‘What to Save’ the options ‘All used data sets’, ‘Only measured data sets’ or ‘Selected data blocks’ are available. Furthermore, for the SPC-134 or other systems operated by the Multi-SPC software a module can be selected the data of which is to be saved.





The default setting is ‘All used data sets’ and ‘All used Modules’, which saves all valid data available in the memory of the SPC modules. These can be measured data, calculated data or data loaded from another file. *Except for special cases (see below) we recommend to use the ‘All used data sets’ and ‘All used Modules’ option.*

‘All used data sets’ and ‘Only measured data sets’

A ‘Data Set’ is the result of a single measurement, e.g.

- a decay curve measured by a single detector in the ‘Single’ mode
- the decay curves measured in a multi-detector configuration in the ‘Single’ or f(t,x,y) mode
- a sequence of decay curves measured in the f(t,T) or f(t,ext) mode
- the time-resolved spectra obtained for the 8 time windows of the fi(T) or fi(ext) mode
- the decay curves for the pixels of an image recorded in the ‘Scan’ modes

‘All used data sets’ saves all data obtained in the current session, data loaded from a file, and results of the 2D and 3D data operations. ‘Only measured data sets’ saves only the data which

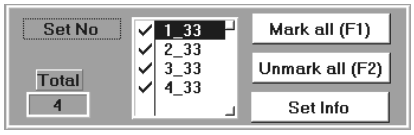
was obtained by *measurements* in the current session. Data loaded from files or results of data operations are *not* saved.

Compressed Data Files

Since 2011 SPCM saves compressed data files of the FIFO imaging mode. This had to be done because the images had become so large that the data file size had become a problem. File compression can be turned on or off in the Application Options panel, see Fig. 976, page 714.

Data Set Info

The save routine saves device number of the SPC modules by which the data were recorded, the time and data of the recording, and the system parameters for individual data sets. The start curve numbers of the available data sets are shown in the lower part of the 'Save' panel, see figure right. For the SPC-134 or other multi-SPC systems operated by the Multi-SPC Software, the data set designator contains the module number and the start curve of the data set.

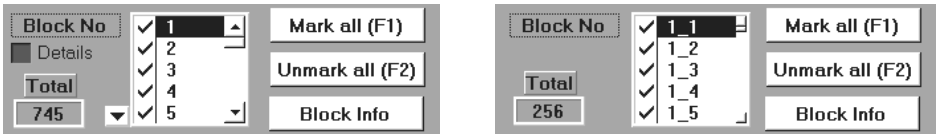


Activating a data set enables the 'Set Info' button. Clicking on this button opens a list that contains the device number of the SPC modules by which the data were recorded, the time and data of the recording, and all system parameters, see Fig. 982. At the end of the block information the minimum and maximum count rates of the corresponding measurement are shown (see Fig. 982, right).

Saving Selected Data Blocks

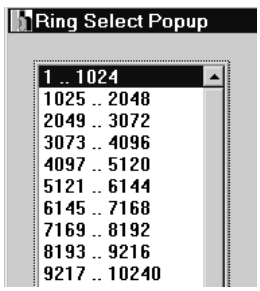
With 'Selected data blocks' a single curve or number of selected curves can be saved. This option is used to create files of selected curves from larger data sets, e.g. to save selected curves of a 'Scan' measurement for processing by an external data analysis program.

The list 'Block No' shows the individual curves which are available in the memory. The desired curves are selected (or deselected) from this list by a mouse click into the marked area. 'Mark all' selects all curves, 'Unmark all' deselects all curves.



Selecting Data Blocks. Left: SPC-6 through -8. Right: SPC-134 or SPC-154

For the SPC-134 or other multi-SPC systems the block designator contains the module number and a curve number. A sequence of blocks can be selected by pressing the 'Shift' key and clicking on the start and stop number.



Creating the 'Block No' list can take some time, especially for modules with large memories in slow computers. Therefore, for high number of blocks the list is created by clicking on the

'Detail' button. When the list is switched on, a menu can be opened from which the location in the block number list can be selected in groups of 1024 blocks.

Predefined Setups

Setups of frequently used system configurations can be added to a list of 'Predefined Setups'. Changing between these setups then requires only a mouse click.

To use the predefined setup option, click on 'Main', 'Load Predefined Setups'. This opens the panel shown right. A setup is loaded by clicking on the button left of the name of the setup.



To add or delete setups to or from the list, or to change the names of the setups, click into one of the name fields with the right mouse key. This opens the panel shown in Fig. 985.

To add a setup, click on the disc symbol right of the 'File Name' filed and select a '.set' file. Default setups coming with the SPCM software are in the 'default setups' folder of the working directory defined during the software installation. Please note that there may by subdirectories for different classes of applications. Select the files you want to put into the list of predefined setups, and click on the 'Add' button. Every setup has a user-defined 'nickname'. The default nickname is the file name of the .set file. To change the nickname, click into the nickname filed and edit the name. Then click on 'Replace'.

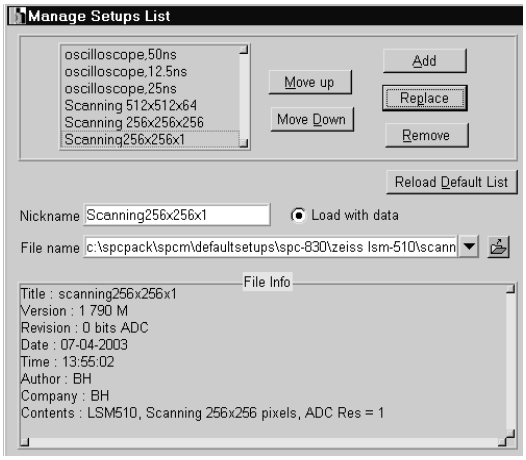


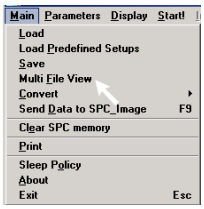
Fig. 985: Editing the list of predefined setups

To create your own predefined setups, first save a setup file of the system configuration you want to add the list. Use the 'Save' panel, option 'setup' as described under 'Save'. Then add the file to the setup list as described above.

You can also add an '.sdt' file to the setup list. The .sdt file contains not only the system setting but also measurement data. You can define whether the file is loaded with or without the data by clicking on the 'load with data' marker. Please note that loading files with data can take a longer time than without, especially for data recorded in the scan modes of the FIFO Imaging Mode.

Multi-File View

Measurements with page stepping or autosave, and measurements in the continuous flow mode can produce a large number of subsequent data files. Loading these data one after another by the 'Load' procedure and comparing them by the standard display routine may be too time-consuming. Moreover, it may be desirable to see the results of a sequential measurement in form of a time-sequence, i.e. as the data were recorded. Therefore SPCM provides a 'Multi File View' function. The function is accessed by clicking into 'Main', 'Multi File View', see Fig. 986, left. The multi-file view panel itself is shown in Fig. 986, right.



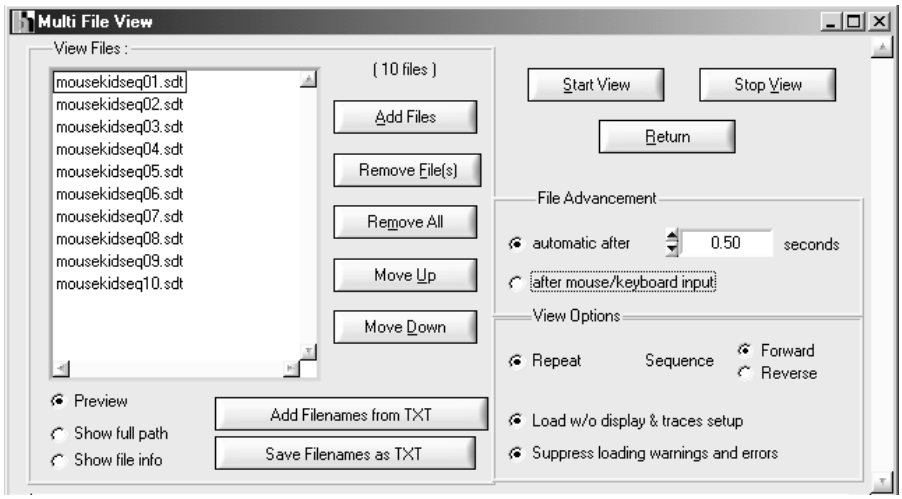


Fig. 986: Control panel of the Multi-File View function

The names of the files to be displayed are specified in a window on the left. Use the 'Add File' or 'Remove File' buttons to add or remove files. The cursor in the list can be moved up and down by the 'Move UP' and 'Move Down' buttons, or by a mouse click on a file name. A list of file names can be imported from a .txt file, or exported to a .txt file.

The display of data in the subsequent files can be advanced by an operator command or automatically in defined intervals. The shortest available interval is 0.1 seconds. For large files, e.g. data of the TCSPC imaging modes loading may take longer than 0.1 s; the view may then advance slower than specified.

The file show can be run only once, or be repeated in a loop ('Repeat' on). It may happen that the subsequent files have different trace or display parameters. In this case activate the 'Load w/o display & traces setup' button. It may also be indicated to switch off possible load warnings, i.e. when data from older software versions are loaded, or the data were measured in a different SPC module.

Data Export and Import: Convert Functions

The 'Convert' functions are used to convert the .sdt data files of the Multi SPC Software into ASCII files or into the files for the Edinburgh Instruments data analysis software. Furthermore, FIFO mode files can be converted into .sdt files containing decay, FCS, PCH, and multichannel scaler data. FIFO mode data can also be converted into 'Continuous Flow' mode files. The Convert panel opens by clicking into 'Main', 'Convert', see Fig. 987, right, left.

Converting .sdt Files

The panel for converting .sdt files is shown in Fig. 987, right. The source file name is selected in a field on top of the Convert panel. After selecting the source file, the corresponding file information text is displayed. The first part of this text was created automatically by the 'Save' function; the last part was written by the operator when the file was saved.

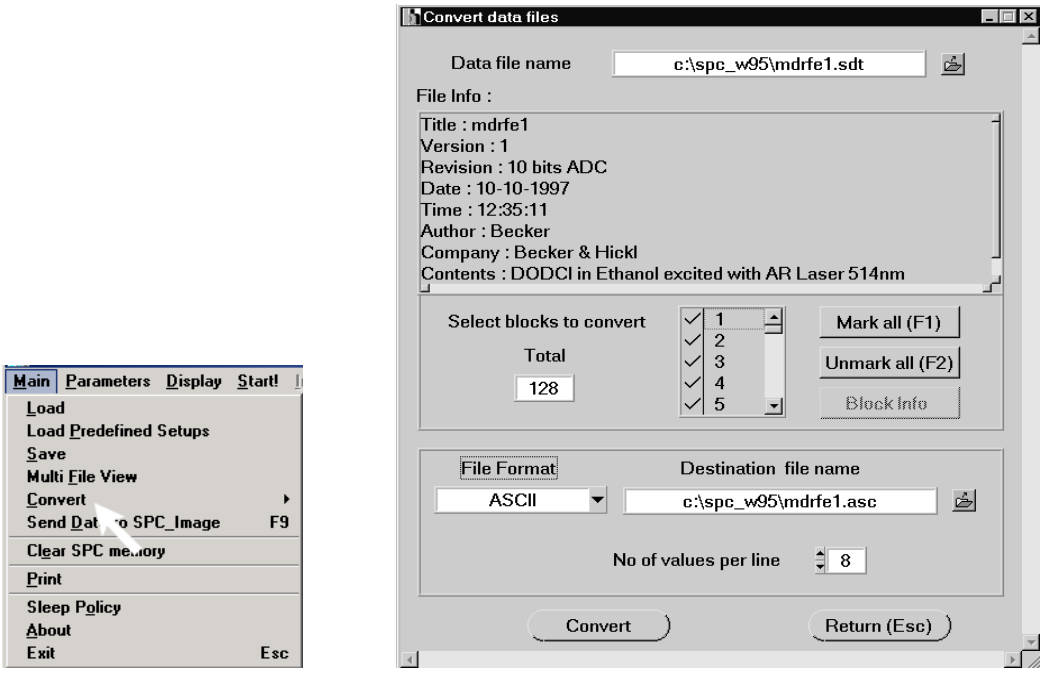


Fig. 987: Conversion of .sdt data into ASCII data

By ‘Select blocks to convert’ specified blocks (curves) from the source file can be selected for conversion. At the beginning all curves of the source file are marked. Thus, no selection is required if all blocks of the source file are to be converted.

The output file format can be ‘ASCII’, ‘ASCII with Setup’ or ‘EI’. ‘ASCII’ converts the measurement data only. ‘ASCII with Setup’ converts the SPC system parameters and the measurement data. For the measurement data part the number of data values per line can be specified. ‘EI’ converts into the format of the Edinburgh Instruments data analysis software.

The entering of the destination file name is optional. If no destination file name is entered the source file name is used with the extension ‘.asc’.

Converting FIFO Files

Measurements in the ‘FIFO’ (time tag) mode deliver an .spc file that contains the micro time, the macro time, and the detector channel for each individual photon. During a FIFO measurement normally decay curves, FCS curves, or photon counting histograms are calculated on-line. These data are saved in normal .sdt files. However, it may happen that not all of the desired functions were calculated during the measurement, or that the calculation was not done with the optimal binning parameters or sampling time intervals. Moreover, on-line data analysis may have not been used altogether to increase the data throughput rate. In these cases, the ‘Convert FIFO File’ function allows you to read the data from the FIFO (.spc) file created during the measurement and calculate the desired correlation functions or histograms. The Convert FIFO panel is shown in Fig. 988.

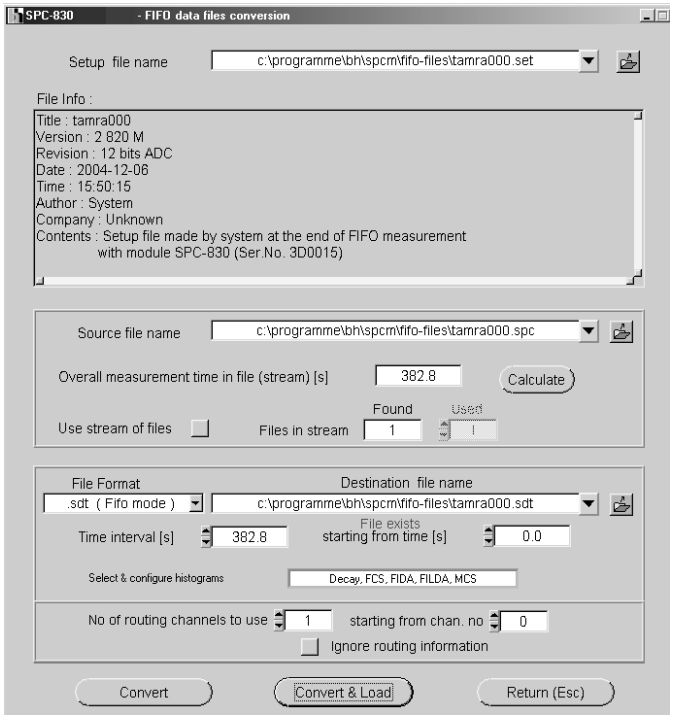


Fig. 988: Conversion of FIFO data into .sdt data

Each FIFO mode measurement creates a setup (.set) file which has the same name as the .spc file (or the last .spc file if several are recorded sequentially). The name of this setup file must be specified under ‘Setup file name’. As in the load and save panels, the file is specified in file name field. Clicking on the disc symbol opens a dialog box that displays the available files. A history of previously used setup files is available by clicking on the button. The ‘File Info’ displays information about the corresponding measurement.

The FIFO (.spc) file is specified under ‘Source file Name’. A FIFO measurement may produce several .spc files. The data of all these files are combined by activating the ‘Use Stream of files’ button. ‘Overall measurement time’ informs about the total time over which the measurement has been run.

The lower part specifies the .sdt file to be created. The file name is specified under ‘Destination file name’. The conversion routine suggests a file with the same name as the .spc file.

The ‘Convert FIFO’ routine allows you to convert .spc files into different destination file types. The destination file type is specified in the ‘File Format’ field in the lower part of the Convert panel. The most frequently used conversion is into .sdt files of the FIFO mode, see Fig. 989.

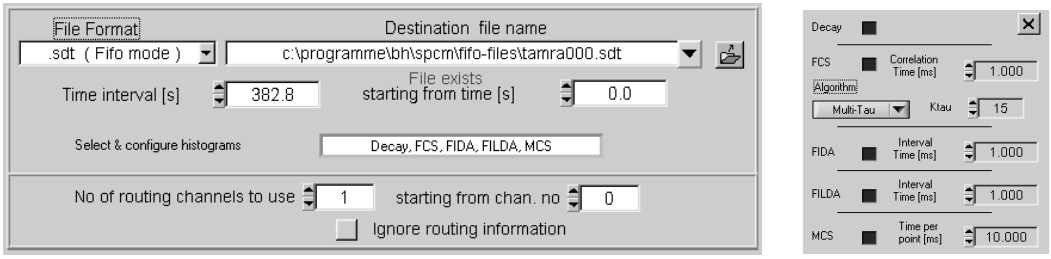


Fig. 989: Conversion of .spc files into .sdt files of the FIFO mode. Left: Configuration of destination data. Right: Selection of the functions to be calculated and calculation parameters.

The functions to be calculated are defined in the ‘Select & configure histograms’ field. A click into this field opens the panel shown in Fig. 989, right. It is the same panel used to configure the online display of the FIFO mode, see page 770. You can specify the calculation of

decay curves, FCS functions, photon counting histograms (FIDA), photon counting lifetime histograms (FILDA), and FCS traces.

A FIFO measurement may have been run over a long acquisition time and contain data from several routing channels (detectors). Therefore, parameters are provided to control the structure of the calculated data. With ‘Time Interval’ and ‘Starting from time’ a time interval within the ‘Overall measurement time’ of the FIFO measurement can be selected. Moreover, if the .spc data were recorded in several detector channels the full routing information may be used, only a specified range of channels may be converted, or the routing information may be ignored altogether, i.e. all detector channels merged.

The results to be calculated from the .spc data are specified under ‘Select & configure histograms’, see Fig. 989, right. The panel opens by clicking into the ‘Select & configure histograms’ field. The options are the same as in the ‘Configure’ menu of the System Parameter panel in the FIFO mode: Decay curves, FCS curves, photon counting histograms and MCS traces can be calculated.

FIFO data can also be converted into data of the Continuous Flow mode, see Fig. 990.

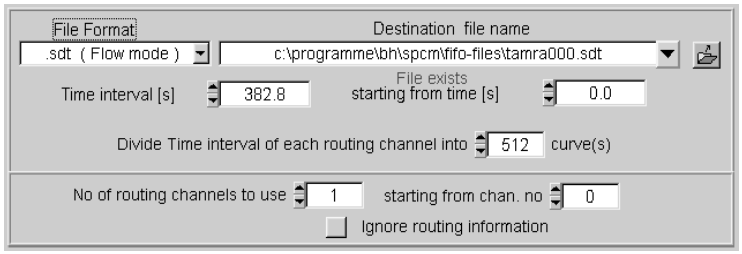


Fig. 990: Conversion of .spc files into .sdt files of the continuous flow mode

With ‘Time Interval’ and ‘Starting from time’ a time interval within the ‘Overall measurement time’ of the FIFO measurement can be selected. This time interval can be divided into a number of subsequent curves by ‘Divide Time Interval of each Routing Channel into ... Curves’. If only one routing channel (one detector) was used this gives a data file which can be displayed in the ‘Continuous Flow’ or f(t,T) mode of the SPC Standard Software. As for conversion into FIFO mode data, the routing information can be used, ignored, or a specified range of detector channel ranges can be converted.

Fig. 991 shows how .sdt data are converted into ASCII data. Several options are available. The macro time in the destination file may be absolute, or the macro-time differences between subsequent photons may be generated. The micro times, the routing channels, and the ‘invalid’ and ‘overrun’ flags may or not be included in the destination file.

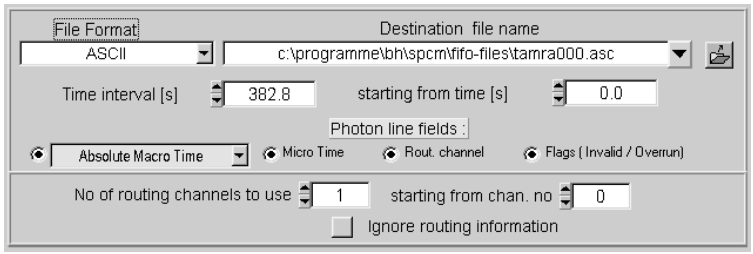


Fig. 991: Conversion of .spc files into ASCII data

Link to SPCImage Data Analysis

There is a direct link to the SPCImage data analysis for single point and fluorescence lifetime imaging decay data, see page 861 of this handbook. Data are sent by clicking on ‘Send Data to SPCImage’, see Fig. 992. middle. This opens the data analysis panel shown on the right.

For a number of instrument configurations several data sets may have been recorded. In the ‘Application Options’ (see page 714) you can select whether you want to send the data of all display windows to SPCImage or only the data of a selected one. For sending selected data click on the display window that shows the data to be analysed before clicking on ‘Send Data to SPCImage’, see Fig. 992, left.

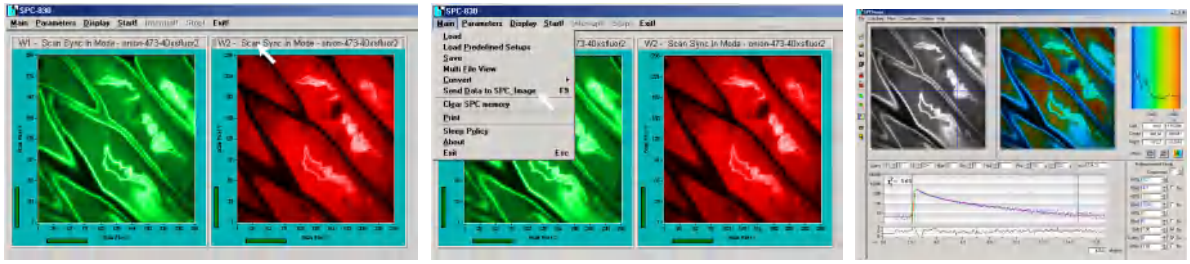


Fig. 992: Sending data to the data analysis. Click on data set to be sent (left), click on ‘send data to SPCImage’ (middle), SPCImage opens with the data selected (right)

The Application Options also allow you so send the data to SPCImage automatically at the end of each measurement. However, not every measurement produces useful data. Opening the analysis window automatically may cause frustration in these cases.

Print

The ‘Print’ function sends the current screen pattern to a printer. You can print either the whole panel or the visible part only. ‘Portrait’ or ‘Landscape’ selects the orientation on the sheet. The dimensions are set by ‘Autoscale’, ‘Full Size’ or ‘Size X’ and ‘Size Y’.

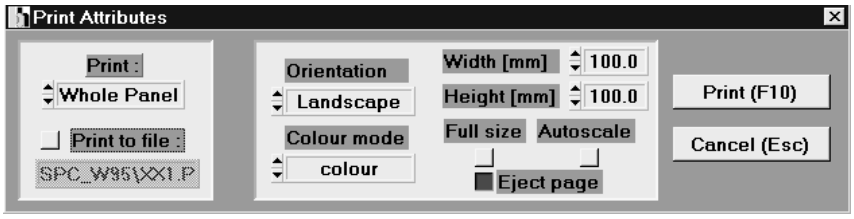


Fig. 993: Print panel

If you want to create a printer file of a screen pattern you can use the ‘Print to file’ option. If you select a postscript-compatible printer the result is a postscript file which can be loaded into many text and image processing programs.

However, another (often more convenient) option to save a screen pattern is the ‘print screen’ key. When this key is pressed, Windows stores the screen pattern to the clipboard from where it can be loaded into an image processing program (Photo Paint, PhotoShop etc.).

Sleep policy

Windows is a multi-task operating systems. However, different applications are not really running simultaneously; the operating system cycles between different applications. The amount of attention the SPCM software gets from the operating system can be changed by setting the ‘Sleep Policy’, see Fig. 994.

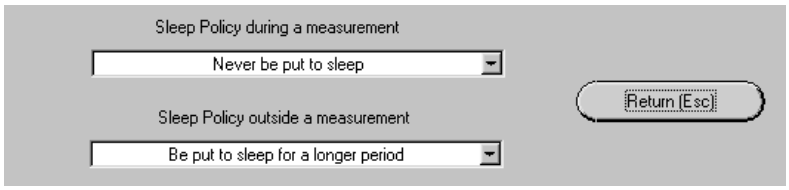


Fig. 994: Sleep policy

The highest level is ‘Never be put to sleep’. On this level the SPCM software claims almost the full power of the CPU. The advantage is short reaction time to any request from the SPC module. The downside is that other applications may be extremely slowed down.

The lowest level is ‘Be put to sleep for a longer period’. It means that the SPCM software claims only a minimum of attention from the CPU. The result are long reaction times. The SPCM software allows you to set different sleep policy during a running measurement and outside a measurement. We recommend to use the settings shown in Fig. 994. The best settings may, however, depend on your operating system and on other applications possibly running in parallel with the SPCM software.

It should be noted here that the data acquisition in the photon distribution (histogram) modes of the bh SPC modules is performed by pure hardware functions. Software activities are only required to read out the data, to initiate the next step of a page stepping sequence, to display status messages, and for operator interactions. Long reaction times of the SPCM software in the ‘Put to sleep’ configurations are therefore rarely a problem.

System Parameters - SPC Series

The ‘System Parameters’ contain all parameters that define the internal functions of the SPC module hardware and the data transfer between the hardware and the software. The system parameter define the operation mode, including the control of sequential measurements, page stepping, repeat, accumulation and autosave functions. Furthermore, the system parameters control the settings of the CFD, SYNC, TAC and ADC parameters as well as the routing and scanning parameters. Because not all parameters may be applicable to all operation modes and SPC modules some details of the system parameter panel change with the operation mode and module type. The typical system parameter panel of the Multi SPC Software is shown Fig. 995.

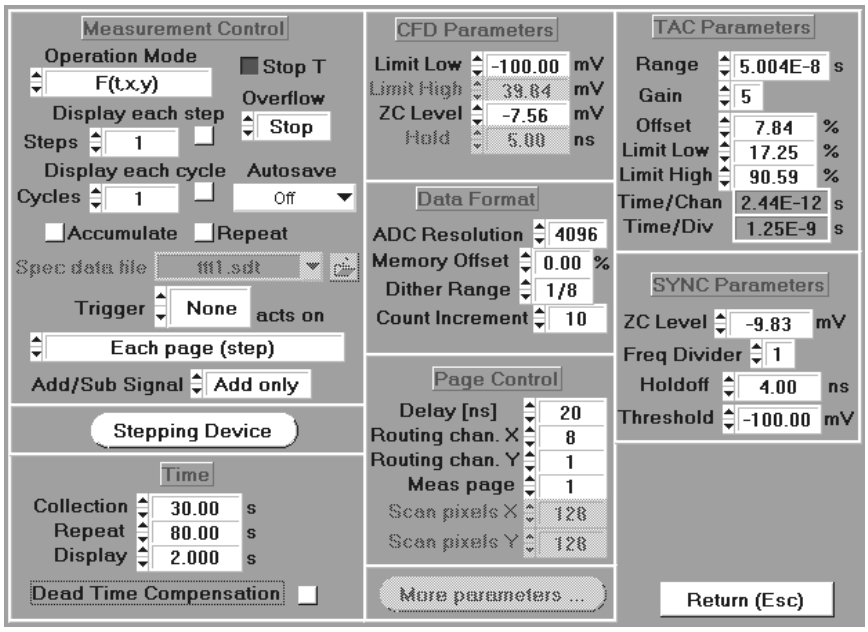


Fig. 995: System parameter panel

The panel contains a measurement control part that allows you to set the operation mode, to configure the measurement procedure by defining page stepping, cycle, accumulate and auto-save functions, and to define the action of the experiment trigger. Due to different hardware in different SPC modules the measurement control part of the panel changes with the module type and with the operation mode selected.

The collection time, repeat time, and display time are defined in the ‘Time’ section below the measurement control parameters.

Under ‘Data Format’ and ‘Page Control’ the ADC resolution and the ADC error correction parameter, the number of detector channels, the number of the pixels of a scan, and the memory page in which a measurement is started are defined. The CFD, SYNC, and TAC parameters are arranged in upper right.

‘More Parameters’ opens an additional panel that contains hardware parameters which are specific for the particular operation mode.

System Parameters - SPC QC Series

The SPC-QC series modules differ from the SPC series in that there are four input channels, and the time-conversion is performed by a TDC. Hence there are four parameter sets for the input discriminators, and different timing-control parameters. The SPC-QC is described in a

separate manual, please see [75]. For information, a typical system-parameter panel for the SPC-QC-104 is shown in Fig. 996.

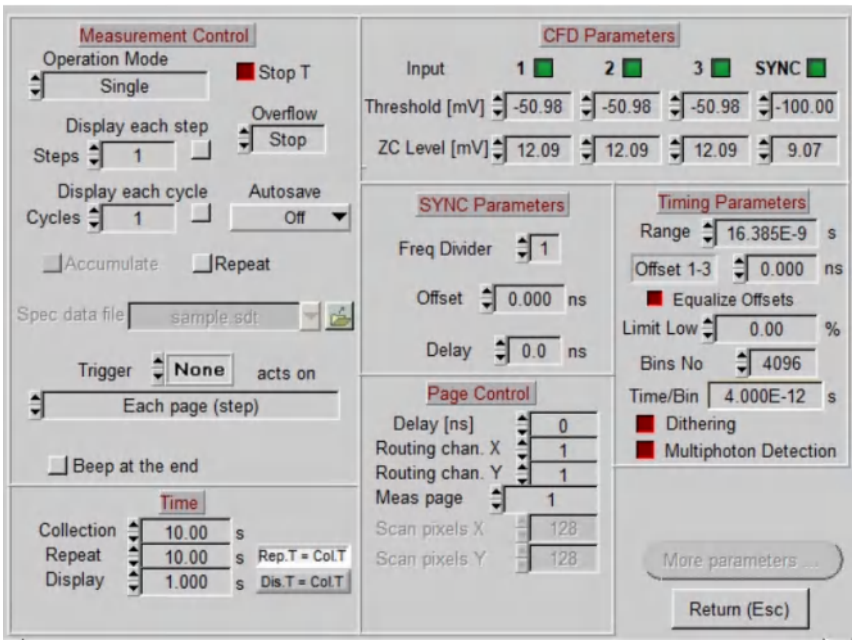


Fig. 996: System Parameter panel for the SPC-QC-104

Operation Modes

When the bh SPC modules are operated via the SPCM software a wide variety of operation modes is available, see Fig. 997.



SPC-130/134 SPC-150/154 SPC150/154N SPC-180/184N SPC-QC SPC-160/164 SPC-830

Fig. 997: Operation modes available in SPC modules. For modules not listed see handbook 9th edition.

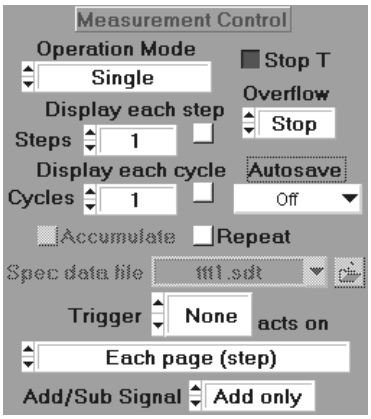
An overview of the operation modes available in different SPC modules is given below.

Mode available for SPC	130, 134	150	150N, NX	180N, NX	QC	730	830	Typical Application
Single	x	x	x	x	x	x	x	Classic fluorescence lifetime
Oscilloscope	x	x	x	x	x	x	x	System adjustment and optimisation
f(t,x,y)	x	x	x	x	x	x	x	Multi-wavelength fluorescence decay
f(t,T)	x	x	x	x	x	x	x	Time-series recording
f(t,EXT)	x	x	x	x	x	x	x	Fluoresc. lifetime with λ scanning
fi(T)	x	x	x	x	x	x	x	Time-gated intensity curves
fi(ext)	x	x	x	x	x	x	x	Time-gated fluorescence spectra
Continuous Flow	x	x	x	x	x			Fast Time series
Scan Sync In		x	x	x	x	x	x	Imaging, laser scanning microscopy
Scan Sync In / Cont. Flow			x	x	x			Fast imaging time series
Scan Sync Out		x	x	x	x	x	x	Imaging, time series of curves
Scan XY Out						x		Imaging with piezo stages
FIFO	x	x	x	x	x		x	FCS, single-molecule spectroscopy
FIFO Imaging			x	x	x		x[1)]	FLIM, large images, complex data
AbsoluteTime					x			Coincidence, FCS
Wide-Field FLIM			x	x				FLIM with delay-line MCP

1) Available for modules from Ser. No. 3D0178 (May 2007). Modules with serial numbers 3D0098 (May 2005) or later can be upgraded.

‘Single’ Mode

The measurement control parameters for the ‘Single’ mode are shown below. With the settings shown a single measurement cycle is performed. Several curves can be measured simultaneously if several detectors and a router are used. Up to eight curves can be displayed simultaneously. The displayed curves are selected in the ‘2D Trace Parameters’, see page 831.



The photon collection is controlled by the parameters ‘Stop T’, ‘Repeat’ and the options under ‘Overflow’. The measurement stops

- at the end of ‘Collection Time’ if ‘Stop T’ is set
- at the first overflow if ‘Stop Ovfl’ is set

If both stop conditions are set the measurement stops in both cases. Without any stop condition the measurement runs until it is stopped by the operator. If the results run out of the data range (65535 counts per time channel) the overflowing parts are clipped.

To collect more than 65535 photons per time channel a ‘Correct Overflow’ function is provided. With ‘Correct Overflow’, the measurement data are transferred to the PC memory at each overflow and accumulated. The measurement data memory is cleared after each overflow and the measurement is restarted. When the collection time is over the result is divided by the number of overflows and written back to the measurement memory. The result has 16 bit resolution and a maximum count number of 65535. However, because several recordings were averaged the standard deviation is reduced by the square root of the number of overflows. The ‘Correct Overflow’ function is available in the ‘Single’ mode only.

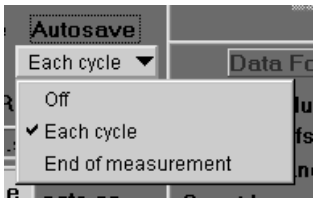
During the measurement intermediate results are shown on the screen in intervals of ‘Display Time’. Up to eight curves can be displayed. The curves are specified in the ‘Trace Parameters’, see page 831.

Stepping through Pages

A ‘Single’ measurement can be repeated in intervals of ‘Repeat Time’ and the results be written into subsequent ‘Pages’ of the memory. The number of subsequent measurements is defined by ‘Steps’. The measurement starts in the ‘Measured Page’ defined in the main panel. The stepping function can be combined with routing, i.e. several detector channels can be measured in each step.

Cycles and Autosave

A stepping sequence (or, if ‘Steps’ = 1, one ‘Single’ measurement) can be repeated for a defined number of ‘Cycles’.



The results of subsequent cycles can be written to the hard disk by using the 'Autosave' function. To activate 'Autosave' for each cycle, click on 'Autosave', 'Each Cycle'.

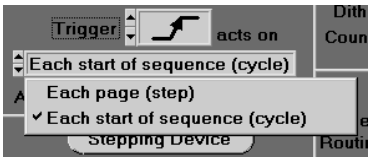
'Autosave' can also be initiated at the end of the measurement, i.e. after the last cycle only.

Repeat

After pushing the 'Repeat' button the complete measurement cycle repeats until the measurement is stopped by the operator.

Trigger

Either the 'Steps' or the 'Cycles' of a page-stepping sequence can be triggered. To activate the trigger, select 'rising edge' or 'falling edge' as 'Trigger Condition', see figure below.

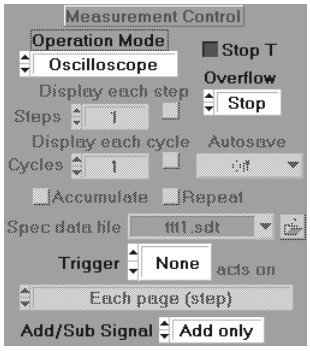


Multi-Detector Operation

Several curves can be measured simultaneously if a multi-channel detector module or several detectors and a router are used. The number of detector channels are defined under 'Page Control', 'Routing Channels X' or 'Routing Channels Y', see page 790. Up to eight curves can be displayed simultaneously during a Single-Mode measurement. The displayed curves are selected in the 'Trace Parameters'.

Oscilloscope Mode

In the 'Oscilloscope Mode' the measurement is repeated automatically at the maximum available speed. The photon collection is controlled by the parameters 'Collection Time', 'Stop T', and the stop condition defined under 'Overflow'.



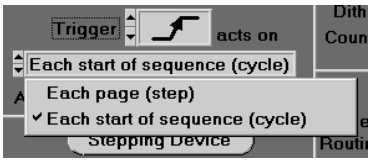
The measurement cycles are finished

- at the end of 'Collection Time' if 'Stop T' is set
- at the first overflow if 'Stop Ovfl' is set

The result is displayed on the screen at the end of each measurement cycle. Please note that at least one stop condition must be set to complete the measurement cycle and to display the data.

Experiment Trigger

The cycles of an 'Oscilloscope' measurement can be triggered. To activate the trigger, select 'rising edge' or 'falling edge' as a Trigger Condition, see figure below.



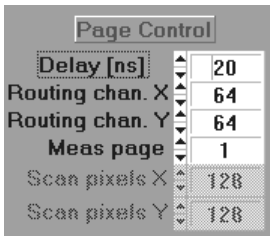
Multi-Detector Oscilloscope Operation

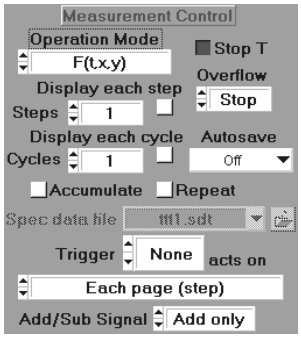
Several curves can be measured simultaneously if a multi-channel detector module or several detectors and a router are used. The number of detector channels are defined under 'Page Control', 'Routing Channels X' or 'Routing Channels Y', see page 790. Up to eight curves can be displayed simultaneously during an Oscilloscope-Mode measurement. The displayed curves are selected in the 'Trace Parameters'.

f(txy) Mode

The f(txy) mode is used for measurements with a multichannel detector module, such as the PML-16, with a large number of individual detectors, and for other applications that control the destination of the photons in the memory via the routing signal inputs. These may be multi-dimensional measurements (page 681), multispectral measurements (page 322), or applications that multiplex a large number of light sources (page 611). In terms of signal acquisition the f(txy) mode is identical with the 'Single' mode. The only difference is that the f(txy) mode interprets the data as a one-dimensional or two-dimensional array of waveform recordings. These are displayed in the 3-D display modes of the SPCM software.

The number of detector channels is defined under 'Page Control' (figure below, see also 'Page Control', page 790). The measurement simultaneously records an array of decay curves defined by 'Routing Channels X' and 'Routing Channels Y'. The maximum number of curves depends on the module type and on the ADC resolution. The photon collection is controlled by the parameters under 'Measurement Control'.





The measurement stops

- at the end of 'Collection Time' if 'Stop T' is set
- at the first overflow if 'Stop Ovfl' is set as overflow option.

If both stop conditions are set the measurement stops in either case. Without any stop condition the measurement runs until it is stopped by the operator. If the results run out of the data range (65535 counts per time channel) the overflowing parts are clipped.

Stepping through Pages

A 'f(txy)' measurement can be repeated in intervals of 'Repeat Time' and the results be written into subsequent 'Pages' of the memory. The number of subsequent measurements is de-

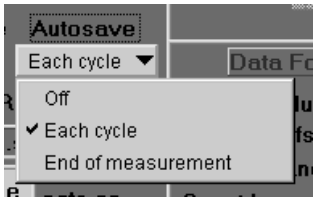
fined by ‘Steps’. The available number of steps depends on the memory size, i.e. on the module type, on ‘Routing Channels X’ and ‘Routing Channels Y’, and on the ADC resolution.

Due to the available memory size, there is a cross-dependence of ‘Routing Channels X’, ‘Routing Channels Y’, ‘Steps’ through subsequent pages, and ‘ADC Resolution’. If one of these parameters is changed beyond the limit set by memory size the software automatically limits it to the maximum possible value.

Cycles and Autosave

A stepping sequence (or, if ‘Steps’ = 1, a single f(txy) measurement) can be repeated for a defined number of ‘Cycles’.

To write the results of subsequent cycles to the hard disk the ‘Autosave’ function is used. To activate Autosave for each cycle, click on ‘Autosave’, ‘Each Cycle’.



‘Autosave’ can also be initiated at the end of the measurement, i.e. after the last cycle only. This is reasonable if the cycling function is used in conjunction with ‘Accumulate’.

Accumulate

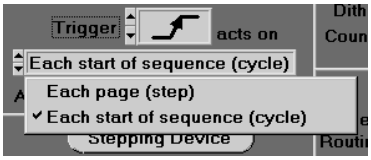
The ‘Accumulate’ function accumulates the results of several ‘Cycles’. It is often used to display intermediate results of a multi-dimensional measurement. After each cycle of the measurement is stopped, and the results are read from the SPC memory and displayed. Then the measurement is continued. The results of all cycles are accumulated. If you want to save the results automatically at the end of the accumulation, use ‘Autosave’, ‘End of Measurement’.

Repeat

After pushing the ‘Repeat’ button the complete measurement sequence repeats until the measurement is stopped by the operator.

Trigger

Either the ‘Steps’ or the ‘Cycles’ of the measurement sequence can be triggered. To activate the trigger, select ‘rising edge’ or ‘falling edge’ as ‘Trigger Condition’.



f(txy) Display

The results of an f(txy) measurement are displayed as a three-dimensional figure. The display style (multiple curve plot or colour intensity plot) is defined in the ‘Display Parameters’. Up to eight display windows can be defined to display the data of different detector or multiplexing channels, data in different time channels, or different sub-sections of a multi-dimensional data set. Please see ‘Display ’, page 797, ‘3D Trace Parameters’, page 836, and ‘Window Intervals’, page 839.

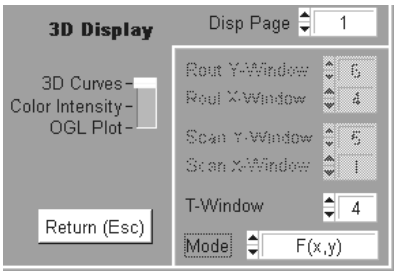
During the individual measurement steps intermediate results are displayed in intervals of ‘Display Time’. Furthermore, the result can be displayed after each step and after each cycle by switching on ‘Display after each Step’ and ‘Display after each Cycle’. However, display-

ing intermediate results requires some time. The ‘Display Time’ and ‘Display after each Step’ options should be used for collection times longer than a few seconds only.

If both ‘Routing Channels X’ and ‘Routing Channels Y’ are greater than one, or if page stepping is used the results are three- or four-dimensional data arrays. Therefore different 3D display modes are possible, e.g.

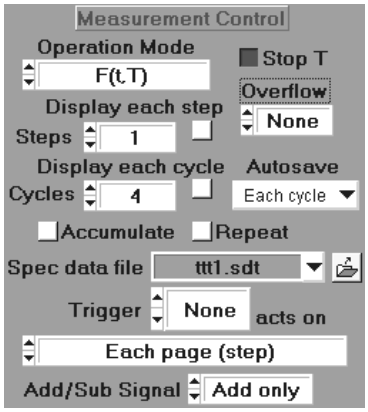
- an f(t,x) display within a selectable ‘Routing y Window’
- an f(t,y) display within a selectable ‘Routing x Window’
- an f(x,y) display within a selectable ‘Time Window’

Furthermore, a ‘Display Page’ can be defined to display a particular step of a stepping sequence. The 3D display plane and the ‘Display Page’ are selected in the ‘Display parameters’, see figure below. For details, please see ‘Display ’, page 797.



f(t,T) Mode

In the f(t,T) mode the measurement of a single curve is repeated in intervals of ‘Repeat Time’, and the results are written into subsequent pages of the memory.



The number of subsequent measurements is defined by ‘Steps’. The measurement starts in the ‘Measured Page’ defined in main panel. The stepping function can be combined with routing, i.e. several detector channels can be simultaneously measured in each step. The measurement sequence is similar to a ‘Single’ measurement with stepping through a number of pages. However, the data are interpreted as a sequence of data blocks and displayed by the 3D display routines of the SPCM software.

Steps

The number of subsequent measurements is defined by ‘Steps’. The measurement starts in the ‘Measured Page’ defined in the main panel.

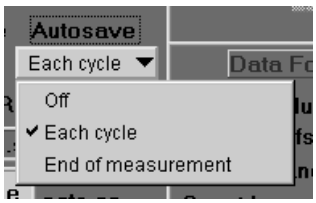
The photon collection for each step is controlled by ‘Stop T’ and the options under ‘Overflow’. The measurement of each particular step stops

- at the end of ‘Collection Time’ if ‘Stop T’ is set
- at the first overflow if ‘Stop Ovfl’ is set

If both stop conditions are set the measurement stops in both cases. If the results run out of the data range 0...65535 the overflowing parts are clipped. Please note that at least one stop condition - usually Stop T - must be set to achieve reasonable operation.

Cycles and Autosave

A stepping sequence can be repeated for a defined number of 'Cycles'. To write the results of subsequent cycles to the hard disk the 'Autosave' function can be used. To activate 'Autosave' for each cycle, click on 'Autosave', 'Each Cycle'.



'Autosave' can also be initiated at the end of the measurement, i.e. after the last cycle only. 'End of Measurement' is normally used in conjunction with 'Accumulate'.

Accumulate

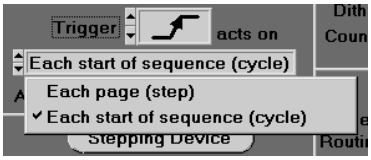
The 'Accumulate' function accumulates the results of several 'Cycles', i.e. several f(t,T) sequences. If you want to save the results automatically at the end of the accumulation, activate 'Autosave', 'End of Measurement'.

Repeat

By pushing the 'Repeat' button the complete measurement sequence can be repeated until the measurement is stopped by the operator.

Trigger

Either the 'Steps' or the 'Cycles' of the measurement sequence can be triggered. To activate the trigger, select 'rising edge' or 'falling edge' as Trigger Condition.



f(t,T) Multidetector Operation

The f(t,T) mode can be combined with multi-detector operation or multiplexing. In this case separate curve sequences are obtained for the individual detector or multiplexing channels, see Fig. 998

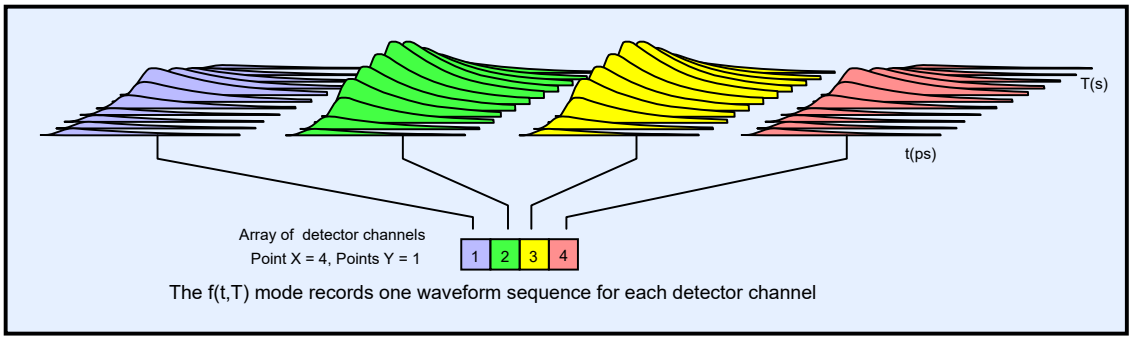


Fig. 998: f(t,T) mode, multi-detector operation

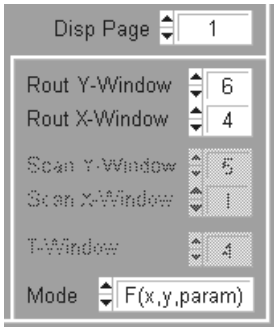
The number of detector channels is defined under 'Page Control', 'Routing Channels X' or 'Routing Channels Y', see page 790.

Due to the available memory size, there is a cross dependence of ‘Routing Channels X’, ‘Routing Channels Y’, ‘Steps’ through subsequent pages, and ‘ADC Resolution’. If one of these parameters is changed beyond the limit set by memory size the software automatically limits it to the maximum possible value. Some combinations are given in the table below.

Module Type	ADC Resol.	Routing Channels	Steps	Module Type	ADC Resol.	Routing Channels	Steps	Module Type	ADC Resol.	Routing Channels	Steps	Module Type	ADC Resol.	Routing Channels	Steps
SPC-8	4096	1	4096	SPC-7	4096	1	1024	SPC-6	4096	1	64	SPC-134	4096	1	32
	4096	8	512	SPC-144	4096	8	128		4096	8	8		4096	8	4
	256	1	65536		256	1	16384		256	1	1024		256	1	512
	256	8	8192		256	8	2048		256	8	128		256	8	64
	64	1	262144		64	1	65636		64	1	4096		64	1	2048
	64	8	32768		64	8	8192		64	8	512		64	8	256

f(t,T) Display

The results of an f(t,T) measurement are displayed as a three-dimensional figure. The display style (multiple-curve plot or colour intensity plot) is defined in the ‘Display Parameters’, see figure below.



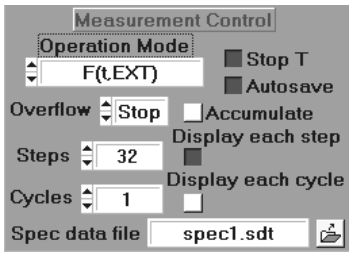
Up to eight display windows can be defined to display the data of different detector or multiplexing channels. Please see ‘Display ’, page 797, ‘3D Trace Parameters’, page 836, and ‘Window Intervals’, page 839.

An f(t,T) measurement can contain a large number of subsequent curves. If the display is in the ‘3D Curve’ mode the finite screen resolution limits the number of curves to 128 curves. To see later parts of a longer sequence, change ‘Display Page’ in the display parameters or in the main panel.

During the individual measurement steps intermediate results can be displayed in intervals of ‘Display Time’. Furthermore, the result can be displayed after each step and after each cycle. However, displaying intermediate results requires some time. The ‘Display Time’ and ‘Display after each Step’ options should be used for collection times longer than a several seconds per step only.

f(t,EXT) Mode

The measurement of a single curve is repeated in intervals of ‘Repeat Time’. The results are written into subsequent pages of the memory.



Simultaneously with the page stepping an external parameter in the measurement setup is varied. The external parameter can be the wavelength of a monochromator or the position of the detector. To control the external parameter the stepping motor controller STP-340 can be used (see data sheet or www.becker-hickl.com). The STP-340 is an additional PC module which is controlled directly by the SPC software. The device is configured by the file STP.CFG which includes minimum and maximum values for the position, step width, motor speed, the unit of the controlled parameter etc. (see STP-340 description). The f(t,ext) mode can also be used to record a sequence of IRF functions for different values of the CFD threshold or the CFD zero cross level.

Steps

The number of subsequent measurements is defined by 'Steps'. The measurement starts in the 'Measured Page' defined in the main panel. The stepping function can be combined with routing, i.e. several detector channels can be measured in each step.

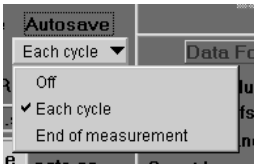
The photon collection for each step is controlled by 'Stop T' and the options under 'Overflow'. The measurement of each step stops

- at the end of 'Collection Time' if 'Stop T' is set
- at the first overflow if 'Stop Ovfl' is set

If both stop conditions are set the measurement stops in both cases. If the results run out of the data range 0...65535 the overflowing parts are clipped. Please note that at least one stop condition - usually Stop T - must be set for reasonable operation.

Cycles and Autosave

The stepping sequence can be repeated for a defined number of 'Cycles'. To write the results of subsequent cycles to the hard disk the 'Autosave' function is provided. To activate Autosave for each cycle, click on 'Autosave', 'Each Cycle'. 'Autosave' can also be initiated at the end of the measurement, i.e. after the last cycle only. 'End of Measurement' is normally used in conjunction with 'Accumulate'.



Accumulate

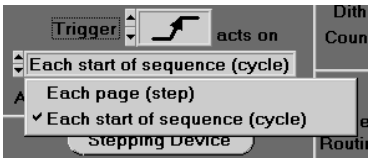
The 'Accumulate' function accumulates the results of several 'Cycles', i.e. several f(t,ext) sequences. It is often used for triggered sequences to acquire more photons than in a single shot. If you want to save the results automatically at the end of the accumulation, use 'Autosave', 'End of Measurement'.

Repeat

By pushing the 'Repeat' button the complete measurement sequence can be repeated until the measurement is stopped by the operator.

Trigger

Either the ‘Steps’ or the ‘Cycles’ of the measurement sequence can be triggered. To activate the trigger, select ‘rising edge’ or ‘falling edge’ as a Trigger Condition.



f(t,EXT) Multi-Detector Operation

As in the f(t,T) mode, multi-detector operation or multiplexing can be used to record several signals in each step of the f(t,EXT), see Fig. 999.

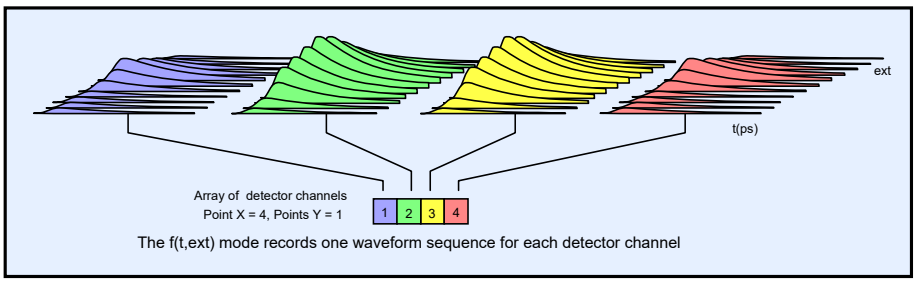


Fig. 999: f(t,EXT) mode, multi-detector operation

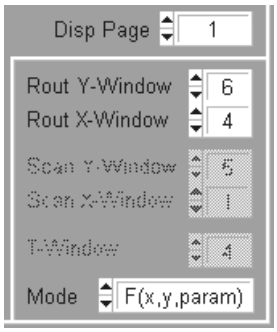
The number of detector channels are defined under ‘Page Control’, ‘Routing Channels X’ or ‘Routing Channels Y’, see page 790.

Due to the available memory size, there is a cross dependence of ‘Routing Channels X’, ‘Routing Channels Y’, ‘Steps’ through subsequent pages, and ‘ADC Resolution’. If one of these parameters is changed beyond the limit set by memory size the software automatically limits it to the maximum possible value. Some combinations are given in the table below.

Modules	ADC Resol.	Rout. Chan.	Steps	Module	ADC Resol.	Rout. Chan.	Steps	Module	Time Bins	Rout. Chan.	Steps	Module	Time Bins	Rout. Chan.	Steps
SPC-150	4096	1	1024	SPC-180	4096	1	1024	SPC-QC	4096	1	256	SPC-QC	4096	1	128
SPC-150N	4096	8	128	N, NX,	4096	8	128	-104	4096	8	32	-106	4096	8	16
SPC-130	256	1	16384	NXX	256	1	16384	-004	256	1	4096	-006	256	1	2048
EM	256	8	2048		256	8	2048		256	8	512		256	8	256
	64	1	65636		64	1	65636		64	1	16384		64	1	8192
	64	8	8192		64	8	8192		64	8	2048		64	8	1024

f(t,EXT) Display

The results of an f(t,ext) measurement are displayed as a three-dimensional figure. The display style (multiple curve plot or colour intensity plot) is defined in the ‘Display Parameters’, see figure below.



Up to eight display windows can be defined to display the data of different detector or multiplexing channels. Please see ‘Display ’, page 797, ‘3D Trace Parameters’, page 836, and ‘Window Intervals’, page 839.

An f(t,EXT) measurement can contain a large number of subsequent curves. If the display is in the ‘3D Curve’ mode the finite screen resolution limits the number of curves to 128 curves. To see later parts of a longer sequence, change ‘Display Page’ in the Display Parameters or in the main panel.

During the individual measurement steps intermediate results can be displayed in intervals of ‘Display Time’. Furthermore, the result can be displayed ‘after each step’ and ‘after each cycle’. Please note that displaying intermediate results requires some time. The ‘Display Time’ and ‘Display after each Step’ options should be used for collection times longer than a several seconds per step only.

fi(T) Mode

The ‘fi’ modes are intended for recording time resolved spectra. A waveform measurement is repeated in intervals of ‘Repeat Time’. The counts in the channels of each curve are averaged within selectable time intervals (see ‘Window Intervals’, page 839). The results of this averaging procedure represent the intensities in the selected time windows. The fi(T) mode records a time-controlled sequence of these intensity values, see Fig. 1000. Up to eight spectra in different time windows are obtained for each detector channel.

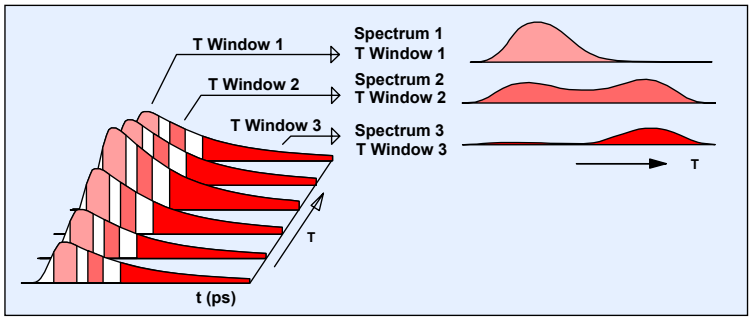
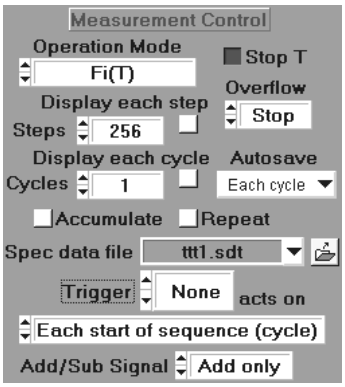


Fig. 1000: fi(T) mode. Intensities within selectable time windows are calculated and displayed as functions of the time from the start of the experiment.

Steps

The number of subsequent intensity values is defined by ‘Steps’. The stepping function can be combined with routing, i.e. several detector channels can be measured in each step.



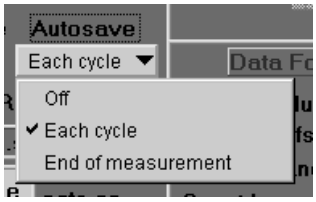
The photon collection for each step is controlled by the parameters ‘Stop T’ and the options under ‘Overflow’. The measurement of each step stops

- at the end of ‘Collection Time’ if ‘Stop T’ is set
- at the first overflow if ‘Stop Ovfl’ is set

If both stop conditions are set the measurement stops in both cases. If the results run out of the data range 0...65535 the overflowing parts are clipped. Please note that 'Stop T' must be set for reasonable operation of the fi(T) mode.

Cycles and Autosave

The sequence described above can be repeated for a defined number of 'Cycles'. The 'Autosave' function can be used to write the results of subsequent cycles to the hard disk. To activate Autosave for each cycle, click on 'Autosave', 'Each Cycle'. 'Autosave' can also be initiated at the end of the measurement, i.e. after the last cycle only. 'End of Measurement' is normally used only in conjunction with 'Accumulate'.

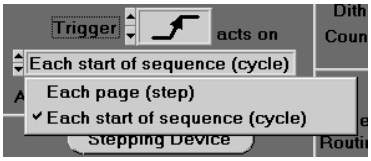


Accumulate

The 'Accumulate' function accumulates the results of several 'Cycles', i.e. several intensity sequences. If you want to save the accumulated results automatically at the end of the measurement, use 'Autosave', 'End of Measurement'.

Trigger

Either the 'Steps' or the 'Cycles' of the measurement sequence can be triggered. To activate the trigger, select 'rising edge' or 'falling edge' as a Trigger Condition.



Repeat

By pushing the 'Repeat' button the complete measurement sequence can be repeated until the measurement is stopped by the operator.

fi(T) Multi-Detector Operation

The fi(T) mode can be used in combination with multi-detector operation or multiplexing. In these cases individual spectra are obtained for the individual detector or multiplexing channels, see Fig. 1001.

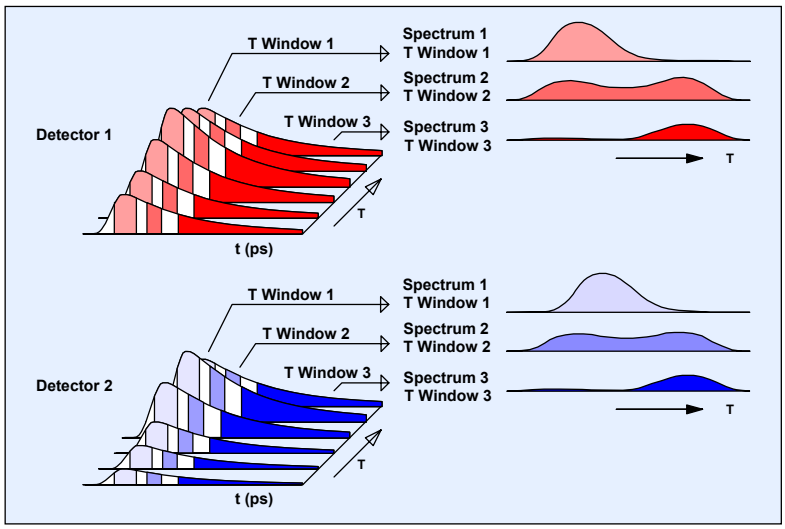


Fig. 1001: fi(T) mode, multi-detector operation

The number of detector channels is defined under ‘Page Control’, ‘Routing Channels X’ or ‘Routing Channels Y’, see page 790. The maximum number of detector channels for an fi(T) measurement depends on the module type, the ADC Resolution, the number of Time Windows and the number of routing channels used.

fi(T) Display

The display of the results is controlled by the ‘Trace Parameters’, see page 831. You can define traces for spectra in different time windows, measurement pages and recorded by different SPC modules and detectors. Two examples are shown in Fig. 1002.

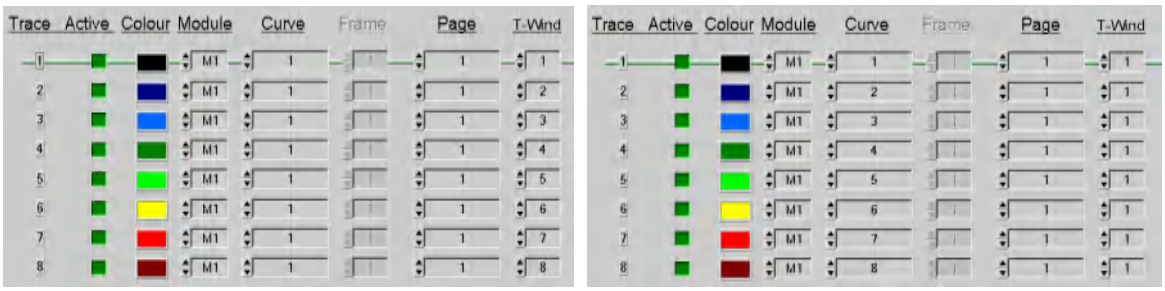


Fig. 1002: Trace parameters for the fi modes. Left: Spectra of detector 1 in subsequent time windows. Right: Spectra in time window 1 for different detectors

Intermediate results can be displayed after each step and after each cycle by switching on ‘Display after each Step’ and ‘Display after each Cycle’. However, displaying intermediate results requires some time. The ‘Display after each Step’ option and should only be used for collection times longer than a few seconds.

fi(EXT) Mode

The measurement of a single waveform is repeated in intervals of ‘Repeat Time’ and for different settings of an externally variable parameter, typically for variable wavelength. The counts in the channels of each curve are averaged within selectable time intervals (see ‘Window Intervals’, page 839). The results of the averaging procedure represent the intensities in the selected time windows. The fi(EXT) mode records of these intensity values versus the external parameter, see Fig. 1003. Up to eight time intervals can be defined. Consequently, to eight spectra are obtained for each detector channel.

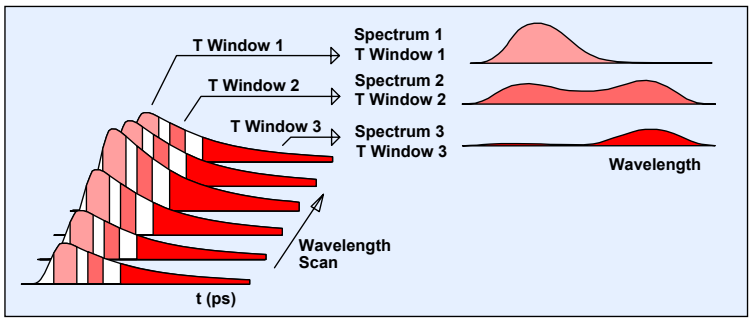
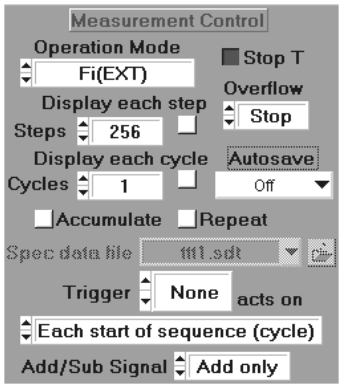


Fig. 1003: fi(EXT) mode. Intensities within selectable time windows are calculated and displayed as functions of an external parameter.

Steps

The number of subsequent intensity values is defined by ‘Steps’. The stepping function can be combined with routing, i.e. several detector channels can be measured in each step.



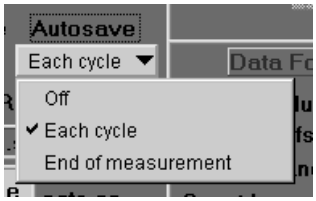
The photon collection for each step is controlled by the parameters ‘Stop T’ and the options under ‘Overflow’. The measurement of each step stops

- at the end of ‘Collection Time’ if ‘Stop T’ is set
- at the first overflow if ‘Stop Ovfl’ is set

If both stop conditions are set the measurement stops in both cases. If the results run out of the data range 0...65535 the overflowing parts are clipped. Please note that ‘Stop T’ must be set for reasonable operation of the fi(ext) mode.

Cycles and Autosave

The sequence described above can be repeated for a defined number of ‘Cycles’. The ‘Autosave’ function can be used to write the results of subsequent cycles on the hard disc. To activate Autosave for each cycle, click on ‘Autosave’, ‘Each Cycle’. ‘Autosave’ can also be used at the end of the measurement, i.e. after the last cycle only. The ‘End of Measurement’ option is normally used in conjunction with ‘Accumulate’.

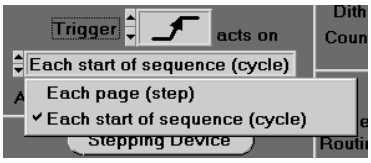


Accumulate

The ‘Accumulate’ function accumulates the results of several ‘Cycles’, i.e. several intensity sequences. If you want to save the results automatically at the end of the accumulation, use ‘Autosave’, ‘End of Measurement’.

Trigger

Either the ‘Steps’ or the ‘Cycles’ of the measurement sequence can be triggered. To activate the trigger, select ‘rising edge’ or ‘falling edge’ as a Trigger Condition.



Repeat

By pushing the ‘Repeat’ button the complete measurement sequence can be repeated until the measurement is stopped by the operator.

fi(EXT) Multidetector Operation

The fi(T) mode can be used in combination with multi-detector operation or multiplexing. In these cases individual spectra are obtained for the individual detector or multiplexing channels, see Fig. 1004.

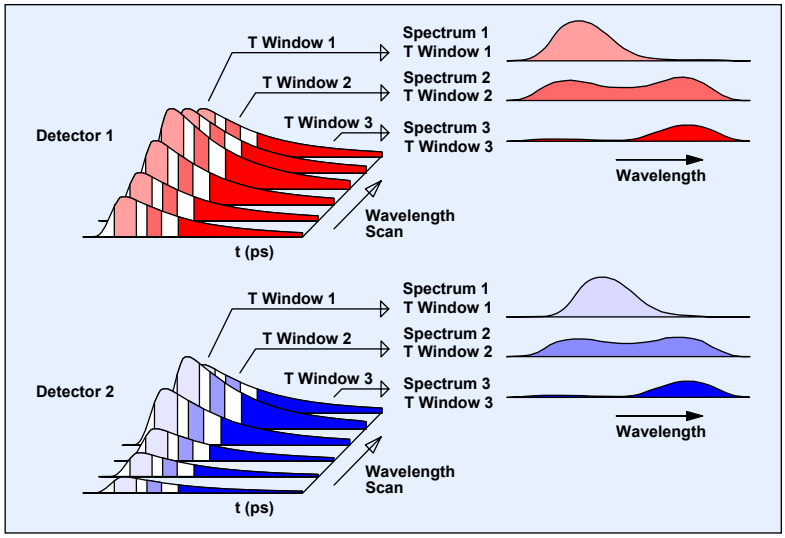


Fig. 1004: fi(EXT mode, multi-detector operation

The number of detector channels is defined under ‘Page Control’, ‘Routing Channels X’ or ‘Routing Channels Y’, see page 790. The maximum number of detector channels for an fi(EXT) measurement depends on the module type, the ADC Resolution, the number of Time Windows and the number of Routing Channels used.

fi(EXT) Display

The display of the results is controlled by the ‘Trace Parameters’. You can select spectra obtained in different time windows and recorded by different detectors of a multi-detector arrangement. Two typical settings are shown in Fig. 1005.

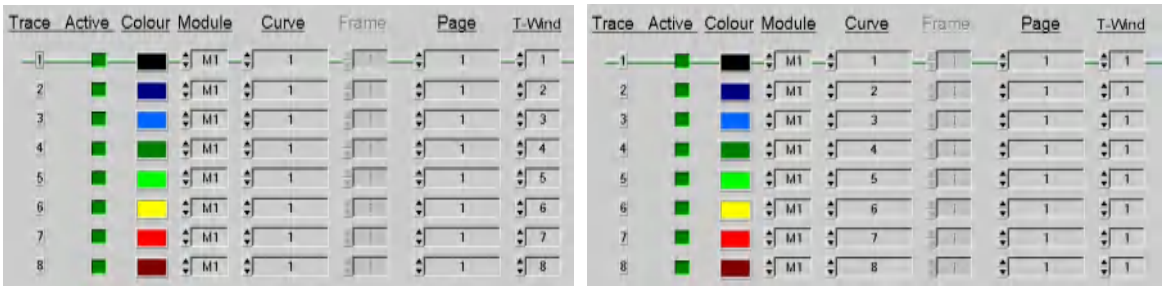


Fig. 1005: Trace parameters for the fi modes. Left: Spectra of detector 1 in subsequent time windows. Right: Spectra in time window 1 for different detectors

Intermediate results can be displayed after each step and after each cycle by switching on ‘Display after each Step’ and ‘Display after each Cycle’. However, displaying intermediate results requires some time. The ‘Display after each Step’ option and should be used for collection times longer than a one second only.

Continuous Flow Mode

The 'Continuous Flow' mode records a sequence of decay curves or other waveforms. Unlike f(t,T), the ‘Continuous Flow’ mode is strictly hardware-controlled and thus provides an extremely accurate recording sequence. Moreover, sequential recording can be combined with memory swapping so that virtually unlimited sequences can be recorded, see ‘Sequential Recording’, page 121. The Continuous Flow mode can also be used to accumulate fast, triggered sequences with stepping times down to a few microseconds. ‘Continuous Flow’ operation requires that the TCSPC module has two independent memory banks. Thus, the mode is available for the SPC-630, SPC-130/134, SPC-150, SPC-160 and SPC-180 modules only.

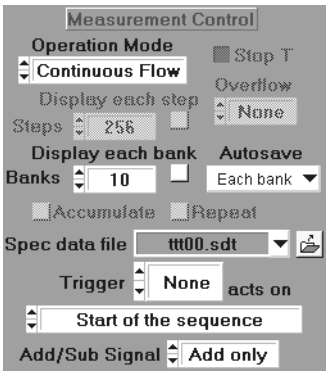


Fig. 1006: Measurement control parameters of the Continuous Flow mode

The principle of the mode is shown in Fig. 216, page 123. Decay curves are measured in time intervals of ‘Collection Time’. The measurement is repeated while the measurement system switches through all memory pages of both memory banks of the TCSPC module. While the measurement is running in one memory bank, the results of the other bank are read and stored on the hard disk. Thus, a virtually unlimited number of decay curves (or other photon distributions) can be recorded without any time gaps between subsequent recordings. In the SPC-150/154 modules continuous flow can even be combined with imaging, see page 758. The measurement control parameters are shown in Fig. 1006.

Banks and Steps

‘Banks’ defines the number of memory banks to be recorded. The number recording steps - or curves - in each memory bank depends on the selected ADC resolution, on the number of detector channels used, and on the module type. Some typical combinations are given in the table below.

SPC-630			SPC-130 SPC-134			SPC-130EM/134EM, SPC-150/154 SPC-160, SPC-180		
ADC Resolution	Routing Channels	Steps per Bank	ADC Resolution	Routing Channels	Steps per Bank	ADC Resolution	Routing Channels	Steps per Bank
4096	1	64	4096	1	32	4096	1	512
4096	8	8	4096	8	4	4096	8	128
1024	1	256	1024	1	128	1024	1	2048
1024	8	32	1024	8	16	1024	8	512
256	1	1024	256	1	512	256	1	16384
256	8	128	256	8	64	256	8	2048
64	1	4096	64	1	2048	64	1	65536
64	8	512	64	8	256	64	8	8192

Collection Time

The photon collection for each step is controlled by ‘Collection Time’. ‘Repeat Time’ and ‘Stop Condition’ are not used in the Continuous Flow mode. ‘Display after each Step’, ‘Accumulate’ and ‘Repeat’ are not available.

Autosave

Normally the ‘Continuous Flow’ mode is used with ‘Autosave’, ‘Each Bank’. That means, while the measurement is running in one memory bank, the results of the other bank are read and saved into an individual data file. The file name is specified under ‘Spec data file’. The software extends the file name with a number that counts up for the subsequent banks. A list of previously used data file names is available by clicking on the ▾ symbol. *Important*: Before starting a new measurement define a new file name for the continuous flow data. If you don’t do so you are in danger to overwrite the data of an earlier measurement.

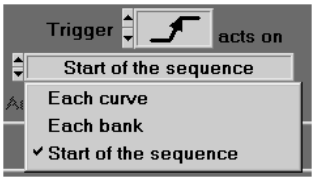
‘Autosave’ in combination with ‘End of Measurement’ is normally used for automatic saving of accumulated sequences, see below.

Accumulate

The ‘Accumulate’ function accumulates the results of repetitive sweeps through one ‘Bank’. It is normally used for fast triggered sequences. If the time per curve is less than a few milliseconds not enough photons are acquired to obtain a reasonable photon distribution in a single sweep. Thus, the stimulation of the experiment is repeated, the start of the sequencer sweep is triggered with the stimulation, and a large number of sweeps are accumulated. For accumulating fast triggered sequences set the trigger to ‘Start of Sequence’, activate the ‘Accumulate’ button, and set ‘Steps’ to a number smaller than the number of curves per memory bank. If you want to save the results automatically at the end of the accumulation, activate ‘Autosave’, ‘End of Measurement’.

Trigger

Either ‘Each Curve’, ‘Each Bank’ or the ‘Start of the Sequence’ can be triggered in the Continuous Flow mode. To activate the trigger, select ‘rising edge’ or ‘falling edge’ as trigger condition.



The trigger functions in the Continuous Flow mode can be used to create extremely powerful measurement procedures. As described above, triggering the ‘start of the sequence’ in combination with ‘accumulate’ can be used to record extremely fast sequences of decay curves, see ‘Transient Fluorescence Phenomena’, page 333.

Fast transient effects can also be recorded by triggering ‘Each bank’. In this case, the recording runs through the current memory bank, and stops. Recording in the next bank is started with the next trigger. Thus the individual sequences are recorded in subsequent banks and stored in subsequent data files. ‘Each bank’ can also be used to synchronise the recording with a two-dimensional scanner. A new bank is triggered at the beginning of each line. The subsequent banks then represent the lines of the scan, the curves within each bank the pixels within the line.

‘Each curve’ triggering can be used to synchronise the recording with the steps of a one-dimensional scan.

Continuous Flow Multidetector Operation

The Continuous Flow mode can be used with multi-detector operation or multiplexing, see Fig. 1007.

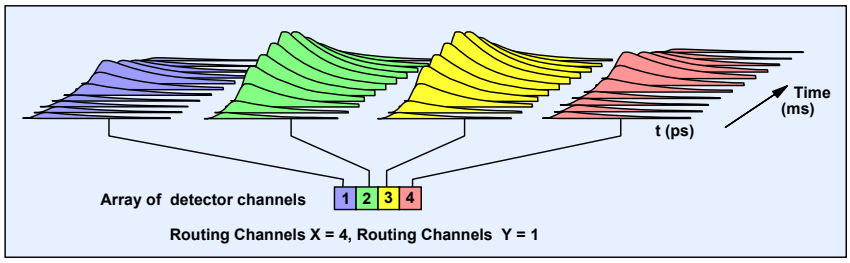


Fig. 1007: Continuous Flow mode, multi-detector operation

The number of detector channels is defined under ‘Page Control’, ‘Routing Channels X’ or ‘Routing Channels Y’, see page 790. Due to the available memory size, there is a cross dependence of ‘Routing Channels X’, ‘Routing Channels Y’, ‘ADC Resolution’ and ‘Steps’ in one memory page. If one of these parameters is changed beyond the limit set by the memory size the software automatically limits it to the maximum possible value. With increasing number of detector channels the number of subsequent recordings per memory bank and consequently the maximum gap-free stepping speed decreases.

Continuous Flow Display

A continuous-flow measurement is usually run through a large number of memory banks, and the results are saved in subsequent files. Only the last memory bank is displayed at the end of the measurement. To display the subsequent files produced by a continuous flow measurement, use the ‘Multi-File View’ function, see page 724.

The results of a continuous-flow measurement are displayed as three-dimensional figures. The display style (multiple curve plot or colour intensity plot) is defined in the ‘Display Parameters’, see figure below. Up to eight display windows can be defined to display the data of different detector or multiplexing channels. Please see ‘Display ’, page 797, ‘3D Trace Parameters’, page 836, and ‘Window Intervals’, page 839.

On bank (or one file) of a continuous-flow measurement can contain a large number of subsequent curves. If the display is in the ‘3D Curve Mode’ a maximum of 128 curves can be displayed due to the finite screen resolution. To see later parts of the sequence, change ‘Display Page’ in the Display parameters or in the Main Panel.

Intermediate results can be displayed after each bank. Displaying intermediate results requires some time and should not be used for time-critical recordings. If the display is not ready to read the data before the recording in this bank is started a gap in the recording sequence appears.

Scan Sync Out Mode

The ‘Scan Sync Out’ mode is used to record time resolved images by sending synchronisation pulses to an external scanner. The mode is implemented in the SPC-830, SPC-700/730, and the SPC-140/144 modules. The principle is shown in Fig. 1008.

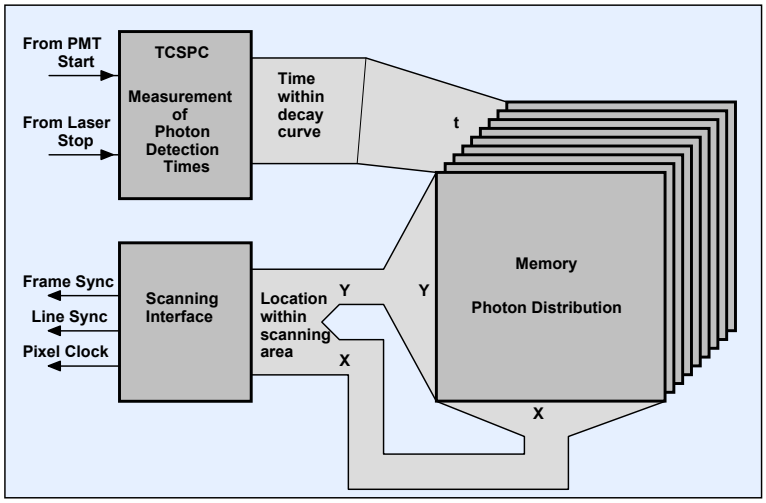


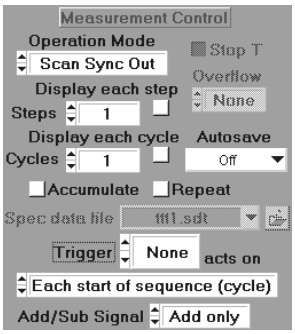
Fig. 1008: Scan Sync Out mode (routing not shown)

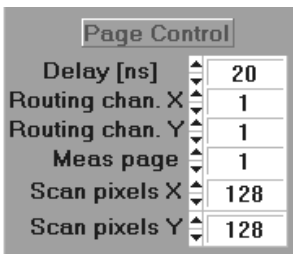
In the ‘Scan Sync Out’ mode the SPC module controls the destination curve number and delivers synchronisation pulses to an external scanning device. For each pixel of the scanned image a complete waveform is recorded. The ‘Scan Sync Out’ mode can be combined with routing, i.e. the photons in several detector channels can be recorded simultaneously. The dwell time for each pixel is ‘Collection Time’. The maximum number of pixels depends on the ADC resolution selected:

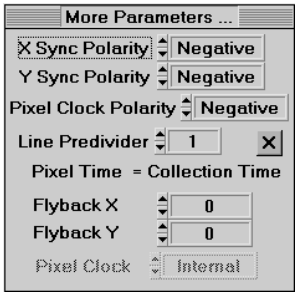
ADC Resolution	1	4	16	64	256	1024	4096
No of Pixels (SPC-730)	n.a.	n.a.	n.a.	65536	16384	4096	1024
No. of Pixels (SPC-830)	16 M	4 M	1 M	262144	65536	16385	4096
No of Pixels (SPC-150)	4 M	1 M	262144	65536	16384	4096	1024
No of Pixels (SPC-154)*	4 M	1 M	262144	65536	16384	4096	1024

* per module

The scan can be either one-dimensional or two-dimensional. The number of steps in X- and Y-direction is specified by the parameters ‘Scan Pixels X’ and ‘Scan Pixels Y’ in the ‘Page Control’ Part of the System Parameters. The definitions for the essential parameters are shown in the figures below.







The scanning parameters are defined under ‘More Parameters’. The meaning of the scanning parameters is as listed below:

X Sync Polarity: Polarity of X Sync Pulses, (H/L or L/H)
YSync Polarity: Polarity of Y Sync Pulses, (H/L or L/H)
Pixel Clock Polarity: Polarity of Pixel Clock Pulses, (H/L or L/H)

Line Predivider:	Values >1 combine several lines of the scanner into 1 line of the result
Flyback X:	Flyback time of the scanner for the X axis, in multiples of 'Collection Time'.
Flyback Y:	Flyback time of the scanner for the Y axis, in multiples of 'Collection Time'.

Stepping through Pages

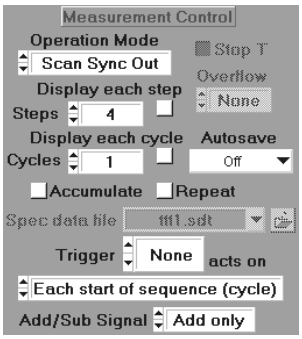
A 'Scan Sync Out' measurement can be repeated after a scan is completed and the results written into subsequent 'Pages' of the memory. The number of subsequent measurements is defined by 'Steps'. The stepping function can be combined with routing, i.e. several detector channels can be simultaneously measured in each step. The available number of steps depends on the memory size, i.e. on the module type, on 'Routing Channels X' and 'Routing Channels Y', and on the ADC resolution.

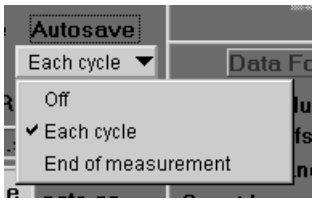
Cycles and Autosave

A stepping sequence (or, if 'Steps' = 1, a single 'Scan Sync Out' measurement) can be repeated for a defined number of 'Cycles'.

To write the results of subsequent cycles to the hard disk the 'Autosave' function is used. To activate 'Autosave' for each cycle, click on 'Autosave', 'Each Cycle'.

'Autosave' can also be initiated at the end of the measurement, i.e. after the last cycle only. This is reasonable if the cycling function is used in conjunction with accumulate.



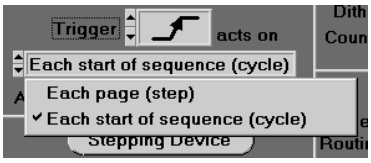


Accumulate

The 'Accumulate' function accumulates the results of several 'Cycles'. It is used to accumulate subsequent scans or to accumulate the results of a triggered stepping sequence. If you want to save the results automatically at the end of the accumulation, use 'Autosave', 'End of Measurement'.

Trigger

Either the 'Steps' or the 'Cycles' of the measurement sequence can be triggered. To activate the trigger, select 'rising edge' or 'falling edge' as Trigger Condition.



Repeat

By pushing the 'Repeat' button the complete measurement sequence can be repeated until the measurement is stopped by the operator.

Multi-Detector Operation

Multi-detector operation and multiplexing is also available in the Scan Sync Out mode. The principles is shown in Fig. 1009. For each PMT pulse, i.e. for each photon, the SPC module determines the time of the photon in the laser pulse sequence, t, and the beam location in the scanning area, X and Y. Furthermore, the detector channel number, n, for the current photon is read into the detector channel register. The obtained values of t, x, y and n are used to address the histogram memory. Thus, in the memory the distribution of the photons over the time, the image coordinates and the detector number builds up. For each detector channel a stack of images for subsequent time channels in the fluorescence decay curve exists.

It should be pointed out that 'Scan Sync Out' multi-detector operation does not involve any time gating or wavelength scanning. Therefore, the method yields a near-perfect counting efficiency and a maximum signal to noise ratio for a given acquisition time.

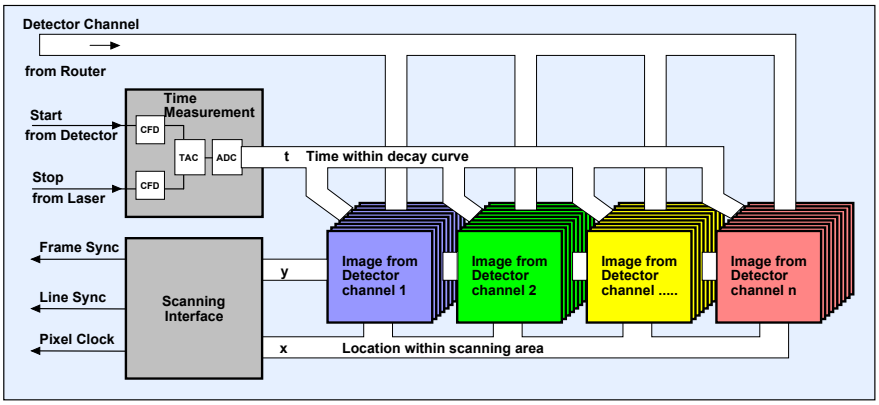
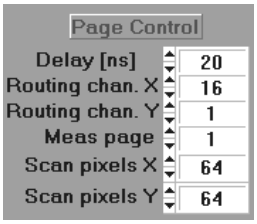


Fig. 1009: Scan Sync Out mode, multidetector operation

The number of detector channels are defined under 'Page Control', 'Routing Channels X' or 'Routing Channels Y', see figure below.



Due to the available memory size, there is a cross dependence of Routing Channels X, Routing Channels Y, Steps through subsequent pages, Scan Pixels X, Scan Pixels Y and ADC Resolution. If one of these parameters is changed beyond the limit set by memory size the software automatically limits it to the maximum possible value. Without stepping through pages the maximum number of pixels is:

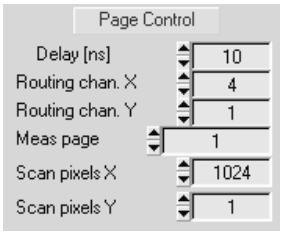
ADC Resolution, Channels	1	4	16	64	256	1024	4096
No of Pixels SPC-7, 1 detector	n.a.	n.a.	n.a.	65536	16384	4096	1024
SPC-7, 4 detectors	n.a.	n.a.	n.a.	16384	4096	1024	256
SPC-7, 16 detectors	n.a.	n.a.	n.a.	4096	1024	256	64
No. of Pixels SPC-8, 1 detector	16 M	4 M	1 M	262144	65536	16385	4096
SPC-8, 4 detectors	4 M	1 M	262144	65536	16385	4096	1024
SPC-8, 16 detectors	1M	262144	65536	16385	4096	1024	256

Sequential Recording in the Scan Sync Out mode

Scanning in the scan sync out mode is fully hardware-controlled. The SPC module uses a sequencer that steps through the memory blocks of the subsequent pixels in accurately defined time intervals. Therefore the Scan Sync Out mode can also be used for sequential recording.

The stepping time can be as short as 100 ns, the start of the sequence can be triggered, and an extremely large number of waveform blocks is available. Thus, the Scan Sync Out mode can be used both for recording single sequences and fast triggered accumulation of sequences.

To record a sequence in the scan sync out mode, define an ‘image’ of one line, with a number of ‘Scan pixels’ corresponding to the desired number of steps. The Page-Control parameters shown below give an example of a sequence of 1024 steps and four detector channels. An SPC-830 allows you to use no less than 4096 time channels under these conditions.



The time per step of the sequence is ‘Collection Time’. To record a fast triggered sequence, set a trigger condition different from ‘None’, ‘Accumulate’, and the desired number of ‘Cycles’.

Scan Sync In Mode

The ‘Scan Sync In’ mode records images in combination with scanners that deliver synchronisation pulses to the SPC module. 'Scan Sync In' is able to work at extremely high pixel rates. It can be used for the fast galvanometer scanner typically used in laser scanning microscopes. It works even with the polygon scanners and resonance scanners used in high-speed tissue imaging systems. The mode is available in the SPC-700/730, SPC-830, SPC-140/144 and SPC-150/154 modules. The principle of the ‘Scan Sync In’ mode is shown in Fig. 1010.

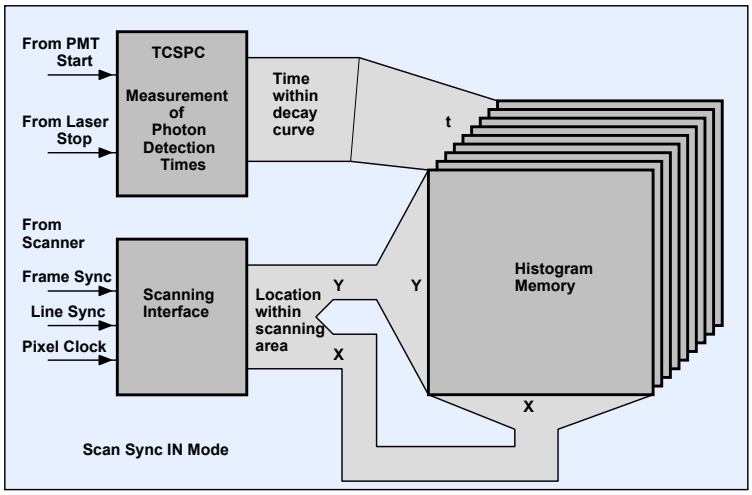


Fig. 1010: Module configuration in the 'Scan Sync In' mode

In the ‘Scan Sync In’ mode the SPC module receives synchronisation pulses from the scanner to control its internal destination curve number. For each PMT pulse, i.e. for each photon, the SPC module determines the time of the photon in the laser pulse sequence and the beam location in the scanning area. These values are used to address the histogram memory in which the events are accumulated. Thus, in the memory the distribution of the photon density over X, Y, and the time within the fluorescence decay function builds up.

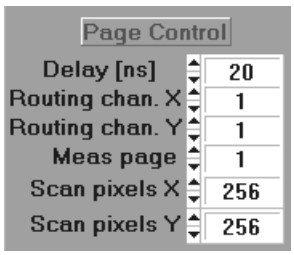
The data acquisition works at any scanning rate of a laser scanning microscope. The acquisition can be run over as many frame scans as necessary to collect enough photons. Due to the

synchronisation via the scan synchronisation pulses, the zoom functions of a scanning microscope automatically act also on the TCSPC recording and can be used in the normal way.

The parameter 'Collection Time' defines the overall image recording time. When the measurement is started the recording starts with the next frame sync pulse, i.e. at the beginning of the next frame. When the collection time is over the measurement stops with the next frame sync pulse, i.e. when the current frame is completed.

Image Format

The number of pixels in X- and Y-direction is specified by the parameters 'Scan Pixels X' and 'Scan Pixels Y' in the 'Page Control' Part of the system parameters, see figure below.



The maximum number of pixels depends on the used ADC resolution. For a single detector measurement without stepping the maximum number of pixels per image is:

ADC Resolution	**1**	**4**	**16**	**64**	**256**	**1024**	**4096**
No of Pixels (SPC-730)	n.a.	n.a.	n.a.	65536	16384	4096	1024
No of Pixels (SPC-150)	4 M	1 M	262144	65536	16384	4096	1024
No of Pixels (SPC-160)	4 M	1 M	262144	65536	16384	4096	1024
No. of Pixels (SPC-830)	16 M	4 M	1 M	262144	65536	16385	4096

Scan Synchronisation Parameters

The synchronisation of the recording process in the SPC module with the operation of the scanner requires a number of hardware parameters to be defined. To define these parameters, click on 'More Parameters'. This opens the panel shown in Fig. 1011. The configuration of the panel changes with the definition of the pixel clock source, compare Fig. 1011 left and right.

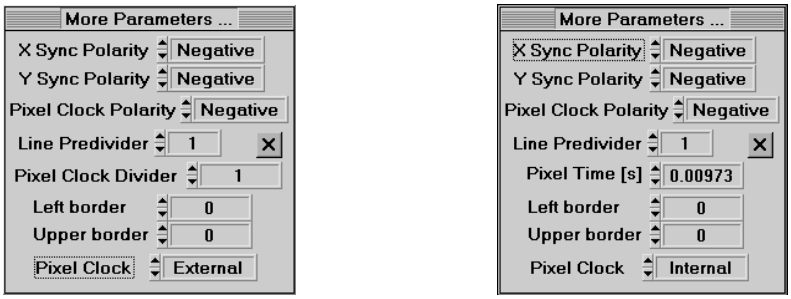


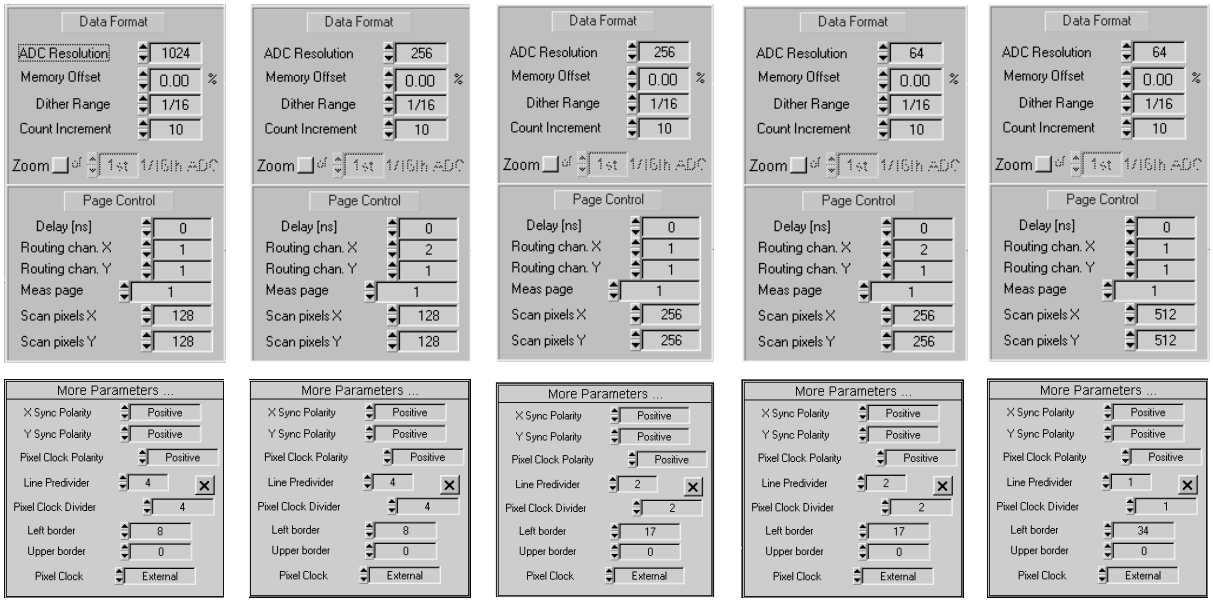
Fig. 1011: Scanning parameters of the Scan Sync In mode. Left: External pixel clock. Right: Internal pixel clock.

The meaning of the scanning parameters is as shown below:

X Sync Polarity:	Polarity of X Sync Pulses, (H/L or L/H)
YSync Polarity:	Polarity of Y Sync Pulses, (H/L or L/H)
Pixel Clock Polarity:	Polarity of Pixel Clock Pulses, (H/L or L/H)
Line Predivider:	Predivider for X Sync. Values >1 merge several lines of the scanner into one line of the result.
Pixel Clock Divider:	Divider for 'Pixel Clock External', values >1 merge several pixels of the scanner into 1 pixel of the result.

Pixel Time:	For ‘Pixel Clock Internal’ only. Dwell Time per pixel for ‘Pixel Clock Internal’ Within one line, the pixel number is counted up in fixed time intervals set by ‘Pixel Time’.
Pixel Clock Predivider:	For ‘Pixel Clock External’ only. For Predivider > 1 several subsequent pixels of the scanner are combined into one result pixel.
Upper Border:	Number of lines which are not recorded at the start of each frame. Used to zoom into the image without changing the scanner operation.
Left Border:	Number of pixels which are not recorded at the start of each line. Used to zoom into the image without changing the scanner operation.
Pixel Clock:	The source of the pixel clock can be external (from the scanner) or internal. The internal pixel clock is derived from the system clock of the SPC board. Internal pixel clock requires that the Xsync frequency from the scanner be constant and stable.

For scanners which deliver a pixel clock the setup of the scan parameters is straightforward. Set the line and pixel clock dividers according to the ratios of the pixel numbers of the scanner and the pixel numbers of the TCSPC image (Scan pixels X and Scan Pixels Y). Possible image shift can be corrected by using the ‘boarder parameters’, see also Fig. 408, page 262. A few combinations of time channel, routing channel, and pixel numbers are shown in Fig. 1012. The parameters refer to an LSM scan of 512 x 512 pixels. As can be seen from Fig. 1012, the available pixel numbers are relatively moderate for modern standards. For higher pixel numbers please see 'FIFO Imaging Mode', page 762.



128 x 128 pixels 1024 time channels 1 detector	128 x128 pixels 256 time channels 2 detectors, routing	256 x 256 pixels 256 time channels 1 detector	256 x 256 pixels 64 time channels 2 detectors, routing	512 x 512 pixels 64 time channels 1 detector

Fig. 1012: Scan parameters in Scan Sync In mode, external pixel clock. Pixel and time channel numbers for an SPC-830. For the SPC-150, SPC-180, or SPC-730 divide the time channels by four or the pixels numbers by two. The LSM scan is 512 x 512 pixels.

For scanners that do not deliver a pixel clock (e.g. the Leica SP2) the internal pixel clock must be used. The pixel time must then be defined correctly. This may be difficult if the speed of the scanner is not known. We suggest to start with an approximate pixel time and then correct the setting by try and error, see Fig. 408, page 262. For video-compatible scanning (64 µs per line) the number of recorded pixels per line is

Pixel Time ns	400	800	1600	3200
Pixels / Line	160	80	40	20

The number of lines in the recorded image is:

Line Predivider	1	2	4	8
Lines / Frame	256	128	64	32

Stepping through Pages

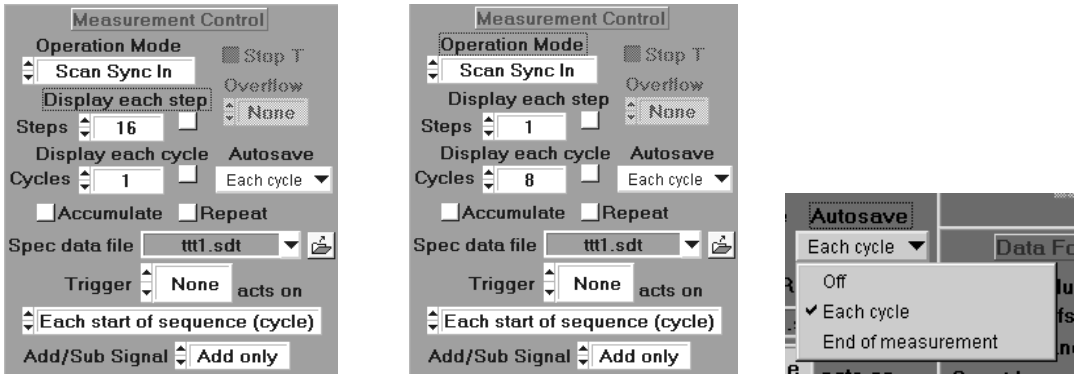
A ‘Scan Sync In’ measurement can be repeated after a scan is completed and the results be written into subsequent ‘Pages’ of the memory. The number of subsequent measurements is defined by ‘Steps’. The stepping function can be combined with routing, i.e. several detector channels can be measured in each step. The available number of steps depends on the memory size, i.e. on the module type, on 'Routing Channels X' and 'Routing Channels Y', and on the ADC resolution.

Cycles and Autosave

A stepping sequence (or, if ‘Steps’ = 1, a single ‘Scan Sync In’ measurement) can be repeated for a defined number of ‘Cycles’.

To write the results of subsequent cycles to the hard disk the ‘Autosave’ function is provided. To activate ‘Autosave’ for each cycle, click on ‘Autosave’, ‘Each Cycle’.

‘Autosave’ can also be initiated at the end of the measurement, i.e. after the last cycle only. This is reasonable if the cycling function is used in conjunction with accumulate.



Definitions for Page Stepping, Cycles, and Autosave

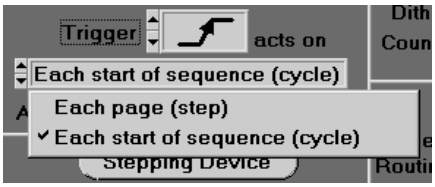
Accumulate

The ‘Accumulate’ function accumulates the results of several ‘Cycles’. It is used to accumulate subsequent scans or to accumulate the results of a triggered stepping sequence. If you want to save the results automatically at the end of the accumulation, use ‘Autosave’, ‘End of Measurement’.

‘Accumulate’ can be used to obtain on-line display during the image acquisition: Define a ‘Collection Time’ of about 10 seconds. Specify a large number of ‘Cycles’. Switch on ‘Accumulate’ and ‘Display each Cycle’. The SPC module will run subsequent acquisition cycles with the specified collection time, accumulate the photons of the cycles, and display the accumulated image.

Trigger

Either the ‘Steps’ or the ‘Cycles’ of the measurement sequence can be triggered. To activate the trigger, select ‘rising edge’ or ‘falling edge’ as Trigger Condition.



Repeat

With ‘Repeat’ the complete measurement or measurement sequence is repeated until the measurement is stopped by the operator.

Multi-Detector Operation

The Scan Sync In mode can be used in combination with multi-detector operation or laser multiplexing. The principle is shown in Fig. 1013. For each PMT pulse, i.e. for each photon, the SPC module determines the time of the photon in the laser pulse sequence, t, and the beam location in the scanning area, X and Y. Furthermore, the detector channel number, n, for the current photon is read into the detector channel register. The obtained values of t, x, y and n are used to address the histogram memory. Thus, in the memory the distribution of the photons over the time, the image coordinates and the detector number builds up. The result can be interpreted as a number of data sets for the individual detectors. Each data set contains a large number of images for consecutive times in the fluorescence decay.

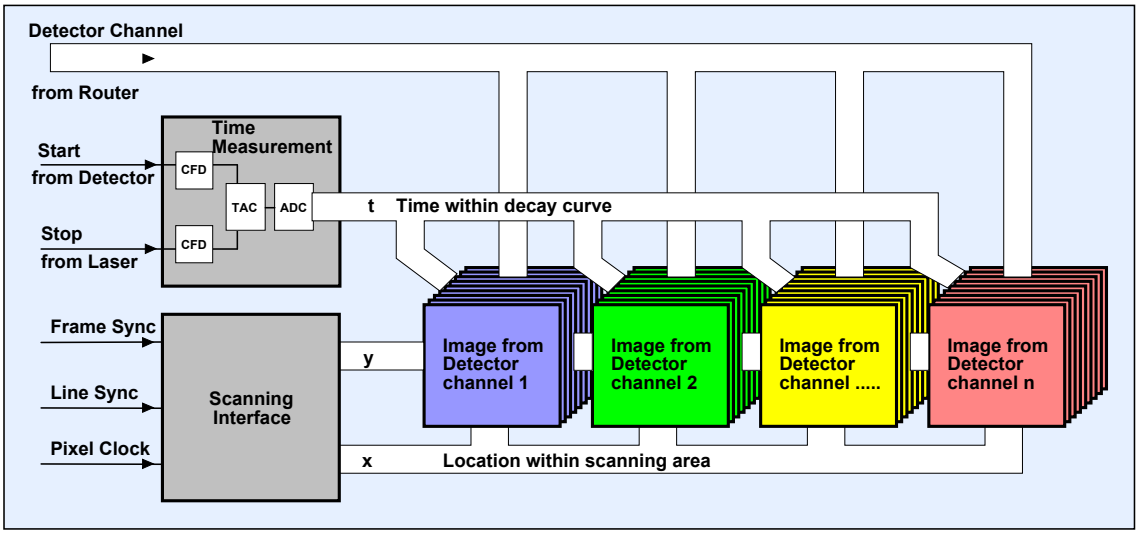
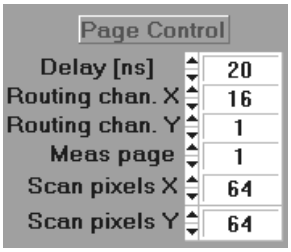


Fig. 1013: Scan Sync In mode, multidetector operation

The number of detector channels are defined under ‘Page Control’, ‘Routing Channels X’ or ‘Routing Channels Y’, see figure below.



Due to the size limitation of the on-board memory, there is a cross dependence of Routing Channels X, Routing Channels Y, steps through subsequent pages, Scan Pixels X, Scan Pixels Y, and ADC Resolution. If one of these parameters is changed beyond the limit set by

memory size the software automatically limits it to the maximum possible value. Without stepping through pages the maximum number of pixels is:

	ADC Resolution, Channels						
Module, no. of detectors	**1**	**4**	**16**	**64**	**256**	**1024**	**4096**
SPC-730							
1 detector	n.a.	n.a.	n.a.	65536	16384	4096	1024
4 detectors	n.a.	n.a.	n.a.	16384	4096	1024	256
16 detectors	n.a.	n.a.	n.a.	4096	1024	256	64
SPC-830							
1 detector	16 M	4 M	1 M	262144	65536	16385	4096
4 detectors	4 M	1 M	262144	65536	16385	4096	1024
16 detectors	1M	262144	65536	16385	4096	1024	256
SPC-150							
1 detector/channel	4 M	1 M	262144	65536	16384	4096	1024
4 detectors/channel	1 M	262144	65536	16384	4096	1024	256
16 detectors/channel	262144	65536	16384	4096	1024	256	64
SPC-154							
4 detectors	4M	1 M	262144	65536	16385	4096	1024
SPC-160, SPC-180							
1 detector/channel	4 M	1 M	262144	65536	16384	4096	1024
4 detectors/channel	1 M	262144	65536	16384	4096	1024	256
16 detectors/channel	262144	65536	16384	4096	1024	256	64
SPC-164							
4 detectors	4M	1 M	262144	65536	16385	4096	1024

Scan Sync In, Continuous Flow Imaging

In the SPC-150/154 modules imaging in the Scan Sync In mode can be combined with ‘continuous flow’ operation. The device memory is split into two memory banks. The banks are used by turns. While the measurement is running in one bank the data of the other bank are read, and vice versa. Thus, an infinite sequence of images is recorded, without gaps between the recordings. The procedure is similar to the ‘continuous flow mode’ for sequences of curves, see page 747. The measurement and page control parameters are shown in Fig. 1014.

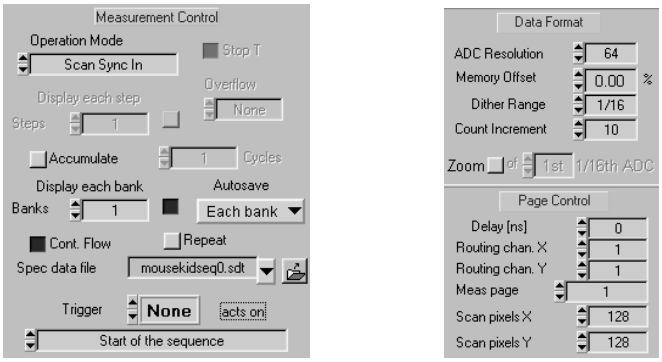


Fig. 1014: Control parameters for continuous flow imaging. Left: Measurement control parameters. Right: ADC and page control parameters

Continuous flow operation of Scan Sync In is activated by clicking on the ‘Cont. Flow’ button in the measurement control parameters.

‘Banks’ defines the number of memory banks to be recorded. The recording in each bank starts with the next frame clock pulse, and continues until the first frame clock pulse after the end of the ‘collection time’. The data of each bank are saved into a separate data file. The name of the files is specified under ‘Spec data file’. The software extends the file name with a number that counts up for the subsequent banks. A list of previously used data file names is available by clicking on the ▾ symbol. *Important*: Before starting a new measurement define

a new file name for the continuous flow data. If you don't do so you are in danger to overwrite the data of an earlier measurement.

To see the results of the individual measurement steps you may activate the 'Display each bank' button. However, please remember that the build-up of the images takes time and computing power. It may therefore reduce the speed at which the image sequence can be recorded.

Continuous-flow operation can be used in combination with the experiment trigger. Either the start of the sequence or the starts of the measurements in the individual memory banks can be triggered.

The ADC and page control parameters are shown in Fig. 1014, right. The numbers of time channels, detectors, and pixels are defined as in the standard Scan-Sync-In mode. Because the device memory of the TCSPC module is split in two banks the maximum images size or the ADC resolution is only 50% of the size in the Scan Sync In mode without continuous flow. This may be considered a drawback. However, continuous-flow operation aims at very fast recording sequences on the order of one second and below. The low photon numbers accumulated within a collection time this short by itself requires a reduction of the pixel number. (For collection times longer than a few seconds you may use the standard Scan-Sync-In mode with autosave.)

To display the subsequent files produced by a continuous flow measurement, use the 'Multi-File View' function, see page 724.

Display of Scan Sync In Data

The display of Scan Sync In data is controlled by the Display Parameters, the 3D Trace Parameters, and the Window Parameters of the SPCM software. Please see 'Display of FLIM Data', page 806.

Scan XY Out Mode (SPC-700/730 only)

The SPC-700/730 modules have a 'Scan XY Out' mode that sends digital X-Y signals to an external scanner. The mode can also be used to record fast hardware-controlled time series of single-point measurements. The principle is shown in Fig. 1015.

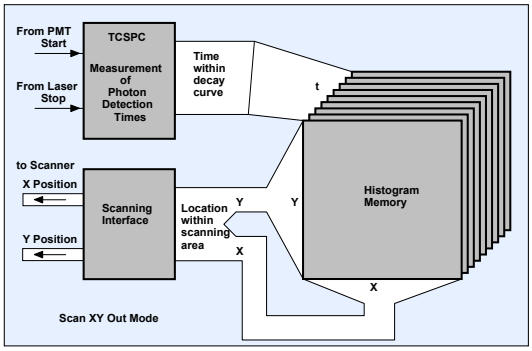


Fig. 1015: Module configuration in the Scan XY Out mode

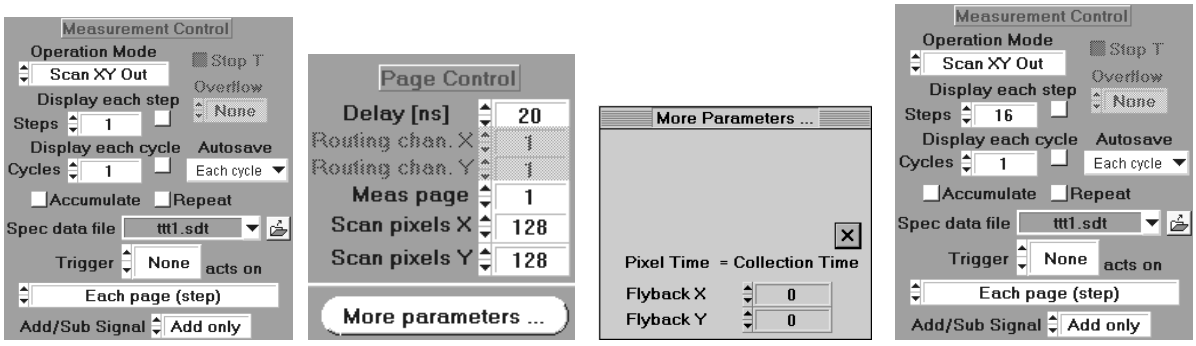
In the 'Scan XY Out' mode the SPC-700 and -730 modules control the destination curve number internally and deliver digital X and Y position signals to an external scanning device.

The XY position is available at the routing connector of the module. Thus, the maximum number of XY bits is 14, and the maximum number of pixels is 16384. Since the routing lines of the SPC modules are used for XY output the 'Scan XY Out' mode cannot be used with routing.

For each pixel of the image a complete waveform is recorded. The dwell time for each pixel is 'Collection Time'. The maximum number of pixels depends on the selected ADC resolution:

ADC Resolution	64	256	1024	4096
No of Pixels	16384	16384	4096	1024

The definitions for the XY Out mode are shown below. The scan can be either one-dimensional or two-dimensional. The number of steps in X- and Y-direction is specified by the parameters 'Scan Pixels X' and 'Scan Pixels Y' in the 'Page Control' Part of the System Parameters.



The scanning parameters are defined under 'More Parameters'. The meaning of the scanning parameters is listed below:

Flyback X: Flyback time of the scanner for the X axis, defined as multiples of 'Collection Time'. After the X position signal has switched back to the '0' position the operation is suspended for the 'Flyback X' time to give the scanner mirror time to settle.

Flyback Y: Flyback time of the scanner for the Y axis, defined as multiples of 'Collection Time'. After the Y position signal has switched back to the '0' position the operation is suspended for the 'Flyback Y' time to give the scanner mirror time to settle.

Stepping through Pages

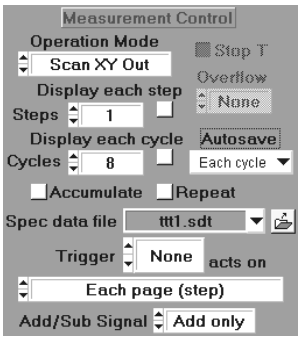
A ‘Scan XY Out’ measurement can be repeated after a scan is completed and the results be written into subsequent ‘Pages’ of the memory. The number of subsequent measurements is defined by ‘Steps’. The available number of steps depends on the memory size, i.e. on the module type, on 'Routing Channels X' and 'Routing Channels Y', and on the ADC resolution.

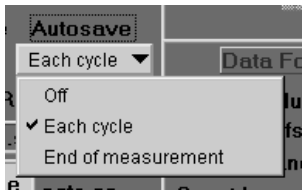
Cycles and Autosave

A stepping sequence (or, if ‘Steps’ = 1, a single ‘Scan XY Out’ measurement) can be repeated for a defined number of ‘Cycles’.

To write the results of subsequent cycles to the hard disk the ‘Autosave’ function is used. To activate ‘Autosave’ for each cycle, click on ‘Autosave’, ‘Each Cycle’.

‘Autosave’ can also be initiated at the end of the measurement, i.e. after the last cycle only. This is reasonable if the cycling function is used in conjunction with accumulate.



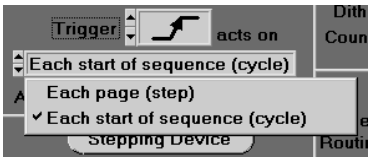


Accumulate

The ‘Accumulate’ function accumulates the results of several ‘Cycles’. It is used to accumulate subsequent scans or to accumulate the results of a triggered stepping sequence. If you want to save the results automatically at the end of the accumulation, use ‘Autosave’, ‘End of Measurement’.

Trigger

Either the ‘Steps’ or the ‘Cycles’ of the measurement sequence can be triggered. To activate the trigger, select ‘rising edge’ or ‘falling edge’ as ‘Trigger Condition’.



Repeat

By pushing the ‘Repeat’ button the complete measurement sequence can be repeated until the measurement is stopped by the operator.

FIFO Imaging Mode

All SPC-150/152/154, SPC-160/162/164, SPC-180 modules, and SPC-830 modules manufactured later than May 2007 have a 'FIFO Imaging' mode built in. The mode records fluorescence lifetime images with pixel numbers or time-channel numbers beyond the limit set by the memory of the SPC module. Moreover, it is able to record MCS lifetime images on the microsecond or millisecond time scale. In terms of photon recording the FIFO Imaging mode is similar to the standard FIFO mode, i.e. it records parameter-tagged data of the individual photons and transfers them into the computer for further processing. However, the FIFO imaging mode also records synchronisation pulses from a scanner via the event marker inputs of the SPC module and builds up FLIM images, PLIM images, combined fluorescence and phosphorescence lifetime (FLIM/PLIM) images, and intensity images from the parallel counter channel of the SPC-160.

Configuration of different image data types

The types of images to be built up are defined in a panel 'Select & Configure Histograms', see Fig. 1016 right. It opens by a click on the 'Configure' button in the measurement control part of the system parameter panel, see Fig. 1016, left.

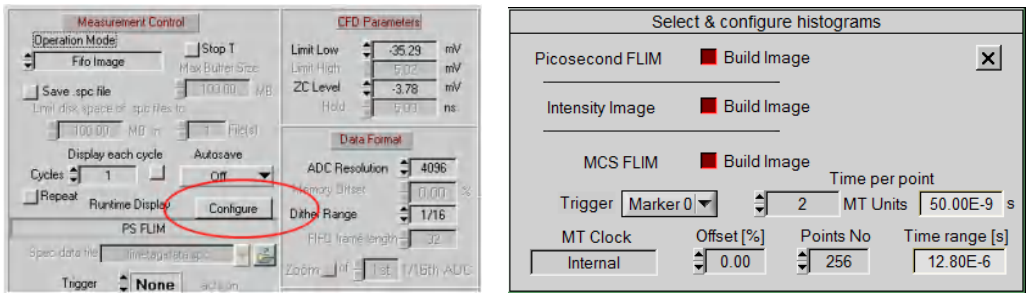


Fig. 1016: Configuring the types of images to be built up in the FIFO Imaging mode.

The 'Picosecond FLIM' button selects normal FLIM. 'Intensity Image' selects the build-up of an intensity image from the parallel counter channel of the SPC-160, see page 428. The MCS FLIM button activates a multi-channel scaler (MCS) imaging mode. Instead of the TAC times it uses macro-time differences of the photons to a reference pulse at one of the marker inputs. In laser scanning microscopes the MCS FLIM mode is used to record PLIM by the procedure described in section 'Simultaneous ', page 434. All three functions can be activated simultaneously, as shown in Fig. 1016.

Display of different image types

Images of different data types are recorded simultaneously and can be displayed simultaneously. Display windows for the images are activated in the '3D Trace Parameters', please see 'Display', page 806.

Measurement Control

The general measurement control parameters of the FIFO Imaging mode are the same as for the basic FIFO mode.

The basic setup for FIFO imaging is shown in Fig. 1017, left. The operation mode is 'FIFO Imaging', the cycle, repeat, and autosave functions are turned off. The .spc (parameter-tagged photon data) are not saved. Instead, the SPCM software analyses the FIFO data online. What the software does with the data is defined in the 'Configure' menu, as described above. Stop T is not set, the measurement is stopped by the operator when an appropriate image quality has been reached. The collection time, display time, and repeat time parameters have the same

effects as in the other operation modes. The Display Time defines how often intermediate images are displayed.

From the point of view of the user the measurement procedure is virtually the same as in the Scan Sync In mode, except for the fact that larger images, more time channels, other types of images, or more detector channels are available. The display parameters, window intervals, and 3D Trace parameters are the same as for the Scan sync In mode (see Display, page 806).

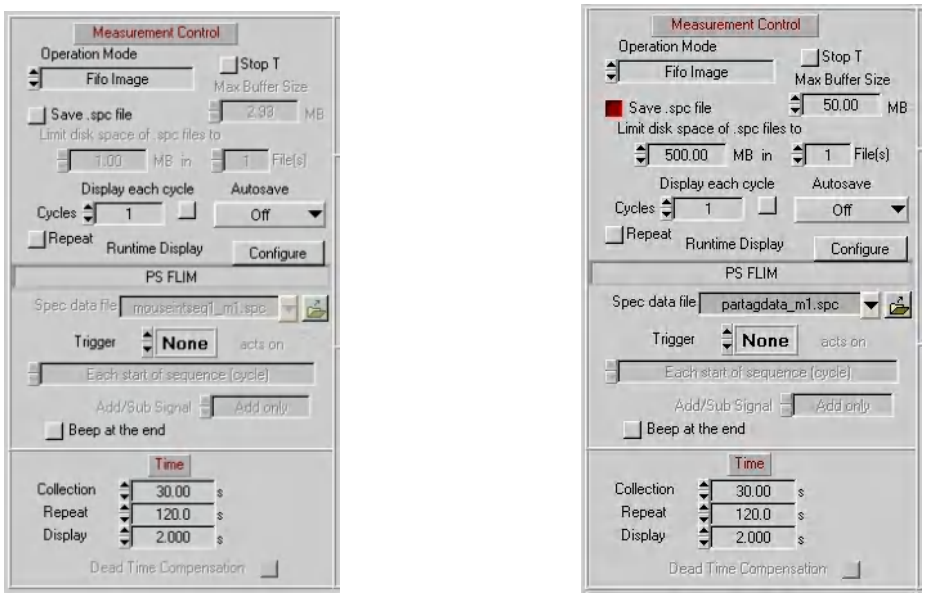


Fig. 1017: Measurement control parameters for FIFO Imaging. Left without, right with saving of time-tag data.

For special data analysis procedures it may be desirable to save not only the final FLIM images but also the parameter-tagged photon data. A measurement control parameter setup with saving of the time-tag data is shown in Fig. 1017, right. Because time-tag data can be extremely voluminous the file size is limited by ‘Limit .SPC File Size’. When this file size is reached the recording stops. The name of the FIFO data file is specified in the ‘Spec Data File’ field. To change the file name, click on the disc symbol right of the name field. A list of previously used data file names is available by clicking on the symbol. *Important*: Before starting a new measurement define a new file name for the FIFO data. If you don’t do so you are in danger of overwriting the FIFO data of an earlier measurement.

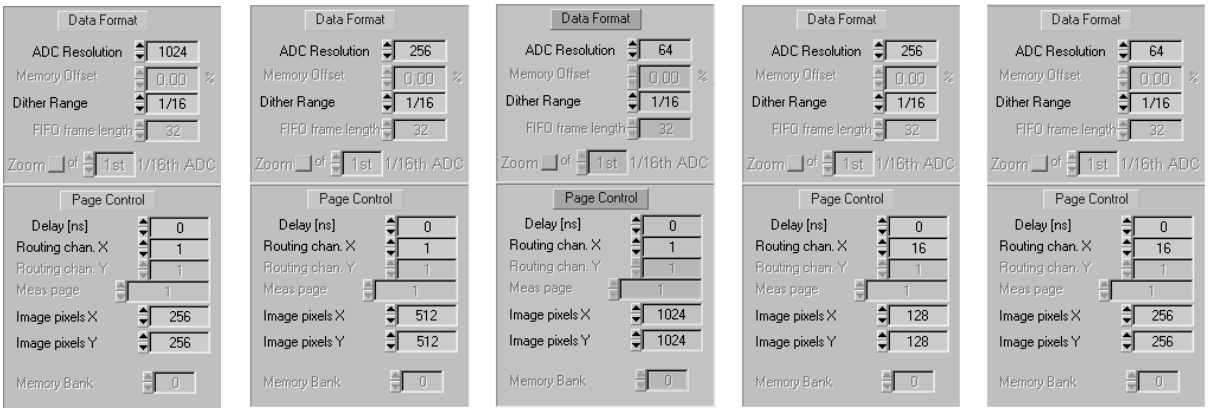
Before the data are written to the hard disk they are buffered in the main memory of the computer. The buffer size is defined by ‘Max Buffer Size’. The SPCM software checks whether enough memory is available; buffers sizes too large are rejected.

Every time the buffer is filled the data are stored on the hard disc. If possible, the buffer size should therefore be large enough to buffer the data of the entire measurement. If not enough buffer is available the computer has to periodically transfer the buffered data on the hard disc. The hard-disk actions may slow down the readout from the FIFO memory of the TCSPC module. It may then happen that the FIFO memory of the TCSPC module overflows. If this happens it may be better to reduce ‘Max Buffer Size’ to a few Megabyte. The data are then written in smaller portions, and within time intervals that are buffered by the FIFO. The better solution is, however, to upgrade your computer with more memory.

Both the start and the stop of a FIFO imaging measurement are synchronised with the frame clock. This avoids intensity steps in the images by recording incomplete frames. An unconditional stop of the measurement can be forced by a click on the stop-measurement button followed by a second click.

Image Format in 32 bit SPCM Software

The number of time channels, number of routing channels, and the number of pixels are defined in the Data Format and Page Control section of the system parameters. Examples for the 32-bit version of SPCM are shown in Fig. 1018.



256 x 256 pixels
1024 time channels
1 detector

512 x 512 pixels
256 time channels
1 detector

1024 x 1024 pixels
64 time channels
1 detector

128 x 128 pixels
256 time channels
16 detector channels

256 x 256 pixels
64 time channels
16 detector channels

Fig. 1018: Time-channel, pixel, and detector channel number of typical FLIM data formats. 32-bit SPCM software.

Image Format in 64-bit SPCM Software

The 64-bit version of the SPCM software achieves much larger image formats than the 32-bit version. The available image size depends on the amount of memory installed in the computer. Combinations of pixels numbers, time-channel numbers, and numbers of routing channels are shown in Fig. 1019. Images with up to 2048 x 2048 pixels can be recorded while maintaining the FLIM-typical ADC resolution of 256 time channels.



Fig. 1019: Time-channel, pixel, and detector channel number of typical FLIM data formats. 64-bit SPCM software.

When SPCM starts it does not automatically allocate memory for the maximum possible image size. The amount of memory Windows reserves for SPCM can be changed manually by clicking on Max Image Size in the Data Format definition. This opens the panel shown in Fig. 1020.

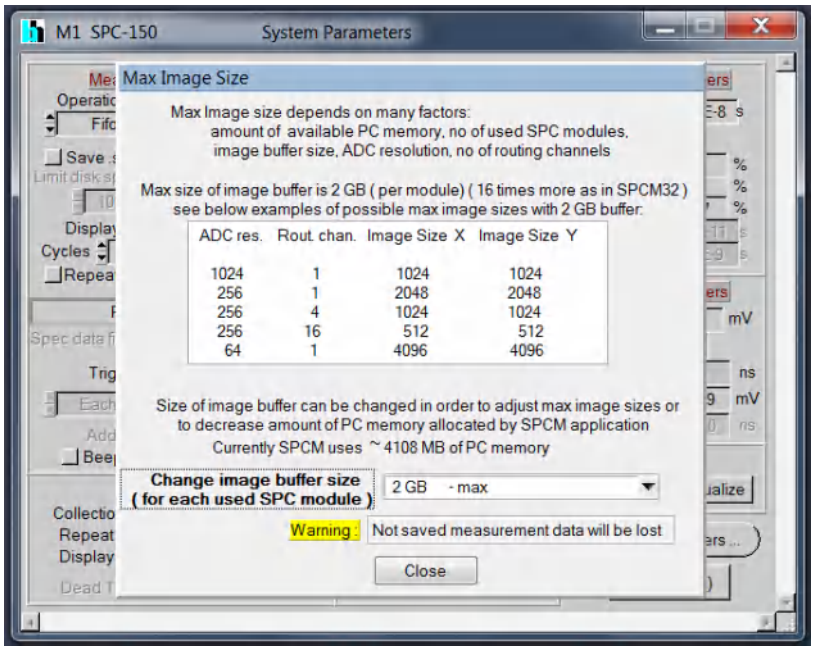


Fig. 1020: Definition of maximum amount of memory reserved for image recording

Mosaic Imaging Function

SPCM 64 bit has a ‘Mosaic Imaging’ function to record arrays of lifetime images. The array can represent a spatial array of images scanned with the ‘Tile Imaging’ function of a laser scanning microscope, images in different depth of a sample, or a time-series of images. Please see page 127 and page 400 for details. The mosaic can also represent images of different wavelength recorded by multi-wavelength FLIM. The definition of the mosaic FLIM parameters is shown in Fig. 1021. Every element of the mosaic has the format defined in the Data Format section, see Fig. 1019. With the parameters shown in Fig. 1021 an array of 64 images of 256 x 256 pixels would be recorded, see Fig. 1021, right. Mosaic data can be accumulated to record fast time series for repeatable processes. The restart of the mosaic recording can be triggered by a signal at the trigger input of the TCSPC module or by a pulse edge at the Marker 3 input.

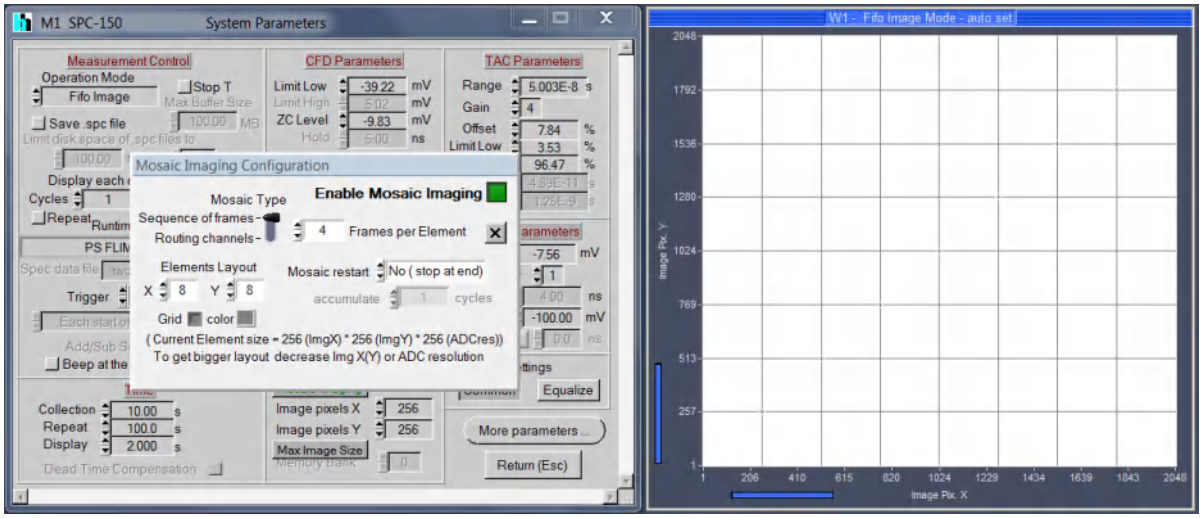


Fig. 1021: Definition of a FLIM mosaic

Scan Synchronisation Parameters

The hardware parameters controlling the synchronisation with the scanner are defined under ‘More Parameters’. The setup panel is shown in Fig. 1022.

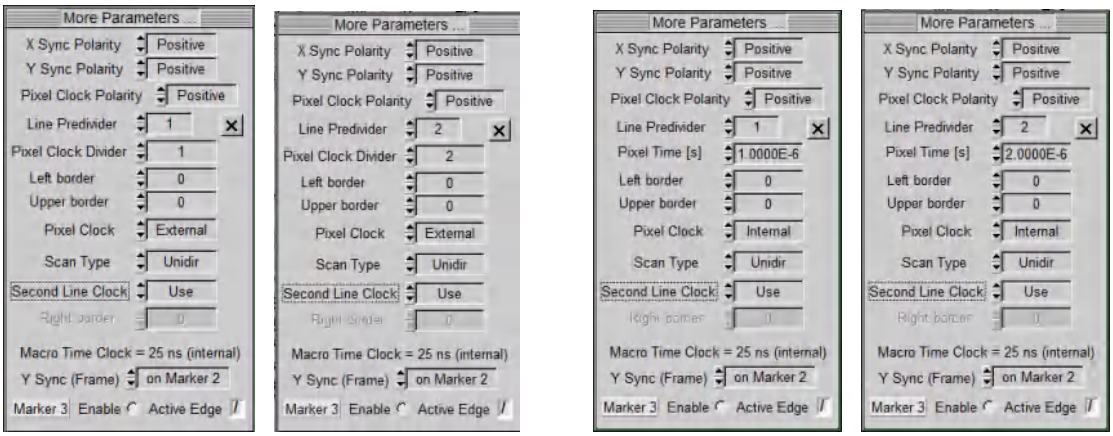


Fig. 1022: Scan synchronisation parameters of the FIFO Imaging mode. Left and second left: External pixel clock, Synchronisation by frame, line and pixel clock, pixel binning 1:1 and 2:1. Right: Internal pixel clock, Synchronisation by frame and line clock only. Pixel binning 1:1 and 2:1

In most FLIM applications recording in the SPC module is synchronised with the scanner via Frame Clock (Y Sync), Line Clock (X Sync) and Pixel Clock pulses. The corresponding scan-parameter setup is shown in Fig. 1022, left and second left. The panel allows you to define the polarity (active edge) of the synchronisation pulses pixel and line binning factors, (line and pixel clock predividers), and a shift of the left and upper border of the recorded image area against the line and frame clock. Please see Fig. 408, page 262 for the effect on the recorded images.

You can define operation with unidirectional (Scan type unidirectional) and bidirectional scanning (Scan type bidirectional). Scanners running in the bidirectional mode normally deliver a line clock at the beginning of the forward scan and at the beginning of the backward scan. 'Second Line Clock' must be set to 'Use'. Scanners running in the unidirectional mode may deliver a line clock at the beginning of each line or at the beginning and at the end of each line. In the second case 'Second Line Clock' must be set to 'Skip' to avoid the recording of ghost images during the beam flyback.

For scanners which do not deliver a pixel clock an internal pixel clock can be used, see Fig. 1022, right. The SPCM software then calculates the position of the current photon within a line from the macro time difference between the photon and the previous line clock. The disadvantage of using an internal pixel clock is that the pixel time has to be individually selected for different scanner speed. Moreover, intensity imaging via the parallel counter channel of the SPC-160 does not work: The counting result of the individual pixels is transferred with the external pixel clock. Without the external pixel clock no counter result is transferred. PLIM by the technique described at page 434 does not work as well: The laser modulation for PLIM must be synchronised with the pixel clock. This is not externally available if the internal pixel clock is used.

Event Markers

The scan clock pulses are detected via the ‘Event Marker’ inputs of the SPC-150 and SPC-830 modules. Normally, Marker 0, 1, and 2 are used for pixel, line, and frame clock, respectively. They are enabled automatically. The fourth marker input (Marker 3) is not normally used for FLIM and therefore not enabled, see Fig. 1022. It can, however, be used for FLITS (see page 410). FLITS requires that the source of the frame clock be switched from the

scanner to the stimulation source. This can be conveniently achieved by connecting the scanner frame clock and the FLITS trigger to Marker 2 and Marker 3, respectively, and selecting between both via the 'Y Sync (Frame)' source parameter in the scan synchronisation panel. Switching from FLIM to FLITS is then only a matter of loading the appropriate predefined setup.

Cycle, Repeat, and Autosave Functions

A FIFO measurement can be repeated for a defined number of cycles, and the results saved into individual data files. For using these functions, please set Stop T to stop the individual cycles after the defined collection time.

Routing

Routing works the same way as in the photon-distribution modes. The number of routing channels and the routing delay are defined in the system parameter panel under 'Page Control', see Fig. 1023.

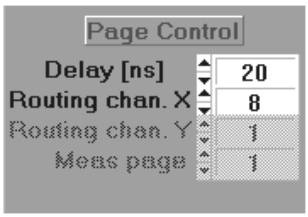


Fig. 1023: Definition of routing in the FIFO Imaging mode

Microsecond Lifetime Imaging: MCS FLIM

Starting form version 9.0 the SPCM software has a 'Triggered Accumulation MCS' option in the FIFO mode. It is available for all SPC-150 modules, all SPC-160 modules, and SPC-830 modules manufactured later than May 2007. The MCS mode uses the macro times of the photons to record decay data at the microsecond or millisecond time scale. The timing reference for the photons is a pulse at one of the 'Marker' inputs of the SPC card. The triggered MCS procedure can also be used to record microsecond or millisecond lifetime images in the FIFO Imaging mode. 'MCS FLIM' is defined in the lower part of the runtime definition panel, see Fig. 1024.

'Trigger' defines which of the marker inputs is used as a timing reference. It is usually Marker 3 because Markers 0, 1, and 2 are used for the scan clocks. However, often the excitation pulses are synchronous with the pixels. 'Trigger' can then be identical with the pixel clock, i.e. Marker 0. Please make sure that the marker input used for trigger is enabled in the 'More Parameters' panel of the 'System Parameters', see, Fig. 1024 right.

The time channel width (Time per point) can be any multiple of the macro time clock period. It is defined by a number of Macro Time units. The number of points of the curves is defined by 'Points No.'. The time range of the curves recorded is then given by the product of Time per Point and Points No. It is displayed under 'Time range'. The recording can be shifted by applying and 'Offset' to the photon times. Both positive and negative offsets are possible.

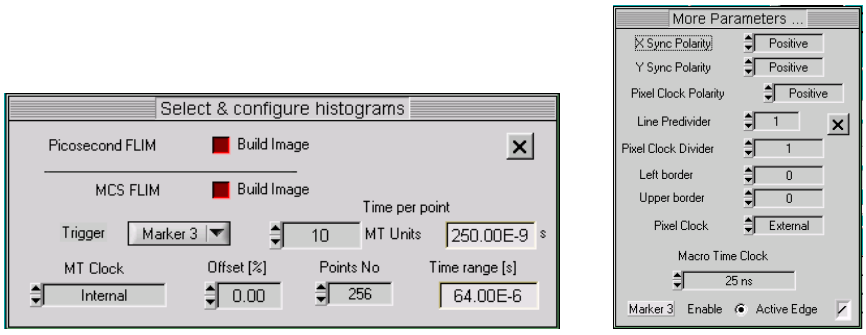


Fig. 1024: Left: Definition of MCS FLIM parameters. Right: Definition of the macro time clock source and the marker clock edge

Normally MCS FLIM recording is done with the internal macro time clock. However, for special applications the SYNC frequency can be used. Using the SYNC frequency does, of course, require that the SYNC signal has a constant period, and is continuously present.

MCS FLIM works in combination with normal FLIM recording, see option ‘ps FLIM’ in the configuration panel. The combination of both requires that a high-frequency pulsed laser is turned on and off at a period in µs or ms range. Please see ‘‘Dual Time-Base Recording’, page 130, or ‘Simultaneous FLIM/PLIM’, page 434. Examples are shown in the applications part of this handbook, please see page 434. MCS FLIM works also in combination with routing.

Delay Correction for 16-Channel Detectors

The individual channels of the multi-anode PMTs of the PML-16 detectors have slightly different transit times. These transit time variations are no problem for conventional multi-wavelength fluorescence decay and FLIM measurements. The bh SPCImage data analysis software calculates a synthetic IRF for each channel. The result is then independent of the delay variation. Problems can, however, occur when global analysis is applied to multi-wavelength data, or when multi-wavelength FLIM by the Mosaic function of the SPCM software is used. SPCM versions later than August 2015 therefore have a channel-delay correction implemented. The feature is available in the FIFO and FIFO Imaging mode. It is reached via the ‘Channel Correction’ button in the page control section of the system parameters, see Fig. 1025, left. The detector correction panel itself is shown in Fig. 1025, right. For each channel, a correction value (in picoseconds) can be typed in. For multi-modules systems with several PML detectors the number of the SPC module (M1, M2, M3, M4) can be selected. The correction data can be saved into a text file. The correction data are local to the SPC system; they are not stored in the sdt files.

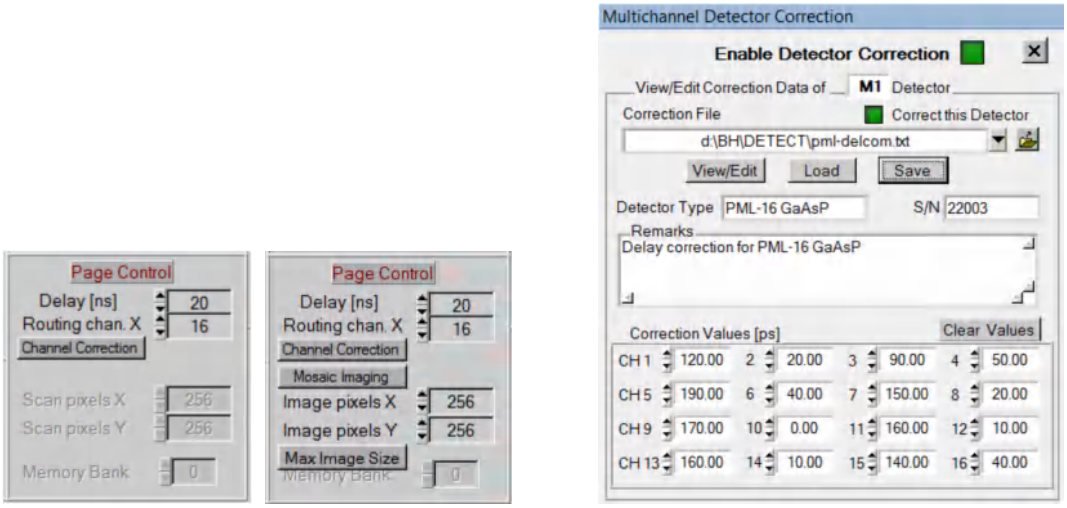


Fig. 1025: Correction of the delay variation of the PML-16 channels. Left: Page control section of the SPCM system parameters, the delay correction is reached via the 'Channel Correction' button. Right: Detector correction panel. The delay correction values for channel 1 to 16 are entered in picoseconds.

The effect of the delay compensation on the IRFs of the channels of a PML-16 GaAsP is shown in Fig. 1026. The left figure is without, the right figure with delay compensation.

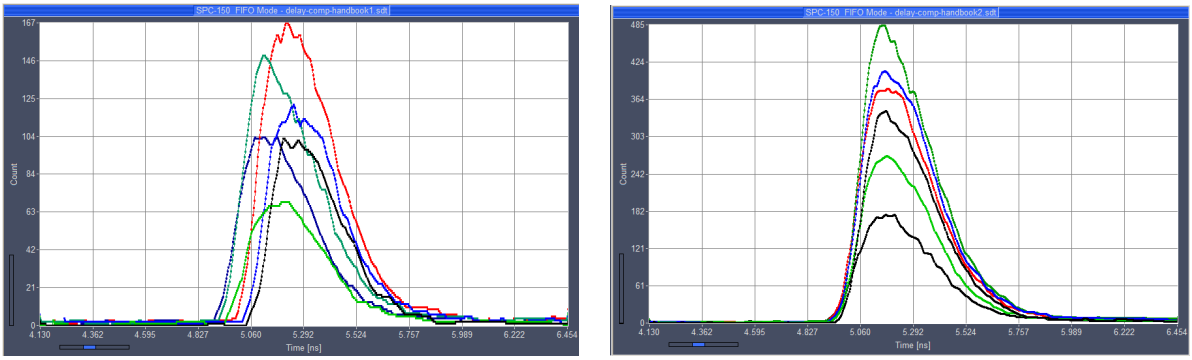


Fig. 1026: Effect of channel-delay compensation. Left without, right with delay compensation. Curves were smoothed by smooth function of 2D data operations.

FIFO Mode

The 'FIFO' mode records ‘Parameter Tagged’ data of the detected photons. It differs from the other modes in that it does not build up any histograms of the photon detection times. Instead, the detection time of each individual photon in the laser pulse sequence is stored together with the time from the start of the experiment and the detector channel number.

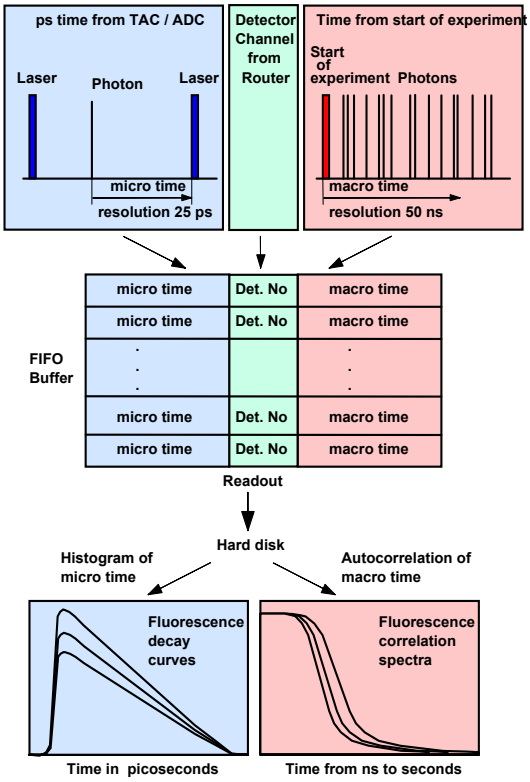


Fig. 1027: Recording in the FIFO Mode

The memory is configured as a FIFO (First In First Out) buffer. It receives the photon data at the input and is continuously read at the output. Therefore, the FIFO mode produces a continuous stream of photon data which is stored on the hard disk or processed on-line (see also ‘Recording Parameter-Tagged ’ page 132).

The 'FIFO' mode is available in the SPC-600/630, SPC-830, SPC-130 / 134, SPC-130 / 134EM, SPC-140 / 144, SPC-150 / 154 and SPC-160/164 modules.

FIFO (parameter-tag) data can be used for a wide variety of fluorescence analysis techniques (see ‘Fluorescence Correlation Spectroscopy’, page 639, and ‘Time-Resolved Single-Molecule Spectroscopy’, page 665.

By calculating a histogram of the ‘Micro Times’, i.e. the times of the photons in the laser pulse sequence, the fluorescence decay functions for the individual detectors are obtained. FCS curves are obtained by calculating the autocorrelation functions of the ‘Macro Times’, i.e. the times from the start of the experiment. Cross correlation curves of different detector channels are obtained by calculating the cross-correlation functions. The data can also be used to calculate photon counting histograms, lifetime histograms, and intensity traces. The SPCM software calculates these functions either on-line from the stream of photon data and off-line from the generated FIFO data files.

System Parameter Setup

FIFO Measurement Control

The measurement control section of the System Parameters for the FIFO mode is shown in Fig. 1028. 'Operation Mode' is set to 'FIFO'. The settings shown on the left calculate and display decay curves, FCS curves, and an MCS (intensity) trace online. The time-tag data are not saved.

The settings shown in Fig. 1028, right, calculate the curves online, but simultaneously save the time-tag data into a file. The name of the FIFO data file is specified in the 'Spec Data File' field. To change the file name, click on the disc symbol right of the name field. A list of previously used data file names is available by clicking on the symbol. *Important*: Before starting a new measurement define a new file name for the FIFO data. If you don't do so you are in danger to overwrite the FIFO data of an earlier measurement.

The measurement data can be stored into several subsequent data files. The file names are then automatically extended with a 3-digit number that is automatically incremented for each subsequent file.

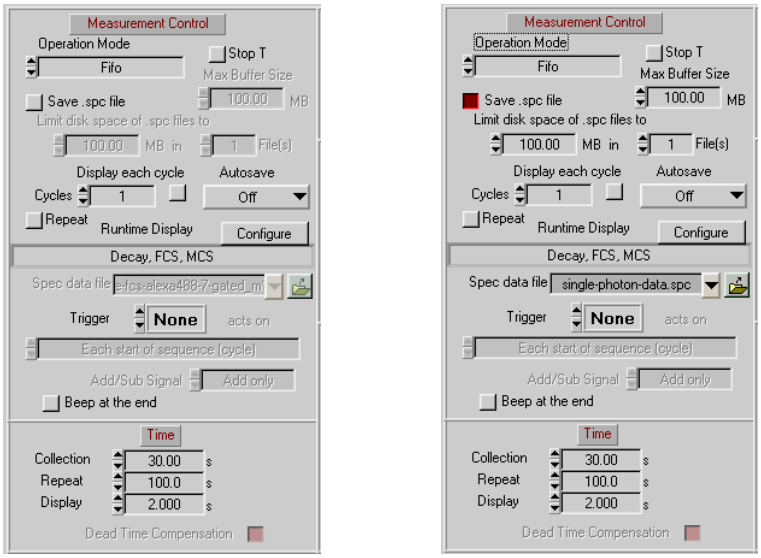


Fig. 1028: Measurement control parameters of the FIFO mode. Left without, right with saving of parameter-tag data

Under 'Limit disk space of .spc File' you can define a maximum file size for the time-tag data. The measurement stops when this file size is reached. The measurement can also be stopped after a defined acquisition time. Activate the 'Stop T' button if you want to stop after a specified time.

'Max Buffer Size' defines a buffer in the RAM of the computer. If enough RAM is available the buffer size should be as large as or larger than the specified file size.

The buffer stores the data before they are saved to the hard disk. If possible, the buffer should be large enough to buffer the FIFO data of the complete measurement. The SPCM software then stores the time-tag data into the RAM before it writes them on the hard disc so that there are no hard disc actions during the measurement. Usually, the buffer size can be as large as 200 to 300 MB for a computer with 1 GB of RAM. Under no circumstances a buffer size larger than the available memory space of the computer should be used. Windows may then attempt to provide virtual memory, i.e. to swap memory space with the hard disc. This makes the computer extremely slow and almost certainly causes problems with the data transfer from the SPC module.

If a sufficiently large buffer is not available use a buffer smaller than the value specified under ‘limit disk space’. Of course, the SPCM software writes to the hard disk when the buffer is full. Although this may slow down the data transfer from the SPC module the loss is by far smaller than for memory swapping.

‘Trigger’ defines whether or not the measurement is started by an experiment trigger. In the examples shown in Fig. 1028 the experiment trigger is not used; the setting is ‘none’. The acquisition then starts by a click on the ‘Start’ button of the SPCM software. Please note that the software does not necessarily start several SPC modules synchronously. For synchronous start either an external trigger or the ‘Trigger Master’ function (see page 795) must be used.

‘Collection time’ defines the acquisition time for the ‘Stop T option. ‘Display Time’ is the update interval for the online display.

Cycle, Autosave Functions

A FIFO measurement can be repeated for a defined number of cycles, and the results saved into individual data files. For using these functions, please set Stop T to stop the individual cycles after the defined collection time.

Source of the Macro Time Clock

FIFO mode measurements can be performed with an internal or with an external macro-time clock. FCS experiments with CW lasers are performed with the internal macro time clock. Also MCS and triggered MCS measurements (see page 775) are usually run with the internal macro time clock.

FCS experiments with pulsed lasers are performed with an external macro time clock. The clock then comes from the SYNC input of the SPC module. The SYNC-synchronous macro time clock prevents that the laser pulse frequency interferes with the macro time clock frequency. The result would be a periodical variation of the number of laser pulses per macro-time period and a periodic ripple in the correlation data. The bh SPC-830, SPC-130/134, SPC-140/144 and SPC-150/154 therefore provide a clock path from the SYNC input to the macro time clock.

The source of the macro time clock is selected via the ‘More Parameters’ button. Clicking on this button opens the panel shown in Fig. 1029. The options for the SPC-830, the SPC-130/134, and the SPC-150/154 are shown left to right.

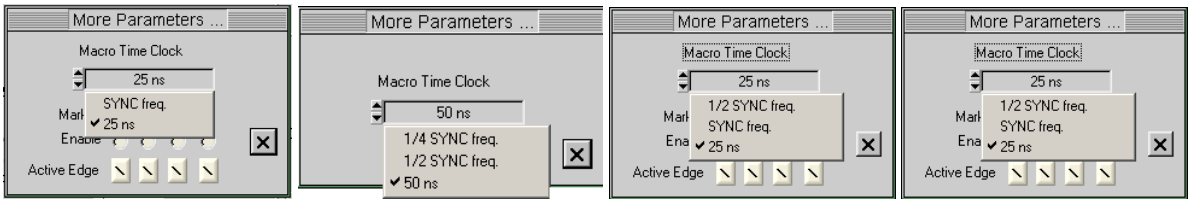
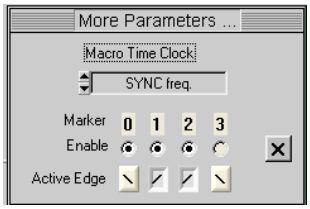


Fig. 1029: Selection of the macro time clock source. Left to right: SPC-830, SPC-130/134, SPC-130/130EM, SPC-150/154 and

Event Markers

The SPC-150 and the SPC-830 modules are able to detect external events at four TTL input lines of their 15-pin connectors, and put these in the data stream of the photons. The markers can be defined under ‘More Parameters’. Event markers are used as a timing reference of the triggered MCS function (see Fig. 1035), and for the scan clocks of the FIFO Imaging mode. The markers can be enabled or disabled, and the active edge of the signal can be selected.



Marker pin assignement, 15-pin connector

Marker 0: Pin 12, same as pxl clk
Marker 1: Pin 9, same as line clk
Marker 2: Pin 8, same as frame clk
Marker 3: Pin 11

Fig. 1030: Definition of event markers

Routing

Routing works the same way as in the photon-distribution modes. The number of routing channels and the routing delay are defined in the system parameter panel under 'Page Control', see Fig. 1031.

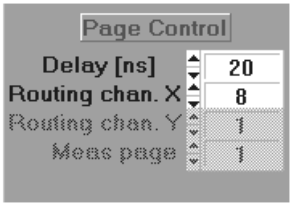


Fig. 1031: Definition of routing in the FIFO mode

Trigger

As in all operation modes, the start of a FIFO measurement can be triggered by a TTL or CMOS signal. To activate the trigger, set the trigger condition to 'rising edge' or 'falling edge'. Triggering is important for parallel FIFO measurements in several SPC modules with synchronised macro time clocks. To obtain comparable macro times all channels must either be started simultaneously by the trigger, or the 'Trigger Master' option (page 795, SPC-150 only) must be used.

Device State

During a FIFO measurement the device state panel of the main window shows the number of collected photons and the amount of used FIFO buffer space, see Fig. 1032.

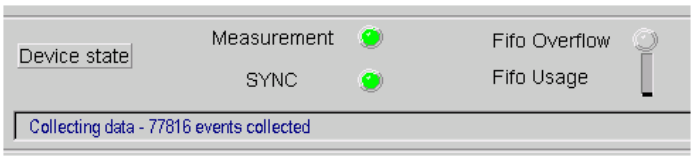


Fig. 1032: Device state during the FIFO mode

FIFO overflow is indicated by a yellow light above FIFO usage bar. FIFO overflow must be avoided in measurements that require absolute photon times over the complete acquisition time period. If you see that the FIFO runs full check whether you can work without some of the functions of the online display, or with a longer Display Time. Please check also the 'Sleep Policy', see page 728. It should be set to 'Never sleep during measurement'.

When you stop a FIFO measurement (by clicking on the 'Stop' button of the main panel) there may still be photon data in the FIFO buffer of the SPC module. You have the option to discard these photons or to continue the readout and the on-line calculation until all photons

have been stored and processed. Please note that this can take some time (the SPC 830 buffers up to 8 million photons!).

FIFO Mode Run-Time Calculations

Calculation of Decay Curves, FCS, Photon Counting Histograms, and MCS traces

The functions calculated on-line are shown in the field under 'Run Time Display'. The run time display can be configured by clicking on the 'Configure' button. This opens the panel shown in Fig. 1033.

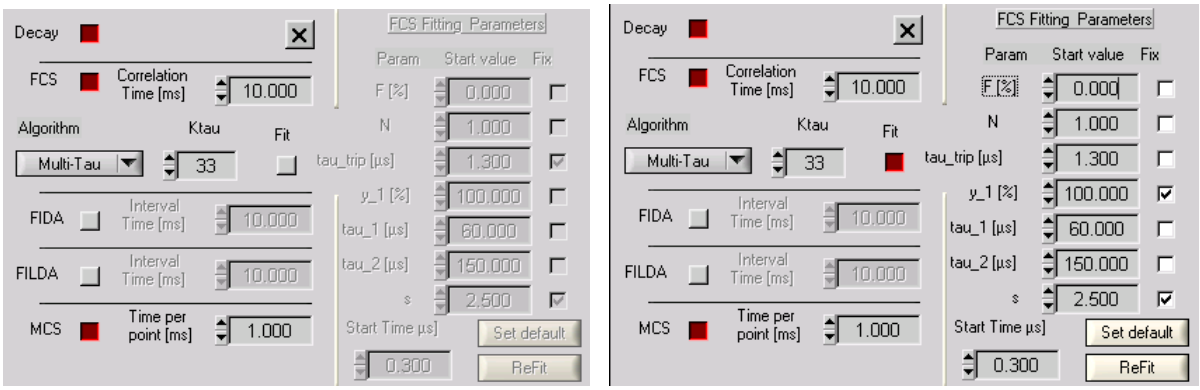


Fig. 1033: Configuration of the runtime display. Left without, right with fitting of FCS data

The available on-line functions are

- Calculation of decay curves for the individual detectors
- FCS by a linear-τ algorithm with subsequent binning or FCS by a multi-τ algorithm. The maximum time up to which the correlation is calculated is defined by 'Correlation Time'. On online fit for FCS data is available, see Fig. 1033, right.
- Fluorescence cross correlation between different detectors. (Use the 2D Trace parameters to define the detector channels to be correlated)
- Calculation of photon counting histograms for the individual detectors ('FIDA'). The sampling time interval is specified on the right.
- Calculation of lifetime histograms (FILDA) for all detectors. The sampling time interval is specified on the right.
- Intensity traces (MCS) for the individual detectors.

For all functions individual display windows are provided in the main panel, see Fig. 960, page 704. For details of FCS display, please see also 'FCS System Parameter Setup', page 645.

For definition of correlation and cross correlation, configure the 'Trace Parameters' to display the appropriate 'Curves' as shown in Fig. 1034. 'Curve' defines the detector numbers of decay functions to be displayed. 'Cross-FCS Curve' defines the detector number to correlate with. If 'Curve' and 'Cross-FCS Curve' are the same the autocorrelation is calculated. For different numbers the cross-correlation of the corresponding detectors is calculated. The configuration shown in Fig. 1034, left calculates the decay functions (histograms) of detector 1 and 2, the autocorrelation of detector 1 and 2, and the cross-correlation of detector 1 and 2.

The configuration shown in Fig. 1034, right, calculates the autocorrelation of detector 1, the cross correlation of detector one versus detector 2, and the fit to the cross correlation of detector one versus detector two.

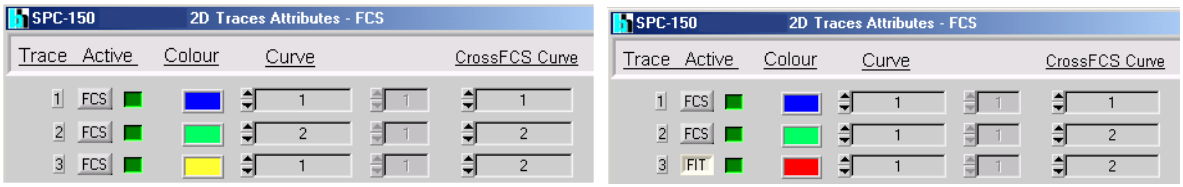


Fig. 1034: Trace Parameters for the FCS display of FIFO mode

On-line calculation and online fit of correlation functions requires a considerable amount of computing power. This can slow down the display sequence below the specified 'Display Time' period. Moreover, the run-time calculations may dramatically reduce the readout rate from the SPC module. This is not really a problem for the modules with large FIFO size and fast bus interface, such as the SPC-830 and SPC-150/154. However, for the SPC-630 and the SPC-134 the on-line display can limit the count rates to 30 to 50 kHz. Therefore, do not define more online-calculations than necessary, and make sure that the FIFO does not overflow when you use the on-line display.

For the same reason, the software calculates only one correlation function per detector channel online. If the Trace Parameters define several correlation functions for one channel, e.g. an autocorrelation and a cross-correlation with another channel, only the first correlation is calculated during the measurement. The other ones are calculated and displayed when the measurement is completed.

Multichannel Scaler, Triggered Accumulation

Starting form version 9.0 the SPCM software has a 'Triggered Accumulation MCS' option in the FIFO mode. It is available for SPC-150 modules and SPC-830 modules manufactured later than May 2007. 'Triggered Accumulation MCS' uses the macro times of the photons to record decay curves on the microsecond or millisecond time scale. The timing reference for the photons is a pulse at one of the 'Marker' inputs of the SPC card, see Fig. 1035.

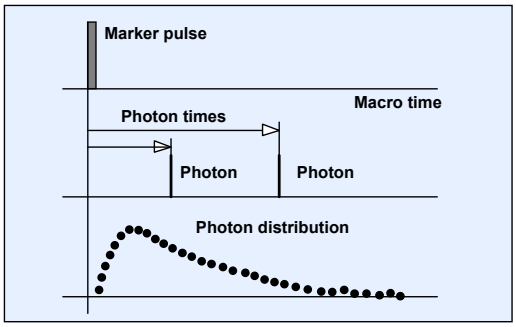


Fig. 1035: Principle of Triggered Accumulation MCS

Triggered accumulation MCS is defined in the lower part of the runtime configuration panel, see Fig. 1036, left. 'Trigger' defines which of the marker inputs are used as a timing reference. Please make sure that the marker input used is enabled in the 'More Parameters' panel of the System Parameters, see Fig. 1036, right. The time channel width (Time per point) can be any multiples of the macro time clock period. It is defined by a number of macro-time units. The number of points of the curves is defined by 'Points No.'. The time range of the curves recorded is then given by the product of Time per Point and Points No. It is displayed under 'Time range'. The recording can be shifted by applying and 'Offset' to the photon times. Both positive and negative offsets are possible.

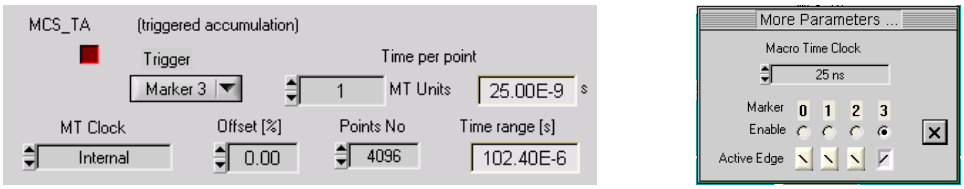


Fig. 1036: Left: Definitions for triggered accumulation multiscaler mode, runtime configuration panel. Right: The marker used as timing reference must be enabled in the 'More Parameters' panel.

Normally triggered accumulation MCS recording is performed with the internal macro time clock. However, for special applications the SYNC frequency can be used. Using the SYNC frequency does, of course, require that the SYNC signal has a constant period, and is continuously present.

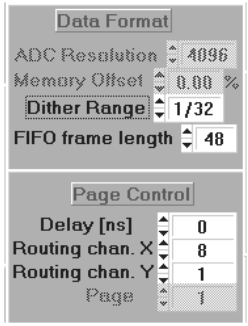
Triggered accumulation MCS works in combination with 'Decay' recording, see Fig. 1033. It works also in combination with routing. Please see 'Simultaneous Measurement of Fluorescence and Phosphorescence Decay', page 340.

Calculating Correlation Functions After the Measurement

If additional correlation functions are specified immediately after a measurement, i.e. before closing the SPCM application, they are calculated when the corresponding traces are activated. If the SPCM application has been closed in the meantime, the FIFO file has to be reloaded by using the 'Convert' function, see 'Converting FIFO Files', page 725.

FIFO Data Format

For the SPC-600/630 two different data formats are available, see figure below, 'FIFO frame length'. You can chose between 4096 time channels plus 256 detector channels or 256 time channels plus 8 detector channels.



Due to the smaller number of bytes per photon the maximum continuous count rate is slightly higher for the second format. For the SPC-134 the data format is fixed to 4096 time channels and 8 detector channels. The formats are shown in the table below.

	FIFO Frame Length byte	Bytes/Photon	ADC Resolution channels	Macro Time Resol. bit	Routing channels
SPC-6	48	6	4096	24	256
SPC-6	32	4	256	16	8
SPC-830	32	4	4096	12	16
SPC-134**	32*	4	4096	12	8**
SPC-144	32*	4	4096	12	16
SPC-155, 180	32*	4	4096	12	16

* Each of the four TCSPC channels delivers its own data file
** Routing requires 8m cable between router and CFD input

Wide-Field FLIM

Principle

The wide-field FLIM mode records fluorescence lifetime images with a position-sensitive detector. For every photon, the detector delivers 5 output pulses, a timing pulse, and two pairs of position pulses. The time of the first pulse determines the time, t, of the photon in the fluorescence decay. The time difference between the pulses of each pair of position pulses, x_2-x_1, and y_2-y_1, determines the location of the photon, x and y, within the image area. The time, t, the x and the y values are measured by separate TCSPC modules. From the information delivered by the individual modules the software builds up the FLIM photon distribution, see Fig. 1037.

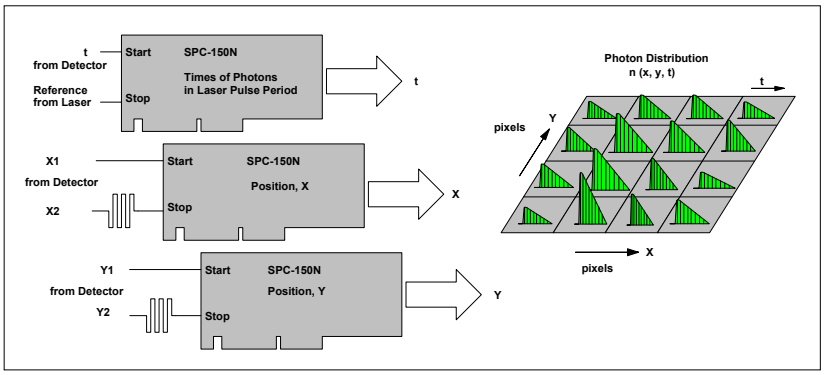


Fig. 1037: TCSPC System for wide-field FLIM

System Parameters

The SPCM system parameter panel for wide-field FLIM is shown in Fig. 1038. Operation mode is 'Wide-Field FLIM'. Stop T is not set - the measurement is started and stopped by the operator. ADC resolution is 1024. That means, the time-measurement channel decay delivers curves of 1024 time channels. Image pixels x and Image pixels y is 512. The recording software bins the data of the position channels down to this value. The pixel number can be increased up to the same value as 'ADC resolution'. The three TCSPC modules have separate system parameters (the 'separate' button is active). This is necessary because the timing and the position SPCs have different discriminators, and the pulse amplitudes at the t, x, and y outputs of the detector are different. The modules therefore need different CFD and SYNC parameters.

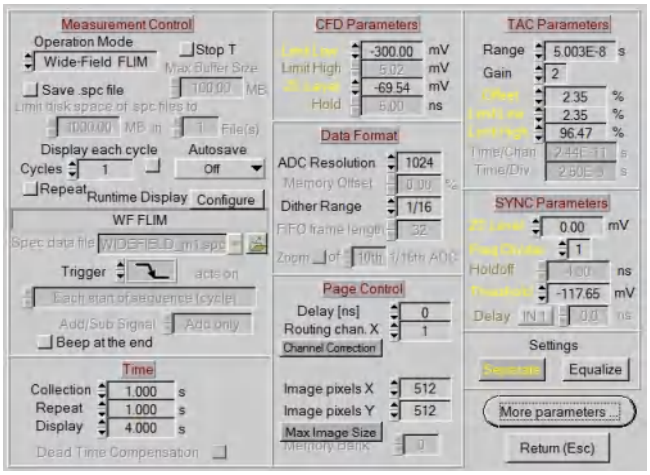


Fig. 1038: System Parameters for wide-field FLIM.

Trigger Master and Master Clock

To associate the events recorded in the three SPC-150N modules to the correct photons the modules must be started synchronously, and be operated from the same master clock. The definitions are shown in Fig. 1039, left and right.

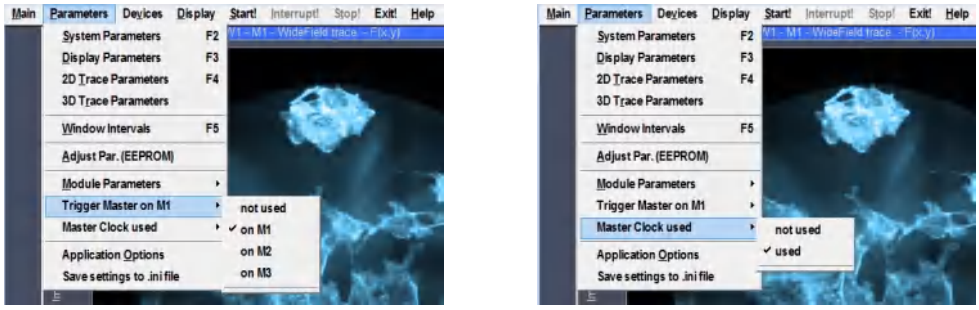


Fig. 1039: Trigger master and master clock must be set to guarantee synchronous operation of the three SPC modules

More Parameters

System-specific parameters are defined under ‘More Parameters’, see button in the system parameter panel, lower right. These parameters control the conversion of the times measured between the X1 and X2, and the Y1 and Y2 signals into spatial information. The More Parameter panel is shown in Fig. 1040.

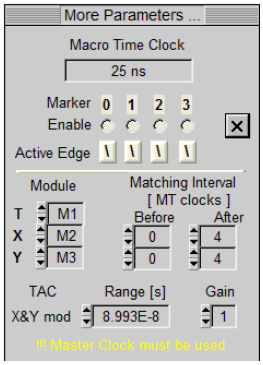


Fig. 1040: More Parameters for wide-field FLIM

Macro time clock is internal, 25 ns. Markers are not used. The individual modules can be freely associated to the T, X, and Y channel. In Fig. 1040 M1 is the T channel, M2 the X channel, and M3 the Y channel. The ‘Matching Intervals’ help associate the information from the T, X, and Y channel to the individual photons. The pulses from the position channels arrive later than the pulses from the T channel. For the Photek FGN 392-1000 detector the time difference can be up to 100 ns. Therefore, position pulses arriving within a macro time interval of 100 ns (4 macro time clocks) of the macro time of a photon in the T channel are associated to one photon.

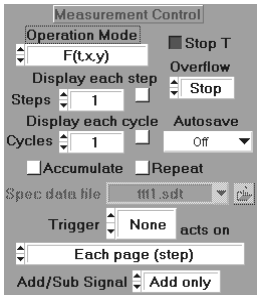
The TAC range and TAC gain of the X and Y modules differ from the values in the T module. (They determine the X and Y scale, not the time scale of the decay curves). The values are defined at the bottom of the more parameters panel. They are specific of the used detector. The values in Fig. 1040 are for the Photek FGN 392-1000 detector.

Display Parameters, Trace and Window Parameters

The display parameters, the 2D Trace Parameters, and the Window parameters are the same as for single-channel FIFO Imaging, see Fig. 1079, page 810.

Control Parameters (Photon Distribution Modes)

The measurement control parameter section of the system parameter panel is shown in the figure below. The effect and availability of the measurement control parameters depend on the module type and the operation mode selected. Therefore the control parameters are described in conjunction with the operation modes in the previous section. The description given here should be considered an overview. For details, please see ‘Operation Modes’.



The FIFO (time-tag) mode has entirely different control parameters. Please see FIFO Mode, page 770.

Stop Condition and Overflow Handling

Stop T

With 'Stop T' the measurement (or the current measurement step) is stopped at the end of 'Collection Time'. ‘Stop T’ can be used together with ‘Stop Overflow’ to stop the measurement either after a defined collection time or at the first overflow.

Stop Ovfl

With 'Stop Ovfl' a ‘Single’, ‘Oscilloscope’ or ‘f(txy)’ measurement stops at the first overflow in the measurement system. Overflow means the count number in one of the time channels exceeds 65635. Please note that the count number is not necessarily the number of photons. There is a parameter ‘Count Increment’ in the ‘Data Format’ section of the system parameters. This parameter allows you to add any number from 1 to 255 at the detection of one photon. You can use this parameter to get a ‘stop on overflow’ for photon numbers as low as 257. With the measurement being stopped on overflow different recordings are normalised to their peak count numbers.

If page stepping is active or one of the f(t,T), f(t,EXT), fi(T) or fi(EXT) is used a ‘stop on overflow’ stops the acquisition for the current step of the sequence. The sequence itself continues as specified by the measurement control parameters.

For multi-detector operation an overflow in any of the detector channels stops the acquisition for all detectors.

‘Stop Overflow’ and ‘Stop T’ can be combined to stop the measurement either after a defined collection time or at the first overflow.

Corr Ovfl

The 'Correct Overflow' function is used in the ‘Single’ mode to record data with more than 65535 photons per channel. The measurement is stopped when an overflow occurs, and the data are transferred into the main memory of the computer. Then the memory of the SPC module is cleared and the measurement is restarted. The data of many such cycles are accumulated in the computer memory. When the collection time is over the result is divided by the

number of overflows and written back into the measurement memory. Although the result has 16 bits again, the standard deviation of the data is reduced by the square root of the number of overflows. The 'Correct Overflow' function is available in the 'Single' mode only. It acts only on the active traces.

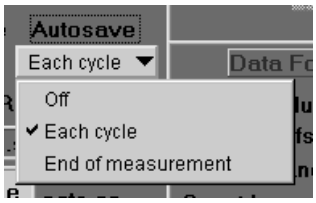
Steps

In most of the operation modes the measurement can be repeated and the results written into subsequent ‘Pages’ of the memory. The number of subsequent measurements is defined by ‘Steps’. The available number of steps depends on the operation mode, on 'Routing Channels X' and 'Routing Channels Y', the ADC resolution and the module type.

In the f(t,T), f(t,Ext) modes 'Steps' is the number of subsequently measured curves. In the fi(T) and fi(Ext) modes ‘Steps’ is the number of intensity values. Please refer to paragraph ‘Operation Modes’.

Cycles and Autosave

A stepping sequence (or, if ‘Steps’ = 1, a single measurement in the selected operation mode) can be repeated for a defined number of ‘Cycles’. To write the results of subsequent cycles to the hard disk an ‘Autosave’ function is provided. In most cases ‘Autosave’ is used for ‘Each cycle’ of a measurement. However, ‘Autosave’ can also be initiated at the ‘End of measurement’, i.e. after the last cycle only. This option is used in combination with ‘Accumulate’.



Accumulate

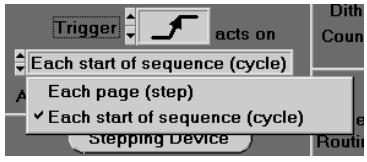
The ‘Accumulate’ function accumulates the results of several ‘Cycles’. If you want to save the results automatically at the end of the accumulation, use ‘Autosave’, ‘End of measurement’.

Repeat

After pushing the ‘Repeat’ button the complete measurement cycle repeats until the measurement is stopped by the operator. The repeat function is often used to run subsequent measurements and display the results in short intervals. The repeat function is an efficient way to obtain online display in multi-dimensional modes, like f(xyt) or Scan Sync In. For the single-curve recording online display can be obtained more efficiently in the ‘Oscilloscope’ mode. In all cases ‘Repeat’ can be used in conjunction with ‘Autosave’.

Trigger

Any single measurement, or the ‘Steps’ or ‘Cycles’ of a measurement sequence can be triggered by the experiment trigger input (see ‘Using the Experiment Trigger’, page 230).



The function of the trigger for the particular mode is described under ‘Operation Modes’. The trigger condition can be set to ‘rising edge’, ‘falling edge’ or ‘None’. ‘None’ means

the measurement is started immediately, without waiting for any trigger signal. The trigger input shared the same line with the ‘Add/Sub’ line used for lock-in-SPC, see ‘External Control Signals’, page 961. Therefore, the trigger is not available when the Add/Sub signal is used and vice versa.

Trigger Synchronisation in Multi-Module Systems

To start the acquisition in a multi-module TCSPC system by an external event a trigger signal must be applied to all modules of the system. This is not only inconvenient, it is also not guaranteed that all SPC module will see the trigger pulse in exactly the same SYNC period. Therefore, the SPC-150 and SPC-130EM modules have a ‘Trigger Master’ function. The trigger is applied to only one module (the master), but all modules are started simultaneously via an internal trigger synchronisation logics. The trigger master option can be set by clicking into ‘Parameters’, ‘Trigger Master’, see page 795.

Display After Each Step and Each Cycle

During the individual measurement steps intermediate results can be displayed ‘after each step’ and ‘after each cycle’. Displaying the results of large multi-dimensional measurement results can take some seconds. Therefore, these online display options should not used for fast sequential recording or other high-throughput applications.

In some operation modes intermediate results can also be displayed in intervals of a specified ‘Display Time’, see ‘Measurement Timing Control Parameters’.

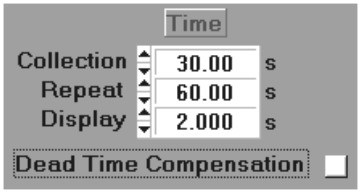
Add/Sub Signal

The ‘Add/Sub’ signal is used for Lock-in SPC, i.e. to externally control whether a photon is added or subtracted. The Add / Sub signal shares one pin of the control signal connector with the ‘Measurement Trigger’ signal, see ‘External Control Signals’, page 961. Therefore, the Add/Sub signal is not available when the trigger is used and vice versa. Add/Sub should be set to ‘Add Only’ when it is not used.

Measurement Timing Control Parameters

Collection Time

In most operation modes 'Collection Time' is the acquisition time of a measurement, a step of a page stepping sequence, or a ‘cycle’ of a repetitive measurement.

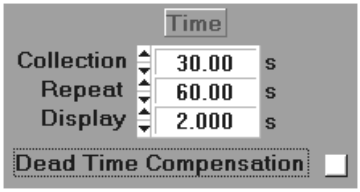


The Collection Time can be ‘dead-time compensated’. With dead-time compensation the collection time automatically increases by the time the system is 'blind' due to the processing of the detected photons, see ‘Dead-Time Compensation’, page 293. The dead time compensation can be switched on and off. Dead-time compensation is available in the Single, Oscilloscope, f(xyt), f(t,T), f(t,EXT), fi(T) and fi(EXT) modes. If sequential modes are used with dead time compensation, or if page stepping or cycling is used, please use a ‘Repeat’ time longer than ‘Collection Time’ to provide some margin for the SPC hardware to extend the effective collection time interval.

In the Scan Sync Out and Scan XY Out modes ‘Collection Time’ is the time to acquire one pixel of the image, in the Scan Sync In mode the total acquisition time of an image.

Repeat Time

The ‘Repeat Time’ controls the repetition of a measurement in the ‘Single’, f(txy), f(t,T), f(t,EXT), fi(T) and fi(EXT) modes.



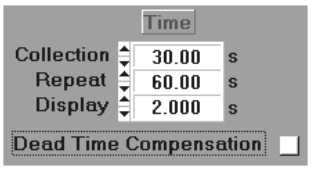
The measurement is repeated in intervals of 'Repeat Time'. If page stepping or cycling is active, or if a sequential mode is used the complete sequence is repeated.

Values smaller than 'Collection time' are rejected by the software to avoid conflicts of the acquisition time with the repeat time. However, if ‘dead time compensation’ is used the effective acquisition time may be longer than the specified ‘collection time’. If the current measurement step or cycle is not finished when 'Repeat Time' is over the next measurement step starts when the current step is complete. If an exact stepping time is important, please use a ‘Repeat’ time longer than ‘Collection Time’ to provide some margin for the SPC hardware to extend the effective collection time interval.

Display Time

Photon Distribution Modes

In the 'Single', f(t,x,y)’, f(t,T), f(t,EXT), fi(T) and fi(EXT) modes intermediate results are displayed in intervals of 'Display Time'. The measurement is stopped, the memory of the SPC module is read, the measurement is continued, and the results are displayed.



Readout and display takes time, especially for multi-dimensional data and 3D display modes. This can slow down the measurement or the time intervals of a page stepping sequence. Therefore unnecessarily short display times should be avoided.

FIFO Mode

In the FIFO mode intermediate results can be are calculated and displayed on-line. The software analyses the photon data when it transfers the FIFO data into the computer memory, continuously builds up histograms and correlation functions, and displays the results (see ‘FIFO Mode’, page 770). Online calculation may consume a substantial amount of computation power, especially for FCS functions of long correlation time. Thus, the actual display rate may be lower than defined by the display time. More important, on-line calculation may slow down the data transfer from the SPC module into the computer. Therefore, please check the FIFO filling status during the measurement if you use the online display features.

On-line results are calculated only if 'Display Time' is set > 1 s. Thus, you can switch off the online display by defining a display time smaller than 1 second.

Dead Time Compensation

The ‘Dead Time Compensation’ function increases the collection time intervals by the sum of the dead time caused by the processing of all recorded photons. Thus, a linear intensity scale is achieved up to extremely high count rates. Please note that dead time compensation results in an effective acquisition time longer than the specified ‘collection time’. The ‘Dead Time Compensation’ is not available in the FIFO mode, the Continuous Flow mode, and in the Scan modes.

CFD Parameters

The bh SPC modules use constant-fraction discriminators (CFDs) both in the detector and at the reference (Sync) input. A CFD triggers at a constant fraction of the pulse amplitude, thus avoiding pulse-height-induced timing jitter. In practice constant-fraction triggering is achieved by triggering on the zero cross point of the sum of the input pulse and the delayed and inverted input pulse, see Fig. 234, page 140. Furthermore, the CFD contains a discriminator that enables the zero-cross trigger only for input pulses larger than a defined discriminator threshold. The CFD threshold is adjusted to reject noise from the environment, noise from preamplifiers or small background pulses from the detector, see ‘CFD and SYNC Inputs’, page 269.

Limit Low

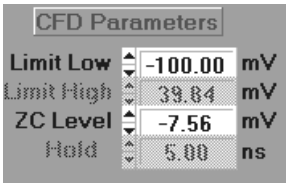
'Limit Low' is the lower discriminator threshold, the ‘CFD threshold’. Pulses with amplitudes smaller than 'Limit Low' are not counted. The parameter range for 'Limit Low' is 5 mV to 80 mV for SPC-x00 modules and 0 to -500 mV for SPC-x30 modules.

Limit High (SPC-x00 only)

'Limit High' is the upper discriminator threshold of the -00 SPC versions. Pulses with amplitudes greater than 'Limit High' are not counted. They do, however contribute to the displayed CFD count rate due to the structure of the CFD (see 'Constant Fraction Discriminator'). The range for 'Limit High' is 5 mV to 80 mV.

ZC Level

'ZC Level' is the reference level of the zero cross trigger in the CFD. The value has a range of -10 mV to +10 mV for the SPC-x00 modules and -100 mV to +100 mV for the SPC-x30 modules.



CFD Parameters. Limit High and Hold are available in older SPC-300 and -400 modules only.

Hold (SPC-x00 only)

When the CFD has detected a pulse within the window 'Limit Low' to 'Limit High' this information is valid for the selected 'Hold' time only. The parameter is normally set to 5 ns. Longer values may be useful for detectors with rise times greater than 5 ns. 'Hold' is available for the SPC-x00 modules only.

SYNC Parameters

The bh SPC modules use constant-fraction discriminators (CFDs) both in the detector and at the reference (SYNC) input. A CFD triggers at a constant fraction of the pulse amplitude, thus avoiding pulse-height-induced timing jitter. In practice constant-fraction triggering is achieved by triggering on the zero cross point of the sum of the input pulse and the delayed and inverted input pulse, see Fig. 234, page 140.

ZC Level

'ZC Level' is the reference level of the zero cross trigger in the SYNC channel. The value has a range of -10 mV to +10 mV for the SPC-x00 modules and -100 mV to +100 mV for the SPC-x30 modules.

Holdoff

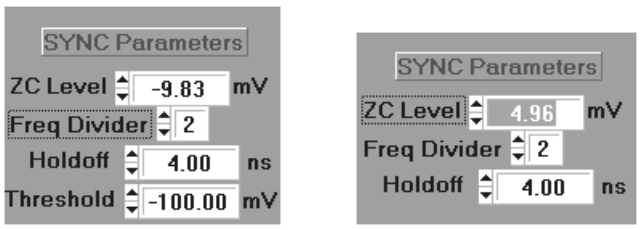
When the SYNC has triggered the detection of an new trigger pulse is rejected for the 'Holdoff' time. 'Holdoff' is used to avoid multiple triggering by pulse ringing or reflections. The 'Holdoff' range is from 4 ns to 16 ns. Please make sure that you don't set 'Holdoff' longer than the period of your SYNC signal. This can produce non-equidistant internal synchronisation signals with correspondingly wrong measurement results.

Threshold (SPC-x30 only)

Input pulses with amplitudes smaller than the selected 'Threshold' are rejected by the SPC-x30 SYNC circuits. The range is from -20 mV to -500 mV. The parameter is available for SPC-x30 modules only.

Freq Div

'Freq Div' is the frequency divider ratio in the SYNC channel. The setting determines the number of signal periods recorded, see 'SYNC Parameters', page 279. Important: 'Freq Div' must be set to 1 for measurements at low repetition rates and for non-reversed start-stop measurements.

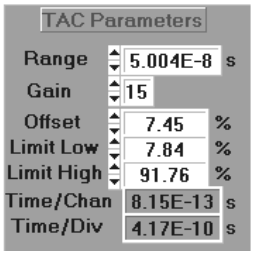


Sync parameters. Left: SPC-x30 modules. Right: Older SPC-0x00 modules

TAC Parameters for SPC Modules

The SPC-130, SPC-150, SPC-150N, and SPC-180N Modules use a Time-to-Amplitude Converter (TAC) to determine the times of the detected photons. The TAC measures the times of the photons from the moment of the detection to the next synchronisation pulse. The core of the TAC is a linear ramp generator. The ramp is started when a photon pulse triggers the CFD of the detector channel and stopped when the next pulse in the reference (SYNC) channel is detected. The output voltage of the ramp generator is amplified by a biased amplifier. The amplifier is used to select a time interval within the range of the ramp generator and stretch it over the full output voltage range. Moreover, the TACs of the SPC-6, -7 and -8 modules have discriminators to reject photons outside a selectable amplitude window of the TAC output signal. The SPC-1 modules have no such discriminators but achieve a similar effect by digital comparators in the ADC data path. The details of the TAC are described under 'Time-to-

Amplitude Converter', page 149. The optimisation of the TAC parameters is described under 'TAC Parameters', page 282. The TAC parameter panel is shown in the figure below.



TAC Parameters

Range

'Range' is the maximum start-stop time of the linear-ramp generator, i.e. the total time interval in which photons can be measured. TAC ranges from 50 ns to 2 µs are available. Internally the setting is accomplished in five steps, in conjunction with a 12-bit fine adjustment within the steps. Therefore virtually any TAC range between 50 ns and 2 us is available.

Gain

'Gain' is the gain of the biased amplifier of the TAC. 'Gain' stretches the time scale of the TAC, see 'TAC Parameters', page 282. Values from 1 to 15 are available.

Offset

With 'Offset' the displayed time range is shifted on the TAC characteristic, see 'TAC Parameters', page 282. The result is shifted in X direction on the screen. 'Offset' can be set to 0...100 % of the overall TAC range. However, the remaining part of the TAC characteristic (from 'Offset' to 100%) should be long enough to fill the display window for the selected TAC Gain. The resolution of 'TAC Offset' is 12 bit for the SPC-6, -7, and -8 modules, and 8 bit for the SPC-1 modules.

Limit Low

The TAC contains a window discriminator to suppress events outside a selected time interval. 'Limit Low' sets the lower limit of this interval. 'Limit Low' can be set from 0% to 100% of the display window, but not higher than 'Limit High'. Typical limit-low values are from 3 to 10%.

Limit High

The TAC contains a window discriminator to suppress events outside a selected time interval. 'Limit High' sets the upper limit of this interval. 'Limit High' can be selected from 0% to 100% of the display window, but not lower than 'Limit Low'. Typical values are 90 to 97%.

Time/Channel

'Time/Channel' is the width of one time channel in the recorded photon distribution. It is

$$Time/Channel = \frac{Range}{Gain \cdot ADCresolution}$$

'Time/Channel' is calculated from the given values of TAC Range, TAC Gain and ADC Resolution (in channels) and displayed for information only. The minimum 'Time/Channel' is 815 femtoseconds.

Time/Div

This value is the time per division. It is displayed for information only. It is calculated from the settings of TAC Range, TAC Gain, ADC Resolution and, for the SPC-830, ADC Zoom.

TDC Parameters for SPC-QC Modules

The SPC-QC modules use a Time-to-Digital Convertion (TDC) principle to determine the times of the detected photons. The TDCS principle differes from the TAC/ADC principle described above. Consequently, also the timing-control parameters are different. The timing parameters are controlled by the TDC-parameter section of the system parameters, see Fig. 1041, Fig. 1042, and Fig. 1043.

'Range' is the time-conversion range, 'Offset' the position of a recorded waveform inside the observation time interval, and 'Range' is the length of the observation time interval. 'Bins. No'. is the number of time channels, and 'Time/Bin' the time-channel width resulting from the selected combination of 'Range' and 'Bins No'. Please note that the minimum time-channel width is 4 ps. Therefore not all combinations of parameters are possible. SPCM therefore corrects the user inputs and suggests parameter combinations which are within the capabilities of the hardware. Examples are shown in Fig. 1041, Fig. 1042, and Fig. 1043.

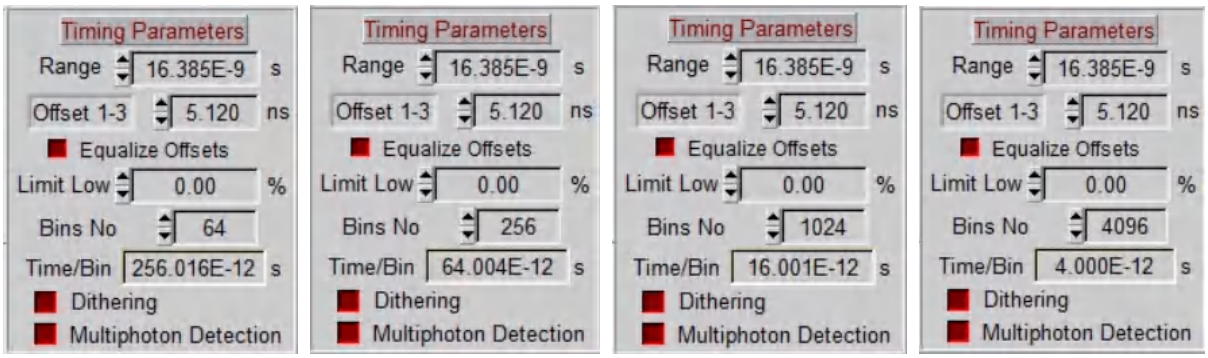


Fig. 1041: TDC settings, different Channel Number with same Range. The combinations yield different Time/Channel.

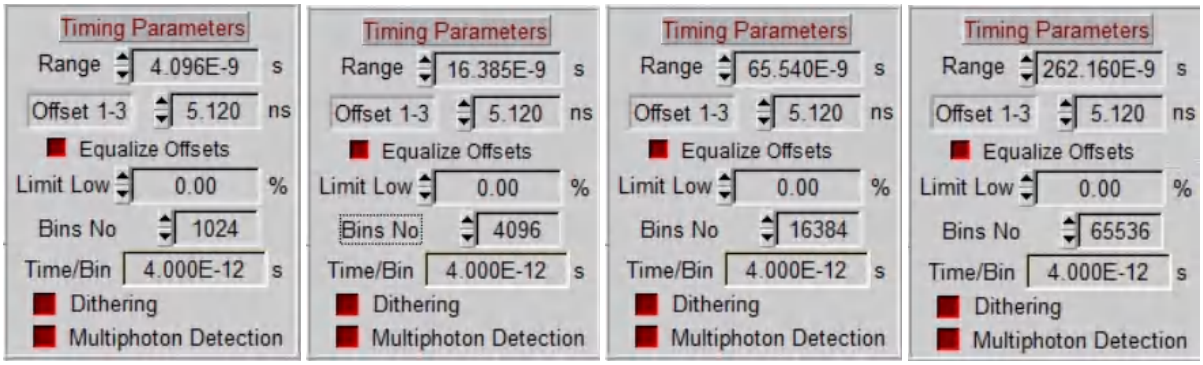


Fig. 1042: TDC settings, different Range with same Time/Channel, different Channel Number.

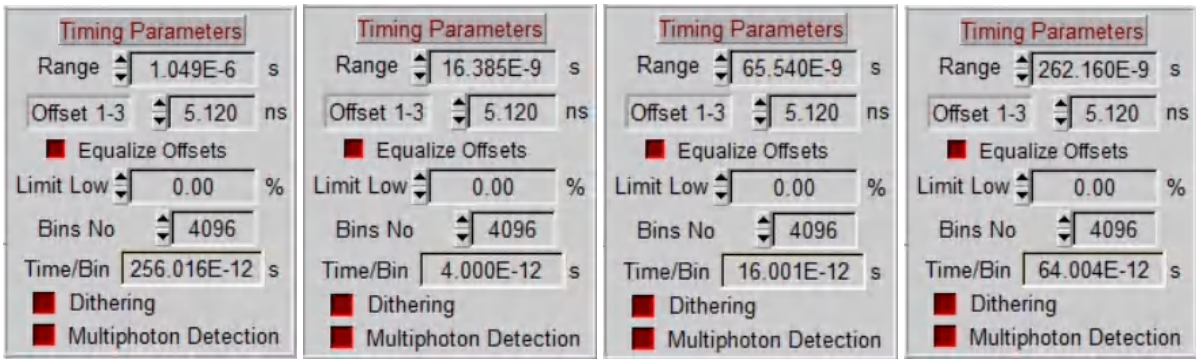


Fig. 1043: TDC settings, different Range with same Channel Number, different Time/Channel

Not all combinations are available for all operation modes. For examples, the maximum channel number for FIFO Imaging is 4096, and for the FIFO mode channel number is always 4096. Please see separate manual for the SPC-QC modules [75].

Data Format

ADC Resolution and ADC Zoom (SPC Modules, Photon Distribution Modes)

'ADC Resolution' defines the number of time channels per curve of a waveform recording. For the SPC-6 and -7 modules and the SPC-134 an ADC Resolution of 64, 256, 1024 or 4096 time channels can be selected, see Fig. 1044.

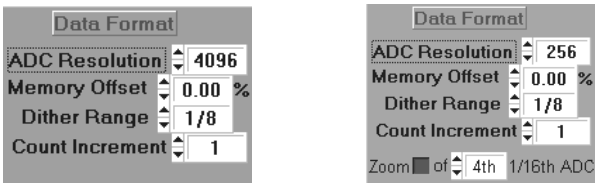


Fig. 1044: Data Format panel for the SPC-6, -7, -130/134 (left) and the SPC-830 and SPC-140/144(right)

For SPC-830 and the SPC-140/144 an ADC resolution of 1, 4, 16, 64, 256, 1024 or 4096 time channels is available. Moreover, the SPC-830 and the SPC-140/144 have an 'ADC Zoom' function to stretch a part of the ADC range over the full display scale. Only the stretched part of the data is recorded. The ADC Zoom function is mainly used to record large images or other multi-curve data simultaneously with a high number of pixels or curves and high time resolution. Please see also 'ADC Zoom', page 153. Fig. 1045 explains the ADC Zoom feature for an ADC resolution of 256 channels.

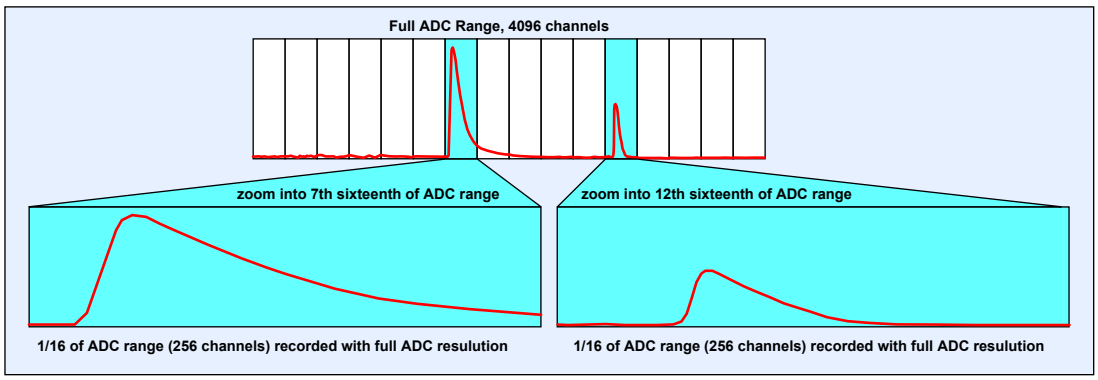


Fig. 1045: ADC Zoom function of the SPC-830 and SPC-140/144

Originally the ADC converts the complete TAC interval (TAC Range / TAC Gain) into 4096 time channels. The zoom function selects 1/16th of the ADC range, i.e. 256 channels. Any 16th part of the ADC range can be selected, and only the selected part is displayed and recorded. The ADC zoom is a powerful function to record ultra-fast signals in high pixel resolution imaging applications.

For single-curve measurements normally an ADC resolution of 4096 or 1024 time channels per curve is used. For sequential measurements, stepping through pages, 'Continuous Flow' measurements and scanning often a trade-off between ADC resolution and number of curves and pages or pixel number must be made. The maximum number of curves for a single detector setup is given below.

SPC-130/134							
ADC Resolution		64		256	1024	4096	
No of Curves		8192		2048	256	64	
No of curves addressed by external routing signal		128		128	128	64	
min. time channel width		52ps		3.26ps	3.26ps	815fs	
SPC-130EM/134EM, SPC-140/144, SPC-150/154							
ADC Resolution	1	4	16	64	256	1024	4096
No of Curves (f(t,T, Scan Sync IN/Out)	16 M	4 M	1 M	65536	16384	4096	1024
No of curves addressed by external routing signal	128	128	128	128	128	128	128
min. time channel width	3.34ns	834ps	209ps	52ps	3.26ps	3.26ps	815fs
min. time channel width, with ADC zoom		52ps	13ps	3.26ps	815fs	815fs	
ADC zoom factor		16	16	16	16	4	
SPC-600/630							
ADC Resolution		64		256	1024	4096	
No of Curves		8192		2048	256	64	
No of curves addressed by external routing signal		128		128	128	64	
min. time channel width		52ps		3.26ps	3.26ps	815fs	
SPC-700/730							
ADC Resolution		64		256	1024	4096	
No of Curves (f(t,T, Scan Sync IN/Out)		65536		16384	4096	1024	
No of curves addressed by external routing signal		16384		16384	4096	1024	
min. time channel width		52ps		3.26ps	3.26ps	815fs	
SPC-830							
ADC Resolution	1	4	16	64	256	1024	4096
No of Curves (f(t,T, Scan Sync IN/Out)	16 M	4 M	1 M	262144	65536	16384	4096
No of curves addressed by ext. routing signal	16384	16384	16384	16384	16384	16384	4096
min. time channel width, without ADC zoom	3.34ns	834ps	209ps	52ps	13ps	3.26ps	815fs
min. time channel width, with ADC zoom		52ps	13ps	3.26ps	815fs	815fs	
ADC zoom factor		16	16	16	16	4	

For multi-detector experiments or measurements with page stepping the memory is shared between the individual detection channels and pages so that the available number of curves is reduced. Please see 'Operation Modes', page 732.

ADC Resolution (SPC modules, FIFO Modes)

The 'Data Format' section of the system parameters for the FIFO mode is shown in Fig. 1046.

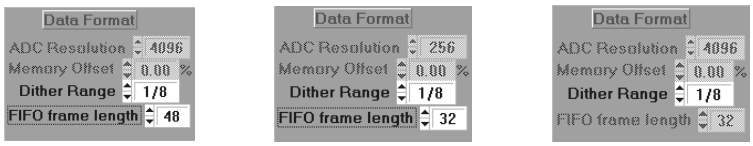


Fig. 1046: ADC Resolution in the FIFO mode for the SPC-630 for 'Frame Length' 48 and 32 and for the SPC-134, SPC-830 and SPC-140/144 (right)

For the SPC-600/630 modules the ADC resolution depends on the 'Frame Length', i.e. on the number of bits per photon saved in the FIFO data file. For the SPC-830, the SPC-130/134 and the SPC-140/144 the frame length and consequently the ADC Resolution are fixed to 32 and 4096, respectively.

Memory Offset (SPC Modules)

When the Lock-in capability of the bh SPC modules is used the light is modulated by a chopper or via on-off modulation of a ps diode laser. The photons in the ‘On’ phases are added and the photons in the ‘Off’ phases subtracted. Consequently, negative photon numbers can occur in the memory. By using a 'Memory Offset' greater then zero the baseline of the recording can be shifted to positive values.

Dither Range (SPC Modules)

'Dither Range' controls the ADC error correction of the bh TCSPC modules. The principle of the error correction is described under ADC Error Correction, page 151. The technique is based on adding an auxiliary signal to the ADC input voltage. The digital equivalent of the signal is subtracted from the ADC output words. Thus, the TAC output voltage is periodically shifted up and down the ADC characteristic. The result is that the non-uniformity of the ADC channels is averaged out. ‘Dither Range’ controls the amplitude of the shift signal. It is defined as a fraction of the total ADC input range.

Larger values of 'Dither Range' improve the differential nonlinearity. However, the sum of the TAC signal and the shift signal is limited to the available ADC input voltage range. Therefore the first and last parts of the ADC characteristic cannot be used for conversion. The effect of ‘Dither Range’ on a recorded curve is shown in Fig. 1047, left.

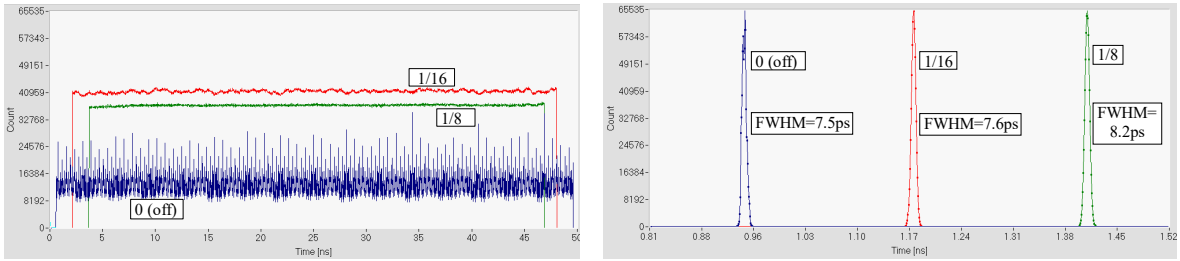


Fig. 1047: ADC error correction. Left: Unmodulated light recorded without error correction, and with ‘Dither Width’ 1/16 and 1/8. right: Corresponding instrument response function for an electrical test signal. SPC-134.

It should be pointed out that large values of 'Dither Range' do *not* impair the time resolution, see Fig. 1047, right. Therefore, use a 'Dither Range' as large as possible. Under normal conditions 1/8 or 1/16 is adequate. Dither Range = 0 switches the error correction off. It is intended for test purposes, not for measurement application.

Count Increment

'Count Increment' is the value which is added in the memory at the detection of each photon. The parameter may look unusual at first glance, especially if you are familiar with conventional NIM TCSPC systems. Of course, a ‘Count Increment’ greater than one does not yield any improvement in accuracy for a given number of photons. It is, however, a convenient means to make the measurement control more flexible.

In ‘Single’ and ‘Oscilloscope’ measurements a Count Increment greater than 1 can be used to reduce the time required to reach the overflow level for a given count rate. If ‘Stop Overflow’ is set instead of ‘Stop T’, a measurement is stopped when the maximum of the curve reaches 65535. Thus, the measured curves are normalised to the same height independently of the pulse shape and the count rate. This normalisation helps to compare different curves in terms of pulse shape or width.

If you run a fitting procedure on SPC data recorded with a Count Increment greater than one, please don't be surprised by the large value of χ^2. To get the true χ^2 you have to divide the value by the Count Increment.

In earlier SPCM versions a Count Increment greater than one had to be used to avoid rounding effects in the display of images. In later versions the pixel intensities are calculated by floating point arithmetics. An increased count increment is therefore not longer needed.

FIFO Frame Length (FIFO Mode)

This parameter sets the data format for the SPC-600/630 in the FIFO Mode. For the SPC-830, SPC-134, SPC-144, SPC-160, and SPC-180 modules the FIFO frame length is fixed.

	FIFO Frame Length byte	Bytes/Photon	ADC Resolution channels	Macro Time Resol. bit	Routing channels
SPC-6	48	6	4096	24	256
SPC-6	32	4	256	16	8
SPC-150, 160, 180	32	4	4096	12	16
SPC-QC-104, 106	32	4	4096	12	12
SPC-134	32*	4	4096	12	8**
SPC-144	32*	4	4096	12	16
SPC-154	32*	4	4096	12	16
SPC-830	32	4	4096	12	16

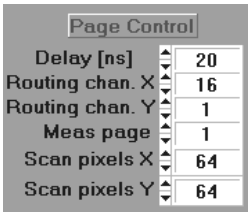
* Each of the four TCSPC channels delivers its own data file

** Routing with the SPC-134 requires 8 m cable between the router and the CFD input

For the SPC-600/630 the 'FIFO Frame Length' determines also the ADC resolution. Please see 'ADC Resolution (SPC modules, FIFO Modes)'.

Page Control

The Page Control section of the system parameters defines the number and the arrangement of the detector channels, the number of pixels in the scan modes, and the memory page in which a measurement starts.



Page Control Parameters

The Page Control parameters are used to define the number and the spatial arrangement of the detector channels or the number and arrangement of the pixels of an image in the SPC-7, SPC-8, SPC-150 and SPC-160 Scan modes. If the number of curves per measurement is less than 50% of the module memory size the memory can hold the results of several measurements. A 'Page' is a memory segment that holds the curves (photon distributions) for all detectors and - in the 'Scan' modes of the SPC-7 and SPC-8 modules - pixels of one measurement or measurement step.

The number of available 'Pages' depends on the used 'ADC Resolution', 'Routing Channels X', 'Routing Channels Y' and, in the 'Scan' modes, on 'Scan Pixels X' and 'Scan Pixels Y'. If one of these parameters is changed beyond the limit set by memory size the software automatically limits it to the maximum possible value.

Delay (Not for SPC-130/134)

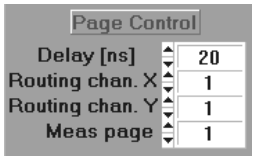
'Delay' determines the moment when the routing and control signals for multidetector measurements are read. The delay is referred to the pulse at the CFD input. For the bh routers and the bh PML-16 multichannel detector the optimum 'Delay' is 0 to 30 ns.

For other applications a 'Delay' in the range from 0 to 60 ns can be used. Please note that an internal delay of the data latch of 5 to 10 ns and the cable transit times must be taken into account.

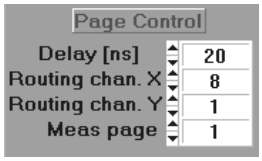
The ‘Delay’ parameter is not available for the SPC-130/134. If you want to use an SPC-134 with a bh router, please connect 7 to 8 m cable between the router and the CFD input of the SPC module. The cable delays the photon pulse. Thus, the routing signal is valid when the photon pulse arrives at the CFD input, and the correct detector number is written into the channel register.

Routing Channels X, Routing Channels Y

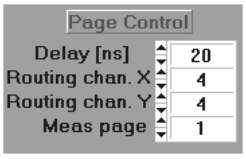
‘Routing Channels X' and 'Routing Channels Y' are the number of rows and columns of a two-dimensional array of detector channels. Some examples are in Fig. 1048.



Single-detector measurement



Multidetector measurement
8 Detectors, linear arrangement



Multidetector measurement
16 detectors, 4x4 arrangement

Fig. 1048: Definition of the number of routing channels

Measured Page

A ‘Page’ is a memory segment that holds the curves (waveforms) for all detectors. If the number of curves per measurement is less than 50% of capacity of the module memory several pages can be defined. Each page holds the data of a complete measurement or step of a page stepping sequence. In the ‘Scan’ modes a page contains the waveforms of all pixels of the image.

For a single-step measurement, ‘Measured Page’ is the memory page in which the result of the measurement is stored. For a measurement with page stepping the measurement starts in ‘Measured Page’ and steps through subsequent pages.

Scan Pixels X, Scan Pixels Y

These parameters are used for the ‘Scan’ modes of the SPC-830, SPC-700/730 and SPC-140/144 modules. ‘Scan Pixels X’ and ‘Scan Pixels Y’ are the number pixels per line and the number of lines per frame in the recorded image.

The ‘Scan’ modes can be used in conjunction with multidetector operation. Therefore a configuration with ‘Scan Pixels X’ and ‘Scan Pixels Y’ greater than one can be used with ‘Routing Channels X' and 'Routing Channels Y' greater than one. Some examples are shown below.

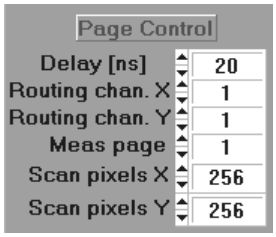


Image of 256 x 256 pixels
Single detector measurement
1 page available for ADC Res = 64

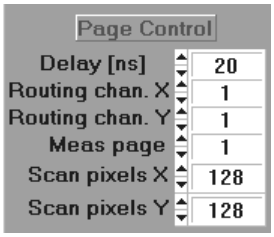


Image of 128 x 128 pixels
Single detector measurement
4 pages available for ADC Res = 64
1 page available for ADC Res = 256

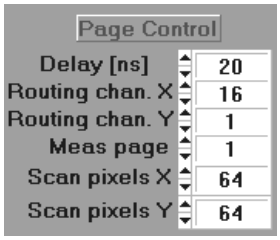
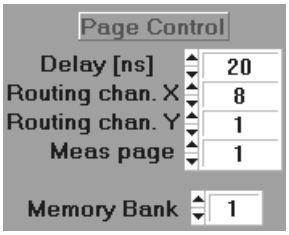


Image of 64 x 64 pixels
16 detector channels
1 page available for ADC Res = 64

Memory Bank (SPC-600/630, SPC-130, -150, -160)

The SPC-600/630 and the SPC-134 have a dual memory, i.e. two memory banks of the same size and configuration. Normally the banks are used for unlimited sequential recording in the ‘Continuous Flow’ mode. You can, however, use the banks to hold the results of two measurements in the SPC memory. 'Memory Bank' = 0 or 1 switches between the two memory banks.



‘More’ Parameters

Depending on the module type and the operation mode special parameters (e.g. to control a scanner) are available. These parameters are described under the ‘Operation Modes’ for these modules.

Adjust Parameters

Most of the required hardware adjustments in the SPC modules are done via the SPCM software. The adjust values are stored in an EEPROM on the SPC module. The SPCM software reads the EEPROM, corrects the setup parameters according to the adjust values, and sends the corrected setup data to the SPC module.

The adjust values are accessible via the adjust parameters menu. To change the adjust parameters a certain knowledge about the SPC hardware is required. Wrong inputs may seriously de-adjust the module. Therefore you can change the adjust parameters, but not save them to the EEPROM. The changed adjust values are used by the device, but they will be replaced with the original values after restarting the SPC software.

The Adjust Parameters for the SPC-630, 730, -830 and the SPC-130/134 and -140/144 modules are shown in Fig. 1049.

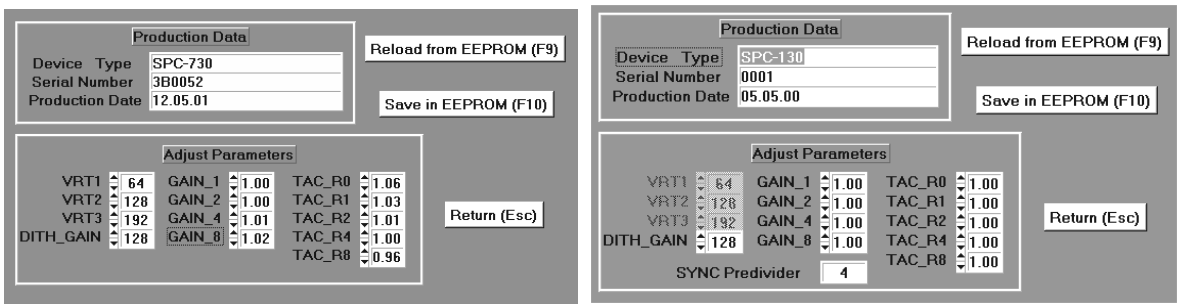


Fig. 1049: Adjust parameters for SPC-6, -7, -8 modules (left) and for SPC-134 and -144 modules (right)

Production Data

This area contains manufacturing information about the particular module: The module type, the serial number, and the manufacturing data. The information is used by the software to recognise different module versions. Please do not change these parameters.

Module Adjust Parameters

VRT1...VRT3 (Voltage of Resistor Tap, SPC-6, -7, -8)

These parameters adjust the large-scale linearity of the ADC. Imagine the ADC characteristic as a rubber band that is fixed at the zero point and the full scale point. At 1/4, 1/2 and 3/4 of this band other bands are fixed which pull the ADC characteristic up or down. The default values are VRT1=64, VRT2=128 and VRT3=192.

Dither Gain

'Dither Gain' changes the gain of the DAC in the error correction part of the ADC (see 'ADC Error Correction', page 151). To adjust the parameter, a short pulse is measured in a slow TAC range with the maximum value of 'Dither Width'. 'Dither Gain' is adjusted to get a minimum pulse width. The range of the parameter is from 0 to 255, the default setting is 128.

Gain1, Gain2, Gain4, Gain8

These parameters correct the time scale of the TAC for different values of 'TAC Gain'. The correction is done by slightly changing the effective TAC range, see below.

Internally the 'TAC Gain' is set by a combination of four binary graded resistors. Therefore, only four parameters are required to set all 15 gain steps. 'Gain1' corrects for errors in the value of TAC Gain = 1, 'Gain2' corrects for errors of TAC Gain = 2, and so on. If the gain is

correct for 1, 2, 4, and 8 also the other values are correct (dynamic errors neglected). The default values are 1, greater values increase the effective TAC Gain, smaller values decrease it.

TAC_R0 toTAC_R8

These adjust values correct the 'TAC Range' parameter. The adjust parameters act on the following TAC Ranges:

	SPC-130, 140, 150, 150N, 160, 180N	SPC-150NX, 180NX	SPC-150NXX, 180NXX
TAC_R0	TAC Range = 50 ns to < 100 ns	25 ns to < 50 ns	12.5 ns to 25 ns
TAC_R1	TAC Range = 1000 ns to < 2000 ns	500 ns to 1000 ns	-
TAC_R2	TAC Range = 500 ns to < 1000 ns	250 ns to 500 ns	-
TAC_R4	TAC Range = 200 ns to < 500 ns	100 ns to 250 ns	50 ns to 125 ns
TAC_R8	TAC Range = 100 ns to < 200 ns	50 ns to 100 ns	25 ns to 50 ns

The default setting is 1. Values >1 increase TAC Range, i.e. decrease the width of a signal recorded, values <1 decrease TAC Range, i.e. increase the with of a signal. Values from 0.9 to 1.1 are accepted.

SYNC Predivider (SPC-130/134 SPC-140/144, SPC-150/154, SPC-180)

In the SPC-134 and SPC-144 modules the internal SYNC frequency is divided by 2 or by 4 before it is fed into the SYNC-Rate Counter. The divider ratio is set by a jumper on the board, see Fig. 1050. To obtain correct SYNC-rate display ‘SYNC Predivider’ must correspond to the jumper setting.

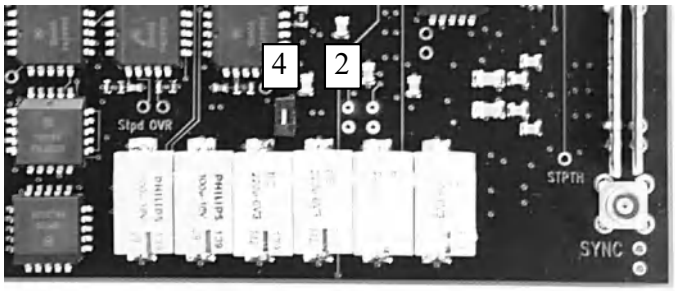
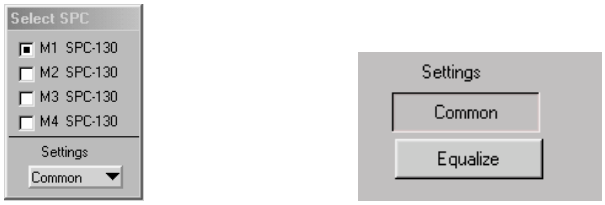


Fig. 1050: SPC-130, -140: Jumpers for SYNC- predivider ratio

Parameter Management for Multi-Module SPC Systems

Module Selection

In multi-module SPC systems each module has its own system parameters, and the currently displayed System Parameter panel refers to one of the modules only. To specify the module to which the parameters refer a small ‘Select SPC’ panel is displayed, see figure right. It can be conveniently placed anywhere in the screen area.



Furthermore, you can decide whether parameter changes apply to all modules or to the specified module only. Use the 'Common/Separate' button in the lower right part of the system parameter panel.

If a parameter has different values in different modules it is highlighted by a different colour in the system parameter panel. If you want to set the equal system parameters for all modules, click on the ‘Equalize’ button. The parameters for the current module are then transferred into the system parameters of all other modules.

Trigger Master and Clock Master Function

These functions allow several SPC-150 modules to start synchronously, and to run on a common (internal) macro time clock. The parameters are selected via the ‘Parameters’ menu.

With the settings shown in Fig. 1051 module 1 is the trigger master. A start in this module starts the other ones synchronously. (That means if an experiment trigger is used it must be connected to module 1.) All modules are using a common clock which comes from module 1.

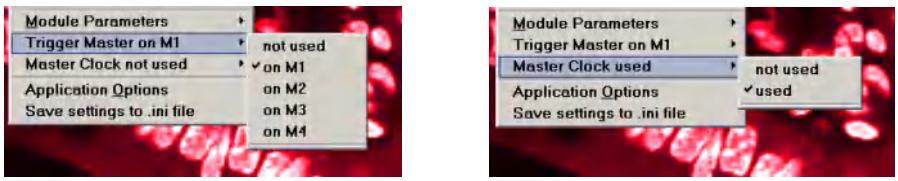


Fig. 1051: Trigger master and clock master definitions

Trigger master and clock master operation is important if data from different modules are to be cross-correlated, e.g. for Cross-FCS with the detectors connected to different modules.

Display Functions

The bh TCSPC modules record multi-dimensional data. In the simplest case, the result of a measurement may just be a single fluorescence decay curve or a single waveform of another optical signal. However, a measurement can also produce several curves simultaneously. The curves can represent data recorded by several SPC modules, data recorded by several detectors connected to a single module, by several channels of a bh multi-wavelength detector, by several multiplexed lasers, or by the steps of a time-series recording procedure. Several such data sets can by recorded in different memory pages. Moreover, the curves may not represent waveforms of light signals at all but FCS curves, photon counting histograms, or time-resolved spectra. A few examples of the display of TCSPC curves are shown in Fig. 1052.

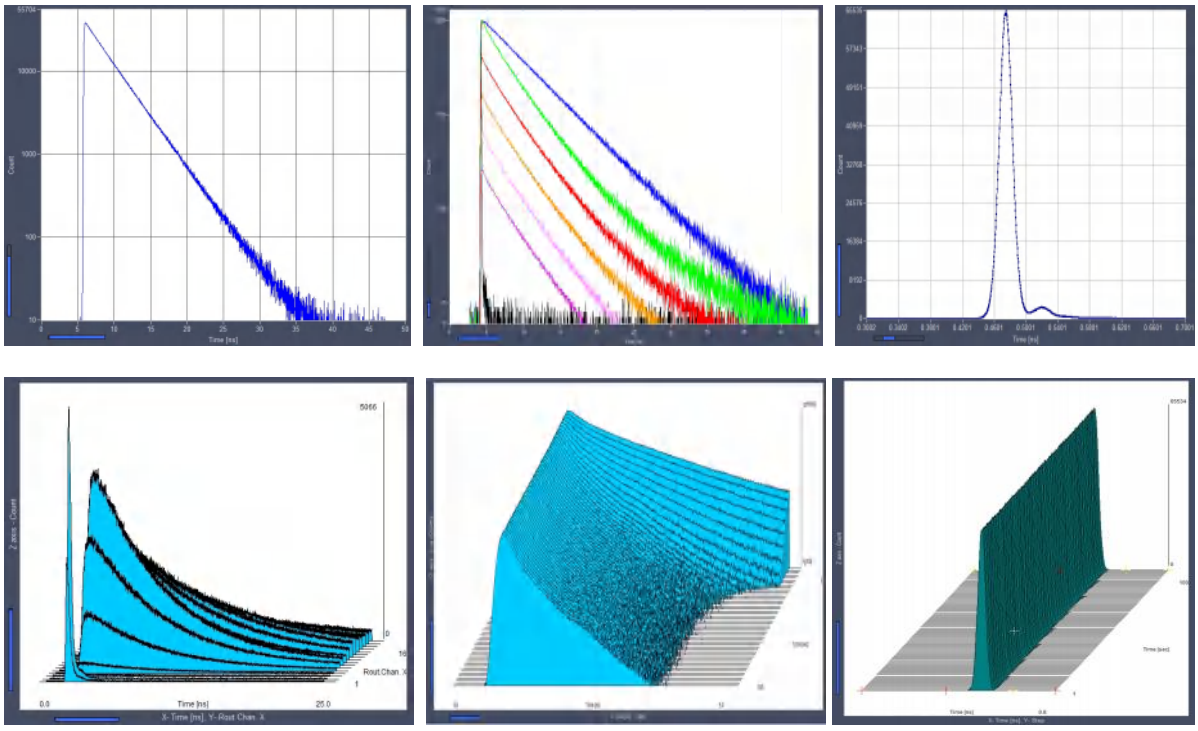


Fig. 1052: Curve display in SPCM. Upper row: 2D curve display. Lower row: 3D curve display.

The structure of TCSPC data becomes even be more complex when the SPC modules are used in the imaging modes. A single TCSPC image is an array of pixels, with each pixel containing a decay curve in the form of photon numbers in consecutive time channels. Several such structures may exist if a multi-wavelength detector is used, or if the measurement system is using routing or laser multiplexing. Mosaic imaging delivers a two-dimensional array of TCSPC images. Data with more than two dimensions cannot easily be displayed by a two-dimensional display device or printer. The data must be projected in a single plane, and the way this projection is performed must be suitably selected. Examples are shown in Fig. 1053.

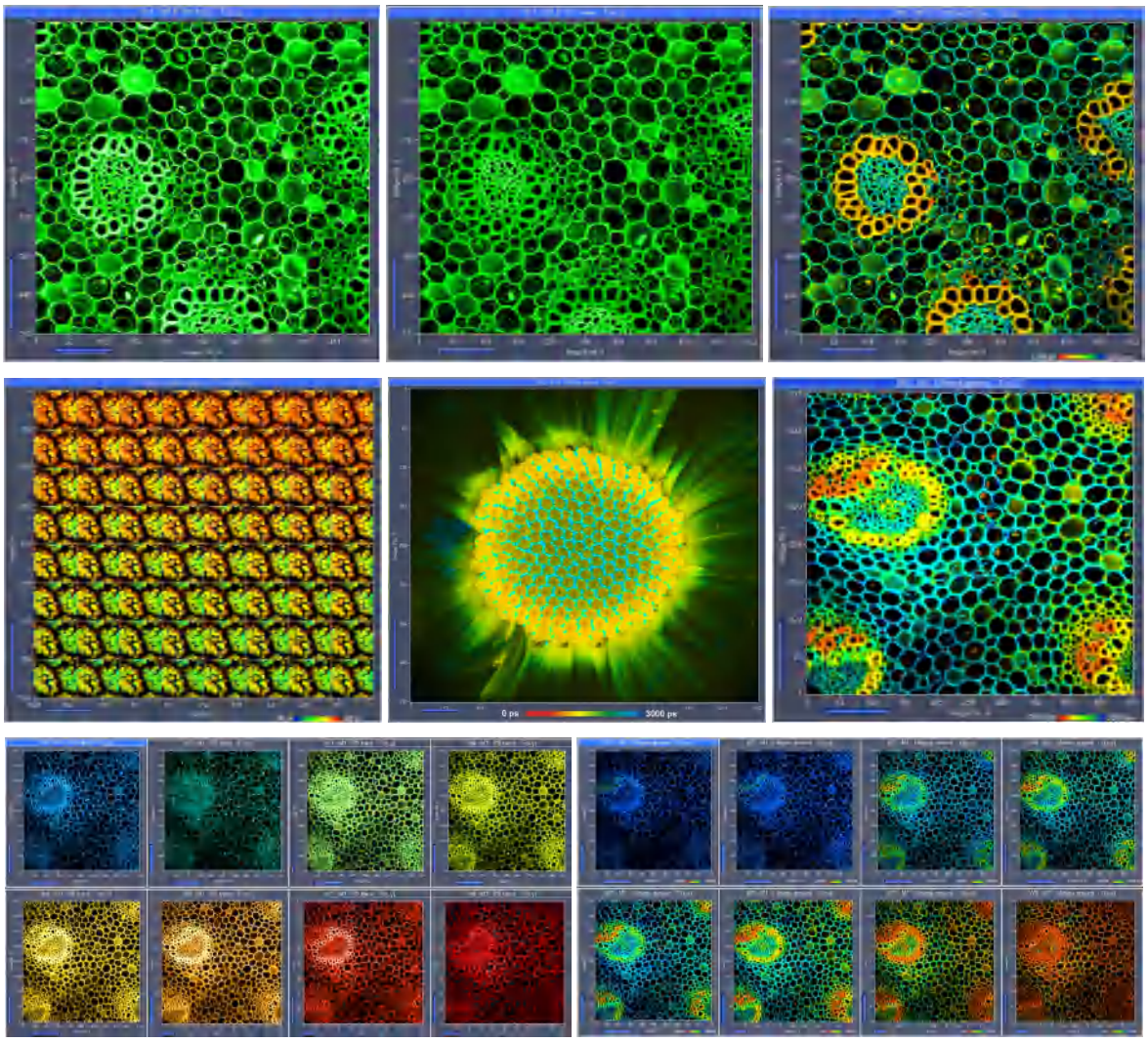


Fig. 1053: Examples of SPCM image display. Upper row: Intensity image, gated intensity image (of late photons), lifetime image. Middle row: Mosaic FLIM image, Image from combined 4 channels of FASTAC system, Image from multi-wavelength FLIM data, channel 9-14 selected by routing window. Lower row: Multi-wavelength intensity image in 8 routing windows selecting 2 adjacent channels each, colours adjusted to real emission wavelengths, multi-wavelength image, colour-coded lifetime.

Display of 2D Data

Decay curves recorded by a single or by several SPC modules, data recorded by several detectors, by several channels of a bh multi-wavelength detector, by several multiplexed lasers, or data from the steps of a time-series recording procedure can be displayed by the 2D display functions of the SPCM software. The 2D function puts the curves in a single t-y diagram, as shown in Fig. 1052. The display of 2D data is controlled by the 2D Trace Parameters in combination with the Display Parameters. The 2D Trace Parameters determine which data are displayed, the Display Parameters determine how they are displayed. The parameters act both on the display of data in the SPCM main window and on the '2D Curve' routine under 'Display' in the top task bar of SPCM.

Selection of the Data to be Displayed

The data to be displayed are selected in the 'Trace Parameter' panel. Up to 16 Traces (curves) can be defined. The traces can be curves from different memory pages into which the data have been recorded ('Pages'), curves from different routing channels of an SPC module ('Curves'), or curves from different SPC modules ('Module'). Three representative examples are shown in Fig. 1054. Different combinations, such as selected curves from a particular

page of a particular module can be selected. The 'Active' button defines whether a curve is displayed or not.



Fig. 1054: Examples of trace parameter definitions. Subsequent measurement pages (left), curves from subsequent routing channels (middle), and curves from subsequent SPC modules (right).

Display Range and Curve Style

The display range, linear or logarithmic scale, and the style of the curves is defined in the Display Parameters. Examples are shown in the figures below. The display parameters also allow the user to define a grid for the display. The autoscale button automatically adjusts the display range to the maximum of the largest curve in the display.

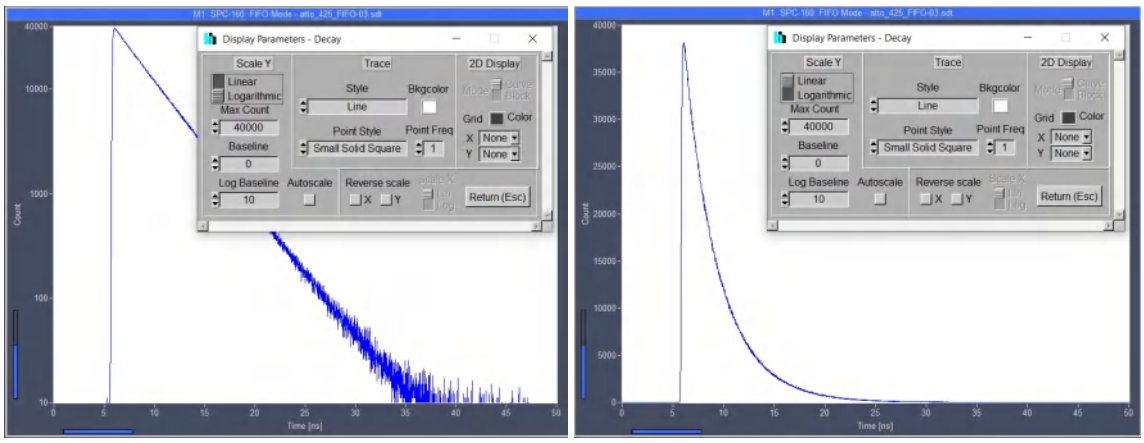


Fig. 1055: Curve display for various display-parameter settings. Linear and logarithmic scale.

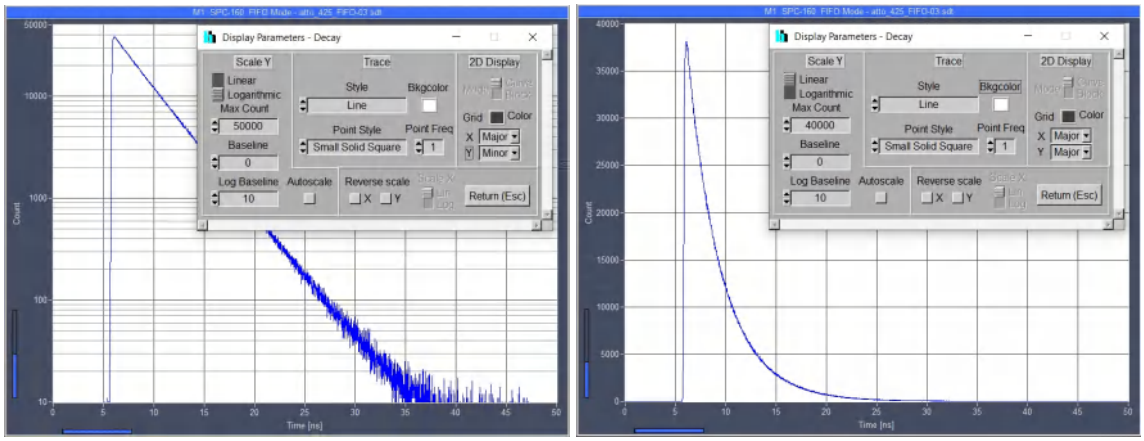


Fig. 1056: Curve display for various display-parameter settings. Linear and logarithmic grid.

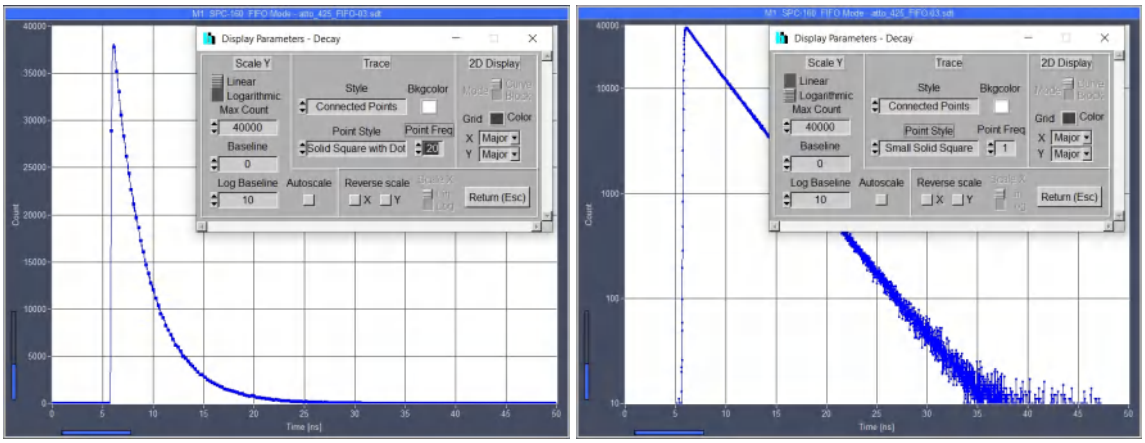


Fig. 1057: Curve display for various display-parameter settings. Curve style '^Connected Points', different point frequency.

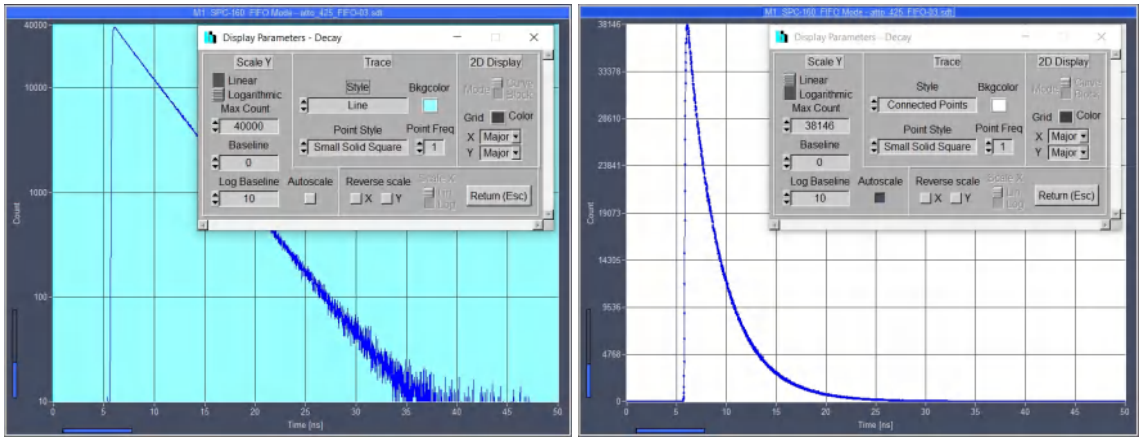


Fig. 1058: 2D display for different display-parameters. Different background colours.

Cursors

Cursors in the SPCM main window are activated by a right mouse click and selecting Enable Cursors. The cursors are shifted by grabbing the cursor lines with the mouse and shifting it over the display. A cursor panel displays the exact location of the cursors see Fig. 1059, left. A 'Data Point' indicator is available to show the contents of individual data points. 'Zoom' magnifies the area enclosed by the cursors to the full display size, see Fig. 1059, right.

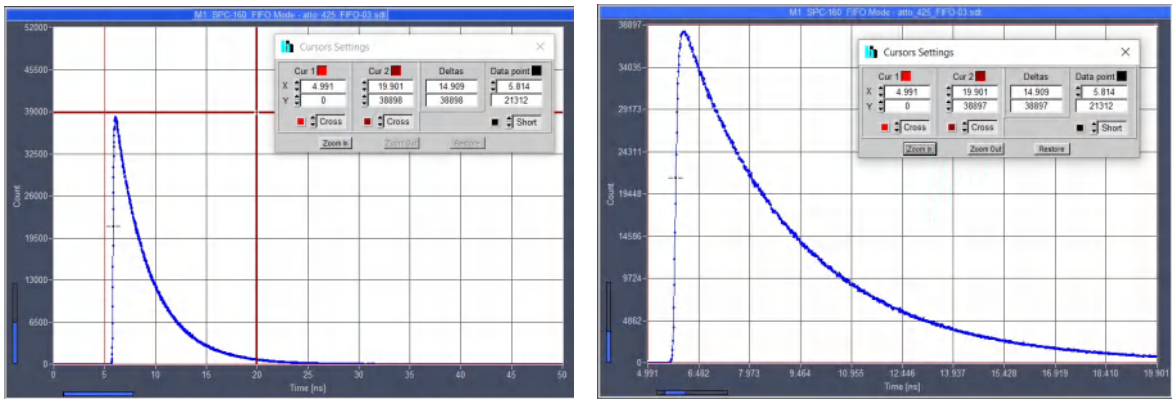


Fig. 1059: Cursors in the SPCM main window. Selection of a t-y parameter range by the cursors (left) and zoom into the corresponding parameter range.

2D Curve Routine

In addition to the curve display in the main panel SPCM has a special '2D Curve' routine. It is similar to the 2D display function of the SPCM main window but contains a few additional functions. The 2D Curve panel opens by a click on 'Display' in the top bar of the main window, and selecting '2D Curve'. The panel is shown in Fig. 1060. In the example shown below five curves are displayed. The corresponding trace parameters are shown on the right.

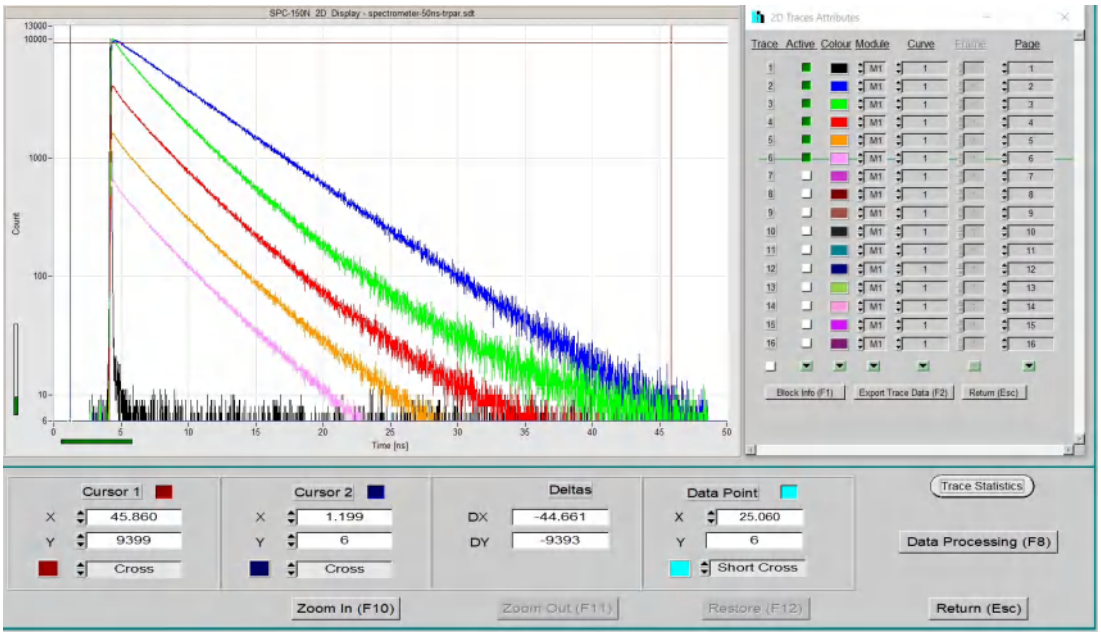


Fig. 1060: 2D Curve routine

2D Data Processing

In addition to the normal curve display functions the 2D Curve routine has a data-processing function, see button in Fig. 1060, lower right. Available data operations are: Clear outside cursors, Reject outliers, Shift in X, Shift in Y, Smooth, Copy, Reverse time axis, Plus, Minus, Multiply, and Divide. A scale factor can be defined to keep the results within reasonable limits. An example is shown in Fig. 1061. The curves in page 2 and page 3 were selected to be added and the result to be written into page 10. Fig. 1059 shows the panel after executing the command.

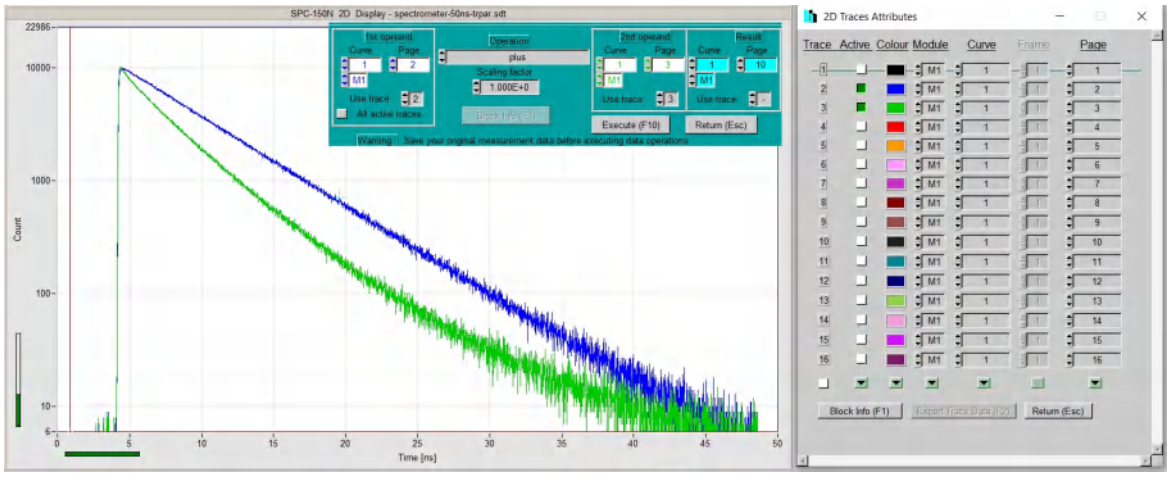


Fig. 1061: 2D data processing. The two curves shown in the upper part of the figure have been selected to be added. The result is shown in the next figure.

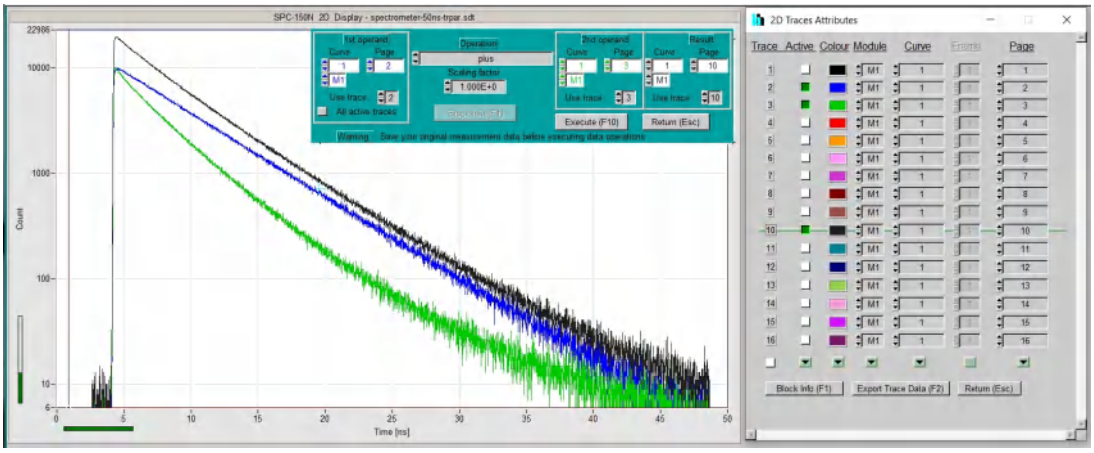


Fig. 1062: Result after executing the data processing command. Curve 2 and Curve 3 were added into Curve 10.

A practical example of a data processing operation to rescue distorted data is shown in Fig. 1063. The decay curve, A, shown left, is badly distorted by an optical reflection. The amplitude of the reflection is about 5.2%, the delay 0.467 ns. An approximate waveform of the reflected part of the signal can be obtained by shifting the curve by 0.467 ns, and multiplying it with 0.052 (use ‘add’ with the original curve for both operands, and a scaling factor of 0.026). The result is curve B. Curve B is then subtracted from curve A. The result is curve C, which is almost free of the reflection.

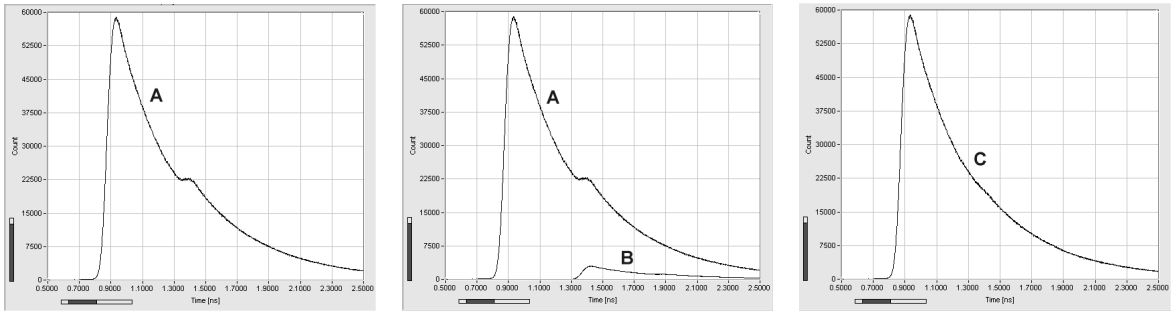


Fig. 1063: Using 2D data processing to remove an optical reflection from a decay curve

Block Mode of the 2D Display

In the 'Block Mode' the 2D Curve function combines several curves from different routing channels. The Block Mode is turned on in the Display Parameters, the curves to be combined are selected by the Window Parameters in combination with the Trace Parameters. An example is given in Fig. 1064. The upper part of the figure shows data from a PML-GaAsP multi-wavelength detector in the curve mode. There are 16 decay curves, all of them are enabled by the Trace Parameters. The lower part of the figure shows the display in the Block mode. The block mode has been selected in the Display Parameters, lower right. The Window Parameters (middle right) define two routing windows. One window contains curves 8 and 9, the other window contains curves 11 to 15. The Trace Parameters (top right) enable two traces for display. One trace contains the data from routing window 1, the other the data from routing window 2. The result are the two curves displayed on the left.

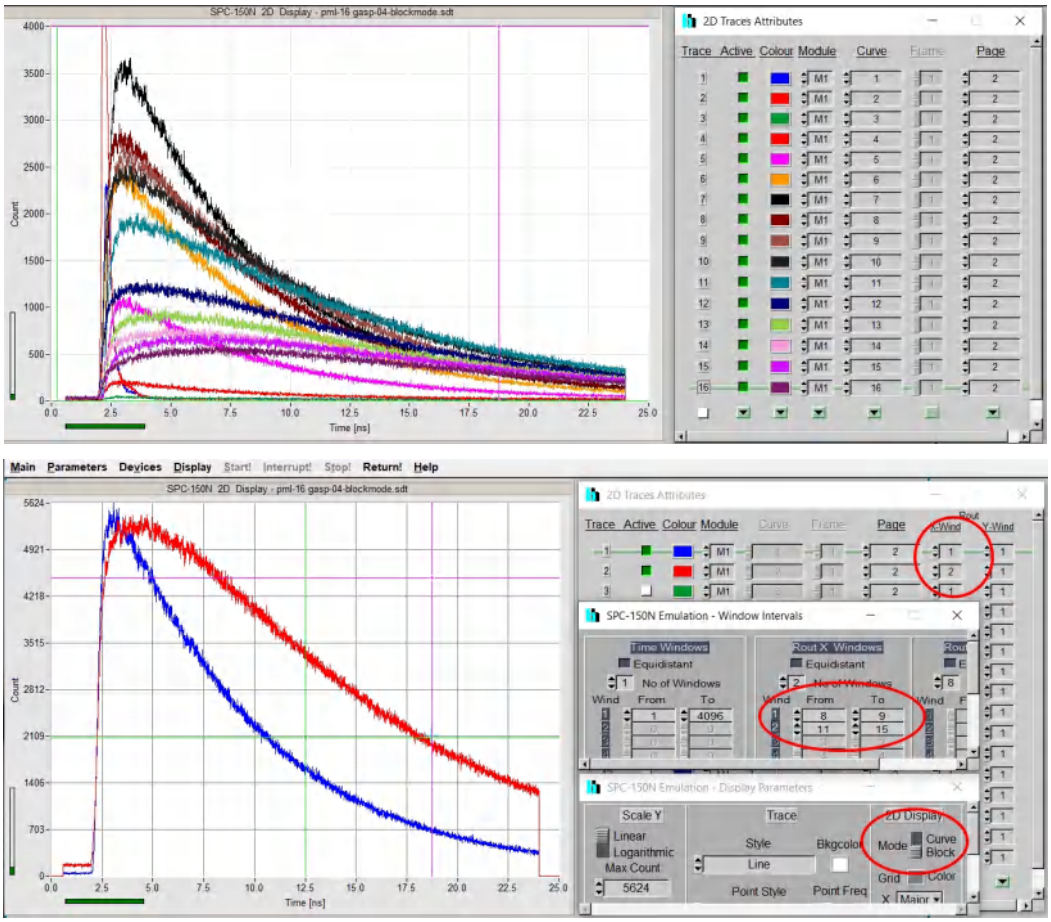


Fig. 1064: 2D Curve display in the curve mode (top) and in the block mode (bottom). The parameters are configures to combine the curves 8 to 9 and 11 to 15 in routing windows 1 and 2, respectively, and to display the combined data as traces 1 and 2.

Display of 3D Data

The 3D display function is used to display data from multi-detector measurements or multi-wavelength measurements, from sequential measurements, or from combinations of these. As the 2D display, the 3D functions are available both in the main window of SPCM and in a special 3D-Display routine.

Configuration of the Display

The corresponding photon distributions may be built up versus several variables, such as an externally varied parameter, the time in a fluorescence decay, the time in a sequence of decay curves, or the wavelength. An example is shown in Fig. 1065. It shows a sequence of curves recorded by scanning the detection wavelength with a monochromator. The data can be displayed both as an array of curves (curve mode, shown left) and as an image in which the brightness and the colour represent the photon numbers (colour-intensity mode, shown right.) The display style is controlled by the settings in the lower part of the Display Parameter panel. The parameters corresponding to the configurations of Fig. 1065 are shown in Fig. 1066. Display mode is 3D Curves (left) and Colour Intensity (right). The third coordinate is the wavelength in the monochromator scan, therefore 'f(x,y,param)' has to be selected in the lower right of the display parameters.

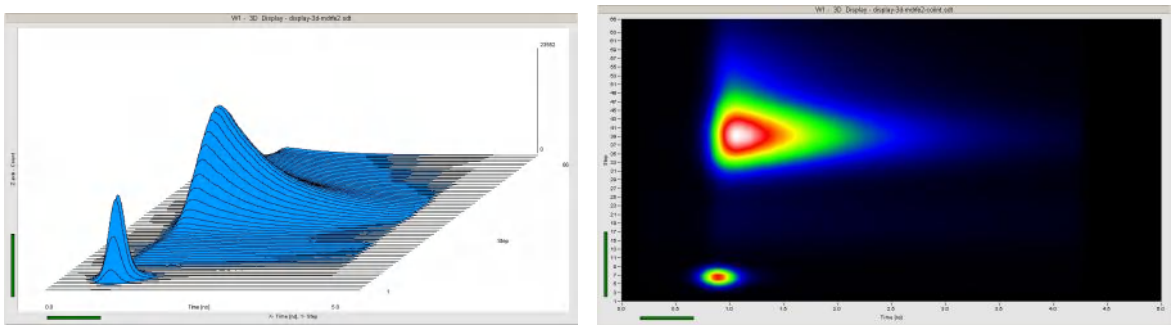


Fig. 1065: Result of f(t,ext) measurement, wavelength scan by monochromator. Left curve mode, right colour intensity mode

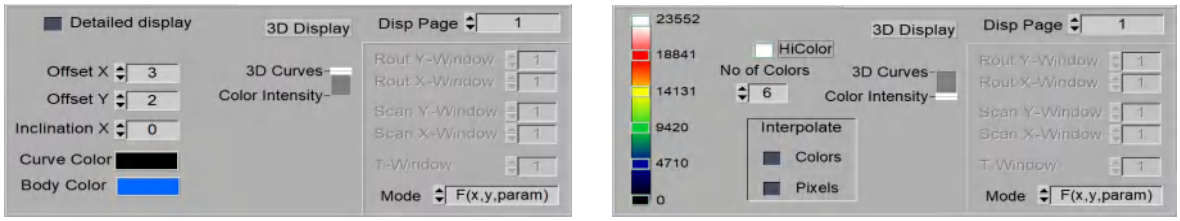


Fig. 1066: Display parameters, 3D section. Left: Curve mode. Right: Colour-intensity mode.

Fig. 1068 shows data recorded with a 16-channel PML-GaAsP detector. The way the data are displayed is similar as for the data in the figure above. However, now the third coordinate is the number of the routing channel, x. Therefore f(t,x) has been selected in the display parameters, see Fig. 1068.

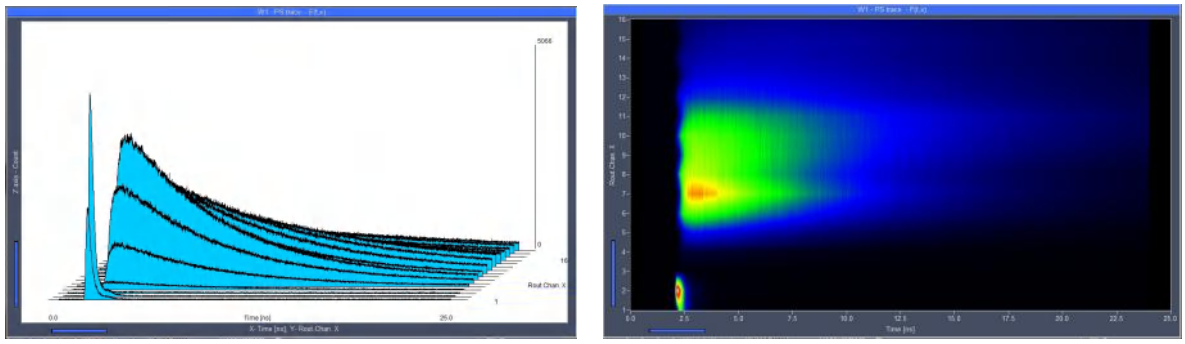


Fig. 1067: Result of f(t,x) multi-wavelength measurement with the PML-16 GaAsP detector. Left Curve Mode, right colour intensity mode

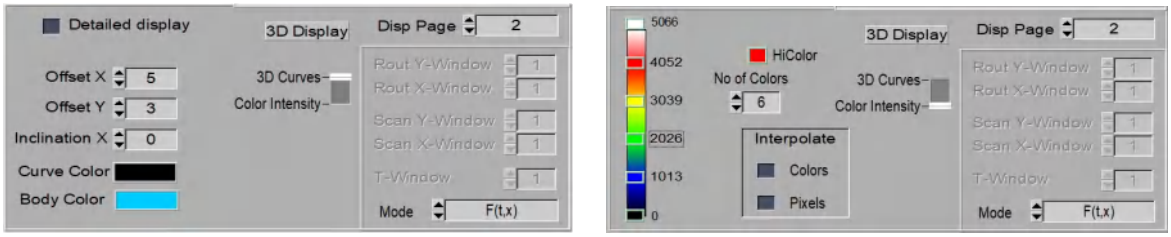


Fig. 1068: Display parameters for the data shown above, 3D section. Left: Curve mode. Right: Colour-intensity mode.

Cursors

Cursors and a data point are available the same way as in the 2D display. Click into the display window by the right mouse key and select Enable Cursors. Cursors can be used both in the 3D Curve display and in the 3D Colour-Intensity display. Using cursors in the 3D Curve mode is difficult, therefore we recommend to switch into the Colour-Intensity mode when cursors are used. An example is shown in Fig. 1069.

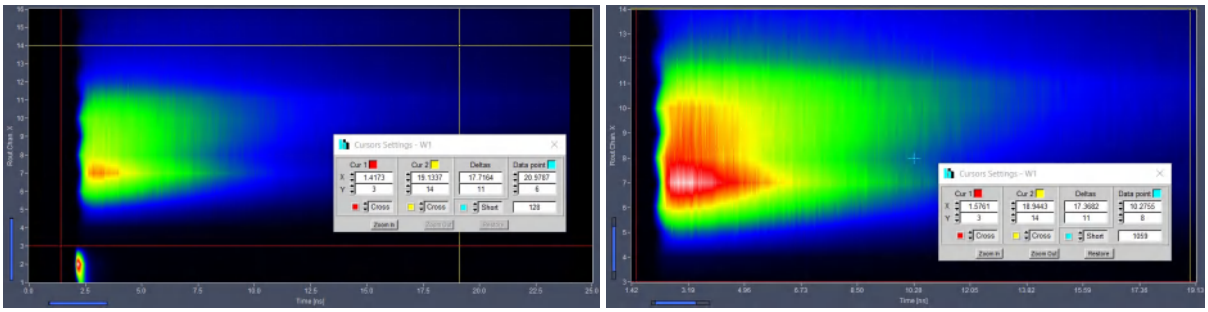


Fig. 1069: Cursors in the 3D display. Left: Cursor panel opened by right mouse click. Right: Zoom into area inside the cursors.

3D Curve Routine

SPCM contains a special '3D Curve' display routine. It is accessible via 'Display' in the top bar, and selecting '3D Curve'. The 3D Curve panel is shown in Fig. 1070. It directly contains the cursor and zoom functions.

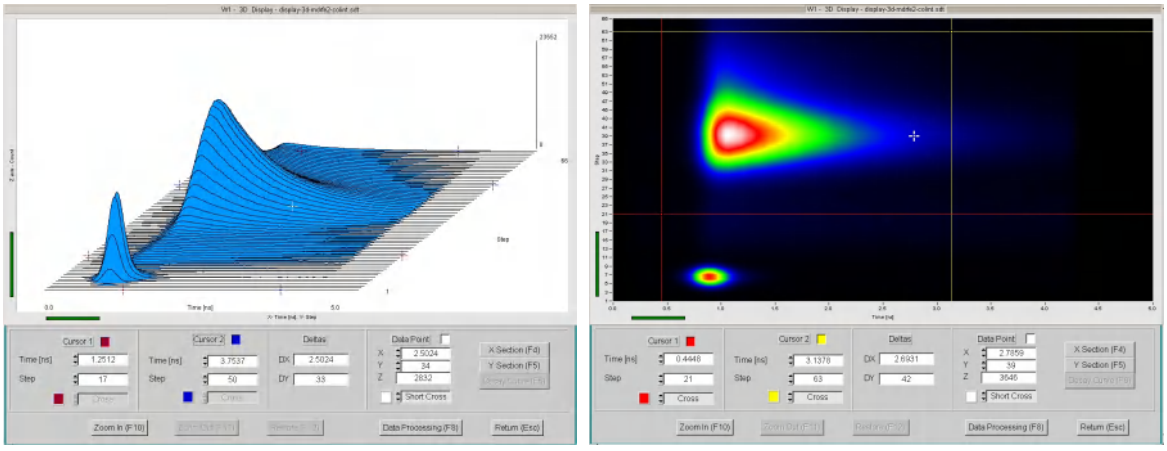


Fig. 1070: 3D Display. Left: 3D Curve mode. Right: Colour-intensity mode

The main difference to the 3D display functions of the main panel is that the 3D Curve routine has a data processing function.

3D Data Processing

The ‘3D Data Processing’ panel is opened by clicking on the ‘Data Processing’ button or by clicking into ‘Display’ in the menu bar and selecting '3D Data Processing'. The 3D data processing panel is shown in Fig. 1071.

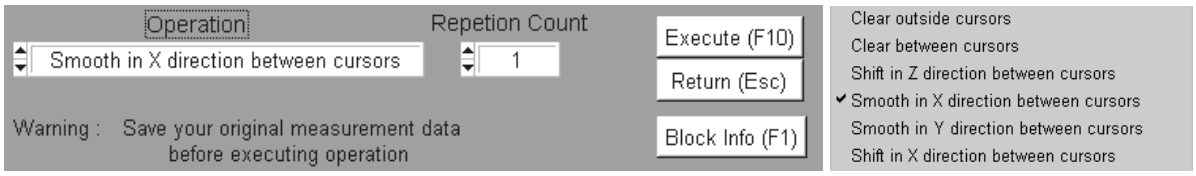


Fig. 1071: 3D Data Processing panel (left) and available operations (right)

All operations are performed in the parameter range defined by the cursors. During the operation the original data is replaced with the result. Therefore, we recommend to store the original data to a file before starting a data processing operation.

Display of FLIM Data

The results of a FLIM measurement are multi-dimensional data arrays. In the simplest case, the dimensions are the two coordinates of the scanning area, X and Y, and the time in a fluorescence of phosphorescence decay, t. However, FLIM data can be more complex. There may be additional coordinates, such as the detector-channel number in multi-wavelength FLIM data, the time step within a series of recordings, or other parameters which were assigned to the photons in the recording process. It may be necessary to display the data in different parameter spaces, e.g. as pure intensity images, as time-gated images, or as colour-coded fluorescence lifetime images. It may even be desired to display the data not as images but as sequences of decay curves integrated over selected spatial windows within the images. The SPCM software allows the user to define up to eight display windows for data of different source, different data type or different projection within the data parameter space. The display of the data is controlled by the '3D Trace Parameters', the 'Window Parameters' and the 'Display Parameters'. This section explains the parameters setup for the display of FLIM data for typical FIFO Imaging measurements and demonstrates it at typical examples.

Definition of the Display Windows

3D Trace Parameters

The 3D trace parameters define how many display windows are opened in the SPCM main panel, which kind of data they are showing, from which TCSPC module or routing channel they are taken, and in which way multidimensional data are projected into the individual display windows. Examples are shown in Fig. 1072 and Fig. 1075.

Fig. 1072 shows a 3D trace parameter setup for displaying images of different data type. The first two windows, W1 and W2, display intensity data of ps FLIM data from two TCSPC modules, M1 and M2. The next two windows, W3 and W4, display the same data as lifetime images. W5 and W 6 display MCS mode (PLIM) images from M1 and M2. Finally, W7 and W8 display intensity images from the direct counter channels of two SPC-160 modules.

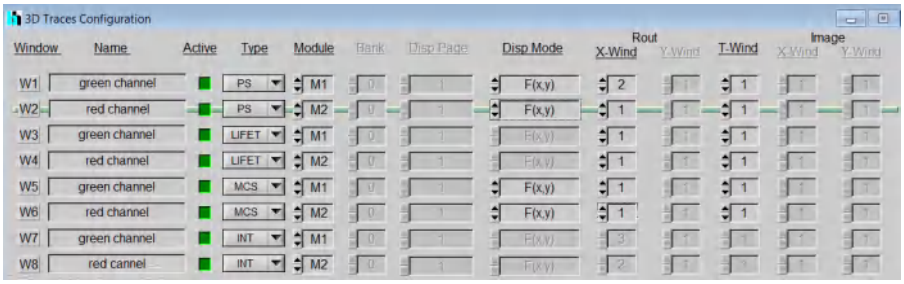


Fig. 1072: 3D Trace parameters for the display of FLIM intensity images, FLIM lifetime images, MCS (PLIM) images, and intensity images from the fast counter channels of two SPC-160 modules

For all definitions shown in Fig. 1072 the 'Display mode' is F(x,y). That means, the data shown in the individual display windows are intensity distributions over the two spatial coordinates, x and y.

However, this is not the only way the data can be displayed. FLIM data are three-dimensional x-y-t arrays. That means, when the FLIM results are displayed different projections of the data can be used. The way the data are projected is selected by 'Display Mode'. The principle is shown in Fig. 1073.

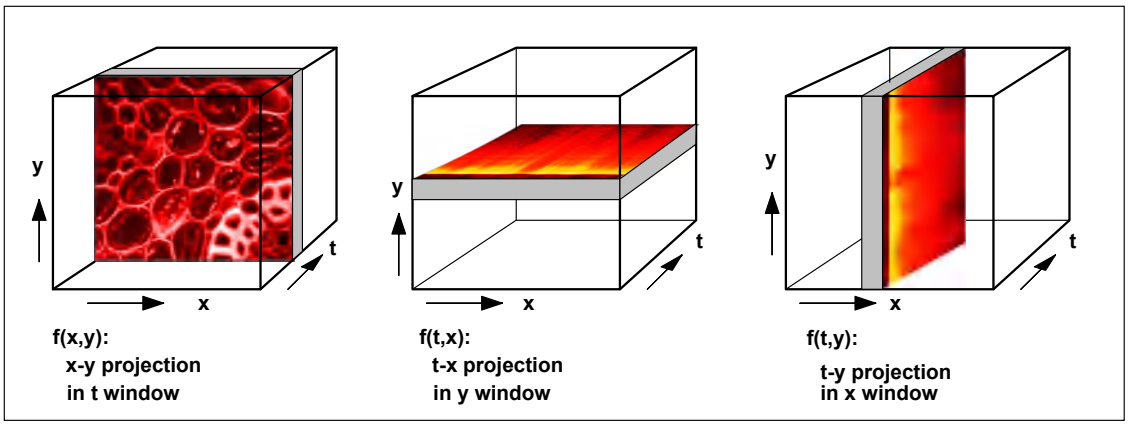


Fig. 1073: Different projections of FLIM data

F(x,y) projects the intensities (photon numbers) of a selected time window in the x-y plane. The result is a time-gated image, or, if the time window covers the entire t axis, an intensity image of the sample.

F(t,x) projects the photon numbers of a selected y window into a t-x plane. The result displays the intensity decay along the t axis versus the location in x for a selected window in y. F(t,y) projects the photon numbers of a selected x window into the t-y plane. The result displays the intensity along the t axis versus the location in x for a selected window in y. In both cases, the spatial window can also cover the entire x or y coordinate. Examples of trace parameters with different projection are shown in Fig. 1075.

A special case is the direct display of the fluorescence lifetime. In this case, the display routine calculates the first moment of the decay data along the t axis of the individual pixels, converts it into the fluorescence lifetime. When ‘Lifetime Display’ is selected (W3 and W4 in Fig. 1072) the colour of the image represents the lifetime, the brightness the total or gated intensity.

So far, things are still relatively straightforward. However, TCSPC data can easily become four-dimensional. This happens especially when the routing function is used. Data in the individual routing channels then represent different detection wavelengths, different excitation wavelengths, or different states of an external signal acting on the sample. The ‘Routing Window’ defines a range of routing channels the data of which are projected into individual x-y, t-x, or t-y planes and displayed as described above. Trace-parameter examples for these situations are shown in Fig. 1074 and Fig. 1075. Please note that time windows cannot be defined for intensity image from the SPC-160 counters and for lifetime display because the counter data do not contain temporal information.

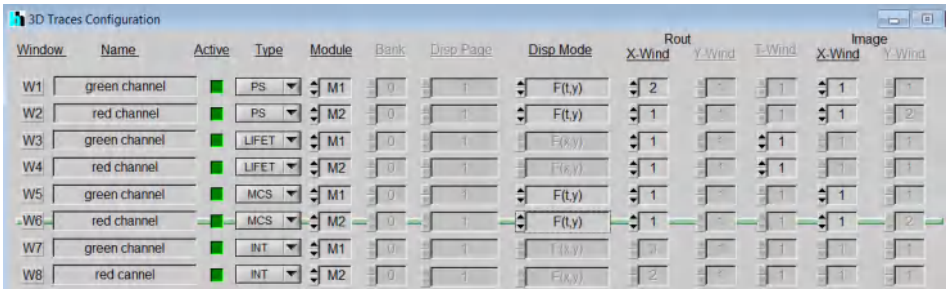


Fig. 1074: 3D Trace parameters for the display of decay functions over one spatial and one temporal coordinate of spatially two-dimensional data. Displayed are functions f(t,y) within different X Windows.

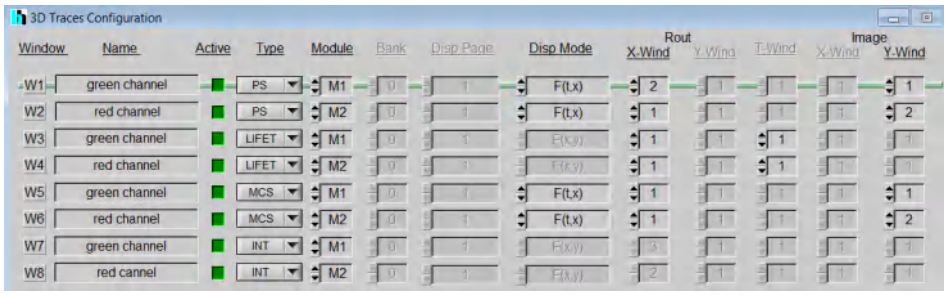


Fig. 1075: Same as figure above but functions f(t,x) within different Y Windows displayed.

Window Parameters

The window parameters define time windows for FLIM, routing windows, time windows for PLIM (MCS windows) and spatial windows in X and Y for displaying multi-dimensional data. Fig. 1076 shows definitions for 8 windows along each coordinate.

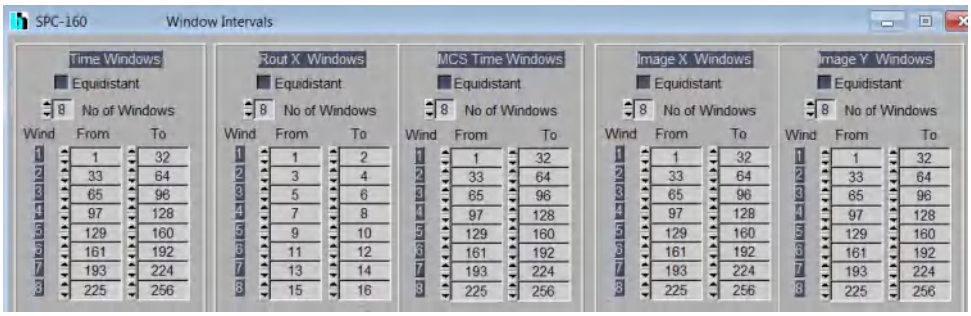


Fig. 1076: Window Parameters. Definitions shown for 8 FLIM time windows, 8 routing windows, 8 PLIM time windows, and 8 windows in x and y.

Basic FLIM and PLIM images are often displayed without the gating functions of the SPCM display routines. In that case, it is enough to define just one windows along each coordinate, covering the entire time axis, all routing channels, and the entire image in x and y. Definitions for data of 256 FLIM time channels, 256 PLIM time channels, and 256 x 256 pixels without routing are shown in Fig. 1077.

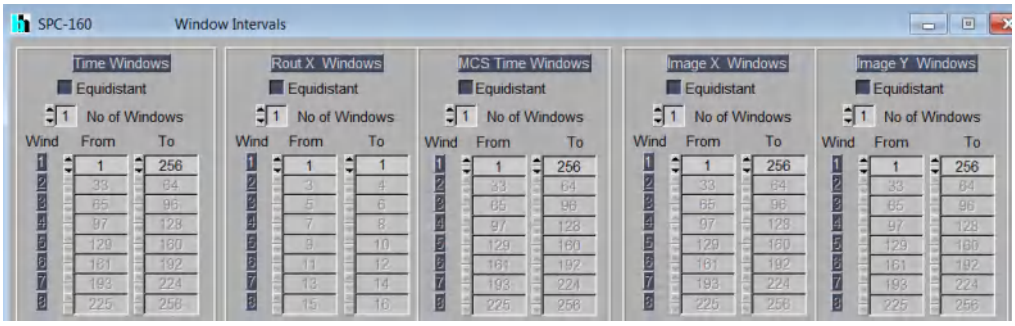


Fig. 1077: Window parameter definitions for 256 FLIM and PLIM time channels 256 x 256 pixels for FLIM and PLIM display without gating functions.

Display Parameters

The display parameters define how the data are displayed in the individual display windows of the SPCM software. Every display window has its own set of display parameters. The parameters define the display range, the colours, the display style (curves or colour-intensity plot), the display mode (f(x,y), f(t,x or f(t,y), and the t, x and y windows in which the data are displayed. Examples are for three different display configurations are shown in Fig. 1078.

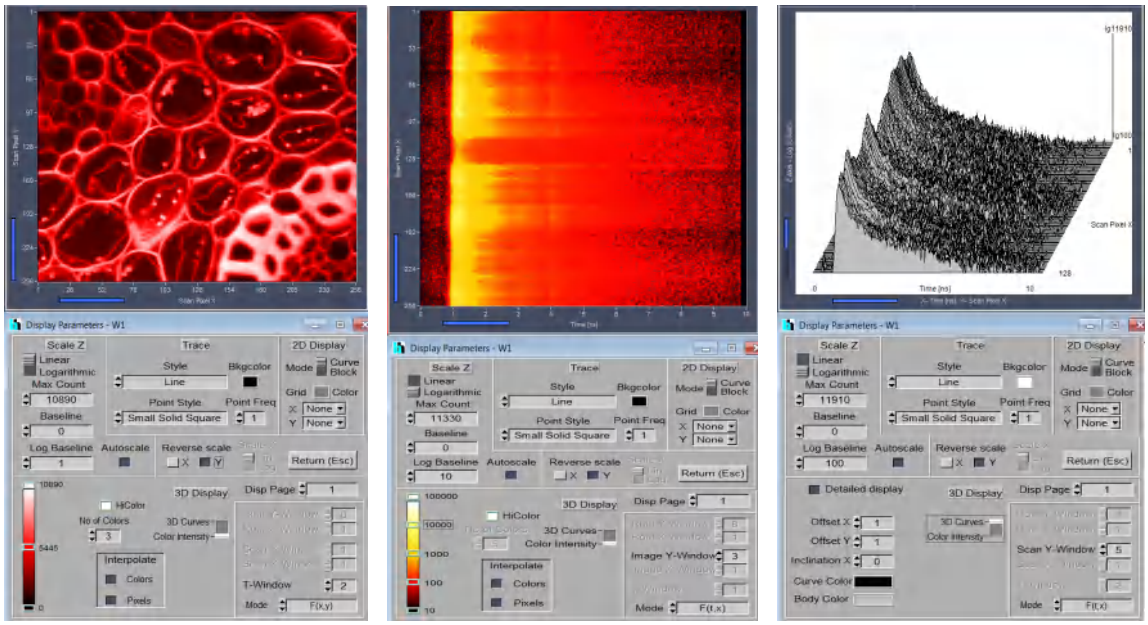


Fig. 1078: Influence of display parameters on the FLIM data display. Left: Image displayed in a selectable time window. Middle: Decay functions over x coordinate in a selectable y window displayed in colour-intensity mode, Right: Decay functions over x coordinate in a selectable y window displayed in curve mode

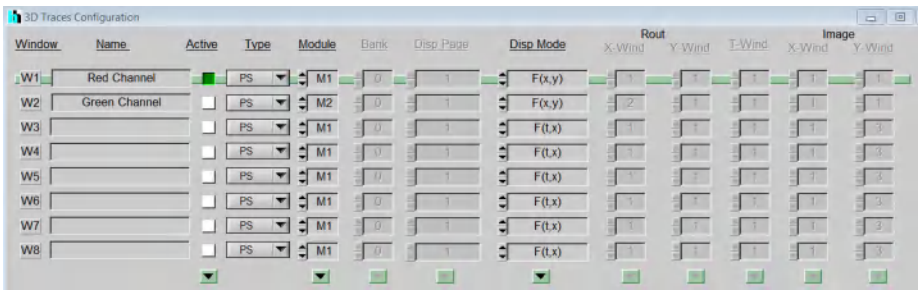
Examples of the display setup for a number of frequently used FLIM configurations are described below.

Intensity Images from FLIM Data

One Image from One SPC Module

Fig. 1079 shows the parameters for displaying an intensity image from the combined photon numbers in all time channels of a single FLIM image. In the 3D Trace parameters, only one display window (W1) is enabled. The data type to be displayed is ps FLIM, the data come from TCSPC module M1, and the display mode is F(x,y). The Window parameters (bottom left) define a single Time Window, from time channel 1 to 256, and two spatial windows, both from pixel 1 to pixel 1024. In other words, the windows incorporate the entire FLIM data array.

The Display Parameters, Fig. 1080, define a colour-intensity image with linear intensity scale. The intensity is coded by colour, the colour scale goes from black over red to white. The image is displayed for Time Window 1 - this is the only time windows defined (see Window Intervals, Fig. 1079). It contains the photons of all time channels (from 1 to 256). The SPC Main panel with an image defined by these parameters is shown in Fig. 1081.



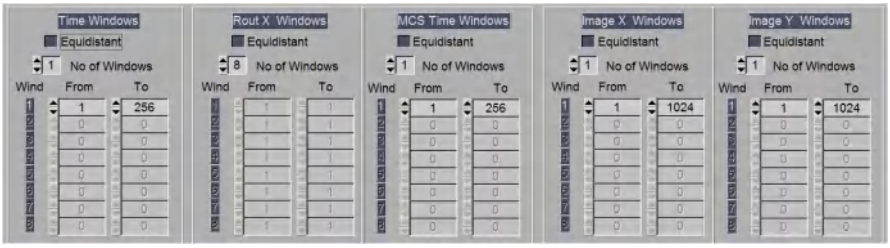


Fig. 1079: 3D Trace parameters and Window Parameters for the display of a single image

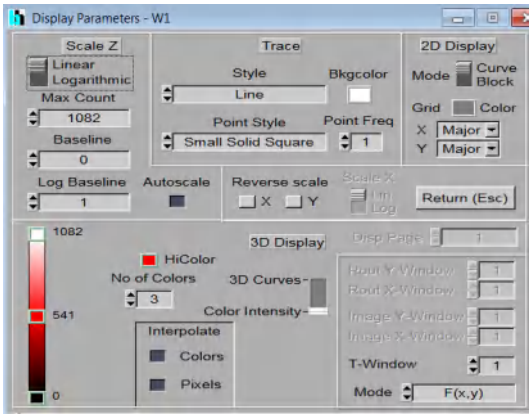


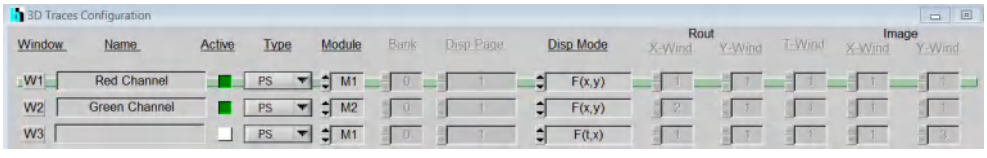
Fig. 1080: Display parameters



Fig. 1081: SPCM Main panel with the image defined by the parameters shown above

Images from Two SPC Modules

The parameter setup for the display of two images from separate SPC modules is shown in Fig. 1082. The Trace Parameters define two display windows. They contain data from two SPC modules, M1, and M2. The window parameters are the same as for a single image - there is only one time window, containing the photons of all TCSPC time channels from 1 to 256.



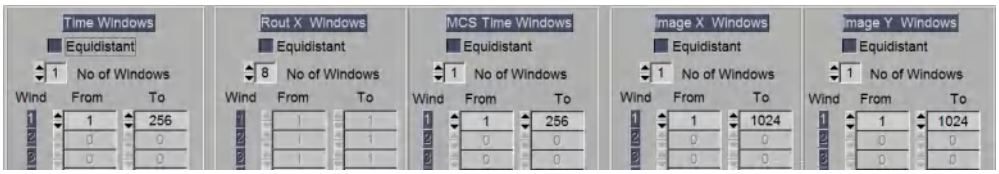


Fig. 1082: 3D Trace parameters and Window parameters for the display of the images from two SPC modules, M1 and M2

The two images are displayed with separate display parameters, see Fig. 1083. The SPCM main panel with the two images is shown in Fig. 1084.

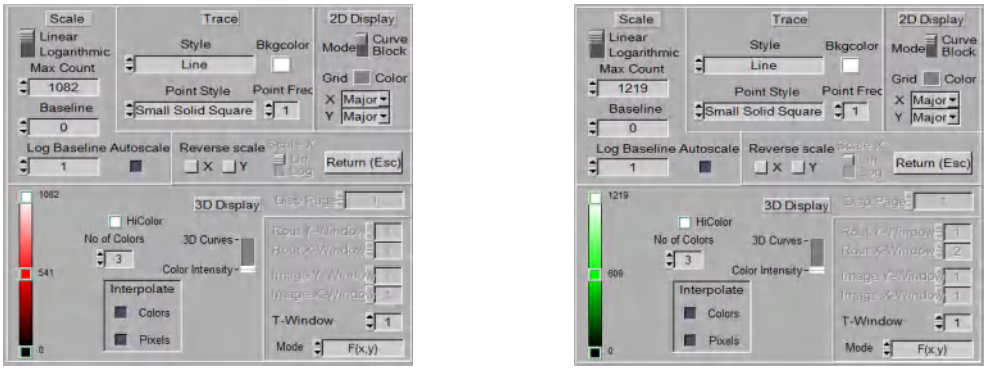


Fig. 1083: Display parameters for the two images defined by the parameters in Fig. 1082

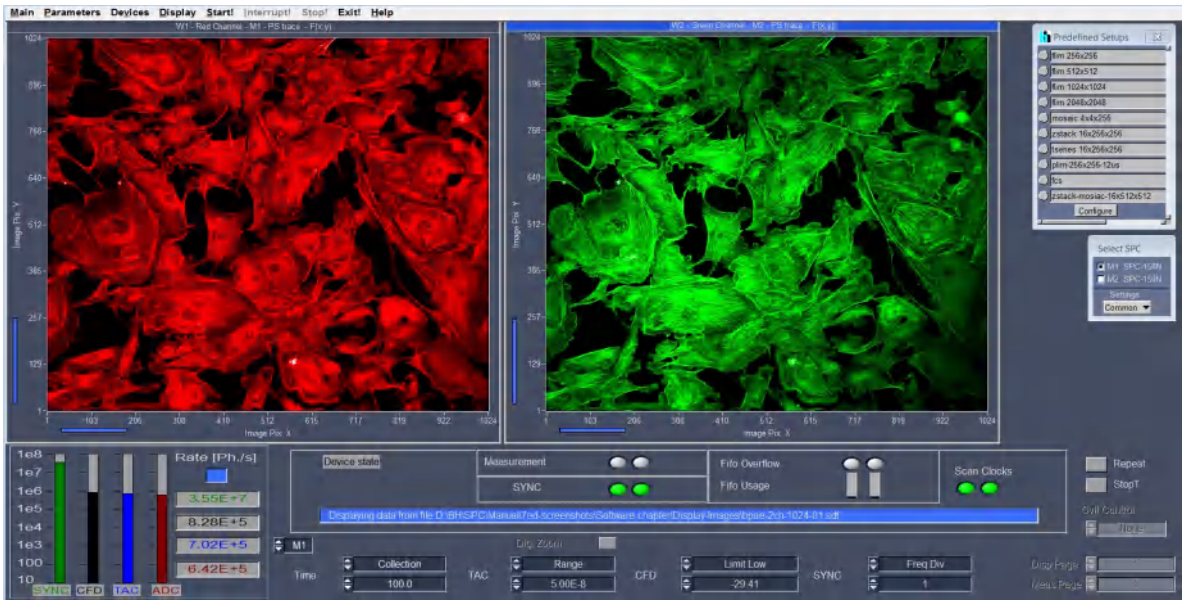


Fig. 1084 SPCM Main panel. Two images for separate SPC modules.

Intensity Images from Routing Channels

Images from several routing channels are displayed as shown in Fig. 1085. The 3D Trace Parameters define several display windows for different routing channels. The data in these channels can come from different detectors connected to the SPC module via a router, or from several multiplexed lasers. The 3D trace parameters define the number of display windows used, and the information to be displayed in the windows. The Window parameters define which routing channels or groups of routing channels are displayed in the windows.

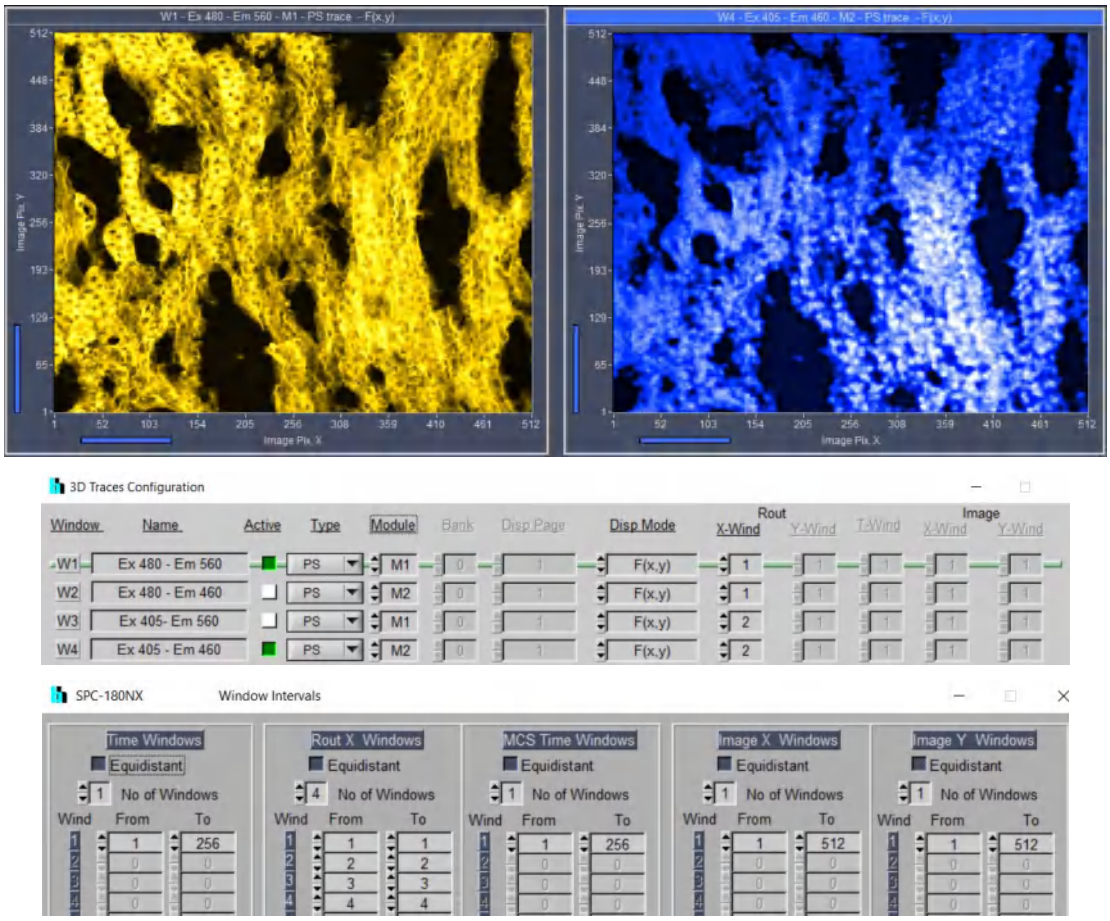


Fig. 1085: Two images from a dual-channel wavelength-multiplexing system, intensity display. 3D trace parameters and Window parameters shown at the bottom. Four combination of excitation and emission wavelength exist, two of them are switched active in the 3D trace parameters.

Multi-Wavelength Intensity Images

The display of multi-wavelength FLIM data from a 16-channel detector is shown in Fig. 1086 trough Fig. 1088. The trace parameters define eight display windows. Data type is ps FLIM. The individual images in the display windows are derived from subsequent 'Routing Windows'. Each routing window contains the data of two subsequent routing channels, see Window Parameters. This way, data of every two wavelength channels are combined in one image.

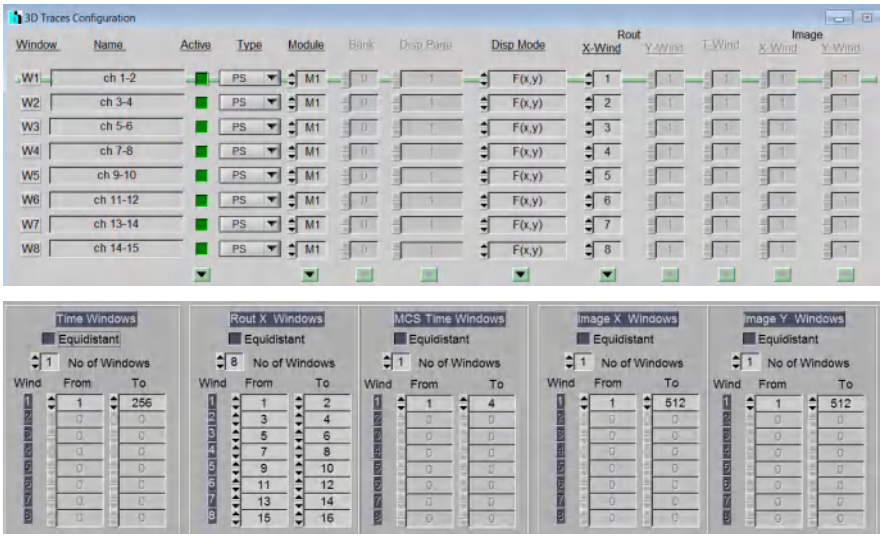


Fig. 1086: 3D Trace Parameters and Window Parameters for multi-wavelength FLIM

As usual, the individual images have separate display parameters. The display parameters for the first three images are shown in Fig. 1087. They contain the colour definition for the individual images, and the routing window. Since the intensities in different wavelength channels can vary over a wide range Autoscale is turned on for all images. The main panel of SPCM with the eight images is shown in Fig. 1088.

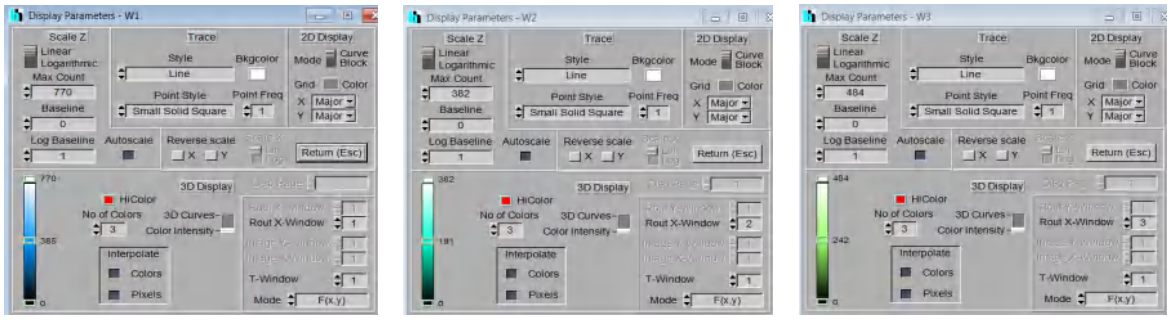


Fig. 1087: Display parameters in the first three display channels of a multi-wavelength measurement

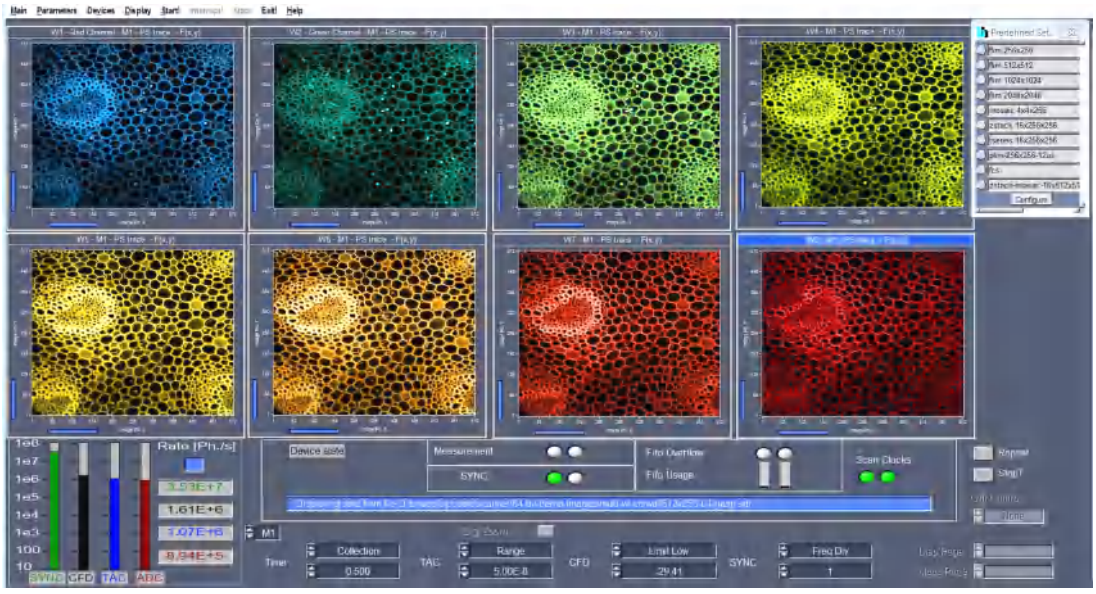


Fig. 1088: SPCM main panel for multi-wavelength FLIM

Intensity Images from Combined Channels of FASTAC System

The SPCM 3D display function is able to combine intensity images, time-gated images, or colour-coded lifetime images from several combined TCSPC channels into a single image. Main application is the bh FASTAC system with its four parallel TCSPC channels. The Trace Parameters are shown in Fig. 1089. The result is a main panel as shown in Fig. 1090, with an image showing an intensity image of the combined data of SPC modules, M1 to M4. In addition to the combined data, it is possible to display also the data of the individual channels. To do so, activate the 'active' buttons for the individual TCSPC modules, M1, M2, M3, M4, in the 3D Trace definitions.



Fig. 1089: Trace parameters for FASTAC system. The data of four TCSPC channels, 1-4, are combined.

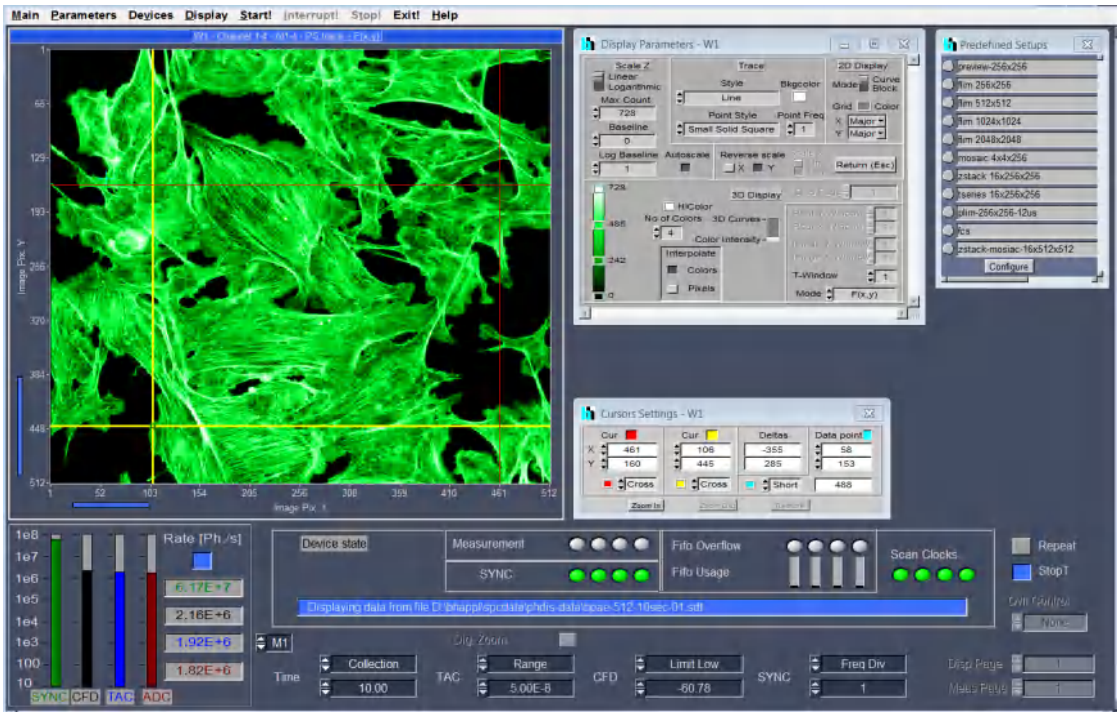


Fig. 1090: Main panel, display of the combined data of four TCSPC FLIM Channels

Time-Gated Intensity Images

Fig. 1091 shows the parameters for the display of four gated images of one TCSPC channel. The 3D trace parameters define four display windows for the data of module M1 in four time windows, 1 to 4. The window parameters define the start and the end channels for the individual time windows.

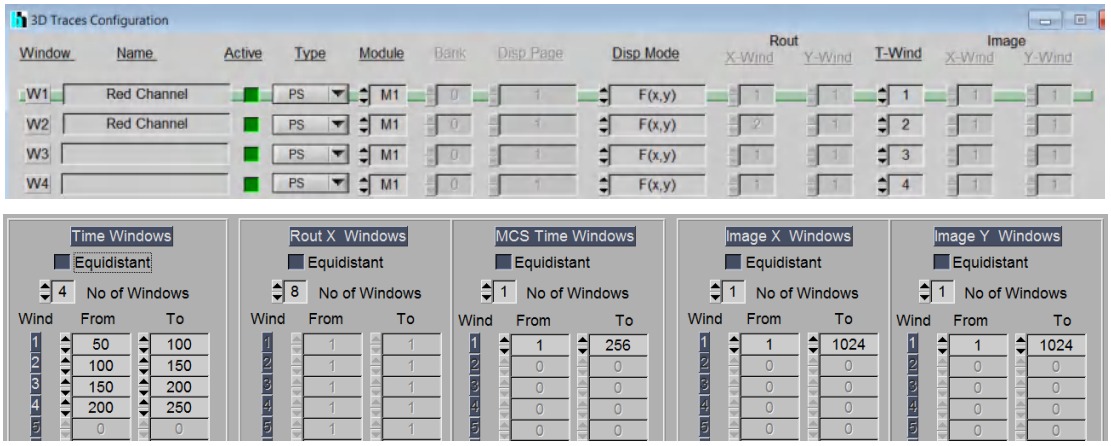


Fig. 1091: 3D Trace parameters and Window parameters for the display of four time-gated images of SPC module M1.

The individual images have separate display parameters, see Fig. 1092. The SPCM main panel with the four gated images is shown in Fig. 1093.

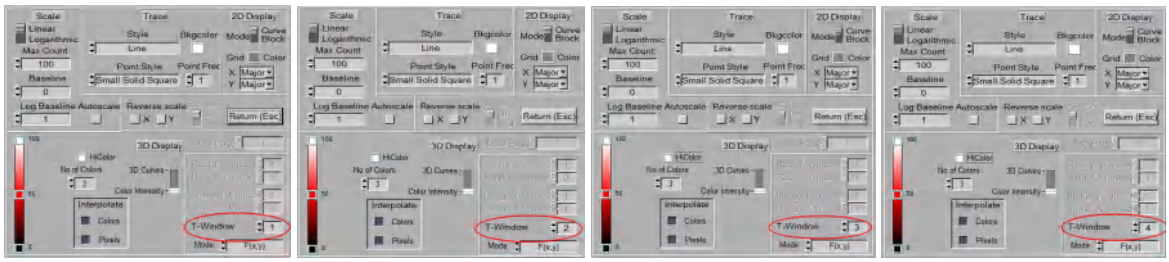


Fig. 1092: Display parameters for the four gated images



Fig. 1093: Four gated images in the main panel of SPCM

Colour-Coded Lifetime Images

Parallel-Channel Systems

The online-lifetime display mode is enabled in the 3D trace parameters. 'Type' defines the type of images to be displayed. 'Type' for online-lifetime display is 'LIFET'. Fig. 1094 shows the definition of the parameters for run-time lifetime display for a one-channel, a two-channel, and a four-channel TCSPC system. Under 'Name', you can assign clear-text names to the individual channels. The name the appears then appears in the top line of the images.

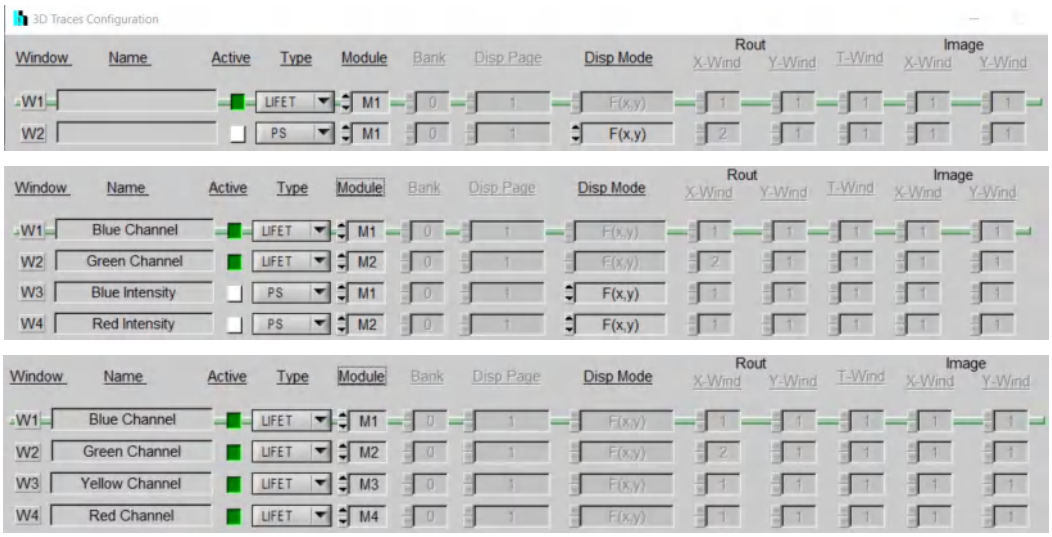


Fig. 1094: 3D trace parameters for run-time display of lifetime images. Top to Bottom: One SPC module, two SPC modules, four SPC modules.

The 'Type' definition need not be identical in all channels. For example, you can display a lifetime in one channel together with an intensity image in the same channel or in another channels, and switch the images 'Active' or inactive on demand.

The display of lifetime-image display requires more parameters than the display of intensity images. The online-lifetime function calculates the first moment of the decay data in the pixels, and subtracts the first moment (the centroid) of the IRF from it. Therefore the temporal location of the IRF must be known. Moreover, the display range for the lifetime, the direction of the colour scale must be known. These parameters are defined in the Display Parameters, see Fig. 1095. As usual, there is a separate set of display parameters for each image. In the lower part of the panels the lifetime range, the direction of the colour bar, the brightness and the contrast, and the reference moment for the IRF is defined. The reference moment can be determined with SPCImage (see SPCImage NG Data Analysis Software, page 861) or calculated from a reference FLIM file of a sample with known fluorescence lifetime. For principle of run-time lifetime calculation please see ‘Fast Online FLIM’, page 415. The main panel of the SPCM software with the lifetime images of two SPC channels is shown in Fig. 1096.



Fig. 1095: Display parameters for run-time lifetime display

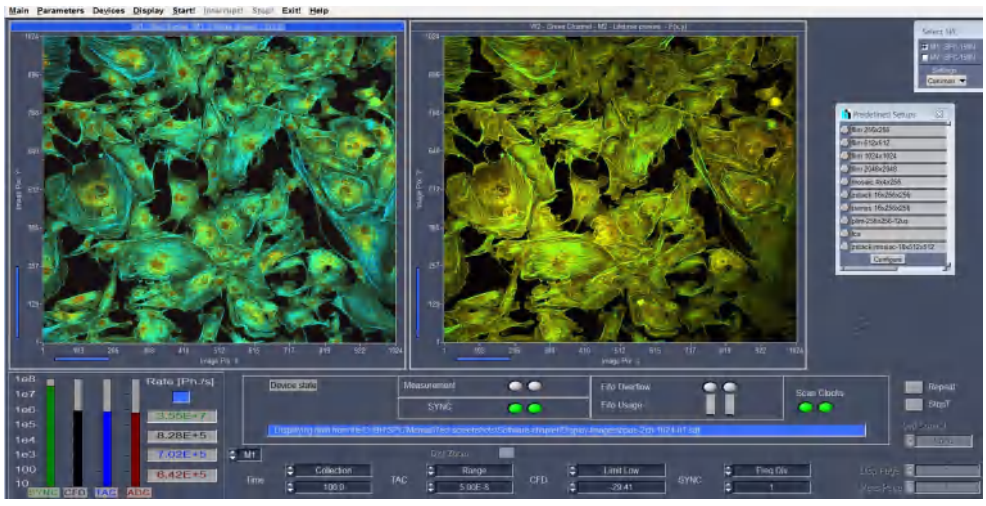


Fig. 1096: SPCM main panel with run-time lifetime calculation

Routing and Multiplexing Systems

Routing is used for excitation-wavelength multiplexing and for multi-wavelength detection. Online-lifetime display is available also for these systems. The channel assignment is the same as for intensity images: Display windows for the routing channels are defined in the 3D

Trace parameters, and routing channels or groups of routing channels are assigned to the display windows by the Window Parameters. Examples of a 2-channel wavelength multiplexing system and for a multi-wavelength system are shown in Fig. 1097 and Fig. 1099.

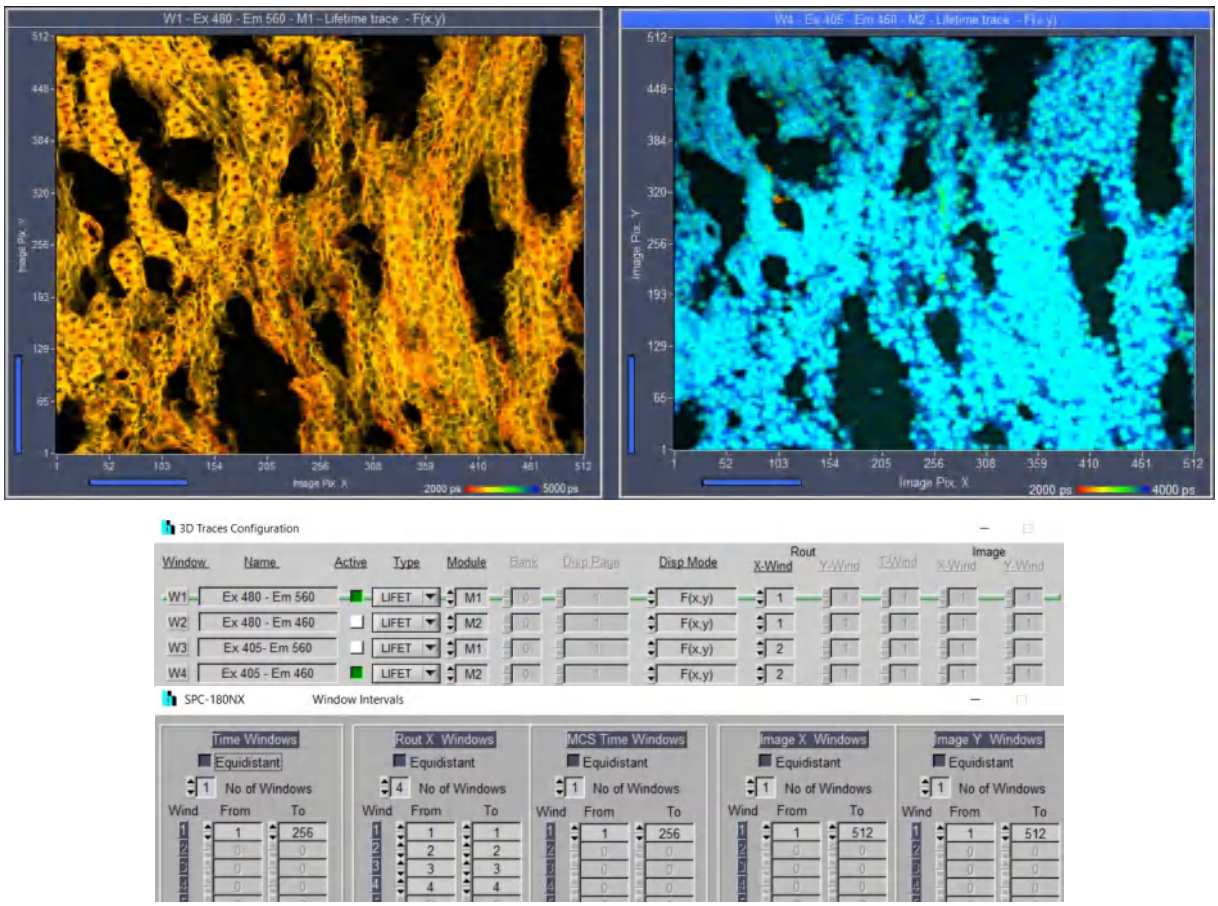


Fig. 1097: Two images from a dual-channel wavelength-multiplexing system, online-lifetime display. 3D trace parameters and window parameters shown at the bottom. Four combination of excitation and emission wavelength exist, two of them are switched active in the 3D trace parameters.

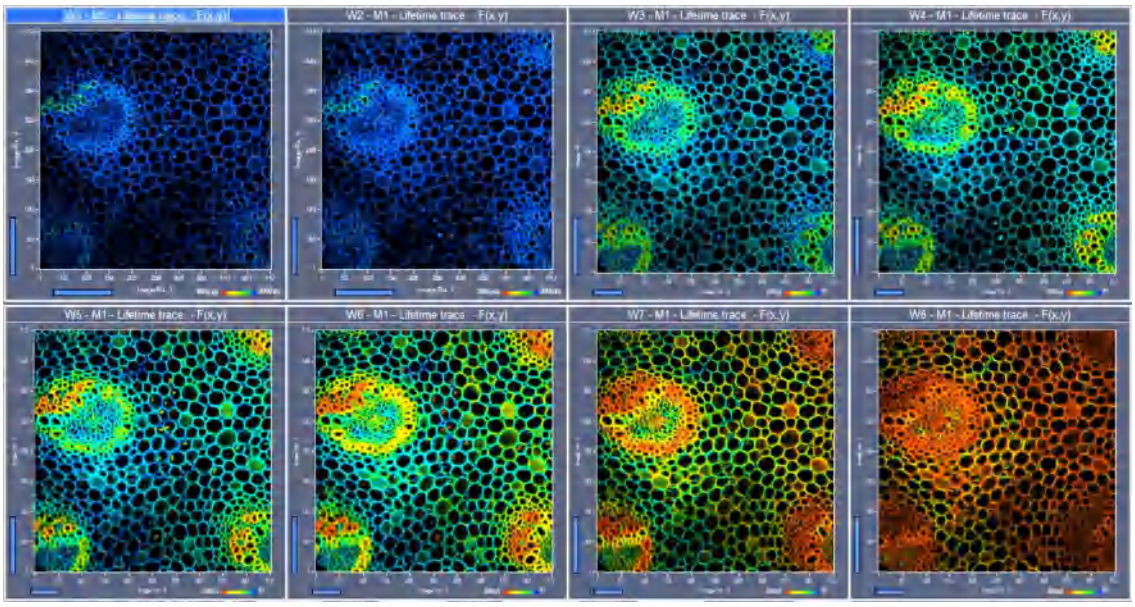


Fig. 1098: Multi-wavelength lifetime-image display. 16-channel detector, 8 images of different wavelength displayed, each image contains 2 combined channels.

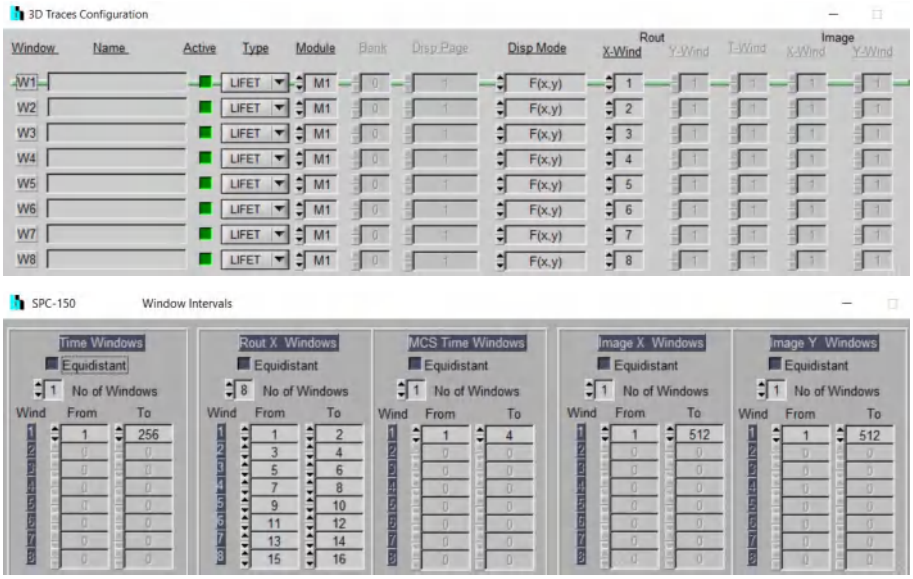


Fig. 1099: Trace parameters and window intervals for Multi-wavelength lifetime-image display. 16-channel detector, 8 images of different wavelength displayed, each image contains 2 combined channels.

FASTAC System

Lifetime display works also for the combined channels of a FASTAC system. The trace parameters are shown in Fig. 1100, the corresponding main panel in Fig. 1101. The Display Parameter panel is open on the right. In its lower part it contains the definitions for the lifetime range, the reference lifetime, binning, and brightness and contrast settings.



Fig. 1100: Trace parameters for lifetime display for the combined channels of a FASTAC system. 'Lifetime' is selected as display data type. The data of four SPC modules, M1-M4, are combined, and displayed in main-panel window W1.

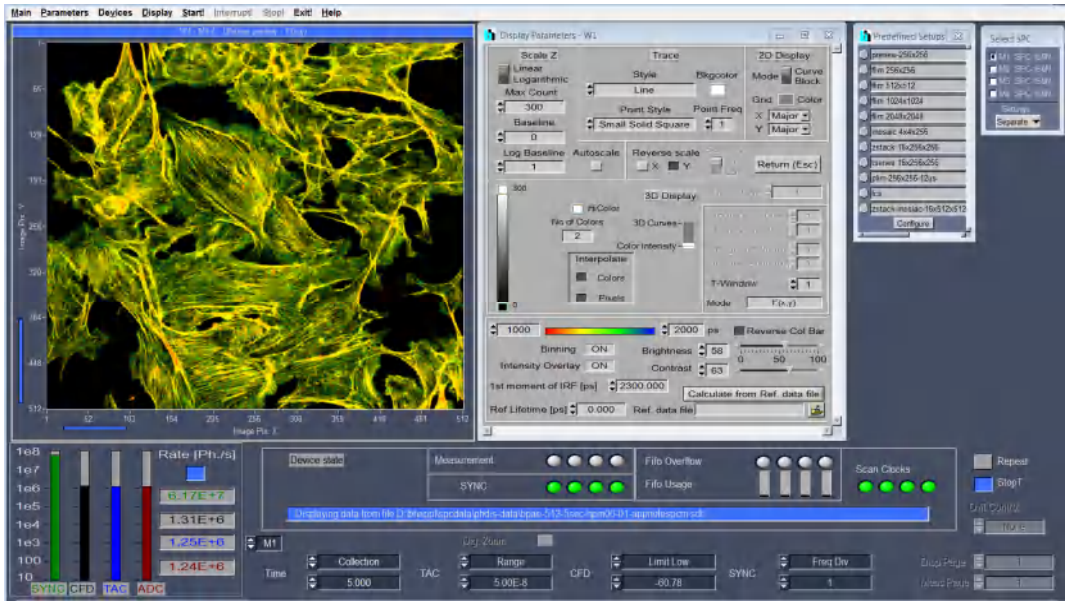


Fig. 1101: SPCM Main panel with lifetime display of combined channels. Colour-coded lifetime image on the left, display parameters on the right.

Images from Lifetime-Intensity Mode

To improve the image contrast at high count rates the SPC-160 and SPC-180 family modules have a fast counter in parallel with the TCSPC timing electronics. The 'Lifetime/Intensity' display mode of bh's SPCM software builds up FLIM images by using pixel intensities from the parallel counter and pixel decay data from the timing electronics. For technical details and for system parameter setup please see section 'Lifetime-Intensity FLIM' page 428. The display type for lifetime-intensity images is 'LIFET+I' see trace parameters in Fig. 1102, bottom.

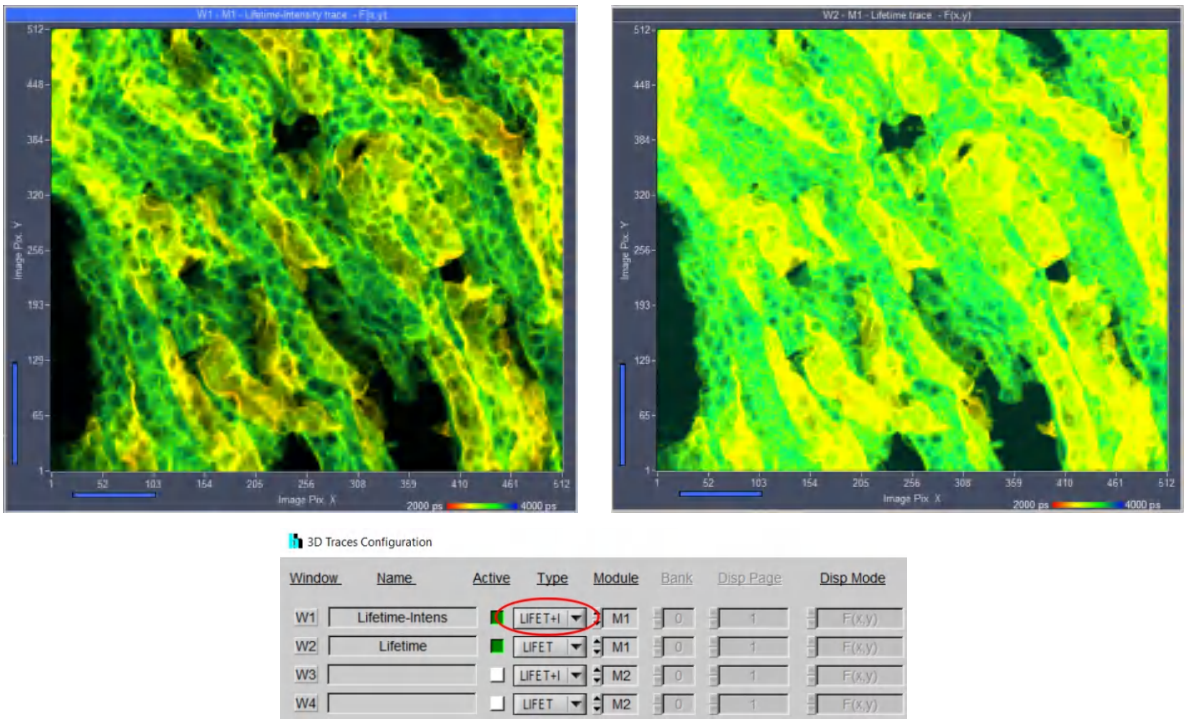


Fig. 1102: Top: Lifetime/Intensity mode image and normal lifetime image. Bottom: 3D trace parameters.

Simultaneous FLIM/PLIM Images

Simultaneous FLIM/PLIM is based on on-off modulation of a pulsed excitation laser. FLIM is recorded in the laser-on phases by the normal FIFO Imaging procedure. PLIM is recorded in the laser-off phases by ‘MCS’ recording, for details please see ‘Simultaneous ’, page 434. To better separate the photons from the laser-on and laser-off phases a routing signal from the laser modulation is sent into the SPC module. Laser-on photons are stored into routing channel 1, laser-off photons into routing channel 2.

Fig. 1103 shows the trace and window parameter setup. The 3D Trace Parameters define three display windows. The first one is the FLIM window, the second and the third one are PLIM windows. Data type for the first window is ps FLIM, for the second and third windows it is MCS imaging. The window intervals define three routing windows. The first one contains the photons from the laser-on phases, the second one the photons from the laser-off phases. The third routing window contains the photons from both phases.

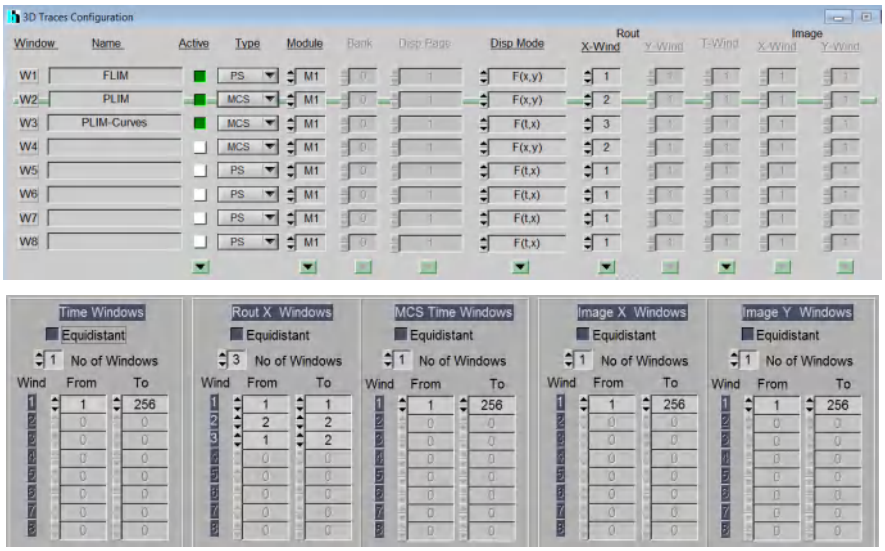


Fig. 1103: 3D Trace Parameters and Window Parameters for simultaneous FLIM / PLIM

The display parameters for the three windows are shown in Fig. 1104. The parameters for W1 display an intensity image for the FLIM data. Colour goes from black over green to white, autoscale is set, intensity scale is linear.

The parameters for W2 display an intensity image of the phosphorescence in the laser off phases. Routing window is 2 (laser off), the colour goes from black over red to white. Window W3 displays the entire signal in both phases of the laser modulation, therefore 'Routing window' is 3. Unlike W1 and W2, W3 does not display an image. Instead, it displays a series of phosphorescence decay curves over the horizontal axis of the image. Therefore, display mode is '3D Curves' and F(t,x), the scale is logarithmic. The curve window helps the user set the correct time scale for PLIM recording. Phosphorescence decay times can vary over orders of magnitude, and the best recording time scale is not a priori known.

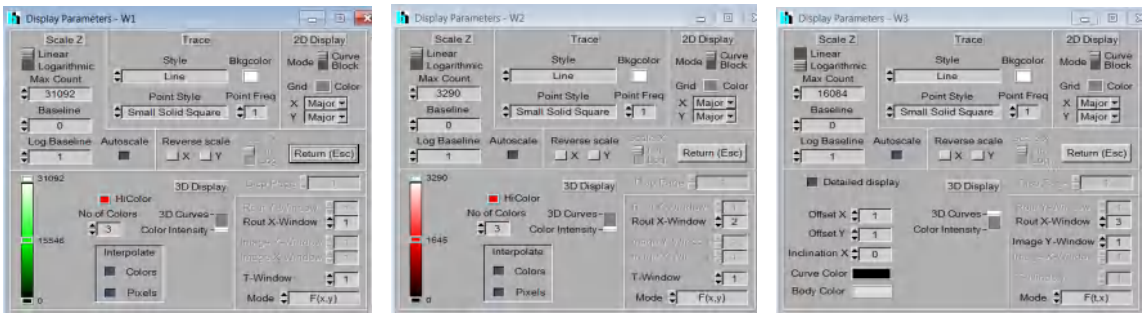


Fig. 1104: Display parameters for fluorescence image, phosphorescence image, and phosphorescence decay curves

The SPCM main panel with these setup parameters is shown in Fig. 1105. The fluorescence image is displayed on the left, the phosphorescence image in the middle, and the window with the phosphorescence decay curves on the right.

Several modifications are possible to this setup. Often the fluorescence and the phosphorescence are recorded at different wavelength, and by different SPC modules. This can be accounted for by changing the Module from M1 to M2 in the trace parameters. It is also possible to activate the run-time lifetime display for the fluorescence and for the phosphorescence. Just change to 'Lifetime' in the trace parameters, and set an appropriate lifetime range and IRF moment in the display parameters.

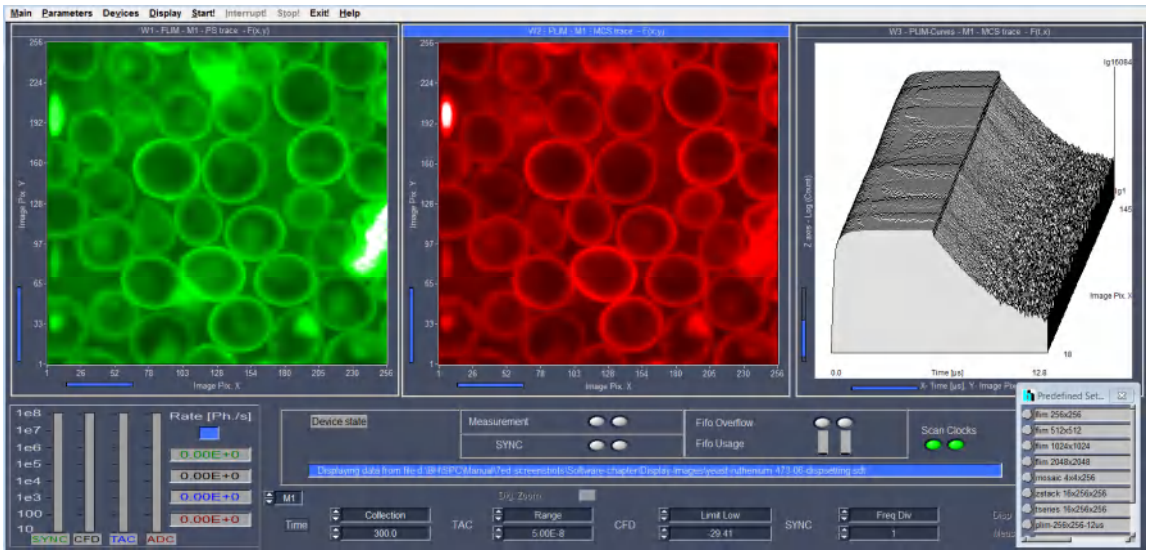


Fig. 1105: SPCM main panel for simultaneous FLIM/PLIM

Display of Decay Data in Point or Region of Interest

A right-mouse click into one of the image in the SPCM main panel opens a small menu from where you can access the image cursors, the display parameters, trace parameters, window parameters, etc. A click into 'Show Decays' opens a decay-curve window as shown in Fig. 1106, right.

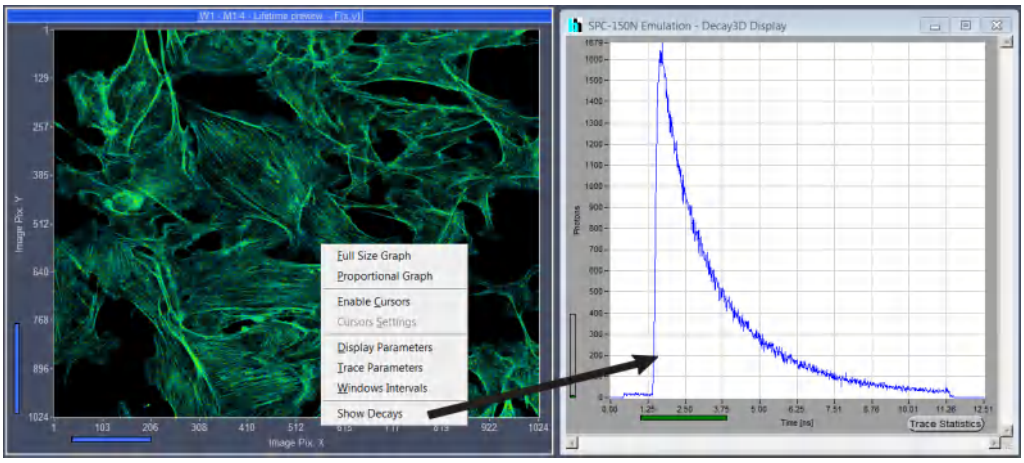


Fig. 1106: A right mouse click into an image and a click on 'Show Decays' opens the decay curve panel shown on the right

The SPCM main panel with the decay curve window is shown in Fig. 1107. The curves can be displayed for all active image windows, and for individual regions or points of interest (ROIs or POIs). The ROIs are defined by the image cursors, the POI by the 'Data Point'. A right mouse click into the decay window opens a panel with the Trace Parameters for the individual curves. The panel can be seen in Fig. 1107, lower right. You can add or remove curves, activate or de-activate curves, define colours for the curves, define whether a curve is from an ROI or a POI, and from which image display window the curve comes. The coordinates of the POI and of the ROI cursors are displayed on the right. As an example, Fig. 1107 displays a lifetime image of the combined channels of a four-channel-fast acquisition system (large image), the lifetime images of the individual channels (small images), and the decay data in an ROI of the combined channels and the individual channels.

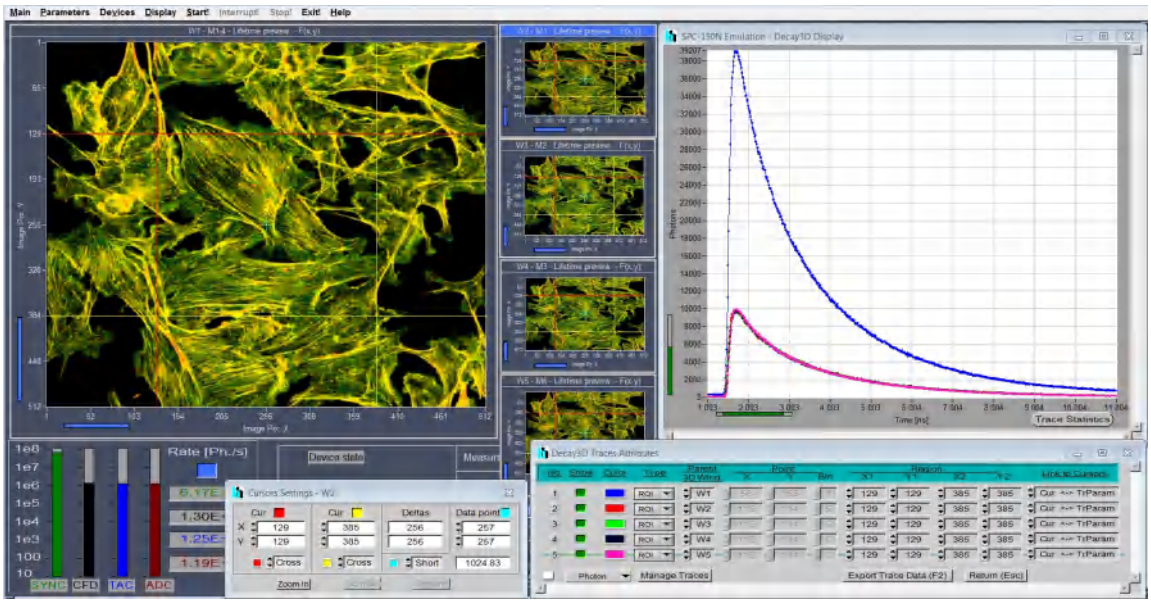


Fig. 1107: SPCM Main Panel with lifetime images and decay curve window

The decay-curve display works for all images that contain decay data in their pixels. These can be intensity images, time-gated intensity images, lifetime images, combined images from several TCSPC modules, or images from different routing channels of a TCSPC module.

The display of the decay curves itself is controlled by the Display Parameters the same way as for decay curves recorded in the Single, Oscilloscope, or FIFO mode. The display scale can be linear or logarithmic, an autoscale function is available, and the curves can be displayed as individual data points, lines, or data points connected by lines. Please see 'Display of 2D Data'.

Resizing and Positioning the Display Windows

Display windows can be shifted and re-sizes as usual in Windows applications. To resize a window, seize the edge of the window with the mouse cursor and drag the panel to the desired size. To shift a window, seize the top bar of the window and shift it into the desired position, see Fig. 1108.

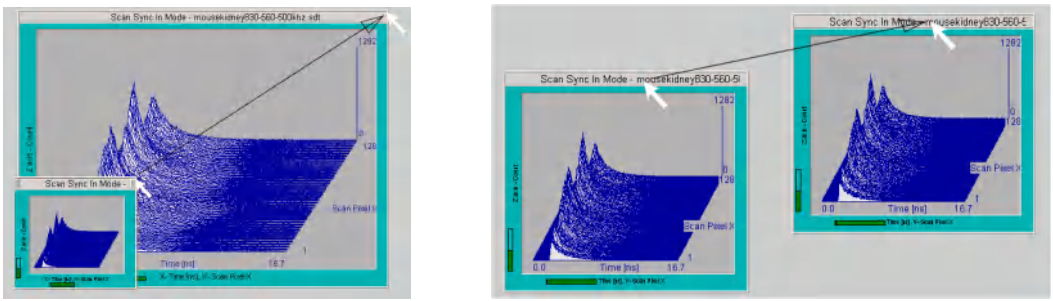


Fig. 1108: Resizing and shifting windows of the main panel

SPCM has a few options for modification of the display windows. Clicking into a display window area by the right mouse key opens the select panel shown in Fig. 1109. ‘Proportional Graph’ sets the display proportions according to the ‘Scan Pixels X’ and ‘Scan Pixels Y’ of a Scan measurement. ‘Full Size Graph’ spreads the display window over the maximum available area.

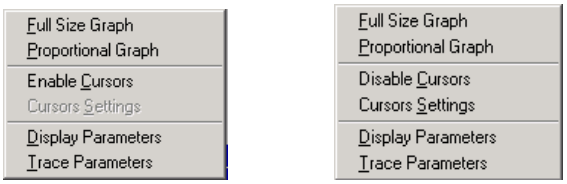


Fig. 1109: Select panel for display size, cursor display, and display and trace parameters

It can happen that a display window has disappeared behind the edge of the screen or otherwise got out of control. (This can happen if a file from a dual-screen system is loaded in a computer with only one screen.) In that case, click into ‘Display’, and ‘Default Size and Position’. When the window is back, set it back to ‘Scale Contents on Resize’.

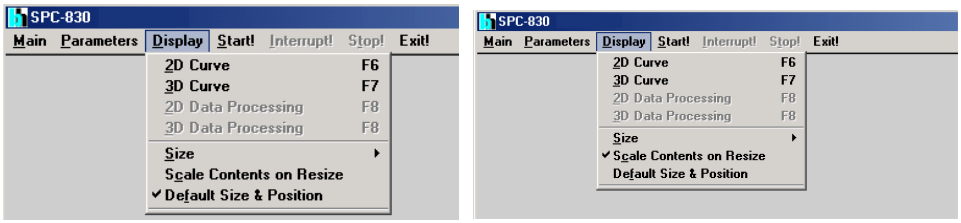


Fig. 1110: Left: Setting window sizes and positions to default. Right: Window sizes user-definable

Until SPCM version 9.8 resizing was available also for most of the parameter windows and the panels for external devices. However, window sizes and font sizes within the windows never were absolutely stable and reprodicible. The problem did not get better with new Windows versions. Trouble with window sizes continued, especially when data were loaded into other computers than they were recorded with. Therefore, in SPCM version 9.92 resizing of parameter windows has been partially abolished. The 'bright' version of 9.92 still has resizing, the 'black version does not. We apologise for the inconveniency.

Display Parameters

SPCM can be configured to show data of different types in different style in several display windows. The ‘Display Parameters’ define in which style (curves, 3D figures, images) the data in these windows are displayed, which display scale is used (linear, logarithmic, minimum, maximum), which parameter is displayed along a particular axis, and in which way subsets of multidimensional data are projected into the display plane. Each of the display windows has its own set of Display Parameters. Typical display parameter panels for 2D and 3D display modes are shown in Fig. 1111 and Fig. 1112. Other examples of display parameters in conjunction with the corresponding display windows are shown in section 'Display Functions'.

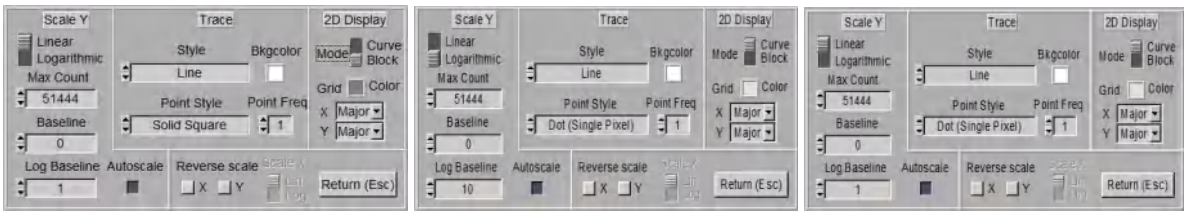


Fig. 1111: Examples of Display Parameters for 2D display modes. Left to right: Linear scale, logarithmic scale, block mode.

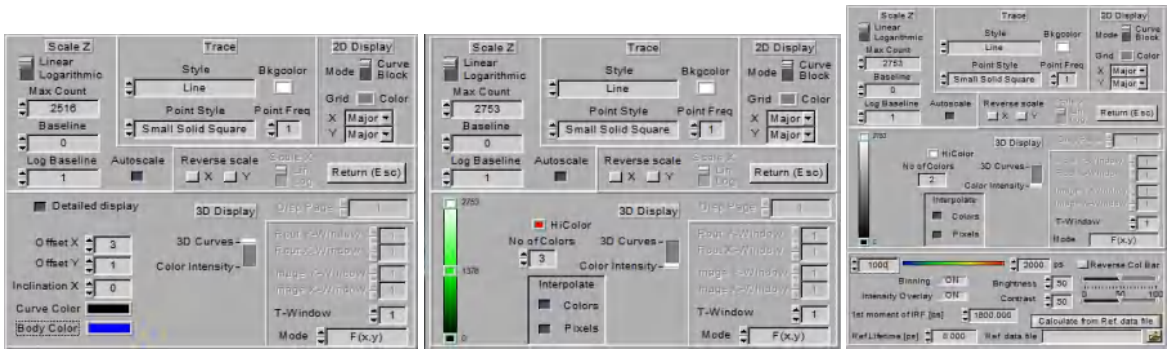


Fig. 1112: Examples of Display Parameters for 3D modes. Left to right: 3D curve figure, intensity image, lifetime image.

General Display Parameters

Scale Y

Under 'Scale Y' you can switch between a linear or a logarithmic scale and set the display range of the photon count number.

Linear / Logarithmic: Linear or logarithmic Y-scale
Max Count: Upper limit of the display range for linear and logarithmic scale
Baseline: Lower limit of the display range for linear scale
Log Baseline: Lower limit of the display range for logarithmic scale

Trace

Bkgcolor: Background colour of the display window to which the display parameters apply.
Style: Display style of the curves. The styles 'Line', 'Points Only' and 'Connected Points' are available.
Point Freq: At values >1 each n^{th} point is displayed only. 'Point Freq' has no influence if 'Line' is selected.

Point Style: Style how data points are displayed. Dot, solid square, empty square, circle, etc.

Autoscale: Normalises the display range to the maximum count number found in the displayed data. Autoscale works both for 2D display modes (curves) and 3D display modes (images or sequences of curves).

Reverse: Reversing one or both axis of the display can be achieved by the two buttons ‘X scale’ and ‘Y scale’. It is often used in the in the ‘Scan’ modes to swap an image into the right orientation. ‘Reverse’ works in all display modes. It acts on the display only, not on the data in the memory.

2D Display Parameters

Grid Color: Grid colour, only if a grid is defined.
Grid X, Grid Y: Different grid sized can be defined by using ‘major’ or ‘minor’. ‘None’ switches the grid off.
Curve Mode: Each curve (trace) on the screen is related to one curve in the memory which is set by the 'Trace Parameters'.

Block Mode: Each curve (trace) on the screen is the average of several curves in the memory. The relation is set by the 'Trace Parameters' and the 'Window Intervals'. The block mode of the display is used to display multichannel measurements in the 2D display mode.

The parameters ‘Curve Mode’ and ‘Block Mode’ are not available in the FIFO Mode.

3D Display Parameters

To display results obtained in the f(t,x,y), f(t,ext), f(t,T) or Scan modes different three-dimensional display modes are provided. Examples of the three display modes are given in Fig. 1113.

The ‘3D Curves’ mode (shown left) displays the results as a set of curves. The Z axis represents the number of photons, the X and Y axis two of the parameters x, y, t or EXT.

The ‘Colour Intensity’ mode (Fig. 1113, middle) transforms the light intensity into a grey scale or colour scale. The X and Y axis represents two of the parameters x, y, t or EXT. Coulor Intensity is also used for the display of scan images, see (Fig. 1113, right)

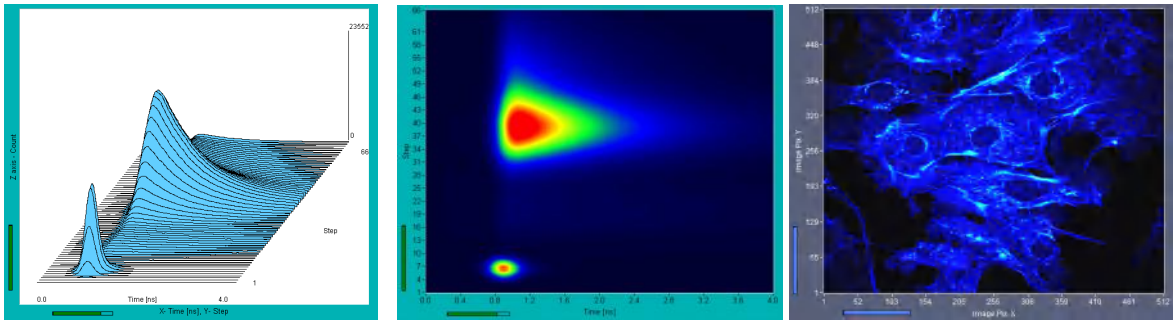


Fig. 1113: 3D display modes. Left: Curve mode. Decay curves along a wavelength axis. Middle: Colour intensity mode, same data as shown left, intensity versus wavelength and time in the fluorescence decay. Right: Image, intensity versus image coordinates, x, y.

3D Curve Mode Parameters

The ‘3D Display’ part of the display parameter menu changes with the display mode selected. When the 3 D display is switched to ‘3D Curves’ the display parameters are as shown in Fig. 1114.

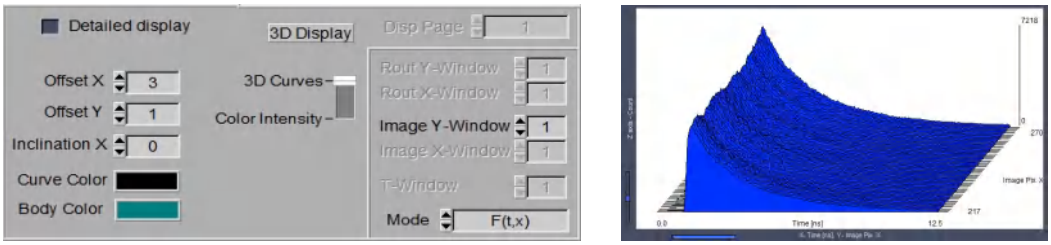


Fig. 1114: Left: 3D display parameters for the 'Curve Mode'. Right: Data displayed in 3D curve mode

Offset X, Offset Y, Inclination X, Curve Color, and Body Color define the layout of the displayed curve sequence. The effect of these parameters is shown in Fig. 1115.

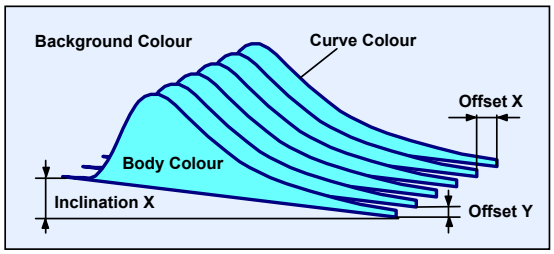


Fig. 1115: Parameters controlling the layout of the 3D curve display

In the 'Detailed Display' mode all points of the result curves are displayed. For a high number of curves and high ADC resolution this can be time-consuming. Moreover, for signals containing a large amount of noise the result may be not satisfactory. Therefore, a compressed display style is available by switching off the 'Detailed Display' function.

The 'Autoscale' function automatically changes 'max count' to fit the data into the display range.

To display subsets of multi-dimensional data arrays different modes, 'Routing Windows', 'Scan Windows' and a 't Window' can be selected. Please see 'Displaying Subsets of Multi-dimensional Data', page 828, and 'Window Intervals', page 839.

3D Colour-Intensity Mode Parameters

In the colour-intensity mode the photon counts are represented by a colour scale. The corresponding display parameters are shown in Fig. 1116, left.

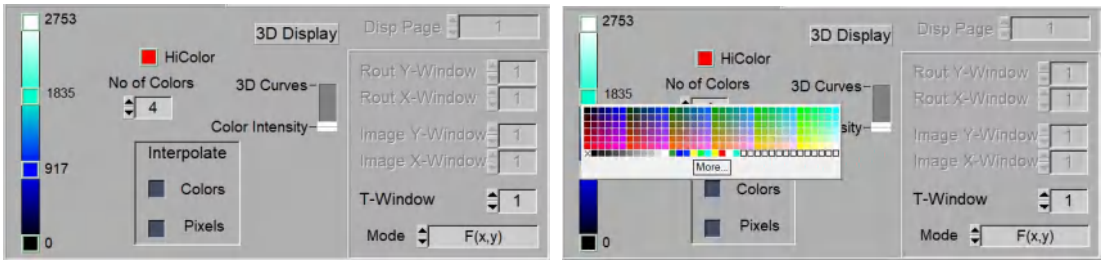


Fig. 1116: Left: Display parameters in the colour-intensity display mode. Right: Selecting the colours for the colour-intensity mode

The colours are selected by clicking on the exaggerated fields in the colour bar. This opens a colour table from which the colours can be selected, see Fig. 1116, right.

For image areas with photon numbers exceeding the range defined by 'Max Count' 'HiColor' is used. The colour can be defined by clicking on the 'HiColor' button.

The 'Interpolate' function is used to deliver intermediate colours ('Interpolate Color' button) and to interpolate the images between the pixels ('Interpolate Pixels' button).

To display subsets of multi-dimensional different display plane within the data (f(x,y), f(x,t), etc, and different 'Routing Windows', 'Scan Windows' and 'T Windows' can be defined. Please see below, 'Displaying Subsets of Multidimensional Data' and 'Window Intervals' page 839.

Displaying Subsets of Multidimensional Data

The sequential modes, the f(txy) mode and the scan modes deliver multi-dimensional data arrays versus time, the coordinates of a scanning area, and the detector number. To display these results subsets of the data in selectable 'Routing Windows', 'Scan Windows' and 't Windows' can be defined. The windows are selected in the right part of the 3D display parameter section and defined in the 'Window Intervals' panel. (Please see 'Window Intervals' page 839)

Mode Selection

The photon density can be displayed versus different coordinates. The corresponding part of the display parameters and the effect on the display are shown in Fig. 1117.

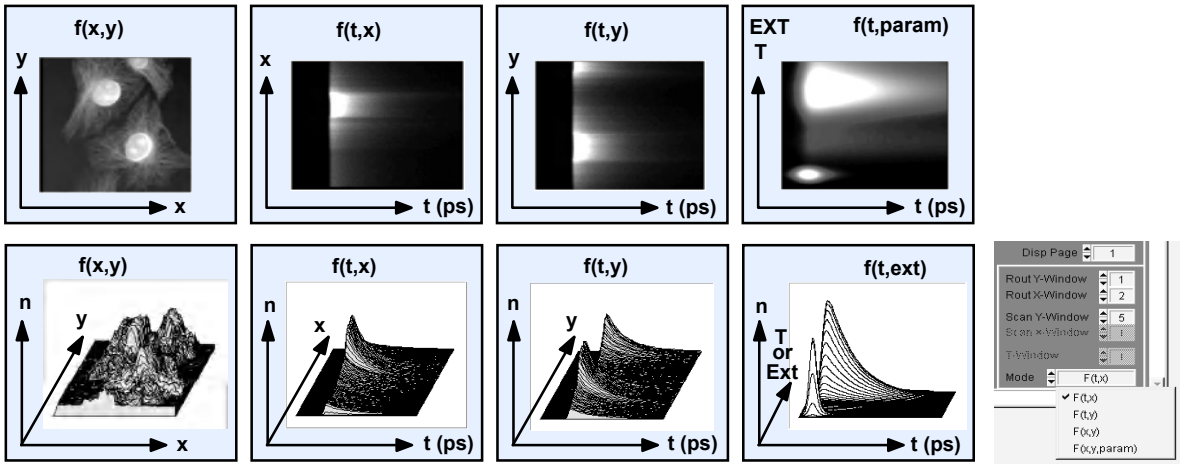


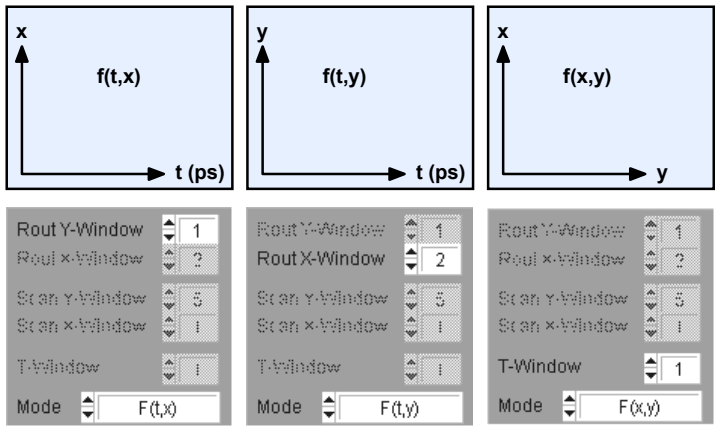
Fig. 1117: Display versus different coordinates of multi-dimensional data. Upper row colour-intensity display, lower row multi-curve display. Left to right: Intensity versus image coordinates, intensity versus time and x coordinate, intensity versus time and y coordinate, Intensity versus time in decay curve and time from start of experiment or external parameter. Far right: Display parameters selecting the display coordinates.

The f(x,y) mode displays the intensity versus the image coordinates, x and y. The intensity is calculated within a window of routing channels, time channels and possibly different memory pages. The result for a FLIM data set is shown in the left column of Fig. 1117.
The same data can be displayed versus the time in the fluorescence decay. Two such displays exist. The intensity can be displayed versus the time, t, and the x coordinate, x, within a 'Scan Y window' f(t,x) or versus the time, t, and the y coordinate, y, within a 'Scan X window' (f(t,y). If several detector channels were used also a window of routing channels can be defined.
The right column shows data measured in a sequential recording mode. The data are displayed versus the time in the fluorescence decay and a second parameter. This may be the time from the start of the experiment or an externally varied parameter, such as the wavelength of a monochromator. Also here several such patterns may exist for different windows of routing channels.

Selection of Routing, Scan, and Time Windows

Depending on the used mode option, 'Routing Windows', 'Scan Windows' and a 't Window' can be selected. The count numbers displayed are calculated within these windows. Further-

more, different ‘Display Pages’ of a multistep measurement can be selected. Depending on the operation mode, the spatial arrangement of the detector channels, possible sequencing or page stepping actions, or scanning multi-dimensional data versus different coordinates are obtained. The effect of the windows for f(txy) mode data is shown in Fig. 1118.



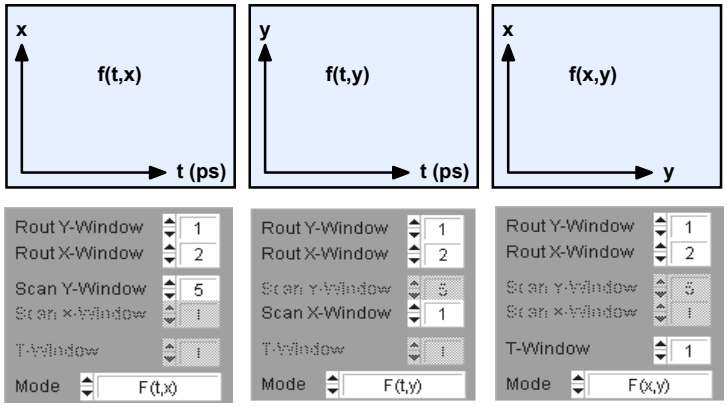
Decay functions over x in Routing Y Window

Decay functions over y in Routing X Window

Intensity over x and y in T Window

Fig. 1118: 3D display options for f(t,x,y) mode data

For the ‘Scan’ modes not only ‘Routing Windows’ but also windows over the scan coordinates exist. The options are shown in Fig. 1119.



Decay functions over x in Scan Y Window and Routing X,Y Windows

Decay functions over y in Scan X Window and Routing X,Y Windows

Intensity over x and y in t Window and Routing X,Y Windows

Fig. 1119: 3D Display options for ‘Scan’ mode data

Display Parameters for Different Display Windows

Several display windows can be defined in the main panel of the SPCM software (see ‘SPCM Main Panel’, page 704. The display windows have separate display parameters. Thus, the windows can be used to display different detector channels, different steps of a page stepping measurements, or different subsets of multi-dimensional data. Moreover, the results can be displayed in the curve mode, the colour-intensity mode, or in linear or logarithmic scale. An example is given in Fig. 1120. The display parameters of the individual display windows are reached by placing the mouse cursor in the display window and clicking on the right mouse key. If a display parameter panel is already open, click into the display window by the left mouse key to get the corresponding parameters displayed.

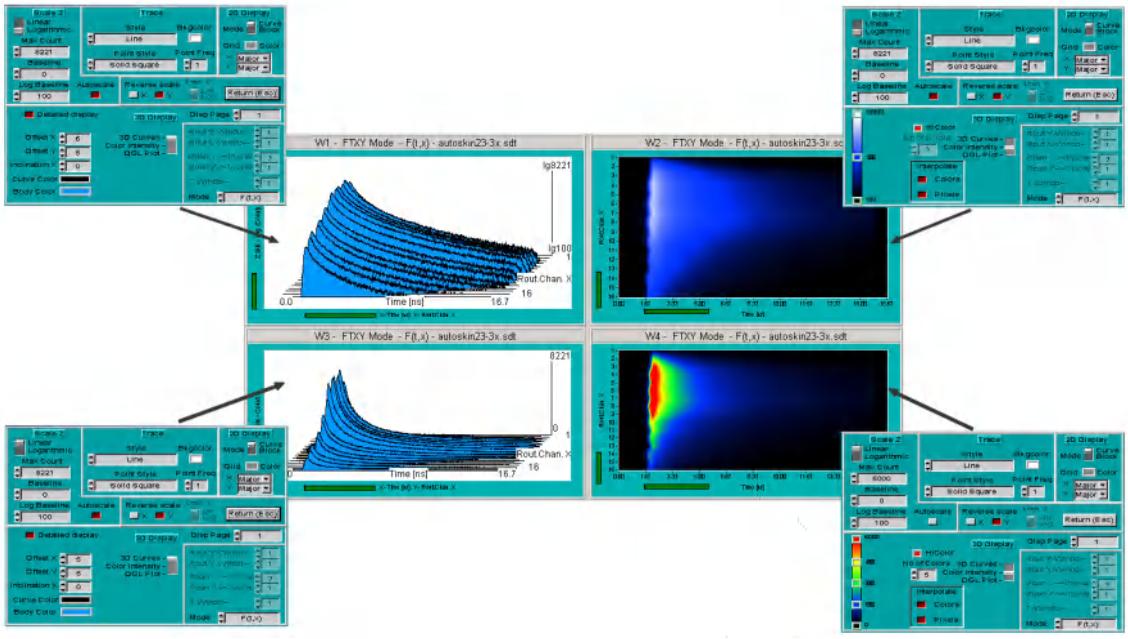


Fig. 1120: The display windows of the main panel have separate display parameters

2D Trace Parameters

The 2D trace parameters control the display of curves. These can be fluorescence decay curves, other optical waveforms, or time-resolved spectral measured in the ‘fi’ modes. Up to 16 curves can be displayed simultaneously. The 2D trace parameters control which curves are displayed, from which module, memory page or routing channel the curves come, and in which colour they are displayed. Please see 'Display Functions', page 797, for examples. In the Block Mode of the display the 2D trace parameters also define from which routing window or image window the data are taken, see 'Block Mode of the 2D Display', page 802 and ‘Window Intervals’, page 839.

Trace Parameters for 2D Curve Mode

The 2D Trace Parameter panel depends on the number of active SPC modules, on the module type, on the operation mode, and on the 2D display mode set in the ‘Display Parameters’. Fig. 1121 shows the trace parameters of a single SPC module (left) and of a multi-module SPC system (right).

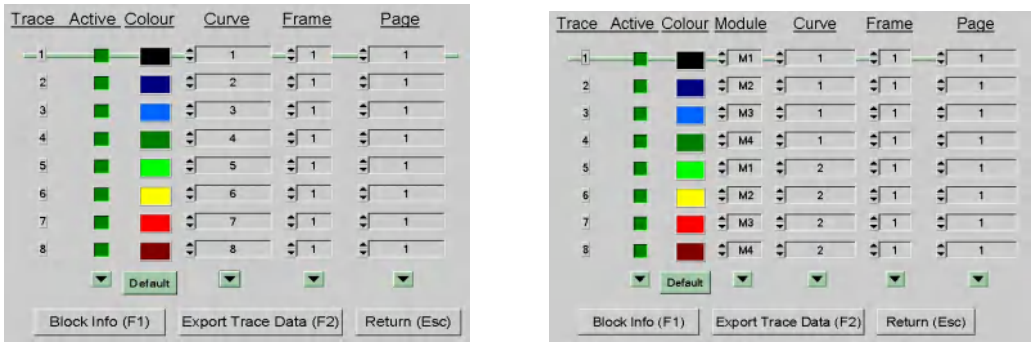


Fig. 1121: Left: Trace parameters for a single SPC module. Right: Trace parameters for a multi-modules system.

The panel contains the definitions for up to 16 traces. For each trace the display can be switched on and off by the ‘Active’ button, and different colours can be defined.

‘Curve’ is used to select a single decay curve from a larger data set. For a ‘Single’, f(xyt), f(t,T), f(t,EXT), fi(T) or fi(Ext) and ‘Continuous Flow’ measurements ‘Curve’ is the number of the detector channel in a multidetector setup. In a ‘Scan’ measurement, ‘Curve’ is the number of the decay curve in the image, i.e. the number of the pixel in the scan.

‘Module’ selects an SPC module of a multi-SPC setup, see Fig. 1121, right. For each of the modules individual frames, pages or time windows may exist.

‘Frame’ is used to select decay curves from the ‘Scan mode’ recorded in a multidetector setup. In this case each pixel of the image contains decay curves from several detectors, i.e. the data array is a stack of images for the individual detectors. ‘Frame’ selects the data from one of the detectors.

‘Page’ defines a step of a page stepping sequence, a step of sequence recorded in one of the sequencer modes, or one of several measurements that were performed in different memory pages.

For the ‘fi’ spectrum scan modes the trace parameters also contain a ‘Time Window’. The ‘Time Window’ is used to select the spectra (i.e. a sequence of intensity values) obtained in different time windows of the decay curve. (Please see also ‘Window Intervals’).

If a curve is activated that has not been used before it may contain random data. The curve is cleared when a measurement is started in the corresponding memory page. The memory can also be cleared by clicking into ‘Main’, ‘Clear TCSPC Memory’.

Some typical examples of the application of the trace parameters are given in Fig. 1122 to Fig. 1125.

The settings shown in Fig. 1122 are normally used for single-detector measurements. The eight pages contain the results of eight individual measurements or eight steps of a page stepping measurement. More pages may exist depending on the module type and the used ADC resolution.

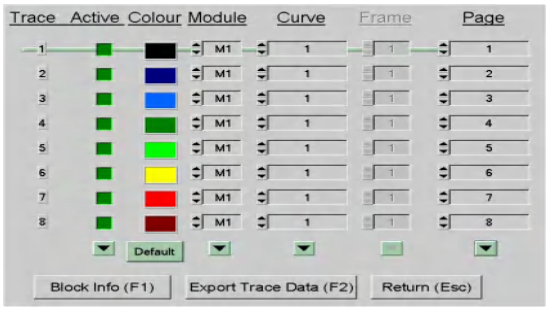


Fig. 1122: Trace Parameters for a single-detector measurement

Fig. 1123 shows trace parameters as they are normally used for multi-detector measurements in the ‘Single’ or ‘Oscilloscope’ mode. The 2D Display shows the first eight detector channels of the first memory page. Other curve numbers can be used within the number of existing detector channels. Different measurements or steps of a page stepping measurement can be displayed by selecting another ‘Page’.

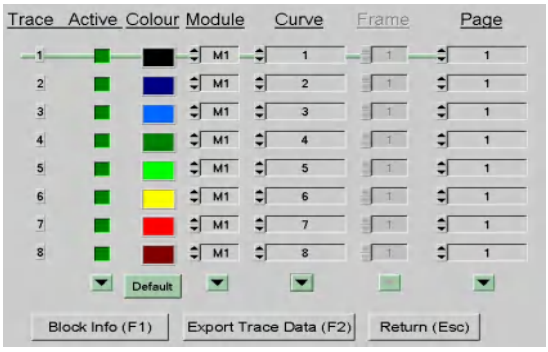


Fig. 1123: Trace parameters for a multi-detector measurement

The Trace Parameters are also used to display time-resolved spectra recorded by the ‘Spectrum’ modes fi(T) and fi(ext). These modes record spectra in the 8 ‘T Windows’ of each detector channel, see ‘Operation Modes’, page 732 and ‘Window Intervals’, page 839. With the setting shown in Fig. 1124, the spectra recorded in the T Windows 1 to 8 are displayed for the detector channel defined by ‘Curve’. Different pages containing different measurements or steps of a page stepping measurement can be selected by selecting another ‘Page’. Different detector channels of a multidetector setup are be selected by ‘Curve’.

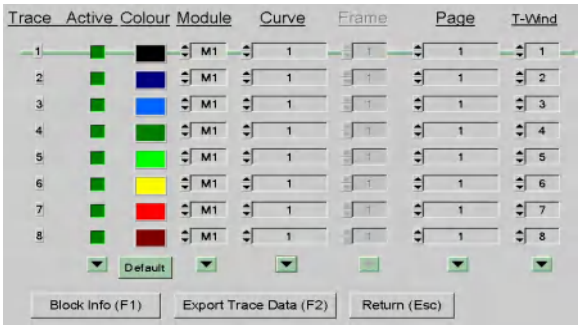


Fig. 1124: Trace Parameters for an fi(T) or fi(EXT) measurement

The trace parameters for the FCS display window of the FIFO mode are shown in Fig. 1125. ‘Curve’ defines a detector number. ‘Cross-FCS Curve’ defines the number of the detector to which the photons of the first one are to be correlated. If the detector numbers of ‘Curve’ and ‘Cross-FCS Curve’ are identical an autocorrelation function is calculated. If the numbers are different the result is a cross-correlation function. The configuration shown right calculates the autocorrelation functions of detector 1 and 2, and the cross correlation function of detector 1 and 2. Trace 4 displays the fit result of the autocorrelation of detector 1.

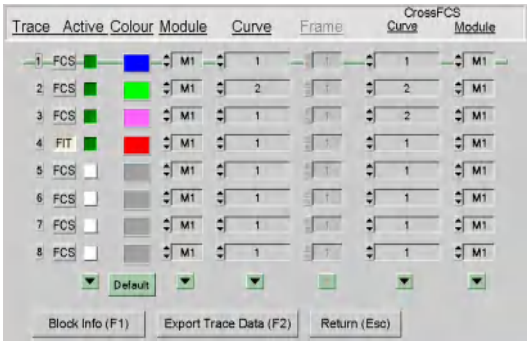


Fig. 1125: Trace Parameters for the FCS display window of a FIFO mode measurement

For reasons of computation speed, the SPCM software calculates only one correlation function per detector channel on-line. If the trace parameters define several correlation functions for one channel, e.g. an autocorrelation and a cross-correlation with another channel, only the first correlation is calculated during the measurement. All other correlation functions are calculated when the measurement is finished.

Trace Parameters for 2D Block Mode

In the ‘Block Mode’ of the 2D display the displayed curves are data from several combined detector channels of a multidetector measurement or from several combined pixels of a ‘Scan’ measurement. The Trace Parameter panel in the ‘Block Mode’ of the 2D Display is shown in Fig. 1126.

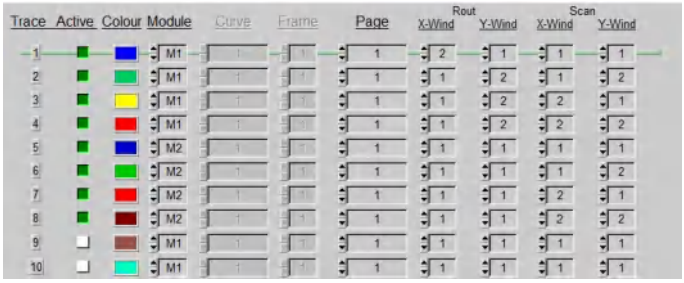


Fig. 1126: 2D Trace Parameters for a system with two SPC modules, Block Mode.

The left part of the panel is the same as for the 2D curve mode. ‘Module’ selects an SPC channel from a multi-module system. If ‘Stepping through Pages’ was used ‘Page’ selects a particular measurement step. If individual measurements were performed in different memory pages ‘Page’ selects the data set of one of these measurements.

The right part of the panel contains the windows from which combined data are calculated. The 'Routing X Windows' and ‘Routing Y Windows’ are used to define a detector channel range in ‘f(t,x,y)’, f(t,T), f(t,ext), fi(T), fi(ext) or Continuous Flow data. For the ‘Scan Sync In’ mode data the ‘Routing Windows’ select images or combined images from different detector channel ranges. Data can also be derived from different image areas. The data of the decay

curves are combined within the ‘Scan X’ and Scan Y’ windows and assigned to the selected trace. Please see also ‘Window Intervals’, page 839.

Two examples of trace parameters in the ‘Block Mode’ of the 2D display are shown in Fig. 1127.

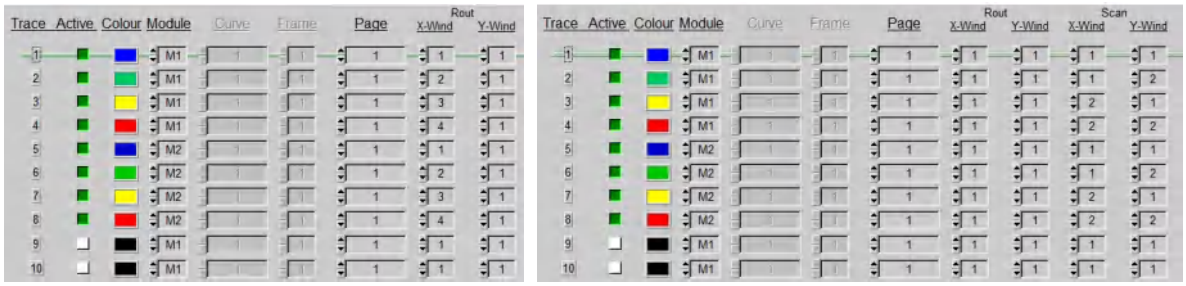


Fig. 1127: Left: Trace Parameters for the ‘Single’, ‘Oscilloscope’, or f(xyt) mode. Different routing windows are selected. Right: Trace parameters for the ‘Scan’ mode. Different image areas are selected.

Fig. 1127, left, shows the selection of a range of routing channels in a f(xyt) measurement or a ‘Single’ or ‘Oscilloscope’ measurement. The routing channels to be combined are defined in the Window Parameters (see page 839). Different combinations of routing channels are selected via ‘Routing X’ and the ‘Routing Y’ window.

Fig. 1127, right, shows the selection of a region of pixels from a ‘Scan Sync In’ measurement. In the Window parameters several windows (image areas) within a scan image have been defined. These windows are selected by ‘Scan X’ and the ‘Scan Y’ window.

Block Info

The ‘Block Info’ button opens a window containing detailed information about a selected data block. The information includes the type and the number of the modules used to measure these data and the corresponding system parameters. The block-info window is shown in Fig. 1128. The block info in the trace parameters is identical with the block info in the load panel, see Fig. 982, page 719.

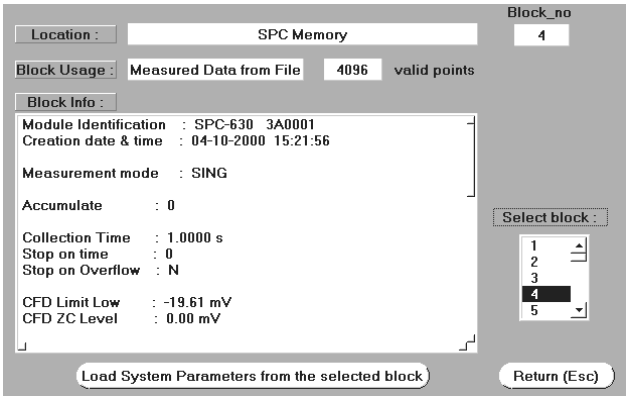


Fig. 1128: Block information panel of the trace parameters

Export of Trace Data

The measurement data contained in a selected trace can be exported into an ASCII file. A click on the ‘Export Trace Data’ button opens dialog box. In this box you can choose a file name and start the conversion.

Exporting trace data is also possible in the ‘Block Mode’ of the display. In this case the trace data are calculated by averaging the set of curves selected for this trace.

Exporting trace data is convenient if selected parts of a ‘Scan’ or ‘Multichannel’ measurement are to be processed by an external data analysis program. For exporting larger data sets, please see ‘Convert’.

3D Trace Parameters

The 3D Trace Parameters organise the display of multi-dimensional TCSPC data in up to eight independent display windows for images and other multi-dimensional data. The parameters define how many display windows are active, from which SPC module they come, of which type the data are, in which display mode they are shown, and from which routing and image windows they come. The 3D trance parameters work in combination with the Display Parameters, see page 825, and the Window Parameters, see page 839. The 3D trace parameter panel is shown in Fig. 1129.

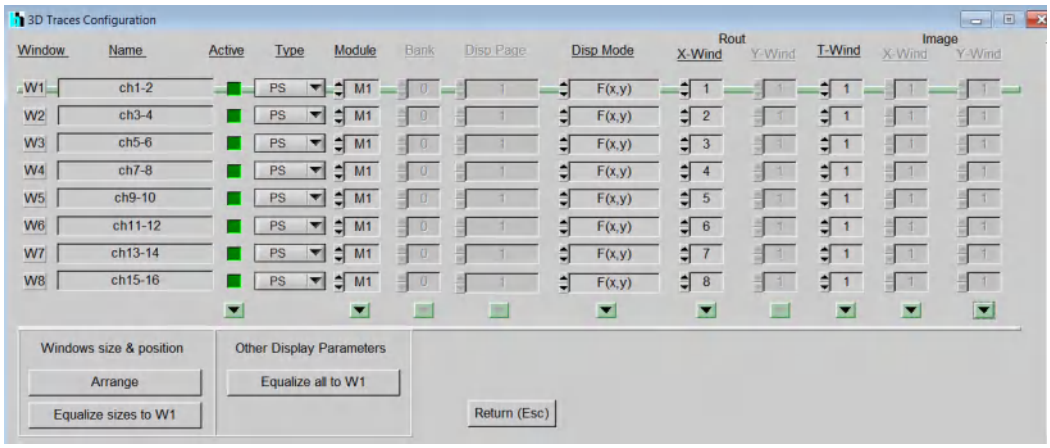


Fig. 1129: 3D Trace parameter panel (parameters are for multi-wavelength FLIM)

The panel defines up to eight display windows, W1 through W8. The windows are activated by the ‘Active’ buttons. ‘Type’ defines the data type to be displayed, ‘Module’ identifies a module of a multi-SPC system. The ‘Display Mode’ fields right of the buttons provide a shortcut to the ‘Mode’ (F(x,y), F(x,t), F(y,t)) in the display parameters. Each window can display data in a specified page (‘Display page’), a specified routing window (‘Rout W Wind’ and ‘Y Wind’), a specified time window of the decay curves (‘T Wind’) or specified spatial windows in an image (‘X Wind’ and ‘Y Wind’). For the definition of the windows, please see ‘Window Intervals’, page 839.

Data Type

‘Type’ can be 'PS' (Intensity from ps FLIM)), ‘LIFET’ (Lifetime), 'LIFET+I' (Lifetime-Intensity), or 'MCS' (Multichannel Scaler, or phosphorescence) imaging. Examples are shown in Fig. 1130. The upper row shows intensity images from picosecond FLIM data of the SPC modules, M1 and M2, of a two-channel FLIM system. The second row shows the same images displayed with ‘LIFET’ in the data type field. The third row shows 'Lifetime - Intensity' display. The image is a combination of an intensity image from the fast counter channels and the decay functions from the TCSPC channels of two SPC-160 or SPC-180 modules. The lower row shows phosphorescence data, ‘Type’ is ‘MCS’. The left window is an image of the phosphorescence intensity, the right window shows the decay curves of the combined lines of the scan over the horizontal axis of the image.

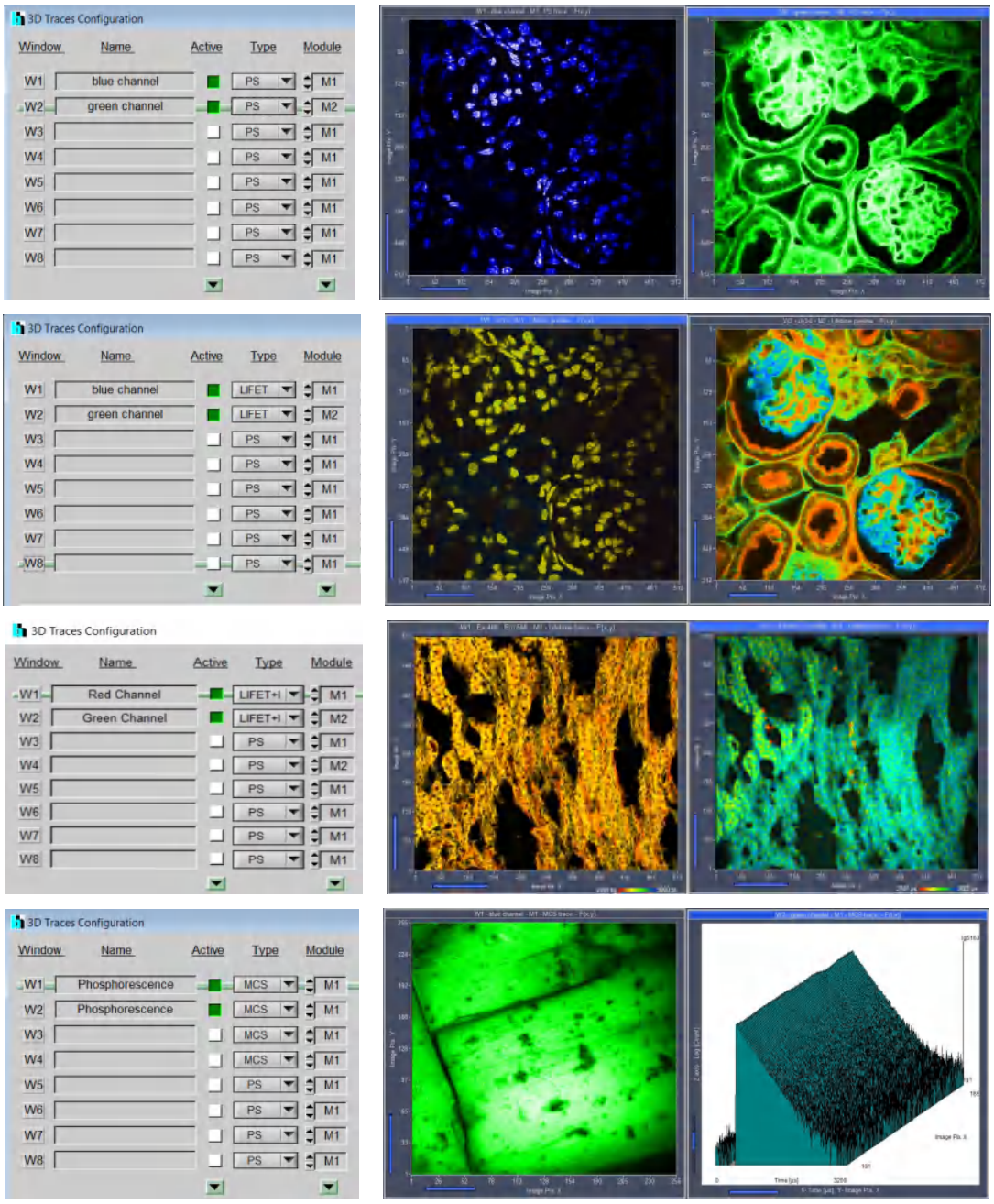


Fig. 1130: Images of different data 'Type' in the 3D Trace parameters. Top to bottom: Intensity images of ps FLIM, lifetime images, lifetime-intensity images (2 channels), MCS Image, Phosphorescence image and decay curves of the one channel.

Display Mode

'Disp Mode' defines subsets of multidimensional data. These may by intensities in specified time windows, the decay function in specified areas of a scan, or decay functions for different time after the start of the experiment. Please see 'Displaying Subsets of Multidimensional Data', page 828.

Some examples of 3D trace parameter settings and the resulting display windows are shown in Fig. 1131. Multi-detector scan mode data are displayed with different 3D trace and display parameters. The upper row shows images in subsequent routing (spectral) windows and the corresponding 3D trace parameters. Images in subsequent time windows within the fluorescence decay are displayed in the middle row. The lower row shows decay curves over the x coordinate for subsequent horizontal stripes (defined by the Y windows) of the image.

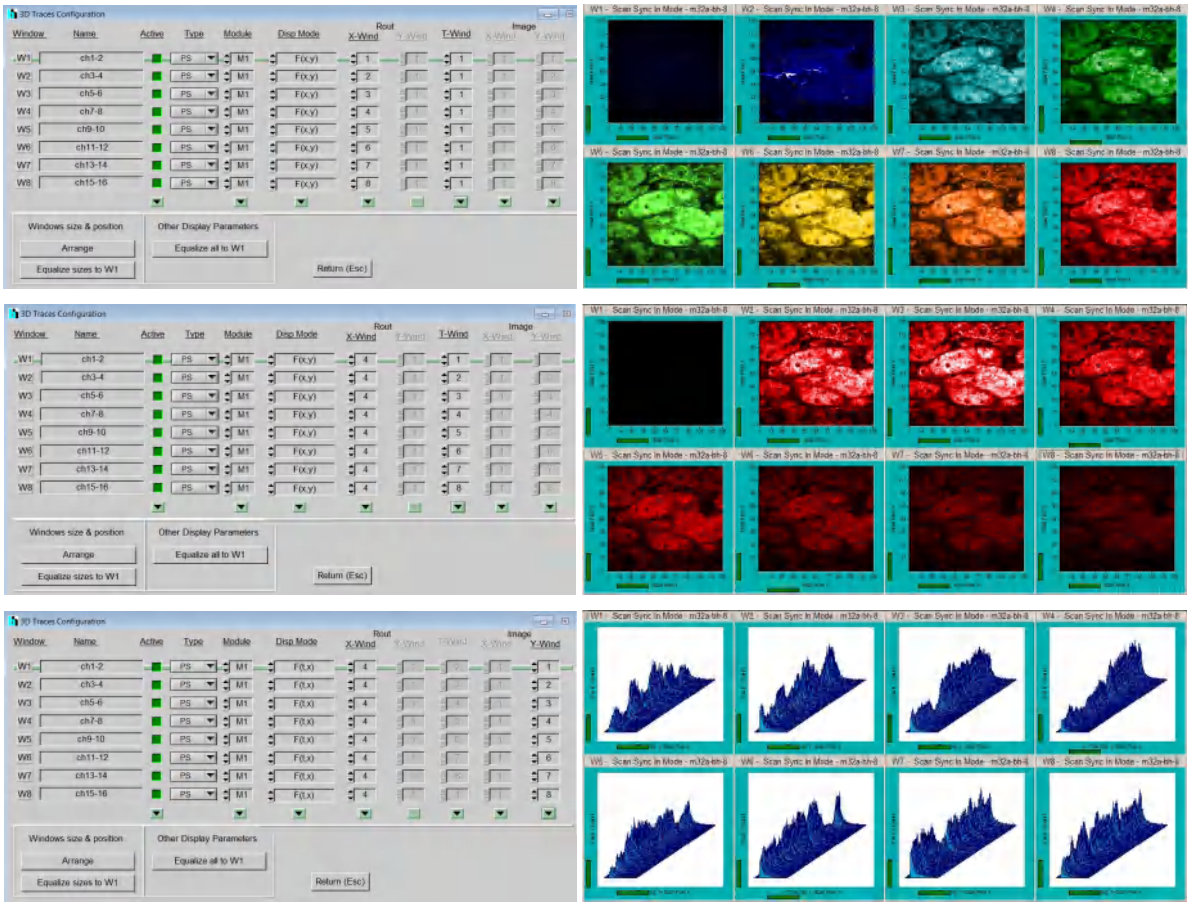


Fig. 1131: Multi-wavelength FLIM data displayed with different 3D trace and display parameters. Top: Images in subsequent routing (spectral) windows. Middle: Images in subsequent time windows of spectral Window 4. Bottom: Decay curves in spectral window 4, over the x coordinate for subsequent horizontal stripes (or Y windows) of the image

Window Sizes and Positions

The buttons in the lower part of the 3D trace parameter panel simplify the configuration of the display windows in the main panel. ‘Arrange’ opens the panel shown right. It helps you arrange to display windows in the main panel. You can also select one of the windows by clicking on the W1 to W8 buttons. You can then equalise the sizes of all other windows to the size of the selected one. Display parameters not shown in the 3D trace parameter panel (such as display scales) can be made equal by clicking on ‘Other Display Parameters’, Equalize to selected Window’.

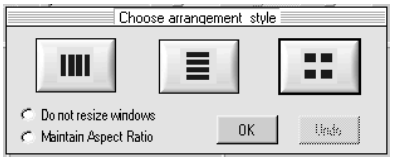


Fig. 1132: Arrangement of the display windows in the Main panel

Window Intervals

The display routines of the SPCM software display subsets of multi-dimensional data arrays. These can be images within specified time windows or ranges of detector channels, decay curves along one coordinate within a spatial interval of another, time-controlled sequences of waveforms within a range of detector channels, or intensity values along a one-dimensional scan within specified time windows. The required window definitions are provided by the 'Window Intervals'. The Window Interval panel for 2D modes is shown in Fig. 1133. It contains Time Windows, Routing X Windows and Routing Y Windows. The windows are used for the 2D display in the 'Block Mode', and for the fi(T) and fi(EXT) spectrum modes.

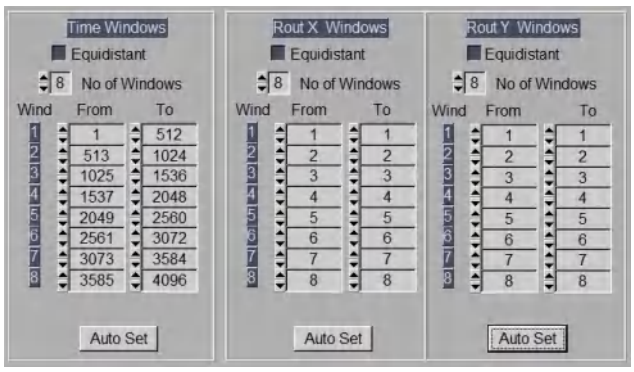


Fig. 1133: Window Interval panel for 2D modes

For the imaging modes 'Window Interval' panel contains also a 'Scan X' and a 'Scan Y' window, see Fig. 1134.

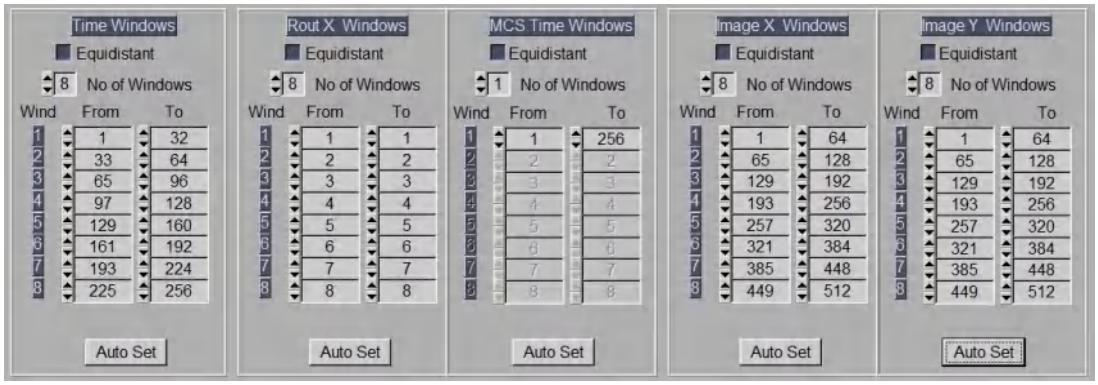


Fig. 1134: Window Interval panel for imaging modes

Time Windows

The 'Time Windows' are used for calculating integral photon numbers in selected time intervals of decay curves or other waveforms. The time windows are used by the 3D display modes and by the spectrum modes fi(ext) and fi(t).

f(xyt) Mode Data

The f(txy) mode delivers a data array for a one- or two-dimensional array of detector channels. For each detector an individual decay curve is obtained. The results are three-dimensional data cubes of photon numbers over the coordinates x, y, and t. To display these data, one of the variables x, y, t is fixed and data are displayed as a function of the other two variables. For the f(x,y) mode of the 3 D display, the 'Time Windows' define intervals in

which integral photon numbers are calculated and displayed as a function of x and y. Fig. 1135 shows how a 4 x 8 pixel intensity pattern is derived from the array 4 x 8 waveforms.

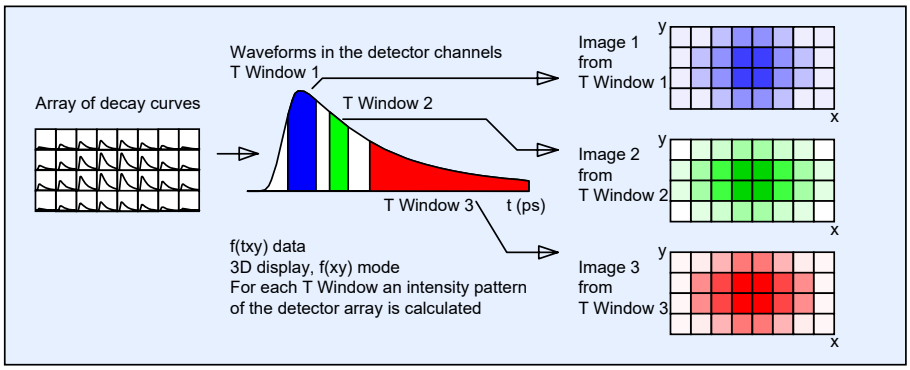


Fig. 1135: Calculating integral photon numbers within time windows of an f(txy) measurement

Scan Mode Data

Images obtained in the ‘Scan’ modes can be five-dimensional data arrays. The coordinates are the time t in the decay curve, the image coordinates X and Y, and the routing channels of a two-dimensional detector array, e.g. an 8 by 2 array for wavelength and polarisation. The images are usually displayed by the f(xy) option of the ‘Colour Intensity’ display mode. The t windows are used to calculate integral photon numbers in selectable time intervals for the individual pixels of the image. The method is the same as for the f(xyt) mode above except that x and y are the coordinates of the pixels in the image.

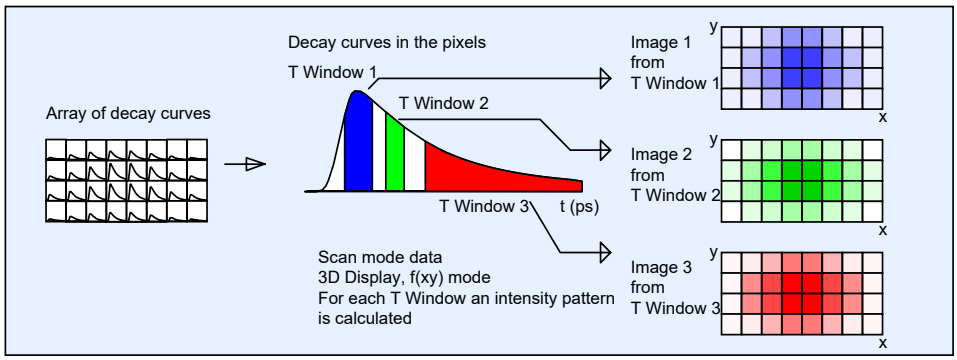


Fig. 1136: Calculating integral photon numbers within time intervals of a scan mode measurement

fi Mode Data

In the ‘fi’ (spectrum) modes the measurement of a single waveform is repeated in intervals of 'Repeat Time' for different settings of an external parameter. From the waveform of each measurement step integral photon numbers are calculated within the ‘T Windows’. The results (i.e. the intensities) are displayed as functions of the time from the start of the measurement or as a function of an external parameter (e.g. wavelength). Up to eight time intervals can be defined. Thus, up to eight spectra can be generated up for each detector channel. The principle is shown in Fig. 1137.

The spectrum modes can be used with routing. In this case individual sets of spectra with different T Windows are calculated for the individual channels or selected ranges of detector channels. Please see also ‘fi(T) Mode’, page 742.

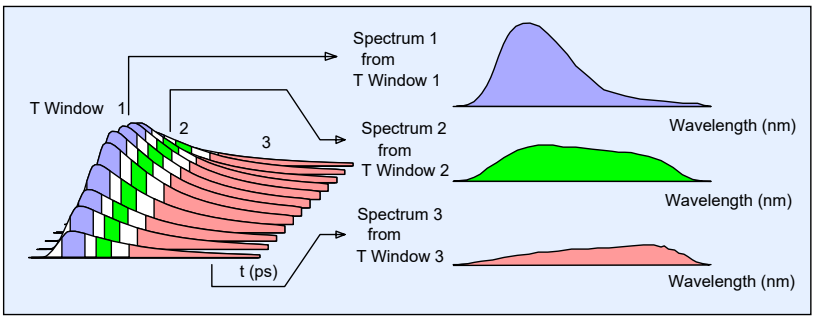


Fig. 1137: A sequence of decay curve is recorded during a wavelength scan. For each decay curve integral photon numbers are calculated within defined time windows and displayed as functions of the wavelength

Routing X and Y Windows

The 'Routing X Windows' and ‘Routing Y Windows’ are used to define detector channels or ranges of detector channels in which integral decay curves are calculated and displayed. Some examples are described below.

f(txy) Mode Data

In Fig. 1138 horizontal stripes of detector channels are selected from a 8 x 8 pixel array of an ‘f(t,x,y)’ mode measurement. The stripes are defined by the ‘Routing Y Windows’. The waveforms are displayed as functions of t and x in the f(t,x) display mode. Depending on the ‘Routing Y Window’ settings up to 8 of these waveform patterns can exist.

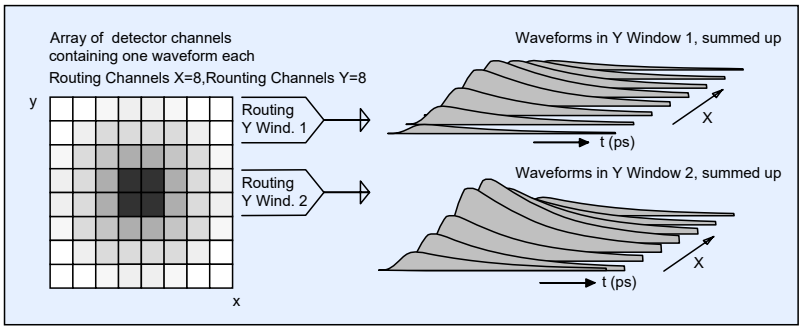


Fig. 1138: Selection of horizontal stripes of detector channels from a two-dimensional array, calculation of integral decay curves over the width of the stripe, and display of decay curves as a function of x

In Fig. 1139 two vertical stripes are selected from the same 8 x 8 pixel array. The waveforms are displayed as functions of t and y. The stripes are defined by the ‘Routing X Windows’.

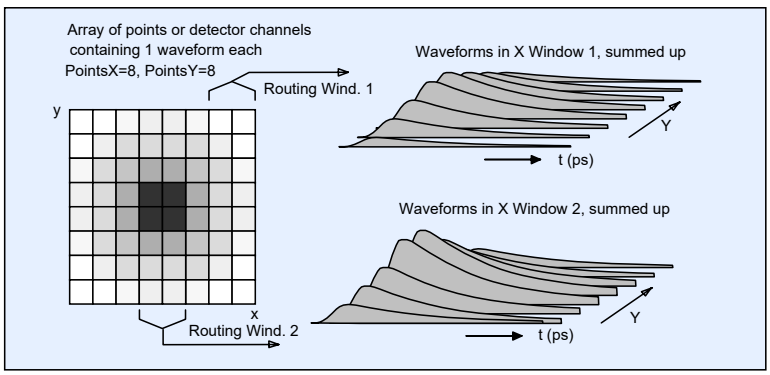


Fig. 1139: Selection of vertical stripes of detector channels from a two-dimensional array, calculation of integral decay curves over the width of the stripe, and display of decay curves as a function of y

Scan Mode Data

In 'Scan' mode data the 'Routing Windows' select different detector channels or ranges of detector channels of a multidetector setup. If the routing window is a single detector channel it defines an image that contains a decay curve of this detector in each pixel. If the window covers several detector channels it defines an image that contains decay curves accumulated for all these detectors.

In most scanning applications the detector channel array is one-dimensional, e.g. for multi-wavelength systems. In these cases only 'Routing X Windows' exist. However, also two-dimensional arrays are possible, e.g. 8 wavelength channels for both directions of polarisation. An example for the f(xy) option of the Colour Intensity display mode is in Fig. 1140.

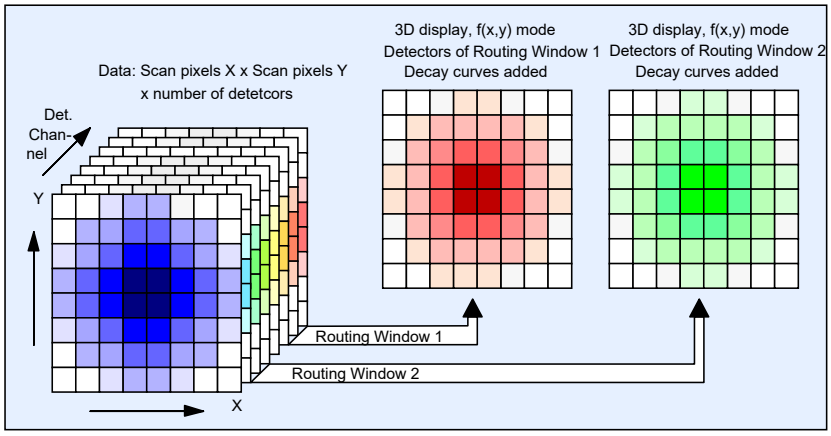


Fig. 1140: Selection of detector channels or ranges of detector channels from multi-detector scan mode data

Data Recorded by Sequential Modes

In data recorded in the sequential modes and spectrum modes the routing windows select different detector channels or ranges of detector channels. If the routing window is a single detector channel it defines a sequence that contains a decay curve of this detector in each step. If the routing window covers several detector channels it defines a sequence that contains curves that are sums of the decay curves of all these detectors.

In most sequencing applications the detector channel array is one-dimensional, e.g. for multi-wavelength systems. In these cases only 'Routing X Windows' exist. The selection of a data subset from a sequential measurement with a linear array of 8 detectors is shown in Fig. 1141.

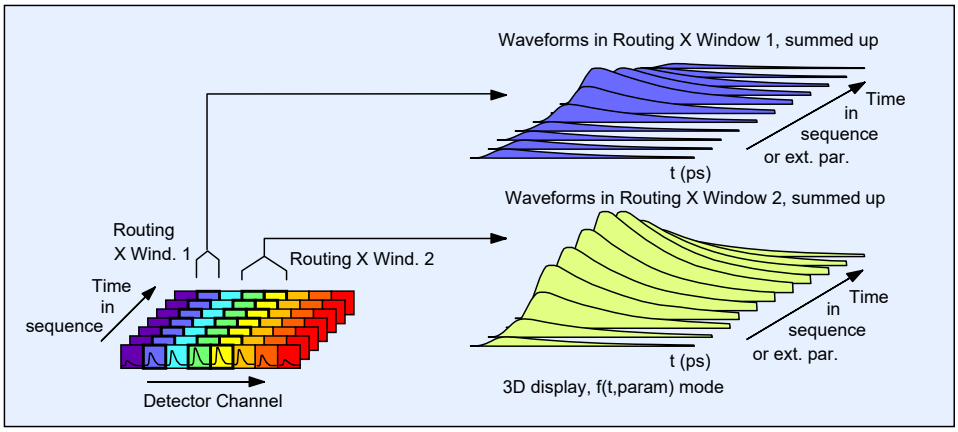


Fig. 1141: Selection of routing channels from sequential multi-detector data, one-dimensional detector array

For a 2-dimensional detector array, a data subset is displayed for the detector channels which are both inside the X Window and the Y Window, see Fig. 1142.

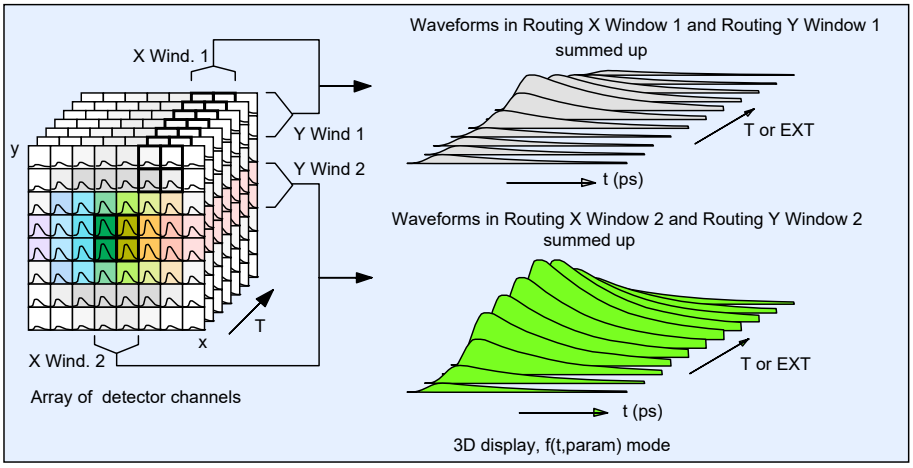


Fig. 1142: Selection of routing channels from sequential multi-detector data, two-dimensional detector array

fi Mode Data

The function of the Routing Windows in the fi (spectrum scan) modes are similar as for the sequential modes. However, instead of integral decay curves integral photon numbers within time windows are calculated. The influence of the X and Y Windows on an fi(T) or fi(ext) measurement is shown in Fig. 1143. The routing windows define either single detector channels or ranges of detector channels. For each routing window and time window a separate spectrum is calculated.

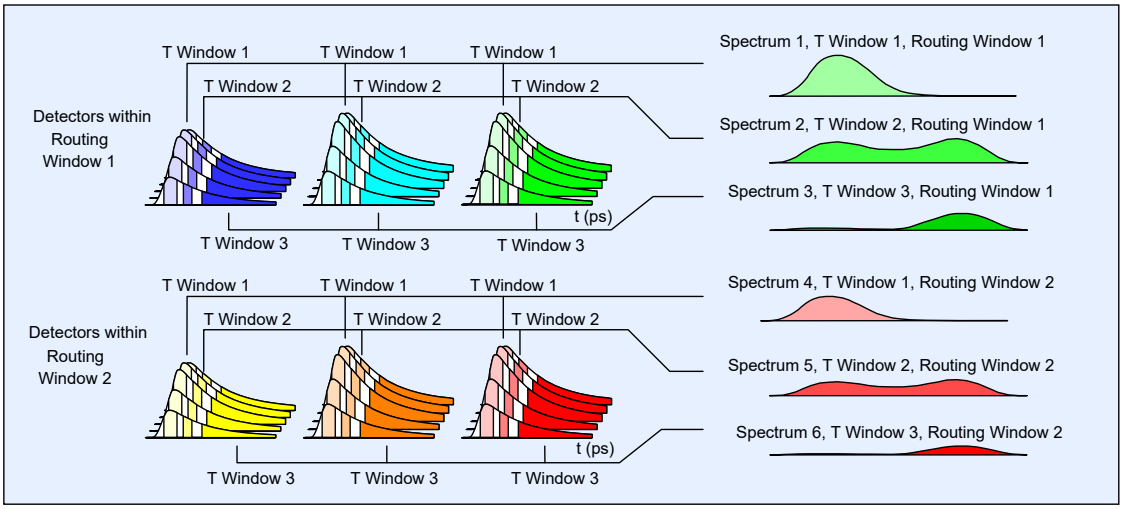


Fig. 1143: Routing Windows in the fi modes. For each routing window and time window a separate spectrum is calculated

2D block mode display

The 2D display of the SPCM software is used to display decay curves in selected ranges of detector channels. Up to eight independent areas can be defined by the Routing X and Routing Y windows. The decay curves in the detector channels of the selected range are summed up and displayed as a trace in the 2D display, see ‘Trace Parameters for 2D Block Mode’, page 833. The principle is shown in Fig. 1144. In scan images the Routing X and Y windows work in conjunction with the Scan X and Scan Y windows, see Fig. 1147.

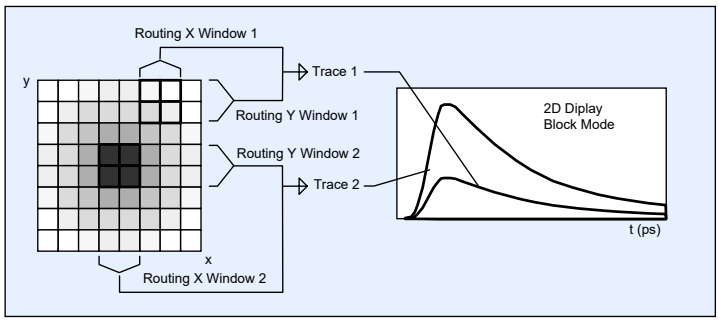


Fig. 1144: Selection of a range of detector channels for the block mode of the 2D display. The decay curves of the detector channels within the selected range are summed up and displayed as a single trace.

Scan X and Y Windows

3D Display of Scan Mode Results

The 'Scan X Windows' and ‘Scan Y Windows’ are used to define spatial (x,y) areas in ‘Scan’ mode results. The effect is very similar as for the Routing X and Y windows in the f(xyt) mode. The 'Scan X Windows' and ‘Scan Y Windows’ are used for the f(t,x) and f(t,y) options of the 3D display and for the 2D display block mode. Fig. 1145 shows how different horizontal stripes are defined in a two-dimensional scan. The results are displayed as a sequence of decay curves versus X.

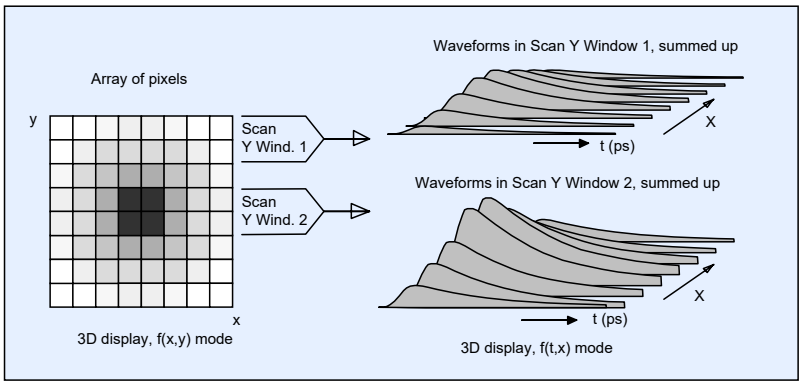


Fig. 1145: Selection of horizontal stripes of pixels from a two-dimensional scan, calculation of integral decay curves over the width of the stripe, and display of decay curves as a function of x

In Fig. 1139 two vertical stripes are selected from the same pixel array. The stripes are defined by the ‘Scan X Windows’; the waveforms are displayed as functions of t and y.

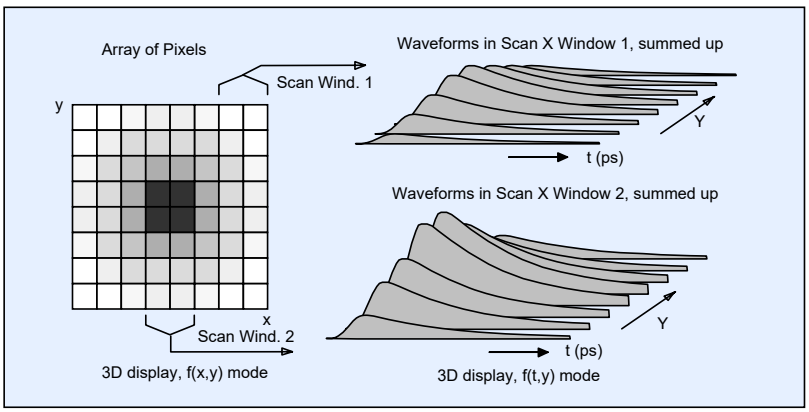


Fig. 1146: Selection of vertical stripes of pixels from a two-dimensional scan, calculation of integral decay curves over the width of the stripe, and display of decay curves as a function of y

2D Block Mode Display

The 2D display of the SPCM software can be used to display decay curves in selected areas of a scan. Up to eight independent areas can be defined by the Scan X and Scan Y windows. The decay curves in the pixels of the selected area are summed up and displayed as a trace in the 2D display, see ‘Trace Parameters for 2D Block Mode’, page 833. The principle is shown in Fig. 1147. The Scan X and Scan Y windows work in conjunction with the Routing X and Routing Y windows, see Fig. 1144.

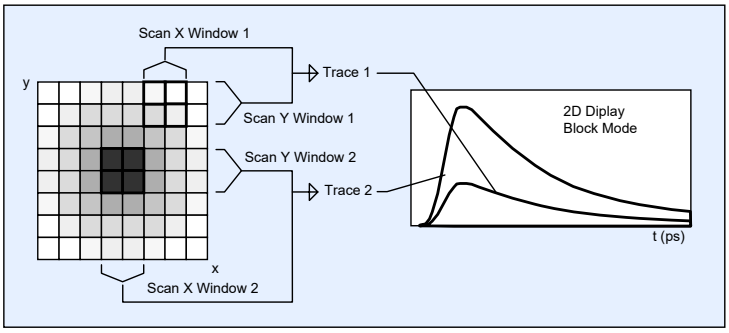


Fig. 1147: Selection of an area within a scan for the block mode of the 2D display. The decay curves of the pixels within the selected area are summed up and displayed as a single trace.

Auto Set Functions

For all window parameters up to eight independent intervals can be defined. The intervals can be defined manually or set automatically by the 'Auto Set' function. To control 'Auto Set' the following options are provided.

Equidistant: The available window range is divided into eight equal intervals. If the number of points cannot divided by 8 (this can happen for X and Y) the last window can be wider than the windows 1 to 7.

Non Equidistant: The start values of the intervals are set by the operator. The end values are set by the autoset function in a way that the intervals fit closely together.

No of Windows: Number of windows to be set by the autoset function.

After a change in the ADC resolution, the number of detector channels, or the number of pixels of a scan the window intervals are re-calculated automatically.

Starting and Stopping a Measurement

Start

The 'Start' button in the menu bar starts the measurement in the selected operation mode. Please note that the measurement may not start immediately. If a trigger condition different from ‘None’ is defined the SPC module waits for an active trigger edge to start the measurement. In the Scan Sync In mode an in the FIFO Imaging mode the module waits until a frame clock indicates the beginning of the next frame.

If the autosave function is active or a mode with automatic writing to the hard disk is used (e.g. FIFO or Continuous Flow) the SPCM software may ask for permission to overwrite the data file specified in the system parameters. Please make sure that this file does not contain valid data of a previous measurement.

During the measurement the main menu remains active and the results are shown in the display window. The rate display gives information about the count rates in the CFD, the TAC and the ADC. The CFD rate represents all pulses with an amplitude greater than 'CFD Limit Low'. The TAC rate is the working rate of the TAC. It is slightly smaller than the CFD rate because the TAC is not started by pulses exceeding the 'CFD Limit High'. 'ADC Rate' is the conversion rate of the ADC. It represents all events inside the selected TAC window.

When a measurement is run in the FIFO mode one or more data files are written which contain the data of the subsequently recorded photons. These measurement data files have the extension ‘.spc’. At the end of the measurement, a setup data file is generated which contains the hardware and software parameter used. The setup data file has the same name as the last measurement data file and has the extension ‘.set’.

Most (though not all) system and display parameters can be changed during the measurement. The effect becomes visible with the display of the next result.

Interrupt

'Interrupt' interrupts a running measurement so that the measurement sequence goes into a ‘hold’ state. 'Interrupt' can be used when the system parameters or an external set-up require re-adjustment. When the measurement is in the ‘hold’ state it can be restarted from the current state by clicking on the 'Start' button. Of course, ‘interrupt’ cannot be used within a sequential measurement, a FIFO measurement or any other recording procedure that requires accurate timing.

Stop

'Stop' aborts a running measurement. After stopping the results are displayed as they were in the moment of stopping. Please note that a sequential measurement or a page stepping sequence may be incomplete. Please note also that the measurement cannot be re-started from the current state after a 'Stop' command.

In some operation modes the measurement may not stop immediately with the stop command. In the Scan Sync In mode and in the FIFO Imaging mode the recording continues until the current frame is complete. When a FIFO mode measurement is stopped the FIFO may still contain valid photon data. The SPCM software then asks you whether these photons are to be processed by the online-calculation and saved in the current data file. Please note also that a FIFO measurement writes a setup file at the end of the measurement. This file contains the hardware and software parameter used. The setup data file has the same name as the FIFO

data file but the extension ‘.set’. Please do not delete this file. It is needed for possible off-line analysis of the FIFO data.

Exit

The SPC software is left by 'Exit'. When the program is left, the system and configuration parameters are saved in a setup file 'auto.set'. This file is automatically loaded at the next program start. Thus, at the next start the SPCM software system will come up with the same hardware and software parameters. If you do not want to save the last settings you can reject the writing of a new auto.set file by switching off the 'Save data on exit' button, see Fig. 1148.

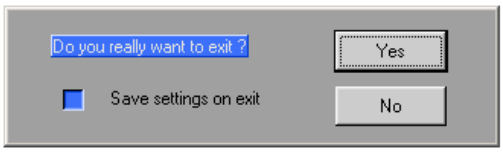


Fig. 1148: Exit panel

Operation of Experiment Control Devices from the SPCM Software

Scanner Control via the GVD-120 Card

The GVD-120 is used to control the scanner of the bh DCS-120 Confocal Scanning FLIM System [68]. However, with appropriate configuration the GVD-120 is able to control also other galvanometer scanners, or piezo scan stages with analog input.

To open the scanner control panel, click on ‘Parameters’ and ‘B&H Galvano Scanner’. The panel allows you to define the number of pixels of the scan, the scan rate, the size and location of a zoom area, or the location where to park the laser beam. Moreover, you can start and stop the scan, run a fast preview, turn on and off the lasers, control the laser power, and define how two lasers are multiplexed. The scanner control panel is shown in Fig. 1149.

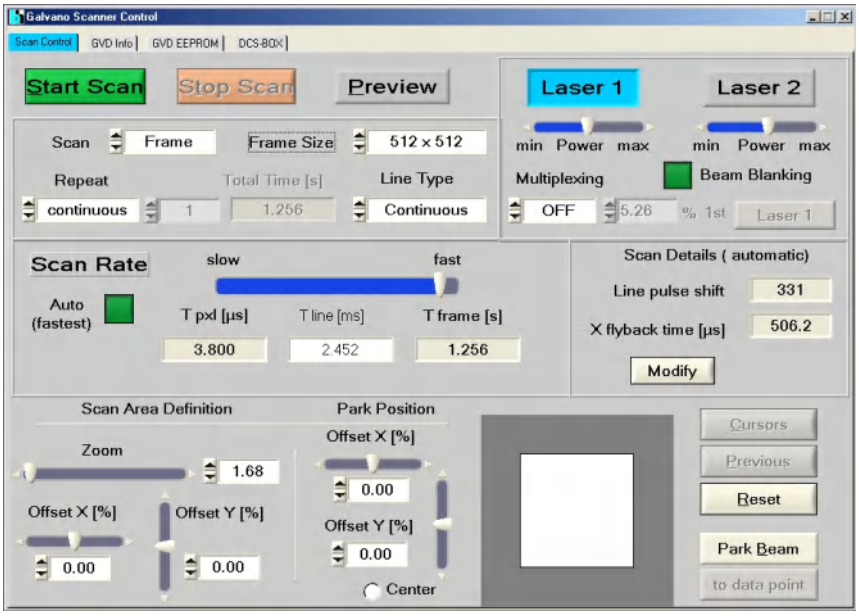


Fig. 1149: DCS-120 scanner control panel of the SPCM software

The scanning is started by clicking on the ‘Start’ button and stopped by clicking on the ‘Stop button. The measurement can be started and stopped with the scan by setting the corresponding buttons in the 'Application Options', see page 714.

General Scan Parameters

Frame Size

The frame size can be defined from 16 x 16 pixels up to 2048 x 2048 pixels. Please note that the ‘Scan Pixels X’ and ‘Scan Pixels Y’ in the TCSPC System Parameters should correspond to the selected image size.

For normal FLIM acquisition the scan format is ‘Frame’. Line scans can be performed by setting ‘Scan’ to ‘Line’. After being started, scanning is normally continuously repeated (Repeat = ‘Continuous’. If necessary, the scan can be stopped after a defined number of frames.

‘Total Time’ is the time to scan one frame. It depends on the used frame size and scan rate. The times of the line and frame flyback are included in the total time.

Normally, the scanner runs along the line continuously. This allows the galvanometer motors to be operated at maximum speed. However, there are applications which require a slow step-

by-step scan along the lines. The operation mode can be changes by setting Line Type to ‘Continuous’ or ‘Steps.

Scan Rate

The scan rate is defined by moving the scan rate slider or be specifying a line time. Please note that the available rates apply to the fast galvanometer scanner of the bh DC-120 scanning system. For other scanners the range of the line and frame times, and the flyback times require to be re-configured, see below, ‘Scanner Configuration’. Please note that for all scanners the applicable scan rate depends on the image size and the zoom state. Therefore the scan rate may change if you change one of these parameters.

If you want to run a fast scan without taking care of these relationships you may activate the ‘Auto’ button. The software then automatically selects the fastest scan rate for the selected frame size, line type, and zoom. The shortest pixel and frame times for the DCS-120 system are shown in Table 2 and Table 3.

Image Size	Zoom = 1	Zoom = 2	Zoom = 4	Zoom = 8
128 x128	12.8 µs	6.4 µs	4.8 µs	3.2 µs
256 x 256	6.4 µs	3.2 µs	2.4 µs	1.6 µs
512 x 512	3.2 µs	1.6 µs	1.2 µs	0.8 µs
1024 x 1024	1.6 µs	1.2 µs	0.8 µs	0.6 µs

Table 2: Minimum pixel time for different image size and zoom

Image Size	Zoom = 1	Zoom = 2	Zoom = 4	Zoom = 8
128 x128	0.367 s	0.184 s	0.120 s	0.074 s
256 x 256	0.640 s	0.643 s	0.259 s	0.173 s
512 x 512	1.24 s	0.636 s	0.480 s	0.320 s
1024 x 1024	2.6 s	2.0 s	1.2 s	1.0 s

Table 3: Minimum frame time for different image size and zoom

Control of Lasers

Two bh BDL or BDS series diode lasers can be controlled from the scan control panel. The lasers can be switched on and off via the ‘Laser 1’ and Laser 2’ buttons. The power can be controlled by the ‘Power’ sliders. Important: The power sliders control the electrical driving power of the laser diode. Therefore also the shape of the laser pulse changes. The power sliders should therefore not be changed within a series of comparable measurements.

For FLIM operation the bh diode lasers can (and should be) used with beam blanking. That means, the lasers are turned off when the system is not scanning and during the line and frame flyback. Please note that beam blanking has to be turned off in the ‘Park Beam’ mode.

If two lasers are operated simultaneously they can be multiplexed within one pixel, or on a line-by-line, or frame-by-frame basis. If only one laser is used ‘multiplexing’ must be ‘off’. Laser multiplexing is also used for phosphorescence lifetime imaging (PLIM). In that case, one of the lasers is turned off optically, and the multiplexing function is used to on-off modulate the other laser [68].

Preview Function

The ‘Preview’ function is used to adjust the focal plane, find the right spot in the sample, identify objects for further investigation, and adjust the zoom and the scan area. Clicking on the ‘Preview’ button starts a fast scan at a resolution of 128 x 128 pixels. Simultaneously a measurement is started, and the results are displayed in one-second intervals. The measurement runs with the defined number of detector channels but with only one time channel.

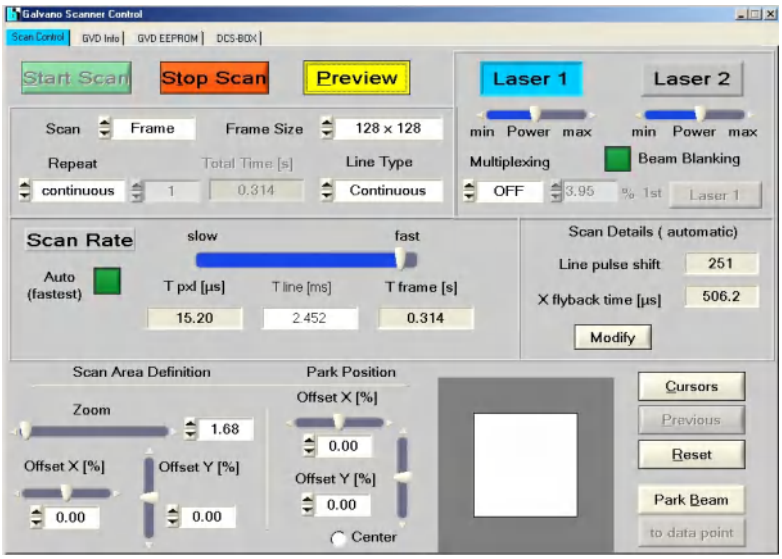


Fig. 1150: Scanner panel in the 'Preview' mode

Scan Area

The scan area can be changed by the parameters under 'Scan Area Definition'. 'Zoom' determines the size of the scan, 'Offset' the centre position, see Fig. 1151. The approximate location of the selected area within the maximum scan area is shown in a graph on the right. You can shift the area with the mouse cursor. 'Reset' resets the scanner to the maximum scan area.

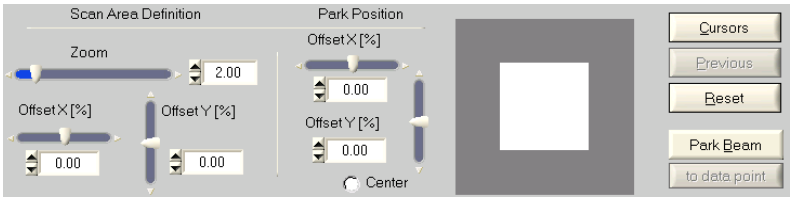


Fig. 1151: Selecting a scan area in the scan control panel

After a preliminary image has been recorded the scan area can be selected from the display window. Enable the cursors in the image by a right-mouse click into the display window, see Fig. 1152, left. Select an image area with the cursors, see Fig. 1152, middle. Then click on 'Cursors' in the area definition part of the scan control panel, see Fig. 1152, right.

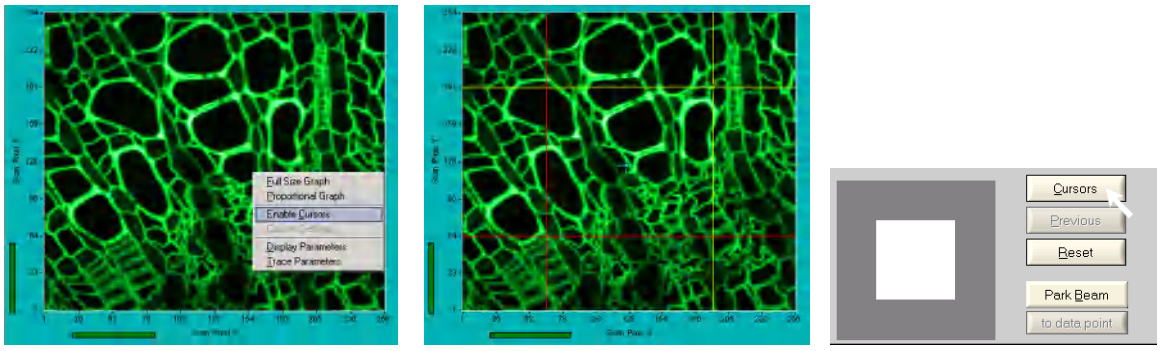


Fig. 1152: Defining a scan area from the display window. Enable cursors (left), select image area (middle), and click on 'Cursors' in the scan area select part of the scanner control panel.

The software then selects the closest possible scan area around the image area selected by the cursors. You can change the scan are even when the scanner is running, as illustrated in Fig. 1153.

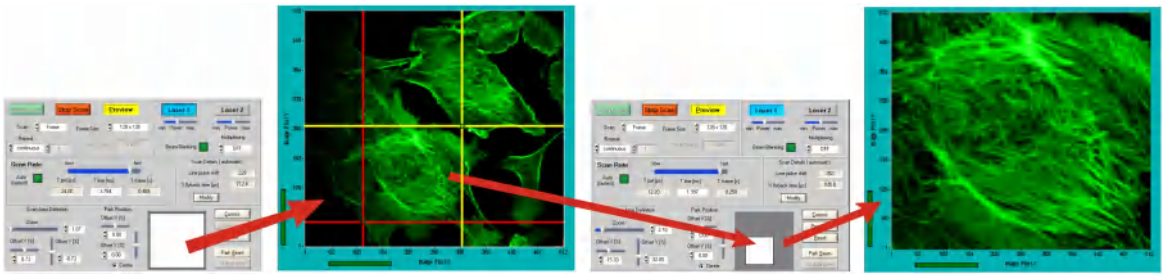


Fig. 1153: The scan are can be adjusted to the area between the cursors even when the scanner is running

Park Beam Function

'Park Beam' places the laser beam in a defined spot of the scan area. Please note that the beam blanking of the laser must be switched off to run a measurement in the beam park mode. In the scanner panel, the location can be set either by changing the 'Offset X' and 'Offset Y' of the park position, or by moving the yellow spot in the image area by the mouse cursor. Please see Fig. 1154.

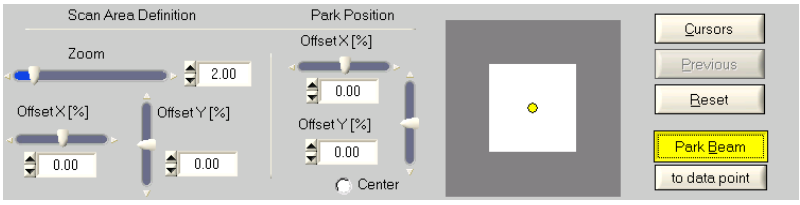


Fig. 1154: Defining the beam position in the Beam Park mode

The beam-park position can also be selected in an image recorded before, see Fig. 1155. Activate the cursors by a right mouse-click into the display window (Fig. 1155, left). Set the 'Data Point' to the desired beam-park position (Fig. 1155, middle). Then click on 'To Data Point' in the area-select part of the scanner panel, see Fig. 1155, right.

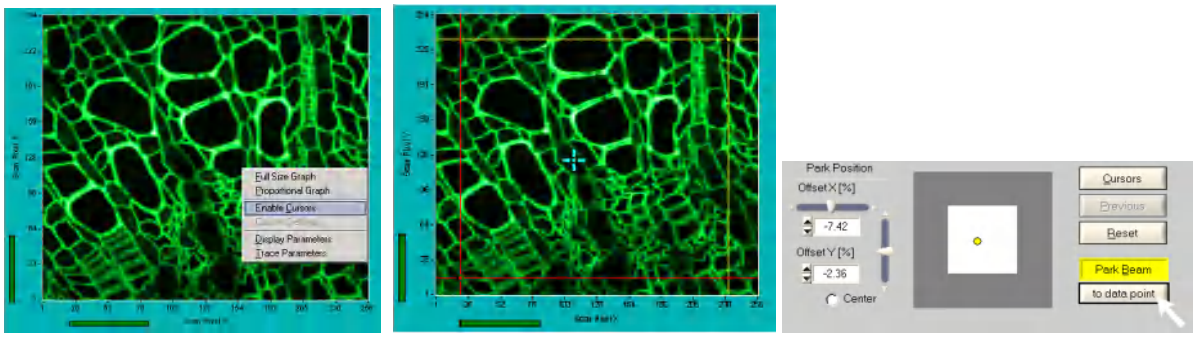


Fig. 1155: Selecting the beam-park position in the display window

Scanner Configuration

The fastest line time and the optimum line flyback time depend on the zoom factor used. Moreover, at high scan rate the scanner lags behind the control voltage ramp. To avoid that a change in the scan rate results in large image shifts the lag is compensated by shifting the line sync pulse that the scan controller sends to the SPC card. All three parameters are calculated automatically from the current zoom factor and line time. The calculation parameters are accessible via the 'Modify' button. The button opens the panel shown in Fig. 1156.

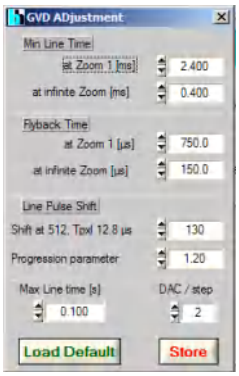


Fig. 1156: Panel for adjusting the details of the scanner control

The parameters are mainly intended for adjusting the GVD-120 scan controller for different scanners. For the DCS-120 system we discourage to change anything but the ‘Max Line Time’. ‘Max Line Time’ determines the range of the scan rate slider (Fig. 1149). Changes may be required if the DCS-120 is to be used for extremely slow scans, or if the GVD-120 scan controller is used in combination with piezo scan stages.

Assigning Names to the Laser Buttons

The laser buttons (in ‘Laser 1’ and ‘Laser 2’ in Fig. 1149) can be assigned user-defined names. The names are defined under ‘GVD EEPROM’, see Fig. 1157.

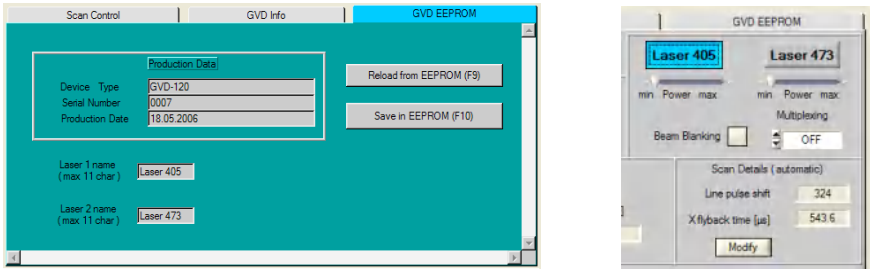


Fig. 1157: Assigning user-defined names to the ‘Laser’ buttons

DCC-100 Detector Controller Card

Control Panel

The DCC-100 card is used to control the detectors of bh TCSPC systems. It is able to control the BDL-SMC, BDL-SMN, and BDS-SM ps diode lasers, and to control electro-mechanical shutters. Please see page 212 for technical details. The software panel of the DCC-100 is shown in Fig. 1158.

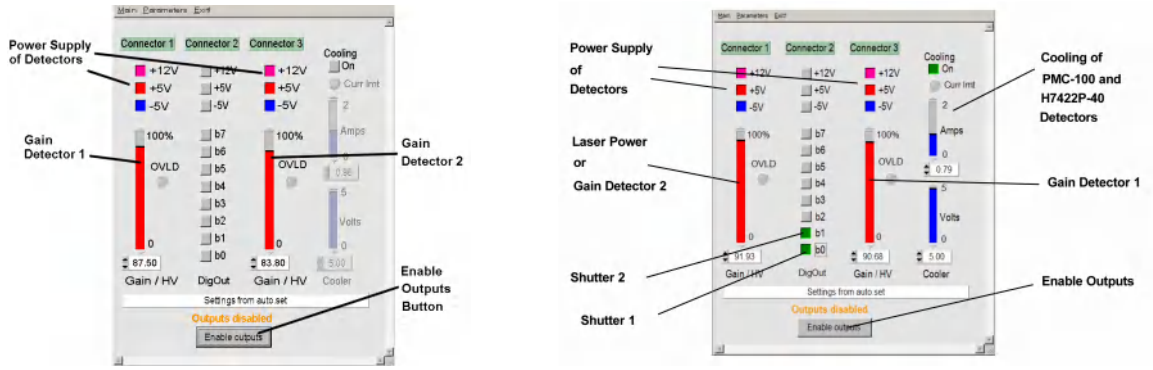


Fig. 1158: Detector control panel. Left: Control of two detectors. Right: Control of one laser and one detector.

Enable Outputs Button

After the start of the DCC-100 software the outputs of the DCC-100 are disabled. Please note that this is a safety function. It avoids unintentionally switching on the output voltage of a high-voltage power supply or unintentional activation of lasers or detectors. Please note: The DCC software can be configured to turn on the outputs automatically (Option 'Enable Outputs on Startup'). This option is *not* intended for operation of PMTs, and should *not* be used in conjunction with lasers.

Power Supply of Detectors

The power supply of the PMC-100, PMC-150, H7422P-40, HPM-100 and PML-16-C detectors is provided by the DCC-100. The DCC also delivers the power to the bh HVM-3000 high voltage module for MCP PMTs. To operate these detectors the corresponding power supply buttons have to be activated.

Cooling of Detectors

The PMC-100, PMC-150, and the H7422P-40 have internal coolers. If you use these detectors, activate the cooling by clicking on the 'Cooling On' and set a cooling current of 0.5 to 1 A. Set the cooling voltage to maximum (5 V). The DCC can be configured to cool either one or both detectors, please see page 88.

Gain of Detectors

The gain of the detectors is set by the sliders under 'Connector 1' and Connector 2'. When changing the detector gain, please remember that the detectors work in the photon counting mode. In other words, the detector delivers a pulse for every photon detected. The data acquisition system counts these single-photon pulses. The light intensity is proportional to the number of pulses per time interval. A change in detector gain changes the amplitude of the single-photon pulses, not their frequency. The detector gain is adjusted in order to obtain a single-photon pulse amplitude well above the threshold of the input discriminator of the TCSPC card (the CFD threshold). With the right combination of CFD threshold and detector gain the count rate (and thus the intensity of the image recorded) becomes almost independent of the detector gain. Please see page 'Detector ', page 269.

Lock Detector Setup Parameters

Once the correct detector gain has been determined, we recommend to lock the detector parameters, see Fig. 1159. This avoids unintentional changes of the detector gain.

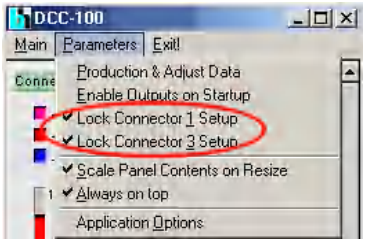


Fig. 1159: Locking the detector setup

Shutters

The shutters of bh detector/shutter assemblies are controlled by the 'Dig. Out' buttons. In case of overload shutdown the shutters are closed and must be opened by clicking on the Dig. Out buttons.

Overload Shutdown

If the light intensity at one or both detectors is too high the DCC-100 shuts down the gain and the +12 V supply voltage, and closes the shutters. In extreme cases this may happen at a gain far below the single-photon detection level, i.e. before the SPC module displays a CFD count rate. The DCC-100 panel after an overload shutdown is shown in Fig. 1160. If an overload shutdown has occurred, first remove the source of the overload. Then click on the 'Reset' button and open the shutters. The detector then resumes normal operation.

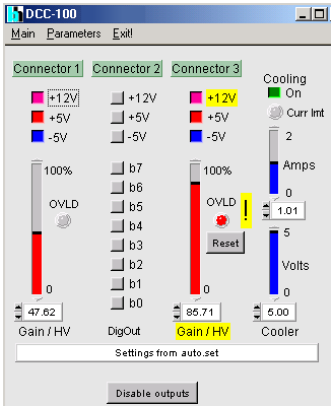


Fig. 1160: DCC-100 panel after an overload shutdown

Maximum Values of Detector Gain

Maximum values of the gain can be defined in the 'Adjust Parameters' panel of the DCC-100. The panel is shown in Fig. 1161. The values are defined under 'C1 Gain HV Limit' and 'C3 Gain HV Limit'. They are automatically saved in a non-volatile memory on the DCC board.

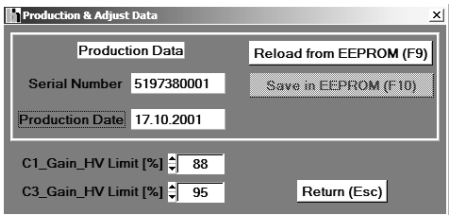


Fig. 1161: DCC-100 Production and adjust data panel, setting maximum values of the detector gain

Control of the Zeiss Axio Observer Z1

The SPCM software is able to control a Zeiss Axio Observer Z1 microscope via a USB bus interface. The function is used for Z-stack FLIM with the DCS-120 system [68]. The Axio Observer control panel is opened by clicking into ‘Parameters’, ‘Zeiss Axio Observer’, see Fig. 1162, left.

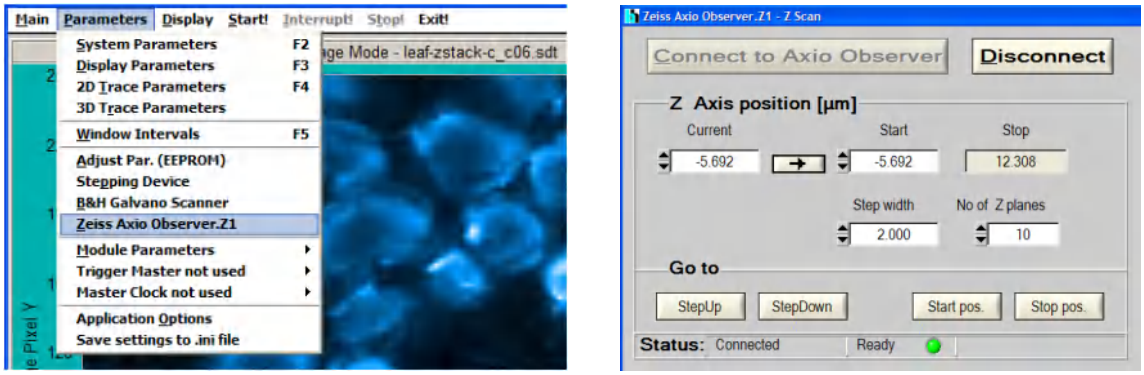


Fig. 1162: Left: Starting the Axio Observer control. Right: Axio Observer Z control panel

The control panel shows the current Z position. The position can be changed by typing in a new position, by clicking on the ⇕ symbols, by clicking on the Step Up or Step Down buttons, or by turning the focusing knob at the microscope. A click on → defines the current position as a start position of the Z scan. ‘Step width’ an ‘No of Z planes’ define the distance and the number of Z steps. ‘No of Z planes’ is automatically connected to the ‘Cycles’ in the system parameters. Please see [68] for details.

Z stack FLIM can be performed both in the Scan Sync In and in the FIFO Imaging mode in combination with the cycle and autosave function. To run a Z scan sequence, first run a fast repetitive scan in the ‘Preview’ mode. Select a Z position to start with. You can do this by turning the focusing knob at the microscope, or by changing the position via the Z control panel. When you have found the right position, define it as a start position and switch off the Preview. Start the ordinary scan, and start the measurement. The SPCM software will record images for the defined number of cycles at subsequent Z positions and save them into consecutive files.

DB-32 SYNC Delay Box

The DB-32 is a USB controlled passive delay box. It is used to adapt the signal transit time in the SYNC path of a TCSPC system to different detectors or optical configurations. The SSYNC-Delay Box is shown in Fig. 1163.



Fig. 1163: Sync Delay Box

Clicking into ‘Devices’, ‘BH Sync delay’ of the SPCM software opens a selection panel in which the connection to the delay box is established. In multi-module TCSPC systems on or several delay boxes can be associated to different SPC modules, see Fig. 1164. Once the delay box has been assigned it is detected automatically at the startup of the SPCM software. The

delay can then be set via a 'Delay' parameter in the SYNC parameter part of the System Parameters, or directly via the SYNC field in the main panel, see Fig. 1165. For delay boxes with two inputs (all newer boxes have two) the active input can be defined in the system parameters.



Fig. 1164: Control of DB-32 SYNC delay box

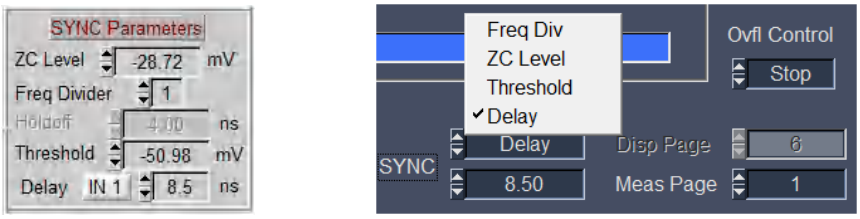


Fig. 1165: Delay setting in the system parameters (left) and in the SYNC field of the main panel (right)

DDG-210 Pulse Generator Card

The DDG-210 pulse generator card is used to on-off modulate BDL and BDS series ps diode lasers lasers for phosphorescence decay measurements and phosphorescence lifetime imaging. The control panel is started as shown in Fig. 1166, left. The DDG-210 panel is shown on the right. The card generates pulses to the laser or to an AOM of a laser, and a routing signal to the SPC module. The pulses can be generated in a free-running mode, or be triggered by the pixel clock of a scanner. The DDG-210 is part of the bh FLIM systems for the Zeiss LSM 710 family microscopes [69]. Please see page 340 and page 434 for further technical details.

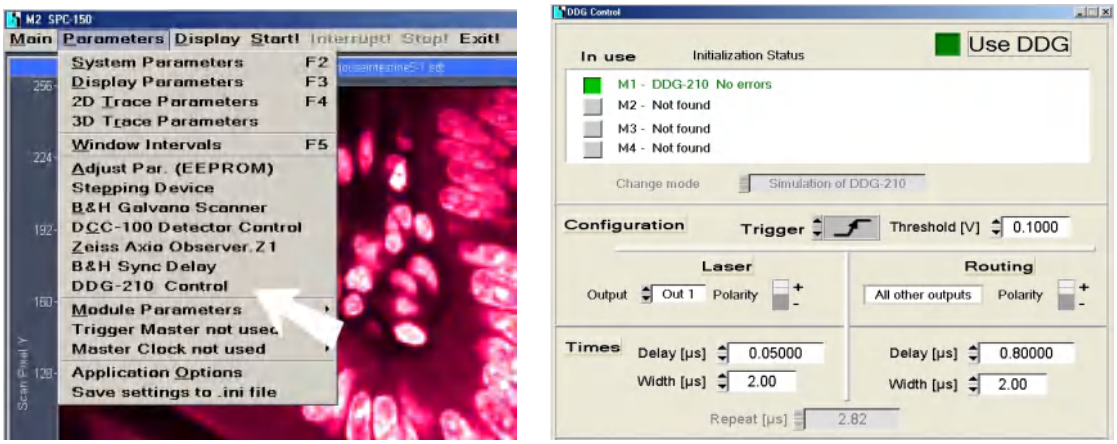


Fig. 1166: Left: Starting the DDG-210 control. Right: DDG-210 control panel

Ti:Sa Laser and AOM Control

The SPCM software is able to control a Ti:Sa laser and an AOM. The control panel opens by a click into ‘Devices’, Ti:Sa laser & AOM Control’. The control panel is shown in Fig. 1167



Fig. 1167: Left: Ti:Sa laser and AOM control panel. Right: Coherent Chameleon laser and bh AOM

The laser is controlled in the upper part of the panel. The type of Ti:Sa laser must be selected under ‘Laser’, ‘Type’. The system computer connects to the laser via a USB interface. If it does not connect automatically you can force the connection by clicking on ‘Refresh’. The laser panel controls the shutter of the laser and the wavelength, and displays the status of the laser.

The lower part of the panel controls the bh AOM. Since an AOM is wavelength-dependent the AOM controller has to know the wavelength selected for the laser. If both the laser and the AOM are controlled from the panel shown in Fig. 1167 the wavelengths for the laser and the AOM are automatically coupled.

The reason why an AOM needs to by tuned to the wavelength of the laser is shown in Fig. 1168. An acoustic wave is excited in the AOM crystal electrically by a high-frequency signal. The wave acts like a grating, and diffracts away a part of the laser light. The amount of diffracted light depends on the amplitude of the high-frequency signal. The angle at which the light is diffracted depends on the frequency and on the wavelength of the light. To obtain a constant diffraction angle the frequency of the electrical signal must be adjusted to the wavelength to maintain a constant angle of the output beam.

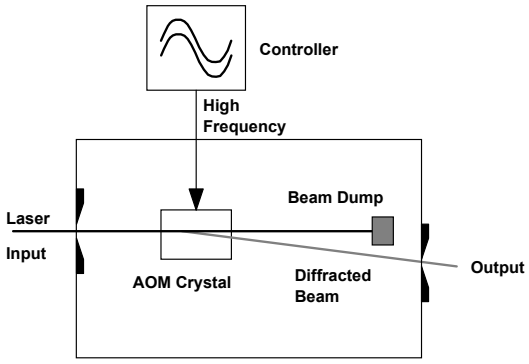


Fig. 1168: Principle of the AOM

Maintaining a constant output beam angle is important especially in multiphoton laser scanning microscopes. If the angle is not constant the laser beam moves out of the optical axis of the scanner and the microscope lens. The result is loss in optical resolution, excitation efficiency, or even failure to record an image at all. Therefore, if you use an AOM with a laser

that is not controlled by SPCM software, you have to type the correct laser wavelength into the AOM control panel.

Motor Stage

Starting from version 9.76, SPCM is able to control a motorised sample stage. So far, the ES 111 motor stages with the ES 11 and Pro Scan III controllers of Prior are integrated but other will possibly follow. The stage can be used to control the position of a sample manually or to record mosaics of images in cooperation with the GVD-120 scan controller of the bh DCS-120 system. A photo of a DCS-120 MACRO system with the motor stage is shown in Fig. 1169.

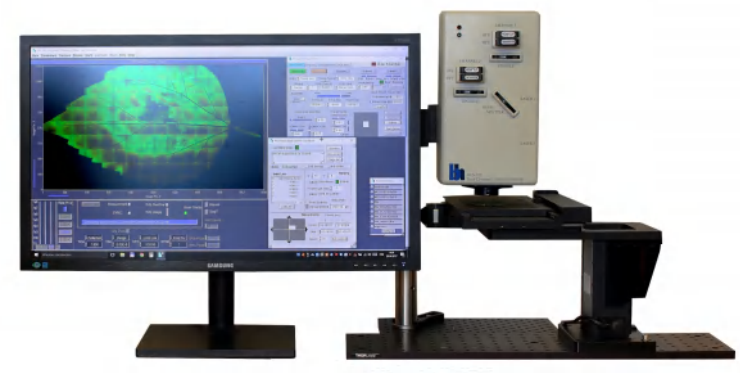


Fig. 1169: DCS-120 MACRO scanner with motor stage

The motor stage control panel is shown in Fig. 1170. The panel shown left has Tile Imaging disabled, i.e. the stage can be controlled manually but does not interact with the DCS-120 scanner. When a DCS scan is started the system records a normal FLIM image in the selected place of the sample. The panel on the right has Tile Imaging enabled. The motor stage interacts with the scanner, and, in cooperation with the DCS scanner, a spatial mosaic of images is recorded.

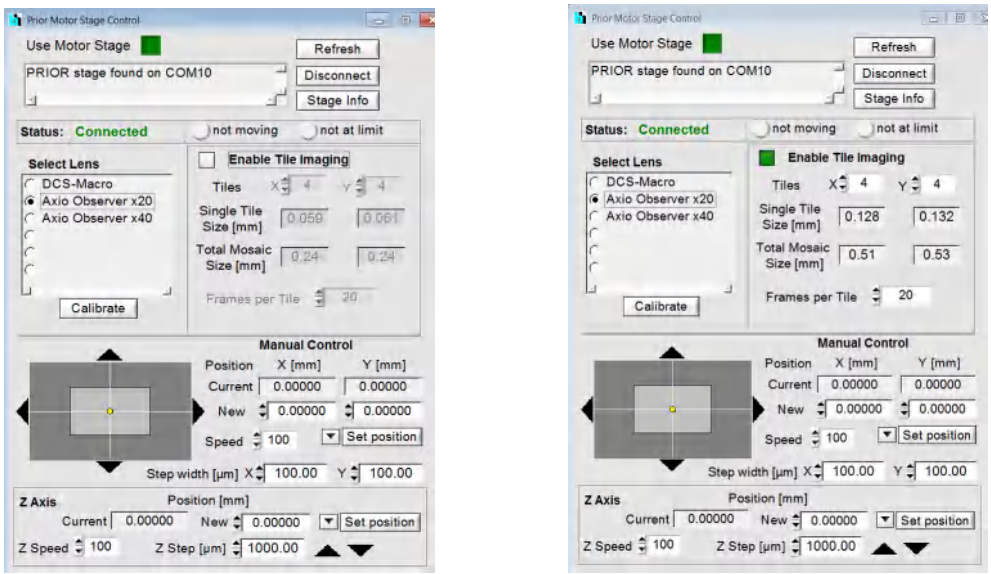


Fig. 1170: Control panel for motor stage. Left: Tile imaging disabled. Normal scanning, manual control of motor stage. Right: Tile imaging enabled. Spatial mosaic scanning and manual control of stage.

Fig. 1171 shows how the optical scanner interacts with the motor stage. When Tile Imaging is enabled the step width of the motor stage automatically adjusts to the scan area (Zoom factor)

selected in the DCS scanner panel. When the measurement is started the SPC system records a mosaic of FLIM images the elements of which have the same x and y size as the step width of the motor stage. The result is a large image consisting of individual scans offset by the motor-stage step width. The data of the individual elements of the mosaic (or tiles) can be accumulated over a selectable number of frames (20 in Fig. 1171). The number of frames per tile can be selected both in the motor stage panel and in the scanner panel. It is automatically adjusted to the same value.

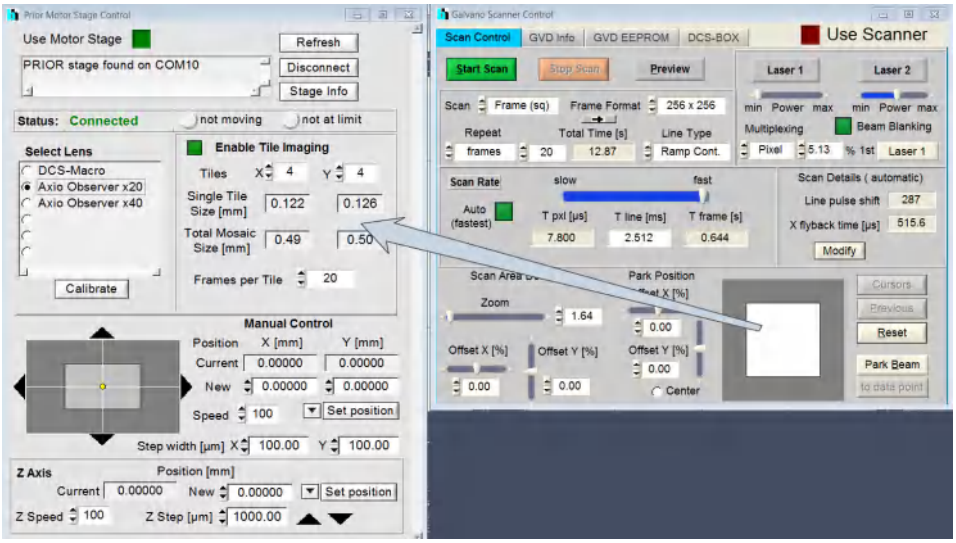


Fig. 1171: Interaction of the motor stage with the DCS-120 scanner

The size of the DCS scan area differs for different optical systems and for different microscope lenses. To guarantee that the individual tiles fit together seamlessly the step width of the motor stage can be calibrated. The calibration panel is shown in Fig. 1172. The calibration table contains the size, X and Y, of the field of view (scan area) of the optical scanner for Zoom = 1. The calibration factors can (but need not) be made different in x and y to account for possible tolerances in the drivers of the galvanometer mirrors. Up to six calibration values can be defined for different microscope configurations or objective lenses. The calibration values are stored in a file. They are local to the particular TCSPC system, and not stored in the sdt files of the measurement data.

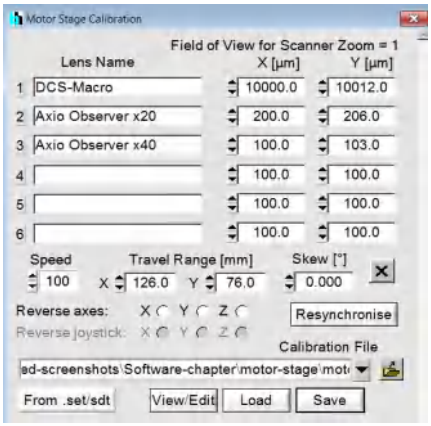


Fig. 1172: Calibration of the motor stage

SPCImage NG Data Analysis Software

Overview

SPCImage NG is a new generation of bh's TCSPC-FLIM data analysis software. It combines time-domain and frequency-domain analysis, uses a maximum-likelihood algorithm to calculate the parameters of the decay functions in the individual pixels, and accelerates the analysis procedure by GPU processing. In addition to FLIM data, SPCImage NG processes single-curve decay data, multi-wavelength data, excitation-multiplexed data, PLIM data, mosaic FLIM data, and other multi-dimensional TCSPC data sets. SPCImage NG provides decay models with one, two, or three exponential components, incomplete-decay models, and a shifted-component model. A global analysis function is available for analysing multi-exponential data with constant component amplitudes. Another important feature is advanced IRF modelling, making it unnecessary to record IRFs for the individual FLIM data sets. 1D and 2D parameter histograms are available to display the distribution of the decay parameters over the pixels of the image or over selectable ROIs. Image segmentation can be performed via the phasor plot or the 2D parameter histograms. Pixels with similar phasor or 2D parameter signature can be combined for high-accuracy time-domain analysis, resulting in photon numbers known only from cuvette-based lifetime experiments. A batch-processing function and a batch export function are available for analysing a large number of FLIM data sets automatically and to convert them into bmp or tif images.

Main Panel

A typical main panel of SPCImage is shown in Fig. 1173. It shows a lifetime image on the left, a parameter histogram in the upper right, and a fluorescence decay curve in the lower right.

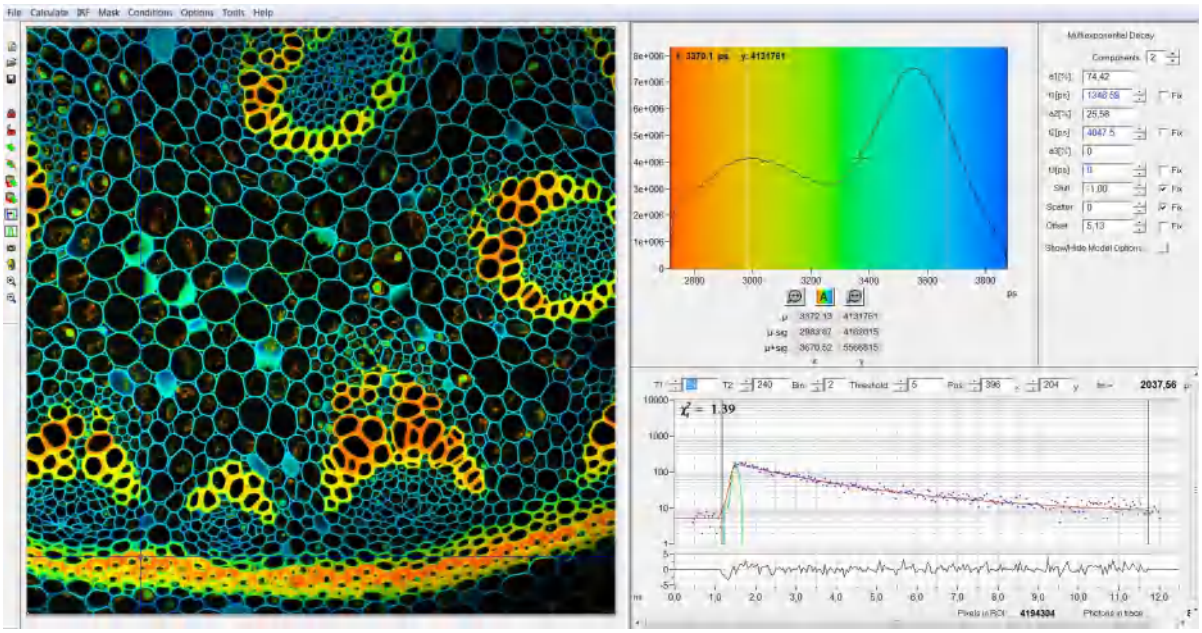


Fig. 1173: Main panel of SPCImage NG

Since version 8.5 SPCImage NG is able to display two lifetime images simultaneously. Typically, these are images of the same sample in different wavelength intervals or for different excitation wavelength. An example is shown in Fig. 1174.

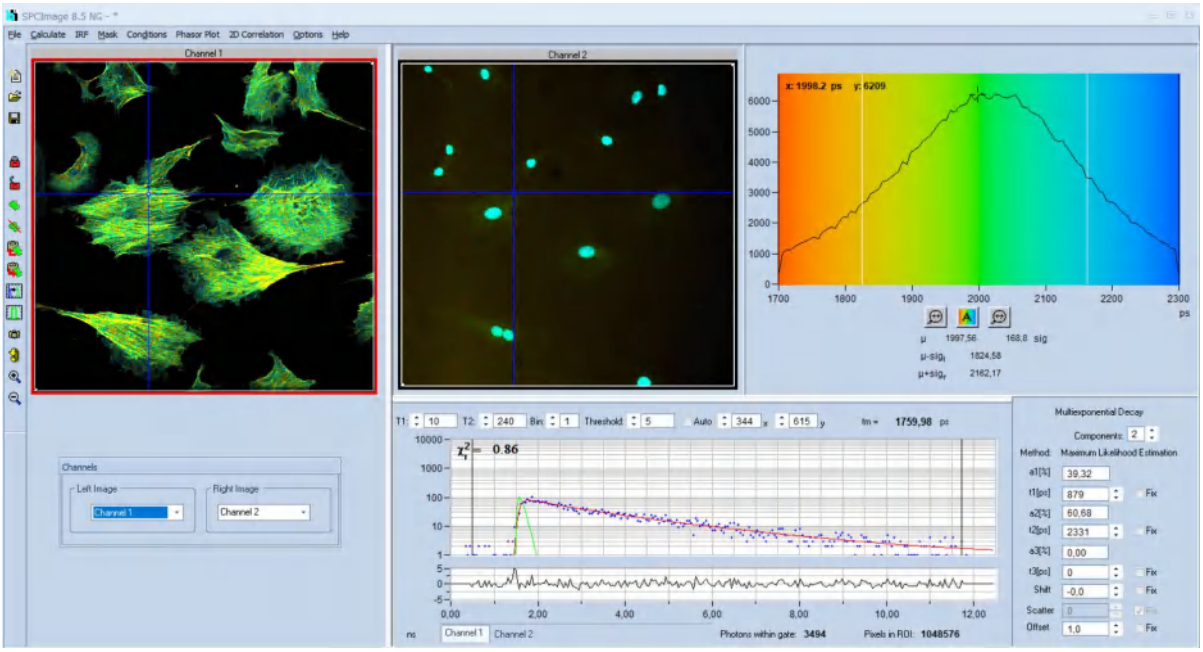


Fig. 1174: SPCImage NG with two images in different wavelength intervals

The upper right part of the SPCImage NG panel can be replaced with a phasor plot. An examples is shown in Fig. 1175

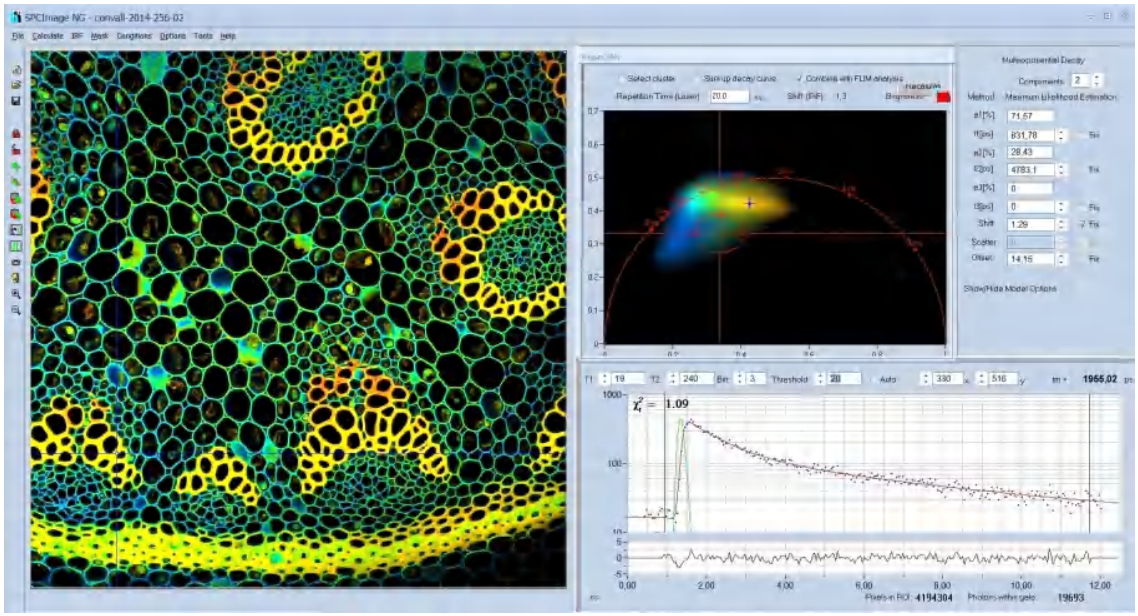


Fig. 1175: SPCImage NG main panel with phasor plot

Other main panel configurations are possible. These include combinations with grey-scale images, with 2-D parameter histograms, and configurations for single-curve analysis. An example is shown in Fig. 1176.

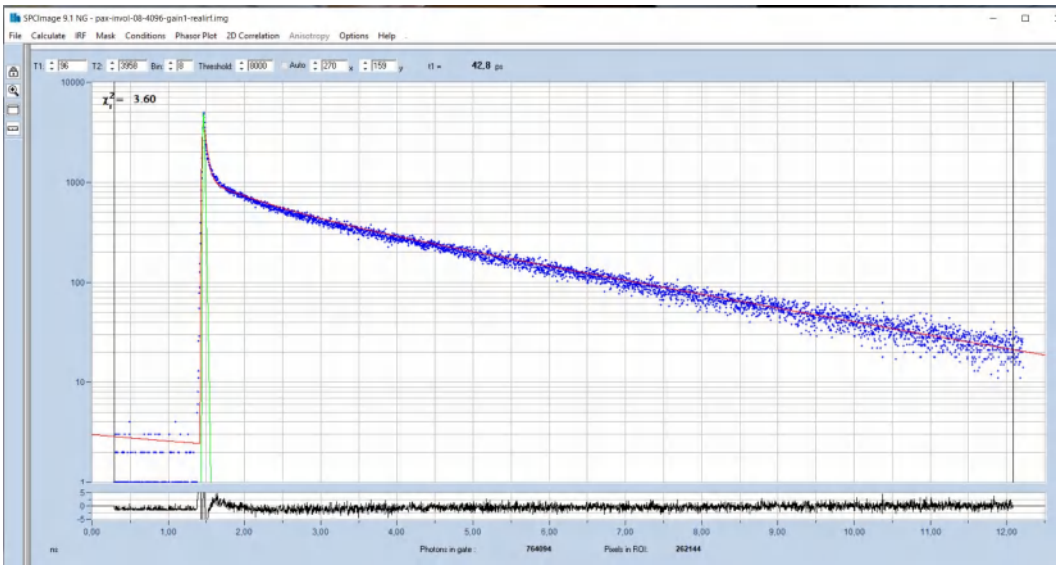


Fig. 1176: Main panel for single-curve analysis

Images of Decay Parameters

In the simplest case, the result of FLIM analysis is the 'lifetime' of the decay functions in the individual pixels. However, in practice the decay functions are not single-exponential. Moreover, the desired biological information often is in the composition of the decay functions, not in the apparent lifetime. For complex decay functions SPCImage delivers the lifetimes and amplitudes of the decay components. SPCImage then creates colour-coded images of the amplitude- or intensity-weighted lifetimes in the pixels, images of the lifetimes or amplitudes of the decay components, images of lifetime or amplitude ratios, and images of other combinations of decay parameters, such as FRET intensities, FRET distances, bound-unbound ratios, or the fluorescence-lifetime redox ratio, FLIRR. Examples are shown in Fig. 1177 through Fig. 1180.

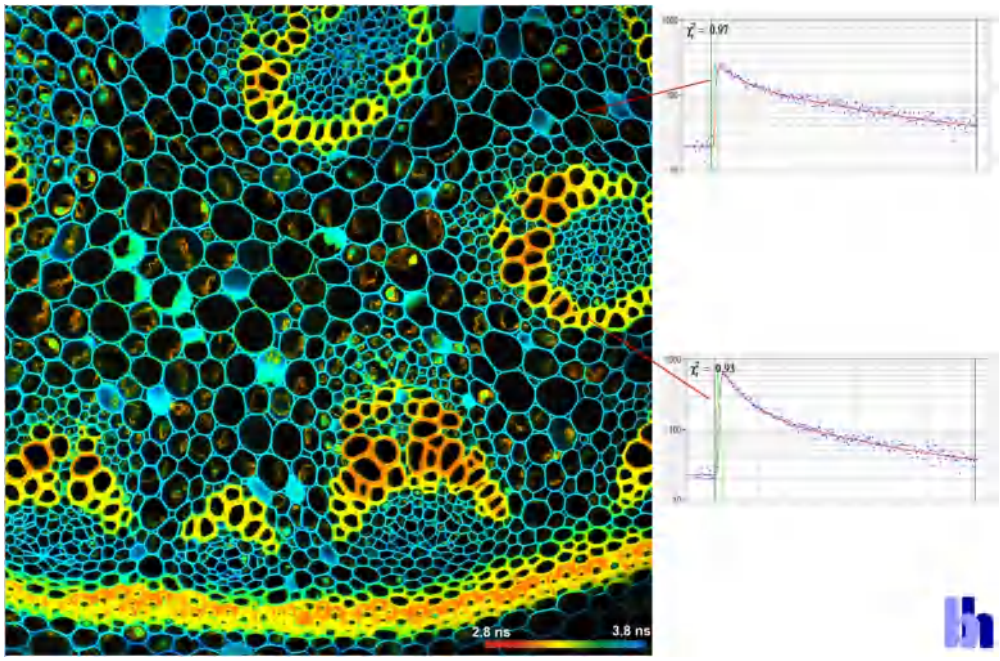


Fig. 1177: Image of the amplitude-weighted lifetime, t_m, of a double-exponential decay. Right: Fluorescence decay curves in selected pixels.

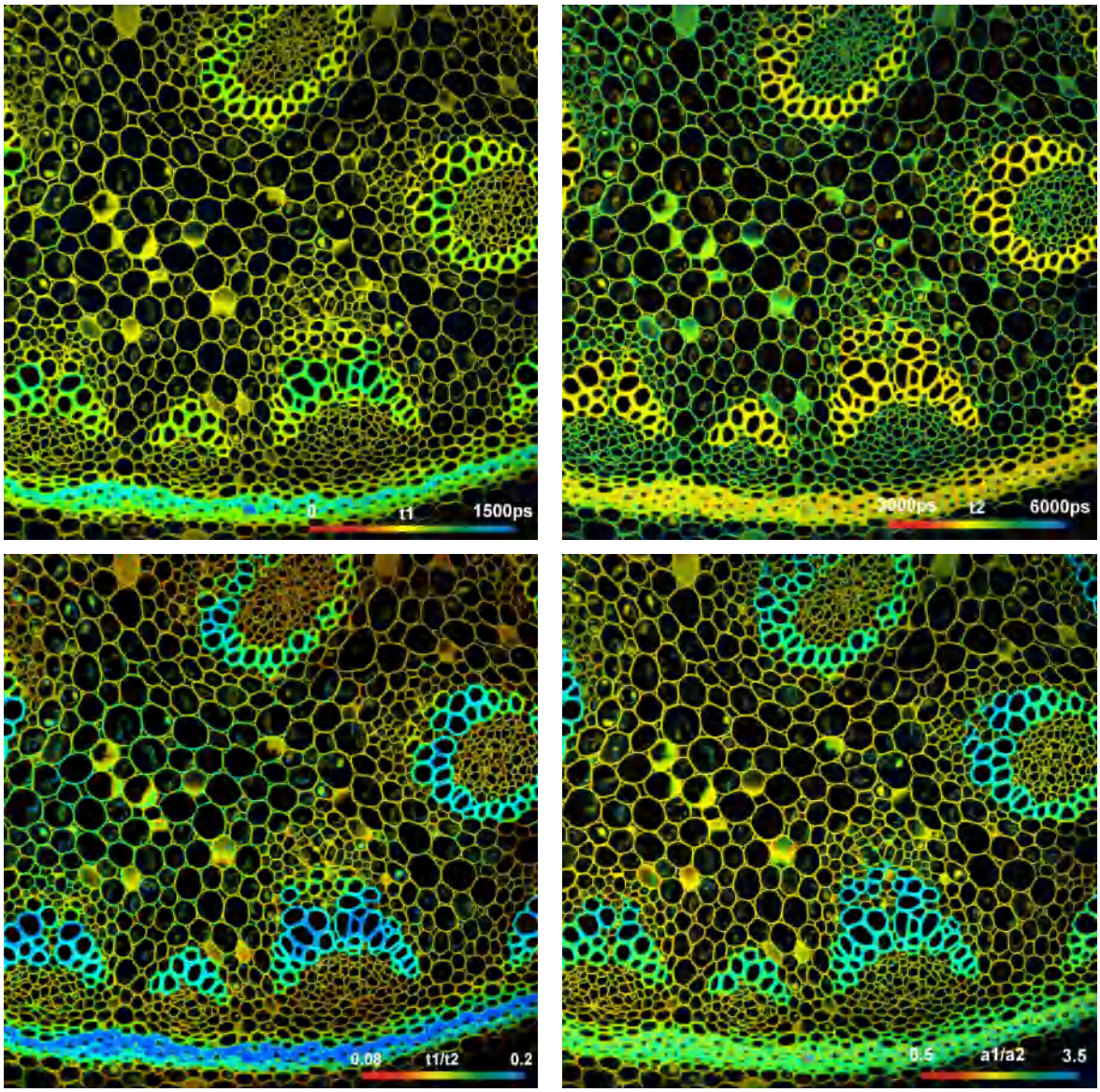


Fig. 1178: Upper row: Images of the lifetimes of the fast component, t_1, and the slow component, t_2, of a double-exponential decay. Lower Row: Images of the amplitude ratio, a_1/a_2, and the lifetime ratio, t_1/t_2, of the fast and the slow decay component.

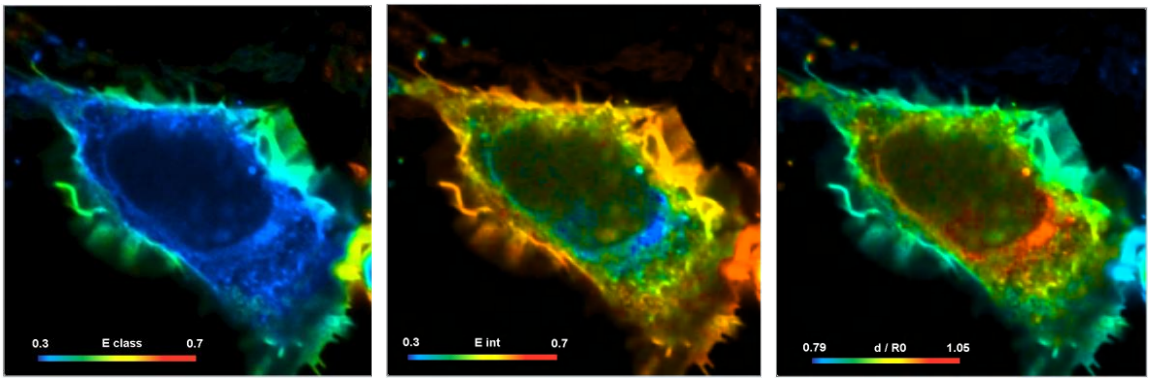


Fig. 1179: Cell with interacting proteins, labelled with a FRET donor and a FRET acceptor. Left to right: Classic FRET efficiency, FRET efficiency of interacting donor fraction, FRET distance

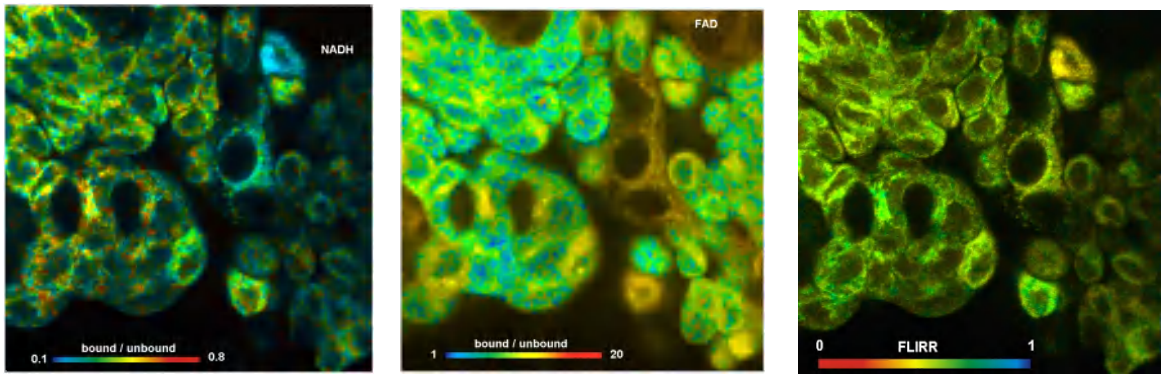


Fig. 1180: Metabolic FLIM. Bound-unbound ratio of NADH, Bound/unbound ratio of FAD, Fluorescence-Lifetime Redox Ratio, FLIRR.

Phasor Plot

SPCImage FLIM analysis software combines time-domain multi-exponential decay analysis with phasor analysis. Phasor analysis expresses the decay data in the individual pixels as phase and amplitude values in a polar diagram, the 'Phasor Plot', page 955. Pixels with similar decay signature form distinct clusters in the phasor plot. Clusters of interest can be selected and back-annotated in the lifetime image for further processing or for combination of pixel data. An example is shown in Fig. 1181.

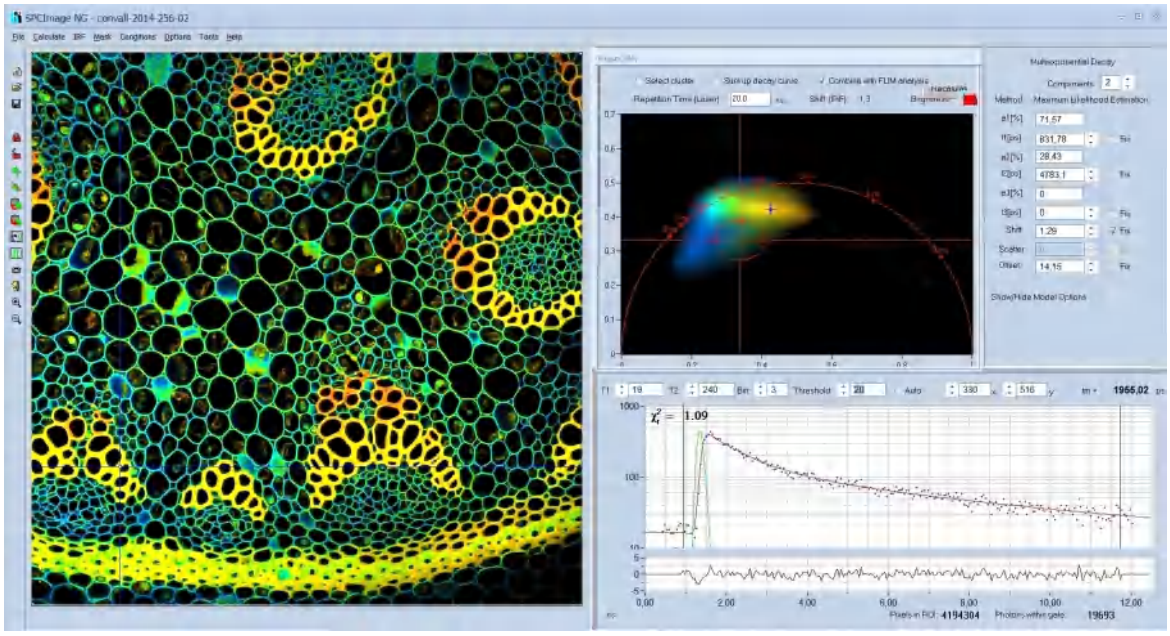


Fig. 1181: Combination of time-domain analysis (left and lower right) and phasor plot (upper right)

Maximum-Likelihood Algorithm

SPCImage NG runs an iterative fit and de-convolution procedure on the decay data of the individual pixels of the FLIM images. Since version 8.5 SPCImage NG uses a maximum-likelihood estimation (MLE) process to determine the decay parameters in the pixels. In contrast to the frequently-used weighted least-square (WLS) fit, MLE is based on calculating the probability that the values of the model function correctly represent the data points of the decay function. Compared to the least-square method, the fit accuracy is significantly improved for multi-exponential decay functions. Moreover, there is no bias toward shorter lifetime as it is unavoidable for the least-square fit. Please see 'Fit Procedures', page 936.

Modelling of the Instrument-Response Function

Recording the 'Instrument Response Function' (IRF) is a permanent problem of time-resolved fluorescence spectroscopy. Recording the IRF in a FLIM system is difficult, and often impossible. As a result, there is rarely an IRF that was recorded in a FLIM system and represents the temporal behaviour of the system correctly. Therefore, SPCImage NG does away with IRF recording altogether. Instead, the IRF is extracted from the FLIM data themselves. Earlier SPCImage versions had an 'Auto IRF', which was derived from the rising edge of the fluorescence decay function. The Auto IRF has been used successfully for more than 20 years. It works well for decay functions which are not too far from a single-exponential function but has deficiencies if very fast decay components are present. A new approach introduced by SPCImage NG is the 'Synthetic IRF'. It is created by modelling the IRF with a generic function. The exact parameters of this function are determined by fitting it to the FLIM data together with the selected decay model, see 'Model Functions', page 877. The results of this procedure are so good that an accurate IRF is obtained even for decay functions containing ultra-fast components, see Fig. 1182.

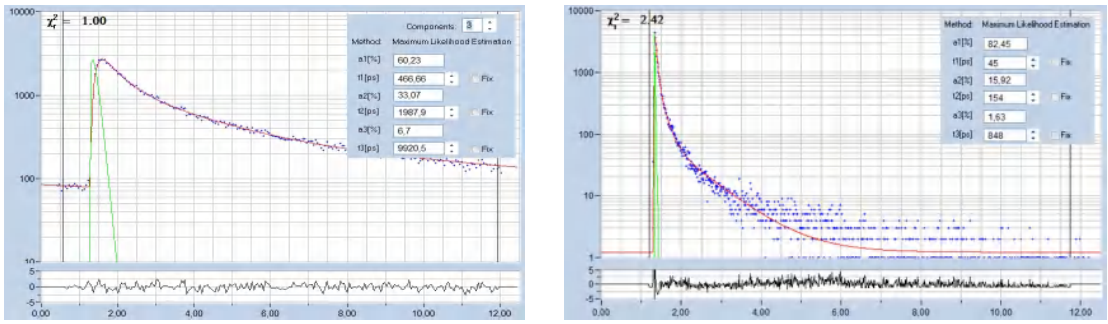


Fig. 1182: Analysis with synthetic IRF. Left: Fluorescence excited by diode laser. Right: Ti:Sa laser, sample with extremely fast decay component. Green curve IRF, blue dots data points, red curve fit with triple-exponential decay model.

Decay Models

SPCImage NG provides single-, double-, and triple-exponential decay models. An ‘Incomplete Decay’ option is available to determine long fluorescence lifetimes within the short pulse period of the Ti:Sa laser of a multiphoton system. SPCImage NG provides also a 'Shifted-Component' model. In this model, the decay components of a multi-exponential model functions can be shifted in time by predefined values. The model is used for ophthalmic FLIM, where different decay components come from different depth within the eye. For details please see 'FLIO Analysis by SPCImage NG', page 598.

GPU Processing

Data recorded with bh FLIM systems can contain an enormous number of pixels and time channels. Images with 1024 x 1024 or even 2048 x 2048 pixels are not uncommon, and time-channel numbers of 1024 are routinely used in combination with fast HPM detectors [122]. Processing such amounts of data by the CPU of even a fast computer would take tens of minutes, and a fit with global parameters would by entirely out of reach. SPCImage NG therefore runs the data analysis on a GPU (Graphics Processor Unit). The image data are transferred into the GPU, which then runs the de-convolution and fit procedure for a large number of pixels in parallel. With the GPU, data processing times are thus massively reduced. The image shown in Fig. 1183 was calculated on an NVIDIA GPU within five seconds.

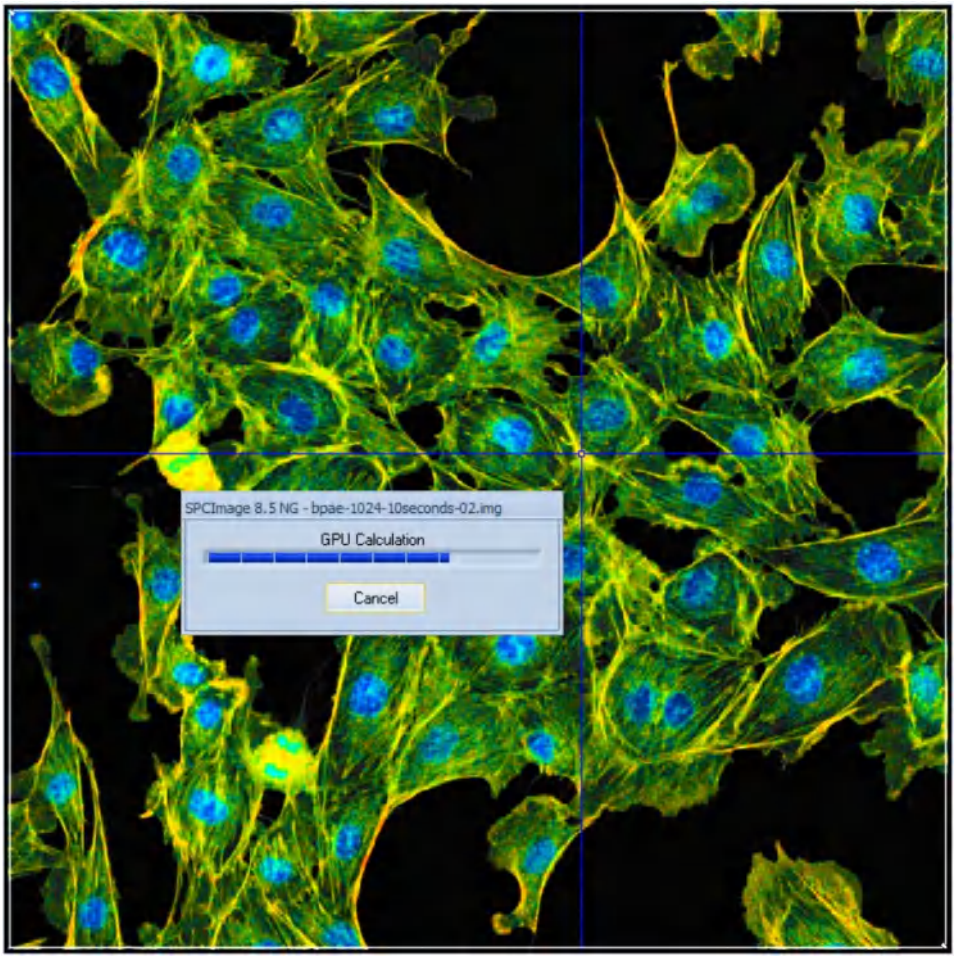


Fig. 1183: A lifetime image with 1024 x 1024 pixels and 1024 time channel per pixel. The image was calculated on an NVIDIA GPU in 5 seconds.

Parameter Histograms

SPCImage has histogram functions for the decay parameters. The histogram shows how often pixels of a given parameter value occur in the lifetime image. The histogram refers either to a selected region of interest or, if no ROI was defined, to the entire lifetime image. Together with the various options to select decay parameters and combinations of decay parameters a wide variety parameter histograms can be obtained. Two examples are shown in Fig. 1184.

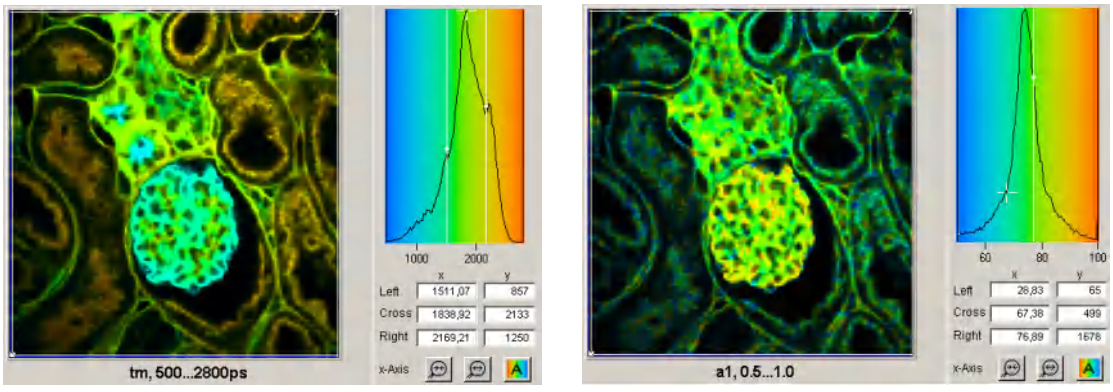


Fig. 1184: Histograms of the mean (amplitude weighted) lifetime of double-exponential fit (left) and of the amplitude of the fast decay component, a_1 (right)

2-D Histograms

2D histograms present density plots of the pixels over two selectable decay parameters. The decay parameters can be lifetimes, t_1, t_2, t_3, or amplitudes, a_1, a_2, a_3, of decay components, amplitude or intensity-weighted lifetimes, t_m or t_i, or arithmetic conjunctions of these parameters. An example is shown in Fig. 1185. A histogram of the amplitude, a_1, of the fast decay component versus the amplitude-weighted lifetime, t_m, has been created. Cursors in the histogram are available to select special parameter combinations and back-annotate the corresponding pixels in the lifetime image.

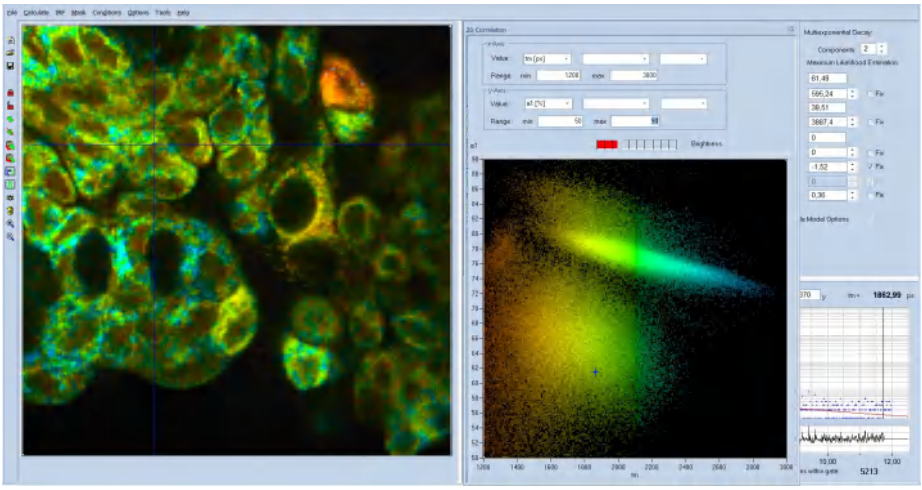


Fig. 1185: 2-D histogram showing density plot of pixels over amplitude-weighted lifetime, t_m, and amplitude of fast component, a_1.

ROIs

SPCImage NG allows the user to define ROIs in the images. Both rectangular and polygonal ROIs can be defined. Parameter histograms are displayed for the selected ROI, see Fig. 1186.

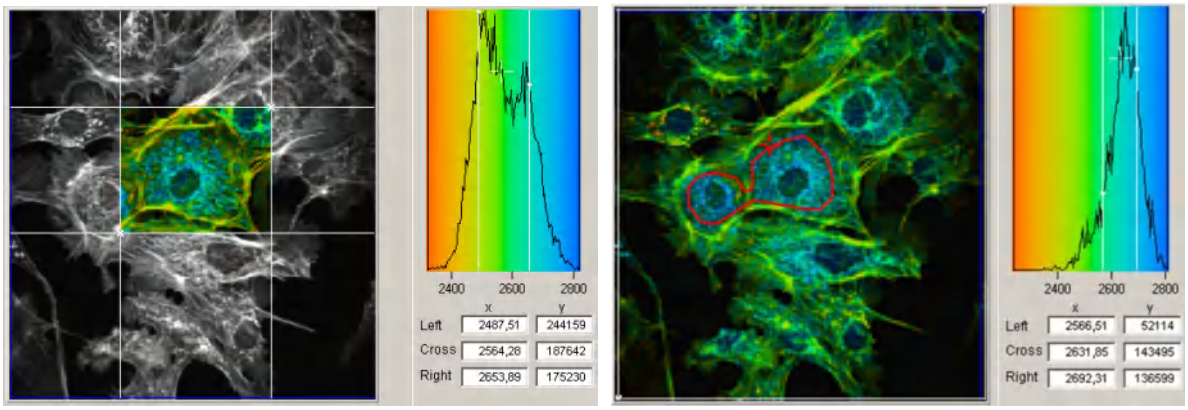


Fig. 1186: ROI Definition. Left: Rectangular ROI. Right: Polygonal ROI

Several polygonal ROIs can be defined, and the corresponding parameter histograms be selected via the buttons on top of the histogram window. Please see Fig. 1187.

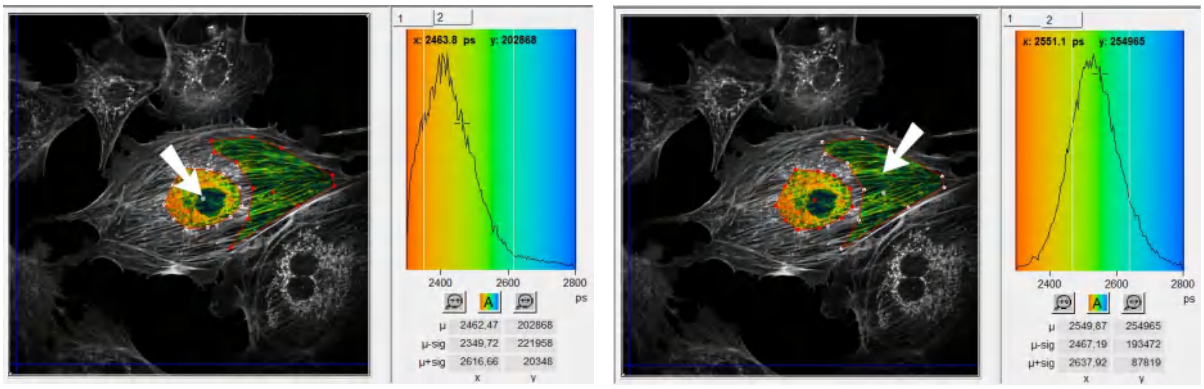


Fig. 1187: Multiple ROIs, with selection of parameter histogram.

Image Segmentation

Images taken at high pixel numbers and Mosaic FLIM images can contain a large number of cells. In these cases, it is time-consuming, if not impossible, to manually select regions of interest for each of the cells in the image. SPCImage NG therefore provides automatic image segmentation functions via the phasor plot and the 2D histograms. Areas with different decay signature form separate clusters in these presentations. Interesting clusters can be selected and back-annotated in the images. An example is shown in Fig. 1188. The image area contains a large number of cells. A phasor plot of the image was calculated, the phasor range of the cell nuclei selected, and the corresponding pixels back-annotated in the lifetime image. The decay data of these pixels were combined. The result is single decay curve, containing an enormous number of photons. This curve can be analysed at high precision with double- and triple-exponential decay models, see Fig. 1188, bottom right. For details please see 'Phasor Plot', page 906.

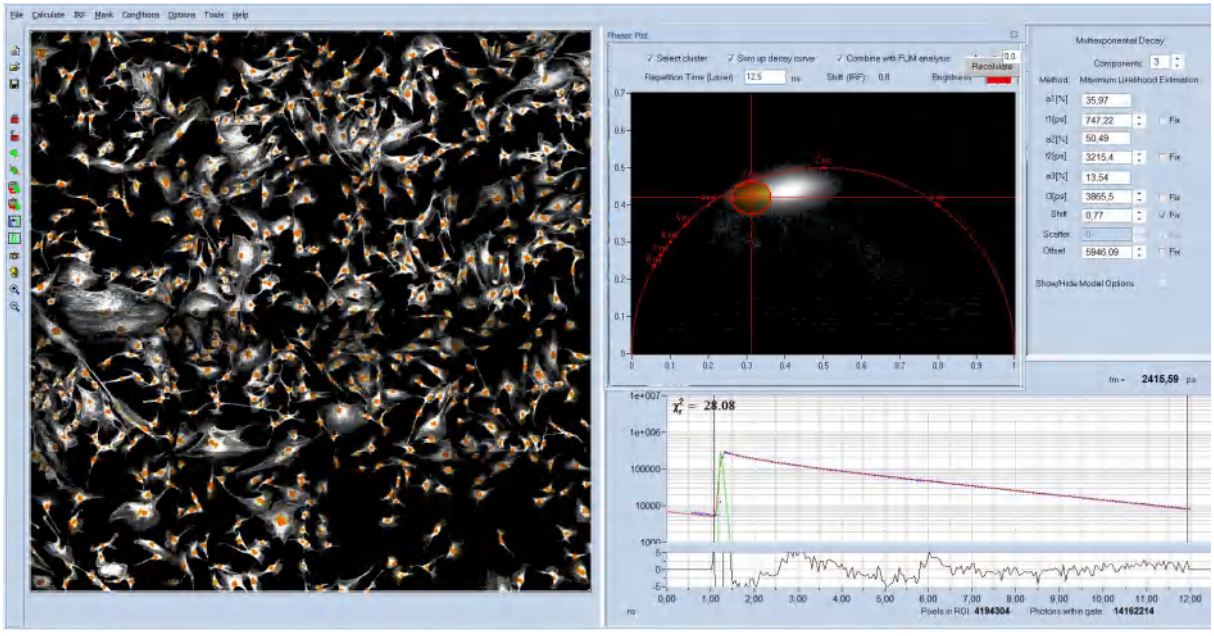


Fig. 1188: The phasor range of the nuclei of the cells has been selected by the 'Select Cluster' Function. The decay-parameter histogram (shown right) refers to the selected pixels. A combined decay curve for the selected pixels is displayed by the 'Sum up decay curves' function.

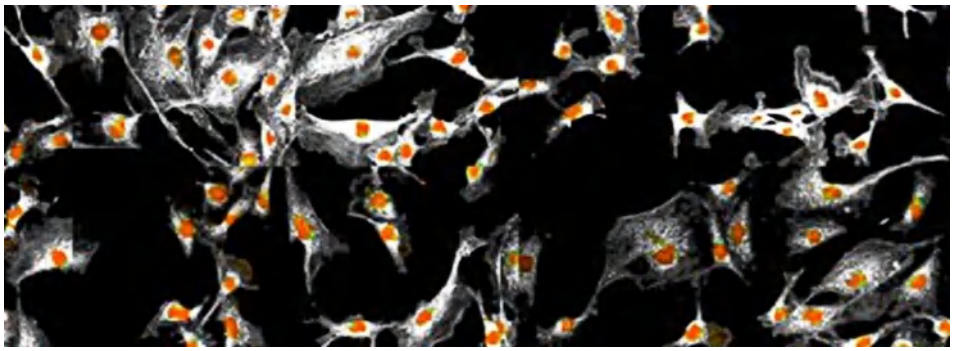


Fig. 1189: Detail from Fig. 1188. The nuclei have been selected by phasor-segmentation.

Analysing FLIM Data with SPCImage

Loading the FLIM Data into SPCImage NG

There are several ways to load FLIM data into SPCImage. You can use the ‘Send Data to SPCImage’ function of the SPCM software, import a .sdt TCSPC data file, or load .img data previously analysed by SPCImage.

Loading of SPCImage Files

Data previously analysed and saved by SPCImage data analysis (.img files) are loaded via the ‘Open’ function. Click into ‘Main’, ‘Open’ as shown in Fig. 1190.

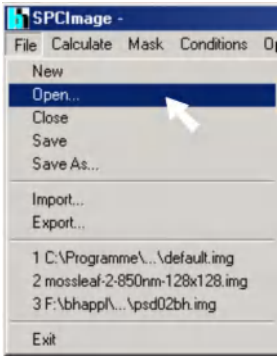


Fig. 1190: Opening .img files generated by SPCImage

After loading the data SPCImage will come up in a configuration as shown in Fig. 1191.

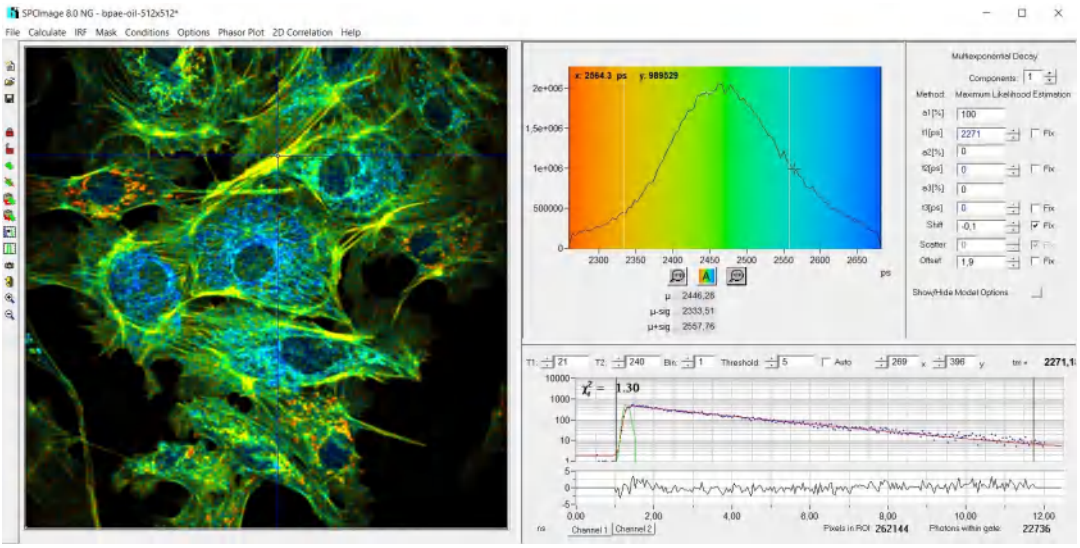


Fig. 1191: SPCIMage NG main panel after loading .img data

Importing Data From SPCM by Send Data Function

Raw data can be send directly from SPCM to SPCImage. The ‘Send Data to SPCImage’ function of the SPCM software is illustrated in Fig. 1192. The function automatically opens SPCImage and transfers the data. In the ‘application options’ of the SPCM software you can select whether you want to transfer the data of all active display windows or only the data of the selected one. To select a display window, first click into the image that you want to analyse,

see Fig. 1192, left. Then transfer the data by clicking into ‘Main’, ‘Send data to SPCImage’, see Fig. 1192, right.

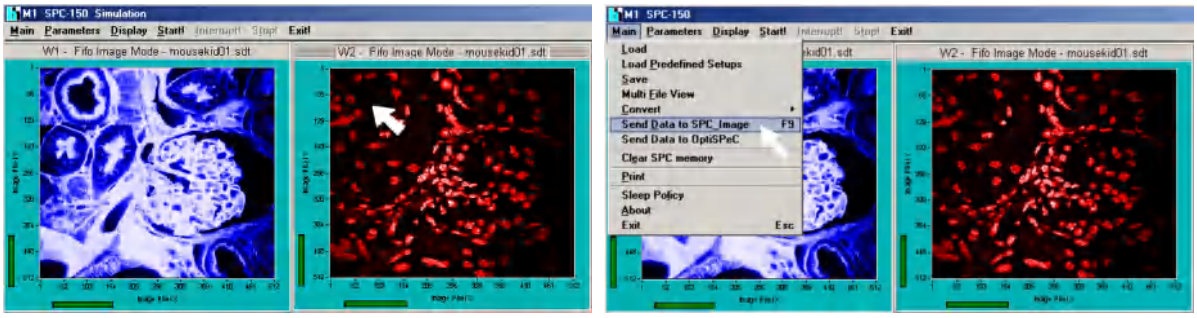


Fig. 1192: Sending data from SPCImage into SPCImage. Left: Selection of the data to be analysed. Right: Sending the selected part of the data to SPCImage

Import of .sdt Files

Files from SPCM (.sdt format) are loaded via the 'Import' function. A click into ‘Main’, ‘Import’, (Fig. 1193, left) opens a file selection panel (Fig. 1193, right). Select the desired file from this panel and click on 'Open'. SPCImage then examines the selected file and opens the Import Options panel for the type of data found in the file.

The 'Import Options' panel for FLIM images is shown in Fig. 1194, left. Top left, it shows the general structure of the data. In the example shown the file contains two FLIM images from different TCSPC / FLIM modules. Upper right, the import panel shows information on the images, such as pixel number and number of time channels. At the bottom of the panel, you can specify subsets of the data for import. For standard applications we recommend to select 'All', and then click on 'OK'. When the import is completed the image and a decay function will show up in the SPCImage main panel. It can happen, however, that the .sdt data contain combinations of modules, routing channels and page numbers which you do not want to import. In that case, you can disable or enable modules, and select ranges of routing channels which you want to import. There is also an option to combine the data of all modules and channels, or to add or subtract data from the data already loaded. These options should be handled with care. They require that all data are recorded with the same time scale, time-channel number, IRF position and IRF shape.

The Import Options for files that contain decay curves are shown in Fig. 1193, right. The file structure window (upper left) indicates that the file contains single decay curves in different 'Traces' of SPCM. The Measurement Info window upper right shows basic information about the data, such as number of time channels and time range. 'Import as' allows you to import the data as normal decay curves or to import a single curve as an Instrument Response Function (IRF). At the bottom of the import panel you can select which curves you want to be import. If in doubt, just select 'All' and proceed by clicking 'OK.

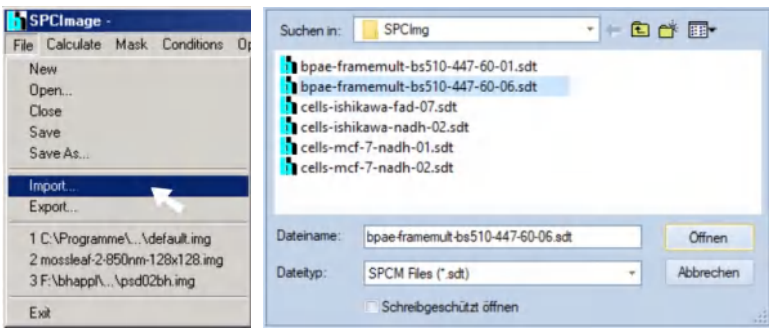


Fig. 1193: Import of FLIM data. Left: Select Import function in 'File' menu. Right: Select the file to be imported.

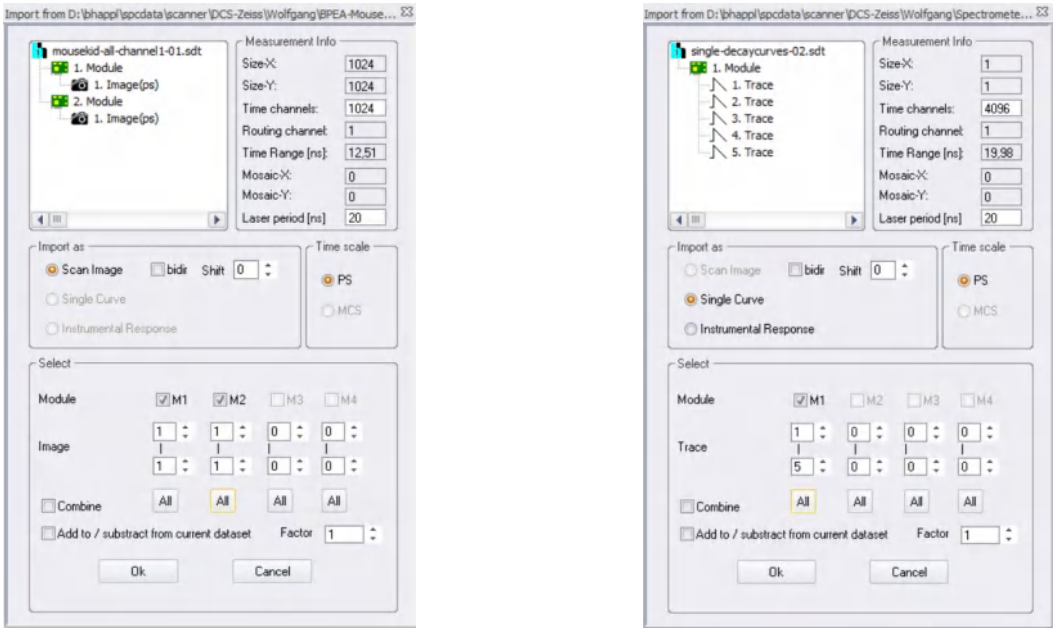


Fig. 1194: Import Options panel for image files (left) and single-curve files (right)

SPCM Panel after Import of Data

After importing .sdt data into SPCImage the main panel comes up as shown in Fig. 1195 or Fig. 1196. Fig. 1195 shows the main panel when image data were imported. An intensity image is shown left, a decay curve at the cursor position bottom right. The image shows only a grey-scale image because these have not been calculated yet. A decay-parameter histogram is shown upper right. It is empty because no decay analysis has been performed yet. In the upper right, the decay model can be specified. After loading new data the model function is single exponential (Components=1), which is the default.

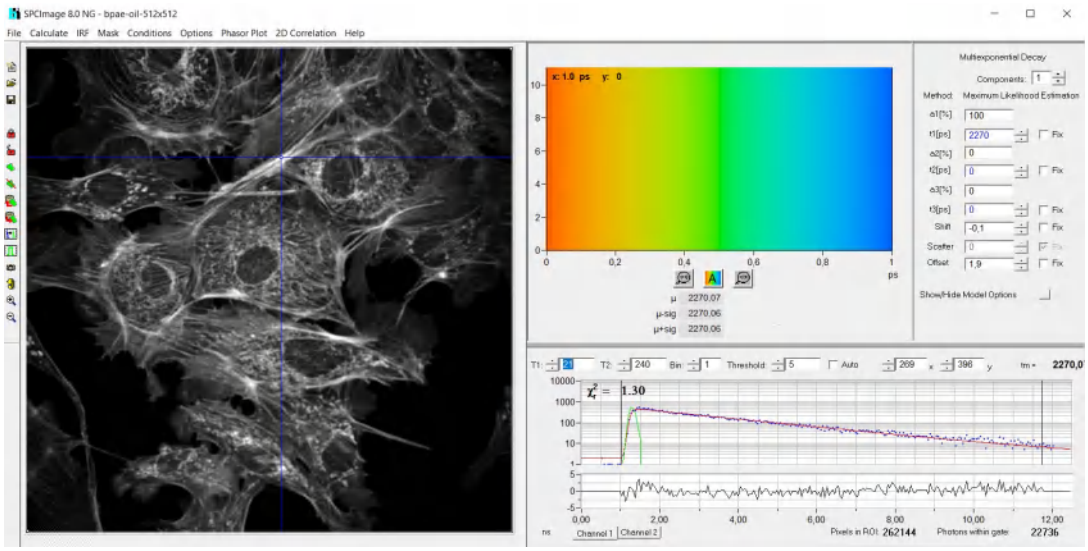


Fig. 1195: SPCImage main panel after importing image sdt data

When single-curve data were imported the main panel comes up as shown in Fig. 1196. The decay-curve window shows a decay curve, the decay parameters are shown upper right. The decay model is single-exponential. If several decay curves were imported these are accessible through the tabs below the decay-curve window. The image window (top left) and the histogram window (top middle) remain empty because the imported file did not contain suitable data for these windows.

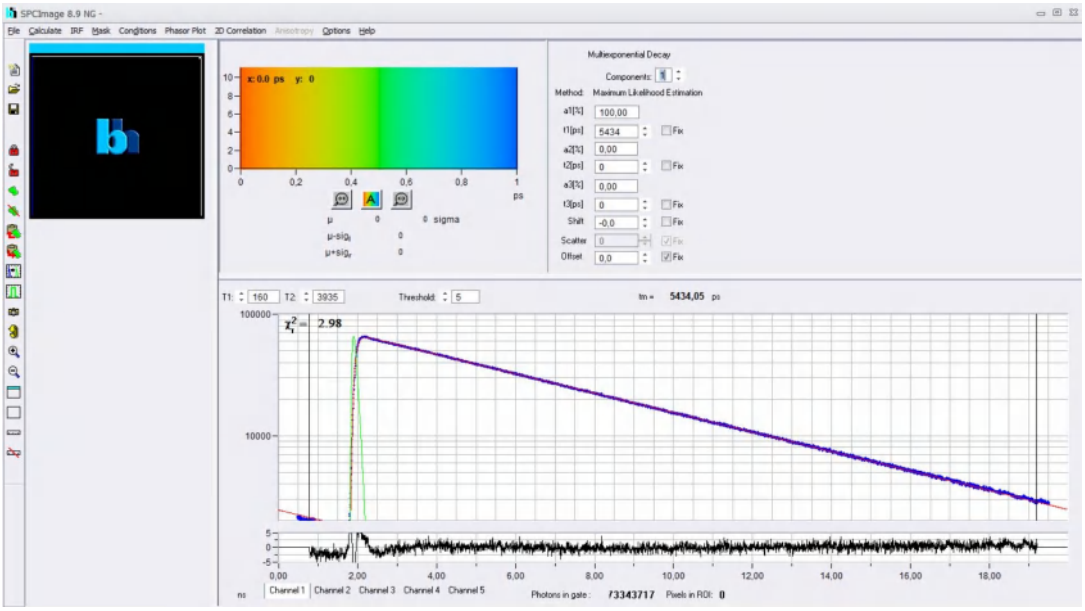


Fig. 1196: SPCImage main panel after importing single-curve sdt data

Initial Check of Decay Data

After importing or loading data you should give the decay data a brief check for integrity. The decay curve should be correctly placed in the decay window (the observation-time interval), as shown in Fig. 1195 and Fig. 1196. The rising edge must be in the decay window, and there should be a few (5 to 10%) of the time channels left of the rising edge. Some unfavourable situations are shown in Fig. 1197 and Fig. 1198. These situations are not necessarily fatal but suggest corrections in the measurement procedure, the measurement setup or the measurement parameters.

In Fig. 1197, left, the decay curve does not contain enough photons. The signal-to-noise ratio of lifetimes obtained from such data is low, and usually not sufficient for the intended application. Increase binning, or record new data with more photons. The decay curve shown in the Fig. 1197, middle, contains large background. SPCImage will extract correct decay parameters from such data, but the signal-to-noise ratio will be sub-optimal [174]. Therefore, find and remove the source of the background. The curve shown in Fig. 1197, right, is not placed well in the observation-time interval. Also here, data analysis will deliver correct data, but with a signal-to-noise ratio below the theoretical limit [174]. Therefore the curve should be shifted in the correct position by changing the TCSPC parameters or the SYNC delay. Please see 'SYNC and CFD Signal Path Length' and 'TAC Parameters'.

The situations shown in Fig. 1198 are more serious or even fatal. In Fig. 1198, left, the decay curve is clipped at the left end, and the rising edge is not in the observation time interval. SPCImage may deliver a reasonable single-exponential lifetime in this case, but multi-exponential decay parameters derived from such data will be entirely wrong. There is no way around taking another measurement with corrected TCSPC system parameters. In Fig. 1198, right, the decay curve does not contain any reasonable decay data at all. The source of the problem is usually that wrong filters had been used, and the FLIM system is detecting scattered laser light.

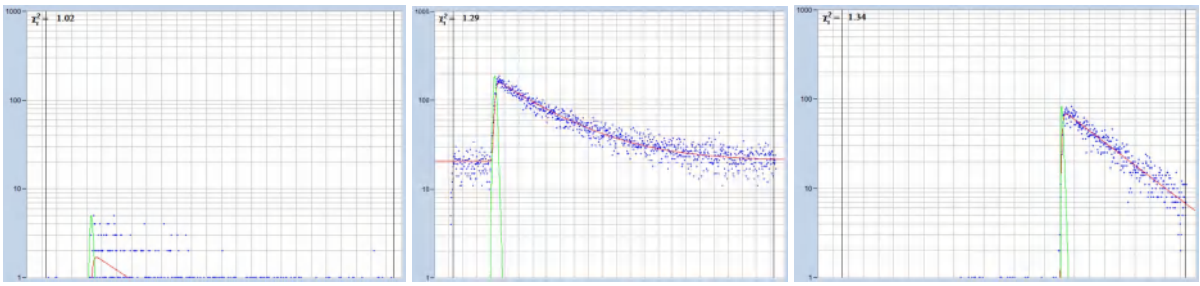


Fig. 1197: Situations where correction is indicated. Left: Not enough photons. Middle: High background. Right: Decay curve shifted in observation-time interval.

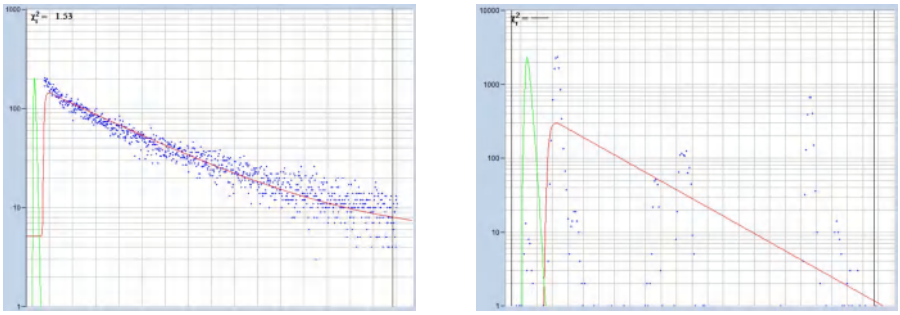


Fig. 1198: Situations which are fatal to FLIM analysis. Left: Decay data clipped at left and, rise of fluorescence not recorded. Right: The recorded signal is scattered laser light.

Calculating the Lifetime Image

Starting the Calculation

In principle, you can start a lifetime analysis immediately from the state shown in Fig. 1195. (There is even an option to do this automatically, see Preferences, page 912.) To start the analysis, click into ‘Calculate’, ‘Decay Matrix’, 'Selected channel' or, if you have loaded data with several channels 'all channels'. This starts the fit process. A progress bar shows the advance of the calculation as the procedure runs through the pixels. If there is a GPU in the computer the calculation will complete within a few seconds, if there is no GPU it can take several minutes. What you get is a colour-coded lifetime image calculated with default parameters of SPCImage. The decay model will be single-exponential, the IRF will be 'Auto', and the lifetime and intensity ranges will be set automatically.

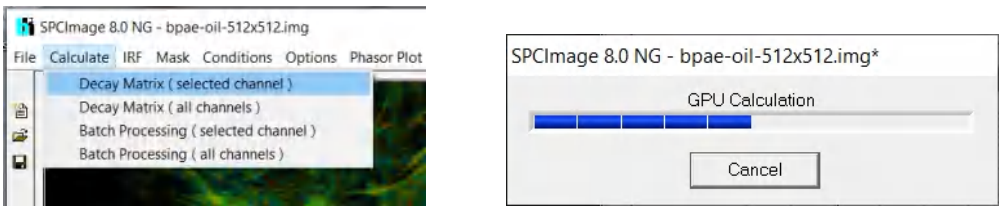


Fig. 1199: Starting the fit procedure for all pixels of the image

Single-Exponential Analysis

The number of decay components used in the analysis is defined in the upper right of the SPCImage panel. FLIM analysis with a single-exponential model (or with default parameters) is shown in Fig. 1200. Number of 'Components' is 1. The procedure delivers a single lifetime, t_1. This lifetime is used for colour-coding the image. The lifetimes in the pixels will be correct and reasonably accurate. However, the fluorescence decay in biological objects is rarely single-exponential. Normally there are several decay components in each pixel, either from different fluorophores, or from one fluorophore in different molecular environment. Often the information is in the composition of the decay rather than in an average ('apparent') lifetime.

Single-exponential analysis is therefore unlikely to deliver the maximum of information you can obtain from your raw data.

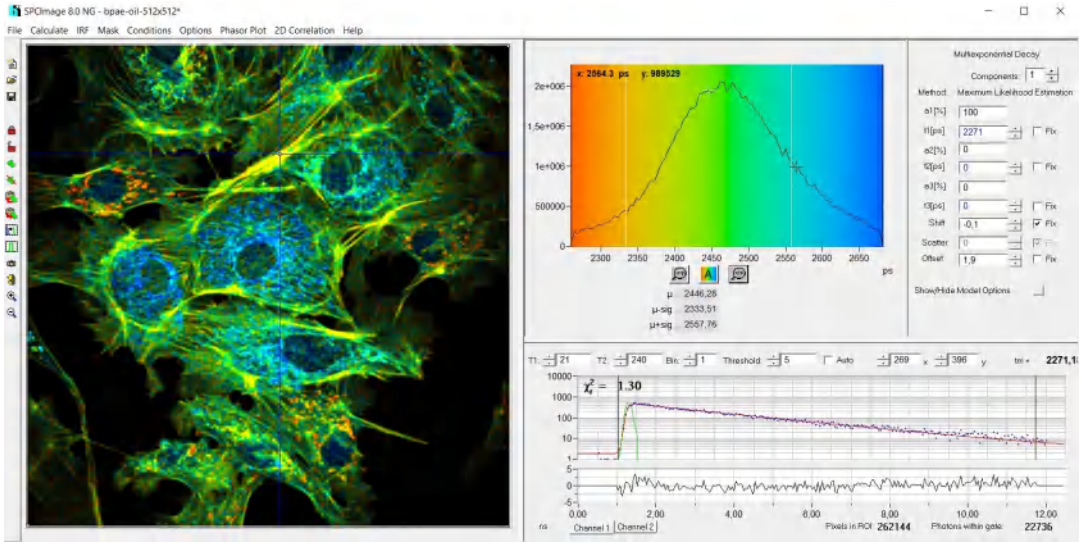


Fig. 1200: SPCImage panel after calculating the lifetime image with the default settings

Multi-Exponential Analysis

Multi-exponential decay analysis is shown in Fig. 1201. In the upper right, analysis with three exponential components has been selected. For every pixel, the analysis procedure delivers three lifetimes, t_1, t_2, t_3, and three amplitudes, a_1, a_2, a_3, for the three decay components. The display routine of SPCImage can display each of these parameters, ratios of the parameters, and intensity- or amplitude-weighted averages of the component lifetimes. The default is the amplitude-weighted mean lifetime, t_m. The display routine has functions to further refine the images, for example by manually adjusting the colour scale and the intensity scale, or by creating time-gated images. Please see page 'Display of Colour-Coded Images'.

Also the model function can be further refined, such as by the 'Incomplete Decay' or the 'Shifted Component' option. It is also possible to fix one or two of the decay components to values which are a priori known. For details please see 'Model Functions', page 877 and 'Model Parameters', page 909.

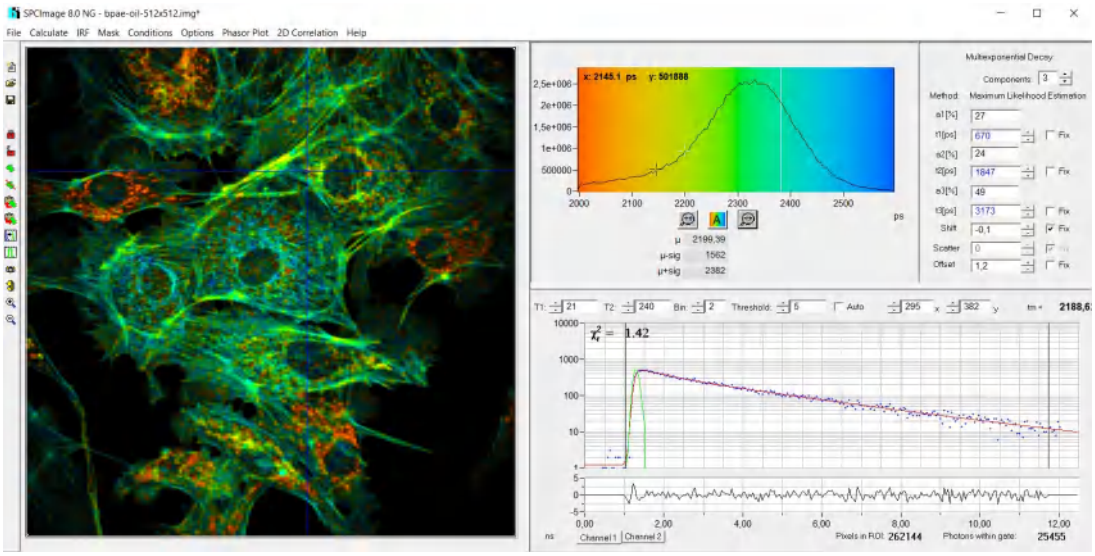


Fig. 1201: Triple-exponential decay analysis. Model selection and decay parameters at cursor position shown in the upper right. Analysis with three exponential components has been selected, the amplitude-weighted lifetime, t_m, is shown.

Parameter Histogram

A histogram of the selected decay parameter over the pixels of the image is shown above the decay-curve window. It shows how frequently a given value of the parameter occurs in the image. The parameter is the same that was selected for colour-coding the image. It can be the amplitude-weighted lifetime (as in Fig. 1201), the intensity-weighted lifetime, a component lifetime, a component amplitude, or a ratio of two of these parameters. The parameter histogram can be displayed for selected regions of interest, please see 'Decay-Parameter Histograms in ROIs', page 902. The parameter histogram has two cursors, which interact with the display function (see 'Interaction with the Colour Parameters', page 896). In combination with the , , and buttons a desired parameter range can be selected, and the colour scale adjusted accordingly. Please see 'Parameter Histogram', page 896.

Model Functions

Basic Decay Models

The fluorescence decay function obtained from a homogeneous population of molecules in the same environment is a single exponential. Decay functions of mixtures of different molecules or of molecules in inhomogeneous environment are sums of exponential functions of different decay time. The basic model functions used in SPCImage are therefore sums of exponential terms:

Single-exponential model: $f(t) = e^{-t/\tau}$

Double-exponential model: $f(t) = a_1 e^{-t/\tau_1} + a_2 e^{-t/\tau_2}$

Triple-exponential model: $f(t) = a_1 e^{-t/\tau_1} + a_2 e^{-t/\tau_2} + a_3 e^{-t/\tau_3}$

The models are characterised by the lifetimes of the exponential components, τ, and the amplitudes of the exponential components, a. In principle, models with any number of exponential components could be defined. However, higher-order models become so similar in curve shape that the amplitudes and lifetimes cannot be obtained at any reasonable certainty. Therefore, SPCImage NG FLIM analysis does not provide model functions with more than three components.

Single, double, and triple-exponential models are selected via the decay-parameter panel on the right of the decay-curve window, see Fig. 1202.

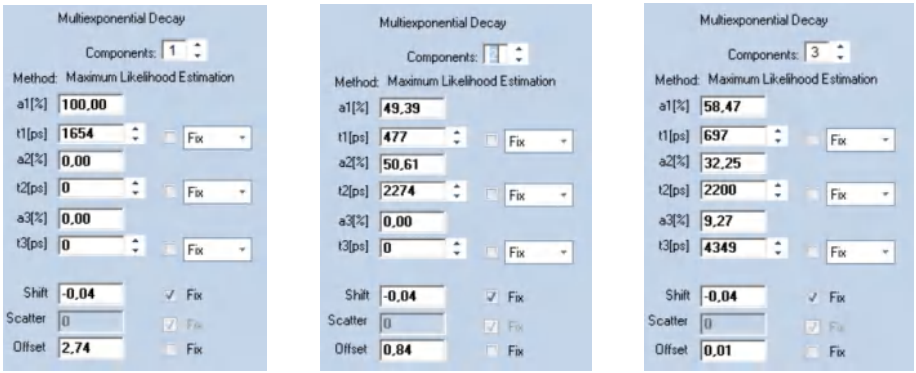


Fig. 1202: Selection of basic single, double, and triple exponential models

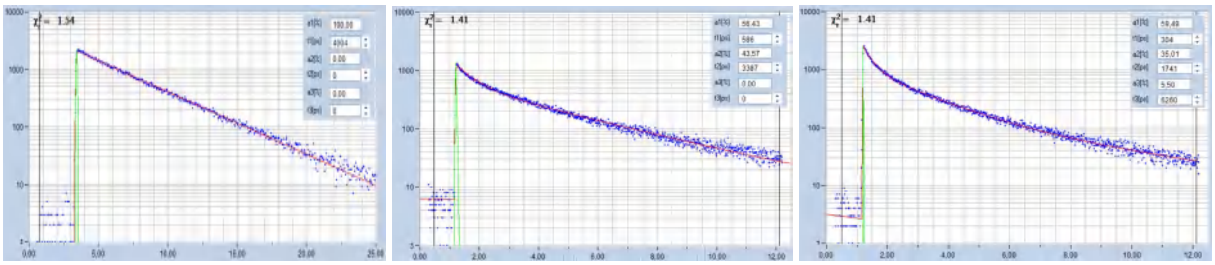


Fig. 1203: Left to right: Fit with Single-, double-, and triple-exponential models. The blue dots are the data in the time channels, the red curve is the model function. The decay parameters are shown upper right.

A shift parameter can be included in the fit procedure. It shifts the IRF in a temporal position that yields the best fit of the decay functions. However, a floating shift decreases the lifetime accuracy and increases the calculation time. We recommend to determine the 'Shift' parameter before starting the analysis and then fix it, or let the analysis procedure fix it automatically when it starts the calculation. Please see Model Parameters, Fig. 1260.

Typical examples of fits with different models are shown in Fig. 1204. The single exponential model (left) does not fit the data. This can be seen from the differences of the model function and the data and from the systematic variation in the residuals. The double-exponential model (middle) fits well, the triple-exponential reveals a weak third component of long lifetime. However, the residuals (the curve below the decay function see 'Fit Quality Indicators', page 886) do not improve substantially for the triple-exponential model. The decay parameters derived by the triple-exponential fit may therefore not exactly represent the real composition of the decay curve.

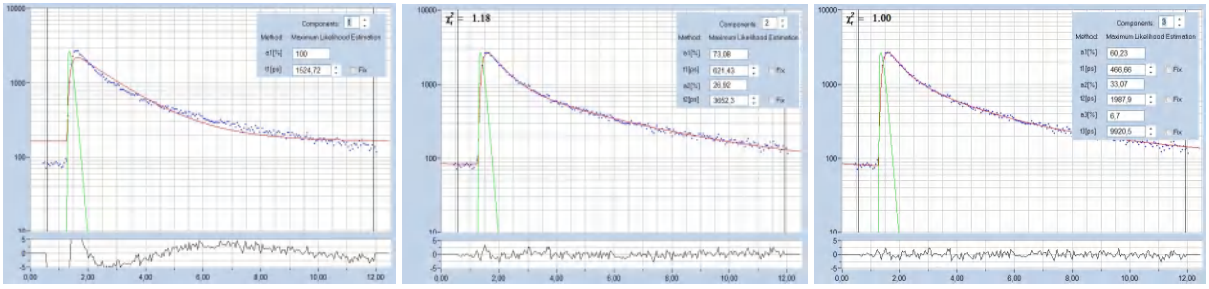


Fig. 1204: Fit of decay data with a single, double, and triple-exponential model.

Incomplete-Decay Model

The basic decay models can be combined with model options provided by the 'Model' parameters, see page 909. The 'Incomplete Multiexponentials' option is used to account for residual fluorescence from previous laser pulses. The corresponding section of the Model Parameters is shown in Fig. 1205. The incomplete decay model needs the period of the excitation pulses, which must be specified in the upper right.

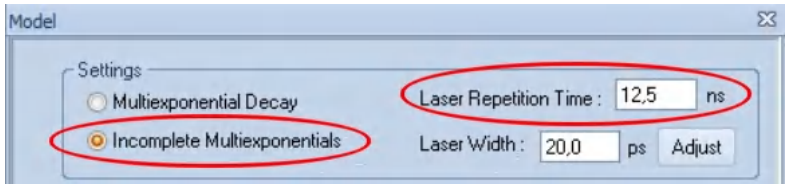


Fig. 1205: Incomplete-decay option in the model parameters.

Fig. 1206 gives a comparison of the ordinary multi-exponential model (left) and the incomplete-decay model (right). The ordinary model interprets the intensity left of the rising edge of the decay curve as offset, the incomplete-decay model fits it correctly with fluorescence from the previous pulses.

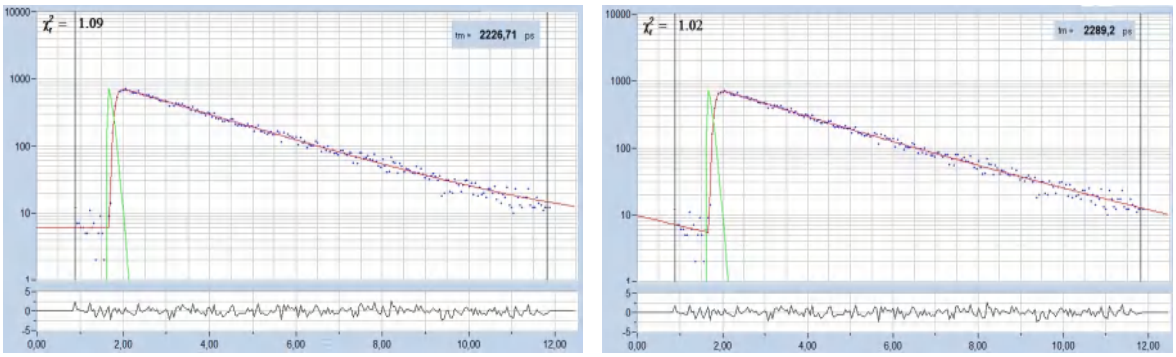


Fig. 1206: Fit of the fluorescence decay of a Calcium sensor, lifetime 2.29 ns, excitation with Ti:Sa laser at 80 MHz. Left: ordinary double-exponential model. Right: Incomplete decay model.

The result is a different lifetime, t_m. The difference is not large as long as the lifetime is short compared to the laser pulse period. The difference can, however, be substantial if the decay time is longer. Fig. 1207 shows an example for a 5.95-ns decay measured with the 12.5 ns repetition time of a Ti:Sa laser. A fit with the conventional model is shown left. The fit delivers a lifetime of 4.05 ns. The large residuals indicate that the model is not able to fit the data correctly. The fit with the incomplete-decay model is shown on the right. The model delivers a perfect fit, and a lifetime of 5.95 ns. The example shows that the use of the incomplete-decay option is mandatory for lifetimes larger than 25% of the laser repetition time.

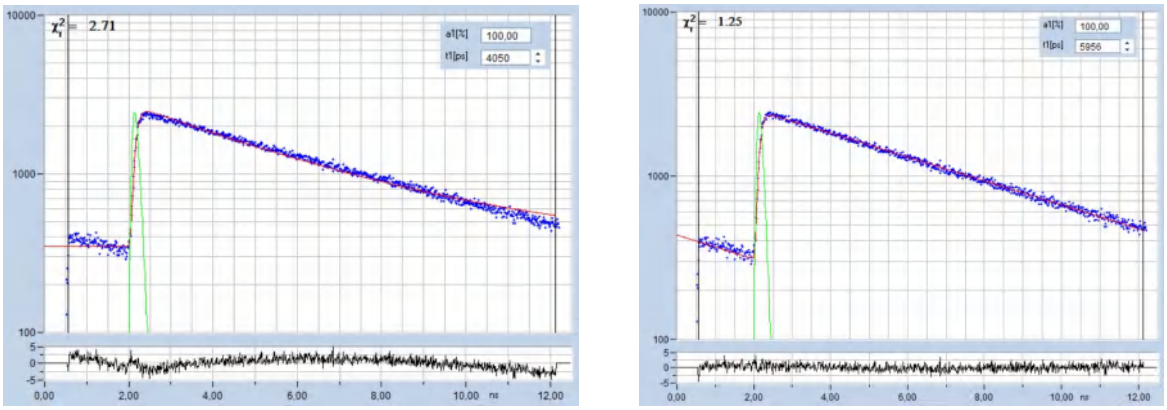


Fig. 1207: A 5.95-ns decay recorded in a two-photon microscope. Laser repetition rate 80 MHz. Left: Fit with conventional model. It does not fit the data correctly. Right: Fit with incomplete-decay model. The incomplete-decay model not only fits the data perfectly but also delivers the correct decay time.

Shifted-Component Model

In clinical FLIM it happens that one or several decay components are shifted in time. A typical example is ophthalmic FLIM (FLIO) where fluorescence from the lens of the eye interferes with fluorescence of the fundus. The lens fluorescence appears about 150 ps before the fundus fluorescence. The shifted-component model takes this shift into account [118, 119].

A demonstration is given in Fig. 1208 and Fig. 1209. A FLIO decay curve together with the model definition is shown in Fig. 1208. A triple-exponential model is used; the lens component is modelled by the third decay component and shifted 150 ps towards earlier times. As a result, the model fits the lens component correctly, including the kink in the rising edge caused by the early arrival of the lens fluorescence.

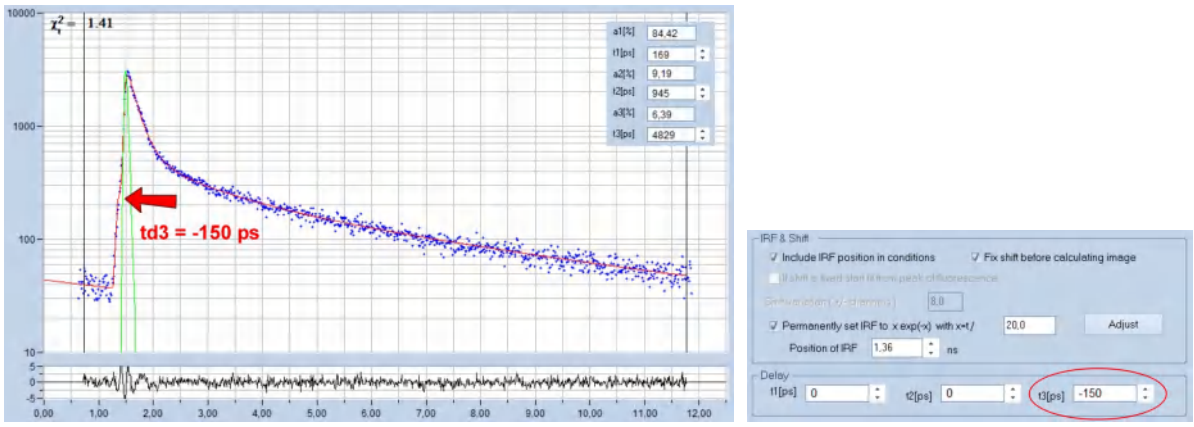


Fig. 1208: Decay curve from FLIO data. Fit with shifted-component model, third decay component shifted by 150 ps to earlier time.

FLIO lifetime images obtained by the ordinary multi-exponential model and by the shifted-component model are compared in Fig. 1209. For the ordinary model, the lens fluorescence causes a substantial shift of the mean lifetime, t_m, to longer values. The shifted-component model is able to deliver an image which contains only the fundus fluorescence, modelled by the components t_1 and t_2. The corresponding image of the lifetime t_{m12} is shown in Fig. 1209, right. It shows the correct lifetime of the fundus of the eye [118, 119]. Please see chapter Ophthalmic FLIM (FLIO).

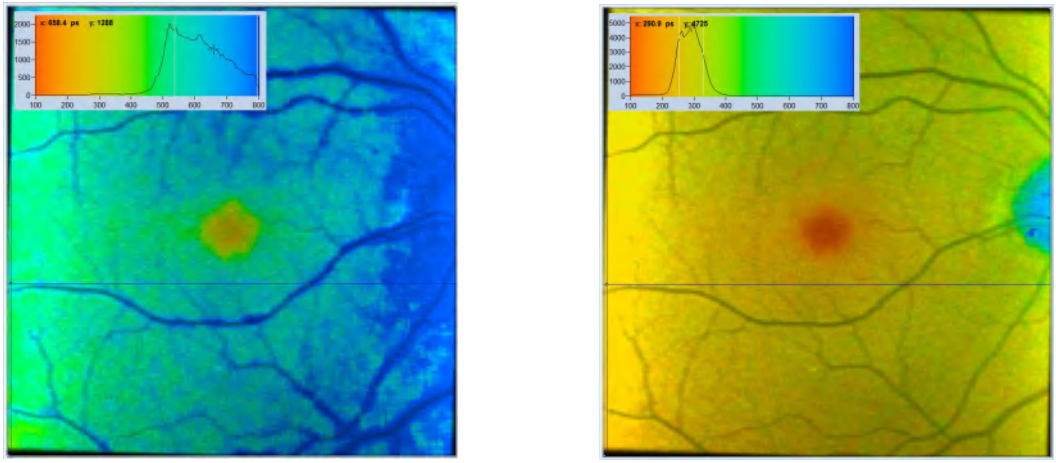


Fig. 1209: Comparison of FLIO analysis with the ordinary 3-component model (left) and with the shifted-component model (right). Due to the contribution of the lens fluorescence, the ordinary image is biased towards long lifetime. The delayed-component model delivers an image that does not contain the lens fluorescence, showing the correct lifetime of the fundus of the eye.

Analysis with fixed or global parameters

The lifetimes of the individual decay components can be fixed to known values or defined as 'Global'. The 'Global' option fits the decay data under the assumption that the component lifetimes are unknown, but otherwise the same in all pixels of the image [135]. Analysis with fixed or global component lifetimes can increase the statistical accuracy of the fit results considerably. It requires, however, that the lifetimes are accurately known or constant over the entire image. For details, please see 'Global Analysis', page 918 The definition of the parameter status is shown in Fig. 1210.

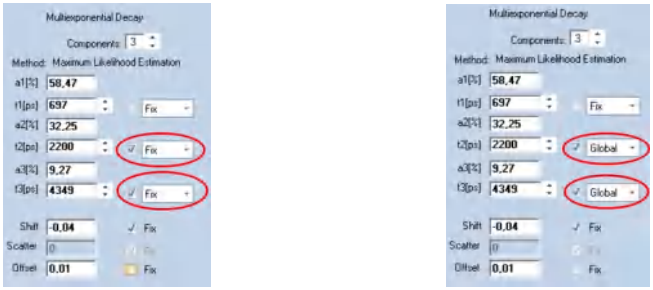


Fig. 1210: Definition of lifetime components as 'Fixed' (left) and 'Global' (right)

IRF Options

The fluorescence waveform the FLIM system records is the convolution of the true fluorescence decay profile with the instrument response function, or 'IRF'. The IRF is the function the FLIM system would record when it detected the laser pulse directly. Decay parameters are derived from the recorded waveforms by convoluting a model function with the IRF, and fitting the result to the data, see 'The Convolution Integral', page 932. Thus, at least an approximate IRF is needed to derive fluorescence decay parameters from the detected fluorescence waveforms. It is often believed that the IRF has to be measured before data can be analysed. However, in a FLIM system this can be difficult or even impossible. SPCImage therefore offers several options to *generate* an IRF from the FLIM data themselves.

Selection of IRF Type

The different IRF types are defined by clicking into 'IRF' in the top bar, and selecting the desired option, see Fig. 1211. The effect of the different options is shown in Fig. 1212.

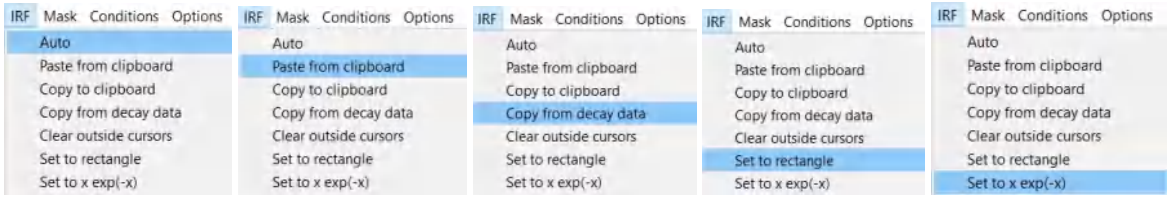


Fig. 1211: Options to generate the IRF

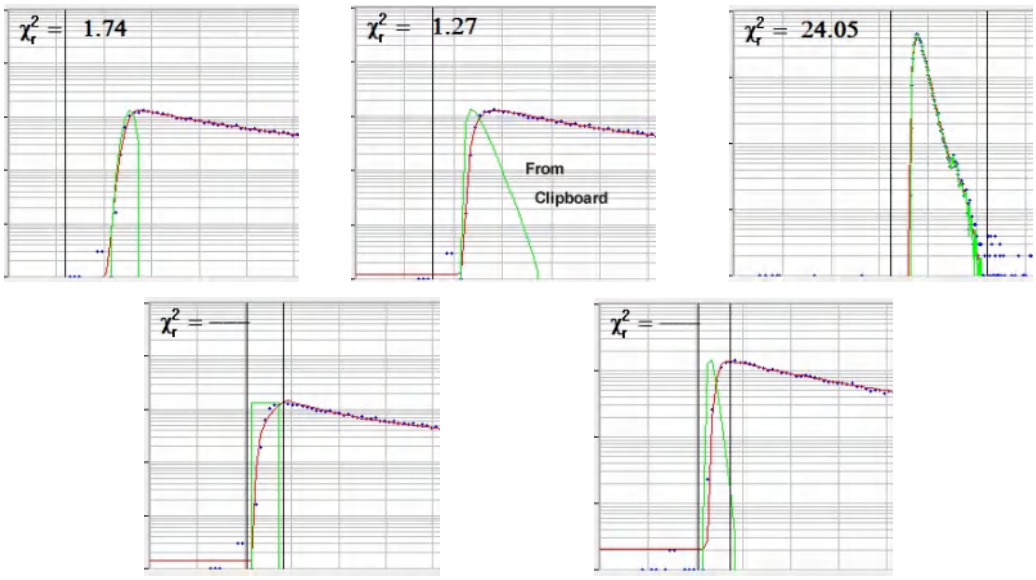


Fig. 1212: Effect of the IRF options. Upper row, left to right: Auto IRF, IRF from Clipboard, IRF copied from recorded data. Lower row left: Rectangular IRF, Right: IRF of type irf(t) = $t/t_0\ e^{-t/t0}$.

'Auto' calculates an IRF from the rising edge of the decay data. The calculation is performed on data from an area around the brightest spot in the image. When 'Auto' has been set the IRF calculation is done automatically after loading data.

'Paste from clipboard' recalls an IRF which has been copied by 'Copy to Clipboard' before.

'Copy from decay data' uses decay data from a selected spot in an image as an IRF. The selected spot can either be a spot in the current image where the decay function is dominated by SHG, or an image that contains only SHG or fast scattering data. The IRF is generated from the data inside the decay cursor interval. Data points outside this interval are set to zero. To transfer the data into a different measurement data set, use 'Copy to clipboard' and, after loading the measurement data file, 'Paste from clipboard'. You can save the IRF by 'Save IRF' in the model parameter panel.

'Set to rectangle' sets a rectangular IRF. Width and location are determined by the cursors in the decay window. The function is often used for PLIM, where the IRF is close to a rectangle.

'Set to x exp (-x)' sets an IRF to a function of the type $irf(t) = t/t_0\ e^{-t/t0}$. The width and the location are selected by the cursors in the decay window, see Fig. 1212, right. You can declare this IRF a permanent one in the 'Model' parameters, and further refine it by an automatic optimisation procedure, see page 942.

Modelling of the Synthetic IRF

Defining a synthetic IRF only by the cursors of the decay window is not quantitative, and leaves room for subjective judgement. SPCImage NG therefore has a function to model the synthetic IRF by fitting it to the recorded decay data. The procedure is described in detail in section 'Instrument Response Function' page 942. Briefly, the width parameter, t_0, of the generic IRF function, $irf(t) = t/t_0\ e^{-t/t0}$ is optimised until the best fit of the convolution integral of the IRF with the selected model to the recorded fluorescence data is obtained. The adjust procedure for the width parameters is accessed under 'Model', section 'IRF & Shift'. A click on the upper 'Adjust' button, Fig. 1213, left, starts the procedure.

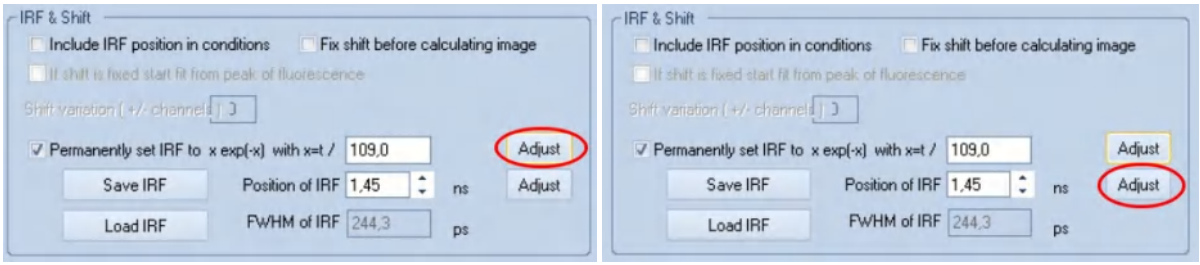


Fig. 1213: IRF Adjust for width (left) and position of IRF (right)

The result of the operation is an IRF with a correct shape, but not necessarily in the correct temporal position. To get the IRF in the correct position, click on the Adjust button for 'Position of IRF', see Fig. 1213, right. The effect of the two adjust operations is demonstrated in Fig. 1214.

Both adjust operations should be performed with a reasonably selected decay model. The reason is obvious: If the model is not able to fit the decay data correctly the IRF adjust procedure compensates for the deficiencies of the model with a change in the IRF. The result may be a reasonably good fit of the decay data but with wrong decay parameters.

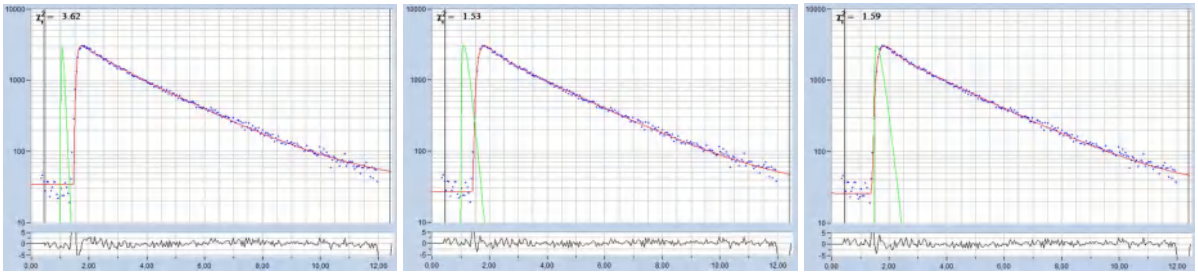


Fig. 1214: Left to right: IRF (green curve) before adjust, after width adjust, and after position adjust.

Permanent IRF

A synthetic IRF, once created, can (and should) be declared 'permanent', see Fig. 1215. The IRF parameters are then taken over in the default parameters of SPCImage, and can be used for other data recorded with the same FLIM system.

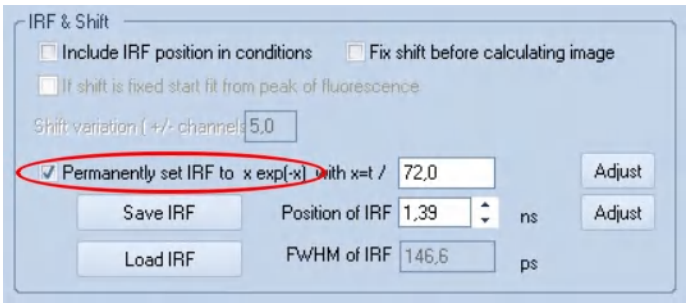


Fig. 1215: Declaring a synthetic IRF 'Permanent'

Saving and Loading IRFs

A synthetic IRF can be saved for future use in a file, and loaded from this file when needed. The function is initiated via the 'Save IRF' and 'Load IRF' buttons (see Fig. 1215). This opens a file selection panel in which the name of a new IRF can be defined or from which an existing IRF can be selected. Please see Fig. 1216.

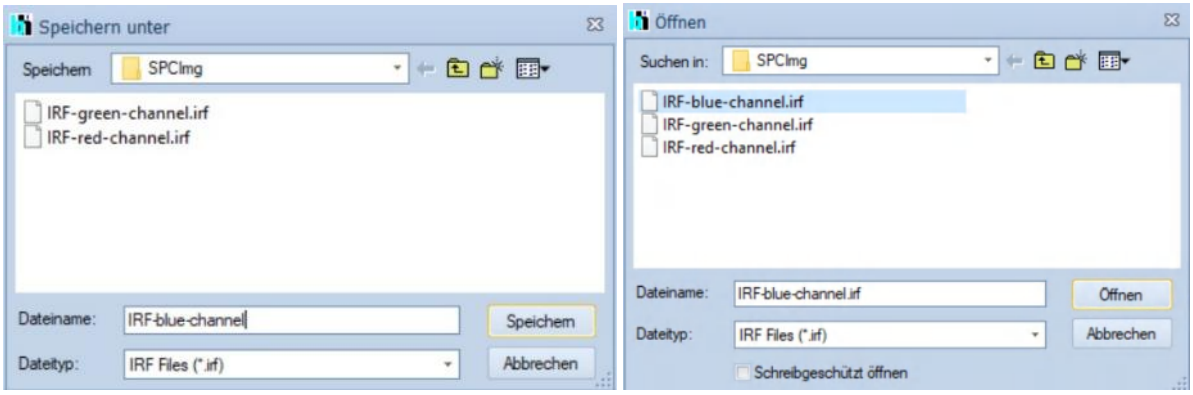


Fig. 1216: File selection panel for saving (left) and loading IRFs (right)

Fit Algorithm

SPCImage NG has three different fit algorithms. 'Weighted Least Squares' (WLS) is the conventional algorithm, based on a minimisation of the sum of the squared differences between the data points and the points of the model function. 'Weighted' means that the differences are weighted with the reciprocal photon number, 1/(n+1). WLS works well for high photon numbers but has deficiencies when the photon number is low.

'Moment' (MOM) is a calculation based on the first moment of the decay curve. MOM is a simple calculation, not a fit algorithm. It is fast and delivers the maximum possible lifetime accuracy. However, it delivers only a single-exponential approximation of the lifetime, and the lifetimes become systematically biased when the tail of the decay function is not entirely in the observation time interval or the data contain background counts [174].

'Maximum-Likelihood Estimation' (MLE) is based on calculating the probability that the values of the model function correctly represent the data points of the decay function. Compared to the least-square method, the fit accuracy is improved especially for low photon numbers, and there is no bias toward shorter lifetime as it is unavoidable for the WLS fit. MLE uses GPU processing, which makes the calculation by a factor of 10 to 100 faster than by WLS. For a detailed description of the algorithms please see 'Fit Procedures', page 936 in section 'Supporting Information'.

The algorithm is selected in 'Algorithmic Setting', in the 'Model' parameters, see Fig. 1217, The default algorithm is MLE.



Fig. 1217: Selection of the fit algorithm in the Model Parameters

Fit Control Parameters

Fit Interval

The fit of the decay data is performed in the interval between the cursors in the decay window. Normally, the fit should be performed over the entire interval where the decay function has valid data, i.e. the cursors should be placed on the first and the last data point, see Fig. 1218, left. After importing data SPCImage runs a check on the data and suggests reasonable cursor positions.

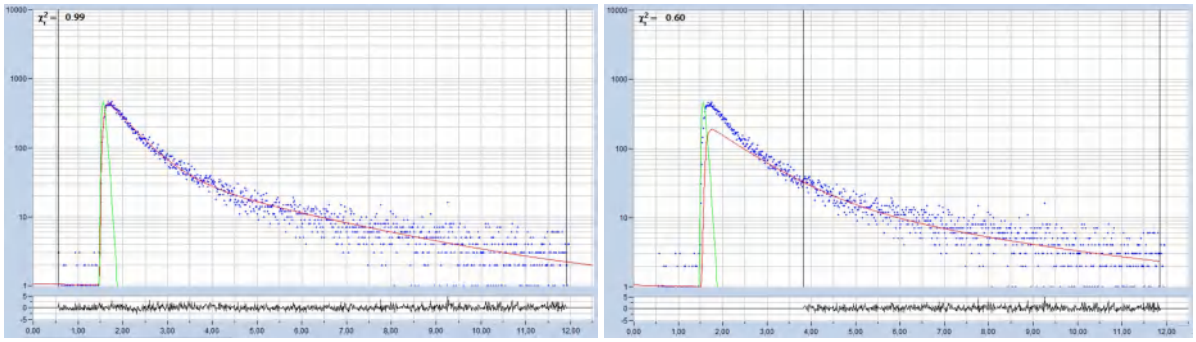


Fig. 1218: Effect of cursors in the decay window. Left: Fit within entire range of valid temporal data. Right: Fit of late part of decay data only. The fast decay component is not correctly reproduced.

The fit can be restricted to a part of the data if necessary, as shown in Fig. 1218, right. However, this should be done as an emergency solution only, e.g. if the decay data contain artefacts. In fact, restricting the fit to the later part of the fluorescence is common practice to solve the problem of a wrong IRF. A wrong IRF leads to large residuals in the rising edge of the decay curve. It is therefore sometimes attempted to exclude this part from the fit. However, excluding the first part of the curve does not make the result any better. On the contrary, the analysis routine is likely to miss fast decay components which may be contained in the

data. An example is shown in see Fig. 1218, right. The fit perfectly reproduces the later part of the decay curve but entirely misses the fast decay component. Another problem of the 'Tail Fit' is that the 'Shift' parameter cannot be reliably determined. The reason is that the shape of later part of the curve is virtually independent of the temporal location of the IRF. Therefore, a tail fit, if ever necessary, must be performed with fixed shift.

Binning

Correct spatial binning is key to good lifetime images [174]. Virtually all microscopy images are over-sampled to obtain maximum spatial resolution. Oversampling means that the point spread function is sampled by several pixels in x and y. Typical (linear) oversampling factors are around 5, that means the point-spread function is sampled by about 25 pixels. Of course, these pixels contain virtually identical lifetime information. Analysing them individually would result in low photon number per pixel, and in unnecessarily high noise in the decay parameters.

The solution to the problem is binning. In SPCImage binning is performed by combining the decay data from a specified binning area and assigning the net decay curve to the central pixel. The process is executed for all pixels of the original image. That means the binning areas overlap, and there is no reduction in the number of effective pixels. For details please see 'Spatial Binning' in section 'Supporting Information'.

Binning is controlled by the 'Bin' parameter on top of the decay-curve window. The parameter should be matched approximately to the radius of the point-spread function, expressed in pixels. An example is shown in Fig. 1219. Two images were recorded with the same count rate and acquisition time. The left image was recorded with 128 x 128 pixels and analysed with bin=0. The right image was recorded with 512 x 512 pixels, and analysed with bin = 3. Due to the binning, the right image has the same number of photons per pixel and the same lifetime accuracy. However, the definition in the image on the right is much better.

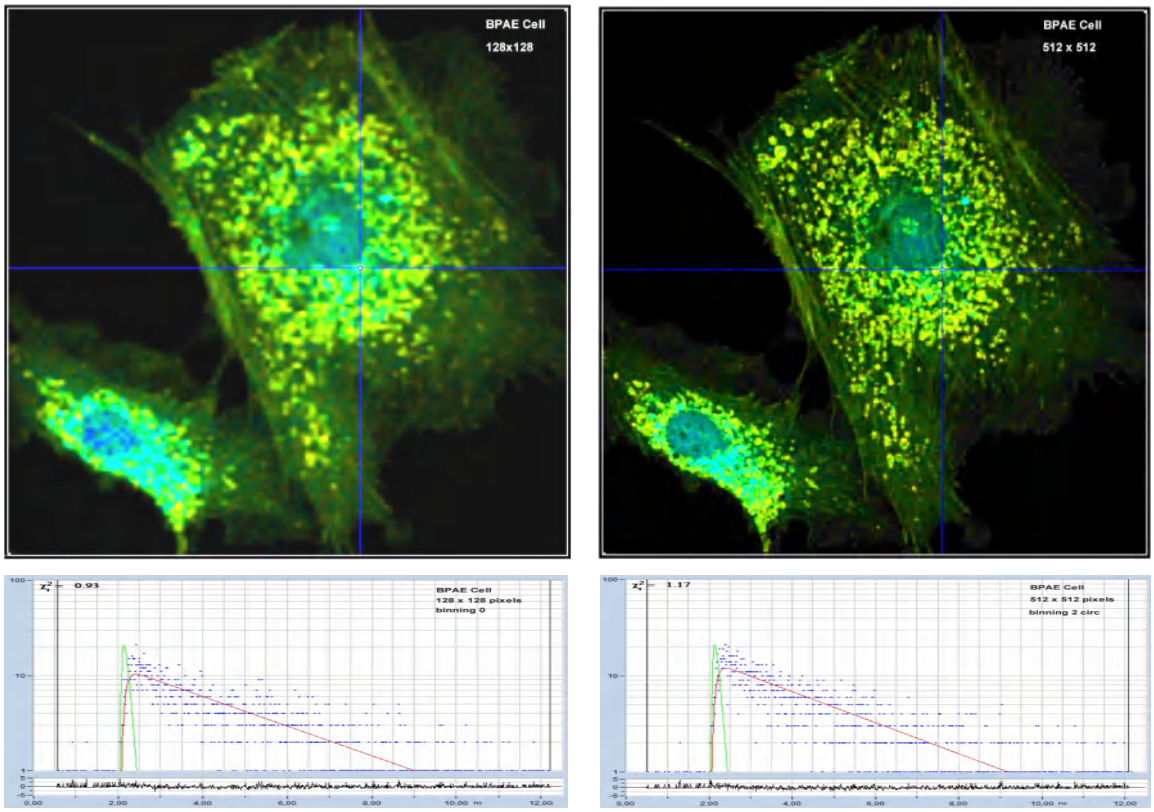


Fig. 1219: Effect of spatial binning. Left: 128 x 128 pixels, bin=0, Right: 512 x 512 pixels, bin=3

The conclusion is that FLIM images should be recorded at sufficiently high pixel numbers to provide spatial resolution, and the resulting decrease in photon numbers per pixel be compensated by binning.

Threshold

The 'Threshold' parameter is used to suppress the analysis of dark pixels. It is located on top of the decay-curve windows, see Fig. 1220. Pixels with photon numbers lower than 'Threshold' are not analysed by the fitting procedure, and do not get a colour assigned in the image. This not only accelerates the calculation process, it also avoids that the parameter histogram is distorted by invalid values from dark pixels. (see ‘Parameter Histogram’, page 902). Suppression of dark pixels is also essential for global analysis. The 'Threshold' value either refers to the maximum of the decay curve or to the total number of photons in it. A selection can be made in the 'Algorithmic Settings' part of the 'Model' panel, see Fig. 1260, page 909.

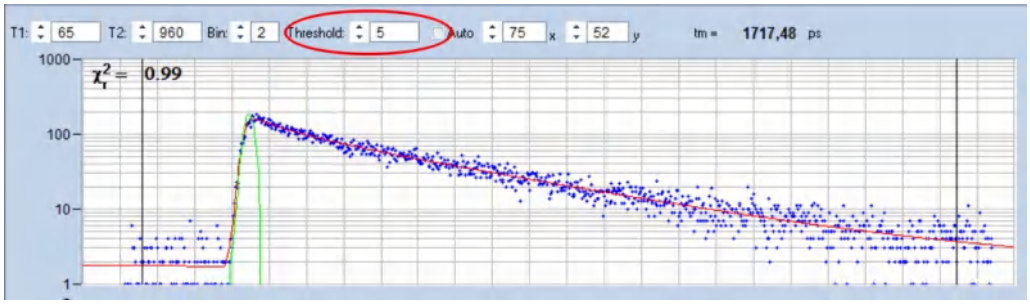


Fig. 1220: Threshold parameter

Fit Quality Indicators

Residuals

The residuals are the differences between the values of the model function (convoluted with the IRF), $f_{mod}(t)$, and the data points of the recorded decay curve, $n(t)$ divided by the square root of $f_{mod}(t)$:

$$R(t) = \frac{f_{\mathrm{mod}}(t) - n(t)}{\sqrt{f_{\mathrm{mod}}(t)}}$$

The background of this expression is as follows. Provided the model function reproduces the shape of decay function properly the differences between $f_{mod}(t)$ and $n(t)$ can be considered the 'noise' in the data. The noise comes from the photon statistics. The average noise amplitude is statistically defined and is $\sqrt{n}$. If the model function is correct the denominator of $R(t)$ is equal to the expectation value of the photon number, n(t). That means the residuals should not depend on the photon number in the respective time channel of the decay function, and vary randomly with a 'Sigma' of one. That means most of the $R(t)$ values are expected within the range from -1 to +1, and virtually all values should be within -5 to +5 (5 Sigma). Any deviation of the convoluted model function $f_{mod}(t)$ from the photon data, $n(t)$ causes systematic wobble in the residuals.

Fig. 1221 shows an example of residuals for a near-ideal fit, a fit with a wrong IRF, and a fit with an inappropriate model function.

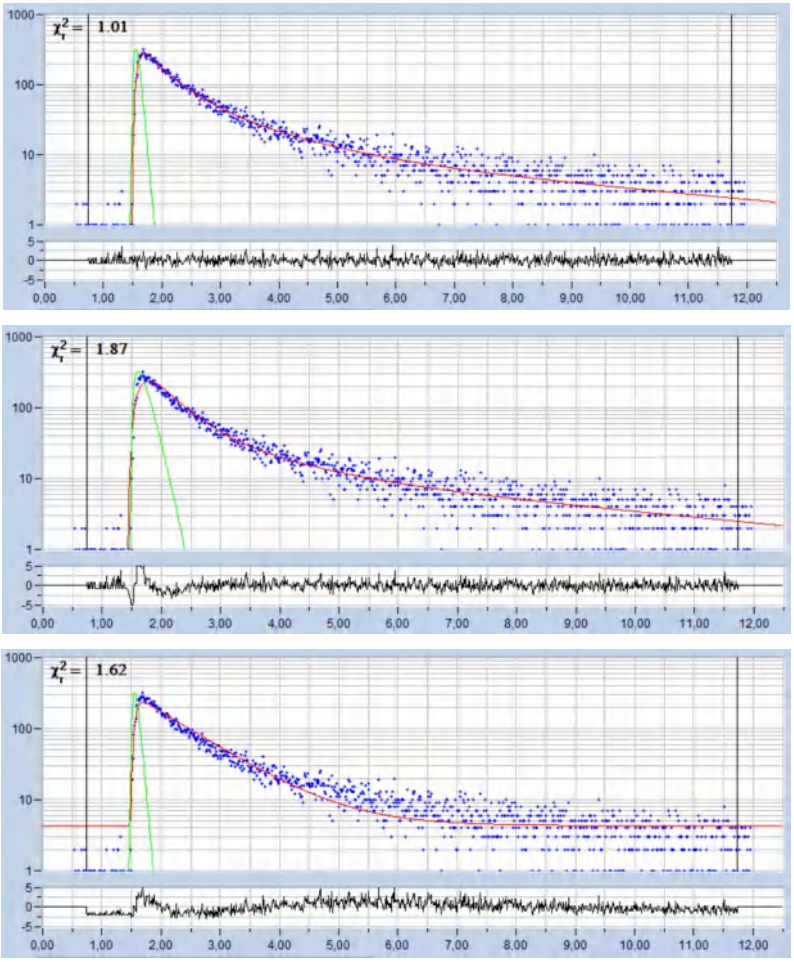


Fig. 1221: Top to bottom: Residuals for a near-ideal fit, for a fit with a wrong IRF, and a fit with a wrong decay model.

There is a feature of the residuals which sometimes causes confusion. When the photon number gets very large the random variation remains in the range of -5 to +5. However, the systematic wobble increases. The reason is that the amplitude of systematic variations increases linearly with the photon number, n, whereas the random variations increase only with $\sqrt{n}$. The result is that residuals for decay data with a high number of photons can look ugly even though the quality of the data is good. Please remember this when you combine pixel data via the phasor plot or via the 'lock' function of SPCImage.

Reduced Chi-Square (χ^2)

The χ^2 parameter is another indicator of the fit quality. It is calculated by

$$\chi^2 = \sum \frac{\left(f_{\mathrm{mod}}(t) - n(t)\right)^2}{k\left(n(t)+1\right)}$$

$f_{mod}(t)$ is the (convoluted) model function, $n(t)$ is the photon number in the time channel t, and k is the number of time channels. The background of the formula is similar as for the residuals. The numerator is the square of the difference between the model function and the photon number in the corresponding time channel. For large n, the denominator, $n(t)+1$, is the square of the expected noise in the photon number. Consequently, an ideal fit should deliver a χ^2 of approximately one.

Unfortunately, the χ^2 has a two unpleasant features. The first one comes from the term *n+1* in the denominator. In fact, the correct term to describe the expected noise would be the photon number, n. However, *n+1* must be used to avoid a singularity for n=0. The result is that χ^2 drops below one when the decay data contain time channels with low photon number or channels with n=0. The other confusing feature is that χ^2 increases for large photon numbers. The reason is the same as for the residuals: The amplitude of systematic variations increases linearly with the photon number, n, whereas the random variations increase only with $\sqrt{n}$. The effect in SPCImage is that χ^2 increases with increased binning. This has led to the misconception that binning has a detrimental effect on the accuracy. This is, of course, not the case. χ^2 is simply not independent of n. It can be used to compare the fit quality for different models and different fit parameters for a given decay data set, but not to compare the quality of decay data which have different photon numbers.

Display of Decay Data

Decay Curve Window

The decay curve window of SPCImage displays the decay data (the photons in the subsequent TCSPC time channels) for a single pixel, the binning area around it, a region of interest, or an area defined by image segmentation. The decay-curve window with decay data is shown in Fig. 1222. The blue dots are the photon numbers in the subsequent time channels, the green curve is the IRF (Instrument-Response Function, see page 942). The red curve is a fit with the model function, the numbers on the right show the fit results for the data in the decay window. The curve at the bottom are the residuals - the deviations of the fit from the real data.

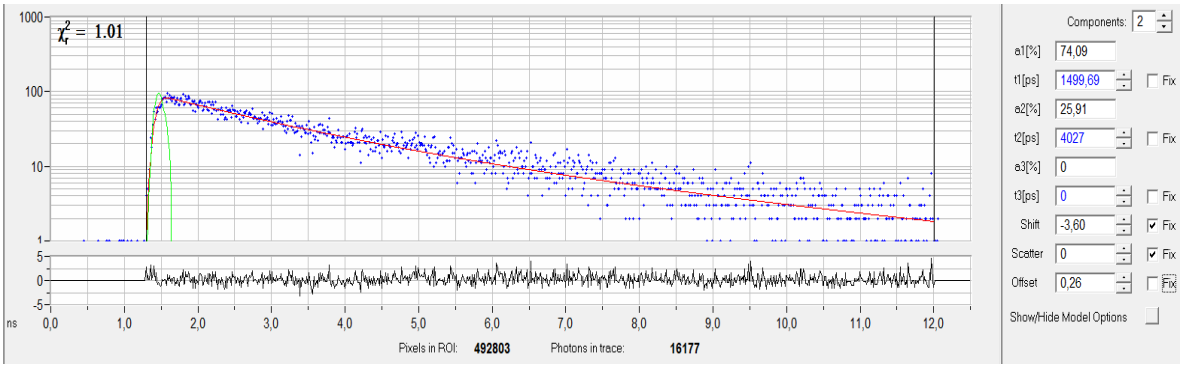


Fig. 1222: Decay curve window of SPCImage

Decay Curve from an ROI

A decay curve can also be displayed for an entire ROI, both for a rectangular one or a polygonal one. To combine the decay data of an ROI into a single decay curve, click on the 'Lock' symbol on the left of the SPCImage main panel, see Fig. 1223. A similar combination can be obtained via the phasor plot, see page 955. The result is a curve with a substantially larger number of photons than in a single pixel. Please don't get frightened by the residuals - they are normalised to the noise (see 'Fit Quality Indicators', page 886). The noise is small in the combined data, so that even minuscule systematic deviations stand out prominently.

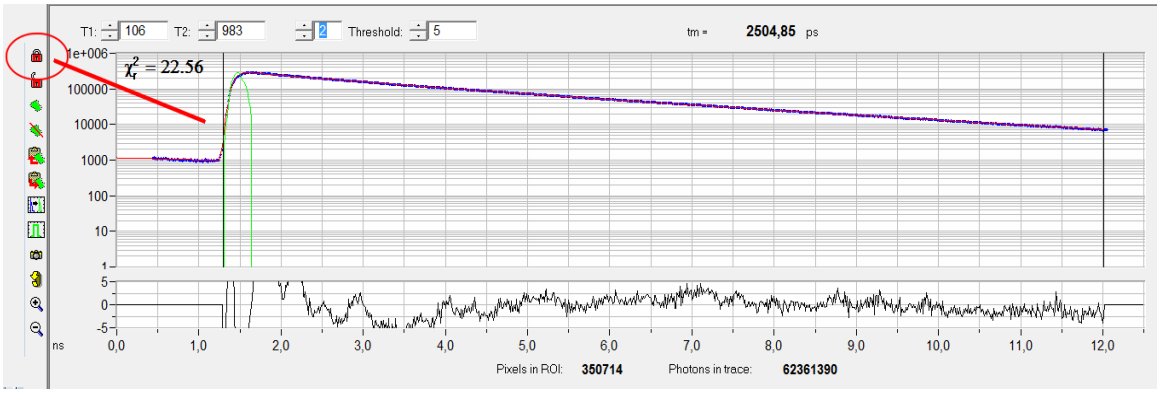


Fig. 1223: Combination of the data of an ROI into a single decay curve

In combined decay data it can happen that the result of the combination exceeds the default Y scale of the decay window. In that case, you can change the scale by a right mouse click into the decay window, and select 'Scale'. This opens a panel in which you can change the x and y scale, as shown in Fig. 1224.

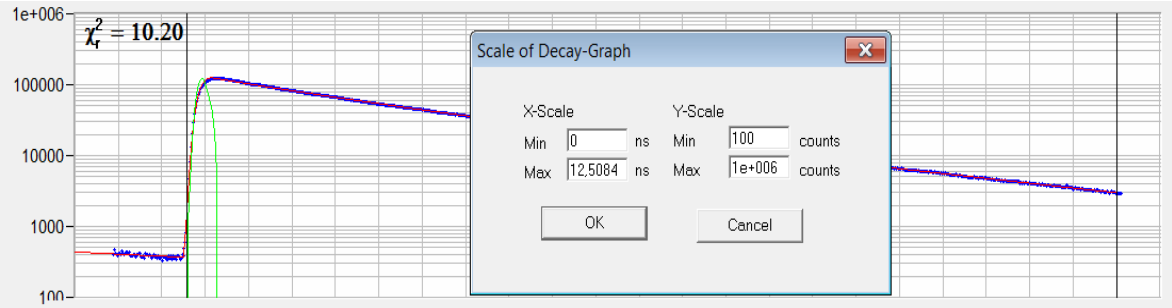


Fig. 1224: Changing the scale of the decay window

Changing the Window Size

The size of the decay-curve window is variable. For FLIM analysis, the decay curve window is normally located under the parameter or intensity histogram and the fit parameter panel. To leave space for these items it is low and wide, as shown in the previous figures. It can, however, be resized to any size within the boarders of the SPCImage panel. An example where the decay curve window fills the entire SPCImage panel is shown in Fig. 1225.

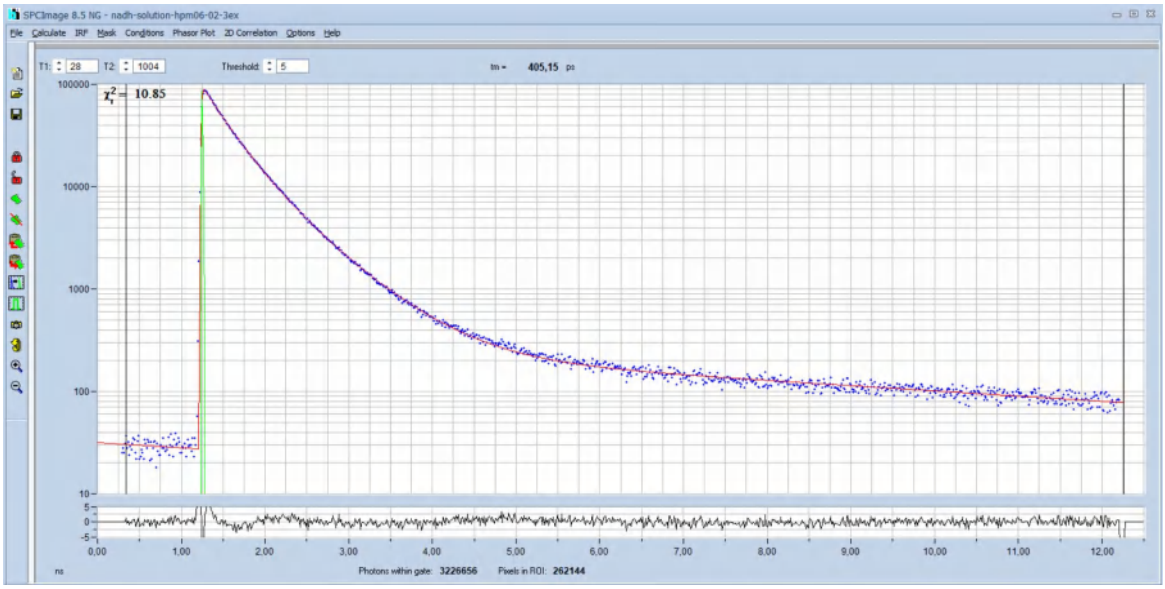


Fig. 1225: Decay curve window, sized up to the entire area of the SPCImage software panel.

Display of Colour-Coded Images

General Configuration

The general configuration of the main panel is defined in the 'Preferences' panel, see page 912. For reasonably modern computers and computer screens we recommend to chose the 'Layout' and 'Lifetime Window' parameters as shown in Fig. 1226. The display configuration then becomes as shown in Fig. 1227. Of course, the colour-coded images does not show up until you have run 'Calculate Decay Matrix', see page 875. Before that, SPCImage displays an gray-scale intensity image, see Fig. 1195, page 873.



Fig. 1226: Recommended 'Layout' and 'Lifetime Window' parameters in the 'Preferences' panel

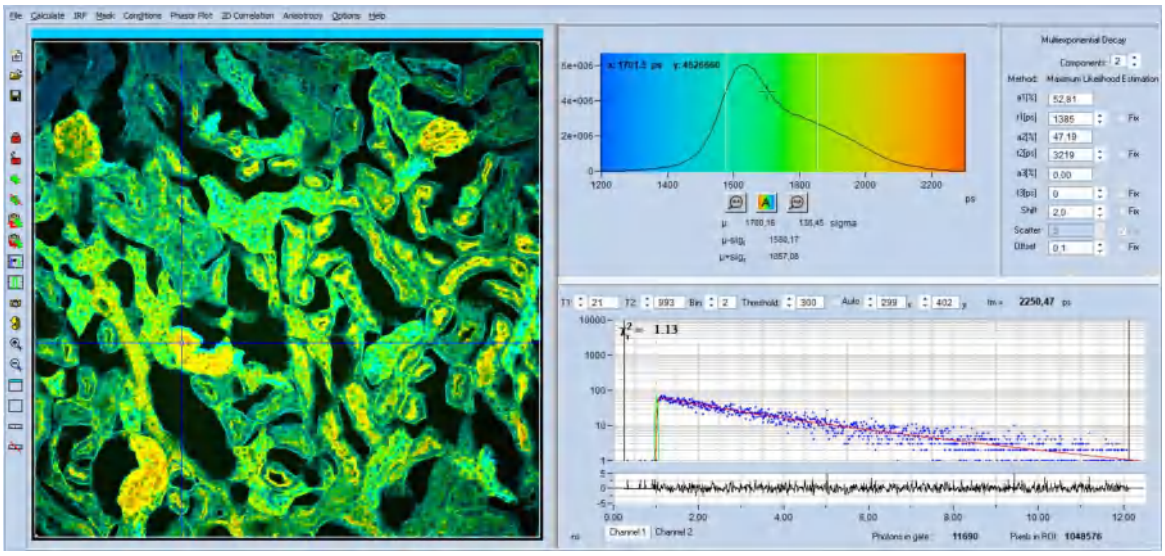


Fig. 1227: Display configuration with the configuration parameters shown above

There are situations when a FLIM data set contains several images, e.g. from different wavelength channels. In that case, you can select the desired image by clicking on one of the tabs below the decay curve windows. Please see Fig. 1228.

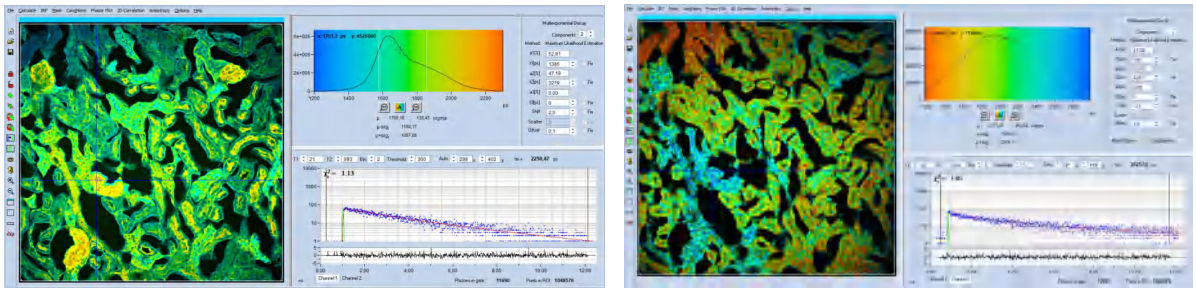


Fig. 1228: Two FLIM images from the same FLIM data set but from different wavelength ranges. Selection by the 'Channel' tabs.

For direct comparison, and for cross-calculation of decay parameters two images can be displayed in one SPCImage main panel. Click into 'Options', 'Channels', and select 'side by side'. An example for simultaneous display of two channels is shown in Fig. 1229.

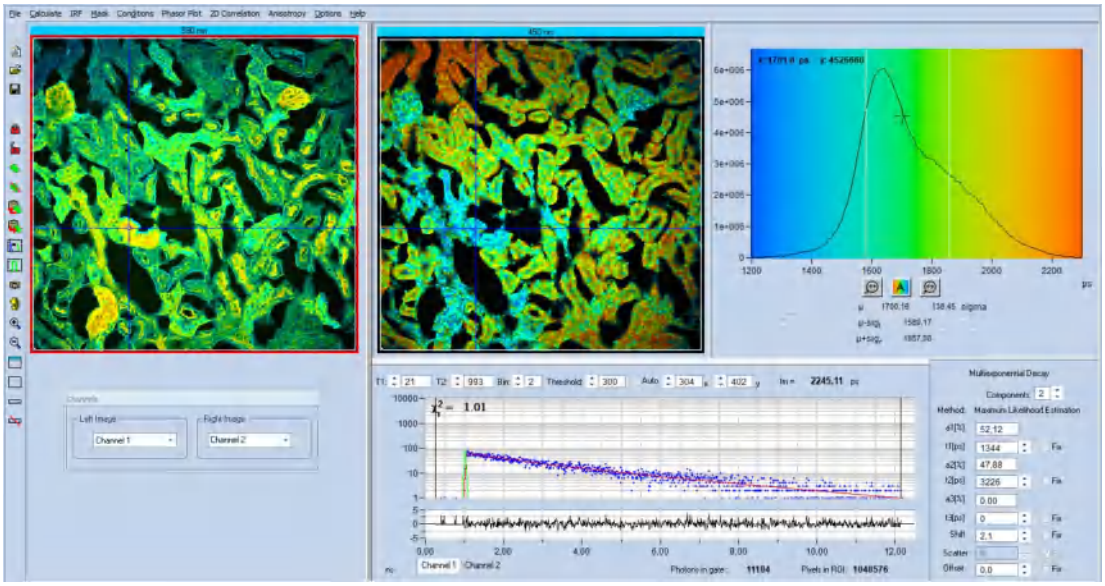


Fig. 1229: Display of two images from two different recording channels

When two images are displayed the images can be given names. Click into the blue bar on top of the images, and type the desired text into the small panel that opens. The text is then displayed on top of the corresponding image, see Fig. 1229.

Intensity Parameters

The display of the lifetime images themselves is controlled by the 'Intensity' parameters and the 'Colour' parameters. Both are accessible via 'Options' in the top bar of the main panel.

The intensity parameters are shown in Fig. 1230. The parameter panel is shown on the right, the corresponding image on the left. There are separate sliders for contrast and brightness of intensity (grey scale) images and lifetime images. 'Intensity Overlay' defined which information is displayed as image intensity. Usually it is the photon number, but other parameters can be selected for special purposes. 'Scaling' is either 'autoscale' or a user-defined number of photons per pixel. 'Other' contains options to reverse images in x and y, to interpolate the intensity between the pixels of low-resolution images, and to time-gate images. Commonly used settings can be seen in Fig. 1230.

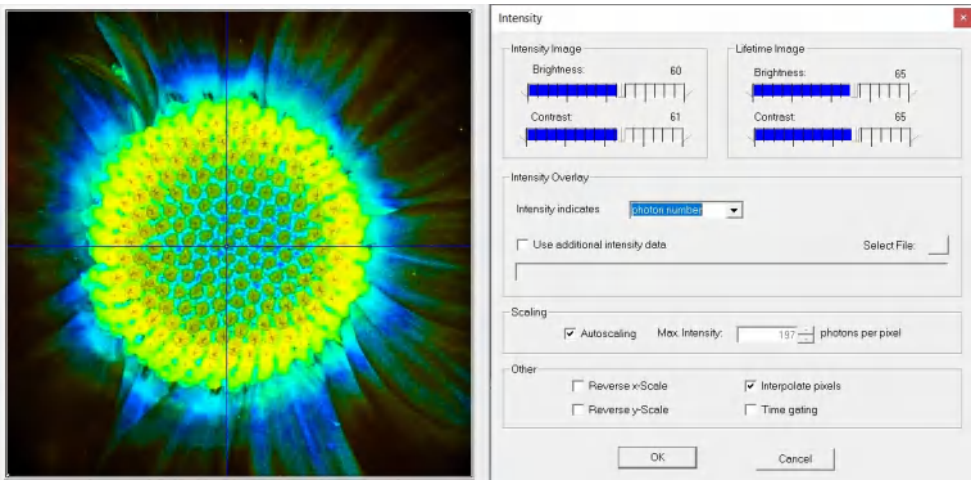


Fig. 1230: Lifetime image with commonly used settings of the intensity parameters

Most of settings can be used more or less intuitively. Normally the images are be displayed with autoscaling. The intensity scale then automatically adjusts to the photon number in the brightest pixel. The autoscaling may fail if there are overexposed spots in the image, such as specks of fluorescent dirt. In that case, turn off autoscaling and set a better intensity range manually or adjust the intensity range via the Intensity Histogram, see page 897.

An example for time-gating of the intensity is shown in Fig. 1231. The time gate is defined by the cursors in the decay window, see Fig. 1231, right. A late time window has been used for gating, therefore pixels with short lifetime appear dark.

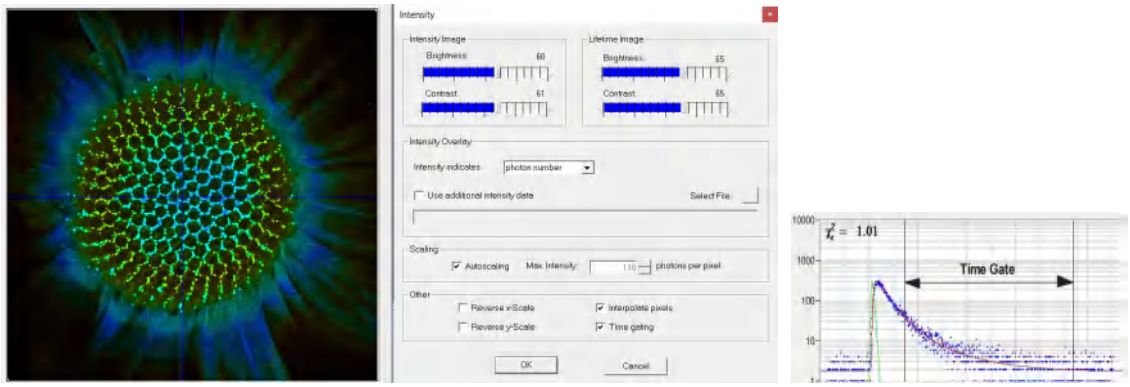


Fig. 1231: Lifetime image with time-gated intensity. The time gate is defined in the decay curve window (right).

Colour Parameters

Colour Coding of Selected Decay Parameters

The 'Colour' parameters define the colour range into which the value of a selected decay parameter is converted. Three examples are shown in Fig. 1232. The figure shows lifetime images of the mean lifetime, t_m, for different settings of the colour parameters. The left and middle image have a continuous colour scale from t_m = 200 to 1000 ps, but the colour scale goes in opposite directions. The image on the right has a discrete colour scale. The ranges for blue, green, and red are shown in the right part of the colour parameter panel.

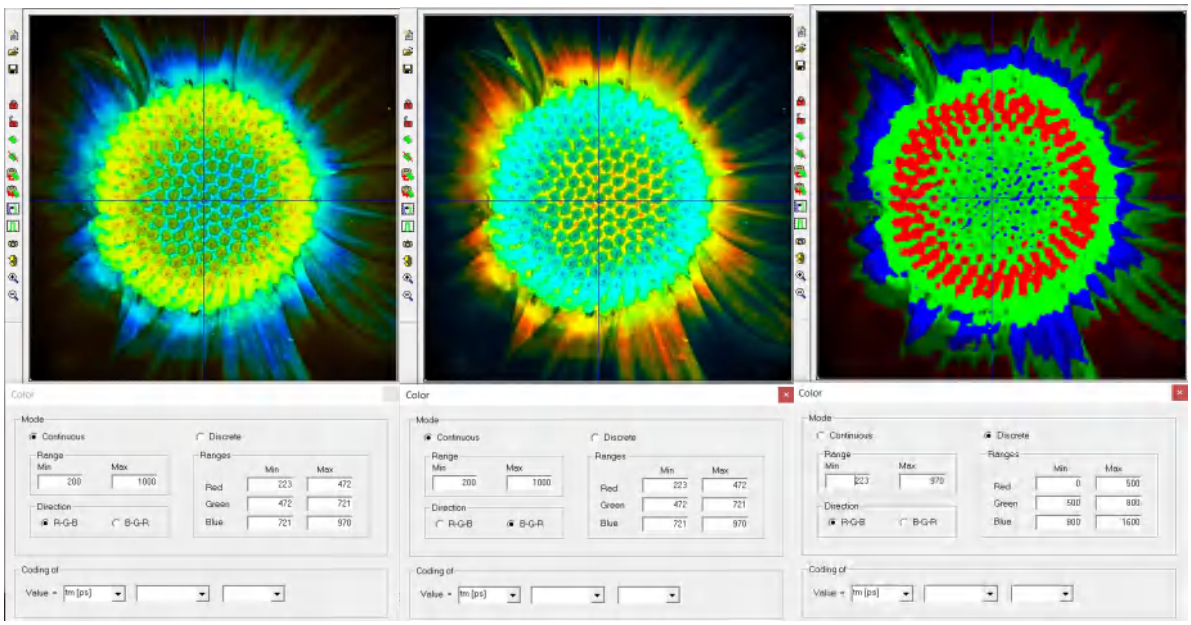


Fig. 1232: Different colour scales. Left: continuous scale, red-green blue. Middle: continuous scale, blue-green-red. Right: Discrete colour scale.

Selection of Parameter for Colour-Coding

'Coding of' in the lower part of the colour panel selects the parameter to be colour-coded in the image. Available parameters are:

t_m	amplitude-weighted lifetime of all decay components enabled in general model parameters
t_{m12}	amplitude-weighted lifetime of the first two decay components of a triple-exponential decay. Used for FLIO analysis.
t_i	intensity-weighted lifetime of all decay components enabled in general model parameters
t_1, t_2, t3	Lifetimes of the individual decay components
a_1, a_2, a_3	Amplitudes of the decay components. $a_1+a_2+a_3=1$
q_1, q_2, q_3	Relative intensity contributions of the decay components. Products of component amplitudes and lifetimes.
N	Number of photons in the pixel. N ratios are used for Redox-Ratio images
Chi^2	χ^2 in the individual pixels
Sca	Amount of scattering or SHG, if scatter enabled in general model parameters
Shift	Shift parameter (if left floating in general model parameters)
E_{int}	FRET efficiency of interacting donor fraction, Eint = 1 - t_1/t_2
E_{class}	Classic FRET efficiency. $E_{class} = 1 - t_m/t_2$
$1-t_i/t_2$	Classic FRET Efficiency calculated from ti. For comparison only.
r/r_0	Ratio of FRET donor-acceptor distance, r, and Förster radius, r0
Offset	Offset parameter, see general model parameters

Three examples are shown in Fig. 1233. The figure shows images of the fast decay component, t_1, of the slow decay component, t_2, and the amplitude of the fast component, a_1, obtained by double-exponential analysis.

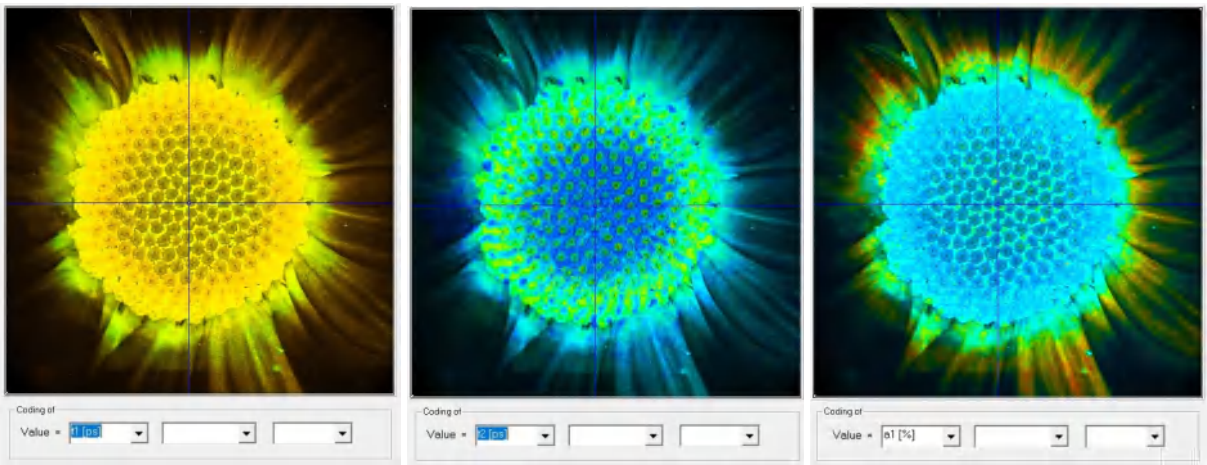


Fig. 1233: Colour coding of t_1, t_2, and a_1. Parameter ranges 0-2ns, 0-2ns, 0.5-1, respectively. Lower part of colour parameters shown only.

Arithmetic Expressions of two Parameters

Colour coding can be performed either by the decay parameters themselves or by arithmetic expressions of decay parameters. Examples are shown in Fig. 1234. It shows the ratios, a_1/a_2, t_1/t_2, and q_1/q_2, of the parameters of double-exponential decay.

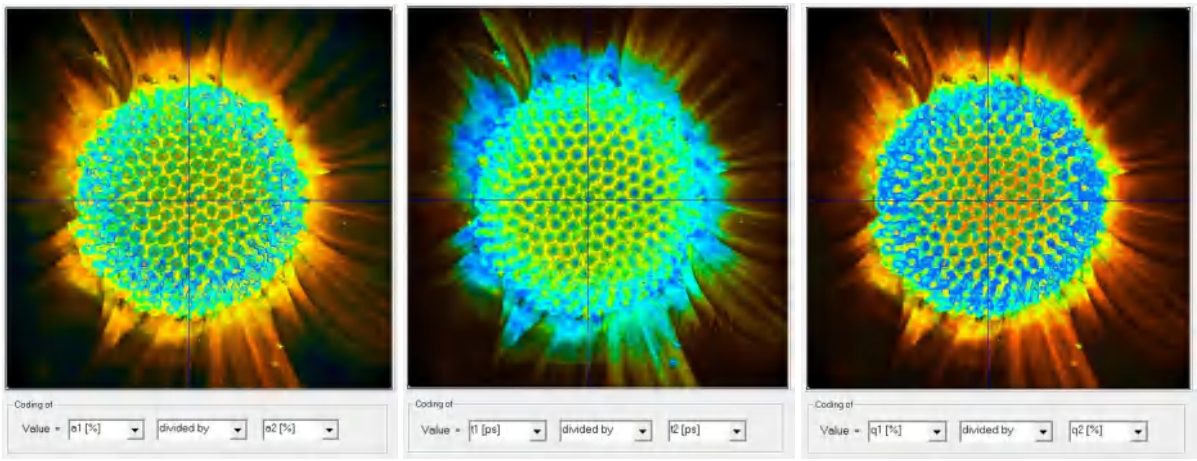


Fig. 1234: colour coding of a_1/a_2, t_1/t_2, q_1/q_2. Parameter ranges 1-20, 0.1-0,5, 1-5, respectively. Lower part of colour parameters shown only.

Linking Parameters from Different Images

If a FLIM data file contains images from two or more detection channels arithmetic expressions of parameters from different channels can be calculated and displayed. An example is shown in Fig. 1235. The FLIM data set contains images from two TCSPC channels, indicated by the tabs below the decay curve window. With the Colour parameters shown SPCImage calculates a_2 from the selected image channel (Channel 2) divided by a_1 of Channel 1. The result is used as colour coding of the selected image channel (Channel 2).

In the example shown Channel 1 contains FAD data and Channel 2 NADH data. The selected expression represents the Fluorescence Lifetime Redox Ratio,

$$FLIRR = a_{2NADH} / a_{1FAD}$$

Please see 'Metabolic Imaging ' page 535.

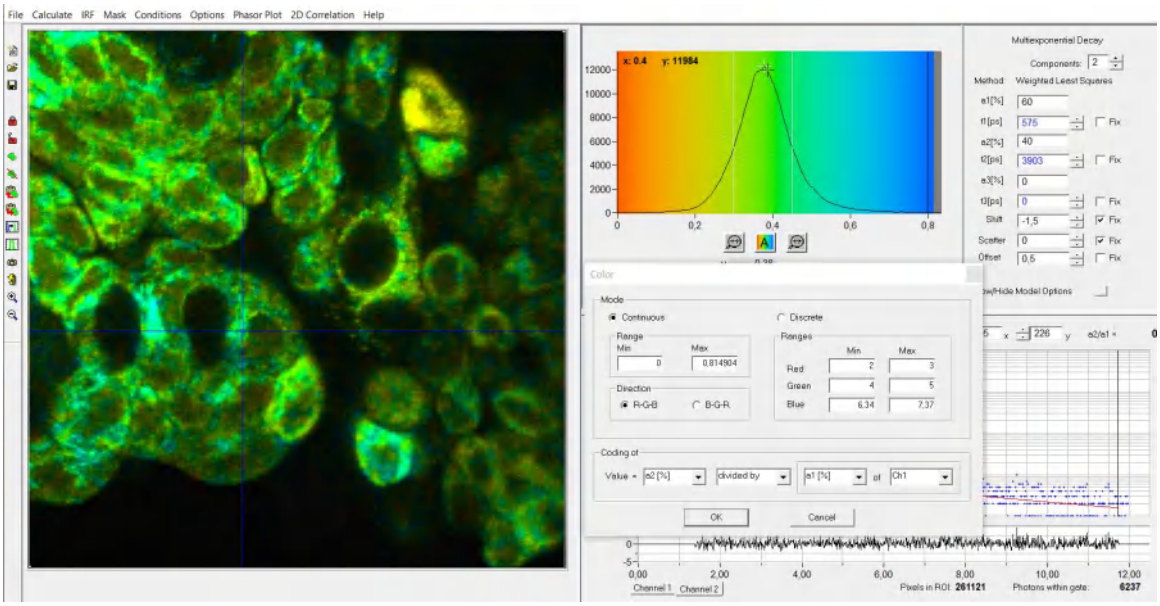


Fig. 1235: Linking parameters from two image channels of one FLIM data set. The example calculates $a_{2channel2}$ divided by $a_{1channel1}$

Parameter Histogram

SPCImage displays a histogram for the decay parameter selected for colour-coding the lifetime image. The histogram shows how often pixels of a given parameter value occur in the lifetime image. Depending on the settings in ‘Preferences’, the histogram either displays the pure pixel frequency or the pixel frequency weighted with the pixel intensity, see 'Preferences', Fig. 1264, upper right. The parameter histogram serves two different purposes.

Interaction with the Colour Parameters

The parameter histogram helps the user conveniently set an appropriate range of the colour parameters of the image. The histogram has two cursors, one for the upper end of the parameter range and one for the lower end, see Fig. 1236. A change in the cursor positions in the histogram (middle) automatically changes the range in the colour parameters (right) and, consequently, the colour coding of the image.

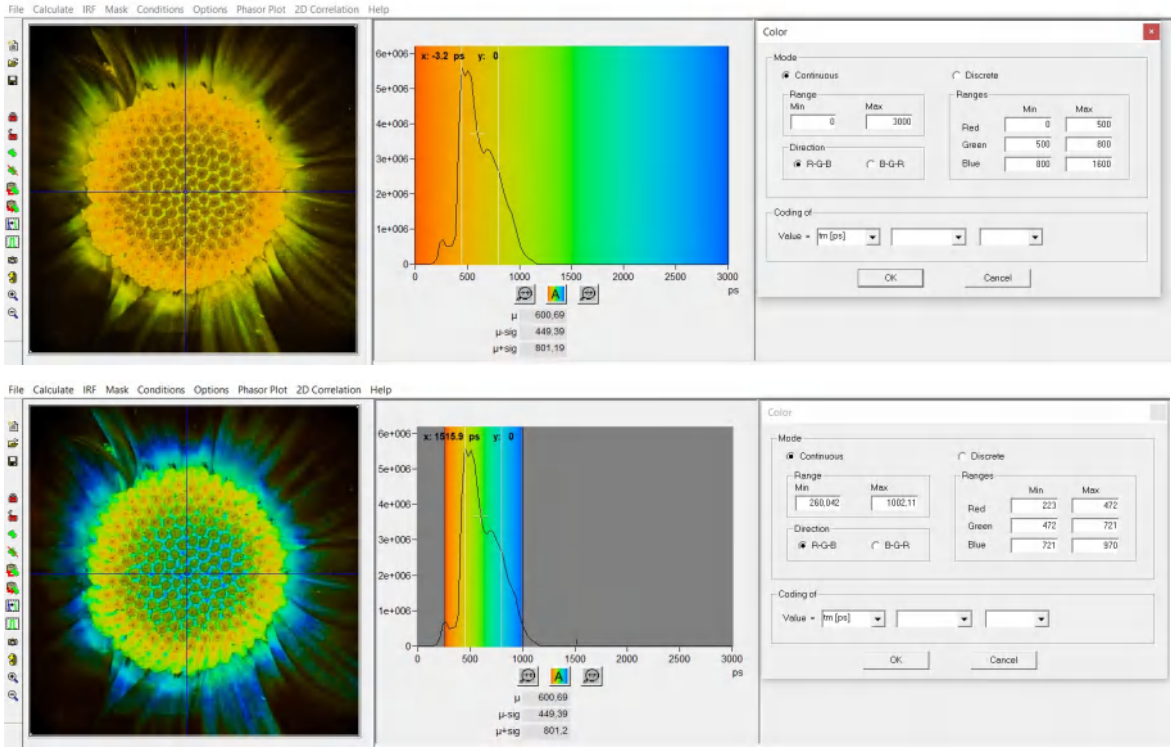


Fig. 1236: Interaction of cursors in the parameter histogram (middle) with colour parameters (right) and colour-coding of the image.

The buttons underneath the histogram help the user define the parameter range. The button zooms the distribution into the selected parameter range, zooms out. The button sets the parameter range automatically.

Estimation of Decay Parameter Values

The parameter histogram shows the distribution of the selected decay parameter in the image. Information from the histogram is therefore more informative than numerical parameter values from a single spot of the image. By giving a graphical overview, the histogram shows what the most frequent value is, how broad the distribution is, and what the shape of the distribution is. The parameter histogram is thus an excellent tool to compare the results of different FLIM measurements. An example is shown in Fig. 1237. The images shows four FLIM data sets obtained from mushroom spores [177]. The images and histograms show the lifetime of the fast decay component, t_1, of triple-exponential decay analysis. The data are for different spore colour, from light brown (upper left) to black (lower right). Although lifetimes in the

range of 20 ps (note the colour scale!) are necessarily a bit uncertain the histograms show a clear trend with the spore colour.

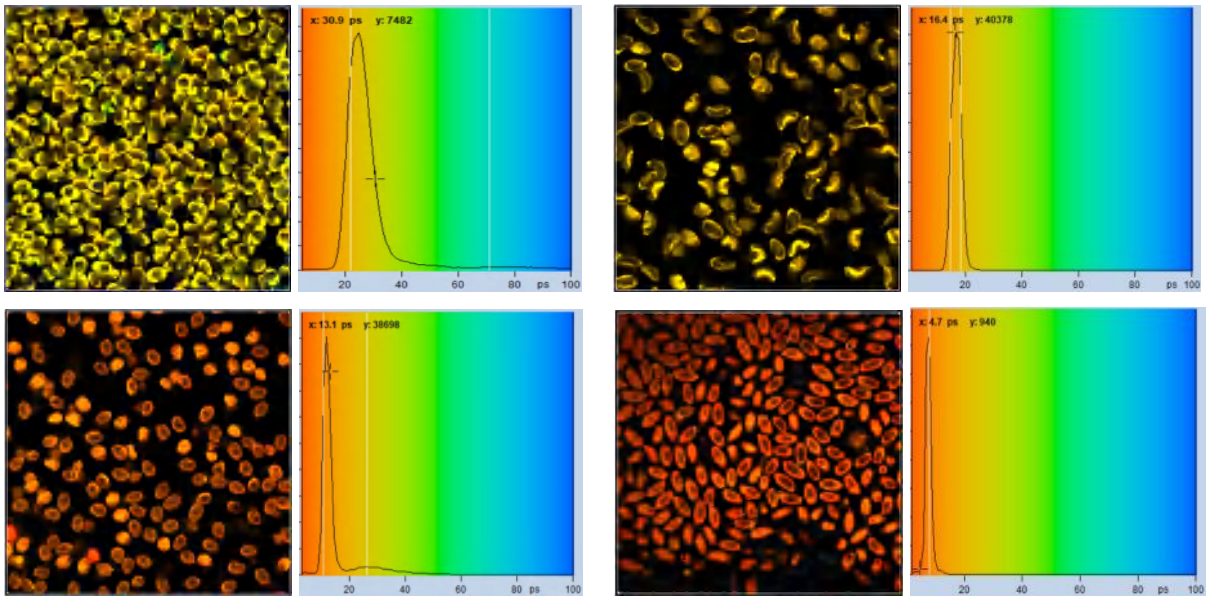


Fig. 1237: t_1 images and t_1 histograms for mushroom spores of different colour. The histograms show a clear trend from upper left to lower right.

Intensity Histogram

Instead of the parameter histogram, SPCImage NG can also display an intensity histogram. The histogram type is switched by a right-mouse click into the image window. This opens a selection panel, from which either 'Parameter Histogram' or 'Intensity Histogram' can be selected, see Fig. 1238. The parameter histogram is shown on the right in Fig. 1238.

The intensity histogram interacts directly with the Intensity Parameters of the image display. The histogram therefore has two cursors by which a suitable intensity range can be selected. An example is shown in Fig. 1238 and Fig. 1239. The image includes a number of extremely bright objects, which are probably dead cells. The normal autoscale procedure (see 'Intensity Parameters', page 892) normalises the image brightness on these cells. The good cells are much dimmer and are therefore displayed at low brightness and contrast. One solution is to open the Intensity Parameter panel, turn off autoscale, and try with a new 'Max Intensity' value.

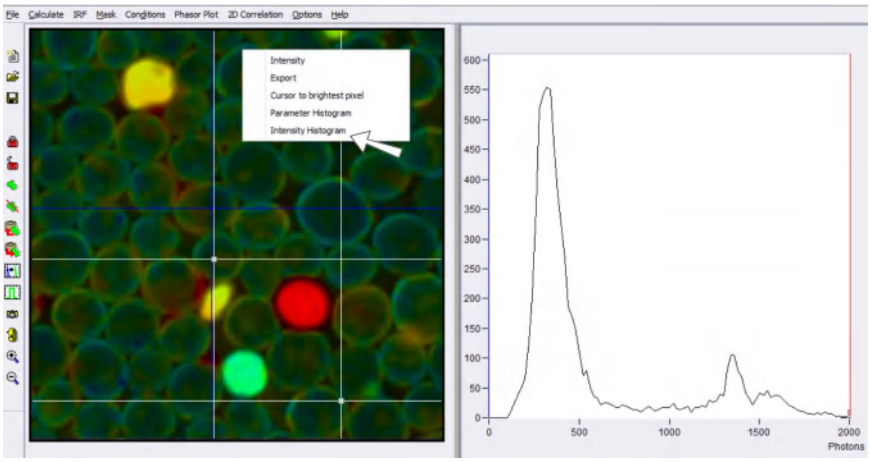


Fig. 1238: Switching from the Parameter Histogram to the Intensity Histogram. Histogram shown on the right.

With the intensity histogram, the intensity range can be adjusted much more easily and quantitatively. Different features form different peaks in the histogram. It is thus easy to identify the peaks of different features, and adjust the intensity range to display the desired feature optimally. In Fig. 1239 the right cursor has been set just above the peak that corresponds to the good cells. The result is that the cells are displayed at a much more favourable brightness.

With the adapted intensity range, it becomes obvious that the background of the image is not entirely dark. The reason in this case is that the image was recorded by simultaneous FLIM/PLIM, and the PLIM signal leaks in the FLIM recording. In Fig. 1240, the background has been suppressed by pulling up the left histogram cursor. The image adjusted this way has a much more favourable appearance than the original image, compare Fig. 1238.

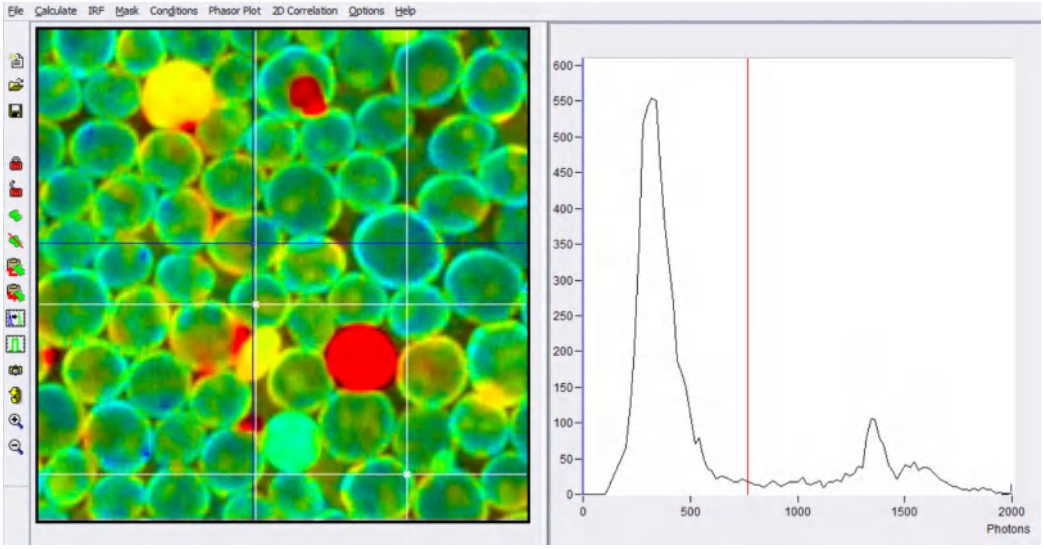


Fig. 1239: Image brightness scale adjusted by histogram cursors. High-Intensity cursor adjusted to brightness peak of good cells.

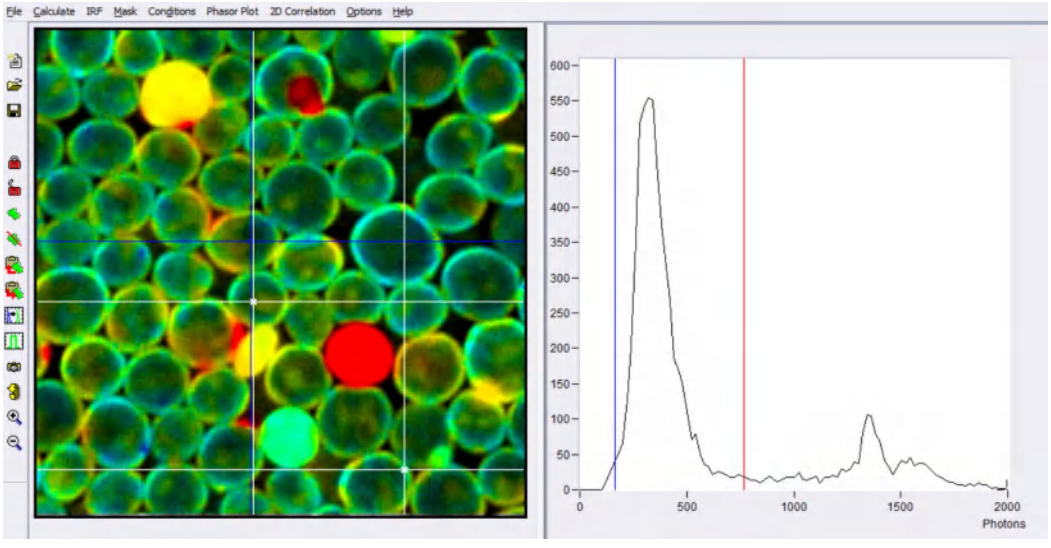


Fig. 1240: Image brightness scale adjusted by histogram cursors. Low-Intensity cursor adjusted to brightness peak of good cells.

ROI Definition

SPCImage has several options to define ROIs. When an ROI is defined the parameter histograms are created from the pixels inside the ROI only. An ROI selection can therefore be used to obtain (and compare) lifetime histograms from different regions of the image. Moreover, decay data from all pixels inside an ROI can be combined into a single decay curve.

Rectangular ROI

The image window of SPCImage contains three cursors. The blue cursor is used to select a spot in the image for which a fluorescence decay curve is displayed. The white cursors are used for region-of-interest (ROI) definition. To define an ROI by the image cursors move the cursors in the desired position, see Fig. 1241. The area between the cursors is the ROI. You can zoom into the selected area by the zoom button on the left of the SPCImage main panel.

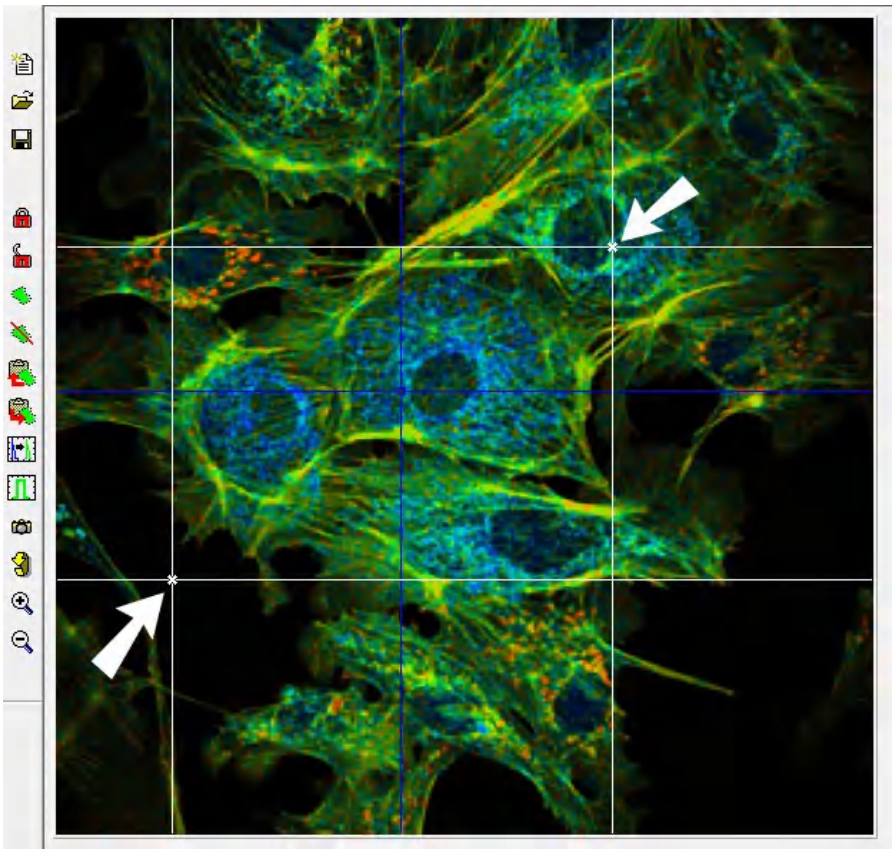


Fig. 1241: Rectangular ROI, definition by image cursors

Polygonal ROI

A polygonal ROI is be defined by clicking on the ('Create ROI') button on the left of the image window. You can also chose 'Mask' in the top bar and select 'New'. This opens the panel shown in Fig. 1242. Select 'Polygon Mask', and find look for the little red cross in the FLIM image.

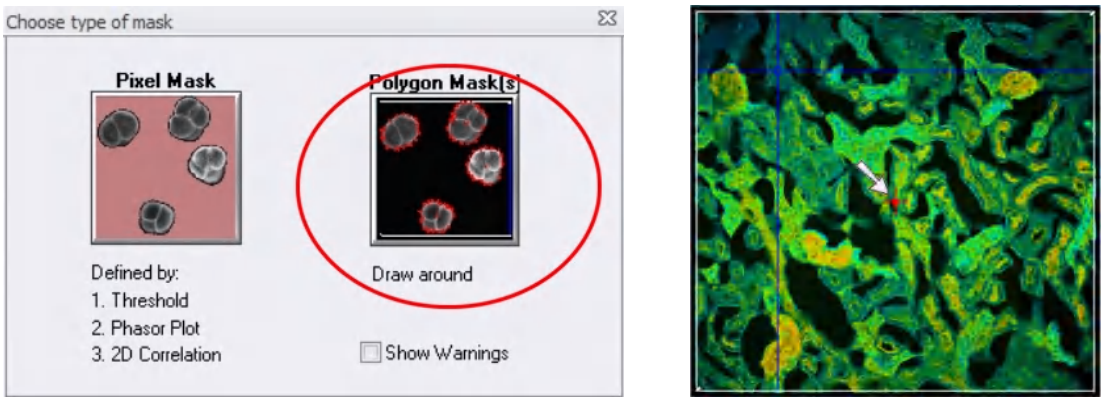


Fig. 1242: Selection of 'Polygon Mask'

The ROI is created by shifting the red cross as shown in Fig. 1243, left. Every mouse click adds a new point to the polygon in the spot where the cross has been placed. You can define several ROIs. To do so, click on the 'Create ROI' button again. This opens a new ROI, see Fig. 1243, middle. To modify an ROI click on 'Mask' in the top bar and select 'Select/Modify'. Click on the ROI you want to modify and shift the points into the desired position, see Fig. 1243, right.

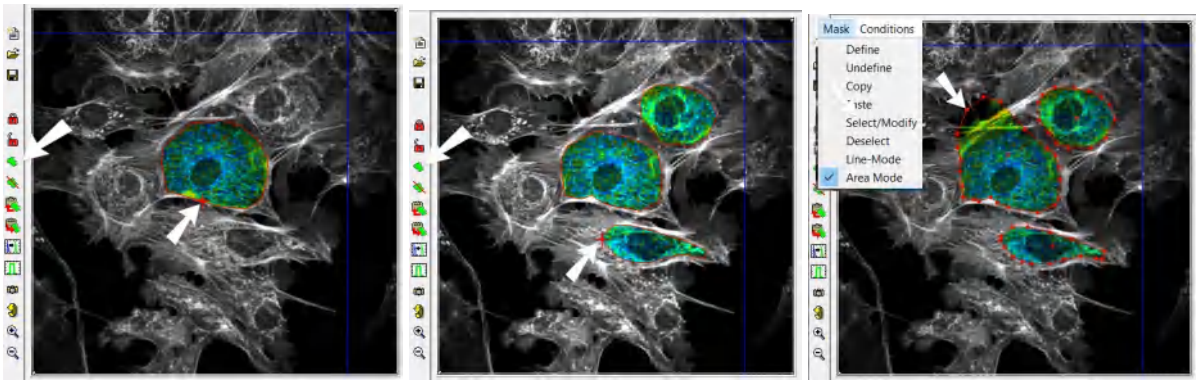


Fig. 1243: Definition of a polygonal ROI. Left: Single ROI. Middle: Several ROIs, every click on the ROI symbol on the left opens a new ROI. Right Modification of an ROI.

Lines of Interest

SPCImage can define ‘Lines of Interest’. Click on ‘Mask’, and select ‘Line Mode’ instead of ‘Area Mode’. Instead of an Area, the ‘Define’ function then defines a line, e.g. along a cell membrane. Also in the ‘Line’ mode you can make several definitions in the same image, select individual histograms for the lines, and combine the decay data of each line in a single decay curve.

ROIs from 2D Histograms and Phasor Plots

ROIs can not only be defined manually but also be obtained from the 2D Histogram and the Phasor Plot of SPCImage, see page 904 and page 906. In these cases the areas are not defined in the images but in two-dimensional histograms of decay or phasor parameters. Areas defined by these functions can be much more complex than manually defined ROIs. In particular, they can contain multiple areas that are not connected to each other, or even disconnected pixels. The associated patterns are therefore also referred to as 'Masks', and the procedures to obtain them as 'Image Segmentation', please see Fig. 1253 and Fig. 1258.

Pixel Masks

Masks are, in principle, ROIs. However, there are differences: A mask can be much more complex than a normal RIO. In particular, it can contain multiple areas that are not connected to each other, or even disconnected pixels. Moreover, a mask can be defined in or derived from one image of a sample and then applied to another image or a series of images of the same sample. These images can be from a time series, from a Z stack, or a multi-wavelength image of the sample. To define a mask, click into 'Mask' in the top bar, and select 'New', see Fig. 1244, left. This opens the selection panel in Fig. 1244, right. A pixel mask can be defined by defining a 'Threshold' of the photon counts per pixel, by selecting a phasor range in the Phasor Plot, or a decay-parameter range in the 2D Correlation histogram.

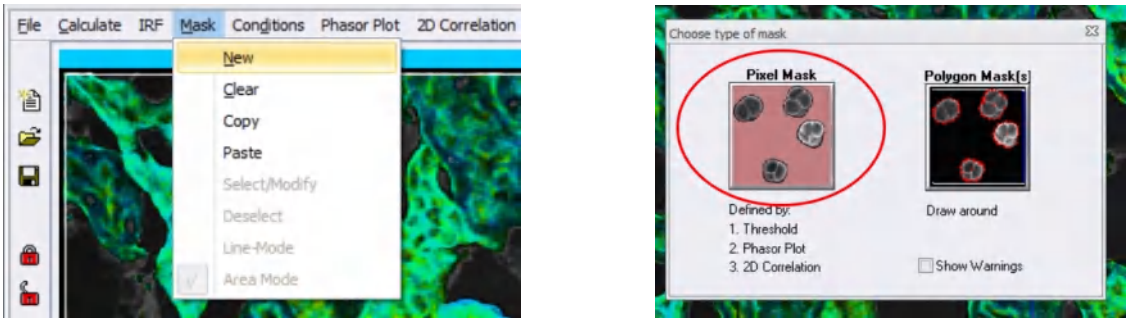


Fig. 1244: Definition of a Mask

'Threshold' creates a mask that contains pixels with numbers exceeding a certain number of photons. The number of photons is defined by the 'Threshold' parameter above the decay curve window, see Fig. 1245, left. The original FLIM image is shown in Fig. 1245, middle. The mask created by a threshold of 3000 (photons in the decay curve of the pixel) is shown in Fig. 1245, right.

Fig. 1246 shows the mask definition via the Phasor Plot. The selection of the desired phasor range in the phasor plot is shown on the left, see small red circle. Fig. 1246, middle shows the FLIM image with the pixels within the selected phasor range highlighted. A mask created from the highlighted pixels is shown on the right.

The mask definition via the 2D parameter histogram is shown in Fig. 1247. The parameter histogram shows the amplitude of the fast decay component, a1, over the amplitude-weighted lifetime, tm. A parameter range covering large a1 with long tm was selected. Fig. 1247, middle, shows the FLIM image with the corresponding pixels highlighted. Fig. 1247, right, shows the mask created from the selection.

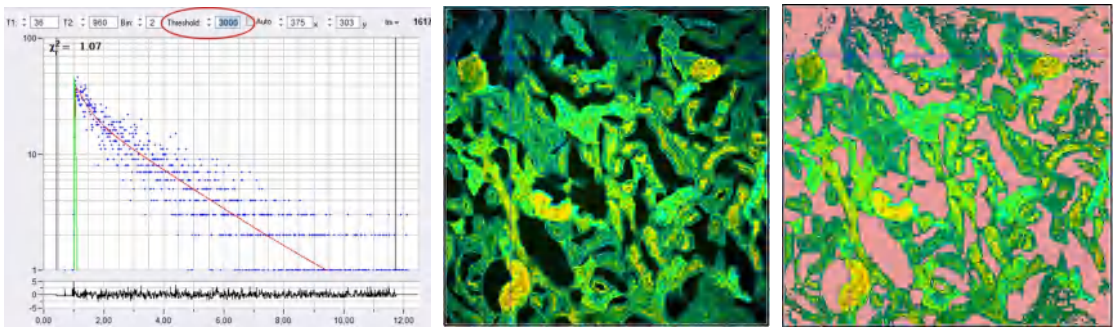


Fig. 1245: Mask definition via 'Threshold'. Left: Threshold definition. Middle. FLIM image. Right: Mask created by Threshold = 3000 photons per pixel.

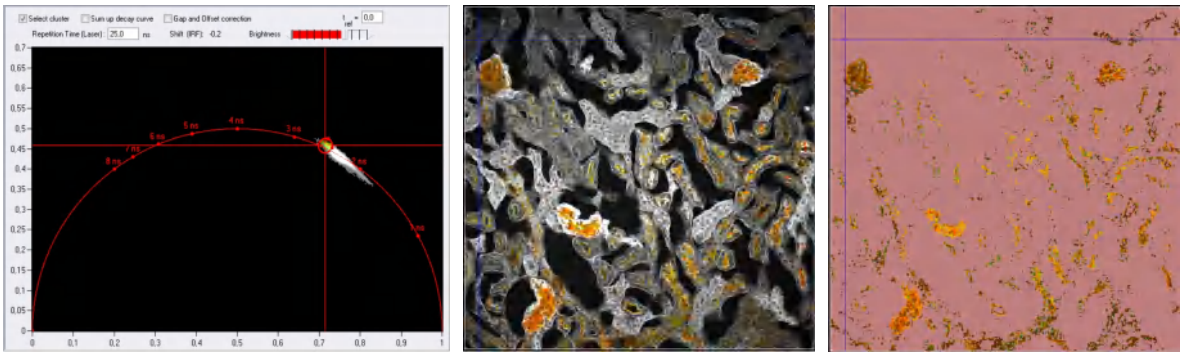


Fig. 1246: Mask definition via Phasor Plot. Left: Selection of phasor range. Middle: Image areas highlighted for selected phasor signature. Right: Mask created from highlighted areas.

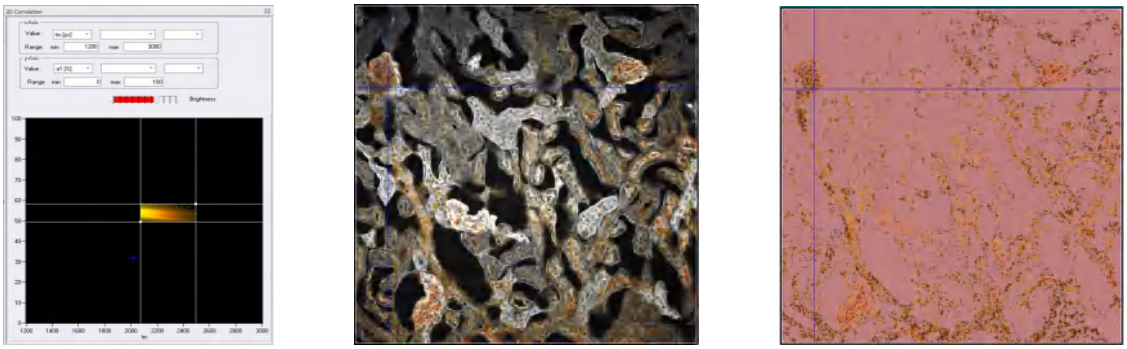


Fig. 1247: Mask definition via 2D-Parameter Histogram. Left: Selection of parameter range, a1 over tm. Middle: Image areas highlighted for selected parameter range. Right: Mask created from highlighted areas.

Decay-Parameter Histograms in ROIs and Masks

If an ROI has been defined or a mask has been created the parameter histogram in the SPCImage main panel refers to the pixels within the ROI or the mask. An example for two different ROI definitions is shown in Fig. 1248. If multiple ROIs have been defined the desired ROI is selected after opening 'Mask' in the top bar and selecting 'Select/Modify'. The ROI is selected either by clicking on the red dot in the centre of it or on one of the tabs on top of the histogram window, see Fig. 1249.

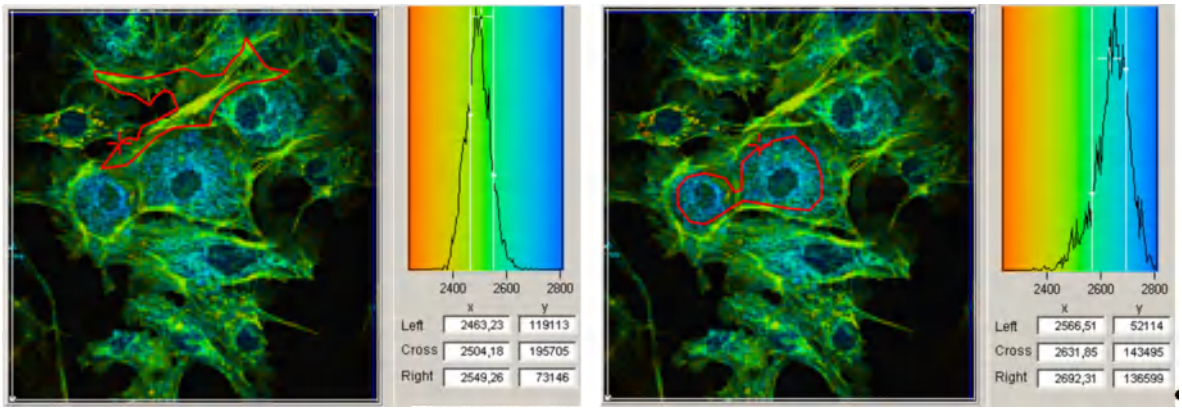


Fig. 1248: Parameter histograms for different definition of the ROI

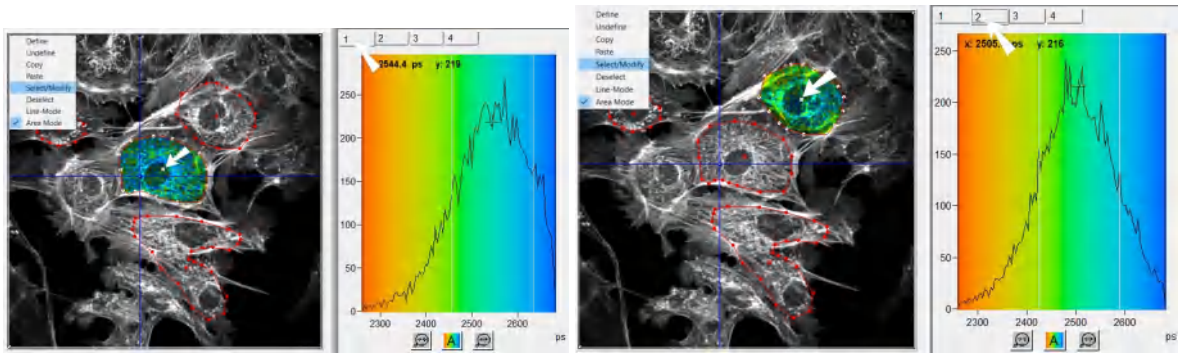


Fig. 1249: Selection of one of several ROIs for display of the parameter histogram

The typical application of a pixel mask is shown in Fig. 1250. The figure shows lifetime images from two wavelength channel of the same FLIM data set. A mask for pixels of long lifetime was created in one wavelength channel (450 nm), see Fig. 1250, left. The mask was copied from this channel to the other (590 nm) by 'Mask', 'Copy', and 'Paste'. The lifetime histogram on the right is thus showing the distribution of the lifetimes of the pixels selected in the image on the left.

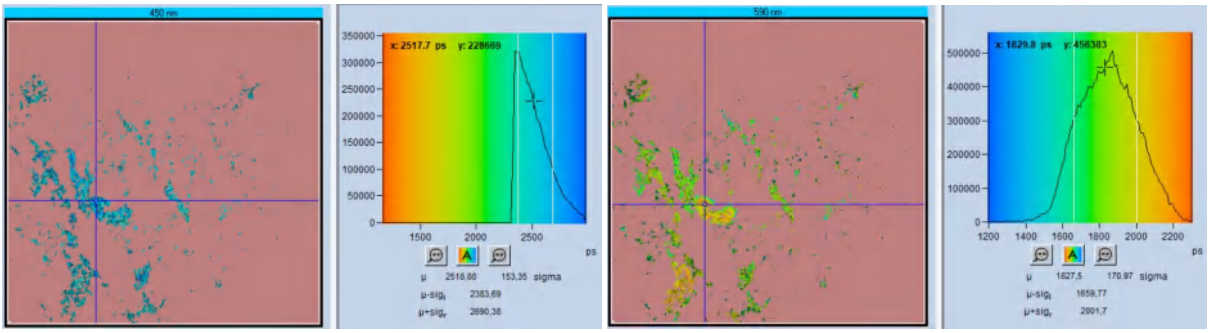


Fig. 1250: Application of a pixel mask to images from different wavelength channels

Combination of Pixel Data into a Single Decay Curve

The (lock) button in the task bar left of the lifetime image combines the decay data of all pixels within an ROI or a mask in a single decay curve. A decay curve for the ROI selected in Fig. 1249, left, is shown in Fig. 1251.

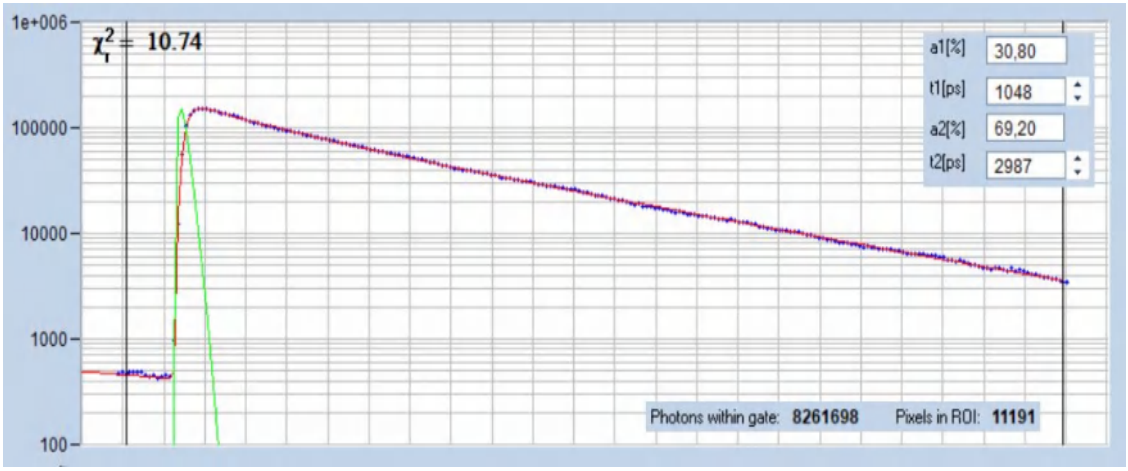


Fig. 1251: Decay curve of combined pixels within ROI of Fig. 1249, left

The resulting decay curve comes from a large number of pixels and thus contains a large number of photons. It can thus be analysed at a an accuracy as it is normally achieved only in cuvette-based experiments.

2D Histograms

SPCImage has a two-dimensional histogram function. It displays a density plot of the pixels over two selectable decay parameters. These can be t_m, t_i, t_1, t_2, t_3, a_1, a_2, a_3, and arithmetic expressions of these parameters. The 2D histogram plot is opened via '2D Correlation' in the top bar. An example is shown in Fig. 1252. The plot has been configured to show the values of t_2 over the values of t_1, see upper part of the 2D histogram panel.

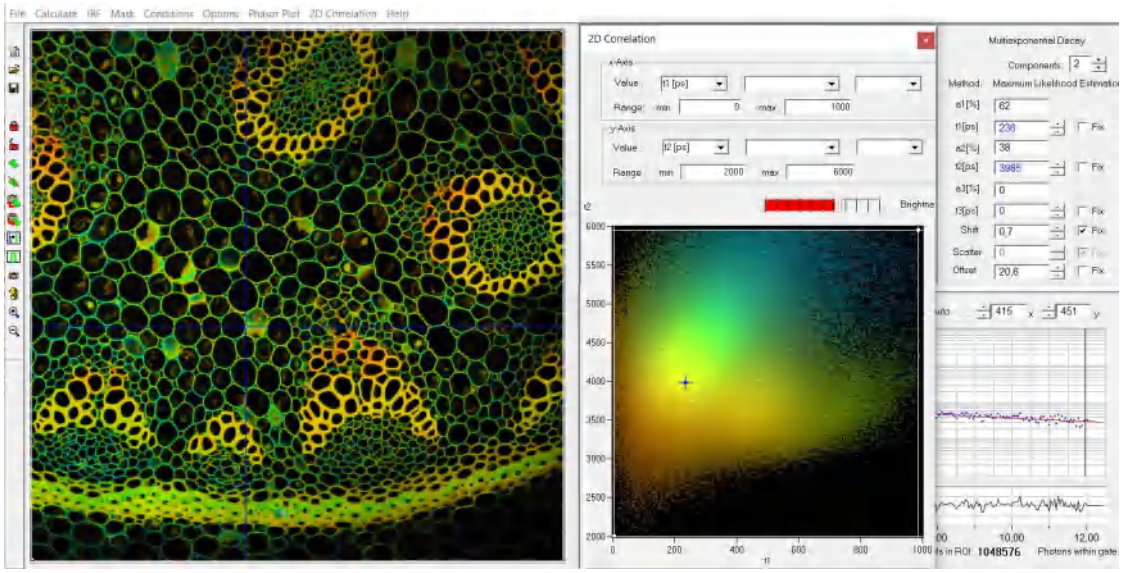


Fig. 1252: 2D histogram of t_2 over t_1

Image Segmentation by 2D Histogram

Cursors in the 2D histogram can be used to select pixels of a specific decay signature and back-annotate them in the image. Pixels with a decay signature within the selected histogram area are shown in the image window normally, pixels outside the area are shown without colour, see Fig. 1253. The selection also acts on the 1D parameter histogram. It is build up for pixels selected in the 2D histogram only.

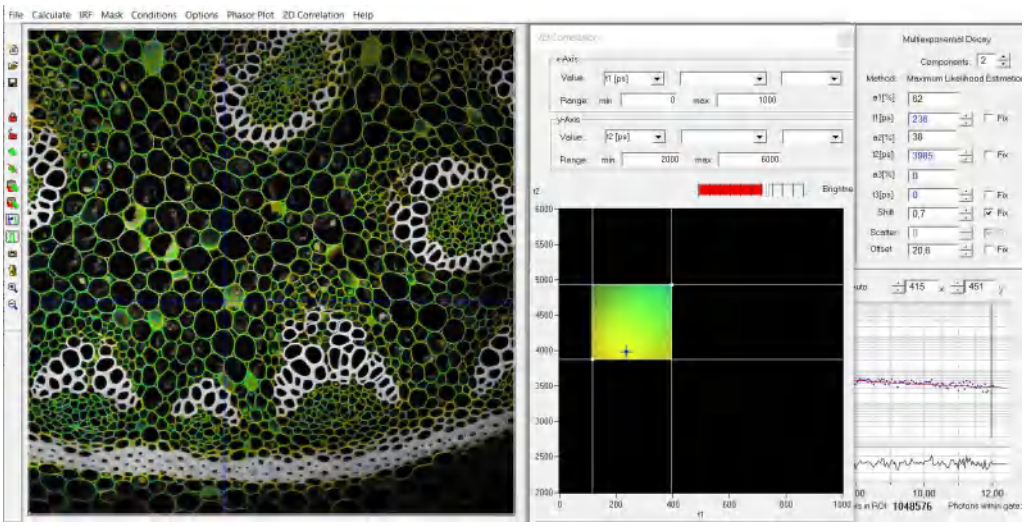


Fig. 1253: Selection of pixels with a specific decay signature in the 2D histogram

Combination of Decay Data Within Selected Parameter Range

The decay data of the pixels within the selected pixels can by combined into a single decay curve. Click on the (lock) button in the task bar left of the lifetime image. The decay curve of the combined pixels of the image features selected in Fig. 1253 is shown in Fig. 1254.

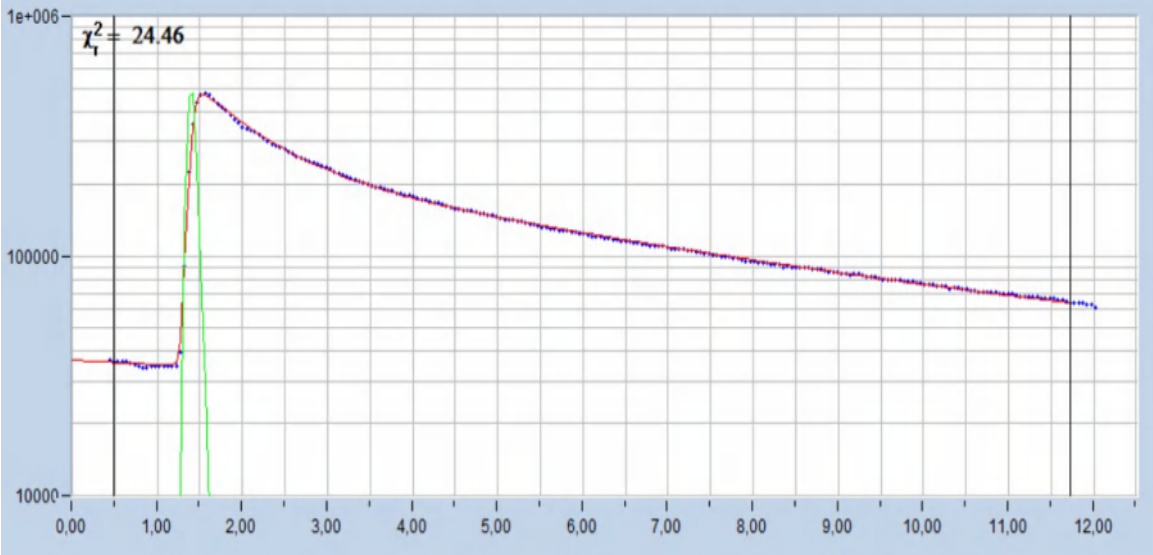


Fig. 1254: Combined decay data from image features selected in Fig. 1253

Phasor Plot

A click on ‘Phasor Plot’ in the top bar of SPCImage opens the phasor plot panel, see Fig. 1255, right. Every pixel in the FLIM image (Fig. 1255, left) is represented by a dot in the phasor plot (right). The location of the pixel in the phasor plot depends on the amplitude and phase of the decay function in the phasor space. To make the correspondence between the image and the phasor plot clearly visible SPCImage can assign the colours of the FLIM image to the dots in the phasor plot. This function is activated by selecting the ‘Combine with FLIM analysis’ option in the phasor plot panel, see Fig. 1255, right.

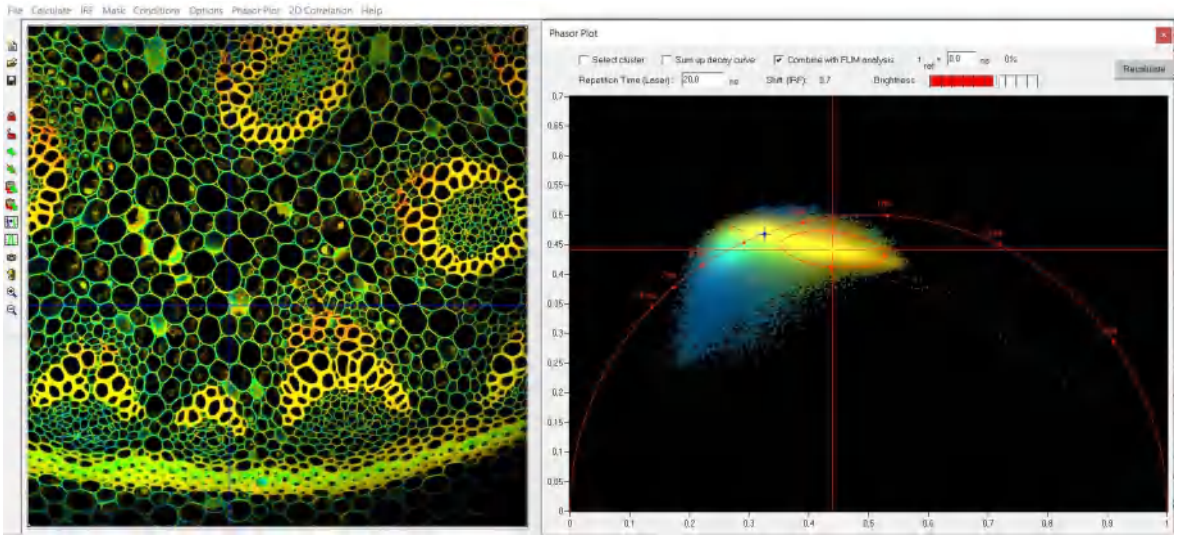


Fig. 1255: Left: Lifetime image (left) and phasor plot (right)

A specific area in the phasor plot can be selected by a selection tool, see red ellipse in Fig. 1255. By 'Select Custer' the corresponding pixels are back-annotated in the FLIM image. Pixels outside the selected phasor range are displayed without colour, see Fig. 1256.

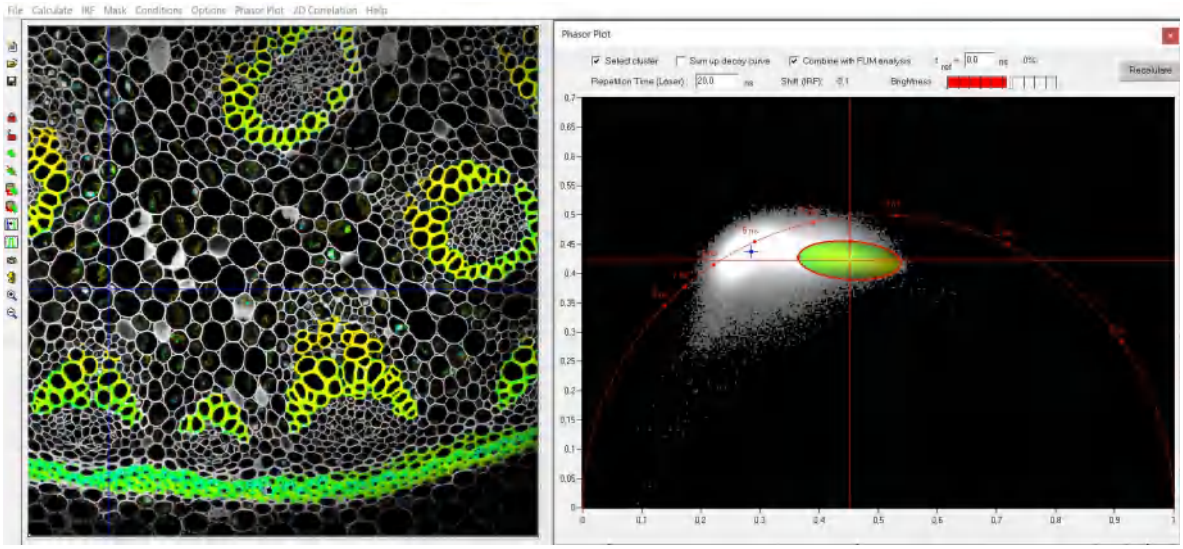


Fig. 1256: Selection of a phasor range and back-annotation of the corresponding pixels in the image

Activation of 'Sum up decay curve' in the phasor plot combines the decay data of all selected pixels in a single decay curve, see Fig. 1257. It represents an average decay curve of all pixels with a phasor signature inside the red ellipse. The curve can contain an enormously high number of photons (more than 88 million in the example, see 'Photons within gate' below decay curve window). It can thus be analysed at extremely high precision.

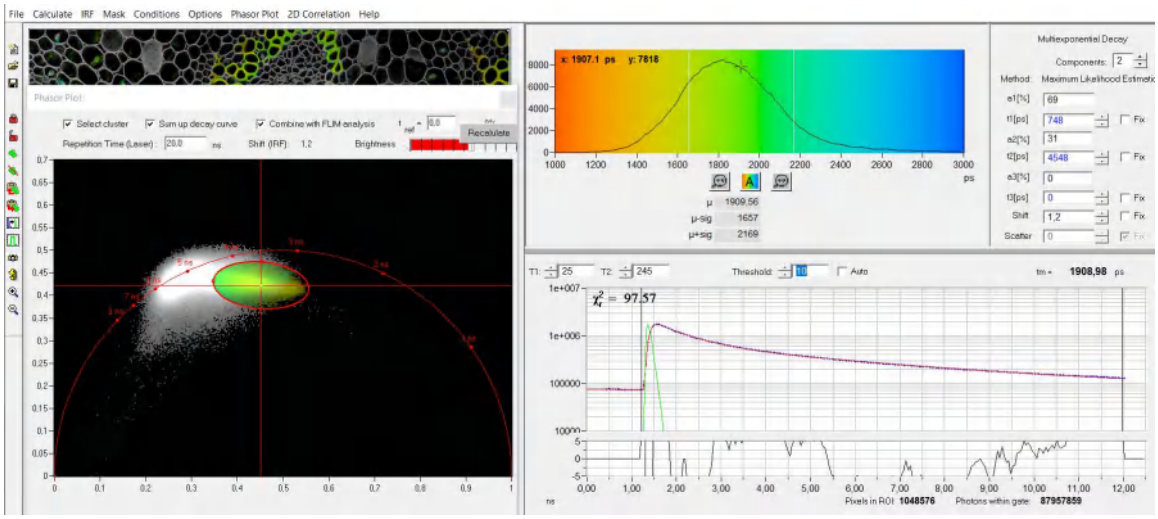


Fig. 1257: Combination of the decay data of all pixels selected in the phasor plot in a single decay curve

Image Segmentation

Selecting a phasor range in the phasor plot and back-annotating the pixels in the FLIM image can be used as an automatic image segmentation function. It is equivalent to a manual ROI selection yet works with far less personal effort. Consider an image as the one shown in Fig. 1258. You want to perform a heterogeneity study on the nuclei of the cells. Creating appropriate regions of interest around all the nuclei manually is almost impossible. But selecting the nuclei in the phasor plot is easy. The result of the selection is a histogram of the lifetime, t_m, of the nuclei, shown in the upper right are of the SPCImage panel.

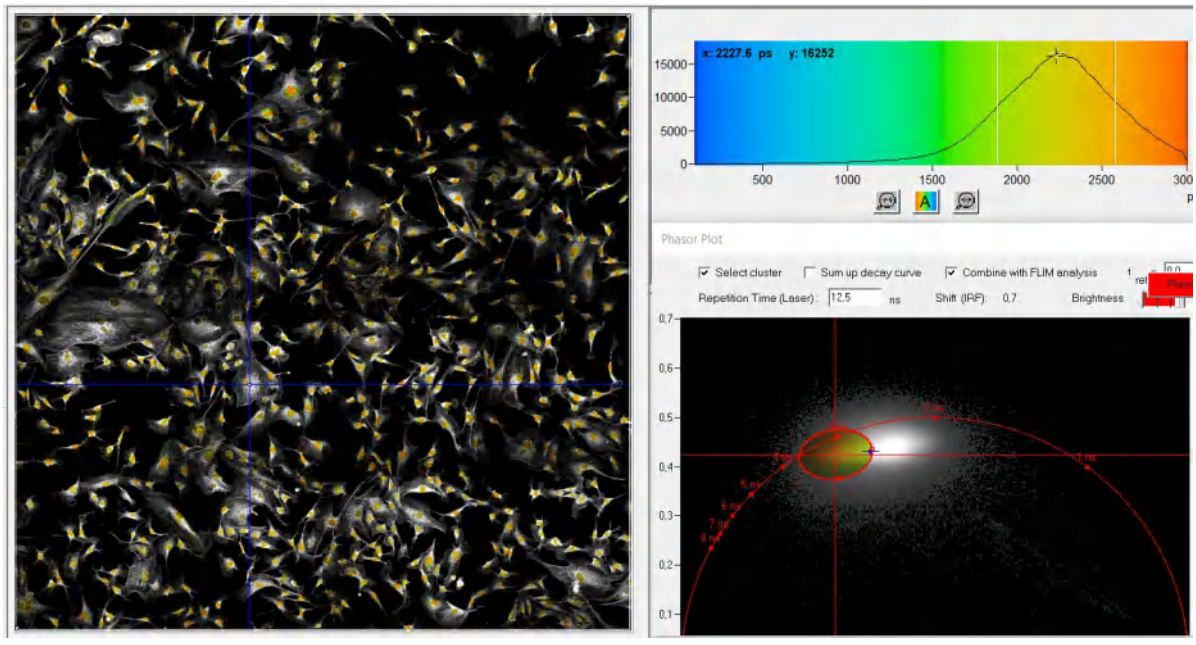


Fig. 1258: Image segmentation by phasor plot.

Analysis of Moving Objects

Biological objects can move during the FLIM acquisition. The images, and, consequently, the fluorescence-decay information, is then smeared out over the a distance the object has moved during the acquisition time. A solution to this problem is provided by the Mosaic FLIM mode of the bh TCSPC modules. A large number of fast scans is performed, and the images are written in a Mosaic FLIM data array. Of course, the number of photons in the individual mosaic elements is too low to obtain precise lifetime information from them. However, if image

segmentation is applied to the entire mosaic, and decay data of the selected image details are combined, a decay curve with a high number of photons is obtained.

An example is shown in Fig. 1259. The mosaic elements are 0.5-second scans of a water flee. The task is to obtain accurate decay parameters from the leg (yellow in the FLIM image) of the water flee. The leg is moving, and thus appears in different locations in the individual images. The number of photons contained in a single mosaic element is not enough for precise decay analysis, see decay curve in Fig. 1259, top. To obtain precise fluorescence-decay information from the leg, load the mosaic in the phasor plot, and select a phasor range that corresponds to the decay signature of the leg, see Fig. 1259, top. Then select 'Select Cluster' and 'Sum up decay curve', see Fig. 1259, bottom. The result is a single decay curve containing an enormous number of photons. It can be analysed at high precision with a multi-exponential decay modes, as shown in the decay parameters in Fig. 1259, bottom.

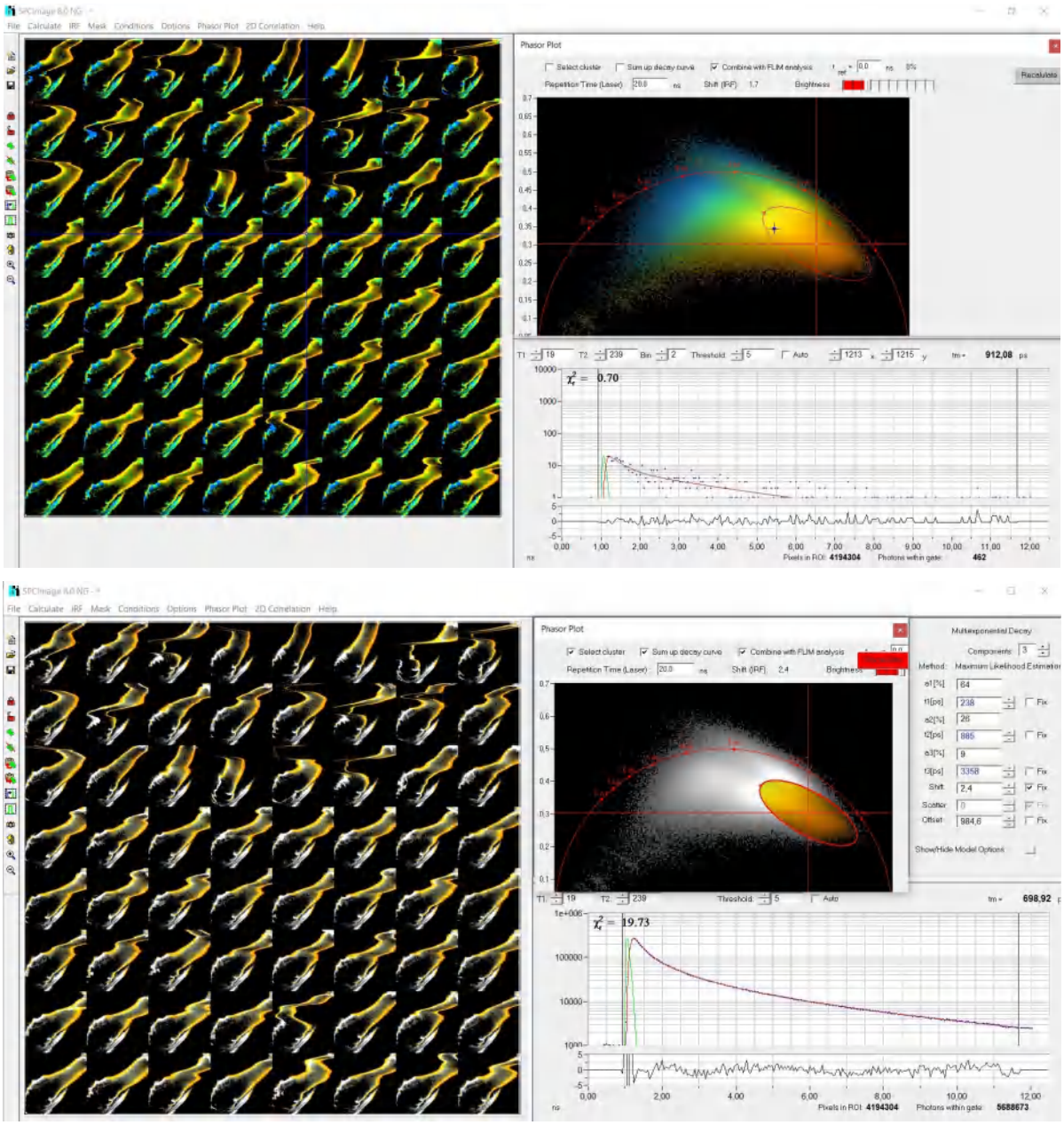


Fig. 1259: Analysis of a moving object by Mosaic FLIM and image segmentation

Model Parameters

Details of the model functions and details of the algorithms, parameter constraints, and IRF definitions are defined in the Model-Parameters panel. The panel differs for the least-WLS (weighted least square) fit and for the MLE (maximum-likelihood estimation) fit, see Fig. 1260, left and right. Fig. 1260 shows the Model Parameter panel as it was in version 9.0 and before. From version 9.1 on the panel has been changed. The new panel is shown in Fig. 1261 and Fig. 1262.

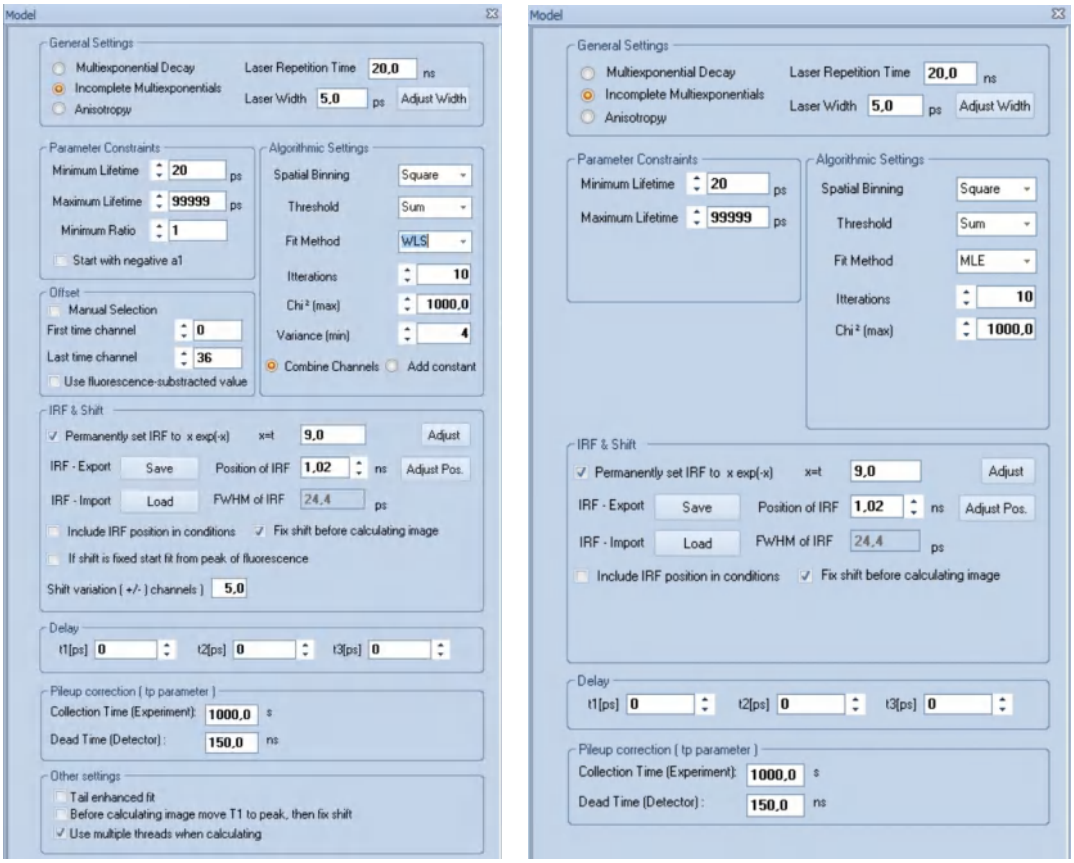


Fig. 1260: Model parameters, version 9.0 and before. Left: Weighted-least-square fit. Right: MLE fit.

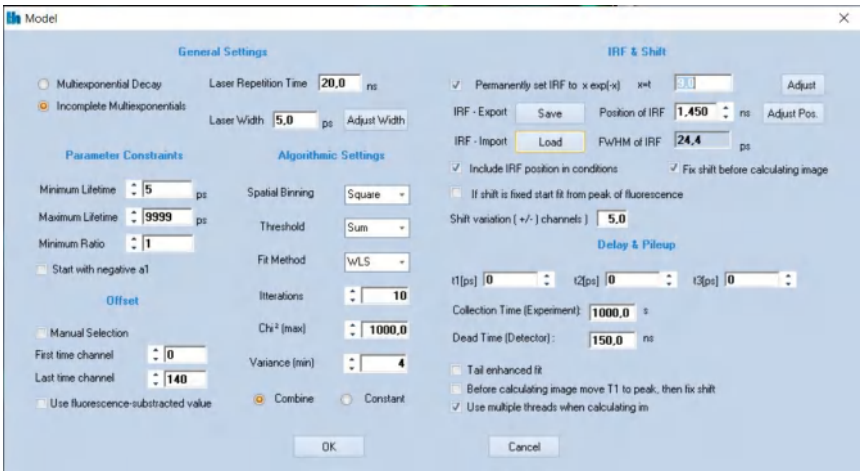


Fig. 1261: Model parameters, version 9.1 and later. Weighted-least-square fit.

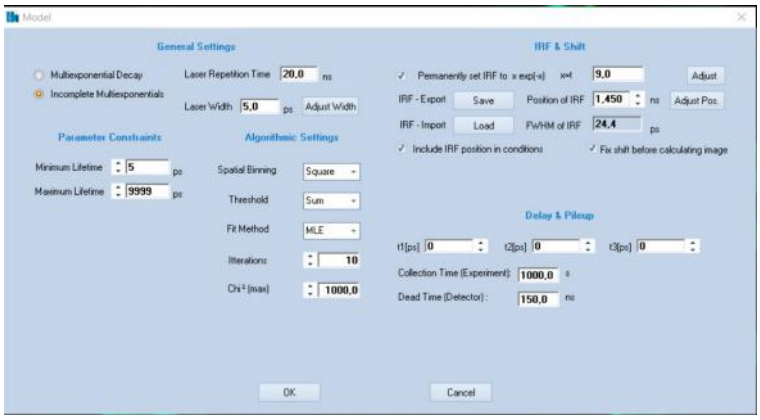


Fig. 1262: Model parameters, version 9.1 and later. MLE fit.

Model Options

'Multiexponential Decay' uses the traditional singe-, double, and triple-exponential decay models, see Fig. 1202. Fluorescence from previous laser pulses is not taken into account. 'Incomplete Multiexponentials' uses the same basic models but takes into account that the fluorescence does not necessarily decay completely within one laser pulse period. It therefore includes residual fluorescence from previous excitation pulse periods. Please see 'Incomplete-Decay Model', page 878.

'Laser Repetition Time' is required for the calculation of incomplete decay and for the phasor plot. 'Laser Width' is the width of the laser pulse. It is used in the determination of the synthetic IRF.

Fit Parameters

'Parameter Constraints' are used to prevent the algorithm from running into irrelevant parameter ranges.

'Offset' is used for WLS only. It allows the user to define a time interval where the counts represent the real counting background. If 'Manual Selection' is not set the offset is determined from the time interval left from the rise of the fluorescence. 'Offset' is irrelevant for MLE because it handles the baseline offset as a real fit parameter.

'Algorithmic Settings' define parameters concerning the fit algorithm. 'Spatial Binning' defines the shape of the area of pixel binning (when used). It can be 'Square' or 'Circle'. 'Threshold' defines whether the 'Threshold' parameter in the decay-curve window is the photon number at the peak of the fluorescence or the total number of photons in the decay function.

'Fit Method' can be 'WLS' (weighted least squares), 'MLE' (maximum likelihood estimation), or MOM (first Moment). Note that only MLE uses GPU processing.

'Iterations' is the maximum number of iterations performed by the fit algorithm. Please note that it refers to the *maximum* number of iterations. In most cases the fit procedure reaches a final fit earlier, and stops when no further improvement is obtained. Chi^2(max) is a maximum of the χ^2 allowed for the WLS algorithm.

'Combine Channels' and 'Add Constant' can be used to tweak the performance of the WLS fit for data with low photon number. Normally 'Combine Channels' is used, i.e. the algorithm uses progressive binning of time channels when the average photon counts per channel approach zero. 'Add Constant' does not bin time channels but adds a 'Minimum Variance' to the least square. The traditional value is '1' but higher values can be used to reduce lifetime bias at low photon number.

IRF Definition

The parameters under 'IRF & Shift' define the IRF and its use in the calculation of the decay functions. We recommend to use 'Fix the shift before calculation'. The IRF is then shifted into an optimum temporal position before the calculation starts, but not shifted any more during the calculation of the entire image. The shift *before the calculation* is limited by 'Shift variation'. In case the fit does not produce reasonable result, please check that 'Shift variation' is large enough.

'Permanently set IRF to x exp(-x)' and the parameter right of it define the synthetic IRF. The 'Adjust' button on the right starts an optimisation procedure for the synthetic IRF. Please see 'Instrument Response Function', page 942. The 'FWHM' of the IRF is displayed for information only. It includes the IRF model function $t/t_0\ e^{-t/t0}$ and the width of the laser pulse defined by 'Laser Width'.

Shifted Component Models

The 'Delay' parameters are used for the shifted-component model. t_1, t_2, t_3, are applied as shifts to the corresponding decay components. Negative values shift the component to the left, positive values to the right. For application of the model please see 'Ophthalmic FLIM', page 590.

Other Settings

'Other Settings' contain a 'Tail-Enhanced Fit' to improve the fit of weak slow decay components, a function that automatically sets of the left cursor of the decay function to the beginning of the rising edge, and multi-threading. Please note that multi-threading is irrelevant for MLE with GPU processing - the GPU processing is parallel by definition. 'Collection Time' and 'Dead Time' are used only to determine pile-up corrected lifetimes, see 'Parameters of the Decay Functions and their Use in SPCImage', page 949. The parameters are not needed under normal conditions.

Enable / Disable User Access to Parameters

In the default state of SPCImage all model parameters are accessible by the users. It is, however, possible to disable user access to selected model parameters. The function was implemented for clinical applications where certain model parameters must not be changed by unauthorised users. To disable access to parameters, open the 'Preferences' panel and switch to 'Expert Mode'. When back in the model parameters, you now can disable parameters by a double click on the parameter name. The parameter name then turns red, meaning that the parameter access has been disabled. Please see Fig. 1263, left and middle. To enable access to disabled parameters double-click again on the name. After switching back to non-expert mode in the Preferences the disabled parameters are greyed out, see Fig. 1263, right.



Fig. 1263: Enable / disable access to selected model parameters. Left: Expert mode in 'Preferences'. Middle: Disabled parameters are shown in red. Right: In non-expert mode the disabled parameters are greyed out.

Preferences

The ‘Preferences’ panel defines general options of SPCImage. The panel is shown in Fig. 1264.

Layout

This part of the preferences defines the layout of the SPCImage main panel.

Extra Intensity Image: In early SPCImage versions a separate greyscale intensity image was displayed together with the lifetime image. In the past 10 years the display of a separate grey scale image came out of use. Unless you are used to the old style we do not recommend to use this option.

Widescreen adapted: This option uses an aspect ratio which is adapted to modern screens with a wide aspect ratio. Unless you have an old computer screen we recommend to turn on this option.

Toolbar: The toolbar on the left of the main panel can be displayed with small icons (Lean Icon Set) or large icons (Extended Icon set). Unless you are very familiar with SPCImage we recommend 'Extended'.

Lifetime Window

‘Zoom in Lifetime Windows only’ restricts zoom operations performed in a lifetime window to this window. If the option is not set a zoom in the lifetime window zooms also the image in an intensity window (if one is displayed).

‘Center ROI to selected pixel’ couples a rectangular ROI (selected by the white image cursors) with the blue image cursor. You can shift the selected area around with the cursor and examine the pixel-parameter histograms for the different areas.

Distribution Window

Pixel parameter histograms can be weighted with the pixel intensity (photon number) or just represent the number of pixels in which a particular parameter value is present. The histograms can be calculated over the full range of the parameter values or only in the parameter range selected in the ‘Colour’ options panel.

Instrumental Response

The IRF can either be displayed or not displayed in the decay curve window. The calculation of an IRF can be performed at the brightest pixel or at a selected cursor position. To get an impression of whether the IRF reasonable fits to the decay data we recommend to always display the IRF in the decay window. 'Always calculate at brightest pixel' determines the IRF at the brightest spot of the image. However, this can lead to an incorrect result if the brightest spot is a speck of dirt or another artefact. So recommend to turn this option off.

Start Properties

New instance when receiving data from SPCM: When SPCImage contains data and a new data transfer from SPCM is started a new instance of SPCImage can be started or previous data can be overwritten. Starting new instances helps the user compare different data. However, old instances should be closed from time to time.

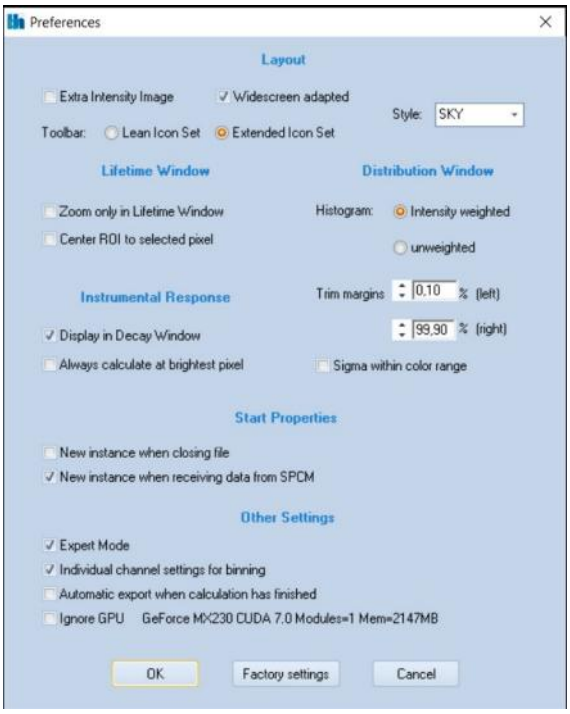


Fig. 1264: Preferences panel of SPCImage, showing parameters and recommended settings.

Other Settings

'Expert Mode' puts SPCImage in a mode where the user can disable and enable the access to certain Model Parameters. There is no need to set 'Expert Mode' unless you want restrict the access to certain model parameters or you want enable the access to parameters which have been disabled before. Please see Fig. 1263.

‘Individual channel settings’ means that the binning factor and the cursor position for IRF calculation are individual for several images (from different SPC modules or from different routing channels) loaded into SPCImage. Otherwise the same binning and the same positions for IRF calculations are used.

'Automatic Export' exports data according to the options in the Export panel when the calculation is finished.

'Ignore GPU' prevents SPCImage from using a GPU. (The type of the GPU is shown on the right). There is no need to use this option unless a GPU in the system is causing trouble.

Configurations

'Configurations' allows you to save and load configuration data of SPCImage. A click into Options, Configurations, opens the panel shown in Fig. 1265, left. To save the current configuration, left-click into one of the empty fields on the left. The field will then show a small icon of the current image for later identification. To load a configuration, left-click into the field that shows the image of the desired configuration. To delete a configuration, right-click on the field with the configuration to be deleted. Configurations can also be stored into and retrieved from files, please use 'Export' and 'Import' to do so. Important: A configuration to be loaded must have the same timing parameters and number of time channels as the current data.

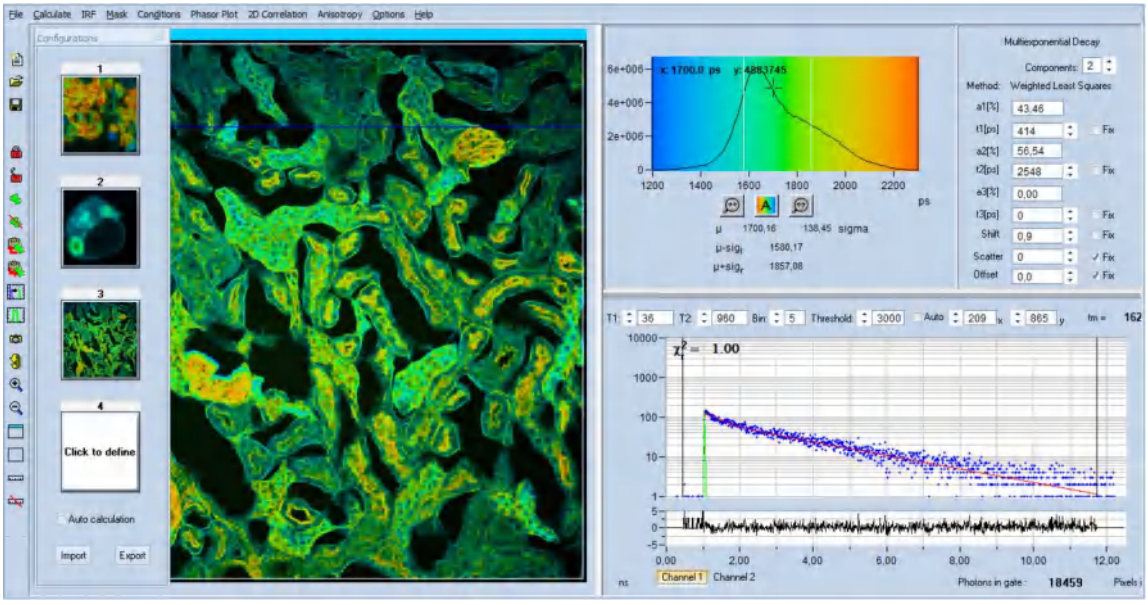


Fig. 1265: Loading and saving Configuration data

Analysis of Special Data Types

Single-Curve Data

Data from Cuvette Experiments

Decay data recorded in traditional cuvette-based setups can be imported into SPCImage and analysed with the normal set of models and model options. There are two ways to import the data into SPCImage. Import via the normal import function of SPCImage is shown in Fig. 1266.

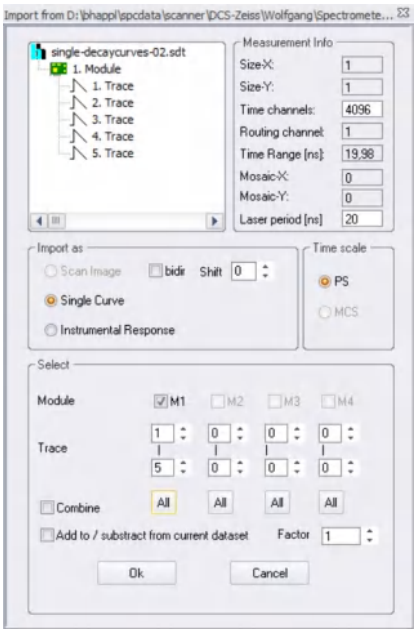


Fig. 1266: Import of single-curve data via the import function of SPCImage

Select 'Single Curve, select the SPC module from which you want to import data, select a range of 'Pages' (see SPCM software) and click OK to import the decay curves.

Data can also be transferred to SPCImage by the 'Send Data' of SPCM. Click into ‘Main’, ‘Send Data to SPCImage’. This opens a select panel in the SPCM curve window, see Fig. 1267. It contains the numbers of pages (traces) which are active in the '2D Trace Parameters'. Select the curves you want to send, and click on ‘OK’.

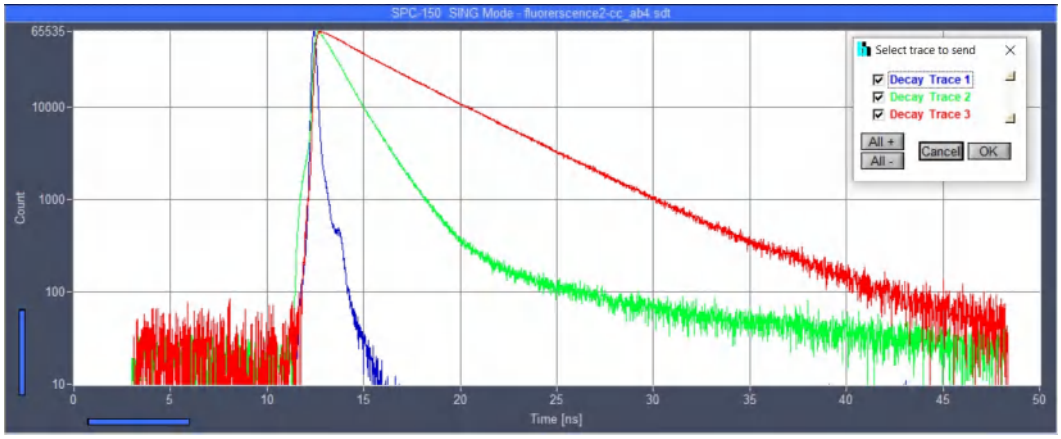


Fig. 1267: Sending single curves from SPCM to SPCImage

The result of the data import is a decay curve window as shown in Fig. 1268. With the 'Channel' tabs bottom left you can switch between the individual curves (pages in SPCM) which you have imported before. In the example there are three of them. If one of the curves contains an IRF which you want to use for the analysis, select the corresponding 'Channel'. In Fig. 1268 it is in 'Channel 1', and 'Channel 1' has been selected.

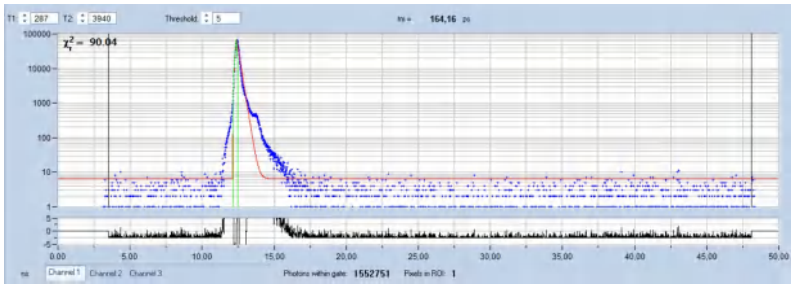


Fig. 1268: Decay window after import of data. If there are several curves the desired one can be selected by the 'Channel' tabs. In the example shown Channel 1 is an IRF.

Enclose the signal peak with the cursors, see Fig. 1269. Then declare it an IRF. Either click 'Copy from Decay Data' under 'IRF' or (data to IRF) in vertical bar on the left.

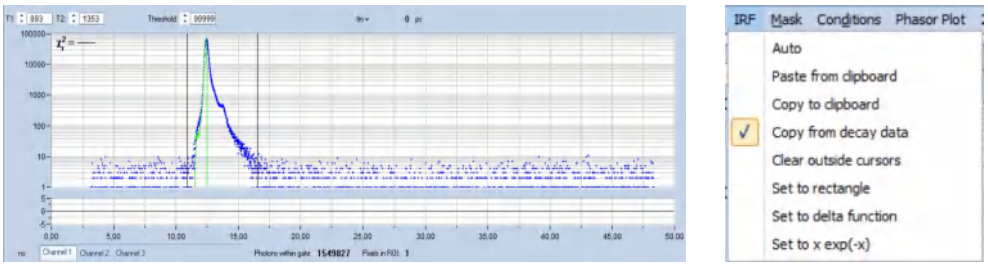


Fig. 1269: Signal peak enclosed by cursors for IRF definition. Right: Decay the selected signal part an IRF.

The result is shown in Fig. 1270, left. The green curve is the IRF. Use 'IRF', 'Copy to clipboard' to have the IRF available for the analysis of decay curves in other channels.

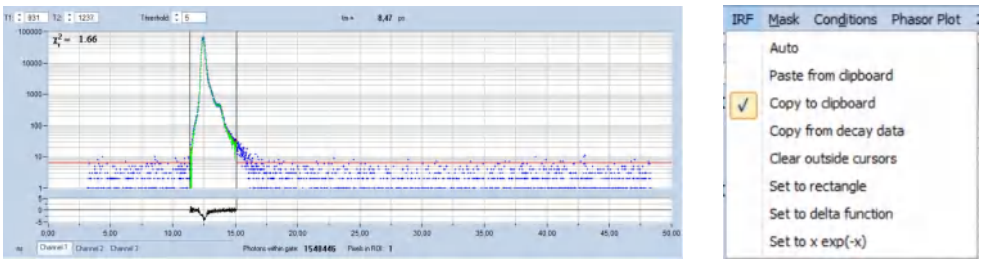


Fig. 1270: The signal peak in Channel 1 has been declared an IRF. Right: 'Copy to clipboard' makes the IRF available for analysis of the decay curves in other 'Channels'.

Then click on a 'Channel' which contains a decay curve to be analysed. The curve is still shown with the 'Auto IRF', as shown in Fig. 1271. To show it with the measured IRF click 'IRF', 'Paste from Clipboard'. The result is shown in Fig. 1272.

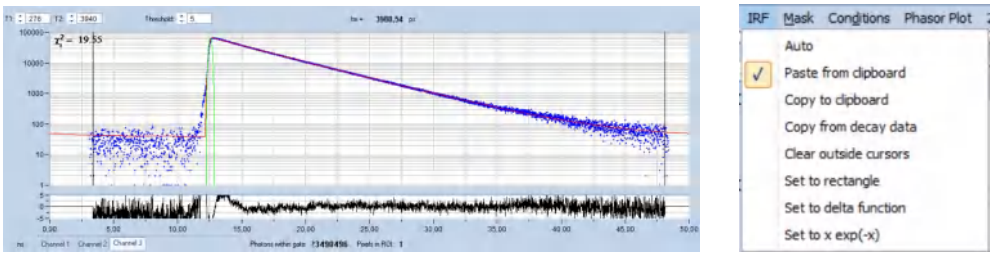


Fig. 1271: 'Channel 3' has been selected by the tab bottom left. It contains a decay curve. It is still shown with the 'Auto' IRF.

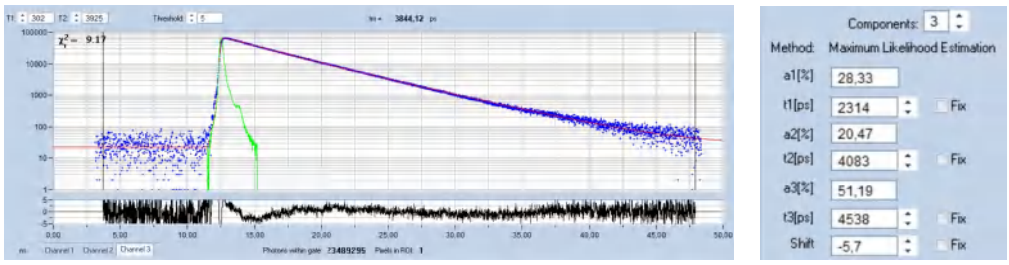


Fig. 1272: 'Paste from clipboard' has been executed to analyse the data in channel 3 with the real IRF.

Single-Curve Data from Scanning Experiments

Single-curve data can also be obtained in a FLIM system. A dish with a solution of the dye to be investigated is placed on the microscope stage, and FLIM data of the solution are recorded. To analyse such data, import them into SPCImage by the normal import procedure for FLIM data. Click the (lock) button to combine the decay data of the entire image area (or of an area selected by the image cursors) into a single decay curve. Select the desired decay model parameters and fit parameters, and choose or create an IRF. The fit process starts instantly (no need to start 'Calculate'), and the decay parameters are shown in the upper right of the SPCImage panel. A result is shown in Fig. 1273.

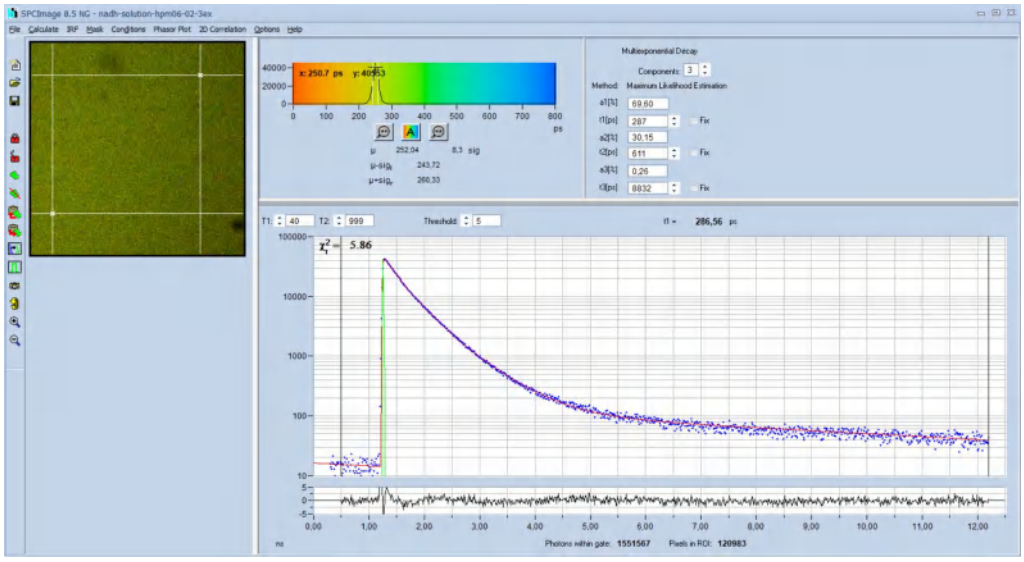


Fig. 1273: Combination of decay data from an image area into a single curve, and data analysis with triple-exponential model. NADH solution, DCS-120 MP system with HPM-100-06 detector.

Pseudo-Global Analysis

SPCImage allows you to fix one or several of the component lifetimes. A typical example is the donor fluorescence in FRET experiments. Theoretically, the slow lifetime component comes from non-interacting donor molecules. In first approximation, it should therefore be constant throughout the image. Another example is autofluorescence FLIM. The variation the mean lifetime is essentially (but not entirely!) caused by variation in the amplitudes of the components.

To use fixed lifetimes of the components, first run a double- or triple-exponential analysis with all lifetimes defined as free fit parameters. Take a look at the lifetime histograms of the component lifetimes. Then fix the lifetimes to the most frequent values found in the histograms, and run a new analysis.

An example for autofluorescence data is shown in Fig. 1274. Fig. 1274, left, shows the result of an analysis with τ_1, τ_2, and τ_3 free. Fig. 1274, left, shows the result of an analysis with τ_1, τ_2, and τ_3 fixed to the maxima of their distributions. The image of the mean lifetime (t_m) is the same. However, the analysis with fixed lifetimes delivers amplitudes at better signal-to-noise ratio.

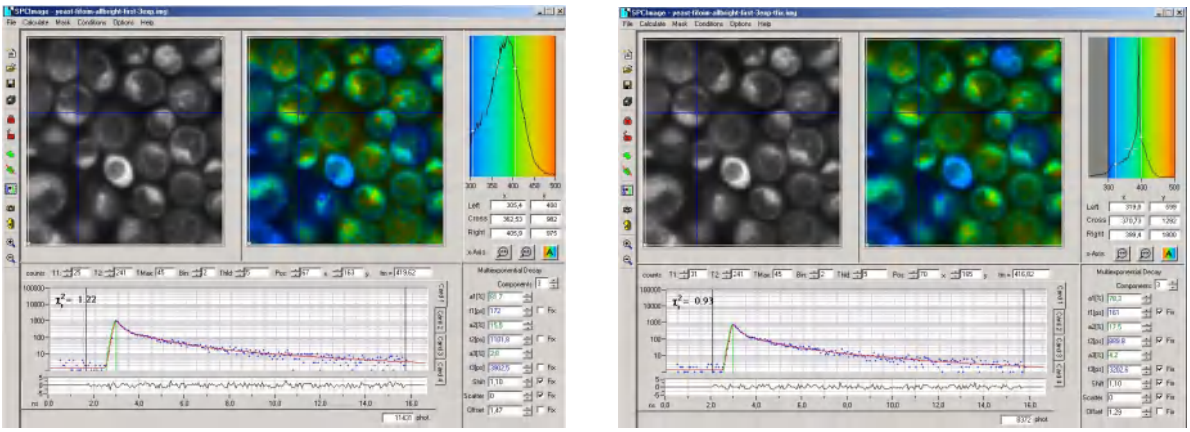


Fig. 1274: Left: Analysis with free τ1, τ2, τ3. Right: Analysis with τ1, τ2, τ3 fixed to the maxima of their distributions. The result is the same. However, the amplitudes are obtained at higher accuracy.

This does not mean that the systematic errors are similarly low. For all lifetime components there are usually subtle lifetime variations, induced by variation in the local environment or the refractive index [153, 1263]. If a lifetime used as fixed parameter is not really constant the fit procedure compensates for the variation by large changes in the amplitude or in the lifetimes of other decay components. The result can be large systematic errors in these parameters.

Global Analysis

Unlike the 'Pseudo-Global' fit described above, a true Global Fit does not use a priori information on the values of any of the component lifetimes. No matter what the component lifetimes are, the global fit only assumes that the lifetimes of one or several decay components *do not vary over the pixels of the image*. That means, the global fit procedure runs iteration cycles each of which is a complete multiexponential fit of all pixels of the entire image. Each cycle uses a different combination of the global parameters until the best possible fit of the entire image is obtained.

Consequently, a global fit is extremely-computation intensive. Assuming that about 20 global iteration cycles are required to obtain the final result the calculation time is 20 times that of a 'normal fit'. In practice, a global fit can therefore only be performed on a GPU. Therefore, please check whether your system has a GPU and whether SPCIMage is using it. You see this from the progress bar during the calculation, see Fig. 1275. It should read 'GPU Calculation', and a normal fit should be finished within a few seconds.

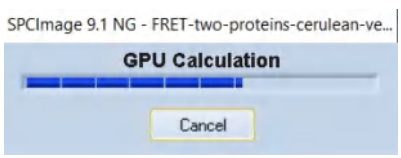


Fig. 1275: Progress bar during the calculation of an image

Global analysis is a powerful technique to obtain accurate amplitude images from multiexponential FLIM data with constant component lifetimes. Different than pseudo-global fitting it does not require that any of the component lifetimes be known. Applications are separation of fluorophores in samples containing mixtures of fluorophores, FLIM-FRET data, and,

especially, metabolic-FLIM data. In FRET-FLIM data the lifetime of the non-interacting donor is constant. In metabolic FLIM data the component lifetimes of bound and unbound NADH and FAD are constant, as are the lifetimes of NADPH and FMN. The observed changes in the net lifetime are caused by changes in the amplitudes of the decay components.

For FAD the situation is especially complicated. The data not only contain the decay components of bound and free FAD but also a noticeable contribution from FMN. Therefore triple-exponential decay analysis has to be used. An example is shown in Fig. 1276 and Fig. 1277. Both images show the amplitudes, a1, a2, and a3 of bound FAD, free FAD, and FMN. Fig. 1276 shows a 'normal' triple-exponential fit of the data. It is evident that the signal-to-noise ratio is not sufficient to derive the metabolic state from the data. Fig. 1277 shows the result of a global fit with the component-lifetimes t1 (bound FAD), t2 (free FAD), and t3 (FMN) defined as global parameters. The improvement in signal-to-noise ratio is amazing. Not only are the amounts of bound and free FAD reproduced clearly, also the amount of FMN is obtained at high accuracy.

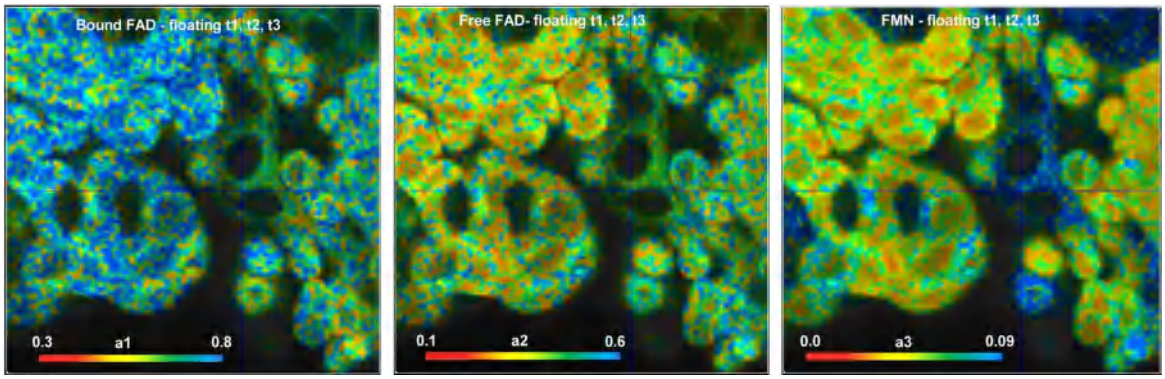


Fig. 1276: Human epithelial bladder cells, amplitudes a1, a2, and a3. Standard MLE fit

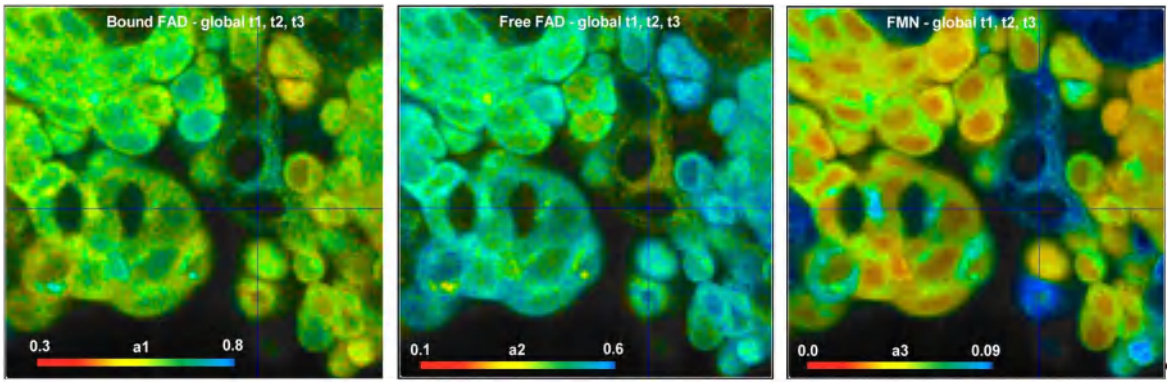


Fig. 1277: Same cells as above. Global fit with global component lifetimes t1, t2, t3.

Multi-Wavelength Lifetime Images

Traditional Multi-wavelength FLIM data from SPCImage represent 16 'channels', each of which holds a complete lifetime image for a particular wavelength interval. The data are imported into SPCImage NG as shown in Fig. 1278, left. After importing, individual channels can by accessed via 16 individual tabs at the bottom of the decay window, see Fig. 1278, bottom right. Individual channels can be selected and analysed individually. However, it is more comfortable to use the ‘Analyse all’ function as shown in Fig. 1278. The function runs the decay fit procedure in all wavelength intervals of the multi-wavelength FLIM data set.

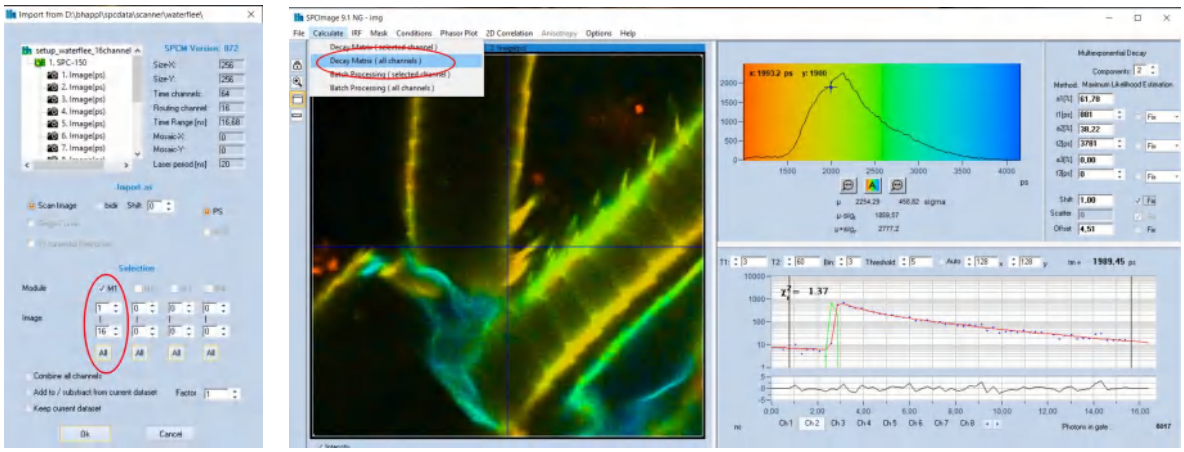


Fig. 1278: Left: Importing multi-wavelength data. Right: The data are analysed by 'Calculate', 'Decay Matrix (all channels)'. Individual wavelength channels can be selected via the tabs below the decay-curve window.

The wavelength channels have separate fit parameters. Before starting the analysis, it is recommended to switch through all wavelength channels and set appropriate fit parameters and fit conditions. When this is done, click on ‘Calculate’, ‘Analyse all’.

Recent SPCM versions have a 'Mosaic Imaging' function which can be used to record multi-wavelength FLIM data. Mosaic Imaging records the wavelength channels into individual mosaic elements of a large data array. When such data are imported via the import function of SPCImage the wavelength channels are treated as routing channels, and show up as individual images, as shown in Fig. 1279.

However, when the data are sent to SPCImage via the 'Send to SPCImage' function of SPCM the entire array set is sent as a single, large FLIM image, see Fig. 1279. Of course, the size of mosaic data is enormous, and the processing effort is high. The analysis can therefore be reasonably performed on systems with a GPU only. The result of the analysis is shown in Fig. 1279.

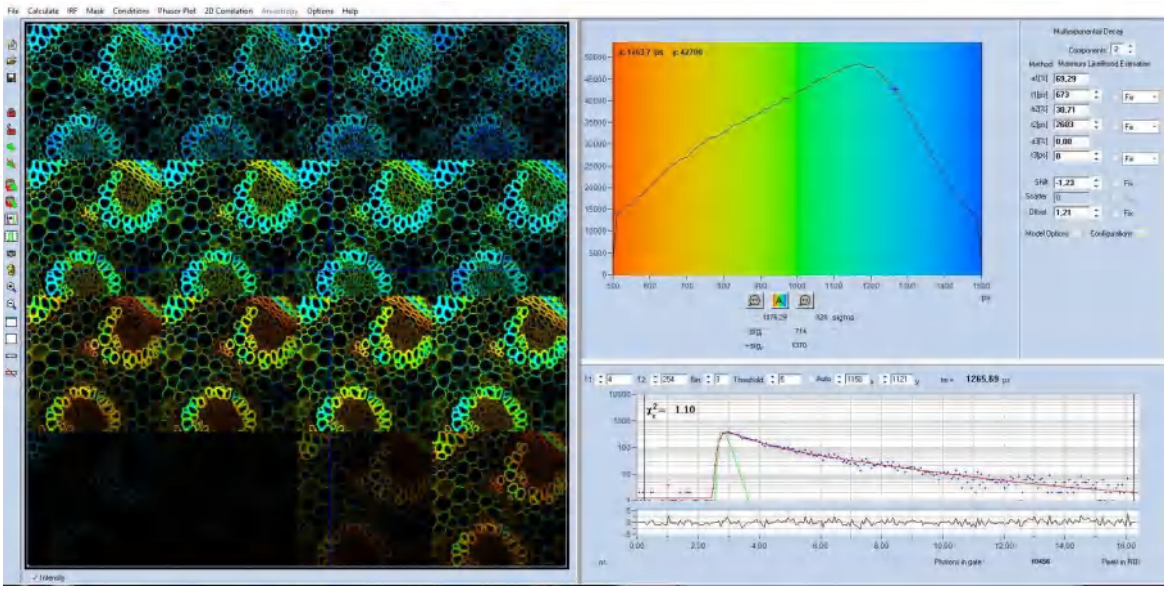


Fig. 1279: Multi-wavelength FLIM mosaic, sent to SPCImage by the 'Send to SPCImage' function of SPCM. The data are treated as a single, large lifetime image. Amplitude-weighted lifetime of double-exponential decay.

Analysing the entire multi-wavelength array at once has two advantages over analysis of the individual images. First, the procedure is more convenient to the user and, second, the array can be analysed with global analysis. This is helpful if there are decay components the lifetimes of which do not change with the wavelength. However, there is also caveat. Multichan-

nel detectors usually display a systematic wobble in the transit time over the channels. This can show up as a systematic lifetime variation over the elements of the mosaic. The analysis should therefore be performed with free 'Shift', see Fig. 1279 upper right. In the Model Parameters, please turn off 'Fix Shift before calculating Image'.

Spatial and Temporal Mosaic FLIM Data

Mosaic FLIM data contain an array of images in a single FLIM data file. The data can represent a spatial mosaic of images, a Z stack of images, time-series images, or multi-wavelength data. Spatial or temporal Mosaic FLIM data have the same data structure as a single, large FLIM image. The data can either by sent to SPCImage via the Send Data to SPCImage' or be loaded into SPCImage via the 'Import' function. Once imported, the data are analysed in a single analysis run. An example is shown in Fig. 1280. The mosaic shows 64 images of a leg of a live water flee, recorded with an acquisition time of 0.5 seconds each. Each element of the Mosaic has 252 x 256 pixels, hence the entire mosaic has 2048 x 2048 pixels. The array was analysed by the MLE algorithm, with a double-exponential model.

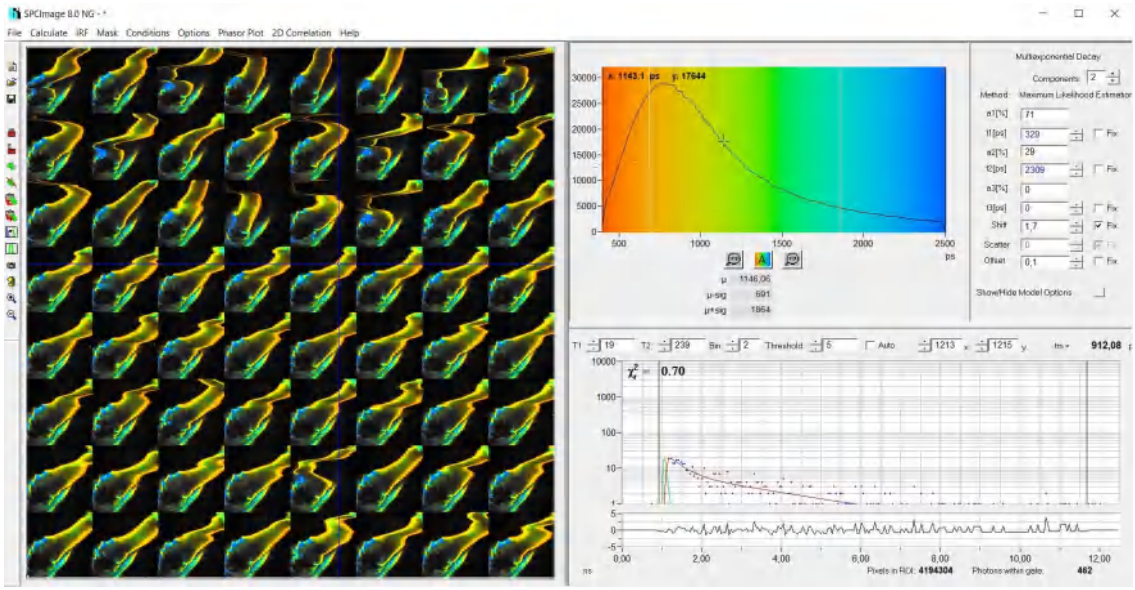


Fig. 1280: Mosaic FLIM of the leg of a water flee, 64 images of 0.5 s acquisition time.

When the data are analysed the traditional way the large image size of a mosaic array may result in very long calculation times. We therefore recommend to run the calculation on a GPU and use the MLE algorithm. The calculation time is then reduced to about 10 seconds.

If there is no GPU in the system we recommend to try an analysis of a small part of the Mosaic image first (e.g. of a single mosaic element). Check the results and make sure that the correct model function and the correct model parameters are selected. When you are satisfied with the result start the analysis of the entire mosaic.

INT FLIM Data

INT FLIM ('Intensity-FLIM') is used to obtain a linear intensity scale of FLIM at high count rates. The data are a combination of normal TCSPC FLIM data and pixel intensity data from a fast counter. Images are created by using the fluorescence-decay curves in the pixels from the

TCSPC channel and the intensities from the counter channel. Please see Lifetime-Intensity FLIM, page 428 for technical details.

INT FLIM data are transferred from SPCM to SPCImage by the 'Send Data' command. SPCM sends both the FLIM data and the intensity data, and SPCImage loads the intensity data as 'Additional Intensity Data', see Intensity Parameters. The corresponding function is activated automatically, see Fig. 1281. Once loaded into SPCIMage, INT FLIM data are processed like standard FLIM data, see Fig. 1282.

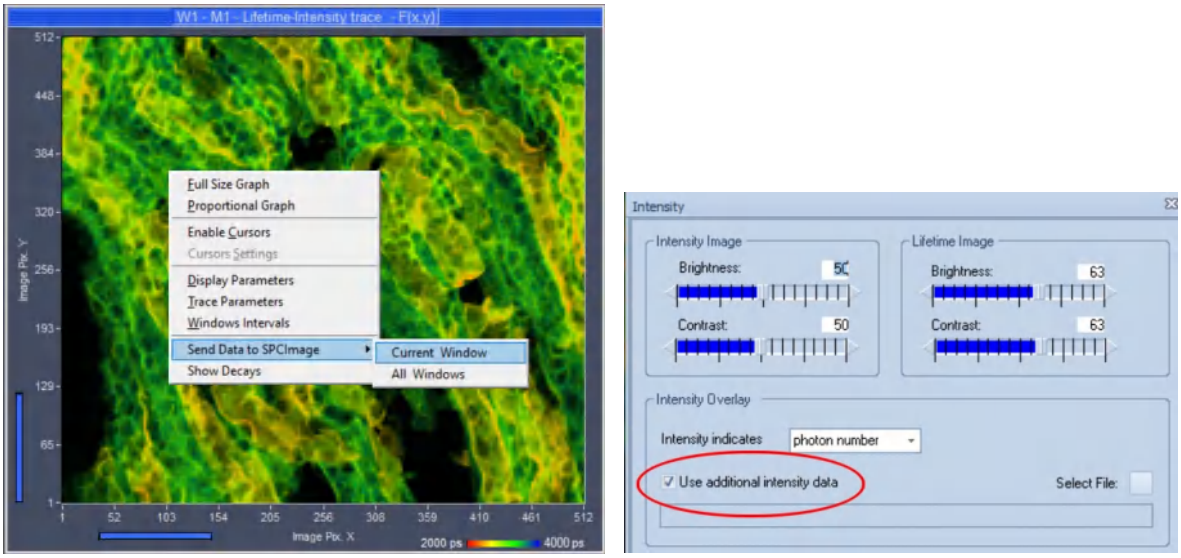


Fig. 1281: Transfer of INT FLIM data to SPCImage. Left: Send Data command in SPCM. Right: SPCImage automatically uses the fast-counter data as 'additional intensity data'.

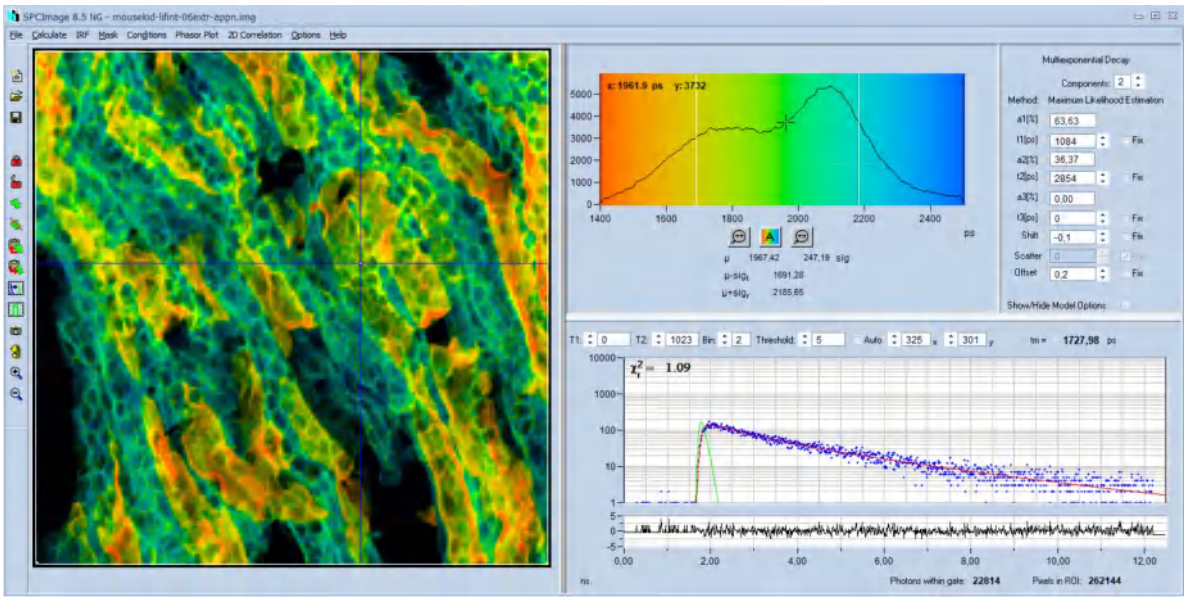


Fig. 1282: SPCImage with INT-FLIM data

Phosphorescence Lifetime Images

Analysis of phosphorescence lifetime images, in principle, works the same way as FLIM analysis. A few differences, do, however, exist.

Sending PLIM Data to SPCImage

The SPCM main panel of a typical FLIM/PLIM setup is shown in Fig. 1283. From left to right, there is a FLIM window, a PLIM window containing only photons in the 'laser-off' periods, and a PLIM window containing the photons both from the laser-on and the laser-off phases, see waveforms above the display windows.

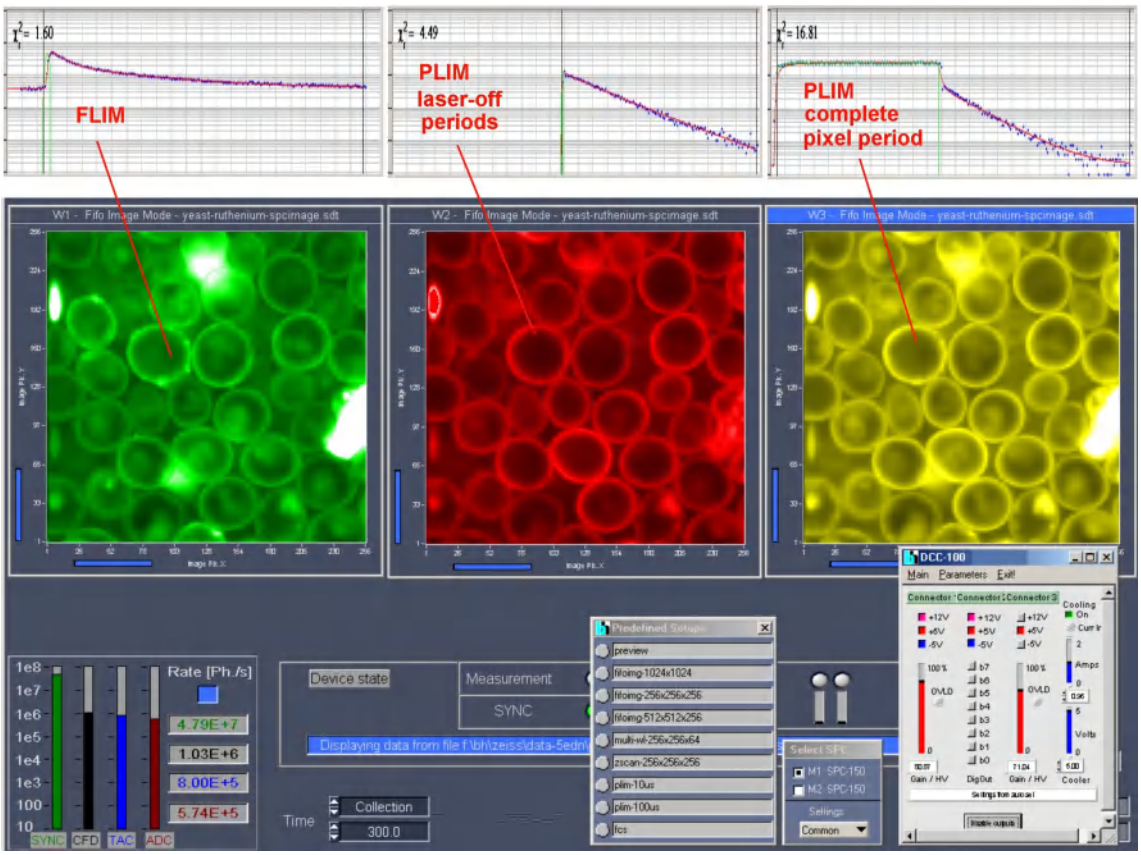


Fig. 1283: Main panel of SPCM, configured to show intensity images of FLIM data, of pure PLIM data in the laser-off intervals, and of FLIM and PLIM data in the complete laser-on-off (pixel time) period. Above: Waveforms seen after sending the data to SPCImage

Because the FLIM and the PLIM data have totally different time scales they cannot be simultaneously loaded into SPCImage. To use the 'Send Data' function of SPCM, select 'Selected Window' in the SPCM Application Options. For sending data, click on the SPCM window you want to analyse, and then transfer it to SPCImage by the 'Send Data' command. Note that you can send data from a FLIM window or from a PLIM window, but not both together. The waveforms you see after sending the data of the windows to SPCImage are shown above the SPCM panel in Fig. 1283.

IRF of PLIM

For PLIM data acquired from samples with pure phosphorescence usually the automatic IRF generated by SPCImage can be used, see page 942. An example can be seen in the PLIM image of an Autumit crystal shown in Fig. 1284.

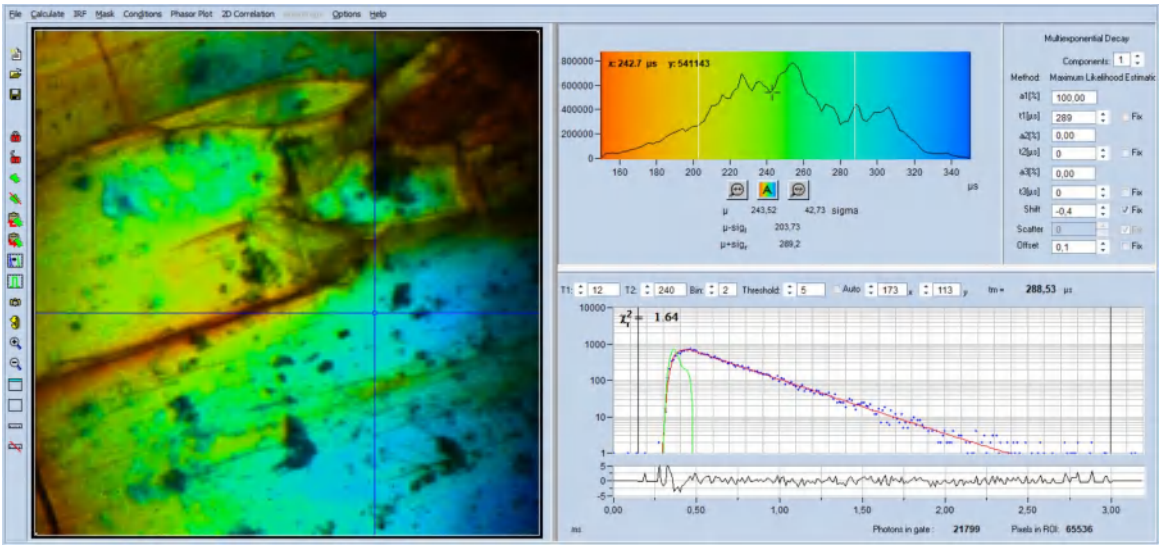


Fig. 1284: Analysis of PLIM data from an Autumit crystal. Synthetic IRF, single-exponential decay model.

If a sample emits also fluorescence, and FLIM is to be measured simultaneously with PLIM the situation can be different. In that case a much longer laser-on phase (extending over a substantial part of the pixel) is used. The IRF of the phosphorescence signal is then no longer a short pulse, and it may not correctly be reproduced by the automatic IRF generation.

There are several ways to obtain an IRF in these cases. One of them is to use the fluorescence pulse present in the data. Phosphorescence is an emission from the triplet state. The triplet state is populated by intersystem crossing from the first singlet state, S1. This is the state from where fluorescence is emitted. Strictly seen, the IRF of fluorescence is therefore the fluorescence pulse. The fluorescence pulse during the laser-on phases can usually be identified in PLIM data. The IRF is then generated by placing the cursors at the beginning and the end of the fluorescence and clicking the ‘curve to IRF’ button. An example is shown in Fig. 1285.

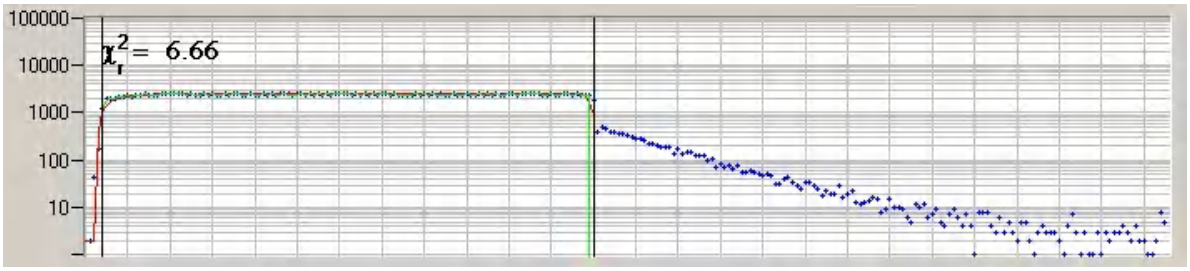


Fig. 1285: IRF from the fluorescence pulse during the laser-on phase. The fluorescence pulse has been selected by the cursors in the curve window, and declared an IRF via the ‘Curve to IRF’ button. The green curve is the IRF.

The procedure shown above works well if the laser-on period is dominated by fluorescence. However, if the dominating signals component in the laser-on phase is phosphorescence (this can happen for phosphorescence labels based on rare-earth chelates) the waveform does not represent the effective IRF. In that case, an IRF can be recorded from a sample showing only fluorescence.

A third way is to set the cursors in the curve window to the beginning and the end of the ‘Laser-on’ phase, and define a rectangular IRF by the (Rectangular IRF) button. Although the generated IRF ignores possible ringing or distortion in the laser-on modulation waveform it usually works reasonably well. A fourth way to deal with the phosphorescence IRF is to ignore it altogether and fit only the phosphorescence data in the laser-off periods, see paragraph below.

Fit Procedure

PLIM data from samples that emit predominately phosphorescence are analysed in analogy to FLIM. The only difference is the time scale, which may require to increase the maximum lifetime in the model parameter panel (see page 909). An example has been shown in Fig. 1284. The automatic IRF was used, and the decay profile was fitted by a single-exponential model.

PLIM data containing also fluorescence pose a bigger challenge to data analysis. To fit both the fluorescence and the phosphorescence the waveforms had to be fitted with a model that contains a component with the shape of the IRF for the fluorescence and one or several decay components for the phosphorescence. A model that takes these components into account is, in principle, available in SPCImage: It is a multi-exponential decay model with ‘Scatter’. The problem of this model is that it is (because of the ‘scatter’) extremely sensitive to the IRF shape. The IRF shape is, however, not accurately known. A better way to fit the data is therefore to restrict the fit to the laser-off phase where the signal does not contain fluorescence.

An example is shown in Fig. 1286. The data from the complete pixel period were sent to SPCImage. The IRF was taken from the fluorescence pulse during the laser-on phase. The phosphorescence data were fitted only in the decaying part of the curve, selected by the cursors in curve window. The intensity options for the lifetime image were set to ‘Gated Intensity’, see 'Intensity Parameters', page 892. The intensity data are therefore only from the interval between the cursors, i.e. from the phosphorescence.

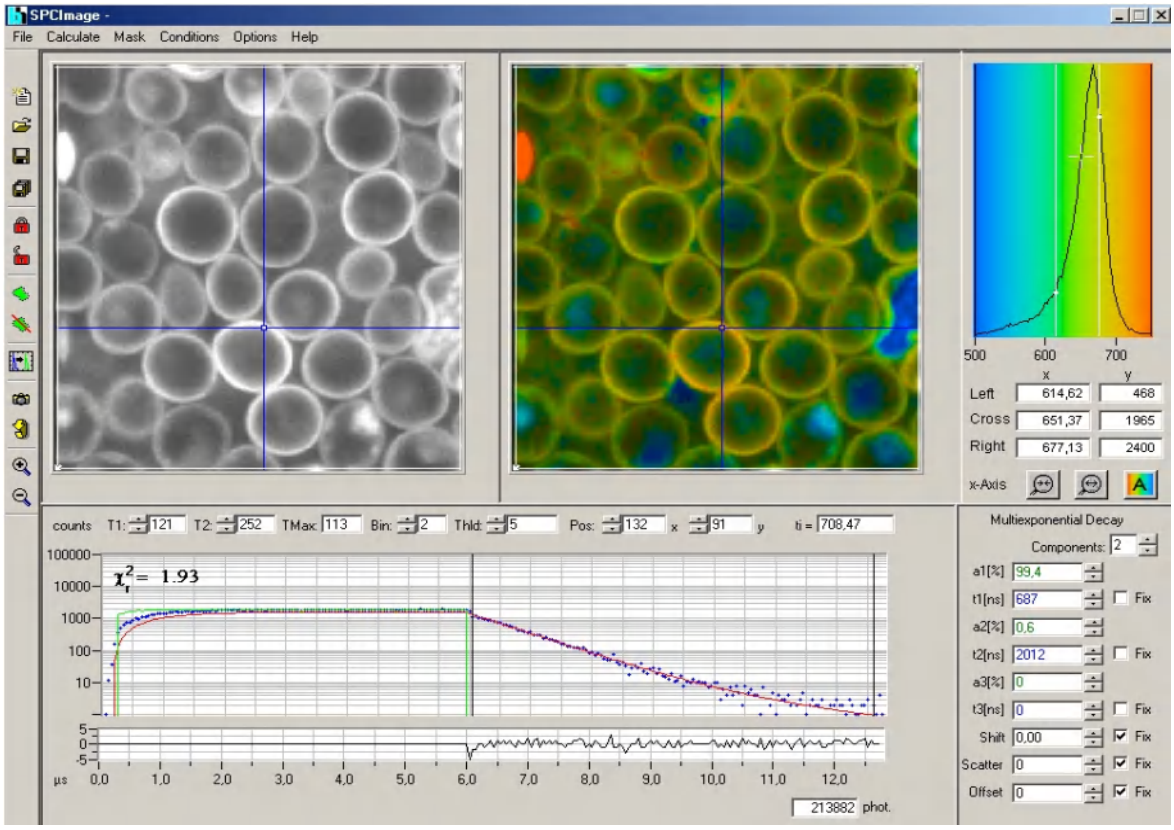


Fig. 1286: Analysis of PLIM data from yeast cells stained with ruthenium dye

FLIM Data Acquired Simultaneously with PLIM

FLIM data acquired simultaneously with PLIM are analysed as normal FLIM data. Send the FLIM data from the FLIM windows of SPCM to SPCImage by the 'Send Data' function. In SPCImage, select the desired model function and model parameters, and start the calculation with 'Calculate Decay Matrix'. It can happen that the FLIM data contain a large counting background. The background can originate from phosphorescence bleedthrough in the fluorescence channel. If fluorescence and phosphorescence were recorded in different TCSPC channels with different detectors the background can often be minimised by using the right filters. However, if the spectral overlap of the signals is large, or if fluorescence and phosphorescence were recorded in the same TCSPC channel some background can be unavoidable. In that case, leave the 'Offset' in the fit conditions floating and use MLE analysis. MLE is less susceptible to high background than WLS. An example is shown in Fig. 1287.

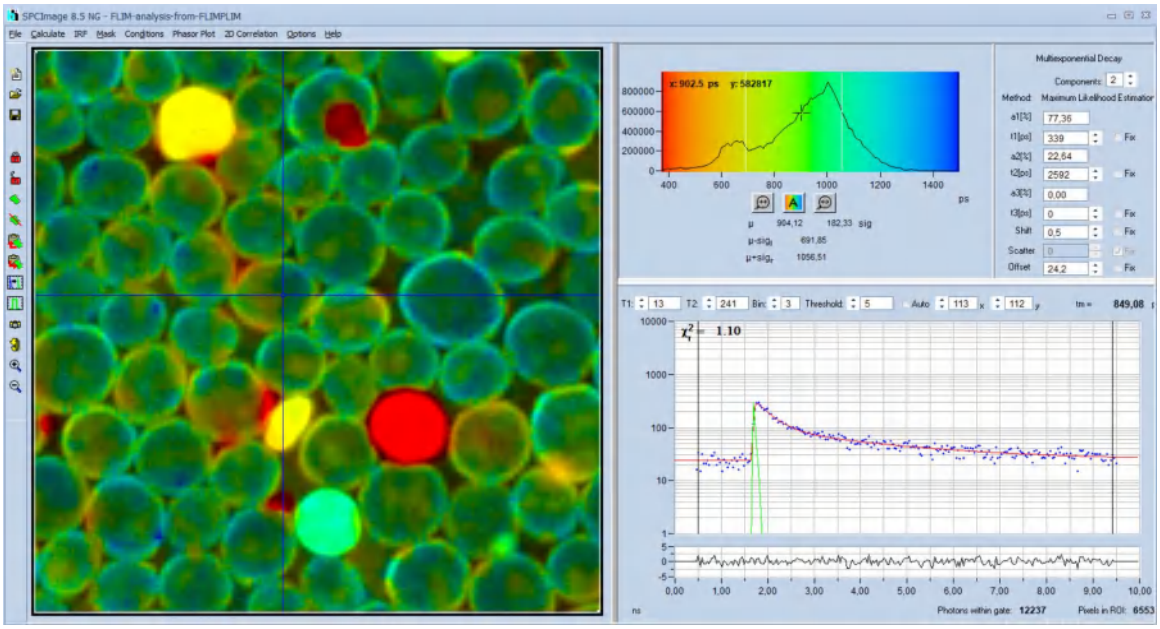


Fig. 1287: FLIM data from simultaneous FLIM/PLIM experiment

Batch Processing

The Batch Processing function allows the user to process a large number of similar FLIM data files automatically. The function is reached via 'Calculate' and 'Batch Processing'. Before you start the function import one of the sdt files you want to analyse and calculate a lifetime image from it. Make sure that you have set all model parameters and colour parameters correctly. When you are satisfied by the result proceed by clicking on 'Batch Processing'. This opens a file selection window as shown in Fig. 1288, upper right. Select the files to be processed.

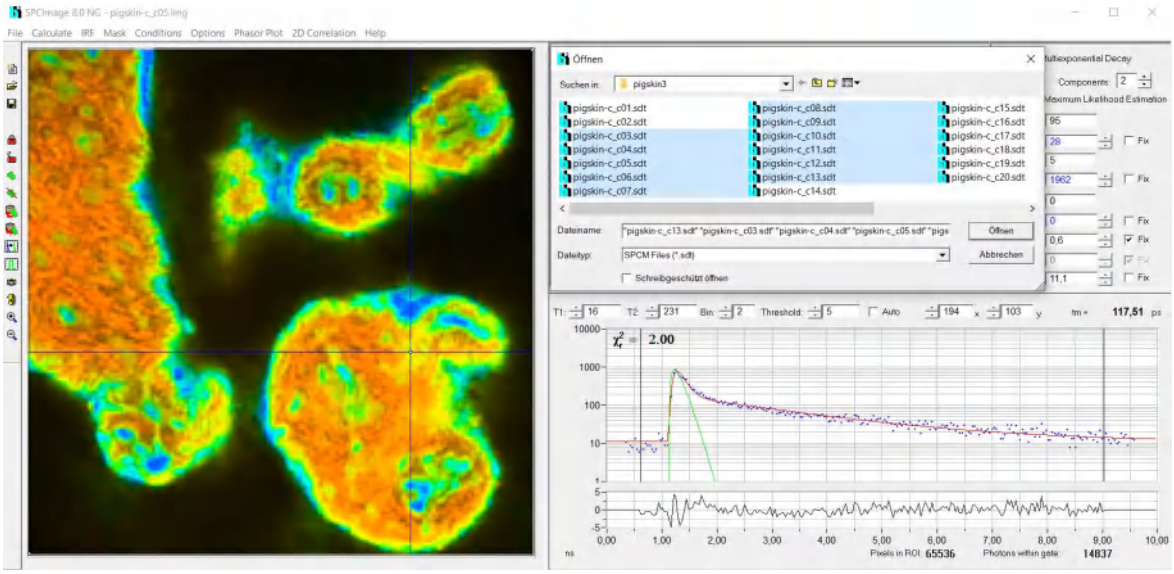


Fig. 1288: Batch Processing, selection of the .sdt files to be processed

Batch processing starts when you click the 'Open File' button in the selection window. One after another, SPCImage loads the selected files, analyses them, and writes the results into .img files. Current results are displayed in the status window in the upper right, see Fig. 1289.

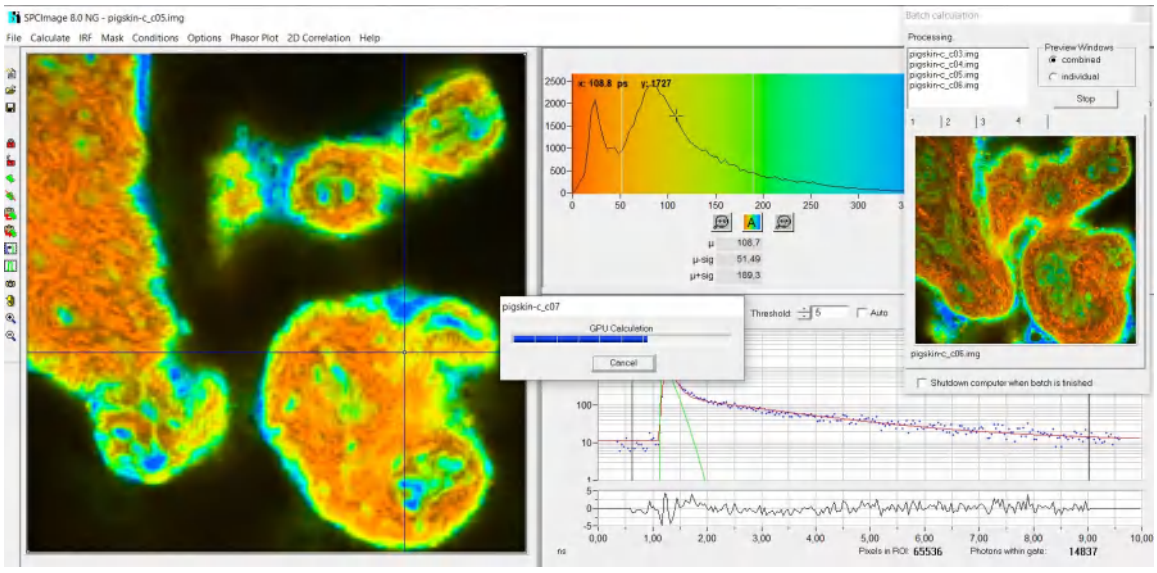


Fig. 1289: Batch Processing in progress. Subsequent files are loaded, analysed, and saved.

Saving SPCImage Data

The analysed data are saved as shown in Fig. 1290. The data file extension is '.img'. The img files contain not only the decay parameters of the individual pixels but also the raw data. Therefore, an img file can be loaded, and the data can be re-analysed with a different model or with different fit parameters.

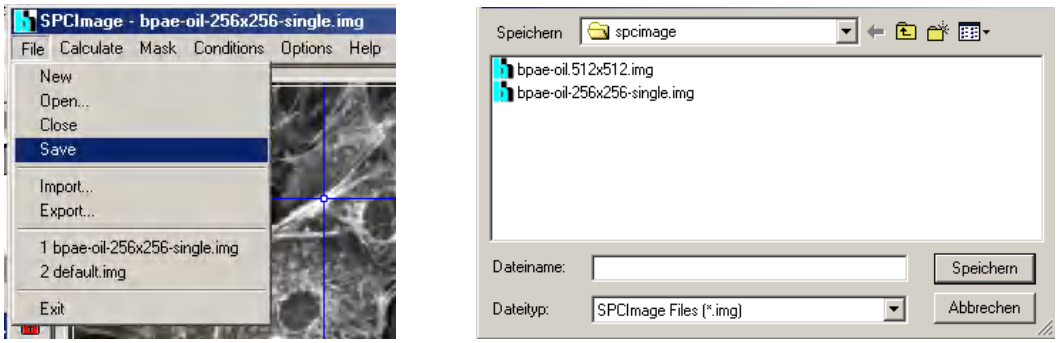


Fig. 1290: Saving the data analysed by SPCImage

Export of Data

FLIM data can be exported into other data formats via the 'Export' panel, see Fig. 1291. The options under 'Matrix' produce ASCII files of the decay parameters in the pixels of the image. 'Traces' generates ASCCII files of the curves displayed in the curve window. 'Image' produces BMP or TIFF files of the intensity or lifetime image. SPCImage versions later than August 2012 have a batch export function. It is used to export data of a series of .img files that have been generated by the Batch Processing function (see page 877). The file selection panel is shown in Fig. 1291, right.

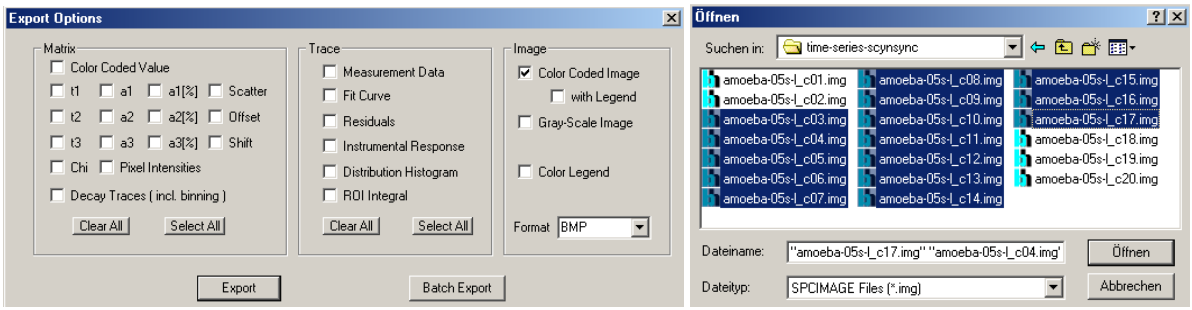


Fig. 1291: Left: Export Options of SPCImage. Right: File selection for Batch Export.

Special Commands

Frequently used commands are accessible in a vertical task bar left of the image window. Turn on 'Extended Icon Set' in the 'Preferences to see all available commands.



Binning of all pixels within a rectangular of polygonal ROI into a single decay curve.



Undo binning of pixels within the ROI.



Defines a polygonal ROI. Decay parameters are calculated only within this ROI.



Discards a previously defined polygonal ROI.



Declares the curve displayed in the decay window an IRF. The parts of the curve outside the cursor range are cut off.



Defines a rectangular IRF. The width and the temporal location are defined by the cursors in the curve window.



The current fit conditions are stored. These include a previously determined IRF, the time-range for the fitting procedure, and the region of interest in the image.



Loads fit the conditions which were stored before.



Zooms into the cursor range of the displayed image or zooms out of the zoomed part of the image.

Supporting Information

Spatial Binning

When an image is recorded by a scanning microscope the point-spread function of the microscope lens is usually 'oversampled' to obtain best spatial resolution. As a rule of thumb, the diameter of the central part of the Airy disc should be sampled by 5 × 5 pixels, see Fig. 1292, left. In practice even higher oversampling factors often occur unintentionally. Under these conditions lifetime data should be calculated from several binned pixels. When the binning function of SPCImage is used the lifetime images are built up from the unbinned intensity pixels and the binned lifetime pixels. This yields substantially improved lifetime accuracy without noticeable loss in spatial resolution [174]. Sampling artefacts are largely avoided by overlapping binning, see Fig. 1292, right.

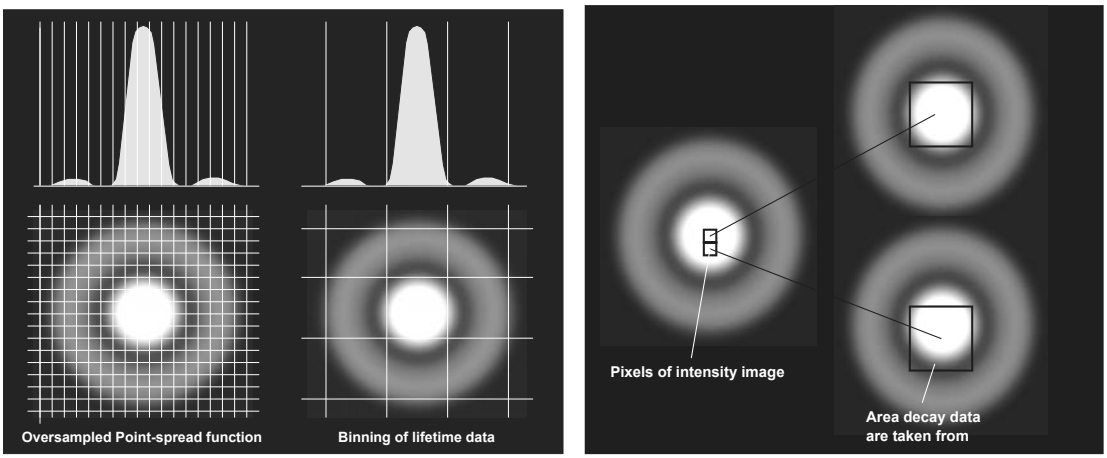


Fig. 1292: Left: Oversampling of the Airy disc in the intensity image and binned pixels for lifetime calculation. Right: Overlapping binning of pixels for lifetime calculation.

The binning is controlled by the 'Bin' parameter above the decay curve window. The function of the parameter is shown in Fig. 1293. 'Bin' defines the number of pixels around the current pixel position. Please note that the number of pixels of the lifetime image is not reduced. Only the lifetimes are calculated from the combined pixels, the intensities remain unbinned.

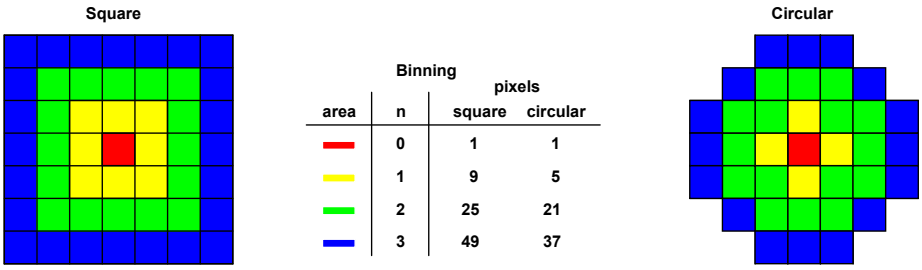


Fig. 1293: Function of the binning parameter, n. Binning 'Square' (left) and 'Circular' (right).

Fig. 1294 shows lifetime images obtained from 256 × 256 pixel raw data. The binning parameter is 0 (left) and 2 (right). The upper row was calculated by the WLS fit, the lower row by MLE. It can be seen from these images that the binning causes no loss in image definition and negligible loss in lifetime detail. However, the binning considerably reduces the noise in the lifetime data.

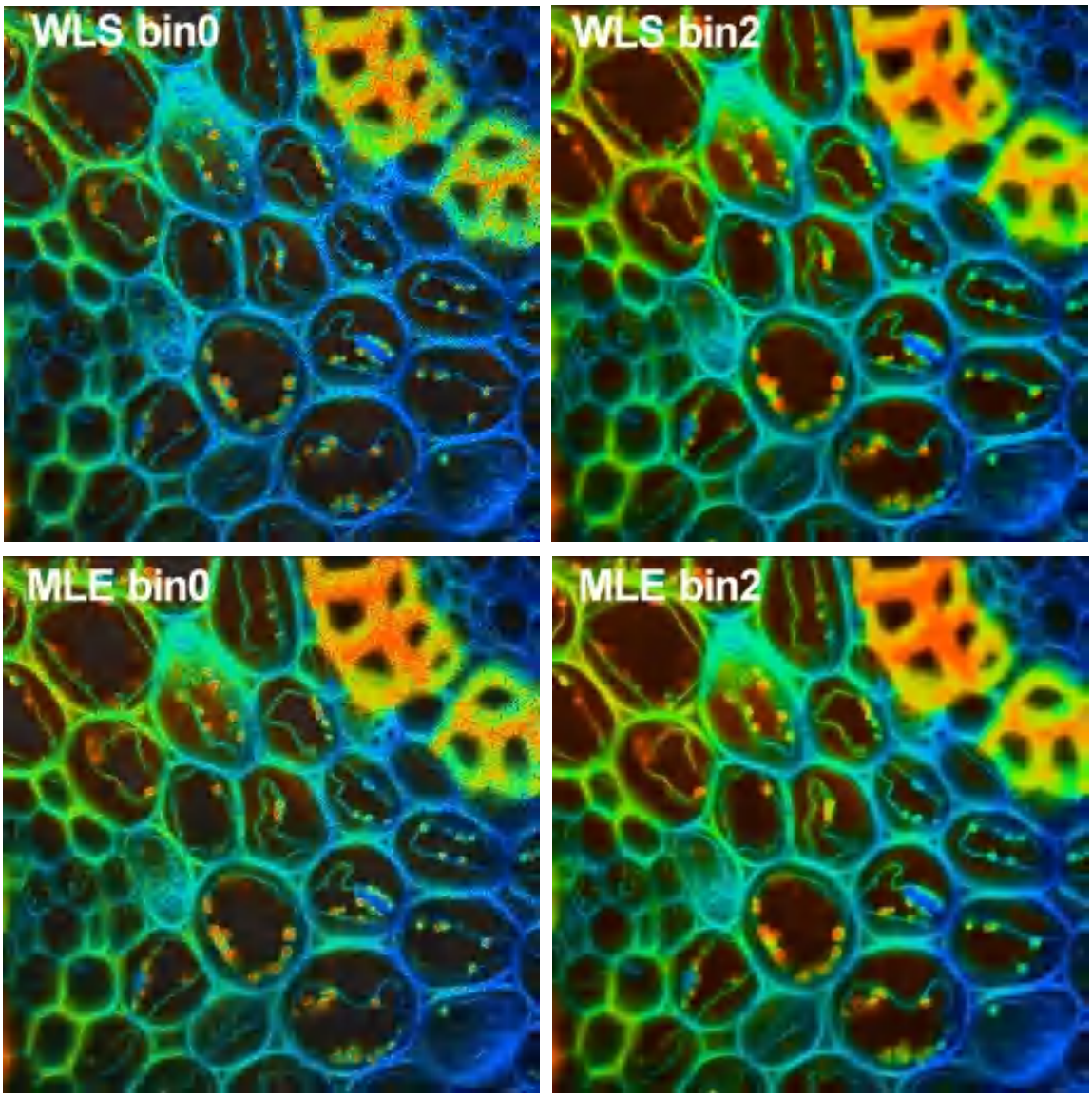


Fig. 1294: Lifetime images of a convallaria sample, 256 x 256 pixels, 256 time channels. Left: Binning parameter 0. Right: Binning parameter 2. Upper row: WLS fit. Lower row: MLE fit. Double-exponential fit, amplitude-weighted lifetime, t_m. Lifetime range from 200 ps (blue) to 600 ps (red)

A conclusion from the figure above is that FLIM should *always* be recorded at sufficiently high pixel number to provide the desired spatial resolution. The resulting decrease in the number of photons per pixel can later be compensated by the binning function of SPCImage [174]. Please see Fig. 1219, page 885.

Of course, an image with a higher pixel number occupies more data space in the computer and on the hard disc. But this is rarely a problem for state-of-the-art computers and data storage devices. Also the data-processing time for the larger number of pixels is no longer a problem. With a GPU, the processing time is rarely more than a few seconds even for the largest images.

Temporal Binning

SPCImage NG has no function for binning of TCSPC time channels. Temporal binning leads to sampling artefacts, such as uncertainty in the position of the IRF and the rising edge of the fluorescence. With the advanced fit algorithms used in SPCImage NG temporal binning is detrimental to the fit accuracy. Please see [174].

The Convolution Integral

In a real FLIM system the fluorescence is excited by laser pulses of non-zero width, and detected by a detector that has a temporal response of non-zero width. The effects on the temporal shape of the recorded signal are shown graphically in Fig. 1295. The laser pulse can be thought to be broken down into a sequence of (infinitely) narrow pulses of different amplitude (Fig. 1295, left). Each of these sub-pulses produces a fluorescence decay of an amplitude proportional to the amplitude of the sub-pulse, and starting at the time of the sub-pulse. The sum of all these decay functions is the real optical waveform of the fluorescence signal, see bottom of Fig. 1295, left.

The real fluorescence signal is measured by a detector the temporal response of which has non-zero width, see Fig. 1295, middle. Again, the detector response can be thought to consist of a sequence of infinitely short pulses. Also here, the measured waveform is the sum of shifted signal components of different amplitude.

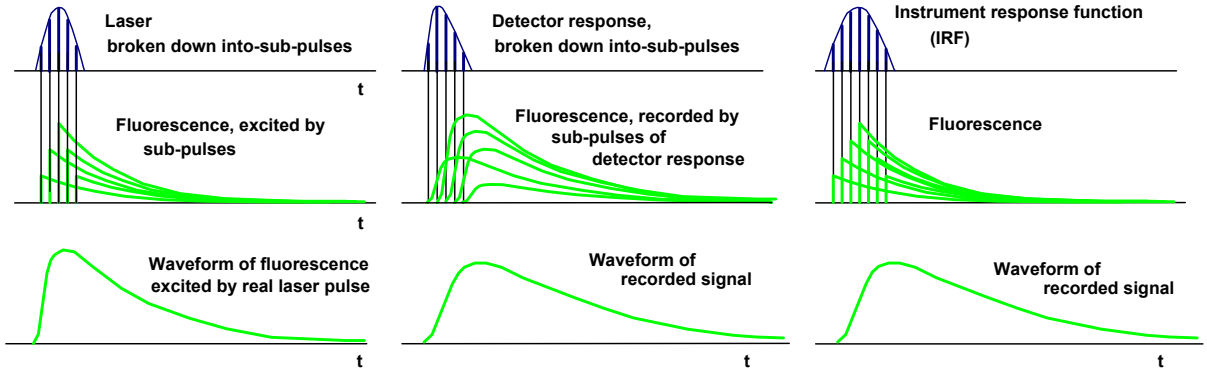


Fig. 1295: Left: Convolution of the laser pulse with the fluorescence decay. Middle: Convolution of the real fluorescence waveform with the detector response. Right: Laser pulse and detector response combined into IRF pulse, convolution of fluorescence decay with IRF.

The transformation of the signal waveforms shown above is called ‘convolution’. In a linear system, the convolution of signal waveforms is a commutative operation. The laser pulse shape and the detector response can therefore be combined in a single ‘instrument response function’, or IRF, see Fig. 1295, right. The IRF is the convolution of the laser pulse shape with the detector response, or the pulse shape the system would record if it directly detected the laser. The convolution of the fluorescence decay function with this IRF delivers the same result as the two subsequent convolution steps shown in Fig. 1295, left and middle.

Mathematically, the convolution of the fluorescence decay with the IRF can be expressed by the convolution integral

$$f_m(t) = \int_{\tau=0}^{t} f(\tau) IRF(t-\tau) d\tau ,$$

with $f_m(t)$ = measured fluorescence function, $f(t)$ = true fluorescence decay function.

The convolution integral cannot be reversed, i.e. there is no analytical expression of $f(t)$ for a given $f_m(t)$ and $IRF(t)$. There is also another implication: The measured data contain noise from the statistics of the photons, i.e. $f_m(t)$ itself is not accurately known. Any attempt to directly *calculate* $f(t)$ from the recorded data is therefore in vain. The standard approach to solve the de-convolution problem is to use a fit procedure: A model function of the fluorescence decay function is defined, the convolution integral of the model function and the IRF is calculated, and the result is compared with the measured data. Then the parameters of the model function are varied until the best fit with the measured data is obtained [924]. This operation is repeated for all pixels of the image.

Decay Models

Basic Multi-Exponential Decay Model

The basic model functions used in SPCImage are sums of exponential terms:

Single-exponential model: $f(t) = e^{-t/\tau}$

Double-exponential model: $f(t) = a_1 e^{-t/\tau_1} + a_2 e^{-t/\tau_2}$ with $a_1 + a_2 = 1$

Triple-exponential model: $f(t) = a_1 e^{-t/\tau_1} + a_2 e^{-t/\tau_2} + a_3 e^{-t/\tau_3}$ with $a_1 + a_2 + a_3 = 1$

The models are characterised by the lifetimes of the exponential components, τ, and the amplitudes of the exponential components, a. In principle, models with any number of exponential components can be defined. However, higher-order models become so similar in curve shape that the amplitudes and lifetimes of the components cannot be obtained at any reasonable certainty. Therefore, FLIM analysis does not use model functions with more than three components.

To account for possible detector background or daylight pickup the models used in SPCImage includes an Offset parameter in the models. The composition of the three basic model functions is illustrated in Fig. 1296.

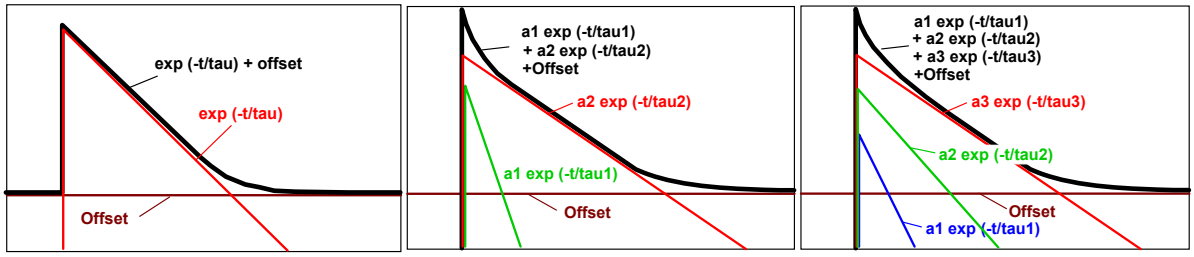


Fig. 1296: Single, double, and triple-exponential decay models

The basic decay models can be combined with a number of options, see below.

Incomplete-Decay Model

The incomplete-decay model includes the fluorescence remaining from the previous laser pulses in the model function, see Fig. 1297.

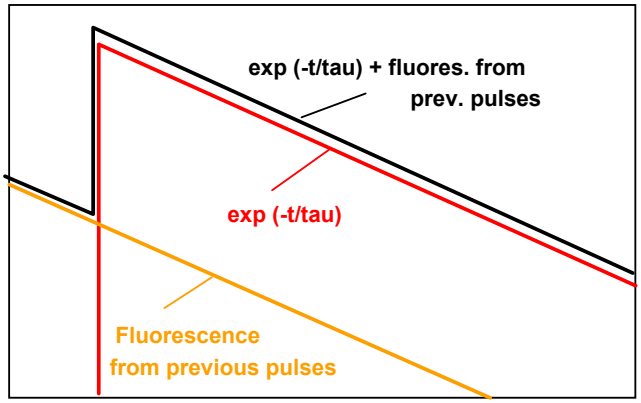


Fig. 1297: Incomplete decay model. Red: Decay function. Orange: Residual fluorescence from previous laser pulses. Black: Sum of decay function and fluorescence from previous laser pulses. Shown for single-exponential decay. Similar models exist for double- and triple-exponential decay functions.

A comparison of the standard decay model and the incomplete decay model is given in Fig. 1298. A single-exponential decay was recorded at 80 MHz repetition rate. The fluorescence lifetime was 4 ns. Consequently, there is a noticeable contribution from fluorescence excited by the previous laser pulses. It can be seen left of the rising edge of the fluorescence pulse. The standard decay model interprets this signal as an offset, see Fig. 1298, top. As a result, an imperfect fit of the fluorescence is obtained. The fluorescence lifetime is determined too short because a fraction of the fluorescence photons in the tail of the decay is interpreted as background signal.

The Incomplete-Decay model interprets the signal correctly. It obtains a near-perfect fit of the decay curve, and delivers the correct lifetime, see Fig. 1298, bottom. The incomplete model also has advantages when a multi-exponential decay has slow lifetime components. According to our own experience, it not only delivers these components with their correct amplitudes and lifetimes but also delivers a more pronounced χ^2 minimum. This is especially the case if the part left of the rising edge of the fluorescence pulses is included in the fit.

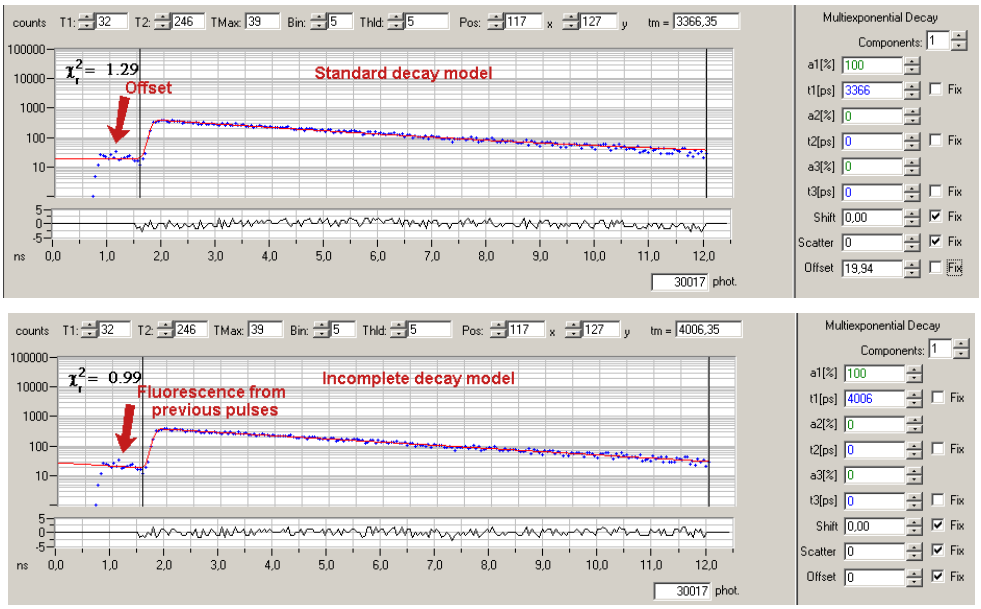


Fig. 1298: Fit of a 4-ns-decay excited at 80 MHz by a standard decay model (top) and an incomplete-decay model (bottom). The incomplete decay model interprets the signal left of the rising edge correctly, and thus obtains a better fit.

Difficulties can arise if the data contain both an offset and a contribution from incomplete decay. The influence on the shape of the model functions is very similar, especially if the incomplete decay is caused by very slow decay components. The advantages of the incomplete decay model can therefore be fully exploited only if there is negligible offset (from daylight, detector dark counts or afterpulses) in the decay signals. The 'Offset' should then be set to zero and fixed. The incomplete decay option is available in SPCImage since 2003. A theoretical evaluation has been published recently by Leung et al. [762].

Shifted-Component Model

The shifted-component model has been developed for analysis of fluorescence-lifetime-ophthalmoscopy (FLIO) data. In FLIO data, the fluorescence of the fundus of the eye is overlaid by fluorescence from the front parts of the eye, especially from the crystalline lens. The lens fluorescence causes unpredictable changes in the detected fundus lifetimes. Moreover, the lens fluorescence causes a distortion in the rising edge of the fluorescence signal. This

makes it difficult to shift the IRF in the correct position. SPCImage NG therefore has a shifted-component model of the form

$$f(t) = a_1\, e^{(-t+td1)/\tau 1} + a_2\, e^{(-t+td2)/\tau 2} + a_3\, e^{(-t+td3)/\tau 3}$$

where t_{d1}, t_{d2}, t_{d3} are temporal shifts of the corresponding decay components. The t_d parameters are fixed parameters which are given by the geometry of the measurement object, in this case the eye.

It turned out that the lens fluorescence in the FLIO data is almost entirely represented by the slow decay component, $e^{(-t+td3)/\tau 3}$. For geometric reasons the lens component arrives about 150 ps before the fundus fluorescence. The data are thus analysed with $t_{d1} = t_{d2} = 0$ and $t_{d3} = -150$ ps. The shifted-component model massively improved the reliability of FLIO analysis. It even made it possible to separate the signals from the fundus form that of the crystalline lens [118, 119]. Please see 'Ophthalmic FLIM', page 590.

Multi-Exponential Models with Fixed Decay Times

Multi-exponential decay analysis, both with the basic models and with the incomplete-decay and shifted-component options, can be performed with fixed decay times of the components. The idea behind this is that the fluorescence lifetimes are often known, or can be determined by independent measurements. Fixing one or several decay times does, of course, result in a substantial increase in accuracy for other decay parameters. Conceivable applications are FRET, where the fluorescence lifetime of the non-interacting donor is supposed to be constant, and NADH and FAD FLIM, where the lifetimes of the unbound components are mostly constant.

Unfortunately the idea has a flaw. Except for a few fluorophores with extremely rigid molecular structure fluorescence lifetimes depend on the molecular environment. They can therefore not a priori be considered to be constant. However, if the value to which the decay time has been fixed is not correct or not constant throughout the sample large systematic errors in the other decay parameters can result. Fixed decay times should therefore used consciously and carefully, and the results be checked versus analysis with free parameters. Please see 'Pseudo-Global Analysis', page 917.

Fixing Shift, Scatter and Offset

Shift, scatter and offset can be fixed in the basic model parameters, see 'Model Functions', page 877. There is no objection against fixing scatter and offset to zero if a look at the decay functions show that their contribution is negligible.

Fixing the 'Shift' can be more problematic. 'Shift' is a temporal offset of the data referred to the IRF. On the one hand, the analysis runs faster and more accurate with fixed shift. On the other hand, a wrong shift directly offsets the obtained decay times. We therefore recommend to leave the shift unfixed but set the option 'Fix shift before calculating image' in the model parameters, see Fig. 1260, page 909. The analysis procedure then determines the optimum shift first, then fixes it to the determined value, and after that performs the decay analysis with the fixed shift.

Fit Procedures

Weighted Least Squares

The principle of the traditional least-square fit is shown in Fig. 1299. The differences, delta(t), between the points of the model function, $f_{mod}(t)$, and the data points, n(t), are calculated. In principle, the squares of the differences, $delta(t)^2$, could be calculated, summed up, and this sum be used as an optimisation parameter.

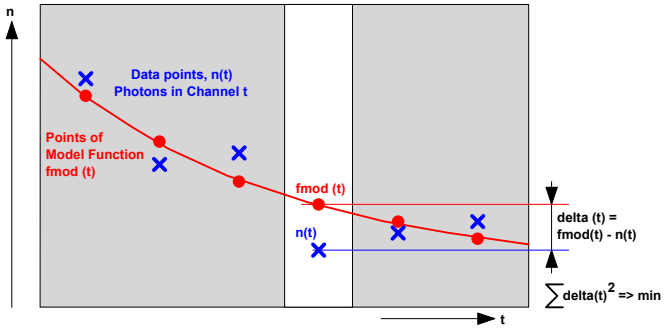


Fig. 1299: Least-square fit

For fluorescence decay curves, this procedure has a flaw. The photon numbers, n(t), are Poisson-distributed. That means the noise is larger in channels with higher photon number: The noise in *n(t)* is $n(t)^{1/2}$. Therefore, the squares of the differences must be weighted with the square of the reciprocal expectation value of the noise, i.e. 1/ *n(t)*.

The correct weighting of the delta-squares is the problem of the least-square fit. The correct weight according to the Poisson distribution would be *1/n(t)*. This is, of course, not possible because there are time channels with *n(t)=0*. The weight of these channels would be infinite, which is a practical impossibility. The commonly used solution is to use a weight of *1/(n(t)+1)*:

$$S = \sum \frac{\Delta(t)^2}{n(t)+1}$$

The weighting with *1/n(t)+1* avoids the singularity problem for *n(t)=0*, but, of course, does not weight the deltas in channels with low *n(t)* or *n(t)=0* correctly. The result is a bias towards shorter lifetimes for decay data of low photon number.

Maximum-Likelihood Estimation

MLE is based on calculating the *probability* that the values of the model function correctly represent the data points of the decay function. The principle is illustrated in Fig. 1300. To each point of the model function, $f_{mod}(t)$, a Poissonian distribution,

$$p(n) = \frac{E^n e^{-E}}{n!}$$

with an expectation value equal to $E=f_{mod}(t)$, is associated, see Fig. 1300, right. From this distribution the probability, *p(n(t))*, is calculated. The probability *p(n(t)* tells how likely it is that the point of the model function is a correct representation of the data point. *p(n(t)* is calculated for all time channels, i.e. for all pairs of data points and model-function points. The product of these probabilities is the probability that the model function represents the data. The parameters of the model functions are then optimised until the maximum probability, $\prod p(n(t))$, is obtained.

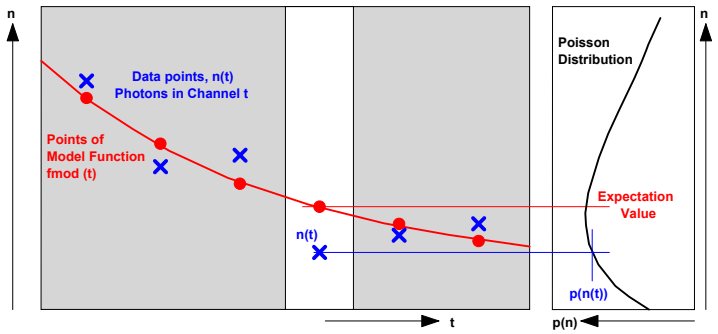


Fig. 1300: Principle of MLE fit. For each point of the model function, $f_{mod}(t)$, a Poissonian distribution is associated. The function delivers a probability p(n(t)), that a given data point, n(t) fits to the corresponding point of the model function. The product of p(n(t)) over all time channels is used for optimising the parameters of the model function.

The MLE fit has no problem with data points with low photon number or even with a photon number of zero. The Poissonian distribution associates correct probabilities to all these situations, and the product of these probabilities correctly describes the quality of the fit. Consequently, there is no bias toward shorter lifetime, as it occurs in the weighted least square fit.

Lifetime Calculation by First-Moment

The first moment of a photon distribution is the average arrival time of the photons. There is a simple relation between the first moment and the fluorescence lifetime: The lifetime is the difference of the first moments of the decay curve and the IRF, see Fig. 1301. The advantage of first-model calculation is that the lifetime is obtained at *ideal accuracy*. There is no error contribution from numerical effects or fit uncertainty.

The disadvantage is that the first moment is correct only if the decay data are free of background and if the entire decay curve is included in the calculation. Moreover, first-moment calculation also does not resolve multi-exponential decay functions into their components. When first-moment calculation is applied to multi-exponential data the result is an 'apparent lifetime' which is close to the lifetime obtained by a single-exponential fit.

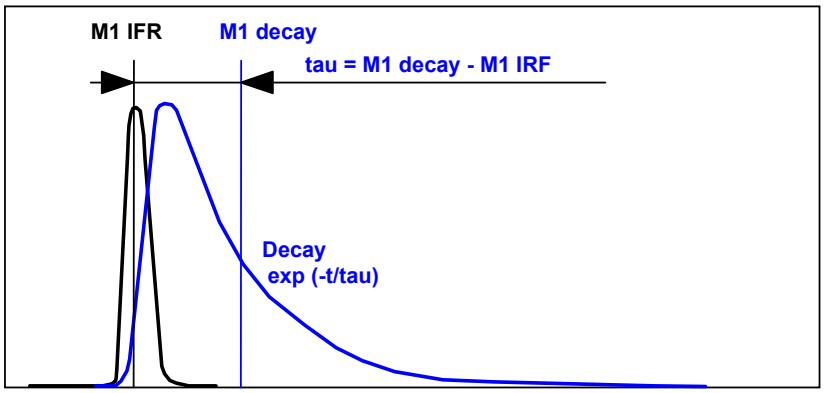


Fig. 1301: First-moment calculation of fluorescence lifetime. The lifetime is the different of the first moments of the decay curve and the IRF.

Two examples of lifetime calculation via the first moment are shown in Fig. 1302. The calculation interval (cursor range) in Fig. 1302, top, includes all photons of the decay data. The lifetime obtained from first-moment calculation is correct. In Fig. 1302, bottom a calculation interval was selected that does not include the later part of the decay function. Consequently, the first moment calculated in the range selected is too small, and the lifetime is determined too short.

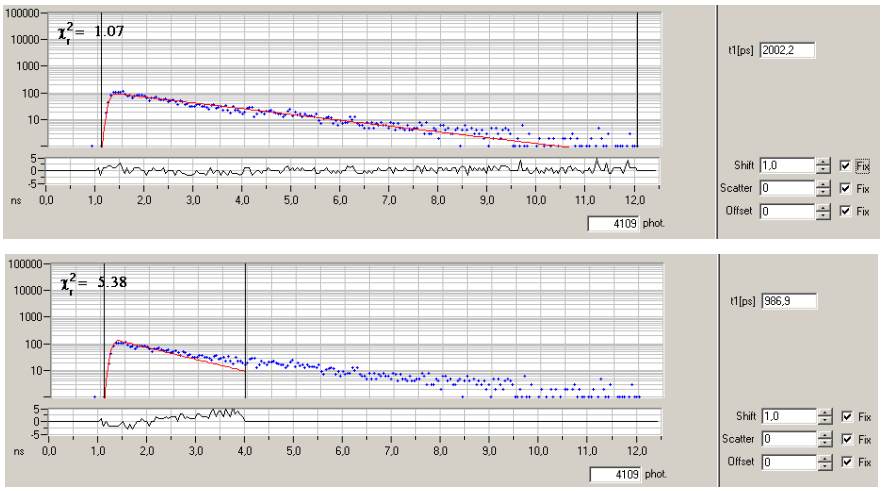


Fig. 1302: Lifetime calculation via the first moment. Top: All photons of the decay function have been included in the moment calculation. The obtained (single-exponential) lifetime is correct. Bottom: If the late photons are not included in the calculation the lifetime is determined too short.

How Many Exponential Components Are Needed?

Users are often uncertain which model, in particular which number of exponential components, they should use to fit the data. In most cases the answer is simple: Use a number of decay components equal to the number of fluorophores or fluorophore fractions you expect to contribute to the fluorescence of the sample.

If there is no a priori knowledge about the fluorescence mechanisms in the sample the model can be found by trial and error. Select a characteristic spot of the sample. Increase the binning factor until you see a clean fluorescence decay function. Then change the number of components and check the displayed χ^2 and the curve of the residuals. A good fit is characterised by a χ^2 close to one, and residuals showing no noticeable systematic variations. Often you see a poor fit already by comparing the fitted curve (red) with the photon data (blue) in the decay window.

In most cases your decay curves will be fitted adequately by a single- or double-exponential model. If you define more exponential components than needed you normally obtain two components of almost identical lifetime, or an additional lifetime component of very long lifetime and low amplitude.

An example is shown in Fig. 1303. Fitting the data with only one component (Fig. 1303, top) delivers a large χ^2 and clearly visible systematic variation in the residuals. With some experience, you may also spot systematic deviations between the decay data and the red curve calculated by the fitting procedure.

Fitting the data with two components delivers a perfect χ^2 and removes any systematic deviations in the residuals. This is an indication that the fit cannot be improved by adding more exponential components.

An attempt to fit the data with three components (Fig. 1303, bottom) indeed does not deliver any improvement. Instead, it delivers a third lifetime component almost identical with the second one. This is a clear indication that the double-exponential model is the right one.

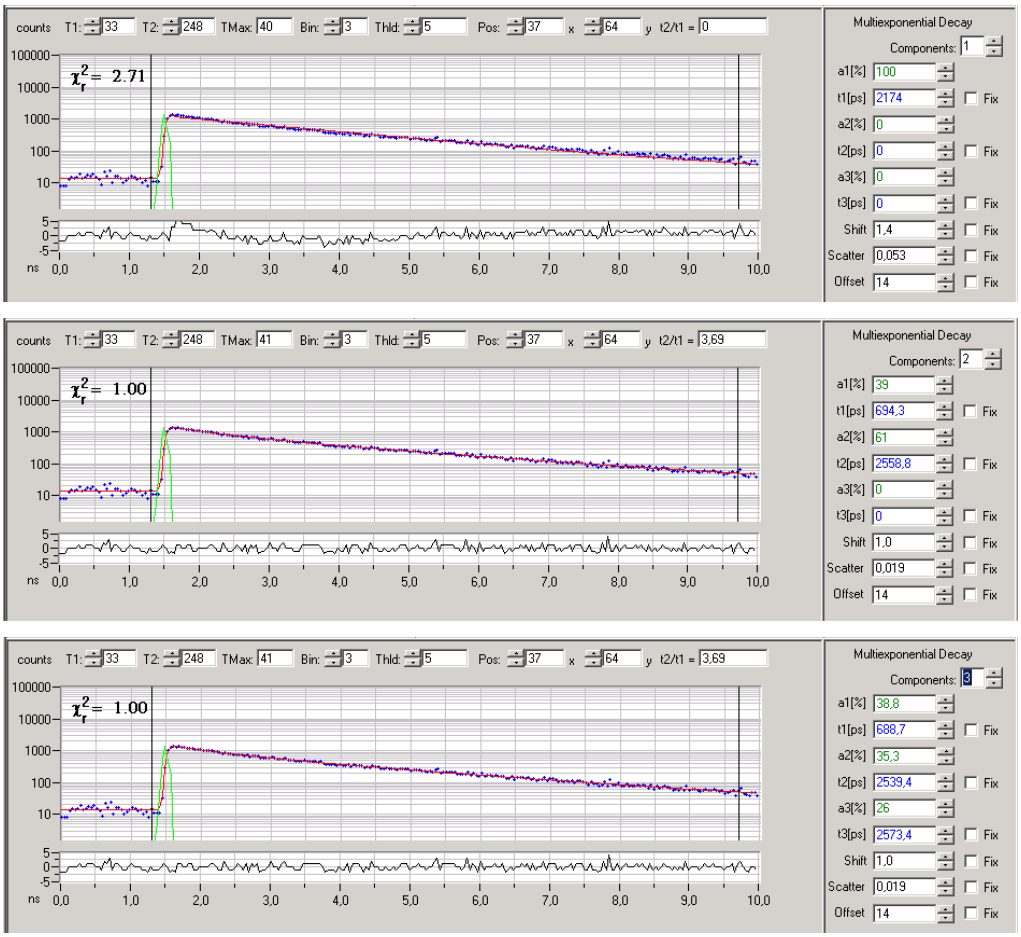


Fig. 1303: Top to bottom: Fitting a decay profile with one, two, and three exponential components

Over-Determined Models

The statistical errors of the fluorescence parameters are, of course, smallest if the correct model function is used. However, the parameters used in the model should be restricted to those actually needed to describe the measured fluorescence waveform. If more parameters are used the fit may achieve a slightly better χ^2 but the individual parameters may vary wildly. This is especially the case if parameters are used that have an almost identical influence on the model function. A few typical cases of over-determined models are described below.

Single-Exponential Decay Fitted with Double-Exponential Model

If a single-exponential decay function is fitted with a double-exponential model the fit procedure delivers two decay components of nearly identical lifetimes. The lifetimes are correct, and an amplitude or intensity-weighted lifetime (t_m or t_i) derived from the components will be correct as well. However, the amplitudes of the two components have no influence on the model function. The amplitudes will thus remain undetermined, and may fluctuate strongly. An example is shown in Fig. 1304. FLIM data of a rhodamine 110 solution were recorded and analysed by a single- and a double-exponential model. The average photon number per pixel is 2700. Rhodamine 110 in water delivers a near-perfect single-exponential decay. Fig. 1304, left shows the result of a single-exponential fit. The lifetime image is nicely homogenous. The lifetime distribution shows a relative variance of about 0.019. This is the theoretical value: The expected relative variance for a photon number N is $1/\sqrt{N}$, i.e. 0.019 for 2700 photons.

The lifetime image and the distribution obtained by a double-exponential model are shown in Fig. 1304, middle. The lifetime distribution has a relative variance of 0.026. This is more than the theoretical value but still reasonably good. However, the amplitudes, a_1 and a_2, are fluctuating wildly because they have no influence on the shape of a double-exponential model with two almost equal lifetimes. See Fig. 1304, right.

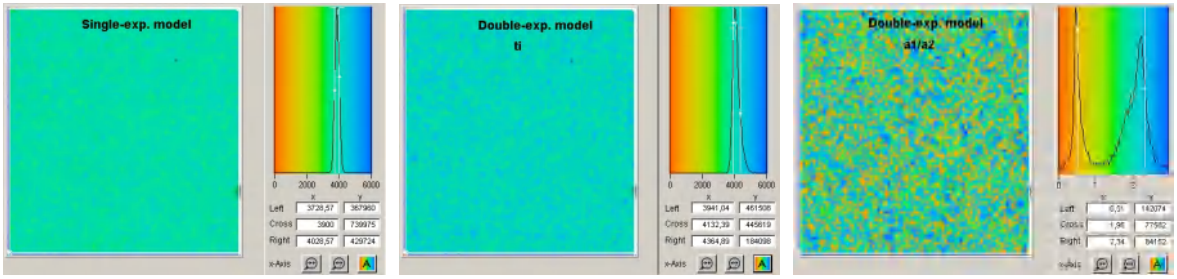


Fig. 1304: Comparison of single-exponential and double exponential model applied to single-exponential decay. Rhodamine 110 solution. Left: Fit with single-exponential model, lifetime image and lifetime distribution. Middle: Double-exponential model, intensity-weighted lifetime. Right: Double-exponential model, amplitude ratio, a_1/a_2.

The situation is similarly difficult for real double-exponential decay profiles with component lifetimes that very close to one another [680]. Also here, reasonably accurate values are obtained for the mean and average lifetime, t_m and t_i, but not necessarily for the lifetimes and amplitudes of the individual components.

Shift Parameter and Extremely Short Lifetime Component

The convolution integral of a lifetime shorter than the width of the IRF is very similar to a shift of the curve, see Fig. 1305. The shift parameter may thus conflict with a short decay component: A slightly shorter lifetime and a slightly larger shift and vice versa deliver almost similar shapes of the model function. The effect is variation of the lifetime and the shift in opposite directions. Therefore, the shift parameter *must* be fixed when lifetimes on the order of the IRF width or shorter are to be determined.

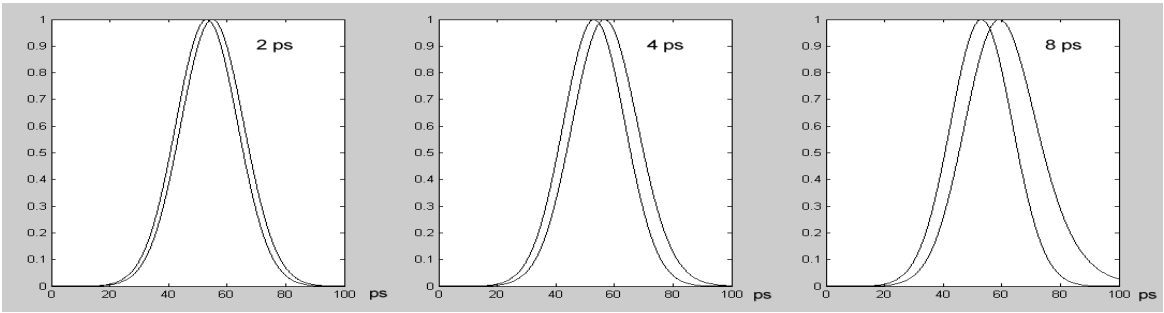


Fig. 1305: The result of a convolution of the IRF with a fast decay function is very similar to a shift. Simulated data, IRF width 25 ps FWHM

Scatter Parameter and an Extremely Short Lifetime

Similar problems can occur if the signal contains SHG components and extremely fast lifetime components. Also here, a change in the amplitude of the fast decay component can be compensated by an opposite change in the scatter. The best advice is record the fluorescence and the SHG signal independently through different filters.

Offset Parameter and Long Lifetime

Long lifetimes are difficult to distinguish from an offset in the signal. This is especially the case when the fluorescence does not fully decay within the recorded time interval or within

the excitation pulse period. The situation is further complicated by the fact that an apparent offset can have different reasons: It can be a real offset caused by daylight pickup or afterpulsing of the detector, or it can be residual fluorescence from the previous pulses. An example is shown in Fig. 1306.

In Fig. 1306, left, the apparent offset left of the rising edge of the fluorescence pulse was fitted by the 'Offset' parameter of SPCImage. The fit quality looks good, although subtle deviations can be seen in the tail of the decay curve. In Fig. 1306, middle, the offset was fixed to zero. The signal part left of the rising edge is not fitted. Nevertheless, the fit of the tail looks better than Fig. 1306, left. The lifetime is determined more than 12% longer than in Fig. 1306, left.

The reason becomes clear when the data are fitted by the 'Incomplete Decay' model, see Fig. 1306, right. The 'Offset' parameter was fixed to zero. The fit is good, and also the signal left of the rising edge fits correctly. The result shows that the apparent offset is fluorescence from the previous pulses that has not completely decayed. Interpreting it as an offset due to background signals (Fig. 1306, left) is wrong and leads to the wrong lifetime.

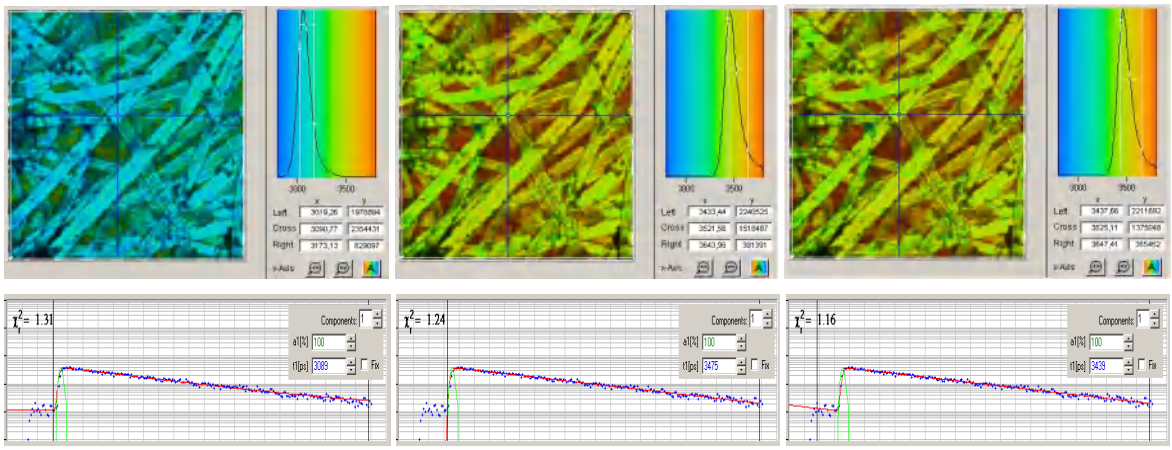


Fig. 1306: Left: 'Offset' parameter used to fit the signal left of the rising edge of the fluorescence pulse. Middle: Offset parameter fixed to zero, signal left of rising edge not fitted. Right: Offset parameter fixed to zero, signal left of rising edge fitted by 'Incomplete Decay' model.

Wrong interpretation of the offset is a frequent source of obtaining 'wrong' lifetimes in two-photon microscopes. 'Lifetime standards', such as fluorescein, have lifetimes on the order of 3 to 5 ns. At 80 MHz repetition rate, the fluorescence does not completely decay between the excitation pulses, causing the problems described above.

To avoid the offset problem we recommend to strictly avoid daylight pickup. If there is still an offset in the signal, check whether it is fitted by the incomplete decay model. In that case, do not forget to set the correct repetition rate in the Model Parameter Options, see Fig. 1260, page 909, and fix the 'Offset' to zero. If the signal part left of the rising edge is fitted correctly by the incomplete decay model the apparent offset is residual fluorescence.

Instrument Response Function

Automatic IRF: Calculating an IRF from Fluorescence Decay Data

SPCImage NG has functions to derive the IRF from recorded FLIM data. The calculation of the 'Auto IRF' is based on the assumption that the fluorescence lifetime is long compared to the width of the IRF. In that case, the rising edge of the fluorescence signal is (almost) the integral of the IRF. The IRF can therefore be obtained from the fluorescence signal: The calculation procedure fits the rising edge of the fluorescence signal with a suitable function, rise(t). The differentiated function, d Rise(t) / dt, is the IRF. Fig. 1307, left, shows how this works. A typical result is shown on the right.

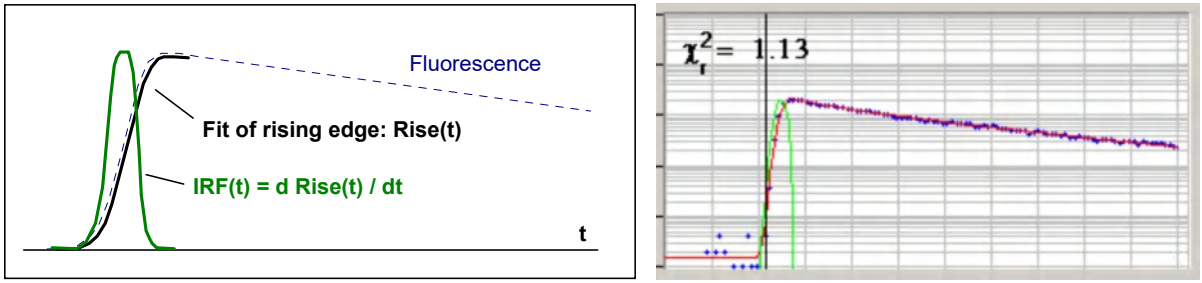


Fig. 1307: Calculation of IRF from fluorescence data. Principle shown left, typical result shown right.

The calculation of the Auto IRF is performed automatically every time raw data are loaded. It is run on combined decay curves from pixels of an area centred around the 'Hot Spot', i.e. from the brightest part of the image. Occasionally, it happens that the hot spot does not contain valid decay curves, e.g. if it is a speck of dust or another contamination. In that case, disable 'Always calculate at brightest pixel' in the preferences panel (see Fig. 1264, page 913), select a better position by the blue image cursor, and click on 'IRF', 'Auto'.

Analysis with the automatic IRF delivers a reasonably good fit and a colour-coded τ_m image virtually identical with an image obtained with the real IRF, compare Fig. 1314, page 946. The τ_m in the selected spot is nearly the same. Even the lifetimes and amplitudes of the decay components do not differ by more than 10%. This is the more surprising as the fastest decay component has a lifetime of only 400 ps, which is not far from the width of the instrument response function.

Nevertheless, there may be cases when the IRF calculation does not deliver the correct result. This can happen when the decay curves contain lifetime components with decay times close to or shorter than the IRF width, or with a contribution from SHG. The rising edge is then faster than the integral of the true IRF. Consequently, the IRF is calculated too short. This may bias fast lifetimes towards longer values, and make it difficult to extract an SHG contribution from the FLIM data.

Fully Synthetic IRF of the Type x exp (-x)

The idea behind the fully synthetic IRF is to model the IRF by a function of the type

$$irf(t) = t/t_0 \, e^{-t/t0}$$

The function has only one parameter, t_0, which determines the width. The function has a steep rise, and a slow, almost single-exponential tail. It closely resembles the IRF of a GaAsP hybrid detector.

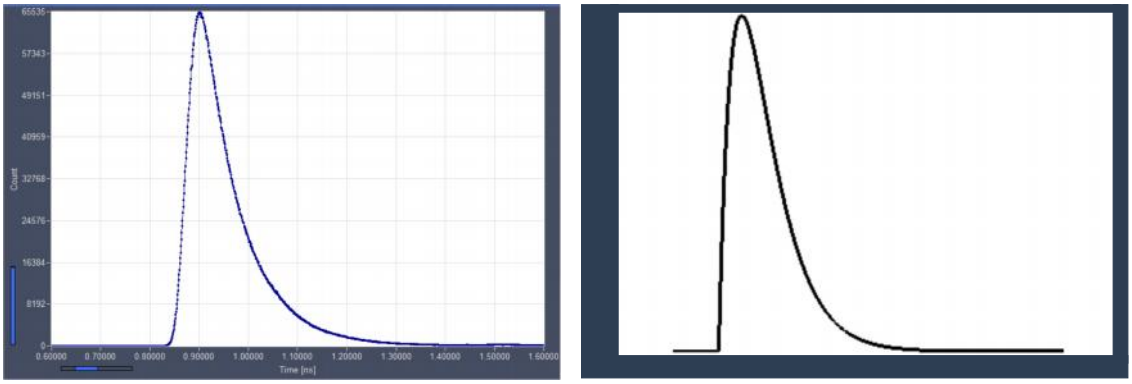


Fig. 1308: IRF of a TCSPC system with HPM-100-40 hybrid detector (left) and shape of the function $irf(t) = t/t_0\ e^{-t/t0}$ (right)

The function is also a good approximation to the IRFs of normal PMTs and most single-photon avalanche photodiodes. To account for possible influence of the laser pulse shape the function is convoluted with a Gaussian curve of the (known) laser pulse width, t_l.

$$f(t) = e^{-(t/tl)^2}$$

The advantage of the fully synthetic IRF is that it works also for short decay times, in presence of ultra-fast components, and in combination with the shifted-component model.

The parameter t_0 can further be refined by an automatic optimisation procedure. The principle is illustrated in Fig. 1309, left. The procedure runs a fit of the fluorescence model parameters together with the parameter t_0 to the decay data. The IRF in subsequent steps of the procedure is shown in Fig. 1309, right. Provided a correct model function is used the result is an optimised IRF function, with the correct width parameter, t_0. The optimisation procedure is accessible via the 'Model' parameters panel, see page 909. Make sure that 'Permanent IRF' is set and that the left decay-window cursor is left of the rising edge of the decay curve.

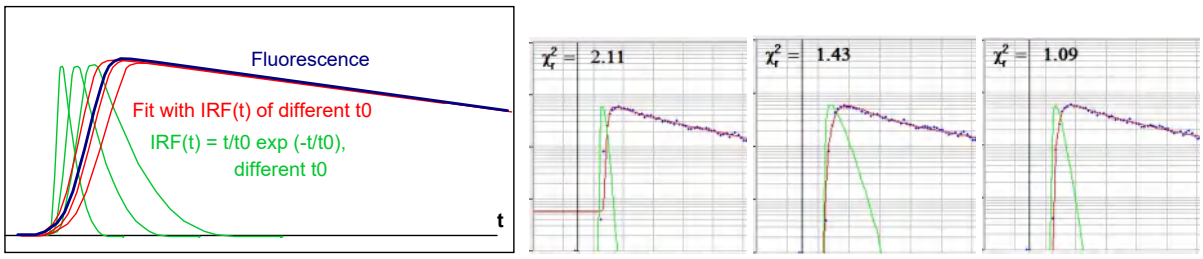


Fig. 1309: Left: IRF optimisation procedure. Right: IRF shape in subsequent steps of the procedure.

For successful IRF optimisation it is important that a reasonable model of the fluorescence decay function is used. If the decay model does not have enough components the IRF optimisation may compensate the deficiency of the decay model with a wrong IRF. On the other hand, if the model is too flexible, the combination of the decay model and the IRF model can become 'over-determined'. The procedure can then fit the data with a small IRF width, t_0, and a large lifetime of the fast decay component, t_1, or vice versa. The situation occurs sometimes with triple-exponential decay models when amplitude of the third component is low. If this happens, go back to a double-exponential model for IRF optimisation, and then switch to a triple-exponential model for decay analysis.

The IRFs from the procedure above yield surprisingly precise fit results. An example of FLIM analysis with a synthetic IRF is shown in Fig. 1310.

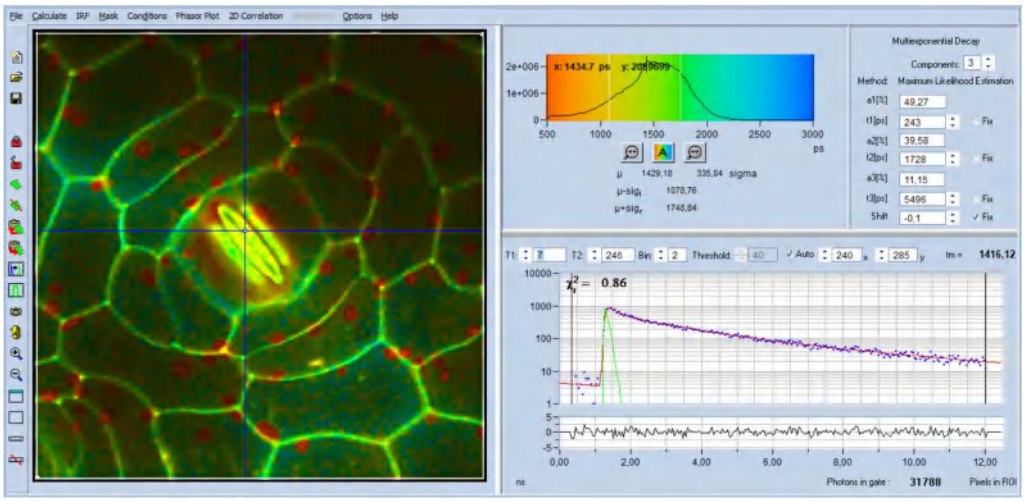


Fig. 1310: Plant tissue FLIM data analysed with synthetic IRF. Amplitude-weighted lifetime of triple-exponential decay model. Autofluorescence, emission wavelength 500 to 550 nm. The result is virtually identical with the result of an analysis with the real IRF, see Fig. 1314.

Measured IRF

Principle

To say it plainly: Most of the measured IRFs are wrong. We therefore do not recommend to use a measured IRF unless this is absolutely unavoidable. IRF measurement and the associated pitfalls are described in section 'IRF Recording', page 481. If you think you need a measured IRF or you can't withstand the temptation to measure one, please follow the instructions given below.

The IRF is obtained from scattering or SHG data. The data must be reasonably free of fluorescence, reflections, and background. It is important that the IRF data be recorded under the same conditions as the FLIM data to be analysed. In particular, TCSPC system parameters affecting the timing and the time scale, such TAC, CFD, SYNC parameters and ADC Resolution, must be the same. Cable lengths, optical path length, delay box settings, DCC detector gain, and electrical laser power (in the scan control panel) must be the same. Needless to say, IRF data must be from the same detector channel as the data to be analysed.

A frequent source of errors in IRF acquisition is baseline shift due to counting background. Surprisingly, the problem is rarely mentioned in the TCSPC literature. If the IRF data contain background - either from room light pickup or from afterpulsing of detectors - the fit of the convoluted model to the fluorescence data delivers wrong lifetimes.

The effect of IRF background is illustrated in Fig. 1311. The convolution of the model function with the true (background-free) IRF yields a waveform that represents the measured fluorescence decay function. Convolution of the model function with a continuous background yields an integral term, see Fig. 1311 middle right. Convolution with an IRF containing background delivers the measured fluorescence decay function plus an integral term, see Fig. 1311, lower right. It does not fit the waveform of the fluorescence data. Even a small IRF background can affect the fit results noticeably: The background extends over far more time channels than the true IRF and thus has a large influence on the convolution integral.

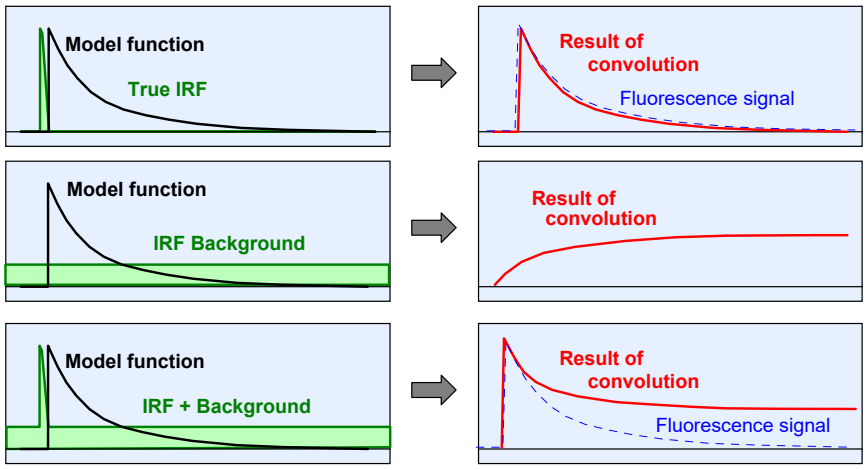


Fig. 1311: Effect of background in a recorded IRF on the result of the convolution with the decay model

Background correction of recorded IRF data is therefore essential. In principle, background could be subtracted from the data. However, the background contains noise. Subtracting the average background from all time channels does not fully clean up the data. Therefore SPCImage allows you to *cut off* the signal portions outside the valid part of the IRF.

Loading a Measured IRF

To generate an IRF from measured data proceed as follows:

- Import or load an .sdt or .img data FLIM file that contains IRF data.
- Use the blue image cursor to select a region that contains good data. Keep away from fluorescent inclusions or suspicious contaminations. Increase the binning until you see a clean waveform in the curve window.
- Place the cursors in the decay-curve window at the beginning and the end of the valid part of the IRF.
- Click on the (Curve to IRF) button. This declares the selected part of the curve an IRF.
- Click on the (Store Conditions) button. This saves the IRF you generated. The IRF will stay in the 'Fit Conditions' until you store a new one.
- To retrieve the IRF after loading new FLIM data click on or ‘Load fit conditions’.
- Alternatively, you can use 'IRF', 'Copy to clipboard', and 'Paste from clipboard'. This saves/retrieves the IRF for the current session.

One-Photon IRF

Fig. 1312 through Fig. 1314 give an example of analysing one-photon FLIM data with an IRF obtained from scattering data.

Fig. 1312, left, is a scattering image obtained from aluminium oxide ceramics. The image was recorded following the instructions under ‘IRF Recording’, page 481. No laser blocking filter was used. To reduce possible fluorescence from contaminations or laser background at longer wavelengths a 460±20 nm bandpass filter was inserted in the detection beam path. The image therefore contains mostly scattered laser light.

A suitable spot was selected in the image (Fig. 1312, left) and the binning factor increased until about 10,000 photons were in the curve. The waveform obtained this way is shown in (Fig. 1312, middle). A click on the (Curve to IRF) button declares the data points within the cursor interval an IRF. See green curve in Fig. 1312, right. The generated IRF can be saved and recalled by 'Save IRF' and 'Load IRF' in the model parameter panel. Within the same SPCImage session, the IRF can be temporarily saved and recalled by 'Copy to Clipboard' and 'Paste from Clipboard' under 'IRF' in the top bar.

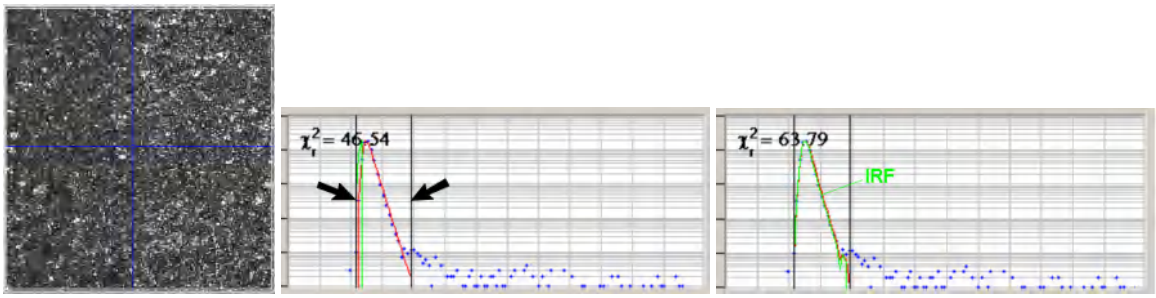


Fig. 1312: Left: Scattering image recorded from Al_2O_3 ceramics. Middle: Waveform in selected spot of the image. Large binning used, cursors pulled to the beginning and the end of the pulse. Right: IRF after clicking the 'Curve to IRF' button. The result is saved by the 'Save IRF' button in the Model Parameters.

Analysis of FLIM data with the IRF generated above is shown in Fig. 1313 through Fig. 1314. The SPCImage main panel after loading the FLIM data is shown in Fig. 1313, left. The IRF is still the Auto IRF or the synthetic IRF. Then the measured IRF is loaded by the 'Load IRF' command. The result is shown in Fig. 1313, right.

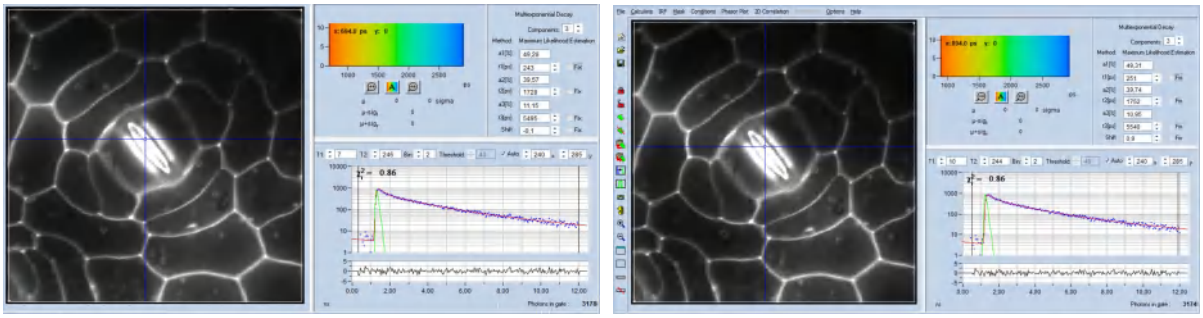


Fig. 1313: Data to be analysed with the measured IRF. Left: After loading the data, synthetic IRF. Right: After loading the real IRF via the 'Load fit conditions' command.

Please notice that there is virtually no difference between the synthetic IRF (left) and the measured IRF (right). Also the decay parameters are closely the same. That means the entire effort to measure the IRF and prepare it for use in SPCImage was unnecessary. The synthetic IRF works equally well.

Once the measured IRF is loaded data analysis is performed the same way as with a synthetic IRF. Analysis with a triple-exponential incomplete decay model is shown in Fig. 1314.

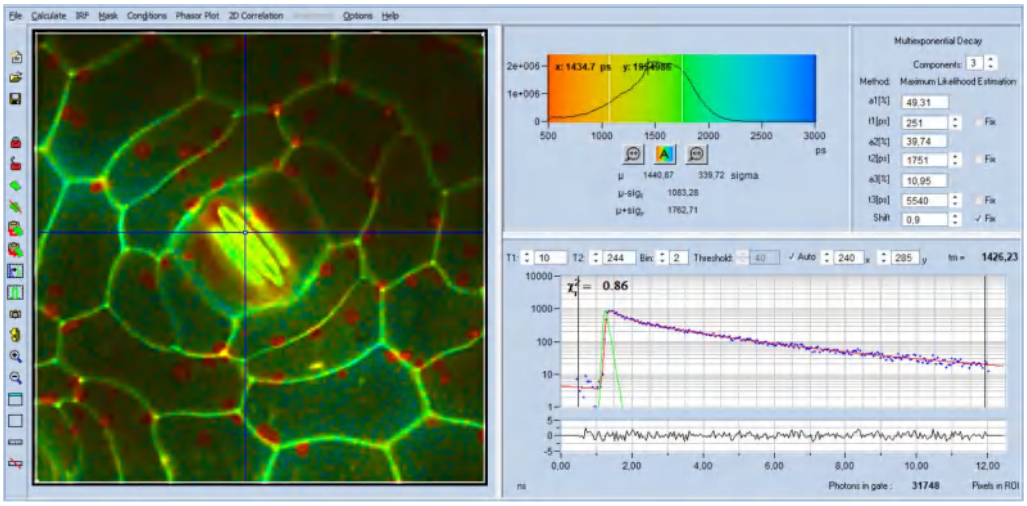


Fig. 1314: Data analysed with measured IRF. Plant tissue, autofluorescence, emission wavelength 500 to 550 nm. Compare with result of analysis with synthetic IRF, Fig. 1310

Two-Photon IRF from SHG Data

In two-photon microscopes a measured IRF is usually obtained from SHG data. Good SHG signals are obtained from crystalline urea or sugar, see 'IRF Recording', page 481. The procedure to generate an IRF from the FLIM data is the same as described for one-photon excitation. Load the data into SPCImage, select a time interval around the signal peak, and declare the data within the cursor interval an IRF. An IRF from SHG of sugar is shown in Fig. 1315.

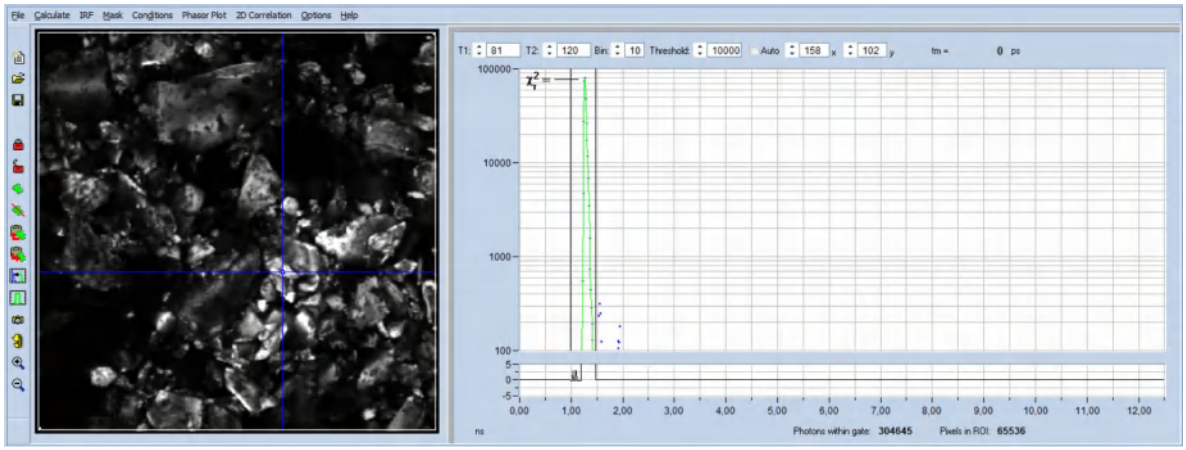


Fig. 1315: IRF from SHG of sugar. DCS-120 MP multiphoton FLIM system, HPM-100-06 detector

Often an IRF can be derived directly from the sample investigated, without data from an external IRF measurement. This is the case when the sample contains collagen, starch or other SHG-active compounds. A spot with a dominating SHG signal can then be selected in the FLIM image and the corresponding waveform declared an IRF.

An example is shown in Fig. 1316. A collagen structure was selected in the intensity image, see Fig. 1316, left. The data shown in the curve window confirm that the selected spot is dominated by an ultra-fast signal, see Fig. 1316, middle. However, the signal is not entirely free of fluorescence, see the tail in the recorded waveform. However, the amplitude of the tail is three orders of magnitude below the peak of the SHG pulse. Consequently, a reasonable IRF is obtained by just deleting the signal outside the SHG pulse. To do so, enclose the SHG pulse by the decay cursors and declare the selected part an IRF, see green curve in Fig. 1316, right.

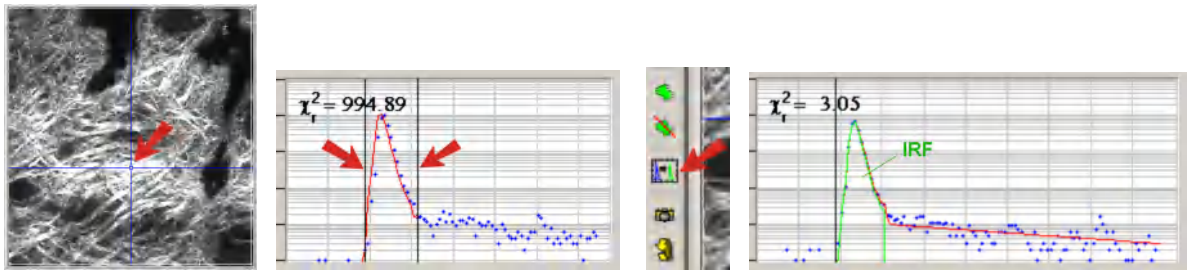


Fig. 1316: Generating an IRF from the SHG signal from collagen in a tissue sample. Left to right: Select a collagen structure in the intensity image, set the cursors in the curve window to the beginning and the end of the SHG pulse, and declare the selected part of the curve an IRF. The IRF is the green curve shown right.

The IRF is then used to analyse the image from which it was extracted. A result is shown in Fig. 1317.

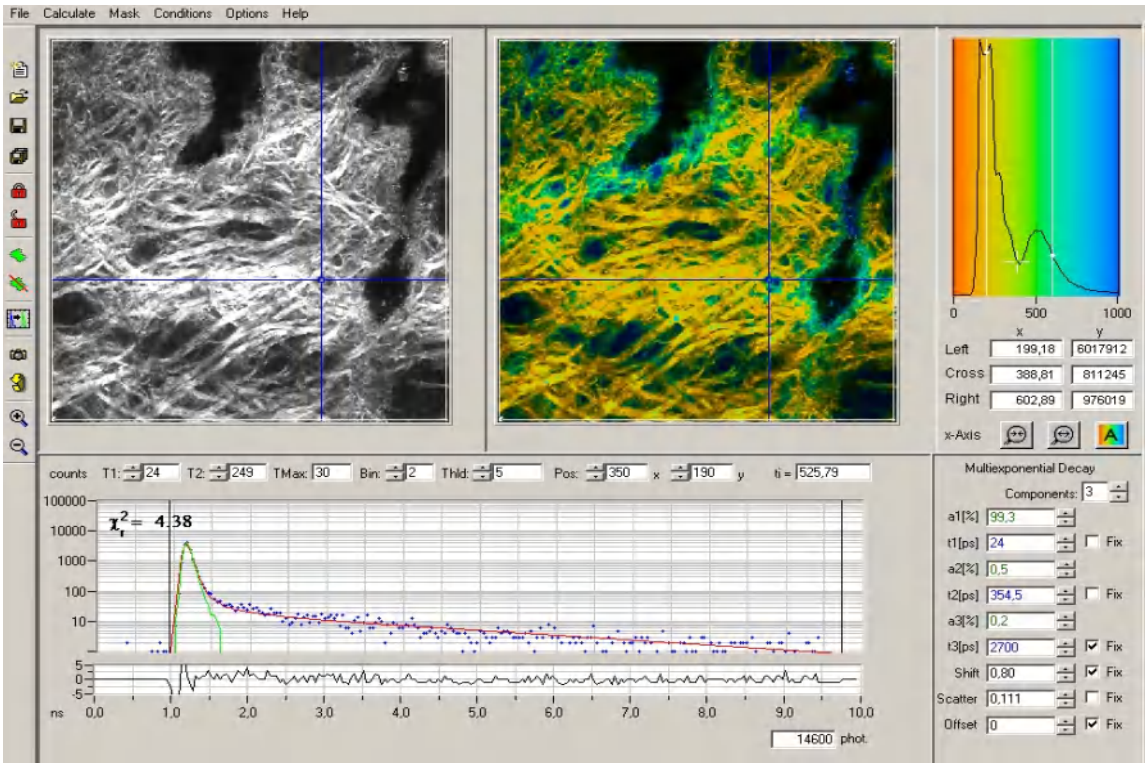


Fig. 1317: Analysis with the IRF derived from SHG in the same image

Parameters of the Decay Functions and their Use in SPCImage

Amplitude-Weighted Mean Lifetime, t_m

The mean lifetime, τ_m, is an average of the lifetimes of the components of a multi-exponential decay weighted by their amplitude coefficients. It is

for a single-exponential decay: $\tau_m = \tau$

for a double-exponential decay: $\tau_m = a_1\tau_1 + a_2\tau_2$ with $a_1 + a_2 = 1$

for a triple-exponential decay: $\tau_m = a_1\tau_1 + a_2\tau_2 + a_3\tau_3$ with $a_1 + a_2 + a_3 = 1$

If a decay function deviates from a single exponential function the mean lifetime τ_m, is *not* the same as the 'apparent' lifetime obtained from a single-exponential fit or from first-moment analysis. To obtain an equivalent of the apparent lifetime the lifetimes of the decay components had to be weighted by their integral intensities, see 'average lifetime'. Calculating a mean lifetime from a multi-exponential decay is therefore often considered incorrect. However, the mean lifetime has a real physical meaning:

The terms $a_n\tau_n$ in the calculation of the mean lifetime are proportional to the intensities contained in the individual decay components. Thus, the mean lifetime is proportional to the total fluorescence quantum efficiency of the emitting species [742]. The mean lifetime is therefore the correct value to calculate classic FRET efficiencies from a multi-exponential decay. Thus, if you use TCSPC FLIM to verify steady-state FLIM results you have to use the mean lifetime. Please note, however, that the FRET efficiency obtained this way averages the emission of all donor molecules, no matter whether they are linked to an acceptor or not. The classic FRET efficiency therefore does not necessarily deliver the correct distance, see 'Förster Resonance Energy Transfer (FRET)', page 507.

Mean Lifetime of the First Two Components, t_{m12}

t_{m12} is the amplitude-weighted lifetime of the first two decay components of a triple-exponential decay:

$$\tau_{m12} = (a_1\tau_1 + a_2\tau_2)/(a_1 + a_2)$$

It is used to display fundus images in FLIO analysis, please see chapter 'Ophthalmic FLIM', page 590.

Intensity-Weighted Average Lifetime, t_i

The average lifetime, t_i, is the average of the lifetimes of the decay components weighted by their integral intensities. The integral intensity of a lifetime component is the product of its lifetime and its amplitude. The intensity-weighted lifetime, ti, is thus

for a single-exponential decay $\tau_i = \tau$

for a double-exponential decay $\tau_i = \dfrac{a_1\tau_1^2 + a_2\tau_2^2}{a_1\tau_1 + a_2\tau_2}$

for a triple-exponential decay $\tau_i = \dfrac{a_1\tau_1^2 + a_2\tau_2^2 + a_3\tau_3^2}{a_1\tau_1 + a_2\tau_2 + a_3\tau_3}$

For a mono-exponential decay, the average lifetime is, of course, identical with the lifetime of the decay. For multi-exponential decay functions the average lifetime comes close to lifetimes obtained by single-exponential analysis or by modulation techniques. t_i is therefore also called 'apparent lifetime'. The average lifetime should therefore be used if a decay profile is not truly single exponential but its lifetime has to be compared with a single 'decay time' given in the literature. Please note also that the average lifetime, ti, is more sensitive to changes in the slow lifetime component while the mean lifetime, t_m, is more sensitive to changes in the fast component.

A practical example is shown in Fig. 1318. The sample has a pronounced double-exponential decay. From left to right, the figure shows the amplitude-weighted lifetime, t_m, the intensity weighted lifetime, ti, (both from a double exponential fit), and the lifetime of a single-exponential fit. Differences are clearly visible.

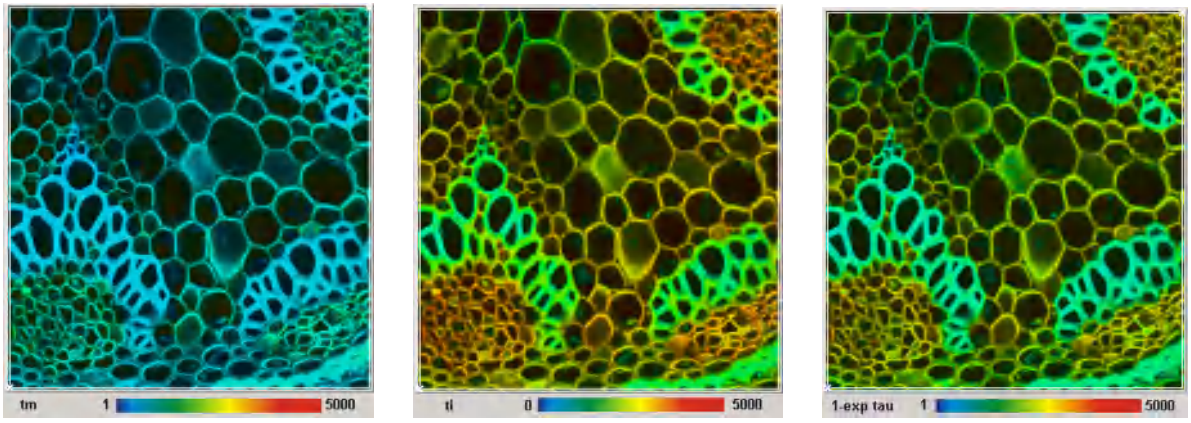


Fig. 1318: Left to right: Lifetime images of the mean (amplitude-weighted) lifetime, the average (intensity-weighted) and the lifetime of a single-exponential fit. Convallaria sample, the decay profiles deviate strongly from single-exponential functions.

Lifetimes of the Decay Components, t_1, t_2, t_3

For a multi-exponential decay model the lifetimes of the individual components, t_1, t_2, or t_3, can be selected and used as colour of the lifetime image. The lifetimes are often used to distinguish several fluorophores or different binding states of a single fluorophore present in the same pixel. For example, in FRET measurements there is usually an interacting and a non-interacting donor fraction. In this case t_1 is the lifetime of the interacting fraction, t_2 is the lifetime of the non-interacting one. In autofluorescence measurements t_1 and t_2 are the lifetimes of unbound and bound NADH fractions [1155, 303].

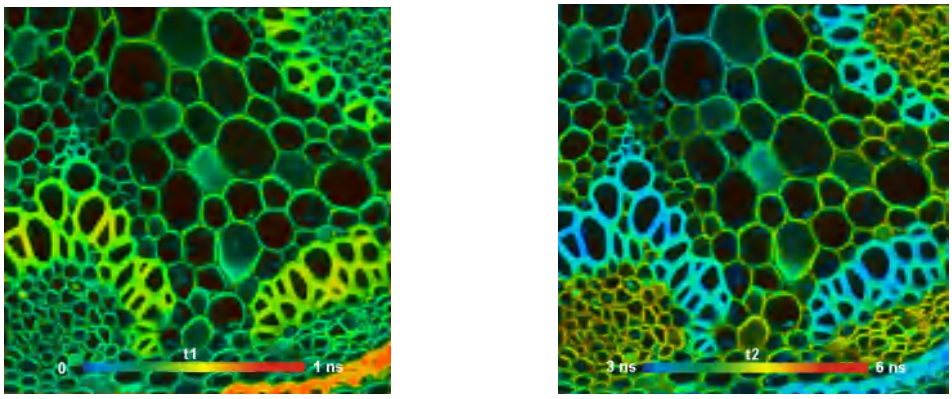


Fig. 1319: Lifetimes of the components of a double-exponential decay. Same data as in Fig. 1318.

Amplitudes of the Decay Components, a_1, a_2, a_3

The colour of the image can be assigned to one of the amplitudes, a_1, a_2, or a_3, of a multi-exponential decay. Amplitude images are used to show the relative concentration of similar fluorophore molecules in different local environment, different binding states, or different states of FRET. Amplitudes of the decay components are often surprisingly stable, with noticeably higher signal-to-noise ratio than the lifetimes.

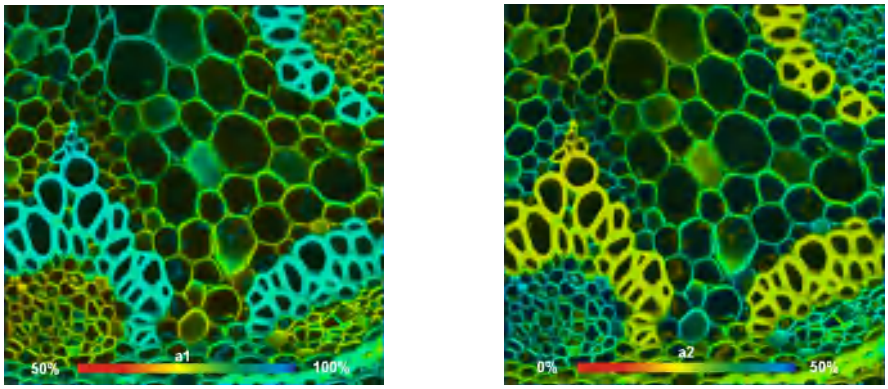


Fig. 1320: Amplitudes of the components of a double-exponential decay. Same data as in Fig. 1318.

Ratios of Lifetimes of Decay Components

SPCImage can display ratios of the lifetimes of different decay components. The lifetime ratio of two decay components is especially useful for FRET. The fast component, t_1, is the lifetime of the interacting donor fraction. The lifetime of the slow component, t_2, is the lifetime of the non-interacting donor. The ratio of both is directly related to the distance of donor and acceptor. The charm of this approach is that it is calibration-free: The reference lifetime is the non-interacting donor lifetime, t_2. t_2 is derived from the same specimen, the same cell, and the same pixels as the interacting-donor lifetime t_2. Variations in t_2, e.g. by variation in the refractive index or in the ph, have no influence on the distance calculation.

Ratios of Amplitudes

Ratios of amplitudes can be used the same way as the amplitudes themselves. For example, the ratio a_1/a_2 of a FRET decay is the concentration ratio of the interacting and non-interacting donor fraction. Amplitude ratio images often have a surprisingly high signal-to-noise ratio. An amplitude ratio image of a FRET measurement is shown in Fig. 732, page 511. In metabolic FLIM the a_1/a_2 ratios of NADH and FAD are indicators of the metabolic state, see chapter 'Label-Free FLIM of Cells and Tissue', page 527.

Classic Redox Ratio

The ratio of the intensities of an NADH image and an FAD image is the 'Redox Ratio, an important indicator of the metabolic state of a cell. In NADH/FAD FLIM data recorded by multiplexed TCSPC the intensities are available via the photon numbers, N_{nadh} and N_{fad} of the corresponding recording channels. The ratio, N_{fad} / N_{nadh} is the redox ratio.

Classic FRET Efficiency, E_{class}

An image of the FLIM-based classic FRET efficiency is obtained by selecting E_{class} from the list of decay parameters. The classic FRET efficiency is

$$E_{class} = 1 - \frac{\tau_m}{\tau_2}$$

τ_m and τ_2 come from an analysis of the donor image with a double-exponential model. E_{class} is the lifetime-based equivalent of the intensity-based classic FRET efficiency. However, please keep in mind that it does not necessarily represent the real FRET efficiency. E_{class} is an average of the real FRET efficiencies of the interacting and the non-interacting donor fraction. This is a general problem of the classic FRET approach, not a problem of SPCImage [188]. Please see 'Förster Resonance Energy Transfer (FRET)', page 507.

Classic FRET Efficiency, Single-Exponential Equivalent

SPCImage offers also a classic FRET efficiency

$$E_{1\exp} = 1 - \frac{\tau_i}{\tau_2}$$

It approximates the FRET efficiency that is obtained if the donor signal is treated as a single-exponential decay or measured with a FLIM system that only delivers single-exponential 'Lifetimes'. The result neither resembles the intensity-based FRET Efficiency nor the real FRET efficiency of the interacting donor fraction. It is simply wrong [188], please see 'Förster Resonance Energy Transfer (FRET)', page 507. SPCImage makes it available to allow the user to compare FRET results with published data based on wrong FRET calculations.

FRET Efficiency of Interacting Donor Fraction, E_{int}

The decay components of the interacting and non-interacting donor fraction can be used to calculate the real FRET efficiency of the interacting donor fraction. The FRET efficiency is

$$E_{\text{int}} = 1 - \frac{\tau_1}{\tau_2}$$

τ_1 and τ_2 are the lifetime components from the interacting and non interacting donor, respectively. Please note that E_{int} is significantly higher than the classic FRET efficiency because it does not include a contribution from the non-interacting donor fraction. Please see 'Förster Resonance Energy Transfer (FRET)', page 507. Of course, E_{int} can only be used if the decay has been analysed by a double-exponential model and the components of the double-exponential decay are clearly resolved.

FRET Distance, r/r0

SPCImage is able to calculate the ratio of the donor-acceptor distance, r, to the Förster radius, r_0. Please see 'Förster Resonance Energy Transfer (FRET)', page 507.

Relative Intensity Contribution, q_1, q_2, q_3

q_1, q_2, and q_3 are the relative intensity contributions of the decay components. The q values are the products of the lifetimes with their amplitude factors. The q values can be useful to visualise the distribution of different fluorophores in autofluorescence images. The q values are especially sensitive to slow lifetime components.

Scatter

The scatter is the amount of light emitted as a prompt response to the laser pulse. Except for directly scattered laser light leaking through improperly selected filters, the source may be Raman scattering, or, in two-photon excitation systems, second-harmonic generation (SHG). An image with the scatter parameter used as colour shows SHG or other prompt effects clearly, see Fig. 1321. A possible fluorescence background can be reduced by using time-gating of the intensity. Please note that exact scatter determination requires the use of the real instrument-response function.

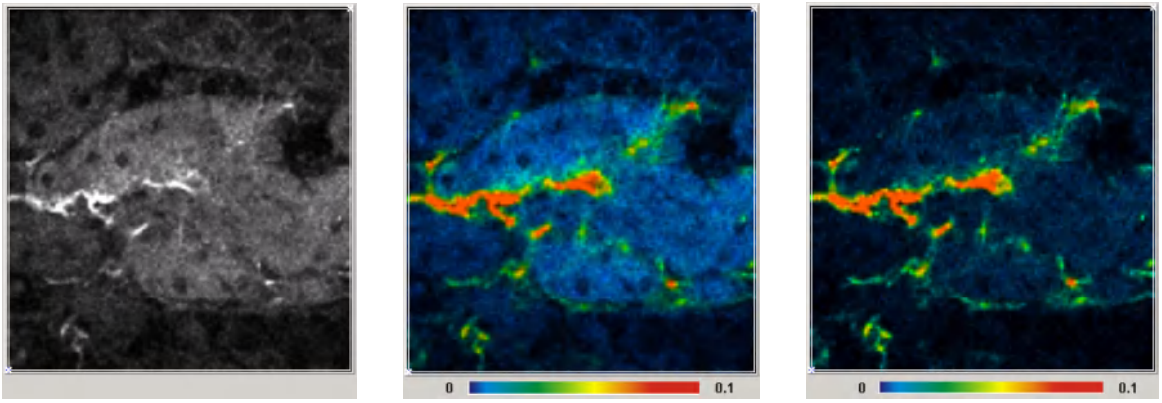


Fig. 1321: Extraction of SHG signals from FLIM data. Left: Intensity image. Middle: Image with colour representing the amount of prompt response. Right: Further suppression of fluorescence background by time-gating the intensity.

Accuracy of the Fit: $\chi 2$

The χ^2 parameter indicates the quality of the fit. A χ^2 image may be used to check whether the used model is appropriate in all areas of the image. An interesting application of the χ^2 image has been described in [629]: The decay data in a lifetime image are expected to be mono-exponential or close to mono-exponential. The data are therefore analysed by a single-exponential model. An increased χ^2 indicates that the corresponding pixels are contaminated by another fluorophore of different lifetime, usually autofluorescence. Autofluorescence by itself deviates so strongly from a single-exponential decay that it shows up clearly in a χ^2 image.

An example of a χ^2 image from a single-exponential analysis is shown in Fig. 1322, left. An a_1/a_2 image of a double-exponential analysis is shown right. It can clearly be seen that large χ^2 correlates with large a_1/a_2, i.e. with strong deviation from the single-exponential decay.

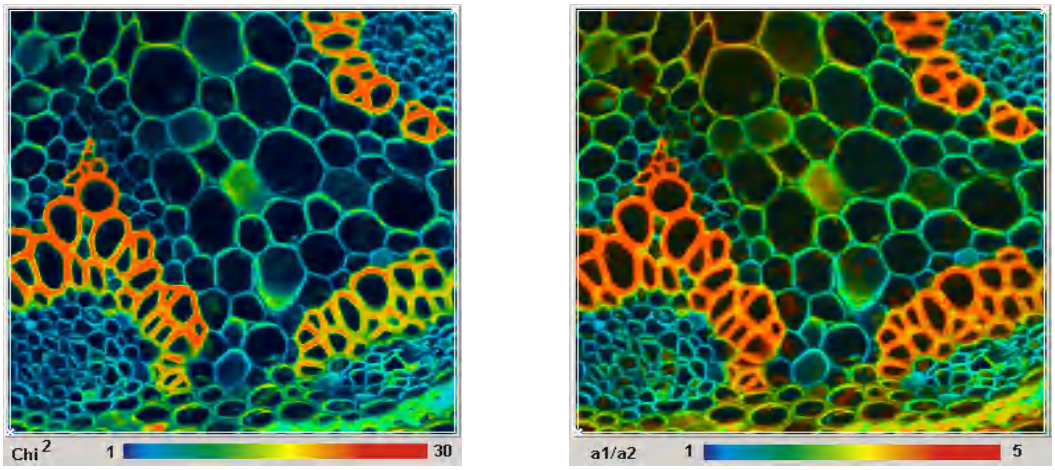


Fig. 1322: χ^2 image (left) of a single-exponential analysis and a_1/a_2 image (right) of a double-exponential analysis. χ^2 is largest where a_1/a_2 is large, i.e. where the decay profile has the strongest deviations from a single-exponential function.

Offset

The offset in the decay data can be used as a colour parameter. This may be considered useless because an offset usually originates from daylight pickup or from detector background. However, an offset may also be phosphorescence. Phosphorescence lifetimes are much longer than the laser pulse period normally used for FLIM. The phosphorescence signal than piles up over many signal periods and causes an baseline offset in the decay data. This can be used to identify phosphorescence, i.e. from Lanthanide dyes or from various nanoparticles. An example is shown in Fig. 1323.

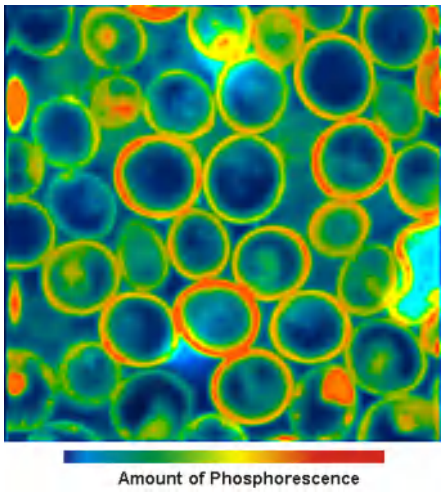


Fig. 1323: Amount of phosphorescence derived from offset in decay data. Yeast cells stained with ruthenium dye.

Phasor Plot

Principle

The phasor plot is based on the analysis of the decay data in the frequency domain. A transformation of the decay data, $n(t)$, into the frequency domain delivers a complex function of frequency, $G(\omega) + iS(\omega)$ with

$$G(\omega) = \frac{1}{N}\sum \cos(\omega t) n(t) \quad \text{and} \quad S(\omega) = \frac{1}{N}\sum \sin(\omega t) n(t)$$

As it turns out, a good representation of the decay function is obtained already if only G and S at the fundamental repetition frequency (the first Fourier component) are used. The decay function is then described by just two numbers, G and S, for $\omega = 2\pi/T$, where T is signal period of the fluorescence signal. Because G and S are no longer functions of ω in this case they can also be considered weighted moments of the decay functions, $n(t)$, where the weight functions are cosine and sine functions.

$$G = \frac{1}{N}\sum \cos(2\pi t / T) n(t) \quad \text{and} \quad S = \frac{1}{N}\sum \sin(2\pi t / T) n(t)$$

The data points $G + iS$, can also be expressed by the magnitude, M, and the phase, φ, in the plane of complex numbers:

$$M = \sqrt{G^2 + S^2} \qquad \varphi = \arctan S / G$$

For analysis of real measurement data still the IRF has to be included in the calculation. In the complex Fourier data plane the convolution integral transforms into a multiplication i.e.

$$G + iS = (G_{fl} + S_{fl}) \cdot (G_{irf} + iS_{irf}) \quad \text{or}$$
$$(G_{fl} + iS_{fl}) = (G + iS) / (G_{irf} + iS_{irf})$$

which can also be written as

$$G_{fl} = G\frac{\cos\varphi_{irf}}{M_{irf}} + S\frac{\sin\varphi_{irf}}{M_{irf}} \qquad S_{fl} = -G\frac{\sin\varphi_{irf}}{M_{irf}} + S\frac{\cos\varphi_{irf}}{M_{irf}}$$

In this form, the representation of a decay curve is called a 'phasor', and a density plot of the phasors of all pixels of an image or an image area is called a 'phasor plot' [383, 384].

The relationship between different decay curves and their phasors is illustrated in Fig. 1324. The phasors of single-exponential decays are located on a semi circle in the G-S plane. The phasor of a fast decay (a) is located on the right, at low phase and large amplitude. The phasor of a slow decay (b) in located farther left, at larger phase and lower amplitude. The phasor of a double-exponential decay (c) is a linear combination of the phasors of the decay components. It is located inside the semicircle.

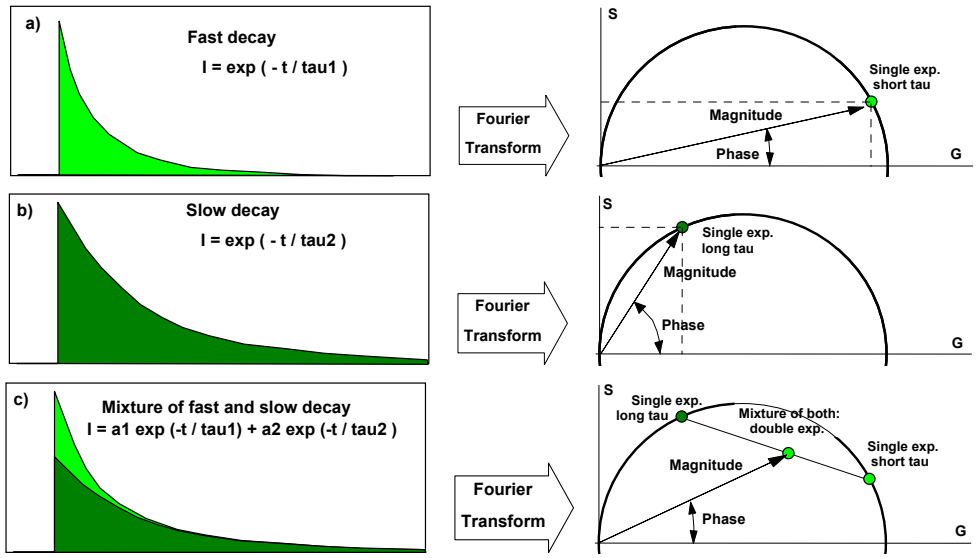


Fig. 1324: Relationship between decay functions in the time domain (left) and phasors in the frequency domain (right)

A fluorescence-lifetime image and the corresponding phasor plot are shown in Fig. 1325. The pixels of objects with different decay functions in the FLIM image (left) form clusters in the phasor plot (right).

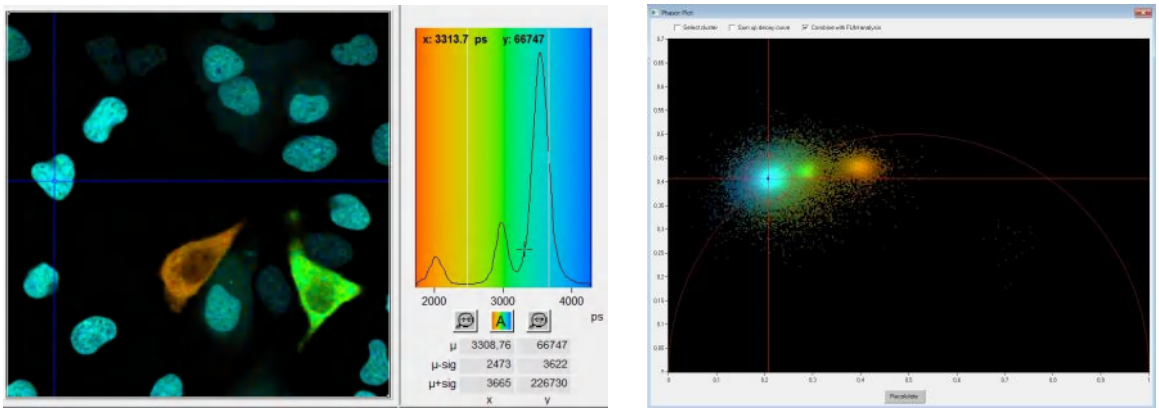


Fig. 1325: Lifetime image (left) and phasor plot (right). Pixels with similar decay profiles form clusters in the phasor plot.

Different phasor clusters can be selected see Fig. 1326 and Fig. 1327 , left, and the corresponding pixels back-annotated in the time-domain FLIM images, see Fig. 1326 and Fig. 1327, right. SPCImage is able to calculate combined decay curves over the selected areas (Fig. 1326 and Fig. 1327, middle), or create decay parameter histograms over the selected areas.

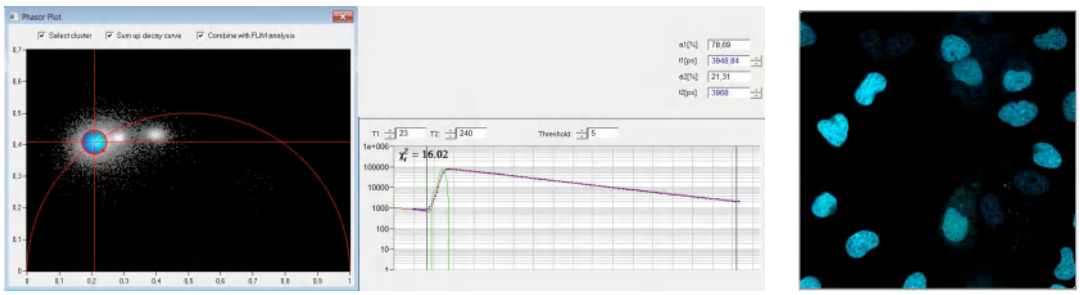


Fig. 1326: Left: Selecting a cluster of phasors in the phasor plot. Middle: Combination of the decay data of the corresponding pixels in a single decay curve. Right: Display of the pixels corresponding to the selected cluster in the phasor plot.

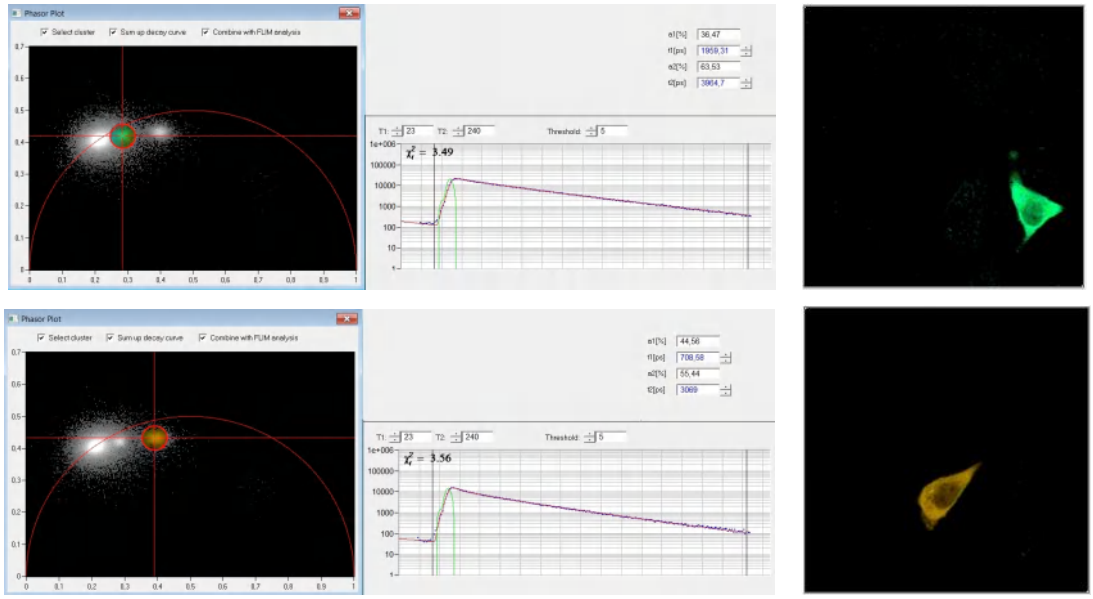


Fig. 1327: As figure above but other phasor clusters selected

Truncation Effects

As all moment-based lifetime techniques, phasor analysis is sensitive to truncation effects. If the signal is not recorded over the full signal period, photons at the end of the period may be not included in the phasor calculation, with the result that the phasor is not correct. Recording intervals shorter than the signal period is a common situation in TCSPC FLIM. The time measurement principle covers just a bit less than one signal period, and recording two signal periods and extracting just one period from the data would dramatically decrease the photon efficiency. Moreover, TCSPC decay functions are usually analysed by fit procedures in the time domain. Recording the full signal period is not necessary in this case. It is more important that the photons are recorded into sufficiently small time channels, especially when fast decay components are present.

The effect of recording an incomplete signal period is illustrated in Fig. 1328. As long as the fluorescence decays completely in the observation time interval (Fig. 1328, left) there are no photons in the last (un-recorded) part of the signal period. Phasors calculated from the data are correct. If the fluorescence does not fully decay within the observation time photons in the last part of the signal period are not included in the calculation of the phasor (Fig. 1328, right). Both G and S become larger (note that the weight function for S is negative in the truncated part), therefore the phasor shifts to left and (to a lesser extend) up in the phasor diagram.

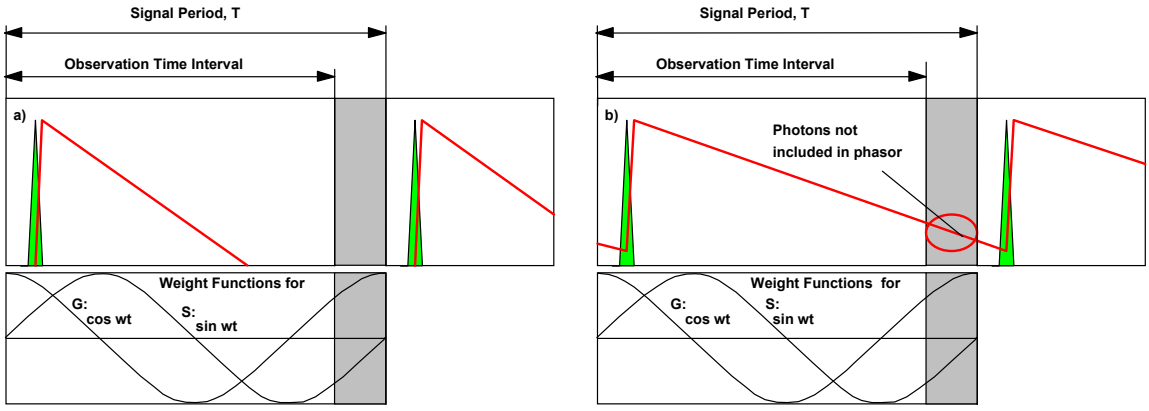


Fig. 1328: Systematic errors can occur if the fluorescence does not entirely decay in the observation time interval

In practice, truncation effects have little influence on the performance of the phasor plot in SPCImage. SPCImage uses the phasor plot mainly for image segmentation. Decay parameters are derived from MLE processing in the time domain. Lifetimes and amplitudes are therefore correct even in presence of truncation effects.

When the phasor plot is used in combination with the incomplete-decay model SPCImage detects possible truncation situations. It then fills the missing part of the decay data by data points from the fitted model function, see Fig. 1329. Of course, this substitution works precisely only if the correct model function is used and a time-domain analysis has been performed before the phasor plot is calculated.

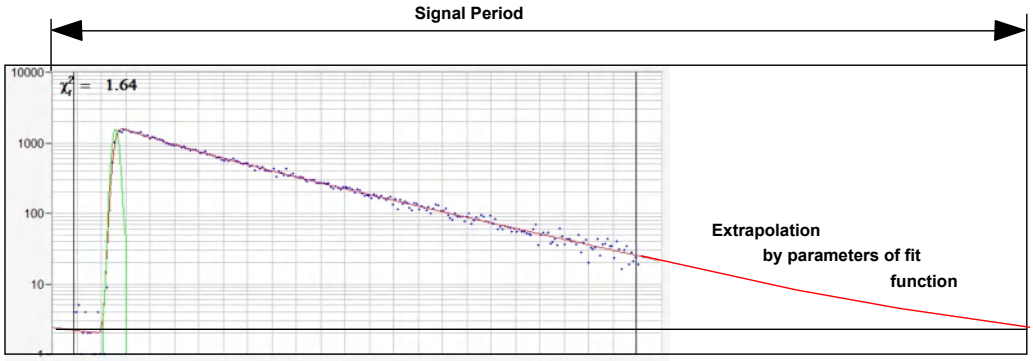


Fig. 1329: Filling of the missing part of the decay data by data points from the fitted model function.

Ambiguity of the Phasor Representation

Another rarely described feature is the ambiguity of the phasor representation. Unless a phasor is located directly on the semicircle (i.e. the decay function is single-exponential) it does not unambiguously represent a particular decay profile. As shown schematically in Fig. 1330, a given phasor can be obtained for different combinations of component lifetimes and amplitudes.

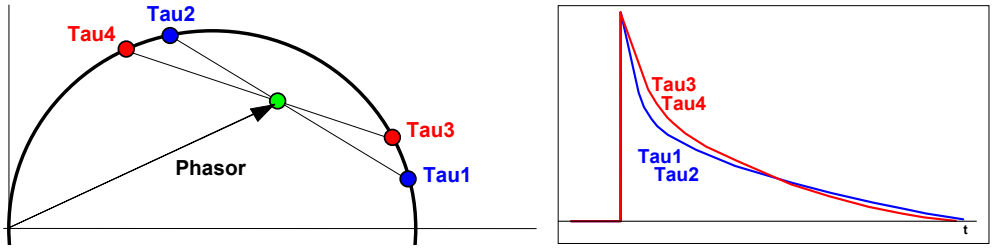


Fig. 1330: Ambiguity of the phasor representation. A given phasor within the semicircle can represent different decay profiles.

Possible ambiguity should be taken into consideration if pixels of similar phasor signature are combined into a single decay curve. The combined curve can, in principle, contain decay components from different decay curves with the same phasor. It need not strictly represent the decay profile of every individual pixel within the selected image area.

Assistance through bh

Software updates, new manual versions and application notes about new applications are available from the bh web site, www.becker-hickl.com. Furthermore, we are pleased to support you in all problems concerning the measurement of fast electrical or optical signals. This includes discussions of new applications, the installation of the SPC modules, their application to your measurement problem, the technical environment and physical problems related to short time measurement techniques. Simply call us or send us an email.

Should there be a problem with your SPC module, please contact us. To fix the problem we ask you to send us a data file (.sdt) of the questionable measurement or (if a measurement is not possible) a setup file (.set) with your system settings. Furthermore, please add the following information:

Description of the Problem
SPC Module Type and Serial Number
Software Version
Detector type, Operating voltage of the detector, PMT Cathode type
Preamplifier type, Gain, Bandwidth etc.
Laser System: Type, Repetition Rate, Wavelength, Power
SYNC Signal Generation: Photodiode, Amplitude, Rise Time
Optical System: Basic Setup, Sample, Monochromator
System Connections: Cable Lengths, Ground Connections. Add a drawing if necessary.
Environment: Possible Noise Sources
Your personal data: E-mail, Telephone Number, Postal Address

The fastest way is to send us an email with the data file(s) attached. We will check your system settings and – if necessary – reproduce your problem in our lab. We will send you an answer within one or two days.

Becker & Hickl GmbH
Nunsdorfer Ring 7-9
12277 Berlin
Tel. +49 / 30 / 212 800 2-0
FAX +49 / 30 / 212 800 2-13
http://www.becker-hickl.de
email: info@becker-hickl.com
or becker@becker-hickl.com

External Control Signals

SPC-630, -730, -830, -130, -150, and -160 modules have one or two 3-row 15 pin Sub-D connectors to connect routing, control signals, and scan control signals to the modules. The SPC-180 and SPC-130IM modules have 2-row micro Sub-D connectors. In any case, the connectors also provide +5 V and +12 V power supply to external amplifiers, routers, PMT heads and photodiodes.

The routing and control signals are the key to the multi-dimensional TCSPC features implemented in the bh SPC modules, see 'Multi-Dimensional TCSPC', page 112. The functions can be used for complex experiments that require to synchronise a measurement with an externally varied parameter, such as sample position, wavelength, temperature or pressure, to record a sequence of measurements for different orientation of a polariser, or to multiplex different light sources or source intensities.

The signals applied to the connectors are key to a wide variety of recording and experiment-synchronisation functions. Admittedly, experiment control functions can also be accomplished by using the SPC DLL or the SPC LabView drivers, i.e. by writing a special windows application. There is certainly no objection against designing special software for complex instruments dedicated to special applications. However, in many (if not in most) cases software control is only used because the multi-dimensional features of the modules are not understood. In other words, the SPC module is used as a software-controlled classic TCSPC device. Software control then not only causes unnecessary development effort but also results in slow and often inefficient data acquisition. Moreover, problems can arise from undefined processing times due to interrupts, hard disk actions, or other applications running on the same computer. Therefore, please check whether you can solve your control problem by using the multi-dimensional features of the SPC modules. Do not hesitate to contact bh for advice.

The paragraphs below describe the control signals of the individual SPC modules. Examples of using of the signals are given under 'Non-Scanning TCSPC Applications' page 311.

Please be careful not to connect a device to the control connectors which is not intended for this purpose. This could damage the connected device or the SPC board.

SPC-600/630

1	+5 V (Load max. 100mA, Rout = 1Ω)
2	Routing Signal, /R 0
3	Routing Signal, /R 1
4	Routing Signal, /R 2
5	Ground
6	-5 V (Load max. 100mA, Rout = 1Ω)
7	Routing Signal, /R 3
8	Routing Signal, /R 4
9	Routing Signal, /R 5
10	+12 V (Load max. 60mA)
11	-12 V (Load max. 60mA)
12	Routing Signal, /R 6
13	ADD or TRIGGER[1] or /R7[2]
14	CNTE
15	Ground

1. If 'Trigger Condition' other than 'none'
2. In the FIFO Mode only

/R0 .. /R13: Routing Inputs. Polarity is 'active low', i.e. /R0 ... /R13 = 'high' will address curve 0. The open input represents a 'high' value.

ADD: The ADD signal is used for the lock-in SPC method. At ADD = 1 the events are added, at ADD = 0 the events are subtracted in the memory. Open inputs repre-

sent a logical ‘1’ value. The ADD input is shared with the TRIGGER input. The ADD function is activated if the trigger condition is set to ‘none’ (please see ‘System Parameters’, ‘More Parameters’). Thus, the trigger cannot be used when the ADD/SUB function is used.

TRIGGER : If a trigger condition is set (see ‘System Parameters’, ‘More Parameters’) the measurement starts when a L/H or H/L transition at the TRIGGER Input is detected. The TRIGGER input is shared with the ADD input. The TRIGGER function is activated if a trigger condition is set to ‘rising edge’ or ‘falling edge’ (please see ‘System Parameters’, ‘More Parameters’). Therefore, the ADD/SUB function cannot be used when the trigger is used.

CNTE: CNTE=L suppresses the storing of the current photon in the SPC memory. In conjunction with a router, the signal is used to reject misrouted events. The open input represents a logical ‘1’ value.

All signals (except the trigger) are read with a selectable ‘Latch Delay’ after a valid photon pulse at the CFD input has been detected (see 'System Parameters', 'Latch Delay').

SPC-700/730 and SPC-830

Connector 1 (lower connector)

1	+5 V (max. 100mA)
2	Routing Signal, /R 0
3	Routing Signal, /R 1
4	Routing Signal, /R 2
5	Ground
6	-5 V (max. 100mA)
7	Routing Signal, /R 3
8	Routing Signal, /R 4
9	Routing Signal, /R 5
10	+12 V (max. 60mA)
11	-12 V (max. 60mA)
12	Routing Signal, /R 6
13	ADD or Marker 3 (SPC-830)
14	CNTE1 (CNTE=CNTE1&CNTE2)
15	Ground

Connector 2 (upper connector)

1	+5 V (max. 100mA)
2	Routing Signal, /R 7 or ARMED[2]
3	Routing Signal, /R 8 or TRGD[2]
4	Routing Signal, /R 9 or MEASURE[2]
5	Ground
6	-5 V (max. 100mA)
7	Routing Signal, /R 10 or ‘Do not Connect’[2]
8	Routing Signal, /R 11 or YSYNC[1] or FBY[2] or Marker 2 (SPC-830)
9	Routing Signal, /R 12 or XSYNC[1] or FBX[2] or Marker 1 (SPC-830)
10	+12 V (max. 60mA)
11	-12 V (max. 60mA)
12	Routing Signal, /R 13 or PxlClk[1,2] or Marker 0 (SPC-830)
13	TRIGGER[3]
14	CNTE2 (CNTE=CNTE1&CNTE2)
15	Ground

The function of the control bits depend on the operation mode:

1. ‘Scan Sync In’ Mode
2. ‘Scan Sync Out’ Mode
3. Used if ‘Trigger Condition’ other than ‘none’ only

Single, Oscilloscope, F(t,x,y), F(t,T), F(t,ext), Fi(T), Fi(ext)

/R0 .. /R13: Routing Inputs. Polarity is ‘active low’, i.e. /R0 ... /R13 = 1 (or open) will address curve 0.

ADD: The ADD signal is used for the lock-in SPC method. At ADD = 1 the events are added, at ADD = 0 the events are subtracted in the memory. Open inputs represent a logical ‘1’ value.

TRIGGER: If a trigger condition is set (see ‘System Parameters’, ‘More Parameters’) the measurement starts when a L/H or H/L transition at the TRIGGER Input is detected.

CNTE1, 2: CNTE=L suppresses the storing of the current photon in the SPC memory. Both CNTE signals are AND connected, i.e. a photon is suppressed when one or both CNTEs are L. In conjunction with a router, the signal is used to reject misrouted events.

All signals (except the trigger) are read with a selectable 'Latch Delay' after a valid photon pulse at the CFD input has been detected (see 'System Parameters', 'Latch Delay').

Scan Sync In

The 'Scan Sync In' mode is used for image recording. The recording procedure is controlled by the scanning device via the 'XSync', 'YSync' and 'Pixel Clock' pulses. The control signals for the 'Scan Sync In' mode are listed below.

/R0 .. /R10: Routing Inputs. Polarity is 'active low', i.e. /R0 ... /R6 = 1 (or open) will address curve 0. The count enable signals CNTE1 and CNTE2 must be both '1' to enable the storing of the currently detected photon. In conjunction with a router, the signal is used to reject misrouted events.

XSync (Input): X synchronisation pulse. XSync forces the start of the next line.

YSync (Input): Y synchronisation Pulse. YSync forces the start of the next frame.

PxlClk (Input): External Pixel Clock. If the source of the pixel clock is set to 'external' the signal starts the measurement of the next Pixel.

CNTE1, CNTE2: CNTE=L suppresses the storing of the current photon in the SPC memory. Both CNTE signals are AND connected, i.e. a photon is suppressed when one or both CNTEs are L.

ADD: The ADD signal is used for lock-in SPC measurements. At ADD = 1 the events are added, at ADD = 0 the events are subtracted in the memory. Open inputs represent a logical 1 (add) value.

TRIGGER: If a trigger condition is set (see 'System Parameters', 'More Parameters') the measurement starts when a L/H or H/L transition at the TRIGGER input is detected. Once triggered, the measurement runs until it is stopped by the collection timer, by an overflow or by the user. After a stop command the measurement stops after the next Ysync pulse. If the 'Repeat' of 'Accumulate' functions are used, a trigger pulse is required to start each repetition or accumulation cycle.

Scan Sync Out

The 'Scan Sync Out' mode is used for image recording. The recording procedure is controlled by the SPC module via the 'Flyback X', 'Flyback X' and 'Pixel Clock' pulses. The control signals for the 'Scan Sync Out' mode are listed below.

/R0 .. /R6: Routing Inputs. Polarity is 'active low', i.e. /R0 ... /R6 = 1 (or open) will address curve 0. The count enable signals CNTE1 and CNTE2 must be both '1' to enable the storing of the currently detected photon. In conjunction with a router, the signal is used to reject misrouted events.

PxlClk (Output): 'Pixel Clock', indicates the start of the measurement of the next pixel. PIXEL is a 50 ns TTT H pulse. The duration of the measurement of each pixel is set by 'Collection Time', the number of points in X and Y direction by 'Scan Pixels X' and 'Scan Pixels Y' (see SPC system parameters).

FBX (Output): 'Flyback X', controls the X flyback phase of the scanner. For polarity and duration please see 'System Parameters'

FBY (Output): 'Flyback Y', controls the Y flyback phase of the scanner. For polarity and duration please see 'System Parameters'

CNTE1, 2: CNTE=L suppresses the storing of the current photon in the SPC memory. Both CNTE signals are AND connected, i.e. a photon is suppressed when one or both CNTEs are L.

ADD: The ADD signal is used for lock-in SPC measurements. At ADD = 1 the events are added, at ADD = 0 the events are subtracted in the memory. Open inputs represent a logical 1 (add) value.

TRIGGER: If a trigger condition is set (see 'System Parameters', 'More Parameters') the measurement starts when a L/H or H/L transition at the TRIGGER input is detected. Once triggered, the measurement runs until it is stopped by the collection timer, by an overflow or by the user. After a command the measurement stops after the next Ysync pulse. If the 'Repeat' of 'Accumulate' functions are used, a trigger pulse is required to start each repetition or accumulation cycle.

The function of the PxlClk, FBX and FBY signals for a simple 8 x 4 matrix is shown in Fig. 1331.

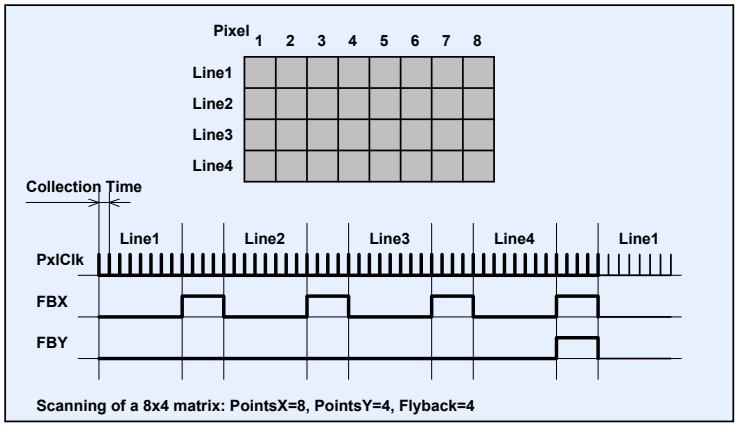


Fig. 1331: Scan clock signals in the Scan Sync Out mode

Scan XY Out (SPC-700/730 only)

The 'Scan XY Out' mode is used for image recording. The recording procedure is controlled by the SPC module via the position signals /R0 through /R13. /R0 through /R13 are outputs and indicate the actual scan position.

/R0 .. /R13: Scan Position Outputs. Polarity is 'active low', i.e. /R0 ... /R13 = 1 sets the scanner position to X=Y=0 and addresses curve 0 in the SPC memory.

ADD: The ADD signal is used for the lock-in SPC method. At ADD = 1 the events are added, at ADD = 0 the events are subtracted in the memory. Open inputs represent a logical '1' value. All signals are read with a selectable 'Latch Delay' after a valid photon pulse at the CFD input has been detected (see 'System Parameters', 'Latch Delay').

TRIGGER: If a trigger condition is set (see 'System Parameters', 'More Parameters') the measurement starts when a L/H or H/L transition at the TRIGGER Input is detected. It stops when the scan of the frame is complete. If the 'Repeat' or 'Accumulate' functions are used, a trigger pulse is required to start each repetition or accumulation cycle.

CNTE1, 2: CNTE=L suppresses the storing of the current photon in the SPC memory. Both CNTE signals are AND connected, i.e. a photon is suppressed when one or both CNTEs are L. In conjunction with a router, the signal is used to reject misrouted events.

SPC-130, SPC-134

1	+5 V (Load max. 100mA, Rout = 1Ω)
2	Routing Signal, /R 0
3	Routing Signal, /R 1
4	Routing Signal, /R 2
5	Ground
6	-5 V (Load max. 100mA, Rout = 1Ω)
7	Routing Signal, /R 3
8	Routing Signal, /R 4
9	Routing Signal, /R 5
10	+12 V (Load max. 60mA)
11	-12 V (Load max. 60mA)
12	Routing Signal, /R 6
13	ADD or TRIGGER
14	CNTE
15	Ground

/R0 .. /R2: Routing Inputs. Polarity is ‘active low’, i.e. /R0 ... /R13 = ‘high’ will address curve 0. The open input represents a ‘high’ value.

ADD: The ADD signal is used for the lock-in SPC method. At ADD = 1 the events are added, at ADD = 0 the events are subtracted in the memory. Open inputs represent a logical ‘1’ value. The ADD input is shared with the TRIGGER input. The ADD function is activated if the trigger condition is set to ‘none’ (please see ‘System Parameters’, ‘More Parameters’). Thus, the trigger cannot be used when the ADD/SUB function is used and vice versa.

TRIGGER: If a trigger condition is set (see ‘System Parameters’, ‘More Parameters’) the measurement starts when a L/H or H/L transition at the TRIGGER Input is detected. The TRIGGER input is shared with the ADD input. The TRIGGER function is activated if a trigger condition is set to ‘rising edge’ or ‘falling edge’ (please see ‘System Parameters’, ‘More Parameters’). Therefore, the ADD/SUB function cannot be used when the trigger is used.

CNTE: CNTE=L suppresses the storing of the current photon in the SPC memory. In conjunction with a router, the signal is used to reject misrouted events. The open input represents a logical ‘1’ value.

The /R0, /R1, /R2, ADD and CNTE signals are read approximately 10ns after a valid photon pulse at the CFD input has been detected. There is no 'Latch Delay' as in the other SPC modules. If the SPC-134 has to be used for multidetector operation 6 to 9 m 50 Ω cable has to be inserted from the timing output of the HRT-41, -81, and -82 router to the corresponding CFD input.

SPC-130EM, SPC-130EMN, SPC-150, SPC-150N, SPC-160

Applies also for SPC-130EMN, SPC-150NX and SPC-150NXX modules

1	+5 V (max. 100mA)
2	Routing Signal, /R 0
3	Routing Signal, /R 1
4	Routing Signal, /R 2
5	Ground
6	-5 V (max. 100mA)
7	Routing Signal, /R 3
8	YSYNC [1)] or FBY [2)], or routing signal, /R 4, or Marker 2 [3)]
9	XSYNC [1)] or FBX [2)], or routing signal, /R 5, or Marker 1 [3)]
10	+12 V (max. 60mA)
11	ADD, or Marker 3 [1,3)]
12	PxlClk[1)], or routing signal,/R 6, or Marker 0 [3)]
13	TRIGGER[4)], or routing signal, /R 7
14	CNTE
15	Ground

1. Scan Sync In Mode and FIFO Imaging Mode
2. Scan Sync Out Mode
3. FIFO Mode
4. If 'Trigger Condition' other than 'None'

The function of the control bits depends on the operation mode:

Single, Oscilloscope, F(t,x,y), F(t,T), F(t,ext), Fi(T), Fi(ext)

/R0 .. /R7: Routing Inputs. Polarity is 'active low', i.e. /R0 ... /7 = 1 (or open) addresses curve 0.

ADD: The ADD signal is used for the lock-in SPC method. At ADD = 1 the events are added, at ADD = 0 the events are subtracted in the memory. Open inputs represent a logical '1' value.

TRIGGER: If a trigger condition is set (see 'System Parameters', 'More Parameters') the measurement starts when a L/H or H/L transition at the TRIGGER Input is detected.

CNTE: CNTE=L suppresses the storing of the current photon in the SPC memory. In conjunction with a router, the signal is used to reject multi-photon events.

All signals (except the trigger) are read with a selectable 'Latch Delay' after a valid photon pulse at the CFD input has been detected (see 'System Parameters', 'Latch Delay').

Scan Sync In

The 'Scan Sync In' mode is used for image recording. The recording procedure is controlled by the scanning device via the 'XSync', 'YSync' and 'Pixel Clock' pulses. The control signals for the 'Scan Sync In' mode are listed below.

/R0 .. /R3: Routing Inputs. Polarity is 'active low', i.e. /R0 ... /R3 = 1 (or open) addresses curve 0. The count enable signal CNTE must be '1' to enable the storing of the currently detected photon. In conjunction with a router, the signal is used to reject multi-photon events.

XSync (Input): X synchronisation pulse. XSync forces the start of the next line.

YSync (Input): Y synchronisation Pulse. YSync forces the start of the next frame.

PxlClk (Input): External Pixel Clock. If the source of the pixel clock is set to 'external' the signal starts the measurement of the next Pixel.

CNTE: CNTE=L suppresses the storing of the current photon in the SPC memory.

ADD: The ADD signal is used for lock-in SPC measurements. At ADD = 1 the events are added, at ADD = 0 the events are subtracted in the memory. Open inputs represent a logical 1 (add) value.

TRIGGER: If a trigger condition is set (see 'System Parameters', 'More Parameters') the measurement starts when a L/H or H/L transition at the TRIGGER input is detected. Once triggered, the measurement runs until it is stopped by the collection timer, by an overflow or by the user. After a stop command in the in the Scan Sync In mode, the measurement stops after the next Ysync pulse. If the 'Repeat' of 'Accumulate' functions are used, a trigger pulse is required to start each repetition or accumulation cycle.

Scan Sync Out

The 'Scan Sync Out' mode is used for image recording. The recording procedure is controlled by the SPC module via the 'Flyback X', 'Flyback X' and 'Pixel Clock' pulses. The control signals for the 'Scan Sync Out' mode are listed below.

/R0 .. /R3: Routing Inputs. Polarity is 'active low', i.e. /R0 ... /R6 = 1 (or open) will address curve 0. The count enable signal CNTE must be '1' to enable the storing of the currently detected photon. In conjunction with a router, the signal is used to reject multi-photon events.

PxlClk (Output): 'Pixel Clock' indicates the start of the measurement of the next pixel. PIXEL is a 50 ns TTT H pulse. The duration of the measurement of each pixel is set by 'Collection Time', the number of points in X and Y direction by 'Scan Pixels X' and 'Scan Pixels Y' (see SPC system parameters).

FBX (Output): 'Flyback X', controls the X flyback phase of the scanner. For polarity and duration please see 'System Parameters'

FBY (Output): 'Flyback Y', controls the Y flyback phase of the scanner. For polarity and duration please see 'System Parameters'

CNTE: CNTE=L suppresses the storing of the current photon in the SPC memory.

ADD: The ADD signal is used for lock-in SPC measurements. At ADD = 1 the events are added, at ADD = 0 the events are subtracted in the memory. Open inputs represent a logical 1 (add) value.

TRIGGER: If a trigger condition is set (see 'System Parameters', 'More Parameters') the measurement starts when a L/H or H/L transition at the TRIGGER input is detected. Once triggered, the measurement runs until it is stopped by the collection timer, by an overflow, or by the user. After a stop command in the in the Scan Sync Out mode, the measurement stops after the next Ysync pulse. If the 'Repeat' of 'Accumulate' functions are used, a trigger pulse is required to start each repetition or accumulation cycle.

FIFO Mode and FIFO Imaging Mode

The 'FIFO Imaging' mode is used for image recording. The recording procedure is controlled by the scanning device via the 'XSync', 'YSync' and 'Pixel Clock' pulses. The control signals are listed below.

/R0 .. /R3: Routing Inputs. Polarity is 'active low', i.e. /R0 ... /R3 = 1 (or open) addresses curve 0. The count enable signal CNTE must be '1' to enable the storing of the currently detected photon. In conjunction with a router, the signal is used to reject multi-photon events.

XSync (Marker1): FIFO mode: General purpose marker input. FIFO Imaging Mode: X synchronisation pulse (line clock) pulse.

YSync (Marker2): FIFO mode: General purpose marker input. FIFO Imaging mode:Y synchronisation (frame clock) pulse.

PxlClk (Marker0): FIFO mode: General purpose marker input. FIFO Imaging mode:pixel clock pulse.

CNTE: Count Enable signal. CNTE=L suppresses the storing of the current photon in the SPC memory.

Marker 3: General purpose marker input. Can be used as an alternative frame clock input in FIFO Imaging mode.

TRIGGER: If a trigger condition is set (see 'System Parameters', 'More Parameters') the measurement starts when a L/H or H/L transition at the TRIGGER input is detected.

FIFO Mode

The 'FIFO' mode records parameter-tagged photon data. The control signals are listed below.

/R0 .. /R3: Routing Inputs. The status of /R0...R3 is attached to the micro- and macrotime data word of the current photon.

Marker0...3: FIFO mode: General purpose marker inputs. L/H or H/L transitions are included in the data stream as individual entries.

CNTE: Marks the currently detected photon as 'invalid'. The status is attached to the data word of the current photon.

TRIGGER: If a trigger condition is set (see 'System Parameters', 'More Parameters') the measurement starts when a L/H or H/L transition at the TRIGGER input is detected.

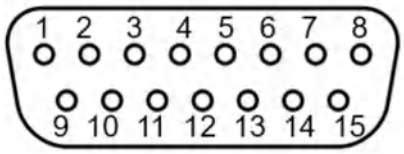
SPC-180N, SPC-180NX, SPC-180NXX, SPC-130IN, SPC-130INX

Different than the SPC-150 and SPC150N family modules which have 3-row sub-D connectors, the SPC-180N and SPC-130IN modules have 2-row micro connectors. Starting from September 2021 the modules have two such connectors, the signals of which are OR-wired. This simplifies the cable connections if both scan clocks and routing signals are connected.

Please note that the pin numbers are not the same as for the SPC-150 and SPC-160.

1 +5 V (max. 100mA)
2 Routing Signal, /R 0
3 Routing Signal, /R 1
4 Routing Signal, /R 2
5 Ground
6 -5 V (max. 100mA)
7 Routing Signal, /R 3
8 YSYNC [1] or FBY [2], or routing signal, /R 4, or Marker 2 [3]
9 XSYNC [1] or FBX [2], or routing signal, /R 5, or Marker 1 [3]
10 ADD, or Marker 3 [1,3]
11 +12 V (max. 60mA)
12 PxlClk[1], or routing signal,/R 6, or Marker 0 [3]
13 TRIGGER[4], or routing signal, /R 7
14 CNTE
15 Ground

1. Scan Sync In Mode and FIFO Imaging Mode
2. Scan Sync Out Mode
3. FIFO Mode
4. If 'Trigger Condition' other than 'none'

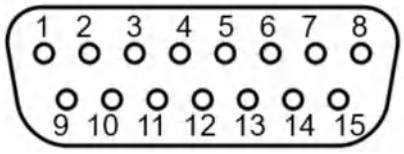


The function of the signals is the same as for the SPC-130EMN, the SPC-150 and the SPC-160. Please see page 967.

SPC-QC-104 and SPC-QC-106 modules

1 +5 V (max. 100mA)
2 Routing Signal, /R 0
3 Routing Signal, /R 1
4 Routing Signal, /R 2
5 Ground
6 -5 V (max. 100mA)
7 Routing Signal, /R 3
8 YSYNC (frame Clock) or Marker 2
9 XSYNC (line clock) or Marker 1
10 Marker 3
11 +12 V (max. 60mA)
12 PxlClk (pixel clock) or Marker 0
13 TRIGGER
14 CNTE (count enable)
15 Ground

Caution: Routing signals /R0 through /R3 act on all channels in parallel



GVD-120 Scan Controller

15-Pin Sub-D Connector

1	+ 5 V
2	Laser-Routing
3	Laser 1 On
4	Laser 2 On
5	GND
6	- do not connect -
7	- do not connect -
8	Frame Clock Out
9	Line Clock Out
10	Laser 1 Power Control, 0...10V
11	Laser 2 Power Control, 0...10V
12	Pixel Clock Out
13	- do not connect -
14	- do not connect -
15	GND

DCC-100 Detector Controller

Connector 1

1	+5 V out switchable
2	Peltier +
3	Peltier +
4	Peltier +
5	GND
6	-5 V out switchable
7	Peltier -
8	Peltier -
9	Peltier -
10	+12 V out switchable, ovld shdwn
11	-12 V out
12	0...+10V HV/gain control signal, shuts down on overload
13	0...+0.9V HV/gain control signal, shuts down on overload
14	/OVLD1 input
15	GND

Connector 2

1	+5 V out switchable
2	Bit0 open drain out
3	Bit1 open drain out
4	Bit2 open drain out
5	GND
6	-5 V out switchable
7	Bit3 open drain out
8	Bit4 open drain out
9	Bit5 open drain out
10	+12 V out switchable
11	-12 V out
12	Bit6 open drain out
13	Bit7 open drain out
14	
15	GND

Connector 3

1	+5 V out switchable
2	Peltier +
3	Peltier +
4	Peltier +
5	GND
6	-5 V out switchable
7	Peltier -
8	Peltier -
9	Peltier -
10	+12 V out, switchable, shuts down on overload
11	-12 V out
12	0...+10V HV/gain control signal, shuts down on overload
13	0...+0.9V HV/gain control signal, shuts down on overload
14	/OVLD3 input
15	GND

DCC-100 modules manufactured before 2014 had only one Peltier cooler supply for connector 1 and connector 3. The corresponding outputs were connected in series. If no cooler was connected to one of the connectors, the corresponding cooler output had to be bridged by a jumper on the DCC board or by a bridge in a blind connector. DCC-100 modules manufactured 2014 or later have two independent cooler supplies. No jumpers or blind connectors are needed for these modules.

Specifications

Due to space limitations the specifications of the SPC modules have been omitted from the current version of the TCSPC Handbook. Please refer to the data sheets on https://www.becker-hickl.com.

Absolute Maximum Ratings (for all SPC modules)

Current into the SYNC and CFD inputs	±50 mA (DC) ±200 mA (pulse, <1us)
Voltage at the routing and control inputs / outputs	-0.5 V ... +5.5 V
Current drawn from the	
+5 V output	200 mA
-5 V output	200 mA
+12 V output	100 mA
-12 V output	100 mA
Supply Voltages at the PCI or PCI-Express Connector	
Vcc (+5 V)	-0.5 ... +5.5 V
Vpp (+12 V)	-0.5 ... +13 V
Signal Voltages at the PCI connector	-0.5 ... +5.5 V
Signal Voltages at the PCI-Express connector	-0.3 ... +1.3 V
Ambient temperature	0°C ... +40°C

Acknowledgements

Work presented under 'Metabolic FLIM with Two-Photon Excitation' has been financially supported by German BMBF, project number 13N14504. Work presented under 'Metabolic FLIM with One-Photon Excitation' has been supported financially by German BMBF, project number 03ZZ0444I. Work presented under 'FLIO Analysis by SPCImage NG' has been financially supported by German BMBF, project number 13N14441. Work presented under 'Oxygen Sensing by PLIM' has been financially supported by German BMWi, project number KF 2122510AK2.

References

1. M. Akatsu,Y. Enari, K. Hayasaka, T. Hokuue, T. Iijima, K. Inami, K. Itoh, Y. Kawakami, N. Kishimoto, T. Kubota, M. Kojima, Y. Kozakai, Y. Kuriyama, T. Matsuishi, Y. Miyabayashi, T. Ohshima, N. Sato, K. Senyo, A. Sugi, S. Tokuda, M. Tomita, H. Yanase, S. Yosino, MCP-PMT timing property for single photons, Nucl. Instr. Meth. A 528, 763-775 (2004)
2. Abberior Instruments STED systems, please see www.abberior-instruments.com
3. E. Abdollahi, G. Taucher-Scholz, M. Durante, B. Jakob, Upgrading the GSI beamline microscope with a confocal fluorescence lifetime scanner to monitor charged particle induced chromatin decondensation in living cells. Nuclear Instruments and Methods in Physics Research B 365, 626-630 (2015)
4. A. M. Adawi, A. Cadby, L. G. Connolly, W.-C. Hung, R. Dean, A. Tahraoui, A. M. Fox, A. G. Cullis, D. Sanvitto, M. S. Skolnick, D. G. Lidzey, Spontaneous Emission Control in Micropillar Cavities Containing a Fluorescent Molecular Dye. Adv. Mater. 18, 742–747 (2006)
5. Z. Ahmed, A. C. Schüller, K. Suhling, C. Tregido, J. E. Ladbury, Extracellular point mutations in FGFR2 elicit unexpected changes in intracellular signalling. Biochem. J. 413, 37–49 (2008)
6. Z. Ahmed, R. George, C.-C. Lin, K. M. Suen, J. A. Levitt, K. Suhling, J. E. Ladbury, Direct binding of Grb2 SH3 domain to FGFR2 regulates SHP2 function. Cellular Signalling 22 23-33 (2010)
7. Z. Ahmed, Z. Timsah, K. M. Suen, N. P. Cook, G. R. Lee, Chi-Chuan Lin, Mihai Gagea, A. A. Marti, J.n E. Ladbury, Grb2 monomer–dimer equilibrium determines normal versus oncogenic function. Nature Communications 6, 7354-1 to -9
8. Z. Ahmed, C.-C. Lin, K. M. Suen, F. A. Melo, J. A. Levitt, K. Suhling, J. E. Ladbury, Grb2 controls phosphorylation of FGFR2 by inhibiting receptor kinase and Shp2 phosphatase activity. J. Cell biol. 200, 493-504 (2013)
9. D. Aigner, R. I. Dmitriev, S. M. Borisov, D. B. Papkovsky, I. Klimant, pH-sensitive perylene bisimide probes for live cell fluorescence lifetime imaging. J. mater. Chem. B (2014)
10. S. R. Alam, H. Wallrabe, Z. Svindrych, A. K. Chaudhary, K. G. Christopher, D. Chandra, A. Periasamy, Investigation of Mitochondrial Metabolic Response to Doxorubicin in Prostate Cancer Cells: An NADH, FAD and Tryptophan FLIM Assay. Scientific Reports 7 (2017)
11. S. R. Alam, H. Wallrabe, K. G. Christopher, K. H. Siller, A. Periasamy, Characterization of mitochondrial dysfunction due to laser damage by 2-photon FLIM microscopy. Scientific Reports 12, 11983 (2022)
12. F. Aletti, R. Re, V. Pace, D. Contini, E. Molteni, S. Cerutti, M. A. Bianchi, A. Torricelli, L. Spinelli, R. Cubeddu, G. Baselli, Deep and surface hemodynamic signal from functional time resolved transcranial near infrared spectroscopy compared to skin flowmotion. Comput Biol Med. 42(3), 282-289 (2012)
13. A. Alex, S. Frey, H. Angelene, C.D. Neitzel, J. Li, A.J. Bower, D.R. Spillman Jr, M. Marjanovic, E.J. Chaney, J.L. Medler, W. Lee, L.S. Vasist Johnson, S.A. Boppart and Z. Arp, In situ biodistribution and residency of a topical anti-inflammatory using fluorescence lifetime imaging microscopy. British Journal of Dermatology 179, 1342-1350 (2018)
14. R.R. Alfano, Ed., The supercontinuum laser source, Springer, New York (2006)
15. W. R. Algar, A. Khachatrian, J. S. Melinger, Alan L. Huston, M. H. Stewart, Ki. Susumu, J. B. Blanco-Canosa, E. Oh, P. E. Dawson, I. L. Medintz, Concurrent Modulation of Quantum Dot Photoluminescence Using a Combination of Charge Transfer and Förster Resonance Energy Transfer: Competitive Quenching and Multiplexed Biosensing Modality, J. Am. Chem. Soc. 2017, 139, 363−372
16. W. Al-Soufi, B. Reija, M. Novo, Suren Felekyan, R. Kühnemuth, C.A.M. Seidel, Fluorescence correlation spectroscopy, a tool to investigate supramolecular dynamics: Inclusion complexes of pyronines with cyclodextrin. J. Am. Chem. Soc. 127, 8775-8784 (2005)
17. K. Amari, E. Boutant, C. Hofmann, C. Schmitt-Keichinger, L. Fernandez-Calvino, P. Didier, A. Lerich, J. Mutterer, C. L. Thomas, M. Heinlein, Y. Mely, A. J. Maule, C. Ritzenthanler, A family of plasmodesmal proteins with receptor-like properties for plant viral movement proteins. PLOS Pathogens 6 e1001119-1 to -10 (2010)
18. K. Amarnath, J. Zaks, S. D. Park, K. K. Niyogi, G. R. Fleming, Fluorescence lifetime snapshots reveal two rapidly reversible mechanisms of photoprotection in live cells of Chlamydomonas reinhardtii. PNAS 109, 8405-8410 (2012)
19. S.M. Ameer-Beg, N. Edme, M. Peter, P.R. Barber, T. Ng, B. Vojnovic, Imaging protein-protein interactions by multiphoton FLIM, Proc. SPIE, 5139, 180-189 (2003)
20. S.M. Ameer-Beg, P.R. Barber, R. Locke, R.J. Hodgkiss, B. Vojnovic, G.M. Tozer, J. Wilson, Application of multiphoton steady state and lifetime imaging to mapping of tumor vascular architecture in vivo, Proc. SPIE, 4620, 85-95 (2002)
21. K. M. Andersen, L. Sauer, R. H. Gensure, M. Hammer, P. S. Bernstein, Characterization of Retinitis Pigmentosa Using Fluorescence Lifetime Imaging Ophthalmoscopy (FLIO). TVST 7 No. 3 (2018)

22. R.M. Anderssen, K. Carlsson, A. Liljeborg, H. Brismar, Characterization of probe binding and comparison of its influence on fluorescence lifetime of two ph-sensitivy benzo[c]xantene dyes using intensity-modulated multiple-wavelength scanning technique, Analytical Biochemistry **283**, 104-110 (2000)
23. N. Anthony, K. Berland, Global Analysis in Fluorescence Correlation Spectroscopy and Fluorescence Lifetime Microscopy. In: S. Y. Tetin, ed., Methods in Enzymology 518, 145-173 Fluorescence Fluctuation Spectroscopy (FFS), Part A, Academic Press (2013)
24. N. R. Anthony, K. M. Berland, Global analysis enhances resolution and sensitivity in fluorescence fluctuation measurements. PLOS ONE 9, e90456, www.plosone.ord
25. M. Antonik, S. Felekyan, A. Gaiduk, and C. A. M. Seidel, Separating Structural Heterogeneities from Stochastic Variations in Fluorescence Resonance Energy Transfer Distributions via Photon Distribution Analysis. J. Phys. Chem. 110, 6970-6978 (2006)
26. H. Aoki, M. Kitamura, S. Ito, Nanosecond Dynamics of Poly(methyl methacrylate) Brushes in Solvents Studied by Fluorescence Depolarization Method. Macromolecules 4, 285-287 (2008)
27. J. Aow, K. Dore, R. Malinow, Conformational signaling required for synaptic plasticity by the NMDA receptor complex. PNAS Early Edition, www.pnas.org/cgi/doi/10.1073/pnas.1520029112
28. C. P. Aplin, R. C. Miller, T. M. Kay, A. A. Heikal, A. J. Boersma, E. D. Sheets, Fluorescence depolarization dynamics of ionic strength sensors using time-resolved anisotropy. Biophys. J. 120, 1417–1430, (2021)
29. Y. Ardeshirpour, V. Chernomordik, R. Zielinski, J. Capala, G. Griffiths, O. Vasalatiy, A. V. Smirnov, J. R. Knutson, I. Lyakhov, S. Achilefu, A. Gandjbakhche, M. Hassan, In Vivo Fluorescence Lifetime Imaging Monitors Binding of Specific Probes to Cancer Biomarkers. Plos ONE 7, e31881 (2012)
30. F. S. Ariola, Z. Li, C. Cornejo, R.t Bittman, A. A. Heikal, Membrane fluidity and lipid order in ternary giant unilamellar vesicles using a new bodipy-cholesterol derivative. Biophys. J. 96, 2696- 2708 (2009)
31. D. Arosio, G. Garau, F. Ricci, L. Marchetti, R. Bizzarri, R. Nifosi, F. Beltram, Spectroscopic and Structural Study of Proton and Halide Ion Cooperative Binding to GFP. Biophys. J. 93, 232-244 (2007)
32. S.R. Arridge, Optical tomography in medical imaging, Inverse Problems, **15**, R41 (1999)
33. S.R. Arridge, M. Cope, D.T. Delpy, The theoretical basis for the determination of optical pathlengths in tissue, temporal and frequency analysis, Phys. Med Biol. **37**, 1531-1560 (1992)
34. S.R. Arridge, J.C. Hebden, M. Schweiger, F.E.W. Schmidt, M.E. Fry, E.M.C. Hillman, H. Dehghani, D.T. Delpy, A method for three-dimensional time-resolved optical tomography, International Journal for Imaging systems and Technology **11**, 2-11 (2000)
35. E. Auksorius, B. R. Boruah, C. Dunsby, P. M. P. Lanigan, G. Kennedy, M. A. A. Neil, P. M. W. French, Stimulated emission depletion microscopy with a supercontinuum source and fluorescence lifetime imaging. Opt. Lett. 33, 113-115 (2008)
36. E. Avezov,. B.C.S. Cross, G.S. Kaminski Schierle, M. Winters, H. P. Harding, E. Pinho Melo, C. F. Kaminski, D. Ron, Lifetime imaging of a fluorescent protein sensor reveals surprising stability of ER thiol redox. J. Cell Biol. 201, 337-349 (2013)
37. K. Awasthi, T. Nakabayashi, L. Li, N. Ohta, Effects of Nanosecond Pulsed Electric Field on Intracellular NADH Autofluorescence: A Comparison between Normal and Cancer Cells. ACS Omega 2, 2916-2924 (2017)
38. D. Axelrodt, Fluorescence Polarisation Microscopy, D.L. Taylor, Y.-L. Wang (eds.), Methods in Cell Biology, Academic Press 1989
39. T. E. Bapiro, S. Martin, Th. S. Blacker, S. D. Wilkinson, A. L. Orton, N. Hariparsad, R. D. O. Jones, M. R. Duchen, S. Harlfinger, A mismatch in enzyme-redox partnerships underlies divergent cytochrome P450 activities between human hepatocytes and microsomes. Communications Biology 8:1539 1-14 (2025)
40. B. J. Bacskai, J. Skoch, G.A. Hickey, R. Allen, B.T. Hyman, Fluorescence resonance energy transfer determinations using multiphoton fluorescence lifetime imaging microscopy to characterize amyloid-beta plaques, J. Biomed. Opt **8**, 368-375 (2003)
41. B. J. Bacskai, J. Skoch, G.A. Hickey, O. Berezovska, B.T. Hyman, Multiphoton imaging in mouse models of Alzheimer's disease, Proc. SPIE, **5323**, 71-76 (2004)
42. W.R.G. Baeyens, D. de Keukeleire, K. Korkidis, Luminescence techniques in chemical and biochemical analysis, M. Dekker, New York (1991)
43. E. Baggaley, S. W. Botchway, J. W. Haycock, H. Morris, I. V. Sazanovich, J. A. G. Williams, J. A. Weinstein, Long-lived metal complexes open up microsecond lifetime imaging microscopy under multiphoton excitation: from FLIM to PLIM and beyond. Chem. Sci. 5, 879-886 (2014)
44. E. Baggaley, M. R. Gill, N. H. Green, D. Turton, I. V. Sazanovich, S. W. Botchway, C. Smythe, J. W. Haycock, J. A. Weinstein, J. A. Thomas, Dinuclear Ruthenium(II) Complexes as Two-Photon, Time-Resolved Emission Microscopy Probes for Cellular DNA. Angew. Chem. Int. Ed. Engl. 53, 3367-3371 (2014)
45. K. Bahlmann, S.W. Hell, Deplorization by high aperture focusing, Appl. Phys. Lett. **77**, 612-614 (2000)

46. R.M. Ballew, J.N. Demas, An error analysis of the rapid lifetime determination method for the evaluation of single exponential decays, Anal. Chem. **61**, 30 (1989)
47. B.P. Barber, R.A. Hiller, R. Lofstedt, S.J. Putterman, K.R. Weninger, Defining the unknowns of sonoluminescence, Phys. Rep. **281**, 65-143 (1997)
48. P.R Barber, S.M Ameer-Beg, J Gilbey, L.M Carlin, M Keppler, T.C Ng, B Vojnovic, Multiphoton time-domain fluorescence lifetime imaging microscopy: practical application to protein -protein interactions using global analysis. J. R. Soc. Interface 6, S93-S105 (2009)
49. D. S. Barkauskas, G. Medley, X. Liang, Y. H. Mohammed, C. A.Thorling, H. Wang, M. S. Roberts, Using in vivo multiphoton fluorescence lifetime imaging to unravel disease-specific changes in the liver redox state. Methods Appl. Fluoresc. 8, 034003 1-18 (2020)
50. T. Basché, W.E. Moerner, M. Orrit, H. Talon, Photon antibunching in the fluorescence of a single dye molecule trapped in a solid, Phys. Rev. Lett. **69**, 1516 (1992)
51. A. Bassi, J. Swartling, C. D'Andrea, A. Pifferi, A. Torricelli, R. Cubeddu, Time-resolved spectrophotometer for turbid media based on supercontinuum generation in a photonic crystal fibre, Opt. Lett. **29**, 2405-2407 (2004)
52. A. Bassi, L. Spinelli, C, D'Andrea, A. Giusto, J. Swartling, A. Pifferi, A. Torricelli, R. Cubeddu, Feasibility of white-light time-resolved optical mammography. J. Biomed. Opt. 11(5) 054035-1 to 5, (2006)
53. A. Bassi, A. Farina, C. D'Andrea, A. Pifferi, G.a Valentini, and R. Cubeddu, Portable, large-bandwidth time-resolved system for diffuse optical spectroscopy. Opt. Expr. 15 14482-14487 (2007)
54. A. Batista, H-G. Breunig A. Uchugonova A. M. Morgado, K. König, Two-photon spectral fluorescence lifetime imaging and second harmonic generation imaging of the porcine cornea with a 12-femtosecond laser microscope. J. Biomed. Opt. 21(3), 036002-1 to -11 (2016)
55. Z. Bay, Calculation of decay times from coincidence experiments. Phys. Rev. 77, 419 (1950)
56. V. Bayle, L. Nussaume, and R. A. Bhat, Combination of Novel Green Fluorescent Protein Mutant TSapphire and DsRed Variant mOrange to Set Up a Versatile in Planta FRET-FLIM Assay. Plant Physiology 148, 51–60 (2008)
57. E. Beaupaire, M. Oheim, J. Mertz, Ultra-deep two-photon fluorescence excitation in turbid media. Optics Communications 188 25-29 (2001)
58. E. Beaurepaire, J. Mertz, Epifluorescence collection in two-photon microscopy. Appl. Opt. 41, 5376-5382 (2002)
59. Becker & Hickl GmbH, SPC-QC-008 8-Channel TCSPC / Time-Tagger Module, user manual. Available on https://www.becker-hickl.com/products/spc-qc-008-tcspc-module/
60. Becker & Hickl GmbH, PMS-800 4-Channel gated photon counter, user manual. Available on https://www.becker-hickl.com/products/pms-800/
61. Becker & Hickl GmbH, Routing modules for time-correlated single photon counting, manual, www.becker-hickl.com
62. Becker & Hickl GmbH, PML-16-C 16 and PML-16 GaAsP 16-channel channel TCSPC / Detectors, PML-SPEC and MW FLIM Multi-Wavelength detectors. User handbook (2016). Available on www.becker-hickl.com
63. Becker & Hickl GmbH, DCC-100 detector control module, manual, www.becker-hickl.com
64. Becker & Hickl GmbH, FLIM in the FIFO Imaging Mode: Large Images with Small TCSPC Modules. Application note, available on www.becker-hickl.com
65. Becker & Hickl GmbH, The DCS-120 Confocal Scanning FLIM System, an Overview. 40-pages brochure, available on www.becker-hickl.com.
66. Becker & Hickl GmbH, The DCS-120 Confocal Scanning FLIM System. Application note, available on www.becker-hickl.com
67. Becker & Hickl GmbH, DCS-120 Confocal FLIM System with Wideband Beamsplitter. Application note, available on www.becker-hickl.com
68. Becker & Hickl GmbH, DCS-120 Confocal and Multiphoton FLIM Systems, user handbook, 9th ed. (2021). Available on www.becker-hickl.com
69. Becker & Hickl GmbH, Modular FLIM systems for Zeiss LSM 710 / 780 / 880 family family laser scanning microscopes. User handbook, 7th ed. (2017). Available on www.becker-hickl.com
70. Becker & Hickl GmbH, FLIM Systems for Zeiss LSM 980 Laser Scanning Microscopes. Addendum to: Handbook for modular FLIM systems for Zeiss LSM 710 / 780 / 880 family laser scanning microscopes. Available on www.becker-hickl.com
71. Becker & Hickl GmbH, FLIM Systems for Zeiss LSM 710 / 780 / 880 / 980 Family Laser Scanning Microscopes. An Overview. 68-pages brochure, available on www.becker-hickl.com
72. Becker & Hickl GmbH, ExpressFLIM Real Time Fluorescence Lifetime Imaging Software. User handbook, available on https://www.becker-hickl.com/products/expressflim-records-real-time-flim-data-stream/

73. Becker & Hickl GmbH, SPCDynamics. User manual, available on https://www.becker-hickl.com/products/spc-dynamics/
74. Becker & Hickl GmbH, LHB-104 Laser Hub. User manual, available on www.becker-hickl.com.
75. Becker & Hickl GmbH, SPC-QC-104 and SPC-QC-106 TCSPC/FLIM Modules, user manual. Available on www.becker-hickl.com.
76. Becker & Hickl GmbH and Leica Microsystems, Leica MP-FLIM and D-FLIM Fluorescence Lifetime Microscopy Systems. User handbook. Available on www.becker-hickl.com
77. Becker & Hickl GmbH, Modular FLIM systems for Olympus laser scanning microscope FV1000. User handbook. Available on www.becker-hickl.com
78. Becker & Hickl GmbH, SPCImage next generation FLIM data analysis software. Overview brochure, available on www.becker-hickl.com
79. Becker & Hickl GmbH, Burst Analyser 2.0, for correlation analysis and single-molecule spectroscopy. Available on www.becker-hickl.com
80. Becker & Hickl GmbH, DPC-230 16 Channel Photon Correlator, www.becker-hickl.com
81. Becker & Hickl GmbH, BDL-375-SMC, BDL-405-SPC, BDL-440-SMC, BDL-473-SMC NUV and blue picosecond diode lasers. Available on www.becker-hickl.com
82. Becker & Hickl GmbH, BDL-SMN series picosecond diode lasers. Available on www.becker-hickl.com
83. Becker & Hickl GmbH, BDS-SM Family Picosecond Diode Lasers. Extended data sheet, available on www.becker-hickl.com
84. Becker & Hickl GmbH, BDS-MM Family Picosecond Diode Lasers. Extended data sheet, available on www.becker-hickl.com
85. Becker & Hickl GmbH, The HPM-100-40 Hybrid Detector. Application note, available on www.becker-hickl.com
86. Becker & Hickl GmbH, The HPM-100-50 Hybrid Detector: Increased Dynamic Range for DOT. Application note, available on www.becker-hickl.com
87. Becker & Hickl GmbH, Non-Descanned FLIM Detection in Multiphoton Microscopes. Application note, available on www.becker-hickl.com
88. Becker & Hickl GmbH, Recording the Instrument Response Function of a Multiphoton FLIM System. Application note, available on www.becker-hickl.com
89. Becker & Hickl GmbH, NDD FLIM Systems for Leica SP2 MP and SP5 MP Multiphoton Microscopes. Application note, available on www.becker-hickl.com
90. Becker & Hickl GmbH, Multiphoton FLIM with the Leica HyD RLD Detectors. Application note, available on www.becker-hickl.com
91. Becker & Hickl GmbH, Non-Descanned FLIM Systems for Olympus FV-1000 and FV-300 Multiphoton Microscopes. Application note, available on www.becker-hickl.com
92. Becker & Hickl GmbH, Tuneable Excitation FLIM with the LSM 710 Intune System. Application note, available on www.becker-hickl.com
93. Becker & Hickl GmbH, DCS-120 Confocal Scanning FLIM System with User-Specific Lasers: FIANIUM SC400 Laser. Application note, available on www.becker-hickl.com
94. Becker & Hickl GmbH, DCS-120 Confocal Scanning FLIM System with User-Specific Lasers: NKT SuperK EXTREME Laser. Application note, available on www.becker-hickl.com
95. Becker & Hickl GmbH, Multiphoton Multiwavelength NDD FLIM with Zeiss LSM 710 NLO. Application note, available on www.becker-hickl.com
96. Becker & Hickl GmbH, FLIM Systems for Zeiss LSM 710 Record Z Stacks. Application note, available on www.becker-hickl.com
97. Becker & Hickl GmbH, An 8-Channel Parallel Multispectral TCSPC FLIM System. Application note, available on www.becker-hickl.com
98. Becker & Hickl GmbH, TCSPC at Wavelengths from 900 nm to 1700 nm. Application note, available on www.becker-hickl.com
99. Becker & Hickl GmbH, Mosaic FLIM: New Dimensions in Fluorescence Lifetime Imaging. Application note, available on www.becker-hickl.com
100. Becker & Hickl GmbH, FLIM with NIR Dyes. Application note, available on www.becker-hickl.com
101. Becker & Hickl GmbH, Multiphoton NDD FLIM at NIR Detection Wavelengths with the Zeiss LSM 7MP and OPO Excitation. Application note, available on www.becker-hickl.com
102. Becker & Hickl GmbH, Zeiss BiG 2 GaAsP Detector is Compatible with bh FLIM Systems. Application note, available on www.becker-hickl.com
103. Becker & Hickl GmbH, Megapixel FLIM with bh TCSPC Modules. The New SPCM 64-bit Software. Application note, available on www.becker-hickl.com
104. Becker & Hickl GmbH, Microsecond Decay FLIM: Combined Fluorescence and Phosphorescence Lifetime Imaging. Application note, available on www.becker-hickl.com
105. Becker & Hickl GmbH, Simultaneous Phosphorescence and Fluorescence Lifetime Imaging by Multi-Dimensional TCSPC and Multi-Pulse Excitation. Application note, available on www.becker-hickl.com

106. Becker & Hickl GmbH, bh TCSPC Systems Record FLIM with Sutter MOM Microscopes. Application note, available on www.becker-hickl.com
107. Becker & Hickl GmbH, SPC Modules Record FLIM with Bidirectional Scanning. Application note, available on www.becker-hickl.com
108. Becker & Hickl GmbH, SPCM Software Runs Online-FLIM at 10 Images per Second. Application note, available on www.becker-hickl.com
109. Becker & Hickl GmbH, Fast-Acquisition TCSPC FLIM System with sub-25 ps IRF width. Application note, available from www.becker-hickl.com
110. Becker & Hickl GmbH, Fast-Acquisition Multiphoton FLIM with the Zeiss LSM 880 NLO. Application note, available from www.becker-hickl.com
111. Becker & Hickl GmbH, bh - Abberior Combination Records STED FLIM at Megapixel Resolution. Application note, available on www.becker-hickl.com
112. Becker & Hickl GmbH, Oline STED FLIM with bh - Abberior Combination. Application note, available on www.becker-hickl.com
113. Becker & Hickl GmbH, Spatially resolved recording of fluorescence-lifetime transients by line-scanning TCSPC. Application note, available on www.becker-hickl.com
114. Becker & Hickl GmbH, 80 ps FHWM Instrument Response with ID230 InGaAs SPAD and SPC 150 TCSPC Module. Application note, available on www.becker-hickl.com
115. Becker & Hickl GmbH, World Record in TCSPC Time Resolution: Combination of bh SPC-150NX with SCONTEL NbN Detector yields 17.8 ps FWHM. Application note, available on www.becker-hickl.com
116. W. Becker, S. Smietana, Fast-Acquisition TCSPC FLIM: What are the Options? Application note, available from www.becker-hickl.com
117. W. Becker, J. Breffke, B. Korzh, M. Shaw, Q-Y. Zhao, K. Berggren, 4.4 ps IRF width of TCSPC with an NbN Superconducting Nanowire Single Photon Detector. Application note, available on www.beker-hick.com
118. W. Becker, A. Bergmann, L. Sauer, Shifted-component model improves FLIO data analysis. Application note, available on www.becker-hickl.com
119. Becker & Hickl GmbH, FLIO data acquisition and analysis. The road to success. Application note in presentation-style, available on www.becker-hickl.com
120. Becker & Hickl GmbH, The PZ-FLIM-110 Piezo-Scanning FLIM System. Application note, available on www.becker-hickl.com
121. Becker & Hickl GmbH, Wide-Field TCSPC FLIM with bh SPC-150 N TCSPC System and Photek FGN 392-1000 Detector. Application note, available on www.becker-hickl.com
122. Becker & Hickl GmbH, Sub-20ps IRF Width from Hybrid Detectors and MCP-PMTs. Application note, available on www.becker-hickl.com
123. Becker & Hickl GmbH, FLIM Systems for Laser Scanning Microscopes. Overview brochure, available on www.becker-hickl.com
124. Becker & Hickl GmbH, New SPCImage Version Combines Time-Domain Analysis with Phasor Plot. Application note, available on www.becker-hickl.com
125. Becker & Hickl GmbH, Photon-Number-Sensitive TCSPC Application note, available on www.becker-hickl.com
126. Becker & Hickl GmbH, Software-Integrated FLIM for Nikon A1+ Confocals. Application note, available on www.becker-hickl.com
127. Becker & Hickl GmbH, Influence of Magnetic Fields on the IRF of High-Speed Detectors for TCSPC. Application note, available on www.becker-hickl.com
128. W. Becker, C. Junghans, H. Netz, Two-Photon FLIM with a Femtosecond Fibre Laser. Application note, available on www.becker-hickl.com
129. Wolfgang Becker, Cornelia Junghans, Lukas Braun, Alexander Jelzow, Two-Photon FLIM with a Small Femtosecond Fibre Laser, Application note, available on www.becker-hickl.com
130. W. Becker, A. Bergmann, L. Braun, Metabolic Imaging with the DCS-120 Confocal FLIM System: Simultaneous FLIM of NAD(P)H and FAD, Application note, available on www.becker-hickl.com (2018)
131. W. Becker, A Differential Discriminator for bh TCSPC Modules. Application note, available on www.becker-hickl.com
132. W. Becker, F. Gramuglia, M.-L. Wu, E. Charbon, C. Bruschini, 8.7 ps FWHM IRF Width from Ultrafast SPAD. Application note, available on www.becker-hickl.com
133. W. Becker, J. Heitz, Two-Photon FLIM of Tryptophan with a Green Femtosecond Laser. Application note, available on www.becker-hickl.com (2025)
134. W. Becker, C. Junghans, A. Bergmann Metabolic FLIM with Simultaneous pH Imaging. Application note, available on www.becker-hickl.com (2024)

135. W. Becker, A. Bergmann, Fast GPU-Based Global Fit of TCSPC FLIM Data. Application note, available on www.becker-hickl.com (2024)
136. W. Becker, A. Bergmann, Detectors for high-speed photon counting, Becker & Hickl GmbH, www.becker-hickl.com
137. W. Becker, A. Bergmann, Detector Assemblies for Picosecond Microscopy, Becker & Hickl GmbH, www.becker-hickl.com
138. W. Becker, H. Stiel, E. Klose, Flexible Instrument for time-correlated single photon counting, Rev. Sci. Instrum. **62**, 2991-2996 (1991)
139. W. Becker, Verfahren und Vorrichtung zur zeitkorrelierten Einzelphotonenzählung mit hoher Registrierrate, Patent DE 43 39 784 (1993)
140. W. Becker, Verfahren und Vorrichtung zur Messung von Lichtsignalen mit zeitlicher und räumlicher Auflösung, Patent DE 43 39 787 (1993)
141. W. Becker, H. Hickl, C. Zander, K.H. Drexhage,M. Sauer, S. Siebert, J. Wolfrum, Time-resolved detection and identification of single analyte molecules in microcapillaries by time-correlated single photon counting, Rev. Sci. Instrum. **70**, 1835-1841 (1999)
142. W. Becker, K. Benndorf, A. Bergmann, C. Biskup, K. König, U. Tirlapur, T. Zimmer, FRET measurements by TCSPC laser scanning microscopy, Proc. SPIE **4431**, 94-98 (2001)
143. W. Becker, A. Bergmann, K. König, U. Tirlapur, Picosecond fluorescence lifetime microscopy by TCSPC imaging, Proc. SPIE **4262**, 414-419 (2001)
144. W. Becker, A. Bergmann, H. Wabnitz, D. Grosenick, A. Liebert, High count rate multichannel TCSPC for optical tomography, Proc. SPIE **4431**, 249-245 (2001)
145. W. Becker, A. Bergmann, C. Biskup, T. Zimmer, N. Klöcker, K. Benndorf, Multi-wavelength TCSPC lifetime imaging, Proc. SPIE **4620** 79-84 (2002)
146. W. Becker, A. Bergmann, G. Weiss, Lifetime Imaging with the Zeiss LSM-510, Proc. SPIE **4620**, 30-35 (2002)
147. W. Becker, A. Bergmann, C. Biskup, L. Kelbauskas, T.Zimmer, N. Klöcker, K. Benndorf, High resolution TCSPC lifetime imaging, Proc. SPIE **4963**, 175-184 (2003)
148. W. Becker, A. Bergmann, M.A. Hink, K. König, K. Benndorf, C. Biskup, Fluorescence lifetime imaging by time-correlated single photon counting, Micr. Res. Techn. **63**, 58-66 (2004)
149. W. Becker, A. Bergmann, G. Biscotti, K. Koenig, I. Riemann, L. Kelbauskas, C. Biskup, High-speed FLIM data acquisition by time-correlated single photon counting, Proc. SPIE 5323, 27-35 (2004)
150. W. Becker, A. Bergmann, G. Biscotti, A. Rück, Advanced time-correlated single photon counting technique for spectroscopy and imaging in biomedical systems, Proc. SPIE 5340, 104-112 (2004)
151. W. Becker, A. Bergmann, E. Haustein, Z. Petrasek, P. Schwille, C. Biskup, T. Anhut, I. Riemann, K. Koenig, Fluorescence lifetime images and correlation spectra obtained by multi-dimensional TCSPC, Proc. SPIE 5700, 144-152 (2005)
152. W. Becker, A. Bergmann, C. Biskup, D. Schweitzer, M. Hammer, Time- and Wavelength-Resolved Autofluorescence Detection by Multi-Dimensional TCSPC, Proc. SPIE 5862, 58620S (2005)
153. W. Becker, A. Bergmann, E. Haustein, Z. Petrasek, P. Schwille, C. Biskup, L. Kelbauskas, K. Benndorf, N. Klöcker, T. Anhut, I. Riemann, K. König, Fluorescence lifetime images and correlation spectra obtained by multi-dimensional TCSPC, Micr. Res. Tech. 69, 186-195 (2006)
154. W. Becker, Advanced time-correlated single-photon counting techniques. Springer, Berlin, Heidelberg, New York, 2005
155. W. Becker, A. Bergmann, Timing stability of TCSPC experiments. Proc. SPIE 6372, 637209-1 to -7 (2006)
156. W. Becker, A. Bergmann, C. Biskup, Multi-Spectral Fluorescence Lifetime Imaging by TCSPC. Micr. Res. Tech. 70, 403-409 (2007)
157. W. Becker, A. Bergmann, Lifetime-resolved imaging in nonlinear microscopy. In: B.R. Masters, P.T.C. So, eds., Handbook of Biomedical Nonlinear Optical Microscopy.Oxford University Press 2008
158. W. Becker, B. Su, A. Bergmann, Fast-acquisition multispectral FLIM by parallel TCSPC. Proc. SPIE 7183 (2009)
159. W. Becker, B. Su, A. Bergmann, Better FLIM and FCS Data by GaAsP Hybrid Detectors, Proc. SPIE 7569 (2010)
160. W. Becker, B. Su, K. Weisshart, O. Holub, FLIM and FCS Detection in Laser-Scanning Microscopes: Increased Efficiency by GaAsP Hybrid Detectors. Micr. Res. Tech. 74, 804-811 (2011)
161. W. Becker, B. Su, A. Bergmann, K. Weisshart, O. Holub, Simultaneous Fluorescence and Phosphorescence Lifetime Imaging. Proc. SPIE 7903, 790320 (2011)
162. W. Becker, B. Su, A. Bergmann, Spatially resolved recording of transient fluorescence lifetime effects by line-scanning TCSPC. Proc. SPIE 8226 (2012)
163. W. Becker, Fluorescence Lifetime Imaging - Techniques and Applications. J. Microsc. 247 (2) (2012)
164. W. Becker, V. Shcheslavkiy, S. Frere, I. Slutsky, Spatially Resolved Recording of Transient Fluorescence-Lifetime Effects by Line-Scanning TCSPC. Microsc. Res. Techn. 77, 216-224 (2014)

165. W. Becker, Fluorescence Lifetime Imaging Techniques: Time-correlated single-photon counting. In: L. Marcu. P.M.W. French, D.S. Elson, (eds.), Fluorecence lifetime spectroscopy and imaging. Principles and applications in biomedical diagnostics. CRC Press, Taylor & Francis Group, Boca Raton, London, New York (2015)
166. W. Becker, Fluorescence lifetime imaging by multi-dimensional time correlated single photon counting. Medical Photonics 27, 41-61 (2015)
167. W. Becker, Introduction to Multi-Dimensional TCSPC. In W. Becker (ed.) Advanced time-correlated single photon counting applications. Springer, Berlin, Heidelberg, New York (2015)
168. W. Becker, V. Shcheslavskiy, H. Studier, TCSPC FLIM with Different Optical Scanning Techniques, in W. Becker (ed.) Advanced time-correlated single photon counting applications. Springer, Berlin, Heidelberg, New York (2015)
169. W. Becker, V. Shcheslavskiy, Fluorescence Lifetime Imaging with Near-Infrared Dyes. Photonics and Lasers in Medicine 4, 73-83 (2015)
170. W. Becker, S. Frere, I. Slutsky, Recording Ca^{++} Transients in Neurons by TCSPC FLIM. In:F.-J. Kao, G. Keiser, A. Gogoi (eds.), Advanced optical methods of brain imaging. Springer (2019)
171. W. Becker, Fluorescence Lifetime Imaging – Applications and Instrumental Principles. In: Ralph A Bradshaw and Philip D Stahl (Editors-in-Chief), Encyclopedia of Cell Biology 2nd ed., Vol 2, Waltham, MA: Academic Press, , pp. 133-151 (2023)
172. W. Becker, L. M. Hirvonen, J. Milnes, T. Conneely, O. Jagutzki, H. Netz, S. Smietana, K. Suhling, A wide-field TCSPC FLIM system based on an MCP PMT with a delay-line anode. Rev. Sci. Instrum. 87, 093710 (2016)
173. W. Becker, R. Suarez-Ibarrola, A. Miernik, L. Braun, Metabolic Imaging by Simultaneous FLIM of NAD(P)H and FAD. Current Directions in Biomedical Engineering 5(1), 1-3 (2019)
174. W. Becker, Bigger and Better Photons: The Road to Great FLIM Results. Education brochure, available on www.becker-hickl.com.
175. W. Becker, Fluorescence-Lifetime Imaging Ophthalmoscopy. Principles, Challenges, Solutions, and Applications. A Guide to Beautiful FLIO Results. 3-hour lecture on FLIO and FLIO data analysis. https://www.becker-hickl.com/literature/application-notes/fluorescence-lifetime-imaging-ophthalmoscopy-lecture-held-april-23-2021/
176. W. Becker, V. Shcheslavskiy, A. Bergmann, FLIM at a Time-Channel Width of 300 Femtoseconds. Application note, available on www.becker-hickl.com
177. W. Becker, C. Junghans, A. Bergmann, Two-Photon FLIM of Mushroom Spores Reveals Ultra-Fast Decay Component. Application note (2021), available on www.becker-hickl.com.
178. W. Becker, T. Saeb-Gilani, C. Junghans, Two-Photon FLIM of Pollen Grains Reveals Ultra-Fast Decay Component. Application note (2021), available on www.becker-hickl.com
179. W. Becker, A. Bergmann, C. Junghans, Ultra-Fast Fluorescence Decay in Natural Carotenoids. Application note, www. becker-hickl.com (2022)
180. W. Becker, C. Junghans, V. Shcheslavskiy, High-Resolution Multiphoton FLIM Reveals Ultra-Fast Fluorescence Decay in Human Hair. Application note, www. becker-hickl.com (2023)
181. W. Becker, J. Heitz, A. Bergmann, Ultra-Fast Fluorescence Decay in Scottish Whiskey. Application note, Becker & Hickl GmbH, available on www. becker-hickl.com
182. W. Becker,V. Shcheslavskiy, V. Elagin, Ultra-Fast Fluorescence Decay in Malignant Melanoma. Application note, available on www. becker-hickl.com
183. W. Becker, L. Braun, DCS-120 FLIM System Detects FMN in Live Cells, application note, available on www.becker-hickl.com.
184. W. Becker, L. Braun, J. Heitz, V. Shcheslavskiy, M. Shirmanova, Metabolic FLIM of Macroscopic Objects. Application note (2022), available on www.becker-hickl.com
185. W. Becker, T. Saeb-Gilani, A. Jelzow, 273 ps FWHM TCSPC Response with Hamamatsu H15620 NIR PMT. Application note (2021), available on www.becker-hickl.com
186. Wolfgang Becker, Axel Bergmann, Measurement of Membrane Potentials in Cells by TCSPC FLIM. Application note (2023), available on www.becker-hickl.com
187. W. Becker, Molecular imaging by TCSPC FLIM - Application to metabolic imaging and FRET imaging. One-day symposium on advanced microscopy techniques in the biomedical sciences, Charlottesville, 2023
188. W. Becker, A Common Mistake in Lifetime-Based FRET Measurements. Application note, Becker & Hickl GmbH (2023)
189. W. Becker, C. Junghans, A. Bergmann, FLIM Finds Fossil Micro-Organisms in Flint Stone. Application note, Becker & Hickl GmbH (2025)
190. J.M. Beechem, Picosecond fluorescence decay curves collected on millisecond time scale: direct measurement of hydodynamic radii, local/global mobility, and intramolecular distances during protein-folding reactions. Meth. Enzymol. 278, 24-49 (1997)

191. A. V. Belashov, A. A. Zhikhoreva, S. S. Kruglov, A. V. Panchenko, I. V. Semenova, O. S. Vasyutinskii, Analysis of In Vivo Radachlorin Accumulation through FLIM-Assisted Examination of Ex Vivo Histological Samples. Photonics 9, 711 1-13 (2022)
192. A.V. Belashov, A.A. Zhikhoreva, A.V. Salova, T.N. Belyaeva, L.K. Litvinov, E.S. Kornilova, I.V. Semenova, O.S. Vasyutinskii, Analysis of Radachlorin localization in living cells by fluorescence lifetime imaging microscopy. J. Photochem Photobiol. B 243, 112699 1-11 (2023)
193. J. Benesch, G. Hungerford, K. Suhling, C. Tregidgo, J. F. Mano, R. L. Reis, Fluorescence probe techniques to monitor protein adsorption-induced conformation changes on biodegradable polymers. Journal of Colloid and Interface Science 312, 193–200 195 (2007)
194. M.Y. Berezin, H. Lee, W. Akers, S. Achilefu, Near infrared dyes as lifetime solvatochromic probes for micropolarity measurements of biological systems. Biophys. J. 93, 2892-2899 (2007)
195. M.Y. Berezin, W. J. Akers, K. Guo, G.M. Fischer, E. Daltrozzo, A. Zumbusch, S. Achilefu, Long lifetime molecular probes based on near-infrared pyrrolopyrrole cyanine fluorophores for in vivo imaging. Biophys. J. 97, L22-L24 (2009)
196. M. Y. Berezin, S. Achilefu, Fluorescence lifetime maesurement and biological imaging. Chem. Rev. 110(5), 2641-2684 (2010)
197. O. Berezovska, P. Ramdya, J. Skoch, M.S. Wolfe, B.J. Bacskai, B.T. Hyman, Amyloid precursor protein associates with a nicastrin-dependent docking site on the presenilin 1-γ-secretase complex in cells demonstrated by fluorescence lifetime imaging, J. Neurosci. **23**, 4560-4566 (2003)
198. O. Berezovska, B.J. Bacskai, B.T. Hyman, Monitoring Proteins in Intact Cells, Science of Aging Knowledge Environment, SAGE KE 14 (2003)
199. O. Berezovska, A. Lleo, L.D. Herl, M.P. Frosch, E.A. Stern, B.J. Bacskai, B.T. Hyman, Familial Alzheimer's disease presenilin 1 mutations cause alterations in the conformation of prenesilin and interactions with amyloid precursor protein, J. Neurosci. **25**, 3009-3017 (2005)
200. A. Bergmann, W. Becker, Multi-wavelength fluorescence lifetime imaging by TCSPC. Proc. SPIE 6372, 637204-1 to -6 (2006)
201. K.M. Berland, P.T.C. So, E. Gratton, Two-photon fluorescence correlation spectroscopy, Method and application to the intracellular environment, Biophys. J. **68**, 694-701 (1995)
202. K.M. Berland, P.T.C. So, Y. Chen, W.W. Mantulin, E. Gratton, Scanning two-photon fluctuation correlation spectroscopy: Particle counting measurements for detection of molecular aggregation. Biophys. J. 71, 410-420 (1996)
203. T. Bernas, M. Zarebski, R.R. Cook, J.W. Dobrucki, Minimizing photobleaching during confocal microscopy of fluorescent probes bound to chromatin, role of anoxia and photon flux, J. Microsc. 215, 281-296 (2004)
204. F. Bestvater, E. Spiess, G. Strobrawa, M. Hacker, T. Feurer, T. Porwolf, U. Berchner-Pfannschmidt, C. Wotzlaw, H. Acker, Two-photon fluorescence absorption and emission spectra of dyes relevant for cell imaging. J. Microsc. 208 Pt. 2, 108-115 (2002)
205. R.A. Bhat, M. Miklis, E. Schmelzer, P. Schulze-Lefert, R. Panstruga, Recruitment and interaction dynamics of plant penetration resistance components in a plasma mebrane microdomain. PNAS 102, 3135-3140, 2005
206. T. Bhatt, K. Patel, Carotenoids: Potent to prevent diseases review. Natural Products and Bioprospecting 10:109-117 (2020)
207. O. Bilsel, Y. Wu, C. Kayatekin, C.R. Matthews, Merging microsecond mixing and time-correlated single-photon counting: Using time-resolved FRET and time-rsolved anisotropy to probe early events in protein folding. Proc. of SPIE 6771, 677103-1 to -8 (2007)
208. O. Bilsel, C. Kayatekin, L.A. Wallace, C.R. Matthews, A microchannel solution mixer for studying microsecond protein folding reactions, Rev. Sci. Instrum. **76**, 014302 (2005)
209. T. Binzoni, A. Torricelli, R. Giust, B. Sanguinetti, P. Bernhard, L. Spinelli, Bone tissue phantoms for optical flowmeters at large interoptode spacing generated by 3D-stereolithogaphy. Biomed. Op. Express 5(8), 2715-2725 (2014)
210. D.J.S. Birch, R.E. Imhof, A. Dutch, Pulse fluorometry using simultaneous acquisition of fluorescence and excitation, Rev. Sci. Instrum. **55**, 1255-1264 (1984)
211. D.J.S. Birch, A.S. Holmes, R.E. Imhof, B.Z. Nadolski, K. Suhling, Multiplexed array fluorometry, Journal of Phys. E. Sci Instrum. **21**, 415 (1988)
212. D.K. Bird, K.W. Eliceiri, C-H. Fan, J.G. White, Simultaneous two-photon spectral and lifetime fluorescence microscopy, Appl. Opt. **43**, 5173-5182 (2004)
213. D.K. Bird , L. Yan , K. M. Vrotsos , K. E. Eliceiri , E. M. Vaughan. Metabolic mapping of MCF10A human breast cells via multiphoton fluorescence lifetime imaging of coenzyme NADH. Cancer Res 65:8766–8773 (2005)
214. D.K. Bird, K.W. Eliceiri, J.G. White, Optimized temporal response in multichannel two-photon fluorescence lifetime microscopy using photonic crystel fibre. J. Microscop. 224(3) 249-225 (2006)

215. D.K. Bird, K.M. Agg, N.W. Barnett, T. A. Smith, Time-resolved fluorescence microscopy of gunshot residue: an application to forensic science. J. Microsc. 226, 18-25 (2007)
216. R.H. Bisby, S.W. Botchway, G.M. Greetham, J.A. Hadfiedl, A.T. McGown, A.W. Parker, K.M. Scherer, M. Towrie, Time-resolved nanosecond fluorescence liftime imaging and picosecond infrared sopectroscopy of combretastatin A-a in solution and in cellular systems. Meas. Sci. Technol. 23, 084001-10 (2012)
217. R.H. Bisby, S.W. Botchway, A.G. Crisostomo, A.W. Parker, K.M. Scherer, Fluorescence lifetime imaging of propranolol uptake in living glia C6 cells. J. Spectrosc. 27, 518353 (2012)
218. C. Biskup, A. Böhmer, R. Pusch, L. Kelbauskas, A. Gorshkov, I. Majoul, J. Lindenau, K. Benndorf, F-D. Böhmer, Visualization of SHP-1-target interaction, J. Cell Sci. **117**, 5155-5178 (2004)
219. C. Biskup, T. Zimmer, K. Benndorf, FRET between cardiac Na^+ channel subunits measured with a confocal microscope and a streak camera, Nature Biotechnology, 22(2), 220-224 (2004)
220. C. Biskup, L. Kelbauskas, T. Zimmer, K. Benndorf, A. Bergmann, W. Becker, J.P. Ruppersberg, C. Stockklausner, N. Klöcker, Interaction of PSD-95 with potassium channels visualized by fluorescence lifetime-based resonance energy transfer imaging, J. Biomed. Opt. **9**, 735-759 (2004)
221. C. Biskup, L. Kelbauskas, Th. Zimmer, S. Dietrich, K. Benndorf, W. Becker, A. Bergmann, N. Klöcker, Spectrally resolved fluorescence lifetime and FRET measurements, Proc. SPIE 5700, 188-196 (2005)
222. C. Biskup, T. Zimmer, L. Kelbauskas, B. Hoffmann, N. Klöcker, W. Becker, A. Bergmann, K. Benndorf, Multi-Dimensional Fluorescence Lifetime and FRET Measurements. Micr. Res. Tech. 70, 403-409 (2007)
223. C. Biskup, B. Hoffmann, K. Benndorf, A. Rueck, Spectrally resolved lifetime imaging microscopy. In: A. Periasamy, R.M. Clegg, eds., FLIM Microscopy in Biology and Medicine. CRC Press 2009
224. C. Biskup, Th. Gensch, Fluorescence lifetime imaging of ions in biological tissue. In: L. Marcu. P.M.W. French, D.S. Elson, (eds.), Fluorecence lifetime spectroscopy and imaging. Principles and applications in biomedical diagnostics. CRC Press, Taylor & Francis Group, Boca Raton, London, New York (2015)
225. T. S. Blacker, Z. F. Mann, J. E. Gale, M. Ziegler, A. J. Bain, G. Szabadkai, M. R. Duchen, Separating NADH and NADPH fluorescence in live cells and tissues using FLIM. Nature Communications 5, 3936-1 to -6 (2014)
226. Th. S. Blacker., M. R. Duchen, Investigating mitochondrial redox state using NADH and NADPH autofluorescence. Free Radical Biology and Medicine 100, 53–65 (2016)
227. Th. S. Blacker, Michael D. E. Sewell, Gyorgy Szabadkai, Michael R. Duchen, Metabolic Profiling of Live Cancer Tissues Using NAD(P)H Fluorescence Lifetime Imaging. In: Majda Haznadar (ed.), Cancer Metabolism: Methods and Protocols, Methods in Molecular Biology, 1928, 365-386 (2019)
228. Th. S. Blacker, N. Mistry, N. Plotegher, E. R. Westbrook, M. D. E. Sewell, J. Carroll, G. Szabadkai, A. J. Bain, M. R. Duchen, Redox-dependent binding and conformational equilibria govern the fluorescence decay of NAD(P)H in living cells. FEBS Letters 599, 2802–2816 (2025)
229. S. Bloch, F. Lesage, L. McIntosh, A. Gandibakhche, K. Liang, S. Achilefu, Whole-body fluorescence lifetime imaging of a tumor-targeted near-infrared molecular probe in mice. J. Biomed. Opt. 10, 054003-1 to -8
230. F. Boal, M. Laguerre, A. Milochau, J. Lang, P. A. Scotti, A charged prominence in the linker domain of the cysteine-string protein Cspα mediates its regulated interaction with the calcium sensor synaptotagmin 9 during exocytosis. The FASEB Journal 25, 132-143 (2011)
231. M. Böhmer, M. Wahl, H-J. Rahn, R. Erdmann, J. Enderlein, Time-resolved fluorescence correlation spectroscopy. Chem. Phys. Lett. 353, 439-445 (2002)
232. M. Börsch, Unraveling the Rotary Motors in FoF1-ATP Synthase by Time-Resolved Single-Molecule FRET. In: W. Becker (ed.) Advanced time-correlated single photon counting applications. Springer, Berlin, Heidelberg, New York (2015)
233. L. M. Bollinger, G. E. Thomas, Measurement of the time dependence of scintillation intensity by a delayed coincidence method. Rev. .Sci. Instrum. 32, 1044-1050 (1961)
234. J. Bordello, M. Novo, W. Al-Soufi, Exchange dynamics of a neutral hydophobic dye in micellar solutions studied by fluorescence correlation spectroscopy. Journal of Colloid and Interface Science 345, 369-376 (2010)
235. F. A. Borges da Silva, J. Batista Florindo, A. Castro de Mattos, F. Ferreira Costa, I. Lorand-Metze, K. Metze, Accompanying Hemoglobin Polymerization in Red Blood Cells in Patients with Sickle Cell Disease Using Fluorescence Lifetime Imaging. Int. J. Mol. Sci. 25,12290 1-12 (2024)
236. F. A. Borges da Silva, A.P. Racanelli, I. Lorand-Metze, K. Metze, Fluorescence lifetime imaging is able to recognize different hematopoietic precursors in unstained routine bone marrow films. Cytometry 99 641 - 646 (2021)
237. J.W. Borst, M.A. Hink, A. van Hoek, A.J.W.G. Visser, Multiphoton spectroscopy in living plant cells, Proc. SPIE 4963, 231-238 (2003)

238. J. W. Borst, S. P. Laptenok, A. H. Westphal, R. Kühnemuth,H. Hornen, N. V. Visser, S. Kalinin,J. Aker, A. van Hoek, C. A. M. Seidel,A. J. W. G. Visser, Structural Changes of Yellow Cameleon Domains Observed by Quantitative FRET Analysis and Polarized Fluorescence Correlation Spectroscopy. Biophys. J. 95, 5399–5411 (2008)
239. M. Bosch, J. Castro, T. Saneyoshi, H. Matsuno, M. Sur, Y. Hayashi, Structural and Molecular Remodeling of Dendritic Spine Substructures during Long-Term Potentiation. Neuron 82, 12059-1 to -16 (2014)
240. G. Boso, A. Dalla Mora, A. Della Frera, A. Tosi, Fast-gating of single-photon avalanche diodes with 200 ps transitions and 30 ps timing jitter, Sensors and Actuators A: Physical 191, 61–67 (2013)
241. S.W. Botchway, A.W. Parker, R.H. Bisby, A.G. Crisostomo, Real-time cellular uptake of serotonin using fluorescence lifetime imaging with two-photon excitation. Microsc. Res. Techn. 71, 267-273 (2008)
242. E. Boutant, P. Didier, A. Niehl, Y. Mely, C. Ritzenthaler, M. Heinlein, Fluorescent protein recruitment assay for demonstration and analysis of in vivo protein interactions in plant cells and its application to Tobacco mosaic virus movement protein. The Plant Journal (2010) 62, 171–177
243. M. Brambilla, L. Spinelli, A. Pifferi, A. Torricelli, and R. Cubeddu, Time-resolved scanning system for double reflectance and transmittance fluorescence imaging of diffusive media. Rev. Sci. Instrum. 79 013103-1 to -9
244. R. Brandenburg, K.V. Kozlov, P. Michel, H-E. Wagner, Diagnostics of the single filament barrier discharge in air by cross-correlation spectroscopy, 53-rd annual gaseous electronics conference, Houston (Texas) (2000)
245. K. Brandner, A. Sambade, E. Boutant, P. Didier, Y. Mély, C. Ritzenthaler, M. Heinlein, Tobacco mosaic virus movement protein interacts with GFP-tagged microtubule end-binding protein 1. Plant Physiology 147, 611-623 (2008)
246. R. Brandenburg, H.-E. Wagner A. M. Morozov, K. V. Kozlov, Axial and radial development of microdischarges of barrier discharges in N2/O2 mixtures at atmospheric pressure. J. Phys. D: Appl. Phys. 38,1649–1657 (2005)
247. R. Brandenburg, H. Grosch, T. Hoder, K.-D. Weltmann, Phase resolved cross-correlation spectroscopy on surface barrier discharges in air at atmospheric pressure. Eur. Phys. J. Appl. Phys. 55, 13813-p1 to -p6 (2011)
248. D. Branning, A.L. Migdall, A.V. Sergienko, Simultaneous measurement of group and phase delay between photons, Phys. Rev. **62**, 063808-1 to -12 (2000)
249. J. L. Brauer, R. Schultz, M. Klemm, M. Hammer, Influence of Lens Fluorescence on Fluorescence Lifetime Imaging Ophthalmoscopy (FLIO) Fundus Imaging and Strategies for Its Compensation. Transl Vis Sci Technol 9 No. 8, Article 13, 1-10 (2020)
250. R.P. Breault, Stray-light suppression, in W.L. Wolfe, Optical engineers's desk reference, OSA Optical society of America, SPIE The International Society for Optical Engineering (2003)
251. P.M. Brenner, S. Hilgenfeld, D. Lohse, Single-bubble sonoluminescence, Rev. Mod. Phys. **74**, 425-484 (2002)
252. H.-G. Breunig, H. Studier, K. König, Multiphoton excitation characteristics of cellular fluorophores of human skin in vivo. Opt. Expr. 18(8) 7857-7871 (2010)
253. S.Y. Breusegem, In vivo investigation of protein interactions in C. Elegans by Förster resonance energy transfer microscopy, University of Illinois at Urbana-Champaign (2002)
254. H. Brismar, B. Ulfhake, Fluorescence lifetime imaging measurements in confocal microscopy of neurons labeled with multiple fluorophores, Nature Biotech. **15**, 373-377 (1997)
255. Broadcom high-sensitivity NUV silicon photomultipliers. https://www.braodcom.com
256. K. Broess, J-W. Borst, H. von Amerongen, Applying two-photon excitation fluorescence lifetime imaging microscopy to study photosynthesis in plant leaves. Phosynth Res 100, 89-96 (2009)
257. S. Brovelli, F. Meinardi, G. Winroth, O. Fenwick, G. Sforazzini, M. J. Frampton, L. Zalewski, J. A. Levitt, F. Marinello, P. Schiavuta, K. Suhling, H. L. Anderson, F. Cacialli, White Electroluminescence by Supramolecular Control of Energy Transfer in Blends of Organic-Soluble Encapsulated Polyfluorenes. Adv. Funct. Mater. 20, 272-280 (2010)
258. J. Bückers, D. Wildanger, G. Vicidomini, L. Kastrup, S.W. Hell, Simultaneous multi-lifetime multi-colour STED imaging for colocalization anlysis. Opt. Expr. 19, 3130-3143 (2011)
259. I. Bugiel, K. König, H. Wabnitz, Investigations of cells by fluorescence laser scanning microscopy with subnanosecond time resolution, Lasers in the Life Sciences 3(1), 47-53 (1989)
260. G.S. Buller, R.D. Harkins, A. McCarthy, P.A. Hiskett, G. R. MacKinnon, G.R. Smith, R. Sung, A. M. Wallace, R.A. Lamb, K.D. Ridley, J.G. Rarity, Multiple wavelength time-of-flight sensor based on time-correlated single-photon counting. Rev. Sci. Instrum. 76, 083112-1 to -7 (2005)
261. G. S. Buller, .A. M. Wallace, Ranging and Three-Dimensional Imaging Using Time-Correlated Single-Photon Counting and Point-by-Point Acquisition. IEEE Journal of Selected Topics in Quantum Electronics 13, 1006-1015 (2007)

262. S. Burgstaller, H. Bischof, T. Gensch, S. Stryeck, B. Gottschalk, J. Ramadani-Muja, E. Eroglu, R. Rost, S. Balfanz, A. Baumann, M. Waldeck-Weiermair, J. C. Hay, T. Madl, W. F. Graier, R. Malli,pH-Lemon, a Fluorescent Protein-Based pH Reporter for Acidic Compartments. ACS Sens. 4, 883-891 (2019)
263. T. Y. Buryakina, P.-T. Su, W.J. Syu, C.A. Chang, H.-F. Fan, F.-J. Kao, Metabolism of HeLa cells revealed through autofluorescence lifetime upon infection with enterohemorrhagic eschericha coli. J. Biomed. Opt. 17(10) 101503-1 to -9
264. M. Butti, D. Contini, E. Molteni, M. Caffini, L. Spinelli, G. Baselli, A. M. Bianchi, S. Cerutti, R. Cubeddu, A. Torricelli, Effect of prolonged stimulation on cerebral hemodynamic: A time-resolved fNIRS study. Med. Phys. 36 4103-4114
265. E. P. Buurman, R. Sanders, A. Draaijer, H. C. Gerritsen, J. J. F. van Ween, P. M. Houpt, and Y. K. Levine, Fluorescence lifetime imaging using a confocal laser scanning microscope, Scanning 14, 155-159 (1992)
266. A. Cadby, R. Dean, A. M. Fox, R. A. L. Jones, D. G. Lidzey, Mapping the Fluorescence Decay Lifetime of a Conjugated Polymer in a Phase-Separated Blend Using a Scanning Near-Field Optical Microscope. Nano Letters 5, 2232-2237 (2005)
267. A. J. Cadby, R. Dean, C. Elliott, R. A. L. Jones, A. M. Fox, D. G. Lidzey, Imaging the Fluorescence Decay Lifetime of a Conjugated-Polymer Blend By Using a Scanning Near-Field Optical Microscope. Adv. Mater. 19, 107–111 (2007)
268. N.I. Cade, G. Fruhwirth, S. J. Archibald, T. Ng, David Richards, A cellular screening assay using analysis of metal-modified fluorescence lifetime. Biophys. J. 98, 2752–2757 (2010)
269. V. Calleja, S. Ameer-Beg, B. Vojnovic, R. Woscholski, J. Downwards, B. Larijani, Monitoring conformational changes of proteins in cells by fluorescence lifetime imaging microscopy, Biochem. J. **372**, 33-40 (2003)
270. D. Campos, W. Peeters, K. Nickel, B. Burkel, J. Bussink, R. J. Kimple, A. van der Kogel, K. W. Eliceiri and M. W. Kissick, Radiation Promptly Alters Cancer Live Cell Metabolic Fluxes: An In Vitro Demonstration. Radiation Research 185, 496-504 (2016)
271. J. Candelario, M.S Chachisvilis, Mechanical Stress Stimulates Conformational Changes in 5-Hydroxytryptamine Receptor 1B in Bone Cells. Cellular and Molecular Bioengineering 5, 277 (2012)
272. T. M. Cannon, J. L. Lagarto, B. T. Dyer, E. Garcia, D. J. Kelly, N. S. Peters, A. R. Lyon, P. M. W. French, and C. Dunsby, Characterization of NADH fluorescence properties under one-photon excitation with respect to temperature, pH, and binding to lactate dehydrogenase. OSA Continuum, 4, No. 5, 1610-1625 (2021)
273. S. Canonica, J. Forrer, U.P. Wild, Improved timing resolution using small side-on photomultilpliers in single photon counting, Rev. Sci. Instrum. 56, 1754-1758 (1985)
274. R. Cao, H. Wallrabe, K. Siller, S. R. Alam, A. Periasamy, Single cell redox states analyzed by fluorescence lifetime metrics and tryptophan FRET interaction with NAD(P)H. Cytometry Part A, 96A, 110-121 (2019)
275. V. Caorsi, E. Ronzitti, G. Vicidomini, S. Krol, G. McConnell, A. Diaspro, FRET measurements on fuzzy fluorescent nanostructures. Micr. Res. Tech. 70, 452-458 (2007)
276. Carl Zeiss Microscopy GmbH, New possibilities for multiphoton microscopy from Carl Zeiss. OPO and simultaneous lasers for LSM 7 series. Press release, www.zeiss.com
277. L. Carlini, J.L. Nadeau, Uptake and processing of semiconductor quantum dots in living cells studied by fluorescence lifetime imaging microscopy (FLIM). Chem Commun (Camb). 49(17), 1714-6 (2013)
278. K. Carlsson, J.P. Philip, Theoretical investigation of the signal-to-noise ratio for different fluorescence lifetime imaging techniques, Proc. SPIE 4622, 70-78 (2002)
279. N. Case, N. Johnston, J. Nadeau, Fluorescence Microscopy with Deep UV, Near UV, and Visible Excitation for In Situ Detection of Microorganisms. Astrobiology 24(3), 300-317 (2024)
280. C. M. Castellani, A. P. Torres-Ocampo, J. Breffke, A. B. White, J. J. Chambers, M. M. Stratton, Th. J. Maresca, Live-cell FLIM-FRET using a commercially available system. Methods in Cell Biology, 158, 63-89 (2020)
281. M. Chachisvilis, Y.-L. Zhang, J. A. Frangos, G protein-coupled receptors sense fluid shear stress in endothelial cells. PMAS 103, 15463-15468 (2006)
282. J.V. Chacko, K.W Eliceiri, Autofluorescence lifetime imaging of cellular metabolism: Sensitivity toward cell density, pH, intracellular, and intercellular heterogeneity. Cytometry Part A 2019, 95, 56–69.
283. B. Chan, K. Weidemaier, W-T. Yip, P.F. Barbara, K. Musier-Forsyth, Intra-tRNA distance measurements for nucleocapsid protein-dependent tRNA unwinding during priming of HIV reverse transcripsion, PNAS 96, 459-464 (1999)
284. B. Chance, Pyridine nucleotide as an indicator of the oxygen requirements for energy-linked functions of mitochondria. Circ Res 38, I31–I38 (1976)

285. B. Chance, B. Schoener, R. Oshino, F. Itshak, Y. Nakase, Oxidation–reduction ratio studies of mitochondria in freeze-trapped samples. NADH and flavoprotein fluorescence signals J. Biol. Chem. 254, 4764–4771 (1979)
286. B. Chance, M. Cope, E. Gratton, N. Ramanujam, B. Tromberg, Phase measurement of light absorption and scatter in human tissue, Rev. Sci. Instrum. 69, 3457-3481 (1998)
287. A. Chanoca, Brian Burkel, N. Kovinich, E. Grotewold, K. W. Eliceiri, Marisa S. Otegui, Using fluorescence lifetime microscopy to study the subcellular localization of anthocyanins. The Plant Journal 88, 895–903 (2016)
288. L.J. Charbonniere, N. Hildebrandt, Lanthanide complexes and quantum dots: A bright wedding for resonance energy transfer. Eur. J. Inorg. Chem. 2008, 3241-3251 (2008)
289. Y. Chen, J.D. Müller, P.T.C. So, E. Gratton, The Photon Counting Histogram in Fluorescence Fluctuation Spectroscopy, Biophys. J. **77**, 553-567 (1999)
290. Y. Chen, J.D. Müller, Q.Q. Ruan, E. Gratton, Molecular brightness characterization of EGFP in vivo by fluorescence fluctuation spectroscopy, Biophys. J. **82**, 133-144 (2002)
291. Y. Chen, A. Periasamy, Characterization of two-photon excitation fluorescence lifetime imaging microscopy for protein localization, Microsc. Res. Tech. **63**, 72-80 (2004)
292. Y. Chen, A. Periasamy, Two-photon FIM-FRET microscopy for protein localization, Proc. SPIE **5323**, 431-439 (2004)
293. Y. Cheng, D. Chorvat, N. Poirier, J. Miro, N. Dahdah, A. Chorvatova, Spectrally and time-resolved study of NAD(P)H autofluorescence in cardiac myocytes from human biopsies. Proc. SPIE 6771, 677104-1 to -13 (2007)
294. W-F. Cheong, S.A. Prahl, A.J. Welch, A review of the optical properties of biological tissue, IEEE Journal of Quantum Electronics **26**, 2166-2185 (1990)
295. V. Chernomordik, D.W. Hattery, A.H. Gandjbakhche, A. Pifferi, P. Taroni, A. Torricelli, G. Valentini, R. Cubeddu, Quantification by random walk of the optical parameters of nonlocalized abnormalities embedded within tissuelike phantoms, Opt. Lett. **25**, 951-953 (2000)
296. V. Chernomordik, D.W. Hattery, D. Grosenick, H. Wabnitz, H. Rinneberg, K.T. Moesta, P.M. Schlag, A. Gandjbakhche, Quantification of optical properties of breast tumor using random walk theory, J. Biomed. Opt. 7 80-87 (2002)
297. W. Cheung, M. Gill, A. Esposito, C. F. Kaminski, N. Courousse, S. Chwetzoff, G. Trugnan, N. Keshavan, A. Lever, U. Desselberger, Rotaviruses Associate with Cellular Lipid Droplet Components To Replicate in Viroplasms, and Compounds Disrupting or Blocking Lipid Droplets Inhibit Viroplasm Formation and Viral Replication. J. Virol. 84, 6782-6798 (2010)
298. C. Cheung, J.P. Culver, K. Takahashi, J.H. Greenberg, A. G. Yodh, In vivo cerebrovascular measurement combining diffuse near-infrared absorption and correlation spectroscopies. Phys Med Biol. 46(8), 2053-2065 (2001)
299. T. H. Chia, A. Williamson, D. D. Spencer, M. J. Levene, Multiphoton fluorescence lifetime imaging of intrinsic fluorescence in human and rat brain tissue reveals spatially distinct NADH binding. Optics Express 16, 4237-4249 (2008)
300. D. Chorvat, A. Chorvatova, Spectrally resolved time-correlated single photon counting: a novel approach for characterization of endogenous fluorescence in isolated cardiac myocytes. Eur. Biophys. J. 36:73-83 (2006)
301. D. Chorvat, A. Mateasik, J. Kirchnerova, A. Chorvatova, Application of spectral unmixing in multi-wavelength time-resolved spectroscopy. Proc. SPIE 6771, 677105-1 to -12 (2007)
302. D. Chorvat Jr., S. Abdulla, F. Elzwei, A. Mateasik, A. Chrovatova, Screening of cardiomyocyte fluorescence during cell contraction by multi-dimensional TCSPC. Proc. SPIE 6860, 686029-1 to -12 (2008)
303. D. Chorvat, A. Chorvatova, Multi-wavelength fluorescence lifetime spectroscopy: a new approach to the study of endogenous fluorescence in living cells and tissues. Laser Phys. Lett. 6 175-193 (2009)
304. D. Chorvat Jr., A. Mateasik, Y.g Cheng, N.y Poirier, J. Miro, N.S. Dahdah3, A. Chorvatova, Rejection of transplanted hearts in patients evaluated by the component analysis of multi-wavelength NAD(P)H fluorescence lifetime spectroscopy. J. Biophotonics 3 646-652 (2010)
305. A. Chorvatova, F. Elzwiei, A. Mateasik, D. Chorvat, Effect of ouabain on metabolic oxidative state in living cardiomyocytes eavaluated by time-resolved spectroscopy of endogenous NAAD(P)H fluorescence. J. Biomed. Opt. 17(10) 101505-1 to -7 (2012)
306. A. Chorvatova, S. Aneba, A. Mateasik, D. Chorvat Jr., B. Comte, Time-resolved fluorescence spectroscopy investigation of the effect of 4-hydroxynonenal on endogenous NAD(P)H in living cardiac myocytes. J. Biomed. Opt. 18(6), 067009-1 to -11 (2013)
307. A. Chorvatova, A. Mateasik, D. Chorvat Jr, Spectral decomposition of NAD(P)H fluorescence components recorded by multi-wavelength fluorescence lifetime spectroscopy in living cardiac cells. Laser Phys. Lett. 10 125703-1 to -10 (2013)

308. A. Chorvatova, Autofluorescence-assisted examination of cardiovascular system physiology and pathology. In: A. A. Heikal and V. Ghukasyan, eds., Natural Biomarkers for Cellular Metabolism: Biology, Techniques and Applications. CRC Press, Taylor & Francis Group, Boca Raton, London, New York (2015)
309. A. Chorvatova, D. Chorvat, Tissue fluorophores and their spectroscopic characteristics. In: L. Marcu. P.M.W. French, D.S. Elson, (eds.), Fluorecence lifetime spectroscopy and imaging. Principles and applications in biomedical diagnostics. CRC Press, Taylor & Francis Group, Boca Raton, London, New York (2015)
310. Y. Chmykh, J. L. Nadeau, The use of fluorescence lifetime imaging (FLIM) for in situ microbial detection in complex mineral substrates. J. Microsc. 294, 36–51 (2024)
311. E. Clancy, S. Ramadurai, S.R. Needham, Karen Baker, T. A. Eastwood, J. A. Weinstein, D. P. Mulvihill, .W. Botchway, Fluorescence and phosphorescence lifetime imaging reveals a significant cell nuclear viscosity and refractive index changes upon DNA damage. Scientific Reports 13:422 (2023)
312. J. Christiansen, M. Mota, A high-resolution time interpolator based on a delay locked loop and an RC delay line, IEEE Journal on solid state circuits **34**, 1360-1366 (1999)
313. G.C. Cianci, K. Berland, Saturation in two-photon microscopy, Proc. SPIE **5323**, 128-135 (2004)
314. R. Cicchi, A. Crisci, A. Cosci, G. Nesi, D. Kapsokalyvas, S. Giancane, M. Carini, F. S. Pavone, Time- and Spectral-resolved two-photon imaging of healthy bladder mucosa and carcinoma in situ. Opt. Express 18, 3840 (2010)
315. A.H.A. Clayton, Q.A. Hanley, D.J. Arndt-Jovin, V. Subramaniam, T.M. Jovin, Dynamic fluorescence anisotropy imaging microscopy in the frequency domain (FLIM), Biophys. J. **83**, 1631-1649 (2002)
316. P.B. Coates, The correction for photon 'pile-up' in the measurement of radiative lifetimes, J. Phys. E. Sci. Instrum. **1**, 878-879 (1968)
317. P.B. Coates, Pile-up corrections in the measurement of lifetimes, J. Phys. E. Sci. Instrum. **5**, 148-150 (1972)
318. P.B. Coates, Pile-up corrections in lifetime experiments, Rev. Sci. Instrum. **43**, 1855-1856 (1972)
319. P.B. Coates, The origin of afterpulses in photomultipliers. J. Phys. D: Appl. Phys. 6, 1159-1166 (1973)
320. S. Coda, A. J. Thompson,1,5 G. T. Kennedy, K. L. Roche, L. Ayaru, D. S. Bansi, G. W. Stamp, A. V. Thillainayagam, P. M. W. French, C. Dunsby, Fluorescence lifetime spectroscopy of tissue autofluorescence in normal and diseased colon measured ex vivo using a fiber-optic probe. Biomed. Opt. Expr. 5, 515-538 (2014)
321. M. Colangelo, B. Korzh, J. P. Allmaras, A. D. Beyer, A. S. Mueller, R. M. Briggs, B. Bumble, M. Runyan, M. J. Stevens, A. N. McCaughan, D. Zhu, S. Smith, W. Becker, L. Narvaez, J. C. Bienfang, S. Frasca, A. E. Velasco, C. H. Pena, E. E. Ramirez, Al. B. Walter, E. Schmidt, E. E. Wollman, M. Spiropulu, R. Mirin, S. Woo Nam, K. K. Berggren, M. D. Shaw, Impedance-matched differential superconducting nanowire detectors. Online arXiv:2108.07962v1 [physics.app-ph] (2021)
322. D. Comelli, A. Bassi, A. Pifferi, P. Taroni, A. Torricelli, R. Cubeddu, F. Martelli, and G. Zaccanti, In vivo time-resolved reflectance spectroscopy of the human forehead. Appl. Opt. 1717-1725 (2007)
323. A. Cong, R. M. L. Pimenta, H. B. Lee, V. Mereddy, Jon Holy, A. A. Heikal. Two-Photon Fluorescence Lifetime Imaging of Intrinsic NADH in Three-Dimensional Tumor Models. Cytometry Part A 95A, 80–92 (2019)
324. A. T. Q. Cong, R. M. L. Pimenta, J. Holy, A. A. Heikal, Associated anisotropy of intrinsic NAD(P)H for monitoring changes in the metabolic activities of breast cancer cells (4T1) in three-dimensional collagen matrix. Phys. Chem. Chem. Phys. 23, 12692-12705 (2021)
325. M. W. Conklin, P. P. Provenzano, K. W. Eliceiri, R. Sullivan, P. J. Keely, Fluorescence Lifetime Imaging of Endogenous Fluorophores in Histopathology Sections Reveals Differences Between Normal and Tumor Epithelium in Carcinoma In Situ of the Breast. Cell Biochem Biophys. 53(3), 145–157 (2009)
326. R. J. Cooper, E. Magee, N. Everdell, S. Magazov, M. Varela, D. Airantzis, A. P. Gibson, J. C. Hebden, MONSTIR II: a 32-channel, multispectral, time-resolved optical tomography system for neonatal brain imaging. Rev. Sci. Instrum. 85(5), 0531052014 (2014)
327. Cornelis J. R. Van Der Oord, Hans C. Gerritsen, Focko F. G. Rommerts, David A. Shaw, Ian H. Munro, and Yehudi K. Levine, Micro-Volume Time-Resolved Fluorescence Spectroscopy Using a Confocal Synchrotron Radiation Microscope. Appl. Spectrosc. **49**, 1469-1473 (1995)
328. M. Cotlet, J. Hofkens, S. Habuchi, G. Dirix, M. Van Guyse, J. Michiels, J. Vanderleyden, F.C. De Schryver, Identification of different emitting species in the red fluorescent protein DsRed by means of ensemble and single molecule spectroscopy, PNAS **98**, 14398-5006 (2001)
329. D. Contini, A. Pifferi, L. Spinelli, A. Torricelli, R. Cubeddu, Multi-channel time-resolved tissue oximeter for functional imaging of the brain. IEEE T. Intrum. Meas. 55, 85-90 (2006)
330. D. Contini, A. Torricelli, A. Pifferi, L. Spinelli, F. Paglia, R. Cubeddu, Multi-channel time-resolved system for functional near infrared spectroscopy. Opt. Expr. 14, 5418-5432 (2006)

331. D.R. Cooper, K. Kudinov, P. Tyagi , C.K. Hill, S.E. Bradforth, J.L.Nadeau, Photoluminescence of cerium fluoride and cerium-doped lanthanum fluoride nanoparticles and investigation of energy transfer to photosensitizer molecules. Phys Chem Chem Phys. 16(24), 12441-53 (2014)
332. T. Costa, M. Peixoto, M. Pineiro, J. S. Seixas de Melo, Solvent-Driven Self-Organization of Meso-Substituted Porphyrins: Morphological Analysis from Fluorescence Lifetime Imaging Microscopy. Langmuir 39, 5727-5737 (2023)
333. M. Cotlet, J. Hofkens, M. Maus, T. Gensch, M. Van der Auweraer, J. Michels, G. Dirix, M. Van Guyse, J. Vanderleyden, A.J.W.G. Visser, F.C. De Schryver, Excited state dynamics in the green fluorescent protein mutant probed by picosecond time-resolved single-photon counting spectroscopy, J. Phys. Chem. B105, 4999-5006 (2001)
334. S. Cova, M. Bertolaccini, C. Bussolati, The measurement of luminescence waveforms by single-photon techniques, Phys. Stat. Sol. 18, 11-61 (1973)
335. S. Cova, A. Longoni, G. Ripamonti, Active-quenching and gating circuits for single-photon avalanche diodes (SPADs), IEEE Trans. Nucl. Sci. **NS29**, 599-601 (1982)
336. S. Cova, G. Ripamonti, S. Lacaita, Avalanche semiconductor detector for single optical photons with a time resolution of 60 ps, Nucl. Instr. Meth. **A253**, 482-487 (1987)
337. S. Cova, S. Lacaita, M. Ghioni, G. Ripamonti, T.A. Louis, 20-ps timing resolution with single-photon avalanche photodiodes, Rev. Sci. Instrum. **60**, 1104-110 (1989)
338. S. Cova, M. Ghioni, A. Lacaita, C. Samori, F. Zappa, Avalanche photodiodes and quenching circuits for single-photon detection, Appl. Opt. **35**, 1954-1976 (1996)
339. S. Cova, M. Ghioni, A. Lotito, I. Rech, F. Zappa, Evolution and prospects for single-photon avalanche diodes and quenching circuits, J. Mod. Opt. **15**, 1267-1288 (2004)
340. G. Cox, Optical imaging techniques in cell biology, Taylor & Francis (2007)
341. R. Cubeddu, A. Pifferi, P. Taroni, A. Torricelli, G. Valentini, Time-resolved imaging on a realistic tissue phantom, $\mu_{s'}$ and μ_a images versus time-integrated images, Appl. Opt. 35 4533-4540 (1996)
342. R. Cubeddu, A. Pifferi, P. Taroni, A. Torricelli, G. Valentini, Imaging with diffusing light: an experimental study of the effect of background optical properties, Appl. Opt. **37**, 3564-3573 (1998)
343. R. Cubeddu, A. Pifferi, P. Taroni, A. Torricelli, G. Valentini, Compact tissue oximeter based on dual-wavelength multichannel time-resolved reflectance, Appl. Opt. **38**, 3670-3680 (1999)
344. R. Cubeddu, A. Pifferi, P. Taroni, A. Torricelli, G. Valentini, Noninvasive absorption and scattering spectroscopy of bulk diffuse media: An application to the optical characterization of human breast, Appl. Phys. Lett. **74**, 874-876 (1999)
345. R. Cubeddu, G. Canti, C. D'Andrea, A. Pifferi, P. Taroni, A. Torricelli, G. Valentini, Effects of photodynamic therapy on the absorption properties of disulphonated aluminum phthalocyanine in tumor-bearing mice, Journal of Photochemistry and Photobiology B: Biology **60**, 73-78 (2001)
346. R. Cubeddu, G. Biscotti, A. Pifferi, P. Taroni, A. Torricelli, M. Ferrari, V. Quaresima, Functional muscle studies by dual-wavelength, 8-channel time-resolved oximetry, Proc. SPIE 5138, 29-34 (2003)
347. R. Cubeddu, G. M. Danesini, F. Messina, A. Pifferi, L. Spinelli, P. Taroni, A. Torricelli, Four-wavelength time-resolved optical mammograph, Proc. SPIE 4955, 203-210 (2003)
348. G. Cui, S.B.Jun, X. Jin, M.D. Pham, S.S. Vogel, D.M. Lovinger, R.M. Costa, Concurrent activation of strial direct and indirect pathways during action initiation. Nature 494, 238-242 (2013)
349. G. Cui, S.B.Jun, X. Jin, G. Luo, M.D. Pham, D.M. Lovinger, S.S. Vogel, R.M. Costa, Deep brain optical measurement of cell type-specific neural activity in behaving mice. Nature Protocols, 9(6) 1213-1228 (2014)
350. M. Currie, H. Leopold, J. Schwarz, A. J. Boersma, E. D. Sheets, and A. A. Heikal, Fluorescence Dynamics of a FRET Probe Designed for Crowding Studies. J. Phys. Chem. B 121, 5688-5698 (2017)
351. A. Dalla Mora, A. Tosi, F. Zappa, S. Cova, D. Contini, A. Pifferi, L. Spinelli, A. Torricelli, R. Cubeddu, Fast-Gated Single-Photon Avalanche Diode for Wide Dynamic Range Near Infrared Spectroscopy. IEEE J. Selected Topics in Quantum Electronics, in press (2010)
352. A. Dalla Mora, D. Contini, A. Pifferi, R. Cubeddu, A. Tosi, F. Zappa, Afterpulse-like noise limits dynamic range in time-gated applications of thin-junction silicon single-photon avalanche diode, Appl. Phys. Lett. 100, 241111 (2012)
353. C. D'Andrea, A. Farina, D. Comelli, A. Pifferi, P. Taroni, G. Valentini, R. Cubeddu, L. Zola, M. Orlandi, A. Kienle, Time-Resolved Optical Spectroscopy of Wood. Appl. Spectrocopy 62, 569-574 (2008)
354. C. D'Andrea, L. Spinelli, A. Bassi, A. Giusto, D. Contini, J. Swartling, A. Torricelli, R. Cubeddu, Time-resolved spectrally constrained method for the quantification of chromophore concentrations and scattering parameters in diffusing media. Opt. Expr. 14, 1888-1898 (2006)
355. C. D'Andrea, A. Nevin, A. Farina, A. Bassi, R. Cubeddu, Assessment of variations in moisture content of wood using time-resolved diffuse optical spectroscopy. Appl. Opt. 48, B87 -B93 (2009)
356. Y. Dancik, A. Favre, C. J. Loy, A.V. Zvyagin, M.S. Roberts, Use of multiphoton tomography and fluorescence lifetime imaging to investigate skin pigmentation in vivo. J. Biomed. Opt. 18(2) 026022-1 to -13 (2013)

357. J. O. Danquah, S. Botchway, A. Jeshtadi, L. A. King, Direct Interaction of Baculovirus Capsid Proteins VP39 and EXON0 with Kinesin-1 in Insect Cells Determined by Fluorescence Resonance Energy Transfer-Fluorescence Lifetime Imaging Microscopy. J. Virol. 86, 844-853 (2012)
358. A.M. Davey, R. P. Walvick, Y. Liu, A. A. Heikal, E. D. Sheets, Membrane Order and Molecular Dynamics Associated with IgE Receptor Cross-Linking in Mast Cells. Biophys. J. 92 343-355 (2007)
359. A.M. Davey, K.M. Krise, E.D.Sheets, A.A. Heikal, Molecular perspective of antigen-mediated mast cell signaling, J. Biol.Chem. (2008) in press
360. R.N. Day, C.F. Booker, A. Periasamy, Characterization of an improved donor fluorescent protein for Förster resonance energy transfer microscopy. J. Biomed. Opt. 13(3), 031203-1 to -9 (2008)
361. R.N. Day, F. Schaufele, Fluorescent protein tools for studying protein dynamics in living cells: A review. J. Biomed. Opt. 13(3), 031202-1 to -6 (2008)
362. P. De Beule, D.M. Owen, H.B. Manning, C.B. Talbot, J. Requejo-Isidro, C. Dunsby, J. McGinty, R.K.P. Benninger, D.S. Elson, I. Munro, M.J. Lever, P. Anand, M.A.A. Neil P.M.W. French, Rapid Hyperspectral Fluorescence Lifetime Imaging. Micr. Res. Tech. 70, 481-484 (2007)
363. P. A. A. De Beule, C. Dunsby, N. P. Galletly, G. W. Stamp, A. C. Chu, U. Anand, P. Anand, C. D. Benham A. Naylor, P. M. W. French, A hyperspectral fluorescence lifetime probe for skin cancer diagnosis. Rev. Sci. Instrum. 78, 123101 (2007)
364. G. Deka, W.W. Wu, F.-J. Kao, In vivo wound healing diagnosis with second harmonic and fluorescence lifetime imaging. J. Biomed. Opt. 18(6), 061222-1 to -8
365. E. Delgado-Pinar, M. Medeiros,T. Costa, J. S. Seixasde Melo, Highly Selective Fluorescent Sensors: Polyethylenimine Derivatives of Triphenylamine and Coumarin for GTP and ATP Interaction via Fluorescence Lifetime Imaging Microscopy. ACS Appl. Polym. Mater. 5, 6167-6185 (2023)
366. W. Denk, J.H. Strickler, W.W.W. Webb, Two-photon laser scanning fluorescence microscopy, Science 248, 73-76 (1990)
367. W. Denk, J. Strickler, W. Webb, Two-photon laser scanning microscopy, Patent WO 91/07651 (1991)
368. E. Deprez, P. Tauc, H. Leh, J-F. Mouscadet, C. Auclair, J-C. Brochon, Oligomeric states of the HIV-1 integrase as measured by time-resolved anisotropy, Biochemistry **39**, 9275-9284 (2000)
369. E. Deprez, P. Tauc, H. Leh, J-F. Mouscadet, C. Auclair, M.E. Hawkins, J-C. Brochon, DNA binding induces dissociation of the multimetric form of HIV-1 integrase: A time-resolved fluorescence anisotropy study, PNAS **98**, 10090-10095 (2001)
370. T. Desmettre, J.M. Devoisselle, S. Mordon, Fluorescence properties and metabolic features of indocyanine green (ICG) as related to angiography, Surv. Ophthalmol. **45**, 15-27 (2000)
371. A. Diaspro, Building a two-photon microscope using a laser scanning confocal architecture, in A. Periasamy (ed.), Methods in Cellular Imaging, Oxford University Press, 162-179 (2001)
372. A. Diaspro, M. Corosu, P. Ramoino, M. Robello, Adapting a compact confocal microscope system to a two-photon excitation fluorescence Imaging architecture, Micr. Res. Tech. **47**, 196–205 (1999)
373. Diaspro A. (ed.). Confocal and two-photon microscopy: Foundations, applications and advances. Wiley-Liss (2001)
374. C. M. Díaz-García, C. Lahmann, J. R. Martínez-François, B. Li, D. Koveal, N. Nathwani, M. Rahman1, J. P. Keller, J. S. Marvin, L. L. Looger, G. Yellen, Quantitative in vivo imaging of neuronal glucose concentrations with a genetically encoded fluorescence lifetime sensor. J. Neuro Res. 97, 946-960 (2019)
375. M.E. Dickinson, C.W. Waters, G. Bearman, R. Wolleschensky, S. Tille, S.E. Fraser, Sensitive imaging of spectrally overlapping fluorochromes using the LSM 510 META, Proc. SPIE, **4620**, 123-136 (2002)
376. Y.T. Didenko, W.B. NcNamara, K.S. Suslick, Molecular emission from single-bubble sonoluminescence, Nature **407**, 877-879 (2000)
377. P. Didier, G. Ulrich, Y. Mely, Raymond Ziessel, Improved push-pull-push E-Bodipy fuorophores for two-photon cell-imaging. Org. Biomol. Chem. 7, 3639-3642 (2009)
378. M. Diez, B. Zimmermann, M. Börsch, M. König, E. Schweinberger, S. Steigmiller, R. Reuter, Suren Felekyan, V. Kudryavtchev, C.A.M. Seidel, P. Gräber, Proton-powered subunit rotation in single membrane-bound F0F1-ATP synthase. Nature Structural & Molecular Biology, 11, No. 2, 135-141 (2004)
379. M. A. Digman, P. Sengupta, P. W. Wiseman, C. M. Brown, A. R. Horwitz and E. Gratton, Fluctuation correlation spectroscopy with a laser-scanning microscope: exploiting the hidden time structure. Biophys. J. 88, L33-L36 (2005)
380. M. A. Digman, C. M. Brown, P. Sengupta, P. W. Wiseman, A. R. Horwitz and E. Gratton, Measuring Fast Dynamics in Solutions and Cells with a Laser Scanning Microscope. Biophys. J. 89, 1317-1327 (2005)
381. M. A. Digman, R. Dalal, A. F. Horwitz, E. Gratton, Mapping the number of molecules and brightness in the laser scanning microscope, Biophys. J. 94, 2320-32 (2008)

382. M. A. Digman, C. M. Brown, A. R. Horwitz, W. W. Mantulin, and E. Gratton, Paxillin dynamics measured during adhesion assembly and disassembly by correlation spectroscopy. Biophys. J. 94, 2819-31 (2008)
383. M. A. Digman, V. R. Caiolfa, M. Zamai, and E. Gratton, The phasor approach to fluorescence lifetime imaging analysis, Biophys J 94, L14-L16 (2008)
384. M.A. Digman, E. Gratton, The phasor approach to fluorescence lifetime imaging: Exploiting phasor linear properties. In: L.Marcu, P.W.M. French, D.S. Elson, Fluorescence lifetime spectroscopy and imaging. CRC Press, Taylor & Francis Group, Boca Raton (2015)
385. E. Dimitrow, I. Riemann, A. Ehlers, M. J. Koehler, J. Norgauer, P. Elsner, K. König, M. Kaatz, Spectral fluorescence lifetime detection and selective melanin imaging by multiphoton laser tomography for melanoma diagnosis. Experimental Dermatology 18, 509-515 (2009)
386. E. Dimitrow, M. Ziemer, M. J. Koehler, J. Norgauer, K. König, P. Elsner, M. Kaatz, Sensitivity and Specificity of Multiphoton Laser Tomography for In Vivo and Ex Vivo Diagnosis of Malignant Melanoma. J. Invest. Dermatol. 12(7) 1752-1758 (2009)
387. M. Diop, K. M. Tichauer, J.T. Elliott , M. Migueis, T.-Y. Lee, K. St. Lawrence, Time-resolved near-infrared technique for bedside monitoring of absolute cerebral blood flow. Proc. SPIE 7555, 75550Z-1 to -9 (2010)
388. M. Diop, K.M. Tichauer, J.T. Elliott, M. Migueis, T.-Y. Lee, K. St. Lawrence, Comparison of time-resolved and continuous-wave near-infrared techniques for measuring cerebral blood flow in piglets. J. Biomed. Opt. 15(5), 057004-1 to -10 (2010)
389. M. Diop, T.-Y. Lee, K. St. Lawrence, Continuous monitoring of absolute cerebral blood flow by combining diffuse correlation spectroscopy and time-resolved near-infrared technology. Proc. SPIE 7896 (2011)
390. L. Di Sieno, H. Wabnitz, A. Pifferi, M. Mazurenka, Y. Hoshi, A. Dalla Mora, D. Contini, G. Boso, W. Becker, F. Martelli, A. Tosi, R. Macdonald, Characterization of a time-resolved non-contact scanning diffuse optical imaging system exploiting fast-gated single-photon avalanche diode detection. Rev. Sci. Instrum. 87, 035118-1 to -11 (2016)
391. P.S. Dittrich, P. Schwille, Photobleaching and stabilization of fluorophores used for single-molecule analysis with one- and two-photon excitation, Appl. Phys. B **73**, 829-837 (2001)
392. R. I. Dmitriev, A. V. Zhdanov, Y. M. Nolan, D. B. Papkovsky, Imaging of neurosphere oxygenation with phosphorescent probes. Biomaterials 34, 9307-9317 (2013)
393. R. I. Dmitriev, S. M. Borisov, A. V. Kondrashina, J. M. P. Pakan, U. Anilkumar, J. H. M. Prehn, A. V. Zhdanov, K. W. McDermot, I. Klimant, D. B. Papkovsky, Imaging oxygen in neural cell and tissue models by means of anionic cell-permeable phosphorescent nanoparticles. Biomaterials 34, 9307-9317 (2013)
394. R. I. Dmitriev, A. V. Kondrashina, K. Koren, I. Klimant, A. V. Zhdanov, J. M. P. Pakan, K. W. McDermott, D. B. Papkovsky, Small molecule phosphorescent probes for O2 imaging in 3D tissue models. Biomater. Sci. 2, 853-866 (2014)
395. R. I. Dmitriev and D. B. Papkovsky, Intracellular probes for imaging oxygen concentrations: how good are they? Methods Appl. Fluoresc. 3, 034001-034010 (2015)
396. R. I. Dmitriev, S. M. Borisov, H. Düssmann, S. Sun, B. J. Müller, J. Prehn, V. P. Baklaushev, I. Klimant, D. B. Papkovsky, Versatile Conjugated Polymer Nanoparticles for High-Resolution O2 Imaging in Cells and 3D Tissue Models. ACS Nano 9, 5275–5288 (2015)
397. R. I. Dmitriev and D. B. Papkovsky, Multi-parametric O_2 Imaging in Three-Dimensional Neural Cell Models with the Phosphorescent Probes. In: Laura Lossi and Adalberto Merighi (eds.), Neuronal Cell Death: Methods and Protocols, Methods in Molecular Biology, vol. 1254, DOI 10.1007/978-1-4939-2152-2_5, Springer Science+Business Media New York (2015)
398. L.A. Donaldson, K. Radotic, Fluorescence lifetime imaging of lignin autofluorescence in normal and compressed wood. J. Microsc. 251, 178-187 (2013)
399. K. Dore, S. Labrecque, C. Tardif, P. De Koninck, FRET-FLIM Investigation of PSD95-NMDA Receptor Interaction in Dendritic Spines; Control by Calpain, CaMKII and Src Family Kinase. PLOS ONE 9(11), e112170 (2014)
400. K. Prinkey, E. Thompson, J. Saikia, T. Cid, K. Dore, Fluorescence lifetime imaging of AMPA receptor endocytosis in living neurons: effects of Aβ and PP1. Frontiers in Molecular Neuroscience 17, 1409401 - 1 to 11
401. K. Dore, J. Aow, R. Malinow, Agonist binding to the NMDA receptor drives movement of its cytoplasmic domain without ion flow. PNAS Early Edition, www.pnas.org/cgi/doi/10.1073/pnas.1520023112
402. L. Dougan, J. Crain, H. Vass, S.W. Magennis, Probing the liquid-state structure and dynamics od aqueous solutions by fluorescence spectroscopy, J. Fluoresc. 14, 91-97 (2004)

403. K. Douma, R.T.A. Megens, S. Reitsma, L. Prinzen, D.W. Slaaf, M.A.M.J. Van Zandvoort, Two-photon lifetime inaging of fluorescent probes in intact blood vessels: A window to sub-cellular structural information and binding status. Micr. Res. Tech. 70, 467-475 (2007)
404. I.N. Druzhkova, M.V. Shirmanova, M.M. Lukina, V.V. Dudenkova, N. M. Mishina, E.V. Zagaynova, The metabolic interaction of cancer cells and fibroblasts – coupling between NAD(P)H and FAD, intracellular pH and hydrogen peroxide. Cell Cycle, 15:9, 1257-1266, (2016)
405. D.R. Drummond, N. Carter, R.A. Cross, Multiphoton versus confocal high resolution z-sectioning of enhanced green fluorescent nanotubules: Increased multiphoton photobleaching within the focal plane can be compensated using a Pockels cell and dual widefield detectors. J. Microsc. 206, 161-169 (2001)
406. K. Drozdowicz-Tomsia, A. G. Anwer, M. A. Cahill, K. N. Madlum, A. M. Maki, M. S. Baker, E. M. Goldys, Multiphoton fluorescence lifetime imaging microscopy reveals free-to-bound NADH ratio changes associated with metabolic inhibition. J. Biomed. Opt. 19, 08601 (2014)
407. M. Düser, Y. Bi, N.d Zarrabi, S. D. Dunn, M. Börsch, The Proton-translocating *a* Subunit of F0F1-ATP Synthase Is Allocated Asymmetrically to the Peripheral Stalk. J. Biol. Chem. 48, 33602-33610 (2008)
408. M. Düser, N.d Zarrabi, D. J. Cipriano, S. Ernst, G. D. Glick, S. D. Dunn, M. Börsch, 36° step size of proton-driven c-ring rotation in FoF1-ATP synthase. The EMBO Journal 28, 2689–2696 (2009)
409. J.M. Dudley, Supercontinuum generation in photonic crystal fibre, Rev. Mod. Phys. 78, 1135-1184 (2006)
410. R.R. Duncan, A. Bergmann, M.A. Cousin, D.K. Apps, M.J. Shipston, Multi-dimensional time-correlated single-photon counting (TCSPC) fluorescence lifetime imaging microscopy (FLIM) to detect FRET in cells, J. Microsc. **215**, 1-12 (2004)
411. R.C. Dunn, Near-field scanning optical microscopy, Chem. Rev. **99**, 2891-2927 (1999)
412. C. Dunsby, P.M.W. French, Single-point probes for lifetime spectroscopy: Time-correlated single-photon counting technique. In: L. Marcu. P.M.W. French, D.S. Elson, (eds.), Fluorecence lifetime spectroscopy and imaging. Principles and applications in biomedical diagnostics. CRC Press, Taylor & Francis Group, Boca Raton, London, New York (2015)
413. T. Durduran, G. Yu, M.G. Burnett, J.A. Detre, J.H. Greenberg, J. Wang, C. Zhou, A. Yodh, Diffuse optical measurement of blood flow, blood oxygenation, and metabolism in a human brain during sensorimotor cortex activation, Opt. Lett. **29**, 1766-1768 (2004)
414. C. Dysli, G. Quellec, M. Abegg, M. N. Menke, U. Wolf-Schnurrbusch, J. Kowal, J. Blatz, O. La Schiazza, A. B. Leichtle, S. Wolf, M. S. Zinkernagel, Quantitative Analysis of Fluorescence Lifetime Measurements of the Macula Using the Fluorescence Lifetime Imaging Ophthalmoscope in Healthy Subjects. IOVS 55, 2107-2113 (2014)
415. C. Dysli, M. Dysli, V. Enzmann, S. Wolf, M. S. Zinkernagel, Fluorescence Lifetime Imaging of the Ocular Fundus in Mice. IOVS 55, 7206-7215 (2014)
416. C. Dysli, S. Wolf, K. Hatz, M. S. Zinkernagel, Fluorescence Lifetime Imaging in Stargardt Disease: Potential Marker for Disease Progression. Invest Ophthalmol Vis Sci. 57, 832-841, (2016)
417. Dysli, C., Wolf, S., Berezin, M.Y., Sauer, L., Hammer, M., Zinkernagel, M.S., Fluorescence lifetime imaging ophthalmoscopy, Progress in Retinal and Eye Research (2017), doi: 10.1016/j.preteyeres.2017.06.005
418. C. Dysli, S. Wolf, M.S. Zinkernagel, Fluorescence lifetime imaging in retinal artery occlusion. Invest Ophthalmol Vis Sci. 2015; 56:3329–3336
419. C. Dysli, S. Wolf, H.V. Tran, M.S. Zinkernagel, Autofluorescence lifetimes in patients with choroideremia identify photoreceptors in areas with retinal pigment epithelium atrophy. Invest Ophthalmol Vis Sci. 2016;57:6714–6721. DOI:10.1167/ iovs.16-20392
420. C. Dysli, M. Dysli, M. S. Zinkernagel, V. Enzmann, Effect of pharmacologically induced retinal degeneration on retinal autofluorescence lifetimes in mice. Experimental Eye Research 153 (2016) 178e185
421. C. Dysli, L. Berger, S. Wolf, M.N S. Zinkernagel, Fundus autofluorescence lifetimes and entral serous chorioretinopathy. Retina 37:2151–2161, 2017
422. C. Dysli, M. Dysli, S. Wolf, M. Zinkernagel, Fluorescence lifetime distribution in phakic and pseudophakic healthy eyes. PLOS ONE, https://doi.org/10.1371/journal.pone.0279158, 1-17, January 6, 2023

423. H-G. Eberle, J. Beuthan, M. Dierolf, D. Felsenberg, W. Gowin, G. Müller, Investigations of the application of a laser radar photogoniometer in the diagnosis of osteoporosis, Proc. SPIE **3259**, 144-153 (1998)
424. H-G. Eberle, J. Beuthan, G. Müller, The propagation of ps-laser-pulses through different bone structure, Z. Med. Phys. **10**, 177 (2000)
425. C. Eggeling, J.R. Fries, L. Brand, R. Günther, C.A.M. Seidel, Monitoring conformational dynamics of a single molecule by selective fluorescence spectroscopy, PNAS **95**, 1556-1561 (1998)

426. C. Eggeling, S. Berger, L. Brand, J.R. Fries, J. Schaffer, A. Volkmer, C.A. Seidel, Data registration and selective single-molecule analysis using multi-parameter fluorescence detection, J. Biotechnol. **86**, 163 (2001)
427. D. Eggert, D. Gaertner, A. Rühm, R. Sroka, C. Arens, N, Davaris, K. Birkmeier, A. Brodschelm, P. Leisching, Hauke Studier, W. Becker, K. König, C. S. Betz, Differentiation of tumors of the upper respiratory tract using optical metabolic imaging. Lasers in Surgery and Medicine, 57, 147–153 (2025)
428. A. Ehlers, I. Riemann, M. Stark, K. König, Multiphoton Fluorescence Lifetime Imaging of Human Hair, Microsc. Res. Tech. 70, 154 - 161 (2006)
429. R. Eichhorn, G. Wessler, M. Scholz, D. Leupold, G. Stankovic, S. Buder, M. Stücker, K. Hoffmann, Early diagnosis of melanotic melanoma based on laser-induced melanin fluorescence. J. Biomed. Opt. 14, 034033-1 to -7 (2009)
430. J.S. Eid, J.D. Müller, E. Gratton, Data acquisition card for fluctuation correlation spectroscopy allowing full access to the detected photon sequence, Rev. Sci. Instrum. **71**, 361-368 (2000)
431. P.A. Ekstrom, Triggered avalanche detection of optical photons, J. Appl. Phys. **52**, 6974-6979 (1981)
432. A.D. Elder, A. Domin, G.S. Kaminski Schierle, C. Lindon, J. Pines, A. Esposito, C.F. Kamiski, A quantitative protocol for dynamic measurements of protein interactions by Förster resonance energy transfer-sensitzed fluorescence emission. J. R. Soc. Interface 6, S59-S81 (2009)
433. K.W. Eliceiri, C.H. Fan, G.E. Lyons, J.G. White, Analysis of histology specimens using lifetime multiphoton microscopy, J. Biomed. Opt. **8**, 376-380 (2003)
434. J.D. Ellis , D. Llères, M. Denegri , A.I. Lamond , J.F. Cáceres, Spatial mapping of splicing factor complexes involved in exon and intron definition. J. Cell Biol. 181, 921-934 (2008)
435. J. Enderlein, M. Sauer, Optimal algorithm for single molecule identification with time-correlated single photon counting, J. Chem. Phys. A **105**, 48-53 (2002)
436. M. Erbakan, Y.-X. Shen, M. Grzelakowski, P.J. Butler, M. Kumar, Molecular cloning, overexpression and characterization of a novel water channel protein from rhodobacter sphaeriodes. PLOS ONE 9, e86830 (2014)
437. R. Esposito, S. De Nicola, M. Brambilla, A. Pifferi, L.o Spinelli, M. Lepore, Depth dependence of estimated optical properties of a scattering inclusion by time-resolved contrast functions. Opt. Expr. 16(22)17667-17685
438. M. Evers, N. Salma, S. Osseiran, M. Casper. R. Birngruber, C.L.Evans, D. Manstein, Enhanced quantification of metabolic activity for individual adipocytes by label-free FLIM. Scientific Reports 8, 8757-1 to 14 (2018)
439. P. G. Falkowski, H. Lin, M. Y. Gorbunov, What limits photosynthetic energy conversion efficiency in nature? Lessons from the oceans. Phil Trans. R. Soc. B. (2017)
440. T.J. Farrel, W.S. Patterson, Diffusion modeling of fluorescence in tissue, in M.-A. Mycek, B.W. Pogue (eds.), Handbook of Biomedical Fluorescence, Marcel Dekker Inc. New York, Basel, 29-60 (2003)
441. J.A. Feeks, J. J. Hunter, Adaptive optics two-photon excited fluorescence lifetime imaging ophthalmoscopy of exogenous fluorophores in mice. Biomed. Opt. Expr. 8(5), 2483-2495
442. S. Felekyan, R. Kühnemuth, V. Kudryavtsev, C. Sandhagen, W. Becker, C.A.M. Seidel, Full correlation from picoseconds to seconds by time-resolved and time-correlated single photon detection, Rev. Sci. Instrum. 76, 083104 (2005)
443. S. Felekyan, Software package for multiparameter fluorescence spcetroscopy, full correlation amd multiparameter imaging. Available from www.mpc.uni-duesseldorf.de/seidel/software.htm
444. S. Felekyan, S. Kalinin, A. Valeri, C.A.M. Seidel, Filtered FCS and species cross correlation function. Proc. SPIE 7183, 71830D (2009)
445. J. A. Fernández-López, V. Fernandez-Lledó, J. M. Angosto, New insights into red plant pigments: more than just natural colorants. RCS Adv. 20, 24669-24682 (2020)
446. A. Ferchner, S.M. Borisov, A. V. Zhdanov, I. Klimant, D.B. Papkovsky, Intracellular O2 sensing probe based on cell-penetrating phosphorescent nanoparticles. ACS Nano 5 5499-5508 (2011)
447. J.L. Fiore, J.H. Hodak, O. Piestert, C.D. Downey, D.J. Nesbitt, Monovalent and divalent promoted GAAA tetraloop-receptor tertiary interactions from freely diffusing single-molecule studies. Biophys. J. 95, 3892-3905 (2008)
448. F. Fischer, B. Volkmer, S. Puschmann, R. Greinert, W. Breitbart, J. Kiefer, R. Wepf, Risk estimation of skin damage due to ultrashort pulsed, focused near-infrared laser irradiation at 800 nm. J. Biomed. Opt. 13(4) 041320 (2008)
449. F. Fischer, B. Volkmer, S. Puschmann, R. Greinert, W. Breitbart, J. Kiefer, R. Wepf, Assessing the risk of skin damage due to femtosecond laser irradiation. J. Biophoton. 1, 470-477 (2008)
450. J. J. Fisz, Fluorescence Polarization Spectroscopy at Combined High-Aperture Excitation and Detection: Application to One-Photon-Excitation Fluorescence Microscopy. J. Chem. Phys. A, 111, 8606-8621 (2007)
451. J.J. Fisz, Another Look at Magic-Angle-Detected Fluorescence and Emission Anisotropy Decays in Fluorescence Microscopy. J. Chem. Phys. A, 111, 12867-12870 (2007)

452. Flint.https://en.wikipedia.org/wiki/Flint
453. Flint and Chert. http://www.quartzpage.de/flint.html
454. Th. Förster, Zwischenmolekulare Energiewanderung und Fluoreszenz, Ann. Phys. (Serie 6) **2**, 55-75 (1948)
455. Th. Förster, Energy migration and fluorescence. Translated by Klaus Suhling. J. Biomed. Opt. 17 011002-1 to -10 (2012)
456. H. Fogel, S. Frere, O. Segev, S. Bharill, I. Shapira, N. Gazit, T. O'Malley, E. Slomowitz, Y. Berdichevsky, D.M. Walsh, E.Y. Isacoff, J.A. Hirsch, I. Slutsky, APP homodimers transduce an amyloid-β-mediated increase in release probability at excitatory synapses. Cell Rep. 7 1560-1576 (2014)
457. A. Dal Fovo, S. Mattana, A. Ramat, P. Riitano, R. Cicchi, R. Fontana, Insights into the stratigraphy and palette of a painting by Pietro Lorenzetti through non-invasive methods. Journal of Cultural Heritage 61, 91–99 (2023)
458. J.H. Fox, T. Connor, M. Stiles, J. Kama, Z. Lu, K. Dorsey, G. Lieberman, E. Sapp, R.A. Cherny, M. Banks, I. Volitakis, M. DiFiglia, O. Berezovska, A.I. Bush, S.M. Hersch, Cysteine Oxidation within N-terminal Mutant Huntingtin Promotes Oligomerization and Delays Clearance of Soluble Protein. J. Biol. Chem. 286, 18320-18330 (2011)
459. M.A. Fox (ed.), Photoinduced electron transfer. Elsevier, Amsterdam, Oxford, New York (1988)
460. M.A. Franceschini, S. Fantini, J.H. Thompson, J.P. Culver, D.A. Boas, Hemodynamic evoked response of the sensorimotor cortex measured noninvasively with near-infrared optical imaging, Psychophysiology **40**, 548-560 (2003)
461. M.A. Franceschini, V. Toronov, M.E. Filiaci, E. Gratton, S. Fantini, On-line optical imaging of the human brain with 160-ms temporal resolution, Opt. Expr. **6**, 49-57 (2000)
462. J.J. Freed, J.L. Engle, Development of the vibrating-mirror flying spot microscope for untraviolet spctrophotometry. Ann. N.Y. Acad. Sci. 97, 412-488 (1962)
463. S. Frere, I. Slutsky, Calcium imaging using Transient Fluorescence-Lifetime Imaging by Line-Scanning TCSPC. In: W. Becker (ed.) Advanced time-correlated single photon counting applications. Springer, Berlin, Heidelberg, New York (2015)
464. M. Frimmer, Y. Chen, A. F. Koenderink, Scanning Emitter Lifetime Imaging Microscopy for Spontaneous Emission Control. Phys. Rev. Lett. 107, 123602-1 to -5 (2011)
465. J. V. Fritz, P. Didier, J.-P. Clamme, E. Schaub, D. Muriaux, C. Cabanne, N. Morellet, S. Bouaziz, J.-L. Darlix, Y. Mély, H. de Rocquigny, Direct Vpr-Vpr Interaction in Cells monitored by two Photon Fluorescence Correlation Spectroscopy and Fluorescence Lifetime Imaging. Retrovirology 8, 87 (2008)
466. J. V. Fritz, D. Dujardin, J. Godet, P. Didier, J. De Mey, J.-L. Darli, Y. Mély, H. de Rocquigny, HIV-1 Vpr oligomerization and not that of Gag directs the interaction between Vpr and Gag. JVI (2009)
467. G. O. Fruhwirth, S. Ameer-Beg, R. Cook, T. Watson, T. Ng, F. Festy, Fluorescence lifetime endoscopy using TCSPC for the measurement of FRET in live cells. Opt. Expr. 18, 11148-11158 (2010)
468. F. Fuchs, B. Stender, M. Trupke, J. Pflaum, D. Dyakonov, G.V. Astakhov, Enineering near infrared singe photon emitters in ultrapure silicon carbide. arXiv:1407.7065v1 [cond-mat.mtrl-sci] (2014)
469. A. Fukasawa, J. Haba, A. Kageyama, H. Nakazawa and M. Suyama, High Speed HPD for Photon Counting, 2006 Nuclear Science Symposium, Medical Imaging Conference, San Diego, CA (2006)
470. A. Fukasawa, J. Haba, A. Kageyama, H. Nakazawa, and M. Suyama, High Speed HPD for Photon Counting. IEEE Trans. Nucl. Sci. 55(2), 758-762 (2008)
471. J. R Fuller, P. A. Rice, Target DNA bending by the Mu transpososome promotes careful transposition and prevents its reversal. eLife 6, e21777 1-20 (2017)
472. K. Funk, A. Woitecki, C. Franjic-Würtz, Th. Gensch, F. Möhrlein, S. Frings, Modulation of chloride homeostasis by inflammatory mediators in dorsal ganglion neurons. Molecular Pain 4:32 (2008)
473. E. Gagnon, D.A. Schubert, S. Gordo, H.H. Chu, K.W. Wucherpfennig, Local Changes in lipid environment of TCR microclusters regulate membrane binding by the CD3ε cytoplasmic domain. J. Eperimental Medicine, 209, 2423 (2012)
474. P. Gallant, A. Belenkov, G. Ma, F. Lesage, Y. Wang, D. Hall, L. McIntosh, A quantitative time-domain optical imager for small animals in vivo fluorescence studies, In OSA Biomedical Optics Topical Meetings on CD ROM (The Optical Sciety of America, Washington, DC,) WD2 (2004)
475. S. Ganesan, S.M. Ameer-beg, T. T. C. Ng, B. Vojnovic, F.S. Wouters, A dark yellow fluorescent protein (YFP)-based Resonance Energy-Accepting Chromoprotein (REACh) for Förster resonance energy transfer with GFP. PNAS 103, 4089–4094 (2006)
476. S. Ganesan, G. Rohde, K. Eckermann, K. Sroka, M.K.E. Schaefer, C.P, Dohm, P. Kermer, G. Haase, F. Wouters, M. Bähr, J.H, Weishaupt, Mutant SOD1 detoxification mechanisms in intact single cells. Cell Death Differ. 15(2) (2008), 312-321
477. I. Gannot, I. Ron, F. Hekmat, V. Chernomordik, A. Ganjbakhche, Functional optical detection based on pH dependent fluorescence lifetime, Lasers in Surgery and Medicine **35**, 342-348 (2004)

478. F. Gao, P. Poulet, Y. Yamada, Simultaneous mapping of absorption and scattering coefficients from a three-dimensional model of time-resolved optical tomography, Appl. Opt. **39**, 5898-5910 (2000)
479. A. Gaiduk, R. Kühnemuth, S. Felekyan, M. Antonik, W. Becker, V. Kudryavtsev, M. Koenig, C. Sandhagen, C.A.M. Seidel, Time-resolved photon counting allows for new temporal and spacial insights imnto the nanoworld. Proc. of SPIE 6372, 637203-1 to -13 (2006)
480. A. Gaiduk, R. Kühnemuth, S. Felekyan, M. Antonik, W. Becker, V. Kudryavtsev, C. Sandhagen, C.A.M. Seidel, Fluorescence Detection With High Time Resolution: From Optical Microscopy to Simultaneous Force and Fluorescence Spectroscopy. Micr. Res. Tech. 70, 403-409 (2007)
481. G. M. Gallego-López, E. Contreras Guzman, D. E. Desa, L. J. Knoll, M. C. Skala, Metabolic changes in Toxoplasma gondii-infected host cells measured by autofluorescence autofluorescence autofluorescence imaging. mbio 15 (8) 1-19 (2024)
482. F. Gao, J. Li, L. Zhang, P. Poulet, H. Zhao, Y. Yamada, Simultaneous fluorescence yield and lifetime tomography from time-resolved transmittances of small-animal-sized phantom. Appl. Opt. 49(16) 3163-3172 (2010)
483. F. Gao, J. Li, W. Zhang, X. Yi, X. Wang, L. Zhang, Z. Zhou, H. Zhao, A CT-analogous scheme for time-domain diffuse tomography. J. of X-Ray Science and Technology 20, 91-105 (2012)
484. S.V. Gaponenko, I.N. Germanenko, E.P. Petrov, Time-resolved spectroscopy of visibly emitting porous silicon, Appl. Phys. Lett. **64**, 85-87 (1994)
485. S.V. Gaponenko, V.K. Kononenko, E.P. Petrov, I.N. Germanenko, A.P. Stupak, Y.H. Xie, Polarization of porous silicon luminescence, Appl. Phys. Lett. **67**, 3019-3021 (1995)
486. S.V. Gaponenko, E.P. Petrov, U. Woggon, O. Wind, C. Klingshirn, Y.H. Xie, I.N. Germanenko, A.P. Stupak, Steady-state and time-resolved spectroscopy of porous silicon. J. Luminesc. **70**, 364-376 (1996)
487. D. I. Garcia, P. Lanigan, M. Webb, T. G. West, J. Requejo-Isidro, E. Auksorius, C. Dunsby, M. Neil, P. French, M. A. Ferenczi, Fluorescence Lifetime Imaging to Detect Actomyosin States in Mammalian Muscle Sarcomeres. Biophys. J. 93, 2091-2101 (2007)
488. C.D. Geddes, H. Cao, I. Gryczynski, J. Fang, J.R. Lakowicz, Metal-enhanced fluorescence (MEF) due to silver colloids on a planar surface: Potential applications of indocyanine green to in vivo imaging, J. Phys. Chem. A **107**, 3443-3449 (2003)
489. C.D. Geddes, H. Cao, I. Gryczynski, J. R. Lakowicz, Enhanced photostability of ICG in close proximity to gold colloids, Stectrochimica Acta **A59**, 2611-2617 (2003)
490. U. Gehlsen, A. Oetke, M. Szaszak, N. Koop, F. Paulsen, Andreas Gebert, G. Huettmann, P. Steven, Two-photon fluorescence lifetime imaging monitors metabolic changes during wound healing of corneal epithelial cells in vitro. Graefes Arch. Clin. Exp. Ophthalmol 250, 1293-1302 (2012)
491. Th. Gensch, V. Untiet, A. Franzen, P. Kovermann, C. Fahlke, Determination of Intracellular Chloride Concentrations by Fluorescence Lifetime Imaging. In: W. Becker (ed.) Advanced time-correlated single photon counting applications. Springer, Berlin, Heidelberg, New York (2015)
492. R. George, H.-L. Chan, Z. Ahmed, K. M. Suen, C. N. Stevens, J. A. Levitt, K. Suhling, J. Timms, J. E. Ladbury, A complex of Shc and Ran-GTPase localises to the cell nucleus. Cell. Mol. Life Sci. 66 711 – 720 (2009)
493. M. Georgin, L. Carlini, D. Cooper, S.E. Bradforth, J.L. Nadeau, Differential effects of β-mercaptoethanol on CdSe/ZnS and InP/ZnS quantum dots. Phys Chem Chem Phys. 15(25), 10418-28 (2013)
494. A. Gerega, N. Zolek, T. Soltysinski, D. Milej, P. Sawosz, B. Toczylowska, A. Liebert, Wavelength-resolved measurements of fluorescence lifetime of indocyanine green. J. Biomed. Opt. 16(6) 067010-1 to -9 (2011)
495. A. Gerega, D. Milej, W. Weigl, M. Botwicz, N. Zolek, M. Kacprzak, W. Wierzejski, B. Toczylowska, E. Mayzner-Zawadzka, R. Maniewski, A. Liebert, Multiwavelength time-resolved detection of fluorescence during the inflow of indocyanine green into the adult's brain. J. Biomed. Opt. 17(8), 087001-1 to -9 (2012)
496. H.C. Gerritsen, R. Sanders, A. Draaijer, Y.K. Levine, Fluorescence lifetime imaging of oxygen in cells, J. Fluoresc. 7, 11-16 (1997)
497. H.C. Gerritsen, M.A.H. Asselbergs, A.V. Agronskaia, W.G.J.H.M. van Sark, Fluorescence lifetime imaging in scanning microscopes: acquisition speed, photon economy and lifetime resolution, J. Microsc. **206**, 218-224 (2002)
498. B. Geusens, M. Van Gele, S. Braat, S.C. De Smedt, M.C.A. Stuart, T.W. Prow, W. Sanchez, M. Roberts, N.N. Sanders, J. Lambert, Flexible nanosomes (SECosomes) enable efficient siRNA delivery in cultured primary skin cells and in the viable epidermis of ex vivo human skin. Adv. Funct. Mater. 20, 4077-4090 (2010)
499. T. Gillbro, R.J. Cogdell, Carotinoid Fluorescence. Chem. Phys. Lett. 158, 312-316 (1989)
500. A. Gilmore, Th. L.Hazlett, Govindgee, Xanthophyll cycle-dependent quenching of photosystem II chlorophyll a fluorescence: Formation of a quenching complex with a short fluorescence lifetime. PNAS 92, 2273-2277 (1995)

501. V. Ghukasyan, Y.-Y. Hsu, S.-H. Kung, F.-J. Kao, Application of fluorescence resonance energy transfer resolved by fluorescence lifetime imaging microscopy for the detection of enterovirus 71 infection in cells, J. Biomed. Opt. 12, 024016-1 to -8 (2007)
502. V. Ghukassian, F.-J. Kao, Monitoring cellular metabolism with fluorescence lifetime of reduced nicotinamide adenine dinucleotide. J. Phys. Chem. C, 113, 11532-11540 (2009)
503. V. Ghukasyan, C.C. Hsu, C.R. Liu, F.J. Kao, T.H. Cheng, Fluorescence lifetime dynamics of enhanced green fluorescent protein aggregates with expanded polyglutamine. J. Biomed. Opt. 15(1) 016008-1 to -11 (2010)
504. V.V. Ghukasyan, A.H. Heikal, Natural biomarkers for cellular metabolism. Biology, techniques, and applications. CRC Press, Taylor and Francis Group, Boca Raton, London, New York (2015)
505. D. Gilbert, C. Franjic-Würtz, K. Funk, T. Gensch, S. Frings, F. Möhrlen, Differential maturation of chloride homeostasis in primary afferent neurons of the somatosensory system. Int. J. Devl. Neuroscience 25, 479-489 (2007)
506. A. A. Gillette, C. P. Babiarz, A. R. VanDommelen, C. A. Pasch, L. Clipson, K. A. Matkowskyj, D. A. Deming, M. C. Skala, Autofluorescence Imaging of Treatment Response in Neuroendocrine Tumor Organoids. Cancers (Basel). 13(8), 1873, 1-17 (2021)
507. V.D. Giorgi, D. Massi, S. Sestini, R. Ricci, F.S. Pavone, T. Lotti, Combined non-linear laser imaging (two-photon excitation fluorescence microscopy, fluorescence lifetime imaging microscopy, multispectral microscopy) in cutaneous tumors: First results. JEADV 23, 314-316 (2009)
508. A. Giusto, C. D'Andrea, L. Spinelli, D. Contini, A. Torricelli, F. Martelli, G. Zaccanti, R. Cubeddu, Monitoring Absorption Changes in a Layered Diffusive Medium by White-Light Time-Resolved Reflectance Spectroscopy. IEEE Trans. Instrum. Measur. (2009)
509. M. Göppert-Mayer, Über Elementarakte mit zwei Quantensprüngen, Ann. Phys. 9, 273-294 (1931)
510. T.Gokus, A. Hartschuh, H.Harutyunyan, M. Allegrini, F. Hennrich, M. Kappes, A.A. Green, M.C.Hersam, P.T. Araujo, A. Jorio, Exiton dynamics in individual carbon nanotubes at room temperature. Appl. Phys. Lett. 92, 153116 (2008)
511. B.R. Gompf, R. Gunther, G. Nick, R. Pecha, W. Eisenmenger, Resolving sonoluminescence pulse width with time-correlated single-photon counting, Phys. Rev. Lett. **79**, 1405-1408 (1997)
512. A. S Goryashchenko, M. G Khrenova, A. P Savitsky, Detection of protease activity by fluorescent protein FRET sensors: from computer simulation to live cells. Methods Appl. Fluoresc. 6, 022001 (2018)
513. G.W. Gordon, G. Berry, X.H. Liang, B. Levine, B. Herman, Quantitative Fluorescence Resonance Energy Transfer Measurements Using Fluorescence Microscopy. Biophys. J. 74, 2702-2713 (1998)
514. Philipp Gorlovoy, Sergey Larionov, Thao Thi Hien Pham, Harald Neumann, Accumulation of tau induced in neurites by microglial proinflammatory mediators. The FASEB Journal 23, 2502-2513 (2009)
515. H.H. Gorris, S.M. Saleh, D.B. Groegel, S. Ernst, K. Reiner, H. Mustroph, O.S. Wolfbeis, Long-wavelength absorbing and fluorescent chameleon labels for proteins, peptides, and amines. Bioconjug Chem. 22(7), 1433-7 (2011)
516. Govindjee, Sixty-three Years Since Kautsky: Chlorophyll α Fluorescence, Aust. J. Plant Physiol. **22**, 131-160 (1995)
517. Govindjee, M.J. Seufferheld, Non-photochemical quenching of chlorophyll α Fluorescence: Early history and characterization of two xanthophyll-cycle mutants of Chlamydomonas Reinhardtii, Funct. Plant Biol. **29**, 1141-1155 (2002)
518. D. Granadero, J. Bordello, M.J. Perez-Alvite, M. Novo, W. Al-Soufi, Host-guest complexation studied by fluorescence correlation spectroscopy: Adamantane-Cyclodextrin Inclusion. Int. J. Mol. Sci. 11, 173-188 (2010)
519. K. J. Grayson, K. M. Faries, X. Huang, P. Qian, P. Dilbeck, E. C. Martin, A. Hitchcock, C. Vasilev, J. M. Yuen, D. M. Niedzwiedzki, G. J. Leggett, D. Holten, C. Kirmaier & C. N. Hunter, Augmenting light coverage for photosynthesis through YFP-enhanced charge separation at the Rhodobacter sphaeroides reaction centre. Nature Communications 8, 13972-1 to -12 (2017)
520. V. J. Greiner, V. Shvadchak, J. Fritz, Y. Arntz, P. Didier, B. Frisch, C. Boudier, Y. Mély, H. de Rocquigny, Characterization of the mechanisms of HIV-1 Vpr(52e96) internalization in cells. Biochimie 93 1647-1658 (2011)
521. F. Gramuglia, E. Ripiccini, C. A. Fenoglio, M.-L. Wu, L. Paolozzi, C. Bruschini, E. Charbon, Sub-10 ps Minimum Ionizing Particle Detection With Geiger-Mode APDs. Frontiers in Physics, 10 (2022) 849237-1 to -10
522. E. Gratton, S. Breusegem, J. Sutin, Q. Ruan, N. Barry, Fluorescence lifetime imaging for the two-photon microscope: Time-domain and frequency domain methods, J. Biomed. Opt. **8**, 381-390 (2003)
523. V. J. Greiner, V. Shvadchak, J. Fritz, Y. Arntz, P. Didier, B. Frisch, C. Boudier, Y. Mély, H. de Rocquigny, Characterization of the mechanisms of HIV-1 Vpr(52e96) internalization in cells. Biochimie 93 1647-1658 (2011)

524. H. Grosch, T. Hoder, K.-D. Weltmann, R. Brandenburg, Spatio-temporal development of microdischarges in a surface barrier discharge arrangement in air at atmospheric pressure. Eur. Phys. J. D 60, 547–553 (2010)
525. D. Grosenick, H. Wabnitz, H. Rinneberg, Time-resolved imaging of solid phantoms for optical tomography, Appl. Opt. **36**, 221-231 (1997)
526. D. Grosenick, H. Wabnitz, H. Rinneberg, K.T. Moesta, P.M. Schlag, Development of a time-domain optical mammograph and first in-vivo applications, Appl. Optics, **38**, 2927-2943 (1999)
527. D. Grosenick, H. Wabnitz, R. MacDonald, H. Rinneberg, J. Mucke, C. Stroszcynski, K.T. Moesta, P.M. Schlag, Determination of in vivo optical properties of breast tissue and tumors using a laser pulse mammograph, Biomedical Topical Meetings, Technical Digest, OSA, 459 (2002)
528. D. Grosenick, K.T. Moesta, H. Wabnitz, J. Mucke, C. Stroszcynski, R. MacDonald, P.M. Schlag, H. Rinneberg, Time-domain optical mammography: initial clinical results on detection and characterization of breast tumors, Appl. Opt. **42**, 3170-3186 (2003)
529. D. Grosenick, H. Wabnitz, K.T. Moesta, J. Mucke, M. Möller, C. Stroszczynski, J. Stößel, B. Wassermann, P.M. Schlag, H. Rinneberg, Concentration and oxygen saturation of haemoglobin of 50 breast tumours determined by time-domain optical mammography, Physics in Medicine & Biology **49**, 1165-1181 (2004)
530. D. Grosenick, K. T. Moesta, M. Möller, J. Mucke, H. Wabnitz, B. Gebauer, C. Stroszczynski, B. Wassermann, P. M. Schlag, and H. Rinneberg, "Time-domain scanning optical mammography: I. Recording and assessment of mammograms of 154 patients," Phys. Med. Biol. 50(11), 2429–2449 (2005)
531. D. Grosenick, H. Wabnitz, K. T. Moesta, J. Mucke, P. M. Schlag, and H. Rinneberg, "Time-domain scanning optical mammography: II. Optical properties and tissue parameters of 87 carcinomas," Phys. Med. Biol. 50(11), 2451–2468 (2005)
532. D. Grosenick, A. Hagen, O. Steinkellner, A. Poellinger, S. Burock, P. M. Schlag, H. Rinneberg and R. Macdonald, A multichannel time-domain scanning fluorescence mammograph: Performance assessment and first in vivo results, Rev. Sci. Instrum. **82**, 024302 (2011)
533. C. Guardia-Laguarta, M. Coma, M. Pera, J. Clarimon, L. Sereno, J.M. Agullo, L. Molina-Porcel, E. Gallordo, A. Deng, O. Berezovska, B. Hyman, R. Blesa, T. Gomez-Isla, A. Lleo, Mild cholesterol depletion reduces amyloid-β production by impairing APP trafficking to the cell surface. J. Neurochem. 110, 220-230 (2009)
534. R. R. Gullapalli, T. Tabouillot, R. Mathura, J. H. Dangaria, P. J. Butler, Integrated multimodal microscopy, time-resolved fluorescence, and optical-trap rheometry: toward single molecule mechanobiology, J. Biomed. Opt. 12, 014012-1 to -17 (2007)
535. H.-W. Guo, C.-T. Chen, Y.-H. Wei, O. K. Lee, V. Gukassyan, F.-J. Kao, H.-W. Wanga, Reduced nicotinamide adenine dinucleotide fluorescence lifetime separates human mesenchymal stem cells from differentiated progenies. J. Biomed. Opt. 13(5) 050505-1 to 3 (2008)
536. Q. Guo , J. E. Jureller, J. T. Warren, E. Solomaha, J. Florian, W.-J. Tang, Protein-Protein Docking and Analysis Reveal That Two Homologous Bacterial Adenylyl Cyclase Toxins Interact with Calmodulin Differently. JBC 283, 23836-23845 (2008)
537. A. Habenicht, J. Hjelm, E. Mukhtar, F. Bergström, L.B-A. Johansson, Two-photon excitation and time-resolved fluorescence: I. The proper response function for analysing single-photon counting experiments, Chem. Phys. Lett. **345**, 367-375 (2002)
538. S. Habuchi, M. Cotlet, J. Hofkens, G. Disix, J. Michiels, J. Vanderleyden, V. Subramaniam, F.C. De Schryver, Resonance Energy Transfer in a Calcium Concentration-Dependent Cameleon Protein, Biophys. J. **83**, 3499-3506 (2002)
539. S. Hackbarth, V. Horneffer, A. Wiehe, F. Hillenkamp, B. Röder, Photophysical properties of pheophorbide-a-substituted diaminobutane poly-propylene-imine dendrimer, Chemical Physics **269**, 339-346 (2001)
540. A. Hagen , D. Grosenick, R. Macdonald, H. Rinneberg, S. Burock, P. Warnick, A. Poellinger, and P. M. Schlag, Late-fluorescence mammography assesses tumor capillary permeability and differentiates malignant from benign lesions, *Opt Express* 2009 , **17** ,17016 – 17033
541. C. K. Haluska, A. P. Schröder, P. Didier, D. Heissler, G. Duportail, Y. Mely, C. M. Marques, Combining Fluorescence Lifetime and Polarization Microscopy to Discriminate Phase Separated Domains in Giant Unilamellar Vesicles. Biophys. J. 95, 5737-5747 (2008)
542. P. Hänninen, S. Hell, Luminescence scanning microscopy process and luminescence scanning microscope, Patent WO 95/30166 (1995)
543. Hamamatsu Photonics K.K., R7400 Series Metal package photomultiplier tube (2001)
544. Hamamatsu Photonics K.K., R3809U-50 series Microchannel plate photomultiplier tube (MCP-PMTs) (2001)
545. Hamamatsu Photonics K.K., R5900U-16 series multianode photomultiplier tube, data sheet
546. Hamamatsu Photonics K.K., R12309U multianode photomultiplier tube, data sheet
547. Hamamatsu Photonics K.K., H5773/H5783/H6779/H6780/H5784 Photosensor modules (2001)

548. Hamamatsu Photonics K.K., H7422 series Metal package PMT with cooler - photosensor modules (2003)
549. Hamamatsu Photonics, R10467 hybrid PMTs, data sheet
550. M. Hammer, R. Schultz, S. Hasan, L. Sauer, M. Klemm, L. Kreilkamp, L. Zweifel, R. Augsten, D. Meller, Fundus Autofluorescence Lifetimes and Spectral Features of Soft Drusen and Hyperpigmentation in Age-Related Macular Degeneration. Translational vision science & technology. 9(5), 1-11 (2020)
551. Q. Han, W. Wu, W. Liu Y. Yang, The peak shift and evolution of upconversion luminescence from $CsPbBr_3$ nanocrystals under femtosecond laser excitation. RSC Adv. 7, 35757-35764 (2017)
552. R. Hanbury-Brown, R.Q. Twiss, Nature **177**, 27-29 (1956)
553. K.M. Hanson, M.J. Behne, N.P. Barry, T.M. Mauro, E. Gratton, Two-photon fluorescence imaging of the skin stratum corneum pH gradient, Biophys. J. **83**, 1682-1690 (2002)
554. G. T. Hanson, R. Aggeler, D. Oglesbee, M. Cannon, R. A. Capaldi,R. Y. Tsien, S. J. Remington, Investigating Mitochondrial Redox Potential with Redox-sensitiveGreen Fluorescent Protein Indicators. J. Biol. Chem., 279, 13044-13053 (2004)
555. Md. E. Haque, L. L. Spremulli, C. J. Fecko, Identification of Protein-Protein and Protein-Ribosome Interacting Regions of the C-terminal Tail of Human Mitochondrial Inner Membrane Protein Oxa1L. J. Biol. Chem. 285, 34991-34998 (2010)
556. I. N. Haridass, J. C. J. Wei, Y.H. Mohammed, M. L. Crichton, C. D. Anderson, J. Henricson, W. Y. Sanchez, S. C. Meliga, J. E. Grice, H. A. E. Benson, M. A. F. Kendall, M. S. Roberts, Cellular metabolism and pore lifetime of human skin following microprojection array mediation. Journal of Controlled Release 306, 59-68 (2019)
557. P.R. Hartig, K. Sauer, Measurement of very short fluorescence lifetimes by singe photon counting, Rev. Sci. Instrum. **47**, 122 (1976)
558. W. Hartmann, F. Bernhard, Fotovervielfacher und ihre Anwendung in der Kernphysik, Akademie-Verlag Berlin (1957)
559. K. Hasegawa, S. J. Ryu, P. Kaláb, Chromosomal gain promotes formation of a steep RanGTP gradient that drives mitosis in aneuploid cells. J. Cell Biol. Vol. 200 No. 2 151–161
560. R.P. Haugland, Handbook of fluorescent probes and research chemicals, 7th Ed. Molecular Probes, Inc. (1999)
561. T. Hayashi, N. Fukuda, S. Uchiyama, N. Inada, A Cell-Permeable Fluorescent Polymeric Thermometer for Intracellular Temperature Mapping in Mammalian Cell Lines. PLOS ONE 0117677-1 to -18 (2015)
562. A. Hayek, A. Grichine, T. Huault, C. Ricard, F. Bolze, B. van der Sanden, J.-C. Vial, Y. Mely, A. Duperray, P. L. Balldeck, J.-F. Nicoud, Cell-Permeant Cytoplasmic Blue Fluorophores Optimized for In Vivo Two-Photon Microscopy With Low-Power Excitation. Micr. Res. Techn. 70 880-885 (2007)
563. T. M. Heaster, M. Humayun, J. Yu, D. J. Beebe, M. C. Skala, Autofluorescence Imaging of 3D Tumor-Macrophage Microscale Cultures Resolves Spatial and Temporal Dynamics of Macrophage Metabolism. Cancer Res. 80 (23) 5408-5423 (2020)
564. T. M. Heaster, A. R. Heaton, P. M. Sondel, M. C. Skala, Intravital Metabolic Autofluorescence Imaging Captures Macrophage Heterogeneity Across Normal and Cancerous Tissue. Front Bioeng Biotechnol. 9, 644648, 1-10 (2021)
565. J.C. Hebden, E.W. Schmidt, M.E. Fry, M. Schweiger, E.M.C. Hillman, D.T. Delpy, Simultaneous reconstruction of absorption and scattering images by multichannel measurement of purely temporal data, Opt. Lett. **24**, 534-536 (1999)
566. J.C. Hebden, H. Veenstra, H. Dehghani, E.M.C. Hillman, M. Schweiger, S.R. Arridge, D.T. Delpy, Three-dimensional time-resolved optical tomography of a conical breast phantom, Appl. Opt. **40**, 3278-3287 (2001)
567. J.C. Hebden, A. Gibson, R.M. Yusof, N. Everdell, E.M.C. Hillman, D.T. Delpy, S.R. Arridge, T. Austin, J.H. Meek, J.S. Wyatt, Three-dimensional optical tomography of the premature infant brain, Phys. Med. Biol. **47**, 4155-4166 (2002)
568. J.C. Hebden, Advances in optical imaging of the newbirn infant brain, Psychophysiology **40**, 501-510 (2003)
569. J.C.Hebden, A. Gibson, T. Austin, R.M. Yusof, N. Everdell, D.T. Delpy, S.R. Arridge, J.H. Meek, J.S. Wyatt, Imaging changes in blood volume and oxygenation in the newborn infant brain using three-dimensional optical tomography, Phys. Med. Biol. **49**, 1117-1130 (2004)
570. A.A. Heikal, S.T. Hess, G.S. Baird, R.Y. Tsien, W.W.W. Webb, Molecular spectroscopy and dynamics of intrinsically fluorescent proteins: Coral red (dsRed) and yellow (Citrine), PNAS **97**, 11996-12001 (2000)
571. A.A. Heikal, S.T. Hess, W.W.W. Webb, Multiphoton molecular spectroscopy and excited-state dynamics of enhanced green fluorescent protein (EGFP): acid-base specificity, Chem. Phys. **274**, 37-55 (2001)
572. A. Heikal, Intracellular coenzymes as natural biomarkers for metabolic activities and mitochondrial anomalies. Biomark. Med. 4(2), 241–263 (2010)

573. S. W. Hell, J. Wichmann, Breaking the diffraction resolution limit by stimulated emission: stimulated-emission-depletion fluorescence microscopy. Opt. Lett. 19, 780-782 (1994)
574. T. Hellerer, New ultrachrome light source for microscopy, Laser+Photonics 4, 36-38, 2009
575. L. Herl, A. V. Thomas, C. M. Lill, M. Banks, A. Deng, P. B. Jones, R. Spoelgen, B.y T. Hyman, O. Berezovska, Mutations in amyloid ceprecursor protein affect its interactions with presenilin/γ-secretase. Molecular and Cellular Neuroscience 41, 166–174 (2009)
576. B. Herman, G. Gordon, N. Mahajan, V. Centonze, Measurement of fluorescence resonance energy transfer in the optical microscope. In A. Periasamy (ed.), Methods of cellular imaging, Oxford University Press (2001)
577. A. I. Herrando, M. Castillo-Martin, A. Galzerano, L. Fernández, P. Vieira, J. Azevedo, A. Parvaiz, R. Cicchi, V. I. Shcheslavskiy, P. G. Silva, and J. L. Lagarto, Dual excitation spectral autofluorescence lifetime and reflectance imaging for fast macroscopic characterization of tissues. Biomed. Opt. Express 15, 3507-3522 (2024)
578. A.M. Heskes, C.N. Lincoln, J.Q.D. Goodger, I.E. Woodrow, T.A. Smith, Multiphoton fluorescence lifetime imaging shows spatial segregation of secondary metabolites in Eucalyptus secretory cavities. J. Microsc. 247, 33-42, (2011)
579. S.T. Hess, E.D. Sheets, A. Wagenknecht-Wiesner, A.A. Heikal, Quantitive Analysis of the Fluorescence Properties of Intrinsically Fluorescent Proteins in Living Cells, Biophys. J. **85**, 2566 (2003)
580. R.A. Hiller, S.J. Putterman, K.R. Weninger, Time-resolved spectra of sonoluminescence, Phys. Rev. Lett. **80**, 1090-1093 (1998)
581. E.M.C. Hillman, J.C. Hebden, M. Schweiger, H. Dehghani, F.E.W. Schmidt, D.T. Delpy, S.R. Arridge, Time resolved optical tomography of the human forearm, Phys. Med. Biol. 46, 1117-1130 (2001)
582. L. M. Hirvonen, W. Becker, J. Milnes, Th. Conneely, S. Smietana, A. Le Marois, O. Jagutzki, K. Suhling, Picosecond wide-field time-correlated single photon counting fluorescence microscopy with a delay line anode detector. Appl. Phys. Lett. 109, 071101 (2016)
583. J. H. Hodak, J. L. Fiore, D. J. Nesbitt, C. D. Downey, and A. Pardi, Docking kinetics and equilibrium of a GAAA tetraloop-receptor motif probed by single-molecule FRET. PNAS 102, 10505-10510 (2005)
584. T. Hoder, M, Sira, K.V. Kozlov, H.-E. Wagner, Investigation of the coplanar barrier discharge in synthetic air at atmospheric pressure by cross-correlation spectroscopy. J. Phys. D: Appl. Phys. 41 035212-1 to -9 (2008)
585. T. Hoder, R. Brandenburg, R. Basner1, K.-D. Weltmann, K. V. Kozlov,H.-E. Wagner, A comparative study of three different types of barrier discharges in air at atmospheric pressure by cross-correlation spectroscopy. J. Phys. D: Appl. Phys. 43 124009-1 to -8 (2010)
586. T. Hoder, M. Cernak, J. Paillol, D. Loffhagen, R. Brandenburg, High-resolution measurements of the electric field at the streamer arrival to the cathode: A unification of the streamer-initiated gas-breakdown mechanism. Phys. Rev. E 86, 055401-1 to -5 (2012)
587. M. Hof, V. Fidler, R. Hutterer, Basics of fluorescence in biosciences, in M. Hof, R. Hutterer, V. Fidler, Fluorescence spectroscopy in biology, Springer Verlag Berlin Heidelberg New York 1-29(2005)
588. M. Hofherr, M. Arndt, K.Il'in, D. Henrich, M. Siegel, J. Toussaint, T. May, H.-G. Meyer, Time-tagged multiplexing of serial biased superconducting nanowire single-photon detectors. IEEE Transactions on Applied Superconductivity 23, 4EPD-10 (2013)
589. B. Hoffmann, Thomas Zimmer, N. Klöcker, L. Kelbauskas, K. König, K. Benndorf, C. Biskup, Prolonged irradiation of enhanced cyan fluorescent protein or Cerulean can invalidate Förster resonance energy transfer measurements. J. Biomed. Opt. 13(3), 031250-1 to -9 (2008)
590. M. Hofherr, D. Rall, K. Ilin, M. Siegel, A. Semenov, H.-W. Hübers, N.A.Gippius, J. Appl. Phys. 108, 014507 (2010)
591. J. Hofkens, M. Cotlet, T. Vosch, P. Tinnefeld, K.D. Weston, C. Ego, A. Grimsdale, K. Müllen, D. Beljonne, J.L. Bredas, S. Jordens, G. Schweitzer, M. Sauer, F.C. De Schryver, Revealing competetive Förster-type resonance energy-transfer pathways in single bichromorphic molecules, PNAS 100, 13146-13151 (2003)
592. A. M. Holmes, J. Lim, H. Studier M.l S. Roberts, Varying the morphology of silver nanoparticles results in differential toxicity against microorganisms, HaCaT keratinocytes and affects skin deposition. Nanotoxixology 10, 1503-1514 (2016)
593. O. Holub, M.J. Seufferheld, C. Gohlke, Govindjee, G.J. Heiss, R.M. Clegg, Fluorescence lifetime imaging microscopy of Chlamydomonas reinhardtii: non-photochemical quenching mutants and the effect of photosynthetic inhibitors on the slow chlorophyll fluorescence transient. J. Microsc. 226, 90–120 (2007)
594. F.G. Holz, R.F. Spaide (eds), Medical retina, Essential in Opthalmology, Springer (2010)
595. A. Hopt, E. Neher, Highly nonlinear Photodamage in two-photon fluorescence microscopy, Biophys. J. 80, 2029-2036 (2002)
596. J. Horilova, B. Cunderlikova, A. Marcek Chorvatova, Time- and spectrally resolved characteristics of flavin fluorescence in U87MG cncer cells in culture. J. Biomed. Opt. 20(5) 051017 -1 to -8 (2015)

597. N. A. Hosny, D. A. Lee, M. M. Knight, Single photon counting fluorescence lifetime detection of pericellular oxygen concentrations. J. Biomed. Opt. 17(1), 016007-1 to -12 (2012)
598. N. A. Hosny, G. Mohamedi, P. Rademeyer, J. Owen, Y. Wu, M. X. Tang, R. J. Eckersley, E. Stride, and M. K. Kuimova, Mapping microbubble viscosity using fluorescence lifetime imaging of molecular rotors. Proc Natl Acad Sci U S A 110, 9225-9230 (2013)
599. N. A. Hosny, C. Fitzgerald, A. Vysniauskas, A. Athanasiadis, T. Berkemeier, N. Uygur, U. Poeschl, M. Shiraiwa, M. Kalberer, F. D. Pope, M. K. Kuimova, Direct imaging of changes in aerosol particle viscosity upon hydration and chemical aging, Chem. Sci. 7, 1357-1367 (2016)
600. D. Hu, M. Micic, N. Klymyshyn, Y.D. Suh, H.P. Lu, Correlated topographic and spectroscopic imaging beyond diffraction limit by atomic force microscopy metallic tip-enhanced near-field fluorescence lifetime microscopy, Rev. Sci. Instrum. **74**, 3347-3355 (2003)
601. C. Huang, P.J. Butler, S. Tong, H.S. Muddana, G. Bao, S. Zhang, Substrate stiffness regulates cellular uptake of nanoparticles. Nano Lett. 13, 1611-1615, (2013)
602. R. Huang, J. Avo, Th. Northey, E. Chaning-Pearce, P. L. dos Santos, J. S. Ward, P. Data, M. K. Etherington, M. A. Fox, Th. J. Penfold, M. N. Berberan-Santos, J. C. Lima, M. R. Bryce, F. B. Dias, The contribution of molecular vibrations and higher triplet levels to the intersystem crossing mechanism in metal-free emitters. J. Mater. Chem. C. 5, 6269-6280 (2017)
603. M.K.Y. Hughes, S. Ameer-Beg, M. Peter, T. Ng, Use of acceptor fluorescence for determining FRET lifetimes, Proc. SPIE **5139**, 88-96 (2003)
604. G. Hungerford, A. Rei, M. I. C. Ferreira, C. Tregidg, K. Suhling, Molecular diffusion within sol-gel derived matrices viewed via fluorescence recovery after photobleaching. Photochem. Photobiol. Sci. 6, 825-828 (2007)
605. A. Hutfilz, S. R. Sonntag, B. Lewke, D. Theisen-Kunde, S. Grisanti, R. Brinkmann, Y. Miura, Fluorescence Lifetime Imaging Ophthalmoscopy of the Retinal Pigment Epithelium During Wound Healing After Laser Irradiation. Trans Vis Sci Tech. 8(5):12, 1-12, (2019)
606. K. T. Huynh, S. Walters, E. K. Foley, J. J. Hunter, Separate lifetime signatures of macaque S cones, M/L cones, and rods observed with adaptive optics fluorescence lifetime ophthalmoscopy. Scientific Reports 13, 2456 (2023)
607. id Quantique, id 100 single photon detection module, data sheet, www.idquantique.com (2005)
608. id Quantique, id 150-8 miniature 8-channel photon counter for OEM applications, www.idquantique.com (2007)
609. id Quantique, id220-FR Cost-effective module for asynchronous single-photon counting at telecom wavelengths. Available on www.idquantique.com
610. B. Ilien, N. Glasser, J.-P. Clamme, P. Didier, E. Piemont, R. Chinnappan, S. B. Daval, J.-L. Galzi, Y. Mely, Pirenzepine Promotes the Dimerization of Muscarinic M1 Receptors through a Three-step Binding Process. J. Biol. Chem. 284(29) 19533–19543, (2009)
611. Inada, N., Fukuda, N., Hayashi, T., Uchiyama, S., Temperature imaging using a cationic linear fluorescent polymeric thermometer and fluorescence lifetime imaging microscopy. Nat Protoc 14, 1293–1321 (2019). https://doi.org/10.1038/s41596-019-0145-7
612. M. Iwai, M. Yokono, N. Inada, J. Minagawa, Live-cell imaging of photosystem II antenna dissociation during state transitions. PNAS 107, 2337-2342 (2010)
613. A. V. Izosimova, M. V. Shirmanova, V. I. Shcheslavskiy, D. A. Sachkova, A. M. Mozherov, G. V. Sharonov, E. V. Zagaynova, D. V. Yuzhakova, FLIM of NAD(P)H in Lymphatic Nodes Resolves T-Cell Immune Response to the Tumor. Int. J. Mol. Sci. 23, 5829-1 to -12 (2022)
614. J.C. Jackson, A.P. Morrison, D. Phelan, A. Mathewson, A novel silicon geiger-mode avalanche photodiode, Proc. IEDM, 32-2 (2002)
615. Jaggi, D., Solberg, Y., Dysli, C., Lincke, J., Habra, O., Wolf, S., & Zinkernagel, M., Ffluorescence Lifetime Imaging Ophthalmoscopy as Predictor of Long-Term Functional Outcome in Maculy-Off Rhegmatogenous Retinal Detachment. Retina, 42(12), 2388–2394. (2022)
616. S. Jakobs, V. Subramaniam, A. Schönle, T. Jovin, S.W. Hell, EGFP and DsRed expressing cultures of *escherichia coli* imaged by confocal, two-photon and fluorescence lifetime microscopy, FEBS Letters 479, 131-135 (2002)
617. M. M. Janas, B. Wang, A. S. Harris, M. Aguiar, J. M. Shaffer, Y. V. B. K. Subrahmanyam, M. A. Behlke, K. W. Wucherpfennig, S. P. Gygi, E. Gagnon, and C. D. Novina, Alternative RISC assembly: binding and repression of microRNA-mRNA duplexes by human Ago proteins. RNA N. Y. N, 18, no. 11, 2041–2055 (2012)
618. G. Jayarai, K. Mapa, S. Maiti, K. Chakraborty, Pulse overlaid excitation (POLEX): A derivative of alternating laser excitation (ALEX) and pulse interleaved excitation (PIE) for single particle fluorescence spectroscopy. ChemPhysChem (2015) in press

619. A. Jelzow, H. Wabnitz, H. Obrig, R. Macdonald, Jens Steinbrink, Separation of indocyanine green boluses in the human brain and scalp based on time-resolved in-vivo fluorescence measurements. J. Biomed. Opt. 17(5) 057003-1 to -4 (2012)
620. A. Jelzow, H. Wabnitz, I. Tachtsidis, E. Kirilina, R. Bruhl, and R. Macdonald, Separation of superficial and cerebral hemodynamics using a single distance time-domain NIRS measurement, Biomedical optics express 5, 1465-1482 (2014)
621. J. Jenkins, R. I. Dmitriev, D. B. Papkovsky, Imaging Cell and Tissue O_2 by TCSPC-PLIM. In: W. Becker (ed.) Advanced time-correlated single photon counting applications. Springer, Berlin, Heidelberg, New York (2015)
622. J. Jenkins, R. I. Dmitriev, K. Morten, K. W. McDermott, D. B. Papkovsky, Oxygen-sensing scaffolds for 3-dimensional cell and tissue culture. Acta Biomaterialia 16, 126–135 (2015)
623. J. Jenkins, D. B. Papkovsky and R. I. Dmitriev, The Ca^{2+} /Mn^{2+}-transporting SPCA2 pump is regulated by oxygen and cell density in colon cancer cells. Biochem. J. 473, 2507-2518 (2016)
624. J. Jenkins, S. M. Borisov, D. B. Papkovsky, R. I. Dmitriev, Sulforhodamine Nanothermometer for Multiparametric Fluorescence Lifetime Imaging Microscopy. Anal. Chem. 88, 10566-10572
625. S. Jentsch, D. Schweitzer, K.-U. Schmidtke, S. Peters, J. Dawczynski, K.-J. Bär, M. Hammer, Retinal fluorescence lifetime imaging ophthalmoscopy measures depend on the severity of Alzheimer's disease. Acta Ophthalmol. (2014)
626. A. Jeshtadi, P. Burgos, C. D. Stubbs, A. W. Parker, L. A. King, M. A. Skinner, S. W. Botchway, Interaction of Poxvirus Intracellular Mature Virion Proteins with the TPR Domain of Kinesin Light Chain in Live Infected Cells Revealed by Two-Photon-Induced Fluorescence Resonance Energy Transfer Fluorescence Lifetime Imaging Microscopy. J. Virol. 84, 12886-12894 (2010)
627. Y. Jiang, L. A. Borrelli, Y. Kanaoka, B. J. Bacskai, J. A. Boyce, CysLT2 receptors interact with CysLT1 receptors and down-modulate cysteinyl leukotriene–dependent mitogenic responses of mast cells. Blood 110, 3263-3270 (2007)
628. K. M. Johnson, L. Swenson, A. W. Opipari, R. Reuter, N. Zarrabi, C. A. Fierke, M. Börsch, G. D. Glick, Mechanistic basis for differential inhibition of the F_1F_0-ATPase by aurovertin. Biopolymers 91, 830-840 (2009)
629. P.B. Jones, A. Rozkalne, M. Meyer-Luehmann, T.L. Spires-Jones, A. Makarova, A.T.N. Kumar, O. Berezovska, B.B. Bacskai, B. Hyman, Two postprocessing techniques for the elimination of background autofluorescence for fluorescence lifetime imaging microscopy. J. Biomed. Opt. 13(1) 014008-1 to -8
630. P. B. Jones, K.W. Adams, A. Rozkalne, T.L. Spires-Jones, T.T. Hshieh, T. Hashimoto1, C.A. F. von Armin, M. Mielke, B.J. Bacskai, B.T. Hyman, Apolipoprotein E: Isoform Specific Differences in Tertiary Structure and Interaction with Amyloid-b in Human Alzheimer Brain. PLoS One 6, e14586 (2011)
631. J. D. Jones, H. E. Ramser, A. E. Woessner K. P. Quinn, In vivo multiphoton microscopy detects longitudinal metabolic changes associated with delayed skin wound healing.Communications Biology 1 198-1 to -8 (2018)
632. V. Jyothikumar, Y. Sun, A. Periasamy, Investigation of tyrptopahn-NADH in live human cells using 3-photon fluorescence lifetime imaging. J. Biomed. Opt. 18(6), 060501 (2013)
633. M. Kacprzak, A. Liebert, P. Sawosz, N. Zolek, R. Maniewski, Time-resolved optical imager for assessment of cerebral oxygenation. J. Biomed. Opt. 12, 034019-1 to -14 (2007)
634. M. Kacprzak, A. Liebert, P.Sawosz, N. Zolek, D. Milej, R. Maniewski, Time-resolved imaging of fluorescent inclusions in optically turbid medium – phantom study. Opto-Electron. Rev. 18(1) 37-47 (2010)
635. L. Abdul Kadir, M. Stacey, R. Barrett-Jolley, Emerging roles of the membrane potential: Action beyond the action potential. Frontiers in Physiology 9:1661 (2018)
636. P. Kalab, A. Pralle, E. Y. Isacoff, R. Heald, K. Weis, Analysis of a RanGTP-regulated gradient in mittotic somatic cells. Nature 440.7084, 697-70 (2006)
637. S. Kalinina, V. Shcheslavskiy, W. Becker, J. Breymayer, P. Schäfer, A. Rück, Correlative NAD(P)H-FLIM and oxygen sensing-PLIM for metabolic mapping. J. Biophotonics 9(8):800-811 (2016)
638. S. Kalinina, C. Freymueller, N. Naskar, B. von Einem, K. Reess, R. Sroka, A. Rueck, Bioenergetic Alterations of Metabolic Redox Coenzymes as NADH, FAD and FMN by Means of Fluorescence Lifetime Imaging Techniques. Int. J. Mol. Sci. 22, 5952, 1-15 (2021)
639. V. P. Kalinushkin, O. V. Uvarov, Two-Photon Confocal Microscopy as a Tool for Nonequilibrium Charge-Carrier Lifetime Tomography in Semiconductor Materials. JETP Letters 104, No. 11, 754–758 (2016)
640. J. Kalisz, Review of methods for time interval measurements with picosecond resolution, Metrologia **41**, 17-32
641. T. Kamali, S. R. M. Farrell, W. H. Baldridge, J. Fischer, B. C. Chauhan Two-Photon Scanning Laser Ophthalmoscope. In: J. F. Bille (ed.), High Resolution Imaging in Microscopy and Ophthalmology, 195-211 (2019)

642. H. Kaneko, I. Putzier, S. Frings, U. B. Kaupp, Th. Gensch**,** Chloride Accumulation in Mammalian Olfactory Sensory Neurons, J. Neurosci., **24** 7931-7938 (2004)
643. S. R. Kantelhardt, J. Leppert, J. Krajewski, N. Petkus, E. Reusche, V. M. Tronnier, G. Hüttmann, A. Giese, Imaging of brain and brain tumor specimens by time-resolved multiphoton excitation microscopy ex vivo. Neuro-Onkology April 2007, 103-112
644. D. Kapsokalyvas, P.M.H. Schiffers, N. Maij, D.P. Suylen, T.M. Hackeng, M.A.M.J. van Zandvoort, J.G.R. DeMey, Imaging evidence for endothelin ETA/ETB receptor heterodimers in isolated rat mesenteric resistance arteries. Life Sciences 111, 36-41 (2014)
645. C.N. Kästner, M. Prummer, B. Sick, A. Renn, U.P. Wild, P. Dimroth, The citrate carrier CitS probed by single molecule fluorescence spectroscopy, Biophys. J. **84**, 1651-1659 (2003)
646. P. Kask, K. Palo, D.Ullmann, K. Gall, Fluorescence-intensity distribution analysis and its application in bimolecular detection technology, PNAS **96**, 13756-13761 (1999)
647. P. Kask, K. Palo, N. Fay, L. Brand, Ü. Mets, D. Ullmann, J. Jungmann, J. Pschorr, K. Gall, Two-dimensional fluorescence intensity distribution analysis: theory and applications, Biophys. J. **78**, 1703-1713 (2000)
648. P. Kask, C. Eggeling, K. Palo, Ü. Mets, M. Cole, K. Gall, Fluorescence intensity distribution analysis(FIDA) and related fluorescence fluctuation techniques: theory and practice, in R. Kraayenhof, A.J.W.G. Visser, H.C. Gerritsen (eds.), Fluorescence spectroscopy inaging and probes, Springer Verlag Berlin Heidelberg New York, 153-181 (2000)
649. H. Kautsky, A. Hirsch, Neue Versuche zur Kohlensäureassimilation, Naturwissenschaften **19**, 964 (1931)
650. S. V. Kathuria, C. Kayatekin, R. Barrea, E. Kondrashkina, R. Graceffa, L. Guo, R. P. Nobrega, S. Chakravarthy, C. R. Matthews, T. C. Irving, O. Bilsel, Microsecond barrier-limited chain collapse observed by time-resolved FRET and SAXS. J Mol Biol 426, 1980-94 (2014)
651. S. V. Kathuria, O. Bilsel, Probing microsecond reactions with microfluidic mixers and TCSPC. In: W. Becker (ed.) Advanced time-correlated single photon counting applications. Springer, Berlin, Heidelberg, New York (2015)
652. V. Katsoulidou, A. Bergmann, W. Becker, How fast can TCSPC FLIM be made? Proc. SPIE 6771, 67710B-1 to 67710B-7 (2007)
653. B. Kaye, T. Y. Yoo, J. Foster, C.-H. Yu, D. J. Needleman, Bridging length scales to measure polymer assembly. Molecular Biology of the Cell 28, 1379-1388 (2017)
654. L. Kelbauskas, W. Dietel, Internalization of aggregated photosensitizers by tumor cells: Subcellular time-resolved fluorescence spectroscopy on derivates of pyropheophorbide-a ethers and chlorin e6 under femtosecond one- and two-photon excitation, Photochem. Photobiol. **76**, 686-694 (2002)
655. T. Kelleher, G. Fruhwirth, G. Patel, E. Ofo, F. Festy, P.R. Barber, S.M. Ameer-Beg, B. Vojnovic, C. Gillett, A. Coolen, G. Kéri, P.A. Ellis, T. Ng, The potential of optical proteomic technologies to individualize prognosis and guide rational treatment for cancer patients. Targ. Oncol. 4, 235–252 (2009)
656. G. T. Kennedy, H. B. Manning, D. S. Elson, M. A. A. Neil, G. W. Stamp, B. Viellerobe, F. Lacombe, C. Dunsby, P. M. W. French, A fluorescence lifetime imaging scanning confocal endomicroscope. J. Biophoton. 3, 103–107 (2010)
657. D. Kepshire, N. Mincu, M. Hutchins, J. Gruber, H. Dehghani, J. Hypnarowski, F. Leblond, M. Khayat, B. W. Pogue, A microcomputed tomography guided fluorescence tomography system for small animal molecular imaging. Rev. Sci. Instrum. 80, 043701-1 to -10 (2009)
658. D. S. Kepshire, S. L. Gibbs-Strauss, J. A. O'Hara, M. Hutchins, N. Mincu, F. Leblond, M. Khayat, H. Dehghani, S. Srinivasan, B. W. Pogue, Imaging of glioma tumor with endogenous fluorescence tomography. J. Biomed. Opt. 14, 030501-1 to -3 (2009)
659. C. Kerbage, C.H. Sadowsky, P.N. Tariot, M. Agronin, G. Alva, F. Darell Turner, D. Nilan, A. Cameron, G. D. Cagle, P.D. Hartung, Detection of Amyloid β signature in the lens and its correlation in the brain to aid the diagnosis of Alzheimer's disease. Americal Journal of Alzheimer's Disease & Other Dementias (2014)
660. S. Khoon Teh, W. Zheng, S. Li, D. Li, Y. Zeng, Y. Yang, J. Y. Qu, Multimodal nonlinear optical microscopy improves the accuracy of early diagnosis of squamous intraepithelial neoplasia. J. Biomed. Opt. 18(3) 036001-1 to -11 (2013)
661. D. J. Killock, M. Parsons, M. Zarrouk, S. M. Ameer-Beg, A. J. Ridley, D. O. Haskard, M. Zvelebil, A. Ivetic, In Vitro and in Vivo Characterization of Molecular Interactions between Calmodulin Ezrin/Radixin/Moesin, and L-selectin. Journal of Biological Chemisty, JBC, 284 8833-8845 (2009)
662. Y. Kim, H. L. Puhl E. Chen, G. H.Taumoefolau, T. A.Nguyen, D. S. Kliger, P. S. Blank, S. S. Vogel, Venus a206 dimers behave coherently at room temperature. Biophys. J. 116:10, 1918-1930 (2019)
663. Y. Kim, S. S. Vogel, Measuring two-photon microscopy ultrafast laser pulse duration at the sample plane using time-correlated single-photon counting. J. Biomed. Opt. 25(1), 014516-1 to 9 (2020)

664. K. Kimura, Ultra fast luminescence in heavy-ion track-cores in insulators: Electron-hole plasma, Nucl. Instr. Meth. Phys. Res. B191, 48 (2002)
665. S. Kinoshita, T. Kushida, Subnanosecond fluorescence-lifetime measuring system using single photon counting method with mode-locked laser excitation, Rev. Sci. Instrum. 52, 572-575 (1981)
666. S. Kinoshita, T. Kushida, High-performance, time-correlated single-photon counting apparatus using a side-on type photomultiplier, Rev. Sci. Instrum. 53, 469-472 (1982)
667. K. Kirchberg, T.-Y Kim, M. Möller, D. Skegro, G. D. Raju, j. Granzin, G. Büldt, R. Schlesinger, U. Alexiev, Conformational dynamics of helix 8 in the GPCR rhodopsin arrestin activation in the desnsitization process. PNAS 108, 18690-18695 (2011)
668. E. Kirilina, A. Jelzow, A. Heine, M. Niessing, H.Wabnitz, R. Brühl, B. Ittermann, A.M. Jakobs, I. Tachtsidis, The physiological origin of task-evoked systemic artefacts in functional near infrared spectrocopy. NeuroImage 61, 70-81 (2012)
669. N. Kitamura, N. Sakata, H-B. Kim, S. Habuchi, Energy gap dependence of the nonradiative decay rate constant of 1-anilino-8-naphthalene sulfonate in reverse micelles, Analytical Sciences 15, 431-419 (1999)
670. T. Kiuchi, E. Ortiz-Zapater, J. Monypenny, D.l R. Matthews, L. K. Nguyen, J. Barbeau, O. Coban1, K. Lawler, B. Burford, D. J. Rolfe, E. de Rinaldis, D. Dafou, M. A. Simpson, N. Woodman, S. Pinder, C.l E. Gillett, V. Devauges, S. P. Poland, G. Fruhwirth, P. Marra, Y. L. Boersma, A. Plückthun, W. J. Gullick, Y. Yarden, G. Santis, M. Winn, B. N. Kholodenko, M. L. Martin-Fernandez, P. Parker, A. Tutt, S. M. Ameer-Beg, T. Ng, The ErbB4 CYT2 variant protects EGFR from ligand-induced degradation to enhance cancer cell motality. Sci. Signal. 7, ra78 1-14 (2014)
671. T. A. Klar and S. W. Hell, Subdiffraction resolution in far-field fluorescence microscopy. Opt. Lett. 24, 954-956 (1999)
672. M. Klemm, A. Dietzel, J. Haueisen, E. Nagel, M. Hammer, D. Schweitzer, Repeatability of autoflurescence lifetime imaging at the human fundus in healthy volunteers. Curr. Eye Res. 38, 793-801 (2013)
673. Klemm M, Blum J, Link D, Hammer M, Haueisen J, Schweitzer D. Combination of confocal principle and aperture stop separation improves suppression of crystalline lens fluorescence in an eye model. Biomed Opt Express. 7(9) 3198 (2016)
674. M. Klemm, L. Sauer, S. Klee, D. Link, S. Peters, M. Hammer, D. Schweitzer, J. Haueisen, Bleaching effects and fluorescence lifetime imaging ophthalmoscopy. Biomedical Optics Express, 10(3), 1446-1461 (2019)
675. P. Kloc, H.-E. Wagner, D. Trunec, Z. Navratil, G. Fedosev, An investigation of dieclectric barrier discharge in Ar and Ar/NH_3 mixture using cross-correlation spectroscopy. J. Phys. D: Appl. Phys. 43, 345205-34514 (2010)
676. J. Klucken, T. F. Outeiro, P. Nguyen, P. J. McLean, B. T. Hyman, Detection of novel intracellular-synuclein oligomeric species by fluorescence lifetime imaging. FASEB J. 20, 2050-2057 (2006)
677. J-P. Knemeyer, N. Marmé, M. Sauer, Probes for detection of specific DNA sequences at the single-molecule level, Anal. Chem. **72**, 3717-3724 (2002)
678. M. J. Koehler, K. König, P. Elsner, R. Bückle, M. Kaatz, In vivo assessment of human skin aging by multiphoton laser scanning tomography, Opt. Lett. 31, 2879-2881 (2006)
679. Z. Kojro, A. Riede, M. Schubert, W. Grill, Systematic and statistical errors in correlation estimators obtained from various digital correlators, Rev. Sci. Instrum. **70**, 4487-4496 (1999)
680. M. Köllner, J. Wolfrum, How many photons are necessary for fluorescence-lifetime measurements?, Phys. Chem. Lett. **200**, 199-204 (1992)
681. K. König, P.T.C. So, W.W. Mantulin, B.J. Tromberg, E. Gratton, Two-Photon excited lifetime imaging of autofluorescence in cells during UVA and NIR photostress, J. Microsc. **183**, 197-204 (1996)
682. K. König, Multiphoton microscopy in life sciences, J. Microsc. **200**, 83-104 (2000)
683. K. König, Laser tweezers and multiphoton microscopes on life science, Histochem. Cell Biol. **114**, 79-92 (2000)
684. K. König, Cellular Response to Laser Radiation in Fluorescence Microscopes, in A. Periasamy, Methods in Cellular Imaging, Oxford University Press, 236-254 (2001)
685. K. König, U. Wollina, I. Riemann, C. Peuckert, K-J. Halbhuber, H. Konrad, P. Fischer, V. Fuenfstueck, T.W. Fischer, P. Elsner, Optical tomography of human skin with subcellular resolution and picosecond time resolution using intense near infrared femtosecond laser pulses, Proc. SPIE **4620**, 191-202 (2002)
686. K. König, I. Riemann, High-resolution multiphoton tomography of human skin with subcellular spatial resolution and picosecond time resolution, J. Biom. Opt. **8**, 432-439 (2003)
687. K. König, I. Riemann, G. Ehrlich, V. Ulrich, P. Fischer, Multiphoton FLIM and spectral imaging of cells and tissue, Proc. SPIE **5323**, 240-251 (2004)
688. K. König, A. Ehlers, F. Stracke, I. Riemann, In vivo drug sceening in human skin using femtosecond laser multiphoton tomography. Skin Pharmakol Physiol 19, 78-88 (2006)
689. K. König, Multiphoton-induced cell damage. In: B.R. Masters, P.T.C. So, eds., Handbook of Biomedical Nonlinear Optical Microscopy.Oxford University Press 2008

690. K. Koenig, Clinical multiphoton tomography. J. Biophoton. 1, 13–23 (2008)
691. K. König, M. Weinigel, D. Hoppert, R. Bückle, H. Schubert, M.J. Köhler, M. Kaatz, P. Elsner, Multiphoton tissue imaging using high-NA microendoscopes and flexible scan heads for clinical studies and small animal research. J. Biophoton. 1, 506-513 (2008)
692. K. Koenig, A. Uchugonova, Multiphoton Fluorescence Lifetime Imaging at the Dawn of Clinical Application. In: A. Periasamy, R.M. Clegg, eds., FLIM Microscopy in Biology and Medicine. CRC Press 2009
693. K. König, A. Uchugonova, E. Gorjup, Multiphoton Fluorescence Lifetime Imaging of 3D-Stem Cell Spheroids During Differentiation. Microsc. Res. Techn. 74, 9-17(2011)
694. A. D. Komarova, S. D. Sinyushkina, I. D. Shchechkin1, I. N. Druzhkova, S. A. Smirnova, V. M. Terekhov, A. M. Mozherov, N. I. Ignatova, E. E. Nikonova, E. A. Shirshin, L. E. Shimolina, S. V. Gamayunov, V. I. Shcheslavskiy, M. V. Shirmanova, Insights into metabolic heterogeneity of colorectal cancer gained from fluorescence lifetime imaging. eLife 13:RP94438, 1-21 (2024)
695. B.A. Korzh et al, Demonstrating sub-3 ps temporal resolution in a superconducting nanowire single-photon detector. ArXiv:1804.06839 (2018)
696. Boris Korzh, Qing-Yuan Zhao, Jason P. Allmaras, Simone Frasca, Travis M. Autry, Eric A. Bersin, Andrew D. Beyer, Ryan M. Briggs, Bruce Bumble, Marco Colangelo, Garrison M. Crouch, Andrew E. Dane, Thomas Gerrits4, Adriana E. Lita, Francesco Marsili, Galan Moody, Cristián Peña, Edward Ramirez, Jake D. Rezac, Neil Sinclair, Martin J. Stevens, Angel E. Velasco, Varun B. Verma, Emma E. Wollman, Si Xie, Di Zhu, Paul D. Hale, Maria Spiropulu, Kevin L. Silverman, Richard P. Mirin, Sae Woo Nam, Alexander G. Kozorezov, Matthew D. Shaw and Karl K. Berggren, Demonstration of sub-3 ps temporal resolution with a superconducting nanowire single-photon detector. Nature Photonics 14, 250–255 (2020)
697. O. Korth, T. Hanke, B. Röder, Photophysical investigations of Langmuir-Blodgett mono- and multilayer films of pheophorbide-a, Thin Solid Films **320**, 305-315 (1998)
698. E. I. Koshel, P. S. Chelushkin, A. S. Melnikov, P. Y. Serdobintsev, A. Yu. Stolbovaia, A. F. Saifitdinova, V. I. Shcheslavskiy, O.r Chernyavskiy, E. R. Gaginskaya, I. O. Koshevoy, S. P. Tunik, Lipophilic phosphorescent gold(I) clusters as selective probes for visualization of lipid droplets by two-photon microscopy. Journal of Photochemistry and Photobiology A: Chemistry 332 (2017) 122–130
699. M. Koshioka, K. Sasaki H. Masuhara, Time-Dependent Fluorescence Depolarization Analysis in Three-Dimensional Microspectroscopy. Appl. Spectr. 49 224-228 (1995)
700. A.S.R. Koti, M.M.G. Krishna, N. Periasamy, Time-Resolved Area-Normalized Emission Spectroscopy (TRANES): A Novel Method for Confirming Emission from Two Excited States, J. Phys. Chem A 105, 1767-1771 (2001)
701. S. V. Koushik, H. Chen, C. Thaler, H. L. Puhl, and S. S. Vogel, Cerulean, Venus, and VenusY67C FRET Reference Standards. Biophys J.: Biophysical Letters L99-L101 (2006)
702. S.V. Koushik, S.S. Vogel, Energy migration alters the fluorescence lifetime of Cerulean: implications for fluorescence lifetime imaging Forster resonance energy transfer measurements. J. Biomed. Opt. 13(3), 031204-1 to -9 (2008)
703. S.V. Koushik, P.S. Blank, S.S. Vogel, Anomalous Surplus Energy Transfer Observed with Multiple FRET Acceptors. www.plosone.org, PLOS ONE 4 Issue 11, e8031 (2009)
704. K.V. Kozlov, R. Brandenburg, H-E. Wagner, A.M. Morozov, P. Michel, Investigation of the filamentary and diffuse mode of barrier discharges in N_2/O_2 mixtrures at atmospheric pressure by cross-correlation spectroscopy, J. Phys. D: Appl. Phys. **38**, 518-529 (2005)
705. K.V. Kozlov, V.V. Dobryakov, A.P. Monyakin, VG- Samoilovich, O.S. Shepeliuk, H-E. Wagner, R. Brandenburg, P. Michel, Cross-correlation spectroscopy in investigations of filamentory gas discharges at atmospheric pressure, Proc. SPIE 4460, 165-176 (2002)
706. K.V. Kozlov, H-E. Wagner, R. Brandenburg, P. Michel, Spatio-temporally resolved spectroscopic diagnostics of the barrier discharge in air at atmospheric pressure, J. Phys. D: Appl. Phys. 34, 3164-3176 (2001)
707. L.J. Kraft, T.A. Nguyen, S.S. Vogel, A.K.Kenworthy, Size, stoichiometry, and organization of soluble LC3-associated complexes. Autophagy 10(5) 861-877 (2014)
708. T. B. Krasieva, C. Stringari, F. Liu, C.-H. Sun, Y. Kong, M. Balu, F.L.Meyskens, E. Gratton, B.J. Tromberg, Two-photon excited fluorescence lifetime imaging and spectroscopy of melanins in vitro and in vivo. J. Biomed. Opt. 18(3), 031107.1 to -9
709. R. Krause-Rehberger, H.S. Leipner, Positron annihilation in semiconductors, Springer Verlag Berlin Heidelberg New York, (1999)
710. M. Kreiter, M. Prummer, B. Hecht, U.P. Wild, Orientation dependence of fluorescence lifetimes near an interface, J. Chem. Phys. **117**, 9430-9433 (2002)
711. M. Krieg, A.R. Dunn, and M.B. Goodman, Mechanical control of the sense of touch by β spectrin. Nat Cell Biol. March ; 16(3): 224–233 (2014)

712. I. S. Kritchenkov, A. I. Solomatina, D. O. Kozina, V. V. Porsev, V. V. Sokolov, M. V. Shirmanova, M. M. Lukina, A. D. Komarova, V. I. Shcheslavskiy, T. N. Belyaeva, I. K. Litvinov, A. V. Salova, E. S. Kornilova, D. V. Kachkin, S. P. Tunik, Biocompatible Ir(III) Complexes as Oxygen Sensors for Phosphorescence Lifetime Imaging. Molecules 26, 2898 1-22 (2021)
713. I. S. Kritchenkov, V. G. Mikhnevich, V. S. Stashchak, A. I. Solomatina , D. O. Kozina, V, V. Sokolov, S. P. Tunik, Novel NIR-Phosphorescent Ir(III) Complexes: Synthesis, Characterization and Their Exploration as Lifetime-Based O2 Sensors in Living Cells. Molecules 27, 3156 1-18 (2022)
714. M. Kröger, J. Scheffel, E. A. Shirshin, J. Schleusener, M. C. Meinke1, J. Lademann, M. Maurer, M. E. Darvin, Label-free imaging of M1 and M2 macrophage phenotypes in the human dermis in vivo using two-photon excited FLIM. eLife11, e72819, 1-23 (2022)
715. M. Kubánková, I. López-Duarte, J. A. Bull, D. M. Vadukul, L. C. Serpell, M. de Saint Victor, E. Stride, M. K. Kuimova, Probing supramolecular protein assembly using covalently attached fluorescent molecular rotors, Biomaterials 139, 195-201 (2017)
716. K.V. Kuchibhotla, C.R. Lattarulo, B. Hyman, B. J. Bacskai, Synchronous hyperactivity and intercellular calcium waves in astrocytes in Alzheimer mice. Science 323, 1211-1215 (2009)
717. J. Kuchlyan, N. Kundu, D. Banik, A. Roy, N. Sarkar, Spectroscopy and fluorescence lifetime imaging microscopy to probe the interaction of bovine serum albumin with graphene oxide. Langmuir 31, 13793-13801 (2015)
718. J. Kuchlyan, S. Basak, D. Dutta, A. Kumar Das, D. Mal a, N. Sarkar, A new rhodamine derived fluorescent sensor: Detection of Hg2+ at cellular level. Chem. Phys. Lett. 673, 84-88 (2017)
719. V. Kudryavtsev, S. Felekyan, A. K. Wozniak, M. König, C.Sandhagen, R.Kühnemuth, C. A. M. Seidel, F. Oesterhelt, Monitoring dynamic systems with multiparameter fluorescence imaging. Anal. Bioanal. Chem. 387, 71–82 (2007)
720. R. Kühnemuth, C.A.M. Seidel, Principles of single molecule multiparameter fluorescence spectroscopy, Single Molecules **2**, 251-254 (2001)
721. M. K. Kuimova, G. Yahioglu, J. A. Levitt, K. Suhling, Molecular Rotor Measures Viscosity of Live Cells via Fluorescence Lifetime Imaging. J. Am. Chem. Soc. 130, 6672–6673 (2008)
722. S. Kumar, C. Dunsby, P. A. A. De Beule, D. M. Owen, U. Anand, P. M. P. Lanigan, R. K. P. Benninger, D. M. Davis, M. A. A. Neil, P. Anand, C. Benham, A. Naylor, P. M. W. French, Multifocal multiphoton excitation and time correlated single photon counting detection for 3-D fluorescence lifetime imaging. Opt. Expr. 15, 12548-12561
723. H. Kume (ed.), Photomultiplier Tube, Hamamatsu Photonics K.K. (1994)
724. H. Kume, K. Koyama, N. Nakatsugawa, S. Suzuki, D. Fatlowitz, Ultrafast microchannel plate photomultipliers, App. Opt. **27**, 1170-1178 (1988)
725. K.T. Kumfer, S.J. Cook, J.M.Squirrell, K.W. Eliceiri, N. Peel, K.F. O'Connel, J.G. White, CGEF-1 and CHIN-1 regulate CDC-42 activity during asymmetric division in the Caenorhabditis elegans embryo. Molecular Biology of the Cell 21, 266-277 (2010)
726. N. Kundu, P. Banerjee, R. Dutta, S. Kundu, R. K. Saini, M. Halder, N. Sarkar, Proton Transfer Pathways of 2,2′-Bipyridine-3,3′-diol in pH Responsive Fatty Acid Self-Assemblies: Multiwavelength Fluorescence Lifetime Imaging in a Single Vesicle. Langmuir 2016, 32, 49, 13284–13295
727. H. Kurokawa, H. Ito, M. Inoue, K. Tabata, Y. Sato, K. Yamagata, S. Kizaka-Kondoh, T. Kadonosono, S. Yano, M. Inoue & T. Kamachi, High resolution imaging of intracellular oxygen concentration by phosphorescence lifetime, Scientific Reports **5**, 1-13 (2015)
728. C. Kurtsiefer, P. Zarda, S. Mayer, H. Weinfurter, The breakdown flash of Silicon Avalance Photodiodes – backdoor for eavesdropper attacks?, J. Mod. Opt. **48**, 2039-2047 (2001)
729. M. Kwaaitaal, N.F. Keinath, Simone Pajonk, C. Biskup, R. Panstruga, Combined Bimolecular Fluorescence Complementation and Förster Resonance Energy Transfer Reveals Ternary SNARE Complex Formation in Living Plant Cells. Plant Physiology 152, 1135-1147 (2010)
730. E.S. Kwak, T.J. Kang, A.A. Vanden Bout, Fluorescence lifetime imaging with near-field scanning optical microscopy, Anal. Chem. **73**, 3257-3262 (2001)
731. P.G. Kwiat, A.M. Steinberg, R.Y. Chiao, P.H. Eberhard, M.D. Petroff, Absolute efficiency and time-response measurement of single-photon detectors, Appl. Opt. **33**, 1844-1853 (1994)
732. Kwon S, Borrelli E, Fan W, Ebraheem A, Marion KM, Sadda SR. Repeatability of Fluorescence Lifetime Imaging Ophthalmoscopy in normal subjects with mydriasis. Trans Vis Sci Tech. 2019;8(3):15, https://doi.org/10.1167/tvst.8.3.15
733. A. Lacaita. S. Cova, M. Ghioni, Four-hundred-picosecond single-photon timing with commercially available avalanche photodiodes, Rev. Sci. Instrum. **59**, 1115-1121 (1988)
734. A. Lacaita. S. Cova, M. Ghioni, Single-photon avalanche diode with ultrafast response free of slow tails. IEEE Electr. Dev. Lett. 14, 360-362 (1993)
735. J. L. Lagarto, V. Shcheslavskiy, F. S. Pavone, R. Cicchi, Real-time fiber-based fluorescence lifetime imaging with synchronous external illumination: A new path for clinical translation. J. Biophotonics e201960119 (2019)

736. J. L. Lagarto, V. Shcheslavskiy, F. S. Pavone, R. Cicchi, Simultaneous fluorescence lifetime and Raman fiber-based mapping of tissues. Opt. Lett. 45, 2247-2250 (2020)
737. A. Laidevant, L. Herve, M. Debourdeau, J. Boutet, N. Grenier, J.-M. Dinten,Fluorescence time-resolved imaging system embedded in an ultrasound prostate probe. Biomed. Opt. Expr. 2, 194-206 (2011)
738. L.H. Laiho, T.M. Hancewicz, P.D. Kaplan, P.T.C. So, Two-photon 3-D mapping of ex-vivo human skin endogenous fluorescence species based on fluorescence emission spectra. J. Biomed. Opt. 10, 024016-1 to 10 (2005)
739. J.R. Lakowicz, I. Gryczynski, W. Wiczk, J. Kusba, M. Johnson, Correction for incomplete labeling in the measurement of distance distributions by frequency-domain fluorometry, Anal. Biochem. **195**, 243-254 (1991)
740. Lakowicz J.R., Szmacinski H., Johnson M.L., Calcium imaging using fluorescence lifetimes an long-wavelength probes. J. Fluoresc. 2, 47-62 (1992)
741. J.R. Lakowicz, H. Szmacinski, K. Nowaczyk, M.L. Johnson, Fluorescence lifetime imaging of free and protein-bound NADH, PNAS **89**, 1271-1275 (1992)
742. J.R. Lakowicz, Principles of Fluorescence Spectroscopy, 3rd edn., Springer (2006)
743. E. Lapointe, J. Pichette, and Y. Berube-Lauziere, A multi-view time-domain non-contact diffuse optical tomography scanner with dual wavelength detection for intrinsic and fluorescence small animal imaging. Rev. Sci. Instrum. 83, 063703-1 to -14 (2012)
744. P. H. Lakner, M. G. Monaghan. Y. Möller, M. A. Olayioye K. Schenke-Layland, Applying phasor approach analysis of multiphoton FLIM measurements to probe the metabolic activity of threedimensional in vitro cell culture models. Scientific Reports 7, 42730-1 to -11
745. G. S. Lakshmikanth, G. Krishnamoorthy, Solvent-exposed tryptophans probe the dynamics at protein surfaces. Biophys. J. 77, 1100-1106 (1999)
746. G. S. Lakshmikanth, K. Sridevi, G. Krishnamoorthy, J. B. Udgaonkar, Structure is lost incrementally during the unfolding of barstar. Nature Structural Biology, 8, 799-804 (2001)
747. D.C. Lamb, A. Schenk, C. Röcker, C. Scalfi-Happ, G.U. Nienhaus, sensitivity enhancement in fluorescence correlation spectroscopy of multiple species using time-gated detection, Biophys. J. 79, 1129-1138 (2000)
748. P. H. Lambrev, M. Nilkens, Y. Miloslavina, P. Jahns, A. R. Holzwarth, Kinetic and Spectral Resolution of Multiple Nonphotochemical Quenching Components in Arabidopsis Leaves. Plant Physiol. 152, 1611-1624 (2010)
749. M. Lampton, R. Raffanti, A high-speed wide dynamic range time-to-digital converter, Rev. Sci. Instrum. 65, 3577-3584 (1994)
750. R.A. La Rue, K.A. Costello, G.A. Davis, J.P. Edgecumbe, V.W. Aebi, Photon Counting III-V Hybrid Photomultipliers Using Transmission Mode Photocathodes. IEEE Transactions on Electron Devices 44, 672-678 (1997)
751. R.A. La Rue, G.A. Davis, D. Pudvay, K.A. Costello, V.W. Aebi, Photon Counting 1060-nm Hybrid Photomultiplier with High Quantum Efficiency, IEEE Electron Device Letters 20, 126-128 (1999)
752. J.R. Lazzari-Dean, A.M.M Gest, E.W. Miller, Optical estimation of absolute membrane potential using fluorescence lifetime imaging
753. A. Y. Lebedev, A. V. Cheprakov, S. Sakadzic, D. A. Boas, D. F. Wilson, Sergei A. Vinogradov, Dendritic Phosphorescent Probes for Oxygen Imaging in Biological Systems. Applied Materials & Interfaces 1, 1292-1304 (2009)
754. F. Leblond, H. Dehghani, D. Kepshire, B. W. Pogue, Early-photon fluorescence tomography: spatial resolution improvements and noise stability considerations, J. Opt. Soc. Am. A/ Vol. 26, 1444-1457 (2009)
755. S. Leistner, T. Sander-Thoemmes, H. Wabnitz, M. Moeller, M. Wachs, G. Curio, R. Macdonald, L. Trahms, and B.-M. Mackert, "Non-invasive simultaneous recording of neuronal and vascular signals in subacute ischemic stroke," Biomed. Tech. Eng. **56**(2), 85–90 (2011)
756. V. R. Leite-Silva, D. C. Liu1, W. Y. Sanchez, H. Studier, Y. H. Mohammed, A. Holmes, W. Becker, J. E. Grice, H. A.E. Benson, M. S. Roberts, Effect of flexing and massage on in vivo human skin penetration and toxicity of zinc oxide nanoparticles. Nanomedicine (Lond.) 11(10), 1193–1205 (2016)
757. V.R. Leite-Silva, W.Y. Sanchez, H. Studier, D.C. Liu, Y.H. Mohammed, A.M. Holmes, E.M. Ryan, I.N. Haridass, N.C. Chandrasekaran, W. Becker, J.E. Grice, H.A.E. Benson, M.S. Roberts, Human skin penetration and local effects of topical nano zinc oxide after occlusion and barrier impairment. European Journal of Pharmaceutics and Biopharmaceutics 104, 140-147 (2016)
758. J. Leppert, J. Krajewski, S.R. Kantelhardt, S. Schlaffer, N. Petkus, E. Reusche, G. Hüttmann, A. Giese, Multiphoton excitation of autofluorescence for microscopy of glioma tissue. Neurosurgery 58, 759-767 (2006)
759. B. Leskovar, C.C. Lo, Photon counting system for subnanosecond fluorescence lifetime measurements, Rev. Sci. Instrum. **47**, 1113-1121 (1976)

760. B. Leskovar, Nanosecond Fluorescence Spectroscopy, IEEE Transactions on Nuclear Science, **NS-32**, 1232-1241 (1985)
761. M. D. Lesoine, S. Bose, J. W. Petrich, E. A. Smith,Supercontinuum Stimulated Emission Depletion Fluorescence Lifetime Imaging. J. Phy. Chem. B, 116, 7821-7826 (2012)
762. R. W. K. Leung, S.-C. A. Yeh, Q. Fang, Effects of incomplete decay in fluorescence lifetime estimation. Biomed. Opt. Expr. 2, 2517-2531
763. J. A. Levitt, M. K. Kuimova, G. Yahioglu, P.-H. Chung, K. Suhling, D. Phillips, Membrane-Bound Molecular Rotors Measure Viscosity in Live Cells via Fluorescence Lifetime Imaging. J. Phys. Chem. C 2009, 113, 11634–11642
764. J. B. Lincke, C Dysli, D Jaggi, R Fink, S. Wolf, M. S. Zinkernagel, The Influence of Cataract on Fluorescence Lifetime Imaging Ophthalmoscopy (FLIO). Transl Vis Sci Technol 10(4), 33, 1-10 (2021)
765. D. J. Liput, T. A. Nguyen, S. M. Augustin, J. O. Lee, S. S. Vogel, Microscopy and Förster's Resonance Energy Transfer in Neuroscience. Current Protocols in Neuroscience, 94, e108, 1-40 (2020)
766. James A Levitt, Daniel R Matthews, Simon M Ameer-Beg, Klaus Suhling, Fluorescence lifetime and polarization-resolved imaging in cell biology. Current Opinion in Biotechnology 20, 28–36 (2009)
767. J. A. Levitt, P.-H. Chung, K. Suhling, Spectrally resolved fluorescence lifetime imaging of Nile red for measurements of intracellular polarity. J. Biomed. Opt. 20(9), 096002-1 to -11 (2015)
768. C. Lewis, W.R. Ware, The Measurement of Short-Lived Fluorescence Decay Using the Single Photon Counting Method, Rev. Sci. Instrum. **44**, 107-114 (1973)
769. L-Q. Li, L.M. Davis, Single photon avalanche diode for single molecule detection, Rev. Sci. Instrum. **64**, 1524-1529 (1993)
770. Q. Li, S. Seeger, Label-free detection of protein interactions using deep UV fluorescence lifetime microscopy. Anl. Biochem. 367 104-110 (2007)
771. D. Li, W. Zheng, .J. Y. Qu, Time-resolved spectroscopic imaging reveals the fundamentals of cellular NADH fluorescence. Opt. Lett. 33, 2365-2367 (2008)
772. D. Li, M.S. Yang, W. Zheng, J.Y. Qu, Study of cadmium-induced cytotoxicity using two-photon excitation endogenous fluorescence microscopy. J. Biomed. Opt. 14(5), 054028-1 to -8 (2009)
773. D. Li, W. Zheng, .J. Y. Qu, Two-photon autofluorescence microscopy of multicolor excitation. Opt. Lett. 34, 202-204 (2009)
774. D. Li, W. Zheng, .J. Y. Qu, Imaging of epithelial tissue in vivo based on excitation of multiple endogenous nonlinear optical signals. Lett. 34, 2853-2855 (2009)
775. D. Li, W. Zheng, Y. Zeng, and J. Y. Qu, In vivo and simultaneous multimodal imaging: Integrated multiplex coherent anti-Stokes Raman scattering and two-photon microscopy. Appl. Phys. Lett 97, 223702-1 to -3 (2010)
776. D. Li, W. Zheng, Y. Zeng, Y. Luo, J. Y. Qu, Two-photon excited hemoglobin fluorescence provides contrast mechanism for label-free imaging of microvasculature in vivo. Opt. Lett. 36, 834-836 (2011)
777. D. Li, W. Zheng, W. Zhang, S. Khoon Teh, Y. Zeng, Y. Luo, J. Y. Qu, Time-resolved detection enables standard two-photon fluorescence microscopy for in vivo label-free imaging of microvasculature in tissue. Opt. Lett. 36, 2638-2640 (2011)
778. J. Li, A.V. Krasavin, L. Webster, P. Egovia, A.V. Zayats, D. Richards, Spectral variation of fluorescence lifetime near single metal nanoparticles. Scientific Reports 6, 21349-1 to -9 (2016)
779. G. Liaugaudas, A.T. Collins, K. Suhling, G. Davies, R. Heitzmann, Luminescence-lifetime mapping in diamond. J. Phys. Condens. Matter 21, 364210-1 to -7 (2009)
780. G. Liaugaudas, G. Davies, K. Suhling, R. U. A. Khan, D. J. F. Evans, Luminescence lifetimes of neutral nitrogen-vacancy centres in synthetic diamond containing nitrogen. J. Phys.: Condens. Matter 24, 435503-7 (2012)
781. A Liebert, H. Wabnitz, J. Steinbrink, H. Obrig, M. Möller, R. Macdonald, H. Rinneberg, Intra- and extracerebral changes of hemoglobin concentrations by analysis of moments of distributions of times of flight of photons, Proc. SPIE **5138**, 126-130 (2003)
782. A. Liebert, H. Wabnitz, D. Grosenick, M. Möller, R.Macdonald, H. Rinneberg, Evaluation of optical properties of highly scattering media by moments of distributions of times of flight of photons, Appl. Opt. **42**, 5785-5792 (2003)
783. A. Liebert, H. Wabnitz, D. Grosenick, R. Macdonald, Fiber dispersion in time domain measurements compromising the accuracy of determination of optical properties of strongly scattering media, J. Biomed. Opt. **8**, 512-516 (2003).
784. A. Liebert, H. Wabnitz, M. Möller, A. Walter, R. Macdonald, H. Rinneberg, H. Obrig, I. Steinbrink, Time-resolved diffuse NIR-reflectance topography of the adult head during motor stimulation, In OSA Biomedical Optics Topical Meetings on CD ROM (The Optical Sciety of America, Washington, DC) WF34 (2004)
785. A. Liebert, H. Wabnitz, J. Steinbrink, H. Obrig, M. Möller, R. Macdonald, A. Villringer, H. Rinneberg, Time-resolved multidistance near-infrared spectroscopy at the human head: Intra- and extracerebral

absorption changes from moments of distribution of times of flight of photons, Appl. Opt. **43**, 3037-3047 (2004)
786. A. Liebert, H. Wabnitz, J. Steinbrink, M. Möller, R. Macdonald, H. Rinneberg, A. Villringer, H. Obrig, Bed-side assessment of cerebral perfusion in stroke patients based on optical monitoring of a dye bolus by time-resolved diffuse reflectance, NeuroImage **24**, 426-435 (2005)
787. A. Liebert, H. Wabnitz, H. Obrig, R. Erdmann, M. Möller, R. Macdonald, H. Rinneberg, A. Villringer, J. Steinbrink, Non-invasive detection of fluorescence from exogenous chromophores in the adult human brain, NeuroImage 31, 600-608 (2006)
788. A. Liebert, P. Sawosz, D. Milej, M. Kacprzak, W. Weigl, M. Botwicz, J. Maczewska, K. Fronczewska, E. Mayzner-Zawadzka, L. Krolicki, R. Maniewski, Assessment of inflow and washout of indocyanine green in the adult human brain by monitoring of diffuse reflectance at large source-detector separation. J. Biomed. Opt. 16(4), 046011-1 to -7 (2011)
789. A. Liebert, M. Kacprzak, D. Milej, W. Becker, A. Gerega, P. Sawosz, R. Maniewski, Dynamic Mapping of the Human Brain by Time-Resolved NIRS Techniques. In: W. Becker (ed.) Advanced time-correlated single photon counting applications. Springer, Berlin, Heidelberg, New York (2015)
790. L.L. Lin, J. E. Grice, M.K. Butler, A.V. Zvyagin, W. Becker, T. A. Robertson, H.P. Soyer, M. S. Roberts, T.W. Prow, Time-correlated single photon counting for simultaneous monitoring of zinc oxide nanoparticles and NAD(P)H in intact and barrier-disrupted volunteer skin. Pharm Res. DOI 10.1007/s11095-011-0515-5 (2011)
791. H. Lin, F. I. Kuzminov, J. Park, S.H. Lee, P. G. Falkowski, M. Y. Gorbunov,The fate of photons absorbed by phytoplankton in the global ocean. Science 351, 264-267 (2016)
792. Y. Liu, S. Walter, M. Stagi, D. Cherny, M. Letiembre. W. Schulz-Schaeffer, H. Heine, B. Penke, H. Neumann, K. Fassbender, LPS receptor (CD 4): a receptor for phagocytosis of Alzheimer's amyliod peptide. Brain 28, 778-789 (2005)
793. Z. Liu, D. Pouli, C. A. Alonzo, A. Varone, S. Karaliota, K. P. Quinn, K. Münger, K. P. Karalis, I. Georgakoudi, Mapping metabolic changes by noninvasive, multiparametric, high-resolution imaging using endogenous contrast. Sci. Adv. 4, eaap9302 (20018)
794. X. Liu, D. Lin, W. Becker, J. Niu, B. Yu, L. Liu, J. Qu, Fast fluorescence lifetime imaging techniques: A review on challenge and development. Journal of Innovative Optical Health Sciences, 1930003-1 to -27 (2019)
795. A. Lleo, O. Berezovska, L. Herl, S. Raju, A. Deng, B.J. Bacskai, M.P. Frosch, M. Irizarry, B.T. Hyman, Nonsteroidal anti-inflammatory drugs lower Aβ42 and change presenilin 1 conformation, Nature Medicine 10, 1065-1066 (2004)
796. D. Lleres, S. Swift, A. I. Lamond, Detecting Protein-Protein Interactions In Vivo with FRET using Multiphoton Fluorescence Lifetime Imaging Microscopy (FLIM). Curr. Protoc. Cytom. 42, 12.10.1-12.10.19 (2007)
797. D. Lleres, J. James, S. Swift, D.G. Norman, A. I. Lamond, Quantitative analysis of chromatin compaction in living cells using FLIM-FRET. J. Cell Biol. 187, 481-191 (2009)
798. D. Lleres, A. P. Bailly A. Perrin, D. G. Norman, D. P. Xirodimas, R. Feil, Quantitative FLIM-FRET Microscopy to Monitor Nanoscale Chromatin Compaction In Vivo Reveals Structural Roles of Condensin Complexes. Cell Reports 18, 1791-1803 (2017)
799. N. Lois, J.V. Forrester, eds., Fundus autofluorescence. Wolters Kluwer, Lippincott Willams & Wilkins (2009)
800. Y. Lu, W. Zhang, L. Wu, L. Zhang, F. Gao, A time-domain optical-fluorescent tomography using multi-dimensional TCSPC design. Proc. SPIE 8572, 85721I-1 to -7
801. M. Lukina, A. Orlova, M. Shirmanova, D. Shirokov, A. Pavlikov, A. Neubauer, H. Studier, W. Becker, E. Zagaynova, T. Yoshihara, S. Tobita, V. Shcheslavskiy, Interrogation of metabolic and oxygen states of tumors with fiber-based luminescence lifetime spectroscopy. Optics Letters 42(4) 731-734 (2017)
802. M. M. Lukina, V. V. Dudenkova, N. I. Ignatovaa, I. N. Druzhkova, L. E. Shimolina, E. V. Zagaynovaa, M. V. Shirmanova, Metabolic cofactors NAD(P)H and FAD as potential indicators of cancer cell response to chemotherapy with paclitaxel. BBA – General Subjects 1862, 1693-1700 (2018)
803. M. M. Lukina, L. E. Shimolina, N. M. Kiselev, V. E. Zagainov, D. V. Komarov, E. V. Zagaynova, M. V. Shirmanova, Interrogation of tumor metabolism in tissue samples ex vivo using fluorescence lifetime imaging of NAD(P)H. Methods Appl. Fluoresc. 8, 014002, 1-11 (2020)
804. M. Lukina, K. Yashin, E. E. Kiseleva, A. Alekseeva, Varvara Dudenkova, E. V. Zagaynova, E. Bederina, I. Medyanic, W. Becker, D. Mishra, M. Berezin, V. I. Shcheslavskiy, M. Shirmanova, Label-Free Macroscopic Fluorescence Lifetime Imaging of Brain Tumors. Frontiers in Oncology 11, 666059, 1-11 (2021)
805. W. Ma, W. Zhang, J. Li, L. Wu, X. Wang, L. Zhang, Z. Zhou H. Zhao, F. Gao, Time-domain fluorescence-guided diffuse optical tomography based on the third-order simplified harmonics approximation. Appl. Opt. 51(36), 8656-8668 (2012)

806. K. Määttä, J. Kostamovaara, A high precision time-to-digital converter for pulsed time-of-flight laser radar applications, IEEE Transactions on Instrumentation and Measurement 47, 521-536 (1998)
807. B.-M. Mackert, S. Leistner,T. Sander, A. Liebert, H. Wabnitz, M. Burghoff, L. Trahms, R. Macdonald, G. Curio, Dynamics of cortical neurovascular coupling analyzed by simultaneous DC-magnetoencephalography and time-resolved near-infrared spectroscopy. NeuroImage 39, 979-986 (2008)
808. S. Mackowski, I. Kaminska, Energy Transfer in Graphene-Based Hybrid Photosynthetic Nanostructures. In: Recent advances in graphene research, http://dx.doi.org/10.5772/64300
809. D. Magde, E. Elson, W.W.W. Webb, Thermodynamic fluctuations ina reacting system - measurement by fluorescence correlation spectroscopy, Phys. Rev. Lett. **29**, 705-708 (1972)
810. K. Magnusson, R. Simon, D. Sjölander, C. J Sigurdson, P. Hammarström, K. P. R. Nilsson, Multimodal fluorescence microscopy of prion strain specific PrP deposits stained by thiophene-based amyloid ligands. Prion 8, Iss. 4 (2014)
811. P. Majumder, Th. S. Blacker, L. S. Nolan, M. R. Duchen, J.n E. Gale, Multiphoton NAD(P)H FLIM reveals metabolic changes in individual cell types of the intact cochlea upon sensorineural hearing loss. Scientific Reports 9, 18907 (2019)
812. K. Makrogianneli, L. M. Carlin, M. D. Keppler, D. R. Matthews, E. Ofo, A. Coolen, S. M. Ameer-Beg, P. R. Barber, B. Vojnovic, T. Ng, Integrating Receptor Signal Inputs That Influence Small Rho GTPase Activation Dynamics at the Immunological Synapse. Mol. Cell. Biol. 29, 2997–3006 (2009)
813. M. Malak, J. James, J. Grantham, M. B. Ericson, Contribution of autofluorescence from intracellular proteins in multiphoton fluorescence lifetime imaging. Scientific Reports 12, 16584 (2022)
814. J. Malicka, I. Gryczynski, C.D. Geddes, J.R. Lakowicz, Metal-enhanced emission from indocyanine green: a new approach to in vivo imaging, J. Biomed. Opt. **8**, 472-478 (2003)
815. M. Manfredini, F. Arginelli, C. Dunsby, P. French, C. Talbot, K. König, G. Pellacani, G. Ponti, S. Seidenari, High-resolution imaging of basal cell carcinoma: a comparison between multiphoton microscopy with fluorescence lifetime imaging and reflectance confocal microscopy. Skin Res. Tech. 19 e433-e443 (2013)
816. C. Mangavel, R. Maget-Dana, P. Tauc, J-C. Brochon, D. Sy, J.A. Reynaud, Structural investigations of basic amphipatic model peptides in the presence of lipid vesicles studied by circular dichroism, fluorescence, monolayer and modeling, Biochimica et Biophysica Acta **1371**, 265-283 (1998)
817. S. E. Mangion, L.Sandiford, Y.Mohammed, M.S. Roberts, A.M. Holmes, Multi-Modal Imaging to Assess the Follicular Delivery of Zinc Pyrithione. Pharmaceutics 14, 1076 1-14, 2022
818. A. K. Mandal, J. Skoch, B. J. Bacskai, B. T. Hyman, P. Christmas, D. Miller, T. D. Yamin, S. Xu, D. Wisniewski, J. F. Evans, and R. J. Soberman, The membrane organization of leukotriene synthesis. PNAS 101, 6587-6592 (2004)
819. J. J. Mancuso, A. M. Larson, T. G. Wensel, P. Saggau, Multiphoton adaptation of a commercial low-cost confocal microscope for live tissue imaging, J. Biomed. Opt. 14(3), 034048 (2009)
820. H.B. Manning, G.T. Kennedy, D.M. Owen, D.M. Grant, A.I. Magee, M.A.A. Neil, Y. Itoh, C. Dunsby, P.M.W. French, A compact, multidimensional spectrofluorometer exploiting supercontinuum generation. J. Biophoton 1, 494-505 (2008)
821. K. Mapa, S. Tiwari, V. Kumar, G.G.Jayarai, S. Maiti, Information encoded in non-native states drives substrate-chaperone pairing. Structure 20, 1562-2573 (2012)
822. A. Marcek Chorvatova, Time-Resolved Spectroscopy of NAD(P)H in Live Cardiac Myocytes. In: W. Becker (ed.) Advanced time-correlated single photon counting applications. Springer, Berlin, Heidelberg, New York (2015)
823. A. Marcek Chorvatova, M. Uherek, A. Mateasik, D. Chorvat Jr, Time-resolved endogenous chlorophyll fluorescence sensitivity to pH: study on Chlorella sp. algae. Methods Appl. Fluoresc. 8 024007 (2020)
824. M. L. Martin-Fernandez, Human epidermal growth factor receptor (HER1) aligned on the plasma membrane adopts key features of *Drosophila* EGFR asymmetry, Biochemical Society Transactions 40, 184–188, (2012)
825. J.S. Massa, G.S. Buller, A.C. Walker, S. Cova, M. Umasuthan, A.M. Wallace, Time-of-flight optical ranging system based on time-correlated single photon counting, Appl. Opt. **37**, 7298-7304 (1998)
826. J.S. Massa, G.S. Buller, A.C. Walker, G. Smith, S. Cova, M. Umasuthan, A.M. Wallace, Optical design and evaluation of a three-dimensional imaging and ranging system based on time-correlated single-photon counting, Appl. Opt. **41**, 1070-1063 (2002)
827. B. R. Masters, P.T.C. So, E. Gratton, Multiphoton excitation fluorescence microscopy and spectroscopy of in vivo human skin. Biophys. J. 72, 2405-2412
828. B. R. Masters, P.T.C. So, Multi-photon excitation microscopy and confocal microscopy imaging of in vivo human skin: A comparison. Microscopy and Microsnalysis 5, 282-289 (1999)
829. B. R. Masters (ed.), Selected papers on multiphoton excitation microscopy. SPIE Milestone Series MS 175, SPIE 2003

830. B. R. Masters, Confocal Microscopy and multiphoton excitation microscopy. The genesis of live cell imaging. SPIE Press (2006)
831. B.R. Masters, P.T.C. So, eds., Handbook of Biomedical Nonlinear Optical Microscopy.Oxford University Press 2008
832. S. Mattana, A. Dal Fovo, J. L. Lagarto, M. C. Bossuto, V. Shcheslavskiy, R. Fontana, R. Cicchi, Automated Phasor Segmentation of Fluorescence Lifetime Imaging Data for Discriminating Pigments and Binders Used in Artworks. Molecules 27, 1475 1-11 (2022)
833. E. G. Maksimov, E. A. Protasova, G. V. Tsoraev, I. A. Yaroshevich, A. I. Maydykovskiy, E. A. Shirshin, T. S. Gostev, A. Jelzow, M. Moldenhauer, Y. B. Slonimskiy, N.i N. Sluchanko, Th. Friedrich, Probing of carotenoid-tryptophan hydrogen bonding dynamics in the single-tryptophan photoactive Orange Carotenoid Protein. Scientific Reports 10, 11729 (2020)
834. K. Maxwell, G.N. Johnson, Chlorophyll fluorescence - a practical guide, Journal of Experimental Botany **51**, 659-668 (2000)
835. M. Mazurenka, A. Jelzow, H. Wabnitz, D. Contini, L. Spinelli, A. Pifferi, R. Cubeddu, A. Dalla Mora, A. Tosi, F. Zappa, R. Macdonald, Non-contact time-resolved diffuse reflectance imaging at null source-detector separation. Opt. Expr. 20, 283-290 (2012)
836. M. Mazurenka, L. Di Sieno, G. Boso, D. Contini, A. Pifferi, A. Dalla Mora, A. Tosi, H. Wabnitz, R. Macdonald, Non-contact in vivo diffuse optical imaging using a time-gated scanning system, Biomed. Opt. Express 4(10), 2257–2268 (2013)
837. T. Maoka, Carotenoids as natural functional pigments. Journal of Natural Medicines 74:1-16 (2020)
838. G. McConnel, Confocal laser scanning fluorescence microscopy with a visible continuum source. Op. Expr. 13, 2844-2850 (2004)
839. G. McConnel, J.M. Girkin , S.M. Ameer-Beg, P. R. Barber, B. Vojnovic,T. Ng, A.Banerjee, T. F. Watson, R.J.Cook, Time-correlated single-photon counting fluorescence lifetime confocal imaging of decayed and sound dental structures with a white-light supercontinuum source. J. Microsc. 225, 126-136 (2007)
840. T.O. McBride, B.W. Pogue, E.D. Gerety, S.B. Poplack, U.L. Österberg, K.D. Paulsen, Spectroscopic diffuse optical tomography for the quantitative assessment of hemoglobin concentration and oxygen saturation in breast tissue, Appl. Opt. **38**, 5480-5490 (1999)
841. I. J. McNeil, D. L. Ashford, H. Luo, C. J. Fecko, Power-Law Kinetics in the Photoluminescence of Dye-Sensitized Nanoparticle Films: Implications for Electron Injection and Charge Transport. J. Phys. Chem. 116, 15888-15899 (2012)
842. R. McQueenie, J. Sutter, J. Karolin, D. J. S. Birch, Eumelanin fibrils. J. Biomed. Opt. 17(7), 075001-1 to -7 (2012)
843. D. X. Medina, A. Caccamo, S. Oddo, Methylene blue reduces Aβ levels and rescues early cognitive deficit by increasing proteasome activity. Brain Pathol. 21, 140–149 (2011)
844. C.N. Medine, A. McDonald, A, Bergmann, R. Duncan, Time-correlated single photon counting FLIM: Some considerations for Physiologists. Micr. Res. Tech. 70, 421-425 (2007)
845. I.L. Medintz, T. Pons, K. Susumu, K. Boeneman, A.M. Dennis, D. Farrel, J.R.Deschamps, J.S. Melinger, G. Bao, H. Mattoussi, Resonance energy trensfer between luminescent quantum dots and diverse fluorescent protein acceptors. J. Phy. Chem. C 113, 18552-18560 (2009)
846. I. L. Medintz, M. H. Stewart, S. A. Trammell, K. Susumu, J. B. Delehanty, B. C. Mei, J. S. Melinger, J. B. Blanco-Canosa, P. E. Dawson, H. Mattoussi, Quantum-dot/dopamine bioconjugates functionas redox coupled assemblies for in vitro and intracellular pH sensing. Natrure Materials, 9, 676-684 (2010)
847. W. Meiling, F. Stary, Nanosecond pulse techniques, Akademie-Verlag, Berlin (1963)
848. E.C. Meister, U.P. Wild, P. Klein-Bölting, A.R. Holzwarth, Time response of small side-on photomultiplier tubes in time-correlated single-photon counting measurements, Rev. Sci. Instrum. **59**, 499-501 (1988)
849. A. V. Meleshina, V. V. Dudenkova, M. V. Shirmanova, V. I. Shcheslavskiy, W. Becker, A. S. Bystrova, E.a I. Cherkasova, E. V. Zagaynova, Probing metabolic states of differentiating stem cells using two-photon FLIM. Scientific Reports 6, 21853-1 to 11 (2016)
850. A. V. Meleshina, V. V. Dudenkova, A. S. Bystrova, D. S. Kuznetsova, M. V. Shirmanova, E. V. Zagaynova, Two-photon FLIM of NAD(P)H and FAD in mesenchymal stem cells undergoing either osteogenic or chondrogenic differentiation. Stem Cell Research & Therapy 8, 15-1 to -10 (2017)
851. J.S. Melinger, L.D. Davis, D. McMorrow, Y. Pan, Z. Peng, Photoluminescence properties of conjugated phenylacetylene monodendrons in thin films, J. Fluoresc. 105-112 (2004)
852. R. Mercadé-Prieto, L. Rodriguez-Rivera, X. D. Chen, Fluorescence lifetime of Rhodamine B in aqueous solutions of polysaccharides and proteins as a function of viscosity and temperature. Photochem. Photobiol. Sci., 16, 1727–1734 (2017)

853. P. Mergenthaler, A. Kahl, A. Kamitz, V. van Laak, K. Stohlmann, Susanne Thomsen, H. Klawitter, I. Przesdzing, Lars Neeb, D Freyer, J Priller, T J. Collins, D. Megow, U. Dirnagl, D. W. Andrews, A. Meisel, Mitochondrial hexokinase II (HKII) and phosphoprotein enriched in astrocytes (PEA15) form a molecular switch governing cellular fate depending on the metabolic state. PNAS 109, 1518-1523
854. J. Meyer, V. Untiet, C. Fahlke, T. Gensch, C.R. Rose, Quantitative determination of cellular [Na^+] by fluorescence lifetime imaging with CoroNaGreen. *Journal of General Physiology*, 151, 1319–1331 (2019)
855. X. Michalet, A. Cheng, J. Antelman, Motohiro Suyama, Katsuhiro Arisaka, Shimon Weiss, Hybrid photodetector for single-molecule spectroscopy and microscopy. Proc. SPIE 6862 (2007)
856. P. Michler, A. Imamoglu, M.D. Mason, P.J. Carson, G.F. Strouse, S.K. Buratto, Quantum correlation among photons from a single quantum dot at room temperature, Nature **406**, 968-970 (2000)
857. M. Micic, D. Hu, Y.D. Suh, G. Newton, M. Romine, H.P. Lu, Correlated atomic force microscopy and fluorescence lifetime imaging of live bacterial cells, Colloids and Surfaces B, Biointerfaces **34**, 205-212 (2004)
858. Micro Photon Devices, PDM Series photon counting modules, www.micro-photon-devices.com
859. K.D. Mielenz, E.D. Cehelink, R.L. McKenzie, Elimination of polarization bias in fluorescence intensity measurements, J. Chem. Phys. **62**, 370-374 (1976)
860. F. Mies, C. Spriet, L. Heliot, S. Sariban-Sohraby, Epithelial Na+ channel stimulation by n-3 fatty acids requires proximity to a membrane-bound A-kinase-anchoring protein complexed with protein kinase A and phosphodiestrase. J. Biol. Chem. 282 18339-18347 (2007)
861. A. Migdall, Absolute quantum efficiency measurements using correlated photons: Toward a measurement protocol, IEEE Trans. on Instrumentation and Measurement **50**, 478-481 (2001)
862. A. Migdall, S. Castelletto, I.P. Degiovanni, M.L. Rastello, Intercomparison of a correlated-photon-based method to measure detector quantum efficiency, Appl. Opt. **41**, 2914-2922 (2002)
863. A.L. Migdall, R.U. Datla, A. Sergienko, J.S. Orszak, Y.H. Shih, Absolute detector quantum-efficiency measurements using correlated photons, Metrologia **32**, 479-483 (1995)
864. E. G. Mik, J. Stap, M. Sinaasappel, J.F. Beek, J.A. Aten, T.G. van Leeuwen, C. Ince, Mitochondrial PO2 measured by delayed fluorescence of endogenous protoporphyrin IX. Nature Methods 11, 939-945 (2006)
865. E. G. Mik, T Johannes, C. J. Zuurbier, A. Heinen, J. H. P. M. Houben-Weerts, G. M. Balestra, Jan Stap, J. F. Beek, Can Ince, In Vivo Mitochondrial Oxygen Tension Measured by a Delayed Fluorescence Lifetime Technique. Biophys. J. 95, 3977-3990 (2008)
866. J. Mik. A. J. Thompson, M. R. Dent, J. Hofkens and M. K. Kuimova, Measuring the viscosity of the Escherichia coli plasma membrane using molecular rotors, Biophys J 111, 1529-1540 (2016)
867. A.J. Miller, S.W. Nam, J.M. Martinis, Demonstration of a low-noise near-infrared photon counter with multiphoton discrimination, Appl. Phys. Lett. **83**, 791-793 (2003)
868. E.W. Miller, J.Y. Lin, E.P. Frady, P.A. Steinbach, W.B. Kristan, R. Y. Tsien, Optically monitoring voltage in neurons by photo-induced electron transfer through molecular wires. PNAS 109 (6), 2114-2119 (2012)
869. R. C. Miller, C. P. Aplin, T. M. Kay, R. Leighton, C. Libal, R. Simonet, A. Cembran, A. A. Heikal, A. J. Boersma, E. D. Sheets, FRET Analysis of Ionic Strength Sensors in the Hofmeister Series of Salt Solutions Using Fluorescence Lifetime Measurements. J. Phys. Chem. B 124, 3447−3458 (2020)
870. D. Milej, M. Kacprzak, N. Zolek, P.Sawosz, A. Gerega, R. Maniewski, A. Liebert, Advantages of fluorescence over diffuse reflectance measurements tested in phantom experiments with dynamic inflow of ICG, Opto-Electron. Rev. 18(2) 208-213 (2010)
871. D. Milej, A. Gerega, N. Zolek , W. Weigl, M. Kacprzak, P. Sawosz , J. Maczewska, K. Fronczewska, E. Mayzner-Zawadzka, L. Krolicki, R. Maniewski, A. Liebert,Time-resolved detection of fluorescent light during inflow of ICG to the brain - a methodological study. Phys. Med. Biol. 57, 6725-6742 (2012)
872. Y. Miloslavina, I. Grouneva, P. H. Lambrev, B. Lepetit, R. Goss, C. Wilhelm, A R. Holzwarth, Ultrafast fluorescence study on the location and mechanism of non-photochemical quenching in diatoms. Biochim. Biophys. Acta 1787, 1189-1197 (2009)
873. W. Min, G. Luo, B. J. Cherayil, S.C. Kou, X.S. Xie, Observation of a power-law memory kernel for fluctuations within a single protein molecule. Phys. Chem. Lett. 94 198302 (2005)
874. M. Minsky, US Patent 3013467, (1957)
875. M. Minsky, Memoir on inventing the confocal microscope, Scanning **10**, 128-138 (1988)
876. A. Minta, J.P.Y. Kao, R.Y. Tsien, Fluorescent indicators for cytosolic calcium based on rhodamine and fluorescein chromophores, J. Biol. Chem. 264, 8171-8178 (1989)
877. S. Miserey-Lenkei, F. Waharte, A. Boulet, M.-H. Cuif, D. Tenza, A. El Marjou, G. Raposo, J. Salamero, L. Heliot, B. Goud, S. Monier, Rab6-interacting protein 1 links Rab6 and Rab 11 function. Traffic 8, 1385-1403 (2007)

878. Y. Miura, G. Hüttmann, R. Orzekowsky-Schroeder, P. Steven, M. Szszak, N. Koop, R. Brinkmann, Two-photon microscopy and fluorescence lifetime imaging of retinal pigment epithel cells under oxydative stress. Invest Ophthalmol Vis Sci, IOVS 54, 3366-3377 (2013)
879. Y. Miura, B. Lewke, A. Hutfilz, R. Brinkmann. Change in Fluorescence Lifetime of Retinal Pigment Epithelium under Oxidative Stress. Nippon Ganka Gakkai Zasshi (J Jpn Ophthalmol Soc) 123, 105-114 (2019)
880. K. Miyashita, S. Kuroda, S. Tajima, K. Takehira, S. Tobita, H. Kubota, Photoluminescence Study of Electron-Hole Recombination Dynamics in the Vacuum-Deposited SiO2/TiO2 Multilayer Film with Photo-Catalytic Activity, Chem. Phys. Lett. **369**, 225-231 (2003)
881. K. Mizukami, A. Katano, S. Shiozaki, T. Yoshihara, N. Goda, S. Tobita, In vivo O2 imaging in hepatic tissues by phosphorescence lifetime imaging microscopy using Ir(III) complexes as intracellular probes. Scientific Reports 10, 21053, 1- 14 (2020)
882. J. Mobley, T. Vo-Dinh, Optical properties of tissue, in T. Vo-Dinh (ed.) Biomedical Photonics Handbook, CRC Press, 53-1 to 53-48 (2003)
883. Y. H. Mohammed, A. Holmes, I. N. Haridass, W. Y. Sanchez, H. Studier, J. E. Grice, H.A.E. Benson, M. S. Roberts, Support for the Safe Use of Zinc Oxide Nanoparticle Sunscreens: Lack of Skin Penetration or Cellular Toxicity after Repeated Application in Volunteers. J. Invest. Dermatol. 139, 308-315 (2019)
884. E. Molteni, D. Contini, M.o Caffini, G. Baselli, L. Spinelli, R. Cubeddu, S. Cerutti, A. M. Bianchi, A. Torricelli, Load-dependent brain activation assessed by time-domain functional near-infrared spectroscopy during a working memory task with graded levels of difficulty. J. Biomed. Opt. 17(5) 056005-1 to -11 (2012)
885. E. Molteni, H. Wabnitz, A. M. Bianchi, O. Steinkellner, T. Sander-Thoemmes, F. Geisler, B.-M. Mackert, S. Leistner, and S. Cerutti, GLM analysis of time resolved NIRS data of motor activation during different motor tasks, Conf. Proc. Annu. Int. Conf. IEEE Eng. Med. Biol. Soc. IEEE Eng. Med. Biol. Soc. Annu. Conf. 2013, 1787–1790 (2013)
886. K. Molugu, G. A. Battistini, T. M. Heaster, J. Rouw, E. C. Guzman, M. C. Skala, K. Saha, Label-Free Imaging to Track Reprogramming of Human Somatic Cells. GEN Biotechnology, 1, No.2, 176-191 (2022
887. S. Mordon, J.M. Devoisselle, S. Soulie-Begu, Indocyanine Green: Physicochemical Factors Affecting Its Fluorescence in Vivo, Microvascular Research **55**, 146 (1998)
888. T. T. Morgan, H. S. Muddana, E. I. Altnoglu, S. M. Rouse, A. Tabakovic, T. Tabouillot, T. J. Russin, S. S. Shanmugavelandy, P. J. Butler, P. C. Eklund, J. K. Yun, M. Kester, J. H. Adair, Encapsulation of Organic Molecules in Calcium Phosphate Nanocomposite Particles for Intracellular Imaging and Drug Delivery. Nano Lett. 8, 4108-4115 (2008)
889. M. P. Mori, R. Penjweini, J. Ma, G.g Alspaugh, A. Andreoni, Y.-C. Kim, P.-Y. Wang, J. R. Knutson , P. M. Hwang, Mitochondrial respiration reduces exposure of the nucleus to oxygen. Redox Biol. 34, 101549, 1-10 (2020)
890. P. Morozov, M. Lukina, M. Shirmanova, A. Divochiy, G. Goltsman,W. Becker, V. Shcheslavskiy, Singlet oxygen phosphorescence imaging by superconducting single photon detector and time-correlated single photon counting.Opt. Lett. 46, No. 4, 1217-1220 (2021)
891. P.E. Morton, T.C. Ng, S.A. Roberts, B. Vojnovic, S.M. Ameer-Beg, Time resolved multiphoton imaging of the interaction between the PKC and NFkB signalling pathways, Proc. SPIE 5139, 216-222 (2003)
892. Y. Mu, M. Niedre, Fast single-photon avalanche photodiode-based time-resolved diffuse optical tomography scanner. Biomed. Opt. Express 6, 3569-3609 (2015)
893. Y. Mu, V. Pera, M. Niedre, Multiplexed fluorescence mediated tomography with temporal and spectral data. J. Biomed. Opt. 21(10), 105001 to -11
894. I. Mueller-Harvey, W. Feucht, J. Polster, L. Trnkova, P. Burgos, A.W. Parker, S.W. Botchway, Two-photon excitation with pico-seond fluorescence lifetime imaging to detect nuclear association of flavanols. Analytica Chimica Acta 719, 68-75 (2012)
895. J.D. Müller, Y. Chen, E. Gratton, Resolving Heterogeneity on the single molecular level with the photon-counting histogram, Biophys. J. 78, 474-586 (2000)
896. R. Müller, C. Zander, M. Sauer, M. Deimel, D-S. Ko, S. Sieberte, J. Arden-Jacob, G. Deltau, N.J. Marx, K.H. Drexhage, J. Wolfrum, Time-resolved identification of single molecules in solution with a pulsed semiconductor diode laser, Chem. Phys. Lett. 262, 716-722 (1996)
897. H. S. Muddana, T. T. Morgan, J. H. Adair, P. J. Butler, Photophysics of Cy3-Encapsulated Calcium Phosphate Nanoparticles. Nano Lett. 9(4) 1559-1556 (2009)
898. H.S. Muddana, S. Sengupta, T.E. Mallouk, A. Sen, P.J. Butler, Substrate catalyis enhances single-enzyme diffusion.J. Am. Chem. Soc. 132, 2110-2111 (2010)

899. S. Mukhopadhyay, P. K. Nayak, J. B. Udgaonkar, G. Krishnamoorthy, Characterization of the Formation of Amyloid Ptotofibrils from Barstar by mapping residue-specific fluorescence dynamics. J. Mol. Biol. 358, 935-942 (2006)
900. I.H. Munro, G.R. Jones, M. Tobin, DA Shaw, Y Levine, H Gerritsen, K van der Oord, F Rommerts, Confocal imaging using synchrotron radiation. Journal of Electron Spectroscopy and Related Phenomena 80, 343–347 (1996)
901. L. Munsie, N. Caron, R. S. Atwal, I. Marsden, E. J. Wild, J. R. Bamburg, S. J. Tabrizi, R. Truant, Mutant huntingtin causes defective actin remodeling during stress: defining a new role for transglutaminase 2 in neurodegenerative disease. Human Molecular Genetics, 2011, Vol. 20, No. 10 1937–1951
902. H. Murakoshi, S-J. Lee, R. Yasuda, Highly sensitive and quantitative FRET–FLIM imaging in single dendritic spines using improved non-radiative YFP. Brain Cell Biol. 36, 31-42 (2008)
903. H. Murakoshi, A.C.E. Shibata, ShadowY: a dark yellow fluorescent protein for FLIM-based FRET measurement. Scientific Reports 7, 6791-1 to 10 (2017)
904. T. Nakabayashi, N. Ohta, Sensing of intracellular environments by fluorescence lifetime imaging of exogenous fluorophores. Analytical Sciences 31, 275-285 (2015)
905. E. Nachliel, N. Pollak, D. Huppert, M. Gutman, Time-Resolved Study of the Inner Space of Lactose Permease, Biophys. J. 80, 1498-1506 (2001)
906. Y. Nakahata, J. Nabekura, H. Murakoshi, Dual observation of the ATP-evoked small GTPase activation and Ca2+ transient in astrocytes using a dark red fluorescent protein. Scientific Reports 6, 39564-1 to -10 (2016)
907. Z. Navratil., R. Josepson, N. Cvetanovic, B. Obradovic, and Pavel Dvořák, Electric field development in γ-mode radiofrequency atmospheric pressure glow discharge in helium. Plasma Sources Sci. Technol. 25, 03LT01-06 (2016)
908. H. Neubauer, N. Gaiko, S. Berger, J. Schaffer, C. Eggeling, J. Tuma, L. Verdier, C.A.M. Seidel, C. Griesinger, A. Volkmer, Orientational and dynamical heterogeneity of Rhodamine 6G terminally attached to a DNA helix revealed by NMR and single-molecule fluorescence spectroscopy. J. Am. Chem. Soc. 129, 12746-12755 (2007)
909. T.A. Nguyen, P. Sarkar, J.V. Veetil, S.V. Koushik, S.S. Vogel, Fluorescence Polarization and Fluctuation Analysis Monitors Subunit Proximity, Stoichiometry, and Protein Complex Hydrodynamics. PLoS ONE 7, e38209-1 to -13 (2012)
910. T. A. Nguyen, P. Sarkar, J. V. Veetil, K. A. Davis,1 H. L. Puhl, S. S. Vogel, Covert Changes in CaMKII Holoenzyme Structure Identified for Activation and Subsequent Interactions. Biophys. J. 108(9) 2158-2170 (2015)
911. T. A. Nguyen, H. L. Puhl, K. Hines, D. J. Liput, S. S. Vogel, Binary-FRET reveals transient excited-state structure associated with activity-dependent CaMKII - NR2B binding and adaptation. Nature Communications 13, 6335-1 to -14 (2022)
912. B. M. Nicola, B. E. Verlinden, M. Desmet, S. Saevels, W.r Saeys, K. Theron, R. Cubeddu, A. Pifferi, A. Torricelli, Time-resolved and continuous wave NIR reflectance spectroscopy to predict soluble solids content and firmness of pear. Postharvest Biology and Technology 47, 68–74 (2008)
913. M. A. Niederschweiberer, P. M. Schaefer, L. N. Singh, L. Lausser, D. Bhosale, R. Hesse, E. Calzia, H. A. Kestler, A. Rueck, D. C. Wallace, B. von Einem, C. A. F. von Arnim, NADH Fluorescence Lifetime ImagingMicroscopy Reveals Selective Mitochondrial Dysfunction in Neurons Overexpressing Alzheimer's Disease–Related Proteins. Frontiers in Molecular Biosciences, Volume 8, Article 671274, 1-12 (2021)
914. M. Niedre, V. Ntziachristos, Comparison of fluorescence tomographic imaging in mice with early-arriving and quasi-continuous photons. Opt. lett. 35, 369-371 (2010)
915. D. Niedzwiedzki, J. F. Koscielecki, H. Cong, J. O. Sullivan, G. N. Gibson, R.t R. Birge, H. A. Frank, Ultrafast Dynamics and Excited State Spectra of Open-Chain Carotenoids at Room and Low Temperatures. J. Phys. Chem. B 111, 5984-5998 (2007)
916. R. Nothdurft, P. Sarder, S. Bloch, J. Culver, and S. Achilefu, Fluorescence Lifetime Imaging Microscopy Using Near-Infrared Contrast Agents. J. Microsc. 247(2) 202-207 (2012)
917. M. Novo, S. Felekyan, C.A.M. Seidel, W. Al-Soufi, Dye-Exchange Dynamics in Micellar Solutions Studied by Fluorescence Correlation Spectroscopy. J. Phys. Chem. B 111, 3614-3624 (2007)
918. S. Nozue, A. Mukuno, Y. Tsuda, T. Shiina, M. Terazima, S. Kumazaki, Characterization of thylakoid membrane in a heterocystous cyanobacterium and green alga with dual-detector fluorescence lifetime imaging microscopy with a systematic change of incident laser power. Biochimica et Biophysica Acta 1857, 46–59 (2016)
919. V. Ntziachristos, X.H. Ma, B. Chance, Time-correlated single-photon counting imager for simultaneous magnetic resonance and near-infrared mammography, Rev. Sci. Instrum. 69, 4221-4233 (1998)
920. V. Ntziachristos, X.H. Ma, A.G. Yodh, B. Chance, Multichannel photon counting instrument for spatially resolved near infrared spectroscopy, Rev. Sci. Instrum. 70, 193-201 (1999)

921. V. Ntziachristos, A.G. Yodh, M. Schnall, B. Chance, Concurrent MRI and diffuse optical tomography of breast after indocyanine green enhancement, PNAS 97, 2767-2772 (2000)
922. V. Ntziachristos, B. Chance, Accuracy limits in the determination of absolute optical properties using time-resolved NIR spectroscopy, Med. Phys. 28, 1115-1124 (2001)
923. A. C. Nyborg, L. Herl, O. Berezovska, A. V Thomas, T. B. Ladd, K. Jansen, B. T. Hyman, T. E. Golde, Signal peptide peptidase (SPP) dimer formation as assessed by fluorescence lifetime imaging microscopy (FLIM) in intact cells. Mol. Neurodegener. 1:16 (2006)
924. D.V. O'Connor, D. Phillips, Time-correlated single photon counting, Academic Press, London (1984)
925. N. O'Donnell, I. A. Okkelman, P. Timashev, T. I. Gromovy, D. B. Papkovsky, R. I. Dmitriev, Cellulose-based scaffolds for fluorescence lifetime imaging-assisted tissue engineering. Acta Biomaterialia 80, 85-96 (2018)
926. M. Oheim, E. Beaurepaire, E. Chaigneau, J. Mertz, S. Charpak, Two-photon microscopy in brain tissue: parameters influencing the imaging depth. Journal of Neuroscience Methods 111, 29–37 (2001)
927. B. Ohnesorge, R. Weigand, G. Bacher, A. Forchel, Minority-carrier lifetime and efficiency of Cu(In, Ga)Se2 solar cells, Appl. Phys. Lett. **73**, 1224-1226 (1998)
928. I. Ohshiro, M. Ikegami, Y. Shinohara, Y. Nishimura, T. Arai, Photochemical Behavior of an Anthracene–Urea Derivative Interacting with Anions. Bull. Chem. Soc. Jpn. 80, 747-751 (2007)
929. K. Okabe, N. Inada, C. Gota, Y. Harada, T. Funatsu, S. Uchiyama, Intracellular temperature mapping with a fluorescent polymeric thermometer and fluorescence lifetime imaging microscopy. Nature Communications (2012)
930. I. A. Okkelman, R. I. Dmitriev, T. Foley, D. B. Papkovsky, Use of Fluorescence Lifetime Imaging Microscopy (FLIM) as a Timer of Cell Cycle S Phase. PLOS ONE 0167285 (Dec. 2016)
931. I. A. Okkelman, A. A. Dolgova, S. Banerjee, J. P. Kerry, A. Volynskii, O. V. Arzhakova, D. B. Papkovsky, Phosphorescent Oxygen and Mechanosensitive Nanostructured Materials Based on Hard Elastic Polypropylene Films. ACS Appl. Mater. Interfaces 9, 13587−13592 (2017)
932. A. Oliveira, R. Yasuda, An improved Ras Sensor for highly sensitive and quantitative FRET-FLIM inaing. PLOS ONE 8 e52874 (2013)
933. L. Olofsson, E. Margeat, Pulsed interleaved excitation fluorescence spectroscopy with a supercontinuum source. Opt. Expr. 21, 3370-3378 (2012)
934. A. Osterrieder, C.M. Carvalho1, M Latijnhouwers, J. N. Johansen1, C. Stubbs, S. Botchway, C. Hawes, Fluorescence Lifetime Imaging of Interactions between Golgi Tethering Factors and Small GTPases in Plants. Traffic 10, 1-13 (2009)
935. M. S. Otegui, Imaging polyphenolic compounds in plant tissues. Recent advances in polyphenol research, 7, 281-295 (2021)
936. S. Pallikkuth, D. J. Blackwell, Z. Hu, Z. Hou, D. T. Zieman, B. Svensson, D. D. Thomas, S. L. Robia, Phosphorylated Phospholamban Stabilizes a Compact Conformation of the Cardiac Calcium-ATPase. Biophys. J. 105, 1812–1821 (2013)
937. Z. J. Palmer, R. R. Duncan, J. R. Johnson, L.-Y. Lian, L. V. Mello, D. Booth., Jeff W. Barclay, M. E. Graham, R. D. Burgoyne, I. A. Prior and Alan Morgan, S-nitrosylation of syntaxin 1 at Cys145 is a regulatory switch controlling Munc18-1 binding. Biochem. J. 413479-491 (2008)
938. K. Palo, L. Brand, C. Eggeling, S. Jäger, P. Kask, K. Gall, Fluorescence intensity and lifetime distribution analysis: Toward higher accuracy in fluorescence fluctuation spectroscopy, Biophys. J. **83**, 605-617 (2002)
939. K. Palo, Ü. Mets, S. Jäger, P. Kask, K. Gall, Fluorescence intensity multiple distribution analysis: concurrent determination of diffusion times and molecular brightness, Biophys. J. **79**, 2858-2866 (2000)
940. D. Papkovsky, A. V. Zhdanov, A. Fercher, R. I. Dmitriev, and J. Hynes, Phosphorescent oxygen-sensitive probes (Springer, 2012)
941. D. B. Papkovsky, and R. I. Dmitriev, Biological detection by optical oxygen sensing, Chem Soc Rev 42, 8700-8732 (2013)
942. D. B. Papkovsky, R. I. Dmitriev, Imaging of oxygen and hypoxia inc cell an tissue samples. Cellular and Molecular Life Sciences 75, 2963-2989 (2018)
943. Y. P. Parshina, A. D. Komarova, L. N. Bochkarev, T. A. Kovylina, A. A. Plekhanov, L. G. Klapshina, A. N. Konev, A. M. Mozherov, I.a D. Shchechkin, M. A. Sirotkina, V. I. Shcheslavskiy, M. V. Shirmanova, Simultaneous Probing of Metabolism and Oxygenation of Tumors In Vivo Using FLIM of NAD(P)H and PLIM of a New Polymeric Ir(III) Oxygen Sensor. Int. J. Mol. Sci. 23, 10263 1 -24
944. Yu. P. Parshina, T. A. Kovylina, A. N. Konev, A. A. Belikov, P. O. Baber, A. D. Komarov, E. A. Romaev, and L. N. Bochkarev, Norbornene-substituted cationic Iridium(III) complex and water-soluble luminescent polymers based on it: Synthesis, photophysical and cytotoxic properties. Russian Journal of General Chemistry 92, No. 12, 2666–2675 (2022)

945. D.A. Parul, S.B. Bokut, A.A. Milyutin, E.P. Petrov, N.A. Nemkovich, A.N. Sobchuk, B.M. Dzhagarov, Time-resolved fluorescence reveals two binding sites of 1, 8-ANS in intact human oxyhemoglobin, Journal of Photochemistry and Photobiology B: Biology **58**, 156-162 (2000)
946. M.N. Pastore, H. Studier, C.S. Bonder, M.S. Roberts, Non-invasive metabolic imaging of melanoma progression. Exp. Dermatol. 26, 607–614 (2017)
947. R. Patalay, C. Talbot, Y. Alexandrov, I. Munro, M. A. A. Neil, K. König, P. M. W. French, A. Chu, G. W. Stamp, C. Dunsby, Quantification of cellular autofluorescence of human skin using multiphoton tomography and fluorescence lifetime imaging in two spectral detection channels. Opt. Expr. 2, 3295-3308 (2011)
948. G.H. Patterson, D.W. Piston, Photobleaching in two-photon excitation microscopy, Biophys. J. **78**, 2159-2162 (2000)
949. M.S. Patterson, B. Chance, B.C. Wilson, Time-resolved reflectance and transmittance for the noninvasive measurement of tissue optical properties, Appl. Opt. **28**, 2331-2336 (1989)
950. R.J. Paul, H. Schneckenburger, Oxygen concentration and the oxidation-reduction state of yeast: Determination of free/bound NADH and flavins by time-resolved spectroscopy, Naturwissenschaften **83**, 32-35 (1996)
951. Z. Pavlinska, D. Chorvat Jr., A. Mateasika, M. Jerigova, Dusan Velic, N. Ivošević DeNardisd, A. Marcek Chorvatova, Fluorescence responsiveness of unicellular marine algae Dunaliella to stressors under laboratory conditions. Journal of Biotechnology, X 6 (2020) 100018, 1-10
952. J. Pawley (ed.), Handbook of biological confocal microscopy, 3rd edn., Springer (2006)
953. S. Pelet, M.J.R. Previte, P.T.C. So, Comparing the quantification of Förster resonance energy transfer measurement accuracies based on intensity, spectral, and lifetime imaging. J. Biomed. Opt. 11 034017-1 to -11 (2006)
954. I. D. Peltan, A.V. Thomas, I. Mikhailenko, D. K. Strickland, B. T. Hyman, C.A.F. von Arnim, Fluorescence lifetime imaging microscopy (FLIM) detects stimulus-dependent phospholylation of the low density lipoprotein receptor-related protein (LRP) in primary neurons. Biochem. Biophys. Res. Commun. 349, 24-30 (2006)
955. R. Penjweini, A. Andreoni, T. Rosales, J. Kim, M. D. Brenner, D. L. Sackett, J. H. Chung, J. R. Knutson, Intracellular oxygen mapping using a myoglobin-mCherry probe with fluorescence lifetime imaging. J. Biomed. Opt.23, 107001-1 to -14 (2018)
956. R. Penjweini, B. Roarke, G. Alspaugh, A. Gevorgyan, A.Andeoni, A. Pasut, D.L. Sacket, J. R. Knutson, Single cell-based fluorescence lifetime imaging of intracellular oxygenation and metabolism. Redox biology 34, 101549 1-10 (2020)
957. R. Penjweini, B. Roarke, G. Alspaugh, K. A. Link, A. Andreoni, M. P. Mori, P. M. Hwang, D. L. Sackett, J. R. Knutson, Intracellular imaging of metmyoglobin and oxygen using new dual purpose probe EYFP-Myoglobin-mCherry. J. Biophotonics e202100166 1-12 (2021)
958. A. Periasamy, Methods in Cellular Imaging. Oxford University Press, Oxford New York (2001)
959. A. Periasamy, R.M. Clegg, eds., FLIM Microscopy in Biology and Medicine. CRC Press 2009
960. A. Periasamy, N. Mazumder, Y. Sun, K. G. Christopher, R. N. Day, FRET Microscopy: Basics, Issues and Advantages of FLIM-FRET Imaging. In: W. Becker (ed.) Advanced time-correlated single photon counting applications. Springer, Berlin, Heidelberg, New York (2015)
961. M.J.B. Pereira, D.A. Harris, D. Rueda, N.G. Walter, Reaction pathway of the trans-acting hepatitis delta virus ribozyme: A conformational change accompanies catalysis, Biochemistry **41**, 730-740 (2002)
962. M. B. M. Pereira, A. M. Santos, D. C. Goncalves, A. C. Cardoso, S. R. Consonni, Fabio C. Gozzo, P. S. Oliveira, A. H. M. Pereira, A. R. Figueiredo, A. O. Tiroli-Cepeda, C. H. I. Ramos, A A. de Thomaz, Carlos L. Cesar, K. G. Franchini, αB-crystallin interacts with and prevents stress-activated proteolysis of focal adhesion kinase by calpain in cardiomyocytes. Nature Communications, 5, 5159 (2014)
963. M. Peter, S.M. Ameer-Beg, Imaging molecular interactions by multiphoton FLIM, Biology of the Cell **96**, 231-236 (2004)
964. M. Peter, S.M. Ameer-Beg, M.K.Y. Hughes, M.D. Keppler, S. Prag, M. Marsh, B. Vojnovic, T. Ng, Multiphoton-FLIM quantifcation of the EGFP-mRFP1 FRET pair for localization of membrane receptor-kinase interactions, Biophys. J. **88**, 1224-1237 (2005)
965. Z. Petrasek, M. Krishnan, I. Mönch, P. Schwille, Simultaneous two-photon fluorescence correlation spectroscopy and lifetime imaging of dye molecules in submicrometer fluidic structures. Micr. Res. Tech. 70, 459-466 (2007)
966. E.P. Petrov, J.V. Kruchenok, A.N. Rubinov, Effects of the external refractive index on fluorescence kinetics of perylene in human erythrocyte ghosts, J. Fluoresc. **9**, 111-121 (1999)
967. Perkin Elmer Optoelectronics, Single photon counting module, SPCM-AQR series. www.perkinelmer.com
968. J.P. Philip and K. Carlsson, Theoretical investigation of the signal-to-noise ratio in fluorescence lifetime imaging, J. Opt. Soc. Am. **A20**, 368-379 (2003)

969. A. Pifferi, A. Torricelli, P. Taroni, R. Cubeddu, Reconstruction of absorber concentrations in a two-layer structure by use of multidistance time-resolved reflectance spectroscopy, Opt. Lett. **26**, 1963-1965 (2001)
970. A. Pifferi, P. Taroni, A. Torricelli, F. Messina, R. Cubeddu, Four-wavelength time-resolved optical mammography in the 680-980-nm range, Opt. Lett. **28**, 1138-1140 (2003)
971. A. Pifferi, A. Torricelli, P. Taroni, A. Bassi, E. Chikoidze, E. Gambatistelli, R. Cubeddu, Optical biopsy of bone tissue: A step toward the diagnosis of bone pathologies. J. Biomed. Opt. **9**, 474-480 (2004)
972. A. Pifferi, J. Swartling, E. Chikoidze, A. Torricelli, P. Taroni, A. Bassi, S. Andersson-Engels, R. Cubeddu, Spectroscopic time-resolved diffuse reflectance and transmittance measurements of the female breast at different interfibre distances, J. Biomed. Opt. **9**, 1143-1151 (2004)
973. Pifferi A, Torricelli A, Bassi A, Taroni P, Cubeddu R, Wabnitz H, Grosenick D, Möller M, Macdonald R, Swartling J, Svensson T, Andersson-Engels S, van Veen RL, Sterenborg HJ, Tualle JM, Nghiem HL, Avrillier S, Whelan M, Stamm H., Performance assessment of photon migration instruments: the MEDPHOT protocol. Appl Opt. 44(11), 2104-2114 (2005)
974. A. Pifferi, A.o Torricelli, P. Taroni, D. Comelli, A. Bassi, R. Cubeddu, Fully automated time domain spectrometer for the absorption and scattering characterization of diffusive media. Rev. Sci. Instrum. 78, 053103-1 to -10 (2007)
975. A. Pifferi, A.o Torricelli, L. Spinelli, D. Contini, R. Cubeddu,1 F. Martelli, G. Zaccanti, A. Tosi, A. Dalla Mora, F. Zappa, and S.o Cova, Time-Resolved Diffuse Reflectance Using Small Source-Detector Separation and Fast Single-Photon Gating. Phys. Rev. Lett. 100, 138101-1 to -4 (2008)
976. L. Pires, M. S. Nogueira, S. Pratavieira, L. T. Moriyama, C. Kurachi, Time-resolved fluorescence lifetime for cutaneous melanoma detection. Biomed. Opt. Expr. 5, 2014, 3080-3089
977. A. Pliss, X. Peng, L. Liu, A. Kuzmin, Y. Wang, J. Qu, Y. Li and P. N. Prasad, Single Cell Assay for Molecular Diagnostics and Medicine: Monitoring Intracellular Concentrations of Macromolecules by Two-photon Fluorescence Lifetime Imaging. Theranostics 5, 919-930 (2015)
978. A. Pliss, S. M. Levchenko, L. Liu, X. Peng, T. Y. Ohulchanskyy, I. Roy, A. N. Kuzmin, J. Qu, P. N. Prasad, Cycles of protein condensation and discharge in nuclear organelles studied by fluorescence lifetime imaging. Nature Communications 10, 455 (2019)
979. A. Poellinger, S. Burock, D. Grosenick, A. Hagen, L. Lüdemann, F. Diekmann, F. Engelken, R. Macdonald, H. Rinneberg, and P.-M. Schlag, "Breast Cancer: Early- and Late-Fluorescence Near-Infrared Imaging with Indocyanine Green - A Preliminary Study," *Radiology* **258**(2), 409–416 (2011)
980. A. Ponjavic, J. Dench, N. Morgan, J. S. S. Wong, In situ viscosity measurement of confined liquids. RSC Adv. 5, 99585-99593 (2015)
981. Point Source Ltd., Kineflex fibre manipulator, operating instructions
982. E. V. Potapova., V. V. Dremin., V. V. Shupletsov, K. Y. Kandurova, A. V. Dunaev, Optical percutaneous needle biopsy in oncology. Light: Advanced Manufacturing 6:72, 1-16 (2025)
983. P.P. Provenzano, C.T. Rueden, S.M. Trier, L. Yan, S.M. Ponik, D.R. Inman, P.J. Keely, K. W. Eliceiri, Nonlinear optical imaging and spectral-lifetime computational analysis of endogenous and exogenous fluorophores in breast cancer. J. Biomed. Opt. 13(3), 031220-1 to -11 (2008)
984. Tarl W. Prow, Jeffrey E. Grice, Lynlee L. Lin, Rokhaya Faye, Margaret Butler, Wolfgang Becker, Elisabeth M.T. Wurm, Corinne Yoong, Thomas A. Robertson, H. Peter Soyer, Michael S. Roberts, Nanoparticles and microparticles for skin drug delivery. Advanced Drug Delivery Reviews 63, 470–491 (2011)
985. M. Prummer, C. Hübner, B. Sick, B. Hecht, A. Renn, U.P. Wild, Single-molecule identification by spectrally and time-resolved fluorescence detection, Anal. Chem. **72**, 433-447 (2000)
986. M. Prummer, B. Sick, A. Renn, U.P. Wild, Multiparameter microscopy and spectroscopy for single-molecule analysis, Anal. Chem. **76**, 1633-1640 (2004)
987. H. Qian, E.L. Elson, Distribution of molecular aggregation by analysis of fluctuation moments, PNAS **87**, 5479-5483 (1990)
988. T. Qian, T. M. Heaster, A. R. Houghtaling, K. Sun, K. Samimi, M. C. Skala, Label-free imaging for quality control of cardiomyocyte differentiation. NATURE COMMUNICATIONS 12, 4580 1-11 (2021)
989. X. Qu, J. Wang, Z. Zhang, N. Koop, R. Rahmanzadeh, G. Hüttmann, Imaging of cancer cells by multiphoton microscopy using gold nanoparticles and fluorescent dyes,. J. Biomed. Opt. 13(3) 031217-1 to 7 (2008)
990. E. Quansah, A. Ramoji, L. Thieme, K. Mirza, B. Goering, O. Makarewicz, A. Heutelbeck, T. Meyer-Zedler, M. W. Pletz, M. Schmitt, Jürgen Popp, Label-free multimodal imaging of infected Galleria mellonella larvae. Scientific Reports 12, 20416 (2022)
991. E. Quansah, E. Gardey, A. Ramoji, T. Meyer-Zedler, B. Goehrig, A. Heutelbeck, S. Hoeppener, Michael Schmitt, M. Waldner, A. Stallmach, J. Popp, Intestinal epithelial barrier integrity investigated by label-free techniques in ulcerative colitis patients. Scientific Reports 13, 2681 (2023)

992. V. Quaresima, M. Ferrari, A. Torricelli, L. Spinelli, A. Pifferi, R. Cubeddu, Bilateral prefocal cortex oxygenation responses to a verbal fluency task: a multichannel time-resolved near-infrared topography study, J. Biomed. Opt. 10 011012-1 to -12 (2005)
993. G. Quarto, A. Torricelli, L. Spinelli, A. Pifferi, R. Cubeddu and P. Taroni, Breast Monitoring by Time-Resolved Diffuse Optical Imaging. In: W. Becker (ed.) Advanced time-correlated single photon counting applications. Springer, Berlin, Heidelberg, New York (2015)
994. M. Rajadhyaksha, S. Gonzalez, J.M. Zavislan, R.R. Anderson, R.H. Webb, In vivo confocal scanning laser microscopy of human skin II: Advances in instrumentation and comparison with histology. J. Investigative Dermatology 113(3) 293-303
995. L. Ramm, S. Jentsch, R. Augsten, M. Hammer, Fluorescence lifetime imaging ophthalmoscopy in glaucoma. Graefes Arch Clin Exp Ophthalmol (2014) 252:2025–2026
996. T. Ramreddy, B. J. Rao, G. Krishnamoorthy, Site-specific dynamics of strands in ss- and dsDNA as revealed by time-domain fluorescence of 2-Aminopurine. J.Phys. Chem. 111, 5757-5766 (2007)
997. J.G. Rarity, K.D. Ridley, P.R. Tapster, Absolute measurement of detector quantum efficiency using parametric downconversion, Appl. Opt. **26**, 4616-4619 (1987)
998. E. Ratajczak, A. Pecherski, J. Ramos-Moreno, M. O. Ruonala, FET-assisted determination of CLN3 membrane topology. PLOS ONE 9, e102593 (2014)
999. R. Re, D. Contini, M. Caffini, R. Cubeddu, L. Spinelli, A. Torricelli, A compact time-resolved system for near infrared spectroscopy based on wavelength space multiplexing. Rev Sci Instrum. 81, 113101 (2010)
1000. R. Re, D. Contini D, M . Turola, L. Spinelli, L. Zucchelli, M. Caffini, R. Cubeddu, A. Torricelli, Multi-channel medical device for time domain functional near infrared spectroscopy based on wavelength space multiplexing. Biomed Opt Express 4(10), 2231-46 (2013)
1001. I. Rech, G. Luo, M. Ghioni, H. Yang, X.S. Xie, S. Cova, Photon-timing detector module for single-molecule spectroscopy with 60-ps resolution, IEEE Journal of selected topics in quantum electronics **10**, 788-795 (2004)
1002. K. Reinhardt, H. G. Breunig, K.König, Autofluorescence lifetime variation in the cuticle of the bedbug Cimex lectularius. Arthropod Structure & Development, 46, 56-62, (2017)
1003. K. Reinhardt, H. G. Breunig, A. Uchugonova, K. König, Sperm metabolism is altered during storage by female insects: evidence from two-photon autofluorescence lifetime measurements in bedbugs. J. R. Soc. Interface 12, 20150609-1 to -9
1004. D. Resnati, I. Rech, A. Geraci, High-linearity analog-to-digital acquisition board for photon counting applications. Rev. Sci. Instrum. 79, 064706 (2008)
1005. B. Richards, E. Wolf, Electromagnetic diffraction in optical systems II. Structure of the image field in an aplanatic system, Proc. Roy. Soc. **A 253**, 358-379 (1959)
1006. L. Richert, P. Didier, H. de Rocquigny, Y. Mély, Monitoring HIV-1 Protein Oligomerization by FLIM FRET Microscopy. In: W. Becker (ed.) Advanced time-correlated single photon counting applications. Springer, Berlin, Heidelberg, New York (2015)
1007. C. Rickman, C.N. Medine, A. Bergmann, R.R. Duncan, Functionally and spatially distinct modes of MUNC18-syntaxin 1 intercation. JBC 282, 12097-12103 (2007)
1008. C. Rickman, C. N. Medine, A. R. Dun, D. J. Moulton, O. Mandula, N. D. Halemani, S. O. Rizzoli, L. H. Chamberlain, and R. R. Duncan, t-SNARE Protein Conformations Patterned by the Lipid Microenvironment. J. Biol. Chem. 285, 13535-13541 (2010)
1009. C. Rickman, R. R. Duncan, Munc18/Syntaxin Interaction Kinetics Control Secretory Vesicle Dynamics. J. Biol. Chem. 285, 3965-3972 (2010)
1010. I. Riemann, P. Fischer, M. Kaatz, T.W. Fischer, P. Elsner, E. Dimitrov, A. Reif, K. König, Optical tomography of pigmented human skin biopies, Proc. SPIE **5312**, 24-34 (2004)
1011. R. Rigler, E.S. Elson (eds), Fluorescence Correlation Spectroscopy, Springer Verlag Berlin, Heidelberg, New York (2001)
1012. R. Rigler, Ü. Mets, J. Widengren, P. Kask, Fluorescence correlation spectroscopy with high count rate and low background: analysis of translational diffusion, European Biophysics Journal **22**, 169-175 (1993)
1013. R. Rigler, J. Widengreen, Utrasensitive detection of single molecules by fluorescence correlation spectroscopy, Bioscience **3**, 180-183 (1990)
1014. R. Richards-Kortum, R. Drezek, K. Sokolov, I. Pavlova, M. Follen, Survey of endogenous biological fluorophores. In M.-A. Mycek, B.W. Pogue (eds.), Handbook of Biomedical Fluorescence, Marcel Dekker Inc. New York, Basel, 237-264 (2003)
1015. A.S. Rinaldi, G. Freund, D. Desplancq, A.P. Sibler, M. Baltzinger, N. Rochel, Y. Mély, P. Didier, E. Weiss, The use of fluorescent intrabodies to detect endogenous gankyrin in living cancer cells. Exp Cell Res. 319(6), 8-49 (2013)
1016. H. Rinneberg, D. Grosenick, K. T. Moesta, J. Mucke, B. Gebauer, C. Stroszczynski, H. Wabnitz, M. Moeller, B. Wassermann, and P. M. Schlag, Scanning time-domain optical mammography: detection and characterization of breast tumors in vivo, Technol. Cancer Res. Treat. 4(5), 483–496 (2005)

1017. H. Rinneberg, D. Grosenick, K.T. Moesta, H. Wabnitz, J. Mucke, G. Wübbeler, R. Macdonald, P. Schlag, Detection and characterization of breast tumours by time-domain scanning optical mammography. Opto-Electron. Rev. 16, 147-162 (2008)
1018. B. Riquelme, D. Dumas, J. Valverde, R. Rasia, J.F. Stoltz, Analysis of the 3D structure of agglutinated erythrocyte using CellScan and Confocal microscopy: Characterisation by FLIM-FRET, Proc. SPIE 5139, 190-198 (2003)
1019. T. Ritman-Meer, N. I. Cade, D. Richards, Spatial imaging of modifications to fluorescence lifetime and intensity by individual Ag nanoparticles. Appl. Phys. Lett. 91, 123122 (2007)
1020. M.B. Rivas Aiello, J.C. Azcárate, E. Zelaya, P.D. Gara, G.N. Bosio, T. Gensch, and D.O. Mártire, Photothermal Therapy with Silver Nanoplates in HeLa cells studied by in situ Fluorescence Microscopy. Biomaterials Science 9, 2608 – 2619 (2021)
1021. M.S. Roberts, M.J. Roberts, T.A. Robertson, W. Sanchez, C. Thörling, Y. Zou, X. Zhao, W. Becker, A. V. Zvyagin, In vitro and in vivo imaging of xenobiotic transport in human skin and in the rat liver. J. Biophoton. 1, 478-493 (2008)
1022. Roberts, M. S., Dancik, Y., Prow, T.W., Thorling, C.A., Li, L., Grice, J.E., Robertson, T.A., König, K., Becker,W. Non-invasive imaging of skin physiology and percutaneous penetration using fluorescence spectral and lifetime imaging with multiphoton and confocal microscopy. European Journal of Pharmaceutics and Biopharmaceutics 77, 469-488 (2011)
1023. T. Robinson, Y. Schaerli, R. Wootton, F. Hollfelder, C. Dunsby, G. Baldwin, M. Neil, P. French, A. deMello, Removal of background signals from fluorescence thermometry measurements in PDMS microchannels using fluorescence lifetime imaging. Lab Chip 9, 3437–3441 (2009)
1024. A. Rochas, A. Pauchard, A. Matteo, P. Trinkler, R. Thew, R. Ribordy, Ultra-compact single photon detector. Proc. SPIE 6372, 6371N-1 to -8
1025. N. Rochel, F. Ciesielski, J. Godet, E. Moman, M. Roessle, C. Peluso-Iltis, M. Moulin, M. Haertlein, P. Callow, Y. Mely, D. I Svergun, D. Moras, Common architecture of nuclear receptor heterodimers on DNA direct repeat elements with different spacings. Nature Structural & Molecular Biology, 18 (5), 564-572 (2011)
1026. C. Rodenbücher, T. Gensch, W. Speier, U. Breuer, M. Pilch, H. Hardtdegen, M. Mikulics, E. Zych, R. Waser, K. Szot, Inhomogeneity of donor doping in SrTiO3 substrates studied by fluorescence-lifetime imaging microscopy. Appl. Phys. Lett. 103, 162904-1 to -4 (2013)
1027. C. Rodenbücher, S. Menzel, D. Wrana, T. Gensch, C. Korte, F. Krok, Kristof Szot, Current channeling along of extended defects during electroreduction of SrTiO3. Scientific Reports 9, 2502, 1-9 (2019)
1028. C. Rodenbücher, D. Wrana, T. Gensch, F. Krok, C. Korte, K. Szot The Electronic Properties of Extended Defects in $SrTiO_3$ - A Case Study of a Real Bicrystal Boundary. *Crystals* 10, 665, 1-19. (2020)
1029. S. Rodimova, D. Kuznetsova, N. Bobrov, V. Elagin, V. Shcheslavskiy, V. Zagainov, E. Zagaynova, Mapping metabolism of liver tissue using two-photon FLIM. Biomed. Opt. Expr. 11, No.8, 4458-4470 (2020)
1030. S. A. Rodimova , D. S. Kuznetsova, N. V. Bobrov, A. A. Gulin, D. G. Reunov, M. M. Karabut, V. I. Shcheslavskiy , N. V. Vdovina, V. E. Zagainov, E. V. Zagaynova, Interrogation of the Liver During Regeneration by Fluorescence Lifetime Imaging and Mass Spectrometry. IEE Journal of Selected Topics in Quantum Electronics, 27 No.4, 6801511 (2021)
1031. S. Rodimova, A. Mozherov, V. Elagin, M. Karabut, I. Shchechkin, D. Kozlov, D. Krylov, A. Gavrina, V. Kaplin, E. Epifanov, N. Minaev, K. Bardakova, A. Solovieva, P. Timashev, E. Zagaynova, D. Kuznetsova, FLIM imaging revealed spontaneous osteogenic differentiation of stem cells on gradient pore size tissue-engineered constructs. Stem Cell Research & Therapy 14:81, 1-23 (2023)
1032. L. Rovati, F. Docchio, Autofluorescence methods in ophthalmology, J. Biomed. Opt. 9, 9-21 (2004)
1033. A. Rudkouskaya, N. Sinsuebphon, X. Intes, J. E. Mazurkiewicz, M. Barroso, Fluorescence lifetime FRET imaging of receptor-ligand complexes in tumpr cells in vitro and in vivo. Proc. of SPIE Vol. 10069, 1006917-1 to -8 (2017)
1034. A. Rück, F. Dolp, C. Happ, R. Steiner, M. Beil, Fluorescence lifetime imaging (FLIM) using ps-pulsed diode lasers in laser scanning microscopes, Proc. SPIE 4962, 160-167 (2003)
1035. A. Rück, F. Dolp, C. Happ, R. Steiner, M. Beil, Time-resolved microspectrofluorometry and fluorescence lifetime imaging using ps pulsed laser diodes in laser scanning microscopes, Proc. SPIE 5139, 166-172 (2003)
1036. A. Rück, F. Dolp, C. Hülshoff, C. Hauser, C. Scalfi-Happ, FLIM and SLIM for molecular imaging in PDT, Proc. SPIE 5700 (2005)
1037. A. Rück, F. Dolp, C. Hülshoff, C. Hauser, C. Scalfi-Happ, Fluorescence lifetime imaging in PDT. An overview. Medical Laser Application 20, 125-129 (2005)
1038. A. Rück, Ch. Hülshoff, I. Kinzler, W. Becker, R. Steiner, SLIM: A New Method for Molecular Imaging. Micr. Res. Tech. 70, 403-409 (2007)

1039. A. Rück, C. Hauser, S. Mosch, S. Kalinina, Spectrally resolved fluorescence lifetime imaging to investigate cell metabolism in malignant and nonmalignant oral mucosa cells. J. Biomed. Opt. 19(9), 096005-1 to -9 (2014)
1040. A.L. Rusanov, A.P. Savitsky, Fluorescence resonance energy transfer between fluorescent proteins as powerful toolkits for in vivo studies. Laser Phys. Lett. 8(2) 91-102 (2011)
1041. S. R. Sadda, E. Borrelli, W.g Fan, A. Ebraheem, K. M. Marion, S. Kwon, Impact of mydriasis in fluorescence lifetime imaging ophthalmoscopy. PLOS ONE, https://doi.org/10.1371/journal.pone.0209194 December 28, 2018
1042. S. R. Sadda, E. Borrelli, W. Fan, A. Ebraheem, K. M. Marion, M. Harrington, S. Kwon, A pilot study of fluorescence lifetime imaging ophthalmoscopy in preclinical Alzheimer's disease. Eye 33, 1271–1279 (2019)
1043. S. Sakadžic, E. Roussakis, M. A. Yaseen, E. T. Mandeville, V. J. Srinivasan1, K. Arai, S. Ruvinskaya, A. Devor, E. H. Lo, S. A. Vinogradov, D. A. Boas, Two-photon high-resolution measurement of partial pressure of oxygen in cerebral vasculature and tissue. Nature Methods 7(9) 755-759 (2010)
1044. M. Salah, N. Samy, M. Fadel, Methylene blue mediated photodynamic therapy for resistant plaque psoriasis. J. Drags Dermatol. 8, 42-49 (2009)
1045. T. Sanchez, T. Wang, M.Venturas Pedro, M. Zhang, E. Esencan, D. Sakkas, D. Needleman, E. Seli, Metabolic imaging with the use of fluorescence lifetime imaging microscopy (FLIM) accurately detects mitochondrial dysfunction in mouse oocytes. Reproductive Science 110, 1387-1397 (2018)
1046. T. Sanchez, M. Venturas, S. A. Aghvami, X. Yang, S. Fraden, D. Sakkas, D. J. Needleman, Combined noninvasive metabolic and spindle imaging as potential tools for embryo and ocyte assessment. Human Reproduction, 1–13 (2019)
1047. W.Y. Sanchez, T.W. Prow, W.H. Sanchez, J.E.Grice, M.S. Roberts, Analysis of the metaboloic deterioration of ex-vivo skin, from ischemic necrosis, through the imaging of intracellular NAD(P)H by multiphoton tomography and fluorescence lifetime imaging microscopy (MPT-FLIM). J. Biomed. Opt. 15, 046008 (2010)
1048. W.Y. Sanchez, C. Obispo, E. Ryan, J. E. Grice, M.S. Roberts, Changes in the redox state and endogenous fluorescence of in vivo human skin due to intrinsic and phot-induced aging, measured by multiphoton tomography with fluorescence lifetime imaging. J. Biomed. Opt. 18(6), 061217-1 to -12 (2013)
1049. W. Y. Sanchez, M. Pastore, I. Haridass, K. König, W. Becker, M. S. Roberts, Fluorescence Lifetime Imaging of the Skin. In: W. Becker (ed.) Advanced time-correlated single photon counting applications. Springer, Berlin, Heidelberg, New York (2015)
1050. A. Sandqvist, J. K. Björk, M. Åkerfelt, Z. Chitikova, A. Grichine, C. Vourch, C. Jolly, T. A. Salminen, Y. Nymalm, L. Sistonen, Heterotrimerization of Heat-Shock Factors 1 and 2 Provides a Transcriptional Switch in Response to Distinct Stimuli. Melecular Biology of the Cell 20, 1340-1347 (2009)
1051. T. H. Sander, A. Liebert, B. M. Mackert, H. Wabnitz, S. Leistner, G. Curio, M. Burghoff, R. Macdonald, L. Trahms, DC-magnetoencephalography and time-resolved near-infrared spectroscopy combined to study neuronal and vascular brain responses, Physiol. Meas. 28 651-664 (2007)
1052. R. Sanders, A. Draaijer, H.C. Gerritsen, P.M. Houpt, Y.K. Levine, Quantitative pH Imaging in cells using confocal fluorescence lifetime imaging microscopy, Analytical Biochemistry 227, 302-308 (1995)
1053. P. Sarkar, S.V. Koushik, S.S. Vogel, I. Gryczynski, Z. Gryczinski, Photophysical properties of Cerulean and Venus fluorescent proteins. J. Biomed. Opt. 14, 034047-1 to -9 (2009)
1054. D.N.S. dos Santos, N. Naskar, E. Delgado-Pinar, K. Reess, J.S. Seixas de Melo, A. Rueck, Bromine indirubin FLIM/PLIM sensors to measure oxygen in normoxic and hypoxic PDT conditions. Photodiagnosis and Photodynamic Therapy 45 103964 -1 to -7 (2024)
1055. Lydia Sauer, Rebekah H. Gensure, PhD,1 Martin Hammer, Paul S. Bernstein, Fluorescence Lifetime Imaging Ophthalmoscopy: A Novel Way to Assess Macular Telangiectasia Type 2. Ophthalmology Retina 2 (6), 587-598 (2018)
1056. Lydia Sauer, Rebekah H. Gensure, Karl M. Andersen, Lukas Kreilkamp, Gregory S. Hageman, Martin Hammer, Paul S. Bernstein, Patterns of Fundus Autofluorescence Lifetimes In Eyes of Individuals With Nonexudative Age-Related Macular Degeneration. IOVS 59 (2018)
1057. L. Sauer, Schweitzer D, Ramm L, Augsten R, Hammer M, Peters S. Impact of macular pigment on fundus autofluorescence lifetimes. Invest Ophthalmol Vis Sci. 2015;56:4668–4679.
1058. L. Sauer, S. Peters, J. Schmidt, D. Schweitzer, M. Klemm, La Ramm, R. Augsten, M. Hammer, Monitoring macular pigment changes in macular holes using lifetime imagingophthalmoscopy. Acta Ophthalmologica 2016
1059. L. Sauer, K.M. Andersen, B. Li, R.H. Gensure, M. Hammer, P.S. Bernstein, Fluorescence Lifetime Imaging Ophthalmoscopy (FLIO) of Macular Pigment. Retina (2018)
1060. L. Sauer, C. B. Komanski, A. S. Vitale, E. D. Hansen, P. S. Bernstein, Fluorescence lifetime imaging ophthalmoscopy (FLIO) in eyes with pigment epithelial detachments due to age-related macular degeneration. IOVS 60, 3054-3063 (2019)

1061. A. M. Saxena, G. Krishnamoorthy, J. B. Udgaonkar, N. Periasamy, Identification of intermediate species in protein-folding by quantitative analysis of amplitudes in time-domain spectroscopy. J. Chem. Sci. 119, 61-69 (2007)
1062. A. M. Saxena, J. B. Udgaonkar, G. Krishnamoorthy, Characterization of intra-molecule distances ans site-specific dynamics in chemically unfolded barstar: Evidence for denaturant-dependent non-random structure. J. Mol. Biol. 359, 174-189 (2006)
1063. A. Saxena, J.B. Udgaonkar, G. Krishnamoorthy, Protein dynamics and protein folding revealed by time-resolved fluorescence, in M. Hof, R. Hutterer, V. Fidler, Fluorescence spectroscopy in biology, Springer Verlag Berlin Heidelberg New York 1-29(2005)
1064. T. Saxl, F. Khan, D.R. Matthews, Z.-L. Zhi, O. Rolinski, S. Ameer-Beg, J. Pickup, Fluorescence lifetime spectroscopy and imaging of nano-engineered glucose sensor microcapsules based on glucose/galactose-binding protein. Biosensors and Bioelectronics 24, 3229–3234 (2009)
1065. M. Sauer, C. Zander, R. Müller, B. Ullrich, S. Kaul, K.H. Drexhage, J. Wolfrum, Detection and identification of individual antigen molecules in human serum with pulsed semiconductor lasers, Appl. Phys. B **65**, 427-431 (1997)
1066. P.M. Schaefer, D. Hilpert, M. Niederschweiberer, L. Neuhauser, S. Kalinina, E. Calzia, A. Rueck, B. von Einem, C.A.F. von Arnim, Mitochondrial matrix pH as a decisive factor in neurometabolic imaging. Neurophotonics 4(4):045004 (2017)
1067. P. M. Schaefer, S. Kalinina, A. Rueck, C.A.F. von Arnim, B. von Einem, NADH Autofluorescence - A Marker on its Way to Boost Bioenergetic Research. Cytometry Part A, 1-13 (2018)
1068. J. Schaffer, A. Volkmer, C. Eggeling, V. Subramaniam, G. Striker, C.A.M. Seidel, Identification of single molecules in aqueous solution by time-resolved fluorescence anisotropy, J. Phys. Chem. A **103**, 331-336 (1999)
1069. H. Scheer, Pigmente und Antennenkomplexe. In: D.-P. Häder (ed.), Photosynthese. Georg Thieme Verlag, Stuttgart, New York. (1999)
1070. R. H. Schirmer, B. Coulibaly, A. Stich, M. Scheiwein, H. Merkle, J. Eubel, K. Becker, H. Becher, O. Müller, T. Zich, W. Schiek, B. Kouyate, Methylene blue as an antimalarial agent. Redox Report 8, 272-275 (2003)
1071. F.E.W. Schmidt, M.E. Fry, E.M.C. Hillman, J.C. Hebden, D.T. Delpy, A 32-channel time-resolved instrument for medical optical tomography, Rev. Sci. Instrum. **71**, 256-265 (2000)
1072. J. Schmidt, S. Peters, L. Sauer, D. Schweitzer, M. Klemm, R. Augsten, N. Müller, M. Hammer, Fundus autofluorescence lifetimes are increased in non-proliferative diabetic retinopathy. Acta Ophthalmologica 2016
1073. R. Schmitz, K. Tweed, C. Walsh, A. J. Walsh, M. C. Skala, Extracellular pH affects the fluorescence lifetimes of metabolic co-factors. J Biomed Opt. 26(5), 056502202-1 to -8
1074. H. Schneckenburger, H.K. Seidlitz, J. Eberz, Time-resolved fluorescence in photobiology, J. Photochem. Photobiol. B:Biol. 2 (1988) 1-19
1075. H. Schneckenburger, M. Frenz: Time-resolved fluorescence of conifers exposed to environmental pollutants, Radiat. Environ. Biophys. 25 (1986) 289-295
1076. H. Schneckenburger, M. Frenz, Y. Tsuchiya, U. Denzer, L. Schleinkofer: Picosecond fluorescence microscopy for measuring chlorophyll and porphyrin components in conifers and cultured cells, Lasers Life Sci. 1 (1987) 299-307
1077. H. Schneckenburger, W. Schmidt: Time-resolving luminescence techniques for possible detection of forest decline (II) Picosecond chlorophyll fluorescence, Radiat. Environ Biophys. 31 (1992) 73-81
1078. H. Schneckenburger, W. Schmidt: Luminescence techniques for monitoring of forest decline, J. Photochem. Photobiol. B: Biol. 13 (1992) 190-193
1079. H. Schneckenburger, W. Schmidt: Time-resolved chlorophyll fluorescence of spruce needles under various light conditions, J. Fluoresc. 5 (1995) 155-158
1080. H. Schneckenburger, W. Schmidt: Time-resolved chlorophyll fluorescence of spruce needles after different light exposure, J. Plant Physiol. 148 (1996) 593-598
1081. A. Schönle, M. Glatz, S.W. Hell, Four-dimensional multiphoton microscopy with time-correlated single photon counting, Appl. Opt. **39**, 6306-6311 (2000)
1082. A. C. Schüller, Z. Ahmed, J. A. Levitt , K. M. Suen, K. Suhling and J. E. Ladbury, Indirect recruitment of the signalling adaptor Shc to the fibroblast growth factor receptor 2 (FGFR2). Biochem. J. 416, 189–199 (2008)
1083. C. Schultz, A. Bartelt, C. Junghans, W. Becker, R. Schlatmann, B. Stegemann, Enhanced recombination next to laser-patterned lines in CIGSe solar cells revealed by spectral and time-resolved photoluminescence. Applied Surface Science 536 147721, 1-7 (2021)
1084. R. Schultz, S. Hasan, L.-S. Schwanengel, M. Hammer, Fluorescence lifetimes increase over time in age-related macular degeneration. Acta Ophthalmologica (2020)

1085. R. Schultz, K. C. L. K. Gamage, J. D. Messinger, C. A. Curcio,M. Hammer Fluorescence Lifetimes and Spectra of RPE and Sub-RPE Deposits in Histology of Control and AMD Eyes. Investigative Ophthalmology & Visual Science. 61(11), 1-9 (2020)
1086. R. Schuyler, I. Isenberg, A Monophoton Fluorometer with Energy Discrimination, Rev. Sci. Instrum. 42 813-817 (1971)
1087. D. Schweitzer, A. Kolb, M. Hammer, E. Thamm, Tau-mapping of the autofluorescence of the human ocular fundus, Proc. SPIE **4164**, 79-89 (2000)
1088. D. Schweitzer, A. Kolb, M. Hammer, Autofluorescence lifetime measurement in images of the human ocular fundus, SPIE **4432**, 29-39 (2001)
1089. D. Schweitzer, A. Kolb, M. Hammer, E. Thamm, Basic investigations for 2-dimensional time-resolved fluorescence measurements at the fundus, Int. Ophthalmol. **23**, 399-404 (2001)
1090. D. Schweitzer, A. Kolb, M. Hammer, R. Anders, Zeitaufgelöste Messung der Autofluoreszenz, Ophthalmologe **99**, 776-779 (2002)
1091. D. Schweitzer, M. Hammer, F. Schweitzer, R. Anders, T. Doebbecke, S. Schenke, E. R. Gaillard, In vivo measurement of time-resolved autofluorescence at the human fundus, J. Biomed. Opt. **9**, 1214-1222 (2004)
1092. Schweitzer D, Hammer M, Schweitzer F. Limits of the confocal laser-scanning technique inmeasurements of time-resolved autofluorescence of the ocular fundus. Biomed Tech (Berl). 50(9), 263–267 (2005)
1093. D. Schweitzer, M. Hammer, F. Schweitzer, S. Schenke, E. Birckner, W. Becker, A. Bergmann, In vivo autofluorescence lifetime imaging at the fundus of the human eye. Proc. SPIE 6138 (2006)
1094. D. Schweitzer, S. Schenke, M. Hammer, F. Schweitzer, S. Jentsch, E. Birckner, W. Becker, Towards Metabolic Mapping of the Human Retina. Micr. Res. Tech. 70, 403-409 (2007)
1095. D. Schweitzer, M. Hammer, S. Jentsch, S. Schenke, Interpretation of dymanic fluorescence of the eye. Proc. SPIE 677108-1 to -12 (2007)
1096. D. Schweitzer, S. Quick, S. Schenke, M. Klemm, S. Gehlert, M. Hammer, S. Jentsch, J. Fischer, Vergleich von Parametern der zeitaufgelösten Autofluoreszenz bei Gesunden und Patienten mit früher AMD. Der Ophthalmologe 8, 714-722 (2009)
1097. D. Schweitzer, Quantifying fundus autofluorescence. In: N. Lois, J.V. Forrester, eds., Fundus autofluorescence. Wolters Kluwer, Lippincott Willams & Wilkins (2009)
1098. D. Schweitzer, Metabolic Mapping. In: F.G. Holz, R.F. Spaide (eds), Medical retina, Essential in Opthalmology, Springer (2010)
1099. D. Schweitzer, S. Quck, M. Klemm, M. Hammer, S. Jentsch, J. Dawczynski, Zeitaufgelöste Autofluoreszenz bei retinalen Gefäßverschlüssen. Der Ophthalmologe 12, 1145-1152 (2010)
1100. D. Schweitzer, E.R. Gaillard, J. Dillon, R.F. Mullins, S. Russell, B. Hoffmann, S. Peters, M. Hammer, C. Biskup, Time-Resolved Autofluorescence Imaging of Human Donor Retina Tissue from Donors with Significant Extramacular Drusen. IOVS, 53, 3376-3386 (2012)
1101. D. Schweitzer, Autofluorescence diagnostics of ophthalmic diseases. In: V.V. Ghukasyan, A.H. Heikal, eds., Natural biomarkers for cellular metabolism. Biology, techniques, and applications. CRC Press, Taylor and Francis Group, Boca Raton, London, New York (2015)
1102. D. Schweitzer, M. Hammer, Fluorescence Lifetime Imaging in Ophthalmology. In: W. Becker (ed.) Advanced time-correlated single photon counting applications. Springer, Berlin, Heidelberg, New York (2015)
1103. D. Schweitzer, Ophthalmic applications of FLIM. In: L. Marcu. P.M.W. French, D.S. Elson, (eds.), Fluorecence lifetime spectroscopy and imaging. Principles and applications in biomedical diagnostics. CRC Press, Taylor & Francis Group, Boca Raton, London, New York (2015)
1104. D. Schweitzer, L. Deutsch, M. Klemm, S. Jentsch, M. Hammer, S. Peters, J. Haueisen, U. A. Müller, J. Dawczynski, Fluorescence lifetime imaging ophthalmoscopy in type 2 diabetic patients who have no signs of diabetic retinopathy. J. Biomed. Opt. 20(6), 061106-1 to 13 (2015)
1105. P. Schwille, Cross-correlation analysis in FCS, in R. Rigler, E.S. Elson (eds.) Fluorescence correlation spectroscopy, Springer Verlag Berlin, Heidelberg, New York, 360-378 (2001)
1106. P. Schwille, F.J. Meyer-Almes, R. Rigler, Dual-color fluorescence cross-correlation spectroscopy for multicomponent diffusional analysis in solution, Biophys. J. **72**, 1878-1886 (1997)
1107. P. Schwille, U. Haupts, S. Maiti, W.W.W. Webb, Molecular Dynamics in Living Cells Observed by Fluorescence Correlation Spectroscopy with One- and Two-Photon Excitation, Biophys. J. **77**, 2251-2265 (1999)
1108. P. Schwille, S. Kummer, A.H. Heikal, W.E. Moerner, W.W.W. Webb, Fluorescence correlation spectroscopy reveals fast optical excitation-driven intramolecular dynamics of yellow fluorescent proteins, PNAS **97**, 151-156 (2000)
1109. SCONTEL Superconducting Nanotechnology, http://www.scontel.ru/sspd

1110. A. J. H. Sedlack, R. Penjweini, K. A. Link, A. Brown, J. Kim, S.-J. Par, J. H. Chung, N. Y. Morgan, J. R. Knutson, Computational Modeling and Imaging of the Intracellular Oxygen Gradient. Int. J.Mol. Sci. 23, 12597-1 to -19 (2022)
1111. S. Seidenari, F. Arginelli, C. Dunsby, P. M. W. French, K. König, C. Magnoni, C. Talbot, G. Ponti, Multiphoton Laser Tomography and Fluorescence Lifetime Imaging of Melanoma: Morphologic Features and Quantitative Data for Sensitive and Specific Non-Invasive Diagnostics. PLOS One, 8(7) e70682-1 to -9 (2013)
1112. A. N. Semenov., E. G. Maksimov, A. M. Moysenovich, M. A. Yakovleva, G. V. Tsoraev, A. A. Ramonova, E. A. Shirshin, N. N. Sluchanko, T. B. Feldman, A. B. Rubin, M. P. Kirpichnikov, M. A. Ostrovsky, Protein-Mediated Carotenoid Delivery Suppresses the Photoinducible Oxidation of Lipofuscin in Retinal Pigment Epithelial Cells. Antioxidants 12, 413, 1-19 (2023)
1113. S. Sengupta, K.K. Dey, H.S. Muddana, T. Tabouillot, M.E. Ibele, P.J. Butler, A. Sen, Enzyme molecules as nanomotors. J. Am. Chem. Soc. 135, 1406-1414 (2013)
1114. S. Sengupta, M.M. Spiering, K.K. Dey, W. Duan, D. Patra, P.J. Butler, R. D. Astumian, S. Benkivic, A. Sen, DNA polymerase as a molecular motor and pump. ACS NANO 8(3) 2410-2418 (2014)
1115. SENSL Technologies Ltd., PCMPlus: Intelligent photon counting module, www.sensl.com
1116. T. F. Sergeeva, M. V. Shirmanova, O. A. Zlobovskaya, A. I. Gavrina, V. V. Dudenkova, M. M. Lukina, K. A. Lukyanov, E. V. Zagaynova, Relationship between intracellular pH, metabolic cofactors, and caspase-3 activation in cancer cells during apoptosis. BBA - Molecular Cell Research (2017)
1117. A.L. Serrano, O. Bilsel, F. Gai, Native State Conformational Heterogeneity of HP35 Revealed by Time-Resolved FRET. J Phys Chem B. 116(35):10631-8 (2012)
1118. S. Sever, J. Skoch, S. Newmyer, R. Ramachandran, D. Ko, M. McKee, R. Bouley, D. Ausiello, B. T Hyman, B. J. Bacskai, Physical and functional connection between auxilin and dynamin during endocytosis. EMBO J. 25, 4163-4174 (2006)
1119. S. Sever, J. Skoch, B. J. Bacskai, S. Newmyer, Assays and functional properties of auxilin-dynamin interactions. Methods Enzymol. 404, 570-585 (2005)
1120. E.M. Sevick-Muraca, A. Godavarty, J.P. Houston, A.B. Thompson, R. Roy, Near-infrared imaging with fluorescence contrast agents. In M.-A. Mycek, B.W. Pogue (eds.), Handbook of Biomedical Fluorescence, Marcel Dekker New York, Basel, 445-527 (2003)
1121. A.T. Shah, K.E. Diggins, A.J. Walsh, J.M. Irish, M.C. Skala, In vivo autofluorescence imaging of tumor heterogeneity in response to treatment. Neoplasia 17, 862-870 (2015)
1122. J. S. Shah, M. Venturas, T. H. Sanchez, A. S. Penzias, D. J. Needleman, D. Sakkas, Fluorescence lifetime imaging microscopy (FLIM) detects differences in metabolic signatures between euploid and aneuploid human blastocysts. Human Reproduction, 37, No.3, 400–410 (2022)
1123. J. R. Shakirova, V. A. Baigildin, A. I. Solomatina, R. Babadi Aghakhanpour, V. V. Pavlovskiy, V. V. Porsev, S. P. Tunik, Intracellular pH Sensor Based on Heteroleptic Bis-Cyclometalated Iridium(III) Complex Embedded into Block-Copolymer Nanospecies: Application in Phosphorescence Lifetime Imaging Microscopy. Adv. Funct. Mater. 2212390 1-17 (2022)
1124. J. T. Sharick, P. F. Favreau, A. A. Gillette, S. M. Sdao, M. J. Merrins, M. C. Skala, Protein-bound NAD(P)H Lifetime is Sensitive to Multiple Fates of Glucose Carbon. Scientific Reports 8, 5456 (2018)
1125. J.T. Sharick, J.J. Jeffery, M.J.Karim, C.M. Walsh, K. Esbona, R.S. Cook, M.C. Skala, Cellular metabolic heterogeneity in vivo is recapitulated in tumor organoids. Neoplasia 21, 615-626 (2019)
1126. J. T. Sharick, Walsh CM, Sprackling CM, Pasch CA, Pham DL, Esbona K, Choudhary A, Garcia-Valera R, Burkard ME, McGregor SM, Matkowskyj KA, Parikh AA, Meszoely IM, Kelley MC, Tsai S, Deming DA, Skala MC, Metabolic Heterogeneity in Patient Tumor-Derived Organoids by Primary Site and Drug Treatment. Front Oncol. 10, 553, 1-17 (2020)
1127. R. Sharma, D.R. Williams, G. Palczewska, K. Palczewki, J.J. Hunter, Two-photon autofluorescence imaging reveals cellular structures throughout the retina of the living primate eye. Invest Ophthalmol Vis Sci. 57, 632-646 (2016)
1128. P.F. Sharp, A. Manivannan, H. Xu, J.V. Forrester, The scanning laser ophthalmoscope - a review of its role in bioscience and medicine, Physics in Medicine & Biology 49, 1085 (2004)
1129. V. Shcheslavskiy, P. Morozov, A. Divochiy, Yu. Vakhtomin, K. Smirnov, W. Becker, Ultrafast time measurements by time-correlated single photon counting coupled with superconducting single photon detector, Rev. Sci. Instrum. 053117 (2016)
1130. V. I. Shcheslavskiy, A. Neubauer, R. Bukowiecki, F. Dinter, W. Becker, Combined fluorescence and phosphorescence lifetime imaging. Appl. Phys. Lett. 108, 091111-1 to -5 (2016)
1131. V. I. Shcheslavskiy, M. V. Shirmanova, V. V. Dudenkova, K. A. Lukyanov, A. I. Gavrina, A. V. Shumilova, E. Zagaynova, W. Becker, Fluorescence time-resolved macroimaging. Opt. Lett. 43, No. 13, 3152-5155 (2018)

1132. V. I. Shcheslavskiy, D. V. Yuzhakova, D. A. Sachkova, M. V. Shirmanova, W. Becker, Macroscopic temporally and spectrally resolved fluorescence imaging enhanced by laser-wavelength multiplexing. Opt. Lett. 48, 20 / 15 (2023)
1133. V. I. Shcheslavskiy, M. V. Shirmanova, K. S. Yashin, A. C. Rück, M. C. Skala, W. Becker, Fluorescence Lifetime Imaging Techniques - A Review on Principles, Applications and Clinical Relevance. J. Biophotonics 0:e202400450, 1-43 (2025)
1134. Q.-H. Shen, Y, Saijo, S. Mauch, C. Biskup, S. Bieri, B. Keller, H. Seki, B. Ülker, I.E. Somssich, P. Schulze-Leftert, Nuclear activity of MLA immune response links isolate-specific and basal resistance responses. Science Express, www.scienceexpress.org / 21 December 2006 / Page 1 / 10.1126/science.1136372
1135. Y.-F. Shen, M.-R. Tsai, S.-C. Chen, Y.-S. Leung, C.-T. Hsieh, Y.-S. Chen, F.-L. Huang, R. P. Obena, M. M. L. Zulueta, H.-Y. Huang, W.-J. Lee, K.-C. Tang, C.-T. Kung, M.-H. Chen, D.-B. Shieh, Y.-J. Chen, T.-M. Liu, P.-T. Chou, and C.-K. Sun, Imaging endogenous bilirubins with two-photon fluorescence of bilirubin dimers. Anal. Chem. 87, 7575-7582 (2015)
1136. P. S. Sherin, I. López-Duarte, M. R. Dent, M. Kubánková, A. Vyšniauskas, J. A. Bull, E. S. Reshetnikova, A. S. Klymchenko, Y. P. Tsentalovich and M. K. Kuimova, Visualising membrane viscosity of porcine eye lens cells using molecular rotors, Chem. Sci. 8, 3523-3528 (2017)
1137. M. Shibata, S. Ichioka, J. Ando, A. Kamiya, Microvascular and interstitial PO2 measurement in rat skeletal muscle by phosphorescence quenching. J. Appl. Physiol. 91, 321-327 (2001)
1138. L. Shimolina, M. A. Izquierdo, I. López-Duarte, J. Bull, M. Shirmanova, L. Klapshina, E. Zagaynova, M. K. Kuimova, Imaging tumor microscopic viscosity in vivo using molecular rotors Sci. Reports 7, 41097-1 to -5 (2017)
1139. L. Shimolina, A. Gulin, N. Ignatova, I. Druzhkova, M. Gubina, M. Lukina, L. Snopova, E. Zagaynov, M. K. Kuimova, M. Shirmanova, The Role of Plasma Membrane Viscosity in the Response and Resistance of Cancer Cells to Oxaliplatin. Cancers 13, 6165 1-18 (2021)
1140. S. Shiobara, R. Kamiyama, S. Tajima, H. Shizuka, S. Tobita, Excited-state proton transfer to solvent of protonated aniline derivatives in aqueous solution: a remarkable effect of ortho alkyl goup on the proton-dissociation rate, J. Photochem. Photobiol. A 154, 53-60 (2002)
1141. S. Shiobara, S. Tajima, S. Tobita, Substituent effects on ultrafast excited-state proton transfer of protonated aniline derivatives in aqueous solution, Chem. Phys. Lett. 380, 673-680 (2003)
1142. M. V. Shirmanova, I. N. Druzhkova, M. M. Lukina, V. V. Dudenkova, N. I. Ignatova, L. B. Snopova, V. I. Shcheslavskiy, V. V. Belousov, E. V. Zagaynova, Chemotherapy with cisplatin: insights into intracellular pH and metabolic landscape of cancer cells in vitro and in vivo. Scientific Reports 7, 8911-1 to -11 (2017)
1143. M. V. Shirmanova, V. I. Shcheslavskiy, M. M. Lukina, W. Becker, E. V. Zagaynova, Exploring Tumor Metabolism with Time-Resolved Fluorescence Methods: from Single Cells to a Whole Tumor. In: Tuchin, V.V., Popp, J., Zakharov, V. (eds) Multimodal Optical Diagnostics of Cancer. Springer, Cham. https://doi.org/10.1007/978-3-030-44594-2_3 (2020)
1144. M. V. Shirmanova, D. A. Gorbachev, K. S. Sarkisyan, A. P. Parnes, A. I. Gavrina, A. V. Polozova, T. F. Kovaleva, L. B. Snopova, V. V. Dudenkova, E. V. Zagaynova, K. A. Lukyanov, FUCCI-Red: a single-color cell cycle indicator for fluorescence lifetime imaging. Cellular and Molecular Life Sciences, https://doi.org/10.1007/s00018-020-03712-7 (2021)
1145. M. V. Shirmanova, D. A. Sachkova, I. D. Shchechkin, E. B. Kiseleva, A. D. Komarova, L. S. Kuhnina, A. S. Grishin, E. L. Bederina, E. V. Pyanova, E. E. Ponomareva, I. A. Medyanik, L. Y. Kravets, V. I. Shcheslavskiy, K. S. Yashin, Optical express-biopsy of gliomas using macroscopic fluorescence lifetime imaging. Biomedical Optics Express 16 (11) 4555-4570 (2025)
1146. E. A. Shirshin, Y. I. Gurfinkel, A. V. Priezzhev, V. V. Fadeev, J. Lademann, M. E. Darvin, Two-photon autofluorescence lifetime imaging of human skin papillary dermis in vivo: assessment of blood capillaries and structural proteins localization. Scientific Reports7, 1171-1 to 10 (2017)
1147. E. A. Shirshin, B. P. Yakimov, S. A. Rodionov, N. P. Omelyanenko, A. V. Priezzhev, V. V. Fadeev, J. Lademann, M. E. Darvin, Formation of hemoglobin photoproduct is responsible for two-photon and single photon-excited fluorescence of red blood cells. Laser Phys. Lett. 15, 075604-1 to -7 (2018)
1148. E. A. Shirshin, Y. I. Gurfinkel, S. T. Matskeplishvili, M. L. Sasonko, N. P. Omelyanenko, B. P. Yakimov, J. Lademann, M E. Darvin, In vivo optical imaging of the viable epidermis around the nailfold capillariesfo r the assessment of heart failure severity in humans. J. Biophotonics (2018)
1149. E. A. Shirshin, B. P. Yakimov1, M. E. Darvin, N. P. Omelyanenko, S. A. Rodionov, Y. I. Gurfinkel, J. Lademann, V. V. Fadeev, and A. V. Priezzhev, Label-Free Multiphoton Microscopy: The Origin of Fluorophores and Capabilities for Analyzing Biochemical Processes. Biochemistry (Moscow) 84, S69-S88 (2019)
1150. E. A. Shirshin, M. V. Shirmanova, A. V. Gayer, M. M. Lukina, E. E. Nikonova, B. P. Yakimov, G. S. Budylin, V. V. Dudenkova, N. I. Ignatova, D. V. Komarov, V. V. Yakovlev, W. Becker, E. V.

Zagaynova, V. I. Shcheslavskiy, Marian O. Scully, Label-free sensing with fluorescence lifetime imaging: The quest for matobilic heterogeneity. PNAS 119 No. 9, e2118241119 (2022)
1151. A. Shivalingam1 M. A. Izquierdo, A. Le Marois, A. Vysniauskas, K. Suhling, M. K. Kuimova, R. Vilar, The interactions between a small molecule and G-quadruplexes are visualized by fluorescence lifetime imaging microscopy. Nature Communications 6, 8178-1 to 10 (2015)
1152. B. Sick, B. Hecht, Orientation of single molecules by annular illumination, Phys. Rev. Lett. 85, 4482-4485 (2000)
1153. B. Sick, B. Hecht, U.P. Wild, L. Novotny, Probing confined fields with single molecules and vice versa, J. Microsc. 202, 365-373 (2001)
1154. D. Singh, H. Sielaff, M. Börsch, G. Grüber, Conformational dynamics of the rotary subunit F in the A_3B_3DF complex of Methanosarcina mazei Gö1 A-ATP synthase monitored by single-molecule FRET.FEBS Letters 591, 854-862 (2017)
1155. M. C. Skala, K. M. Riching, D. K. Bird, A. Dendron-Fitzpatrick, J. Eickhoff, K. W. Eliceiri, P. J. Keely, N. Ramanujam, In vivo multiphoton fluorescence lifetime imaging of protein-bound and free nicotinamide adenine dinucleotide in normal and precancerous epithelia. J. Biomed. Opt. 12 02401-1 to 10 (2007)
1156. M. C. Skala, K. M. Riching, A. Gendron-Fitzpatrick, J. Eickhoff, K. W. Eliceiri, J. G. White, N. Ramanujam, In vivo multiphoton microscopy of NADH and FAD redox states, fluorescence lifetimes, and cellular morphology in precancerous epithelia, PNAS 104, 19494-19499 (2007)
1157. M.C. Skala, A. Fontanella, L. Lan, J.A. Izatt, M.W. Dewhirst, Longitudinal optical imaging of tumor metabolism and hemodynamics. J. Biomed. Opt. 15(1) 011112-1 to -8 (2010)
1158. M.C. Skala, N. Ramanujam, Multiphoton Redox Ratio Imaging for Metabolic Monitoring in vivo. Methods Mol. Biol. 594, 155-162 (2010)
1159. A. M. Smyth, C. Rickman, R. R. Duncan, Vesicle Fusion Probability Is Determined by the Specific Interactions of Munc18. J. Biol. Chem. 285, 38141-38148 (2010)
1160. M. Snippe, J.W. Borst, R. Goldbach, R. Kormelik, The use of fluorescence microscopy to visualise homotypic interactions of tomato spotted wilt virus nucleocapsid protein in living cells, J. Vir. Meth. **125**, 12-15 (2005)
1161. P.T.C. So, K.H. Kim, L. Hsu, P. Kaplan, T. Hacewicz, C.Y. Dong, U. Greuter, N. Schlumpf, C. Buehler, Two-photon microscopy of tissues, in M.-A. Mycek, B.W. Pogue (eds.), Handbook of Biomedical Fluorescence, Marcel Dekker, New York, Basel, 181-208 (2003)
1162. J. F. Soderholm, S. L. Bird, P. Kalab, Y.i Sampathkumar, K Hasegawa, M. Uehara-Bingen, Karsten Weis, R. Heald, Importazole, a small molecule inhibitor of the transport receptorimportin-β. ACS Chem Biol. 15, 6, 700–708 (2011)
1163. U. Solbach, C. Keilhauer, H. Knabben, S. Wolf, Imaging of retinal autofluorescence in patients with age-related macular degenderation, Retina **17**, 385-389 (1997)
1164. P.V. Solntsev, K.L.Spurgim, J.R. Sabin, A.A. Heikal, V.N.Nemykin, Photoinduced charge transfer in short-distance ferrocenylsubphtahlocyanine dyads. Inorg. Chem. 51, 6537-6547 (2012)
1165. A. I. Solomatina, P. S. Chelushkin, D. V. Krupenya, I. S. Podkorytov,T. O. Artamonova,V. V. Sizov, A. S. Melnikov, V. V. Gurzhiy, E. I. Koshel, V. I. Shcheslavskiy, S. P. Tunik, Coordination to Imidazole Ring Switches on Phosphorescence of Platinum Cyclometalated Complexes: The Route to Selective Labeling of Peptides and Proteins via Histidine Residues.Bioconjugate Chem. 282, 426-437 (2017)
1166. A. I. Solomatina, S.-H. Su, M. M. Lukina, V. V. Dudenkova, V. I. Shcheslavskiy, C.-H. Wu, P. S. Chelushkin, P.-T. Chou, I. O. Koshevoy, S. P. Tunik, Water-soluble cyclometalated platinum(II) and iridium(III) complexes: synthesis, tuning of the photophysical properties, and in vitro and in vivo phosphorescence lifetime imaging. RSC Adv. 8, 17224-17236 (2018)
1167. S. R. Sonntag, E. Seifert, M. Hamann, B. Lewke, D. Theisen-Kunde, S. Grisanti, R. Brinkmann, Y. Miura, Fluorescence Lifetime Changes Induced by Laser Irradiation: A Preclinical Study towards the Evaluation of Retinal Metabolic States. Life 11, 555, 1-13 (2021)
1168. S. R. Sonntag, M. Kreikenbohm, G. Böhmerle, J. Stagge, S. Grisanti, Y. Miura, Impact of cigarette smoking on fluorescence lifetime of ocular fundus. Scietific Reports 13, 11484 1-12 (2023)
1169. L. Song, C.A.G.O. Varma, J.W. Verhoeven, H.J. Tanke, Influence of the triplet excited state on the photobleaching kinetics of fluoresceien in microscopy. Biophys. J. 70, 2959-2968 (1996)
1170. L. Spantzel, I. Pérez, Th. Heitkamp, A. Westphal, S. Reuter, R. Mrowka, M. Börsch, Monitoring oligomerization dynamics of individual human neurotensin receptors one in living cells and in SMALP nanodiscs. Proc. SPIE 12384, Multiphoton Microscopy in the Biomedical Sciences XXIII; 1238407 (2023)
1171. R.D. Spencer, G. Weber, Influence of brownian rotations and energy transfer upon the measurement of fluorescence lifetime, J. Chem. Phys. 52 1654-1663 (1970)
1172. A. Spinelli, M. Ghioni, S.Cova, L.M. Davis, Avalanche detector with ultraclean response for time-resolved photon counting. IEEE J. Quant. Electr. 34, 817-821 (1998)

1173. L. Spinelli, A. Torricelli, A. Pifferi, P. Taroni, R. Cubeddu, Experimental test of a perturbation model for time-resolved imaging in diffuse media, Appl. Opt. **42**, 3145-3153 (2003)
1174. L. Spinelli, A. Torricelli, A. Pifferi, P. Taroni, R. Cubeddu, Bulk optical properties and tissue componenty in the female breast from multiwavelength time-resolved optical mammography, J. Biomed. Opt. **9**, 1137-1142 (2004)
1175. L. Spinelli, F. Martelli, S.e Del Bianco, A. Pifferi,1 A. Torricelli, R. Cubeddu, G. Zaccanti, Absorption and scattering perturbations in homogeneous and layered diffusive media probed by time-resolved reflectance at null source-detector separation. Phys. Rev. 74, 021919-1 to -8 (2006)
1176. C. Spriet, D. Trinel, S. Laffray, M. Landry, B. Vandenbunder, L. Heliot, J. Barbillat, Setup of a fluorescence lifetime and spectral correlated acquisition system for two-photon microscopy, Rev. Sci. Instrum. 77, 123702-1 to -6 (2006)
1177. C. Spriet, D. Trinel, F. Waharte, D. Deslee, B. Vandenbunder, J. Barbillat, L. Heliot, Correlated Fluorescence Lifetime and Spectral Measurements in Living Cells, Micr. Res. tech. 70, 85-94 (2007)
1178. K. Sridevi, G. S. Lakshmikanth, G. Krishnamoorthy, J. B. Udgaonkar, Increasing stability reduces conformational heterogeneity in a protein folding intermediate ensemble. J. Mol. Biol. 337, 699-711 (2004)
1179. Srinagesh V. Koushik, Huanmian Chen, Christopher Thaler, Henry L. Puhl III, and Steven S. Vogel, Cerulean, Venus, and VenusY67C FRET Reference Standards. Biophys J.: Biophysical Letters L99-L101 (2006)
1180. M. Stagi, P. Gorlovoy, S. Larionov, K. Takahashi, H. Neumann, Unloading kinesin transported cargoes from the tubulin track via the inflammatory c-Jun N-terminal kinase pathway. The FASEB Journal 20, E1-E12 (2006)
1181. M. Stark, B. Manz, A. Ehlers, M. Küppers, I. Riemann, F. Volke, U. Siebert, W. Weschke, K. König, Multiparameter high-resolution imaging of barley embryos by multiphoton microscopy amd magnetic resonance imaging. Mircr. Res. Techn. 70, 426-432 (2007)
1182. F. Stefani, K. Vasilev, N. Bocchio, F. Gaul, A. Pomozzi, M. Kreiter, Photonic mode density effects on single-molecule fluorescence blinking. New Journal of Physics 21 (2007)
1183. J. Steinbrink, H. Wabnitz, H. Obrig, A. Villringer, H. Rinneberg, Determining changes in NIR absorption using a layered model of the human head, Phys. Med. Biol. **46**, 879-896 (2001)
1184. J. Steinbrink, A. Liebert, H. Wabnitz, R. Macdonald, H. Obrig, A. Wunder, R. Bourayou, T. Betz, J. Klohs, U. Lindauer, U. Dirnagl, A. Villringer, Towards Noninvasive Molecular Fluorescence Imaging of the Human Brain. Neurodegenerative Dis. 5, 296-303 (2008)
1185. O. Steinkellner, C. Gruber, H. Wabnitz, A. Jelzow, J. Steinbrink, J. B. Fiebach, R. Macdonald, and H. Obrig, Optical bedside monitoring of cerebral perfusion: technological and methodological advances applied in a study on acute ischemic stroke, J Biomed Opt 15, 061708 (2010)
1186. O. Steinkellner, H. Wabnitz, A. Jelzow, R. Macdonald, C. Gruber, J. Steinbrink, and H. Obrig, Cerebral Perfusion in Acute Stroke Monitored by Time-domain Near-infrared Reflectometry, Biocybernetics and Biomedical Engineering 32, 3-16 (2012)
1187. E.H.K. Stelzer, The intermediate optical system of laser scanning confocal microscopes. In J. Pawley (ed.), Handbook of biological confocal microscopy, 3rd edn., Springer (2006)
1188. P. Steven, M. Müller, N. Koop, C. Rose, G. Hüttmann, Comparison of Cornea Module and DermaInspect for noninvasive imaging of ocular surface pathologies. J. Biomed. Opt. 14(6), 064040-1 to 8
1189. M. Stevens, R.H. Hadfield, R.E. Schwall, S.W. Nam, R.P. Mirin, Time-correlated single-photon counting with superconducting detectors. Proc. of SPIE 6372, 63720U-1 to -10
1190. M. Stevens, R.H. Hadfield, R.E. Schwall, S.W. Nam, R.P. Mirin, Fast lifetime measurements of infrared emitters using low-jitter superconducting single-photon detectors. Appl. Phys. Lett. 89, 031109-1 to -3 (2006)
1191. M. H. Stewart, A. L. Huston, A. M. Scott, A. L. Efros, J. S. Melinger, K. Boeneman Gemmill, S. A. Trammell, J. B. Blanco-Canosa, P E. Dawson, I. L. Medintz, Complex Förster energy transfer interactions between semiconductor quantum dots and a redox-active osmium assembly. ACS Nano 6, 5330-5347 (2012)
1192. M. Straub, S.W. Hell. Fluorescence lifetime three-dimensional microscopy with picosecond precision using a multifocal multiphoton microscope. Appl. Phys. Lett. 73/13 (1998): 1769-1771
1193. D. Strat, F. Dolp, B. von Einem, C. Steinmetz, C. A. F. von Arnim, A.a Rueck, Spectrally resolved fluorescence lifetime imaging microscopy: Förster resonant energy transfer global analysis with a one- and two-exponential donor model. J. Biomed. Opt. 16(2), 026002-1 to -19
1194. S. J. Strickler, R. A. Berg, Relationship between absorption intensity and fluorescence lifetime of molecules, J. Chem. Phys. 37, 814–822 (1962)
1195. C. Stringari, L Abdeladim, G. Malkinson, P. Mahou, X. Solinas, I. Lamarre, S. Brizion, J-B. Galey, W. Supatto, R. Legouis, A.-M. Pena, E. Beaurepaire, Multicolor two-photon imaging of endogenous fluorophores in living tissues by wavelength mixing. Scientific Reports 7, 3792 (2017)

1196. C. Strohhöfer, T. Förster, D. Chorvat, P. Kasak, I. Lacik, M. Koukaki, S. Karamanou A.s Economoude, Quantitative analysis of energy transfer between fluorescent proteins in CFP–GBP–YFP and its response to Ca^{2+}. Phys. Chem. Chem. Phys. 13 17852-17863 (2011)
1197. C.D. Stubbs, S.W. Botchway, S.J. Slater, A.W. Parker, The use of time-resolved fluorescence imaging in the study of protein kinase C localisation in cells. BioMed Central 6:22 (2005), available on www.biomedcentral.com/1471-2121/6/22
1198. H. Studier, W. Becker, Megapixel FLIM. Proc. SPIE 8948 (2014)
1199. E. Stuntz, Y. Gong1, D. Sood, V. Liaudanskaya, D. Pouli, K. P. Quinn, C. Alonzo, Z. Liu1, D. L. Kaplan, I. Georgakoudi, Endogenous Two-Photon Excited Fluorescence Imaging Characterizes Neuron and Astrocyte Metabolic Responses to Manganese Toxicity. Scientific Reports 7, 1041-1 to -15 (2017)
1200. G.-C. Su, Y.-H.i Wei, .H.-W. Wang, NADH fluorescence as a photobiological metric in 5-aminolevlinic acid (ALA)-photodynamic therapy. Opt. Expr. 19, 21145-21154
1201. A. Sudakou, F. Lange, H. Isler, P. Lanka, S. Wojtkiewicz, P. Sawosz, D. Ostojic, M. Wolf, A. Pifferi, I. Tachtsides, A. Liebert, A. Gerega, Time-domain NIRS system based on supercontinuum light source and multi-wavelength detection: validation for tissue oxygenation studies. Biomed. Opt. Express 12, No. 10, 6629-6650 (2021)
1202. K. Suhling, D. McLoskey, D.J.S.Birch, Multiplexed single-photon counting. II. The statistical theory of time-correlated mesurements. Rev. Sci. Instrum. 67, 2230-2246, (1996)
1203. K. Suhling, D.M. Davis, Z. Petrasek, J. Siegel, D. Phillips, The influence of the refractive index on EGFP fluorescence lifetimes in mixtures of water and glycerol, Proc. SPIE **4259**, 91-101 (2001)
1204. K. Suhling, J. Siegel, D. Phillips, P.M.W. French, S. Lévêque-Fort, S.E.D. Webb, D.M. Davis, Imaging the environment of green fluorescent protein, Biophysical J. **83**, 3589-3595 (2002)
1205. K. Suhling, L. M. Hirvonen, J. A. Levitt, P.-H. Chung, C. Tregido, A. le Marois, D. Rusakov, K. Zheng, Fluorescence Lifetime Imaging (FLIM): Basic Concepts and Recent Applications. In: W. Becker (ed.) Advanced time-correlated single photon counting applications. Springer, Berlin, Heidelberg, New York (2015)
1206. Y. Sun, J. Qu, G. Xu, L. Zhao, H. Niu, Autofluorescence lifetime imaging of Lipofuscin and melanin in retinal pigment epithelium cells. Invest Ophthalmol Vis Sci, IOVS 48, 2965 (2007)
1207. Y. Sun, C.F. Booker, S. Mumari, R.N. Day, M. Davidson, A. Periasamy, Characterisation of an orange acceptor fluorescent protein for sensitzed spectral fluorescence resonance energy transfer microscopy using a white light laser. J. Biomed. Opt. 14(5) 054009-1 to 11 (2009)
1208. Y. Sun, A. Periasamy, Additional correction for energy transfer efficiency calculation in filter-based Förster resonance energy transfer for a more accurate result. J. Biomed. Opt. 15(2), 020513 (2010).
1209. Q. Sun, Y. Li, S. He, C. Situ, Z. Wu, J. Y. Qu, Label-free multimodal nonlinear optical microscopy reveals fundamental insights of skeletal muscle development. Biomed. Opt. Expr. 5, 158-166 (2013)
1210. Y. Sun, C. Rombola, V. Jyothikumar, A. Periasamy, Förster resonance energy transfer microscopy and spectroscopy to localize protein-protein interactions in live cells. Cytometry A, 83A(9), 780-793 (2013)
1211. R. Suarez-Ibarrola, L. Braun, P. Fabian Pohlmann, W. Becker, A. Bergmann, C. Gratzke, A. Miernik, K. Wilhelm, Metabolic Imaging of Urothelial Carcinoma by Simultaneous Autofluorescence Lifetime Imaging (FLIM) of NAD(P)H and FAD. Clinical Genitourinary Cancer (2020)
1212. D. Suraci, E. Baria, L. Tirloni, J.L. Lagarto, S. Buccianti, C. Agostini, S. Pillozzi, L. Antonuzzo, A. Taddei, and R. Cicchi, Delineation of gastrointestinal tumors biopsies using a fluorescence lifetime imaging optical fiber probe, J. Biophotonics J. e202400122 (2024)
1213. Sutter Instrument, Movable Objective Microscope. www.sutter.com/microscopes
1214. T. Svensson, J. Swartling, P. Taroni, A. Torricelli, P. Lindblom, C. Ingvar, S. Andersson-Engels, Characterization of normal breast tissue heterogeneity using time-resolved near-infrared spectroscopy. Phy. Med. Biol. 50, 2559-2571 (2005)
1215. T. Svensson, S. Andersson-Engels, M. Einarsdottir, K. Svanberg, In vivo optical characterisation of human prostate tissue using near-infrared time-resolved spectroscopy. J. biomed. Opt. 12(1), 014022 (2007)
1216. M. Szalkowski, J. D. J. Olmos, D. Buczyńska, S. Maćkowski, D. Kowalska, J. Kargul, Plasmon-induced absorption of blind chlorophylls in photosynthetic proteins assembled on silver nanowires. Nanoscale 9, 10475-10486 (2017)
1217. M. Szaszak, P. Steven, K. Shima, R. Orzekowsky-Schröder, Gereon Hüttmann, I.R. König, W. Solbach, J. Rupp, Fluorescence Lifetime Imaging Unravels C. trachomatis Metabolism and Its Crosstalk with the Host Cell. PLOS Pathogens 7, e1002108-1 to 12 (2011)
1218. H. Szmacinski, I. Gryczynski, J.R. Lakowicz, Three-photon induced fluorescence of the calcium probe Indo-1, Biophys. J. 70, 547-55 (1996)
1219. J. M. Szulczewski, D. R. Inman, D. Entenberg, S. M. Ponik, J. Aguirre-Ghiso, J. Castracane, J. Condeelis, K. W. Eliceiri, P. J. Keely, In vivo visualization of stromal macrophages via label-free FLIM-based metabolite imaging.Scientific Reports 6, 25086-1 to -9

1220. T. Tabouillot, H.S. Muddana, P.J. Butler, Endothelial membrane sensitivity to shear stress is lipid domain dependent. Cell. Mol. Bioeng. 4(2), 169-181 (2011)
1221. S. Tajima, S. Shiobara, H. Shizuka, S. Tobita, Excited-state proton-dissociation of N-alkylated anilinium ions in aqueous solution studied by picosecond fluorescence measurements Phys. Chem. Chem. Phys. **4**, 3376-3382 (2002)
1222. C, B. Talbot, R. Patalay, I. Munro, S. Warren, F. Ratto, P. Matteini, R. Pini, H. G. Breunig, K. König, A. C. Chu, G. W. Stamp, M. A. A. Neil, P. M. W. French, C. Dunsby, Application of ultrafast gold luminescence to measuring the instrument response function for multispectral multiphoton fluorescence lifetime imaging. Opt. Expr. 19, 13484-13861 (2011)
1223. C. Tardif, G. Nadeau, S. Labrecque, D. Côté, F. Lavoie-Cardinal, P. De Koninckа, Fluorescence lifetime imaging nanoscopy for measuring Förster resonance energy transfer in cellular nanodomains. Neurophotonics 6(1), 015002-1 to -16 (2019)
1224. P. Taroni, G. Danesini, A. Torricelli, A. Pifferi, L. Spinelli, R. Cubeddu, Clinical trial of time-resolved scanning optical mammography at 4 wavelengths between 683 and 975 nm, J. Biomed. Opt. **9**, 464-473 (2004)
1225. P. Taroni, A. Pifferi, A. Torricelli, L. Spinelli, G.M. Danesini, R. Cubeddu, Do shorter wavelength improve contrast in optical mammography?, Phys. Med. Biol. **49**, 1203-1215 (2004)
1226. P. Taroni, A. Torricelli, L. Spinelli, A. Pifferi, F. Arpaia G. Danesini and R. Cubeddu, Time-resolved optical mammography between 637 and 985 nm: Clinical study on the detection and identification of breast lesions, Phys. Med. Biol. **50**, 2469-2488 (2005)
1227. P. Taroni, D. Comelli, A. Farina, and A. Pifferi, A. Kienle, Time-resolved diffuse optical spectroscopy of small tissue samples. Opt. Expr. 15, 3301-3311 (2007)
1228. P. Taroni, D. Comelli, A. Pifferi, A. Torricelli, R Cubeddu, Absorption of collagen: effects on the estimate of breast composition and related diagnostic implications. J. of Biomed. Opt. 12(1) 014021-1 to -4 (2007)
1229. P. Taroni, A. Bassi, D. Comelli A. Farina, R. Cubeddu, A, Pifferi, Diffuse optical spectroscopy of breast tissue extended to 1100 nm, J. Biomed. Opt. 14(5) 1-1 to -7
1230. P. Taroni, A. Pifferi, G. Quarto, L. Spinelli, A. Torricelli, F. Abbate, A. Villa, N. Balestreri, S. Menna, E. Cassano and R. Cubeddu, Non-invasive assessment of breast cancer risk using time-resolved diffuse optical spectroscopy, J. Biomed. Opt., 15, 060501 (2010)
1231. P. Taroni, G, Quarto, A. Pifferi, F. Ieva, A.M.Paganoni, F. Abbate, N. Balestreri, S. Menna, E. Cassano, R. Cubeddu, Optical identification of subjects at high risk for developing breast cancer. J. Biomed. Opt. 18(6) 060507-1 to -3 (2013)
1232. T. A. Tasmi, L. Singh, A. J. Walsh, Fluorescence lifetime imaging to investigate propofol-induced metabolic alterations in MDA-MB-231 cells. Biomedical Optics Express 16(11) 4470-4482 (2025)
1233. P. Tauc, C.R. Mateo, J-C. Brochon, Pressure effects on the lateral distribution of cholesterol in lipid bilayers: A time-resolved spectroscopy study, Biophys. J. 74, 1864-1870 (1998)
1234. P. Tauc, C.R. Mateo, J-C. Brochon, Investigation of the effect of high hydrostatic pressure on proteins an lipidic membranes by dynamic fluorescence spectroscopy, Biochim. Biophys. Acta **1595**, 103-115 (2002)
1235. J. Teister, A. Liu, D. Wolters, N. Pfeiffer, F.H. Grus, Peripapillary fluorescence lifetime reveals age-dependent changes using fluorescence lifetime imaging ophthalmoscopy in rats. Exp. Eye Res. 176, 110-120 (2018)
1236. T. Teplicky, M. Danisova1, M. Valica, D. Chorvat Jr., A. Marcek Chorvatova, Fluorescence Properties of Chlorella sp. Algae. Appl. Phys. 15, 352-357 (2017)
1237. K. Teuchner, J. Ehlert, W. Freyer, D. Leupold, P. Altmeyer, M. Stücker, K. Hoffmann, Fluorescence studies of melanin by stepwise two-photon femtosecond laser excitation. J. Fluoresc. 10, 275-281 (2000)
1238. I. Texier, M. Goutayer, A. Da Silva, L. Guyon, N. Djaker, V. Josserand, E. Neumann, J. Bibette, F. Vinet, Cyanine-loaded lipid nanoparticles for improved in vivo fluorescence imaging. J. Biomed. Opt. 14(5), 054005-1 to 11 (2009)
1239. C. Thaler, S.V. Koushik, H.L. Puhl, P.S. Blank, S.S. Vogel, Structural rearrangement of CaMKIIα catalytic domains encodes activation. PNAS 0901913106 (2009)
1240. P. Theer, M.T. Hasan, W. Denk, Multi-photon imaging using a Ti:sapphire regenerative amplifier, Proc. SPIE **5139**, 1-6 (2003)
1241. N.L. Thomson, J.L. Mitchell, High order autocorrelation, in R. Rigler, E.S. Elson (eds.), Fluorescence Correlation Spectroscopy, Springer Verlag, Berlin, Heidelberg, New York 438-458 (2001)
1242. R.M. Thompson, R.M. Stevenson, A.J. Shields, I. Farrer, C.J. Lobo, D.A. Ritchie, M.L. Leadbeater, M. Pepper, Single-photon emission from exciton complexes in individual quantom dots, Physical Review B 64, 1-4 (2001)
1243. A.J. Thompson, S. Coda1, M. Brydegaard Sorensen, G. Kennedy, R. Patalay, U.a Waitong-Brämming, P.A.A. De Beule, M.A.A. Neil, S. Andersson-Engels, N. Bendsoe, P.M.W. French, K. Svanberg, C. Dunsby, In vivo measurements of diffuse reflectance and time-resolved autofluorescence emission spectra of basal cell carcinomas. J. Biophotonics 5, No. 3, 240–254 (2012)

1244. C.A. Thorling, X. Liu, F.J. Burczynski, L.M. Fletcher, M.S. Roberts, W.Y. Sanchez, Intravital multiphoton microscopy can model uptake and excretion of fluorescein in hepatic ischemia reperfusion injury. J. Biomed. Opt.18(10), 101306-1 to - 11
1245. C. A. Thorling, A. Holmes, H. Studier, D. Liu, X. Liang, M. S. Roberts, Multiphoton and Fluorescence Lifetime Imaging Microscopy in Studying Nanoparticle Pharmacokinetics in Skin and Liver. In: Micro and Nanotechnologies for Biotechnology, http://dx.doi.org/10.5772/63452
1246. C. A. Thorling, D. Crawford, F. J. Burczynski, X. Liu, I. Liau, M. S. Roberts, Multiphoton microscopy in defining liver function. J. Biomed. Opt. 19(9), 09090-1 (2014)
1247. Z. Timsah, Z. Ahmed, C.-C. Lin, F. A. Melo, L. J. Stagg, P. G. Leonard, P. Jeyabal, J. Berrout, R. G. O'Neil, M. Bogdanov, J. E. Ladbury, Competition between Grb2 and Plcγ1 for FGFR2 regulates basal phospholipase activity and invasion. Nature Structural & Molecular Biology 21, 180-188 (2014)
1248. P. Tinnefeld, V. Buschmann, D-P. Herten, K.T. Han, M. Sauer, Confocal fluorescence lifetime imaging microscopy (FLIM) at the single molecule level, Single Mol. **1**, 215-223 (2000)
1249. U.K. Tirlapur, K. König, Targeted transfection by femtosecond laser, Nature **418**, 290-291 (2002)
1250. L.M.M. Tijskens, P. E. Zerbini, R.E. Schouten, M. Vanoli, S. Jacob, M. Grassi, R. Cubeddu, L. Spinelli, A. Torricelli, Assessing harvest maturity in nectarines. Postharvest Biology and Technology 45, 204–213 (2007)
1251. C. Toncelli, O. V. Arzhakova, A. Dolgova, A. L. Volynskii, N. F. Bakeev, J. P. Kerry, D. B. Papkovsky, Oxygen-sensitive phosphorescent nanomaterials produced from high density polyethylene films by local solvent-crazing. Anal. Chem. 86(3), 1917-23 (2014)
1252. V. Toronov, M.A. Franceschini, M. Filiaci, S. Fantini, M. Wolf, A. Michalos, E. Gratton, Near-infrared study of fluctuations in cerebral hemodynamics during rest and motor stimulation. Med. Phys. **27**, (801-815) (2000)
1253. V. Toronov, A. Webb, J. H. Choi, M. Wolf, L. Safonova, U. Wolf, E. Gratton, Study of local cerebral hemodynamics by frequency-domain near-infrared spectroscopy and correlation with simultaneously acquired functional magnetic resonance imaging, Opt. Expr. **9**, 417-427 (2001)
1254. A. Torricelli, A. Pifferi, P. Taroni, E. Giambattistelli, R. Cubeddu, In vivo optical characterization of human tissue from 610 to 1010 nm by time-resolved reflectance spectroscopy, Phys. Med. Biol. **46**, 2227-2237 (2001)
1255. A. Torricelli, L. Spinelli, A. Pifferi, P. Taroni, R. Cubeddu, Use of a nonlinear perturbation approach for in vivo breast lesion characterization by multi-wavelength time-resolved optical mammography, Opt. Expr. **11**, 853-867 (2003)
1256. A. Torricelli, V. Quaresima, A. Pifferi, G. Biscotti, L. Spinelli, P. Taroni, M. Ferrati, R. Cubeddu, Mapping of calf muscle oxygenation and haemoglobin content during dynamic plantrat flexion exercise by multi-channel time-resolved near-infrared spectroscopy, Phys. Med. Biol. **49**, 685-699 (2004)
1257. A. Torricelli, A. Pifferi, Spinelli, R. Cubeddu, F. Martelli, S. Del Bianco, G. Zaccanti, Time-Resolved Reflectance at Null Source-Detector Separation: Improving Contrast and Resolution in Diffuse Optical Imaging. Phys. Rev. Lett. 95, 078101-1 to -4 (2005)
1258. A. Torricelli, D. Contini, A. Pifferi, L. Spinelli, R. Cubeddu, Functional brain imaging by multi-wavelength time-resolved near infrared spectroscopy. Opto-Electronic Rev. 16(2) 131-135 (2008)
1259. A. Torricelli, D. Contini, A. Pifferi, M. Caffini, R. Re, L. Zuchelli L. Spinelli, Time domian functional NIRS imaging for human brain mapping. Neuroimage 85, 28-50 (2014)
1260. A. Tosi, A. Dalla Mora, F. Zappa, A. Gulinatti, D. Contini, A. Pifferi, L. Spinelli, A. Torricelli, R. Cubeddu, Fast-gated single-photon counting technique widens dynamic range and speeds up acquisition time in time-resolved measurements. Opt. Expr. 19, 10735-10746 (2011)
1261. J. Tousaint, R. Grüner, M. Schubert, T. May, H.-G. Meyer, B. Dietzek, J. Popp, M. Hofherr, M. Arndt, D. Henrich, K. Ilin, M. Siegel, Superconductiong single-photon counting system for optical experiments requiring time-resolution in the picosecond range. Rev. Sci. Instrum. 83, 123103-1 to -5 (2012)
1262. J. Toussaint, S. Dochow, I. Latka, A. Lukic, T. May, H.-G. Meyer, K. Il'in, M. Siegel, J. Popp, Proof of concept of fiber dispersed Raman spectroscopy using superconducting nanowire single-photon detectors. Opt. Expr. 23, 5078-5090 (2015)
1263. B. Treanor, P.M.P. Lanigan, K. Suhling, T. Schreiber, I. Munro, M.A.A. Neil, D. Phillips, D.M. Davis, P.M.W. French, Imaging fluorescence lifetime heterogeneity applied to GFP-tagged MHC protein at an immunological synapse, J. Microsc. **217**, 36-43 (2005)
1264. C. Tregido, J.A. Levitt, K. Suhling, Effect of refractive index on the fluorescence lifetime of green fluorescent protein. J. Biomed. Opt. 13(3), 031218-1 to -8 (2008)
1265. C.-C. Tu, K. Awasthi, K.g-Po Chen, C.h-H. Lin, M. Hamada, N. Ohta, Y.-K. Li, Time-Gated Imaging on Live Cancer Cells Using Silicon Quantum Dot Nanoparticles with Long-Lived Fluorescence. ACS Photonics (May 2017)

1266. C. J. Tynan, S. K. Roberts, D. J. Rolfe, D. T. Clarke, H. H. Loeffler, J. Kästner, M. D. Winn, P. J. Parker, M. L. Martin-Fernandez, Human Epidermal Growth Factor Receptor (EGFR) Aligned on the Plasma Membrane Adopts Key Features of Drosophila EGFR Asymmetry. Mol. Cell. Biol 31(11) 2241-2252 (2011)
1267. A. Uchugonova, K. König, Two-photon autofluorescence and second-harmonic imaging of adult stem cells. J. Biomed. Opt. 13(5) 054068-1 to 8 (2008)
1268. Y. Ueda, S. Kwok, Y. Hayashi, Application of FRET probes in the analysis of neuronal plasticity, Frontiers in neural circuits 7, 163 (2013)
1269. Y. Ueda, Y. Hayashi, PIP_3 regulates spinule formation in dentritic spines structural long-term potentiation. J. Neurosci. 33(27) 11040-11047 (2013)
1270. K. Uemura, C. M. Lill, M. Banks, M. Asada, N. Aoyagi, K. Ando, M. Kubota, T. Kihara, T. Nishimoto, H. Sugimoto, R. Talahashi, B. T. Hyman, S. Shimohama, O. Berezovska, A. Kinoshita, N-cadherin-based adhesion anhances Aβ releases and decreases $A\beta_{42/40}$ ratio. J. Neurochem. 108, 350-360 (2009)
1271. M. Uherek, O. Ulicna, O. Vancova, J. Muchova, Z. Ďuračková, L. Šikurová, D. Chorvat1, Alteration of time-resolved autofluorescence properties of rat aorta, induced by diabetes mellitus. Laser Physics 26, (2016)
1272. V. Ulrich, P. Fischer, I. Riemann, K. König, Compact multiphoton / single photon laser scanning microscope for spectral imaging and fluorescence lifetime imaging, Scanning **26**, 217-225 (2004)
1273. G. Ulu, A.V. Sergienko, M.S. Ünlü, Influence of hot-carrier luminescence from avalanche photodiodes on time-correlated photon detection, Opt. Lett. **25**, 758-760 (2000)
1274. M. Umasuthan, A.M. Wallace, J.S. Massa, G.S. Buller, A.C. Walker, Processing time-correlated single photon counting data to acquire range images, IEEE Proc. Vis. Image Signal Process. **145**, 237-243 (1998)
1275. G. Valentini, C. D'Andrea, R.e Ferrari, A.o Pifferi, R.o Cubeddu, M. Martinelli, C. Natoli, P. Ubezio and R. Giavazzi, In Vivo Measurement of Vascular Modulation in Experimental Tumors Using a Fluorescent Contrast Agent. Photochem. Photobiol. 84, 1249-1256 (2008)
1276. N. Valim, J. Brook, M. Niedre, Experimental measurement of time-dependant photon scatter for diffuse optical tomography. J. .Biomed. Opt. 15(6), 065006-1 to -8 (2010)
1277. M. Valkonen., E. R. Kalkman, M. Saloheimo1, M. Penttilä1, N. D. Read, R. R. Duncan, Spatially segregated snare protein interactions in living fungal cells. J. Biol. Chem. 282 22775-22785 (2007)
1278. VALO Femtosecond Series -Aalto with SHG Option, https://hubner-photonics.com/products/lasers/femtosecond-lasers/valo-series/
1279. P.A.W. Van den Berg, A. van Hoek, C.D. Walentas, R.N. Perham, A.J.W.G. Visser, Flavin Fluorescence Dynamics and Photoinduced Electron Transfer in Escherichia coli Glutathione Reductase, Biophys. J. **74**, 2046-2058 (1998)
1280. P.A.W. van den Berg, K.A.Feenstra, A.E. Mark, H.J.C.Berendsen, A.J.W.G. Visser, Dynamic Conformations of Flavin Adenine Dicucleotide: Simulated molecular dynamics of the flavin cofactor related to the time-resolved fluorescence characteristics. J. Phys. Chem. 106, 8858-8869 (2002)
1281. C.J.R. Van der Oord, J.R. Jones, D.A. Shaw, I.H. Munro, Y.K. Levine, H.C. Gerritsen, High-resolution confocal microscopy using synchrotron radiation. J. Microsc. 182 217-224 (1996)
1282. M.A.M.J. Van Zandvoort, C.J. de Grauw, H.C. Gerritsen, J.L.V. Broers, M.G.A. Egbrink, F.C.S. Ramaekers, D.W. Slaaf, Discrimination of DNA and RNA in cells by a vital fluorescent probe: Lifetime imaging of SYTO13 in healthy and apoptotic cells, Cytometry **47**, 226-232 (2002)
1283. M. Valkonen, E. R. Kalkman, M. Saloheimo, M. Penttilä, N. D. Read, R. R. Duncan, Spatially segregated snare protein interactions in living fungal cells. JBC 282, 22775-22785 (2007)
1284. K. Verdeccia, M. Diop, T.-Y. Lee, K. St. Lawrence, Quantifying the cerebral metabolic rate of oxygen by combining diffuse correlation spectroscopy and time-resolved near-infrared spectroscopy. J. Biomed. Opt. 18(2) 027007 (2013)
1285. A. Verevkin, A. Pearlman, W. Slysz, J. Zhang, M. Currie, A. Korneev, G. Chulkova, O. Okunev, P. Kouminov, K, Smirnov, B. Voronov, G. Goltsman, R. Sobolewski, Untrafast superconducting single-photon detectors for near-infrared-wavelength quantum communications. J. Mod. Op. 51, 1447-1458 (2004)
1286. M. Venturas, X. Yang, K. Kumar, D. Wells, C. Racowsky, D. J. Needleman, Metabolic imaging of human cumulus cells reveals associations among metabolic profiles of cumulus cells, patient clinical factors, and oocyte maturity. Reproductive Science 116 No. 6 1651-1662 (2021)
1287. M. Venturas, J. S. Shah, X. Yang, T. H. Sanchez , W. Conway, D. Sakkas, Dan J. Needleman, Metabolic state of human blastocysts measured by fluorescence lifetime imaging microscopy. Human Reproduction, 1–17 (2022)
1288. M. Venturas, X. Yang, D. Sakkas, D. Needleman, Noninvasive metabolic profiling of cumulus cells, oocytes, and embryos via fluorescence lifetime imaging microscopy: a mini-review. Human Reproduction, 1–12 (2023)

1289. M. L. Viger, W. Sheng, K. Dore, A. H. Alhasan, C.-J. Carling, J. Lux, C. de Gracia Lux, M. Grossman, R. Malinow, A. Almutairi, Near-Infrared-Induced Heating of Confined Water in Polymeric Particles for Efficient Payload Release. ACS NANO 8(5), 4815–4826 (2014)
1290. H.D. Vishwasrao, A. A. Heikal, K.A. Kasischke, W. W. Webb, Conformational Dependence of Intracellular NADH on Metabolic State Revealed by Associated Fluorescence Anisotropy. J. Biol. Chem. 280, 25119-25126 (2005)
1291. S. S. Vogel, C. Thaler, S. V. Koushik, Fanciful FRET. Sci. STKE 2006, re2 (2006)
1292. S.S. Vogel, C. Thaler, P.S. Blonk, S.V. Koushik, Time-Resolved Fluorescence Anisotropy. In: A. Periasamy, R.M. Clegg, FLIM microscopy in Biology and medicine. Taylor & Francis (2009)
1293. S. S. Vogel, T.A. Nguyen, P.S. Blank, W. van der Meer, An introduction to interpreting time-resolved fluorescence anisotropy curves. In: W. Becker (ed.) Advanced time-correlated single photon counting applications. Springer, Berlin, Heidelberg, New York (2015)
1294. A. Volkmer, D.A. Hatrick, D.J.S. Birch, Time-resolved nonlinear fluorescence spectroscopy using femtosecond multiphoton excitation and single-photon timing, Meas. Sci. Technol. **8**, 1339-1349 (1997)
1295. A. Volkmer, V. Subramaniam, D.J.S. Birch, T.M. Jovin, One- and two-photon excited fluorescence lifetimes and anisotropy decays of green fluorescent proteins, Biophys. J. **78**, 1589 (2000)
1296. C.A. von Arnim ,A. Kinoshita ,I.D. Peltan ,M.M. Tangredi ,L. Herl ,B.M. Lee ,R. Spoelgen, T.T. Hshieh, S. Ranganathan, F.D. Battey, C.X. Liu, B.J. Bacskai, S. Sever,M.C. Irizarry, D.K. Strickland, B.T. Hyman, The low density lipoprotein receptor-related protein (LRP) is a novel beta-secretase (BACE1) substrate. J Biol Chem. 280, 7777-7785 (2005)
1297. A. Vyšniauskas, M. Qurashi and M. K. Kuimova, A Molecular rotor that measures dynamic changes of lipid bilayer viscosity caused by oxidative stress, Chem. Eur. J. 22, 13210–13217 (2016)
1298. A. Vyšniauskas, I. López-Duarte, N. Duchemin, T.-T. Vu, Y. Wu, E. M. Budynina, Y. A. Volkova, E. Peña Cabrera, D. E. Ramírez-Ornelas and M. K. Kuimova, Exploring viscosity, polarity and temperature sensitivity of BODIPY-based molecular rotors, Phys. Chem. Chem. Phys. (2017)
1299. A. Vyšniauskas, D. Ding, M. Qurashi, I. Boczarow, M. Balaz, H. L. Anderson; and M. K. Kuimova, Tuning the sensitivity of fluorescent porphyrin dimers to viscosity and temperature, Chem. Eur J 23, 11001 – 11010 (2017)
1300. H. Wabnitz, H. Rinneberg, Imaging in turbid media by photon density waves: spatial resolution and scaling relations, Appl. Opt. 36(1), 64-74 (1997)
1301. H. Wabnitz, A. Liebert, M. Möller, D. Grosenick, R. Model, H. Rinneberg, Scanning laser-pulse mammography: matching fluid and off-axis measurements. Biomedical Topical Meetings, Technical Digest, OSA 686 (2002)
1302. H. Wabnitz, D. Grosenick, M. Möller, J. Stössel, B. Wassermann, R. Macdonald, K.T. Moesta, H. Rinneberg, Scanning laser-pulse mammography: matching fluid and off-axis measurements, In OSA Biomedical Optics Topical Meetings on CD ROM (The Optical Sciety of America, Washington, DC) (2004)
1303. H. Wabnitz, M. Möller, A. Liebert, A. Walter, R. Erdmann, O. Raitza, C. Drenkhahn, J.P. Dreier, H. Obrig, J. Steinbrink, R. Macdonanld, A time-domain brain imager applied in functional stimulation experiments. Proc. SPIE 5859, 58590H-1 to -9 (2005)
1304. H. Wabnitz, M. Moeller, A. Liebert, H. Obrig, J. Steinbrink, R. Macdonald, Time-Resolved Near-Infrared Spectroscopy and Imaging of the Adult Human Brain. Adv. Exp. Med. Biol. 662 143-148 (2010)
1305. H. Wabnitz, D. R. Taubert, M. Mazurenka, O. Steinkellner, A. Jelzow, R. Macdonald, D. Milej, P. Sawosz, M. Kacprzak, A. Liebert, R. Cooper, J. Hebden, A. Pifferi, A. Farina, I. Bargigia, D. Contini, M. Caffini, L. Zucchelli, L. Spinelli, R. Cubeddu, A. Torricelli., Performance assessment of time-domain optical brain imagers, part 1: basic instrumental performance protocol. J. Biomed. Opt. 19(8), 086010 (2014)
1306. H. Wabnitz, A. Jelzow, M. Mazurenka, O. Steinkellner, R. Macdonald, D. Milej, N. Zolek, M. Kacprzak, P. Sawosz, R. Maniewski, A. Liebert, S. Magazov, J. Hebden, F. Martelli, P. Di Ninni, G. Zaccanti, A. Torricelli, D. Contini, R. Re, L. Zucchelli, L. Spinelli, R. Cubeddu, A. Pifferi, Performance assessment of time-domain optical brain imagers, part 2: nEUROPt protocol. J. Biomed. Opt. 19(8), 086012 (2014)
1307. H. Wabnitz, M. Mazurenka, L. Di Sieno, G. Boso, W. Becker, K. Fuchs, D. Contini, A. Dalla Mora, A. Tosi, R. Macdonald, A. Pifferi, Time-domain diffuse optical imaging of tissue by non-contact scanning. In: W. Becker (ed.) Advanced time-correlated single photon counting applications. Springer, Berlin, Heidelberg, New York (2015)
1308. H.E. Wagner, R. Brandenburg, K.V. Kozlov, Cross correlation emission spectroscopy: application to non-equilibrium plasma diagnostics, Proceedings of Frontiers in Low Temperature Plasma Diagnostics V (2003)
1309. H.E. Wagner, R. Brandenburg, K.V. Kozlov, A. Sonnenfeld, P. Michel, J.F. Behnke, The barrier discharge: Basic properties and applications to surface treatment, Vacuum **71**, 417-436 (2003)

1310. H.E. Wagner, R. Brandenburg, K.V. Kozlov, Progress in the visualisation of filametary gas discharges, part1: Milestones and diagnostics of dielectric-barrier discharges by cross-correlation, Journal of Advanced Oxidation Technologies **7**, 11-19 (2004)
1311. F. Waharte, C. Spriet, L. Heliot, Setup and Characterization of a Multiphoton FLIM Instrument for Protein–Protein Interaction Measurements in Living Cells, Cytometry Part A 69A 299–306 (2006)
1312. P. Walczysko, U. Kuhlicke, S. Knappe, C. Cordes, T.R. Neu, In Situ Activity of Suspended and Immobilized Microbial Communities as Measured by Fluorescence Lifetime Imaging. Appl. Environ. Mocrobiol. 74, 294-299 (2008)
1313. A.M. Wallace, G.S. Buller, A.C. Walker, 3D imaging and ranging by time-correlated single photon counting, Computing & Control. IEE Computing and Control Engineering Journal 12, 157-168 (2001)
1314. H. Wallrabe, Z. Svindrych, S. R. Alam, K. H. Siller, T. Wang, D. Kashatus, S. Hu, A. Periasamy, Segmented cell analyses to measure redox states of autofluorescent NAD(P)H, FAD & Trp in cancer cells by FLIM. Sci. Reports 8:79, 1-11 (2018)
1315. A. Walsh, R.C. Cook, B. Rexer, C.L. Arteaga, M.C. Skala, Optical Imaging of metabolism in HER2 overexpressing breast cancer cells. Biomedical Optics Express 3(1), 75-85 (2012)
1316. A. J. Walsh, R. S. Cook, H. C. Manning, D. J. Hicks, A. Lafontant, C. L. Arteaga, M. C. Skala, Optical Metabolic Imaging Identifies Glycolytic Levels, Subtypes, and Early-Treatment Response in Breast Cancer. Cancer Res. 73, 6164-6174 (2013)
1317. A. J. Walsh, R. S. Cook, M. E. Sanders, L. Aurisicchio, G. Ciliberto, C. L. Arteaga, M. C. Skala, Quantitative Optical Imaging of Primary Tumor Organoid Metabolism Predicts Drug Response in Breast Cancer. Cancer Res 74, OF1-OF11 (2014)
1318. A. J. Walsh, A. T. Shah, J. T. Sharick, M. C. Skala, Fluorescence Lifetime measurements of NADH in live cells and tissue. In: W. Becker (ed.) Advanced time-correlated single photon counting applications. Springer, Berlin, Heidelberg, New York (2015)
1319. A. J. Walsh, M. C. Skala, Optical metabolic imaging quantifies heterogeneous cell populations. Biomed. Opt. Expr. 6, 559-573 (2015)
1320. A.J. Walsh, K.P. Mueller, K. Tweed, I. Jones, C.M. Walsh, N.J. Piscopo, N.M. Niemi, D.J. Pagliarini, K. Saha, M.C. Skala, Classification of T-cell activation via autofluorescence lifetime imaging. Nat Biomed Eng. 5(1), 77-88 (2021)
1321. H-W. Wang, V. Ghukassyan, C.T. Chen, Y.H. Wei, H.W. Guo, J.S. Yu, F.J. Kao, Differentiation of appoptosis from necrosis by dynamic changes of reduced nicotinamide adenine dinucleotide fluorescence lifetime in live cells. J. Biomed. Opt. 13(5), 054011-1 to 9 (2008)
1322. H. Wang, R. Zhang, K. R. Bridle, A. Jayachandran, J. A. Thomas, W. Zhang, J. Yuan, Z. P. Xu, D. H. G. Crawford, X. Liang, X. Liu, M. S. Roberts, Two-photon dual imaging platform for in vivo monitoring cellularoxidative stress in liver injury. Scientific Reports 7, 45374-1 to -11 (2017)
1323. H. Wang, X. Liang, G. Gravot, C.A Thorling, D. H. G. Crawford, Z. P.Xu, X. Liu, M. S. Roberts, Visualizing liver anatomy, physiology and pharmacology using multiphoton microscopy. J. Biophotonics 10, 46-60 (2017)
1324. M. Wang, F. Tang, X. Pan, L. Yao, X. Wang, Y. Jing, J. Ma, G. Wang, L. Mi, Rapid Diagnosis and Intraoperative Margin Assessment of Human Lung Cancer with Fluorescence Lifetime Imaging Microscopy. BBA Clinical (2017)
1325. S. Wang, Y. Li, Y. Zhao, F. Lin, J. Qu, L.I Liu, Investigating tunneling nanotubes in ovarian cancer based on two-photon excitation FLIM-FRET. Biomedical Optics Express, 12(4), 1962-1971 (2021)
1326. O. Warburg, On the origin of cancer cells. Science 123, 309-314 (1956)
1327. O. Warburg, On respiratory impairment in cancer cells. Science 124, 269-270 (1956)
1328. R.E. Warburton, A. McCarthy, A.M. Wallace, S. Hernandez-Marin, S. Cova, R.A. Lamb, G.S. Buller, Enhanced performance photon-counting time-of-flight sensor. Opt. Expr. 15, 423-429 (2007)
1329. M. Ware, A. Migdall, Single-photon detctor characterization using correlated photons: The march from feasibility to metrology, Journal of Modern Optics 51, 1549-1557 (2004)
1330. S. Weidkamp-Peters, S. Felekyan, A. Bleckmann, R. Simon, W. Becker, R. Kühnemuth, C.A.M. Seidel. Multiparameter fluorescence image spectroscopy to study molecular interactions. Photochem. Photobiol. Sci. 8, 470-480 (2009)
1331. M. Weinigel, H.-G. Breuning, A. Uchugonova, K. König, Multipurpose nonlinear optical imaging system for in vivo and ex vivo multimodal histology. Journal of Medical Imaging 2, 016003-1 to -10 (2015)
1332. M. Weissman, H. Schindler, G. Feher, Determination of molecular weights by fluctuation spectroscopy. PNAS 73, 2776-2780 (1976)
1333. J. H. Werner, R. Joggerst, R.B. Dryer, P.M. Goodwin, A two-dimensional view of the folding energy landscape of cytochrome c. PNAS 103, 11130-11135 (2005)
1334. K.D. Weston, M. Dyck, P. Tinnefeld, C. Müller, D.P. Herten, M. Sauer, Measuring the number of independent emitters in single molecule fluorescence images and trajectories using coincident photons, Anal. Chem. 74, 5342-5349 (2002)

1335. D. Wickramasinghe, R. Timerman, J. Bartusek, A. Heikal. Partitioning and Diffusion of Fluorescently Labelled FTY720 in Resting Epithelial Cells. In: W. Becker (ed.) Advanced time-correlated single photon counting applications. Springer, Berlin, Heidelberg, New York (2015)
1336. J. Widengren, V. Kudryavtsev, M. Antonik, S. Berger. M. Gerken, C. A. M. Seidel, Single-molecule detection and identification of multiple species by multiparameter fluorescence detection. Anal.Chem. 78, 2039-2050 (2006)
1337. J. G. Wieland, N. Naskar, Kirsten Reess, D. Nobre Sarmento dos Santos, J. M. Weise, Th. Blatt, S. Kordes, P. Walther, A. Rück, Impact of Coenzyme Q10 on Mitochondrial Metabolism: A Complementary Study Using Fluorescence Lifetime Imaging and Electron Microscopy. Front. Biosci. (Landmark Ed), 29(11) 383-1 to -9 (2024)
1338. R.W. Wijnaendts van Resandt, R.H. Vogel, S.W. Provencher, Double beam fluorescence lifetime spectrometer with subnanosecond resolution: Application to aqueous tryptophan, Rev. Sci. Instrum. **53**, 1392-1397 (1982)
1339. O.M. Williams, W.J. Sandle, A ‚pile-up' gate generator for removing distortion in multichannel delayed coincidence experiments, Phys. Sci. Instrum. **3**, 741-743 (1970)
1340. C.D. Wilms, H. Schmidt, .J Eilers, Quantitative two-photon calcium imaging via fluorescence lifetime analysis, Cell Calcium 49, 73-9 (2006)
1341. C.D. Wilms, J. Eilers, Photo-physical properties of calcium indicator dyes suitable for two-photon fluorescence-lifetime recordings, J. Microsc. 225, 209-13 (2007)
1342. J.G. White, W.B. Amos, M. Fordham, An evaluation of confocal versus conventional imaging of biological structures by fluorescence light microscopy, J. Cell Biol. **105**, 41-48 (1987)
1343. B.C. Wilson, A.L. Jaques, Optical reflectance and transmittance of tissues: Principles and application, IEEE Journal of Quantum Electronics **26**, 2186-2199 (1990)
1344. C. D. Wilms, H. Schmidt, and J. Eilers, Quantitative two-photon Ca^{2+} imaging via fluorescence lifetime analysis, Cell Calcium 40, 73-79 (2006).
1345. T. Wilson, C. Sheppard, Theory and practice of scanning optical microscopy. Academic Press (1984)
1346. G. T. Wondrak, NQQO1-activated phenothiazinium redoc cyclers for the targeted bioreductive induction of cancer cell apaptosis. Free Radic. Biol. Med. 15, 178-190 (2007)
1347. A.K. Wozniak, S. Nottrott, E. Kühn-Hölsken, G. F. Schröder, H. Grubmüller, R. Lührmann, C.A.M. Seidel, F. Oesterheld, Detecting protein-induced folding of the U4 snRNA kink-turn by single-molecule multiparameter FRET measurements. RNA 11, 1545-1554 (2005)
1348. D. Wrobel, I. Hanyz, Charged porphyrin - dopa melanin interaction at varied pH: Fluorescence lifetime and photothermal studies, J. Fluoresc. **13**, 169-177 (2003)
1349. Y. Wu, Y. Qu, Combined depth- and time-resolved autofluorescence spectroscopy of epithelial tissue. Opt. Lett. 31, 1833-1835 (2006)
1350. Y. Wu, W. Zheng, Y. Qu, Sensing cell metabolism by time-resolved autofluorescence. Opt. Lett. 31 3122-3124 (2006)
1351. Y. Wu, E. Kondrashkina, C. Kayatekin., C. R. Matthews, O. Bilsel, Microsecond acquisition of heterogeneous structure in the folding of a TIM barrel protein. PNAS 105 no. 36, 13367–13372 (2008)
1352. C. Xu, W.W. Webb, Measurement of two-photon excitation cross sections of molecular fluorophores with data from 690 to 1050 nm. J. Opt. Soc. Am. B 13, 481-491 (1996)
1353. Flavonoids. https://lpi.oregonstate.edu/mic/dietary-factors/phytochemicals/flavonoids
1354. J. Yabuzaki, Carotenoids Database: structures, chemical fingerprints and distribution among organisms. Database, 2017, 1–11, doi: 10.1093/database/bax004
1355. B. Yakimov, A. Komarova, E. Nikonova, A. Mozherov, L. Shimolina, M. Shirmanova, W. Becker, E. Shirshin, V. Shcheslavskiy, Simultaneous assessment of NAD(P)H and flavins with multispectral fluorescence lifetime imaging microscopy at a single excitation wavelength of 750 nm. J. .Biomed. Opt. 29(10), 106501-1 to -14 (2024)
1356. I. Yamazaki, N. Tamai, H. Kume, H. Tsuchiya, K. Oba, Microchannel-plate photomultiplier applicability to the time-correlated photon-counting, Rev. Sci. Instrum. **56**, 1187-1194 (1985)
1357. H. Yang, X.S. Xie, Probing single-molecule dynamics photon by photon, J. Chem. Phys. **117**, 10965-10979 (2002)
1358. H. Yang, G. Luo, P. Karnchanaphanurach, T.-M. Louie, I. Rech, S. Cova, L. Xun, X.S. Xie, Protein conformational dynamics probed by single-molecule electron transfer. Science 302, 262-266 (2003)
1359. M.S. Yang, D. Li, T, Lin, J.J. Zheng, W. Zheng, J.Y. Qu, Increase in intracellular free/bound NAD[P]H as a cause of Cd-induced oxidative stress in the $HepG_2$ cells. Toxicology247, 6-10 (2008)
1360. H. Yang, G. Luo, P. Karnchanaphanurach, T.-M. Louie, I. Rech, S. Cova, L. Xun, X.S. Xie, Protein conformational dynamics probed by single-molecule electron transfer. Science 302, 262-266 (2003)
1361. F. Yang, F. Gao, P. Ruan, H. Zhao, Combined domain decomposition and matrix decomposition scheme for large-scale diffuse optical tomography. Appl. Opt. 49(16) 3111-3126

1362. X. Yang, G. Ha, D. J. Needleman, A coarse-grained NADH redox model enables inference of subcellular metabolic fluxes from fluorescence lifetime imaging. eLife 10, e738082021, 1-44
1363. M.A. Yaseen, S. Sakadzic, w. Wu, W. Becker, K.A. Kasischke, D.A. Boas, In vivo imaging of cerebral enery matabolism with two-photon fluorescence lifetime imaging microscopy of NADH. Biomed. Opt. Expr. 4, 307-321 (2013)
1364. M. Yaseen, J. Sutin, W. Wu, B. Fu, H. Uhlirova, A. Devor, D.A. Boas, S. Sakadzic, Fluorescence lifetime microscopy of NADH distinguishes alterations in cerebral metabolism in vivo. Biome. Opt. Expr. 8, 2368-2385 (2017)
1365. R. Yasuda, C.D. Harvey, H. Zhong, A. Sobczyk, L. van Aelst, K. Svoboda, Supersensitive Ras activation in dendrites and spines revealed by two-photon fluorescence lifetime images. Nature Neuroscience 9 (2), 238-291 (2006)
1366. G. Yazgan, R. I. Dmitriev, V Tyagi, J.Jenkins, G-M. Rotaru, M.Rottmar, R. . Rossi, C. Toncelli, D. B. Papkovsky, K. Maniura-Weber, G. Fortunato, Steering surface topographies of electrospun fibers: understanding the mechanisms. Scietific Reports 7, 158-1 to -13 (2017)
1367. J. Yguerabide, Nanosecond fluorescence spectroscopy of macromolecules, Meth. Enzymol. **26**, 498-578 (1972)
1368. H. Yokota, A. Fukasawa, M. Hirano, T. Ide, Low-Light Photodetectors for Fluorescence Microscopy. Microscopy. Appl. Sci., 11, 2773, 1-20 (2021)
1369. T. Yoshihara, H. Shimada, H. Shizuka, S. Tobita, Internal conversion of o-aminoacetophenone in solution, Phys. Chem. Chem. Phys. **3**, 4972-4978 (2001)
1370. K.S. Youngworth, T.G. Brown, Focusing of high numerical aperture cylindrical-vector beams, Opt. Expr. **7**, 77-87 (2000)
1371. S.Yazdanfar, C. Joo, C. Zhan, M.Y. Berezin, W.J. Akers, S. Achilefu, Multiphoton microscopy with near infrared contast agents. J. Biomed. Opt. 15(3), 030505-1 to -3 (2010)
1372. G. Yu, T.F. Floyd, T. Durduran, C. Zhou, J. Wang, J.A. Detre, A.G. Yodh, Validation of diffuse correlation spectroscopy for muscle blood flow with concurrent arterial spin labeled perfusion MRI. Opt. Expr. 15, 1064-1075 (2007)
1373. Q. Yu, A. A. Heikal, Two-photon autofluorescence dynamics imaging reveals sensitivity of intracellular NADH concentration and conformation to cell physiology at the single-cell level. J. Photochem. Photobiol. B 95, 46-57 (2009)
1374. Z. Yuan, B. Kardynal, R.M. Stevenson, A.J. Shields, C.J. Lobo, K. Cooper, N.S. Beattie, D.A. Ritchie, M. Pepper, Electrically driven Single-Photon Source, Science **295**, 102-105 (2002)
1375. I. Yudushkin, R.D.Vale, Imaging T-cell receptor activation reveals accumulation of tyrosine-phosphorylated CD3ζ in the endosomal compartment. PNAS 107, 22128-22133 (2010)
1376. D. Yuzhakova, E. Kiseleva, M. Shirmanova, V. Shcheslavskiy, D. Sachkova, L. Snopova, E. Bederina, M. Lukina, V. Dudenkova, G. Yusubalieva, T. Belovezhets, D. Matvienko, V. Baklaushev, Highly Invasive Fluorescent/Bioluminescent Patient-Derived Orthotopic Model of Glioblastoma in Mice. Frontiers in Oncology 12, 897839 1-16 (2022)
1377. Yuzhakova DV, Sachkova DA, Shirmanova MV, Mozherov AM, Izosimova AV, Zolotova AS, Yashin KS. Measurement of Patient-Derived Glioblastoma Cell Response to Temozolomide Using Fluorescence Lifetime Imaging of NAD(P)H. Pharmaceuticals 16(6), 796 1-14 (2023)
1378. C. Zander, M. Sauer, K.H. Drexhage, D-S. Ko, A. Schulz, J. Wolfrum, L. Brand, C. Eggeling, C.A.M. Seidel, Detection and characterisation of single molecules in aqueous solution, Appl. Phys. B **63**, 517-523 (1996)
1379. C. Zander, K.H. Drexhage, K-T. Han, J. Wolfrum, M. Sauer, Single-molecule counting and identification in a microcapillary, Chem. Phys. Lett. **286**, 457-465 (1998)
1380. N. Zarrabi, M. G. Düser, S. Ernst, R. Reuter, G. D. Glick, S. D. Dunn, J. Wrachtrup, M. Börsch, Monitoring the rotary motors of single F_oF_1-ATP synthase by synchronized multi channel TCSPC, Proc. SPIE 6771, 677110F-1to -12 (2007)
1381. N. Zarrabi, M. G. Düser, R. Reuter, S. D. Dunn, J. Wrachtrup, M. Börsch, Detecting substeps in the rotary motors of F_oF_1-ATP synthase by Hidden Markov Models, Proc. SPIE 6444 (2007)
1382. N. Zarrabi, S. Ernst, B. Verhalen, S. Wilkens, M. Börsch, Analyzing conformational dynamics of single P-glycoprotein transporters by Förster resonance energy transfer using hidden Markov models, Methods, 65, in press (2014)
1383. Y.-L. Zhang, H. Tavakoli, M. Chachisvilis, Apparent PKA activity responds to intermittent hypoxia in bone cells: A redox pathway? Am. J. Physiol. Heart Circ. Physiol. 299, H225–H235 (2010)
1384. Y. Zeng, B. Yan, Q. Sun, S. Khoon Teh, W. Zhang, Z. Wen, Jianan Y. Qu, Label-free in vivo imaging of human leukocytes using two-photon excited endogenous fluorescence. J. Biomed. Opt. 18(4), 040103-1 to -3 (2013)
1385. Y.-L. Zhang, J. A. Frangos, M.S Chachisvilis, Mechanical stimulus alters conformation of type 1 parathyroid hormone receptor in bone cells. Am. J. Physiol. Cell Physiol. 296, C1391-C1399 (2009)

1386. S. Zhang, M. Hosaka, T. Yoshihara, K. Negishi Y. Iida S. Tobita T. Takeuchi, Phosphorescent light-emitting iridium complexes serve as a hypoxia-sensing probe for tumor imaging in live animals. Cancer res. 70, 4490-4498 (2010)
1387. X. Zhang, S. Shastry, S.E. Bradforth , J.L.Nadeau, Nuclear uptake of ultrasmall gold-doxorubicin conjugates imaged by fluorescence lifetime imaging microscopy (FLIM) and electron microscopy. Nanoscale 7(1), 240-251 (2014)
1388. W. Zhang, L. Wu, J. Li, X.Wang, Y, Lu W. Chen, Z. Zhou, L. Zhang, H. Zhao, F. Gao, Combined hemoglogin and fluorescence diffuse optical tomography for breast tumor diagnosis: a pilot study on time-domain methodology.
1389. B. Zhang, C. Yang, Y. Gao, Y. Wang, C. Bu, S. Hu, L. Liu, H. V. Demir, J. Qu and K.-T. Yong, Engineering Quantum Dots with Different Emission Wavelengths and Specific Fluorescence Lifetimes for Spectrally and Temporally Multiplexed Imaging of Cells. Nanotheranostics 1, 131-140 (2017)
1390. A. V. Zhdanov, A. V. Golubeva, I. A. Okkelman, J. F. Cryan, D. B. Papkovsky, Imaging of oxygen gradients in giant umbrella cells: an ex vivo PLIM study. Am J Physiol Cell Physiol 309, 2015
1391. A. V. Zhdanov, I. A. Okkelman, F. W. J. Collins, S. Melgar, D.i B. Papkovsky, A novel effect of DMOG on cell metabolism: direct inhibition of mitochondrial function precedes HIF target gene expression. Biochimica et Biophysica Acta 1847, 1254–1266 (2015)
1392. A. V. Zhdanov, I. A. Okkelman, A. V. Golubeva, B. Doerr, N. P. Hyland, S. Melgar, F. Shanahan, J. F. Cryan, D. B. Papkovsky, Quantitative analysis of mucosal oxygenation using ex vivoimaging of healthy and inflamed mammalian colon tissue. Cell. Mol. Life Sci. 74, 141–151 (2017)
1393. W. Zheng, D. Li, J.Y. Qu, Monitoring changes of cellular metabolism and microviscosity in vitro based on time-resolved endogenous fluorescence and its anisotropy decay dynamics. J. Biomed. Opt. 15(3), 037013-1 to 11 (2010)
1394. W. Zheng, D. Li, Y.Zeng, Y. Luo, J. Y. Qu, Two-photon excited hemoglobin fluorescence. Biomed. Opt. Expr. 2, 71-79 (2011)
1395. K. Zheng, T. P. Jensen, L. P. Savtchenko, J. A. Levitt, K. Suhling, D. A. Rusakov, Nanoscale diffusion in the synaptic cleft and beyond measured with time-resolved fluorescence anisotropy imaging. Scientific Reports 7, 42022-1 to 9
1396. C. Zhou, G. Yu, D. Furuya, J.H. Greenberg, A.G. Yodh, T. Durduran, Diffuse optical correlation tomography of cerebral blood flow during cortical spreading depression in rat brain. Opt. Expr. 14, 1125-1144 (2006)
1397. Y. Zhu, C.-S. Choe, S. Ahlberg, M. C. Meinke, U. Alexiev, J. Lademann, M. E. Darvina, Penetration of silver nanoparticles into porcine skin ex vivo using fluorescence lifetime imaging microscopy, Raman microscopy, and surface-enhanced Raman scattering microscopy. J. Biomed. Opt. 20(5), 051006-1 to -8 (2015)
1398. G. Zou, W.i Yu, Y. Xu, Y. Li, R. Hu, J. Qu, L. Liu, Investigation of apoptosis based on fluorescence lifetime imaging microscopy with a mitochondria-targeted viscosity probe. RSC Adv. 11, 38750-38758 (2021)
1399. B. Zimmermann, M. Diez, N. Zarrabi, P. Gräber, M. Börsch, Movements of the ε-subunit during catalysis and activation in single membrane-bound H^+-ATP synthase. EMBO J. 24 (2005) 2053-2063
1400. V. Zherdeva, N. I. Kazachkina, V. Shcheslavskiy, A. P. Savitsky, Long-term fluorescence lifetime imaging of a genetically encoded sensor for caspase-3 activity in mouse tumor xenografts. J. Biomed. Opt. 23(3), 035002 -1 to -11 (2018)
1401. E. A. Zherebtsov, E. V. Potapova, A. V. Mamoshin, V. V. Shupletsov, K. Y. Kandurova, V. V. Dremin, A. Y. Abramov, and A. V. Dunaev, Fluorescence lifetime needle optical biopsy discriminates hepatocellular carcinoma. Biomed. Opt. Express 13, 633-646 (2022)
1402. O.A. Zlobovskaya, T. F. Sergejeva, M. V. Shormanova, V.V. Dundenkova, G. V. Sharonov, E. V. Zagaynova, K. Lukyanov, Genetically encoded far-red fluorescent sensors for caspase-3 activity. Biotechniques 60, 62-68 (2016)
1403. K. M. Zoltowska, M.o Maesako, I. Lushnikova, S. Takeda, Laura J. Keller, G, Skibo, B. T. Hyman, O. Berezovska, Dynamic presenilin 1 and synaptotagmin 1 interaction modulates exocytosis and amyloid β production. Molecular Neurodegeneration 12, 15 (2017)
1404. M. Zude, L. Spinelli, A. Torricelli, Approach for non-destructive pigment analysis in model liquids and carrots by means of time-of-flight and multi-wavelength remittance readings. Analytica Chimia Acta 623, 204-212 (2008)
1405. V. Zwiller, H. Blom, P. Jonsson, N. Panev, S. Jeppesen, T. Tsegaye, E. Goobar, M.E. Pisto, L. Samuelson, G. Björk, Single quantum dots emit single photons at a time: Antibunching experiments, Appl. Phys. Lett. 78, 2476-2478 (2001)

Index

2D Curve Routine 801
2D Data Processing 801
2D Display Parameters 826
2D FIDA 676
2D histograms in SPCImage 904
2D histograms of single-molecule burst parameters 669
3D Curve Display, display parameters 826
3D curve mode 826
3D Data Processing 805
3D Display 803
3D Display Parameters 826
3D display parameters, mode selection 828
3D display parameters, window selection 828
3D trace parameters 264, 806, 836
Abberior STED microscopes 71
Absorption coefficient 611
Absorption of biological tissue 605
Acceptor, of FRET 507
Accumulate function 736, 738, 740, 743, 745, 748, 751, 756, 761, 780
Accumulation
- of FLIM data, by hardware 125
- of FLIM data, by software 125
- of FLITS data 130
- of temporal mosaic FLIM data 403, 409

Acousto-optical modulator, see AOM 80
Acquisition time
- dynamic brain imaging 613
- FASTAC FLIM system 422
- of FLIM 56, 130, 444, 453, 470, 474, 480
- of TCSPC 105, 130
- ophthalmic FLIM 592
- scanning mammography 610
- static brain imaging 612

Active quenching of SPAD 158
Adapters
- A-PPI-D 92
- beamsplitter assemblies 86
- detector/shutter assemblies 86
- electrical 92
- fibre adapter of laser 75
- FV-1000 confocal 68
- FV1000 NDD 69
- FV300 NDD 69
- HPM detector 83
- LSM 710/780/880 confocal 52
- LSM 710/780/880 NDD 52

ADC 107, 140, 151, 152
- dither range 141, 151, 789
- dithering 141, 150, 151, 789
- error correction 151
- Resolution 152, 787
- TAC-ADC priciple 140
- variable resolution 152
- zoom function 153, 787

ADC principle 153
Add / Sub Signal 781
Adjust Parameters 793
Afterpulsing 167, 182, 660
Afterpulsing background 168, 277, 299
Aggregates 497, 583
Amplifiers
- biased, in TAC 107
- for detector signals 211
- preamplifers 88, 211

Amplitude distribution
- of single photon pulses 161, 271

Amplitude jitter, of detector pulses 147
Amplitudes of decay components 951
- autofluorescence 556
- FAD 366, 529
- FRET 510, 511
- NADH 366, 529

Analog-to-digital conversion 151
Analog-to-digital converter 107
Anisotropy 314
- anisotropy decay 307, 551
- fluorescence, at high NA 308, 485
- of fluorescence 307, 328, 485

Anode luminous sensitivity 164
Anti-bunching 111, 635
- by CW excitation 636
- by pulsed excitation 636
- technical aspects 637

AOM 80, 858
- control from SPCM software 858
- control panel 858
- principle 858

APD 637, 659
- gain 157
- geiger mode 157
- light emission from 158
- quenching 158
- single-photon 157

Aperture Stops 306
Apparent lifetime 949
A-PPI-D pulse inverter 92, 223, 226
Application options 251, 714, 728, 871
Assistance through bh 959
ATP synthase 672
- conformational changes, by lifetime 672
- conformational changes, by single-molecule FRET 672, 673
- c-ring rotation 673
- in cardiac myocytes 673

Autocorrelation function 134, 640
- calculation from TCSPC FIFO data 641
- diffuse optical correlation 619
- efficiency, autocorrelation vs. crosscorrelation 661
- normalisation 641

Autofluorescence 527
- fluorophores 590
- lifetime imaging 587
- lifetimes 529, 577, 590
- metabolic imaging 375, 535
- multi-wavelength FLIM 549
- multi-wavelength measurement 324
- NADH/FAD 375, 535
- of ocular fundus 560
- of plant tissue 577
- of skin 556, 587
- of stem cells 555
- ophthalmic FLIM 590
- single-point measurement 324
- tissue spectrometer 324

– Tryptophan 381, 517
– two-photon excitation 587
– Z-stack FLIM 558
Autosave 780
– (f(t,T) mode 738
– continuous flow mode 748
– f(t,EXT) mode 740
– f(txy) mode 736
– fi modes 743, 745
– FIFO imaging mode 767
– FIFO mode 772
– scan sync in mode 756
– scan sync out mode 751
– scan xy out mode 761
– single mode 733
Autoscale function
– of display parameters 799, 813, 826, 827
– of print function 728
– of SPCImage 892
– of SPCM 799, 813, 826, 827
Avalanche Photodiodes 193
Average lifetime, ti 949
Axio Observer 856
Background suppression 331
Background, caused by afterpulsing 168, 277, 299
Baffles 306
Ballistic photons 605
Banks, of memory 123, 145, 747, 748, 758
Barrier discharges 681
BCECF 498, 543
BDL series diode lasers
– in phosphorescence systems 230
BDL series ps diode lasers 75, 76
– control by DDG-210 card 230, 857
– control by GVD-120 card 435, 850
– excitation of fluorescent proteins 349
– fibre coupling 75
– in DCS-120 system 242
– in FLIM systems 242, 352
– in phosphorescence systems 857
– PLIM 435
BDS series ps diode lasers 77, 78
– control by DDG-210 card 857
– control by GVD-120 card 435, 850
– excitation of fluorescent proteins 349
– fibre coupling 77
– in DCS-120 system 242
– in FLIM systems 242
– in phosphorescence systems 857
– PLIM 435
BDS-MM ps diode lasers 78
BDU-SM ps diode lasers 78
Beam blanking 850
Beam combiner for lasers 80
Beam park function 852
Beam scanning 35, 243
Beamsplitters, dichroic 315, 639, 668
Biased amplifier 107
Bidirectional scanning 57, 432
BIFL 665
Binning
– pixels, during image acquisition 754, 766
– pixels, effect on acquisition time 475
– pixels, in lifetime analysis 475, 479, 885, 930
Block Info 718, 834
Block mode, of 2D display 802, 826, 833
BOB-101 box 93, 232
BOB-104 box 93, 232
Brain activation measurement, in mice 622
Brain imaging 605
Brain imaging, dynamic 613
Brain imaging, static 611
Breakdown flash of SPADs 197, 697
Broken cables, electrical shock 215
Burst analyser 99
Burst analysis 136, 672
Ca^{2+} imaging 499
Ca^{2+} transients 66, 403, 409, 415, 500
Cardiac myocytes
– single-molecule FRET of ATP 673
Carotenoids 563
Cathode luminous sensitivity 164
Cathode quantum efficiency 165, 183, 186, 191
Cathode radiant sensitivity 164
Cerulean 520
CFD 139
Change Modes 56
Channel delay correction for 16 channel detector 768
Channel PMT 155
Channel register 142
Channel Uniformity
– of ADC channels 141
– transit time of multi-anode PMT 190, 768
Chi square 887, 938, 953
Chlorophyll 333, 412, 577
Chlorophyll transients 402, 412, 578
Cl^- ion concentration 500
Classic TCSPC 106
– acquisition time 105
– applications 110
– architecture 106
– count rate 105
– implementation with SPC modules 217
– IRF 103
– lifetime spectrometer 312, 319
– modern implementations 108
– photon distribution 102
– photon efficiency 104
– principle 102, 106
– reversed start-stop 107
– SNR 104
– time resolution 103, 313
Clock master function 795
Clock signals, from scanner 124
Coenzyme Q10 551
Collection time 731, 781
– continuous flow mode 747
– dead time compensation 293
– f(t,EXT) mode 740
– f(t,T) mode 737
– f(txy) mode 735
– FCS 646
– fi modes 742, 745
– FIFO imaging 762
– FIFO mode 767, 772
– oscilloscope mode 734
– scan sync in mode 754
– scan sync out mode 750, 963
– scan xy out mode 760
– single mode 733

– triggered sequence 753
Colour coding of decay parameters 949
Colour intensity mode 826, 827
Configuration of SPCM software 94, 704
Confocal detection
– 1p excitation 345
– DCS-120 scan head 34, 243
– ophthalmic scanner 591
– piezo stages 451
– sample scanning 451
– single-molecule detection 668
– STED 455
Confocal FLIM systems
– 8 channel parallel FLIM 397
– DCS-120 system 32, 242
– DIC FLIM 430
– endoscopes 443
– FV1000 68
– IRF measurement 482
– LSM 710/780/880 inverted 50
– LSM 710/780/880 upright 51
– macroscopic FLIM 439
– multispectral 366
– NIR FLIM 384
– optical principle 345
– polygon scanners 449
– tuneable excitation 353
– wideband beamsplitter 353
– with ps diode lasers 352
– with supercontinuum laser 353
– with synchrotron radiation 353
– Zeiss Intune system 355
– Zeiss LSM 710/780/880/980 family 50
Confocal microscope 343, 344
Conformational changes 672
– ATP synthase 672
– full correlation 645
Connectors, pin assignment
– DCC-100 972
– GVD-120 971
– SPC-130 966
– SPC-130EM 967
– SPC-130EMN 967
– SPC-130IN 970
– SPC-150 967
– SPC-150N 967
– SPC-160 967
– SPC-180N 970
– SPC-630 961
– SPC-730, 830 962
– SPC-QC 970
Constant Fraction Disciminator 147
– amplitude jitter 147
– CFD cable length 279
– configuration 269
– for wide-field FLIM 461
– hold 783
– limit high 783
– limit low 783
– of SPC-130 and SPC-150 148
– of SPC-160, SPC-150N, SPC-80N 148
– pactical implementation 148
– parameters 783
– principle 147
– threshold 148, 269, 783
– zero cross level 148, 274, 783
Constant Fraction Disciminator and SYNC circuits 139
Continuous flow mode 145
– accumulate 748
– Banks and Autosave 748
– curves 747
– display 749
– imaging 758
– in DOT 614
– in scan sync in mode 124, 399, 758
– multidetector operation 749
– principle 123
– recording of chlorophyll transients 335
– single molecule detection 665
– stopped flow 337
– system setup parameters 747
– trigger 748
Control Parameters, in SPCM software 779
Control signals of SPC modules 961
Convert
– FIFO files 725
– into ASCII 724
– into EI format 724
– single traces 834
Convolution integral 932
Cooling, of PMT 88, 301, 854
Corr Ovfl 779
Correlation
– diffuse optical correlation 619
– down to picosonds 657
– FCS 133, 639
– Hanbury-Brown-Twiss 635
– of detector afterpulsing 167
– of fluorescence lifetimes 674
– online calculation 774
Count Increment 789
Count rate
– background by afterpulsing 167, 168, 182, 276, 277, 299, 660
– count rate display 713
– counting loss 292
– dark count rate of PMTs 166
– dependence on CFD threshold 271
– DOT 611, 614
– influence on IRF of H5773 173
– influence on IRF of R3809 170
– influence on pile-up error 295
– maximum 293
– maximum count rate of detector 274
– maximum useful 292
– of MCP-PMT 170
– of multi-detector TCSPC 119
– of multi-module FLIM 5
– of multi-module systems 138
– of SPADs 158
– of TCSPC 105
– of TCSPC in FIFO mode 147
– ophthalmic FLIM 592
– pile-up effects 294
– recorded vs. detected 292
– SPC modules 5
Count rates 474, 478, 479
Counting efficiency 292
– of multi-detector TCSPC 118
Counting loss 279, 292, 477

Cross-correlation function 640
– calculation from TCSPC FIFO data 641
– normalisation 641
Cursors
– during measurement 710
– in 2D display 800
– in 3D display 804
– in lifetime analysis 899
– in the display window 710
– interaction with scanner 851
Curve mode, of 2D display 826, 831
Curve mode, of 3D display 826
Cycles of measurement 733, 736, 738, 740, 743, 745, 780
Damage
– by wrong routing cable 961
– photodamage 472
– TCSPC module, by charged cables 216
Dark count rate 166, 301
Data Analysis
– Burst analyser 99
– of Scan mode data 95, 728
– of Single-molecule burst data 99
– SPCImage 95, 728
Data and Setup File Formats 718, 721
Data Point
– in SPCM 2D display 800, 821
– in SPCM 3D display 804
– interaction with scanner 852
Data Processing
– Burst analyser software 99
– first moment algorithm 415
– MLE algorithm, see SPCImage 415
– Online lifetime display 415
– SPCDynamics 98
– SPCImage software 95
– SPCM software, 3D processing 805
– WLS algorithm, see SPCImage 415
DB-32 SYNC delay box 92, 280
– control by SPCM software 856
DCC-100 88, 212, 237, 854
– control of H7422 224
– control of PMC-100 223, 227
– control of R3809 225
– Cooler Control 214
– cooling current 214
– cooling voltage 214
– detector gain 854
– detector gain control 213
– detector gain, maximum 855
– detector overload shutdown 213, 855
– detector power supply 854
– high-current switches 214
– lock detector setup 855
– peltier current 214
– peltier voltage 214
– shutter control 214, 855
DCS-120 44, 242, 263, 265
DCS-120 system
– basic confocal system 32
– beam park function 852
– configurations 243
– confocal scanning FLIM system 32
– DCS box 244
– DCS-120 CMI 32
– DCS-120 DMP 33
– DCS-120 MACRO 34
– DCS-120 MP 33
– DCS-20 Super MPC 33
– examples of FLIM images 352, 367, 397, 399
– Express FLIM 39
– fast scanning 35
– FCS 48, 656
– FLITS 48
– integrated scanner control 37
– laser control 850
– Laser Wavelength Multiplexing 43
– macroscopic objects 47
– main panel 244
– Megapixel FLIM 40
– metabolic FLIM 44, 535
– Mosaic FLIM 41
– Mosaic FLIM, temporal 44
– motor stage 48
– multiphoton FLIM system 32
– multiphoton systems 33
– multiphoton systems 45
– multi-wavelength FLIM 41
– near-infrared FLIM 47
– Online Lifetime Display 38
– optical principle 242
– preview function 37, 45, 850
– ps FCS 657
– scan control panel 263
– scan rate 850
– scanner control 91, 849
– simultaneous FLIM/PLIM 39
– system architecture 242
– system connections 244
– Time-series FLIM 44
– ultra-fast decay 46
– wideband system 353
– Z stack recording 856
– Z-Stack FLIM 45
DCU-400 detector controller 88
DDG-210 91
– control by SPCM software 857
– for laser modulation 230, 240, 341, 436
– for PLIM laser control 240, 436
– phosphorescence decay recording 230, 240, 341, 436
DDG-210 module 435
DDG-220 91
Dead time 279, 290, 477
Dead time compensation 150, 293, 783
Decay function
– amplitudes of components 951
– amplitude-weighted lifetime 949
– average lifetime 949
– decay components 950, 951
– display in SPCImage 889
– intensity-weighted lifetime 949
– lifetimes of components 950
– mean lifetime 949
– model definition 933
– over-determined models 939
– recorded by FLIM system 317
– relative intensity of components 953

Decay models 877
Delay
– channel correction for multi-anode PMT 768
– delay lines, for SYNC and CFD 270
– delay of stop signal 281
– delay switch box 92, 280
– of stop signal 220
– routing signals) 790
Delayed coincidence method 102
Delayed fluorescence of PpIX 574
Delayed start-stop operation 220, 281
Depolarisation of fluorescence 307, 314, 328, 485
Depth resolution
– by confocal detection 344, 346
– by two-photon excitation 346
– effect on fluorescence decay data 469
– in DOT 606
Dermainspect system 587
Descanned detection 345, 348
Detector Control 88, 212, 854
Detector signal 101, 223, 469
Detector, shielding 287
Detectors
– 16 channel 83, 189
– 8-channel SPAD 85
– afterpulsing 167, 660
– cathode efficiency 164
– dark count rate 166
– detector control 212, 854
– detector principles 154
– eight-channel SPAD 197
– for DOT 631
– for FCS 659
– for FLIM 350
– for photon correlation 637
– for TCSPC 154
– gain 160, 854, 855
– gated SPAD 198
– H10467 178
– H10720 / H10721 173
– H10770A 176
– H11900 / H11901 173
– H15620 IR PMT 177
– H5773, H5783 172
– H7421 177
– H7422 176
– H8632 176
– HPM-100 83, 178, 273, 351, 632, 633, 661
– HVM-100 module 82
– hybrid detectors 83, 155, 178, 273, 351, 453, 632, 633, 660, 661
– InGaAs SPAD 85, 199, 201, 392
– MCP PMTs 82, 169
– microchannel PMTs 155
– NbN, SCONTEL 206
– NbN, single nanowire 207
– NbN, superconducting 86, 204, 206, 207
– overload shutdown 855
– PMC-100 174
– PMC-150 175
– PMCS-150 175
– PMH-100 174
– PML-16 83
– PML-16 GaAsP 84, 189
– PML-16C 189
– PML-SPEC 83
– PML-SPEC GaAsP 84
– PMTs 81, 154
– PMZ-100 174
– power supply 854
– preamplifiers 211
– pulse height distribution 161
– quantum efficiency 164
– R10467 178, 661
– R11322 178
– R3809U 169
– R5600, R7400 171
– safety advice 215
– SER 160, 219
– shielding 285
– shutter assemblies 86
– side-window PMT 185
– silicon photomultipliers 159, 196
– SIPMs 159, 196
– SPADs 84, 157, 193
– SSPDs 159, 204
– superconducting 204, 207
– transit time 163
– Transit time spread 163
– TTS 163
– ultrafast HPMs 181, 365
Device State 713, 773
DIC FLIM 430
Dichroic beamsplitters 315, 639, 668
Diethylthiatricarbocyanine 386
Differential Nonlinearity 288
Diffuse correlation 619
Diode laser
– BDL-SMN ps diode lasers 76
– BDS-MM ps diode lasers 78
– BDS-SM ps diode lasers 77
– BDU-SM ps diode lasers 78
– connection to SPC 223, 227
– fast switching 335
– in DOT systems 612, 613
– in FLIM systems 242, 352
– in lifetime spectrometer 312
– laser multiplexing 75, 371
– laser switch box 79
– multiplexing 452
– pulse-interleaved operation 127, 371
– two-photon excitation 685
Diode-Laser FLIM 352
Direct detection 347, 357, 367
Display
– 3D colour-intensity mode 826
– 3D curve mode 826
– 3D display parameters 828
– 3D display parameters, mode selection 828
– 3D display parameters, window selection 828
– after display time 782
– after each cycle 781
– after each step 781
– amplitudes of decay components 951
– autoscale 826
– colour intensity mode 826, 827
– curve style 825
– display time 782
– display windows in main panel 704
– during measurement 781

– FCS, off-line 776
– FCS, on-line 774
– FRET efficiency of interacting donor 952
– grid colour 826
– in scan modes 806
– intensity contribution of decay components 953
– lifetime images, SPCM 809
– lifetime of decay components 950
– lifetime ratio of decay components 951
– multidimensional data 828
– multi-file show 724
– of average lifetime 949
– of Chi square 953
– of curve maximum 711
– of first moment 711
– of FWHM 711
– of gated images, SPCM 953
– of mean lifetime 949
– of scatter contribution 953
– of total counts 711
– parameters for different windows 829
– parameters, 3D 826
– parameters, 3D curve mode 826
– Parameters, colour intensity mode 827
– photon counting histograms, on-line 774
– ratio of decay amplitudes 951
– resizing of display window 822
– reverse axis 826
Display functions 797, 891
– 2D Curve Routine 801
– 2D data processing 801
– 2D display 798
– 3D curve mode 803
– 3D display 803
– 3D display, configuration 803
– block mode 826
– block mode of 2D display 802
– colour intensity mode 803
– cursors, 2D display 800
– cursors, 3D display 804
– parameters, 2D 826
– SPCImage 891
– SPCM 797
Display parameters 709, 808
– background colour 825
– f(xyt) mode 257
– FIFO imaging mode 265, 809, 811, 813, 814, 816
– FIFO imaging mode, PLIM 820
– runtime lifetime display 816
– scale 825
Display time 731
Distance Measurement 689
Dither gain 793
Dither width 151, 152, 789
Dithering 141, 150, 151
DNA-RNA ratio 505
DNL 288
Donor, of FRET 507
DOT 605
– absorption 605
– cerebral blood flow 616
– count rates 611
– detector area 633
– detector background 631
– detector efficiency 632
– detectors 631
– diffuse correlation 619
– dynamic brain imaging 613
– endoscopes 620
– fluorescence 617
– fluorescence lifetime 626
– haemodynamic response 614
– hybrid detector 632, 633
– ICG absorption 615
– ICG bolus 615
– ICG fluorescence 615
– moments of time-of-flight 614
– of muscles and bones 626
– optical fibres 629
– perfusion measurement 615
– pulses shapes 605
– scanning mammography 608
– scanning systems 623
– scattering coefficient 605
– small animals 627
– small distance 620
– SPAD detector 633
– spatial resolution 606
– static brain imaging 611
– supercontinuum laser 623
– technical aspects 629
– time resolution 631
– time-of-flight distribution 610, 612
– timing stability 631
– tissue scanning 623
– tissue spectrometers 621
– tomographic fluorescence systems 627
– wavelength multiplexing 623
DPC-230 16-channel photon correlator 17, 656, 657
DTTCC 386
Dual-module FLIM systems 58
– FCS system parameters 646
– FCS, cross correlation 649
– synchronous start 646
EEPROM Parameters 793
Efficiency
– cathode efficiciency 164
– comparison of detectors 186
– comparison of PML-16 C and PML-16 GaAsP 191
– counting efficiency 292
– of FLIM systems 468
– of multi-detector TCSPC 118
– photon efficiency 104, 468
Electrical shock, by broken cables, 215
Electron transfer 497
Emulation Mode 717
Endogenous fluorophores 527, 559
Endoscopes
– 2p FLIM 445
– DOT 620
– fibre bundle 443
– FLIM 443
– optical principle 443
– rigid 443
– single-point multi-wavelength 324
Error correction, ADC 151
Event markers 766, 767, 772

Excitation power
– endoscopic FLIM 1p 444
– endoscopic FLIM 2p 445
– fibre laser 2p FLIM 350
– fibre laser, 2p FLIM 382
– tryptophan FLIM, 2p 382
– tryptophan FLIM, 3p 381
Excitation spectra
– FAD 349, 528
– fluorescent proteins 349
– NADH 349, 528
Excitation wavelength multiplexing 26, 126, 336, 371, 375, 378, 535
Exit, the SPC software 848
Experiment trigger 122, 124, 230, 751, 756, 761, 773, 780, 962, 966, 967
Export
– FIFO files 725
– into ASCII 724
– into EI format 724
– single traces 834
– SPCImage data 928
Export, data from SPCM 724
Express FLIM 29, 39, 98, 424
External Control of SPC modules 961
External photoeffect 157
f(t,EXT) mode 739
– accumulate 740
– autosave 740
– cycles 740
– display 741
– multidetector operation 741
– repeat 740
– steps 740
– trigger 741
f(t,T) mode 737
– accumulate 738
– autosave 738
– cycles and autosave 738
– display 739
– multidetector operation 738
– Repeat 738
– steps 737
– trigger 738
f(txy) mode 735
– accumulate 736
– autosave 736
– cycles 736
– display 736
– repeat 736
– stepping through pages 735
– trigger 736
f(xyt) mode 256
FAD 370, 375, 495
– contribution from FMN 547
– decay function 375, 529, 547
– metabolic FLIM 375, 376
– redox ratio 528, 531
– spectra 375, 528
– unmixing components 549
FAD 527
FAD FLIM 375, 527, 529
Fast Counter Channel 428
Fast FLIM 409
– Ca^{2+} transients 409, 415
– Express FLIM 424
– FASTAC system 420
– FLITS 410
– Time-tag recording, offline processing 427
– triggered mosaic FLIM 409
Fast preview 55
FASTAC FLIM system 73, 420
– acquisition time 422
– images 422
– principle 420
– time resolution 421
FBX 963, 968
FBY 963, 968
FCS 48, 67, 133, 639
– afterpulsing of detectors 660
– autocorrelation function 134, 640
– background signals 662
– beam jitter 662
– calculation from TCSPC FIFO data 133, 640, 641
– clock from SYNC input 659
– cross correlation 660
– cross-correlation function 640
– CW operation, stop pulse for 659
– DCS-120 656
– detectors 659
– display of fit results 648, 711
– display parameters 650
– efficiency, autocorrelation vs. crosscorrelation 661
– FCS down to picosecond times 136, 644
– fit of FCS curves 647
– Fit results 648
– from parameter-tag data 133, 640
– full correlation 136, 644
– gated FCS 652
– global fit with decay data 136, 644
– in cells 658
– lifetime-filtered 136, 644
– linear-tau algorithm 641
– LSM 510 651
– LSM 710 651
– macro time clock source 647, 659
– main panel configuration 648, 705
– matching of refractive index 662
– multi-tau algorithm 642
– normalisation 641
– off-line display 776
– online display 646, 774
– online fit 647, 774
– optical aberrations 662
– ps correlation 657
– sample setup 663
– sample volume 662
– saturation 653
– saving time-tag data 646
– synchonous start of modules 649
– system parameters 771
– time gating 135, 644
– trace parameters 648
– trigger master 649
– two-photon 639
– two-photon FCS 654
– using micro times of photons 135
– with CW laser 654
– with hybrid detector 652, 654, 656, 657, 661
– with Intune laser 652
– with laser scanning microscopes 651

– with ps diode laser 653
– ZEN software setup for FCS 652
fi(EXT) mode 744
– accumulate 745
– autosave 745
– cycles 745
– display 746
– multidetector operation 746
– repeat 746
– steps 745
– trigger 746
fi(T) mode 742
– accumulate 743
– autosave 743
– cycles 743
– display 744
– multidetector operation 743
– repeat 743
– steps 742
– trigger 743
Fibres 305, 609
– coupling into SSPD detector 394
– fibre based TCSPC systems 325, 622
– fibre switches 611, 613, 621
– fibre system with implantable tip 623
– in DOT applications 609
– laser output 75
– multi-mode 305
– principle of light transmission 305
– pulse dispersion 305
– single mode 75, 306
Fibres, optical 611, 613, 621, 622
FIDA 675
FIFO 132
– buffer size 147
– FIFO files 725
– FIFO imaging mode 25, 762
– FIFO mode 132, 146, 676
– frame length 790
– Overflow 713
FIFO data, setup files 726
FIFO imaging 762
FIFO imaging mode 762
– autosave 767
– display of images 806
– event markers 766
– image format 32bit software 764
– image format 64bit software 764
– image format parameters 764
– measurement control parameters 762
– microsecond lifetime 130, 434, 767
– mosaic FLIM 765
– parameter setup 762
– routing 767
– scan clock pulses 766
– synchronisation with scanners 766
FIFO mode 132, 770
– autosave 772
– buffer size 147
– calculation of FCS 640
– count rate, burst 147
– count rate, continuous 147
– cycle function 767, 772
– data file 771
– data format selection 776
– disk space 771
– event markers 772
– FCS fit 774
– FIFO imaging mode 762
– frame length 790
– microsecond decay 775
– off-line display 776
– online display 774
– routing 773
– software buffer 771
– source of macro-time clock 659, 772
– trigger 773
– triggered MCS mode 775
FILDA 676
File Formats, Data and Setup 718, 721
File Info 718, 721
Files
– conversion of FIFO files 725
– convert into ASCII 724
– exporting traces 834
– FIFO 725
– loading of 718
– of screen pattern 728
– saving of 720
Filters
– absorptive 303
– in IRF recording 484
– interference 303
– reflections 303
First moment
– display of 711
– for online lifetime display 416
– of IRF 631
– of time-of-flight distribution 606
– SPCImage 937
Fit of FCS data 647
Fit with global parameters 548, 918
Fixed decay parameters 917, 935
FLIM 343
– 1000nm and beyond 392
– acquisition time 56, 130, 444, 453, 470, 474, 480
– aggregates 583
– applications 491
– at 300 femtoseconds channel width 364
– autofluorescence 527
– autofluorescence of tissue 587
– beam scanning 35, 243
– Ca^{2+} imaging 499
– Ca^{2+} transients 500
– carotenoids 563
– charge cariier lifetime 679
– Chloride ions 500
– chlorophyll 577
– chlorophyll transients 580
– confocal 352
– count rate 474, 478, 479
– counting loss 477
– DCC-100 detector controller 237
– Dermainspect 587
– DIC 430
– diode laser excitation 352
– dual-wavelength FLIM 234, 243, 360
– efficiency 468

– endocopes 443
– endogenous fluorophores 527, 559
– excitation wavelength multiplexing 126, 452
– Excitation wavelength multiplexing 371, 372
– Express FLIM 29, 39, 98, 424
– Exress FLIM 424
– FASTAC system 73, 420
– FIFO imaging 762
– FIFO imaging mode 25
– FLIO system 593
– FLITS 129, 410
– fluorescence quenching 498
– fossil bacteria in flint 569
– FRET measurements 507
– high resolution 58
– high speed 395
– image size 125, 126, 480
– in NSOMs 458
– influence of anisotropy decay 485
– Intune laser 355
– ion concentrations 498
– lable-free imaging 527
– laser multiplexing 371
– Laser multiplexing 376
– Lifetime-intensity mode 428
– line scanning 129
– macroscopic 439
– macroscopic objects 47
– main panel configuration 705
– malignant melanoma 566
– MCS FLIM 130, 434, 767
– megapixel FLIM 58
– Megapixel FLIM 40
– metabolic FLIM 375, 527, 535
– microsecond decay 434
– microsecond FLIM 130, 434
– mosaic FLIM 400
– Mosaic FLIM 27
– MPT Flex 589
– multi-beam scanning 451
– multi-dimensional TCSPC 124
– multiphoton 45, 59, 357
– multispectral confocal 366
– multispectral multiphoton 367
– multi-wavelength 125, 549
– multi-wavelength FLIM 41
– Multi-wavelength FLIM 25
– NDD 50, 69, 237, 347, 357, 367
– NIR dyes 384
– non-descanned detection 50, 69, 237, 347, 357, 367
– NSOM 458
– of rotating object 447
– ophthalmic FLIM 590
– ophthalmic imaging 590
– OPO excitation 389
– parallel channel 397
– perovskite 679
– perovskite, voltage dependent 680
– pH imaging 498
– photobleaching 472
– photon number 471
– photosensitisers 583
– pile-up 477
– PLIM combined with FLIM 130
– polygon scanners 449
– preview function 55
– pulse-interleaved excitation 127, 371
– scan rate 488
– Scan Sync In mode 23
– semiconductors 679
– SHG 549
– shutter control 237
– signal-to-noise ratio 470
– single PMC-100 detector 237
– skin 444
– STED FLIM 454
– supercontinuum laser 353
– synchrotron radiation 353
– system architecture 124
– system parameters 753
– Temperature measurement 584
– time resolution 467
– time series 580
– time-series 398
– triggered accumulation 130
– Tryptophan 381
– tuneable excitation 45, 62
– tuneable excitation confocal 353
– ultra-fast decay 46, 60, 362, 561, 562, 563, 565, 566
– ultra-fast detectors 362
– upgrading laser scanning microscopes 234
– viscosity 501
– well plates 446
– wideband beamsplitter 353
– wide-field FLIM 31, 460, 777
– wiring diagrams of FLIM systems 237
– Z scanning 26, 45, 63, 391, 406
– Z stacks 391
– Z-Stack recording 558
FLIO 590
– 2p excitation 604
– analysis, cataract 600
– analysis, normal patient 602
– data analysis 598
– data analysis 596
– FLIO system 593
– images 594
– IRF position 596
– IRF shape 596
– IRF, synthetic 598
– lens fluorescence 597, 600, 603
– model function 597, 598
– phasor plot 604
– shifted component model 598
– suppresion of lens component 600
– system architecture 593
FLIRR 534, 895
FLITS 29, 48, 66, 129, 410
– chlorophyll transients 412, 581
– frame clock 411
– photon distribution 129, 410
– principle 129
– procedure 411
– recording speed 130
– triggered accumulation 130, 411
Flourescence
– ultra-fast decay 561, 562

Fluorescence
– anisotropy 307, 328, 485
– anisotropy decay 307, 314, 485, 551
– carotenoids 563
– chlorophyll 412
– decay functions 108, 110, 467
– decay measured by FLIM system 317
– decay models 933
– depolarisation 307, 314, 328, 485
– electron transfer 497
– fluorescence correlation, ps 635
– fluorescence decay 311
– fluorophores bound to proteins 495
– FRET 352, 361, 494, 507
– FRET donors 348
– FRET efficiency 507, 508
– ion concentrations 493
– Kautsky effect 333
– lifetime 108, 110, 136, 644
– lifetime spectrometers 311
– local refractive index 496
– local viscosity 495
– metal surfaces 496
– of aggregates 497
– of chlorophyll 333
– of protonated and deprotonated forms 493
– oxygen concentration 495
– oxygen effect on NADH 495
– pH sensors 493
– protonation 493
– quenching 493, 498
– re-absorption 309
– resonance energy transfer 494, 507
– solvent effects 496
– transient effects 410
– transient phenomena 333
– transients, of chlorophyll 333
– ultra-fast decay 46, 60, 362, 563, 565, 566
Fluorescence correlation spectroscopy, see FCS 639
Flyback X 751, 760, 963, 968
Flyback Y 751, 760, 963, 968
FMN 547
Forensic FLIM applications 586
Förster resonance energy transfer, see FRET 494, 507
Frame clock 124, 130, 452
FRAP 584
Freq Div (SYNC) 784
FRET 507
– acceptor decay function 514
– acceptor photobleaching 508
– Alzheimer desease 523
– amplitudes of decay components 510, 511
– basics 494
– by double-exponential lifetime analysis 508, 510, 511, 952
– by MFD 668
– by multi-wavelength FLIM 516
– by single-exponential lifetime 508
– classic FRET efficiency 508, 949, 952
– contamination by autofluorescence 521
– dark acceptors 516
– decay function of CFP 513, 520
– diffraction limited spots 518
– donor decay function 508, 509, 510, 520
– endogenous fluorophores 517
– examples 352, 361, 511
– fixed samples 520
– for infection mechanisms 524
– FRET distance 512
– FRET efficiency 507, 508
– FRET efficiency by mean lifetime 949
– FRET efficiency of interacting donor 512, 952
– homo FRET 518
– Huntington desease 523
– intensity based 507
– interacting donor fraction 510, 512
– lifetime based 508
– lifetimes of decay components 510, 511
– literature 522
– multi-exponential donor decay 520
– photobleaching 521
– photo-induced changes 522
– plant cells 525
– protein interaction 494, 511
– samples 520
– shear forces 524
– single molecule FRET 668, 672
– single-exponentail 508
– SNARE proteins 524
– tryptophan to NADH 517
– ultra-fast 518
FRET efficiency 507, 508
– classic, intensity 507
– classic, lifetime 508
– intensity based 507, 508
– interacting donor 512
– lifetime based 508
– ti based 509
– tm based 509, 512
FWHM, display of 711
G factor 328
Gain
– detector gain, optimisation 269
– of APDs 157
– of PMTs 160, 269
– TAC gain 785
Galvanometer scanner 130
Geiger mode 157
Global analysis 918
Global fit 548, 918
GPU processing 97, 866
Ground loops 286
Grounding 285
GVD-120 scan controller 91
– beam blanking 850
– beam park function 852
– configuration for different scanners 852
– control by SPCM software 849
– control of lasers 850
– control panel 849
– cooperation with motor stage 859
– DOT scanner 624
– driving piezo stages 452
– frame size 849
– laser multiplexing 850
– operation from SPCM software 849
– preview function 850
– scan rate 850

– scan waveform 91
– zoom function 851
GVD-140 scan controller, see GVD-120 91
H10720 / H10721 173
H10770A 176
H11900 / H11901 173
H15620 177
H5773 163, 172
H5773, high count rates 173
H5773, IRF 172
H5783 172, 701
H5783, high count rates 173
H5783, IRF 172
H7421 177
H7422 161, 163, 176, 637, 659
H7422, connection to SPC 224
H8632 176
Hanbury-Brown-Twiss experiment 635
HFAC series preamplifiers 88, 211
HFAH series preamplifiers 88, 211
High resolution FLIM 58
High voltage module, for PMT 82
High voltage, for PMT 163, 215
High-current switches of DCC100 214
Histogram
– 2D histogram 868
– decay parameters 867, 896, 902
– decay parameters in ROI 867
– intensity histogram 897
Hold (CFD) 783
Holdoff (SYNC) 784
HPM-100 hybrid detector 178, 273, 351, 632, 633, 661
HPM-100, sensitivity comparison 186
HPM-100-06 179, 181, 365
HPM-100-07 179, 181, 365
HPM-100-40 179
HPM-100-41 179
HPM-100-50 179, 180
HRT series routers 89
– cable diagrams 227
– principle 117
HVM-100 high voltage module 82
Hybrid detectors 155, 178, 273, 351, 453, 632, 633, 660, 661
Hydrant 276
ICG 385, 615, 617
Id 220 199
Id 230 201
Image Format
– FIFO Imaging 764
– Scan Sync In 758
– Scan Sync Out 752
– Scan XY Out 760
Image segmentation by phasor plot 402, 404, 907
Image size 480, 849
Imaging 124, 343
– advantage of scanning 344
– beam scanning 236
– clinical FLIM 587
– control Signals 963, 967
– FIFO imaging mode 762
– FLIM systems 234
– imaging modes 750
– microsecond decay 130, 767
– Ophthalmic FLIM 590
– scanning vs. wide field 344
– wide field FLIM 460
– with scanning microscope 343
Import, data into SPCM 724
Import, FLIM data into SPCImage 871
Incomplete decay model 878, 933
Indicators of cell metabolism 531
– amplitude ratios 533
– amplitudes 534
– CMR 533
– FLIRR 534
– lifetimes 532
– OMI index 532
– redox ratio 531
Indocyanine green 385, 615, 617
InGaAs SPAD 85
Input signals of SPC modules 217, 223
Installation
– setup service 249
Intensity contribution of decay components 953
Intensity gating in SPCImage 893
Intensity images
– intensity histogram 897
– SPCM, gated images 808
– SPCM, trace parameters 806
– SPCM, window parameters 808
Internal photoeffect 157
Interrupt, a measurement 847
Intune laser FLIM 62
Inverters, APPI, for pulses 92
Ion concentrations 493, 498
IRF 300
– auto IRF from data 942
– define curve as IRF 929
– define rectangular IRF 929
– from recorded data 944
– from scattering data 945
– from SHG data 947
– H5773 172
– H5773, H5783 173
– H5783 172
– HPM-100 hybrid detector 179
– HPM-100-06 and -07 181
– illuminated detector area 300
– IRF modelling 866, 881
– measuring an IRF, one-photon 482
– measuring an IRF, procedure 484
– measuring an IRF, two-photon 485
– of bh FLIM systems 481
– of detector, measurement 694
– of FLIM systems 942
– of PLIM 923
– one-photon 945
– photosensor modules 172
– R3809U 169
– R5600 171
– R7400 171
– side-window PMTs 185
– stability vs. count rate 173
– synthetic IRF 96, 483, 866, 881, 942
– synthetic vs. measured 483
– TO-8 PMTs 171
– two-photon 947
– ultrafast HPMs 181
– use in data analysis 942
– voltage divider 300
Jitter

– amplitude, detector pulses 147
– of detector transit time 163
– of pulse period 281
– of SER amplitude 161, 271, 302
Kautsky effect 333, 578
Label-free imaging 527
– bladder tissue 537
– epthelium cells 537
– glioblastoma 542
– malignant melanoma 566
– mouse tumor 542
– multi-wavelength 549
– ocular fundus 560
– of skin 556
– stem cells 555
– ultra-fast fluorescence decay 561
Laser
– BDL-SMC and SMN series 75, 76
– BDS-MM series 78
– BDS-SM series 77
– BDU-SM series 78
– beam blanking 850
– beam combiner 80
– control from GVD-120 81
– control via DCS-120 panel 850
– diode lasers 75
– femtosecond fibre lasers 350
– fibre coupling 75
– Intune laser 355
– LHB-104 Laser Hub 79
– LSB laser switch boxes 79
– modulation, for PLIM 435
– multiplexed TCSPC 119
– multiplexing 59
– multiplexing 81
– multiplexing 298
– multiplexing 336
– multiplexing 630
– multiplexing, in DOT 607
– multiplexing, in FLIM 371, 609, 850
– power control 850
– ps diode lasers 352
– supercontinuum laser 325, 353, 454, 621, 623, 624
– TiSa, 1-photon excitation 385
– TiSa, 2-photon excitation 346, 349
– TiSa, control from SPCM software 858
– tuneable fibre laser 355
Laser multiplexing 376
– BDL-SMC laser 75
– by DCS-120 system 371, 850
– chlorophyll fluorescence 336
– DCS-120 43
– DDG-210 card 81
– in DOT 607, 609, 614, 623, 630
– in FLIM 43, 355, 371
– metabolic FLIM 375, 376, 378, 535
– multiplexed TCSPC operation 115, 119
– pulse by pulse vs. pulse group 298
– supercontinuum laser 355, 623
Laser pulse duration, measurement 686
Laser scanning microscopes
– A1 70
– C1 70
– confocal 344, 345
– DCS-120 32
– detectors for FLIM 350
– excitation lasers 348
– femtosecond fibre lasers 350
– FLIM upgrade 234
– FV 1000 68
– FV 300 68
– multiphoton 346
– principle 345
– ps diode lasers 348
– supercontinuum lasers 349
– Sutter MOM 71
– TiSa lasers 349
– Zeiss LSM 710/780/880/980 family 50
Laser scanning microscopes, see also FLIM 345
Leica SP2 68
Leica SP5 68
Leica SP8 68
Lens
– NDD transfer lens 357, 358
– objective lens 345, 347, 357
– scan lens 345, 443
Lenses 303
LHB-104 Laser Hub 53, 59, 79, 244
LIDAR Systems 689
Lifetime
– amplitudes of decay components 951
– apparent lifetime 949
– average lifetime, ti 949
– Chi square 953
– FRET efficiency of interacting donor 952
– histograms for single molecules 672
– intensity contibution of components 953
– lifetime ratios of decay components 951
– mean lifetime, tm 949
– of decay components 950
– pile-up error 478
– ratios of amplitudes 951
– scatter contribution 953
Lifetime images
– calculation of 875, 919
– calculation, first moment 416
– online calculation 418
Lifetime Imaging, applications 491
Lifetime spectrometers 311
– anisotropy 328
– fibre-based systems 325
– filter-based 312
– implantable fibres 325
– micro spectrometers 326
– micro spectrometers, multi-wavelength 327
– monochromators 319
– multi-wavelength 322
– polarisation 314
– time resolution 313
– time-resolved spectra 320
– tissue, multi-wavelength 324
– use of FLIM systems 317
Lifetime-intensity mode 428, 921
Lifetimes of decay components
– autofluorescence 556
– FAD 545
– FRET 510, 511
– NADH 545

– SPCImage 863, 949
Light emission from SPADs 697
Limit High (CFD) 783
Limit High (TAC) 785
Limit Low (TAC) 785
Limit Low, CFD 783
Line clock 124, 130, 452
Load 718
– data files, SPCM 718
– FIFO files 725
– File Formats 718
– files from older software versions 720
– img data files into SPCImage 871
– predefined setups 706, 723
– selected parts of a file 719
– setup files, SPCM 718
Loading of FLIM data into SPCImage 871
Lock detector setup 855
Lock-in SPC 331, 781
Luminescence decay 311
Luminous sensitivity 164
Macro time clock 647
Macro-time clock, synchronisation of 659, 772
Magic angle 308, 485
Magnetic field, infuence on detector 187
Main (in menue bar) 718
Main Panel 703
– configuration of 704
– count rate display 713
– cursors 710
– device state 713
– dual-channel FLIM 811
– examples 704
– F(xyt) mode 256
– FCS 648
– FLIM/PLIM 820
– gated images 814
– module select 712
– mosaic FLIM 265
– multi-wavelength FLIM 263, 813
– multi-wavelength fluorescence lifetime 255
– one-channel FLIM 809
– runtime FLIM 816
– scanning systems 259
– single-channel fluorescence lifetime 250
– trace statistics 711
Malignant melanoma 566
Mammography, optical 605
Markers 766, 767, 772
Maximum Ratings of SPC modules 973
MCP 301
MCP PMT 82
– comparison with HPM-100-40 179
– comparison with SPADs 194
– detector assemblies 87
– FV-1000 68
– in laser scanning microscopes 351
– IRF 169
– IRF with SPC-150NX 170
– position-sensitive 460
– principle 155
– R3809U 169
MCS FLIM 767
Mean lifetime, tm 949
Mean lifetime, tm12 949
Measurement
– dead time compensation 783
– display during measurement 781, 782
– imaging modes 791
– lock-in TCSPC 331
– multi-detector 791
– normalisation to maximum 789
– repeat 782
– Stop T 733, 735, 737, 740, 742, 745, 779, 781
Measurement modes 732
– continuous flow mode, curves 747
– continuous flow mode, images 758
– f(t,EXT) mode 739
– f(t,T) mode 737
– f(txy) Mode 735
– fi(EXT) mode 744
– fi(T) mode 742
– FIFO imaging mode 762
– FIFO mode 770
– MCS FLIM 767
– mosaic FLIM 765
– oscilloscope mode 734
– Overview 18
– Scan Sync In continuous flow mode 758
– Scan Sync In mode 753
– Scan Sync Out mode 750
– Scan XY Out mode 760
– single mode 733
– Triggered accumulation MCS 775
– wide-field FLIM 777
Megapixel FLIM 40, 58, 400
Melanoma
– FLIM 371, 566
Membrane Potential 496, 502
Memory Banks 123, 145, 747, 758, 792
Memory control 142
– Add/Sub 146
– Count Enable 146
Memory Offset 789
Memory Page 790
Memory swapping in TCSPC 123
Metabolic FLIM 527
– amplitude ratios 530, 533
– amplitude, a1 534
– amplitudes of decay components 530
– bladder tissue 537
– brain tissue 554
– cell cycle 555
– clinical application 539
– combination with SHG 557
– comparison with histology 539
– FAD data 540
– FLIRR 534
– FMN 547
– glioblastoma 542
– laser multiplexing 375, 376, 378
– lifetimes 532
– literature 550
– liver tissue 553
– MACRO FLIM 542
– macrophages 552
– MCR 533
– mouse tumor 542
– NADH and FAD lifetimes 529
– NADH/FAD amplitude histogram 540
– neurons 554

– OMI index 532
– one-photon 375
– oocytes 553
– redox ratio 531
– response to chemotherapy 551
– response to drugs 552
– T cells 552
– tumor identification 539, 551
– two-photon 378
Metabolic imaging 527
– amplitude ratios 530, 533
– amplitudes of decay components 530, 534, 535
– bladder tissue 537
– clinical application 539
– comparison with histology 539
– FAD data 540
– FLIRR 534
– FMN 547
– glioblastoma 542
– lifetimes 532
– literature 550
– MACRO FLIM 542
– metabolic indicators 531
– mouse tumor 542
– NADH and FAD decay components 535
– NADH and FAD decay functions 529
– NADH and FAD lifetimes 529, 532
– OMI index 532
– redox ratio 528, 531
– tumor identification 539
– with bh systems 535
– with simultaneous pH imaging 543
Methylene blue 387
MFD 459, 667
– data analsyis 669, 670
– imaging 670
– in cells 671
– molecules in solution 668
– optical principle 668
Microchannel PMT 155
Microfluidic channels 585
Microscope, confocal 343
Microscope, multiphoton 346
Microsecond decay 23, 341, 775
Microsecond lifetime imaging 130, 434, 767
Mixing techniques 338
MLE fit 96, 865, 884, 936
Model function 933
– 1,2,3-exponential models 877
– fixed decay parameters 917, 935
– global analysis 918
– incomplete decay model 934
– number of components 938
– over-determined models 939
– pseudo-global analysis 917
– shifted-component model 879
Model parameters 939
Module types
– DCC module 88, 212, 854
– DDG module 81, 91
– DPC modules 17
– GVD module 91
– other photon counters 17
– power-tau systems 16
– Simple-Tau systems 15
– SPC modules 7
Molecular brightness 675
Molecular environment
– Ca^{2+} imaging 499
– Ca^{2+} transients 500
– Chloride ions 500
– Hg2+ 505
– membrane potential 502
– Na+ concentraion 504
– pH imaging 498
– viscosity 501
Moments
– display of M1 711
– in DOT 606
– of time-of-flight distribution 606
– online-lifetime calculation 416
Monochromators 304, 319
More Parameters 792
Mosaic FLIM 27, 64, 127, 400, 765
– data processing 921
– lateral 64, 127
– moving objects 403, 907
– parameter setup 765
– spatial 127
– SPCImage 921
– temporal 44, 64, 128, 402, 580
– temporal, accumulation 403, 409
– z-stack 128, 391
Motor stage 446, 859
– calibration 860
– cooperation with optical scanner 446, 859
– in DCS-120 systems 446, 859
Moving objects
– by mosaic FLIM 403
– decay analysis 907
– image segmentation 404, 907
MPT Flex 589
Multi SPC systems
– equalize parameters 795
– module select 712
– Module Select 795
– Parameters 795
– setup 229
Multi-beam scanning FLIM 451
Multichannel System, pile-up 298
Multi-detector operation
– continuous flow mode 749
– data display 808
– efficiency 118
– f(t,T) mode 738, 741
– fi modes 743, 746
– FIFO imaging mode 767
– FIFO mode 773
– in DOT 621, 628
– of TCSPC 115, 116
– oscilloscope mode 735
– principle 116
– scan modes 752, 757
– single mode 734
Multidimensional data, display of subsets 828
Multi-dimensional TCSPC 112
– architecture 113
– excitation multiplexed FLIM 126

– FLIM 124
– FLITS 129, 410
– hardware accumulation 114
– mosaic FLIM 127
– multiplexing 119
– multi-wavelegth FLIM 125
– multi-wavelength 116
– PLIM combined with FLIM 130
– principle of data acquisition 112
– sequential recording 121
– software accumulation 114
– spatial multiplexing 121
Multi-file view 724
Multi-module TCSPC systems 137, 795
– 8-channel FLIM 397
– DCS-120 243, 352
– DOT 609, 613
– FLIM 234, 395
– multiphoton FLIM 357
– principle 137
– Simple-tau systems 137
– Trigger synchronisation 781, 795
– wiring diagrams 241
Multi-parameter fluorescence detection 459, 667
Multi-parameter TCSPC 115, 682
Multi-photon detection 278
Multiphoton excitation 346
– non-descanned detection 347, 357, 367
Multiphoton FLIM systems 59
Multiphoton tomography of human skin 371
Multiplexed TCSPC 119, 144, 298, 609, 630
Multiplexing
– excitation wavelength 126
– in TCSPC 115
– of lasers 298, 609, 630
Multi-spectral FLIM, see multi-wavelength FLIM 366
Multi-spectral TCSPC 116
Multi-wavelength FLIM 25, 41, 366
– 3D trace parameters 264
– 64-bit software 369
– applications 370
– confocal 366
– large images 41
– mosaic FLIM function 265
– NDD 367
– system parameters 263
– TCSPC principle 125
– window parameters 264
Multi-wavelength NDD FLIM 61
Multi-wavelength operation 116, 324
– in DOT 621
– Scan Sync In FLIM 125
– single-point tissue fluorescence 324
MW FLIM GaAsP system 84
MW FLIM system 69, 84, 191, 366, 367
– autofluorescence detection 549
– unmixing 549
NADH 370, 371, 375, 495, 527, 550
– decay function 375, 529, 545
– metabolic FLIM 375, 376
– redox ratio 528, 531
– spectra 375, 528
– unmixing components 549
NADH FLIM 375, 527, 535
– a1/a2 ratio 366, 529
– brain tissue 554
– cell cycle 555
– combination with SHG 557
– decay funtions 366, 529
– FLIRR 534
– infection mechanisms 552
– literature 550
– liver tissue 553
– metabolic FLIM 375
– neurons 554
– OMI index 532
– oocytes 553
– response to chemotherapy 551
– response to drugs 552
– stem cells 555
– tumor identification 551
– with ultrafast detectors 365
– wound healing 553
Nanoparticles 497
– detection in skin 559
NbN detectors 86
– IRF 204
– IRF 86, 204
– IRF 206
– IRF 207
– recording of fluorescence decay 208
– single nanowire 207
– test setup 204, 208
NDD
– beamsplitters 358
– examples of FLIM images 59, 360
– multi-wavelength detection 367
– NDD detectors 367
– principle 347
– Principle 357
– principle of beam path 357
Near-Field Microscope 458
Nikon A1 70
Nikon A1 integrated FLIM 70
Nikon C1 70
NIM modules 108
NIR dyes
– DTTCC 386
– FLIM 384
– ICG 385, 615, 617, 626
– methylene blue 387
NIR FLIM 384
– 1000nm and beyond 392
– 2-photon, with OPO 389
– confocal 384
– diode laser 385
– DTTCC 386
– ICG 385
– Intune laser 388
– methylene blue 387
– TiSa laser, one-photon excitation 385
– wideband beamsplitter 385
Noise
– electromagnetic shielding 285
– ground loops 286
– in multi-detector systems 118
– signal-to-noise ratio of FLIM 470
Non-descanned detection, see NDD 347, 357, 367
NSOM 458
OEM TCSPC boards 10, 13
Offset

– counting background 275
– DOT, effect on accuracy 631
– in SPCImage 910, 933, 954
– MCS mode 767, 775
– TAC offset 785
Olympus FV1000 68
Olympus FV300 68
OMI index 532
Online FLIM 57
Online Lifetime Display 38, 415
Operating voltage, of PMT 163
Operation Modes 732
– continuous flow mode, curves 747
– continuous flow mode, images 758
– f(t,EXT) mode 739
– f(t,T) mode 737
– f(txy) Mode 735
– fi(EXT) mode 744
– fi(T) mode 742
– FIFO imaging mode 762
– FIFO Mode 770
– MCS FLIM 767
– MCS, triggered accumulation 775
– oscilloscope mode 734
– overview 18, 732
– Scan Sync In mode 753
– Scan Sync Out mode 750
– Scan XY Out mode 760
– single mode 733
– wide-field FLIM 777
Ophthalmic FLIM 590
– 2p excitation 604
– background 590
– data analysis 596
– FLIO system 593
– fluorophores 590
– shifted-component model 598
– suppresion of lens component 600
– system architecture 591
OPO 389
Optical fibres 305, 609, 611, 613, 621, 622, 629
Optical fibres, single mode 75, 306
Optical oscilloscope 701
Optical reflections 299, 306
Optical sectioning
– by confocal detection 344
– by multiphoton excitation 344
Optical System 303
Optical System, influence on system response 303
Optical tomography see DOT 605
Optimising the CFD Parameters 269
Optimising the SYNC Parameters 279
Optimising the TAC parameters 282
Oscilloscope Mode 269, 275, 734
– application 701
– detectors 701
– multidetector operation 735
– trigger 735
Over-determined models 939
Overflow
– correct overflow option 779
– overflow handling 779
– Stop on overflow option 733, 735, 737, 740, 742, 745, 779
Overload Flip-Flop of DCC-100 214
Overload shutdown 214, 855
Overload Signal 214
Overload, of PMT 301
Oxygen sensing 572
Oxygen sensing by FLIM 504
P box 237
Page Control 790
Page in memory 791
Page stepping 733, 735, 751, 756, 761, 780
Parameter histogram 902
Parameter-tag data
– Burst analyser software 99
– calculation of FCS 640
– conversion into sdt files 725
– export and import 725
– saving into file 763, 771
Parameter-tag mode 114, 132
– buffer size 147
– burst analysis 136
– calculation of FCS 133, 640
– configure online display 774
– data structure 132
– FCS fit 774
– FIDA 676
– FIFO imaging 762
– FIFO mode 770
– MCS trace 774
– memory control 146
– PCH 676
– principle 132
– system parameter setup 770
– TCSPC architecture 132
Parametric downconversion, for QE measurement 698
Passive quenching, of SPAD 158
PCH 675
PDT 583
Peltier Control 214
Perovskite 679
– voltage dependent FLIM 680
pH imaging 498
pH sensors 493
Phasor plot 97
– ambiguity of phasor representation 958
– chlorophyll 402
– cluster selection 906, 956
– combine decay curves 906, 956
– correction of truncation effects 958
– equations 955
– FLIO 604
– image segmentation 404, 869, 907
– in SPCImage 865, 906
– principle 955
– truncation effects 957
Phosphorescence 434, 572
– data analysis 923
– decay 434
– IRF 923
– phosphorescenc decay 130, 340, 341
– phosphorescence decay 23
– phosphorescence decay imaging 434
– PpIX 574
– quenching by oxygen 434, 572
– singlet oxygen 394
Phosphorescence Lifetime Imaging, see PLIM 434
Photobleaching 468, 472, 489

Photodamage 472
Photodiode Modules 89, 216, 218
Photodynamic therapy 583
Photomultiplier Tubes 154
Photon
– detection 101, 154
– distribution 3, 102, 112, 116, 118, 121, 122, 124, 125, 129, 131
– efficiency 104
– pulses 101, 102, 147, 160, 219
– timing 1, 103, 147
Photon correlation
– anti-bunching 635
– detectors 637
– Hanbury-Brown-Twiss experiment 635
– start-stop experiment 635
Photon Counting Histograms 675
Photon distribution
– built up in computer 114
– built up in TCSPC device 114
– classic TCSPC 102
– FLITS 129
Photon migration, see DOT 605
Photon-number sensitive TCSPC 699
Photosensor modules 172
PIE 371
Piezo scan stages 853
Piezo stage scanning systems 240
Piezo stages 240, 451
– combination with TCSPC 72, 452
– control from FLIM system 452
– GVD-120 scan controller 452
– PZ-FLIM-110 system 72
– STED FLIM 455
Pile-up 105, 478
– avoiding pile-up errors 297
– classic pile-up 294
– for laser multiplexing 298
– in FLIM 477
– in multi-detector systems 298
– in multi-module systems 298
– influence on recorded lifetime 295
– inter-pulse 295
– size of pile-up error 295
Pin assignment, of connectors
– DCC-100 972
– GVD-120 971
– SPC-130 966
– SPC-130EM 967
– SPC-130EMN 967
– SPC-130IN 970
– SPC-150 967
– SPC-150N 967
– SPC-160 967
– SPC-180N 970
– SPC-630 961
– SPC-730, 830 962
– SPC-QC 970
Pinhole 243, 345, 346, 451, 668
Pixel clock 124, 130, 452, 963, 967, 968
Pixels
– binning, effect on acquisition time 475
– FIFO imaging mode 764
– max. pixel numbers 754, 764
– number of, effect on acquisition time 474
– pixel binning during image acquisition 754
– Scan Sync In mode 754, 766
Plant physiology 577
PLIM 30, 39, 65, 434
– applications 576
– data analysis 923
– DCS-120 435
– DDG-210 module 435
– delayed fluorescence of PpIX 574
– display setup 819
– examples 436
– fit proccedure 925
– IRF 923
– laser control 435
– laser modulation 435
– oxygen imaging 573
– photon timing 435
– principle 130, 434
– recording process 435
– send data to SPCImage 923
– simultaneos O2 and NADH imaging 573
– simultaneous FLIM/PLIM 30, 39, 65
– singlet oxygen detection 394
– TCSPC process 130
PMC-100 detector 174
– connection to SPC 223, 227, 237, 246
PMC-150 detector 175
PMCS-150 detector 175
PMH-100 detector 174
PMH-100, connection to SPC 223
PML-16 detector 83
PML-16 GaAsP detector 84, 189
PML-16C detector 189
PML-SPEC detector 191
PMT
– afterpulsing 167, 182, 660
– anode luminous sensitivity 164
– cathode luminous sensitivity 164
– cathode quantum efficiency 165
– cathode radiant sensitivity 164
– cooling 88, 214, 301, 854
– dark count rate 166
– focusing voltages 300
– gain 160
– H10770A 176
– H5773, H5783 172
– H7422 176
– illuminated area 300
– measurement of quantum efficiency 698
– measurement of SER 301
– operating voltage 163, 215
– optimisation 300
– overload 301
– PMC-100 PMT Module 174
– PMC-150 PMT Module 175
– PMCS-150 PMT Module 175
– PML-16 GaAsP 189
– PML-16C 189
– PMZ-100 PMT Module 174
– pre-pulses 168, 172
– principle 154
– pulse amplitude distribution 161, 271
– quick test 302
– R3809U MCP PMT 169
– R5600, R7400 171
– recovery after overload 301

– Safety 215
– SER 160, 219
– shielding 287
– side-window 185
– single electron response 160, 219
– single-photon pulses 101, 160, 219
– timing stability 173
– transit time 163
– transit time spread 163
– treatment for bad 276
– TTS 163
– voltage divider 300
PMZ-100 detector 174
Polarisation 314
Polarisation, of fluorescence 328
Polariser
– in detection path 308, 485
– magic angle 308, 485
– rotating 331
Polychromators 304, 322
Polygone definition 929
Positron Lifetime 687
Power splitters 92
Power Supply to external units 961
Power-Tau TCSPC systems 16
PpIX, delayed fluorescence 574
Preamplifiers 211
– HFAC series 88, 211
– HFAH series 88, 211
Predefined setups 706, 723
– definition of 723
– switching instrument configuration 56, 706
Pre-pulses, of PMT 168
Preview function 37, 55
Preview function of scanner 850
Print function 728
Printing, into files 728
Production Parameters 793
Protein interaction 494, 511
ps FCS 657
Pseudo-global analysis 917
Pulse amplitude distribution, of SER pulses 161, 271
Pulse period jitter 281
Pulse-interleaved excitation 127, 371
PxlClk 963, 967, 969
Quantum efficiency
– comparison of detectors 186
– of detectors 165, 183, 191
– of photocathodes, measurement 698
Quenching
– fluorescence quenching 333, 493, 498, 578
– of SPAD 158
– phosphorescence quenching 434, 572
R10467 178
R11322 178
R3809U 169
– connection to SPC 225
– HVM-100 power supply modue 82
– IRF 169
– IRF with SPC-150NX 170
– transit time 163
R5600 162, 163, 171
R7400 163, 171
R928 163
Radiant sensitivity, of photocathodes 164
Random signals detected by TCSPC 221
Range (TAC) 785
Ranging Systems 689
Rates 713
Ratio of component amplitudes 951
Ratio of component lifetimes 951
Re-absorption 309
Redox ratio 528, 531
Redox Ratio 952
Reference Photodiodes 89, 218
Reference signal
– delay 281
– for reversed start-stop 281
– from laser 217
– from photodiodes 218
Reflections
– in optical systems 306
– on SYNC line 279
Refractive index imaging 501
Region of interest, see ROI 929
Repeat 734, 736, 738, 740, 743, 746, 751, 757, 780
Repeat time 731, 782
Repetition Rate, measurement at low 220
Residuals 886
Resizing Panels 822
Resolution
– ADC 152, 787
– time resolution of TCSPC 103, 163
– TTS of detectors 103, 163
Reversed start-stop
– at low repetition rate 281
– delayed stop operation 282, 795
– effect of SYNC delay 280
– principle 107
– reference signal 281
– SYNC delay 281
– TAC operation 140, 282
RF noise 286
RNA-DNA ratio 505
ROI 899, 902
– combination into single curve 903
– parameter histogram of 867
– polygonal 899, 929
Rotational relaxation 307, 328, 485
Router
– cable diagrams 227
– for multi-anode PMTs 118
– noise accumulation 118
– principle 117
– routing devices 89
Routing 116
– by photon number 699
– efficiency 118
– FIFO mode 773
– FIFOimaging mode 767
– multiplexing 119
– multi-wavelength detection 118
– multi-wavelength FLIM 125
– principle 117
– Routing Channels X 791
– Routing Channels Y 791
– routing delay 790
– routing devices 89
– routing signals 961
– routing windows 807

– Routing XY windows 841
Runtime FLIM 57
Runtime Lifetime Display 38, 415, 418
Safety Recommendations 215
Sample rate 701
Save 720
– autosave function, see autosave 780
– calibration of motor stage 860
– calibration of PML-16 channel delay 768
– data files, SPCImage 928
– data files, SPCM 721
– file formats 721
– options 721
– selected data blocks 722
– setup files 721
Save, screen pattern 728
Scan
– frame size 849
– frame time 849
– line scan 849
– line type 849
– park beam 852
– pixel time 850
– scan area 851
– scan controller 91
– scan parameters 849
– scan rate 488, 850
– scan waveform 91
– scanner control panel 849
– Z scan 26, 45, 406, 856
– Z scan control panel 856
– Z step width 856
– Z steps 856
– zoom 851
Scan clock pulses 124, 130, 132, 237, 452, 754, 766
Scan Controller 91, 624, 849
Scan head, DCS-120 32, 242
Scan lens 443
Scan Modes 791
Scan parameters 849
Scan Pixels X 750, 754, 760, 791
Scan Pixels Y 750, 754, 760, 791
Scan rate 453, 488
Scan stages 240
Scan Sync In mode 753, 963, 967
– accumulate 756
– autosave 756
– continuos flow operation 758
– cycles 756
– display 806
– multidetector operation 757
– stepping through pages 756
– trigger 756
Scan Sync Out mode 750, 963, 968
– accumulate 751
– autosave 751
– cycles 751
– display 806
– multidetector operation 752
– repeat 751, 757
– stepping through pages 751
– trigger 751
– use for fast sequential recording 752
Scan XY Out mode 760, 964
– accumulate 761
– autosave 761
– cycles 761
– display 806
– repeat function 761
– stepping through pages 761
– trigger 761
Scan XY windows 844
Scanning 609
– advantages over wide-field imaging 344
– bidirectional 432
– by galvanometer mirrors 243
– confocal 345
– DCS-120 32
– DCS-120 scanner 849
– in DOT 608, 623
– laser scanning microscope 345
– measurement of barrier discharges 683
– multi-beam 451
– multiphoton 346
– near-infrared FLIM 384
– non-descanned detection 347
– out-of focus suppression 344
– scan rate 453
– scanning interface 124
– scanning mammography 608
– scanning microscopes 32, 68, 345
– scanning techniques for TCSPC 124
– suppression of scattered light 344
– with multidimensional TCSPC 115, 124
Scanning microscope, see laser scanning microscope 343
Scatter 953
Scattering coefficient 605, 611
Secondary emission 160
Second-Harmonic Generation, see SHG 497, 557
Selection of fit model 933
Select-SPC Panel 712
Send data to SPCImage 871, 923
Sequencer 142
Sequential recording 115, 121, 144, 321, 333
– chlorophyll transients 335
– in DOT 614
– in FLIM 398
– in single molecule spectroscopy 665
– phosphorescence decay 340
– stopped flow 337
SER 160, 219
– amplitude jitter 161, 271, 302
– measurement of 301
– of PMT 301
Setup of FLIM system
– setup service 249
SHG 371, 497
– for IRF recording 947
– in tissue 360, 407, 497
SHG imaging 557
Shielding 285
– detectors 287
– ground loops 286
Shifted-component model 879, 934
Shifting the Signal by cable length 279
Shutdown, of detectors 214
Shutter 86, 855
– control by DCC100 214, 237
– wiring diagrams 237, 241
Signal bandwidth 701
Simple-Tau II TCSPC systems 15
Simple-Tau TCSPC systems 15

Single Electron Response 160, 219
Single Mode 733
– cycles and autosave 733
– multidetector operation 734
– repeat 734
– stepping through pages 733
– trigger 734
Single molecule detection 635
Single molecule FRET 668, 672
Single molecule spectroscopy 665
– BIFL 665
– burst analysis 136
– correlation of lifetimes 674
– diffusing molecules 136
– FRET 672
– FRET density plot 673
– identification of molecules 674
– lifetime histogram 675
– multi-parameter detection 136
– photon counting histogram 675
Single-photon APD, see SPAD 157
Single-photon pulses 301
Singlet oxygen detection 394
SIPMs 159, 196
Skin
– Dermainspect 587
– FLIM and SHG of pig skin 557
– FLIM of human skin 556
– FLIM of human skin in vivo 588
– FLIM of papilloma 444
– FLIM of pig skin with NIR dye 47
– FLIM through periscope 444
– MPT Flex 589
– Multiphoton tomography 587
– Multi-wavelength FLIM 588
– z-stack 558
Sleep policy 728
SLIM 125
Small animal imaging 627
Small distance DOT 620
SNOM 458
SNR of FLIM data 470
Software, SPCM 703
– 2d trace parameters 831
– 3D trace parameters 264, 836
– application options 714
– autosave function 580
– Axio Observer control 856
– changing between instrument configurations 706
– control of DB-32 SYNC delay box 856
– control of TiSa laser 858
– conversion of files 724
– DDG-210 control 857
– display functions 797
– emulation mode 717
– export and import 724
– GVD-120 control 849
– Loading of files 718
– Main 718
– Main panel 703
– main panel configuration 256, 263, 265
– operation modes 732
– predefined setups 56, 706, 723
– preview function 55
– print function 728
– resizing panels 822
– Saving of files 720
– Scanner control 849
– send data to SPCImage 728
– sleep policy 728
– start without module 717
– status infornation 713
– system parameters - QC 731
– trace statistics 711
– Window intervals 839
– window parameters 264
SPAD-8 detector 197
SPADs 157, 637, 659
– 8-channel 85
– 8-channel SADP module 197
– breakdown flash 197, 697
– diffusion tail 195
– gated SPAD 198
– id100-20 84, 193
– in DOT, comparison with HPM 633
– InGaAs 199, 201, 392
– light emission from 158, 697
– PDM 50CT 193
– principle 157
– quenching 158
– spatially resolved characterisation 695
– SPCM-AQR 193
– wavelength dependence of IRF 195
SPC modules
– maximum ratings 973
SPC modules
– 12-channel systems 15
– connection to diode laser 223, 227
– control signals 961
– delayed stop operation 220
– detector signal 223
– experiment trigger 230
– FLIM systems 234
– input signals 217
– low repetition rates 220
– module types 7
– multi-module packages 9
– multi-module systems 795
– OEM boards 10, 12, 13
– panel configuration for startup 250
– random signals 221
– routing signals 961
– setup for H7422 224
– setup for phosphorescence systems 229
– setup for PMC-100 223
– setup for PMH-100 223
– setup for R3809 225
– setup for several detectors 227
– setup for several PMC-100 227
– setup for several SPC modules 229
– setup for single detector 223
– setup for SPCM-AQR 226
– setup for SPC-QC 227
– setup of FLIM systems 237
– Simple-tau II systems 15
– Simple-Tau systems 15
– SPC-130 12

– SPC-130EM 13
– SPC-130EMN 11
– SPC-150 13
– SPC-150N 10
– SPC-150NX 11
– SPC-150NXX 11, 207
– SPC-160 12
– SPC-160pcie 12
– SPC-180N 7
– SPC-180NI 8
– SPC-180NX 7
– SPC-180NXX 7
– SPC-630 14
– SPC-730 14
– SPC-830 13
– SPC-QC-008 9
– SPC-QC-104 8
– SPC-QC-106 9
– stand-alone systems 15
– startup of TCSPC systems 249
– SYNC signal 217
– system parameters for startup 249
SPC-130 12
SPC-130EM 13
SPC-130EMN 11
SPC-150 13
SPC-150N 10
SPC-150NX 11
SPC-150NXX 11, 207
SPC-160 12
SPC-160pcie 12
SPC-180N 7
SPC-180NI 8
SPC-180NX 7
SPC-180NXX 7
SPC-630 14
SPC-730 14
SPC-830 13
SPCImage 95, 861
– 2D histograms 868, 904
– analyse-all function 919
– analysis of PLIM data 923
– auto IRF 942
– Batch processing 927
– binning 885
– binning of pixels 930
– calculating the lifetime image 875
– Chi square 887
– colour coding of decay parameters 893, 949
– colour parameters 893
– combination into single curve 903, 905, 906
– convolution integral 932
– decay model 877, 933
– decay parameters 894
– decay-curve window 889
– export of data 928
– first-moment calculation 937
– fit control parameters 884
– fit interval 884
– fixed decay parameters 935
– FLIRR 895
– gated intensity 893
– global analysis 918
– GPU processing 97, 866
– image cursors 899
– image segmentation 904
– image segmentation by phasor plot 869, 907
– images of decay parameters 863
– import of data 871
– incomplete decay model 878, 933
– intensity gating 893
– intensity histogram 897
– intensity parameters 892
– IRF 942
– IRF auto 882
– IRF copy from decay data 882
– IRF from recorded data 944
– IRF modelling 866, 881
– IRF of PLIM 923
– IRF options 881
– IRF rectangular 882
– IRF xe-x 882, 942
– lifetime-image window 891
– Lifetime-intensity data 921
– lines of interest 900
– linking parameters from different images 895
– load/save IRF 883
– MLE algorithm 865, 884, 936
– MLE fit 936
– model definition 933, 938
– model functions 877
– model parameters 877, 909, 933
– moment caculation 884
– mosaic FLIM data 921
– moving objects 907
– multi-exponential decay model 933
– multiple ROIs 902
– multi-wavelength FLIM data 919
– offset, as an image parameter 954
– over-determined models 939
– overview 861
– parameter histograms 867, 896, 902
– phasor analysis 865, 906
– phasor plot 97, 906, 955
– pixel masks 901
– polygonal ROI 899
– preferences 912
– pseudo-global analysis 917
– rectangular ROI 899
– residuals 886
– ROIs 868, 899, 902
– ROIs from 2D histograms 900
– ROIs from phasor plot 900
– saving data 928
– selection of fit model 938
– send data to SPCImage 728, 871
– send PLIM data to SPCImage 923
– shifted-component model 879, 934
– single-curve analysis 97
– single-curve data 915
– special commands 929
– synthetic IRF 866, 882, 942
– threshold 886
– WLS fit 883, 936
SPCM main panel configuration
– examples 704
– f(xyt) mode 256
– FIFO imaging mode 263
– FLIM, gated images 814

– FLIM, multi-wavelength 813
– FLIM, one detector 809
– FLIM, runtime lifetime images 816
– FLIM, two parallel channels 811
– FLIM/PLIM 820
– mosaic FLIM function 265
– multi-wavelength 255
– multi-wavelength FLIM 263
– scanning systems 259
SPCM software, see software 94, 703
SPCM-AQR 193, 637, 659
– single, connection to SPC 226
SPC-QC-008 9
SPC-QC-104 8
SPC-QC-106 9
Special commands, in data analysis 929
Spectra, recording in fi Modes 744
Spectral lifetime imaging 125
Spectrum modes 742
SSPD 159, 204
– IRF 204, 206, 207
– principle 159
– single nanowire 207
– singlet oxygen detection 394
Stage scanning systems 240
Stand-alone TCSPC systems 15
Start, a measurement, see also experiment trigger 847
Start-Stop Time 290
Start-stop, reversed 140
Startup
– panel configuration for 250
– system parameters for 249
STED FLIM 71, 454
– dual-wavelength 454
– gated images 456
– principle of STED 454
– with Abberior system 455
– with runtime lifetime display 456
– with supercontinuum laser 454
– with TiSa laser 454
Stem cells 555
Stepping through Pages 733, 735, 751, 756, 761, 780
Steps 780
Stop Condition 779
Stop Ovfl 733, 735, 737, 740, 742, 745, 779
Stop pulse, for CW FCS 659
Stop signal
– delay of stop pulses 281
– for reversed start-stop 281
– from photodiode modules 89, 218
– from PMT 221, 635, 681, 687
– stop pulse from correct pulse period 281
Stop T 646, 733, 735, 737, 740, 742, 745, 779
Stop, a measurement 847
Stop, after collection time 733, 735, 737, 740, 742, 745, 779, 781
Stop, on overflow 733, 735, 737, 740, 742, 745, 779
Stopped flow techniques 337
Sub-D connector 961
Superconducting detectors 204
– IRF 204, 206
– principle 159
– single nanowire 207
Supercontinuum laser 325, 353, 371, 621, 624
Superresolution 454
Sutter MOM microscope 71
Switching operation modes 56, 723
SYNC
– configuration 269
– delay 281
– for reversed start-stop 281
– frequency divider 140, 784
– generation of signal 217
– Holdoff 784
– No SYNC 713
– parameters 784
– setting the SYNC parameters 279
– SYNC cable length 279
– SYNC OK 713
– SYNC overload 713
– threshold 784
– ZC level 784
SYNC delay box, DB-32 92, 280
Synchronisation
– PLIM, with laser modulation 435
Synchronisation signal, see SYNC 217, 285
Synchronous start of modules 649, 781, 795
Synchrotron radiation 353
Synthetic IRF 96, 598, 866, 881, 882
System Parameters - QC 731
System Parameters - SPC 731
System Response, Influence of optical system 303
System Response, PMT 300
System setup
– multi-wavelength FLIM systems 263
– multi-wavelength systems 255
– scanning systems 258
– setup service 249
– single-detector systems 249
SYTO13 505
T Geometry 330
TAC 107, 109, 140, 149
– architecture 149
– biased amplifier 107
– dead time 290
– dead time compensation 150, 293
– DNL 288
– linearity 288
– optimising the TAC parameters 282
– overrange reset 150
– recovery time 290
– reset time 290
– start-stop sime 290
– TAC Gain 283, 785
– TAC Limit High 785
– TAC Limit Low 785
– TAC Offset 282, 785
– TAC Range 283, 785
– TAC Window 150
– timing diagram 290
Tail matching 329
TCSPC 101
– architecture of bh SPC modules 139
– CFD 139
– channel register 142
– classic architecture 106
– continuous flow mode 123, 145, 665
– count rate 105
– counting efficiency 292

– counting loss 477
– dead time 477
– delayed stop 220
– detectors 154
– direct start-stop 109
– excitation wavelength multiplexing 126
– FIFO mode 146, 656
– FLIM 124
– general principle 102
– hardware accumulation 114
– Lock-in SPC 331
– memory control 142
– memory swapping 123
– mosaic FLIM 127
– multi-detector operation 115, 116, 143, 227
– multi-dimensional 112, 124
– multi-module 137
– multi-module operation 229
– multi-parameter 115, 682
– multiplexed 115, 119, 144, 609
– multiplexing 336
– multi-spectral 116
– multi-wavelength 322, 469
– non-reversed start stop 109
– parameter-tag mode 114, 132
– phosphorescence systems 229
– photon distribution 102, 109, 129
– photon-number sensitive 699
– pile-up effect 478
– pulse-interleaved excitation 127, 371
– random signals 221
– reversed start-stop 107
– router 117
– routing 116
– scanning techniques 115, 124, 145, 609
– sequencer 142
– sequential recording 115, 121, 144, 333
– single molecule detection 635
– software accumulation 114
– spatial multiplexing 121
– TAC / ADC principle 109, 139, 151
– TDC principle 109, 139
– time resolution 103
– time-tag mode 114, 132, 146, 656
TCSPC Imaging 343
TCSPC system parameters 712, 731
– CFD parameters 783
– channel delay correction 266, 768
– data format parameters 787
– display parameters 257, 265
– experiment trigger 780
– f(xyt) mode 256, 257
– FIFO imaging mode 263
– for wide-field FLIM 777
– in main panel 712
– measurement control 779
– mosaic FLIM function 265, 266
– mosaic imaging 765
– operation modes 732
– page control 790
– scan synchronisation parameters 766
– SPC-QC series 731
– Sync parameters 784
– TAC parameters 784
– timing control parameters 781
– trigger master 778, 795
TCSPC, Laser Scanning Microscope 343
TDC 109, 141
Temperature measurement 584
Test
– of a PMT 302
Thermoelectric cooling 214
Threshold
– CFD threshold 140, 269, 783, 854
– SYNC threshold 140, 784
Time gating
– in SPCImage 953
– in SPCM 807, 814
– of lifetime images 814
– of PIE recordings 372
– STED images 456
Time per Channel 785, 788
Time per Division 786
Time resolution of TCSPC 103, 163
Time windows 839
Time-correlated single photon counting, see TCSPC 101
Time-of-flight distribution, in DOT 610, 612
Time-resolved spectra 320
Time-series FLIM 44, 63, 580
– by record and save procedure 398
– by temporal mosaic FLIM 128, 402
– by temporal mosaic FLIM, accumulation 403, 409
– of Ca^{2+} transient FLIM 409, 500
– of chlorophyll transients 580
Time-tag data, see parameter-tag mode 646
Time-tag mode, see parameter-tag mode 114, 132, 770
Time-to-amplitude converter 107, 149
Timing
– CFD parameters 783
– SYNC parameters 784
– TAC parameters 784
– time-tagged data 641
– timing control parameters 781
Timing stability
– electrically 2
– H5773, H5783 173
– magnetic field 187
TiSa laser
– control from SPCM software 858
– multiphoton excitation 349
– one-photon excitation for NIR FLIM 385
Tissue spectrometers 621
Tomography, optical 605
Trace parameters 709, 831
– 2D 709, 831
– 3D 710, 836
– 3D, data type 836
– 3D, display mode 837
– 3D, display of FLIM data 806
– 3D, window sizes and positions 838
– block info 834
– block mode 833
– curve mode 831
– export of traces 834
Trace Statistics 711
Traces 831
Traces, export of 834
Transit time of PMTs 163
Transit time spread 163, 694
Trigger
– continuous flow sequence 124, 748

– experiment trigger 780
– FIFO mode 773
– for FLITS 130, 411, 413
– from experiment 114
– MCS trigger 341, 775
– of recording sequence 122
– oscilloscope mode 735
– page stepping 734, 736, 738, 741, 743, 746, 751, 756, 761
– recording cycles 734, 736, 738, 741, 743, 746, 751, 756
– scan sync in mode 756
– SPC-130 966
– SPC-150 967
– SPC-160 967
– SPC-630 962
– SPC-730 962
– Synchronous start of modules 781, 795
– to start a measurement 967
– Trigger Condition 780
– trigger master function 649, 781, 795
– Trigger synchronisation 781, 795
Trigger master 649, 781, 795
Trigger synchronisation 781, 795
Triggered accumulation 411, 413
– chlorophyll transient 334
– fast time series 316
– FLITS 411, 413
– MCS imaging mode 767
– MCS mode 23, 341, 775
– multiwavelength time series 323
– of recording sequence 122
– of sequence 122
– temporal mosaic FLIM 64, 129, 403, 409
Triggered accumulation MCS mode 775
Triggered sequential recording 122
Triplet accumulation 488
Trouble Shooting
– assistance through bh 959
Tryptophan 371, 381, 517
– FLIM with DCS-120 system 382
– Tryptophan FLIM 381
– Two-Photon Excitation 381
TTS 163, 694
Tuneable excitation FLIM 45, 62, 353
Tuneable fibre laser 355
Two-photon absorption 346
Two-photon excitation 346, 685
– descanned detection 348
– examples of images 357, 367, 407
– NDD principle 357
– non-descanned detection 347, 357, 367
– two-photon FCS 639, 654
– Z stack recording 406
Two-photon microscope 343
Ultra-fast fluorescence decay 561
– carotenoids 563
– human hair 565
– malignant melanoma 566
– mushroom spores 561
– pollen grains 562
Viscosity 501
Viscosity sensors 495
Warburg effect 528
Wavelength multiplexing
– PIE 127, 371
– pulse-group multiplexing 126
Weighted least squares 936
Well plates 446
Wide-field FLIM 31, 460, 777
– CFDs 461
– data analysis 464
– detector 460
– implementation in SPCM 462
– optical system 462
– principle 460, 777
– resolution 465
– system parameters 777
– TCSPC system 460
Window intervals 839
– auto set function 845
– routing XY windows 841
– scan XY windows 844
– time windows 839
Window parameters 264, 808
WLS fit 883, 936
XP2020 163
XSync 963, 967, 968, 969
YSync 963, 967, 969
Z scan 26, 45, 63, 406, 856
Z- Stack FLIM 26, 391
Zeiss LSM 710/780/880/980 50
– beamsplitter, NDD ports 358
– bidirectional scanning 57
– dual-channel FLIM 58
– FCS 67, 651
– FLIM detectors 52
– FLIM lasers 53
– FLIM systems 50
– FLITS 66
– Intune FLIM 355, 388
– Laser Hub 59
– laser multiplexing 59
– Meagapixel FLIM 58
– Metabolic FLIM 61
– Mosaic FLIM 64
– multiphoton FLIM 59
– multi-wavelength FLIM 368
– Multi-wavelength NDD FLIM 61
– NDD FLIM 59, 360
– near-infrared FLIM 64
– NIR FLIM 386
– online FLIM 57
– optical configuration 50
– PLIM 436, 857
– Preview function 55
– Runtime Display 57
– simultaneous FLIM/PLIM 65
– time-series FLIM 63
– ultra-fast FLIM 60
– ZEN Integrated FLIM 54
– Z-Stack FLIM 63, 406
ZEN software setup for FCS 652
Zero cross level, CFD 274, 783
Zero cross level, SYNC 784
Zero-distance DOT 620
Zoom
– ADC 153, 787

– by scan parameters 851
– during preview 851
– in FLIM recording 480
– in SPCImage 899
– into parameter histograms 896
Z-Stack FLIM 45, 63, 406, 558
– by integrated microscope control 408
– by mosaic FLIM 128, 391
– by record and save procedure 406
– NIR dyes 391
– pig skin 558
– with DCS-120 408